15 APRIL 1996
PART 2B

VOLUME 79 NUMBER 8

# JOURNAL OF APPLIED PHYSICS

Proceedings of the 40th Annual Conference on Magnetism and Magnetic Materials

AMERICAN INSTITUTE OF PHYSICS

DISTRIBUTION STATEMENT A
Approved for public release;
Distribution Unlimited

# JOURNAL OF APPLIED PHYSICS

CODEN: JAPIAU
ISSN: 0021-8979

**Editor**
Steven J. Rothman
Argonne National Laboratory
Argonne, IL

**Associate Editors at Argonne National Laboratory**
Roy Benedek
Robert C. Birtcher
Gian P. Felcher
John N. Mundy
Simon R. Phillpot

**Editorial Board**

*Term ending 31 December 1996*
Gene F. Dresselhaus (MIT, Cambridge, MA)
Allen M. Goldman (Univ. Minnesota, Minneapolis)
Klaus H. Ploog (Paul Drude Inst., Berlin, Germany)
Robert Sinclair (Stanford Univ., Stanford, CA)

*Term ending 31 December 1997*
Federico Capasso (AT&T Bell Labs, Murray Hill, NJ)
Esther M. Conwell (Xerox Corp., Rochester, NY)
C. Y. Fong (University of California, Davis, CA)

*Term ending 31 December 1998*
Dieter M. Gruen (Argonne Nat'l Lab., Argonne, IL)
James S. Williams (The Australian Nat'l Univ., Canberra, Australia)
Patricia M. Mooney (IBM Corp., Yorktown Heights, NY)

**Editorial Office**
Diane M. Kurtz, *Editorial Supervisor*
**Editorial Staff:** Catherine M. Dial, *Assistant to the Editor;* Jennifer A. Smeets, *Secretary*

**AIP Production**
Deborah McHone, *Editorial Supervisor*
Margaret Reilly, *Journal Coordinator*
Janet Panarelli, *Chief Production Editor*
Cindy Klingensmith, *Senior Production Editor*
Daniela Boscia, *Production Editor*

**Submit manuscripts (3 copies)** to Editor, *Journal of Applied Physics,* Argonne National Laboratory, Bldg. 203, Room R-127, 9700 South Cass Avenue, P.O. Box 8296, Argonne, IL 60439-8296.

**Physics Auxiliary Publication Service (PAPS) and/or Electronic PAPS (E-PAPS):** For a nominal fee, authors may submit material that is part of and supplemental to a paper, but is too long to be included in the journal. PAPS deposits may be on paper or in electronic media, and can include text, data in graphic or numeric form, computer programs, etc. Retrieval instructions are footnoted in the related published paper. Direct requests to the editor.

The *Journal of Applied Physics* (ISSN: 0021-8979) is published semimonthly by the American Institute of Physics, 500 Sunnyside Blvd., Woodbury, NY 11797-2999. Second-class postage paid at Woodbury, NY, and additional mailing offices. POSTMASTER: Send address changes to *Journal of Applied Physics*, AIP, 500 Sunnyside Blvd., Woodbury, NY 11797-2999.

The *Journal of Applied Physics* is the American Institute of Physics' (AIP) archival journal for significant new results in applied physics. The journal publishes articles that emphasize understanding of the physics underlying modern technology. There are two issues per month. The subject coverage includes, but is not limited to, experimental or theoretical physics applied to all aspects of materials: for example, charge and mass transport, superconductivity, magnetism; surfaces, interfaces, thin films, crystal lattice defects; electrical, optical, magnetic, and structural properties; processing; ion implantation. Materials covered include semiconductors, superconductors, metals and alloys, amorphous materials, and oxides. Other important topics are: electrical, optical, and magnetic devices; optics and lasers; nonlinear optics; electrical discharges; acoustics. The Proceedings of the Annual Conference on Magnetism and Magnetic Materials is a regular feature. *Applied Physics Reviews* is a series of occasional review articles on similar subjects.

**Publication Charge:** To support the cost of wide dissemination of research results through publication of journal pages and production of a database of articles, the author's institution is requested to pay a page charge of $55 per page (with a one-page minimum) and an *article charge* of $20 per article. For any regular, published article that exceeds 10 journal pages, a mandatory $150 page charge will be added for each page in excess of 10 pages. For Errata the minimum page charge is $10, with no article charge.

| **Subscription Prices*** (1996) | U.S.A. & Poss. | Can., Mex., Central & S. Amer. & Caribbean | Foreign Surface Mail | Air Freight — Europe, Asia, Africa & Oceania | Optional Air Freight |
|---|---|---|---|---|---|
| Members† | $210 | $295 | $295 | — | $480 |
| Nonmembers | $2045 | $2130 | — | $2315‡ | — |

*The journal is available on microfiche at $210 per year to members and $2045 per year at the nonmember rate.
†AIP Member and Affiliated Societies. ‡Includes air freight service.

**Back-Number Prices:** 1996 single copies: $95. Prior to 1996 single copies: $26 for members; $95 for nonmembers. Prices for conference supplements available on request.

**Subscription, renewals, and address changes** should be addressed to *AIP Circulation and Fulfillment Division (CFD), 500 Sunnyside Blvd., Woodbury, NY 11797-2999.* Allow at least six weeks advance notice. For address changes please send both old and new addresses and, if possible, include a mailing label from a recent issue.

**Claims, Single Copy Replacement and Back Volumes:** Missing issue requests will be honored only if received within six months of publication date (nine months for Australia and Asia). Single copies of a journal may be ordered and back volumes are available in print or microform. Members—contact AIP Member Services at (516) 576-2288; (800) 344-6901. Nonmember subscribers—contact AIP Subscriber Services at (516) 576-2270; (800) 344-6902; Internet: subs@aip.org.

**Page Charge and Reprint Billing:** Contact: AIP Publication Page Charge and Reprints—CFD, 500 Sunnyside Blvd., Woodbury, NY 11797-2999; (516) 576-2234; (800) 344-6909.

**Copying:** Single copies of individual articles may be made for private use or research. Authorization is given (as indicated by the Item Fee Code for this publication) to copy articles beyond the use permitted by Sections 107 and 108 of the U. S. Copyright Law, provided the copying fee of $10 per copy per article is paid to the Copyright Clearance Center, 222 Rosewood Drive, Danvers, MA 01923, USA. Persons desiring to photocopy materials for classroom use should contact the CCC Academic Permissions Service. The Item Fee Code for this publication is 0021-8979/96 $10.00.
Authorization does not extend to systematic or multiple reproduction, to copying for promotional purposes, to electronic storage or distribution, or to republication in any form. In all such cases, specific written permission from AIP must be obtained.

**Permission for Other Use:** Permission is granted to quote from the journal with the customary acknowledgment of the source. To reprint a figure, table, or other excerpt requires the consent of one of the authors and notification to AIP.

**Requests for Permission:** Address requests to AIP Office of Rights and Permissions, 500 Sunnyside Boulevard, Woodbury, NY 11797-2999; Fax: 516-576-2327; Telephone: 516-576-2268; Internet: rights@aip.org.

**Publisher Item Identifier:** A Publisher Item Identifier (PII) has been adopted by AIP and other publishers to provide unique and concise identification of individual published documents. The PII appears at the end of the abstract of each article. The PII should be included in all document requests for copies of the article.

**Document Delivery:** Copies of articles can be ordered for $15 per copy from the AIP/Member Society document delivery service, "Articles in Physics," 1722 Gilbreth Road, Burlingame, CA 94010-1305; Fax: 415-259-6044; Telephone: 800-480-PHYS (in U.S. and Canada), or 415-259-6002; Internet: articles@aip.org.

**Reprints:** Reprints can be ordered with or without covers only in multiples of 50 (with a minimum of 100 in each category) from AIP, Circulation & Fulfillment/Reprints, 500 Sunnyside Boulevard, Woodbury, NY 11797-2999; Fax 516-349-9704; Telephone: 800-344-6909 (in U.S. and Canada), or 516-576-2234.

**Microform:** *Journal of Applied Physics* is available on microfiche issued at the same frequency as the printed journal and annually on microfilm. A microform catalog is available from AIP, Circulation & Fulfillment/Single Copy Sales, 500 Sunnyside Boulevard, Woodbury, NY 11797-2999; Fax: 516-349-9704; Telephone: 800-344-6908 (in U.S. and Canada), or 516-576-2277.

**Online Availability:** Abstracts of journal articles published by AIP and Member Societies (and several other physics publishers) are available in the SPIN database via the AIP online service PINET. Also available on PINET are *Advance Abstracts*, a current awareness

# PROCEEDINGS OF THE FORTIETH ANNUAL CONFERENCE ON MAGNETISM AND MAGNETIC MATERIALS

## PART B

November 6–9, 1995
Philadelphia, Pennsylvania

Edited by E. Dan Dahlberg, W.-Y. Ching,
J. K. Howard, Y. Idzerda, M. Lederman, and J.-G. Zhu

DISTRIBUTION STATEMENT A
Approved for public release;
Distribution Unlimited

19960424 113

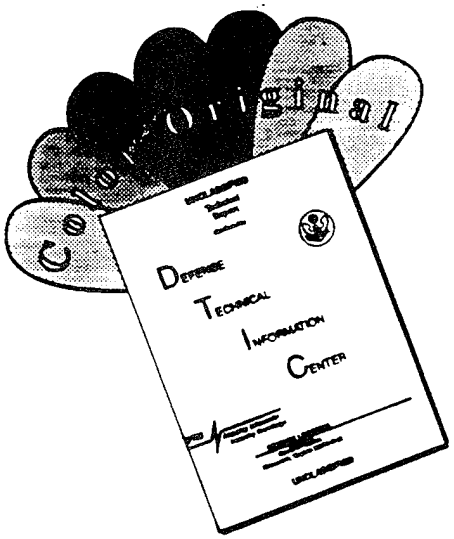
DTIC QUALITY INSPECTED 1

Journal of Applied Physics
Volume 79, Number 8, Part 2, 1996

International Standard Serial Number: 1087-3848
International Standard Book Number: 1-56396-613-1
CONF-951101—Vol. 2
Copyright © 1996 by the American Institute of Physics
Published by the American Institute of Physics
500 Sunnyside Blvd., Woodbury, New York 11797-2999
Printed in the United States of America

All papers in this volume, and in previous Proceedings of the Conference on Magnetism and Magnetic Materials published in this series, have been reviewed for technical content. The selection of referees, review guidelines, and all other editorial procedures are in accordance with standards prescribed by the American Institute of Physics.

# DISCLAIMER NOTICE




THIS DOCUMENT IS BEST QUALITY AVAILABLE. THE COPY FURNISHED TO DTIC CONTAINED A SIGNIFICANT NUMBER OF COLOR PAGES WHICH DO NOT REPRODUCE LEGIBLY ON BLACK AND WHITE MICROFICHE.

**Symposium on 10 GB/in.$_2$ Magnetic Recording**


4485 Approaches to 10 Gbit/in.$^2$ recording (invited) — M. H. Kryder, W. Messner, L. R. Carley

4491 Impact of new magnetoresistive materials on magnetic recording heads (invited) — J. A. Brug, L. Tran, M. Bhattacharyya, A. Jander, J. H. Nickel, T. C. Anthony

4496 Media for 10 Gb/in.$^2$ hard disk storage: Issues and status (invited) — D. N. Lambeth, E. M. T. Velu, G. H. Bellesis, L. L. Lee, D. E. Laughlin

4502 Signal processing for 10 GB/in.$^2$ magnetic disk recording and beyond (invited) — Kevin D. Fisher, Cory S. Modlin

4508 Head/disk tribology: Toward 10 Gb/in.$^2$ (invited) (abstract) — B. Marchon


**Interlayer Coupling**


4509 Quantum oscillations of properties in magnetic multilayers (invited) — G. Bayreuther, F. Bensch, V. Kottler

4515 Calculated spacer-layer Friedel oscillations in Co/Cu(001) — Lars Nordström, David J. Singh

4518 Interface alloying at Fe/Cr interfaces and its role in exchange coupling, angular resolved Auger electron, magneto-optic Kerr effect, and Brillouin light scattering studies (invited) — B. Heinrich, J. F. Cochran, D. Venus, K. Totland, D. Atlan, S. Govorkov, K. Myrtle

4524 Suppression of biquadratic coupling at the Cr Néel temperature in Fe/Cr(001) superlattices (invited) (abstract) — Eric E. Fullerton, S. Adenwalla, G. Felcher, C. H. Sowers, S. D. Bader, J. L. Robertson, A. Berger

4525 Interlayer thickness Dependence of the strong 90° coupling in epitaxial CoFe/Mn/CoFe trilayers — J. J. Krebs, G. A. Prinz, M. E. Filipkowski, C. J. Gutierrez

4528 Dependence of the interlayer exchange coupling on the constitution of the magnetic layers — K. Ounadjela, Li Zhou, R. Stamps, P. Wigen, M. Hehn, J. Gregg

4531 Domain structure and anisotropy of exchange coupled Co/Cr/Fe multilayers (abstract) — Th. Kleinefeld, M. Figge, K. Theis-Bröhl, R. Scheidt, Th. Zeidler, Ch. Mathieu, B. Hillebrands

4532 Magnetic coupling in Co/face-centered-cubic Fe/Co sandwiches — R. K. Kawakami, Ernesto J. Escorcia-Aparicio, Z. Q. Qiu


**Colossal Magnetoresistance in Perovskite Oxides I**


4535 Transport and magnetism correlations in thin-film ferromagnetic oxides — M. F. Hundley, J. J. Neumeier, R. H. Heffner, Q. X. Jia, X. D. Wu, J. D. Thompson

4538 Colossal magnetoresistance in the antiferromagnetic $La_{0.5}Ca_{0.5}MnO_3$ system — G. Q. Gong, C. L. Canedy, Gang Xiao, J. Z. Sun, A. Gupta, W. J. Gallagher

4541 Lattice effects on the magnetoresistance in doped manganese perovskites (abstract) — H. Y. Hwang, S-W. Cheong, P. G. Radaelli, M. Marezio, T. T. M. Palstra, B. Batlogg

4542 Electrical conductivity in ferromagnetic perovskite structures — Shufeng Zhang

4545 Response to an electric field of $Nd_{0.7}Sr_{0.3}MnO_3$ films in a MOSFET configuration (abstract) — S. B. Ogale, V. Talyansky, G. C. Xiong, R. P. Sharma, R. Ramesh, R. L. Greene, T. Venkatesan

4546 Magnetotransport and hysteretic behavior in epitaxial $La_{0.67}Ca_{0.33}MnO_{3-\delta}$ films — C. L. Canedy, K. B. Ibsen, Gang Xiao, J. Z. Sun, A. Gupta, W. J. Gallagher

4549 Magnetoresistance and magnetic properties of $La_{1-x}\square_xMnO_{3-\delta}$ thin films — T. R. McGuire, A. Gupta, P. R. Duncombe, M. Rupp, J. Z. Sun, R. B. Laibowitz, W. J. Gallagher, Gang Xiao


*(Continued)*

4552 Superparamagnetic behavior and giant magnetoresistance in oxygen deficient $R_{0.67}Sr_{0.33}MnO_z$ (R=Nd, Pr) epitaxial films (abstract) — H. L. Ju, Qi Li, G. C. Xiong, T. Venkatesan, R. L. Greene

4552 Role of lattice distortions in the transport property of $R_{0.7}Me_{0.3}MnO_3$ (R=Pr,Nd,La and Me=Ba,Sr,Ca) (abstract) — R. P. Sharma, G. C. Xiong, S. B. Ogale, R. L. Greene, T. Venkatesan

4553 The effect of disorder and fluctuations on the magnetotransport of a double-exchange ferromagnet (abstract) — Jeff M. Byers

4553 Ozone assisted, block-by-block, molecular beam epitaxy of La–M–Mn–O (M=Ca,Ba,Sr) thin films and La–M–Mn–O/Dy–Ba–Cu–O multilayers (abstract) — V. A. Vas'ko, P. A. Kraus, V. S. Achutharaman, C. A. Nordman, A. M. Goldman

4554 Transport properties and magnetic behavior of $La_{1-x}Sr_xMnO_3$ single crystals (abstract) — A. Anane, C. Dupas, K. Le Dang, J. P. Renard, P. Veillet, A. M. de Leon Guevarra, F. Millot, L. Pinsard, A. Revcolevschi

4555 Density-functional studies of the electronic structure of the perovskite oxides: $La_{1-x}Ca_xMnO_3$ — S. Satpathy, Zoran S. Popović, Filip R. Vukajlović

4558 Electron spectroscopic studies of colossal magnetoresistance material $La_{1-x}Ca_xMnO_3$ — J.-H. Park, C. T. Chen, S.-W. Cheong, W. Bao, G. Meigs, V. Chakarian, Y. U. Idzerda


**Soft Ferrites and Alloys I**


4561 Cation distribution in NiZn-ferrite films determined using x-ray absorption fine structure — V. G. Harris, N. C. Koon, C. M. Williams, Q. Zhang, M. Abe

4564 Possible nearly loss-free ferrimagnetic resonance in small samples — J. B. Sokoloff

4567 Anomalous low dimensional system: Study of magnetism and electrical conductivity in $Na_2Ru_4O_{9-\delta}$ — G. Cao, S. McCall, F. Freibert, M. Shepard, P. Henning, J. E. Crow

4570 Growth of epitaxial films of iron oxide, nickel oxide, cobalt oxide, strontium hexagonal ferrite, and yttrium iron garnet by laser ablation (abstract) — Robin J. Kennedy

4570 Resolution of conflicts concerning $Fe_{16}N_2$ (abstract) — A. S. Arrott

4571 Influence of the plastic anisotropy on the magnetic properties of a nonoriented 3% silicon iron — E. Hug, O. Hubert, M. Clavel

4574 Magnetic properties of 3%Si-Fe thin sheets annealed in Ar atmosphere (abstract) — Y. Yamashiro, A. Yonesu, S. Hashi, K. Ishiyama, K. I. Arai

4575 Power losses in thick steel laminations with hysteresis — C. Appino, G. Bertotti, O. Bottauscio, F. Fiorillo, P. Tiberto, D. Binesti, J. P. Ducreux, M. Chiampi, M. Repetto

4578 High temperature magnetic properties of 49%Co–2%V–Fe alloy — Lin Li

4581 Effect of nucleating layers on the soft magnetic properties of multilayer permalloy films — Craig A. Grimes


**Hard Magnet Nitrides, Carbides, and Hydrides**


4584 A spin reorientation in $Pr_2Fe_{17}D_3$ as revealed by Mössbauer spectroscopy — F. Grandjean, Dimitri Hautot, Gary J. Long, O. Isnard, S. Miraglia, D. Fruchart

4587 Neutron diffraction and Mössbauer spectral study of the $Nd_2Fe_{16}TiC_x$ solid solutions — G. K. Marasinghe, Peter C. Ezekwenna, W. J. James, Gary J. Long, O. A. Pringle, Z. Hu, W. B. Yelon, F. Grandjean

4590 Mössbauer study of permanent-magnet $R_2Fe_{17-x}M_xC_y$ compounds — I. A. Al-Omari, E. W. Singleton, Y. Zheng, G. C. Hadjipanayis, D. J. Sellmyer

4593 Crystal field induced anisotropy in rare earth intermetallics as studied by $^{155}Gd$ Mössbauer spectroscopy — D. P. Middleton, F. M. Mulder, D. A. van de Straat, R. C. Thiel, K. H. J. Buschow

4596 Study of the nitrogen diffusion mechanism in $R_2Fe_{17}$ — Y. D. Zhang, J. I. Budnick, W. A. Hines, D. P. Yang


*(Continued)*

4599 Nuclear magnetic resonance study of expanded lattice permanent magnet nitrides and carbides at high pressure — Cz. Kapusta, J. S. Lord, G. J. Tomka, P. C. Riedi, K. H. J. Buschow

4602 Band theoretical investigation of the Curie temperatures of modified $R_2Fe_{17}$-based intermetallic compounds — W. Y. Ching, Ming-Zhu Huang

4605 Metastable $RFe_7$ compounds (R=rare earths) and their nitrides with $TbCu_7$ structure — O. Mao, J. Yang, Z. Altounian, J. O. Ström-Olsen

4608 High field magnetization isotherms of the $Pr_2Fe_{17}D_5$ system — O. Isnard, M. Guillot, S. Miraglia, D. Fruchart

4611 Structural and magnetic properties of rapidly quenched $(R,Zr)(Fe,Co)_{10}N_x$ (R=Nd,Sm) — S. Sakurada, A. Tsutai, T. Hirai, Y. Yanagida, M. Sahashi, S. Abe, T. Kaneko

4614 Aligned high magnetization $Nd(Fe,Co,Mo)_{12}$ films nitrided by N ion implantation — X. R. Qian, H. Hegde, F. J. Cadieu

4616 Magnetic and phase transformation studies in $Nd_{15}DyFe_{75}(C,B)_9$ cast alloys — A. S. Murthy, I. Panagiotopoulos, G. C. Hadjipanayis

4619 Characteristics of $Sm_2Fe_{17}C_x$ compounds prepared from ball-milled blends of $Sm_2Fe_{17}$ and graphite — O. Mao, J. O. Ström-Olsen, Z. Altounian, J. Yang

4622 Exchange and crystal-field interactions in $R_3(Fe,Ti)_{29}$ and $R_3(Fe,Ti)_{29}N_y$ (R=Nd,Sm) — Hong-Shuo Li, D. Courtois, J. M. Cadogan


**Critical Phenomena I**


4625 Magnetic ordering in clustered Fe-based materials synthesized from laser plasma (abstract) — Yuri Blyakhman, N. I. Polushkin, A. D. Akhsakhalyan, S. A. Gusev, N. N. Salashchenko, V. G. Semenov

4626 Magnetization processes of free- and fixed-single-crystal antiferromagnets — Z. G. Zhao, P. F. de Châtel, F. R. de Boer, K. H. J. Buschow

4629 Dynamics of quantum spin systems in dimer and valence-bond-solid ground states stabilized by competing interactions — Yongmin Yu, Gerhard Müller

4632 Spin correlation functions in random-exchange $s=1/2$ $XXZ$ chains — Heinrich Röder, Joachim Stolze, Richard N. Silver, Gerhard Müller

4635 Rotational hysteresis and self-organized criticality in magnetic recording media — T. L. Templeton, A. S. Arrott

4638 Quantum correction to the BKT transition for 2D easy-plane antiferromagnets — Cristiano Biagini, Alessandro Cuccoli, Valerio Tognetti, Ruggero Vaia, Paola Verrucchi

4641 Homogeneous magnetization dynamics below $T_c$ of EuO: Effects of spin waves and anisotropy — A. Flosdorff, D. Görlitz, J. Kötzler

4644 Concentration-dependent critical behavior in dilute ferromagnetic $Fe_{1-x}As_x[S_2CN(C_2H_5)_2]_2Cl$ — G. C. DeFotis, G. A. Coffey, G. S. Coker, J. L. Marmorino, K. L. Beers, S. Chandarlapaty, W. W. Brubaker, V. J. Pugh, S. A. Carling, P. Day


**Magnetoelastic Effects**


4647 Magnetovolume effects of $MnAs_{1-x}Sb_x$ — O. Nashima, T. Suzuki, H. Ido, K. Kamishima, T. Goto

4650 Transmission electron microscopy of Terfenol-D crystals — A. P. Holden, D. G. Lord, P. J. Grundy

4653 Propagation and reflection properties of magnetoelastic wave in FeSiB amorphous wire — Y. Takemura, S. Masuda, T. Yamada, K. Kakuno

4656 Anomalous compressibility and magnetovolume effects in $Ce_3(FeTi)_{29}$ — J. Kamarád, Z. Arnold, L. Morellon, P. A. Algarabel, M. R. Ibarra, C. D. Fuerst

4659 Magnetostriction and thermal expansion measurements on $FeRh_{1-x}Pt_x$ alloys — P. A. Algarabel, M. R. Ibarra, C. Marquina, S. Yuasa, H. Miyajima, Y. Otani


*(Continued)*

4662 Magnetostriction of a superconductor: Results from the critical-state model — Z. Koziol, R. A. Dunlap

4665 Magnetostriction and anisotropy of twin-free single-crystals $Tb_{0.5}Dy_{0.5}(Fe_{0.9}Mn_{0.1})_2$ — Jinghua Wang, Guangheng Wu, Xuegen Zhao, Kechang Jia, Wenshan Zhan

4668 Magnetic properties and magnetostriction of twin-free single-crystal $Tb_{0.27}Dy_{0.73}(Fe_{1-x}Al_x)_2$ — Jinghua Wang, Guangheng Wu, Xuegen Zhao, Kechang Jia, Wenshan Zhan

**Numerical Methods and Design Techniques**

4671 Perfect conductivity approximation: Modification for polyphase systems — K. V. Namjoshi, J. D. Lavers, P. P. Biringer

4674 Dual-complementary variational methods in eddy currents (abstract) — P. Lois, D. Baldomir, J. Rivas

4675 Solution of induction heating problems involving media with hysteresis — A. A. Adly

4678 Solution of magnetic field and eddy current problem induced by rotating magnetic poles (abstract) — Z. J. Liu, T. S. Low

4679 Nonlinear flux diffusion and ac susceptibility of superconductors: Exact numerical results — Z. Kozioł, R. A. Dunlap

4682 New method of evaluating the explicit magnetic-state-dependent energy of iron in semiempirical calculations — Genrich L. Krasko

4685 Three-dimensional modeling techniques applied to regions with small susceptibility variations (abstract) — R. J. Hill-Cottingham, J. F. Eastham, I. R. Young, J. V. Hajnal

4685 An efficient three-dimensional demagnetizing field calculation scheme (abstract) — A. S. Kazmi, R. C. Giles

4686 Computational calculations of magnetic relaxation and viscosity in small magnetic grains — J. M. Hernàndez, X. X. Zhang, J. Tejada

4689 Loss simulations in magnetostrictive actuators — G. Engdahl, A. Bergqvist

4692 Analysis and optimization of synchronous magnetic couplings — E. P. Furlani

4695 Irregular grain structure in micromagnetic simulation — D. G. Porter, E. Glavinas, P. Dhagat, J. A. O'Sullivan, R. S. Indeck, M. W. Muller

**Biochemical Magnetism**

4698 Low temperature magnetic properties of a molecular compound (abstract) — J. L. Tholence, M. Novak, D. Luneau, P. Rey, E. Belorisky

4699 An application of the wavelets to the magnetic field source searching — T. Doi, S. Yoshida, Y. Nakaya, S. Hayano, Y. Saito

4702 Functionalization and applications of nanosized $\gamma$-$Fe_2O_3$ particles — Qingxia Liu, Zhenghe Xu

4705 Catalytic activity of catalase under strong magnetic fields of up to 8 T — S. Ueno, M. Iwasaka

4708 Measurement of clottability of fibrin polymers using magnetic orientation — M. Iwasaka, S. Ueno, H. Tsuda

4711 Analysis of extremely low frequency brain magnetic fields associated with short-term memory and recognition processes (abstract) — Hideki Yoshida, Shoogo Ueno, Douglas Cheyne, Harold Weinberg

4712 Artifacts in magnetic resonance imaging from metals — L. H. Bennett, P. S. Wang, M. J. Donahue

4715 Magnetic phase transitions in perovskite-type anilinium-based tetrachlorocuprates — D. J. Nelson, K. Chan, F. Cervantes-Lee, L. W. ter Haar

4718 $NiBr_2 \cdot 3H_2O$, a lower dimensional antiferromagnet — G. C. DeFotis, J. R. Goodey, A. A. Narducci, M. H. Welch

4721 Magnetic field effect on interface profile between immiscible nonmagnetic liquids—Enhanced Moses effect — Hiroharu Sugawara, Noriyuki Hirota, Takuro Homma, Masayuki Ohta, Koichi Kitazawa, Hiroyuki Yokoi, Yozo Kakudate, Shuzo Fujiwara, Mitsutaka Kawamura, Shoogo Ueno, Masakazu Iwasaka


*(Continued)*

**Symposium on Spin Tunneling and Injection Phenomena**

| | | |
|---|---|---|
| 4724 | Ferromagnetic–insulator–ferromagnetic tunneling: Spin-dependent tunneling and large magnetoresistance in trilayer junctions (invited) | Jagadeesh S. Moodera, Lisa R. Kinder |
| 4730 | Theory of spin-dependent tunneling and transport in magnetic nanostructures (invited) | S. Maekawa, J. Inoue, H. Itoh |
| 4733 | Spin-dependent tunneling effect and GMR in metal–nonmetal granular systems (invited) (abstract) | H. Fujimori, S. Mitani, S. Ohnuma |
| 4734 | Spin-dependent transmission of free electrons through ultrathin cobalt layers (invited) | H.-J. Drouhin, A. J. van der Sluijs, Y. Lassailly, G. Lampel |

**Instrumentation and Measurement Techniques**

| | | |
|---|---|---|
| 4740 | The vibrating sample magnetometer: Experiences of a volunteer (invited) | S. Foner |
| 4746 | Measurement of texture in magnetic recording media using a biaxial vibrating sample magnetometer | F. Schmidlin, P. R. Bissell, J. A. Gotaas |
| 4749 | Application of Barkhausen effect measurements for detection of near surface stress (abstract) | D. A. Kaminski, D. C. Jiles |
| 4750 | Nondestructive inspection of a fractured nickel bar by Barkhausen and magnetoacoustic emissions | C. C. Yu, C-D. Qin, D. H. L. Ng |
| 4753 | A two-dimensional single sheet tester incorporating controlled magnetization direction | J. J. Dalton, J. Liu, A. J. Moses, D. H. Horrocks, A. Basak |
| 4756 | A magnetoelastic torque transducer utilizing a ring divided into two oppositely polarized circumferential regions | I. J. Garshelis, C. R. Conto |
| 4759 | Hall-effect characterization in semiconductor heterostructure junctions using polarized laser signal | Hoton How, Ta-Ming Fang, Feng Lu, Brian Ahern |

**Giant Magnetoresistance and Anisotropy in Multilayers**

| | | |
|---|---|---|
| 4762 | Nature of the interlayer coupling in annealed $Ni_{80}Fe_{20}$/Ag multilayers | J. A. Borchers, P. M. Gehring, R. W. Erwin, C. F. Majkrzak, J. F. Ankner, T. L. Hylton, K. R. Coffey, M. A. Parker, J. K. Howard |
| 4765 | Magnetization, magnetoresistance, and x-ray diffraction measurements of discontinuous [$Ni_{80}Fe_{20}$/Ag] multilayers (abstract) | T. Lorenz, M. Moske, A. Käufler, H. Geisler, K. Samwer |
| 4766 | Exchange coupling in sputtered giant magnetoresistance NiFe/Cu/CoFe/Cu multilayers | M. T. Kief, J. Bresowar, Q. Leng |
| 4769 | Spin polarized neutron scattering study of NiCo/Cu multilayers | Ming Mao, S. H. Nguyen, B. D. Gaulin, Z. Tun, X. Bian, Z. Altounian, J. O. Ström-Olsen |
| 4772 | Magnetic properties of epitaxial and polycrystalline Fe/Si multilayers | A. Chaiken, R. P. Michel, C. T. Wang |
| 4775 | Anomalous temperature dependence of interlayer coupling in Fe/Si multilayers (abstract) | R. P. Michel, A. Chaiken, M. A. Wall, J. W. Dykes, J. F. Ankner, H. Kaiser |
| 4776 | Antiferromagnetic coupling in magnetic multilayers with a narrow gap semiconductor spacer | Zhu-Pei Shi, Barry M. Klein |
| 4779 | Magnetic properties of $(11\bar{2}0)$ Dy/Y superlattices | K. Theis-Bröhl, K. A. Ritley, C. P. Flynn, K. Hamacher, H. Kaiser, J. J. Rhyne |
| 4782 | Structural, field, and temperature dependence of noncollinear magnetic coupling in Fe/Cr(001) superlattices (abstract) | J. F. Ankner, H. Kaiser, K. Hamacher, A. Schreyer, Th. Zeidler, H. Zabel, C. F. Majkrzak, M. Schäfer, P. Grünberg |
| 4783 | Structural and magnetic properties of fcc Pt/Fe(111) multilayers | Ruqian Wu, Lujun Chen, Nicholas Kioussis |
| 4786 | Magnetic properties and magnetization reversal in Co/Au multilayers (abstract) | Z. S. Shan, J. X. Shen, R. D. Kirby, D. J. Sellmyer |
| 4787 | Coordinated RHEED, XRD, and FMR investigations of MBE grown Co–Cu (100) superlattices | R. A. Lukaszew, R. Naik, K. R. Mountfield, J. O. Artman |

*(Continued)*

4790 Studies of the magnetic anisotropies of Co($1\bar{1}00$)/Cr(211) and Co($11\bar{2}0$)/Cr(100) multilayers — J. C. A. Huang, F. C. Tang, W. W. Fang, R. L. Liu, Y. M. Hu, C. K. Lo, Y. Liou, Y. D. Yao, W. T. Yang, C. P. Chang, S. Y. Liao

4793 Reorientational transition of the magnetic anisotropy and antiferromagnetic coupling of Co/Cr(001) superlattices — Th. Zeidler, F. Schreiber, H. Zabel

**Itinerant Magnetism**

4796 Spin-resolved density of states of 3*d* magnets — A. K. See, L. E. Klebanoff

4799 Electronic structure and exchange interactions in fcc Fe — M. van Schilfgaarde, V. P. Antropov, B. N. Harmon

4802 Critical dynamics at the spin-density-wave transition of chromium — B. J. Sternlieb, J. P. Hill, T. Inami, G. Shirane, W.-T. Lee, S. A. Werner, Eric Fawcett

4805 Theory of non-Heisenberg exchange: Results for localized and itinerant magnets — O. N. Mryasov, A. J. Freeman, A. I. Liechtenstein

4808 Local density approximation of magnetocrystalline anisotropy: An approach for narrowband materials — R. P. Erickson

4811 Magnetic properties of melt-quenched Ni-rich amorphous and bcc Zr–Ni alloys (abstract) — László F. Kiss, Lajos K. Varga, Imre Bakonyi

4812 Specific heat and magnetization of $Co_{2-x}Sc_{1+x}Sn$ — Z. W. Chen, C. L. Lin, T. Mihalisin, J. T. Wang, X. Q. Wang

4815 On the conduction band polarization in metallic systems with a periodic array of localized magnetic moments — A. Hernando, J. M. Rojo, J. C. Gómez Sal, J. M. Novo

4818 Electronic and magnetic properties of the 4*d* itinerant ferromagnet $SrRuO_3$ — David J. Singh

4821 Magnetic and transport properties of Na doped $SrRuO_3$ and $CaRuO_3$ — M. Shepard, G. Cao, S. McCall, F. Freibert, J. E. Crow

4824 Goldstone modes of incommensurate chromium alloys — R. S. Fishman, S. H. Liu

**Hard Magnets, Borides, and Exchange Coupling**

4827 Magnetic hardening of melt-spun nanocomposite $Nd_2Fe_{14}B$/Fe magnets — I. Panagiotopoulos, L. Withanawasam, A. S. Murthy, G. C. Hadjipanayis, E. W. Singleton, D. J. Sellmyer

4830 Microstructural control of NdFeB cast ingots for achieving 50 MGOe sintered magnets — D. W. Scott, B. M. Ma, Y. L. Liang, C. O. Bounds

4833 Formation of $Nd(Fe_{1-y}Co_y)_2$ in rapidly quenched $Nd_{13.75}(Fe_{1-x}Co_x)_{80.25}B_6$ ($x$=0–0.5) alloys — Er. Girt, M. Koknaeva, Z. Altounian

4836 Hard and soft magnetic properties of nanocrystalline Fe–Nd–Zr–B alloys containing intergranular amorphous phase (abstract) — A. Inoue, A. Kojima, A. Takeuchi, T. Masumoto, A. Makino

4837 Melt-spun $Pr_2Co_{14}B$/Co nanocomposite magnets — L. Withanawasam, I. Panagiotopoulos, G. C. Hadjipanayis

4840 Hydrogen induced corrosion mechanism in NdFeB magnets — A. S. Kim, F. E. Camp, T. Lizzi

4843 Magnetic properties and transmission electron microscopy microstructures of exchange coupled $Nd_{12-x}Fe_{82+x}B_6$ melt spun ribbons — W. C. Chang, D. M. Hsing

4846 Microstructure of flash and conventionally annealed melt spun NdFeB (abstract) — M. V. P. Altoé, M. Chandramouli, G. Thomas

4847 A metallurgical approach toward alloying in rare earth permanent magnet systems (abstract) — D. J. Branagan, K. W. Dennis, M. J. Kramer, R. W. McCallum

4848 Microstructure and composition in rapidly quenched NdFeB-based hard magnet alloys — Tai D. Nguyen, Kannan M. Krishnan, Laura Henderson Lewis, Yimei Zhu, David O. Welch

4851 Explosive compaction of Magnequench Nd–Fe–B magnetic powders — S. Guruswamy, M. K. McCarter, J. E. Shield, V. Panchanathan

4854 The protective coatings of NdFeB magnets by Al and Al(Fe) — C-D. Qin, A. S. K. Li, D. H. L. Ng

*(Continued)*

**Magnetic Recording Media I**


| | | |
|---|---|---|
| 4857 | Twin screw extrusion of a metal particle dispersion | H. Göktürk, K. Maki |
| 4860 | Preparation of acicular iron nanoparticles by the reduction of ferrous salt in the presence of tubular lecithin assemblies | Jason L. Cain, David E. Nikles |
| 4863 | Iron particle surface chemistry and corrosion protection by amine-quinone polyurethanes | Antony P. Chacko, David E. Nikles |
| 4866 | Synthesis and magnetic properties of electrodeposited metal particles on anodic alumite film | Xiaohua Bao, Feiyue Li, Robert M. Metzger |
| 4869 | Lanthanide and boron oxide-coated $\alpha$-Fe particles | Feiyue Li, Xiaohua Bao, Robert M. Metzger, Massimo Carbucicchio |
| 4872 | Time effects in exchange anisotropy-affected metal-evaporated tapes | G. Bottoni, D. Candolfo, A. Cecchetti |
| 4875 | The archival stability of metal evaporated tape for consumer digital VCRs | Seiichi Onodera, Tsutomu Takeda, Takahiro Kawana |
| 4878 | Effects of $Cr_2O_3$ or $Y_2O_3$ doping in barium ferrite thin-film medium for high-density recording | Y. J. Chen, M. H. Kryder |
| 4881 | Sputtered hexagonal Ba-ferrite films for high-density magnetic recording media | Akimitsu Morisako, Mitsunori Matsumoto, Masahiko Naoe |
| 4884 | Recording characteristics of Co-$\gamma Fe_2O_3$ perpendicular magnetic recording media | S. Yamamoto, T. Andou, H. Kurisu, M. Matsuura, T. Doi, K. Tamari |
| 4887 | Preparation and the magnetic properties of Co-$\gamma$-$Fe_2O_3$ perpendicular magnetic films on NiO underlayer | T. Doi, K. Tamari |
| 4890 | Determination of local order in the amorphous precursor to Ba-hexaferrite thin-film recording media | J. E. Snyder, V. G. Harris, B. N. Das, N. C. Koon, X. Sui, M. H. Kryder |
| 4893 | Fabrication and magnetic properties of metal/cobalt ferrite composite thin films | J. G. Na |


**Magnetic Recording Media II**


| | | |
|---|---|---|
| 4896 | Co–Cr films prepared by sputtering using electron cyclotron resonance microwave plasma | S. Yamamoto, K. Sato, H. Kurisu, M. Matsuura |
| 4899 | Magnetic viscosity and switching volumes of annealed Fe/Pt multilayers | C. P. Luo, Z. S. Shan, D. J. Sellmyer |
| 4902 | Seed layer induced (002) crystallographic texture in NiAl underlayers | Li-Lien Lee, David E. Laughlin, David N. Lambeth |
| 4905 | Plastic substrate preembossed 100 kbpi, 3.4 $\mu$m track width magnetic disk (abstract) | O. Ishizaki, T. Ohnuki, K. Adachi, K. Akagi, H. Momiji, O. Komoda, N. Ohta |
| 4906 | Nonlinear partial erasure and its correlation with transition noise in longitudinal thin-film media | Jian-Gang Zhu, Terence Lam, Yansheng Luo, Xiao-Guang Ye |
| 4909 | Magnetic force microscopy study of submicron track width recording in thin-film media | Yansheng Luo, Terence T. Lam, Jian-Gang Zhu, Hua-Ching Tong, Robert Rottmayer |
| 4912 | Magnetic force microscopy images of ultrahigh-density bit patterns recorded on high-coercivity longitudinal and perpendicular thin-film media | Xing Song, John Sivertsen, Jack Judy |
| 4915 | The effect of physical structure on $\delta I$ curves of longitudinal thin film (abstract) | N. S. Walmsley, A. Hart, D. A. Parker, C. Dean, R. W. Chantrell |
| 4916 | Micromagnetic studies of inhomogeneous CoPtCr bicrystal thin-film media | Qingzhi Peng, H. Neal Bertram, Mary Doerner |
| 4919 | Multilevel master equation for bicrystal clusters | I. Klik, Y. D. Yao, C. R. Chang |
| 4922 | Coercivity mechanism in CoPt alloy films with perpendicular magnetic anisotropy (abstract) | Th. Kleinefeld, J. Heimel, D. Weller |
| 4923 | Grain morphology and magnetic properties of CoCrPt/Cr(Si,Ti) films sputtered at room temperature | G. Choe |


*(Continued)*

**Thin Films, Interfaces, and Anisotropy**


| | | |
|---|---|---|
| 4926 | Ultrahigh vacuum SQUID magnetometry study of the magnetic properties of Co/Co-oxide thin films | S. Spagna, M. B. Maple, R. E. Sager |
| 4929 | Ferromagnetic resonance of sputtered Co/Mn multilayers | D. Spoddig, F. Schreiber, J. Pflaum, J. Pelzl, Q. Wang, H. Zabel |
| 4932 | Structural and magnetocrystalline anisotropy contributions to the blocking temperatures of $Ni_xCo_{(1-x)}O$ exchange couples (abstract) | Kentaro Takano, Ami E. Berkowitz, Wei Cao, Gareth Thomas |
| 4933 | Rotatable anisotropy in radio frequency diode sputtered iron thin films | W. Win, E. J. Yun, R. M. Walser |
| 4936 | Coupling effects in Fe/CoNbZr and Fe/Ag/CoNbZr sandwiches studied by magneto-optical techniques | M. C. Contreras, J. F.-Calleja, M. O. Gutiérrez, M. Rivas, R. Krishnan |
| 4939 | Low-energy ion beam-assisted deposition of giant magnetoresistive thin films | S. J. Guilfoyle, R. J. Pollard, P. J. Grundy |
| 4942 | Dynamic hysteresis of two-dimensional magnetic islands with uniaxial anisotropy | C. N. Luse, A. Zangwill |
| 4945 | Uniaxial magnetic anisotropy of iron thin films deposited by oblique incidence of deposition particles | Y. Hoshi, E. Suzuki, M. Naoe |
| 4948 | Complex anisotropies in sputtered $Co_{90}Fe_{10}$ alloy thin films (abstract) | E. J. Yun, W. Win, R. M. Walser |
| 4949 | Ferromagnetic resonance studies of noble metals based sandwiches | Y. D. Wang, L. Y. Chen, Y. X. Sui, S. M. Zhou, Y. Wang, Y. X. Zheng, Y. H. Qian, Q. Y. Jin |
| 4951 | Finite temperature magnetization reversal in ultrathin magnetic films | S. T. Chui |
| 4954 | The growth of magnetic Fe overlayers on sulphur passivated GaAs(100) | G. W. Anderson, M. C. Hanf, P. R. Norton, M. Kowalewski, K. Myrtle, B. Heinrich |
| 4957 | Epitaxial ferromagnetic MnAs thin films grown on Si (001): The effect of substrate annealing | K. Akeura, M. Tanaka, T. Nishinaga, J. De Boeck |
| 4960 | Thickness dependence of effective magnetic anisotropy | Ching-Ray Chang |
| 4963 | Uniaxial and planar magnetic anisotropy of thin transition-metal films (abstract) | R. Lorenz, J. Hafner |
| 4964 | Structural and magnetic properties of face-centered-cubic Fe films grown on Co(100) | Ernesto J. Escorcia-Aparicio, R. K. Kawakami, Z. Q. Qiu |
| 4967 | Galvanomagnetic properties and magnetic domain structure of epitaxial MnAs films on GaAs(001) | M. C. Park, Y. Park, T. Shin, G. M. Rothberg, M. Tanaka, J. P. Harbison |
| 4970 | GMR properties of spin valves using multilayered $Co_{90}Fe_{10}$ for free magnetic layer | Koichi Nishioka, Takayuki Iseki, Hideo Fujiwara, Martin R. Parker |
| 4973 | Micromagnetics of uneven ultrathin film trilayers | A. S. Arrott |
| 4976 | Magnetization of two-dimensional *XY* magnets with symmetry breaking fields: Relevance to ultrathin magnetic films (abstract) | J. Rothman, P. C. W. Holdsworth, S. T. Bramwell |
| 4976 | Characterization of iron-oxide films grown on Cu(001) and Ag(001) (abstract) | L. Scipioni, B. Sinkovic |
| 4977 | Thickness dependence of magneto-optical properties in face-centered-cubic Co/Cu(001) ultrathin films | K. Nakajima, T. Miyazaki |
| 4980 | Investigation of magnetic coupling in sputtered epitaxial Fe/Cr and Co/Cu wedged structures | X. Bian, H. T. Hardner, S. S. P. Parkin |
| 4983 | Enhancement of orbital magnetism at surfaces: Co on Cu(100) (abstract) | M. Tischer, F. May, K. Baberschke, O. Hjortstam, D. Arvanitis, J. Hunter Dunn, J. Trygg, B. Johansson, O. Eriksson, J. M. Wills |
| 4984 | Critical phenomena in the two-dimensional *XY* magnet Fe(100) on W(100) | H. J. Elmers, J. Hauschild, G. H. Liu, U. Gradmann |
| 4987 | *In situ* Brillouin light scattering from ultrathin epitaxial Fe/Ag(100) films with Cr and Ag overlayers | R. J. Hicken, A. Ercole, S. J. Gray, C. Daboo, J. A. C. Bland |


*(Continued)*

4990 Magneto-optical investigation of the fcc–bcc phase transition of Fe wedges sandwiched between CuNi alloys (abstract) — H. Theuss, D. Weller, A. Carl

4991 Dependence of structural and magnetic properties on deposition angle in electron-beam evaporated Co/Pt multilayer thin films — Ki-Seok Moon, Sung-Chul Shin

4994 Simulations of inhomogeneous magnetization processes in ultrathin films with growth-induced roughness (abstract) — A. Moschel, A. Zangwill, M. D. Stiles

**Recording Heads and Materials**

4995 Measurement of the crystalline anisotropy in sputtered single-crystal FeTaN thin films — L. Varga, W. D. Doyle

4998 Magnetic properties and crystal structure of FeTaAlN soft magnetic materials for MIG head (abstract) — Yiqun Li, Bingchu Cai, Xianglin Zeng, Dong Xu

4999 Magnetic domain control of thick Fe-M(Zr,Ta)-N films for digital VCR metal in gap heads — M. Uchizawa, J. Fujita, H. Kobayashi, S. Tanabe

5002 Contact magnetoresistive head for perpendicular magnetic recording — Ken-ichi Takano, Hiroaki Muraoka, Yoshihisa Nakamura

5005 Magnetostriction and thin-film stress in high magnetization magnetically soft FeTaN thin films — M. K. Minor, B. Viala, J. A. Barnard

5008 Exchange coupling between NiO and NiFe thin films — J. X. Shen, M. T. Kief

5011 Search for high moment soft magnetic materials: FeZrN (abstract) — A. Chakraborty, G. H. Bellesis, K. R. Mountfield, D. N. Lambeth, M. H. Kryder

5011 Magnetic properties of CoFeB sputtered films for high Bsat applications (abstract) — Durga Ravipati, Hua-Ching Tong, Lena Miloslavsky

5012 Exchange coupling of sputter deposited NiCo–O/NiFe thin films — Minshen Tan, Hua-Ching Tong, Swie-In Tan, Robert Rottmayer

5015 Preparation of soft magnetic Fe/Ta and Fe:N/Ta:N multilayered films with large magnetization for inductive recording head — Masahiko Naoe, Shigeki Nakagawa

5018 Cr\(CoPtCr,$CoPt_x$) layered film studies for hard bias applications — A. Tsoukatos, S. Gupta, D. Marx

**Commemorative Symposium on Neutron Scattering**

5021 Early development of neutron scattering by magnetic materials (invited) (abstract) — C. G. Shull

5022 Magnetic scattering of neutrons (invited) (abstract) — R. M. Moon

5022 Neutron scattering as a probe of unconventional superconductivity in $YBa_2Cu_3O_7$ (invited) (abstract) — B. Keimer

5023 Strong magnetic fluctuations in transition metal oxides (invited) — C. Broholm, G. Aeppli, S.-H. Lee, W. Bao, J. F. DiTusa

**Symposium on High Performance Permanent Magnets and Coercivity**

5029 Overview of Nd–Fe–B magnets and coercivity (invited) — J. Fidler, T. Schrefl

5035 High performance NdFeB magnets (invited) — A. S. Kim, F. E. Camp

5040 Anisotropic Nd–Fe–B bonded magnets made from HDDR powders (invited) — T. Takeshita, K. Morimoto

5045 $Sm_2Fe_{17}$ interstitial magnets (invited) — K.-H. Müller, Lei Cao, N. M. Dempsey, P. A. P. Wendhausen

5051 Disorder and noncollinear magnetism in permanent-magnet materials (invited) — R. Lorenz, J. Hafner

**Small Particles/Lithography**

5056 Long range order in 2-D arrays of nanometer-sized Fe islands on $CaF_2$/Si(111) (invited) (abstract) — M. R. Scheinfein, K. E. Schmidt, K. R. Heim, G. G. Hembree

5057 Fabricating nanoscale magnetic mounds using a scanning probe microscope — K. Bessho, Y. Iwasaki, S. Hashimoto

5060 Magnetic properties of nanometer-size CoPt particles — S. H. Liou, Y. Liu, S. S. Malhotra, M. Yu, D. J. Sellmyer


*(Continued)*

5063 Oxidation states and magnetism of Fe nanoparticles prepared by a laser evaporation technique — B. J. Jönsson, T. Turkki, V. Ström, M. S. El-Shall, K. V. Rao

5066 65 Gbits/in.$^2$ quantum magnetic disk (abstract) — Stephen Y. Chou, Peter R. Krauss

5066 Quantized writing processes in quantum magnetic disks (abstract) — Usman Suriono, Stephen Y. Chou

5067 Nonmonotonic length dependence of switching field of nanolithographically defined single-domain nickel and cobalt bars (abstract) — Linshu Kong, Stephen Y. Chou

5067 Ultramicro fabrications on Fe-Ni alloy films using electron-beam writing and reactive-ion etching (abstract) — I. Nakatani

5068 Structural and magnetic study of submicronic single crystal cobalt box arrays — M. Hehn, K. Ounadjela, S. Padovani, J. P. Bucher, J. Arabski, N. Bardou, B. Bartenlian, C. Chappert, F. Rousseaux, D. Decanini, F. Carcenac, E. Cambril, M. F. Ravet

5071 High field irreversibility in $NiFe_2O_4$ nanoparticles (abstract) — R. H. Kodama, A. E. Berkowitz, E. J. McNiff, Jr., S. Foner

5072 Sputter deposited Co/CoO composite materials — J. Y. Yi, C. L. Platt, M. L. Rudee, A. E. Berkowitz, T. L. Cheeks

5075 High-resolution observation of magnetization processes in 2 $\mu$m $\times$ 2 $\mu$m $\times$ 0.04 $\mu$m permalloy particles — K. Runge, Y. Nozaki, Y. Otani, H. Miyajima, B. Pannetier, T. Matsuda, A. Tonomura


**Critical Phenomena II**


5078 Neutron diffraction determination of the nuclear spin ordering in Cu and Ag at nano- and subnano-K temperatures (invited) — M. Steiner, A. Metz, K. Siemensmeyer, O. V. Lounasmaa, J. T. Tuoriniemi, K. K. Nummila, R. T. Vuorinen, K. N. Clausen, K. Lefmann, F. B. Rasmussen

5081 Critical properties of the spin Peierls transition in $CuGeO_3$ — M. D. Lumsden, B. D. Gaulin, H. Dabkowska

5084 Evidence for crossover effects in the spin dynamics of the two-dimensional antiferromagnet $Sr_2CuO_2Cl_2$ from $^{35}Cl$ nuclear magnetic resonance — B. J. Suh, F. Borsa, L. L. Miller, D. C. Johnston, D. R. Torgeson, M. Corti

5087 Magnetic and nonmagnetic glass transitions in the Blume–Emery–Griffiths model with competing biquadratic interactions (abstract) — Daniel P. Snowman, Susan R. McKay

5087 The three-dimensional RFIM: Existence of a tricritical point? (abstract) — Laura Hernandez, H. T. Diep

5088 $m$=3 Ashkin–Teller-like cubic model on an FCC lattice — Ron ald Fisch

5091 Phase transitions in disordered systems: Exactly solvable model — D. Nicolaides, A. A. Lisyansky

5094 Effect of exchange anisotropy on susceptibility of one-dimensional spin 1/2 ferromagnets — Ying Liu, John E. Drumheller

5096 Effects of randomness in gapped antiferromagnetic quantum spin chains — Kun Yang, R. A. Hyman, R. N. Bhatt, S. M. Girvin

5099 Competition between spin-Peierls phase and three-dimensional antiferromagnetic order in $CuGe_{1-x}Si_xO_3$ — J. P. Renard, K. Le Dang, P. Veillet, L. P. Regnault, G. Dhalenne, A. Revcolevschi


**Exchange Bias and Interface Roughness**


5102 Domain structure in NiO biasing layers (abstract) — R. W. Erwin, J. A. Borchers, D. M. Lind, E. Lochner, K. A. Shaw, B. Singer, P. Stoyonov, R. C. DiBari, S. D. Berry

5103 Exchange biasing in MBE grown $Fe_3O_4$/CoO bilayers: The antiferromagnetic layer thickness dependence — P. J. van der Zaag, A. R. Ball, L. F. Feiner, R. M. Wolf, P. A. A. van der Heijden

5106 Magnetic properties of exchange-coupled Fe/FeO bilayers — D. V. Dimitrov, A. S. Murthy, G. C. Hadjipanayis, C. P. Swann


*(Continued)*

5109 Effects of cooling field strength on exchange anisotropy at permalloy/CoO interfaces — Timothy J. Moran, Ivan K. Schuller

5112 The role of interface crystalline and magnetic structure in exchange anisotropy (abstract) — J. Nogués, D. Lederman, Ivan K. Schuller, K. V. Rao

5113 Topological coupling in magnetic multilayer films — J. Zhang, R. M. White

5116 Surface roughness in Cu(100)/$[Co/Cu]_n$ systems grown by ion-beam sputtering — Timothy J. Minvielle, Robert L. White, Robert J. Wilson

5119 $^{59}Co$ nuclear magnetic resonance studies of the effect of annealing molecular beam epitaxy grown Co/Cu(111) multilayers — T. Thomson, P. C. Riedi, B. J. Hickey

5122 Field dependent resonance frequency of hysteresis loops in a few monolayer thick Co/Cu(001) films — Q. Jiang, H.-N. Yang, G.-C. Wang

5125 Fe adsorption and film growth on GaAs(001) (2×4)-As (abstract) — E. Kneedler, P. M. Thibado, B. T. Jonker, B. R. Bennett, L. J. Whitman, B. V. Shanabrook, J. J. Krebs

5126 Magnetic properties and Pd–H miscibility gap in Ni/Pd composite fine particles — Takashi Manago, Yoshichika Otani, Hideki Miyajima, Etsuo Akiba

5129 Magnetic impurities and clusters on Ag, Pd, and Pt surfaces (abstract) — V. S. Stepanyuk, K. Wildberger, P. Lang, R. Zeller, P. H. Dederichs


**Soft Amorphous and Nanocrystalline Materials I**


5130 High-frequency magnetic properties in metal–nonmetal granular films (invited) — S. Ohnuma, H. Fujimori, S. Mitani, T. Masumoto

5136 Giant magnetoimpedance effect in soft and ultrasoft magnetic fibers — P. Ciureanu, P. Rudkowski, G. Rudkowska, D. Menard, M. Britel, J. F. Currie, J. O. Ström-Olsen, A. Yelon

5139 Giant magneto-impedance effects in Metglas 2705M — R. L. Sommer, C. L. Chien

5142 Barkhausen noise in FeCoB amorphous alloys (abstract) — G. Durin, G. Bertotti

5143 Magnetism and microstructure of nanocrystalline nickel — H. Kisker, H. Kronmüller, H.-E. Schaefer, T. Suzuki

5146 Small-angle neutron scattering behavior of $Fe_{91}Zr_9$ glass under magnetic field — L. Fernández Barquín, J. C. Gómez Sal, S. N. Kaul, J. M. Barandiarán, P. Gorría, J. S. Pedersen, R. Heenan

5149 Time-temperature-transformation study of a nanocrystalline $Fe_{91}Zr_7B_2$ soft magnetic alloy — K. Suzuki, J. M. Cadogan, V. Sahajwalla, A. Inoue, T. Masumoto

5152 Soft magnetic properties of Fe–Zr–B thin films (abstract) — N. B. Shevchenko, J. A. Christodoulides, X. Meng-Burany, A. S. Murthy, G. C. Hadjipanayis

5153 The change of magnetic properties in nanocrystalline $Fe_{88}Zr_7B_4Cu_1$ alloy by cooling rate — K. S. Kim, V. Ström, J. Wittborn, K. V. Rao, K. Y. Kim, T. H. Noh, S. C. Yu

5156 Improvement of soft magnetism of $Fe_{90}Co_{10}$ sputtered films by addition of N and Ta — Shigeki Nakagawa, Satoshi Tanaka, Katsumi Suemitsu, Masahiko Naoe

5159 Effect of nitrogen interstitial in $\alpha$-Fe crystalline on the magnetic soft properties of FeTaN thin films — W. C. Chang, D. C. Wu, J. C. Lin, C. J. Chen


**Colossal Magnetoresistance in Perovskite Oxides II**


5162 Giant magnetoresistance induced by spin-correlation scattering in magnetic thin films and other compounds — Liang-Jian Zou, X. G. Gong, Qing-Qi Zheng, C. Y. Pan

5165 Giant magnetoresistive memory effect in $Nd_{0.7}Sr_{0.3}MnO_z$ (abstract) — G. C. Xiong, Q. Li, H. L. Ju, R. L. Greene, T. Venkatesan, M. Dominguez, S. E. Lofland, S. M. Bhagat


*(Continued)*

5166 Ferromagnetic resonance and intrinsic properties of $La_{0.67}Ba_{0.33}MnO_z$ — S. E. Lofland, S. M. Bhagat, H. L. Ju, G. C. Xiong, T. Venkatesan, R. L. Greene, S. Tyagi

5169 Role of epitaxy and polycrystallinity in the magnetoresistance and magnetization of $La_{0.8}Sr_{0.2}MnO_3$ thin films — Kannan M. Krishnan, A. R. Modak, C. A. Lucas, R. Michel, H. B. Cherry

5172 Magnetic exchange and charge transfer in mixed-valence manganites and cuprates — Gerald F. Dionne

5175 Correlation between magnetovolume and giant magnetoresistance effects in doped $La_{2/3}Ca_{1/3}MnO_3$ perovskites — J. M. De Teresa, J. Blasco, M. R. Ibarra, J. García, C. Marquina, P. Algarabel, A. del Moral

5178 Pressure effect on the resistivity in GMR $La_{0.60}Y_{0.07}Ca_{0.33}MnO_3$ compound (abstract) — Z. Arnold, K. Kamenev, M. R. Ibarra, P. A. Algarabel, C. Marquina, J. Blasco, J. García

5179 Hall effect and giant magnetoresistance in lanthanum manganite thin films — J. E. Núñez-Regueiro, D. Gupta, A. M. Kadin

5182 Magnetic properties of colossal magnetoresistive manganese oxides — J. Fontcuberta, B. Martínez, A. Seffar, S. Piñol, A. Roig, E. Molins, X. Obradors, J. Alonso, J. M. González-Calbet

5185 Magnetic and magnetoresistance studies on radio frequency sputtered La–Pb–Mn–O films — G. Srinivasan, T. E. Brusca, A. S. Fisher, V. Suresh Babu, M. S. Seehra

5188 Composition dependence of giant magnetoresistance in $(La_{1-x}Y_x)_{2/3}Ca_{1/3}MnO_\delta$ $(0 \leq x \leq 1)$ — Zisen Li, X. T. Zeng, H. K. Wong

**Magnetic Semiconductors**

5191 Effects of high-temperature annealing on the optical absorption of Ca:YIG films — R. E. Bornfreund, P. E. Wigen

5193 Determination of Mn composition in $Zn_{1-x}Mn_xSe$ from Faraday rotation analysis — Yu-Xiang Zheng, Liang-Yao Chen, Shi-Ming Zhou, Ya-Dong Wang, Yu Wang, You-Hua Qian, Jie Wang, Cai-Xia Jin, Xun Wang

5195 Microstructural properties of (ZnSe/FeSe) and (ZnSe/MnSe) diluted magnetic semiconductor superlattices (abstract) — K. Park, L. Salamanca-Riba, B. T. Jonker

5196 Polaron-polaron interactions in diluted magnetic semiconductors — P. A. Wolff, R. N. Bhatt, A. C. Durst

**Instrumentation and Measurement Techniques II**

5199 Hybrid pole pieces for permanent magnets — M. G. Abele, J. H. Jensen

5202 Method based on the saturation approach law for monitoring the quality of texture in 3% Si–Fe — M. Birsan, J. A. Szpunar

5205 Construction of novel magnets for generating astatic fields in x-ray topography — Tetsuo Nakajima, Masami Yoshizawa

5208 Automized magnetic hysteresis measurement system — Rolf Disselnkötter

5211 Alternating current-excited magnetoresistive sensor — P. Ripka

5214 Magnetic field distribution caused by a notebook computer and its source searching — T. Doi, S. Hayano, Y. Saito

5217 Highly sensitive magneto-optic transverse Kerr effect measurement system for the detection of perpendicular anisotropy and magnetic phases in thin films — J. A. Corrales, M. Rivas, J. F.-Calleja, I. Iglesias, M. C. Contreras

**Itinerant Magnetism and Other Fundamental Properties**

5220 First-order magnetic phase transition in (Er, Tb)$M_2$(M=Co, Ni) (abstract) — A. Y. Takeuchi, F. Garcia, S. F. da Cunha

5221 Magnetism in URhSi — K. Prokeš, E. Brück, K. H. J. Buschow, F. R. de Boer, V. Sechovský, P. Svoboda, X. Hu, H. Maletta, T. J. Gortenmulder


*(Continued)*

5224 Magnetic and crystallographic properties of $CrAs_{1-x}S_x(0 \leqslant x < 1)$ — Takanobu Suzuki, Hideaki Ido

5227 Impact of criticality and phase separation on the spin dynamics of the one-dimensional $t-J$ model — Shu Zhang, Gerhard Müller, Joachim Stolze

5230 Rapid loss of magnetic order in Ni on alloying with Cr, Mo, Re, and Si — V. Suresh Babu, A. S. Pavlovic, Mohindar S. Seehra

5233 Magnetic properties of the $SmMn_2(Ge_{1-x}Si_x)_2$ system — Shibaji Saha, Naushad Ali

5236 Remanent magnetization in the linear chain antiferromagnet $(CH_3NH_3)Mn_{1-x}M_xCl_3 \cdot 2H_2O$, M=Cd or Cu — A. Paduan-Filho, C. C. Becerra, F. Palacio

5238 Magnetic properties of $Ni_2In$ type $(Co_{1-x}Mn_x)_{65}Ge_{35}$ compounds — Hiroshi Shiraishi, Tomiei Hori, Yasuo Iguchi, Yasuo Yamaguchi, Masayoshi Ohashi, Kazuo Kanematsu

5241 Magnetism of the solid solution $GdGa_{1-x}Ge_x$ (abstract) — A. Leithe-Jasper, K. Hiebl

5242 Neutron scattering and magnetization clouds in dilute Pd based alloys — R. E. Parra, A. C. González

5245 Polarization analysis of the electron spin resonance lines in the $S=1$ one-dimensional antiferromagnet $Ni(C_3H_{10}N_2)_2NO_2ClO_4$ — M. Hagiwara, K. Katsumata


**New Materials**


5247 Highly crystallized $(La,Sr)MnO_3$ films deposited by facing targets sputtering apparatus — N. Matsushita, K. Noma, S. Nakagawa, M. Naoe

5250 $\alpha''$-$Fe_{16}N_2$ phase epitaxially grown by sputter beam method — Satoshi Okamoto, Osamu Kitakami, Yutaka Shimada

5253 The formation of stable $Co/Co_2MnSn$ two phase magnets — T. W. Kim, R. J. Gambino

5256 Magnetic phase transitions in $RENi_2B_2C$ (RE=Ho,Dy,Tb) studied by $^{57}Fe$ Mössbauer spectroscopy (abstract) — D. Sánchez, H. Micklitz, M. B. Fontes, S. L. Bud'ko, E. Baggio-Saitovitch

5257 Morin-like spin reorientation in BiPb-2201 ferrates with iron in octahedral oxygen coordination — M. Rosenberg, Th. Sinnemann, G. Filoti, S. Kemmler-Sack

5260 Magnetization behavior of $(NBu_4)_2Mn_2[Cu(opba)]_3$ and related solvated ferromagnets — S. A. Chavan, R. Ganguly, V. K. Jain, J. V. Yakhmi

5263 Magnetic properties and grain growth stability of nanocomposite $Fe-ZrO_2$ granular solids prepared by mechanical milling — S. C. Axtell, R. Schalek

5266 The macroscopic ferri-ferromagnetic transition in amorphous Y–Co/Gd–Co bilayers — T. Yonamine, Y. Souche, A. D. Santos

5269 Weak ferromagnetic resonance of $Gd_2CuO_4$ small particles (abstract) — J. Mira, J. Rivas, A. Butera, M. Tovar, C. Vázquez-Vázquez, J. Mahía, M. A. López-Quintela, S. B. Oseroff


**Symposium on Giant and Colossal Magnetoresistance**


5270 Inverse giant magnetoresistance (invited) — J.-P. Renard, P. Bruno, R. Mégy, B. Bartenlian, P. Beauvillain, C. Chappert, C. Dupas, E. Kolb, M. Mulloy, J. Prieur, P. Veillet, E. Vélu

5276 *Ab initio* calculations of spin-dependent transport properties (invited) (abstract) — I. Mertig

5277 Optimizing the giant magnetoresistance of symmetric and bottom spin valves (invited) — W. F. Egelhoff, Jr., P. J. Chen, C. J. Powell, M. D. Stiles, R. D. McMichael, C.-L. Lin, J. M. Sivertsen, J. H. Judy, K. Takano, A. E. Berkowitz, T. C. Anthony, J. A. Brug

5282 First principles calculations of electrical conductivity and giant magnetoresistance of periodic multilayers and spin valves (invited) — W. H. Butler, X.-G. Zhang, D. M. C. Nicholson, T. C. Schulthess, J. M. MacLaren

5288 Origins of colossal magnetoresistance in perovskite-type manganese oxides (invited) — Y. Tokura, Y. Tomioka, H. Kuwahara, A. Asamitsu, Y. Moritomo, M. Kasai


*(Continued)*

5292 Colossal magnetoresistivity in manganese-based perovskites (invited) (abstract) — R. Ramesh, T. Venkatesan, S. B. Ogale, R. L. Greene, S. M. Bhagat

**Small Particles/Nanocrystals**

5293 Magnetic properties of monodomain Nd-Fe-B-C nanoparticles — E. M. Brunsman, J. H. Scott, S. A. Majetich, M. E. McHenry, M.-Q. Huang

5296 Magnetic properties and imaging of Mn-implanted GaAs semiconductors — Jing Shi, J. M. Kikkawa, D. D. Awschalom, G. Medeiros-Ribeiro, P. M. Petroff, K. Babcock

5299 Finite size effects in nanoscale Tb particles — D. Johnson, P. Perera, M. J. O'Shea

5302 Effect of preparation technique on the structural and magnetic properties of granular Fe-$SiO_2$ (abstract) — J. A. Christodoulides, N. B. Shevchenko, A. S. Murthy, G. C. Hadjipanayis

5303 Preparation and quantitative magnetic studies of single-domain nickel cylinders — R. O'Barr, M. Lederman, S. Schultz, Weihua Xu, A. Scherer, R. J. Tonucci

5306 Magnetic domain percolation in granular Co-Ag — A. Gavrin, M. H. Kelley, J. Q. Xiao, C. L. Chien

5309 Observation of perpendicular anisotropy in granular magnetic solids — John Q. Xiao, C. L. Chien, A. Gavrin

5312 Self-stabilized magnetic colloids: Ultrafine Co particles in polymers — Diandra L. Leslie-Pelecky, X. Q. Zhang, Reuben D. Rieke

5315 Complementary imaging of granular Co-Ag films with magneto-optical indicator film technique and magnetic force microscopy — M. J. Donahue, L. H. Bennett, R. D. McMichael, L. J. Swartzendruber, A. J. Shapiro, V. I. Nikitenko, V. S. Gornakov, L. M. Dedukh, A. F. Khapikov, V. N. Matveev, V. I. Levashov

5318 Perpendicular spin valve behavior in a microstructured Co/Cu-Cu oxide/Co trilayer — K. Matsuyama, H. Asada, I. Matsuguma, T. Saeki, K. Taniguchi

5321 Epitaxial $Fe_{16}N_2$ films grown on Si(001) by reactive sputtering — M. A. Brewer, Kannan M. Krishnan, C. Ortiz

5324 Classical and quantum magnetism in synthetic ferritin proteins — S. Gider, D. D. Awschalom, T. Douglas, K. Wong, S. Mann, G. Cain

**Magnetic Recording Media III**

5327 Magnetic recording measurements of high coercivity longitudinal media using magnetic force microscopy (MFM) — P. Giljer, J. M. Sivertsen, J. H. Judy, C. S. Bhatia, M. F. Doerner, T. Suzuki

5330 Grain growth and ordering kinetics in CoPt thin films — K. Barmak, R. A. Ristau, K. R. Coffey, M. A. Parker, J. K. Howard

5333 Co-Sm $(\bar{1}100)[0001]$//Cr $(\bar{1}2\bar{1})[\bar{1}01]$ epitaxy and its effects on magnetic properties of Co-Sm//Cr films — Y. Liu, D. J. Sellmyer, B. W. Robertson

5336 Magnetic and recording properties of monolayer and multilayer thin-film media by using composite targets — Brij B. Lal, A. Bourez, Michael A. Russak

5339 Dependence of media noise on grain size and intergranular coupling in thin-film media — Akira Kikuchi, Shinya Kawakita, Junichi Nakai, Takehito Shimatsu, Migaku Takahashi

5342 The role of stress-induced anisotropy in longitudinal thin film magnetic recording media — C. A. Ross, M. E. Schabes, R. Ranjan, G. Bertero, T. Chen

5345 The role of Ta and Pt in segregation within Co-Cr-Ta and Co-Cr-Pt thin film magnetic recording media — K. M. Kemner, V. G. Harris, V. Chakarian, Y. U. Idzerda, W. T. Elam, C.-C. Kao, Y. C. Feng, D. E. Laughlin, J. C. Woicik

*(Continued)*

5348 Microstructure and magnetic properties of CoCrPt/Cr films on ultrasmooth NiP/AlMg substrates — Li Tang, David E. Laughlin, David N. Lambeth, Mary F. Doerner

5351 Reduction of Co–Cr–Pt media noise by addition of Ti to Cr underlayer — Y. Matsuda, Y. Yahisa, J. Inagaki, E. Fujita, A. Ishikawa, Y. Hosoe

5354 Magnetic and crystallographic properties of CoCrPt thin films formed on Cr–Ti single crystalline underlayers — N. Inaba, A. Nakamura, T. Yamamoto, Y. Hosoe, M. Futamoto

5357 Magnetic and microstructural properties of CoCrTa/Cr/Al thin films (abstract) — H. S. Chang, T. D. Lee, J. K. Park, K. H. Shin, K. Park

5358 Influence of sputter gas and sputter pressure on the structure and magnetic properties of Co–Pt–Cr thin films (abstract) — A. Roshko, L. L. Dulcie, T. Nguyen, T. Yogi

5359 Improvement of $Co_{71}Cr_{19}Pt_{10}/Ti_{90}Cr_{10}$ perpendicular recording media by independent optimization of film nucleation and growth processes — T. P. Nolan, Y. Hirayama, M. Futamoto

5362 High recording performance of Co–Cr medium sputter-deposited at high Ar pressure and high substrate temperature — Naoki Honda, Satoshi Yanase, Kazuhiro Ouchi, Shun-ichi Iwasaki


**Magnetic Excitations I**


5365 Microwave solitons in magnetic films (invited) (abstract) — A. D. Boardman, K. Xie, H. Mehta, S. A. Nikitov

5366 Thresholds of spin wave envelope soliton formation in magnetic films with dissipation (abstract) — A. N. Slavin

5367 Phase properties of microwave magnetic envelope dark solitons in yttrium iron garnet thin films (abstract) — J. M. Nash, P. Kabos, C. E. Patton, R. Staudinger

5368 Two-dimensional solitons in the classical Heisenberg antiferromagnet with nonmagnetic impurities — Kala Subbaraman, Craig E. Zaspel, John E. Drumheller

5371 Interaction of light with a nonlinear spin wave in a normally magnetized ferromagnetic film — A. A. Stashkevich, M. G. Cottam, A. N. Slavin

5374 Variations in auto-oscillation frequency at the main resonance in rectangular yttrium–iron–garnet films — A. Prabhakar, D. D. Stancil

5377 Driven spin-wave dynamics in yttrium–iron–garnet films (abstract) — D. J. Mar, T. L. Carroll, L. M. Pecora, J. F. Heagy, F. J. Rachford

5378 Synchronization of chaos in circular yttrium iron garnet films — D. W. Peterman, M. Ye, P. E. Wigen

5381 Experimental observation of the longitudinal resonance mode in ferromagnets with random anisotropy — G. Suran, E. Boumaiz, J. Ben Youssef

5384 Investigation of the spin-Peierls phase diagram of $CuGeO_3$: Far-infrared electron spin resonance in high field — W. Palme, G. Ambert, J. P. Boucher, G. Dhalenne, A. Revcolevschi

5387 Magnetic anisotropies in thick body centered cubic Co — X. Liu, R. L. Stamps, R. Sooryakumar, G. A. Prinz

5390 Two magnon ferromagnetic resonance linewidths in uniaxial and planar single crystal hexagonal ferrites (abstract) — D. R. Franklin, M. J. Hurben, C. E. Patton


**One-Dimensional Magnetism and Other Cooperative Phenomena**


5391 Finite temperature effects in the $S=1/2$ Heisenberg chain $Cu(C_6D_5COO)_2 \cdot 3D_2O$ (abstract) — D. Dender, D. H. Reich, C. Broholm, K. Lefmann, G. Aeppli

5392 $Cu_2$(1,4-diazacycloheptane)$_2Cl_4$: A quasi-one-dimensional $S=1/2$ spin liquid system — Philip R. Hammar, Daniel H. Reich

5395 Magnetic fluctuation spectrum of $CuGeO_3$: Raman scattering — P. H. M. van Loosdrecht, J. P. Boucher, G. Martinez, G. Dhalenne, A. Revcolevschi

5398 Neutron diffraction study of the magnetic structures of $CeMn_2Ge_2$ and $CeMn_2Si_2$ — J. A. Fernandez-Baca, Peggy Hill, B. C. Chakoumakos, Naushad Ali

5401 Magnetic studies of the metal–insulator transition in $CuIr_2S_{4-x}Se_x$ ($x=0$, 0.1, and 4) — P. Somasundaram, J. M. Honig, T. M. Pekarek, B. C. Crooker

5403 Magnetization and specific heat studies of $Gd_2In$ — Chan-Soo Jee, C. L. Lin, T. Mihalisin, Xue-Qin Wang


*(Continued)*

5406 Magnetic viscosity far and close to equilibrium in the superparamagnetic alloy — A. Maraner, X. Zhang, A. Cavalleri, J. Tejada, S. Vitale

5409 Simultaneous molecular and spin dynamics: Quasiclassical approximation and quantum effects — V. P. Antropov, B. N. Harmon

5412 Magnetic exchange coupling mediated by bound states — C. A. R. Sá de Melo

5415 Phenomenological description of the magnetization relaxation (abstract) — V. L. Sobolev, Huei Li Huang

5416 Atomic magnetic moments and spin notion — Xavier Oudet

5419 Aharonov–Bohm oscillations at finite temperature — P. Schlottmann, A. A. Zvyagin

**Soft Ferrites and Alloys II**

5422 Study of the frequency dependence of the ferromagnetic resonance linewidths of nickel ferrites from 8–60 GHz — L. Torres, M. Zazo, A. G. Flores, V. Raposo, J. Iñiguez

5425 Variable texture $NiOFe_2O_3$ ferrite films prepared by pulsed laser deposition — P. Samarasekara, R. Rani, F. J. Cadieu, S. A. Shaheen

5428 Atomic migration in Ni–Co ferrite — Chul Sung Kim, Seung Wha Lee, Seung Iel Park, Jae Yun Park, Young Jei Oh

5431 EXAFS and magnetic characterization of inverted ball milled zinc ferrite powders (abstract) — S. A. Oliver, V. G. Harris, H. H. Hamdeh, J. C. Ho

5432 High-power-use Mn–Zn ferrites with monodomain structure prepared by low-temperature sintering — C. S. Liu, J. M. Wu, I. Nan Lin, C. J. Chen

5435 Magnetic properties of Zn–Mg ferrite fine powders (abstract) — H. H. Hamdeh, J. C. Ho, S. A. Oliver, R. J. Willey, M. J. O'Shea

5436 Comparison between disaccommodation and ferromagnetic resonance measurements in polycrystalline yttrium–iron–garnet samples — L. Torres, M. Zazo, J. Iñiguez, C. de Francisco, J. M. Muñoz, P. Hernandez

5439 Magnetic properties of $BaFe_{12-(x+y)}Sn_xCo_yO_{19}$ single crystals (abstract) — R. Solé, X. X. Zhang, X. Ruiz, M. Aguiló, F. Díaz, J. Tejada

5440 Epitaxial single crystal $Fe_{16}N_2$ films grown by facing targets sputtering — D. C. Sun, E. Y. Jiang, M. B. Tian, C. Lin, X. X. Zhang

5443 (100)-textured 3% silicon steel sheets by manganese removal and decarburization — Toshiro Tomida

5446 Deposition condition and thickness dependence on magnetic properties of sputtered NiFeCo thin films — A. Tsoukatos, S. Gupta, Y. K. Kim

5449 Ferromagnetism of $Y_2(Fe_{1-y}Co_y)_{17-x}Al_x$ — N. Ohkubo, K. Kanematsu

5452 Ferromagnetism of deuterides $YFe_2D_x$ (abstract) — K. Kanematsu, N. Ohkubo, K. Itoh, S. Ban, T. Miyajima, Y. Yamaguchi

5453 Hydrogen charging in nickel and iron and its effect on their magnetic properties — A. Ramesh, M. R. Govindaraju, D. C. Jiles, S. B. Biner, J. M. Roderick

**Soft, Amorphous, and Nanocrystalline Materials II**

5456 Magnetic viscosity investigations of nanograin iron powder — U. Atzmony, Z. Livne, R. D. McMichael, L. H. Bennett

5459 Magnetic properties and the crystallization of amorphous $Fe_{83}B_9Nb_7Cu_1$ — Chul Sung Kim, Sung Baek Kim, J. S. Lee, T. H. Noh

5462 Resonant microwave cavity response of amorphous ribbons — A. N. Medina, M. Knobel, S. Salem-Sugui, F. G. Gandra

5465 Coercivity and remanence of amorphous and nanocrystalline Fe–(Cu,Ta)–SiB ribbons — N. Murillo, J. González, J. M. Blanco, J. M. González

5468 NMR study of the local inhomogeneities in the soft magnetic alloy $Co_{74.26}Fe_{4.74}Si_{2.1}B_{18.9}$ (abstract) — L. Iannarella, C. Kim, R. C. O'Handley, A. P. Guimarães

5469 Evolution from soft to hard magnetic behavior in Co-based devitrified glassy alloy — G. Bottoni, D. Candolfo, A. Cecchetti

5472 Nanocrystalline Fe-M-B-Cu (M=Zr, Nb) alloys with improved soft magnetic properties (abstract) — A. Makino, T. Bitoh, A. Inoue, T. Masumoto


*(Continued)*

5472 Comparison of experimental and theoretical initial permeability taking into account anistropy dispersion in CoNbZr thin films (abstract) — M. C. Contreras, M. Rivas, J. F. Calleja, I. Iglesias, M. Guyot, V. Cagan, R. Krishnan

5473 Crystallization behavior of a mechanically alloyed amorphous $Fe_{80}Zr_8B_{11}Cu_1$ alloy — Jianqiang Zhang, Bingyao Wu, Xiaohua Wu, Guiqin Wang, Jiwan Zhao

5476 Microstructure and magnetic properties of $Cu_{0.8}(Fe_{1-x}Co_x)_{0.2}$ alloy powders manufactured by a mechanical alloying process — Yong Goo Yoo, Seong Cho Yu, Won Tae Kim

5479 Mechanically ground $Fe_{73.5}Cu_1Nb_3Si_{13.5}B_9$: A soft magnetic material in powdered form — Anit K. Giri, P. García Tello, J. González, J. M. González

5482 Correlation of magnetic and mechanical properties of hydrogenated, compositionally modulated, amorphous $Fe_{80}Zr_{20}$ films (abstract) — S. Rengarajan, E. J. Yun, B. H. Lee, B. I. Cho, R. M. Walser

**Soft Materials—Applications and Other Properties**

5483 Application of Co-based amorphous ribbon to a noise filter and a shielded cable — Osamu Ishii, Masakatsu Senda, Koji Takei, Yasuhiro Koshimoto, Toshinori Mori

5486 A gigahertz-range electromagnetic wave absorber with wide bandwidth made of hexagonal ferrite — Morihiko Matsumoto, Yoshimori Miyata

5489 Rapidly solidified Fe–6.5%Si alloy powders for high frequency use (abstract) — Seung Duk Choi, Choong Jin Yang

5490 Large shielding factor obtained by a multiple-shell magnetic shield having separate magnetic shaking — I. Sasada, T. Yamamoto, T. Yamauchi

5493 The magnetomechanical effect in electrolytic iron — M. K. Devine, D. C. Jiles

5496 Effect of cutting techniques on local magnetic characteristics of SIFE (abstract) — D. A. Philips, L. R. Dupre, K. Eloot, J. A. Melkebeek

5497 The soft magnetic properties of stripes fabricated using laser ablation of multilayer thin films — Craig A. Grimes, Janet K. Lumpp

5500 Magnetic garnet film epitaxy on nonsingular faces (abstract) — S. S. Gorelik, L. M. Letyuk, A. T. Morchenko

**Hard Magnets, 2-14-1, Interstitials**

5501 The effects of average grain size on the magnetic properties and corrosion resistance of NdFeB sintered magnets — D. W. Scott, B. M. Ma, Y. L. Liang, C. O. Bounds

5504 Unusual magnetic behavior in Nd–Fe–B alloy powder compacts — H. Wan, F. T. Parker, F. F. Putris, A. E. Berkowitz

5507 Magnetocrystalline anisotropy and spin reorientation in $Gd_{1-x}Dy_xCo_4B$ — T. Ito, H. Asano, H. Ido, M. Yamada

5510 Dependence of energy dissipation on annealing temperature of melt–spun NdFeB permanent magnet materials — Z. Gao, D. C. Jiles, D. J. Branagan, R. W. McCallum

5513 Quantitative characterization of additional ferromagnetic phase in melt-quenched and sintered Nd–Fe–B-based magnets — L. H. Lewis, D. O. Welch, F. Pourarian

5516 Crystallographic and magnetic properties of $NdFe_{10.7}TiM_{0.3}$(M=B, Ti) — Chul Sung Kim, Young Jong Lee, Seung Wha Lee, Y. B. Kim, C. S. Kim

5519 Structure and magnetic properties of mechanically alloyed $Nd(Fe,V)_{12}N_x$ compounds — Jun Yang, Ou Mao, Z. Altounian

5522 Neutron diffraction and magnetic studies of $RFe_{12-x}T_xC_y$ (R=Y,Er; T=V,Ti,Mo) alloys — Z. Hu, W. B. Yelon, X. Zhang, W. J. James

5525 Structure and magnetic properties of mechanical alloyed Nd–Fe–Ti compounds and their nitrides — Zhi-qiang Jin, X. K. Sun, W. Liu, X. G. Zhao, Q. F. Xiao, Y. C. Sui, Z. D. Zhang, Zhi-gang Wang

5528 High coercivity of melt–spun $Sm_2Fe_{15}Al_2C_{1.5}$ compound — Jun-Xian Zhang, Zhao-Hua Cheng, Bao-Gen Shen

5530 Nuclear magnetic resonance study of $R_2Fe_{17}$ (R=Y, Sm, and Gd) hydrides — N. X. Shen, Y. D. Zhang, J. I. Budnick, W. A. Hines, U. Binninger

5533 Structural and magnetic studies of $Er_2Fe_{17-x}M_xC_y$ (M=Ga and Al) compounds — W. C. Chang, S. L. Lu, S. K. Chen, Y. D. Yao


*(Continued)*

5536 Thermal stability of nanostructured $Sm_2Fe_{17}C_x$ compounds prepared by ball milling — O. Mao, Z. Altounian, J. Yang, J. O. Ström-Olsen

5539 Synthesis and magnetic properties of rare earth–iron–chromium phases and their nitrides — O. Kalogirou, V. Psycharis, M. Gjoka, D. Niarchos, C. D. Fuerst

5542 High field magnetization measurements of $SmFe_{11}Ti$ and $SmFe_{11}TiH_{1-\delta}$ — O. Isnard, M. Guillot, S. Miraglia, D. Fruchart

5545 First-principles calculation of the electronic and magnetic properties of $Nd_2Fe_{17-x}M_x$ (M=Si, Ga) solid solutions — Ming-Zhu Huang, W. Y. Ching

**Applications of Hard Materials**

5548 A novel integrated electric motor/pump for underwater applications — C. Peter Cho, Barry K. Fussell, John Y. Hung

5551 Imposition of periodic magnetization patterns on high-energy-product magnetic plates — H. A. Leupold, A. S. Tilak, E. Potenziani II

5554 Effects of slot closure by soft magnetic powder wedge material in axial-field permanent magnet brushless machines — S. Gair, J. F. Eastham, A. Canova

5557 An efficient design to reduce the flux leakage of a spindle motor — T. F. Ying, C. M. Chen, C. P. Liao, M. D. Wu, D. R. Huang

5560 Magnetic profiles of bonded magnets affected by the magnetizing fixtures — Donyau Chiang, Shyh-Jier Wang, Der-Ray Huang

5563 Magnetic multipole cylinders from mould-injection $Nd_2Fe_{14}B$ plastic bonded magnets (abstract) — G. K. Nicolaides, D. Niarchos, D. Tsamakis, I. Koubouros, A. Mitsis

**Symposium on Magnetism of Fe–N and fcc Fe**

5564 Structure and magnetic moment of $\alpha''$-$Fe_{16}N_2$ compound films: Effect of Co and H on phase formation (invited) — Migaku Takahashi, H. Takahashi, H. Nashi, H. Shoji, T. Wakiyama, M. Kuwabara

5570 Electronic and magnetic structure of iron nitride, $Fe_{16}N_2$ (invited) — Akimasa Sakuma

5576 Magnetic and electrical properties of single-phase, single-crystal $Fe_{16}N_2$ films epitaxially grown by molecular beam epitaxy (invited) — Yutaka Sugita, Hiromasa Takahashi, Matahiro Komuro, Masukazu Igarashi, Ryo Imura, Takashi Kambe

5582 Mössbauer-effect study of face-centered-cubic-like Fe on Cu(001) (invited) (abstract) — W. Keune, A. Schatz, R. D. Ellerbrock, A. Fuest, K. Wilmers, R. A. Brand

5583 Magnetic properties of fcc-Fe multilayer (invited) (abstract) — M. Matsui, M. Doi, A. Kida, Y. Yamada

**Giant Magnetoresistance–Granular Systems**

5584 Giant magnetoresistance and high sensitivity in annealed NiFeCo/Ag multilayers — J. W. Dykes, Y. K. Kim, A. Tsoukatos, S. Gupta, S. C. Sanders

5587 Finite-size effect and its temperature dependence of giant magnetoresistance in magnetic granular materials — Jian-Qing Wang, Gang Xiao

5590 Thickness dependence of giant magnetoresistance of AgNiFe heterogeneous alloys films — J. Wiggins, M. L. Watson, P. A. Gago-Sandoval, K. O'Grady

5593 Jitterbug spin channel mixing in heterogeneous giant magnetoresistive material — J. F. Gregg, W. Allen, S. M. Thompson, M. L. Watson, G. A. Gehring

5596 Modeling effects of temperature annealing on giant magnetoresistive response in discontinuous multilayer NiFe/Ag films — J. O. Oti, Y. K. Kim

5599 Giant magnetoresistance in melt-spun $Cu_{80}Ni_{10}Fe_{10}$ ribbons — L. H. Chen, S. Jin, T. H. Tiefel, S. Y. Liao, Y. D. Yao

5602 Giant magnetoresistance properties in multilayered Co-Ag/Cu granular alloys — Makoto Iijima, Yutaka Shimizu, Naomi Kojima, Atsushi Tanaka, Kazuo Kobayashi


*(Continued)*

5605 Modeling giant magnetoresistance and magnetization of $Ag_{1-x}Ni_{x-y}Fe_y$ heterogeneous alloy films (abstract) — J. Wiggins, M. L. Watson, P. A. Gago-Sandoval, X. Batlle, F. Badia, A. Labarta

5606 Structural evolution in sputtered $Co_{90}Fe_{10}$/Ag giant magnetoresistance multilayers — J. D. Jarratt, J. A. Barnard

**Ultra-Thin Films**

5609 Magnetic domain structure in ultrathin Cu/Ni/Cu/Si(001) films (invited) — Hans J. Hug, B. Stiefel, A. Moser, I. Parashikov, A. Klicznik, D. Lipp, H.-J. Güntherodt, Gabriel Bochi, D. I. Paul, R. C. O'Handley

5615 Magnetization and finite-size effects in Gd/W multilayers — J. Samuel Jiang, C. L. Chien

5618 Magnetism and structure of ultrathin fcc $Fe_xCo_{1-x}$ films on Cu(001) (abstract) — A. Dittschar, M. Zharnikov, W. Kuch, C. M. Schneider, J. Kirschner

5619 Magnetization reversal properties near the reorientation phase transition of ultrathin Fe/Ag(100) films — A. Berger, H. Hopster

5622 Structure and magnetism in fcc magnetic transition metals on (001) diamond (abstract) — J. A. Wolf, J. J. Krebs, Y. U. Idzerda, G. A. Prinz, K. M. Kemner

5623 Anomalous perpendicular magnetism in Ni/Cu(001) films and the effects of capping layers — W. L. O'Brien, B. P. Tonner

5626 Magnetic x-ray linear dichroism in the photoelectron spectroscopy of ultrathin magnetic alloy films — J. G. Tobin, K. W. Goodman, G. J. Mankey, R. F. Willis, J. D. Denlinger, E. Rotenberg, A. Warwick

5629 New magnetic phases of Fe on fcc Co(001) and Ni(001) — W. L. O'Brien, B. P. Tonner

5632 Nonlinear magneto-optical Kerr effect study of quantum-well states in a Au overlayer on a Co(0001) thin film — M. Groot Koerkamp, A. Kirilyuk, W. de Jong, Th. Rasing, J. Ferré, J. P. Jamet, P. Meyer, R. Mégy

5635 Growth and magnetic properties of $Fe_xNi_{1-x}$ ultrathin films on Cu(100) — F. O. Schumann, S. Z. Wu, G. J. Mankey, R. F. Willis

5638 Quantum well states and interlayer coupling: Co/Cu(100) — L. Nordström, P. Lang, R. Zeller, P. H. Dederichs

5641 The growth of Fe on sulphur passivated Ge(100): A technique for avoiding intermixing — G. W. Anderson, P. Ma, P. R. Norton

**Recording Phenomena and Modeling**

5644 Data storage based on proximal probe techniques (invited) (abstract) — H. J. Mamin, B. D. Terris, D. Rugar

5645 Recording performance of submicron track width thin film heads — T. T. Lam, Y. Luo, J.-G. Zhu, H.-C. Tong, R. Rottmayer

5648 Effects of write current switching time on recording characteristics (abstract) — F. Tomiyama, H. Takano, Y. Shiroishi, M. Suzuki, Y. Sugita

5649 Bit-shift performance investigations at different skew angles and for different media orientations — S. B. Hu, B. Liu, C. S. Lee

5652 Track-width dependence of transition jitter — P. Dhagat, E. Glavinas, A. Jander, D. G. Porter, R. S. Indeck, M. W. Muller

5655 Trilayer media for high track density longitudinal recording — J. Akiyama, Y. Ohinata, T. Hikosaka, T. Taguchi, Y. Tanaka

5658 Experimental analysis of the effects of tape thickness on magnetic recording — A. Friedmann, D. Wei, H. N. Bertram, J. K. Wolf, R. Swanson, F. Jeffers

5661 Signals and nonlinearities in thin metal-particle tape — Dan Wei, H. Neal Bertram, A. Friedmann

5664 Computer simulation of ultrahigh-density perpendicular magnetic recording — K. Yoshida, M. Hara, Y. Hirayama, Y. Sugita

5667 Barkhausen jumps during domain wall motion in thin magneto-optical films — S. Gadetsky, M. Mansuripur

5670 Simulation of magneto-optic readout signal spectrum using digitized mark and beam patterns (abstract) — S. Jo, J. W. Sohn, S. K. Lee, S. G. Kim


*(Continued)*

| | | |
|---|---|---|
| 5671 | Prediction of the limitations placed on magnetoresistive head servo systems by track edge writing for various pole tip geometries | R. Davidson, R. Simmons, S. Charap |
| 5674 | Autotuning of a servowriter head positioning system with minimum positioning error | Y. H. Huang, S. Weerasooriya, T. S. Low |

**Magneto-Optic Recording Media III**

| | | |
|---|---|---|
| 5677 | The effect of additives on MSR performance of GdFeCoM/TbFeCo (M=Ta, Pt) double layer | Isao Moritani, Koyata Takahashi, Akio Kondo, Takao Suzuki |
| 5680 | Exchange coupling in rare-earth/transition-metal multilayers for magnetic super-resolution | A. M. Ayres, E. E. Marinero |
| 5683 | Transition from in-plane to perpendicular magnetization in MSR magneto-optical disks | Naoki Nishimura, Tomoyuki Hiroki, Takeshi Okada, Shigeru Tsunashima |
| 5686 | Magnetic parameter control for high-density quadrivalued MO recording (invited) (abstract) | N. Ohta, K. Shimazaki, M. Yoshihiro, N. Nagai, S. Ohnuki |
| 5687 | Magneto-optical recording on patterned substrates (invited) | S. Gadetsky, J. K. Erwin, M. Mansuripur, T. Suzuki |
| 5693 | Comparison of the magneto-optical figure of merit of NdFeCo and TbFeCo alloys | W. A. Challener |
| 5696 | Effect of sputtering condition on dynamic characteristics and microstructures of magneto-optical 5.25 in. SiN/TbFeCo/SiN/Al disks for 532 nm recording media | M. D. Ro, B. I. Cho, M. J. Kim, S. S. Kim, Y. M. Ahn, K. G. Lee, B. L. Gill |
| 5699 | A study on the Kerr angle enhancement by the magnetic image effect (abstract) | S. P. Chang, Y. P. Lee, D. R. Huang |
| 5700 | A dynamic study of domain formation mechanism during thermomagnetic recording based on micro-Hall effect measurements | Yung-Chieh Hsieh, S. N. Gadetsky, M. Mansuripur, M. Takahashi |
| 5703 | The rate of domain growth in magneto-optic recording media (abstract) | J. Earl, A. Lyberatos, R. W. Chantrell |
| 5704 | Sensitivity enhancement of Co/Pt superlattices through underlayer composition modification | T. K. Hatwar, C. F. Brucker |

**Magnetic Excitations II**

| | | |
|---|---|---|
| 5707 | Magnetic circular x-ray dichroism in $Fe_7S_8$ and $Fe_7Se_8$ (abstract) | T. Koide, H. Miyauchi, T. Shidara, N. Nakajima, H. Kawabe, H. Fukutani, K. Shimada, A. Fujimori, K. Iio, T. Kamimura |
| 5708 | Magnetic circular x-ray dichroism in Co/Pt multilayers (abstract) | T. Koide, N. Nakajima, T. Shidara, H. Miyauchi, H. Kawabe, H. Fukutani, A. Fujimori, K. Iio, T. Katayama, Y. Suzuki |
| 5709 | Mössbauer and x-ray diffraction studies of the phase composition of crystallized $Nd_xFe_{81.5-x}B_{18.5}$ alloys with $7 \leq x \leq 16$ (abstract) | Zhao-hua Cheng, Bao-gen Shen, Jun-xian Zhang, Ming-xi Mao, Ji-jun Sun, Fa-shen Li, Yi-de Zhang |
| 5710 | Superexchange interactions in $Ni_{0.5}Co_{0.5}Fe_2O_4$ | Choong Sub Lee, Chan Young Lee |
| 5713 | A $^{57}Fe$ Mössbauer study of $Gd_2Fe_{17-x}Ga_xC_2$ ($x=0-6$) | Bo-Ping Hu, Hong-Shuo Li, Bao-Gen Shen, Suharyana, Fang-Wei Wang, J. M. Cadogan, Wen-Shan Zhan |
| 5716 | The low-temperature rate of electron capture beta decay in magnetic materials | L. M. Folan, V. I. Tsifrinovich, V. A. Sheverev |
| 5718 | Bragg diffraction of laser light by magnetostatic forward volume waves in a layered yttrium–iron–garnet film geometry | Liang-Ping Peng, J. P. Parekh, H. S. Tuan |
| 5721 | Modulation of magnetostatic surface wave in garnet film by optical pulses | Y. K. Fetisov, A. V. Makovkin |
| 5724 | Dipole-exchange spin wave spectra of exchange-coupled magnetic multilayers calculated by transfer matrix formalism | I. V. Rojdestvenski, M. G. Cottam, A. N. Slavin |
| 5727 | Nonlinear magneto-acoustic waves in ferromagnets | G. T. Adamashvili, A. A. Maradudin |

*(Continued)*

5730 Parametrical interaction of magnetostatic volume waves in a space-time periodic magnetic field — Y. K. Fetisov, N. V. Ostrovskaya, A. F. Popkov

5733 Characteristic analysis of coupled microstrip patch resonators on ferrimagnetic substrates — Kunquan Sun, Yinchao Chen, Walter Barry, John Corlett

5736 Characteristics of microstrip directional coupler on magnetized ferrites — E. L. Albuquerque, M. R. M. L. Albuquerque, A. G. d'Assunção

5739 Magnetic losses in stripline/microstrip circulators — H. How, T. M. Fang, C. Vittoria, R. Schmidt

5742 Experimental determination of an effective demagnetization factor for nonellipsoidal geometries — Guobao Zheng, M. Pardavi-Horvath, Xiaohua Huang, B. Keszei, J. Vandlik

5745 Quantum fluctuations in antiferromagnets of the $BX_2$ family (abstract) — E. Rastelli, A. Tassi

5745 Spin configurations in $VBr_2$ supported by uniaxal anistropy and quantum fluctuations (abstract) — E. Rastelli, A. Tassi

**Micromagnetics and Hysteresis**

5746 Henkel plots and the Preisach model of hysteresis — C. J. Buehler, I. D. Mayergoyz

5749 Kinetic Ising systems as models of magnetization switching in submicron ferromagnets — Howard L. Richards, Scott W. Sides, Mark A. Novotny, Per Arne Rikvold

5752 Simple function for a complex domain configuration — A. S. Arrott, J.-G. Lee

5755 Dynamical micromagnetics of a ferromagnetic particle: Numerical studies — Bo Yang, Donald R. Fredkin

5758 Anomalous time-induced curvature in Henkel plots based on the Preisach model — P. D. Mitchler, E. Dan Dahlberg, E. Wesseling, R. M. Roshko

5761 Magnetization reversal and small lancettes calculated by statistic domain behavior (abstract) — Paul L. Fulmek, Hans Hauser

5762 Surface anisotropy of a fine $\gamma$-$Fe_2O_3$ particle — Kezhao Zhang, Donald R. Fredkin

5764 Random free energy model for the description of hysteresis — G. Bertotti, V. Basso, G. Durin

5767 Micromagnetics of polycrystalline two-dimensional platelets — K. M. Tako, M. A. Wongsam, R. W. Chantrell

5770 Three-dimensional analysis of the magnetization process of thin-film media — E. Miyashita, Y. Yoneda, J. Numazawa

5773 Characterization of minor loops using Preisach-based models — Ferenc Vajda, Edward Della Torre

**Head–Media Interface and Tribology**

5776 Radio frequency ion beam deposition of diamond-like carbon for sliders and heads — Lien-Chang Wang, Gary Halada, Richard J. Gambino, Alan Hayes, Sal DiStefano

5779 Nanoindentation study of the mechanical properties of metal evaporated magnetic tapes — Hong Deng, John A. Barnard

5782 Comparison of tribological performance of pure carbon and carbon-nitrogen coated thin film head sliders — Geng Wang, John M. Silversten, Jack H. Judy, Ga-Lane Chen

5785 Transient response of ultralow flying sliders over contaminated and textured surfaces — Paul R. Peck, Ki-Ook Park, Myung S. Jhon, Soo-Choon Kang, Tom I.-P. Shih

5788 Surface diffusion of thin perfluoropolyalkylether films — Teresa M. O'Connor, Young R. Back, Myung S. Jhon, Byung G. Min, Do Y. Yoon, Thomas E. Karis

5791 Wear studies of contact recording interface with a microfabricated head — Bharat Bhushan, Youlin Li

5794 Non-Gaussian surface roughness distribution of magnetic media for minimum friction/stiction — Bharat Bhushan, Sameera Chilamakuri

5797 A micro-remote centered compliance suspension for contact recording head (abstract) — M. Nakao, S. Sugiyama, Y. Hatamura, T. Hamaguchi, K. Watanabe

5798 Micro/nanoscale studies of boundary layers of liquid lubricants for magnetic disks (abstract) — Vilas N. Koinkar, Bharat Bhushan


*(Continued)*

5799 Rough surface contact analysis and its relation to plastic deformation at the head–disk interface — Chin Y. Poon, Bharat Bhushan

5802 Environmental effects on the pause mode performance of metal-evaporated and metal-particle tapes — Steven T. Patton, Bharat Bhushan

**Giant Magnetoresistance and Magnetic Multilayers**

5805 Spin-dependent interface transmission and reflection in magnetic multilayers (invited) — M. D. Stiles

5811 How predictable is the current perpendicular to plane magnetoresistance? (invited) — W. P. Pratt, Jr., Q. Yang, L. L. Henry, P. Holody, W.-C. Chiang, P. A. Schroeder, J. Bass

5816 The role of impurity scattering in Co/Cu (111) M.B.E. multilayers (abstract) — K. P. Wellock, B. J. Hickey

5817 Giant magnetoresistance multilayers of high thermal stability with thicker magnetic layers — S. A. Hossain, B. H. Pirkle, J. Yang, M. R. Parker

5820 Relaxation in NiFe/Ag giant magnetoresistive devices — R. W. Cross, A. B. Kos

5823 New methods to measure the current perpendicular to the plane magnetoresistance of multilayers — P. Dauguet, P. Gandit, J. Chaussy

5826 Engineering coercivities by dual ion beam sputtering for synthesizing soft permalloy-based spin-valve multilayers (abstract) — C. J. Gutierrez, R. Dail, R. Selestino, L. Tristan, M. Khater, Steve Michel

**Electronic Structure and Anisotropy**

5827 First principles determination of magnetocrystalline anisotropy for surfaces and interfaces using a torque method (abstract) — Xindog Wang, A. J. Freeman, R. Wu, D. S. Wang

5828 Theoretical predictions of magnetic interface anisotropy in (Pd/Co/Pd)/X superlattices — J. M. MacLaren

5831 Orientation and structure dependence of interface magnetocrystalline anisotropy of Co/Cu overlayers and superlattices — Lieping Zhong, Miyoung Kim, Xindong Wang, Dingsheng Wang, A. J. Freeman

5834 Onset of C(2×2) ferrimagnetic order in Cr islands deposited on Fe(001) as a function of island size — L. Pizzagalli, D. Stoeffler, A. Vega, S. Bouarab, C. Demangeat, H. Dreyssé, F. Gautier

5837 On the $\gamma$-like surface of $\alpha$-Ce: Theory (abstract) — O. Hjortstam, J. Trygg, B. Johansson, O. Eriksson, J. M. Wills

5838 Spin polarization of the conduction bands and secondary electrons of Gd(0001) — Dongqi Li, J. Pearson, S. D. Bader, D. N. McIlroy, C. Waldfried, P. A. Dowben

5841 Spin-resolved electron spectroscopies of epitaxial magnetite (001) (abstract) — Kimberly A. Shaw, Eric Lochner, David M. Lind, Rebecca C. DiBari, Plamen Stoyanov, Brian Singer

5841 Origins of giant biquadratic coupling in CoFe/Mn/CoFe sandwich structures (abstract) — Norman C. Koon

5842 New estimation of surface anisotropy — Xiao Hu, Yoshiyuki Kawazoe

5845 Perpendicular magnetization and surface magnetoelastic anisotropy in epitaxial Cu/Ni/Cu (001) — Gabriel Bochi, C. A. Ballentine, H. E. Inglefield, C. V. Thompson, R. C. O'Handley

5848 Magnetization reversal in patterned Co(0001) ultrathin films with perpendicular magnetic anisotropy — N. Bardou, B. Bartenlian, C. Chappert, R. Mégy, P. Veillet, J. P. Renard, F. Rousseaux, M. F. Ravet, J. P. Jamet, P. Meyer

5851 Magnetic force microscopy of single-domain single-crystal iron particles with uniaxial surface anisotropy — R. M. H. New, R. F. W. Pease, R. L. White, R. M. Osgood, K. Babcock

5854 Surface-induced miscibility gap in vapor deposited $Co_{1-x}Pt_x$ (abstract) — M. Q. Tran, A. L. Shapiro, P. W. Rooney, F. Hellman

5855 Effects of magnetostatic interaction between two single-domain cobalt bars on crystal anisotropy and switching field (abstract) — Stephen Y. Chou, Linshu Kong


*(Continued)*

**Superconductivity**


| | | |
|---|---|---|
| 5856 | Synthesis and physical properties of $RNi_2B_2C$ and related materials (invited) (abstract) | R. J. Cava |
| 5857 | Neutron scattering studies of the magnetic order in $RNi_2B_2C$ | J. W. Lynn, Q. Huang, S. K. Sinha, Z. Hossain, L. C. Gupta, R. Nagarajan, C. Godart |
| 5860 | Superconducting metastable phase in rapid quenched Y–Pd–B–C borocarbides | Valter Ström, K. S. Kim, A. M. Grishin, K. V. Rao |
| 5863 | Field dependence of magnetic transitions for magnetic superconductors $RNi_2B_2C$ (R=Dy, Ho) | H. C. Ku, M. S. Lin, Y. Y. Hsu, J. H. Shieh, Y. B. You |
| 5866 | Systematic variation of $T_N$(Pr) for the two-$CuO_2$-layer cuprate $m$212 ($m$=1, 2, 3) systems | H. C. Ku, C. L. Yang, C. H. Chou, Y. Y. Hsu, Y. B. You, J. H. Shieh |
| 5869 | Magnetic structure and ordering of Nd ions in Ga substituted $NdBa_2Cu_3O_7$ (abstract) | A. M. Niraimathi, E. Gmelin, P. Allenspach, C. Ritter |
| 5869 | Influence of the crystalline electric field on the magnetic properties of Ga-doped $NdBa_2Cu_3O_x$ (abstract) | P. Allenspach, A. M. Niraimathi, E. Gmelin |
| 5870 | Synthesis and superconductivity of intermetallic compounds $Y_2Ni_xB_{8-x}C_2$, $YNi_xCu_{2-x}B_2C$, and $YNi_xCu_{2-x}Si_2C$ | Wei Zhao, Jinke Tang, Young-sook Lee, Charles J. O'Connor |
| 5873 | Oxygen dependence of the Josephson weak link effect, specific heat, and the transition temperature of $YBa_2Cu_3O_x$ | S. Glenis, G. Choi, C. L. Lin, T. Mihalisin, X. Q. Wang |
| 5876 | Effects of Pr, Tb, and Zn doping into $YBa_2Cu_3O_7$ on magnetoresistivity and magnetic phase boundaries | F. Freibert, G. Cao, S. McCall, M. Shepard, J. E. Crow |
| 5879 | Rotational magnetic measurements of vortex pinning in polycrystalline superconductors (abstract) | M. K. Hasan, S. J. Park, J. S. Kouvel |


**Recording Heads and Materials**


| | | |
|---|---|---|
| 5880 | 4 Gbit/in.$^2$ inductive write heads using high moment FeAlN poles | W. P. Jayasekara, S. Wang, M. H. Kryder |
| 5883 | Experimental studies of nonlinearities in MR heads | Xinzhi Xing, H. Neal Bertram |
| 5886 | Micromagnetics of dual spin-valve GMR heads | Jian-Gang Zhu, Xiao-Guang Ye, Samuel W. Yuan, Hua-Ching Tong, Robert Rottmayer |
| 5889 | Experimental and analytical properties of 0.2-$\mu$m-wide, end-on, multilayer, giant magnetoresistance, read head sensors | A. V. Pohm, R. S. Beech, J. M. Daughton, E. Y. Chen, M. Durlam, K. Nordquist, T. Zhu, S. Tehrani |
| 5892 | Magnetization reversal processes of NiFe elements exchange coupled by NiO antiferromagnetic films | Juren Ding, Jian-Gang Zhu |
| 5895 | Domain structures at the cross sections of thin film inductive recording heads | Francis H. Liu, Hua-Ching Tong, Lena Milosvlasky |
| 5898 | Picosecond time-resolved magnetization dynamics of thin-film heads | M. R. Freeman, J. F. Smyth |
| 5901 | Stress and magnetic properties in high moment FeN thin films | Kyusik Sin, Shan X. Wang |
| 5904 | Effect of base layers on the soft magnetic properties of FeTaN films | V. R. Inturi, J. A. Barnard |
| 5907 | Soft magnetic properties of nanocrystalline FeRuGaSi-Hf alloy films and head characteristics for the embedded thin film tape head | H. Ohmori, M. Shoji, T. Kobayashi, T. Yamamoto, Y. Sugiyama, K. Hayashi, K. Hono |
| 5910 | Theory, fabrication and testing of dual track complimentary type of thin-film recording heads for perpendicular magnetic recording system | T. Ichihara, S. Nakagawa, N. Matsushita, M. Naoe |
| 5913 | Permeability of microstrip thin films of various materials | Kiyoshi Yamakawa, Kazuyuki Ise, Naoki Honda, Kazuhiro Ouchi, Shun-ichi Iwasaki |
| 5916 | Pole tip recession studies of hard carbon-coated thin-film tape heads | Bharat Bhushan, Steven T. Patton, Ramesh Sundaram, Subrata Dey |


*(Continued)*

**Exchange Coupling in Oxides and Composites**


5919 Heat capacity measurements of NiO/CoO superlattices (invited) (abstract) — E. N. Abarra, K. Takano, F. Hellman, A. E. Berkowitz

5920 Finite-size scaling in thin antiferromagnetic CoO layers — T. Ambrose, C. L. Chien

5923 Magnetic properties of epitaxial ferrite multilayer films — Y. Suzuki, R. B. van Dover, E. M. Gyorgy, Julia M. Phillips, V. Korenivski, D. J. Werder, C. H. Chen, R. J. Felder, R. J. Cava, J. J. Krajewski, W. F. Peck, Jr.

5926 Interlayer exchange coupling in amorphous/crystalline $NiFe_2O_4$ thin-film bilayers — V. Korenivski, R. B. van Dover, Y. Suzuki, E. M. Gyorgy, J. M. Phillips, R. J. Felder

5929 Magneto-optic properties and exchange interaction of the macroscopic ferrimagnet $Co_{1-x-y}Tb_x(EuS)_y$ — P. Fumagalli, A. Schirmeisen, R. J. Gambino

5932 Bi–DyIG films: Enhancement of the Dy contribution to the Faraday rotation — M. Guillot, H. Le Gall, J. Gouzerh, J. M. Desvignes, M. Artinian

5935 Microstructural characterization of ferrimagnetic substituted iron garnet heterostructures for magneto-optical applications (abstract) — B. M. Simion, R. Ramesh, G. Thomas

5936 A study of the magneto-optical Kerr spectra of bulk and ultrathin $Fe_3O_4$ — P. J. van der Zaag, W. F. J. Fontijn, P. Gaspard, R. M. Wolf, V. A. M. Brabers, R. J. M. van de Veerdonk, P. A. A. van der Heijden


**Other Hard Magnetic Materials I**


5939 Site affinity of substituents in $Nd_2Fe_{17-x}T_x$ (T=Cu,Zr,Nb,Ti,V) alloys — W. B. Yelon, Z. Hu, W. J. James, G. K. Marasinghe

5942 Electronic structure and magnetism in $Sm_2Fe_{17-x}A_x$ (A=Al,Ga,Si) — R. F. Sabirianov, S. S. Jaswal

5945 of the $Ce_2Fe_{17-x}Al_x$ solid solutions (abstract) — Sanjay R. Mishra, Gary J. Long, O. A. Pringle, Z. Hu, W. B. Yelon, D. P. Middleton, K. H. J. Buschow, F. Grandjean

5946 Magnetization and coercivity of $Mn_{3-\delta}Ga$ alloys with a $D0_{22}$-type structure — Hiroshi Niida, Tomiei Hori, Hideya Onodera, Yasuo Yamaguchi, Yasuaki Nakagawa

5949 Magnetic characteristics of $RCo_{13-x}Si_x$ alloys (R=La, Pr, Nd, Gd, and Dy) — M. Q. Huang, W. E. Wallace, R. T. Obermyer, S. Simizu, M. McHenry, S. G. Sankar

5952 First-principles calculation of the 3*d* magnetocrystalline anisotropy energy of $YCo_5$ — M. Yamaguchi, S. Asano

5955 Magnetic viscosity and microstructure: Particle size dependence of the activation volume — J. M. González, C. de Julián, Anit K. Giri, S. Castro, M. Gayoso, J. Rivas

5958 High coercivity rare earth–cobalt films — S. S. Malhotra, Y. Liu, Z. S. Shan, S. H. Liou, D. C. Stafford, D. J. Sellmyer

5961 High-temperature magnetic properties of $TbCu_7$-type SmCo-based films — H. Hegde, X. R. Qian, Jong-Guk Ahn, F. J. Cadieu

5964 Nanocomposite $Sm_2Co_{17}$/Co permanent magnets by mechanical alloying — S. K. Chen, J. L. Tsai, T. S. Chin

5967 Control of the axis of chemical ordering and magnetic anisotropy in epitaxial FePt films — R. F. C. Farrow, D. Weller, R. F. Marks, M. F. Toney, A. Cebollada, G. R. Harp

5970 Ba ferrite films with large saturation magnetization and high coercivity prepared by low-temperature sputter deposition — K. Noma, N. Matsushita, S. Nakagawa, M. Naoe

5973 Characterization of $Fe_{17}R_2$ phases (R=Pr and Sm) oxidized at 200 °C — S. Gama, C. A. Ribeiro, F. A. O. Cabral, C. C. Colucci, E. de Morais, N. L. Sanjurjo, C. Campos, J. D. Ardisson, A. I. C. Persiano


*(Continued)*

**Magneto-Optical Materials**


| | | |
|---|---|---|
| 5976 | Magneto-optical properties of (BiGdY) iron garnets for optical magnetic field sensors | O. Kamada |
| 5979 | An investigation on the magneto-optical enhancement in Ni-substituted barium ferrites | Xijuan Zhang, You Xu, Mingqian Duan, Maurice Guillot |
| 5982 | Second harmonic investigation of ac magnetized in-plane anisotropic garnet film | Sergey V. Lebedev |
| 5985 | Magneto-optical properties of Sc-substituted holmium iron garnet single crystals | J. Ostoréro, M. Guillot |
| 5988 | Effect of structural irregularity on propagation properties of optical waves in discontinuous magneto-optical media with one-dimensional quasirandom array structures | Mitsuteru Inoue, Takeshi Yamamoto, Keiji Isamoto, Toshitaka Fujii |
| 5991 | Magneto-optic and microwave properties of epitaxial garnet thin film heterostructures and superlattices (abstract) | R. Ramesh, T. Venkatesan, S. Lofland, M. Dominguez, S. M. Bhagat, B. M. Simion, G. Thomas |


**New Magnetic Materials**


| | | |
|---|---|---|
| 5992 | Mössbauer effect and electronic transport studies of icosahedral $Al_{50}Pd_{10}Mn_{25-x}Fe_xB_{15}$ alloys | M. Yewondwossen, J. E. Jagger, Z. Koziol, R. A. Dunlap |
| 5995 | Magnetic and electronic properties of the magnetically ordered quasicrystalline alloys $Al_{70-x}Pd_{15}Mn_{15}B_x$ | M. Yewondwossen, Z. Koziol, D. Bahadur, Z. J. Yang, M. Foldeaki, R. A. Dunlap |
| 5998 | Structural, magnetic, and magnetocaloric properties of $(Hf_{0.83}Ta_{0.17})Fe_{2+x}$ materials | J. F. Herbst, C. D. Fuerst, R. D. McMichael |
| 6001 | Magnetic properties of a high $T_c$ superconductivity related system $Y_{1-x}Pr_xBa_2Fe_3O_8$ | T. Yuen, M. Seyedahmadian, R. E. Salomon, G. H. Myer, G. Cao |
| 6004 | Observation of independent iron and rare-earth ordering in $RFe_6Ge_6$ (R= *Y*, Gd–Lu) compounds | D. H. Ryan, J. M. Cadogan |


**Small Particles/Ferrofluids**


| | | |
|---|---|---|
| 6007 | Cobalt-doped carbon nanotubes: Preparation, texture, and magnetic properties | K. Lafdi, A. Chin, N. Ali, J. F. Despres |
| 6010 | Magnetic properties of nanosized wires | J. Meier, B. Doudin, J.-Ph. Ansermet |
| 6013 | Negative remanence in magnetic nanostructures | X. Yan, Y. Xu |
| 6016 | Preparation of Co–Fe–P amorphous fine needles with anodization technique and measurement of demagnetizing factor | A. Tayaoka, E. Tayaoka, J. Yamasaki |
| 6019 | Nonhomogeneous magnetization reversal in 2D Ising clusters | D. García-Pablos, P. García-Mochales, N. García, P. A. Serena |
| 6022 | Alternating current (ac) susceptibility studies in Ni-$SiO_2$ granular film | B. Zhao, Jeff Y. Chow, X. Yan |
| 6025 | High coercivity single-domain particles in glass matrix | C. Tsang, H. D. Gafney, D. Sunil, M. Rafailovich, J. Sokolov, R. J. Gambino |
| 6028 | Identification of a high-temperature magnetic phase transition in ball-milled and compacted nanocrystalline Fe-Cu alloys | R. D. Shull, J. P. Cline, I. Baker, F. Liu |
| 6031 | Steps in the hysteresis loops of a high-spin molecule | Jonathan R. Friedman, M. P. Sarachik, J. Tejada, J. Maciejewski, R. Ziolo |
| 6034 | Computer simulation of microstructure and interaction effects in fine particle systems (abstract) | G. N. Coverdale, R. W. Chantrell, M. El-Hilo, K. O'Grady |
| 6034 | Periodic breathing oscillations and instabilities in ferrofluids (abstract) | Weili Luo, Tengda Du |
| 6035 | Effects of Zn ion on magnetic properties of $Fe_3O_4$ magnetic colloids (abstract) | C. H. Lin, P. C. Kuo, J. L. Pan, D. R. Huang |


*(Continued)*

**Domains and Magnetization Processes**

6036 Measurements of local magnetization by Kerr effect on Si-Fe nonoriented sheets — S. Defoug, R. Kaczmarek, W. Rave

6039 The energy loss per cycle in bar domain Si–Fe — Bryen E. Lorenz

6042 Correlation between the Barkhausen noise power and the total power losses in 3% Si–Fe — M. Birsan, J. A. Szpunar, T. W. Krause, D. L. Atherton

6045 Effects of surface condition on Barkhausen emissions from steel — A. P. Parakka, D. C. Jiles, H. Gupta, S. Jalics

6047 Simultaneous Barkhausen discontinuities of multiple die-drawn Fe-Si-B amorphous wires connected with amorphous ribbons (abstract) — M. Soeda, J. Yamasaki

6048 The influence of domain activities on MR head performance — Weichun Ye, Jinyue Yu, Bingchu Cai

6051 Iron whisker domain patterns imaged by garnet films — J.-G. Lee, S. A. Govorkov, A. S. Arrott

6054 Temperature and field dependence of domain wall dynamics up to the Curie point of EuO — A. Flosdorff, D. Görlitz, J. Kötzler

6057 The dependence of magnetoacoustic emission on magnetizing frequency in nickel and mild steel — D. H. L. Ng, C. C. Yu, C-D. Qin, C. C. H. Lo, J. P. Jakubovics

6060 180° domain wall with the coordinate dependent azimuthal angle of magnetization — V. L. Sobolev, C. T. Teh, H. L. Huang

**Imaging and Applied Magnetics**

6063 Modeling MFM images of periodic magnetization patterns (abstract) — R. Madabhushi, R. D. Gomez, E. R. Burke, I. D. Mayergoyz

6064 Magnetic force microscope study of domain wall structures in magnetite — Taras G. Pokhil, Bruce M. Moskowitz

6067 A scanning microscope using a magnetoresistive head as the sensing element — R. O'Barr, M. Lederman, S. Schultz

6070 Surface deformations and domains in Terfenol-D by scanning probe microscopy — A. P. Holden, D. G. Lord, P. J. Grundy

6073 Magneto-optical indicator film (MOIF) microscopy of granular and layer structures (abstract) — V. I. Nikitenko, V. S. Gornakov, L. M. Dedukh, A. F. Khapikov, L. H. Bennett, R. D. McMichael, L. J. Swartzendruber, A. J. Shapiro, M. J. Donahue, V. N. Matveev, V. I. Levashov

6074 High density recorded patterns observed by high-resolution Bitter scanning electron microscope method — O. Kitakami, T. Sakurai, Y. Shimada

6077 A new magnetic bar code system based on a magnetic anisotropy detection (abstract) — I. Sasada, N. Watanabe

**Symposium on Magnetic Nanostructures**

6078 Giant magnetoresistance as a probe of interfacial electronic character (invited) (abstract) — S. S. P. Parkin

6079 Nanostructure fabrication via laser-focused atomic deposition (invited) — R. J. Celotta, R. Gupta, R. E. Scholten, J. J. McClelland

6084 Perpendicular transport and magnetic properties in patterned multilayer magnetic microstructures (invited) — J. J. Krebs, W. Vavra, G. A. Prinz, S. F. Cheng, Anita Fink

6090 Arrays of multilayered nanowires (invited) — B. Doudin, A. Blondel, J.-Ph. Ansermet

6095 Femtosecond near-field spin microscopy in digital magnetic heterostructures (invited) — J. Levy, V. Nikitin, J. M. Kikkawa, D. D. Awschalom, N. Samarth

6101 The energy loss per cycle in bar domain Si–Fe — Bryen E. Lorenz

**Macroscopic Quantum Tunneling and Transport Properties**

6107 Chiral quantum spin solitons — Hans-Benjamin Braun, Daniel Loss

*(Continued)*

6110 Quantum dynamical calculations in clusters of spin 1/2 particles: Resonant coherent quantum tunneling on the magnetization reversal — D. García-Pablos, N. García, P. A. Serena, H. De Raedt

6113 Frequency mixing phenomena in a bistable system — A. N. Grigorenko, P. I. Nikitin, G. V. Roschepkin

6116 Low temperature magnetic relaxation and quantum tunneling in nanocrystalline particles (abstract) — X. X. Zhang, J. M. Hernandez, E. C. Kroll, R. Ziolo, J. Tejada

6117 Annealing and geometric effects in the magneto-impedance of amorphous $Co_{70.4}Fe_{4.6}Si_{15}B_{10}$ alloys — R. L. Sommer, C. L. Chien, R. Hasegawa

6120 Size dependence of the magnetoresistance in submicron FeNi wires — A. O. Adeyeye, J. A. C. Bland, C. Daboo, Jaeyong Lee, U. Ebels, H. Ahmed

6123 Effect of interstrip gap on the sensitivity of high sensitivity magnetoresistive transducers — Bharat B. Pant

6126 Large magnetic Hall effect in ferromagnetic $Fe_xPt_{100-x}$ thin films — C. L. Canedy, G. Q. Gong, J. Q. Wang, Gang Xiao

6129 Resistivities of sputtered Ag(3.3 nm)/Cu($t_{Cu}$), Ag(3.3 nm)/Au($t_{Au}$), and Ni(4.2 nm)/Co($t_{Co}$) multilayers at 4–5 and 295 K — L. L. Henry, M. Oonk, R. Loloee, Q. Yang, W.-C. Chiang, W. P. Pratt, Jr., J. Bass

6132 Resonant near-sound reorientation of the domain wall plane in yttrium orthoferrite — M. V. Chetkin, Yu. N. Kurbatova, A. I. Akhutkina

6134 Approach to the anhysteretic surface — M. J. Sablik, R. A. Langman

6137 Studies of remanence in granular Ni–$SiO_2$ films — Y. Xu, B. Zhao, X. Yan

6140 Observation of giant Hall effect in granular magnetic films — A. B. Pakhomov, X. Yan, Y. Xu


**Spin Glasses and Frustrated Ferromagnets**


6143 Freezing of the extended state in the random local field theory of Ising spin glasses with long range interactions — B. E. Vugmeister, D. Nowakowski, D. L. Huber

6146 Criticality of the fully frustrated *XY* model: A study using Monte Carlo hard-spin mean-field theory (abstract) — James E. Tesiero, Susan R. McKay

6147 Magnetization and dynamics of reentrant ferrimagnetic spin-glass $[MnTPP]^{\cdot+}[TCNE]^{\cdot-}\cdot 2PhMe$ — W. B. Brinckerhoff, B. G. Morin, E. J. Brandon, Joel S. Miller, A. J. Epstein

6150 The anhydrous alums: A versatile new series of model triangular lattice magnets (abstract) — S. T. Bramwell, L. Nixon, I. P. Parkin, B. M. Kariuki, K. D. M. Harris, S. G. Carling, C. J. Harding

6151 Finite size effects in thin NiMn spin glass layers — L. Hoines, J. A. Cowen, J. Bass

6154 A new type of spin glass in spin-density-wave CrMn alloys (abstract) — V. Yu. Galkin, P. C. de Camargo, Naushad Ali, J. Schaf, E. Fawcett

6155 Magnetic phase diagram of the $Fe_xMn_{0.6-x}Al_{0.40}$ alloys series — G. A. Pérez Alcázar, Ligia E. Zamora, A. Bohórquez, E. González, J. M. González

6158 Ferromagnetic critical correlations and dynamics in AuFe reentrant ferromagnets — C. Pappas, M. Alba, A. Brulet, V. Viel, F. Mezei

6161 Neutron depolarization study of magnetic order in *a*-$Fe_xZr_{100-x}$ ($x$=90–93), *a*-$Fe_{90}Sc_{10}$ and their hydrides — D. H. Ryan, J. M. Cadogan, S. J. Kennedy

6164 Spin glass behavior of $Zn_{1-x}Mn_xTe$ — P. M. Shand, A. D. Christianson, L. S. Martinson, J. W. Schweitzer, T. M. Pekarek, I. Miotkowski, B. C. Crooker

6167 Observation of spin-glass freezing in the $S$=1 linear-chain Heisenberg antiferromagnet NENP — M. Hagiwara, K. Katsumata, S. Sasaki, N. Narita, I. Yamada, T. Yosida

6170 Nonlinear susceptibility measurements at the spin-glass transition of the pyrochlore antiferromagnet $Y_2Mo_2O_7$ — M. J. P. Gingras, C. V. Stager, B. D. Gaulin, N. P. Raju, J. E. Greedan


*(Continued)*

6173 Magnetic ordering in pyrochlore $Ho_2Mn_2O_7$ — N. P. Raju, J. E. Greedan, J. S. Pedersen, Ch. Simon, A. Maignan, A. M. Niraimathi, E. Gmelin, M. A. Subramanian

6176 λ-$MnO_2$, a new frustrated antiferromagnet with the defect spinel structure (abstract) — J. E. Greedan, Guo Liu, N. P. Raju, J. N. Reimers, Zin Tun

**Magneto-Optic Kerr Effect: Theory and Experiment**

6177 Theory of nonlinear magneto-optics (invited) — U. Pustogowa, T. A. Luce, W. Hübner, K. H. Bennemann

6181 Giant nonlinear magneto-optical Kerr effects from Fe interfaces (invited) — Th. Rasing, M. Groot Koerkamp, B. Koopmans, H. v.d. Berg

6186 Symmetry of the magneto-optic response of the Sagnac interferometer — J. S. Dodge, L. Klein, M. M. Fejer, A. Kapitulnik

6189 Second-order magneto-optic effects in anisotropic thin films (abstract) — R. M. Osgood III, B. M. Clemens, R. L. White

6190 Spectroscopic Kerr investigations of CoNi/Pt multilayers — W. P. Van Drent, T. Suzuki, Q. Meng, J. C. Lodder, Th. J. A. Popma

6193 *In situ* and *ex situ* optical characterization of electro deposited magneto-optic materials — James N. Hilfiker, Darin W. Glenn, Scott Heckens, John A. Woollam, Kurt W. Wierman

6196 Theoretical predictions of the polar Kerr effect in Fe and Co — J. M. MacLaren, W. Huang

6199 First principles calculations of the Kerr effect in MnBi, MnSb, and $Mn_2BiSb$ (abstract) — W. Huang, J. M. MacLaren, R. H. Victora

6200 Dielectric tensor characterization of $Mn_{0.53}Bi_{0.47}$ and $Mn_{0.52}Bi_{0.44}Sb_{0.04}$ films — Z. Celinski, Zheng Yan

6203 Influence of Al capping layers on growth, topography, and magnetic properties on MnBi thin films — U. Rüdiger, P. Fumagalli, P. Dworak, A. Schirmeisen, G. Güntherodt

6206 Magnetic and magneto-optical properties of $Mn_xPt_{1-x-y}Zn_y$ — Kurt W. Wierman, Roger D. Kirby

**Magnetostriction**

6209 First principles determinations of magnetostriction in transition metals (invited) — Ruqian Wu, A. J. Freeman

6213 Zero field damping capacity in $(Tb_xDy_{1-x})Fe_y$ — J. P. Teter, K. B. Hathaway, A. E. Clark

6216 Anomolous $\Delta E$ effects in TbDyZn alloys — J. R. Cullen, M. Wun-Fogle, J. B. Restorff, J. P. Teter, A. E. Clark

6219 Enhancement of piezomagnetic response of highly magnetostrictive rare earth-iron alloys at kHz frequencies — P. P. Pulvirenti, D. C. Jiles, R. D. Greenough, I. M. Reed

6222 Texture in magnetic annealed Terfenol-D films — M. Loveless, S. Guruswamy

6225 Stress dependence of magnetostrictions and strains in ⟨111⟩-oriented single crystals of Terfenol-D — Xuegen Zhao, Guangheng Wu, Jinghua Wang, Kechang Jia, Wenshan Zhan

**Giant Magnetoresistance in Multilayers and Granular Systems**

6228 Effects of surface topology and texture on exchange anisotropy in NiFe/Cu/NiFe/FeMn spin valves — C.-M. Park, K.-I. Min, K. H. Shin

6231 High sensitivity in magnetoresistance of epitaxial NiFe/Cu/Co (/Cu) (100) superlattices — Y. Kawawake, H. Sakakima, Y. Irie, M. Satomi

6234 Factors affecting performance of NiO biased giant magnetoresistance structures — S. F. Cheng, J. P. Teter, P. Lubitz, M. M. Miller, L. Hoines, J. J. Krebs, D. M. Schaefer, G. A. Prinz

6237 Giant magnetoresistance effect and electric conduction in amorphous-CoFeB/Cu/Co sandwiches — M. Jimbo, K. Komiyama, S. Tsunashima

*(Continued)*

| | | |
|---|---|---|
| 6240 | Size effects and giant magnetoresistance in unannealed NiFe/Ag multilayer stripes | S. C. Sanders, R. W. Cross, S. E. Russek, A. Roshko, J. O. Oti |
| 6243 | Effect of sputter gas on the physical and magnetic microstructure of Co/Cu multilayers | D. M. Donnet, K. Tsutsumi, P. de Haan, J. C. Lodder |
| 6246 | Giant thermopower in 3D-magnetic multilayers. Structural and electron band effects (abstract) | M. M. P. de Azevedo, B. G. Almeida, V. S. Amaral, M. E. Braga, J. B. Sousa, P. P. Freitas, R. Krishnan |
| 6247 | Structural characterization of epitaxial Co–Ag | A. Azizi, L. El Chahal, K. Ounadjela, J. P. Deville, S. M. Thompson, J. F. Gregg |
| 6250 | Spin-dependent scattering in the nonmagnetic layers of annealed Co/Cu multilayers | H. Laidler, B. J. Hickey |
| 6253 | Interfacial roughness of Fe–Cr GMR superlattices (abstract) | W. Dmowski, T. Egami, D. Kelly, I. Schuller |
| 6254 | Giant magnetoresistance in evaporated NiFe/Cu and NiFeCo/Cu multilayers (abstract) | A. M. Zeltser, Neil Smith |
| 6255 | Giant magnetoresistance in magnetic granular systems | L. Sheng, R. Y. Gu, D. Y. Xing, Z. D. Wang, Jian-Xin Zhu |
| 6258 | Giant magnetoresistance in granular Fe–$MgF_2$ films | T. Furubayashi, I. Nakatani |
| 6261 | The influence of Ni on the microstructure and GMR of the Co–Cu alloy granular films (abstract) | S. Y. Zhang, Q. Q. Cao |
| 6261 | Real-space analysis of inhomogeneous scattering versus superlattice-potential effects for magnetotransport (abstract) | Horacio E. Camblong |
| 6262 | Magnetic tunneling effect in $Fe/Al_2O_3/Ni_{1-x}Fe_x$ junctions | N. Tezuka, T. Miyazaki |
| 6265 | Spin polarized tunneling in half-metallic ferromagnets (abstract) | C. T. Tanaka, J. S. Moodera |
| **Anisotropy, Magnetoresistance, and Interface Coupling** | | |
| 6266 | Ferromagnetic resonance of sputtered Co/Mn multilayers (abstract) | D. Spoddig, F. Schreiber, J. Pflaum, Q. Wang, H. Zabel, J. Pelzl |
| 6266 | Thermal effects in magnetization, anisotropy, and interface width in Fe/Cu multilayers (abstract) | Michael J. Pechan, Eric E. Fullerton, Ivan K. Schuller |
| 6267 | Study of magnetic reorientation phenomenon and magnetic properties of Pd/(Pt/Co/Pt) multilayers | Ying Xiao, Jun-Hao Xu, K. V. Rao |
| 6270 | Structural anisotropy of Tb/Fe multilayers | Y. Fujiwara, X. Y. Yu, S. Tsunashima, S. Iwata, M. Sakurai, K. Suzuki |
| 6273 | Occurrence of large perpendicular magnetic anisotropy in bilayered films with nanometer-thick TbFeCo and Al layers | H. Ito, K. Song, M. Naoe |
| 6276 | Studies of anisotropic and giant magnetoresistance in Co/Cu(111) epitaxial multilayers | J. C. A. Huang, Y. H. Lee, Y. M. Hu, T. C. Chang |
| 6279 | Effects of discharge pressure on the properties of Ag/Ni superlattices prepared by facing-target sputtering | X. T. Zeng, H. K. Wong |
| 6282 | Influence of the crystal structure on the magnetic property of Co/Cr superlattices | Y. Liou, J. C. A. Huang, Y. D. Yao, W. T. Yang, S. Y. Liao, C. P. Chang |
| 6285 | Magnetoresistance in NiFe/Au multilayers and spin-valve structures (abstract) | K. T. Wu, R. J. Gambino |
| 6286 | Temperature dependence of the pinning field and coercivity of NiFe layers coupled with an antiferromagnetic FeMn layer | H. Fujiwara, K. Nishioka, C. Hou, M. R. Parker, S. Gangopadhyay, R. Metzger |
| 6289 | Magnetic and magnetotransport properties of Ni/Fe multilayers | M. Cai, T. Veres, R. Morel, R. W. Cochrane |
| 6292 | Studies of Fe/Cr multilayer and trilayer films | E. M. Ho, A. C. Daykin, A. K. Petford-Long |


*(Continued)*

6295 Spin orientation in an exchange coupled Fe/Cr/Fe trilayer determined by polarized neutron reflection — J. A. C. Bland, H. T. Leung, S. J. Blundell, V. S. Speriosu, S. Metin, B. A. Gurney, J. Penfold

6298 Superconductivity and magnetic properties of Fe/Nb multilayers (abstract) — Th. Mühge, I. Zoller, K. Westerholt, H. Zabel, Yu. V. Goryunov, N. N. Garif'yanov, G. G. Khaliullin, I. A. Garifullin, L. R. Tagirov

6299 A comparison of structure and magnetoresistance in Fe/(Ag–Cu) films (abstract) — S. J. Kwon, S. J. Choi

6300 $^{59}Co$ and $^{55}Mn$ NMR of CoMn alloys and multilayers — T. Thomson, P. C. Riedi, Q. Wang, H. Zabe

6303 Study of interface structure of Fe/Al multilayers — Ataur R. Chowdhury, Andrea E. Freitag

6306 Effect of ion beam mixing on microstructure and magnetic properties of Gd-Co multilayer films — G. Choe, R. M. Walser

6309 Nonlinear dynamics in microwave driven coupled magnetic multilayer systems — S. M. Rezende, F. M. de Aguiar

**Other Hard Magnetic Materials II**

6312 Magnetic interactions in nanocrystalline SmFeCo — D. R. Cornejo, F. P. Missell, J. M. González

6315 Neutron diffraction studies of $Nd_nFe_{m-x-y}V_xAl_y$ [$(n,m)=(1,12)$, (2,17), (3,29)] — Z. Hu, W. B. Yelon, W. J. James

6318 Neutron diffraction structural study of $Ce_2Fe_{17-x}Ga_x$ — H. Luo, Z. Hu, W. B. Yelon, S. R. Mishra, G. J. Long, O. A. Pringle, D. P. Middleton, K. H. J. Buschow

6321 Magnetic properties of $DyCo_{10-x}Ni_xSi_2$ compounds — Z. G. Zhao, N. Tang, E. Brück, K. H. J. Buschow, F. R. de Boer

6324 Magnetic properties of $R(Fe,Mn)_{11}Ti$ compounds — T. Zhao, X. C. Kou, Z. D. Zhang, X. K. Sun, Y. C. Chuang, F. R. de Boer

6327 Temperature and field-induced spin reorientations in $NdFe_{10-x}Co_xMo_2$ single crystals — W. A. Mendoza, S. A. Shaheen

6330 Magnetic anisotropy and spin reorientation transition in a $TbFe_{11}Ti$ single crystal (abstract) — C. Abadía, P. A. Algarabel, M. R. Ibarra, C. Marquina, N. V. Kudrevatykh, P. E. Markin

6331 Magnetic and structural characteristics of $LaCo_{9+\delta}Si_4$ and $LaCo_{8.5+\delta}Si_{4.5}$ alloys ($\delta$=0–4) — M. Q. Huang, Jason Wolf, W. E. Wallace

6334 Magnetic and crystallographic properties of $R_2Fe_{14}Si_2$ ($R$=Y, Gd, Dy, Er, and Tm) compounds (abstract) — K. Konno, H. Ido, F. Pourarian, R. T. Obermyer, S. G. Sanker

6335 Effect of Fe and/or Cu contents on the intrinsic coercivity of $Sm_2Co_{17}$-type coercive powders for the bonded magnet application — W. L. Liu, Y. L. Liang, D. W. Scott, B. M. Ma, C. O. Bounds

6338 $CoFe_2O_4$ thin films grown on (100) MgO substrates using pulsed laser deposition — P. C. Dorsey, P. Lubitz, D. B. Chrisey, J. S. Horwitz

6341 Optical and magnetic studies of SmCo and SmFe films (abstract) — K. T. Wu, Y. D. Yao, T. C. Chen

6341 Aspects of sintering barium hexaferrite with $SiO_2$, $Al_2O_3$, $CaCO_3$, and $Y_6Fe_{10}O_{24}$ additions for microwave applications (abstract) — J. G. Fagan, R. L. Snyder, C. Hach, L. Jones, J. B. Ings, J. May, J. J. Simmins

6342 Finite element modeling of powder aligning and multipole magnetizing systems for anisotropic bonded permanent magnets — C. D. Riley, G. W. Jewell, D. Howe

**Kondo, Mixed Valence, and Heavy Fermions I**

6345 Metal-insulator transition in the presence of excitonic correlation — Mucio A. Continentino, Gloria M. Japiassú, Amós Troper

6347 Resistivity and $L_{III}$-edge absorption studies in valence fluctuation system $Ce_2Ni_3Si_5$ — Chandan Mazumdar, R. Nagarajan, C. Godart, L. C. Gupta, B. D. Padalia, R. Vijayaraghavan


*(Continued)*

6349 Transport, magnetic, and $^{119}Sn$ Mössbauer studies on magnetically ordered valence fluctuating compound $SmRuSn_3$ — Chandan Mazumdar, Z. Hossain, R. Nagarajan, C. Godart, S. K. Dhar, L. C. Gupta, B. D. Padalia, R. Vijayaraghavan

6352 Kondo behavior in $CeNi_{0.4}Cu_{0.6}$ — J. I. Espeso, J. García Soldevilla, J. C. Gómez Sal, M. Reiffers, J. A. Blanco

6355 Temperature dependence of the electrical resistivity and thermopower of $U_2Ni_2In$ and $Nd_2Ni_2Sn$ — R. P. Pinto, M. M. Amado, M. E. Braga, J. B. Sousa, B. Chevalier, D. Laffargue, J. Etourneau

6358 Thermal expansion of single-crystalline UNiAl — K. Prokeš, A. de Visser, A. A. Menovsky, E. Brück, F. R. de Boer, V. Sechovský, T. J. Gortenmulder

6361 Electronic properties of $U_2Pt_2Sn$ — K. Prokeš, F. R. de Boer, H. Nakotte, L. Havela, V. Sechovský, P. Svoboda, J. M. Winand, J. Rebizant, J. C. Spirlet, X. Hu, T. J. Gortenmulder

6364 The spin-glass state of $Y_{1-x}U_xPd_3$ — M. A. Lopez de la Torre, J. Rodriguez Fernandez, K. A. McEwen

6367 Search for hybridization gap in the electronic density of states in CeNiSb — Latika Menon, S. K. Dhar, S. K. Malik, W. B. Yelon

**Giant Magnetoresistance of Magnetic Multilayers II**

6370 Anisotropy and angular variation of the giant magnetoresistance in magnetic multilayers (invited) — B. Dieny, C. Cowache, A. Nossov, P. Dauguet, J. Chaussy, P. Gandit

6376 Theory of the temperature dependence of giant magnetoresistance (invited) — Hideo Hasegawa

6382 Currents at angle to the planes of the layers (abstract) — P. M. Levy, S. Zhang, T. Ono, T. Shinjo

6383 Oblique electron transport in the presence of collinear and noncollinear magnetizations — Horacio E. Camblong

6386 Simulating device size effects on magnetization pinning mechanisms in spin valves — J. O. Oti, R. W. Cross, S. E. Russek, Y. K. Kim

6389 Exploration of magnetization reversal and coercivity of epitaxial NiO {111}/NiFe films — Chih-Huang Lai, Hideo Matsuyama, Robert L. White, Thomas C. Anthony, Gary G. Bush

6392 Change of magnetoresistance characteristic and crystal structure by ion bombardment to interfaces in $[Ni_{81}Fe_{19}/Cu]$ multilayers (abstract) — Y. Miyamoto, T. Yoshitani, S. Nakagawa, M. Naoe

6393 Structural comparisons of ion beam and dc magnetron sputtered spin valves by high-resolution transmission electron microscopy — William E. Bailey, Nan-Chang Zhu, Robert Sinclair, Shan X. Wang

6396 Giant magnetoresistance and magnetic phase diagram of UNiGa — K. Prokeš, E. Brück, F. R. de Boer, M. Mihálik, A. Menovsky, P. Burlet, J. M. Mignot, L. Havela, V. Sechovský

6399 Giant magnetoresistance and soft magnetic properties of $Co_{90}Fe_{10}/Cu$ spin-valve structures — Y. Kamiguchi, K. Saito, H. Iwasaki, M. Sahashi, M. Ouse, S. Nakamura

6402 Giant magnetoresistance effect in multilayered wire arrays — Minoru Kume, Atsushi Maeda, Toshio Tanuma, Kazuhiko Kuroki

**Kondo, Mixed Valence, and Fermions II**

6405 Superconductivity and structural transformation in $HfV_2$ and Nb-doped $HfV_2$ — F. Chu, Z. W. Chen, C. J. Fuller, C. L. Lin, T. Mihalisin

6408 Electronic properties of UCuSn — H. Nakotte, A. Purwanto, R. A. Robinson, K. Prokeš, F. R. de Boer, L. Havela, V. Sechovský, I. P. Swainson

*(Continued)*

6411 Crystallographic and magnetic structure of $UCu_{1.5}Sn_2$ — A. Purwanto, R. A. Robinson, H. Nakotte, I. P. Swainson, M. S. Torikachvili

6414 Metal-insulator transition in dirty Kondo insulators — P. Schlottmann, C. S. Hellberg

6417 Tb impurities in Th: A Kondo system with undercompensated magnetic moment? — J. G. Sereni, P. Schlottmann

6420 Hybridization-induced magnetism in correlated cerium systems — Nicholas Kioussis, J. Thevenot, Bernard R. Cooper, Q. G. Sheng

6423 Theoretical interpretation of optical conductivity of $YbCu_4Ag$,Au — A. Continenza, P. Monachesi, M. Galli, F. Marabelli, E. Bauer

6426 Magnetic dichroism study of the relativistic electronic structure of perpendicularly magnetized Ni/Cu(001) — W. Kuch, M. Zharnikov, A. Dittschar, K. Meinel, C. M. Schneider, J. Kirschner, J. Henk, R. Feder

6429 Density functional study of fcc iron and iron particles in copper — Diana Guenzburger, D. E. Ellis

6432 The magnetic response at the metal–insulator transition in $La_{1-x}Sr_xTiO_3$ (abstract) — R. Osborn, M. C. Aronson, E. A. Goremychkin, J. E. Greedan

6433 On perturbation theory for the three-band model of cuprates — T. A. Kaplan, S. D. Mahanti, Yen-Sheng Su, K. Kubo

6436 Magnetic measurements on $Cd_{1-x}Cr_xTe$ and $Zn_{1-x}Cr_xTe$ — T. M. Pekarek, I. Miotkowski, B. C. Crooker

6439 Specific heat of $R_3Co$ (R: La,Pr, and Nd) (abstract) — I. Umehara, K. Nakano, Q. F. Lu, K. Sato


**Magnetic Microscopy and Imaging**


6440 Submicron characterization of recording media using magnetic force microscopy (invited) (abstract) — K. Babcock, S. Manalis, V. Elings, M. Dugas, W. Challener

6441 Magnetic imaging in the presence of external fields: Technique and applications (invited) — Romel D. Gomez, Edward R. Burke, Isaak D. Mayergoyz

6447 Domain structure of iron single crystals grown on Si(111) investigated by magnetic force microscopy (abstract) — S. Foss, R. Proksch, K. Moloni, E. D. Dahlberg, Y. Cheng

6447 Force gradient mapping of domain wall structures in magnetite (abstract) — Roger Proksch, Tilman E. Schäffer, Sheryl Foss

6448 Superparamagnetic magnetic force microscopy tips — P. F. Hopkins, John Moreland, S. S. Malhotra, S. H. Liou

6451 Sensitive detection of magnetic field distribution using scanning interference electron microscope (abstract) — Y. Yajima, Y. Takahashi, K. Kuroda, Y. Sugita

6452 Magnetization reversal process in TbCo-biased spin valves — J. N. Chapman, M. F. Gillies, P. P. Freitas

6455 Direct observation of domain walls in NiFe films using high-resolution Lorentz microscopy — Bunsen Y. Wong, David. E. Laughlin


**Computational Magnetics**


6458 Numerical micromagnetics in hard magnetic and multilayer systems (invited) — T. Schrefl, J. Fidler

6464 Simulation of three-dimensional nonperiodic structures of $\pi$-vertical Bloch line and $2\pi$-vertical Bloch line in magnetic garnet — M. Redjdal, F. B. Humphrey

6467 Simulations of highly anisotropic Co–Cr–Ta thin films — C. Dean, R. W. Chantrell, H. Suzuki, N. Kodama, P. R. Bissell

6470 Modeling of permanent magnets: Interpretation of parameters obtained from the Jiles–Atherton hysteresis model — L. H. Lewis, J. Gao, D. C. Jiles, D. O. Welch

6473 Superconducting hysteresis and the Preisach model — I. D. Mayergoyz

6476 A model for magnetomechanical hysteresis and losses in magnetostrictive materials — A. Bergqvist, G. Engdahl

6479 On the relaxation of simple magnetic systems — J. M. González, R. Ramírez, R. Smirnov-Rueda, J. González


*(Continued)*

6482 Response of a kinetic Ising system to oscillating external fields: Amplitude and frequency dependence — S. W. Sides, R. A. Ramos, P. A. Rikvold, M. A. Novotny

6485 Study of residual magnetization of hard steel samples — M. Saadi, F. Jellali, A. Delmas, G. Quichaud

**Magnetic Circular Dichroism and Hyperfine Fields**

6488 Magnetic reversal in perpendicularly oriented thin films subjected to picosecond magnetic fields (abstract) — Juergen Heidmann, Dieter Weller, Hans C. Siegmann, E. L. Garwin

6489 A theoretical description of magnetic switching experiments in picosecond field pulses — L. He, W. D. Doyle

6492 Structural and magnetic studies of heteromagnetic multilayers by reflectivity of circularly polarized soft x rays (abstract) — Y. U. Idzerda, V. Chakarian, C. J. Gutierrez, G. A. Prinz, C.-C. Kao, J.-H. Park, G. Meigs, C. T. Chen

6493 Giant magnetic effects in the $L$-edge extended x-ray absorption fine structure of $3d$ transition metals — V. Chakarian, Y. U. Idzerda, K. M. Kemner, J.-H. Park, G. Meigs, C. T. Chen

6496 Magnetic circular dichroism in EELS (abstract) — G. R. Harp, R. F. C. Farrow, R. F. Marks

6497 Temperature and field-induced magnetization flips in amorphous Er–Fe alloys evidenced by x-ray magnetic circular dichroism — L. M. Garcia, S. Pizzini, J. P. Rueff, J. Vogel, R. M. Galéra, A. Fontaine, J. P. Kappler, G. Krill, J. Goedkoop

6500 Magnetic circular dichroism at the $K$ and $L$ edges of Co and Cu in Co/Cu(001) — Ruqian Wu, A. J. Freeman

6503 Determination of the energy dependence of the off-diagonal terms of the dielectric tensor by means of $M_{2,3}$ reflection MCD measurements (abstract) — Hartmut Höchst, Dai Zhao, David Huber

6504 Magnetic dichroism in angle-resolved UV photoemission from valence bands, using linearly polarized light — D. Venus, W. Kuch, A. Dittschar, M. Zharnikov, C. M. Schneider, J. Kirschner

6507 Spin polarized photoemission studies of the $3s$ core level in ferromagnetic systems (abstract) — Y. Liu, J. Xu, D-J. Huang, P. D. Johnson

6508 Magnetic dichroism in the soft x-ray regime for magnetic domain imaging by total yield microscopy (abstract) — F. U. Hillebrecht, T. Kinoshita, Ch. Roth, H. B. Rose, D. Spanke, J. Dresselhaus, E. Kisker

6509 Spin resolved resonant Raman scattering — W. A. Caliebe, C.-C. Kao, L. E. Berman, J. B. Hastings, M. H. Krisch, F. Sette, K. Hämäläinen

6512 Raman heterodyne detection of magnetic resonance in a phosphate glass — G. K. Liu, C.-K. Loong, James V. Beitz, Ruoxin Cao, Y. H. Chen, K. Suzuya

6515 Magnetic and Mössbauer studies of hot-pressed MnZnNi ferrites (abstract) — V. K. Babbar, R. K. Puri

**Transport—Mostly Magnetoresistance**

6516 Quantum vortex motion in high-$T_c$ superconductors — A. García, X. X. Zhang, J. Tejada

6519 An ultrasonic study of spin-density-wave effects in a Cr+0.2 at. % Ir alloy single crystal — J. Martynova, H. L. Alberts, P. Smit

6522 Hall-effect measurements on Cr films deposited on Ge substrates — Chien-Sheng Hsieh, Klaus Schröder

6525 Modeling the stress dependence of Barkhausen phenomena for stress axis linear and noncollinear with applied magnetic field (abstract) — M. J. Sablik, B. Augustyniak, M. Chmielewski

6526 Magnetovolume and magnetoelastic effects in ternary Cr–Ru–Mo alloys — J. T. Mochele, P. Smit, H. L. Alberts

6529 Magnetoelastic energy in domains separated by 90° walls — A. S. Arrott

6532 High frequency (1–1200 MHz) magnetoimpedance in CoFeSiB amorphous wires (abstract) — V. P. Paramonov, A. S. Antonov, A. N. Lagarikov, L. V. Panina, K. Mohri

6533 Enhancement of magnetoresistance in Co($1\bar{1}00$)/Cr(211) bilayered films on MgO(110) — Y. D. Yao, Y. Liou, J. C. A. Huang, S. Y. Liao, I. Klik, W. T. Yang, C. P. Chang, C. K. Lo


*(Continued)*

6536 Magnetic and electrical properties of CoFeSiB:O thin films near the percolation threshold — R. Banerjee, A. P. Valanju, G. Choe, R. M. Walser

6539 Circumferential magnetization processes in CoFeBSi wires — L. Domínguez, J. M. Blanco, P. Aragoneses, J. González, R. Valenzuela, M. Vázquez, A. Hernando

6542 Measurements of magnetization dynamics and magnetoimpedance in FeCoSiB and FeSiB amorphous wires — S. Masuda, K. Komatsu, Y. Takemura, T. Yamada, K. Kakuno

6545 Transport properties of amorphous CoZrNd thin films with very low Nd content (abstract) — C. de Francisco, J. M. Muñoz, J. F. Calleja, M. Rivas, M. C. Contreras

6546 Domains and giant magneto-impedance in amorphous ribbons by magneto-optical Kerr effect — A. D. Santos, L. G. C. Melo, C. S. Martins, F. P. Missell, Y. Souche, F. L. A. Machado, S. M. Rezende

6549 A position sensor based on magnetoimpedance — R. Valenzuela, M. Vazquez, A. Hernando

6552 The field-annealing effect on magnetoimpedance of a zero magnetostrictive metallic glass — S. U. Jen, Y. D. Chao

6555 Giant transversal magnetoimpedance and Hall-effect measurements in $Co_{70.4}Fe_{4.6}Si_{15}B_{10}$ — K. C. Mendes, F. L. A. Machado, L. G. Pereira, S. M. Rezende, F. C. Montenegro, M. V. P. Altoé, F. P. Missell

6558 A theoretical model for the giant magnetoimpedance in ribbons of amorphous soft-ferromagnetic alloys — F. L. A. Machado, S. M. Rezende


**Superconductivity and Applied Superconductivity**


6561 Superconducting properties of Fe-doped $YNi_2B_2C$ — X. Z. Zhou, H. P. Kunkel, P. A. Stampe, Gwyn Williams

6564 Magnetic properties of polycrystalline $Sm_{2-x}Ce_xCuO_{4-y}$ at high magnetic fields — R. F. Jardim, C. H. Westphal, C. H. Cohenca, L. Ben-Dor, M. B. Maple

6567 Thermal conductivity of $Bi_2Sr_2Ca_nCu_{n+1}O_x$ bulk superconductors in high magnetic fields (abstract) — S. C. Nakamae, J. Schwartz

6568 Cu spin reorientation in Tl(BaSr)$PrCu_2O_7$ — W.-H. Li, Y. F. Lin, S. Y. Wu, W. T. Hsieh, K. C. Lee, J. W. Lynn, C. C. Lai, H. C. Ku

6571 Alternating current susceptibility studies of Tb ordering in $Pb_2Sr_2TbCu_3O_8$ — S. Y. Wu, W.-H. Li, K. C. Lee, T. H. Meen, H. D. Yang

6574 Field dependence of magnetic relaxation in BiPbSrCaCuO superconductors — V. Raposo, A. G. Flores, M. Zazo, L. Torres, J. Iñiguez

6577 Gd concentration dependence of the spin reorientation critical field in $Eu_{2-x}Gd_xCuO_4$ — A. Butera, A. Fainstein, M. Tovar, Z. Fisk, S. B. Oseroff

6580 Magnetization of $HgBa_2CuO_{4+\delta}$ with $0.03 \leqslant \delta \leqslant 0.4$ — Q. Xiong, S. Afonso, Y. Q. Tang, F. T. Chan, G. Salamo, Y. Y. Xue, C. W. Chu

6583 Superconducting properties of Hg-1223 prepared by using fluorides — B. J. Jönsson, T. Turkki, V. Ström, Z. Iqbal, K. V. Rao

6586 Vortex pinning in layered organic superconductors: $\kappa$-$(BEDT\text{-}TTF)_2Cu[N(CN)_2]Br$ — S. Khizroev, F. Zuo, G. C. Alexandrakis, J. A. Schlueter, U. Geiser, J. M. Williams

6589 Experimental evidence of a crossover in the vortex dimensionality in high-$T_c$ superconductors — A. García, X. X. Zhang, J. Tejada

6592 Vortex gliding between Cu–O planes in an anisotropic high temperature superconductor (abstract) — C. A. Durán, P. L. Gammel, D. J. Bishop

6593 Magnetic field and temperature dependence of critical current densities in multilayer $YBa_2Cu_3O_{7-\delta}$ films — S. Afonso, F. T. Chan, K. Y. Chen, G. J. Salamo, Y. Q. Tang, R. C. Wang, X. L. Xu, Q. Xiong, G. Florence, S. Scott, S. Ang, W. D. Brown, L. W. Schaper


*(Continued)*

6596 Flux trapping and levitation forces in directionally solidified superconducting $YBa_2Cu_3O_7$ ingots — J. Mora, M. Carrera, X. Granados, J. Fontcuberta, S. Piñol, X. Obradors

6599 Magnetostatic effect on magnetic flux penetration in superconducting Nb film covered with a micron–size magnetic particle array — Yukio Nozaki, Yoshichika Otani, Katharina Runge, Hideki Miyajima, Bernard Pannetier, Jean Pierre Nozières

6602 "Standing" diffusion of electromagnetic fields in superconductors with gradual resistive transitions — I. D. Mayergoyz, M. Neely

6605 Low-temperature specific heat of the degenerate supersymmetric *t-J* model in one dimension — Kong-Ju-Bock Lee, P. Schlottmann

**Spin Glasses and Frustrated Magnets**

6608 Magnetic and thermodynamic properties of $Sr_2LaFe_3O_9$ — J. T. Wang, C. L. Lin, T. Mihalisin

6611 Low-temperature Mössbauer study of the mechanically alloyed $Fe_xMn_{0.7-x}Al_{0.3}$ ($0.4 \leq x \leq 0.5$) series — J. M. González, Anit K. Giri, G. A. Pérez Alcázar, Ligia E. Zamora

6614 Magnetic and crystal phase transitions in $KNiCl_3$ — O. A. Petrenko, M. F. Collins, C. V. Stager, B. F. Collier, Z. Tun

6617 New spin glass $Fe_{0.67}Cr_{1.33}Sn_{0.67}S_4$ with magnetic ions in tetrahedral and octahedral sublattices (abstract) — L. I. Koroleva, L. N. Lukina, A. G. Odintsov, T. V. Virovets

6618 Scaling of the thermoremanent relaxation in FeNiCr — D. Li, R. M. Roshko

6621 $^7$Li nuclear magnetic resonance spectra and relaxation in $Ni_{1-x}Li_xO$ — M. Corti, S. Marini, A. Rigamonti, V. Massarotti, D. Capsoni

6624 Susceptibility and $^{89}$Y nuclear magnetic resonance in $Y_{1-x}Ca_xVO_3$ — F. Cintolesi, M. Corti, A. Rigamonti, G. Rossetti, P. Ghigna, A. Lascialfari

6627 Spin glass behavior of amorphous $Fe_5(InTe_4)_3$ — Jian H. Zhang, Damon Williams, Cuihong Tao, Charles J. O'Connor

6630 Order-parameter fluctuations in the frustrated Heisenberg model on the square lattice — Shu Zhang, Gerhard Müller

6633 Mictomagnetism of $\epsilon$-MnZn alloys — T. Hori, H. Shiraishi, Y. Nakagawa

6636 Low temperature spin dynamics of geometrically frustrated antiferromagnets $Y_2Mo_2O_7$ and $Y_2Mo_{1.6}Ti_{0.4}O_7$ studied by muon spin relaxation — S. R. Dunsiger, R. F. Kiefl, K. H. Chow, B. D. Gaulin, M. J. P. Gingras, J. E. Greedan, A. Keren, K. Kojima, G. M. Luke, W. A. MacFarlane, N. P. Raju, J. E. Sonier, Y. J. Uemura, W. D. Wu

**Alternative Memories, Concepts, and Bubbles**

6639 Quarternary giant magnetoresistance random access memory — Zhigang Wang, Yoshihisa Nakamura

6642 Important factors included in nondestructive readout of GMR MRAM (abstract) — Y. Nakamura, Z. Wang

6642 Domain collapse in grooved magnetic garnet material (abstract) — J. C. Peredo, G. N. Patterson, Y. N. Fedyunin

6643 Fundamental studies of stripe-domain chopping in the presence of magnetic fields — K. J. Fogarty, K. Matsuyama, H. Asada, W. W. Clegg

6646 Micromagnetic study on write operation in submicron magnetic random access memory cell — H. Asada, K. Matsuyama, K. Taniguchi

6649 Analytical model in a weakly coupled sandwich for memory purposes — Zhigang Wang, Yoshihisa Nakamura


AUTHOR INDEX

**A publication of the American Institute of Physics, 500 Sunnyside Blvd., Woodbury, NY 11797-2999**

# Magnetic domain structure in ultrathin Cu/Ni/Cu/Si(001) films (invited)

Hans J. Hug
*Institute of Physics, University of Basel, Klingelbergstrasse 82, CH-4056 Basel, Switzerland*

B. Stiefel, A. Moser, I. Parashikov, A. Klicznik, D. Lipp, and H.-J. Güntherodt
*Institute of Physics, University of Basel, Klingelbergstrasse 82, CH-4056 Basel, Switzerland*

Gabriel Bochi and D. I. Paul
*Massachusetts Institute of Technology, Cambridge, Massachusetts 02139*

R. C. O'Handley
*Massachusetts Institute of Technology, Cambridge, Massachusetts 02139*

We present a series of magnetic force microscope (MFM) images of epitaxial magnetic thin films. The films studied, Ni/Cu/Si(001) capped by 2 nm of Cu, exhibit perpendicular anisotropy over an exceptionally broad thickness range, 2 nm$<h<$14 nm. The magnetic domain structure of the as-grown films shows a sharp transition to a finer length scale above a finite critical thickness of 12 nm. Micromagnetic theory provides the first quantitative description for these general but previously unexplained phenomena. Further we discuss MFM data obtained on films with a thickness larger than 14 nm. These films show a pronounced in-plane anisotropy. © *1996 American Institute of Physics.* [S0021-8979(96)19308-3]

## I. INTRODUCTION

The study of magnetic thin films in which perpendicular magnetization is realized is of particular importance in many applications such as information storage media and diverse sensors for magnetic field, strain and acceleration. A perpendicular orientation of **M** defies the magnetostatic energy which tends to keep the magnetic moments in plane. The study of thin film systems in which perpendicular magnetization is realized, e.g., fcc Fe/Cu(001),[1–3] bcc Fe/Ag,[4] Co/Pt,[5] Co/Au,[6,7] Ni/Cu,[8–11] remains very active. In many cases the behavior of the magnetization with field is modeled assuming the ultrathin film is comprised of a single magnetic domain. However, in some ultrathin film cases such as Co/Cu,[12] Co/Au,[13,14] and Cu/Ni/Cu[15,16] where domains have been observed, this assumption is not correct. Further, it is expected that as film thickness increases domain size should first decrease then increase.[17] Also, at sufficiently large film thickness the magnetostatic energy increases to a level at which **M** falls into the film plane. There is as yet no clear understanding of the conditions under which domains should exist in ultrathin films or of the evolution of their domain structure with film thickness. Further, the mode by which the magnetization reverts to an in-plane orientation with increasing film thickness (coherent rotation, domain wall expansion, or formation of surface layers with perpendicular magnetization, while the magnetization inside of the film falls in-plane) has not been resolved.

We have made an extensive magnetic force microscopy study of the magnetic domain structure in Cu/Ni/Cu/Si(001) over a Ni thickness range of 2 nm$<h<$17.5 nm. The samples studied are a series of MBE-grown, epitaxial Ni/Cu/Si(001) films capped with 2 nm of Cu. These films had previously been fully characterized *in situ*, before capping, using RHEED[18,19] and after capping by magneto-optic Kerr effect[8,10] and *ex situ* after capping using vibrating sample magnetometry[11] and optical interferometry (for strain measurements).[18,19] The Cu/Ni/Cu/Si(001) system shows an extremely broad thickness range (2 nm to 14 nm) over which perpendicular magnetization is observed.[9,11] Here we show that a magnetic force microscope (MFM) can resolve domains in magnetic films as thin as 2 nm and report the first detailed experimental confirmation of a micromagnetic model predicting a transition to an essentially infinite domain size below a critical thickness of a magnetic film. Finally, the MFM images indicate that the perpendicular to in-plane transition with increasing film thickness is not achieved by coherent rotation of domain magnetization but by a more complex process which is not yet fully understood. We propose a first model which explains both, the MFM data and the magnetization measurements.

## II. MFM ON PERPENDICULARLY MAGNETIZED THIN FILMS

We use a new, sophisticated MFM which was built for low temperature and ultrahigh vacuum (UHV) use. The small size of the instrument (diameter: 40.4 mm, length: 120 mm), the thermally well compensated construction not containing any ferromagnetic materials allows its use in a magnetic field produced by a Cu-wire-solenoid. The technical details and properties of the microscope will be published later. All measurements presented here are taken in air, at room temperature and in zero magnetic field (no special precautions were taken to shield the earths magnetic field). The MFM is operated in the static, variable deflection mode which is well suited for high-speed images of large areas.[20,21] The force on a magnetic force microscope tip in the magnetic stray field of a sample is given by

 0021-8979/96/79(8)/5609/6/$10.00 © 1996 American Institute of Physics 

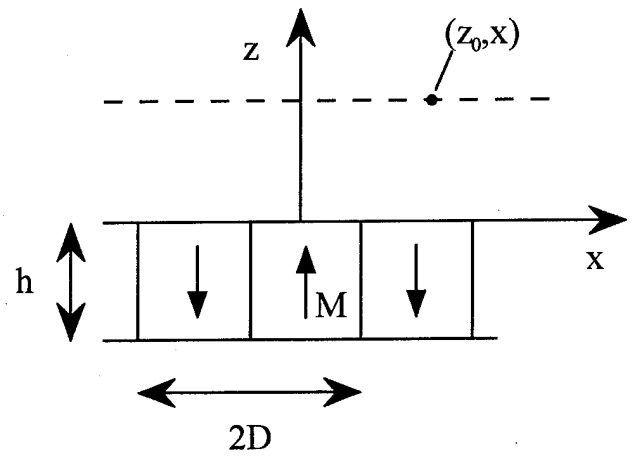



FIG. 1. Model domain structure with the coordinate system. $M$—magnetization (arrow up=1, arrow down=−1); $h$—film thickness; $2D$—domain size; $(z_0,x)$—position of MFM tip.

$$F_z = -\mu_0 \cdot \int_{V_{\mathrm{Tip}}} \left[ \mathbf{M}_{\mathrm{Tip}} \cdot \frac{\partial}{\partial z} \mathbf{H}_{\mathrm{Sample}}(x,y,z) \right] dV. \tag{1}$$

To obtain a tip with a well defined direction of the magnetization we have used an electron microscope to grow a deposition tip on a standard pyramid tip of a commercially available cantilever. The needle like tip was grown in an angle of approximately ten degrees to the vertical axis of the pyramid tip to have the needle like tip perpendicular to the surface of the sample. The tip is made sensitive to magnetic stray fields by a 25-nm-thick Co film which was deposited on the side of the needle like tip by thermal evaporation.[22] The strong shape anisotropy of the thin film keeps the magnetization along the tip axis

$$\mathbf{M}_{\mathrm{Tip}} = (0,0,M_{z,\mathrm{Tip}}). \tag{2}$$

With the tip magnetization being purely along the $z$-axis Eq. (1) can be rewritten as

$$F_z = \oint_{A_{\mathrm{Tip}}} [\rho_{m,\mathrm{Tip}} \cdot H_{z,\mathrm{Sample}}(x,y,z)] dA, \tag{3}$$

where $\rho_{m,\mathrm{Tip}}$ is the magnetic surface charge density of the tip. Approximating the tip as a long and thin, homogeneously magnetized cylinder with magnetic charges at the bottom surface, $A_{\mathrm{bottom}}$ and the top surface, $A_{\mathrm{top}}$ Eq. (3) simplifies to

$$F_z = \mu_0 \cdot M_{z,\mathrm{Tip}} \cdot \left( \int_{A_{\mathrm{bottom}}} H_{z,\mathrm{Sample}} dA - \int_{A_{\mathrm{top}}} H_{z,\mathrm{Sample}} dA \right). \tag{4}$$

Since the distance of the top surface of the tip to the surface of the sample is about 1 $\mu$m larger than the one of the bottom surface to the sample. Thus the part of the force produced by the top surface can be neglected. Then the force, $F_z$ [Eq. (4)] reflects the local stray field averaged over the area of the bottom surface of the tip. The size of the bottom surface sets a natural limit to the resolution of the stray field of the MFM experiment. However, for all images presented in this work the distance between two image points is approximately 60 nm and therefore about a factor of two larger than the diameter of the bottom area, $A_{\mathrm{bottom}}$ of the tip. Equation (4) further simplifies to

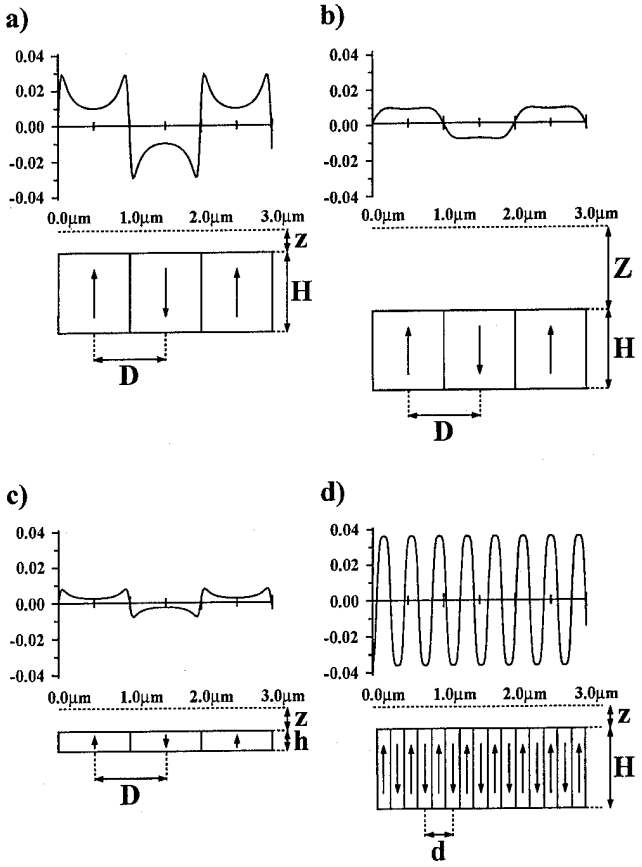



FIG. 2. Model calculation of the stray field above a periodical domain structure in a perpendicularly magnetized thin film. Magnetization—arrow up=1, arrow down=−1; field in same units as the magnetization; domain size—$D=1$ $\mu$m, $d=0.2$ $\mu$m; film thickness—$H=10$ nm, $h=2.5$ nm; tip-to-sample distance—$Z=200$ nm, $z=50$ nm. (a) Stray field above model structure. (b) Stray field for a larger tip-to-sample distance ($Z=200$ nm). (c) Stray field for a thinner film ($h=2.5$ nm). (d) Stray field for smaller domains ($d=0.2$ $\mu$m).

$$F_z = q_{\mathrm{Tip}} \cdot H_z, \tag{5}$$

where $q_{\mathrm{Tip}} = \mu_0 \cdot M_{z,\mathrm{Tip}} \cdot A_{\mathrm{bottom}}$ is the magnetic charge of the bottom surface of the magnetic tip. Note that, within these limits the magnetic force microscope image is proportional to the $z$ component of the stray field of the sample.

To have a better understanding of the MFM images obtained on the Ni sandwiches we analytically calculate the stray field of a periodical, perpendicularly magnetized model thin film sample (Fig. 1).[20,23] For a film thickness, $h$, a domain period, $2D$, and a tip-to-sample distance, $z_0$, we obtain

$$H_z(x,z=z_0) = \frac{2}{\pi} \cdot M_{z,\mathrm{Tip}} \cdot \sum_{n=0}^{\infty} \frac{(-1)^n}{2n+1} \left[ 1 - \exp\left( -(2n+1) \frac{2\pi h}{2D} \right) \right] \exp\left[ -(2n+1) \frac{2\pi z_0}{2D} \right] \times \cos\left[ (2n+1) \frac{2\pi x}{2D} \right]. \tag{6}$$

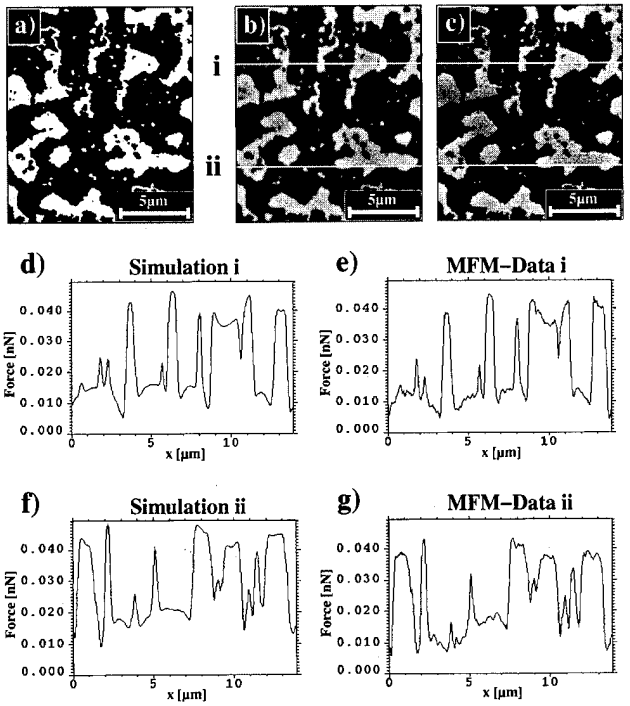



FIG. 3. Simulation of MFM data. (a) Domain Structure. (b) Calculated stray field (force) using the domain structure (a) and a film thickness of 10 nm. (c) MFM data acquired on a film with a thickness of 10 nm [the domain structure of Fig. 3(a) was derived from this data]. (d and f) Cross sections of simulation to be compared with (f) and (g) cross section of MFM data.

From Eq. (6) we learn that the stray field becomes smaller towards the center of a domain [Fig. 2(a)], for increasing tip-to-sample distance [Fig. 2(b)] and for decreasing film thickness [Fig. 2(c)]. Note that the force contrast does not decreased as the domain size is decreased by a factor of four [Fig. 2(d)]. This rather unexpected behavior is a special property of thin films. For an infinitely thick sample the decay of the force contrast with decreasing domain size is governed by the first exponential factor in the second line of Eq. (6). Clearly a domain structure of smaller size (in an infinitely thick sample) produces a smaller force contrast. In thin films, however, the situation can be different, as shown in Fig. 2(d). The difference is due to the two magnetic charges of opposite sign induced on the top and bottom surface of the film. Thus a small distance above the center of a large domain we expect to have a very small stray field [Fig. 2(a)]. In contrast to the large domain, the field above the small domain is mainly dominated by the fringe fields at the site of the domain wall and can therefore be larger [Fig. 2(d)].

Using a new theoretical approach[24] the stray field for an arbitrary complex two-dimensional perpendicularly magnetized domain pattern [Fig. 3(a)] can be calculated. The obtained stray field [Fig. 3(b)] perfectly matches the measured MFM data [Fig. 3(c)]. This is impressively demonstrated by comparing the calculated cross sections (i,ii) [Figs. 3(d) and 3(f)] with experimental cross sections [Figs. 3(e) and 3(g)].

## III. DOMAIN STRUCTURES OF FILMS CONTAINING 2 nm TO 12.5 nm OF Ni

The MFM images confirm dramatically that the magnetization is indeed strongly held to a perpendicular direction as indicated by magneto-optic KERR effect measurements[8,10] and vibrating sample magnetometry.[4] In these images the contrast is due to magnetization into and out of the plane; no regions of in-plane magnetization were observed other than the domain walls themselves.

It is noteworthy that the domain walls show no orientational correlation with the easy in-plane ⟨110⟩ crystallographic directions in these epitaxial Ni films. This will be the subject of a forthcoming paper. The domain walls are Bloch walls, not Néel walls, so the wall magnetization runs along the wall length with no cost in magnetostatic energy. (Néel walls are preferred only in thin films exhibiting in-plane magnetization.) Based on our magnetic anisotropy measurements,[11] the wall width, $\delta_{dw}=\pi(A/K)^{1/2}$ should be of order 30 nm for a Ni thickness of 8.5 nm and increases for thinner or thicker films.

The domain structure of the as-grown films is characterized by two types of behavior in different thickness ranges. At and below 8.5 nm of Ni the domain patterns are irregularly spotted [Figs. 4(a)–4(d)] and tend toward serpentine patterns at larger thickness, $h$ [Fig. 4(e)]. The length scale of this coarse structure is poorly defined but its average decreases with increasing thickness, $h$. Relative to the film thickness, these patterns are essentially infinite in lateral scale (1–4 $\mu$m) and so may be characterized by a reduced domain size parameter $D/h\approx\infty$. The weak energies that govern these features are not yet well understood. Above 8.5 nm the relatively large serpentine domains begin to break down by internal fragmentation (submicron bubble domain formation) as seen in Figs. 4(e) and 4(f). It is noteworthy that the larger domain features that characterize the thinner Ni films [Figs. 4(a)–4(d)] are preserved even as the internal fragmentation of the domains progresses with increasing thickness above 8.5 nm [Figs. 4(e) and 4(f)]. This suggests that these separate-scale structures may be governed by different energies and/or kinetics. As the Ni thickness increases, magnetostatic energy is reduced by refinement of the interior bubble domain structure rather than by more complex contortions of the existing domain walls. This occurs because the magnetostatic energy well inside a domain is $(\mu_0/2)M_z^2$ while it is significantly reduced near an existing domain wall. We can calculate the transition to this finer domain structure and its length scale by extensions of domain theory as outlined by Kittel[25] and developed by others.[17,26] As shown in Ref. 2, the energy difference between stripe and checker domain patterns is small. Neglecting the finite width of the domain walls, we may use the expression for the energy per unit surface area for a stripe domain structure, i.e.,

$$u=16M_S^2\frac{D}{\pi^2}\cdot\sum_n^{\text{odd}}\frac{1-\exp(-n\pi h/D)}{n^3}+\frac{h\sigma_{dw}(h)}{h}, \qquad (7)$$

where we write the domain wall energy density, $\sigma_{dw}(h)=4(AK_{eff})^{1/2}$ as a function of Ni thickness because of the strong dependence of the measured effective anisotropy, $K_{eff}$, on thickness.[9,10] We have numerically minimized Eq. (7) with respect to the domain size,[27] using the methods of Malek and Kambersky.[28] For the range of interest here, $h<14$ nm, we have plotted the numerical solution in Fig. 5 using the experimentally measured[10] effective anisotropy,

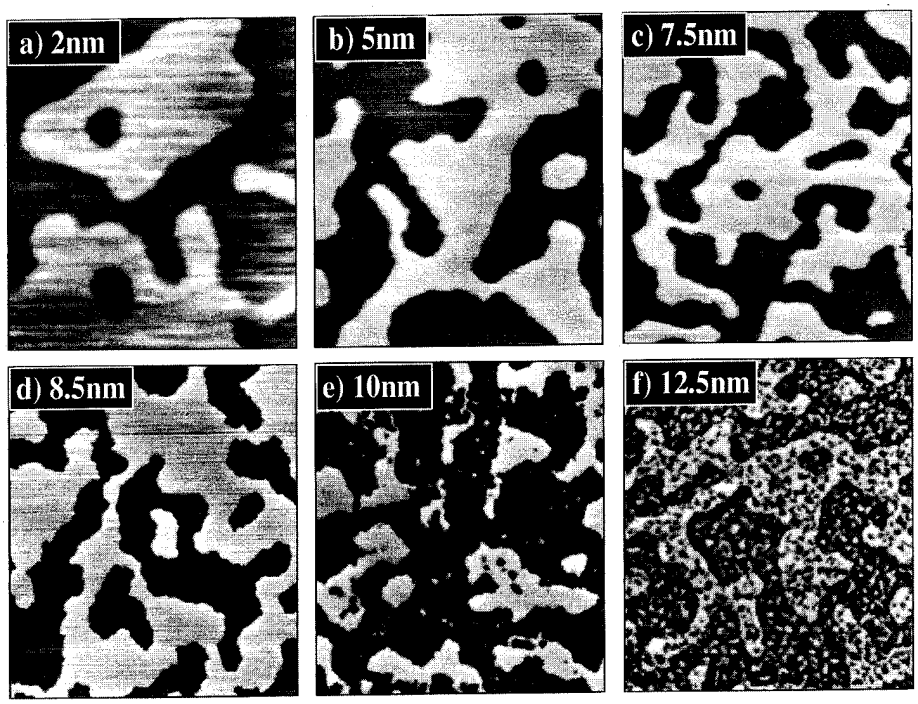



FIG. 4. MFM data acquired on Cu/Ni/Cu films containing (a) 2 nm, (b) 5 nm, (c) 7.5 nm, (d) 8.5 nm, (e) 10 nm, (f) 12.5 nm Ni. (Image size: 13.9 $\mu$m×15.8 $\mu$m.)

$K_{eff}$, in $\sigma_{dw}$, $A=1\cdot10^{-6}$ erg/cm and $M_S\approx435$ emu/cm$^3$. This magnetization density is smaller than the bulk value for Ni, 485 emu/cm$^3$, but is typical of that measured for our films in this thickness range.

The thickness, $h$, corresponding to the onset of domain fragmentation is calculated to be approximately 8.5 nm and the average domain spacing is calculated to decrease to about 0.6 $\mu$m for $h=12$ nm. The domain images indicate that between $h=8.5$ and 10 nm [Figs. 4(d) and 4(e)] the fine domains first appear in our Cu/Ni/Cu sandwiches but a complete breaking up into submicron domains occurs between $h=10$ and 12.5 nm [Figs. 4(e) and 4(f)]. Thus the observed domain structure breaks up into small bubbles at a thickness, $h$, where the domain-size vs thickness function develops a pronounced energy minimum (Fig. 5, insets). Below 10 nm film thickness, the minimum of the energy, $u$, vs the domain size, $D$, from Eq. (7) is extremely shallow, suggesting that at finite temperatures a broad range of $D$ values would be allowed. Indeed the measured domain size for films with thicknesses below 8.5 nm is smaller than expected from our model. The model is only valid for a thickness $h$ above 10 nm where the energy minimum becomes well defined.

## IV. TRANSITION OF THE EASY AXIS OF MAGNETIZATION ABOVE 14 nm Ni-FILM THICKNESS

Above a Ni thickness of 14 nm where magnetometry[9–11] indicates the easy magnetization axis is in plane (Fig. 6), the

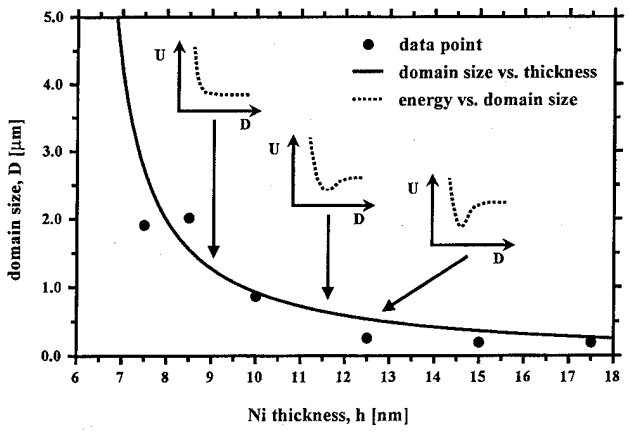



FIG. 5. Domains size versus Ni film thickness. — domain size versus Ni film thickness; ··· energy versus domain size; and ● experimental value.

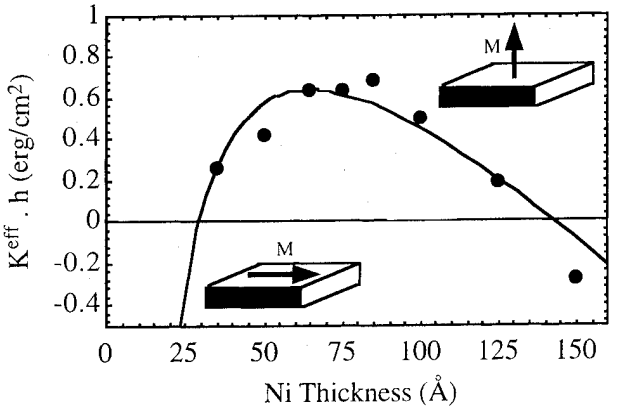



FIG. 6. Dependence of $k^{\text{eff}}\cdot h$ on Ni film thickness in Cu/Ni/Cu/Si(001) sandwiches. The perpendicular magnetic anisotropy dominates over a large Ni thickness range from 2 nm to 14 nm.

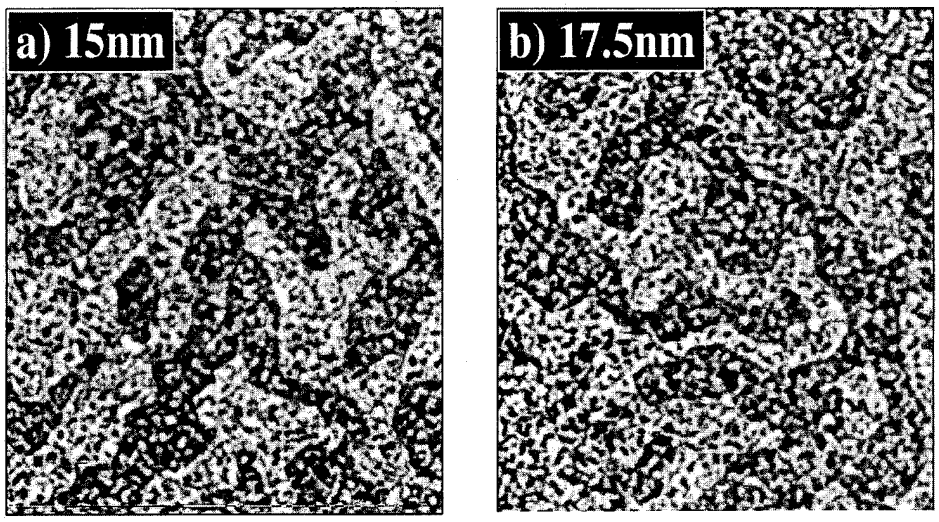



FIG. 7. MFM data acquired on Cu/Ni/Cu films containing (a) 15 nm and (b) 17.5 nm of Ni. (Image size: 13.9 $\mu$m×15.8 $\mu$m.)

MFM data reveals small bubbles still magnetized perpendicularly (Fig. 7). This suggest that the net in-plane magnetization measured by magnetometry at 15 nm Ni may be due to a layer of in-plane magnetization burried inside the Ni film and/or due to the broad Bloch walls between smaller, perpendicularly magnetized regions at the surface of the film. Magnetization measurements reveal the net in-plane moment whereas MFM detects the $z$ component of the fringe field above the small perpendicularly magnetized regions. From Refs. 9, 10, and 11 we know that the strong perpendicular anisotropy observed in Cu/Ni/Cu-sandwiches with an Ni thickness between 2 and 14 nm (Fig. 6) is mainly caused by the magnetocrystalline surface anisotropy and the combination of misfit strain and the large positive bulk magnetoelastic coupling coefficient.

In sandwiches with a sufficiently large Ni thickness[9] the misfit strain decays towards the inside of the film due to misfit dislocations. Thus, perpendicular anisotropy caused by the bulk magnetoelastic coupling becomes less important inside the film whereas the positive magnetocrystalline surface anisotropy still keeps the magnetization perpendicular at the surface of the film.

Thus the easy axis transition in these films appears to be the result of wall broadening of the perpendicularly magnetized surface regions and possibly a complex rotation of the magnetization into the film plane in the inside of the film. This is the subject of a forthcoming publication.

## V. CONCLUSION

We have measured the domain size in a series of epitaxial Cu/Ni/Cu films over the Ni thickness range 2 nm$<h<$17.5 nm using a high-resolution MFM. From 2 nm up to 10 nm of Ni the domains are large and of a relatively irregular size; their average size decreases with increasing Ni thickness. Between 8.5 and 10 nm of Ni internal fragmentation of the larger domains into sub-micron bubble domains begins. The size and spacing of these internal bubble domains decreases to approximately 0.3 $\mu$m at $h=12.5$ nm for the as-grown films. In contrast, the demagnetized films show such a small domain size already at smaller Ni thicknesses around 10 nm. These finer domains are more uniform in their spacing than are the coarser domains observed below 8.5 nm. All of these features in films with Ni thicknesses up to 12.5 nm are well described by micromagnetic domain theory. At larger Ni-thicknesses the MFM data indicates that the transition of the easy axis of magnetization from out-off-plane to in-plane as revealed by magnetometry is due to a rather complex interplay of perpendicularly magnetized surface layers and laterally magnetized regions in the inside of the film. Further MFM studies on much thicker sandwiches as well as MFM measurements searching for domain walls of the laterally magnetized regions in the inside are underway.

## ACKNOWLEDGMENTS

This work was supported by the Swiss National Science Foundation and in part by NSF Grant No. DMR 9410943. We thank Leon Ablemann, Steffen Porthun and Cock Lodder (University of Twente, The Netherlands) for the electron-beam fabrication of the MFM tip.

[1] D. Pescia, M. Stampanoni, G. L. Bona, A. Vaterlaus, R. F. Willis, and F. Meier, Phys. Rev. Lett. **58**, 2126 (1987).
[2] C. Liu, E. R. Moog, and S. Bader, Phys. Rev. Lett. **60**, 2422 (1988).
[3] D. P. Pappas, K. P. Kämper, and H. Hopster, Phys. Rev. Lett. **64**, 3179 (1990).
[4] M. Stampanoni, A. Vaterlaus, M. Aeschlimann, and F. Meier, Phys. Rev. Lett. **59**, 2483 (1987).
[5] B. N. Engle, C. D. England, R. Leeuwen, and M. H. Wiedemann, Phys. Rev. Lett. **67**, 1910 (1991).
[6] F. den Broeder, D. Kuiper, A. de Mosselaer, and W. Hoving, Phys. Rev. Lett. **60**, 2769 (1988).
[7] C. H. Lee, H. He, F. J. Lamelas, W. Vavra, C. Uher, and R. Clark, Phys. Rev. B **42**, 1066 (1990).
[8] G. Bochi, C. A. Balletine, H. E. Inglefield, S. S. Bogomolov, C. V. Thompson, and R. C. O'Handley, Mater. Res. Soc. Proc. **313**, 309 (1993).
[9] G. Bocci, C. A. Ballentine, H. E. Inglefield, C. V. Thompson, and R. C. O'Handley, Phys. Rev. B (to be published).

[10]G. Bochi, Magnetic anisotropy in epitaxial Ni/Cu(001) thin films and Cu/Ni/Cu(001) sandwiches Ph.D. thesis, M.I.T., 1995.
[11]G. Bocci, C. A. Ballentine, H. E. Inglefield, C. V. Thompson, and R. C. O'Handley, Phys. Rev. B **52**, 7311 (1995).
[12]H. P. Oepen, M. Benning, H. Ibach, C. M. Schneider, and J. Kirschner, J. Magn. Magn. Mater. **86**, 137 (1990).
[13]R. Allenspach, M. Stampanoni, and A. Bischof, Phys. Rev. Lett. **65**, 3344 (1990).
[14]R. Allenspach and A. Bischof, Phys. Rev. Lett. **69**, 3385 (1992).
[15]G. Bocci, H. J. Hug, D. I. Paul, B. Stiefel, A. Moser, I. Parashikov, H.-J. Güntherodt, and R. C. O'Handley, Phys. Rev. Lett. **75**, 1839 (1995).
[16]B. Kaplan and G. A. Gehring, J. Magn. Magn. Mater. **128**, 111 (1993).
[17]H. Inglefield, C. Ballentine, G. Bochi, S. Bogomolov, R. C. O'Handley, and C. Thompson, Mater. Res. Soc. Symp. Proc. **308**, 765 (1993).
[18]H. Inglefield, G. Bochi, C. Ballentine, R. C. O'Handley, and C. V. Thompson, Mater. Res. Soc. Symp. Proc. **365** (1995).
[19]H. J. Hug, Low Temperature Magnetic Force Microscopy. Application on Magnetic Materials and Superconductors, Ph.D. thesis, Universität Basel, 1993.
[20]H. J. Hug, A. Moser, Th. Jung, A. Wadas, and I. H.-J. Güntherodt, Rev. Sci. Instrum. **64**, 2920 (1993).
[21]M. Rührig, S. Porthun, and J. C. Lodder, Rev. Sci. Instrum. **165**, 3225 (1994).
[22]A. Wadas and H.-J. Güntherodt, Phys. Lett. A **146**, 277 (1990).
[23]H. J. Hug (to be published).
[24]C. Kittel, Phys. Rev. **70**, 945 (1946).
[25]Y. Yafet and E. M. Gyorgy, Phys. Rev. B **38**, 9145 (1988).
[26]Z. Malek and V. Kambersky, Czech. J. Phys. 8 **102**, 416 (1958).

# Magnetization and finite-size effects in Gd/W multilayers

J. Samuel Jiang and C. L. Chien
*Department of Physics and Astronomy, The Johns Hopkins University, Baltimore, Maryland 21218*

We have studied the magnetization and finite-size effects of thin Gd layers in sputter-deposited Gd/W multilayers. The interfacial Gd atoms lose about 9% of their moment, as the result of being in proximity with W. Annealing the multilayers at high temperatures improves the crystalline quality and sharpens the susceptibility peaks. The Curie temperature $T_C$ decreases with decreasing $d_{Gd}$ according to the finite-size scaling relation $[T_C(\infty)-T_C(d)]/T_C(\infty)=(d/d_0)^{-\lambda}$. The shift exponent $\lambda$ has been found to be $1.5\pm0.1$ and the constant $d_0$ to be 13 Å. © *1996 American Institute of Physics.* [S0021-8979(96)19408-X]

Magnetic multilayers with ferromagnetic metals separated by thin nonmagnetic spacer layers have attracted much attention recently in the investigation of oscillatory interlayer exchange coupling,[1] a phenomenon where the exchange interaction between the adjacent magnetic layers alternates between ferromagnetic and antiferromagnetic, and decays with increasing spacer layer thickness. Multilayers containing gadolinium (e.g., Gd/Y) are the first systems in which the RKKY-like interlayer exchange coupling was clearly demonstrated.[2] It has recently been reported that the saturation magnetization of Gd oscillates as the intervening W layer thickness is varied,[3] and an enormous enhancement of the saturation magnetization has been claimed in Gd/W multilayers at thin Gd thickness.[4] It has been postulated that the exchange interaction induces a moment in the W layers by polarizing the conduction band,[3] or the induced moment comes from the polarization of a hybrid band of Gd and W.[4] However, this does not seem very likely since the amount of enhancement, in excess of $6\mu_B$ per W atom, would require a complete mixing of Gd and W and a very substantial polarization of the conduction band. Furthermore, a recent photoemission study of Fe on Pd has shown that even for Pd, which has a very large magnetic susceptibility, an interfacial hybrid state provides an induced moment of only $0.32\mu_B$ for Pd at the interface.[5] On the other hand, when the magnetic layers are as thin as a few atomic planes, surface and interface effects may play an important role in affecting the magnetism. Polarized neutron diffraction studies of the magnetization profile in Gd/Y have shown a significant reduction of the interfacial Gd moment, which cannot be explained by alloying alone.[6] In light of these results, it is important to ascertain the magnetic properties of thin Gd layers.

We have prepared Gd/W multilayers to investigate the thickness dependence of the magnetic properties. Multilayer films with uniform layers for one component and wedge-shaped layers for the other component have been made, so that samples taken from different positions in the film differ only in the thickness of one component layer. This eliminates inconsistencies in material parameters that might arise if the samples were prepared separately. We will denote the samples as $Gd_{d_{Gd}}/W_{d_W}$, where $d_{Gd}$ and $d_W$ are Gd and W layer thicknesses. Here we present results from two series of samples: $Gd_{37\ Å}/W_{0-40\ Å}$ (*series A*) and $Gd_{0-50\ Å}/W_{26\ Å}$ (*series B*), both have 30 bilayers.

The Gd/W multilayers were deposited on Si(100) substrates using dc magnetron sputtering from 99.9% pure solid Gd and W targets. The deposition chamber was evacuated to $10^{-8}$ Torr prior to sputtering. Deposition was carried out in 99.9995% argon atmosphere at 4 mTorr. A liquid nitrogen-cooled Meissner trap was used during sputtering. The substrates were at ambient temperature and the Gd and W deposition rates were kept at 5 Å/s. The multilayers were sandwiched between two 350 Å W layers to protect the Gd layers from substrate reaction and oxidation. Some of the films were subsequently annealed in a high vacuum at 600 °C for 20 min, with a temperature ramping rate of 15 °C/min, to improve the crystalline quality and to relieve interfacial strain. Each of the films, 50 mm long in the wedge direction, was cut into 2 mm wide stripes perpendicular to the wedge direction for measurements. The area of each sample was determined optically. Because of the finite width of the samples, the wedge layers have a built-in thickness variation of about 1.6 Å (*series A*) or 2 Å (*series B*) from edge to edge.

The structural properties of the multilayers have been characterized using $\theta$-2 $\theta$ x-ray diffraction. Figure 1 shows

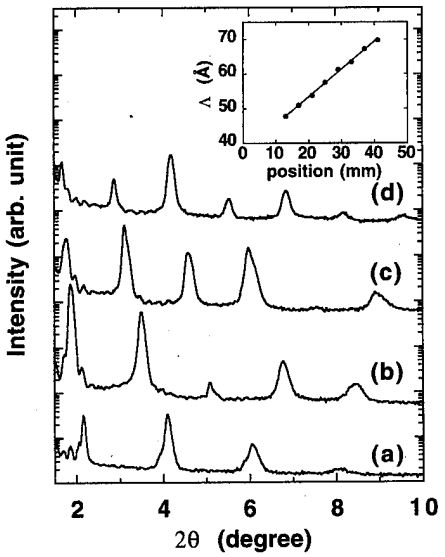



FIG. 1. Low-angle x-ray diffraction patterns of four Gd/W multilayers annealed at 600 °C with $d_{Gd}=37$ Å and $d_W=8$ Å (a), 17 Å (b), 24 Å (c), and 30 Å (d). Inset: The bilayer thickness Λ as a function of position for the same series of wedged multilayers.

 0021-8979/96/79(8)/5615/3/$10.00 © 1996 American Institute of Physics 

the low-angle diffraction patterns of four multilayers with $d_{Gd}$=37 Å and $d_W$=8, 17, 24, and 30 Å from *series A* after annealing at 600 °C. Several orders of low-angle diffraction peaks are seen, indicating that the layered structure remains intact after annealing. In fact, Gd and W are mutually insoluble at the equilibrium condition, annealing at high temperatures might improve the interface sharpness. The bilayer thickness $\Lambda$ can be calculated from the position of the low angle diffraction peaks. In the inset of Fig. 1, we plot $\Lambda$ as the function of the position of the multilayers within the series. The linear relation indicates a constant thickness gradient as intended. The W thickness gradient from least square fit is 0.80 Å/mm, and the Gd layer thickness is 37 Å, both agree well with the designed values. In the *B series*, the Gd layer thickness gradient as 1.06 Å/mm and $d_W$=26 Å. The good agreement between the measured and designed thicknesses and the linearity of the wedge layer profile have allowed us to determine the layer thicknesses in each sample accurately. This is of crucial importance if magnetization and magnetic moments are to be determined.

High-angle x-ray diffraction patterns indicate that W layers are (110) textured. We did not observe any gadolinium oxide phase. The Gd layers in the as-deposited sample are mostly (002) oriented, with a low and broad (101) contribution that is almost indistinguishable from the background. Upon annealing at 600 °C, the (002) peak grows sharper and significantly higher in intensity, indicating an increase in Gd crystallite size and relief of interfacial strain. The absence of high-angle satellite peaks suggests that although the samples have a very well-defined layered structure, they are not structurally coherent. Annealing at high temperatures improves the crystallinity of the Gd layers. As will be seen later, this has great ramifications on the magnetic properties of the multilayers.

The dc magnetization and ac susceptibility of the multilayers have been measured using a Quantum Design SQUID magnetometer, which has been calibrated against a platinum reference issued by NBS. It has been reported that in Gd/Y supperlattices, the interfacial Gd moments do not order ferromagnetically, and the magnetization shows a linear rise with the applied field when measured at 25 K and relatively low fields (15 kOe) due to the paramagnetic Gd moments at the interface.[7,8] Since the Brillouin function for paramagnetic Gd moments ($J$=7/2) reaches 99.5% saturation at an $H/T$ of 3 T/K, we have measured the dc magnetization of the multilayers at 1.7 K, so that the magnetization at 5 T can be used to approximate the saturation magnetization. We have also measured at 1.7 K the susceptibilities of W metal and the Si substrate used. From the known thicknesses of the layers and the sample area, the magnetization of Gd can be calculated after correcting the measured total magnetic moment from the paramagnetic contribution of W and the diamagnetic contribution of Si.

The as-deposited samples are quite difficult to saturate even at 1.7 K with an in-plane field, similar to what has been observed in Ref. 4. However, after annealing at 600 °C, the hysteresis loops become more square, especially for samples with thicker Gd layers. All samples with $d_{Gd} \geq 9$ Å have nonzero remanence and coercivity, indicating ferromagnetic ordering. Figure 2 shows the M–H curves of the sample $Gd_{32\ Å}/W_{26\ Å}$, with the applied field parallel and perpendicular to the sample plane. In an ideal thin film, the parallel and perpendicular saturation fields differ by $H_K = 4\pi M_S$ due to the shape anisotropy. As seen in Fig. 3, the saturation magnetization is 1900 emu/cm$^3$ and the difference in saturation fields is about 23 kOe. The fact that the demagnetization factor is to a good approximation equal to $4\pi$ confirms that the layered structure is preserved during annealing. However, the saturation magnetization is slightly less than the Gd bulk magnetization of 2060 emu/cm$^3$. In fact, in the thickness range studied ($d_{Gd} \leq 50$ Å), none of the samples reaches the bulk Gd saturation magnetization, as shown in the inset of Fig. 2 for multilayers with $d_{Gd}$=8.7, 13, 17, and 40 Å measured at 1.7 K. As the Gd thickness is decreased, the Gd saturation magnetization decreases. This feature becomes more evident in Fig. 3, where we plot the Gd saturation magnetization ($M_S$) as a function of inverse Gd layer thickness ($1/d_{Gd}$). The data points in Fig. 3 can be fitted to a linear relation:

$$M_s = 2017 - 2112 \times \left(\frac{1}{d_{Gd}}\right). \tag{1}$$

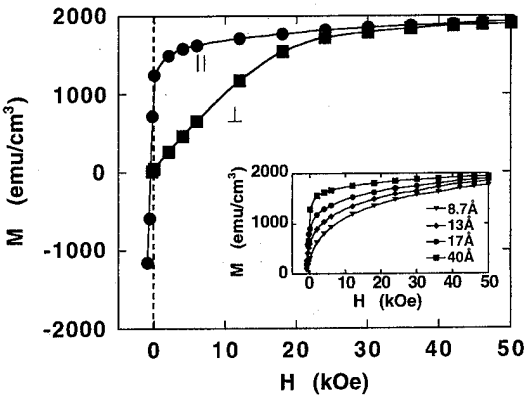



FIG. 2. The Gd Magnetization curves at 1.7 K for annealed $Gd_{32\ Å}/W_{26\ Å}$ with the field applied parallel and perpendicular to the sample plane. Inset: Magnetization of Gd for multilayers with 8.7, 13, 17, and 40 Å Gd layers.

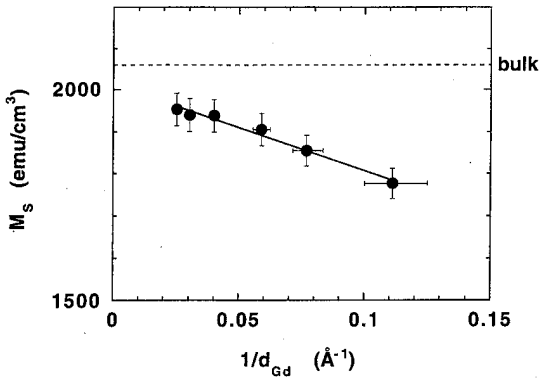



FIG. 3. Saturation magnetization of Gd ($M_S$) as a function of inverse Gd layer thickness ($1/d_{Gd}$) for a series of annealed multilayers. The dotted line represent the bulk Gd magnetization.

In an approach similar to that used by Kwo *et al.*,[7] we model this behavior by assuming that two interfacial regions of thickness $t$ in the Gd layers have a reduced magnetization of $M'$, whereas the interior of the Gd layers retains the bulk magnetization $M_{\text{bulk}}$. The Gd saturation magnetization $M_S$ can then be expressed as

$$M_S = M_{\text{bulk}}\left(1-\frac{2t}{d_{\text{Gd}}}\right)+M'\frac{2t}{d_{\text{Gd}}}. \tag{2}$$

Comparing Eq. (2) with Eq. (1) gives $M_{\text{bulk}}=2017$ emu/cm$^3$, which is only about 2% less than the bulk value, and is within experimental error. Polarized neutron diffraction studies of the magnetization profile in Gd/Y indicate that two atomic layers of Gd have reduced moments,[6] and since the Gd layers here are mostly (002) oriented, we assume $t\approx c=5.78$ Å. This gives an $M'$ of 1834 emu/cm$^3$, i.e., the interfacial Gd atoms have lost about 9% of their moment. The bulk saturation moment of Gd is $7.63\mu_B$ per atom, of which $7\mu_B$ comes from the localized $4f$ core, and the excess moments of $0.63\mu_B$ represents the polarization of the conduction electrons. The 9% reduction in magnetization suggests that the conduction electrons of the interfacial Gd atoms possibly lose the polarization as the result of their local environment.

Magnetization measurements on sample series A with fixed $d_{\text{Gd}}=37$ Å but varying $d_{\text{W}}$(0–40 Å) did not show evidence of antiferromagnetic exchange coupling. The Gd layers behave independently, and the Gd saturation magnetization is constant with no indication oscillation, contrary to what has been reported.[3]

In thin magnetic films, the surface energy contribution causes the decreasing of the ordering temperature. Finite-size scaling theory predicts that the Curie temperature $T_C$ of magnetic films will decrease from the bulk value $T_C(\infty)$ with decreasing thickness $d$, following a power law: $[T_C(\infty)-T_C(d)]/T_C(\infty)=(d/d_0)^{-\lambda}$, where $d_0$ is a characteristic length scale and $\lambda$ is the shift exponent.[9] In the ideal case, the susceptibility in a second-order phase transition diverges at the critical temperature as the coherence length diverges. However, it has been pointed out that a number of factors, such as dislocations, lattice defects, and locally varying strains restrict the divergence of coherence length at $T_C$, and this cluster-size effect influences the ordering temperature.[10] The ferromagnetic ordering in a real sample shows up as a peak in the temperature dependence of the susceptibility, and the Curie temperature can be determined from the susceptibility peak position.

To study the finite-size effect on the ferromagnetic ordering temperature of Gd/W multilayers, we have measured the AC susceptibility as a function of the temperature for multilayers with different $d_{\text{Gd}}$. The low excitation filed (0.5 Oe in amplitude and 11 Hz) lies in the film plane. The inset of Fig. 4 shows the temperature dependence of the susceptibility of the as-deposited and annealed $Gd_{40\ Å}/W_{26\ Å}$ samples. The as-deposited film has a low Curie–Weiss susceptibility peak at 200 K, while for the annealed sample the susceptibility peak increases by a factor of 4, and is shifted to

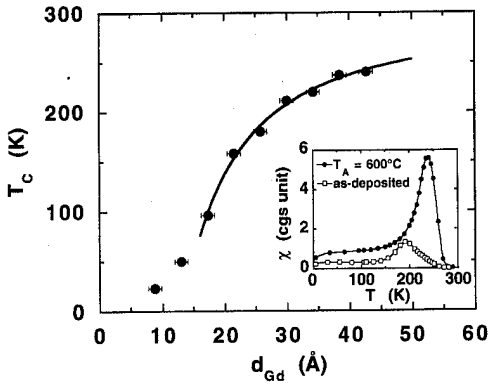



FIG. 4. Curie temperature as a function of the Gd layer thickness for a series of multilayers with $d_{\text{W}}=26$ Å annealed at 600 °C. The solid curve is a fit to the finite-size scaling law. Inset: Temperature dependence of the AC susceptibility (in cgs units) of the as-deposited and annealed $Gd_{40\ Å}/W_{26\ Å}$ samples.

235 K. This is a clear demonstration that ferromagnetic ordering depends sensitively on the crystalline quality. We have determined the Curie temperatures from the position of the susceptibility peaks for a series of multilayers. In Fig. 4 we plot $T_C$ of the annealed multilayers as a function of Gd layer thickness. It is seen that the Curie temperature decreases as the thickness of the Gd layer is reduced, and the multilayer films order ferromagnetically down to a Gd thickness of 9 Å. A similar behavior has also been observed in Gd/Nb multilayers.[11] Fitting the results at large Gd thicknesses with the scaling relation gives the shift exponent $\lambda=1.5\pm0.1$ and $d_0=13$ Å. It has been shown that the shift exponent $\lambda$ is the inverse of the correlation length $\nu$.[12,13] Renormalization group calculations indicate $\nu=0.687$, and thus $\lambda=1.456$. Our result is in agreement with the expectation of scaling theory.

This work has been supported by National Science Foundation Grant No. DMR-9501195.

[1] S. S. P. Parkin, Phys. Rev. Lett. **67**, 3598 (1991).
[2] C. F. Majkrzak, J. W. Cable, J. Kwo, M. Hong, D. B. McWhan, Y. Yafet, J. V. Waszczak, and C. Vettier, Phys. Rev. Lett. **56**, 2700 (1986).
[3] A. Heys and P. E. Donovan, J. Magn. Magn. Mat. **126**, 326 (1993).
[4] A. Heys, P. E. Donovan, A. K. Petford-Long, and R. Cywinski, J. Magn. Magn. Mat. **131**, 265 (1994).
[5] O. Rader, E. Vescovo, J. Redinger, S. Blügel, C. Carbone, W. Eberhardt, and W. Gudat, Phys. Rev. Lett. **72**, 2247 (1994).
[6] C. F. Majkrzak, J. W. Cable, J. Kwo, M. Hong, D. B. McWhan, Y. Yafet, J. V. Waszczak, H. Grimm, and C. Vettier, J. Appl. Phys. **61**, 4055 (1987).
[7] J. Kwo, E. M. Gyorgy, D. B. McWhan, M. Hong, F. J. DiSalvo, C. Vettier, and J. E. Bower, Phys. Rev. Lett. **55**, 1402 (1985).
[8] J. Kwo, E. M. Gyorgy, F. J. DiSalvo, M. Hong, Y. Yafet, and D. B. McWhan, J. Magn. Magn. Mat. **54–57**, 771 (1986).
[9] M. N. Barber, in *Phase Transitions and Critical Phenomena*, edited by C. Domb and J. L. Lebowitz (Academic, New York, 1983), Vol. 8.
[10] U. Stetter, M. Farle, K. Baberschke, and W. G. Clark, Phys. Rev. Rapid Commun. B **45**, 503 (1992).
[11] J. S. Jiang, D. Davidovic, D. H. Reich, and C. L. Chien, Phys. Rev. Lett. **74**, 314 (1995).
[12] M. E. Fisher and A. E. Ferdinand, Phys. Rev. Lett. B **6**, 3461 (1972).
[13] D. S. Fisher and D. A. Huse, Phys. Rev. B **36**, 8937 (1987).

# Magnetism and structure of ultrathin fcc $Fe_xCo_{1-x}$ films on Cu(001) (abstract)

A. Dittschar, M. Zharnikov, W. Kuch, C. M. Schneider, and J. Kirschner
*Max-Planck-Institut für Mikrostrukturphysik, Weinberg 2, D-06120 Halle, Germany*

Ultrathin films of 3*d*-transition metal alloys, and in particular FeCo alloys, currently receive considerable interest because of their potential technological application and the possibility to adjust magnetic properties via the variation of composition and structure. To study magnetic and structural properties of the otherwise unstable fcc phase of FeCo, this structural phase was stabilized by epitaxial growth on Cu(001). Ultrathin $Fe_xCo_{1-x}$ films were deposited at room temperature by coevaporation from two separate Knudsen cells, operated under stabilized conditions. The film thickness was varied between 2 and 9 monolayers (ML) and the Fe concentration between $x=0.2$ and $x=0.95$. The growth process was monitored by medium energy electron diffraction (MEED). Auger electron spectroscopy and low energy electron diffraction (LEED) were employed to analyze the composition and structure of the films. A nearly perfect layer-by-layer growth up to at least 9 ML, as seen by MEED, is encountered for $x \leqslant 0.7$. For higher Fe concentrations and thicknesses greater than 4 ML, deviations from the layer-by-layer growth are observed, indicating a structural rearrangement. LEED-I(V) curves reveal the coexistence of two structural phases with different interlayer spacings, the relative amount of which depends on the composition. Magnetic properties were characterized by the magneto-optical Kerr effect (MOKE). The remanent magnetization was found to lie within the film plane over the whole range of thicknesses and concentrations investigated. A linear increase of the Kerr signal at saturation magnetization with increasing thickness indicates that practically the whole film is magnetic. As a function of composition, the saturation Kerr signal develops continuously with increasing Fe content. This suggests that in fcc FeCo alloys the contribution of Fe and Co to the total magnetic moment is nearly constant over the whole compositional range. © *1996 American Institute of Physics.* [S0021-8979(96)42908-5]

 0021-8979/96/79(8)/5618/1/$10.00 © 1996 American Institute of Physics

# Magnetization reversal properties near the reorientation phase transition of ultrathin Fe/Ag(100) films

A. Berger[a] and H. Hopster
*Department of Physics and Institute for Surface and Interface Science, University of California, Irvine, California 92717*

We have measured the magnetization reversal properties of ultrathin Fe/Ag(100) films in the vicinity of the reorientation phase transition using the magneto-optical Kerr effect. Near the reorientation temperature $T_r$, we observe a characteristic change in the perpendicular magnetization curves $M(H)$ from a strongly nonlinear behavior for $T<T_r$ to a simple linear field dependence above $T_r$. The experimental observations are discussed within the context of the expected temperature-dependent magnetization structure and the corresponding magnetization reversal processes. © *1996 American Institute of Physics.* [S0021-8979(96)19508-6]

## I. INTRODUCTION

Ultrathin ferromagnetic films have been found to exhibit a much stronger magnetocrystalline anisotropy than their bulk counterparts due to the broken crystallographic symmetry at the surface.[1] The magnetocrystalline anisotropy can even be sufficient to overcome the demagnetizing field and align the magnetization perpendicular to the surface.[1] For films in which the magnetocrystalline and dipolar self-energy are of comparable size, the so-called reorientation phase transition (RPT) can be observed as a function of film thickness or temperature.[2] The occurrence of this phase transition is caused by the different thickness or temperature dependence of these two competing energies. Both the temperature as well as the thickness-dependent reorientation transition have attracted a large amount of attention lately.[3] From an experimental point of view, the investigation of the temperature effect has the advantage of being measured on one particular sample, whereas thickness-dependent studies have to be performed on a series of samples. Thus, these samples are not necessarily comparable with regard to film morphology, etc., and we focus on the temperature-dependent RPT henceforth.

The temperature-dependent reorientation transition is characterized by two major experimental observations, as shown in Fig. 1. With increasing temperature, one first observes that the remanent out-of-plane magnetization is vanishing at a characteristic temperature $T^*$, with no in-plane magnetization found yet. At temperatures $T>T_r$ with $T_r$ significantly larger than $T^*$, an in-plane magnetization occurs and increases strongly in a narrow temperature range, above which it saturates. Thus, for an intermediate temperature range $T^*<T<T_r$, no remanent magnetization can be observed.

Performing microscopic studies, Allenspach *et al.*[4] have been able to confirm that samples exhibit a multidomain state with alternating (see the inset in Fig. 1) out-of-plane domain magnetization in this intermediate temperature region. The domain state reduces the dipolar energy and therefore represents the lowest-energy state for films with an out-of-plane magnetization. In a recent study, we have been able to demonstrate that the occurrence of the remanent out-of-plane magnetization at low temperatures is actually a nonequilibrium effect, caused by the activation energy necessary to initially form domains.[5] Thus, the occurrence of the in-plane magnetization marks the real reorientation transition.

## II. EXPERIMENT

In this paper, we investigate the characteristics of perpendicular magnetization curves $M(H)$ in the vicinity of the reorientation transition at $T_r$. For this purpose, we performed magneto-optical Kerr effect (MOKE) measurements for Fe/Ag(100) films with a thickness of approximately four monolayers, which exhibit a reorientation transition in an easily accessible temperature range of $T_r=200-400$ K. Similar to the results of previous experimental investigations, we observe that $T_r$ decreases strongly with increasing thickness.[6] The complete experiment, i.e., film preparation and magnetic characterization, were done under ultrahigh vacuum conditions. The Fe films were grown by evaporation from an $e$-beam evaporator onto a clean and well annealed Ag(100)

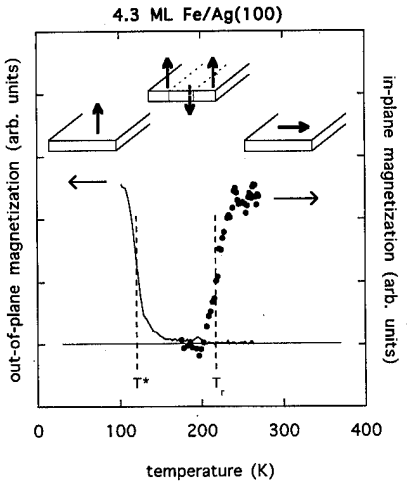



FIG. 1. Temperature-dependent magnetization in remanence for a 4.3 ML Fe/Ag(100) film (solid line: out of plane; circles: in plane); the thin solid line represents $M=0$ for both quantities. The corresponding magnetization states are illustrated.

[a]Present address: Department of Physics, University of California—San Diego, La Jolla, California 92093-0319.

 0021-8979/96/79(8)/5619/3/$10.00 © 1996 American Institute of Physics 

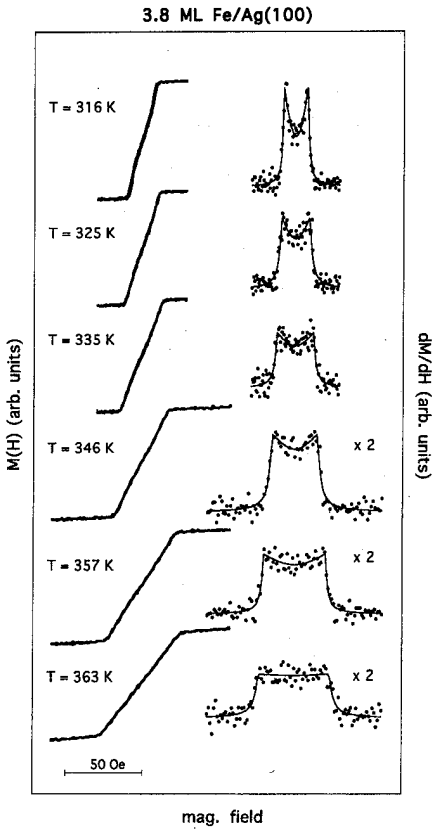



FIG. 2. Field-dependent out-of-plane magnetization curves $M(H)$, measured for a 3.8 ML Fe/Ag(100) film (temperatures $T$ as indicated): original $M(H)$—data (left); $dM/dH$—values (right).

substrate, held at room temperature. The growth rate was chosen to be approximately one monolayer per minute and was controlled *in situ* by a quartz monitor. After deposition, the films were heated to 440 K for 30 mins, which improved the sharpness of the LEED spots significantly, as previously demonstrated by Qiu *et al.*[6] Using two sets of coreless coils and a conventional MOKE setup,[7] we were able to measure the in-plane as well as out-of-plane magnetization.

## III. RESULTS AND DISCUSSION

Figure 2 shows a set of perpendicular magnetization curves for a 3.8 monolayer Fe/Ag(100) film, measured at various temperatures in the vicinity of the reorientation transition temperature $T_r = 370 \pm 10$ K, which has been determined by measurements of the in-plane magnetization. As one can easily see from the data in Fig. 2, there is a quite extended temperature range in which no hysteresis effect is observed for the out-of-plane magnetization curves. Therefore, these curves can actually be compared to theoretical predictions derived from a thermodynamic treatment of the RPT phenomenon. For $T<316$ K, hysteresis effects occur due to the increasing significance of activation barrier limited processes, which eventually result in a metastable remanent out-of-plane magnetization at low temperatures.[5] It is obvious from Fig. 2 that the remanent magnetization is zero in the entire temperature range shown, but a very small magnetic field in the 10 Oe range is sufficient to fully saturate the sample. This observation is in excellent agreement with predictions for the multidomain state with domain magnetization perpendicular to the surface.[8] The reason for such a small value of the critical field $H_{cr}$ at which saturation occurs is the fact that the energy gain of a multidomain structure is very small in ultrathin films.[9] Thus, a small external field already destabilizes the domain structure and produces a saturated single domain state. Furthermore, one can see from the curves in Fig. 2 that the critical field $H_{cr}$ for the phase transition between the multidomain, and the single domain state is decreasing with decreasing temperature. This is also consistent with theoretical predictions, because at lower temperatures one expects an enhanced effective anisotropy, which corresponds to a reduced energy gain by domain formation.[9] Therefore, at lower temperatures an even smaller critical field $H_{cr}$ is already sufficient to produce the saturated single domain state.

On evaluation of the detailed shape of the $M(H)$ curves in Fig. 2, one finds that the transition region between positive and negative saturation is not simply a straight line but has some curvature, at least for the low-temperature curves. To visualize this nonlinearity, we have determined the derivative $dM/dH$ from our $M(H)$ data, which is shown in Fig. 2 as well. For low temperatures, the $dM/dH$ curves exhibit a double peak structure in the magnetization reversal region; i.e., the susceptibility $dM/dH$ has a strongly enhanced value at the critical field $H_{cr}$, where the system undergoes the phase transition to the saturated out-of-plane state. As the temperature increases, the peak structure at $H_{cr}$ decreases gradually and cannot be observed anymore for temperatures $T \geqslant 363$ K. In this high-temperature range only a steplike structure is found. These measurements of $M(H)$ clearly demonstrate that the magnetization reversal process undergoes a qualitative change in the vicinity of $T_r$, which should be associated with the observed reorientation phase transition itself. To discuss these magnetization reversal properties in more detail, we compare our experimental data to the available theoretical models. Figure 3 shows the essential features for the magnetization states and magnetization reversal that one expects in the vicinity of $T_r$. For temperatures above $T_r$, the film is in a single domain state with in-plane magnetization. Under the assumption that an applied field (perpendicular to the surface) preserves the existence of a uniform state, one expects the out-of-plane magnetization to linearly increase with the applied field strength up to the critical field $H_{cr}$, where the magnetization is saturated. Thus, the susceptibility $dM/dH$ should simply follow a steplike structure, as shown in Fig. 3. For temperatures below $T_r$, the magnetization behavior is very different. Due to the existing domain structure, the sample contains domains in which the magnetization is already aligned along the magnetic field direction. Thus, the magnetization reversal is associated with domain growth or domain wall displacement processes, which is fundamentally different from the rotation process occurring at higher temperatures $T>T_r$. So, it is not surprising that the $M(H)$ characteristic is very different for this domain state, resulting in a pronounced nonlinear behavior of the $M(H)$ curve. Kashuba *et al.* have evaluated the $M(H)$ behavior be-

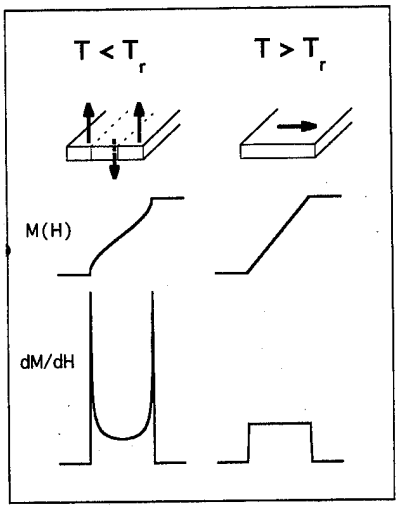



FIG. 3. Schematic of the expected magnetization states and the corresponding magnetization reversal properties in the vicinity of the reorientation phase transition.

low $T_r$ for a simple stripe domain structure.[8] In their calculation they derived

$$M(H)=\frac{2}{\pi}M_S \arcsin\left(\frac{H}{H_{cr}}\right)$$

for the magnetization reversal region, resulting in a singularity of the susceptibility at the critical field $H_{cr}$ (see Fig. 3). Thus, our measurements show exactly the features one expects for the magnetization reversal in the vicinity of the reorientation transition, namely, a linear $M(H)$ dependency for $T>T_r$ corresponding to a uniform rotation of the film magnetization, and a nonlinear $M(H)$ behavior associated with a domain structure and domain wall displacement processes for $T<T_r$. Therefore, our results do not only represent a study of the reversal process in the vicinity of the RPT, but they also confirm the existence of an equilibrium domain structure for $T<T_r$. But, even though the measurements exhibit the most essential features one expects in the vicinity of $T_r$, there are also some discrepancies between our measurements and the present theoretical description. First, calculations predict that very close to $T_r$, the critical field $H_{cr}$ should decrease again with increasing temperature.[10] We do not observe this behavior. All our measurements show only a monotonic increase of $H_{cr}$ with temperature. Second, we observe a gradual decrease of the peak height in the $dM/dH$ data with temperature, which is also not expected within the available theoretical description. To our understanding, these discrepancies are caused by the fact that the theoretical model describing the magnetization reversal is restricted to a perpendicular magnetization direction within the domains, independent of the temperature.[8] It has been shown that the total energy of a stripe domain structure can actually be reduced by an inclined domain magnetization near the RPT.[9] Thus, one expects the magnetization state to show a gradual transition from an out-of-plane domain state to an in-plane uniform state. In this case, one would also expect that the magnetization reversal process gradually changes from a pure domain wall displacement to a pure magnetization rotation, producing the gradual alteration of the $M(H)$ and $dM/dH$ characteristics we have found in our experiments. The observed discrepancies also imply that recent evaluations of the phase diagram in the immediate vicinity of $T_r$ are insufficient because they do not include the possibility of a gradual change in the domain magnetization direction.[10]

## ACKNOWLEDGMENTS

This work was supported by the National Science Foundation through Grant No. DMR 9500213. One of us (A.B.) also gratefully acknowledges support from the Alexander von Humboldt-Stiftung through a Feodor Lynen Research Fellowship.

[1] See, for example, W. J. M. de Jonge, P. J. H. Bloemen, and F. J. A. den Broeder, in *Ultrathin Magnetic Structures I*, edited by J. A. C. Bland and B. Heinrich (Springer, Berlin, 1994).
[2] D. P. Pappas, K. P. Kaemper, and H. Hopster, Phys. Rev. Lett. **64**, 3179 (1990).
[3] See S. D. Bader, D. Li and Z. Q. Qiu, J. Appl. Phys. **76**, 6419 (1994), and references therein.
[4] R. Allenspach and A. Bischof, Phys. Rev. Lett. **69**, 3385 (1992).
[5] A. Berger and H. Hopster, Phys. Rev. Lett. **76**, 519 (1996).
[6] Z. Q. Qiu, J. Pearson, and S. D. Bader, Phys. Rev. Lett. **70**, 1006 (1993).
[7] S. Bader, J. Magn. Magn. Mater. **100**, 440 (1991).
[8] A. B. Kashuba and V. L. Pokrovsky, Phys. Rev. B **48**, 10 335 (1993).
[9] Y. Yafet and E. M. Gyorgy, Phys. Rev. B **38**, 9145 (1988).
[10] Ar. Abanov, V. Kalatsky, V. L. Pokrovsky, and W. M. Saslow, Phys. Rev. B **51**, 1023 (1995).

# Structure and magnetism in fcc magnetic transition metals on (001) diamond (abstract)

J. A. Wolf,[a] J. J. Krebs, Y. U. Idzerda, G. A. Prinz, and K. M. Kemner[a]
*Naval Research Laboratory, Washington, DC 20375*

We have prepared single crystal face centered cubic (fcc) magnetic transition metal films (Co,Ni,Fe) on (001) diamonds, the thickness of the films varying between a few tenths of a nanometer to over 100 nm. The crystalline quality and fourfold symmetry of these layers was monitored *in situ* during the film growth with RHEED and a chemical analysis was performed using Auger spectroscopy. In addition, the structure of the samples was investigated *ex situ* using X-ray diffraction and EXAFS, demonstrating the single crystal, fcc (001) structure throughout each entire film. The magnetic characterization was performed with Ferromagnetic Resonance (FMR) and Superconducting Quantum Interference Device (SQUID) hysteresis loops. The saturation magnetization of the Co films is only slightly lower than the literature values. The coercive fields are very small (~25 Oe) and the magnetization reversal very sharp. The FMR yielded a fourfold anisotropy comparable to literature values. The observation of the first standing spinwaves underlines the good quality. The Ni films are tetragonally distorted due to the 1.2% mismatch. The FMR data indicate a significant perpendicular anisotropy slightly smaller than $4\pi M$, the fourfold in-plane anisotropy being comparable to the bulk value. The saturation magnetization is reduced by 30% compared to bulk values, probably due to nickel-carbide which was observed in the XRD data from some samples. Neither the in-plane ⟨110⟩ nor the in-plane ⟨100⟩ axis show an easy axis behavior and both require fields in excess of 6000 Oe to saturate, the coercive fields being about 200 Oe. The RHEED patterns of the Fe films show single crystal growth with a lattice constant comparable to diamond, indicating an fcc structure. A similar structural and magnetic characterization of these films will also be presented. © *1996 American Institute of Physics.* [S0021-8979(96)43008-9]

This work has been supported by the Office of Naval Research.

[a]NRC-NRL Research Associate.

 0021-8979/96/79(8)/5622/1/$10.00 © 1996 American Institute of Physics

# Anomalous perpendicular magnetism in Ni/Cu(001) films and the effects of capping layers

W. L. O'Brien
*Synchrotron Radiation Center, University of Wisconsin—Madison, 3731 Schneider Drive, Stoughton, Wisconsin 53589*

B. P. Tonner
*Department of Physics, University of Wisconsin—Milwaukee, 1900 East Kenwood Blvd., Milwaukee, Wisconsin 53211 and Synchrotron Radiation Center, University of Wisconsin—Madison, 3731 Schneider Drive, Stoughton, Wisconsin 53589*

X-ray magnetic circular dichroism (XMCD) measurements on wedges of Ni grown on Cu(001) are used to investigate magnetic properties in Ni/Cu(001) ultrathin films. A sharp transition from in-plane to perpendicular magnetization is found near 7 ML, and a gradual transition back to in-plane magnetization begins near 37 ML. The critical thickness for epitaxial growth, 13 ML, is determined from a rapid rise in the coercive field versus film thickness. Both transitions in the direction of easy axis are well explained by considering the effects of the surface, shape, and the strain-induced magnetoelastic anisotropies. The critical layer thickness of 13 ML plays a critical role in understanding the transition near 37 ML. Capping the Ni wedge with 2 ML of Co increases the magnitude of the surface anisotropy, forcing the magnetization to remain in plane for thickness up to at least 18 ML. Addition of an Fe capping layer has no effect on the direction of magnetization, suggesting the importance of interface anisotropies or intermixing. © *1996 American Institute of Physics.* [S0021-8979(96)19608-2]

Ultrathin films and multilayers possessing easy axes of magnetization perpendicular to the surface have recently attracted much interest[1–4] due to their potential advantages in magneto-optical recording. The existence of perpendicular magnetization is determined by the combined effects of all the magnetic anisotropies present. These anisotropies include shape, surface, interface, and crystalline anisotropies, strain-induced magnetoelastic anisotropy, and anisotropies due to roughness and atomic mixing at the interfaces. An important goal in the research on these thin films and multilayers is to understand which anisotropies are important in determining the easy axes of magnetism.

In the past few years a number of studies have been performed on the magnetism of Ni/Cu(001) thin films.[1–3] Ni/Cu(001) films show a transition from in-plane magnetization to perpendicular magnetization as the film thickness increases. This unusual behavior is opposite to what would be predicted by the effects of a surface anisotropy by itself. Schulz and Baberschke,[2] using FMR, showed that the unusual magnetic behavior of Ni/Cu(001) could be explained by the competition between a negative surface/interface anisotropy and a uniaxial magnetoelastic volume anisotropy due to the strain caused by psuedomorophic growth. For films less than ~7 ML thick the surface anisotropy dominates and the films have an in-plane easy axis of magnetization. Films thicker than ~7 ML have an easy axis of magnetization perpendicular to the surface due to the volume effect of the magnetoelastic anisotropy, which favors perpendicular magnetization.

In this paper we discuss the results of experiments designed to more fully understand the magnetic anisotropies in Ni/Cu(001) thin films. The experiments were performed on the 10 m TGM beamline located at the Synchrotron Radiation Center, Stoughton, WI. All magnetic measurements were made using x-ray magnetic circular dichroism (XMCD), which gives element specific magnetic information. Details of the XMCD measurements are published separately.[5] Measurements were made at room temperature on Ni wedges grown on a clean Cu(001) single crystal at a base of $2\times10^{-10}$ Torr. The pressure during film growth was $8\times10^{-10}$ Torr. Five different wedges, with overlapping thickness ranges were used in this study.

Hysteresis curves obtained for different Ni thicknesses are shown in Fig. 1 for magnetization applied perpendicular to the sample surface. The curves were obtained by setting the photon energy to the Ni $L_3$ absorption maximum and sweeping the magnetic field. The height of the loops are normalized to the total Ni $L_3$ cross section and are propor-

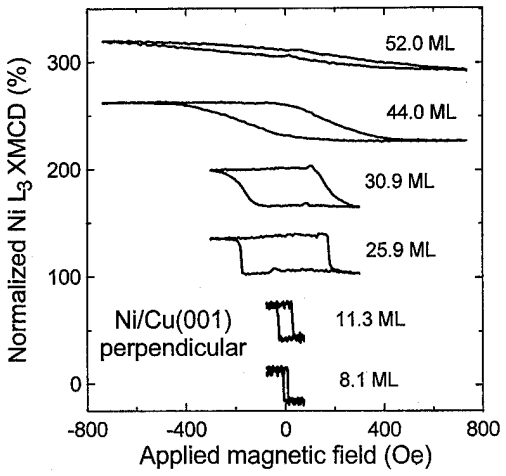



FIG. 1. Hysteresis curves for different Ni film thicknesses from Ni/Cu(001) wedges. The magnetic field was applied perpendicular to the film surface.

 0021-8979/96/79(8)/5623/3/$10.00 © 1996 American Institute of Physics 

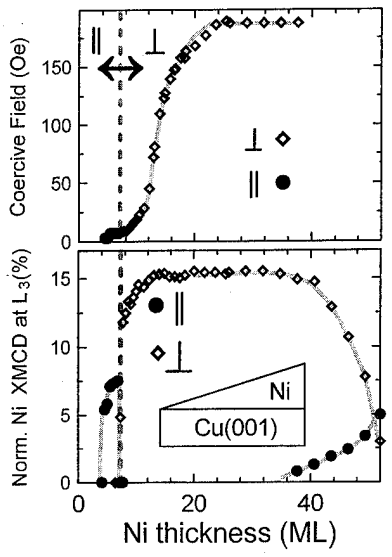



FIG. 2. Coercive field (top) and normalized remanent dichroism intensity (bottom) vs thickness across Ni/Cu(001) wedges. There is sharp transition from an in-plane to perpendicular easy axis of magnetization at 7 ML and a gradual transition from a perpendicular to an in-plane easy axis of magnetization beginning near 37 ML. Note the sharp increase in $H_c$ beginning near 13 ML.

tional to the average magnetization per Ni atom. In Fig. 2(a) the coercive field, $H_c$, is plotted versus film thickness. $H_c$ increases rapidly beginning near 13 ML, and reaches a constant value of ~190 Oe near 24 ML. In Fig. 2(b) the normalized dichroism intensity is plotted versus film thickness. Below 7 ML the easy axis of magnetization is in plane, between 7 and 36 ML the easy axis of magnetization is perpendicular to the surface, for thicknesses greater than 37 ML the film could be magnetized both in plane and perpendicular to the surface.

Following Schulz and Baberschke,[2] the easy axis of magnetization for Ni/Cu(001) is determined by the surface, interface, and magnetoelastic anisotropies. Perpendicular magnetization in the Ni/Cu(001) films will result when

$$K_{\mathrm{ME}} > \frac{-K_S - K_I}{d} + 2\pi M^2, \tag{1}$$

where $K_{\mathrm{ME}}$, $K_S$, and $K_I$ are the magnetoelastic, surface and interface anisotropy constants, respectively, $d$ is the film thickness, and $M$ is the magnetization. The use of (1) is complicated due to the dependence of $T_c$ on film thickness and of $M$ on $T_c/T$. At room temperature, $K_{\mathrm{ME}}=29$ $\mu$eV/atom in the pseudomorphic region and $K_I+K_S=-154$ $\mu$eV/atom.[2] Using experimental values[3] of $M$ and $T_c$ versus film thickness we find that the transition from in-plane to perpendicular magnetization should take place near 6 ML at room temperature. This is consistent with the results in Fig. 2 and with the results of Schulz and Baberschke.[2]

Both Ni and Cu crystallize in the fcc structure with the Ni lattice constant being 2.5% smaller than the Cu lattice constant. Structural investigations[6,7] of Ni growth on Cu(001) show that the Ni films initially grow pseudomorphically. This growth mode continues up to a critical thickness, $d_c$, where the onset of strain relaxation causes the formation of misfit dislocations. Strain relaxation also reduces the magnetoelastic energy, causing the magnetism to switch back to in plane for thicker films. In magnetoelastic theory, the magnetoelastic anisotropy is proportional to the strain, $\epsilon$. In the pseudomorphic growth region $\epsilon=-\eta$, where $\eta$ is the lattice misfit. Chappert and Bruno[8] have derived an expression for the residual strain for film thicknesses greater than $d_c$, $\epsilon=-\eta\, d_c/d$. Using this and the value of $K_{\mathrm{ME}}$ for $d<d_c$ determined by Schulz and Baberschke,[2] we obtain $K_{\mathrm{ME}}=29\, d_c/d$ $\mu$eV/atom for $d>d_c$.

The transition from perpendicular to in-plane magnetization at higher coverages due to strain relaxation can now be determined. Assuming $d_c=8$ ML[6] we find that the magnetization in the film should be in plane again above 14 ML. This is clearly not in agreement with the results in Fig. 2, which show that the perpendicular to in-plane transition occurs at ~37 ML. Either the assumption that $\epsilon=-\eta\, d_c/d$ or that $d_c=8$ ML must be incorrect. This value of $d_c=8$ ML is the generally accepted value of $d_c$.[2,3] It comes from an *ex-situ* TEM study of a Ni/Cu(001) wedge.[6] The Cu(001) substrate was grown on a NaCl surface in high vacuum ($10^{-7}$ Torr). After Ni deposition ($2\times10^{-8}$ Torr) the bilayer was floated off the NaCl surface and examined by TEM and diffraction. Due to the greatly different techniques and conditions in film preparation between our experiment and the TEM experiment we suspect that the value of $d_c=8$ ML may not be valid for our experiment. In fact, recent XPD experiments on 10 ML Ni/Cu(001)[7] are well explained by assuming that no strain relaxation has taken place. This sets a lower limit of 10 ML on $d_c$.

The need for an accurate value of $d_c$ is apparent. We look again at the $H_c$ results presented in Fig. 2. It is well known that the strain in pseudomorphic films is relieved by the formation of misfit dislocations once the critical thickness for epitaxial growth has been exceeded. It is equally well known that defects and dislocations in magnetic single crystals increase the coercive field.[9] These two arguments taken together allow us to interpret the rapid rise in the coercive field vs Ni film thickness as being due to the formation of misfit dislocations. We can also take the onset of the rapid rise in $H_c$ as an estimate for $d_c$. From Fig. 2 $d_c\sim13$ ML for Ni/Cu(001). Using $d_c=13$ ML, we determine that the crossover from perpendicular to in-plane magnetization should occur at 34 ML, in better agreement with the results in Fig. 2.

To show that the rapid increase in $H_c$ versus film thickness is a general phenomena that is useful for measuring $d_c$, we have investigated the magnetism in Co wedges grown on Cu(001). We find a trend in $H_c$ versus film thickness similar to that shown in Fig. 2, with a rapid increase from $H_c=20$ Oe to $H_c=100$ Oe, beginning at 12 ML. Co grows pseudomorphically on Cu(001) in a metastable face centered tetragonal structure up to a critical thickness of ~11 ML, as determined by TEM.[10] The onset of the rapid rise in $H_c$ near 12 ML is consistent with $d_c$ measurements by TEM. We have performed similar experiments on a number of other thin film systems, including Fe/Pd(001) and Fe/Ag(001). In each case we find a trend in $H_c$ versus film thickness similar to that shown in Fig. 2. For each system studied, the onset in

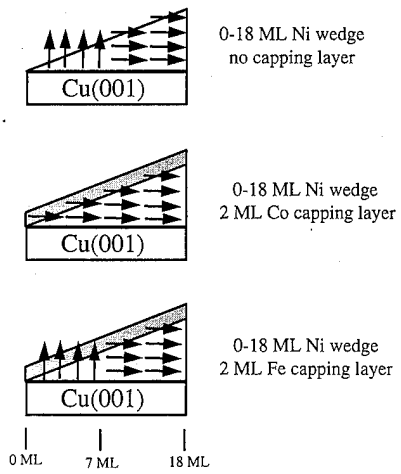



FIG. 3. Effects of capping layers on an easy axis of magnetization for a 0–18 ML Ni/Cu(001) wedge. Addition of 2 ML Co causes the magnetization direction to lie in plane along the entire wedge while the addition of 2 ML Fe has no effect on the direction of magnetization vs film thickness.

the rapid rise of $H_c$ can be equated with the critical thickness for epitaxial growth.

Both transitions in the direction of magnetization, Fig. 2, are now explained using (1). It would be informative to measure the changes in magnetization influenced by altering one or more of the anisotropy constants in (1). Toward this purpose we have studied the magnetization of Ni/Cu(001), wedges, 0–18 ML, capped with a 2 ML film of either Co or Fe. This should alter the value of $K_S$ in (1). The Ni wedge capped with Co has an in-plane easy axis of magnetization over the entire Ni thickness range, while capping with Fe has no effect on the magnetization direction versus Ni thickness. These results are summarized in Fig. 3. For each position on both wedges the magnetic bilayers were ferromagnetically coupled, as determined by measuring the hysteresis curves of each element separately, which is possible using XMCD.

To discuss the effects of the capping layers (1) must be modified to include an additional interface anisotropy term, and $K_S$ is now dependent on the capping layer. Fe has a positive surface anisotropy[4] and Co has a large negative surface anisotropy, $\sim -400$ $\mu$eV/atom,[11] for growth on Cu(001). As a starting point, we assume that $K_S$ of Fe and Co are the same for growth on Ni(001) and Cu(001), and consider only the effects of changing $K_S$ (we assume intermixing is negligible and that $|K_S| \gg |K_I|$). Capping with Co increases $K_S$ by a factor of $\sim 2.5$ and should cause the transition from in-plane to perpendicular magnetization to shift to higher Ni thicknesses. This is consistent with our experiment. Capping with Fe changes the sign of $K_S$, which should cause Ni films less than 7 ML thick to magnetize perpendicular to the surface. This is not consistent with our experiment. Interface anisotropies or intermixing are apparently important and need to be considered.

This work was supported by Research under Grant No. DMR-94-13475. The Synchrotron Radiation Center is a national facility supported by the National Science Foundation Division of Materials Research.

[1] W. L. O'Brien and B. P. Tonner, Phys. Rev. B **49**, 15 370 (1994).
[2] B. Schulz and K. Babershke, Phys. Rev. B **50**, 13 467 (1994).
[3] F. Huang, M. T. Kief, G. J. Mankey, and R. F. Willis, Phys. Rev. B **49**, 3962 (1994).
[4] D. qi Li, M. Freitag, J. Pearson, Z. Q. Qiu, and S. D. Bader, Phys. Rev. Lett. **72**, 3112 (1994).
[5] W. L. O'Brien and B. P. Tonner, Phys. Rev. B **52**, 15 332 (1995).
[6] J. W. Matthews and J. L. Crawford, Thin Solid Films **5**, 187 (1970).
[7] J. Zhang, Z.-L. Han, S. Varma, and B. P. Tonner, Surf. Sci. **298**, 351 (1993).
[8] C. Chappert and P. Bruno, J. Appl. Phys. **64**, 5736 (1988).
[9] C.-W. Chen, in *Magnetism and Metallurgy of Soft Magnetic Materials* (General Publishing, Ontario, 1986), pp. 286–295.
[10] W. A. Jesser and J. W. Matthews, Philos. Mag. **17**, 461 (1968).
[11] P. Krams, F. Lauks, R. L. Stamps, B. Hillebrands, and G. Güntherodt, Phys. Rev. Lett. **69**, 3674 (1992).

# Magnetic x-ray linear dichroism in the photoelectron spectroscopy of ultrathin magnetic alloy films

J. G. Tobin and K. W. Goodman
*Lawrence Livermore National Laboratory, Livermore, California 94550*

G. J. Mankey[a] and R. F. Willis
*Physics Department University Park, Pennsylvania State University, Pennsylvania 16802*

J. D. Denlinger, E. Rotenberg, and A. Warwick
*Advanced Light Source, Lawrence Berkeley Laboratory Berkeley, California 94720*

The magnetic structure of nanoscale alloy films has been probed using the magnetic x-ray linear dichroism in photoelectron spectroscopy. FeNi and CoFe epitaxial films were grown on Cu(001), *in situ* and using molecular beam epitaxy techniques. The magnetic x-ray linear dichroism measurements were made at the Spectromicroscopy Facility of the Third Generation Advanced Light Source. Because soft x-rays were used to generate photoemission from the $3p$ core levels, both elemental selectivity and magnetic sensitivity were achieved simultaneously. © *1996 American Institute of Physics.* [S0021-8979(96)41808-9]

A full elucidation of the underlying principles driving magnetic properties in complex systems will require the applications of probes which couple elemental specificity and magnetic sensitivity. Two important classes of magnetic devices, spin valves[1] and giant magnetoresistance (GMR) materials,[2] are typically composed of several nanoscale layers or aggregations[3] composed of different elements or alloys. The ultra-thin nature of these films or clusters further complicates the picture by introducing the impact of interfacial effects, including pseudomorphic strain and spin-specific scattering at the interfaces.[4] One avenue to address such issues is to build epitaxial ultrathin alloy films and probe them directly using techniques that are both elementally selective and magnetically sensitive. Here we report the beginnings of such a study, using CoFe and FeNi films grown with molecular beam epitaxy (MBE) techniques and investigated with magnetic x-ray linear dichroism[5–7] (MXLD) in the core-level photoelectron spectroscopy of the $3p$ states of Fe, Co, and Ni. (See Fig. 1).

The measurements were made at the Spectromicroscopy Facility (Beamline 7) of the Advanced Light Source at Lawrence Berkeley Laboratory.[8] Extraordinarily bright, linearly polarized x-rays were generated by the U 5.0 undulator and wavelength selection was achieved using the spherical grating monochromator, with a resolving power of over 8000. The photoelectrons were detected using the angle-resolving, multichannel, 5.4 in. radius, Perkin–Elmer hemispherical deflector system. Sample alignment (including pseudomorphic growth), cleanliness, and composition were measured using the hemispherical deflector and a separate Mg K$\alpha$ source, thus freeing up the beamline for other uses during our periods of sample preparation. The actual MXLD measurements (Fig. 2) used the highly polarized synchrotron radiation and were performed with a total instrumental energy resolution bandpass of $<100$ meV and angular resolution of 2°. The angle of incidence of the x-rays was 30° relative to the surface plane. The electrons were collected along the surface normal, i.e., "normal emission." Typically, the magnetic alloy was magnetized in the plane of the surface but perpendicularly to the plane containing the emission direction (surface normal) and the Poynting vector and electric polarization vector of the x-rays. Thus, the "transverse-chiral" condition necessary for MXLD was achieved: reversing the magnetic field causes two mirror-image configurations which are equivalent but totally nonsuperimpossible. By comparing spectra from these configurations, it is possible to directly probe the magnetic perturbations of the elementally specific electronic structure of the systems.

The alloy systems under consideration were CoFe and FeNi. Ultra-thin films of each were grown on Cu(001) at room temperature, using well-developed MBE techniques.[9] Studies of the bulk electronic structures have been performed,[10–13] but the properties of these pseudomorphic overlayers are further complicated by epitaxial strain and other nanoscale effects. Examples of our spectroscopic results are shown in Figs. 3 and 4. In this energy regime, the

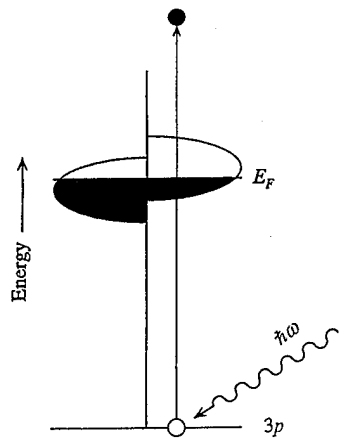



FIG. 1. The ejection of a $3p$ electron by a linearly polarized x-ray is shown here. The spin-polarized $d$-states, near the Fermi level, are also included. The presence of these magnetically polarized valence bands are the root cause of the MXLD effect.

[a]Present address: Louisiana State University, Baton Rouge, LA.

 0021-8979/96/79(8)/5626/3/$10.00 © 1996 American Institute of Physics

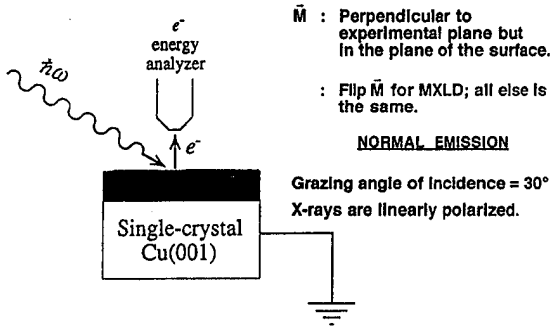



FIG. 2. The experimental configuration is schematically shown here. The grazing angle of incidence of the linearly polarized x-rays was 30°, relative to the surface plane. Electrons injected perpendicularly to the surface were collected by the angle resolving detector (i.e., normal emission). The plane containing the ejected electron and the Poynting vector of the x-ray also contained the electric polarization vector of the x-ray as well. The magnetization vector was perpendicular to this experimental plane, but in the plane of the surface. To achieve MXLD, comparisons were made between spectra in which only the direction of the magnetization was reversed; all else was kept the same.

cross sections for the Fe, Co, and Ni $3p$ are strongly photon-energy dependent:[14] hence, the peaks do not scale with concentration without further correction. The asymmetry in the case of the Fe and Co in Fig. 3 is actually underestimated. It would be appropriate to set the prepeak region, before the Co and Fe, respectively, to zero for that calculations. (See Figs. 3 and 4.)

Presently, we are pursuing studies of these systems where we vary the thickness and composition of the magnetic overlayers and probe the $3p$ levels of each element. In essence, we are attempting to use the MXLD measurements as element-specific, surface magnetometers. Our initial studies suggest a concentration dependent quenching similar to that observed in bulk Invar but with different elementally specific contributions than those of the bulk.[10–13] It appears that template and thickness dependent relaxation effects may be competing in this system. Additional studies will include not only MXLD but also surface magneto-optic Kerr effect

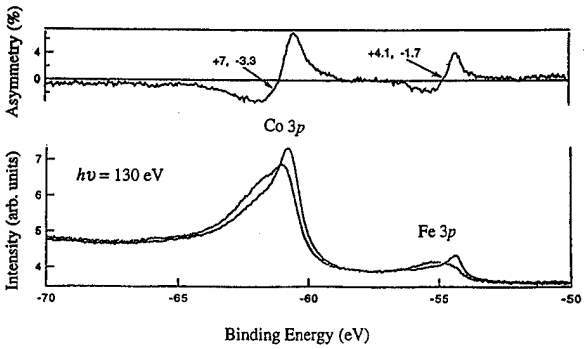



FIG. 3. Photoelectron spectra of Fe[1]Co[8]/Cu(001), taken using a photon energy of 130 eV. Also shown is the asymmetry for these two spectra. The asymmetry is equal to $(I^+ - I^-)$ divided by $(I^+ + I^-)$. The asymmetry values shown here, positive peaks of 7% for Co and 4% for Fe, are the most conservative estimates. These were calculated using the entire underlying electron background in $I^+$ and $I^-$ (see vertical scale). If one instead uses the prepeak (lower binding energy) regions as an estimate of zero intensity, values near 40% for Fe and 15% for Co are found.

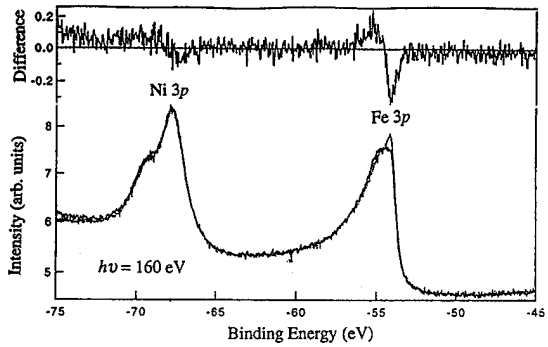



FIG. 4. Photoelectron spectra of Fe[1]Ni[4]/Cu(001), taken using a photon energy of 160 eV. Here, a difference spectrum is also shown. Using the prepeak regions as estimates of zero intensity, asymmetry values near 5% for Fe and 2% for Ni can be obtained. The relatively larger spin-orbit effect in Ni results in a more consistent structure with a peak and shoulder, compared to the Fe spectra.

(SMOKE) measurements.[9,15] Furthermore, analysis based upon the MXLD effects may not be quite as straightforward as it might seem: it is not clear that simple perturbative models are accurate.[16,17] In fact, for the $3p$ levels of Fe, Co, and Ni, it may be that simple perturbative pictures fail and that both the spin-orbit and exchange splitting need to be dealt with on an equal footing[16,17] (Fig. 5). However, as one moves across the series from Fe to Ni, the ratio of magnetic moment to spin orbit splitting decreases substantially, suggesting the plausibility of a perturbative approach for Ni (Table I). This is reflected also in Fig. 4. Thus, our initial results are promising in terms of understanding key effects in magnetic nanoscale films, including such possibilities as strain-modified invar quenching, but it may require more sophisticated analysis, including multiple-scattering calculations[16,17] and more extensive examination of thickness and composition effects.

We are using the elementally specific and magnetically sensitive technique of MXLD photoelectron spectroscopy to probe nanoscale magnetic alloys. These structures are the building blocks of many new magnetic devices, including spin-value and GMR materials. The variation of classical

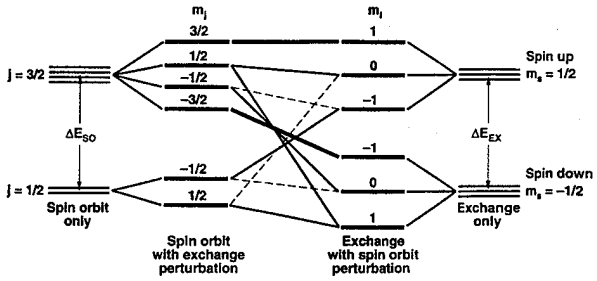



FIG. 5. The effect of spin-orbit and exchange splitting upon a $p$ core-level is illustrated here. Two perturbative approaches are shown: Large spin-orbit and small exchange splitting (left hand side) and small spin-orbit and large exchange splitting (right hand side). The Ni $3p$ would fall to the left while the Fe $3p$ is near the center, where spin-orbit and exchange effects are nearly equal and a nonperturbative approach is required. State mixing is indicated by dashed and solid lines (Table I).

TABLE I. A rough comparison of exchange and spin orbit splittings in Fe, Co, and Ni is shown here. Assuming that the spin-orbit splitting scales as $z$, the atomic number, to the fourth power,[18] it is possible to crudely estimate the spin-orbit splitting in Fe and Co from spectroscopic data (Ref. 19) for Ni, Cu, and Zn. By comparison to the ratio of the magnetic moment (Ref. 20) vs the spin orbit splitting in Ni, we see that such a ratio is seven times larger for Fe than Ni. Thus, while it might be possible to view the Ni $3p$ from the limiting case of an exchange splitting perturbing a larger spin-orbit splitting, such an approach is unlikely to be appropriate for the Fe $3p$.

| | $\mu^a$ ($\mu_B$) | $\Delta E_{SO}{}^b$ (eV) | Ratio[c] |
|---|---|---|---|
| Fe | 2.2 | (~1.0) | (~7) |
| Co | 1.7 | (~1.3) | (~4) |
| Ni | 0.6 | 1.8 | 1 |
| Cu | ··· | 2.2 | |
| Zn | ··· | 2.8 | |

[a]Bulk magnetic moment values from "Materials Sciences" by Anderson *et al.* (Ref. 20).

[b]$\Delta E_{SO}=B^F(3p_{1/2})-B^F(3p_{3/2})$. From X-Ray Data Booklet by Kirz *et al.* (Ref. 19). The Fe and Co values were obtained by extrapolation from the Zn, Cu, and Ni values, assuming $\Delta E_{SO}$ is proportional to $Z^4$, with $Z$=atomic number.

[c]Ratio $=(\mu/\Delta E_{SO})i/(\mu/\Delta E_{SO})\text{Ni}=(\mu/\Delta E_{SO})i*3(\mu_B{}^{-1}\text{ eV})$.

magnetic effects, such as Invar quenching, due to pseudomorphic strain and other nanoscale perturbations, is being investigated.

This work was performed under the auspices of the U. S. Department of Energy by the Lawrence Livermore National Laboratory under Contract No. W-7405-ENG-48. The Spectromicroscopy Facility and the Advanced Light Source were constructed with support from the U.S. Department of Energy.

[1] B. A. Gurney, V. S. Speriosu, J. P. Nozieres, H. F. Lefakis, D. R. Wilhoit, and D. U. Need, Phys. Rev. Lett. **71**, 4023 (1993); B. Dieny, V. S. Speriosu, S. Metin, S. S. Parkin, B. A. Gurney, P. Baumgart, and D. R. Wilhoit, J. Appl. Phys. **69**, 4774 (1991); B. Dieny, V. S. Speriosu, S. S. P. Parkin, B. A. Gurney, D. R. WIlhoit, and D. Mauri, Phys. Rev. B **43**, 1297 (1991).

[2] S. S. P. Parkin, Phys. Rev. Lett. **71**, 1641 (1993); A. C. Ehrlich, *ibid.* **71**, 2300 (1993); V. Grolier, D. Renard, B. Bartenlian, P. Beauvillian, C. Chappert, C. Dupas, J. Ferre, M. Galtier, E. Kolb, M. Mulloy, J. P. Renard, and P. Veillet, *ibid.* **71**, 3023 (1993).

[3] R. F. Marks, R. F. C. Farrow, G. R. Harp, S. S. P. Parkin, T. A. Rabedeau, M. F. Toney, A. Cebollada, N. Thangaray, and K. M. Krishnan, Mater. Res. Soc. Symp. Proc. **313**, 411 (1993).

[4] N. M. Rensing and B. M. Clemens, Mater. Res. Soc. Symp. Proc. **313**, 197 (1993); J. M. George, A. Barthelemy, O. Durand, J. L. Ouvail, A. Fert, P. Galtier, O. Heckmann, L. G. Pereira, F. Petroff, and T. Valet, *ibid.* **313**, 737 (1993).

[5] C. H. Roth, F. U. Hillebrecht, H. B. Rose, and E. Kisker, Phys. Rev. Lett. **70**, 3479 (1993); Solid State Commun. **86**, 647 (1993).

[6] W. Kuch, M. T. Lin, W. Steinhogl, C. M. Schneider, D. Venus, and J. Kirschner, Phys. Rev. B **51**, 609 (1995).

[7] G. Rossi, F. Sirotti, N. A. Cherepkov, F. Cambet-Farnoux, and G. Panaccione, Solid State Commun. **90**, 557 (1994); F. Sirotti and G. Rossi, Phys. Rev. B **49**, 15 682 (1994).

[8] J. D. Denlinger, E. Rotenberg, T. Warwick, G. Visser, J. Nordgren, J. H. Guo, P. Skytt, S. D. Kevan, K. S. McCutcheon, D. Shuh, J. Bucher, N. Edelstein, J. G. Tobin, and B. P. Tonner, Rev. Sci. Instrum. **66**, 1342 (1995).

[9] G. J. Mankey, M. T. Kief, and R. F. Willis, J. Vac. Sci. Technol. A **9**, 1595 (1991); F. Huang, M. T. Kief, G. J. Mankey, and R. F. Willis, Phys. Rev. B **49**, 3962 (1994).

[10] D. D. Johnson, F. J. Pinski, and J. B. Staunton, J. Appl. Phys. **61**, 3715 (1987).

[11] I. A. Abrikosov, O. Eriksson, P. Soderlind, H. L. Skiver, and B. Johansson, Phys. Rev. B **51**, 1058 (1995).

[12] P. Soderlind, O. Eriksson, B. Johansson, R. C. Albers, and A. M. Boring, Phys. Rev. B **45**, 12 911 (1992).

[13] C. Kittel, *Introduction to Solid State Physics*, 6th ed. (Wiley, New York, 1953).

[14] J. J. Yeh and I. Lindau, At. Data Nucl. Data Tables **32**, 1 (1985).

[15] S. Z. Wu, G. J. Mankey, F. O. Schumann, and R. F. Willis (unpublished).

[16] E. Tamura, G. D. Waddill, J. G. Tobin, and P. A. Sterne, Phys. Rev. Lett. **63**, 3642 (1992).

[17] J. G. Tobin, G. D. Waddill, E. Tamura, P. A. Sterne, P. J. Bedrossian, X. Guo, and S. Y. Tong, Surf. Rev. Lett. (in press).

[18] E. E. Anderson, *Modern Physics and Quantum Mechanics* (Saunders, Philadelphia, 1971).

[19] J. Kirz, D. Attwood, B. L. Henke, M. R. Howells, K. D. Kennedy, K.-J. Kim, J. B. Kortright, R. C. Perera, P. Pianetta, J. C. Riordan, J. H. Schofield, G. L. Straling, A. C. Thompson, J. H. Underwood, D. Vaughan, G. P. Williams, and H. Winick, *X-Ray Data Booklet* (LBL, Berkeley, CA, 1987).

[20] J. C. Anderson, K. D. Leaver, J. M. Alexander, and R. D. Rowlings, *Materials Science* (Wiley, New York, 1974).

# New magnetic phases of Fe on fcc Co(001) and Ni(001)

W. L. O'Brien
*Synchrotron Radiation Center, University of Wisconsin—Madison, 3731 Schneider Drive, Stoughton, Wisconsin 53589*

B. P. Tonner
*Department of Physics, University of Wisconsin—Milwaukee, 1900 East Kenwood Blvd., Milwaukee, Wisconsin 53211, and Synchrotron Radiation Center, University of Wisconsin—Madison, 3731 Schneider Drive, Stoughton, Wisconsin 53589*

A sequence of three distinct magnetic phases of Fe are found for growth on both fcc Co(001) and Ni(001) using x-ray magnetic circular dichroism. For Fe coverages below 5 ML the films are ferromagnetic, with the magnetic moments aligned perpendicular to the surface for growth on Ni and parallel to the surface for growth on Co. Between 5 and 11 ML the Fe films are nonferromagnetic at room temperature. Above 11 ML the Fe films are once again ferromagnetic. An identical sequence of magnetic phase transitions is known to occur for Fe growth on Cu(001). Based on this comparison and on the nearly identical lateral lattice constants of fcc Co, Ni, and Cu, we conclude that Fe growth on fcc Co(001) and Ni(001) follows the same sequence of crystalline phase transitions as Fe growth on Cu(001). © *1996 American Institute of Physics.*
[S0021-8979(96)19708-9]

Metastable magnetic phases of Fe grown on Cu(001) are perhaps the most intensely studied thin film magnetic system.[1–5] These films exhibit a variety of different magnetic properties and crystalline structures, depending on film thickness and temperature. Three phases of Fe, identified by their different magnetic properties, are found in films grown at room temperature using physical vapor deposition. Fe films less than five monolayers (ML) thick are ferromagnetically ordered, with an easy axis of magnetization perpendicular to the surface.[1,2] Films between 5 and 11 ML thick are antiferromagnetic with a Néel temperature below room temperature. The outer two surface layers of this antiferromagnetic phase are ferromagnetically aligned with the moment oriented perpendicular to the surface.[1,2] Films thicker than 11 ML are ferromagnetic with an in-plane moment.[1,2]

These three regions of different magnetic behavior correspond to three distinct surface structures, which can be identified by their low-energy electron diffraction (LEED) patterns.[3] The ferromagnetic phase present at coverages below 5 ML has an $(n\times 1)$ LEED pattern, where $n=4$ or 5.[1–3] The antiferromagnetic phase has been reported by various groups to have either a $(1\times 1)$[2] or $(2\times 1)$[1,3] LEED pattern. For coverages above 11 ML, a $(3\times 1)$ LEED pattern is observed.[1–3] The crystalline structure of these three phases has been investigated by a number of techniques, including x-ray photoelectron diffraction,[6] scanning tunneling microscopy (STM),[5] and extended x-ray absorption fine structure (EXAFS).[4] EXAFS and STM both find evidence of a fcc to bcc phase transition as the film thickness increases beyond 10 ML. This identifies the antiferromagnetic Fe phase present between 5 and 11 ML as fcc Fe and the ferromagnetic phase present at coverages above 11 ML as bcc Fe. The low coverage (<5 ML) ferromagnetic phase has been identified as a face-centered-tetragonal, fct, structure by EXAFS.[4]

An important open question is whether the metastable fct and fcc structures of Fe can be observed on other substrates, or if they are only present in the Fe/Cu(001) system. We have chosen to investigate both fcc Ni(100) and metastable fcc Co(100) as substrates for Fe epitaxy, where the substrates are in the form of films grown on Cu(100). For Co/Cu(001) the growth mode is nearly perfectly layer by layer, resulting in metastable fcc Co films with the same surface unit cell as Cu(001)[6] for films below the critical layer thickness for dislocation formation. Ni on Cu(001) also grows in the fcc structure,[7] owing to the close lattice match between Ni and Cu. Because of the nearly identical surface unit cell of Cu(001), metastable fcc Co(001), and Ni(001), we expect that there is a strong likelihood that the Fe/Co(001) and Fe/Ni(001) structures are very similar to those of Fe/Cu(100).

In this paper we report on the magnetism and structure of ultrathin Fe films grown on the ferromagnetic substrates, fcc Co(001) and fcc Ni(001). The experiments were performed on the 10 M toroidal grating monochromator beamline located at the Synchrotron Radiation Center. The fcc Co(001) (10 ML) and fcc Ni(001) (15 ML) thin-film substrates were grown on a clean Cu(001) crystal at room temperature by evaporation from pure Co and Ni wires. These film thicknesses were chosen to reduce the possibility of Cu diffusion to the surface. Both of these substrates are ferromagnetic with the magnetization vector lying in plane for Co and perpendicular to the surface for Ni. Fe films of different thickness were deposited at room temperature, by evaporation from a pure Fe wire. The base pressure of the vacuum chamber was $2\times 10^{-10}$ Torr, and the pressure during evaporation was below $2\times 10^{-9}$ Torr. LEED was used to determine substrate and film order.

X-ray magnetic circular dichroism (XMCD) measurements were made with the sample located between the poles of an electromagnet. Two geometries were used for the XMCD measurements, as shown in Fig. 1. The photon angle of incidence was 45° for both perpendicular and in-plane measurements. XMCD spectra were taken at room temperature by switching the direction of the magnetic field and measuring the total electron yield, $Y(\hbar\omega)$, while sweeping the incident photon energy at a fixed polarization. Dichroism

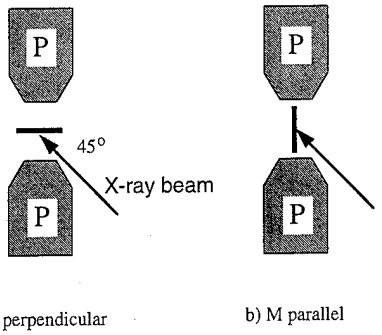



FIG. 1. Experimental geometry for (a) magnetization perpendicular to the sample surface and (b) parallel to the sample surface. The sample is rotated 90° to change the measurement geometry.

intensities were normalizing to the total absorption cross section and are proportional to the magnetization.

There are a number of important reasons why the specific measurement geometry of Fig. 1 was chosen. We have shown earlier[8] that the approximation $\sigma(\hbar\omega) \propto \hbar\omega \cdot Y(\hbar\omega)$, where $\sigma(\hbar\omega)$ is the absorption cross section, is not always valid for studies of magnetic films with photon angles of incidence greater than 50°. This is due to saturation effects in the total electron yield. Our geometry was chosen so that the approximation $\sigma(\hbar\omega) \propto \hbar\omega \cdot Y(\hbar\omega)$ is valid to within 5%.[8] The symmetry of our experimental geometry allows a direct comparison of the XMCD intensities between the parallel and perpendicular magnetization cases. This geometry, together with azimuthal rotation, also allows the easy axis of magnetization to be determined unambiguously.

The normalized Fe dichroism intensities at $L_3$ measured at remanence, $\Sigma_R$(Fe), were found to vary greatly depending on Fe film thickness and substrate. Figure 2 shows a graph of $\Sigma_R$(Fe) as a function of Fe film thickness on the three substrates we studied. For Fe growth on Cu(001), no ferromagnetic ordering is observed for films less than 11 ML thick. Above 11 ML the films are ferromagnetically ordered in-plane, as shown by the nonzero dichroism intensity. The saturation in $\Sigma_R$(Fe) at 14 ML shows that the entire film is magnetized at this thickness.

Three regions of different magnetic behavior are found for Fe growth on the ferromagnetic substrates fcc Co(001) and fcc Ni(001). These regions are characterized by different values of $\Sigma_R$(Fe). For coverages less than 4 ML, the Fe is ferromagnetically aligned, as determined by the large value of $\Sigma_R$(Fe) ~32%. The easy axis of magnetization is in plane along ⟨110⟩ for 1–4 ML of Fe on Co(001). At the same thickness range on Ni(100), the easy axis is perpendicular to the surface.

Between 5 and 11 ML, $\Sigma_R$(Fe) is reduced to nearly zero for growth on both Co and Ni. The easy axis of magnetization for this thickness range remains in plane for growth on Co, ⟨110⟩, and perpendicular to the surface for growth on Ni. For coverages greater than 11 ML, $\Sigma_R$(Fe) increases. For growth on Co, $\Sigma_R$(Fe) at 16 ML coverage is nearly equal to $\Sigma_R$(Fe) for thick bcc Fe films grown on Cu(001). For growth on Ni, $\Sigma_R$(Fe) gradually increases over the thickness range from 12 to 18 ML, but does not quite reach the value of

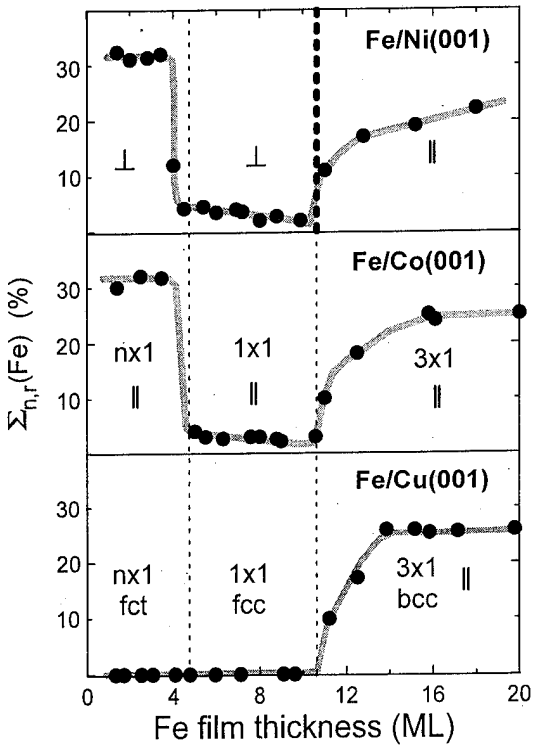



FIG. 2. Normalized dichroism intensities of Fe measured at remanence, $\Sigma_R$(Fe), which is proportional to the average vector magnetic moment per Fe atom, vs the film thickness for growth on Cu(001), Co(001), and Ni(001). The vertical dashed lines represent regions of different growth for Fe/Cu(001), fct, fcc, and bcc. Different surface reconstructions, as observed by LEED, are given for Fe growth on Cu(001) and Co(001). The symbols ⊥ and ∥ signify magnetic alignment perpendicular and parallel to the sample surface, respectively.

$\Sigma_R$(Fe) for thick bcc Fe films grown on Cu(001). The easy axis of magnetization for Fe films thicker than 11 ML switches from perpendicular to the surface to in plane for Fe films grown on Ni, and remains in plane for Fe films grown on Co(001). Element specific hysteresis measurements show predominantly square hysteresis loops, $M_R > 0.9M_S$, with ferromagnetic coupling between the substrate and Fe for all Fe thicknesses.

It is important to examine the magnetization of the substrate before discussing the results presented in Fig. 2. In Fig. 3 we show the values of $\Sigma_R$(Co) and $\Sigma_R$(Ni) vs Fe coverage. $\Sigma_R$(Co) does not change with Fe coverage, and the easy axis of magnetization is always in the surface plane. For Fe/Ni, $\Sigma_R$(Ni) is 18% for Fe coverages less than 11 ML and 12% for Fe coverages greater than 11 ML. This change in $\Sigma_R$(Ni) is accompanied by a change in the easy axis of magnetization, which is perpendicular to the surface for coverages below 11 ML and in plane for coverages above 11 ML. The decrease in $\Sigma_R$(Ni) may be due to complex magnetic domain structures in the Ni films magnetized in plane. The sharp decline in the Fe magnetization near 5 ML has no counterpart in the substrate signals. The rise in Fe magnetization above 11 ML is absent in the Co data, and for Ni there is an opposite behavior at this point. This means that the magnetization changes seen in the Fe films at 5 and 11 ML must be

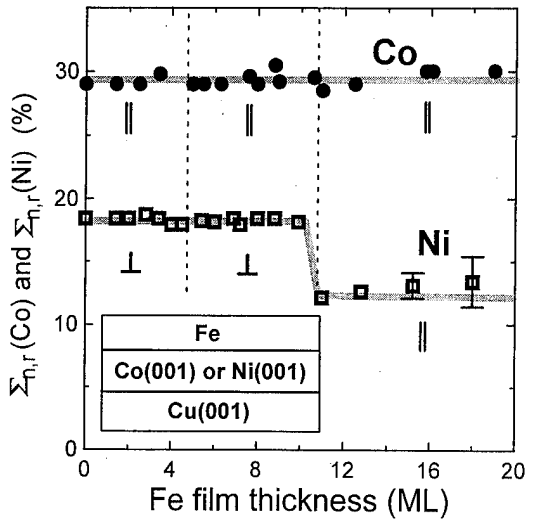



FIG. 3. Normalized dichroism intensities of the Co and Ni substrates vs Fe coverage.

due to phase changes in the Fe itself, rather than arising from changes in the substrate magnetization.

The dashed lines in Fig. 2, at 5 and 11 ML, separate the regions of different crystal structures found for Fe growth on Cu(001).[1,2] The onset of ferromagnetic ordering at 11 ML for Fe/Cu(001) is due to the antiferromagnetic fcc to ferromagnetic bcc phase transition. We do not see magnetic ordering in the fcc phase (5–11 ML), since we are measuring at room temperature. Both the Néel temperature of the fcc phase ($T_N$=200 K) and the Curie temperature of the live surface bilayer ($T_C$=250 K) are below room temperature.[2] Similarly, we observe no perpendicular magnetization for fct Fe/Cu(001) films (5 ML and below), since room temperature is only slightly below the Curie temperature of these films.

The regions of different magnetic behavior of Fe for growth on Co and Ni nearly coincide with the regions of different crystal structure for Fe growth on Cu. This is strong evidence that Fe has the growth mode on Cu(001), Co(001), and Ni(001). Further evidence comes from LEED. For Fe growth on Co, we observe $(n\times1)$, $n$=4 or 5, diffraction patterns for Fe coverages less than 5 ML, $(1\times1)$ diffraction patterns for Fe coverages between 5 and 11 ML, and $(3\times1)$ diffraction patterns for coverages greater than 11 ML. This is identical to the LEED results we obtain for Fe growth on Cu(001), and is in agreement with published LEED results for Fe/Cu(001).[2] For Fe growth on Ni(001), we do not observe sharp higher-order diffraction spots, just intensity modulated streaks along the ⟨110⟩ directions. Given the identical surface unit cells of the three substrates, the coincidence of the changes in magnetism with anticipated changes in crystalline structure, and the identical surface reconstructions for growth on Cu(001) and Co(001), we propose that the sequence of structures for Fe grown on Ni(001) and Co(001) is the same as for Fe growth on Cu(001).

The magnetic transitions of the Fe/Co and Fe/Ni thin films (Fig. 2) can now be explained in terms of the structural changes in the films and the influence of the magnetic substrates. At coverages below 5 ML, the Fe films grow in the fct structure, which is ferromagnetic. Ferromagnetic ordering is evident in the large dichroism intensity we find for films between 1 and ~4 ML thick. Between 5 and 11 ML, the Fe films grow with a fcc structure. For growth on Cu(001), fcc Fe is an antiferromagnet ($T_N$=200 K). Since $T_N$ for the Fe/Cu(001), Fe/Co(001), and Fe/Ni(001) films are likely to be similar, at room temperature these films will be nonmagnetic. However, the dichroism signal in this phase is greatly reduced, but does not go to zero. This nonzero dichroism intensity is most likely due to magnetism at the Fe/Co and Fe/Ni interfaces. Above 11 ML, the critical thickness for fcc Fe growth is exceeded, and the Fe films gradually transform into the bcc structure. This is the room temperature stable crystal structure, and it is ferromagnetic, which is evident in the increase in the dichroism intensity. The larger value of $\Sigma_R$(Fe) for fcc Fe may be due to an enhanced surface moment, or complex domain structures in the bcc Fe/fcc Ni and bcc Fe/fcc Co films.

This work was supported by the National Science Foundation, Contract No. DMR-94-13475. The Synchrotron Radiation Center is a national facility supported by the National Science Foundation Division of Materials Research.

[1] J. Thomassen, F. May, B. Feldmann, M. Wuttig, and H. Ibach, Phys. Rev. Lett. **69**, 3831 (1992).
[2] D. Li, M. Freitag, J. Pearson, Z. Q. Qiu, and S. D. Bader, Phys. Rev. Lett. **72**, 3112 (1994).
[3] P. Xhonneux and E. Courtens, Phys. Rev. B **46**, 556 (1992).
[4] H. Magnan, D. Chandesris, B. Villette, O. Heckmann, and J. Lecante, Phys. Rev. Lett. **67**, 859 (1991).
[5] K. Kalki, D. D. Chambliss, K. E. Jonson, R. J. Wilson, and S. Chiang, Phys. Rev. B **48**, 18 344 (1993).
[6] M. T. Kief and W. F. Egelhoff, Phys. Rev. B **47**, 10 785 (1993); D. A. Steigerwald and W. F. Egelhoff, Jr., Surf. Sci. **192**, L887 (1987).
[7] J. Zhang, Z.-L. Han, S. Varma, and B. P. Tonner, Surf. Sci. **298**, 351 (1993).
[8] W. L. O'Brien and B. P. Tonner, Phys. Rev. B **50**, 12 672 (1994).

# Nonlinear magneto-optical Kerr effect study of quantum-well states in a Au overlayer on a Co(0001) thin film

M. Groot Koerkamp, A. Kirilyuk, W. de Jong, and Th. Rasing
*Research Institute for Materials, University of Nijmegen, Toernooiveld 1 NL-6525 ED Nijmegen, The Netherlands*

J. Ferré, J. P. Jamet, and P. Meyer
*Laboratoire de Physique des Solides, Université Paris Sud, 91405 Orsay Cédex, France*

R. Mégy
*Institut d'Electronique Foundamentale, Université Paris Sud, 91405 Orsay Cédex, France*

We have measured the polar nonlinear magneto-optical Kerr rotation and the total generated second harmonic intensity from a perpendicularly magnetized Co(0001)/Au(111) thin film (6 ML) versus the thickness of a Au overlayer. For both experiments we find a clear oscillation with a period of about 13.5 ML. This behavior can be interpreted as arising from quantum-well states (QWSs) in the Au overlayer, though interestingly, the observed period is twice the expected one. Especially for the reflected intensity this oscillation is very pronounced: the intensity changes by a factor of 10 when the Au overlayer thickness changes from 7 to 13 ML. These strong effects make this nonlinear technique very suitable for the study of these QW oscillations. © *1996 American Institute of Physics.* [S0021-8979(96)19808-5]

Since the discovery that magnetic films separated by a nonmagnetic spacer layer could be coupled antiferromagnetically,[1] and the subsequent discovery that this coupling could oscillate between ferromagnetic and antiferromagnetic,[2] there have been intense efforts to understand these phenonema. It was shown that in ultrathin films, due to the electronic potential discontinuities experienced by electronic states at interfaces, the perpendicular component of the wave vector can become quantized, giving rise to resonances in the density of states. Those quantum-well states (QWSs) may act as the mediator for this magnetic coupling.[3] Magneto-optical Kerr effect (MOKE) and direct- and inverse photo emission experiments have shown direct evidence of such QWSs in thin noble metal films on magnetic substrates (Fe and Co),[4–6] and in a bcc Fe(100) layer on Au(100).[7,8] More recently, oscillations of the Kerr angle with changes of overlayer film thickness have been observed for a Au/Co/Au system.[9] These results showed the existence of quantum size effects in the thin Au overlayer and also gave an indication of possible interface contributions.

Due to the fact that optical second harmonic generation (SHG) is known to be surface sensitive on an atomic scale, it seems that SHG studies might be particularly suitable for improving our knowledge of the electrodynamics of ultrathin metallic films. Though the absolute nonlinear signals are small, the nonlinear magneto-optical effects can be large: compared to the linear Kerr angle, enhancements up to a factor of 1000 have been observed.[10] Wierenga *et al.*[11] were the first to report about the possibilities of this nonlinear optical technique for detecting QW oscillations. They have found very strong oscillations in the magnetization-induced SHG signal for the Cu/Co/Cu system as a function of the thickness of the Cu overlayer, which are probably related to QWSs in these films.[11] These strong effects are directly related to the extreme interface localization of the nonlinear response.

In this paper we report the unambiguous observation of QWSs in a Au(111) overlayer on Co(0001). The oscillations are found in both the polar nonlinear MOKE as well as in the total generated second harmonic intensity, as measured as a function of the Au overlayer thickness. These are the first nonlinear MOKE results in the polar geometry, showing an enhancement of two orders of magnitude with respect to its linear equivalent.

For our experiments we used a Ti:sapphire (Tsunami) laser operating at a repetition rate of 82 MHz and a pulse width of about 100 fs. The incoming laser light was filtered and focused onto the sample. Polarization control of both incident fundamental and reflected SH light was achieved by means of polarizers. Appropriate optical filtering was used before the signal was detected by a photon counter. Our sample consists of a six monolayer (ML) Co(0001) film on a 30 nm thick Au buffer layer, covered with a stepped Au wedge, consisting of 13 terraces of $t_{Au}=6-18$ ML. The terraces have a width of 1.5 mm, so the laser beam can easily be focused on each separate step. Details about the sample preparation can be found in Ref. 9. Note that this sample has a perpendicular easy magnetization axis.

SHG arises from the nonlinear polarization $\mathbf{P}(2\omega)$ induced by an incident laser field $\mathbf{E}(\omega)$. In the electric dipole approximation, this polarization can be written as

$$P_i(2\omega)=[\chi^{+}_{ijk}(M)+\chi^{-}_{ijk}(M)]E_j(\omega)E_k(\omega), \tag{1}$$

where $\chi^{+}_{ijk}(M)$ and $\chi^{-}_{ijk}(M)$ are the even and odd elements of the nonlinear susceptibility tensor that fulfill $\chi^{\pm}_{ijk}(-M)=\pm\chi^{\pm}_{ijk}(M)$, as suggested by Pan *et al.*[12] Since this susceptibility tensor has to reflect the symmetry of the crystal,[13] the nonzero elements are easily derived from the invariance of $\boldsymbol{\chi}(M)$ under symmetry operations. Table I

 0021-8979/96/79(8)/5632/3/$10.00 © 1996 American Institute of Physics

TABLE I. The nonzero elements of the SH susceptibility tensor for an isotropic surface in the polar ($\mathbf{M}\|z$) configuration and for a nonmagnetized interface. The two columns list the elements that are even and odd in the magnetization, respectively.

| Nonmagnetized | |
|---|---|
| $xxz=xzx=yyz=yzy$ | |
| $zxx=zyy$ | |
| $zzz$ | |
| Polar ($\mathbf{M}\|z$) | |
| Even in **M** | Odd in **M** |
| $xxz=xzx=yyz=yzy$ | $xyz=xzy=-yxz=-yzx$ |
| $zxx=zyy$ | $zxy=zyx$ |
| $zzz$ | |

shows the relevant tensor elements for our experiments. For $s$-polarized incident light (i.e., parallel to the $y$ axis, see the inset to Fig. 1), only the even element can be excited. Therefore, no Kerr rotation can be expected for this configuration. For $p$-polarized incident light the Co/Au interfaces have two odd components, both giving rise to $s$-polarized SHG, and three even components, which produce $p$-polarized SHG. From this it follows that the SHG polarization ellipses for $\pm\mathbf{M}$ are each other mirror images in the plane of incidence, and we can define a nonlinear Kerr angle $\Phi_K^{(2)}$, analogous to the linear Kerr rotation. Experimentally, the Kerr angle is found by fitting a $\cos^2\alpha$ dependence to the measured intensity as a function of the analyzer angle $\alpha$, for opposite directions of the magnetic field. This leads to a precision in the nonlinear Kerr angle of $\pm 0.12°$.

The experimental variation of $\Phi_K^{(2)}$ vs $t_{\mathrm{Au}}$ is given in Fig. 1, showing a clear oscillatory behavior. These measurements have been done with $p$-polarized incident light at a wavelength of 740 nm and at an angle of incidence of 45°. The observed amplitude of the oscillation is about two orders of magnitude larger than its linear counterpart, as measured on the same sample.[9] The solid line in the figure is a least-squares fit to the expression

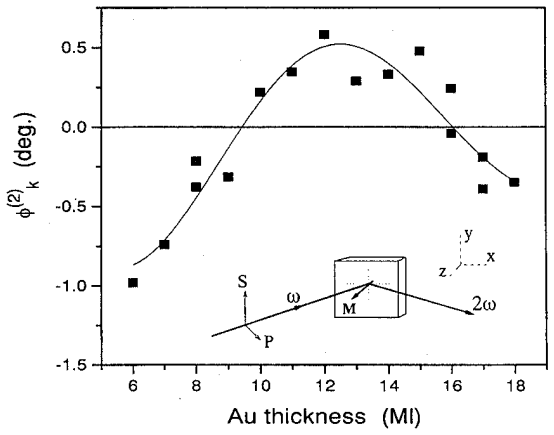



FIG. 1. Nonlinear polar Kerr rotation as a function of the Au overlayer thickness. The solid line is a fit to Eq. (2). The inset shows the experimental configuration.

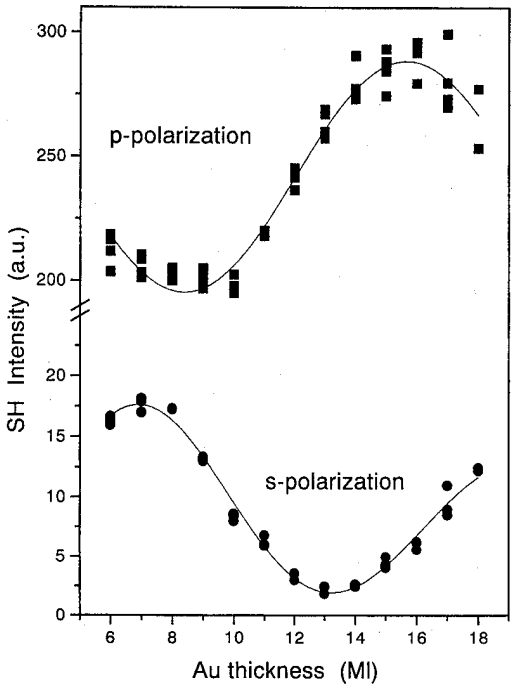



FIG. 2. Total generated SH intensity as a function of the Au overlayer thickness. Dots: $s$-polarized incoming light, squares: $p$-polarized incoming light. The solid lines are fits to Eq. (2).

$$\Phi_{\mathrm{K}}^{(2)}=A\times\exp\frac{-t_{\mathrm{Au}}}{\delta}\times\cos\left(2\pi\frac{t_{\mathrm{Au}}}{\Lambda}+\gamma\right)+\beta. \tag{2}$$

From this fit the period $\Lambda$ of the oscillation is found to be $14\pm3$ ML with an attenuation length $\delta$ of $18\pm4$ ML. The maximum measured Kerr angle is about 1.0°. Although this value is a factor of 10 larger than its linear counterpart, the rotation is not as large as one would expect from earlier nonlinear Kerr experiments.[10] One reason for this is the 180° phase difference between the tensor components of the symmetric interfaces Au/Co and Co/Au. Because of the small thickness of the Co film (6 ML), the SH signals from these interfaces partly cancel each other and reduce the nonlinear magneto-optical effects.

The observed oscillatory character of the Kerr angle suggests that the quantum size effects have an influence on the tensor components. Since these effects will not only appear in the magnetic (odd), but particularly in the nonmagnetic tensor elements, the QWSs should also be observable in the total SH intensity. In Fig. 2 it can be seen that for both $s$- and $p$-input polarizations we found a clear oscillation in the total reflected SH signal. In the case of $s$-polarized incident light, we only have one nonzero tensor element $\chi_{zyy}$ present at both the Au/air and Au/Co interfaces, which explains the small signals here. The oscillation, however, comes out much more pronounced than in the Kerr measurements. By varying the Au overlayer thickness from 7 to 13 ML, the generated SH intensity drops by a factor of 10. The solid line in the figure is a least squares fit of the measured data according to Eq. (2). From this fit the period is found to be 12.6 ML, with an attenuation length of 18.3 ML. For $p$-polarized incident light, a clear oscillation can be seen on top of a large offset.

The solid line is again a fit by Eq. (2) with a period of 13.9 ML. In contrast with the $s$-input configuration, now no damping is found in the oscillation. This can possibly be explained by the different ways of penetration of the $s$- and $p$-polarized light into the material. For comparison we also measured the linear reflection as a function of the Au thickness. Within the experimental uncertainty of $\pm 2\%$, we found a constant value. Our observed period of about 13.5 ML is quite remarkable, as earlier linear Kerr measurements (at 632 nm) on the same sample gave a period of 7.8 ML.[9] Experiments on the oscillatory interlayer coupling between Co films across Au(111) gave a period of 6.5 ML.[14] The difference between the oscillation period in the linear and nonlinear Kerr rotation could possibly be due to the fact that these measurements were not done at the same wavelength, as Suzuki *et al.*[15] have shown that the period of the oscillation in the magneto-optical effect is energy dependent. To find out if there is any strong wavelength dependence, we repeated our Kerr and SH intensity measurements at different wavelengths between 740 and 1000 nm (the tuning range of our Ti:sapphire laser). In this range, however, no wavelength dependence of the period could be measured. A more likely explanation could be the difference between the selection rules involved in the linear and nonlinear optical response. However, this point needs more theoretical investigations. A final point of discussion is the interface roughness, as SHG is known to be extremely sensitive for this. The high quality of the thickness dependence fits suggests that the Co/Au interfaces are very smooth. The latter was also confirmed by other measurements.

In conclusion, we have observed large oscillations in both the nonlinear polar Kerr rotation and in the total generated SH intensity from a perpendicularly magnetized Au/Co/Au(111) sandwich versus the Au overlayer thickness. The period of the oscillation is for both experiments about 13.5 ML. The oscillations are believed to originate from QWSs in the Au overlayer. Specially for the total generated SH intensity, the quantum size effects can be very large: for the $s$-input polarization, the SH intensity drops by a factor of 10 when the Au overlayer thickness changes from 7 to 13 ML. These large effects make this nonlinear technique very suitable for detecting QW oscillations.

Part of this work was supported by the Stichting Fundamenteel Onderzoek der Materie (FOM) which is financially supported by the Nederlandse Organisatie voor Wetenschappelÿk Onderzoek (NWO), by Brite Euram II FFR CT 930569 and by HCM ERBCH.BGCT930444.

[1] P. Grünberg, R. Schreiber, Y. Pang, M. B. Brodsky, and H. Sowers, Phys. Rev. Lett. **57**, 2442 (1986).
[2] S. S. P. Parkin, N. More, and K. P. Roche, Phys. Rev. Lett. **64**, 2304 (1990).
[3] M. D. Stiles, Phys. Rev. B **48**, 7238 (1993).
[4] J. E. Ortega, F. J. Himpsel, G. J. Mankey, and R. F. Willes, Phys. Rev. B **47**, 1540 (1993).
[5] D. Hartmann, W. Weber, A. Rampe, S. Popovic, and G. Güntherodt, Phys. Rev. B **48**, 16 837 (1993).
[6] T. Katayama, Y. Suzuki, M. Hayashi, and A. Thiaville, J. Magn. Magn. Mater. **126**, 527 (1993).
[7] F. J. Himpsel, Phys. Rev. B **44**, 5966 (1991).
[8] W. Geerts, Y. Suzuki, T. Katayama, K. Tanada, K. Audo, and S. Yoshida, Phys. Rev. B **50**, 12 581 (1994).
[9] R. Mégy, A. Bounouh, Y. Suzuki, P. Beauvillain, P. Bruno, C. Chappert, B. Lecuyer, and P. Veillet, Phys. Rev. B **51**, 5586 (1995).
[10] B. Koopmans, M. Groot Koerkamp, Th. Rasing, and H. v.d. Berg, Phys. Rev. Lett. **74**, 3692 (1995).
[11] H. A. Wierenga, W. de Jong, M. W. J. Prins, Th. Rasing R. Volmer, A. Kirilyuk, H. Schwabe, and J. Kirschner, Phys. Rev. Lett. **74**, 1462 (1995).
[12] R.-P. Pan, H. D. Wei, and Y. R. Shen, Phys. Rev. B **39**, 1229 (1989).
[13] J. F. Nye, *Physical Properties of Crystals* (Oxford University Press, Oxford, 1957).
[14] V. Grolier, D. Renard, B. Bartenlian, P. Beauvillain, C. Chappert, C. Dupas, J. Ferré, M. Galtier, E. Kolb, M. Mulloy, J. P. Renard, and P. Veillet, Phys. Rev. Lett. **71**, 3023 (1993).
[15] Y. Suzuki and P. Bruno, J. Magn. Magn. Mater. **140–144**, 651 (1995).

# Growth and magnetic properties of $Fe_xNi_{1-x}$ ultrathin films on Cu(100)

F. O. Schumann, S. Z. Wu, G. J. Mankey,[a] and R. F. Willis
*Department of Physics, The Pennsylvania State University, University Park, Pennsylvania 16803*

We have investigated ultrathin $Fe_xNi_{1-x}$ films grown epitaxially on Cu(100) with different stochiometry. With the surface magneto-optic Kerr effect (SMOKE) we measured the variation of the Curie temperature $T_C$ as a function of the film thickness $n$ in monolayers (ML). Using the results of our previous investigations on finite-size scaling (Huang *et al.*), we are able to extrapolate the value $T_C(\infty)$ for samples with different Fe content. In particular, alloy films with Fe concentrations close to 65% remain ferromagnetic. This is in contrast to bulk $Fe_{65}Ni_{35}$, which shows a collapse of long range order, which is the so-called invar effect associated with a fcc to bcc structural transition. Growing these alloy films on a Cu(100) substrate forces them to adapt the Cu lattice spacing, thereby suppressing the structural relaxation. © *1996 American Institute of Physics.* [S0021-8979(96)19908-1]

## I. INTRODUCTION

Molecular beam epitaxy (MBE) has offered the possibility of stabilizing materials as thin films in new metastable phases, e.g., fcc Co/Cu(100) and fcc Fe/Cu(100). Theoretical studies reveal that fcc Fe can have several magnetic states.[1] Depending on the lattice constant (or atomic volume) antiferromagnetic (AF), nonmagnetic (NM) or ferromagnetic with high spin (HS)/low spin (LS) phases are stable. At the Cu lattice constant, these magnetic phases are very close in energy, which made the Fe/Cu(100) system very attractive for experimental studies.[2–9] The LEED *I-V* study by Müller *et al.*[10] shows that Fe/Cu(100) films with thicknesses up to 4 ML order in a heavily distorted fcc structure, where the atomic volume of Fe is increased with respect to Cu. This has the result that the whole film is in a ferromagnetic state.[9,11] Going to higher thicknesses at 300 K, Fe adopts the Cu atomic volume, except for the top layer, which still has an increased atomic volume before Fe transforms into the bcc phase. This means that the ferromagnetism is only located in the top layer[9] while the rest of the film is antiferromagnetically ordered.[8] In simple terms one can say that the Fe atoms try to adopt the bulk bcc crystal atomic volume while at the same time fulfilling the constraints imposed by the Cu substrate.

A well-known moment instability in the bulk is the invar effect in $Fe_xNi_{1-x}$ alloys. At a Fe concentration of 65% the magnetic moment deviates strongly from the Slater–Pauling curve, dropping quickly to zero, as does the Curie temperature, at which point a structural transition from the fcc into the bcc phase is observed.[12] Also, the thermal expansion is very low.[12] From a comparison with FePt and FePd alloys, which do not show a collapse of the magnetic moment, but have a small thermal expansion and strong reduction of the Curie temperature[12] it seems that the moment instability is not an invar relevant feature. A recent study[13] of 200 nm thick as-grown $Fe_{65}Ni_{35}$ films revealed that the magnetic moment follows the Pauling–Slater curve, but a small thermal expansion was still present. Again, stressing the point that the collapse of the magnetic moment is not an invar relevant feature.

The bulk lattice constants of fcc $Fe_xNi_{1-x}$ vary between 3.55–3.59 Å for concentrations $0.7>x>0.2$.[14] This gives only a very small lattice mismatch with Cu. This fact motivates the growth of $Fe_xNi_{1-x}$ films on Cu(100), for which we can expect good epitaxy with the above lattice matching argument. Furthermore, "clamping" $Fe_xNi_{1-x}$ films on Cu(100) should extend the concentration range for which the fcc structure prevails.

At this point it is important to refer to the work of Abrikosov *et al.*,[15] which discusses bulk fcc $Fe_xNi_{1-x}$ through the whole concentration range. They find that the magnetic moment collapses at $x=0.75$ and the lattice parameter drops noticeably, this is due to the fact that the LS/NM solution becomes lower in energy. We see that "clamping" $Fe_xNi_{1-x}$ to a fcc structure alone does not prevent the deviation from the Slater–Pauling curve, but by keeping the lattice constant fixed we expect a suppression of the invar effect.

## II. EXPERIMENTAL

The experiments were performed in an UHV apparatus previously described[16] with a base pressure of $1\times10^{-10}$ mbar, which was better than $4\times10^{-10}$ mbar during Fe, Ni codeposition. The Cu(100) crystal was mechanically polished and electropolished before inserting into the vacuum system. A few cycles of $Ar^+$ sputtering and annealing re-

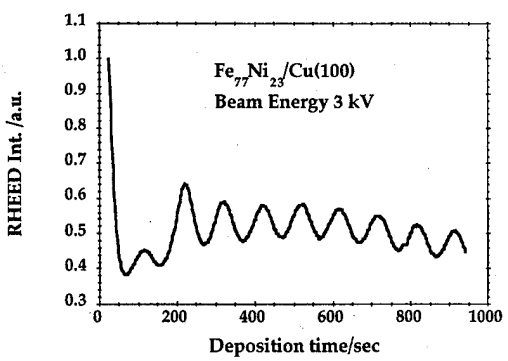



FIG. 1. Variation of the specular RHEED intensity during $Fe_{77}Ni_{23}$ growth.

[a]Present address: Dept. of Physics, Louisiana State University, Baton Rouge, LA 70803.

 0021-8979/96/79(8)/5635/3/$10.00 © 1996 American Institute of Physics 

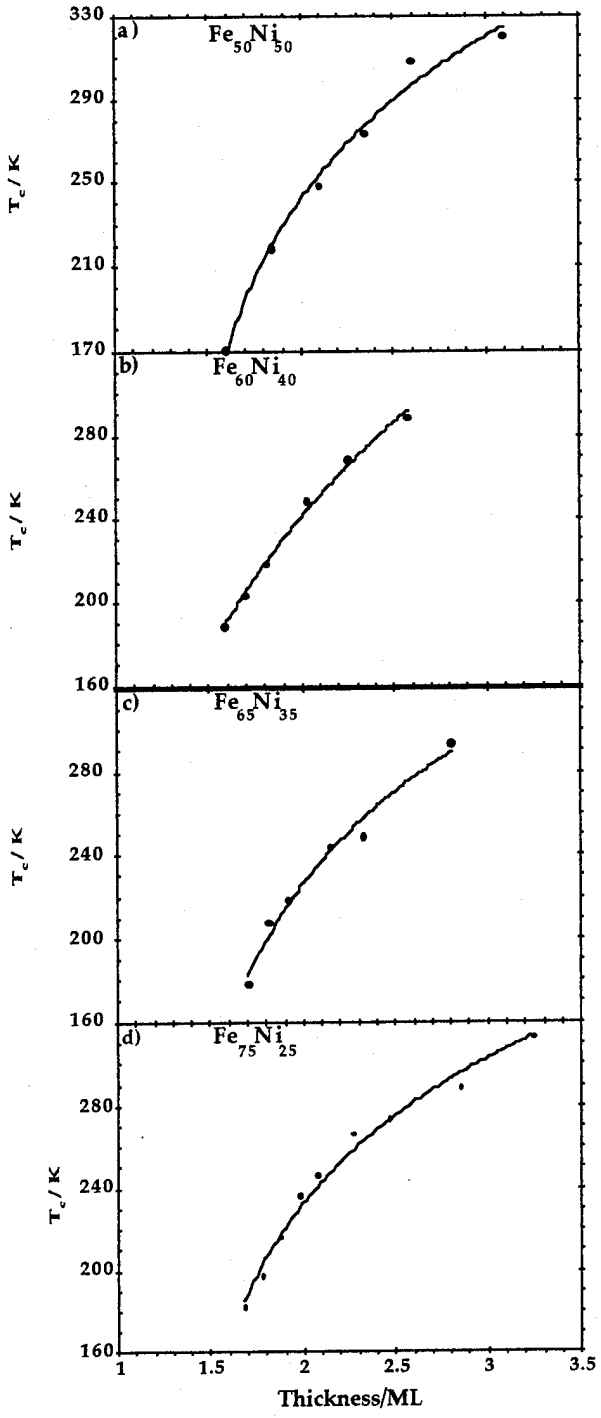



FIG. 2. Thickness dependence of $T_C$ for different alloy concentrations. The solid line represents the fit to the scaling law; see the text.

sulted in an ordered and clean sample, as judged from LEED and Auger spectroscopy. The growth rate of the Fe and Ni sources were controlled by quartz crystal monitors (QCM), which were calibrated via RHEED oscillations of Fe/Cu(100) and Ni/Cu(100).[16]

The alloy films were grown at 350 K in order to avoid Cu segregation, we also observed RHEED oscillations during the growth of $Fe_xNi_{1-x}$ films, which indicates good layer-by-layer growth; see Fig. 1. The thickness determined

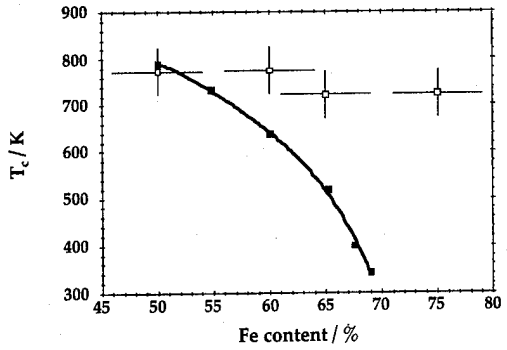



FIG. 3. Comparison between bulk Curie temperatures[12] (solid squares) and $T_C(\infty)$ of the thin film data (open squares). Error bars show variation of $T_C$ on fit parameters and accuracy of composition.

by the calibrated QCM and by the RHEED oscillations of the $Fe_xNi_{1-x}$ films agree to within 3%. This confirms our ability to control the thickness and the stochiometry very accurately.

The presence of $p(1\times1)$ LEED patterns confirmed pseudomorphic growth, which agrees with the observation of Dresselhaus *et al.*, who investigated 30 ML thick $Fe_xNi_{1-x}$/Cu(100) films, with $x=0.47$, 0.64, and $x=0.87$.[17]

Small C,O contamination were detectable at the end of the experimental run. With the surface magneto-optical Kerr effect (SMOKE) we measured the remanence as a function of temperature, thereby determining the Curie temperature $T_C$.

## III. RESULTS AND DISCUSSION

Although the magnetic measurements focused on the invar concentration at $x\approx0.65$, we investigated the growth of $Fe_xNi_{1-x}$/Cu(100) through the whole concentration range. We found RHEED oscillations of the (0,0) beam for up to 10 ML, which is exceptional in metal epitaxy and confirms good epitaxial growth even better than, e.g., Ni/Cu(100). As an example we show the RHEED oscillation for a $Fe_{77}Ni_{23}$/Cu(100) film. This concentration is above the bulk invar concentration, where the transition to bcc has already occurred. This curve is qualitatively identical with the

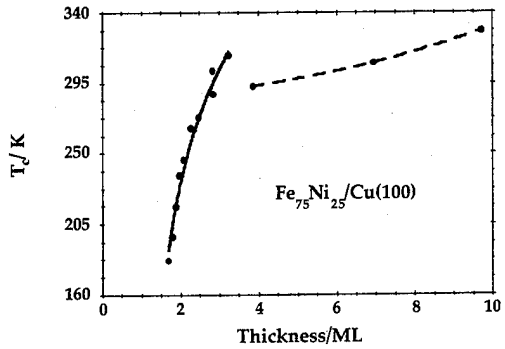



FIG. 4. Thickness dependence of $T_C$ for a $Fe_{75}Ni_{25}$ alloy in the thin film limit and intermediate thickness. The solid line is fit to scaling law; the dashed line is a guide for the eye.

RHEED data for $Fe_xNi_{1-x}$ films, with $x$ below 65%. We can therefore rule out a sudden transformation into the bcc phase, which would also be accompanied by a drop in the RHEED intensity, like for Fe/Cu(100).[9,18]

In our previous studies,[16,19] we have shown that the variation of the Curie temperature $T_C(n)$ with film thickness $n$ can be described with the empirical scaling law:

$$\frac{T_C(n)}{T_C(\infty)} = \frac{1}{1+[(n-n')/n_0]^{-\lambda}}. \quad (1)$$

Here $n'$ is an empirical constant approximately equal to 1.[16] The value of $n'$ determines the thickness for which $T_C$ starts to be finite. $n_0$ is another empirical constant, which has a value of approximately 3.5.[16] $T_C(\infty)$ and $\lambda$ are treated as independent fit parameters.

Equation (1) allows us to determine the $T_C(\infty)$ and compare this value with the bulk $T_C$ of a given alloy concentration. Obviously, it would be desirable to measure $T_C$ for very thick alloy films. This would give us directly $T_C(\infty)$, but the experimental window is limited, since at 400 K, Cu segregation is noticable, as Auger spectra show. In Fig. 2 we show $T_C$ as a function of the number of monolayers for several alloy films near the invar concentration. The solid line represents the fit to Eq. (1). We see that all these curves show a large slope near the onset of long-range order. We can now plot $T_C(\infty)$ as a function of concentration and compare it with the Curie temperature of bulk $Fe_xNi_{1-x}$ alloys,[12] see Fig. 3. The vertical error bars reflect the uncertainty of the determination of $T_C(\infty)$, whereas the horizontal error bars indicate the variation of the concentration during the deposition. The important point here is that $T_C(\infty)$ does not follow the bulk behavior and varies little within the accuracy of the fit with Eq. (1). Also important is that the alloy films are all ferromagnetic, even beyond the invar concentration, which is in contrast to the bulk behavior, but is also at odds with the theoretical work of Abrikosov and co-workers.[15]

Extending the measurements for a $Fe_{75}Ni_{25}$ alloy film up to 10 ML thickness reveals a strong deviation from the scaling law; see Fig. 4. At 4 ML $T_C$ has dropped when compared with the scaling curve, and increases only slowly with further deposition. These results indicate a structural relaxation/spin reduction occurring between 3 and 4 ML thickness.

## ACKNOWLEDGMENT

This work was funded via National Science Foundation Grant No. DMR-94-21728.

[1] V. L. Moruzzi, P. M. Marcus, and J. Kübler, Phys. Rev. B **39**, 6957 (1989).
[2] D. Pescia, M. Stampanoni, G. L. Bona, A. Vaterlaus, R. F. Willis, and F. Meier, Phys. Rev. Lett. **58**, 2126 (1987).
[3] R. Allenspach and A. Bischof, Phys. Rev. Lett. **69**, 3385 (1992).
[4] A. Brodde and H. Neddermayer, Surf. Sci. **287/288**, 987 (1993).
[5] M. T. Kief and W. F. Egelhoff, Jr., Phys. Rev. B **47**, 10 785 (1993).
[6] G. L. Nyberg, M. T. Kief, and W. F. Egelhoff, Jr., Phys. Rev. B **48**, 14 509 (1993).
[7] D. P. Pappas, K. P. Kämper, and H. Hopster, Phys. Rev. Lett. **64**, 3179 (1991).
[8] D. Li, M. Freitag, J. Pearson, Z. Q. Qiu, and S. D. Bader, Phys. Rev. Lett. **72**, 3112 (1994).
[9] J. Thomassen, F. May, B. Feldmann, M. Wuttig, and H. Ibach, Phys. Rev. Lett. **69**, 3831 (1992).
[10] S. Müller, P. Bayer, C. Reischl, K. Heinz, B. Feldman, H. Zillgen, and M. Wuttig, Phys. Rev. Lett. **74**, 765 (1995).
[11] H. Zillgen, B. Feldmann, and M. Wuttig, Surf. Sci. **321**, 32 (1994).
[12] E. F. Wassermann, J. Magn. Magn. Mater. **100**, 33 346 (1991).
[13] G. Dumpich, J. Kästner, U. Kirschbaum, H. Mühlbauer, J. Liang, T. Lübeck, and E. F. Wassermann, Phys. Rev. B **46**, 9258 (1992).
[14] D. Bonnenberg, K. A. Hempel, and H. P. J. Wijn, in *Landolt–Börnstein New Series*, Vol. III/19a.
[15] I. A. Abrikosov, O. Erikson, P. Söderling, H. L. Skriver, and B. Johansson, Phys. Rev. B **51**, 1058 (1995).
[16] F. Huang, M. T. Kief, G. J. Mankey, and R. F. Willis, Phys. Rev. B **49**, 3962 (1994).
[17] J. Dresselhaus, M. Möller, T. Kleemann, and E. Kisker, J. Magn. Magn. Mater. **148**, 172 (1995).
[18] J. Thomassen, B. Feldmann, and M. Wuttig, Surf. Sci. **264**, 406 (1992).
[19] G. J. Mankey, S. Z. Wu, F. O. Schumann, F. Huang, M. T. Kief, and R. F. Willis, J. Vac. Sci. Technol. A **13**, 1531 (1995).

# Quantum well states and interlayer coupling: Co/Cu(100)

L. Nordström
*Institute for Computational Sciences and Informatics, George Mason University, Fairfax, Virginia 22030-4444 and Complex Systems Theory Branch, Naval Research Laboratory, Washington, DC 20375-5345*

P. Lang, R. Zeller, and P. H. Dederichs
*Institut für Festkörperforschung, Forschungszentrum Jülich, D-52425 Jülich, Germany*

The electronic states that mediate the interlayer exchange coupling and the corresponding coupling strengths are calculated for Co/Cu(100). It is found that some states are strongly confined within the spacer layer. This is shown to lead to a strong RKKY-like coupling, but also to some weak contributions from higher harmonics. Weaker confined states only contribute by a rather weak RKKY coupling. © *1996 American Institute of Physics.* [S0021-8979(96)20008-1]

## I. INTRODUCTION

The experimental observation of interlayer exchange coupling (IXC) of two magnetic layers through a nonmagnetic spacer layer in numerous systems has influenced much theoretical work. Out of these there are two models that have attracted most attention: the RKKY model[1] at one hand and the quantum well model (QW)[2,3] at the other. These models have many properties in common, especially that the coupling oscillates with periods given by the Fermi surface of the spacer layer, but they have two different physical origins. The RKKY model can be viewed as that one magnetic layer induces a magnetization in the spacer layer, which interacts with the second layer. In the QW model some Bloch states of the spacer layer are confined between the two magnetic layers. Often this confinement only occurs when the two magnetic layers have parallel magnetization, which then gives rise to a magnetic interaction of the two layers. In a more general formulation, both these two models appear as two limits of the same theory.[4] The significant quantity that enters this theory is the strength of the interface scattering, or, correspondingly, the degree of "confinement" of the electrons within the spacer layer.

In this paper we present a realistic calculation of the electronic states that are responsible for the IXC, and further on we analyze how the two "models," RKKY and QW, are describing these. The method we use here has recently been used successfully to calculate the IXC of Co/Cu sandwiches in different orientations[5–7] and to calculate the size-quantized states within a Cu overlayer on fcc Co.[8] The computational method we use is in many respects closely related to the general formulation by Bruno, and is hence very suitable for the present study of the size-quantized states coupling the two layers.

The system we have chosen to study here is fcc Co/Cu/Co(100), partly because our earlier work has shown that the method we employ is able to reproduce experimental results for this system. But also because neither the RKKY model, the QW model, nor our calculation take into account exchange enhancements within the spacer layer that might become of importance when it is consisting of a transition metal, instead of a noble metal as in the present case. It is also a natural choice, since due to its favorable properties, this system has become *the* standard model system in the field of IXC, both for theoretical work as well as for different experimental investigations.

## II. INTERACTION-INDUCED DENSITY OF STATES

In this study we are focusing on the electronic states that arise from the scattering between two magnetic layers embedded in the nonmagnetic host. The magnetic layers are both consisting of five atomic layers, while the distance in between them is varied.

The change of the electronic structure when the interaction between the two layers is allowed for compared to the case of two independent layers is calculated in the way described in Ref. 7. There it is derived that the change of the integrated density of states (CIDOS) due to the interaction of the two magnetic layers with alignment $\alpha$ (F or AF), is given by

$$\Delta N_{\rm int}^{\sigma,\alpha}(\mathbf{k}_\parallel,\omega) = -\frac{1}{\pi}\,\mathrm{Im}\,\ln\det(1-G^n\tau_\sigma^{(1)}G^{-n}\tau_\sigma^{(2)}), \quad (1)$$

where $\omega$ is the energy and $\tau_\sigma^{(i)}(\mathbf{k}_\parallel,\omega)$ is the spin- ($\sigma$) and $\mathbf{k}_\parallel$-dependent $t$ matrix of the magnetic layer, which takes care of all multiple scattering processes within the magnetic layer $i$. In Eq. (1), the Green's function matrix of the spacer, $G^n(\mathbf{k}_\parallel,\omega)$, describes a propagation from one layer to the other separated by $n$ ML of unperturbed spacer material. It is worthwhile pointing out that all quantities entering Eq. (1) have been calculated from first principles (local spin density approximation to density functional theory) in the way described in Ref. 7.

In order to properly get the CIDOS we should work with the retarded Green's functions, which in turn means that $\omega=\epsilon+i\delta$, where $\delta$ is an infinitesimal imaginary part. For numerical reasons however, $\delta$ is here taken as a finite constant. By numerical differentiation of Eq. (1) with respect to the real part of the energy, $\epsilon$, we finally obtain the change in the density of states (CDOS).

In Fig. 1 the CDOS is shown in an energy window around the Fermi energy for the case of spacer layers with thicknesses of 6 and 10 ML and for $\mathbf{k}_\parallel$ corresponding to one of the two RKKY calipers of the "dog-bone" of the Cu Fermi surface, i.e., $q_2=(1.08,0)\pi/a$, where $a$ is the lattice constant of fcc Cu. In both curves in the region from 1 eV below to 1 eV above the Fermi energy, there are several

 0021-8979/96/79(8)/5638/3/$10.00 © 1996 American Institute of Physics

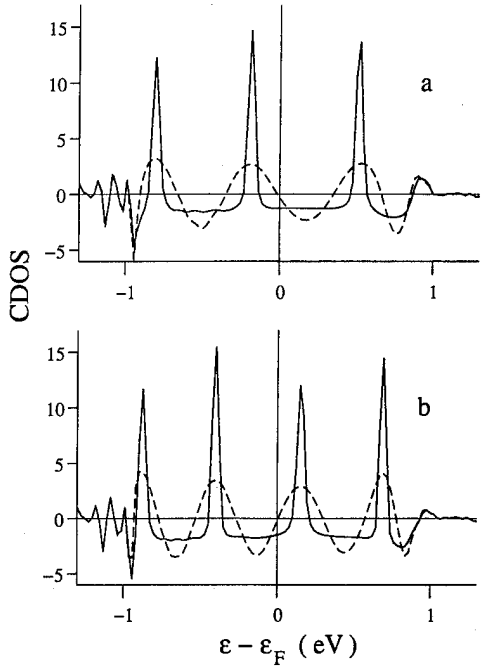



FIG. 1. The calculated CDOS for $q_2$, minority spin, ferromagnetic alignment, and with interlayer distances of (a) 6 ML and (b) 10 ML. Both the full calculation (solid curve) and its first-order approximation (dashed curve) is plotted. The Fermi energy is at zero energy.

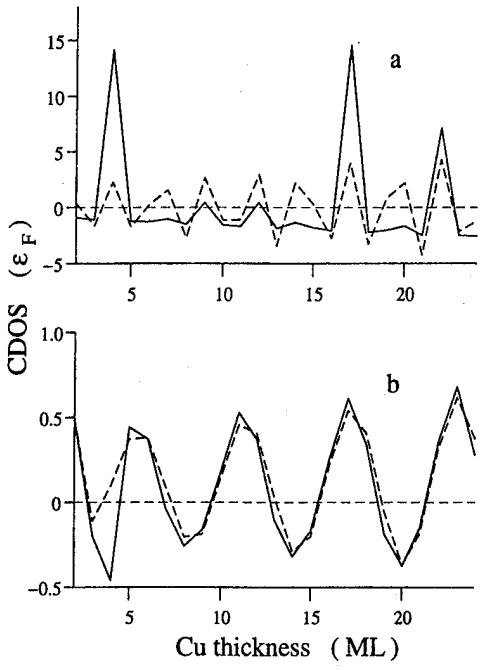



FIG. 2. The CDOS at the Fermi energy as a function of interlayer distance for the two stationary $\mathbf{k}_\parallel$ points: (a) $q_2$ and (b) $q_1$. The solid curves is for the full calculation and the dashed curve is for the first-order approximation.

sharp peaks. These CDOS was calculated for the states corresponding to the minority spin states of Co, and with ferromagnetic alignment. For majority spin states or antiferromagnetic alignment, the CDOS is much smaller without any sharp peaks. These peaks corresponds to electronic states strongly confined to the spacer layer due the presence of a partial gap in the minority spin states of the cobalt layer.[6] All this is in accordance with the QW models.[2,3] Also shown in Fig. 1 are the first-order approximations (FOA) to Eq. (1) when expanding the logarithm of the determinant according to

$$\ln \det(1-x) = \mathrm{Tr} \ln(1-x) = -\mathrm{Tr} \sum_{n=1} \frac{x^n}{n}. \tag{2}$$

These curves are smoothly oscillating as a function of the energy and may be viewed as rising from the interference when states are reflected only once at each layer. To be noted is that the maxima of the oscillations occur at exactly the same energies as the sharp peaks.

Almost bound states also exist for $q_1=(0,0)$, but only for larger binding energies. At the Fermi energy the full CDOS is here rather small and is oscillating smoothly. In Fig. 2 the CDOS at the Fermi energy is plotted as a function of the interlayer distances for the two stationary $\mathbf{k}_\parallel$, together with their respective FOA. For the $q_1$ curve it is clear that the two curves are in close agreement, and that a maximum occur about every 6 ML. On the other hand, for $q_2$, the FOA curve has a period close to 2.6 ML while the full calculation curve, due to its sharp peaks, has an effective period of ca. 13 ML. So while the $q_1$ indeed has a CDOS at Fermi energy oscillating with the corresponding RKKY period, 5.9 ML, as was suggested in Ref. 3, this is only true for the FOA in the case of $q_2$, or if the sharp peaks would be broadened. Also to be noted is that while the maxima of the CDOS are 30 times larger for $q_2$ than for $q_1$, the FOA is only five to eight times larger.

## III. COUPLING ENERGY

From the CDOS one can also calculate the interlayer coupling energy (see, e.g., Ref. 7). To calculate the free energy for one alignment $\alpha$ of the two magnetic layers, we integrate the CIDOS over the two-dimensional Brillouin zone (BZ) and the occupied part of the energy,

$$\Omega_{\mathrm{int}}^{\alpha} = -\sum_{\sigma} \int^{\mu} d\omega \int_{\mathrm{BZ}} d\mathbf{k}_\parallel \, f(\omega) \Delta N_{\mathrm{int}}^{\sigma,\alpha}(\mathbf{k}_\parallel, \omega), \tag{3}$$

where $f$ is the Fermi–Dirac distribution function. While maybe looking straightforward, this is a numerically demanding task. In order to avoid numerical problems the energy integral is here solved by a contour integral in the complex energy plane and the BZ integration is performed with a very dense mesh of special points.

For large interlayer distances it is possible to show that the contribution to this integral only will come from the Fermi energy and there from stationary calipers of the Fermi surface of the pure spacer layer. The fact that these calipers govern the asymptotic behavior of the IXC has been verified by direct calculation.[6]

The IXC energy is calculated for the same system as before. By dividing the BZ into two parts, the $q_2$ contribution is separated out as in Ref. 6. By expanding the logarithm of the determinant of Eq. (3), one can show that the FOA only contributes to the bilinear coupling, while in second

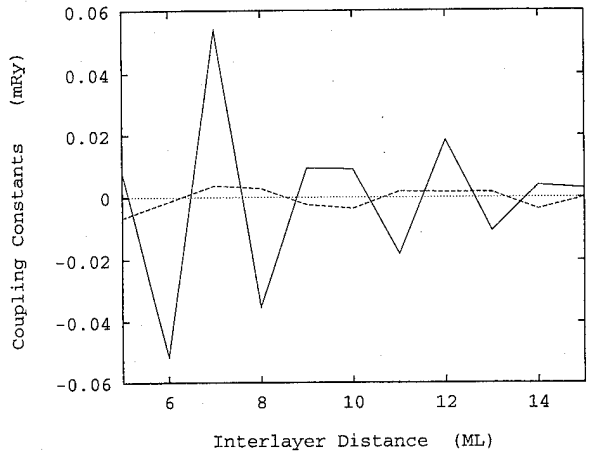



FIG. 3. The first- (solid curve) and second- (dashed) order contribution to the coupling constant $J$ are plotted as a function of interlayer distance.

order (SO, the $n=2$ term) there are both contributions to bilinear, $-J\cos(\theta)$, and biquadratic, $-J_2\cos(2\theta)$, coupling ($\theta$ is the angle between the magnetic moments of the two layers). In Fig. 3 the two first contributions to the bilinear coupling constant $J$ are plotted for the $q_2$ part of the coupling. As has been observed before, the largest part that is from the FOA follows closely the RKKY oscillation, with a period 2.6 ML. The SO contribution is much weaker and has a period between 4 and 5 ML, in good agreement with the expected 4.3 ML. This is the second harmonic of the RKKY period when the aliasing effect is taken into account. The calculated SO biquadratic contribution is of the same magnitude as the bilinear contribution, and has a similar period. Although small, the SO contribution to $q_2$ is almost of the same size as the FOA of $q_1$, for which the SO is truly negligible. The existence of higher-order contributions has been predicted within the QW model.[2]

In the calculations of IXC coupling here we have introduced a temperature of 1 mRy, which leads to a broadening of the CIDOS entering Eq. (3). A systematic investigation of the temperature effects will be published elsewhere.

## IV. CONCLUSIONS

From a calculation of the electronic states mediating the IXC, it is found to be a fundamental difference of the nature between the states at the two different stationary $\mathbf{k}_\parallel$ points. First, for the $q_1$ point the confinement is small and a FOA describes the states well. On the other hand, due to the development of a partial gap in the Co layer,[6] there is a strong confinement for $q_2$ that leads to almost bound states, or "true" QW states.

Since it is the FOA part of the CDOS that gives rise to the RKKY-like IXC with $2k_Fd$ oscillations, the $q_1$ contribution is purely RKKY. However, also for $q_2$ the RKKY part is dominating, since the higher harmonics are largely canceled when the BZ integration is performed. Only a weak SO harmonic is found with the expected $4k_Fd$ oscillation. The intrinsic biquadratic coupling appears first in SO, and is therefore only found for $q_2$, where it is of the same magnitude as the SO contribution to the bilinear coupling, i.e., much weaker than the full bilinear coupling.

As a summary, although some IXC-mediating states are found to be confined QW states, their extra contribution to the IXC beyond the RKKY coupling is rather small for Co/Cu(100). But, since it is not much smaller than the $q_1$ contribution it could be possible to experimentally observe it, which has not been done hitherto.

## ACKNOWLEDGMENTS

The work at the Naval Research Laboratory was financed by the Office of Naval Research. The calculations were performed on the CRAY computers of Höchstleistungsrechenzentrum (HLRZ), Forschungszentrum Jülich, and the NAVO center of the Department of Defense.

[1] P. Bruno and C. Chappert, Phys. Rev. Lett. **67**, 1602 (1991); Phys. Rev. B **46**, 261 (1992).
[2] D. M. Edwards and J. Mathon, J. Magn. Magn. Mater. **93**, 85 (1991); D. M. Edwards, J. Mathon, R. B. Muniz, and M. S. Phan, Phys. Rev. Lett. **67**, 493 (1991).
[3] J. E. Ortega and F. J. Himpsel, Phys. Rev. Lett. **69**, 844 (1992).
[4] P. Bruno, J. Magn. Magn. Mater. **121**, 248 (1993).
[5] P. Lang, L. Nordström, R. Zeller, and P. H. Dederichs, Phys. Rev. Lett. **71**, 1927 (1993).
[6] L. Nordström, P. Lang, R. Zeller, and P. H. Dederichs, Phys. Rev. B **50**, 13 058 (1994).
[7] P. Lang, L. Nordström, R. Zeller, and P. H. Dederichs, submitted to Phys. Rev. B (in press).
[8] L. Nordström, P. Lang, R. Zeller, and P. H. Dederichs, Europhys. Lett. **29**, 395 (1995).

# The growth of Fe on sulphur passivated Ge(100): A technique for avoiding intermixing

G. W. Anderson,[a] P. Ma, and P. R. Norton
*Interface Science Western, The University of Western Ontario, London, Ontario N6A 5B7, Canada*

The growth of Fe on Ge(100) surfaces results in the intermixing of Ge with the Fe overlayer, producing relatively thick magnetic dead layers. In this paper we describe a new technique, the growth of Fe overlayers on S-passivated Ge(100), which successfully prevents the intermixing of Ge with the Fe overlayer. Bcc Fe(100) is observed to grow epitaxially on this substrate, with the S floating out as an ordered overlayer. The S prevents intermixing by acting as a surfactant, holding the Fe on top of the substrate and preventing interdiffusion. The Fe overlayers are observed to be ferromagnetic in nature, displaying sharp hysteresis loops with easy axes along the Fe[010] directions. A uniaxial in-plane anisotropy is observed, which results in the two easy axes being inequivalent. © *1996 American Institute of Physics.* [S0021-8979(96)20108-8]

## I. INTRODUCTION

There is great interest in developing simple and efficient methods for growing magnetic overlayers directly on semiconductors because of the potential for integrating the desired magnetic properties of these systems with computer circuitry. However, problems usually arise because of intermixing of the semiconductor elements into the overlayer, which results in a degradation of the magnetic properties of these systems.

Interest in the growth of Fe on Ge stems from the good lattice match between the materials (1.3% mismatch) and the fact that high purity, low defect Ge wafers are readily available. However, previous investigations of the growth of Fe on Ge(100) have shown significant difficulties, due to the fact that Ge and Fe form many alloys.[1] For Fe growth at 150 °C, while the films are well ordered, a large amount of Ge interdiffusion was observed. This resulted in layers up to 100 Å showing no magnetic moment.[2] For growth at lower temperatures, the amount of interdiffusion was not as great, but the overlayers were rough and highly defected.[2]

In this investigation, the use of sulphur passivated Ge(100) substrates has been examined as a means to prevent this interdiffusion. Treatment of Ge(100) samples in an aqueous ammonium sulphide solution has previously been shown to result in the formation of a S-passivating layer, which prevents surface oxidation in air.[3] It is hoped that, in the same manner as the growth of Fe on S-passivated GaAs(100),[4] this passivation layer would act to prevent Ge intermixing and permit the growth of a magnetic, epitaxial Fe overlayer.

In this investigation the growth of Fe overlayers on S-passivated Ge(100) substrates at 25 °C and 150 °C has been investigated with Auger electron spectroscopy (AES), angle resolved AES (ARAES), low-energy electron diffraction (LEED), and magneto-optic Kerr effect (MOKE) measurements. We will show that this method successfully prevents the intermixing of Ge with the Fe overlayer. Bcc Fe(100) is observed to grow epitaxially on this substrate, with the S floating out as an ordered overlayer. The S prevents intermixing by acting as a surfactant, holding the Fe on top of the substrate and preventing interdiffusion. The Fe overlayers are observed to be ferromagnetic in nature, displaying sharp hysteresis loops with easy axes along the Fe[010] directions. A uniaxial in-plane anisotropy is observed, which results in the two easy axes being inequivalent.

## II. EXPERIMENT

The experiments were carried out on a two-chamber UHV system. The main growth/analysis chamber is diffusion and sublimation pumped, achieving a base pressure $<1\times10^{-10}$ Torr. The chamber is equipped with a Fe evaporation source, a four-grid retarding field analyzer for LEED measurements, and a CLAM electron energy analyzer (Fisons Instruments) for AES and ARAES measurements. It is also interfaced, via a two stage differential pumping station, to a 2.5 MV van de Graaff accelerator, which can be utilized for ion beam measurements. The LEED images were collected with a CCD camera from the LEED screen and recorded on videotape. The VCR is interfaced to a computer system, allowing subsequent analysis of the LEED spot intensities and widths.

The second chamber is a UHV loadlock chamber, pumped with a diffusion pump backed turbo pump (base pressure $2\times10^{-10}$ Torr). This chamber has a magnetic transfer arm for sample transfer between the two systems and is equipped with the MOKE apparatus for magnetic characterization of the samples.

Ge wafers [aligned to within 0.25° of the (100) direction] from the Semiconductor Processing Company, were utilized in this investigation. The samples were prepared by an *ex-situ* S-passivation treatment. First, the samples were degreased in hot methanol (50 °C–60 °C) and then immersed in an aqueous ammonium sulphide $[(NH_4)_2S]$ solution at 65 °C for 20 min. At the end of this treatment the samples were rinsed in methanol, blown dry with He, and inserted into the loadlock chamber. Samples prepared in this manner exhibit a (1×1) LEED pattern without any further preparation. The presence of a small amount of C and O contamination was detected. Prior to Fe deposition the samples were

[a]Present address: Dept. of Physics, University of California, Davis, CA 95616.

 0021-8979/96/79(8)/5641/3/$10.00 © 1996 American Institute of Physics 

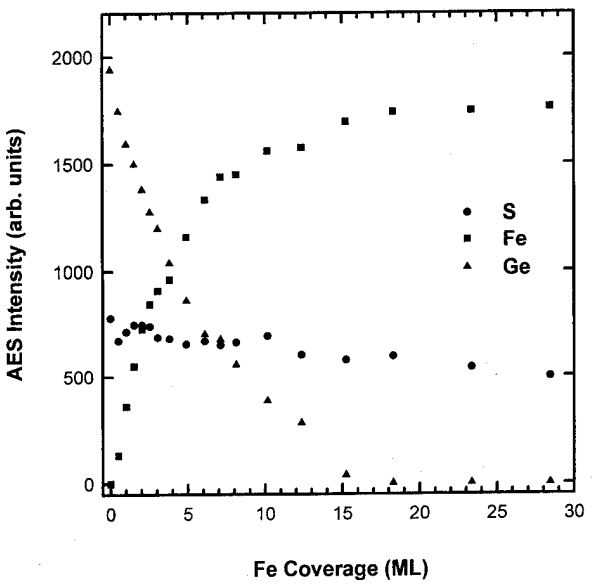



FIG. 1. The S, Fe, and Ge AES intensities during Fe deposition at 25 °C.

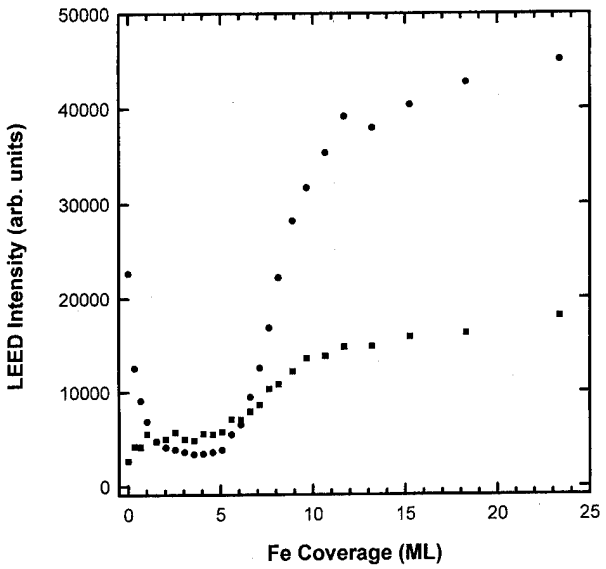



FIG. 2. The change in intensity of two LEED spots during Fe deposition at 150 °C. The circles represent the Ge[2,0] and Fe[1,1] LEED spots, while the squares represent the S/Fe(100) [1/2,1/2] LEED spots.

annealed to 190 °C, which results in an improvement in the surface order[3] and removal of the surface contamination.

The Fe was deposited from a liquid nitrogen shrouded sublimation source onto the substrate, at a rate of 1.6 ML min [where 1 ML corresponds to the Fe(100) surface density]. The Fe coverages were determined via a Rutherford backscattering calibration of the evaporation rate onto an Al substrate.[5]

## III. RESULTS AND DISCUSSION

AES measurements were utilized to look for Ge interdiffusion into the Fe overlayer during Fe deposition. Figure 1 illustrates the intensity of the S (152 eV), Fe (703 eV), and Ge (1147 eV) AES signals during Fe deposition, with the substrate held at 25 °C. The Fe signal is observed to increase with coverage as expected, beginning to level off at about 7 ML. The S signal is observed to decrease slightly for Fe coverages up to 25 ML. This suggests that, as in the growth of Fe/S/GaAs(100),[4] the S floats out on top of the Fe surface during overlayer growth, perhaps helping to stabilize the high-energy Fe surface. The Ge signal is observed to decrease exponentially with Fe coverage, being undetectable by a coverage of about 18 ML. These results indicate that Ge is not intermixed through the Fe overlayer. For growth with the substrate held at 150 °C, similar results were observed, indicating that the interdiffusion is also prevented at elevated temperatures.

As most of the S floats out on top of the film, the most likely mechanism by which the S prevents interdiffusion is by acting as a surfactant. Thus, as Fe is deposited the S preferentially bonds to the Fe, holding it on top of the Ge substrate, preventing any chemical interaction. As further Fe is deposited, the S floats out, and is no longer attached to the Fe at the Fe/Ge interface. However, now the Ge can only diffuse into the overlayer by bulk diffusion (as opposed to surface diffusion in the absence of S). Bulk diffusion is a more highly activated process, and does not appear to be energetically feasible at these temperatures.

The structure of the Fe overlayers were investigated with LEED and ARAES experiments. LEED was used to examine the long range order of the samples during Fe deposition. Initially, the S/Ge(100) substrate showed a good, sharp (1×1) LEED pattern. As Fe was deposited at 25 °C the substrate pattern was observed to fade into an increasing background, completely disappearing by the time 2 ML of Fe had been deposited. As more Fe was deposited an overlayer pattern begins to develop at a coverage of approximately 5 ML. The diffraction beams were extremely broad, with the spots being approximately four times the width of the substrate pattern. As further Fe was deposited, the pattern increased in strength, but was never observed to sharpen. Thus, while growth at 25 °C proceeds without any significant interdiffusion, the overlayer is not well ordered and likely highly defected, as observed in the previous study of Fe/Ge(100).[2]

Figure 2 displays the intensity of two LEED spots during Fe deposition at 150 °C. As for deposition at 25 °C, the substrate LEED pattern is observed to fade into an increasing background during the initial phase of deposition, disappearing completely by an Fe coverage of 2 ML. With further Fe deposition, a pattern due to the Fe overlayer begins to form at a coverage of 4.5 ML. However, at this temperature the pattern is considerably sharper, with the spot widths being comparable to those of the initial substrate pattern, indicating that the Fe overlayer is as well ordered as the substrate. Comparison of the observed energy dependence of the pattern with previous LEED IV data[6] identified this pattern as being due to $c(2\times2)$S Fe(100).

ARAES measurements have proven to be a useful technique in examining the short range order of metal overlayer systems.[7] In this technique, modulations in the angular dis-

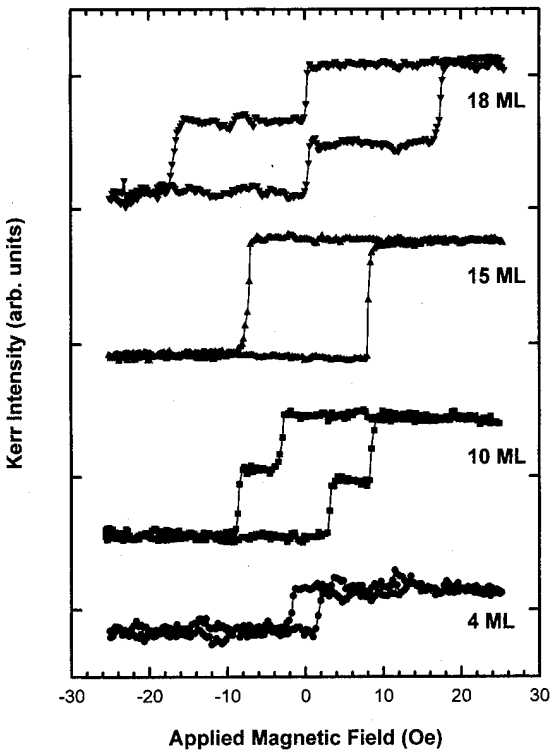



FIG. 3. MOKE hysteresis loops for various Fe films grown at 25 °C. The effect of the uniaxial anisotropy can be seen in the presence of two-step hystersis loops.

tribution of the AES electrons are used to gain information about the local structural environment of the emitting atoms. ARAES measurements of this system show that the Fe overlayers grow as bcc Fe(100) on the S/Ge(100) substrate.

The magnetic properties of the samples were determined by MOKE measurements. Ferromagnetic behavior is observed for samples grown at both temperatures for coverages above 3 ML, with the magnetic signal increasing in strength as the Fe coverage increases. The easy axes are located along the [010] directions, as expected. Figure 3 displays the hysteresis loops for some Fe overlayers. In some of the MOKE data a two-step hysteresis loop is observed. We propose that this is due to the presence of a uniaxial anisotropy (as previously observed for growth on GaAs[8] and MgO[9] substrates), which makes the two easy axes inequivalent (one is easier than the other). When the applied magnetic field is along the easier axis, a sharp, square hysteresis loop is observed. When it is along the less easy axis, the two-step loop is observed. In this loop, the outer transitions represent the switching to domains aligned with the magnetic field. The inner transitions represent the magnetic domains aligning along the easier axis in the low-field condition, only aligning with the applied field when it is strong enough to overcome the uniaxial anisotropy. The variation of the apparent coercivity of the inner-loop is puzzling and of unknown origin. Further FMR experiments are planned to investigate the presence of this anisotropy directly.

## IV. CONCLUSIONS

We have shown that the use of S-passivated Ge(100) as a substrate for the growth of Fe overlayers, successfully prevents the interdiffusion of Ge into the overlayer at temperatures of 25 °C and 150 °C. Bcc Fe(100) is observed to grow on this surface, being stabilized by the continual segregation of the S into an ordered $c(2\times2)$ overlayer. The S prevents intermixing by acting as a surfactant, holding the Fe on top of the substrate and preventing interdiffusion. For deposition at 25 °C, the Fe overlayer is poorly ordered and likely highly defected. However, for deposition at 150 °C, the Fe overlayer is as well ordered as the initial substrate. The Fe overlayers are ferromagnetic in nature, displaying good MOKE hysteresis loops. The [010] directions are the easy axes, however, the presence of an uniaxial anisotropy results in the two (010) directions being inequivalent (one is magnetically easier than the other). A possible interpretation of these observations would be in terms of an in-plane anisotropy.

## ACKNOWLEDGMENTS

Support of the Natural Sciences and Engineering Research Council of Canada (NSERCC) is gratefully acknowledged. The authors would also like to thank B. Heinrich for helpful discussions.

[1] M. Richardson, Acta Chem. Scand. **21**, 2305 (1967).
[2] G. A. Prinz, in *Ultrathin Magnetic Structures II: Measurement Techniques and Novel Magnetic Properties*, edited by B. Heinrich and J. A. C. Bland (Springer, New York, 1994), p. 35.
[3] G. W. Anderson, M. C. Hanf, P. R. Norton, Z. H. Lu, and M. J. Graham, Appl. Phys. Lett. **66**, 1123 (1995).
[4] G. W. Anderson, M. C. Hanf, and P. R. Norton, Phys. Rev. Lett. **74**, 2764 (1995).
[5] G. W. Anderson and P. R. Norton, Surf. Sci. **336**, 267 (1995).
[6] K. O. Legg, F. Jona, D. W. Jepsen, and P. M. Marcus, Surf. Sci. **66**, 25 (1977).
[7] W. F. Egelhoff, Jr., Solid State Mater. Sci. **16**, 213 (1990).
[8] J. J. Krebs, B. T. Jonker, and G. A. Prinz, J. Appl. Phys. **61**, 2596 (1987).
[9] J. R. Childress, A. Schuhl, J.-M. George, O. Durand, P. Galtier, V. Cros, K. Ounadjela, R. Kergoat, and A. Fert, in *Magnetism and Structure in Systems of Reduced Dimension*, Proceedings of the 1992 NATO Advanced Workshop in Cargèse, France (Plenum, New York, 1993).

# Data storage based on proximal probe techniques (invited) (abstract)

H. J. Mamin, B. D. Terris, and D. Rugar
*IBM Research Division, Almaden Research Center, 650 Harry Rd., San Jose, California 95120*

Recently, there has been considerable interest in examining the feasibility of using proximal probe techniques as the basis for a data storage device. These techniques, derived from the scanning tunneling microscope (STM) and atomic force microscope (AFM), provide a potential pathway to reaching the ultrahigh densities needed in the decades ahead. While these techniques offer high areal density, a number of formidable technical challenges must be met, however, in order to produce a device with realistic data rate, error rate, and overall reliability. In this talk we will review some of the approaches that have been taken, including those based on the STM, the AFM, and near-field optics. We will focus on the efforts in our laboratory to demonstrate realistic data rates at reasonably high densities using thermomechanical writing with an AFM tip,[1] and near-field recording with a solid immersion lens.[2] The prospects for parallel tip arrays and issues of overall implementation will also be addressed. © *1996 American Institute of Physics.* [S0021-8979(96)46108-6]

[1]H. J. Mamin and D. Rugar, Appl. Phys. Lett. **61**, 1003 (1992).
[2]B. D. Terris, H. J. Mamin, D. Rugar, W. R. Studenman, and G. S. Kino, Appl. Phys. Lett. **65**, 388 (1995).

 0021-8979/96/79(8)/5644/1/$10.00 © 1996 American Institute of Physics

# Recording performance of submicron track width thin film heads

T. T. Lam, Y. Luo, and J.-G. Zhu
*Department of Electrical Engineering, University of Minnesota, Minneapolis, Minnesota 55455*

H.-C. Tong and R. Rottmayer
*Read-Rite Corporation, 44100 Osgood Road, Fremont, California 94539*

This spin-stand measurement study focuses on recording characteristics at submicron scale track width. The pole tips of a set of identical thin film heads were trimmed from the air-bearing surface by focused ion beam etching. A set of thin film heads with track widths ranging from $W=2$ $\mu$m to $W=0.5$ $\mu$m were produced. Recording experiments were performed on a high precision spin-stand tester using these heads. Both on-track and off-track performances were studied and analyzed. As the track width is scaled down, degrading of recording performance is observed. When the width of a recording head is decreased, the onset of partial erasure occurs at a lower density, and the noise power per unit head track width increases. Further investigation on the track profiles reveals that the extent of partial erasure is higher at the track edge as density increases, and this phenomenon is more pronounced in narrower track width heads. © *1996 American Institute of Physics.* [S0021-8979(96)10208-0]

## I. INTRODUCTION

In the recent IBM 3 Gbits/in.$^2$ recording demonstration, it was shown that high track density approach seemed to have a fundamental advantage over high linear density approach.[1,2] In order to achieve high tracks per inch (TPI), understanding of the recording performance of narrow track thin film heads becomes critical. Here, we present an experimental study on recording and side writing properties of submicron track width thin film heads. Focused ion-beam etching process was employed to trim the pole tips from the air bearing surface (ABS). The recording characteristics at submicron scale track width were investigated by spin-stand measurements using the trimmed heads. The performance of the test heads was first evaluated in terms of their frequency responses, which include frequency domain partial erasure,[3,4] resolution, and integrated noise power measurements. Comparison among the test heads was made based on these basic signal and noise measurements. Finally, the use of frequency domain partial erasure measurement was extended to off-track measurements. Combining partial erasure and track profile measurements, the actual track width and the integrity of the track edge of narrow tracks at different linear densities were compared.

## II. EXPERIMENT

The pole tips of two sets of identical thin film inductive heads, 4.5 $\mu$m wide each, were trimmed from the ABS by high precision focused ion beam etching with a beam diameter less than 10 nm. The final widths of the trimmed heads ranged from $W=2$ $\mu$m to $W=0.5$ $\mu$m. The trimming depth was about 1 $\mu$m, approximately equals to the throat height of the heads. One head in each set was left untrimmed for comparison of recording performance. The sliders of the heads in set A are conventional designs with a fly height of about 3 $\mu$in. The sliders of the heads in set B are of "tripad" type with a fly height less than 1 $\mu$in. The parameters of the heads and disk are given in Table I.

The recording experiments were performed on a high precision spin-stand tester with a close loop laser interferometer positioning mechanism, which had a resolution of 0.026 $\mu$m. The linear velocity between the head and medium was kept at 12 m/s in each test, and the same head was used for writing and playback. Write current was adjusted to obtain the best overwrite for each head.

## III. SPIN-STAND TEST RESULTS AND DISCUSSION

### A. Nonlinear partial erasure and resolution

The recording performance of the test heads was first examined by a partial erasure measurement. Nonlinear partial erasure is defined as the nonlinear amplitude reduction of playback voltage at high recording densities. In this measurement, all 1's patterns were recorded at two recording densities $D$ and $D'$, such that the higher density was three times greater than the lower one ($D'=3D$). By comparing the amplitude of the fundamental component of the voltage spectrum for the high density ($3D$) pattern to that of the 3rd harmonic for the low density ($D$) pattern, the nonlinear partial erasure can be measured by the ratio $R$, defined as

$$R=V_{3D}(1\text{st})/3V_{1D}(3\text{rd}) \tag{1}$$

where $V_{3D}(1\text{st})$ is the amplitude of the 1st harmonic of a squarewave track written at density $3D$, and $V_{1D}(3\text{rd})$ is the amplitude of the 3rd harmonic of a track written at density $D$. In the experiments, density $D$ was kept low enough to ensure that linear superposition was valid for the lower density track. Figure 1(a) shows the measured partial erasure ratio as a function of the density ($D'$) for the three heads in set A (high fly height). The partial erasure ratio $R$ is unity at low density when linear superposition still holds for both tracks, then it starts to drop below unity as density increases, indicating the onset of partial erasure for the high density track. It is interesting to note that the onset of the partial erasure for narrower heads occurs at significantly lower recording densities. The slope of the partial erasure drop also becomes slightly steeper for narrower heads at high densities. Figure 1(b) shows the partial erasure curves for the three heads in set B (low fly height). At this lower fly height, similar dependence of the onset of the partial erasure is ob-

 0021-8979/96/79(8)/5645/3/$10.00 © 1996 American Institute of Physics 

TABLE I. Parameters of the heads and disk used in the experiments.

| Head | $P1/P2$ width($\mu$m) $W$ | Gap($\mu$m) $g$ | Fly height($\mu$in.) $y$ |
|---|---|---|---|
| $A1$ | 4.50 | 0.25 | 3 |
| $A2$ | 2.00 | 0.25 | 3 |
| $A3$ | 0.50 | 0.25 | 3 |
| $B1$ | 4.50 | 0.22 | 1 |
| $B2$ | 2.00 | 0.22 | 1 |
| $B3$ | 0.75 | 0.22 | 1 |
| Disk | Hc(Oe) | MrT(memu/cm$^2$) | $S^*$ |
| | 2200 | 0.79 | 0.87 |

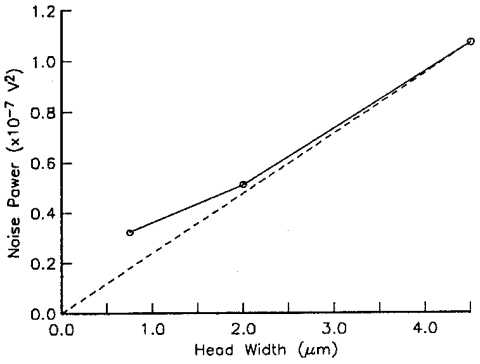



FIG. 2. Measured noise power (at 3900 fr/mm) as a function of head width. Dashed line represents the expected noise power using the 4.5 $\mu$m head as a reference. Excess noise is sensed by the head as head width decreases.

served, which is the quickening of the onset of partial erasure with reducing head width. Comparing the two sets of heads, lower fly height delays the onset of partial erasure, while the rate of partial erasure drop remains virtually unchanged.

The strong dependence of the onset of partial erasure on head width can be accounted for by two factors: (1) As head width decreases, the on-track field gradient is degraded, resulting in intertransition percolation at lower recording densities; (2) partial erasure can be dominated by transition percolation near the track edges which results in an effective track width reduction. Since the fly height and gap length of the heads in the experiments are still significantly smaller than the head width, the on-track field gradient should not be seriously affected by the width, and the dependence is most likely to be attributed to the second factor: transition percolation at the track edges.

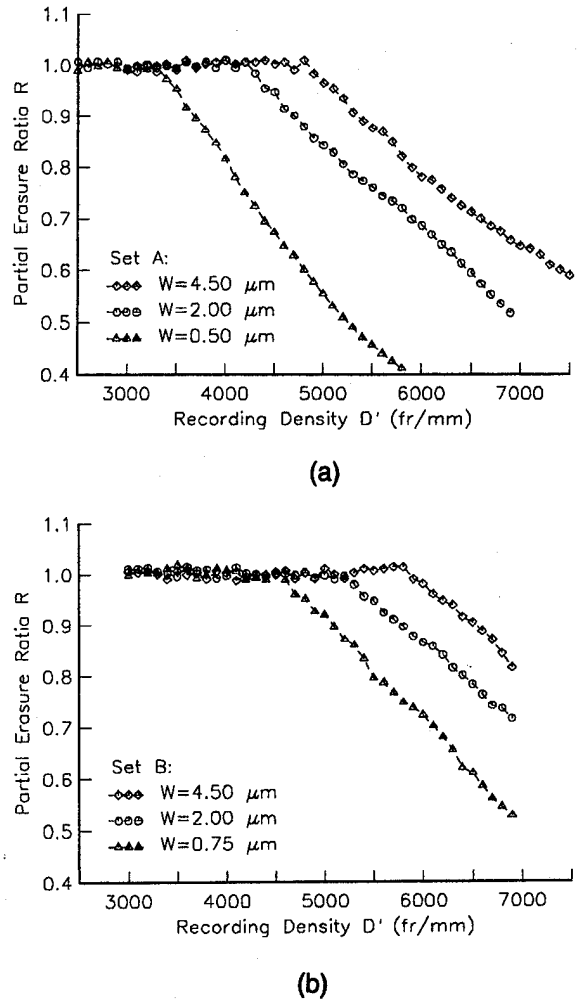



FIG. 1. Partial erasure vs recording density for the (a) high flying heads (set A), and (b) low flying heads (set B).

Since better performance was obtained for the heads in set B, only these heads were used in further signal and noise measurements. Resolution measurements show the $D_{50}$ (density at which the signal amplitude drops to half of its low density value) for heads $B1$, $B2$, and $B3$ are 5200, 4600, and 3400 fr/mm, respectively, which again indicates recording performance degrades with decreasing head width. The differences among the resolution curves can be explained by the differences in the isolated pulse width. For heads $B1$, $B2$, and $B3$, the widths are 358, 403, and 546 nm, respectively. Therefore, the degrading of recording performance can be attributed to an effective broadening of transitions, probably due to edge percolation caused by the poor writability of the saturated corners of the pole tips.

### B. Medium noise power

Since edge effects become significant for these narrow heads, noise near the track edge can be a significant portion of the total amount of medium noise. Transition noise can increase significantly in submicron tracks due to the mentioned edge transition broadening effects. In addition, as the head width is reduced to submicron scale, the so-called erased band, in which track edge noise manifest itself,[5] can have a width comparable to the recorded track. Therefore, the measured medium noise power at a high density (3900 fr/mm) no longer scales linearly to zero with the head width, as shown in Fig. 2. The "expected" noise power, or linear extrapolation of noise power against head width is obtained using the 4.5 $\mu$m wide head as a reference. As the head width is reduced, the measured medium noise power exceeds the linear extrapolation by an increasing amount. This indicates the medium noise power sensed by the narrower heads

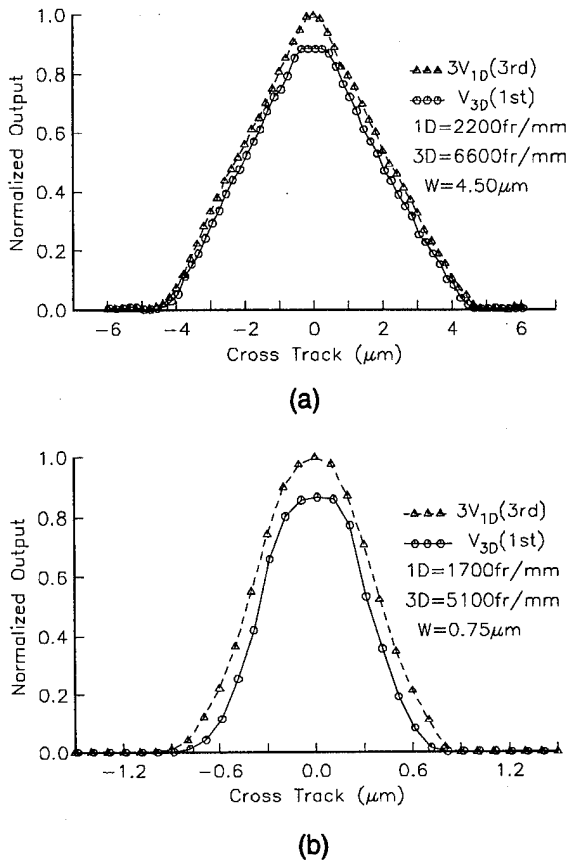



FIG. 3. Track profiles of the $1D$ and the $3D$ tracks. 3rd harmonic of the $1D$ track and 1st harmonic of the $3D$ track are measured using the (a) 4.50 $\mu$m wide and (b) 0.75 $\mu$m wide low flying heads.

is dominated by the noise near the track edge, which includes noise from broadened edge transitions and track edge noise.

### C. Cross-track profile

In order to examine the integrity of recorded transitions in the cross-track direction, the same technique as used in the partial erasure measurements was employed to study the cross-track profiles at different recording densities. Figure 3(a) shows two measured cross-track profiles for head $B1$ ($W$=4.50 $\mu$m), measured using a step size of 0.2 $\mu$m. The triangular symbols represent the 3rd harmonic voltage amplitude for a track recorded at density $D$=2200 fr/mm and the amplitude is scaled up by a factor of three. The circular symbols represent the fundamental component of the voltage amplitude for a track recorded at density $D'=3D=6600$ fr/mm, at which the partial erasure ratio $R$ is 0.88. Since the voltage harmonics were measured at the same frequency, the same head sensitivity functions were assured for these two different recording densities. In the absence of partial erasure, the two profiles should coincide with each other. However, in our case, the cross-track profile for the higher density track exhibits a plateau in the center, whereas the plateau is much less significant for the lower density track. Also, the slopes beyond the plateau of the cross-track profiles are similar for the two recording densities. The triangular shaped profile for the lower density track indicates that the read and write widths are essentially the same. The pronounced plateau for the higher density track indicates that the actual track width becomes smaller than the read track width. This measurement confirms that the onset of the partial erasure shown in Fig. 1(b) is mainly due to transition percolation at track edges. In other words, partial erasure starts from the track edge and yields an effective track width reduction.

Figure 3(b) shows similar track profiles measured using head $B3$ ($W$=0.75 $\mu$m). In this case, $D$=1700 fr/mm and the step size is decreased to 0.1 $\mu$m. A reduction in track width in the higher density track is again observed, as indicated by the increased plateau width and narrow base. The extent of the reduction, however, is relatively more significant in this case of a much narrower track. The decrease in the width of the higher density track is much more pronounced, and there is also an increase in the curvature of the slopes near the base of the profile. This increased curvature indicates the signal near the edge of the higher density track is weaker compared to the rest of the track, due to track edge percolation.

The track profile measurement confirms the poor writability of the edges of the heads, which is likely to be caused by the saturation at the corners of the pole tips. This corner saturation degrades the effective write field gradient, reduces track width, and essentially broadens transitions. As the saturated corners become a significant portion of the head as head width decreases, the edge field dominates the performance of the head. As a result, partial erasure at high densities mainly comes from edge erasure in submicron tracks. The narrower the track, the worse the effective field gradient because of the increase in proportion of the poor writing corners. It is the degraded write field that quickens the onset of partial erasure in narrower tracks. The degradation is also reflected in the medium noise measurement, and eventually confirmed by the track profile measurement.

## IV. CONCLUSION

Recording performance of submicron track thin film heads was systematically examined by spin-stand measurements. As head width is reduced, the onset of partial erasure shifts to lower densities, and an excess amount of noise is sensed by the narrow heads. Analysis of track profiles shows that the degradation of performance originates at the edge of a recorded track. It is concluded that for the narrow track heads, partial erasure starts from the track edge and effectively reduces the track width at high recording densities. It is believed that the head corner saturation is partially responsible for the degradation of recording performance for the narrow heads. High moment write heads may be necessary to keep the corners of the pole tips free of saturation.

[1] C. Tsang, H. Santini, D. McCown, J. Lo, and R. Lee, TMRC'95 (to be published).
[2] C. Tsang, J. Appl. Phys. **69**, 5393 (1991).
[3] X. Che, IEEE Trans. Magn. **31**, 3021 (1995).
[4] J.-G. Zhu, T. T. Lam, Y. Luo, and X. Ye, these proceedings.
[5] J.-G. Zhu, X.-G. Ye, and T. C. Arnoldussen, IEEE Trans. Magn. **29**, 324 (1993).

# Effects of write current switching time on recording characteristics (abstract)

F. Tomiyama, H. Takano, and Y. Shiroishi
*Central Research Laboratory, Hitachi, Ltd., Kokubunji, Tokyo 185, Japan*

M. Suzuki
*Data Storage and Retrieval Systems Division, Hitachi, Ltd., Odawara, Kanagawa 256, Japan*

Y. Sugita
*Central Research Laboratory, Hitachi, Ltd., Kokubunji, Tokyo 185, Japan*

High-frequency recording is essential for a recording channel with both a high data rate and a high linear recording density, and this study examined the ways in which performances are affected by the switching time of the write current, $t_s$, and the disk velocity, $v$. The switching time, defined as $(t_r+t_f)/2$, where $t_r$ and $t_f$ are the rise time and the fall time of the write current, was changed from 5 to 20 ns, while $v$ was changed from 12 to 26 m/s. Co-based thin-film media with a coercivity of about 2.5 kOe and a remanence-thickness product of about 100 G $\mu$m were used for recording the data. The flying height of the head was maintained at 50 nm regardless of disk velocity. This study confirmed that the overwrite characteristics are strongly related to the product of $t_s$ and $v$. Overwrite here was defined as the ratio of the residual fundamental frequency component amplitude of a 21 kFCI signal to the original one after overwriting with a 86 kFCI signal. Suitable overwrite characteristics were obtained when $t_s^* v$ was smaller than $\pi a$, where $a$ is the transition parameter derived from the equation proposed by Williams and Comstock.[1] The transition length on the medium was determined primarily by $\pi a$ when $t_s^* v$ was smaller than $\pi a$, but was determined by $t_s^* v$ when $t_s^* v$ was larger than $\pi a$. Linear density characteristics and noise characteristics and their relationship to the medium properties will also be addressed in this talk. © *1996 American Institute of Physics.* [S0021-8979(96)46208-2]

[1]M. L. Williams *et al.*, Am. Inst. Phys. Conf. Proc. **5**, 738 (1972).

 0021-8979/96/79(8)/5648/1/$10.00 © 1996 American Institute of Physics

# Bit-shift performance investigations at different skew angles and for different media orientations

S. B. Hu and B. Liu
*Magnetics Technology Centre, National University of Singapore, Singapore 0511*

C. S. Lee
*Western Digital (S) Pte Ltd., 750-B Chai Chee Road, Singapore 1646*

Bit-shift performance was investigated at different skew angles and for media with different orientation. Results indicate that the bit-shift value increases as the skew angle increases for both planar orientated media and near-isotropic media. As the skew angle increases, the off-track capability, described by the bit shift at different off-track distances, decreases and the bit-shift profile becomes asymmetric. Comparison of normalized bit-shift values (normalized according to the bit shift at 0° skew angle) shows that the bit shift of the near-isotropic media is not as sensitive to skew angle variation as the media with strong orientation. © *1996 American Institute of Physics.* [S0021-8979(96)10308-7]

## I. INTRODUCTION

Rotary actuators are used in most of today's disk drives for the positioning of read/write heads. The rotary actuator introduces a varying skew angle at different radii. The skew angle, the angle between track direction and slider direction, can vary by as much as 25°–30° in present disk drive design.[1] It has been reported that a nonzero skew angle will make recording performance asymmetric from the track center. Reported results also show that a nonzero skew angle will also induce offset of transitions from the track center and an increase in side reading.[2]

Bit shift, which occurs in closely spaced data bits, affects performance of various detection schemes. Bit-shift analysis measures the timing aperture of a recording system and evaluates the expected error rate. Bit-shift testing and characterization are important parts in recording system design.

Though bit-shift performance at different recording conditions has been studied,[3] a report on the bit-shift performance at different skew angles has not been seen yet. Furthermore, not much work on the relationship between media orientation and bit-shift performance at different skew angles has been addressed, even though the effects of media orientation on transition noise and the signal-to-noise ratio have been reported.[4,5]

This paper presents results of experimental investigations on the bit-shift performance at different skew angles. Special attention is also paid to the impact of the skew angle on the off-track capability and media with different orientations.

## II. EXPERIMENT

### A. Bit-shift profile and off-track capability

Both track profiles and bit-shift profiles can be used to describe the off-track capability of a given head-disk integration. The bit-shift profile is a plot of the bit shift at different off-track distances, while the track profile is a plot of track average amplitude (TAA) at different off-track distances. The main advantage of bit-shift profile is that it describes the off-track capability from error rate viewpoint, which is of special importance in achieving a reliable disk drive design.

### B. Experimental setup

All experimental investigations were conducted with a selected set of transverse pressure contour (TPC) sliders. Testing was carried out at a fixed testing radius ($r$=1.65 in.) of 3.5 in. disks. The coding scheme used is (1,7) code. Bit-shift is measured at analysis level of $10^{-6}$, with a sample level of $10^8$.

#### 1. Media

Two types of media were used: near-isotropic media (media *A*) and orientated media (media *B*). All media used are of similar *Hc*, *MrT* values: $Hc=1800\pm50$ Oe and $MrT=2.20\pm0.1$ m emu/cm$^2$. Here, *Mr* and *T* are the the remanence and media thickness, respectively. Typical *Hc* orientation ratios of the near-isotropic media and the orientated media are $1.01\pm0.01$ and $1.4\pm0.05$, respectively. The *Hc* orientation ratio is the ratio of *Hc* in track direction to that in radial direction: $Hc_{\parallel}/Hc_{\perp}$.

#### 2. Positioning accuracy

To obtain a reliable bit-shift profile, the testing system itself must have high linear positioning accuracy and low hysteresis in positioning operation. A Guzik 1701 MP micropositioning spin stand with air bearing spindle was used in all experiments to be reported. The linear positioning accuracy and positioning hysteresis of such a system are 1.2 and 0.4 $\mu$in., respectively.

TABLE I. Spindle speed for 1.5 $\mu$in. gap flying height and testing parameter setup.

| $\theta$ | rpm | Bit cell (ns) | *M*-frps |
|---|---|---|---|
| 0° | 3077 | 37.15 | 13.46 |
| 5° | 3391 | 33.69 | 14.84 |
| 10° | 4136 | 27.62 | 18.1 |
| 15° | 4895 | 23.34 | 21.42 |
| 20° | 5499 | 20.7 | 24.16 |

 0021-8979/96/79(8)/5649/3/$10.00 © 1996 American Institute of Physics 

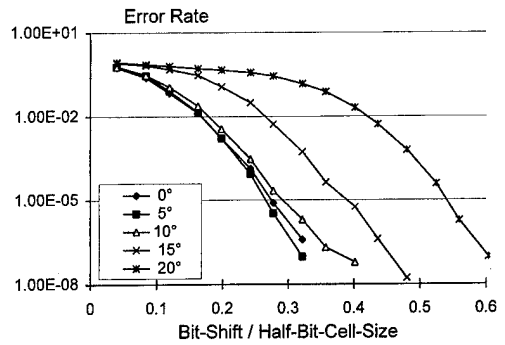



FIG. 1. Bit-shift plots at different skew angles (for media A: the orientated media).

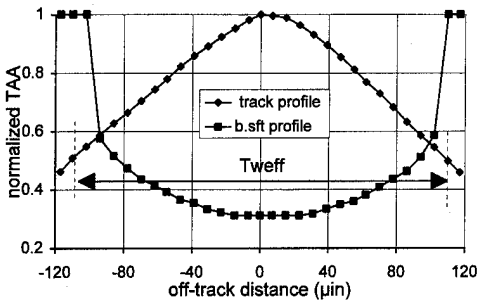



FIG. 3. Comparison between the normalized bit-shift profile and the track profile of the orientated media.

### 3. Constant flying height

The gap flying height used in all experiment reported in this paper is 1.5 $\mu$in. The flying height is measured by the dynamic flying height tester of phase metrics.

The gap flying height of TPC sliders is a function of skew angle. The spindle speed is adjusted so as to achieve 1.5 $\mu$in. flying height at different skew angles. The spindle speed, bit cell size and flux reversal rate used for one of the testing HGAs (head-gimbal assembly) is illustrated in Table I.

## III. RESULTS AND DISCUSSION

### A. Bit-shift plot

Figure 1 illustrates bit-shift plots at different skew angles. Figure 2 shows the relationship between the skew angle and the normalized bit shift at an analysis level of $10^{-6}$. The bit shift is normalized so that one unit corresponds to half of the bit cell size. A few degrees of skew angle shift was noticed from the experimental results. The shift value is fixed and is toward the positive direction. Such a shift is believed to be from alignment error in the testing system.

The following two conclusions can be drawn from the obtained results. (1) An increase in skew angle value will increase the bit-shift value at all bit-shift analysis levels investigated and for both positive and negative skew angles. (2) From a bit-shift viewpoint, it is better to restrict skew angle within 15°, as the bit shift will be increased significantly when skew angle value is above 15°.

### B. Bit-shift profile and track profile

Figure 3 compares the bit-shift profile and the track profile at a 0° skew angle. The track average amplitude (TAA) at the track center is normalized as one unit. The following can be observed from Fig. 3. (1) Though TAA reduces rapidly as off-track distance increases, the corresponding increase in the bit-shift value is not so significant when the off-track distance is not long. (2) The bit-shift value increases rapidly when the off-track distance is approaching 50% of effective track width (Tweff). Here, the effective track width is the distance measured between the two points corresponding to 50% of the maximum TAA value on the track profile.

### C. Bit-shift profiles at different skew angles

Figure 4 gives bit-shift profiles at different skew angles. The following have been noticed in all comparisons conducted between bit-shift profiles obtained at small skew angles (around 0°) and that at high skew angles (above 15°). (1) The bit-shift profile obtained at small skew angles is always below the bit-shift profile obtained at large skew angles if the off-track distance is not so long (say, 90 $\mu$in. in Fig. 4). (2) The bit-shift profile becomes asymmetric when skew angle is high.

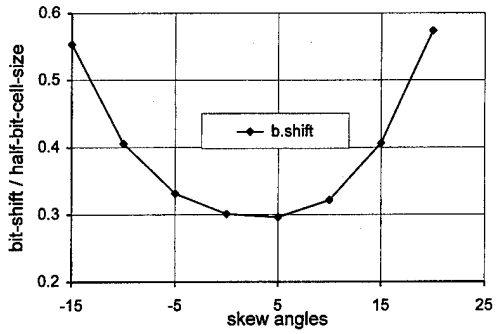



FIG. 2. Normalized bit-shift values at different skew angles (media A: the orientated media).

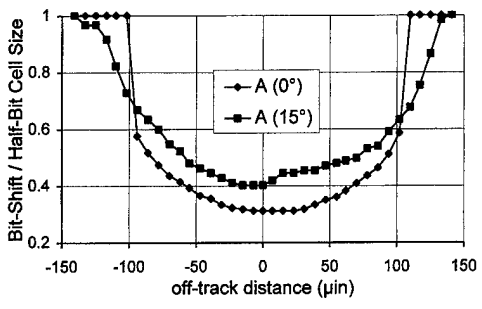



FIG. 4. Normalized bit-shift profile comparison at different skew angles (media A: the orientated media).

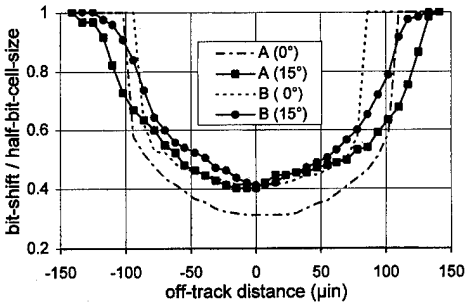



FIG. 5. Comparison of the bit-shift profiles between the near-isotropic media (B) and the orientated media (A) at 0° and 15° skew angles.

### D. Bit-shift profile and medium orientation

Bit-shift profiles for the two types of media were measured at different skew angles. Figure 5 compares the bit-shift profiles of the near-isotropic media and the orientated media at both 0° and 15° skew angles. The following observations can be made from Fig. 5. (1) The bit-shift profile becomes asymmetric for both types of media, as the skew angle goes to higher values (15° or above). (2) The bit-shift profile of the near-isotropic media is narrower than that of the orientated media. (3) The normalized bit-shift value of the near-isotropic media (media B) is not as sensitive to skew angle variation as the orientated media (media A).

## IV. CONCLUSIONS AND DISCUSSIONS

(1) Both the value of the bit shift and the shape of the bit-shift profile vary when skew angle is changed. Increased skew angle will increase bit-shift value, especially when skew angle is above 15°.

(2) The bit shift increases as the off-track distance increases and the bit-shift profile becomes asymmetric when skew angle is high. However, the increasing rate of the bit shift as the off-track distance increases is smaller than the TAA reducing rate, when the off-track distance is not too long.

(3) The bit-shift value of the near-isotropic media is higher than that of the media with strong orientation, when those media are of comparable *Hc* and *MrT* values.

## ACKNOWLEDGMENTS

The authors thank S. H. Soh of the Magnetics Technology Centre for his assistance in flying height measurement and Janice Yip of the Magnetics Technology Centre for her assistance in media magnetic property measurement.

[1] G. Clifford and D. Henze, IEEE Trans. Magn. **25**, 3713 (1989).
[2] K. Wiesen, R. M. Lansky, and C. Sobey, IEEE Trans. Magn. **29**, 4002 (1993).
[3] N. Bertram, *Theory of Magnetic Recording* (Cambridge University Press, Cambridge, MA, 1994).
[4] J. G. Zhu and X. G. Ye, IEEE Trans. Magn. **29**, 324 (1993).
[5] H. Aoi and F. Tomiyami *et al.*, IEEE Trans. Magn. **29**, 3715 (1993).

# Track-width dependence of transition jitter

P. Dhagat, E. Glavinas, A. Jander, D. G. Porter, R. S. Indeck, and M. W. Muller
*Magnetics and Information Science Center, Department of Electrical Engineering, Washington University, St. Louis, Missouri 63130-4899*

A simple model that represents the microstructure of magnetic medium as a rectangular tesselation predicts that the mean-square jitter is inversely proportional to the track width. We test this prediction using different width heads as well as creating different track widths by partially erasing the original track. We also simulate these experiments using a micromagnetic model. Our experimental and simulation results are found to be in agreement with the prediction. © *1996 American Institute of Physics.* [S0021-8979(96)06208-8]

## I. INTRODUCTION

Increasing the storage density of magnetic recording media requires both shortening the bit length and narrowing the track width. Density limits are set by noise levels and the inevitable loss of signal associated with the reduction of the storage medium per bit. Transition jitter is a major component of medium noise. We show in this article experimentally and by modeling that, as expected,[1] the transition jitter associated with permanent microstructural medium irregularities[2–4] and with relaxation statistics increases with decreasing track width. This finding emphasizes the importance of exploiting the microstructural permanence in adaptive noise compensation.[5]

In this article we investigate the track-width dependence of jitter. The observed transition jitter is an average, over the track width, of local deviations of the magnetization reversal from the intended transition center. The local deviations are determined by the down track and cross track dimensions of the magnetic units constituting the medium.

The medium may be represented by a brick wall model with bricks representing fixed magnetic microstructural units. As shown in Fig. 1, transitions are locally recorded at the nearest edge of the underlying magnetic unit. The mean-square transition jitter of this model is[6,7]

$$\langle \sigma_t^2 \rangle = \left(\frac{c}{W}\right)(\sigma_s^2), \tag{1}$$

where $(c)/(W)$ is the number of subtransitions, given a medium with transverse coherence length, $c$, and track width $W$.

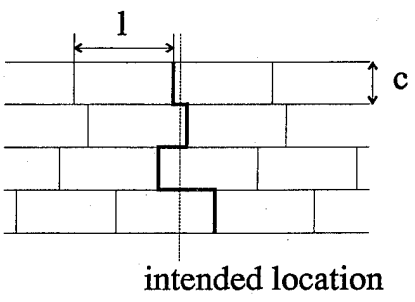



FIG. 1. Brick wall model of a magnetic medium.

$\sigma_t^2$ and $\sigma_s^2$ represent the variance of transition and subtransition positions, respectively. A detailed derivation of the above is presented in Ref. 7.

## II. EXPERIMENT

Our experiments were performed using a precision spin stand with accurate spatial positioning, a variety of thin-film and ferrite heads, and oxide and longitudinal thin-film disks. To establish the track-width dependence of transition jitter we wrote transitions at 100 preselected locations on the medium. Multiple writes at each location ensured minimization of write uncertainty and 128 read acquisitions provided small read uncertainty. We determined the actual position of the transition by fitting each transition output to a standard transition waveform. The position of maximum cross correlation of these waveforms is defined as the transition position. The standard transition waveform was obtained by averaging several read averaged transitions written at different locations. Such ensemble averaging minimized both read/write inaccuracy as well as position dependence of the standard transition waveform.

The displacement of the actual position of the transition from its intended position is defined as jitter. For each of the 100 preselected locations mean jitter is computed (from multiple writes at that location). Histograms of these mean jitter

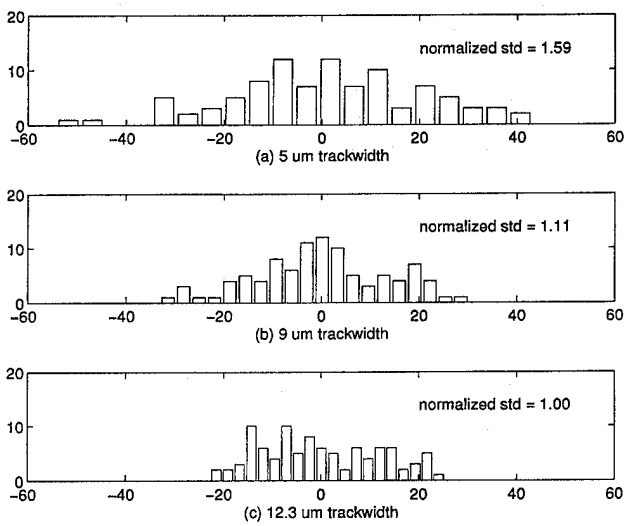



FIG. 2. Histogram plots for track widths of 5, 9, and 12.3 $\mu$m.

 0021-8979/96/79(8)/5652/3/$10.00 © 1996 American Institute of Physics

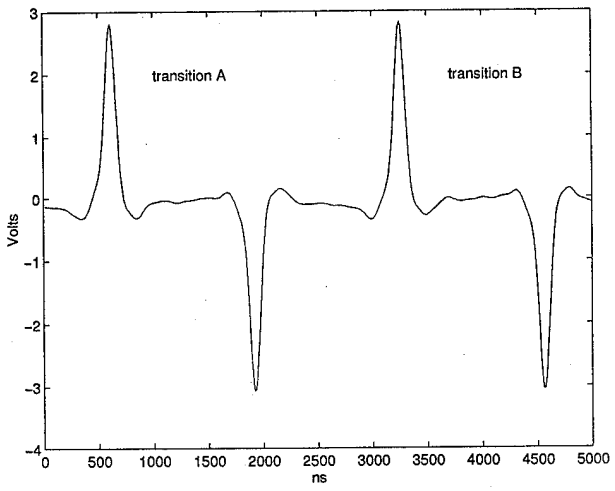



FIG. 3. Consecutive dibits for center-to-center measurements.

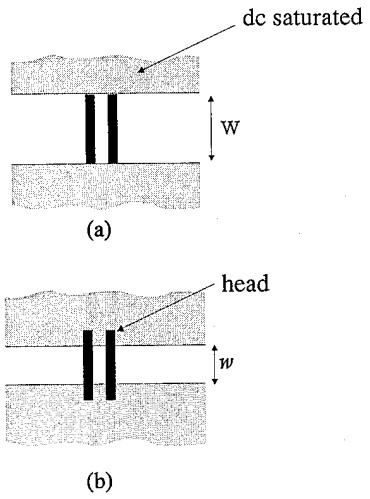



FIG. 5. (a) Original track width $W$. (b) Partially erased track width $w$ ($w<W$).

values are plotted in Fig. 2. The above approach measures jitter relative to the reference trigger which may vary from write to write due to limitations in the instrumentation. To eliminate the effect of a variable reference trigger we employed a center-to-center measurement technique, measuring the distance between two transitions. We wrote two consecutive dibits (Fig. 3) at randomly selected locations on the medium and determined their position jitter by correlating the first transition (A) and the third transition (B) with a standard transition waveform. The difference between the actual positions of transition (A) and transition (B) gives a measure of the actual distance between them. Jitter is computed as the difference between the actual distance and the intended distance. Presented in Fig. 4 are histograms of jitter values.

We repeated this experiment with heads of the same track-width and number of turns but with different structural parameters (e.g., pole thickness). We found that the standard deviation of jitter was unaffected by these parameters; no systematic error, such as amplitude effects, was seen. We also used a single head (thereby keeping flying height, gap

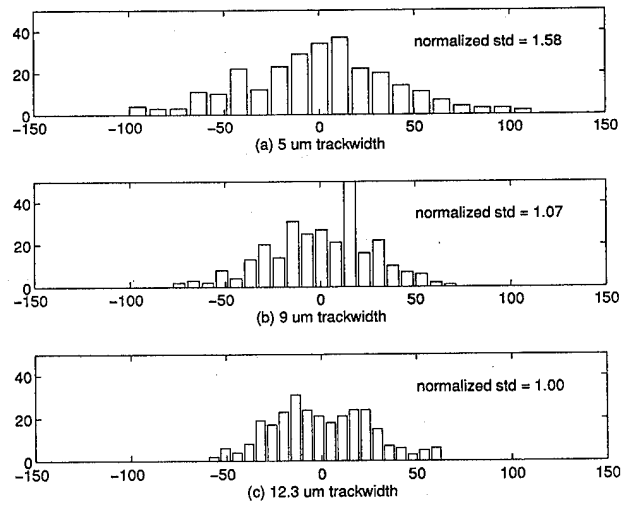



FIG. 4. Histogram plots for track widths of 5, 9, and 12.3 $\mu$m using center-to-center measurements.

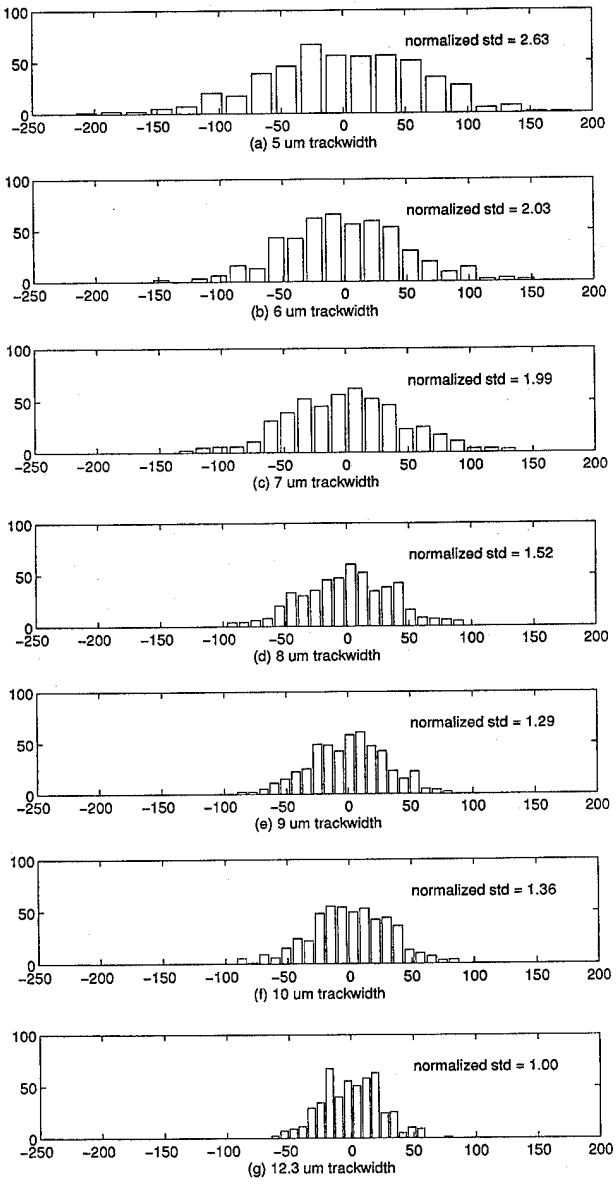



FIG. 6. Histogram plots for partially erased tracks with width $w=5$, 6, 7, 8, 9, and 10 $\mu$m. Original track=12.3 $\mu$m.

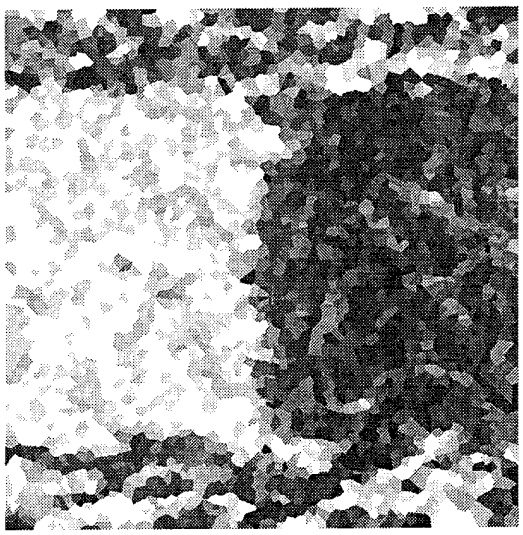


FIG. 7. An isolated transition in a partially erased track using a Voronoi tesselation medium.

width, and pole thickness identical from one run to another) to create tracks of different widths by partially erasing a track to various widths (see Fig. 5). Position jitter was determined as before by correlating transition A and transition B with a standard transition waveform. Figure 6 shows histogram plots for different track widths. In order to achieve the accurate placement of the transitions it was imperative to maintain control over tracking and down track timing. Accurate timing was maintained by phase locking an oscillator to a signal on the disk. We measured thermal variations every 10 min, over the span of the experiment. Using the permanent physical microstructure of the underlying medium we infer thermal drifts to be less than 5% of the read track width.

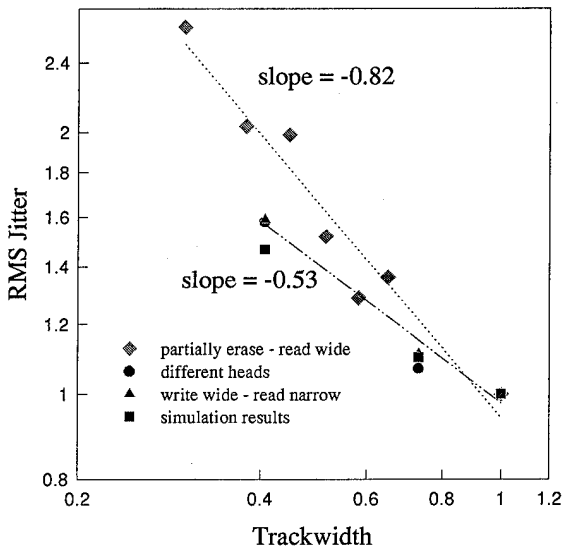



FIG. 8. rms jitter as a function of track width.

## III. RESULTS AND DISCUSSION

To augment our recording tests we simulated these experiments using a Voronoi tesselation medium (see Fig. 7). From the histogram plots for each track width we obtain a mean-square value for transition jitter. Equation (1) predicts that ratios of mean-square values plotted against the ratios of corresponding track widths on a log scale follow a slope of $-\frac{1}{2}$. A modification of Eq. (1) predicts more rapid increase of jitter with decreasing track width for partially erased tracks. To account for side writing, edge effects, and erased medium noise we assume the effective track width to be linearly proportional to the signal amplitude and plot in Fig. 8 mean-square ratios versus corresponding effective track width ratios (base track width=12.3 $\mu$m) for experimental data. It is found that experimental and simulated results[8] closely follow theoretical predictions, supporting the proposed model of transition jitter.

Transition jitter measurements by Huang *et al.*[9] are also consistent with expectation and show increasing jitter with decreasing track width.

## IV. CONCLUSIONS

We have shown that transition jitter increases with decreasing track widths and validated our theoretical predictions with experimental results. These results provide valuable input to real-time pre-compensation schemes which aim at improving signal-to-noise ratio and recording densities by using the repeatability of medium induced effects.

## ACKNOWLEDGMENT

This work is supported in part by NSF Grants No. NCR-94-06197 and No. ECS-94-06198.

[1] H. N. Bertram, *Theory of Magnetic Recording* (Cambridge University Press, New York, 1994), p. 315ff, and references therein.
[2] R. S. Indeck and E. Glavinas, IEEE Trans. Magn. **29**, 4095 (1993).
[3] J. R. Hoinville, R. S. Indeck, and M. W. Muller, IEEE Trans. Magn. **28**, 3398 (1992).
[4] E. Glavinas *et al.*, IEEE Trans. Magn. (in press).
[5] J. A. O'Sullivan *et al.*, in *Proc. 28th CISS* (Princeton University, Princeton, NJ, 1994), pp. 1152–1155.
[6] H. N. Bertram and R. Arias, J. Appl. Phys. **71**, 3439 (1992).
[7] P. Dhagat, Master's thesis, Washington University, St. Louis, MO, 1995.
[8] D. G. Porter *et al.*, J. Appl. Phys. (in press).
[9] M. Huang, R. Chu, Y. Hsia, and T. Tran, IEEE Trans. Magn. **30**, 4281 (1994).

# Trilayer media for high track density longitudinal recording

J. Akiyama, Y. Ohinata, T. Hikosaka, T. Taguchi, and Y. Tanaka
*Communication and Information Systems Research Laboratories, Toshiba R&D Center, 1 Komukai Toshiba-cho, Saiwai-ku, Kawasaki 210, Japan*

This paper introduces a new recording method using a trilayer medium (recording layer/nonmagnetic layer/soft magnetic layer/substrate) to diminish the side written band width ($\Delta W$). Magnetostatic coupling between the soft magnetic layer in the media and the write head poles decreases the side fringing field off the track edges. Off-track overwrite experiments revealed that the trilayer media reduced $\Delta W$ by 40%–60% compared to the monolayer medium while maintaining the effective write track width and the linear resolution. © *1996 American Institute of Physics.* [S0021-8979(96)15608-5]

## I. INTRODUCTION

In order to achieve high track density in longitudinal recording, aiming at a level of 10 Gbits/in.$^2$ or higher, the side written band degradation near the track edges needs to be effectively suppressed. This paper introduces a new trilayer medium structure to diminish the side written band width ($\Delta W$) for conventional ring head writing.

Figure 1 shows the configuration of the new medium. The trilayer structure consists of a recording layer at the top, a nonmagnetic control layer underneath, and a soft magnetic layer at the bottom. Magnetostatic coupling between the write head poles and the soft magnetic layer in the media sharpens the write field distribution along and across the track resulting in a decrease of the side fringing field off the track edges. The nonmagnetic control layer is indispensable for adequately controlling the balance between effective head-to-medium magnetostatic coupling and undesired downward flux leakage from the recorded magnetization to the soft magnetic layer.

The side written band widths were measured using off-track overwrite experiments[1] developed by the authors. The effective write track widths ($TW_{\text{eff}}$) were measured by the conventional off-track profile method. The measured $\Delta W$ and $TW_{\text{eff}}$ of the trilayer medium (CoPtCr/Ti/CoFeTa) were compared with those of a CoPtCr monolayer medium. The on-track read/write performances including overwrite and linear resolution were also evaluated for both media.

## II. EXPERIMENT

A FeTaN metal-in-gap (MIG) head with a high $Bs$ of 1.6 T and coils of 50 turns was used for writing in this experimental study. The widths of top and bottom poles were both 5.5 $\mu$m, and the gap length was 0.3 $\mu$m. A 4.5-$\mu$m-wide MR head with 0.7 $\mu$m shield-to-shield gap was used only for evaluating on-track read/write performances. The head flying height was set to be 75 nm at a head-to-medium relative velocity of 7.38 m/s.

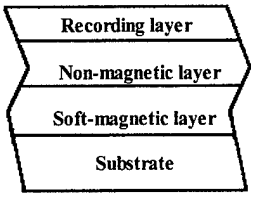



FIG. 1. Schematic view of the trilayer medium.

Two trilayer longitudinal media with different nonmagnetic Ti layer thickness and a monolayer longitudinal medium with almost the same magnetic properties were made by rf sputtering. The magnetic properties of all the media were measured using a vibrating sample magnetometer. The media specifications are shown in Table I.

The off-track overwrite recording was performed to measure the side written band width. Figures 2(a) and 2(b) show the schematic diagram of the off-track overwrite method and the measured off-track overwrite profile, respectively. At first, a signal (sig−1:60 kFCI) was recorded with the MIG head at a fixed position on the previously dc-erased medium. Then the head was displaced in the cross track direction and the old signal was partially erased by another signal (sig−2:42 kFCI) with the same write current as the sig−1 writing. This displacement ($x$) is the variable of the experiment. The fundamental of the residual sig−1 was read out with a spectrum analyzer (resolution band width: 30 kHz, video band width: 10 Hz) by the same head at the track center where the read sensitivity distribution was uniform. If all the above mentioned procedure is iterated with increasing the displacement ($x$), the off-track overwrite profile shown in Fig. 2(b) can be obtained. The head position was precisely controlled by a piezoelectric actuator, with an error of less

TABLE I. Media specifications.

| | Trilayer medium *A* | Trilayer medium *B* | Monolayer medium |
|---|---|---|---|
| ⟨Overcoated layer: *C*⟩ | | | |
| thickness (nm) | 20 | 20 | 20 |
| ⟨Recording layer: CoPtCr⟩ | | | |
| Hc (Oe) | 2000 | 1820 | 2000 |
| Mrt (memu/cm$^2$) | 1.54 | 1.63 | 1.5 |
| $S^*$ | 0.92 | 0.83 | 0.92 |
| ⟨Nonmagnetic layer: Ti⟩ | | | |
| thickness ($\mu$m) | 0.2 | 0.5 | ··· |
| ⟨Soft-magnetic layer: CoFeTa⟩ | | | |
| Bs (T) | 1.4 | 1.4 | ··· |
| Thickness ($\mu$m) | 0.5 | 0.5 | ··· |

 0021-8979/96/79(8)/5655/3/$10.00 © 1996 American Institute of Physics 

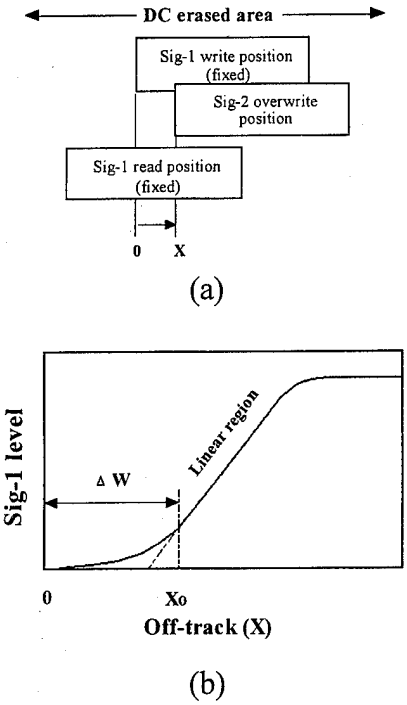



FIG. 2. Off-track overwrite method: (a) schematic diagram, (b) off-track overwrite profile.

than 25 nm. Furthermore, for all the media, the sig−1 level at $x=0$ was equal to the noise at the sig−1 frequency, which was about 10 dB larger than the electronic noise and little depended on the displacement. Then, the distance between the origin and the point ($x=x_0$) where the sig−1 begins to increase linearly was defined as the side written band width ($\Delta W$). The error in $\Delta W$ was estimated to be less than 0.1 $\mu$m.

In addition, the conventional off-track profiles were measured with the MIG head in order to examine the effective write track width ($TW_{\text{eff}}$) of the 60 kFCI signal.

## III. RESULTS AND DISCUSSION

### A. On-track read/write performances

On-track read/write performances were measured with the MIG write head and MR read head. Figure 3 shows the

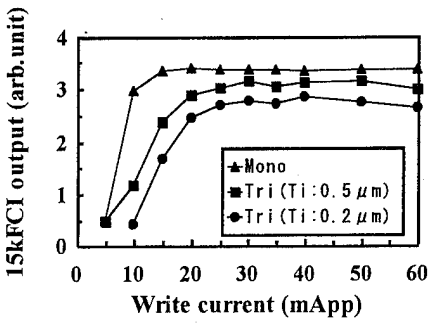



FIG. 3. Write current dependence of 15 kFCI signal output.

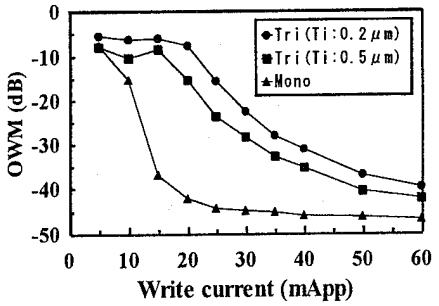



FIG. 4. Write current dependence of OWM. 15 kFCI signal is overwritten by 60 kFCI signal.

write current dependence of the reproduced output of the 15 kFCI signal. The current required to saturate the output increased in order of monolayer medium, trilayer medium $B$ with Ti:0.5 $\mu$m and trilayer medium $A$ with Ti:0.2 $\mu$m. The saturation output level also decreased in the same order as above. Figure 4 shows the write current dependence of the overwrite modulation (OWM). The OWM was defined as the reduction of the 15 kFCI signal fundamental after overwriting by the 60 kFCI signal. The write current needed to saturate the OWM increased in the order of monolayer medium, trilayer medium $B$, and trilayer medium $A$. However, it should be noted that both the trilayer media still had the level of less than −30 dB enough for practical use.

The above-mentioned write efficiency degradation of the trilayer media is thought caused by the decrease of the write field intensity due to the collimation of the head field bubble by the soft magnetic layer.[2]

In order to obtain the saturation output level and the OWM of less than −30 dB, the write currents ($Iw$: shown in Table II) for the subsequent experiments were set to be 20 $mA_{pp}$, 35 $mA_{pp}$, and 40 $mA_{pp}$, for monolayer medium, trilayer medium $B$, and trilayer medium $A$, respectively.

Figure 5 shows the measured recording roll-off curves for the sample media. The $D_{50}$'s were almost the same for the three media. The results showed that there was no significant difference in the linear resolution among the three media, and that the write head could generate enough field gradient to create a sharp transition even for the trilayer media. The results can be supported by the previous work[2] on the shaping of the head field by the soft magnetic layer, explaining that the presence of the soft magnetic layer decreases the write field intensity, but can maintain the write field gradient.

TABLE II. Measured on-track read/write performances.

| | Trilayer medium $A$ | Trilayer medium $B$ | Monolayer medium |
|---|---|---|---|
| Write current ($mA_{pp}$) | 40 | 35 | 20 |
| Normalized output | 0.83 | 0.93 | 1 |
| $D_{50}$ (kFCI) | 76 | 72 | 76 |
| OWM (dB) | −31.0 | −32.0 | −42.5 |

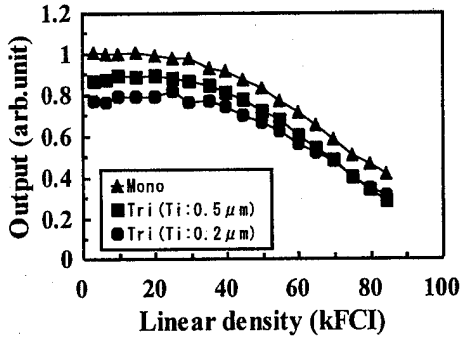



FIG. 5. Measured roll-off curves.

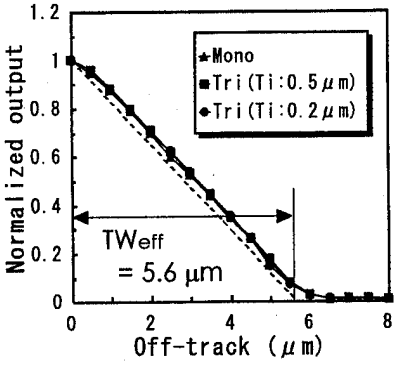



FIG. 7. Off-track profiles.

By the way, the saturation output decrease of the trilayer media can be thought caused by the downward flux leakage from the recorded magnetization to the soft magnetic layer rather than the decrease of write field intensity, because the write head could generate enough field gradient even for the two trilayer media, as above mentioned.

Furthermore, through the experiments, the reproduced wave forms for the trilayer media were extremely stable and no spike noise occurred, even in the presence of an external dc field of a few Oe applied to the soft magnetic layer using a permanent magnet. The results may reveal that the MR head was not sensitive to any magnetic change in the soft magnetic layer because the presence of the relatively thick nonmagnetic layer enough weakened the magnetostatic coupling between the MR head and the soft magnetic layer.

The on-track read/write performances are summarized in Table II.

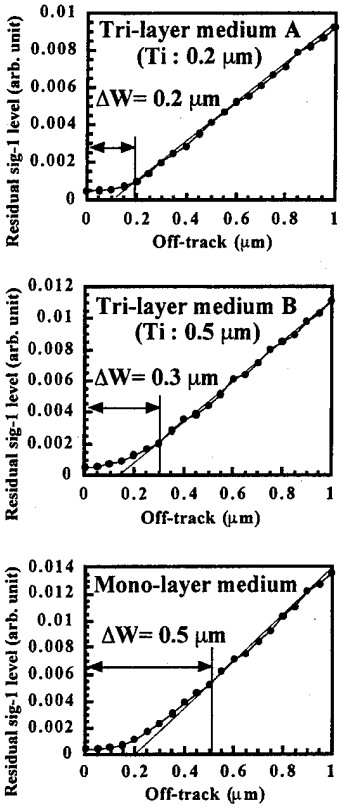



FIG. 6. Off-track overwrite profiles (sig−1:60 kFCI, sig−2:42 kFCI).

### B. Side writing performances

Figure 6 shows the off-track overwrite profiles measured with the MIG head. The side written band widths ($\Delta W$) were 0.2 $\mu$m for trilayer medium $A$, 0.3 $\mu$m for trilayer medium $B$, and 0.5 $\mu$m for monolayer medium. Both of the trilayer media thus effectively reduced $\Delta W$ by 40%–60% compared to the monolayer medium, and $\Delta W$ decreased with the decrease in thickness of the nonmagnetic layer of the trilayer medium. The $\Delta W$ reduction for the trilayer media is believed to be caused by the sharp fringing field distribution off the track edges due to the magnetostatic coupling between the write poles and the soft magnetic layer in the media. In addition, it is thought that the decrease of the nonmagnetic layer thickness increased the magnetostatic coupling and then more sharply decreased the fringing field resulting in the $\Delta W$ decrease.

Figure 7 shows the measured off-track profiles. The effective write track width ($TW_{\text{eff}}$) was defined as the distance between the origin and the point where the straight line through the point (0,1) and parallel to the linear region of the measured curves crosses the horizontal axis in Fig. 7. The results showed that all the three media had almost the same $TW_{\text{eff}}$ of 5.6 $\mu$m.

## IV. CONCLUSIONS

A novel trilayer medium structure was developed, to diminish the side written band width ($\Delta W$). Off-track overwrite experiments revealed that the trilayer media effectively reduced the $\Delta W$ by 40%–60% relative to the monolayer medium while maintaining the effective write track width and the linear resolution. This fundamental feature of thenew trilayer medium makes it a strong candidate medium for high track density longitudinal recording.

[1] Y. Tanaka and T. Taguchi, IEEE Trans. Mag. **31**, 2684 (1995).
[2] D. S. Bloomberg, IEEE Trans. Mag. **19**, 1493 (1983).

# Experimental analysis of the effects of tape thickness on magnetic recording

A. Friedmann,[a] D. Wei, H. N. Bertram, and J. K. Wolf
*Center for Magnetic Recording Research, University of California, San Diego, Mail Code 0401, La Jolla, California 92037*

R. Swanson and F. Jeffers
*Eastman Kodak Company, 3985 Sorrento Valley Blvd., San Diego, California 92121*

Advances in magnetic tape recording have produced media with magnetic layers as thin as 0.1 $\mu$m. In this article, a metal particulate tape with a magnetic layer thickness of ~0.37 $\mu$m is compared to a standard thick media tape with a magnetic layer thickness of ~4 $\mu$m. Measurements of the isolated pulse are made and shown to compare well with micromagnetic simulations. The replay voltage versus current is measured with a 4 $\mu$m track width, shielded magnetoresistive head at various densities. The thin tape shows better high density response at high currents than the thick tape. The simulations show that the transitions are sharper on the thin tape due to both the reduction in thickness, and an improvement in the particle orientation. The better oriented particles yield narrower pulses, thereby improving the high frequency response of the tape. Frequency response measurements are also taken with the magnetoresistive head, which yield a signal to noise ratio of >20 dB at 200 kfci. Last, overwrite performance versus current is compared for the two tapes plus a metal-evaporated (ME) tape with a 0.2 $\mu$m thick layer. A significant improvement in overwrite is seen on the ME tape. © *1996 American Institute of Physics.* [S0021-8979(96)10408-3]

## I. INTRODUCTION

One historical drawback of high density tape recording has been the thickness of the recording layer. Until recently, the magnetic layer thickness was always greater than the depth of the recorded transitions. This resulted in wider transitions and reduced high frequency response.[1,2] Recently, manufacturers have been able to reduce the magnetic layer thickness of tape to <0.5 $\mu$m, to as low as 0.1 $\mu$m.[3] In this article we will examine one such tape and compare it to a standard, thick media (SVHS) tape. The thin tape analyzed here is a Fuji double-coated, metal–particulate tape. The double coating refers to a process where first a nonmagnetic layer is deposited on the backing material for smoothness, and then the magnetic layer is added. The experimental results are compared with micromagnetic simulations to better understand the findings, as well as to calibrate the simulations.

## II. EXPERIMENTAL SYSTEM

A Honeywell 7600 reel-to-reel recorder was used for the measurements. The recording was done with a 15-turn, thin-film inductive head. The track width was 125 $\mu$m, the gap length was 0.3 $\mu$m, and the efficiency was 80%. The readback was performed using both an inductive head and a shielded magnetoresistive (MR) head. The inductive readback head had: 200 turns, a gap length of 0.27 $\mu$m, a track width of 250 $\mu$m, and an efficiency of 72%. The MR head was used for the frequency response measurements while the inductive head was used to measure the isolated pulses. It was necessary to use the inductive head for the isolated pulse measurements because of saturation of the MR head at low frequencies. The MR head was originally designed for disk recording, but a satisfactory mounting arrangement was found for the Honeywell system. The MR head had a shield-to-shield spacing of 0.55 $\mu$m and a track width of 4 $\mu$m.

The thin tape was a Fuji metal particle (MP) tape with a magnetic layer thickness of ~0.37 $\mu$m, a coercivity of 1780 Oe, and a remanence of 3000 G. The thick tape was a 3M SVHS tape with a thickness of about 4 $\mu$m, a coercivity of 935 Oe, and a remanence of 1390 G. The tape speed was 7.5 ips for the inductive readback head and 3.75 ips for the MR readback head.

## III. MEASUREMENTS AND ANALYSIS

For the measurements that will be presented, a simplified model of tape recording wherein the tape is viewed as having a number of laminae, each at a different depth, will help explain the different response characteristics of the two tapes. Each lamina is assumed to have its own transition with a fixed transition shape and center. The widths and centers of these transitions vary from lamina–lamina. With this model, it has been shown that the demagnetization fields from the back layers of the tape influence the front layers and increase the transition parameter (also referred to as the $a$ parameter), thereby reducing the sharpness of the transition.[2] In addition, the transition width increases for deeper laminae, and their respective centers shift further downtrack. Since the readback head sums the voltages from each layer, this shifting and broadening in the back layers produces asymmetries and widens the overall pulse, yielding a reduction in the high frequency response. From this model, it is clear that reducing the thickness of the magnetic layer will improve the high frequency response if the new thickness is smaller than the depth of recording. In essence, this will limit the demagnetization field and effectively remove the contributions from the deeper layers that broaden the pulse.

[a]Kodak student fellow.

 0021-8979/96/79(8)/5658/3/$10.00 © 1996 American Institute of Physics

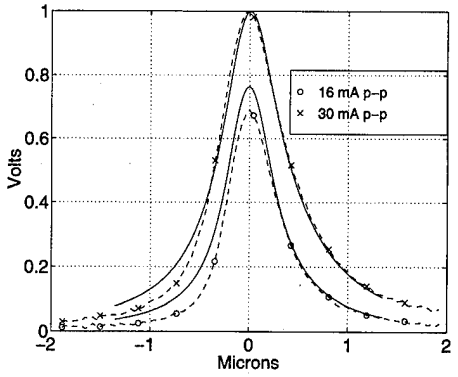



FIG. 1. Measures (dashed line) and simulated (solid line) isolated pulses on SVHS tape for two write currents.

The first measurement presented is a plot of isolated pulses at different write currents. Figures 1 and 2 show measured and simulated isolated pulses written at two currents for the two tapes. The simulation results are plotted in solid lines, while the measured values are given as $x$'s and $o$'s (with a dotted line plot for SVHS). For the measurements, a 10 kHz square wave was recorded on each tape, for each current, at a tape velocity of 7.5 ips. The pulses were then averaged on a Lecroy 9314 sampling digital oscilloscope. The simulation results are from a micromagnetic model developed at CMRR.

The first difference to note is the increase in the peak voltage versus current. This increase is much larger for the two pulses on the SVHS tape (~40%) than for the first two pulses on the MP tape (~20%). Since the readback voltage is directly proportional to the record depth, this implies that the record depth has increased more in the SVHS tape. The depth of recording is approximately equal to the depth at which the recording head field is equal to the coercivity, minus the head-to-tape spacing.[1,4] A good approximation of the record depth is

$$y = g \times \left( \frac{1}{2.95} \times \frac{H_g}{H_c} - 0.15 \right),$$

where $y$ is the depth of recording, $g$ is the gap length, $H_g$ is the deep gap field, and $H_c$ is the coercivity of the tape.[5] The low current isolated pulses were recording at $H_g/H_c$ equal to

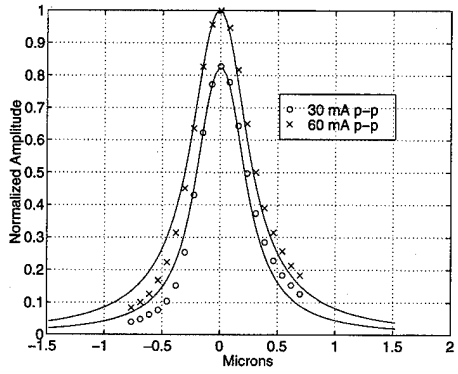



FIG. 2. Measures ($x$'s and $o$'s) and simulated (solid line) isolated pulses on MP tape for two write currents.

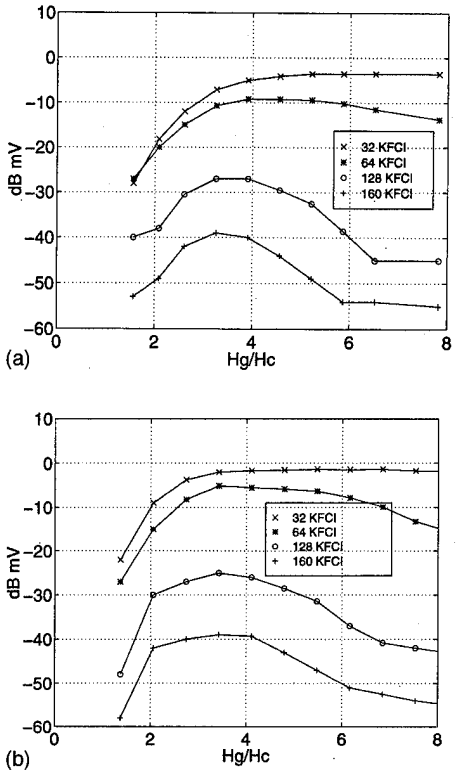



FIG. 3. Voltage vs $H/H_c$ for four densities (a) on SVHS tape and (b) on MP tape.

four for both tapes. Assuming a spacing of 0.125 $\mu$m, this yields a record depth of 0.2 $\mu$m. For the higher current, the record depth is 0.64 $\mu$m. This analysis shows that the MP tape has been recorded through and therefore its output did not increase as much as in the SVHS tape.

Another obvious difference is the width of the pulses. The $PW_{50}$ at 16 mA for the SVHS tape is 11% wider than that of the MP tape at 30 mA, but the $PW_{50}$ of the SVHS increases 38% at 30 mA, while the $PW_{50}$ of the MP (thin) tape increases only 15% from 30 to 60 mA. This is partly due to the recording layer thickness difference, and partly due to particle orientation. To accurately model the MP tape, the particle orientation for the MP tape in the simulation was made more uniform in the longitudinal direction. This translated to less broadening in the MP tape as a function of depth, and consequently, less increase in the $PW_{50}$.[2]

Figures 3(a) and 3(b) show the effect of increasing write current on the output response of the two tapes for four frequencies. For each plot, the frequency is set and the write current is varied from 0 to 90 mA peak to peak. At each current, a reading is taken from an HP 3586 selective level meter with a bandwidth of 3100 Hz. The MR head was used for the signal reproduction and the tape speed was 3.75 ips. Figures 3(a) and 3(b) show the output as a function of the ratio of the deep gap field (which is proportional to the write current) to the coercivity of the tape. Because the depth of recording varies as a function of this ratio, the plots are essentially normalized to each other. Figure 3(a), the SVHS tape, shows the characteristic output versus current relationship for tape recording. The low frequency output increases

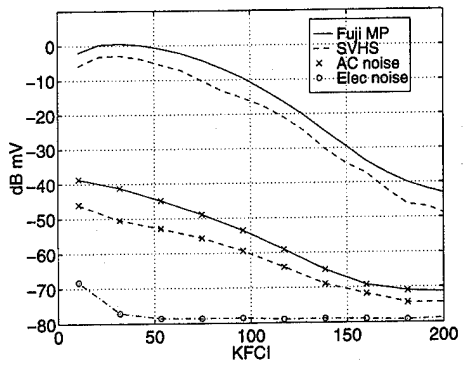



FIG. 4. Frequency response curves for both tapes at two currents. Also shown is the ac-erased noise and the electronics noise.

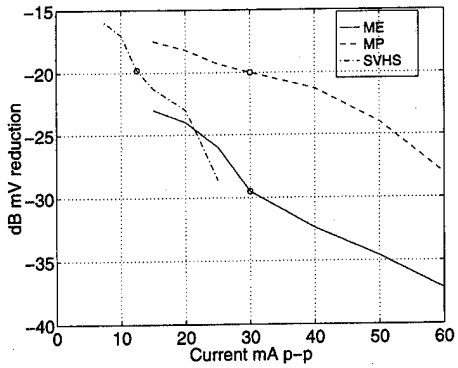



FIG. 5. $4F/1F$ overwrite vs current for SVHS, MP, and ME tape.

as the current increases, and the high frequency output peaks and subsequently declines. The low frequency output increases because as the write current is increased, the depth of recording increases and a stronger field is emitted from the tape. The degradation in high frequency output with increasing current is mainly due to three phenomena. The first is the result of the influence of the deeper layers; the broadening due to the back layers reduces the high frequency output. The second effect is a write process phenomena. The increase in the write current causes a reduction in the gradient of the record head field and results in an increase in the width of the record zone. The increase in the width of the record zone results in a wider pulse and less high frequency response. The third cause is also the result of the write process. As the density is increased, the head field for writing subsequent transitions broadens the previously recorded transitions.[6]

Figure 3(b), the MP tape, shows that the write process is the dominant cause of the degradation of the high frequency response for large currents. The general output characteristics for the MP tape are approximately the same as for the thicker, SVHS tape. The MP tape is recorded through at $\sim H_c/H_g=5.25$, but the high frequency output continues to degrade beyond this point. If the thickness of the magnetic layer was the dominant cause of the high frequency degradation, the output would have leveled off after it had been recorded through. There is improvement, however, which can be seen by comparing the optimum high density output to the output at a ratio of $H_c/H_g=6$ for both tapes. At 160 kfci, this difference is ~16 dB for the SVHS tape and 11 dB for the MP tape.

Figure 4 shows the frequency response of both tapes. The write current was chosen for maximum high frequency response for each tape. The top two curves show the output at the given density to a square wave recording. The middle two curves show the ac-erased noise for the two tapes, and the bottom curve shows the electronics noise. All measurements were taken at a tape speed of 3.75 ips. This plot shows that the signal to noise ratio for the two tapes is about equal. It is interesting to note the high density resolution of the MR head. At 200 kfci, the signal is still ~20 dB above the noise floor. This is impressive for tape recording, considering that the track width is only 4 $\mu$m.

The last plot, Fig. 5, shows overwrite characteristics for the tapes, as well as for a metal-evaporated tape. This overwrite test consists of first writing a 25 kfci square wave and measuring the output. Next, a 100 kfci square wave is recorded over the original square wave and the remaining power at 25 kfci is measured. The record current is the same for both frequencies. Since the ratio of the two frequencies is 4:1, this is referred to as $4F/1F$ overwrite. It is important to note that the $x$ axis is the current in mA and that the range was quite different for the SVHS tape. This was also true in Figs. 3(a) and 3(b), but those plots were normalized. The circles represent the currents at which the high frequency output is optimized. The overwrite performance at this current is the same for both the SVHS and the MP tape. In both cases the current would have to be at least double the optimum to reach the 30 dB overwrite seen in the ME tape. The thickness of the recording layer for the ME tape is only 0.2 $\mu$m. Micromagnetic simulations of overwrite have shown that overwrite performance is not improved until the thickness of the magnetic layer is less than the gap length of the record head,[7] as is the case with the ME tape. This explains why the thin MP tape did not perform better than the thick SVHS with this write head. Use of newer, thinner, MP tapes should show significant overwrite improvement for narrow gap recording.

For the thin particulate media tested here, there is little improvement in recording characteristics over the thicker media when the record current is optimized for both tapes. Improvement in the signal to noise ratio at high densities was seen in simulations with a 0.1-$\mu$m-thick tape,[6] suggesting that the performance will continue to improve as the magnetic layers become thinner and the optimal write current is able to record through the entire layer.

[1] H. N. Bertram, *Theory of Magnetic Recording* (Cambridge University Press, Cambridge, 1994).
[2] D. Wei and H. N. Bertram, IEEE Trans. Magn. **30**, 2739 (1994).
[3] H. Inaba, K. Ejiri, N. Abe, K. Masaki, and H. Araki, IEEE Trans. Magn. **29**, 3607 (1993).
[4] H. J. Richter and R. J. Veitch, IEEE Trans. Magn. **31**, 2883 (1995).
[5] F. Jeffers, Proc. IEEE **74**, 1540 (1986).
[6] D. Wei, A. Friedmann, and H. N. Bertram, J. Appl. Phys. **79**, 1996 (in press).
[7] D. Wei, H. N. Bertram, and R. Dee (unpublished).

# Signals and nonlinearities in thin metal-particle tape

Dan Wei, H. Neal Bertram, and A. Friedmann[a)]
*Center for Magnetic Recording Research, University of California at San Diego, La Jolla, California 92093-0401*

A new type of metal-particle tape, whose thickness is thinner and whose particles are better oriented than traditional thick particulate media, is simulated and analyzed. Signals at high densities are much larger in the thin tape than in the traditional tape. Nonlinearities at high densities are dominated by transition width increases. Signals and nonlinearities in even thinner media are studied versus record gap length to investigate proper system parameters. © *1996 American Institute of Physics.* [S0021-8979(96)13908-0]

## I. INTRODUCTION

In a proposed high-density tape project,[1] the volume density will reach 1 *Terabyte*/in.$^3$ and the linear density will be 256 K BPI. Traditional particulate or ME tape media cannot yield sufficiently large signals at such high densities. Recently, new thin metal-particle tape media have been developed.[2] We have simulated these metal-particle (MP) tapes by a three-dimensional micromagnetic simulation model.[3,4]

Square wave signals are simulated at various densities (15–250 KFCI) to calculate the voltage output curves in the thin MP tape tape.[2] The simulated output curve utilizing a magnetoresistance (MR) head for a Fuji dc tape is in very good agreement with the experiment. Nonlinearities at high densities are calculated and analyzed by an analytical formula. Signals and nonlinearities versus record gap lengths are studied.

In Sec. II, system parameters and a simulation model will be introduced. In Sec. III, signals and nonlinearities in thin MP tape media are analyzed.

## II. SYSTEM PARAMETERS AND SIMULATION MODEL

Thin MP tape media are simulated with $N\sim2000$ particles. The thickness of the medium is about 5–8 $\mu$in. The particle width is about 0.6–0.8 $\mu$in. and the particle length is 3–4 $\mu$in. We utilize a three-dimensional micromagnetic simulation model for particulate tape media.[3,4] For simplicity, the medium is modeled by a three-dimensional sample of 5:1 ellipsoidal particles. The particle centers are randomly distributed. Particles are very well oriented so that the noninteracting squareness $S_0=0.83$. The cross section of the simulated medium is shown in Fig. 1. The sample size is typically 5 $\mu$m in the down-track direction and 8 $\mu$in. in width. The packing fraction is about 0.4. The record gap length $g$ is varied from 6–12 $\mu$in. and the head-medium spacing $d$ is 2–3 $\mu$in. The shield to element spacing in the playback shielded MR head is in the range 4.5–10 $\mu$in. Periodic boundary conditions were applied in the width direction.

Magnetostatic interactions dominate the computational time. Due to the spatial random placement of particles, fast Fourier transform (FFT) techniques cannot be used.[3,4] In this article, interactions are approximated by exact interactions from neighbor particles plus a mean-field contribution from nonneighbor particles. The scaled magnetostatic interacting field $\mathbf{h}_m^i$,[3] Eq. (3) acting on $i$'th particle is calculated approximately as[6]

$$\mathbf{h}_m^i = -\sum_{j,\langle j,i\rangle}^{N} (R_j N_{ij} R_j^T)\cdot \mathbf{m}_j + \mathbf{h}_{\text{mean}}^i. \tag{1}$$

The matrix $N_{ij}$ is a 3×3 dimensionless interaction matrix between $i$'th and $j$'th particles. The term $\langle j,i\rangle$ indicates that the $j$'th particle is a neighbor of the $i$'th particle (about 30 neighbors are included for each particle). The term $\mathbf{h}_{\text{mean}}^i$ is the mean-field contributions from the nonneighbor particles. In a uniform external field, $\mathbf{h}_{\text{mean}}^i$ is a constant and only a function of the average magnetization. In a spatially nonuniform external field, $\mathbf{h}_{\text{mean}}^i$ depends on the magnetization pattern of the nonneighbor particles. This approximation decreases the memory by 20–30 times and the simulation time by a factor of 8.

The $M$-$H$ loop was calculated utilizing the above parameters; the interacting coercivity $H_c=9.82M_r$ (or $4\pi M_r/H_c=1.3$)[6] and squareness $S=0.86$ (neglecting interactions, $H_c=4\pi M_r$ and $S=0.83$).[6] The loop fits typical media neglecting a crystalline anisotropy field.

## III. RESULTS

Square waves are recorded separately on ac-erased media at various densities. The voltage spectrum is calculated by performing the direct spectral sum of all particles in the recorded magnetization pattern.[3,7] Here, we use a MR head response function $h_s^*(k)$, where the surface field function $h_s(x)$ is given by[8]

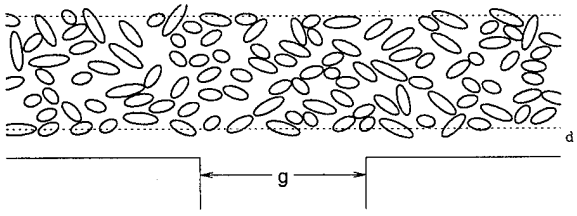



FIG. 1. Cross section of a simulated thin MP tape and the record head.

[a)]Manuscript received November 15, 1995. Kodak student fellow.

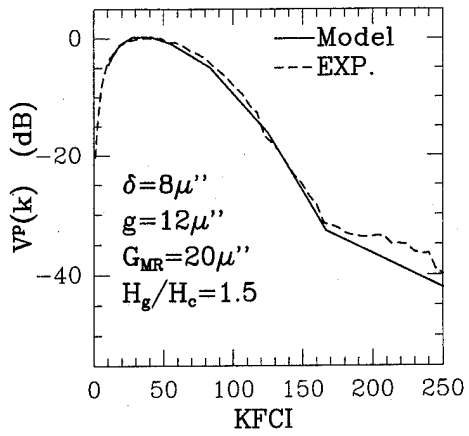



FIG. 2. Simulated and experimental output curve in a Fuji dc tape.

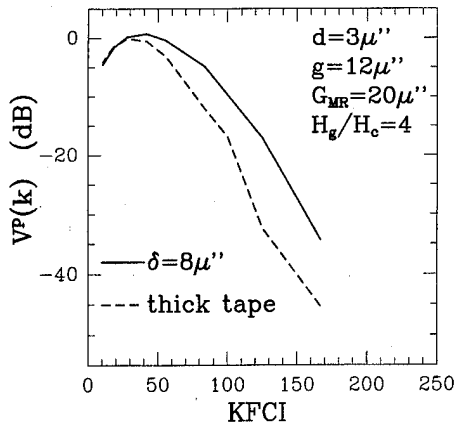



FIG. 3. Output curves for the thick and 200 nm thin MP tapes. All other parameters are fixed for both media.

$$h_s(x)=\frac{1}{2}\left(\frac{1}{1-\alpha}+\frac{C_{\text{nor}}}{\sqrt{(1-x^2)(x^2-\alpha^2)}}\right), \tag{2}$$

where the down-track distance $x$ is normalized by $G_{MR}/2$, half of the shield to shield MR gap length; $\alpha$ is the ratio of MR element thickness $t$ to $G_{MR}$, usually chosen as 0.1; the constant $C_{\text{nor}}$ will normalize the integration of the second part to be one.[8]

The output curve for square wave recording in a tape medium is a function of signal (fundamental peak voltage) versus density. In Fig. 2, a simulated output curve is compared with experiment[5] in a Fuji dc tape. The thickness of the simulated tape medium is chosen to be 8 $\mu$in. and the 5:1 ellipsoidal particle length is 4 $\mu$in. The record gap length is $g=12$ $\mu$in. and the MR head gap length is 20 $\mu$in., as in the experiment. The flying height is set to be 3 $\mu$in. The experimental deep gap field $H_g$ has a small value of $1.5H_c$. The simulated output curve fits very well with the experiment. The isolated pulse is also studied, and fits very well with the experiment.[9] The recording depth is about 6 $\mu$in. Because of the small deep gap field, the transition width increases rapidly versus depth into the medium: the $a$ parameter increases from 1.4 $\mu$in. at the surface to 6 $\mu$in. at a depth of 3.6 $\mu$in. into the tape. If the peak voltage is analyzed by assuming a constant $a$ parameter over the depth, the estimated recording depth will be less than 3.6 $\mu$in.

The thin metal-particle tape has a much better high-frequency performance than the traditional thick tape. In Fig. 3, computed output curves in the two media are compared. The thin medium is better oriented. The record gap length $g$, the flying height $d$, and the MR gap length $G_{MR}$ have the same values as in Fig. 2. The deep gap field is chosen as $H_g/H_c=4$. The dash curve is the output for traditional thick tape media ($4\pi M_r/H_c=1.6$, $S=0.83$).[2,3] The solid curve is for the Fuji dc tape of similar size particles with smaller thickness $\delta=8$ $\mu$in. and better orientation. At extremely low densities ($k<20$ KFCI), signals in two media are almost the same. At the density of 150 KFCI, the voltage for the Fuji dc tape is $-29$ dB, which is much better than $-42$ dB for the thick tape. We also calculated the output curve for the same system parameters in a thinner MP tape ($\delta=5$ $\mu$in.) and the result is almost the same as the solid curve in Fig. 3.

The recording depth in the thick medium is about 9.6 $\mu$in. with $H_g/H_c=4$.[3] For an isolated transition in thick tape,[2] the transition center shifts and the transition width increases with depth. However, the $a$ parameter is virtually a constant versus depth in the thin MP tape with $H_g/H_c=4$. For an isolated transition, the average $\langle a\rangle$ (over depth) for the thick tape is larger than that for the thin tape, but is still much less than the gap length. Therefore, at very low densities, signals in the two media are almost the same.

At high densities, nonlinearity will occur. We have found the transition width will increase with the recording density because of the demagnetizing interactions among neighbor transitions and the spatial extent of the record head field (at previously recorded transitions). We calculate the average transition width $\langle a(k)\rangle$ by fitting the magnetization $m(x)$ for various density $k$, shown in Fig. 4 for the thick and thin MP tapes. The symbol $\langle\ \rangle$ means averaging over transitions, but also averaging through the depth for the thick tape. The $a$

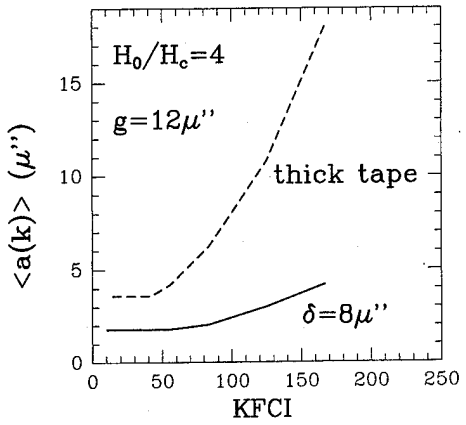



FIG. 4. The transition width of square waves vs density for the thick and thin particulate tape media.

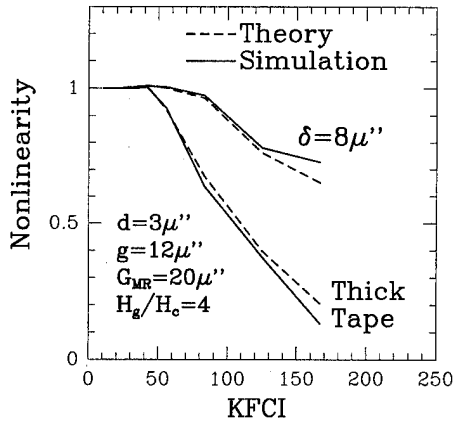



FIG. 5. Nonlinearity curves of the thin and thick particulate tapes. Two solid curves are simulation results, and two dash curves are theoretical estimates.

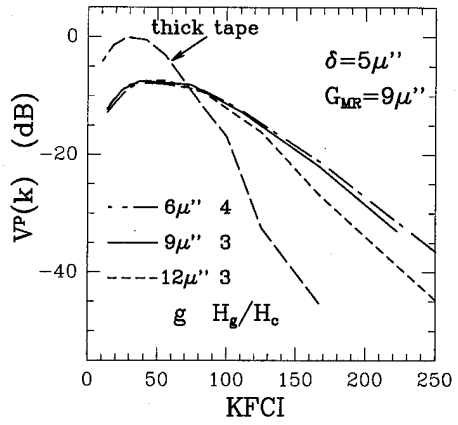



FIG. 7. Output curves with three record gap lengths 6, 9, and 12 $\mu$in. in a 130 nm thin MP tape.

parameter is not only larger, but also increases much faster in the thick tape than in the thin tape, which results in the voltage difference at high densities.

Our assessment of nonlinearity at a square wave density $k$ is defined as $V_1(k)/3V_3(k/3)$, where $V_1(k)$ is the fundamental peak with a bit length $B=\pi/k$ and $V_3(k/3)$ is the third harmonic peak with a bit length $3B$.[5] $V_1(k)$ and $V_3(k)$ can be obtained by integrals

$$V_m(k)=\int_0^{B/2} dx\ \sin(mkx)\tanh\frac{2x}{\pi\langle a(k)\rangle}, \tag{3}$$

where the integer $m=1,3,5,\ldots$ ; and $\langle a(k)\rangle$ is the fitted average transition width versus density plotted in Fig. 4. In Fig. 5, the simulated (solid) and analytical (dash) nonlinearity curves are plotted for the thick and thin particulate tape media. The theoretical nonlinearity curves, calculated by utilizing Eq. (3) and Fig. 4, fit very well with the simulated curves for both media. Therefore, the nonlinearity in tape is due to transition width increase rather than "percolation" as seen in disk recording.[7]

The output and nonlinearity curves in a thinner MP tape media are also studied with three different record gap lengths. The thickness of the media is $\delta=5$ $\mu$in. The 5:1 ellipsoidal particle length is $l=3$ $\mu$in. The shield-to-shield MR gap length is chosen as $G_{MR}=9$ $\mu$in. The $I$-$O$ curve with $g=6$ $\mu$in. is shown in Fig. 6 at two high densities 93 KFCI and 185 KFCI. From Fig. 6, the optimum deep gap fields are chosen as $H_g/H_c=4,3,3$ for $g=6,9,12$ $\mu$in., respectively. Note for the thin media, the optimized record current is approximately independent of the density.

In Fig. 7, three output curves for the $\delta=.13$ $\mu$m thin tape are plotted with $g=6$ $\mu$in. (dash-dot), $g=9$ $\mu$in. (solid) and $g=12$ $\mu$in. (dash), respectively. The signal curve (long-dash) for the thick tape (the same as in Fig. 3) is plotted for a reference. At a low density of 40 KFCI, the output voltages are almost identical for three different gaps, but are about 7 dB lower than the signal in the thick tape: this result is due to a thickness of $\delta=5$ $\mu$in. which is about half of the recording depth in the thick tape. The signals in the thin MP medium are $-18$ dB, $-19$ dB, $-22$ dB at 150 KFCI; and $-27.5$ dB, $-29$ dB, $-34$ dB at 200 KFCI for $g=6,9,12$ $\mu$in., respectively. The high-frequency response for the thin tape is about 20 dB better than the thick tape at 150 KFCI.

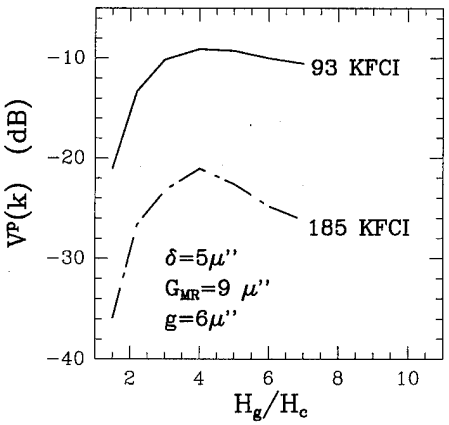



FIG. 6. The $I$-$O$ curve with $g=6$ $\mu$in. in the 130 nm thin MP tape.

## ACKNOWLEDGMENTS

The authors are grateful to the San Diego Supercomputer Center for supporting their research. They would also like to thank Bill Doyle for helpful discussions. This research is sponsored by Storage Technology Corporation, NSIC/ARPA program (MDA972-93-1-009) and NSF/MRG fund (NSF-DMR 90-10908).

[1] NSIC/ARPA tape project.
[2] For example, new Fuji thin metal-particle tape; S. Saitoh, H. Inaba, and A. Kashiwagi, Intermag'95, EA-02.
[3] D. Wei, H. N. Bertram, A. Friedmann, and R. H. Dee, Intermag'95, HD-04.
[4] D. Wei and H. N. Bertram (to be published).
[5] X. Che, Intermag'95, CB-01.
[6] H. N. Bertram and A. K. Bhatia, IEEE Trans. Magn. **MAG-9**, 127 (1973).
[7] H. N. Bertram, *Theory of Magnetic Recording* (Cambridge University Press, 1994), Chaps. 9 and 11.
[8] Y. Zhang, H. N. Bertram, and S. Shtrickman, preprints.
[9] A. Friedmann, *et al.* (to be published).

# Computer simulation of ultrahigh-density perpendicular magnetic recording

K. Yoshida, M. Hara, Y. Hirayama, and Y. Sugita
*Central Research Laboratory, Hitachi, Ltd., Tokyo 185, Japan*

The possibility of ultrahigh-density recording higher than 10 Gb/in.$^2$ with perpendicular magnetic recording is investigated by computer simulation for a ring-type head and single-layer medium combination. A nucleation model is used as a media model because it incorporates a nucleation site, which causes irreversible magnetization switching. Fundamental read–write characteristics are found to be entirely different from those of longitudinal recording. Recorded magnetization strongly depends on head field strength; the maximum magnetization appears around the head field strength of media coercivity, and beyond this the recorded magnetization decreases abruptly. Spacing loss in the recording process also depends on head field strength and recording density. However, saturation recording can be attained even at an ultrahigh recording density of 600 kFCI with a spacing of 30 nm. Also, a higher signal-to-noise ratio than in longitudinal recording can be obtained by introducing weak intergrain exchange interaction with a relatively large grain size in the media film. This suggests that perpendicular magnetic recording is stable in thermal fluctuation. © *1996 American Institute of Physics.* [S0021-8979(96)10508-X]

## I. INTRODUCTION

The recording density of hard disk drives is increasing. In the near future, areal recording density is expected to approach up to 10 Gb/in.$^2$. Beyond 10 Gb/in.$^2$, however, longitudinal magnetic recording may encounter serious problems, as a result of residual magnetization that is too low, coercivity that is too high, and strong thermal fluctuation[1] due to thin film thickness. Perpendicular magnetic recording, on the other hand, has the potential to attain an ultrahigh recording density of over 10 Gb/in.$^2$ because of its stable recorded mode at a high recording density region.[2] This type of recording has two magnetic head and medium combinations; the first is a single-pole-type head and a double-layered medium (SPT/DL),[3] and the second is a ring-type head and a single-layered medium (RT/SL). The latter combination is better from a practical point of view, although the former is thought to be an ideal combination for perpendicular magnetic recording.

The purpose of this study is to investigate by computer simulation the possibility of ultrahigh-density recording with the RT/SL combination. Zhu and Ye[4] and Che and Bertram[5] performed simulations for perpendicular magnetic recording, however, their studies focused on the SPT/DL combination. In our studies, we simulate the fundamental read–write characteristics of perpendicular magnetic recording, and compare them with longitudinal recording. The possibility of an ultrahigh-density recording with perpendicular magnetic recording of the RT/SL combination is discussed.

## II. CALCULATION METHOD

In computer simulations of magnetic recording, the recording media usually consist of a closely packed regular array of hexagonal prisms. However, magnetization curves calculated with this model never agree with experimental results. The calculated switching fields ($H_{sw}$) are always larger than those of the experiments, resulting in a higher coercivity and squareness. Thus, for the calculation and experiment to agree, a much lower anisotropy field ($H_k$) or stronger exchange interaction constant has to be used. To solve this problem, we used the nucleation model, proposed by Chang and Zhu[6] for magnetization reversal simulation of Ba–ferrite platelet particles. In this model, each grain is divided into smaller subgrains. The subgrain with the lowest anisotropy field ($H_{kn}$) is located on the outermost side, as shown in Fig. 1, and functions as a nucleation site. Based on the model, the switching field ($H_{sw}$) and perpendicular coercivity decreased considerably, although the effects depend on grain size and the number of subgrains.

The following calculation conditions were chosen for the simulation; the saturation magnetization ($M_s$) was 440 emu/cm$^3$; the anisotropy field ($H_k$) of the normal subgrain was 5750 Oe, and that of the nucleation site ($H_{kn}$) was 500 Oe. The average $H_k$ was 5000 Oe. The exchange interaction constant acting within one grain and the constants acting between the neighboring grains are defined as $A_i$ and $A_b$, respectively. $A_i$ was set at $0.3\times10^{-6}$ erg/cm and $A_b$ was varied from 0 to $0.3\times10^{-6}$ erg/cm. The value of $A_i$ was the most effective in decreasing $H_{sw}$ and squareness. The diameter of the grain was 30 nm and each grain was divided into seven subgrains with a diameter of 10 nm. The dimensions of the medium were 1.2 $\mu$m in length (track direction) and 0.26 $\mu$m in width (track width direction), and the thickness was 50 nm. The boundary condition for the track width direction was periodic. The surface charges of the track direction side were erased. The head field was calculated by the Lindholm equation. The head field ($H_h$) means a vertical

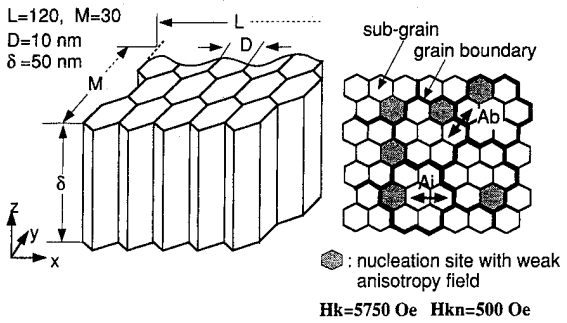



FIG. 1. Media model (nucleation model).

 0021-8979/96/79(8)/5664/3/$10.00 © 1996 American Institute of Physics

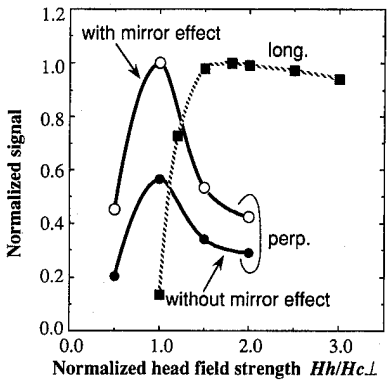



FIG. 2. Dependence of signal output on head field strength.

field strength at the middle of the media. The track width was 1.0 $\mu$m and the gap length 0.3 $\mu$m. The interaction between the head and media was calculated by the mirror effect.

## III. RESULTS

### A. Head field strength dependence

We investigated the dependence of the signal output on the head field strength at the middle of a medium. Figure 2 shows the calculated results. The recording density was 170 kFCI and the spacing was 5 nm. The unshaded circles indicate results with the mirror effect and the shaded circles indicate results without the mirror effect. For comparison, we included the results for longitudinal recording, indicated by a broken line. The maximum output for perpendicular recording with the mirror effect and that of longitudinal recording were equated. For perpendicular recording the signal has maximum output around the head field strength ($H_h$) of media coercivity ($H_{c_\perp}$), but it decreases abruptly with a stronger field than the $H_{c_\perp}$. This is different from the characteristics of longitudinal recording in which the maximum signal output appears at twice the field strength of the media coercivity, and the amplitude changes little in stronger fields. The output of the signal with the mirror effect is about twice that without the mirror effect, meaning that the interaction between the recording head and the media facilitates magnetic recording, although the mirror effect may overestimate the interaction.

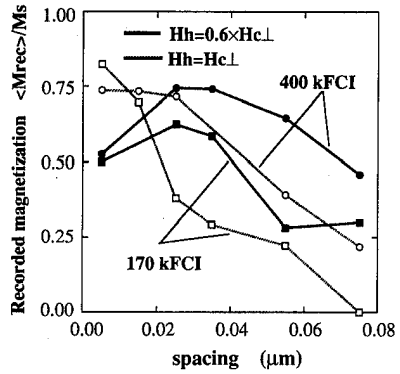



FIG. 3. Dependence of recorded magnetization on head-medium spacing.

TABLE I. Dependence of magnetic properties on intergrain exchange interaction strength.

| $A_b$ ($\times 10^6$ erg/cm) | $H_{c_\perp}$ (Oe) | Squareness | Switching field (Oe) |
|---|---|---|---|
| 0 | 3400 | 0.60 | 3500 |
| 0.1 | 2750 | 0.63 | 3800 |
| 0.2 | 2200 | 0.62 | 3800 |
| 0.3 | 1300 | 0.52 | 4000 |

### B. Spacing dependence

The spacing loss of perpendicular magnetic recording for the RT/SL combination is an important issue. Several experiments have suggested that the spacing loss, especially in the recording process, is very large and the spacing loss coefficient $K$ is over 100 dB.[7] This is one reason for the necessity of proximate recording. Figure 3 shows the recorded magnetization ($M_{\text{rec}}$) dependence at 170 and 400 kFCI on the spacing. Here, $M_{\text{rec}}$ means the magnetization averaged over a recorded bit area. The head field strength is $1.0H_{c_\perp}$ and $0.6H_{c_\perp}$. The spacing dependence strongly relies on head field strength and recording density. The $M_{\text{rec}}$ larger than $0.6M_s$ can be obtained by adjusting a head field strength for the recording density of 170 kFCI and of 400 kFCI in a spacing region narrower than 30 nm. But, the spacing loss increases abruptly over a spacing of 30 nm, especially for $1.0H_{c_\perp}$. The spacing loss for 400 kFCI is smaller than for 170 kFCI. This strong dependence of $M_{\text{rec}}$ on head field strength and spacing is a serious problem for practical use. This dependence may result from an insufficient head field gradient of the $z$ component at the trailing edge of a ring-type head.

### C. Effect of exchange interaction

In longitudinal recording, reducing exchange interaction is necessary to decrease media noise. Reducing exchange interaction may also be effective in attaining a high signal-to-noise ratio in perpendicular recording, however, this has not been confirmed. In this section, we examine the effects of exchange interaction on signal output and media noise.

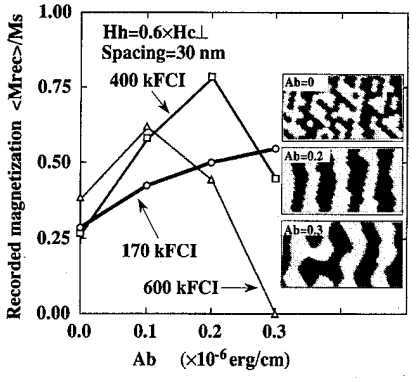



FIG. 4. Relationships between intergrain exchange interaction and recorded magnetization.

TABLE II. Comparison of signal-to-noise ratios of perpendicular recording and longitudinal recording at ultrahigh density.

| | $M_s$ | $H_k$ | $A_b$ | $H_c$ | Thickness | Grain size | Relative SN (dB) | | |
|---|---|---|---|---|---|---|---|---|---|
| | (emu/cc) | (Oe) | ($\times 10^{-6}$ erg/cm) | (Oe) | (nm) | (nm) | 400 kFCI | 600 kFCI | KuV/kT |
| Perp 1 | 440 | 5000 | 0.2 | 2200 | 50 | 30 | +5.5 | ··· | ~800 |
| Perp 2 | 440 | 5000 | 0.1 | 2750 | 50 | 30 | +4 | +1 | ~800 |
| Long. | 360 | 8320 | 0 | 4000 | 20 | 10 | 0 | ··· | ~50 |

Intergrain exchange interaction ($A_b$) was varied from 0 to $0.3\times10^{-6}$ erg/cm. Along with the changes in the exchange strength, the coercivity changed as shown in Table I. Figures 4 and 5 show the relationships between $A_b$ and recorded magnetization, and $A_b$ and media noise, respectively. The insets in Fig. 4 show recorded magnetization patterns at 400 kFCI. At any linear recording density, the introduction of a weak $A_b$ such as 0.1 and $0.2\times10^{-6}$ erg/cm increases the recorded magnetization. The introduction of a stronger interaction, such as $0.3\times10^{-6}$ erg/cm, decreases the recorded magnetization, especially at high recording densities of 400 and 600 kFCI. The weak interaction also tends to reduce media noise, and strong interaction abruptly increases the media noise for 400 and 600 kFCI. This suggests that moderate intergrain exchange interaction is favorable for attaining a high signal-to-noise ratio.

Signal-to-noise ratios (SNRs) of perpendicular magnetic recording and longitudinal recording at recording densities of 400 and 600 kFCI are compared in Table II. The spacing is assumed to be 30 nm. The SNRs of perpendicular recording with weak exchange interaction are much higher than those of longitudinal recording, despite the larger grain size of the perpendicular media. Also, the ratio of anisotropy energy to thermal energy ($kT$; $k$ is the Boltzmann constant and $T$ is temperature) is about 800, which is much larger than that of longitudinal media. This means that perpendicular recording is very stable in thermal fluctuation.

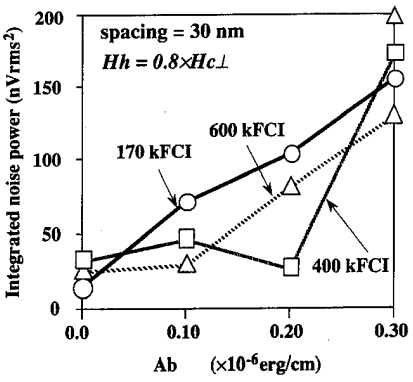



FIG. 5. Dependence of media noise power on intergrain exchange interaction.

## IV. CONCLUSION

Read–write characteristics for perpendicular magnetic recording for a ring-type head and single-layer medium combination were investigated using computer simulation. The following results were obtained.

(1) Recorded magnetization strongly depended on head field strength and spacing between head surface and media surface. However, magnetic recording could be attained at an ultrahigh-density of 600 kFCI by carefully adjusting the recording head field and writing at a proximate spacing of 30 nm.

(2) A high SNR ratio could be obtained with a medium having a grain size of 30 nm and a weak intergrain exchange interaction. Thus, perpendicular magnetic recording is stable in thermal fluctuation.

## ACKNOWLEDGMENTS

We would like to express our gratitude to Dr. N. Hayashi and Dr. Y. Nakatani of University of Electro-Communications at Tokyo for their invaluable information on the calculation method. We are also indebted to Dr. Y. Shiroishi and Dr. M. Futamoto of Central Research Laboratory for their invaluable discussions on the calculation results.

[1] P.-L. Lu and S. H. Charap, IEEE Trans. Magn. **30**, 4230 (1994).
[2] S. Yamamoto, Y. Nakamura, and S. Iwasaki, IEEE Trans. Magn. **MAG-23**, 2070 (1987).
[3] S. Iwsaki, Y. Nakamura, and K. Ouchi, IEEE Trans. Magn. **MAG-15**, 1456 (1979).
[4] J.-G. Zhu and X.-G. Ye, IEEE Trans. Magn. **29**, 3736 (1993).
[5] X. Che and H. N. Bertram, IEEE Trans. Magn. **29**, 3739 (1993).
[6] T. Chang and J.-G. Zhu, IEEE Trans. Magn. **29**, 3619 (1993).
[7] K. Yoshida, Y. Honda, T. Kawsaki, M. Kiozumi, F. Kugiya, M. Futamoto, and A. Tonomura, IEEE Trans. Magn. **MAG-23**, 2073 (1987).

# Barkhausen jumps during domain wall motion in thin magneto-optical films

S. Gadetsky and M. Mansuripur
*Optical Sciences Center, University of Arizona, Tucson, Arizona 85721*

A method with high spatial resolution is developed to study wall motion in thin magnetic films with perpendicular anisotropy. Barkhausen jumps during domain wall motion in amorphous TbFeCo films and polycrystalline Co/Pd multilayer films have been observed. The average distance between strong pinning sites in Co/Pd was found to be around 0.3–0.4 $\mu$m. Maximum pinning times as long as several seconds were observed. Magnitudes of major jumps in TbFeCo were around 0.7 $\mu$m.
© *1996 American Institute of Physics.* [S0021-8979(96)05908-0]

## I. INTRODUCTION

Jaggedness of a recorded domain causes additional noise during magneto-optical (MO) readout. The jaggedness is produced by Barkhausen jumps during domain wall motion within a nonuniform medium containing pinning sites.[1] When a domain wall climbs out of one pinning site and falls into an adjacent trap, it produces a Barkhausen jump. The wall can get over the energy barrier due to an energy supply from an external magnetic field,[2] due to increased surface tension of the wall itself,[3] by thermal activation,[4] and through certain tunneling mechanisms.[5] The average wall velocity depends on the average distance between pinning sites and also on the average time it takes the wall to overcome pinning. Therefore, experimental measurements of average wall velocity [6–8] generally produce the ratio of average Barkhausen jump distance to average pinning time, rather than the values of each parameter individually.

In this article we study domain wall motion in Co/Pd multilayers and in amorphous TbFeCo thin films using a focused laser beam in a magneto-optical Kerr loop tracer.

## II. EXPERIMENT

Co/Pd multilayers were sputtered in an argon environment onto Si(111) substrates coated with 85 nm of SiN sublayer. Individual layer thicknesses of Co and Pd were 1.6 and 6.3 Å, respectively. In this study we used samples having 10 and 20 Co/Pd pairs of layers; we will refer to these films as Co/Pd-80 Å and Co/Pd-160 Å, respectively. The TbFeCo film was also fabricated by sputtering in an argon environment onto a Si substrate. The film had a TM-rich composition and was approximately 100 nm thick.

The experimental setup for this study is described in detail in Ref. 9. The motion of domain walls was monitored with a 780 nm diode laser whose beam was focused onto an approximately 2 $\mu$m diam spot (1/$e$ intensity radius $\approx$1 $\mu$m). The reflected beam was picked up by a differential detector. When the domain wall was moving under the focused spot, the differential output signal was sampled by a computer at equal time intervals. The estimated spatial resolution in measuring the position of a given domain wall was about 50 nm.

Figure 1(a) shows a jagged domain wall whose profile is described by the function $x(y)$, and is assumed to be moving with an average velocity $v$ from right to left. The average distance between the wall and the $Y$ axis will be denoted by $x_0$. The circle with radius $R_0$ represents the focused laser spot, which is assumed to have a Gaussian intensity profile with a 1/$e$ radius of $R_0$. The apparent Kerr rotation angle $\alpha$ measured at an arbitrary position $x_0$ of the wall is given by

$$\alpha/\alpha_{\max}=2\int_0^{x_0}\exp(-x^2/R_0^2)dx/(\sqrt{\pi}R_0), \tag{1}$$

where $\alpha_{\max}$ is the Kerr rotation angle of the saturated sample. Figure 1(b) shows the theoretical dependence of $\alpha/\alpha_{\max}$ on $x_0=vt$, obtained from Eq. (1). Here $v$ is the wall velocity and $t$ is the time relative to the instant at which the wall crosses the center of the focused spot. In our experiments $R_0$ was about 1 $\mu$m (measured directly using the knife-edge method). Figure 1(b) has been used throughout this article to determine domain wall velocities.

Figure 2 shows domain structures in two different Co/Pd multilayer films. In (a) the domain structure within the Co/Pd-80 Å film is seen to be solid and free from mazelike patterns. On a micrometer scale (the size of the focused spot) the wall is fairly straight, thus justifying the approach taken in arriving at Eq. (1). [Our TbFeCo film also possesses a domain structure similar to that shown in Fig. 2(a).] In the Co/Pd-160 Å film, the mazelike domain structure of Fig. 2(b) is observed. Thus, Eq. (1) is not applicable to this film.

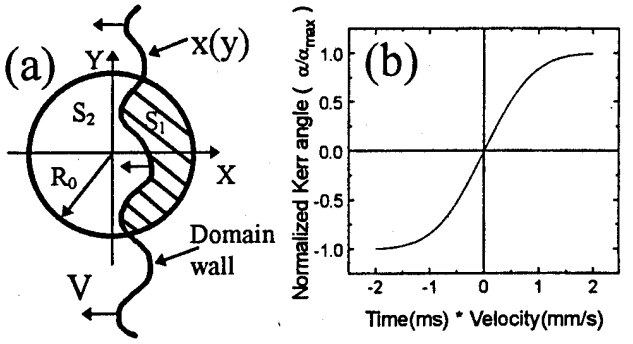



FIG. 1. (a) Schematic diagram showing the passage of a wall through a region of MO film illuminated by a focused laser beam. $R_0$ is the 1/$e$ radius of the focused spot. (b) Normalized differential detector output during the uniform motion of a straight domain wall under the focused spot having $R_0$=1 $\mu$m.

 0021-8979/96/79(8)/5667/3/$10.00 © 1996 American Institute of Physics 

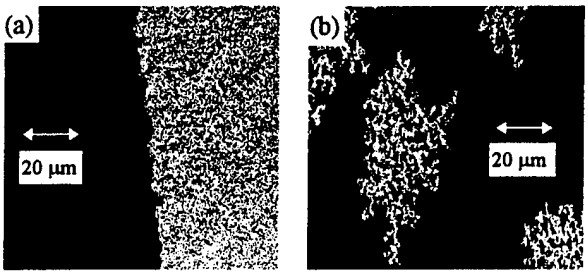



FIG. 2. (a) Domain structure developing in Co/Pd-80 Å film under a bias magnetic field of 1.2 kOe. (b) Domain structure developing in Co/Pd-160 Å film under a bias field of 2.0 kOe.

## III. RESULTS AND DISCUSSION

### A. Wall motion in Co/Pd-80 Å film

Figure 3 shows the differential signals during the passage of a domain wall under the focused spot. The shape of the curve indicates that the wall motion is not smooth, but rather consists of jumps separated by pinnings at certain locations. The average number of large jumps is typically five or six, indicating that the distance between strong pinning sites is around 0.3–0.4 $\mu$m. With the magnetic field of 1.02 kOe applied in this experiment, pinning times as long as several s were observed. During a jump the wall velocity is greater than the average wall velocity. The ratio of maximum velocity ($V_{max}$) to average velocity ($V_{ave}$) of the wall in Fig. 3(a) is about six. Between strong pinning sites there exist weaker sites that cause short delays in the wall motion. Figure 3(b) is an enlarged view of the encircled region in Fig. 3(a). Figure 3(a) shows a number of different pinning times and different magnitudes of jumps.

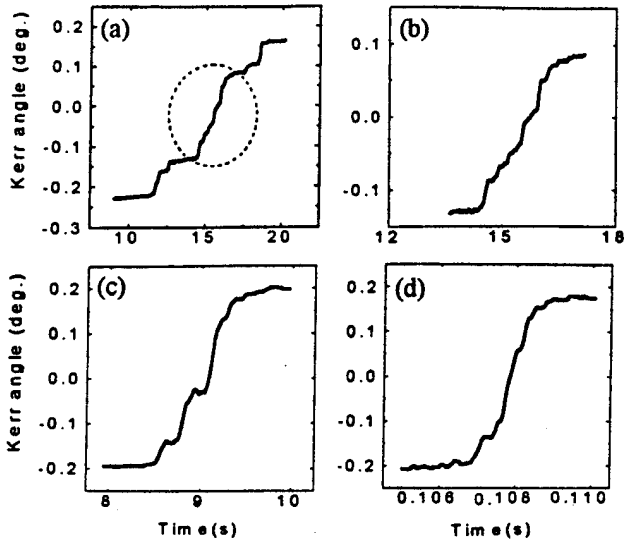



FIG. 3. Differential signals obtained during the passage of a wall under a focused spot in the Co/Pd-80 Å film under an external magnetic field. (a) $H=1.02$ kOe. (b) Enlarged view of the encircled region in (a). (c) $H=1.05$ kOe. (d) $H=1.25$ kOe.

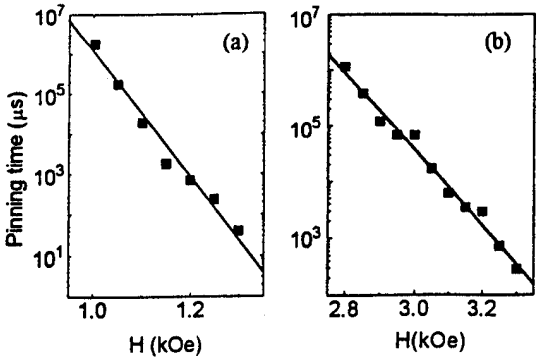



FIG. 4. Maximum domain wall pinning time vs the strength of the magnetic field. (a) in the Co/Pd-80 Å film; (b) in the TbFeCo film.

At higher magnetic fields the wall velocity increases and the wall passes under the focused spot in shorter times [see Figs. 3(c) and 3(d)]. The pinning times become shorter at higher fields, and there are fewer large jumps. Figure 4(a) shows the magnetic-field dependence of the maximum pinning time experienced by the wall. Clearly there is an exponential decrease of the pinning time with the increasing magnetic field. Figure 4(b) shows the similar behavior of the TbFeCo sample which will be discussed later in the article.

Both $V_{max}$ and $V_{ave}$ increase exponentially with H in the range of 1.0–1.3 kOe, as shown in Fig. 5(a). The slope of $V_{ave}$ on a logarithmic scale is slightly larger than that of $V_{max}$, indicating that the ratio of $V_{max}$ to $V_{ave}$ must decrease with the increasing magnetic field [see Fig. 5(b)].

### B. Wall motion in amorphous TbFeCo film

Figure 6 shows the differential signals obtained during the passage of a domain wall under the focused spot in TbFeCo film. As in the Co/Pd-80 Å film, the motion consists of jumps separated by pinnings at certain locations. Unlike the Co/Pd-80 Å film, however, there are fewer strong pinning sites within the illuminated area. In Fig. 6(a), where the applied field is $H=2.8$ kOe, we observe only three major jumps, implying that the average distance between strong pinning sites is about 0.7 $\mu$m. Between strong pinning sites

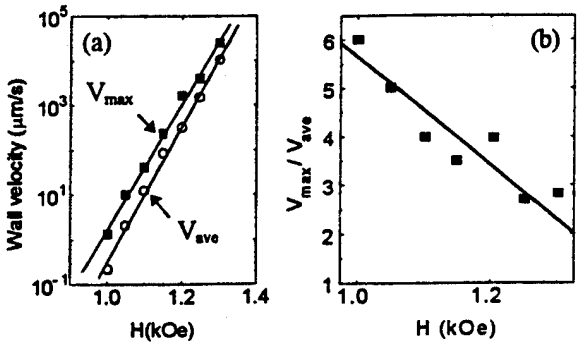



FIG. 5. (a) Maximum and average wall velocities in Co/Pd-80 Å film vs the applied magnetic field. (b) Ratio of the velocities.

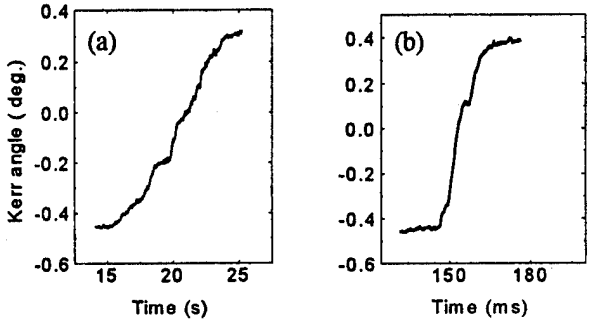



FIG. 6. Differential signals during the passage of a domain wall under the focused spot in TbFeCo film in the presence of an external magnetic field. (a) $H=2.8$ kOe. (b) $H=3.2$ kOe.

there exist weak sites which block the wall motion for short periods of time. In the TbFeCo film during and in between major jumps, the wall experiences rather strong pinning from weak sites as compared with the Co/Pd-80 Å film. This leads to a lower $V_{max}$ during the major jumps in TbFeCo. At the higher magnetic field of 3.2 kOe, shown in Fig. 6(b), the wall velocity increases while the pinning times decrease.

Figure 4(b) shows the magnetic-field dependence of the maximum pinning time experienced by the wall in TbFeCo film; clearly, there is an exponential decrease of the pinning time with the increasing field. The slope of this curve is smaller than that in Fig. 4(a), which corresponds to Co/Pd-80 Å. Within a 300 Oe range of magnetic fields, the pinning time changes by four orders of magnitude in Co/Pd-80 Å, whereas it changes by only two orders in TbFeCo.

In the TbFeCo film, $V_{max}$ and $V_{ave}$ increase exponentially with H in the range of 2.8–3.3 kOe [see Fig. 7(a)]. On a logarithmic scale the slope of $V_{ave}$ is slightly larger than that of $V_{max}$, indicating that the ratio $V_{max}/V_{ave}$ must decrease with the increasing field [see Fig. 7(b)]. The slopes of both $V_{ave}$ and $V_{max}$ for TbFeCo shown in Fig. 7(a) are much smaller than those of Co/Pd-80 Å shown in Fig. 5(a). This implies significantly lower wall mobilities for the TbFeCo sample. The highest $V_{max}/V_{ave}$ in TbFeCo is about 2.5,

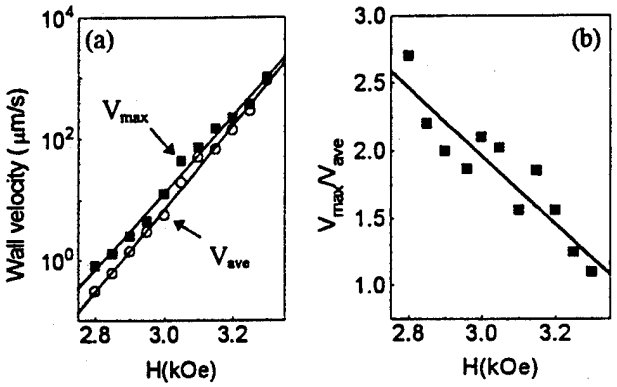



FIG. 7. (a) Maximum and average wall velocities in TbFeCo film vs the applied magnetic field. (b) Ratio of the velocities.

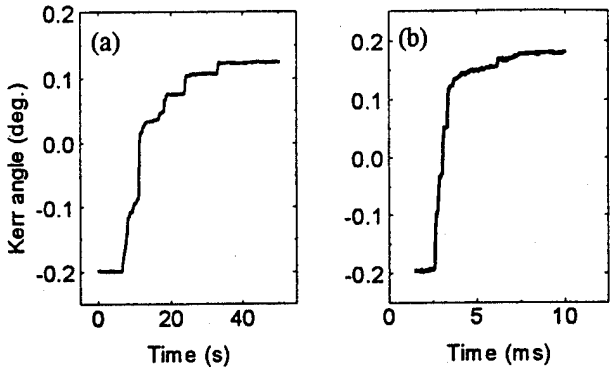



FIG. 8. Differential signals during the passage of a domain structure under the focused spot in Co/Pd-160 Å film in the presence of an external magnetic field. (a) $H=2.25$ kOe. (b) $H=3.1$ kOe.

whereas that in Co/Pd-80 Å is about 6. (These ratios are evaluated at similar values of $V_{ave}$, namely, at 0.3 and 0.2 $\mu$m/s, respectively.) We conclude that $V_{ave}$ in Co/Pd is controlled primarily by pinnings at randomly distributed, strong pinning sites. In contrast, TbFeCo has more frequent pinnings and the pinning strength is distributed more uniformly.

### C. Wall motion in Co/Pd-160 Å film

As mentioned earlier, we cannot apply Eq. (1) to determine wall velocity in this sample, which has the complicated domain structure shown in Fig. 2(b). Therefore, in this section we provide only general considerations on wall motion in this film. Figure 8 shows the differential readout signal during the passage of a domain structure under the focused spot. The plots consist of jumps separated by wall pinnings at certain points. Both plots are asymmetric, having a smaller slope at the end of the process (where the signal level is close to $+0.2°$) rather than in the beginning. The pinning times also become longer towards the end of the process. Moreover, at the lower field shown in Fig. 8(a), the region under the focused spot remains partially unreversed after the passage of the domain structure. (To see this, note that a maximum Kerr angle of 0.12° is achieved compared to the saturation value of 0.2°.) In the case of the higher magnetic field, shown in Fig. 8(b), the final signal is close to the saturation level, indicating that the illuminated area is fully reversed after the passage of the domain structure.

[1] Hong Fu, R. Giles, M. Mansuripur, and G. Patterson, Comput. Phys. **6**, 610 (1992).
[2] J. A. Jatau and E. Della Torre, J. Appl. Phys. **75**, 6846 (1994).
[3] Hong Fu, R. Giles, and M. Mansuripur, Comput. Phys. **8**, 80 (1994).
[4] R. Street and S. D. Brown, J. Appl. Phys. **76**, 6386 (1994).
[5] W. Riehemann and E. Nembach, J. Appl. Phys. **55**, 1081 (1984).
[6] T. G. Pokhil and E. N. Nikolaev, IEEE Trans. Magn. **MAG-29**, 2536 (1993).
[7] M. Labrune, S. Andrieu, F. Rio, and P. Bernstein, J. Magn. Magn. Mater. **80**, 211 (1989).
[8] A. Kirilyuk, J. Ferre, and D. Renard, IEEE Trans. Magn. **MAG-29**, 2518 (1993).
[9] S. Gadetsky, T. Suzuki, J. K. Erwin, and M. Mansuripur, these proceedings.

# Simulation of magneto-optic readout signal spectrum using digitized mark and beam patterns (abstract)

S. Jo and J. W. Sohn
*Department of Electronic Engineering, Soong Sil University, Seoul 156-743, Korea*

S. K. Lee and S. G. Kim
*Materials Design Laboratory, Korea Institute of Science and Technology, Seoul 136-791, Korea*

This paper describes a simple and convenient simulation method, which uses analytical models[1] for mark and beam patterns. The readout signal of optical disk system is obtained by two-dimensional convolution of Gaussian intensity beam pattern and elliptical mark pattern. Then, signal spectrum is obtained by executing a fast Fourier transform algorithm after adding quantitative MO noise sources within bandwidth. For simulation, the two-dimensional distributions of mark reflectivity and beam intensity were digitized, which enabled us to use easily available algorithm routines in digital signal processing. The resolution of the beam and mark patterns can easily be adjusted by changing the number of bits representing the patterns. Also, various noise sources in the MO disk system can be selectively added using random function generator. Simulated signal spectra were compared with experimental results.[2] The parameters used were as follows: laser beam width was 780 nm, NA was 0.55, signal frequency was 9.4 MHz, duty ratio was 38%, and minimum mark dimension was 0.6 $\mu$m by 0.75 $\mu$m. Simulated C/N ratio was 50 dB, which was very close to the experimental value of 52 dB. © *1996 American Institute of Physics.* [S0021-8979(96)46308-9]

[1] T. Tanabe, Y. Tanaka, and R. Arai, Proc. SPIE **1663**, 196 (1992).
[2] H. Miyamoto, M. Ojima, T. Toda, T. Niihara, T. Maeda, J. Saito, H. Matsumoto, T. Hosokawa, and H. Akasaka, Jpn. J. Appl. Phys. **32**, 5457 (1993).

 0021-8979/96/79(8)/5670/1/$10.00 © 1996 American Institute of Physics

# Prediction of the limitations placed on magnetoresistive head servo systems by track edge writing for various pole tip geometries

R. Davidson[a] and R. Simmons
*Hewlett Packard Company, Disk Memory Division, P. O. Box 15, Boise, Idaho 83707-0015*

S. Charap
*Carnegie Mellon University, Pittsburgh, Pennsylvania 15213-3890*

The typical configuration for inductive write/magnetoresistive read heads used in hard disk applications involves a shared pole (shield) between the write transducer and the read transducer. The shared pole forms the leading pole of the write portion of the head. The write track width is primarily determined by the width of the trailing pole, however, the leading pole geometry has an important influence on track-edge writing effects and, therefore, on embedded servo system performance. This effect is simulated for shared pole, trimmed pole, and, for comparison, conventional inductive head pole geometries. The merits of each geometry and impact of side writing on servo is discussed. © *1996 American Institute of Physics.* [S0021-8979(96)28108-2]

## I. INTRODUCTION

The continuous increase in areal density required by industry demands narrower tracks and magnetoresistive (MR) heads. Narrower tracks increase the importance of track edge effects in the design of recording systems. The use of MR heads introduces new physics to the readback process. The MR readback element responds to the flux from the track directly in contrast to the inductive case where it is the partial derivative of the flux taken in the down-the-track direction that is transduced. The result is that the MR head responds to the track-edge charge created during the write process,[1] an edge effect one does not have to consider with inductive heads.

The goal of this work is to analyze the dependency of track-edge writing on pole geometry and the effect that the track-edge charge has on servo gain linearity and position error signal (PES) noise. The patterns of track-edge charge created in the write process vary for each pole geometry; the effect this has on the servo system gain depends on the servo detector method. Two detection schemes are discussed, area integrate and peak-peak amplitude demodulation. For the purpose of this analysis, media noise is assumed to be proportional to $1-m^2$.[2] All predictions are based upon a three-dimensional (3D) self-consistent recording model.

## II. MACROMAGNETIC MODELING

The simulation consists of a 3D macromagnetic media model and nonlinear finite element model (FEM) 3D head field models.[3] The macromagnetics of unoriented thin film media is simulated with a new vector Preisach hysteresis model.[4] The hysteresis model uses a biaxial switching function in place of the classic square loop switching function normally associated with the Preisach model. The advantage of this approach is speed since micromagnetic detail can be treated in terms of the aggregate or macromagnetic response.

Three pole geometries were considered including the most common implementation of the write portion of a MR head, the shared pole geometry, as shown in Fig. 1. The corresponding head fields, including saturation effects, were computed for the midplane of the medium, which is 75 nm from the poletips in this case. The head fields are then used to self-consistently compute the resulting magnetization pattern as the head (field) is translated down the track. To compute a representative servo magnetization pattern, dibits were recorded for each of the three pole geometries. The MR output is proportional to the flux from the media and, therefore,

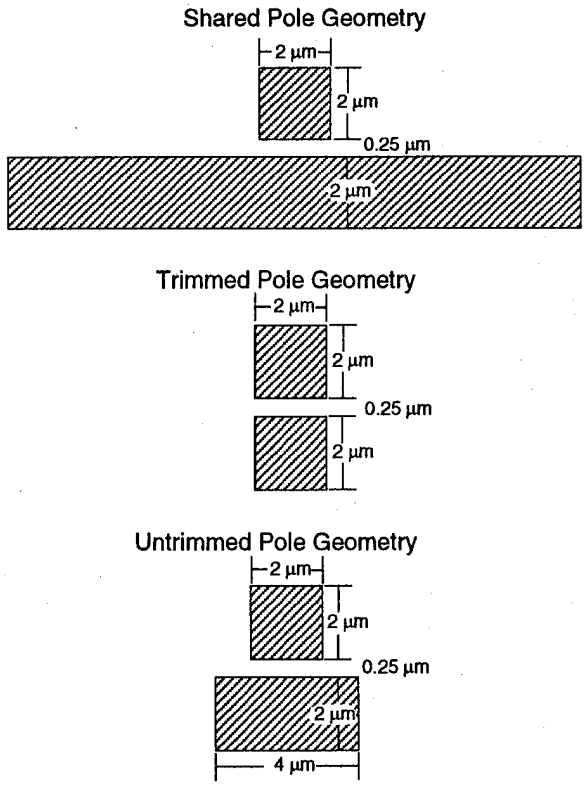



FIG. 1. Pole geometries simulationed.

[a]Author to whom correspondence should be addressed. Present address: Hewlett Packard Company, PO Box 15, Boise, ID 83707. Electronic mail: bjd@boi.hp.com

 0021-8979/96/79(8)/5671/3/$10.00 © 1996 American Institute of Physics 

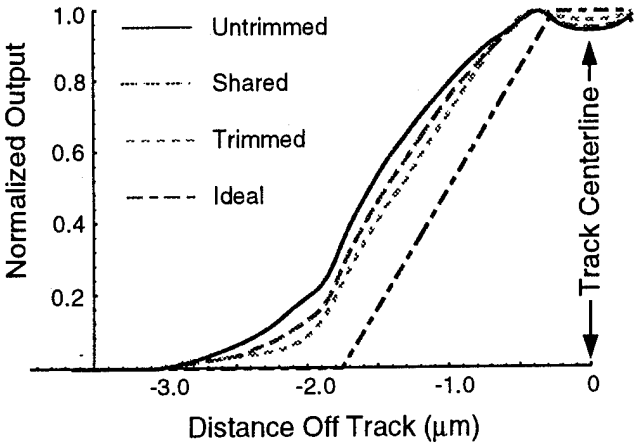



FIG. 2. Area integrated PES for various poletip geometries.

to the equivalent magnetic charge density, $\rho_m$, associated the written magnetization patterns.

In the case of a servo demodulation scheme using area integration of the servo burst, the signal from the MR head is proportional to the integral of the magnitude of $\rho_m$ from the beginning of the servo field to the end. In this simulation the integral is over one dibit. The PES signal read from the dibit, i.e., the readback signal versus position across the track, would then be the correlation of down-the-track integral of $|\rho_m|$ and the 3D MR head sensitivity function. To avoid the complication of the spatial variation of the MR sensitivity functions, a simple rectangular response function is assumed, the width being 0.75 of the 2 $\mu$m trailing write pole width. This approach is appropriate for a DSMR or spinvalve head and can be applied, with modifications, to a SAL MR head.[6] The ideal case would yield a PES that is the correlation of two rectangular functions, one equal to the pole width for the write and the other to the MR width for the read. In this analysis, any deviation from this ideal straight line response would be considered PES gain nonlinearity as shown in Fig. 2.

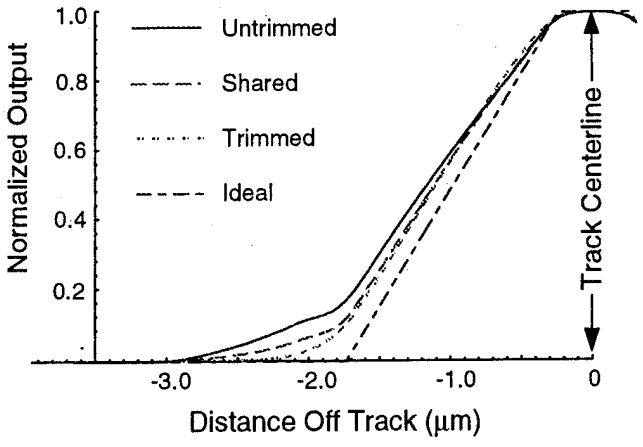



FIG. 3. Peak detected PES for various poletip geometries.

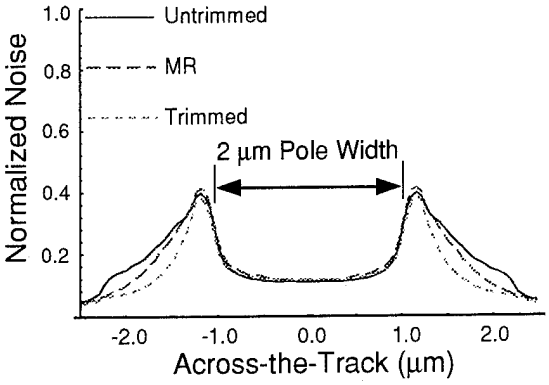



FIG. 4. Integrated noise proportional to $1-m^2$.

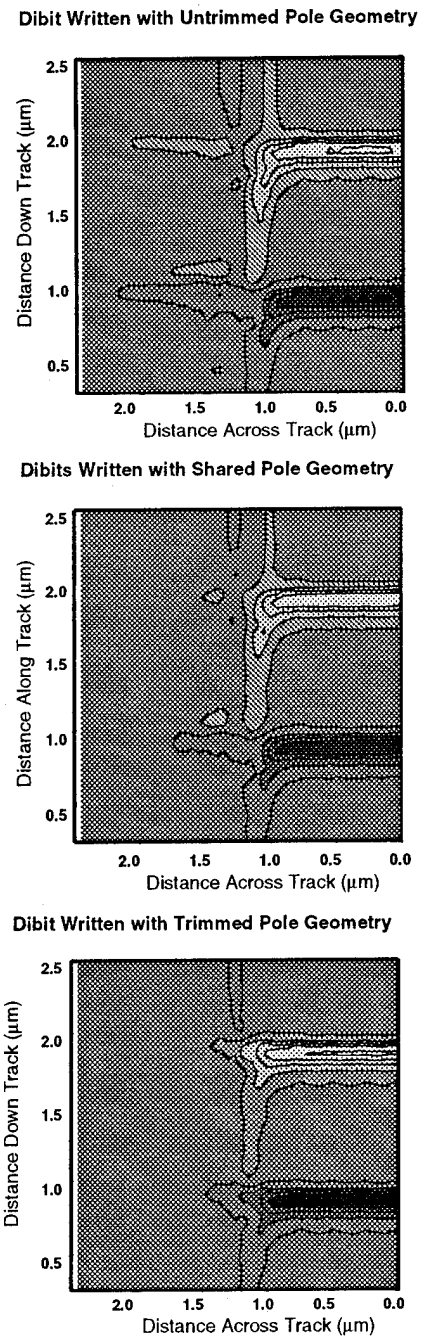



FIG. 5. Resulting $\rho_m$ for various poletip geometries.

In the case of a servo demodulation scheme which uses peak-to-peak output, the down-the-track peak-to-peak value of $\rho_m$ for the dibit is used. The PES is computed as in the previous case, and the results are shown in Fig. 3. Deviation from the ideal appears as nonlinear gain variations to the servo system.

In addition to PES nonlinearity, PES noise must be considered. The fluctuation of the magnetization at the track edge contributes to the noise on PES. The total PES noise must be included in the off-track error budget. To determine this, the normalized noise function, $\text{noise}(x,y,z)=1-m^2$, where $m=M(x,y,z)/M_{\text{sat}}$, is computed. Finally, noise $(x,y,z)$ is integrated down the track to yield the total noise across-the-track corresponding to the written transitions as shown in Fig. 4.

## III. RESULTS AND DISCUSSION

The head fields differ mainly in the spatial distribution of the edge fields due to the pole geometry differences, the gap length and head/medium separation being held constant. The difference in the edge fields can most easily be seen in $H_z$, the across-the-track component. For the trimmed pole configuration, the peak in the $H_z$ component occurs at the same distance from the track edge for the leading as for the trailing pole. For the shared pole case, there is only a $H_z$ component for the trailing pole at the same distance from the track edge as for the trimmed pole case. The untrimmed pole case, however, has a much wider distribution in $H_z$, the peak in $H_z$ for the leading pole being offset from the trailing pole by the geometric difference in the leading to trailing pole widths.

In Fig. 5, the spatial distributions of $\rho_m$ corresponding to the written magnetization patterns for each geometry are shown. The variation in writing beyond the edge of the dibit and the charge along the edge of the dibit are visible in the contour plots. The slow decay to the side of the track and the spike at the track edge visible in the untrimmed case would contribute significant nonlinearity in the servo gain as the head is moved onto the track using the area integrate servo detection scheme. For example, the change in the output per unit track width would increase sharply when the edge of the read head is in the neighborhood of 1.9 $\mu$m in Fig. 2, i.e., high gain. However, as the head is moved further onto the track, to 1.0 $\mu$m, the increase in output per unit track width is much less. For the area integrate scheme, the trimmed pole geometry is best. In the case of peak-to-peak detection, note that the track edge charge does not contribute, but the slow decay to the side is still present. The nonlinearity would only occur when the read head is almost completely off the servo field, so the relative impact to the system design would be a narrower range for the servo.

## IV. CONCLUSIONS

Leading pole geometry has an important effect on side writing. High track density MR designs must take this into account. Trimmed poles are best at reducing side writing and peak-to-peak servo demodulation is more immune to side-writing. Partially trimmed poles for MR heads need to be evaluated. It is sufficient to consider the macromagnetics of the recording system to see this.

## ACKNOWLEDGMENTS

This work is supported in part by National Science Foundation Grant No. ECD-8907068.

[1] J. L. Su and K. Ju, IEEE Trans. Magn. **25**, 3384 (1989).
[2] T. Silva and H. N. Bertram, IEEE Trans. Magn. **26**, 3129 (1990).
[3] MAGNET. Montreal, Quebec Canada: Infolytica, Inc., Version 5.1, 1994.
[4] R. Davidson, S. Charap, and R. Simmons, these proceedings.
[5] D. Heim, IEEE Trans. Magn. **30**, 1453 (1994).
[6] D. Cahalan and K. Chopran, IEEE Trans. Magn. **30**, 4203 (1994).

# Autotuning of a servowriter head positioning system with minimum positioning error

Y. H. Huang, S. Weerasooriya, and T. S. Low
*Magnetics Technology Center, Faculty of Engineering, National University of Singapore, 10 Kent Ridge Crescent, Singapore 0511, Singapore*

This paper proposes a servopositioning system of a servowriter with autotuning capability. The position feedback is obtained through an interferometry-based laser positioning system. The retroreflector is mounted directly on the disk drive arm for hard coupling. The dynamics of the actuator are now included in the servopositioning loop. Since drive dynamics vary from drive to drive, a fixed controller may not provide optimal settling performance for a series of drives. In the proposed control method, the actuator dynamics are identified by injecting a pseudorandom binary sequence into a coarsely tuned feedback servoloop. The resulting frequency domain identification results are used to fine tune the compensator to enable faster settling and better following. Using this information in the servodesign, settling times of 9 ms and a following accuracy of 1 $\mu$in. seem achievable using existing hardware. © *1996 American Institute of Physics.*
[S0021-8979(96)10608-6]

The primary concern in designing a servowriter is head positioning accuracy. In the hard disk drive industry at present, the physical head position accuracy required when servowriting is typically 1% of the track pitch. With a track density of 10 000 TPI, the position accuracy requirement in servowriting is translated to less than 1 $\mu$in.

With such stringent position accuracy requirements in servowriting, a precision position sensing scheme is imperative.[1–6] Laser-interferometry-based position measurement is the most widely used technique today. In this technique, a glass prism called a retroreflector is attached to a moving part of the actuator system. Depending on how the retroreflector is attached there are two head positioning techniques that have been successfully used: (1) servowriting using the heads of the head disk assembly (HDA) pushed by an external stage, and (2) servowriting using the HDA's own heads with a retroreflector attached to the actuator.[1]

The main disadvantage of the first method is that the dynamic effects of having the actuator driven by the push pin are not compensated for by the servoloop.

In the second method, the highest confidence in head positioning results.[1] The position of the arm is now inside the servoloop. With future hard disk drive's track density climbing to above 10 000 TPI, actuator dynamics and thermal deformation of the actuator structure can no longer be ignored in servopositioning, therefore this method seems to have a better chance of survival in the long term.

However, as a result of including the drive dynamics in the servoloop in the second method, a controller that is tuned for one drive may not achieve the same performance for another drive. One parameter which primarily affects the closed-loop system performance is the acceleration constant of the Amplifier/VCM Actuator Structure (AAS). From the control system point of view, the change in AAS is equivalent to the change in the dc gain of the plant, which has the effect of moving the position of the closed-loop dominant poles.[2]

In this paper, the effects of variations in the AAS of individual drive on track to track seek is investigated. In order to achieve fast settling and accurate following, it is desirable to autotune the servoloop on a drive by drive basis so that the closed-loop dominant pole locations are maintained at the specified position in the $z$ plane. This is the motivation of the research performed in this paper. The test stand for the proposed servopositioning control system is illustrated in Fig. 1. The system consists of a laser position measurement system, a VCM current driver, a spindle motor speed controller, a 3.5 in. disk-drive assembly, and an IBM-compatible PC.

The block diagram of the servoloop with the rigid body plant model of the VCM actuator is given in Fig. 2.[8] The specifications of interest are settling time and overshoot in time responses. As servowriters mainly operate on one-half or one-quarter track seek mode, the filter $F(z)$ in the block diagram is a discrete time linear IIR filter which can facilitate the required closed-loop operation. The digital-to-analog-converter DAC gain and the laser position transducer gain $K_t$ are specified by the laser measurement electronics. The amplifier gain $K_a$ is selected by the transconductance of the voice coil motor driver. The rigid body model of the VCM actuator/retroreflector structure is a double integrator with an acceleration constant $K_m$. The last block $K_d$ is determined by the relative position of the retroreflector on the actuator.

The AAS of the system in Fig. 2 can be defined as a series gains of $K_a$, $K_m$, and $K_d$. It is equivalent to the dc gain of the rigid body model of the amplifier/VCM actuator structure. It is seen that AAS changes with the moment of inertia to the pivot of the actuator/retroreflector structure, as well as with the force constant of the VCM. Because these parameters vary from drive to drive, the optimal controller may not be obtained without prior knowledge of the AAS of the particular drive. Therefore, system identification is introduced to provide information on fine tuning of the controller.

The target of the system identification is the VCM actuator/retroreflector structure of the new drive being servowritten. From the system identification, the AAS of the drive can be reliably obtained. Pseudorandom binary sequences (PRBS) detection have long been used in system

 0021-8979/96/79(8)/5674/3/$10.00 © 1996 American Institute of Physics

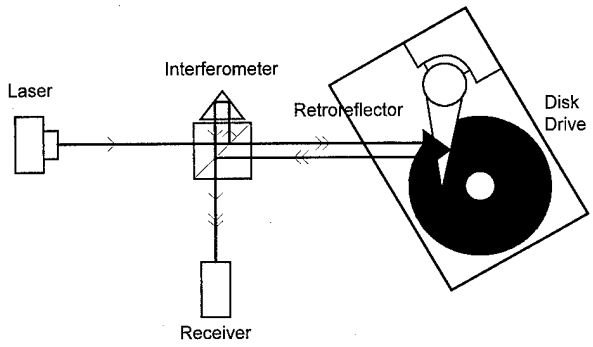



FIG. 1. Head-disk assembly with laser positioning system.

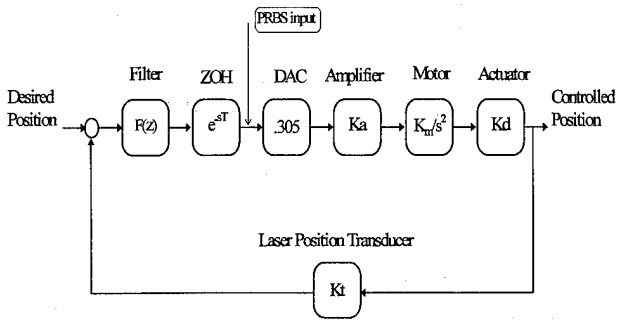



FIG. 2. System block diagram of servowriter positioning system.

identification problems in place of white noise.[4] PRBS signals are simple to generate in the present hardware/software platform. This method is an effective alternative to swept-sine identification which is normally used for such applications.

The identification is done under closed loop. The test signal is injected after the filter output; see Fig. 2. The corresponding controller output and actuator position are captured and used as the input–output pair for system identification. The frequency response of the plant transfer function is then calculated by comparing the spectrum of the input–output data. The reader is referred to Ref. 4 for details of this method. Once the plant transfer function frequency response is available, both the rigid body and flexible body model of the plant can be estimated. This is illustrated bellow.

Let $\{\omega_i, G(j\omega_i)\}$ be the experimental frequency response data of the plant. We would like to fit the experimental data with a polynomial rational transfer function $P(s)$,

$$P(s)=\sum_{i=0}^{m} b_i s^{m-i} \Big/ \left( s^n+\sum_{i=1}^{n} a_i s^{n-i} \right), \tag{1}$$

where $b_i,\ldots,b_m$ and $a_0,\ldots,a_n$ are real coefficients, $m$ and $n$ are the estimated order of the numerator and denominator, respectively. We wish to find the above-mentioned parameters $m,n,b_i,\ldots,b_m$ and $a_0,\ldots,a_n$ so that for each particular frequency $\omega$,

$$\sum_{i=0}^{m} b_i(j\omega)^{m-i} \Big/ \left( (j\omega)^n+\sum_{i=1}^{n} a_i(j\omega)^{n-i} \right) = G(j\omega) \quad \text{for all } \omega=\omega_i. \tag{2}$$

However, Eq. (2) is the ideal case which is either unachievable or too costly to achieve with the computing resource given. A practical solution can be to select the coefficients of Eq. (1) such that the tolerance for Eq. (2) to hold is in some way minimized.

Rewrite Eq. (2) as

$$\sum_{i=0}^{m} b_i(j\omega)^{m-i}-G(j\omega)\sum_{i=1}^{n} a_i(j\omega)^{n-i}=(j\omega)^n G(j\omega). \tag{3}$$

The identification task now becomes minimizing

$$\left\| \left\{ \sum_{i=0}^{m} b_i(j\omega)^{m-i}-G(j\omega)\sum_{i=1}^{n} a_i(j\omega)^{n-i} \right\} -(j\omega)^n G(j\omega) \right\| \quad \text{for all } \omega=\omega_i. \tag{4}$$

Selecting the rms norm the above equation transforms into a standard least-square minimization problem.[5]

In the proposed system, a fourth-order model in the form below is used to represent the system identified,

$$\frac{k}{s^2}\,\frac{b_1 s+a_0}{s^2+a_1 s+a_0}. \tag{5}$$

The above model can be considered as a double integrator model plus one high frequency resonance mode. The AAS of the nominal plant is therefore equivalent to $k$ in Eq. (5).

In the $s$ plane, the model shown in Eq. (5) has two poles at the origin and two zero-pole pairs near the imaginary axis. The controller design is then to select the proper controller zero/pole locations as well as the appropriate gain to obtain desired closed-loop performances. This is illustrated in Sec. III B.

With the nominal model of the plant, a linear second-order IIR filter is designed in time using MATLAB.[2,3] The controller is a combination of a PI and a lead compensator. The transfer function of the filter is

$$\frac{C(s)}{E(s)}=K\,\frac{s+z_1}{s}\,\frac{s+z_2}{s+p_1}, \tag{6}$$

where the zeros $z_1$ and $z_2$, and pole $p_1$ are so selected that the root locus of the control system has the desired shape. The gain $K$ in Eq. (6) is chosen so that the dominant closed-loop poles are placed at the desired position on the root locus.

The ideal closed-loop dominant poles are the key factors in determining the system time responses. At the preliminary stage of design, the controller chooses its controller gain according to the AAS of the nominal plant model. For a drive with an AAS different from the nominal value, such selected controller gain will not give the same time response as desired. However, with the identified AAS of each drive from Sec. III A, the controller gain can be adjusted so that the dominant poles of the closed-loop system with the new drive are the same as that with the nominal one.

The discrete time IIR filter in Fig. 2 can be derived from the continuous time controller model demonstrated below.

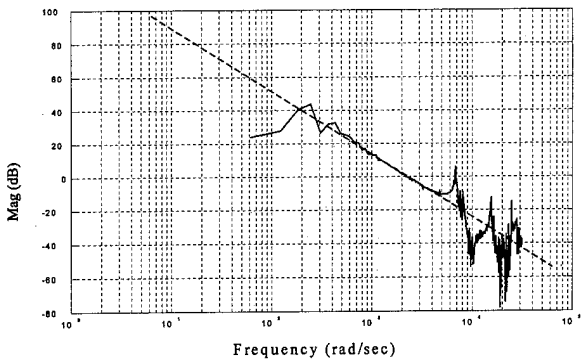



FIG. 3. Frequency response plot of identification.

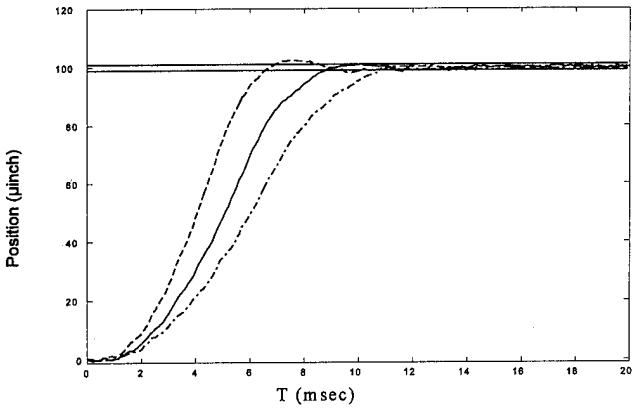



FIG. 4. A 100 $\mu$in. move of the servosystem.

Assuming a sampling interval of $T$, the backward rectangular rule is used to discretize the model by substituting

$$s=(1-z^{-1})/T. \tag{7}$$

As a result, the IIR filter equation of the digital controller is obtained as[8]

$$\frac{C(z)}{E(z)}=\frac{K_{x0}+K_{x1}z^{-1}+K_{x2}z^{-2}}{1+K_{y1}z^{-1}+K_{y2}z^{-2}}, \tag{8}$$

where

$$\begin{aligned} K_{x0}&=K(1+Tz_1)(1+Tz_2)/(1+Tp_1),\\ K_{x1}&=-K(2+Tz_1+Tz_2)/(1+Tp_1),\\ K_{x2}&=K/(1+Tp_1),\\ K_{y1}&=-2-Tp_1,\\ K_{y2}&=1//(1+Tp_1). \end{aligned} \tag{9}$$

Before servowriting a new drive, a maximal length PRBS signal of 1023 time points is first applied to the servoloop. Figure 3 shows the frequency responses of both the identified plant and the estimated rigid body model. The dashed line is the estimated value of the rigid body model, while the solid line represents the experimental values. Due to system nonlinearities such as the significant effect of pivot friction in disk drives of 3.5 in. and below, the low frequency responses (below 100 Hz) deviate significantly from the rigid body model of the plant. The rigid body model of the plant matches the experimental data only in the midfrequency range.

With the identified system model, the AAS of the new plant is compared with that of the nominal value used in the preliminary design stage. The controller gain and reference input are then adjusted accordingly to give the desired performance of the closed-loop system.

Figure 4 shows a 100 $\mu$in. move of the closed-loop system with 1% error tolerance lines. A profiled reference input is used instead of a step input in order to suppress the excitation of the high frequency components of the system. Equal acceleration commands in opposite directions are applied in the two halves of the reference input. The amplitude of the acceleration is adjusted proportionally to the AAS of the plant.

The same control is applied to three drive sets of different AAS gains. The dashed line shows the case where the previous controller gain is large. An undesirable larger overshoot is observed. The dot-dashed line shows the case where the previous controller gain is small. The system seems overdamped and an improvement in settling time is expected. The solid line gives a time response of the tuned system. Compared with the two cases before controller tuning, the tuned system has the fast settling time while the overshoot is sufficiently suppressed.

Note that although other system dynamics like resonance mode and low frequency nonlinearity are available from the system identification, only the gain is used in tuning the controller. The first resonance mode identified, however, aids mainly in the preliminary design stages in selecting the controller. Future development on direct on-line tuning of a higher order system model can be achieved without modifications of the system identification scheme.

[1]Helios Incorporated, Servowriter Technical Journal, 1994, Vol. 1, No. 2.
[2]G. F. Franklin, J. D. Powell, and A. E. Naeini, *Feedback Control of Dynamic Systems* (Addison-Wesley, Reading, MA, 1986).
[3]G. F. Franklin, J. D. Powell, and M. L. Workman, *Digital Control of Dynamic Systems* (Addison-Wesley, Reading, MA, 1990).
[4]W. D. T. Davies, *System Identification for Self-Adaptive Control* (Wiley-Interscience, New York, 1970).
[5]L. Ljung, *System Identification: Theory for the User* (Prentice-Hall, Engelwood Cliffs, NJ, 1987).
[6]Laser and Optics, User Manual, Hewlett–Packard, 05517–90033.
[7]HP10889B PC-servo Axis Board, Operating and Service Manual, Hewlett–Packard, 10889–90006.
[8]Submicron Positioning, Hewlett–Packard, 325-10.

# The effect of additives on MSR performance of GdFeCoM/TbFeCo (M=Ta, Pt) double layer

Isao Moritani
*Information Storage Materials Laboratory, Toyota Technological Institute, 2-12-1, Hisakata, Tempaku, Nagoya 468, Japan*

Koyata Takahashi and Akio Kondo
*Tokyo Research Center, Tosoh Corporation, Ayase 252, Japan*

Takao Suzuki
*Information Storage Materials Laboratory, Toyota Technological Institute, 2-12-1, Hisakata, Tempaku, Nagoya 468, Japan*

Magnetically induced super-resolution performance for a center aperture detection scheme in a double layered magneto-optical storage is discussed. In order to make a readout layer thinner for better media lifetime, the effect of Ta and Pt additive elements in a readout layer GdFeCo on recording performance is systematically studied. Ta is found to be most effective in making it possible to reduce the readout layer thickness for an acceptable recording performance. For the mark length of 0.5 $\mu$m, the thickness can be reduced to 60 nm with Ta (1.9 at. %) from 80 nm without Ta for carrier-to-noise ratio (CNR)$\geq$42 dB. © *1996 American Institute of Physics.*
[S0021-8979(96)10708-2]

## INTRODUCTION

Magnetically induced super-resolution (MSR), through which marks smaller than a diffraction limited size can be read, is one of the schemes for future high-density magneto-optical recording.[1] There are several proposals for MSR. One of them is a so-called "center aperture detection scheme (CAD)," which consists of an exchange coupled double layer. A readout layer has the magnetic anisotropy which changes from in-plane to perpendicular at higher temperatures.[2] Inside a heated laser beam spot of reading, the magnetization direction tends to be along the film normal because the perpendicular magnetic anisotropy becomes predominant, whereas outside the spot the magnetization is in-plane. Therefore, only the perpendicular component of the magnetization in the locally heated center region can be detected as signal.

Previous work[3] on the relation between magnetic properties and readout characteristics of MSR with a GdFeCo readout layer showed that the readout layer thickness larger than 80 nm was necessary for CNR higher than 35 dB at 0.4 $\mu$m mark length. Thicker magnetic layer requires higher writing power due to larger heat capacity. Therefore, the writing power must be lowered for practical applications in order to avoid the degradation of a media lifetime. One way to overcome this drawback is to make a readout layer thickness smaller. (However, it should not be too thin, since one should avoid the readout signal from the magnetization of a recording layer.) Through the exchange coupling, the direction of the magnetization near the interface between the recording and readout layers is not completely in-plane, but has a component along the film normal. It gradually changes in going from the interface through the readout layer thickness direction. Because of this gradual change, the thickness of more than at least 80 nm was found to be necessary to keep the polar Kerr rotation of GdFeCo at room temperature small enough so that little signal can be detected. It is believed that a steep change of the direction in the readout layer is essential for high performance MSR.

The present study discusses the effect of additives in a readout layer on performance so that one can decrease a readout layer thickness.

## EXPERIMENT

Thin films of SiN(80 nm)/GdFeCoM($d$)/TbFeCo(50 nm)/SiN(30 nm)/Al(20 nm) (M=Ta, Pt) were sputter deposited on polycarbonate (PC) substrates with a track pitch of 1.6 $\mu$m. GdFeCoM layers were deposited by co-sputtering of Gd and FeCo targets. Chips of additive, M, were placed on a Gd target. The deposition rate was 0.2 nm/s and the Ar pressure was 0.7 Pa. SiN films were deposited by reactive sputter deposition of Si in (Ar+$N_2$) gases, where the total gas pressure was kept 0.76 Pa. The compositions of GdFeCoM were (a) $(Gd_{94}Ta_6)_{32}(Fe_{60}Co_{40})_{68}$, (b) $(Gd_{88}Ta_{12})_{31}(Fe_{60}Co_{40})_{69}$, (c) $(Gd_{94}Pt_6)_{32}(Fe_{60}Co_{40})_{68}$, and their Curie temperatures, $T_c$, were about 370, 350, and 380 °C for (a), (b), and (c), respectively. The composition of recording layer was fixed for the above samples, which was $Tb_{19}(Fe_{87}Co_{13})_{81}$ with $T_c$ of 270 °C. A sample with nondoped $Gd_{27}(Fe_{50}Co_{50})_{73}$ readout layer was also prepared as reference.

Writing and reading performances were examined using an optical tester with $\lambda$=780 nm, NA=0.55, and linear velocity 7.5 m/s.

 0021-8979/96/79(8)/5677/3/$10.00 © 1996 American Institute of Physics 

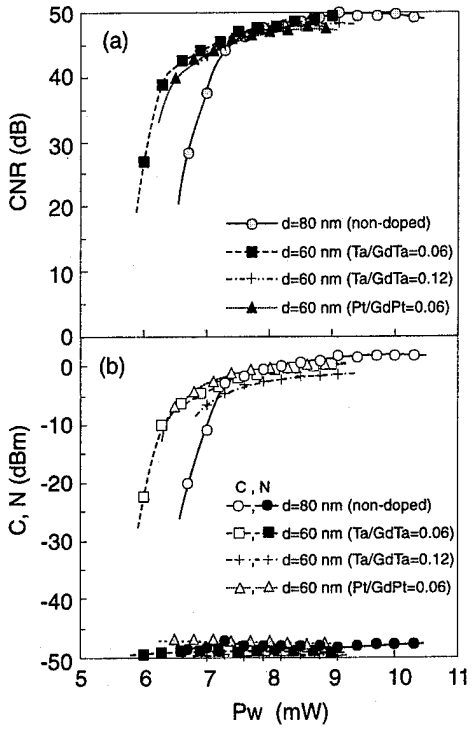



FIG. 1. Writing power dependence of (a) CNR and (b) C and N levels for mark length of 0.76 $\mu$m at 7.5 m/s.

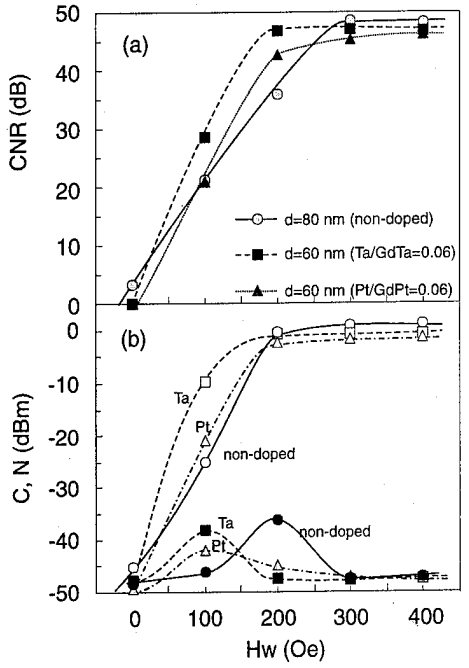



FIG. 2. Writing field dependence of (a) CNR and (b) C and N levels for mark length of 0.76 $\mu$m at 7.5 m/s.

## RESULTS AND DISCUSSION

Figure 1(a) shows the writing power dependence of CNR, where the mark length is 0.76 $\mu$m, the readout power is 2.5 mW, and the writing magnetic field is 500 Oe. Figure 1(b) is the carrier and noise levels as a function of the writing power. The samples with a 60-nm-thick readout layer show nearly the same CNR in a range from 7.5 to 9 mW as that with a 80-nm-thick nondoped one. A slight difference between the nondoped and doped samples in a low writing power region is believed to be due to a difference in thermal capacity through the thickness difference. The writing powers corresponding to minima of a second harmonic amplitude of carrier for the doped samples were lower than that for nondoped one by about 1 mW. [The actual powers were 9.7, 8.7, 8.5, and 8.6 mW for nondoped of $d$=80 nm, (a) of $d$=60 nm, (b) of $d$=60 nm, and (c) of $d$=60 nm, respectively.] A slight difference of CNR between Ta and Pt in a low power region is due to a lager noise of the Pt additive one, as shown in Fig. 1(b).

Figure 2(a) shows the writing field dependence of CNR, where the mark length is 0.76 $\mu$m and readout power is 2.5 mW. Figure 2(b) is the result of carrier and noise. When the thickness of the readout layer decreases, and when the Curie temperature of the readout layer also decreases with the additives, the writing process becomes less influenced by the magnetization of the readout layer. Therefore, the field dependence is improved, as given in Fig. 2(a). The saturation writing field for the doped samples is smaller than that of nondoped one. The effect of the additive is more clearly seen in Fig. 2(b), where the peaks of the noise level for the doped samples are smaller by 100 Oe than that of the nondoped one.

Figures 3(a) and 3(b) show the readout power dependences of CNR and carrier and noise, respectively for 0.5 $\mu$m marks. The sample with a Ta-doped 60-nm-thick readout layer (a) exhibits nearly the same CNR as that for nondoped one with a 80-nm-thick readout layer in a range from 2 to 4

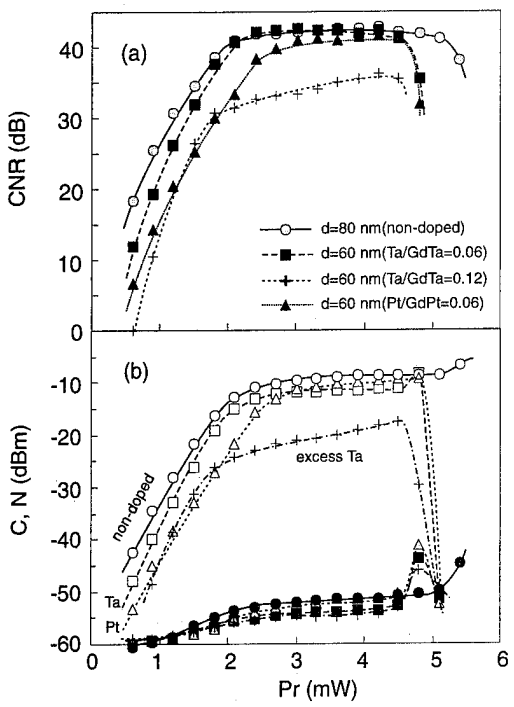



FIG. 3. Readout power dependence of (a) CNR and (b) C and N levels for mark length of 0.5 $\mu$m at 7.5 m/s. Excess Ta means Ta/GdTa=0.12.

mW of the readout power. The readout power margin (CNR>40 dB) for the Ta doped sample is about 2 mW, which is quite reasonable for practical use. The CNR of the Pt doped sample (c) is less by a few dB than those with and without Ta. An excess amount of Ta doping to the readout layer (b) reduces CNR as shown in Fig. 3(a). The Ta doped samples show lower noise level than other samples, as shown in Fig. 3(b).

The present result indicates that there might be a further possibility for reducing a readout layer thickness. In order to examine how thin the thickness can be made for acceptable performance, another experiment was performed. A sample with a 40-nm-thick readout layer (Ta/GdTa=0.06) was tested. Although the writing power sensitivity was improved by 1 mW under the same condition as indicated in Fig. 1, the CNR value was 37 dB for 0.5 $\mu$m marks. Thus, this result implies that there is a limit for reducing a readout layer thickness, which is around 50 nm for the composition of Ta/GdTa=0.06.

As to the effect of the exchange constant, $A$, and the perpendicular magnetic anisotropy, $Ku$, on the reduction of a readout layer, it is conjectured that a smaller $A$ and $Ku$ are favorable, since a sharper transition of the magnetization direction near the interface of the two layers takes place for smaller $A$ and $Ku$.[4] The present result is consistent with this argument, where the sample with Ta has smaller $A$ and $Ku$ than those for nondoped one. A preliminary calculation was made to examine the effect of $A$ and $Ku$ on the spin distribution for two cases:

(i) reduction of $A$ by 1/2, and
(ii) reduction of $Ku$ by $1 \cdot 10^5$ ergs/cm$^3$.

For both the cases the spin distribution was found to become equally sharper. It is not clear, however, at this moment what are the optimum values of $A$ and $Ku$ for best CNR performance at small mark size. The change of $Ku$ with temperature is also strongly related to MSR performance. A detail study on the effect of $A$ and $Ku$ relating to MSR performance is in progress.

## CONCLUSION

The present study has demonstrated that the readout layer can be made as thin as 60 nm for acceptable performance with adding Ta. It is found that the writing power can also be made lower by 1 mW as compared to the case for the nondoped sample. Improvement of the writing field dependence of CNR was demonstrated, which results from a lower Curie temperature of the Ta-doped readout layer.

[1] M. Ohta, A. Fukumoto, K. Aratani, M. Kaneko, and K. Watanabe, J. Magn. Soc. Jpn. **15**, Suppl. S1, 319 (1991).
[2] Y. Murakami, N. Iketani, J. Nakajima, A. Takahashi, K. Ohta, and T. Ishikawa, J. Magn. Soc. Jpn. **17**, Suppl. S1, 201 (1993).
[3] I. Moritani, K. Takahashi, and A. Kondo, J. Magn. Soc. Jpn. **19**, Suppl. S1, 327 (1995).
[4] H. Wakabayashi, H. Notarys, and T. Suzuki, J. Magn. Soc. Jpn. **15**, Suppl. S1, 87 (1991).

# Exchange coupling in rare-earth/transition-metal multilayers for magnetic super-resolution

A. M. Ayres
*Department of Materials Science and Engineering, Stanford University, Stanford, California 94305-2205*

E. E. Marinero
*IBM Almaden Research Center, San Jose, California 95120*

We study exchange coupling in rare-earth/transition-metal multilayers in which one layer has perpendicular magnetization and a second layer has in-plane magnetization at room temperature. The exchange coupling between these layers is mediated by a thinner intermediate layer, and we investigate the dependence of the exchange on the magnetic properties of this intermediate layer from room temperature through the compensation and Curie temperatures of the layers. The structures of interest consist of a 400 Å TbFeCo layer with perpendicular magnetization, a 400 Å GdFeCo layer with in-plane magnetization, and a GdFe intermediate layer of variable composition and thickness. The results indicate that the structures are well-described by either a two-layer or a three-layer coherent rotation model (depending on intermediate-layer thickness) and that the influence of the intermediate layer is a function of its anisotropy energy, its thickness, and the identity of its dominant atomic moment. © *1996 American Institute of Physics.*
[S0021-8979(96)10808-9]

## INTRODUCTION

Ferrimagnetic amorphous alloys of the rare-earth and transition-metal groups are the media of choice in today's magneto-optical storage technology. Sequential layering of such alloys permits additional control of their magnetic behavior through interlayer exchange coupling. As the intrinsic properties of the constituent layers are strongly temperature dependent, the exchange coupling exhibits unique dynamic effects when such structures are rapidly heated and cooled. An elegant example of such effects has been demonstrated in recent years through the concept of magnetic super-resolution (MSR).[1–5]

In one MSR scheme, Murakami *et al.*[4] used two layers, one (the storage layer, SL) having perpendicular magnetization and the other (the readout layer, RL) having in-plane magnetization at room temperature. The temperature response of this system depends strongly on the exchange interactions between the RL and the SL. Recent results by Nishimura *et al.*[5] suggest that better control of the exchange process can be achieved by using an intermediate layer (IL). This motivated us to understand the exchange interactions between the RL and SL as a function of the composition and thickness of the IL.

## EXPERIMENTAL TECHNIQUES

RE–TM alloys are sputtered onto glass substrates in a system equipped with six magnetron sources and a rotating sample turntable. The system's base pressure is around $6\times10^{-8}$ Torr and films are grown in a 3 mT argon atmosphere. Deposition takes place at the chamber's ambient temperature (estimated to be 70–80 °C) with no bias voltage applied to the substrates. SiN underlayers and overcoats are grown during the same pumpdown by reactive sputtering.

Magneto-optical Kern effect (MOKE) measurements are conducted in a 20 kG electromagnet equipped with a heating stage and a MOKE setup consisting of a He–Ne laser and a Wollaston prism/differential detector combination. Measurements are conducted from both sides of the trilayer samples to obtain hysteresis loops for both RL (glass interface) and SL (air interface) at the same temperature. A combined vibrating-sample magnetometer/torque system is employed to measure saturation magnetizations in the films as a function of temperature.

## RESULTS AND DISCUSSION

In Fig. 1, representative MOKE loops for the RL in a bilayer structure as well as those of the single RL and SL are shown for various sample temperatures (expressed as a frac-

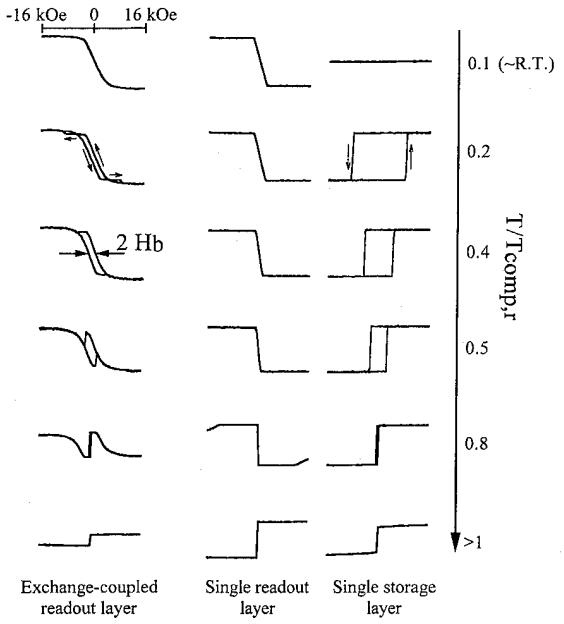



FIG. 1. Representative MOKE loops vs temperature for experimental bilayer and corresponding RL and SL single layers.

 0021-8979/96/79(8)/5680/3/$10.00 © 1996 American Institute of Physics

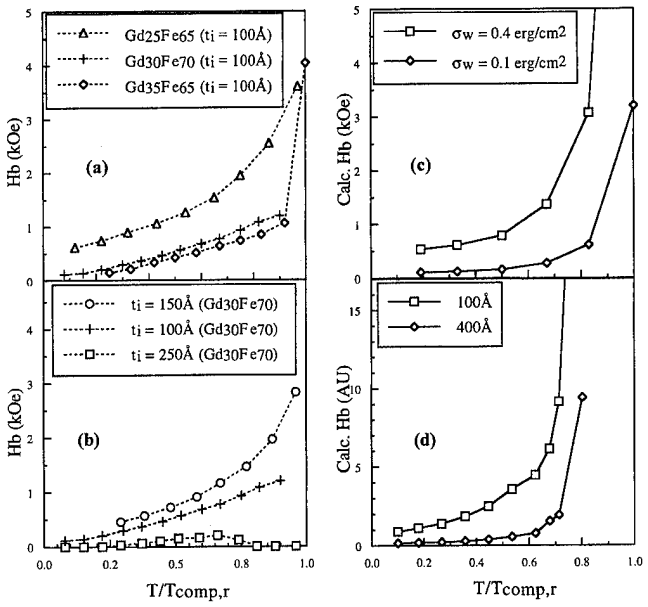



FIG. 2. $H_b$ vs temperature. (a) and (b) Experimental. (c) Results from two-layer (Esho) model. (d) Results from the three-layer model.

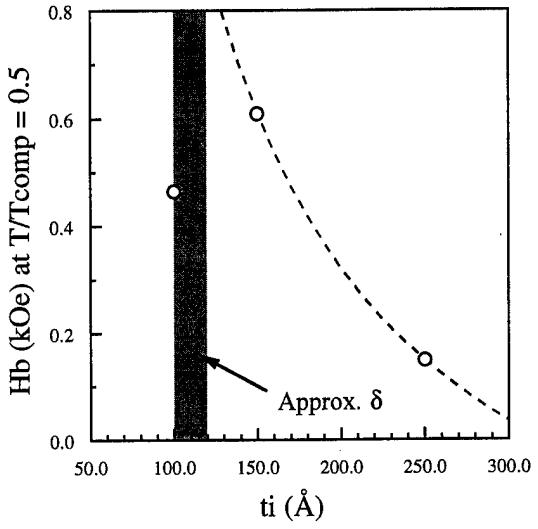



FIG. 3. $H_b$ vs intermediate-layer thickness. The dashed line illustrates the decrease in $H_b$ above $t_i \sim \delta$; it is not a fit.

tion of the RL compensation temperature). The SL composition $[Tb_{24}(Fe_{70}Co_{30})_{76}]$ is TM-dominated and exhibits room-temperature compensation and 100% remanence hysteresis loops through its Curie temperature of about 400 °C. The RL composition $[Gd_{31}(Fe_{60}Co_{40})_{69}]$ is RE-dominated and has in-plane magnetization for all temperatures below 0.8 $T/T_{comp}$. It has a $T_{comp}$ value of about 225 °C and a Curie temperature above 400 °C. The exchange coupling between the two layers manifests itself as a bias field which displaces the hysteresis curve of the RL from the $H$, $\theta$ origin. When the field sweep exceeds the SL coercivity, the MOKE signal from the RL traces out an inverted loop whose zero crossings give the magnitude of the exchange bias field $H_b$. Above $T_{comp}$ the films are strongly exchange coupled for all applied field values.

The exchange bias represents the value of the applied field at which the Zeeman energy per unit area ($E_j = \mathbf{H}_{applied} \cdot \mathbf{M}_j t_j$ for each layer $j$) favoring rotation of net moments in all layers toward the applied field direction balances the energy of the interface domain wall that accommodates nonparallel TM moment alignment in the various layers. This domain wall is a 180° head-on wall whose energy is considered to be equivalent to that of a 180° Bloch wall, $\sigma_w = 4(AK_{eff})^{1/2}$, in which $A$ is the exchange stiffness constant and $K_{eff} = (K_u - 2\pi M_s^2)$ is the effective uniaxial anisotropy energy of the layer in which the wall resides. The thickness of a Bloch wall is given by $\delta = \pi(A/K_{eff})^{1/2}$; for typical values of $A$ and $K_{eff}$, a lower bound for $\delta$ is about 100 Å for our films.

This work dealt with samples in which either the composition of 100 Å intermediate layers or the thickness of $Gd_{30}Fe_{70}$ intermediate layers was varied. Plots of $H_b$ versus reduced temperature for both sets of samples [Figs. 2(a) and 2(b)] show the increase in $H_b$ with temperature observed in Fig. 1. The results of Figs. 2(a) and 2(b) can be categorized into two classes, one in which the IL thickness is comparable to $\delta$ and one in which it is larger.

For the case in which the IL thickness is less than about 100 Å, the situation is equivalent to the bilayer case considered by Esho,[6] for which the exchange bias is described by

$$H_b = \sigma_w / 2M_s t. \tag{1}$$

Here $\sigma_w$ is the energy per unit area of the domain wall between the two layers and $M_s$ and $t$ are the saturation magnetization and thickness of the layer which feels the exchange bias (the RL). The $H_b$ results of Fig. 2(a) can be understood by considering that the domain wall is energetically favored to lie in the layer with the lowest value of $(AK_{eff})$. IL compositions $Gd_{35}Fe_{65}$ and $Gd_{30}Fe_{70}$ both have higher $K_{eff}$ values than the RL, so energy considerations suggest that the wall will tend to reside in the RL for these samples. Consequently, $\sigma_w$ is the same in both cases, so the $H_b$ behavior is similar. The observed $H_b$ data can be fit using a value of $\sigma_w = 0.1$ erg/cm$^2$, as shown in Fig. 2(c). Since the $Gd_{25}Fe_{75}$ IL is TM-dominated we observe a higher $H_b$, for which experimental results are shown in Fig. 2(a) and fit in Fig. 2(c) using an effective value of $\sigma_w = 0.4$ erg/cm$^2$.

The second category of trilayers includes those in which the IL thickness is larger than $\delta$. In this case, the experimental $H_b$ results shown in Fig. 3, which plots exchange bias at a given temperature versus IL thickness, are consistent with a three-layer coherent rotation model. In the three-layer model, we express the energy of the generic trilayer of Fig. 4(b) as the sum of six terms describing the Zeeman, exchange, anisotropy, and magnetostatic energies of the IL and the RL. The full energy expression is

$$\frac{E}{\text{area}} = -M_{s,r} H t_r (1 - \cos\theta_r) + \sigma_{w,r} \sin^2\left(\frac{\theta_r - \theta_i}{2}\right) + K_{\text{eff},r} t_r \sin^2\theta_r - M_{s,i} H t_i (1 - \cos\theta_i) + \sigma_{w,i} \sin^2\left(\frac{\theta_i}{2}\right) + K_{\text{eff},i} t_i \sin^2\theta_i, \tag{2}$$

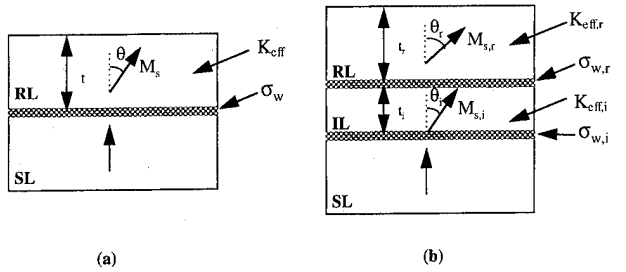



FIG. 4. Geometries for (a) two-layer and (b) three-layer coherent rotation models.

where the subscripts $i$ and $r$ indicate values for the IL and the RL, respectively. The bias field is found by minimizing the energy with respect to both angles $\theta_i$ and $\theta_r$, setting $\theta_r$ equal to $\pi/2$, and eliminating $\theta_i$. This yields an equation that is fourth order in $H_b$. We recover the prior solution for $H_b$ [Eq. (1)]. as well as a new solution which allows for an arbitrary direction of IL magnetization; the exchange bias is then described by

$$H_b = \frac{\sigma_{w,i}\sigma_{w,r}}{2t_i(M_{s,i}\sigma_{w,r} - 4K_{\mathrm{eff},i}t_r M_{s,r})}. \tag{3}$$

This equation has an explicit $1/t_i$ dependence, but it should be noted that $K_{\mathrm{eff},i}$ is also a function of $t_i$.

Figure 2(d) shows simulated data using Eq. (3) to find $H_b$ for triple-layer films. The model indicates that the temperature dependence of $H_b$ stems from the individual temperature dependencies of $M_{s,i}$ and $K_{\mathrm{eff},i}$ of the IL; both of these vanish at the Curie temperature, so the model predicts that $H_b$ will go to infinity at the IL's $T_C$ (190–205 °C depending on composition). However, the $H_b$ curve appears to be insensitive to the Curie temperature of the IL. Magnetostatic coupling can be ruled out because of the different dominant submoments in the SL and RL. Thus it is apparent that coupling persists beyond the temperature at which the IL is expected to become paramagnetic, in contrast to the "switching off" of exchange that is proposed in Ref. 5.

The model also predicts a monotonic decrease in exchange bias as a function of IL thickness, while Fig. 3 indicates that the exchange bias increases in the thickness range from 100 to 150 Å before decreasing with further thickness increases. The physical interpretation is that there is some threshold thickness of the IL at which it begins to behave as a coherent magnetic layer bounded by two domain walls. This critical thickness corresponds to a balance between the energetic cost of building two 90° domain walls (one in the high-anisotropy IL) and the energetic benefit of allowing the IL to assume its lower-energy state of in-plane magnetization. This means that the three-layer model is valid only above a certain threshold IL thickness, so the $1/t_i$ dependence of the exchange bias is observed only above this thickness.

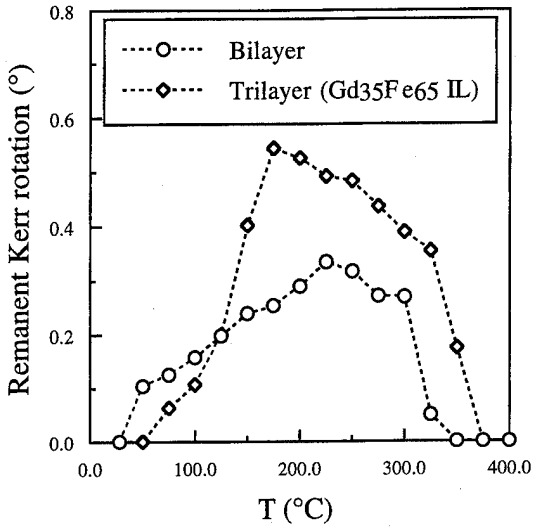



FIG. 5. Comparison of temperature response of bilayer and trilayer structures.

Since the shifting of the magnetization curve of the RL causes a finite remanence (related to the magnetization direction of the SL) at zero field, and since this shifting increases with temperature, the films exhibit the temperature-dependent remanent Kerr rotation that is necessary for MSR. As shown in Fig. 5, the influence of the IL is to sharpen the temperature response of the remanent Kerr rotation in comparison with that of the two-layer system.

## CONCLUSION

We observe exchange coupling in RE–TM bilayers in which one layer has in-plane magnetization and a second layer has perpendicular magnetization at room temperature, and we investigate the influence of an intermediate layer on the strength of the exchange coupling between the two layers.

## ACKNOWLEDGMENT

This material is based upon work supported under a National Science Foundation Graduate Research Fellowship.

[1] K. Aratani, A. Fukumoto, M. Ohta, M. Kaneko, and K. Watanabe, Proc. SPIE **1499**, 209 (1991).
[2] A. Fukumoto, S. Yoshimura, T. Udagawa, K. Aratani, M. Ohta, and M. Kaneko, Proc. SPIE **1499**, 216 (1991).
[3] M. Ohta, A. Fukumoto, K. Aratani, M. Kaneko, and K. Watanabe, J. Magn. Soc. Jpn. **15**, Suppl. S1, 319 (1991).
[4] Y. Murakami, N. Iketani, J. Nakajima, A. Takahashi, K. Ohta, and T. Ishikawa, J. Magn. Soc. Jpn. **17**, Suppl. S1, 201 (1993).
[5] N. Nishimura, T. Hiroki, and T. Okada, J. Magn. Soc. Jpn. **19**, Suppl. S1, 417 (1995).
[6] S. Esho, Jpn. J. Appl. Phys. **15**, Suppl. 15-1 93 (1976).

# Transition from in-plane to perpendicular magnetization in MSR magneto-optical disks

Naoki Nishimura, Tomoyuki Hiroki, and Takeshi Okada
*Imaging Research Center, Canon Inc., 30-2, Shimomaruko 3-Chome, Ohta-ku, Tokyo 146, Japan*

Shigeru Tsunashima
*Department of Electronics, Nagoya University, Nagoya 464-01, Japan*

Transition from in-plane to perpendicular magnetization caused by temperature changes have been investigated for double-layer (GdFeCo/TbFeCo) and triple-layer (GdFeCo/GdFe/TbFeCo) magneto-optical recording films. The transition in the GdFeCo layer occurs mainly as a result of change in the demagnetizing energy of the GdFeCo layer having compensation temperature. Such transition occurs more rapidly in the triple-layer film than that in the double-layer film. Micromagnetic calculation showed that in the double-layer film the interface wall penetrates deeply into the GdFeCo readout layer, while in the triple-layer film the wall is almost completely confined within the GdFe intermediate layer having a large $Ms$ and a low $T_c$. The triple-layer film is found to improve the characteristics of magnetically induced super resolution (MSR). © *1996 American Institute of Physics.* [S0021-8979(96)15708-1]

Magnetically induced super resolution (MSR) is a promising technology for achieving super high-density magneto-optical recording media.[1] Recently, a new type of MSR double layer film has been proposed.[2,3] In the film, the magnetization orientation of the readout layer changes from in-plane to perpendicular with the raise of the temperature, and hence the marks in the most heated area can be detected while the adjacent marks are masked. However in such double-layer film, it is difficult to achieve sharp transition from in-plane to perpendicular magnetization, resulting in insufficient MSR characteristics.

The present authors adopted a magnetic triple-layer film instead of the double-layer film and allowed a sharper transition from in-plane to perpendicular magnetization, and then succeeded to improve the MSR characteristics.[4,5]

In this paper we investigate the mechanism of the transition from in-plane to perpendicular magnetization, and clarify the effect of the intermediate layer on the magnetization transition both by micromagnetic calculation and by magnetic and magneto-optic measurements.

Magnetic layers were deposited by dc co-sputtering from elemental targets on glass or polycarbonate substrates. GdFeCo (readout) and GdFe (intermediate) layers were rare-earth (RE) rich alloys. TbFeCo (memory) layers were $3d$ transition metal (TM) rich alloys.

Saturation magnetization $Ms$ was obtained by using a vibrating-sample magnetometer and mean-field theory. The Kerr rotation $\theta k$ and the anisotropy field $Hk$ were measured from Kerr hysteresis loops, which were measured from the substrate (GdFeCo) side for the wavelength of 830 nm. All of the magnetic layers were sandwiched between SiN layers, and samples have a reflectivity of 19%. The uniaxial perpendicular anisotropy constants $Ku$ of respective layers were obtained from the expression $Ku-2\pi Ms^2=-MsHk/2$.

In magnetic thin films the orientation of the magnetization is determined by the effective perpendicular anisotropy constant $K$ given by

$$K=Ku-2\pi Ms^2, \tag{1}$$

where $2\pi Ms^2$ is demagnetizing energy. When $K$ is negative, the magnetic film exhibits in-plane magnetization. On the other hand, when $K$ is positive, the magnetic film exhibits perpendicular magnetization.

In both single and double layer films, the effective perpendicular anisotropy $K$ changes its sign from negative to positive at a certain temperature, resulting in a transition from in-plane to perpendicular magnetization [Fig. 1(a)]. When the GdFeCo layer is coupled with the TbFeCo layer,

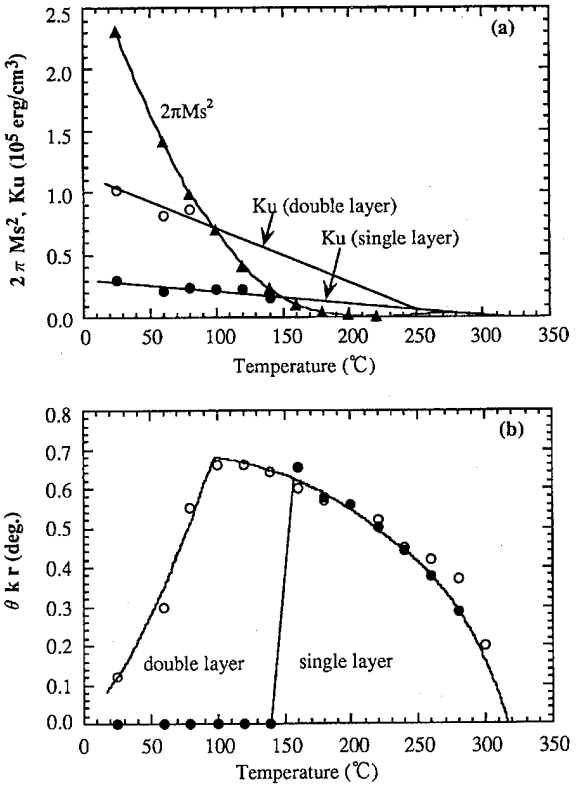



FIG. 1. Temperature dependence of magnetic and magneto-optical properties for single layer $Gd_{28}(Fe_{60}Co_{40})_{72}$ (80 nm) and double layer $Gd_{28}(Fe_{60}Co_{40})_{72}$ (50 nm)/$Tb_{20}(Fe_{80}Co_{20})_{80}$ (30 nm). (a) $2\pi Ms^2$ and $Ku$ for $Gd_{28}(Fe_{60}Co_{40})_{72}$, which has a compensation temperature of 220 °C and $Tc$ of 320 °C. (b) Remanent Kerr rotation $\theta kr$.

 0021-8979/96/79(8)/5683/3/$10.00 © 1996 American Institute of Physics 

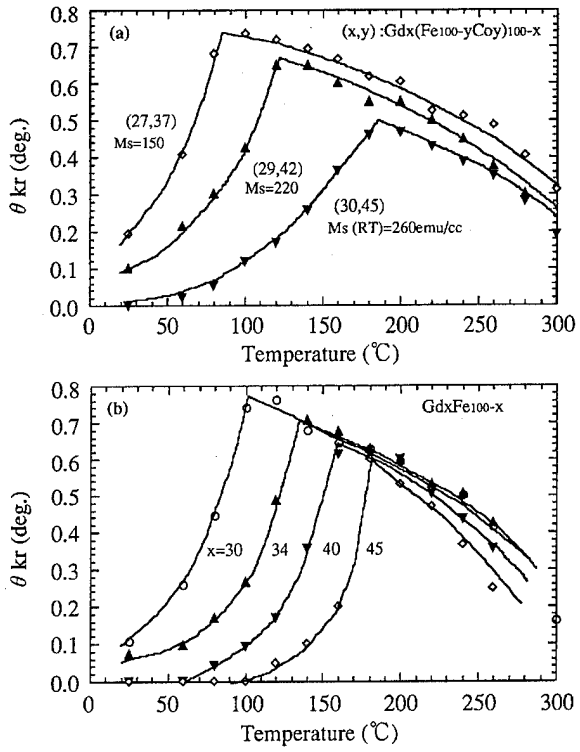



FIG. 2. Temperature dependence of $\theta kr$ for (a) double layer: $Gd_x(Fe_{100-y}Co_y)_{100-x}$ (50 nm)/$Tb_{20}(Fe_{80}Co_{20})_{80}$ (30 nm), where $Tc$ of the GdFeCo layers was adjusted to 320 °C by controlling Co content and (b) triple layer: $Gd_{28}(Fe_{60}Co_{40})_{72}$ (40 nm)/$Gd_xFe_{100-x}$ (10 nm)/$Tb_{20}(Fe_{80}Co_{20})_{80}$ (30 nm).

$Ku$ is apparently increased due to the large perpendicular anisotropy of the TbFeCo layer. As a result, the transition occurs at lower temperature [Fig. 1(b)]. It should be noted here that, in double-layer films, the transition does not occur suddenly at a temperature but does occur gradually over a wide range of temperature.

In double-layer films, as the Gd content becomes higher, the transition point shifts to higher temperatures due to larger demagnetizing energy [Fig. 2(a)]. Although $\theta kr$ at room

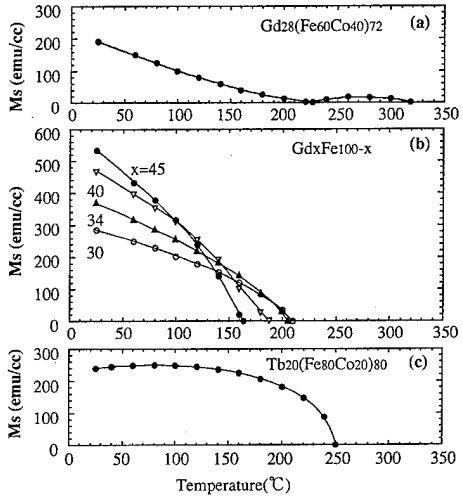



FIG. 3. Saturation magnetization $Ms$ as a function of temperature.

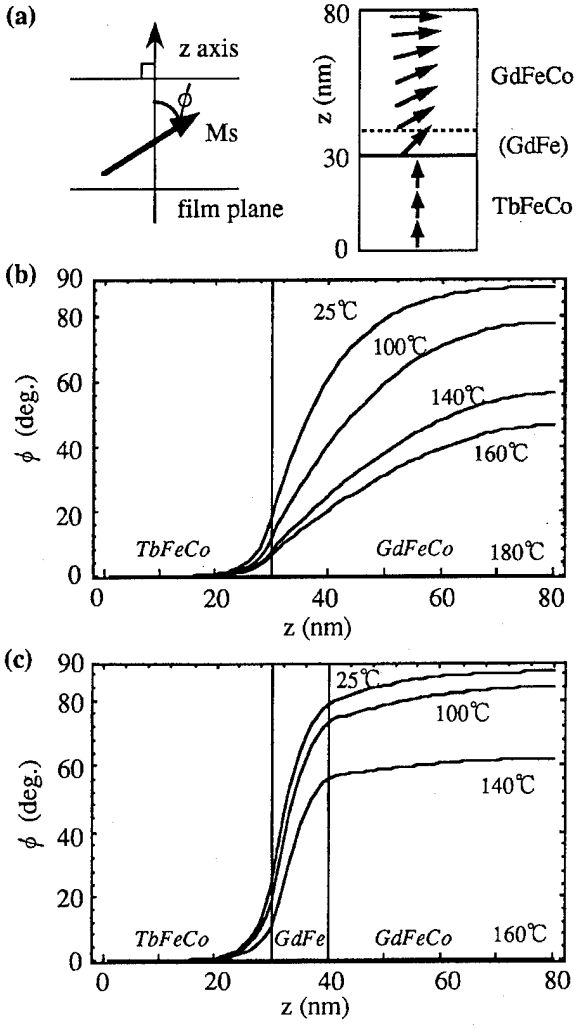



FIG. 4. (a) Schematic diagram of the magnetization direction. (b) Calculated profile of magnetization direction at various temperatures for double layer $Gd_{30}(Fe_{55}Co_{45})_{70}$/$Tb_{20}(Fe_{80}Co_{20})_{80}$ and (c) triple layer $Gd_{28}(Fe_{60}Co_{40})_{72}$/$Gd_{40}Fe_{60}$/$Tb_{20}(Fe_{80}Co_{20})_{80}$ whose properties are listed in Table I.

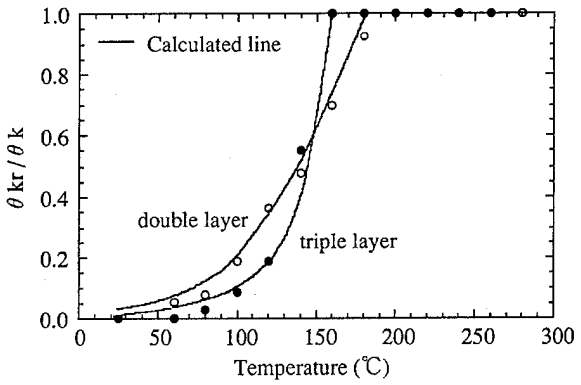



FIG. 5. Measured and calculated results of $\theta kr/\theta k$ as a function of temperature for double layer and triple layer shown in Fig. 4. Optical constants used were: $n^+=3.607-3.817i$ and $n^-=3.698-3.875i$ for GdFeCo and GdFe layers, $n^+=3.475-4.122i$ and $n^-=3.625-4.084i$ for the TbFeCo layer.

TABLE I. Magnetic constants at room temperature.

| | $Gd_{30}(Fe_{55}Co_{45})_{70}$ | $Gd_{28}(Fe_{60}Co_{40})_{72}$ | $Gd_{40}Fe_{60}$ | $Tb_{20}(Fe_{80}Co_{20})_{80}$ |
|---|---|---|---|---|
| $Ms$ (emu/cm$^3$) | 260 | 191 | 466 | 238 |
| $Ku$ (ergs/cm$^3$) | $1.00\times10^4$ | $2.90\times10^4$ | $6.65\times10^4$ | $4.00\times10^6$ |
| $A$ (ergs/cm) | $4.00\times10^{-7}$ | $4.00\times10^{-7}$ | $2.80\times10^{-7}$ | $3.00\times10^{-7}$ |

temperature (RT) can be made almost zero by increasing the Gd content up to 30 at. %, the transition takes place more gradually and $\theta kr$ does not reach its saturation value even at 180 °C. This is because, as we will describe in a later section, the interface wall appearing around the boundary between the two layers considerably penetrates into the GdFeCo layer.

For the ideal MSR media, the penetration of the interface wall is not desired and furthermore the transition should occur suddenly at an appropriate temperature. Therefore, we controlled the behavior of the interface wall by inserting an intermediate layer between the readout and memory layers. For high speed recording,[4] the lower part (intermediate layer side) of the GdFeCo layer was removed to maintain the total thickness of magnetic layers constantly. We adopted the intermediate layers of GdFe having a low Curie temperature ($T_c$) and a large $Ms$ as shown in Fig. 3.

Figure 2(b) shows that the transition temperature in triple-layer films becomes higher as the higher Gd content of the intermediate layer. A more important point is that in the case of higher Gd content, the triple-layer films show a sudden transition, namely, a very steep slope of $\theta kr$ while attaining zero $\theta kr$ at RT.

To analyze the effect of the intermediate layer on magnetization transition, we calculated the profile of the magnetization direction using the noncontinuous model.[6] In this model, the total free energy per unit area $E$ is expressed as a function of the magnetization direction $\Phi=(\phi_1,\phi_2,,,\phi_N)$ of $N$ homogeneously magnetized sheets

$$E(\Phi)=\sum_{i=1}^{N-1}\frac{2A_i}{d_i}[1-\cos(\phi_{i+1}-\phi_i)]+\sum_{i=1}^{N}[d_i(Ku_i-2\pi Ms_i^2)\sin^2\phi_i], \quad (2)$$

where $A_i$ is the exchange stiffness of the coupling between the $n$th and the $(n+1)$th sheet, and $d_i$ and $\phi_i$ are the sheet thickness (0.5 nm) and angle of the magnetization with respect to the film's normal direction [Fig. 4(a)], respectively. The equilibrium magnetization orientation is obtained by minimizing $E$ with respect to $\Phi$.

Kerr rotation $\theta k$ can also be obtained by Kerr enhancement calculation with $\phi$ and refractive index $n^{\pm}$ derived from

$$n^{\pm}(T)=n_0\pm\delta n\times\cos(\phi)\times m^{\mathrm{TM}}(T)/m^{\mathrm{TM}}(\mathrm{RT}), \quad (3)$$

where $n_0$ is the average of refractive index for right circularly polarized light $n^+$ and for left circularly polarized light $n^-$, and $\delta n$ is the difference between $n^+$ and $n^-$, and $m^{\mathrm{TM}}(T)$ and $m^{\mathrm{TM}}(\mathrm{RT})$ are magnitudes of TM magnetic moment at the temperature and RT, respectively.

We applied these micromagnetic calculations to double and triple layer films both of which have almost zero $\theta kr$ at RT. The calculated results show that the interface wall of the double-layer film significantly penetrates into the GdFeCo layer which has a small effective magnetic anisotropy [Fig. 4(b)]. As the temperature increases, the interface wall spreads into the GdFeCo layer, and as a result, the transition from in-plane to perpendicular magnetization does not occur suddenly.

On the other hand, in the case of triple-layer film, the interface wall is almost confined within the intermediate layer, and the direction of the magnetization in the GdFeCo layer is almost completely in-plane at low temperatures [Fig. 4(c)]. This can be attributed to the strong effective in-plane anisotropy of the intermediate layer. When the temperature is increased, the transition of the GdFeCo layer to perpendicular magnetization occurs very rapidly. This seems to be attributed to the rapid decrease of the effective in-plane anisotropy of the intermediate layer below and near the Curie temperature. Figure 5 shows that the calculation results are in good agreement with experimental results. The triple-layer film is seen to exhibit very rapid transition around 140 °C.

The triple-layer media was confirmed to achieve CN ratio at least 4 dB higher than the double-layer media for a mark length of 0.40 $\mu$m using a conventional optical unit with a wavelength of 780 nm and numerical aperture of 0.55.

Transition from in-plane to perpendicular magnetization of GdFeCo layers occurs as a result of the changes in the sign of the effective perpendicular anisotropy. In the triple-layer films, the transition occurs more rapidly than double-layer films. A micromagnetic calculation showed that the interface wall is almost completely confined within the intermediate layer while, in the case of the double-layer films, the wall penetrates into the GdFeCo layer. The triple-layered films make it possible to improve the MSR characteristics.


[1] K. Aratani, A. Fukumoto, M. Ohta, M. Kaneko, and K. Watanabe, Proc. SPIE **1499**, 209 (1991).
[2] Y. Murakami, N. Iketani, J. Nakajima, A. Takahashi, K. Ohta, and T. Ishikawa, J. Magn. Soc. Jpn. **17**, S1, 201 (1993).
[3] A. Takahashi, J. Nakajima, Y. Murakami, K. Ohta, and T. Ishikawa, IEEE Trans. Magn. **30**, 232 (1994).
[4] N. Nishimura, T. Hiroki, and T. Okada, J. Magn. Soc. Jpn. **19**, S1, 417 (1995).
[5] N. Nishimura, T. Hiroki, T. Okada, and S. Tsunashima, Jpn. J. Appl. Phys. **35**, 145 (1996).
[6] W. Andra, IEEE Trans. Magn. **2**, 560 (1966).

# Magnetic parameter control for high-density quadrivalued MO recording (invited) (abstract)

N. Ohta, K. Shimazaki, M. Yoshihiro, N. Nagai, and S. Ohnuki
*Engineering Research Laboratory, Hitachi Maxell Ltd., 6-20-1 Kinunodai, Yawara-mura, Tsukuba-gun, Ibaraki, 300-24 Japan*

To increase recording density of MO media, several schemes have been proposed. Among them, magnetic multivalued (MMV) recording is one of the most promising methods. We have first realized the quadrivalued MMV media using a field modulation method.[1] Such media is composed of an exchange coupled TbFeCo/PtCo bilayer. By switching the external field in four levels, the separated signal corresponding to the each field is obtained as a four leveled output. For the acutal device application for high-density and high-speed recording, it is necessary to reduce the external field as small as possible. In the previous experiment, about ±900 Oe was necessary to record the whole levels. For such MMV media, the quadrivalued signal response depends on the magnetic characteristics of the TbFeCo/PtCo bilayer, which is so called dual write state.[1] The higher field level on the MMV media is defined by the threshold field of the dual write state. It is found that the threshold field is controllable to tune the magnetic parameter, especially the exchange coupling force between the TbFeCo and PtCo. As a result, the reduction of the recording field less than 350 Oe is realized on a new media. Using such tuned media, high-density quadrivalued recording is experimentally carried out. © *1996 American Institute of Physics.* [S0021-8979(96)46408-5]

[1]K. Shimazaki, M. Yoshihiro, O. Ishizaki, S. Ohnuki, and N. Ohta, J. Magn. Soc. Jpn. **19**, 429 (1995).

 0021-8979/96/79(8)/5686/1/$10.00 © 1996 American Institute of Physics

# Magneto-optical recording on patterned substrates (invited)

S. Gadetsky, J. K. Erwin, and M. Mansuripur
*Optical Sciences Center, University of Arizona, Tucson, Arizona 85721*

T. Suzuki
*Toyota Technological Institute, Nagoya, Japan*

Patterning of glass or plastic substrates in the form of shallow square patches is a promising method of increasing the storage density for magneto-optical disks. The sidewalls of the patches pin the reverse-magnetized domains that develop in these samples. Confinement of domains within the patch boundaries during thermomagnetic recording has also been demonstrated. We have measured polarization conversion of the incident light on the sidewalls of the patches; a method to reduce the amount of such polarization conversion is proposed in this article. © *1996 American Institute of Physics.* [S0021-8979(96)06008-5]

## I. INTRODUCTION

To keep pace with present hard magnetic drives, magneto-optical (MO) recording technology must increase recording density to 10 Gb/in.$^2$. Such densities imply recorded domain diameters of the order of 0.25 $\mu$m. From a micromagnetic point of view, such domains are stable in the current MO media, which are based on amorphous rare-earth transition metal alloys.[1] The problem is how to write and read back such small domains considering the fact that, even for the blue light, the focused spot at the disk surface is about twice the size of the desired domains. Reading of small marks may be possible with a three-beam scheme[2] in conjunction with partial response signaling.[3] As for writing and erasure, patterning of disk substrates[4,5] promises to confine reverse-magnetized domains within areas that are as small as (or even smaller than) the focused laser spot.

Figure 1 presents the main idea behind the confinement of domains on patterned disks. The circle with a radius of 0.4 $\mu$m represents the Airy disk for the laser spot with a wavelength of 400 nm, focused through an objective lens with NA=0.6. The disk substrate is patterned by 0.25×0.25 $\mu$m$^2$ shallow square patches in the form of a checkerboard. When the laser beam is focused at the center of a patch it nucleates a reverse domain which subsequently expands (under the influence of an externally applied magnetic field) towards the patch borders. The sidewalls of the patch prevent the domain wall from crossing the patch boundary. This confinement is caused by the increased coercivity of the MO film at the sidewalls. The increased coercivity is probably rooted in the tilt of the easy axis of magnetization on the sidewalls, as well as in the reduced film thickness there.[6] Thus, this technique should allow the writing of magnetic domains smaller than the laser spot. Another advantage of patterned substrates is that the laser beam does not interfere with previously recorded domains since the patch sidewalls prevent the expansion or contraction of existing domains in the neighborhood of the focused spot.

In this article we provide experimental evidence for the strong pinning of domain walls on the sidewalls of shallow patches. Thermomagnetic recording performed on several patterned samples indicates that recorded domains can form within the confines of patches that have a height (or depth) as low as 10 nm. Scanning optical microscopy has been used to identify the source of noise introduced during readout of patterned samples.

## II. EXPERIMENT

Corning 7059 glass substrates were patterned using a photolithographic method.[4] The patterns in the photoresist layer were produced by exposure to optical interference fringes in two orthogonal directions. 2.5×2.5 $\mu$m$^2$, 1×1 $\mu$m$^2$, and 0.5×0.5 $\mu$m$^2$ square patches having height (or depth) of 10, 20, or 30 nm were produced by argon–ion etching through the developed photoresist mask.[7,8] The samples used in our study are listed in Table I. The resulting surface features are shown in two typical atomic force micrographs in Fig. 2. If the exposed photoresist is underdeveloped, wells appear in the photoresist film, which, upon ion etching, are replicated into the glass substrate [see Fig. 2(a)]. On the other hand, if the exposed photoresist is overdeveloped, isolated islands remain on the glass substrate [see Fig. 2(b)]. A thin film stack was subsequently deposited on these substrates as follows: substrate/SiN(10 nm)/TbFeCo(either 25 nm or 50 nm)/SiN(80 nm). The MO layer in this stack was an amorphous Tb-rich TbFeCo film having a saturation moment $Ms$=190 emu/cm$^3$ and a coercivity $Hc$=3 kOe at $T$=300 K (see Table I).

Figure 3 is a schematic diagram of our custom-built microscope for domain observations, Kerr loop tracing (with a resolution approaching one wavelength of the light), wall motion studies, and scanning optical microscopy. Domain structures were observed in this polarized-light microscope

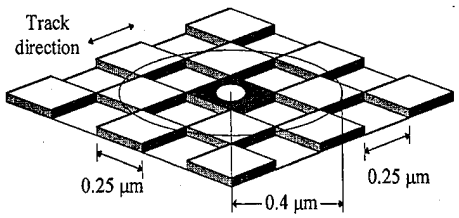



FIG. 1. Schematic diagram showing a checkerboard pattern of 0.25×0.25 $\mu$m$^2$ square patches on a disk substrate. The 0.8 $\mu$m diam circle represents the Airy disk of the focused laser spot, produced with a 0.6 NA objective lens at a wavelength of 400 nm. The small white circle in the middle represents a domain nucleus.

 0021-8979/96/79(8)/5687/6/$10.00 © 1996 American Institute of Physics 

TABLE I. Characteristics of the samples used in experiments.

| Sample | Patch size ($\mu m^2$) | Patch height (nm) | TbFeCo thickness (nm) | Etched areas |
|---|---|---|---|---|
| A | 2.5×2.5 | 30 | 50 | Low |
| B | 1×1 | 20 | 50 | Low |
| C | 1×1 | 10 | 50 | Low and high |
| D | 0.5×0.5 | 10 | 25 | Low and high |

using a 100× oil immersion objective. The observations were recorded with a TV camera and a PC-based frame grabber that allowed image processing for noise reduction.[9] An electromagnet, having a maximum field capability of 9 kOe and a rise time of 50 ms, was mounted under the microscope's XY stage to provide the necessary fields for domain nucleation and wall motion studies, for thermomagnetic recording, and for loop tracing. The microscope was supplemented with a laser diode operating at $\lambda=780$ nm. The laser beam was focused onto the sample by the microscope's objective lens. The reflected beam was picked up by a differential detection module (polarizing-beam splitter and two photodiodes). The difference and sum signals from the detectors were sampled by an A/D board and were sent to the computer for further processing.

For Kerr loop tracing with submicron resolution, the sampling of detector outputs was synchronized with the sweeping magnetic field. For every value of the magnetic field, the differential and sum signals were sampled and an apparent Kerr rotation angle was calculated. (Faraday rotation in the objective lens was taken into account when the final Kerr angle was determined.) Kerr hysteresis loops obtained with this loop tracer will be discussed later in the article.

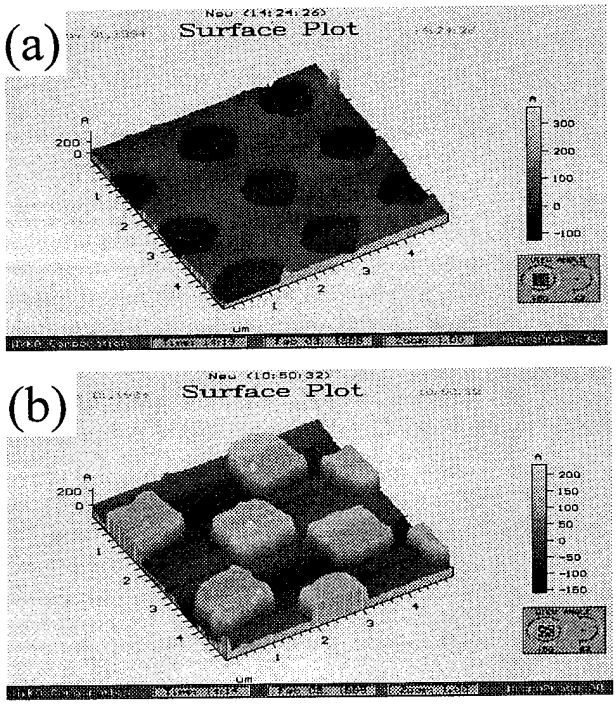



FIG. 2. AFM pictures of 1×1 $\mu m^2$ patches on Corning 7059 glass substrates obtained by a photolithographic process and argon–ion milling. (a) Lowered patches having a depth of 10 nm. (b) Raised patches having a height of 20 nm.

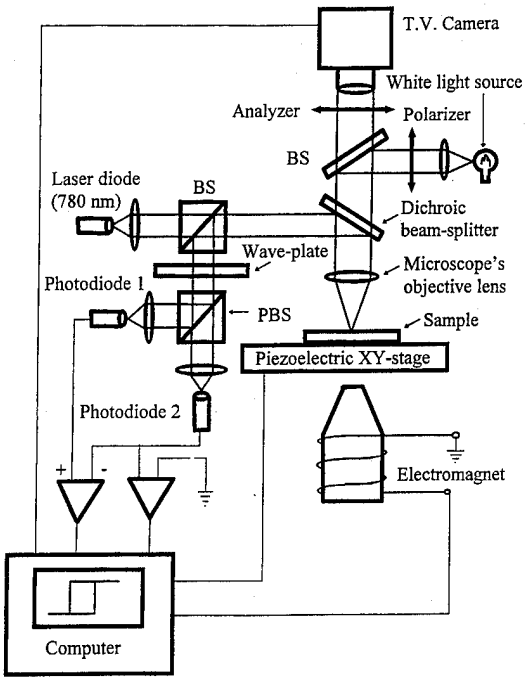



FIG. 3. Experimental setup used in observations of domain nucleation and wall propagation, scanning optical microscopy, and micro-Kerr loop tracing.

To study the peculiarities of domain wall motion with a spatial resolution of better than 50 nm, the magnetic field was brought up to a constant level that allowed a single domain wall to move under the laser spot. The differential output signal was then sampled at equal time intervals (maximum sampling rate=$10^5$/s) and plotted as a function of time. This method allows observation of small Barkhausen jumps during wall motion.[10]

For scanning optical microscopy, the polarized-light microscope was equipped with a piezo stage. The piezo stage was computer controlled, its steps being synchronized with the sampling instances of the differential and sum signals from the photodetectors. A two-dimensional plot of the sum signal would represent a reflectivity map of the sample. The corresponding plot of the differential signal would yield a map of the polarization rotation angles occurring at the sample's surface.

## III. EXPERIMENTAL RESULTS AND DISCUSSION

### A. Scanning optical microscopy of patterned samples

Figure 4 shows scanning photomicrographs of patterned samples that were saturated prior to scanning (i.e., there was no magnetic structure within the scanned area). The micrographs were obtained using the differential signal from the detector module. The gray level represents the degree of rotation of polarization. In Figs. 4(a) and 4(b), where the patch size is 2.5×2.5 $\mu m^2$ and the patch height is 30 nm (sample A), black corresponds to a minimum rotation of −3.0° and white corresponds to a maximum rotation of +3.0°. Figure

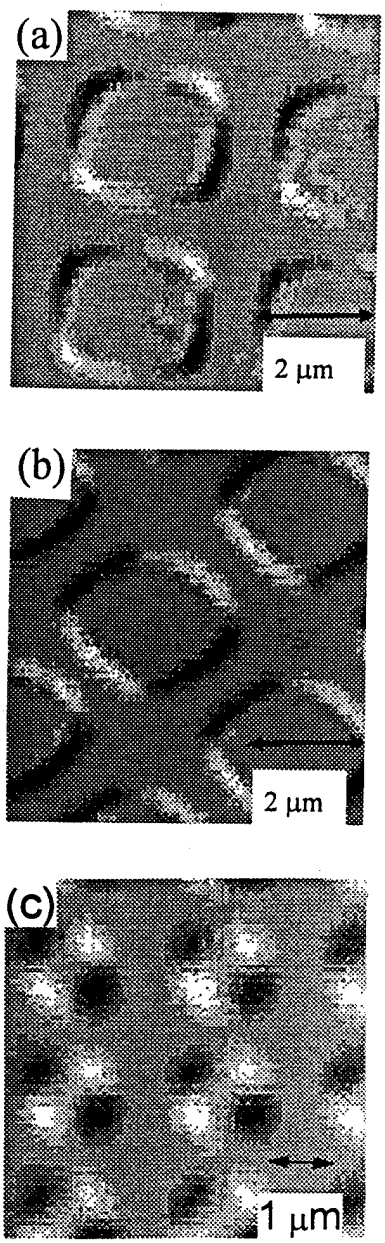



FIG. 4. Scanning photomicrographs of patterned samples. The samples were saturated in a strong magnetic field prior to scanning. The differential signal picked up during scanning (and used to produce these images) was proportional to the angle of rotation of polarization. The incident polarization was linear along the Y axis. (a) $2.5\times2.5$ $\mu m^2$ patches having a height of 30 nm. (b) Same sample as in (a) but rotated 45° around the Z axis. (c) $1\times1$ $\mu m^2$ patches having a height of 10 nm.

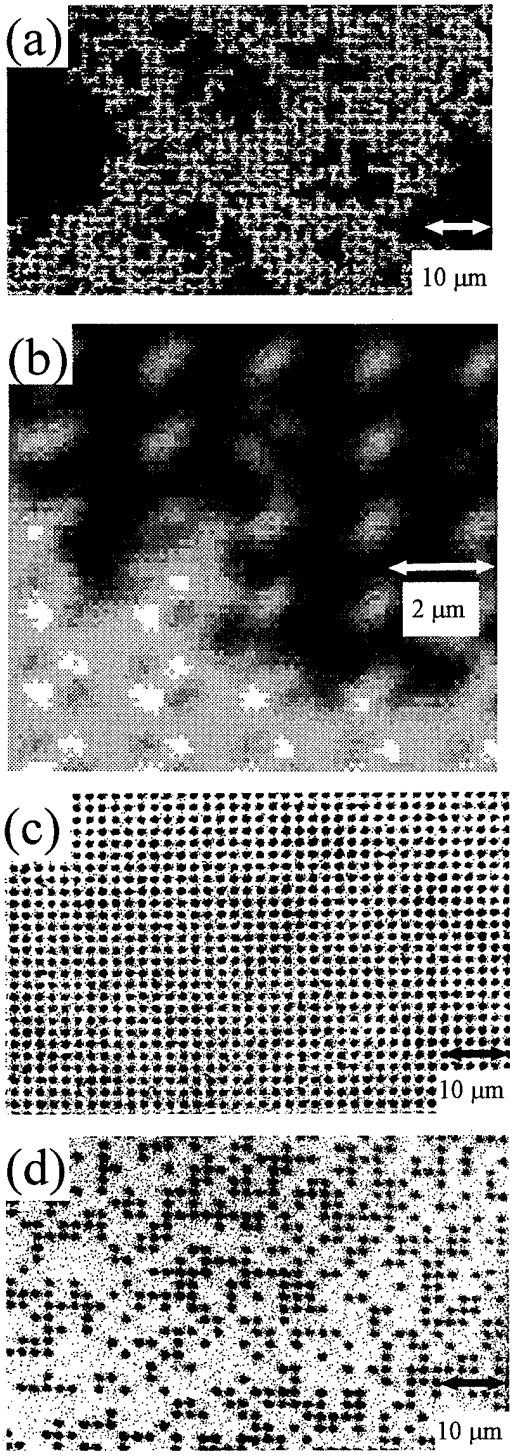



FIG. 5. Domain structure developing under a bias magnetic field in a TbFeCo film on a patterned substrate having 10 nm high, $1\times1$ $\mu m^2$ patches: (a) at $H=2.8$ kOe; (b) scanned photomicrograph showing a close-up of a small region in (a); (c) at $H=3.4$ kOe; (d) at $H=4.5$ kOe.

4(a) indicates that the patch borders cause a fairly significant rotation of polarization. Specifically, the sidewalls of the patches aligned at ±45° to the direction of incident polarization (which is along the Y axis) produce the strongest rotations. If the orientation of the sidewall relative to the incident polarization is +45° (upper left and lower right corners of each patch) the sidewalls produce negative rotation. For −45° orientation (lower left and upper right corners of each patch) the sense of rotation is positive. The observed rotations are caused by different reflectivities for the p and s components of polarization, where s is perpendicular and p is parallel to the sidewall. If the incident polarization happens to be either parallel or perpendicular to the sidewall, then there would be no rotations at all. The patches in Fig. 4(a) are visible in this differential scanning micrograph essentially because they have rounded corners (at ±45° to the incident polarization). If we rotate the sample by 45°, then

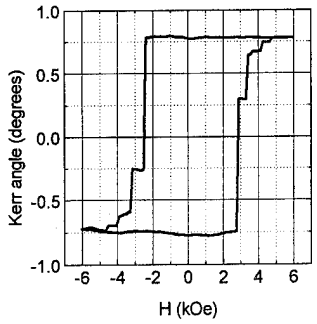



FIG. 6. Micro-Kerr loop measured on the sample of Fig. 5 using a loop tracer with a 2 $\mu$m diam focused spot.

the sidewalls themselves become oriented at $\pm 45°$ to the incident polarization, which is the case presented in Fig. 4(b). In Fig. 4(c), where the patches are $1\times1$ $\mu m^2$ and the patch height is only 10 nm (sample C), the minimum rotation angle (black) is $-0.3°$ and the maximum rotation angle (white) is $+0.3°$. The order of magnitude reduction in the polarization rotation angles in the case of Fig. 4(c) as compared to those in Figs. 4(a) and 4(b) indicates that polarization rotation on the sidewalls dramatically decreases with a reduction of the patch height.

### B. Magnetic domain structures in patterned samples

Figure 5 shows domain structures developing in the patterned sample C [i.e., the sample with the surface topography of Fig. 2(b)] under a bias magnetic field. At first the magnetic reversal occurs due to nucleation followed by wall motion in the connected areas of the sample, namely in the region between the patches, as shown in the polarized-light micrograph of Fig. 5(a). The scanning optical micrograph of Fig. 5(b) shows how the domain structure bends its way around the patches, leaving behind unreversed islands. In this picture, the advancing domains are black, while the four corners of individual patches appear as two pairs of bright and dark spots. The surviving domains appear as elongated bright spots oriented at 45° to the X axis. This apparent elongation of the domain is an illusion caused by the surrounding pairs of bright and dark spots arising from the patch corners: the dark spots compress the domain image in one direction, while the bright spots stretch it in the perpendicular direction. At a certain magnetic field the entire region in-between the patches becomes saturated, while within the patches magnetization remains unreversed [see Fig. 5(c)]. Apparently, the patch sidewalls prevent domain walls from entering the patches. At higher magnetic fields the domains confined within the patches begin to collapse either by domain wall penetration through the sidewalls or by nucleation of reverse domains from within the patches [see Fig. 5(d)].

Figure 6 shows a micro-Kerr loop, measured in sample C, using a 2 $\mu$m diam probe laser beam ($1/e$ intensity radius $\approx 1$ $\mu$m). The beam covers a region that contains only a few patches (a minimum of one and a maximum of four), thus allowing us to obtain information about individual patch reversals. The sharp drop in the Kerr signal in the vicinity of 2.8 kOe corresponds to magnetization reversal in the connected regions between the patches. The three jumps that follow the first one at magnetic fields between 2.8 and 4.8 kOe correspond to individual reversals within the three patches that are apparently illuminated by the focused beam in this experiment. The different heights of the jumps are due to uneven illumination of the patches.

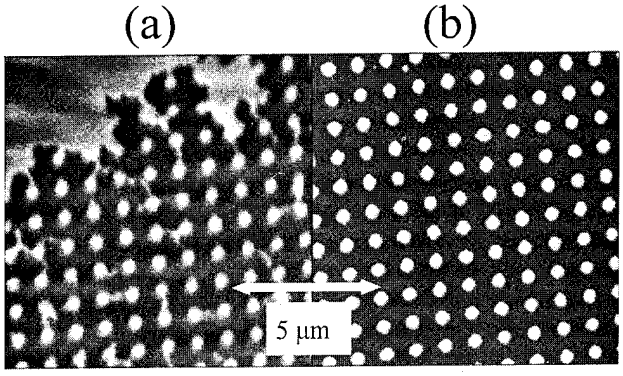



FIG. 7. (a) Magnetic force microscope image of domain structure developing under a bias magnetic field in a TbFeCo film on a patterned substrate having 10 nm high, $0.5\times0.5$ $\mu m^2$ patches. (b) Atomic force micrograph of the same region of the sample.

The domain structure under a bias magnetic field in sample D, which has $0.5\times0.5$ $\mu m^2$ patches, is shown in Fig. 7(a). Since optical microscopy fails to resolve domain features on such a small scale, we employed an atomic force microscope (AFM) and a magnetic force microscope (MFM) for these observations. In Fig. 7(a) the MFM picture shows domains expanding in the connected areas between the patches. [The AFM picture of Fig. 7(b) shows the same region of the sample where the patches are white and the space between them is black.] In a good portion of the MFM picture, the black domain structure has developed in the connected areas of the sample, but it has not penetrated through the patch borders.

Figure 8 shows a micro-Kerr loop, measured for sample D, using a 2 $\mu$m diam probe beam. The first jump of the Kerr signal in the vicinity of $H=2.6$ kOe corresponds to fast domain expansion in the connected areas between the patches.

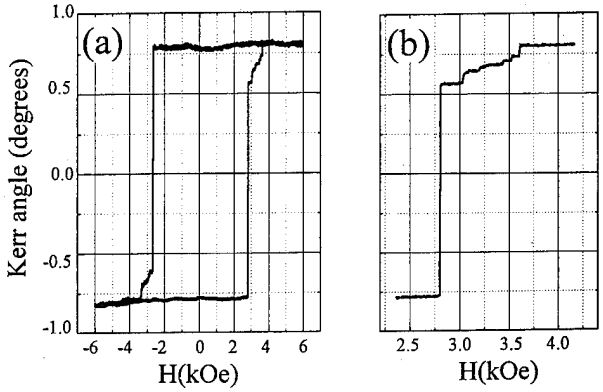



FIG. 8. (a) Micro-Kerr loop measured on the sample of Fig. 7 using a loop tracer with a 2 $\mu$m diam focused spot. (b) Enlarged view of the section of the loop between $H=2.5$ and $H=4.0$ kOe.

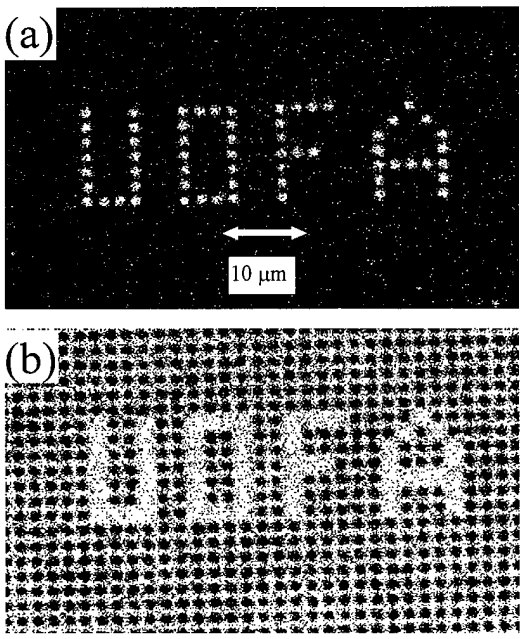



FIG. 9. (a) Domains written on $1\times1$ $\mu m^2$ patches having a height of 20 nm at $H=1.3$ kOe using 200 ns, 10 mW laser pulses. (b) Domains erased at $H=1$ kOe by 200 ns, 10 mW laser pulses from a sample having 10 nm high, $1\times1$ $\mu m^2$ patches.

The next five jumps between $H=2.6$ and $H=3.6$ kOe correspond to individual patch reversals. As before, different magnitudes of the jumps are caused by uneven illumination of the patches within the focused beam.

These observations of magnetization reversal on patterned substrates indicate that the patch sidewalls prevent domain walls from entering the patches. At room temperature the strength of this sidewall pinning varies from a maximum of 1 kOe in the $0.5\times0.5$ $\mu m^2$ patches to a maximum of 2 kOe in the $1\times1$ $\mu m^2$ patches (both patches having a height of 10 nm). This difference may be due to the better quality of the $1\times1$ $\mu m^2$ patches fabricated with our photolithographic process. One conclusion that we may draw from this study is that pinning on the sidewalls should also occur when a domain nucleates inside a patch and proceeds to expand towards the sidewalls. It must therefore be possible to confine such domains within the patch borders.

### C. Thermomagnetic recording and erasure experiments on patterned samples

Figure 9 shows results of thermomagnetic recording and erasure on patterned samples. The 780 nm laser beam was directed through a 1.25 NA immersion oil objective onto individual patches and, with the aid of an externally applied magnetic field, effected the writing and/or erasing of domains. The domains in Fig. 9(a) were written inside the patches of the initially saturated sample B under a reverse field of 1.3 kOe using a 10 mW, 200 ns laser pulse. Good confinement of domains within individual patches is observed. In Fig. 9(b), the application of 10 mW, 200 ns laser pulses has produced erasure of selected domains on sample

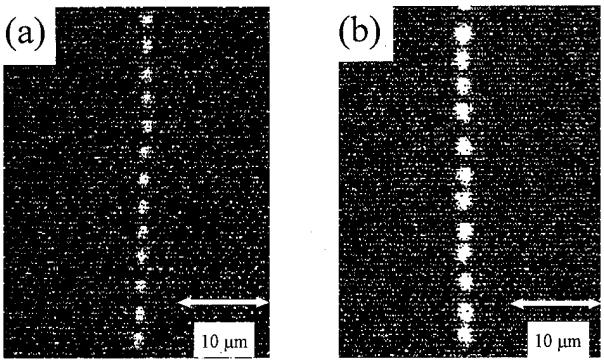



FIG. 10. (a) Domains written on $1\times1$ $\mu m^2$ patches having a height of 20 nm at $H=1.3$ kOe using 200 ns, 10 mW laser pulses. (b) Domains written on a flat area of the same sample under identical recording conditions.

C, which was described earlier in conjunction with Fig. 5; the pattern of domains before erasure of selected patches may be seen in Fig. 5(c).

Figure 10(a) shows domains written on $1\times1$ $\mu m^2$, 20 nm high patches (sample B) under a reverse field of 1.3 kOe, using 10 mW, 200 ns laser pulses. Compare this with Fig.

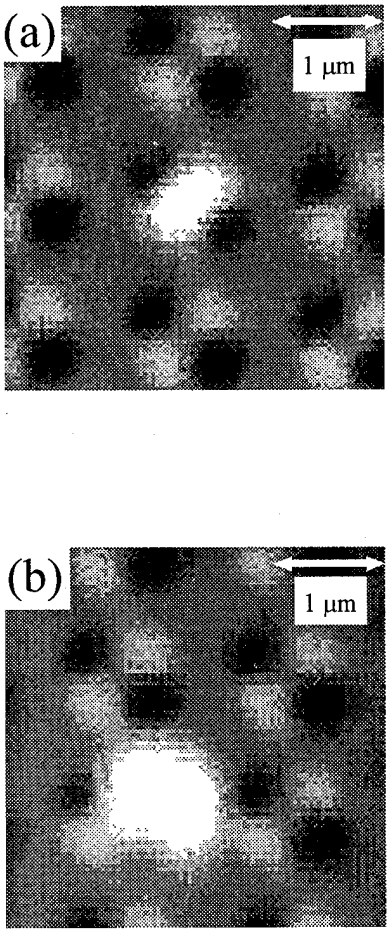



FIG. 11. (a) Scanning photomicrograph of a domain recorded on a $1\times1$ $\mu m^2$ patch. The focused beam was aimed at the center of the patch during recording. (b) Same as (a) but the beam was intentionally offset from the patch center.

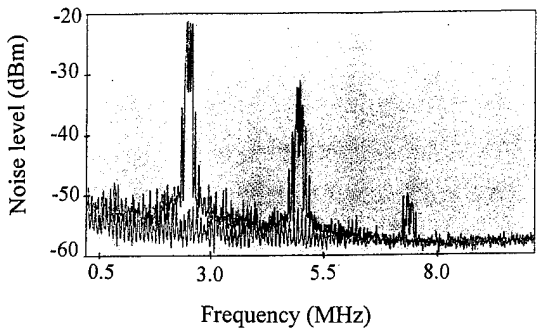



FIG. 12. Noise spectra measured on the flat region (bottom trace) and patterned region (top trace) of the sample having $1\times1$ $\mu m^2$, 10 nm high patches. The sample was fully saturated in a strong magnetic field prior to these measurements. The sample's linear velocity during these measurements was 5 m/s.

10(b), which shows domains written under identical conditions on the flat area outside the patterned region of the same sample. The domains on the flat region are much larger, thus implying confinement on the part of domains written onto the patches.

Figure 11(a) shows a domain written on a $1\times1$ $\mu m^2$ patch on sample C using the same conditions as those described earlier in conjunction with Figs. 9 and 10. This scanning optical micrograph shows that the recorded domain is located symmetrically with respect to the two pairs of bright and dark spots corresponding to the patch corners. The size of the domain is similar to those shown in Fig. 5(b). If we intentionally miss a patch during thermomagnetic writing, as we did in the case of Fig. 11(b), the resulting domain becomes considerably larger, reminding us, once again, of the lack of confinement.

The noise spectrum measured in a dynamic tester[11] on sample C is shown in Fig. 12. The sample was magnetically saturated before the measurement. The peaks at 2.5, 5.0, and 7.5 MHz correspond to the first three harmonics of the 2 $\mu$m period pattern at the measurement velocity of 5 m/s. Shown below the spectrum of the patterned region is the noise spectrum obtained from the flat region of the same sample. Note that the additional wideband noise introduced by the patches is about 5 dB. This noise is believed to have arisen from the induced roughness on the substrate by our primitive photolithographic and ion-etching processes. Improvements in the patterning process should reduce this component of the media noise. The various harmonics of the periodic pattern appearing in the differential channel output are caused by polarization rotation at patch corners, as discussed earlier. To prevent the signal of the patches from appearing alongside the MO signal in the differential channel output, one must fabricate perfectly square patches whose sides are aligned strictly parallel and perpendicular to the direction of polarization of the incident beam.

## IV. CONCLUSIONS

Kerr loop tracing on micrometer-sized regions and scanning optical microscopy with polarization detection have been employed to study magnetization reversal on patterned substrates. Pinning of domain walls in TbFeCo films by the sidewalls of shallow patches on patterned glass substrates has been demonstrated. Also, thermomagnetically written domains have been shown to be successfully confined within the patches. The angle of rotation of polarization, caused by different reflectivities of the patch corners for $p$- and $s$-polarized light was measured, and a method to eliminate this undesirable signal was proposed.

## ACKNOWLEDGMENTS

The authors are grateful to W. McChesney, J. Hurst, and B. Urison of the IBM Almaden Research Center for deposition of the films and for dynamic noise measurements. They also wish to thank Dr. T. Pokhil of the Institute for Rock Magnetism in Minneapolis for the use of their Atomic and Magnetic Force Microscope facility. Thanks are also due to Warren Bletscher of the Optical Sciences Center for his technical assistance.

[1] Hong Fu, R. Giles, M. Mansuripur, and G. Patterson, Comput. Phys. **6**, 610 (1992).
[2] M. Yamamoto, A. Watabe, and I. Yamada, IEEE Trans. J. Magn. Jpn. **8**, 277 (1993).
[3] Lu Cheng, M. Mansuripur, and D. G. Howe, Appl. Opt. **34**, 5153 (1995).
[4] S. Gadetsky, T. Suzuki, J. K. Erwin, and M. Mansuripur, IEEE Trans. Magn. **MAG-30**, 4404 (1994).
[5] K. Wakabayashi, H. Sugiyama, T. Maeda, A. Saitou, H. Miyamoto, and H. Awano, Proceedings of SOM'94, article MoB3.
[6] Y.-C. Hsieh and M. Mansuripur, J. Appl. Phys. **78**, 380 (1995).
[7] S. Gadetsky, T. Suzuki, J. K. Erwin, and M. Mansuripur, J. Magn. Soc. Jpn. **19**, suppl. S1, 91 (1995).
[8] S. Gadetsky, T. Suzuki, J. K. Erwin, and M. Mansuripur, these proceedings.
[9] B. E. Bernacki and M. Mansuripur, J. Appl. Phys. **69**, 4960 (1991).
[10] S. Gadetsky and M. Mansuripur, these proceedings.
[11] J. E. Hurst, D. Weller, and H. A. Notarys, J. Magn. Soc. Jpn. **17**, suppl. S1, 299 (1993).

# Comparison of the magneto-optical figure of merit of NdFeCo and TbFeCo alloys

W. A. Challener
*Basic Materials Laboratory, 3M, St. Paul, Minnesota 55144*

Due to the magneto-optical (MO) activity of light rare earths, NdFeCo alloys have been suggested as candidates for use in future high density MO media designed for use at shorter wavelengths. We have measured the MO indices of refraction and computed the maximum Kerr rotation figure of merit as a function of wavelength from 400 to 900 nm for a wide range of NdFeCo and TbFeCo alloys. Only a marginal gain in MO media performance is expected by incorporating NdFeCo into optimized TbFeCo thin film stacks. © *1996 American Institute of Physics.* [S0021-8979(96)10908-5]

## INTRODUCTION

Magneto-optic (MO) materials suitable for future high density MO media will be designed for use with shorter wavelength lasers. Rare-earth–transition-metal (RE–TM) alloys in general and TbFeCo in particular have been found quite suitable for use in media designed to operate at red and near-IR wavelengths. These alloys can be tailored to exhibit perpendicular anisotropy, high coercivity, and Curie temperatures that are suitable for the recording powers available with current semiconductor lasers. While the MO signal is not particularly large, an optimized thin film stack typically exhibits about 20% reflectance and 1° Kerr rotation. This together with the amorphous nature of the MO film, which eliminates grain boundary noise, generally provides an excellent signal-to-noise ratio. In addition, TbFeCo can be sputtered from an alloy target, making it more easily manufactured than a nanolayered MO material such as PtCo.

Concern has been expressed in the MO community about ways to increase the MO signal, especially at shorter wavelengths. As a result, a variety of materials[1–5] have been proposed as replacements for TbFeCo, or as "enhancement layers." The latter typically lack certain desirable properties such as perpendicular anisotropy and/or high room temperature coercivity, and so must be laminated with another material like TbFeCo to obtain a suitable recording medium.

An enhanced Kerr rotation has been reported for NdFeCo alloys.[6–10] It was initially suggested that a Nd spin–polarized $4f$ band was within about 2 eV of the Fermi level, closer than that of the heavy rare earths, and could therefore contribute to the increase in Kerr rotation.[7,11] Subsequent electronic structure calculations,[12] however, indicated that transitions from Fe $d$ states at the Fermi level to Nd $f$ states about 3.85 eV above the Fermi level are primarily responsible for the MO activity. This information is not sufficient, however, to determine if NdFeCo alloys can be used in optimized thin film stacks to give a larger signal in MO media than that which can be obtained with TbFeCo alloys.[13] The correct figure of merit (FOM) for comparing different MO materials is not the Kerr rotation of the thick film, but rather the potential Kerr coefficient[14,15] or maximum Kerr rotation.[16] These FOMs can only be calculated by first completely determining the MO refractive indices of the materials. The maximum Kerr rotation FOM is[13]

$$\mathrm{FOM}=\frac{1-R}{2\sqrt{R}}\sqrt{\left(\frac{1}{n^2}+\frac{1}{K^2}\right)(\Delta n^2+\Delta K^2)}, \tag{1}$$

where $R$ is the reflectance of the film stack, and the refractive index of the MO layer is $(n\pm\Delta n)+i(K\pm\Delta K)$ where the "+" and "−" signs refer to right and left circular polarizations, respectively. The potential Kerr coefficient FOM in other publications[14,17] may be directly compared to the maximum Kerr rotation FOM in this article after multiplying by $(360°/2\pi)(1-R/\sqrt{R})=102.5°$ for $R=0.2$.

## EXPERIMENT

Samples with a variety of NdFeCo and TbFeCo compositions were dc magnetron sputtered in Ar gas at a pressure of 2.5 mTorr from elemental targets in a vacuum chamber with a base pressure of $1.5\times10^{-7}$ Torr. Silicon wafers and glass microscope slides were used as substrates. They were mounted on a planetary and its speed of revolution could be controlled to obtain either complete mixing or nanolayering. The typical sample consisted of 180–200 Å of SiC, 150–200 Å RE–TM deposited in an alloylike film, and 180–200 Å SiC. Film thicknesses were measured by a stylus profilometer. The SiC was used as an environmental barrier to oxidation of the MO. Separate glass slides of SiC alone were also prepared for optical characterization.

The composition of the samples was measured by XRF on the Si wafers. Reflectance and transmittance measurements were made from both the air-incident and substrate-incident side of the thin films on the glass slides from 400 to 900 nm to determine the average value of the index of refraction.[18] The MO indices of refraction were calculated from polar Kerr rotation and ellipticity, measured from 400 to 900 nm from the air-incident side only to minimize effects of Faraday rotation in the glass substrate. Room temperature magnetization was measured on a vibrating-sample magnetometer.

Three optimized film stacks were also deposited. The first of these was a standard quadrilayer consisting of 60 Å $YO_x$/200 Å TbFeCoTa/400 Å $YO_x$/ and 1000 Å AlCr. In the other two film stacks the MO layer was replaced by a trilayer film stack with 50 Å TbFeCoTa on either side of a 100 Å NdFeCo layer to obtain perpendicular anisotropy and 100%

 0021-8979/96/79(8)/5693/3/$10.00 © 1996 American Institute of Physics 

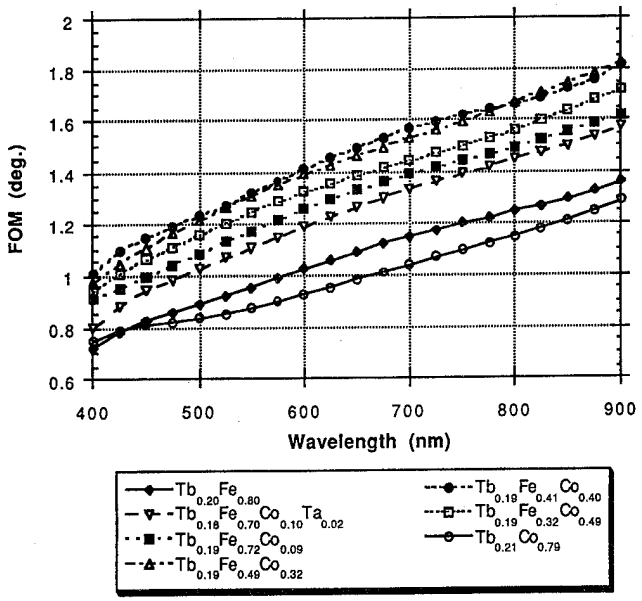



FIG. 1. Figure of merit vs wavelength for various TbFeCo alloys.

remanence for the MO trilayer. For these two film stacks, the NdFeCo layers were deposited in a nanolayered structure to enhance perpendicular anisotropy.[19]

## RESULTS AND DISCUSSION

The wavelength dependence of the maximum Kerr rotation FOM for a film stack with 20% reflectance is shown for several $Tb_{0.2}(FeCo)_{0.8}$ alloys in Fig. 1. The standard deviation in the measurements from random error is less than $\pm 0.05$. Systematic error in the film thickness or optical measurements is more difficult to assess, but is probably no larger than the random error. The FOM decreases monotonically with decreasing wavelength, as found previously.[13,17] The maximum FOM occurs for an Fe/Co ratio close to 1, which also corresponds to maximum room temperature magnetization. $Tb_{0.18}Fe_{0.70}Co_{0.10}Ta_{0.02}$, used in current MO media, has a FOM of 0.8° at 400 nm.

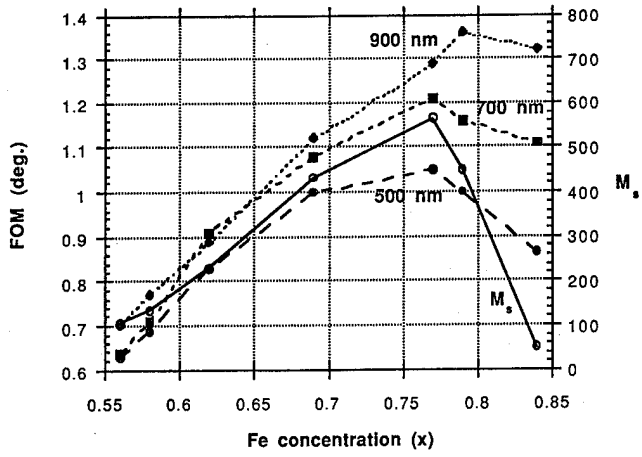



FIG. 2. Figure of merit and $M_s$ vs composition for various $Nd_{1-x}Fe_x$ alloys.

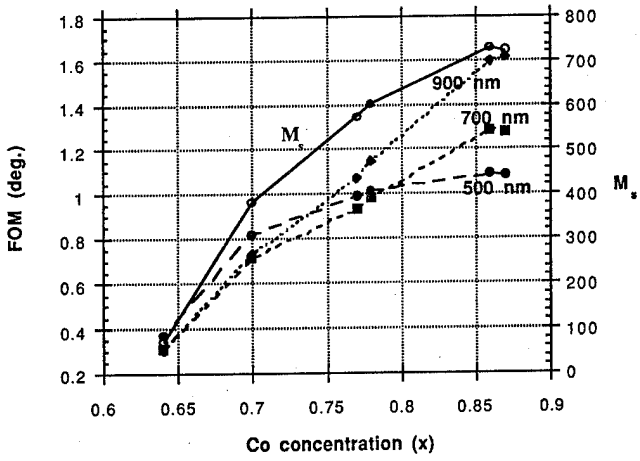



FIG. 3. Figure of merit and $M_s$ vs composition for various $Nd_{1-x}Co_x$ alloys.

The FOM and room temperature $M_s$ for NdFe alloys are graphed as a function of Fe concentration in Fig. 2 and for NdCo alloys as a function of Co concentration in Fig. 3. The FOM for all NdFe and NdCo alloys are generally smaller than that of $Tb_{0.19}Fe_{0.41}Co_{0.40}$ at essentially all wavelengths, although at wavelengths below 550 nm there are NdFe and NdCo compositions with FOMs larger than the standard MO media alloy of TbFeCoTa. The FOM and room temperature magnetization for NdFe are directly correlated and are maximized for Fe concentrations slightly less than 80%. The FOM and room temperature magnetization for NdCo alloys both increase with increasing Co concentration. The Curie points of $Nd_{0.14}Fe_{0.56}$ and $Nd_{0.36}Co_{0.64}$ are only slightly above room temperature, resulting in small FOMs.

FOMs significantly larger than those of TbFeCo can be obtained with NdFeCo alloys. The FOMs versus wavelength for $Nd_{0.2}(FeCo)_{0.8}$ alloys are shown in Fig. 4, and for $Nd(Fe_{0.5}Co_{0.5})$ alloys are shown in Fig. 5. As before, room temperature magnetization is found to be directly correlated with FOM. The FOM for some of these alloys is larger at all

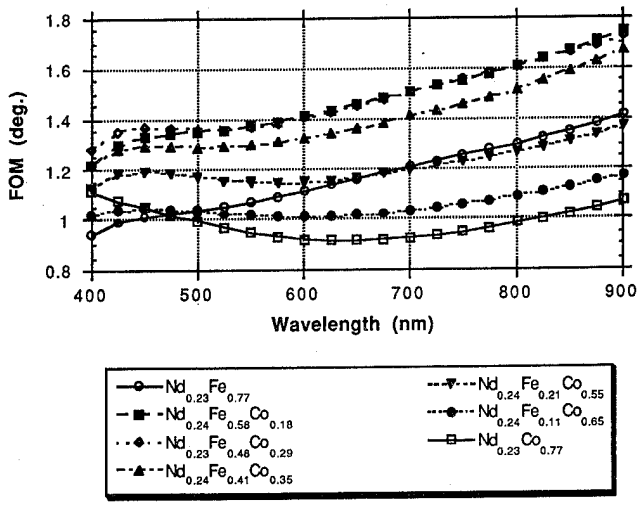



FIG. 4. Figure of merit vs wavelength for various NdFeCo alloys.

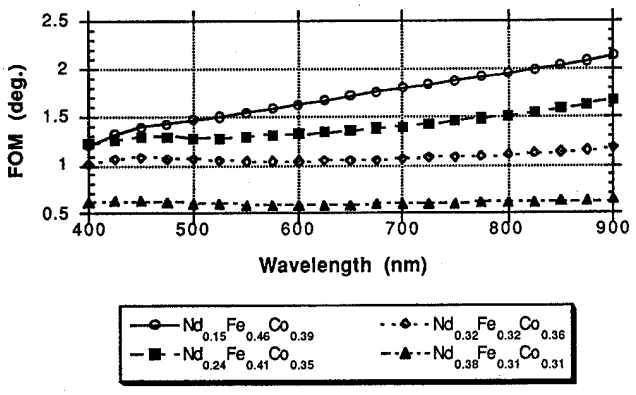



FIG. 5. Figure of merit vs wavelength for various NdFeCo alloys.

visible wavelengths than that of the best TbFeCo alloy. At 515 nm the largest FOM for a NdFeCo alloy is 1.5°, compared to 1.25° for TbFeCo. Alloys with 20% Nd exhibit a peak in the FOM for an Fe/Co ratio of about 2. Alloys with Fe/Co≈1 show a monotonic decrease in FOM with increasing Nd concentration.

Using the measured indices of refraction for TbFeCoTa, a substrate-incident thin film stack optimized for maximum effective Kerr rotation at 515 nm was designed and deposited. It had a total reflectance of 26% (including the 4% front surface reflectance of the glass substrate) and an effective Kerr rotation of 0.75°. The disparity from the predicted value of 1.04° in Fig. 2 is due to three factors. The FOM in Fig. 2 is calculated for a 20% inside surface reflectance, but for this sample the inside surface reflectance is actually 24%, which accounts for a reduction in the FOM of 0.87 according to Eq. (1). Absorption losses in the AlCr reflector account for a reduction of 0.90 and in the dielectric of 0.91 as determined by computer modeling.

Two additional samples were deposited using the same thin film stack design, but in which the center 100 Å of TbFeCoTa was replaced by $Nd_{0.23}Fe_{0.54}Co_{0.23}$ in one case, with a FOM of 1.36° at 515 nm, and $Nd_{0.15}Fe_{0.46}Co_{0.39}$ in the other case with a FOM of 1.47°. The first sample had a measured total reflectance of 26% and an effective Kerr rotation of 0.80° at 515 nm. The FOM for this trilayer stack can be no larger than the simple average of the FOMs of the two alloys, or 1.2° for a 20% reflectance stack. This is 7% larger than the measured value after including the previously discussed correction factors. The second sample had a measured total reflectance of 24% and effective Kerr rotation of 0.94° at 515 nm. In this case, the expected FOM average at 20% reflectance is 1.26°. The reflectance correction factor is 0.94, so the measured value is only 3% smaller than the expected value.

## CONCLUSION

TbFeCo has proven over the years to be an excellent MO material for optical recording, and it will require strong incentives to incorporate new materials into future MO thin film stacks. Although it has been suspected that TbFeCo is not capable of providing the MO signal required at shorter wavelengths, the FOM results demonstrate that at 400 nm a fully optimized thin film stack, using the standard TbFeCoTa composition, with 20% reflectance will have an adequate Kerr rotation of 0.8°. Even with a nonideal absorbing dielectric and reflector, a thin film stack with 0.75° effective Kerr rotation and 24% reflectance at 515 nm has been made. From a MO signal standpoint, TbFeCo should be adequate for any future visible wavelength MO media.

Nevertheless, an appropriate choice of NdFeCo alloy will indeed enhance the MO signal for an optimized film stack at all visible and near-IR wavelengths over that obtainable with the standard TbFeCo composition. The main drawback with NdFeCo is that its magnetic properties (anisotropy, coercivity) by itself are not suitable for MO media, and therefore it must be laminated with TbFeCo in order to obtain a suitable thin film stack. Lamination not only increases the complexity of the manufacturing process, but also significantly reduces the enhancement effect. In particular, an optimized MO trilayer stack at 515 nm would exhibit an MO signal increase of only 1.5 dB over that of an optimized TbFeCo film stack.

[1] N. Imamura, S. Tanaka, F. Tanaka, and Y. Nagao, IEEE Trans. Magn. **MAG-21**, 1607 (1985).
[2] P. Hansen, D. Raasch, and D. Mergel, J. Appl. Phys. **75**, 5267 (1994).
[3] S. Funada, S. Shimokawato, M. Ishida, and T. Shimoda, IEEE Trans. Magn. **MAG-23**, 2602 (1987).
[4] M. Sato, S. Tatskawa, H. Niwa, N. Tsukane, T. Mitani, and H. Toba, IEEE Trans. Magn. **MAG-23**, 2617 (1987).
[5] H.-P. D. Shieh, J. Yamasaki, and M. H. Kryder, IEEE Trans. Magn. **MAG-23**, 3208 (1987).
[6] R. J. Gambino and T. R. McGuire, J. Appl. Phys. **57**, 3906 (1985).
[7] R. J. Gambino, and T. R. McGuire, J. Magn. Magn. Mater. **54–57**, 1365 (1986).
[8] T. R. McGuire, R. J. Gambino, T. S. Plaskett, and W. Reim, J. Appl. Phys. **61**, 3352 (1987).
[9] T. Suzuki, A. Murakami, and T. Katayama, IEEE Trans. Magn. **MAG-23**, 2958 (1987).
[10] D. Weller, W. Reim, and P. Schrijner, IEEE Trans. Magn. **MAG-24**, 2554 (1988).
[11] T. Suzuki and T. Katayama, IEEE Trans. Magn. **MAG-22**, 1230 (1986).
[12] H. Tanaka and S. Takayama, J. Appl. Phys. **67**, 5334 (1990).
[13] W. A. Challener, J. Phys. Chem. Solids **56**, 1499 (1995).
[14] R. Gamble, P. H. Lissberger, and M. R. Parker, IEEE Trans. Magn. **MAG-21**, 1651 (1985).
[15] M. Mansuripur, Appl. Phys. Lett. **49**, 19 (1986).
[16] R. Atkinson, P. J. Grundy, C. M. Hanratty, R. J. Pollard, and I. W. Salter, J. Appl. Phys. **75**, 6861 (1994).
[17] H. Fu, Z. Yan, S. K. Lee, and M. Mansuripur, J. Appl. Phys. **78**, 4076 (1995).
[18] W. A. Challener and S. L. Grove, Appl. Opt. **29**, 3040 (1990).
[19] Z. S. Shan, S. Nafis, K. D. Aylesworth, and D. J. Sellmyer, J. Appl. Phys. **63**, 3218 (1988).

# Effect of sputtering condition on dynamic characteristics and microstructures of magneto-optical 5.25 in. SiN/TbFeCo/SiN/Al disks for 532 nm recording media

M. D. Ro, B. I. Cho, M. J. Kim, S. S. Kim, Y. M. Ahn, K. G. Lee, and B. L. Gill
*Optical Storage Media Laboratory, Samsung Advanced Institute of Technology, P.O. Box 111, Suwon 440-600, Korea*

A systematic study of the effect of sputtering conditions, for each layer of the magneto-optical SiN 500 Å/TbFeCo 200 Å/SiN 200 Å/Al 600 Å disks, such as power and Ar gas flow rate on the noise levels (NL) and carrier-to-noise ratio (CNR) was performed for the 532 nm high density storage media in this work. The NL dropped to its minimum value of −71.3 dB as the sputtering power for the first SiN increased from 0.5 to 1.5 kW. With a further increase in sputtering power to 2.5 kW, it sharply increased to −64.5 dB. This was ascribed to the smooth and dense surface of the first layer at 1.5 kW, as was observed in the atomic forces microscopy images. The spherical, isotropic, fine grains with a diameter of about 0.2–0.7 $\mu$m at 1.5 kW were found, while the longitudinal, directional granular features with a length of 2.5 $\mu$m were seen at 2.5 kW. The highest CNR of 46.3 dB was observed at 0.6 kW with a constant sputtering Ar gas flow rate of 25 sccm for the magneto-optical layer. The sputtering conditions for other layers are as follows: 1.5 kW with sputter $Ar/N_2$ gas flow rate of 30 sccm/11 sccm for the first and third SiN layer, and 0.6 kW with 25 sccm of Ar for the Al reflection layer. This is due to the smooth surface morphologies of the magneto-optical layer at this optimum sputtering pressure, as previously reported in similar research. To obtain a high readout signal, the phase compensation for the elliptic laser beam has been considered. © *1996 American Institute of Physics.* [S0021-8979(96)11008-X]

## I. INTRODUCTION

Transition-metal-rich Tb–Fe–Co amorphous thin film alloys have received considerable attention from technological and scientific points of view for the following reasons: (1) the high perpendicular magnetic anisotropy and high coercivity make it possible to greatly enhance areal storage density,[1] compared to that of the longitudinal magnetic recording media; (2) the strong magneto-optical response produces good dynamic characteristics such as high carrier levels. Recently, a comparably increased information storage capacity of the magnetic recording media due to persistent research and development motivated the use of short wavelength lasers for writing and reading in the magneto-optical media.[2–4] However, the readout carrier-to-noise ratio (CNR) is known to decrease due to a deteriorated Kerr rotation angle at the short wavelengths. It has been reported that the static magnetic properties of Tb–Fe–Co thin films are influenced to a large extent by the sputtering parameters of the magneto-optical layer.[5,6] To further explore this possibility and increase the CNR, extensive and systematic research to correlate main sputtering parameters (power and gas flow rate) for the SiN, TbFeCo, Al layers with dynamic characteristics [C.L. noise level (NL), CNR] of 5.25 in. SiN 500 Å/TbFeCo 200 Å/SiN 200 Å/Al600 Å disks for the high density media using a green laser (wavelength, $\lambda$=532 nm) was conducted in this work. This study was partially focused on reducing the NL for the maximum CNR by determining optimal sputtering conditions through investigating the relationships between morphology of the first SiN film and the NL. The film structure and surface mophology were examined by transmission electron microscopy and atomic force microscopy, respectively. The dynamic characteristics of the magneto-optical disks using glass substrates with a narrow track pitch of 1.0 $\mu$m were measured by an optical pickup system which was made by the authors' institution.[7]

## II. EXPERIMENT

The thin film layers consisting of the magneto-optical 5.25 in. SiN 500 Å/TbFeCo 200 Å/SiN 200Å/Al 600 Å disk were magnetron rf-dc sputter side deposited onto the pregrooved photopolymer (2P) glass substrates with a narrow track pitch of 1.0 $\mu$m using a continuous in-line sputtering system (model—Balzers SDS-130). The magneto-optical and reflection films were sputtered from hot isostatic pressed $Tb_{20.7}Fe_{71}Co_{8.3}$ alloy and Al targets with a diameter of 8 in. The chemical composition of the magneto-optical films was analyzed with an inductively coupled plasma (ICP) and was almost the same as that of target. A good uniformity of both thin film layer thickness and magneto-optical properties in disks was confirmed. For the dielectric and antioxidation SiN films, an elemental Si target was reactively sputtered with $N_2$ gas mixed with Ar gas. Sputtering for the first SiN layer was carried out at the different powers. For morphological study, the first SiN films with a thickness of 500 Å were deposited on the rock salt for a transmission electron microscopy (TEM) operating at 300 kV, and were deposited on a Si wafer for a contact-type atomic force microscopy (AFM) with a 4 $\mu$m piezo cantilever. The AFM was also used for measuring film thickness. The Kerr rotation angle and coercivity of the four layered films were measured at 532 nm at the room temperature with a Kerr spectrometer. The reflectivity was measured with an UV-VIS scanning spectrophotometer (model UV-2101PC). The dynamic characteristics were measured at the following conditions: constant angular

 0021-8979/96/79(8)/5696/3/$10.00 © 1996 American Institute of Physics

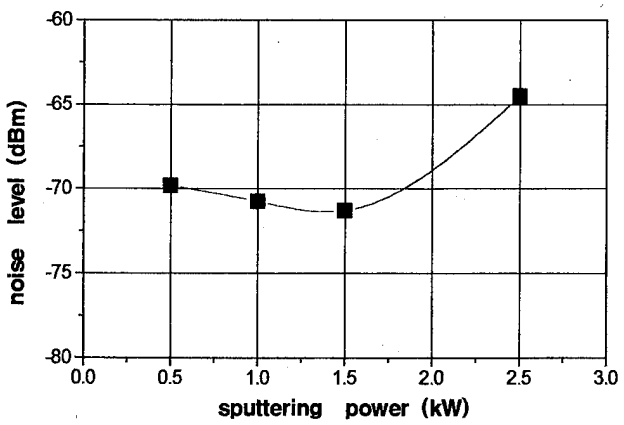



FIG. 1. Noise level of the magneto-optical 5.25 in. SiN 500 Å/TbFeCo 200 Å/SiN 200 Å/Al 600 Å disks as a function of sputtering power for the first SiN thin film layer.

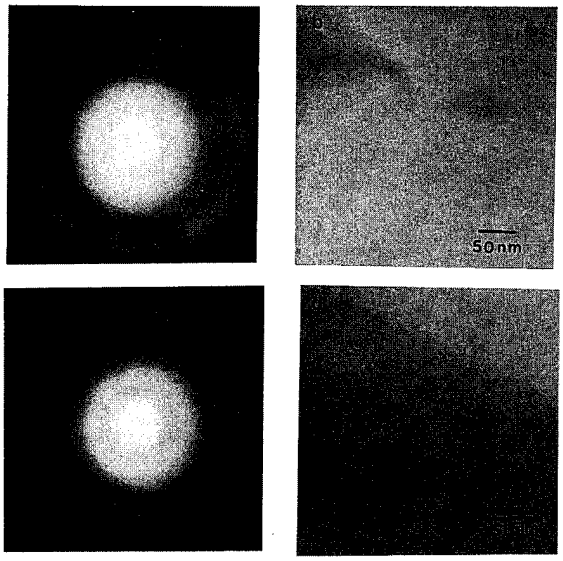



FIG. 2. TEM diffraction patterns and bright field images of the as-deposited SiN films at different sputtering powers: (a), (b) 1.5 kW and (c), (d) 2.5 kW, respectively.

velocity—1800 rpm, frequency—6.27 MHz, writing power ≤4.5 mW, reading power—1.2 mW, erasing power—5.0 mW, and duty—37.5%. For the high information storage density, the mark edge recording method has been adopted.

## III. RESULTS AND DISCUSSION

The NL of the magneto-optical 5.25 in. SiN 500 Å/TbFeCo 200 Å/SiN 200 Å/Al 600 Å disks was measured as a function of sputtering power for the first SiN thin film layer and is plotted in Fig. 1. Sputtering conditions for the SiN, TbFeCo, and Al layers are shown in Table I. Experimental results show that variation in the sputtering power resulted in a significant change in the NL, as similarly suggested in previous investigations.[8,9] The NL decreased to its minimum value of −71.3 dB as the sputtering power increased from 0.5 to 1.5 kW. With a further increase in sputtering power to 2.5 kW, it sharply increased to −64.5 dB. Transmission electron microscopy (TEM) diffraction patterns confirmed the typical amorphous structures of the first SiN film as shown in Fig. 2(a) for 1.5 kW and Fig. 2(c) for 2.5 kW, respectively. No big difference in TEM bright field images [Figs. 2(b) and 2(d)] was observed at two different sputtering powers. Considering an important effect of the sputtering power on atomic arrangements in the SiN film surface, a further examination of film surface morphology was conducted with a contact-type AFM. The experimental results showed that the surface consists of spherical, isotropic, fine grains with a diameter of ~0.7 μm when the film with a thickness of 500 Å [Fig. 3(a)] was sputter deposited at 1.5 kW. As the film thickness increased to 2700 Å at the same power level, the structures became dense with fine grains with a diameter of ~0.2 μm as shown in [Fig. 3(b)]. At 2.5 kW, however, the longitudinal, directional, granular features with a length of 2.5 μm were observed for both 500- and 2500-Å-thick films [Figs. 3(c) and 3(d), respectively]. Therefore, it appeared that the desirable lowest NL at 1.5 kW was ascribed to the relatively dense and smooth surface morphologies of the first SiN film layer, compared to those at 2.5 kW. In the second set of experiments, the dynamic characteristics such as CL, NL, and CNR were measured as a function of sputtering power for the $Tb_{20.7}Fe_{71}Co_{8.3}$ film at a constant sputtering Ar gas flow rate of 25 sccm [Fig. 4]. The sputtering conditions for the first and third SiN layer and Al layer are listed in Table II. At 0.6 kW, the maximum CL (−22.2 dB) and minimum NL (−68.5 dB) resulted in the highest CNR of 46.3 dB. Figure 5 also shows the dynamic characteristics of disks as a function of Ar gas flow rate for the magneto-optical layer at 0.6 kW. The same sputtering conditions as in the above experiment were used for the first and third SiN, and Al reflection layers. As the Ar gas flow rate increased from 15 to 25 sccm, the noise level greatly

TABLE I. Sputtering conditions for the third SiN, TbFeCo, and Al film layers with variation in sputtering power for the first SiN layer.

| Layer | Sputtering power (kW) | Ar gas flow rate (sccm) |
|---|---|---|
| First SiN | 0.5–2.5 | ··· |
| TbFeCo | 0.6 | 25 |
| Third SiN | 1.5 | ··· |
| Al | 0.6 | 25 |

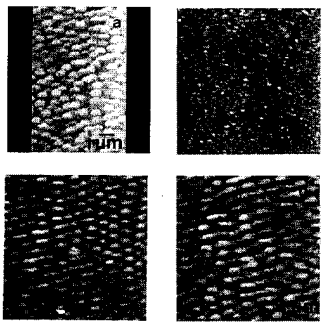


FIG. 3. AFM surface morphologies of the as-deposited first SiN films with variation in sputtering power and film thickness: (a) 1.5 kW, 500 Å, (b) 1.5 kW, 2700 Å, (c) 2.5 kW, 500 Å, and (d) 2.5 kW, 2500 Å.

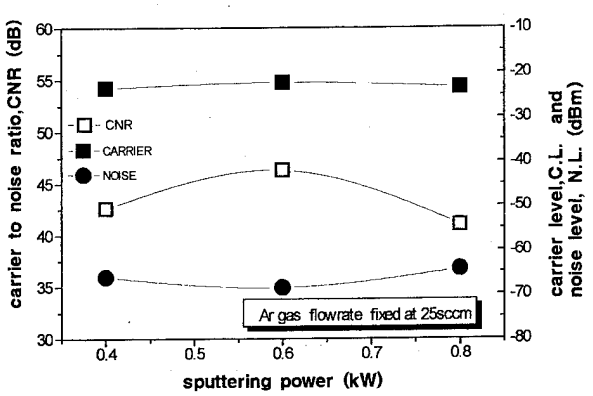



FIG. 4. Dependence of CL, NL, and CNR on the sputtering power for magneto-optical TbFeCo film in SiN 500 Å/TbFeCo 200 Å/SiN 200 Å/Al 600 Å disks at a constant sputtering Ar gas flow rate of 25 sccm. Sputtering powers for the first and third SiN layer were fixed at 1.5 kW with sputter $Ar/N_2$ gas flow rate of 30 sccm/11 sccm, and for Al layer at 0.6 kW with 25 sccm, respectively.

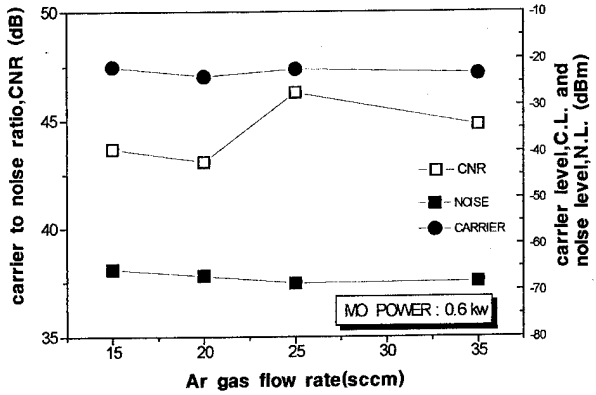



FIG. 5. Dependence of CL, NL, and CNR on the Ar gas flow rate for magneto-optical TbFeCo film in SiN 500 Å/TbFeCo 200 Å/SiN 200 Å/Al 600 Å disks at fixed 0.6 kW. Sputtering conditions for the first and third SiN and Al layer are as same as above in Fig. 4.

improved from −65.5 dB to the lowest value of −68.5 dB. This seems to be attributed to the previous experimental results: The film surface morphologies of the magneto-optical layers were smooth and featureless at an optimum sputtering pressure for the high CNR. However, they were rough at the high pressure because the film contained microvoid-surrounding amorphous structures.[5,6] So far the optimum sputtering conditions for the maximum CNR such as power levels and gas flow rates for the first dielectric, the third antioxidation SiN film layers, and the $Tb_{20.7}Fe_{71}Co_{8.3}$ film have been determined experimentally. Based on these results, the effect of the Al sputtering conditions on CNR of the magneto-optical disks was investigated. The data revealed that the highest CNR of 46.3 dB (=CL −22.2 dB, NL −68.5 dB) was observed at 0.6 kW with 25 sccm. The influence of the sputtering conditions for the Al layer on the CNR was little, compared to that of the sputtering conditions for the SiN layers and magneto-optical layers. The static magneto-optical properties of the four layered SiN/TbFeCo/SiN/Al deposited on the Corning glass under these sputtering conditions were measured at 532 nm by the Kerr spectrometer and are as follows: coercivity—7.63kOe; Kerr rotation angle—0.913°, ellipticity—0.407°, reflectivity—16°–38%.

TABLE II. Sputtering conditions for the first and third SiN and Al film layers with variation in sputtering power for the TbFeCo layer.

| Layer | Sputtering power (kW) | Ar gas flow rate (sccm) |
|---|---|---|
| First SiN | 1.5 | ··· |
| TbFeCo | 0.4–0.8 | 25 |
| Third SiN | 1.5 | ··· |
| Al | 0.6 | 25 |

## IV. CONCLUSIONS

Based on the experimental results and discussion, it has been concluded that the dynamic characteristics measured at a green laser ($\lambda$=532 nm) of the 5.25-in.-diam TbFeCo magneto-optical disks are substantially influenced by the sputtering parameters. Especially, the lowest NL resulting in a CNR as high as 46.3 dB is attributed to the isotropic, fine, spherical grains in the first SiN film deposited at 1.5 kW as evidenced from the surface morphologies of the AFM. The CNR was affected by the sputtering power and Ar gas flow rate for the magneto-optical layer, but it was little dependent on the sputtering power for the reflection Al layer.

[1] F. Tanaka, Y. Nagao, and N. Imamura, IEEE Trans. Magn. **MAG-20**, 1033 (1984).
[2] I. Ichimura, Y. Sabi, Y. Takeshita, A. Fukumoto, M. Kaneko, and H. Owa, Jpn. J. Appl. Phys. **32**, 5312 (1993).
[3] M. Oka and S. Kubota, Jpn. J. Appl. Phys. **31**, 513 (1992).
[4] K. Tatsuno, M. Takahashi, K. Muraoka, H. Sugiyama, J. Nakamura, T. Andou, and T. Miyai, Jpn. J. Appl. Phys. **31**, 601 (1992).
[5] M. Hong, E. M. Gyorgy, R. B. Van Dover, S. Nakahara, D. D. Bacon, and P. K. Gallaghen, J. Appl. Phys. **59**, 551 (1986).
[6] J. W. Lee, H.-P. D. Shieh, M. H. Kryder, and D. E. Laughlin, J. Appl. Phys. **63**, 3624 (1988).
[7] I. S. Park, J. E. Seo, J. K. Kim, K. H. Rim, and D. H. Shin, ISOM 47, 1994 (unpublished).
[8] G. Choe, J. K. Magn. Soc. **2**, 56 (1992).
[9] J. E. Hurst, Jr. and W. J. Kozlovsky, Jpn. J. Appl. Phys. **32**, 5301 (1993).

# A study on the Kerr angle enhancement by the magnetic image effect (abstract)

S. P. Chang and Y. P. Lee
*Department of Applied Physics, Chung Cheng Institute of Technology, Tahsi 335, Taiwan, Republic of China*

D. R. Huang
*Opto-Electronics & Systems Laboratory, ITRI, Chutung, Hsinchu 310, Taiwan, Republic of China*

Recently, new mechanisms have been proposed to explain the giant enhancements of M-O Kerr effect.[1] In this work, we use magnetic image effect to explain the Kerr angle enhancement of M-O media on Co-base amorphous films. The M-O layer and reflection layer were produced by using conventional dc magnetron sputtering processes. The Kerr hysteresis loops of M-O films were measured with wavelength from 500 to 860 nm, and the peak applied field was 9 kOe. We have studied the enhancements of Kerr angle in TbFeCo amorphous film which sandwiched by AlN layers and backed with Co-base amorphous film. There is a remarkable increase of Kerr angle with value 1.85° at wavelength 640 nm. At wavelength 780 nm, the Kerr angle of magneto-optic medium on Co-base amorphous ribbon has been significantly enhanced by a factor of 3.1 as compared to that on Al foil. Because of its high permeability and low coercivity, the Co-base amorphous film serve as a magnetic shielding material which can induce the magnetic image effect for M-O film. Theoretical calculations show that the Kerr angle can be enhanced by the image magnetic field. The calculated values of Kerr angle are in good agreement with experiment results. An explicit equation to calculate the Kerr angle will be discussed. © *1996 American Institute of Physics.* [S0021-8979(96)80808-4]

[1] Y. P. Lee, D. R. Huang, T. C. Hsiao, and S. P. Chang, Dig. Magneto-Optical Recording International Symposium '94 Japan, 1994, p. 74.

# A dynamic study of domain formation mechanism during thermomagnetic recording based on micro-Hall effect measurements

Yung-Chieh Hsieh, S. N. Gadetsky, and M. Mansuripur
*Optical Sciences Center, University of Arizona, Tucson, Arizona 85721*

M. Takahashi
*Central Research Laboratory, Hitachi Ltd., Kokubunji, Tokyo 185, Japan*

A method for analyzing the dynamics of domain formation during the thermomagnetic recording process has been developed based on the extraordinary Hall effect.[1,2] A magnetic domain is written at the center of a cross-shaped magneto-optical sample having an area of $5\times5$ $\mu m^2$, and the Hall voltage is monitored during the recording process. As far as domain nucleation is concerned, we find that the temperature gradient around the transition region (i.e., the region whose temperature is between the critical temperature for magnetization reversal and the Curie point) is very important. Under the conditions of high power and short pulse-width laser, a domain can form only during the cooling period. However, it is possible for a domain to form during the heating cycle under a low power, long pulse laser beam. © *1996 American Institute of Physics.* [S0021-8979(96)06108-1]

## I. INTRODUCTION

In thermomagnetic recording, a focused laser beam creates a hot spot in a thin magnetic film, thus allowing an external magnetic field to reverse the direction of local magnetization. This is a very complex dynamic phenomenon involving the nucleation of one or more domains, followed by domain expansion and/or contraction.[3] The details of this process depend on the recording conditions and the composition of the recording material. To enhance recording density, one must write domains as small as possible under the constraint of an acceptable signal-to-noise ratio in readout. To achieve this goal, one may reduce the laser wavelength and increase the numerical aperture of the objective lens in order to attain a small, diffraction-limited focused spot. Alternatively, one might strive to develop a technique that allows the writing of small domains even when the focused light spot is not as small. In the latter case, the mechanism of domain formation will have to be better understood, and the most suitable combination of material properties and recording conditions must be adopted. For example, we have observed that under certain conditions the newly formed domains shrink during the cooling cycle. In such cases, the small size of the final domain might be misleading, since it may have damaged an adjacent domain while it was being recorded. Because the existing "static" methods of domain observation and measurement monitor only the final state of a recorded domain, they are incapable of providing insight into problems that are of a "dynamic" nature. On the other hand, dynamic measurement techniques, such as the one described in this article, are quite attractive since they enable the sensing and monitoring of a domain while it is being written.

In this article, we describe a micro-Hall effect measurement scheme for the study of domain formation mechanism. The Hall voltage is proportional to the instantaneous average magnetic moment within the measured area of the sample. By monitoring the Hall signal during thermomagnetic recording, we observe the process of domain formation in real time.

## II. EXPERIMENTAL SETUP

A schematic diagram of the experimental setup is shown in Fig. 1(a). The laser beam is focused at the center of the magneto-optical (MO) sample, and a perpendicular magnetic field is applied by a small coil having a diameter of 2 mm. The maximum available field is 750 Oe, which corresponds to a current of 2.5 A through the coil. In order to monitor the variations of Hall voltage caused by the formation of a single domain, a cross-shaped sample, shown in Fig. 1(b), was prepared. The central part of the cross, which has an area of $5\times5$ $\mu m^2$, is made of TbFeCo film. Two different magnetic

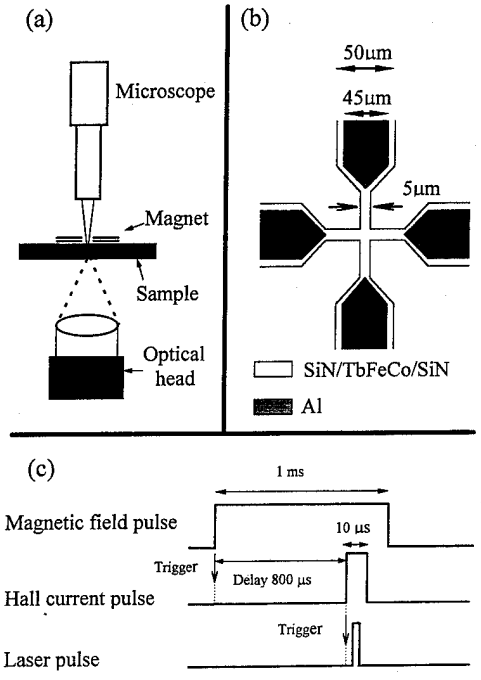



FIG. 1. (a) Schematic diagram showing the experimental setup for micro-Hall effect measurements. (b) Cross-shaped sample used in the experiments. (c) Temporal relationship among the magnetic field pulse, the Hall current pulse, and the laser pulse.

 0021-8979/96/79(8)/5700/3/$10.00 © 1996 American Institute of Physics

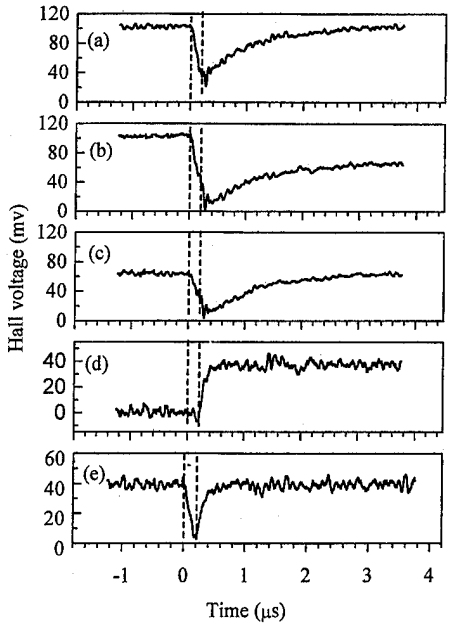



FIG. 2. Hall signals for a Fe-rich sample obtained in several kinds of measurements with a laser pulse having $P=8$ MW and $T=200$ ns. (a) In the presence of a +750 Oe field along the direction of initial magnetization, no domain is being formed. (b) Domain-writing signal in the presence of a −300 Oe field. (c) Domain-rewriting signal under $H=-300$ Oe. (d) The difference between signals shown in (a) and (b), containing information about magnetization reversal. (e) The difference between signals shown in (a) and (c).

films were used in our studies. Sample 1 had a thickness of $\delta=25$ nm, coercivity $H_c \geq 25$ kOe at room temperature, and Curie and compensation point temperatures of $T_c=230$ °C and $T_{comp}=-50$ °C, respectively. Sample 2 had $\delta=100$ nm, $T_c=260$ °C, $T_{comp}=190$ °C, and $H_c=5$ kOe. The results presented in Secs. III A and III B were obtained using sample 1, while those in Sec. III C correspond to sample 2. In both samples, the magnetic film was sandwiched between a 75 nm thick SiN underlayer and a 200 nm thick SiN overlayer. The four aluminum electrodes, having a thickness of 300 nm each, were connected to the four sides of the MO film. The Hall signal was measured using the four-point probe method. The magnitudes of the applied magnetic field $H$, the laser power $P$, and the laser pulse duration $T$ were all adjustable. Temporal relations among the magnetic field pulse, the Hall current pulse, and the laser current pulse are shown in Fig. 1(c). The Hall current pulse has been delayed by 800 $\mu$s in order to avoid perturbations caused by the induced voltage from the magnetic field pulse.

## III. RESULTS AND DISCUSSION

### A. Recording with a short laser pulse

Here the laser power $P=8$ MW and its pulse width $T=200$ ns. One set of our measurement results is shown in Fig. 2. In Fig. 2(a) the laser pulse is turned on, but no domain is being formed. For this measurement, we saturate the magnetic moment of the sample in the $+Z$ direction, and maintain a +750 Oe field on the sample in order to prevent domain formation during the experiment. The vertical dash lines in Fig. 2 show the duration of the laser pulse. The laser creates a time-dependent temperature profile in the film. We define the Curie disk as the region where at any given instant of time the temperature is higher than the Curie temperature. In the early stages of heating, the radius of the Curie disk is zero, but once formed, it rapidly increases with time. The Hall signal drops quickly during the heating cycle because the magnetization decreases with the rising of temperature. Once the laser is turned off, the signal gradually returns to its original level. In Fig. 2(b) a domain is being written in the presence of a −300 Oe field. The signal in this case also decreases when the laser is first turned on, but it does not return to the original level since a domain is now formed in the region of the hot spot. The voltage difference between the initial and final levels is proportional to the size of the written domain. Figure 2(c) represents the case of domain rewriting. Following the writing of a domain, we turn on the laser once again with the same power and pulse duration, and without changing the magnetic field. Observe that the initial signal level in Fig. 2(c) is the same as the final level in Fig. 2(b). During the heating period the signal decreases, but it recovers to its original level after cooldown. This indicates that the size of the domain remains the same after rewriting.

Variations of the Hall voltage with time shown in Fig. 2(b) are caused both by the variations of the magnitude of magnetization due to the temperature change, and by the formation of a reverse domain after a certain point in time. To obtain the signal caused by magnetization reversal alone, we subtract the signal in Fig. 2(a) from that in Fig. 2(b) and refer to the difference, shown in Fig. 2(d), as the differential writing signal. This differential Hall signal indicates that the signal arising from domain formation does not have any significant value until after the laser has been turned off. Under these recording conditions, therefore, domain formation must occur during the cooling period. The reason for this behavior may be speculated to be as follows. The temperature of the region in which the domain nucleates should be greater than some critical temperature, $T_{crit}$, which is a function of the strength of the applied magnetic field $H$, and is lower than the Curie temperature. We define the region in which the temperature is higher than $T_{crit}$ as the critical disk. By definition, the critical disk is always greater than the Curie disk. A domain can form only in the annular region between the Curie disk and the critical disk. If the temperature gradient is so large that this annular region is narrower than the width of a magnetic domain wall, then no domains can form. In the cooling process, however, temperature gradients are on the decline, and nucleation should occur more readily.

Figure 2(e) shows the difference between the signals in Figs. 2(a) and 2(c). Observe that, in the rewriting process, the signal arising from the reversed domain reaches a minimum and then returns to its initial value. The nonzero value of the minimum signal in this case indicates that a certain part of the domain survives during the heating period.

### B. Recording with a long laser pulse

The pulse width $T$ used in this case was 1 $\mu$s, and the applied magnetic field $H$ was −450 Oe. Figures 3(a)–3(c) show the differential writing signals during recording experi-

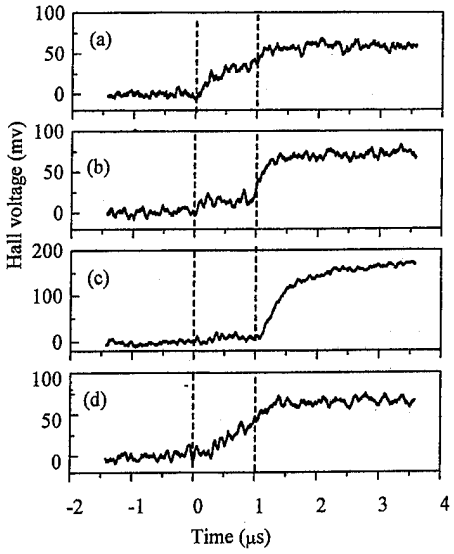



FIG. 3. Differential writing Hall signals for a Fe-rich sample obtained during recording with a $T=1$ $\mu$s laser pulse and in the presence of a magnetic field $H=-450$ Oe. (a) $P=1$ MW; the domain is formed early in the heating cycle. (b) $P=2$ MW; the domain signal during the heating period is smaller than that in (a) due to the higher temperature levels. (c) $P=5$ MW; the domain no longer forms during the heating cycle. (d) $P=5$ MW, but the laser is slightly out of focus. In the first 300 ns, no region of the MO film reaches $T_{crit}$. After that, the critical disk is formed and expands rapidly.

ments corresponding to laser power levels of $p=1$, 2, and 5 MW, respectively. In Fig. 3(a), we observe that a domain forms in the beginning of the heating period and that it continues to grow afterwards. This result can be explained as follows. Because of the low level of laser power being used, it takes the magnetic film a long time to reach the Curie temperature. But, during this period, heat diffusion broadens the temperature profile. The time duration in which the Hall signal increases rapidly corresponds to a rapidly expanding critical disk. In Fig. 3(b) essentially the same phenomena occur, but the signal during the heating cycle is smaller than that in Fig. 3(a). This is due to the fact that the magnetization decreases with a rising temperature. In Fig. 3(c), the domain differential writing signal does not have a significant value before the laser is turned off. This is similar to the behavior described in Sec. III A in conjunction with a short laser pulse. Note in Fig. 3 that the final domain size is increasing with the increase of the laser power. Figure 3(d) shows the Hall signal during writing under the same conditions as in Fig. 3(c) except for a slight defocusing of the laser beam. This figure indicates that the domain has formed during the heating cycle. The reason for this behavior is that, as a result of defocusing, the temperature profile has broadened.

### C. Domain size variations during the cooling period

In this section, the Tb-rich samples are measured. As in the preceding experiments, the saturated state of the magnetization is along the $+Z$ direction. Figure 4 shows the differential writing and rewriting signals for two different magnetic fields when the laser pulse width $T=530$ ns and the laser power $P=9.3$ MW. The heavy curves show the differential writing signals, while the light curves are the differential rewriting signals. In both cases, the level of the rewriting signal immediately after heating is greater than its initial level. This indicates that the written domain expands somewhat during rewriting. In Fig. 4(a), where $H=+300$ Oe, the writing signal slowly decreases after reaching a maximum value. The fact that the initial level of the rewriting signal is below the maximum value of the writing signal indicates a shrinkage of the recorded domain during the cooling cycle. In case Fig. 4(b), where $H=+600$ Oe, the domain does not shrink significantly during the cooling phase of the writing process. This is due to the presence of a stronger magnetic field in this case compared to Fig. 4(a). The strong magnetic field in Fig. 4(b) also causes the domain to expand during rewriting.

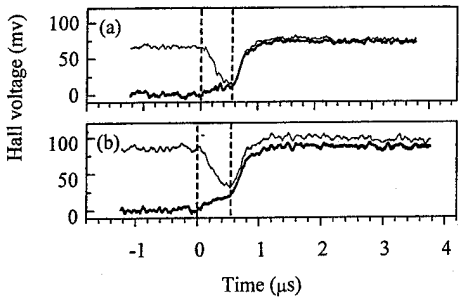



FIG. 4. Differential writing (dark) and rewriting (light) signals for a Tb-rich sample in the presence of two different magnetic fields. (a) With $H=+300$ Oe the domain shrinks somewhat during cooling. (b) With $H=+600$ Oe, the domain does not shrink during writing, but expands during rewriting.

## IV. CONCLUDING REMARKS

From the type of measurement described in this article, in addition to the above information, one can reconstruct the temperature profile within the sample by employing the known dependence of magnetization on temperature. This is a helpful step in furthering our understanding of the recording mechanism. We will concentrate on studying the measurements of the thermal constants of MO media in the future.

## ACKNOWLEDGMENTS

The authors thank Junko Ushiyama of the Hitachi Central Research Laboratory for preparing the samples, and Warren Bletscher of the Optical Sciences Center for design and construction of the electronic subsystem.

[1] B. C. Webb, IEEE Trans. Magn. **MAG-26**, 1715 (1990).
[2] M. Takahashi, S. N. Gadetsky, and M. Mansuripur, J. Magn. Soc. Jpn. **19**, 395 (1995).
[3] M. Mansuripur, *The Physical Principles of Magneto-optical Recording* (Cambridge University Press, London, 1995).

# The rate of domain growth in magneto-optic recording media (abstract)

J. Earl, A. Lyberatos, and R. W. Chantrell
*Physics Department, Keele University, Keele, ST5 5BG, United Kingdom*

The magnetization reversal in magneto-optic media occurs in general by a process of nucleation followed by domain growth. The rate of domain growth is of importance in thermomagnetic recording. Under steady external field conditions, a slow thermoactivated domain growth is observed[1] and the time dependence curves $M(t)$ are often described[1] using a theory by Fatuzzo.[2] The Fatuzzo theory assumes a constant rate of expansion $v$ of cylindrical domains; however, it does not consider the dispersion in the energy barriers or the formation of dendritic domain structures that may arise, for example, from the spatial and temporal variations of the demagnetizing field. Monte Carlo simulations of domain growth were performed using a model that considers distinct intrinsic energy barriers for nucleation and wall motion and incorporates the contribution of the demagnetizing and domain wall energy in the computation of the energy barriers. The rate of domain expansion, $v = dR_g/dt$, where $R_g$ is the radius of gyration, was found to be constant during the initial stage of the growth process but decreases for large $R_g$ as a result of the reduction in demagnetizing strength. Small fluctuations in $v$ are observed arising from the variation of the domain shape during the growth process. The simulations have also shown that the dependence on the applied field is exponential, $v = v_0 \exp(H/H_f)$, where $H_f$ is the fluctuation field, in good agreement with experiment.[1,3,4] The exponential dependence was found to be valid even in the case of dendritic domain growth, suggesting that the Fatuzzo theory may be useful in the description of the growth of domains of irregular shape. © *1996 American Institute of Physics.* [S0021-8979(96)46508-1]

[1] M. Labrune, S. Andrieu, F. Rio, and P. Bernstein, JMMM **80**, 211 (1989).
[2] E. Fatuzzo, Phys. Rev. **127**, 1999 (1962).
[3] T. G. Pokhil, B. S. Vvedensky, and E. N. Nikolaev, Mater. Sci. Forum **62–64**, 619 (1990).
[4] A. Kirilyuk, J. Ferré, J. Pommier, and D. Renard, JMMM **121**, 536 (1993).

# Sensitivity enhancement of Co/Pt superlattices through underlayer composition modification

T. K. Hatwar and C. F. Brucker
*Optical Recording Materials Laboratory, Imaging Research and Advanced Development, Eastman Kodak Company, Rochester, New York 14650-2017*

Co/Pt superlattice films for magneto-optical recording have a relatively high Curie temperature compared to rare earth-transition metal films, which has led to criticism of their recording sensitivity at higher disk velocities. We have prepared high-performance Co/Pt disk recording media using $(In_2O_3)_{100-x}(SnO_2)_x$ (ITO) as the underlayer. We have observed a two-fold increase in recording sensitivity as $x$ is increased from 0 to 75 mol % $SnO_2$. We have correlated measured sensitivity behavior with composition-induced changes in the microstructure and electrical resistivity in the ITO underlayer. ITO deposited with low $SnO_2$ content exhibits crystalline microstructure and low electrical resistivity, whereas ITO deposited with high $SnO_2$ content exhibits amorphous microstructure and high electrical resistivity. The reduction in crystallinity with increasing $SnO_2$ content is expected to decrease the ITO thermal conductivity, which can explain the increase in recording sensitivity. Small changes in Co/Pt coercivity as a function of $x$ can easily be compensated by adjusting the ITO sputtering pressure. The optimum combination of Co/Pt sensitivity and coercivity can be readily achieved by controlling the ITO underlayer composition and sputtering pressure. © *1996 American Institute of Physics.* [S0021-8979(96)28308-5]

## I. INTRODUCTION

Co/Pt multilayers have been investigated as a future generation magneto-optical (MO) recording media using blue lasers. These films exhibit large perpendicular anisotropy, which depends on the film composition, deposition conditions, quality of the substrate surface, and the underlayer.[1,2] Recently, we have shown that Co/Pt media with high perpendicular anisotropy and high coercivity can be achieved through microstructural modification of the underlayer.[3] A smooth $(In_2O_3)_{100-x}(SnO_2)_x$ (ITO) underlayer deposited at low sputtering pressure results in high squareness and anisotropy of the multilayers. These multilayers also possess a higher Curie temperature than the rare earth-transition metal alloys, resulting in low recording sensitivity (i.e., requires high write power). Higher writing sensitivity is desirable for future generation disk drives to permit higher rotation speed for reduced access time and faster data rate. Also, write/erase cyclability depends on the writing threshold power. Efforts have been made to improve the writing sensitivity of these Co/Pt media by lowering the Curie temperature via adjusting the Co/Pt ratio, and by addition of an element in the Co layer such as Ni or Re, etc.[4,5] However, these approaches reduced the Kerr rotation of the Co/Pt multilayer. We enhanced the sensitivity of the Co/Pt media by modifying the composition of the ITO underlayer, with no degradation in Kerr rotation. In this article, we present both the static and dynamic performance of the Co/Pt multilayer disks using ITO underlayers of varying composition.

## II. EXPERIMENT

Co/Pt multilayers were prepared by dc magnetron sputtering Co and Pt targets using Kr gas. ITO films were prepared by dc sputtering homogeneous targets of $In_2O_3$ and $SnO_2$. Targets of varying amounts of $In_2O_3$ and $SnO_2$ prepared by a hot press method were used to obtain films of various ITO compositions. The deposition pressure for the Co/Pt superlattice was 10 mT Kr, and that for the ITO underlayer was 5 mT Ar+1% $O_2$. Structural properties of ITO and Co/Pt films were measured by x-ray diffraction. The magnetic and magneto-optic properties were measured with a vibrating sample magnetometer and a polar Kerr loop tracer using a 780 nm wavelength laser. An UV-cured lacquer protective overcoat of 5–10 $\mu$m was formed by a spin coating method on the Co/Pt multilayer to improve the mechanical durability of the disk. The dynamic measurements were made using a 780 nm wavelength laser, 0.75 $\mu$m mark length, 6.03 m/s disk velocity, 3.87 MHz carrier frequency, 90 ns pulse, 30 kHz bandwidth, 300 Oe bias field, 0–10 mW write power, and 1.5–2.0 mW read power. This mark length and carrier frequency correspond to standard international standard organization (ISO) test conditions for first generation 130 mm MO media, for which a narrow band signal-to-noise ratio of >45 dB is specified. Optimum recording power (ORP) was obtained using 3.5 $\mu$m marks, 7 m/s linear velocity, 1 MHz carrier frequency, and 50% duty cycle.

## III. RESULTS AND DISCUSSION

The crystallanity of the ITO films was analyzed by x-ray diffraction and found to vary with the composition of the film. Figure 1 shows the x-ray diffraction pattern of the ITO films as a function of $SnO_2$ content. The $In_2O_3$ film is found to be crystalline, whereas the $SnO_2$ film is amorphous. ITO with 10% $SnO_2$ is crystalline, but less so than the $In_2O_3$ film. With increasing $SnO_2$ content, the film becomes less crystalline or becomes amorphouslike. Finally, ITO films with greater than 50% $SnO_2$ are completely amorphous, similar to $SnO_2$.

It is known that the coercivity of Co/Pt films depends on the type of underlayer. Previously, underlayers of poly-

 0021-8979/96/79(8)/5704/3/$10.00 © 1996 American Institute of Physics

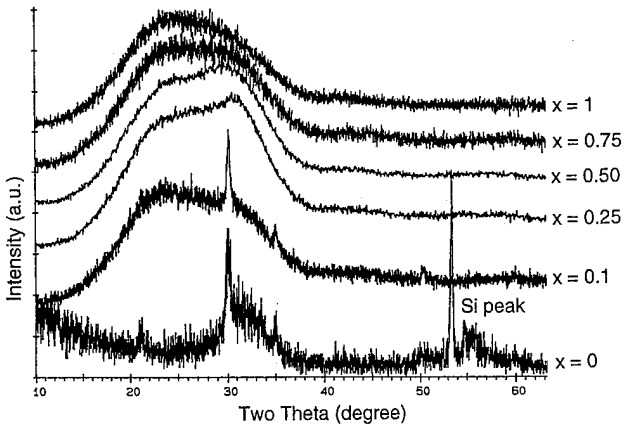



FIG. 1. X-ray diffraction pattern of $(In_2O_3)_{1-x}$ $(SnO_2)_x$ films deposited using Ar+1% $O_2$ gas. All films were deposited on glass substrates except $In_2O_3$, which was deposited on a silicon substrate.

crystalline materials, such as ZnO or $In_2O_3$, were found to be the most effective in enhancing the coercivity (1). The texture and epitaxial growth of the multilayer film was improved. We recently reported that amorphous ITO films also enhance the coercivity, anisotropy, as well as Kerr loop squareness of the Co/Pt superlattice structure. This enhancement depends on the deposition conditions of the ITO underlayer. The coercivity was found to increase monotonically with increasing pressure. For the purpose of comparison here we sputter deposited all the ITO compositions at a fixed pressure of 5 mT Ar+1% $O_2$. Twelve bilayers of Co 4 Å/Pt 8 Å were deposited on the ITO underlayers deposited on the glass substrate. Figure 2 shows the variation of coercivity as a function of ITO composition. Coercivities on the orders of 2400 Oe were obtained for the ITO films with 10–50 % $SnO_2$.

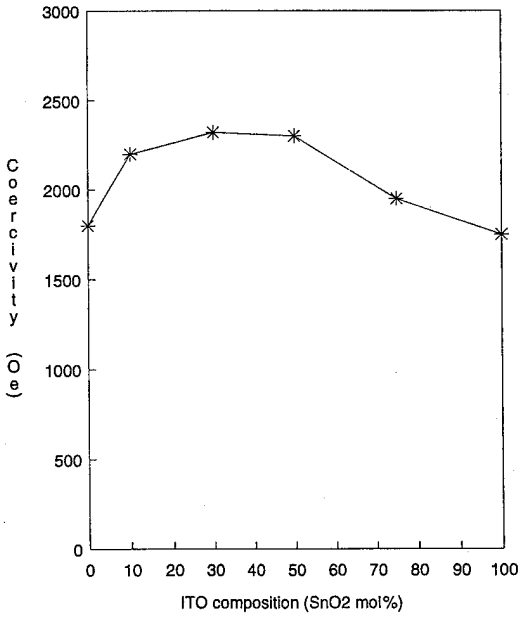



FIG. 2. Variation of coercivity of the Co/Pt multilayer as a function of composition of the ITO underlayer.

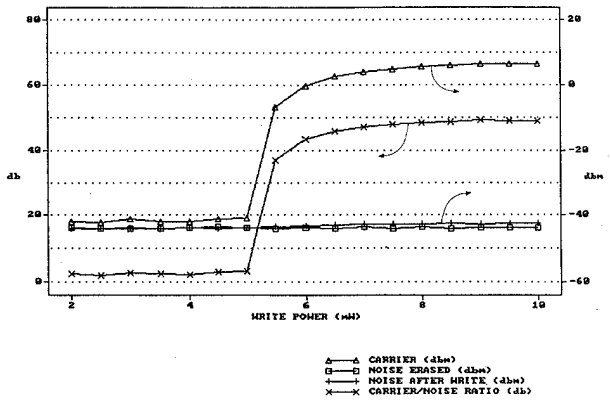



FIG. 3. Recording power dependence of carrier-to-noise ratio using a simple bilayer structure disk with ITO underlayer containing 30% $SnO_2$. The recording was done at a linear velocity of 5.66 m/s and mark length of 0.75 $\mu$m.

Full structure disks were prepared by depositing 12 bilayers of Co 4 Å/Pt 8 Å on 1000 Å ITO underlayers using polycarbonate (PC) and glass substrates. PC substrates with pregrooves of 1.6 $\mu$m pitch were used for testing recording properties. All the disks using various ITO compositions exhibited similar carrier levels as well as Kerr rotation, but they were obviously different in the noise level and the writing sensitivity. The disks with crystalline $In_2O_3$ underlayer were very noisy, whereas the disks with amorphous underlayers showed lower noise. The lower disk noise in the case of amorphous underlayers is attributed to their finer microstructure and smoother surface. Figure 3 shows the dependence of the recording performance on the writing laser power of the disk using ITO underlayer with 30% $SnO_2$. It shows that a CNR of greater than 48 dB is obtained for a 0.75 $\mu$m mark length, exceeding ISO specifications. Also, it is noteworthy that the unwritten and written noise levels are as low as those obtained from conventional rare earth-transition metal alloy disks, such as TbFeCo. Previously, the noise in the Co/Pt disk has been lowered by an additional step of sputter etching the substrate surface.[6,7]

Significant differences are also observed in the writing sensitivity. Figure 4 shows the optimum recording power for these disks as a function of ITO composition. The sensitivity of the disk is much higher for the high $SnO_2$ content disk. In fact a two-fold increase in recording sensitivity is observed as $SnO_2$ content is increased from 0 to 75%. This behavior is correlated to the composition-induced changes in the microstructure and thermal conductivity of the ITO underlayer. As noted above, ITO deposited with low $SnO_2$ content exhibits crystalline microstructure and low electrical resistivity, whereas ITO deposited with high $SnO_2$ content exhibits amorphous microstructure and high electrical resistivity. The change in resistivity is considerable, e.g., 0.017 $\Omega$ cm to 400 $\Omega$ cm for ITO with 10% $SnO_2$ and 50% $SnO_2$, respectively. The density of conduction electrons is much too low, however, to make any significant contribution to the ITO thermal conductivity. Rather, the ITO should be regarded as an electrical insulator whose lattice thermal conductivity depends primarily on the phonon mean free path. Increased phonon scattering due to irregular crystal structure can dramatically reduce the thermal conductivity coefficient. For ex-

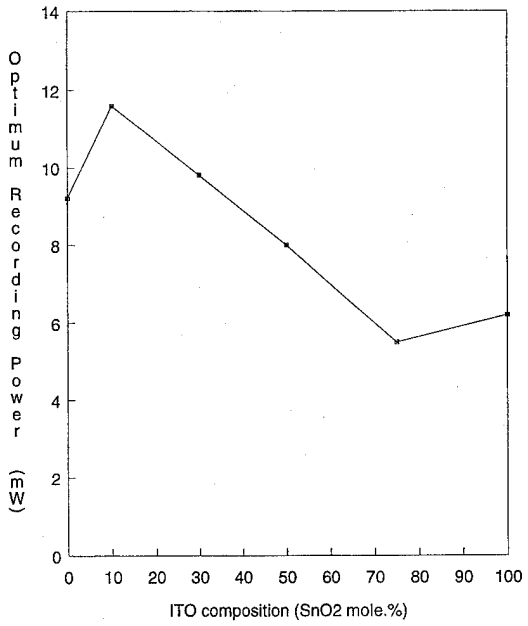



FIG. 4. Variation of the optimum recording power as a function of ITO composition of the underlayer.

ample, the random network of silicon-oxygen bonds in clear, fused quartz glass leads to an eight-fold reduction in thermal conductivity compared to crystalline quartz along the $c$ axis.[8] In general, the thermal conductivity values of amorphous glasses at room temperature run about an order of magnitude below those of crystalline insulators. Although detailed thermal modeling has not been carried out, we note that the thickness of the ITO layer is substantially greater than the thermal diffusion length given the marking time employed in our experiment. The ITO layer thus acts as a "thermal barrier" between the MO layer and the substrate. Thus, we conclude that the reduction in crystallinity with increasing $SnO_2$ content decreases the ITO thermal conductivity, increasing its effectiveness as a thermal barrier, which results in the increase in recording sensitivity. Acting as it does as a "nucleation layer," the ITO film probably influences the microstructure of the MO layer as we observed in our previous studies.[3] As ITO amorphizes it is likely that the microstructure changes it induces in the MO layer alter the thermal and electrical conductivity of that layer as well.

## IV. CONCLUSIONS

In conclusion, we have prepared a high performance Co/Pt multilayer media with high coercivity and high sensitivity. This was achieved by an optimum combination of composition and microstructure of the ITO underlayer. ITO films with higher $SnO_2$ content are amorphous in structure and appear to have lower thermal conductivity, which results in lower disk noise and higher recording sensitivity.

## ACKNOWLEDGMENTS

We would like to thank Dr. Y. S. Tyan, Dr. R. H. Victora, and Dr. B. Bartholomeusz for useful discussions, G. Farruggia for technical help, and T. Blanton for x-ray diffraction.

[1] P. F. Carcia, M. Reiley, W. B. Zeper, and H. W. van Kersteren, Appl. Phys. Lett. **58**, 191 (1991).
[2] C. H. Chang and M. H. Kryder, J. Appl. Phys. **75**, 6864 (1994).
[3] T. K. Hatwar and C. F. Brucker, IEEE Trans. Magn. **31**, 3256 (1995).
[4] S. Hashimoto, J. Appl. Phys. **75**, 438 (1994).
[5] H. W. van Kesteren and W. B. Zeper, J. Magn. Magn. Mater. **120**, 271 (1993).
[6] S. Sumi, K. Tanase, Y. Teragaki, K. Torazawa, S. Tsunashima, and S. Uchiyama, Jpn. J. Appl. Phys. **31**, 3328 (1992).
[7] A. Maesaka, K. Bessho, and S. Hashimoto, Jpn. J. Appl. Phys. **32**, 3160 (1993).
[8] *CRC Handbook of Chemistry and Physics*, 72nd edition (Chemical Rubber, Boca Raton, 1992), pp. 15–36, 12–139.

# Magnetic circular x-ray dichroism in $Fe_7S_8$ and $Fe_7Se_8$ (abstract)

T. Koide
*Photon Factory, National Laboratory for High Energy Physics, Tsukuba, Ibaraki 305, Japan*

H. Miyauchi
*Institute of Physics, University of Tsukuba, Tsukuba, Ibaraki 305, Japan*

T. Shidara
*Photon Factory, National Laboratory for High Energy Physics, Tsukuba, Ibaraki 305, Japan*

N. Nakajima
*Department of Physics, Tokyo Institute of Technology, Meguro-ku, Tokyo 152, Japan*

H. Kawabe and H. Fukutani
*Institute of Physics, University of Tsukuba, Tsukuba, Ibaraki 305, Japan*

K. Shimada and A. Fujimori
*Department of Physics, University of Tokyo, Bunkyo-ku, Tokyo 113, Japan*

K. Iio
*Department of Physics, Tokyo Institute of Technology, Meguro-ku, Tokyo 152, Japan*

T. Kamimura
*Department of Physics, Tohoku University, Sendai, Miyagi 980, Japan*

Magnetic circular dichroism (MCD) in core-level absorption provides insights into the element-specific and site-selective magnetic states of various magnetic materials. $Fe_7S_8$ and $Fe_7Se_8$ have the pseudo-NiAs-type crystal structure and are ferrimagnetic below 578 and ~450 K, respectively. We have measured MCD spectra in the Fe $2p$ ($L_{2,3}$) and Fe $3p$ ($M_{2,3}$) core-level absorption of these compounds. The $L_{2,3}$ MCD spectra were taken at ~80 K with the total electron yield method. The $M_{2,3}$ MCD spectra were measured at room temperature with the reflection method using the magnetic-field modulation technique. Both experiments were made using circularly polarized undulator radiation. The $L_{2,3}$ MCD spectra were found to exhibit a negative peak at the $L_3$ edge with a maximum intensity of $\sim 10^{-2}$ and a weaker positive peak at the $L_2$ edge. The MCD spectrum of $Fe_7S_8$ showed sideband features near the $L_3$ edge. Utilization of the magnetic-field modulation method allowed a detection of small MCD signals around the $M_{2,3}$ edges; the maximum signal intensity was of the order of $\sim 3\times 10^{-3}$. The $M_{2,3}$ MCD spectrum of $Fe_7S_8$ showed a MCD signal for a prethreshold multiplet, while that of $Fe_7Se_8$ exhibited no appreciable MCD signal for a prethreshold multiplet. The features observed in the $L_{2,3}$ MCD and $M_{2,3}$ MCD are consistent with an electronic band-structure calculation reported recently.[1] © *1996 American Institute of Physics.*
[S0021-8979(96)69508-4]

[1] H. Ikeda, M. Shirai, N. Suzuki, and K. Motizuki, J. Magn. Magn. Mater. **140–144**, 159 (1995).

# Magnetic circular x-ray dichroism in Co/Pt multilayers (abstract)

T. Koide
*Photon Factory, National Laboratory for High Energy Physics, Tsukuka, Ibaraki 305, Japan*

N. Nakajima
*Department of Physics, Tokyo Institute of Technology, Meguro, Tokyo 152, Japan*

T. Shidara
*Photon Factory, National Laboratory for High Energy Physics, Tsukuba, Ibaraki 305, Japan*

H. Miyauchi, H. Kawabe, and H. Fukutani
*Institute of Physics, University of Tsukuba, Tsukuba, Ibaraki 305, Japan*

A. Fujimori
*Department of Physics, University of Tokyo, Bunkyo-ku, Tokyo 113, Japan*

K. Iio
*Department of Physics, Tokyo Institute of Technology, Meguro, Tokyo 152, Japan*

T. Katayama and Y. Suzuki
*Electrotechnical Laboratory, Tsukuba, Ibaraki 305, Japan*

A Co/Pt multilayer is one of the most attractive candidates for next-generation high-density magneto-optical recording media. With a decreasing Co layer thickness, the direction of the easy axis of magnetization changes from in-plane to out-of-plane. We have measured core-level MCD of Co/Pt multilayers. Six Co/Pt multilayer samples were prepared which had Co layer thicknesses from 3 to 14 Å. The MCD experiments were made using circularly polarized undulator radiation. The spectra were taken separately for the energy regions around the Co $M_{2,3}$ (and Pt $O_3$) and Pt $N_{6,7}$ (and Pt $O_2$) edges. The dichroic signals in reflectivity were recorded for two opposite directions of an external magnetic field of 2 T. We have also measured the reflectivity spectra down to 4 eV and have made Kramers–Kronig analyses to obtain the dielectric tensor. The dielectric tensor element which represents absorption MCD shows a dramatic change at the Co $M_{2,3}$ edges. The MCD spectra of thinner Co-layer samples are more asymmetric than those of thicker ones. This shows that the orbital magnetic moment of Co is enhanced as the Co layer thickness decreases. The MCD spectra become sharper and narrower with a decreasing Co layer thickness. This feature strongly reflects a band narrowing of the Co $3d$ state at or around the Co/Pt interfaces. The MCD spectra at the Pt $N_{6,7}$ edges show little dependence on the Co layer thickness. This can be explained by assuming that Pt atoms only at the interfaces are responsible for the MCD signals, since the surface density of Pt atoms is equal for all the samples. Combining the result at the Co $M_{2,3}$ edges with that at the Pt $N_{6,7}$ edges leads to the conclusion that perpendicular magnetic anisotropy mainly depends on the electronic structure of Co at Co/Pt interfaces and that Pt atoms at the interfaces play a partial role in magnetic anisotropy. © *1996 American Institute of Physics.* [S0021-8979(96)69608-0]

 0021-8979/96/79(8)/5708/1/$10.00 © 1996 American Institute of Physics

# Mössbauer and x-ray diffraction studies of the phase composition of crystallized $Nd_xFe_{81.5-x}B_{18.5}$ alloys with $7 \leqslant x \leqslant 16$ (abstract)

Zhao-Hua Cheng, Bao-gen Shen, and Jun-Xian Zhang
*State Key Laboratory of Magnetism, Institute of Physics, Chinese Academy of Sciences, P.O. Box 603, Beijing 100080, People's Republic of China*

Ming-xi Mao, Ji-jun Sun, Fa-shen Li, and Yi-de Zhang
*Department of Physics, Lanzhou University, People's Republic of China*

In previous work, the phase composition of melt-spun Nd-Fe-B with a low Nd concentration ($X \leqslant 6$ at. %) have been extensively investigated by means of x-ray diffraction, spin echo nuclear magnetic resonance, and Mössbauer spectra.[1] However, the phase composition of melt-spun Nd-Fe-B with intermediate and high Nd concentration has not been studied by Mössbauer effect. Based on the knowledge of the $^{57}Fe$ hyperfine parameters for $Nd_2Fe_{14}B$, $Nd_{1.1}Fe_4B_4$ and $Nd_2Fe_{23}B_3$, the phases produced during annealing Nd-Fe-B amorphous alloys can be identified with greater sensitivity by Mössbauer spectroscopy than by x-ray diffraction. In the present work, a combination of x-ray diffraction experiments and Mössbauer spectroscopy has been performed on annealed $Nd_xFe_{81.5}B_{18.5}$ ($7 \leqslant x \leqslant 16$). It is found that the samples with $7 \leqslant x \leqslant 9$ contain $Nd_2Fe_{23}B_3$ metastable phase and $Nd_{1.1}Fe_4B_4$ paramagnetic phase. The body-centered-cubic structure of $Nd_2Fe_{23}B_3$ cannot generate the hard magnetic properties. The samples with $12 \leqslant x \leqslant 16$ consist of $Nd_2Fe_{14}B$ magnetically hard phase and $Nd_{1.1}Fe_4B_4$ paramagnetic phase. The large coercivity for the high Nd content Nd-Fe-B originates from the very fine size of $Nd_2Fe_{14}B$ crystallites below the critical size of single domain particle, which has a pinning domain wall effect. © *1996 American Institute of Physics.* [S0021-8979(96)69708-7]

This work is supported by the National Natural Science Foundation of China.

[1] Z. H. Cheng *et al.*, J. Appl. Phys. **76**, 2981 (1994).

# Superexchange interactions in $Ni_{0.5}Co_{0.5}Fe_2O_4$

Choong Sub Lee and Chan Young Lee
*Department of Physics, National Fisheries University of Pusan, Pusan 608-737, Korea*

Slowly cooled $Ni_{0.5}Co_{0.5}Fe_2O_4$ has been investigated over a temperature range from 13 to 880 K using the Mössbauer technique. X-ray diffraction shows that it has an inverse spinel structure and a lattice constant of $a=8.346\pm0.005$ Å. The Mössbauer spectra that are laid less overlapping at low temperature have been fitted with two sextets in the ferrimagnetic state. The iron ions at both $A$ (tetrahedral) and $B$ (octahedral) sites are found to be in ferric high-spin states. Its Néel temperature $T_N$ is found to be $865\pm3$ K. As the temperature increases toward $T_N$ a more overlapping effect of the six-line patterns in $A$ and $B$ sites is observed and interpreted to have originated from different temperature dependencies of the magnetic hyperfine fields at $A$ and $B$ iron sites. Assuming that $A$–$B$ magnetic interactions are stronger than $A$–$A$ and $B$–$B$ interactions, we have calculated the hyperfine fields at the $A$ and $B$ iron sites in ionic distribution $(Fe)_A[Ni_{0.5}Co_{0.5}Fe]_BO_4$ as a function of temperature. The theoretical Mössbauer spectra from the above calculated hyperfine fields are obtained and compared with experimental spectra. © *1996 American Institute of Physics.* [S0021-8979(96)74508-9]

$NiFe_2O_4$ is completely inverse spinel[1,2] and has the ionic distribution $(Fe^{3+})_A[Ni^{2+}Fe^{3+}]_BO_4$, where $A$ and $B$ indicates tetrahedral site and octahedral site in spinel structure, respectively. This was verified by measuring the area ratio $I_A/I_B=1.0$ of the Mössbauer patterns (two well-resolved sextets) corresponding to $^{57}Fe$ in $A$ and $B$ sites. $CoFe_2O_4$ is not completely inverse, and x-ray and magnetic studies report that the degree of inversion depends on the heat treatment.[3,4] Kim *et al.*[5,6] suggested that the atomic migration (cationic exchange of $A$ and $B$ site in $CoFe_2O_4$ and $Ni_{0.5}Co_{0.5}Fe_2O_4$) results from the area ratio analysis of two overlapped sextets of $A$ and $B$ Mössbauer pattern. This is different from the atomic migration that accompanied by the change of crystal structure.[7]

In this study Mössbauer spectra of $Ni_{0.5}Co_{0.5}Fe_2O_4$ have been collected over a wide temperature range 13–880 K. The subspectrum of $A$ and $B$ site at 13 K is well resolved and the overlapping effect of subspectra increases with increasing temperature. This overlapping effect is interpreted to originate from different temperature dependencies of the magnetic hyperfine fields at $A$ and $B$ site.

The sample $Ni_{0.5}Co_{0.5}Fe_2O_4$ was prepared by grinding together appropriate proportions of ferric oxide, nickel oxide, and cobalt oxide powders of 99.995%, 99.999%, and 99.999% purity, respectively, pressing the resulting mixture into pellets at 6000 kg/cm$^2$, firing in an evacuated and sealed quartz ampoule at 1000 °C for 3 days, and then slowly cooled to room temperature at a rate of 10 °C/h. The sample was $^{57}Fe$ enriched to 5 at. % of the metal atoms for Mössbauer measurements.

X-ray diffraction patterns of $Ni_{0.5}Co_{0.5}Fe_2O_4$ showed that the sample had the cubic spinel of a single phase. We could not find out a single diffraction peak of $Fe_2O_3$, NiO, CoO, Fe, $NiFe_2O_4$, $CoFe_2O_4$, $NiFe_2O_4$, etc. The lattice constant, $a=8.346\pm0.005$ Å, at room temperature was found by using Nelson–Riley function[8] and extrapolating to the backward diffraction ($\theta=90°$).

Mössbauer spectra were recorded using a conventional Mössbauer spectrometer of the electromechanical type with a 10-mCi $^{57}Co$ source in a Rh matrix.

Figure 1 shows some of the Mössbauer spectra of $Ni_{0.5}Co_{0.5}Fe_2O_4$ below the Néel temperature. The Néel temperature, $T_N=865\pm3$ K, was measured using the thermal scan method. Mössbauer absorption lines are two hyperfine-split sextets and they overlap increasingly with increasing temperature. Two sets of six Lorentzian lines were fitted to the Mössbauer spectra under the valid constraints, which are $\Gamma_j=\Gamma_{7-j}(j=1,2,3)\Gamma_j=\Gamma_{7-j}(j=1,2,3)$ of line-width and $I_j=I_{7-j}$ of intensity with $I_1:I_2:I_3=3:2:1$ when the electric quadrupole interaction is much weaker than the magnetic hyperfine interaction. The solid line on data points is sum of dot lines originated from $Fe^{3+}$ of $A$ and $B$ sites. The results of computer analysis for two well-resolved sextets at low temperatures are presented in Table I.

We neglected the recoil-free fraction for intensity ratios in Table I. These intensity ratios confirm that $Ni_{0.5}Co_{0.5}Fe_2O_4$ is an inverse spinel of the cation distribution

$$(Fe^{3+})_A[Ni^{2+}_{0.5}Co^{2+}_{0.5}Fe^{3+}]_BO_4. \quad (1)$$

The isomer shift values at room temperature for the $A$ and $B$ subspectrum are found to be $0.15\pm0.01$ and $0.26\pm0.01$ mm/s relative to the Fe metal, respectively, which are consistent[1] with the high spin $Fe^{3+}$ state. The smaller value of $A$ site isomer shift is due to a larger covalency at the $A$ site. The ferric character of the Fe ions is also manifested by the magnitudes of the magnetic hyperfine field; the field values at 13 K of the $A$ and $B$ patterns are found to be $511\pm2$ and $553\pm2$ kG, respectively, which are typical values for $Fe^{3+}$ ions.

As can be seen in Fig. 1, the Mössbauer absorption lines overlap increasingly as the temperature approaches the Néel temperature $T_N$ from below. The overlapping of the Mössbauer spectral lines may result from different temperature dependencies of the magnetic hyperfine fields at $A$ and $B$ iron site using the molecular field theory.[9,10]

In the spinel ferrites, the $A$–$B$ magnetic interactions between the magnetic atoms on the $A$ and $B$ sites are stronger than $A$–$A$ and $B$–$B$ interactions.[11] According to the cation distribution Eq. (1), the molecular field acting on $A$-site

 0021-8979/96/79(8)/5710/3/$10.00 © 1996 American Institute of Physics

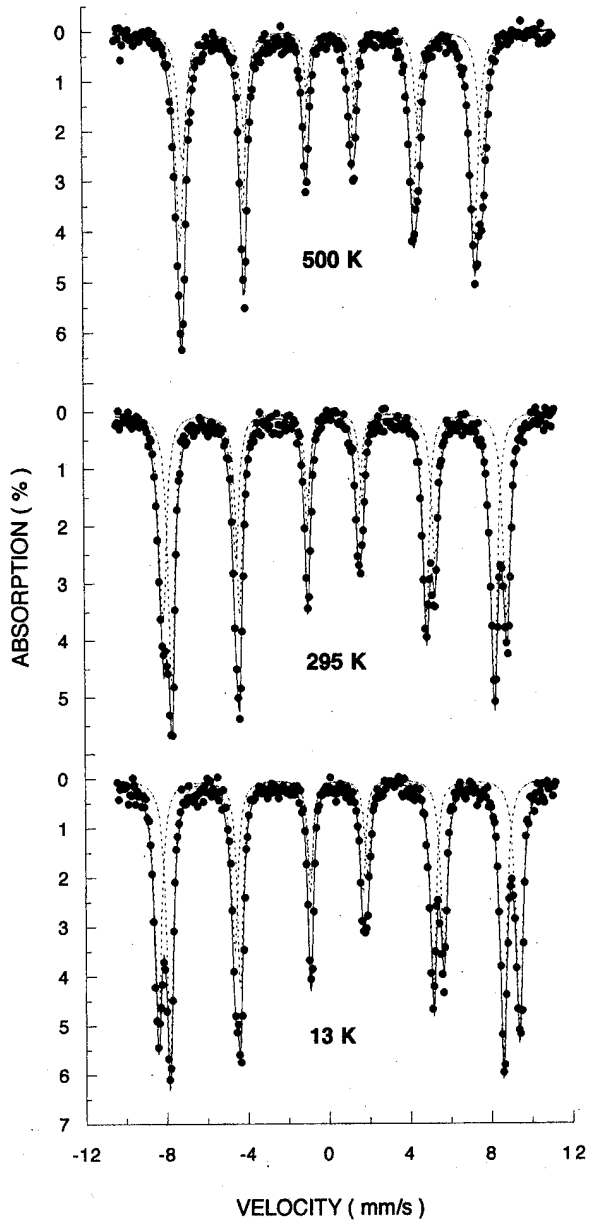



FIG. 1. Mössbauer spectra of $Ni_{0.5}Co_{0.5}Fe_2O_4$ below the Néel temperature.

$Fe^{3+}$ ions with 12 next nearest neighbor $B$ site ions ($Ni^{2+}$, $Co^{2+}$, and $Fe^{3+}$), is approximated by

$$H=-\frac{2}{g\mu_B}J\times 12\times\langle\bar{S}'\rangle. \tag{2}$$

Here, $J$ is an exchange integral between $Fe^{3+}$ and $Ni^{2+}$, $Co^{2+}$, or $Fe^{3+}$ ions, $\mu_B$ is Bohr magneton, $\langle\bar{S}'\rangle$ is the average value of the $B$-site ion spin taken over all environments, and $\bar{S}'$ is the average value of $S_z'$ for a particular environment. $g$ is the $g$ factor of an $A$-site $Fe^{3+}$ ion.

On the other hand, the molecular field acting on $B$-site $Fe^{3+}$ ions with 6 next nearest neighbor $A$-site $Fe^{3+}$ ions is approximated by

$$H'=-\frac{2}{g'\mu_B}J\times 6\times\langle\bar{S}\rangle, \tag{3}$$

TABLE I. Magnetic hyperfine field $H$, electric quadrupole shift $\Delta E_Q$, isomer shift $\delta$, and intensity ratio $R(=I_A/I_B)$ at low temperatures $T$ for $Ni_{0.5}Co_{0.5}Fe_2O_4$. $\delta$ is relative to the iron metal.

| | $H$ (kG) | | $\Delta E_Q$ (mm/s) | | $\delta$ (mm/s) | | |
|---|---|---|---|---|---|---|---|
| $T$ (K) | $B$ | $A$ | $B$ | $A$ | $B$ | $A$ | $R(=I_A/I_B)$ |
| 13 | 553 | 511 | −0.01 | 0.00 | 0.37 | 0.25 | 1.08 |
| 77 | 552 | 511 | −0.01 | 0.00 | 0.37 | 0.25 | 1.05 |
| 130 | 549 | 508 | −0.01 | 0.00 | 0.35 | 0.23 | 1.01 |
| 180 | 545 | 506 | −0.01 | 0.00 | 0.33 | 0.21 | 1.14 |
| (Error) | ±2 | ±2 | ±0.01 | ±0.01 | ±0.01 | ±0.01 | ±0.05 |

where $S$ stands for the $Fe^{3+}$ spin, and $g'$ is the $g$ factor of $B$-site ions.

It is true that the approximations given by Eqs. (2) and (3) are somewhat crude, because the exchange integrals are $J_{Fe-Fe}\cong J_{Fe-Ni}\cong J_{Fe-Co}$; the Néel temperature of 858 K[12] for $Fe_3O_4$ is nearly equal to 862 K[13] for $NiFe_2O_4$ and 870 K[5] for $CoFe_2O_4$. Now the average value of a $A$-site $Fe^{3+}$ spin $S$ can be written as

$$\langle\bar{S}\rangle=\bar{S}=-SB_S\left(\frac{g\mu_BSH}{k_BT}\right), \tag{4}$$

where $B_S(x)$ is the Brillouin function for a spin $S$. $k_B$ and $T$ represent the Boltzmann constant and temperature, respectively. Similarly, the average value of a $B$-site ion spin $S'$ can be written as

$$\langle\bar{S}'\rangle=\bar{S}'=-S'B_{S'}\left(\frac{g'\mu_BS'H'}{k_BT}\right). \tag{5}$$

The magnetic ordering temperature can be easily derived from Eqs. (4) and (5) to be

$$T_N=\frac{2|J|}{3k_B}[S(S+1)S'(S'+1)\times 12\times 6]^{1/2}. \tag{6}$$

Introducing the reduced variables $\sigma=\langle\bar{S}\rangle/S$, $\sigma'=\langle\bar{S}'\rangle/S'$ and $\tau=T/T_N$, Eqs. (4) and (5) are combined to give the equations:

$$\sigma=-B_S\left(12\times a\times\frac{\sigma'}{\tau}\right), \tag{7}$$

$$\sigma'=-B_{S'}\left(6\times a\times\frac{\sigma}{\tau}\right), \tag{8}$$

where $a$ is a constant given by

$$a=\frac{3SS'}{[S(S+1)S'(S'+1)\times 12\times 6]^{1/2}}. \tag{9}$$

For each reduced temperature $\tau$, the reduced spin $\sigma$ and $\sigma'$ proportional to the reduced magnetic hyperfine field at the $A$ and $B$ site are calculated numerically by solving Eqs. (7) and (8) simultaneously.

Figure 2 shows that the temperature dependencies of the reduced hyperfine fields at the $A$ and $B$ site in $Ni_{0.5}Co_{0.5}Fe_2O_4$ are different. To compare the temperature dependencies of the hyperfine fields at the $A$ and $B$ site in detail, we put on $H_A(0)=511$ kG for $A$ site and $H_B(0)=553$ kG for $B$ site. Figure 3 presents the magnetic

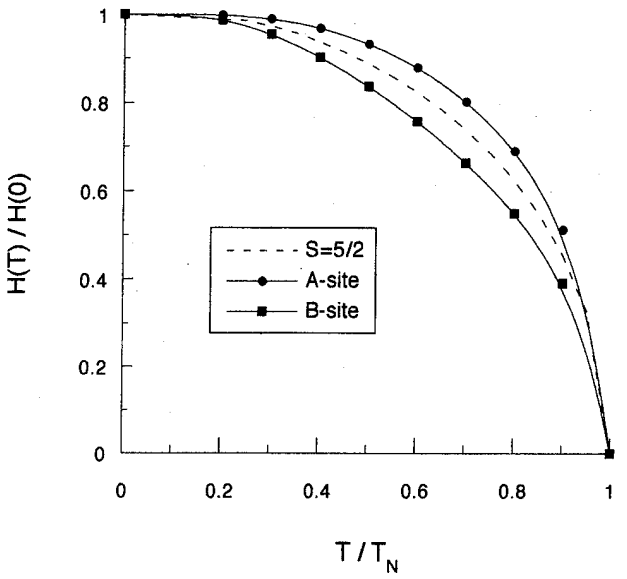



FIG. 2. Reduced hyperfine fields at the $A$ and $B$ site as a function of reduced temperature. The dash line is Brillouin function for spin $S$=5/2.

hyperfine fields at the $A$ and $B$ site as a function of reduced temperature and the hyperfine fields at the $A$ and $B$ site crossing each other.

As can be seen in Fig. 4, we calculated the theoretical Mössbauer spectra at various reduced temperatures using the hyperfine fields of Fig. 3 and line-width=0.38 mm/s, isomer shift=0.25 mm/s for $A$ site and line-width=0.41 mm/s, isomer shift=0.37 mm/s for $B$ site of the 13 K experimental parameters in Fig. 1. The calculated Mössbauer spectra are nearly consistent with those in Fig. 1, but 0.25 $T_N$ (216 K) and 0.35 $T_N$ (303 K) are not in accord with 295 K and 500 K, respectively. We may interpret this discord in the magnetic ions of lowest level by Hund's rule.

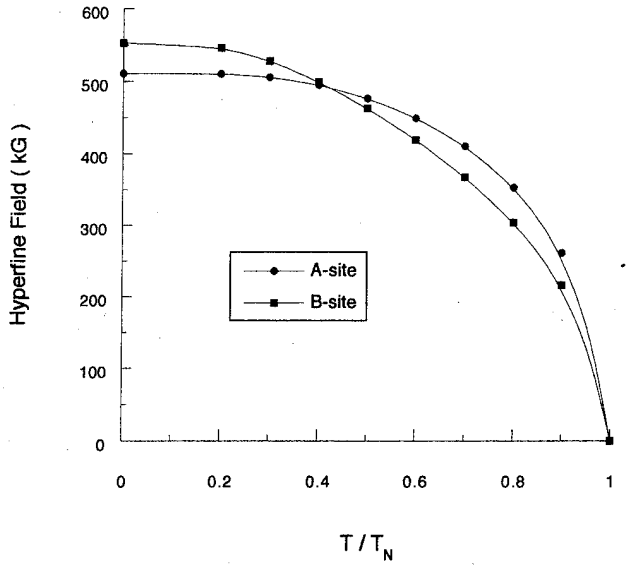



FIG. 3. Magnetic hyperfine fields at the $A$ and $B$ site as a function of reduced temperature.

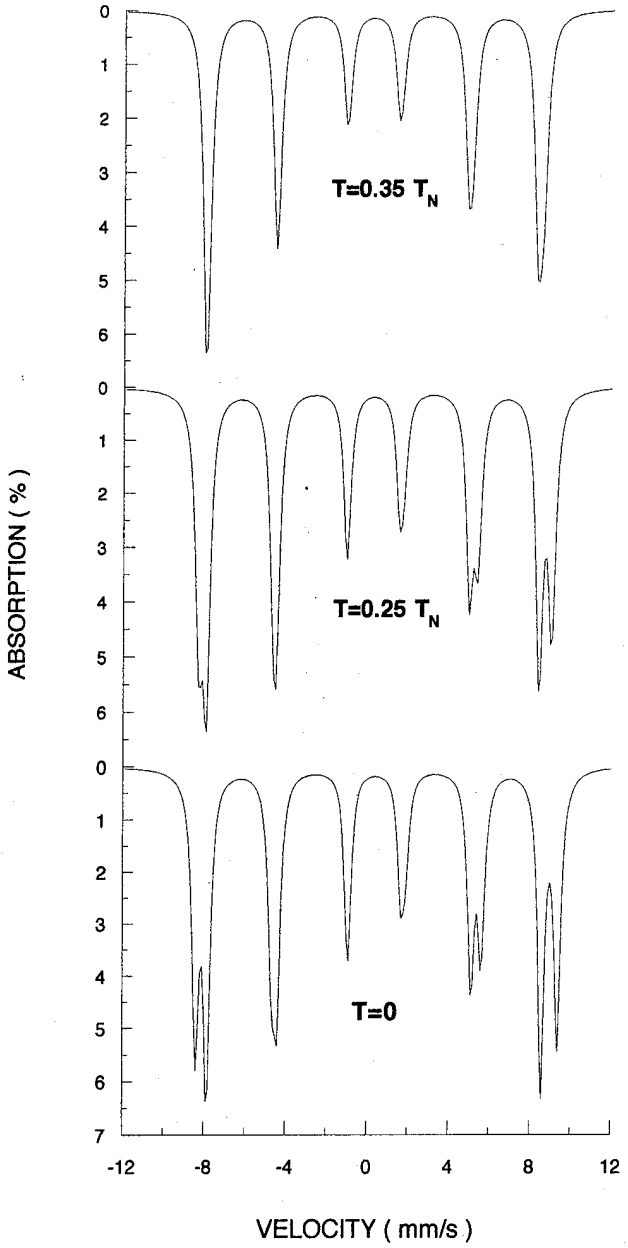



FIG. 4. Mössbauer spectra calculated by the molecular field theory at various reduced temperatures.


[1] G. A. Sawatzky, F. van der Woude, and A. H. Morrish, J. Appl. Phys. **39**, 1204 (1968); Phys. Rev. **187**, 747 (1969).
[2] D. Kedem and T. Rothem, Phys. Rev. Lett. **18**, 165 (1967).
[3] K. Haneda and A. H. Morrish, J. Appl. Phys. **63**, 4258 (1988).
[4] M. R. De Gurie, R. C. O'Handley, and G. Kalonji, J. Appl. Phys. **65**, 3167 (1989).
[5] Chul Sung Kim, Seung Iel Park, Young Lang Um, Young Jong Lee, Seung Wha Lee, and Sung Real Hong, J. Korean Phys. Soc. **27**, 323 (1994).
[6] Seung Wha Lee, Sung Real Hong, Seung Iel Park, and Chul Sung Kim, J. Korean Mag. Soc. **5**, 58 (1995).
[7] Hang Nam Ok and Yun Kon Kim, Phys. Rev. B **36**, 5120 (1987).
[8] J. B. Nelson and D. P. Riley, Proc. Phys. Soc. London **57**, 160 (1945).
[9] J. M. Daniels and A. Rosencwaig, Canadian J. Phys. **48**, 381 (1970); J. K. Srivastava, K. Muraleedharan, and R. Vijayaraghavan, Phys. Lett. **24**, 482 (1984).
[10] Choong Sub Lee and Chan Young Lee, J. Korean Mag. Soc. **3**, 173 (1993).
[11] C. M. Srivastava, G. Srinivasan, and N. G. Nanadikar, Phys. Rev. B **19**, 499 (1979).
[12] S. Geller, J. P. Remeika, H. J. Williams, G. P. Espinosa, and R. C. Sherwood, Phys. Rev. A **137**, 1034 (1965).
[13] T. M. Uen and F. H. Yang, Jpn. J. Appl. Phys. **27**, 955 (1988).

# A $^{57}$Fe Mössbauer study of $Gd_2Fe_{17-x}Ga_xC_2$ ($x$=0–6)

Bo-Ping Hu
*San Huan Research Laboratory, Chinese Academy of Sciences, Beijing 100080, People's Republic of China*

Hong-Shuo Li
*School of Physics, The University of New South Wales, Sydney NSW 2052, Australia and Southern Research Institute of Pure and Applied Sciences, Southern University, Baton Rouge, Louisiana 70813*

Bao-Gen Shen
*Magnetism Laboratory Institute of Physics, Chinese Academy of Sciences, Beijing 100080, People's Republic of China*

Suharyana
*School of Physics, The University of New South Wales, Sydney, NSW 2052, Australia*

Fang-Wei Wang
*Magnetism Laboratory, Institute of Physics, Chinese Academy of Sciences, Beijing 100080, People's Republic of China*

J. M. Cadogan
*School of Physics, The University of New South Wales, Sydney, NSW 2052, Australia*

Wen-Shan Zhan
*Magnetism Laboratory, Institute of Physics, Chinese Academy of Sciences, Beijing 100080, People's Republic of China*

A $^{57}$Fe Mössbauer study of $Gd_2Fe_{17-x}Ga_xC_2$ ($x$=0–6) has been carried out in order to reveal the effects of Ga substitution on the Fe-sublattice magnetic properties. We have used a simplified fitting model which uses six broadened sextets in the theoretical fit to the spectra of $Gd_2Fe_{17-x}Ga_xC_2$. Our results suggest that the electronic factor plays an important role in determining the Fe magnetism in the substituted $R_2Fe_{17-x}T_x$ (T=Al,Ga,Si,Ti,...) compounds and their carbides. The average Fe magnetic moment in $Gd_2Fe_{17-x}Ga_xC_2$ varies from $1.99\mu_B$ for $x$=0 to $0.94\mu_B$ for $x$=5 at room temperature. Therefore, the optimum substituent concentration would be $1 \leqslant x \leqslant 3$ for the substituted $R_2Fe_{17-x}T_x$ compounds as potential permanent magnet materials. © *1996 American Institute of Physics.* [S0021-8979(96)74608-5]

## I. INTRODUCTION

The substitution of Ga for Fe in $R_2Fe_{17}$ (2:17) phase has been shown[1,2] to enhance both the Curie temperature and uniaxial anisotropy of 2:17 phase. In particular, the $Sm_2Fe_{17-y}Ga_y$ compounds exhibit uniaxial anisotropy for $y$ in the range of $1 \leqslant y \leqslant 5$[1] but have a planar anisotropy without the Ga substitution. The Curie temperature shows a maximum at $y \sim 3$, and reaches 635 K. In addition, this substitution facilitates the formation of interstitial carbides $R_2Fe_{17}C_x$ directly by conventional arc-melting[3] with higher carbon content, $x$, reaching about 2.5 (otherwise it is only about $x \sim 1.0$ without Ga substitution). A uniaxial anisotropy field $B_a$ greater than 9 T at 293 K for $Sm_2Fe_{14}Ga_3C_2$ is observed.[1] Moreover, a room temperature coercivity of $\mu_{0i}H_c$=1.5 T has been obtained in $Sm_2Fe_{14}Ga_3C_{1.5}$ prepared by melt spinning.[4,5] These results suggest that $Sm_2Fe_{14}Ga_3C_x$ might be a possible new material for sintered permanent magnets.

Here we present a $^{57}$Fe Mössbauer study of $Gd_2Fe_{17-x}Ga_xC_2$ ($x$=0–6). The effect of Ga on the magnetism of Fe sublattice will be discussed through the hyperfine parameters obtained.

## II. RESULTS AND DISCUSSION

This work is a part of our systematic study of the $R_2Fe_{17-y}Ga_yC_x$ series of compounds. The bulk magnetic properties of $Gd_2Fe_{17-x}Ga_xC_2$ ($x$=0–6) compounds have been studied in detail previously.[6] The sample preparation techniques are described in Ref. 6. $^{57}$Fe Mössbauer spectroscopy was carried out at 293 K in a standard transmission geometry using a $^{57}$CoRh source, calibrated with an $\alpha$-Fe foil.

In order to determine the number of magnetic sextets needed in the theoretical fitting, we need to consider the local environment of each Fe site in the rhombohedral $Th_2Zn_{17}$ structure. There are four Fe sites, namely 6*c*, 9*d*, 18*f*, and 18*h*; the carbon atoms occupy the 9*e* site. Therefore for the case of $R_2Fe_{17}$, the required number of sextets is four for easy-axis magnetization and seven for easy-plane ordering.[7,8] In the rhombohedral $Th_2Zn_{17}$ structure with the interstitial carbon atoms occupying 9*e* site, both the 18*f* and 18*h* Fe sites have one neighboring carbon atom. Thus, the introduction of the carbon atoms splits further each of the 18*f* and 18*h* sites' spectra into two subspectra. Since all $Gd_2Fe_{17-x}Ga_xC_2$ compounds have a planar easy magnetization direction, the total of number of sextets needed is eleven for fitting the spectra of $Gd_2Fe_{17}C_2$. Introduction of Ga atom further complicates the situation due to preferential site occupation of the Ga atoms. Previous neutron diffraction[9–11] and $^{57}$Fe Mössbauer studies[12–14] on $R_2Fe_{17-y}Ga_y$ suggest that the Ga atoms preferentially occupy mainly the 18*h* site of the $Th_2Zn_{17}$ structure when $x \leqslant 4$ and occupy the 18*h*, 18*f*,

 0021-8979/96/79(8)/5713/3/$10.00 © 1996 American Institute of Physics 

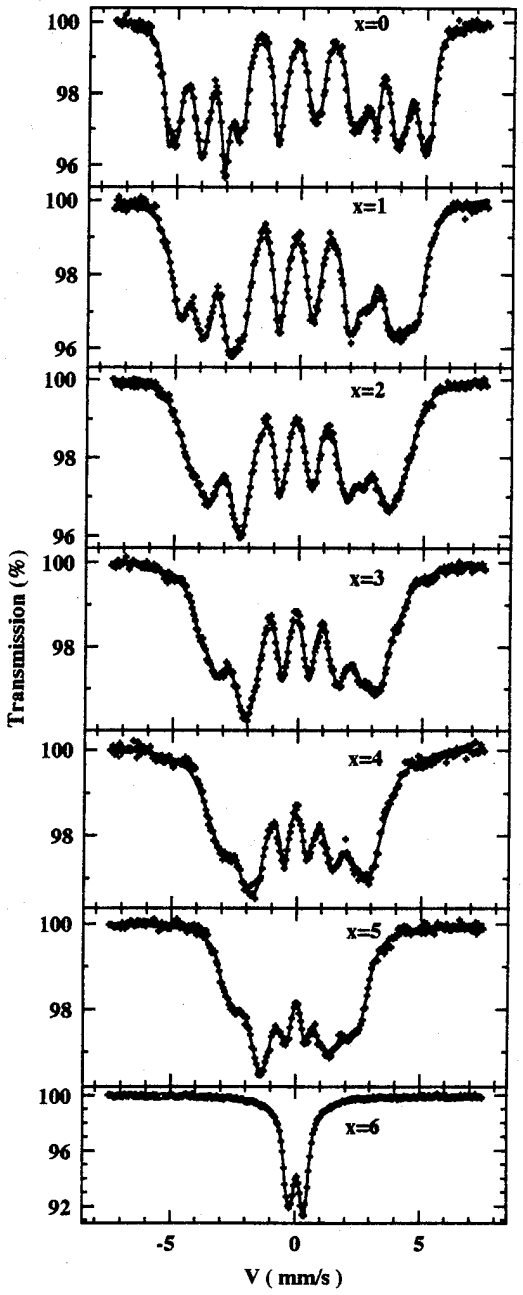



FIG. 1. The Mössbauer spectra of $Gd_2Fe_{17-x}Ga_xC_2$ ($x$=0−6) at room temperature with the fits shown as full curves.

TABLE I. Hyperfine parameters: isomer shift (IS), quadrupole splitting (QS), hyperfine field ($\mu_0 H_{hf}$) and relative area ($I$), deduced from the theoretical fits to the Mössbauer spectrum of $Gd_2Fe_{15}Ga_2C_2$ at room temperature.

| Site | IS (mm/s) | QS (mm/s) | $\mu_0 H_{hf}$ (T) | $I$ (%) |
|---|---|---|---|---|
| 6*c* | −0.01(3) | −0.01(5) | 27.8(2) | 18(5) |
| 9*d* | −0.18 | 0.28 | 25.5 | 14 |
| 18*f* | −0.17 | 0.05 | 22.6 | 23 |
| | −0.13 | 0.41 | 19.4 | 14 |
| 18*h* | 0.16 | 0.02 | 22.7 | 19 |
| | 0.17 | 0.20 | 16.8 | 12 |

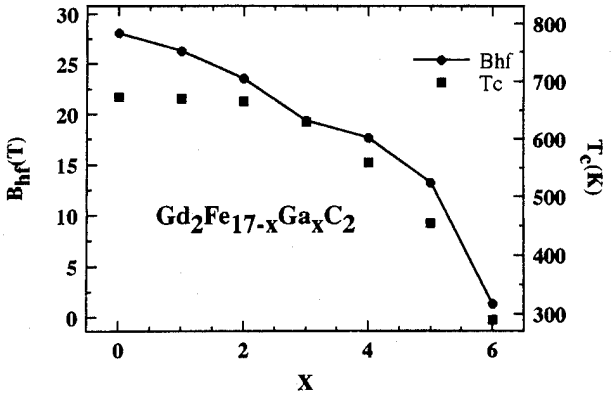



FIG. 2. Ga concentration dependence of average hyperfine field of $Gd_2Fe_{17-x}Ga_xC_2$ ($x$=0−6) at room temperature.

and 6*c* sites for $x>4$. The number of sextets thus needed is more than twenty if we intend to analyze the experimental spectra of $Gd_2Fe_{17-y}Ga_y$ in terms of an exact binomial distribution of the nearest-neighbor Ga environments. From the point of view of fitting the spectra, this is an unmanageable situation; some simplification must be introduced. Therefore, we have used a simplified fitting model[13] using six broadened sextets in the theoretical fit to the spectra of $Gd_2Fe_{17-y}Ga_yC_2$ compounds which ignores the local Ga and C environment of each Fe site. For $Gd_2Fe_{11}Ga_6C_2$ only one doublet is needed since it is paramagnetic at room temperature. This model reproduces the experimental absorption well, but some problems are found with the relative intensities.[15]

Figure 1 shows the Mössbauer spectra of $Gd_2Fe_{17-x}Ga_xC_2$ ($x$=0−6) collected at room temperature, together with the theoretical fits shown as solid lines. It is clear from this figure that the theoretical fits are satisfactory. Table I gives the hyperfine parameters resulting from the fits to the Mössbauer spectrum of $Gd_2Fe_{15}Ga_2C_2$ as a typical example of the $Gd_2Fe_{17-y}Ga_yC_2$ series. These results indicate that the Ga atoms preferentially occupy the 18*h* site as revealed by above mentioned Neutron diffraction studies[9–11] and $^{57}$Fe Mössbauer studies.[12–14]

The average hyperfine field $\langle B_{hf} \rangle$ as a function of Ga concentration is shown in Fig. 2. It can be seen that the $\langle B_{hf} \rangle$ decreases with Ga concentration which corresponds mainly to the decrease of the Curie temperature due to the Ga substitution (also shown in Fig. 2 for comparison). Of particular interest is the hyperfine field behavior at low Ga concentrations (there is a kink for $x\sim3$) where the field increases with decreasing $x$ while the Curie temperature remains essentially constant. This observation suggests that electron transfer effects between the Fe and Ga are important in determining the Fe magnetism in these compounds. In fact, recent theoretical studies[16,17] suggest that the enhancement of Curie temperature observed in the $R_2Fe_{17-x}T_x$ systems by any substituent, T=Al,Ga,Si,Ti... is attributed to be electronically in origin other than due to the simple volume expansion effect. The effect of the substitution is to fill out

the Fe $3d$ spin-up subband and the substituted compound thus becomes a strong magnet.[18]

Finally, using a conversion factor of 14.1 $T/\mu_B$ for 2:17 carbides,[19] the average Fe atomic magnetic moment in $Gd_2Fe_{17-x}Ga_xC_2$ varies from 1.99$\mu_B$ ($x$=0) to 0.94$\mu_B$ ($x$=5) at room temperature. Therefore, only those compounds with the low substituent concentration ($x<3$) have useful magnetization as potential permanent magnet materials.

## III. CONCLUSION

Our present $^{57}$Fe Mössbauer study on $Gd_2Fe_{17-x}Ga_xC_2$ ($x$=0−6) compounds suggests that the electronic factor plays an important role in determining the Fe sublattice magnetism in the substituted $R_2Fe_{17-x}T_x$ (T=Al,Ga,Si,Ti...) compounds and their carbides. The observed kink at $x\sim3$ in the Ga concentration dependence average hyperfine field indicates that there exist electron transfer effects between the Fe and Ga. The optimum substituent concentration would be $1\leqslant x\leqslant 3$ for the substituted $R_2Fe_{17-x}T_x$ compounds as potential permanent magnet materials.

## ACKNOWLEDGMENTS

This work was mainly supported by Research grants from the Australian Research Council. HSL would also like to acknowledge partial financial support from the U.S. Department of Energy, through the Grant No. DEFG 05-94ER 45505 to Southern University.

[1] Bao-Gen Shen, Fang-Wei Wang, Lin-Shu Kong, and Lei Cao, J. Phys.: Condens. Matter **5**, L685 (1993).
[2] J.-L. Wang, R.-W. Zhao, N. Tang, W.-Z. Li, H. Gao, and F.-M. Yang, J. Appl. Phys. **76**, 6740 (1994).
[3] Bao-Gen Shen, Fang-Wei Wang, Lin-Shu Kong, Lei Cao, and Hui-Qun Guo, J. Magn. Magn. Mater. **127**, L267 (1993).
[4] Bao-Gen Shen, Fang-Wei Wang, Lin-Shu Kong, and Lei Cao, Appl. Phys. Lett. **63**, 2288 (1993).
[5] Lin-Shu Kong, Bao-Gen Shen, Fang-Wei Wang, Lei Cao, Hui-Qun Guo, and Tai-Shan Ning, J. Appl. Phys. **75**, 6250 (1994).
[6] Bao-Gen Shen, Fang-Wei Wang, Lin-Shu Kong, Lei Cao, Bo Zhang, and Jian-Gao Zhao, J. Appl. Phys. **75**, 6259 (1994).
[7] Bo-Ping Hu, Hong-Shuo Li, Hong Sun, and J. M. D. Coey, J. Phys.: Condens. Matter **3**, 3983 (1991).
[8] W. Steiner and R. Haferl, Phys. Status Solidi A **42**, 739 (1977).
[9] Q. W. Yan, Q. W. Yan, P. L. Zhang, B. G. Shen, F. W. Lang, L. S. Kong, C. Gou, D. F. Chen, and Y. F. Cheng, J. Phys.: Condens. Mater. **6**, 3567 (1994).
[10] Z. Hu, W. B. Yelon, S. Mishra, Gary J. Long, O. A. Pringle, D. P. Middleton, K. H. J. Buschow, and F. Grandjean, J. Appl. Phys. **76**, 443 (1994).
[11] Z. Hu, W. B. Yelon, W. J. James, and G. K. Marasinghe, "Site Affinity of Substituents in $Nd_2Fe_{17-x}T_x$ (T=Cu, Zr, Nb, Ti, V) Alloys," these proceedings, paper FF-01.
[12] M. Morariu and M. S. Rogalski, Phys. Status Solidi A **141**, 223 (1994).
[13] J. M. Cadogan, Hong-Shuo Li, A. Margarian, and J. B. Dunlop, Mater. Lett. **18**, 39 (1993).
[14] Hong-Shuo Li, Suharyana, J. M. Cadogan, Bo-Ping Hu, Bao-Gen Shen, Fang-Wei Wang, and Wen-Shan Zhan, IEEE Trans. Mag. **31**, 3716 (1995).
[15] G. K. Marasinghe, S. Mishra, O. A. Pringle, G. J. Long, Z. Hu, W. B. Yelon, F. Grandjean, D. P. Middleton, and K. H. J. Buschow, J. Appl. Phys. **76**, 6133 (1994).
[16] W. Y. Ching and Ming-Zhu Huang, "Band Theoretical Investigation of Curie Temperatures of Modified $R_2Fe_{17}$-Based Intermetallic Compounds," these proceedings, paper AE-07.
[17] R. F. Sabirianov and S. S. Jaswal, "Theory of Magnetism in $Sm_2Fe_{17-x}A_x$ (A=Al, Ga, Si)," these proceedings, paper FF-02.
[18] Hong-Shuo Li and J. M. D. Coey, in *Handbook of Magnetic Materials,* edited by K. H. J. Buschow (Elsevier, Amsterdam, 1991), Vol. 6, Chap. I, p. 1.
[19] Q.-N. Qi, H. Sun, R. Skomski, and J. M. D. Coey, Phys. Rev. B **45**, 12278 (1992).

# The low-temperature rate of electron capture beta decay in magnetic materials

L. M. Folan, V. I. Tsifrinovich, and V. A. Sheverev
*Department of Applied Mathematics and Physics, Polytechnic University, 6 Metrotech Center, Brooklyn, New York 11201*

Electron capture $\beta$-decay in $^{54}Mn^{2+}$ ions in solids is analyzed. It is shown that the decay rate of $^{54}Mn^{2+}$ should decrease significantly at low temperatures, approaching a limit of 35% of its room temperature value. It is also shown that the decay rate at low temperatures can be manipulated using resonant electromagnetic fields and the rate can be modulated by a factor of four. Extension to other species is suggested and potential applications are described. © *1996 American Institute of Physics.* [S0021-8979(96)74708-2]

It was pointed out recently that the rate of electron capture beta decay of paramagnetic atoms and ions, confined in atom and ion traps, can be effectively controlled when their temperature is comparable to the hyperfine splitting of the ground state.[1,2] This provides opportunities to create modulated gamma ray and neutrino sources and for the development of new probes of both nuclear decay and hyperfine transitions. In this paper we show that the possibility exists to observe similar phenomenon for dilute magnetic impurities in solids, in the presence of an external magnetic field. The control of a nuclear decay in solids has many more potential applications than trapped atoms or ions because of the large density of radioactive nuclei achievable in solids and the ability to exploit long-lived isotopes.

As a simple example, for both theoretical analysis and experimental verification, we will consider divalent $^{54}Mn$ ions in a diamagnetic host. We will show that the decay rate of $^{54}Mn^{2+}$ depends significantly on the populations of the hyperfine levels of the system and consequently the decay rate can be manipulated using temperature or resonant electromagnetic fields. $^{54}Mn$ has spin $I=3$ and magnetic moment $\mu=+3.28$[3,4] The disintegration scheme is extremely simple, $^{54}Mn$ decays by electron capture to the first excited state of the stable isotope $^{54}Cr$:

$$^{54}_{25}\mathrm{Mn}+e^{-}\rightarrow{}^{54}_{24}\mathrm{Cr}^{*}+\nu, \tag{1}$$

where $\nu$ denotes a neutrino, and no other decay branches have been detected.[5] The daughter nuclear state has spin $I=2$ and the same (positive) parity as the parent. Such a transition is caused by the Gamow–Teller interaction, which changes the nuclear spin by one unit but preserves the parity of the nucleus.[6,7]

In divalent manganese ions the $3d$-electron shell is half filled with electrons. The ground state has electronic spin $S=5/2$ and no net orbital angular momentum. The hyperfine fields at the nuclei of these ions have been extensively studied.[8] The fields are caused mainly by exchange polarization of the internal $s$-shells. In particular, according to spin-polarized Hartree–Fock calculations,[9] the $1s$-shell gives a contribution of $-3$ T, the $2s$-shell gives $-141$ T and the $3s$-shell yields $+74$ T. The resultant field of $-70$ T is close to the value $-65$ T derived from the analysis of experimental data.[10] The negative sign means that the hyperfine field is oriented opposite to the electronic magnetic moment.

Consider a sample of divalent manganese ions in a diamagnetic solid and assume the $^{54}Mn^{2+}$ ions are very dilute, so that dipolar and exchange interactions between them can be ignored. In the presence of an external magnetic field **H**, the electronic magnetic moment in the ground Zeeman state is oriented along **H**. Because the electron gyromagnetic ratio is negative, the electronic spin direction is opposite **H**. The first (lowest) hyperfine level of the ground state has the nuclear magnetic moment $\boldsymbol{\mu}$ oriented in the direction of the hyperfine field $\mathbf{H_n}$, i.e., opposite **H** (we assume $H<H_n$). Because the $^{54}Mn$ gyromagnetic ratio is positive, the nuclear spin has the same direction as $\boldsymbol{\mu}$.

Let the $+z$-axis be oriented in the direction of the external field **H**. Then the $z$-projection of the total angular momentum of the system $F_z$ is a conserved quantity. There are seven hyperfine levels in the ground Zeeman state of the $^{54}Mn^{2+}$ ion, having $F_z$ values from $-11/2$ to $+1/2$. The first hyperfine level $F_z=-11/2$ corresponds to the state

$$|S_z,I_z\rangle=|-5/2,-3\rangle. \tag{2}$$

The second level $F_z=-9/2$ is approximately $|-5/2,-2\rangle$ (we assume, as usual, that the Zeeman splitting for the electronic system is large compared to the hyperfine splitting, and therefore the admixture of the state $|-3/2,-3\rangle$ with the same value $F_z$ is small). The remaining levels follow appropriately.

Following a nuclear decay, one has a $^{54}Cr$ nucleus with spin $I'=2$ (primed quantities refer to final states), a neutrino with spin 1/2 and an electronic system with total spin $S'=2$ or $S=3'$, corresponding to the capture of an $s$-electron with spin parallel or antiparallel to the electronic spin of the parent ion. The lowest hyperfine level of the daughter system has a $z$-projection of the total angular momentum $F'_z = -11/2$. This corresponds to the state

$$|S'_zI'_z\nu'_z\rangle=|-3,-2,-1/2\rangle, \tag{3}$$

where $\nu'_z$ denotes the $z$-projection of neutrino spin. The next value, $F'_z=-9/2$, corresponds to three states, which can be written approximately as

$$|-3,-2,+1/2\rangle,|-3,-1,-1/2\rangle \text{ and } |-2,-2,-1/2\rangle. \tag{4}$$

We neglect "shake-up" processes in the electronic system and in particular, we ignore transitions which involve a change of spin state for the $3d$-electrons.

 0021-8979/96/79(8)/5716/2/$10.00 © 1996 American Institute of Physics

It is easy to show that any of the values $F_z' = -7/2, -5/2, -3/2$ corresponds to four possible final states, $F_z' = -1/2$ to three and $F_z' = +1/2$ to only one final state. The number of decay channels $N_i$ for the $i$th hyperfine level of the initial system is equal to the number of final states with $F_z' = F_z$. This is because the $z$-projection of the total angular momentum is conserved during an electron capture decay. Therefore, the first hyperfine level of the initial system has one channel for decay, the second level has three channels, the third has four channels and so on.

One can intuitively understand this result by taking into consideration the four possibilities encountered in an electron capture decay:

(1) Annihilation of an electron with spin "up" and emission of a neutrino with spin "down"—the spin projection of the nucleus $I_z$ must increase by one unit to conserve $F_z$;

(2) Annihilation of an electron with spin "down" and emission of a neutrino with spin "up"— the value of $I_z$ must decrease by one unit to conserve $F_z$;

(3) and (4) Absorption and emission of leptons with the same spin ("up" or "down") with no change in $I_z$.

If the initial state of a $^{54}Mn^{2+}$ system corresponds to the first hyperfine level with $I_z = -3$, and the daughter nucleus has spin $I' = 2$, the value $I_z$ must increase by one unit. Thus in the decay only the first possibility described above is allowed. If the initial state corresponds to the second hyperfine level $I_z = -2$, the second possibility (decrease of $I_z$ by one unit) is forbidden but the other three possibilities are allowed. For the initial state $I_z = -1$ all the possibilities are allowed and similar considerations apply to the other levels.

Assuming, for simplicity, equal decay probabilities for all the channels, we obtain the ratio of decay probabilities for the seven hyperfine levels as 1:3:4:4:4:3:1. The temperature dependence of the decay rate is then given for the case of $^{54}Mn^{2+}$ by

$$W/W_\infty = (7/20)\left[\sum_{i=1}^{7} N_i \exp\left(\frac{-E_i}{kT}\right)\right] \Big/ \left[\sum \exp\left(\frac{-E_i}{kT}\right)\right], \tag{5}$$

where $W_\infty$ is the decay rate for $T \to \infty$ (i.e., $T \gg E_i/k$) and $E_i$ is the energy of the $i$th level

$$E_i = \Delta(i-1), \Delta = (\mu/I)(H_n - H). \tag{6}$$

Putting $H = 5$ T, $H_n = 65$ T for our example, one obtains $\Delta/k \approx 24$ mK. The temperature dependence of $W/W_\infty$ is plotted for this value of $\Delta/k$ in Fig. 1. One can see that the decay rate decreases with temperature, approaching its minimum value $W_{\min} = 0.35 W_\infty$ when the temperature approaches zero. For $T \ll \Delta/k$ one can transfer the initial system to the second and third hyperfine levels using nuclear magnetic resonance techniques. As a result, the decay rate can be increased by a factor of four, to its maximum value $W_{\max} = 1.4 W_\infty$.

In summary, we estimated the decay rate of $^{54}Mn$ nuclei in divalent Mn ions for magnetically dilute solids in an external magnetic field. It was shown that at temperatures comparable to the hyperfine splitting of the ground state, the electron capture decay rate may be controlled effectively with temperature and resonant electromagnetic fields. According to our estimates, the electron capture rate of $^{54}Mn$ can be decreased to 0.35 times and increased to 1.4 times its high temperature value of 0.81/yr. Techniques of microwave and optical pumping could be used to align the spins and produce significant dynamic nuclear polarization.

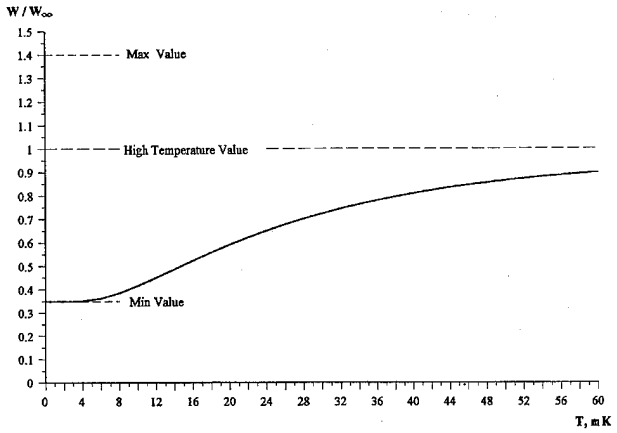



FIG. 1. The temperature dependence of the electron capture decay rate of $^{54}Mn^{2+}$ assuming $\Delta/k = 24$ mK.

Similar considerations are valid for many other isotopes which decay by electron capture, i.e., their decay rates in paramagnetic ions depend significantly on the populations of the hyperfine levels and can consequently be controlled. We also suspect that the same effect could be observed in magnetically ordered media in spite of large exchange interaction between the ions. Potential applications of phenomenon considered here for solids are very promising. These include artificially induced changes of decay rate for transportation and utilization of radioactive isotopes, modulated long-lived sources of gamma rays and neutrinos, and new methods for detection of nuclear magnetic resonance, among others. The authors are delighted to acknowledge the assistance of Robert Lee, a YES program summer researcher.

[1] L. M. Folan and V. I. Tsifrinovich, Phys. Rev. Lett. **74**, 499 (1995).
[2] L. M. Folan, V. I. Tsifrinovich, and V. A. Sheverev, Trans. Am. Nucl. Soc. **72**, 103 (1995).
[3] *Table of Isotopes*, edited by C. M. Lederer and V. S. Shirley (Wiley, New York, 1978).
[4] N. E. Holden, in *CRC Handbook of Chemistry and Physics*, 75th ed. edited by D. R. Lide (CRC, Boca Raton, 1994).
[5] M. T. F. Dacruz, Y. Chan, A. Garcia, M. M. Hindi, G. Kenchian, R. M. Larimer, K. T. Lesko, E. B. Norman, R. G. Stokstad, F. E. Wietfeldt, and I. Zlimen, Phys. Rev. C **48**, 3110 (1993).
[6] C. S. Wu and S. A. Moszkowski, *Beta Decay* (Wiley, New York, 1966).
[7] K. Grotz and H. V. Klapdor, *The Weak Interaction in Nuclear, Particle and Astrophysics* (Adam Hilger, Bristol, 1990).
[8] A. J. Freeman and R. E. Watson, in *Magnetism*, edited by G. T. Rado and H. Suhl (Academic, New York, 1965), Vol. IIA.
[9] R. E. Watson and A. J. Freeman, Phys. Rev. **123**, 2027 (1961).
[10] A. Abragam, J. Horowitz, and M. H. L. Pryce, Proc. Roy. Soc. A **230**, 169 (1955).

# Bragg diffraction of laser light by magnetostatic forward volume waves in a layered yttrium–iron–garnet film geometry

Liang-Ping Peng, J. P. Parekh, and H. S. Tuan
*Electrical Engineering Department, State University of New York at Stony Brook, Stony Brook, New York 11794*

The present article reports a theoretical study of Bragg diffraction of laser light by magnetostatic forward volume waves (MSFVWs) in a double-yttrium–iron–garnet(YIG)-film-layered structure. The layering provides a means of achieving a significant enhancement in bandwidth for nondispersive MSFVW propagation, leading in turn to a significant enhancement in bandwidth for magneto-optic (MO) coupling. Numerical computations comparing bandwidth for MO coupling between a single-YIG-film geometry and a double-YIG-film geometry are presented. © *1996 American Institute of Physics.* [S0021-8979(96)74808-1]

## INTRODUCTION

Interest in Bragg diffraction of laser light by magnetostatic waves in epitaxial yttrium–iron–garnet (YIG) films arises from the potential for large time-bandwidth and tunable optical signal processing at microwave frequencies in the range from about 2 GHz to about 20 GHz.[1–6] The bandwidth for magneto-optic (MO) coupling is limited primarily by the bandwidth of magnetostatic wave (MSW) propagation. The use of an *inhomogeneous* bias field as a means of enhancing the bandwidth for MSW propagation, and thereby the bandwidth for magneto-optic (MO) coupling, has previously been reported[6] for the case of magnetostatic forward volume waves (MSFVWs) in a single YIG-film geometry. The present article reports an alternative approach also employing MSFVWs for enhancing the bandwidth for MO coupling through enhancement of bandwidth for nondispersive MSFVW propagation, i.e., the use of a layered YIG-film in conjunction with a separated ground plane. The computations presented here show a significant improvement in bandwidth for MO coupling arising from the use of a layered YIG-film geometry.

## THEORY AND NUMERICAL RESULTS

A double-YIG-film-layered structure supporting MSFVWs is treated in which the top YIG-film layer (labeled YIG1) is Bi-doped and the lower layer (labeled YIG2) is pure YIG as shown in Fig. 1. The MO coupling effect is accentuated in the YIG1 region by choosing it to be Bi-doped. The dc bias magnetic field $\mathbf{H}_0$ is applied normal to the YIG films so that the MSW wave-type supported by the structure is MSFVW. In Fig. 1, the ground plane placed above the YIG1 Bi-doped film is omitted for the sake of simplicity. An *orthogonal* MO coupling geometry is treated, with the incident light wave essentially trapped within the YIG1 film propagating orthogonal to the MSFVW. The TM→TE mode coupling treated here assumes the lowest optical waveguide modes of the structure.

The MO coupling efficiency $\eta$ is found to assume the standard expression

$$\eta = \sin^2(K_{\pm} L), \tag{1}$$

where $K_{\pm} = k_1 \pm k_2$ is the MO coupling coefficient representing the Stokes and anti-Stokes conditions, respectively. The quantities $k_1$ and $k_2$ depend upon the magnitudes of the components of the rf magnetization $\mathbf{m}$ and their distribution across the YIG1 film. The expressions for $k_1$ and $k_2$ differentiate the present geometry from previous studies since the field distributions in the YIG1 film vary with geometry.

Sample computations of the frequency-variation of the MO coupling efficiency $\eta$ are presented in Figs. 2–5. In each of these figures, two curves are plotted, one for the present double-YIG-film-layered geometry and the other for a single-YIG-film geometry. The computations in the layered-YIG-film case are for YIG1 film thickness $d_1 = 9$ $\mu$m, YIG2 film thickness $d_2 = 60$ $\mu$m, saturation magnetizations of the two films $\mu_0 M_{01} = 1{,}750$ G and $\mu_0 M_{02} = 1{,}878$ G, ground plane separation from YIG1 film $h = 625$ $\mu$m, aperture of MSFVW microstrip transducer $L = 0.88$ cm, and applied bias field $\mu_0 H_0 = 3{,}678$ G. These parameter values are also the ones used in the single-YIG-film geometry computations except that in the latter geometry $d_2$ is set to zero. The computations also employ the same value $\mu_0 m_x = 68$ G for the $x$-component of rf magnetization in the YIG1 film for both the layered-film and single-film geometries, thereby maintaining the same rf power in the YIG1 film for the two geometries.

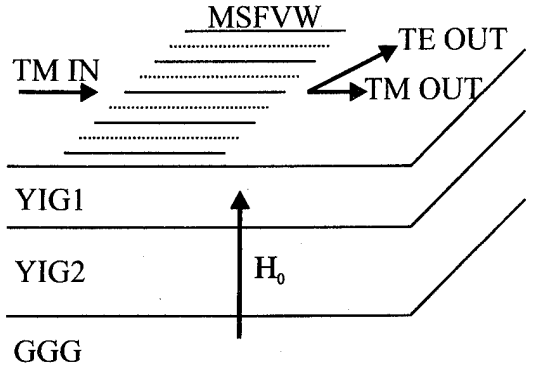



FIG. 1. Double-YIG-film geometry showing the directions of MSFWV propagation and of incident and scattered laser waveguide modes.

 0021-8979/96/79(8)/5718/3/$10.00 © 1996 American Institute of Physics

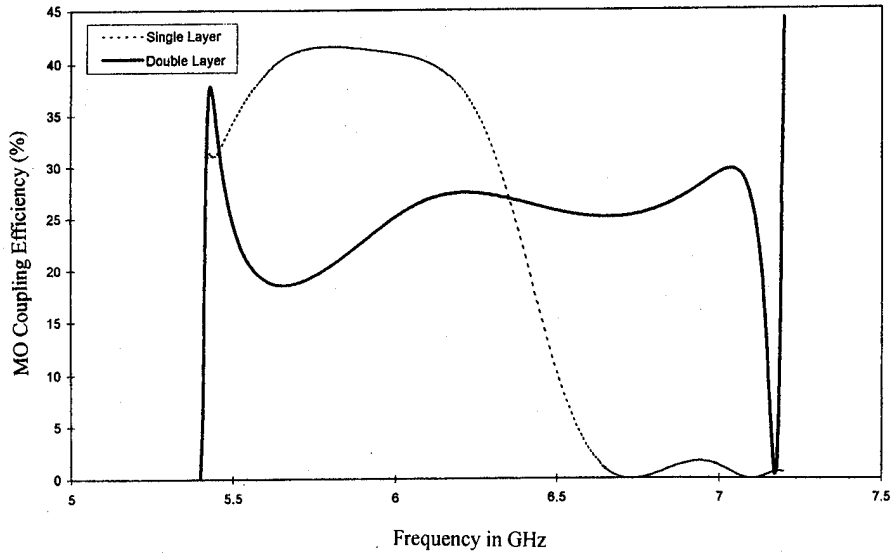



FIG. 2. Computed frequency variation of MO coupling efficiency for the case of MSFVW transducer width of 25 $\mu$m.

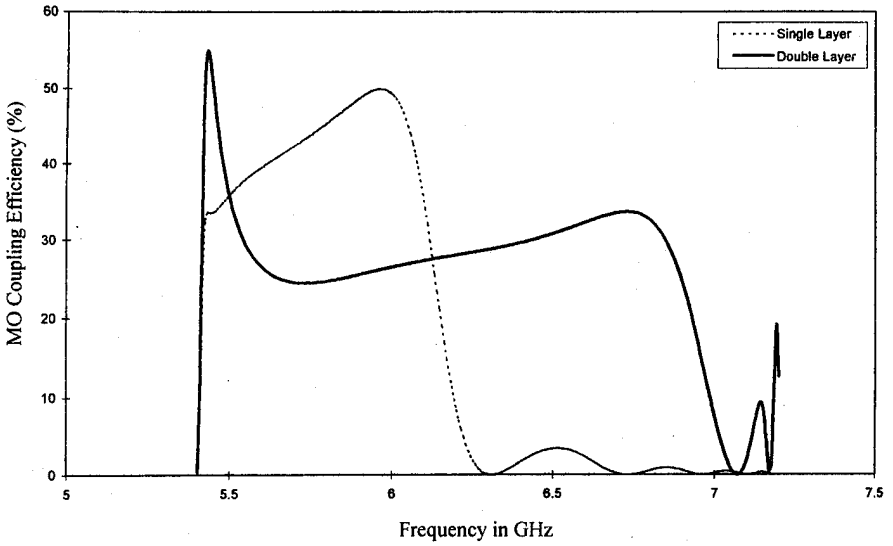



FIG. 3. Computed frequency variation of MO coupling efficiency for the case of MSFVW transducer width of 50 $\mu$m.

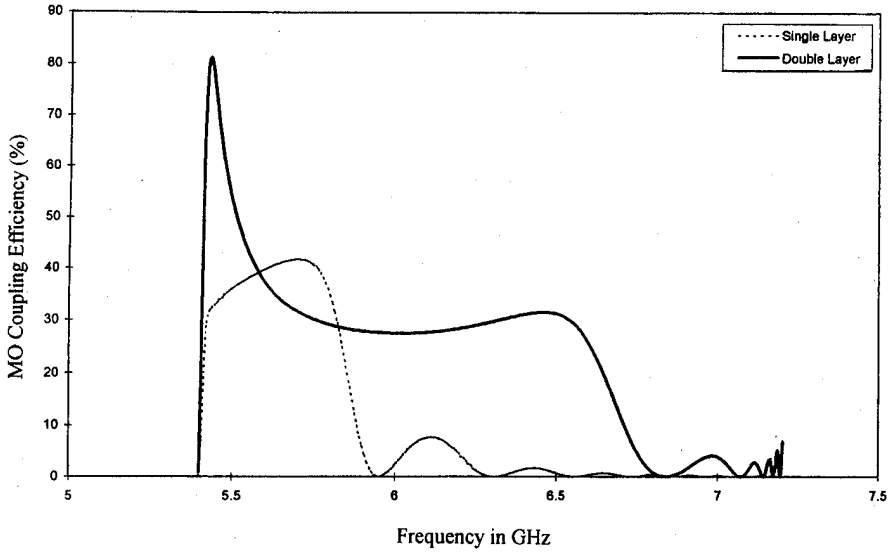



FIG. 4. Computed frequency variation of MO coupling efficiency for the case of MSFVW transducer width of 100 $\mu$m.

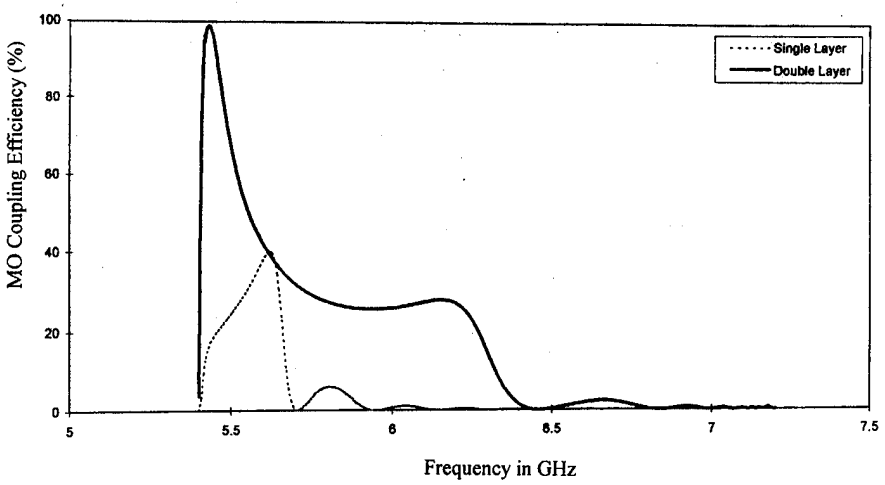



FIG. 5. Computed frequency variation of MO coupling efficiency for the case of MSFVW transducer width of 200 $\mu$m.

In going from Fig. 2 to Fig. 5 sequentially, the width of the microstrip transducer is incremented in the following order: $w=25$ $\mu$m (Fig. 2), $w=50$ $\mu$m (Fig. 3), $w=100$ $\mu$m (Fig. 4) and $w=200$ $\mu$m (Fig. 5). The computations presented in Figs. 2–5 contain two salient features:

(i) For a given value of microstrip transducer width $w$, a significant improvement in bandwidth for MO coupling takes place with the use of a layered YIG-film structure over a single YIG-film structure.

(ii) The bandwidth for MO coupling goes down monotonically with increase in the microstrip transducer width $w$ for both the single-film and layered-film geometries. This effect is, of course, consistent with the *antenna array* effect associated with the *extended* nature of a microstrip transducer[7] relative to a line-current source.

## CONCLUSION

The present article reports theoretical computations demonstrating that a layered-YIG-film MSFVW geometry provides a method of achieving a *significant* enhancement in the bandwidth for MO coupling over a single-YIG-film geometry. One advantage of the present method over the use of an inhomogeneous bias field is the practical difficulty implicit in the latter method of implementing an accurate inhomogeneous bias-field profile.

[1] A. D. Fischer, Circuits, Systems and Signal Processing **4** (1985) [Special issue on Magnetostatic Waves and Applications to Signal Processing].
[2] D. Young and C. S. Tsai, Appl. Phys. Lett. **53**, 1696 (1988).
[3] A. D. Fischer, S. Gaynor, and J. N. Lee, Proceedings of 1983 IEEE Ultrasonics Symposium, pp. 226–231.
[4] C. T. Wey, Ph.D. dissertation, State University of New York at Stony Brook, 1986.
[5] S. H. Talisa, IEEE Trans. Magn. **24**, 2811 (1988).
[6] C. S. Tsai and D. Young, IEEE Trans. MTT **38**, 560 (1990).
[7] J. P. Parekh, J. Appl. Phys. **50**, 2452 (1979).

# Modulation of magnetostatic surface wave in garnet film by optical pulses

Y. K. Fetisov and A. V. Makovkin
*Moscow Institute of Radioengineering, Electronics and Automation, Vernadskogo 78*
*Moscow 117454, Russia*

Microwave power modulation in a magnetostatic surface wave (MSSW) transmission line containing an yttrium-iron-garnet film of thickness 20 $\mu$m in the 3–4 GHz frequency band with optical pulses of duration 2 ms and energy of 20 $\mu$J has been investigated. At microwave powers less than 1 mW a slow thermal modulation with magnitude up to 4% and characteristic time of 0.5 ms took place. At power levels 1–100 mW a fast modulation of the transmitted signal with magnitude up to 10% and characteristic time of about 1 $\mu$s caused by nonlinear properties of MSSW was observed. © *1996 American Institute of Physics.* [S0021-8979(96)74908-0]

## INTRODUCTION

Magnetostatic spin waves (MSWs) propagating in microwave region in magnetically biased planar magnetic structures containing epitaxial yttrium-iron-garnet (YIG) films are widely used in microwave signal processing devices.[1] Characteristics of the waves such as wave length, velocity of propagation, efficiency of excitation, and propagation losses depend strongly on magnetic and electrical parameters of the structure. It is of great interest to use these dependences to design optically controlled microwave devices.

The basic mechanism by which light influence on MSW characteristics is a heating of the YIG film due to absorption of light energy. The heating results in a decrease in the YIG magnetization and gives rise to a change in MSW dispersion characteristics. The irradiation of garnet structure with short high-energy laser pulses gives rise to considerable heating of the film, that may be used to control the wave length, velocity of propagation, and MSW frequency as well.[2]

This paper presents results of experimental investigation of modulation of magnetostatic surface waves (MSSW) propagating in a free YIG film by low energy optical pulses. The measurements have been carried out for linear as well as for nonlinear regimes of MSSW propagation.

## MSSW TRANSMISSION LINE

A schematic of MSSW transmission line used in the experiments is shown in Fig. 1. The YIG film of thickness $d=20$ $\mu$m, saturation magnetization $4\pi M=1750$ G, and uniform FMR line width $\Delta H\simeq 0.6$ Oe was grown by the LPE method on a gadolinium-gallium-garnet (GGG) substrate of thickness 0.5 mm and dimensions of 2 mm×20 mm. Two microstrip transducers of width 50 $\mu$m and length 2.5 mm evaporated on two alumina substrates were used to excite and to receive MSSW. The alumina substrates were placed in close contact with the film surface so that the distance between the transducers was equal to 5 mm. The structure was placed in a uniform dc magnetic field of $H=630$ Oe applied tangentially to the film plane and parallely to the transducers.

The upper surface of the YIG film was irradiated with optical pulses of wave length $\lambda=0.44$ $\mu$m, duration 2 ms, and rise time of 0.1 ms from a He-Cd laser with output power up to $I=10$ mW. A lens allowed focusing of the optical beam to a circle of 0.1 mm diameter at any point of the film.

A microwave signal $P_{in}(f)$ of frequency $f=3$–4 GHz and power up to 1 W was applied to the input transducer. The signal excited a MSSW of the same frequency $f$ with a wave number $k$, which propagated in the YIG film toward the output transducer. An output microwave signal $P_{out}(f)$ was registered for different optical powers $I$ and different positions of the beam on the film surface.

Figure 2 shows the measured dependence of the output microwave signal power $P_{out}(f)$ versus the wave frequency $f$ (frequency response of transmission line) at low power of the input microwave signal $P_{in}\lesssim 1$ mW. One can see, that MSSWs propagate within a frequency band between the lower $f_L=3555$ MHz and the upper $f_U\sim 4000$ MHz boundary frequencies. At low power the minimal insertion loss was equal to $L(f) = 10\ \lg\{P_{out}(f)/P_{in}(f)\} = -6.8$ dB.

For MSSW propagating in a linear regime in an infinite ferrite film the boundary frequencies can be found using the well-known dispersion equation:[3]

$$f_L(k=0)=\gamma\sqrt{H(H+4\pi M)}$$

and

$$f_U(k=\infty)=\gamma(H+2\pi M),$$

where $\gamma=2.8$ MHz/Oe is the gyromagnetic ratio. Calculated and measured values for $f_L$ will coincide if an effective magnetic field in the film is taken to be equal to $H=667$ Oe. The insignificant difference between calculated and measured fields may be due to anisotropy of YIG and demagnetizing effects. The ripple in the frequency response with a period of ~40–10 MHz is conditioned by an interference between MSSW and a direct electromagnetic induction. The ripple with a period of ~4–5 MHz in a narrow lower frequency region (see inset in Fig. 2) may be due to a change in the wave dispersion in this region or due to interference between a main mode and higher-order transverse MSSW modes propagating in the structure of finite width.

At input signal powers $P_{in}\simeq 1$–100 mW an increase in the transmission loss near the upper edge of the MSSW band (curve 2 in Fig. 2) as well as a shift of the lower boundary frequency of up to $\Delta f_L\simeq 1$ MHz toward smaller frequencies were observed. Increase in the loss was due to nonlinear three-wave decay processes allowed for MSSW only in the frequency range $f\geq 2\gamma H$ ($f\geq 3.73$ GHz for $H=667$ Oe).[4] The

 0021-8979/96/79(8)/5721/3/$10.00 © 1996 American Institute of Physics 

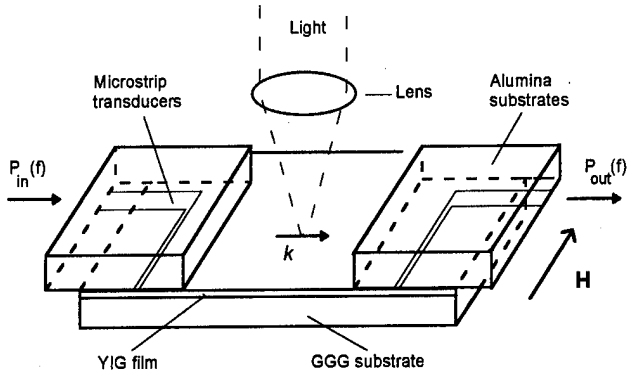



FIG. 1. Experimental set-up.

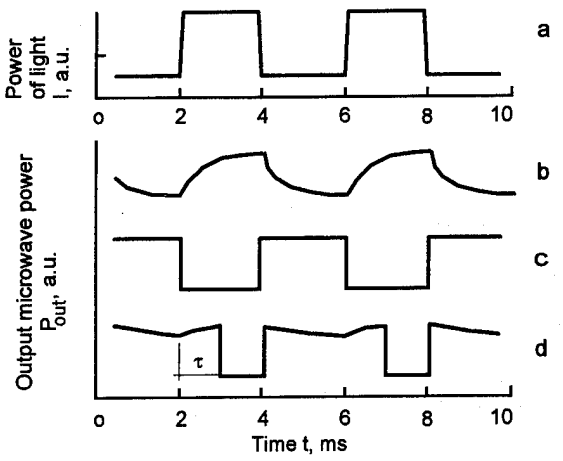



FIG. 3. Time-dependences for optical MSSW modulation in YIG film: (a) envelope of optical pulses; (b) envelope of output signal for "slow" modulation, $f$=3624 MHz; (c) and (d) envelope of output signals for "fast" modulation, $f$=3563 MHz.

shift of the lower boundary frequency was evidenced of a decrease in the YIG film magnetization of about $\Delta(4\pi M) \simeq 0.7$ G at high powers of input microwave signal.

## EXPERIMENTAL RESULTS AND DISCUSSION

Two kinds of MSSW modulation have been observed by irradiating the YIG structure with optical pulses.

At low levels of input microwave power $P_{in} \leqslant 1$ mW, when MSSW frequency was positioned within the regions $A$ or $B$ on the frequency response (see Fig. 2), a "slow" amplitude modulation of MSSW signal with the magnitude $\eta=(\Delta P_{out}/P_{out})100\%$ of up to 4% and characteristic relaxation time about of $\tau_1 \simeq 0.5$ ms was observed [see Fig. 3(b)]. The magnitude of modulation was increased linearly with the increase in the optical power (see Fig. 4) and depended critically on the light beam position on the film surface.

This type of MSSW modulation was conditioned by a local heating of the garnet film due to absorption of optical energy. The heating resulted in a local decrease in the YIG magnetization $\Delta(4\pi M)$ and provided a downward shift of the whole frequency response, which gave rise to an increase or decrease in the output microwave signal power. Numerical calculations showed, that under the influence of optical pulses with energy of $W=20$ $\mu$J and duration of $\tau=2$ ms a YIG film area of ~0.1 mm diameter was heated by $\Delta T \approx 10$ K and then cooled with a characteristic time of about $\tau_1 \approx 0.5$ ms. Such variation in the temperature corresponded to a local changing in the YIG film magnetization by $\Delta(4\pi M) \approx 30$ G.

The real spatial distribution of MSSW high-frequency magnetization $m(r,f)$ over the plane of a garnet structure of finite dimensions is essentially nonuniform. So, to provide maximum efficiency of thermal MSSW modulation, a laser beam should be focused on the film regions where the magnetization $m(r,f)$ is a maximum. It seems, this approach may be used as an indirect method to measure a spacial distribution of MSW fields in planar ferrite structures.[5]

For the first time, at high levels of microwave power $P_{in}>1$ mW a new "fast" modulation of MSSW amplitude has been observed in a narrow frequency region (~10 MHz) just above the lower boundary frequency $f_L$ of the transmis-

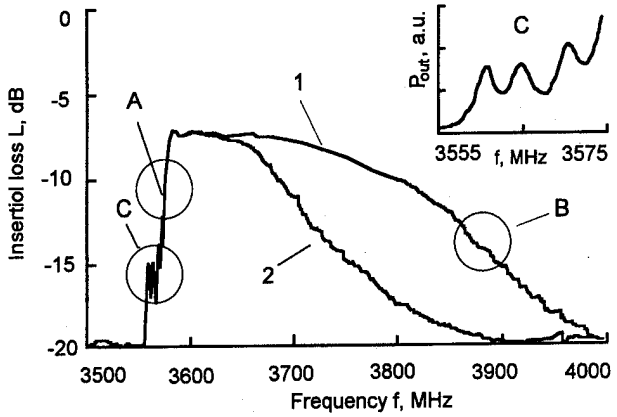



FIG. 2. Measured frequency responses of MSSW transmission line at different levels of input microwave power $P_{in}$, mW: 1–0.5, 2–500.

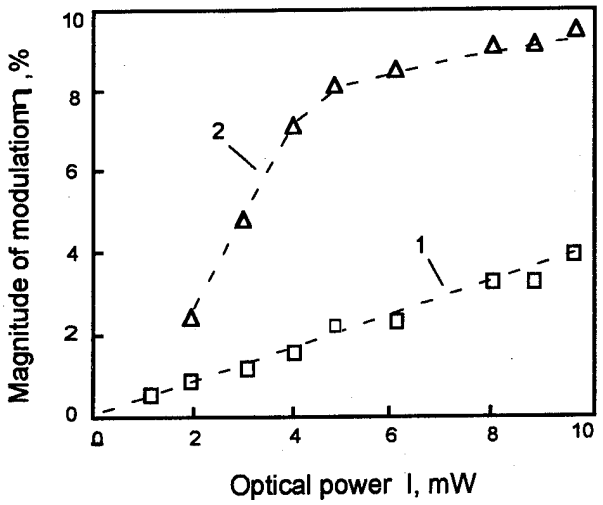



FIG. 4. Magnitude of MSSW modulation $\eta$ as a function of power $I$ of optical pulses: 1: thermal modulation; 2: "fast" modulation.

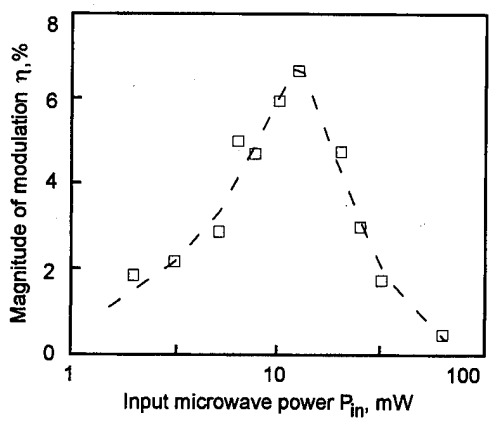



FIG. 5. Magnitude of "fast" MSSW modulation $\eta$ as a function of input microwave power $P_{in}$.

sion band (region $C$ in Fig. 2). Characteristic rise time and fall time for such a modulation were equal to $\tau_2 \simeq 1$ $\mu$s. This was approximately $10^2$ times less than the rise time for optical pulses [Fig. 3(c)]. For certain positions of optical beam on the film surface the microwave pulse was delayed with respect to the optical pulse by time of about 0.1–2 ms [see Fig. 3(d)].

Figure 4 shows a typical threshold-like dependence of magnitude of modulation $\eta$ versus the optical power $I$. The "fast" modulation was observed only for optical powers $I \geqslant 2$–3 mW. The magnitude of modulation was increased almost linearly with the increase in $I$ and was saturated at the maximum level of $\eta \approx 10\%$. Figure 5 shows a typical dependence of modulation magnitude $\eta$ versus input microwave power $P_{in}$, measured at maximum power and fixed position of optical beam on the film surface. The modulation appeared at microwave powers of about $P_{in} \simeq 1$ mW, its magnitude reached a maximum at $P_{in} \simeq 10$ mW, the modulation was completely vanished for microwave power $P_{in} > 100$ mW.

The results described led to the conclusion that "fast" modulation of output microwave power with optical pulses is conditioned by nonlinear properties of MSSW. The modulation was observed in the frequency region, where such nonlinear phenomena as auto-oscillations, formation of solitons, and self-channelizing of MSW can take place. As shown,[6] the Lighthill criterion

$$[\partial^2 f(k)/\partial k^2][\partial f(k)/\partial(|u|^2)] < 0,$$

(where $|u|^2$ is the dimensionless power of the wave) is not satisfied for MSSW in a free infinite film and the wave is stable with respect to longitudinal perturbations of amplitude. However, when the structure has a finite width and a metal screen is present, then near the lower boundary frequency $f_L$ (where $k \to 0$) the MSSW dispersion law is considerably modified and multimode propagation of MSSW takes place.[7] This can create conditions such that the Lighthill criterion is satisfied and a self-modulation of MSSW appears.[8]

Besides that, as it is seen from the inset of Fig. 2, that frequency response of MSSW line is well modulated in this region. Such a shape of transmission characteristic together with a high nonlinearity in the system can result in a bistability and arising of the self-pulsations in the transmitted microwave power is analogous with bistability in optical systems.[9] It seems, in both cases a heating of garnet film with optical pulses stimulated transitions in the system from one stable state to another resulting in a modulation of output microwave power. A small value of transition time $\tau_2$ was determined by the microwave characteristics of the garnet film, not by the velocity of the film heating. A theory describing stimulated transitions in bistable MSW lines and resonators is under development now.

## ACKNOWLEDGMENTS

The research was made possible in part by grant M6Q300 from the International Science Foundation and Russian Government.

[1] W. S. Ishak, Proc. IEEE **76**, 17 (1988).
[2] Y. K. Fetisov, I. G. Romanov, and V. B. Studenov, Electron. Lett. **31**, 1168 (1995).
[3] R. W. Damon and J. R. Eshbach, J. Phys. Chem. Solids **19**, 308 (1961).
[4] J. D. Adam, IEEE Trans. Magn. **MAG-16**, 1168 (1980).
[5] N. I. L'yashenko, M. Y. Hvastukhin, and S. V. Yakovlev, Sov. Tech. Phys. Lett. **17**, 90 (1991) (in Russian).
[6] A. K. Zvezdin and A. F. Popkov, Sov. Phys. JETP **57**, 350 (1983).
[7] T. W. O'keffe and R. W. Patterson, J. Appl. Phys. **49**, 4886 (1972).
[8] S. A. Nikitov, Su Jun, R. Marcelli, and P. De Gasperis, J. Magn. Magn. Mater. **145**, L6 (1995).
[9] H. M. Gibbs, *Optical Bistability: Controling Light with Light* (Academic, New York, 1985).

# Dipole-exchange spin wave spectra of exchange-coupled magnetic multilayers calculated by transfer matrix formalism

I. V. Rojdestvenski and M. G. Cottam
*Physics Department, University of Western Ontario, London, Ontario N6A 3K7, Canada*

A. N. Slavin
*Physics Department, Oakland University, Rochester, Michigan 48309*

We employ a transfer matrix formalism to study dipole-exchange spin waves in a perpendicularly magnetized multilayered structure consisting of identical magnetic layers alternated by nonmagnetic spacers, assuming both intralayer and interlayer exchange interactions. The interlayer exchange and the anisotropies at the magnetic layer boundaries are taken into account via linearized Hoffman boundary conditions. The bulk-mode bands for the case of infinite multilayers and the bulk and surface modes for semi-infinite multilayers are derived. Applications are made to recent ferromagnetic resonance data for Co/Pt multilayers. The extension of our theory to finite multilayers is discussed. © *1996 American Institute of Physics.* [S0021-8979(96)75008-9]

## I. INTRODUCTION

The spectra of microwave excitations in magnetic multilayers and superlattices provide valuable information about the structural and magnetic parameters of the sample. In particular, characteristic parameters of exchange coupling between magnetic layers can be deduced.[1–3] Typically, the spectra of magnetic excitations in multilayers have been studied experimentally by either ferromagnetic resonance (FMR) [wave number $k\sim 0$] or Brillouin light scattering (BLS) [$k\sim 10^5$ cm$^{-1}$]. It is important to have a theory that covers all the experimentally accessible wave numbers.

In previous related work[4,5] we developed an analytic theory of BLS in magnetic multilayers. The purpose of the present paper is to give a variant of this approach that applies to FMR. We take into account both dipole-dipole and exchange interactions within each magnetic layer. The interlayer exchange coupling through a nonmagnetic spacer is incorporated phenomenologically through linearized Hoffman boundary conditions.[1] Here we are not concerned with the mechanism of this coupling or its oscillations (see, e.g., Ref. 6). We assume that the phenomenological quantity $A_{12}$ characterizing the strength of interlayer exchange coupling depends exponentially on the spacer thickness $\ell$ as

$$A_{12}=A_{12}^0 \exp(-\ell/b), \tag{1}$$

where the interaction amplitude $A_{12}^0$ and characteristic length $b$ are the fitting parameters in our theory.

In contrast with existing theories of FMR spectra in magnetic multilayers[3] we do *not* assume uniformity of the variable magnetization across the thickness of a magnetic layer, but rather calculate this distribution for each value of a spacer thickness $\ell$ assuming that the interlayer exchange leads to a renormalization of interface pinning.[4] Also we do not introduce effective volume uniaxial anisotropies in the magnetic layer depending on interlayer exchange interaction, as was done in Ref. 3.

Comparing our theory with recent FMR experiments in Co/Pt multilayers,[2,3] we find that we can explain the behavior of the collective quasi-surface mode of the FMR as a function of the spacer thickness $\ell$ and we determine the characteristic parameters $A_{12}^0$ and $b$.

## II. TRANSFER MATRIX FORMALISM FOR A MULTILAYER

We use a traditional transfer matrix formalism (e.g., see Ref. 7 for a general review and Refs. 8 and 9 for specific applications to magnetic multilayers) to derive the spectrum of dipole-exchange spin waves in infinite and semi-infinite magnetic multilayers consisting of identical magnetic layers of the thickness $L$ separated by nonmagnetic spacers of thickness $\ell$. For waves propagating within any magnetic layer $j$ we write the wave variables (i.e., variable magnetizations in the case of spin waves) in the form:

$$n(\mathbf{r},z)=\exp(i\mathbf{k}\cdot\mathbf{r})[A_+^j f_+(z,q_z)+A_-^j f_-(z,q_z)], \tag{2}$$

where $\mathbf{r}$ and $\mathbf{k}$ denote the in-plane position vector and wave vector, respectively, while $z$ and $q_z$ are the coordinate and wave number in the perpendicular direction. Also $f_\pm$ are appropriate single-layer eigenfunctions representing waves propagating in the $\pm z$ directions. We define a vector representation for the transverse wave amplitudes in the form:

$$|A^j\rangle=\begin{bmatrix}A_+^j\\ A_-^j\end{bmatrix}, \tag{3}$$

Using the boundary conditions to account for the interaction of adjacent magnetic layers via the spacer, we obtain $|A^{j+1}\rangle=T|A^j\rangle$, where $T$ is a $2\times 2$ transfer matrix[7] of the system. On the other hand, the translational symmetry of an infinite superlattice yields Bloch's theorem, i.e., $|A^{j+1}\rangle=\exp(iQL_0)|A^j\rangle$, where $Q$ is the Bloch vector (or the wave vector of a collective excitation envelope in a multilayer) and $L_0=L+\ell$ is the periodicity length in our problem. Combining the above relationships we obtain an equation for $Q$ and $q_z$ in the form:

$$\cos(QL_0)=\frac{1}{2}\mathrm{Tr}\ (\mathbf{T}(q_z)), \tag{4}$$

 0021-8979/96/79(8)/5724/3/$10.00 © 1996 American Institute of Physics

The modes form continuous bands with $Q$ real. The boundaries correspond to putting $\cos(QL_0)=\pm 1$ in Eq. (4), yielding conditions satisfied by wave number $q_z$.

In the case of a semi-infinite multilayer there may also be surface-like solutions with imaginary $Q$ in addition to the bulk-like (real $Q$) modes. The presence of a surface yields the boundary condition at the top surface, having the general form of $C_+A_+ + C_-A_- = 0$, giving

$$C_-(T_{11} - \exp(-iQL_0)) - C_+T_{12} = 0. \tag{5}$$

The solution of Eqs. (4) and (5) yield the values of $q_z$ and $Q$ for the surface and bulk modes of a semi-infinite multilayer. If the structure is finite, the formalism can be extended to account for another boundary condition at the lower surface of the multilayer. This makes the bulk modes quantized and also modifies the surface mode frequencies.

We now assume that the normal spin wave (SW) modes in each layer are eigenfunctions of the intralayer exchange operator, i.e., $f_\pm(z,q_z)=\exp(\pm iq_z z)$ as in Ref. 10. This yields the dispersion relationship in the form:

$$\omega_{\mathbf{k}n} = \omega_H + \alpha\omega_M(\mathbf{k}^2 + q_z^2), \tag{6}$$

where $\omega_H = \gamma(H - 4\pi M_0)$, $\omega_M = \gamma(4\pi M_0)$, $\gamma$ is the gyromagnetic ratio, $\alpha = A/(2\pi M_0^2)$ is the exchange constant, $4\pi M_0$ is the saturation magnetization, and $H$ is the external bias magnetic field (directed perpendicular to the layers).

With surface anisotropy and interlayer exchange included and following the notations of Ref. 6, we may write the linearized Hoffman boundary conditions[1,4] in the form:

$$\left[-\frac{dm_{j+1}}{dz} + (d^U + \beta)m_{j+1}\right]_{\text{upper}} - [\beta m_j]_{\text{lower}} = 0;$$
$$\left[\frac{dm_j}{dz} + (d^L + \beta)m_j\right]_{\text{lower}} - [\beta m_{j+1}]_{\text{upper}} = 0 \tag{7}$$

for the bulk layers, and

$$\left[-\frac{dm_1}{dz} + d^{SU}m_1\right]_{\text{upper}} = 0; \quad \left[\frac{dm_N}{dz} + d^{SL}m_N\right]_{\text{lower}} = 0 \tag{8}$$

for the external surfaces of the multilayer. Here $m_j$ is the variable magnetization in layer $j$, $d^U$, and $d^L$ are the pinning parameters at the upper and lower surfaces of each magnetic layer, while $d^{SU}$ and $d^{SL}$ are the pinning parameters at the upper and at the lower external surfaces of the multilayer, respectively. Pinning parameters $d = K_S/A$, measured in $\text{cm}^{-1}$ units,[10] are determined by the ratio between the constant of surface anisotropy $K_s$ and the exchange constant $A$. Parameter $\beta = A_{12}/A$ is also measured in $\text{cm}^{-1}$ and characterizes exchange coupling between the magnetic layers.[4]

Equations (7) and (8) correspond to the SW modes in an exchange approximation, with the dipole-dipole interaction taken into account only in the lowest order. This approximation is adequate in two physical situations:

(1) *FMR and Long-wavelength SW.* In this case $\mathbf{k} \cong 0$; the dipole interaction is close to saturation and results only in an effective renormalization of the uniform Zeeman field by a demagnetization field (in $\omega_H$).

(2) *Short-wavelength exchange waves,* $\mathbf{k} \gg 1$ (normally, of order of magnitude $10^6$ $\text{cm}^{-1}$ and larger). In this case the dipolar contribution to the energy of the wave is small because of the long-range character of the weak dipole-dipole interaction.

Using the perturbation theory developed in Ref. 10 it is possible to obtain SW dispersion relations in magnetic multilayers for any values of $\mathbf{k}$. In particular, this was done in Ref. 5 for the interpretation of BLS experiments.

With the assumed form for $f_\pm(z,q_z)$ and denoting $d_{L,U} = d^{L,U} + \beta$, we get the following equations for $q_z$ and $Q$ in the case of a semi-infinite multilayer:

(1) *Bulk band boundaries* ($q_z$ and $Q$ real, $\cos(QL_0)=\pm 1$):

$$(d_L + d_U)\frac{\cos(q_z L)}{2\beta} + (q_z^2 + \beta^2 - q_L d_U)\frac{\sin(q_z L)}{2\beta q_z} = \pm 1 \tag{9}$$

(2) *Surface-type solutions* ($q_z = i\kappa$, $Q = iK$):

$$[\beta^2 + (\kappa - d_U)(\kappa + d_L)]\Big[\cosh(\kappa)[\beta^2 - (d^{SU} + d_U) \times (d_L - d^{SU})] + \frac{\sinh(\kappa)}{\kappa}[\beta^2 d^{SU} + (d^{SU} + d_U) \times (\kappa^2 - d_L d^{SU})]\Big] = 0 \tag{10}$$

$$\frac{\exp(-\kappa L)}{\beta(d^{SU} + \kappa)}[\beta^2 - (d^{SU} + d_U)(d_L + \kappa)] = -\exp(KL_0) \tag{11}$$

Now, solving Eqs. (10) and (11), we obtain the values of $K$ and $\kappa$ for a quasi-surface collective mode. Equation (10) holds in either of two cases:

(1) $\beta^2 + (\kappa - d_U)(\kappa + d_L) = 0$, which gives

$$\kappa_{1,2} = \frac{1}{2}[d_U - d_L \pm \sqrt{(d_U - d_L)^2 + 4(\beta^2 - d_U d_L)}], \tag{12}$$

(2)

$$\cosh(\kappa)[\beta^2 - (d^{SU} + d_U)(d_L - d^{SU})] + \frac{\sinh(\kappa)}{\kappa} \times [\beta^2 d^{SU} + (d^{SU} + d_U)(\kappa^2 - d_L d^{SU})] = 0. \tag{13}$$

Case (1) represents solutions independent of the value of the first layer surface anisotropy $d^{SU}$, while Case (2) accounts for it. The question of which solutions really exist in the system depends on the consistency condition for $K > 0$.

## III. COMPARISON WITH FMR EXPERIMENTS

The above formalism is now applied to interpret the FMR results obtained by Zhang *et al.*[3] for Co/Pt multilayers with different values of the spacer (Pt) thickness.

We assume that pinning conditions on both sides of each individual layer are the same, $d^U = d^L \equiv d$. In this case the dispersion relation at $\mathbf{k}=0$, corresponding to the solution of Eq. (12), reads:

$$\omega = \omega_H - \alpha\omega_M(d + \beta(\not{\ell}))d, \tag{14}$$

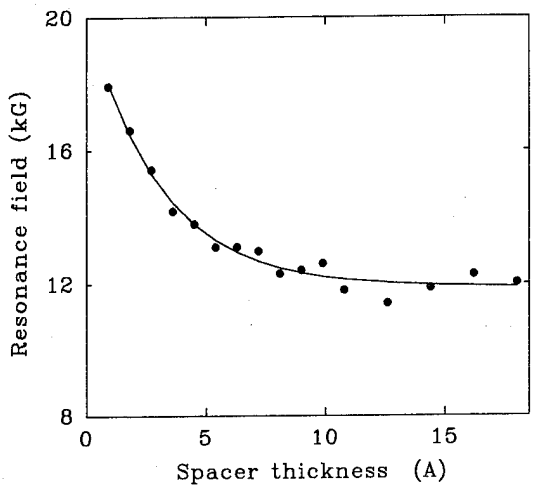



FIG. 1. FMR resonance field vs spacer thickness for a Co/Pt multilayer for a quasi-surface collective mode. Circles–experimental data [Ref. 3]; solid line–theory [Eq. (14)]. See text for the parameters.

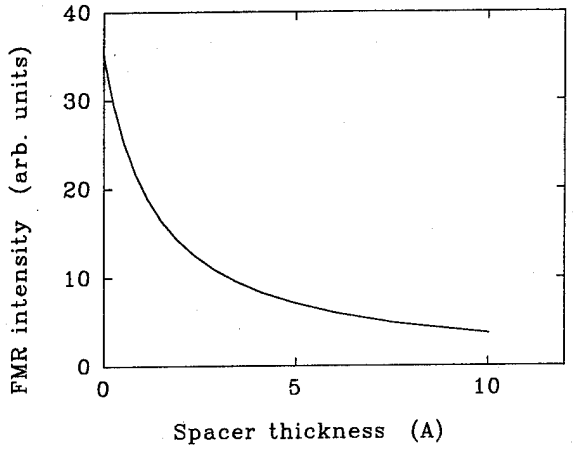



FIG. 2. Theoretical FMR response intensity vs spacer thickness for a Co/Pt multilayer. See text for the parameters.

where $\beta(\ell)=A_{12}(\ell)/A$ depends on the spacer thickness $\ell$ in accordance with Eq. (1).

Equation (14) describes correctly all the main features of the behavior of the quasi-surface collective FMR mode in a Co/Pt multilayer observed in Refs. 2 and 3. In particular, it accounts for the decrease of the resonance field with increasing spacer thickness, which was not explained by the theory of FMR presented in Ref. 3.

The results of fitting Eq. (14) to the experimental data[3] are shown in Fig. 1. We took $A=2.84\times10^{-6}$ erg/cm for the intralayer exchange constant in Co layers of thickness $L=25$ Å, the surface anisotropy constant at the Co/Pt interface to be $K_s\equiv Ad=0.4$ erg/cm$^2$, and $\omega/\gamma=3.5$ kG. The best fit was obtained for the following values of the parameters: $A_{12}^0=20$ erg/cm$^2$, $b=3.7$ Å, and $4\pi M_0=7900$ Oe. Differences in our values and the values quoted in Ref. 3 [$A_{12}^0=(70\pm5)$ erg/cm$^2$, $b=(7\pm1)$ Å] can be attributed to the fact that our theory accounts for the nonuniform distribution of variable magnetization within the magnetic layers, which effectively renormalizes the parameters of exchange coupling between the layers.

Another characteristic feature of the quasi-surface collective mode of FMR, for which the frequency is given by Eq. (14), is that its intensity, calculated as a normalized overlap integral of the magnetization distribution in this mode and the uniform magnetic field exciting the FMR in a multilayer, decreases with increasing spacer thickness (see Fig. 2). This is also in agreement with experiment.[3]

## IV. CONCLUSION

By applying the transfer matrix formalism to semi-infinite magnetic multilayers, we obtained a simple analytical expression for the spectrum of a quasi-surface collective mode of FMR, which turns out to be in good qualitative agreement with the experimental data for the behavior of a quasi-surface collective mode of FMR in a Co/Pt multilayer when the spacer (Pt) thickness is varied.

## ACKNOWLEDGMENT

This work has been supported in part by grant CC-3401 from the Research Corporation, by Oakland University Foundation, and by NSERC of Canada.

[1] M. Vohl, J. Barnas, and P. Grunberg, Phys. Rev. B **39**, 12003 (1989).
[2] Z. Zhang, P. E. Wigen, and S. S. P. Parkin, J. Appl. Phys. **69**, 5649 (1991).
[3] Z. Zhang, P. E. Wigen, and T. Suzuki, J. Magn. Soc. Jpn. **17**, Suppl. S1, 119 (1993).
[4] A. N. Slavin, I. V. Rojdestvenski, and M. G. Cottam, J. Appl. Phys. **75**, 6443 (1994).
[5] A. N. Slavin, I. V. Rojdestvenski, and M. G. Cottam, J. Appl. Phys. **76**, 6549 (1994).
[6] P. Bruno and C. Chappert, Phys. Rev. Lett. **67**, 1602 (1991).
[7] E. L. Albuquerque and M. G. Cottam, Phys. Rep. **233**, 2 (1993).
[8] E. L. Albuquerque, P. Fulco, E. F. Sarmento, and D. R. Tilley, Solid State Commun. **58**, 41 (1986).
[9] S. W. McKnight and C. Vittoria, Phys. Rev. B **36**, 8574 (1987); C. Vittoria, Phys. Rev. B **37**, 2387 (1988).
[10] B. A. Kalinikos and A. N. Slavin, J. Phys. C **19**, 7013 (1986).

# Nonlinear magneto-acoustic waves in ferromagnets

G. T. Adamashvili
*Tbilisi State University, Tbilisi, Republic of Georgia 380079*

A. A. Maradudin
*University of California, Irvine, California 92717*

The nonlinear coherent interaction of a high-frequency acoustic wave pulse with a magnetically ordered medium is studied theoretically. We consider both microscopic and phenomenological theories of the formation of nonlinear magneto-acoustic waves in a ferromagnet. A self-consistent determination of the dispersion law for nonlinear magneto-acoustic waves in a ferromagnet is carried out. It is shown that in both of these theories nonlinear excitations arise which can be of the form of a periodic nonlinear wave, a soliton, or a kink. The nature of the change of polarization of transverse linearly polarized magneto-acoustic waves is also investigated. © *1996 American Institute of Physics.* [S0021-8979(96)75108-5]

## I. INTRODUCTION

The propagation of an acoustic wave in a magnetically ordered medium (MOM) is accompanied by its interaction with spin waves, which leads to the formation of a bound magneto-acoustic wave (MAW). When the acoustic wave is weak, the degree of excitation of the magnetic system of the MOM is sufficiently low that properties of the MAW can be adequately described within the framework of the linear theory of these waves, which has been extensively developed.[1,2] With an increase of the intensity of the acoustic wave the situation changes significantly. Under the action of a strong acoustic wave a macroscopically large number of excitations occur, at least locally. In a MOM under strong excitation of the spin system various nonlinear phenomena can arise, which are due to nonlinear magneto-acoustic interactions. Some of them have been investigated in detail in Refs. 3 and 4. In addition to these nonlinear phenomena, great interest attaches to nonlinear effects which arise due to the nonlinear coherent resonant interaction of an acoustic wave with a MOM, and lead to the formation of nonlinear MAW of an invariable profile. Such a wave, for example, can have the form of a soliton. Some properties of these nonlinear waves have been investigated in considerable detail. In particular, in Refs. 5–7 a microscopic theory of nonlinear MAW was constructed on the basis of the Heisenberg model of a ferromagnet. In these papers, for a self-consistent determination of the dispersion law of these waves the method of Goll and Haken, applied earlier for the investigation of nonlinear optical waves in the exciton region of the optical spectrum,[8] was used. However, in the corresponding equations in Refs. 5–7 the speed of magnons was not taken into account. With the phase plane method it was shown that nonlinear waves having the forms of a soliton, a kink, and a nonlinear periodic wave can occur in this system, but explicit expressions for the forms of the parameters on which these waves depend were not presented. This was also the case in the presentation of a corresponding phenomenological theory that proceeded from the Landau–Lifshitz equations and the equations of the theory of elasticity.[9,10]

In the present paper we present microscopic and phenomenological theories of the formation of nonlinear MAW, and the nature of the change of their polarization, when the speeds of magnons as well as the speeds of coherent phonons are taken into account. Explicit expressions for the parameters of these nonlinear MAW are also presented.

## II. MICROSCOPIC THEORY OF NONLINEAR MAW

For a microscopic determination of the basic features of the formation of nonlinear MAW in a ferromagnet we proceed from the Heisenberg model of a cubic ferromagnet. We assume that a transversely polarized MAW propagates in it along a constant magnetic field $\mathbf{H}_0$ which is parallel to the $z$-axis. The duration of the pulse is $T \ll T_{1,2}$, where $T_1$ and $T_2$ are the longitudinal and transverse relaxation times, and its frequency is $\omega \gg T^{-1}$. We consider the nonlinear coherent interaction of this pulse with the ferromagnet.

The Hamiltonian of the model investigated has the form

$$H=\hbar\omega_0\sum_i S_i^2-\Lambda\sum_i (S_i^z)^2+\hbar\sum_k \omega_k a_k^+ a_k$$

$$-\sum_{i\neq j} g_{ij}S_i^zS_j^z-\sum_{i\neq j}\eta_{ij}S_i^+S_j^-$$

$$-b\int_V\sum_{i\neq j}(S_i^+S_j^z\epsilon^-+S_i^-S_j^z\epsilon^+)dv, \qquad (1)$$

where

$$g_{ij}=J_{ij}-I_{ij}^d, \quad \eta_{ij}=J_{ij}+1/2I_{ij}^d, \quad b=\gamma_2(\hbar\gamma/VM_0)^2,$$

$$\epsilon^{\pm}=\epsilon_{xz}\pm i\epsilon_{yz}=\pm i\sum_k \bar{\kappa}a_k^{\pm}\exp[\pm i(\omega_k t-kl)],$$

$$\bar{\kappa}=k\left(\frac{N_0\hbar}{8\rho\omega V}\right)^{1/2}, \quad \Lambda=2\mu\frac{\beta^2}{v_0}.$$

$\omega_0=\gamma H_0$ is the Zeeman frequency of the spins, where $\gamma$ is the magnetomechanical ratio; $\mathbf{S}_i$ is the spin of the atom which is at the $i^{\text{th}}$ site of the crystal; $J_{ij}$ is the coefficient of the exchange interaction between spins ($J_{ij}>0$ for a ferromagnet); $I_{ij}^d$ is the coefficient of the magnetic dipole-dipole interaction; $\beta$ is the Bohr magneton; $\gamma_2$ is the magneto-acoustic coupling constant; $M_0$ is the saturation magnetization; $\epsilon_{ik}(i,k=x,y,z)$ are the components of the strain tensor; $\rho$ is the mass density of the medium, $v_0$ is the volume of a

 0021-8979/96/79(8)/5727/3/$10.00 © 1996 American Institute of Physics 

primitive unit cell of the crystal, and $V$ is the volume of the crystal; $a_k^+$ and $a_k$ are the creation and annihilation operators of the phonon with wave vector $\mathbf{k}$, while $\omega_k$ is the frequency of the $k^{\text{th}}$ phonon mode; $\hbar$ is the Planck constant; $\mu$ is the anisotropy parameter; $\ell$ is the discrete coordinate along the $z$-axis; and $N_0$ is the number of lattice sites in the crystal.

From the expression (1), we obtain the equations of motion,

$$\begin{aligned}
&\alpha^*\dot{m}^{\pm}=\pm i(\omega_0-\omega-qN)m^{\pm}\pm i\beta_0[2N^2\mathscr{E}^{\pm}\\
&\qquad -m^{\pm}m^{\mp}\mathscr{E}^{\pm}-(m^{\pm})^2\mathscr{E}^{\mp}]\\
&\alpha^*\dot{N}=i\beta_0 N(m^+\mathscr{E}^- - m^-\mathscr{E}^+) \qquad (2)\\
&\alpha\dot{\mathscr{E}}^{\pm}=\mp i(\omega-c_t k)\mathscr{E}^{\pm}\mp i\beta_0\bar{\kappa}^2 N m^{\pm},
\end{aligned}$$

where $\alpha=1-c_t/v$, $\alpha^*=1-u_m/v$, with $v$ the velocity of the nonlinear wave; $c_t$ is the speed of transverse acoustic waves, and $u_m$ is the speed of magnons; $\beta_0=b/\hbar$; $q=2[G(0)-M(k)]$, and $M(k)$ and $G(k)$ are the Fourier transforms of the quantities $\eta_{il}$ and $g_{il}$, respectively.[7] The quantities $N, m^{\pm}$, and $\mathscr{E}^{\pm}$ are defined by $N=\langle S_l^z\rangle$, $\langle S_l^{\pm}\rangle = m^{\pm}e^{\pm i(\omega t-kl)}$, $\langle \epsilon^{\pm}\rangle=\mathscr{E}^{\pm}e^{\pm i(\omega t-kl)}$. The coordinate $\tau$ is defined by $\tau=t-l/v$, and the dot denotes differentiation with respect to $\tau$. Using the initial conditions for the acoustic wave and magnetization that no magnons are excited before the acoustic wave impinges on the medium, i.e., at $t\to-\infty$, $\mathscr{E}^{\pm}\to 0$, $N=-1/2$, then from Eqs. (2) we obtain

$$m^+m^- + N^2=\frac{1}{4}, N=-\frac{1}{2}+g\mathscr{E}^+\mathscr{E}^-,$$

where $g=-\alpha/\alpha^*\bar{\kappa}^2$.

Taking into account these relations and decomposing the complex amplitudes $\mathscr{E}^{\pm}=ae^{\pm i\Phi}$ into their modulus $a$ and phase $\Phi$, from Eqs. (2) we obtain the following differential equation for the phase,

$$\dot{\Phi}=\frac{1}{2\alpha}\left(\tilde{\Delta}-\frac{\alpha}{\alpha^*}\Delta\right)-\mathrm{Ga}^2,$$

where $\tilde{\Delta}=\omega-c_t k$, $\Delta=\omega_0-\omega+q/2$, $G=q\alpha/4\bar{\kappa}^2\alpha^{*2}$. We assume that $k$ is the central momentum and $\omega$ the central frequency of the pulse. Therefore $\dot{\Phi}$ must not contain a constant part. Consequently

$$\dot{\Phi}=-\mathrm{Ga}^2,$$

and

$$\frac{\tilde{\Delta}}{\alpha}=\frac{\Delta}{\alpha^*}, \qquad (3)$$

which is the dispersion law for the nonlinear wave.

From Eqs. (2) we also obtain the equation for the amplitude of the pulse

$$(\dot{a})^2=T^{-2}a^2+c_1a^4+c_2a^6+c_3a^8, \qquad (4)$$

where

$$T^{-2}=-\frac{G_0^2}{\alpha}-\left(\frac{\tilde{\Delta}}{\alpha}\right)^2,\quad c_1=-\frac{5}{4}\left(\frac{\beta_0}{\alpha^*}\right)^2-\frac{\tilde{\Delta}q}{2\bar{\kappa}^2\alpha^{*2}},$$

$$c_2=\frac{2\beta_{0s}^2 g}{\alpha^{*2}}-G^2,\quad c_3=-\left(\frac{\beta_{0s}g}{\alpha^*}\right)^2,\quad G_0^2=\frac{\beta_{0s}^2\bar{\kappa}^2}{4\alpha^*}, \qquad (5)$$

and the quantity $G_0$ is the magnon-phonon coupling constant. Expressions (3) and (5) contain the velocities $u_m$, $v$, and $c_t$ as parameters. An analysis of Eq. (4) can be carried out in the same way as this was done in Ref. 7, where it was shown that nonlinear MAW having the form of a soliton, a kink, or a nonlinear periodic wave can occur.

## III. PHENOMENOLOGICAL THEORY OF NONLINEAR MAW

In the phenomenological theory it is assumed that the state of a MOM can be described by the magnetic moment density $\mathbf{M}(z)$. The macroscopic energy density of the medium can be represented as $W=W_p+W_m+W_{mp}$, where $W_p$, $W_m$, $W_{mp}$ are the densities of the elastic energy, the magnetic energy, and the energy of the magnon-phonon interaction, whose forms can be found in the monographs.[1,2]

The equations of motion for the magnetization $\mathbf{M}$ and for the acoustic wave have the forms

$$\begin{aligned}
&\frac{\partial M^{\pm}}{\partial t}=\pm i\omega_0 M^{\pm}\pm iF_1\left(\frac{\partial^2 M_z}{\partial z^2}M^{\pm}-M_z\frac{\partial^2 M^{\pm}}{\partial z^2}\right)\\
&\qquad \pm iF_2\left[\left(M_z^2-\frac{1}{2}M^+M^-\right)\epsilon^{\pm}-\frac{1}{2}(M^{\pm})^2\epsilon^{\mp}\right],\\
&\frac{\partial M_z}{\partial t}=i\frac{F_1}{2}\left(M^-\frac{\partial^2 M^+}{\partial z^2}-M^+\frac{\partial^2 M^-}{\partial z^2}\right)\\
&\qquad +i\frac{F_2}{2}M_z(M^+\epsilon^- - M^-\epsilon^+),\\
&\frac{\partial^2\epsilon^{\pm}}{\partial t^2}=c_t^2\frac{\partial^2\epsilon^{\pm}}{\partial z^2}+\tilde{G}\frac{\partial^2}{\partial t^2}(M_z M^{\pm}),
\end{aligned}$$

where

$$\tilde{G}=\frac{\gamma_2}{2\rho M_0^2},\quad F_1=\frac{2A\gamma}{M_0^2},\quad F_2=\frac{2\gamma\gamma_2}{M_0^2},$$

and

$$M^{\pm}=M_x\pm iM_y.$$

The constant $A$ appearing in the definition of the coefficient $F_1$ is the coefficient of rigidity of the medium.

We can simplify these equations significantly by using the method of slowly changing profile. For this purpose, we represent the functions $M^{\pm}$, $M_z$, and $\epsilon^{\pm}$ in the forms

$$M^{\pm}=m^{\pm}e^{\pm i(\omega t-kz)},\quad M_z=M_0+m_z,\quad \epsilon^{\pm}=\mathscr{E}^{\pm}e^{\pm i(\omega t-kz)},$$

where $m^{\pm}$, $m_z$, $\mathscr{E}^{\pm}=ae^{\pm i\Phi}$ are slowly varying amplitudes.

Substituting these expressions in the equations of motion we obtain

$$\begin{aligned}
&\widetilde{\alpha^*}\dot{m}^{\pm}=\pm i(\omega_0-\omega+\tilde{q}M_z)m^{\pm}\\
&\qquad \pm i\tilde{\beta}[(2M_z^2-m^{\pm}m^{\pm})\mathscr{E}^{\pm}-(m^{\pm})^2\mathscr{E}^{\mp}],\\
&\widetilde{\alpha^*}\dot{M}_z=i\tilde{\beta}M_z(m^+\mathscr{E}^- - m^-\mathscr{E}^+), \qquad (6)
\end{aligned}$$

$$\tilde{\alpha}\dot{\mathscr{E}}^{\pm}=\mp i\Delta_0\mathscr{E}^{\pm}\pm i\tilde{g}M_z m^{\pm},$$

where $\tilde{q}=F_1k^2$, $\tilde{g}=\gamma_2k^2/4\rho\omega M_0^2$, $\tilde{\alpha}=1-c_t^2k/\omega v$, $\tilde{\alpha}^*=1-v_m/v$, $v_m=4A\gamma k/M_0$ is the magnon velocity, $\Delta_0=(\omega^2-c_t^2k^2)/(2\omega)$, and $\tilde{\beta}=F_2/2$. Using the initial conditions for the acoustic wave and magnetization in the same way as this was done in Sec. II, from the set of equations (6) we obtain the differential equation satisfied by the phase function

$$\dot{\Phi}=\tilde{G}a^2,$$

the dispersion law

$$\frac{\Delta_0}{\tilde{\alpha}}=\frac{\tilde{\Delta}_0}{\tilde{\alpha}^*}, \tag{7}$$

and the equation for the amplitude of the nonlinear wave

$$(\dot{a})^2=T_0^{-2}a^2+C_1a^4+C_2a^6+C_3a^8,$$

where

$$T_0^{-2}=-\frac{R^2}{\tilde{\alpha}^*\tilde{\alpha}}-\left(\frac{c_t^2k^2-\omega^2}{2\omega\tilde{\alpha}}\right)^2,$$

$$C_1=-\left(5g_0^2M_0^2\frac{\tilde{g}^2}{\tilde{\alpha}^2}-2\frac{\Delta_0}{\tilde{\alpha}}\tilde{G}\right),\quad C_2=4\frac{g_0^3M_0\tilde{g}^2}{\tilde{\alpha}^2}-\tilde{G}^2, \tag{8}$$

$$C_3=\left(\frac{\tilde{g}g_0^2}{\tilde{\alpha}}\right)^2,$$

$$\tilde{G}=\frac{\tilde{q}g_0^2\tilde{g}}{4\tilde{\beta}\tilde{\alpha}},\quad \tilde{\Delta}_0=\omega_0-\omega+\tilde{q}M_0,\quad R=2\tilde{g}\beta M_0^3,$$

$$\tilde{g}_0=-\frac{\tilde{\alpha}\tilde{\beta}}{\tilde{\alpha}^*\tilde{g}}.$$

Comparing Eqs. (3) and (5) with Eqs. (7) and (8) we see that the results of the microscopic and phenomenological theories are quite similar to each other.

## IV. POLARIZATION OF NONLINEAR MAW

For describing the state of polarization of the nonlinear MAW we consider a linearly polarized transverse wave (LPTW) which propagates along an external constant magnetic field of magnitude $H_0$. By the use of the methods of Ref. 11, we obtain the following expression for the angle of rotation of the plane of polarization of the nonlinear MAW,

$$\psi_{n\ell}=-\frac{G_0^2}{2c_t}\frac{\tilde{\tilde{\Delta}}T^2}{1+\tilde{\tilde{\Delta}}^2T^2}z, \tag{9}$$

where

$$\tilde{\tilde{\Delta}}=\frac{\Delta}{\alpha^*}.$$

As the nonlinear MAW propagates, it becomes elliptically polarized as well. The ratio of the lengths of the small $b$ and large $a$ elliptic axes follows from

$$\left(\frac{b}{a}\right)_{n\ell}=\frac{|f_+-f_-|}{f_++f_-}, \tag{10}$$

where $f_+$ and $f_-$ are to within a constant factor the forms (shapes) of the clockwise and counterclockwise polarized components of the LPTW pulse. In the linear limit the angle of rotation of the plane of polarization is

$$\psi_\ell=-\frac{G_0^2}{2c_t\tilde{\tilde{\Delta}}}z, \tag{11}$$

and the ratio of the lengths of the small and large elliptic axes in the absence of dissipation is equal to zero, i.e., the linear wave remains linearly polarized as it propagates. In the presence of dissipative effects $f_+=1$, $f_-=\exp(-\alpha_0z)$ (where $\alpha_0$ is the absorption coefficient) and we have

$$\left(\frac{b}{a}\right)_\ell=\left(\frac{\cosh(\alpha_0z)-1}{\cosh(\alpha_0z)+1}\right)^{1/2},$$

i.e., in the general case elliptic polarization of the wave occurs.

From expressions (9) and (11) for the angle of rotation of the plane of polarization it is seen that the values of $\psi$ in the linear and nonlinear limits differ considerably in their dependences on $\Delta$. In particular, in the linear limit, with the frequency $\omega$ approaching $\omega_0+1/2q$, the angle $\psi_\ell$ increases and tends to its maximum value while, on the other hand, for a nonlinear magneto-acoustic wave, as $\Delta\to0$ the angle $\psi_{n\ell}$ tends to zero, i.e., there is no rotation of the plane of polarization.

The nature of the variation of the ratio $b/a$ is also significantly different in the linear and nonlinear limits. From Eq. (10) it is seen that as the nonlinear LPTW propagates, it transforms into an elliptically polarized wave. In this case the nature of the transformation depends on the form of the pulse $f_\pm$. At the values of $z$ for which $f_+=f_-$ the magneto-acoustic wave is linearly polarized.

## V. CONCLUSION

In the present paper we have shown that, due to the nonlinear coherent interaction of an acoustic pulse with a ferromagnet, nonlinear MAW of the type of a soliton, kink, or nonlinear periodic waves can arise. The nonlinear dispersion laws (3) or (7) are valid for these waves, which contain the speed of the nonlinear wave as well as the speeds of magnons and coherent phonons.


[1] J. W. Tusker and V. W. Rampton, *Microwave Ultrasonics in Solid State Physics* (North-Holland, Amsterdam, 1972).
[2] A. I. Akhiezer, V. G. Bar'yakhtar, and S. V. Peletminsky, *Spinovie Volny* (Spin Waves) (Nauka, Moscow, 1967) in Russian.
[3] I. A. Monosov, *Nelineiny Ferromagnitny Resonans* (Nonlinear ferromagnetic resonance) (Nauka, Moscow, 1971) in Russian.
[4] V. S. Lvov, *Nelineinie Spinovie Volni* (Nonlinear spin waves) (Nauka, Moscow, 1987) in Russian.
[5] G. T. Adamashvili, Solid State Commun. **40**, 623 (1981).
[6] G. T. Adamashvili, Preprint N7, Institute of Spectroscopy, Academy of Sciences of the USSR, Troitsk, Moscow Region, 1981.
[7] G. T. Adamashvili, Teor. Mat. Fiz. **80**, 461 (1989).
[8] J. Goll and H. Haken, Phys. Rev. A **18**, 2241 (1978).
[9] G. T. Adamashvili, G. G. Uturashvili, D. M. Zviadadze, and Z. M. Shengelia, Transactions Georgia Technical University **392**, 16 (1992).
[10] G. T. Adamashvili, G. G. Uturashvili, D. M. Zviadadze, and Z. V. Gongadze, Transactions Georgia Technical University **395**, 19 (1993).
[11] G. T. Adamashvili, Phys. Lett. A **158**, 81 (1991).

# Parametrical interaction of magnetostatic volume waves in a space-time periodic magnetic field

Y. K. Fetisov
*Moscow Institute of Radioengineering, Electronics and Automation, Vernadskogo 78, Moscow 117454, Russia*

N. V. Ostrovskaya and A. F. Popkov
*Zelenograd Research Institute of Physical Problems, Moscow 103460, Russia*

The theory describing parametrical interaction of magnetostatic backward volume waves (MSBVW) in a space-time periodic magnetic field was developed. Forward and backward scattering of MSBVW propagating in a 20-$\mu$m-thick yttrium-iron-garnet film at a central frequency of 3 GHz was observed. A space-time periodic magnetic field with a spatial period of 500 $\mu$m, a frequency in the range 20–150 MHz, and a magnitude up to 10 Oe was created by ac current passing through a meander line placed on the film surface. An interaction bandwidth of 20 MHz and an efficiency of up to 10% have been obtained in accordance with theoretical predictions. © *1996 American Institute of Physics.* [S0021-8979(96)75208-1]

## INTRODUCTION

Magnetostatic spin waves (MSW) propagating in ferrite films are very sensitive to conditions at the film surface and to the external magnetic field. These properties may be used to control the propagation and the interaction of MSWs by means of weak nonuniformities created in the film. The efficient reflection of MSW in a periodically corrugated[1] or periodically ion-implanted[2] films and the scattering in a static space-periodic magnetic field[3] have been demonstrated. A dynamic nonuniformity, such as surface acoustic wave, propagating in the same film may be used to control MSW propagation as well.[4]

This paper presents the theory describing parametrical interaction of magnetostatic backward volume waves (MSBVWs) in a ferrite film placed in a weak space-time periodic magnetic field. Such a field may be easily created by passing an ac current through a meander line conductor placed near the film surface.[5] The collinear MSBVW scattering accompanied by conversion of the wave number and the frequency has been investigated.

## THEORY OF COLLINEAR MSBVW INTERACTION

Consider a $y$-$z$ plane oriented ferrite film of the thickness $d$, saturation magnetization $4\pi M$, and FMR line width $\Delta H$, which is saturated with an external dc magnetic field $H$ along the $z$ axis. A metal lattice of the period $\Lambda$, strip width $a$, and thickness $b$ is placed at a distance $t$ above the film surface.

The characteristics of MSW propagating in a free film are found by solving the Maxwell's equations (without retardation) and the linearized equation of motion of the magnetization with boundary conditions at the film surfaces.[6] The dispersion equation for MSBVW propagating along the $z$ axis has the form:

$$tg(kd/\sqrt{-\mu}) = -2\sqrt{-\mu/(1+\mu)}, \tag{1}$$

where $\mu = 1 + \omega_H\omega_M/[\omega^2(k) - \omega_H{}^2]$, $\omega_0 = \sqrt{\omega_H(\omega_H + \omega_M)}$, $\omega_H = \gamma H$, and $\omega_M = \gamma(4\pi M)$, $\gamma$ is the gyromagnetic ratio.

Equation (1) gives the dependence of the wave frequency $\omega(k)$ versus the wave number $k$ for eigenmodes with numbers $n = 1,2,...$ having symmetrical or antisymmetrical distributions of magnetostatic potential $\Psi_n$ across the film thickness.

Let an ac current $I = I_0\cos(\Omega t)$ with the frequency $\Omega$ pass through the metal lattice so that currents in the neighboring strips flow in opposite directions. Such a current distribution creates a space-time periodic magnetic field in the film that may be represented as a sum of "magnetic waves" propagating in opposite directions along the $z$ axis:

$$h(z,t) = \sum_{l=1}^{\infty} \sum_{s=\pm 1} h_{ls} e^{i(sK_l z - \Omega t)} + c.c., \tag{2}$$

where $K_1 = \pi l/\Lambda$ and $s$ determines the direction of propagation.

The amplitudes of the magnetic waves $h_{l,s} = (h_x^{1,s}, 0, h_z^{1,s})$ are determined by the current magnitude $I_0$ and by the geometrical parameters of the structure.

In the presence of the modulating field the MSW potential $\Psi$ should be represented as a sum of the harmonics:[7]

$$\Psi = \sum_{m=-\infty}^{m=\infty} \sum_{l=1}^{\infty} \sum_{s=\pm 1} A_{mls} e^{i(smK_l z - m\Omega t)} e^{i(kz - \omega t)} + c.c., \tag{3}$$

where $A_{mls}$ are the amplitudes of the harmonics. The harmonics are shifted relative to each other in frequency and wave number by the vector $(smK_1,\ m\Omega)$. In the zero approximation for the small parameter $\varepsilon = h/H \ll 1$ the harmonics do not interact and their dispersion is given by Eq. (1). When terms which are first order in $\varepsilon$ are considered, the modulating field results in the interaction of harmonics. The strongest interaction takes place for harmonics with the neighboring numbers $m = 0$ and $m = \pm 1$ and $K = \pi/\Lambda$, when the following phase-matching conditions are satisfied:

$$k_\pm = k \pm K, \quad \omega(k_\pm) = \omega(k) \pm s\Omega, \quad s = \pm 1. \tag{4}$$

Figure 1 shows the MSBVW dispersion curves and demonstrates that the character of interaction depends on the

 0021-8979/96/79(8)/5730/3/$10.00 © 1996 American Institute of Physics

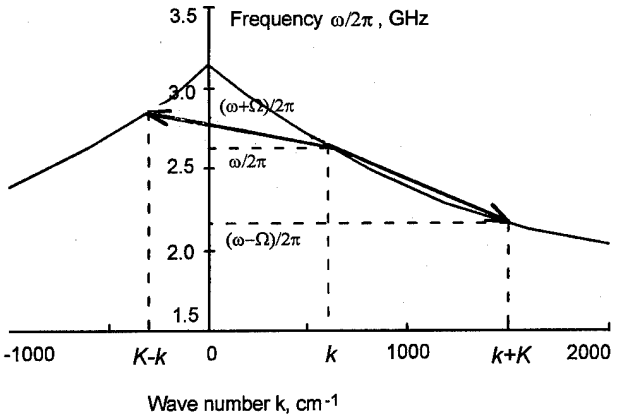



FIG. 1. Diagram for MSBVW scattering in a space-time periodic magnetic field.

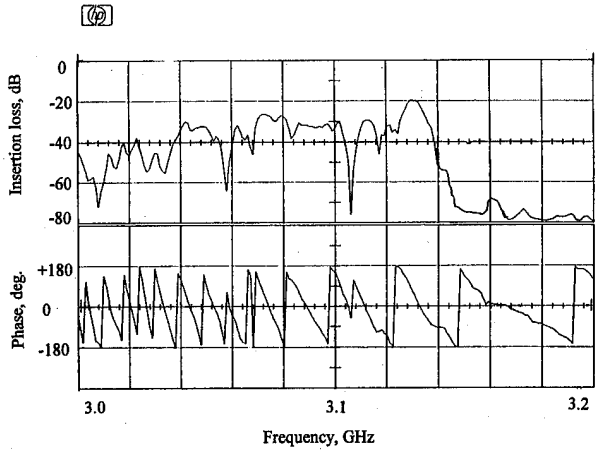



FIG. 2. Frequency response (a) and phase response (b) of the MSBVW transmission line containing a 500 $\mu$m-period meander imposed on the YIG film surface in the absence of modulation magnetic field.

value of the magnetostatic wave number $k$ and the lattice wave number $K$. If $k>K$ only forward scattering takes place. If $k<K$ forward as well as backward scattering is allowed. In general the offsets of scattered wave frequencies $\omega_+$ and $\omega_-$ from the incident wave frequency $\omega$ are different.

Interaction in a weak modulating field ($h/H \ll 1$) is well described by the theory of coupled waves. Solution of the problem to the first order in $\varepsilon$, gives the system of coupled equations:

$$i\frac{dA_+}{dt}+V_+\frac{dA_+}{dz}+i\delta\omega_+A_++\omega_C^+A_-=0, \tag{5a}$$

$$i\frac{dA_-}{dt}\pm V_-\frac{dA_-}{dz}+i\delta\omega_-A_-+\omega_C^-A_+=0, \tag{5b}$$

where $A_\pm$, $V_\pm=d\omega_\pm/dk$, $\delta\omega_\pm=\gamma\Delta H$, and $\omega_{C\pm}=\omega_C$ are the amplitudes, group velocities, damping coefficients, and coupling coefficients of interacting waves, respectively. The signs + and − in the second equation correspond to the forward and backward scattering, respectively.

The coupling coefficients for waves with identical ($\omega_{CS}$) and different ($\omega_{CA}$) symmetries are given by the expressions:

$$\omega_{CS}=\frac{h_z}{4\pi M}\frac{\omega_M(\omega_H^2+\omega_0^2)}{2\omega_H\omega_0}, \quad \omega_{CA}=\frac{ih_x}{4\pi M}\frac{\omega_M^2}{\omega_0}\sqrt{\frac{kd}{2}}. \tag{6}$$

From Eq. (6) one can see that coupling is strongest for identical modes and is almost independent on the frequency. The coupling for different modes, on the other hand, sharply decreases with decreasing wave number.

The efficiency $\eta$ of the MSBVW interaction can be found by solving Eq. (6) with the proper boundary conditions at $z=0$ and $z=L$. For forward scattering and a strong coupling ($\omega_C \gg \delta\omega$) one can obtain the following expressions:

$$\eta_{F+}=\left|\frac{A_+(z=L)}{A(z=0)}\right| = \sqrt{\cos^2(\xi_1L)+\frac{\Delta_\omega^2\Delta_V^2}{1+\Delta_\omega^2\Delta_V^2}\sin^2(\xi_1L)}\cdot e^{-\xi_2L}, \tag{7a}$$

$$\eta_{F-}=\left|\frac{A_-(z=L)}{A(z=0)}\right|=\frac{|\sin(\xi_1L)|}{\sqrt{1+\Delta_\omega^2\Delta_V^2}}e^{-\xi_2L}, \tag{7b}$$

where $\xi_1=(\omega_C/V)(1+\Delta_\omega^2\cdot\Delta_V^2)^{1/2}$, $\xi_2=\delta\omega V$, $\Delta_\omega=\Delta\omega/\omega$, $\Delta_V=\Delta V/V$, and $\Delta\omega=\omega_\pm-\omega$ and $\Delta V=V_\pm-V$ are the frequency detuning and difference in the group velocities of the interacting waves respectively, $V=(V_++V_-)/2$. The efficiency reaches its maximum at exact frequency matching condition $\Delta\omega=0$ for $\omega_CL\ll\pi/2$, and it may have a maximum at $\Delta\omega\neq0$ when $\omega_CL\gg\pi/2$ is fulfilled. Amplitudes of the interacting waves decay and oscillate along the $z$ axis as the group velocity $V$ decreases due to the decrease of the effective interaction length. For the backward single-mode scattering on a long magnetic lattice ($L/V\gg\sqrt{\omega^2+\delta\omega^2}$), the efficiency is given as

$$\eta_B(L=\infty)\simeq\frac{\omega_B}{|\Delta\omega+i\delta\omega+\sqrt{(\Delta\omega+i\delta\omega)^2-\omega_C^2}|}. \tag{8}$$

From Eq. (8) it follows that the frequency detuning is $\Delta\omega\approx\omega_C$ in the case of strong coupling, and $\Delta\omega\approx\delta\omega$ in the case of strong damping. Estimation of the coupling coefficient and the efficiency of MSBVW scattering from Eqs. (6) and (7) and the values of parameters listed below give the following results: $\omega_C/2\pi\approx30$ MHz, $\eta\approx100\%$.

## EXPERIMENTAL RESULTS AND DISCUSSION

The MSBVW transmission line containing an yttrium-iron-garnet (YIG) film ($d=20$ $\mu$m, $4\pi M=1750$ G, $\Delta H=0.5$ Oe), an alumina substrate with two microstrip transducers, and a meander line conductor deposited between them was used in the experiment. The length of the meander line was 7 mm with an aperture of 6 mm and a period of 100, 200, or

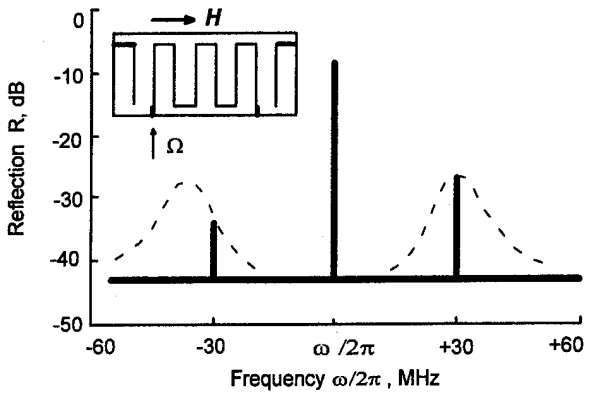



FIG. 3. Spectrum of a microwave signal reflected from the MSVBW line. The inset shows the geometry of experiment.

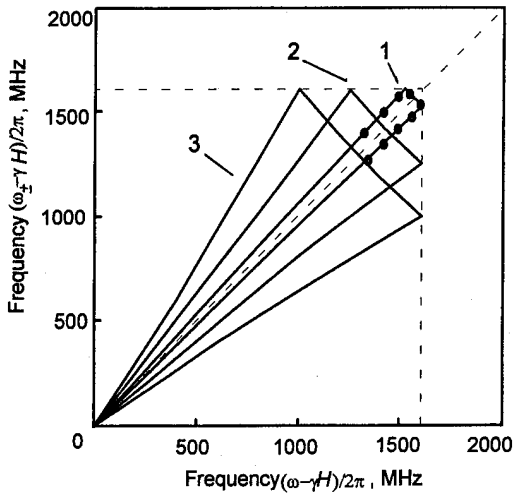



FIG. 4. Frequency synchronization curves for MSBVW scattering. Solid lines are calculation, dots are experimental data. Period of the lattice Λ is: 1–500 $\mu$m, 2–200 $\mu$m, and 3–100 $\mu$m.

500 $\mu$m. An ac current with magnitude up to 2 A and frequency of $\Omega/2\pi=20-150$ MHz was passed through the meander line, creating the modulation field with magnitude of up to $h\approx 10$ Oe. The structure was tangentially magnetized with an external dc magnetic field $H=550$ Oe. The MSBVW was excited by a continuous signal with a carrier frequency of $\omega/2\pi=2-3.5$ GHz. Spectra of transmitted and reflected signals were registered.

Figure 2 shows a frequency response (upper trace) and a phase response (lower trace) for the MSBVW line with the meander's period of 500 $\mu$m under stationary conditions (in the absence of modulating field). Imposing of the meander on the ferrite surface increased the ripple in the line frequency response and resulted in changes in the dispersion for the waves with wave numbers $k\Lambda<1$. One can see formation of rejection peaks resulting from MSBVW reflection by the meander conductors at the frequencies when the following condition is fulfilled:

$$k(\omega_N)=(\pi/2\ \Lambda)+2\pi N, \quad \text{where } N=1,2\ldots \tag{9}$$

Note, that the frequencies defined by Eq. (9) do not coincide with the frequencies defined by Eq. (4) for MSBVW scattering in a space-time periodic magnetic field.

Figure 3 shows a typical spectrum of a microwave signal reflected from the line in the presence of modulating magnetic field. Two lateral harmonics appeared in the spectrum due to MSBVW scattering in a space-time periodic magnetic field. The dashed curves in Fig. 3 show the resonance variation of the harmonics' power as a function of the modulation frequency. Different offsets of the harmonics' maxima from the input signal frequency were observed.

Figure 4 shows dependences of scattered wave frequencies $\omega_\pm$ versus the incident wave frequency $\omega$ (synchronization curves) calculated from Eq. (4) and Eq. (1). The main MSBVW mode and parameters which are corresponded to the experimental structure were used. Frequencies of backward scattered waves lie on the upper parts of the curves. The decrease of the meander line period leads to the broadening of the synchronization curve, so that the frequencies of the scattered waves $\omega_\pm$ are moved apart from the carrier frequency $\omega$. The points in Fig. 4 correspond to experimentally observed MSBVW forward and backward scattering. Only the lower frequency $\omega_+$ was observed in the spectrum of the transmitted signal when the input signal excited the wave with $k=K$. In this case the frequency $\omega_-$ corresponded to the wave with $k\approx 0$ and was not detected by the transducer.

The interaction bandwidth, defined as a half-height width of the resonance curve in Fig. 3, was equal to $\Delta\omega/2\pi\simeq 20$ MHz, which agrees with the calculation. The maximum interaction efficiency, calculated from experimental data and taking into account the MSBVW excitation losses, was equal to $\eta\simeq 10\%$.

Note that the considered effects may be used for effective excitation of higher order magnetostatic volume modes. From Eq. (7b) it follows that in the case of strong coupling ($\omega_C\gg\delta\omega$) the mode conversion with almost 100% efficiency takes place at the distance $L=(V/\Delta\omega_C)\ \mathrm{arctg}(2\omega_C/\delta\omega)\simeq(\pi/2)(V/\omega_C)$. For the YIG film thickness of 20 $\mu$m and modulation field amplitude of $h=10$ Oe the conversion distance will be about $L\simeq 1$ mm.

This research was made possible in part by grant M6Q300 from the International Science Foundation and the Russian Government.

[1] C. G. Sykes, J. D. Adam, and J. H. Collins, Appl. Phys. Lett. **29**, 388 (1976).
[2] R. L. Carter, J. M. Owens, C. V. Smith, and K. W. Reed, J. Appl. Phys. **53**, 2655 (1982).
[3] A. V. Voronenko, S. V. Gerus, and V. D. Haritonov, Sov. Phys. J. **31**, 76 (1988).
[4] A. M. Mednikov, S. A. Nikitov, and A. F. Popkov, Sov. Phys. Solid State **24**, 3008 (1982).
[5] A. N. Myasoedov and Y. K. Fetisov, Sov. Phys. Tech. Phys. **34**, 666 (1989).
[6] R. W. Damon and J. R. Eshbach, J. Phys. Chem. Solids **19**, 308 (1961).
[7] M. V. Vinogradova, O. V. Rudenko, and A. P. Sukhorukov, *Theory of Waves* (Nauka, Moscow, 1979).

# Characteristic analysis of coupled microstrip patch resonators on ferrimagnetic substrates

Kunquan Sun
*Department of Technology, Jackson State University, Jackson, Mississippi 39217*

Yinchao Chen
*Department of EE, The Hong Kong Polytechnic University, Hong Kong*

Walter Barry and John Corlett
*Center for Beam Physics, Lawrence Berkeley Laboratory, Berkeley, California 94720*

This paper is to use the spectral-domain technique to perform characteristic analysis of coupled microstrip patch resonators on ferrimagnetic substrates. Our formulation has been validated by comparing our result with the published data and showing an excellent agreement between them. Numerical computations have been performed to obtain dependence of resonant frequency on patch dimensions, offset and separation between the two patches, thicknesses of ferrimagnetic film and substrate. It has been seen that as the length of the patch increases the resonant frequency decreases. The larger the offset between the two patches the lower the resonant frequency. The separation between the two patches strongly affects the resonant frequency. It is also found that the resonant frequency increases as the width of the patch decreases. For the fixed dimensions, separation and offset, a thinner substrate results in a higher resonant frequency, and in contrast, a thinner ferrimagnetic film results in a lower resonant frequency. © *1996 American Institute of Physics.* [S0021-8979(96)75308-8]

## I. INTRODUCTION

Recently there is a growing interest[1–4] in microwave integrated circuits (MICs) on ferrimagnetic substrates, especially on epitaxially grown yttrium iron garnet (YIG)/gadolinium gallium garnet (GGG) films due to rapid advances of material technology that makes it possible to contiguously grow and deposit magnetic thin films on different substrates. It is known that a variety of applications of MICs such as filters, oscillators, and tuned amplifiers are directly involved with utilizing microwave resonators.[5] It is the new material technology and demand of MICs on magnetized ferrites that drive investigation of microwave resonators on ferrimagnetic substrates. Great efforts have been made to study microwave resonators with different geometries on YIG/GGG structures.[6,7] It is of our interest in this work to investigate a new configuration of coupled microstrip patch resonators on YIG/GGG with an offset between the two coupled patches as illustrated in Fig. 1.

This paper is to use the spectral-domain technique[8] to study the coupled microstrip patch resonators on YIG/GGG structures. The boundary value problem of the coupled patch resonators is formulated in the spectral domain by the two-dimensional (2D) Fourier-transform. Then Galenkin's method is applied to obtain a system of matrix equations. As a result a secular equation is generated based on the determinant of the system equation and the resonant frequency of the coupled patch resonator can be solved for a given set of dimensions. To assure accuracy of numerical results and efficiency of numerical computations, a set of basis functions is chosen, which accurately represent expected resonant currents on each patch. Numerical computations have been performed. Our results have revealed that resonant frequency depends on patch dimensions, offset and separation between the two patches, and thicknesses of YIG and GGG.

## II. FORMULATION

The geometry of the shielded structure of the coupled microstrip patch resonator on YIG/GGG is illustrated in Fig.

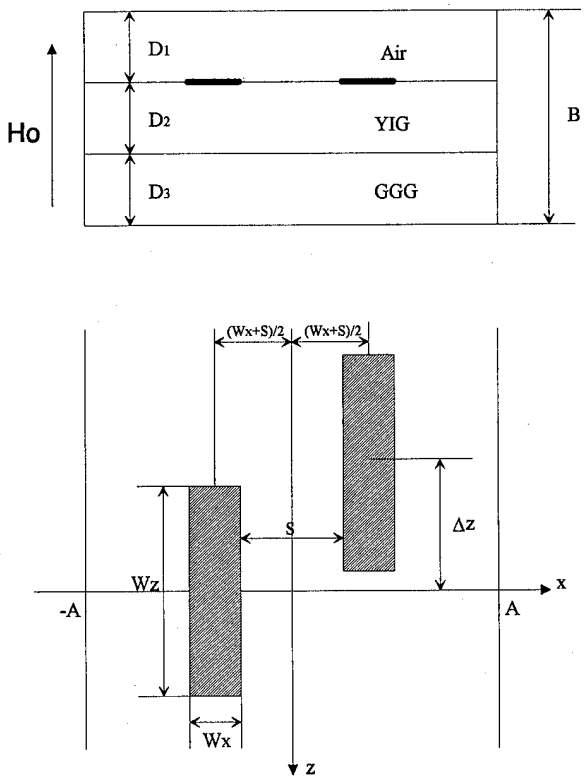



FIG. 1. Cross section and top views of coupled microstrip patch resonator. $2A$ and $B$ the waveguide dimensions, $(W_x, W_z)$ the patch width and length, $S$ the separation between the two patches, $\Delta z$ the offset between the two patches along the $z$-axis, and $D_1$, $D_2$, and $D_3$ thicknesses of air region, YIG, and GGG, respectively.

 0021-8979/96/79(8)/5733/3/$10.00 © 1996 American Institute of Physics 

1. Two rectangular patches have dimensions of $W_x$ and $W_z$, and are separated by a distance of $S$ with an offset of $\Delta z$. Thicknesses of YIG and GGG are $D_2$ and $D_3$, respectively. A dc magnetic field is applied normal to the plane of YIG film, which is characterized by its static magnetization. Accordingly the permeability tensor of YIG is given as

$$\vec{\vec{\mu}}=\mu_0\begin{bmatrix}\mu & 0 & -j\kappa\\ 0 & 1 & 0\\ j\kappa & 0 & \mu\end{bmatrix} \tag{1}$$

with $\mu = 1 + \omega_h\omega_m/\omega_h^2 - \omega^2$, $\kappa = \omega\omega_m/\omega_h^2 - \omega^2$, where $\omega_h=\gamma\mu_0 H_0$, $\omega_m=\gamma\mu_0 M$, and $\gamma$, $\mu_0$, $\omega$, and $H_0$ are the gyromagnetic ratio, the free-space permeability, the operating frequency, and the internal field, respectively.

In order to formulate the boundary problem in the spectral-domain, the 2D Fourier transforms of every field component and patch currents in $xz$ plane are taken:

$$\tilde{f}(\alpha_n,\gamma,\beta)=\int_{-\infty}^{\infty}\int_{-a}^{a} f(x,y,z)e^{j\alpha_n x+j\beta z}dxdz. \tag{2}$$

In this case summation index $n$ takes on all integer values from minus to plus infinity, since the symmetry of the Green's function is perturbed by the off-diagonal terms in $\vec{\vec{\mu}}$ of YIG. The above definition of the transform allows the first derivatives with respect to $x$ and $z$ in the space domain to be converted to multiplicative factors in the spectral-domain.

With the transformation defined in Eq. (2) field components of $E_x$ and $E_z$ in YIG film are transformed into the spectral-domain and two coupled equations for $\tilde{E}_x$ and $\tilde{E}_z$ can be obtained to determine the solution to Maxwell's equation. Other field components can be found based on $\tilde{E}_x$ and $\tilde{E}_z$. The electric and magnetic fields in regions of air and GGG can be written as a superposition of TE$y$ and TM$y$ modes.[10] By enforcing the boundary conditions at each of interfaces the Green's function is yielded as follows:

$$\begin{bmatrix}\tilde{E}_z(\alpha_n,\beta)\\ \tilde{E}_x(\alpha_n,\beta)\end{bmatrix}=\begin{bmatrix}\tilde{Z}_{zz}(\alpha_n,\beta) & \tilde{Z}_{zx}(\alpha_n,\beta)\\ \tilde{Z}_{xz}(\alpha_n,\beta) & \tilde{Z}_{xx}(\alpha_n,\beta)\end{bmatrix}\begin{bmatrix}J_z(\alpha_n,\beta)\\ J_x(\alpha_n,\beta)\end{bmatrix}. \tag{3}$$

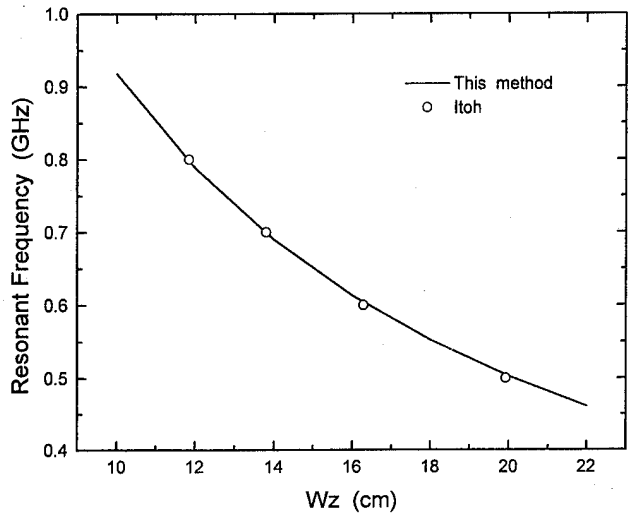



FIG. 2. Resonant frequency vs the patch length $W_z$ with $\epsilon_{xx}=\epsilon_{yy}=\epsilon_{zz}=2.65$, $D_1=8.89$ cm, $D_2=1.27$ cm, $D_3=0$, $B=15.5$ cm, and $W_x=2$ cm.

The remaining task is to employ Galerkin's method along with Paserval's theorem to set up a system equation which includes two sets of homogeneous linear equations. These equations can be solved by setting the determinant of coefficients to zero and searching for the root to find the resonant frequency.

To successfully solve the system equation one must have a proper choice of basis functions that satisfy the edge conditions and have fast convergence properties. In this study the basis functions which are chosen to expand the patch currents are presented below:

$$\begin{aligned}J_x^{(e/o)}(x,z)&=J_x^-(x,z)\mp J_x^+(x,z),\\ J_z^{(e/o)}(x,z)&=J_z^-(x,z)\pm J_z^+(x,z),\end{aligned} \tag{4}$$

with

$$\begin{cases} J_x^-(x,z)=\dfrac{\sin\{(2\pi/W_x)[x+\frac{1}{2}(S+W_x)]\}}{\sqrt{1-\{(2\pi/W_x)[x+\frac{1}{2}(S+W_x)]\}^2}}\times\dfrac{\sin(\pi z/W_z)}{\sqrt{1-(2z/W_z)^2}}, & -\left(\dfrac{S}{2}+W_x\right)<x<-\dfrac{S}{2} \text{ and } -\dfrac{W_z}{2}<z<\dfrac{W_z}{2}\\ J_x^+(x,z)=\dfrac{\sin\{(2\pi/W_x)[x-\frac{1}{2}(S+W_x)]\}}{\sqrt{1-\{(2\pi/W_x)[x-\frac{1}{2}(S+W_x)]\}^2}}\times\dfrac{\sin[(\pi/W_z)(z-\Delta z)]}{\sqrt{1-[(2(z-\Delta z)/W_z)]^2}}, & \dfrac{S}{2}<x<\dfrac{S}{2}+W_x \text{ and } \Delta z-\dfrac{W_z}{2}<z<\Delta z+\dfrac{W_z}{2}\end{cases}$$

$$\begin{cases} J_z^-(x,z)=\dfrac{1}{\sqrt{1-\{(2\pi/W_x)[x+\frac{1}{2}(S+W_x)]\}^2}}\times\dfrac{\cos(\pi z/W_z)}{\sqrt{1-(2z/W_z)^2}}, & -\left(\dfrac{S}{2}+W_x\right)<x<-\dfrac{S}{2} \text{ and } -\dfrac{W_z}{2}<z<\dfrac{W_z}{2}\\ J_z^+(x,z)=\dfrac{1}{\sqrt{1-\{(2\pi/W_x)[x-\frac{1}{2}(S+W_x)]\}^2}}\times\dfrac{\cos\left[\dfrac{\pi}{W_z}(z-\Delta z)\right]}{\sqrt{1-[2(z-\Delta z)/W_z]^2}}, & \dfrac{S}{2}<x<\dfrac{S}{2}+W_x \text{ and } \Delta z-\dfrac{W_z}{2}<z<\Delta z+\dfrac{W_z}{2}\end{cases}$$

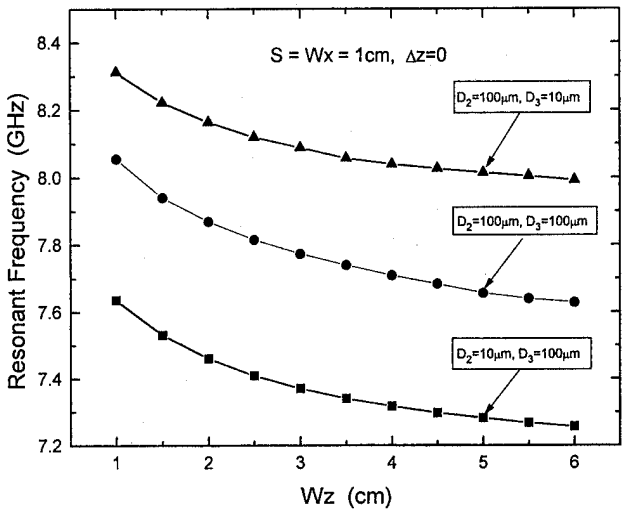



FIG. 3. Dependence of the patch length $W_z$ on resonant frequency as well as impacts of thicknesses of YIG and GGG on resonant frequency.

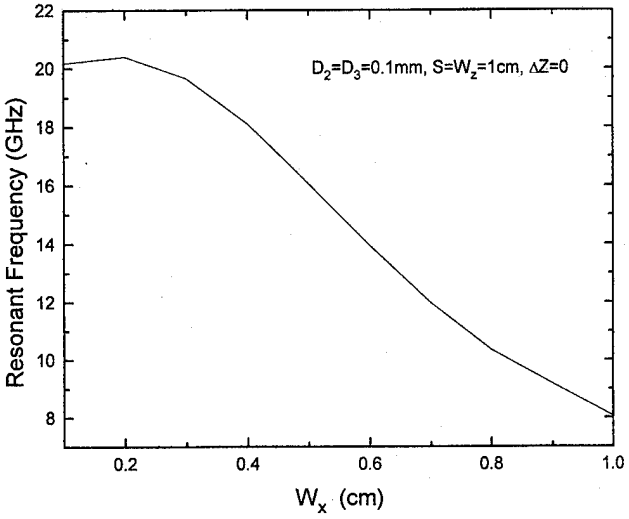



FIG. 5. Resonant frequency vs the patch width $W_x$.

where the superscription $(e/o)$ denotes even and odd modes, respectively.

## III. NUMERICAL RESULTS

In order to validate our formulation and numerical results we simplify the configuration, in which the thickness of GGG is reduced to zero, $S+W_x$ is set to be zero such that the two patches overlap, permeability tensor of YIG is chosen to be that utilized in Ref. 9. Comparison is made between our results and those in Ref. 9 and illustrated in Fig. 2. It is clear that our results agree very well with the published data.

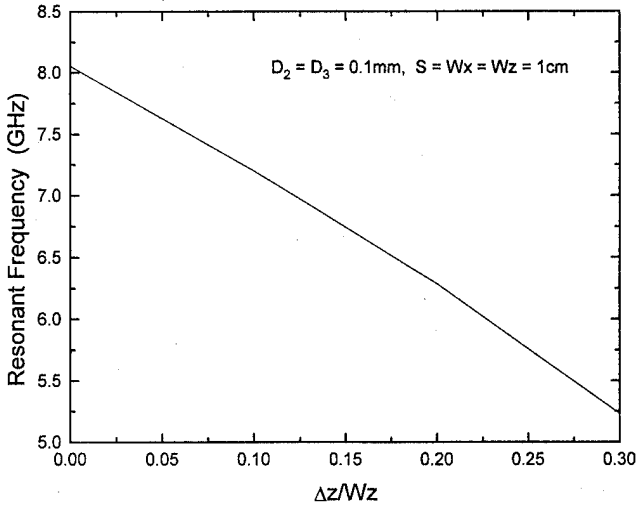



FIG. 4. Resonant frequency vs offset $\Delta z$.

Numerical computations have been performed with $\mu_0 H_0=0.1T$, $\mu_0 M=0.175T$, permittivity for YIG and GGG $\epsilon_r=12.3$, $A=7.75$ cm and $B=6$ cm throughout this paper unless stated elsewhere. Both even and odd modes of resonance were calculated. Since there is a slight difference between them, only is the even mode presented in this paper. Figure 3 demonstrates dependence of resonant frequency on the patch length $W_z$. It is observed that the resonant frequency decreases with $W_z$. Impacts of thicknesses of YIG and GGG on resonant frequency are illustrated in Fig. 3. For a given set of patch dimensions $(W_x, W_z)$, separation $(S)$ and offset $(\Delta z)$, a thinner substrate GGG results in a higher resonant frequency, and in contrast, a thinner YIG film results in a lower resonant frequency. Influence of offset between the two patches on resonant frequency was investigated. Figure 4 shows that the resonant frequency decreases with $\Delta z$ for a given set of $(W_x, W_z)$, $S$, and thicknesses ($D_2$ and $D_3$) of YIG and GGG. Width $(W_x)$ of the resonant patch has the same impact on the resonant frequency as $W_z$ except for $W_x<0.2$ cm (see Fig. 5). The resonant frequency slightly increase with $W_x$ as $W_x$ is less than 0.2 cm, and then decreases with $W_x$ rapidly.


[1] J. D. Adam, Proc. IEEE **76**, 159 (1988).
[2] D. C. Webb, IEEE Trans. Magn. **24**, 2799 (1988).
[3] E. Schloemann, IEEE Trans. MTT **34**, 1394 (1986).
[4] C. S. Teoh and L. E. Davis, IEEE International Magnetics Conference Digest, April 1995, FD-03.
[5] R. C. Collin, *Foundation for Microwave Engineering* (McGraw-Hill, New York, 1992), Chap. 7.
[6] T. D. Poston and D. D. Stancil, J. Appl. Phys. **53**, (1984).
[7] R. Marcelli, R. Rossi, and P. De Gasperis, IEEE International Magnetics Conference Digest, April 1995, FD-08.
[8] T. Itoh and R. Mittra, IEEE Trans. MTT **21**, 496 (1973).
[9] T. Itoh, IEEE Trans. MTT **22**, 946 (1974).
[10] T. Itoh, *Numerical Techniques for Microwave and Millimeter-Wave Passive Structures* (Wiley, New York, 1989).

# Characteristics of microstrip directional coupler on magnetized ferrites

E. L. Albuquerque[a)]
*Department of Physics, Harvard University, Cambridge, Massachusetts 02138*

M. R. M. L. Albuquerque and A. G. d'Assunção
*Departamento de Engenharia Elétrica, Universidade Federal do Rio Grande do Norte, Natal, RN 59072-970, Brazil*

We have studied the physical properties of a high directivity microstrip directional coupler on a single-layered ferrite substrate under the influence of an external dc magnetic field $H_0$. We also present an analysis of the coupled microstrip lines on a ferrite-dielectric substrate. Our method of calculation, which is done in the spectral domain, is based upon a combination of the Hertz vector potentials and the Galerkin numerical technique. The dyadic Green functions for the coupled microstrip lines are also obtained. We consider the even and odd modes of propagation, with the characteristic impedances and normalized phase constants of these artificial structures obtained as a function of their geometry. Special attention is given to the determination of a high directivity for the coupler, by equating the phase velocity of the even and odd modes of propagation which, in turn, is obtained throughout the variation of the applied magnetic field $H_0$. © *1996 American Institute of Physics.* [S0021-8979(96)75408-X]

The development of microstrip circuits on magnetized ferrimagnetic layers, such as microstrip antennas and resonators, is presently receiving a growing interest. This is mainly due to the fact that these devices/circuits performance can be tailored by changing the external dc magnetic field magnitude or orientation.[1] In this context, many works were devoted not only to the analysis of finlines and slotlines, but also to study microstrip lines with several layers, including magnetic ones (see Refs. 2 and 3, and the references therein). Furthermore, the study of microstrip lines and its application in the development of planar phase shifters was reported and discussed by Bolioli *et al.*,[4] taking into account the advantage of the nonreciprocal transmission effects, which could be controlled by an externally dc magnetic bias field.

The aim of this work is to study the properties of a microstrip directional coupler on a single-layered ferrite substrate under the influence of an external dc magnetic field $H_0$, with a special attention to the case depicted in Fig. 1, which guarantees its high directivity. Our analysis is done in two steps: in the first one, we characterize the coupled microstrip lines in order to determine the characteristic impedances and the normalized phase constants as a function of the frequency and its geometry. We achieve these expressions by using a combination of the Hertz vector potentials, Parseval's theorem and the Galerkin method within the spectral domain.[3,5] The analysis is performed by considering that the ferrite substrate is magnetized by an external dc magnetic field applied perpendicularly to the ground plane. The symmetry of the structure allows us to study the even and odd modes of propagation. In the second step, the theory of transmission lines is used to express the main parameters of the directional coupler, namely the coupling factor and the directivity, in terms of its physical characteristic and geometry. Numerical results are then shown to illustrate our theoretical predictions.

The multilayered geometry under consideration is depicted in Fig. 1. The coupled strips of width $w$ and uniform spacing $s$ are assumed to be infinitely thin and perfectly conducting. Region 1 is occupied with the ferrite layer, and it has thickness $d$, scalar permittivity $\epsilon_1$ and a tensor permeability $\vec{\vec{\mu}}$. We also assume that a uniform external magnetic field $H_0$ is applied perpendicularly to the substrate to saturate the sample, and then removed, so that the magnetic permeability tensor is given by:

$$\mu=\begin{bmatrix} \mu & 0 & ik \\ 0 & \mu_0 & 0 \\ -ik & 0 & \mu \end{bmatrix}, \tag{1}$$

where the components $\mu$ and $k$ depend on the ferrite characteristics and operating frequency, i.e.:

$$\frac{\mu}{\mu_0}=1-\frac{\gamma^2 H_0 4\pi M_s}{\omega^2-(\gamma H_0)^2}; \quad \frac{k}{\mu_0}=\frac{\gamma 4\pi M_s}{\omega^2-(\gamma H_0)^2}. \tag{2}$$

Here, the saturation magnetization of the ferrite is $4\pi M_s$, and $\gamma$ and $\omega$ are the gyromagnetic ratio and the operating frequency, respectively. Region 2, which has a thickness $h$, is filled up with a dielectric material, whose permittivity is given by $\epsilon_2$. Region 3 is the air with parameters $\epsilon_0$ and $\mu_0$ denoting the free-space values of permittivity and permeability, respectively.

The analysis in the spectral domain is carried out initially for the determination of the impedance matrix, through the use of the Hertz vector potentials oriented along the $y$-axis (the same orientation of the magnetic field $H_0$). The components of the electrical field can be given in terms of the current density at one of the conducting lines. Taking into

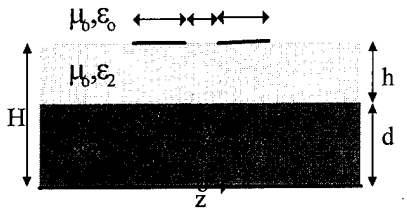



FIG. 1. Schematic representation of the coupled microstrip line supported by a ferrite substrate used in this paper.

[a)]On sabbatical leave from Departamento de Física, Universidade Federal do Rio Grande do Norte, Natal, RN 59072-970, Brazil.

 0021-8979/96/79(8)/5736/3/$10.00 © 1996 American Institute of Physics

account the spectral domain formulation, these components can be determined after using the appropriate continuity and boundary conditions in Fourier transform domain, i.e.:

$$\begin{bmatrix}\tilde{E}_x(\alpha,H)\\ \tilde{E}_z(\alpha,H)\end{bmatrix}=\begin{bmatrix}\tilde{Z}_{xx}(\alpha,H) & \tilde{Z}_{xz}(\alpha,H)\\ \tilde{Z}_{zx}(\alpha,H) & \tilde{Z}_{zz}(\alpha,H)\end{bmatrix}\begin{bmatrix}\tilde{J}_x(\alpha,H)\\ \tilde{J}_z(\alpha,H)\end{bmatrix}, \quad (3)$$

where $\alpha$ represents the spectral variable, $\tilde{E}_x$, $\tilde{E}_z$, and $\tilde{J}_x$, $\tilde{J}_z$ are the Fourier transforms of the tangential electrical field and the current density components in the conducting strip. The elements of the dyadic impedance Green's function can now be found, and are given by:

$$\tilde{Z}_{xx}(\alpha,\beta,H)=i\frac{\alpha\beta}{\omega(\alpha^2+\beta^2)}\left[F_1+\frac{\beta}{\alpha}F_2-F_3+\frac{\alpha}{\beta}F_4\right], \quad (4)$$

$$\tilde{Z}_{xz}(\alpha,\beta,H)=-i\frac{\alpha\beta}{\omega(\alpha^2+\beta^2)}\left[\frac{\beta}{\alpha}F_1+F_2-\frac{\beta}{\alpha}F_3+F_4\right], \quad (5)$$

$$\tilde{Z}_{zx}(\alpha,\beta,H)=i\frac{\alpha\beta}{\omega(\alpha^2+\beta^2)}\left[\frac{\alpha}{\beta}F_1-F_2+\frac{\beta}{\alpha}F_3-F_4\right], \quad (6)$$

$$\tilde{Z}_{zz}(\alpha,\beta,H)=i\frac{\alpha\beta}{\omega(\alpha^2+\beta^2)}\left[-F_1-\frac{\alpha}{\beta}F_2+F_3+\frac{\beta}{\alpha}F_4\right], \quad (7)$$

where $\beta$ is the single microstrip phase constant, and

$$F_1=i\omega^2\mu_0\epsilon_1\frac{k}{\mu}\frac{g_3g_5}{g_1g_2};\quad F_2=\omega^2\mu_0\frac{g_5}{\gamma_0 g_2} \quad (8)$$

$$F_3=i\omega^2\mu_0\epsilon_1\frac{k}{\mu}\frac{\gamma_0}{\gamma_2\gamma_{e1}g_1}\coth(\gamma_{e1}d)\tanh(\gamma_2h);$$

$$F_4=\frac{\gamma_0 g_4}{g_1}\coth(\gamma_{e1}d)\tanh(\gamma_2h). \quad (9)$$

Also, the remaining parameters appearing in Eqs. (4) to (9) are given by

$$g_1=\epsilon_0+\frac{\epsilon_1}{\gamma_{e1}}\left[\frac{\epsilon_0}{\epsilon_2}\gamma_2\tanh(\gamma_2h)+\gamma_0\right]\coth(\gamma_{e1}d)+\epsilon_2\frac{\gamma_0}{\gamma_2}\tanh(\gamma_2h), \quad (10)$$

$$g_2=\frac{\mu}{\mu_0}+\gamma_{h1}\left[\frac{1}{\gamma_2}\tanh(\gamma_2h)+\frac{1}{\gamma_0}\right]\coth(\gamma_{h1}d)+\frac{\mu}{\mu_0}\frac{\gamma_2}{\gamma_0}\tanh(\gamma_2h), \quad (11)$$

$$g_3=\frac{1}{\gamma_{e1}}\left[1+\frac{\gamma_0}{\gamma_2}\tanh(\gamma_2h)\right]\coth(\gamma_{e1}d), \quad (12)$$

$$g_4=\frac{\gamma_2}{\gamma_{e1}}\left[\frac{\epsilon_1}{\epsilon_2}+\frac{\gamma_{e1}}{\gamma_2}\tanh(\gamma_{e1}d)\coth(\gamma_2h);\right.$$

$$g_5=\left[\frac{\mu}{\mu_0}+\frac{\gamma_{h1}}{\gamma_2}\coth(\gamma_{h1}d)\tanh(\gamma_2h)\right]. \quad (13)$$

Here,

$$\gamma_0^2=(\alpha^2+\beta^2-k_0^2);\quad \gamma_{h1}^2=\frac{\mu}{\mu_0}(\alpha^2+\beta^2-k_1^2);$$

$$\gamma_e^2=(\alpha^2+\beta^2-k_2^2) \quad (14)$$

$$\gamma_1^2=(\alpha^2+\beta^2-k_3^2);\quad k_0^2=\omega^2\mu_0\epsilon_0;\quad k_1^2=\omega^2\mu_0\epsilon_1 \quad (15)$$

$$k_2^2=\omega^2\left(\frac{\mu^2-k^2}{\mu}\right)\epsilon_1;\quad k_3^2=\omega^2\mu_0\epsilon_2. \quad (16)$$

In order to obtain the characteristic equation for the propagation constants, we use Galerkin's procedure along with Parseval's theorem. The solution of Eq. (3) depends upon a reasonable choice of basis functions, and they should contain the edge conditions of the currents. It is considered that the current distribution on each strip is the same as those given for a single strip.[6] Once the propagation constant is available, the characteristic impedance can be evaluated based on the power-current definition.[7]

The study of the coupling among transmission lines, as the microstrips shown in Fig. 1, requires the coupling factor in a frequency-dependent form be written like:[8]

$$C(\theta)=\frac{iC\sin\theta}{(1-C^2)^{1/2}\cos\theta+i\sin\theta}, \quad (17)$$

where $C$, the coupling factor at the central frequency, is given by

$$C=\frac{Z_{0e}-Z_{0o}}{Z_{0e}+Z_{0o}}. \quad (18)$$

Here, $Z_{0e}$ and $Z_{0o}$ are the even and odd mode characteristic impedances, respectively, and $\theta=\beta l$, $l$ being the length of the coupled region which is determined from the average of the even and odd phase constants, $\beta_e$ and $\beta_o$.

The directivity, which is the coupling which can occur to the theoretically isolated port, is:[8]

$$D=\left|\frac{\chi Z_{0e}-\psi Z_0 Z_{0o}}{\chi(Z_{0e}Z_0\cos\Theta_e+iZ_{0e}^2\sin\theta_e)-\psi(Z_{0o}Z_0\cos\theta_o+iZ_{0o}^2\sin\theta_o)}\right|, \quad (19)$$

where

$$\chi=2Z_{0o}Z_0\cos\theta_o+i(Z_{0o}^2+Z_0^2)\sin\Theta_o, \quad (20)$$

$$\psi=2Z_{0e}Z_0\cos\theta_e+i(Z_{0e}^2+Z_0^2)\sin\theta_e, \quad (21)$$

with $Z_0$ being the characteristic impedance of each individual line and $\theta_e$ and $\theta_o$ being the even and odd electrical lengths, respectively.

We show now numerical results for microstrip directional couplers containing a magnetized ferrite perpendicu-

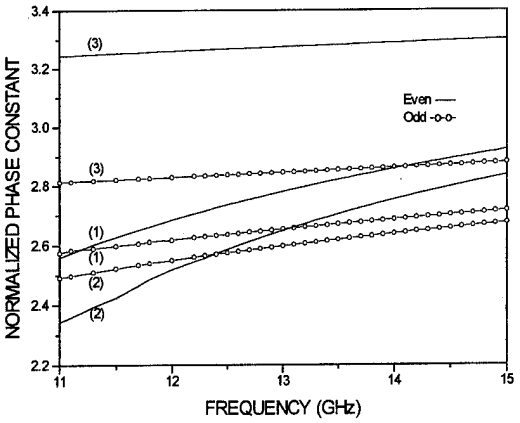



FIG. 2. Normalized phase constant as a function of the frequency for the parameters given in the main text. The labels (1), (2), and (3) refer to the cases where $H_0$=900 Oe, $H_0$=1300 Oe, and the isotropic situation.

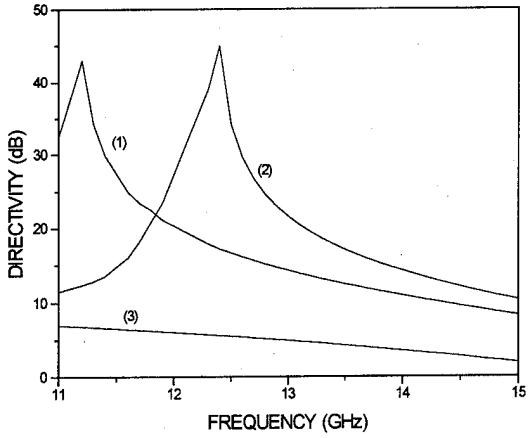



FIG. 4. Directivity as a function of the frequency for the same parameters and cases presented in Fig. (2).

larly to the substrate surface. We present results for the even and odd modes of propagation as well as for the coupler's parameters as a function of the frequency, various structural parameters, and the biasing magnetic field.

A ferrite substrate, with a saturation magnetization $4\pi M_s$=2150 G, a gyromagnetic ratio $\gamma$=2.855 MHz/Oe, a relative dielectric permittivity $\epsilon_{rl}=\epsilon_l/\epsilon_0=12.7$, and a thickness $d$=1.0 mm, was considered. The coupled strips have $w$=1.0 mm and $s$=0.5 mm.

Figure 2 presents the normalized phase constants for the odd and even modes of propagation in parallel coupled microstrip lines. The cases labeled (1) and (2) correspond to the utilization of a ferrimagnetic substrate with $h$=0 in Fig. 1, and the external magnetic field equal to 900 and 1300 Oe, respectively. The case with the label (3) corresponds to a numerical convergence for the isotropic case, which is obtained from (1) provide $\mu=\mu_0$ and $k$=0. Observe that the utilization of a ferrite substrate permits a reduction, and even an equalization, in the difference between the values of the phase velocities of the coupled modes. This represents a very interesting result, mainly if one is interested on the project of high directivity couplers.

In Fig. 3 we show the behavior of the coupling factor against the frequency, for the same cases discussed in Fig. 2. The coupled region length is 2.35 mm. As we expected, the strength of the coupling shows a significant dependence with the frequency, particularly for lower frequencies.

Figure 4 shows the curves obtained for the directivity as a function of the frequency, considering again the same three situations discussed in the previous figures. The best values of the directivity were obtained when it was considered a ferrite substrate, especially in the vicinities of the frequencies which equalize the phase velocities of the even and odd modes of propagation, observed in Fig. 2.

We have performed an analysis, within the spectral domain regime, for microstrip directional couplers supported by a ferrite material. It was shown that the utilization of this kind of substrate allows the development of high directivity couplers, through the variation of the magnitude of $H_0$. Agreement was observed when we compare our results with those presented by Janiczak and Kitlinski[9] for coupled symmetric microstrip lines, and by Alexópoulos[10] for the coupling factor and directivity.

We thank the Brazilian Research Agency CNPq for partial financial support.

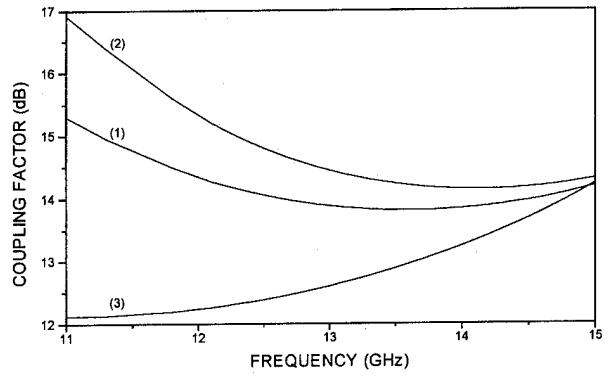



FIG. 3. Coupling factor as a function of the frequency for the same parameters and cases presented in Fig. (2).

[1] A. G. d'Assunção and E. J. Dantas, IEEE/AP-S International Symposium, Ann Arbor, MI **3**, 1508 (1993).
[2] M. Geshiro and T. Itoh, IEEE Trans. Microwave Theory Tech. **40**, 765 (1992).
[3] M. R. M. L. Albuquerque, A. G. d'Assunção, and A. J. Giarola, Int. Journal of Infrared and Millimeter Waves **14**, 1531 (1993).
[4] S. Bolioli, H. Benzina, and H. Baudrand, IEEE Trans. Microwave Theory Tech. **37**, 698 (1989).
[5] H. Lee and V. K. Tripathi, IEEE Trans. Microwave Theory Tech. **30**, 1188 (1982).
[6] K. C. Gupta, R. Garg, and I. J. Bahl, *Microstrip Lines and Slotlines* (Artech, Dedham, 1979).
[7] J. R. Brews, IEEE Trans. Microwave Theory Tech. **35**, 30 (1987).
[8] T. C. Edwards, *Foundations for Microstrip Circuit Design* (Wiley, NY, 1981).
[9] B. Janiczak and M. Kitlinski, Electron. Lett. **19**, 779 (1983).
[10] N. G. Alexópoulos, IEEE Trans. Microwave Theory Tech. **33**, 847 (1985).

# Magnetic losses in stripline/microstrip circulators

H. How and T. M. Fang
*Massachusetts Technological Laboratory, Inc., Belmont, Massachusetts 02178*

C. Vittoria
*Northeastern University, Boston, Massachusetts 02115*

R. Schmidt
*Microelectronics Products Division, M/A-COM, Inc., Burlington, Massachusetts 01803*

We have included losses in the analysis of a $3N$-port stripline/microstrip circulator and have reformulated the circulation conditions previously postulated for the lossless case. Our calculations have been compared to three published data on circulator designs biased below and above ferrimagnetic resonance. Scattering parameters at each port have been calculated as a function of assumed material losses and coupling capacitance of a multiport circulator. Wide transmission band or wide stop bands may be possible for a six port circulator biased above ferrimagnetic resonance.
© *1996 American Institute of Physics.* [S0021-8979(96)75508-6]

## INTRODUCTION

The present theory is able to calculate reasonably well the required external magnetic field and operating frequency at which the circulation condition of a stripline/microstrip circulator is obeyed. However, the present theory is not able to predict insertion loss or the coupling efficiency between ports at circulation. Clearly, the insertion loss must somehow be related to the intrinsic losses of the ferrite, both magnetic and electric losses. In this paper, we want to elevate this qualitative notion to a more precise quantitative prediction of insertion loss at circulation based upon intrinsic loss of the ferrite and external microwave loading to the circulator. We have avoided the traditional approach which relies on the use of Bessel functions which take only real numbers as arguments, since in the previous calculations intrinsic losses are assumed to be zero. Instead, new computational algorithms have been developed which directly process complex numbers upon which the circulator's interport impedances can be conveniently calculated. Also, previous theoretical formulations was based upon the assumption that at the circulation condition the transmission efficiency between the input and the circulation ports was 100% and the isolation port was zero. This assumption cannot be applied here. We need to relax this principle by allowing the circulation transmission to be a maximum, since there may be dissipation included in the ferrite. This suggests a theoretical formalism in which some sort of mathematical extremum conditions are derived from the equation of motion of the magnetization. We find that our formulation predicts exactly the same circulation conditions as derived by previous papers using the conventional formalism.[1–3] Once we were able to predict the circulation conditions calculated by others, we then calculated the insertion loss, isolation efficiency, and circulation transmission efficiency for various cases by including the ferrite losses in the formalism. Calculations compare quite well with measurements.[1–3]

## FORMULATION

In this paper we define a $3N$-port circulator to be a multi-port ferrite-junction circulator in which three ports are through ports capable of signal circulation in the normal sense and the other $(3N\text{-}3)$ ports are open-circuited ports which are used to provide additional capacitance tuning. The threefold symmetry of the junction requires ports $m$, $m+N$, and $m+2N$ to be characterized by the same parameters. Here $m$ is an integer and $1\leqslant m\leqslant N$. The azimuthal angle at the center of port $\alpha$ is denoted as $\phi_\alpha$ and $\phi_\alpha=2\pi(\alpha-1)/3N$ for $1\leqslant\alpha\leqslant 3N$. The port suspension angle at port $\alpha$ is $2\theta_\alpha$. Port 1 will be considered as the input port, and ports $1+N$ and $1+2N$ are either the transmission port or the isolation port, respectively.

The ferrite disk is of radius $R$, height $h$, whose dielectric constant, dielectric loss tangent, saturation magnetization, ferrimagnetic resonance (FMR) linewidth are denoted as $\epsilon_i$, $\tan\delta$, $4\pi M_i$, $\Delta H$, respectively. The ferrite disk is surrounded by a dielectric matching material filling the space between the metal strip and the ground plane(s) making up for the stripline/microstrip feeder lines. The dielectric constant of the dielectric filling material is denoted as $\epsilon_i$.

The six-port circulator has been previously formulated and reported in Ref. 3. We derive in this paper the formulation of a general $3N$-port circulator in which the ports may not necessarily have the same port angles. Denote $a_{\text{in}}$ as the incident rf-magnetic field at port 1 and $a_\alpha$, $1\leqslant\alpha\leqslant 3N$, as the average rf-magnetic field at port $\alpha$. Analogous to the derivations in Ref. 3 $a_\alpha$ can be solved in terms of $a_{\text{in}}$ from the following $3N$ coupled linear equations:

$$\sum_{\beta=1}^{3N}(Z_\alpha\delta_{\alpha\beta}+G_{\alpha\beta})a_\beta=2a_{\text{in}}Z_a\delta_{\alpha 1},\qquad \text{for } 1\leqslant\alpha\leqslant 3N, \tag{1}$$

where $G_{\alpha\beta}$ are the interport impedances given by

$$G_{\alpha\beta}=-iZ_f\left(\frac{\theta_\beta}{\pi}\right)\sum_{n=-\infty}^{\infty}\left[\frac{n}{x}\left(1-\frac{\kappa}{\mu}\right)-\frac{J_{n+1}(x)}{J_n(x)}\right]^1\left(\frac{\sin n\theta_\alpha}{n\theta_\alpha}\right)\left(\frac{\sin n\theta_\beta}{n\theta_\beta}\right)e^{\text{in}(\phi_\alpha-\phi_\beta)},$$

$$x=kR,\quad k=\omega(\mu_{\text{eff}}\epsilon_f)^{1/2}/c,$$

$$Z_d=(\mu_0/\epsilon_d\epsilon_0)^{1/2},\quad Z_f=(\mu_{\text{eff}}\mu_0/\epsilon_f\epsilon_0)^{1/2},$$

 0021-8979/96/79(8)/5739/3/$10.00 © 1996 American Institute of Physics 

$$\mu_{\text{eff}}=(\mu^2-\kappa^2)/\mu, \quad \mu=1+f_0 f_m(f_0^2-f^2),$$
$$\kappa=f f_m/(f_0^2-f^2),$$
$$f_m=4\pi\gamma M_s, \quad f_0=\gamma H_i. \tag{2}$$

$H_i$ is the internal dc magnetic field, $c$ denotes the speed of light in vacuum, $\gamma$ the gyromagnetic ratio, and $\delta_{\alpha\beta}$ is the Kronecker delta function. Finally, the wave impedance viewed at port $\alpha$ is

$$Z_\alpha=iZ_d \cot(x_\alpha\omega\sqrt{\epsilon_{re}}/c).$$

For stripline port $\epsilon_{rc}=\epsilon_d$, and for microstrip port $\epsilon_{rc}=1+q(\epsilon_d-1)$, where $q$ denotes the filling factor of the dielectric in the microstrip transmission line.

We note that Eq. (2) can be evaluated only if $x(=kR)$ is real. However, when material becomes lossy, both dielectric and magnetic imperfections need to be accounted for explicitly. For lossy ferrites the dielectric constant $\epsilon_f$ shall be replaced by $\epsilon_f(1+i\tan\delta)$ and the internal field $H_i$ by $H_i-(i\Delta H/2)f/f_i$, where $f_i$ denotes the frequency at which the linewidth $\Delta H$ was measured (usually at 10 GHz). As such, $x$ becomes a complex number and Eq. (2) can no longer be appropriate for numerical evaluation. Other numerical schemes have to be used as an alternative. Actually, Eq. (2) has been purposely cast in the form which facilitates complex-number calculation. That is, the ratio between two Bessel functions of subsequent orders can be expressed in a form involving continued fractions:[4]

$$\frac{J_\nu(z)}{J_{\nu-1}(z)}=\frac{1}{2\nu z^{-1}-}\,\frac{1}{2(\nu+1)z^{-1}-}\,\frac{1}{2(\nu+2)z^{-1}-}\cdots, \tag{3}$$

in which $z$ can be a complex number and $\nu$ a real number (not necessarily an integer). Equation (3) converges rather rapidly and the radii of convergence in the $z$ and the $\nu$ variables are both infinite.

The scattering parameters can now be calculated as

$$S_{11}=1-a_1/a_{\text{in}}, \quad S_{(1+N)1}=-a_{1+N}/a_{\text{in}},$$
$$S_{(1+2N)1}=-a_{1+2N}/a_{\text{in}}. \tag{4}$$

The circulation conditions in the presence of material imperfections are rephrased as

$$|a_{11}|=\text{maximum},$$
$$|a_{1+N}|=\text{minimum (or maximum)}, \tag{5}$$
$$|a_{1+2N}|=\text{maximum (or minimum)}.$$

Equation (5) describes the case when port $1+N$ is the transmission (isolation) port and port $1+2N$ is the isolation (transmission) port. We note that Eq. (5) needs to be maximized/minimized for at least two conditions, the third one will hold automatically due to the three-fold symmetry of the ferrite junction. Optimization of scattering parameters, or searching for circulation conditions, Eq. (5), needs to be performed with respect to, at least, two independent circulator variables with others being treated as parameters. Traditionally, $\epsilon_i$ and $R$ were used as variables to solve for the "lossless" circulation conditions, $|a_{11}|=1$ and, say, $|a_{1+N}|=0$, other parameters are specified beforehand, such as the desired circulation frequency, port suspension angle(s), internal field, and other parameters characterizing the ferrite material. In this paper we may use any of the quantities, $f$, $\theta_\alpha$, $\epsilon_i$, $R$, and/or $H_i$ as the independent variables exploiting the so-called multidimensional simplex method in optimizing the circulation conditions, Eq. (5). Multidimensional simplex method,[5] although it is relatively slow in comparison with other slope-related methods, is quite robust and efficient in the present calculations.

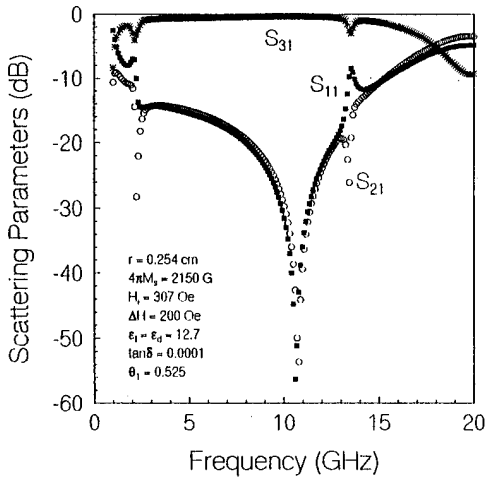



FIG. 1. Optimization of Wu and Rosenbaum's circulator design for better isolation and insertion loss.

## RESULTS

Figure 1 shows the calculated scattering parameters of the optimized design of the three-port circulator proposed by Wu and Rosenbaum.[1] In this design the ferrite used was magnesium ferrite (TT1-390, Trans-Tech, MD) possessing the following parameters: $4\pi M_i=2150$ G, $\Delta H=540$ Oe, $\epsilon_f=12.7$ $(=\epsilon_d)$, and $\tan\delta=2.5\times10^{-4}$. In the calculation we also use $r=0.254$ cm, and $\theta_1=0.525$ rad. After optimization of Eq. (5) with respect to $H_i$ and $f$, we obtain $H_i=307$ Oe

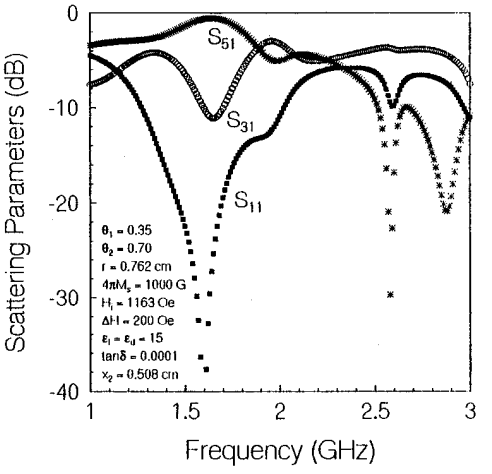



FIG. 2. Optimization of Riblet's sixport circulator design allowing for wideband transmission operation.

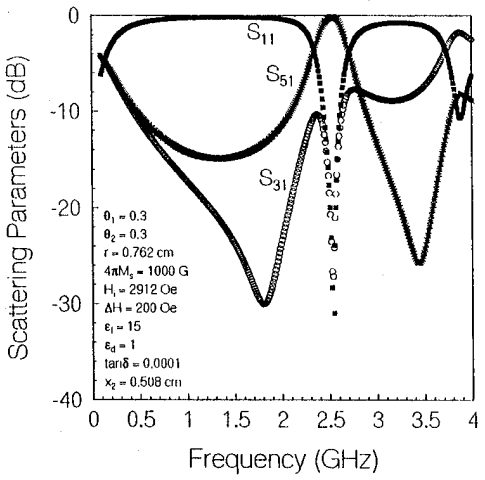



FIG. 3. Optimization of Riblet's sixport circulator design allowing for wide stop band protection.

with an insertion loss $-0.255$ dB at the central circulation frequency $f_0=10.629$ GHz. The transmission band extends from 2.615 to 12.97 GHz with insertion loss $-1.01$ and $-0.595$ dB, respectively. The measured absorption peak in $S_{11}$ at 13.2 GHz due to excitation of second-order harmonic can also be identified in Fig. 1. However, the wide-band feature of the above circulator was not measured experimentally. It was realized that the internal field has to be uniformized before the real bandwidth of the circulator can be measured.[6]

Figure 2 shows the calculated scattering parameters for a six-port stripline circulator operating above FMR. This design was originally proposed by Riblet which was intended for high power wideband operation.[2] For this design $r=0.762$ cm, $4\pi M_1=1000$ G, $\epsilon_1=\epsilon_d=15$, $\Delta H=200$ Oe, $\tan\delta=0.0001$, and $x_1=0.508$ cm. The external field used by Riblet was 2000 Oe and the port suspension angles were $\theta_1=\theta_2=0.425$. However, we found that Riblet's design has not been optimized. After optimizing the circulation conditions, Eq. (5), using $H_i$, $\theta_1$, $\theta_2$, and $f$ as the independent variables we found that $\theta_1=0.35$ rad, $\theta_2=0.70$ rad, $H_i=1163$ Oe with the central transmission frequency located at 1.64 GHz ($-0.56$ dB insertion loss). The transmission band extends from 1.37 to 1.77 GHz and the bandwidth is about 24.4% of the transmission frequency.

Another circulator design using Riblet's parameters which may have potential applications is shown in Fig. 3. In this design $\theta_1=\theta_2=0.3$, $\epsilon_d=1$ ($\neq\epsilon_1$), and $H_i=2912$ Oe. As shown in Fig. 3 the calculated insertion loss minimum locates at 2.528 GHz with a value of $-0.193$ dB. The design does not show wideband operation, since the bandwidth is only about 6.1% of the transmission frequency. However, the advantage of using the design of Fig. 3 is that it is easy to be fabricated, since air can be conveniently used as the dielectric filling material providing the greatest dielectric breakdown voltage. Furthermore, it is seen in Fig. 3 that the transmission band is surrounded by two wide stopbands where the circulator becomes highly reflective (reflection loss $-0.3$ and $-1$ dB, respectively). The circulator can be thus deployed in front of a frequency selective radome which, while it is intended to transmit/receive signals at the desirable frequencies near 2.528 GHz, blocks effectively other unwanted jamming/interfering signals above and below the transmission band in wide frequency ranges to protect the electronics inside the radome.


[1] Y. S. Wu and F. J. Rosenbaum, IEEE Trans. Microwave Theory Tech. **MTT-22**, 894 (1974).

[2] C. P. Riblet, IEEE Trans. Microwave Theory Tech. **MTT-28**, 125 (1980).

[3] H. How, T. M. Fang, C. Vittoria, and R. Schmidt, IEEE Trans. Microwave Theory Tech. **42**, 1272 (1994).

[4] *Handbook of Mathematical Functions with Formulas, Graphs, and Mathematical Tables*, edited by M. Abramowitz and I. A. Stegun (National Bureau of Standards, , Washington, DC, 1964), Applied Mathematics Series, 55, p. 363.

[5] W. H. Press, S. A. Teukolsky, W. T. Vetterling, and B. P. Flannery, *Numerical Recipes* (Cambridge University Press, New York, 1992), Chap. 10.

[6] E. Schloemann and R. E. Blight, IEEE Trans. Microwave Theory Tech. **MTT-34**, 1394 (1986).

# Experimental determination of an effective demagnetization factor for nonellipsoidal geometries

Guobao Zheng, M. Pardavi-Horvath, and Xiaohua Huang
*Institute for Magnetics Research, The George Washington University, Washington, DC 20052*

B. Keszei and J. Vandlik
*Institute for Materials Science, H-1525 Budapest, P.O.B. 49, Hungary*

For a nonellipsoidal magnetic sample, the internal magnetic field $\mathbf{H}_{\text{int}}(\mathbf{r})$ is inhomogeneous even when a uniform external magnetic field $\mathbf{H}_{\text{app}}$ is applied to it. In such a case the elements of the demagnetizing tensor become position-dependent, $\mathbb{N}=\mathbb{N}(\mathbf{r})$. The knowledge of the *local* demagnetization tensor is important for the analysis and design of devices using finite size and shape magnetic elements. The demagnetizing tensor elements can be calculated analytically and/or numerically, however, often a quick check of the extent of the inhomogeneity of the magnetization distribution of a sample, or a single approximate value of the demagnetizing factor for the given non-ellipsoidal geometry, would be satisfactory. Therefore a method to define and measure an effective demagnetizing tensor element $N_{\text{eff}}$ for rectangular and circular shapes has been developed. Experiments, performed on $2\times4$ mm$^2$ yttrium iron garnet samples up to 220 $\mu$m thickness, show that the analytical approximation can be used to define an $N_{\text{eff}}$. But even for a length/thickness ratio of 200, the thin film approximation still is in an error of 3.7%. © *1996 American Institute of Physics.* [S0021-8979(96)75608-9]

## I. INTRODUCTION

Ferrite elements are widely used in microwave devices, isolators, circulators, and phase shifters. The traditional elements have a spherical shape and uniform magnetization.

As the industry turns to monolithic integrated/hybrid nonreciprocal microwave devices, planar geometries have to be used. At microwave frequencies, the size of a distributed microstrip circulator is related to the wavelength in the ferrite ($\sim r/2$).

The magnetization distribution in modern planar ferrite elements, due to the nonellipsoidal shape of the ferrite, is no more uniform. This gives rise to nonuniform internal fields, affecting the operation of the device. In planar microwave devices, the thickness of the layers is in the range of 100 $\mu$m, and the lateral dimensions are comparable to the thickness so, the aspect ratio cannot be regarded as infinite. As a result, demagnetizing effects cannot be neglected. Due to inhomogeneous demagnetizing fields, the value of the external bias field in general has to be increased as compared to the case of the spherical geometry. Another problem, arising from the fact that the ferrite element is not a thin film, is that one has to solve the problem in three dimensions. The distribution of the internal magnetization of the ferrite and the electromagnetic field around the edges has a great important for device performance.[4] In designing magnetic devices, the range of $N_{zz}$ is the measure of the inhomogeneity of the internal field in the sample.

The inhomogeneity of magnetization should be taken into account in device design, i.e., the knowledge of *local* distribution of demagnetization factors $N_{ij}(x,y,z)$ is necessary. If the *local* demagnetizing tensor is known, the equilibrium distribution of the magnetization can be calculated by micromagnetic methods.

The demagnetizing correction is nontrivial for samples in open magnetic circuits. An exact correction can be obtained only for ellipsoids, where both the magnetization $\mathbf{M}$ and the demagnetizing field $\mathbf{H}_d$ are uniform under a uniform applied field $\mathbf{H}_{\text{app}}$.[5–7] If the three principal ellipsoid axes coincide with the $x$, $y$, and $z$ axes, then the internal field is:

$$\mathbf{H}_{in}=\mathbf{H}_{\text{app}}+\mathbf{H}_d=\mathbf{H}_{\text{app}}-\mathbb{N}\mathbf{M} \tag{1}$$

where $\mathbb{N}$ is a diagonal demagnetizing tensor, and $N_{xx}+N_{yy}+N_{zz}=1, 0\leqslant N\leqslant 1$ in SI units, and $0\leqslant N\leqslant 4\pi$ in CGS units.

For nonellipsoidal samples, if the sample is placed in a uniform applied field $\mathbf{H}_{\text{app}}$ along its axis, a demagnetization factor $N$ can be defined as the ratio of the average demagnetizing field to the average magnetization of the entire sample:[8]

$$\int_S \mathbf{H}_d(\mathbf{r})d\mathbf{S}=-N\int_S \mathbf{M}(\mathbf{r})d\mathbf{S}. \tag{2}$$

But now $N$ is the function of the aspect ratio, $m=L/D$ (length to diameter). So, the ellipsoidal approximation is no longer suitable and a relationship between the shape and size of the ferrite element and the demagnetizing factors should be developed. The demagnetizing factors, and/or the local demagnetizing tensor elements have been calculated analytically in Refs. 1–3 using various approximations. Nonuniform demagnetizing factors have been calculated in Ref. 1, based on a first order approximation, that the direction of the magnetization coincides with the direction of the local magnetic field at any point within the sample. This approximation may cause a 20% error. It is desirable to know the difference between the real demagnetizing factors and that calculated by Ref. 1.

In the present work an experimental method was developed to determine an *effective* demagnetizing factor $N_{\text{eff}}$ for thick, small rectangular and circular ferrite samples. The results are compared to $N_{\text{eff}}$, derived from Ref. 1, based on a technique of statistical averaging over the volume.

 0021-8979/96/79(8)/5742/3/$10.00 © 1996 American Institute of Physics

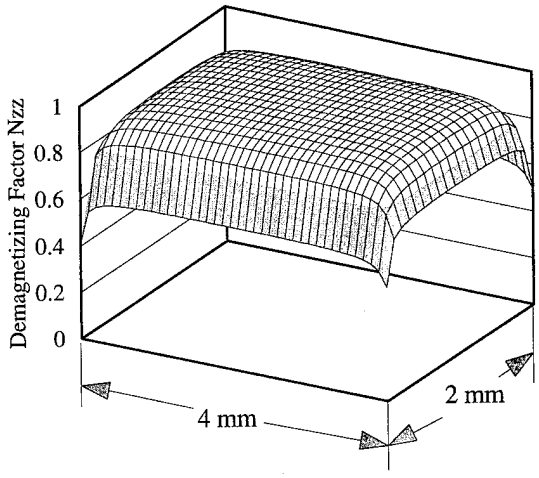



FIG. 1. Calculated distribution of local demagnetization factors $N_{zz}(x,y)$ on the center plane, $z=0$, of a $2\times4\times0.135$ mm$^3$ YIG sample.

## II. EXPERIMENTS

The method to determine an *effective* demagnetizing factor for a nonellipsoidal sample is based on the measurement of the in-plane and out-of-plane major hysteresis loops using a vibrating sample magnetometer (VSM). Experiments were performed on $4\times2$ mm$^2$ rectangular yttrium iron garnet (YIG) films ($4\pi M_s$ = 1780 G), in the thickness range from 4.7 to 220 $\mu$m; on 3–5 mm square YIG films of 140 $\mu$m thickness; and on round polycrystalline MnMg ferrites ($4\pi M_s$ = 2350 G) of 0.15 in. diameter, thickness from 0.005 in. to 0.025 in. The measured YIG samples were grown by liquid phase epitaxy on (111) GGG substrates. All samples were cut from the same wafer, and polished to the final thickness. The measured magnetization curves have been corrected for the paramagnetic contribution of the GGG substrate.

The procedure is illustrated for the case of the rectangular geometry. The dimensions of the rectangular sample are: $2a\times2b\times2h=2\times4\times0.135$ mm$^3$. For this configuration, the 3D distribution of demagnetizing factors, $N_{ij}(x,y,z)$ has been calculated. Figure 1 illustrates $N_{zz}(x,y)$ in the central plane ($z=0$) of the YIG sample. For this geometry the distribution of the magnetization is mostly uniform; inhomogeneous fields occur only around the edges of the sample.

The maximum $N_{zz}$ is at the center on the top surface. The smallest value is at the corners of the sample. If $N_{zz}(x,y)$ is calculated over planes, corresponding to different $z$, then after averaging $N_{zz}(x,y)$ over the plane, the maximum average Max $N_{zz}$ will appear on the top and bottom planes of sample, while the minimum $N_{zz}$ will be on the center plane of the sample. We expect that the experimentally determined $N_{zz,\mathrm{eff}}$ will correspond to the average of $N_{zz}(x,y,z)$ all over the sample.

$N_{\mathrm{eff}}$ can be determined from in-plane and out-of-plane hysteresis loops. For the case of negligible anisotropy (as compared to $4\pi M_s$), the loops are expected to be congruent after correcting for the demagnetizing factors. Based on this assumption, the expression $H_{\mathrm{in}} = H_{\mathrm{app}} - 4\pi M_s N_{\mathrm{eff}}$ has been used to find $N_{\mathrm{eff}}$, i.e., to correct the in-plane and out-of-plane loops until they coincide. First, it is assumed that the samples are thin enough, therefore, $N_{xx}$ approaches zero; i.e., the in-plane hysteresis loop is not corrected. Then, the out-of-plane loop should be corrected with a proper $N_{zz}$ until it overlaps with the in-plane loop. This procedure gives the minimum of $N_{zz}$. Next, it is considered that the inhomogeneous field exists not only in the out-of-plane direction, but also in-plane. So, both hysteresis loops should be corrected by $N_{zz}$ and $N_{xx}$ to arrive to the same loop. The final hysteresis loops, after corrected by demagnetizing factors, should not "overshoot," i.e., have a negative slope. This limiting $N_{zz}$ is the maximum $N_{zz}$, and Max $N_{zz}$ = Min $N_{zz}$ + $N_{xx}$. The values of Max $N_{zz}$ and Min $N_{zz}$, determined experimentally, are used to verify the numerical results of Refs. 1–3.

TABLE I. Thickness dependence of demagnetizing factors for MgMn-ferrite discs, diameter: $D=0.15$ in., height: $L=0.010$, 0.015, and 0.020 in.

| | $N$ | $D/L=15$ | $D/L=10$ | $D/L=7.5$ |
|---|---|---|---|---|
| $N_{xx}$ | Theory (2) | 0.0482 | 0.0696 | 0.0894 |
| | Measured | 0.0562 | 0.0785 | 0.0955 |
| $N_{zz}$ | Theory (2) | 0.904 | 0.861 | 0.821 |
| | Theory (3) | 0.8478 | 0.7967 | 0.7533 |
| | Measured | 0.758 | 0.725 | 0.698 |

## III. RESULTS AND DISCUSSION

The correction procedure has been applied to a series of YIG samples of same size, but having different thickness, and same thickness but different size; and circular MgMn ferrites of different thickness.

### A. Circular ferrite samples

Figures 2(a) and 2(b) illustrate the in-plane hysteresis loops before and after the correction was performed for circular ferrite samples of different aspect ratios ($D=0.15$ in.) and are given in Table I. Theoretical values for $N_{xx}$ in Table 1 are calculated by Eq. (2), and the corresponding $N_{zz}$ = $1-2N_{xx}$ are given in Table I. The difference between the experimental data and the theoretical results of the ellipsoidal approximation (2) is much larger than expected. Therefore, the solenoid approximation of Eq. (3) has been used to calculate the effective demagnetizing factors of circular samples:

$$N_{zz}=1-4LL_s/(\mu_0\pi D^2), \tag{3}$$

where $L_s$ contains the complete elliptic integrals, and $\mu_0$ is the permeability of vacuum. Table I shows that both Eqs. (2) and (3) underestimate the effect of the shape, i.e., the inhomogeneity of the internal field for disk shaped samples.

### B. Rectangular YIG samples

Measurements were done on $4\times2$ mm$^2$ YIG films up to 220 $\mu$m thickness. The theoretical results for the local demagnetizing tensor element $N_{zz}(x,y,z)$, are based on the first order approximation of Ref. 1. Calculated and measured demagnetizing factors are given in Table II and Fig. 3. In the theoretical estimation column, Max $N_{zz}$ is the average of

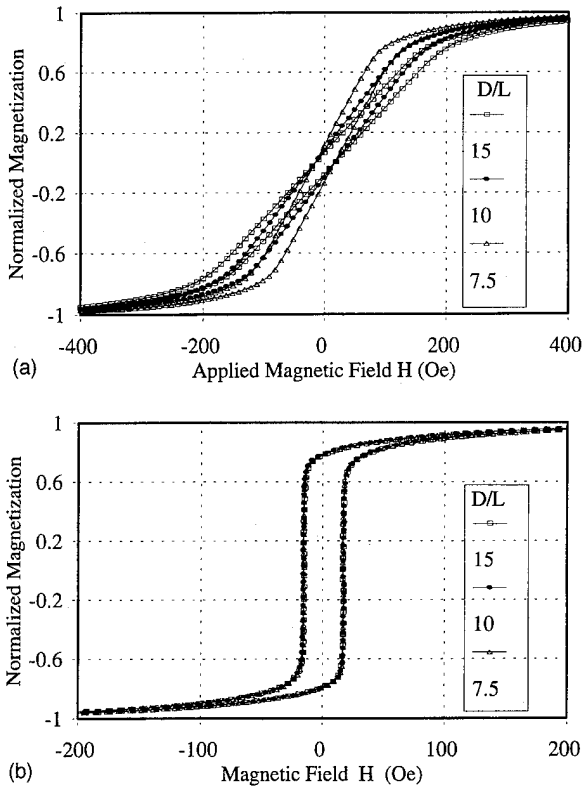



FIG. 2. In plane hysteresis loops for MnMg ferrite disks, $D$=0.15 in., $L$=0.010, 0.015, and 0.020 in.; (a) as measured, (b) after correcting by the demagnetizing factors $N_{xx}$ and $N_{zz}$.

demagnetization factors on the top (bottom) plane, min $N_{zz}$ is on the center plane; Avg $N_{zz}$ is the average all over the sample. The agreement between the averaged values of the first order approximation of Ref. 1 and the measured demagnetization factors is in good agreement with Ref. 1, however the experimental data suggest a different slope of the curve.

### C. Shape dependence of the demagnetizing factor

Measurements of the shape dependence of the magnetization curves are performed on $h$=140-$\mu$m-thick square ($L$=3, 4, and 5 mm) YIG samples with aspect ratio of $20 \leqslant L/h \leqslant 200$. The calculated and measured values of $N_{zz}$ are given in Table III. The difference between the measured Max $N_{zz}$ and the calculated value is 3% for the smallest

TABLE II. Shape dependence of demagnetizing factors for square YIG samples (side $L$, thickness $h$=140 $\mu$m).

| Demagnetization factor $N$ | | | $L/h$=21.4 | $L/h$=28.6 | $L/h$=35.7 | $L/h$=214.2 |
|---|---|---|---|---|---|---|
| $N_{xx}$ | Measured | | 0.042 | 0.0368 | 0.030 | (theor.) |
| $N_{zz}$ | Theory | Max | 0.864 | 0.867 | 0.868 | 0.964 |
| | | Min | 0.814 | 0.817 | 0.818 | 0.956 |
| | | Ave | 0.828 | 0.830 | 0.831 | 0.960 |
| | Measured | Max | 0.840 | 0.856 | 0.873 | |
| | | Min | 0.798 | 0.820 | 0.843 | |
| | Error | | 3.0% | 1.2% | 0.6% | ... |

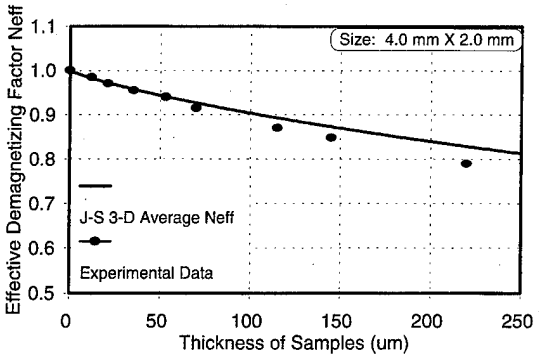



FIG. 3. Thickness dependence of the measured effective demagnetizing factor $N_{zz}$ of 2×4 mm$^2$ epitaxial YIG films (solid circles), compared to the averaged values calculated from Ref. 1 (solid line).

sample, and it is less than 1% for the 5 mm sample. However, for $L/h$=214 the calculated Max $N_{zz}$ is only 0.964, i.e., the validity of the thin film approximation is still worse than 3%.

## V. CONCLUSIONS

The internal field of a finite size, finite thickness magnetic material is nonuniform, which affects the operation of microwave ferrite devices. The knowledge of the *local* demagnetizing tensor elements $N_{ij}(x,y,z)$ is necessary to analyze and design such devices. Analytical calculations of the demagnetizing tensor elements are based on approximations. To investigate the applicability of these theories, a method, based on in-plane and out-of-plane hysteresis loop measurements, has been developed to define and measure an effective demagnetizing factor for nonellipsoidal samples. The measurements dependence of the effective $N_{zz}$, $N_{xx}$ on thickness, sample size, and shape have been performed on rectangular YIG and circular MgMn ferrite samples. The measured data have been compared to the properly averaged, calculated results, and it is concluded, that the agreement between the calculated and measured $N_{\text{eff}}$ values for rectangular YIG samples is very good, however, the available analytical calculations underestimate the inhomogeneity for the case of disc-shaped samples.

## ACKNOWLEDGMENTS

Stimulating discussions with colleagues from the Ferrite Development Consortium and the Magnetics Research Institute are appreciated. This work was partially supported by ARPA Ferrite Development Consortium.

[1] R. I. Josephs and E. Schloemann, J. Appl. Phys. **36**, 1579 (1965).
[2] R. M. Bozorth, *Ferromagnetism* (IEEE, New York, 1993), pp. 848–849.
[3] D-X. Chen, J. A. Brug, and R. B. Goldfarb, IEEE Trans. Magn. **27**, 3601 (1991).
[4] G. Vertesy, M. Pardavi-Horvath, L. Bodis, and I. Pinter, J. Magn. Magn. Mater **75**, 389 (1988).
[5] J. Clerk Maxwell, *A Treatise on Electricity and Magnetism*, 3rd ed., (Oxford, Clarendon, 1892), Vol. 2, pp. 66–73.
[6] H. Zijlstra, *Experimental Methods in Magnetism* (North-Holland, Amsterdam, 1967),Vol. 2, pp. 69–72.
[7] J. A. Osborn, Phys. Rev. **67**, 35 (1945).
[8] E. C. Stoner, Philos. Magn. Ser. 7 **36**, 803 (1945).

# Quantum fluctuations in antiferromagnets of the $BX_2$ family (abstract)

E. Rastelli and A. Tassi
*INFM, Dipartimento di Fisica, Università di Parma, 43100 Parma, Italy*

The hexagonal antiferromagnets of the $BX_2$ family, where B is a magnetic ion, and X a halogen, are characterized by an in plane exchange interaction $J$ much stronger than the exchange interaction $J'$ along the $c$ axis, so that some features of the triangular antiferromagnet (TA) could survive in these real compounds. In particular we are interested to investigate a possible "planar" phase with the spins lying in the $c$ plane supported by quantum fluctuations when an external magnetic field $H$ is applied perpendicular to the $c$ axis. We find that such a phase is stable for sufficiently small interplane coupling owing to the zero point motion energy, whereas an "umbrella" phase would be expected on the basis of the classical approximation for any nonzero interplane coupling. Notice that for the TA model the planar and umbrella configurations are degenerate in classical approximation for any $H$ and infinite isoenergetic planar configurations exist. Quantum fluctuations select a planar configuration with a spin over three opposite to the field.[1] We find that the classical scenario itself is substantially different for any $j=J'/J\neq 0$, because only a planar configuration with a spin over three nearly perpendicular to the field and the umbrella configuration minimize the energy of the model and the umbrella is stable. However, quantum fluctuations stabilize the planar configuration for any $H$ below a critical interplane coupling $j^*$. For intermediate $j$ the planar configuration is stable for low and high fields, whereas only the umbrella phase is stable of $j$ large enough. © *1996 American Institute of Physics.* [S0021-8979(96)69808-3]

[1] A. V. Chubukov and D. I. Golosov, J. Phys. CM **3**, 69 (1991).

# Spin configurations in $VBr_2$ supported by uniaxal anistropy and quantum fluctuations (abstract)

E. Rastelli and A. Tassi
*INFM, Dipartimento di Fisica, Università di Parma, 43100 Parma, Italy*

Small single ion anisotropy is believed to play an important role in selecting the plane where the spins lie in hexagonal anitferromagnets on the basis of the classical approximation. For instance, in $VBr_2$ a small easy-axis single ion anisotropy is expected to force the spins in a plane containing the $c$ axis and the classical approximation suggests that the spin configuration should be an "umbrella" configuration with axis along the external magnetic field perpendicular to the $c$ axis.[1] However, the classical expectation is questionable because the zero point motion energy supports spin configurations with the spins lying in a plane containing the magnetic field. We find that the "planar" configuration with the spins in the plane containing the $c$-axis and the external magnetic field is stable for interplane coupling and anisotropy sufficiently small. Since this is the case of $VBr_2$, our results rise some doubts about the interpretation of experimental data in $VBr_2$ when an external magnetic field is applied. © *1996 American Institute of Physics.*
[S0021-8979(96)69908-X]

[1] H. Kadowaki, K. Ubukoshi, and K. Hirakawa, J. Phys. Soc. Jpn. **54**, 363 (1985).

 0021-8979/96/79(8)/5745/1/$10.00 © 1996 American Institute of Physics 

# Henkel plots and the Preisach model of hysteresis

C. J. Buehler and I. D. Mayergoyz
*Department of Electrical Engineering, University of Maryland, College Park, Maryland 20742*

Interpretation of Henkel plots in terms of the Preisach model is revisited. The Preisach model is treated as a purely phenomenological one and the Henkel plots are directly related to experimental data, namely, to the first-order transition curves. © *1996 American Institute of Physics.* [S0021-8979(96)20208-4]

Henkel plots have been the focus of considerable research in magnetics in recent years. This is because these plots can provide some insights concerning interaction mechanisms that govern magnetization processes.[1,2] In a ground breaking paper of Basso and Bertotti,[3] the classical Preisach model has been used for the interpretation of Henkel plots. This line of research has been further extended in subsequent publications (see, for instance, Refs. 4 and 5). In all of these publications, the Preisach model has been viewed as a physical model. For this reason, the distribution (weight) function $p(\alpha,\beta)$ [or $\mu(\alpha,\beta)$] has been given a probabilistic interpretation, and it has been assumed to be positive. It has been shown by Basso and Bertotti that, under this assumption, the classical Preisach model imposes some restrictions on the possible configurations of Henkel plots. It has been suggested that these restrictions on Henkel plots can be removed by using the moving Preisach model.[6]

In this paper, the interpretation of Henkel plots in terms of the Preisach model is revisited. The Preisach model is treated as a purely phenomenological one for which the question of its applicability can be posed and answered on solely mathematical grounds without invoking any physical arguments. For this reason, no *a priori* assumptions are made concerning the weight function $\mu(\alpha,\beta)$ except those that are imposed by the experimental data used for the identification of the model. By using this approach, we relate the Henkel plots directly to first-order transition curves. These curves constitute the experimental data used for identification.[7] In this way, it is demonstrated that under some conceivable conditions on the first-order transition curves, the classical Preisach model can yield Henkel plots that may lie outside the constrained region established by Basso and Bertotti. Another (and probably more important) benefit of this approach is the ability to compute the Henkel plots directly in terms of first-order transition curves without numerical "preparation" of the ac demagnetized state. This is important because the shape of the Henkel plots is very sensitive to the precise method by which the ac demagnetized state is prepared.[4] This sensitivity has been one reason (among other things) why a "thermally" demagnetized state has been introduced.[5]

To start the discussion, we recall that Henkel plots represent the $\tilde{f}_d$ vs $\tilde{f}_r$ relationship, where $\tilde{f}_d=f_d/f_\infty$ and $\tilde{f}_r=f_r/f_\infty$ and where the physical meaning of $f_d$, $f_r$ and $f_\infty$ is demonstrated by Fig. 1. It is customary to associate the linear Wohlfarth relation

$$f_d(u)=f_\infty-2f_r(u) \tag{1}$$

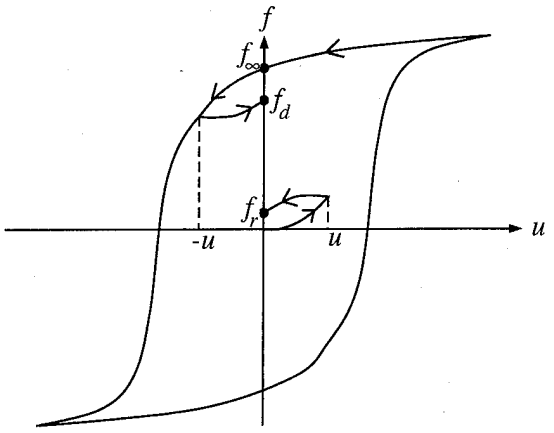



FIG. 1. Definition of Henkel plot variables $f_d$, $f_r$, and $f_\infty$.

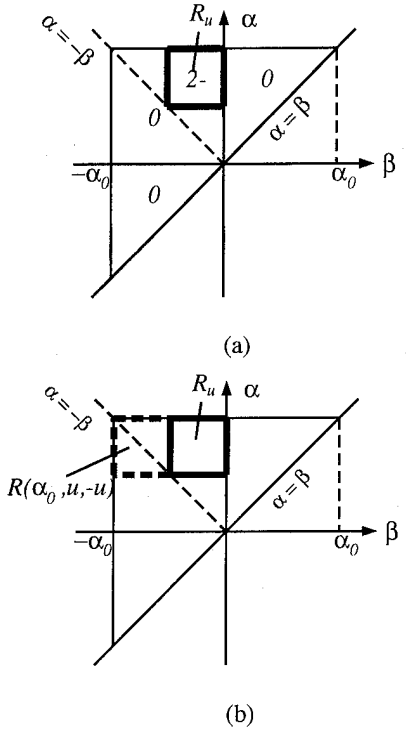



FIG. 2. Rectangular regions of integration.

 0021-8979/96/79(8)/5746/3/$10.00 © 1996 American Institute of Physics

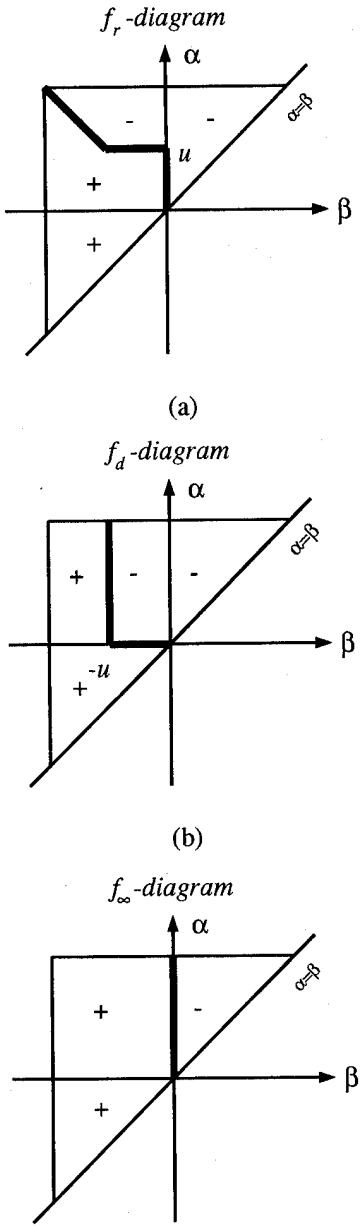



FIG. 3. (a) $f_r$ diagram, (b) $f_d$ diagram, and (c) $f_\infty$ diagram.

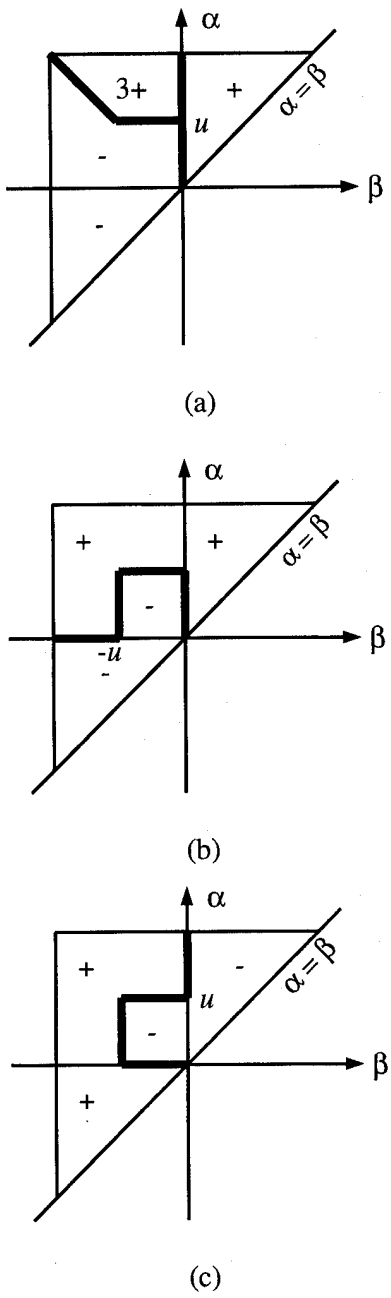



FIG. 4. Intermediate steps in manipulations of $(f_\infty - 2f_r)$ diagrams.

with noninteracting "particles," while inequalities

$$f_d(u) > f_\infty - 2f_r(u), \tag{2}$$

$$f_d(u) < f_\infty - 2f_r(u) \tag{3}$$

are associated with positive (magnetizing-like) and negative (demagnetizing-like) interactions, respectively. It has been shown[3] that the classical Preisach model,

$$f(t) = \iint_{\alpha \geqslant \beta} \mu(\alpha,\beta)\hat{\gamma}_{\alpha\beta}u(t)d\alpha\, d\beta, \tag{4}$$

imposes the restriction (3) on Henkel plots under the assumption that $\mu(\alpha,\beta)$ is positive. To revisit this issue, we introduce

$$\Delta f = f_d - (f_\infty - 2f_r), \tag{5}$$

and shall next derive the expression for $\Delta f$ in terms of first-order transition curves. To this end, we first show that

$$\Delta f = -2\iint_{R_u} \mu(\alpha,\beta)d\alpha\, d\beta, \tag{6}$$

where $R_u$ is the rectangle pictured in Fig. 2(a).

The proof of (6) is based on the symmetry of the weight function,

$$\mu(\alpha,\beta) = \mu(-\beta,-\alpha), \tag{7}$$

and the careful manipulation of Preisach diagrams that correspond to $f_r$ and $f_d$ "states," respectively. Diagrams shown

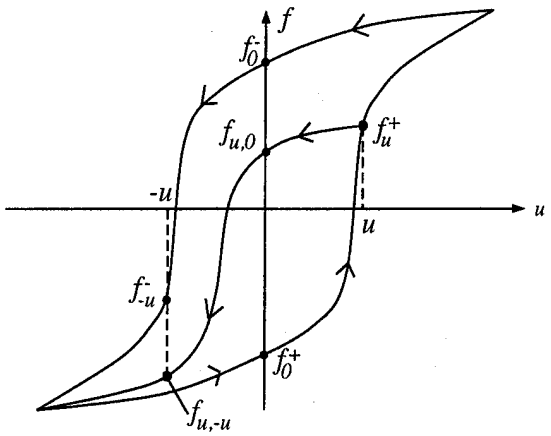



FIG. 5. Illustration of relevant first-order transition curve values.

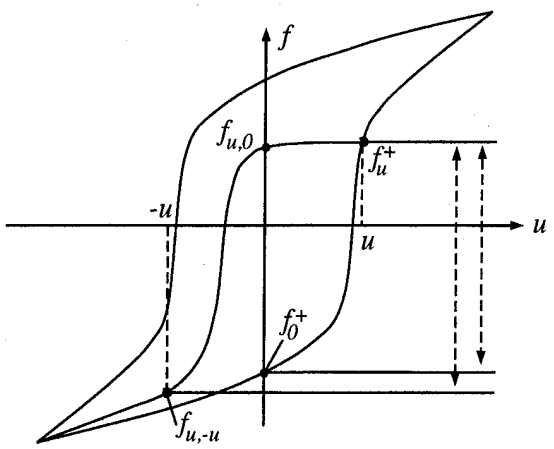



FIG. 6. Example first-order transition curves, which satisfy the conditions for a demagnetizing-like Henkel plot.

in Figs. 3(a)–3(c) correspond to $f_r$, $f_d$, and $f_\infty$ "states." Subtracting twice the $f_r$ diagram from the $f_\infty$ diagram yields the intermediate result shown in Fig. 4(a). By using the symmetry property of $\mu(\alpha,\beta)$, we can simplify this diagram to the one shown in Fig. 4(b). By using transposition about the symmetry line $\alpha=-\beta$, we end up with the diagram shown in Fig. 4(c). Now, we notice that the $f_d$ diagram and the $(f_\infty-2f_r)$ diagram differ only in a rectangular region. By performing one more subtraction, we arrive at the final Preisach $\Delta f$ diagram [Fig. 2(a)]. This diagram leads to the expression (6).

Clearly, if $\mu(\alpha,\beta)$ is assumed to be positive, then the integral in (6) must always be negative, leading to the conclusion[3] that the classical Preisach model always produces demagnetizing-like Henkel plots. However, we shall not use any *a priori* assumption concerning $\mu(\alpha,\beta)$, but rather relate the integral in (6) directly to first-order transition curves.

To achieve this, we transform Eq. (6) as follows:

$$\Delta f=-2\left(\iint_{R(\alpha_0,u,0)}\mu(\alpha,\beta)d\alpha\,d\beta-\iint_{R(\alpha_0,u,-u)}\mu(\alpha,\beta)d\alpha\,d\beta\right), \tag{8}$$

where rectangles $R(\alpha_0,u,0)$, $R(\alpha_0,u,-u)$, and $R_u$ are related by the expression $R(\alpha_0,u,0)=R(\alpha_0,u,-u)+R_u$ and rectangle $R(\alpha_0,u,-u)$ is outlined in Fig. 2(b).

It can be shown (see Ref. 7 p. 68) that the integrals in (8) can be directly related to the first-order transition curves as follows:

$$2\iint_{R(\alpha_0,u,0)}\mu(\alpha,\beta)d\alpha\,d\beta=f_0^--f_{u,0}, \tag{9}$$

$$2\iint_{R(\alpha_0,u,-u)}\mu(\alpha,\beta)d\alpha\,d\beta=f_{-u}^--f_{u,-u}, \tag{10}$$

where the meaning of $f_0^-$, $f_{-u}^-$, $f_{u,0}$, and $f_{u,-u}$ is demonstrated by Fig. 5. By substituting (9) and (10) in (8), we obtain

$$\Delta f=(f_{-u}^--f_0^-)+(f_{u,0}-f_{u,-u}). \tag{11}$$

By using symmetry, we easily find

$$f_{-u}^--f_0^-=-(f_u^+-f_0^+). \tag{12}$$

From (11) and (12), we derive the final expression:

$$\Delta f=(f_{u,0}-f_{u,-u})-(f_u^+-f_0^+). \tag{13}$$

It is clear that the classical Preisach model can produce a magnetizing-like Henkel plot if

$$f_{u,0}-f_{u,-u}>f_u^+-f_0^+. \tag{14}$$

As shown in Fig. 6, it is conceivable to have the first-order transition curves, which satisfy inequality (14).

Next, we shall demonstrate that the Henkel plots can be directly computed in terms of the first-order transition curves. The calculation of these plots in terms of the first-order transition curves is based on the following observations. First, $f_d$ can be construed as $-f_{u,0}$, and $f_\infty$ as $-f_0^+$. Second, by using these facts and substituting (5) into (13), we derive the following expression for $f_r$ in terms of the first-order transition curves:

$$f_r=f_{u,0}-\frac{1}{2}(f_{u,-u}+f_u^+). \tag{15}$$

Thus, $f_r$ can be computed by using first-order transition curves, i.e. without numerical preparation of the demagnetized state.


[1] O. Henkel, Phys. Status Solidi **7**, 919 (1964).
[2] E. P. Wohlfarth, J. Appl. Phys. **29**, 595 (1958).
[3] V. Basso and G. Bertotti, IEEE Trans. Magn. **30**, 64 (1994).
[4] F. Vajda, E. Della Torre, and R. D. McMichael, J. Appl. Phys. **75**, 5689 (1994).
[5] P. D. Mitchler, E. Dan Dahlberg, E. Engle, and R. M. Roshko, IEEE Trans. Magn. **31**, 2499 (1995).
[6] E. Della Torre, IEEE Trans. Audio Electroacoust. **14**, 86 (1966).
[7] I. D. Mayergoyz, *Mathematical Models of Hysteresis* (Springer, New York, 1991).
[8] I. D. Mayergoyz and G. Freidman, IEEE Trans. Magn. **24**, 212 (1988).

# Kinetic Ising systems as models of magnetization switching in submicron ferromagnets

Howard L. Richards,[a] Scott W. Sides,[a] Mark A. Novotny,[b] and Per Arne Rikvold[a]
*Supercomputer Computations Research Institute, Florida State University, Tallahassee, Florida 32306-3016*

Experimental techniques, such as magnetic force microscopy (MFM), have recently enabled the magnetic state of individual submicron particles to be resolved. Motivated by these experimental developments, we use Monte Carlo simulations of two-dimensional kinetic Ising ferromagnets to study the magnetic relaxation in a negative applied field of a grain with an initial magnetization $m_0=+1$. The magnetostatic dipole–dipole interactions are treated to lowest order by adding to the Hamiltonian a term proportional to the square of the magnetization. We use droplet theory to predict the functional forms for some quantities, which can be observed by MFM. One such quantity is the probability that the magnetization is positive, which is a function of time, field, grain size, and grain dimensionality. The relaxation is characterized by the number of droplets larger than a field-dependent critical size, which form during the switching process. Our simulations of the kinetic Ising model are in excellent agreement with droplet-theoretical predictions. The qualitative agreement between experiments and our simulations of switching in individual single-domain ferromagnets indicates that the switching mechanism in such particles may involve local nucleation and subsequent growth of droplets of the stable phase. © *1996 American Institute of Physics.* [S0021-8979(96)20308-0]

## I. INTRODUCTION

The processes by which magnetization reversal occurs in the nanoscale ferromagnets that will make up the next-generation recording media are the subject of active research. One quantity for which theory and experiment often disagree is the lifetime $\tau$, which is the time required for a particle with initial magnetization $m_0=+1$ to reach $m=0$ when a magnetic field in the $-\hat{z}$ direction is applied. Micromagnetics,[1] a theoretic technique in which differential equations are numerically solved on a lattice that is coarse grained compared to the physical lattice, predicts that the lifetime is given by the Arrhenius equation,

$$\tau \propto \exp(\beta\, \Delta F), \tag{1}$$

with $\Delta F \propto L^d$. Here $d$ is the dimension, $\beta^{-1}$ is the temperature in units of energy, $\Delta F$ is the free-energy barrier between the stable and metastable phases, and $L$ is the linear system size. [Equation (1) must be appropriately generalized if there is more than one barrier or path between the stable and metastable states.] This same prediction is made by the standard Néel–Brown theory of single-domain ferromagnets.[2,3] The evident failure of Eq. (1) with $\Delta F \propto L^d$ for somewhat larger grains is ascribed to the existence of more than one domain in larger particles, as is a corresponding peak in plots vs. $L$ of the switching field $H_{\rm sw}$, which is the field required to yield a given lifetime.

Recently, techniques such as MFM have been used to resolve the magnetic properties of *isolated, well-characterized* single-domain particles (see, e.g., Ref. 4). This is an important advance, since previous experiments on ferromagnetic powders left uncertainties due to the range of grain sizes and orientations and the local magnetic environments. Observations of individual particles by MFM have made it clear that even for many *single-domain* particles, Néel–Brown theory is inadequate.

We have applied the statistical-mechanical droplet theory of metastable decay to nanoscale ferromagnets with large uniaxial anisotropy, and compared Monte Carlo simulations of square-lattice Ising systems with droplet-theory predictions.[5] (For a review of droplet theory, see Ref. 6.) The agreement between theory and simulation is quite good, and despite the crudeness of the Ising model as a model for real magnets, it shows good qualitative agreement with the MFM experiments. We find rich $L$-dependent behavior in the standard Ising model, even though its equilibrium structure is a single domain for all $L$. This suggests that for some strongly anisotropic magnetic materials, magnetization reversal may occur through the nucleation and growth of nonequilibrium droplets. Details of our work are given in Refs. 5 and 7, including formulas for general dimensionality. For simplicity, we only discuss the two-dimensional case here.

## II. APPLIED DROPLET THEORY

To be concrete, consider a kinetic Ising ($s_i=\pm 1$) ferromagnet evolving under Metropolis single-spin-flip dynamics on a square lattice ($d=2$) with periodic boundary conditions. In addition to terms arising from the nearest-neighbor (n.n.) coupling $J$ and applied field $H$, the Hamiltonian, $\mathcal{H}=-J\Sigma_{\rm n.n.}s_is_j-H\Sigma_i s_i+L^{-d}D(\Sigma_i s_i)^2$, includes a term ($\propto D$) representing a mean-field approximation for the dipole–dipole interaction energy. Unless noted, we set $D=0$. The critical radius of a "droplet" of $s_i=-1$ spins surrounded by $s_i=+1$ spins occurs when the free energy of the droplet ($2\pi R\sigma-\pi R^2 2|H|$) is maximum: $R_c\approx\sigma/2|H|$, where $\sigma$ is the surface tension per unit length. Droplets smaller than this will very probably shrink and vanish; larger droplets will very probably grow and reverse the magnetiza-

[a]Center for Materials Research and Technology and Department of Physics.
[b]Also, Department of Electrical Engineering, Florida A&M University—Florida State University, Tallahassee, Florida 32310-6046.

 0021-8979/96/79(8)/5749/3/$10.00 © 1996 American Institute of Physics 

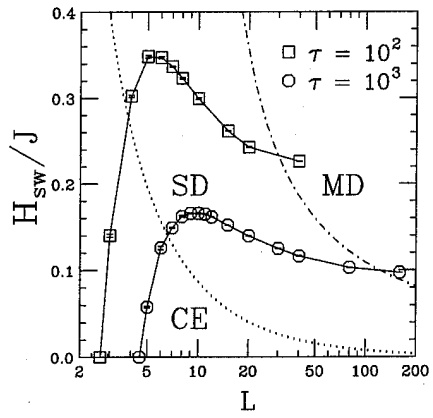



FIG. 1. The relation between the switching field $H_{sw}$ and the system width $L$ for two different fixed lifetimes (solid curves), calculated by kinetic Ising model simulations at $k_BT=0.8k_BT_c\approx 1.815$ J. The dotted curve is near the crossover between the CE and SD regions;[5] the dash–dotted curve is near the crossover between the SD and MD regions.[5]

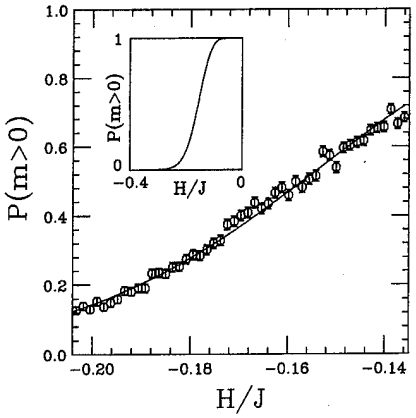



FIG. 2. The probability that $m>0$ for a kinetic Ising system in the SD region. $T=0.8T_c$, for fixed time $t=914$ Monte Carlo steps per spin (MCSS) and $L=10$. The solid curve is a fit of $\exp(-t/\tau)$ to the MC data, where $\tau$ is given by Eq. (4). The inset figure shows the fitted curve over a wider range in $H$.

tion of the system. In a sufficiently large system, the probability per unit time that a critical droplet forms, centered at a given site, is given by droplet theory as[6]

$$I\propto|H|^3\exp(-\beta\pi\sigma^2/2|H|). \tag{2}$$

The details of the magnetization reversal depend on the number of critical droplets the system forms.

For weak fields or small systems ($L<R_c$), no critical droplet can form. This is called the coexistence (CE) Region, and since two interfaces (remember periodic boundary conditions) must form to reverse the magnetization,

$$\tau\propto\exp\{\beta[2\sigma L-O(HL^2)]\}. \tag{3}$$

For slightly larger $L$, the first supercritical droplet will grow to the size of the system before another one can form. The lifetime in this Single Droplet (SD) Region is

$$\tau\approx[L^dI]^{-1}. \tag{4}$$

In both the CE and SD regions, switching is a Poisson process, so the standard deviation of the lifetime is comparable to $\tau$. Both Eq. (3) and Eq. (4) are actually special cases of the Arrhenius equation, Eq. (1), but in neither case is $\Delta F$ proportional to $L^d$. Note that if $\tau$ is held constant and the system size is increased, Eq. (3) implies that the magnetic field must *increase*, whereas Eq. (4) implies that the magnetic field must *decrease*. This shows that the peak in $H_{sw}$ occurs near the crossover between the CE and SD regions (see Fig. 1).

The probability that the magnetization is greater than zero $P(m>0)$ is shown as a function of field in Fig. 2 for a system in the SD region. This probability is what is most easily observed in MFM experiments, and it decays exponentially with time in both the CE and SD regions. In the SD region, the system is very unlikely to return to the metastable state from the stable state, so

$$P(m>0)=\exp(-t/\tau). \tag{5}$$

In the CE region such backward switching takes place on a time scale comparable with the initial decay, so the situation is more complicated.

For sufficiently large $L$ or $H$, several supercritical droplets may form before any one of them has grown to the size of the system. This is the Multi-Droplet Region (MD). Such systems were first studied by Kolmogorov,[8] Johnson and Mehl,[9] and Avrami,[10] and have a lifetime

$$\tau\approx[I\pi v^2/3\ \ln 2]^{-1/3}, \tag{6}$$

where the radial growth velocity $v$ is assumed to be proportional to $|H|$. Although $\tau$ is independent of $L$, the variance of the lifetime is proportional to $(v/L)^2$. Measuring $P(m>0)$ as a function of $H$ or $t$ thus provides a means of estimating the proportionality constant between $v$ and $H$ (see Fig. 3). Details are given in Ref. 5.

To first approximation, the effects of dipole–dipole interactions on the switching behavior can be studied through inclusion of the term $L^{-d}D(\Sigma_i s_i)^2$ in the Hamiltonian. The system then evolves in an *effective* field, $H_{\text{eff}}\equiv H-2Dm$. In the CE and SD regions, the values of $m$ that enter in $H_{\text{eff}}$ depend only on the volume of the critical fluctuation, and the modified $\Delta F$ in Eq. (1) can be easily evaluated through a

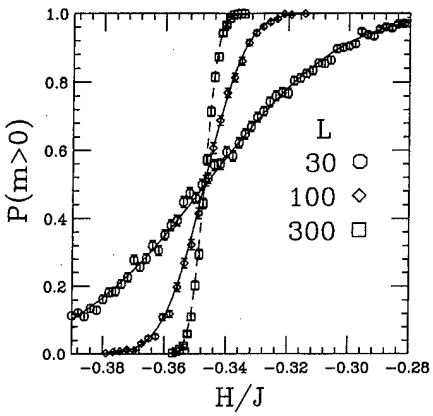



FIG. 3. The probability that $m>0$ for a kinetic Ising system in the MD region. $T=0.8T_c$, $\tau=40.7$ MCSS and $L=30$, 100, and 300. The solid curves are fits of droplet theory predictions to the MC data. The dashed curve is the fit of the droplet-theory prediction for $L=100$ extrapolated to $L=300$.

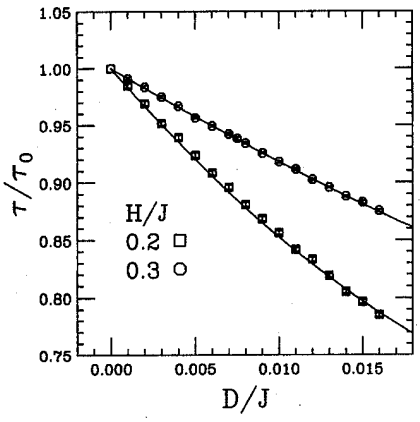



FIG. 4. The lifetime $\tau$ for a kinetic Ising system in the MD region, normalized by the lifetime in a similar system with $D=0$. $T=0.8T_c$, and $L=100$. The solid curves are droplet-theory predictions.

continued-fraction expansion. The switching remains a Poisson process, so Eq. (5) still applies in the SD region. In the MD region, $H_{\text{eff}}$ involves the time-dependent magnetization $m(t)$. This can be evaluated analytically to $O(D)$. The resulting analytic expression for $\tau$ to $O(D)$, plus small nonlinear corrections obtained by a numerical iteration procedure, give very good agreement with simulation results (Fig. 4). A detailed treatment of the $D>0$ case is given in Ref. 7.

## III. CONCLUSION

We have used Monte Carlo methods to simulate magnetization switching in two-dimensional kinetic Ising ferromagnets. The results of the simulations can be well explained by droplet theory and show good qualitative agreement with experiments, despite the comparative simplicity of the Ising model. This simplicity, in turn, allows us to develop an understanding of the underlying statistical mechanics. Particular features to make the model more realistic, such as appropriate boundary conditions, quenched randomness, and less rigorous anisotropy will be added in later studies.

## ACKNOWLEDGMENTS

We thank S. von Molnár, D. M. Lind, J. W. Harrell, and W. D. Doyle for useful discussions. This research was supported in part by FSU-MARTECH, by FSU-SCRI under Department of Energy Contract No. DE-FC05-85ER25000, and by National Science Foundation Grants No. DMR-9315969 and No. DMR-9520325.

[1] W. F. Brown, *Micromagnetics* (Wiley, New York, 1963).
[2] L. Néel, Ann. Géophys. **5**, 99 (1949).
[3] W. F. Brown, J. Appl. Phys. **30**, 130S (1959); Phys. Rev. **130**, 1677 (1963).
[4] M. Lederman, G. A. Gibson, and S. Schultz, J. Appl. Phys. **73**, 6961 (1993); M. Lederman, D. R. Fredkin, R. O'Barr, and S. Schultz, *ibid.* **75**, 6217 (1994); M. Lederman, S. Schultz, and M. Ozaki, Phys. Rev. Lett. **73**, 1986 (1994).
[5] H. L. Richards, S. W. Sides, M. A. Novotny, and P. A. Rikvold, J. Magn. Magn. Mat. **150**, 37 (1995).
[6] P. A. Rikvold and B. M. Gorman, in *Annual Reviews of Computational Physics I*, edited by D. Stauffer (World Scientific, Singapore, 1994), p. 149.
[7] H. L. Richards, M. A. Novotny, and P. A. Rikvold, submitted to Phys. Rev. B.
[8] A. N. Kolmogorov, Bull. Acad. Sci. USSR, Mat. Ser. **1**, 355 (1937).
[9] W. A. Johnson and P. A. Mehl, Trans. Am. Inst. Mineral Mining Eng. **135**, 365 (1939).
[10] M. Avrami, J. Chem. Phys. **7**, 1103 (1939); **8**, 212 (1940); **9**, 177 (1941).

*Published without author corrections*

# Simple function for a complex domain configuration

A. S. Arrott and J.-G. Lee
*Department of Physics, Simon Fraser University, Burnaby, British Columbia, V5A 1S6, Canada*

A complex domain configuration found in an iron whisker can be generated by a function with three parameters. The configuration is generated by passing a current along the axis of a {100} whisker with a square cross section. It has four domains in which the magnetization circulates about a central domain magnetized along the $z$ axis. There are four {110} 90° walls and four {100} 90° walls separating these domains. Two of the parameters are known *a priori* from micromagnetics: $a_1$ describes type I 90° walls between two domains with in-plane magnetization; and $a_2$ describes type II 90° walls between the domains with in-plane magnetization and the central domain with the magnetization out of the plane. The third parameter $h$, which determines the width of the central domain, is adjustable to minimize the total micromagnetic energy in response to magnetic fields. The magnetization pattern is generated from a vector potential $A(x,y)\hat{z}$. Calculating $M_s$ curl $A(x,y)\hat{z}$ produces $M_x$ and $M_y$. Then $M_z$ is found from $M_x^2+M_y^2+M_z^2=M_s^2$. The potential has four parts: $A(x,y)=A_x+A_z+A_h+A_c$, where $A_x$ and $A_y$ are the same function (with $x$ and $y$ interchanged) used to create the in-plane domains and the type I walls, $A_h$ generates the type II walls, and $A_c$ describes the outer corners. The resulting magnetization is divergence free. The analytic functions are convenient for calculation of the magnetic response to applied fields.
© *1996 American Institute of Physics.* [S0021-8979(96)20408-7]

When a {100} iron whisker with a square cross section is fitted with lead wires to pass a current along its axis, it is possible to achieve the structure illustrated in Fig. 1. This is a conjecture for which there is considerable experimental evidence from measurement of the ac response of the magnetization to ac fields along the whisker axis ($z$ axis) for values of the currents and dc fields, also along the whisker axis.[1] The change in these responses on application of additional fields perpendicular to the $z$ axis also supports this picture.

The description of the magnetization in the cross section midway between the ends of the whisker is simpler than for the cross sections away from the midplane. By symmetry there are no first derivatives with respect to $z$. Furthermore, there is no need to have any magnetic charge; that is, div $\mathbf{M}=0$ within the whisker and $\hat{\mathbf{n}}\cdot\mathbf{M}=0$ at the four surfaces. For the midplane cross section one can pretend that the whisker is infinitely long, except for considerations of the demagnetizing fields coming from the charges away from the midplane. The pattern has four domains in which the magnetization circulates about a central domain magnetized along the $z$ axis. There are four {110} 90° walls and four {100} 90° walls separating these domains. In addition, the magnetization lies along the edges of the whisker at the corners of the central cross section.

The magnetization at one of the corners is illustrated in Fig. 1 and Fig. 2. There are eight distinct patterns depending on the directions of the magnetization at the corners. As the magnetic responses of these are almost identical, the only cases considered are where all four corners have their magnetization parallel or antiparallel to the magnetization of the central domain. The in-plane components of the conjectured magnetization pattern are shown in Fig. 2. With standard expressions from one-dimensional models it is possible to describe this pattern by dividing it into the five domains and the eight walls, but this does not take into account either the four outside corners or the four inside corners. Because the experiments[1] indicate quite singular behavior as the area of the central domain approaches zero, one might wonder if the energetics of the inside corners are responsible. This possibility led to the detailed study of this configuration.[2] The cause of the singular behavior is the magnetoelastic energy[3] and is not due to the energetics of the inside corners. Nevertheless, this did lead to the description of the configuration presented here.

Because there have been no direct observations of the inner domain pattern it is necessary to rely on agreement between model calculations and experiments. There are many terms in the expression for the energy of a whisker with such a domain pattern. There are the magnetostatic terms of interaction between the magnetization and the various applied fields, including the field from the current. There are the micromagnetic terms from the wall energies, including exchange and anisotropy, the magnetoelastic energy from the strains resulting from the conflicting directions of magnetization in the five domains, and the demagnetizing field energy from the interaction of the magnetization with itself.

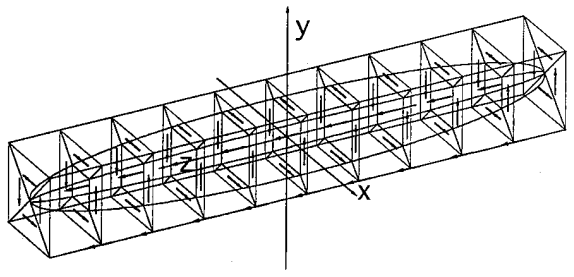



FIG. 1. Domain structure for a {100} iron whisker fitted with lead wires to pass a current along its axis.

 0021-8979/96/79(8)/5752/3/$10.00 © 1996 American Institute of Physics

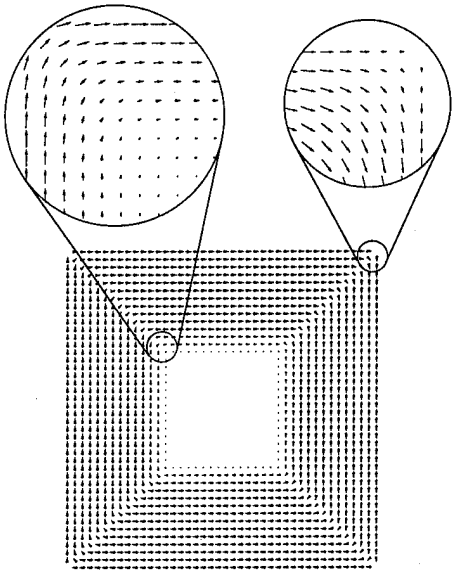


FIG. 2. In-plane components of the conjectured magnetization pattern.

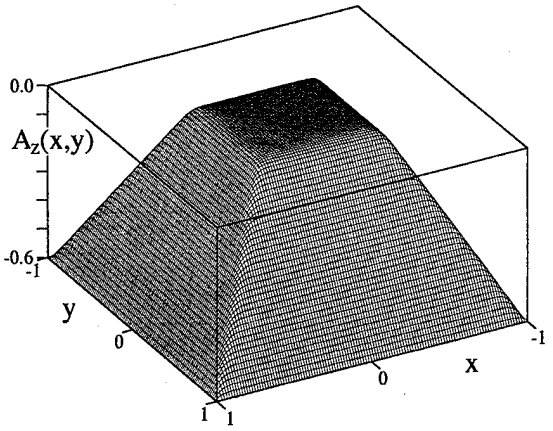



FIG. 3. Vector potential used to generate the complex domain pattern. Equation (9) is illustrated for greatly exaggerated ratios of $a_1/d$ and $a_2/d$, taken here to be 1/20 and 1/30, respectively, whereas they should be two orders of magnitude smaller for a typical whisker.

To describe all of these terms analytically it is convenient to have a mathematical description of the conjectured magnetization pattern. Such a pattern can be characterized by three parameters. These are the area of the central domain $A_c=h^2$, the thickness of the {110} walls $a_2=a_{110}$ and the thickness of the {100} walls $a_1=a_{100}$. As the wall thicknesses are already known, the pattern is a function of $h$.

A functional form for this pattern is given here using a vector potential $\mathbf{A}=f(x,y)\hat{\mathbf{z}}$ to generate the in-plane components of the magnetization from $\mathbf{M}=\text{curl}\,\mathbf{A}$. The $z$ components are found by the condition that $M_s^2=M_x^2+M_y^2+M_z^2$. The functional form $f(x,y)$ is illustrated in Fig. 3. The main structure is a truncated pyramid. The coordinates $(x',y')$ used to generate the pyramid are rotated by 45° with respect to the edges of the whisker and the pyramid. This puts the edges of the pyramid (and the {110} walls) in the planes $x'=0$ or $y'=0$. The total function has four parts. The main part is given by

$$f_m(x',y') = a_1 \ln\left(\tan\left\{\frac{\pi}{4}+\frac{1}{2}\arctan\left[\exp\left(\frac{|x'|+|y'|-h}{a_1}\right)\right]\right\}\right), \quad (1)$$

which can also be expressed as

$$f_m(w)=a_1 \ln\left\{\frac{\sqrt{e^{2w}+1}+e^w}{\sqrt{e^{2w}+1}-e^w}\right\}, \quad (2)$$

where $w=(|x'|+|y'|-h)/a_1$ and $|x'|+|y'|=h$ is the equation of the center of the 90° {100} domain wall. The function $f_m(w)$ is zero for sufficiently negative argument and is asymptotic to $w+\ln 2$ for sufficiently positive argument. The crossover occurs for $w=0$ where $|x'|+|y'|=h$. The parameter $a_1$ makes the truncation smooth and determines the width of the {100} domain walls.

The main function would produce infinitely sharp {100} domain walls corresponding to the edges of the truncated pyramid. The domain wall widths are made finite by rounding the edges of the pyramid using the functions $f_{x'}(x',y')$ and $f_{y'}(x',y')=f_{x'}(y',x')$, where

$$f_{x'}(x',y')=a_2 \sin(\arctan e^{(|y'|-h)/a_1}) \times\left\{\ln\left(2\cosh\frac{|x'|}{a_2}\right)-\frac{|x'|}{a_2}\right\}. \quad (3)$$

The sin (arctan $u$) function appears in the theory of 90° {100} walls. It is also the derivative of the principal term in the function for the truncated pyramid. It is replaced by using the relation $\sin(\arctan u)=u/\sqrt{u^2+1}$.

The term in brackets { } in Eq. (3) produces sharp edges that cancel the sharp edges of the pyramid. The parameter $a_2$ determines the width of the {110} domain walls. The function sin(arctan $u$) turns off the rounding functions for $|y'|<h$ and $|x'|<h$.

Finally, one adds a function that flattens the potential in the corners so that the in-plane components of the magnetization will vanish there as they do in the central region:

$$f_c(x',y')=a_2 \ln\left[\frac{\cosh[(x'-\sqrt{2}d)/a_2]\cosh[(x'+\sqrt{2}d)/a_2]\cosh[(y'-\sqrt{2}d)/a_2]\cosh(y'+\sqrt{2}d)/a_2}{\cosh^4(2\sqrt{2}d/a_2)}\right]. \quad (4)$$

The vector potential **A** has only a $z$ component given by

$$A_z=\frac{1}{\sqrt{2}}\,[f_m(x',y')+f_{x'}(x',y')+f_{y'}(x',y') +f_c(x',y')], \tag{5}$$

where $x'=(x+y)/\sqrt{2}$ and $y'=(-x+y)/\sqrt{2}$, with the boundaries of the whisker cross section at $x=\pm d$ and $y=\pm d$.

It should be noted that $a_1$ and $a_2$ will be the wall widths as normally determined in one-dimensional domain theory. There are no extra parameters to describe the four corners of the whisker cross section. There are no extra parameters to describe the details of the intersection of the {100} walls with the {110} walls. The model is highly constrained, with only the area of the inner domain $h^2$ as a parameter to change with application of applied fields or changes in the current along the whisker. We show elsewhere that the energy has terms in $h^4$, $h^3$, $h^2$, $h$, and $h\ln h$ coming from the demagnetizing field, the field from the current, the applied field, the wall energy, and the magnetoelastic energy, respectively. All are important in one range or another as the applied field and the current are varied.

The magnetization is given by

$$M_x=\frac{1}{2}\,(\sqrt{2}M_{x'}-\sqrt{2}M_{y'}),$$
$$M_y=\frac{1}{2}\,(\sqrt{2}M_{x'}+\sqrt{2}M_{y'}), \tag{6}$$

where the components in the rotated coordinate system are given by

$$\sqrt{2}M_{x'}=(M_1+M_{2x'}+M_{3x'})\operatorname{sgn} y'-M_{cx'}$$
$$\sqrt{2}M_{y'}=-(M_1+M_{2y'}+M_{3y'})\operatorname{sgn} x'+M_{cy'}, \tag{7}$$

where

$$M_1=\frac{e^{(|x'|+|y'|-h)/a_1}}{\sqrt{e^{[2(|x'|+|y'|-h)/a_1]}+1}}, \tag{8}$$

$$M_{2x'}=\frac{a_2}{a_1}\,\frac{e^{(|y'|-h)/a_1}}{(e^{2(|y'|-h)/a_1}+1)^{3/2}} \times\left(\ln\left(2\cosh\frac{|x'|}{a_2}\right)-\frac{|x'|}{a_2}\right), \tag{9}$$

$$M_{3x'}=\frac{e^{(|x'|-h)/a_1}}{\sqrt{e^{2(|x'|-h)/a_1}+1}}\left(\tanh\frac{|y'|}{a_2}-1\right), \tag{10}$$

and

$$M_{cx'}=\tanh\frac{y'-d\sqrt{2}}{a_2}+\tanh\frac{y'+d\sqrt{2}}{a_2}. \tag{11}$$

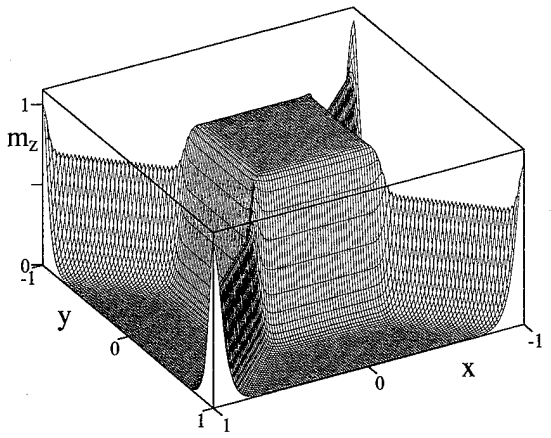



FIG. 4. Analytic expressions Eqs. (6)–(11) are used to plot $M_z$ for the same parameters as Fig. 3.

Equations for the $M_{y'}$ functions in Eq. (7) are not shown. They are given by interchanging $x'$ and $y'$ in Eqs. (9), (10), and (11). These analytic expressions were used to draw Fig. 2 for the in-plane components and Fig. 4 for $M_z$. In order to demonstrate the geometry it was necessary to greatly exaggerate the ratios of $a_1/d$ and $a_2/d$ taken here to be 1/20 and 1/30, respectively, whereas for a typical whisker they should be two orders of magnitude smaller.

This is a fully analytic expression. It has just one variable $h$, as long as $d\gg a_1$ and $d\gg a_2$, so that $a_1$ and $a_2$ are not affected by the energy of the corners at each end of the {110} domain walls. Such a simple function is not a solution of the full micromagnetic equations. For example, the function chosen for the {110} walls is not the solution for the one-dimensional wall. The analytic expression is the first step in developing a Ritz method for calculating the energy of this complex structure. It incorporates the constraint that $\operatorname{div} M=0$, which is an approximation that takes into account the dominance of magnetostatic energies as long as $d\gg a_1$ and $d\gg a_2$. (In relaxation calculations it would be necessary to consider all the dipole–dipole interactions in order to recover the effects that are legislated by the functions used here.)

For each choice of $h$ one can calculate each of the terms in the micromagnetic energy. The total energy can be compared with models where the energy is assumed to be the energy per unit length of the walls times the lengths of the wall sections. It was found that the effects of the intersections can be safely ignored. As mentioned above, there was a strange effect that was unaccounted for when this calculation was carried out, but which later was found to be the result of magnetostriction. The approach given here may be useful in describing the entire three-dimensional structure shown in Fig. 1, but this has not been done.

[1] J.-G. Lee and A. S. Arrott, J. Appl. Phys. **75**, 7006 (1994).
[2] J.-G. Lee, Ph.D. thesis, Simon Fraser University, 1994.
[3] A. S. Arrott, these proceedings.

# Dynamical micromagnetics of a ferromagnetic particle: Numerical studies

Bo Yang and Donald R. Fredkin
*Department of Physics, University of California, San Diego, La Jolla, California 92093*

We have developed a general purpose dynamical micromagnetic code to solve the damped Gilbert equation using the finite element method. We report a study of magnetization switching in a ferromagnetic prolate ellipsoid with aspect ratio of 4.6:1. Switching starts with curling at the middle of the particle, then continues with more complex magnetization configurations, heavily influenced by the damping constant. In general, lighter damping produces more sharply defined domain walls. The critical field for switching has a mild dependence on the damping constant. © *1996 American Institute of Physics.* [S0021-8979(96)20508-3]

We solve Gilbert's equation[1] for a continuous magnetic medium, including all interactions in standard micromagnetic theory in three-dimensional regions of arbitrary geometrical and physical properties. We handle submicrosecond to nanosecond processes. In this paper we use the code to study magnetization switching in an ellipsoidal particle. We concentrate on dynamical aspects of the processes: Larmor precession and Gilbert damping.

## I. NUMERICAL MODEL

We start with Gilbert's equation,[1] written here as

$$\frac{1}{\gamma}\frac{\partial \mathbf{M}}{\partial t}=\mathbf{M}\times\mathbf{H}_{\text{eff}}-\eta\mathbf{M}\times\frac{\partial \mathbf{M}}{\partial t}, \tag{1}$$

where $\mathbf{M}$ is the magnetization density with constant magnitude $M_s$ and $\eta$ is a positive constant associated with dissipation. The effective field $\mathbf{H}_{\text{eff}}=-\delta E/\delta\mathbf{M}$ is defined as the variational derivative of the free energy,[2]

$$E=\int\left[\frac{A}{2M_s^2}|\nabla\cdot\mathbf{M}|^2-\frac{1}{2}\mathbf{H}_d\cdot\mathbf{M}-\mathbf{H}_0\cdot\mathbf{M}\right]dV.$$

The first term is the exchange energy. $\mathbf{H}_0$ is the applied magnetic field and $\mathbf{H}_d$ is the demagnetizing field. For simplicity we omit crystalline anisotropy energy; its inclusion does not lead to any complications. Appropriate boundary conditions are imposed. At constant $\mathbf{H}_0$ and in the absence of random thermal noise, $E$ decreases until an equilibrium is reached.[2]

Gilbert's equation (1) is discretized by the Galerkin method, using the piecewise linear basis functions associated with a tetrahedral mesh as test functions. Let $\varphi_i(\mathbf{r})$ be the basis function at node $i$ that is linear in each element and such that $\varphi_i(\mathbf{r}_j)=\delta_{ij}$. The magnetization can be approximately represented as $\mathbf{M}(\mathbf{r})=\Sigma_i\mathbf{M}_i\varphi_i(\mathbf{r})$ and, similarly, the potential for the demagnetizing field ($\mathbf{H}_d=-\nabla\phi$) can be approximated by $\phi(\mathbf{r})=\Sigma_i\phi_i\varphi_i(\mathbf{r})$. This is the same representation of $\mathbf{M}(\mathbf{r})$ as was used by Chen, Fredkin, and Koehler[3] for static micromagnetic calculations using the finite element method. The dynamical equation is then discretized with the Galerkin method with $\varphi_i$ as test functions,

$$\frac{1}{\gamma}\int\varphi_i\frac{\partial \mathbf{M}}{\partial t}dV=\int\varphi_i\mathbf{M}\times\left(\mathbf{H}_{\text{eff}}-\eta\frac{\partial \mathbf{M}}{\partial t}\right)dV,$$

where $i$ runs from 1 to the number of nodes, $N$. All the dependence on geometry is included in integrals of products of $\varphi_i(\mathbf{r})$, and these are computed analytically. The boundary conditions are brought in by a partial integration of the exchange term. This leads to a system of coupled ordinary differential equations that are solved with a custom variant of LSODI.[4]

Demagnetization fields are computed on the fly by the solution of Poisson's equation with absorbing boundary conditions[5] using a finite element method and a preconditioned conjugate gradient method. Because of space limitations, details will be given elsewhere. We mention here that, for an $N$ point mesh, our method has time complexity $O(N\log N)$ and storage cost $O(N)$. Our use of the finite element method with a tetrahedral mesh gives us the flexibility to handle any finite magnetic region of arbitrary shape, morphology, and connectivity, with possibly inhomogeneous physical properties.

## II. RESULTS

The first application of our code is a study of switching of an ellipsoid modeled after a $\gamma$-$Fe_2O_3$ particle used in an experimental study.[6] It is a prolate ellipsoid 3000 Å long and 650 Å wide, with $M_s=350$ emu/cm$^3$. The exchange constant $A$ is unknown experimentally, and an approximate value is used such that the exchange length $A^{1/2}/M_s=338$ Å. The field direction $\hat{\mathbf{n}}_H$ is along the long axis of the ellipsoid, $\hat{\mathbf{z}}$, tilted 0.1° to a short axis, $\hat{\mathbf{x}}$, to break the initial symmetry around $\hat{\mathbf{z}}$. The initial state is prepared by applying a large ($6M_s$) external field along $-\hat{\mathbf{n}}_H$ until saturation is reached. Then the field is reversed and kept at a constant value $H_0$ along $\hat{\mathbf{n}}_H$. To avoid excessive transients, the reversal of $\mathbf{H}_0$ is completed in time $\tau$ with a cosine function for the transition. The field switching time, $\tau$, is relatively short at this stage of the study (up to $10/\gamma M_s$), so switching of the magnetization occurs mostly after the field is reversed.

Little is known about the value of $\eta$ and its effect.[7] To investigate both over-damped and lightly-damped systems, we have set $\eta$ to values ranging from $3.0/\gamma M_s$ to $0.01/\gamma M_s$. Different values of $H_0$ are used, and for each $\eta$ we found one field value $H_c$ below which the particle is not switched. Figure 1 is a linear-log plot of the component of total magnetization, $\mathcal{M}$, along $\hat{\mathbf{n}}_H$ as a function of time at various values of $H_0$ and $\eta$. On most of the curves three segments are found with distinctive slopes, which suggests that we divide the dynamics of switching into three stages, each found to be

 0021-8979/96/79(8)/5755/3/$10.00 © 1996 American Institute of Physics 

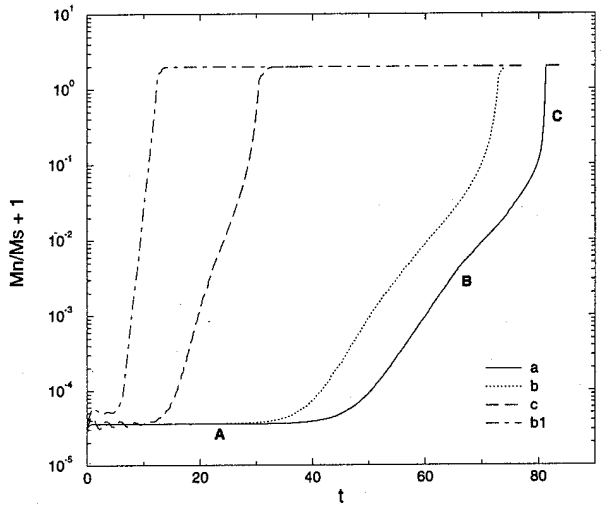



FIG. 1. Component of total magnetization along the applied field versus time in units of $1/\gamma M_s$. $M_n = \mathcal{M}_n/V$, $V$ is the volume of the particle. Note that one has been added to permit a logarithmic axis. (a) $\eta = 3/\gamma M_s$, $H_0 = 3.493 M_s$. (b) $\eta = 0.3/\gamma M_s$, $H_0 = 3.493 M_s$. (c) $\eta = 0.1/\gamma M_s$, $H_0 = 3.493 M_s$. (b1) $\eta = 0.3/\gamma M_s$, $H_0 = 3.700 M_s$.

characterized by one physical process: (A) precursor, (B) curling, and (C) switching and damping.

The precursor stage is characterized by small movements of $\mathbf{M}$, and almost stationary $\hat{\mathbf{n}}_H$ component of total magnetization $\mathcal{M}$. Motion of $\mathcal{M}$ can best be illustrated by tracing the projection of $\mathcal{M}$ on the $xy$ plane. We found that when $\eta$ is small, $\mathcal{M}$ initially precesses around what looks like a local minimum of the energy, designated by $\mathcal{M}_s$, while moving toward it. The direction of $\mathcal{M}_s$ is very close to $-\hat{\mathbf{n}}_H$. When $H_0$ is lower than a critical value, $H_c$, $\mathcal{M}$ eventually settles at $\mathcal{M}_s$, and the particle is not switched [Fig. 2(a)]. When $H_0 > H_c$, after some revolutions, $\mathcal{M}$ is able to escape from the trap and exits to the curling stage [Fig. 2(b)], which, without observed exception, leads to switching. We found that the exit point is closer to $\mathcal{M}_s$ when $H_0$ is closer to

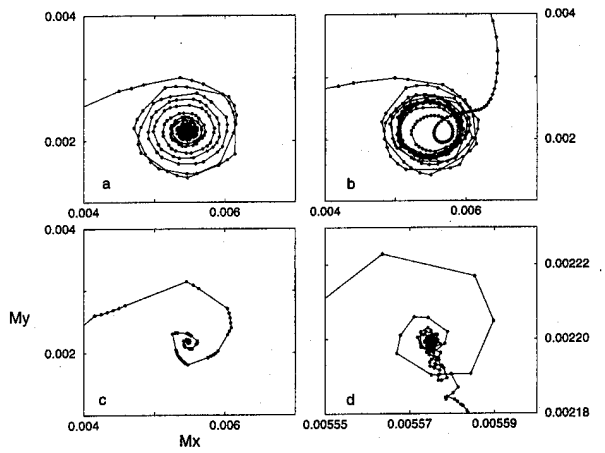



FIG. 2. Small movements of total magnetization. $\mathcal{M}_x$ and $\mathcal{M}_y$ in units of $M_s V$. The vector enters from left when the field is being switched. (a) $\eta = 0.03/\gamma M_s$, $H_0 = 3.469 M_s$. (b) $\eta = 0.03/\gamma M_s$, $H_0 = 3.475 M_s$. The vector exits to the top, starting a curling process. (c) $\eta = 0.3/\gamma M_s$, $H_0 = 3.475 M_s$. (d) $\eta = 0.3/\gamma M_s$, $H_0 = 3.486 M_s$. Note the change in scale.

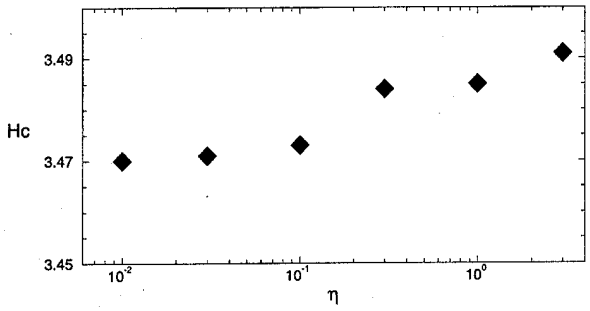



FIG. 3. Critical switching field as a function of damping constant, $H_c/M_s$ vs $\gamma M_s \eta$.

$H_c$. At higher $\eta$, the path to $\mathcal{M}_s$ is shorter, as energy is quickly dissipated. At some field values causing switching, if $\eta$ is increased the particle can no longer exit from the trap [Fig. 2(c)].

We need a criterion to mark a system as being in equilibrium so that we can decide if a value of $H_0$ eventually causes a reversal. We have chosen the total free energy, since it is consistently decreasing until equilibrium is reached. However, when the system is close to equilibrium, energy changes become small and are subject to numerical errors, which we believe are responsible for some switching when $H_0$ is very close to $H_c$ [Fig. 2(d)]. This may correspond to thermal noise in a real particle, but the exact relation between the two, and the possibility of using this relation to

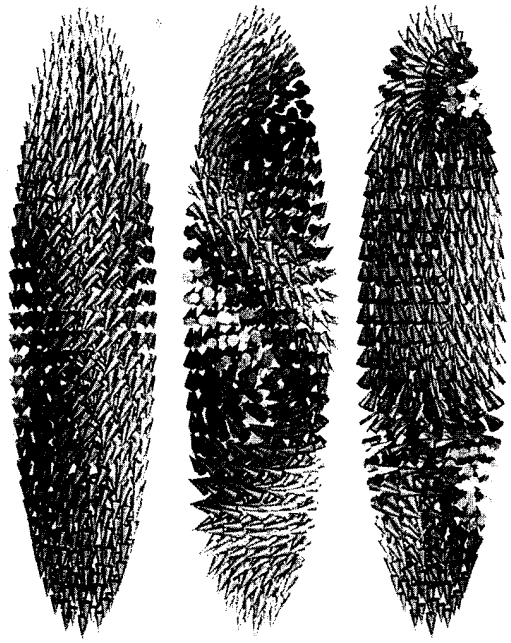


FIG. 4. Magnetization at switching, viewed from $+\hat{\mathbf{x}}$. $\mathbf{H}_0$ is pointing up. (a) curling pattern before switching. This is found for all values of $H_0$ and $\eta$ for which switching occurs. (b) $H_0 = 3.493 M_s$, $\eta = 3/\gamma M_s$. During switching a vortex with an axis on the $xz$ plane is formed in the middle of the ellipsoid; it travels transversely along $+\hat{\mathbf{y}}$. A smaller vortex forms closer to the top and travels along $-\hat{\mathbf{y}}$. When both vortices exit, magnetization of the whole particle is reversed. (c) $H_0 = 3.492 M_s$, $\eta = 0.3/\gamma M_s$. The middle part switches first, followed by the two ends.

simulate thermal noise, remains to be investigated. For the present we compute a moving average of the free energy and consider the system to be in equilibrium when that average stops decreasing for a fixed period of time. We estimate the error of $H_c$ caused by this choice of criterion to be less than $0.01M_s$. Figure 3 shows $H_c$ found as a function of $\eta$. We conclude that over-damping slightly increases the switching field. And that damping has no observable effect on the critical switching field when $\eta$ is lower than one-tenth of $1/\gamma M_s$.

The curling stage starts with an exponential increase of $\mathcal{M}_n$, the component of the total magnetization along the applied field. The magnetization moves to a configuration that mostly resembles curling, with $M_z$ gradually increasing, but stops before it switches. This curling process starts from center of the ellipsoid and expands to the whole middle part [Fig. 4(a)]. Curling stops at this configuration, and other more complicated processes take over. Parts of the ellipsoid, usually close to the center, switch first. This results in the appearance of domain walls and the subsequent events vary with the values of $H_0$ and $\eta$. The behavior can be best described as a continuous spectrum between two extreme cases. In a highly damped system ($\gamma M_s \eta > 1$), when $H_0$ is only slightly higher than the critical switching field, vortices with axes close to $\hat{\mathbf{x}}$ are formed [Fig. 4(b)]. This is similar to a configuration found in a static calculation.[8] When the damping is light ($\gamma M_s \eta < 1$), or $H_0$ is much higher than critical value, the whole middle part suddenly switches, and produces two sharp domain walls parallel to the $xy$ plane [Fig. 4(c)], which eventually leave the particle through the surface. Generally speaking, the switching patterns at lower $\eta$ are configurations with higher exchange energy, characterized by abrupt changes of magnetization in space.

In conclusion, we remark that, since the computational cost, both in time and in memory, of our method scales almost linearly with geometric size, it is quite feasible to treat larger systems than the one discussed here.


[1] T. Gilbert, Phys. Rev. **100**, 1243 (1955).
[2] W. F. Brown, *Micromagnetics* (Interscience, New York, 1963).
[3] W. Chen, D. R. Fredkin, and T. R. Koehler, IEEE Trans. Magn. **29**, 2124 (1993).
[4] A. C. Hindmarsh, in *Scientific Computing*, edited by R. S. Stepleman (North-Holland, Amsterdam, 1983), p. 55.
[5] A. Khebir, A. Kouki, and R. Mittra, IEEE Trans. Microwave Theory Technol. **38**, 1427 (1990).
[6] M. Lederman, D. R. Fredkin, R. O'Barr, S. Schultz, and M. Ozaki, J. Appl. Phys. **75**, 6217 (1994).
[7] W. F. Brown, Phys. Rev. **130**, 1677 (1963).
[8] D. R. Fredkin and T. R. Koehler, J. Appl. Phys. **67**, 5554 (1990).

# Anomalous time-induced curvature in Henkel plots based on the Preisach model

P. D. Mitchler
*Department of Physics, University of Manitoba, Winnipeg, Manitoba, R3T 2N2, Canada*

E. Dan Dahlberg, E. Wesseling, and R. M. Roshko[a)]
*School of Physics and Astronomy, University of Minnesota, 116 Church St. S.E., Minneapolis, Minnesota 55455*

We have used a finite-temperature version of the Preisach model, in which thermally activated switching events supplement those induced by an applied field $h_a$, to calculate the magnetizing and demagnetizing remanences, $i_r(h_a)$ and $i_d(-h_a)$, respectively, assuming a Preisach distribution that is Gaussian in both the coercive field $h_c$ and the shift field $h_s$. Since $T\neq 0$, the time $t$ that the magnetization is permitted to relax influences the shape of the hysteresis loop and the Henkel plots constructed from the remanences. If the effective time for relaxation is specific to a given branch of the cycle, due perhaps to the way the system reacts to a given experimental procedure, it is possible to generate Henkel plots with curvature suggestive of mean field interaction effects, even if no such effects are actually present, or with such extreme demagnetizing-like curvature that the plot actually crosses the nominal lower boundary $i_d=-i_r$. Experimental instances of this behavior are discussed.
© *1996 American Institute of Physics.* [S0021-8979(96)20608-X]

## I. INTRODUCTION

The Henkel plot[1] was originally proposed as an experimental technique for analyzing a magnetic system for the presence of interparticle interaction effects. If the magnetizing remanence, $i_r(h_a)$ of a system of single-domain particles is measured by applying and then removing positive fields $h_a$ to the unmagnetized state until the remanence is saturated at $i_\infty \equiv i_r(h_a\rightarrow\infty)$, and then the demagnetizing remanence $i_d(-h_a)$ is measured by applying and removing negative fields $-h_a$ to the saturated remanence state $i_\infty$ until negative saturation $-i_\infty$ is reached, then, according to Wohlfarth,[2] *noninteracting* systems will be characterized by the linear relation $i_d(-h_a)=i_\infty-2i_r(+h_a)$. Thus, a Henkel plot of $i_d/i_\infty$ vs $i_r/i_\infty$ with $h_a$ as the matching variable, which curves above or below the Wohlfarth straight line $i_d/i_\infty=1-2i_r/i_\infty$, may be interpreted as evidence of either magnetizing-like or demagnetizing-like interactions, respectively, between the particles. This technique is now widely used, even in continuous systems,[3] which are only figuratively particulate by virtue of their domain wall motions,[4] and its interpretation has been formalized[5–7] through numerical calculations based on the Preisach model[8] of hysteresis. This model treats macroscopic hysteresis phenomena as a superposition of elementary rectangular hysteresis loops with individual coercive fields (or half-widths) $h_c$, with centers offset from the origin $h_a=0$ by a shift field $h_s$ due to interactions between loops, and with two possible outputs, $\pm 1$. The fields $h_c$ and $h_s$ are generally assumed to be distributed independently according to the Preisach distribution, $p(h_c,h_s)=f(h_c)g(h_s)$, and symmetry arguments[9] require that $g(h_s)$ be symmetric about $h_s=0$. In the moving Preisach model,[10] $h_s\rightarrow h_s+km$, where $m$ is the magnetization and $k$ is the mean field constant, in order to account, in an average sense, for the effect on the interaction field distribution of magnetizing the system. Numerical calculations have shown that, for ac and dc demagnetized systems,[5,6] curvature in a Henkel plot is produced by *both* mean field effects ($k\neq 0$) *and* by "disorder," that is, by a nonzero width to the shift field distribution $g(h_s)$. Only in the case of thermal demagnetization[7] is curvature produced *only* by a nonzero mean field parameter $k$. Furthermore, as long as $T=0$, all Henkel plots must lie above a lower boundary $i_d(-h_a)=-i_r(+h_a)$, independent of the details of their initial demagnetized state.

In this paper, we will use a generalized, finite-temperature version of the Preisach model[11,12] to show that the time that the system is permitted to relax may have a profound influence on the shapes of Henkel plots, and that varying this relaxation time from one branch to another of a given hysteresis cycle can produce spurious mean field-like curvature or even violations of the nominal lower boundary $i_d=-i_r$, as observed in some canonical spin glasses.

## II. MODEL CALCULATIONS

Figure 1(a) shows the effect of applying a positive field $h_a$ to an initially unmagnetized Preisach plane at $T=0$. For purposes of reference we have included both the $(h_c,h_s)$ axes and the alternate $(\alpha,\beta)$ axes, where $\alpha=h_c+h_s$ and $\beta=h_c-h_s$ are the up and down switching fields, respectively, for an elementary loop. The signs indicate the current state of each loop. All the loops with $\alpha>h_a$ *and* $\beta<h_a$ are double well potentials like that illustrated in Fig. 1(a), while the rest of the loops outside this region are single well potentials. The symbol $\pm$ in the fourth quadrant means that one or both of the wells may have been occupied in the initial unmagnetized state, depending on the specific demagnetization technique; ac demagnetization leaves only the $-(+)$ well occupied above (below) the $h_c$ axis, while for a thermally demagnetized system,[7] the $+$ and $-$ wells are both occupied with equal probability, $p(h_c,h_s)/2$.

[a)]Permanent address: Department of Physics, University of Manitoba, Winnipeg, Manitoba, R3T 2N2, Canada.

 0021-8979/96/79(8)/5758/3/$10.00 © 1996 American Institute of Physics

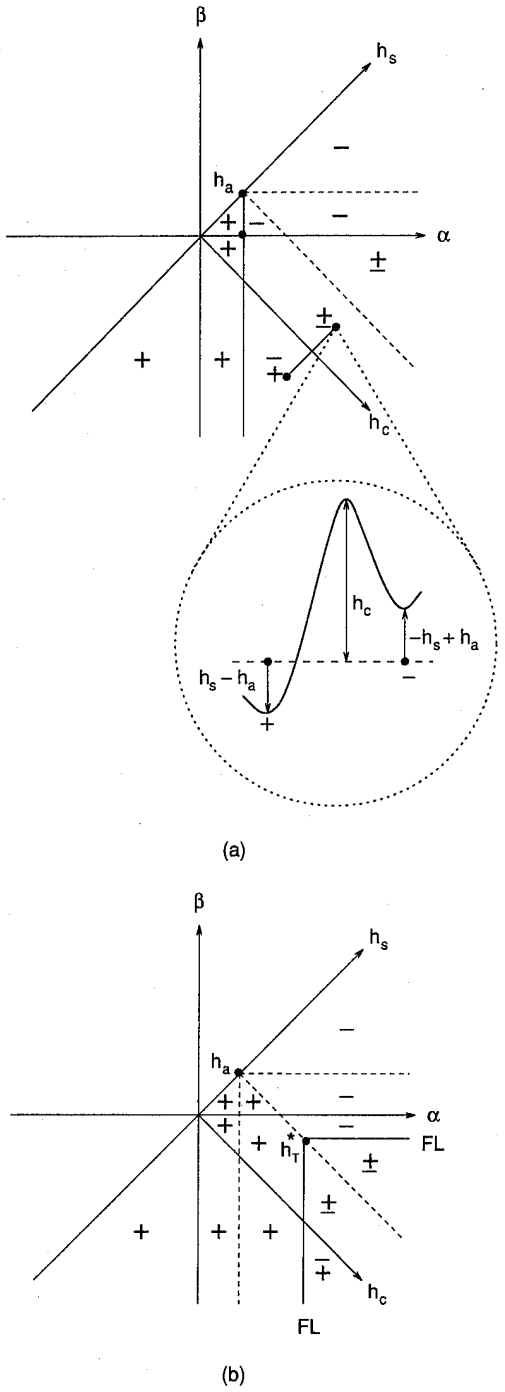



FIG. 1. (a) The effect of applying a positive field $h_a$ to an initially unmagnetized Preisach plane at $T=0$. The double well representation of one of the elementary loops is shown on the right. (b) The same plane at a finite temperature $T\neq 0$. FL is the frontier line and $h_T^*$ is the thermal field.

If the temperature $T$ is not zero, we must take account of the effect of thermal overbarrier activation on the state of each loop.[11] More specifically, if an elementary loop is "trapped" in the higher-energy state of the double well potential in Fig. 1(a), this is regarded as an unstable configuration, and it is assumed that a transition will eventually occur over the smaller of the two barriers, which "switches" the loop to its lower-energy (or ground) state. Since the time $\tau$ for a thermally activated transition over an energy barrier $W$ is

$$\tau=\tau_0 \exp(W/k_B T), \tag{1}$$

where $\tau_0^{-1}$ is a microscopic attempt frequency, then we expect that in a finite observation time $t$, all of the smaller barriers $W=h_c\pm h_s\mp h_a<W^*\equiv k_B T \ln(t/\tau_0)$ will have been overcome. This defines a frontier line,

$$h_c=W^*\pm h_s\mp h_a, \tag{2}$$

with its vertex on $h_s=h_a$, as shown in Fig. 1(b), which separates those regions "behind" the line that have reached equilibrium within the observation time $t$, from those "in front" of the line that have not. From a technical perspective the effect of the critical barrier height $W^*$ on the Preisach plane is equivalent to an *effective thermal field* $h_T^*=W^*$ (since the loop moment is unity), which can act simultaneously along the $\alpha$ and $\beta$ axes via two coupled flipping lines, to supplement the switching events induced by the applied field $h_a$.

Numerical calculations[12] of the remanences $i_r(h_a)$ and $i_d(-h_a)$, which assume that the Preisach distribution is a product of two Gaussians:

$$p(h_c,h_s)=\frac{1}{2\pi\sigma_c\sigma_s}\exp\left[-\frac{(h_c-\bar{h}_c)^2}{2\sigma_c^2}\right]\exp\left[-\frac{(h_s+km)^2}{2\sigma_s^2}\right], \tag{3}$$

and that all branches of a given hysteresis cycle have a common thermal field parameter $h_T^*$ corresponding, for example, to a fixed temperature $T$ and a single time constant $t$, have shown that the Henkel plots for a thermally demagnetized system with no mean field interactions ($k=0$) are Wohlfarth straight lines, independent of $h_T^*$, while those for an ac demagnetized system with $k=0$ always have demagnetizing-like curvature, which increases with increasing $h_T^*$, but never violates $i_d=-i_r$.

If, however, a common *experimental* time constant does *not* imply a common relaxation rate for the magnetization, then the effective time constant for relaxation $t_{\text{eff}}$ may vary from branch to branch of the cycle, as will the effective thermal field parameter, $h_T^*$, and the Henkel plots will show anomalous structure. Field cooled spin glasses are a particularly good instance of this temporal "asymmetry." It is now widely accepted that, if a spin glass is cooled from above to below its ordering temperature $T_{SG}$ in the presence of a field, it attains its equilibrium magnetization essentially instantaneously, independent of the actual measuring time $t$, as if the effective time constant for relaxation was infinite. However, all subsequent field reversals, such as those required to reach the remanent state or the demagnetizing branch, are governed by a necessarily much shorter time constant, close to the actual, finite experimental one. We have replicated this behavior in the finite temperature Preisach model by assigning a very large value $h_{T1}^*\gg\bar{h}_c$ to the thermal field parameter along the virgin magnetizing curve, and another smaller value $h_{T2}^*<h_{T1}^*$ to the remanence (in this case the thermoremanence or TRM), the descending branch of the major loop, and the demagnetizing remanence.

Figure 2 shows a sequence of Henkel plots generated for a *thermally demagnetized* system with a Preisach distribution

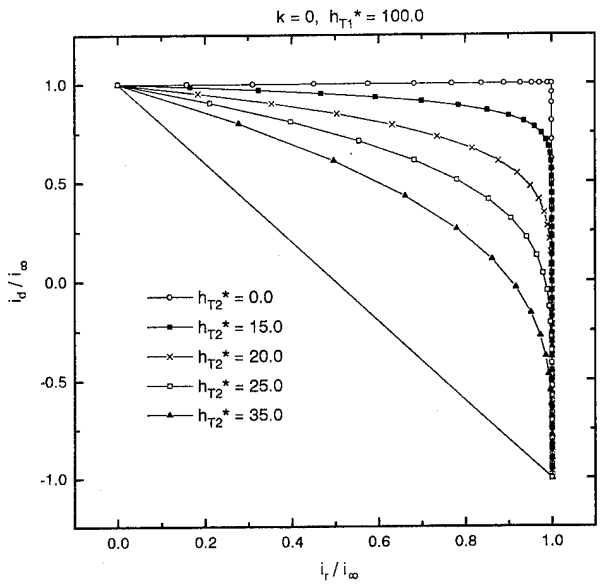



FIG. 2. Henkel plots for a thermally demagnetized, field cooled system with Preisach distribution parameters $\bar{h}_c=12$, $\sigma_c=4$, $\sigma_s=1$, $k=0$, for thermal fields $h^*_{T1}=100$ and $h^*_{T2}=0, 15, 20, 25, 35$.

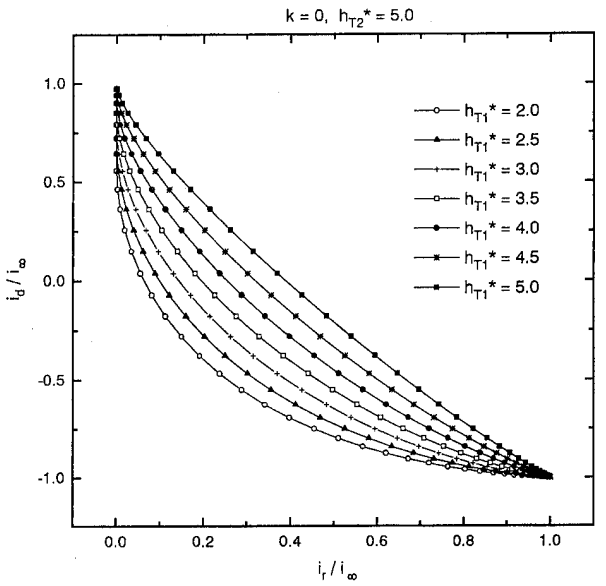



FIG. 3. Henkel plots for an ac demagnetized system with Preisach distribution parameters $\bar{h}_c=10$, $\sigma_c=3$, $\sigma_s=1$, $k=0$, for thermal fields $h^*_{T1}=2.0$, 2.5, 3.0, 3.5, 4.0, 4.5, 5.0, and $h^*_{T2}=5.0$.

with parameters $\bar{h}_c=12$, $\sigma_c=4$, $\sigma_s=1$, $k=0$, for thermal fields $h^*_{T1}=100$ and $h^*_{T2}=0, 15, 20, 25, 35$. All the Henkel plots show magnetizing-like curvature, which for thermally demagnetized systems would be unambiguous evidence of positive mean field interactions $k>0$, but that is actually an artificial consequence of the variation in time constants related to the experimental procedure of field cooling. In real spin glasses, the situation is further complicated by the existence of a peak in the field dependence of the TRM, which is difficult to accommodate within the usual Henkel analysis.

The inverse configuration of time constants yields anomalous structure of a different kind and may also be physically relevant to spin glasses. If we assume that the relaxation time constant is shorter along the virgin magnetizing curve than it is for the rest of the cycle, corresponding to $h^*_{T1}<h^*_{T2}$, then, in the absence of mean field effects, Henkel plots will always show demagnetizing-like curvature, as illustrated in Fig. 3 for an ac demagnetized system with Preisach distribution parameters $\bar{h}_c=10$, $\sigma_c=3$, $\sigma_s=1$, $k=0$, for thermal field parameters $h^*_{T1}=2.0, 2.5, 3.0, 3.5, 4.0, 4.5, 5.0$, and $h^*_{T2}=5.0$. Moreover, if the difference between the two thermal fields (or time constants) is sufficiently large, the Henkel plots will actually cross the nominal $T=0$ lower boundary $i_d=-i_r$, as observed in canonical spin glass systems like AgMn[13] and CuMn[14] at low reduced temperatures $T/T_{SG}$, when they have been *zero field cooled* through their glass temperature. As $h^*_{T1}\to h^*_{T2}$, this effect becomes weaker and eventually disappears, which is precisely what happens experimentally with increasing temperature. If the theoretical and experimental behaviors are indeed related, then it would mean that zero field cooling has essentially the opposite effect of field cooling, and "traps" the system in a region of its complicated configuration space, which requires relatively long times and high reduced temperatures for "escape."

In summary, numerical calculations based on a finite temperature version of the Preisach model show that, when $T\neq 0$, the effective time in which the magnetization relaxes becomes an important factor in shaping Henkel plots, and may lead to anomalous curvature that imitates mean field effects, or that violates zero temperature boundaries.

## ACKNOWLEDGMENT

This work was supported in part by a grant from the Natural Sciences and Engineering Research Council of Canada.

[1] O. Henkel, Phys. Status Solidi **7**, 919 (1964).
[2] E. P. Wohlfarth, J. Appl. Phys. **29**, 59 (1958).
[3] V. Basso, M. Lo Bue, and G. Bertotti, J. Appl. Phys. **75**, 5677 (1994).
[4] L. Neel, Cah. Phys. **12**, 1 (1942).
[5] V. Basso and G. Bertotti, IEEE Trans. Magn. **30**, 64 (1994).
[6] F. Vajda, E. Della Torre, and R. D. McMichael, J. Appl. Phys. **75**, 5689 (1994).
[7] P. D. Mitchler, E. Dan Dahlberg, E. Engle, and R. M. Roshko, IEEE Trans. Magn., **31**, 2499 (1995).
[8] F. Preisach, Z. Phys. **94**, 277 (1935).
[9] I. D. Mayergoyz, Phys. Rev. Lett. **56**, 1518 (1986).
[10] E. Della Torre, IEEE Trans. Audio Electroacoust. **14**, 86 (1966).
[11] J. Souletie, J. Phys. **44**, 1095 (1983).
[12] P. D. Mitchler, E. Dan Dahlberg, E. Wesseling, and R. M. Roshko, IEEE Trans. Magn. (in press).
[13] E. Dan Dahlberg, E. Wesseling, and R. M. Roshko, unpublished.
[14] I. S. Jacobs and R. W. Schmitt, Phys. Rev. **113**, 459 (1959).

# Magnetization reversal and small lancettes calculated by statistic domain behavior (abstract)

Paul L. Fulmek and Hans Hauser
*Institut für Werkstoffe der Elektrotechnik, Technische Universität Wien Gusshausstrasse 27–29, A-1040 Wien, Austria*

The energetic model of ferromagnetic hysteresis calculates the magnetic state of anisotropic ferromagnetic materials by minimizing the total energy function $E_T = E_H + E_M$. The energy of the material $E_M$ is divided into reversible (statistic domain behavior) and irreversible terms.[1,2] The applied field $H$ (energy $E_H$) causes reversible domain wall displacements $s_i$ until an individual Barkhausen jump starting position $s_A$ is reached. The probability density $p_a(s_A)$ is assumed to be decreasing with increasing $s_A$: $p_a = (K_a/K_c)\exp[-(K_a/K_c)s_A]$ (adaptive constant $K_a$). $K_c$ describes the influence of the total magnetic state on $p_a$ at points of magnetization reversal; $K_c = 1$ for the initial magnetization curve. The losses $E_r$ during an irreversible Barkhausen jump (wall friction $K_r$) are increasing with $s_i$: $E_r = K_r[s_i - s_A - (K_c/K_a)(K_c - 1)]$ and $K_c$ depends on the covered displacements $s_i$ at a point of field reversal: $K_c^{\text{new}} = 2 - K_c^{\text{bold}}\exp[-(K_a/K_c^{\text{old}})s_i]$. This follows from the condition of steadiness at these points. The physical constants of this model are derived from anisotropic energy contributions, initial susceptibility, coercivity, and saturation magnetization. The approach shows a good agreement to measurements to the stability of small lancettes of (110)[001] 3.5% FeSi steel sheets, magnetized in the rolling direction. © *1996 American Institute of Physics.* [S0021-8979(96)82508-9]

[1]H. Hauser, J. Appl. Phys. **75**, 2584 (1994).
[2]H. Hauser, J. Appl. Phys. **77**, 2625 (1995).

 0021-8979/96/79(8)/5761/1/$10.00 © 1996 American Institute of Physics 

# Surface anisotropy of a fine $\gamma$-$Fe_2O_3$ particle

Kezhao Zhang and Donald R. Fredkin
*Physics Department, University of California, San Diego, La Jolla, California 92093*

We investigate the effects of surface anisotropy of a single-domain $\gamma$-$Fe_2O_3$ fine particle (length 3000 Å, aspect ratio 4.6:1) using micromagnetics and the finite element method. We add surface anisotropy energy, axially symmetric about the surface normal, to the total magnetic energy of the particle. We show that surface anisotropy of the appropriate sign enhances the coercivity. Further, the surface magnetization tends to be tangential to the surface and the magnetization reversal starts from the surface. Our simulation suggests that surface anisotropy might be an important mechanism for the coercivity enhancement in the surface-modified iron oxides. © *1996 American Institute of Physics.* [S0021-8979(96)20708-6]

## I. INTRODUCTION

Surface effects of fine particles in high density magnetic recording media become very pronounced because of the large surface-to-volume ratio. Experiments have shown that modification of fine $\gamma$-$Fe_2O_3$ particles with Co[1,2] or sodium polyphosphate[3,4] can enhance the coercivity. A variety of possible mechanisms for and numerical simulations of the enhancement of coercivity have been discussed. For example, the particle volume can be divided into a low crystalline anisotropy core region and a high crystalline anisotropy shell region.[5–7] In another approach, a mechanism for surface anisotropy is suggested[8] and a quantum theory of the surface anisotropy of ferrimagnetic $\gamma$-$Fe_2O_3$ has been developed.[9] Dimitrov and Wysin[10] have numerically investigated the effects of surface anisotropy on hysteresis in a simplified case where the magnetic particles are spins on two- and three-dimensional finite lattices; each element in the system represents a single magnetic ion rather than a finite volume as in micromagnetics. In their simulation, magnetic dipole interactions are neglected.

In this paper we describe our micromagnetic study of the effects of surface anisotropy of a fine single-domain $\gamma$-$Fe_2O_3$ particle.

## II. MICROMAGNETIC MODEL

We formulate the problem in terms of micromagnetics.[11] To investigate the effects of surface anisotropy, we add surface anisotropy energy to the total magnetic energy,

$$E_{\text{total}}=E_{\text{ex}}+E_{\text{demag}}+E_{\text{anis}}+E_{\text{Zeem}}+E_{\text{surface}}, \tag{1}$$

where $E_{\text{ex}}$ is the exchange energy, $E_{\text{demag}}$ is the magnetostatic interaction energy, $E_{\text{anis}}$ is the crystalline anisotropy energy in the bulk of the particle, and $E_{\text{Zeem}}$ is the Zeeman energy describing the interaction of the magnetization in the particle and an applied field. The surface anisotropy energy is

$$E_{\text{surface}}=K_s'\int [\mathbf{M}(\mathbf{r})\cdot\hat{\mathbf{n}}]^2\, dS=K_s\int \cos^2\theta\, dS, \tag{2}$$

where $\mathbf{M}(\mathbf{r})$ is the magnetization vector, $\hat{\mathbf{n}}$ is the unit vector normal to the surface, $\theta$ is the angle between $\mathbf{M}$ and $\hat{\mathbf{n}}$, and the surface anisotropy constant is $K_s = K_s'|\mathbf{M}|^2$. The integration is carried out over the surface of the particle.

We use the finite element method (FEM) to discretize the continuous magnetization field.[12,13] The magnetic region is decomposed into tetrahedral elements and the magnetization within an element is interpolated linearly from its values at the nodes of the mesh. The magnitude of the magnetization is fixed, $|\mathbf{M}(\mathbf{r})|=M_s$, where $M_s$ is the saturation magnetization. Finally, the total magnetic energy is expressed as a quadratic polynomial of the magnetization vectors on the nodal points of the FEM mesh,

$$E_{\text{total}}=\sum_{i,j}\tfrac{1}{2}\mathbf{M}_i\cdot\mathbf{K}_{ij}\cdot\mathbf{M}_j-\sum_i Z_i\mathbf{M}_i\cdot\mathbf{H}_{\text{ext}}. \tag{3}$$

The $\mathbf{K}$ matrix contains all information about the long range magnetostatic interaction, the anisotropy energy (including surface and crystalline anisotropies), and the exchange energy. $Z_i$ gives the weights of external field on the nodes.

We use the Landau–Lifshitz equation without the procession term to monotonically reduce the system energy to a local minimum, corresponding to a metastable magnetization configuration.

## III. RESULTS

We investigate a fine single-domain ellipsoidal $\gamma$-$Fe_2O_3$ particle with a long axis of 3000 Å and a short axis of 650 Å. The saturation magnetization $M_s=350$ emu/cm$^3$; the crystalline anisotropy constant $K_1=-4.6\times10^4$ ergs/cm$^3$.[14] The crystalline anisotropy constant is negligible compared to the shape anisotropy energy of an ellipsoid with an aspect ratio of 4.6:1 which is $0.81\pi M_s^2=3.2\times10^5$ ergs/cm$^3$.[15] Therefore we neglect crystalline anisotropy, $K_1=0$. The value of the exchange constant is known only approximately; we use $A=5.0\times10^{-7}$ ergs/cm in our calculation.

We calculate the hysteresis loops (Fig. 1) with different surface anisotropy constants. Surface anisotropies on the order of 1 erg/cm$^2$ have been reported for iron.[16,17] We choose $K_s$ within the range of 0–50 ergs/cm$^2$.

Figure 1 shows the increase of coercivity due to the surface anisotropy. The relationship of these two quantities is summarized in Fig. 2. For $K_s\approx20$ ergs/cm$^2$, the coercivity is about double of the value when $K_s=0$.

The computed magnetization configuration just before the switching indicates that magnetization reversal starts from the surface where the magnetization vectors form a wavelike pattern [Fig. 3(b)], while in the bulk magnetization is almost pointing in the same direction [Fig. 3(a)]. Surface

 0021-8979/96/79(8)/5762/2/$10.00 © 1996 American Institute of Physics

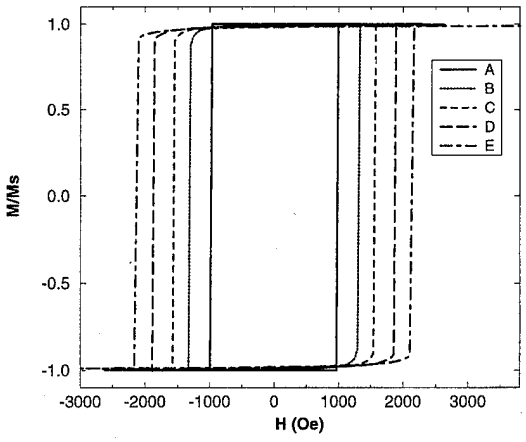



FIG. 1. Hysteresis loops of an ellipsoidal $\gamma$-$Fe_2O_3$ particle (aspect ratio 4.6:1) with various surface anisotropy constants $K_s$. The magnetization is along the long axis of the particle. The angle between the external field and the long axis is 1°. (A) $K_s=0$; (B) $K_s=3.98$ ergs/cm$^2$; (C) $K_s=7.96$ ergs/cm$^2$; (D) $K_s=19.91$ ergs/cm$^2$; (E) $K_s=39.81$ ergs/cm$^2$.

magnetization tends to be tangential to the surface, which requires a larger applied field during the switching, hence the enhancement of coercivity.

We have also investigated the effects of $K_s<0$. Negative $K_s$ is found experimentally to be much smaller than the positive $K_s$ for iron.[16] Our simulation shows that negative surface anisotropy does not effectively enhance the coercivity and in many cases decreases it. However, $K_s<0$ makes the surface magnetization perpendicular to the surface and aids formation of nucleation centers on the surface.

## IV. CONCLUSION

We added a surface anisotropy energy term to the total magnetic energy in the micromagnetic model in order to understand the effects of the surface anisotropy in a fine surface-modified $\gamma$-$Fe_2O_3$ particle. Our simulation shows that with positive surface anisotropy ($K_s>0$), magnetization reversal starts from the surface. Coercivity is doubled when $K_s\approx 20$ ergs/cm$^2$ for an ellipsoidal particle with a 3000-Å-long axis. This suggests that surface anisotropy might be an important mechanism for the coercivity enhancement in fine surface-modified iron oxide particles. The increase of coercivity can be attributed to the energy barrier, which requires a larger applied field during the switching, due to the positive surface anisotropy. For smaller particles that have a larger surface-to-volume ratio, the effects of surface anisotropy could be more prominent.

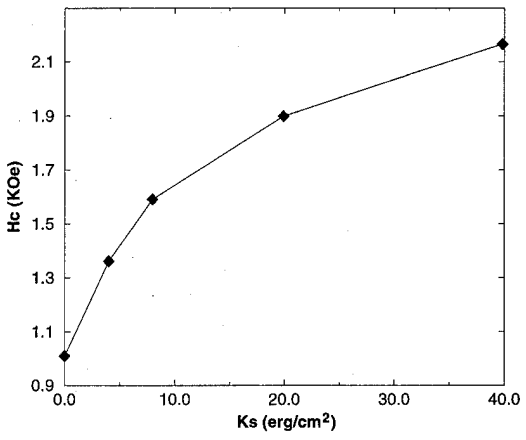



FIG. 2. Coercivity vs surface anisotropy constant. The values of the coercivity are obtained from the computed hysteresis loops.

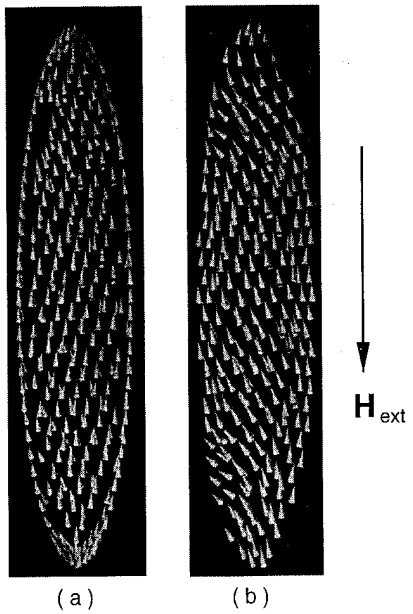



FIG. 3. Magnetization configurations on different cross sections just before switching. The surface anisotropy $K_s=19.91$ ergs/cm$^2$ and the applied magnetic field $H_{ext}=1869$ Oe. The arrows represent the magnetization vector **M**—sections (a) through the center, and (b) closer to the surface of the particle.


[1] A. E. Berkowitz, F. E. Parker, E. Hall, and G. Podolsky, IEEE Trans. Magn. **24**, 2871 (1988).
[2] Z. Lin, J. Magn. Magn. Mater. **116**, 147 (1992).
[3] F. Itoh and M. Satou, Jpn. J. Appl. Phys. **14**, 2091 (1975).
[4] F. E. Spada, F. T. Parker, C. Y. Nakakura, and A. E. Berkowitz, J. Magn. Magn. Mater. **120**, 129 (1993).
[5] A. Aharoni, J. Appl. Phys. **62**, 2576 (1987).
[6] A. Aharoni, J. Appl. Phys. **63**, 4605 (1988).
[7] M. E. Schabes and H. N. Bertram, J. Appl. Phys. **67**, 5149 (1990).
[8] F. Itoh, M. Satou, and Y. Yamazaki, IEEE Trans. Magn. **13**, 1385 (1977).
[9] J. C. Slonczewski, J. Magn. Magn. Mater. **117**, 368 (1992).
[10] D. A. Dimitrov and G. M. Wysin, Phys. Rev. B **50**, 3077 (1994).
[11] D. R. Fredkin and T. R. Koehler, J. Appl. Phys. **67**, 5554 (1990).
[12] W. Chen, D. R. Fredkin, and T. R. Koehler, IEEE Trans. Magn. **29**, 2124 (1993).
[13] D. R. Fredkin and T. R. Koehler, IEEE Trans. Magn. **28**, 1239 (1992).
[14] E. Köster and T. C. Arnoldussen, in *Magnetic Recording*, edited by C. D. Mee and E. D. Daniel (McGraw-Hill, New York, 1987), p. 98.
[15] D. J. Craik, *Structure and Properties of Magnetic Materials* (Pion, London, 1971).
[16] U. Gradmann, J. Magn. Magn. Mater. **54–57**, 733 (1986).
[17] K. B. Urquhart, B. Heinrich, J. F. Cochran, A. S. Arrott, and K. Myrtle, J. Appl. Phys. **64**, 5334 (1988).

# Random free energy model for the description of hysteresis

G. Bertotti, V. Basso, and G. Durin
*IEN Galileo Ferraris, INFM and GNSM, Corso M. d'Azeglio 42, I-10125 Torino, Italy*

The connection between hysteresis phenomena and free energy metastable states in magnetic systems is discussed. A random free energy model is introduced, which leads to a stochastic differential equation for the evolution of magnetization in time. We show that the solutions of this equation are equivalent to the Preisach model of hysteresis. The analytical form of the Preisach distribution is calculated. © *1996 American Institute of Physics.* [S0021-8979(96)20808-2]

## I. INTRODUCTION

Hysteresis, and in particular ferromagnetic hysteresis, has its origin in the multiplicity of metastable states in the system free energy. The consequences of such a general statement are usually very difficult to translate into quantitative predictions. An intermediate, more viable approach pursued by several authors has been to introduce phenomenological models, where all the basic hysteretic features are a direct consequence of a few simple initial assumptions. In this respect, a powerful tool is the Preisach model,[1] where hysteresis is described by a collection of a large number of elementary bistable units, each characterized by the values $\alpha$ and $\beta$, $\alpha>\beta$, at which the external field $H_a$ makes the unit switch up or down. A given system is fully described by the switching field distribution $p(\alpha,\beta)$. The Preisach model clarifies several important aspects of hysteresis phenomena, but its relation to the system free energy properties still presents several unresolved aspects. The most remarkable result in this respect is still perhaps Néel's derivation of the Rayleigh law of ferromagnetic hysteresis,[2] where he showed that the behavior of a magnetic domain wall under small fields is approximately equivalent to a Preisach description with a constant Preisach density.

In this paper we analyze the properties of a simple single-degree-of-freedom system which sheds new light on this problem. The model is based on a stochastic description of the system free energy $F(I)$ as a function of the magnetization $I$, characterized by the presence of a great number of local minima. We will show that the evolution of the system through the metastable states landscape results in a random sequence of irreversible jumps and that the associated hysteresis properties, once averaged over a proper statistical ensemble, are equivalent to a Preisach description with an exponential Preisach distribution of the form $p(\alpha,\beta) \propto \exp[-(\alpha-\beta)/2A\chi]$, where $A$ and $\chi$ are suitable constants. The model shows how the Preisach description arises from the stochastic dynamics of the system and thus represents an important result in the direction of clarifying the physical meaning and limits of the Preisach model itself.

## II. MODEL

We will consider a ferromagnetic system, described by its magnetization $I$, evolving under the action of a time-dependent external field $H_a(t)$, where internal heat is produced as a consequence of irreversible processes. The rate of heat production per unit volume during a given isothermal transformation is

$$\frac{dQ_i}{dt}=H_a(t)\frac{dI}{dt}-\frac{dF}{dt}=\left[H_a(t)-\frac{\partial F}{\partial I}\right]\frac{dI}{dt}, \tag{1}$$

where $H_a dI/dt$ is the power injected into the system and $F(I)$ is the system free energy. We consider the case where the system is not brought too far from equilibrium, so that there exists a linear relationship between the thermodynamic flux $dI/dt$ and the thermodynamic force $H_a(t)-\partial F/\partial I$,

$$\gamma\frac{dI}{dt}=H_a(t)-\frac{\partial F}{\partial I}. \tag{2}$$

In the case of a quadratic dependence of $F$ on $I$, i.e., $F=I^2/2\chi$, Eq. (2) gives the well-known exponential relaxation equation $\gamma dI/dt=H_a-I/\chi$. This equation predicts a linear quasistatic behavior of the form $I=\chi H_a$ (no hysteresis). Under stationary conditions, if $H_a$ increases at constant rate, $dI/dt=\chi dH_a/dt$, and the heat production per unit magnetization change is $dQ_i/dI=\gamma dI/dt=\gamma\chi dH_a/dt$.

Moving from these well-known results, we now consider the case where $F$ exhibits random fluctuations around the large-scale parabolic behavior, as a consequence of the presence of some quenched-in disorder in the system. We thus consider $F=I^2/2\chi+F_p(I)$, where $F_p(I)$ describes the random fine structure of the free energy. This leads to the formation of many metastable states. The precise functional dependence of $F_p(I)$ on $I$ is different for different systems. We assume that $F_p(I)$ is continuous and has a continuous first derivative, so that the random pinning field $H_p(I)=\partial F_p/\partial I$ exists and is continuous, but otherwise random. The simplest stochastic process having such properties is an $I$-random-walk characterized by independent increments $dH_p$, with $\langle dH_p\rangle=0$ and $\langle|dH_p|^2\rangle=2A\,dI$. Some cutoff in this behavior is expected for sufficiently small or large $I$ variations. These complications are not considered here and will be addressed in subsequent more refined treatments. By introducing the dimensionless variables $u=t/\gamma\chi$, $x=I/A\chi^2$, $v=dx/du$, $h_a=H_a/A\chi$, $h_p=H_p/A\chi$, we obtain

$$\begin{aligned} &v=h_a(u)-[x+h_p(x)],\\ &\langle dh_p\rangle=0,\quad \langle|dh_p|^2\rangle=2dx. \end{aligned} \tag{3}$$

The random nature of $h_p(x)$ is responsible for the corresponding stochastic evolution of $v$. As shown in the following sections, there is an intimate connection between the statistical properties of the $v$ process and the hysteresis properties of the system.

 0021-8979/96/79(8)/5764/3/$10.00 © 1996 American Institute of Physics

## III. ENERGY DISSIPATION

Let us consider the $v$ process as a function of the dimensionless coordinate $x$.[3] By deriving Eq. (3) with respect to $x$ in the case where the external field increases at the constant time rate $c=dh_a/du$, we obtain

$$\frac{dv}{dx}+\left(1-\frac{c}{v}\right)=-\frac{dh_p(x)}{dx}. \tag{4}$$

The associated Fokker–Planck equation for the $v$ transition density $P(v,x|v_0)$ is

$$\frac{\partial P}{\partial x}-\frac{\partial}{\partial v}\left[\left(1-\frac{c}{v}\right)P\right]-\frac{\partial^2 P}{\partial v^2}=0. \tag{5}$$

From Eq. (5), the stationary distribution turns out to be

$$P_x(v)=\frac{1}{\Gamma(c+1)}\,v^c\exp(-v), \tag{6}$$

where the subscript $x$ recalls the fact that $P_x$ represents the distribution of $v$ values picked up at random $x$ positions. In the limit of quasistatic excitation ($c\ll 1$), the system evolves by a sequence of well-separated Barkhausen jumps, responsible for the quasistatic hysteretic behavior of the system.[4,5] The corresponding heat production $\langle dQ_i/dI\rangle_I=\gamma$ $\langle dI/dt\rangle_I=\chi A\langle v\rangle_x$ can be calculated from Eq. (6) as

$$\begin{aligned}\left\langle\frac{dQ_i}{dI}\right\rangle&=\chi A\langle v\rangle_x=\chi A\int_0^\infty vP_x(v)dv\\&=\frac{\chi A}{\Gamma(c+1)}\int_0^\infty v^{c+1}\exp(-v)dv\\&=\chi A\,\frac{\Gamma(c+2)}{\Gamma(c+1)}=\chi A(1+c)\\&=\chi A+\gamma\left\langle\frac{dI}{dt}\right\rangle.\end{aligned} \tag{7}$$

The heat production per unit average magnetization change has the dimensions of a field and represents the half-width of the corresponding hysteresis loop. The first term in the last expression of Eq. (7) represents the quasistatic dissipation associated with a hysteresis loop of half-width $H_0=A\chi$, while the second one is the dynamic dissipation expected when fluctuations can be neglected, so that $F=I^2/2\chi$, as calculated above. The fact that these two terms are simply summed up is what is commonly termed loss separation. Our result shows that this is a rigorous property of a certain class of dynamical systems, rather than, as is often assumed, a useful empirical assumption for the description of experimental results.

## IV. EQUIVALENCE WITH THE PREISACH MODEL

As shown by Eq. (7), the model predicts the existence of rate-independent hysteresis in the limit of vanishing magnetization rates. We will show that these hysteresis effects can be described by the Preisach model. Mayergoyz proved that a system with hysteresis is equivalent to the Preisach model if it obeys the so-called "wiping out or return-point-memory" and "congruency" properties.[6] We will prove that the system described in the preceding sections obeys these properties.

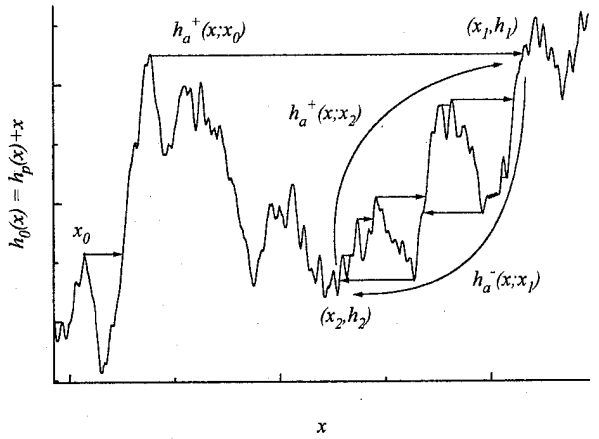



FIG. 1. Example of evolution of the system over $h_0(x)=h_p(x)+x$ with a field rate $dh_a/du=c\ll 1$. $h_a^+(x;x_0)$ is an ascending branch starting from the point $x_0$. The wiping out property assures the closure of the minor loop between the $h_1$ and $h_2$ fields.

*Wiping out or return-point-memory property*: If we consider a nonmonotone applied field with two subsequent reversal points $h_1$ and $h_2$, as the field goes back from $h_2$ to $h_1$ and reaches $h_1$ again, the system returns to exactly the same state it was at the first reversal point.

We prove this property in the limit of the low applied field rate $dh_a/du=c\ll 1$. In this limit, the behavior of the system depends only on the sign of $dh_a/du$. Irreversible jumps correspond to horizontal $h_a$ segments starting from local maxima of $h_0(x)=h_p(x)+x$ (see Fig. 1). The evolution of the system is described by the $h_a(x)$ line. We indicate by $h_a^+(x;x_0)$ and $h_a^-(x;x_0)$ generic monotone branches originating from the point $x_0$, and associated with increasing (+) or decreasing (−) field. The system must be at rest at the point $x_0$, which means that $h_a^+(x_0;x_0)=h_0(x_0)$, $h_a^-(x_0;x_0)=h_0(x_0)$. Monotone branches satisfy the following laws:

(1) $h_a^+(x;x_0)\geq h_a^-(x;x_1)$ for any $x_0$ and $x_1$. This is the immediate consequence of the fact that, by definition, $h_a^+(x;x_0)\geq h_0(x)$ and $h_a^-(x;x_1)\leq h_0(x)$ for any $x$.

(2) $h_a^+(x;x_0)\geq h_a^+(x;x_1)$ for any $x_1\geq x_0$ and $h_a^-(x;x_0)\leq h_a^-(x;x_1)$ for any $x_1\leq x_0$. Let us consider the first inequality and suppose it is not obeyed. Then there exists a local maximum of $h_0(x)$ exceeding $h_a^+(x;x_0)$, with $x>x_0$. But this is not possible, because, as illustrated above, $h_a^+(x;x_0)\geq h_0(x)$ for any $x>x_0$.

The two inequalities (1) and (2) imply the wiping out property. In fact, let us consider a branch $h_a^+(x;x_0)$, up to the turning point $h_a^+(x_1;x_0)=h_0(x_1)$, $x_1>x_0$, and the subsequent decreasing branch $h_a^-(x;x_1)$ down to the second turning point $h_a^-(x_2;x_1)=h_0(x_2)$, $x_1>x_2>x_0$. Let us consider the branch $h_a^+(x;x_2)$. By inequality (1), $h_a^+(x;x_2)\geq h_a^-(x;x_1)$. On the other hand, since $x_2>x_0$, inequality (2) gives $h_a^+(x;x_0)\geq h_a^+(x;x_2)$. Thus $h_a^+(x;x_0)\geq h_a^+(x;x_2)\geq h_a^-(x;x_1)$. Since $h_a^+(x_1;x_0)=h_a^-(x_1;x_1)=h_0(x_1)$, also $h_a^+(x_1;x_2)=h_0(x_1)$. This proves the wiping out property.

*Congruency property*: All minor loops delimited by the same peak field values are geometrically congruent.

In order to prove this property, we have to properly define minor loops. Let us consider an applied field oscillating between the two reversal points $h_1$ and $h_2$. Because of the wiping-out property, cycling between $h_2$ and $h_1$ will eventually generate a closed minor loop in all cases. Individual minor loops between the same peak fields will have in general different shapes, so that congruency can hold only for the average loop obtained after statistical average over the subensemble of $h_0(x)$ portions selected by the applied field history. After the average, the minor loop shape can only depend on the difference $h=h_2-h_1$, and not on $h_1$ or $h_2$ separately. This occurs because the increments of $h_0(x)=x+h_p(x)$ for a given $x$ increment $\Delta x$ have a statistical distribution only dependent on $\Delta x$ and otherwise completely independent of $h_0$ and $x$. Thus average minor loops associated with the same $\Delta h$ difference are identical in shape. This proves the congruency property.

The fact that minor loops characterized by the same $\Delta h$, with different $h_1$ and $h_2$, are congruent implies that the Preisach distribution $p(\alpha,\beta)$ associated with the system is a function of $(\alpha-\beta)$ only. The analytic dependence on $(\alpha-\beta)$ can be determined by considering the rate of energy dissipation predicted by the model. According to the Preisach model, the energy dissipated during a given field change $dH_a$ is

$$dQ_i=dH_a\int_{-\infty}^{H_a}d\beta(H_a-\beta)p(H_a-\beta)$$

$$=4dH_a\int_0^{\infty}dh_c h_c p(h_c), \tag{8}$$

where $h_c=(\alpha-\beta)/2$ represents the half-width of each elementary Preisach loop. Let us compare this expression with the term of Eq. (7) where the dissipation is expressed in terms of $P_x(v)$. The quantity $h_c$ plays, in the Preisach model, the same role of $\gamma dI/dt$, i.e., of $v$, since it measures the rate of energy dissipation. Therefore, from Eqs. (7) and (8), by taking the limit $c\to 0$ and by exploiting the correspondence $h_c\leftrightarrow\gamma dI/dt=A\chi v$, $p(h_c)\leftrightarrow\exp(-v)=\exp(-h_c/A\chi)$ and the fact that $dI=\chi dH_a$, we obtain

$$p(\alpha-\beta)=\frac{1}{4A}\exp\left(-\frac{\alpha-\beta}{2A\chi}\right). \tag{9}$$

It is worth noticing that this distribution has no dependence on $h_u=(\alpha+\beta)/2$, as our model describes nonsaturating hysteresis. Furthermore, in the case of small applied fields the Rayleigh law $I=aH+bH^2$ holds with $a=0$ and $b=1/(2A)$.

## V. CONCLUSIONS

The physical picture here proposed gives a convincing interpretation of several experimental observations. The model predicts Barkhausen jump properties which are in good agreement with recent experiments.[4,5] The Preisach description mentioned above predicts a hysteresis loop half-width proportional to $A\chi$. As shown in Sec. II, the parameter $\chi$ describes the curvature of the large-scale potential well in which a given domain wall is trapped. This curvature can be experimentally modified by various means, and the dependence of coercivity on $\chi$ has actually been observed and interpreted by methods similar to the ones discussed in Sec. III.[7] Finally, the Preisach density of Eq. (9) obeys the factorization $p(\alpha,\beta)=f(\alpha)f(-\beta)$, with $f(x)$ proportional to $\exp(-x)$. Recently, there has been some debate about the fact that such factorization might be the natural one when domain wall motion is the basic magnetization mechanism.[8,9] The present results make clear the context and the limits within which this assumption is acceptable.


[1] F. Preisach, Z. Phys. **94**, 277 (1935).
[2] L. Néel, Cahiers de Phys. **12**, 1 (1942).
[3] This basic equation has been considered in the past to describe the properties of the Barkhausen effect (see Refs. 4 and 5 and references therein). An analytic solution as a function of the time exits in closed form in the case where the external field increases at constant rate.
[4] B. Alessandro, C. Beatrice, G. Bertotti, and M. Montorsi, J. Appl. Phys. **64**, 5355 (1988); **68**, 2901 (1990); **68**, 2908 (1990).
[5] G. Durin, G. Bertotti, and A. Magni, Fractals **3**, 351 (1995).
[6] I. D. Mayergoyz, *Mathematical Models of Hysteresis* (Springer, New York, 1991).
[7] L. Pust and G. Bertotti, IEEE Trans. Magn. **30**, 834 (1994).
[8] V. Basso and G. Bertotti, IEEE Trans. Magn. **30**, 64 (1994).
[9] R. D. McMichael, F. Vajda, and E. Della Torre, J. Appl. Phys. **75**, 5692 (1994).

# Micromagnetics of polycrystalline two-dimensional platelets

K. M. Tako, M. A. Wongsam, and R. W. Chantrell
*Physics Department, Keele University, Keele, Staffordshire ST5 5GB, United Kingdom*

A numerical micromagnetic technique is used to simulate magnetization processes in two-dimensional thin metallic platelets. The platelets are modeled as an array of interacting polycrystalline grains. The technique assumes a triangular discretization at the subgrain level with the magnetization varying linearly over each triangle. The coupling between the grains has a profound effect on the magnetic structure of the platelets as does the grain size. For systems with strongly exchange coupled grains, approximately solenoidal magnetization structures exist. A single domain behavior exists for systems with weakly coupled grains. The magnetization pattern of the platelets has been characterized by the vorticity of the magnetization vector field. © *1996 American Institute of Physics.* [S0021-8979(96)20908-9]

## I. INTRODUCTION

Since the theory of micromagnetics was formulated by Brown,[1,2] numerical techniques have become an everyday tool in solving micromagnetic problems. Then, only particles with the simplest of geometries were considered enabling analytical techniques to be employed. It is, however, apparent that for present day technological applications these particles generally have a wide distribution of complicated geometries. The demagnetizing field within the particles is generally nonuniform. This gives rise to nonuniform magnetization states. It is therefore not surprising that for particles with more complicated morphology, the idea of nonuniform magnetization within the particles cannot be ignored. The intergranular correlations in materials with nonuniform magnetization properties within grains is of great significance. Shape[3] and size[3,4] have been found to influence the magnetic behavior of these systems. Effort has been made by different authors to investigate the magnetization processes associated with such complicated shapes.

In this paper, we present a dynamic finite element method which is used to study magnetization processes in polycrystalline two-dimensional (2D) platelets with a realistic grain structure. The grains which are irregularly shaped, have been produced by the Voronoi construction[4] and have easy anisotropy axes oriented at random. The Landau–Lifschitz (LL) equation is used. We give a brief description of the model in Sec. II and we present some results in Sec. III.

## II. MICROMAGNETIC MODEL

Since the bulk of the micromagnetic model has been described elsewhere,[4] we shall limit ourselves to a brief description. The 2D platelet is modeled as an array of irregularly shaped interacting polycrystalline grains produced using the Voronoi construction.[4] Each grain, assumed to be a single crystal, is assigned a random in-plane uniaxial anisotropy easy axis. The approach assumes a triangular discretization at the subgrain level with the magnetization allowed to vary linearly within each triangle. We have discretized each grain by joining its nodes to its seed point (center). The total magnetic field at each point within the platelet is made up of contributions from external, exchange, anisotropy, and magnetostatic sources. The formulation of all the field terms has been given in our previous work.[4]

The time evolution of the magnetization of the system is governed by the LL equation which can be written as

$$\frac{d\mathbf{m}}{d\tau}=\mathbf{m}\times\mathbf{h}-\alpha\mathbf{m}\times(\mathbf{m}\times\mathbf{h}), \tag{1}$$

where $\mathbf{h}=\mathbf{H}/H_k$ is the total reduced effective field from all sources, $\mathbf{m}=\mathbf{M}/M_s$ the reduced magnetization, $\alpha$ the reduced damping constant, and $\tau$ the reduced time. $H_k=2K/M_s$, $K$ being the uniaxial anisotropy constant and $M_s$ the saturation magnetization. A fourth-order predictor–corrector algorithm with error control capability and step size adjustment is used to solve the system of coupled differential equations (1). A suitable convergence criterion is adopted by limiting the angle between $\mathbf{m}$ and $\mathbf{h}$ to within 0.01 rad.

The magnetic structure is characterized by the vorticity ($\Gamma$) of the magnetization field vector. The vorticity defines the sense of rotation of the magnetization vector as well as the extent to which it is tilted in the vortex regions. It is defined as the line integral of the magnetization field vector along a chosen path in the film plane scaled with respect to the length of the path.[5,6] For convenience, we chose a circular path. Thus $\Gamma_i(r)=\oint\mathbf{m}\cdot d\boldsymbol{\lambda}/\oint\hat{p}\cdot d\boldsymbol{\lambda}$, defines the vorticity at points lying on the circumference of a circle of radius $r$ centered on the seed point of grain $i$. $\hat{p}$ is a unit vector tangential to the path. Given that $\oint\mathbf{m}\cdot d\boldsymbol{\lambda}=\int_s(\nabla\times\mathbf{m})ds$ by Stoke's theorem, it is more convenient in practice to calculate the vorticity function via the curl of $\mathbf{m}$. Because of the presence of vortices with positive and negative sense, the most sensible system average is the absolute value of $\Gamma$. Thus we define the system vorticity as

$$\Gamma(r)=\frac{1}{N}\left|\sum_{j=1}^{N}\frac{\oint\mathbf{m}\cdot d\boldsymbol{\lambda}}{\int\hat{p}\cdot d\boldsymbol{\lambda}}\right|, \tag{2}$$

where $N$ is the number of seed points considered. The vorticity function as defined is an extension of the previous definition[5,6] and is potentially sensitive to the magnetic microstructure of the films.

## III. RESULTS AND DISCUSSION

We have simulated structures in Co platelets with different grain sizes and degree of intergranular exchange coupling. There are free boundary conditions. The predicted

 0021-8979/96/79(8)/5767/3/$10.00 © 1996 American Institute of Physics 

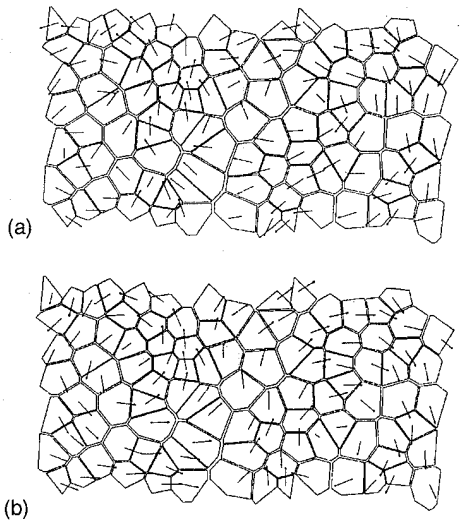



FIG. 1. (a) $C^*=0.0$, $h=0.23$, grain size=400 Å, thickness=1000 Å. (b) $C^*=0.4$, $h=0.15$, grain size=400 Å, thickness=1000 Å.

structures agree with the experiments of Wong *et al.*[7] The choice of material parameters is as follows: $\alpha=1.0$, $A=10^{-6}$ ergs/cm, $C^*$ is in the range of 0.0–0.4, $K=4.2\times10^6$ ergs/cm$^3$, and $M_s=1.4\times10^3$ emu/cm$^3$. $A$ is the exchange constant and $C^*$ defines the strength of the intergranular exchange coupling. Films with an aspect ratio of 2:1 have been used with thicknesses of 125 Å for grains averaging 50 Å in diameter and 1000 Å for 400 Å grains. We have calculated hysteresis loops and obtained magnetization plots. The vorticity function has been used to characterize the magnetic structure and investigate the nature of magnetization reversal.

### A. Magnetization structure

In Figs. 1(a) and 1(b), the arrows represent the vector average of the magnetization within the grains. The state of the system close to the coercive field for grains averaging approximately 400 Å in size are shown for $C^*=0.0$ and $C^*=0.4$. Clearly, the magnetic behavior of the systems differ. For low $C^*$, the magnetic structure is not well defined.

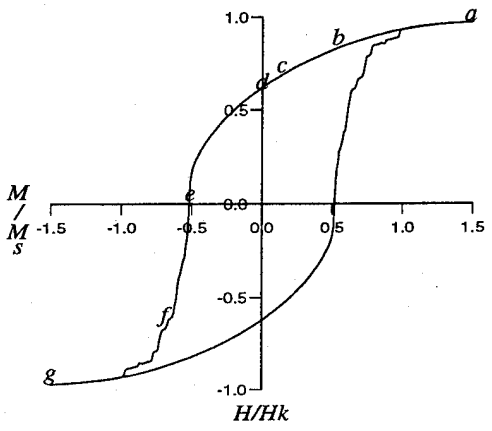



FIG. 2. $C^*=0.0$. No magnetostatic interactions.

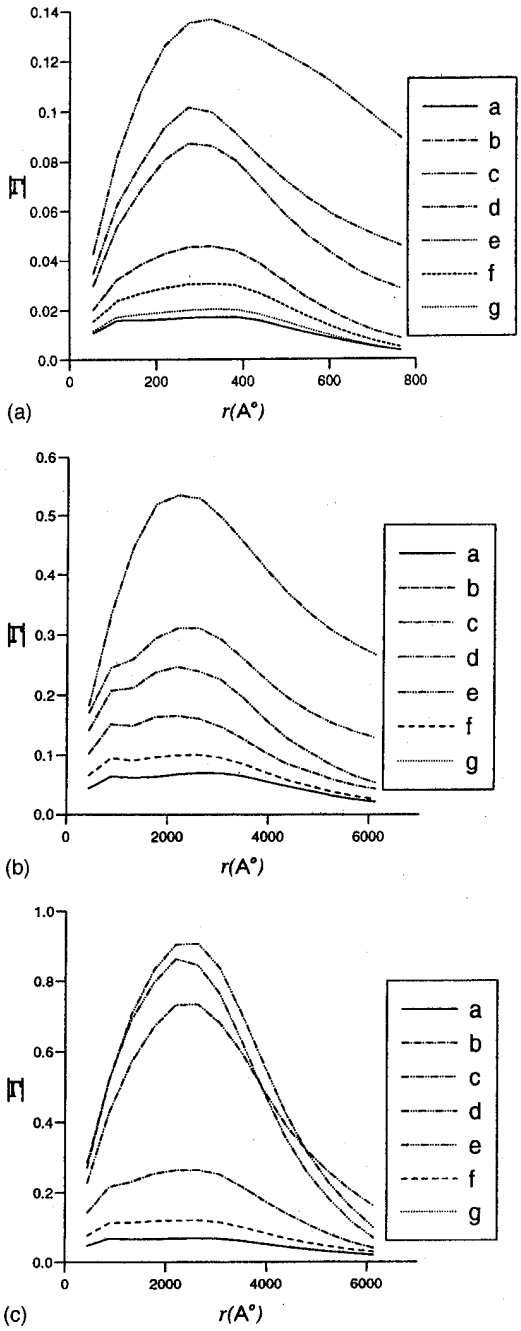



FIG. 3. (a) $|\Gamma|$ vs $r$, $C^*=0.4$, grain size=50 Å, thickness=125 Å. (b) $|\Gamma|$ vs $r$, $C^*=0.0$, grain size=400 Å, thickness=1000 Å. (c) $|\Gamma|$ vs $r$, $C^*=0.4$, grain size=400 Å, thickness=1000 Å.

There is considerable disorder in the flux pattern although a tendency to form a weak solenoidal structure can be discerned. This is due to the weak coupling between the grains. For high $C^*$, regions of flux closure exist. Local irregularities in the magnetization structure are minimal. The magnetization structure is approximately solenoidal. Similar to Ref. 8, similar behavior was observed for other grain sizes and is consistent with experimental data. The magnetic structure is not perfectly solenoidal probably due to the polycrystalline nature of the system.

### B. Characterization of magnetization structures

The process of vortex formation and its subsequent expansion can be characterized by the vorticity of the magnetization distribution. $\Gamma(r)$ has a very characteristic behavior as can be seen by studying its variation with $r$ at different points on the hysteresis loop, an example of which is given in Fig. 2. This loop (calculated for zero magnetostatic and exchange interactions) serves to define seven characteristic points at which the vorticity has been calculated for a number of simulations.

Figures 3(a)–3(c) show the absolute vorticity ($|\Gamma|$) versus the radii of the circular path. In Fig. 3(a), $C^*=0.4$ and the grain size is 50 Å. In Figs. 3(b) and 3(c), $C^*=0.0$ and 0.4, respectively, while the grain size is 400 Å.

The plots clearly demonstrate vortex formation in these systems and can be related to the magnetization structures and reversal mechanism as follows.

At saturation, the vorticity is quite close to zero in Figs. 3(a)–3(c). The fact that it is not exactly zero indicates the effects of the demagnetizing field at the ends which result in bending nonuniform magnetization structures. As the external field is reduced from saturation, a peak appears indicating the onset of vortex formation. The peak becomes more pronounced as the applied field is further reduced, indicating the subsequent expansion of the vortex as it moves inwards from the ends. The maximum vorticity reaches a peak close to the coercive field indicating that the vortices are fully expanded. For high values of $C^*$, the vorticity peaks sharply for systems with larger grain sizes [Fig. 3(c)] compared to Fig. 3(a) in which the average grain size is smaller and where the peak broadens. In addition, the peak value of the vorticity is significantly higher ($\approx 1.0$) in Fig. 3(c). Thus at the coercive force, peaks are pronounced in those systems where vortex formation occurs readily. For lower values of $C^*$ as in Fig. 3(b), the peak is less pronounced and broadens, indicating that there is little sign of vortex formation. Further reduction in the applied field results in a gradual disappearance of the peak as the vortex moves through the particle and subsequently disappears at negative saturation. The maximum vorticity increases with increasing grain size. Thus $\Gamma$ seems to be reflecting the form of the microstructure and magnetization reversal.

## IV. CONCLUSION

A dynamic finite element method in micromagnetics has been described. The magnetic structures are profoundly influenced by the strength of the magnetic interactions and the shape and size of the grains. The structures have been characterized by the vorticity of the magnetization field vector. The magnitude and variation of the vorticity are strongly influenced by the grain size and the magnetic interactions. The solenoidal magnetization structures predicted by our theoretical model have been observed experimentally.


## ACKNOWLEDGMENTS

This work was supported by EPSRC and carried out within the EU CAMST project.



[1] W. F. Brown Jr., *Micromagnetics* (Wiley-Interscience, New York, 1963).
[2] W. F. Brown Jr., J. Appl. Phys. **30**, 8 (1959).
[3] M. E. Schabes, J. Magn. Magn. Mater. **95**, 249 (1991).
[4] K. M. Tako, M. A. Wongsam, and R. W. Chantrell, J. Magn. Magn. Mater. (to be published).
[5] M. E. Schabes and H. N. Bertram, J. Appl. Phys. **64**, 3 (1988).
[6] M. E. Schabes and H. N. Bertram, J. Appl. Phys. **64**, 10 (1988).
[7] H. Y. Wong, J. N. Chapman, S. McVitie, and S. J. Hefferman, J. Magn. Magn. Mater. **104–107**, 329 (1992).
[8] D. R. Fredkin and T. R. Koehler, IEEE Trans. Magn. **26**, 5 (1990).

# Three-dimensional analysis of the magnetization process of thin-film media

E. Miyashita, Y. Yoneda, and J. Numazawa
*NHK Science and Technical Research Labs, 1-10-11 Kinuta, Setagaya-ku, Tokyo 157, Japan*

A calculation model in which the medium is considered as a set of many fine magnetic particles is applied to thin-film media. The magnetic characteristics are calculated for a particle with an initial layer, a particle without an initial layer, and media composed of the particles of either type. The results show that the switching mode of both particles is a quasi-coherent rotation but the switching field dependence of the particle with an initial layer has curlinglike characteristics. The perpendicular medium with an initial layer is over corrected by $4\pi M_s$ demagnetization correction.
© *1996 American Institute of Physics.* [S0021-8979(96)21008-3]

## I. INTRODUCTION

All kinds of recording media have intrinsic particle structures, sizes and shapes, and interactions between them. When analyzing media, we must consider the characteristics of fine magnetic particles of which they are constituted. In order to analyze a medium microscopically the authors have proposed a new medium model for calculating the magnetic characteristics of recording media.[1] Several calculation models have been proposed,[2,3] but they have assumed either that the magnetization in a particle is uniform or that the switching field characteristics of a particle are curling. In this model, no assumptions are made about either the magnetization in a particle or the reversal mode. The medium is considered as a many-body system of fine magnetic particles and the magnetic characteristics of the media are calculated from the magnetic properties of the isolated fine particles and interparticle interactions. The authors have previously calculated the characteristics of metal-particle and barium–ferrite-particle media and showed the effect of the interactive field on the magnetization process.[1]

We have now improved this model for application to thin-film media. In the improved model, the initial layer of a fine particle can be considered for calculation of the switching process. To calculate the medium magnetization process, the exchange and demagnetization fields are also considered. Using this model, we calculate the magnetization curves for perpendicular thin-film media. Perpendicular media have an initial layer which is semihard and has easy axis in the plane, because the surface roughness or adatoms of the substrate throw an initial crystal growth into disorder. In order to study the effect of initial layer on the magnetization process, we calculate the magnetization curves of perpendicular media both with and without an initial layer. The validity of a demagnetization correction for perpendicular media is also discussed.

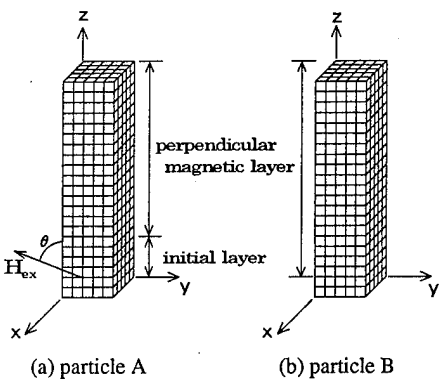



FIG. 1. Calculated particles.

## II. CALCULATION MODEL

### A. Calculation model for the switching process of an isolated fine particle

The switching process of an isolated fine particle was calculated numerically by use of the Landau–Lifshitz–Gilbert equation.[4] The fine particles are assumed to be hexahedral, as shown in Fig. 1. The particle is divided into $n_x \times n_y \times n_z$ cubic cells. The cell size is set sufficiently small for the magnetization in the cell to be considered uniform. The easy axis of each cell can be set independently for consideration of not only the perpendicular layer but also the initial layer. The forward differential method was used because the algorithms are simple and the free boundary condition was imposed. The calculation parameters are shown in Table I.

### B. Calculation model for magnetization process of the medium

The medium model is shown in Fig. 2. The thin-film medium is composed of fine particles located on $N_x \times N_y$

TABLE I. Calculation parameters of particles.

| | Particle A | Particle B |
|---|---|---|
| Division number $n_x \times n_y \times n_z$ | 5×5×26 | 5×5×26 |
| Cell size [nm] | 9 | 9 |
| Exchange in a particle $A$ [$\times 10^{-6}$ erg/cm] | 0.6 | 0.6 |
| Magnetocrystalline anisotropic constant | | |
| $K_{u1}$ [$\times 10^4$ erg/cc] | 142–342 | 142–342 |
| $K_{u2}$ [$\times 10^4$ erg/cc] | 36–85 | 36–85 |
| Initial layer | | |
| $K_{u1}$ [$\times 10^4$ erg/cc] | 48–114 | |
| $K_{u2}$ [$\times 10^4$ erg/cc] | 12–28 | |
| Saturation magnetization $M_s$ [emu/cc] | 570 | 570 |

 0021-8979/96/79(8)/5770/3/$10.00 © 1996 American Institute of Physics

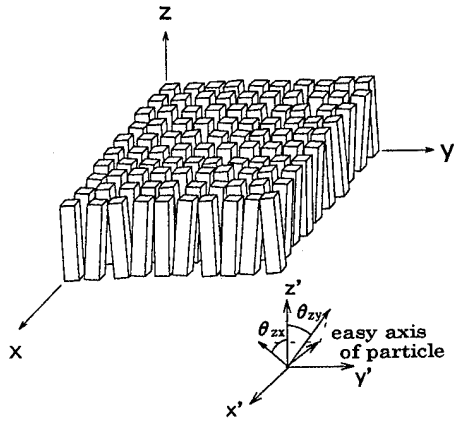



FIG. 2. Medium model.

lattice points with each easy axis direction. The characteristics of the isolated particle have already been calculated in (a), and now the interactive field must be calculated. This includes considerations of the magnetostatic interactive field from other particles, the exchange field from the nearest neighboring particles, and the demagnetization field. For simplicity, the magnetostatic field was calculated on the assumption that the magnetization of the particles is uniform. The demagnetization field coefficient in the $z$-axis direction is equal to 1. The calculation range of the magnetostatic interactive field is to the sixth nearest neighboring particles. The periodic boundary condition was imposed. The calculation's parameters are shown in Table II. All distribution is assumed to be Gaussian.

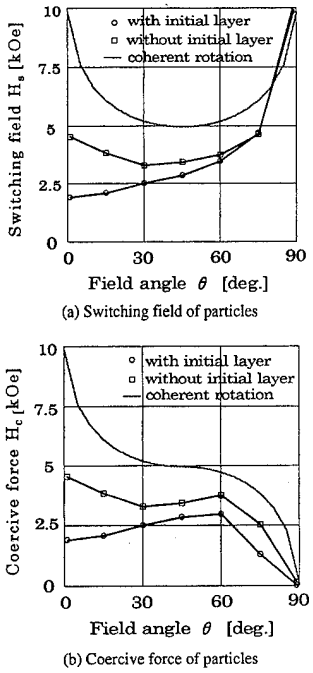
## III RESULTS AND DISCUSSION

### A. Switching process of an isolated fine particle

Figure 3 shows the dependence of the switching field and coercive force on the angle of the external field with a crystalline anisotropic field strength of 8000 Oe. The switching mode of both particle **A** with an initial layer and particle **B** without an initial layer is a quasi-coherent rotation. The curve of particle **A**, however, is similar to a curling mode curve. Magnetization reversal of both particles starts at one end of the particle, with the reversal then gradually moving to the other end. This switching mode is taken because in the

TABLE II. Calculation parameters of media.

| | Medium A | Medium B |
|---|---|---|
| Particle number $N_x \times N_y$ | 50×50 | 50×50 |
| Lattice distance $dx \times dy$ [nm] | 50×50 | 50×50 |
| Interparticle exchange $A_{\text{pmean}}$ [$\times 10^{-6}$ erg/cm] | 0.2 | 0.2 |
| $\sigma_{Ap}$ [$\times 10^{-6}$ erg/cm] | 0.2 | 0.2 |
| Easy axis dispersion $\sigma_{zx}, \sigma_{zy}$ [deg] | 4,4 | 4,4 |
| Average anisotropic field $H_{\text{kmean}}$ [Oe] | 7500 | 7500 |
| Anisotropic field dispersion $\sigma_{Hk}$ [Oe] | 500 | 500 |



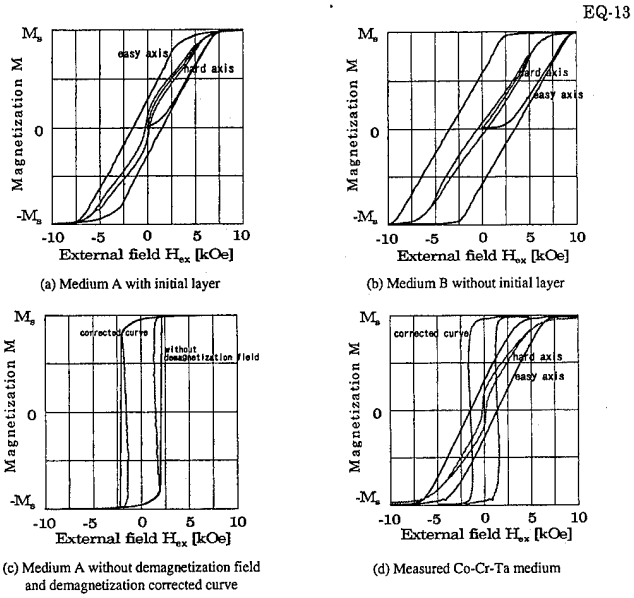

(a) Switching field of particles

(b) Coercive force of particles

FIG. 3. Switching field and coercive force.

case of long and thin particles less total energy is used than in other switching modes. The switching field of particle **A** is much smaller than that of particle **B** in the small field angle. For particle **A**, the magnetization layer is in-plane by the easy axis in the plane in the initial layer and out of plane by the easy axis out of the plane in the perpendicular. The angle of magnetization in both layers is nearly 90°. Accordingly, a large torque acts on the initial layer in the low field angle.

EQ-13




(a) Medium A with initial layer

(b) Medium B without initial layer

(c) Medium A without demagnetization field and demagnetization corrected curve

(d) Measured Co-Cr-Ta medium

FIG. 4. Calculated and measured magnetization curves.

### B. Magnetization curves of the media

These magnetization curves were calculated for perpendicular medium **A** composed of particle **A** and medium **B** composed of particle **B**. Figure 4(a) and 4(b) show the magnetization curves of media **A** and **B** with the demagnetization field. Figure 4(c) shows magnetization curves of medium A both without the demagnetization field and after demagnetization correction of the curve in Fig. 4(a). (The curve of medium **A** is shown (c) without the demagnetization field and the corrected curve (a) is shown after demagnetization field correction.) Calculated magnetization curves (a) agree quite well with the measured curves. The coercive force of medium **A** is much smaller than that of **B**. The measured magnetization curves of the perpendicular Co–Cr–Ta film media are also shown in Fig. 4(d) for comparison with the calculated curves. The magnetization curve in the hard axis direction jumps near the zero field shown in Fig. 4(d) because the real perpendicular medium has an initial layer. The curve of the easy axis direction has a slope of nearly $4\pi M_s$ because of the demagnetization field. The dashed line in Fig. 4(d) is the corrected measured curve. Both corrected curves are over corrected after simple demagnetization correction. The switching field of the fine particle depends on not only the strength of the field but also on the angle between the magnetization and the field. The magnetostatic and exchange fields take various directions, so the switching field of each particle in the medium varies. The demagnetization field is uniform but the total field applied to particles exhibits various strengths and directions. The result is that the magnetization curve is not corrected precisely by simple demagnetization. The reason for over correction is that the magnetization process depends strongly on both the switching field characteristics and the magnetostatic interactive field.

## IV. CONCLUSION

The improved fine particle model was applied to thin-film media and the magnetization curves were calculated. The following results were obtained:

(1) The switching field characteristics of the particle with the initial layer has curlinglike characteristics.
(2) The coercive force in the perpendicular direction of the medium is considerably reduced by the initial layer.
(3) The perpendicular medium with initial layer is over corrected by $4\pi M_s$ demagnetization.


## ACKNOWLEDGMENT

The authors would like to thank Hideo Oshima, the director of their research division, for his helpful advice on their studies.



[1] E. Miyashita, Y. Yoneda, and J. Numazawa, J. Mag. Soc. Jpn. **18**, Suppl. No. S1, 125 (1994).
[2] J.-G. Zhu and H. N. Bertram, J. Appl. Phys. **63**, 3248 (1988).
[3] I. Tagawa, A. Takeo, Y. Shimizu, and Y. Nakamura, J. Magn. Soc. Jpn. **18**, Suppl. No. S1, 129 (1994).
[4] Y. Nakatani, Y. Uesaka, and N. Hayashi, Jpn. J. Appl. Phys. **28**, 2485 (1989).

# Characterization of minor loops using Preisach-based models

Ferenc Vajda and Edward Della Torre
*Institute for Magnetics Research, The George Washington University, Washington, DC 20052*

This paper gives a theoretical analysis of recently reported experimental hysteresis data by O'Grady and Greaves [J. Magn. Magn. Mater. **138**, L233 (1994)] performed on a variety of thin film and particulate recording samples. Using recently developed hysteresis models, it is shown that the nonzero area of their measured minor loop is due to hysterons in the media that switch to the up state in negative field. Using the accommodation model, it is shown that, when cycling the applied field, the computed magnetization drifts up or down and approaches a stable minor loop. The direction of the drift depends on the accommodating magnetizing process. © *1996 American Institute of Physics.* [S0021-8979(96)21108-X]

## I. INTRODUCTION

O'Grady and Greaves[1,2] recently reported experimental hysteresis data on a variety of thin film and particulate recording samples that they called anomalous effects in minor hysteresis loops. Using recently developed hysteresis models, this paper presents a theoretical explanation of the observed phenomena.

One of the experiments they performed was a magnetizing process that started from positive saturation, followed by the application of a negative field $H_1$ and then $H_2$ which in the experimental data they always set to zero. They observed that, for the samples considered, the magnetization of this first-order reversal curve increased as the negative filed $H_1$ was being removed. It was also observed that, when cycling between $H_1$ and $H_2$, the area enclosed by the stable minor loop was not zero. The experimental results also indicated that the minor branches closed only after the applied field had been cycled a sufficient number of times between $H_1$ and $H_2$ and that during this process, the magnetizations at the end points, denoted $M(H_1)$ and $M(H_2)$, decreased with each cycle until the stable cycle was reached. In our theoretical analysis, we will call these observations 1, 2, and 3, respectively.

In this paper we will show that observations 1 and 2 can be explained by the complete moving hysteresis (CMH) model.[3] The explanation of observation 3 requires the additional refinement of an accommodation model. The measured results can be explained by the accommodating complete hysteresis (MACH) model.[4] The parameters of the models are based on the statistical analysis of the interaction field and critical field in medium hard materials and accurately predict complex high-order reversal curves that include both locally reversible and irreversible processes.[3–5] It is emphasized that, since the reported experimental results are not sufficient to identify the parameters of the models, the goal of this paper is to show that the observed but unexplained phenomena are in agreement with our models.

## II. STABLE MINOR LOOPS

In this section, we will show that it is necessary to use Preisach-based models[3,6] to explain observations 1 and 2 summarized above.[1,2] Since the measured minor loops are noncongruent, the classical Preisach model[7] cannot describe them. In order to characterize noncongruent minor loops, one has to use a magnetization-dependent model,[8] the simplest of which is the moving model. However, in order to compute minor loops with nonzero slope at the field reversal point, the locally reversible magnetization also has to be modeled. Since the observed data has a variable slope at the same applied field, the model must have a magnetization-dependent locally reversible magnetization, such as the DOK model[6] and the CMH models.[3]

### A. The moving model

The moving model is a Preisach-based magnetization-dependent hysteresis model that computes the irreversible component of the magnetization and was developed based on the statistical analysis of the interaction field in longitudinal media. Using $U$ and $V$ to denote the "up" and "down" switching fields and $\alpha$ to denote the material-dependent moving constant, the operative Preisach plane, whose axes are the operative up and down switching fields $u=U+\alpha M$ and $v=V+\alpha M$, is illustrated in Fig. 1. The active region of the Preisach plane corresponding to the cycling between $H_1<0$ and $H_2=0$ for an initially up saturated sample is illustrated by the cross-hatched region in Fig. 1. The magnetization of all the other regions will remain unchanged after the first traversal of the minor loop. The active region is magne-

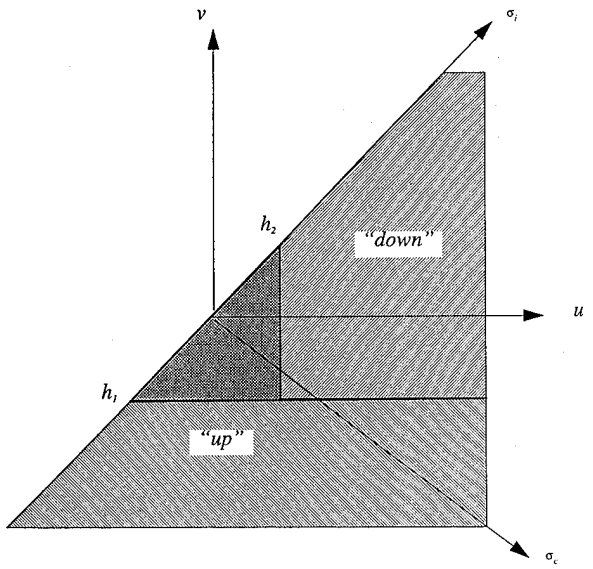



FIG. 1. Active region of the operative Preisach plane corresponding to a cyclical field between $H_1<0$, $H_2=0$. The initial magnetization state is up saturation.

 0021-8979/96/79(8)/5773/3/$10.00 © 1996 American Institute of Physics 

tized down when $H=H_1$ and it is magnetized up when $H=H_2$. However, since the moving Preisach hysterons experience the operative field $h=H+\alpha M$, the active region in the moving model will be bounded by

$$h_1=H_1+\alpha M(H_1), \quad h_2=\alpha M(H_2), \tag{1}$$

where $M(H_1)$ and $M(H_2)$ are the magnetizations at $H_1$ and $H_2$, respectively.

The state of hysterons in the classical Preisach model is independent of the magnetization, that is, since $H_2$ is equal to 0, for any value of the applied field it is equal to $H$. This means that, as long as $H_1<0$ and $H_2=0$, the triangular actively switched region in Fig. 1 encompasses only quadrant III of the Preisach plane. Therefore, the classical Preisach function has to be nonzero in this quadrant to describe observations 1 and 2. In case of the moving model, the situation is more complex. During the experimental analysis of various longitudinal media we always observed, $\alpha>0$; therefore, if $M(H_2)>0$, as is the case in the experimental data presented,[1,2] then the vertical side of the actively switched triangular region lies in quadrant I of the Preisach plane. If $|\alpha M(H_1)|\mp hH_1$ then $h_1<0$ and the active region encompasses parts of quadrants III, IV, and I of the operative Preisach plane, as illustrated in Fig. 1. If $\alpha M(H_1)$ is sufficiently large so that $h_1>0$, then the active region may be entirely contained in quadrant I. In summary, the location of the actively switched triangular region computed by the moving model depends on the magnetization, as well. Therefore, it is not necessary for the operative Preisach function to be nonzero outside quadrant IV for the moving model to describe observations 1 and 2. Using the experimental data[2] one can only determine that $M(H_1)>0$ which is not sufficient to decide which case occurs for the specific samples. However, as discussed below, the moving model is generally applicable to characterize all possible cases. Thus

$$M(h_2)-M(h_1)=2\int_R\int p(u,v)dudv, \tag{2}$$

and the region of integration, $R$, is the cross-hatched triangular region illustrated in Fig. 1.

The above Preisach integrand is always non-negative; therefore, in agreement with observation 1, the computed magnetization increases as the applied negative field, $H_1$ is being removed. This is not surprising, since one expects the susceptibility to increase (decrease) as the applied field increases (decreases). This is true regardless of the sign of the applied field, since this susceptibility increases (decreases) depending on only the relative change in the applied field.

When the applied field is cycled between $H_1$ and $H_2$, the change in the irreversible magnetization is partially due to switching in quadrants I and III of the operative Preisach plane. Thus, the nature of the stable minor loop is dependent on how much the operative Preisach function extends into quadrants I and III. Therefore, the measured nonzere minor loop area,[2] also called the eye, is due to the relatively large interaction in these media.

Minor loops computed by the moving model for increasing values of $\sigma_i$ corresponding to the magnetizing process $+H_{sat}$, $H_1<0$, $H_2=0$, $H_1<0$ are shown in Fig. 2. The aim of the computations, in which only $\sigma_i$ was varied, was to show that the moving model can compute minor loops with a nonzero eye, and no attempt was made to fit the measured data presented in Ref. 2. Although the moving model computes the irreversible magnetization $m_i$ only, it is seen that at $H_2=0$ the magnetization of the descending major irreversible branch decreases as $\sigma_i$ increases. This is due to the increasing apparent reversible contribution of quadrants I and III of the operative Preisach plane for increasing values of $\sigma_i$. Although the apparent reversible contribution causes the magnetization to decrease (increase) when a positive (negative) operative field is being removed, it is different from locally reversible contributions in which no energy is dissipated during the process.[9] The computed magnetization at the reversal field, $H_1$, decreases as $\sigma_i$ increases, which is due to the increasing apparent reversible contribution of the entire quadrant I of the Preisach plane. However, as seen in the inset in Fig. 2, the slope of all the computed minor loops is zero at the turning points, which is a property of all Preisach-type models.[6] Since the measured slopes at the reversal points are not zero, an accurate model of the observed phenomena must include the locally reversible magnetization, as well.

### B. The DOK and CMH models

The DOK[6] and CMH[3] models are seven-parameter scalar hysteresis models developed for medium hard materials that add a state-dependent reversible magnetization to the moving model. Thus, these models compute both the irreversible and the state-dependent locally reversible magnetization. A parametric identification method of the models was developed and verified for a variety of recording materials in which the operative Preisach function is zero outside quadrant IV of the Preisach plane.[3] Such a Preisach function is commonly referred to as a IV quadrant Preisach function.

Minor loops computed by the CMH model for increasing values of $\sigma_i$ corresponding to the magnetizing process $+H_{sat}$, $H_1<0$, $H_2=0$, $H_1<0$ are shown in Fig. 3. It is noted that, like the measured data,[2] the computed curves include both the irreversible and the locally reversible components of the magnetization. It is seen that, in agreement with experi-

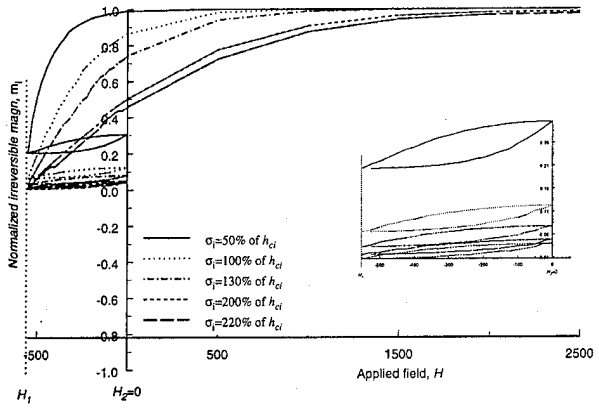



FIG. 2. Minor loops computed by the moving model for increasing values of $\sigma_i$ corresponding to the magnetizing process $+H_{sat}$, $H_1<0$, $H_2=0$, $H_1<0$. The inset is an enlargement of the computed minor loops.

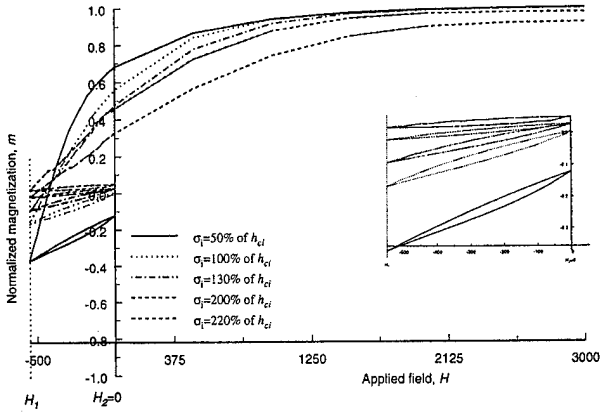



FIG. 3. Minor loops computed by the CMH model for increasing values of $\sigma_i$ corresponding to the magnetizing process $+H_{sat}$, $H_1<0$, $H_2=0$, $H_1<0$ (a). The inset is an enlargement of the computed minor loops.

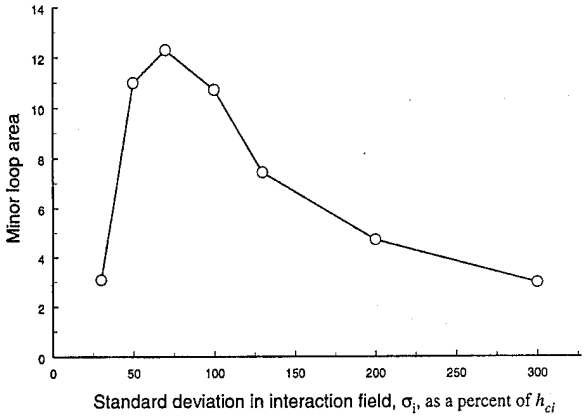



FIG. 4. The computed area of minor loops for increasing values of $\sigma_i$ using the CMH model.

mental results, the minor loops have a nonzero slope at the reversal points. At smaller values of $\sigma_i$, a larger number of hysterons switch from the down state to the up state as the field $H_1$ is being removed. Therefore, since the slope of the individual hysteron loops is greater in the up state than in the down state, there will be a greater increase in the state-dependent reversible magnetization resulting in a larger relative increase in magnetization when removing the field, $H_1$. As $\sigma_i$ is increased, a smaller portion of the hysterons switch to the up state while removing $H_1$; therefore, the relative change in magnetization decreases, as seen in the inset on Fig. 3.

The computed minor loop area for increasing values of $\sigma_i$ is shown in Fig. 4. It is seen that, for small interactions, since the Preisach function is negligible in the active region illustrated in Fig. 1, there is a small change in the irreversible state during the magnetizing process. Thus, the area of the minor loop will also be small. As $\sigma_i$ increases, the actively switched region will include an increasing portion of the Preisach function; therefore, the area will increase. At even greater values of $\sigma_i$, a considerable portion of the Preisach function will lie outside the actively switched region; therefore, after reaching a peak, the area of the minor loop will decrease. It is noted that the value of $\sigma_i$ at which the peak area occurs is a function of all the other model parameters, as well as the reversal field, $H_1$.

## III. ACCOMMODATION PHENOMENA

Observation 3 shows that, as the applied field is cycled between $H_1<0$ and $H_2=0$, the magnetization drifts down and the minor loop closes only after the field has been cycled a sufficient number of times,[2] a phenomenon known as the accommodation or reptation. As discussed in the MACH model,[4] accommodation is due to the interaction between the particles that comprise the medium. Using the MACH model it has been shown that, in agreement with measured results,[10] the measured accommodation is due to the change in the interaction field during the magnetizing process. In agreement with observation 3, the MACH model computes accommodating minor loops that approach a stable limiting cycle. The model also shows that, for the magnetizing process used to obtain observation 3, the magnetization drifts down at each cycle until the minor loop stabilizes. Using the MACH model, it can also be shown that, if the reversible magnetization is negligible then the accommodation in the minor loop is driven by the eye of the minor loop. Thus, for such materials, there would be no accommodation if the eye in the minor were zero. It has also between shown that the direction of the magnetization drift is dependent on the reversal field, $H_1$ and that the amount of accommodation can be maximized by selecting a magnetizing process that maximizes regions $R_1$ and $R_4$. This latter property of the model has been shown to be important when identifying the parameters of the MACH model.[10]

## IV. CONCLUSIONS

This paper gave a theoretical explanation of recently reported experimental hysteresis data by O'Grady and Greaves[1,2] performed on a variety of thin film and particulate recording samples. Using recently developed hysteresis models,[3] it was shown that the nonzero area of the measured minor loop when cycling between a negative field, $H_1$ and zero field, $H_2$, is due to hysterons in the media that switch to the up state in negative field. It was also shown that, one does expect the measured magnetization to increase while the applied field is increased but is negative throughout the process, since a change in the magnetization is caused by a changing field regardless of its sign. Using the accommodation model,[4] it was shown that, in agreement with the measured data, when cycling the applied field, the computed magnetization drifts up or down and approaches a stable minor loop. The direction of the drift depends on the accommodating magnetizing process.

[1] K. O'Grady and S. J. Greaves, J. Magn. Magn. Mater. **138**, L233 (1994).
[2] K. O'Grady and S. J. Greaves, IEEE Trans. Magn. (in press).
[3] E. Della Torre and F. Vajda, IEEE Trans. Magn. **30**, 4987 (1994).
[4] E. Della Torre, IEEE Trans. Magn. **30**, 2701 (1994).
[5] F. Vajda and E. Della Torre, IEEE Trans. Magn. (in press).
[6] E. Della Torre, J. Oti, and G. Kadar, IEEE Trans. Magn. **26**, 3052 (1990).
[7] G. Schwantke, Frequenz **12**, 383 (1958) [English translation in J. Aud. Eng. Soc. **9**, 37 (1961)].
[8] G. Kádár and E. Della Torre, IEEE Trans. Magn. **23**, 2820 (1987).
[9] G. R. Kahler, E. Della Torre, and F. Vajda, IEEE Trans. Magn. **30**, 4374 (1994).
[10] F. Vajda and E. Della Torre, IEEE Trans. Magn. **30**, 4371 (1994).

# Radio frequency ion beam deposition of diamond-like carbon for sliders and heads

Lien-Chang Wang, Gary Halada, and Richard J. Gambino,
*Department of Materials Science and Engineering, State University of New York, Stony Brook, New York 11794-2275*

Alan Hayes and Sal DiStefano
*Veeco Instruments, Plainview, New York 11803-2313*

Diamond-like carbon prepared by direct ion beam deposition from a filamentless rf ion source has been found to have properties suitable for protective coatings on sliders and heads. One advantage of the rf inductively coupled plasma source used in this study is that it can be operated reliably for hundreds of hours with high concentrations of hydrocarbon gas. We have studied deposition from argon-$CH_4$ mixtures with 28% to 100% $CH_4$ and beam energies mainly in the 100 to 400 eV range. X-ray photoemission spectra analysis shows that films prepared with pure $CH_4$ have less $sp^3$ (diamond-like) bonding than films prepared from mixtures with argon. © *1996 American Institute of Physics.* [S0021-8979(96)15808-8]

## I. INTRODUCTION

It has been estimated that the head/media separation may be as little as 20 nm in 10 Gbit/in.$^2$ disk products[1] which are expected to be in production in the next five to ten years. This flying height puts extraordinary demands on the wear, tribological, and electric properties of the protective coating on the slider and head. Diamond-like carbon (DLC) films have been prepared by many different methods and the properties vary widely depending on the process and on specific process parameters. Direct ion beam deposition from low pressure hydrocarbon-rich atmospheres has been found to produce films with properties suitable for this application.[2] This article reports, for the first time, direct ion beam deposition of DLC films from a filamentless rf ion source. One advantage of the rf inductively coupled plasma source used for this study is that it can be operated reliably for hundreds of hours with high concentrations of hydrocarbon gas. In this paper we report on the effects of varying the fraction of argon in the hydrocarbon gas mixture used in the gun on the rate and film properties. We have also studied the influence of ion energy.

## II. EXPERIMENTAL PROCEDURE

The vacuum chamber used for deposition of the DLC films is equipped with a Veeco RIM 210 rf inductively coupled plasma (ICP) ion source and a 1000 ℓ/s turbo pump. The base pressure of the system prior to deposition was less than $2\times10^{-6}$ Torr. Substrates of Si and $SiO_2$ were cleaned prior to deposition by immersion in acetone, spray-rinsed with acetone, then with methanol, and blown dry. The substrates were mounted on a helium gas cooled wafer stage which was oriented during deposition so that the ion beam is normal to the substrate surface. A Kapton tape mask was put on each wafer to provide a step for thickness measurements. After the system reached base pressure the substrates were precleaned for 20 s with a 300 mA argon ion beam at 750 eV. The substrate holder was rotated during ion cleaning and deposition.

The deposition rate was determined by measuring the film thickness at a masked step using a Dektak, DT3 surface profiler. Film stress was determined from the curvature of the Si substrate after deposition, measured using the Dektak in a broad scan. Vickers microhardness measurements were made on selected films on Si. The films on Si were also used for x-ray photoemission spectra (XPS). The index of refraction ($n$) of the films on $SiO_2$ were measured on a Nanospec Microspectrophotometer. A Rudolph Research ellipsometer was used to get the index of films on Si. Optical absorption was also measured on a few films on $SiO_2$.

## III. ION SOURCE

The RIM-210 ion source used in this study is briefly described as follows. A rf plasma is generated by a helical rf coil external to the quartz plasma chamber and is operated at 1.8 MHz. The 180-mm diameter ion beam is extracted from the plasma by a three grid set of ion optics fabricated from molybdenum. The inductively coupled plasma has been shown to provide a very uniform ion beam for etching.[3]

We have studied deposition from $CH_4$-argon mixtures with 28% to 100% $CH_4$ and beam energies of 100, 200, 300, and 400 eV. In these experiments, the gas flow rate was held constant at 20 sccm and the beam current was 250 mA. Under these conditions the pressure in the chamber was 3 to $4\times10^{-4}$ Torr. A few experiments were carried out with beam energies of 50 and 100 eV and 150-mA beam current and flow rates of 6 to 10 sccm as noted below.

## IV. RESULTS

Qualitatively hard, scratch resistant, transparent films typical of DLC were deposited by this process. The refrac-

 0021-8979/96/79(8)/5776/3/$10.00 © 1996 American Institute of Physics

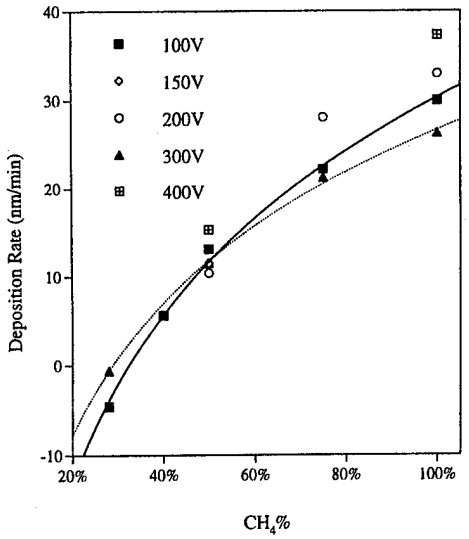



FIG. 1. Dependence of deposition rate on $CH_4$ percent with beam energies in the range 100 to 400 eV. The beam current was 250 mA and the gas flow rate was fixed at 20 sccm for these experiments.

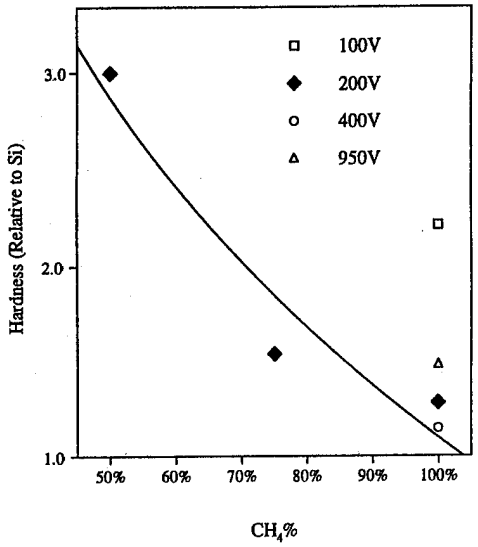



FIG. 3. Hardness vs $CH_4$ percent with various beam voltages. The trend line is for the 200-eV data.

tive index of the films is relatively high, typically about 1.8 to 2.0 as measured by both ellipsometry and Nanospec methods. Films about 100-nm thick show 90% transmission at a wavelength of 500 nm.

The dependence of the deposition rate on $CH_4$ percentage and beam energy are shown in Fig. 1. The rate decreases with decreasing $CH_4$ percent from about 30 nm/min at 100% $CH_4$ to about zero at 28%. These rates were measured on Si substrates but the rates on $SiO_2$ were the same within experimental error. The deposition rate is only weakly dependent on beam energy in this series of experiments with constant beam current. No clear trend with beam energy is seen in this data. The deposition rate of samples prepared with a beam current of 150 mA was in the 3 to 10 nm/min range.

Figure 2 shows stress and hardness as a function of beam energy up to 1000 eV. The lines are logarithmic fits to the data to show the trends. Figure 3 shows the hardness relative to the hardness of the Si substrate plotted against the $CH_4$ percent in the gas mixture for films prepared with various beam energies. The microhardness was measured with a 10-gram load, the lowest available load on our Vickers instrument. Measurements of the hardness of films are difficult in this thickness and hardness range.[4] The film was always extensively cracked and spalled in the region of the indent so the measured indent was actually in the silicon substrate. The penetration of the indenter was greater than the film thickness so the hardness was corrected for the fact that only part of the area of the indenter is pushing on the DLC film. The measured thickness of the film and the geometry of the indenter were used to calculate the area of the indenter in con-

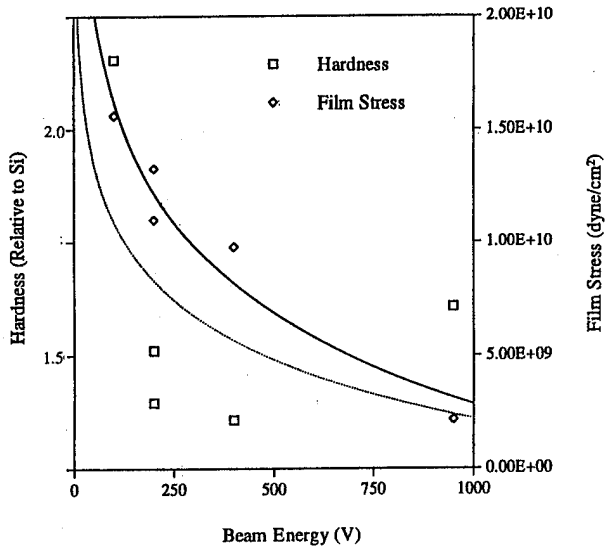



FIG. 2. Dependence of relative film hardness and stress on beam energy for samples prepared with pure $CH_4$.

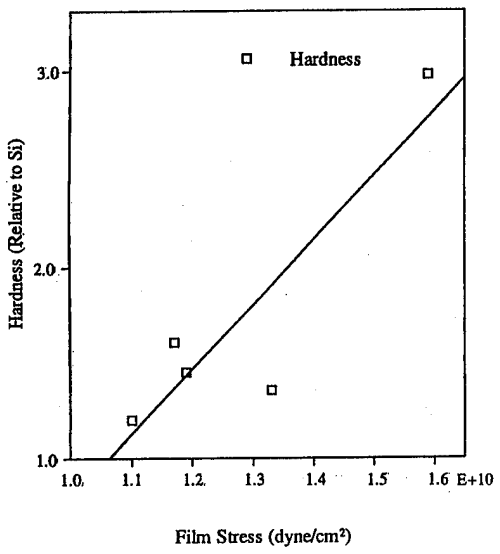



FIG. 4. The dependence of hardness on film stress for samples prepared at 200 eV, 250 mA, and 20 sccm with various argon-$CH_4$ mixtures.

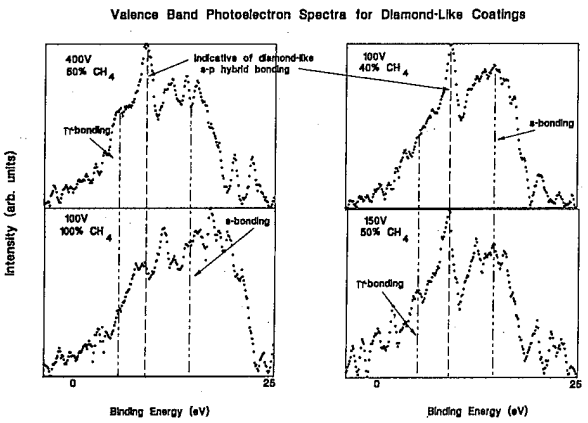



FIG. 5. The valence band photoelectron spectra of four DLC films prepared under different conditions. The spectra were taken using Mg $K\ \alpha$ radiation (1253.6 eV) with a hemispherical analyzer having a 20-eV pass energy.

tact with DLC and the corrected hardness. The measured hardness, therefore, is reported relative to the hardness measured on the Si substrate to show trends with processing conditions. The dependence of microhardness on film stress is shown in Fig. 4. Hardness and film stress appear to be strongly correlated.

Samples analyzed by XPS show less $sp^3$ (diamond-like) bonding when prepared from 100% $CH_4$ than from gas mixtures with argon. The XPS spectra of four DLC films prepared under different conditions are shown in Fig. 5. High levels of $sp^3$ bonding indicative of the diamond-like structure were observed in general. The sample prepared with pure $CH_4$ has significantly less $sp^3$ bonding than the samples prepared with argon-$CH_4$ mixtures. Among the samples prepared with argon-$CH_4$ mixtures, the 100-eV sample has slightly less $sp^3$ character than the 400- and 150-eV samples. On the other hand, the $\pi$ bonding peak appears to be weaker in the 100- and 150-eV samples as indicated by the height of the low energy peak labeled $\pi$ bonding. The sample prepared with an argon-$CH_4$ mixture at 150 eV shows both a strong $sp^3$ diamond-like peak and a weak $sp^2$ graphitic peak.

## V. DISCUSSION AND CONCLUSIONS

This paper, for the first time, reports ion beam deposition of diamond-like carbon films from a rf ion source. The films have a high $sp^3$ fraction, refractive index of up to 2.0, and are highly transparent. Although we were not able to obtain accurate absolute hardness values with our equipment, we were able to show that the hardness is several times greater than that of the Si substrate. These properties show that DLC films prepared by rf ion beam deposition are suitable for coating heads and sliders.

DLC consists of an amorphous network of covalently bonded carbon with a mixture of $sp^3$ and $sp^2$ bonding.[4] The understanding of the relationship between processing conditions and the formation of $sp^3$ bonds has been advanced by recent models.[5,6] According to these models $sp^3$ bonds form when carbon atoms are forced into close proximity either by direct implantation of a carbon atom into the carbon network or by a knock-on process. This suggests a possible beneficial role of argon bombardment, that is the generation of additional knock-ons by argon ion impact. Another feature of the model is the effect of the "thermal spike" associated with the damage track along the ions implantation path. The interstitials and knock-ons form, for the most part, at the end of the implantation track. The track itself is treated as a region which has been thermally relaxed by the thermal spike. Since the $sp^3$ bonded regions are metastable at low pressures the thermal spike promotes the formation of the more stable $sp^2$ bonds. According to this model the optimum energy for high $sp^3$ bond fraction is between 100 and 200 eV. We do not observe a major difference in $sp^3$ bond fraction between 150 and 400 eV; however, more $sp^2$ bond character is seen at the high beam energy. This model and others also predict a correlation of high $sp^3$ bond fraction with high compressive stress[5] which we observe.

## ACKNOWLEDGMENTS

The authors thank Veeco Instruments for financial support of this work. We especially thank Emmanuel Lakios for supporting and encouraging this research. The authors gratefully acknowledge Veeco colleagues Boris Druz, Kurt Williams, Ed Ostan, and Ralph Ruf (now at Stony Brook) for assistance in sample preparation and helpful discussions.

[1] E. S. Murdock, R. F. Simmons, and R. Davidson, IEEE Trans. Magn. **28**, 3078 (1992).
[2] D. Bogy, X. Yum, and B. Knapp, IEEE Trans. Magn. **30**, 369 (1994).
[3] A. Hayes and E. Ostan, 40th National Symposium of the American Vacuum Sociedty, Orlando, FL, 15–19 November 1993 (unpublished), Paper VT-WeP15, Abstract 1138.
[4] R. J. Gambino and J. A. Thompson, Solid State Commun. **34**, 15 (1980).
[5] J. Robertson, J. Non-Cryst. Solids **164–166**, 1115 (1993).
[6] C. A. Davis, Thin Solid Films **226**, 30 (1993).

# Nanoindentation study of the mechanical properties of metal evaporated magnetic tapes

Hong Deng and John A. Barnard
*Department of Metallurgical and Materials Engineering and Center for Materials for Information Technology, The University of Alabama, Tuscaloosa, Alabama 35478-0202*

Nanoindentation techniques have been used to examine hardness ($H$), Young's modulus ($E$), and strain rate sensitivity ($m$) in three types of commercial unaged and aged metal evaporated (ME) magnetic tapes. The aged tape samples were aged at 75 °C for 60 weeks at 5% and 90% humidity. The hardness of the ME layer can be determined at a depth of 30–50 nm, but for deeper penetrations the hardness value is increasingly affected by the soft polymer substrate. H and $E$ are essentially the same for the unaged samples and the samples aged at 5% humidity but greatly decreased for the tapes aged at 90% humidity. The creep behavior (the time-dependent deformation) of these tapes was also characterized for the first time using the nanoindenter. Strain rate sensitivity increases with maximum applied load. On the other hand, a decrease in the strain rate sensitivity is observed for the tapes aged at 5% humidity. For the tapes aged at 90% humidity it is very difficult to obtain the strain rate sensitivity due to the excessive brittleness of the samples. Nanoindentation creep measurements appear to be quite sensitive to the degradation of ME tape caused by adverse environmental conditions. © *1996 American Institute of Physics.* [S0021-8979(96)11108-6]

## I. INTRODUCTION

Metal evaporated (ME) magnetic tape is a most promising candidate for high-density audio/video recording, especially for small cassette digital video tape recorders (SCD-VTR).[1,2] With ever increasing magnetic recording densities the flying heights will be reduced to near zero. Therefore, wear and friction problems for both head and medium have to be minimized to meet durability requirements. The hardness ($H$), Young's modulus ($E$), and strain rate sensitivity ($m$) of magnetic tapes are important mechanical properties related to the wear and friction of the head/medium interface. Nanoindentation has been successfully used to determine the hardness and elastic modulus of thin films and coatings.[3,4] More recently, this technique has been employed to characterize the time dependent properties of thin films and to determine their strain rate sensitivity.[4,5] In this work, nanoindentation techniques are employed to characterize the mechanical properties of ME tapes. Preliminary results obtained using a newly developed approach[4,5] to the strain rate sensitivity of thin films are reported in this article.

## II. EXPERIMENT

Three kinds of commercial ME tapes labeled as Tape 1, 2, and 3 obtained from the National Media Laboratory (NML) were studied. The tapes consist of a polymer substrate with a thickness of 10 $\mu$m and a magnetic metal layer which is about 150 nm without an overcoat. Because the effect of adverse environmental conditions on the durability of the ME tapes is always a major concern in practical applications, we also examined the aging effects of temperature and humidity on the mechanical properties of these ME tapes. For this purpose, several pieces of the tape samples were aged at 75 °C with 5% and 90% humidity for 60 weeks. Then, both unaged and aged samples were characterized using a Nano Indenter® II Mechanical Properties Microprobe (Nano Instruments, Inc. Oak Ridge, TN).

Nanoindentation experiments were carried out with two different methods. For $H$ and $E$ measurements, a constant displacement loading approach was used. The $H$ and $E$ were determined at six indenter penetration depths: 30, 40, 50, 60, 80, and 120 nm, with indenter descent rates from 3 to 10 nm/s depending upon the maximum depths. A 6×6 matrix indentation configuration with a 50 $\mu$m spacing was used for $H$ and $E$ evaluation. In the indentation creep test a constant load loading segment and a long time hold are employed for characterization of the strain rate sensitivity. In this experiment, the maximum loads used are 0.05, 0.1, 0.2, and 0.3 mN and the loading rate is 10 $\mu$N/s. A 600 s hold was used in this work. All the indentation tests were performed at room temperature.

The strain rate sensitivity was calculated using the data collected in the long time hold segment after loading. The elastic contribution has to be eliminated from the total displacement; only plastic deformation is considered in this work. 2500–3000 data points were collected in the hold segment. They were divided into about 40 groups. For each group the slope of a linear fitting line and an averaged depth were calculated. The stress for a given indentation plastic depth is defined as $\sigma=P/A$, in which $P$ is the maximum load and $A$ is the indenter projected area corresponding to the averaged plastic depth and can be calculated with the indenter tip area function determined by calibration experiments. The strain rate ($\dot{\epsilon}$) is defined as the plastic descent rate divided by the plastic indentation depth $h$, $\dot{\epsilon}=(1/h)(dh/dt)$. Thus, strain rate sensitivity ($m$) is obtained from the slope of a log-log plot for the creep equation, $\sigma=C(\dot{\epsilon})^m$.[5]

## III. RESULTS AND DISCUSSION

The results of the nanoindentation hardness and Young's modulus measurements for the three ME tapes are shown in Fig. 1–3. The apparent hardness of the metal layer can be determined at a depth of 30–50 nm but for deeper penetrations the hardness value will be affected by the soft polymer

 0021-8979/96/79(8)/5779/3/$10.00 © 1996 American Institute of Physics 

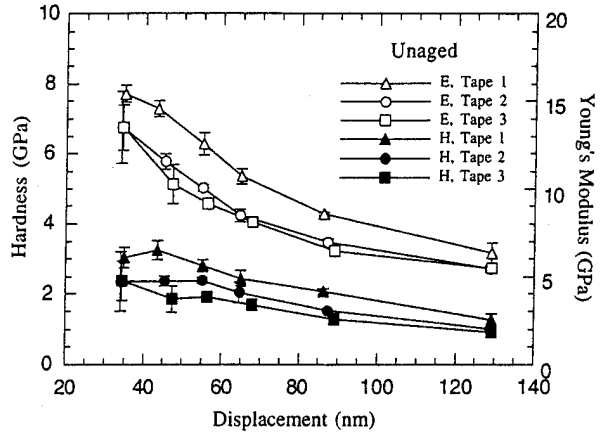



FIG. 1. Hardness and Young's modulus of the three unaged ME tapes.

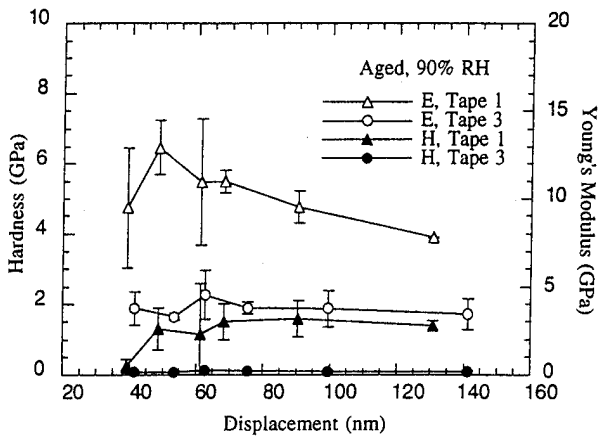



FIG. 3. Hardness and Young's modulus of the two ME tapes aged at 75 °C and 90% humidity.

substrate which has a hardness of 0.5 GPa and Young's modulus of 5 GPa. The hardnesses of the metal layers of the three unaged tapes are ~3.0, ~2.4, and ~2.0 GPa, and the Young's moduli are 15, 13.5, and 13.5 GPa. The hardnesses and Young's moduli are essentially the same for the unaged samples and the samples aged at 5% humidity but greatly decreased for the tapes aged at 90% humidity. The hardness values obtained in this test may not be the inherent hardness of the metallic layers of the tapes because the metal layer is very thin. The measurement of the inherent hardness of the magnetic layer on the polymer substrate is one of the subjects of our continuing research. In addition, the soft substrate effect on the elastic modulus is greater than on the hardness as we have reported before.[6]

A typical time dependent deformation experiment is shown in Fig. 4. This figure illustrates the indentation plastic depth as a function of time under two different maximum initial load. It can be seen that the deformation behavior depends on the maximum initial load. The effect of aging at 75 °C and 5% humidity on the deformation is also shown in the figure. It is obvious that aging at 75 °C and 5% humidity for 60 weeks makes these tapes much less deformable. This deformation capacity can be quantified by the strain rate sensitivity. An example of the log(strain rate) versus log(stress) plots from which the strain rate sensitivity is obtained by a linear fit is given in Fig. 5. The strain rate sensitivity of the unaged and aged ME tapes as a function of load are summarized in Fig. 6. The strain rate sensitivity of these ME tapes is strongly dependent on the initial loads. Increasing the maximum initial load increases the strain rate sensitivity. On the other hand, a decrease in the strain rate sensitivity is observed on aging. Aging generally shifts the load required for a given $m$ to higher values. This is consistent with the polymer substrate becoming more brittle and less deformable on aging. Because the properties of the metal layer and the polymer substrate of a ME tape are very different the change in strain rate sensitivity with load probably indicates the different responses from the two different materials. The polyethylene terephthalate (PET) polymer substrate ($H$ is 0.5 GPa and $E$ is 5 GPa) is definitely superplastic. As can be seen in Fig. 7, even measured at a very low load such as 0.05 mN its

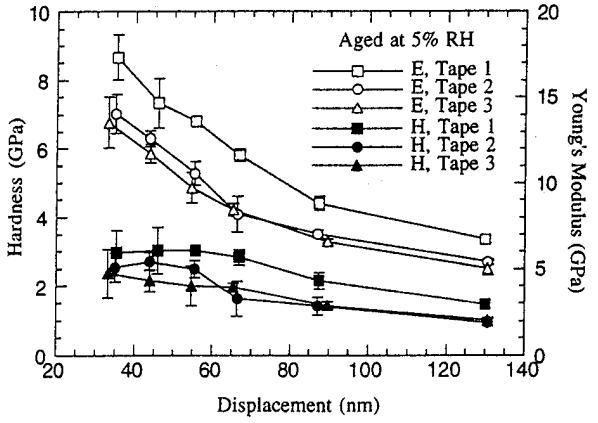



FIG. 2. Hardness and Young's modulus of the three ME tapes aged at 75 °C and 5% humidity.

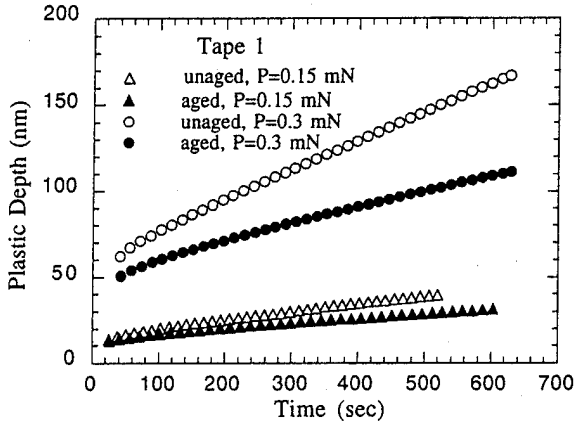



FIG. 4. The indentation plastic depth as a function of the holding time for tape 1 (aging conditions: 75 °C and 5% humidity).

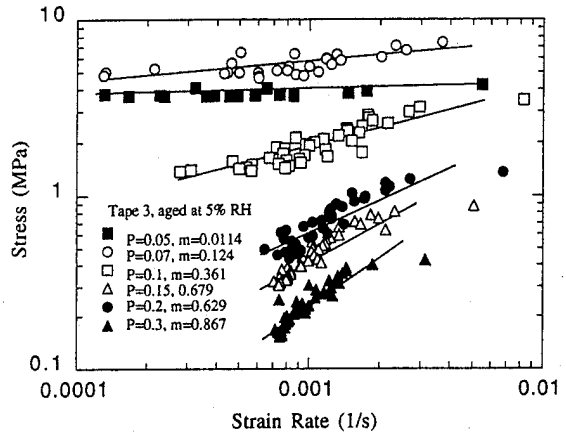



FIG. 5. Stress-strain rate for tape 3 aged at 5% humidity.

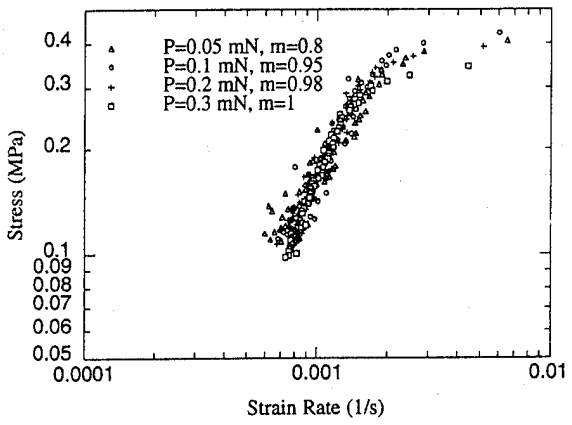



FIG. 7. Stress vs strain rate curves for the polymer substrate.

strain rate sensitivity is almost unity. According to the literature,[4] if the strain rate sensitivity of a given material is equal to or greater than 0.4, the material exhibits superplastic behavior and is capable of elongations of 100%–5000%. In this study, loads >0.1 mN result in $m>0.4$ for unaged samples. Therefore, it can be concluded that the time dependent deformation behavior of the metal layer of the ME tapes will be affected by the soft polymer substrate if the maximum initial load is above a certain load. In other words, the superplastic behavior above a certain load reflects the response from the polymer substrate rather than from the metal layers.

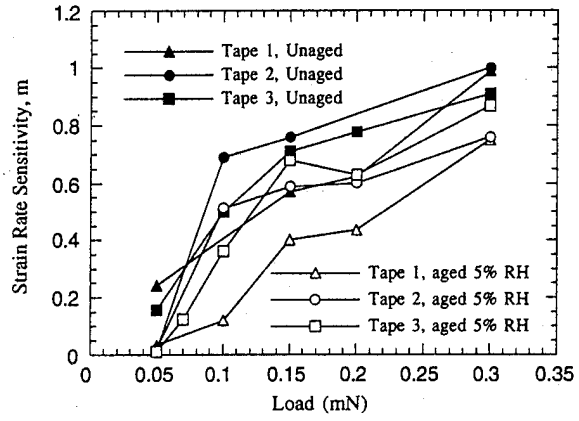



FIG. 6. Strain rate sensitivity as a function of load for ME tapes.

## IV. CONCLUSIONS

The mechanical properties of three kinds of commercial ME tapes were characterized using nanoindentation techniques. The hardness of the metal layers can be measured at 30–50 nm penetration depths. Aging is expected to make the tapes more brittle even at 75 °C and 5% humidity. However, this property change is not sensitively detected by the hardness tests. Hardness and elastic modulus were found essentially the same for the unaged samples and the samples aged at 5% humidity. However, nanoindentation creep measurements appear to be quite sensitive to the degradation of ME tape caused by even mildly adverse environmental conditions. A clear decrease in the strain rate sensitivity is observed for the tapes aged at 75 °C and 5% humidity.

## ACKNOWLEDGMENTS

This work was supported by the National Media Laboratory (NML). Thanks are also due to Dr. Roger Anderson and his colleagues at the NML for their assistance.

[1] H. J. Richter, IEEE Trans. Magn. **29**, 21 (1993).
[2] H. Fujiwara, J Appl. Phys. **73**, 5757 (1993).
[3] W. C. Oliver and G. M. Pharr, J. Mater. Res. **7**, 1564 (1992).
[4] M. I. Mayo, R. W. Siegel, A. Narayanasamy, and W. D. Nix, J. Meter. Res. **5**, 1073 (1990).
[5] K. M. O'Connor and P. A. Cleveland, Mater. Res. Soc. Symp. Proc. **308**, 495 (1993).
[6] H. Deng, V. R. Inturi, and J. A. Barnard, IEEE Trans. Magn. **31**, 2697 (1995).

# Comparison of tribological performance of pure carbon and carbon-nitrogen coated thin film head sliders

Geng Wang and John M. Silversten
*The Center for Micromagnetic and Information Technologies (MINT), Department of Chemical Engineering and Materials Science, University of Minnesota, Minneapolis, Minnesota 55455*

Jack H. Judy
*The Center for Micromagnetic and Information Technologies (MINT), Department of Electrical Engineering, University of Minnesota, Minneapolis, Minnesota 55455*

Ga-Lane Chen
*Conner Peripherals, Milpitas, California 95035*

The wear performance of pure carbon and carbon nitrogen (C:N) coated thin film head sliders was evaluated by continuous drag testing (CDT). Comparison was made in light of protection of these two various carbon films. By studying the air bearing surfaces of the heads under atomic force microscopy (AFM) and secondary electron microscopy (SEM), it was found that during the CDT test, the head may fail before the disk fails and the area of $Al_2O_3$ is the most possible place where wear begins. There were small amounts of material transferred from head slider to disk, although no evidence of opposite transfer was found. © *1996 American Institute of Physics.*
[S0021-8979(96)11208-2]

## I. INTRODUCTION

Increasing the amount of information that can be stored in a thin magnetic film is one of the key technological challenges facing the data storage industry. The areal recording density of stored information in today's state-of-the-art disk drive products is typically a few hundred megabits per square inch. Over the next decade, the data storage industry expects to increase this areal recording density by at least an order of magnitude, reaching several gigabits per square inch. To achieve this dramatic increase, the current flying height will need to be substantially decreased. Reducing the separation distance between the head slider and disk surfaces will place even more extreme tribological demands on the hard carbon overcoats. It has been demonstrated that a significant improvement in wear performance of the head–disk interface can be obtained by coating thin film head sliders with a carbon thin film.[1–3] However, the role of a carbon film remains unanswered. The purpose of this article is to present the results of atomic force microscopy (AFM) and secondary electron microscopy (SEM) mapping studies of the air bearing surface of head sliders uncoated and coated with pure carbon and carbon nitrogen after continuous drag testing. The possible mechanisms of the wear performance enhancements is explored.

## II. EXPERIMENTAL PROCEDURES

The pure carbon and carbon nitrogen thin films were deposited on head sliders using a facing target sputtering (FTS) system which had a background pressure less than $5\times10^{-7}$ Torr. The pure argon, or argon-nitrogen gas mixture (40%-$N_2$) was used as the sputtering gas. The resulting carbon nitrogen film has a 22 at. % nitrogen which was determined by Auger electron spectroscopy (AES). No adhesion layer was deposited under the carbon coatings. Continuous drag tests (CDT) were conducted with 50% $Al_2O_3$-TiC type thin film head sliders having a normal load of 4 gms dragged on 3.5″ unlubricated (H:C)-coated commercial disks. The radius at which to perform the CDT tests was chosen to be 1″ on the 3.5″ disks. The linear velocity was fixed at 26.60 cm/s. The average kinetic friction was measured every 500 revolutions at a speed of 0.1 rpm for one complete revolution. After the test was terminated, the head slider air bearing surfaces were carefully studied using AFM and SEM, and images of the most severe wear damage were taken for each sample.

## III. RESULTS AND DISCUSSION

Figure 1 shows a comparison of the friction versus the number of revolutions for the cases of an uncoated slider and sliders coated with 90 Å of FTS sputtered pure carbon and carbon nitrogen. After a total of 23 000 revolutions in each CDT test, only that disk paired with an uncoated head exhibited any visible wear marks which indicate that the head–disk interface had failed at this point. The SEM micrograph of the disk surface around the wear track associated with wear testing with the uncoated head was shown in Fig. 2. For comparison purposes, we note that the coefficient of kinetic friction versus the number of revolutions increases rapidly

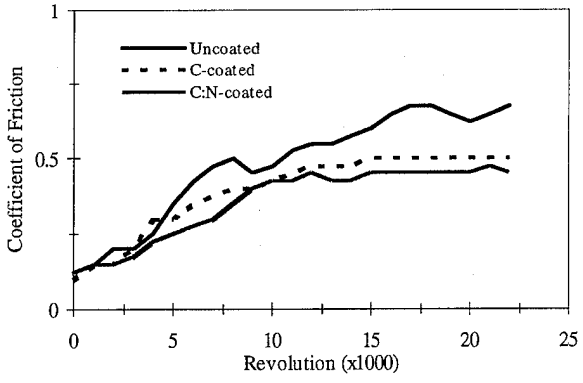



FIG. 1. The coefficient of friction vs number of revolutions with and without carbon coating on sliders.

 0021-8979/96/79(8)/5782/3/$10.00 © 1996 American Institute of Physics

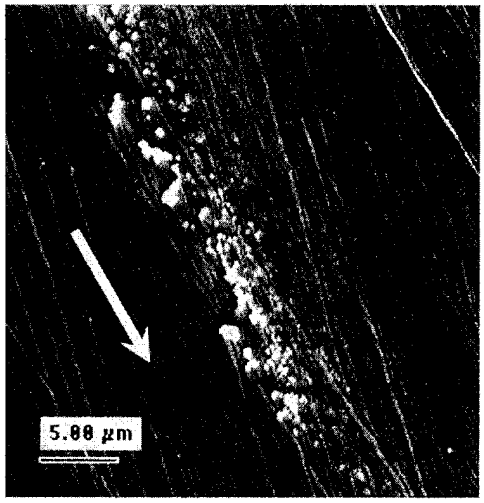



FIG. 2. The SEM image of disk wear track area associated with wear testing with the uncoated head.

from 0.12 initially to about 0.7 at 23 000 revolutions for the head slider which was uncoated. On the other hand, the kinetic friction coefficient of the head coated with 90 Å pure carbon increases from 0.1 initially to 0.5 at 15 000 revolutions and remained constant, whereas that for the head coated with 90 Å carbon nitrogen increases from 0.1 to a constant value of 0.45.

Upon completing the CDT tests, the head surfaces were observed using AFM and SEM and the resulting micrographs are shown in Figs. 3 and 4. In Fig. 3, all of the three testing heads exhibited some degree of wear damage where that of the uncoated head was the most severe and that of the carbon nitrogen coated head was the least. This is in agreement with the studies of Torng *et al.*[4] and Yeh *et al.*[5] which showed that carbon nitrogen has more $sp^3$ bonding and better wear performance than pure carbon. Figure 4 shows the SEM mapping results of the uncoated head surface, in which Al, Ti, and Cr were mapped. We see that there are a lot of wear particles on the air bearing surface [as shown in Fig. 4(a)], TiC was well separated from $Al_2O_3$ and no Cr was found.

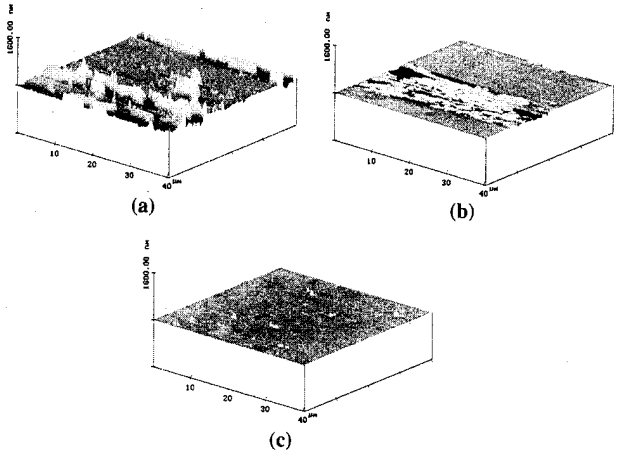



FIG. 3. The AFM images of the air bearing surfaces of (a) uncoated, (b) pure carbon, and (c) carbon nitrogen coated head sliders after 23 000 revolutions of CDT test runs.

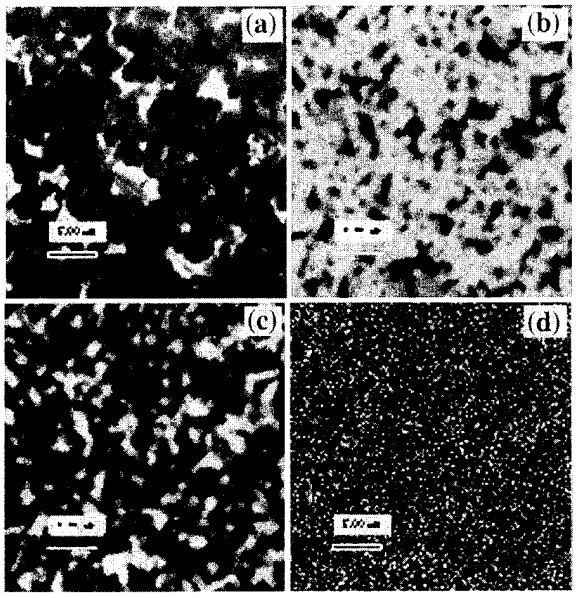



FIG. 4. The SEM mapping results of the uncoated head surface: (a) corresponding secondary electron image; (b) Al distribution; (c) Ti distribution; (d) Cr distribution. The scale bar is 5.00 $\mu$m.

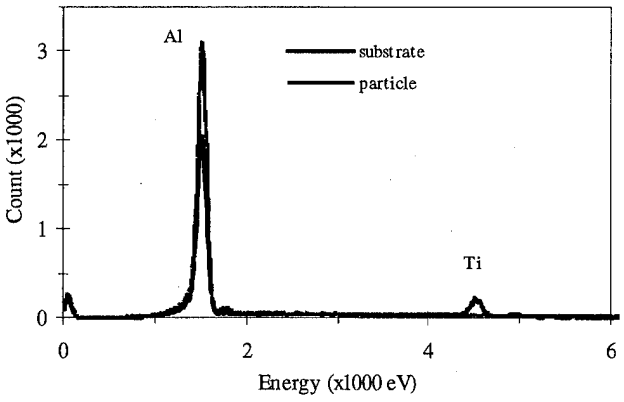



FIG. 5. The EDX spectrum of the uncoated head surface after CDT test.

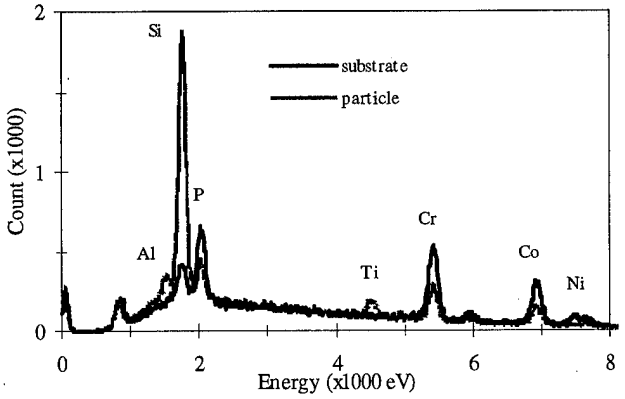



FIG. 6. The EDX spectrum of the disk surface around wear track after CDT test.

Figure 5 shows a typical energy-dispersive x-ray (EDX) spectrum of the testing head air bearing surfaces. Only Al had been detected from the wear particle which means that they were mainly composed of Al and came from the slider itself. In all cases being studied, there was no evidence that Cr was transferred to the sliders. On the other hand, Al and Ti (as shown in Fig. 6) particles were found on the surface around the wear track of the disk paired with the uncoated head slider.

Comparing Fig. 2 with Fig. 4(a), we note that the wear damage of the disk was less severe than that of the head. We also found that by dragging an uncoated head slider on a disk for 12 000 revolutions, although there was no visible wear marks on the disk surface, the head exhibited wear features under both AFM and SEM.

In summation, we can say that during the CDT test, the head may fail before the disk fails and the area of $Al_2O_3$ is the most possible place where wear begins. Since the $Al_2O_3$ is relatively softer than TiC, this conclusion is not unreasonable. Both the pure carbon and carbon nitrogen behave like a protective coating for the head slider where the carbon nitrogen is better than the pure carbon in light of the protection.

## IV. CONCLUSION

Both FTS sputtered pure carbon and carbon nitrogen films can protect head slider from wear failure to some extent during CDT tests and carbon nitrogen is better than pure carbon. In CDT tests, the head may fail before the disk fails and the area of $Al_2O_3$ is the most possible place where wear begins.


[1] Grill, C. T. Horng, B. S. Meyerson, V. V. Patel, and M. A. Russack, US Patent No. 5,159,508, October 27, 1992.
[2] D. B. Bogy, X. Yun, and B. J. Knapp, IEEE Trans. Magn. **30**, 369 (1994).
[3] G. Wang, T-A. Yeh, J. M. Sivertsen, J. H. Judy, and G.-L. Chen, IEEE Trans. Magn. **30**, 4125 (1994).
[4] C. J. Torng, J. M. Sivertsen, J. H. Judy, and C. Chang, J. Mater. Res. **5**, 2490 (1990).
[5] T. Yeh, C.-L. Lin, J. M. Sivertsen, and J. H. Judy, IEEE Trans. Magn. **27**, 5163 (1991).

# Transient response of ultralow flying sliders over contaminated and textured surfaces

Paul R. Peck, Ki-Ook Park,[a] and Myung S. Jhon
*Department of Chemical Engineering, Carnegie Mellon University, Pittsburgh, Pennsylvania 15213-3890*

Soo-Choon Kang and Tom I.-P. Shih
*Department of Mechanical Engineering, Carnegie Mellon University, Pittsburgh, Pennsylvania 15213-3890*

The transient flying dynamics of positive and negative pressure sliders over nonsmooth surfaces were investigated. Surface roughness was modeled by variously oriented sinusoidal waves, and contaminated surfaces were modeled as series of asperities and pits. A finite element algorithm was used which incorporates a generalized form of the Reynolds equation based upon the linearized Boltzmann equation. A new kinetic equation descriptive of ultralow flying was also discussed. Spectral analysis using fast Fourier transformation was adopted to explore the transient behavior of sliders in the frequency domain. © *1996 American Institute of Physics.* [S0021-8979(96)11308-9]

## I. INTRODUCTION

In the magnetic storage industry, higher information storage densities are achieved by reducing the slider–disk separation. At ultralow flying heights, the effect of surface topography on transient slider dynamics becomes a critical issue in the dynamic stability due to the increase in the risk of detrimental slider–disk collisions.

Surface roughness effects have been previously studied either experimentally,[1] numerically,[2–4] or semianalytically.[5,6] Most of the previous investigations focused on IBM 3370 positive pressure sliders and utilized the first-order modified Reynolds equation. In this paper, we simulated positive and negative pressure "bow tie" shaped sliders[7] over various surface topographies and disk defects using a finite element algorithm. As a new methodology to analyze transient dynamic behavior of sliders, spectral analysis was introduced using fast Fourier transformation (FFT) into a time-dependent transient simulation code.

## II. MATHEMATICAL MODELING OF THE HEAD–DISK INTERFACE (HDI)

Bow tie shaped positive and negative pressure sliders, shown in Fig. 1(a), were introduced to simulate ultralow flying slider dynamics over rough surfaces. These sliders are meant to serve as an illustrative example for nonrectangular shaped rail geometry, even though they may not be feasible for operational use. The negative pressure bow tie slider has the same configuration as the positive one with the addition of a cross rail between the side rails, which generates a suction force.

Sinusoidal roughness of several amplitudes oriented in various directions relative to the slider length (see Table I), was placed on either the slider or the disk to study the effects of moving and stationary roughness on flying characteristics. For a sinusoidal varying surface, the change in vertical displacement ($z$) was calculated using

$$z_{\text{rough}}=z_{\text{smooth}}-z_s^{\max}\sin\Phi_1(x)\sin\Phi_2(y). \tag{1}$$

The effects of contaminants on the disk were studied by introducing various configurations of ellipsoidal asperities and pits onto the simulated disk surfaces.

The equation governing the pressure distribution between the slider and disk surface is the modified Reynolds equation which incorporates kinetic theory based on the Bhatnagar–Gross–Krook's (BGK) approximation to the linearized Boltzmann equation (LBE).[8] A closed form[9] (no database lookup procedures) for this equation was used in the present simulations.

Under ultralow flying conditions, molecule–surface collisions occur more often than intermolecular collisions. The BGK theory is invalid under these conditions. A rigorous kinetic equation is currently being developed, which is structurally similar to the Fokker–Planck (FP) equation.[10]

The dynamics of a one particle distribution function in dimensionless velocity form, $f(\mathbf{r},\zeta,t)$, is described by the following kinetic equation:

$$\left(\frac{\partial}{\partial t}+v_0\zeta\frac{\partial}{\partial \mathbf{r}}\right)f(\mathbf{r},\zeta,t)=A(f). \tag{2}$$

$A(f)$ contains the collisional information of the gas molecules and depends on the kinetic model chosen.

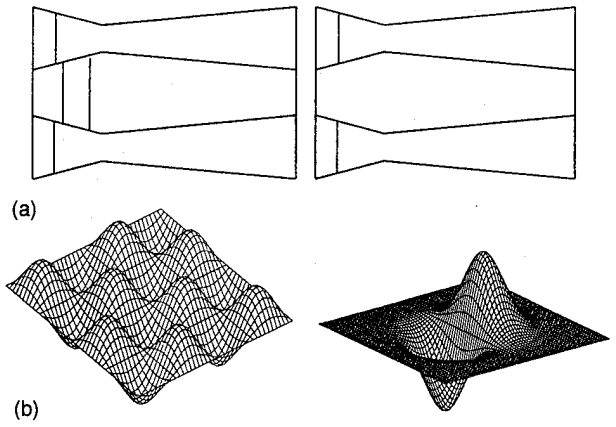



FIG. 1. (a) Bow tie shaped negative and positive pressure sliders and (b) surface topography of a two-dimensional surface and an asperity-pit combination.

[a]Samsung Advanced Institute of Technology, Suwon, Korea.

 0021-8979/96/79(8)/5785/3/$10.00 © 1996 American Institute of Physics 

TABLE I. Expression of surface roughness topology.[a]

| Surface roughness | Stationary | Moving |
|---|---|---|
| Transverse | $\Phi_1=2\pi\omega x/U$<br>$\Phi_2=\pi/2$ | $\Phi_1=2\pi\omega x/U-t$<br>$\Phi_2=\pi/2$ |
| Longitudinal | $\Phi_1=\pi/2,\ \Phi_2=2\pi\omega y/U$ | |
| Two dimensional | $\Phi_1=2\pi\omega x/U$<br>$\Phi_2=2\pi\omega yW/UL$ | $\Phi_1=2\pi\omega x/U-t$<br>$\Phi_2=2\pi\omega yW/UL$ |

[a]$\omega$ is the wave number of the surface roughness, $U$ is the disk velocity, $W$ is the width of the slider, and $L$ is the length of the slider.

Instead of comparing numerical results between several kinetic equations, the mathematical structures of the BGK approximation (LBE/BGK), an alternative kinetic equation (FP), and the collisionless kinetic equation (CL) are compared by expanding $A(f)$ in terms of the generalized orthogonal Hermite polynomial tensors $H^{(n)}_{i_1,i_2,\Lambda,i_n}(\zeta)$,[10]

$$A(f)=\int d^3\zeta' \Xi(\zeta,\zeta')f(\mathbf{r},\zeta';t), \tag{3}$$

with $\Xi(\zeta,\zeta')=\Sigma\lambda_n\varphi(\zeta)H^{(n)}_{i_1,\Lambda,i_n}(\zeta)H^{(n)}_{i_1,\Lambda,i_n}(\zeta')$.

The eigenvalues, $\lambda_n$, for the three models and the range of application of the equations are qualitatively summarized in Table II. Note that all of the models satisfy conservation laws, implying five zero eigenvalues.

## III. NUMERICAL SIMULATION

Numerical simulations were performed for positive and negative pressure nano (50%) bow tie sliders. The length and width of the sliders are 2.0 and 1.5 mm, respectively. The recess depth of the negative pressure slider is 4.44 $\mu$m. In all simulations, the air inflow velocity is 10 m/s, the mass of the slider is 0.0125 g, the rotational speed is 5400 rpm, the skew angle is zero, the linear spring stiffness is 11 N/m, the torsional spring stiffness is 0.0006 N m/rad, and the moment of inertia is $9.2\times10^{-11}$ kg m$^2$. The applied normal load is 5 g for the positive pressure slider and 1 g for the negative pressure slider.

TABLE II. Eigenvalues for three different kinetic models and illustration of the applicable HDI spacing ranges.

| Fluid mechanics (Navier–Stokes) | Applicable spacing ranges |
|---|---|
| $\lambda_n$ ; 2 1 0 | $h$ ; $h\gg\lambda$ |
| LBE/BGK | |
| $\lambda_n$ ; 4 3 2 1 0 | $h$ ; $h\geqslant\lambda$ |
| Fokker–Planck | In between LBE/BGK |
| $\lambda_n$ ; 4 3 2 1 0 | and collisionless $h\leqslant\lambda$ |
| Collisionless | |
| $\lambda_n$ ; 3 2 1 0 | $h$ ; $h\ll\lambda$ |
| × Conserved | $h$: head–disk spacing |
| ○ Nonconserved | $\lambda$: mean free path |

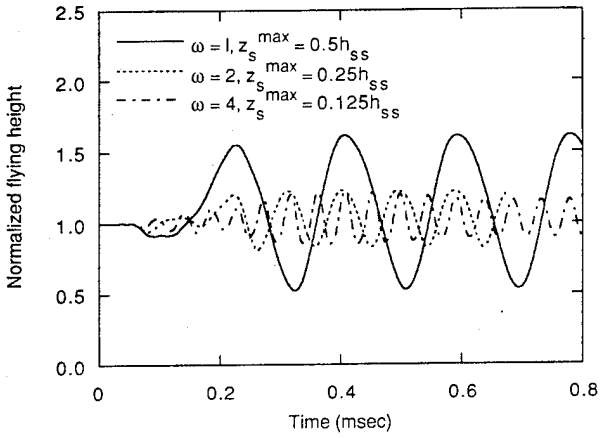



FIG. 2. Surface roughness wave number effects on the dynamic response over transverse sinusoidal surfaces.

### A. Effects of sinusoidal surface roughness

The effects of roughness orientation and dimension on the slider flying characteristics were studied using sinusoidal surfaces. Simulations were performed with wave numbers, $\omega$ (inverse wavelength), equaling different multiples of the slider length. The ratio of the wavelength to the amplitude of the surface roughness was kept constant to be consistent with slider miniaturization. For a wave number of 1, the amplitude of the roughness is half of the smooth surface steady state flying height ($h_{ss}$).

Flying height variations normalized to $h_{ss}$ are shown in Fig. 2 for transverse surface roughness. The slider follows the large wave form at the large wavelength, but as the size of the roughness is decreased, the flying height does not follow the surface roughness contour.

Transient dynamics of the bow tie negative pressure slider were simulated over the two-dimensional surface roughness shown in Fig. 1(b). The amplitude of the roughness is half of $h_{ss}$, and the wave number is 8 in the longitudinal direction and 6 in the transverse direction (to make the wave form square). The three-dimensional pressure distribution underneath the slider is shown in Fig. 3.

Dynamic responses show that the negative pressure slider does not follow the surface roughness as regularly as the positive pressure slider, however it does oscillate with smaller amplitude. This is attributed to the higher air bearing stiffness of the negative pressure slider.

### B. Effects of multiple asperities

Contaminated particles which adhere to the moving disk surface can be modeled as multiple asperities randomly distributed over the disk surface. When a slider passes over a series of asperities, its behavior is affected by the time history. This non-Markovian behavior may cause sudden deviations from the designed flying characteristics.

To simulate possible scenarios of slider–contaminant interaction, two isolated ellipsoidal asperities and an asperity-

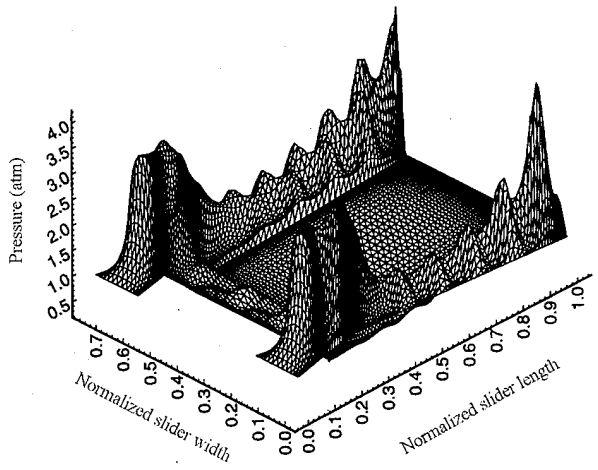



FIG. 3. Three-dimensional pressure distribution underneath a negative pressure slider flying over two-dimensional surface roughness.

pit combination were positioned beneath the center of the left rail (upstream to downstream) of a positive pressure slider. The amplitude of the asperity (or pit), $h_a$, was 20 nm and the radius of the asperity (or pit), $r_a$, was 100 $\mu$m. The separation distance between the centers of adjacent asperities (or the asperity and pit), $L_a$, was increased from 1 to 3 times the radius of the asperity. We refer to $L_a = r_a$ as a double asperity. Results for these simulations are shown in Fig. 4.

At smaller separations, a large amount of dynamic coupling occurs between the two asperities, while at larger separations ($L_a \geq 2r_a$), the coupling diminishes.

The effects of multiple asperities were examined in the frequency domain using FFT. A typical frequency spectra for the flying height mode is given in Fig. 5 for a double asperity, an asperity-pit, and two asperities with $L_a = 3r_a$. There are only a couple of dominant frequencies for each asperity

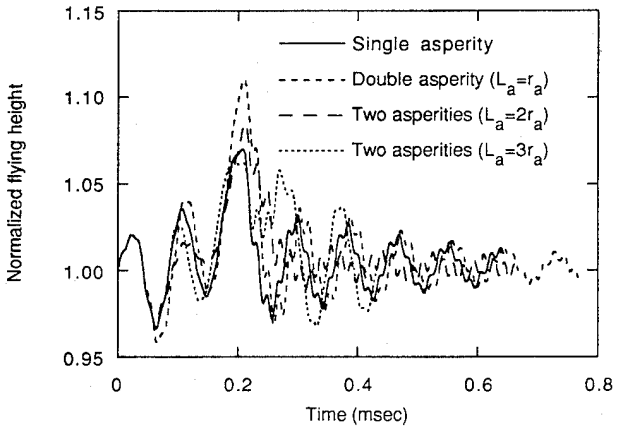



FIG. 4. Transient response of sliders flying over multiple asperities.

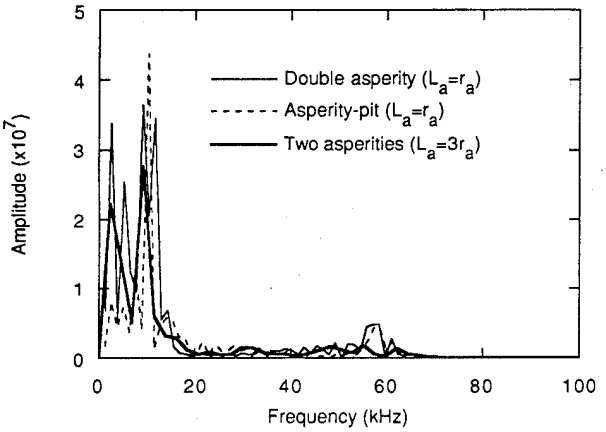



FIG. 5. Frequency spectra in the flying height mode.

set. The response for the double asperity shows a unique mode split phenomena at the dominant low frequency region.

## IV. CONCLUSIONS

Transient dynamic responses of ultralow flying sliders were investigated over contaminated and textured surfaces using the LBE/BGK equation. A critique of this equation and the mathematical structure of the collision integral of an advanced kinetic equation descriptive of ultralow flying are given. Simulations were performed with positive and negative pressure nano bow tie sliders flying over various sinusoidal rough surfaces.

To simulate the effects of rough surfaces on the flying characteristics, multiple asperities and asperity-pit combinations were introduced. Non-Markovian memory effects of the slider response were prominent. As the asperity separation distance increased, coupling effects diminished. The asperity-pit combination showed the least disturbance to the dynamics of the slider.

Spectral analysis was introduced using FFT to characterize the dynamic response of sliders over various rough surfaces. This analysis showed the negative pressure slider to be more stable than the positive pressure slider in response to surface roughness.

## ACKNOWLEDGMENT

This work was supported in part by the National Science Foundation under Grant No. ECD-8907068.

[1] Y. Mitsuya, T. Ohkubo, and H. Ota, ASME J. Trib. **111**, 495 (1989).
[2] J. W. White, P. E. Raad, A. H. Tabrizi, and S. P. Ketkar, ASME J. Trib. **108**, 171 (1986).
[3] R. M. Crone, M. S. Jhon, B. Bhushan, and T. E. Karis, Adv. Info. Storage Syst. **1**, 189 (1991).
[4] O. J. Ruiz and D. B. Bogy, ASME J. Trib. **112**, 593 (1990).
[5] R. M. Crone, P. R. Peck, M. S. Jhon, T. E. Karis, and B. Bhushan, Adv. Info. Storage Syst. **4**, 123 (1992).
[6] B. Bhushan and K. Tonder, ASME J. Trib. **111**, 228 (1989).
[7] P. R. Peck, B. S. Wang, K. O. Park, and M. S. Jhon, Adv. Info. Storage Syst. (in press).
[8] S. Fukui and R. Kaneko, ASME J. Trib. **110**, 253 (1988).
[9] R. M. Crone, P. R. Peck, M. S. Jhon, T. E. Karis, and B. Bhushan, J. Magn. Soc. Jpn. **15**, 525 (1991).
[10] M. S. Jhon and D. Forster, Phys. Rev. A **12**, 254 (1975); J. Chem. Phys. **74**, 279 (1981).

# Surface diffusion of thin perfluoropolyalkylether films

Teresa M. O'Connor, Young R. Back, and Myung S. Jhon
*Department of Chemical Engineering, Carnegie Mellon University, Pittsburgh, Pennsylvania 15213-3890*

Byung G. Min
*Korea Institute of Science and Technology, P.O. Box 131, Cheongryang, Seoul, Korea 305-701*

Do Y. Yoon and Thomas E. Karis
*IBM Research Division, Almaden Research Center, 650 Harry Road, San Jose, California 95120-6099*

The spreading characteristics of thin polymeric liquid films of perfluoropolyalkylethers (PFPEs) Fomblin Z15 and Fomblin Zdol (hydroxyl terminated PFPE) on silica surfaces have been measured by scanning microellipsometry (SME). We estimated the surface diffusion coefficients and propose a modified diffusion equation to interpret the spreading phenomenon from film thickness profiles measured with SME. We investigated the spreading of Z15 as a function of binary blend ratio of monodisperse Z15 fractions and found that the surface diffusion coefficients of the blends do not obey a simple linear mixing rule. A summary of thin PFPE film spreading characteristics as a function of molecular weight, film thickness, chain-end functionality, temperature, and humidity is presented. © *1996 American Institute of Physics.* [S0021-8979(96)11408-5]

## I. INTRODUCTION

In magnetic hard disk drive systems, an ultrathin layer (~5–20 Å) of perfluoropolyalkylether (PFPE) is applied to the thin-film media surface to prevent wear of the media. In order to advance magnetic disk media technology, it is necessary to understand the interaction between the lubricants and the solid surface (retention), and the mobility of the lubricant molecules (replenishment). Only limited quantitative work has been reported on the mobility or diffusion of polymers in thin films on solid surfaces. Microscopic spreading characteristics of thin films[1–4] and small drops[5–7] of polymeric liquids on flat surfaces has gained considerable interest.

Surface diffusion of nearly monodisperse ($M_w/M_n<1.1$) PFPE films cast from solution onto the surface of silicon wafers was investigated as a function of molecular weight, film thickness, chain-end functionality, temperature, and humidity.[3,4] Scanning microellipsometry (SME) was used to measure the thickness profiles as the film spreads with time. The spreading of nonfunctional PFPE (Z15), a random copolymer of $CF_2O$ and $CF_2CF_2O$ moieties, and hydroxyl terminated PFPE (Zdol) exhibit distinctly different thickness profiles and mobilities. Spreading of Z15 occurs mainly by the diffusionlike movement of the fast moving front or foot of gradually decreasing thickness, and displays a greater mobility than Zdol. Zdol exhibits a characteristic shoulder by forming an apparent monomolecular "anchored" layer, which separates out from the initial film layer with a sharp boundary. The apparent surface diffusion coefficients of Z15 and Zdol increase with decreasing molecular weight and increasing film thickness (particularly for films <50 Å). Surface diffusion of 50 Å Z15 ($M_w$=13 800 g/mol) and Zdol ($M_w$=3400 g/mol) films were evaluated at temperatures ranging from 25 to 50 °C.[3] The activation energy for surface diffusion $E_d$ of Zdol (50.6 kJ/mol) is higher than that of Z15 (20.6 kJ/mol), reflecting the stronger affinity of its hydroxyl end groups for the substrate. The bulk viscosity flow activation energies $E_\eta$ were compared with $E_d$ yielding $E_d \cong E_\eta$ for Z15 (neutral polymer–substrate interaction), and $E_d \cong 1.5E_\eta$ for Zdol (positive polymer–substrate interaction). Z15 is not significantly affected by humidity, whereas the PFPEs with functional chain-ends (i.e., Zdol, Ztetraol, and AM2001) exhibit a dramatic increase in mobility with increasing relative humidity.[4] In this paper, we introduce a full scale theoretical development of a modified diffusion equation to describe the spreading rate of the lubricant front. Using a finite difference scheme with the modified diffusion equation, the calculated positions of the moving front agree well with the measured data for a wide range of time. We focus on a binary blend system of Z15 monodisperse fractions to illustrate the essence of the experiments and theoretical development. This paper reports the first systematic study of lubricant thin film spreading behavior as a function of blend ratio, and the results presented may be useful in the development of advanced lubricant systems for hard disk drives.

## II. EXPERIMENTATION

The commercially available Fomblin Z and its derivative Fomblin Zdol (products of Ausimont USA, Inc.) have the following random copolymer linear backbone chain structure:

$$X\text{–}CF_2\text{–}[(OCF_2\text{–}CF_2)_p\text{–}(OCF_2)_q]\text{–}OCF_2\text{–}X,$$

where X is F and $p/q \cong 2/3$ in Z15, and X is $CH_2OH$ and $p/q \cong 1$ in Zdol.

Binary blends of monodisperse Z15 fractions were dip coated onto the surface of single-side polished silicon wafers. The silicon wafers were 25.4 mm in diameter and 0.2–0.3 mm thick having a native oxide $SiO_2$ (silica) layer of ~16 Å. Prior to coating, the wafer is cleaned by sequentially rinsing with isopropanol and perfluorohexane (FC-72, product of 3M). Half of the wafer is then immersed in a dilute solution of Z15 blend in FC-72 in order to form a film having a sharp step on one part of the substrate. The initial film thickness $h_0$ is controlled through solution concentration and

 0021-8979/96/79(8)/5788/3/$10.00 © 1996 American Institute of Physics

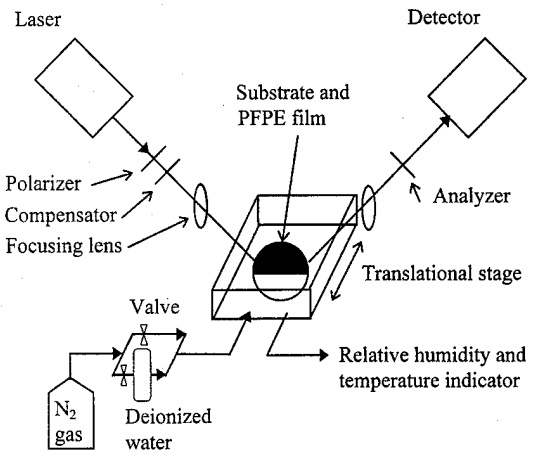



FIG. 1. Schematic of the SME setup.

the rate of drawing the wafer out of solution. The time-dependent thickness profiles of the films were measured using a SME (spot size 20×60 $\mu$m) having a translational stage with a temperature and humidity controlled environment as depicted in Fig. 1. The sample is oriented so that the steplike film boundary is parallel to the plane of incident light. All experiments were performed for $h_0$=50 Å films under a continuous stream of clean nitrogen gas at room temperature (≅26 °C) and 0% relative humidity.

## III. RESULTS

### A. Experiment

After dip coating, the PFPE film spreads with time along the surface of the silicon wafer and the thickness profiles are monitored using SME.[3,4] To determine the spreading rate of the lubricant, we focused on the leading edge of the advancing film front. The length that the front travels $L$ is defined as the difference between the initial position of the lubricant front and each position in the subsequent profiles. Lengths $L$ and corresponding travel times $t$ are plotted as shown in Fig. 2 for Z15 $M_w$=13 800 g/mol. In the $L-t$ plot, the spreading

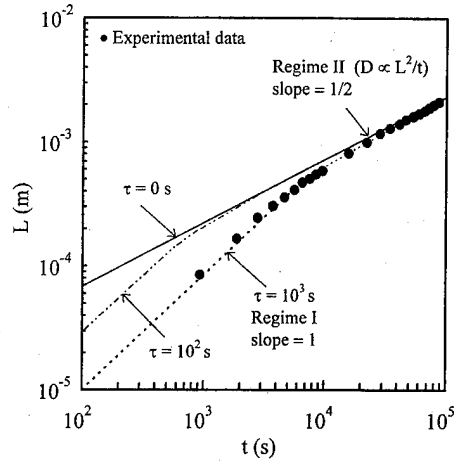



FIG. 2. $L-t$ plot of experimental data for Z15 over 24 h, and numerical $L-t$ curves obtained from Eq. (3) for different values of $\tau$.

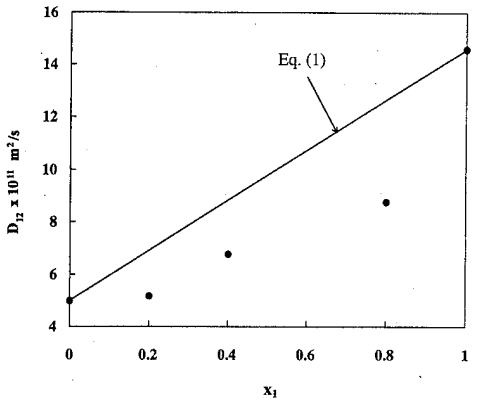



FIG. 3. Plot of $D_{12}$ vs $x_1$ for binary blends of Z15.

phenomenon demonstrates $L \propto t$ for short times (Regime I) and after a gradual transition $L \propto t^{1/2}$ (Regime II; diffusion region). The surface diffusion coefficient $D$ is estimated from the data in Regime II using[7] $D=L^2/t$. Film thickness profiles were monitored over 24 h for 0, 20, 40, 80, and 100 mol % ratios of Z15 monodisperse fractions $M_w$=5400 g/mol (component 1) and $M_w$=35 600 g/mol (component 2). As shown in Fig. 3, surface diffusion coefficients $D_{12}$ were calculated for each of the binary Z15 blends of the low molecular weight fraction component 1 and high molecular weight fraction component 2. Applying a simple linear mixing rule for a binary mixture, the diffusion coefficient of an "ideal" mixture $D_{12}^{id}$ may be expressed as

$$D_{12}^{id}=(D_1-D_2)x_1+D_2, \tag{1}$$

where $D_i$ and $x_i$ denote surface diffusion coefficient and mole fraction of pure component $i(i=1,2)$, respectively. For Z15 blends, $D_{12}$ does not obey the ideal mixing rule, i.e., $\Delta D=D_{12}-D_{12}^{id}<0$ where $\Delta D$ is the excess quantity due to nonideality, as illustrated in Fig. 3.

Monodisperse fractions of Z15 $M_w$=5400 g/mol and Zdol $M_w$=4700 g/mol were blended in a 1:1 ratio by weight. From the characteristic shapes of the profiles shown in Fig. 4 and relative mobilities of Z15 and Zdol, the advancing front

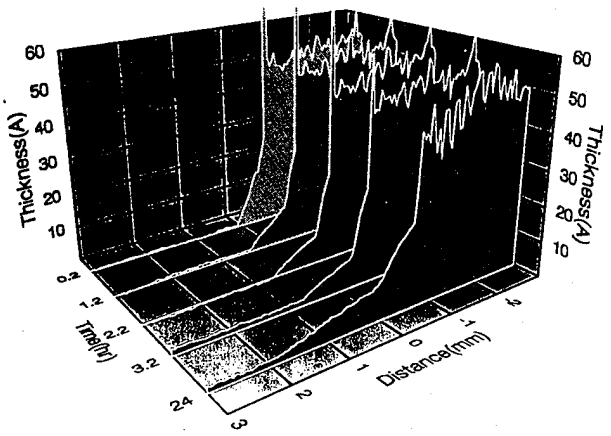



FIG. 4. Spreading profiles of a Z15/Zdol binary blend.

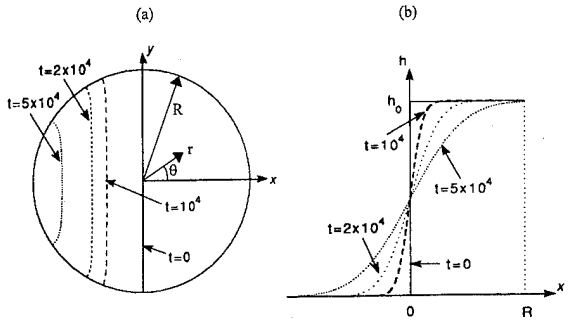



FIG. 5. Plots of $h(r,\theta,t)$: (a) contour of $h/h_0=0.01$ and (b) $h$ at $y=0$ for $t=0$, $1\times10^4$, $2\times10^4$, and $5\times10^4$ s.

region of the film appears to be the relatively fast-moving Z15 and the remaining region, which exhibits a shoulder, should be the less mobile Zdol.

Two monodisperse fractions of Zdol ($M_w=1600$ g/mol and $M_w=4700$ g/mol) were blended in a 1:1 ratio by weight. Relative to its pure components, the Zdol blend shows a drastic increase in the dewetting exhibited on the film side of the profile which may be due to phase separation of its two components. The intermediate shoulder height of the blend is less distinct as compared to the shoulder heights of the anchored layers corresponding to the pure components.

### B. Theory

To interpret experimental data shown in Fig. 2, the leading edge movement of the advancing film front was calculated with the conventional diffusion equation

$$\frac{\partial h(\mathbf{r},t)}{\partial t}=\nabla\cdot[D(h)\nabla h(\mathbf{r},t)], \tag{2}$$

where $h(\mathbf{r},t)$ is the thickness of the film ($h$=volume/area), and $D(h)$ is the thickness-dependent surface diffusion coefficient. Using a finite difference scheme, we solve for Eq. (2) in cylindrical form $h(r,\theta,t)$, for the system geometry in Fig. 5(a), assuming constant $D$, initial conditions $h(x>0,r\leqslant R;t=0)=h_0$, $h(x<0,r\leqslant R;t=0)=0$, and zero flux boundary conditions $\partial h/\partial r]_{r=R}=0$, $\partial h/\partial\theta]_{\theta=0,\pi}=0$. The numerical results shown in Fig. 5(a) of typical film thickness contours for the lubricant front assigned as $h/h_0=0.01$ at different times demonstrate $D\propto L^2/t$, and in Fig. 5(b) show the change in $h$ with respect to time at $y=0$.

Although applicable in Regime II, the results obtained from Eq. (2) do not describe the $L\propto t$ behavior in Regime I. Therefore, we propose a modified diffusion equation given as

$$\tau\frac{\partial^2 h(\mathbf{r},t)}{\partial t^2}+\frac{\partial h(\mathbf{r},t)}{\partial t}=\nabla\cdot[D(h)\nabla h(\mathbf{r},t)], \tag{3}$$

where $\tau$ is a parameter related to the crossover time of the transition between Regimes I and II. Using a finite difference numerical scheme Eq. (3) can be used to describe the behavior of experimental data as shown in Fig. 2 for several different values of $\tau$; note Eq. (3) reduces to Eq. (2) at $\tau=0$. The parameter $\tau$ can aid in characterizing microscopic spreading behavior of ultrathin polymeric films.

## IV. DISCUSSION AND CONCLUSIONS

From Regime II of $L$–$t$ plots for films of binary Z15 blend ratios ranging from 0 to 100 mol %, surface diffusion coefficients were estimated using the relationship $D=L^2/t$. We found that surface diffusion of the Z15 blend deviates from an ideal mixture. Spreading of a 1:1 Z15/Zdol binary blend showed profiles in which the mobility of the individual PFPEs spread somewhat independently of each other. Thus, surface diffusion of a thin-film lubricant depends on its molecular weight distribution which should be one of the factors considered when selecting a lubricant. Since the conventional diffusion theory does not account for spreading in Regime I, a modified diffusion equation was proposed to more accurately describe and fit experimental data obtained from spreading profiles of PFPE films. The new term accounts for the early spreading where $L\propto t$. By analogy, the physical origin of $\tau$ can be understood in terms of the Deborah number commonly used in polymer rheology. Defining the "Deborah number of diffusion" as $\mathrm{De}_d\equiv\beta\tau/t$ (for Z15 $\beta\cong10$), then for $\mathrm{De}_d<1$ conventional diffusion ($L\propto t^{1/2}$) is applicable, and for $\mathrm{De}_d>1$ the new term in Eq. (3) becomes dominant ($L\propto t$) and describes the mobility of the lubricant front. Equation (3) was rigorously derived from Ficks law by introducing a delayed flux response, i.e., $j(\mathbf{r},t+\tau)=-D(h)\nabla h(\mathbf{r},t)$, for small $\tau$. The details of this new theoretical investigation will be provided in a future publication.

## ACKNOWLEDGMENTS

We would like to thank Dr. H. R. Brown, Dr. A. M. Homola, Dr. C. M. Mate, and Dr. C. L. Bauer for valuable discussions which contributed to this work. We gratefully acknowledge Dr. P. H. Kasai who provided us with the monodisperse PFPEs and NMR measurements, and Dr. P. M. Cotts who provided GPC measurements of the PFPEs. This work was supported in part by the National Science Foundation under Grant No. ECD-8907068.

[1] V. J. Novotny, J. Chem. Phys. **92**, 3189 (1990).
[2] C. M. Mate, J. Appl. Phys. **72**, 3084 (1992).
[3] T. M. O'Connor, M. S. Jhon, C. L. Bauer, B. G. Min, D. Y. Yoon, and T. E. Karis, Tribol. Lett. **1**, 219 (1995).
[4] B. G. Min, J. W. Choi, H. R. Brown, D. Y. Yoon, T. M. O'Connor, and M. S. Jhon, Tribol. Lett. **1**, 225 (1995).
[5] F. Heslot, N. Fraysse, and A. M. Cazabat, Nature **338**, 640 (1989).
[6] M. P. Valignat, N. Fraysse, A. M. Cazabat, and F. Heslot, Langmuir **9**, 601 (1993).
[7] A. M. Cazabat, N. Fraysse, F. Heslot, and P. Carles, J. Phys. Chem. **94**, 7581 (1990).

# Wear studies of contact recording interface with a microfabricated head

Bharat Bhushan and Youlin Li
*Computer Microtribology and Contamination Laboratory, Department of Mechanical Engineering, The Ohio State University, Columbus, Ohio 43210-1107*

In contact recording devices, a head is designed to remain in continuous contact with the disk surface. Friction/stiction and wear issues in continuous contact are critical to interface reliability. Objective of the present research is to study the wear mechanisms responsible for the wear of a microfabricated *a*-C:H contact pad sliding against a smooth disk surface. Wear rate of the contact pad was measured using a faceted technique. Disk wear track was measured using an atomic force microscope. After initial run-in, wear rate increased slightly with sliding distance. Wear rate at contact pressure when the pad is in complete contact with the disk is about 0.015 nm/h. Optical microscopy showed small accumulation of wear debris at the leading edge of the pad. The dominant wear mechanism initially is adhesive followed by some contribution by three-body abrasive wear caused by fine debris produced at the interface. Particulate contamination in the environment significantly increased the wear rate. Tests in various gaseous environments showed that wear rates in argon and in nitrogen are lower than that in ambient air, suggesting that tribochemical oxidation of carbon plays an important role in wear of carbon pad. © *1996 American Institute of Physics.* [S0021-8979(96)11508-1]

## I. INTRODUCTION

In order to enable continued increase in storage density, one method is to minimize the head-disk separation (e.g., flying height) and ideally reduce it to zero. While a contact recording device (where the flying fight is zero) would be highly attractive from the perspective of magnetic performance, the tribological issues have to date discouraged their introduction into the commercial drives.[1] A number of contact recording devices are currently under development. In one of the most advanced designs, the contact pad consisting of Censtor MicroFlex head is substantially smaller (17 $\mu$m×36 $\mu$m) than the conventional heads.[2] During operation, the contact pad remains in contact with the disk at a typical applied normal load of 40 mg and at linear velocity of 3–8 m/s. A perpendicular-probe-type configuration can tolerate as much as 7 $\mu$m of vertical pole tip wear over the life of the drive (~5 y) without significant signal degradation.[3] Friction/stiction and wear problems associated with the continuous contact at head-disk interface become important. The objectives of the research are to study the wear mechanisms relevant to the pad/disk interface and the influence of the environments on the wear rate of the contact pad.

## II. EXPERIMENT

The read-write heads used here were two-piece Censtor MicroFlex heads with gold contact on top of head body soldered to one end of a triangular stainless steel flexure beam. The laminated beam contains 25-$\mu$m-thick stainless steel with a polymeric layer topped with two parallel gold leads connecting the read-write element at the free end to bonding pads at the other end. The length and thickness of the flexure beam are 10 mm and 30 $\mu$m, respectively. The width ranges from 1.5 mm (head end) to 0.7 mm (free end). The flexure beam has an effective mass of about 600 $\mu$g with a spring constant of around 1.75 $Nm^{-1}$. The flexure is epoxy bonded to an alumina diving board which is then epoxy bonded to an anodized aluminum arm. A perpendicular-probe-type head, with a flux return pole and multilayered pancake coil, is fabricated using photolithographic techniques. The Co-Nb-Zr alloy pole and front yoke reside vertically along the center line of the head body with the coil placed orthogonally, and the gold contacts on the top. The head construction contains layers of SiC, $Al_2O_3$, and Si and the head is buried in a layer of plasma-enhanced chemical-vapor deposited (PECVD) *a*-C:H, which forms a contact pad with a cross section of 17 $\mu$m×36 $\mu$m with about 7 $\mu$m thickness.[4]

The magnetic disks used in this study were made of 0.635-mm-thick Al-Mg substrate with an outer diameter of 48 mm and an inner diameter of 12 mm. The disks were coated with 6-$\mu$m-thick electroplated Ni-Fe underlayer, 75-nm-thick sputtered Co-Cr-Ta magnetic layer, 10-nm-thick sputtered *a*-C:H overcoat and 1-nm-thick bonded perfluropolyether lubricant overlayer. The disks passed 38 nm glide height test. Roughness parameters of the disk surface measured using AFM are as follows: rms=0.55 nm, peak-mean distance=2.1 nm, *P-V* distance=4.2 nm, and $\beta^*$ (correlation length)=0.3 $\mu$m.

Two tribotest apparatuses were used in this study to measure the wear rate of the contact pad. The wear tests in ambient air were conducted in a modified Seagate drive (ST-225), schematically shown in Fig. 1. The head-suspension assembly was mounted at an angle of about 8°–10°, on an actuator arm which is mounted on a vertical linear stage on a tower. The tower was actuated by a rotary actuator. The rotating speed of the disk was 3600 rpm and the applied normal force was 40 mg. Typical test duration was 120 h. The influence of various environments on the wear rate of the contact pad was studied using an ultra-high vacuum (UHV) environmental tribotester.[5,6] The experiments were performed in various environments of air (RH=65%), dry air (RH=10%), Ar, and $N_2$. The rotating speed of the disk, the applied load, and the test duration were 500 rpm, 40 mg, and 170 h, respectively. For experiments in environments other than in ambient air, the vacuum chamber was initially evacuated to a pressure of about $10^{-6}$ Torr and then backfilled with the desired gas.

 0021-8979/96/79(8)/5791/3/$10.00 © 1996 American Institute of Physics 

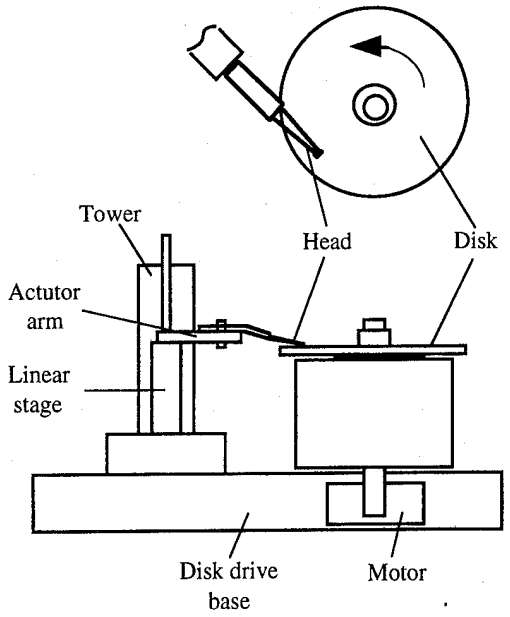



FIG. 1. Schematic of the disk drive for ambient wear test.

In these tests, the pad was brought in contact with the disk surface and was lowered by a known displacement to exert a desired normal load (normal spring stiffness is 1.75 $Nm^{-1}$). Displacement was measured by a noncontact fiber optic probe placed above the pad. Wear tests were conducted

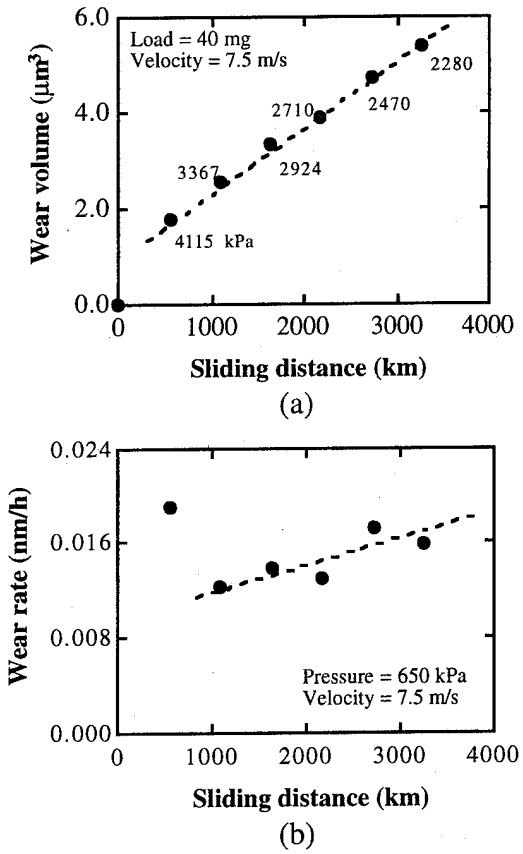



FIG. 2. Wear as a function of sliding distance (a) at pressures as shown in the figure, (b) at a normal pressure of 650 kPa.

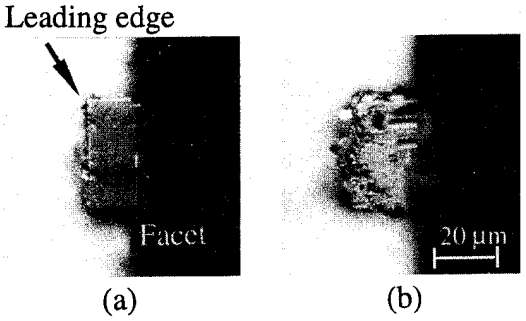



FIG. 3. Optical micrographs of the contact pads after 3250 km of test (a) in class 100 environment, (b) in class 10 000 environment.

by sliding the pad tilted with the disk surface to develop a facet on the pad surface. The wear rate of the contact pad was determined by measuring the growth in the size of the wear facet generated on the pad. The head was first loaded onto the coarse lapping disk (rms=235 nm) at a pre-test load (~58 mg) and ran for 10 s to create a single facet on the contact pad. It was then loaded onto the fine lapping disk (rms=1.4 nm) at the same load and ran for 120 min to remove the scratches on the pad surface. After that, the head was run on a test disk at the same load for 60 min and then repositioned to a new track, tilted about −0.75° (trailing edge in contact with disk surface) by decreasing the load to 40 mg and run for the test duration to create a new facet on the pad surface. Tilt angle was determined from the vertical displacement of the pad multiplied by the bending stiffness of the beam (7.4 degree/mm). The wear volume of the pad was calculated from the pad width, tilt angle and length of the new facet. The wear track on the disk surface was measured using AFM. All tests were conducted at ambient temperature of 22±1 °C. Humidity in the clean room environment was 50±5% RH.

## III. RESULTS AND DISCUSSION

The wear volume of the contact pad as a function of sliding distance for the tests conducted at a normal load of 40 mg and tilt angle of −0.75° in class 100 environment is shown in Fig. 2(a). After the first 540 km of sliding at higher pressure, the wear volume increases at a nearly constant rate. Note that during the wear test, the facet gradually grew and

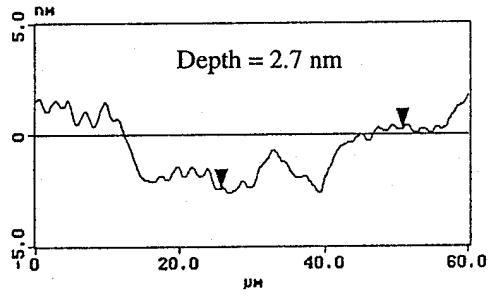



FIG. 4. AFM profile of the wear track in the disk surface after 3250 km of test.

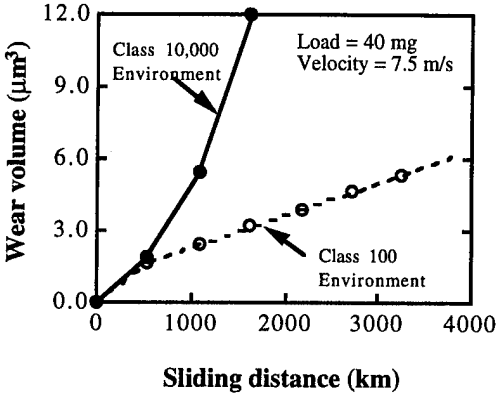



FIG. 5. Wear volume as a function of sliding distance in two environments.

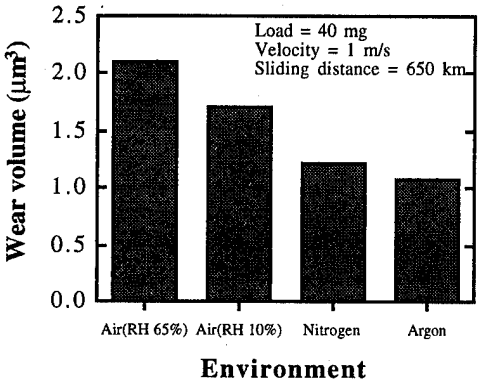



FIG. 6. Wear volume data in different environments after 650 km of sliding at 40 mg of load.

thus the contact pressure decreased with the test time. At the beginning of the test, the wear pad makes a line contact with the disk surface, and thus the contact pressure is very high. Optical microscopy of the head surface during initial sliding showed light burnishing of the pad, which suggests that wear was dominated by plastic deformation. Absence of any abrasion marks suggests that dominant wear mode was adhesive. Optical microscopy of the worn surfaces after considerable sliding (>2000 km) revealed very fine scratching of the pad surface and some debris accumulation at the leading edge of the contact pad, Fig. 3(a). EDX analysis of the debris revealed that the debris contains C, Si, and Al, which suggests that one source of the debris is the contact pad. Some of the debris accumulated at the leading edge of the pad, and some re-entered the contact region between the head and disk, causing the three-body abrasive wear.

Since the rate of wear volume was constant after initial run-in, Archard's wear law is applicable. From simple geometry, square root of wear volume is proportional to the contact pressure. Using this relationship, the equivalent wear rate at a contact pressure of 650 kPa as a function of sliding distance was obtained, as shown in Fig. 2(b). A pressure of 650 kPa corresponds to the pressure when the pad is in complete contact with the disk at 40 mg of load. The contact pressure at the beginning of the test was underestimated, which gives a high wear rate. The wear rate at 2700 km is about 0.017 nm/h. Assuming that the hardness of the carbon pad is 15 GPa, the wear coefficient for the contact pad at 2700 km of sliding is about $8\times10^{-11}$, which is extremely low for dry sliding conditions.[1] After the run-in period, an increase in the wear rate with sliding distance is consistent with the contribution by the three-body abrasive wear.

Figure 4 shows the AFM measurement of the disk after 125 h of sliding against the head at a normal load of 40 mg and disk rotating speed of 3600 rpm (7.5 m/s). The wear track depth ranges from 2.5 to 3.5 nm.

The effect of the particulate contamination in environment on the wear volume is shown in Fig. 5, under the test conditions of normal load of 40 mg and disk rotating speed of 3600 rpm (7.5 m/s). The wear volume increased with sliding distance more quickly in class 10 000 environment than in the class 100 environment. After 1620 km of sliding, the wear volume in class 10 000 is about 12.0 $\mu m^3$, as compared to 3.3 $\mu m^3$ in class 100 environment. Figures 3(a) and 3(b) show the typical optical images of the worn pads in class 100 and in class 10 000 environments. Severe scratches are clearly observed on the worn area in class 10 000 environment, which suggests that the particulate contamination in ambient environment caused severe abrasive wear and therefore increased the wear volume to a high value. The smaller scratches on the worn area in class 100 environment are caused by the contaminants and/or the fine debris generated during sliding wear.

Figure 6 shows the wear volumes in various gaseous environments under the test conditions of normal load of 40 mg, disk rotating speed of 500 rpm (1 m/s) and sliding distance of 650 km. These tests were conducted in the UHV tribotester. The wear volume in air with relative humidity of 65% is higher than in argon and in nitrogen. Tribochemical oxidation of carbon may be responsible for the higher wear rate in ambient environment, as compared to that in nitrogen or in argon environment.[5–7] The effect of environment on carbon pad sliding against carbon coated disk is not as significant as $Al_2O_3$-TiC slider sliding against carbon disk.[6,7] Catalytic effect of $Al_2O_3$-TiC slider is known to be responsible for very high wear rates in oxidizing environments. Further reduction in the interface wear will undoubtedly be desirable. Wear performance improvements may be accomplished by the use of alternative coatings, such as $SiC_4$ and cathodic arc carbon coatings[8] for the construction of contact pad and disk overcoat, and by the use of super smooth disks.

## ACKNOWLEDGMENTS

We thank Dr. Mike H. Azarian of Censtor Corporation for providing the samples and technical guidance and support throughout the research. Financial support was provided by NSIC/ARPA.

[1] B. Bhushan, *Tribology and Mechanics of Magnetic Storage Devices* (Springer, New York, 1990).
[2] H. Hamilton, J. Magn. Soc. Jpn. **18**, 171 (1994) (Suppl. S1).
[3] C. Foster, Data Storage January/February, 23 (1995).
[4] B. Bhushan, B. K. Gupta, and M. H. Azarian, Wear **181-183**, 743 (1995).
[5] B. Bhushan and J. Ruan, Surf. Coat. Technol. **68/69**, 644 (1994).
[6] B. Bhushan *et al.*, Wear **190**, 44 (1995).
[7] B. Marchon, M. Khan, and N. Heiman, IEEE Trans. Magn. **26**, 168 (1990).
[8] B. K. Gupta and B. Bhushan, Thin Solid Films (in press).

# Non-Gaussian surface roughness distribution of magnetic media for minimum friction/stiction

Bharat Bhushan and Sameera Chilamakuri
*Department of Mechanical Engineering, The Ohio State University, Columbus, Ohio 43210*

Contact of two rough surfaces at an interface occurs at a small fraction of the nominal area. The real area of contact and interfacial adhesion primarily control the friction of an interface. With the presence of a thin film of liquid lubricant or adsorbed water layer at the interface, menisci form around the contacting and near-contacting asperities. The meniscus formation results in stiction problems in the head–medium interfaces. The objective of this research is to predict optimum surface roughness for minimum friction/stiction. For the first time, the effects of skewness and kurtosis of surfaces with non-Gaussian distribution on contact area and meniscus contribution have been studied. A numerical model that accounts for the effects of roughness distribution and liquid film was used for this study. Based on this study, a surface with non-Gaussian distribution with positive skewness between 0 and 0.2 and/or with high values of kurtosis ($K \geqslant 5$) should be used for low friction and stiction. © *1996 American Institute of Physics.* [S0021-8979(96)11608-8]

## I. INTRODUCTION

High magnetic storage density in modern disk drives is achieved by the use of very smooth thin-film rigid disks that allow ultralow flying of read/write head sliders over the disk surface. However smooth surfaces result in high stiction during rest and high stiction/friction during the contact start/stop (CSS) operation, especially with the presence of a thin film of liquid lubricant or adsorbed water vapor at the head–disk interface.[1] Disk surfaces are textured to minimize stiction/friction. There is a critical $h/\sigma$ (total liquid film thickness/standard deviation of surface heights) above which the stiction increases rapidly with an increase in the liquid film thickness.[1,2] Distribution of local roughness plays an important role in friction/stiction and wear. Thus optimization of roughness distribution on the disk surface is required. In the past few decades many analytical and numerical models have been developed for contact simulation of rough surfaces.[1,3] In most models surface height distribution is assumed to follow a Gaussian distribution. In the present model for the first time the effect of non-Gaussian distribution of roughness on real area of the contact and meniscus contribution have been systematically studied. Non-Gaussian surfaces were computer generated.

## II. CONTACT MODEL

A Gaussian surface can be represented by two surface roughness parameters—$\sigma$ (standard deviation of surface heights) or $R_q$ (rms value) and $\beta^*$ (correlation length).[1,3,4] A non-Gaussian surface may exhibit skewness (Sk) and kurtosis ($K$). Skewness is a parameter which defines the asymmetric spread and it is given by

$$\mathrm{Sk}=\frac{1}{\sigma^3}\int_{-\infty}^{\infty} z^3 p(z)\,dz, \tag{1}$$

where $p(z)$ is the probability density function of variable, $z$ (the height distribution). A Gaussian surface has zero skewness. Kurtosis represents the peakedness of the distribution and it is given by

$$K=\frac{1}{\sigma^4}\int_{-\infty}^{\infty} z^4 p(z)\,dz. \tag{2}$$

A Gaussian surface has a kurtosis of 3. Figure 1 shows the probability density functions for surface heights with different skewness and kurtosis values. An algorithm suggested by Hu and Tonder[5] has been used for the generation of non-Gaussian surfaces with given skewness and kurtosis. By using a two-dimensional digital filter technique combined with fast Fourier transform, rough surfaces with any given $\sigma$, $\beta^*$, Sk, and $K$ can be generated efficiently using a computer. A

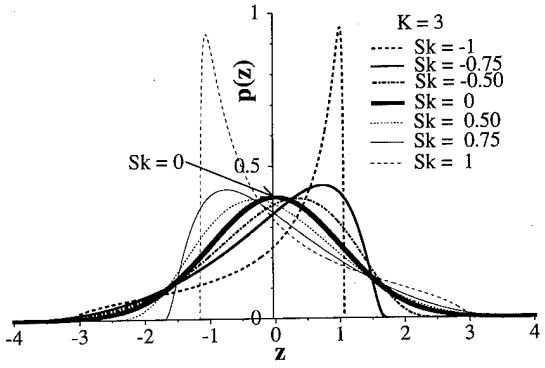



FIG. 1. Probability density function for surfaces with (a) different skewness and (b) different kurtosis.

 0021-8979/96/79(8)/5794/3/$10.00 © 1996 American Institute of Physics

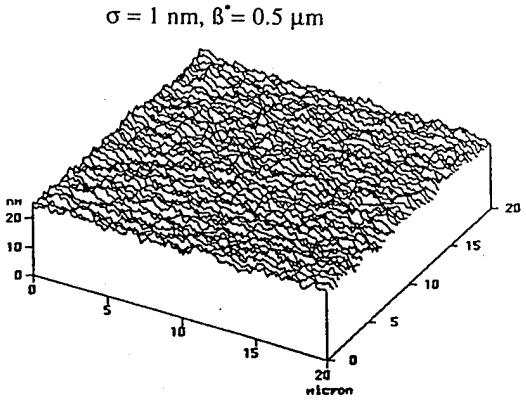



FIG. 2. Three-dimensional surface height profile of a computer generated Gaussian surface.

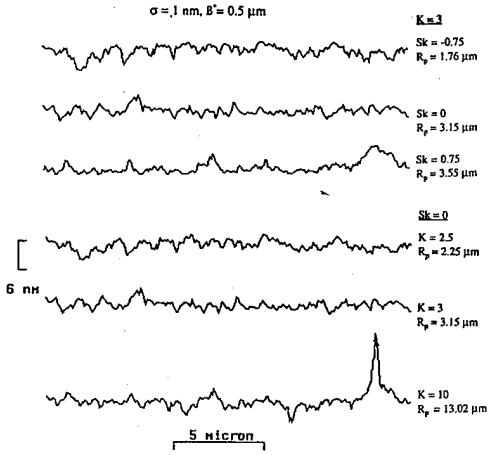



FIG. 3. Two-dimensional height profiles of surfaces with different skewness and kurtosis values.

computer generated three-dimensional Gaussian surface profile is shown in Fig. 2. The heights of the surface profiles consists of 256×256 data points. Figure 3 shows relative features of different non-Gaussian surfaces. A Gaussian surface with zero skewness and kurtosis of 3 has an equal number of peaks and valleys at a certain height. A surface with high negative skewness is almost flat with a relatively large number of peaks whereas a surface with high positive skewness consists of few high peaks. A surface with low kurtosis ($K<3$) has a relatively large number of peaks as compared to that of surface with high kurtosis.

A numerical model developed by Tian and Bhushan[6] has been used for the dry contact analysis of rough surfaces. The method is based on variational principle in which the real area of contact and contact pressure distribution are those which minimize the total complementary potential energy. The effect of meniscus force due to the presence of a thin liquid film is studied using the meniscus model developed by Tian and Bhushan.[7] Surfaces with different skewness and kurtosis were generated using a scan size of 20 $\mu$m×20 $\mu$m. Analyses were carried out using mechanical properties of Al–Mg/Ni–P disk with $E$ (elastic modulus)=110 GPa, Poisson ratio=0.36, and $H$ (hardness)=7 GPa against $Al_2O_3$–TiC slider with $E$=450 GPa and Poisson ratio=0.23 and perfluoropolyether lubricant with $\gamma$ (surface tension)=25 dyn/cm and $\theta$ (contact angle)=10°. The composite modulus of elasticity of the interface was 101.6 GPa. Computer runs were made for a range of pressures. A pressure of 32.8 kPa corresponds to nominal pressure of a nanoslider (50%). Most computations were performed for $h/\sigma$=1 where $h$ is the liquid film thickness.

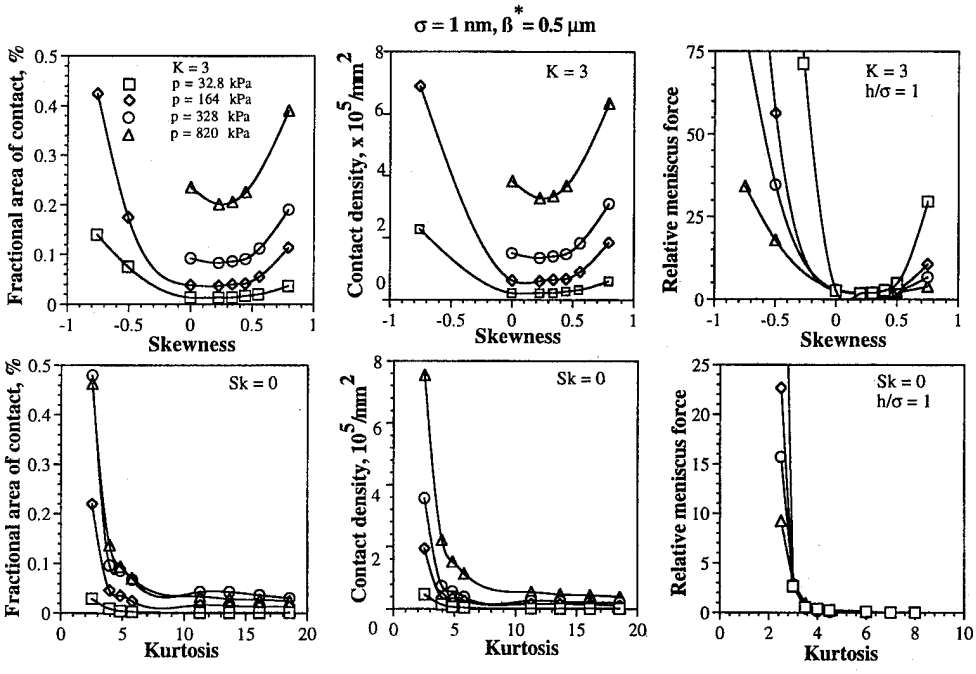



FIG. 4. Effect of skewness and kurtosis on fractional area of contact, contact density, and relative meniscus force.

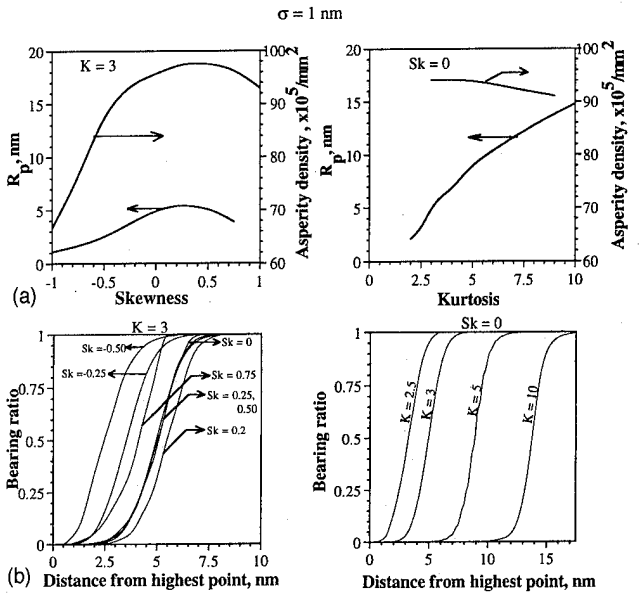



FIG. 5. (a) Peak-mean distance ($R_p$) and asperity density as a function of skewness and kurtosis. (b) Bearing ratio curves at different skewness and kurtosis values.

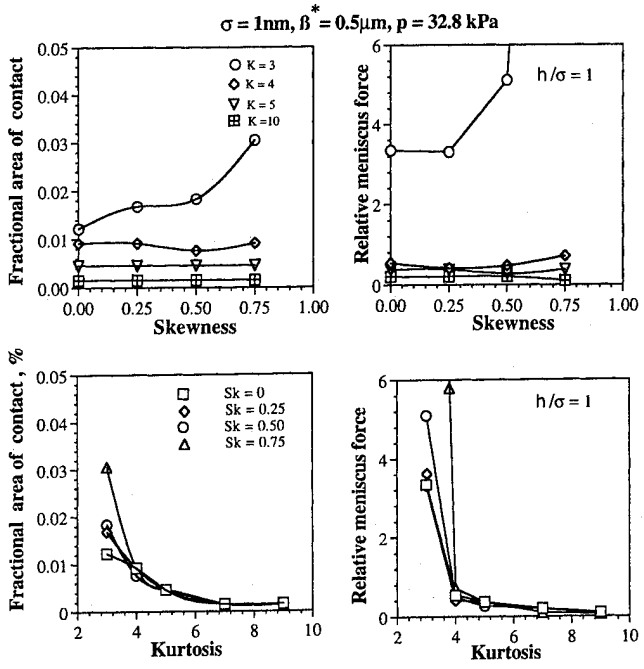



FIG. 7. Interplay of skewness and kurtosis on fractional area of contact and relative meniscus force.

## III. RESULTS AND DISCUSSION

Figure 4 shows the variation of fractional real area of contact, contact density, and relative meniscus force with skewness and kurtosis. A positive skewness between 0 and 0.2 at low pressures and of 0.2 at high pressures, results in lowest real area of contact, contact density, and meniscus force. Fewer peaks in a surface with positive skewness as shown in Fig. 3 account for low real area of contact and meniscus force. Slightly positive skewness gives optimum number of peaks and the highest peak-mean value as shown in Fig. 5(a) which can support the applied load. Thus, it is clear that a positive skewness in the range of 0–0.2 is desirable with 0.2 being the optimum value. Figure 5(b) shows bearing ratio curves at different skewness values. Bearing ratio increases with an increase in negative skewness value, whereas it attains a minimum value at a positive skewness of 0.2 and increases again with further increase in skewness value. Figure 4 also shows that fractional area of contact, contact density, and relative meniscus force decrease with an increase in kurtosis of the surface. A higher kurtosis results in higher peak-mean value ($R_p$) and lower asperity density as shown in Fig. 5(a), which gives lower real area of contact and meniscus force. As shown in Fig. 5(b) bearing ratio increases with increase in kurtosis which again supports the trends observed in Fig. 4.

Figure 6 shows the variation of relative meniscus force with $h/\sigma$ ratio at different values of skewness and kurtosis. We note that sensitivity of $h/\sigma$ to meniscus force decreases at a range of positive skewness and kurtosis greater than 3.

Next we study the interplay of skewness and kurtosis to predict an optimum roughness distribution. Figure 7 shows the combined effect of skewness and kurtosis on real area of contact and meniscus force. For a zero or positive skewness, a kurtosis larger than 3 results in lower real area of contact and relative meniscus force. The plots of fractional area of contact and relative meniscus force are almost flat at kurtosis values greater than 5. So the effect of skewness ($\geq 0$) is negligible at kurtosis greater than 5. However at $K<5$, zero skewness is optimum. Based on this study, we conclude that a surface with a kurtosis of about 5 or larger with a skewness greater than or equal to zero (positive skewness has little effect) is optimum. However, if a surface with large kurtosis cannot be manufactured, then a skewness of 0–0.2 is desirable for surface with $K$ equal to 3–5. Surfaces with negative skewness and kurtosis less than 3 must be avoided.

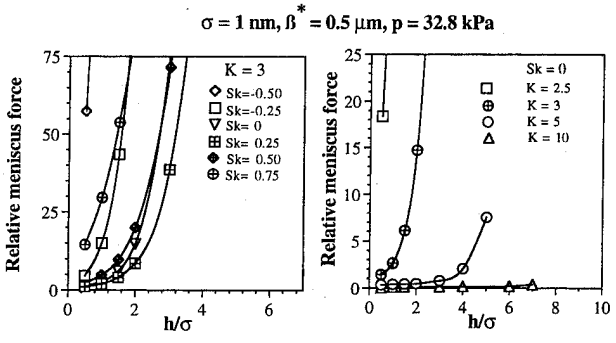



FIG. 6. Effect of skewness and kurtosis on relative meniscus force as a function of $h/\sigma$.


[1] B. Bhushan, *Tribology and Mechanics of Magnetic Storage Devices* (Springer, New York, 1990).
[2] C. Gao and B. Bhushan, Wear **190**, 60 (1995).
[3] *Rough Surfaces*, edited by T. R. Thomas (Longman, London, 1982).
[4] D. J. Whitehouse, *Handbook of Surface Metrology* (IOP, Bristol, UK, 1994).
[5] Y. Z. Hu and K. Tonder, Int. J. Mach. Tool Manuf. **32**, 82 (1992).
[6] X. Tian and B. Bhushan, ASME J. Tribol. **118**, 1996.
[7] X. Tian and B. Bhushan, J. Phys. D: Appl. Phys. **29**, 163 (1996).

# A micro-remote centered compliance suspension for contact recording head (abstract)

M. Nakao, S. Sugiyama, and Y. Hatamura
*The University of Tokyo, Faculty of Engineering, Department of Engineering Synthesis, Tokyo, Japan*

T. Hamaguchi and K. Watanabe
*Mechanical Engineering Research Laboratory, Hitachi, Ltd., Japan*

Nowadays contact recording has become one of the most important mechanisms for high-density recording of HDD. The contact recording head is always subject to friction when sliding. If the friction causes vibration on the sliding head, the swaying of the head is likely to lead to some undesirable bit shifts. The authors previously measured the head movement in sliding with a Watrous-type suspension where it was verified that the front edge of the head fell down to the disk surface because the rotational center of the pitching motion of the head was located above the sliding surface, inducing a heavy sticking. In order to prevent the sticking from occurring, we have already proposed RCC (remote centered compliance) suspension (15 mm in thickness) which consists of a pair of inclined plates.[1] With this suspension, the front edge of the head is raised up because of the enhanced location of the rotational center which is now below the sliding surface. In this article we present a newly designed micro-RCC suspension (125 $\mu$m in thickness) for an acutal small MR head ($1\times1\times0.5$ mm) of the contact recording. It has two pairs of the inclined plates structure for two-axis frictions which are caused by seeking and tracking motions of the head, respectively. This suspension is fabricated from a 125 $\mu$m thick sheet of polyimide using the ultraviolet laser beam. We evaluate its movement in sliding at low speed (50 $\mu$m/s) and at high speed (2 m/s) under a 10 mN load on a sputtered disk, respectively. The normal and frictional forces are measured by a micro two-axis force sensor (0.01 mN resolution) with parallel-plate structure and the pitching motion of the head is measured by an inclination sensor by means of laser reflection angle measurement (10 $\mu$rad resolution). From the experiment at low speed, we have clarified that the head yields a stable friction ($0.15\pm0.02$ mN) and has the nose-up attitude (0 to + 100 $\mu$rad). In addition, from the evaluation at high speed, we have observed the stable read-back signal ($\pm7\%$ modulation) because of the stable motion without any sticking. As a reference suspension, we prepare a micro-Winchester-type suspension. From the similar evaluation, we have identified that the reference head shows unstable friction ($0.25\pm0.1$ mN) with the nose-down attitude (0 to $-500$ $\mu$rad) and an unstable signal ($\pm50\%$ modulation). We have confirmed through these observations that the micro-RCC suspension will be an indispensable tool for contact recording in order to realize a stable recording against the friction. © *1996 American Institute of Physics.* [S0021-8979(96)46608-8]

[1] Y. Hatamura *et al.*, IEEE Trans. Magn. **26**, 2483 (1990).

# Micro/nanoscale studies of boundary layers of liquid lubricants for magnetic disks (abstract)

Vilas N. Koinkar and Bharat Bhushan
*Computer Microtribology and Contamination Laboratory, 206 W. 18th Avenue, The Ohio State University, Columbus, Ohio 43210-1107*

The atomic force/friction force microscope is used to study the micro/nanotribiological properties of perfluoropolyether lubricants. Single-crystal silicon wafers were lubricated with nonpolar (Fomblin Z-15) and polar (Fomblin Z-DOL and Demnum S-100) lubricants. The nanowear tests show that the nonpolar (Z-15) lubricant depleted from the wear track within few cycles whereas polar (Z-DOL) lubricant exhibits excellent nanowear resistance with no degradation. The polar lubricant results in a lower value of microfriction as compared to the nonpolar lubricant and unlubricated silicon sample. The effect of thickness of polar lubricant is studied for the thermally bonded Z-DOL lubricant before and after wash. Unwashed polar lubricant film with unbonded fraction exhibited better resistance to wear than that of washed lubricant film. Thicker films are also more durable. Wear experiments with magnetic disks show that lubricant film on a supersmooth disk is more effective in reduction of friction and wear than a smooth disk. Coefficients of friction on micro- and macroscales are compared. Variation in lubricant film thickness results in variation in the coefficient of friction. Thus, friction force microscopy can be used to measure lubricant uniformity with spatial resolution on the order of tens of nanometers. Finally, adhesive experiments show that bonded film behaves as a soft polymeric solid. © *1996 American Institute of Physics.*
[S0021-8979(96)11708-4]

 0021-8979/96/79(8)/5798/1/$10.00 © 1996 American Institute of Physics

# Rough surface contact analysis and its relation to plastic deformation at the head–disk interface

Chin Y. Poon and Bharat Bhushan
*Computer Microtribology and Contamination Laboratory, Department of Mechanical Engineering, The Ohio State University, Columbus, Ohio 43210-1107*

Ni–P coated Al–Mg (Ni–P) and glass–ceramic (GC) substrates for magnetic recording are measured by an atomic force microscope (AFM) using different scan sizes and sampling resolution. AFM measurements of the Ni–P and GC surfaces at smaller sampling intervals reveal finer details. The GC surface contains more high frequency details than the Ni–P surface. The correlation length $\beta^*$, a spatial parameter, is used in addition to the rms roughness $R_q$ to characterize the surfaces. Contact analysis using a three-dimensional elastic-plastic rough surface contact model shows that the asperity pressure of the GC surface increases more rapidly than the Ni–P surface as the sampling interval decreases. For both surfaces, asperity contact starts from plastic deformation, the scale of which depends on different surface topographical structures. The GC surface is shown to have higher asperity pressure because it has higher frequency structures. The high frequency structure will facilitate plastic deformation, and it can help explain previously published results why the disk with Ni–P substrate has better durability than the disk with GC substrate in different environments.
© *1996 American Institute of Physics.* [S0021-8979(96)11808-0]

## I. INTRODUCTION

Contacts at head–disk interface on a microscale are generally elastic.[1] But real surfaces consist of a broad range of wavelengths and high magnification reveals more of the fine structures. Therefore when contacts are examined on a nanoscale, asperity contact size becomes smaller and asperity contact pressure becomes higher. Therefore, results of rough surface contact analysis depend on sampling resolution. In this article, a three-dimensional numerical rough surface contact model[2] is used to examine the contact of Ni–P and GC surfaces and study the effect of sampling resolution on contact pressure and contact area.

## II. MEASUREMENT AND CHARACTERIZATION

Rough surfaces of Ni–P and GC substrates are measured by an atomic force microscope (AFM) using different square scan areas with scan length of $L$=64, 32, 16, 8, 4, 1, 0.5, 0.25, and 0.1 $\mu$m. Each scan area contains 256×256 data points. Therefore, the sampling interval $\tau$ decreases linearly with $L$. Figure 1 shows the AFM surface maps of both surfaces for $L$=1 and 16 $\mu$m. The GC surface appears to be smoother but contains higher frequency structures than the Ni–P surface.

Whitehouse and Archard[3] showed that the standard deviation of height distribution $\sigma$ and the correlation length $\beta^*$ can be used to characterize a rough surface. $\sigma$ is equal to rms of height distribution $R_q$ for zero mean. $\beta^*$ gives information about spatial distribution of a surface. The knowledge of spatial variation of surface is essential, as it affects the distribution and density of asperity contacts. A surface with shorter wavelength structures has smaller $\beta^*$.

$\beta^*$ is given by the autocorrelation function (ACF). For a two-dimensional profile $z(x)$, normalized ACF, $R(\tau)$, is defined as

$$R(\tau)=\frac{1}{\sigma^2 L}\int_L z(x)z(x+\tau)\,d\tau. \tag{1}$$

For many engineering surfaces, an exponential function $\rho$ is found to fit the ACF. We have

$$R(\tau)=\rho(\tau)=\exp\left(\frac{-\tau}{\beta^*}\right), \tag{2}$$

where $1/\beta^*$ is the decay rate of the function. The correlation length can be defined as $\rho(\tau)$=0.1 (when $\tau$=2.3$\beta^*$) or $\rho(\tau)$ =1/$e$ (when $\tau$=$\beta^*$). Both forms are considered to be a measure of the length at which single height readings become statistically independent of one another. In this article, $\beta^*$ is given by $\rho(\tau)$=1/$e$.

The variation of $R_q$ and $\beta^*$ with scan size for the Ni–P and the GC surfaces is shown in Fig. 2. $R_q$ of each surface initially increases with $L$ and approaches a constant value when $L$ reaches about 16 $\mu$m. This indicates that both sur-

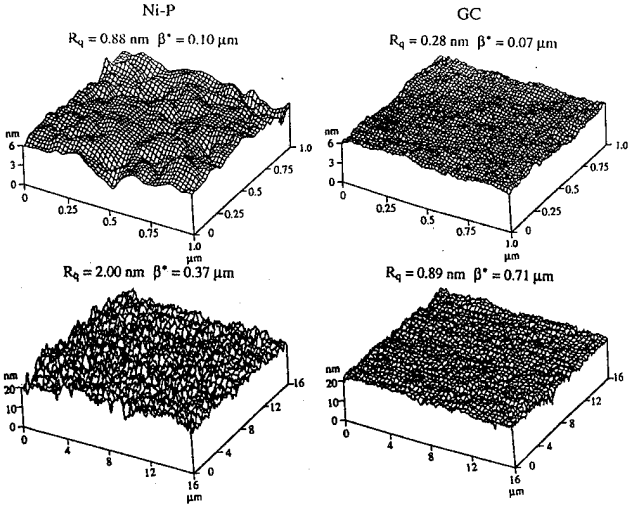



FIG. 1. AFM surface maps of Ni–P and GC surfaces for $L$=1 and 16 $\mu$m.

 0021-8979/96/79(8)/5799/3/$10.00 © 1996 American Institute of Physics 

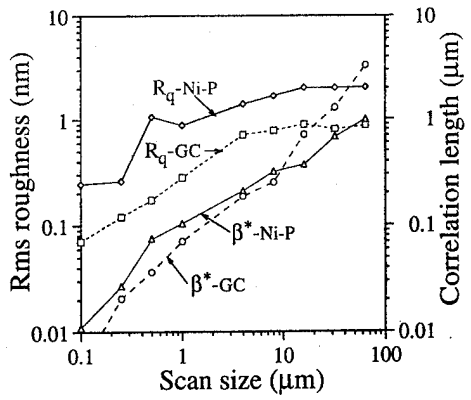



FIG. 2. Variation of rms roughness and correlation length with scan size.

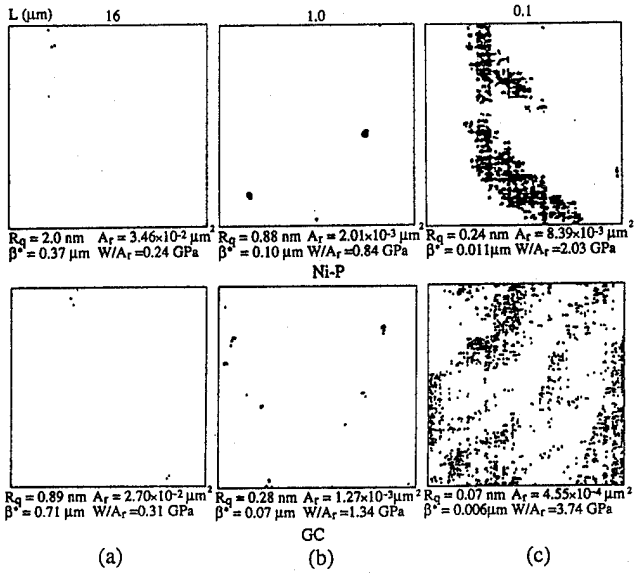



FIG. 3. Contact area of Ni–P and GC surfaces for $L=16$, 1, and 0.5 $\mu$m. $p_n=32.8$ kPa for $L\geq 16$ $\mu$m and $W=1.7$ $\mu$N for $L\leq 8$ $\mu$m.

faces contain a long-wavelength limit of 16 $\mu$m. Therefore, $\beta^*$, which represents the wavelength structure of a random surface, should approach a constant value as $L$ reaches 16 $\mu$m for measurements made at constant $\tau$. But in the AFM measurements, $\tau$ increases with an increase in $L$, which is responsible for an increase in $\beta^*$ with $L$, observed in Fig. 2. As $\tau$ increases, the higher frequencies in the surface cannot be recorded[4] and error in sampling occurs. The surfaces being studied contain predominantly submicron details. Increasing $\tau$ will result in loss of high frequencies information. As $\tau$ increases, high frequency details of the original profile gradually disappear resulting in high $\beta^*$. $R_q$ is a vertical parameter not sensitive to $\tau$ but is generally increasing with $L$. $\beta^*$ is a spatial parameter affected by both $\tau$ and $L$.

## III. CONTACT OF Ni–P AND GC SURFACES

A three-dimensional (3D) numerical rough surface contact model[2] is used to study the contact of a head slider on the Ni–P and the GC surfaces. This model analyzes elastic/plastic contact of two rough surfaces and predicts the contact statistics and contact pressure. Roughness data used in the model are the 3D roughness maps obtained at a given scan size and sampling interval. For the asperity undergoing plastic deformation, the asperity pressure is taken to be the hardness of the softer body, which is 8.0 GPa. The head slider is a 50% size slider made of $Al_2O_3$–TiC and is taken as perfectly smooth. The Young's modulus and Poisson's ratio for the slider, the Ni–P surface, and the GC surface are 450 GPa and 0.23, 130 GPa and 0.36, and 130 GPa and 0.25, respectively. The nominal load $W_n$ is 3 g and the nominal area $A_n$ is 0.915 mm$^2$, which gives the nominal pressure $p_n$ of 32.8 kPa. In the contact analysis, the applied load is changed for different scan sizes according to different bandwidths involved in the nominal contact.

In Fig. 2, $R_q$ of each surface approaches a constant value when $L\geq 16$ $\mu$m, which indicates that the surfaces contain a long-wavelength limit of 16 $\mu$m. Therefore, the applied load can be reasonably assumed to distribute evenly over the surface for $L\geq 16$ $\mu$m and is given by $W=p_n\times L^2$. $p_n$ is equal to 32.8 kPa. For $L=64$, 32, and 16 $\mu$m, the load $W$ are 134, 33.6, and 8.4 $\mu$N, respectively. The contact areas of the Ni–P and GC surfaces for $L=16$ $\mu$m are shown in Fig. 3(a). However, for $L<16$ $\mu$m, $R_q$ increases with $L$ because of different bandwidth structure for $L<16$ $\mu$m; therefore, the load cannot be calculated based on assumption of uniform distribution of load over the slider area.

From Fig. 3(a), the contact areas for the Ni–P and the GC surfaces are 0.035 and 0.027 $\mu$m$^2$, respectively. The number of contacts for both surfaces is five. Therefore, the average contact width for each asperity contact of both surfaces is about 0.08 $\mu$m and the average asperity contact load is 8.4/5 or 1.7 $\mu$N. Now, this particular asperity contact is examined in finer detail by reducing the scan size using the same number of discretized data points and assuming that each scan size contains asperity contacts. In this way, the scan size can go down to 0.08 $\mu$m using the same asperity contact load. For a range of scan sizes 16 $\mu$m$>L\geq 0.1$ $\mu$m, the load is taken as $W=1.7$ $\mu$N. The contact areas of Ni–P and GC surfaces for $L=8$, 4, 1, 0.5, 0.25, and 0.1 $\mu$m are calculated and the contact areas for $L=1.0$ and 0.1 $\mu$m are shown in Figs. 3(b) and 3(c). The contact areas of Ni–P and GC are significantly different; the contact area of the Ni–P surface is almost twice the GC surface, and the individual asperity contact of GC is much smaller.

Next, the effect of sampling interval on contact area and contact pressure is studied. The contact area calculated for different scan sizes is modified so that it can be compared based on a particular scan size. For surfaces with $L\geq 16$ $\mu$m, the contacts are taken as distributed evenly over the surface; therefore the contact area of the surfaces with $L=64$ and 32 $\mu$m can be divided by 16 and 4, respectively, to compare with the surface with $L=16$ $\mu$m. The number of contacts at $L=16$ $\mu$m is five, therefore at $L=8$ $\mu$m about one contact is expected. Therefore, the contact area for $L\leq 8$ $\mu$m is considered as the higher magnification of one of the five contact spots at $L=16$ $\mu$m and it should therefore be multiplied by

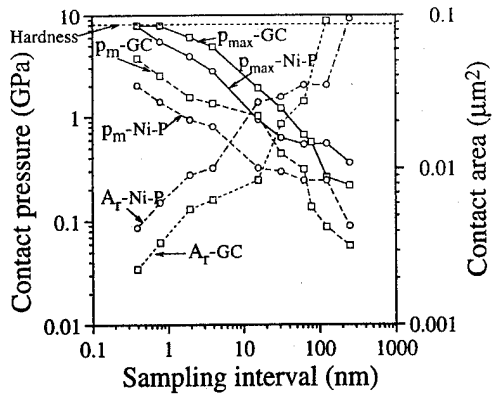



FIG. 4. Variation of mean contact pressure, maximum contact pressure and contact area with sampling interval for Ni–P and GC surfaces.

five to compare with the surface using $L=16$ $\mu$m. However, the mean contact pressure $p_m = W/A_r$, does not need to be modified with $L$ because $W$ and $A_r$ will change by the same factor for different $L$. Using the preceding argument, the variation of contact area and contact pressure with sampling interval is shown in Fig. 4. For both surfaces, the contact area decreases and contact pressure increases as the sampling interval decreases. The contact pressure of the GC surface is always higher than that of the Ni–P surface. As the sampling interval becomes smaller, the maximum contact pressure $p_{max}$ can reach the hardness. The subsurface stress is always higher than the surface stress and plastic deformation is expected to occur before surface stress reaches the hardness.

## IV. DISCUSSION

Surface texture plays an important role in controlling friction and durability at the head–disk interface (HDI).[1] In general, friction and durability have been qualitatively related to vertical roughness parameters such as rms roughness $R_q$, center-line-average roughness $R_a$, peak-to-mean distance $R_p$, peak-to-valley distance $P$-$V$, and bearing ratio. On the other hand, spatial parameters have rarely been used. Since the complex nature of surface roughness covers a broad bandwidth of wavelengths, the measured surface profile depends on the scale of measurement and the surface measuring instruments.[5] In particular, spatial parameters are very sensitive to the sampling resolution.

Whitehouse and Archard[3] used a statistical approach for a gaussian surface and showed that the distribution of peak heights, curvatures, slopes, and peak density could be expressed in terms of $R_q$ and $\beta^*$. Their expressions have shown a broad agreement with surface measurements of different surfaces used for magnetic recording.[6] Whitehouse and Archard further expressed the plasticity index in terms of $R_q$ and $\beta^*$. Later, Onions and Archard[7] combined the approaches of Greenwood and Williamson[8] and Whitehouse and Archard.[3] They expressed the contact pressure in terms of $R_q/\beta^*$. Hirst and Hollander[9] provided experimental evidence that surface damage can be related to $R_q$ and $\beta^*$. It appears that $\beta^*$ can be used in addition to $R_q$ to assess the disk's friction and durability at HDI.

From Fig. 2, $R_q$ of the Ni–P surface is always higher than that of the GC surface. Based on $R_q$ alone, it is expected that the contact pressure for the Ni–P surface is higher. On the contrary, Fig. 4 shows that contact pressure for the GC surface is always higher, except for larger $L$. But the results for larger $L$ (higher $\tau$) are not representative because much of the high frequency structures in the GC surface are excluded in the contact analysis. Figure 4 shows that for both surfaces, the contact pressure increases and the contact area decreases as $\tau$ decreases because finer asperities become involved in the contact. The GC surface contains more higher frequency structures than the Ni–P surface, which explains why the contact pressure for the GC surface is higher than the Ni–P surface. Results show that a spatial parameter such as $\beta^*$ is also needed to characterize a rough surface.

From Fig. 4, the asperity contact pressure of both surfaces reaches the hardness of the softer material at low $\tau$. This implies that the contact of real surfaces starts from plastic deformation on a nanoscale. The GC surface experiences a larger degree of plastic deformation than Ni–P surface because GC has higher frequency structures compared to the Ni–P surface. Bhushan *et al.*[10] have reported that the durability of Ni–P was generally better than the GC surface in different environments. In their paper, the $R_p$ values of Ni–P and GC surfaces were comparable but the corresponding AFM surfaces showed that the GC surface contained much higher frequency details. The wear track on the GC surface showed a few very thin continuous scratches and the corresponding head slider contained a trail of wear particles after test. The wear particles may be generated from shearing of the asperities by plastic deformation which can get trapped at the interface resulting in the three-body abrasion.[1] Based on the contact analysis and the earlier tests on Ni–P and GC surfaces, the high frequency structure in the GC surface will facilitate the plastic deformation and form wear particles, which in turn take part in the three-body abrasion process. Therefore, the high frequency structure in the GC surface is not desired.


[1] B. Bhushan, *Tribology and Mechanics of Magnetic Storage Devices* (Springer, New York, 1990).
[2] X. Tian and B. Bhushan, ASME J. Tribol. **118** (1996).
[3] D. J. Whitehouse and J. F. Archard, Proc. R. Soc. London Ser. A **316**, 97 (1970).
[4] D. J. Whitehouse, in *Rough Surfaces*, edited by T. R. Thomas (Longman, London, 1982).
[5] T. R. Thomas, *Rough Surfaces* (Longman, London, 1982).
[6] C. Y. Poon and B. Bhushan, Wear **190**, 89 (1995).
[7] R. A. Onions and J. F. Archard, J. Phys. D **6**, 289 (1973).
[8] J. A. Greenwood and J. B. P. Williamson, Proc. R. Soc. London Ser. A **295**, 300 (1966).
[9] W. Hirst and A. E. Hollander, Proc. R. Soc. London Ser. A **337**, 379 (1974).
[10] B. Bhushan, L. Yang, C. Gao, S. Suri, R. A. Miller, and B. Marchon, Wear **190**, 44 (1995).

# Environmental effects on the pause mode performance of metal-evaporated and metal-particle tapes

Steven T. Patton and Bharat Bhushan
*Department of Mechanical Engineering, The Ohio State University, Columbus, Ohio 43210*

A commercial *Hi*-8 VCR was instrumented to measure the friction force between the rotary heads and tape and rms head output. Pause mode experiments using metal-evaporated (ME) and metal-particle (MP) tapes were performed at design tension under equilibrium conditions inside of an environmental chamber at various temperatures and specific humidities (SH is the ratio of the weights of water vapor to dry air in the mixture). ME tape performed well only at high humidity [on the order of 80% relative humidity (RH)] in the operating temperature range of 15.6–32.2 °C. Under all conditions, lubricant was removed from the ME tape surface, which resulted in increased signal amplitude (due to decreased head medium spacing) and friction during individual experiments. For fixed temperature, increased SH reduced both the lubricant depletion rate and the number and magnitude of spacing loss signal dropouts. The thicker water film maintained on the interface components acted as an additional replenished lubricant, which reduced the displacement of the perfluropolyether lubricant from the tape surface and acted as a mediator for solid debris to traverse the contact region of the head and tape. For fixed SH, reduced temperature led to the same improvements due to increased lubricant viscosity at lower temperatures. Increased lubricant viscosity reduced the displacement of lubricant from the tape surface, and displaced lubricant remained on the tape contact region of the head surface and acted as a mediator for solid debris to traverse the contact region of the head and tape. Tests with MP tape showed a relative insensitivity to the environment. © *1996 American Institute of Physics.* [S0021-8979(96)11908-7]

Metal-evaporated (ME) and metal-particle (MP) tapes are leading candidates for high-density recording applications such as consumer digital audio, video, and data processing. The effects of temperature and specific humidity (SH is the ratio of the weights of water vapor to dry air in the mixture) on the performance of these tapes must be understood to ensure that the tapes can operate satisfactorily in the operating envelope for a given application. Previous studies showed that ME tape performance improved when operated above a threshold humidity for a given temperature (with a threshold value that increased with temperature), and that MP tape performance was relatively insensitive to the environment.[1,2] However, the effect of temperature on ME tape performance and the underlying mechanisms which improved performance above the threshold humidity are not known.

A commercial *Hi*-8 VCR (Sony EV-C100) with four heads was instrumented to measure the friction force between the rotary heads and tape and root mean square (rms) head output. The relative speed between a rotary head and tape is 3.8 m/s with an inlet tension of 0.1 N.[2] The average pressure at the contact region of the head and tape is about 100 kPa.[2] The two read/write metal in gap heads have a core material of single-crystal Mn–Zn ferrite with crystalline Sendust metal alloy (Fe–Si–Al) in the gap. Commercially available *Hi*-8 ME and MP tapes were used in this study.[3]

The data processing operating envelope is 15.6–32.2 °C

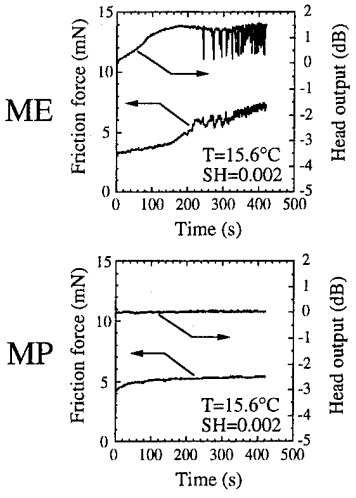



FIG. 1. Friction force and head output during testing with ME and MP tape in the same environment.

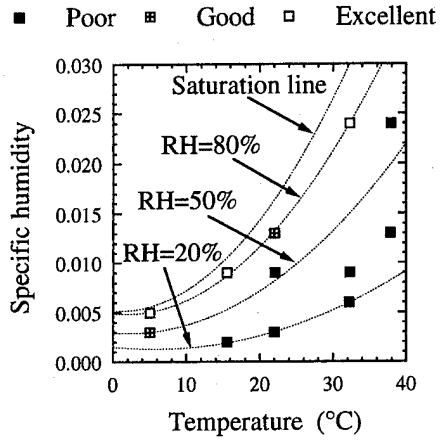



FIG. 2. Comparative durability results of pause mode experiments using ME tape at various temperatures and specific humidities.

 0021-8979/96/79(8)/5802/3/$10.00 © 1996 American Institute of Physics

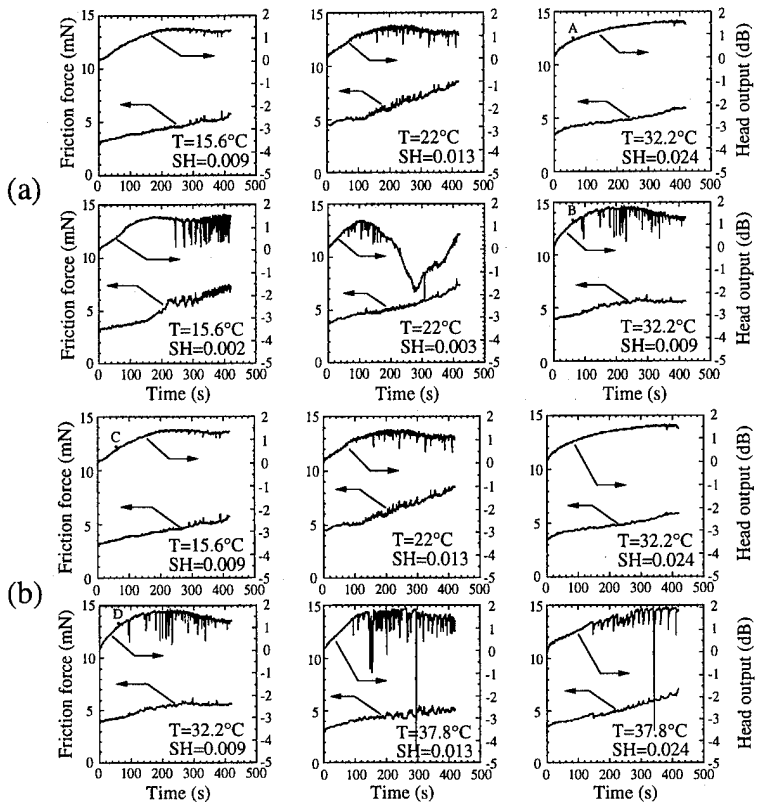



FIG. 3. Friction force and head output during testing with ME tape at (a) various specific humidities at constant temperature and (b) various temperatures at constant specific humidity.

and 20%–80% relative humidity (RH) with a maximum wet bulb temperature of 25.6 °C. Pause mode experiments were conducted at design tension under equilibrium conditions inside of an environmental chamber in a broader envelope at temperatures ranging from 5 to 37.8 °C (±1 °C) and relative humidity ranging from 20%–80% RH (±1% RH). The VCR and tape samples were placed in the chamber 24 h prior to experimentation at a given condition which allowed the components to come to equilibrium. The friction force was measured by monitoring the voltage across the motor used for drum rotation, and the friction force was obtained using a previously developed calibration procedure.[3] The calibration constant was 54 mV/mN. The head output was measured in a rms voltage format using a rms signal converter. A sine wave was recorded on the tape at a wavelength of 0.6 $\mu$m using VCR electronics. The motor voltage and rms head output were sampled at a rate of 4 Hz over the duration of seven minute pause mode experiments using an analog to digital converter, and the data were stored in a personal computer. The head and tape samples were observed with an optical microscope after selected experiments.

Figure 1 shows the friction force and head output during testing with ME and MP tapes in the same environment. ME tape lacked the stability in friction and head output exhibited by MP tape. Head output for ME tape shows a rapid increase to about +1 dB, implying a decrease in the head–medium spacing of about 10 nm for a recorded wavelength of 0.6 $\mu$m based on the Wallace equation. Since the lubricant thickness is also 10 nm, this implies the removal of essentially all of the lubricant from the ME tape surface. After lubricant depletion, interaction of the rotary heads with the metallic layer prevented the rapid increase in head output observed during lubricant removal and generated solid tape debris, which, at this environmental condition, caused signal dropouts upon

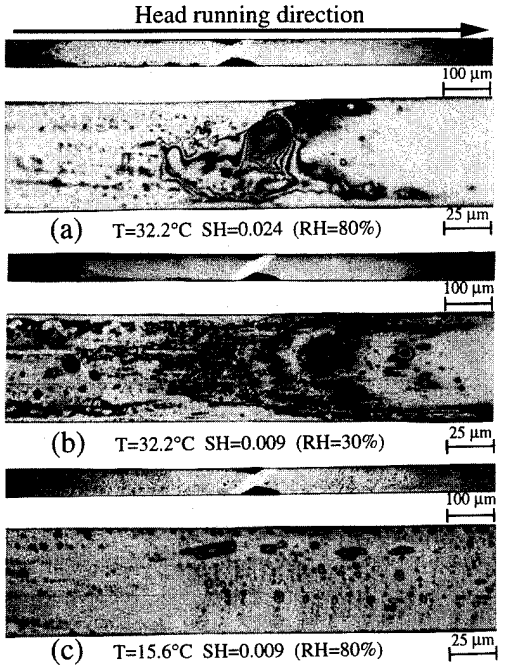



FIG. 4. Optical micrographs of the entire head surface (top) and magnified view of the trailing edge (bottom) after running to (a) point A in Fig. 3(a), (b) point B in Fig. 3(a) or point D in Fig. 3(b), and (c) point C in Fig. 3(b).

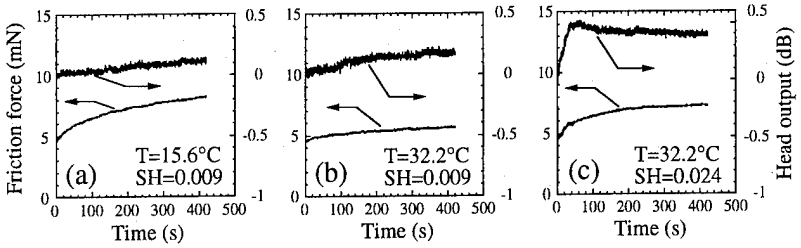



FIG. 5. Friction force and head output during testing with MP tape at various temperatures and specific humidities.

traversing the tape contact region of the head surface. The friction force increased as the lubricant was removed, and further increased and became unstable after lubricant depletion with friction spikes temporally correlated to signal dropouts.

Figure 2 shows durability results of pause mode experiments using ME tape at various temperatures and SHs. At constant temperature, increased SH improved tape performance. At constant SH, decreased temperature improved tape performance. At a given temperature more water vapor improved performance, and the amount of water vapor needed for improved performance decreased at lower temperatures. Experiments performed at various SH on the RH =80% line yielded good or excellent results in the operating temperature range of 15.6–32.2 °C. However, at temperatures lower than 15.6 °C, ME tape performed satisfactorily at lower humidity to RH=50%.

Figure 3(a) shows the friction force and head output at selected SH at constant temperature. At three different temperatures, increased SH improved the performance of ME tape. Increased SH reduced the lubricant removal rate, and improved signal stability after the lubricant depletion. The thicker water film maintained on the interface components acted as an additional replenished lubricant and a mediator for solid debris to smoothly traverse the contact region of the head and tape. Optical micrographs in Figs. 4(a) and 4(b) of the head surface after testing to points A and B in Fig. 3(a) show a relatively clean tape contact region for the head. Lubricant transferred to the leading edge from the tape, and collected on the trailing edge of the tape contact region. The amount of lubricant transferred to the head was greater after running at SH=0.009 than at SH=0.024, and thus the lubricant removal rate decreased at higher values of SH. The clean tape contact region of the head at points A and B suggests that the water film on the interface components must be the mediator which assisted solid debris in traversing the contact region of the head and tape.

Figure 3(b) shows friction force and head output at selected temperature at constant SH. At three different values of SH, decreased temperature reduced the lubricant removal rate and improved signal stability after lubricant depletion, due to increased lubricant viscosity at lower temperature. The average lubricant removal rate decreased from 10 to 4.3 nm/min, 10 to 5 nm/min, and 6.25 to 5 nm/min for SH equal to 0.009, 0.013, and 0.024, respectively, as the temperature was reduced in each case. In the cases of SH=0.009 and 0.013, the average lubricant removal rate was halved with a reduction in temperature of about 15 °C. Viscosity–temperature relations for perfluropolyether lubricants show that kinematic viscosity increases by about a factor of 2 with a 15 °C decrease in temperature within the range of temperatures used in these experiments.[4] For SH=0.024, the lubricant removal rate was reduced by about 20% for a smaller temperature reduction of about 5 °C. The data are consistent with the lubricant removal rate being inversely proportional to the viscosity. Figures 4(b) and 4(c) show optical micrographs of the head surface after testing to points D and C, respectively, in Fig. 3(b). The amount of lubricant transferred to the head was greater after running at 32.2 °C than at 15.6 °C, and lubricant remained on the tape contact region of the head after running at 15.6 °C. At lower temperatures, the lubricant removal rate decreased and lubricant persisted on the tape contact region of the head and acted as a mediator for solid debris to traverse the contact region of the head and tape.

Figure 5 shows friction force and head output in different environment using MP tape. Figures 5(a) and 5(b) show that MP tape performance was insensitive to changes in temperature at constant SH, and both friction and head output increased during each experiment due to mild burnishing of the tape surface. Figures 5(b) and 5(c) show that a thicker water film resided on the interface components with increased SH at constant temperature. The rapid increase in head output in Fig. 5(c) to 0.5 dB over the first 40 s of running suggests that about 2.5 nm of the water film on each interface component was removed by the friction force exerted on the components during this time. Subsequent head output decreased slightly as the water film partially reestablished on the head and tape surfaces.

[1] A. Tomago, T. Suzuki, S. Kawase, and Y. Kai, Polymer Preprints (Jpn.) **36**, 3483 (1987).
[2] T. Tsuchiya and B. Bhushan, IEEE Trans. Mag. **30**, 4177 (1994).
[3] S. T. Patton and B. Bhushan, ASME J. Tribol. **117** (1996).
[4] B. Bhushan, *Tribology and Mechanics of Magnetic Storage Devices* (Springer, New York, 1990).

# Spin-dependent interface transmission and reflection in magnetic multilayers (invited)

M. D. Stiles
*Electron Physics Group, National Institute of Standards and Technology, Gaithersburg, Maryland 20899*

First-principles calculations of transmission and reflection from Ag/Fe, Au/Fe, Cu/Co, and Cu/Ni interfaces show very strong spin dependence that differs significantly from expectations based on free electron approximations. The results can be used to understand both the giant magnetoresistance and the oscillatory exchange coupling observed in magnetic multilayers of these materials. The spin dependence of the reflection probabilities is strong enough to give a large giant magnetoresistance even if there is no spin-dependent defect scattering. The calculated reflection amplitudes determine the strength of the oscillatory exchange coupling. [S0021-8979(96)79608-8]

## I. INTRODUCTION

Magnetic multilayers, in which magnetic layers are separated by nonmagnetic spacer layers, exhibit two effects in which there has been significant recent interest: giant magnetoresistance (GMR)[1] and oscillatory exchange coupling.[2] The GMR is the change in resistance when the relative orientation of the magnetizations in neighboring layers is switched by applying a magnetic field. When the magnetizations are parallel, there is a "short circuit" effect; electrons of one spin have a lower average resistance. They carry more of the current, lowering the total resistance of the structure compared to the total resistance for antiparallel magnetizations. The spin dependence of the resistance can come from spin-dependent defect scattering or spin-dependent interface reflection. The oscillatory exchange coupling is the coupling between the magnetic layers that oscillates in sign as a function of the spacer layer thickness. In magnetic multilayers, multiple reflection from the interfaces produces quantum well states, which are spin polarized because the reflection amplitudes are spin dependent. The quantum well states increase or decrease in energy as the thickness of the spacer layer increases. When they cross the Fermi level, the energy gained or lost from filling them changes the relative energies of the configurations with parallel and antiparallel magnetizations.

Both GMR and oscillatory exchange coupling have been the subject of many model and first-principles calculations.[3] Model calculations, usually based on the free electron approximation, can be easy to interpret and give insight into the important mechanisms, but many important details, related to neglecting the appropriate band structure, are not included. First-principles calculations implicitly include many of these details, but extracting underlying mechanisms from the results can be difficult. It can be quite useful to combine the best of both approaches and carry out first-principles calculations of the band-structure-related details used in model calculations. Among such details, spin-dependent transmission and reflection probabilities, particularly those for Fermi surface electrons, play an important role in both the GMR and the oscillatory exchange coupling.

Here, I present first-principles calculations of the spin-dependent transmission and reflection probabilities for the (001) interfaces of Ag/Fe, and Au/Fe and the (001), (111), and (110) interfaces of Cu/Co and Cu/Ni. I discuss the implications of the results for the transport properties of these systems and compute the strengths of the oscillatory exchange coupling.

## II. TRANSMISSION AND REFLECTION PROBABILITIES

In structures in which there is a single interface between two materials, an electron propagating toward the interface can either transmit or reflect. If the interface is coherent, that is, the two materials are well lattice matched, then the momentum parallel to the interface is conserved during transmission and reflection. Far enough from the interface, the time-independent scattering states for this process consist of linear combinations of bulk Bloch states. On one side of the interface, they each consist of one Bloch state propagating toward the interface plus one or more reflected Bloch states propagating away from the interface, and on the other side, they consist of zero or more transmitted Bloch states propagating away from the interface. Close to the interface, the scattering states consist of these Bloch states plus evanescent contributions that decay exponentially with distance from the interface. The transmission and reflection probabilities are just the flux in the transmitted and reflected Bloch states divided by the flux in the incident Bloch state. The two probabilities sum to one.

The calculation[4] of the time-independent scattering states starts by breaking space up into layers. The potential is computed for each layer from a bulk electronic structure calculation (a linearized-augmented-plane-wave implementation of the local spin-density approximation). Generalized Bloch states for a layer are computed from the potential in the layer. Generalized Bloch states are related to Bloch states by allowing the component of the wave vector normal to the interface to be complex. They form a complete set of states,

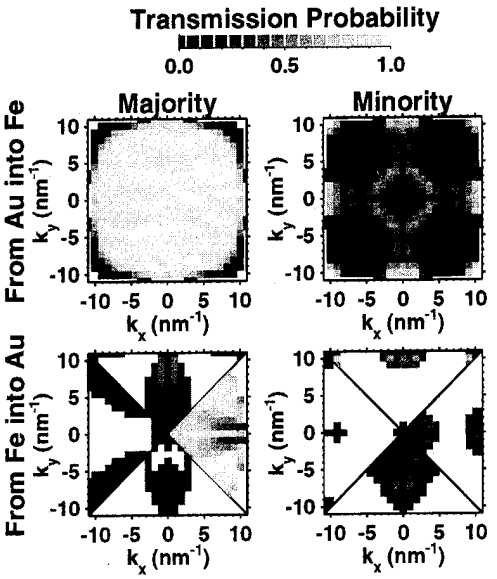



FIG. 1. Spin-dependent transmission probabilities for Au/Fe(001). The transmission probabilities are shown for various points on the Fermi surface projected onto the interface Brillouin zone. The gray scale for the transmission probability is at the top. The top (bottom) two panels show the transmission for electrons from the Au (Fe) into the Fe (Au). The two right (left) panels show the transmission probabilites for the minority (majority) electrons.

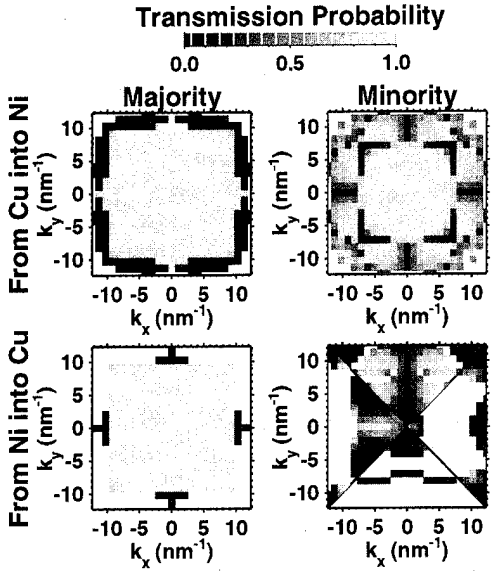



FIG. 3. Spin-dependent transmission probabilities for Cu/Ni(001). See Fig. 1.

which includes the usual Bloch states and all evanescent states, and consequently describe any time-independent solution of Schrödinger's equation for arbitrary boundary conditions. The generalized Bloch states for the two materials are matched together across the interface to construct the electron scattering states, giving the reflection and transmission amplitudes directly.

The calculations for Cu/Ni and Cu/Co, where the Co is face-centered cubic, use the bulk lattice constant of Cu for both materials. Face-centered cubic Ag and Au are quite well lattice matched with body-centered cubic Fe is the (001) planes are rotated 45° with respect to each other. The calculations for Au/Fe and Ag/Fe use the bulk lattice constant for Fe and a very slight tetragonal distortion, based on their bulk elastic constants, for Au and Ag.

Figures 1–4 show the transmission probabilities across interfaces between these pairs of materials calculated for states on the Fermi surfaces of both materials. The Fermi surfaces are shaded according to the transmission probability for each state, and then they are projected into the interface Brillouin zone. For simple Fermi surfaces and certain interface orientations, there is only one state moving toward the interface at each parallel wave vector. Grouped together, these states form a sheet of the Fermi surface. For the interfaces with only one sheet of states moving toward the interface, that sheet is shown in the whole interface Brillouin

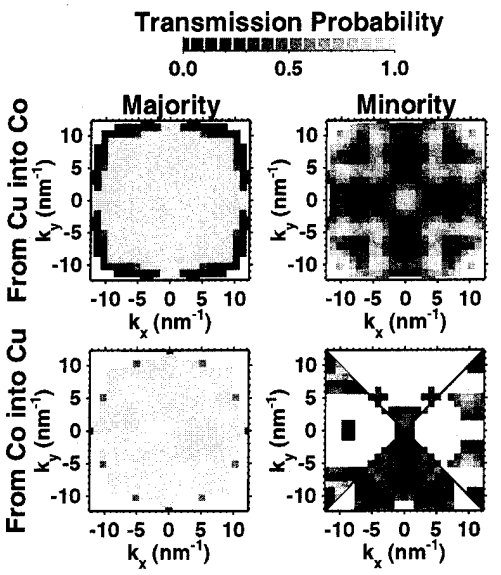



FIG. 2. Spin-dependent transmission probabilities for Cu/Co(001). See Fig. 1.

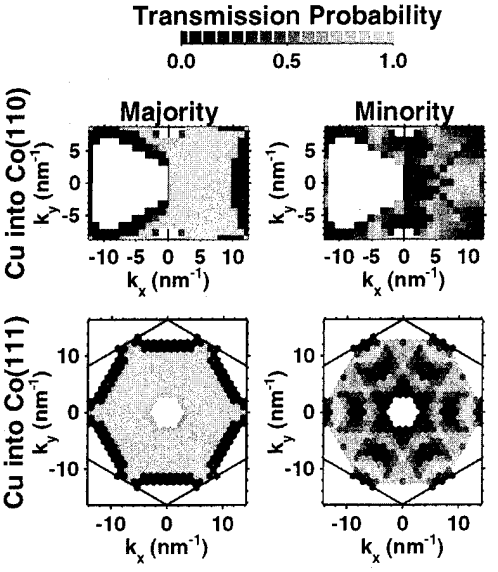



FIG. 4. Spin-dependent transmission probabilities for Cu/Co(110) and Cu/Co(111). See Fig. 1.

TABLE I. Transmission probabilities averaged over the Fermi surface.

| | Into | | From | |
|---|---|---|---|---|
| | minority | majority | minority | majority |
| Ag/Fe(001) | 0.16 | 0.86 | 0.14 | 0.36 |
| Au/Fe(001) | 0.17 | 0.84 | 0.16 | 0.37 |
| Cu/Co(001) | 0.49 | 0.79 | 0.27 | 0.95 |
| Cu/Co(111) | 0.54 | 0.73 | 0.33 | 0.94 |
| Cu/Co(110) | 0.44 | 0.66 | 0.29 | 0.92 |
| Cu/Ni(001) | 0.72 | 0.73 | 0.33 | 0.93 |
| Cu/Ni(111) | 0.80 | 0.67 | 0.38 | 0.92 |
| Cu/Ni(110) | 0.62 | 0.63 | 0.31 | 0.60 |

zone. For other interface orientations, or for complicated Fermi surfaces, the Fermi surface has several sheets. That is, at some parallel wave vectors there is more than one state moving toward the interface. For Fe, minority Co and Ni, Cu(110), and majority Co(110), each sheet is shown in a fraction of the Brillouin zone. The behavior over the full Fermi surface is found by rotating each sheet into each fraction of the Brillouin zone and stacking the sheets on top of each other. Table I gives the average over the Fermi surface of the transmission probabilities.

Some general features of these results are straightforward to understand. For example, states reflect completely if there are no states in the other material with the same parallel momentum. In addition, the symmetry of the states is important. Fermi surface states have $s-p$ character for noble metals and majority states in Co and Ni, but they have mainly $d$ character for minority states and Fe majority states. States with $s-p$ character tend to couple well to one another and to states with $dz^2$ character, but couple weakly to other $d$-like states. At high symmetry points, like the zone center, $\bar{\Gamma}$, these symmetry requirements become strict and some states, like the minority states in Au/Fe, reflect completely even though there are states with the same parallel wave vector.

Au/Fe (Fig. 1) and Ag/Fe (similar, but not shown) both show very good transmission into the majority states of Fe and poor transmission into the minority states. In the reverse direction the difference is much smaller, because there are many majority states that have very small transmission probabilities. These systems contain minority electrons that are largely confined to each separate material, majority electrons that transmit freely between them, and majority electrons confined to the ferromagnetic material.

The potentials in Cu are very similar to the potentials for the majority electrons in Co and Ni, but significantly different from those for the minority. This spin dependence leads to strongly spin-dependent scattering from substitutional impurities in these systems,[5,6] and strongly spin-dependent transmission across interfaces, Figs. 2–4. The majority Fermi surfaces in Co and Ni are similar to the Fermi surfaces in Cu, but are smaller. The similarities lead to almost complete transmission from the majority states in the ferromagnet into the nonmagnetic material, but the smaller sizes lead to complete reflection for the states in Cu with group velocities parallel to the interface. The transmission from Cu into minority states is not simply characterized. Some electrons transmit well, some completely reflect, but most exhibit intermediate behavior. The complicated behavior arises from the complicated nature of the minority Fermi surfaces of Co and Ni. Overall, the results do not vary much with interface orientation. It seems likely that transport calculations, which average in some way over all of the states, will have only a weak orientation dependence.

These transmission probabilities can be contrasted with those from free electron approximations. Projecting spherical free-electron Fermi surfaces on to the interface Brillouin zone gives circles of different radii. States with parallel wave vectors less than the Fermi wave vectors of the materials on either side of the interface transmit well. When the parallel wave vector becomes close to the smaller of the two Fermi wave vectors, the transmission goes to zero, and reflection is complete for states with a parallel wave vector greater than the smaller Fermi wave vector. This free electron behavior is a reasonable description of the behavior for the majority states in Cu/Co and Cu/Ni, but not for the minority states, or for Au/Fe(001) or Ag/Fe(001).

## III. GIANT MAGNETORESISTANCE

Strongly spin-dependent interface reflection can lead to a GMR effect even if there is no spin dependence to the defect scattering. For the case of current perpendicular to the interfaces, a contribution to the GMR comes from the spin dependence of the resistance associated with each interface. For current flow parallel to the interface there is no resistance associated with reflection. However, if the defect scattering rates are different in the ferromagnetic layers and nonmagnetic layers, spin-dependent interface reflection will still contribute to the GMR as discussed below.

GMR is usually observed in samples in which the elastic mean free paths and the thicknesses of the layers are comparable and both lengths are much less than the spin diffusion length. The essential physics is most easily understood from semiclassical calculations, which are valid when the layer thicknesses are much greater than the mean free paths. Here, I discuss GMR from such a semiclassical perspective, and note some corrections that are a consequence of the mean free paths being comparable to the thicknesses. I also assume that the spin diffusion length is infinite. Throughout this discussion, GMR is caused by a short circuit effect. When the magnetizations are antiparallel, electrons of both spins have the same average resistance. When the magnetizations are parallel, electrons of one spin have a higher resistance and those of the other a lower resistance. The electrons with the lower resistance carry more of the current, lowering the resistance of both spins taken together. Thus the resistance of the structure is lower than the magnetizations are parallel.

Current flow perpendicular to interfaces that reflect electrons requires that there be a chemical potential difference across the interface, even if there is no defect scattering at the interface.[7] For interface separated by much more than the mean free path, the amount of current crossing the interface is proportional to the chemical potential difference across the interface. This proportionality means that there is a resistance associated with each interface even if the momentum randomization occurs elsewhere in the sample. This resis-

tance is independent of the separation of the interfaces and the bulk scattering rates, provided the interfaces are sufficiently far apart.

If the reflection probability is spin dependent, the resistance of the interface is also. Thus, if electrons of only one spin transmit freely through all the interfaces in the structure, those electrons will have a lower resistance when the magnetizations in the ferromagnetic layers are parallel. They cause the short circuit effect that gives the GMR. The interface resistance is dominated by electrons moving perpendicular to the interface; these tend to be close to the zone center. It is clear from Figs. 1 and 2 that this effect will give a large contribution to the GMR for Au/Fe(001), Ag/Fe(001), and Cu/Co(001), but from Fig. 3 it will be much smaller for Cu/Ni(001). For most of these systems, the spin dependence of the interface resistance is much greater than it would be in free electron models. In those models, the electrons close to the zone center reflect only weakly from both the majority and the minority states and do not contribute to the GMR.

When the separation between interfaces becomes comparable to the mean free path in the material between them, interference between electrons reflecting from different interfaces modifies the transport so that the interface resistance is no longer associated with a single interface. For periodic interfaces closer than a mean free path, the Bloch states of the superlattice become the appropriate basis for treating the scattering. In this regime, which has been used in all first-principles calculations to date,[5,6,8] the contribution to the resistance from the interfaces becomes obscured, but is still present.

The electronic structure of multilayers and superlattices can be constructed piecewise from the electronic structures of the bulk materials and the interface reflection amplitudes.[9] Such a construction allows the electronic structure of multilayers and superlattices to be understood in terms of these simpler parts. Where the reflection probability is small, the states tend to propagate readily through the whole structure, but when the reflection probabilities are large, the states tend to localize in one material. In superlattices, reflection from the interfaces produces gaps in the Fermi surface of the superlattice. When states are freely propagating through the superlattice, these gaps are small, but when the states are localized the gaps become large. The results shown in Fig. 2 explain the spin-dependent gaps found for Cu/Co(001) superlattices.[10] That calculation shows that even when there is no defect scattering, this spin dependence leads to a GMR effect in a point contact.[10]

For current parallel to the interface, "channeling" can make an important contribution to the GMR, as seen in studies based on free-electron models.[11] Channeling occurs for any multilayer in each layer in which electrons are strongly reflected from both its interfaces. If the scattering rate in that layer is lower than it is in neighboring layers, electrons in that layer which strongly reflect see a lower effective scattering rate than they would in the absence of reflection. In magnetic multilayers, channeling contributes to the GMR only for parallel wave vectors for which there is strong reflection for one spin, but not the other. In this case, channeling does not occur for electrons of either spin in antiferromagnetic alignment because both transmit through one or the other interface. On the other hand, for ferromagnetic alignment, electrons of one spin are confined to the layer, and if that layer has a lower scattering rate, these electrons cause a short circuit effect, giving a GMR.

In the Cu/Co and Cu/Ni systems, the electrons in Cu with the largest velocities parallel to the interfaces reflect completely from the majority states due to the mismatch in the Fermi surfaces. Since the same states transmit well into the minority states, channeling by these electrons will give a large contribution to the GMR if the scattering rate in Cu is much smaller than it is in Co. Closer to, but not at, the zone center, there are additional channeling contributions to the GMR from states that are strongly reflected from the Co minority states, but are readily transmitted into the Co majority states.

Free electron models will not correctly describe these channeling effects. In free electron models, the minority Fermi surface is smaller than the majority Fermi surface. Thus, the electrons in Cu with the largest velocities parallel to the interfaces will reflect completely from both the majority and the minority states and not contribute to the GMR. On the other hand, there will be a contribution, not found in the present results, from electrons with parallel wave vectors between the majority and minority Fermi wave vectors. Finally, free electron models will not include the contribution for electrons closer to the zone center found in the present results.

For the Au/Fe(001) and Ag/Fe(001), the difference in reflectivity is so large over the Fermi surface that channeling will be a very big effect, even though the electrons in the noble metal that are moving parallel to the interface reflect strongly from both majority and minority states and do not give a channeling contribution to the GMR.

There is an additional interface contribution to the GMR for parallel transport in supercell calculations.[8,10] Here, the group velocities of the states at the Fermi surface *of the supercell* are modified by the multiple reflection at the interfaces. This effect is related to the gaps in superlattice Fermi surfaces discussed above. The different group velocities at the spin-dependent Fermi surfaces in different configurations lead to a GMR.

The results presented there make it clear that free-electron models will not accurately predict the size of either the interface resistance or the channeling effect. Free electron descriptions are reasonable only for majority electrons in Cu/Co and Cu/Ni, but the contribution to the GMR depends on the difference in reflection between majority and minority systems.

## IV. OSCILLATORY EXCHANGE COUPLING

The exchange coupling between ferromagnetic layers separated by nonmagnetic spacer layers is a product of geometrical properties of the Fermi surface of the spacer layer material and the reflection amplitudes from the interfaces.[12,13] There are oscillatory contributions to the coupling from parallel wave vectors where two sheets of the Fermi surface are parallel to each other and have opposite group velocities in the interface direction. For large spacer

TABLE II. Coupling strength due to various stationary points on the spacer layer Fermi surfaces, see Eq. (1).

| Interface | $k_x$ ($nm^{-1}$) | $k_y$ ($nm^{-1}$) | Period (nm) | Period (layers) | $J^\alpha/(1.0\ nm)^2$ ($mJ/m^2$) |
|---|---|---|---|---|---|
| Ag/Fe(001) | 0.00 | 0.00 | 1.34 | 6.5 | 3.1 |
| Ag/Fe(001) | 9.41 | 0.00 | 0.50 | 2.44 | 0.36 |
| Au/Fe(001) | 0.00 | 0.00 | 2.12 | 10.3 | 1.1 |
| Au/Fe(001) | 9.12 | 0.00 | 0.51 | 2.49 | 2.0 |
| Cu/Co(001) | 0.00 | 0.00 | 1.16 | 6.4 | 0.12 |
| Cu/Co(001) | 9.92 | 0.00 | 0.47 | 2.58 | 11 |
| Cu/Co(111) | 14.22 | 0.00 | 0.90 | 4.3 | 0.67 |
| Cu/Co(110) | 0.00 | 0.00 | 0.26 | 2.07 | 27 |
| Cu/Co(110) | 0.00 | 12.31 | 0.34 | 2.65 | 0.029 |
| Cu/Co(110) | 8.71 | 12.31 | 0.32 | 2.52 | 0.16 |
| Cu/Co(110) | 8.71 | 12.31 | 1.23 | 9.7 | 1.3 |
| Cu/Ni(001) | 0.00 | 0.00 | 1.16 | 6.4 | 0.005 |
| Cu/Ni(001) | 9.92 | 0.00 | 0.47 | 2.58 | 10 |
| Cu/Ni(111) | 14.22 | 0.00 | 0.90 | 4.3 | 0.26 |
| Cu/Ni(110) | 0.00 | 0.00 | 0.26 | 2.07 | 1.2 |
| Cu/Ni(110) | 0.00 | 12.31 | 0.34 | 2.65 | 0.003 |
| Cu/Ni(110) | 8.71 | 12.31 | 0.32 | 2.52 | 0.008 |
| Cu/Ni(110) | 8.71 | 12.31 | 1.23 | 9.7 | 0.07 |

layer thicknesses, $D$, each of these critical spanning vectors, indexed by $\alpha$, makes a contribution, $J^\alpha$ of the form

$$\frac{J^\alpha}{D^2}\sin(q_\perp^\alpha D+\phi^\alpha)=\frac{\hbar v_\perp^\alpha \kappa^\alpha}{4\pi^2 D^2}\,\mathrm{Im}[\Delta r_A^\alpha \Delta r_B^\alpha e^{iq_\perp^\alpha D}e^{i\chi^\alpha}], \tag{1}$$

where $v_\perp^\alpha$ is the component of the effective group velocity in the interface direction, $\kappa^\alpha$ is the radius of curvature of the Fermi surface, $\Delta r_{A(B)}^\alpha$ is the spin difference in the reflection amplitude for the left (right) interface, $q_\perp^\alpha$ is the critical spanning vector, which determines the period of the oscillation $L^\alpha=2\pi/q_\perp^\alpha$, $\chi^\alpha$ is a phase from the type of critical point (maximum, minimum, saddle point), and $\phi^\alpha$ is the resulting phase. (The reflection amplitudes are complex.)[14] Table II gives the coupling strengths for all of the critical points for these systems. These critical points are the same as those identified from experimental Fermi surfaces by Bruno and Chappert.[15]

For Ag/Fe and Au/Fe the critical point at $\bar{\Gamma}$ (the interface zone center) gives a long-period oscillation. Here the reflection probability for the minority spins is exactly one and for the majority spins it is close to zero. The other critical points, along the $\bar{\Delta}$ line close to the zone boundary, produce a short-period oscillation. At these points, the reflection probability is increasing rapidly as a function of parallel wave vector for the majority states and decreasing rapidly for the minority states. These rapid changes lead to a large uncertainty in the coupling strengths for these critical points. For Au/Fe, the ratio of the strengths for the two periods happens to be close to the experimentally determined ratio of 2.1,[16] but for Ag/Fe the ratio is very far from the experimental ratio of 1.0.[17] All the coupling strengths are roughly an order of magnitude larger than measured values.[18]

The Cu/Co systems have been extensively studied experimentally[19] and theoretically.[20–24] Previous theoretical results are similar to the results found here. For the (001) interface, the critical points along $\bar{\Delta}$ give a strong short-period oscillation and the critical point at $\bar{\Gamma}$ gives a long-period oscillation that is weak because both spins reflect weakly. For the (111) interface the critical points at the necks along the zone boundary give strong coupling. For the (110) interface, there are four critical spanning vectors, including one at the zone boundary which gives a strong long-period oscillation and one at $\bar{\Gamma}$ which gives an extremely strong short-period oscillation. The Cu/Ni systems have received much less attention. The differences in coupling strength compared to Cu/Co are due to the differences in reflection amplitudes.

As was the case for the Au/Fe and Ag/Fe systems, the calculated coupling strengths for Cu/Co are much stronger than those measured experimentally. In my opinion, the difference results from calculations being done for ideal interfaces while measurements are made on systems with interdiffusion and steps and other defects at the interfaces. Interface defects reduce reflection amplitudes by scattering electrons into all parallel wave vectors. Reduced reflection amplitudes lead to reduced coupling strengths. The experimental determination of the structural properties of the interfaces will allow a more detailed comparison between theory and experiment.

The major source of error in this work is the deviation of the Fermi surfaces calculated in the local spin-density approximation from the actual Fermi surfaces. Comparing predicted periods with those found from the measured Fermi surfaces[15] gives an estimate of this error. Differences range up to ±20%. Lee and Chang[23] compute coupling strengths for Cu/Co using empirical tight binding and Eq. (1). Since they fit their band structures for Cu to de Haas–van Alphen data, the contributions to the coupling from the geometrical factors are more accurate in their calculations. On the other hand, the reflection probabilities, which they calculate in a parametrized tight-binding approach, are less reliable. Their results disagree with the present calculations by up to a factor of 2. A less significant source of error in this work is the neglect of self-consistency in the interface potential. Experience[4] suggest that introducing a self-consistent potential leads to only small changes in the reflection and transmission amplitudes.

## V. SUMMARY

First-principles calculations of transmission and reflection from Ag/Fe, Au/Fe, Cu/Co, and Cu/Ni interfaces show very strong spin dependence. The behavior of the spin-dependent transmission and reflection probabilities is significantly more complicated than expected from free electron models. The complications arise because many of the relevant Fermi surfaces are significantly more complicated than spheres. The spin-dependence of the reflection from interfaces is enough to give a large GMR even if there is no spin-dependent defect scattering. For perpendicular transport, it leads to a spin-dependent resistance associated with each interface. For parallel transport, it leads to channeling, which gives a GMR if the scattering rates are different in the two materials. The calculated reflection amplitudes predict strengths of the oscillatory exchange coupling which are

much greater than those observed experimentally. This disagreement is probably due to the assumed perfection of the interfaces.

## ACKNOWLEDGMENTS

I thank R. J. Celotta, W. F. Egelhoff, D. R. Penn, D. T. Pierce, J. Unguris, E. L. Shirley, Z. H. Levine, A. Zangwill, S. P. Hershfield, H. E. Camblong, and P. M. Levy, for either useful discussions, critical reading of the manuscript, or both.

[1] M. N. Baibich, J. M. Broto, A. Fert, F. Nguyen Van Dau, F. Petroff, P. Etienne, G. Creuzet, A. Friederich, and J. Chazelas, Phys. Rev. Lett. **61**, 2472 (1988); G. Binasch, P. Grünberg, F. Saurenbach, and W. Zinn, Phys. Rev. B **39**, 4828 (1989).

[2] P. Grünberg, R. Schreiber, Y. Pang, M. B. Brodsky, and H. Sowers, Phys. Rev. Lett. **57**, 2442 (1986); S. S. P. Parkin, N. More, and K. P. Roche, *ibid.* **64**, 2304 (1990).

[3] For reviews of exchange coupling and GMR see A. Fert, P. Grünberg, A. Barthelemy, F. Petroff, and W. Zinn, J. Magn. Magn. Mater. **140-144**, 1 (1995); *Ultrathin Magnetic Structures II*, edited by B. Heinrich and J. A. C. Bland (Springer, Berlin, 1994), Chap. 2, p. 45; for a more complete review of the GMR see P. M. Levy, Solid State Phys. **47**, 367 (1994).

[4] M. D. Stiles and D. R. Hamann, Phys. Rev. B **38**, 2021 (1988); **40**, 1349 (1989).

[5] W. H. Butler, J. M. MacLaren, and X.-G. Zhang, Mater. Res. Soc. Symp. Proc. **313**, 59 (1993); W. H. Butler, X.-G. Zhang, D. M. C. Nicholson, and J. M. MacLaren, *ibid.* (in press).

[6] R. K. Nesbet, J. Phys. Condens. Matter **6**, L449 (1994); Int. J. Quantum Chem. Symp. **28**, 77 (1995).

[7] A. Fert, T. Valet, and J. Barnaś, J. Appl. Phys. **75**, 6693 (1994); J. Barnaś and A. Fert J. Magn. Magn. Mater. **136**, 260 (1994); Phys. Rev. B **49**, 12835 (1994); A. Vedyayev, C. Cowache, N. Ryzhanova, and B. Dieny, Phys. Lett. A **198**, 267 (1995).

[8] P. Zahn, I. Mertig, M. Richter, and H. Eschrig, Phys. Rev. Lett. **75**, 2996 (1995).

[9] M. D. Stiles and D. R. Hamann, Phys. Rev. B **41**, 5280 (1990).

[10] K. M. Schep, P. J. Kelley, and G. E. W. Bauer, Phys. Rev. Lett. **74**, 586 (1995).

[11] R. Q. Hood and L. M. Falicov, Phys. Rev. B **46**, 8287 (1992); A. Vedyayev, C. Cowache, N. Ryzhanova, and B. Dieny, J. Phys. Condens. Matter **5**, 8289 (1993); B. R. Bulka and J. Barnaś, Phys. Rev. B. **51**, 6348 (1995).

[12] P. Bruno, J. Magn. Magn. Mater. **121**, 238 (1993).

[13] M. D. Stiles, Phys. Rev. B **48**, 7238 (1993).

[14] I have used the notation of Refs. 23 and 24 which differs slightly from that of Ref. 13.

[15] P. Bruno and C. Chappert, Phys. Rev. Lett. **67**, 1602 (1991).

[16] J. Unguris, R. J. Celotta, and D. T. Pierce, J. Appl. Phys. **75**, 6437 (1994).

[17] J. Unguris, R. J. Celotta, and D. T. Pierce, J. Magn. Magn. Mater. **127**, 205 (1993).

[18] Q. Leng, V. Cros, R. Schafer, A. Fuss, P. Grünberg, and W. Zinn, J. Magn. Magn. Mater. **126**, 367 (1993); Z. Celinski, B. Heinrich, and J. F. Cochran, J. Appl. Phys. **73**, 5966 (1993).

[19] M. T. Johnson, S. T. Purcell, N. W. E. McGee, R. Coehoorn, J. aan de Stegge, and W. Hoving, Phys. Rev. Lett. **68**, 2688 (1992); M. T. Johnson, R. Coehoorn, J. J. de Vries, N. W. E. McGee, J. aan de Stegge, and P. J. H. Bloemen, *ibid.* **69**, 969 (1992); Z. Q. Qui, J. Pearson, and S. D. Bader, Phys. Rev. B **46**, 8659 (1992); A. Cebollada, R. Miranda, C. M. Schneider, P. Schuster, and J. Kirschner, J. Magn. Magn. Mater. **103**, L221 (1992); P. J. H. Bloemen, R. van Dalen, W. J. M. de Jonge, M. T. Johnson, and J. aan de Stegge, J. Appl. Phys. **73**, 5972 (1993); P. J. H. Bloemen, M. T. Johnson, M. T. H. van de Vorst, R. Coehoorn, J. J. de Vries, R. Jungblut, J. aan de Stegge, A. Reinders, and W. J. M. de Jonge, Phys. Rev. Lett. **72**, 764 (1994); W. Weber, R. Allenpach, and A. Bischof, Europhys. Lett. **31**, 491 (1995).

[20] F. Herman, J. Sticht, and M. van Schilfgaarde, J. Appl. Phys. **69**, 4783 (1991).

[21] P. Lang, L. Nordström, R. Zeller, and P. H. Dederichs, Phys. Rev. Lett. **71**, 1927 (1993); L. Nordström, P. Lang, R. Zeller, and P. H. Dederichs, Phys. Rev. B **50**, 13058 (1994).

[22] J. Mathon, M. Villeret, R. B. Muniz, J. d'Albuquerque e Castro, and D. M. Edwards, Phys. Rev. Lett. **74**, 3696 (1995).

[23] B. Lee and Y.-C. Chang, Phys. Rev. B **51**, 316 (1995).

[24] P. Bruno, Phys. Rev. B **52**, 411 (1995).

# How predictable is the current perpendicular to plane magnetoresistance? (invited)

W. P. Pratt, Jr., Q. Yang, L. L. Henry, P. Holody, W.-C. Chiang, P. A. Schroeder, and J. Bass

*Department of Physics and Astronomy and Center for Fundamental Materials Research, Michigan State University, East Lansing, Michigan 48824-1116*

Prior measurements of the current perpendicular to the layer planes (CPP) resistances, taken on Co/Cu/Py/Cu (Py=$Ni_{84}Fe_{16}$) multilayers with a single pair of Co and Py thicknesses, are extended to three additional pairs of thicknesses. The same parameters, obtained from independent measurements on Co/Cu and Py/Cu multilayers that fit the original pair reasonably well, fit the three new pairs almost as well, from which we conclude that there is substantial predictability in the CPP magnetoresistance (MR). Because the predictability is not perfect, we examine the extent to which we can improve the fits to the Co/Cu/Py/Cu data by varying the Py/Cu and Co/Cu parameters within their uncertainties, without substantially weakening the fits to the original Co/Cu and Py/Cu data. We conclude by presenting the first CPP-MR measurements on Co/Ag/Py/Ag multilayers. The data are similar to those for Co/Cu/Py/Cu multilayers, but the Co/Ag/Py/Ag MRs are noticeably larger.
© *1996 American Institute of Physics.* [S0021-8979(96)54508-1]

## I. INTRODUCTION

For both scientific and technological reasons, the giant (G) magnetoresistance (MR) in magnetic multilayers consisting of alternating layers of ferromagnetic (F) and nonmagnetic (N) metals continues to be a topic of great interest.[1,2] Since tailoring of F/N systems for specific uses will likely require new combinations of F and N elements, one major goal of GMR studies is to be able to predict the behavior of samples involving these new combinations, using parameters derived from old ones. The fundamental parameters are those that characterize the magnitude and spin asymmetry of electron scattering in the bulk of the F metal and at the F/N interfaces.[2–5]

In the present paper, we extend a prior test,[6,7] of the predictability at 4.2 K of the current perpendicular to the layer planes (CPP)[8] specific resistances, $AR_t$ (area $A$ times total resistance $R_t$), of three-component Co/Cu/Py/Cu multilayers using parameters determined without adjustment from measurements of the two-component multilayers Co/Cu[9,10] and Py/Cu[10,11] (Py=$Ni_{84}Fe_{16}$).

Quantitative tests of predictability are easier in the CPP geometry than in the usual geometry with current in the layer planes (CIP),[2] because the analytical expressions are much simpler. We have shown that the CPP $AR_t$s at 4.2 K of Co/Ag,[3,12] Co/Cu,[9,10] and Py/Cu[10,11] multilayers can be described rather well by a phenomenological two-current, series-resistor model,[3,10–12] that has now been well validated theoretically[4,13,14] in the experimentally relevant limit where the electron spin-flip diffusion length is much larger than the F and N metal layer thicknesses, $t_F$ and $t_N$. Electrons in the multilayer can then be divided into two classes that do not mix–spin up (+) and spin down (−) relative to the direction of the applied magnetic field $H$. $AR(\pm)$ for each spin direction is then the series sum over the multilayer of the ARs of all the interfaces and the resistivities times layer thicknesses of all the layers. $AR_t$ is simply the parallel combination of $AR(+)$ and $AR(-)$.[3,4,13] The equivalent expressions for the CIP geometry are much more complex; in addition to parameters like those for the CPP ARs, they also contain exponential factors involving ratios of the electron mean-free paths in given layers to the layer thicknesses.[5]

The standard models of GMR[2,5] assume that the reduction in resistance as the magnetic field $H$ increases is due to a field-induced reorientation of the magnetizations $M_i$ of adjacent F layers, from an antiparallel (AP) alignment (total magnetization $M=0$) at small $H$ to a parallel (P) alignment (maximum $M$) at large $H$. We thus want to measure $AR_t$(AP) and $AR_t$(P). However, most two-component F/N multilayer systems exhibit a complete AP state—if at all—only when the exchange coupling between adjacent F layers is strongly antiferromagnetic ($af$) in zero field; and, unfortunately, such strong $af$ coupling occurs only at a single value of $t_N$ for fixed $t_F$.[15] To extract the parameters of interest from our simple model, we need to use a range of $t_F$ and $t_N$ values, and we need for each $t_F$ and $t_N$ pair an $AR_t$ that approximates well that for a true AP state. We have argued elsewhere[3,9,16] that the $AR_t$ values for our virgin, as-sputtered samples (a state designated by $H_0$) approximate well those of the AP state, so long as $t_N$ is large enough to magnetically decouple the F layers. This $H_0$ state was used to fix the Co/Cu and Py/Cu parameters for our analysis. For these decoupled F layers, the P state is attained when $H$ exceeds $H_s$, the field at which the $M_i$s of the F-layers saturate.

A positive feature of our three-component Co/Cu/Py/Cu multilayers is that there is a large difference in $H_s$ between sputtered Co ($H_s^{Co} \approx 200$ Oe) and Py ($H_s^{Py} \leqslant 10$ Oe). This naturally leads to a closely AP alignment of the $M_i$ for the Co and Py layers when $H$ (applied parallel to the layers) is taken from above $+ H_s^{Co}$ to just below $- H_s^{Py}$.

We recently showed[6,7] that $AR_t$(AP) and $AR_t$(P) for a set of Co/Cu/Py/Cu multilayers with $t_{Co}=3$ nm, $t_{Py}=8$ nm, and $t_{Cu}=20$ nm (large enough to magnetically decouple the Co and Py layers) could be reasonably well described by parameters previously determined from independent measurements of the $AR_t$s at $H_0$ and $H_s$ for Co/Cu and Py/Cu. These values of $t_{Co}$ and $t_{Py}$ were chosen to give nearly equal layer magnetizations (i.e., total magnetization $M \approx 0$ for AP Co and Py magnetization alignment) and to be comparable to those in the Co/Cu and Py/Cu multilayers from which the parameters

 0021-8979/96/79(8)/5811/5/$10.00 © 1996 American Institute of Physics 

TABLE I. Fitting parameters and independent measurements. Column 1: Constrained fits to Co/Cu and Py/Cu (Ref. 6). Column 2: Co/Cu and Py/Cu parameters adjusted to fit better the Co/Cu/Py/Cu data. Column 3: Independent measurements of $2AR_{Nb/Co}$ (Ref. 22) and $2AR_{Nb/Py}$ (Ref. 11) and of $\rho_{Co}$, $\rho_{Py}$, and $\rho_{Cu}$ from films sputtered with the Co/Cu and Py/Cu multilayers. Column 4: Independent measurements of $\rho_{Co}$, $\rho_{Py}$, and $\rho_{Cu}$ from films sputtered with the Co/Cu/Py/Cu multilayers.

| | "Best-fit" parameters | Adjusted Co/Cu and Py/Cu parameters | Indep. meas. Co/Cu;Py/Cu | Indep. meas. Co/Cu/Py/Cu |
|---|---|---|---|---|
| $2AR_{Nb/Co}$ (f$\Omega$m$^2$) | $6.1^{+1}_{-0.3}$ | | $6.1^{+1}_{-0.3}$ | |
| $2AR_{Nb/Py}$ (f$\Omega$m$^2$) | 7±1.5 | | 5.7–8.5 | |
| $\rho^*_{Co}$ (n$\Omega$m) | 76±5 | 81 | | |
| $\rho_{Co}=\rho^*_{Co}(1-\beta^2_{Co})$ | 60±9 | 60 | 60±10 | 51±3 |
| $\rho^*_{Py}$ (n$\Omega$m) | 164±20 | 159 | | |
| $\rho_{Py}=\rho^*_{Py}(1-\beta^2_{Py})$ | 123±40 | 111 | 137±30 | 111±8 |
| $\rho_{Cu}$ (n$\Omega$m) | 4.5±0.5 | 4.5 | 6±1 | 5.5±1 |
| $\beta_{Co}$ | 0.46±0.08 | 0.51 | | |
| $\gamma_{Co/Cu}$ | 0.75±0.05 | 0.76 | | |
| $\beta_{Py}$ | 0.50±0.16 | 0.55 | | |
| $\gamma_{Py/Cu}$ | 0.81±0.12 | 0.85 | | |
| $2AR^*_{Co/Cu}$ (f$\Omega$m$^2$) | 1.05±0.05 | 1.04 | | |
| $2AR_{Co/Cu}=2AR^*_{Co/Cu}(1-\gamma^2_{Co/Cu})$ | 0.46±0.10 | 0.43 | | |
| $2AR^*_{Py/Cu}$ (f$\Omega$m$^2$) | 1.00±0.08 | 1.08 | | |
| $2AR_{Py/Cu}=2AR^*_{Py/Cu}(1-\gamma^2_{Py/Cu})$ | 0.34±0.22 | 0.30 | | |

of interest were derived.[9–11] This agreement supported our argument that $AR_t(H_0)$ is close to $AR_t$(AP) for our Co/Cu and Py/Cu multilayers.

This agreement, however, was not perfect in that the difference $[AR_t(\mathrm{AP})-AR_t(\mathrm{P})]$ was about 20% larger than that predicted by the previously determined parameters. We argued that such a modest difference was reasonable, given that we had no adjustable parameters and also required all common parameters ($\rho_{Cu}$ appears in all three sets, and most other parameters in two) to be the same for data sets taken years apart. In fact, those parameters that could be independently measured ($\rho_{Cu}$, $\rho_{Co}$, and $\rho_{Py}$) were found to be slightly different (compare columns 3 and 4 of Table I).

In the present paper we further test the CPP predictability.

First, we extend the measurements of the Co/Cu/Py/Cu $AR_t$s in two directions: (a) to a Co-Py pair where $M\approx 0$ in the AP state, but $t_{Co}$ and $t_{Py}$ are twice as large as in the prior fits, and (b) to two Co-Py pairs where $t_{Co}$ and $t_{Py}$ are closer to those used in the prior fits, but $M\neq 0$ in the AP state. The unadjusted parameters continue to predict $AR_t$(AP) and $AR_t$(P) for the new samples reasonably well, but also underestimate $[AR_t(\mathrm{AP})-AR_t(\mathrm{P})]$ now by 25–35%.

Second, we examine whether, by modifying the Co/Cu and Py/Cu parameters within their uncertainties, we can improve our fits to the Co/Cu/Py/Cu data, without excessively weakening those to the original Co/Cu and Py/Cu data.

Third, to test the sensitivity of the MRs of the three-component systems to the N-metal component, we measure, for the first time, the MRs of a set of Co/Ag/Py/Ag multilayers. We find MRs larger than those for Co/Cu/Py/Cu with the same nominal layer thicknesses.

## II. SAMPLE PREPARATION

Our Co/Cu/Py/Cu multilayers were sputtered onto sapphire substrates in an ultrahigh-vacuum compatible, four-target system, using preparation conditions and procedures already described.[17] The base pressure before sputtering was $\leq 2\times 10^{-8}$ Torr; the sputtering pressure was held constant at $\approx$2.5 mTorr, and the sputtering rates were all $\approx$1 nm/s.[18] We used an *in situ* mask changing system[18] to fabricate the crossed-superconducting-strip geometry described elsewhere,[17] where the multilayer of interest is sandwiched between two $\approx$1.1-mm-wide, 300-nm-thick Nb strips, deposited at right angles to each other, that serve as both current and voltage leads. At the measuring temperature of 4.2 K, the Nb strips superconduct, becoming equipotential contacts, thereby ensuring that a uniform current passes through the overlap areas of the strips, $A\approx 1.25$ mm$^2$. To avoid proximity effects in the Cu layers, the first and last layers are Co at least 3 nm thick.[19] A sample thus consists of two Nb strips, the multilayer, and a "cap" Co layer just below the top Nb strip. In the CPP geometry, we measure the specific resistance $AR_t$, the overlap area $A$ of the Nb strips times the voltage across the sample divided by the current through it. The measuring current was held constant at 50 mA, and the resistances of the reported samples were all current independent. The measuring system was the same as that already described.[17]

## III. TWO-CURRENT MODEL

The two-current, series resistor model used here assumes that the electrons in the spin-up and spin-down channels are independent in that they do not flip their spins or mix. For $T=4.2$ K and N layers that are free of magnetic impurities and strong spin-orbit scatterers,[20] the assumed independence of the currents is a good approximation. For each spin channel the AR is a series sum of layer resistivities times layer thicknesses and the ARs for each interface. $AR_t$ is then just the parallel combination of the ARs for each channel.[3] Using the notation of Valet and Fert[4] for a simple F/N multilayer, we denote the F-metal resistivities as $\rho^{\uparrow}_F(\rho^{\downarrow}_F)$ for electron

spin parallel (antiparallel) to the local F-layer $M_i$, and F/N interface resistance as $R^{\uparrow}_{F/N}(R^{\downarrow}_{F/N})$. The Nb/F interface resistances and the N-layer resistivities are assumed to be spin independent. That is, $R^{\uparrow}_{Nb/F}=R^{\downarrow}_{Nb/F}=2R_{Nb/F}$, and $\rho^{\uparrow}_N=\rho^{\downarrow}_N=2\rho_N$. We make these definitions: $\rho^{\uparrow(\downarrow)}_F=2\rho^*_F[1-(+)\beta]=2\rho_F/[1+(-)\beta]$ and $R^{\uparrow(\downarrow)}_{F/N}=2R^*_{F/N}[1-(+)\gamma]=2R_{F/N}/[1+(-)\gamma]$. For a thick F film, $\rho_F$ would be its bulk resistivity. For the simple F/N multilayer, we obtain that the six fitting parameters of the two-current-model equations are the following: $2AR_{Nb/F}$, $\rho_N$, $\rho^*_F=\rho_F/(1-\beta^2)$, $AR^*_{F/N}=(AR_{F/N})/(1-\gamma^2)$, $\beta$, and $\gamma$. A constrained set of these parameters, derived from measurements on Co/Cu and Py/Cu samples, is presented in column 1 of Table I.[6]

For the more complex multilayer consisting of $N$[Co/Cu/Py/Cu] quadrilayers, the ARs for the up (+) and down (−) spin channels in the AP state are

$$AR^{AP(+)}=4AR_{Nb/Co}+4N\rho_{Cu}t_{Cu}+(N+1)\rho^{\uparrow}_{Co}t_{Co}+2NAR^{\uparrow}_{Co/Cu}+N\rho^{\downarrow}_{Py}t_{Py}+2NAR^{\downarrow}_{Py/Cu}, \quad (1)$$

$$AR^{AP(-)}=4AR_{Nb/Co}+4N\rho_{Cu}t_{Cu}+(N+1)\rho^{\downarrow}_{Co}t_{Co}+2NAR^{\downarrow}_{Co/Cu}+N\rho^{\uparrow}_{Py}t_{Py}+2NAR^{\uparrow}_{Py/Cu}. \quad (2)$$

$AR^{AP}_t$ is then obtained by adding $AR^{AP(+)}$ and $AR^{AP(-)}$ in parallel, and the dependence of $AR^{AP}_t$ on parameters $\rho^*_{Co}$, $\rho^*_{Py}$, $\beta_{Co}$, $\beta_{Py}$, $AR^*_{Co/Cu}$, $AR^*_{Py/Cu}$, $\gamma_{Co/Cu}$, and $\gamma_{Py/Cu}$ can be obtained by substituting in the above definitions. Here, unlike the simple F/N multilayer, we have $AR^{AP(+)}\neq AR^{AP(-)}$. For the P state, $AR^{P(+)}$ and $AR^{P(-)}$ will have only ↑ and ↓ terms, respectively, and then are combined in parallel to produce $AR^P_t$.

## IV. DATA AND ANALYSIS

For most of the samples in this paper, the Cu layer thickness is held fixed at $t_{Cu}=20$ nm, a value that our previous data indicate[3,7–9,16] should be large enough to magnetically decouple the Co and Py layers. As mentioned earlier, because $H^{Co}_s \gg H^{Py}_s$, an AP alignment of $M_i$ for the Co and Py layers should naturally occur when $H$ is taken from above $+H^{Co}_s$ to slightly less than $-H^{Py}_s$. This formation of the AP state is illustrated in Fig. 1(a) for a Co/Cu/Py/Cu sample with $t_{Co}$ and $t_{Py}$ chosen so that $M\approx 0$ for the AP state. Indeed as $H$ decreases toward −10 Oe, $M$ rapidly decreases to zero as the $M_i$'s of Py layers reverse. Thereafter $M$ decreases more slowly, as the Co layers reorient over a larger field range. The behavior of $M$ for this sample is very similar to that of the Co/Cu/Py/Cu sample shown in Fig. 2 of Ref. 6, where $t_{Co}$ and $t_{Py}$ were half those of the sample in Fig. 1. The main difference is that $H^{Co}_s$ is somewhat smaller in the present sample due to its thicker Co layers. Figure 1(b) shows that $AR_t$ rises rapidly over the same small field range (where $M$ drops sharply), reaches a peak value, and then falls slowly along with $M$. For AP alignment, we choose $AR_t$(AP) at the peak of the curve in Fig. 1(b). For P alignment of the Co and Py magnetizations, $AR_t$(P) is measured at $H > H^{Co}_s$.

Figures 2 and 3 show $AR_t$(AP) and $AR_t$(P) versus quadrilayer number $N$ for our published set[6,7] of Co/Cu/Py/Cu

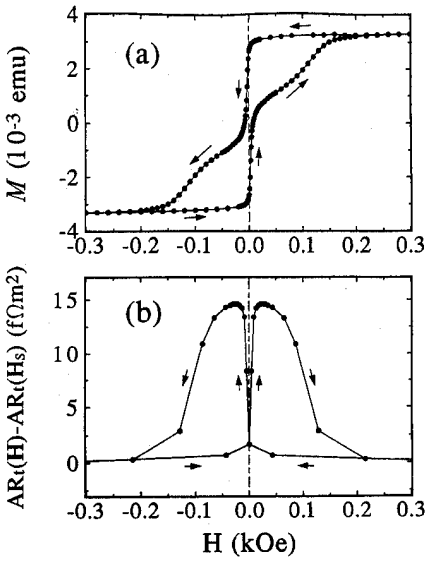



FIG. 1. (a) $M(H)$ vs $H$ for a [Co(6 nm)/Cu(20 nm)/Py(16 nm)/Cu(20 nm)]$_8$ multilayer. (b) $[AR_t(H)-AR_t(H_s)]$ vs $H$ for the same multilayer.

samples [Fig. 2(b)] and for three new sets of data [Figs. 2(a), 3(a), and 3(b)]. As shown in Fig. 2, changing $t_N$ to 10 or 40 nm (+ and × symbols, respectively) does not significantly change the data. The no-free-parameter predictions, $AR^{AP}_t$ and $AR^P_t$, from the independently derived parameters for Co/Cu and Py/Cu listed in column 1 of Table I, are shown as solid curves. The predictions fit all of the data reasonably well, but not perfectly. Figure 4 shows that for these column 1 parameters the quantity $[AR_t(AP)-AR_t(P)]/[AR^{AP}_t - AR^P_t]$, the ratio of the measured difference to the

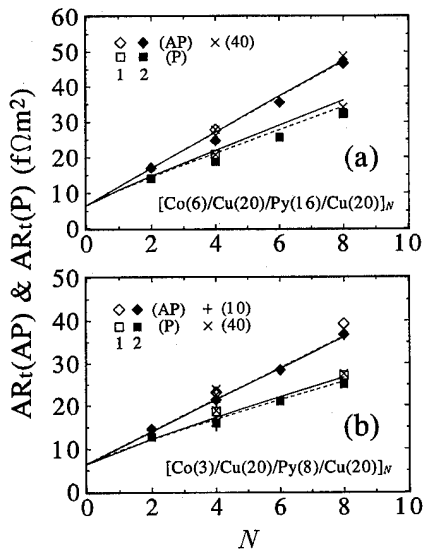



FIG. 2. $AR_t$(AP) and $AR_t$(P) vs quadrilayer number $N$ for multilayers of (a) [Co(6 nm)/Cu(20 nm)/Py(16 nm)/Cu(20 nm)]$_N$ and (b) [Co(3 nm)/Cu(20 nm)/Py(8 nm)/Cu(20 nm)]$_N$ with nearly equal magnetizations in the Co and Py layers. Open and filled symbols refer to samples made in differing sputtering runs. The + and × symbols are for $t_{Cu}=10$ and 40 nm, respectively. The solid curves are predicted from the independently determined parameters listed in column 1 of Table I. The dashed curves are determined by the parameters in column 2 of Table I.

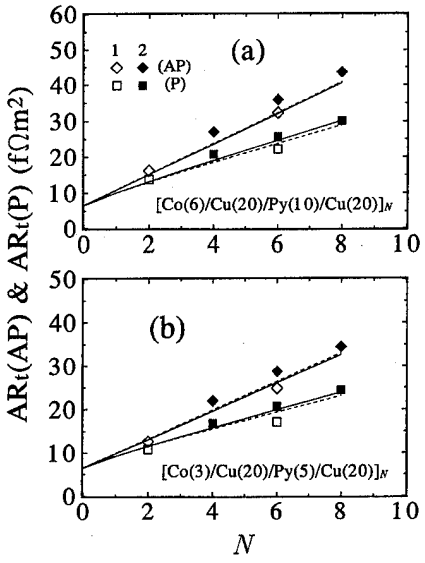



FIG. 3. $AR_t$(AP) and $AR_t$(P) vs quadrilayer number $N$ for multilayers of (a) [Co(6 nm)/Cu(20 nm)/Py(10 nm)/Cu(20 nm)]$_N$ and (b) [Co(3 nm)/Cu(20 nm)/Py(5 nm)/Cu(20 nm)]$_N$ with different magnetizations in the Co and Py layers. Open and filled symbols refer to samples made in different sputtering runs. The solid curves are predicted from the independently determined parameters listed in column 1 of Table I. The dashed curves are determined by the parameters in column 2.

predicted one, averages about 1.3 (open symbols), with the ratios for the newer samples [Figs. 4(a)–4(c)] being a bit larger than for the old ones [Fig. 4(d)].

This systematic discrepancy between measurement and prediction led us to ask how much we could improve the fits in Figs. 2–4, within the uncertainties of the parameters in

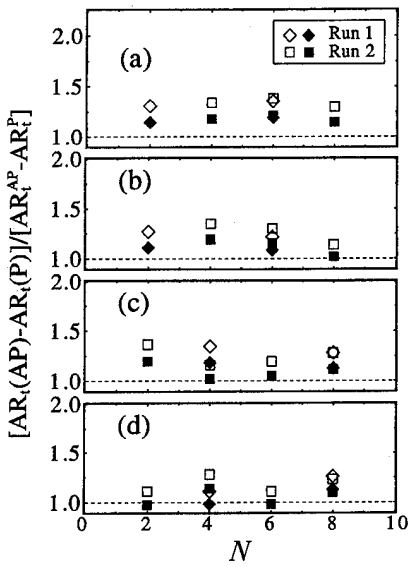



FIG. 4. $[AR_t(\mathrm{AP})-AR_t(\mathrm{P})]/[AR_t^{\mathrm{AP}}-AR_t^{\mathrm{P}}]$ vs $N$ for all four data sets. Open symbols are for $AR_t^{\mathrm{AP}}$ and $AR_t^{\mathrm{P}}$ values determined from the parameters in column 1 of Table I. Filled symbols are determined from column 2 of Table I. (a) [Co(6 nm)/Cu(20 nm)/Py(10 nm)/Cu(20 nm)]$_N$, (b) [Co(3 nm)/Cu(20 nm)/Py(5 nm)/Cu(20 nm)]$_N$, (c) [Co(6 nm)/Cu(20 nm)/Py(16 nm)/Cu(20 nm)]$_N$, and (d) [Co(3 nm)/Cu(20 nm)/Py(8 nm)/Cu(20 nm)]$_N$.

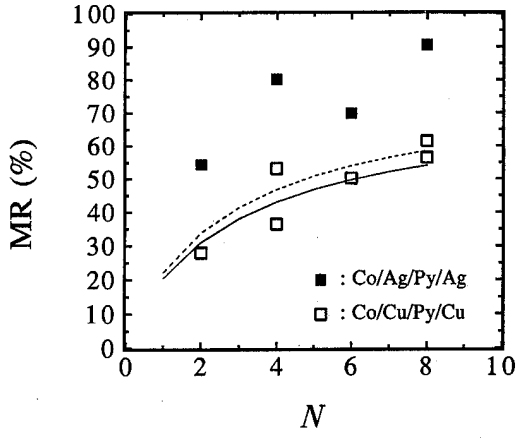



FIG. 5. Comparison of corrected MR vs $N$ for [Co(3 nm)/Ag(20 nm)/Py(8 nm)/Ag(20 nm)]$_N$ and [Co(3 nm)/Cu(20 nm)/Py(8 nm)/Cu(20 nm)]$_N$ multilayers. Solid curve is determined from parameters in column 2 of Table I. The dashed curve is produced by replacing Co/Cu parameters in column 2 by Co/Ag ones.

column 1 of Table I. In previous papers,[6,7] we noted that the ratios in Fig. 4(d) could be reduced to about 1.1 by increasing $\rho_{\mathrm{Py}}^{*}$, $\beta_{\mathrm{Co}}$, and $\beta_{\mathrm{Py}}$, well within their uncertainties, without excessively degrading the fits to the original Co/Cu and Py/Cu data. Those same parameters only reduced the average ratio for all of the samples in Fig. 4 to about 1.2. We thus searched for a set of parameters giving a better fit to all of our data, using the ratios in Fig. 4 (which emphasize the difference $[AR_t(\mathrm{AP})-AR_t(\mathrm{P})]$) as a guide for improving the fit to the Co/Cu/Py/Cu data. Such a set is given in column 2 of Table I. This new parameter set gives an average ratio for all four data sets that is now very close to 1.1 and is shown as filled symbols in Fig. 4. The fits of these column 2 parameters to the Co/Cu/Py/Cu $AR_t$s are shown as dashed curves in Fig. 2 and 3 and are better (smaller total $\chi^2$) than those for the column 1 parameters. The parameters of column 2 lie within—usually well within—the uncertainties of the nonadjusted ones of columns 1, and only modestly degrade the fits to the original Co/Cu and Py/Cu data.[21]

Lastly, we recently started to examine the behavior of Co/Ag/Py/Ag multilayers with layer thicknesses similar to those for the Co/Cu/Py/Cu multilayers described above. We will show elsewhere that the $M_s$ and $AR_t$s for these multilayers look very similar to those in Figs. 1 and 2.[21] Here, we focus upon the relative MRs of the two different systems. For this purpose, we compare the corrected multilayer MRs.

$$\mathrm{MR}\% = [AR_t(\mathrm{AP})-AR_t(\mathrm{P})]/[AR_t(\mathrm{P})-6.1\ \mathrm{f\Omega m^2}]. \tag{3}$$

In the denominator, the two Nb/Co interface resistances[22] $\sim$6.1 f$\Omega$m$^2$ have been subtracted from $AR_t$(P) to give the AR due to the multilayer alone (i.e., without the superconducting contact resistance). As shown in Fig. 5, the MRs for Co/Ag/Py/Ag are considerably larger than those for Co/Cu/Py/Cu, even though the nominal layer thicknesses are identical. The solid curve in Fig. 5 shows the computed MR for the adjusted parameters in column 2 of Table I. The dashed curve is generated by combining the column 2 parameters for

Py/Cu with the previously determined Co/Ag parameters.[3,18] The dashed curve still clearly falls below the Co/Ag/Py/Ag data. This disagreement implies that the Py/Ag parameters must be noticeably different from those for Py/Cu.

## V. SUMMARY AND CONCLUSIONS

We have shown that the CPP specific resistance, $AR_t$, of Co/Cu/Py/Cu multilayers with four different pairs of Py and Co thicknesses can all be fit reasonably well with parameters obtained with no adjustment from independent measurements on Py/Cu and Co/Cu multilayers. Even the more challenging difference $[AR_t(\mathrm{AP})-AR_t(\mathrm{P})]$ is correctly given to within 20–35%. We have, thus, shown that the CPP-MR of a three-component system is fairly well predictable from parameters for the two-component multilayers of which it is composed. We have found also that the fit to the Co/Cu/Py/Cu data can be made better by modifying the Co/Cu and Py/Cu parameters well within their respective uncertainties, without substantially weakening the fits to the original Co/Cu and Py/Cu data. We conclude that the Co/Cu/Py/Cu, Co/Cu, and Py/Cu data are mutually consistent to within their uncertainties and reproducibilities. Lastly, we have shown that a set of Co/Ag/Py/Ag multilayers gives significantly larger MRs than those for Co/Cu/Py/Cu multilayers with identical nominal layer thicknesses, which leads us to predict that the as yet unknown CPP-MRs for uncoupled Py/Ag multilayers will be larger than those for Py/Cu.

## ACKNOWLEDGMENTS

This work was supported in part by the National Science Foundation under Award No. DMR-9423795 and through the MRSEC Program under Award No. DMR-9400417, by the MSU Center for Fundamental Materials Research, and by Ford Research Laboratory.

[1] L. M. Falicov, D. T. Pierce, S. D. Bader, R. Gronsky, K. B. Hathaway, H. J. Hopster, D. N. Lambeth, S. S. P. Parkin, G. Prinz, M. Salamon, I. K. Schuller, and R. H. Victora, J. Mater. Res. **5**, 1299 (1990).
[2] M. N. Baibich, J. M. Broto, A. Fert, F. Nguyen Van Dau, F. Petroff, P. Etienne, G. Creuzet, A. Friederich, and J. Chazelas, Phys. Rev. Lett. **61**, 2472 (1988).
[3] S.-F. Lee, W. P. Pratt, Jr., Q. Yang, P. Holody, R. Loloee, P. A. Schroeder, and J. Bass, J. Magn. Magn. Mater. **118**, L1 (1993).
[4] T. Valet and A. Fert, J. Magn. Magn. Mater. **121**, 378 (1993); Phys. Rev. B **48**, 7099 (1993).
[5] See, e.g., P. M. Levy, *Solid State Physics Series*, Vol. 47, edited by H. Ehrenreich and D. Turnbull (Academic, New York, 1994), p. 367, and references therein.
[6] Q. Yang, P. Holody, R. Loloee, L. L. Henry, W. P. Pratt, Jr., P. A. Schroeder, and J. Bass, Phys. Rev. B **51**, 3226 (1995).
[7] J. Bass, P. A. Schroeder, W. P. Pratt, Jr., S.-F. Lee, Q. Yang, P. Holody, L. L. Henry, and R. Loloee, Mater. Sci. Eng. B **31**, 77 (1995).
[8] W. P. Pratt, Jr., S.-F. Lee, J. M. Slaughter, R. Loloee, P. A. Schroeder, and J. Bass, Phys. Rev. Lett. **66**, 3060 (1991).
[9] P. A. Schroeder, J. Bass, P. Holody, S.-F. Lee, R. Loloee, W. P. Pratt, Jr., and Q. Yang, NATO ASI Series "Magnetism and Structure in Systems of Reduced Dimension," Vol. 309 of *NATO Advanced Study Institute, Series B: Physics*, edited by R. F. C. Farrow, B. Dieny, M. Donath, A. Fert, and B. D. Hermsmeier (Plenum, New York, 1993), p. 129.
[10] P. A. Schroeder, J. Bass, P. Holody, S.-F. Lee, R. Loloee, W. P. Pratt, Jr., and Q. Yang, in *Magnetic Ultrathin Films: Multilayers and Surfaces/ Interfaces and Characterization*, edited by B. T. Jonker, S. A. Chambers, R. F. C. Farrow, C. Chappet, R. Clarke, W. J. M. de Jonge, T. Egami, P. Grunberg, K. M. Krishnan, E. E. Marinero, C. Rau, and S. Tsunashima, MRS Symposium Proceedings No. 313 (Materials Research Society, Pittsburgh, 1993), p. 47.
[11] P. Holody, Q. Yang, S.-F. Lee, R. Loloee, W. P. Pratt, Jr., P. A. Schroeder, and J. Bass (unpublished).
[12] W. P. Pratt, Jr., S.-F. Lee, P. Holody, Q. Yang, R. Loloee, P. A. Schroeder, and J. Bass, J. Appl. Phys. **73**, 5326 (1993); J. Magn. Magn. Mater. **126**, 406 (1993).
[13] S. Zhang and P. M. Levy, J. Appl. Phys. **69**, 4786 (1991).
[14] H. E. Camblong, S. Zhang, and P. M. Levy, J. Appl. Phys. **75**, 6906 (1994); Phys. Rev. B **47**, 4735 (1993).
[15] See, e.g., S. S. P. Parkin, N. More, and K. P. Roche, Phys. Rev. Lett. **64**, 2304 (1990); D. H. Mosca, F. Petroff, A. Fert, P. A. Schroeder, W. P. Pratt, Jr., and R. Loloee, J. Magn. Magn. Mater. **94**, L1 (1991).
[16] P. A. Schroeder, S.-F. Lee, P. Holody, R. Loloee, Q. Yang, W. P. Pratt, Jr., and J. Bass, J. Appl. Phys. **76**, 6610 (1994).
[17] J. M. Slaughter, W. P. Pratt, Jr., and P. A. Schroeder, Rev. Sci. Instrum. **60**, 127 (1989).
[18] S.-F. Lee, Q. Yang, P. Holody, R. Loloee, J. H. Hetherington, S. Mahmood, B. Ikegami, K. Vigen, L. L. Henry, P. A. Schroeder, W. P. Pratt, Jr., and J. Bass, Phys. Rev. B **52**, 15426 (1995).
[19] J. M. Slaughter, J. Bass, W. P. Pratt, Jr., P. A. Schroeder, and H. Sato, Proc. of LT-18 [Jpn. J. of Appl. Phys. **26**, Suppl. 26-3, 1451 (1987)].
[20] Q. Yang, P. Holody, S.-F. Lee, L. L. Henry, R. Loloee, P. A. Schroeder, W. P. Pratt, Jr., and J. Bass, Phys. Rev. Lett. **72**, 3274 (1994).
[21] W.-C. Chiang, Q. Yang, P. Holody, L. L. Henry, R. Loloee, W. P. Pratt, Jr., P. A. Schroeder, and J. Bass (unpublished).
[22] C. Fierz, S.-F. Lee, W. P. Pratt, Jr., P. A. Schroeder, and J. Bass, J. Phys.: Cond. Matter **2**, 9701 (1990).

# The role of impurity scattering in Co/Cu (111) M.B.E. multilayers (abstract)

K. P. Wellock and B. J. Hickey
*The Department of Physics, The University of Leeds, Leeds LS2 9JT, United Kingdom*

The origin of spin-dependent scattering (sds) within magnetic/nonmagnetic systems is a controversial issue which has attracted much attention in recent years. There is now a consensus of opinion that sds is necessary for the giant magnetoresistance (GMR) and most work suggests that this scattering occurs at the interface, but the details have yet to be discovered. Numerous studies have been performed placing impurities within the multilayer and in nearly all cases a reduction in MR is observed. The only exceptions to this are the cases where magnetic impurities are used. We have observed the first enhancement of MR for the Co/Cu system using nonmagnetic impurities. In the case of a simple trilayer system up to an eightfold increase in MR is observed while for a multilayer system up to 40% increase is recorded. Impurities have been introduced during sample growth in a controlled manner using a shutter arrangement such that a direct comparison of impurity-doped and an undoped sample can be made. In previous impurity studies changes in coupling have given rise to confusing results. In order to avoid this we have used relatively thick Cu spacer layers and very small levels of impurities so that no magnetic coupling changes are induced by doping. All samples were characterized by x-ray diffraction and *in situ* RHEED where we found no evidence of structural changes induced by the Au impurities. We discuss these results in the light of current theories of spin-dependent scattering. © *1996 American Institute of Physics.*
[S0021-8979(96)60808-7]

 0021-8979/96/79(8)/5816/1/$10.00 © 1996 American Institute of Physics

# Giant magnetoresistance multilayers of high thermal stability with thicker magnetic layers

S. A. Hossain, B. H. Pirkle, J. Yang, and M. R. Parker[a)]
*The University of Alabama, MINT/MRSEC Center, P. O. Box 870209, Tuscaloosa, Alabama 35487*

The problem of poor thermal stability in NiFeCo/Cu multilayers can be resolved by utilizing thicker magnetic layers than those giving optimum giant magnetoresistance (GMR), in the as-deposited state. This type of structure exhibits very little GMR in the as-deposited state, but upon appropriate post-deposition anneal, produces huge improvements in GMR magnitude and sensitivity. The described technique provides an improvement necessary for retaining the magnetic properties of the multilayers at temperatures that would be encountered in the fabrication and operation of GMR field sensors. © *1996 American Institute of Physics.* [S0021-8979(96)54608-8]

## I. INTRODUCTION

A variety of multilayers with large giant magnetoresistance (GMR) values and low saturation fields have been made in these laboratories.[1,2] The poor thermal stability of these structures has, however, been a critical issue in our earlier work,[2] as well as in that of other groups.[3] High-temperature anneal causes serious degradation of the GMR magnitude and field sensitivity. GMR multilayers have been identified as long-term candidates for ultrahigh density heads in the data storage industry. Fabrication of any field-sensor microdevice would require thermal processing of materials at temperatures of 200 °C or thereabouts. No practical technique has been proposed until now to deal with this critical issue. Thermally induced reduction of GMR has been attributed to an enhanced interdiffusion at the interfaces of magnetic/nonmagnetic structures. Reasonable thermal stability has been identified in NiFeCo/Cu/Co/Cu structures[3] with, however, GMR properties worse than those of conventional NiFeCo/Cu structures. In the present study, a methodology is introduced for enhancement of the thermal characteristics of GMR multilayer films. The Cu spacer thickness is first optimized in the as-deposited state at approximately 23 Å. A corresponding optimization of magnetic layer thickness is then determined (~21 Å). Multilayers sputtered with ~21 Å magnetic layer thickness or less show good as-deposited GMR characteristics (GMR magnitude and field sensitivity), and multilayers with significantly thicker magnetic layers (>23 Å) show very poor (<2%) GMR characteristics, being dominated in the as-deposited state by positive exchange coupling. As expected, samples with NiFeCo layers of thickness <21 Å show a decrease in the GMR properties upon high-temperature anneal (>200 °C). By contrast, high temperature anneal of the samples with significantly thicker NiFeCo layers produces a marked improvement in GMR properties. This improvement appears to originate from a transformation to a minimum energy configuration in the antiferromagnetic (AFM) state at zero external field, which is induced by the high-temperature anneal. Subsequent annealing of these samples does not effect their GMR characteristics significantly. This technique, therefore, provides GMR multilayers with excellent thermal stability. The underlying mechanism(s) causing this thermal stability enhancement remain(s) unclear. It is obviously tempting to attribute the behavior described in the following sections to discontinuous multilayers of the sort normally associated with the NiFe/Ag system.[4] The experimental evidence discussing this issue is described below.

## II. EXPERIMENT

Preparation conditions and experimental analysis of NiFeCo/Cu multilayers have been described in detail previously.[1,2] The GMR field sensitivity is defined as $S$=GMR%/FWHM of GMR field profile).

Six-bilayer (bl) structures with optimum Cu spacer thickness and various magnetic layer thicknesses (from 17 through 37 Å) have been investigated. In the as-deposited state, an optimum GMR effect occurs for a magnetic layer thickness around 21 Å. Multilayers with magnetic layers thinner than ~21 Å exhibit excellent GMR characteristics (~9% GMR, ~0.11%/Oe sensitivity for 10bl samples and ~8% GMR, ~0.22%/Oe sensitivity for 6bl) in the as-deposited state. An abrupt decrease in the as-deposited GMR magnitude and sensitivity is observed for magnetic layers thicker than this optimum. This observation is consistent with magnetization loop data, which indicates AFM and FM coupling in this sample and thicker magnetic layer samples,

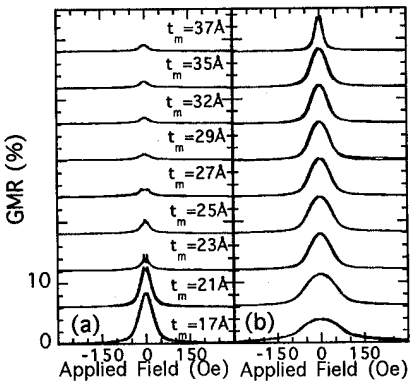



FIG. 1. GMR loops for (a) as-deposited and (b) annealed (300 °C) samples as a function of the NiFeCo layer thickness.

[a)]Corresponding author: Department of Electrical Engineering, 317 Houser, P. O. Box 870286, The University of Alabama, Tuscaloosa, AL 35487-0286; Electronic mail: mparker@coe.eng.ua.edu

 0021-8979/96/79(8)/5817/3/$10.00 © 1996 American Institute of Physics 

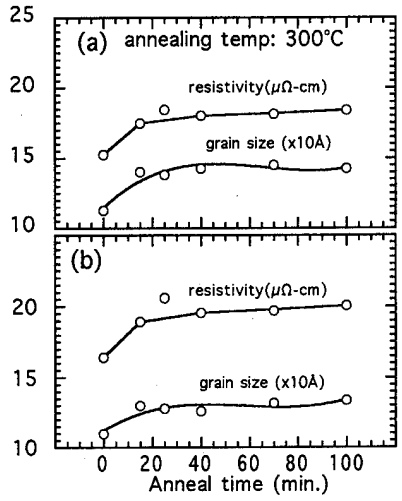



FIG. 2. The change in the grain size and resistivity as a function of annealing time for NiFeCo/Cu ML samples with (a) 17 Å and (b) 26-Å-thick magnetic layers.

respectively. High-temperature anneal (300 °C) rapidly degrades the above-mentioned GMR characteristics in samples with magnetic layer thicknesses of ~21 Å or less. By contrast, samples with magnetic layers of thicknesses >23 Å, with insignificant GMR characteristics in the as-deposited state [Fig. 1(a)], show a drastic improvement [Fig. 1(b)] upon annealing. Annealing at 300 °C also results in an increase in grain size and resistivity for all samples (Fig. 2). A linear extrapolation of the inverse of resistance versus the magnetic layer thickness is plotted in Fig. 3. The resistivity of the Cu spacer layers and the interfaces has been estimated from the intercepts at zero magnetic layer thickness. Our data indicates an approximately 26% increase in this resistivity after annealing. The low-angle x-ray diffraction (LXRD) data shows, following anneal, about a 5% reduction in effective bilayer thickness as well as a small change of the interface (see Fig. 4). This 5% thickness reduction does not equate directly to the 26% change in the resistivity. The additional increase in resistivity must therefore be attributed to other effects. Summary plots of GMR in the as-deposited and annealed states are given in Fig. 5 for a set of ten 6bl samples. Thin NiFeCo samples show increased AFM coupling with no significant uniaxial anisotropy in the annealed

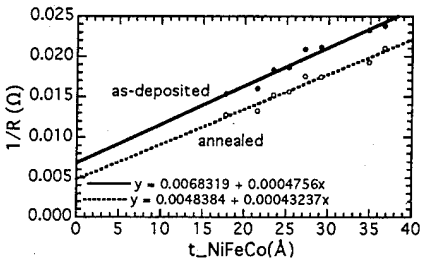



FIG. 3. Linear fit to the inverse of the resistance as a function of the magnetic layer thickness.

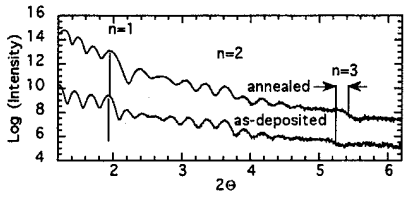



FIG. 4. As-deposited and annealed low-angle x-ray diffraction scans for a multilayer sample with 25-Å-thick NiFeCo layers.

state. Ferromagnetic resonance (FMR) data indicates a decrease in anisotropy upon annealing for the thick samples. An indication of a small decrease in magnetization is also observed, which is consistent with vibrating sample magnetometer (VSM) data.

## III. ANALYSIS

One method for calculating the bilinear and biquadratic exchange fields $H_1$ and $H_2$ has been proposed earlier.[5] In our present study, we estimated the exchange fields, and hence the exchange constants $J_1$ and $J_2$ as a function of magnetic layer thickness (given in Table I) by a slightly different approach, as shown below.

From the experimentally determined full width half maxima (FWHM) of the GMR field profiles, the transverse (hard axis) and parallel (easy axis) fields can be related to $H_1$ and $H_k$ conveniently. These fields are given[6] by the following equations:

$$H_{\perp 50}=\frac{1}{\sqrt{2}}(H_1+H_k) \tag{1a}$$

and

$$H_{\parallel 50}=\frac{1}{\sqrt{2}}(H_1-H_k), \tag{1b}$$

where

$$H_1=\frac{2(2N-1)}{N}\left(\frac{J_1}{M_s t}\right). \tag{2}$$

$H_{\perp 50}$ and $H_{\parallel 50}$ are, respectively, the FWHM field values in the hard and easy directions, $2N$ is the total number of magnetic layers, $J_1$ is the bilinear exchange constant, $M_s$ is the saturation magnetization, and $t$ is the magnetic layer thick-

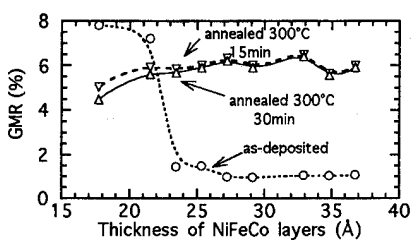



FIG. 5. GMR in as-deposited and annealed states as a function of the magnetic layer thickness.

TABLE I. Exchange constants $J_1$, $J_2$, and anisotropy field $H_k$.

| NiFeCo thickness (Å) | $H_1$ (Oe) | $H_2$ (Oe) | $H_k$ d(Oe) | $J_1$ ($\mu$J/m$^2$) | $J_2$ ($\mu$J/m$^2$) |
|---|---|---|---|---|---|
| 18 | 109.6 | 11.4 | 10.6 | 5.73 | 0.60 |
| 21 | 77.8 | 8.1 | 7.1 | 4.74 | 0.49 |
| 23 | 55.9 | 7.5 | 6.4 | 3.73 | 0.50 |
| 25 | 56.2 | 8.3 | 7.4 | 4.08 | 0.60 |
| 27 | 58.0 | 8.0 | 5.7 | 4.55 | 0.62 |
| 33 | 40.3 | 5.5 | 7.8 | 3.86 | 0.53 |
| 35 | 38.2 | 5.3 | 5.7 | 3.88 | 0.54 |

ness. $H_k(=2K_u/M_s)$ is the field induced anisotropy field, where $K_u$ is the uniaxial anisotropy constant. Clearly, it follows from Eqs. (1a), (1b), and (2) that $\sqrt{2}H_{\perp 50,\parallel 50}$ vs $1/t$ should be a linear curve of positive slope. From Eqs. (1a) and (1b) we can determine $H_1$ and $H_k$ as follows:

$$H_1=\frac{1}{\sqrt{2}}(H_{\perp 50}+H_{\parallel 50}) \tag{3}$$

and

$$H_k=\frac{1}{\sqrt{2}}(H_{\perp 50}-H_{\parallel 50}). \tag{4}$$

Now, $J_1$ and $H_k$ can be evaluated by inserting experimental data for $H_{\perp 50,\parallel 50}$ into Eq. (2), (3), and (4). Table I lists $J_1$ and $H_k$ values after annealing for various magnetic layer thicknesses and $J_2$ is included for completeness. The data in Table I indicates that the $J_1$, $J_2$ values are effectively constant for magnetic layer thicknesses from 23 to 35 Å. The linear dependence of $H_{\parallel 50}$ and $H_{\perp 50}$ on the inverse of magnetic layer thickness (Fig. 6) also supports the conclusion that interlayer interactions remain constant as the thickness increases. A small reduction in the thickness of the bilayer stack was observed. $H_{\parallel 50}$ and $H_{\perp 50}$ decrease in accordance with the model of Ref. 5 accordingly for an increase in GMR sensitivity given that GMR magnitude is approximately constant. Calculation of $J_1$ as described in Eq. (2) is based on a continuous-layer model. This model predicts that $H_{\parallel 50}$ and $H_{\perp 50}$ should increase with the increase in inverse of the magnetic layer thickness. Our data in Fig. 6 show reasonable agreement with the model (using average values of $J_1$ and $H_k$ from Table I for thicknesses in the range 23–35 Å) and, therefore, explains the decrease in saturation field with increasing magnetic layer thickness.

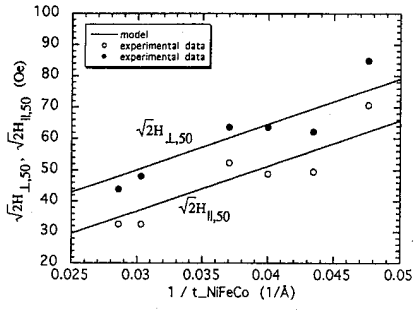



FIG. 6. $\sqrt{2}H_{\perp 50}$ and $\sqrt{2}H_{\parallel 50}$ as a function of the inverse of the magnetic layer thickness.

## IV. RESULTS

We have developed a methodology to improve the thermal stability of magnetoresistive NiFeCo/Cu multilayers. Multilayers with "optimum" or thinner magnetic layers decrease in both GMR magnitude and field sensitivity upon high-temperature anneal. Samples with thicker magnetic layers (>23 Å) exhibit a huge improvement in GMR characteristics upon post-deposition anneal with enhanced thermal stability.

After much experimentation, the reasons for the dramatic post-anneal effects of Fig. 1 remain unclear. On one hand, the magnetization, as determined from FMR and from vibrating sample magnetometry, appears to decline following anneal, suggesting, possibly, fragmentation of the magnetic layers. Conversely, however, the low-angle x-ray patterns of these MLs before and after anneal (see Fig. 4) show little evidence of this. Additionally, the decrease of GMR saturation field (and, concomitantly, the magnitudes of $H_{\parallel 50}$, $H_{\perp 50}$) with increasing magnetic layer thickness seems consistent with theoretical expectations[5] for a continuous-layer GMR system. GMR enhancement, increase in resistivity, and grain growth all appear independent of the number of bilayers; similar enhancement is seen in 10- and 20-bilayer stacks. We conclude that the magnetic and spacer materials do not necessarily have to be immiscible to produce multilayers of high thermal stability.

## ACKNOWLEDGMENTS

This work was supported in part by a grant from ATP administered by the National Storage Industry Consortium and by NSF-MRSEC Grant No. DMR-9301648. We would like to thank Professor Chester Alexander for his help with FMR measurements and Dr. Mark Kief and Dr. Timothy Klemmer for helpful discussions.

[1] M. R. Parker, S. Hossain, D. Seale, J. A. Barnard, M. Tan, and H. Fujiwara, IEEE Trans. Magn. **MAG-30**, 358 (1994).
[2] S. Hossain, D. Seale, G. Qiu, J. Jarratt, J. A. Barnard, H. Fujiwara, and M. R. Parker, J. Appl. Phys. **75**, 7067 (1994).
[3] M. Satomi and H. Sakakima, J. Magn. Magn. Mater. **126**, 504 (1993).
[4] T. L. Hylton, K. R. Coffey, M. A. Parker, and J. K. Howard, Science **261**, 1021 (1993).
[5] H. Fujiwara and M. R. Parker, J. Magn. Magn. Mater. **135**, L23 (1994).
[6] N. Smith (private communication).

# Relaxation in NiFe/Ag giant magnetoresistive devices

R. W. Cross and A. B. Kos
*Electromagnetic Technology Division, National Institute of Standards and Technology, Boulder, Colorado 80303*

Giant magnetoresistance was measured as a function of time and device size for patterned NiFe/Ag multilayer films. The sputtered NiFe/Ag multilayers were postannealed at 340 °C for 5 min in order to produce a change in resistivity $\Delta\rho/\rho$ of 5% in a saturating field of 4 kA/m (50 Oe). The microstructure of these films is believed to be discontinuous due to Ag bridging through the NiFe grain boundaries after the anneal. The films were fabricated into rectangular stripes with Au current lead, and then exposed to a magnetic field pulse to measure the time response of the resistance, characterized by a time constant $\tau$, from the relation $\Delta R(t)=\Delta R_0 e^{-t/\tau}$. An apparatus was developed to produce a magnetic field pulse up to 8 kA/m (100 Oe) with a turn-on/off time constant of 10 $\mu$s. The response of the NiFe/Ag devices saturated quickly with the turn-on step with a time constant nearly equal to that of the field pulse. The response to the turn-off step, however, had a time constant of nearly 300 $\mu$s. When the field is first applied, the torque on the magnetic moments quickly aligns the magnetization. When the field is shut off, however, the torque due to the field drops to 0, so interacting magnetostatic fields from the grains and thermal energy dominate the relaxation process. The average time constant depends on the device size and the applied current density. Relaxation may be detrimental for using this type of material for read heads where very high data rates are required. [S0021-8979(96)54708-4]

## I. INTRODUCTION

Research in giant magnetoresistance (GMR) materials is moving toward device applications. Device-level characterization of different GMR systems is becoming more important with the goal of achieving the largest GMR with the smallest saturation field in micrometer size devices. The NiFe/Ag system is formed by sputtering bilayers of NiFe/Ag and then postannealing the films until the Ag diffuses into the NiFe grain boundaries and separates the grains to form a discontinuous structure. We have reported on the transport properties of micrometer-size discontinuous multilayer devices where noise, size, and self-field effects become important.[1,2] These effects may limit the usefulness of discontinuous GMR materials in applications like magnetic recording where very small devices are needed.

Relaxation in discontinuous films plays an important role in device performance as well. We report results of relaxation measurements on NiFe/Ag films fabricated into devices with micrometer dimensions. Relaxation rates are measured by exposing a device to a very fast turn-on/off field pulse while monitoring the response versus time. Long relaxation rates are observed in annealed NiFe/Ag devices due to the discontinuous structure compared to continuous films of NiFe. We find that the device response is very fast in large saturating fields, but long time constants are observed when the saturating field is removed. In addition, discrete structure and nonlogarithmic behavior are observed in the time response for submicrometer devices due to discrete switching of magnetic grains.

## II. MATERIALS

The NiFe/Ag discontinuous system is interesting from a device point of view because of its low saturation field. Most GMR systems with large changes in resistivity $\Delta\rho/\rho$ of 50%–90%, like Fe/Cr or Co/Cu multilayers, have very large saturation fields, typically 800 kA/m (10 000 Oe).[3] This is not useful for recording applications, where the field from the bits is typically 0.8–8 kA/m (10–100 Oe) at the sensor. One requirement for GMR is antiparallel alignment of the magnetization between neighboring domains. A way of achieving this is to antiferromagnetically (AF) couple the layers using exchange interactions.[4] The layers can be engineered to obtain the strongest AF coupling, which in turn produces the largest GMR. However, to saturate the material, it is necessary to overcome this large exchange force, requiring very large saturation fields. The lesson is that the largest GMR is not necessarily the best for some applications like read heads, where high sensitivity is needed at low fields. High sensitivity at low field can be achieved by setting the AF coupling to a weaker level, or by using some other form of coupling to obtain antiparallel alignment. In the NiFe/Ag system, the coupling is magnetostatic, which is accomplished by annealing the multilayer into a discontinuous structure. This system has exhibited some of the highest sensitivities at low fields.[5]

The NiFe/Ag films were made following the original prescription outlined in Ref. 5. The films consisted of seven sputtered bilayers with a 4.4 nm layer of Ag and a 2 nm layer of $Ni_{82}Fe_{18}$. The films were annealed at 340 °C for 5 min to obtain a $\Delta R/R$ of 4.5%. The thickness of the Ag layer is such that the layers are not exchange-coupled. The microstructure of similar films has been studied in detail by Parker *et al.*[6] using scanning electron microscopy and cross-sectional transmission electron microscopy, and they determined that Ag bridges form during the anneal through the NiFe grain boundaries. This is important in the NiFe/Ag multilayers because magnetic poles can form along the edges of the grains and couple by magnetostatic fields to grains in adjacent layers, producing antiparallel alignment.[7] We have worked on simulating the response using a micromagnetic model of the magnetostatic interactions of a matrix of NiFe grains in Ag,

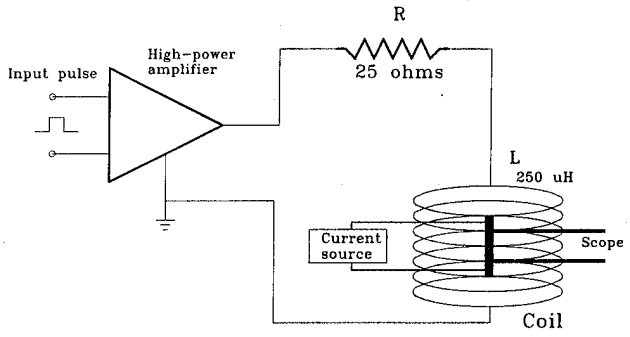



FIG. 1. Schematic diagram of field-pulse apparatus. The time constant of the field coil is determined by the inductance $L$ and resistance $R$, and is 10 $\mu$s. The maximum field amplitude of the pulse is 8 kA/m (100 Oe).

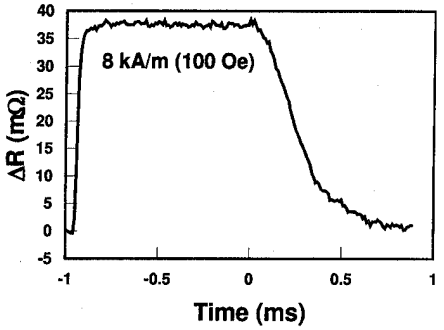



FIG. 2. Time response to the field pulse for a 4×4 $\mu$m (active area) NiFe/Ag device. The turn-on time constant of the device is nearly the same as that of the field pulse. However, the turn-off time constant is approximately 300 $\mu$s.

and found some agreement with experimental results.[8]

The films were fabricated into devices with Au current leads. Track widths, defined as the distance between the Au leads, varied from 1 to 16 $\mu$m. The total width of the stripe was typically much longer than the track width. The height of the stripes varied from 0.5 to 16 $\mu$m. The active area of the device is defined as the stripe height times the track width.

## III. RELAXATION

The frequency response of NiFe read heads is generally limited by eddy currents, which reduce the permeability of the NiFe. The strength of the eddy currents depends on the size, thickness, and conductivity of the element as well as the strength and frequency of the external field. Presently, the permeability of NiFe read heads remains high up to 100 MHz, which is adequate for recording applications. The intrinsic limitation of NiFe devices is related to the relaxation time of the ferromagnetically coupled spin system and is on the order of $10^{-9}$ s, suggesting that these devices could be used up to 1 GHz. However, for the NiFe/Ag discontinuous GMR devices, the granular structure leads to other relaxation effects. In this case, the magnetostatic fields from the magnetic grains interact, causing the magnetization distribution to thermally relax into a metastable configuration. When one grain switches, it changes the field distribution and the relaxation conditions of the other grains, which in turn may switch, and the process continues until equilibrium is reached.

To measure the frequency response of the GMR devices, we constructed an apparatus that can supply a longitudinal field pulse up to 8 kA/m (100 Oe) with a turn-on/off time constant of 10 $\mu$s. The apparatus is shown in Fig. 1. The time constant of the field pulse is determined by $L/R$, making it necessary to use a small inductance $L$ and a large resistance $R$. However, to get enough field from the coil, high voltage is needed to produce a large current. We use a low duty cycle for the pulse (one pulse per second) so that coil heating is kept small. A GMR device is placed at the center of the coil and exposed to the longitudinal field pulse while the output of the sensor is monitored using a high-frequency 16 bit digital oscilloscope. To remove any background signal due to the small inductance of the current leads and the sensor, two measurements are made, one with current applied to the device and the other without. There are typically 20 curves taken and averaged to improve the signal-to-noise level.

To test the system, we measured a continuous NiFe device and found that the output follows the applied field pulse with a time constant of 10 $\mu$s. The relaxation is described by a time constant $\tau$ in the relation $\Delta R(t)=\Delta R_0 e^{-t/\tau}$, where $\Delta R(t)$ is the change in resistance versus time and $\Delta R_0$ is the characteristic GMR of the device.

The response of a 4×4 $\mu$m (active area) NiFe/Ag GMR device is shown in Fig. 2. The turn-on time of the response nearly coincides with that of the applied field pulse. The output remains flat until the turn-off step (see Fig. 2) at time $t=0$, where a decay time constant of 300 $\mu$s is observed. The fast turn-on time of the device is due to the large torque exerted on the magnetic moments of the grains from the applied longitudinal field, which is large enough to saturate the magnetization. For the turn-off step, however, the torque from the applied field suddenly goes to zero and all of the magnetic grains thermally relax to the zero-field condition. The interacting magnetostatic fields from the magnetic grains affect this process (this is not the case for continuous NiFe devices) because the field emanating from a given grain changes the relaxation conditions of neighboring grains. Long time constants may limit the usefulness of this type of material in applications like magnetic recording.

Device size also affects the GMR response to the field pulse, as shown in Fig. 3 for a 0.7×1 $\mu$m device. In Fig. 3(a), the response is shown for a slowly changing field cycle. The main things to note are the structure and hysteresis in the response, which are due to the discontinuous microstructure of the film. Discrete switching of magnetic grains or clusters produce jumps in the response.[1,2] The 0.7×1 $\mu$m device was then exposed to the field pulse and the output is shown in Fig. 3(b). The turn-off response is not an exponential decay as observed for the larger devices, but rather has steps or bends. The steps are not as sharp as they might be due to the curve averaging. Note that the output voltage does not return to the initial value in the time period shown in the figure (eventually it does relax back to $\Delta R=0$). Single-shot measurements would show more distinct switching events as

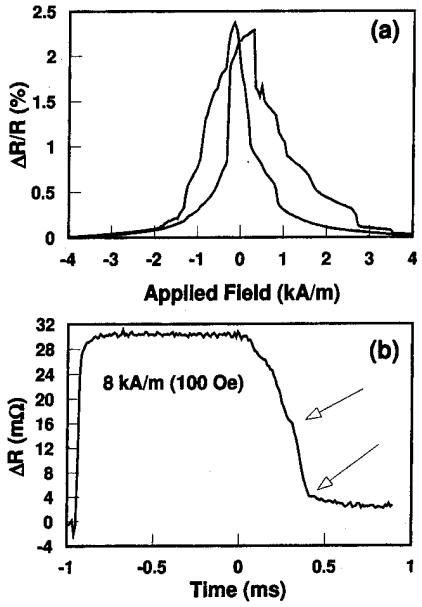



FIG. 3. (a) GMR response to a slowly changing applied field cycle for a $0.7\times1$ $\mu$m NiFe/Ag device, and (b) time response of the device to the field pulse. Note the structure in the relaxation curve.

jumps in the relaxation, but the noise was not low enough to observe this.

If a constant field is always applied to the device then the magnetic grains would partially align along the field direction, reducing the noise and relaxation rate. The magnetic field due to the applied current flowing through the device may be used to do this.[9] The current density produces a constant field transverse to the current flow that can be used to align the moments. The turn-off response of a $4\times4$ $\mu$m device to the field pulse is shown in Fig. 4 for low and high current densities for single-shot measurements. The curves were normalized so that the decay rates could be compared. (The values of $\Delta R/R$ are not the same because the high current density causes a 12% reduction in GMR response.) The time constant of the $5\times10^5$ A/cm$^2$ curve is greater than 300 $\mu$s and reduces to approximately 150 $\mu$s at $1\times10^7$ A/cm$^2$.

## IV. CONCLUSIONS

We measured the time response of NiFe/Ag discontinuous GMR devices to a sharp field pulse and observed relaxation time constants greater than 300 $\mu$s when the applied field switches from saturation to zero. When the field is applied, the torque on the magnetic grains composing the discontinuous film causes the moments to respond quickly. However, when the field is turned off, interacting magnetostatic fields from the grains and thermal activation dominate the response, causing the long relaxation rates. We observed size effects in the response for devices approaching 1 $\mu$m in size. In addition, the relaxation rate depends on the magnetic field, whether due to an external field or self fields from the applied current. Application of a current density $1\times10^7$ A/cm$^2$ halved the time constant for a $4\times4$ $\mu$m active area device. The long time constants observed in the discontinuous NiFe/Ag system may limit their usefulness as read-head sensors where high bit rates are used.

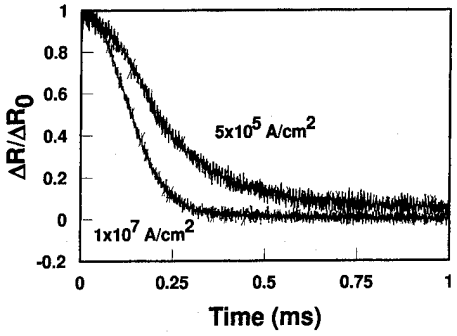



FIG. 4. The turn-off time response to the field pulse for a $4\times4$ $\mu$m (active area) NiFe/Ag device at low and high current densities. The self field due to the applied current density of $1\times10^7$ A/cm$^2$ halves the relaxation rate.


[1] R. W. Cross, S. E. Russek, S. C. Sanders, M. R. Parker, J. A. Barnard, and S. A. Hossain, IEEE Trans. Magn. **30**, 3825 (1994).
[2] S. E. Russek, R. W. Cross, S. C. Sanders, and J. O. Oti, IEEE Trans. Magn. **31**, 3939 (1995).
[3] M. N. Baibich, J. M. Broto, A. Fert, F. Nguyen, Van Dau, F. Petroff, P. Etienne, G. Creuzet, A. Friederich, and J. Chazelas, Phys. Rev. Lett. **61**, 2472 (1988).
[4] S. S. P. Parkin, N. More, and K. P. Roche, Phys. Rev. Lett. **64**, 2304 (1990).
[5] T. L. Hylton, K. R. Coffey, M. A. Parker, and J. K. Howard, J. Appl. Phys. **75**, 7058 (1994).
[6] M. A. Parker, T. L. Hylton, K. R. Coffey, and J. K. Howard, J. Appl. Phys. **75**, 6382 (1994).
[7] J. C. Slonczewski, J. Magn. Magn. Mater. **129**, 123 (1994).
[8] O. Oti, R. W. Cross, S. K. Russek, and S. Sanders, IEEE Trans. Magn. (to be published).
[9] N. Smith, IEEE Trans. Magn. **30**, 3822 (1994).

# New methods to measure the current perpendicular to the plane magnetoresistance of multilayers

P. Dauguet, P. Gandit, and J. Chaussy
*Centre de Recherches sur les Très Basses Températures, Centre National de la Recherche Scientifique, BP, 38042 Grenoble Cedex 09, France*

The experimental devices presented here enable us to measure variations with magnetic field of electrical resistances in the range (0.1 nΩ, 1 μΩ), for applied magnetic fields up to 3 T, and for temperatures less than 9 K. The setups work with three measurement methods. Two provide direct access to $R(H)$, one in constant current, the other in alternating current. Their absolute sensitivity is about 1 pΩ, and their relative resolution $\Delta R/R$ is limited to 0.3%. The third method is a sinusoidal field modulation technique giving the field derivative of the resistance: $dR/dH$. It is sensitive to variations of the resistance as small as 1 pΩ independent of the absolute resistance of the sample, thus the resulting resolution $\Delta R/R$ is, for example, $10^{-6}$ for a 1 μΩ sample. With these devices, the magnetoresistance of multilayers can be studied with the current perpendicular to the plane. © *1996 American Institute of Physics.* [S0021-8979(96)54808-0]

## I. INTRODUCTION

Since the discovery in 1988 of the giant magnetoresistance (GMR) of Fe/Cr multilayers,[1] many multilayer systems composed of ferromagnetic layers alternating with nonmagnetic layers have been found to exhibit the same effect, as for example Co/Cu, Co/Ag, NiFe/Ag. Their electrical transport properties have been extensively studied with the current flowing in the multilayer plane.[2] This geometry yields sample resistances in the range (1 mΩ–1 Ω) and the GMR effect can be investigated with standard measurement techniques. Whereas numerous theoretical models have been developed to describe the GMR effect with the current flowing perpendicular to the multilayer plane (CPP-MR),[3] few experimental results have been obtained,[4,5] the measurements being difficult. The square resistance of the samples is indeed about $10^{-8}$ Ω mm$^2$ in this geometry. For samples of surfaces 0.1–1 mm$^2$, the resistances to be measured range from $10^{-8}$ to $10^{-7}$ Ω. If biased with a 10 mA current, the voltage appearing across the sample is $10^{-10}$–$10^{-9}$ V and to study the magnetoresistance effects properly, the measurement method must have at least a $10^{-2}$ resolution. So the sensitivity of the measurement method has to be better than $10^{-12}$ V.

In this paper, we describe techniques which allow such measurements. The first two give a direct access to $R(H)$, the third one yields $dR/dH$. All are original in this investigation field and achieve high sensitivities not attainable with commercial instruments. We present the principles of the three methods, the experimental setups, their resulting performances, and the conditions required to get them. Then we show some CPP-MR measurements made on multilayer samples.

## II. $R(H)$ MEASUREMENTS WITH CONSTANT CURRENT

The setup is designed to measure $R(H)$ from 50 mK to 9 K. A constant current is applied to the sample and a constant voltage appears across it. Because this voltage is very low ($10^{-10}$ V), it is amplified at low temperature and as close to the sample as possible to avoid the appearance of parasitic thermoelectric voltages than can be far bigger than the signal. To do this, the constant voltage is first made alternating by means of a superconducting chopper[6] which consists of a superconducting bridge, two opposite branches of which are made normal alternatively with the aid of heating light-emitting diodes (LED) at a frequency of about 30 Hz (see Fig. 1). The alternating voltage is amplified with a transformer of amplification rate 25 000 working at 4.2 K, and then with a low-noise amplifier with a field-effect transistor (FET) working at 150 K. Finally, the signal is detected with a lock-in amplifier. This system is placed in a dilution refrigerator equipped with a superconducting magnet delivering fields up to 0.7 T. Its input noise voltage is $10^{-12}$ V/$\sqrt{\text{Hz}}$ in working conditions and in the maximum field. Averaging the signal over 100 s, the sensitivity of the method in thus $10^{-13}$ V. With a sample current of 0.1 A, the absolute sensitivity in terms of resistance is thus $10^{-12}$ Ω, the resolution of the method $\Delta R/R$ being to 0.3%.

## III. $R(H)$ MEASUREMENTS WITH ALTERNATING CURRENT

It consists in detecting the ac voltage that appears across a sample supplied with a known ac current $i$ of frequency $f$, and placed in a constant magnetic field $H$. The voltage to be measured $V$ is amplified with a transformer of ratio 25 000 working at 4.2 K and then with a low-noise FET amplifier at room temperature, before being detected with a lock-in amplifier. This voltage $V$ follows the equation:

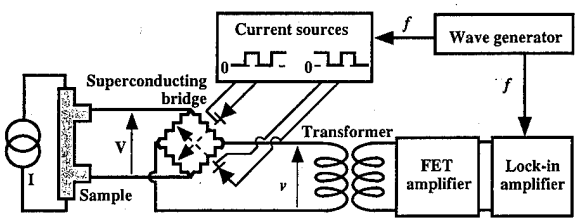



FIG. 1. Schematic diagram of the constant current $R(H)$ measurement method.

 0021-8979/96/79(8)/5823/3/$10.00 © 1996 American Institute of Physics 

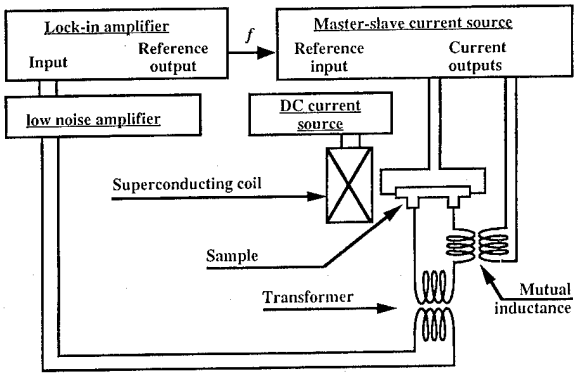



FIG. 2. Schematic diagram of the alternating current $R(H)$ measurement method.

$$V=R(H)i+M_p\frac{di}{dt}, \tag{1}$$

where $M_p$ is the parasitic mutual inductance coupling the current injection circuit and the voltage measurement circuit at the sample level. $M_p$ is about $10^{-10}$ H. As $(M_p\, di/dt)$ is proportional to $f$, we should work with a frequency as small as possible. But lowering $f$, the noise of the electronics grows (it is proportional to $1/f$ at low frequencies). So we work at the frequency where the white noise regime of our apparatus is reached, that is 9 Hz. At this frequency $(M_p\omega)$ is about $5\times10^{-9}$ Ω, which is far bigger than the desired sensitivity in terms of resistance. Noticing that the perturbating voltage is in quadrature with the one of interest, it can be avoided using a lock-in amplifier phase locked to the sample current. The error it induces is thus reduced by a factor $10^3$–$5\times10^{-12}$ Ω. Injecting in the circuit a signal in opposition to $(M_p\, di/dt)$ with the aid of a mutual inductance allows it to be reduced below the required level of 1 pΩ equivalent.

A schematic diagram of the measurement setup is presented in Fig. 2. It works at 4.2 K with fields up to 3 T. Its noise voltage measured in working conditions under a field of 1 T is $7\times10^{-13}$ V/$\sqrt{\text{Hz}}$, which corresponds to an absolute sensitivity of 0.7 pΩ in terms of resistance, the resolution of the method $\Delta R/R$ being limited to 0.3%. This setup has been designed to permit the rotation of the sample in the field. It allows the study of the angular dependence of the CPP-MR of spin-value multilayers like, for example, Ag/NiFe/Ag/Co.

## IV. ($dR/dH$) MEASUREMENTS

With the method we describe now, we get $dR/dH(H)$. The sample is subjected to a constant field $H$ to which is superposed a small modulation $dH$ at frequency $f_1$. The idea is to detect the response of the sample resistance to the field modulation. If the current biasing the sample is a constant current, the voltage appearing across the sample is the sum of a constant term:

$$V_{\text{dc}}=R(H)I, \tag{2}$$

and an alternating term at the frequency $f_1$:

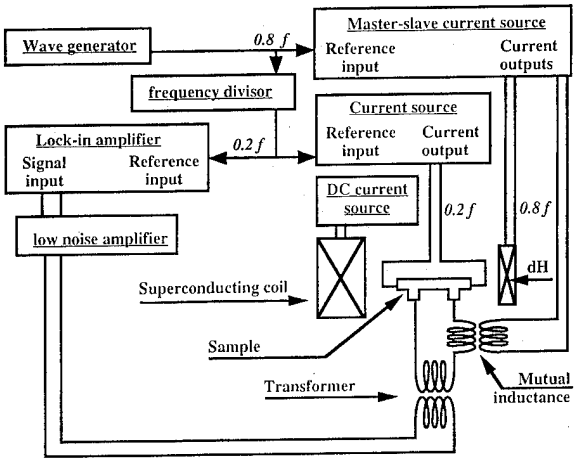



FIG. 3. Schematic diagram of the $dR/dH$ measurement method. The numerical lock-in amplifier detects the signal at $f$ (which is five times its reference frequency).

$$V_{f1}=\left(\frac{dR}{dH}\right)_H dH\, I+\frac{d\Phi}{dt}, \tag{3}$$

where $d\Phi/dt$ is the flux variation created by the field modulation and seen by the voltage measurement circuit. Working at 9 Hz with a field modulation of 10 Oe, this perturbating term is about $10^{-7}$ V which is $10^5$ times the required sensitivity. To avoid $d\Phi/dt$, the first idea is to inject a voltage in opposition to it using a mutual inductance placed in the detection circuit. This way, it is reduced by a factor $10^3$, which is still not sufficient to achieve the minimum required sensitivity of $10^{-12}$ V. So, the second idea is to supply the sample with a sinusoidal current $i$ of frequency $f_2$. The voltage appearing across the sample is thus

$$V=R(H)i+\left(\frac{dR}{dH}\right)_H dH\, i+\frac{d\Phi}{dt}+M_p\frac{di}{dt}. \tag{4}$$

The perturbating terms are then at frequencies $f_1$ and $f_2$, and the term of interest is at $(f_1+f_2)$ and $(f_1-f_2)$. Amplifying $V$ the same way as in the $R(H)$ method, and detecting its $(f_1+f_2)$ component $(V_{f1+f2})$ with a lock-in amplifier, we get $dR/dH(H)$. In fact, the rejection of the lock-in amplifier between the signals at different frequencies is $10^4$, and the component of $V$ at $f_1$ $(d\Phi/dt)$ is more than $10^4$ times the required sensitivity level, so the rejection of the lock-in amplifier is not sufficient. $d\Phi/dt$ has to be first opposed using a mutual inductance, and then $V_{f1+f2}$ can be measured without any error induced by $V_{f1}$ and $V_{f2}$.

For this measurement, the detection frequency $f$ we use is 9 Hz. The way to avoid any perturbations produced by the small harmonic distortion of the $d\Phi/dt$ term induced by Foucault currents in the calorimeter, is to choose $f_1+f_2$ different from any higher harmonic of $f_1$. In what follows, the detection frequency $f_1+f_2$ is called $f$. Practically, we took $f_1$ equal to $0.8\,f$ and $f_2$ equal to $0.2\,f$.

A block diagram of the setup is presented in Fig. 3. It works at 4.2 K with fields up to 3 T. Its noise voltage measured in working conditions under a field of 1 T is

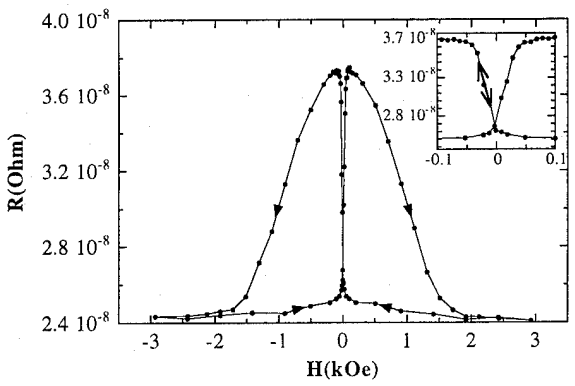



FIG. 4. CPP-MR of (Ag 40 Å/Co 4 Å/Ag 40 Å/NiFe 20 Å)$_{20}$ at 4.2 K obtained with both $R(H)$ methods. The double arrow in the inset indicates for comparison the $dR/dH$ value measured at one point.

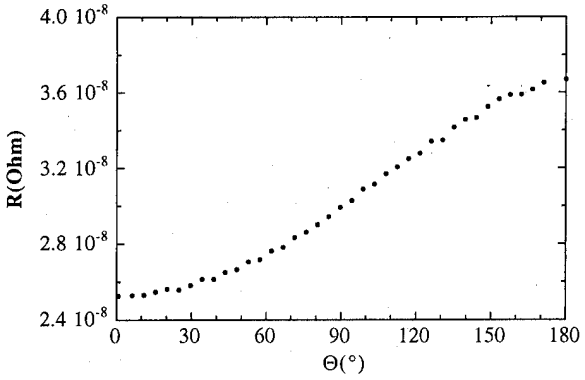



FIG. 5. Angular dependence of the CPP-MR of (Ag 40Å/Co 4Å/Ag 40Å/NiFe 20Å)$_{20}$ at 4.2 K.

$7\times10^{-13}$ V/ $\sqrt{\text{Hz}}$. It is sensitive to variations of the resistance as small as 0.7 pΩ independent of the absolute resistance of the sample, thus the resulting resolution $\Delta R/R$ is, for example, better than $10^{-6}$ for a 1 μΩ sample. This ultrahigh resolution has the advantage of allowing magnetoresistance studies of systems with very low magnetoresistances.

## V. PRECAUTIONS

In order to achieve the sensitivities presented in Secs. II to IV, all sources of noise present in the circuits have been reduced.

To minimize the *thermal noise*, the transformer is placed in the helium bath. This reduces the Nyquist noise of its copper secondary, and enables the use of superconducting wires at primary. The total resistance of the measurement circuit seen from its input is about $10^{-6}$ Ω, which generates a total Nyquist noise of $2\times10^{-14}$ V/$\sqrt{\text{Hz}}$.

The *electromagnetic perturbations* are minimized. Electrostatic shielding is ensured by the stainless-steel Dewar and a metallic shielding of the cables outside of it. The length and surface of each circuit are reduced to their minimum in order to reduce the effect of the electromagnetic perturbations coming from electronic devices, radio waves, and the Earth's magnetic field. Moreover, the transformers and mutual inductances are shielded from field variations by putting them in superconducting containers. These boxes at the same time shield out the constant field $H$, in which the transformers cannot work properly.

The last type of noise we had to deal with is *microphonic*. To reduce the vibration transmitted by the building, the Dewar is set on pneumatic shock absorbers. Some cables used are totally rigid, and the others are partially tied up. Despite this, the resulting noise level (see Secs. II to IV) is mainly due to the motion of the wires in the magnetic field. This noise voltage is proportional to the field and is about $10^{-12}$ V/$\sqrt{\text{Hz}}$ per T.

## VI. MEASUREMENTS

To illustrate the high sensitivity of the setups presented above, we have measured the CPP-MR of Ag/Co/Ag/NiFe multilayers deposited between two superconducting leads by sputtering on Si(100) substrates. They were prepared and supplied by Schroeder and co-workers. A typical $R(H)$ curve at 4.2 K is given in Fig. 4, the two $R(H)$ methods gave the same result.

For the first time, the angular dependence of the giant magnetoresistance of multilayers has been measured with the current applied perpendicular to the multilayer plane. In the sample studied, the magnetization of the $Ni_{80}Fe_{20}$ layers can be rotated by rotating the sample in a small field, without affecting the remanent magnetization of the Co layers.[7] The sample is saturated in a field of 5000 Oe and then rotated in 150 Oe. The magnetization of the Co follows the sample rotation, whereas the magnetization of $Ni_{80}Fe_{20}$ remains parallel to the applied field. The angle between the magnetizations is called Θ. A $R(\Theta)$ curve is presented in Fig. 5. Analysis and physical interpretations of these measurements will be presented elsewhere.

We have tested the $dR/dH$ method on these samples. A measure at one point is given by the double arrow in the inset of Fig. 4. We see that the results obtained with the $dR/dH$ method are consistent with the $R(H)$ measurements.

## ACKNOWLEDGMENT

This work is partially supported by the European Community through the Brite Euram Contract No. BRE2-CT94-0546.

[1] M. N. Baibich, J. M. Broto, A. Fert, F. Nguyen Van Dau, F. Petroff, P. Eitenne, G. Creuzet, A. Friederich, and J. Chazelas, Phys. Rev. Lett. **61**, 2472 (1988).
[2] B. Dieny, J. Magn. Magn. Mater. **136**, 335 (1994) (review article).
[3] G. E. W. Bauer, Phys. Rev. Lett. **69**, 1676 (1992); H. E. Camblong, S. Zhang, and P. M. Levy, Phys. Rev. B **47**, 4735 (1993); T. Valet and A. Fert, *ibid.*, **48**, 7099 (1993); J. Inoue, H. Itoh, and S. Maekawa, J. Magn. Magn. Mater. **126**, 413 (1993).
[4] W. P. Pratt, Jr., S. F. Lee, J. M. Slaughter, R. Loloee, and P. A. Schroeder, Phys. Rev. Lett. **66**, 3060 (1991); S. F. Lee, W. P. Pratt, Jr., Q. Yang, P. Holody, R. Loloee, P. A. Schroeder, and J. Bass, J. Magn. Magn. Mater. **118**, L1 (1993); J. Bass, Q. Yang, S. F. Lee, P. Holody, R. Loloee, P. A. Schroeder, and W. P. Pratt, Jr., J. Appl. Phys. **75**, 6699 (1994).
[5] M. A. M. Gijs, S. K. J. Lenczowski, and J. B. Giesbers, Phys. Rev. Lett. **70**, 3343 (1993).
[6] Y. N. G. Tong, Ph.D. thesis, Grenoble, 1980; and Patent ANVAR-CNRS.
[7] L. B. Steren, A. Barthelemy, J. L. Duvail, A. Fert, R. Morel, F. Petroff, P. Holody, R. Loloee, and P. A. Schroeder, Phys. Rev. B **51**, 292 (1995).

# Engineering coercivities by dual ion beam sputtering for synthesizing soft permalloy-based spin-valve multilayers (abstract)

C. J. Gutierrez, R. Dail, R. Selestino, L. Tristan, and M. Khater
*Physics Department, Southwest Texas State University,*

Steve Michel
*Commonwealth Scientific Corporation*

Thin permalloy ($Ni_{80}Fe_{20}$) single-layer films and multilayers were fabricated onto Ta-buffered oxidized silicon substrates using a prototype dual ion beam sputtering system (Commonwealth Scientific Corporation). The room temperature substrates were placed in a uniform in-plane magnetic field during growth (~150 Oe) yielding a uniaxial magnetic anisotropy in the permalloy films (typically ~6 Oe). An examination of single-layer permalloy films with thicknesses from 20–50 nm indicated that the presence of an ~100 eV ion-beam assist beam focused directly onto the substrate during film growth consistently modified the coercive and remnant characteristics of the films. Typically, the nonion beam assist modified NiFe films exhibited a coercivity ~1 Oe, while the ion beam assist modified films exhibit a slightly larger coercivity (~1.5 Oe). Based on this apparent influence of the assist ion beam treatment on the film coercivity, the fabrication of soft spin-valve multilayer structures exploiting differences in the ion beam treatment of chemically identical ferromagnetic layers seemed plausible. To test this idea ,two parallel series of multilayers composed of [2.5 nm permalloy]-[Cu (2.5 nm, 4 nm, or 5.5 nm)] or [0.3 nm Co-1.9 nm permalloy -0.3 nm Co]-[Cu (2.5 nm, 4 nm, or 5.5 nm)] were fabricated. In these 30 cycle multilayers, alternating ferromagnetic layers were subjected to a 150 eV assist ion beam treatment during growth (higher coercivity layer), or to NO assist ion beam treatment during growth (lower coercivity layer). VSM analysis revealed that the simplest uncoupled spin-valve multilayer configuration consisted of the [2.5 nm permalloy]-[4 nm Cu] multilayer with Hc1 ~0.8 Oe and Hc2 ~2.2 Oe, and the [0.3 nm Co - 1.9 nm permalloy - 0.3 nm Co] - [4 nm Cu] multilayer with Hc1 ~ 3 Oe and Hc2 ~ 15 Oe. Film analysis by low-angle x-ray diffraction and reflectivity, as well as the effect of the Co interface layer on GMR properties will also be reported. © *1996 American Institute of Physics.* [S0021-8979(96)60908-0]

CJG acknowledges support from the Texas Coordinating Board ATP program and the Office of Naval Research.

 0021-8979/96/79(8)/5826/1/$10.00 © 1996 American Institute of Physics

# First principles determination of magnetocrystalline anisotropy for surfaces and interfaces using a torque method (abstract)

Xindog Wang and A. J. Freeman
*Department of Physics and Astronomy, Northwestern University, Evanston, Illinois 60208-3112*

R. Wu
*Department of Physics, California State University, Northridge, California 91330-8268*

D. S. Wang
*Institute of Physics, Academia Sinica, Beijing 100080, People's Republic of China*

Perpendicular magnetic alignment is vital for high density magneto-optical recording materials. Despite the tremendous theoretical/computional advances made during the last few decades, the determination of magnetocrystalline anistropy (MCA) from first principles still remains a great challenge for complex systems. We will describe our recently proposed torque method for the first principles determination of MCA. In the usual first principles methods, one calculates the band energies associated with two magnetization directions and substracts one from the other. Within this approach, one has the difficulty of getting rid of the random fluctuations arising from the two different Fermi surfaces due to different magnetization directions. We show that to accurately determine the spin-orbit induced uniaxial ansisotropy energy for surfaces/interfaces, calculation of the torque at a specific angle is sufficient and one avoids the complexities associated with two Fermi surfaces by employing the Feynman-Hellman theorem. In the $k$-space integrations, we used both linear and quadratic interpolation schemes and convergence is assured when these two schemes agree to the accuracy desired. Examples, including Fe and Co multilayer systems, will be presented to demonstrate the efficiency and precision of this method. Detailed comparisons with previously proposed state-tracing method by Wang *et al.*[1] are also made and discussed. © *1996 American Institute of Physics.* [S0021-8979(96)43108-0]

This work was supported by the ONR (N 00014-94-1-0030).

[1]D. S. Wang, R. Wu, and A. J. Freeman, Phys. Rev. Lett. **70**, 869 (1993).

# Theoretical predictions of magnetic interface anisotropy in (Pd/Co/Pd)/X superlattices

J. M. MacLaren
*Department of Physics, Tulane University, New Orleans, Louisiana 70118*

We present first principles electronic structure calculations of the magnetic interface anisotropy for several (1Pd/1Co/1Pd)/$n$X superlattices with X=Pt, Pd, Ag, or Cu. The calculated anisotropies are compared to those found in Co/X and (1Pt/1Co/1Pt)/$n$X superlattices. The predicted anisotropies for monolayer spacers of Ag or Cu are similar in magnitude to those computed for Co/Pd or Co/Pt multilayers. In the case of (1Pd/1Co/1Pd)/1Pt, the anisotropy is enhanced when compared to either Co/Pt or Co/Pd superlattices, though to a lesser extent than that computed for (1Pt/1Co/1Pt)/1Pd. Surprisingly, increasing the number of spacer layers to three, results in a suppression of the perpendicular anisotropy in (1Pd/1Co/1Pd)/3X and (1Pt/1Co/1Pt)/3Cu superlattices. This result is inconsistent with a near-neighbor Neel model, which would predict little sensitivity to the number of X layers. The Neel model has been shown to work quite well on average for many fcc-based Co/Pt and Co/Pd multilayers. This suggests that the details of the superlattice electronic structure are important in these systems. © *1996 American Institute of Physics.* [S0021-8979(96)21208-6]

Magneto-optic data storage, using the polar Kerr effect to read stored data, requires a media with both perpendicular magnetic anisotropy and a satisfactory Kerr rotation. In order to achieve future aerial densities, the wavelength of the laser used to read data will need to be about 400 nm. Both Co/Pt and Co/Pd superlattices have been the focus of recent work since they exhibit large perpendicular anisotropies and significant Kerr rotations at wavelengths around 400 nm.[1] The magnitude of the magnetic anisotropy measured in a particular superlattice depends crucially upon sample preparation. Superlattices with sharper, more ideal interfaces, such as those made by molecular beam epitaxy, have the largest anisotropies, while those grown by sputtering have significantly smaller anisotropies because of diffuse interfaces. As an example of this, several 1 Co/5Pd superlattices have been prepared under different growth techniques. The observed magnetocrystalline anisotropies range from $5.9\times10^7$ ergs/cm$^3$ (Ref. 2) for a sample grown by molecular beam epitaxy, to $2.6\times10^7$ ergs/cm$^3$ (Ref. 3) for a sputtered sample. Theoretical values for a perfect 1Co/5Pd superlattice with ideal interfaces show even larger anisotropies, namely $6.6\times10^7$ ergs/cm$^3$ (Ref. 4) and $8.7\times10^7$ ergs/cm$^3$.[5] Within a nearest-neighbor Néel model of magnetocrystalline anisotropy,[6,7] we have previously shown that the magnitude of the interface anisotropy is always reduced by the presence of interfusion at the interfaces[7,8]—a result consistent with many experimental observations. In fact, Bertero and Sinclair[9] have stressed that, based upon their experiments for Co/Pt superlattices, the most important parameter controlling the magnitude of the anisotropy is the sharpness of the interfaces present. Thus, because of the inevitable loss of anisotropy associated with the presence of imperfect interfaces in the superlattice, it is clearly desirable to have a structure with a large intrinsic magnetocrystalline anisotropy.

In a recent experimental study, Bertero and Sinclair[10] observed improved coercivities and perpendicular anisotropies in sputtered (Pt/Co/Pt)/X superlattices, where X=Pd, Ag, or Cu, as compared to equivalent Co/X superlattices. The origin of the enhanced anisotropy was thought to result from either sharper interfaces, or an intrinsic property of (Pt/Co/Pt)/X superlattices. Bertero and Sinclair noted that in high resolution transmission electron microscopy images that the interfaces in the (Pt/Co/Pt)/Pd and Co/Pt superlattices appeared to be chemically sharp and of a similar quality, suggesting that the enhancement was an intrinsic property of the (Pt/Co/Pt)/Pd superlattice rather than through the production of better interfaces. However, this issue could not be unambiguously resolved, since reducing the number of Pt layers in the structure might be expected to improve the quality of the interface in Ar sputtered samples because of the reduction of backscattered Ar from the Pt target. First-principles electronic structure calculations predicted anisotropies of (1Pt/1Co/1Pt)/$n$Pd that were several times larger than equivalent 1Co/$n$Pt or 1Co/$n$Pd superlattices.[11] The calculated enhancements were similar to those seen experimentally. Since the calculations all assumed perfect interfaces, it was concluded that this was an intrinsic effect.

In this paper, we use first-principles electronic structure calculations to study similar (Pd/Co/Pd)/X superlattices and compare the anisotropies to both Co/X and (Pt/Co/Pt)/X superlattices. In common with our previous first-principles studies of magnetic anisotropy we have used the layer Korringa–Kohn–Rostoker technique. This approach and its application to the calculation of magnetocrystalline anisotropy has been discussed in detail in several other publications.[4,7,12] In summary, the electronic structure for a perpendicular magnetization direction is solved self-consistently within the local spin density approximation, using the Janak, Moruzzi, and Williams parametrized functional to describe electronic exchange and correlation.[13] The muffin-tin approximation to the crystalline potential is assumed. The scalar relativistic Schrödinger equation including the spin–orbit term was solved within each muffin-tin sphere using the approach of Koelling and Harmon,[14] leading to a set of coupled differential equations. The longitudinal direction is then computed as a perturbation on the self-consistent perpendicular solution. The magnetic anisotropy is found from the force theorem by considering only the difference in

 0021-8979/96/79(8)/5828/3/$10.00 © 1996 American Institute of Physics

TABLE I. Superlattice anisotropy energies per Co atom.

| System | Energy (Mergs/cm$^3$) | System | Energy (Mergs/cm$^3$) | System | Energy (Mergs/cm$^3$) |
|---|---|---|---|---|---|
| 1Co/3Pt | 110 | | | | |
| 1Co/3Pd | 90 | 1Co/3Ag | −33 | 1Co/3Cu | −2.6 |
| 1Pd/1Co/1Pd/1Pt | 130 | 1Pd/1Co/1Pd/1Ag | 107 | 1Pd/1Co/1Pd/1Cu | 67 |
| 1Pt/1Co/1Pt/1Pd | 320 | 1Pt/1Co/1Pt/1Ag | 110 | 1Pt/1Co/1Pt/1Cu | 76 |
| 1Pd/1Co/1Pd/3Pt | 21 | 1Pd/1Co/1Pd/3Ag | 8 | 1Pd/1Co/1Pd/3Cu | 29 |
| 1Pt/1Co/1Pt/3Pd | 240 | 1Pt/1Co/1Pt/3Ag | 120 | 1Pt/1Co/1Pt/3Cu | 23 |

the eigenvalue sum that is corrected for small changes in Fermi level associated with the change in magnetization direction.[15] This includes all first-order changes in the total energy. The approach yields essentially identical results compared to the difference in total energies of self-consistent calculations for perpendicular and longitudinal magnetization directions. Note that this is not quite the same as using the force theorem on calculations converged without the spin–orbit interaction. In the case of Co/Pt, we have found that this other approach introduces errors of about 10% in the anisotropy energy. As in previous work, care was taken to ensure convergence in all calculational parameters. The calculations[4] use 1620 special $k$ points in the two-dimensional Brillouin zone, 48 energy points, and 13 plane waves. This Brillouin zone sampling corresponds roughly to 80 000 wave vectors in the three-dimensional Brillouin zone. The errors in the calculated anisotropies are estimated at about 7%. Convergence was demonstrated for Co/Pd superlattices by making comparisons to calculations which used larger basis sets.

All of the superlattices considered in this paper were assumed to be unstrained and to have a [111] orientation. The atomic positions are those of a fcc lattice whose lattice constant for each different structure was chosen to be a composition average of the elemental lattice constants. This choice of lattice constant is consistent with those lattice constants deduced from x-ray diffraction studies of [111] Co/Pt[16] and [111] Co/Pd systems.[17] In the results presented here, the demagnetization energy was not included. Since in a cubic system the demagnetization energy represents the dominant contribution to the volume anisotropy, the calculated anisotropies are, therefore, a measure of the interface anisotropies. In the superlattice geometry, the demagnetization energy always favors an in-plane anisotropy.

The calculated magnetic anisotropies of all the superlattices studied are shown in Table I. A positive (negative) number corresponds to perpendicular (in-plane) magnetocrystalline anisotropy. With the exception of 1Co/3Ag and 1Co/3Cu, all of the superlattices are computed to have perpendicular anisotropy, though in the case of 1Co/3Cu the anisotropy is smaller than the expected accuracy of the calculations. Superlattices with monolayers of the spacer all exhibit enhanced perpendicular anisotropy when compared to similar Co/X structures, and in the case where X is a noble metal the anisotropies are similar to those expected in Co/Pd or Co/Pt structures. The calculated anisotropy of (1Pd/1Co/1Pd)/1Pt is larger than that of either Co/Pt or Co/Pd, though it is significantly smaller than that seen in (1Pt/1Co/1Pt)/1Pd, a fact which probably reflects the smaller size of the spin–orbit interaction in Pd. The large enhancement calculated for (1Pt/1Co/1Pt)/$n$Pd was first observed experimentally by Bertero and Sinclair;[10] these authors also found improved anisotropies and coercivities for (1Pt/1Co/1Pt)/Ag and (1Pt/1Co/1Pt)/Cu. Surprisingly, in (1Pd/1Co/1Pd)/3X superlattices, the anisotropy is sharply reduced. In contrast for (1Pt/1Co/1Pt)/3X superlattices, only the superlattice with a Cu spacer causes a similar reduction in anisotropy. In previous work,[4,7,8] we have used a near-neighbor Néel model to describe the magnetic anisotropy of fcc-based Co/Pd and Co/Pt superlattices. This model sums a pairwise interaction of the form $L(\mathbf{M}\cdot\mathbf{R})^2$ over all near-neighbor bonds ($\mathbf{M}$ and $\mathbf{R}$ are unit vectors representing the magnetization and interatomic separations). The interaction strength $L$ depends only on the type of atoms under consideration. The Néel model reproduces the anisotropy of the Co/Pd and Co/Pt systems on average. Microscopic details of the electronic structure have been averaged into the interaction parameters which depend only on atomic type and not atomic environment. This model is applicable when the electronic structure of the superlattice is somewhat insensitive to the number and ordering of the constituent layers. Co/Pd and Co/Pt superlattices show this behavior, except for those structures containing a monolayer of Co. However, in (Pd/Co/Pd)/X and (Pd/Co/Pd)/X superlattices, the electronic structure is very sensitive to the number and ordering of the layers and thus a simple two-parameter Néel model is inadequate, not because the interaction is long ranged, but rather because the interaction parameters are not transferrable.

In Table II, we show the Co spin and orbital moments for all the superlattices studied. The Co layer contributes the dominant contribution to the anisotropy. Some insight into the calculated anisotropies can be obtained from Table II. The spin and orbital moments in all superlattices containing Cu are quite small. The size and anisotropy of the orbital moments and the magnetocrystalline anisotropy also depend upon the strength of spin–orbit coupling,[18] thus reduced orbital moments are concomitant with reduced anisotropy. In the other superlattices, where the Co $l_z$ orbital moment is significant, it is found that the change in orbital moment between perpendicular and longitudinal magnetization directions correlates roughly with the size of the Co contribution to the magnetocrystalline anisotropy.

In conclusion, the anisotropy of (Pd/Co/Pd)/X and (Pt/Co/Pt)/X superlattices seem more sensitive to the environ-

TABLE II. Spin and orbital moments, and anisotropy energy for the Co atom in Co/X, (Pd/Co/Pd)/X, and (Pt/Co/Pt)/X superlattices.

| System | $S_z$ | $l_z$ | $l_x$ | (Mergs/cm$^3$) |
|---|---|---|---|---|
| 1Co/3Pt | 2.061 | 0.106 | 0.032 | 66 |
| 1Co/3Pd | 2.020 | 0.122 | 0.104 | 41 |
| 1Pd/1Co/1Pd/1Pt | 2.131 | 0.129 | 0.012 | 46 |
| 1Pt/1Co/1Pt/1Pd | 1.992 | 0.101 | 0.012 | 170 |
| 1Co/3Ag | 1.801 | 0.138 | 0.185 | −35 |
| 1Pd/1Co/1Pd/1Ag | 1.994 | 0.140 | 0.122 | 58 |
| 1Pt/1Co/1Pt/1Ag | 1.945 | 0.122 | 0.030 | 100 |
| 1Co/3Cu | 1.398 | 0.074 | 0.101 | −6.8 |
| 1Pd/1Co/1Pd/1Cu | 1.735 | 0.093 | 0.010 | 31 |
| 1Pt/1Co/1Pt/1Cu | 1.735 | 0.086 | 0.024 | 57 |
| 1Pd/1Co/1Pd/3Pt | 2.195 | 0.142 | 0.122 | 23 |
| 1Pt/1Co/1Pt/3Pd | 1.987 | 0.100 | 0.010 | 47 |
| 1Pd/1Co/1Pd/3Ag | 1.884 | 0.119 | 0.141 | 0.3 |
| 1Pt/1Co/1Pt/3Ag | 1.970 | 0.122 | 0.116 | 93 |
| 1Pd/1Co/1Pd/3Cu | 1.678 | 0.082 | 0.007 | 14 |
| 1Pt/1Co/1Pt/3Cu | 1.565 | 0.057 | 0.025 | 33 |

ment than Co/X structures. Enhanced anisotropies are predicted for monolayers of X in both (Pd/Co/Pd)/X and (Pt/Co/Pt)/X systems. In the latter, there is experimental evidence of enhanced anisotropies and coercivities. The loss of anisotropy in the (Pd/Co/Pd)/3X superlattices is surprising and reflects the details of the electronic structure in these systems. Changes in Co orbital moment provide some insight into the subtle changes in electronic structure found in these sets of superlattices.

J.M.M. acknowledges the support of the Louisiana Quality Education Support Fund under Grant No. LEQSF (1991-94)-RD-A-30, the Center for Photoinduced Processes (funded under a NSF EPSCoR Program), and the Eastman Kodak Company.

[1] W. B. Zeper, F. J. A. M. Greidanus, and P. F. Carcia, IEEE Trans. Magn. **MAG-25**, 3764 (1989); S. Hashimoto, Y. Ochiai, and K. Aso, J. Appl. Phys. **67**, 2136 (1990).
[2] B. N. Engel, C. D. England, R. A. Van Leeuwen, M. H. Wiedmann, and C. M. Falco, Phys. Rev. Lett. **67**, 1910 (1991).
[3] H. J. G. Draaisma, W. J. M. de Jonge, and F. J. A. den Broeder, J. Magn. Magn. Mater. **66**, 351 (1987).
[4] R. H. Victora and J. M. MacLaren, Phys. Rev. B **47**, 11583 (1993); J. M. MacLaren and R. H. Victora, IEEE Trans. Magn. **29**, 3034 (1993).
[5] G. H. O. Daalderop, P. J. Kelly, and M. F. H. Schuurmans, in *Science and Technology of Nanostructured Magnetic Materials*, edited by G. C. Hadjipanayis and G. A. Prinz (Plenum, New York, 1991), p. 185; G. H. O. Daalderop, P. J. Kelly, and M. F. H. Schuurmans, Phys. Rev. B **42**, 7270 (1990).
[6] L. Néel, J. Phys. Radium **15**, 225 (1954).
[7] R. H. Victora and J. M. MacLaren, J. Appl. Phys. **75**, 6428 (1994).
[8] J. M. MacLaren and R. H. Victora, J. Appl. Phys. **76**, 6069 (1994).
[9] G. A. Bertero and R. Sinclair, J. Magn. Magn. Mater. **134**, 174 (1994).
[10] G. A. Bertero and R. Sinclair, Appl. Phys. Lett. **64**, 3997 (1994).
[11] R. H. Victora and J. M. MacLaren, J. Appl. Phys. **73**, 6415 (1993).
[12] J. M. MacLaren, S. Crampin, D. D. Vvedensky, and J. B. Pendry, Phys. Rev. B **40**, 12164 (1989); J. M. MacLaren, S. Crampin, D. D. Vvedensky, R. C. Albers, and J. B. Pendry, Comput. Phys. Commun. **60**, 365 (1990).
[13] J. F. Janak, V. L. Moruzzi, and A. R. Williams, Phys. Rev. B **12**, 1257 (1975).
[14] D. D. Koelling and B. N. Harmon, J. Phys. C **10**, 3107 (1977).
[15] A. R. MacKintosh and O. K. Anderson, in *Electrons at the Fermi Surface*, edited by M. Springford (Cambridge University Press, Cambridge, 1980).
[16] C.-J. Lin, G. L. Gorman, C. H. Lee, R. F. C. Farrow, E. E. Marinero, H. V. Do, H. Notarys, and C. J. Chien, J. Magn. Magn. Mater. **93**, 194 (1991).
[17] B. N. Engel, M. H. Wiedmann, R. A. Van Leeuwen, C. M. Falco, L. Wu, N. Nakayama, and T. Shinjo, Appl. Surf. Sci. **60-61**, 776 (1992); B. N. Engel, C. D. England, R. A. Van Leeuwen, M. H. Wiedmann, and C. M. Falco, J. Appl. Phys. **70**, 5873 (1991).
[18] D. Weller, G. R. Harp, R. F. C. Farrow, A. Cebollada, and J. Sticht, Phys. Rev. Lett. **72**, 2097 (1994).

# Orientation and structure dependence of interface magnetocrystalline anisotropy of Co/Cu overlayers and superlattices

Lieping Zhong, Miyoung Kim, and Xindong Wang
*Department of Physics and Astronomy, Northwestern University, Evanston, Illinois 60208-3112*

Dingsheng Wang
*Department of Physics and Astronomy, Northwestern University, Evanston, Illinois 60208-3112 and Institute of Physics, Academia Sinica, Beijing 100080, People's Republic of China*

A. J. Freeman
*Department of Physics and Astronomy, Northwestern University, Evanston, Illinois 60208-3112*

The full potential linearized augmented plane wave method and atomic force approach are employed for the theoretical determination of interface magnetocrystalline anisotropy (MCA) for superlattice systems of Co/Cu in (001), (110), and (111) orientations, and overlayer systems of the monolayer Co on Cu (111) substrate adsorbed by different further coverage of Cu. It is found in superlattices that the interface MCA is sensitive to the geometry arising from different orientations. In good agreement with experiment, the interface MCA with Cu overlayers is found to peak at 1 monolayer of Cu-coated Co/Cu(111) and then to decrease with further Cu deposition. In addition to the hybridization of electronic states at the Co/Cu interface, the interaction between the interface layers and the next-to-interface layers in superlattices and structure relaxation in overlayers may have a significant influence on the MCA of the Co layer. © *1996 American Institute of Physics.* [S0021-8979(96)21308-2]

A fundamental understanding of the magnetocrystalline anisotropy (MCA) arising from the interface between magnetic and nonmagnetic metal films is an important problem in magnetism that continues to receive a great deal of attention. Of particular interest are systems that display perpendicular magnetic orientations which are highly desirable for high density recording media. Examples of such systems include some Co/X (X=Cu,Ag,Pd,Pt) multilayers and short periodic superlattices, where for Co film thicknesses below a few atomic layers the magnetic easy axis is found to align perpendicular to the film plane.[1] The key to understanding interface MCA appears to be the clarification of structural and electronic influences. Experimentally, the study of the role of crystal orientation on the interface MCA of single-crystal Co/Pd superlattices grown along different crystal directions shows the interface contribution to MCA as independent of crystal structure.[2] On the other hand, an explicit demonstration of the orientational dependence was given by experiments on Co/Ni superlattices.[3] More interestingly, by an *in situ* polar Kerr effect measurement, it was found that the interface MCA shows anomalous changes in ultrathin molecular-beam-epitaxy-grown Co films with and without overlayers of various nonmagnetic metals (Ag,Cu,Pd). The perpendicular MCA is strongly peaked near 1 monolayer (ML) coverage, which is most pronounced for Cu, and the further Cu deposition causes a drastic decrease.[4]

Stimulated by these exciting experimental findings, we here present calculated MCA results for superlattice systems of Co/Cu with (001), (110), and (111) orientations, and overlayer systems of a Co ML on a Cu(111) substrate, and with ML and bilayer Cu depositions. The lattice constant is set equal to the ideal cubic Cu lattice ($a=4.83$ a.u.). For the superlattices, we use structures consisting of the repetition of magnetic Co MLs separated by $n$ layers ($n\leqslant 5$) of nonmagnetic fcc (001), (110), and (111) Cu slabs. For the overlayers, the adatoms are put pseudomorphically over the fcc sites on the Cu(111) substrate and the vertical positions of all the atoms are optimized by calculating the atomic force acting on each atom based on the full potential linearized augmented plane wave (FLAPW) method. When self-consistency for the semirelativistic calculation is achieved, i.e., the average root mean square distance between the input and output charge densities and spin densities are less than $2\times10^{-4}$ $e$/(a.u.)$^3$, the interface MCA is determined by calculating the torque at $\theta=45°$, where $\theta$ is the angle between the magnetization direction and the film plane.[5] As in the previous state-tracking approach (STA) treatment,[6] the occupancies of the perturbed states are determined by tracking the correct states from the unperturbed wave functions, owing to the adoption of self-consistent scalar relativistic charge/spin density. The convergence of the MCA energy with respect to the number of $k$ points has been checked; we found that 120 $k$ points in the irreducible Brillouin zone (Bz) is sufficient if an error bar of 0.025 meV/adatom for the MCA energy is allowed.

The calculated MCA can be simply related to the spin–orbit coupling (SOC) between the occupied and empty valence states. From a fundamental point of view, it is natural that the MCA should be sensitive to the geometry arising from different orientations. Owing to the spin–orbit interaction, the splitting and the shifting of electronic states depend on the magnetization direction. In the simple ML case, the lifting of twofold degeneracies is found to play an important role in determining the interface MCA of (001)- and (111)-oriented Co MLs.[7] It is therefore anticipated that a lower-symmetry interface, such as (110), which has no degeneracies, will exhibit a very different interface MCA. As shown in Table I, the calculated MCA shows an appreciable orientation dependence, and the most pronounced negative MCA

 0021-8979/96/79(8)/5831/3/$10.00 © 1996 American Institute of Physics 

TABLE I. Orientation dependence of the interface (surface) MCA, $\Delta E^{sl}$ in meV (and in mJ/m$^2$ in parenthesis), and spin magnetic moment $M$ (in $\mu_B$) in isolated monolayer and superlattices.

| Orientation | System | $M$ | $\Delta E^{sl}$ | Exp. $(2K_s)$[a] |
|---|---|---|---|---|
| (001) | Co ML | 2.06 | −1.25(−3.07) | |
| | $Co/Cu_1$ | 1.67 | 0.02(0.05) | |
| | $Co/Cu_3$ | 1.65 | 0.31(0.76) | |
| | $Co/Cu_5$ | 1.63 | 0.46(1.13) | 0.21 |
| (110) | Co ML | 2.20 | −2.40(−4.18) | |
| | $Co/Cu_1$ | 1.67 | −0.01(−0.02) | |
| | $Co/Cu_3$ | 1.52 | −0.12(−0.21) | −0.86 |
| (111) | Co ML | 1.83 | −0.85(−2.41) | |
| | $Co/Cu_2$ | 1.51 | 0.06(0.17) | |
| | $Co/Cu_5$ | 1.58 | 0.10(0.28) | 0.15 |

[a]From Ref. 1 in mJ/m$^2$ units.

is for (110), which gives almost twice as large a value as in the (001) case.

Upon contact with a nonmagnetic substrate at the interface, the energies and wave functions of the Co states, which are mainly out of plane $d_{z^2}$ and $d_{xz,yz}$ states, will be changed by interfacial hybridization, which is expected to affect the strength of the SOC perturbation between these states, and thus the MCA energy. For the superlattices considered, the difference in geometry arising from different orientations will lead to different hybridization strength, and this is also confirmed by the calculated magnetic moments given in Table I. In fairly good agreement with experiment, the easy axes for (001)- and (111)-oriented Co/Cu superlattices are perpendicular, while the (110)-oriented Co/Cu gives an in-plane one.

More interestingly, for (001)-oriented Co/Cu superlattices, when the Cu spacer increases from 1 to 3 MLs, the interface MCA changes appreciably. The reason is that when the spacer Cu slab becomes thicker than 1 ML, the Cu $d$ band is broadened due to the Cu–Cu interaction, and the top of the Cu $d$ band is brought closer to the bonding Co $d$ bands. These Cu bands strongly interact with the bonding Co bands, resulting in an upward shift of these Co bands. Now, the direct interaction between the Co layer and its next-nearest neighbor (nnn) layer is expected to be weak; however, this nnn layer strongly influences the interface Cu layer. It is this influence which leads, in turn, to the appreciable change of the Co bands and to the prominent change of the interface MCA.

For clean, ML and bilayer Cu-coated Co/Cu overlayers, the theoretical interface MCA is found to be highly sensitive to the presence of the Cu adsorbate and to structural relaxation. The clean Co/Cu(111) results show that the easy axis is in-plane, and switches to perpendicular when capped with 1 ML of Cu. Deposition of the second Cu layer leads to a decrease of the interface MCA. From the comparison with the calculated MCA for unrelaxed structures, it is found that the peaked feature is more pronounced owing to the interface relaxation, as can be seen from Table II.

In Fig. 1, we present the calculated density of states (DOS) for spin down $d$ states of Co atoms. The different hybridization between Co and Cu due to structural changes

TABLE II. Calculated $\Delta E^{sl}$ (in meV) and spin magnetic moment $M$ (in $\mu_B$) of Co atoms in Co/Cu with different Cu coverage; the results for unrelaxed structures are shown in parenthesis.

| Cu coverage | Clean | 1 ML | 2 ML |
|---|---|---|---|
| $M$ | 1.57(1.60) | 1.26 (1.40) | 1.37(1.41) |
| $\Delta E^{sl}$ | −0.30(−0.31) | 0.23 (0.08) | −0.02(−0.05) |

in the interface is clearly shown by the DOS peaks in the range of −1.0 to 1.0 eV with respect to $E_F$. Especially for the peak just below the $E_F$, there is an abrupt change versus Cu coverage, namely, when the Cu coverage varies, the location and the height of this peak is greatly enhanced and reaches a maximum with 1 ML coverage. This feature is consistent with the magnetic moment of Co in these systems. As shown in Table II, for the clean case, the magnetic Co is at the surface, and the hybridization between magnetic Co and nonmagnetic Cu atoms is expected to be weak. The presence of the interface Cu atom instead of vacuum is shown to reduce the magnetic moment of Co, through the strong interaction and hybridization.

Now it is clear that the effects of the nonmagnetic substrates on the Co MCA arise mainly from the hybridization with the Co-$d_{z^2}$ and Co-$d_{xz,yz}$ states. Obviously, as revealed in an effective ligand interaction model (ELIM),[8] (i) the energy separation between the Co and substrate $d$ bands and (ii) the strength of the interfacial hybridization plays a key role in determining the MCA energy. The stronger the hybridization, the more the perpendicular MCA prevails. This makes a connection between the interface MCA and the above DOS features, i.e., through hybridization. The presence of the Cu overlayer results in an upward shift of these bonding Co states, which mainly are out-of-plane Co-$d_{z^2}$ and Co-$d_{xz,yz}$ states in the Bz, and a strongly positive MCA con-

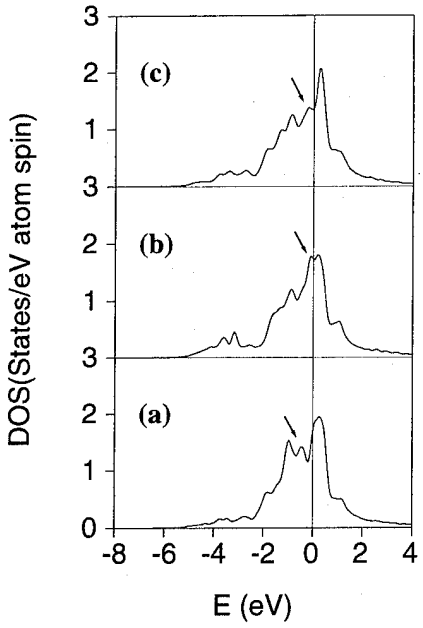



FIG. 1. Projected density of states for Co spin down $d$ states for: (a) clean Co/Cu; (b) 1 ML Cu-coated Co/Cu; (c) 2 ML Cu-coated Co/Cu.

tribution exists through $l_z$ coupling between occupied $d_{xz}$ and empty $d_{yz}$ bands. The presence of a Cu adsorption layer instead of vacuum is somewhat similar to the Co/Pd case,[9] where, due to hybridization, the large $d$—$d$ bonding strength and high energy of the Pd $d$ band cause a substantial component of the out-of-plane bonding Co states to be shifted upward, and thus lead to a strong perpendicular interface MCA.

A similar argument can be applied to explain why the second Cu layer deposition leads to a decrease in the interface MCA. Note that for bilayer Cu coverage, the interface Cu is located at subsurface, while in ML Cu coverage, the interface Cu is at the surface. Obviously, the energies of the $d$ orbitals for surface Cu atoms are higher than those of subsurface Cu atoms, because the subsurface Cu atom is more bulklike. The strength of the Co–Cu hybridization will be stronger if the interface Cu atom is located at the surface, and thus a more positive MCA results.

When relaxation is introduced, the positive MCA is enhanced for the 1 ML Cu coverage (cf. Table II). This can be understood from the strength of the interfacial hybridization. Owing to the relaxation, the interatomic distance between Co and Cu in the ML Cu-coated case is the smallest, and then has the strongest hybridization. For bilayer Cu, the relaxation of Co and interface Cu atoms is released by the screening, the interatomic distance between Co and interface Cu is increased, and then weakens the interaction, and thus the positive contribution to interface MCA is expected to become smaller.

This is to be compared with the Co/Cu(001) overlayer and sandwich systems,[8] where the downward shift of out-of-plane states responsible for the interface MCA changes the result from a more negative MCA ($-0.38$ meV) in the overlayer to near zero ($-0.01$ meV) in sandwich. Here in the Co/Cu(111) overlayer with different Cu coverage, the MCA change is caused by two effects, the presence of the interface and relaxation. On the Co/Cu surface, due to the surface effect the energy of the coated Cu $d$ band was brought closer to the bonding Co $d$ bands and thus have strong interaction with the out-of-plane Co states; this results in an upward shift of these Co bands, and a strong positive MCA contribution exists through $l_z$ coupling between occupied $d_{xz}$ and empty $d_{yz}$ bands. More Cu deposition is expected to decrease the surface effect on the Co/Cu interface and then weaken the interaction strength, and thus the interface MCA decreases drastically.

This work was supported by the Office of Naval Research (Grant No. N00014-94-1-0030) and a grant of computer time at the Arctic Region Supercomputer Center and the Pittsburgh Supercomputing Center (through the NSF Division of Advanced Scientific Computing).

[1] M. T. Johnson, R. Jungblut, P. J. Kelly, and F. J. A. den Broeder, J. Magn. Magn. Mater. **148**, 118 (1995), and references therein.
[2] B. N. Engel, C. D. England, M. H. Wiedmann, R. A. Van Leeuwen, and C. M. Falco, Phys. Rev. Lett. **67**, 1910 (1990).
[3] M. T. Johnson, J. J. Vries, N. W. E. McGee, J. Stegge, and F. J. A. den Broeder, Phys. Rev. Lett. **69**, 3575 (1992).
[4] B. N. Engel, M. H. Wiedmann, and C. M. Falco, J. Appl. Phys. **75**, 6401 (1994); F. Huang, G. J. Mankey, and R. J. Willis, *ibid.* **75**, 6406 (1994).
[5] X. D. Wang, D. S. Wang, R. Wu, and A. J. Freeman, Bull. Am. Phys. Soc. **40**, 528 (1995).
[6] D. S. Wang, R. Wu, and A. J. Freeman (to be published).
[7] M. Y. Kim, L. P. Zhong, X. D. Wang, and A. J. Freeman, Phys. Rev. B (to be published).
[8] D. S. Wang, R. Wu, and A. J. Freeman, J. Magn. Magn. Mater. **129**, 237 (1994).
[9] D. S. Wang, R. Wu, and A. J. Freeman, Phys. Rev. B **48**, 15886 (1993).

# Onset of C(2×2) ferrimagnetic order in Cr islands deposited on Fe(001) as a function of island size

L. Pizzagalli and D. Stoeffler
*IPCMS-GEMME, UMR 46 du CNRS-Université Louis Pasteur, 23 rue du Loess, F-67037 Strasbourg, France*

A. Vega and S. Bouarab
*Departamento de Física Teórica, Universidad de Valladolid, C/Prado de la Magdalena s/n, E-47011 Valladolid, Spain*

C. Demangeat, H. Dreyssé, and F. Gautier
*IPCMS-GEMME, UMR 46 du CNRS–Université Louis Pasteur, 23 rue du Loess, F-67 Strasbourg, France*

We present a study of the magnetic properties of compact Cr clusters deposited on Fe(001). A Cr monolayer deposited on Fe(001) is found to be $c(2\times2)$ ferrimagnetic ($AP$) and the moments of a single adatom and very small clusters are antiferromagnetically aligned with the Fe substrate moments ($P$). Therefore a transition from $P$ to $AP$ order is expected when the cluster size increases. An Ising model is used to model the magnetic energy of two geometric configurations, a square-shaped and a diamond-shaped cluster. Self-consistent tight-binding calculations allow us to determine the $P$ to $AP$ transition which is obtained for a 400 adatoms square-shaped cluster. The pair magnetic energies have been estimated to $-105.7$ meV for the first neighbors Fe–Cr interaction and to $-111.3$ meV for the second neighbors Cr–Cr interaction in the Ising model. © *1996 American Institute of Physics.* [S0021-8979(96)21408-9]

## I. INTRODUCTION

The magnetic behavior of chromium deposited on a ferromagnetic iron substrate has been extensively studied during the last decade,[1–17] because of the interesting properties of Fe/Cr superlattices. First theoretical studies with tight-binding[1] and FLAPW band structure calculations[2] predicted that the monolayer (001) Cr is ferromagnetic and antiferromagnetically aligned with Fe(001), with large Cr moments nearly equal to 3 $\mu_B$. Nevertheless, either the most recent experimental studies cannot estimate the moment[3] or are in discrepancy on its value.[4,8] Hence, Jungblut *et al.*[4] found an average Cr moment of 1 $\mu_B$ and Idzerda *et al.*[8] found 0.6 $\mu_B$ for low coverages, whereas several authors[5–6,9] supposed a giant moment or observed Cr magnetic "dead layer".[10] Following Blügel,[11] who displayed within FLAPW an antiferromagnetic $c(2\times2)$ configuration as the most stable solution for the free-standing Cr monolayer and a $c(2\times2)$ ferrimagnetic solution for Cr on Pd and Ag, tight-binding studies[12,15] predicted a $c(2\times2)$ ferrimagnetic solution as the most stable state for the Cr monolayer on Fe(001). The energy difference per adatom with the usual $p(1\times1)$ ferromagnetic solution is found to be small ($\simeq$20 meV) and of the order of the room temperature excitation energy. Following Vega *et al.*,[12] both solutions can coexist at room temperature and the experimental determinations of both the chromium magnetic structure and magnetic moment may become harder. In this paper, we investigate the magnetic transition from the ferromagnetic small clusters toward the $c(2\times2)$ ferrimagnetic monolayer of Cr deposited on Fe(001), increasing the size of the clusters for two different shapes (square, diamond). Section II is devoted to the model of the magnetic configurations with a two parameters Ising model. Tight-binding calculation results are summarized in Sec. III and we conclude in Sec. IV.

## II. ISING MODEL

Our aim is to determine which of the $p(1\times1)$ ferromagnetic ($P$) and of the $c(2\times2)$ ferrimagnetic ($AP$) case is the most stable state for a given two-dimensional (2D) cluster. The relative stability is obtained by calculating the difference $\delta E_{P-AP}=E_P-E_{AP}$ between the band energy of both magnetic configurations. The lattice parameter of Fe and Cr being very similar, we do not expect buckling like in the case of Mn on Fe(001).[16]

If we consider a closed packed 2D cluster with any shape, the inner adatoms look like monolayer adatoms and the $AP$ configuration should be more stable than the $P$ one. On the other hand, adatoms located at the cluster sides look like less-coordinated adatoms in the small ferromagnetic clusters. Therefore a competition between these two contributions occurs: (i) one contribution favors the $AP$ configuration and is proportional to the cluster area (surface effect) and (ii) the second one favors the $P$ configuration and is proportional to the perimeter area (side effect). In order to confirm this phenomenological description, we derive the analytical expressions for $\delta E_{P-AP}$ using a simple Ising model. We consider only the Cr–Fe first neighbors ($J_1$) and Cr–Cr second neighbors ($J_2$) magnetic interactions. We expect $J_1<0$ favoring the antiferromagnetic coupling between the Cr adatom and the Fe surface and $J_2<0$ favoring the $c(2\times2)$ antiferromagnetic order in the cluster. The magnetic energy for a given configuration is

$$E_m=\sum_{i=1}^{N_{\mathrm{ad}}}\left(-\sum_{\langle i,j\rangle}J_1\mathbf{S}_i^{\mathrm{Cr}}\mathbf{S}_j^{\mathrm{Fe}}-\frac{1}{2}\sum_{\langle i,j\rangle}J_2\mathbf{S}_i^{\mathrm{Cr}}\mathbf{S}_j^{\mathrm{Cr}}\right) \tag{1}$$

with $N_{\mathrm{ad}}$ being the adatoms number in the cluster. We consider two different configurations, a square-shaped cluster (Fig. 1) and a diamond-shaped cluster. We expect a strong side effect for the first one because of several Cr adatoms

 0021-8979/96/79(8)/5834/3/$10.00 © 1996 American Institute of Physics

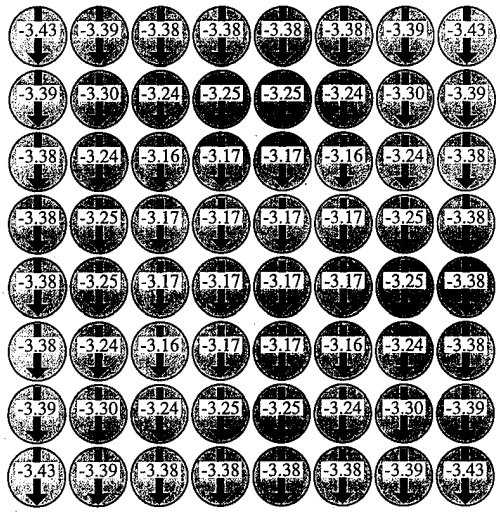



FIG. 1. Magnetic moments of a Cr 64 adatoms square-shaped cluster with a ferromagnetic order and antiferromagnetically aligned with Fe(001) ($P$ configuration). The arrows display magnitude and direction of the local magnetic moment.

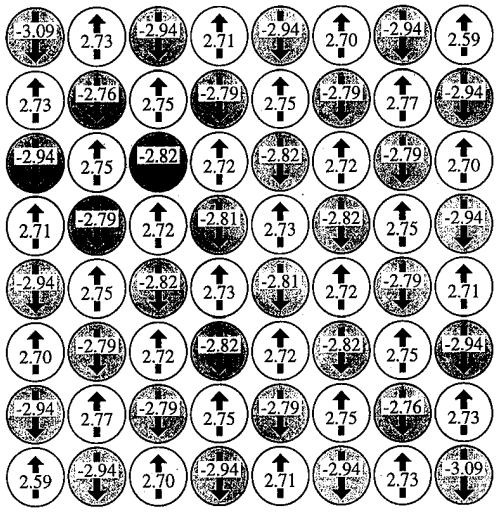



FIG. 2. Magnetic moments of a Cr 64 adatoms square-shaped cluster with a $c(2\times2)$ ferrimagnetic order ($AP$ configuration).

located on the edges and ferromagnetically aligned with Fe (Cr–Fe frustrated link). On the other hand we consider diamond-shaped clusters which keep the $c(2\times2)$ magnetic order and include only Cr adatoms antiferromagnetically aligned with Fe (Cr–Fe nonfrustrated link) on the edges. Therefore the side effect must be very weak.

If $x$ is the cluster size parameter (in units of $a_0$ for square-shaped clusters and $\sqrt{2}a_0$ for diamond-shaped clusters), we derive the following expression for the square:

$$\delta E_{P-AP}=4x^2(J_1-J_2)+4x(2J_1-J_2)+4J_1 \tag{2}$$

and, for the diamond,

$$\delta E_{P-AP}=4x^2(J_1-J_2). \tag{3}$$

The surface effect depends on the competition between $J_1$ and $J_2$ in both geometries. It is expected that the Cr–Cr interaction $J_2$ is stronger than the Cr–Fe one and the surface effect contribution is positive ($|J_1|<|J_2|$) to favor the $AP$ configuration. We also note that (i) the constant term in the square case comes from the corners and (ii) the $AP$ configuration is already the most stable state for the smallest diamond cluster (5 adatoms).

## III. TIGHT-BINDING CALCULATIONS

We report here the results of tight-binding calculations with the two cluster geometries considered above. This study is still our of reach for *ab initio* techniques[17] due to the large number of inequivalent atoms. For example, we investigate a cluster composed of 400 Cr adatoms which yield about 1100 inequivalent atoms in the Cr/Fe system. The self-consistent calculations have been done in the mean-field approximation, with the local neutrality approximation.[13] The Cr and Fe lattice parameters being very close, we assume that the atoms are located on a perfect Fe lattice and are not allowed to relax.[1,2,11–13] Calculations made with our parameters[13] give a Cr $AP$ monolayer deposited on Fe(001) as the most stable state, the energy difference per adatom with P being $\delta E_{P-AP}=22.4$ meV. The Cr magnetic moments are equal to $-3.19\ \mu_B$ in the P state and $-2.81\ \mu_B$ and $2.72\ \mu_B$ in the $AP$ state. These value agree with *ab initio* calculations of Freeman *et al.*[2] who found $-3.1\ \mu_B$ ($P$ case).

The $x$ parameter of the first section is the square or diamond side length. For both cases, we compute for $P$ (Fig. 1) and $AP$ (Fig. 2) magnetic configurations with $x$ ranging from 1 until an asymptotic value for which the monolayer properties are recovered. Figure 1 shows the Cr adatoms magnetic moments for $x=7$ (64 adatoms square) in the $P$ configuration. The adatoms located in the center of the cluster carry a magnetic moment close to the $P$ monolayer values. The $AP$ configuration in Fig. 2 also shows the same feature. This shows that the magnetic interaction is short ranged and this justifies the use of only nearest-neighbor interactions in the Ising model. The empirical rule predicting an enhanced moment for less-coordinated atoms is here well suited for the nonfrustrated adatoms. On the contrary, in the wedges for example, the frustrated less-coordinated adatoms carry a reduced moment (Fig. 2). The calculations for large $x$ do not lead to strong modifications of these conclusions. We only note that we have to compute clusters with very large $x$ in order to recover the exact monolayer magnetic moment in the cluster center. For the diamond-shaped configuration the same main features remain valid.

Figures 3 and 4 show the energy difference between $P$ and $AP$ configurations versus the size parameter $x$ for both the square and diamond geometries. A quadratic expression fits our calculated data with an excellent agreement in both cases. We deduce that the phenomenological argument exposed in the second section and the Ising expressions derived are well suited for this problem. For the diamond curve, we found that the transition $P-AP$ ($\delta E=0$) does not happen for $x=0$ as expected but for $x\simeq1.7$. In fact, for small clusters, there are large variations of the Cr adatoms magnetic moment whereas the Ising model suppose $J$ parameters are constant. Large clusters are more suited for such a description.

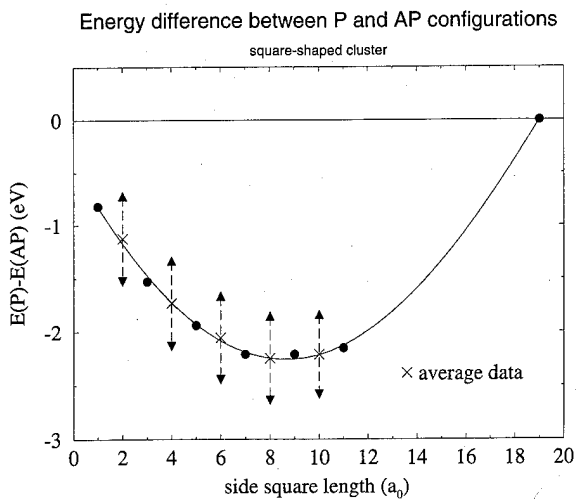



FIG. 3. Energy difference between $P$ and $AP$ configurations (square-shaped cluster) vs the length of one edge (size parameter $x$). The filled circles show the results of the tight-binding calculations and the curve is the quadratic fit. For an odd number of adatoms, there are two possible $AP$ configurations, one with one more spin up atom (filled triangle up) and the other with one more spin down atom (filled triangle down). The analytical expressions of the first section being derived for geometries with an even number of adatoms, we use the arithmetical mean (crosses). Note that the transition ($\delta E = 0$) happens for a large size (400 adatoms cluster).

Anyhow it does not matter since the considered energy difference in this range is small. For the other case, we investigated a 400 adatoms square ($x=19$) and more than 1100 inequivalent atoms to get a transition for $x \simeq 19$. The curves associated with expressions (2) and (3) allow us to determine the $J_1$ and $J_2$ parameters. We found that $J_1=-105.7$ meV and $J_2=-111.3$ meV. As explained in Sec. II, both are negative to favor antiparallel coupling between Cr and Fe on the one hand, and between Cr and Cr on the other hand. Moreover, we get $|J_1|<|J_2|$ meaning that the Cr–Cr interaction is stronger than the Cr–Fe interaction and the $AP$ configuration is favored for the monolayer as expected.

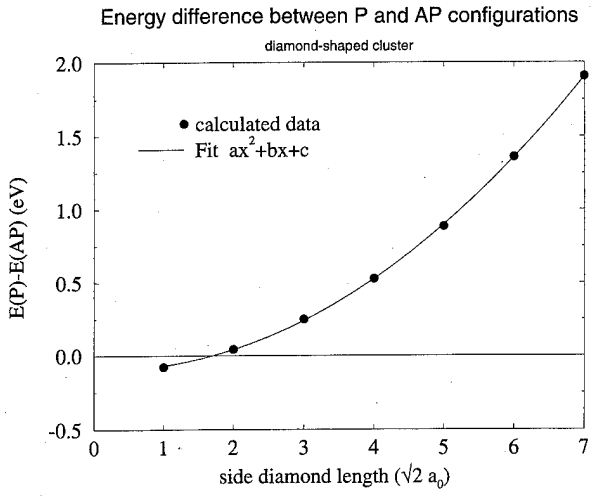



FIG. 4. Energy difference between $P$ and $AP$ configurations (diamond-shaped cluster) vs the length of one edge (size parameter $x$). The filled circles show the results of the tight-binding calculations and the curve is the quadratic fit.

## IV. CONCLUSION

In spite of the lack of experimental confirmations, the most stable state for a Cr monolayer adsorbed on Fe(001) was expected to be ferromagnetic. But recent theoretical investigations have suggested that the $c(2\times2)$ ferrimagnetic configuration may be the most stable state. In this framework, we have investigated the onset of $c(2\times2)$ magnetism in small clusters as a function of their sizes. First we model the magnetic interactions with a simple two-parameters Ising model, for two geometries (a square and a diamond). Then self-consistent tight-binding calculations have been done for each cluster as a function of the size from which we deduced the magnetic transition for a 400 adatoms square-shaped cluster. The Ising parameters, i.e., the pair magnetic energy, have been estimated to $J_1=-105.7$ meV for the first neighbor Fe–Cr interaction and to $J_2=-111.3$ meV for the second neighbor Cr–Cr interaction.

New magnetic configurations are under study and may give us more insights for the magnetism of Cr/Fe(001). In spite of its crudeness, the Ising model accurately reproduces the magnetic properties. However, for more complex structures, it seems necessary to take into account more parameters as the third-neighbor Cr–Cr interaction for example. Results about these calculations will be reported soon.


[1] R. H. Victoria and L. M. Falicov, Phys. Rev. B **31**, 7335 (1985).
[2] C. L. Fu, A. J. Freeman, and T. Oguchi, Phys. Rev. Lett. **54**, 2700 (1985).
[3] C. Carbone and S. F. Alvarado, Phys. Rev. B **36**, 2433 (1987).
[4] R. Jungblut, Ch. Roth, F. U. Hillebrecht, and E. Kisker, J. Appl. Phys. **70**, 5923 (1991).
[5] J. Unguris, R. J. Celotta, and D. T. Pierce, Phys. Rev. Lett. **69**, 1125 (1992).
[6] T. G. Walker, A. W. Pang, H. Hopster, and S. F. Alvarado, Phys. Rev. Lett. **69**, 1121 (1992).
[7] J. Xu and A. J. Freeman, Phys. Rev. B **47**, 165 (1993).
[8] Y. U. Ydzerda, L. H. Tjeng, H.-J. Lin, C. J. Gutierrez, G. Meigs, and C. T. Chen, Phys. Rev. B **48**, 4144 (1993).
[9] C. Turtur and G. Bayreuther, Phys. Rev. Lett. **72**, 1557 (1994).
[10] S. Miethaner and G. Bayreuther, J. Magn. Magn. Mater. **148**, 42 (1995).
[11] S. Blügel, M. Weinert, and P. H. Dederichs, Phys. Rev. Lett. **60**, 1077 (1988); S. Blügel, D. Pescia, and P. H. Dederichs, Phys. Rev. B. **39**, 1392 (1989).
[12] A. Vega, S. Bouarab, H. Dreyssé, and C. Demangeat, Thin Solid Films (in press).
[13] D. Stoeffler and F. Gautier, J. Magn. Magn. Mater. **147**, 260 (1995).
[14] A. Vega, S. Demangeat, H. Dreyssé, and A. Chouairi, Phys. Rev. B **51**, 11546 (1995).
[15] D. Stoeffer (unpublished).
[16] R. Wu and A. J. Freeman, Phys. Rev. B **51**, 17131 (1995).
[17] K. Wildberger, V. S. Stepanyuk, P. Lang, R. Zeller, and P. H. Dederichs, Phys. Rev. Lett. **75**, 509 (1995).

# On the $\gamma$-like surface of $\alpha$-Ce: Theory (abstract)

O. Hjortstam, J. Trygg, B. Johansson, and O. Eriksson
*Department of Physics, Uppsala University, Box 530, S-751 21 Uppsala, Sweden*

J. M. Wills
*Theoretical Division, Los Alamos National Laboratory, Los Alamos, New Mexico 87544*

We have shown theoretically, by means of a full-potential LMTO method in a slab geometry, that the topmost surface layer of $\alpha$-Ce is $\gamma$-like. The calculations are fully relativistic and include all electrons. Also an orbital correction to the $f$-electron states is included to allow for $f$ localization. For the topmost layer the spin moment is found to be 0.70 $\mu_B$ for the $f$ electrons and 0.08 $\mu_B$ for the $d$-electron states while the orbital moment from the $f$ electrons is found to be $-1.07$ $\mu_B$. These moments correspond well to the moments calculated for bulk $\gamma$-Ce which are 0.63, 0.07, and $-0.87$ $\mu_B$, respectively. The subsurface and lower lying layers are calculated to have spin and orbital moments close to zero. We therefore conclude that the topmost layer on the $\alpha$-Ce surface is $\gamma$-like while the subsurface and lower lying layers are similar to bulk $\alpha$-Ce. Our findings explain recent photoemission experiments on this material and provide a theoretical foundation for the interpretation of these experiments. The fact that our theory assumes that $\alpha$-Ce has delocalized $f$ electrons, and the agreement with the interpretation of photoemission experiments, gives support that the Mott transition model for the $\alpha \rightarrow \gamma$ phase transition is correct. © *1996 American Institute of Physics.* [S0021-8979(96)43208-7]

 0021-8979/96/79(8)/5837/1/$10.00 © 1996 American Institute of Physics 

# Spin polarization of the conduction bands and secondary electrons of Gd(0001)

Dongqi Li, J. Pearson, and S. D. Bader
*Materials Science Division, Argonne National Laboratory, Argonne, Illinois 60439*

D. N. McIlroy, C. Waldfried, and P. A. Dowben
*Department of Physics, University of Nebraska, Lincoln, Nebraska 68588*

Angle- and spin-resolved photoemission was utilized to investigate the $5d$ bulk bands and the surface state of Gd(0001) in the temperature range of 130–350 K. The bulk bands at 1–2 eV below the Fermi energy $E_F$ show Stoner-like behavior, while the temperature dependence of the surface state near $E_F$ indicates spin-mixing behavior due to fluctuating local $5d$ moments. The secondary electron spectra of the Gd surfaces both before and after initial oxygen adsorption show a polarization dip at low kinetic energies due to the extra scattering channel for minority electrons via the unoccupied $4f$ level. The temperature dependencies of the surface and bulk magnetization are separated using the spin polarization of the surface state and the bulk exchange splitting. © *1996 American Institute of Physics.* [S0021-8979(96)21508-5]

Surface magnetism of the heavy rare earth metals has been the subject of great interest because of the unique phenomena exhibited. The Curie temperature $T_C$ of the Gd and Tb surfaces are reported to be significantly higher than that of the bulk.[1–4] There is also evidence that the magnetic moments at the surface are canted out of the surface plane,[3,5] while the bulk of the Gd(0001) films, <400 Å thick, have in-plane anisotropy.[6] The enhanced surface magnetic order is believed to originate from the surface electronic structure, namely, a magnetic surface state near the Fermi energy $E_F$ located around the Brillouin zone center.[7–9] The $5d$ bulk bands appear in spin-integrated photoemission at binding energies of 1–2 eV and exhibit a temperature-dependent exchange splitting $\Delta_b$.[10,11]

The study of surface magnetic order depends on separating the surface signal from that of the bulk. This has been accomplished previously by comparing relatively surface-sensitive techniques, like spin-polarized low energy electron diffraction,[1] spin-polarized secondary electron spectroscopy,[3] to a bulk measurement, or taking advantage of the surface core level shift of the Gd $4f$ levels.[3–5] Even with these techniques, it is still difficult to unambiguously distinguish the surface and the bulk. In the present work, we use the spin polarization of a magnetic surface state as an indicator of the surface magnetic order, and $\Delta_b$ as the bulk indicator to separate the two. The temperature dependance of the exchange splitting itself is a very interesting issue, since theories for finite temperature magnetism of itinerant electron systems are less developed than ground state theories. In addition, we examine the spin polarization of the secondary electrons, both as an additional indicator of the magnetization and to understand the anomalous polarization dip at low energy.[12]

Spin-polarized photoemission experiments were performed on the U5 undulator beamline of NSLS at Brookhaven National Laboratory. The ultrahigh vacuum chamber is equipped with low energy electron diffraction and a hemispherical electron energy analyzer with a low-energy spin detector. The details of the experimental setup are described elsewhere.[13] The sample preparation followed previous procedures.[10,14] The W(110) single-crystal substrate was cleaned by flashing and annealing in oxygen. The nominally 80-Å-thick epitaxial Gd(0001) films were deposited thermally onto the room-temperature substrate and subsequently annealed to 780 K to improve the structural ordering and magnetic properties.[15] The chamber pressure remained $<5\times10^{-11}$ Torr during the process to ensure cleanliness. Films made by similar procedures are known to have single domains with in-plane magnetization and low coercivities. The spin polarization was measured in the remanent state after the sample was magnetized in-plane with a pulse field. The samples show no sign of hydrogen or carbon contamination, although the annealed films have a trace amount of oxygen that is equivalent to <0.05 L (1 L$=1\times10^{-6}$ Torr s) oxygen exposure at room temperature. All photoemission spectra were taken at normal emission with the light incident at an angle of 65°. The photoemission spectra of the conduction bands were taken at $h\nu=32.7$ eV and the secondary electrons at 69.5 eV. The sample was biased to −30 V to minimize the stray field effects.

Typical spin-polarized photoemission spectra at different temperatures are shown in Fig. 1. The peak near $E_F$ is the surface state of Gd(0001), which is responsible for the enhanced magnetic ordering of the Gd surface.[7–9] This feature is strongly spin polarized at low temperature, and the polarization has the same sign as that of the occupied $4f$ feature at 8.6 eV binding energy (not shown in the figure). With increased temperature, the spin polarization of the surface state decreases and approaches zero, while the peak position and intensity show no change. The minority-spin counterpart of this state has been observed as an unoccupied state above $E_F$ with inverse photoemission.[16,17]

The bulk bands at 1–2 eV exhibit a different temperature dependence. At low temperature there are two well-defined peaks with opposite spin polarization. They are the majority and minority spin branches of the $5d$ bulk band at $\Gamma$, separated by $\Delta_b$ (with the former at higher binding energy). Note that the sign of the spin polarization of the surface state is the same as that of the majority-spin bulk band. This confirms that the surface state is of majority spin character and that the surface couples to the bulk ferromagnetically[5,18] instead of

 0021-8979/96/79(8)/5838/3/$10.00 © 1996 American Institute of Physics

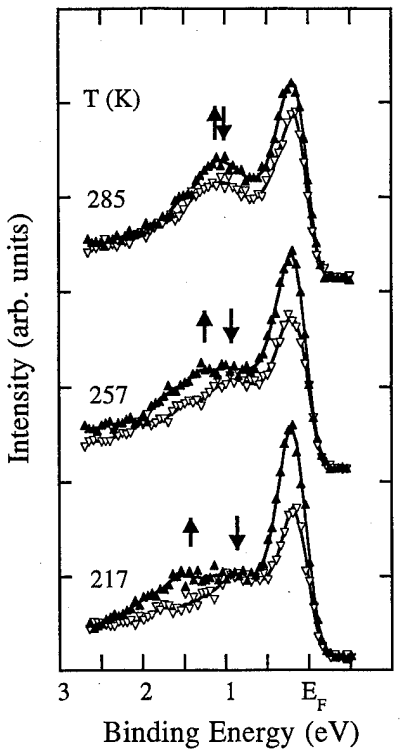



FIG. 1. Spin-polarized photoemission spectra at different temperatures at normal emission. The majority- and minority-spin components are shown with solid (up) and open (down) triangles, respectively. The majority- and minority-spin bulk bands are marked with up and down arrows. The solid lines are to guide the eye.

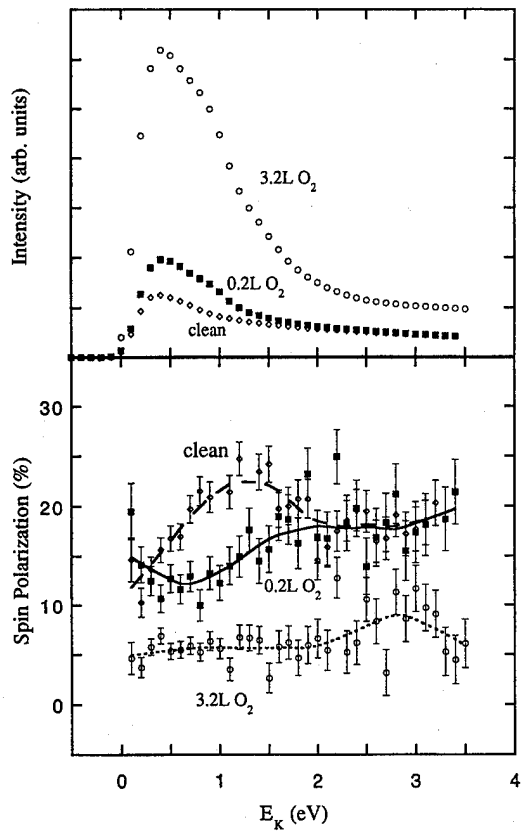



FIG. 2. Intensity and spin polarization of the secondary electron emission vs electron kinetic energy $E_k$. The measurements were taken at 130 K on clean Gd(0001) and after 0.2 and 3.2 L of oxygen exposure. The lines are to guide the eye.

antiferromagnetically.[1] With increased temperature the two peaks with distinct spin character shift toward each other and eventually overlap to form one peak with no spin polarization. In other words, $\Delta_b$ decreases and approaches zero upon warming to $T_C$.

The temperature dependence of the bulk bands is characteristic of Stoner-like[19] behavior, where the exchange splitting $\Delta$ of the itinerant electrons directly correlates with the macroscopic magnetization and approaches zero as $T \rightarrow T_C$. The surface state, however, does not show an energy shift or intensity change near $T_C$, while the spin polarization varies significantly. This suggests that, instead of Stoner-like behavior, the local $\Delta$ of the surface state ($\Delta_s$) does not go to zero at the surface Curie temperature $T_{Cs}$. Such non-Stoner-like behavior is common among transition metals, although they were the original subject of the Stoner model.[19] This is usually attributed to the existence of local moments or short range order above $T_C$.[20–22] We believe that the difference originates from the different degree of itinerancy of the electrons, as discussed elsewhere.[14]

The secondary electrons are also spin polarized, as shown in Fig. 2. The intensity of the secondary electron emission increases with oxygen exposure as oxygen atoms enhance the inelastic scattering in Gd. For the clean Gd(0001) surface, the spin polarization shows a dip when the kinetic energy of the electrons $E_k < 1.5$ eV. This polarization anomaly, first observed by Tang *et al.*,[12] is in contrast to the polarization increase at low $E_k$ for transition metal surfaces. Tang *et al.* suggested that an additional channel for the emission of minority spin electrons exists. The ordinary inelastic scattering of the hot electrons is determined by the unoccupied conduction bands, which provides the available states to scatter into. The unoccupied $4f$ state above the vacuum level, i.e., $4f$,[8] could behave as an additional intermediate, where the minority hot electrons experience quasielastic scattering and emit to vacuum. This channel should selectively enhance the emission of minority spin electrons with $E_k \sim E_{4f} - E_v$, where $E_{4f}$ is the energy of the empty $4f$ level above $E_F$ and $E_v$ is the vacuum level. For the clean Gd surface, the unoccupied $4f$ level is at 4.1 eV above $E_F$ and $\sim$0.8–0.9 eV above $E_v$. Taking the width of the empty $4f$ levels ($\sim$1.5 eV)[23] into consideration, this possible mechanism explains the drop of spin polarization for $E_k < 1.5$ eV. Our data from the samples with initial oxygen adsorption supports such a hypothesis. Figure 2 shows that 0.2 L of oxygen exposure causes the onset of the spin-polarization dip to shift to higher energy by $\sim$0.6 eV. This is consistent with the shift of the empty $4f$ level away from the $E_F$ with oxygen adsorption due to reduced screening.[23] With 0.2 L of oxygen, the empty $4f$ levels shift away from $E_F$ by 0.2–0.3 eV (Ref. 23) while the work function drops by 0.2–0.3 eV.[24] This results in the empty $4f$ levels shifting up $\sim$0.5 eV with respect to $E_v$, consistent within experimental error with the 0.6 eV shift of the onset of the polarization dip. Other pos-

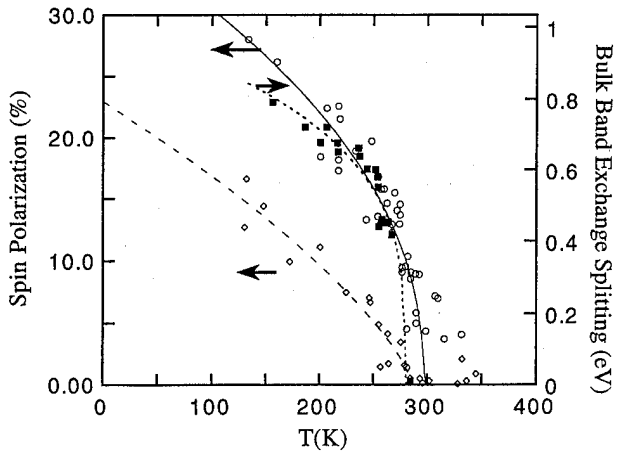



FIG. 3. Temperature dependence of the bulk band exchange splitting (squares), and the spin polarization of the surface state (circles) and secondary electrons (diamonds). The lines are to guide the eye.

sible scattering channels fail to provide the correct energy or the oxygen-induced shift of the dip. With additional oxygen dosing, the overall spin polarization drops further as the oxygen destroys the surface magnetic order of Gd, and the dip disappears as both the $4f$ and the valence band lose the net spin polarization. The effect of oxygen adsorption on the surface magnetization of Gd(0001) will be discussed further elsewhere.[25]

The spin polarization of the surface state and the secondary electrons and $\Delta_b$ are all correlated to the magnetization of the Gd(0001), though in somewhat different ways. The surface-state polarization reflects the purely magnetic order of the surface, and $\Delta_b$ reflects that of the bulk. The polarization of the secondary electrons should provide the mixed information from both the surface and the bulk. Figure 3 shows the temperature dependence of all three quantities. The spin polarization of the secondary electrons was measured at $E_k=3-4$ eV to avoid the anomaly at low energy, as discussed above. All quantities decrease with increasing temperature. The spin polarization of the secondary electrons and $\Delta_b$ approach zero before the surface-state polarization, as is consistent with $T_{Cs}>T_{Cb}$. This enhanced magnetic order can also be seen from Fig. 1, where $\Delta_b=0$ within experimental error, while the surface state and the background remain spin polarized. From Fig. 3, we find $T_{Cb}=283\pm10$ K and $T_{Cs}=297\pm10$ K, with the accuracy limited by the signal-to-noise ratio.

In conclusion, we have studied the spin polarization of the conduction bands and secondary electrons of Gd(0001) at different temperatures. The $5d$ bulk band shows Stoner-like behavior at the Brillouin zone center, while the surface state has a nonzero exchange splitting even above $T_C$. The anomaly in secondary electron polarization for both the clean and oxygen-adsorbed surfaces is discussed in terms of an extra scattering channel via the empty $4f$ levels. The shift in the polarization dip to higher kinetic energy with initial oxygen adsorption is consistent with the chemical shift of the empty $4f$ levels. In addition, our results are consistent with the enhanced magnetic order of the Gd(0001) surface.

We thank D.-J. Huang and Q. Dong for technical assistance and P. D. Johnson for valuable discussions. The work at Argonne is supported by DOE BES-MS Contract No. W-31-109-ENG-38 and ONR Contract No. N-00014-94-F-0085; the work at Nebraska is supported by NSF Grant No. DMR-92-21655.

[1] D. Weller, S. F. Alvarado, W. Gudat, K. Schröder, and M. Campagna, Phys. Rev. Lett. **54**, 1555 (1985).
[2] C. Rau, C. Jin, and M. Robert, Phys. Lett. A **138**, 334 (1989).
[3] H. Tang, D. Weller, T. G. Walker, J. C. Scott, C. Chappert, H. Hopster, A. W. Pang, D. S. Dessau, and D. P. Pappas, Phys. Rev. Lett. **71**, 444 (1993).
[4] E. Vescovo, C. Carbone, and O. Rader, Phys. Rev. B **48**, 7731 (1993).
[5] D. Li, J. Zhang, K. Garrison, and P. A. Dowben, J. Phys. Condens. Matter **5**, L73 (1993).
[6] A. W. Pang, A. Berger, and H. Hopster, Phys. Rev. B **50**, 6457 (1994).
[7] D. Li, C. W. Hutchings, P. A. Dowben, C. Hwang, R.-T. Wu, M. Onellion, A. B. Andrews, and J. L. Erskine, J. Magn. Magn. Mater. **99**, 85 (1991).
[8] D. Li, J. Zhang, P. A. Dowben, and M. Onellion, Phys. Rev. B. **48**, 5612 (1993).
[9] R. Wu and A. J. Freeman, J. Magn. Magn. Mater. **99**, 81 (1991).
[10] D. Li, J. Zhang, P. A. Dowben, and M. Onellion, Phys. Rev. B **45**, 7272 (1992).
[11] B. Kim, A. B. Andrews, J. L. Erskine, K. J. Kim, and B. N. Harmon, Phys. Rev. Lett. **68**, 1931 (1992).
[12] H. Tang, T. G. Walker, H. Hopster, D. P. Pappas, D. Weller, and J. C. Scott, Phys. Rev. B **47**, 5047 (1993).
[13] P. D. Johnson, N. B. Brookes, S. L. Hulbert, R. Klaffky, A. Clarke, B. Sinkovic, N. V. Smith, R. Celotta, M. H. Kelly, D. T. Pierce, M. R. Scheinfein, B. J. Waclawski, and M. R. Howells, Rev. Sci. Instrum. **63**, 1902 (1992).
[14] D. Li, J. Pearson, S. D. Bader, D. N. McIlroy, C. Waldfried, and P. A. Dowben, Phys. Rev. B **51**, 13895 (1995).
[15] M. Farle, K. Baberschke, U. Stetter, A. Aspelmeier, and F. Gerhardter, Phys. Rev. B **47**, 11571 (1993).
[16] D. Li, P. A. Dowben, J. E. Ortega, and F. J. Himpsel, Phys. Rev. B **49**, 7734 (1994).
[17] A. V. Fedorov, K. Starke, and G. Kaindl, Phys. Rev. B **50**, 2739 (1994).
[18] G. A. Mulhollan, K. Garrison, and J. L. Erskine, Phys. Rev. Lett. **69**, 3240 (1992).
[19] E. C. Stoner, Proc. R. Soc. London Ser. A **154**, 656 (1936).
[20] V. Korenman, J. L. Murray, and R. E. Prange, Phys. Rev. B **16**, 4032 (1977).
[21] A. J. Pindor, J. Staunton, G. M. Stocks, and H. Winter, J. Phys. F **13**, 979 (1983).
[22] H. Hasegawa, J. Phys. Soc. Jpn. **46**, 1504 (1979).
[23] J. E. Ortega, F. J. Himpsel, D. Li, and P. A. Dowben, Solid State Commun. **91**, 807 (1994).
[24] J. Zhang, D. Li, M. Onellion, and P. A. Dowben, Surf. Sci. **329**, 177 (1995).
[25] D. N. McIlroy, C. Waldfried, D. Li, J. Pearson, S. D. Bader, D.-J. Huang, P. D. Johnson, R. F. Sabirianov, S. S. Jaswal, and P. A. Dowben (unpublished).

# Spin-resolved electron spectroscopies of epitaxial magnetite (001) (abstract)

Kimberly A. Shaw, Eric Lochner, David M. Lind, Rebecca C. DiBari, Plamen Stoyanov, and Brian Singer
*Florida State University, Department of Physics, MARTECH, and the National High Magnetic Field Laboratory, Tallahassee, Florida 32306-3016*

We will present the first spin-resolving electron spectroscopic studies of a magnetite ($Fe_3O_4$)(001) surface. Magnetite is a semimetal with a high density of states in the minority band, but a large band gap in the majority states at the Fermi energy. The polarization of the secondary emission cascade is measured using spin-resolved secondary electron emission spectroscopy (SRSEES), and reflects the semimetallic spin structure of $Fe_3O_4$. The polarization plateau of spin-resolved secondary emission (29.8%) matches the average 3D band polarization of stoichiometric $Fe_3O_4$ as determined from spin-resolved band structure calculations (34.2%). An enhancement of the polarization of the secondary electrons at lowest energies will also be discussed. Spin-resolved Auger emission spectroscopy (SRAES) of the $Fe_3O_4$ films have been measured and show correlation effects in the valence-valence Auger transitions. Suppressed intensity and polarization of $M_{23}M_{45}M_{45}$ Auger emission relative to $M_1M_{45}M_{45}$ Auger emission is observed, as well as strong resonant emission with shake-up. Conversely, no spin polarization is detected in the spin-resolved oxygen *LMM* Auger features, although oxygen Auger emission (in which we can distinguish between adsorbed and bonded oxygen) is used to verify surface cleanliness of the samples. The synthesis of $Fe_3O_4$ films grown on magnesium oxide (001) substrates using oxygen plasma-assisted molecular beam epitaxy will be discussed, as will thin-film characterization using SQUID magnetometry and x-ray and electron diffraction. A unique angle-, energy-, and spin-resolved electron spectrometer has been designed and built for the study of magnetic surfaces, and these studies represent its' first use. That spectrometer is based on a tandem configuration of an energy-dispersive energy analyzer and Mott spin polarimeter. © *1996 American Institute of Physics.* [S0021-8979(96)82608-0]

[1]Research supported by ONR Grant No. N00014-92-J-1356 and NSF Grant No. DMR-9206870.

# Origins of giant biquadratic coupling in CoFe/Mn/CoFe sandwich structures (abstract)

Norman C. Koon
*Code 6342, Naval Research Laboratory, Washington, DC 20375*

Recently Filipkowski *et al.*[1] reported extremely strong, near 90 degree coupling of 2.5 erg/cm$^2$ for epitaxial sandwiches of CoFe/Mn/CoFe, where the CoFe composition was chosen to be a good lattice match to Mn. Both CoFe and Mn have the bcc structure, but Mn is antiferromagnetic while CoFe is ferromagnetic. It was found that the data were very well described by a simple model due to Slonczewski,[2] in which the interlayer coupling is given by $F_c = C_+(\varphi 1 - \varphi 2)^2 + C_-(\varphi 1 - \varphi 2 - \pi)^2$. While this model describes the data much better than the usual biquadratic form, it still does not connect directly to the microscopic origins of the effect. In the present work we seek to explain the results[1] in terms of normal bilinear exchange and magnetocrystalline anisotropy, together with reasonable assumptions about the structure of the interfaces. We obtain excellent agreement with both the experimental results and the Slonczewski model under the assumptions that at least one of the two CoFe/Mn interfaces is smooth (i.e., atomically flat) on a length scale comparable to or greater than the thickness of the Mn layer and at least one interface is rough on a scale less than approximately a domain wall thickness. © *1996 American Institute of Physics.* [S0021-8979(96)43308-3]

[1]M. E. Filipkowski, J. J. Krebs, G. A. Prinz, and C. J. Gutierrez, Phys. Rev. Lett. **25**, 1847 (1995).
[2]J. C. Slonczewski, J. Magn. Magn. Mater. (to be published).

# New estimation of surface anisotropy

Xiao Hu
*Institute for Materials Research, Tohoku University, Sendai 980-77, Japan and National Institute of Standards and Technology, Boulder, Colorado 80303*

Yoshiyuki Kawazoe
*Institute for Materials Research, Tohoku University, Sendai 980-77, Japan*

A micromagnetic study for the spin–reorientation transition in ultrathin magnetic films is reported. Phase diagrams of the magnetization configuration are presented. Scaling relations among the film thickness, exchange coupling, and magnetic anisotropies are revealed. Formulas are given for the energy stored in the film per unit area, which enable one to evaluate the surface anisotropy by ferromagnetic resonance techniques. © *1996 American Institute of Physics.*
[S0021-8979(96)21608-1]

## I. INTRODUCTION

Much attention has been paid to metallic thin films in recent years, since sophisticated epitaxial techniques enable one to control the film thickness, surface condition, and interface smoothness between films, and many new phenomena such as giant magnetoresistance[1] and square hysteresis loops and giant magneto-optical effects[2] have been observed. It is found experimentally in ultrathin transition metals sandwiched by noble metals that the easy-axis direction of magnetization changes as a function of thickness of the magnetic films:[3] At lower thickness it is normal to the film plane, while at higher thickness it lies in the film plane. This spin–reorientation transition is the result of competition between two different magnetic anisotropies: a surface anisotropy normal to the film exists because of the breaking of translational symmetry in the electronic structure at the interface,[4] and it has been measured by ferromagnetic resonance techniques.[5] On the other hand, the dipole–dipole interaction in thin films produces a strong in-plane shape anisotropy. The understanding of the stable magnetization state and magnetization reversal by external field is the most important issue of magnetism of ultrathin film. In this paper we concentrate on the zero-field case.

## II. DISCRETE MODEL

The energy per unit area of a thin magnetic film with normal surface anisotropy can be described by the following discrete model:[6]

$$\gamma = -JM_s^2 \sum_{i=1}^{N-1} \cos(\varphi_i - \varphi_{i+1}) - K_v' \sum_{i=2}^{N-1} \sin^2 \varphi_i + K_s'(\sin^2 \varphi_1 + \sin^2 \varphi_N), \quad (1)$$

where the direction of magnetization is measured from the normal of film plane. The first term covers the exchange coupling between magnetizations on adjacent atomic layers. The second and third terms are for the in-plane shape anisotropy and the normal surface anisotropy, respectively. The stable magnetization configuration is determined by minimizing the energy functional (1). For numerical calculation in this section, we take $\frac{1}{2}JM_s^2 = 1$ and $\hat{a} = 1$ (lattice constant).

Fixing the magnetic constants, we have found a spin–reorientation transition from the perpendicular uniform configuration to a canting one as the number of layers increases from $N=2$. A further transition has also been observed, where the canting configuration is switched into the uniform in-plane one. The phase diagram with the number of atomic layers and the surface anisotropy as variables is depicted in Fig. 1 for two different values of volume anisotropy. The region below/above and to the right/left of the right/left phase boundary is one of perpendicular/in-plane magnetization, the region in between is one of canting magnetic structure. The phase boundaries consist of steps, as a result of the discrete variation of the number of atomic layers. The locations of the phase boundaries depend sensitively on the value of volume anisotropy. We have calculated magnetic configurations in films of $N=2$–$20$ and various values of $K_s'$ and $K_v'$. We then find that scaling into variables $(N - \Delta N)\sqrt{K_v'}$ and $K_s'/\sqrt{K_v'}$, where $\Delta N$ is a fitting parameter, all the phase boundaries for $K_v' \leqslant 0.1$ in units of $JM_s^2$ such as those shown in Fig. 1 fall into two smooth curves as in Fig. 2. Here $\Delta N = 2.2$ is selected in order to obtain the best fitting.[6] For realistic materials like Fe, one has $K_v' \simeq 0.003$ in unit of $JM_s^2$ and thus the criterion on the volume anisotropy for scaling is satisfied well. This fact implies the presence of the following two scaling relations in spin–reorientation transitions, one among the film thickness, volume anisotropy, and exchange stiffness: $(N-\Delta N)\sqrt{K_v'/(JM_s^2)}$, the other among the surface anisotropy, volume anisotropy, and exchange stiffness: $K_s'/\sqrt{K_v' JM_s^2}$.[6]

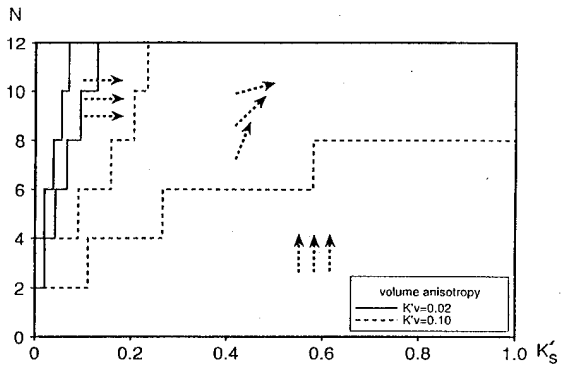



FIG. 1. Phase diagram with the volume anisotropy as a parameter. The dashed arrows denote the magnetization configuration in each phase (Ref. 6).

 0021-8979/96/79(8)/5842/3/$10.00 © 1996 American Institute of Physics

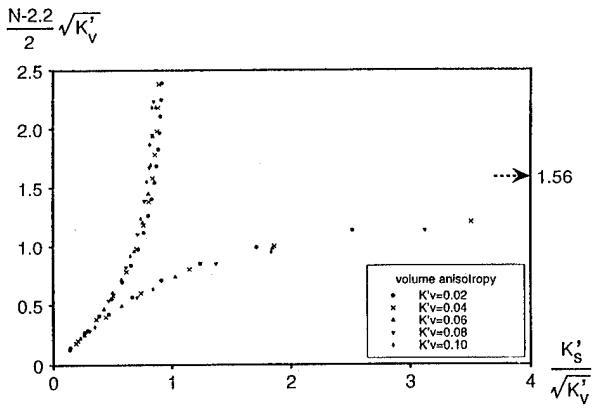



FIG. 2. Scaled phase diagram (Ref. 6).

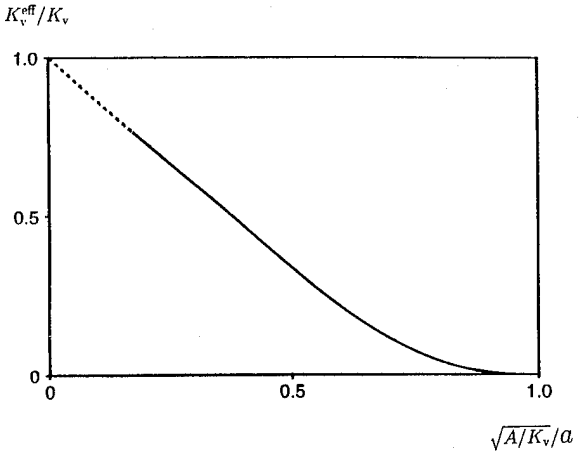



FIG. 4. Thickness dependence of the effective anisotropy (Ref. 9).

## III. CONTINUUM MODEL

In order to understand the above numerical results, we introduce the continuum model. Consider a thin magnetic film of thickness $2a$: On the surfaces there exist perpendicular anisotropies $K_s$. Within the film the volume anisotropy $K_v$ is in the film plane. The exchange stiffness $A$ is ferromagnetic and finite. We assume that the magnetization is uniform in the in-plane directions. Then, half of the total magnetic energy per unit area is expressed by[7–9]

$$\gamma=\int_0^a\left[A\left(\frac{d\varphi}{dz}\right)^2-K_v\sin^2\varphi\right]dz+K_s\sin^2\varphi(0), \qquad (2)$$

where the $z$ axis is taken to be normal to the film plane and the origin at the bottom surface. The relations among the magnetic quantities in functionals (1) and (2) are given as

$$\tfrac{1}{2}JM_s^2\hat{a}=A,\quad K_v'/\hat{a}=K_v,\ \text{and}\ K_s'=K_s.$$

The stable magnetization configuration is determined by solving the variational problem for energy functional (2). It is then revealed that there exists the first critical thickness[9,8] $a_{c1}=\sqrt{A/K_v}\tan^{-1}(K_s/\sqrt{AK_v})$, so that for $a\leqslant a_{c1}$ the stable configuration is uniform and magnetization stands normally to the film plane. For materials with surface anisotropy satisfying $K_s<\sqrt{AK_v}$, there exists the second critical thickness[9,8] $a_{c2}=\sqrt{A/K_v}\tanh^{-1}(K_s/\sqrt{AK_v})$, so that for $a\geqslant a_{c2}$, the magnetization is aligned uniformly within the film plane. For $a_{c1}<a<a_{c2}$, the spin configuration is not uniform in the vertical direction: The spin direction at $z=a$ is determined by[9]

$$\frac{K_s}{\sqrt{AK_v}}=\frac{\mathrm{sn}[a\sqrt{K_v/A},\sin\varphi_a]\,\mathrm{dn}[a\sqrt{K_v/A},\sin\varphi_a]}{\mathrm{cn}[a\sqrt{K_v/A},\sin\varphi_a]}, \qquad (3)$$

with $\varphi_a\equiv\varphi(a)$, and the magnetization configuration is expressed by $\varphi_a$ as[9]

$$\varphi(z)=\sin^{-1}\left\{\sin\varphi_a\,\frac{\mathrm{cn}[(a-z)\sqrt{K_v/A},\sin\varphi_a]}{\mathrm{dn}[(a-z)\sqrt{K_v/A},\sin\varphi_a]}\right\}$$

$$\text{for}\ 0\leqslant z\leqslant a, \qquad (4)$$

where $\mathrm{sn}[x,k]$, $\mathrm{cn}[x,k]$, and $\mathrm{dn}[x,k]$ are Jacobi elliptic functions. The phase diagram of magnetization configuration obtained from the above formalism is given in Fig. 3. The dashed arrow in Fig. 3 denotes $a\sqrt{K_v/A}=\pi/2$, where the phase boundary $a_{c1}$ saturates. Good coincidence is found between the phase diagrams in Figs. 2 and 3. Thus, the results derived by the discrete model have been explained analytically. On the other hand, this coincidence implies the sufficiency of the continuum approach in study of magnetic properties of ultrathin magnetic films of several atomic layers.

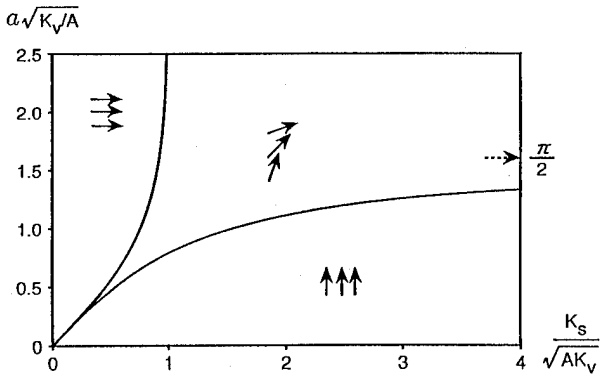



FIG. 3. Phase diagram derived by the continuum model (Ref. 6).

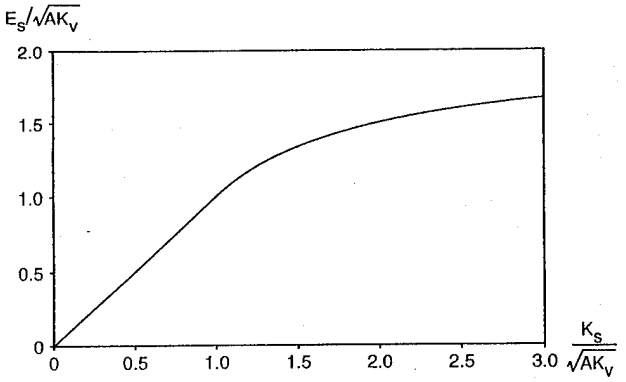



FIG. 5. Relation between the surface anisotropy and surface energy.

## IV. ESTIMATION OF SURFACE ANISOTROPY

Let us investigate the energy stored in the film per unit area at large thicknesses. For this purpose, we only have to study the continuum model, since for film thicknesses much larger than the lattice spacing the continuum approximation is sufficient. Integrating Eq. (2) one obtains the following expression for magnetic energy as a function of $\varphi_a$ for $a > a_{c1}$:[9]

$$\gamma = -aK_v \sin^2\varphi_a + K_s\left(\frac{\mathrm{cn}[a\sqrt{K_v/A},\sin\varphi_a]}{\mathrm{dn}[a\sqrt{K_v/A},\sin\varphi_a]}\right)^2 \sin^2\varphi_a + 2\left\{E\left[\frac{\pi}{2},\sin\varphi_a\right] - E\left[\sin^{-1}\left(\frac{\mathrm{cn}[a\sqrt{K_v/A},\sin\varphi_a]}{\mathrm{dn}[a\sqrt{K_v/A},\sin\varphi_a]}\right),\sin\varphi_a\right]\right\}$$
$$-2\cos^2\varphi_a\left\{F\left[\frac{\pi}{2},\sin\varphi_a\right] - F\left[\sin^{-1}\left(\frac{\mathrm{cn}[a\sqrt{K_v/A},\sin\varphi_a]}{\mathrm{dn}[a\sqrt{K_v/A},\sin\varphi_a]}\right),\sin\varphi_a\right]\right\}, \tag{5}$$

where $F[x,k]$ and $E[x,k]$ are elliptic integrals of the first and second kind, respectively. As $\varphi_a$ can be determined by Eq. (3) as a function of film thickness, we can evaluate the thickness dependence of the effective anisotropy $K_v^{\mathrm{eff}}$ defined by $K_v^{\mathrm{eff}} \equiv -\gamma/a$ using the above relation. The result is depicted in Fig. 4. It is found that the asymptote of the effective anisotropy for large thickness is given as

$$K_v^{\mathrm{eff}} \simeq K_v - \frac{E_s}{a}, \tag{6}$$

where $\varphi_a = \pi/2$ for large thicknesses has been used.[9]

The coefficient $E_s$ in Eq. (6) is the physical quantity observed in ferromagnetic resonance experiments,[5] which should be considered as a surface energy. In the case of $K_s > \sqrt{AK_v}$, where the canting configuration remains stable even at large thicknesses, we obtain[9]

$$E_s = 2\sqrt{AK_v} - \frac{AK_v}{K_s}. \tag{7}$$

Since the large surface anisotropy is relaxed into the canting structure, the surface energy has two contributions, one from the surface anisotropy and the other from wall energy of the canting structure. The surface anisotropy, usually defined in the same way as in energy functionals (1) and (2), is not equal to the slope $E_s$ of extrapolation formula (6) in the case of $K_s > \sqrt{AK_v}$. Instead it should be estimated from $E_s$ as

$$K_s = \frac{AK_v}{2\sqrt{AK_v} - E_s}. \tag{8}$$

In the case of $K_s < \sqrt{AK_v}$, uniform in-plane magnetic configuration is stable for $a > a_{c2}$ and Eq. (6) is established exactly in this region of thickness. Since no wall energy is involved in this case, one has simply

$$K_s = E_s. \tag{9}$$

For iron in Fe(100)/Ag(100) superlattice, one has $K_s/\sqrt{AK_v} \simeq 0.14$. Therefore, relation (9) is applicable for samples of transition metals. Relation (8) should be used where the wall energy $\sqrt{AK_v}$ is small, the case possibly realized in samples of rare earth metals. The relation between the surface energy and the surface anisotropy is summarized in Fig. 5.

## V. SUMMARY

Spin–reorientation transitions with the variation the film thickness and the magnetic constants are clarified. Scaling relations among the relevant quantities in these transitions are derived. It is shown that the continuum approximation is sufficient in the study of the spin–reorientation transitions in magnetic ultrathin films of several atomic layers. A complete formula is presented for the evaluation of surface anisotropy via ferromagnetic resonance techniques.


[1] M. N. Baibich, J. M. Broto, A. Fert, F. Nguyen van Dau, F. Petroff, P. Etienne, G. Creuzet, A. Friederich, and J. Chazelas, Phys. Rev. Lett. **61**, 2472 (1988).
[2] J. Ferré, G. Pénissard, C. Marliere, D. Renard, P. Beanvillain, and J. P. Renard, Appl. Phys. Lett. **56**, 1588 (1990).
[3] S. D. Bader, D. Q. Li, and Z. Qui, J. Appl. Phys. **76**, 6419 (1994).
[4] L. Néel, J. Phys. Rad. **15**, 376 (1954).
[5] C. Chappert and P. Bruno, J. Appl. Phys. **64**, 5736 (1988).
[6] X. Hu, R. B. Tao, and Y. Kawazoe (unpublished).
[7] Continuum models have been used for study of magnetic structures in semi-infinite systems with surface anisotropy by several authors: D. L. Mills, Phys. Rev. B **39**, 12306 (1989); R. C. O'Handley and J. P. Woods, *ibid.* **42**, 6568 (1990); A. Aharoni, *ibid.* **47**, 8296 (1993).
[8] A. Thiaville and A. Fert, J. Magn. Magn. Mater. **113**, 161 (1992).
[9] X. Hu and Y. Kawazoe, Phys. Rev. B **51**, 311 (1995).

# Perpendicular magnetization and surface magnetoelastic anisotropy in epitaxial Cu/Ni/Cu (001)

Gabriel Bochi, C. A. Ballentine, H. E. Inglefield, C. V. Thompson, and R. C. O'Handley
*Massachusetts Institute of Technology, Cambridge, Massachusetts 02139*

Epitaxial Ni films (2.0 nm$<h<$14 nm) have been grown on Cu/Si (001) and capped with 2.0 nm of Cu in a molecular beam epitaxy chamber. Their magnetic anisotropy has been measured *ex situ* in a vibrating sample magnetometer. Perpendicular magnetization is preferred over a broad Ni-thickness range: 25$\leqslant h\leqslant$140 Å. The quantitative anisotropy data are not well described by a model including bulk and surface magnetocrystalline anisotropy, $K^b+K^s h$, magnetostatic energy, and bulk magnetoelastic energy, $B^b e(h)$. If surface magnetoelasticity $B^s e/h$ is considered, the data are well described and values for $K^s$ and $B^s$ consistent with Néel's model are determined. © *1996 American Institute of Physics.* [S0021-8979(96)21708-8]

The effective magnetic anisotropy in thin films is altered due to reduced atomic coordination symmetry at the surface,

$$K^{\text{eff}}=K^{\text{bulk}}+\frac{K^{\text{surface}}}{h}. \tag{1}$$

Magnetic surface anisotropy is often justified in terms of Néel's phenomenological model.[1] It is not widely recognized that strain-dependent magnetic surface anisotropy comes as naturally from Néel's pair-interaction model as does the strain-dependent surface magnetocrystalline anisotropy of Eq. (1),[2]

$$B^{\text{eff}}=B^{\text{bulk}}+\frac{B^{\text{surface}}}{h}. \tag{2}$$

Here, $B$ is the magnetoelastic (ME) coupling coefficient related to the negative of the magnetostriction constant by elastic moduli. The total magnetic surface anisotropy energy is then given by a relation of the form $E^{\text{surface}}=K^s+B^s e$, where $e$ represents the appropriate components of the strain tensor in the magnetic thin film.[3]

Several experimental results have unambiguously demonstrated that ME interactions at surfaces and in thin films can be significantly different than in the bulk. Zuberek *et al.*[4] found that the effective magnetostriction constant of Ni/Ag multilayers goes from negative to positive values as the Ni film thickness approaches zero. Sun and O'Handley[5] found that the surface ME coupling coefficient can differ sharply from the bulk value in Co-rich and Fe-rich amorphous alloys. More recently, Song *et al.*[6] measured the effective ME coupling coefficient in polycrystalline NiFe/Ag/Si, NiFe/Cu/Si, and Ni/$SiO_2$/Si thin films by a direct *in situ* method. $B^{\text{eff}}$ was shown to diverge from the bulk value to more positive values for film thicknesses below 150 Å and to take giant positive values in films thinner than 40–60 Å due to a significant surface contribution. The magnetostriction of ultrathin polycrystalline Fe films has also been measured directly *in situ*.[7] Significant deviations from the bulk value were observed for Fe film thicknesses below 100 Å. The effective magnetostriction constant was shown to change sign when the Fe film thickness was between 80 and 30 Å. Bochi *et al.*[8] showed that published data on the magnetic anisotropy in epitaxial fcc (111) Co/Cu superlattices can be more effectively interpreted by inclusion of a surface ME term. Their analysis implied that the effective ME coupling coefficient of fcc Co/Cu (111) multilayers changes sign around a Co thickness of 9 Å.

In the present work, we report the behavior of both the magnetic anisotropy and the ME coupling in epitaxial Cu/Ni/Cu/Si(001) sandwiches. We show that the interpretation of the dependence of the magnetic anisotropy energy on Ni film thickness is severely wanting without the inclusion of a strain-dependent magnetic surface anisotropy term (the surface ME anisotropy energy). Using a phenomenological model developed recently,[8] we are able to determine the surface magnetocrystalline ($K^s$) and surface ME ($B^s e_0$) anisotropy energies corresponding to the Ni/Cu (001) interface. The variation of the effective ME coupling coefficient, $B^{\text{eff}}$, with Ni film thickness is also determined.

Our (20 Å Cu)/Ni/(2000 Å Cu) sandwiches were deposited at room temperature on Si (001) substrates by molecular beam epitaxy. The details of the experimental procedures are given elsewhere.[9–11] The crystallographic quality of the sandwiches was studied *in situ* by reflection high-energy electron diffraction and *ex situ* by x-ray diffraction and transmission electron microscopy (TEM). Using plan-view TEM, we observed both 60° and 90° misfit dislocations (MDs) at the Ni/Cu (001) interface and we measured their densities as a function of Ni film thickness.[10,11] MDs were present in Ni/Cu (001) thin films with Ni thicknesses of 25 Å and greater but not in the 15-Å-thick films. This indicates that the critical thickness $h_c$ for the onset of MDs is between 15 and 25 Å. For Cu/Ni/Cu (001) sandwiches, we observed dislocations in Ni films as thin as 30 Å, indicating that $h_c<30$ Å.[12] We also measured the average in-plane biaxial tensile misfit strain in the Ni films as a function of film thickness in Ni/Cu/Si (001) epitaxial thin films by measuring the substrate curvature using an optical interferometry technique.[9,11] The effective magnetic anisotropy, $K^{\text{eff}}$, of Cu/Ni/Cu (001) was measured *ex situ* as a function of Ni film thickness, $h$, using a vibrating sample magnetometer where 10 kOe fields were available to saturate the sandwiches both in-plane and perpendicular to the plane. *In situ* magneto-optic Kerr effect measurements on Ni/Cu/Si (001) were reported earlier.[9]

Our measurements of $K^{\text{eff}}h$ vs $h$ are shown in Fig. 1. The

 0021-8979/96/79(8)/5845/3/$10.00 © 1996 American Institute of Physics 

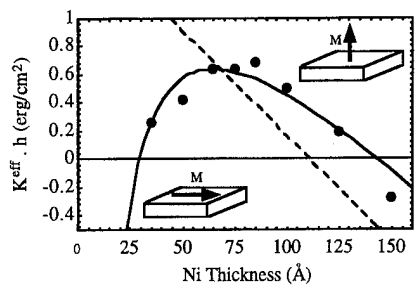



FIG. 1. $K^{\text{eff}}h$ vs Ni film thickness for our Cu/Ni/Cu (001) sandwiches. The solid curve is a plot of $K^{\text{eff}}(h)$ vs $h$ using Eq. (6) and the magnetic surface energies in the first row of Table I. The dashed straight line is the best fit to the data using Eq. (3).

first important result is that perpendicular magnetic anisotropy dominates up to Ni thicknesses of approximately 135 Å in Cu/Ni/Cu (001) sandwiches. This is in agreement with the results of Naik *et al.*[13] and the ones of Jungblut *et al.*[14] The region of perpendicular magnetization is exceptionally broad in Cu/Ni/Cu (001) and is twice as large as the one of Ni/Cu (001) thin films.[9] The second important result of Fig. 1 is that the magnetization easy axis exhibits *two* switching thicknesses: one near 135 Å, which our measurements confirm, and another one near 20 Å.[14] Two switching thicknesses for the magnetization easy axis have also been reported for Ni/Cu(001) thin films.[9]

It is common practice to explain the behavior of the magnetic anisotropy of epitaxial (001) thin films sandwiched between two identical nonmagnetic layers in terms of a phenomenological model, where $K^{\text{eff}}$ is the sum of the bulk magnetostatic (MS) energy, $2\pi M_s^2$, the bulk ME anisotropy energy, and a magnetic surface anisotropy energy $K^s$,[8]

$$K^{\text{eff}}h=[2B_1e_0(h)-2\pi M_s^2]h+2K^s. \tag{3}$$

In Eq. (3), we omitted the bulk magnetocrystalline anisotropy because it is negligible for Ni/Cu (001) thin films. $B_1$ is the Ni bulk ME coupling coefficient and $e_0(h)$ is the average biaxial in-plane misfit strain in the magnetic film. For $h<h_c$, $e_0(h)=\eta$, the film–substrate lattice mismatch [$\eta$=2.6% in Ni/Cu (001)]. Equation (3) then predicts $K^{\text{eff}}h$ to be a linear function of $h$ with a slope given by $2B_1\eta-2\pi M_s^2$ and intercept equal to $2K^s$. For $h>h_c$, $e_0(h)$ decreases with film thickness as the misfit strain is accommodated by MDs. Using the form of strain suggested by Chappert and Bruno,[15] $e_0(h)=\eta h_c/h$, Eq. (3) predicts that, for $h>h_c$, a plot of $K^{\text{eff}}h$ vs $h$ is a straight line with a slope of $-2\pi M_s^2$ and intercept $2[B_1\eta h_c+K^s]$. The above two straight lines would intersect exactly at $h_c$, thus forming a kink in the $K^{\text{eff}}h$ vs $h$ data. Although the model of Eq. (3) could fit to our data reasonably well, a major problem exists. The change in slope in our data is centered at $h\approx 75$ Å but the critical thickness was observed to be below 30 Å.[12] Since our data points are all above 35 Å, they should fall along a straight line of slope $-2\pi M_s^2$ according to Eq. (3). The best fit to the data with such a model is the dashed line in Fig. 1. The model of Eq. (3) is therefore clearly inadequate for Cu/Ni/Cu (001).

The inadequacy of the model is not related to the fact that the bulk MS energy of Ni does not apply to Ni thin films. Our films show essentially constant magnetization (±10% relative to bulk) with thickness down to 30 Å. Further, a careful study by Huang *et al.*[16] showed that the Curie temperature of bulk Ni is valid for Ni films as thin as 35 Å. Another possible source of discrepancy between the model of Eq. (3) and the data could be the $1/h$ film thickness dependence generally accepted for the misfit strain $e_0(h)$. Our own measurements of the thickness dependence of the strain in Ni/Cu/Si (001) thin films yield[9,11]

$$e_0(h)\approx\frac{0.2}{h^{0.7}}, \tag{4}$$

expressed in percent with $h$ in Å. Whether we use the strain of Eq. (4) or other powers of $h$, there remains a strong divergence between the measured effective magnetic anisotropy energy of Fig. 1 and the model of Eq. (3). The source of discrepancy in the interpretation of Fig. 1 must therefore lie elsewhere.

By including in the free energy the surface ME anisotropy term predicted by the strain-dependent Néel model,[2] we obtain the following phenomenological equation for (001) epitaxial films sandwiched between two identical nonmagnetic layers:[8,9]

$$K^{\text{eff}}h=-2\pi M_s^2h+2\left(B_1+\frac{B^s}{h}\right)e_0(h)h+2K^s. \tag{5}$$

Substituting in the Chappert–Bruno strain[15] yields

$$K^{\text{eff}}h=-2\pi M_s^2h+2(B_1\eta h_c+K^s)+2\frac{B^s\eta h_c}{h}. \tag{6}$$

Fitting our data points with Eq. (6), we obtain the solid line shown on Fig. 1. The figure clearly shows that the presence of the $B^s/h$ term significantly improves the fit to the data and offers a rational explanation for the behavior of the data. Comparing the equation of the solid line and Eq. (6), and using $B_1=6.2\times10^7$ ergs/cm$^3$ and $h_c=18$ Å, we obtain $B^s$(Ni/Cu)(001)$\approx-67$ ergs/cm$^2$ and $K^s$(Ni/Cu)(001)$\approx+0.98$ erg/cm$^2$.

We have also fit our experimental data using the measured strain of Eq. (4). In this case, we obtained the following surface energies: $B^s$(Ni/Cu)(001)$\approx-52$ ergs/cm$^2$ and $K^s$(Ni/Cu)(001)$\approx+0.88$ erg/cm$^2$. Clearly, the thickness dependence of the misfit strain in the magnetic thin film affects the parameters deduced. We have also analyzed the data of Jungblut *et al.*[14] using the strain $e_0(h)=\eta h_c/h$ (with $h_c=15$ Å) in our phenomenological model, and found a good fit of

TABLE I. Magnetic surface anisotropy energies of the Ni/Cu(001) interface. The results obtained by applying Eq. (6) to our data and to those of Jungblut *et al.* (Ref. 14) are summarized in the first three rows. The energies reported by Jungblut *et al.* using the model of Eq. (3) are shown in the last row.

| Cu/Ni/Cu (001) | $B^s$ (ergs/cm$^2$) | $K^s$ (erg/cm$^2$) |
|---|---|---|
| $e_0(h)=\eta h_c/h$ | −67 | +0.98 |
| $e_0(h)=0.2/h^{0.7}$ | −52 | +0.88 |
| Jungblut *et al.* data | −37 | +0.73 |
| $e_0(h)=\eta h_c'/h$ Results of Jungblut *et al.* (Ref. 14) | ... | −0.40 |

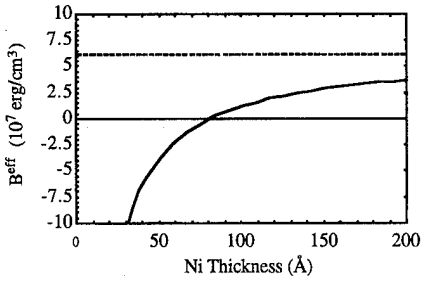



FIG. 2. Dependence of the effective ME coupling coefficient on Ni film thickness in Cu/Ni/Cu (001) sandwiches. We used the average value $B^s$(Ni/Cu)(001)$\approx -50$ ergs/cm$^2$ obtained from the data in Table I. The dashed line indicates the bulk ME coupling coefficient of Ni.

their data only if we included a surface ME term with $B^s$(Ni/Cu)(001)$\approx -37$ ergs/cm$^2$ and $K^s$(Ni/Cu)(001)$\approx +0.73$ erg/cm$^2$. When Jungblut *et al.* analyzed their data with Eq. (3), they found $K^s$(Ni/Cu)(001)$\approx -0.40$ erg/cm$^2$, assuming that $h_c \approx 40$ Å.

The above results on the surface magnetocrystalline anisotropy energy and the surface ME coupling coefficient of the Ni/Cu (001) interface are summarized in Table I. The surface magnetocrystalline anisotropy energies are all large and positive indicating that $K^s$(Ni/Cu)(001) together with the *bulk* ME anisotropy energy, $2B_1 e_0(h)$, account for the remarkable perpendicular magnetic anisotropy in Cu/Ni/Cu (001) sandwiches. On the other hand, the surface ME coupling coefficients are negative indicating that the *surface* ME anisotropy energy $2B^s e_0(h)/h$ favors an in-plane magnetization. At small Ni thicknesses ($h<20$ Å), this term becomes very large and is responsible for keeping the magnetization in plane. The magnetostatic energy, $2\pi M_s^2$, on the other hand, is responsible for bringing the magnetization back in plane for $h>135$ Å. Our model therefore gives a consistent explanation as to why the magnetization easy axis changes orientation twice. Double magnetization easy-axis transitions are also observed in bcc Fe/Ag (001)[17] and fcc Fe/Cu (001)[18] thin films. In both cases, both transitions occur for $h<h_c$, which means once again that they cannot be explained by Eq. (3) and that Eq. (5) or Eq. (6) does not apply.

The average values of the surface energies in the first three rows of Table I are $B^s \approx -50$ ergs/cm$^2$ and $K^s \approx +0.85$ erg/cm$^2$. In agreement with the predictions of the strain-dependent Néel model[2] for fcc (001) interfaces, $K^s$ and $B^s$ have opposite signs. Using the average surface ME coupling coefficient, we plot $B^{\text{eff}} = B_1 + B^s/h$ for Cu/Ni/Cu (001) sandwiches in Fig. 2. The figure indicates that significant deviations from the bulk value $B_1$ occur for films as thick as 200 Å and that $B^{\text{eff}}$ changes sign around 80 Å. This striking result questions the assumption, often encountered in the literature, that bulk ME coupling coefficients apply to ultrathin films and is supported by the recent direct measurements of magnetostriction by Song *et al.*[6] and Weber *et al.*[7] We emphasize that ME coupling in ultrathin films depends strongly on the *symmetry and chemistry* of the interfaces, not just on the film thickness, $h$.[9]

This work was supported by NSF Grants Nos. DMR 9022572 and 9410943 and ARO Contract No. DAAL-03-91-G0156.

[1] L. Néel, Compt. Rend. **237**, 1468 (1953); J. Phys. Radium **15**, 225 (1954).
[2] D. S. Chuang, C. A. Ballentine, and R. C. O'Handley, Phys. Rev. B **49**, 15084 (1994).
[3] R. C. O'Handley, O. Song, and C. A. Ballentine, J. Appl. Phys. **74**, 6302 (1993); E. du Trémolet de Lacheisserie, Phys. Rev. B **51**, 15925 (1995).
[4] R. Zuberek, H. Szymczak, R. Krishnan, and M. Tessier, J. Phys. C **49**, 1761 (1988).
[5] S. W. Sun and R. C. O'Handley, Phys. Rev. Lett. **66**, 2798 (1991); R. C. O'Handley and S. W. Sun, Mater. Res. Soc. Symp. Proc. **231**, 485 (1992).
[6] O. Song, C. A. Ballentine, and R. C. O'Handley, Appl. Phys. Lett. **64**, 2593 (1994).
[7] M. Weber, R. Koch, and K. H. Rieder, Phys. Rev. Lett. **73**, 1166 (1994).
[8] G. Bochi, O. Song, and R. C. O'Handley, Phys. Rev. B **50**, 2043 (1994).
[9] G. Bochi, C. A. Ballentine, H. E. Inglefield, C. V. Thompson, R. C. O'Handley, H. J. Hug, B. Stiefel, A. Moser, and H. J. Güntherodt, Phys. Rev. B **52**, 7311 (1995); G. Bochi, C. A. Ballentine, H. E. Inglefield, S. S. Bogomolov, C. V. Thompson, and R. C. O'Handley, Mater. Res. Soc. Symp. Proc. **313**, 309 (1993).
[10] H. E. Inglefield, C. A. Ballentine, G. Bochi, S. S. Bogomolov, R. C. O'Handley, and C. V. Thompson, Mater. Res. Soc. Symp. Proc. **308**, 765 (1993).
[11] H. E. Inglefield, G. Bochi, C. A. Ballentine, R. C. O'Handley, and C. V. Thompson, Mater. Res. Soc. Symp. Proc. **356** (1995).
[12] H. E. Inglefield, G. Bochi, R. C. O'Handley, and C. V. Thompson (unpublished).
[13] R. Naik, C. Kota, J. S. Payson, and G. L. Dunifer, Phys. Rev. B **48**, 1008 (1993).
[14] R. Jungblut, M. T. Johnson, J. aan de Stegge, A. Reinders, and F. J. A. den Broeder, J. Appl. Phys. **75**, 6424 (1994).
[15] C. Chappert and P. Bruno, J. Appl. Phys. **64**, 5736 (1988); P. Bruno and J.-P. Renard, Appl. Phys. A **49**, 499 (1989).
[16] F. Huang, M. T. Kief, G. J. Mankey, and R. F. Willis, Phys. Rev. B **49**, 3962 (1994).
[17] M. Stampanoni, A. Vaterlaus, M. Aeschlimann, and F. Meier, Phys. Rev. Lett. **59**, 2483 (1987).
[18] C. Liu, E. R. Moog, and S. D. Bader, Phys. Rev. Lett. **60**, 2422 (1988); D. P. Pappas, K.-P. Kämper, and H. Hopster, *ibid.* **64**, 3179 (1990).

# Magnetization reversal in patterned Co(0001) ultrathin films with perpendicular magnetic anisotropy

N. Bardou, B. Bartenlian, C. Chappert,[a] R. Mégy, P. Veillet, and J. P. Renard
*Institut d'Electronique Fondamentale, URA CNRS 022, Université Paris-Sud, 91405 Orsay, France*

F. Rousseaux and M. F. Ravet
*Laboratoire de Microstructures et Microelectronique, UPR CNRS 020, 196 Av. H. Ravera, BP107, 92225 Bagneux, France*

J. P. Jamet and P. Meyer
*Laboratoire de Physique des Solides, URA CNRS 002, Université Paris-Sud, 91405 Orsay, France*

Using x-ray lithography we have patterned dot arrays in Au/Co/Au(111) sandwiches based on ultrathin Co layers with perpendicular anisotropy. Large area arrays of dots with diameters of 1 and 2 $\mu$m have been obtained, keeping mostly undamaged the ultrathin Co layer. Hysteresis loops of the arrays depend drastically on the dot diameter. Magneto-optical domain visualization experiments confirm a magnetization reversal mechanism based on a large distribution of nucleation fields in the film, with complete reversal of the magnetization of one dot through the domain wall propagation after a local nucleation process. This could give information on the magnetization reversal processes in Au/Co/Au(111) continuous films. © *1996 American Institute of Physics.*
[S0021-8979(96)21808-4]

The study of magnetization reversal processes in thin and ultrathin (a few atomic layers thick) magnetic films is of wide interest both for fundamental research and for applications to magnetic recording and sensors. One way to get information on the intrinsic processes could be to reduce the lateral dimensions of the films to values comparable to the fundamental lengths of magnetism, like domain wall width or minimum domain size.[1] Such patterned films have also been proposed as new media for magnetic[2] or magneto-optical[3] recording. Defining geometrically the magnetic bit borders could indeed be a path toward drastic reduction of the bit size, without increasing the wall jaggedness, detrimental to the signal-to-noise ratio.[3]

We present a magnetic study of dot arrays patterned in Au/Co/Au(111) sandwiches based on ultrathin Co layers with perpendicular magnetic anisotropy. Large area arrays of dots with diameters of 1 and 2 $\mu$m have been obtained using x-ray lithography and ion-beam etching. Hysteresis loops of the arrays depend drastically on the dot diameter. Domain visualization experiments confirm a magnetization reversal mechanism based on a large distribution of nucleation fields in the film, coupled to complete reversal of the magnetization of one dot through domain wall propagation after a local nucleation process, in agreement with previous similar measurements on continuous films.[4]

Preparation techniques and the crystalline structure of our Au/Co/Au samples have already been published.[5,6] Depositions are made in a ultrahigh vacuum unit (below $5\times10^{-10}$ mbar) using Joule heating and electron beam evaporation. The first step is to grow a polycrystalline, atomically flat, fully textured, 28-nm-thick Au(111) buffer layer on a flat amorphous substrate. For regular magnetic studies we use float glass platelets. For the present study, float glass was replaced by a thermally oxidized Si(001) wafer, without loss of structural quality. On this Au(111) buffer, Co grows nearly layer by layer under its stable hcp(001) structure. The Co layer is then covered by a 7.5-nm-thick Au coverage to ensure protection during patterning processes and magnetic studies. Magnetic and magneto-optical properties of this Au/Co/Au(111) system have been extensively studied (cf. Ref. 7 and references herein). Note that up to about 10 atomic layers (AL) of Co, the easy magnetization axis remains perpendicular due to strong magnetic interface anisotropy. The magnetization reversal process shows two different behaviors, depending on the structural quality and Co thickness of the sample.[4] On top quality samples with up to about 7 AL of Co, one observes rare nucleation of reverse domains followed by rapid domain wall propagation throughout the sample. This gives almost perfectly square hysteresis loops in the perpendicular applied field. On "bad" samples, for instance deposited on a rough Au buffer, domain wall propagation is blocked by the defects and magnetization reversal occurs mostly through nucleation processes, which results in rounded hysteresis loops.

The magnetic properties thus depend drastically on the interface quality. Due probably to the polycrystalline character of the Au buffer layer, further heat treatment of the sample above 100 °C can easily damage it. Moreover, the adhesion of the Au layer on the amorphous substrate is very weak.[8] Patterning the sample without modifying its magnetic properties thus required careful adaptation of all microtechnology processes.[9]

X-ray lithography was used to define the structure of the dot arrays. This technique has demonstrated excellent resolution as low as 50 nm,[10] which will allow the exploration of mesoscopic magnetic phenomena from the classical to the quantum limit. It is furthermore a parallel process (like optical lithography), allowing us to rapidly treat large areas with a high throughput, which is of crucial importance for applications. Exposures were done using synchrotron radiation in the L2M facility at Super-ACO (Lure—orsay), through a mask realized using a current technology[11] based on a silicon carbide membrane and tungsten or gold absorber patterns.

[a]Electronic mail: chappert@ief-paris-sud.fr

 0021-8979/96/79(8)/5848/3/$10.00 © 1996 American Institute of Physics

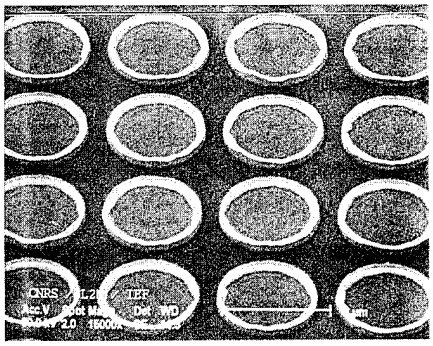


FIG. 1. Scanning electron microscopy view of a 2 $\mu$m diam by 2.2-$\mu$m spacing dot array, patterned on a Au/Co/Au(111) sandwich.

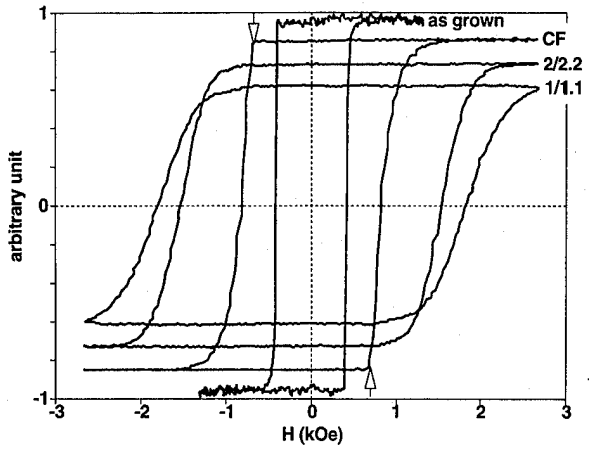



FIG. 2. Evolution of hysteresis loops vs dot diameter, for an Au/Co/Au(111) sample with 5 AL Co thickness.

Resist dot arrays were obtained on the magnetic sandwiches with a positive resist PMMA/MAA.

Ion milling was then used as the etching technique, with $Ar^+$ ions at 500 eV and 0.5 mA/cm$^2$, which corresponds to an Au etch rate of about 40 nm/min at normal incidence. Being anisotropic, this technique is in principle well adapted to image transfer down to nanometer scale, as it preserves very well the lateral dimensions and shape of the mask. However, it produces some Au redeposition on the resist walls.[9] After resist removal in a 20% $O_2$ plasma, thin Au "crowns" remain on top of the dots, as shown in Fig. 1. These crowns should be of no importance to the standard magnetization measurements reported here (polar magneto-optical Kerr effect at normal incidence), and are not expected to change the magnetic properties of the dots. Besides that, excellent topological qualities of the patterned structures could be obtained (Fig. 1 and Ref. 9).

For this study, a mask with four $1\times1$ mm$^2$ arrays has been used. Each array is composed of round dots with respective diameter over lattice spacing ratios of 1/1.1, 2/2.2, 1/2, and 2/4, all lengths given in $\mu$m. Finally, all etching processes have been performed through a metallic aperture, which keeps unetched a large area of the sample. This unetched part, which has nevertheless undergone all other nanofabrication steps, will hereafter be referred to as "continuous film" (CF), as opposed to the "as-grown" sample coming out of the deposition chamber.

Hysteresis loops were taken on each sample, using a sensitive magnetoptical Kerr effect experiment[7] with a laser beam focused to a diameter of 0.4 mm, for all different configurations of the samples (as grown, CF, and dot arrays). Typical results are displayed in Fig. 2 for a sample with 5 AL Co thickness and an excellent as-grown quality. Note first that we could find no significant effect of the dot spacing, as expected for such ultrathin films for which dipolar coupling is negligible. The hysteresis loop of the as-grown film appears perfectly square.[4] The loop measured on the CF is already quite rounded, with a surprisingly much higher coercive field. However, the beginning of the magnetization reversal remains abrupt, which could indicate that some initial domain propagation still exists in part of the sample, together with the existence of hard centers responsible for the slow approach to saturation. This shows that limited structural modifications have been induced in our samples by the nanofabrication process (a similar behavior was induced by substrate patterning in Ref. 3). The loops measured on the dot arrays are much more rounded, the coercive field increasing dramatically with decreasing dot diameter (Fig. 2). However, the magnetization reversal starts for CF and dot arrays at the same value $H_N$, a sign of some intrinsic origin for the process.

Indeed, one expects that, in micrometer size dot arrays patterned in high quality samples, the global magnetization reversal will be modified through the blocking of the domain wall propagation by the border of the dot. Assuming that each dot has its magnetization fully reversed by wall propagation following a nucleation event, the behavior will depend on the dot diameter through the spatial distribution of nucleation centers, leading to more rounded hysteresis loops and higher coercive fields with decreasing dot diameter. This looks like the crossover from a continuous film behavior to that of an assembly of magnetically independent grains with a large distribution of nucleation fields.

This picture has been confirmed by domain visualization experiments. For these experiments, we have used a polarization microscope. A cooled charge-coupled device camera acquires the images which are stored and processed in the camera's processing unit and a linked microcomputer. The spatial resolution of the camera (1 pixel) corresponds to 0.2 $\mu$m on the sample, but due to diffraction effects, the resolution is of the order of 0.5 $\mu$m. The light source is a high intensity blue light emitting diode (Nichia Chemical). Our experimental setup allows us to obtain images of the magnetization state of the sample by using an image of the saturated sample as a reference in order to cancel out intensities of nonmagnetic origin. Besides, analysis of the images yields hysteresis loops of an assembly of dots as well as of single dots.

We now present polar Kerr measurements on the 1/2 and 2/4 arrays. Figure 3(a) displays the magnetic image of the unetched part of the sample (CF) obtained after partial reversal of the saturation magnetization following the application of a bias field $H_b$ of 700 Oe for 1 s. One observes many nucleation centers, together with a large domain developing by propagation of its domain wall. The presence of numerous

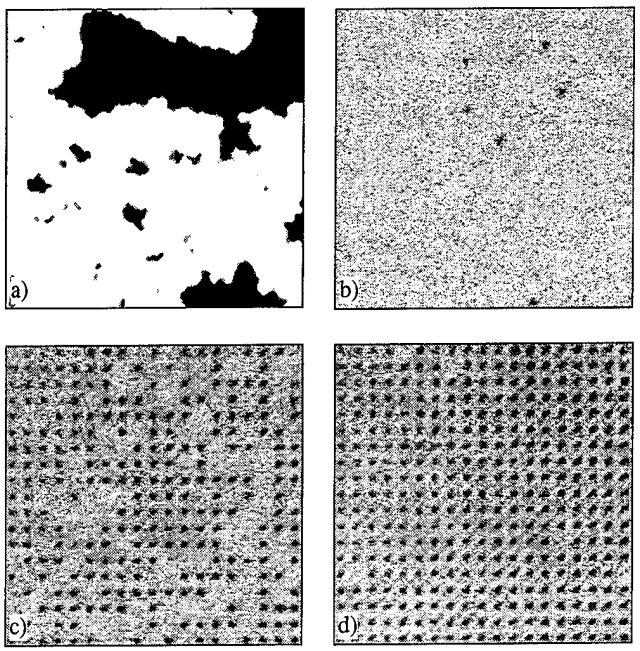



FIG. 3. Magneto-optic images of a 1/2 array of dots, taken after applying a bias field $H_b$ for 1 s: (a) unetched part with $H_b=0.96$ kOe; (b) $H_b=0.96$ kOe; (c) $H_b=1.44$ kOe; (d) $H_b=2.35$ kOe.

nucleation centers confirms that the photolithographic process has somewhat damaged the sample, as suggested by Fig. 2, but without totally suppressing domain wall propagation. Figures 3(b)–3(d) present magnetic images of large areas (including several hundred dots) of the 1/2 array, taken for increasing values of a bias field $H_b$ applied for 1 s, after saturation in reverse field. In these images, one observes an increase of the number of reversed dots with an increase of $H_b$.

From the images obtained for increasing values of $H_b$, one can rebuild the hysteresis loop of the sample: The result is in perfect agreement with the loops displayed in Fig. 2. But it is also important to measure the hysteresis loops of individual dots which have been seen to reverse their magnetization for different field values. As an example, Figs. 4(a) and 4(b) display the hysteresis loops of dots which flip for different values of the reversed bias field. These last pictures demonstrate that each dot has its own and very well-defined coercive field, with a square hysteresis loop which confirms that a dot is fully reversed by wall propagation once a nucleation event has occurred. Repeating the same experiment several times shows that each dot always reverses its magnetization for the same value of the coercive field. Thus, the spread of the coercive field which is observed on an assembly of dots, Fig. 2, comes from the distribution of the individual nucleation fields of the dots. Also, the above results confirm that there is no detectable magnetic coupling between the dots, contrary to other observations.[3]

It is also easy to reconcile the partial domain wall blocking on defects observed for the CF [Fig. 3(a)], and the picture developed above of complete magnetization reversal of individual dots through domain wall propagation. Indeed, as can be seen in Fig. 2, due to the large distribution of nucleation fields, most of the dots begin to reverse their magnetization at high fields—higher than the propagation field necessary to overcome the blocking on defects in the CF area.

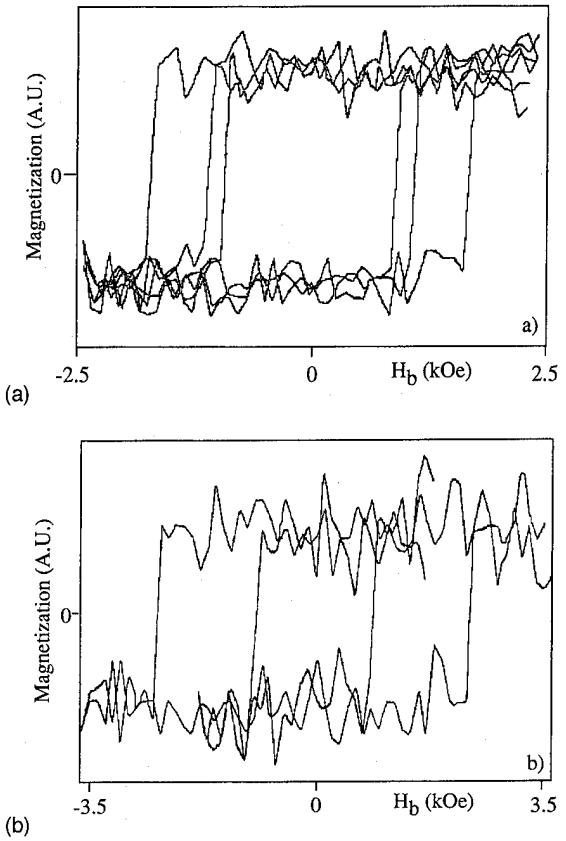



FIG. 4. Examples of hysteresis loops of individual dots: (a) single dots of a 2/4 array; (b) single dots of a 1/2 array.

Numerical simulations are in progress on the theoretical basis outlined above that will allow us to extract the distribution of nucleation fields in the films.

J. Ferré is acknowledged for fruitful discussions. This work was supported in part under the HCM grant "Magnetic Properties of Novel Ultrathin Films" of the European Union and by the DRET Contract No. 90 126.

[1] A. D. Kent, S. von Molnar, S. Gider, and D. D. Awschalom, J. Appl. Phys. **76**, 6656 (1994).
[2] P. R. Kraus, P. B. Fischer, and S. Y. Chou, J. Vac. Sci. Technol. B **12**, 3639 (1994).
[3] S. Gadetsky, T. Suzuki, J. K. Erwin, and M. Mansuripur, IEEE Trans. Magn. **30**, 4404 (1994); these proceedings.
[4] J. Pommier, P. Meyer, G. Penissard, J. Ferré, P. Bruno, and D. Renard, Phys. Rev. Lett. **65**, 2054 (1990).
[5] C. Cesari, J. P. Faure, G. Nihoul, K. Le Dang, P. Veillet, and D. Renard, J. Magn. Magn. Mater. **78**, 296 (1989).
[6] S. Ould-Mahfoud, R. Mégy, N. Bardou, B. Bartenlian, P. Beauvillain, C. Chappert, J. Corno, B. Lécuyer, G. Sczigel, P. Veillet, and D. Weller, Mater. Res. Soc. Symp. Proc. **313**, 251 (1993).
[7] R. Mégy, A. Bounouh, Y. Suzuki, P. Beauvillain, P. Bruno, C. Chappert, B. Lécuyer, and P. Veillet, Phys. Rev. B **51**, 5586 (1995).
[8] F. Didier and J. Jupille, Surf. Sci. **314**, 378 (1994).
[9] F. Rousseaux, D. Decanini, F. Carcenac, E. Cambril, M. F. Ravet, C. Chappert, N. Bardou, B. Bartenlian, and P. Veillet, J. Vac. Sci. Technol. B **13**, 2787 (1995).
[10] Y. Chen, R. K. Kupka, F. Rousseaux, F. Carcenac, D. Decanini, M. F. Ravet, and H. Launois, J. Vac. Sci. Technol. B **12**, 3959 (1994).
[11] A. M. Haghiri-Gosnet, F. Rousseaux, B. Kebabi, F. R. Ladan, C. Mayeux, A. Madouri, D. Decanini, J. Bourneix, F. Carcenac, H. Launois, B. Wieniewski, and E. Gat, J. Vac. Sci. Technol. B **8**, 1565 (1990).

# Magnetic force microscopy of single-domain single-crystal iron particles with uniaxial surface anisotropy

R. M. H. New, R. F. W. Pease, and R. L. White
*Department of Electrical Engineering, Stanford University, Stanford, California 94305*

R. M. Osgood
*Department of Applied Physics, Stanford University, Stanford, California 94305*

K. Babcock
*Digital Instruments Inc., 520 East Montecito Street, Santa Barbara, California 93103*

Lithographic patterning techniques have been used to fabricate arrays of submicron particles from a [110] single-crystal iron thin film with a strong uniaxial surface anisotropy and with an easy axis of magnetization lying in the [001] direction (in the plane of the film). Magnetic force microscopy images indicate that these islands are single domain over a wide range of island shapes and sizes. The uniaxial surface anisotropy is stronger than the shape anisotropy for the island geometries used, so the easy axes of the islands all lie roughly in the [001] direction, regardless of the island shape. Magnetic force images were also taken as both the magnetic tip and sample were subjected to a gradually increasing externally applied field. This technique allows us to monitor the magnetization reversal of individual islands and provides a direct measure of their switching fields. © *1996 American Institute of Physics.* [S0021-8979(96)21908-0]

## INTRODUCTION

The application of lithographic patterning techniques to the study of fine magnetic particles has permitted experimental measurements of single-domain magnetic islands with well-controlled sizes and shapes.[1,2] Most of these experiments have used soft magnetic materials with negligible magnetocrystalline anisotropy,[1–5] so the easy axis of magnetization of each patterned island was determined solely by its shape, and could be controlled by lithography. For hard magnetic materials with strong magnetocrystalline anisotropy it is more difficult to obtain small particles with predictable and well-defined easy axes: one must control not only particle shape, but also the crystallographic structure of the magnetic material.

In previous work, we studied the behavior of single-domain islands fabricated from a hard polycrystalline magnetic film.[6] Because of the inherent microstructural inhomogeneities in these polycrystalline films, the magnetic islands did not have predictable magnetic properties.[7,8] To obtain single-domain particles with more predictable magnetic properties, we have patterned islands from a 200-Å-thick single-crystal [110] iron film with an easy axis of magnetization (due to surface anisotropy) along the [001] direction.

## MAGNETIC FILM PREPARATION AND CHARACTERIZATION

The magnetic film to be patterned was deposited in a custom-built dc magnetron sputtering system using a procedure similar to that outlined in Refs. 9 and 10: a 200-Å-thick layer of single-crystal [110] iron was deposited onto an 890-Å-thick seed layer of [110] molybdenum, which was in turn deposited on a $[11\bar{2}0]$ sapphire substrate. Both the molybdenum and iron layers are bcc, and grow with their $[\bar{1}11]$ axes parallel to the [0001] axis of the sapphire. The sapphire substrate was a 2-in.-diam wafer with its wafer flat perpendicular to the [0001] direction. The orientation of the the iron [001] direction (which turns out to be the easy axis of magnetization) was therefore roughly 35° away from the wafer flat as shown in Fig. 1.

The crystal structure of the [110] iron film was examined using x-ray diffraction. Figure 2 shows the stereographic projection of a cubic system onto a [110] plane, as well as the locus of scattering vectors sampled during the x-ray scan. This locus intercepts only four allowed scattering vectors which are separated by 70° and 110°. The experimental data (Fig. 3) show peaks at the appropriate locations, indicating that the film is single crystal. Rocking curves taken across the [011] peak showed a full width at half-maximum width of 1.7°, consistent with good quality epitaxial growth.

Previous experiments[10] have shown that iron/molybdenum multilayers have a strong uniaxial anisotropy with an easy axis oriented along the [001] direction in the iron. Figure 4(a) shows a torque curve obtained from a multilayer sample. It has been shown that the anisotropy is due to surface effects and is not due to either bulk magnetocrystalline anisotropy or strain-induced anisotropy.[10] For a single-layer 200-Å-thick iron film, the anisotropy is also uniaxial and still believed to be due primarily to surface

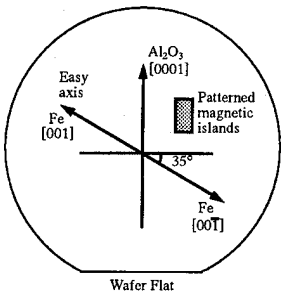



FIG. 1. This diagram indicates the orientation of the easy axis of magnetization with respect to the sapphire wafer flat. Note that the edges of the patterned features (to be shown later) will lie parallel and perpendicular to the wafer flat, and will not be aligned with the easy axis of magnetization.

 0021-8979/96/79(8)/5851/3/$10.00 © 1996 American Institute of Physics 

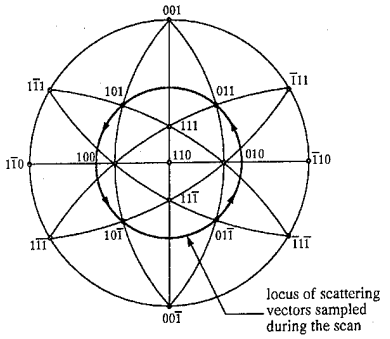



FIG. 2. The stereographic projection of a cubic system onto the [110] plane. The heavy line shows the locus of x-ray scattering vectors probed during the x-ray scan. For a single-crystal substrate, the scan should yield four peaks ([001], [101], [$10\bar{1}$], and [$01\bar{1}$]) separated from each other by 70° and 100°.

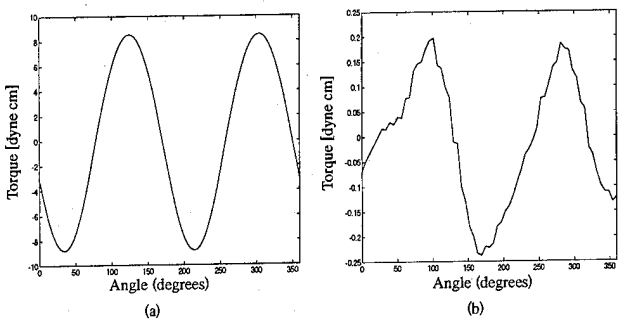



FIG. 4. Graph (a) is a torque curve for a [110] Fe/Mo multilayer film consisting of 40 bilayers, with each bilayer containing 25 monolayers of Fe and 25 monolayers of Mo. The combined thickness of Fe is 2030 Å. Graph (b) is a torque loop taken from a 9 $mm^2$ section of a 200-Å-thick [110] single-layer iron film on a molybdenum underlayer. The applied field was 15000 Oe.

effects. Figure 4(b) shows a torque loop from a single 200-Å-thick iron layer. The size of the anisotropy in a single layer is much smaller than for multilayers, however it is still significantly larger than the expected contribution from bulk magnetocrystalline anisotropy. For both single and multilayers, the easy axis is along the [001] axis of the iron. Hysteresis loops (not shown) were also used to confirm the easy-axis direction. Classic easy- and hard-axis loops were obtained for fields applied along the [001] and [$1\bar{1}0$] directions, respectively, and the coercivity for the easy axis loop was 60 Oe.

The sample used to obtain the torque loop of Fig. 4(b) was a 9 $mm^2$ area of 200-Å-thick iron with a total magnetic volume of $1.8\times10^{-7}$ $cm^3$. A frequency domain analysis of the torque loop indicates that the strongest harmonic (which gives rise to the uniaxial anisotropy) has an amplitude of 0.50 dyn cm. As long as the magnetization remains in plane, the anisotropy energy of the magnetic sample will be of the form $E=VK\sin^2\theta$, where $\theta$ is the angle between the magnetization and the [001] easy axis, $V$ is the magnetic volume of the sample, and $K$ is a uniaxial anisotropy constant. The torque measured by the torque magnetometer is $\tau=-VK\sin 2\theta$, so we have $VK=0.50$ dyn cm, and the uniaxial anisotropy constant is therefore $K=28\times10^5$ ergs/$cm^3$. This value is the bulk magnetocrystalline anisotropy constant which is equivalent to the surface anisotropy for a film thickness of 200 Å.

The patterning procedure of Ref. 11 was applied to the single-crystal iron films described above. A large area of film was patterned with rectangles of various shapes, sizes, and aspect ratios, with dimensions ranging from 0.1 to 3 $\mu$m.

## MAGNETIC FORCE MICROSCOPY

Atomic and magnetic force images of the magnetic islands (Figs. 5–7) were obtained using a commercial Nanoscope III scanning probe microscope. Two striking features emerge from these images. The first is that all of the particles, even the very large 1.0 by 3.0 $\mu$m islands, appear to be single domain. The second is that the magnetizations of the particles are all oriented roughly along the [001] or [$00\bar{1}$] directions (that is along the easy axis defined by the surface anisotropy of the unpatterned film) regardless of particle shape.

We can compare the shape and magnetocrystalline anisotropies for a 0.2 by 0.6 $\mu$m iron island patterned from a 200 Å thin film. We treat the island as an ellipsoid so that we can easily calculate demagnetizing coefficients. If $\alpha$ is the angle between the magnetization (assumed uniform) and the long axis of the island then the shape anisotropy energy density can be written as $E_{\text{shape}}=(1/4)M^2(N_a-N_b)\cos 2\alpha$, where $N_a$ and $N_b$ are demagnetizing factors for the long and

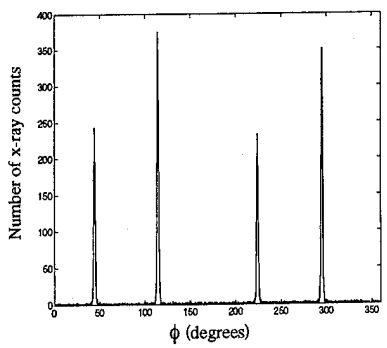



FIG. 3. An x-ray scan of the [110] iron film. There are four peaks, separated by 70° and 110° (see Fig. 2).

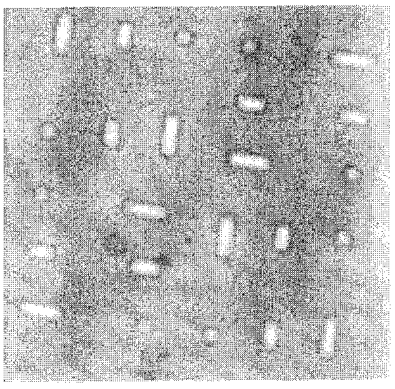


FIG. 5. Topographical atomic force microscopy image of single-crystal iron islands ranging in size from 0.2 by 0.2 $\mu$m to 0.2 by 0.6 $\mu$m.

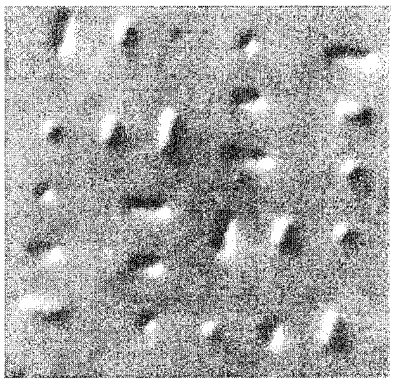


FIG. 6. Magnetic force image of the patterned islands shown in Fig. 5. The orientation of the easy axis of magnetization with respect to the edges of the patterned features is shown in Fig. 1. All of the particles are single domain, and the magnetizations are all directed roughly along the easy axis defined by the 001 crystallographic direction.

short axes of the island, respectively. Using $N_a=0.07\pi$ and $N_b=0.34\pi$, we obtain $E_{\text{shape}}=6\times10^5$ ergs/cm$^3$ $(\cos 2\alpha)$. We can compare this with the surface anisotropy energy density: $E_{\text{surface}}=-(1/2)K\cos 2\theta=-14$ ergs/cm$^3$ $(\cos 2\theta)$, where $\theta$ is the angle between the magnetization and the [001] axis of the iron. Since the surface anisotropy is larger than the shape anisotropy, we expect the easy axis to be determined primarily by the crystalline orientation rather than island shape.

Magnetic images were also taken as the sample and tip were subjected to a gradually increasing externally applied field. Although we observed that switching fields generally increased with particle size, we attribute this to tip-induced switching: fields from the imaging tip have a greater effect on smaller islands. Interpretation of images such as those of Fig. 8 is complicated by the effect of the external field on the magnetic tip. At high fields the tip magnetization is almost horizontal and images of single-domain particles are quite different from those of Figs. 6 and 7 in which the tip is vertically magnetized.[12,13]

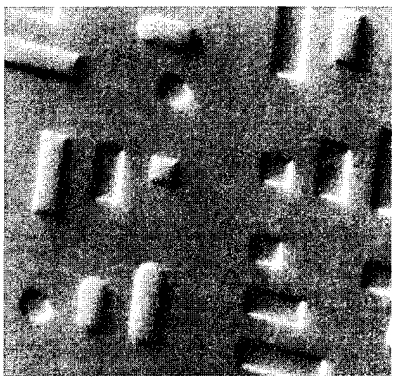


FIG. 7. Magnetic force images of single-crystal iron islands with sizes ranging from 1.0 by 1.0 $\mu$m to 1.0 by 3.0 $\mu$m. Some of the islands have deliberately smoothed corners or serrated edges. Unlike polycrystalline cobalt islands (Ref. 6), the patterned features are single domain even for large island sizes. For this sample, the silicon dioxide mask was not completely removed, so the magnetic signal is slightly stronger at the edges of the islands. The islands appear to be either sticking up out of the surface or receding into the surface, depending on their magnetization state.

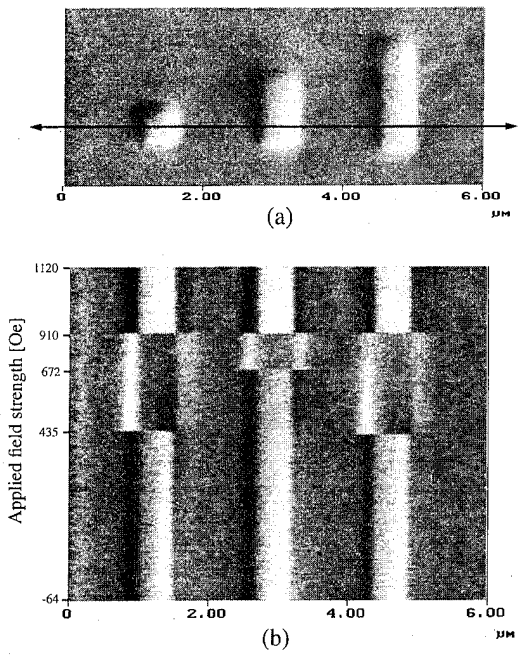



FIG. 8. Figure (a) shows a magnetic force image of three islands, each with a width of 0.5 $\mu$m, but with different lengths. In (b), the vertical scan direction has been turned off, and the magnetic tip moves back and forth along a horizontal line ($\leftrightarrow$) as an externally applied field from an electromagnet is ramped up. The field is applied within five degrees of the easy axis of magnetization as shown in Fig. 1. Both the electromagnet and the islands are initially in a saturation remanent state [at the bottom of (b)]. As the field is increased, the left and right islands are the first to reverse their magnetizations (at 435 Oe) followed by the center island (at 672 Oe). At 910 Oe, the magnetization of the tip reverses so as to align itself with the applied field.

## ACKNOWLEDGMENTS

This work was performed under NSF Grant No. ECS8920652 and JSEP Grant No. DAAH 04-94-6-0058, with the assistance of an IBM fellowship, and with support from Hewlett–Packard. Electron beam exposures were performed by Judith Seeger at Hewlett–Packard.

[1] J. F. Smyth, S. Schultz, D. R. Fredkin, D. P. Kern, S. A. Rishton, H. Schmid, M. Cali, and T. R. Koehler, J. Appl. Phys. **69**, 5262 (1991).
[2] G. A. Gibson, J. F. Smyth, and S. Schultz, IEEE Trans. Magn. **27**, 5187 (1991).
[3] S. Y. Chou, M. Wei, P. R. Krauss, and P. B. Fisher, J. Appl. Phys. **76**, 6673 (1994).
[4] M. S. Wei and S. Y. Chou, J. Appl. Phys. **76**, 6679 (1994).
[5] A. D. Kent, S. von Molnár, S. Gider, and D. D. Awschalom, J. Appl. Phys. **76**, 6656 (1994).
[6] R. M. H. New, R. F. W. Pease, and R. L. White, J. Vac. Sci. Technol. B **13**, 1089 (1995).
[7] R. M. H. New, R. F. W. Pease, and R. L. White, IEEE Trans. Magn. **31**, 3805 (1995).
[8] R. M. H. New, R. F. W. Pease, and R. L. White, Sixth International Conference on Magnetic Recording Media, Oxford, July 1995 (unpublished).
[9] B. M. Clemens, R. M. Osgood, A. P. Payne, B. M. Lairson, S. Brennan, R. L. White, and W. D. Nix, J. Magn. Magn. Mater. **121**, 37 (1993).
[10] R. M. Osgood III, B. M. Clemens, R. L. White, and S. Brennan, Proc. Mat. Res. Soc. **317**, 439 (1994).
[11] R. M. H. New, R. F. W. Pease, and R. L. White, J. Vac. Sci. Technol. B **12**, 3196 (1994).
[12] R. D. Gomez, I. D. Mayergoyz, and E. R. Burke, IEEE Trans. Magn. **31**, 3346 (1995).
[13] R. Proksch, E. Runge, P. K. Hansma, S. Foss, and B. Walsh, J. Appl. Phys. **78**, 3303 (1995).

# Surface-induced miscibility gap in vapor deposited $Co_{1-x}Pt_x$ (abstract)

M. Q. Tran, A. L. Shapiro, P. W. Rooney, and F. Hellman
*Department of Physics, University of California at San Diego, La Jolla, California 92093-0139*

We have deposited (100) and (111) oriented single-crystal $Co_{1-x}Pt_x$ films ($x$=0.65, 0.75, and 0.86) over a range of growth temperatures from −50 to 800 °C. The Curie temperature is increased by up to 200 °C over the value expected for the homogeneous, chemically disordered alloy in the as-deposited films (of both orientations) grown near 400 °C. Measurements of the onset of magnetic ordering below the Curie temperature indicate separation into Co-rich and Pt-rich regions. High resolution x-ray measurements show no shift in the lattice constant or broadening of the x-ray peaks, and no observable strain for $x$=0.75, suggesting that the separated regions are small and epitaxially coherent. We interpret this as evidence for a previously unobserved miscibility gap. The bulk phase diagram shows no phase separation, but magnetic energy tends to drive the system toward immiscibility as demonstrated by the calculations of several workers. We suggest that the observed miscibility gap is an equilibrium *surface* effect, trapped into the bulk film by low bulk mobility.[1] Preliminary work by Rosengren and Kundrotas supports this idea. Large perpendicular magnetic anistropy is found in those films that exhibit an anomalously high Curie temperature (films grown near 400 °C). This anisotropy is likely related to the phase separation. After annealing at high temperatures, the Curie temperature approaches the homogeneous values and the anisotropy relaxes. © *1996 American Institute of Physics.* [S0021-8979(96)43408-X]

Work supported by DOE Grant No. DE-FG03-95ER45529 and the NSF-MRL program through the Center for Materials Research at Stanford University.

[1] P. W. Rooney, A. L. Shapiro, M. Q. Tran, and F. Hellman, Phys. Rev. Lett. **75**, 1843 (1995).

 0021-8979/96/79(8)/5854/1/$10.00 © 1996 American Institute of Physics

# Effects of magnetostatic interaction between two single-domain cobalt bars on crystal anisotropy and switching field (abstract)

Stephen Y. Chou and Linshu Kong
*NanoStructure Laboratory, Department of Electrical Engineering, University of Minnesota, Minneapolis, Minnesota 55455*

Understanding the magnetostatic field effects of a single-domain particle on its neighbors during thin film deposition and magnetic recording is essential to the development of magnetic recording media. Here, we present a unique study of such effects using nanofabrication technology and magnetic force microscopy (MFM). We fabricated pairs of single-domain cobalt bars. Each bar is 35 nm thick, 50 nm wide, and 1 $\mu$m long. The twin bars were oriented side-by-side on a silicon substrate with a spacing that varied from 50 to 1000 nm. In fabrication, a resist template was first created on a silicon substrate, followed by e-beam evaporation of cobalt into the bar-shaped openings of the template as well as on the top of the template. Then, the resist was dissolved making the cobalt on top of the template lift off. MFM showed that as-fabricated bars are single magnetic domain. We polarized the magnetic moment of the twin single-domain bars in the same direction and measured the magnetic field needed for the following three cases: (a) switching the magnetization direction of only one of the twin bars, $H_a$; (b) switching both bars, $H_b$; and (c) switching one bar after the other bar was physically removed by a nanotechnique, $H_c$. Two important facts can be seen. First, for a given bar spacing, $H_a<H_c<H_b$. The difference is due to the demagnetization field of the neighbor which is on the order of 150 Oe depending upon the bar spacing. Second, all three switching fields decrease significantly as the bar spacing becomes larger. For example, $H_c$ is 2050 Oe for a 300 nm bar spacing and 1700 Oe for 1000 nm spacing. The spacing dependence of $H_c$ clearly indicates that the intrinsic switching field of a bar has been significantly affected, during the cobalt deposition, by the demagnetization field of its neighbors. One explanation is that as soon as the first few atomic layers of cobalt were deposited into a nanoscale bar shaped opening in the resist template, a single domain is formed immediately creating a magnetostatic field. This field forces the $c$ axis of the cobalt that was later deposited into the neighboring bar to align with the field, therefore enhancing the crystal anisotropy and intrinsic coercivity of the neighboring bar. This study implies that a small topology variation on a magnetic disk substrate may cause a large local coercivity variation due to the enhancement of crystal anisotropy and coercivity induced during the deposition by the demagnetization field of neighboring single-domain particles. © *1996 American Institute of Physics.* [S0021-8979(96)43508-6]

# Synthesis and physical properties of $RNi_2B_2C$ and related materials (invited) (abstract)

R. J. Cava
*AT&T Bell Laboratories, Murray Hill, New Jersey 07974*

Copper oxides have dominated superconductivity research since 1987. The interplay between superconductivity and magnetism lies at the center of the controversy concerning the appropriate microscopic model for their superconductivity. We have recently been exploring a broad new family of materials which represent the first true quaternary intermetallic superconductors. Although their superconducting $T_c$'s are not competitive with the copper oxides, several of the members of the family have $T_c$'s equivalent to the highest $T_c$'s ever reported for intermetallic compounds. The materials are especially surprising in that they are not based on niobium alloys, but rather are based on the borides of nickel, palladium, and platinum. The presence of square planes of the normally magnetic transition metals nickel and palladium suggests that magnetism might play some role in the superconducting mechanism. There are experimental results on both sides of the magnetic/conventional mechanism question, and although at this time the community is leaning largely toward a conventional mechanism, this should still be considered an open question. The presence of superconductivity for some of the magnetic rare earth analogs results in interesting phenomena, especially in the case of $HoNi_2B_2C$ where the magnetic transition on the Ho sublattice is very close to the superconducting $T_c$. This talk will serve as an introduction to the chemistry, structure, and basic physical properties of these new materials, and will draw on the results of other groups, as well to present a summary view of these materials. © *1996 American Institute of Physics.*
[S0021-8979(96)63108-4]

 0021-8979/96/79(8)/5856/1/$10.00 © 1996 American Institute of Physics

# Neutron scattering studies of the magnetic order in $RNi_2B_2C$

J. W. Lynn and Q. Huang
*Reactor Radiation Division, National Institute of Standards and Technology, Gaithersburg, Maryland 20899 and University of Maryland, College Park, Maryland 20742*

S. K. Sinha
*Advanced Photon Source, Argonne National Laboratory, Argonne, Illinois 60439*

Z. Hossain, L. C. Gupta, and R. Nagarajan
*Tata Institute of Fundamental Research, Bombay 400 005, India*

C. Godart
*CNRS, UPR-209, 92195 Meudon, Cedex, France*

Neutron diffraction has been used to investigate the magnetic order of $RNi_2B_2C$. For R=Er the system orders antiferromagnetically at $T_N$=6.8 K, and this long range order coexists with superconductivity ($T_c$=11 K). The magnetic structure is an incommensurate, transversely polarized spin-density-wave state, with the modulation wave vector $\delta$ along the $a$ axis and the moments along $b$. $\delta$ has a temperature-independent value of 0.5526 ($2\pi/a$), with the structure squaring up at low temperatures. For R=Ho the moments also prefer to reside in the $a-b$ plane, but initially an incommensurate $c$-axis spiral state forms upon cooling, with $T_N \approx T_C \approx 8$ K. This $c$-axis spiral consists of ferromagnetic sheets of holmium moments in the $a-b$ plane, but with each sheet rotated by ~163° as one proceeds along the $c$ axis. Small $a$-axis peaks are also observed above the reentrant superconducting transition over a narrow temperature range, but the $c$-axis peaks dominate. Just below the reentrant transition at ~5 K the magnetic system locks-in to a simple commensurate antiferromagnetic structure, which permits superconductivity to be restored. The $c$-axis spiral, the $a$-axis component, the commensurate antiferromagnetic structure, and the superconducting phase are all in a delicate balance energetically, and this balance may be easily shifted by subtle changes in composition, magnetic field, and pressure. $DyNi_2B_2C$ orders antiferromagnetically at $T_N$=11 K, with the same commensurate antiferromagnetic structure as found for the holmium material at low temperature. The existence of superconductivity in some samples of $DyNi_2B_2C$ is consistent with the antiferromagnetic structure observed. © *1996 American Institute of Physics.*
[S0021-8979(96)02008-8]

## I. INTRODUCTION

The interaction between magnetic long range order and superconductivity has been an active area of interest for many years. In the Chevrel-phase and related compounds[1] the magnetic ordering temperatures are typically much lower than the superconducting transitions, and are in the temperature range where dipolar interactions play a crucial role. An even more extreme situation is found for the high-$T_c$ cuprate superconductors, where the rare earth ordering is typically ~1 K while the superconducting transitions are one to two orders of magnitude higher in temperature.[2] The new classes of quaternary intermetallic borocarbide superconductors such as the $RNi_2B_2C$ (R=magnetic rare earth ion) materials[3] have therefore attracted considerable attention because the magnetic ordering of the rare earth ions typically occurs at a much higher temperature,[4–12] which requires that exchange interactions dominant the energetics rather than dipolar interactions. The $T_c$'s are also comparable to the magnetic transition temperatures so that the interplay between these two cooperative phenomena is enhanced. Moreover, the evidence to date suggests that the superconductivity is three-dimensional in nature, unlike the layered cuprates, and that it originates from a relatively strong electron–phonon interaction so that the theories advanced to explain the original systems can be more readily compared and tested experimentally in these new materials. We have therefore been carrying out neutron scattering experiments to explore the nature of the magnetism and its interaction with superconductivity.[4–8]

The samples were prepared by melting the elements Y, Er, Ho, Dy, or Ce (purity 99.9%), Ni (99.9%), B (99.8%), and C (99.7%) in an arc-furnace under a protective atmosphere of flowing argon. The $^{11}B$ isotope was used to reduce the effects of nuclear absorption in the samples. The powder diffraction measurements were carried out on the diffractometers at National Institute of Standards and Technology (NIST), and more recently at the high-flux-isotope reactor (HFIR) spectrometers at the Oak Ridge National Laboratory when the NIST facilities were unavailable. A standard top-loading pumped He cryostat with a low $T$ capability of 1.7 K was employed to control the sample temperature. Data were collected on samples of Er, Ho, Dy, Ce, and Y. No magnetic order was found in either the Y[6] or Ce systems, and so no further discussion of these materials will be given here.

## II. RESULTS AND DISCUSSION

### A. $HoNi_2B_2C$

The first system to be investigated with neutrons was $HoNi_2B_2C$ because of the doubly reentrant superconducting behavior exhibited by this material.[3] Both the magnetic order and the superconductivity begin to develop at ~8 K, and

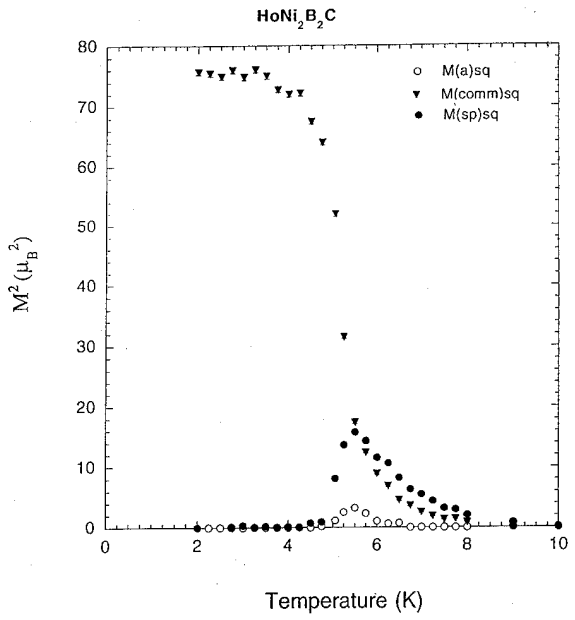



FIG. 1. Temperature dependence of the commensurate antiferromagnetic (▼) Bragg peaks, the incommensurate $c$-axis spiral peaks (●), and incommensurate the $a$-axis magnetic peaks (○) for this sample of $HoNi_2B_2C$. These data were taken on cooling.

initially two types of magnetic peaks were observed.[4] One set of peaks originates from a long-wavelength $c$-axis spiral antiferromagnetic structure, where the moments in the tetragonal plane are ferromagnetically aligned, but they spiral along the $c$ axis with a relative alignment of 163°. Thus this magnetic periodicity is incommensurate with the underlying chemical unit cell. The second set of peaks originates from a commensurate magnetic structure in which the Ho moments are again ferromagnetically aligned within the tetragonal plane, but are antiferromagnetically coupled along the $c$ axis (i.e., a relative alignment of 180°). The temperature evolution of these two types of peaks is shown in Fig. 1, where the intensities have been normalized to the nuclear peaks. Upon cooling through the ordering temperature we see that the intensity of the spiral peak in this sample is about twice the intensity of the (001) commensurate antiferromagnetic peak, which is quite different than found for other samples.[4,5,7–9] Thus the relative ratio of these two types of peaks varies dramatically from sample to sample, and demonstrates that these two types of magnetic order occur in distinct regions of the sample. Indeed, it is now clear[12] that both the magnetic and superconducting states are very sensitive functions of the sample composition for all these materials.

Upon further cooling the antiferromagnetic intensity begins to rapidly increase, while the intensity of the spiral state drops rapidly. This is just the temperature regime where the reentrant superconductivity is observed; the superconducting state that initially forms on cooling is quenched, but then is regained at lower temperature as the spiral intensity disappears and the antiferromagnetic state becomes fully established. At low $T$ only the commensurate antiferromagnetic order survives in this sample, and this magnetic order readily coexists with the superconductivity. Hence we believe that the spiral magnetic order and superconductivity are strongly coupled and competing states, with the development of the spiral amplitude driving the system normal.[4,5,7,8,13] The simple commensurate antiferromagnetic state, on the other hand, is not strongly coupled to the superconductivity, which allows the coexistence at low temperature.

Finally, we note that there is also a small component of the magnetism associated with an incommensurate $a$-axis modulation found by Goldman *et al.*,[9] as also shown in Fig. 1. The intensity of this peak is much smaller than for the spiral peaks, and exists over a narrower temperature range. In particular, note that the development of the $c$ axis and antiferromagnetic intensities occur together, and they start at a higher temperature where the $a$-axis intensity is zero. We also note that the maximum in intensity for the $a$-axis and $c$-axis reflections occurs at about the same temperature for this particular sample, while for other samples they occur at quite different temperatures. The relative intensity of these $a$-axis peaks and the temperature range where they appear also vary substantially from sample to sample. These results suggest that these $a$-axis peaks again originate from separate regions of the sample, and emphasizes that the antiferromagnetic, $c$-axis spiral, $a$-axis, and superconducting states are all delicate functions of the sample composition.

### B. $DyNi_2B_2C$

The Dy ions in $DyNi_2B_2C$ order antiferromagnetically at a $T_N$ just above 10 K. Within the $a-b$ plane the moments are ferromagnetically aligned, while the structure is antiferromagnetic along the $c$ axis.[10] This is the same commensurate, collinear antiferromagnetic structure that is found in the $HoNi_2B_2C$ material at low temperature. The superconducting state is very sensitive to the precise composition of the sample, and is present in some samples while absent in others.[14,15] If the superconducting state is present then there appears to be little interaction between it and the magnetic order parameter, with the two coexisting to low temperatures as found for $HoNi_2B_2C$.

The intensity of the (001) antiferromagnetic Bragg peak is shown in Fig. 2 as a function of temperature. The intensity varies smoothly with temperature, with no evidence of any hysteresis (in contrast to the case of $HoNi_2B_2C$). The solid curve is a fit to the $S=1/2$, $2d$ Ising model, with the fit being restricted to the data below 9 K to avoid the effects of critical scattering. The overall fit is relatively good, with $T_N=10.16$ K. However, this curve should be regarded primarily as a "guide-to-the-eye" rather than as establishing the $2d$ Ising model as appropriate; a more definitive test could be made with an extinction-free single crystal. We also tried fitting the data to a mean field model with a variable spin, but the fitted curve was not steep enough and the fit was not nearly as good. Finally, we obtained a low temperature ordered moment of 8.47(9) $\mu_B$ from the profile refinements of the full diffraction pattern.

### C. $ErNi_2B_2C$

For the Er system the superconducting transition occurs at $T_c \approx 11$ K, and superconductivity persists to low temperatures with no reentrant transitions or evidence of strong cou-

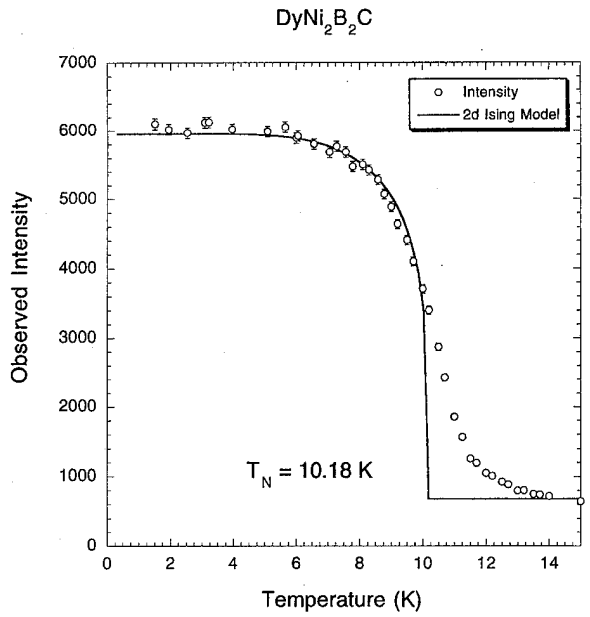



FIG. 2. Temperature dependence of the intensity of the (001) magnetic reflection for $DyNi_2B_2C$. The solid curve is a fit to the $2d$ Ising model.

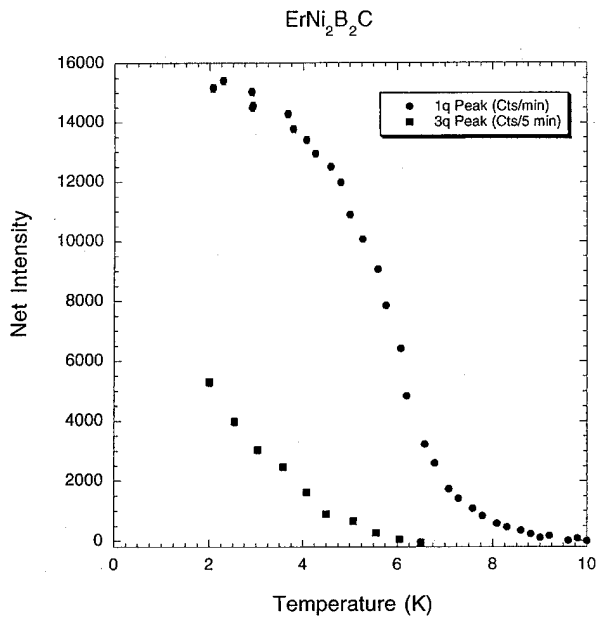



FIG. 3. Temperature dependence of the primary spin density wave intensity, and the third harmonic, in $ErNi_2B_2C$.

pling to the magnetic state. The antiferromagnetic ordering develops at $T_N$=6.8 K,[6,11] with the Er ions forming a transversely polarized, incommensurate spin density wave state. The modulation wave vector for this state is $\delta$=0.5526 ($2\pi/a$) and is approximately temperature independent, with the direction along the $a$ axis (or equivalently along the $b$ axis in this tetragonal system) with the spins directed along $b$ (or $a$). The staggered magnetization increases smoothly as the temperature is decreased below $T_N$ as shown in Fig. 3, and is nonhysteretic. Higher-order harmonics of $\delta$ also develop at lower temperatures, as also shown in Fig. 3, and indicate a squaring-up of the magnetic structure as we go to low $T$. This squaring-up of the spin density wave is expected, since a purely sinusoidal spin density wave cannot be the ground state of a local-moment system because this leaves many of the moments in a partially disordered state.

A refinement of the magnetic structure gives an ordered moment of 7.8 $\mu_B$/Er ion. There is also evidence of an induced moment of $-0.35$ $\mu_B$ on the Ni ions, as the refinement gives a small improvement when a Ni moment is included. However, such a small Ni moment is difficult to resolve unambiguously from the large Er moment, and it might indicate that a small adjustment in the model is needed rather than an actual Ni moment. In particular, from a physical standpoint an ordered Ni moment is difficult to reconcile with the coexistent superconducting state since it is believed that the Ni electrons are the ones that are predominantly involved in the Cooper pairing. The spin-depairing would then be expected to suppress the superconductivity if indeed the superconducting state originates from conventional BCS-type electron–phonon pairing. Clearly additional work will be needed to clarify this issue.

We note that the magnetic structure observed in $ErNi_2B_2C$ is reminiscent of the small $a$-axis peaks found in the $HoNi_2B_2C$ material as discussed above. Since this large-moment magnetic structure readily coexists with superconductivity in the Er system, it seems unlikely that the weak $a$-axis peaks in the Ho material could be the cause of the reentrant behavior in $HoNi_2B_2C$. Thus this is additional evidence that the reentrant superconducting behavior in the holmium system is associated with the incommensurate $c$-axis magnetic ordering.

## ACKNOWLEDGMENTS

We would like to thank Bryan Chakoumakos, Jaime Fernandez-Baca, and Brent Taylor for their generous assistance while we were visiting Oak Ridge National Laboratory. Research at the University of Maryland is supported in part by NSF, DMR 93-02380.

[1] *Topics in Current Physics*, edited by Ø. Fischer and M. B. Maple (Springer, New York, 1983), Vols. 32 and 34.
[2] *High Temperature Superconductivity* edited by J. W. Lynn (Springer, New York, 1990), Chap. 8.
[3] H. Eisaki *et al.*, Phys. Rev. B **50**, 647 (1994); R. J. Cava *et al.*, Nature (London) **367**, 252 (1994); R. Nagarajan *et al.*, Phys. Rev. Lett. **72**, 274 (1994).
[4] T. E. Grigereit *et al.*, Phys. Rev. Lett. **73**, 2756 (1994); **75**, 2629 (1995).
[5] Q. Huang *et al.*, Phys. Rev. B **51**, 3701 (1995).
[6] S. K. Sinha *et al.*, Phys. Rev. B **51**, 681 (1995).
[7] T. E. Grigereit *et al.*, Physica C **248**, 382 (1995).
[8] J. W. Lynn *et al.*, Phys. Rev. B **53**, 802 (1996).
[9] A. I. Goldman *et al.*, Phys. Rev. B **50**, 9668 (1994).
[10] J. Zarestky *et al.*, Phys. Rev. **51**, 678 (1995).
[11] P. Dervenagas, J. Zarestky, C. Stassis, A. I. Goldman, P. C. Canfield, and B. K. Cho, Physica B **212**, 1 (1995).
[12] H. Schmidt, M. Weber, and H. F. Braun, Physica C **235–240**, 779 (1994).
[13] M. S. Lin *et al.*, Phys. Rev. B **52**, 1181 (1995).
[14] Z. Hossain, R. Nagarajan, L. C. Gupta, S. K. Dhar, C. Godart, and R. Vijayaraghavan, these proceedings.
[15] B. K. Cho, P. C. Canfield, and D. C. Johnston, Phys. Rev. B **52**, 3844 (1995).

# Superconducting metastable phase in rapid quenched Y–Pd–B–C borocarbides

Valter Ström, K. S. Kim, A. M. Grishin, and K. V. Rao
*Department of Condensed Matter Physics, Royal Institute of Technology, S-100 44 Stockholm, Sweden*

Rapid quenched (RQ) palladium-based borocarbides with large fractions of the superconducting phase ($T_c$>20 K) have been obtained. Superconductivity is found to exist only in the RQ state. Thus, while the as cast $YPd_2B_2C$ is nonsuperconducting, the RQ material superconducts and has an x-ray diffraction (XRD)-pattern characteristic of a face-centered cubic fcc lattice with a lattice parameter of 4.15 Å. A sequential annealing study shows decay of the superconducting phase above 750 °C which correlates well with the reduction in the integral intensities of the XRD fcc peaks. A tentative phase diagram for superconductivity in the Y–Pd–B–C systems is presented. © *1996 American Institute of Physics.* [S0021-8979(96)40708-3]

## I. INTRODUCTION

In early 1994 a new family of intermetallic superconductors named *borocarbides* was discovered. Among these materials, the Pd-based borocarbide, i.e., $YPd_5B_3C_{0.35}$, has the highest reported $T_c$ (=23 K) for any intermetallic bulk superconductor.[1] Soon after, the crystal structure for Ni-based $LuNi_2B_2C$ was reported suggesting that the superconducting phase in the Pd system has a similar structure to that of the Ni-based borocarbides.[2–4] However, few studies have been reported on Pd-based borocarbides, because superconductivity in this system is due to a metastable phase for which conventional synthesizing methods like arc-melting will not be efficient yielding only a minor superconducting fraction if at all.

We use rapid quenching technique to identify the metastable superconducting phase. This approach makes it possible to suppress phase separation and obtain a more homogeneous material. As far as we know there are no other reports on RQ borocarbides except our earlier study on melt-spun $YNi_2B_2C$-ribbons.[5,6] In this article we present a detailed study of rapid quenched $YPd_2B_2C$ in which we find the x-ray diffraction (XRD)-pattern characteristic for a face-centered cubic (fcc)-structure ($a$=4.15 Å). The thermal stability of this phase shows that superconductivity is suppressed simultaneously with the intensities of the peaks of the fcc-like XRD-pattern. We also present a phase-diagram showing the optimum composition regimes for superconductivity in the Y–Pd–B–C system.

## II. EXPERIMENT

Ingots were prepared by arc-melting in pure (99.9997%) Ar gas. Bulk pieces, (99.9+% Y, C, Pd, 99.7% B), were used with sample batches of ~3 g. Ingots were remelted several times. Splat-quenching as well as melt spinning methods have been used. Melt-spinning was performed in pure Ar on a copper wheel with a peripheral velocity of 47 m/s. Splat-quenching was performed in an arc melter with a copper rod impinging at a hammer blow on a small droplet of the molten sample.

Magnetization was measured in a Quantum Design SQUID. XRD data were obtained in a Siemens D5000 diffractometer with Cu anode. For the annealing sequence we used the same sample of splat-quenched material with nominal composition $YPd_2B_2C$. The annealing was performed in a Perkin Elmer thermo-gravimetry instrument (TGS) in pure Ar atmosphere. The annealing system was purged with pure Ar for 7 h prior to each annealing (1 h).

## III. RESULTS AND DISCUSSIONS

### A. Rapid quenched Y–Pd–B–C

The pseudo-ternary phase-diagram in Fig. 1 shows the $T_c$'s for the as-melted and RQ samples. In Table I the $T_c$'s and zero-field cooled susceptibility (M/H) at 5 K are given. The as-melted Pd-samples show superconductivity only when the compositions lie *outside* the composition region around $YPd_2B_2C$ and $YPd_3B_3C$ (hereafter referred to as the "1221 region") of the phase-diagram and in these cases displaying a very shallow fraction of the superconducting phase. A $T_c$ as high as 21.5 K is found in the as-melted $YPd_5B_3C_{0.35}$, consistent with i.e., Ref. 1.

In contrast to what is observed in as-melted ingots, the best RQ Pd samples are found *within* the 1221 region. The compositions on the verge to superconductivity in the as-melted state are no longer superconducting. This may be understood in terms of two mechanisms: initial formation and the subsequent transformation of a superconducting

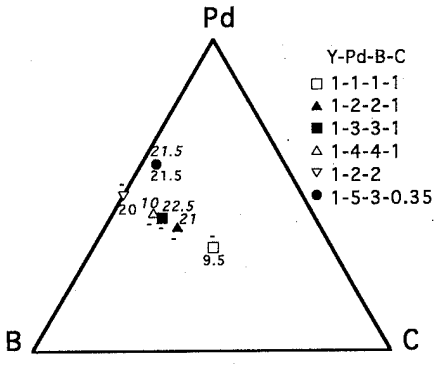



FIG. 1. Pseudoternary phase diagram showing the investigated compositions. $T_c$ (K) for RQ samples are in italics above symbol, for "as-melted" samples below symbol. "–" means $T_c$<5 K. Solid symbols denote large fractions of the superconducting phase when RQ.

 0021-8979/96/79(8)/5860/3/$10.00 © 1996 American Institute of Physics

TABLE I. $T_c$ and zero-field cooled magnetic susceptibility normalized to sample mass at 5 K, $-M_{mass}(5\text{ K})/H$, measured in 10 G. "−" means $T_c<5$ K. Note: demagnetization corrections have not been made.

| | $T_C$ (K) as-cast | $T_C$ (K) RQ | $-M(5\text{ K})/H$ (10−5 emu/g/G) as-cast | $-M(5\text{ K})/H$ (10−5 emu/g/G) RQ |
|---|---|---|---|---|
| YPdBC | 9.5 | ··· | 1 | 0 |
| $YPd_2B_2C$ | ··· | 21 | 0 | 1400 |
| $YPd_3B_3C$ | ··· | 22.5 | 0 | 30 |
| $YPd_4B_4C$ | ··· | 10 | 0 | 8 |
| $YPd_2B_2$ | 20 | ··· | 1 | 0 |
| $YPd_5B_3C_{0.35}$ | 21.5 | 21.5 | 30 | 270 |

metastable phase. Since the formation and transformation occur sequentially, a dynamic equilibrium will develop yielding both the metastable phase and its derivatives depending on the time-scale of the cooling. During the natural cooling of the as-melted samples with compositions from outside the 1221 region, we expect a multiphase situation, which slows down the crystallization process. Even a relatively slow cooling after arc-melting is enough to prevent the crystallization to reach the ground state. In this case long-term annealing should put the system into the ground state which means complete transformation of the superconducting phase. This is in agreement with the observation of vanishing superconductivity in as-melted $YPd_5B_3C_{0.35}$ after annealing.[1,3,4] When RQ, the time-scale is too short for transformations so the originally formed metastable phase is retained.

The XRD-spectra for melt-spun ribbon and splat-quenched samples before and after annealing at 900 °C are shown in Fig. 2. The main feature of the spectra for the RQ samples are peaks at positions characteristic for a fcc lattice. The fcc line spectrum ($a$=4.15 Å) is also shown. The spectra for the nonsuperconducting material after annealing above

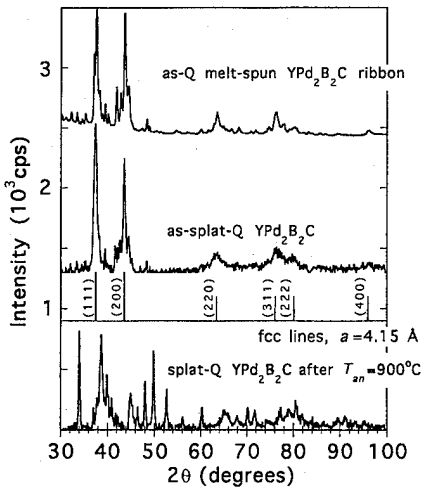



FIG. 2. XRD spectra for as-Q ribbons and splat-Q samples before and after annealing at 900 °C. Background contribution from the sample holder has been subtracted. For clarity the curves are offset. Also inserted is the line spectrum for a fcc lattice ($a$=4.15 Å).

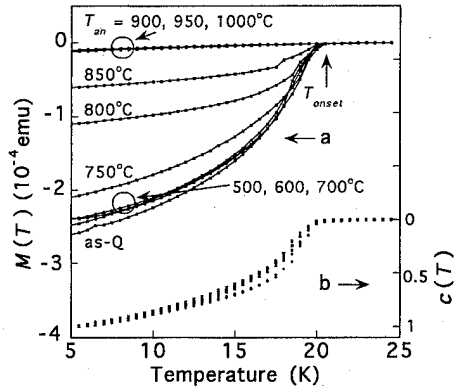



FIG. 3. (a) Zero-field cooled response in 10 G field of RQ $YPd_2B_2C$ prior to and after each annealing. (b) The same data but now normalized with respect to its value at 5 K.

900 °C are quite different. This transformation has been studied by a step-by-step annealing sequence.

### B. Thermal stability of the metastable phase in rapid quenched $YPd_2B_2C$

As-melted $YPd_2B_2C$- and $YPd_3B_3C$-ingots are not superconducting. However, on RQ large fractions of the superconducting phase are found. Therefore, we have investigated the anticipated decay of this metastable phase upon annealing by monitoring the relevant intensities in the XRD-spectra and quantify the changes of superconductivity. This is done by annealing an originally superconducting sample at increasingly higher temperatures ($T_{an}$=400, 500, 600, 700, 750, 800, 850, 900, 950, and 1000 °C) and after each stage take an XRD pattern and measure the magnetic properties of the superconducting state. To quantify the decrease of intensity of the peaks in the original spectrum, the peaks were integrated and normalized with respect to their original values as-Q yielding XRD integral intensity as a function of annealing temperature:

$$I(T_{an})/I(\text{as-Q}). \tag{1}$$

The first three peaks were measured, and the $2\theta$ intervals integrated were 36.7°–38.1°, 43.1°–44.3°, and 61.2°–64.4°. We deduce the loss of superconducting fraction upon annealing from the magnetization in 10 G field in zero-field cooled state. The full set of zero-field cooled curves is presented in Fig. 3(a). Above $T_{an}$=750 °C, the superconducting fraction begins to decrease and totally disappears on annealing at $T_{an}$=900 °C. When the magnetization data for samples annealed up to 850 °C is normalized with respect to the value at $T$=5 K they essentially collapse into a universal curve, Fig. 3(b), indicating that the superconducting phase has the same $T_c$ during the various annealing states.

To quantify the decrease of superconducting fraction as a function of annealing temperature, we normalize the moment at 5 K after each annealing with respect to the as-Q value

$$c(T_{an})=M(T_{an})/M(\text{as-Q}) \quad \text{at 5 K.} \tag{2}$$

In Fig. 4 we plot XRD integral intensities and superconducting fraction versus annealing temperature. The close cor-

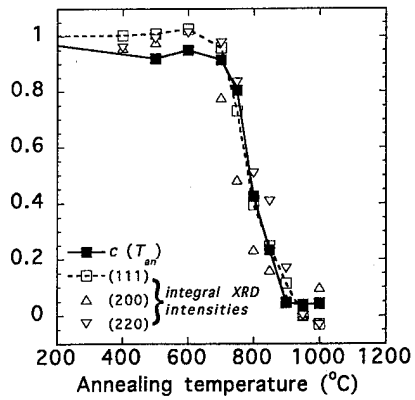



FIG. 4. XRD integral intensities $I(T_{an})/I(\text{as-Q})$, and superconducting fraction $c(T_{an})$ vs annealing temperature for RQ $YPd_2B_2C$.

respondence between the two quantities implies that *the phase responsible for these fcc-peaks corresponds to the superconducting phase in this system.*

There are two reports on superconductivity and structure determination in Pd-based borocarbides.[3,4] From Fig. 5, the XRD-spectra for our three RQ superconducting Pd-based samples, we cannot identify the *tetragonal 1221-phase* suggested in Refs. 3 and 4 neither in $YPd_2B_2C$ nor in the other compositions. Moreover, we observe that the $YPd_2B_2C$ composition has the simplest XRD-pattern which suggests that this composition is closest to the stoichiometry of the fcc-like phase. However, when we try to deduce the existence of this fcc-phase in the other two XRD-patterns, we are unable to identify this phase except for the (111)-peak.

Thus, while our study is consistent with Refs. 3 and 4, in that superconductivity in Pd-based borocarbides is metastable and found in the composition regime close to $YPd_2B_2C$, our XRD analysis *appears to contradict* the suggestions of a tetragonal structure. We cannot find this structure in *any* of our samples.

## IV. CONCLUSIONS

We show that superconductivity in rapid quenched $YPd_2B_2C$ is related to a metastable phase which closely correlates with an XRD pattern which is characteristic for a

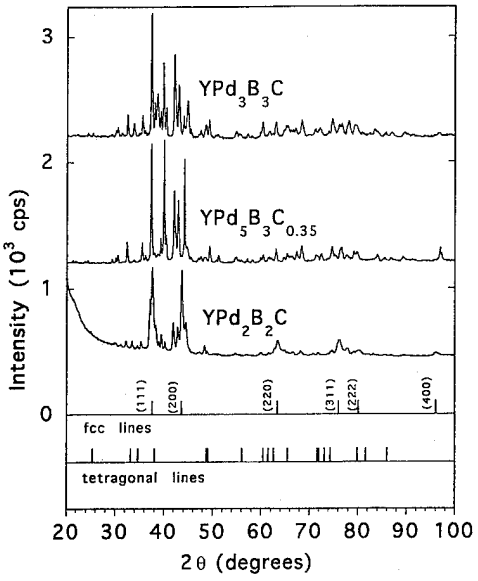



FIG. 5. XRD spectra for the three RQ superconducting compositions. The spectra are offset for clarity. Also inserted are the linespectra for a fcc lattice ($a$=4.15 Å) and the tetragonal structure from Refs. 3 and 4 ($a$=3.71 Å, $c$=10.81 Å).

fcc-structure with a lattice parameter of $a$=4.15 Å. The compositions having the best superconducting properties are found to lie in the $YPd_2B_2C$ region of the pseudoternary phase-diagram.

## ACKNOWLEDGMENTS

This research has been financially supported by the Swedish funding Agencies NUTEK and NFR.

[1] R. J. Cava, H. Takagi, B. Batlogg, H. W. Zandbergen, J. J. Krajewski, W. F. Peck, Jr., R. B. van Dover, R. J. Felder, T. Siegrist, K. Mizuhashi, J. O. Lee, H. Eisaki, S. A. Carter, and S. Uchida, Nature **367**, 146 (1994).
[2] T. Siegrist, H. W. Zandbergen, R. J. Cava, J. J. Krajewski, and W. F. Peck, Jr., Nature **367**, 254 (1994).
[3] Y. Y. Sun, I. Rusakova, R. L. Meng, Y. Cao, P. Gautier-Picard, and C. W. Chu, Physica C **230**, 435 (1994).
[4] H. W. Zandbergen, W. G. Sloof, R. J. Cava, J. J. Krajewski, and W. F. Peck, Jr., Physica C **226**, 365 (1994).
[5] V. Ström, T. Turkki, A. M. Grishin, and K. V. Rao, Fourth Conference NSSC, 25–28 May 1994, Varberg, Sweden (unpublished).
[6] V. Ström, K. S. Kim, A. Mouroux, T. Turkii, A. M. Grishin, and K. V. Rao, Physica C **235–240**, 2537 (1994).

# Field dependence of magnetic transitions for magnetic superconductors $RNi_2B_2C$ (R=Dy, Ho)

H. C. Ku, M. S. Lin, Y. Y. Hsu, J. H. Shieh, and Y. B. You
*Department of Physics, National Tsing Hua University, Hsinchu, Taiwan 300, Republic of China*

High field (up to 5 T) magnetization measurements were performed on both bulk and field-aligned powder samples of $RNi_2B_2C$ (R=Dy, Ho) magnetic superconductors. For $T_c=3.8$ K, a $DyNi_2B_2C$ superconductor with antiferromagnetic Néel temperature $T_N$ of 10–11 K, and anomalous field-induced weak-ferromagnetic transitions were observed above the superconducting upper critical field $H_{c2}$(2 K) of 1.75 kG. The aligned powders show distinct hysteresis characteristics for both fields applied parallel and perpendicular to the tetragonal basal plane. For $T_c=7.8$ K, $HoNi_2B_2C$ has an incommensurate magnetic ordering temperature $T_m$ of 6 K and $T_N$ of 5.2 K. Anomalous field-induced weak-ferromagnetic transitions were also observed below $T_N$. No hysteresis can be detected for $T_N<T<T_m$. © *1996 American Institute of Physics.*
[S0021-8979(96)02108-4]

The coexistence of antiferromagnetic ordering and superconductivity, with Néel temperature ($T_N$) higher than superconducting transition temperature ($T_c$), was first observed in the metastable ternary boride $HoIr_4B_4$ and the related pseudoternary boride systems $R(Rh_{1-x}Ir_x)_4B_4$ (R=Ho, Dy) with composition factor $x>0.6$.[1–3] For example, in the partial Rh-substituted $Ho(Rh_{0.3}Ir_{0.7})_4B_4$ compound, $T_c$ (1.6 K) was below $T_N$ (2.7 K).[2]

Recently, a new magnetic superconducting system was reported in the quaternary borocarbide $RNi_2B_2C$ compounds (R=Sc, Y, Th, U, or a rare earth).[4–11] Among nonmagnetic compounds, $LuNi_2B_2C$ exhibits the highest $T_c$ of 16.6 K,[5] followed by 15–16 K for $YNi_2B_2C$ and metastable $ScNi_2B_2C$,[4,5,7] 8 K for $ThNi_2B_2C$, and no superconducting transition was found down to 2 K for $LaNi_2B_2C$.[9–11] For compounds containing magnetic rare earth elements such as R=Dy, Ho, Er, and Tm, lower $T_c$ values were observed due to the magnetic pair breaking effect.[5–8] A nearly reentrant superconductivity was observed for $HoNi_2B_2C$ with $T_c=8$ K, which is higher than the $T_N$ of 5.2 K associated with commensurate magnetic structure and $T_m$ of 6 K due to a transition to an incommensurate state.[5,8,12–16]

For a magnetic $DyNi_2B_2C$ compound, $T_c$ of 3.8 K with onset around 5.2 K was observed below $T_N$ around 10–11 K, which provides another interesting example of the coexistence of superconductivity and antiferromagnetism.[8,17] The low-temperature electrical resistivity shows no reentrant behavior down to 0.3 K and indicates a perfect coexistence between superconductivity and antiferromagnetism below $T_c$.[17] The observed $T_N$ around 10–11 K from magnetic measurements is associated with the long-range $Dy^{3+}$ magnetic ordering through the RKKY indirect exchange interaction. The magnetic transition can be clearly corroborated by low-temperature specific heat data $C(T)$ where a very distinct transition peak was observed around 10 K.[17] The magnetic entropy $S_m$ of 10.3 J/mol K is close to 90% of R ln 4 and indicates the antiferromagnetic ordering of $Dy^{3+}$ with a possible quadruplet ground state in the tetragonal crystal field.

Magnetic hysteresis $M(H)$ data at temperature below $T_c$ for $DyNi_2B_2C$ provide the precise information on the temperature dependence of superconducting upper critical field $H_{c2}(T)$ and lower critical field $H_{c1}(T)$. The $DyNi_2B_2C$ samples were prepared using high-purity elements under an argon atmosphere in a Zr-gettered arc furnace. As shown in Fig. 1, the upper critical field $H_{c2}(T)$ of 1.75 kG at 2 K and 750 G at 3 K were determined from the merging point of the hysteresis curve. Similarly, $H_{c2}$ of 1.25 kG at 2.5 K, 450 G at 3.3 K, and 100 G at 3.7 K were obtained. Lower critical field $H_{c1}(T)$ is defined as the deviation from linearity in the initial magnetization in each $M(H)$ curve. The values thus obtained are 100 G at 2 K and 30 G at 3 K. Similarly, $H_{c1}$ of 50 G at 2.5 K and 10 G at 3.3 K were obtained. From the temperature dependence of critical fields, the extrapolated $H_{c2}(0)$ of 3 kG and the extrapolated $H_{c1}(0)$ of 200 G are derived. From $H_{c1}(0)$ and $H_{c2}(0)$, the Ginzburg–Landau parameter $\kappa=3.7$ is evaluated.[17] As a comparison, the $\kappa$ value of 3.5 was reported for $HoNi_2B_2C$.[16] The relative low $H_{c2}$ in all quaternary borocarbides implies a long coherence length $\xi$, and three-dimensional superconductivity.

Since each $M(H)$ curve at 2 or 3 K has a slightly nonlinear background due to the field dependence of antiferromagnetic order with $T_N$(Dy) of 10–11 K, high field $M(H)$ isotherm data up to 5 T were measured for bulk sample at 2 K to understand the normal state magnetism and possible field-induced magnetic transitions. As shown in Fig. 2, above

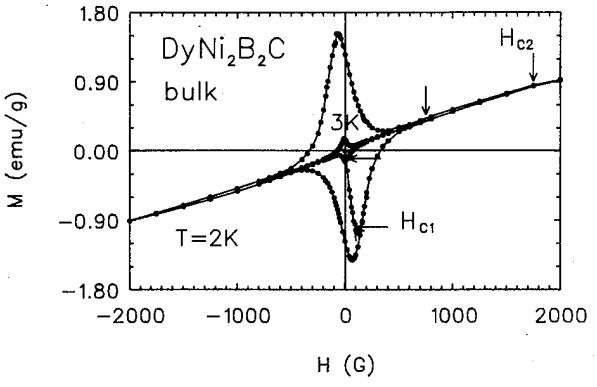



FIG. 1. Intermediate field (up to ±2 kG) magnetic hysteresis curves $M(H)$ at 2 and 3 K for $DyNi_2B_2C$ bulk sample. Upper critical field $H_{c2}$ and lower critical field $H_{c1}$ are indicated by arrows.

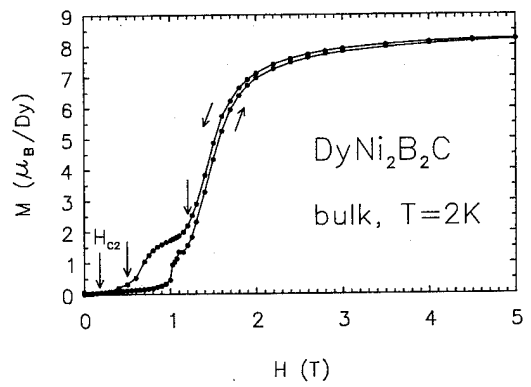



FIG. 2. High field (up to 5 T) magnetic hysteresis curve $M(H)$ at 2 K$<T_N$ for a $DyNi_2B_2C$ bulk sample.

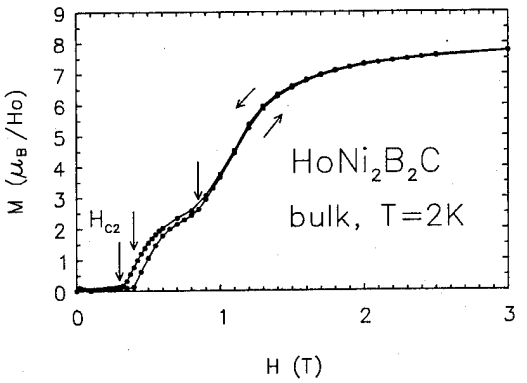



FIG. 4. High field (up to 3 T) magnetic hysteresis curve $M(H)$ at 2 K$<T_N$(5.2 K) for a bulk $HoNi_2B_2C$ sample.

$H_{c2}$(2 K) of 1.75 kG where the sample is no longer superconducting, two distinct weak-ferromagnetic-like hysteresis curves were observed indicating two possible field-induced magnetic transitions at 5 kG and at 1.2 T, respectively. The hysteresis characteristics persist up to a maximum applied field of 5 T where a saturated magnetic moment of 8.3 $\mu_B$ per Dy is achieved, very close to the calculated free ion $Dy^{3+}$ $g_J J=10$ $\mu_B$ magnetic moment.

The anisotropy of these magnetic transitions with field applied parallel and perpendicular to the tetragonal basal plane is studied by using aligned $DyNi_2B_2C$ powder at 2 K as shown in Fig. 3. Farrell's method was employed for the powder alignment. Powders were first obtained by grinding the bulk sample into fine microcrystalline grains with average size 1–10 $\mu$m, then mixed with SPAR-5-min epoxy/hardener in a 8 mm quartz holder, with a typical powder-epoxy ratio of 1:7, and then aligned in a 9.4 T magnetic field at room temperature. Because of the intrinsic normal-state magnetic anisotropy, the degree of easy tetragonal basal plane alignment is close to 90%. Slightly higher $T_N$ around 13 K was observed from magnetic measurement for aligned powder. Below $T_N$, for field $H$ perpendicular to the easy basal plane, initial magnetization curve increases slowly to magnetic moment 0.5 emu at 1.7 T, then increases sharply to 2.7 emu at 1.8 T, and then saturates to 3.0 emu at 5 T. Broad hysteresis behavior occurs only below 1.8 T with two distinct magnetic transitions at 5 kG and 1.2 T as observed in bulk samples. For field parallel to the basal plane, initial magnetization increases sharply above 8 kG with fairly broad low field and very narrow high field hysteresis features. The same magnetic transition fields were observed. The preliminary $M(H)$ data at other temperatures below $T_N$(Dy) indicate that there are weak temperature dependencies associated with these transitions.

For a nearly reentrant $HoNi_2B_2C$ superconductor with a $T_c$ of 8 K, a $T_N$ of 5.2 K, a $T_m$ of 6 K, and a complex $H_{c2}(T)$ upper critical field curve,[16] a coexistence between superconductivity and antiferromagnetism will prevail only below 5.2 K. Magnetism above $H_{c2}(T)$ will create a very complex phase diagram. As shown in Fig. 4, the magnetization measurement $M(H)$ of bulk sample at 2 K with field higher than $H_{c2}$(2 K) of 3 kG shows similar field-induced magnetic transitions around 4 and 8.5 kG, respectively.[16] A saturated magnetic moment of 7.8 $\mu_B$ per Ho is achieved at 3 T field and is very close to the calculated free ion $Ho^{3+}$ $g_J J=10$ $\mu_B$ magnetic moment. At higher temperature of 4.6 K which is close to $T_N$ and with a low $H_{c2}$(4.6 K) of 500 G, these field-induced transitions decrease to around 3 and 6 kG, respectively. For $T=T_N=5.2$ K with a minimum, nearly reentrant $H_{c2}$(5.2 K) of 400 G,[16] field-induced transitions decrease further to around 1 and 3 kG, respectively. Above $T_N$

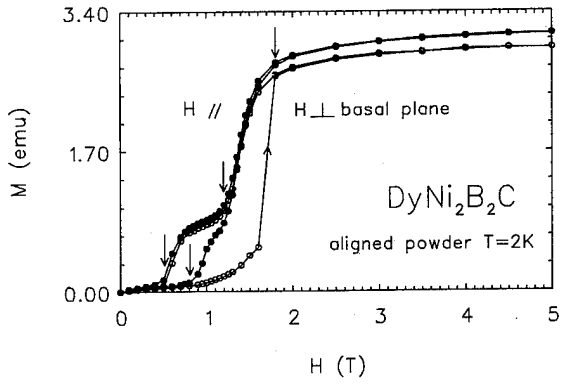



FIG. 3. Anistropic high field (up to 5 T) magnetic hysteresis curve $M(H)$ at 2 K for $DyNi_2B_2C$ aligned powder, with field parallel and perpendicular to the tetragonal basal plane.

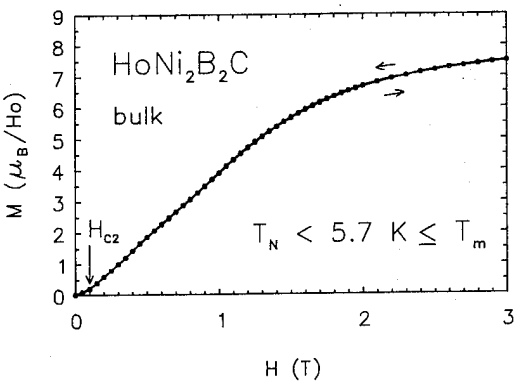



FIG. 5. High field (up to 3 T) magnetic hysteresis curve $M(H)$ at 5.7 K$<T_m$(6 K) for a bulk $HoNi_2B_2C$ sample.

at 5.7 K but is still lower than $T_m = 6$ K as shown in Fig. 5, no hysteresis or a very small effect can be detected above $H_{c2}$(5.7 K) of 1 kG due to the intrinsic, complex incommensurate magnetic structure.

In conclusion, field-induced weak-ferromagnetic transitions were observed only at a temperature below the antiferromagnetic ordering temperature $T_N$ for both $DyNi_2B_2C$ and $HoNi_2B_2C$ magnetic superconductors. No hysteresis can be detected for $HoNi_2B_2C$ at temperature below the higher incommensurate ordering temperature $T_m$.

This work was supported by the National Science Council of Republic of China under Contract NSC85-2112-M007-043 and -044PH.

[1] H. C. Ku, B. T. Matthias, and H. Barz, Solid State Commun. **32**, 937 (1979).
[2] H. C. Ku, F. Acker, and B. T. Matthias, Phys. Lett. A **76**, 399 (1980).
[3] H. C. Ku and F. Acker, Solid State Commun. **35**, 937 (1980).
[4] R. Nagarajan, C. Mazumdar, Z. Hossain, S. K. Dhar, K. V. Gopalakrishnan, L. C. Gupta, C. Godart, B. D. Padalia, and R. Vijayaraghavan, Phys. Rev. Lett. **72**, 274 (1994).
[5] R. J. Cava *et al.*, Nature **367**, 252 (1994).
[6] T. Siegrist, H. W. Zandbergen, R. J. Cava, J. J. Krajewski, and W. F. Peck, Jr., Nature **367**, 254 (1994).
[7] H. C. Ku, C. C. Lai, Y. B. You, J. H. Shieh, and W. Y. Guan, Phys. Rev. B **50**, 351 (1994).
[8] H. Eisaki, H. Takagi, R. J. Cava, B. Batlogg, J. J. Krajewski, W. F. Peck, Jr., K. Mizuhashi, J. O. Lee, and S. Uchida, Phys. Rev. B **50**, 647 (1994).
[9] J. L. Sarrao, M. C. de Andrade, J. Herrmann, S. H. Han, Z. Fisk, M. B. Maple, and R. J. Cava, Physica C **229**, 65 (1994).
[10] T. Takabatake, Y. Maeda, T. Konishi, and H. Fujii, J. Phys. Soc. Jpn. **63**, 2853 (1994).
[11] C. C. Lai, M. S. Lin, Y. B. You, and H. C. Ku, Phys. Rev. B **51**, 420 (1995).
[12] P. C. Canfield, B. K. Cho, D. C. Johnston, D. K. Finnemore, and M. F. Handley, Physica C **230**, 397 (1994).
[13] T. E. Grigereit, J. W. Lynn, Q. Huang, A. Santoro, R. J. Cava, J. J. Krajewski, and W. F. Peck, Jr., Phys. Rev. Lett. **73**, 2756 (1994).
[14] A. I. Goldman, C. Strassis, P. C. Canfield, J. Zarestky, P. Dervenagas, B. K. Cho, D. C. Johnston, and B. Sternlieb, Phys. Rev. B **50**, 9668 (1994).
[15] H. Schmidt and H. F. Braun, Physica C **229**, 315 (1994).
[16] M. S. Lin, J. H. Shieh, Y. B. You, W. Y. Guan, H. C. Ku, H. D. Yang, and J. C. Ho, Phys. Rev. B **52**, 1181 (1995).
[17] M. S. Lin, J. H. Shieh, Y. B. You, Y. Y. Hsu, J. W. Chen, S. H. Lin, Y. D. Yao, Y. Y. Chen, J. C. Ho, and H. C. Ku, Physica C **249**, 403 (1995).

# Systematic variation of $T_N$(Pr) for the two-$CuO_2$-layer cuprate $m212$ ($m=1, 2, 3$) systems

H. C. Ku, C. L. Yang, C. H. Chou, Y. Y. Hsu, Y. B. You, and J. H. Shieh
*Department of Physics, National Tsing Hua University, Hsinchu, Taiwan 300, Republic of China*

The systematic variation of anomalous Pr antiferromagnetic ordering temperature $T_N$(Pr) for the two-$CuO_2$-layer cuprate system $MA_2PrCu_2O_y$ (M=Cu, Hg, Tl, Pb; A=Ba, Sr) was verified through the observation of a new Hg-1212 $HgSr_2PrCu_2O_{6+\delta}$ tetragonal compound with a $T_N$(Pr) of 6 K and a Pr—O bond length of 2.492 Å between Pr and oxygen in the adjacent $CuO_2$ layers. For the tetragonal/orthorhombic 1212 compounds including the $PrBa_2Cu_3O_{7-y}$ system, $T_N$(Pr) was found to decrease monotonically with increasing Pr—O distance. The importance of Pr-O-Pr superexchange magnetic coupling is expected for all two-$CuO_2$-layer $M_mA_2PrCu_2O_y$ $m212$-type ($m=1, 2, 3$) compounds. A similar Pr anomaly in the 2212-type system was first observed on the new tetragonal $(Pb_{0.5}Cu_{0.5})_2(Ba_{0.5}Sr_{0.5})_2PrCu_2O_8$ compound with a high $T_N$(Pr) of 9 K. © *1996 American Institute of Physics.* [S0021-8979(96)02208-0]

The orthorhombic $PrBa_2Cu_3O_7$ compound with an anomalously high Pr antiferromagnetic ordering temperature $T_N$(Pr) of 17 K is the only nonsuperconducting member of the $RBa_2Cu_3O_7$ system (R=Y or a rare earth).[1–6] With further oxygen deficiency, $T_N$ decreases to 10 K in tetragonal $PrBa_2Cu_3O_6$.[5,7] In comparison, other magnetic rare earth compounds have a maximum $T_N$(R) of 2.2 K in $GdBa_2Cu_3O_7$.[8,9] Since Pr is one of the lightest elements of rare-earth series, its $4f$ wave function is more extended and the anomalously high $T_N$ observed indicates the importance of the quasi-two-dimensional (quasi-2D) Pr-O-Pr superexchange magnetic coupling through the strong hybridization between the Pr $4f$ and the eight O $2p_\pi$ orbitals in the adjacent two-$CuO_2$ layers.[6]

From the structural viewpoint, the 123-type $PrBa_2Cu_3O_{7-y}$ system can be recategorized as either the Cu-1212C-type (C stands for chain) for orthorhombic $[Cu]Ba_2PrCu_2O_7$ (space group $Pmmm$) or Cu-1212 $TlBa_2CaCu_2O_{7-\delta}$-type for tetragonal $[Cu]Ba_2PrCu_2O_6$ (space group $P4/mmm$),[10] analogous to other two-$CuO_2$-layer Pr compounds in the Tl-1212 $Tl(Ba,Sr)_2PrCu_2O_{7-\delta}$ system[11–15] and (Pb,Cu)-1212 $(Pb,Cu)Sr_2PrCu_2O_{7-\delta}$.[13] They also exhibit the common feature of having anomalous high $T_N$(Pr) values ranging from 4 to 8 K. The 12 K tetragonal $PrBa_2Cu_2NbO_8$ or $[Nb]Ba_2PrCu_2O_8$ compound can also be recategorized as the Nb-1212 $TlBa_2CaCu_2O_{7-\delta}$-type compound.[16]

Recently, a new Hg-1212 compound $HgSr_2PrCu_2O_{6+\delta}$ with the tetragonal $HgBa_2CaCu_2O_{6+\delta}$-type structure was reported where the mercury sample was prepared by two-stage solid-state reaction techniques where the precursor $Sr_2PrCu_2O_y$ powders were mixed with HgO powder, pressed into pellets, sealed in a 2 mm wall quartz tube in vacuum, and reacted at 1000 °C in vacuum for 8 h then quenched in liquid nitrogen.[17] A similar Pr anomaly is expected for this new compound. As shown in Fig. 1, a $T_N$(Pr) value of 6 K was identified from the minimum in the temperature derivative of the molar magnetic susceptibility $d\chi_m/dT$ in 1 T applied magnetic field. At higher temperatures, the temperature dependence of the magnetic susceptibilities indicates a magnetic $Cu^{2+}$ ordering near 300 K or above. A simple Curie–Weiss fit $\chi_m=C^*/(T+\theta_p)$ below 200 K gives an antiferromagnetic-like, negative paramagnetic intercept $\theta_p=-13$ K and an effective magnetic moment of 3.31 $\mu_B$ per Pr from the Curie constant $C^*$ if the small $Cu^{2+}$ moment is neglected.[17] As in many other Pr cuprates, this effective moment is closer to that of the free $Pr^{3+}$ ion (3.58 $\mu_B$) rather than the $Pr^{4+}$ ion (2.54 $\mu_B$). Indeed, most experimental results on such compounds imply a $Pr^{3+}$ state. The Pr magnetic transition of $HgSr_2PrCu_2O_{6+\delta}$ is clearly corroborated by low-temperature specific heat data $C(T)$ which show a distinct but broad magnetic transition prevails at $T_N$(Pr)=6 K and a very high onset around 11 K.[16] The broad transition indicates that a truly three-dimensional (3D) or quasi-2D long-range magnetic ordering set in at $T_N$(Pr)=6 K, while the 2D ordering effect persists up to the onset near 11 K.

The high $T_N$(Pr) observed in $HgSr_2PrCu_2O_{6+\delta}$ again indicates the importance of the quasi-2D Pr-O-Pr superexchange magnetic coupling through the strong hybridization between the Pr $4f$ and the eight O $2p_\pi$ orbitals in the adjacent $CuO_2$ layers. This degree of hybridization can be readily reflected in the Pr—O bond length, which can be accurately derived from the Rietveld analysis. X-ray Rietveld refinement on powder samples of tetragonal $HgSr_2PrCu_2O_{6+\delta}$ ($a=3.8532$ Å and $c=12.1199$ Å) gives a refined bond length $d$(Pr—O) between Pr and O(1) in the adjacent two-$CuO_2$ layers of 2.492 Å and the O(1)—Pr—O(1) bond angle is

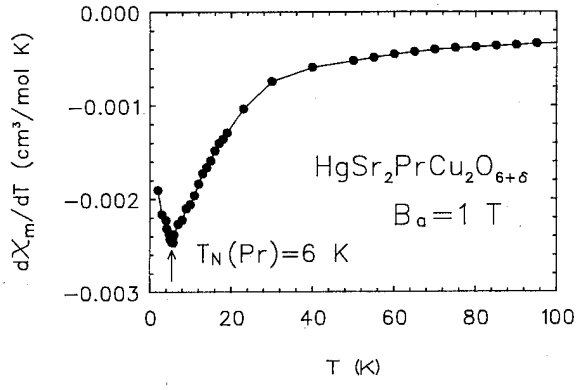



FIG. 1. Low-temperature differential molar magnetic susceptibility $d\chi_m/dT$ for a Hg-1212 $HgSr_2PrCu_2O_{6+\delta}$ compound revealing a $T_N$(Pr)=6 K.

 0021-8979/96/79(8)/5866/3/$10.00 © 1996 American Institute of Physics

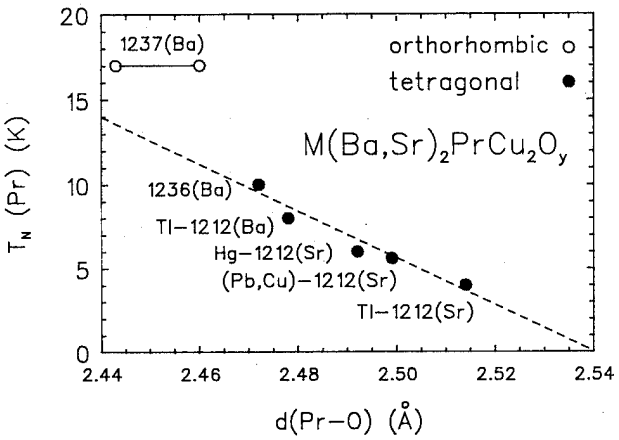



FIG. 2. $T_N$(Pr) vs Pr—O distance in various M(Ba,Sr)$_2$PrCu$_2$O$_y$ (M=Cu, Hg, Tl, Pb) 1212-type compounds. The dashed line is a guide to the eyes only.

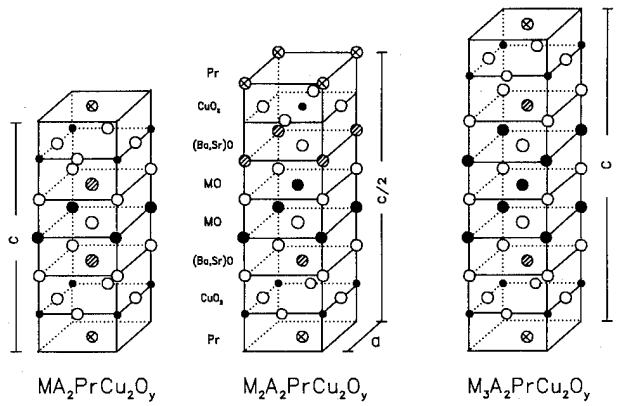



FIG. 3. Crystal structures of $M_mA_2PrCu_2O_y$ $m212$ ($m=1, 2, 3$; M=Cu, Hg, Tl, Pb; A=Ba, Sr) systems.

101.3°.[17] The $d$(Pr—O) for $HgSr_2PrCu_2O_{6+\delta}$ with $T_N$(Pr)=6 K, is shorter than 2.514 Å for Tl-1212(Sr) $TlSr_2PrCu_2O_{7-\delta}$ with $T_N$=4 K or 2.499 Å for (Pb,Cu)-1212 $(Pb_{0.6}Cu_{0.4})Sr_2PrCu_2O_{7-\delta}$ with $T_N$=5.6 K, but is longer than 2.478 Å for Tl-1212(Ba) $TlBa_2PrCu_2O_{7-\delta}$ with $T_N$=8 K.[13,14] This regularity forces us to study the systematic variation of $T_N$(Pr) for all reported M(Ba,Sr)$_2$PrCu$_2$O$_y$ (M=Cu, Hg, Tl, Pb) 1212-type compounds as a function of the Pr—O bond length as shown in Fig. 2. Note that for the orthorhombic $T_N$(Pr)=17 K 1237(Ba) $PrBa_2Cu_3O_7$ (Cu-1212C), instead of a single Pr—O bond length, there are two Pr—O bond lengths of 2.443 and 2.460 Å, respectively. For the oxygen-depleted tetragonal 1236(Ba) $PrBa_2Cu_3O_6$ (Cu-1212) compound, a single long Pr—O bond length of 2.472 Å with lower $T_N$(Pr) of 10 K was observed.[7] Clearly, $T_N$(Pr) decreases monotonically with increasing Pr—O bond length which reflects the degree of Pr $4f$–O $2p_\pi$ orbital hybridization or the strength of Pr-O-Pr superexchange coupling. Meanwhile, an effective coupling occurs between Cu and Pr moments through oxygen $2p_\pi/2p_\sigma$ as revealed by preliminary neutron and nuclear magnetic resonance studies on Tl-1212 Tl(Ba,Sr)$_2$PrCu$_2$O$_{7-\delta}$ system.[17] This competition should be taken into account before a final conclusion can be reached.

Various types of experiments have been performed to substantiate these anomalous Pr phenomena in the 123 or 1212 system to clarify the mechanism of magnetic order and/or superconductivity suppression, but a clear picture is still elusive. Obviously, additional information from more diverse systems would be extremely helpful toward delineating the various factors which may play crucial roles in this regard. Since in the high $T_c$ cuprate systems, a total replacement of Ca by Pr between the $CuO_2$ layers can be achieved only in the tetragonal/orthorhombic two-$CuO_2$-layer $M_mA_2PrCu_2O_y$ $m212$-type structures ($m=1$, 2, 3; M=Cu, Hg, Tl, Pb and A=Ba, Sr), where the schematic structure comparison is shown in Fig. 3. Questions arise naturally whether the anomalous Pr effect occurs in 2212 $M_2A_2PrCu_2O_y$ or 3212 $M_3A_2PrCu_2O_y$ compounds. Only one 3212-type compound with a $T_N$(Pr) of 6–14 K was reported so far in the orthorhombic (Pb,Cu)-3212 $(Pb_2Cu)Ba_{2-x}Sr_xPrCu_2O_8$ system ($0\leqslant x\leqslant 1$), or commonly known as the 2213-type $Pb_2Ba_{2-x}Sr_xPrCu_3O_8$ system.[18] For the 2212-type compounds, no Pr ordering was observed down to 1.6 K for the orthorhombic Bi-2212 compound $Bi_2Sr_2PrCu_2O_8$.[19] However, via proper substitution, we are able to observe the first Pr anomaly in the tetragonal (Pb,Cu)-2212 $(Pb_{0.5}Cu_{0.5})_2(Ba_{0.5}Sr_{0.5})_2PrCu_2O_8$ compound ($a$ =3.878 Å and $c$=27.594 Å). The sample was prepared by two-stage solid-state reaction techniques where the precursor $BaSrPrCu_3O_y$ powders were mixed with PbO powder and heated at 730 °C for 1 day and then pressed into pellets and sintered at 825–830 °C in flowing Ar for 3 days, then quenched in liquid nitrogen.[19] A fairly high $T_N$(Pr) value of 9 K was identified from the minimum in the temperature derivative of the molar magnetic susceptibility $d\chi_m/dT$ as shown in Fig. 4. In comparison, the isostructural compound $(Pb_{0.5}Cu_{0.5})_2(Ba_{0.5}Sr_{0.5})_2GdCu_2O_8$ exhibits a lower $T_N$(Gd) of only 2.2 K.[19] The magnetic transition can also be corroborated by low-temperature specific heat data $C(T)$ which show a distinct magnetic transition at $T_N$(Pr)=9 K with onset around 11 K.[19] The temperature dependence of the magnetic susceptibilities below 200 K indicates a simple Curie–Weiss fit $\chi_m=C^*/(T+\theta_p)$ which yields a negative paramagnetic

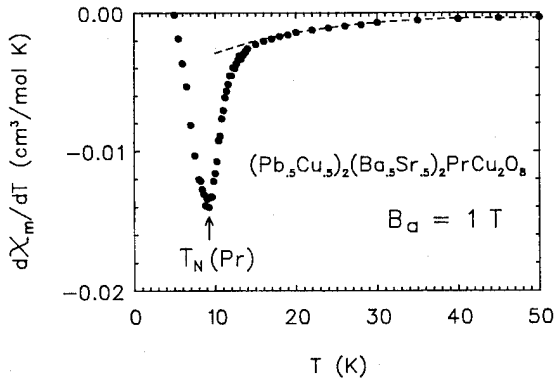



FIG. 4. Low-temperature differential molar magnetic susceptibility $d\chi_m/dT$ for (Pb,Cu)-2212 $(Pb_{0.5}Cu_{0.5})_2(Ba_{0.5}Sr_{0.5})_2PrCu_2O_8$ compound revealing a $T_N$(Pr)=9 K.

intercept $\theta_p = -10$ K and an effective magnetic moment of 3.22 $\mu_B$ per Pr.[19] The effective moment again is closer to that of the free $Pr^{3+}$ ion. The magnetic entropy $S_m$ associated with the Pr ordering has a lower limit, ~20% of $R \ln 3$ expected for $Pr^{3+}$ with a quasi-triplet ground state. Accordingly, it seems reasonably to categorize the Pr ordering in this (Pb,Cu)-2212 compound as a three-dimensional-like ordering process. Confirmation requires detailed neutron diffraction studies.

The current results of anomalous Pr ordering on the new Hg-1212 compound $HgSr_2PrCu_2O_{6+\delta}$ and (Pb,Cu)-2212 compound $(Pb_{0.5}Cu_{0.5})_2(Ba_{0.5}Sr_{0.5})_2PrCu_2O_8$, along with earlier reports on other 1212- and 3212-type compounds, complete the demonstration of systematic of anomalous Pr ordering in all two-$CuO_2$-layer $M_mA_2PrCu_2O_y$ $m212$ ($m=1, 2, 3$) systems. Anomalously high $T_N$(Pr) observed for all compounds indicates the importance of the quasi-2D Pr-O-Pr superexchange magnetic coupling mechanism through the strong hybridization between the Pr $4f$ and the eight O $2p_\pi$ orbitals in the adjacent two-$CuO_2$ layers.

We thank Professor J. C. Ho and H. D. Yang for helpful discussions. This work was supported by the National Science Council of Republic of China under Contract Nos. NSC85-2112-M007-043 and -044PH.

[1] L. Soderholm, K. Zhang, D. G. Hinks, M. A. Beno, J. D. Jorgensen, C. U. Segre, and I. K. Schuller, Nature **328**, 604 (1987).
[2] J. K. Liang, X. T. Xu, S. S. Xie, G. H. Rao, X. Y. Shao, and Z. G. Duan, Z. Phys. B **69**, 137 (1987).
[3] Y. Dalichaouch, M. S. Torikachvili, E. A. Early, B. W. Lee, C. L. Seaman, K. N. Yang, H. Zhou, and M. B. Maple, Solid State Commun. **65**, 101 (1988).
[4] H. C. Ku, C. C. Chen, and S. W. Hsu, Int. J. Mod. Phys. B **2**, 1411 (1988).
[5] H. B. Radousky, J. Mater. Res. **7**, 1917 (1992), and references cited therein.
[6] R. Fehrenbacher and T. M. Rice, Phys. Rev. Lett. **70**, 3471 (1993).
[7] S. Uma, T. Sarkar, M. Seshasayee, G. Rangarajan, C. R. V. Rao, and C. Subramanian, Solid State Commun. **87**, 289 (1993).
[8] J. C. Ho, P. H. Hor, R. L. Meng, C. W. Chu, and C. Y. Huang, Solid State Commun. **63**, 711 (1987).
[9] J. W. Lynn, in *High Temperature Superconductivity*, edited by J. W. Lynn (Springer, Berlin, 1990), Chap. 8, p. 268, and references cited therein.
[10] H. Shaked, P. M. Keane, J. C. Rodriguez, F. F. Owen, R. L. Hitterman, and J. D. Jorgensen, *Crystal Structure of the High-$T_c$ Superconducting Copper-Oxides* (Elsevier, Amsterdam, 1994).
[11] C. C. Lai, B. S. Chiou, Y. Y. Chen, J. C. Ho, and H. C. Ku, Physica C **202**, 104 (1992).
[12] W. T. Hsieh, K. J. Chang, W. H. Li, K. C. Lee, J. W. Lynn, C. C. Lai, and H. C. Ku, Phys. Rev. B **49**, 12200 (1994).
[13] H. C. Ku, C. C. Lai, J. H. Shieh, J. W. Liou, C. Y. Wu, and J. C. Ho, Physica B **194–196**, 213 (1994).
[14] C. C. Lai, T. J. Lee, H. K. Fun, H. C. Ku, and J. C. Ho, Phys. Rev. B **50**, 4092 (1994).
[15] H. K. Fun, P. Yang, C. C. Lai, H. C. Ku, and T. J. Lee, Physica C **223**, 267 (1994).
[16] N. Rosov, J. W. Lynn, H. B. Radousky, M. Bennahmias, T. J. Goodwin, P. Klavins, and R. N. Shelton, Phys. Rev. B **47**, 15256 (1993).
[17] C. H. Chou, Y. Y. Hsu, J. H. Shieh, T. J. Lee, H. C. Ku, J. C. Ho, and D. H. Chen (unpublished).
[18] J. H. Shieh, H. C. Ku, and J. C. Ho, Phys. Rev. B **50**, 3288 (1994), and references cited therein.
[19] C. L. Yang, J. H. Shieh, Y. Y. Hsu, H. C. Ku, and J. C. Ho, Phys. Rev. B **52** (in press).

# Magnetic structure and ordering of Nd ions in Ga substituted $NdBa_2Cu_3O_7$ (abstract)

A. M. Niraimathi and E. Gmelin
*Max-Planck-Institut für Festkörperforschung, 70569 Stuttgart, Germany*

P. Allenspach
*Laboratory for Neutron Scattering, ETH Zürich & PSI, 5232 Villigen PSI, Switzerland*

C. Ritter
*Insitut-Laue-Langevin, Grenoble Cedex 9, France*

Magnetic ordering of $Nd^{3+}$ ion changes with oxygen concentration in $NdBa_2Cu_3O_{7-x}$.[1] In the oxygen-rich sample $NdBa_2Cu_3O_{6.9}$, $Nd^{3+}$ ion orders antiferromagnetically with 2D-Ising type of ordering. Whereas, in the oxygen reduced compound $NdBa_2Cu_3O_{6.2}$ Nd ion orders three dimensionally at 1.73 K. Similar effects has been observed by specific heat measurements performed on $NdBa_2Cu_{3-y}Ga_yO_7$ ($0<y<0.5$).[2] In these samples, a small amount of Ga substitution changes the magnetic ordering of Nd ions from 2D Ising ($y=0$) to 1D or magnetic clusters ($y=0.01$, 0.03). With higher Ga substitution, the third magnetic ordering is restored.[2] The magnetic ordering seen in $NdBa_2Cu_{3-y}Ga_yO_7$ ($y=0.5$) is more isotropic in nature compared to $NdBa_2Cu_3O_{6.2}$. The critical exponent derived from the specific data show a 3D spherical type of ordering. Magnetic neutron diffraction are performed at low and high temperatures for $y=0.5$ to deduce the magnetic structure, which are compared with the unsubstituted compounds and to verify the isotropic nature. The second-order CEF parameter $A_2^0$ decreases for $NdBa_2Cu_{3-y}Ga_yO_7$ ($y=0.5$) which in turn reduces the magnetic anisotropy constant,[3] consistent with magnetic specific heat results. © *1996 American Institute of Physics.* [S0021-8979(96)80908-0]

[1] P. Allenspach *et al.*, Z. Phys. B **96**, 455 (1995).
[2] A. M. Niraimathi *et al.*, Phys. Rev. B **51**, 8503 (1995).
[3] A. M. Niraimathi *et al.*, submitted to PRB.

# Influence of the crystalline electric field on the magnetic properties of Ga-doped $NdBa_2Cu_3O_x$ (abstract)

P. Allenspach
*Laboratory for Neutron Scattering, ETH Zurich & PSI, 5232 Villigen PSI, Switzerland*

A. M. Niraimathi and E. Gmelin
*Max-Planck-Institut für Festkörperforschung, 70569 Stuttgart, Germany*

Crystal electric field (CEF) effects are of essential importance for the magnetic properties of rare-earth ions. For $NdBa_2Cu_3O_x$ the variation of the CEF due to a reduction of oxygen directly influences the character of the magnetic ordering[1] and partially explains the peculiar magnetic behavior of this system:[2] Oxygen reduction transforms the 2D-Ising system just below $x=6.9$ into a (short-range) 2D-Heisenberg system due to a reduction of the single-ion anisotropy. Since, magnetic specific heat data for Ga-doped $NdBa_2Cu_3O_x$[3] resemble very much the oxygen reduced data, neutron CEF spectroscopy of $Nd^{3+}$ in $NdBa_2(Cu_{3-y}Ga_y)O_x$ was performed to deduce the behavior of the single-ion anisotropy. These neutron data in conjunction with paramagnetic susceptibility and specific heat data[4] confirm the strong influence of the CEF on the magnetic ordering of the Nd ions. © *1996 American Institute of Physics.* [S0021-8979(96)81008-5]

[1] P. Allenspach *et al.*, Z. Phys. B **96**, 455 (1995).
[2] B. W. Lee *et al.*, in *Oxygen disorder effects in high-Tc Superconductor*, edited by J. L. Moran-Lopez and I. K. Schuller (Plenum, New York, 1990), p. 151.
[3] A. M. Niraimathi *et al.*, Phys. Rev. B **51**, 8503 (1995).
[4] A. M. Niraimathi *et al.*, Phys. Rev. B (submitted).

 0021-8979/96/79(8)/5869/1/$10.00 © 1996 American Institute of Physics 

# Synthesis and superconductivity of intermetallic compounds $Y_2Ni_xB_{8-x}C_2$, $YNi_xCu_{2-x}B_2C$, and $YNi_xCu_{2-x}Si_2C$

Wei Zhao and Jinke Tang
*Department of Physics, University of New Orleans, New Orleans, Louisiana 70148*

Young-sook Lee and Charles J. O'Connor
*Department of Chemistry, University of New Orleans, New Orleans, Louisiana 70148*

Borocarbide and silicocarbide intermetallic $Y_2Ni_xB_{8-x}C_2$ ($x=1$, 2, 3, 5), $YNiCuB_2C$, and $YNi_xCu_{2-x}Si_2C$ ($x=0$, 2) were prepared and their superconductivity was studied. The results indicated that with the change of the ratio of Ni to B in $Y_2Ni_xB_{8-x}C_2$, secondary phases were introduced into $YNi_2B_2C$ phase. A $T_c$ of 15.0 K was observed for the compounds $x=2$, 3, and 5, which originated from the major phase $YNi_2B_2C$ in these samples. Partial substitution of Ni by Cu reduced the $T_c$ to 11.0 K for $YNiCuB_2C$. For Si substitution system, no bulk superconductivity was found in $YNi_2Si_2C$ and $YCu_2Si_2C$. But a minor superconducting phase ($T_c \sim 4$ K) with a volume fraction of the order of near 1% was observed in them. It was noticed that for the temperature-dependent magnetization of superconducting compounds containing Ni, a significant difference between zero-field cooling and field cooling curves before $T_c$ was always observed, which was tentatively attributed to Ni-containing impurity. © *1996 American Institute of Physics.*
[S0021-8979(96)02308-7]

## I. INTRODUCTION

Superconductivity has been discovered recently in borocarbide intermetallic $YNi_2B_2C$ with $T_c=15.6$ K.[1] Like $LuNi_2B_2C$, $YNi_2B_2C$ displays a tetragonal body-centered layerlike structure with a $I_4/mmm$ symmetry.[1,2] It may be viewed as alternate stackings of the NaCl-type (YC) and the inverse PbO-type ($Ni_2B_2$) layers. In the $Ni_2B_2$ layers, a Ni atom is tetrahedrally coordinated by four boron atoms. It is interesting to inspect the possibility of increasing $T_c$ in this system through substitution of Ni and B by other elements such as Cu and Si and through changing the ratio of Ni and B. In this work, borocarbide and silicocarbide intermetallic $Y_2Ni_xB_{8-x}C_2$ ($x=1$, 2, 3, 5), $YNiCuB_2C$, and $YNi_xCu_{2-x}Si_2C$ ($x=0$, 2) have been prepared and their superconductivity is studied.

## II. EXPERIMENT

Samples were prepared by the arc-melt technique. The starting materials were Y (Aldrich, 99.9%), Ni (Aldrich, 99.95%), Cu (Aldrich, 99.99%), B (99.999%), C (99.9%), and Si (99.9%). Stoichiometric amounts of the starting materials were melted under argon atmosphere on a standard water-cooled copper hearth at least four times, with the melted button turned over between melts in order to ensure homogeneity. The overall loss in weight of the samples during arc melting was less 1%.

The magnetic susceptibility was measured by a SQUID magnetometer (Quantum Design). The resistance was determined by the standard four-lead method. The x-ray diffraction patterns of samples were obtained on a SCINTAG powder diffractometer using Cu $K\alpha$ radiation.

## III. RESULTS AND DISCUSSION

For $Y_2Ni_xB_{8-x}C_2$ ($x=1$, 2, 3, 5) system, their x-ray diffraction patterns indicated that all samples were multiphased. Except for the sample with $x=1$, all other three samples showed major diffraction patterns characteristic of $YNi_2B_2C$. Figure 1(a) shows the normalized x-ray diffraction patterns of $Y_2Ni_3B_5C_2$. One can see that the main peaks can be attributed to the $YNi_2B_2C$ phase with lattice parameters $a=3.53$ Å and $c=10.57$ Å, agreeing with the data in Ref. 1. For $Y_2Ni_2B_6C_2$ ($YNiB_3C$) and $Y_2Ni_5B_3C_2$ samples, their major diffraction patterns can also been indexed with the $YNi_2B_2C$ of the same lattice parameters. For the sample

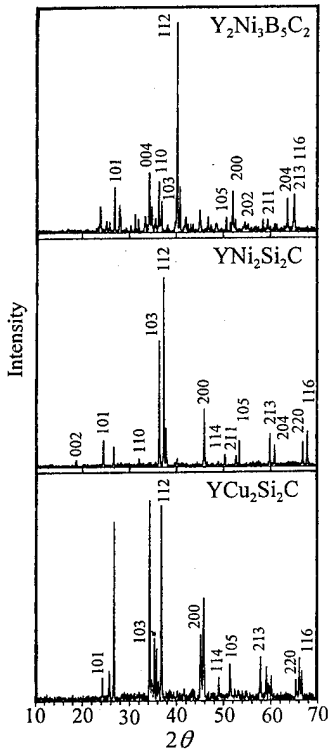



FIG. 1. The x-ray diffraction patterns of $Y_2Ni_3B_5C_2$, $YNi_2Si_2C$, and $YCu_2Si_2C$.

 0021-8979/96/79(8)/5870/3/$10.00 © 1996 American Institute of Physics

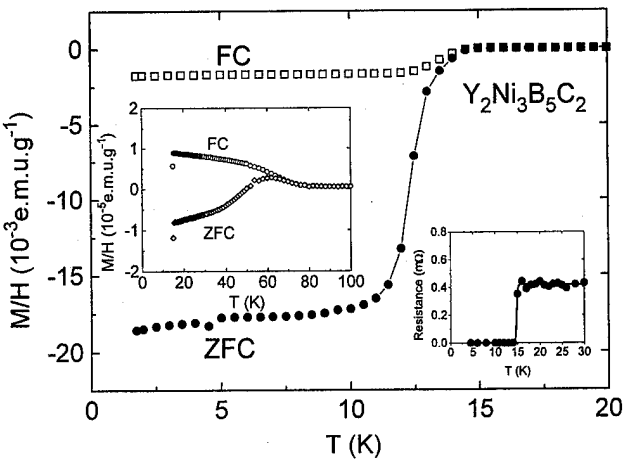



FIG. 2. Temperature-dependent magnetization (applied field $H=10$ G) for $Y_2Ni_3B_5C_2$. The left inset, expended view showing the magnetization before $T_c$. The right inset shows the resistance for this sample.

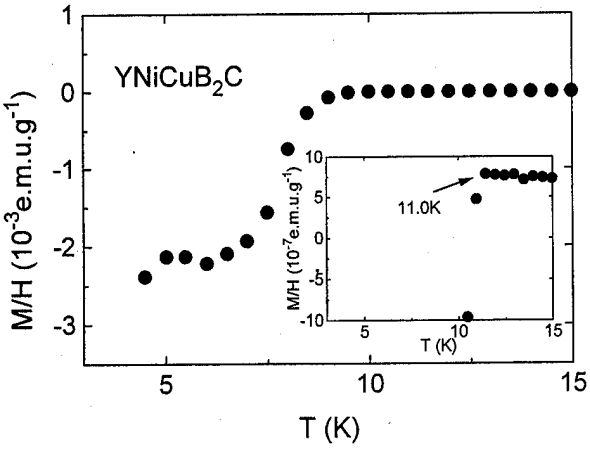



FIG. 3. Temperature-dependent magnetization ($H=20$ G) for $YNiCuB_2C$, showing the superconducting transition. The data were obtained during warming after zero-field cooling.

$Y_2NiB_7C_2$, no $YNi_2B_2C$ phase was observed. The analysis of the secondary phases in these samples has been proven to be a difficult task and will be discussed elsewhere. The above results were consistent with those of Buchgeister *et al.*[3] and Chakoumakos and Paranthaman,[4] who reported that excess amounts of both Ni and B introduced secondary phases into the samples. These results also confirmed that defects such as planar defects or intergrowths were hard to exist in the $YNi_2B_2C$ structure.[2]

The x-ray diffraction pattern of Cu-substituted $YNiCuB_2C$ consisted of a major pattern with tetragonal structure with lattice parameters $a=3.54$ Å and $c=10.63$ Å and some additional peaks which could not be identified. Gangopadhyay *et al.*[5] found that there was limited solubility in $YNi_2B_2C$ for Cu and that with increasing the doping level of Cu, the impurity peaks grew stronger. Our data agreed with their results.

Silicocarbides $YNi_2Si_2C$ and $YCu_2Si_2C$ were prepared as shown in Figs. 1(b) and 1(c). In Fig. 1(b), most of the diffraction peaks can be indexed to the $YNi_2B_2C$-type structure with lattice parameters $a=3.94$ Å and $c=9.55$ Å. This suggests that a new silicocarbide intermetallic $YNi_2Si_2C$ compound with $YNi_2B_2C$-type structure was formed. For $YCu_2Si_2C$, the diffraction pattern [Fig. 1(c)] showed that this sample was multiphased. The main peaks were identified to the $YNi_2B_2C$-type structure with $a=3.95$ Å and $c=9.98$ Å. There also existed peaks of secondary phases in Fig. 1(c) whose indentification is needed. The result of $YCu_2Si_2C$ is similar to that of Cu-substituted $YNiCuB_2C$ in which pure, Cu-containing intermetallic compounds with a $YNi_2B_2C$-type structure are difficult to synthesize by means of an arc-melting technique.

Figure 2 shows the temperature dependence of the magnetization measured at 10 G and the resistance for the $Y_2Ni_3B_5C_2$ sample. The superconducting transition is seen at 15.0 K with a broader transition width as compared with that of the pure $YNi_2B_2C$ sample.[1] The sample cooled in zero field shows a magnetic shielding equal to ~80%–100% of that of a perfect superconductor. On cooling in the field, it displays a Meissner effect of ~10% of that expected for perfect diamagnetism. The broader transition width may result from the secondary phases already seen in the x-ray pattern which separate the $YNi_2B_2C$ phase grains so that weak links form. We found that before $T_c$, positive, upgrown field cooling and zero-field cooling curves were always observed in these Ni-containing samples. As shown in the left inset of Fig. 2, the zero-field cooling curve shows a broad maximum at ~60 K. More interestingly, for this sample, its ZFC susceptibility became negative at a lower temperature. Although ac susceptibility conducted on the sample indicated that this negative ZFC dc susceptibility was not due to a superconducting phase transition, its origin is yet

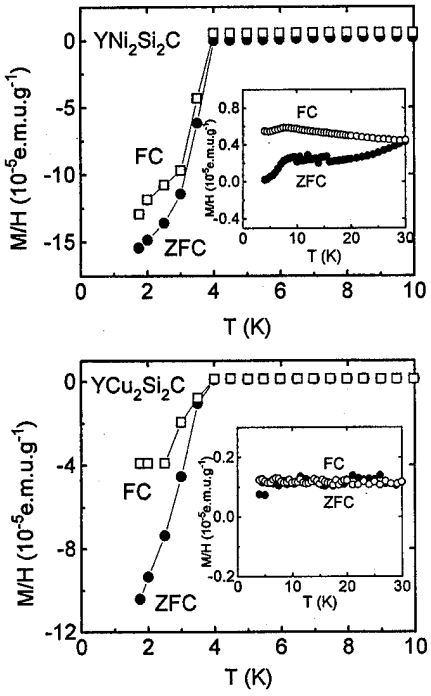



FIG. 4. Temperature-dependent magnetization ($H=10$ G) for $YNi_2Si_2C$ and $YCu_2Si_2C$. The insets, expended view showing the magnetization before $T_c$.

to be found out. Its FC susceptibility, on the other hand, continued to increase with decreasing temperature until $T_c$ was reached. This novel behavior is most likely to be associated with a Ni-containing impurity. For $Y_2Ni_2B_6C_2$ ($YNiB_3C$) and $Y_2Ni_5B_3C_2$ samples, they possess the same onset temperature at 15.0 K with a broader transition width. This result is consistent with the x-ray data which indicate that $YNi_2B_2C$ is the major phase in these samples. For the sample $Y_2NiB_7C_2$, no superconductivity was found. Its susceptibility (in the order of $10^{-5}$) seems to follow the Curie–Weiss law. Such a behavior may be due to a residual magnetic moment of Ni.[6]

The temperature-dependent magnetization data measured at 20 G for Cu-substituted $YNiCuB_2C$ are given in Fig. 3. The shield signal corresponds to ~25% of perfect diamagnetism. The inset to Fig. 3 shows an onset temperature at 11.0 K, indicating that Cu substitution for Ni reduces $T_c$, agreeing with that of Gangopadhyay *et al.*[5]

Superconductivity in small quantities can be observed in silicocarbides $YNi_2Si_2C$ and $YCu_2Si_2C$. The temperature dependence of the magnetization at 10 G for both samples is shown in Fig. 4. The onset temperature is ~4 K for both samples. The magnitudes of the shielding and Meissner effect signals correspond to ~1.5% and ~1.2% of perfect diamagnetism for $YNi_2Si_2C$ and ~1% and ~0.4% for $YCu_2Si_2C$, respectively. This suggests that the superconducting phase is a minor phase with a volume fraction of the order of 1%. From the insets of Fig. 4, the hysteresis between field cooling and zero-field cooling curves before $T_c$ can also be seen in $YNi_2Si_2C$. While such curves were not observed in $YCu_2Si_2C$, which is Ni free, further suggesting that this history-dependent hysteretic magnetic behavior is associated with a Ni-containing impurity.

## IV. CONCLUSIONS

Deviation from the stoichiometric composition of $YNi_2B_2C$ by changing the ratio of Ni to B introduced impurity phases into the major phase $YNi_2B_2C$. In $Y_2Ni_xB_{8-x}C_2$ ($x=2$, 3, 5), the major phase $YNi_2B_2C$ was responsible for superconductivity with $T_c=15.0$ K. For Cu-substituted $YNiCuB_2C$, an expansion in lattice was observed due to the substitution of Ni with Cu. Secondary phases emerged because of the limited solubility of Cu in this compound. The Cu substitution reduced the $T_c$ to 11 K, in agreement with the argument that the Fermi level in the parent compound lies very near to a peak in the density of states so that further enhancement in $T_c$ by chemical modification is rather unlikely.[5] For new silicocarbides $YNi_2Si_2C$ and $YCu_2Si_2C$, they were not bulk superconductors. But there existed superconducting minor phases with $T_c=\sim 4$ K.

## ACKNOWLEDGMENTS

This work was supported by National Science Foundation, Department of Energy, and Louisiana Education Quality Support Fund.

[1] R. J. Cava *et al.*, Nature **367**, 252 (1994).
[2] T. Siegrist, H. W. Zandbergen, R. J. Cava, J. J. Krajewski, and W. F. Peck Jr., Nature **367**, 254 (1994).
[3] M. Buchgeister, A. Handstein, J. Klosowski, N. Mattern, P. Verges, and U. Wiesner, Mater. Lett. **22**, 203 (1995).
[4] B. C. Chakoumakos and M. Paranthaman, Physica C **227**, 143 (1994).
[5] A. K. Gangopadhyay, A. J. Schuetz, and J. S. Schilling, Physica C **246**, 317 (1995).
[6] H. Schmidt, M. Muller, and H. F. Braun, Physica C **235–240**, 779 (1994).

# Oxygen dependence of the Josephson weak link effect, specific heat, and the transition temperature of $YBa_2Cu_3O_x$

S. Glenis, G. Choi, C. L. Lin, and T. Mihalisin
*Department of Physics, Temple University, Philadelphia, Pennsylvania 19122*

X. Q. Wang
*Department of Materials Science and Engineering, University of Pennsylvania, Philadelphia, Pennsylvania 19104*

We have measured $\chi(T)$ for oxygen-annealed $YBa_2Cu_3O_x$ samples and observed a glass-like behavior at low magnetic fields which can be explained in terms of a Josephson weak link effect. The glass transition temperature $T_g$ depends on the oxygen annealing temperature and sample pellet pressure. $T_g$ disappears when a sample was powdered after receiving an oxygen anneal, indicating that the Josephson weak link effect occurs between intergranular boundaries. In addition, $T_c$ shifts from 93 K for the air-sintered samples to 90 K for the oxygen-annealed materials. Under vacuum annealing, $T_g$ disappears and $T_c$ first shifts back to 93 K. Prolonged vacuum annealing or vacuum annealing at higher temperatures depresses $T_c$ to below 90 K. The temperature dependence of the specific heat shows a single anomaly for samples sintered in air or annealed under high vacuum. But a double-peak specific heat anomaly occurs for the oxygen-annealed samples. © *1996 American Institute of Physics.* [S0021-8979(96)02408-3]

## I. INTRODUCTION

Although the high $T_c$ cuprate superconductors[1,2] were discovered in 1986, the thermodynamic, electric, and magnetic properties are not clearly understood. From the magnetization $\chi(T)$ measurements on good quality oxygen-annealed $YBa_2Cu_3O_x$ ($x\approx7$) samples we have observed[3] a glass transition at low magnetic fields which is different from the vortex glass–fluid transition at high fields.[4,5] This glass behavior can be explained in terms of Josephson weak link effects proposed by several theoretical researchers.[6,7] These effects may also explain the so-called "paramagnetic Meissner effect",[8,9] where the field-cooled magnetization below $T_c$ becomes paramagnetic for very low fields. Whether the weak links originate from intergranular or intragranular junctions is not clear.

$T_c$ as determined from the Meissner effect "onset" temperature is about 90 K for oxygen-annealed samples. This value differs significantly from the 93 K value which has usually been reported for $YBa_2Cu_3O_x$ with $x\approx7$, but agrees with that observed for some single crystals.[10] The electrical resistivity measurements on oxygen-annealed samples have shown a two-step transition[11] with the first step at 93 K. Moreover, double-peak specific heat anomalies have been reported for both single-crystal and polycrystalline $YBa_2Cu_3O_x$ ($x\approx7$) samples.[11–13] This double-peak behavior has led some researchers[14] to propose different pairing mechanisms to explain high $T_c$ cuprate superconductors.

We have prepared $YBa_2Cu_3O_x$ samples sintered in air, annealed in oxygen at different temperatures, and annealed under high vacuum. The temperature dependence of the magnetic susceptibility and the specific heat has been measured. The results for these samples are discussed in terms of variations in their oxygen content.

## II. EXPERIMENT

Polycrystalline $YBa_2Cu_3O_x$ samples were prepared using the solid-state reaction technique. The appropriate amounts of high-purity $Y_2O_3$, $BaCO_3$, and CuO were thoroughly mixed and then pressed into pellets 1/2 in. in diameter. The pellets were reacted in air at 950 °C for 24 h. They were then ground to a fine powder and the entire procedure was repeated twice. After the materials were sintered in air three times, they were again ground to a fine powder, pressed into pellets, and finally annealed in flowing oxygen at atmospheric pressure. The oxygen annealing temperature varied from 300 to 950 °C. X-ray diffraction measurements at room temperature were used to check sample homogeneity and determine lattice parameters. The results showed that the lattice parameters are essentially the same for all samples annealed in oxygen irrespective of the annealing temperatures and time intervals, and are consistent with those previously published.[15] We also investigated the microstructure and grain sizes of these samples using a scanning electron microscope. The typical grain size was found to be about 10 $\mu$m. A terrace-like circularly layered microstructure was observed and reported.[3] The temperature dependence of the magnetic susceptibility was measured using a commercial SQUID magnetometer. Since these measurements were performed in low fields, certain precautions were taken. In particular, a "zero-field" calibration was obtained by using a high-purity Pd sphere to determine the residual field in the magnetometer solenoid. The specific heat was measured from 15 to 150 K using a semiadiabatic heat pulse method.

## III. RESULTS AND DISCUSSION

Shown in Fig. 1 curve (a) is the temperature dependence of the zero-field-cooled (ZFC) magnetic susceptibility $\chi(T)$ measured at $H=10$ Oe for a sample that was sintered in air without receiving the final oxygen anneal. It shows a typical diamagnetic behavior for superconductors. The absolute value of $\chi$ at 10 K is close to $1/4\pi$ indicating a good quality sample. $T_c$ is defined from the temperature where the onset of $\chi(T)$ occurs and is found to be about 93 K for this sample. Curve (O1), for a sample annealed in oxygen at 450 °C for

 0021-8979/96/79(8)/5873/3/$10.00 © 1996 American Institute of Physics 

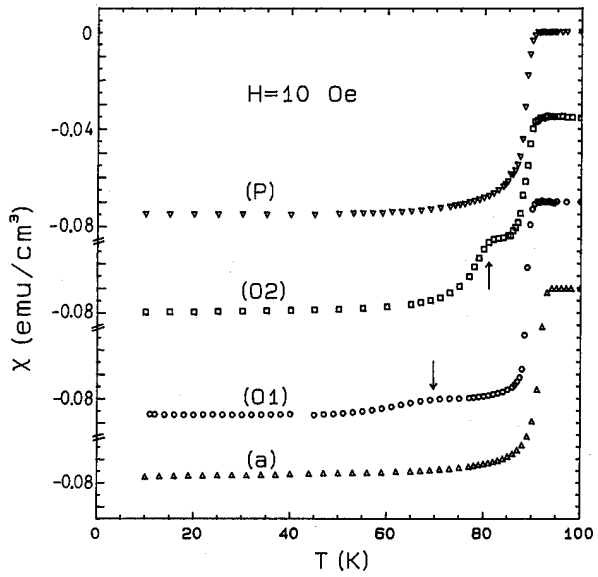



FIG. 1. The $\chi(T)$ data measured at $H=10$ Oe for samples (a) annealed in air, (O1) annealed in oxygen at 450 °C for 10 h, (O2) annealed in oxygen at 950 °C for 10 h and (P) powdered after receiving final oxygen anneal.

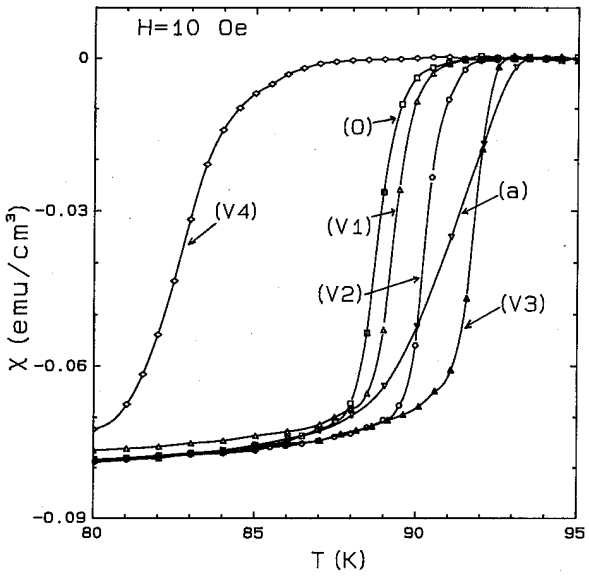



FIG. 3. The $\chi(T)$ data measured at $H=10$ Oe. (a) sample sintered in air. (O) sample annealed in oxygen at 450 °C for 10 h. (V1), (V2), and (V3) samples annealed under vacuum at 375 °C for 1, 3, and 5.5 h, respectively, after being fully oxygenated, and (V4) sample annealed under vacuum at 450 °C for 5 h.

10 h, shows a kink at $T_g=70$ °C. This kink can be attributed to a glass transition which will be discussed later. Note that $T_c$ shifts from 93 to 90 K for this oxygen-annealed sample. Curve (O2), for a sample annealed in oxygen at 950 °C for 10 h, is similar to curve (O1), except $T_g$ shifts to a higher temperature. We have measured $\chi(T)$ for several samples annealed in oxygen between 300 and 950 °C, and found that $T_g$ increases monotonically with increasing oxygen annealing temperature.

We have performed thermal cycling measurements of $\chi(T)$ in order to understand the magnetic response below and above $T_g$. Shown in Fig. 2 is the $\chi(T)$ data for a sample annealed in oxygen at 950 °C for 10 h. The sample was first cooled to 5 K (point A) in zero field. Then a field of $H=5$ Oe was applied and held fixed for the remainder of the cycle. The sample was then taken through a heating–cooling reheating trajectory. It can be seen that the heating–cooling cycle (e.g., $A\rightarrow B\rightarrow C$) is far more irreversible than the cooling–reheating cycle ($B\rightarrow C\rightarrow B'$). However, the heating–cooling–reheating trajectory that starts at $D$, i.e., $D\rightarrow E\rightarrow D\rightarrow E$, is entirely reversible. Note that point $D$ is at the kink temperature $T_g$. Hence it appears that $\chi(T)$ shows irreversible behavior below $T_g$ and reversible behavior above $T_g$ characteristic of a glass transition. Note that the value $H=5$ Oe is smaller than the lower critical field $H_{c1}$ and hence this glass transition is completely different from the vortex–glass–fluid transition[4,5] observed at higher fields. It has been proposed by several theoretical groups[6,7] that this glass behavior at low fields can be explained in terms of Josephson weak link effects. We have shown[3] that $T_g$ initially increases with increasing pellet pressure but saturates at high pressures, and that $T_g$ decreases with increasing applied fields and in fact disappears at sufficiently high field.

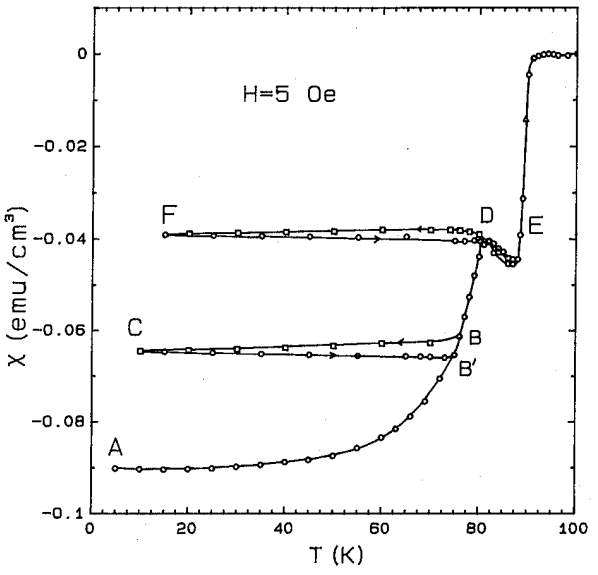



FIG. 2. The thermal cycling magnetic susceptibility measured at $H=5$ Oe for a sample annealed at 950 °C for 10 h.

Returning to Fig. 1, curve $(P)$ shows $\chi(T)$ for a sample which was powdered after receiving an oxygen anneal at 950 °C for 10 h. The kink disappears suggesting that the glass behavior is due to Josephson weak link effects which occur at intergranular boundaries. However, $T_c$ for the powdered samples remains at 90 K indicating that during the oxygen anneal oxygen not only enters the grain boundaries but also enters the entire material resulting in a change of the bulk superconducting properties.

In order to understand $T_c$ as a function of oxygen content, we have measured $\chi(T)$ for several samples annealed in air, in oxygen, and under high vacuum at 375 °C. In Fig. 3 curve (a) shows $\chi(T)$ for an air-sintered sample. Curve $(O)$ shows $\chi(T)$ for a sample annealed in oxygen at 450 °C for

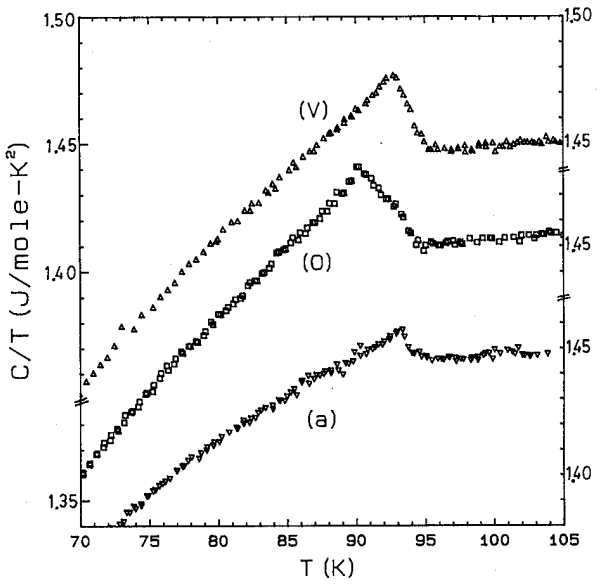



FIG. 4. The $C(T)/T$ data for samples (a) sintered in air, (O) annealed in oxygen at 450 °C for 10 h, and (V) annealed under vacuum at 375 °C for 5.5 h after being fully oxygenated.

10 h. Curves (V1), (V2), and (V3) show $\chi(T)$ for samples that were fully oxygenated by a 10 h oxygen anneal at 450 °C and then vacuum annealed at 375 °C for 1, 3, and 5.5 h, respectively. Curve (V4) shows $\chi(T)$ for a sample that was vacuum annealed at 450 °C for 5 h. Weight measurements before and after oxygen annealing allowed us to determine how the oxygen content varies with the temperature and time (duration) of the oxygen anneal. The oxygen content rises rapidly and saturates presumably at a value corresponding to $\approx 7$. The time required for saturation depends on the anneal temperature. We found the saturation time to be about 3 h at 450 °C but only 30 min at 950 °C. It should be noted that a number of samples (not shown in Fig. 3) were annealed in oxygen for very long times (up to 60 h) at varying temperatures (from 300 to 950 °C). These samples as well as the sample shown in curve (O) of Fig. 3 (annealed in oxygen for 10 h at 450 °C) all show a $T_c$ of 90 K indicating that 90 K is the $T_c$ for fully saturated $YBa_2Cu_3O_7$.

Curves (V1), (V2), and (V3) are for samples that were first fully oxygenated and then vacuum annealed at 375 °C for 1, 3, and 5.5 h, respectively, to drive out oxygen. Note from Fig. 3 that $T_c$ rises from 90 to 93 K. Finally curve (V4) of Fig. 3 shows a sample that was first fully oxygenated and then vacuum annealed at a higher temperature, namely, 450 °C for 5 h. This sample shows a considerably lower $T_c$ presumably because too much oxygen has been removed. The $T_c$ variation observed here is in good agreement with recently published results.[10,12,16]

Shown in Fig. 4 is specific heat data plotted as $C(T)/T$ vs $T$. Curve (a) is the data for a sample sintered in air. A small specific heat anomaly is present at about 93 K which is associated with the superconducting transition. After the sample was annealed in oxygen at 450 °C for 10 h the specific heat anomaly became more pronounced as seen in curve (O). In fact, curve (O) consists of a main peak at about 90 K and a shoulder at 93 K. Samples annealed in oxygen for 10 h at temperatures between 450 and 950 °C show the same behavior. This double-peak specific heat anomaly has been observed previously.[11–13] Curve (V) shows the data for a fully oxygenated sample that was then annealed under vacuum at 375 °C for 5.5 h. The anomaly shifts back to 93 K, but still remains more pronounced [than curve (a)]. A more extensive analysis of the specific heat data is under way and will be presented in a future paper. However, it seems clear at this point that a number of interesting phenomena besides the value of $T_c$ are closely tied to the oxygen content including the presence of a weak link glass state and a double-peaked specific heat behavior.

## ACKNOWLEDGMENTS

C. L. Lin and T. Mihalisin acknowledge support from the Materials Research Center at Temple University and DOD-AFOSR under Grant No. F49620-93-1-0018. X. Q. Wang acknowledges support from NSF-MRL under Grant No. DMR91-20668.

[1] J. G. Bednorz and K. A. Muller, Z. Phys. B **64**, 189 (1986).
[2] M. K. Wu, J. R. Ashburn, C. J. Torng, P. H. Hor, R. L. Meng, L. Gao, Z. J. Huang, Y. Q. Wang, and C. W. Chu, Phys. Rev. Lett. **58**, 408 (1987).
[3] C. L. Lin, X. Q. Wang, S. Kotowich, N. Bykovetz, T. Mihalisin, F. Chu, and J. T. Wang, Phys. Rev. B **51**, 8390 (1995).
[4] K. A. Muller, M. Takashige, and J. G. Bednorz, Phys. Rev. Lett. **58**, 1143 (1987).
[5] D. S. Fisher, M. P. A. Fisher, and D. A. Huse, Phys. Rev. B **43**, 130 (1991).
[6] F. V. Kusmartsev, Phys. Rev. Lett. **69**, 2268 (1992).
[7] D. Dominguez, E. A. Jagla, and C. A. Balseiro, Phys. Rev. Lett. **72**, 2773 (1994).
[8] W. Braunisch *et al.*, Phys. Rev. B **48**, 4030 (1993).
[9] P. Svedlindh, K. Niskanen, P. Norling, P. Nordblad, L. Lundgren, B. Lonnberg, and T. Lundstrom, Physica C **164**, 1365 (1989).
[10] H. Claus *et al.*, Physica C **200**, 271 (1992).
[11] Y. Nakazawa, J. Takeya, and M. Ishikawa, Physica C **225**, 71 (1994).
[12] E. Janod, A. Junod, T. Graf, K. Q. Wang, G. Triscone, and J. Muller, Physica C **216**, 129 (1993).
[13] M. Ishikawa, Y. Nakazawa, T. Takabatake, A. Kishi, R. Kato, and A. Maesono, Physica C **153–155**, 1089 (1988).
[14] T. Pavlopoulos, P. L. Christiansen, and M. P. Soerensen, Z. Phys. B **91**, 43 (1993).
[15] See, for example, *Chemical and Structural Aspects of High Temperature Superconductors*, edited by C. N. R. Rao (World Scientific, Singapore, 1988).
[16] H. Claus *et al.*, Physica C **198**, 42 (1992).

# Effects of Pr, Tb, and Zn doping into $YBa_2Cu_3O_7$ on magnetoresistivity and magnetic phase boundaries

F. Freibert, G. Cao, S. McCall, M. Shepard, and J. E. Crow
*National High Magnetic Field Laboratory, Florida State University, Tallahassee, Florida 32306-4005*

Transverse $AB$-plane magnetoresistivity $\rho_{AB}$ ($C$ axis $\|H$) of $(Y_{1-X}Pr_X)Ba_2Cu_3O_{7-\delta}$ and $YBa_2(Cu_{1-X}Zn_X)_3O_{7-\delta}$ thin films and $(Y_{1-X}Tb_X)Ba_2Cu_3O_{7-\delta}$ thin films and single crystals has been measured as a function of $0.0<X<X_C$, $2\text{ K}<T<300$ K, and $0\text{ T}<H<20$ T. Mean-field upper critical field $H_{C2}$ and irreversibility field $H_I$ phase boundaries have been determined and are discussed in terms of proposed theories. Tb doping of $YBa_2Cu_3O_7$ reflects an enhanced pinning or "stiffening" of the vortex system without apparent alteration to $T_C$ or the slope of the mean-field normal phase-mixed phase boundary line, $dH_{C2}/dT|_{T=T_c}$. However, Pr and Zn doping of $YBa_2Cu_3O_7$ tends to depress both $T_C$ and $dH_{C2}/dT|_{T=T_c}$ and shows a "softening" of the vortex system. This behavior may be understood in terms of the magnitude of the superconducting pair coherence length, which is controlled by doping, and the divergence of the vortex-glass correlation length as it relates to flux line coupling of vortices in the $CuO_2$ planes. These systems are compared with other high $T_C$ superconducting systems which possess similar phase boundary properties.
© *1996 American Institute of Physics.* [S0021-8979(96)02508-X]

## I. INTRODUCTION

Magnetoelectronic transport measurements of selectively doped high $T_C$ superconductors can provide a direct gauge of structural and magnetic alterations as sensed by vortices in the superconducting state and electrons in the normal state. Local disorder introduced into the structure by doping has a great consequence both for the $H-T$ (magnetic field–temperature) phase diagram of the vortex system and for its dynamical properties. This is evidenced by shifts and novel structures seen in the magnetic phase boundaries of the $H-T$ plane, since these boundaries mark transition points between the different vortex system states within the superconductor. The magnitude of the extrapolated residual resistivity $\rho_O(T=0\text{ K})$ is indicative of electron-defect and electron-impurity scattering lifetimes and the temperature dependence of the normal state resistivity of characteristic of electron-exitation or electron-magnetic impurity spin scattering.

$YBa_2Cu_3O_{7-\delta}$ (YBCO) and the other Cu-based high $T_C$ oxide superconductors have many features in common, including large anisotropies in their magnetic and transport properties, which reflect the role played by the $CuO_2$ planes common to all these systems. This article focuses on portions of a magnetotransport properties study of YBCO doped with Pr, Tb, and Zn where particular attention is devoted to dissipative properties of the normal and superconducting states, the onset of superconductivity $H_{C2}$, and the formation of the vortex–solid phase $H_I$. Many similarities and many differences exist between the impact of impurities on the normal and superconducting properties upon entering the lattice and preferentially perturbing the system. The superconducting properties of YBCO are insensitive to Y-site trivalent substitutions, except in the case of Ce, Pr, and Tb. Of these three exceptions, Pr and Tb can be doped onto the Y-site accompanied by altered superconducting and normal state properties. Increasing Pr concentration from $X=0.0$ to $X_C=0.55$ in $(Y_{1-X}Pr_X)Ba_2Cu_3O_{7-\delta}$ (YPBCO) produces a monotonic decrease in $T_C$ and a monotonic increase in $\rho_O$ from 90 to 0 K. However, Tb doped into $(Y_{1-X}Tb_X)Ba_2Cu_3O_{7-\delta}$ (YTBCO) epitaxial thin films and crystals shows $T_C$ to be independent of doping up to the highest concentration measured, i.e., $X=0.50$. These differences are unusual since Pr- and Tb-doped YBCO have many features in common, e.g., both Pr and Tb appear to hybridize with carriers in the $CuO_2$ planes as reflected by large enhancements in $\gamma$ (coefficient of the linear temperature-dependent contribution of the specific heat) and the large anisotropies in the normal state magnetic susceptibilities.[1–4] In contrast to the impact on the normal and superconducting properties due to Pr and Tb doping of YBCO, which indirectly modify the $CuO_2$ planes through hybridization, the impact due to Zn doping of YBCO accomplished by substitution for the Cu in the $CuO_2$ planes leads to a precipitous drop in $T_C$ with $T_C\rightarrow 0$ K for $X_C=0.10$ in $YBa_2(Cu_{1-X}Zn_X)_3O_{7-\delta}$ (YBCZO). This behavior indicates the importance of the Cu ion magnetic moment to the superconducting mechanism in YBCO, since Zn is diamagnetic and isovalent with $Cu^{+2}$ and distorts the unit cell volume less than 0.5% at $X_C$.

## II. THEORETICAL BACKGROUND

All high $T_C$ superconductors are anisotropic type II superconductors whose reduced dimensionality and high $T_C$ have greatly enhanced the thermal fluctuations of the order parameter and altered the mixed phase behavior. These effects are apparent in the electrical resistivity of the superconductor cooled in a magnetic field. Near $T_C$, the fluctuation enhancement in the resistivity obeys scaling relations as expected on the basis of Ginzburg–Landau fluctuation theory for a three-dimensional superconducting system in a high magnetic field.[5] This scaling behavior provides a consistent method of determining the second-order mean-field upper critical field transition temperature, $T(H_{C2})$, and offers an alternative, more physically significant method to that of obtaining $T(H_{C2})$ from $0.5\rho(H)|_{T=T_c}$.

 0021-8979/96/79(8)/5876/3/$10.00 © 1996 American Institute of Physics

As the cooling process continues in field ($H_{C1}<H<H_{C2}$) below $T_C$, a vortex–liquid phase appears, and is soon replaced as vortex–vortex and vortex–defect interactions act collectively to bring about the transition from a vortex-liquid to a vortex-glass at a well-defined temperature $T_G$ (in a dc measurement $T_G=T_I$). The vortex–glass phase onset is signaled by a vanishing electrical resistivity $\rho=|T-T_G|^{-s}$, where $s=\nu(z-1)$ for critical exponent $\nu$ and dynamical exponent $z$.[6] Thus, the $H-T$ (magnetic field–temperature) phase diagram possesses a vortex state ($H_{C1}<H<H_{C2}$) with regions of reversible and irreversible magnetic behavior separated by an "irreversibility" line. The theoretical vortex–glass transition line obeys the low-field ($H_{C2}\gg H>H_{C1}$) power-law temperature dependence $H_G = H_O(1 - T/T_C)^{2\nu'}$, where $\nu'=2/3$ for the zero-field critical region and is true for vortex systems in YBCO single crystals and thin films.[7,8] This temperature dependence is related to divergence in the correlation length of the order parameter, $\xi_G = |T - T_G|^{-\nu'}$, as $T_G$ is approached from either higher or lower temperatures.

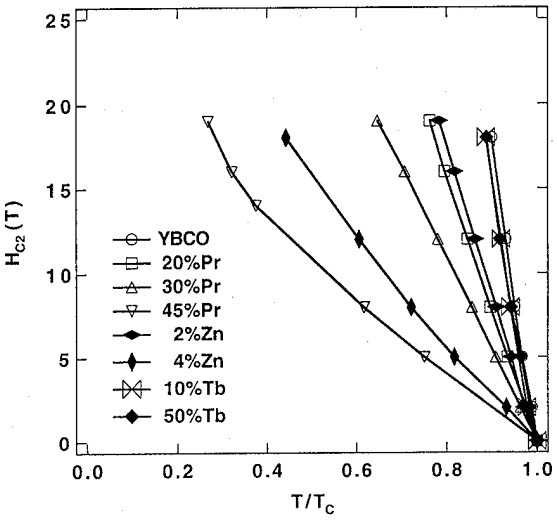



FIG. 1. Mean-field upper critical field $H_{C2}$ phase boundaries for various dopant concentrations vs normalized temperature. (Solid lines are guides to the eye.)

## III. EXPERIMENTS AND RESULTS

Thin films of YPBCO, YTBCO, and YBCZO were grown by laser ablation, each of average thickness 1.5 mm.[1,2] Since the films were epitaxially deposited on twinned single-crystal $LaAlO_3$ substrates, transport measurements are representative of collective $AB$-plane behavior. Single crystals of YTbCO were grown by the self-flux growth technique.[2] Resistivity measurements $\rho_{AB}(X,H,T)$ for $0<X<X_C$, 2 K$<T<$300 K and 0 T$<H<$20 T were made using an in-line four-probe method for the thin film samples and the Montgomery technique for the single crystals. In all cases, corrections for thermal EMFs were applied with current densities of 1 A/cm$^2<J<$50 A/cm$^2$. These measurements allow determination of such physical quantities as the mean-field upper critical field $H_{C2}$ and irreversibility field $H_I$, and their dependence on temperature $T$, dopant concentration $X$ and magnetic field $H$.

This study has revealed that an increase in Tb doping appears to shift the vortex–glass transition line to higher temperatures or "stiffening" as compared to undoped YBCO, while leaving $T_C$ and the slope of the mean-field normal phase-mixed phase boundary line, $dH_{C2}/dT|_{T=T_c}$, relatively unchanged [$\Delta T(H_{C2})$ and $\Delta dH_{C2}/dT|_{T=T_C}$ $<2\%$] as seen in Fig. 1. The absence of change in $\xi_{GL}$, the Ginzburg–Landau superconducting pair coherence length ($H_{C2}=\phi_0/2\pi\xi_{GL}^2$, $\phi_0$ is the flux quanta), implies some possible vortex-impurity interactions causing an enhanced pinning or "stiffening" of the vortex system and bringing about the transition to the vortex–solid phase at higher temperatures. Fitting the power-law temperature dependence of the irreversibility line shows an increase in $\nu'$ of 20% with increased Tb doping (Fig. 2). Co-doped $YBa_2(Cu_{1-X}Co_X)_3O_{7-\delta}$ (YBCCO-chain site doping) single crystals at concentrations less than $X=0.025$ show a similar behavior with an increase in $\nu'$ ($\nu'=0.55$ at $X=0.01$ to $\nu'=0.66$ at $X=0.02$); but no significant shift in temperature of the irreversibility line as measured by dc magnetization.[9] However, at $X=0.025$ doping this system undergoes an orthorhombic-to-tetragonal phase transition, resulting in behavior similar to the Pr- and Zn-doped systems. Magnetization studies show oxygenation of as-grown polycrystalline $HgBa_2CaCu_2O_{6+\delta}$ introduces small displacements to higher temperatures in the irreversibility line and increases in $\nu'$ ($\nu'=1.2$ to $\nu'=1.3$) which are attributed to variations in $CuO_2$ planar coupling with planar separation distances.[10]

In contrast to the phase diagram of the Tb-doped system, increased Pr and Zn doping of YBCO tends to depress both $T_C$ and $dH_{C2}/dT$ (Fig. 3), but to increase $\nu'$ (Fig. 2). The depression of $dH_{C2}/dT$ has been seen in other $H_{C2}$ studies of YPBCO and is attributed to hole filling and/or hybridization.[1,4] The enlargement in the size of $\xi_{GL}$ with increased doping (Fig. 3) redefines the length scales in the vortex system resulting in an inability of the quenched dis-

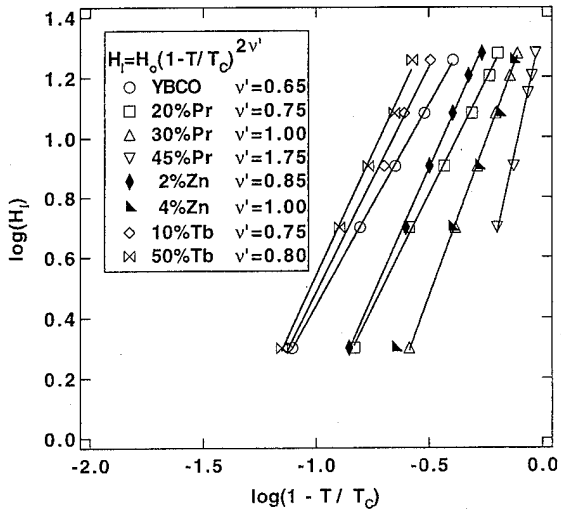



FIG. 2. Log–log plot of $H_I$ vs $1-T/T_C$ for thin film samples of Pr-, Tb-, Zn-doped YBCO. (Solid lines represent power-law fits with given exponents.)

order (twinning and point defects) to reduce thermally activated vortex motion thus "softening" the vortex system. As mentioned above, single crystals of YBCCO at dopant concentrations of greater than $X=0.025$ have a similar behavior with the irreversibility line shifted to lower temperatures and increasing $\nu'$ ($\nu'=0.75$ at $X=0.025$ to $\nu'=1.3$ at $X=0.04$ for $H>1$ T) which has been attributed to decoupling of the vortices between $CuO_2$ planes.[9] Thickness dependence studies of YBCO thin films by ac magnetization show a progressive depression in transition temperature $T_I$ with $\nu'$ increasing from $\nu'=0.66$ to $\nu'=0.86$ as film thickness decreased from 1000 to 20 nm, respectively.[11] Although no explanation was afforded, the reduction in the number of possible $CuO_2$ planes coupled by flux lines from 30 000 to 60, results in similar behavior seen in Pr-, Zn-, and Co-doped YBCO with increased doping. From a magnetoresistivity study of YBCO thin films with decreasing strip width from 5.6 to 0.54 mm, evidence was offered that size effects were responsible for softening of the vortex system elasticity.[12] This evidence took the form of an increase in the dynamical exponent $z$ by some 70% ($z=5.6$ to $z=9.7$) with an associated increase in $\nu'$ of 40% ($\nu'=0.75$ to $\nu'=1.07$).

These systems were chosen for study based on the need to understand the effects magnetic and nonmagnetic impurities have on the mechanisms responsible for the depression of superconductivity and on the fundamental phenomena which underlies the vortex state in these unconventional type II superconductors. Within this and similar studies, alterations of the structure in and around the $CuO_2$ planes have redefined the boundaries of the $H-T$ phase plane. This phenomenon is intimately tied to the manner in which the vortex system detects these changes and adapts its dynamical properties. The questions brought up and left unanswered here will provide an area for more detailed investigation in future work.


[1] G. Cao, J. Bolivar, J. W. O'Reilly, J. E. Crow, R. J. Kennedy, and P. P. Wise, Physica B **186–188**, 1004 (1993), and references therein.
[2] G. Cao, J. W. O'Reilly, J. E. Crow, R. J. Kennedy, and D. H. Nichols, J. Appl. Phys. **75**, 6326 (1994), and references therein.
[3] G. Cao, F. Freibert, P. F. Henning, S. McCall, M. Shepard, and J. E. Crow, Physica B **206 & 207**, 749 (1995), and references therein.
[4] Y. X. Jia, J. Z. Liu, M. D. Lan, P. Klavins, R. N. Shelton, and H. B. Radousky, Phys. Rev. B **45**, 10609 (1992).
[5] S. Ulah and T. Dorsey, Phys. Rev. B **44**, 262 (1991).
[6] D. S. Fisher, M. P. A. Fisher, and D. A. Huse, Phys. Rev. B **43**, 130 (1991).
[7] R. H. Koch, V. Foglietti, W. J. Gallgher, G. Koren, A. Gupta, and M. P. A. Fisher, Phys. Rev. Lett. **63**, 1511 (1989).
[8] D. S. Reed, N. Yeh, W. Jiang, U. Kriplani, D. A. Beam, and F. Holtzberg, Phys. Rev. B **49**, 4384 (1994).
[9] R. L. Neiman, J. Giapintzakis, and D. M. Ginsberg, Phys. Rev. B **50**, 16028 (1994).
[10] Z. J. Huang, Y. Y. Xue, R. L. Meng, and C. W. Chu, Phys. Rev. B **49**, 4218 (1994).
[11] L. Chivale, T. K. Worthington, and A. Gupta, Phys. Rev. B **43**, 5425 (1991).
[12] Y. Ando, H. Kubota, and S. Tanaka, Phys. Rev. Lett. **69**, 2851 (1992).


*Published without author corrections*

# Rotational magnetic measurements of vortex pinning in polycrystalline superconductors (abstract)

M. K. Hasan, S. J. Park, and J. S. Kouvel
*Department of Physics, University of Illinois, Chicago, Illinois 60607-7059*

Magnetization-vector measurements were made at various temperatures on polycrystalline disks of $YBa_2Cu_3O_7$ and $(Ba,K)BiO_3$ as each was rotated about its axis in a fixed field **H** along the disk plane. For hysteretic starting states, the vortex flux density vector **B** is found to bifurcate into a $\mathbf{B}_R$ component that rotates rigidly with the sample and a $\mathbf{B}_F$ component that stays at a fixed angle ($\theta_F$) relative to $H$, thus turning frictionally relative to the sample, as seen earlier.[1] With increasing H, $B_R$ decreases and $B_F$ increases in size, indicating a distribution in the strength of the vortex pinning torques. After $B_R$ has vanished, the frictional angle $\theta_F$ decreases rapidly. Thus, the quantity $H\mu \sin \theta_F$ ($\mu$ being the quantized vortex moment), which equals the average pinning torque ($\tau_p$) on each vortex, does not remain constant but diminishes with increasing $H$. This decrease of $\tau_p$ is consistent with the collective pinning phenomenon known as vortex bundling. At fixed $H$, $\tau_p$ diminishes rapidly with increasing temperature, reaching very low values well below $T_c$. These results are compared with those derived from critical-state model interpretations of conventional hysteresis loop data. © *1996 American Institute of Physics.* [S0021-8979(96)63208-4]

Work supported by NSF Grant No. DMR-92-21901.

[1] H. P. Goeckner and J. S. Kouvel, Phys. Rev. B **50**, 3435 (1994).

# 4 Gbit/in.$^2$ inductive write heads using high moment FeAlN poles

W. P. Jayasekara, S. Wang,[a] and M. H. Kryder
*Data Storage Systems Center, Carnegie Mellon University, Pittsburgh, Pennsylvania 15213*

Thin film inductive write heads incorporating 2-$\mu$m-thick single and multilayer FeAlN/$SiO_2$ poles were fabricated. The poles were trimmed to 1 $\mu$m trackwidth using focused ion beam etching from the air bearing surface of the sliders. Tests on 2950 Oe media show satisfactory media saturation. Overwrite in excess of $-43$ dB and hard transition peak shift $<2$ nm were measured for wide trackwidth heads with 0.2 $\mu$m gap lengths. Tracks written using a 1 $\mu$m track width head were imaged using magnetic force microscopy, showing well defined transitions at linear densities up to 6600 flux changes per millimeter. A written track width of approximately 1.1 $\mu$m and a side erase band of less than 0.1 $\mu$m were observed. Assuming a coding scheme with a density ratio of 1.33, these heads promise a recording density of over 4 Gbit/in.$^2$ © *1996 American Institute of Physics.* [S0021-8979(96)12008-1]

## I. INTRODUCTION

Achieving high areal density magnetic recording requires writing data at high track density as well as high linear density. The former requires write heads with very narrow track widths, while the latter calls for narrow gap heads capable of both saturating high coercivity media as well as generating a high write field gradient. Recording heads capable of 1–3 Gbit/in.$^2$ areal density recording have been discussed in the past.[1–3] In this article we discuss the performance of narrow and wide track width write heads with poles made of FeAlN high moment material. These heads are capable of saturating 2950 Oe media. The narrow track heads are shown to write at an areal density of over 4 Gbit/in.$^2$

## II. EXPERIMENT

The write heads were made with poles consisting of 2-$\mu$m-thick single and multilayer FeAlN/$SiO_2$ films. This material was deposited in a Perkin Elmer 2400 system by rf-diode sputtering an FeAl target in an Ar/$N_2$ ambient. FeAlN films deposited on glass wafers were reported earlier.[4] These showed coercivity $H_c<1$ Oe, anisotropy field $H_k$ of 6 Oe, saturation magnetization of 20 kG (yielding a permeability of 3400), near zero magnetostriction, and, for laminated films, a permeance roll-off frequency of over 200 MHz. Wafer level testing of FeAlN write heads have shown satisfactory magnetic behavior.[5] The poles were defined by ion milling through a photoresist mask. Track widths of 10–24 $\mu$m were defined in this manner. The gap consisted of 0.2 $\mu$m sputtered $Al_2O_3$. The heads incorporated 15 turn plated copper coils and hard cured photoresist insulators. The heads were subsequently machined into two rail sliders. The magnetic separations quoted below are based on air bearing simulations, and 38 nm for the sum of carbon overcoat, half media thickness, and pole tip recession. The heads were lapped to a target throat height of 0.5–1.0 $\mu$m. The poles of the wide track width heads were trimmed from the air bearing surface (ABS) of the slider using focused ion beam etching (FIBE). A 0.7 $\mu$m track width defined by trimming a 12 $\mu$m track width head is shown in Fig. 1.

The recording data presented in this article pertain to a 22 $\mu$m track width head and a 1 $\mu$m track width focused ion beam etched head. For the latter, the etch depth was 1 $\mu$m, which previous modeling showed to be adequate to prevent disturbing adjacent data tracks.[6] These heads had poles consisting of two 1-$\mu$m-thick laminations. The two cobalt based thin film media used in this experiment had coercivities of 2500 and 2950 Oe. Both had an $M_rt$ of 0.65 memu/cm$^2$ and a carbon overcoat of 7.5 nm. The written pattern was read back with a separate magnetoresistive sensor with a read trackwidth of 2.8 $\mu$m and a shield to shield gap spacing of 0.36 $\mu$m.

## III. RESULTS AND DISCUSSION

The signal read back using the MR head as a function of the write current for the 22 $\mu$m track width and the 1 $\mu$m track width write heads on 2950 Oe coercivity media is shown in Fig. 2. Complete media saturation is accomplished for both heads. The media saturation onset currents for both heads are quite similar, indicating that the pole trimming has

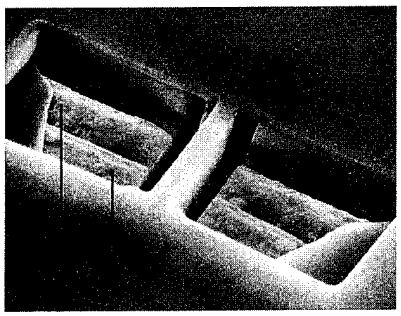


FIG. 1. 0.7 $\mu$m track width defined by focused ion beam etching from the ABS.

[a]Now at Stanford University.

 0021-8979/96/79(8)/5880/3/$10.00 © 1996 American Institute of Physics

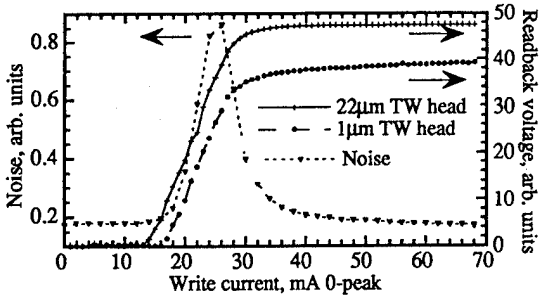



FIG. 2. Readback voltage and reverse dc erase noise as a function of write current, on 2950 Oe media.

had no detrimental effects on head performance. The efficiency of the heads was evaluated using the reverse dc erase noise method.[7] In this measurement the media is dc erased with one polarity, and then the media noise is measured as a function of the dc write current applied to the head with opposite polarity. The reverse dc erase noise exhibits a maximum at the current at which the field in the media equals the remanent coercivity of the media. This is also depicted in Fig. 2, for the 22 $\mu$m track width head on 2950 Oe media. The nominal magnetic separation (fly height, overcoat, half media thickness, plus pole tip recession) in this case was 105 nm. Using the Karlqvist relationship between deep gap field and field at the media, a relatively low efficiency of approximately 27% is calculated for this head.

Overwrite results at the same fly height are presented in Fig. 3. In this measurement, a 625 flux changes per millimeter (fc/mm) pattern was overwritten by a 2500 fc/mm pattern, and the reduction in signal amplitude at the fundamental frequency of the overwritten pattern was determined. The wide track width head demonstrates very good overwrite on 2950 Oe coercivity media. However, the overwrite for the 1 $\mu$m track width head (not shown) was much lower. This is attributed to the 2.8 $\mu$m track width MR read head sensing incompletely overwritten track edges of the 1-$\mu$m-wide track. Hard transition peak shift (HPS) was measured using overwrite spectra.[8] An HPS of less than 2 nm is obtained at a write current over 55 mA and a magnetic separation of 80 nm, as shown in Fig. 3. It was observed that at separations over 100 nm an HPS of less than 5 nm could not be achieved, inspite of the good overwrite observed earlier. This is attributed to the lower write field gradient experienced at the larger separations.

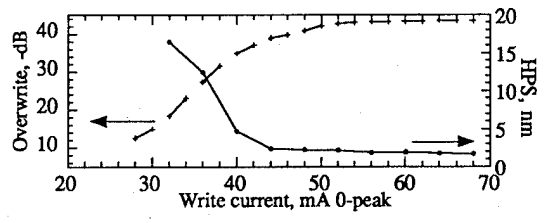



FIG. 3. Overwrite and hard transition peak shift as a function of write current for 22 $\mu$m head on 2950 Oe media.

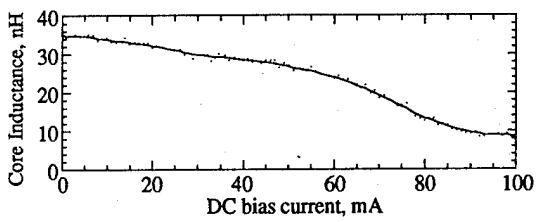



FIG. 4. Core inductance of the write head as a function of applied dc bias current.

Core inductance of the head as a function of applied dc bias current is shown in Fig. 4. Up to a current of approximately 60 mA, the inductance rolls off gradually, indicating that no severe saturation is occurring in this regime. However, a sharper drop in inductance is observed beyond 60 mA, indicative of possible saturation of the neck region. The core inductance at zero bias current is lower than in a conventional NiFe head, indicating lower core permeability. This is consistent with the low efficiencies observed, and has been reported earlier.[9] This low permeability could be due to low substrate temperature when FeAlN was deposited without substrate preheating on $Al_2O_3$–TiC wafers,[10] and/or due to the high anisotropy of the FeAlN deposited on nonplanar surfaces of the head.[11] Core inductance measured as a function of frequency for heads with poles with 20 laminations does not show any appreciable roll off in the measured range of 1–50 MHz.

Roll-off measurements were done on 2950 Oe media at a magnetic separation of 80 nm. As shown in Fig. 5, $D_{50}$, the linear density at which the readback amplitude falls to 50% of that at low density, is 5200 fc/mm. The signal from the 1-$\mu$m-wide tracks shows slightly different characteristics, possibly due to track edge effects detected by the wider track width read head. Assuming $D_{50}\approx 1.44/\mathrm{PW}_{50}$,[12] where $\mathrm{PW}_{50}=[g^2+4(a_x+d)^2]^{0.5}$ is the width at half maximum amplitude of the readback pulse, $g=0.18$ $\mu$m is half the read gap, $a_x$ is the transition parameter of the written pattern, and $d\sim 60$ nm is the magnetic separation during readback, $a_x\sim 40$ nm. This is consistent with calculations based on the Williams–Comstock model. This also predicts a $D_{50}$ of 6200 fc/mm if the read gap is reduced to 0.2 $\mu$m.

Tracks written using the 1 $\mu$m track width head at a magnetic separation of 94 nm on 2500 Oe coercivity media were imaged using magnetic force microscopy (MFM). The MFM lift height was 25 nm. An all-ones pattern written at a linear density of 6600 fc/mm, shown in Fig. 6, has been

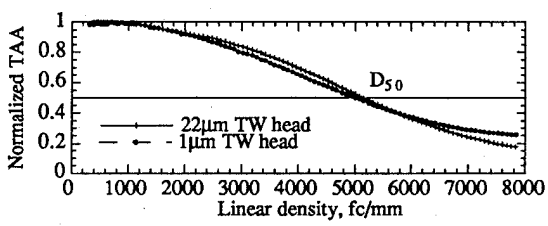



FIG. 5. Roll-off curves for FeAlN write heads on 2950 Oe media.

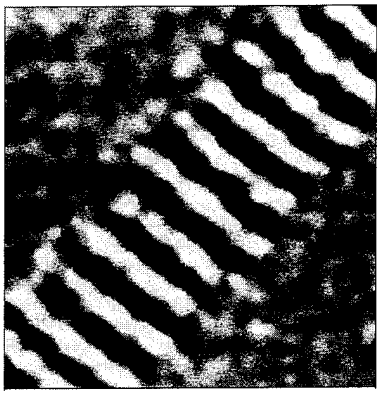


FIG. 6. MFM image of 6600 fc/mm pattern written with 1 $\mu$m track width head. Total field width is 2.5 $\mu$m.



FIG. 8. MFM image of offtrack overwrite test showing side erase band. Total field width is 5 $\mu$m.

defined well. In contrast, a track written at a linear density of 8800 fc/mm, shown in Fig. 7, is showing some transition percolation. The written track width is observed to be approximately 1.1 $\mu$m. An off-track overwrite image, where a track was written at a low density and partly overwritten by another track at twice that density after stepping the head half a track width, is shown in Fig. 8. A narrow erase band of $<0.1$ $\mu$m is observed between the tracks. This is consistent with modeling results (cf. 6).

Allowing $\pm 0.1$ $\mu$m for track misregistration, these images show that a track pitch of 1.35 $\mu$m can be achieved with these heads. Using a coding scheme with a density ratio of 1.25 (bits/fc), the 6600 fc/mm tracks correspond to a user bit density of 8250 bits/mm, while a code with a density ratio of 1.33 would yield 8800 bits/mm. These correspond to areal densities of 6.1 and 6.5 Mbit/mm$^2$, or 3.95 and 4.2 Gbits/in.$^2$, respectively.

## IV. CONCLUSIONS

Write heads using FeAlN high moment pole material were fabricated and tested. These heads are capable of saturating 2950 Oe media. MFM imaging showed clearly defined transitions in tracks written at a linear density of 6600 fc/mm. Wide track width heads demonstrated overwrite of over $-43$ dB and a hard transition peak shift of $<2$ nm. Inductance measurements indicate that the heads were not undergoing severe saturation in the operating regime. The heads were observed to have somewhat low efficiencies. This is attributed to low permeability of FeAlN deposited without substrate heating and/or deposited on nonplanar surfaces. Narrow track width heads were defined by pole trimming wide trackwidth heads from the ABS. These were demonstrated to be capable of writing at an areal density of 4 Gbits/in.$^2$

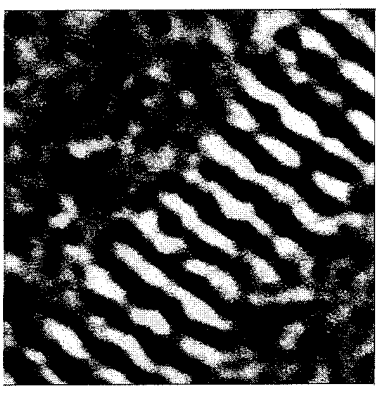


FIG. 7. MFM image of 8800 fc/mm pattern written with 1 $\mu$m track width head. Total field width is 2.5 $\mu$m.

## ACKNOWLEDGMENTS

The authors gratefully acknowledge Dr. P. Frank, Dr. G. Roberts, Dr. S. Liao, and J. Stocker of Applied Magnetics Corporation for assistance in fabricating the write heads, P. Williams and T. Woodward of Materials Analytical Services for FIBE services, and Dr. G. Spratt, J. Gorczyca, D. Karns, Dr. G. Bellesis, Dr. J. Bain, and Dr. R. Jones for assistance with measurements and useful discussion. The authors also wish to thank Dr. S. Bhatia of IBM Corporation for supplying media, Dr. E. Murdock of Seagate Technology, Rocky Mountain Magnetics, and IBM Corporation for supplying MR read heads. This work was supported by the National Science Foundation under Grant No. ECD-8907068, and the National Storage Industry Consortium.

[1] C. Tsang, M. Chen, T. Yogi, and K. Ju, IEEE Trans. Magn. **26**, 1689 (1990).
[2] H. Takano, H. Fukuoka, M. Suzuki, K. Shiiki, and M. Kitada, IEEE Trans. Magn. **27**, 4678 (1991).
[3] C. Tsang, H. Santini, D. McCown, J. Lo, and R. Lee, IEEE Trans. Magn. **32**, 7 (1996).
[4] M. H. Kryder, S. Wang, and K. Rook, J. Appl. Phys. **73**, 6212 (1993).
[5] S. Wang, F. Liu, K. D. Maranowski, and M. H. Kryder, IEEE Trans. Magn. **30**, 281 (1994).
[6] M. H. Kryder and W. Lai, IEEE Trans. Magn. **30**, 3873 (1994).
[7] G. Tarnopolsky, L. Tran, A. Barany, H. Bertram, and D. Bloomquist, IEEE Trans. Magn. **25**, 3160 (1989).
[8] C. Tsang and Y. Tang, IEEE Trans. Magn. **24**, 3087 (1988).
[9] H. Hu, L. Vo, and T. Nguyen, IEEE Trans. Magn. **30**, 3870 (1994).
[10] J. Bain and M. H. Kryder, IEEE Trans. Magn. **31**, 2703 (1995).
[11] P. Zheng, J. Bain, and M. H. Kryder, IEEE Trans. Magn. **31**, 2700 (1995).
[12] H. Bertram, *Theory of Magnetic Recording* (Cambridge University Press, Cambridge, 1994), p. 159.

# Experimental studies of nonlinearities in MR heads

Xinzhi Xing and H. Neal Bertram
*Center for Magnetic Recording Research, University of California at San Diego, La Jolla, California 92093-0401*

Magnetoresistive (MR) heads have been widely developed for high density digital magnetic recording. The nonlinear MR head response causes nonlinear distortion in the playback signals, and this results in a degradation of system performance. In this work, techniques for identifying the nonlinearity due to the playback process have been developed. Different levels of nonlinear distortion in the playback signals were observed for different head/disk combinations. The behavior of the MR nonlinear distortion as a function of flying height and recording density was also examined. © *1996 American Institute of Physics.* [S0021-8979(96)28708-0]

## I. INTRODUCTION

In magnetic recording, nonlinear distortions in the playback signals cannot generally be corrected by equalization; therefore it is particularly important to correctly characterize these effects. For rigid disk and magnetoresistive (MR) head combinations, both the write and read process can cause nonlinear distortion in the playback signals. Previous studies[1–4] explored nonlinearities induced by the write process. Few studies have been done on readback induced nonlinearities. This work concentrates on investigating the nonlinear distortion in the playback signals due to the readback process of MR heads. The nonlinear response of an asymmetric MR (AMR) head is due to the fact that the playback output is proportional to $\langle \cos^2 \theta \rangle$,[5] where $\theta$ is the angle between the magnetization and the current direction. The average is over the active read region of the head. When the head is properly biased ($\theta \sim 45°$), and the signal field from the medium is small, the head response can be considered approximately linear, and linear analysis applies.[4] However, when this is not the case, the nonlinear terms contribute significantly, the playback wave form will deviate from linearity and eventually saturate. The level of this nonlinear distortion changes with the head and disk parameters, the recording density, and flying height $d$. In our investigation, the playback nonlinearity was examined in both the time and frequency domain in order to obtain a more complete understanding of the playback distortion.

## II. EXPERIMENTAL TECHNIQUES

### A. Time domain measurements

For a linear system,

$$V_r(t) = \sum_i a_i V_{\mathrm{is}}(t - iT) \tag{1}$$

where $V_r(t)$ represents the playback signal of the recorded data pattern, $V_{\mathrm{is}}(t)$ is the playback pulse of an isolated transition, and $T$ is the bit separation. $a_i$, the write sequence, can take three values for each $i$, 1, 0, $-1$. From Eq. (1), the playback wave form of the recorded pattern at a given density is predictable once the isolated playback pulse is known. On the other hand, by reversing the linear superposition process, the isolated playback pulse can be determined from the playback wave form of a recorded data pattern.

The area under the recorded playback wave form is simply the weighted sum of the areas of the isolated pulses:

$$A_r = \int V_r(t)dt = \sum a_i \int V_{\mathrm{is}}(t - iT)dt = \sum a_i A_{\mathrm{is}}(i) \tag{2}$$

where $A_{\mathrm{is}}(i)$ is the area of the $i$th isolated pulse. For a data pattern with an odd number of transitions, $A_r$ is independent of $T$, and $A_r = A_{\mathrm{is}}$. From an approximate linear analysis,[6] this area is

$$A_{\mathrm{is}} = 4IR \frac{\Delta\rho}{\rho} \langle \sin \theta \rangle E \frac{M_r \delta}{M_s t} (g + t)/v \tag{3}$$

where $I$ is the sense current, $R$ is the resistance of the MR element, $\Delta\rho/\rho$ is the fractional change in the resistivity, $E$ is the efficiency of the MR head, $g$ is the element to shield spacing, $t$ is the thickness of the MR element, and $v$ is the relative velocity between the head and disk. It should be noted that the area under the playback pulse depends only on the head parameters and disk $M_r\delta$, and is totally independent of the flying height $d$ and the recorded transition shape.

In order to identify the nonlinear distortion from the area of playback wave form, an experimental technique based on Eqs. (2) and (3) was developed. In this method, three adjacent transitions (tribit) were recorded at different bit separations. Areas under tribits of two polarities (Fig. 1) versus recording density were determined. The variation of these two areas represents how the total nonlinear distortion in the playback signal changes with the recording density.

Another method of characterizing the nonlinearity is the shape analysis of the playback signal. A data pattern containing two adjacent transitions (dibit) were recorded at different densities. The measured amplitudes of the recorded dibits were compared with two different reference dibits. The first reference was obtained by linearly superimposing the measured isolated pulses. The second reference utilized a linear superposition of theoretically obtained isolated pulses. In this way the nonlinear distortion was identified.

### B. Frequency domain measurement

In the frequency domain measurement, square waves were utilized to study the head nonlinearities. In a linear system, the spectrum of the playback signal is

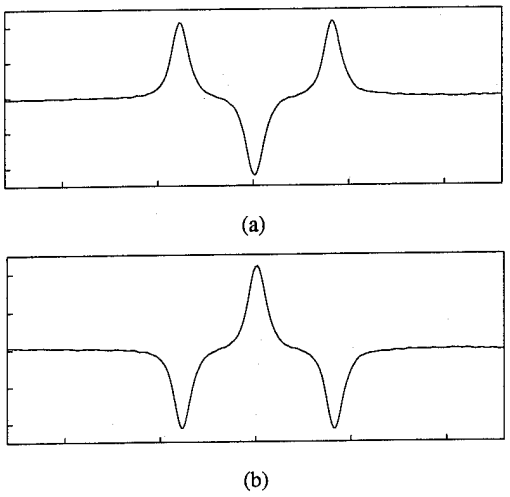



FIG. 1. (a) Positive tribit. (b) Negative tribit.

$$V(k)=2k_0V_{is}(k)\sum_{-\infty}^{\infty}\delta(k-(2m+1)k_0) \tag{4}$$

where $k_0=\pi/B$ and $V_{is}(k)$ is the Fourier transform of the isolated playback signal.[5] Only odd harmonics exist.

Our measurement utilizes a previously developed method for analyzing nonlinearities.[7] Two square waves were recorded, one at a lower frequency $f$, the other at a higher frequency $(2n+1)f$, where $n$ is an integer. The $(2n+1)$th harmonic of the low frequency signal was compared with the fundamental of the high frequency signal. To maximize the sensitivity of the measurement, $n=1$ was chosen. The ratio

$$R31=\frac{V(3f,1)}{V(f,3)} \tag{5}$$

is defined as the three to one ratio. $V(3f,1)$ represents the fundamental of the high frequency and $V(f,3)$ represents the third harmonic of the low frequency.

From Eq. (4), the $R31$ of a linear system is 3. Nonlinearity in the play back signals results in a deviation of the $R31$ value from 3. Since head nonlinearities occur at low density and medium nonlinearities occur at high density, these two effects can be distinguished by using this method.

## III. MEASUREMENTS

The measurements were performed on a Guzik spinstand tester. An MR head with a read track width of 3.75 $\mu$m, MR element thickness of 25 nm, and shield to shield spacing of 0.55 $\mu$m was used. Two thin film disks with $M_r\delta$ equal 0.9 memu/cm$^2$ (disk 1) and 0.65 memu/cm$^2$ (disk 2) were selected for this investigation. Since high coercivity, low moment disks were used, the medium nonlinearities do not appear until the density reaches approximately 100 kfci. Thus, in this density range, we can exclude the medium effects and only consider the head nonlinearities.

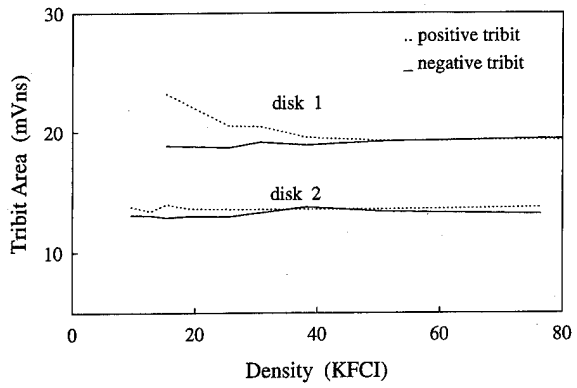



FIG. 2. Tribit areas vs recording density for disk 1 and disk 2.

## IV. DISCUSSION AND RESULTS

### A. Tribit area measurement

Measured tribit areas of both polarities versus recording density for disk 1 and disk 2 at a 4.5 $\mu''$ flying height are shown in Fig. 2. For disk 1, the areas of the positive tribit and negative tribit are quite different at low recording densities since this is where large head nonlinearities occur. When the bit separation decreases, overlapping of the adjacent transitions causes a smaller signal field. The less distorted MR head response results in a smaller difference between the two polarities at a higher recording density. These two curves converge at 50 kfci and remain constant at higher densities, which suggests that nonlinear head distortion disappears above 50 kfci. In the linear region, the area under the tribit from measurement is 19 mV ns, and from the linear analysis,[6] we expect 20 mV ns. Nonlinearity is not observed for the low moment disk 2. The area under the tribit for disk 2 obtained from measurement is 13.5 mV ns, and agrees well with 14.4 mV ns given by the theory.

The tribit areas vs recording density at different flying heights for disk 1 are shown in Fig. 3. At a low flying height of 3.5 $\mu''$, a larger separation between positive and negative areas was observed, and the convergence occurred at a higher density of 70 kfci. This result is understandable, be-

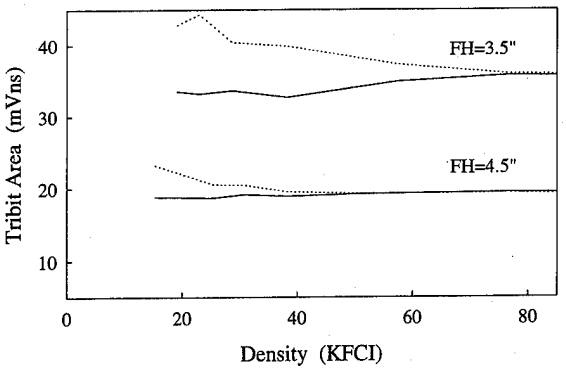



FIG. 3. Tribit areas vs recording density for disk 1. Solid curve and dashed curves correspond respectively to negative and positive tribit.

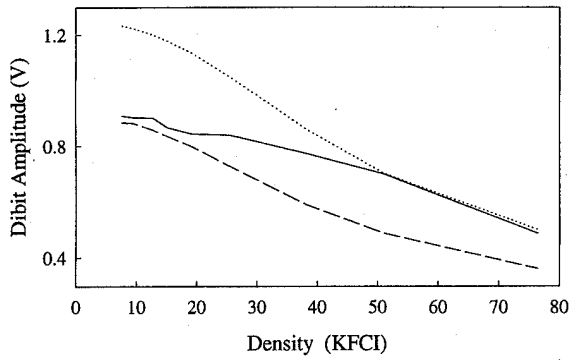



FIG. 4. Dibit amplitude vs recording density. Solid curve (—) shows the experimental results for disk 1; dashed curve (---) is the linear superposition of measured isolated pulses; dotted curve (···) is the linear superposition of calculated pulses.

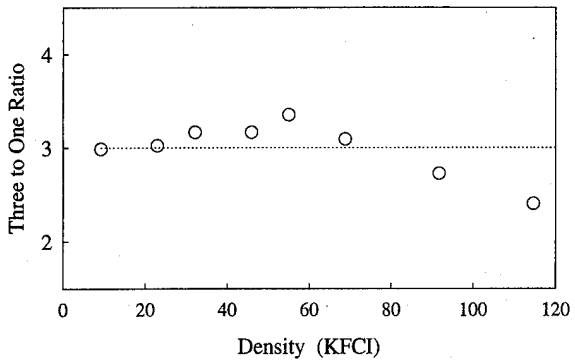



FIG. 5. Three to one ratio vs recording density for disk 1.

cause the head senses a larger signal field at a lower flying height; therefore, the nonlinear distortion in the playback signal is more severe.

### B. Dibit measurement

Figure 4 shows the dibit measurement results for disk 1. The solid curve is the amplitude of the measured dibits versus recording density and the dashed curve is the amplitude of dibits from the linear superposition of measured isolated pulses. For comparison, a pulse calculated from the linear analysis theory was used to create linear dibits. The result from this calculation is plotted in Fig. 4 as the dotted curve and represents the behavior of a linear system.

The measured curve is close to the dashed curve at low density, where large nonlinearities exist. With increasing density, the measured curve becomes close to the linear curve as nonlinear distortion decreases. Linear head response is observed when the density is larger than 50 kfci, where the measured curve joins the linear curve.

### C. Frequency domain measurement

The three to one ratio versus density for disk 1 is plotted in Fig. 5. The curve increases with density and peaks at 50 kfci. The nonlinear distortion decreases at lower density in the high frequency signal than in the low frequency case. The peak occurs where the nonlinear distortion in the high frequency signal disappears which is 50 kfci in this case. Media nonlinearities enter the results above 80 kfci where $R31$ falls below 3.

## V. CONCLUSIONS

In this work, techniques for characterizing the playback process induced nonlinearity in both time and frequency domains have been developed. Various head/disk combinations were examined by using these techniques. For the head 1/disk 1 combination, nonlinearity was observed below 50 kfci at a 4.5 $\mu''$ flying height. A lower flying height will worsen the nonlinear distortion. The linear analysis of MR heads agrees well with the experimental results when the head is operating in the linear region.

## ACKNOWLEDGMENTS

The authors would like to thank the IBM Corp. for supporting this research, and thank Dr. Herbert G. Lin and Eric Champion for helpful discussions.

[1] H. E. Melbye and C. S. Chi, IEEE Trans. Magn. **14**, 746 (1978).
[2] P. Newby and R. Wood, IEEE Trans. Magn. **22**, 1203 (1986).
[3] D. Palmer and P. Ziperovich, IEEE Trans. Magn. **23**, 2377 (1987).
[4] Y. Tang and C. Tsang, IEEE Trans. Magn. **27**, 5316 (1991).
[5] H. N. Bertram, *Theory of Magnetic Recording* (Cambridge University Press, New York, 1993), Chap. 7.
[6] H. N. Bertram, IEEE Trans. Magn. **31**, 2573 (1995).
[7] C. Che, IEEE Trans. Magn. **31**, 3021 (1995).

# Micromagnetics of dual spin-valve GMR heads

Jian-Gang Zhu and Xiao-Guang Ye
*MINT, Department of Electrical Engineering, University of Minnesota, Minneapolis, Minnesota 55455*

Samuel W. Yuan, Hua-Ching Tong, and Robert Rottmayer
*Read-Rite Corp., Milpitas, San Jose, California*

Micromagnetic simulations were performed to study the biasing characteristics and playback performance of actual dual spin-valve GMR heads. Both symmetric and asymmetric dual spin valve heads were analyzed. The study shows that the symmetric dual spin-valve head is not properly biased in its patterned form, without any additional transverse biasing schemes. On the other hand, the asymmetric dual spin valve head is self-biased since in this form, the free layer is free from the demagnetizing fields arising from the pinned layers. However, opposite GMR effects with similar magnitudes would be required for the two spin valve structures in the same multilayer film.
© *1996 American Institute of Physics.* [S0021-8979(96)15908-4]

## I. INTRODUCTION

The spin-valve head has emerged as one of the most promising read sensors employing the giant magnetoresistive effect in magnetic recording applications. The dual spin-valve (DSV) structures that further enhance the GMR effect have been proposed and fabricated.[1,2] While the magnetic properties look promising at the sheet film level,[2] the actual device performance of such structures has not been analyzed or demonstrated.

In this work, micromagnetic simulations are performed to address the above issues. The modeling is performed on narrow track dual spin valve heads intended for future high density rigid disk recording applications.

## II. MODEL AND SIMULATION

The most basic dual spin valve consists of a five layer GMR film sandwiched by two antiferromagnetic films. The five layer GMR film consists of three ferromagnetic layers separated by two thin conductive metallic layers. The two outer magnetic layers are exchange coupled to the antiferromagnetic films. The center ferromagnetic layer rotates freely, acting as flux sensing layer. Figure 1 shows the schematics of the symmetric dual spin-valve structures. The symmetric DSV head has the magnetizations of the outer magnetic layers pinned in the same direction, vertical to the air bearing surface (ABS), by the antiferromagnetic films. A GMR ratio above 14% has been obtained experimentally at the sheet film level with additional thin ferromagnetic layers added on each side of the each conductive interlayer to enhance the GMR effect.[2]

Here, only the most basic DSV structures were modeled. The three magnetic layers are assumed to be made of Permalloy with $M_s = 800$ emu/cm$^3$ and unaxial anisotropy field $H_k = 5$ Oe. The thicknesses of the multilayer structure are assumed to be 4(nm)/2(nm)/7(nm)/2(nm)/4(nm) for the NiFe/Cu/NiFe/Cu/NiFe structure respectively, unless mentioned otherwise. The three magnetic layers of the GMR film are discretized into three two dimensional arrays of elements. The thickness of each element is the same as the layer thickness and the size of each element is 5 nm×5 nm. Besides the inclusion of the magnetostatic interaction, ferromagnetic interlayer exchange coupling between the three magnetic layers is assumed. The interlayer exchange field $H_{fe}$ is defined as

$$\mathbf{H}_{1,or3} = H_{fe}\hat{m}_2$$

and

$$\mathbf{H}_2 = H_{fe}(\hat{m}_1 + \hat{m}_3),$$

where $\mathbf{H}$ are the interlayer exchange field acts on one of the layers and $\hat{m}$ is the unit vector of local magnetization. $H_{fe}$ defines the magnitude of the interlayer exchange field. Between each pair of adjacent layers, same magnitude of the exchange field $H_{fe} = 10$ Oe is assumed. The interfacial exchange coupling fields provided by the two antiferromagnetic films on the two outer magnetic layers were modeled by unidirectional fields of a magnitude 500 (Oe) along the pinning direction.

The head transfer curve is calculated with the excitation field calculated from a step transition in the presence of the soft magnetic shields. For all the calculations, the shield-to-shield spacing is $G = 0.2$ $\mu$m. The sensor structure has a track width of $W = 0.5$ $\mu$m and stripe height of $h = 0.3$ $\mu$m, unless mentioned otherwise.

Both types of DSV heads utilize abutted permanent magnet (PM) films as longitudinal domain stabilization. The de-

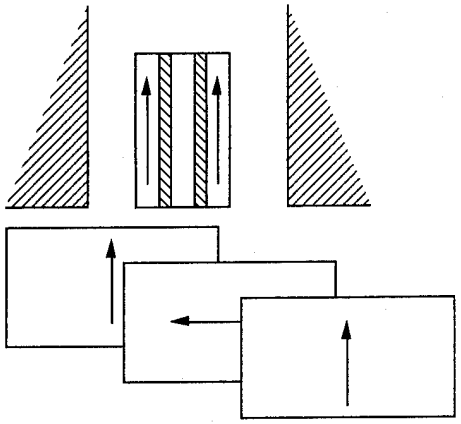


FIG. 1. Schematics of the symmetric dual spin-valve structure.

 0021-8979/96/79(8)/5886/3/$10.00 © 1996 American Institute of Physics

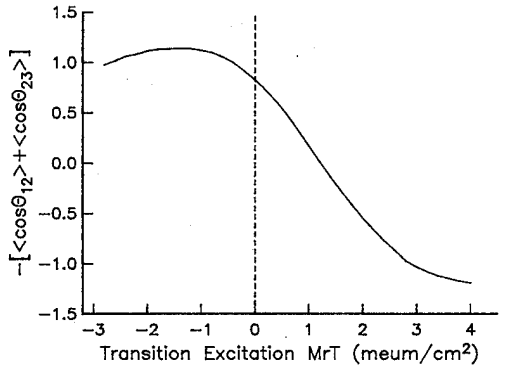



FIG. 2. Calculated transfer curve of the symmetric dual spin-valve head. $\langle\cos\theta_{12}\rangle+\langle\cos\theta_{23}\rangle$ is the GMR output averaged over the entire active region where $\theta_{12}$ and $\theta_{23}$ denote the angles between the magnetizations in the layers 1 (pinned) and 2 (free) and layers 2 and 3 (pinned), respectively.

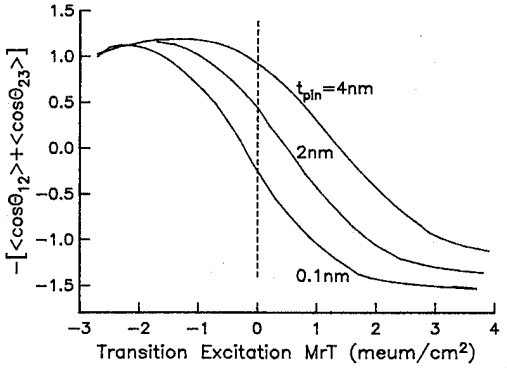



FIG. 4. Transfer curves calculated for different pinned layer thickness. The thickness of the free layer is 7 nm.

tail of the modeling with abutted PM film is described in Ref. 3. The PM moment is optimized for maximum head sensitivity while maintain head stability without any hysteresis and irreversible jumps in the calculated transfer curve.

## III. RESULTS AND DISCUSSIONS

### A. Symmetric dual spin valve structure

Figure 2 shows the calculated transfer curve for the symmetric DSV. As shown by the curve, the head is not properly biased. This phenomenon is due to the demagnetizing fields arising from the two pinned layers acting on the center free layer. Since the magnetizations of the two outer layers are exchange pinned in the same vertical direction, the demagnetizing field are reinforcing each other and rather strong. Due to this field, at the quiescent state, the magnetization of the free layer is oriented towards the opposite direction of the magnetizations in the pinned layer, as clearly shown in Fig. 3. The properly biased free layer should have the magnetization orient in the horizontal direction.

Reducing pinned layer thickness improves the biasing condition to a certain degree. As shown in Fig. 4, transfer curves were calculated for three different pinned layer thickness, assuming that both pinned layers are equally thick and the free layer thickness remains the same ($\delta_f=7$ nm). However, optimum biasing was obtained only when the pinned layer thickness is nearly zero.

Since the demagnetizing field acting on the free layer is in the opposite direction of the magnetizations of the pinned layers, bias condition can be improved by increasing the interlayer ferromagnetic exchange coupling between the free and pinned layers. Figure 5 shows three transfer curves with different interlayer ferromagnetic exchange field. As the exchange field increases, the bias condition does increase, but not without reducing the linear dynamic range of the output. At $H_{fe}=80$ Oe interlayer exchange coupling field, the head become properly biased, but the linear dynamic range of the output has decreased by near 50%.

The most effective way to bias the symmetric spin valve head is to apply an external field, e.g., by employing a current carrying conducting film near the sensor film which provide a rather uniform external field to the sensor. Here, a

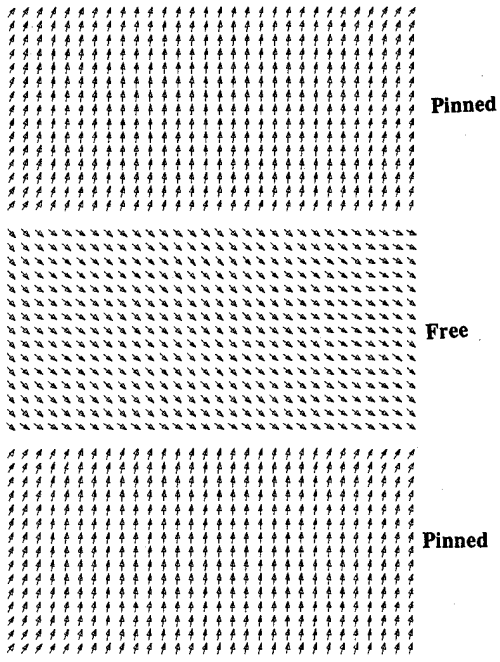



FIG. 3. Magnetization configurations at quiescent state of a symmetric dual spin valve head. Due to the demagnetizing field, the magnetization of the free layer rotates downward away from the horizontal.

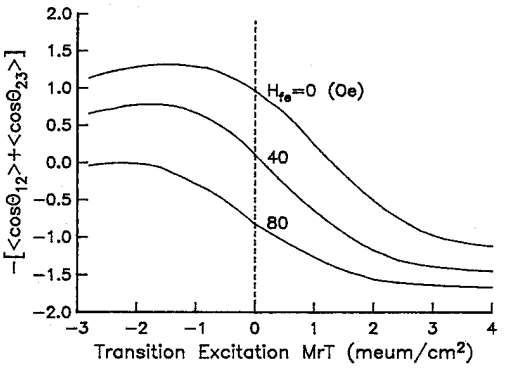



FIG. 5. Transfer curves calculated for three different interlayer ferromagnetic exchange coupling strength. Same coupling field is assumed between the free and the pinned layers across the two conductive interlayers.

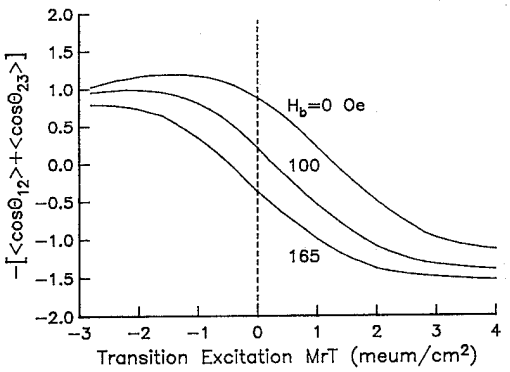



FIG. 6. Transfer curves calculated for three magnitudes of the external transverse bias field: $H_b=0$ Oe, $H_b=100$ Oe, and $H_b=165$ Oe.

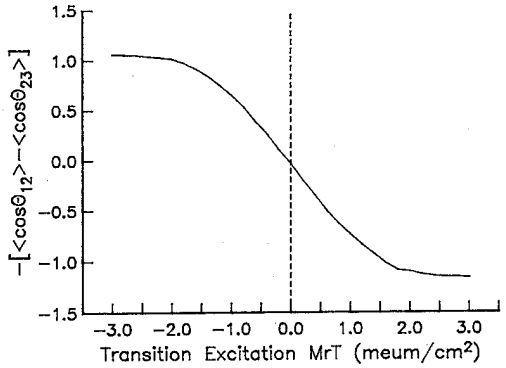



FIG. 8. Calculated transfer curve of the asymmetric dual spin valve head. The output is calculated according to $\langle\cos\theta_{12}\rangle-\langle\cos\theta_{23}\rangle$, assuming the dual spin valve has opposite GMR effect with same magnitude.

series of transfer curves are calculated with different magnitudes of an uniform external field, applied in the upward vertical direction, as shown in Fig. 6. For the head geometry simulated here, an external field magnitude of $H_b=165$ Oe is needed to properly bias the head.

### B. Asymmetric dual spin valve structure

Figure 7 shows the schematics of the asymmetric dual spin-valve structures. The asymmetric DSV has the magnetizations of the outer magnetic layers pinned in the opposite vertical direction. For the asymmetric DSV, the GMR effect between the two pairs of magnetic layers is assumed to have opposite sign with exact same magnitude, even though to date, observed inverse GMR effects are significantly smaller than the ordinary GMR effect.[4] The thickness of the free layer is 7 nm and the thicknesses of the pinned layers are 4 nm with same magnetic parameters (used for symmetric DSV calculation). The output is calculated as

$$\mathrm{GMR}_{\mathrm{output}}=-(\langle\cos\theta_{12}\rangle-\langle\cos\theta_{23}\rangle).$$

Figure 8 shows a calculated transfer curve for the asymmetric dual spin-valve head structure. As shown by the transfer curve, the head is self biased, because the demagnetizing fields arising from the oppositely pinned outer magnetic layers cancel each other at the free layer. In another words, the magnetizations of the two outer layers form a flux closure with little impact to the free layer. If the sense current flows in the direction such that it reinforces the flux closure rather than opposing it, the self biasing is stable and efficient.

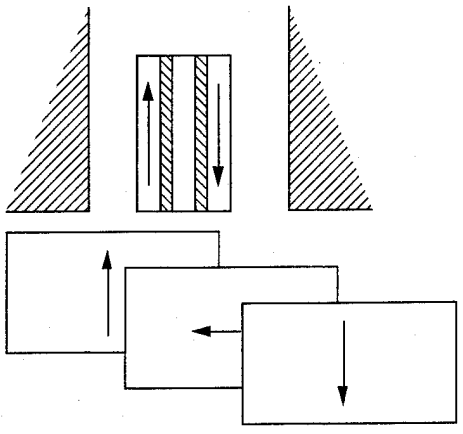


FIG. 7. Schematics of the asymmetric dual spin-valve head structure.

## IV. SUMMARY

Micromagnetic simulations were performed to study the biasing characteristics and playback performance of actual dual spin valve GMR heads. Both symmetric and asymmetric dual spin-valve heads were analyzed. The study shows that the symmetric dual spin-valve head is poorly biased in its patterned form, without any additional transverse biasing schemes. This phenomenon is seen on both unshielded and shielded devices and is due to the demagnetizing field acting on the free layer from the pinned layers on both sides. The existing interlayer ferromagnetic exchange coupling is too small to counterbalance the demagnetizing field. On the other hand, the asymmetric dual spin-valve head is self-biased since in this form, the free layer is free from the demagnetizing fields arising from the pinned layers. However, opposite GMR effect with similar magnitudes would be required for the two spin valve structures in the same multilayer film.

## ACKNOWLEDGMENTS

This research is supported in part by the National Science Foundation under Grant No. ECS 9358309 and by the NIST/NSIC. Simulation studies were performed on the Cray/C90 supercomputers with grants provided by Minnesota Supercomputer Institute at the University of Minnesota and San Diego Supercomputer Center.

[1] P. M. Baumgart *et al.*, U.S. patent 5,287,238, Feb. 1994.
[2] T. C. Anthony, J. A. Brug, and S. Zhang, IEEE Trans. Magn. **30**, 3819 (1994).
[3] D. Lu and J.-G. Zhu, IEEE Trans. Magn. **31** (to be published).
[4] J. M. George *et al.*, Phys. Rev. Lett. **72**, 408 (1994).

# Experimental and analytical properties of 0.2-$\mu$m-wide, end-on, multilayer, giant magnetoresistance, read head sensors

A. V. Pohm, R. S. Beech, and J. M. Daughton
*Nonvolatile Electronics, 11409 Valley View Rd., Eden Prairie, Minnesota 55344*

E. Y. Chen, M. Durlam, K. Nordquist, T. Zhu, and S. Tehrani
*Motorola, Inc., Phoenix Corporate Research Laboratory, 2100 E. Elliot Rd., Tempe, Arizona 85284*

Sensing elements which are 0.20 $\mu$m wide have been fabricated from giant magnetoresistance material that has four magnetic layers separated by 16–17 Å copper alloy layers. The material has a bulk magnetoresistive coefficient of 12%–15%, and when etched into the 0.2-$\mu$m-wide stripes, the stripe material has a shifted linear response range of about 8%, extending from −140 to +140 Oe, for example. Empirical models have been developed for both the bulk material and the stripe material. Using the stripe material model, a numerical analysis was performed for end-on, 0.2-$\mu$m-wide, read head sensors in a shielded read head with a 0.25 $\mu$m head gap. The analysis shows that with input fields of ±100 Oe from transitions, a peak to peak output of 0.85 mV can be achieved in the assumed read head structure with a 0.20-$\mu$m-wide tip. If a 0.25 $\mu$m flux gathering tip is used, the peak to peak output can be increased to 1.3 mV. © *1996 American Institute of Physics.* [S0021-8979(96)12108-8]

## I. INTRODUCTION

An experimental and analytical investigation has been made on the use of 0.2-$\mu$m-wide, four magnetic layer, giant magnetoresistance (GMR) stripes in end-on read head sensors in which the stripes are perpendicular to the recording surface.[1] Figure 1 depicts such a head sensor structure with a flux gathering front tip and contact at the air bearing surface. The figure also illustrates the use of the sense current in a 0.2 $\mu$m winding to generate a bias field. The front contact protects the active part of the sensor from abrasion but at the expense of signal attenuation. A numerical analysis was performed for the end-on read head sensors using this material in a shielded read head with a 0.25 $\mu$m head gap. A 0.2 $\mu$m contact at the air bearing surface and a 1.25 mA sense current also were assumed. The analysis also included the effects of a field dependent permeability. Assuming state of the art lithography and advanced fabrication methods, this work shows that with signal fields of ±100 Oe from recorded transitions, peak to peak signal swings of 1 mV can be achieved for submicron sensors and track widths.

Electron ($e$) beam lithography was employed to define the 0.2 $\mu$m stripes used to perform the experimental measurements. However, the fabrication capability to form the 0.2-$\mu$m-wide front contact and the 0.2-$\mu$m-wide bias winding was not available. The effects of the front contact and bias winding were treated analytically.

## II. EXPERIMENTAL RESULTS

Experimentally, 0.20-$\mu$m-wide sensing elements were fabricated from GMR materials that contained four magnetic structures separated by 16–17-Å-thick copper alloy layers (Cu, Ag, Au). The outside magnetic structures were 55 Å thick and had 40-Å-thick ternary layers (65% Ni, 15% Fe, 20% Co) and 15-Å-thick cobalt-rich layers (95% Co, 5% Fe) at the interfaces. The two interior magnetic structures were 50 Å thick with a 20 Å ternary layer sandwiched between two 15-Å-thick cobalt-rich layers. The material has a bulk magnetoresistive coefficient of 12%–15% and a sheet resistance of 12–14 Ω per square.

Figures 2(a) and 2(b) illustrate typical $M-R$ responses for sheet samples using a four-point probe method. The saturation field typically could be varied from 100 to 500 Oe depending on deposition conditions and the nonmagnetic layer thickness. The small switching transitions occurring at field magnitudes of 5–10 Oe correspond with the coercive force of the bulk sample. The measured remnant magnetization was approximately 25% of the saturated value.

Figure 3 shows a scanning electron microscope picture of a section of a nominal 0.2-$\mu$m-wide, six-contact, 100-$\mu$m-long test structure used for the measurements. Structures varied in width from 0.17 to 0.22 $\mu$m. When etched into the 0.2-$\mu$m-wide stripes, the material illustrated in Fig. 2(a) had a linear range of about 8% extending from about −140 to +140 Oe, as illustrated in Fig. 4. Note that the switching is very abrupt and occurs at the ±140 Oe values. On other 0.2 $\mu$m samples, switching occurred in the 100–150 Oe range.

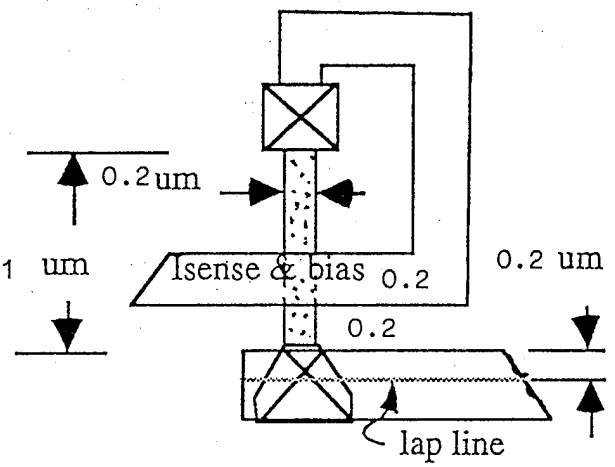



FIG. 1. Head sensor configuration.

 0021-8979/96/79(8)/5889/3/$10.00 © 1996 American Institute of Physics 

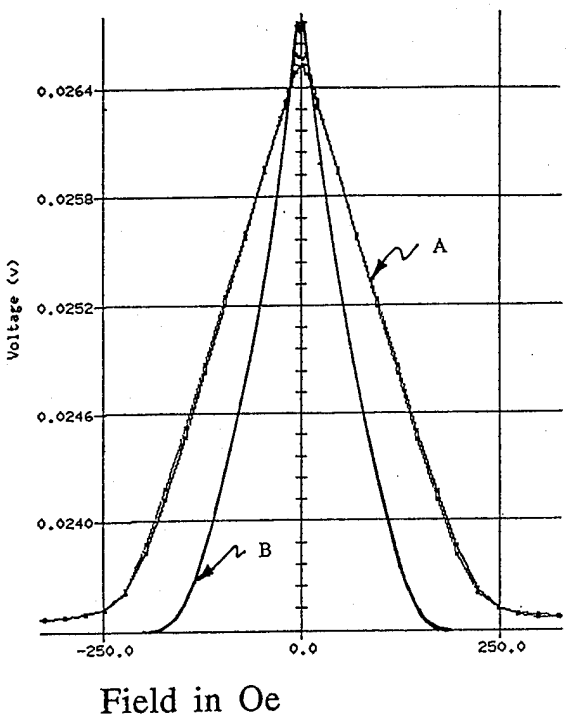



FIG. 2. Bulk sample GMR response.

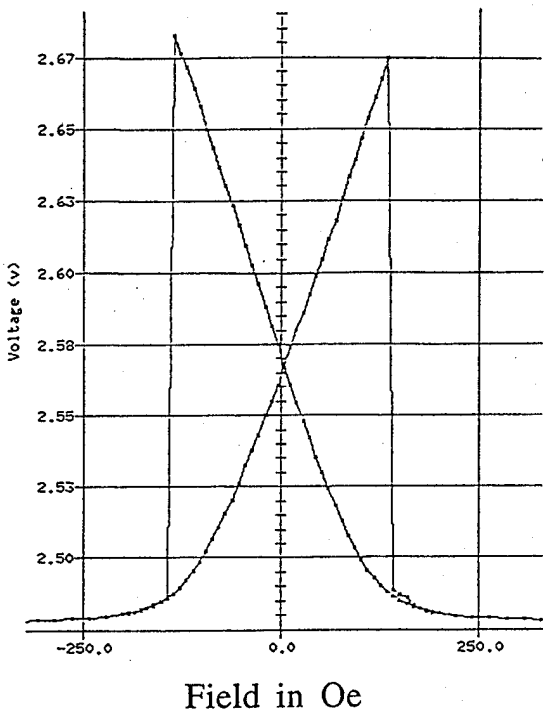



FIG. 4. Stripe $M-R$ response.

## III. EMPIRICAL MODELS AND ANALYSIS

### A. Bulk model

Generally within a 10% experimental error, the bulk magnetic properties of the GMR material examined could be characterized by assigning to every magnetic layer the same antiparallel coupling field $H_3$ and the same parallel coupling field $H_2$ with their axes perpendicular to one another.[2] These two parameters were suffice to characterize the $M-R$ response to the field, the field to saturate the response, the remnant magnetization, the magnetization curve, the rest directions of the magnetization, and the field at which switching occurs. If $H_w$ is the drive field and $M$ is the saturation magnetization, the energy density ($E$ in erg/cm$^3$) is given by

$$E=H_3M|\sin^3\Theta|/3-H_2M\sin^2\Theta/2-H_wM\sin\Theta,$$

where $\Theta$ is the angle of the magnetization with respect to an axis perpendicular to the applied field and the material anisotropy constant is lumped into the $H_2$ constant. With no field applied, the two rest directions of the magnetization are given by $|\sin\Theta|=H_2/H_3$ and switching occurs when the reversing field is given by $|H_w|=H_2H_2/(4H_3)$. The $\sin^3\Theta$ term was chosen on the basis of a simple fit to the experimental data. The bulk curve of Fig. 5 illustrates the calcu-

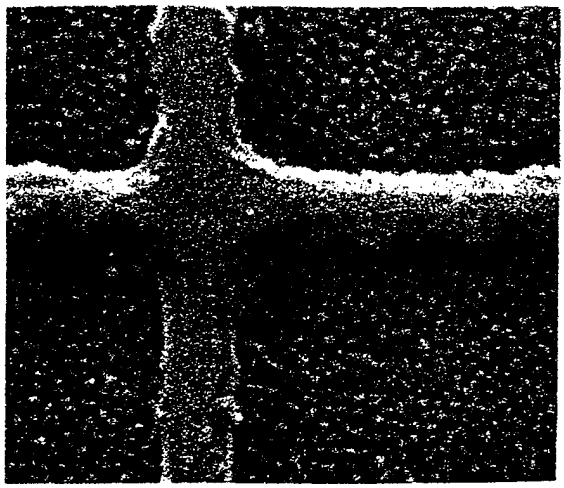


FIG. 3. Scanning electron microscope picture 0.2 $\mu$m stripe.

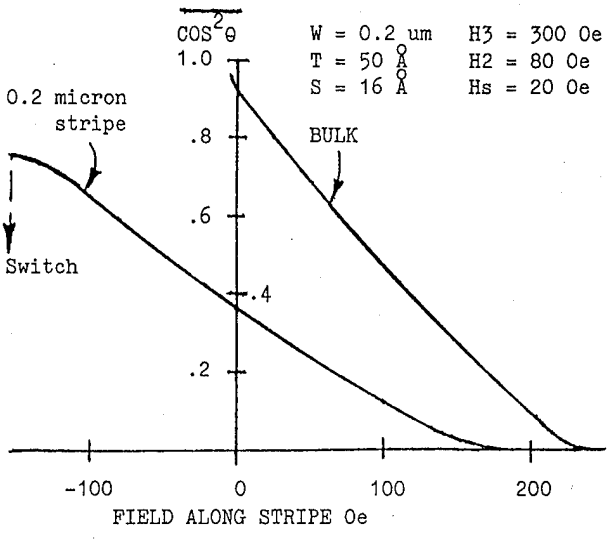



FIG. 5. Calculated stripe response.

lated response for material with parameters close to those measured for the experimental sample indicated in Fig. 2(a).

### B. Stripe model

When the material is etched into narrow stripes, exchange energy and demagnetizing effects from the curling of the magnetization at the edges greatly alter the $M-R$ behavior of the material as noted in the experimental results indicated in Fig. 4. The four magnetic layer stripe structure was modeled as two identical, paired, magnetic layers coupled by a common demagnetizing field arising at the edges. It was also assumed that alternate magnetic layers rotated with equal magnitude but in opposite directions. Because the equivalent magnetic poles at the layer edges are of alternate polarity, the demagnetizing field diminishes rapidly with distance into the material; the effective range of the field is less than 50 Å. The same, average, short range, field value was used for all layers in the analysis. Also, the net field from the sense current ($H_s$) assumed a uniform current density.

The maximum torque which can be sustained from the edge demagnetizing field occurs when the edge magnetization makes a 45° angle with the edge. If this value is exceeded, the edge magnetization flips. The 0.2 $\mu$m stripe curve of Fig. 5 shows the calculated response and switching behavior for the parameters given. Stripe response was calculated from the torque equation[3] for the magnetization with the constraint that the torque from the edge demagnetizing field be sufficient for equilibrium. At the end of a stripe, the edge magnetization tips out and the magnetization in the center of the stripe tips back in response to the end demagnetizing field. For the 0.2-$\mu$m-wide tip with pinned edges, the equilibrium end demagnetizing field is 50–75 Oe and for the 0.25 $\mu$m tip it is 25–50 Oe.

Because of the effects of exchange and the edge demagnetizing fields, the average permeability of the stripe material in response to a field along the stripe is a nonlinear function of the applied field. Figure 6 depicts the calculated average permeability of a 0.2-$\mu$m-wide stripe with unpinned edges and a 0.25-$\mu$m-wide stripe with pinned edges. To prevent switching, the edges must be pinned in the sensor contact area (a proprietary process).

### C. Head sensor response

To calculate the response of a 0.2-$\mu$m-wide sensor, a 0.25 $\mu$m gap between shields was assumed with the shield separation distance increasing to 0.50 $\mu$m immediately after the front contact in an arrangement where the front contact is integral with the top pole piece.[4] A nonuniform transmission line model was used which took into account the pinned edges in the contact area, the increased gap beyond the contact area, and the field dependent permeability. Calculations were performed for tip widths of 0.2 and 0.25 $\mu$m. The 0.2-$\mu$m-wide bias winding was assumed to be located 0.2 $\mu$m behind the front contact midway between the $M-R$ stripe and the shield. The method of images was used to calculate the field from the bias winding.

For the 0.25-$\mu$m-wide flux gathering tip with pinned edges, an average permeability of 60 and a decay length of

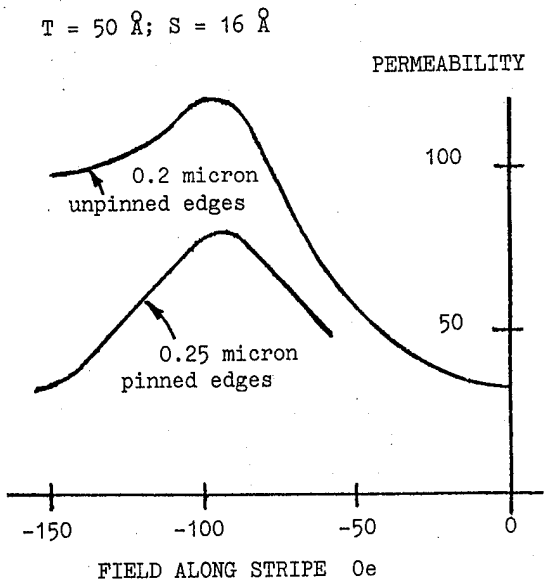



FIG. 6. Stripe average permeability.

0.28 $\mu$m was used in the simulation. For the case of the 0.20-$\mu$m-wide pinned tip, an average permeability of 45 and a decay length of 0.25 $\mu$m were assumed. Beyond the contact area, the 0.2-$\mu$m-wide stripe with unpinned edges was assumed to have a permeability of 80 for fields above 50 Oe and a permeability of 40 for fields below 50 Oe. The corresponding decay lengths were 0.45 and 0.32 $\mu$m. These average values were calculated for materials with $H_3=200$ Oe and $H_2=75$ Oe, values similar to those of the material indicated in Fig. 2(b). The analysis showed that with input fields of $\pm 100$ Oe from transitions and a sense current of 1.25 mA, the calculated peak to peak output for the 0.20-$\mu$m-wide tip is 0.85 mV. If a 0.25 $\mu$m flux gathering tip is used, the peak to peak output is 1.3 mV.

## IV. SUMMARY

The experimental and analytical results obtained in this work show that with advanced fabrication methods and existing four magnetic layer GMR materials with 12%–15% $M-R$ coefficients, shielded, end-on read head sensors with tip widths of 0.2 and 0.25 $\mu$m can be made to yield peak to peak outputs of approximately 1 mV for an input field of $\pm 100$ Oe when operating at a 1.25 mA sense current.

## ACKNOWLEDGMENTS

This work was supported by the National Science Foundation and Department of Defense grants.

[1] E. Y. Chen, A. V. Pohm, J. M. Daughton, J. Brown, and W. Black, IEEE Trans. Magn. **30**, 3816 (1994).
[2] H. Fujiwara and M. R. Parker, J. Magn. Magn. Mater. **135**, L23-L9, (1994).
[3] H. Y. Yoo, A. V. Pohm, J. H. Hur, S. W. Kenkare, and C. S. Comstock, IEEE Trans. Magn. **25**, 4269 (1989).
[4] T. Shibata, N. Saito, H. Narisawa, Y. Sada, and T. Sekiya, IEEE Trans. Magn. **30**, 3843 (1994).

# Magnetization reversal processes of NiFe elements exchange coupled by NiO antiferromagnetic films

Juren Ding and Jian-Gang Zhu
*MINT, Department of Electrical Engineering, University of Minnesota, Minneapolis, Minnesota 55455*

The magnetic domain structures and their switching processes of small peamalloy (NiFe) elements exchange coupled by antiferromagnetic (NiO) thin films were studied using magnetic force microscopy. A uniform external magnetic field generated by an electromagnet was applied to the magnetic force microscopy so that the domain switching processes could be observed *in situ*. The effects of NiFe film thickness, element size, and aspect ratio on domain behavior were investigated. It was found that the unidirectional exchange coupling field of small elements was much greater than that measured on the sheet bilayer films. The results of this study showed little indication of the existence of domain structure in NiO antiferromagnetic film. © *1996 American Institute of Physics.* [S0021-8979(96)12208-4]

## I. INTRODUCTION

Antiferromagnetic films are used in variety of applications. One of their main applications is to generate an unidirectional exchange anisotropy within adjacent soft magnetic films, either stacked on top or underneath, through the interfacial exchange coupling, i.e., to maintain the magnetization configuration of a soft film in a single domain state, such as used for domain stabilization in a magnetoresistive head for magnetic recording a pplications.[1] However, the interfacial exchange coupling is usually two to three orders of magnitude smaller than the interatomic spin-to-spin exchange coupling. The interfacial exchange coupling field is only at the order of tens to hundreds of oersteds. The properties of the exchange coupling have been studied extensively and various mechanisms have been proposed.[2,3] Some antiferromagnetic films not only yield pure shifts of the easy axis hysteresis loops, but also expansion of the hysteresis loop; i.e., the coercivity of the adjacent soft film is increased. A NiO antiferromagnetic film is one such example. Whether the interfacial exchange coupling affects the magnetization switching processes of the adjacent soft magnetic film in addition to the shift due to the ideal unidirectional exchange anisotropy has remained unclear.

In attempting to address these issues, we investigated the magnetization switching processes of NiFe/NiO bilayer films which were patterned to micronscale rectangular elements via the magnetic force microscopy (MFM) technique. The focus was to understand the domain reversal processes of various NiFe elements in the presence of interfacial exchange coupling under an uniform external field.

## II. EXPERIMENT

Thin films were deposited on Si substrates using rf sputtering. The base pressure before sputtering was about $4\times10^{-7}$ Torr. All films were deposited at room temperature. The Ar pressure was 10 mTorr for all film depositions except NiO. During the deposition of the NiFe thin film, a magnetic field (about 20 Oe) was applied to the sample by using two permanent magnets resulting in an unidirectional anisotropy along the field direction.

NiO antiferromagnetic thin films were deposited using reactive sputtering. The deposited NiO thin films were measured using a vibrating-sample magnetometer (VSM) and the presence of the antiferromagnetic phase was confirmed. In this study, all NiO thin films were prepared under the same conditions and the thicknesses of all NiO films were 80 nm. The grain size of the NiO thin film was about 20 nm measured by atomic force microscopy. It was found that the NiO grains were elongated.

After the deposition, small elements with varying sizes ranging from 2 $\mu$m to 200 $\mu$m and varying aspect ratios were fabricated using photolithography and ion milling. In the photolithographic process, the samples were heated at 90 °C for 30 min.

All domain structures were imaged using a Digital Instrument Nanoscope III. An electromagnet was designed to attach to the MFM to apply an uniform magnetic field to the samples so that domain switching processes could be observed *in situ*. Magnetic fields as high as 500 Oe could be obtained by controlling an applied current. The lift height of the MFM tip was 100 nm for all images shown in this paper. The tips were magnetized in a large field in the direction parallel to the film plane and perpendicular to the cantilever.

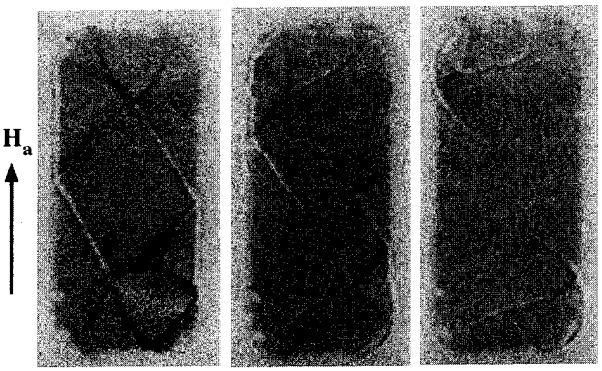



FIG. 1. Domain structures of NiFe single layer (20 nm thick) element (10 $\mu$m×20 $\mu$m) under external magnetic field. The arrow shows positive external field direction and also corresponds to the magnetic easy axis of the element (likewise in the following figures).

 0021-8979/96/79(8)/5892/3/$10.00 © 1996 American Institute of Physics

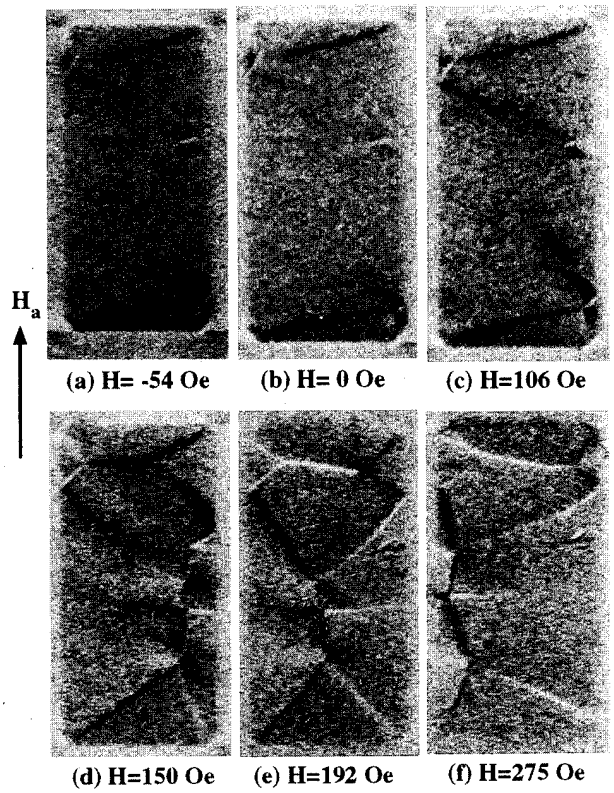



FIG. 2. Magnetization switching process of 20 nm thick NiFe element (10 $\mu$m×20 $\mu$m) exchange-coupled with a 80 nm NiO antiferromagnetic layer. The unidirectional exchange coupling field was antiparallel to the arrow direction (likewise in the following figures). The exchange coupling field of the sheet film was about 14 Oe.

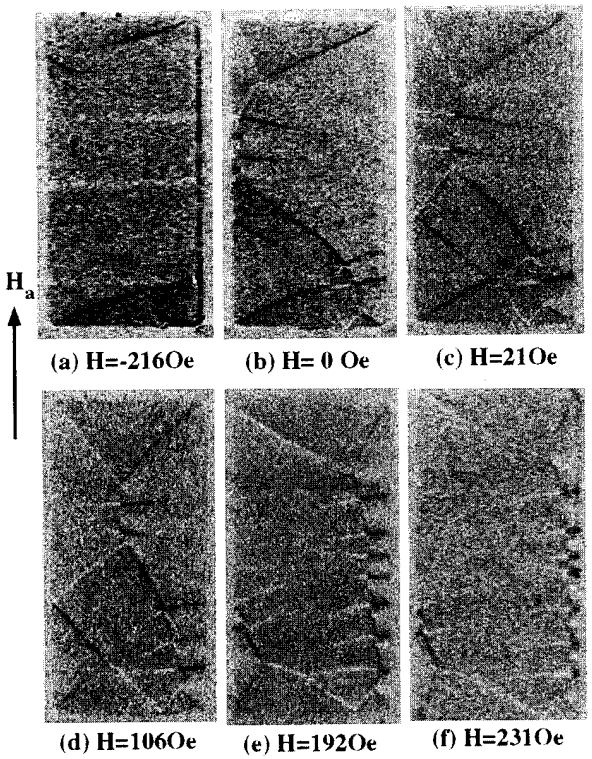



FIG. 3. Magnetization switching process of a 30 nm thick NiFe element (10 $\mu$m×20 $\mu$m) exchange coupled with a 80 nm NiO antiferromagnetic layer. The exchange coupling field of the sheet film was about 9 Oe.

## III. MAGNETIZATION REVERSAL OF NiFe SINGLE LAYER FILM

Figure 1 shows three MFM images of the magnetic domain configurations for a patterned NiFe single layer film element (10 $\mu$m×20 $\mu$m). The three images correspond to three different magnitudes of the external field, which was applied along the film easy axis direction. At zero external field [Fig. 1(a)], a typical closure domain configuration is observed and the film is in a self-demagnetized state. As the external field increases, the domains with magnetization parallel to the field expand [Fig. 1(b)]. At $H=106$ Oe [Fig. 1(c)], a quasisingle domain state is reached with only edge domains remaining at both ends of the element.

## IV. MAGNETIZATION REVERSAL OF NiFe/NiO BILAYER FILM

Three different NiFe/NiO bilayer films were deposited, with thickness of the NiFe layer 10 nm, 20 nm, and 30 nm respectively while keeping the NiO layer the same thickness. The exchange fields, measured by the shift of the easy axis hysteresis loop with a VSM, are 24, 14, and 9 Oe, respectively for the three sheet films before patterning. The coercivities of the NiFe films expanded a little (by about 5 Oe).

### A. Comparison with NiFe single layer film

Figure 2 shows a series of MFM images of the bilayer film element. The thickness of the NiFe film was 20 nm same as that in the single layer film with the same element size (10 $\mu$m×20 $\mu$m). The interfacial exchange field was in the opposite direction of the positive external field. At zero external field [Fig. 2(b)], a quasisingle domain configuration with edge domains remaining at the ends was observed. This indicates that the magnitude of the interfacial exchange field is greater than 106 Oe which kept the single layer element in a similar single domain state. The complete demagnetized state with closure domains is formed at a field magnitude of 192 Oe [Fig. 2(e)]. It is interesting to note that the interfacial exchange field in the patterned elements is nearly one order of magnitude greater than that measured on the sheet films. Two other elements of the same size on the same bilayer film were examined and similar results were obtained. This surprising difference between the interfacial exchange field of the sheet film and the small element was not caused by the patterning process. The exchange field of a sheet film subjected to a the heating procedure similar to that in the patterning process did not exhibit any significant change.

### B. Effect of NiFe film thickness

Figure 3 shows the domain configurations in a bilayer film element with a NiFe film thickness of 30 nm. In this case, at zero external field, the quasisingle domain state could no longer be achieved [Fig. 3(b)]. This is due to the combined factors of stronger demagnetizing field in the single domain state and an effective reduction of the interfacial exchange coupling field due to the thicker NiFe film

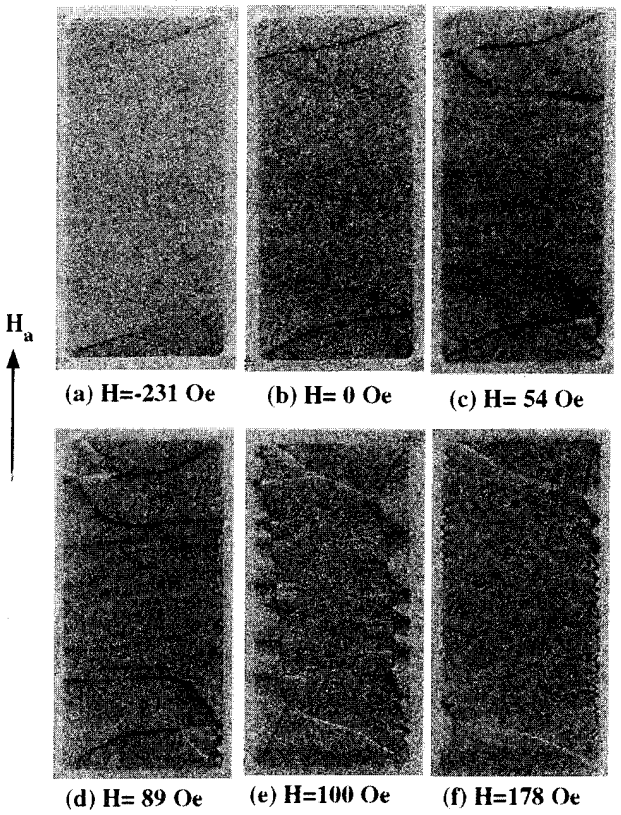



FIG. 4. Magnetization switching process of a 30 nm thick NiFe element (20$\mu$m×40 $\mu$m) exchange coupled with a 80 nm NiO antiferromagnetic layer.

since the exchange coupling field arises only from interfacial energy. The coercive state [Fig. 3(e)] occurs at an external field of 106 Oe which is smaller than that for 20 nm thick NiFe film with same element size (192 Oe) mainly due to the smaller exchange coupling field.

For the 10 nm thick NiFe film, the domain switching process was very difficult to observe because of the large exchange coupling field. The single domain state was broken at about 400 Oe applied external field.

### C. Effect of element size

Figure 4 shows the magnetization switching process of a bilayer film element with a size of 20 $\mu$m×40 $\mu$m. The thickness of NiFe layer was 30 nm. In contrast to the 10 $\mu$m×20 $\mu$m element (Fig. 3), the quasisingle domain is formed in the 20 $\mu$m×40 $\mu$m element at zero external field due to a smaller demagnetization field in the middle of the element. It should be noticed that a central domain is formed at coercive state in the big element while the closure domain structure is formed in the small element. Cross-tie structures are almost evenly distributed.

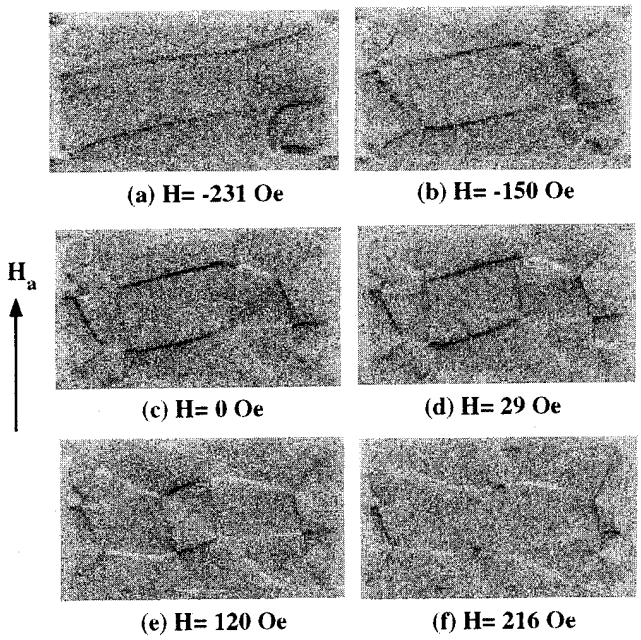



FIG. 5. Magnetization switching process of a 30 nm thick NiFe element (20 $\mu$m×10 $\mu$m) exchange coupled with a 80 nm NiO antiferromagnetic layer.

### D. Effect of aspect ratio

Figure 5 shows the magnetization reversal process of a 20 $\mu$m×10 $\mu$m element with 30 nm thick NiFe layer. At zero external field, a multidomain structure is formed due to the large demagnetization field. In order to achieve a single domain state, an external field of about 200 Oe needs to be applied in the exchange coupling field direction.

## V. CONCLUSIONS

Magnetic domain reversal processes in patterned exchange coupled NiFe/NiO bilayer film elements have been investigated via *in situ* magnetic force microscopy. It was found that the unidirectional exchange anisotropy field of the patterned small elements, arising from the interfacial exchange coupling, is significantly greater than that measured on the sheet bilayer films. For multidomain states, cross-tie structures were particularly prominent in the NiFe layer of the NiFe/NiO bilayer film elements while they were rarely observed in the NiFe single-layer film for identical film thicknesses. The "well-behaved" domain configurations in the NiFe layer of the exchange-coupled bilayer film elements gave little indication of the existence of antiferromagnetic domains in the NiO film.

[1] T. C. Anthony, J. A. Brug, and S. Zhang, IEEE Trans. Magn. **30**, 3819 (1994).
[2] A. P. Malozemoff, Phys. Rev. B **35**, 3679 (1987).
[3] C. Schlenker, S. S. P. Parkin, J. C. Scott, and J. K. Howard, J. Magn. Magn. Mater. **54–57**, 801 (1986).

# Domain structures at the cross sections of thin film inductive recording heads

Francis H. Liu, Hua-Ching Tong, and Lena Milosvlasky
*Read-Rite Corporation, Fremont, California 94539*

Using a scanning Kerr effect microscope with external ac-tickle field excitation, zigzagged and slanted intersections of domain walls were observed at the symmetry-axis cross sections of thin film inductive heads. These domain walls are believed to be the intersections of edge-closure domain walls, with the magnetization on the two sides of the walls (or lines) oriented in "head-to-head" or "tail-to-tail" configurations. They are thus slanted or zigzagged in order to spread the charges along the walls over a larger region, thereby reducing magnetostatic energy. This interpretation is further evident by the observation that upon applying a small dc bias field in the symmetry-axis direction, the slanted or zigzagged intersections of domain walls were observed to displace according to the field direction, and sometimes deformed to different configurations. Upon lapping the heads from their air-bearing surfaces, slanted domain walls at the sloped backgap cross sections were occasionally observed. © *1996 American Institute of Physics.* [S0021-8979(96)12308-0]

## INTRODUCTION

The readback noise in thin film inductive recording heads, such as popcorn and wiggle noise, has been correlated with magnetic domains and their dynamic behavior.[1,2] However, only the dynamic response of domain walls at the top-yoke surfaces, sloped pole-tip surfaces and air-bearing surfaces (ABS) were typically observed. Domain walls at various depth of thin film heads have been observed by using an electron microscope;[3] complete depth profiles of domain walls in thin film heads, however, have yet to be reported. In this report, for the first time, we report the domain wall depth profiles observed directly, by using scanning Kerr effect microscopy (SKEM), at the symmetry-axis cross sections of top (P2) and bottom (P1) permalloy yokes, as well as at the ABS-side cross sections of sloped backgap region.

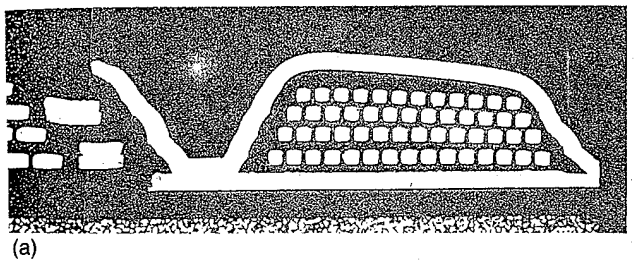
## EXPERIMENTAL METHODS

A SKEM was used to image the dynamic domain structures in thin film heads. A ferrite-core electromagnet, attached to the objective, was used to generate uniform external magnetic tickle field of 50 Oe peak to peak at 0.5 MHz, which in turn modulate the magnetization in thin film heads. Using longitudinal Kerr effect, average magnetization dynamics in response to the high frequency tickle field was thus mapped out. A lapping and polishing process similar to that in throat height definition was typically used to obtain the cross sections at symmetry axis and that lapped from ABS. With external field excitation and the plane of laser beam incidence both in the direction of symmetry axis, dynamic domain wall structures observed at the symmetry-axis cross section can thus be obtained.

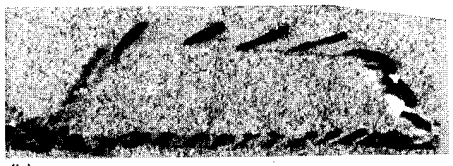
## RESULTS

The symmetry-axis cross section of head A and its corresponding domain configuration are shown in Figs. 1(a) and 1(b), respectively. In head A, domain walls were observed to be slanted all in the same orientation (yet with slightly different angles), as shown in Fig. 1(b). The corresponding domain structures of Fig. 1(b) imaged from the deposition side, both before and after lapping, are shown in Figs. 2(a) and 2(b), respectively. Closure domain structures were observed before and after cross sectioning. Based on the domain images observed in Figs. 1(b) and 2(b), a schematic interpretation of a section of the P2 domain structure is shown in Fig. 3.

The domain configuration of the symmetry-axis cross section of head B is shown in Fig. 4(a). As opposed to the domain configuration of head A, as shown in Fig. 1(b), domain walls were observed to be slanted in the alternating orientations in the top pole of head B, as shown in Fig. 4(a). Upon +15 Oe of dc bias field applied to head B, the slanted walls were observed to displace according to the field direction, in that one domain wall was displaced in one direction and the adjacent walls were observed to displace in the opposite direction, as shown in Fig. 4(b). Upon −15 Oe of dc bias field applied to head B, however, a new wall with a kink in the middle was observed to form, in addition to the displacements of slanted domain walls, as shown in Fig. 4(c).



(a)



(b)

FIG. 1. Thin film inductive head, head A, (a) viewed from the symmetry-axis cross section and (b) its corresponding domain configuration.

 0021-8979/96/79(8)/5895/3/$10.00 © 1996 American Institute of Physics 

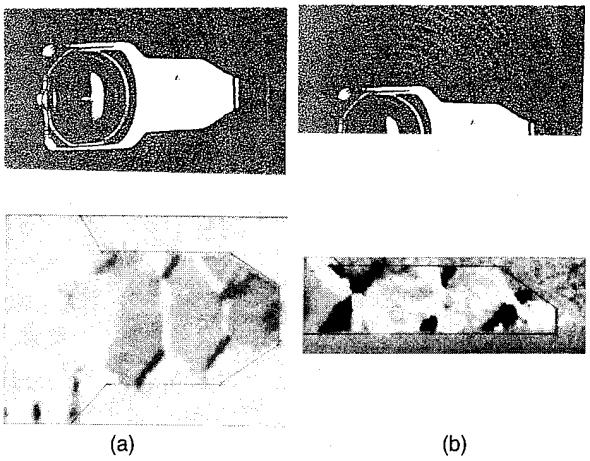



FIG. 2. Top-view (P2 deposition-side) domain structure of head A (a) before cross section and (b) after cross section.

The domain configuration of the symmetry-axis cross section of head C is shown in Fig. 5(a). In this case, both zigzagged and slanted domain walls were observed. Even more complicated domain wall deformations were observed with a small dc bias field applied to head C, as shown in Figs. 5(b), 5(c), and 5(d). In addition to the slanted domain walls connecting the top and bottom surfaces of P2, V-shaped and upside down V-shaped domain walls were observed in head C upon a small dc bias field, as shown in Figs. 5(b)–5(d). In particular, the two ends of V-shaped walls were observed to terminate only at the top surface of P2, whereas the two ends of upside down V-shaped walls were observed to terminate only at the bottom surface of P2. Upon removing the small dc bias field, the remanent domain structure of head C is shown in Fig. 5(e). Comparing with the domain structure as shown in Fig. 5(a), the remanent domain structure in head C is now completely different from that before applying dc bias field.

It is interesting to note that very few or no domain walls were observed at the sloped backgap regions of symmetry-axis cross sections of heads A, B, and C, as shown in Figs. 1, 4, and 5, respectively. In an attempt to observe the domain configurations at the sloped backgap region directly, head D was lapped from its ABS and toward its backgap. In this case, slanted domain walls were observed at the sloped backgap region, as shown in Fig. 6(b). The corresponding P2 domain structure before cross sectioning and its schematic interpretation is depicted in Fig. 6(a) and 6(c), respectively.

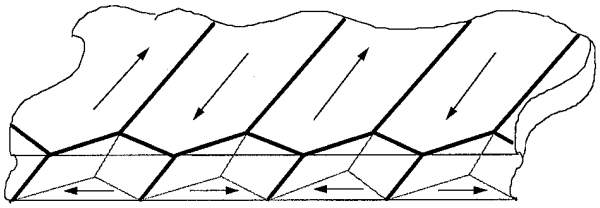


FIG. 3. Schematic interpretation of the P2 domain structure observed in head A.

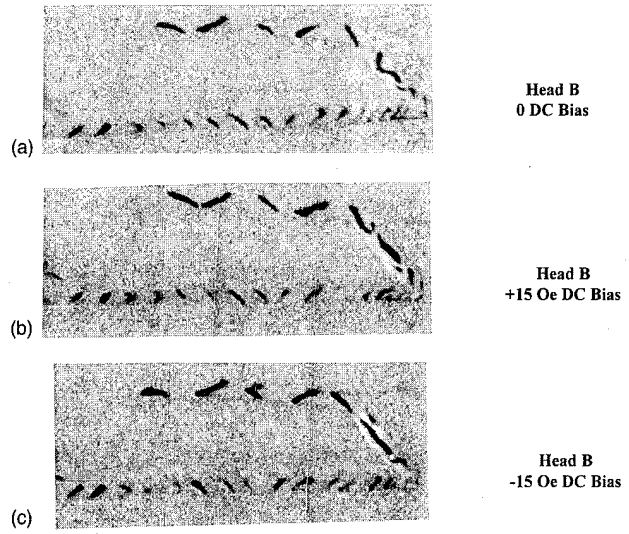



FIG. 4. Domain structure at the symmetry-axis cross section of head B, with (a) 0 Oe, (b) +15 Oe, and (c) −15 Oe of dc bias field.

## DISCUSSION

Based on the domain images observed at the symmetry-axis cross section, as shown in Fig. 1(b), and at the P2 deposition side after cross sectioning, as shown in Fig. 2(b), it is clear that the domain walls observed at the symmetry-axis

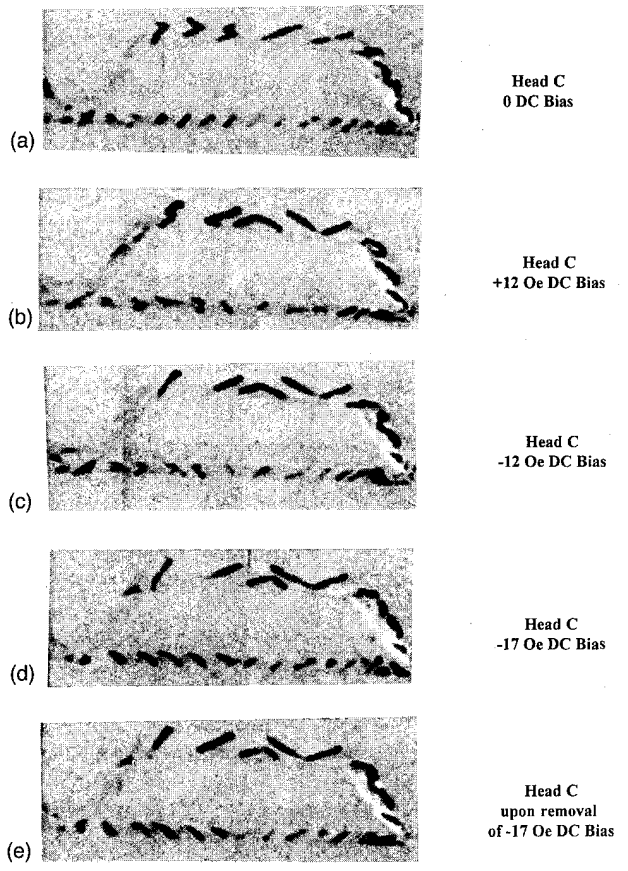



FIG. 5. Domain structure at the symmetry-axis cross section of head C, with (a) 0 Oe, (b) +12 Oe, and (c) −12 Oe, (d) −17 Oe of dc bias field, and (e) upon removal of −17 Oe of dc bias field.

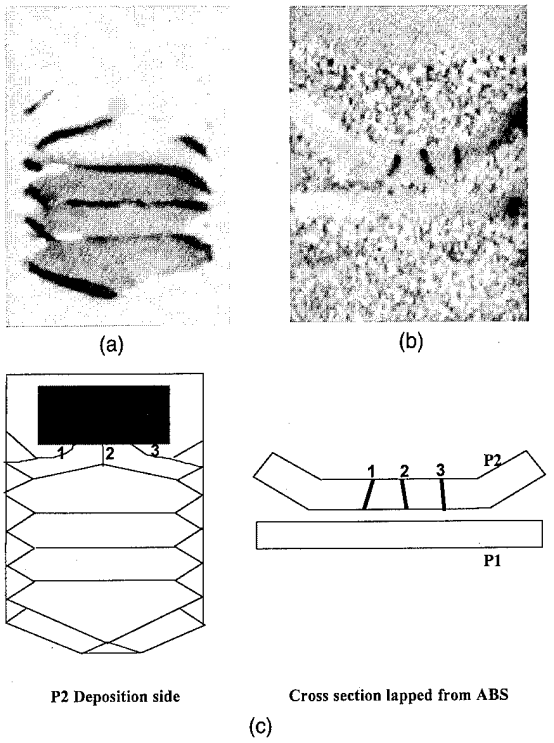



FIG. 6. Domain structure of head D as observed (a) at the P2 deposition side, before cross section, and (b) at the cross section of sloped backgap region, lapped from ABS, and (c) its schematic interpretation of the backgap domain walls.

cross section are the intersections of edge-closure domain walls, as schematically illustrated in Fig. 3. This observation is expected since soft ferromagnetic material, such as permalloy, usually form flux closure domain structures in a specific geometry to minimize its total energy. This interpretation is further evident by the observation that these walls were typically observed to displace according to a small external dc bias field in the symmetry-axis direction, as shown in Figs. 4 and 5. Here, when one wall was observed to displace in one direction, the adjacent walls were typically observed to displace in the opposite direction, as one edge-closure domain expands and the adjacent edge closure domains shrink in response to a dc bias field.

The intersections of closure domain walls are believed to be charged domain walls (or lines, strictly speaking), with the magnetization on the two sides of the domain walls oriented either "head-to-head" or "tail-to-tail," as shown schematically in Fig. 3. These domain walls are thus slanted or zigzagged in order to spread the charges along the walls over a larger region, thereby reducing magnetostatic energy.[2] Furthermore, it has been theoretically predicted[4] and experimentally inferred[5] that 90° walls in Fe films of up to 0.7 $\mu$m thick are slanted at their cross sections. It is thus plausible to observe the intersections of two 90° walls to be slanted as well. In consistence with the above observation and interpretation, slanted domain walls were also observed at the air-bearing surfaces of some thin film inductive heads.[2]

Various angles, length, and structures of domain walls, however, have been observed at the symmetry-axis cross sections, as shown in Figs. 4 and 5. It is believed that the exact angles, length, and structures of domain walls are the results of total energy minimization, which includes wall energy and the associated magnetostatic energy. The wall energy in turn depends on the distribution of stress and magnetostriction products in the permalloy yokes. It is thus reasonable to expect the domain walls at the specific locations of symmetry-axis cross sections to reflect the local distribution of stress and magnetostriction products, not only in the symmetry-axis direction, but also in the film thickness direction. Upon small dc bias field, the charge distributions along the walls may alter, resulting in deformation to again minimize the total energies, as shown in Figs. 4 and 5. Deformations and instabilities of domain walls in the thickness direction, as shown in Figs. 5(a) and 5(e), can thus be another sources of wiggle or popcorn noise in thin film inductive recording heads. The effective anisotropy of sloped backgap region was also observed, in some cases, to be transverse to that of other regions of the heads. They may thus also be a source of readback noise.[1]

## CONCLUSIONS

Using SKEM, domain structures of thin film inductive recording heads were observed from three principal perspectives: the deposition side, the symmetry-axis cross section and the ABS-side cross section. Thus, domain structures at the bottom poles (P1) and backgap closures, which previously cannot be observed at finished head form, can now be observed directly. Various slanted and zigzagged intersections of domain walls were observed at the symmetry-axis cross sections of thin film heads. Upon small dc bias field, even more complicated domain wall deformations in the thickness direction were observed. It is thus speculated that deformations and instabilities of domain walls in the film thickness direction can be another sources of readback noise, such as popcorn and wiggle noise. Domain walls at the sloped backgap regions that are longitudinal to the flux conduction direction were also observed occasionally. They may thus also cause readback noise.[1]

## ACKNOWLEDGMENT

Helpful discussions with Erich Valstyn are appreciated.

[1] F. H. Liu and M. H. Kryder, J. Appl. Phys. **75**, 6391 (1994).
[2] X. Shi, F. H. Liu, and M. H. Kryder, J. Appl. Phys. **75**, 6394 (1994).
[3] K. Kobayashi, IEEE Trans. Magn. **30**, 3933 (1994).
[4] A. Aharoni and J. P. Jakubovics, IEEE Trans. Magn. **26**, 2810 (1990).
[5] S. Tsukahara and H. Kawakatsu, J. Phys. Soc. Jpn. **32**, 72 (1972).

# Picosecond time-resolved magnetization dynamics of thin-film heads

M. R. Freeman
*Department of Physics, University of Alberta, Edmonton, Canada T6G 2J1*

J. F. Smyth
*IBM Storage Systems Division, 5600 Cottle Road, San Jose, California 95123*

The application of picosecond magneto-optic sampling techniques to studies of the magnetization dynamics of thin-film recording heads is described. Time-resolved magnetization measurements are performed using picosecond stroboscopic scanning Kerr microscopy. A Faraday probe is used to monitor the coil excitation current with the same optical setup, yielding a direct measure of the magnetic propagation delay through the head. This delay is found to have a marked spatial dependence across the face of the pole tips. As an aid to visualization of the spatial dependence, scanned images of the polar Kerr rotation at fixed time delays are acquired. © *1996 American Institute of Physics.* [S0021-8979(96)16008-9]

## I. INTRODUCTION

The dynamical properties of small magnetic structures represent problems of great current interest, both because of the implications for magnetic recording and due to the rapid improvements in experimental and computational attacks on the fundamental issues.[1–5] Just as there has been continual focus on the intrinsic limitations that size may impose on the recording process,[6] fundamental speed limitations are of concern as well.[7] In this paper we report novel measurements of the fast (subnanosecond regime) time response of the complex micromagnetic circuit which makes up a thin-film inductive write head. Picosecond magneto-optic sampling measurements[8] have been performed which yield a direct time-domain comparison of the excitation current in the coil with the magnetization response anywhere across the pole tips (P1 and P2) on the air-bearing surface.

## II. THE EXPERIMENTS

Details of the experimental setup are shown schematically in Fig. 1. The optical measurements are performed with picosecond pulses delivered by a synchronously pumped, cavity dumped dye laser. A polarizing beamsplitter and differential diode detection scheme is used to monitor the polar Kerr rotation. Ordinary low-speed signal diodes can be used as the picosecond-scale information is all obtained via the timing of the optical probe pulses relative to the excitation of the head. The heads are driven by electronically generated and time-delayed current pulses, synchronized to the cavity dumper. Two pulses of opposite polarity are superposed to create a bipolar waveform to simulate actual write conditions (albeit with much shorter transition times). The typical "pulse sequence" consists of a 5-ns duration positive pulse placed in the center of a 75-ns-width negative pulse of half the amplitude, repeated at 631.7 kHz. The time resolution in this configuration is limited to 50 ps by trigger jitter of the electronic pulsing circuit. The electronic pulse risetime at the head itself is still significantly larger than this in these measurements, limited by the coil inductance. To minimize this risetime, the head is mounted on a circuit board with the twisted pair leads normally running to the harness truncated to a few millimeters in length, and connected to a coplanar transmission line which delivers the current pulses. In practice, the current waveform is toggled on and off at 2 kHz such that the actual Kerr signal measured arises from the difference in the perpendicular magnetization under drive to that in the remanent state (where the magnetization is almost entirely in-plane.)

The current waveform is monitored by a small sample of thin-film bismuth-doped yttrium–iron–garnet, placed next to one of the coplanar lines. The garnet, with low perpendicular anisotropy and magnetization lying in the plane of the film in zero applied field, is situated such that the stray magnetic field from the lead is perpendicular to the film. The perpendicular component of magnetization is then proportional to the coil current (provided the transition times are within the bandwidth established by the ferromagnetic resonance of the garnet.) The perpendicular magnetization is measured "instantaneously" by sampling with a picosecond probe pulse at normal incidence to the film. A local in-plane field of 0.1 T, created by a small NdFeB permanent magnet, stiffens the

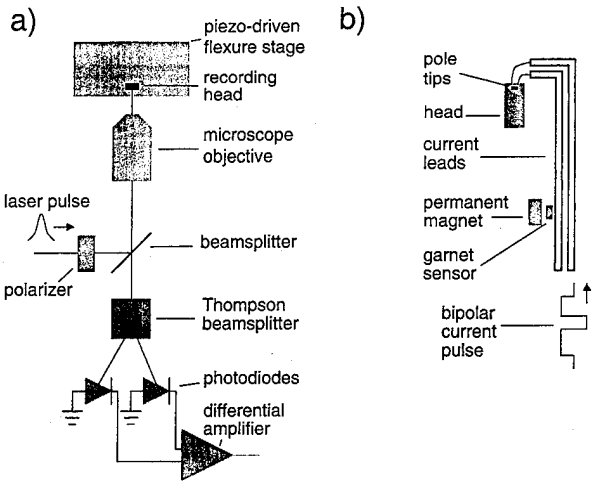



FIG. 1. Schematic layout of the experiment. (a) The heads are scanned under the focussed laser using a piezo-driven stage. The Kerr signal is analyzed using a polarizing beamsplitter (here a Thompson prism—Melles Griot 03PTB001—similar to a Wollaston prism but yielding larger beam separation.) (b) The head is mounted on a circuit board incorporating the time-resolved Faraday current probe.

 0021-8979/96/79(8)/5898/3/$10.00 © 1996 American Institute of Physics

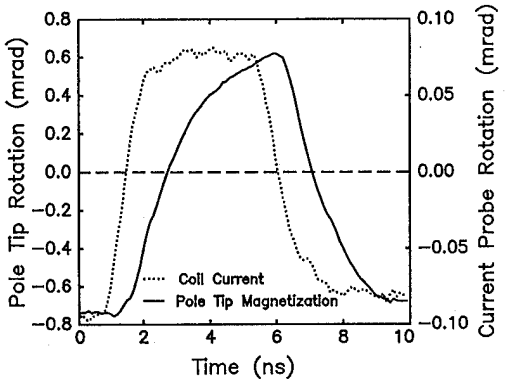



FIG. 2. A time-resolved optical measurement of the perpendicular magnetization at P2 on a 10-turn recording head, with the corresponding optical measurement of the coil current for absolute timing comparisons.

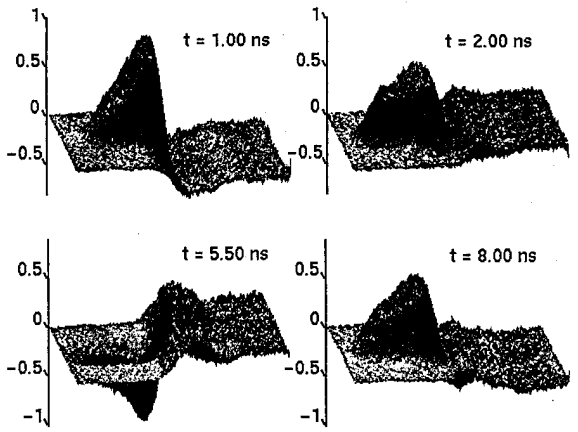



FIG. 3. A collection of stroboscopic scanned images of the perpendicular magnetization in a 12-$\mu$m-square region centered on the gap, with P2 to the left and P1 on the right. The labels correspond to time positions during a write cycle as shown in Fig. 2.

restoring force on the garnet magnetization to raise the ferromagnetic resonance frequency. This resulting Faraday current probe has a bandwidth of almost 5 GHz, corresponding to a risetime of 65 ps. The electrical pulse propagation delay along the line separating the Faraday probe and the head itself is approximately 80 ps.

## III. RESULTS

An example of the time-domain measurements is shown in Fig. 2. Here, a bipolar current waveform of nominal operating amplitude, $\pm 61$ mA, has been applied to a permalloy head having a 10-turn input coil. The dotted line illustrates the time dependence of the actual write current as sampled by the Faraday probe. The corresponding response of the perpendicular magnetization recorded by the polar Kerr effect is shown by the solid line, measured here for the bottom of the pole tip P2. The 80-ps time shift from the line length between the garnet and the head has been removed in this plot. The data indicate a 1.6-ns time constant for the magnetization change, combined with an apparent 0.7-ns magnetic propagation delay between the arrival of current at the coil and the onset of magnetization change at the pole tip.

The instantaneous spatial dependence of the perpendicular magnetization during the write cycle is acquired by scanning the sample under a laser spot produced by focussing the 585-nm wavelength beam using a 0.6 numerical aperture microscope objective. The resulting spatial resolution is close to the diffraction-limited value of 0.8 $\mu$m. This spatial resolution is sufficient to allow us to resolve many interesting position-dependent features in the magnetization, although it is clearly insufficient to resolve all of the detail in the magnetization near the gap. Representative images from a permalloy head taken at four different instants along a time-span similar to that of Fig. 2 are shown in Fig. 3. The shape of the current waveform in this case is the same as in Fig. 2, but the amplitude is now $\pm 94$ mA. The images are three-dimensional renderings in which the topography corresponds to the local perpendicular magnetization. The spatial window is 12 $\mu$m on a side, approximately centered on the write gap between P1 and P2. Of particular note is the fact that under these extreme drive conditions, significant differences in the response time at different spatial locations arise, to the extent that there exist instants at which the net perpendicular magnetization has the same phase on both pole tips. A sequence of such images has been stitched together into a "slow-motion" video[9] having an effective frame rate of 20 billion per second. Our interest in strong drive conditions also stems from a desire to use the heads as high-speed field transducers in research applications.

The spatial dependence is further highlighted by the spot measurements of the time dependence of the magnetization at different locations compared in Fig. 4. Very dramatic differences can be observed, for example, by comparing the responses on P2 (solid curve) to those near the far edges of P1 (dot–dashed curve). Even at the nominal drive current of 61 mA one observes very rapid time response on P1 far from P2, approaching the rise time of the current pulse at the coil as determined by the current probe. To some degree this is understandable in that the extremal regions of P1 remain everywhere well below saturation, hence a continuous high permeability path for rapid flux transport is assured. However, by simply reducing the amplitude of the drive current, comparably fast response is not achieved at P2, suggest-

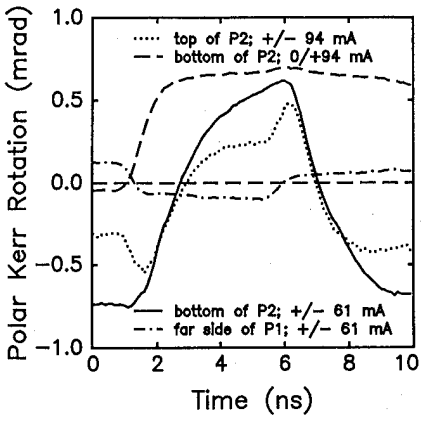



FIG. 4. Time-resolved magnetization measurements at different spatial locations on the pole tips, and for different current pulsing conditions.

ing that eddy currents (perhaps screening currents induced in P1) play a more important role there. Illustrative time-domain observations made using larger drive currents are also shown in Fig. 4. The dashed curve indicates that P2 can be forced from the remanent state to saturation very quickly at a 94-mA drive level with unipolar current pulses. The onset of slow decays of the magnetization from the saturated to remanent states is also made visible by our method in this case. Finally, an apparent nonmonotonic response of the perpendicular magnetization has been observed at the top of P2 (away from the gap; dotted curve in Fig. 4.) The equilibrium magnetization under drive this far from the gap includes a substantial in-plane component, however, and this observation should be complemented with a transverse Kerr measurement. Diffraction effects can also affect the purity of the polar Kerr measurement near the edges of the pole tips, and it would be desirable to repeat these measurements with higher spatial resolution.

## IV. SUMMARY

In summary, a picosecond time-domain technique has been described which enables very high-speed measurements of the magnetic dynamics underlying the thin-film inductive write process. A key feature of the technique is the ability to monitor the coil current on precisely the same time axis, yielding direct measurements of magnetic propagation delays in the head. The data therefore contain all of the information that could be obtained in frequency-dependent phase sensitive measurements of the same response.[1,2] The measurements can easily be extended to much shorter time scales through the use of photoconductive switches to generate the current waveforms[8] (producing faster risetimes and eliminating jitter); this will be done as the speed of the technology increases to demand it. In addition, transverse Kerr measurements can be performed to probe the other components of the pole tip magnetization, and external ("media-like") sensors could be incorporated to monitor components of the magnetic field external to the poles themselves.

## ACKNOWLEDGMENTS

M.R.F. thanks B. Argyle, B. Petek, J. Slonczewski, P. Trouilloud, and B. Webb of the IBM T. J. Watson Research Center for valuable discussions. This work is supported by IBM and by the Natural Sciences and Engineering Research Council, Canada.

[1] B. Petek, P. L. Trouilloud, and B. E. Argyle, IEEE Trans. Magn. **26**, 1328 (1990).
[2] X. Shi, F. H. Liu, Y. Li, and M. H. Kryder, J. Appl. Phys. **75**, 6394 (1994).
[3] J. C. Slonczewski, IEEE Trans. Magn. **27**, 4784 (1991); N. Smith, *ibid.* **27**, 4754; J.-G. Zhu and H. N. Bertram, *ibid.* **27**, 3553.
[4] Z. Guo and E. Della Torre, J. Appl. Phys. **75**, 5712 (1994).
[5] A. Aharoni and J. P. Jakibovics, IEEE Trans. Magn. **29**, 2527 (1993).
[6] D. D. Awschlom, D. P. DiVincenzo, and J. F. Smyth, Science **258**, 414 (1992).
[7] R. Wood, M. Williams, and J. Hong, IEEE Trans. Magn. **26**, 2954 (1990).
[8] M. R. Freeman, R. R. Ruf, and R. J. Gambino, IEEE Trans. Magn. **27**, 4840 (1991); M. R. Freeman, J. Appl. Phys. **75**, 6194 (1994).
[9] With the assistance of C. Pickover, Visualization Laboratory, IBM T. J. Watson Research Laboratory.

# Stress and magnetic properties in high moment FeN thin films

Kyusik Sin
*Center for Research on Information Storage Materials (CRISM), Dept. of Materials Science and Engineering, Stanford University, Stanford, California 94305*

Shan X. Wang
*Dept. of Electrical Engineering, Stanford University, Stanford, California 94305*

Single layer FeN films with low coercivity and low residual stress were prepared on Corning 0211 glass and Si substrates using rf diode sputtering without postannealing. Substrates and a small amount of nitrogen in the film had a significant effect on the magnetic properties and residual stress of FeN films. The residual stress in the pure Fe films showed tensile characteristics due to thermal stress. The stress decreased with increasing $N_2$/Ar flow ratio and passed a zero point at a flow rate ratio of ~3.5%, accompanied with a low coercivity. The stress changed to compressive with further increasing nitrogen in the lattice. The tensile-to-compressive transition in residual stress can be explained by the increase in lattice constant in FeN films. The lattice constant increased with increasing nitrogen flow during deposition, which was probably due to more nitrogen incorporation in the bcc Fe lattice. © *1996 American Institute of Physics.* [S0021-8979(96)06508-7]

## I. INTRODUCTION

In recent years there has been significant interest in ferromagnetic FeN films for head core materials because of their high saturation magnetization which is necessary for writing on media possessing very high coercivity (2500–4500 Oe).[1] It has been reported that high saturation magnetization ($4\pi M_s$=18–22 kG), low coercivity (<1.5 Oe), and low saturation magnetostriction ($<2\times10^{-6}$) can be obtained by the addition of a few percent of N into bcc Fe.[2] However, as-deposited FeN films often possess a large residual stress which causes low adhesion and makes head fabrication process very difficult. The residual stress also produces additional magnetic anisotropy other than induced magnetic anisotropy in the film head structures. The purpose of this article is to report the influence of substrates and $N_2$/Ar flow rate ratio on the coercivity and residual stress of single layer FeN films prepared using rf reactive sputtering without postannealing.

## II. EXPERIMENTAL PROCEDURES

Single layer FeN films, 6000 Å in thickness, were prepared on Corning 0211 glass, (111) Si, and $Al_2O_3$–TiC substrates using a Perkin–Elmer 4400 rf diode sputtering system. The base pressure of the system was below $3\times10^{-7}$ Torr. The FeN films were prepared from an 8 in. diam Fe target in Ar+$N_2$ plasma. A total gas pressure of 3 m Torr was used. The $N_2$/Ar flow rate ratio was varied to control the nitrogen content in the FeN films and to obtain optimum coercivity of the films. A magnetic field of about 50 Oe was applied parallel to the film plane during sputter deposition.

The microstructure of the films was determined using an x-ray diffractometer ($\theta$–$2\theta$ scan). The magnetic properties of the films were determined using a magneto-optic Kerr effect $M$-$H$ loop tracer. The saturation magnetostriction constant ($\lambda_s$) was measured using an ac magnetostriction tester. The residual stress in the films was determined from curvature measurements using the laser scanning technique[3] on (111) Si wafers and glass plates before and after film deposition.

## III. RESULTS AND DISCUSSION

X-ray diffraction results on 6000 Å thick FeN films on Corning 0211 glass with various $N_2$/Ar flow ratios are shown in Fig. 1. The films exhibit strong (110) texture of $\alpha$-Fe when the $N_2$/Ar flow rate ratio is small. As the $N_2$/Ar flow ratio increases, $\gamma'$-$Fe_4N$ phase is formed and the intensity of $\gamma'$-$Fe_4N$ peak increases. One of the interesting results is that the (200) $\gamma'$-$Fe_4N$ peak is dominant whereas Wang *et al.* reported that the (111) $\gamma'$-$Fe_4N$ peak was dominant in FeN films. The full width at half maximum (FWHM) of the (110) $\alpha$-Fe peak increases with increasing $N_2$/Ar flow ratio, indicating a probable decrease in grain size. The decrease in grain size is attributed to the existence of $\gamma'$-$Fe_4N$ at the grain boundaries inhibiting grain growth during sputtering.[4]

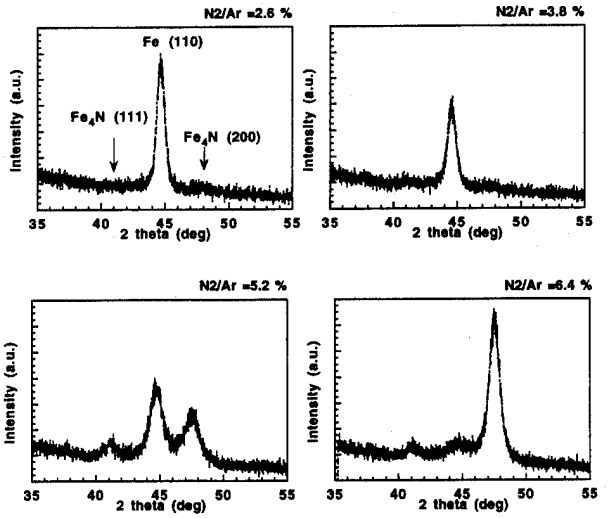



FIG. 1. X-ray diffraction spectra of 6000 Å FeN/glass films sputtered at various $N_2$/Ar flow rate ratios (input power: 0.64 kW, gas pressure: 3 m Torr).

 0021-8979/96/79(8)/5901/3/$10.00 © 1996 American Institute of Physics 

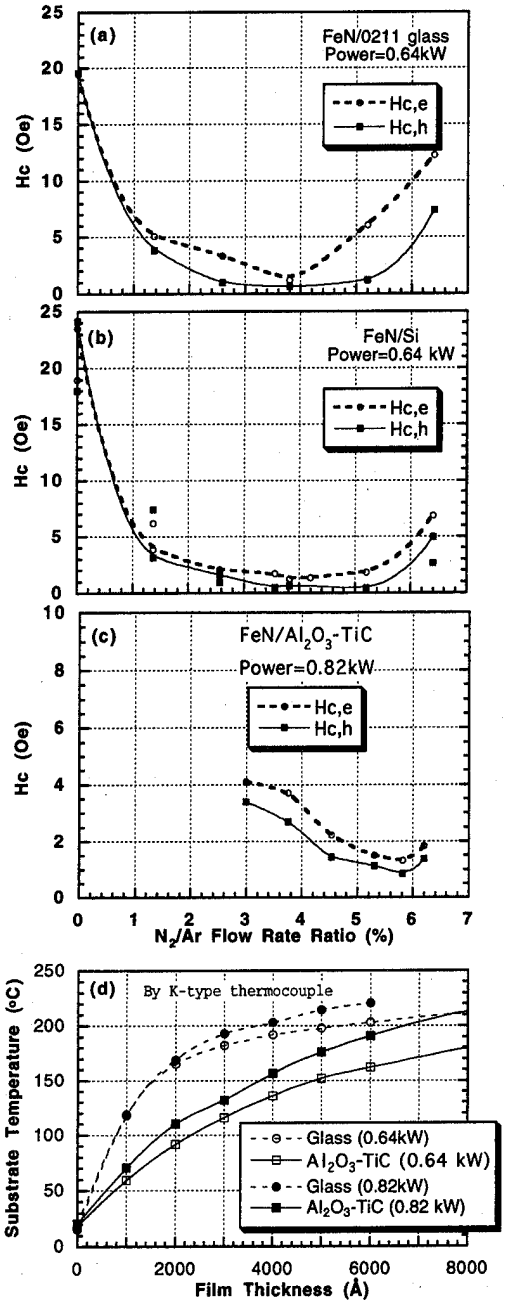



FIG. 2. Effect of $N_2$/Ar flow rate ratio on the coercivity of 6000 Å FeN films on (a) 0211 glass, (b) (111) Si, and (c) $Al_2O_3$–TiC substrates. (d) The changes in surface temperature of glass and $Al_2O_3$–TiC substrates during sputtering.

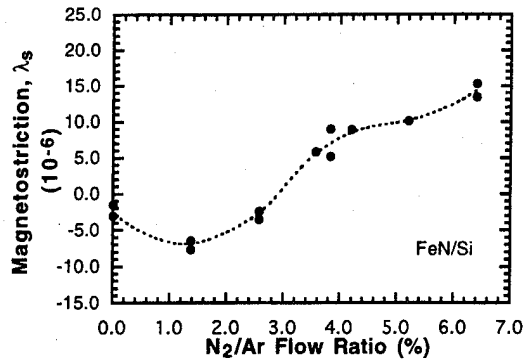



FIG. 3. Effect of $N_2$/Ar flow rate ratio on the saturation magnetostriction ($\lambda_s$) of FeN films on Si substrates.

The coercivity of pure Fe films on glass in Fig. 2(a) is about 20 Oe. As $N_2$ is introduced, both easy axis coercivity ($H_{c,e}$) and hard axis coercivity ($H_{c,h}$) decrease significantly. At a $N_2$/Ar flow ratio of 3.8% and an input power of 0.64 kW, the easy axis and hard axis coercivities are 1.2 and 0.6 Oe, respectively. The x-ray intensity of $\gamma'$-$Fe_4N$ at the minimum coercivity is very small indicating an optimum amount of $\gamma'$-$Fe_4N$ phase for the minimum $H_c$. Further increases in $N_2$/Ar flow ratio increase coercivity. The increase in coercivity beyond the optimum $N_2$/Ar flow ratio might be related to the increase in grain size. The transmission electron microscopy study showed that the average grain size of FeN/glass at 3.8% $N_2$/Ar flow ratio was about 90 Å. The average grain size increased to about 320 Å at 6.4% due to the formation of a large amount of $\gamma'$-$Fe_4N$.

As shown in Figs. 2(a) and 2(b), both FeN films on 0211 glass and Si substrates show similar coercivities at the $N_2$/Ar flow ratio of 3.8% and the input power of 0.64 kW. However, FeN/Si have a broader range of low coercivity. In the case of $Al_2O_3$–TiC substrates [see Fig. 2(c)], the input power was optimized to be 0.82 kW due to the larger thermal mass of $Al_2O_3$–TiC substrates. Figure 2(d) is the actual surface temperature during sputtering measured using a *K*-type thermocouple attached to the surface of the substrate. The surface temperature of the $Al_2O_3$–TiC substrate rises very slowly compared with that of glass substrate. The final surface temperature of $Al_2O_3$–TiC substrate at 0.82 kW becomes close to that of glass substrate at 0.64 kW. The optimum $N_2$/Ar flow ratio was also shifted from 3.8% to 5.8% due to a larger sputtering rate of Fe at 0.82 kW.

The saturation magnetostriction ($\lambda_s$) of the FeN on Si substrates is shown in Fig. 3. The $\lambda_s$ is negative for pure Fe films as expected.[5] An increase in $N_2$/Ar flow rate ratio increases $\lambda_s$ and there is a transition from negative to positive at a flow rate ratio of 2.8%. This behavior is consistent with other results and can be attributed to the increase in the amount of $Fe_4N$ phase in the films[2,6] or incorporation of nitrogen atom in $\alpha$-Fe lattice.[7] The $N_2$/Ar flow rate ratio at the zero magnetostriction point was lower than that at the minimum coercivity.

The residual stress in the films on Si substrate is tensile (240–450 M Pa) when the $N_2$/Ar flow ratio is 0, as shown in Fig. 4(a). It decreases as $N_2$/Ar flow ratio increases and reaches a zero point at a $N_2$/Ar flow ratio of ~3.8%, which corresponds to the minimum coercivity. It has a broad range of low stress (<100 M Pa). The sign of residual stress changes to compressive with further increasing nitrogen flow (−330 to −450 M Pa at $N_2$/Ar of 6.4%). The residual stress of FeN/glass in Fig. 4(b) shows similar profile but with steeper transition from tensile to compressive stress. The profiles of residual stress are well correlated with those of coercivity shown in Figs. 2(a) and 2(b). The residual stress ($\sigma_{total}$) is composed of thermal stress ($\sigma_{th}$) and internal stress ($\sigma_{int}$). The thermal stress is due to the difference in thermal

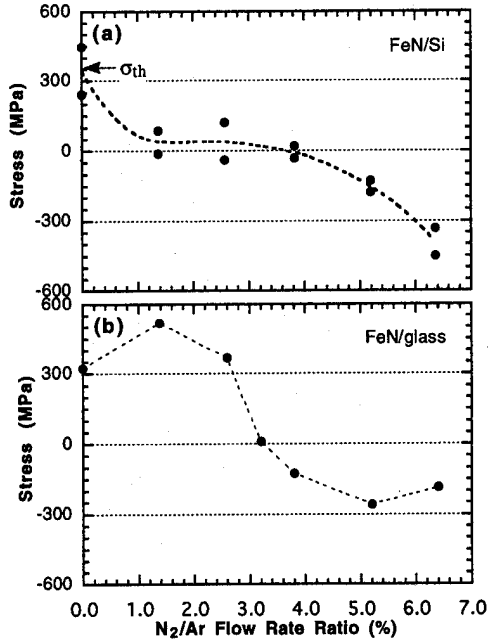



FIG. 4. Effect of $N_2$/Ar flow rate ratio on the residual stress of 6000 Å FeN films on (a) Si and (b) glass substrates.

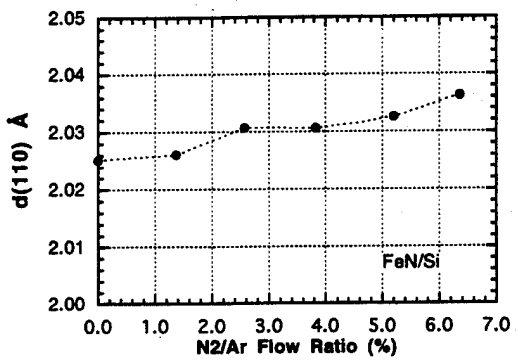



FIG. 5. Effect of $N_2$/Ar flow rate ratio on the $d(110)$ of bcc Fe in FeN films on Si substrates.

expansion coefficient between the film and the substrate: $\sigma_{th}=E_f(\alpha_f-\alpha_s)\Delta T/(1-\nu_f)$, where $E_f$ is the Young's modulus of the film, $\alpha_f$ and $\alpha_s$ are the thermal expansion coefficient of the film and the substrate, respectively, and $\Delta T$ is the temperature difference between the sputtering and room temperature. Assuming that the Young's modulus and the thermal expansion coefficient of Fe do not change significantly with the addition of a few percent of N into Fe, the thermal stress is calculated to be ~360 M Pa (tensile) using $E_{f(Fe)}$ = 205 G Pa, $\alpha_{f(Fe)}$ = 11.7 × $10^{-6}$ °$C^{-1}$, $\alpha_{s(Si)}$ = 2.6 × $10^{-6}$ °$C^{-1}$, $\Delta T$=135 °C, $\nu_f$=0.3. Thus, the residual stress at zero $N_2$/Ar flow rate is caused mostly by thermal stress. The decrease in tensile stress and the transition from tensile to compressive stress are explained by an increase in the lattice spacing of (110) $\alpha$-Fe planes [$d(110)$]. The peak position of (110) $\alpha$-Fe was calibrated by the (111) peak of Si. As shown in Fig. 5, the values of $d(110)$ increase with increasing nitrogen flow rate during deposition which results in more nitrogen being incorporated in the interstitial sites of bcc Fe lattice.[8,9] It is to be noted that $d(110)$ still increases even though $\gamma'$-$Fe_4N$ is formed in the film. This result suggests that N atoms are still incorporated in $\alpha$-Fe lattice during the formation of $\gamma'$-$Fe_4N$, resulting in a monotonic increase in residual stress.

## IV. CONCLUSIONS

Single layer FeN films with low coercivity ($H_{c,e}$=1.2 Oe, $H_{c,h}$=0.6 Oe) and low residual stress (<100 M Pa) were prepared using a rf diode sputtering without postannealing. Substrate and a small amount of nitrogen in the film had a significant effect on the magnetic and mechanical properties of FeN films. The stress in the films was tensile when $N_2$/Ar flow ratio was 0. It decreased as the ratio increased and passed a zero point at a $N_2$/Ar flow rate of ~3.5%. The stress changed to compressive with further increasing nitrogen in the lattice. The tensile-to-compressive transition in residual stress can be explained by the change in lattice constant in FeN films. The lattice constant increased with increasing nitrogen flow during deposition, probably due to more nitrogen incorporated in the lattice.

## ACKNOWLEDGMENTS

The authors would like to acknowledge the help of Dr. Hua-Ching Tong at Read-Rite for measuring the saturation magnetostriction of FeN films. This work was supported in part by the National Science Foundation under Grant No. ECS-9409805, the Terman Fellowship endowed by W. Hewlett and D. Packard, and the Center for Materials Research at Stanford University.

[1] E. S. Murdock, R. F. Simons, and R. Davidson, IEEE Trans. Magn. **MAG-28**, 3079 (1992).
[2] S. Wang and M. H. Kryder, J. Appl. Phys. **67**, 5134 (1990).
[3] P. A. Flinn, D. S. Gardner, and W. D. Nix, IEEE Trans. Electron Devices **ED-34**, 689 (1987).
[4] M. H. Kryder, S. Wang, and K. Rook, J. Appl. Phys. **73**, 6212 (1993).
[5] N. Ishiwata, C. Wakabayashi, and T. Matsumoto, IEEE Trans. Magn. **MAG-24**, 3078 (1988).
[6] M. A. Russak, C. V. Jahnes, E. Klokholm, J.-W. Lee, M. E. Re, and B. C. Webb, J. Appl. Phys. **70**, 6427 (1990).
[7] J. C. Cates, C. Alexander, Jr., E. Haftek, and J. A. Barnard, IEEE Trans. Magn. **MAG-29**, 3105 (1993).
[8] K. H. Jack, J. Appl. Phys. **76**, 6620 (1994).
[9] C. Barrett and T. Massalski, *Structure of Metals*, 3rd rev. ed. (Pergamon, Oxford, 1980), p. 259.

# Effect of base layers on the soft magnetic properties of FeTaN films

V. R. Inturi and J. A. Barnard
*Department of Metallurgical and Materials Engineering and Center for Materials for Information Technology, The University of Alabama, Tuscaloosa, Alabama 35487-0202*

The effects of base layers with different crystal structures and well defined growth textures on the soft magnetic properties of FeTaN films have been studied. Broadly speaking, base layers with fcc or hcp crystal structures and having predominantly (111) and (0002) growth textures, respectively, significantly improve the soft magnetic properties of the subsequently deposited (110) textured bcc FeTaN films. Base layers with bcc crystal structures and (110) growth textures either degrade the soft magnetic properties or have little effect. © *1996 American Institute of Physics.* [S0021-8979(96)12408-7]

## I. INTRODUCTION

In our continuing efforts to improve the soft magnetic properties of high moment (~20 kG) FeTaN films, we have noticed that certain base layers can have substantial beneficial effects. To determine the origin of these effects (assumed to be crystallographic), identically processed FeTaN films of varying thickness have been prepared with and without selected base layers.

In previous work,[1] the effect of N content on the soft magnetic properties of FeTaN films (no base layers) has been systematically documented. $\lambda_s$ was found to vary linearly with N (negative for zero N but crossing zero and becoming increasingly positive with increasing N). The initial permeability also increased linearly with N up to the onset of stripe domains. $H_{ce}$ varied in a more complex manner, decreasing strongly on initial incorporation of N, then remaining constant over a broad range of N content, finally increasing dramatically as stripe domains appeared. For FeTaN grown without a base layer, processing conditions which produce acceptably small $\lambda_s$ often do not coincide with those yielding a small enough coercivity and sufficient permeability.

FeTaN films were deposited reactively by dc magnetron sputtering using an Ar and $N_2$ gas mixture and a 4 in diam Fe—10 w/o Ta target. The base vacuum was $\sim 3.6\times10^{-7}$, the Ar+$N_2$ total pressure was 3 mTorr, and the power was 220 W. The sputtering rate was ~12 Å/s. All the films were grown in an aligning field of 80 Oe to induce uniaxial in-plane magnetic anisotropy. The substrate materials used were 7059 Corning glass, oxidized Si (111), and oxidized Si (100). Thicknesses were measured by DekTak IIA surface profilometer, coercivity with a SHB 10 Hz loop tracer, saturation magnetostriction with an high precision optical magnetostriction unit, growth texture with a Rigaku D/max-B x-ray diffractometer, and initial permeability with a permeameter. All the base layers were deposited by dc magnetron sputtering using 3 mTorr Ar pressure and 220 W power. All the measurements reported were made on as-deposited films. The saturation magnetization, $M_s$, for all the films, independent of base layer, was found to be ~1650 emu/cc.

## II. RESULTS AND DISCUSSION

Preliminary measurements of the effect of Cr and Ta (bcc), Cu (fcc), and Hf (hcp) base layers on the magnetostriction of FeTaN films are summarized in Fig. 1. The FeTaN films were grown with a fixed Ar+$N_2$ gas mixture (known to produce good soft magnetic properties in thicker films) and with varying thickness. The base layer thicknesses are fixed at ~1000 Å for this set of films. It is very clear that the base layers having fcc (Cu) and hcp (Hf) crystal structures and close packed plane growth textures [i.e., (111) and (0002)] significantly improve the magnetostriction. Of the two bcc base layers examined Cr, with a (110) texture, clearly increases $\lambda_s$ while Ta with a complex texture (and a mixture of bct $\beta$-Ta and bcc $\alpha$-Ta phases), has a beneficial effect on thin FeTaN films which does not persist to large thicknesses. The general decrease of $\lambda_s$ with increasing FeTaN thickness is attributed to a decrease in average N content with increasing thickness as monitored by lattice parameter measurements.[2] Films with lower N content (i.e., smaller $d$ spacing) should have lower $\lambda_s$ as noted previously.[1]

Based on the clear effects illustrated in Fig. 1, a more systematic study was undertaken using Ti (hcp) and Ag (fcc) base layers (both ~600 Å thick) with well defined growth textures. Figures 2(a)–(c) illustrates the effect of these base layers on $\lambda_s$, $H_{ce}$, and $\mu_i$, all of which are clearly and sig-

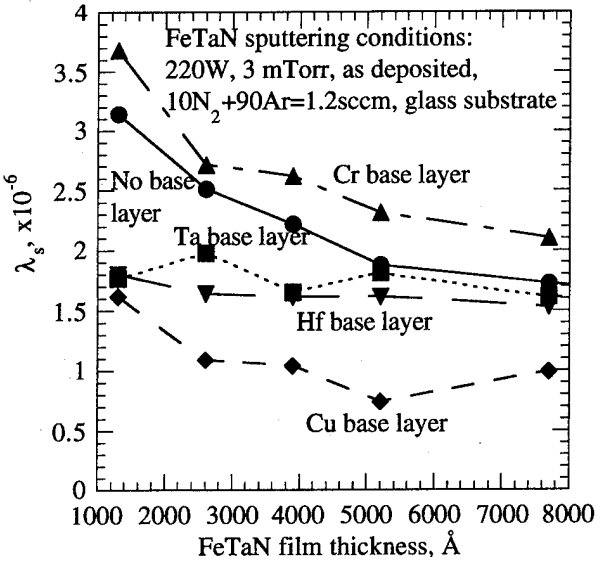



FIG. 1. The effect of base layers on the saturation magnetostriction, $\lambda_s$, of FeTaN films of varying thickness.

 0021-8979/96/79(8)/5904/3/$10.00 © 1996 American Institute of Physics

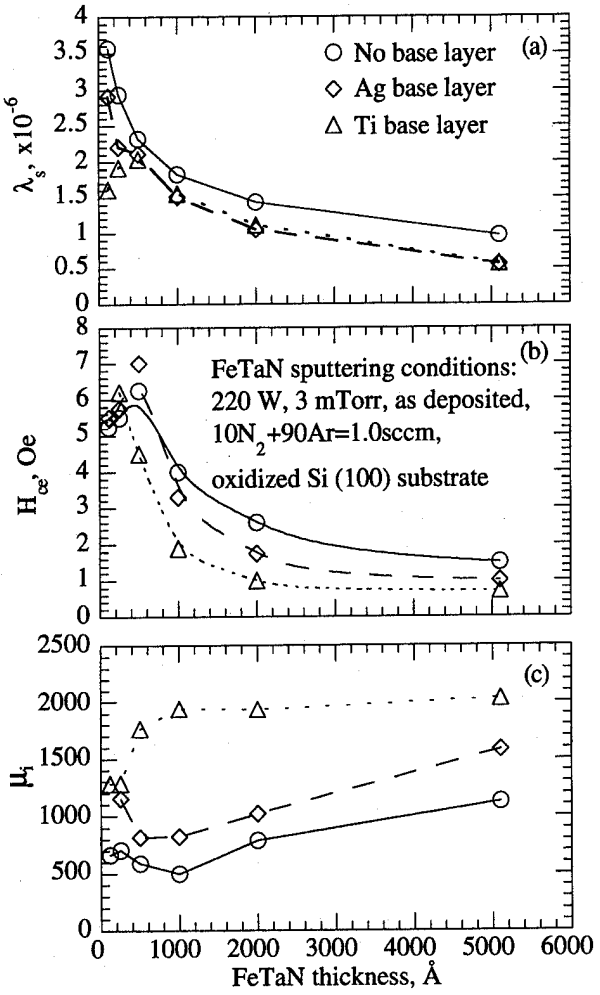



FIG. 2. The effect of Ti and Ag base layers on the (a) saturation magnetostriction, $\lambda_s$, (b) coercivity, $H_{ce}$, and (c) initial permeability, $\mu_i$, of FeTaN films.

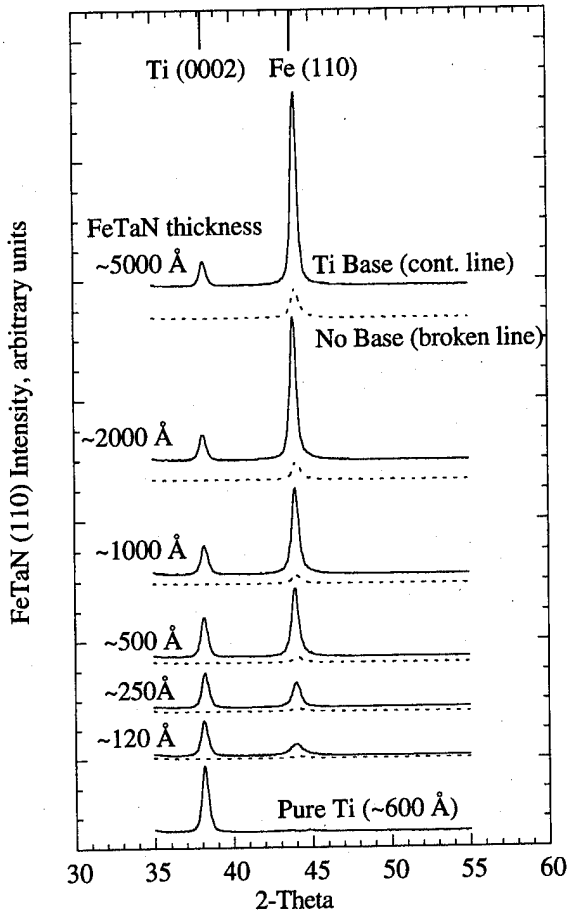



FIG. 3. $\theta$–$2\theta$ XRD scans of FeTaN films with and without a 600 Å Ti base layer.

nificantly improved (the $\lambda_s$ values for the no base layer films are slightly lower than those plotted in Fig. 1 because the sputtering conditions were slightly different). Figure 2(a) shows the effects of Ti and Ag base layers on $\lambda_s$. Both Ti and Ag substantially reduce $\lambda_s$ and the beneficial effect persists to 5000 Å films where almost a 50% reduction is observed. The effect of Ti and Ag base layers on coercivity is plotted in Fig. 2(b). Generally, the coercivity decreases with increasing FeTaN thickness. Both base layers improve coercivity but Ti is more effective, reducing the coercivity at 5000 Å by ~50%. Figure 2(c) shows the dependence of initial permeability on FeTaN thickness and the presence of Ti and Ag base layers. $\mu_i$ improvement with the base layers is quite remarkable, particularly for Ti, where $\mu_i$ is doubled for the 5000 Å films. In summary, by using a 600 Å Ti base layer with strong (0002) growth texture, 5000 Å thick FeTaN films with extremely good soft magnetic properties ($\lambda_s = 0.5\times10^{-6}$, $H_{ce}$=0.6 Oe, $\mu_i$=2000) can be grown.

Some of these results can be explained by the dramatic effects that the base layers have on the growth texture of FeTaN films. These effects are summarized in Fig. 3 for the case of Ti (similar results were found for Ag but we focus on Ti for clarity). In Fig. 3, $\theta$-$2\theta$ x-ray diffraction (XRD) scans (Bragg–Brentano mode[3]) of FeTaN films of varying thicknesses grown using identical sputtering conditions with and without a Ti base layer are plotted along with the XRD scan of the bare Ti base layer. A remarkable improvement in the FeTaN (110) texture which persists up to 5000 Å thickness is caused by the Ti base layer. This can be observed by comparing the FeTaN (110) intensities with and without the Ti base layer. The XRD scan of the bare Ti base layer clearly shows a very strong (0002) growth texture. The effect of Ti on the FeTaN crystallography can be quantitatively described by plotting the FeTaN (110) peak intensity measured in both $\theta$–$2\theta$ and fixed incidence (Seemann–Bohlin) modes[3] vs FeTaN thickness [Fig. 4(a) and 4(b)]. In the $\theta$–$2\theta$ mode, the (110) intensity is proportional to the fraction of (110) planes parallel to the substrate (the textured portion of the film), while in fixed incidence mode, the (110) intensity is due to those (110) planes not parallel to the substrate. From Fig. 4(a), it is clear that the FeTaN (110) peak intensity with a Ti base layer is several times greater than the FeTaN (110) peak intensity without a base layer. Furthermore, from the intensities obtained in the fixed incidence XRD mode [Fig. 4(b)], one sees that the number of FeTaN (110) planes nonparallel to the surface of the film is significantly reduced by the Ti base layer. Taken together, this is strong evidence that Ti

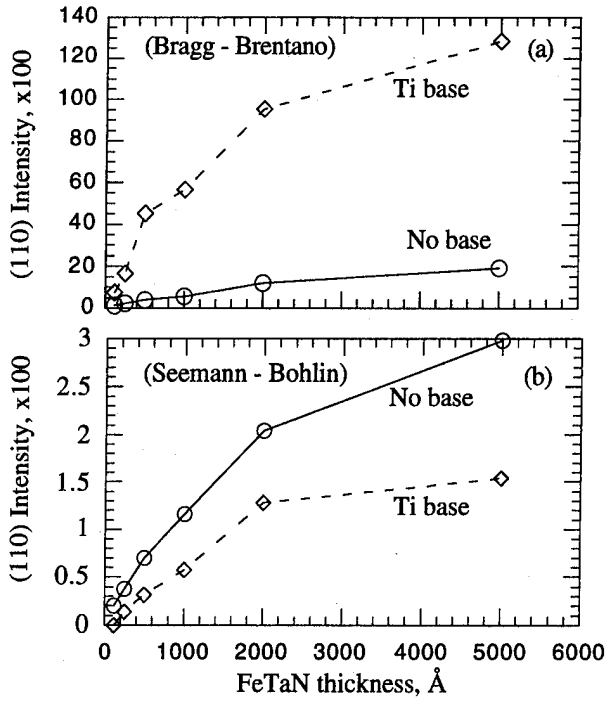



FIG. 4. (110) peak intensity of FeTaN films with and without a Ti base layer in two XRD modes.

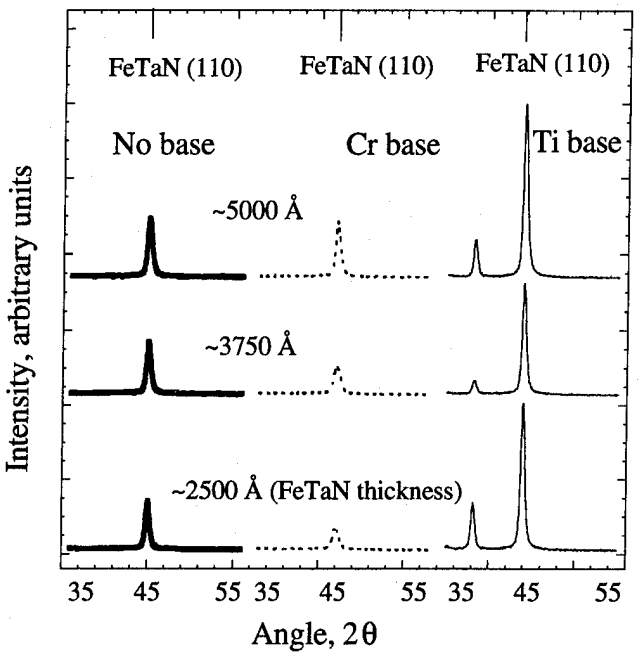



FIG. 5. Comparison plot of $\theta$–$2\theta$ XRD scans of FeTaN films with no base layer and with Cr and Ti base layers.

(and Ag base layers, not shown here) strongly enhance the (110) texture of FeTaN films.

Ti base layers do cause an increase of ~25% in FeTaN grain size as determined by full width half maximum (FWHM) measurements of the FeTaN (110) peak. However, the contribution of this grain size increase (which decrease the amount of disordered material having positive magnetostriction[4]) to the change in $\lambda_s$ is only ~6%.[1] The enhancement of (110) growth texture in FeTaN films may be understood on the basis of standard metallurgical arguments. At interfaces between two crystal structures, orientation relationships are often formed which have the closest packed planes in each structure parallel to the another. For bcc:fcc and bcc:hcp orientation relationships two classical variants are known, Nishiyama–Wasserman (NW) and Kurdjumow–Sachs (KS) which predict (110) bcc‖ (111) fcc [or (0002) hcp].[5,6]

At this point, it is useful to recall that Cr base layers had a deleterious effect on $\lambda_s$ in FeTaN. This result requires an explanation as there is good lattice matching between Cr and FeTaN and a Cr (110) base layer might be expected to promote FeTaN (110) growth texture. In fact, the opposite is true. In Fig. 5, a series of XRD scans are plotted which clearly demonstrate that the Cr (110) base layer actually inhibits FeTaN (110) texture. Note that the Cr (110) peak overlaps the FeTaN (110) peak and contribute to the observed intensity further demonstrating the deleterious effect of Cr (110) base layer on FeTaN (110) growth texture. The reasons for this phenomenon are not clear at this time.

The improvement of $\lambda_s$ can be directly attributed to the enhancement of the (110) texture. As calculated earlier,[1,7] (110) textured polycrystalline Fe-based films should have lower $\lambda_s$ than randomly oriented Fe-based films and the stronger the texture the lower the $\lambda_s$. Crystallographic texture may also be at the root of the permeability increase. For Fe–Si alloy films multilayered with permalloy spacers, a strong correlation between improved (110) texture and increased $\mu_i$ has been reported.[8] Although it is not surprising that $H_c$ should decrease as the other soft magnetic properties improve, there is no obvious crystallographic origin to this effect.

## ACKNOWLEDGMENTS

This work is supported mainly by the National Storage Consortium—Advanced Technology Program funded through the Department of Commerce and partially by Storage Technology Corporation, Kodak, and NSF Grant No. DMR - 9157402.

[1] V. R. Inturi and J. A. Barnard, IEEE Trans. Magn. **31**, 2660 (1995).
[2] G. Qiu and J. A. Barnard, J. Appl. Phys. **75**, 6934 (1994).
[3] P. A. Flinn and G. A. Waychunas, J. Vac. Sci. Technol. B **6**, 1749 (1988).
[4] K. Nago, H. Sakakima, and K. Ihara, J. Magn. Soc. Jpn. **15**, 365 (1991).
[5] J. H. van der Merwe and G. J. Shiflet, Acta Metall. Mater. **42**, 1173 (1994).
[6] Y. Mou and H. I. Aaronson, Acta. Metall. Mater. **42**, 2133 (1994).
[7] J. C. Cates and C. Alexander, Jr., J. Appl. Phys. **75**, 6754 (1994).
[8] H. Ohji, S. Tanabe, M. Kataoka, and T. Ozeki, J. Magn. Magn. Mater. **134**, 292 (1994).

# Soft magnetic properties of nanocrystalline FeRuGaSi-Hf alloy films and head characteristics for the embedded thin film tape head

H. Ohmori, M. Shoji, T. Kobayashi, T. Yamamoto, Y. Sugiyama, and K. Hayashi
*Sony Corp. Research Center, 174 Fujitsuka-cho, Hodogaya-ku, Yokohama 240 Japan*

K. Hono
*National Research Institute for Metals, 1-2-1 Sengen, Tsukuba 305 Japan*

The Hf-added FeRuGaSi alloy film has an amorphous structure in the as-deposited state and becomes nanocrystalline after annealing. Due to this structure change from crystalline to amorphous by the addition of Hf, soft magnetic degradation of the film deposited on the slant grooved substrate, which is necessary for the sophisticated embedded thin film (ETF) head structure, is greatly suppressed and the undesirable film stress is relieved. The FeRuGaSi-Hf alloy film has higher resistivity and permeability at high frequencies than those of sendust film, and the read/write characteristics of this alloy film show better performance than sendust film. © *1996 American Institute of Physics.* [S0021-8979(96)12508-3]

## I. INTRODUCTION

The embedded thin film (ETF) head with a rubbing surface similar to a TSS (tilted sputtered sendust) head and an embedded thin film coil in between the gap, has potential characteristics for high frequency tape recording systems because of its small magnetic core size.[1] The read/write characteristics of this head reflect directly film core permeability. The FeRuGaSi alloy, which has high permeability, high wear resistivity, and high magnetization, is a very attractive candidate for the core material of this head.[2] The thick film deposited on the slant groove substrate, however, gives rise to film cracking/peeling due to the large internal stress accompanied with undesirable growth anisotropy.[3] To overcome these problems, we introduce an additive element to the FeRuGaSi alloy system with the aim of inhibiting the grain growth by annealing. Among the elements studied, we found Hf is the most effective one to reduce film stress as well as to improve high frequency permeability.

## II. EXPERIMENT

Thin films were prepared by dc magnetron sputtering method using alloy sputtering target of 100 mm in diameter. The sputtering conditions are 0.5 Pa in Ar gas pressure and 400 W of incident power. The thermal treatment was performed in vacuum without a magnetic field for one hour at a fixed temperature. Coercivity and magnetostriction are measured by a $B-H$ loop tracer. Permeability was measured by a figure-eight-coil permeance tester. The magnetic induction was measured by a vibration sample magnetometer. The x-ray diffractions are measured by $\theta$–$2\theta$ method using Co–$K\alpha$ radiation. The transmission electron microscope (TEM) observation was also performed to clarify the film microstructure. The embedded thin film (ETF) head with a FeRuGaSi-Hf film core was fabricated by the same process as the prior study[1] except for thermal treatment at 700 °C before glass molding. Read/write characteristics were measured with a conventional drum tester.

## III. RESULTS AND DISCUSSION

### A. Magnetic properties

Figure 1 shows the effects of Hf content on the coercivities of $Fe_{74.5-x}Ru_{4.5}Ga_3Si_{18}Hf_x$ alloy films for the annealing temperatures of 600 °C, 700 °C, and 800 °C. All the films were deposited on flat substrates. Coercivities increase with Hf additions up to 3 at. %, while in the region from 3.5 at. % to 5.5 at. %-Hf very small coercivities are observed. Coercivities minima are obtained for the 700 °C annealing. With the fixed contents of 3.5 at. %-Hf and 4.5 at. %-Ru, the compositional contours of coercivity, magnetic induction, permeability, and zero magnetostrictive lines are shown in Fig. 2. All the specimens were annealed at 700 °C. There was no film crack/peeling for all the specimens. Eventually, a coercivity of 16 A/m, permeability of 1700, and magnetic induction of 1.1 T are obtained for the $Fe_{71}Ru_{4.5}Ga_3Si_{18}Hf_{3.5}$ alloy film with a 10 $\mu$m thickness.

### B. Microstructure

In order to observe the microscopic structure of the FeRuGaSi-Hf alloy film, x-ray diffraction and TEM observation were performed. Figure 3 shows the x-ray diffraction patterns of the various Hf content films for the as deposited state and after annealing ones at 700 °C. The structure of the as deposited films changes from crystalline to amorphous

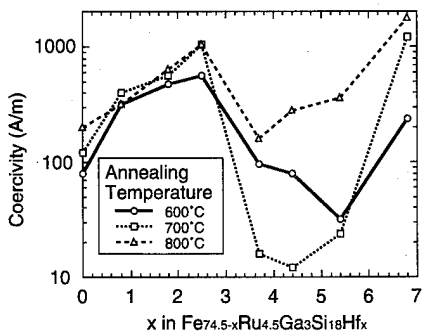



FIG. 1. Hf composition dependence of coercivity for various annealing temperatures.

 0021-8979/96/79(8)/5907/3/$10.00 © 1996 American Institute of Physics 

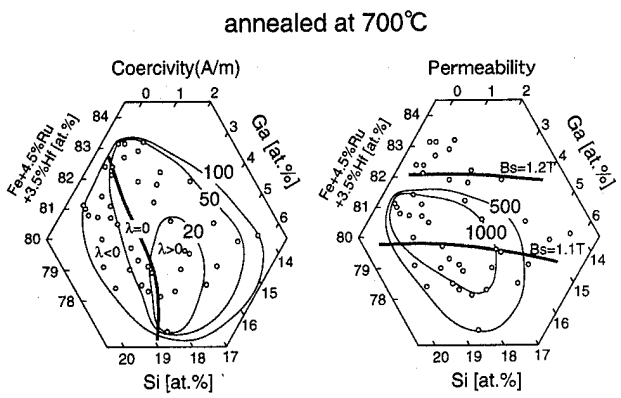



FIG. 2. Compositional contours of coercivities, permeability, magnetic induction, and zero magnetostrictive line.

with increasing Hf content. The annealed film structure becomes nanocrystalline with increasing Hf composition, and crystalline orientation of (110) is remarkably suppressed due to random orientation of the crystallites. In the system with a small Hf content, diffraction peaks of ordered $DO_3$ phase such as (111) are not observed because of preferred orientation of (110), while in Hf-rich film the $DO_3$ peaks are recognized.

Figure 4 shows bright field TEM images in the as-deposited film (a) and the annealed ones at 600 °C (b) and 700 °C (c).[4] Hf-free FeRuGaSi film shows enormous crystal growth by annealing, and crystal structure changes from B2 to $DO_3$ with increasing annealing temperature. For the Hf-added film, on the other hand, only slight crystal growth is observed and the average crystal sizes are 12 and 24 nm for 600 and 700 °C annealing, respectively. The crystal structure of the FeRuGaSi-Hf film changes from B2 to $DO_3$, which is the same character as in the FeRuGaSi alloy film. Thus, major reasons for the soft magnetic character in the Hf added system are (a) because of the $DO_3$ ordered phase and (b) due to the nanocrystalline structure.[5]

### C. Head characteristics

FeRuGaSi-Hf film is suitable for a magnetic recording head with a slant groove such as an embedded thin film

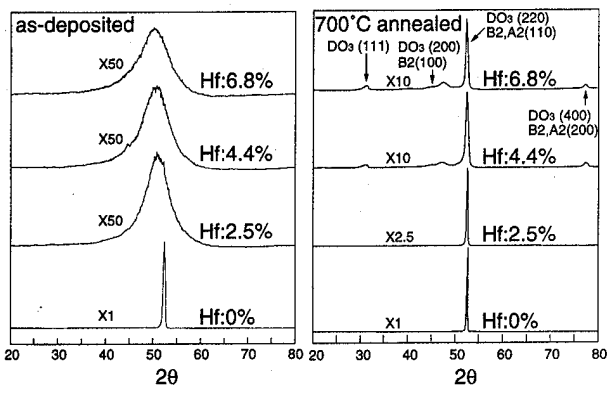



FIG. 3. X-ray diffraction patterns of the as-deposited and annealed films for various Hf contents.

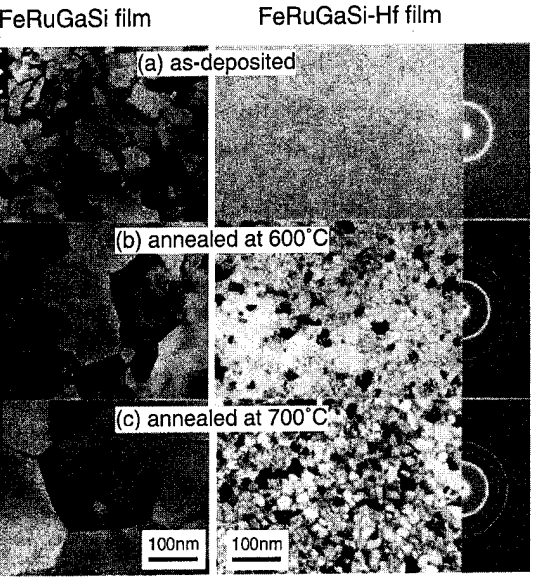



FIG. 4. TEM images for the films of as-deposited (a) and annealed at 600 °C (b), 700 °C (c).

(ETF) head, because the amorphous structure of the as-deposited film can reduce anisotropy by diminishing columnar structure and crystal orientation. A schematic view of the embedded thin film head and its abbreviated manufacturing process is shown in Fig. 5. The permeability of thin film *on the slant grooved part* is measured after glass molding. Figure 6(a) shows frequency dependence of permeability in the Hf-FeRuGaSi film and sendust film with the thickness of 15 $\mu$m. FeRuGaSi-Hf film has higher permeability compared with that of sendust film, especially in high frequencies.

Frequency dependence of the reproducing voltage by the read/write measurement is shown in Fig. 6(b) for the ETF head utilizing the sendust film and FeRuGaSi-Hf film. Experimental specifications of the recording measurements are 14 $\mu$m in track width, 18 $\mu$m in gap depth, 0.2 $\mu$m in gap length, 16 turns in coil turns, commercial metal particle (MP)

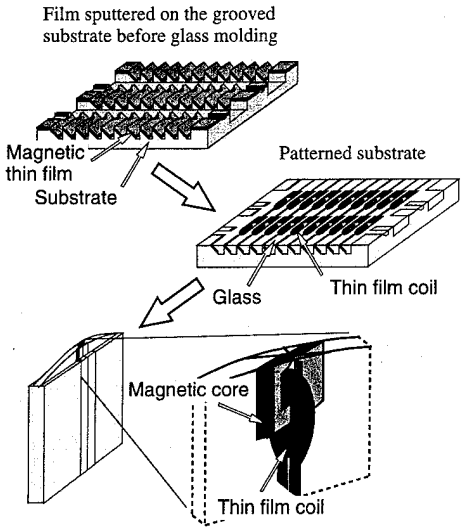



FIG. 5. Schematic view of the embedded thin film head.

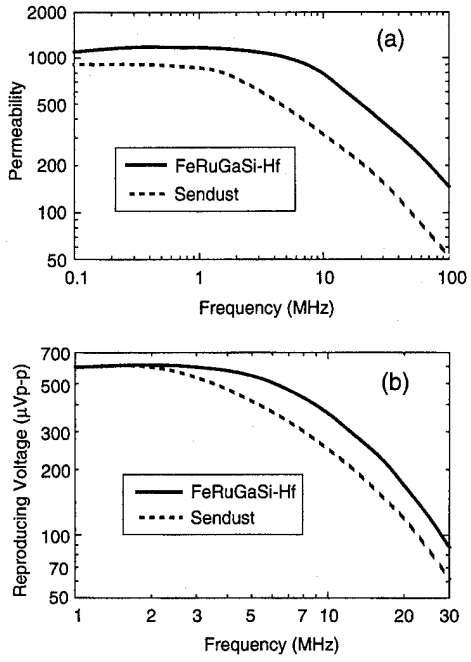



FIG. 6. (a) Frequency dependence of permeability in the FeRuGaSi-Hf and sendust films. (b) Frequency dependence of reproducing voltage in the ETF heads with FeRuGaSi-Hf and sendust films.

tape for a Hi-8 VCR (video cassette recorder), and 10 m/s head-tape speed. Although both the heads have almost the same reproducing voltage at low frequencies, the FeRuGaSi-Hf head show higher output than that of the sendust head at high frequencies. These results correspond to the permeabilities differences of the films.

One of the possibilities for the FeRuGaSi-Hf film having high permeability at high frequencies is considered to be the high resistivity of the film. Film resistivities are shown in Fig. 7 for the as deposited and 700 °C annealed films with various Hf contents. Hf-rich films show higher resistivities of 130–140 $\mu\Omega$ cm after annealing at 700 °C, which is about 40% higher than that of sendust film annealed at the optimum temperature of 600 °C. Improvement of the high frequency permeability, however, cannot be well-explained solely from the resistivity increase. The magnetic flux mostly concentrates on the thin skin depth of the film in high frequencies. The magnetic uniformity of the soft magnetic character of the FeRuGaSi-Hf alloy film, without any initial and surface degraded layer, is better than that of sendust film, because the as-deposited FeRuGaSi-Hf film is amorphous and then crystallized. The flux path, therefore, may be better for the FeRuGaSi-Hf alloy film. The detailed analysis of the high frequency character, including magnetic domain structure, should be subjects for future research.

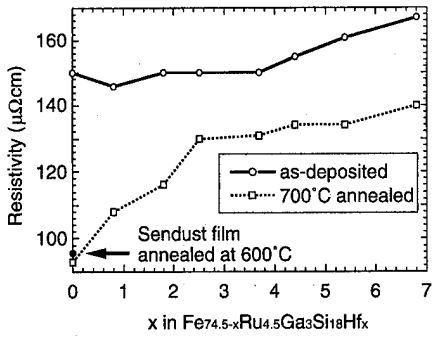



FIG. 7. Hf composition dependence of resistivity.

## IV. CONCLUSION

The FeRuGaSi-Hf alloy film shows good soft magnetic properties with a Hf content of 3.5–4.5 at. %. The as-deposited FeRuGaSi-Hf film is amorphous and becomes nanocrystalline after annealing. The origin of magnetic softness is considered due to the nanocrystalline structure as well as the $DO_3$ ordered structure. The ETF head with this film realized better high frequency recording performance.

## ACKNOWLEDGMENTS

The authors wish to gratefully acknowledge the encouragements of Professor T. Sakurai of Tohoku University and Dr. J. Seto of Sony Research Center.

[1] H. Ohmori *et al.*, IEEE Trans. Magn. **30**, 3903 (1994).
[2] K. Hayashi *et al.*, J. Appl. Phys. **64**, 772 (1988).
[3] Y. Iwasaki *et al.*, J. Appl. Phys. **2**, 64 (1993).
[4] K. Hono *et al.* (unpublished).
[5] G. Herzer, IEEE Trans. Magn. **26**, 1397 (1990).

# Theory, fabrication and testing of dual track complimentary type of thin-film recording heads for perpendicular magnetic recording system

T. Ichihara, S. Nakagawa, N. Matsushita, and M. Naoe
*Department of Physical Electronics, Tokyo Institute of Technology, 2-12-1, O-okayama, Meguro, Tokyo 152, Japan*

A new type of recording head for a perpendicular magnetic recording system, a dual track complimentary (DTC) type of thin-film head, was proposed in this study. The magnetic core of the head has a "*U*" character shape which is provided with "a pair of" recording tracks and the efficiency to detect flux reversal in the media will become high enough to achieve high linear density. The two-dimensional analysis of DTC heads implied that the perpendicular component of the head field should become larger by using the double-layered media under a narrower spacing condition. Recording characteristics using conventional ring head were evaluated in order to determine the principle of DTC configuration. Several DTC heads were prepared using photolithography technique and their performances were examined. A typical DTC head has inductance of about 500 nH, which is relatively low, and constant up to 10 MHz. DTC heads seems to be one of the most hopeful candidates as the heads useful for perpendicular magnetic recording systems. © *1996 American Institute of Physics.* [S0021-8979(96)06608-3]

## I. INTRODUCTION

A perpendicular magnetic recording system with a single pole-type (SPT) head and double-layered thin-film media has a high potential which exceeds the longitudinal magnetic recording systems in both linear and track recording densities.[1] However, the reproducing efficiency is still insufficient because of the relatively opened magnetic circuit system, as shown in Fig. 1(a). We have proposed a new type of recording head for perpendicular magnetic recording system, named as a dual track complimentary (DTC)-type of head,[2] as illustrated schematically in Figs. 1(b) and 1(c). In this system, the magnetic core in the head (the head core) has a "*U*" character shape and it is provided with "a pair of"recording tracks. As shown in Fig. 1(c), the reproducing flux from one pole returns to another pole in the head through the perpendicularly magnetized recording layer and the soft magnetic backlayer of the medium. So the closed short magnetic circuit is formed and the efficiency to detect flux reversal in the media will become high enough to achieve high linear density. Furthermore, both of the poles of the magnetic core are always contacted with the recorded bits, so the head is free from interference of external field. It seems that the track density advantage of perpendicular recording is reduced by a factor of 2. However, if the reproducing output becomes much higher, the total track width will become narrower than the SPT head configuration.

In this study, first a theoretical consideration based on a two-dimensional model was performed to determine the efficiency of DTC head. Secondly, using a conventional ring type of thin-film head, the read/write characteristics in the DTC head-media system were evaluated in order to recognize the recording mechanism of this system. Then, a DTC-type of several thin-film heads were prepared using photolithography techniques and their performances were evaluated.

## II. THEORETICAL ANALYSIS OF DTC HEAD CONFIGURATION

It is important to calculate the magnetic field originating from recording heads in order to determine the efficiency of the writing and reading process. Although the magnetic fields of the DTC head should be calculated in three-dimensional analysis, especially in a thin-film-type of DTC head configuration, two-dimensional analysis is convenient to calculate the field more easily. Four assumptions were made for the calculation: (1) the head field can be calculated from magnetic scalar potential $V$, (2) the head core and the backlayer are perfectly soft magnetic materials with infinite permeability, (3) the thickness of the backlayers is infinite, and (4) the relative permeability of the recording layer is unity. Then, the magnetic potential caused by the head field can be expressed as a two-dimensional Laplace equation. However, this kind of two-dimensional analysis is valid only when there is no change in the field in the third dimension, i.e., the direction along the recording track. The solution, therefore, is only approximation for a thin-film head with DTC con-

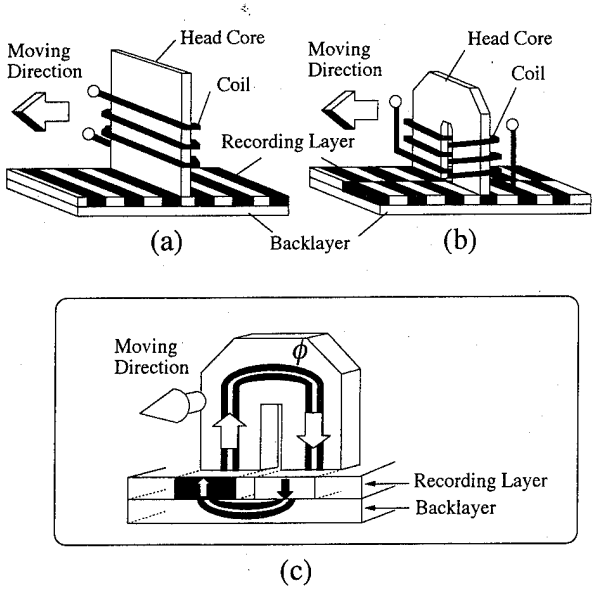



FIG. 1. Schematic illustrations of perpendicular magnetic recording heads: (a) Single pole type (SPT) of recording head, (b) and (c) Dual track complimentary (DTC) type of head.

 0021-8979/96/79(8)/5910/3/$10.00 © 1996 American Institute of Physics

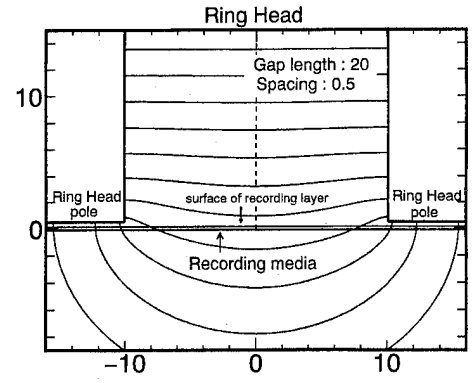



FIG. 2. Magnetic force line distribution around gap region of conventional recording head.

figuration. Then, the magnetic force line can be calculated analytically by using a conformal mapping with Schwarz–Christoffel transformation.

Figure 2 shows the magnetic force line distribution around the poles in a conventional ring-type of head derived by Westmijze.[3]

The transformation from $w$-plane to a $z$ one in the gap region of the DTC head was expressed as follows, using the coordinate as illustrated in Fig. 3(a):

$$z = i\frac{g}{\pi}\log\left(\frac{i\sqrt{P}+t}{i\sqrt{P}-t}\right) - \frac{g}{\sqrt{P}\pi}\log\left(\frac{1+t}{1-t}\right) - g + ih \qquad (1)$$

$$t = \sqrt{\frac{\zeta - P}{\zeta + 1}}, \quad \zeta = -\exp\left(-\frac{\pi}{V_0}w\right), \qquad (2)$$

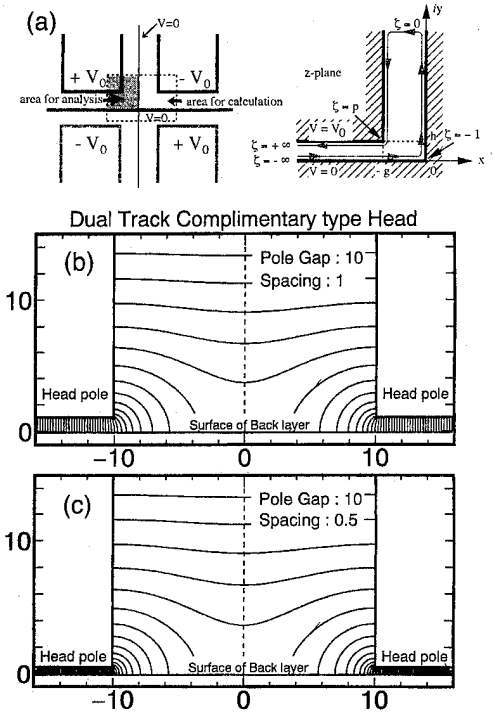



FIG. 3. (a) Coordinate for calculation of conformal mapping, (b),(c) Magnetic force line distribution around gap and head tip region of DTC recording head.

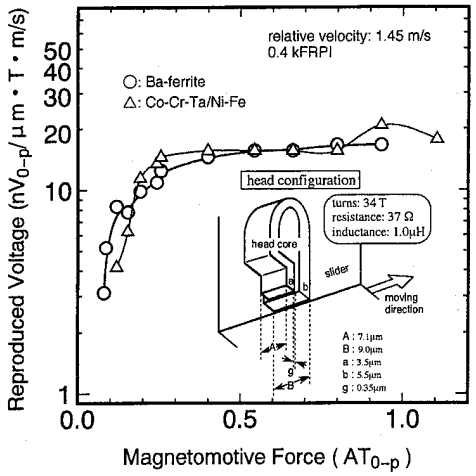



FIG. 4. Dependence of reproduced voltage on magnetomotive force of DTC head configuration using a conventional thin-film-type of recording head.

where $P$ is determined by boundary condition. Figures 3(b) and 3(c) show the magnetic force line distribution around the head poles of a DTC head. The pole gap of 20 in Figs. 3(b) and 3(c) was the same with that of the ring head in Fig. 2 and the head-backlayer spacing corresponded to 1 and 0.5, respectively. It has been recognized that the field beneath the poles of the DTC head should be stronger than that of the ring head, as shown in Fig. 2. In addition, the perpendicular component of the magnetic field around the tips of the head is very large and dominant. The perpendicular component of the head field seems to be so appropriate to enhance the writing and reproducing efficiency. Consequently, it was concluded that the DTC head configuration may be very applicable for the perpendicular magnetic recording system using the double-layered media.

## III. RECORDING CHARACTERISTICS OF DTC SYSTEM USING CONVENTIONAL THIN-FILM HEAD

A conventional ring-type of head was used to detect written magnetic transitions from the DTC head structure. The moving direction of the head was rotated through 90° from the conventional moving direction, as shown in the insets in Fig. 4. Ba–ferrite floppy disks (type ED) and Co–Cr–Ta/Ni–Fe double-layered thin-film media for perpendicular recording were used for evaluating the recording characteristics. Several parameters of the Co–Cr–Ta media were listed in Table I.

Figure 4 shows the dependence of the reproduced voltage on the motive force of the DTC head configuration at linear recording density of 400 frpi using a conventional

TABLE I. Parameters of Co–Cr–Ta/Ni–Fe double-layered media.

| | $Co_{85}Cr_{13}Ta_2$ | | $Ni_{81}Fe_{19}$ | |
|---|---|---|---|---|
| $Co_{85}Cr_{13}Ta_2$ | Thickness | 200 [nm] | Thickness | 200 [nm] |
| $Ni_{81}Fe_{19}$ | $M_s$ | 5.5 [kG] | $H_{c//}$ | 1.2 [Oe] |
| Glass substrate | $H_{c\perp}$ | 1.6 [kOe] | $\mu_r$ | $1.1\times10^3$ |
| | $H_k$ | 6.0 [kOe] | | |

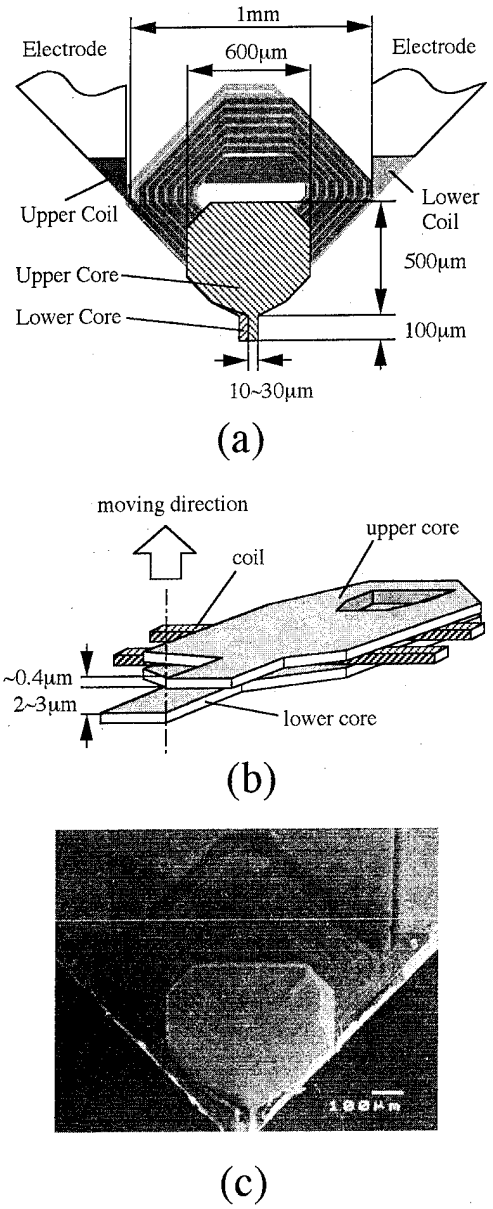



FIG. 5. (a) Top view (b) cross section, and (c) SEM image of DTC-type of thin-film head.

ring-type of thin-film head and Ba–ferrite floppy disk or Co–Cr–Ta/Ni–Fe double-layered media. In both cases, the output voltages were not so high because the conditions of spacing between head and media and the measurement apparatus could not be optimized. Furthermore, it was considered that the perpendicular component of recording field was relatively weak because 0.35 $\mu$m of the gap of two poles was too short. However, it was confirmed that saturation recording could be performed using the DTC head configuration and the perpendicular media such as Co–Cr–Ta/Ni–Fe thin-film media.

## IV. PREPARATION OF DTC THIN-FILM HEADS

Figures 5(a) and 5(b) show the typical configuration of the DTC head and Fig. 5(c) shows the scanning electron micrograph (SEM) images of the head, respectively, prepared in this study.

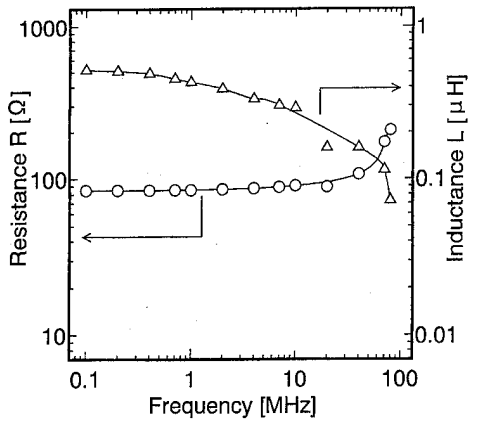



FIG. 6. Change of impedance of head as a function of frequency of 100 kHz–80 MHz.

Ni–Fe thin films for magnetic core layers and Al layers for electric coils were deposited by using the facing target sputtering (FTS) apparatus. Insulating layers were made of photoresist. The fabrication procedure is similar to one for a conventional ring-type of thin film head. However, the upper magnetic pole was not put above the lower pole in order to construct a pair of recording tracks, and then they performed totally as a DTC head.

Figure 6 shows the change of the head impedance as a function of frequency in the range from 0.1 to 80 MHz. The head inductance is relatively low and almost constant up to 10 MHz. These results insist that the heads of DTC configuration can be applicable at relatively high frequency.

## V. CONCLUSION

A dual track complimentary (DTC)-type of thin-film recording heads was proposed in this study.

Theoretical calculation implied that the perpendicular component of the head field becomes larger by using the double-layered media under narrower spacing condition. These results suggested that the heads of DTC configuration are suitable to apply for the perpendicular magnetic recording system.

Read/write characteristics using a conventional ring-type of thin-film head and the Ba–ferrite or Co–Cr–Ta/Ni–Fe media implied that the DTC head should be applicable to the perpendicular recording system.

The head composed of Ni–Fe core layers and Al spiral coils has relatively low and constant inductance up to 10 MHz. These results insist that the DTC heads can be applicable at high frequency, which is required for higher recording density and higher transfer rate of data.

In conclusion, the DTC-type of recording heads may be one of the candidates for use in perpendicular magnetic recording systems in the near future.

[1] S. Iwasaki, Y. Nakamura, S. Yamamoto, and K. Yamanaka, IEEE Trans. Magn. **MAG-19**, 1713 (1983).
[2] S. Nakagawa, Y. Miyamoto, and M. Naoe, J. Magn. Soc. Jpn. **17**, 97 (1993).
[3] W. K. Westmijze, Philips Res. Rep. **8**, 161 (1953).

# Permeability of microstrip thin films of various materials

Kiyoshi Yamakawa, Kazuyuki Ise, Naoki Honda, and Kazuhiro Ouchi
*Akita Research Institute of Advanced Technology, Akita 010-16, Japan*

Shun-ichi Iwasaki
*Tohoku Institute of Technology, Sendai 982, Japan*

Soft magnetic bilayered microstrip films have been studied for various materials such as Ni–Fe–Mo–Cu, Co–Zr–Mo–Ni, Fe–Si–N, and Ni–Fe in terms of their magnetization dynamics. Effects of the strip width and the interlayer thickness on permeability were investigated. An optimum interlayer thickness was found for obtaining the maximum permeability for those films except Fe–Si–N, but the optimum value differs in magnetic film material. A scanning Kerr effect microscope observation reveals that permeability variations with strip width related to changes of the dynamic domain configurations of the strips. All magnetic film materials except Fe–Si–N show a high permeability of more than 1000 at 2 $\mu$m strip width at each optimum interlayer thickness. When the film width is reduced to 1 $\mu$m, however, the permeability decreases significantly regardless of the interlayer thickness and kinds of the film materials. For such narrow strip film, a higher permeability is obtained for higher anisotropy field. It is concluded that the shape anisotropy of the micropatterned films must be controlled for achieving a higher permeability. © *1996 American Institute of Physics.* [S0021-8979(96)12608-X]

## I. INTRODUCTION

Sliding contact recording is attractive for high density recording because of the minimum spacing loss. A contact recording head such as a single pole head for perpendicular recording or a MR head with a recessed MR sensor is inevitable to have a flux conducting yoke. To improve recording performances, especially, reproducing sensitivity, a very narrow strip-shaped thin film with a high permeability is required for such the yoke. We have recently reported that permeability variation with respect to the strip width is affected by the interlayer thickness for Ni–Fe bilayered strip films.[1] In this paper, microstrip soft magnetic films of various materials of Ni–Fe–Cu–Mo, Co–Zr–Mo–Ni (Ref. 2) and Fe–Si–N have been studied in terms of their permeability and domain magnetization behavior. Such magnetic behaviors of microrectangular films with various aspect ratios are also discussed from the view point-of-head yoke application.

## II. EXPERIMENTS

The films were deposited using an rf sputtering method onto Si substrates with an applied magnetic field. The sputtering conditions are listed in detail in Table I along with those for Ni–Fe films[3] deposited by ion-beam sputtering (IBS). The bilayered film was composed of two magnetic layers of 20 nm thick and a nonmagnetic interlayer. The interlayer thickness was varied from 2 to 5 nm, where the bilayered sheet films exhibited no changes in coercivity or anisotropy field, representing no exchange coupling between magnetic layers. A 5 nm thick underlayer and overlayer of the same material as interlayer shown in the table were formed. The sheet film of about 9 mm square was etched by ion milling into an array of strips with different widths keeping a constant strip packing density of 50%. The anisotropy field *Hk* of the film was in the range from 2.5 to 4 Oe.

Permeability in the strip length direction, namely, the hard axis of magnetization in the original sheet film, was measured by an eight-figured coil method with a driving magnetic field of 5 mOe at 10 MHz. Dynamic domain behavior was observed by a scanning Kerr effect microscope (SEKM) with a driving field frequency of 0.5 MHz.

## III. RESULTS AND DISCUSSIONS

### A. Bilayered strips of moderate width

The strip width dependence of the permeability for the bilayered film is shown in Fig. 1 along with the previous

TABLE I. Sputtering conditions.

| Target (Interlayer) | Ni–Fe–Mo–Cu/(Ti) | Co–Zr–Mo–Ni/($SiO_2$) | Fe–Si–N/($Si_3N_4$) | Ni–Fe/(Ti) |
|---|---|---|---|---|
| Composition | 78:14:4.5:3.5 (wt %) | 79:10:9:2 (at. %) | 98.5:1.5 (wt %) | 81.2:18.8 (wt %) |
| Ms of film (emu/cc) | 490 | 590 | 1500 | 800 |
| Sputtering method | rf | rf | rf | IBS |
| Target diameter (mm) | 100 | 100 | 100 | 150 |
| Total pressure (Pa) | 0.5 | 0.5 | 0.4 | 0.032 |
| $N_2$ partial pressure (Pa) | 0 | 0 | 0.04 | 0 |
| Power (W) | 200/(50) | 200/(50) | 200/(50) | 1 kV/150 mA |
| Substrate temperature (°C) | water cooled | water cooled | 150 | water cooled |
| Target-Subst. distance (mm) | 60 | 60 | 60 | 250 |
| Substrate | Si | Si | Si | corning 7059 |

 0021-8979/96/79(8)/5913/3/$10.00 © 1996 American Institute of Physics 

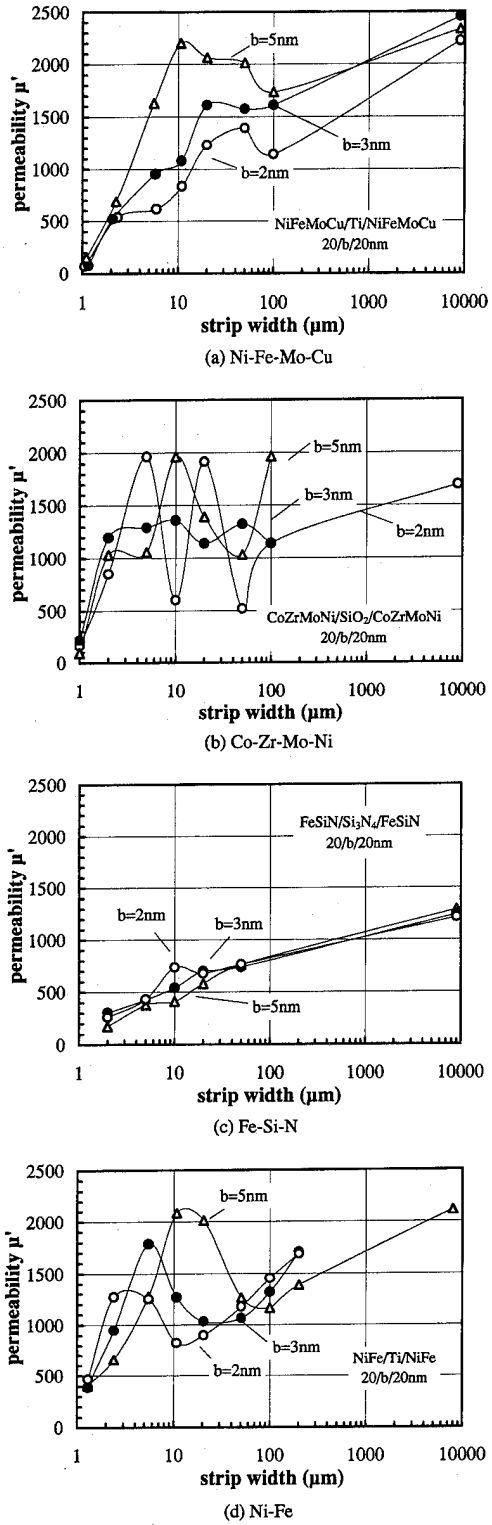



FIG. 1. Dependence of permeability of bilayered strip films on strip width as a parameter of interlayer thickness.

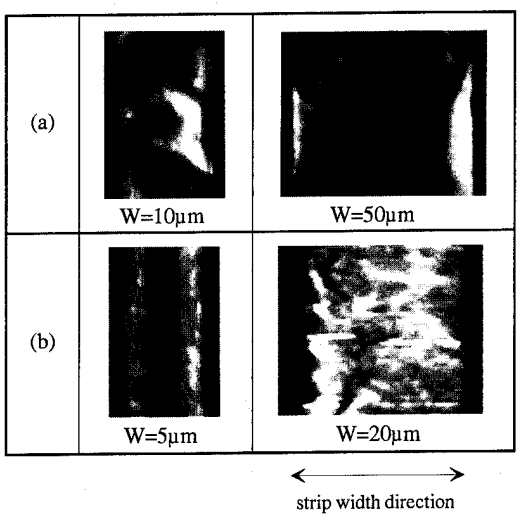



FIG. 2. Scanning Kerr effect microscope images of Co–Zr–Mo–Ni bilayered strip films of width for (a) minimum and (b) maximum permeability.

results in Fig. 1(d) for the Ni–Fe bilayered film. For any of the materials, the permeability decreased as the strip width $W$ decreased from 9000 $\mu$m (sheet state) to around 100 $\mu$m. For further reduction of the strip width, the permeability undulated and the manner depends on the interlayer thickness $b$. It is noted that the permeability variation with respect to the interlayer thickness in the region below 100 $\mu$m is quite different in the magnetic materials as seen between Fig. 1(a) and Fig. 1(d).

For the Ni–Fe–Mo–Cu bilayered film with Ti interlayer, the permeability changes with the strip width, in the same manner as NiFe film, exhibiting a peak value as shown in Fig. 1(a). However, the strip width for the maximum permeability decreases with increasing interlayer thickness in Fig. 1(a), while it increases in Fig. 1(d). The tendency in Fig. 1(a) was similarly observed for the Ni–Fe–Mo–Cu bilayered films deposited on glass substrates by either ion-beam sputtering or rf sputtering. As reported by the authors,[4] the increase in permeability with decreasing strip width can be explained by the domain configuration transition from the multidomain state to the single-domain-like state, namely the easy-axis state.[5]

On the other hand, the Co–Zr–Mo–Ni bilayered film showed a complicated tendency as shown in Fig. 1(b), where the $SiO_2$ interlayer was used. For the 2 nm thick interlayer, the permeability change displayed a oscillatory curve according to the strip width exhibiting the minima and the maxima. In order to investigate this phenomenon, Scanning Kerr images of the strips were observed at a driving field of 1 Oe. The results are shown in Fig. 2. The films with minimum permeability exhibited a multidomain configuration accompanied by large domains insensitive to the applied field. To the contrary, although small variation of contrast was observed, the strip films for the maximum permeability responded uniformly throughout the whole strip, similarily to the Ni–Fe–Mo–Cu films and the Ni–Fe films of strip width for the maximum permeability. Therefore, the oscillatory change of the permeability for the Co–Zr–Mo–Ni film is attributed to the domain structure, though the mechanism of change in domain configuration is not clear.

As for the Fe–Si–N films, the permeability decreased monotonically with decreasing the strip width regardless of the interlayer thickness. This may be due to the fact that magnetic interaction between the layers is rather weak owing

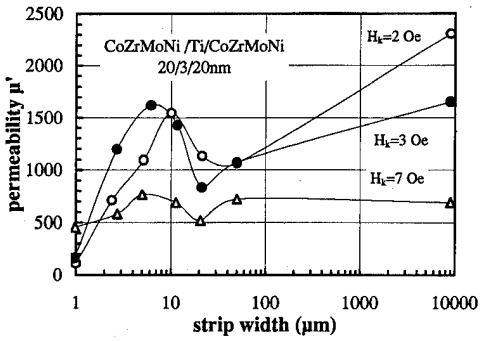



FIG. 3. Effect of anisotropy field on permeability of Co–Zr–Mo–Ni bilayered strip films.

to a relatively high *Hc* of around 0.5 Oe and generally seen large dispersion of anisotropy of the intrinsic sheet film.

### B. Very narrow bilayered strips

When a proper interlayer thickness is chosen, the permeability more than 2000 as the same value of the original sheet film could be obtained for the 10 $\mu$m width in any film material except Fe–Si–N. However, as the strips become narrower than 10 $\mu$m, the permeability rapidly decreases and finally drops to the value as low as few hundred at 1 $\mu$m width. According to the edge-curling wall theory by Slonczwski *et al.*[5] and by Ruhrig *et al.*,[6] the easy-axis state changes into the hard-axis state at the critical strip width *Wc*. The calculated values of *Wc* range between 1.4 and 2.1 $\mu$m for our experimental *Hk*'s. Therefore, it is easily understood that the lowest permeability was obtained at 1 $\mu$m strip width for every kinds of materials. On the other hand, when the anisotropy field *Hk* is increased, the *Wc* should decrease, then, permeability would be improved even for 1 $\mu$m strips. Figure 3 shows the effect of the *Hk* on the permeability for the Co–Zr–Mo–Ni bilayered strip films. A Ti interlayer and glass substrates are used in this case. The permeability changes differently from that in Fig. 1(b). As the *Hk* is increased up to 7 Oe, a higher permeability than the previously mentioned strips is obtained for the very narrow strip width of 1 $\mu$m. Besides edge-curling wall, other possible origins of the low permeability for 1 $\mu$m strip are the increase in coercivity and the localized insensitive domains.[4] For example, the coercivity reaches to about 10 Oe at around 1 $\mu$m of the strip width. Therefore, it seems difficult to further improve the permeability for such very narrow long strips by adjusting the material parameters.

### C. Aspect ratio of strip

Figure 4 shows the scanning Kerr images for the Ni–Fe–Mo–Cu bilayered strip film which were measured before and after forming the array of rectangular-shaped patterns

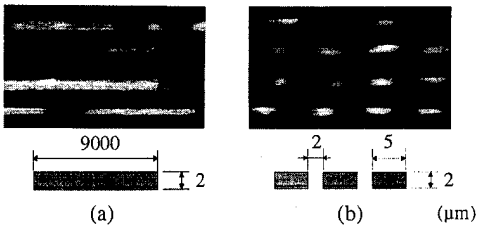



FIG. 4. Scanning Kerr effect microscope images of (a) long strip-shaped and (b) microrectangular Ni–Fe–Mo–Cu bilayered films.

whose size is 2 $\mu$m in width and 5 $\mu$m in length. It was found that the microrectangular shape films with a small shape anisotropy, whose size is the same order as actual head elements, respond more uniformly to the driving field, comparing with the continuously long strip-shaped films. This has been prospected by the partial response of magnetization for a narrowest film.[4] Therefore, the shape anisotropy of the strip is one of the factors to define the magnetization configurations. It is safe to say that the optimization of the shape anisotropy of the patterned film could give rise to a high effective permeability.

## IV. CONCLUSIONS

The permeability of the microstrip bilayered films of Ni–Fe–Cu–Mo, Co–Zr–Mo–Ni, and Fe–Si–N was investigated. An optimum interlayer thickness was found for obtaining the maximum permeability and is determined by the film material itself. When the interlayer thickness was kept at the optimum, similar value of permeability to that for the original sheet film could be obtained except for a Fe–Si–N film. For very narrow and long strips of 1 $\mu$m width, it is necessary to increase the *Hk* for a high permeability. Further investigations regarding multilayered strip films with thinner magnetic layers is also necessary. As a highly homogeneous response was obtained for a small aspect ratio pattern, the shape anisotropy has a key effect to improve magnetic sensitivity of the micropatterned film.

## ACKNOWLEDGMENT

The author would like to express thanks to S. Takahashi of AIT for technical assistance.

[1] S. Takahashi, K. Yamakawa, N. Honda, and K. Ouchi, J. Magn. Magn. Mater. **148**, 88 (1995).
[2] M. Nose, K. Esashi, J. Kanehira, K. Shirakawa, and T. Masumoto, Proc. 4th Int. Conf. on Rapidly Quenched Materials, Sendai, 1981.
[3] S. Takahashi, K. Yamakawa, N. Honda, K. Ouchi, and S. Iwasaki, J. Magn. Soc. Jpn. Supp. **18**, 385 (1994).
[4] S. Takahashi, K. Yamakawa, N. Honda, and K. Ouchi, IEEE Trans. Magn., Proc. of INTERMAG'95 (1995).
[5] J. C. Slonczewski, B. Petek, and B. E. Argyle, IEEE Trans. Magn. **MAG-24**, 2045 (1988).
[6] M. Ruhrig, W. Rave, and A. Hubert, J. Magn. Magn. Mater. **84**, 102 (1990).

# Pole tip recession studies of hard carbon-coated thin-film tape heads

Bharat Bhushan and Steven T. Patton
*Department of Mechanical Engineering, The Ohio State University, Columbus, Ohio 43210-1107*

Ramesh Sundaram and Subrata Dey
*Storage Technology Corporation Louisville, Colorado 80028-8110*

Hard carbon coatings were deposited by cathodic arc and direct ion beam deposition techniques on thin-film $Al_2O_3$–TiC heads and by the latter technique on thin-film Ni–Zn ferrite heads. Functional accelerated tests were conducted against metal particle tapes in a linear tape drive. Ion beam carbon coatings on Ni–Zn ferrite and $Al_2O_3$–TiC heads substantially reduced the pole tip recession observed with uncoated heads. Cathodic arc carbon coated $Al_2O_3$–TiC heads performed better than uncoated heads, but were less effective than the ion beam coating. Pole tip recession increased only if carbon was removed from the pole tip. This suggests that coating effectiveness is determined by its adherence to the pole tip. In two-wide pole tip heads, wear of the pole adjacent to the substrate was less than that of the other pole. Coatings withstood accelerated tests and may meet life time requirements of future heads. © *1996 American Institute of Physics.* [S0021-8979(96)12708-6]

A major problem in thin-film recording heads is pole tip/gap recession in inductive heads.[1] Pole tip recession (relative wear of the pole tip with respect to the air bearing surface or ABS) and other damage to the head structure, which may result in signal degradation, can be minimized by depositing a thin (~5 to 20 nm) hard carbon coating over the entire ABS, including the head structure.[2–4] Sputter deposited carbon coatings are currently used in MR heads.[3,4] Cathodic arc and direct ion beam deposition techniques are highly energetic processes which are known to produce a dense and hard coating with good adhesion to the substrate.[5,6] Recent screening studies[5,6] have shown that cathodic arc and ion beam carbon coatings are superior in mechanical properties and scratch and wear resistance to sputtered and plasma-enhanced chemical vapor deposition (PECVD) carbon coatings. The objective of this research was to conduct functional tape drive tests with coated dummy $Al_2O_3$–TiC and Ni–Zn ferrite heads with thin-film head structure.

$Al_2O_3$–TiC and Ni–Zn ferrite heads (rms=1.5 nm) with IBM 3480/3490 type of construction were selected for this study, Fig. 1. One of the two modules (19 mm×3.8 mm) had the thin-film construction of an inductive write head, whereas the second module was a dummy module. The radius of the modules was 20 mm. Thick films of NiFe were electroplated and $Al_2O_3$ and thin films of NiFe were rf sput-

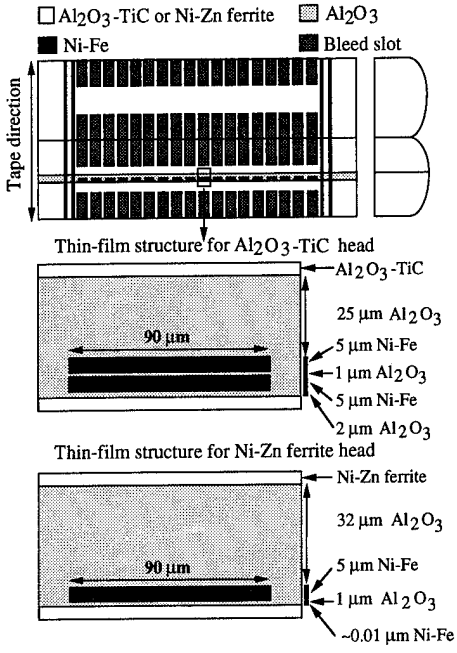



FIG. 1. Top view schematic of IBM 3480/3490 type of head and expanded view of the thin-film structure for each substrate.

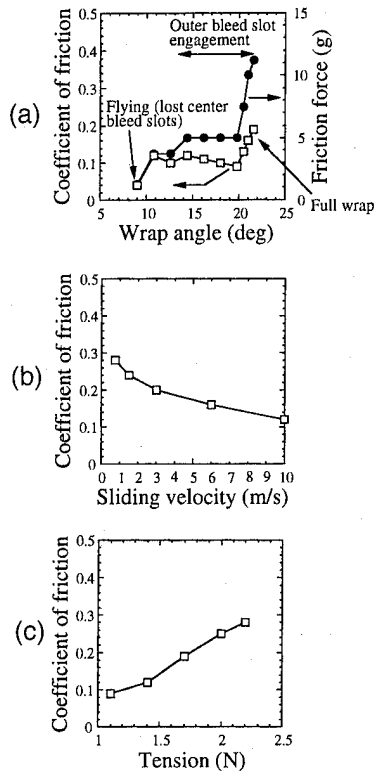



FIG. 2. Coefficient of friction and friction force at nominal experimental conditions as a function of (a) wrap angle, (b) sliding velocity, and (c) tape tension.

 0021-8979/96/79(8)/5916/3/$10.00 © 1996 American Institute of Physics

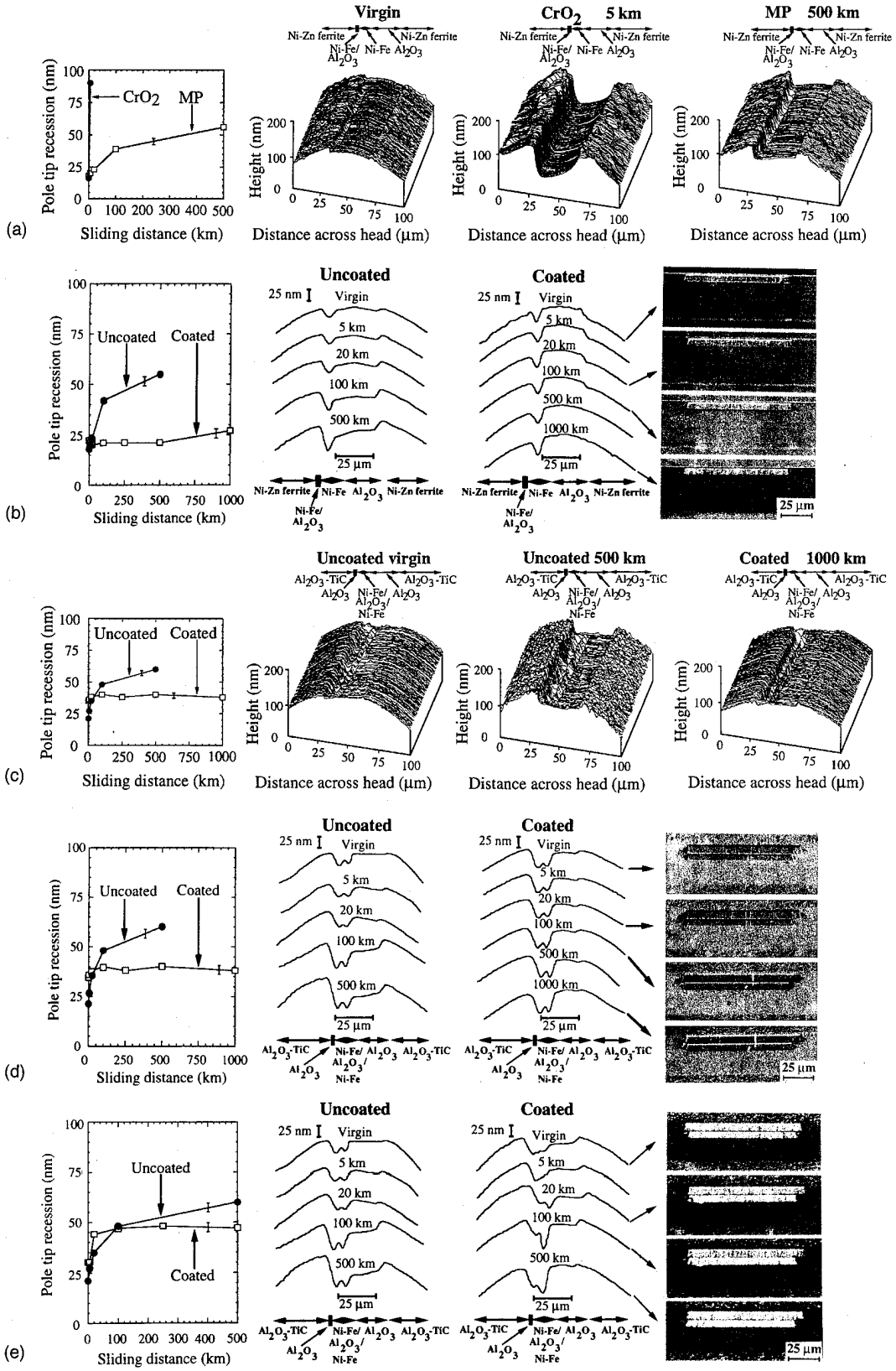



FIG. 3. Pole tip recession vs sliding distance as measured with an AFM. AFM scans across the thin-film structure at various sliding distances and optical micrographs [except (a) and (c)] of the coated thin-film structure at various sliding distances for (a) uncoated Ni–Zn ferrite heads before and after being run against $CrO_2$ and MP tapes, (b) uncoated and ion beam carbon coated Ni–Zn ferrite heads run against MP tape, (c) and (d) uncoated and ion beam carbon coated $Al_2O_3$–TiC heads run against MP tape, and (e) uncoated and cathodic arc carbon coated $Al_2O_3$–TiC heads run against MP tape.

tered. $Al_2O_3$–TiC heads have two poles with thin-film structure, and Ni–Zn ferrite heads utilize a single pole tip (Fig. 1). The hard amorphous carbon ($a$–C) (also referred to as diamondlike carbon) coatings with 20 nm thickness were deposited by cathodic arc and ion beam deposition techniques.[5,6] Nanoindentation hardness values of cathodic arc and ion beam carbon coatings are 38 and 19 GPa, respectively, whereas, hardness of commonly used sputtered carbon is about 15 GPa.[5] The critical load required to damage cathodic arc and ion beam coatings in microscratch experiments is more than a factor of two higher than that of the sputtered coatings.[5] The sliding tests on coated heads run against Fuji Atomm double layer video grade (substrate/total thickness $=9.8/13.2$ $\mu$m) metal particle (MP) magnetic tapes (rms=4 nm, $P-V=37$ nm)[7] were carried out using a linear tape drive (Honeywell 96) at 1.7 N of tape tension and 3 m/s sliding velocity in an ambient environment ($22\pm1$ °C and $45\pm5$% RH) to sliding distances of 500–1000 km.[7] In normal drive operation, the tape wraps 17° over the head and engages one half of the outer bleed slots (Fig. 1), which results in a flying height of less than 100 nm. In these experiments, about 90% of the outer bleed slots were engaged by wrapping the head to increase the minimum film thickness region (which may accelerate wear by particle entrapment) and to increase the friction force (which may accelerate wear). Data in Fig. 2(a) shows an increase in both the friction force and coefficient of friction at large wrap angles. Since at low sliding velocity and high tape tension, the coefficient of friction is higher than that under the condition of entire slot engagement as shown in Figs. 2(b) and 2(c), it appears that air bearing effect is still present at the test conditions.

The pole tip recession was measured by atomic force microscope (AFM) imaging before and after the sliding tests. For recession measurements, the head was placed on a linear stage. A pole on one end was first located in an optical microscope, and then the others were located with respect to that pole. Typically, poles numbered 3, 7, 11, and 15 (out of 1 to 18) were imaged and photographed in this study to account for any variability across the tape width (Fig. 1). Pole tip recession was referenced to the substrate nearest to the pole, and the average was taken over each pole. Pole tip recession for a given condition is the average over the four chosen poles.

Figure 3(a) shows a comparison of the results obtained by running $CrO_2$ (rms=17.1 nm, $P-V=161$ nm) and MP tapes against uncoated Ni–Zn ferrite heads.[7] $CrO_2$ tape caused a large pole tip recession and catastrophic wear of the thin-film region after only 5 km of sliding distance, whereas MP tape produced smaller pole tip recession and relatively minor damage primarily in the form of scratching to the thin-film region after 500 km of sliding distance. MP tape was selected since this tape is considered for advanced thin-film head applications.

Figure 3(b) shows a comparison of the performance of uncoated and ion beam carbon coated Ni–Zn ferrite heads during sliding experiments. The pole tip recession increased with sliding distance for the uncoated head, but remained essentially constant over a larger sliding distance for the coated head (error bars in the left block represent the variability in the average pole tip recession over the four chosen poles). The 2D AFM line scans of the uncoated head show that the entire thin-film region recessed from the ABS with increased sliding distance. Optical micrographs of the coated head show that the coating remained on the pole tips through 1000 km of sliding distance which prevented growth of pole tip recession.

Figures 3(c) and 3(d) show a comparison of the performance of uncoated and ion beam carbon coated $Al_2O_3$–TiC heads during sliding experiments. The pole tip recession increased with sliding distance for the uncoated head, but remained essentially constant over a larger sliding distance for the coated head. The 3D [Fig. 3(c)] and 2D [Fig. 3(d)] AFM line scans show that the coating reduced the growth of recession of the entire thin-film region from the ABS with increased sliding distance as compared to that observed with the uncoated head. Optical micrographs in Fig. 3(d) show that the coating remained on the pole tips through 1000 km of sliding.

Figure 3(e) shows a comparison of the performance of uncoated and cathodic arc carbon coated $Al_2O_3$–TiC heads during sliding experiments. The performance of the cathodic arc carbon coated head in preventing pole tip recession was better than the uncoated head, but was less effective than the ion beam carbon coating. The 2D AFM line scans and optical micrographs of the coated head show that the coating was removed from the pole farthest from the substrate (bottom pole in optical micrographs) after sliding between 5 and 100 km. Further growth in recession of this pole tip after 100 km observed with the uncoated head did not occur. Further note that wear of carbon coating, when it occurred, was initiated at the pole tips which is related to the adhesion of carbon to various layers present on the substrate. Finally, no loose debris was found on the thin-film region near the pole tips in tests with uncoated and coated heads.

We thank Paul D. Reader of Ion Tech Inc. and S. Anders of Lawrence Berkeley Laboratory for coating of the heads.

[1] B. Bhushan, *Tribology and Mechanics of Magnetic Storage Devices* (Springer, New York, 1990).
[2] V. Zieren *et al.*, IEEE Trans. Magn. **30**, 340 (1994).
[3] H. C. Chang *et al.*, U.S. Patent 5,175,658 (29 December 1992).
[4] A. Grill *et al.*, U.S. Patent 5,159,508 (27 October 1992).
[5] B. Bhushan *et al.*, IEEE Trans. Magn. **31**, 2976 (1995)
[6] B. K. Gupta and B. Bhushan, Wear **190**, 110 (1995).
[7] B. Bhushan and J. A. Lowry, Wear **190**, 1 (1995).

# Heat capacity measurements of NiO/CoO superlattices (invited) (abstract)

E. N. Abarra, K. Takano,[a] F. Hellman, and A. E. Berkowitz[a]
*Department of Physics, University of California at San Diego, La Jolla, California 92093-0319*

We present heat capacity measurements of NiO/CoO superlattices grown by reactive sputtering. Neutron diffraction studies of similar superlattices have shown antiferromagnetic ordering through several bilayers despite the short-range nature of the spin interaction in the constituent materials.[1] Specific heat measurements were made using a unique thin film microcalorimeter capable of measuring the heat capacity of thin films from 1.5 K to well above room temperature.[2] We examine the effect of exchange coupling at the interfaces by varying the thickness of the bilayers. For thin bilayers (26 Å), we observe a single broad heat capacity peak similar to a $Ni_{0.5}Co_{0.5}O$ alloy. This peak is at a temperature which corresponds to the superlattice magnetic blocking temperature. For thicker bilayers (>50 Å), two broad maxima occur which approach the individual Néel temperatures of CoO and NiO with increasing bilayer thickness. The ordering temperature of the NiO layers is more suppressed than expected, indicating a more pronounced size effect compared to the CoO layers. The magnetic entropy $S=R(\ln 3+\ln 2)/2$ for the superlattices, within the uncertainties of the measurement, is conserved. We compare the temperature dependences of the specific heats to various models. © *1996 American Institute of Physics.* [S0021-8979(96)43608-2]

This work was supported by the DOE, Grant No. DE-FG03-95ER45529.
[a]Also at Center for Magnetic Recording Research, CMRR-0401, University of California at San Diego, La Jolla, CA 92093-0401.

[1]J. A. Borchers, M. J. Carey, R. Erwin, C. F. Majkrzak, and A. E. Berkowitz, Phys. Rev. Lett. **70**, 1878 (1993).
[2]D. W. Denlinger, E. N. Abarra, K. Allen, P. W. Rooney, M. T. Messer, S. K. Watson, and F. Hellman, Rev. Sci. Instrum. **65**, 946 (1994).

 0021-8979/96/79(8)/5919/1/$10.00 © 1996 American Institute of Physics 

# Finite-size scaling in thin antiferromagnetic CoO layers

T. Ambrose and C. L. Chien
*Department of Physics and Astronomy, The Johns Hopkins University, Baltimore, Maryland 21218*

Finite-size scaling effects in CoO, an antiferromagnetic insulator with localized moments, have been observed in $CoO/SiO_2$ multilayers. The Néel temperatures of the CoO layers, as determined by susceptibility measurements, shows a finite-size scaling relation with a shift exponent of $\lambda=1.6\pm0.1$. © *1996 American Institute of Physics.* [S0021-8979(96)22008-5]

Thin films are suitable media for studying finite-size effects, where the correlation length in the lateral dimensions are not limited but clamped in the direction of the layer thickness. Near the bulk ordering temperature $T_0(\infty)$, the temperature dependence of the correlation length has a power-law dependence of

$$\xi(T)=\xi_0\left[1-\frac{T}{T_0(\infty)}\right]^{-\nu}, \tag{1}$$

where $\xi_0$ is the correlation length at $T=0$ K, and $\nu$ is the critical exponent for the correlation length $\xi$.[1] From Eq. (1), the ordering temperature $[T_0(t)]$ of a thin layer of thickness $t$ varies as

$$\frac{T_0(\infty)-T_0(t)}{T_0(\infty)}=\left(\frac{\xi_0}{t}\right)^{\lambda}, \tag{2}$$

where $\lambda$ is the shift exponent for finite-size scaling, $\lambda=1/\nu$, and $T_0(t)$ is less than $T_0(\infty)$.

In a low $T_c$ superconductor where the coherence length is hundred of Å long, a reduction in $T_c$ can be more easily observed in superconducting thin films a few hundred of Å in thickness.[2] For strongly correlated systems, such as ferromagnets, where the correlation length is of the order of atomic spacing, only when the thickness is a few times of $\xi_0$ would $T_C(t)$ be significantly lower than $T_C(\infty)$. Because of the high Curie temperature ($T_C$) of common ferromagnets (e.g., Co and Fe with $T_C>1000$ K) and the inability to measure $T_C(t)$ at high temperatures without destroying thin films, $T_C(t)$ can only be measured in ultrathin films only a few atomic layers thick.[3,4] Consequently, there are few such studies reported.

Conspicuously lacking is the studies of finite-size effects of antiferromagnetic (AF) materials, despite the promise of more interesting features because the AF order is realized by compensation of two or more sublattice magnetizations. The studies of AF layer is even more challenging because the AF order with no net magnetization responds only very weakly to the external magnetic field. The only reports of finite-size scaling effects in AF materials have been by indirect determination of the Neel temperature in the $FeF_2/ZnF_2$ system by thermal expansion measurements[5] and most recently in the Fe/Cr system using transport measurements.[6] In this work, we report the first observation of finite-size effects in CoO, an AF insulator with localized moments, using dc susceptibility measurements.

We have chosen CoO because it is a well-known AF insulator with conveniently accessible $T_N(\infty)$ near room temperature. It has a simple fcc NaCl-type crystal structure with a lattice parameter of $a_0=4.26$ Å. The $Co^{2+}$ moments, with 3.8 $\mu_B$ in magnitude, form a fcc lattice.[7] The intrinsically weak response to an external magnetic field requires multilayer samples of CoO with an inert spacer layer. After exploring various materials, $SiO_2$ was chosen as a space layer, resulting in multilayers with oriented CoO layers. The $SiO_2$ layers, being insulting, nonmagnetic, and thick (50 or 75 Å), have the added benefit of completely confining the magnetic interactions within the CoO layer. Multilayers of $CoO/SiO_2$ have been fabricated by multi-source magnetron sputtering using a computer-controlled substrate platform. The CoO layer thickness has been varied from 5 to 125 Å, while keeping the total CoO thickness in the multilayers to be 5000 Å by appropriately controlling the total number of bilayers.

X-ray diffraction data of a representative $CoO/SiO_2$ sample are shown in Fig. 1. The low-angle data [see Fig. 1(a)] shows many orders of diffraction peaks indicating a good quality multilayer. In the high-angle diffraction, a predominantly oriented film of (100)CoO is observed. The $SiO_2$ layers are amorphous, with a very broad peak near $2\theta=25°$.

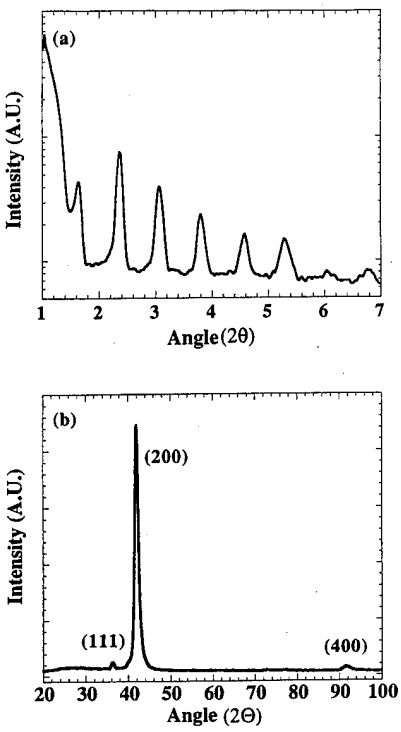



FIG. 1. (a) small-angle and (b) large-angle x-ray diffraction results of a $CoO(65\ Å)/SiO_2(50\ Å)]_{77}$ multilayer.

 0021-8979/96/79(8)/5920/3/$10.00 © 1996 American Institute of Physics

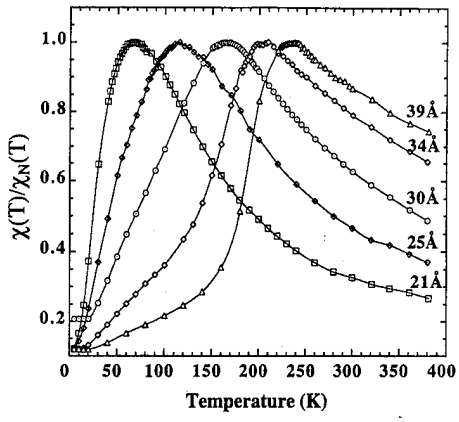



FIG. 2. Temperature dependence of dc susceptibility at $H=100$ Oe of representative multilayer samples of CoO/$SiO_2$ with a fixed $SiO_2$ thickness of 75 Å. For clarity, the results are normalized to the susceptibility at the Néel temperature.

Magnetic susceptibility under an external field of $H=100$ Oe has been used to measure the Néel temperature. Although a larger external field would increase the signal, it tends to distort the susceptibility peak, especially for thin CoO layers. Representative results of susceptibility data, normalized to $\chi(T_N)$ for clarity, are shown in Fig. 2. The susceptibility data clearly show that as the CoO thickness ($t$) is reduced, the susceptibility peak, at which the Neel temperature $[T_N(t)]$ is located, progressively shifts to lower temperatures.

The results of $T_N(t)$ for CoO layer thickness ($t$) are shown in Fig. 3(a). The values of $T_N(t)$ deviate appreciably from $T_N(\infty)$ for thicknesses $t<80$ Å. The solid curve in Fig. 3(a) is the best-fit results of the finite-size scaling relation[8]

$$\frac{T_N(\infty)-T_N(t)}{T_N(\infty)}=\left(\frac{\xi_0}{t}\right)^{\lambda}, \tag{3}$$

with $\lambda=1.6\pm0.1$, $\xi_0=18\pm2$ Å and $T_N(\infty)=315\pm5$ K. The scaling relation of Eq. (3), as described previously, comes from the critical behavior of the correlation length. It is strictly valid for $T_N(t)$ less than, but close to, $T_N(\infty)$.[8] Nevertheless, Eq. (3) adequately describes the results of a wide range of thicknesses. Only for $t<22$ Å do the values of $T_N(t)$ clearly deviate from the scaling relation. To further illustrate the scaling relation, in Fig. 3(b), a log–log plot of the reduced temperature versus CoO thickness is shown. A straight line with a slope of 1.6 fits the data for $t>22$ Å. Our results also show that AF ordering with $T_N(t)\geq5$ K persists down to a thickness of at least 10 Å.

Theoretical studies indicate that the shift exponent has a value of $\lambda=1.5587$ for Ising systems,[9] and $\lambda=1.419$ for Heisenberg systems.[10] Apparently, the value of $\lambda$ is not sensitive to the types of interactions. Our determined values of $\lambda=1.6\pm0.1$ are in good agreement with these theoretical values.

It should be mentioned that, although there are not many studies of finite-size scaling in magnetic systems, considerable confusion already exists in the scaling relation with which to analyze the data. While many have used Eq. (2), some, unfortunately, have used

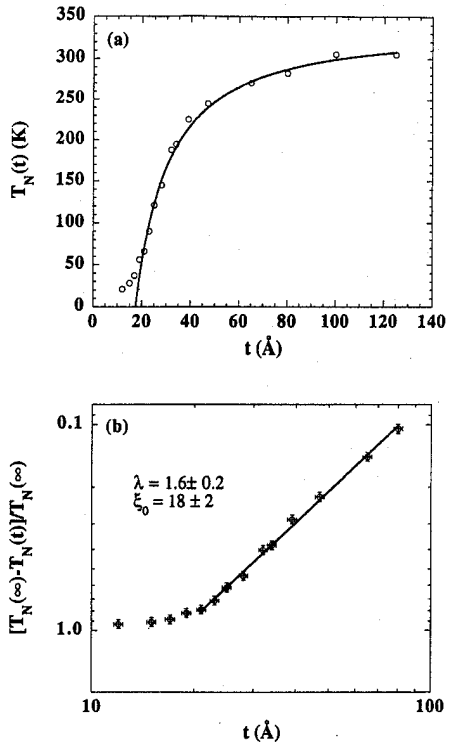



FIG. 3. (a) Néel temperature $T_N(t)$ of CoO/$SiO_2$ multilayers vs CoO thickness ($t$). The solid curve is the result of finite-size scaling relation Eq. (3) with $\lambda=1.6$, $\xi_0=18$ Å and $T_N(\infty)=315$ K. (b) Log–log plot of $[T_N(\infty)-T_N(t)]/T_N(\infty)$ vs CoO layer thickness $t$, where the straight line has a slope of 1.6.

$$\frac{T_0(\infty)-T_0(t)}{T_0(t)}=\left(\frac{\xi_0'}{t}\right)^{\lambda'}. \tag{4}$$

The difference between Eq. (3) and Eq. (4) lies in the denominator on the left-hand side being $T_0(\infty)$ or $T_0(t)$. In Eq. (4), $\xi_0'$ is not the correlation length at $T=0$ K, but the thickness at which $T_N(\xi_0')=T_N(\infty)/2$, and furthermore, one obtains $T_N(t)=0$ *only* for $t=0$. As pointed out previously, data in some thickness range can be reasonably described by *either* Eq. (3) *or* Eq. (4).[11] But the resultant values of $\lambda'$ and $\xi_0'$ using Eq. (4) are very different from $\lambda$ and $\xi_0$ using Eq. (3). This led to the unfortunate confusion of claiming the experimentally determined value of $\lambda'$ using Eq. (4) to be in agreement, or disagreement, with the theoretical value of $\lambda$ using Eq. (3). We illustrate this point by fitting the same data in Fig. 3(a) to Eq. (4), and the results are shown in Fig. 4(a). A reasonable fit can *also* be obtained for $t\geq15$ Å, as shown by the solid line in Fig. 4(a), although the fit in Fig. 3(a) is clearly better. A comparison of Figs. 3(a) and 4(a) shows that a power-law dependence exists in Fig. 3(b), but less so in Fig. 4(b). However, most importantly, the best-fit values of $\lambda'=3.4\pm0.3$ is very different from $\lambda=1.6\pm0.1$, which is close to the theoretical value. The value of $\xi_0'=30\pm3$ Å is also different from $\xi_0=18\pm2$ Å.

Originally, Eq. (4) was suggested to improve the description of the scaling relationship which showed deviation at smaller thickness range due to nonasymptotic character in the Monte Carlo studies of finite Ising films.[12] It was also found that Eq. (4) can extend the thickness range in which a

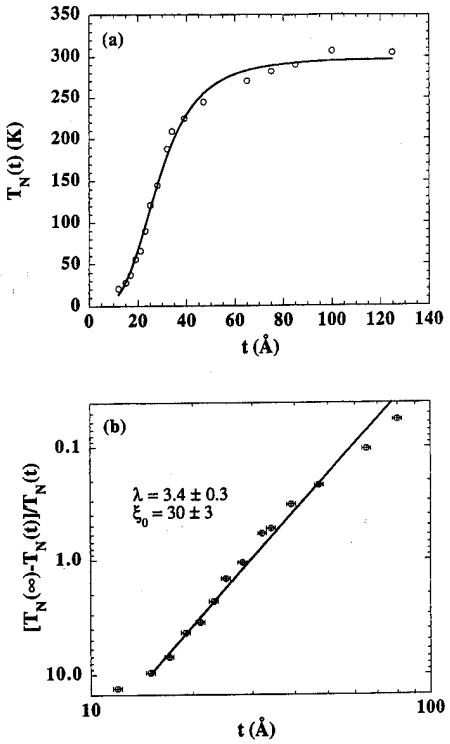



FIG. 4. (a) Néel temperature $T_N(t)$ of $CoO/SiO_2$ multilayers vs CoO thickness ($t$). The solid curve is the result of finite-size scaling relation Eq. (4) with $\lambda'=3.4$, $\xi_0'$ = 30 Å and $T_N(\infty)=300$ K. (b) Log–log plot of $[T_N(\infty)-T_N(t)]/T_N(t)$ vs CoO layer thickness $t$, where the straight line has a slope of 3.4.

single scaling relation can adequately describe the data.[13] This point can be illustrated in the present data. As shown in Fig. 3(a), the data points with $t \leqslant 20$ Å clearly deviate from Eq. (3), whereas practically all data points in the low thickness range can be described by Eq. (4), as shown in Fig. 4(a). However, as mentioned earlier, finite-size scaling is the result of the critical behavior of the correlation length near bulk $T_N(\infty)$. The actual data of $T_N(t)$ in very thin films, much smaller than $T_N(\infty)$, are expected to deviate from the scaling relation.

Finally, we comment on the value of $\xi_0$. For ferromagnets, $\xi_0$ is quite small. Observation of finite-size effects are difficult except in ultrathin ferromagnetic films. For spin glasses, $\xi_0$ is much longer at about 20 Å. Together with a shift exponent of $\lambda=0.64\pm0.07$, finite-size scaling effects can be observed in layers a few hundred Å thick.[14,15] Antiferromagnetic CoO has an intermediate $\xi_0 \approx 18$ Å, exhibiting finite-size effects in CoO films of the order of 50 Å.

In conclusion, we have made, to the best of our knowledge, the first observation of finite-size scaling in CoO, an insulating antiferromagnet with localized moment, using $CoO/SiO_2$ multilayers. A shift exponent of $\lambda=1.6\pm0.1$, in good agreement with theoretical calculations, has been determined.

This work has been supported by ONR Grant No. N00014-91-J-1633.

[1] See, e.g., H. E. Stanley, *Introduction to Phase Transition and Critical Phenomena* (Oxford University Press, New York, 1971), p. 46.
[2] See, e.g., B. Y. Jin and J. B. Ketterson, Adv. Phys. **38**, 189 (1989).
[3] C. Lu and S. D. Bader, in *Magnetic Properties of Low Dimensional Systems II*, edited by L. Falicov, F. Mejia-Lira, and J. L. Moran-Lopez (Springer, Berlin, 1990).
[4] C. M. Schneider, P. Bressler, P. Schuster, J. Kirchner, J. J. de Miguel, and R. Miranda, Phys. Rev. Lett. **64**, 1059 (1990).
[5] D. Lederman, C. A. Ramos, V. Jaccarino, and J. L. Cardy, Phys. Rev. B **48**, 8365 (1993).
[6] E. E. Fullerton, K. T. Riggs, C. H. Sowers, S. D. Bader, and A. Berger, Phys. Rev. Lett. **75**, 330 (1995).
[7] C. G. Shull, W. A. Strauser, and E. O. Wollan, Phys. Rev. **83**, 333 (1951).
[8] M. E. Fisher and M. N. Barder, Phys. Rev. Lett. **28**, 1516 (1972).
[9] A. M. Ferrenberg and D. P. Landau, Phys. Rev. B **44**, 5081 (1991).
[10] K. Chen, A. M. Ferrenberg, and D. P. Landau, Phys. Rev. B **48**, 3249 (1993).
[11] J. R. Childress, C. L. Chien, and A. F. Jankowski, Phys. Rev. B **45**, 2855 (1992).
[12] K. Binder and P. C. Hohenberg, Phys. Rev. B **9**, 2194 (1974).
[13] F. Huang, G. J. Manley, M. T. Kief, and R. F. Willis, J. Appl. Phys. **73**, 6760 (1993).
[14] G. G. Kenning, J. M. Slaughter, and J. A. Cowen, Phys. Rev. Lett. **59**, 2596 (1987).
[15] A. Gavrin, J. R. Childress, C. L. Chien, B. Martinez, and M. B. Salamon, Phys. Rev. Lett. **64**, 2438 (1990).

# Magnetic properties of epitaxial ferrite multilayer films

Y. Suzuki, R. B. van Dover, E. M. Gyorgy,[a] Julia M. Phillips,[b] V. Korenivski, D. J. Werder, C. H. Chen, R. J. Felder, R. J. Cava, J. J. Krajewski, and W. F. Peck, Jr.
*AT&T Bell Labs, 600 Mountain Ave., Murray Hill, New Jersey 07974*

We have fabricated and studied the structure and magnetic properties of high quality single crystalline (Mn,Zn)$Fe_2O_4$, $NiFe_2O_4$, and $CoFe_2O_4$ films. Although (Mn,Zn)$Fe_2O_4$ and $NiFe_2O_4$ films grown directly on $SrTiO_3$ and $MgAl_2O_4$ show mediocre structural and magnetic properties, these same films grown on $SrTiO_3$ and $MgAl_2O_4$ buffered with $CoCr_2O_4$ or $NiMn_2O_4$ exhibit excellent crystallinity and bulk saturation magnetization values, thus indicating the importance of lattice match and structural similarity between the film and the underlying layer. X ray, Rutherford backscattering spectroscopy, atomic force microscopy, and transmission electron microscopy analysis provide a consistent picture of the structural properties of these ferrite films. © *1996 American Institute of Physics.* [S0021-8979(96)22108-1]

## I. INTRODUCTION

There has been much investigation of exchange-coupled biasing as an alternative to the application of a small external field to magnetically saturate thin films. For magnetoresistive sensor or read head applications, a bias field due to an antiferromagnetic layer or a magnetically hard ferromagnetic layer will suppress Barkhausen noise induced by domain wall motion in the adjacent magnetically soft layer. To obtain strong exchange coupling across the interface, one needs a clean interface with minimal strain and roughness. Most magnetic data storage studies of exchange-coupling biasing involve a magnetically soft metallic ferromagnet such as permalloy (Ni–Fe alloy) biased by an antiferromagnet such as a Mn–Fe alloy.[1] The values of the exchange constant deduced from this and similar polycrystalline systems are much smaller than expected, thus suggesting the nonoptimal quality of the interface.

For the fabrication of thin-film inductors, however, metallic ferromagnets such as permalloy are not suitable due to eddy current losses. Low conductivity exchange-coupled magnetic oxide layers are promising for this purpose. There are, however, very few studies of exchange coupling in oxide systems. Notably Wolf *et al.* have investigated CoO/$Fe_3O_4$ bilayers where CoO is an antiferromagnet with $T_N \sim 295$ K and $Fe_3O_4$ is a relatively soft ferrimagnet.[2] Exchange biasing in this system is obviously possible only below room temperature. We have studied spinel structure ferrites of $CoFe_2O_4$(CF), (Mn,Zn)$Fe_2O_4$(MZF) and $NiFe_2O_4$(NF) films, all of which have Curie temperatures well above room temperature. We have optimized growth of single-crystal ferrite films to avoid the high temperatures of 800–1000 °C required in previous work.[3,4] Here we report on the growth of single-crystal MZF, NF, and CF films on CCO($CoCr_2O_4$) and $NiMn_2O_4$(NMO) buffered (100)$SrTiO_3$(STO) as well as (110)STO and (110)$MgAl_2O_4$(MAO) at low temperatures with good crystallinity and magnetic properties approaching bulk values.[5]

[a]Deceased.
[b]Presently at Sandia National Laboratories, Albuquerque, NM 87185.

## II. EXPERIMENTAL PROCEDURE

All films except NF were deposited in a pulsed laser deposition (PLD) system with a KrF excimer laser (248 nm) operating at 10 Hz with an energy density of ~3 J/cm$^2$ for CCO and NMO and ~4 J/cm$^2$ for MZF and CF. The CCO films were deposited at 600 °C in 1 mTorr atmosphere of 1% $O_2$ and 99% $N_2$. The NMO films were deposited at 600 °C in 1 mTorr of $O_2$. The MZF and CF films were deposited at 400 °C in a 1 mTorr $O_2$ atmosphere. The NF films were grown in an off-axis sputtering chamber in a 100 mTorr Ar atmosphere and at 400 °C. The two buffer materials with thicknesses varying from 500–1500 Å promote good crystalline growth of a subsequent ferrite film. We grew ferrite films with thicknesses varying from 700–3000 Å and found no degradation of ferrite crystal quality in this range. The ferrite films discussed in this article are all ~2000 Å thick with buffer layers ~1000 Å thick. Crystal orientation and rocking curve widths were determined by a four-circle x-ray diffractometer with a monochromatic beam and a resolution of ~0.3°. In Rutherford backscattering spectroscopy (RBS), the ratio of backscattering signal of 1.8 MeV $^4He^+$ ions aligned with the [100] direction and along a random direction gives a figure of merit $\chi_{min}$ for the crystallinity. Magnetization data were taken on a Lake Shore vibrating-sample magnetometer (VSM) at fields of up to 1.4 kOe at room temperature and on a Quantum Design superconducting quantum interference device (SQUID) magnetometer at fields of up to 5.5 T at room temperature and at 10 K.

## III. STRUCTURAL CHARACTERIZATION

Structural characterization of CCO and NMO buffer films on (100)STO reveal the (100) plane to be parallel to the plane of substrate and in-plane alignment of the [001] directions of the buffer and substrate. RBS channeling yields a $\chi_{min}$ of 25%–30% for these films. Films grown on (110) STO have a (110) orientation and have the [$\bar{1}$10] direction aligned with that of STO in the plane of the substrate. The full widths at half maximum (FWHM) of the $\omega$ rocking curves of the (400) and (440) buffer peaks in the respective films show moderately good crystallinity of $\Delta\omega \sim 1.0°$. Since the spinel lattice constant of the buffer is twice that of the STO substrate, coalescence of neighboring nucleation sites of the

 0021-8979/96/79(8)/5923/3/$10.00 © 1996 American Institute of Physics 

TABLE I. The crystalline quality of three types of (100) oriented ferrite films on (100) $SrTiO_3$ and $CoCr_2O_4$ buffered (100) $SrTiO_3$ as described by the FWHM $\Delta\omega$ of the (400) rocking curve from x-ray analysis and $\chi_{min}$ from Rutherford backscattering analysis.

| | $(Mn,Zn)Fe_2O_4$ | | $CoFe_2O_4$ | | $NiFe_2O_4$ | |
|---|---|---|---|---|---|---|
| | Buffered | No buffer | Buffered | No buffer | Buffered | No buffer |
| $\Delta\omega$ | 0.9° | 2.5° | 0.6° | 1.3° | 0.7° | 1.0° |
| $\chi_{min}$ | 21% | 30% | ··· | ··· | 18% | 35% |

buffer on the STO results in antiphase boundaries.[6] These antiphase boundaries give rise to grains on the order of a few hundred Å on a side. To improve the crystalline quality of the buffer, we subsequently annealed CCO and NMO on STO at 1000 °C in air for 30 min. Such an anneal not only oxidizes the sample but also promotes grain growth. Atomic force microscopy (AFM) imaging of annealed CCO on STO reveals typical grains on the scale of 5000 Å. After annealing, rocking curves of the (400) buffer peaks have a much sharper FWHM of $\Delta\omega$=0.5–0.7°. RBS channeling analysis of the buffer layers show a decrease of $\chi_{min}$ to 10%–14%, indicating excellent crystallinity. Similarly (110) oriented buffer layers on (110) oriented substrates have improved crystallinity after annealing ($\Delta\omega$~0.7°). A way of avoiding antiphase boundaries is to use spinel structure MAO substrates.

These annealed buffered substrates served as templates to grow spinel structure MZF, NF, and CF ($CoFe_2O_4$) single-crystal films. The buffered substrates gives rise to high quality ferrite films at 400 °C. MZF, NF, and CF grow with the (100) and (110) orientation on (100) and (110) STO substrates, respectively. All three types of ferrite films show excellent crystalline quality as seen from x-ray and RBS analysis. In Table I, the crystallinity of the ferrites buffered with CCO is compared with that of unbuffered ferrites. The buffered ferrites have far better crystallinity than the corresponding unbuffered ferrites as measured by the FWHM of the rocking curves ($\Delta\omega$) from x-ray analysis and $\chi_{min}$ from RBS analysis. The similarity of the $\Delta\omega$ and $\chi_{min}$ values of the buffered ferrites and underlying buffer indicates excellent epitaxial growth of the ferrites on the buffers. Since MZF films are better lattice matched to NMO than to CCO, the $\Delta\omega$ and $\chi_{min}$ values of MZF/NMO/STO ($\Delta\omega$=0.5° and a $\chi_{min}$~16%) are consistently smaller than those of MZF/CCO/STO. However, this difference does not affect any magnetic properties, as shown later. Growth of NF films in a reducing argon atmosphere at 400 °C is incompatible with highly crystalline NMO.

Ferrite films grown on top of buffered substrates have grain sizes on the order of 5000 Å similar to those of the buffer layers. For comparison, we have also deposited MZF, CF, and NF films directly on (100) STO under the same conditions as the above samples. AFM images indicate that grains are less than 100 Å on a side and are consistent with plan view transmission electron microscopy (TEM) images.

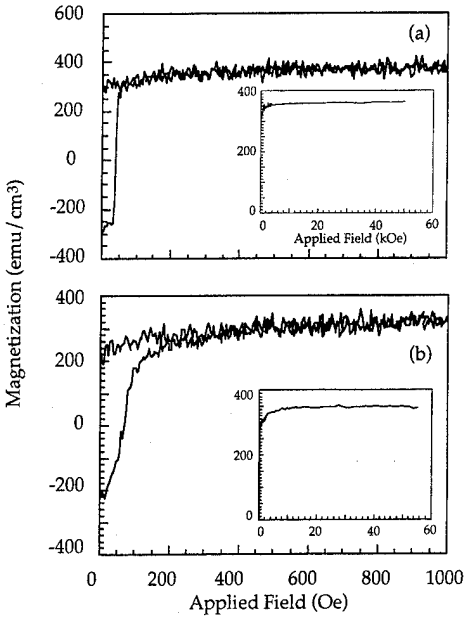



FIG. 1. Magnetization vs field of (100) $(Mn,Zn)Fe_2O_4$ films measured on a VSM up to 1 kOe and on a SQUID magnetometer up to 5.5 T (insets) at room temperature with the field applied parallel to the film surface: (a) on $CoCr_2O_4$ buffered (100) $SrTiO_3$ and (b) on $NiMn_2O_4$ buffered (100) $SrTiO_3$.

## IV. MAGNETIC PROPERTIES

Magnetic properties of MZF, CF, and NF films grown on buffered substrates are comparable to those of bulk MZF, CF, and NF. The magnetization loops of (100) and (110) MZF films have saturation magnetizations ($M_s$) of approximately 320 emu/cm$^3$ at room temperature. The magnetization of (100) MZF films on CCO and NMO buffered STO was measured on a VSM up to fields of 1 kOe applied in the plane of the substrate [see Figs. 1(a) and 1(b)]. The insets of Fig. 1 are magnetization curves of the same samples measured in the same field configuration on a SQUID magnetometer. The similarity of the magnetization loops of the two films indicates that slight differences in the crystallinity of the films due to buffer layer choice do not affect the magnetization properties. Magnetization loops of (100) MZF films mea-

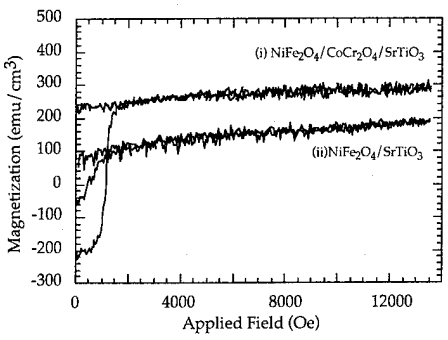



FIG. 2. Magnetization vs field of a (100) $NiFe_2O_4$ film on $CoCr_2O_4$ buffered and unbuffered (100) $SrTiO_3$ with the field applied parallel to the film surface as measured on a VSM. While buffered $NiFe_2O_4$ films reach saturation by ~1 kOe, unbuffered films do not reach saturation even at 5.5 T.

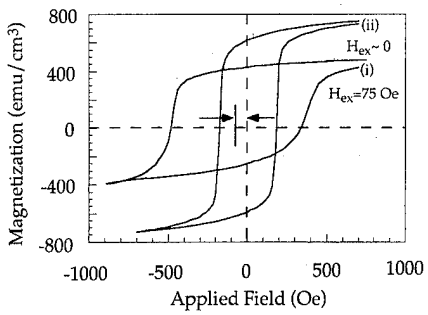



FIG. 3. Magnetization loops of (i) a MZF film on (100) $SrTiO_3$ field cooled in 10 kOe–10 K and (ii) a MZF film on $CoCr_2O_4$ buffered (100) $SrTiO_3$ field cooled in 10 kOe–10 K. The unbuffered MZF film shows an exchange bias field of 75 Oe, thus indicating the presence of regions with antiferromagnetic or glassy properties and exchange coupling across boundaries between ordered and disordered regions.

sured with the field applied parallel to the film surface and in various directions in the plane of the film reveal no easy axes.

NF films on CCO buffered STO show $M_s$ values of 300 emu/cm$^3$ as compared to bulk values of 270 emu/cm$^3$ (see Fig. 2). Such a high moment may be attributed to nonequilibrium site occupation quenched into the film. Venzke *et al.* have also observed $M_s$ values greater than that of bulk in NF films homoepitaxially grown on annealed NF films.[7] NF films grown at 600 °C on CCO buffered STO exhibit similar saturation magnetization values; however, their coercive fields are consistently smaller and range from 300–400 Oe. Fewer microstructural defects in the 600 °C samples may present fewer pinning defects and therefore lower coercive field.

Magnetization loops of (100) and (110) CF films on buffered STO and MAO reach bulk $M_s$ values of 400 emu/cm$^3$. Coercive fields range from 3800–4400 Oe for films grown at 400 °C. Loops of CF on CCO buffered (110) STO and (110) MAO with the field applied in the plane of the substrate reveal an easy axis along the [001] direction. From torque magnetometer measurements, the anisotropy constant of (110) CF films is $K_1 \sim 4.3 \times 10^6$ ergs/cm$^3$ with the field rotating in the plane of the film. This value is in good agreement with $K_1 \sim 3 \times 10^6$ ergs/cm$^3$ for bulk CF.[8]

MZF and NF films grown directly on STO and MAO never reach bulk $M_s$ values (see Fig. 2). While buffered NF films reach saturation by ~1 kOe, unbuffered films do not reach saturation even at 5.5 T. In MZF films, x-ray fluorescence spectroscopy indicates similar Zn fractions for MZF films grown with and without a buffer layer. Therefore variations in Zn fractions cannot account for the differences in $M_s$ values of buffered and unbuffered MZF films. MZF films grown on STO and MAO have lattice mismatches of 8% and 4%, respectively. Therefore lattice mismatch and thermally induced strain may give rise to disordered regions in MZF films during low-temperature growth, thus resulting in a reduced $M_s$. When these MZF films are field cooled in 10 kOe–10 K, magnetization loops show an offset of 75 Oe [see Fig. 3, curve (i)]. This offset is indicative of disordered regions with antiferromagnetic or glassy magnetic behavior and exchange coupling between these structurally and/or chemically disordered regions and crystalline regions of MZF.[7,8] For MZF films grown on buffered substrates, similar field cooled magnetization loops show no offset, indicating a negligible amount of disordered material in buffered MZF films [see Fig. 3, curve (ii)]. In NF films grown directly on STO, a similar effect is seen.[7] Thus we correlate the presence of the offset in field cooled magnetization loops with regions with antiferromagnetic or glassy magnetic properties and with exchange coupling across boundaries between ordered and disordered regions.

We are able to grow CF films on STO with $M_s$ values approaching the bulk values whether or not there is a buffer on the substrate and in spite of measurable differences in the structural quality in the two cases. However, the magnetic properties of MZF grown on top of CF are sensitive to whether the structure is buffered or not and hence to the microstructure. MZF/CF bilayers grown directly on STO have reduced magnetization compared to their buffered counterparts, but nevertheless exhibit exchange coupling.

## V. CONCLUSION

In conclusion, we have fabricated high quality single crystalline ferrite thin films of MZF, NF, and CF by using CCO and NMO buffered STO and MAO. The nonmagnetic spinel structure buffer layers are essential in the low-temperature growth of ferrite thin films with magnetic properties approaching the bulk because they take up the strain at the buffer/substrate interface and provide an improved coincidence site in the case of an STO substrate. The resulting films will be suitable for studies of exchange coupling between oxide films, because nearly perfect single-crystal structural integrity occurs at a substrate temperature low enough (400 °C) to preclude interdiffusion at the boundary.

## ACKNOWLEDGMENTS

The authors would like to thank Paula Trevor for x-ray fluorescence spectroscopy and Khiem B. Do and Lydia L. Sohn for AFM imaging. V. K. gratefully acknowledges financial support from the Swedish Natural Science Research Council.

[1] R. D. Hempstead, S. Krongelb, and D. A. Thompson, IEEE Trans. Magn. **14**, 521 (1978).
[2] R. M. Wolf, A. E. M. de Veirman, P. J. van der Zaag, P. van der Sluis, and J. B. F. aan de Stegge, Mater. Res. Soc. Symp. Proc. **341**, 23 (1994).
[3] C. M. Williams, D. B. Chrisey, P. Lubitz, K. S. Grabowski, and C. M. Cotell, J. Appl. Phys. **75**, 1676 (1994).
[4] R. B. van Dover, S. Venzke, E. M. Gyorgy, T. Siegrist, J. M. Phillips, J. H. Marshall, and R. J. Felder, Mater. Res. Soc. Symp. Proc. **341**, 41 (1994).
[5] Y. Suzuki, R. B. van Dover, E. M. Gyorgy, Julia M. Phillips, V. Korenivski, D. Werder, C. H. Chen, R. J. Cava, J. J. Krajewski, and W. F. Peck (unpublished).
[6] D. Margulies, F. T. Parker, F. E. Spada, and A. E. Berkowitz, Mater. Res. Soc. Symp. Proc. **341**, 53 (1994).
[7] S. Venzke, R. B. van Dover, E. M. Gyorgy, Julia M. Phillips, T. Siegrist, C. H. Chen, D. Werder, R. M. Fleming, R. J. Felder, E. Coleman, and R. Opila (unpublished).
[8] V. Korenivski, R. B. van Dover, Y. Suzuki, E. M. Gyorgy, J. M. Phillips, and R. J. Felder, J. Appl. Phys. (to be published).

# Interlayer exchange coupling in amorphous/crystalline $NiFe_2O_4$ thin-film bilayers

V. Korenivski, R. B. van Dover, Y. Suzuki, E. M. Gyorgy,[a] J. M. Phillips, and R. J. Felder
*AT&T Bell Laboratories, Murray Hill, New Jersey 07974*

Amorphous/crystalline bilayers of $NiFe_2O_4$ exhibit interlayer magnetic exchange coupling, which results from an interaction between a spin-glass material and a ferrimagnetic material. The observed effect is reminiscent of the well-known exchange coupling effect between an antiferromagnet and a ferromagnet, which is widely used in applications where field biasing of thin magnetic films is desirable. © *1996 American Institute of Physics.* [S0021-8979(96)22208-8]

## I. INTRODUCTION

Bulk ferrites are widely used in discrete microwave devices owing to their high magnetization and low electrical conductivity. For integrated planar circuits operating at high frequencies, however, designs based on thin ferrite films are expected to have important applications. Generally, magnetic properties of ferrite films are more sensitive to crystalline disorder than those of metal films, such as permalloy. Studying the relationship between the structure and magnetic properties of thin films is an important step in the realization of planar ferrite devices, and is also potentially interesting for tailoring magnetic properties of thin ferrite films. There have been a number of studies addressing this issue. Booth and Crangle[1] have investigated cobalt–zinc mixed ferrite and found that the magnetic properties of their bulk specimens—low magnetization values with extremely high saturation fields—were consistent with superparamagnetism of strongly magnetic particles of diameter about 4 nm dispersed in a nonmagnetic matrix. Moreover, they found that cooling the samples in an applied field down to helium temperature produced a displaced hysteresis loop characteristic of unidirectional exchange anisotropy, and suggested that this effect may be due to the presence of antiferromagnetic regions at low temperatures. Berkowitz *et al.*[2] prepared $NiFe_2O_4$ in the form of ultrafine particles with an average diameter of 8 nm coated with an organic surfactant and observed a small low-temperature magnetization and very high saturation field. They attributed this behavior to extremely strong pinning of the ferrite surface spins to the organic molecules. Recent studies have revealed similar effects in thin films. Margulies *et al.*[3] argued that the reduced magnetization with only asymptotic saturation observed in their sputtered nickel ferrite films may be due to anisotropy caused by compressive strain normal to the film plane, which results from the film/substrate lattice mismatch present in $NiFe_2O_4$ on MgO. They pointed out, however, that the observed behavior could as well be caused by structural defects. We have previously reported epitaxial growth of $NiFe_2O_4$ films on $SrTiO_3$.[4,5] Films grown at 600 °C consist of small crystalline grains surrounded by thin regions of amorphous material.[5] These disordered regions strongly affect the magnetic behavior, resulting in extremely high saturation fields and giving rise to unidirectional anisotropy when the films are cooled in a field. Postdeposition annealing improves the crystallinity of the films, at the same time reducing the field required for saturation and eliminating the exchange anisotropy at low temperature. The anomalous magnetic behavior was therefore attributed to magnetic interactions between the crystalline and defective regions.[5] In this report we present direct evidence for magnetic exchange coupling between crystalline and amorphous components in nickel ferrite. We observe interlayer exchange coupling in amorphous/crystalline bilayers of $NiFe_2O_4$, which results from an interaction between a spin-glass material and a ferrimagnetic material. However, the exchange anisotropy is absent above 150 K and therefore cannot explain the anomalous magnetic behavior at room temperature reported in Refs. 3–5.

## II. EXPERIMENTAL PROCEDURE

The films were deposited by rf magnetron sputtering using a stoichiometric $NiFe_2O_4$ target (see Refs. 4 and 5 for details). The chamber was evacuated to the base pressure of $10^{-7}$–$10^{-6}$ Torr, and the sputtering was performed at a pressure of 100 m Torr of argon gas and rf power of 100 W. Silver paste was used to attach the (001)-oriented $SrTiO_3$ substrates to a heated block, which was kept at room temperature for deposition of amorphous films and 600 °C for deposition of crystalline films. The films deposited at 600 °C were postannealed at 1000 °C in air for 3 h to improve their crystallinity and magnetic properties. Our previous structural studies[5] showed that the films deposited at room temperature are amorphous and the films deposited at 600 °C and subsequently annealed at 1000 °C are essentially single crystal with bulklike magnetic properties. Amorphous/crystalline bilayers were formed by depositing at room temperature an overlayer of $NiFe_2O_4$ on the postannealed crystalline films. For the bilayers used in this study the thickness of the single films was 100–150 nm. Amorphous films of 1 $\mu$m in thickness were prepared in order to resolve the weak paramagnetic component in the measured dc magnetic moment. Magnetic properties of the films were measured using a superconducting quantum interference device (SQUID) magnetometer in the temperature range of 5–350 K with fields up to 55 kOe. The magnetic field was applied in the plane of the films along the [100] direction. Field-cooled magnetization loops were taken after the films were cooled in 55 kOe from 350 K to a given temperature.

[a]Deceased.

 0021-8979/96/79(8)/5926/3/$10.00 © 1996 American Institute of Physics

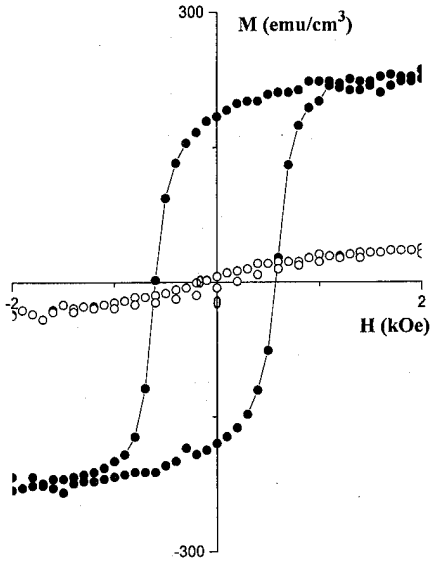



FIG. 1. Magnetization curves recorded at 10 K for crystalline (solid circles) and amorphous (open circles) $NiFe_2O_4$ films.

## III. RESULTS AND DISCUSSION

Shown in Fig. 1 are magnetization curves recorded at 10 K for the crystalline and amorphous films (solid and open circles, respectively). The data shown are subsets of the major loops taken with field excursions of ±55 kOe. The saturation magnetization of the crystalline film approaches 270 emu/cc, the bulk $NiFe_2O_4$ saturation magnetization. In contrast, the amorphous film is disordered magnetically and exhibits only ~15% of the bulk saturation magnetization value. Figure 2 shows magnetization loops taken at 10 K for the crystalline film before and after the deposition of the amorphous overlayer. The saturation magnetization is practically unaffected. However, the initially symmetric field-cooled magnetic loop of the crystalline film is found to be offset by

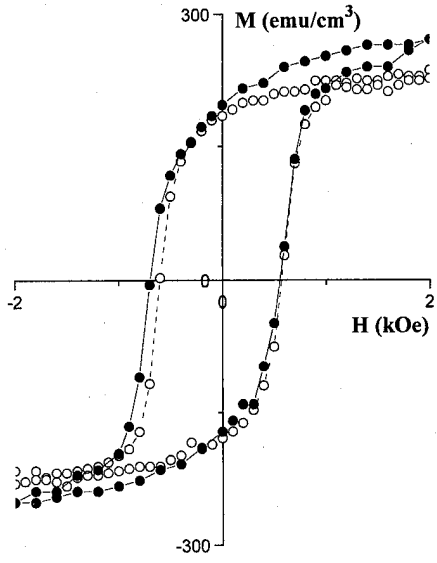



FIG. 2. Field-cooled magnetization curves recorded at 10 K for a crystalline $NiFe_2O_4$ film before (open circles) and after (solid circles) deposition of an amorphous $NiFe_2O_4$ overlayer.

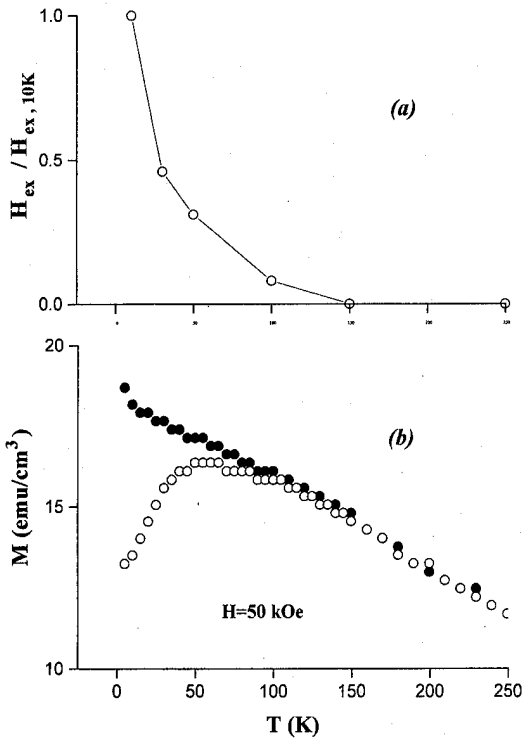



FIG. 3. (a) Normalized exchange field, $H_{ex}$, vs temperature for an amorphous/crystalline $NiFe_2O_4$ bilayer; (b) zero-field-cooled (open circles) and field-cooled (solid circles) $M$ vs $T$ data for an amorphous $NiFe_2O_4$ film.

~75 Oe after the deposition of the amorphous film, indicating unidirectional magnetic anisotropy caused by magnetic interaction between the layers. This exchange interaction takes place at the interface between the layers and causes the surface spins of the crystalline film to be pinned in the direction of the applied field when the bilayer is cooled to low temperature. For this to occur the amorphous film must be magnetically of antiferromagnetic or spin-glass character, i.e., have "magnetic memory" and retain the spin pattern once cooled below the transition temperature of the antiferromagnetic or spin-glass component. Then the interface spins of the amorphous film aligned by magnetic exchange with the interface spins of the saturated crystalline film would be "frozen in" when the bilayer is cooled through the transition temperature and create unidirectional magnetic anisotropy that would bias the magnetization. Such effect was first reported by Meikeljohn and Bean[6] for an antiferromagnetic/ferromagnetic interface and is now extensively used for field biasing of thin magnetic films. The offset field, $H_{ex}$, which is characteristic of the strength of the interlayer magnetic exchange interaction, is shown in Fig. 3(a) as a function of temperature. Each data point in Fig. 3(a) represents the displacement in the $M$-$H$ loop taken after the bilayer was cooled in 55 kOe from 350 K to a given temperature, normalized to the displacement at 10 K. The exchange field differs from zero below ~150 K and increases with decreasing temperature, indicating a magnetic transition in the amorphous component at around 150 K. Antiferromagnetic order is not expected in our amorphous films because of the lack of any crystal structure. Spin-glass behavior, on the other hand, is likely to arise from competing local magnetic interactions

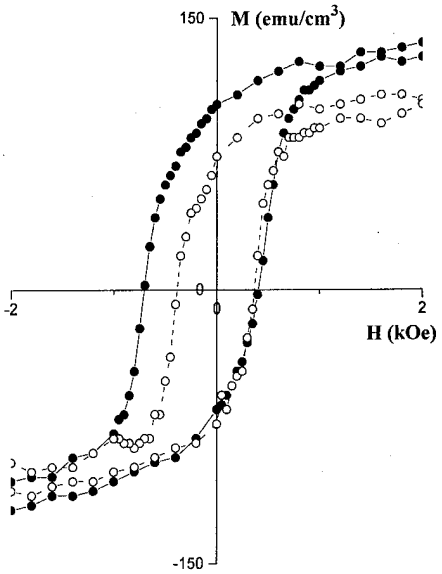



FIG. 4. Field-cooled magnetization loops taken at room temperature (open circles) and 10 K (solid circles) for an amorphous/crystalline $NiFe_2O_4$ bilayer annealed at 550 °C. The magnetization is normalized to the total volume of the bilayer.

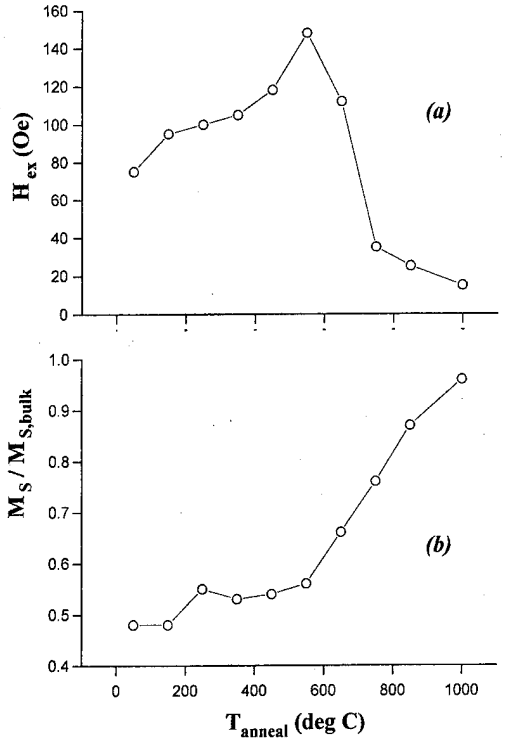



FIG. 5. (a) Exchange field, $H_{ex}$, and (b) saturation magnetization, $M_s$, for an amorphous/crystalline $NiFe_2O_4$ bilayer as a function of annealing temperature. The bilayer saturation magnetization is normalized to 270 emu/cc.

as a result of structural disorder. Figure 3(b) shows zero-field-cooled and field-cooled magnetization versus temperature curves for the amorphous film recorded with $H=50$ kOe. The data are typical of spin-glass material. The magnetization exhibits substantial relaxation below ~100 K (not shown), which is also an indication of a spin-glass behavior. The glass transition temperature correlates well with the point where the unidirectional anisotropy starts to be observed [see Figs. 3(a) and 3(b)]. We, therefore, attribute the observed interlayer exchange coupling in amorphous/crystalline bilayers of $NiFe_2O_4$ to an interaction between a spin-glass material and a ferrimagnetic material.

Annealing makes amorphous structure crystallize and is, therefore, expected to eliminate the effect we observe. We have carried out a series of annealing experiments and found that the interlayer exchange coupling increases when the bilayer film is annealed at temperatures below 600 °C. Figure 4 shows the field-cooled $M$-$H$ loops taken at room temperature and 10 K for the bilayer annealed at 550 °C. The room-temperature loop is symmetric, while the exchange field at 10 K is 150 Oe—double the value of $H_{ex}$ in the as-prepared bilayer. The results of the annealing experiments are summarized in Fig. 5. The exchange field increases with $T_{anneal}$ for $T_{anneal}<600$ °C. This is attributed to improved contact between the ferrimagnetic and spin-glass layers. At higher annealing temperatures the overlayer crystallizes and becomes ferrimagnetic with the bulk magnetization of $NiFe_2O_4$. As this happens, the exchange field quickly decreases to zero.

## IV. CONCLUSIONS

We have shown that a significant exchange anisotropy can be obtained in amorphous/crystalline $NiFe_2O_4$ bilayers, which can explain the unusual low-temperature magnetic properties reported previously.[5] However, because the glass transition temperature of the amorphous layer is only ~150 K, the observed exchange anisotropy is not likely the source of the anomalous room-temperature magnetization loops reported in Refs. 3–5. Our results nevertheless demonstrate exchange coupling in a model system relevant to the properties of bulk as well as thin-film oxides.

## ACKNOWLEDGMENT

V. K. gratefully acknowledges financial support from the Swedish Natural Science Research Council.

[1] J. G. Booth and J. Crangle, Proc. Phys. Soc. **79**, 1278 (1962).
[2] A. E. Berkowitz, J. A. Lahut, I. S. Jacobs, L. M. Levinson, and D. W. Forester, Phys. Rev. Lett. **34**, 594 (1975).
[3] D. T. Margulies, F. T. Parker, F. E. Spada, and A. E. Berkowitz, Mater. Res. Soc. Symp. Proc. **341**, 53 (1994).
[4] R. B. van Dover, S. Venzke, E. M. Gyorgy, J. M. Phillips, J. H. Marshall, and R. J. Felder, Mater. Res. Soc. Symp. Proc. **341**, 41 (1994).
[5] S. Venzke, R. B. van Dover, J. M. Phillips, E. M. Gyorgy, T. Siegrist, C.-H. Chen, D. Werder, R. M. Fleming, R. J. Felder, E. Coleman, and R. Opila (unpublished).
[6] W. H. Meikeljohn and C. P. Bean, Phys. Rev. **102**, 1413 (1956).

# Magneto-optic properties and exchange interaction of the macroscopic ferrimagnet $Co_{1-x-y}Tb_x(EuS)_y$

P. Fumagalli and A. Schirmeisen
*2. Physikalisches Institut, RWTH Aachen, D-52056 Aachen, Germany*

R. J. Gambino
*Department of Materials Science & Engineering, State University of New York at Stony Brook, Stony Brook, New York 11794*

Polar Kerr-rotation spectra and hysteresis loops have been measured in $Co_{1-x-y}Tb_x(EuS)_y$, with $0 \leqslant x \leqslant 0.21$ and $0 \leqslant y \leqslant 0.21$, and compared to the macroscopic ferrimagnet $Co_{1-y}(EuS)_y$ and to amorphous $Co_{1-x}Tb_x$. The measurements were taken at room temperature and at 7 K over a wide photon energy range of 1.1–4.6 eV in fields up to 2.77 T. The addition of Tb retains the phase-separated nature yielding a material consisting of a Co–Tb matrix containing crystalline EuS precipitate particles with about 2 nm diameter. Up to 8% Tb is substituted for Eu in the EuS phase. The Kerr rotations are rather small reaching $-0.25°$ at room temperature and increasing to $-0.85°$ at 7 K, i.e., no optical enhancement is observed as in Co(EuS). This is most likely due to the much smaller size of the EuS crystallites. An "*s*"-shaped feature in the Kerr-rotation spectra can be assigned to an $Eu^{2+}$ $4f \rightarrow 5d$ transition while a contribution from the $Tb^{3+}$-$4f$ states shows up as a decrease with increasing photon energies. At 7 K, the Tb and Eu magnetic moments are found to be parallel while the Co moment is believed to be antiferromagnetically exchange coupled to both. At room temperature, the Co moment is dominating the Tb moment which is antiferromagnetically coupled as in $Co_{1-x}Tb_x$. © *1996 American Institute of Physics.* [S0021-8979(96)22308-4]

## I. INTRODUCTION

Magnetic thin films are of continuous interest to the scientific community as they have a high technological potential. They are widely used in conventional mass storage devices and—more recently—in magneto-optic data-storage devices. With the discovery of the giant magnetoresistance (GMR) effect in magnetic multilayers,[1] an application of magnetic thin films as a sensor in disk reading heads seems likely in the near future. The fact that the interface plays a crucial role in producing GMR effects has prompted interest in granular or phase-separated systems where the interface-to-volume ratio is increased as compared to multilayers.[2] A new class of such phase-separated materials has recently been found and named macroscopic ferrimagnets.[3] In these materials two magnetic phases couple antiferromagnetically across the phase boundary. An example is $Co_{1-y}(EuS)_y$ consisting of a Co matrix containing crystalline precipitate particles of EuS with 10 nm diameter. Due to a strong magnetic exchange, the Curie temperature of the EuS phase is enhanced to at least 60 K.[3] In addition, these materials exhibit a magnetoresistance effect of 2%.[4] At low temperatures, the thin films show growth-induced perpendicular magnetic anisotropy. At room temperature, the magnetization direction is in plane and an optical-enhancement effect is observed which leads to Kerr rotations up to $-2°$ at 4.5 eV.[5]

We present magneto-optic Kerr spectra of the "ternary" system $Co_{1-x-y}Tb_x(EuS)_y$ where $0 \leqslant x \leqslant 0.21$ and $0 \leqslant y \leqslant 0.21$. The motivation for adding Tb to Co(EuS) is an antiferromagnetic exchange in $Co_{1-x}Tb_x$[6] which leads to a ferrimagnetic compound with a compensation point above room temperature for $x \cong 0.2$. The single-ion anisotropy of Tb causes perpendicular magnetic anisotropy in $Co_{1-x}Tb_x$.[7] A combination of Tb with Co(EuS) promises, therefore, interesting magnetic and magneto-optic effects.

## II. EXPERIMENT

Films of 200 nm thickness were prepared by co-evaporation of Co and Tb metal and EuS powder from separate crucibles at a deposition rate of 0.3 nm $s^{-1}$ as described in more detail elsewhere.[3] The fused $SiO_2$ substrates were cooled to $-15$ °C by passing helium gas at liquid-$N_2$ temperature through the substrate support block. The films were characterized by x-ray diffraction analysis and vibrating-sample magnetometry. Polar Kerr-rotation spectra were taken at photon energies ranging from 1.1 to 4.6 eV using a fully automated Kerr spectrometer with an electromagnet allowing fields up to 2.77 T. In order to eliminate possible rotations of optical components within stray fields of the magnet, the rotation of an Al reference mirror was subtracted from the sample rotation at each photon energy. All spectra were measured in both positive and negative fields and then averaged to eliminate rotations of nonmagnetic origin as, e.g., stress-induced birefringence. Reflectivity spectra were taken relative to an Al mirror and corrected for the reflectivity of the Al.

## III. RESULTS

The addition of Tb to the macroscopic ferrimagnet Co(EuS) retains the phase-separated nature of the material. X-ray diffraction analysis shows broadened EuS diffraction peaks with full width at half-maximum (FWHM) of 4°. From the peak position, a lattice constant of 5.90 Å for a NaCl structure is derived showing clearly a phase separation between the CoTb phase and EuS precipitate particles. In comparison to Tb-doped EuS films,[8] this indicates that about 8% of the Eu is replaced by Tb. The line broadening, on the other hand, corresponds to a crystallite size of the EuS–Tb

 0021-8979/96/79(8)/5929/3/$10.00 © 1996 American Institute of Physics 

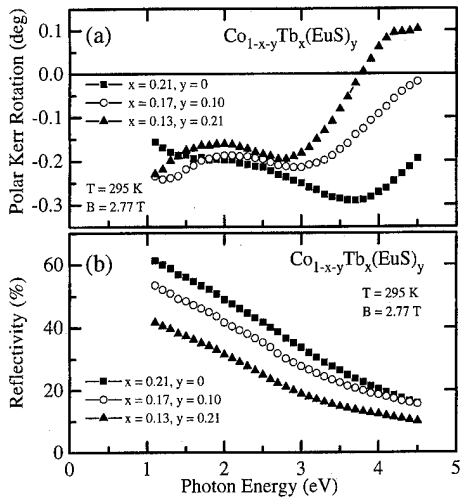



FIG. 1. Polar Kerr rotation (a) and reflectivity (b) at room temperature for $Co_{0.79}Tb_{0.21}$ (■), $Co_{0.73}Tb_{0.17}(EuS)_{0.10}$ (○), and $Co_{0.66}Tb_{0.13}(EuS)_{0.21}$ (▲).

precipitate particles of about 2 nm which is much smaller than in Co(EuS), where a crystallite size of 10 nm has been derived.[4]

In Fig. 1 the polar Kerr rotation (a) and reflectivity (b) spectra at room temperature (RT) are shown in a magnetic field of 2.77 T for three samples, $Co_{0.79}Tb_{0.21}$, $Co_{0.73}Tb_{0.17}(EuS)_{0.10}$, and $Co_{0.66}Tb_{0.13}(EuS)_{0.21}$. The Kerr rotation, $\theta_K$, of the samples containing EuS reaches $-0.25°$. This is considerably smaller than the $-2°$ found in $Co_{1-y}(EuS)_y$.[5] The spectral dependence is rather similar to Co or Co–Tb except for a zero crossing in $\theta_K$ above 3.5 eV. For increasing photon energies, the reflectivity of all samples decreases. Contrary to Co(EuS), the reflectivity does not show a pronounced minimum with values less than 10%.[5]

In order to discuss the magnetic properties at RT, polar Kerr hysteresis loops are plotted for three samples in Fig. 2 at a photon energy of 1.5 eV. A striking asymmetry is observed in $Co_{0.79}Tb_{0.21}$ and $Co_{0.73}Tb_{0.17}(EuS)_{0.10}$ violating time-reversal invariance. The loops are shifted along the positive $x$ axis. $Co_{0.79}Tb_{0.21}$ exhibits an additional step at $-1$ T. The sample containing 21% EuS (c) shows a symmetric loop with just a small coercive field, $H_c$. All samples have perpendicular magnetic anisotropy at RT.

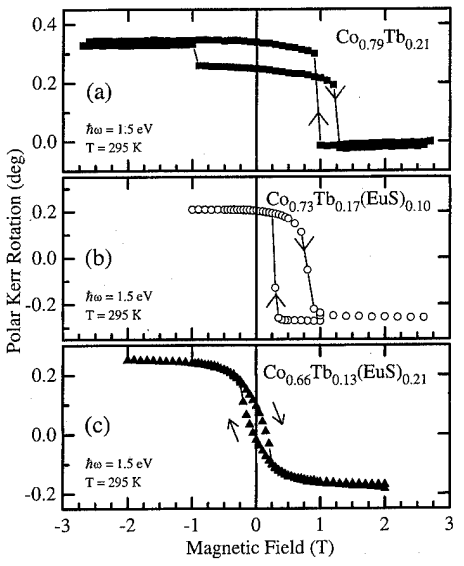



FIG. 2. Polar Kerr hysteresis loops at room temperature for (a) $Co_{0.79}Tb_{0.21}$, (b) $Co_{0.73}Tb_{0.17}(EuS)_{0.10}$, and (c) $Co_{0.66}Tb_{0.13}(EuS)_{0.21}$.

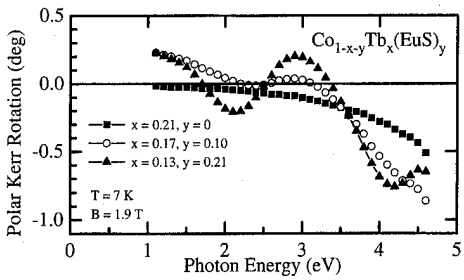



FIG. 3. Polar Kerr rotation at 7 K for $Co_{0.79}Tb_{0.21}$ (■), $Co_{0.73}Tb_{0.17}(EuS)_{0.10}$ (○), and $Co_{0.66}Tb_{0.13}(EuS)_{0.21}$ (▲).

Low-temperature (7 K) polar Kerr-rotation spectra are plotted in Fig. 3. In contrast to the RT measurements, $\theta_K$ reaches values up to $-0.85°$. For all samples, an increase in absolute value of $\theta_K$ is observed at higher photon energies. This is also true for the $Co_{0.79}Tb_{0.21}$ composition indicating a contribution of Tb-4$f$ electronic transitions. Besides this increase, an "$s$"-shaped feature is apparent in the (EuS)-containing films, e.g., in a 21% EuS sample a negative peak at 2.1 eV in combination with a positive one at 2.9 eV. A third peak is seen in the 21% EuS sample at 4.2 eV.

## IV. DISCUSSION

$Co_{1-x}Tb_x$ is known to be a sperimagnetic material,[6] i.e., the Tb spins couple antiferromagnetically to the Co but scatter about an average direction. The antiferromagnetic exchange leads to a compensation point, $T_{comp}$, which is for $x \cong 0.2$ above RT. $T_{comp}$ varies rapidly with composition, at a rate of about 50 K/at. %.[9] Near $T_{comp}$, the total magnetization vanishes and the coercivity, $H_c$, increases to infinity. The strong asymmetry of the loops in the samples with 0% and 10% EuS can be explained if the films are assumed to be composed of regions with slightly varying composition. Let us suppose a region (A) with $T_{comp}$ near RT. It will be impossible to switch this domain. The neighboring region, say (B), has $H_c$ small enough to be overcome by an applied field. If the regions are exchange coupled they will act like a spin-valve system,[10] i.e., the magnetic moment of (B) will couple to a magnetic sublattice of (A) which is not reversed in an external field since $H_c$(A) is infinite. From Fig. 2 we can estimate a value of 1 and 0.5 T for the exchange field in the 0% and 10% EuS-doped samples, respectively. In $Co_{0.79}Tb_{0.21}$ there must exist a third region (C) weakly coupled to region (B) in order to explain the partial reversal of the loop at $-1$ T. The 21% EuS sample has a $T_{comp}$ lower than RT since the Tb/(Co+Tb) ratio is only 0.16 causing finite $H_c$ and a symmetric loop.

Let us now focus on the spectral dependence of the polar Kerr spectra at RT (Fig. 1). In Co(EuS) thin films we had previously found a strong optical-enhancement (OE) effect at 4.5 eV leading to a pronounced minimum in the reflectivity

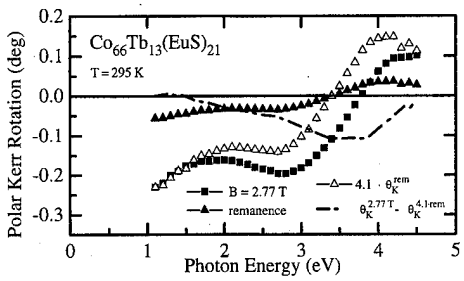



FIG. 4. Polar Kerr rotation at room temperature for $Co_{0.66}Tb_{0.13}(EuS)_{0.21}$ in a field of 2.77 T (■) and in the remanence state (▲). Dash-dotted line is the difference between the 2.77 T spectrum and 4.1 times the remanence spectrum.

spectra and to $\theta_K$ values of up to $-2°$ at RT.[5] The OE effect is most likely dependent on the size of the EuS precipitate particles as indicated by model calculations[11] and it will shift to higher energies with smaller particle size. As the size of the EuS particles of 2 nm in the CoTb(EuS) system is much smaller than the 10 nm found in Co(EuS), an OE effect is expected to occur at energies above 5 eV. This would explain the small Kerr-rotation values in the photon-energy range measured. However, the zero crossing in $\theta_K$ above 3.5 eV in the EuS-containing samples could hint to the onset of an OE effect at higher photon energies.

At 7 K, the Kerr spectra change considerably, as demonstrated in Fig. 3. In Co(EuS) a strong antiferromagnetic exchange exists between the Co and the EuS phase leading to an increase of the Curie temperature, $T_C$, of the EuS phase. In the CoTb(EuS) system, we find the signature of the $Eu^{2+}$ $4f \rightarrow 5d$ transition, an "$s$"-shaped feature with a negative peak in $\theta_K$ at 2.1 eV and a positive one at 2.9 eV, in all EuS-containing samples. Another strong evidence for such a transition is the existence of a third peak in the 21% EuS sample at 4.2 eV belonging to the crystal-field split $Eu^{2+}$ $4f \rightarrow 5d(e_g)$ transition. The difference of 2.1 eV is in good agreement with the crystal-field splitting found in EuS.[12] From a comparison of the sign of the feature with EuS spectra,[8] we find that the magnetic moment of the EuS phase is parallel to the applied field. From the Tb/(Tb+Co) ratio, it is evident that at 7 K the Tb moment dominates the Co moment in all three samples. Hence, the Tb and EuS magnetic moments are parallel to each other at 7 K and the Co moment is antiparallel because of the negative exchange between Tb and Co,[6] and between EuS and Co.[3] This interpretation is corroborated by a positive $\theta_K$ at low photon energies in the 10% and 21% EuS samples. At these energies, merely Co transitions contribute to $\theta_K$.[3]

In Fig. 4 the polar Kerr spectra at RT is plotted for the sample with 21% EuS in a field of 2.77 T and in the remanence state. Using the argument that at low photon energies only Co transitions contribute to $\theta_K$, the remanence spectra is multiplied by a factor of 4.1 ($\Delta$) in order to overlap with the 2.77 T spectra at low photon energies. Subtracting the two spectra (dash-dotted line) eliminates the Co contributions and shows a continuous decrease with increasing photon energies reaching a minimum at 3.8 eV. Comparing this to the spectra at 7 K, we find that the $Co_{0.79}Tb_{0.21}$ sample exhibits a similar energy dependence, except for the minimum, indicating that the difference is mainly due to Tb-4$f$ transitions. Photoemission studies find the location of the Tb-4$f$ states in Tb–Fe at 3 eV below the Fermi energy.[13] In conclusion, the Co moment is dominating at RT, leading to a negative $\theta_K$, as seen in Co metal, and the Tb moment is antiferromagnetically coupled to the Co. Applying a magnetic field will drag the Tb spins toward the field direction, breaking the coupling.

What can we say about a contribution of the EuS phase to $\theta_K$ at RT? A close look at Fig. 4 reveals a positive peak at 2.0 eV and a negative peak at 2.8 eV in the high field and the remanence spectra. This is opposite in sign to the spectrum at 7 K (see Fig. 3) suggesting that the EuS magnetic moment is antiparallel to the field at RT indicating a strong antiferromagnetic exchange to the Co. This implies that $T_C$ of the EuS phase is enhanced up to RT. An alternative explanation is that the feature is due to the Co contribution. The Kerr spectrum of Co metal has a shallow minimum at 1.5 eV and a maximum at 2.7 eV. Since $\theta_K$ is dependent on $n$ and $k$ (index of refraction and absorption), the shallow features of the Co contribution could shift due to a change in $n$ and $k$.

## ACKNOWLEDGMENT

This work has been supported in part by the German BMBF.

[1] M. N. Baibich, J. M. Broto, A. Fert, F. Nguyen Van Dau, F. Petroff, P. Etienne, G. Creuzet, A. Friederich, and J. Chazelas, Phys. Rev. Lett. **61**, 2472 (1988).
[2] A. E. Berkowitz, J. R. Mitchell, M. J. Carey, A. P. Young, S. Zhang, F. E. Spada, F. T. Parker, A. Hutten, and G. Thomas, Phys. Rev. Lett. **68**, 3745 (1992).
[3] R. J. Gambino and P. Fumagalli, IEEE Trans. Magn. **MAG-30**, 4461 (1994).
[4] R. J. Gambino and J. Wang, Acta Metall. (in press).
[5] P. Fumagalli, C. Spaeth, U. Rüdiger, and R. J. Gambino, IEEE Trans. Magn. **MAG-31**, 3319 (1995).
[6] J. M. D. Coey, J. Appl. Phys. **49**, 1646 (1978).
[7] R. J. Gambino, P. Chaudhari, and J. J. Cuomo, AIP Conf. Proc. **18**, 578 (1974).
[8] R. J. Gambino, P. Fumagalli, R. R. Ruf, T. R. McGuire, and N. A. Bojarczuk, IEEE Trans. Magn. **MAG-28**, 2973 (1992).
[9] Y. Mimura, N. Imamura, T. Kobayashi, A. Okada, and Y. Kushiro, J. Appl. Phys. **49**, 1208 (1978).
[10] B. Dieny, V. S. Speriosu, S. S. P. Parkin, B. A. Gurney, D. R. Wilhoit, and D. Mauri, Phys. Rev. B **43**, 1297 (1991).
[11] M. Quinten, 1. Physikalisches Institut, RWTH Aachen, D-52056 Aachen, Germany (private communication).
[12] J. Schoenes, Z. Phys. B **20**, 345 (1975).
[13] K. Starke, E. Navas, E. Arenholz, L. Baumgart, and G. Kaindl, IEEE Trans. Magn. **MAG-31**, 3313 (1995).

# Bi–DyIG films: Enhancement of the Dy contribution to the Faraday rotation

M. Guillot
*Laboratoire des Champs Magnétiques Intenses, CNRS/MPI, 38042 Grenoble, France*

H. Le Gall, J. Gouzerh, J. M. Desvignes, and M. Artinian
*Laboratoire des Matériaux Isolants, Magnétiques et Semi-Conducteurs, CNRS, EP95, 92195 Meudon, France*

The Faraday rotation of epitaxial garnet films of composition $\{R_{3-x}Bi_x\}[Fe_2](Fe_3)O_{12}$ with R=Dy, Y, and high Bi content ($x \cong 1.30$) has been measured in the temperature range 10 K$<T<$600 K at $\lambda$=1155 nm. The analysis of the data in terms of the sublattice magnetization reveals a strong contribution of the {Dy} sublattice. The "electric" dipole Faraday rotation per Dy ion has been determined and compared to its value in the bismuth-free dysprosium garnet. It turns out that Bi gives rise to a pronounced enhancement of this contribution. This result is compared with that observed for other Bi-substituted rare-earth iron garnets in the visible band. © *1996 American Institute of Physics.* [S0021-8979(96)22408-0]

## I. INTRODUCTION

The garnet system allows on its three nonequivalent crystallographic sites a great variety of cation species of different valences.[1] Among these different substitutions in rare-earth iron garnets (REIG), diamagnetic $Bi^{3+}$ and $Pb^{2+}$ ions and some lighter rare-earth ions like $Ce^{3+}$, $Pr^{3+}$, and $Nd^{3+}$ strongly enhance the magneto-optical (MO) activity in the wavelength range 0.4–2 $\mu$m (see Refs. 2–4 and references therein). Since the observation of large Faraday rotation (FR) without a noticeable increase of the optical absorption, there has been much work devoted to the fundamental properties of bismuth-doped iron garnets. On the other hand, these materials have been expected to be promising materials for different MO devices, especially in magneto-optical recording.[5,6]

Relevant investigations of garnet films of composition $Y_{3-x}Bi_xFe_5O_{12}$ reported earlier in the literature have been performed in the visible range by Hansen *et al.*[7] We have extended such experiments to the infrared range ($\lambda$=1150 nm) in order to confirm that the Bi ions stimulate the MO activity of the $Fe^{3+}$ ions at both the octahedral and tetrahedral sites of the garnet.[4] At $\lambda$=633 nm, the studies of the MO properties of various Bi-substituted rare-earth iron garnets have led to the following conclusion: the bismuth affects the iron transition only, the enhancement of the iron contribution to FR being independent of the nature of the rare-earth ion.[8]

In this article, we intend to probe the intrinsic MO properties of garnet films of composition $Dy_{3-x}Bi_xFe_5O_{12}$ and $Y_{3-x}Bi_xFe_5O_{12}$ for $x \cong 1.30$ at $\lambda$=1155 nm and to quantitatively analyse the effect of bismuth presence on the MO activity of the $Dy^{3+}$ ion.

Note that prior to this work, the FR of single crystals of $Dy_{3-x}Bi_xFe_5O_{12}$ and of $Tb_{3-x}Bi_xFe_5O_{12}$ was studied for $x=0.42$.[9,10]

We have sought to increase the amount of Bi using epitaxial thin films, the $Dy^{3+}$ ion being chosen because of its large magnetostriction constant which induces a positive uniaxial anisotropy favorable for MO recording.

## II. EXPERIMENT

Garnet films of composition $Y_{3-x}Bi_xFe_5O_{12}$ (YBiIG) and $Dy_{3-x}Bi_xFe_5O_{12}$ (DyBiIG) were grown by liquid phase epitaxy onto (111) oriented cation-doped gadolinium gallium garnet ($Gd_3Ga_5O_{12}$) substrates with a lattice parameter equal to 12.498 Å. A $PbO/Bi_2O_3/B_2O_3$ based flux was used, the Bi content being controlled by the growth rate to adjust the lattice mismatch. The growth temperatures ranged between 1000 and 1200 K and the thicknesses of the films between 5.9 (YBiIG) and 12.9 $\mu$m (DyBiIG) within an accuracy of ±1%. X-ray diffraction studies confirmed the high crystalline quality of the films. The lattice constants being equal to 12.493 Å (YBiIG) and to 12.497 Å (DyBiIG), the misfits $\Delta a$ are small. The film compositions were determined by electron probe analysis, the amount of Bi achieved in the two preparations was 1.30±0.03 (YBiIG) and 1.27±0.03 (DyBiIG). Note that the measured "$a$" lattice constant data are in very good agreement with the values calculated from the ionic radii using the previous composition determinations.[11] On the other hand, the amount of lead entering the crystals as an impurity is negligible.

Using polarization modulation techniques, very accurate FR measurements have been performed at 1155 nm wavelength in the 10–610 K range and under magnetic field along the direction [111] up to 20 kOe. Special attention was paid during the experiments to eliminate the influence of internal reflections and multilayer structures on the measurements.[12,13]

The crystallographic symmetry of pure and bismuth-substituted garnets is usually described by the cubic space group $O_h^{10}$–Ia3$d$. Within the general formula $\{RE_3\}[Fe_2](Fe_3)O_{12}$, the trivalent RE (and Bi) ions are dodecahedrally coordinated (24$c$) with $O^{-2}$ ions while the iron ions occupy two different sites: octahedral (16$a$) sites and tetrahedral (24$d$) sites. The magnetic properties are interpreted in terms of a ferrimagnetic arrangement of the three corresponding sublattice magnetizations $M_c$, $M_a$, and $M_d$.[14] $M_d$ and $M_a$ are strongly coupled antiferromagnetically and $M_c$ is antiparallel to the resultant $Fe^{3+}$ magnetization. In heavier rare-earth garnets the macroscopic garnet magnetization which is given by $|M_c - M_{YIG}|$ vanishes at the compen-

 0021-8979/96/79(8)/5932/3/$10.00 © 1996 American Institute of Physics

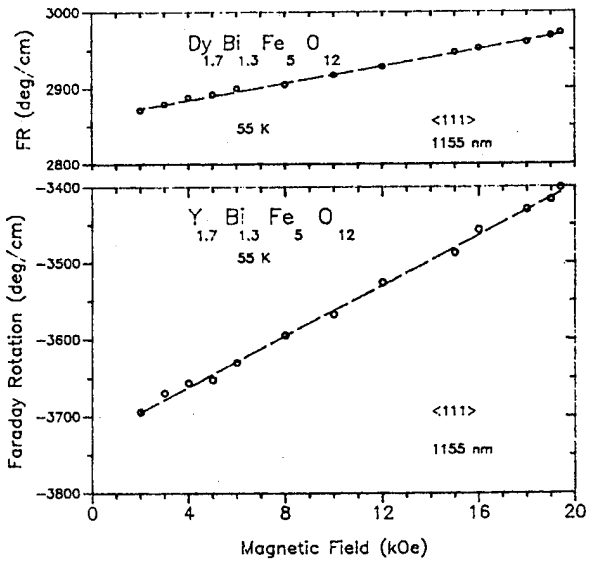



FIG. 1. Faraday rotation vs applied field at 55 K in DyBiIG and YBiIG films.

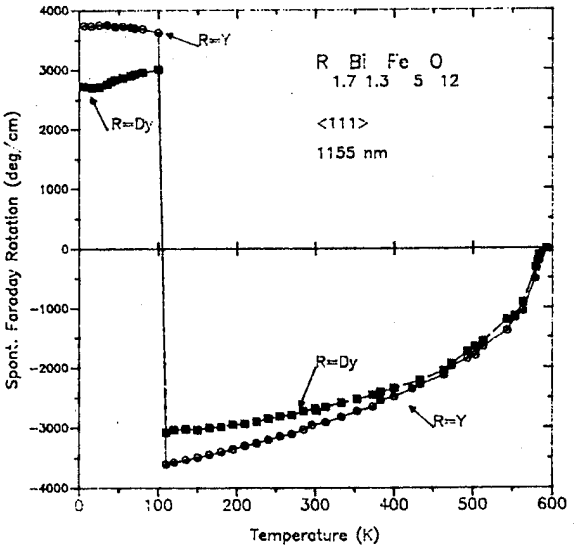



FIG. 2. Temperature dependences of the spontaneous Faraday rotation at $\lambda=1155$ nm for DyBiIG and YBiIG films. Note that below $T_{comp}$, the values of BiYIG films have been changed.

sation temperature $T_{comp}$. In pure DyIG, $T_{comp}$ is equal to $(223\pm1)$ K.[15] The iron garnets are known to present a large circular magnetic birefringence in the infrared and in the visible part of the spectrum as reviewed by Dillon.[16]

The FR is induced by the electric and magnetic dipole transitions and is proportional to the three sublattice magnetizations as discussed by Cooper and his co-workers.[17,18]

## III. RESULTS AND DISCUSSION

The isothermal variations $FR_T(H)$ present a linear magnetic field dependence whatever the temperature (Fig. 1), and the spontaneous Faraday rotation, $FR^S$, defined as the FR associated with the spontaneous ferrite magnetization, was immediately deduced using a least-squares refinement technique.

The temperature dependences of the $FR^S$ that are displayed in Fig. 2 confirm that the MO properties are strongly affected by the bismuth incorporation. The Curie temperature was found to be $(600\pm5)$ K for the two films in accordance with magnetic and MO measurements performed at $\lambda=633$ nm on bismuth-substituted yttrium iron garnets.[19] These data lead to a change $\Delta T_c/x$ of 34 K/Bi formula unit in thin films, while in a crystal the increase in $T_c$ was evaluated to be 38 K.[20] In the YBiIG film, FR shows an important increase towards a large negative value (for bismuth-free YIG, the FR is equal to 250 deg cm$^{-1}$ and is only weakly temperature dependent); the contribution $\Delta FR^S/x$ at 4.2 and 300 K is $-3060$ and $-2460$ deg cm$^{-1}$/Bi/f.u., respectively. Note that the MO intrinsic efficiency of Bi is not exactly proportional to the Bi content since for $x\leqslant0.6$, $\Delta FR^S/x$ was observed to be equal to $-3200$ and $-2600$ deg cm$^{-1}$.[4] This effect of saturation was not observed in the visible band,[7] where FR is about 10 times larger than in the infrared.

The absolute value of $FR^S$ of DyBiIG film is smaller than that of the YBiIG film at $T<400$ K (see Fig. 2), indicating that the contribution of the $Dy^{3+}$ sublattice is large as it is observed for bismuth-free dysprosium iron garnet.[15] A compensation temperature $T_{comp}$ of the spontaneous FR occurs at $(110\pm5)$ K, causing a change of sign of $FR^S$. Note that in Fig. 2, we have changed the sign of $FR^S$ values measured on YBiIG films to respect the change of orientation of the iron sublattices in DyBiIG at $T_{comp}$. Furthermore, it should be pointed out that the Bi free DyIG exhibits a higher $T_{comp}$ value $(220\pm2$ K). The shift of $T_{comp}$ towards lower temperature with increasing bismuth content ($T_{comp}=178$ K for $x=0.43$[9]) results from the presence of diamagnetic $Bi^{3+}$ ions in the $\{c\}$ sublattice.

The contribution to the Faraday rotation of DyBiIG by iron ions is well represented by that of BiYIG measured in the same experimental conditions.[20] The total contribution to FR of the $Dy^{3+}$ sublattice is given by

$$\mathrm{FR}(Dy^{3+})=\mathrm{FR}(\mathrm{BiDyIG})-\mathrm{FR}(\mathrm{BiYIG})$$
$$=\pm(C_e+C_m)|M_c|, \quad (1)$$

where $C_e$ and $C_m$ are the respective magneto-optical electric "$e$" and magnetic "$m$" dipole coefficients. The upper (rep lower) sign is valid for $T<T_{comp}$ (rep $T>T_{comp}$). As in the $\{c\}$ sublattice, only the $Dy^{3+}$ ions contribute to FR, $C_m$ is proportional to the Landé $g$-factor of the rare earth and is equal to 6.1 deg cm$^{-1}$ $\mu_B^{-1}$ (references reviewed in Ref. 4). Knowing $M_c$ from direct magnetization measurements, the $m$ dipole contribution in the $\{c\}$ sublattice is easily calculated, and the $e$ dipole transitions contribution is then deduced. The analysis of the observed data indicates that (i) the $\{c\}$ sublattice FR originates mainly from $e$ transitions as in bismuth-free dysprosium iron garnet, (ii) the Bi substitution has no effect on the sign of this $e$ contribution which remains negative as in DyIG; on the contrary, the $e$ contributions of the $Fe^{3+}$ sublattices have a resultant which changes sign under Bi substitution,[4] (iii) as shown in Fig. 3, the FR of the $\{c\}$ sublattice is strongly reduced by the Bi incorporation.

To understand precisely the influence of bismuth, we calculated the $e$ Faraday rotation per $Dy^{3+}$ ion in Bi free and substituted garnets and then deduced the ratio R of these two contributions. The temperature dependence of R shown in

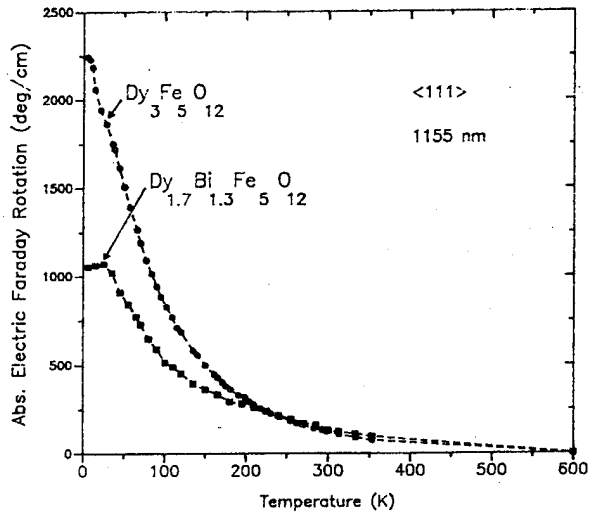



FIG. 3. Temperature dependences of the electric dipole transitions contribution of the {c} sublattice in bismuth-free and bismuth-substituted dysprosium iron garnets at $\lambda=1155$ nm.

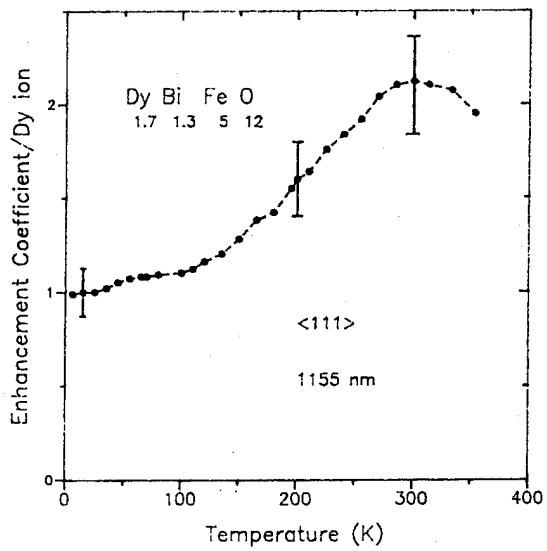



FIG. 4. Temperature dependence of electric dipole transitions contribution per $Dy^{3+}$ ion in DyBiIG divided by the same contribution in bismuth-free DyIG.

Fig. 4 clearly demonstrates that the $Dy^{3+}$ *e* Faraday rotation is affected by the bismuth except for the low-temperature range. It turns out that the enhancement of R is strongly temperature dependent and presents a maximum near room temperature.

Geller *et al.* have determined how the increase of $T_c$ observed in BiYIG is directly related to a change of the super exchange geometry.[21] A refinement of the crystal structure has shown evidence of a small decrease of the [Fe]–O distance and of a weak increase of the (Fe)–O separation. An increase of $J_{ad}$ (and of $T_c$) results from the noncompensated variations of the *d-p* wave function overlap between $Fe^{3+}$ ions and nearest oxygen. An oxygen is, however, at the corner of four polyhedra: a tetrahedron, an octahedron, and two dodecahedra, the last involving two different $\{M\}$–O distances. In YBiIG crystals ($x\cong 1.8$), the {BiY}–O distance of the smallest dodecahedron is very close to the value of bismuth-free YIG, namely 2.37(9) Å, but for the second dodecahedron, the same distance (2.493 Å) is significantly larger than that of YIG (2.43 Å). It is worth noting that the effects of a small admixture of the Bi wave function into the iron orbitals and of covalency between $Fe^{3+}$ ions are analyzed in Refs. 23 and 24. Although an in-depth analysis of the crystal structure of DyBiIG has not yet been performed, to our knowledge, this gives credence to a change of the super exchange interaction between $Dy^{3+}$ and $Fe^{3+}$ ions which can explain the enhancement of FR. Note that generally the dominant interaction is of {Dy}–O–[Fe] type.

At the end of this section, it seems useful to discuss briefly the possible pollution by lead of our films, since the $Pb^{2+}$ contribution to FR was found to be comparable, in the visible range, with that of bismuth.[22] Taking into account the following data, we have concluded that the amount of lead is too weak to affect the discussion developed in this article: (i) electron probe analysis has not revealed any trace of lead, (ii) in the visible, the transparency of our films is very high, although lead is known to increase the optical absorption much more than bismuth, (iii) our YBiIG films present a monotonic decrease of FR with the temperature; with a small amount of lead, the FR variation would show an additional minimum at low temperature (iv) at $\lambda=633$ nm, we have measured, over the whole 10–600 K temperature range, a temperature variation of FR in YBi films that is in very good agreement with the data of Hansen *et al.*[19] It is noticeable that all the results observed on the two films remain unchanged after a long annealing (10 h) at 1000 °C of the two samples.


[1] S. Geller, Z. Kristall. **125**, 1 (1967).
[2] P. Hansen and J. P. Krumme, Thin Solid Films **114**, 69 (1984).
[3] J. P. Krumme, V. Doormann, P. Hansen, H. Baumgart, J. Petruzello, and M. P. A. Viegers, J. Appl. Phys. **66**, 4393 (1989).
[4] H. Le Gall, M. Guillot, A. Marchand, Y. Nomi, M. Artinian, and J. M. Desvignes, J. Magn. Soc. Jpn. **11**, 235 (1987).
[5] M. Abe and M. Gomi, J. Magn. Soc. Jpn. **11**, 299 (1987).
[6] Proceedings of the Magneto-optical Recording International Symposium 1994, J. Magn. Soc. Jpn. **19**, 51 (1995).
[7] P. Hansen, K. Witter, and W. Tolksdorf, J. Appl. Phys. **55**, 1052 (1984).
[8] P. Hansen, C. P. Klages, and K. Witter, J. Appl. Phys. **60**, 721 (1986).
[9] M. Guillot, Y. Braik, H. Le Gall, M. Artinian, and J. M. Desvignes, IEEE Trans. Magn. **29**, 3396 (1993).
[10] M. Guillot, H. Le Gall, J. M. Desvignes, and M. Artinian, IEEE Trans. Magn. **30**, 4419 (1994).
[11] B. Strocka, P. Holst, and W. Tolksdorf, Philips J. Res. **33**, 186 (1978).
[12] G. B. Scott and J. L. Page, J. Appl. Phys. **48**, 1342 (1977).
[13] H. Takeuchi, Jpn. J. Appl. Phys. **14**, 1903 (1975).
[14] R. Pauthenet, Ann. Phys. (N.Y.) **3**, 424 (1958).
[15] P. Feldmann, H. Le Gall, M. Guillot, and M. Artinian in *The Rare Earths in Modern Science and Technology*, edited by G. J. McCarthy and J. J. Rhyne (Plenum, New York, 1978), p. 481.
[16] J. F. Dillon in *Physics of Magnetic Garnets*, edited by A. Paoletti (North-Holland, Amsterdam, 1978).
[17] R. W. Cooper, W. A. Crossley, J. L. Page, and R. F. Pearson, J. Appl. Phys. **39**, 565 (1968).
[18] W. A. Crossley, R. W. Cooper, J. L. Page, and R. P. Stapele, Phys. Rev. **181**, 896 (1969).
[19] P. Hansen, K. Witter, and W. Tolksdorf, Phys. Rev. B **27**, 4375 (1983).
[20] M. Guillot, P. Feldmann, and H. Le Gall, J. Phys. (Paris) **40**, 17 (1979).
[21] S. Geller, G. P. Espinosa, H. J. Williams, R. C. Sherwood, and E. A. Nesbitt, J. Appl. Phys. **35**, 570 (1964).
[22] P. Hansen, M. Rosenkranz, and K. Witter, Phys. Rev. B **25**, 4396 (1982).
[23] P. Novak, Czech. J. Phys. B **34**, 1060 (1984).
[24] G. F. Dionne and G. A. Allen, J. Appl. Phys. **73**, 6127 (1993).

# Microstructural characterization of ferrimagnetic substituted iron garnet heterostructures for magneto-optical applications (abstract)

B. M. Simion
*Department of Materials Science and Mineral Engineering, University of California, Berkeley, California 94720*

R. Ramesh
*Department of Materials Science and Nuclear Engineering, University of Maryland, College Park, Maryland 20742*

G. Thomas
*Department of Materials Science and Mineral Engineering, University of California, Berkeley, California 94720*

Multilayered garnet heterostructures of $Y_3Fe_5O_{12}$ (YIG) and $Eu_1Bi_2Fe_5O_{12}$ (EBIG) have been deposited on single crystalline [111] oriented $Gd_3Ga_5O_{12}$ (GGG) substrates, pulsed laser deposition (PLD). Magnetic (vibrating sample magnetometer) and magneto-optical (reflective Faraday effect) measurements have indicated out-of-plane magnetization for all YIG/EBIG films, coercivities up to 1.2 kOe, and Faraday rotations as high as 50 000 deg/cm.[1] According to x-ray diffraction experiments, all films are single crystalline, [111] oriented. Initial high resolution transmission electron microscopy studies have shown epitaxial growth of both YIG and EBIG layers. All samples had YIG deposited as the first layer of the heterostructure because of its small lattice mismatch with the substrate. As a consequence, all films showed sharp interfaces between the substrate and the first YIG layer. At the second interface, between the YIG layer and the first EBIG layer, structural defects were noted to form in the EBIG film. The thickness ratios between YIG and EBIG layers were intentionally changed during the processing to study the effect on magneto-optical properties. Transmission electron microscopy characterization indicated changes in the interface morphology, with some films displaying high coherence and sharpness of the interfaces, while others showed wavy and very incoherent interfaces. The films with sharp interfaces showed the highest values of Faraday rotation. Since there were no processing parameter changes from one film to another, the results appear to indicate that the morphology of the interfaces is the result of thickness variations in the heterostructures. © *1996 American Institute of Physics.* [S0021-8979(96)43708-9]

[1] B. M. Simion, R. Ramesh, V. G. Keramidas, R. L. Pfeffer, G. Thomas, and E. Marinero, J. Appl. Phys. **76**, 6287 (1994).

# A study of the magneto-optical Kerr spectra of bulk and ultrathin $Fe_3O_4$

P. J. van der Zaag,[a] W. F. J. Fontijn, P. Gaspard,[b] and R. M. Wolf
*Philips Research Laboratories, Professor Holstlaan 4, 5656 AA Eindhoven, The Netherlands*

V. A. M. Brabers, R. J. M. van de Veerdonk, and P. A. A. van der Heijden
*Department of Physics, Eindhoven University of Technology (EUT), 5600 MB Eindhoven, The Netherlands*

An analysis of the complete dielectric tensor of bulk magnetite, $Fe_3O_4$, and of $Fe_3O_4$ substituted with a variable degree of $Mg^{2+}$ or $Al^{3+}$ allowed the assignment of the main magneto-optical (MO) transitions in $Fe_3O_4$ between 0.5 and 4.0 eV. This assignment is consistent with our reinterpretation of the $MgFe_2O_4$ and $Li_{0.5}Fe_{2.5}O_4$ MO-Kerr spectra. An analysis of the stoichiometry of a thin $Fe_3O_4$ layer is made, based on the Kerr spectrum, which is compared to an analysis based on the Verwey transition. The Kerr spectrum is also used to compare wavelengths for MO-Kerr effect studies of wedge-shaped samples. © *1996 American Institute of Physics.* [S0021-8979(96)22508-7]

## I. INTRODUCTION

The interpretation of the magneto-optical (MO) Kerr spectrum of spinel ferrites, and notably magnetite, has been a subject of debate.[1–3] Some authors have explained the part of the spectrum around 2.0 eV in terms of $3d$ crystal field transitions of $Fe^{3+}$ ions on the tetrahedral ($A$-) sites.[1] Others have assigned the major peaks in the MO-Kerr spectrum of $Fe_3O_4$ to $3d^n \rightarrow 3d^{n-1}4s$ orbital promotion processes.[2] The problem with these interpretations, however, is that they are based on forbidden transitions, whereas $Fe_3O_4$ has relatively strong MO transitions and absorption peaks with an oscillator strength of about $10^{-3}$ below 4.0 eV. Hence, Feil proposed that the main MO-active transitions between 0.5 and 4.0 eV are intervalence charge transfer (IVCT) transitions ($Fe^{2+}+Fe^{3+} \rightarrow Fe^{3+}+Fe^{2+}$).[3] As the $Fe^{2+}$–$Fe^{3+}$ pair involved does not posses inversion symmetry, the parity selection rule is relaxed. Consequently, IVCT transitions should have much higher oscillator strengths than the transitions previously proposed.

We will show that IVCT transitions indeed explain the MO-Kerr spectrum of $Fe_3O_4$ between 0.5 and 4.0 eV. Key to the unraveling of the complicated $Fe_3O_4$ MO-Kerr spectrum were: first, the fitting of all four relevant elements of the dielectric tensor $\epsilon'_{xx}$, $\epsilon''_{xx}$, $\epsilon'_{xy}$ and $\epsilon''_{xy}$ *simultaneously* with one set of transitions. Secondly, the systematic substitution with nonmagnetic ions, $Mg^{2+}$ and $Al^{3+}$, which allows the determination of trends in the Kerr spectra with a reduction in $[Fe^{2+}]$ and $[Fe^{3+}]$ content (round brackets denote ions on $A$-sites, square brackets ions on $B$-sites). Of these substitutions, the $Mg^{2+}$ substitution is of special significance as it reduces the intense $Fe^{2+}$-dependent IVCT transitions, allowing the detection of other, overlapping transitions such as the intersublattice charge transfer (ISCT) transitions ($Fe^{3+}+Fe^{3+} \rightarrow Fe^{2+}+Fe^{4+}$). Finally, the usefulness of this understanding of the MO spectra of $Fe_3O_4$ in the field of thin oxidic films will be discussed.

[a]Author to whom correspondence should be addressed. Electronic-mail: ZAAG@PRL.PHILIPS.NL
[b]Permanent address: UFR de Physique, Université Joseph Fourier-Grenoble I, 38041 St. Martin d'Heres, France.

## II. RESULTS AND DISCUSSION

To arrive at a consistent transition assignment for $Fe_3O_4$, we determined the complete dielectric tensor for synthetic crystals of $Fe_3O_4$, and $Mg^{2+}$- and $Al^{3+}$-substituted $Fe_3O_4$, prepared by a floating zone technique.[4] The diagonal element of the dielectric tensor was determined by ellipsometry between 0.5 and 5.0 eV.[5] The polar MO-Kerr spectrum was measured between 0.7 and 4.0 eV.[6,7] From these spectra the off-diagonal element was calculated between 0.7 and 4.0 eV. Thus, for each sample the complete dielectric tensor was obtained, amounting to four spectra: $\epsilon'_{xx}$, $\epsilon''_{xx}$, $\epsilon'_{xy}$, and $\epsilon''_{xy}$. As these spectra consist of many overlapping bands, partly of opposing sign,[2,7] inspection of the spectra does not yield proper transition identification. To achieve this, rigorous fitting, using equations describing the basic line shapes of transitions in the microscopic theory of the dielectric tensor,[6] is needed. The complete dielectric tensor of $Fe_3O_4$ and of the $Mg^{2+}$- or $Al^{3+}$-substituted $Fe_3O_4$ were least-square fitted with one set of transitions for all samples. The criterion for a good fit was that the difference between the measured spectrum and the fit was on average less than 1% of the tensor element.[7]

Trends in MO-peak intensity and energy shift could be established due to the variable degree of substitution. Furthermore, as $Mg^{2+}$ and $Al^{3+}$ both preferentially occupy only the octahedral site, we are able to establish the nature of the MO-active transitions. The key results are summarized in Fig. 1, which depicts $\epsilon_{xy,\max}$ vs $[Fe^{2+}]$ and $[Fe^{3+}]$ content for the four major transitions which depend strongly on the $Fe^{2+}$ content. The nonlinear dependence on $[Fe^{2+}]$ points to a pair interaction for all these transitions.[8] Given their behavior on substitution of $[Fe^{3+}]$ with $Al^{3+}$ the transitions at 0.56 and 1.94 eV involve also this ion, while the transitions at 3.11 and 3.93 eV involve $(Fe^{3+})$. Consequently, four of the main transitions are assigned to intervalence charge transfer transitions (0.56 eV: $[Fe^{2+}]t_{2g} \rightarrow [Fe^{2+}]t_{2g}$, 1.94 eV: $[Fe^{2+}]t_{2g} \rightarrow [Fe^{2+}]e_g$, 3.11 eV: $[Fe^{2+}]t_{2g} \rightarrow (Fe^{2+})e$ and 3.93 eV: $[Fe^{2+}]t_{2g} \rightarrow (Fe^{2+})t_2$). For the three major transitions remaining we propose a new assignment. These transitions are assigned to intersublattice charge transfer transitions (2.61 eV: $(Fe^{3+})t_2 \rightarrow [Fe^{2+}]t_{2g}$, 3.46 eV: $[Fe^{3+}]e_g \rightarrow (Fe^{2+})t_2$ and 3.94 eV: $(Fe^{3+})t_2 \rightarrow [Fe^{2+}]e_g$), since the relative peak positions, the relative strengths and the linewidths of these transitions

 0021-8979/96/79(8)/5936/3/$10.00 © 1996 American Institute of Physics

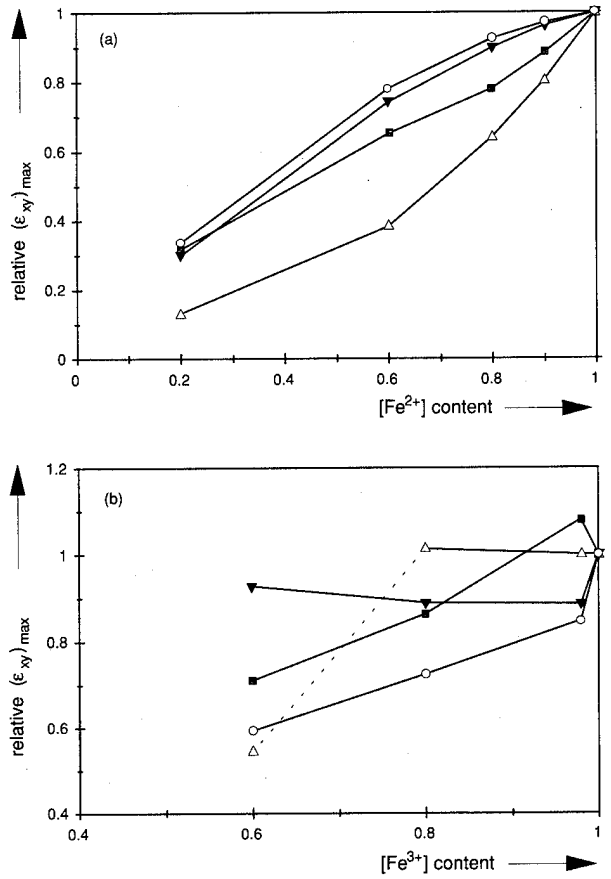



FIG. 1. Relative maximum $\epsilon'_{xy}$ value (a) vs [$Fe^{2+}$] and (b) [$Fe^{3+}$] content for the IVCT transition; (○) 0.56 eV, (□) 1.94 eV, (△) 3.11 eV, and (▼) 3.93 eV.

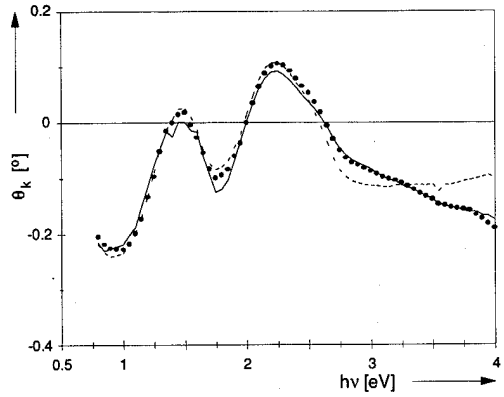



FIG. 2. The measured Kerr rotation spectrum of 115 nm $Fe_3O_4$ layer on $MgAl_2O_4$ (100) (—) vs the theoretical spectrum of a perfect layer (----) and the fitted spectrum (···).

are consistent with the results reported for YIG.[8] From this transition assignment for $Fe_3O_4$ the transition assignment for related ferrites such as $MgFe_2O_4$ and $Li_{0.5}Fe_{2.5}O_4$ can be derived. This assignment should be the same as that of $Fe_3O_4$ without the IVCT transitions as these involve $Fe^{2+}$, although one should allow for some shift in transition energy and differences in intensity. We used the dielectric tensor of $MgFe_2O_4$ from the literature[9] and applied the same fit procedure. This yields three major MO transitions consistent with the ISCT transitions found in $Fe_3O_4$ and in YIG. Hence our assignment: 2.64 eV $(Fe^{3+})t_2 \rightarrow [Fe^{2+}]t_{2g}$, 3.48 eV: $[Fe^{3+}]e_g \rightarrow (Fe^{2+})t_2$ and 3.97 eV: $(Fe^{3+})t_2 \rightarrow [Fe^{2+}]e_{2g}$. The same transitions are observed in $Li_{0.5}Fe_{2.5}O_4$,[2,10] however, at increased intensity and at higher energies compared to $MgFe_2O_4$. The increased intensity is in part due to the increased amount of $Fe^{3+}$ and in part due to the perturbation of the octahedral symmetry as a result of the small ion radius of $Li^+$. The latter is also responsible for the increase in transition energy. The same shift in transition energy is observed for $Al^{3+}$ substitution of $Fe_3O_4$.[7] Thus, also the MO-Kerr spectra of $MgFe_2O_4$ and $Li_{0.5}Fe_{2.5}O_4$ can be interpreted in a consistent manner with the proposed transition assignment given for $Fe_3O_4$.

The data obtained for the transition assignment of $Fe_3O_4$ and the assignment itself can be applied to the investigation of the stoichiometric quality of thin layers of $Fe_3O_4$. The polar Kerr spectra between 0.7 and 4.0 eV were measured of thin layers of $Fe_3O_4$ deposited by oxidic molecular beam epitaxy (MBE)[11] on $MgAl_2O_4$ (100) with thicknesses of 40, 115 (see Fig. 2), and 360 nm. The polar Kerr spectra of these layers are distorted by interference. From the dielectric tensor of $Fe_3O_4$ we were able to calculate the theoretical polar Kerr spectra of these layers (dashed line in Fig. 2), thereby isolating the interference effects from true changes in the dielectric tensor. In the measured spectra (solid line) an energy shift and a reduced intensity for the IVCT transitions is observed. Based on the transition assignment for $Fe_3O_4$ we could identify oxidation of part of the layer as the cause of these changes. Subsequent model calculations (leading to the dotted line in Fig. 2) enabled us to localize and quantify this oxidation to the upper 2–4 nm of the layer.[12,13]

Since the Verwey transition is often taken as an indication for the stoichiometric quality of $Fe_3O_4$,[14,15] we also determined the Verwey temperature, $T_V$, of the 40, 115, and 360 nm thick layers on $MgAl_2O_4$; see Fig. 3. $T_V$ was identified through changes in resistivity, $\rho$, with temperature, $T$. We take as a measure for $T_V$ the temperature at which the derivative of the $\rho/T$ vs $T^{-1}$ is maximum.[16] For the 360 nm thick layer this leads to $T_V = 122 \pm 1$ K, equal to the bulk value. For the 115 nm layer $T_V$ is $109 \pm 1$ K. For the 40 nm thick layer a barely discernable $T_V$ at $107 \pm 1$ K is found. In addition to the shift to lower transition temperature for thinner films, also a broadening of the transition and changes in the high temperature $\rho$ are found.

Oxidation of the *total* layer might lead to the observed reduction in $T_V$.[14] However, the Kerr measurements point to an oxidized surface layer. The changes observed are, therefore, better explained by the influence of the substrate on the conductance of the film. As the perpendicular lattice parameter at room temperature of the 115 nm thick $Fe_3O_4$ layer is $8.398 \pm 0.004$ Å, which is within the experimental accuracy equal to the bulk lattice parameter, epitaxial strain is ruled out as the prime cause for the reduced $T_V$ in this case. However, the difference in thermal expansion coefficients between substrate and the $Fe_3O_4$ film could give rise to the observed increased reduction of $T_V$ for thinner layers. Hence,

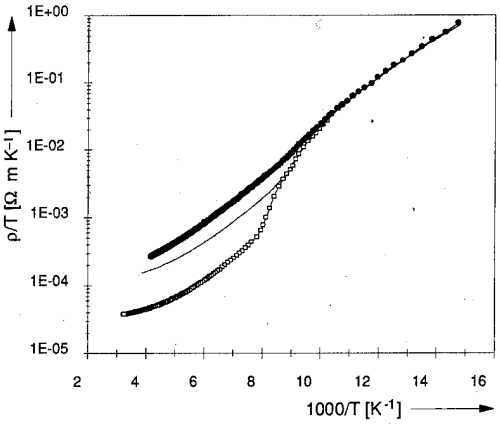



FIG. 3. Specific resistivity divided by temperature, $\rho/T$, of thin layers of $Fe_3O_4$ on $MgAl_2O_4$ as a function of inverse temperature, $T^{-1}$. (●) 40 nm, (–) 115 nm, and (□) 360 nm.

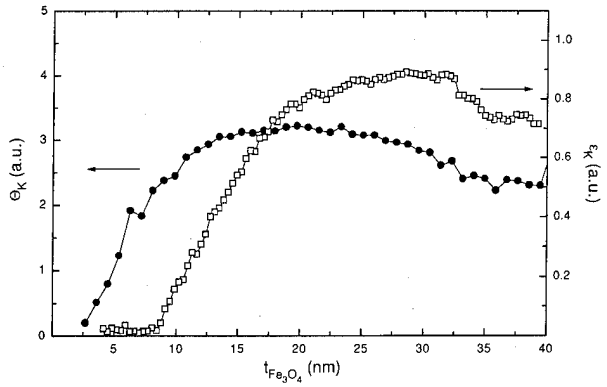



FIG. 4. Comparison of the Kerr effect vs $Fe_3O_4$ layer thickness, $t_{Fe_3O_4}$, for a wedge-shaped $Fe_3O_4$ sample at two wavelengths, λ. (□) ellipticity $\epsilon_K$ at 633 nm; (●) rotation $\Theta_K$ at 514 nm.

as strain due to differences in thermal expansion coefficient influences $T_V$,[17] this parameter may not be suited to assess the stoichoimetric quality of epitaxial thin $Fe_3O_4$ layers. In addition, it does not provide depth dependent information as the Kerr spectrum does.

Finally, we wish to point out the importance of spectral variations in MO-Kerr effect (MOKE) experiments to determine the magnetic anisotropy in ferrite layers grown on a certain substrate. As an example we give the Kerr ellipticity and rotation at a wavelength $\lambda=514$ and 633 nm versus the $Fe_3O_4$ thickness, $t_{Fe_3O_4}$, for a wedge of $Fe_3O_4$ grown on MgO (100) covered with a 2 nm MgO/3 nm NiO capping layer. MgO was chosen as substrate as previous work has shown that growth on this substrate results in proper $Fe_3O_4$.[18] Figure 4 shows that $\lambda=633$ nm (HeNe laser) and $\lambda=514$ nm (the green line of an $Ar^+$ laser) allow the polar MOKE detection of hysteresis loops down to 9 and 2.5 nm, respectively. We should remark that reliable hysteresis loops for anisotropy analysis are only obtained at somewhat larger thicknesses than those listed above, e.g., 12 nm for $\lambda=633$ nm and 8.5 nm for 514 nm. The fact that 514 nm allows the detection at lower thickness is caused by several effects. We have found that interference shifts the MO-Kerr spectrum of thin $Fe_3O_4$ layers to the blue; a capping layer may enhance this effect. Furthermore, the $Fe_3O_4$ absorption is larger at shorter wavelengths. From Fig. 4 we conclude that for studies of wedged-shaped samples judicious selection of the wavelength is important.

## III. CONCLUSIONS

We have found through systematic substitution with $Mg^{2+}$ and $Al^{3+}$ that the main transitions in the magneto-optical (MO)-Kerr spectrum of $Fe_3O_4$ can be assigned to intervalence charge transfer transitions at 0.56, 1.94, 3.11, and 3.93 eV and intersublattice charge transfer transitions at 2.61, 3.46, and 3.94 eV. Also the MO-Kerr spectra of $MgFe_2O_4$ and $Li_{0.5}Fe_{2.5}O_4$ can be assigned consistently. Two applications of this understanding of the MO-Kerr spectrum of $Fe_3O_4$ have been shown in the field of thin oxidic films: first in a stoichiometry analysis of an $Fe_3O_4$ layer, second, in the wavelength selection in MO-Kerr effect studies of such layers.


[1] Z. Šimša, H. LeGall, and P. Široký, Phys. Status Solidi B **100**, 665 (1980).
[2] X. X. Zhang, J. Schoenes, W. Reim, and P. Wachter, J. Phys. C **16**, 6055 (1983).
[3] H. Feil, Solid State Commun. **69**, 245 (1989).
[4] V. A. M. Brabers, T. E. Whall, and P. S. A. Knapen, J. Cryst. Growth **69**, 101 (1984).
[5] J. C. Jans, Philips J. Res. **47**, 347 (1993).
[6] F. J. Kahn, P. S. Pershan, and J. P. Remeika, Phys. Rev. **186**, 891 (1969).
[7] W. F. J. Fontijn, P. J. van der Zaag, M. A. C. Devillers, V. A. M. Brabers, and R. Metselaar (to be published).
[8] G. B. Scott and D. E. Lacklison, IEEE Trans. Magn. **MAG-12**, 292 (1976).
[9] G. B. Scott and J. L. Page, Phys. Status Solidi B **79**, 203 (1977).
[10] Š. Višňovsky, V. Prosser, R. Krishnan, V. Parízek, K. Nitsch, and L. Svobodová, IEEE Trans. Magn. **MAG-17**, 3205 (1981).
[11] R. M. Wolf, A. E. M. De Veirman, P. van der Sluis, P. J. van der Zaag, and J. B. F. aan de Stegge, Mater. Res. Soc. Symp. Proc. **341**, 23 (1994).
[12] W. F. J. Fontijn, R. M. Wolf, R. Metselaar, and P. J. van der Zaag (to be published).
[13] Interestingly, preliminary magnetization and resistivity data as a function of $Fe_3O_4$ layer thickness suggest a "dead" layer of a similar thickness of about 3 nm.
[14] J. P. Shepherd, J. W. Koenitzer, R. Aragón. J. Spalek, and J. M. Honig, Phys. Rev. B **43**, 8461 (1991).
[15] E. Lochner, K. A. Shaw, R. C. DiBari, W. Portwine, P. Stoyonov, S. D. Berry, and D. M. Lind, IEEE Trans. Magn. **MAG-30**, 4912 (1994).
[16] Note that in inhomogeneously strained systems the normal definition of $T_V$ loses meaning due to the broadening of the Verwey transition.
[17] J. S.-Y. Feng and M.-A. Nicolet, J. Phys. Chem. Solids **36**, 835 (1975).
[18] P. A. A. van der Heijden, J. J. Hammink, P. J. H. Bloemen, R. M. Wolf, M. G. van Opstal, P. J. van der Zaag, and W. J. M. de Jonge, Mater. Res. Soc. Symp. Proc. **384**, 27 (1995).

# Site affinity of substituents in $Nd_2Fe_{17-x}T_x$ (T=Cu,Zr,Nb,Ti,V) alloys

W. B. Yelon and Z. Hu
*Research Reactor Center, University of Missouri–Columbia, Columbia, Missouri 65211*

W. J. James and G. K. Marasinghe
*Graduate Center for Materials Research, University of Missouri–Rolla, Rolla, Missouri 65401*

In order to understand the magnetic properties of the substituted rare-earth-iron alloys, it is especially important to know the location of the substitutional atoms within the iron lattice. The site distributions of some nontransition-metal substituents in the substituted $Nd_2Fe_{17-x}T_x$ alloys have previously been reported. Here we report the site distributions of some transition-metal substituents (Cu,Zr,Nb,Ti,V) in the $Nd_2Fe_{17-x}T_x$ alloys and compare them with those of the nontransition-metal substituted compounds. Rietveld analysis of neutron powder diffraction data indicates that the nontransition-metal substituents show very similar site affinity at low substituent content. For example Al, Ga, and Si all prefer the 18*h* sites. The transition-metal substituents show a more complex site affinity. Ti and V atoms strongly prefer the 6*c* sites, Cu atoms prefer the 9*d* and 18*f* sites, Nb atoms prefer the 6*c* and 18*h* sites, and Zr atoms prefer 6*c* and 18*f* sites. It was also noted that the site affinity can change if carbon is included in the melting procedure of the sample preparation. The superconducting quantum interference device measurements show that all the substituted compounds have a Curie temperature higher than the unsubstituted parent compound. The relationship between the site distribution of substituents and the magnetic properties of the substituted $Nd_2Fe_{17-x}T_x$ alloys is discussed. © *1996 American Institute of Physics.*
[S0021-8979(96)33208-3]

## INTRODUCTION

High performance permanent magnets should exhibit a Curie temperature ($T_c$) high enough to ensure the stability of the magnetic properties under operating conditions. Moving more and more of the iron–iron bonds into the optimum ferromagnetic exchange distance range while leaving a sufficiently concentrated iron lattice is one possible way of improving the Curie temperature of the rare-earth-iron compounds. Intensive research on enhancing the magnetic properties of the rare-earth-iron compounds by incorporation of interstitial atoms[1–6] and incorporation of substitutional atoms[7–15] (or by a combination of those two methods)[16,17] has been carried out recently.

It is well accepted that different Fe sites are of differing importance in the magnetic exchange coupling. Thus, it is especially important to know the location of substituents because new materials may be optimized by the elimination of particular exchange interactions detrimental to strong ferromagnetic interaction. The only tool capable of extracting this information directly is neutron diffraction. Analysis of the site substitution mechanism may lead to substituted compounds in which the desirable Fe–Fe bond lengths are maintained while the Fe atoms of the less desirable bonds are replaced by nonmagnetic species to give Curie temperatures high enough to be of technological interest.

We have previously reported the site distribution of some nontransition-metal substituents[6–8,14,15] in the substituted $Nd_2Fe_{17-x}T_x$ alloys. Little is known about the site distributions for most transition-metal substituents except Co.[18] The site distributions of some transition metal substituents (Cu,Zr,Nb,Ti,V) in $Nd_2Fe_{17-x}T_x$ alloys are reported. Our focus is on low substituent content because high substituent content will result in a larger reduction of magnetization.

## EXPERIMENT

Samples of $Nd_2Fe_{17-x}T_x$ (T=Ti,V,Cu,Zr,Nb) were prepared from 99.9% or higher purity elements by rf induction melting in a flowing argon atmosphere at the Materials Research Center of the University of Missouri–Rolla. After melting, the ingots were wrapped in tantalum foil and were vacuum annealed at 950 °C for one week. The ingots were then crushed and ground finely in an acetone bath.

The powder neutron diffraction patterns were collected at the Missouri University Research Reactor Center by using a linear position sensitive detector with a wavelength of 1.4783 Å. The data for each sample were collected at room temperature on ~2 g of a finely powdered sample placed in a thin wall vanadium container. The two-theta range is from 5° to 105°.

Refinements of the neutron diffraction data were carried out using the program FULLPROF, which permits multiple phase refinement as well as magnetic structure refinement of each of the coexisting phases. In each of the samples, a small amount of $\alpha$-Fe, ranging from 0.5% to 5% in volume, was the only detectable second phase. The Curie temperatures were measured by a superconducting quantum interference device using a Quantum Design MPMS system.

 0021-8979/96/79(8)/5939/3/$10.00 © 1996 American Institute of Physics 

TABLE I. Site occupancies of substituents in 2:17 compounds.

| Compound | Lattice parameter | | | | $\chi^2$ | Substituent occupancies (%) | | | | $T_C$ (K) |
|---|---|---|---|---|---|---|---|---|---|---|
| | $a$ (Å) | $c$ (Å) | $c/a$ | $V$ (Å$^3$) | | $6c$ | $9d$ | $18f$ | $18h$ | |
| $Nd_2Fe_{16.03}Ti_{0.97}$ | 8.6135(1) | 12.5244(2) | 1.4540 | 804.723 | 2.24 | 34.1 | 1.2 | 2.4 | 1.4 | 383 |
| $Nd_2Fe_{16.03}V_{0.97}$ | 8.5993(2) | 12.5109(4) | 1.4549 | 801.211 | 1.69 | 38.9 | 0.0 | 3.2 | 0.0 | 365 |
| $Nd_2Fe_{16.29}Cu_{0.71}$ | 8.5727(2) | 12.4530(2) | 1.4526 | 792.575 | 1.97 | 0.0 | 7.6 | 8.0 | 0.0 | 360 |
| $Nd_2Fe_{16.12}Zr_{0.88}$ | 8.5903(3) | 12.4730(5) | 1.4520 | 797.100 | 2.24 | 7.8 | 0.0 | 12.0 | 0.0 | 375 |
| $Nd_2Fe_{15.99}Nb_{1.01}$ | 8.5971(2) | 12.4912(3) | 1.4530 | 799.527 | 1.54 | 16.2 | 0.0 | 7.0 | 4.4 | 370 |
| $Nd_2Fe_{15}Al_2$ | 8.6569(1) | 12.5782(3) | 1.4530 | 814.300 | 2.18 | 4.0 | 0.0 | 7.0 | 24.8 | 435 |
| $Nd_2Fe_{14.8}Si_{2.2}$ | 8.5524(3) | 12.4988(5) | 1.4614 | 791.724 | 3.80 | 0.0 | 7.2 | 0.0 | 33.5 | 470 |
| $Nd_2Fe_{14.9}Ga_{2.1}$ | 8.6281(1) | 12.5531(2) | 1.4549 | 809.304 | 3.34 | 0.0 | 0.0 | 8.8 | 25.6 | [a] |
| $Nd_2Fe_{15.99}Ti_{1.01}$ | 8.6042(3) | 12.5133(5) | 1.4543 | 802.271 | 2.42 | 37.7 | 0.0 | 2.6 | 1.6 | [a] |
| $Nd_2Fe_{15.94}Ti_{1.06}C_{0.29}$ | 8.6452(5) | 12.4875(9) | 1.4444 | 808.270 | 3.82 | 1.2 | 4.8 | 6.4 | 8.4 | [a] |

[a]Have not been measured.

## RESULTS AND DISCUSSION

The site occupancies of the transition-metal substituents and the lattice parameters of $Nd_2Fe_{17-x}T_x$ (T=Ti, V, Cu, Zr, and Nb), obtained from neutron diffraction data, are given in Table I. For comparison, the site occupancies of some nontransition-metal substituents and their lattice parameters in $Nd_2Fe_{17-x}T_x$ (T=Al,Si,Ga), obtained in previous studies, are also given in Table I.

The unsubstituted parent compound $Nd_2Fe_{17}$ has a unit cell volume of 799.7 Å$^3$. The substituents will change the unit cell volume due to the different "size" of different substituents and/or some other chemical/electronic effects. Previous studies showed that the nontransition-metal Al and Ga will increase the unit cell volume[6–8] while Si will decrease it.[14,16] That behavior can be explained by the "size effect" because Al and Ga have an atomic radius larger than that of Fe while Si has a radius smaller than that of Fe. However, the case of transition metal substitution is complex. Although most of the transition metals, such as Ti, V, Zr, and Nb, have a free atom radius much bigger than Al or Ga, the volume effect of the transition-metal substitutions are much weaker than those of the nontransition-metal substitutions. The Al or Ga expands the unit cell of $Nd_2Fe_{17}$ compound by more than 8.5 Å$^3$/per substituent atom.[6–8] In contrast, the first-row transition metals Ti and V only increase the unit cell by 1.4 Å$^3$/V atom and 5.0 Å$^3$/Ti atom, respectively, while the second-row transition metals Zr and Nb even decrease the unit cell slightly (Table I). This behavior strongly suggests that the transition-metal substituents bond to Fe and Nd atoms in the 2:17 compound more strongly than do the nontransition metals.

For a singly substituted compound, the site distribution of substituents can be determined directly from the neutron diffraction data. From Table I, we see that nontransition metal substituents have a strong preference for the $18h$ site, which can be explained by the coordination effect, because $18h$ sites have the most rare earth neighbors (three) and the fewest transition neighbors (nine). Nontransition metal substituents show a preference for bonding to rare earth atoms. The transition metal substituents show more complex site affinities. For the first-row transition metals Ti, V, and Cu, the steric effect alone can be used to explain the site affinity. For the Cu compound, the small atom radius of Cu results in Cu occupancy of the $9d$ (which has the smallest size) and the $18f$ sites (which have the second smallest size). For the Ti and V compounds, the large atom radii of Ti and V force them to occupy the largest $6c$ sites and leave the other sites almost empty of substituents. For the second-row transition-metal substituents Zr and Nb, the site affinities of the transition-metal substituents appear to be the result of a combination of the steric effect and the coordination effect. Because they have large atom radii, the steric effect will promote occupancy of the largest $6c$ sites or the second largest $18h$ sites. However, because of their negative affinity for rare-earth neighbors, they avoid the $18h$ site, but take the $18f$ site. While Nb has a stronger affinity for the $6c$ site than for the $18f$ site, Zr shows an inverse site affinity.

Another interesting behavior which has recently been observed is also given in Table I. When carbon is included in the melt, the site affinity of Ti is totally changed. As can be seen from Table I, the Ti atoms strongly prefer the $6c$ sites if the sample contains no C. However, if C is introduced into the sample by melting (not the gas phase reaction method), the Ti atoms prefer the $18h$ and $18f$ sites. This phenomenon does not occur for nontransition-metal substituents.[19] A broader and deeper study of this phenomenon is underway.

The Curie temperatures of some samples were measured by a superconducting quantum interference device and the results are given in Table I. All the substituted samples have a Curie temperature higher than that of the unsubstituted parent compound $Nd_2Fe_{17}$ (330 K) regardless of the unit cell size.

## CONCLUSIONS

The nontransition-metal substituents show very similar site affinities at low substitutent content: all prefer the $18h$ sites. The transition-metal substituents show a more complex site affinity, e.g., Ti and V atoms prefer the $6c$ sites, Cu atoms prefer the $9d$ and $18f$ sites, Zr and Nb atoms prefer the $6c$ and $18f$ sites. The site affinity of the transition-metal substituent can change if carbon is included in the sample preparation by melting. All the substituted compounds have Curie temperatures higher than the unsubstituted parent compound.

## ACKNOWLEDGMENTS

The authors would like to thank the Division of Materials Research of the National Science Foundation, for Grant No. DMR 9305782 and the Missouri University Research Board.

[1] D. B. de Mooij and K. H. J. Buschow, J. Less-Common Met. **142**, 349 (1988).
[2] R. B. Helmholdt and K. H. J. Buschow, J. Less-Common Met. **155**, 15 (1989).
[3] J. M. D. Coey and H. Sun, J. Magn. Magn. Mater. **87**, 1251 (1990).
[4] H. Sun, J. M. D. Coey, Y. Otani, and D. P. F. Hurley, J. Phys. Condens. Matter **2**, 6465 (1990).
[5] Y. C. Yang, X. D. Zhang, L. S. Kong, Q. Pan, J. L. Yang, Y. F. Ding, B. S. Zhang, and C. T. Ye, Solid State Commun. **78**, 313 (1991).
[6] W. B. Yelon, H. Xie, G. J. Long, O. A. Pringle, F. Grandjean, and K. H. J. Buschow, J. Appl. Phys. **73**, 6029 (1993).
[7] G. J. Long, G. K. Marasinghe, Z. Hu, W. B. Yelon, D. P. Middleton, K. H. J. Buschow, and F. Grandjean, J. Appl. Phys. **76**, 5383 (1994).
[8] Z. Hu, W. B. Yelon, S. Mishra, G. J. Long, O. A. Pringle, D. P. Middleton, K. H. J. Buschow, and F. Grandjean, J. Appl. Phys. **76**, 443 (1994).
[9] R. van Mens, J. Magn. Magn. Mater. **61**, 24 (1986).
[10] E. E. Alp, A. M. Umarji, S. K. Malik, G. K. Shenoy, M. Q. Huang, E. B. Boltich, and W. E. Wallace, J. Magn. Magn. Mater. **68**, 305 (1987).
[11] P. C. M. Gubbens, A. M. van der Kraan, T. H. Jacobs, and K. H. J. Buschow, J. Less-Common Met. **159**, 173 (1990).
[12] C. Lin, Y. X. Sun, Z. X. Liu, H. W. Jiang, G. Jiang, Y. L. Yang, B. S. Zhang, and Y. F. Ding, Solid State Commun. **81**, 299 (1992).
[13] F. Pourarian, R. Obermyer, Y. Zhang, S. G. Shankar, and W. E. Wallace, J. Appl. Phys. **73**, 6272 (1993).
[14] G. J. Long, G. K. Marasinghe, S. Mishra, O. A. Pringle, F. Grandjean, K. H. J. Buschow, D. P. Middleton, W. B. Yelon, F. Pourarian, and O. Isnard, Solid State Commun. **88**, 761 (1993).
[15] D. P. Middleton, S. Mishra, G. L. Long, O. A. Pringle, Z. Hu, W. B. Yelon, F. Grandijean, and K. H. J. Buschow, J. Appl. Phys. (to be published).
[16] W. B. Yelon, Z. Hu, E. W. Singleton, and G. C. Hadjipanayis, J. Appl. Phys. (submitted).
[17] G. K. Marasinghe, P. C. Ezekwenna, W. J. James, G. J. Long, O. A. Pringle, Z. Hu, and W. B. Yelon, these proceedings.
[18] J. Herbst, J. Croat, and W. B. Yelon, J. Appl. Phys. **53**, 250 (1982).
[19] H. Luo, Z. Hu, and W. B. Yelon (unpublished).

# Electronic structure and magnetism in $Sm_2Fe_{17-x}A_x$ (A=Al,Ga,Si)

R. F. Sabirianov and S. S. Jaswal
*Behlen Laboratory of Physics and Center for Materials Research and Analysis, University of Nebraska, Lincoln, Nebraska 68588-0111*

Self-consistent spin–polarized electronic structure calculations have been carried out to derive the magnetic properties of the $Sm_2Fe_{17-x}A_x$ (A=Al, Ga, Si and $x=0$ and 1). The influence of impurities on the Curie temperature ($T_C$) of $Sm_2Fe_{17}$ has been studied using the spin–fluctuation approach of Mohn and Wohlfarth. The calculated $T_C$ generally goes up with the addition of each impurity but the relative increase in $T_C$ depends on the type of the impurity and its site. The calculated $T_C$ enhancement weighted with the impurity-site occupancy from Mössbauer data are in good agreement with the experimental data. © *1996 American Institute of Physics.*
[S0021-8979(96)33308-X]

Recently a substantial enhancement in $T_C$ has been observed with a low concentration of impurities substituting for Fe in $R_2Fe_{17}$ compounds.[1–8] For example a substitution of Al, Ga, and Si for one of the Fe atoms in $Sm_2Fe_{17}$ raises its $T_C$ from 391 (Refs. 2–5) to 410 (Ref. 7) to 417 (Ref. 2), 468 (Ref. 5) to 512 (Ref. 6), and 490 (Ref. 7), respectively. In this paper we start with the study of the magnetovolume effect of the parent compound $Sm_2Fe_{17}$. Then we examine how various impurities substituting for Fe in $Sm_2Fe_{17}$ modify its magnetization and Curie temperature ($T_C$). Calculated results are compared with the available data.

We employ the linear-muffin-tin-orbitals (LMTO) method in the atomic sphere approximation to calculate the self-consistent spin–polarized electronic structure and magnetic properties of ferromagnetic (FM) $Sm_2Fe_{17-x}A_x$ (A =Al, Ga, Si and $x=0,1$) alloys. Sm $4f$ electrons are treated as core electrons with their spins antiparallel to those of the majority of Fe electrons (Total energy calculations show that this state is more stable than the parallel–spin-alignment state.) We use the linear tetrahedron method with 65 $k$ points in the irreductible part of the Brillouin zone for $Sm_2Fe_{17}$. The calculations with impurities were carried out for the same cell as for $Sm_2Fe_{17}$. Because of the changes in the point-group symmetry due to a large number of the impurities considered here we performed all the impurity calculations at 64 $k$ points distributed throughout the entire Brillouin zone. The lattice parameters for the various alloys were taken from Refs. 1–8.

The $Sm_2Fe_{17}$ has a rhombohedral $Th_2Zn_{17}$ structure. The unit cell contains 19 atoms with 1 Sm and 4 Fe sites. The number of nearest neighbors is 12 for $d$, $f$, and $h$ Fe sites, and 14 for $c$ Fe sites. The relative positions of neighbors are similar for $d$, $f$, and $h$ sites with icosahedral symmetry environment. The $d$ site has some rotational distortion and distortion in interatomic distances, but $f$ and $h$ sites are almost ideally icosahedrally coordinated.

Self-consistent spin–polarized electronic structure calculations are used to calculate the magnetic moments at various sites in $Sm_2Fe_{17}$ as a function of the volume. The magnetization decreases rapidly with decreasing volume [Fig. 1(a)]. This behavior is similar to the magnetovolume effect in fcc Fe, but transition to the state with low magnetic moment is not as steep. Beuerle *et al.* obtained similar results for $Y_2Fe_{17}$.[9] The site decomposed magnetic moments are presented in Fig. 1(b). The $c$ site has the largest while the $d$ site has the smallest magnetic moment of all the Fe atoms. This is the expected magnetovolume effect because the $c(d)$ site has the largest (smallest) Wigner–Seitz (WS) volume of all the Fe atoms. Finally the induced non-$4f$ spin moment on Sm is antiparallel to those of Fe moments, the well-known hybridization effect.

Substitutional impurities modify hard-magnet properties due to changes in hybridization produced by changes in bonding and volume. We use the Mössbauer data as a guide to study the effect of impurities on the magnetic properties of $Sm_2Fe_{17}$. Due to the complexity of this problem we consider a single impurity per cell, i.e., $Sm_2Fe_{16}A$ (A=Al, Ga, Si). Furthermore we consider one site at a time for each impurity. The calculated magnetization results are compared with the

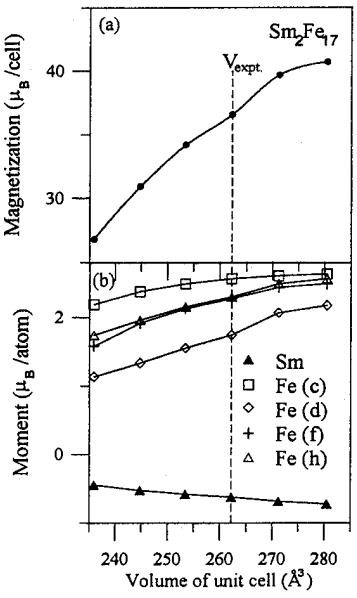



FIG. 1. (a) Magnetization and (b) site decomposed magnetic moment per atom as a function of the cell volume for $Sm_2Fe_{17}$.

 0021-8979/96/79(8)/5942/3/$10.00 © 1996 American Institute of Physics

TABLE I. Magnetization in $Sm_2Fe_{16}A(\mu_B/atom)$.

| A→ | Fe | Al($c$) | Al($f$) | Al($h$) | Ga($c$) | Ga($f$) | Ga($h$) | Si($c$) | Si($f$) | Si($h$) |
|---|---|---|---|---|---|---|---|---|---|---|
| Theory[a] | 2.001 | 1.924 | 1.950 | 1.969 | 1.944 | 1.972 | 1.972 | 1.871 | 1.884 | 1.930 |
| Expt. | 1.868[b] | | 1.642[b](4.2 K) | | | 1.68[c](300 K) | | | 1.312[d](300 K) | |

[a]Calculated magnetization values include a Sm $4f$ contribution of 0.715 $\mu_B$/atom.
[b]Reference 1.
[c]Reference 4.
[d]Reference 8.

available experimental data in Table I. In this comparison one should keep in mind that the 0 K calculated results depend on the degree of $4f$ polarization and the experimental data depend on the temperature.

Finally, we consider the enhancements in $T_C$ due to various impurities in $Sm_2Fe_{17}$. The exchange–parameter analysis described earlier gives only a qualitative description of magnetism in $Sm_2Fe_{17}$ but the $T_C$ estimated from this model is too high. The spin–fluctuation model of Mohn and Wohlfarth[11] has been reasonably successful[12] in predicting the changes in $T_C$. We use this model here to study the changes in $T_C$. In this model

$$T_C \propto \frac{M_0^2}{\chi_0}, \tag{1}$$

where $M_0$ is the Fe magnetization per unit cell and $\chi_0$ is the enhanced ferromagnetic susceptibility, both at 0 K,

$$\frac{1}{\chi_0} = \frac{1}{4\mu_B^2}\left(\frac{1}{N^{\uparrow}(E_F)} + \frac{1}{N^{\downarrow}(E_F)} - 2I\right), \tag{2}$$

where $N^{\uparrow}(E_F)$ and $N^{\downarrow}(E_F)$ are, respectively, the average spin-up and spin-down density of states (DOS) per Fe atom at the Fermi energy ($E_F$) and $I$ is the Stoner parameter. Our calculations give $I$=0.91 eV. As can be seen from Table I, the changes in the calculated magnetization for the various impurities are quite small. Thus most of the changes in $T_C$ must come from the changes in $N^{\uparrow}(E_F)$ and $N^{\downarrow}(E_F)$. In general, a decrease in DOS at $E_F$ enhances $T_C$ as can be seen from Eqs. (1) and (2). To qualitatively see how impurities enhance $T_C$ we show the site-projected DOS for $Sm_2Fe_{17}$ in Fig. 2. The result for the four Fe sites are qualitatively similar with the DOS near $E_F$ dominated by the $d$ states. An impurity modifies the width of the Fe $d$ band and promotes new Fe states at the impurity $p$ band (~8 eV below $E_F$) through magnetovolume and hybridization effects. These changes lead to changes in $M_0$ and $\chi_0$ and hence $T_C$. Since $E_F$ is located at different points along a steep edge of majority DOS for different Fe sites, the narrowing of their bands due to volume expansion and lower impurity–Fe ($s$–$d$) hybridization compared to that of Fe–Fe ($d$–$d$) will lower $N^{\uparrow}(E_F)$ (raise $T_C$) by varying amounts. As can be seen from Fig. 2, the $c(d)$ sites will make the least (most) contribution. Also while volume expansion enhances $M_0$, the promotion of new unpolarized Fe $p$ states by the impurity lowers $M_0$.

The overall effect on $T_C$ of the various changes in the electronic structure produced by different impurities is shown in Table II. All three impurities at $c$, $f$, and $h$ sites enhance $T_C$ with the enhancement being minimum for the $c$ site and the maximum for the $h$ site. The result for the $c$ site is in agreement with the prediction in the last paragraph. No calculations were carried out for the $d$ site because the Mössbauer data, also shown in Table II, do not give any occupancy for this site. The calculated ratios of $T_C$ weighted with the experimental site occupancy are also shown in Table II along with the experimental data. The reasonable agreement between theory and experiment supports the Mössbauer results for the relative site occupancies. What determines the relative site occupancies for different impurities is an interesting but difficult question.

Finally it is interesting that $T_C$ increases by ~21% with the Si impurity even though the volume decreases slightly.[7] This is primarily due to the narrowing of $d$ bands of Fe atoms surrounding the impurity because the Si–Fe hybridization is lower than that of Fe–Fe.

In conclusion we have used the changes in electronic structure in going from $Sm_2Fe_{17}$ to $Sm_2Fe_{16}A$ (A=Al, Ga, Si) and the spin–fluctuation theory to explain substantial enhancements in the Curie temperature.

We are thankful to I. A. Al-Omari and Professor D. J. Sellmyer for many helpful discussions. This work is supported by the U.S. Department of Energy under Grant No.

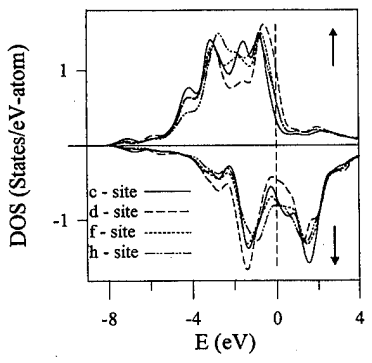



FIG. 2. Site-projected spin–polarized density of states of $Sm_2Fe_{17}$ for the various Fe sites. The zero along the $x$ axis corresponds to the Fermi energy.

TABLE II. The Curie temperature ratio and site occupancies for $Sm_2Fe_{16}A$.

| A→ | Al($c$) | Al($f$) | Al($h$) | Ga($c$) | Ga($f$) | Ga($h$) | Si($c$) | Si($f$) | Si($h$) |
|---|---|---|---|---|---|---|---|---|---|
| $\left(\frac{T_c^{imp}}{T_C^{Sm_2Fe_{17}}}\right)_{calc}$ | 1.15 | 1.51 | 1.53 | 1.25 | 1.52 | 1.52 | 1.04 | 1.16 | 1.29 |
| Occupancy, (%)[a] | 93 | 0 | 7 | 69.4 | 0 | 30.6 | 19.3 | 61.4 | 19.3 |
| $\left(\frac{T_c^{imp}}{T_C^{Sm_2Fe_{17}}}\right)_{weight}$ | | 1.17 | | | 1.33 | | | 1.17 | |
| $\left(\frac{T_c^{imp}}{T_C^{Sm_2Fe_{17}}}\right)_{expt}$ | | 1.07[b] | | | 1.32[c], 1.20[d] | | | 1.20[e] | |

[a]From Mössbauer data in Refs. 7 and 10.
[b]Reference 2.
[c]Reference 6.
[d]Reference 5.
[e]Reference 7.

DE-FG2-86ER45262 and the National Science Foundation under Grant No. OSR-925525.

[1]D. McNeely and H. Oesterreicher, J. Less-Common Met. **44**, 183 (1976).
[2]Z. Wang and R. A. Dunlap, J. Phys. Cond. Matter **5**, 2407 (1993).
[3]X. Li, N. Tang, Z. Lu, T. Zhao, W. G. Lin, and R. Zhao, J. Appl. Phys. **73**, 5890 (1993).
[4]N. Tang, J. L. Wang, Y. H. Gao, W. Z. Li, F. Yang, and F. R. de Boer, J. Magn. Magn. Mater. **140–144**, 979 (1995).
[5]Z. Wang and R. A. Dunlap, Philos. Mag. B **69**, 103 (1994).
[6]B. G. Shen, F. W. Wang, L. S. Kong, and L. Cao, J. Phys. Cond. Matter **5**, L685 (1993).
[7]Z. W. Li, X. Z. Zhou, and A. H. Morrish, Phys. Rev. B **51**, 2891 (1995), and reference therein.
[8]B. Liang, B. Shen, Z. Cheng, J. Zhang, H. Gong, F. Wang, S. Zhang, and W. Zhan, Solid State Commun. **95**, 301 (1995).
[9]T. Beuerle, P. Braun, and M. Fähnle, J. Magn. Magn. Mater. **94**, L11 (1991).
[10]I. A. Al-Omari, S. S. Jaswal, A. S. Fernando, and D. J. Sellmyer, J. Appl. Phys. **76**, 6159 (1994); I. A. Al-Omari, S. S. Jaswal, E. W. Singleton and D. J. Sellmyer, J. Magn. Magn. Mater. (in press).
[11]P. Mohn and E. P. Wohlfarth J. Phys. F Met. Phys. **17**, 2421 (1987).
[12]S. S. Jaswal, W. B. Yelon, G. C. Hadjipanayis, Y. Z. Wang, and D. J. Sellmyer, Phys. Rev. Lett. **67**, 644 (1991).

# A magnetic, neutron diffraction, and Mössbauer spectral study of the $Ce_2Fe_{17-x}Al_x$ solid solutions (abstract)

Sanjay R. Mishra, Gary J. Long, and O. A. Pringle
*Departments of Physics and Chemistry, University of Missouri-Rolla, Rolla, Missouri 65409-0010*

Z. Hu and W. B. Yelon
*University of Missouri Research Reactor, University of Missouri-Columbia, Columbia, Missouri 65211*

D. P. Middleton
*Philips Research Laboratories, P.O. Box 80000, NL-5600 JA Eindhoven, The Netherlands*

K. H. J. Buschow
*Van der Waals-Zeeman Laboratory, University of Amsterdam, NL-1018 XE Amsterdam, The Netherlands*

F. Grandjean
*Institute of Physics, B5, University of Liége, B-4000 Sart-Tilman, Belgium*

The magnetic properties of a series of $Ce_2Fe_{17-x}Al_x$ solid solutions with $x$ equal to 0.0, 0.88, 2.06, 2.80, 3.98, 5.15, 6.08, 7.21, 8.20, 9.08, 9.84, and 10.62 have been studied by magnetic measurements, neutron diffraction, and Mössbauer spectroscopy. Neutron diffraction data indicate that the compounds all crystallize in the rhombohedral $Th_2Zn_{17}$-type structure. The aluminum atoms are excluded from the 9*d* site and show a distinct preference for the 6*c* site for $x$ greater than 6. The substitution of aluminum leads to an expansion of the $a$ and $c$ axis by 0.5% and 0.4% per aluminum atom. The unit cell volume increases by approximately 1.4% per aluminum atom. The magnetic moment per formula unit, measured at 295 K, shows very little change for $x$ less than or equal to 4, but decreases rapidly with increasing aluminum content for higher values of $x$, indicating that aluminum acts as a magnetic hole at the lower concentrations. The Curie temperature increases from 238 K in $Ce_2Fe_{17}$ to a maximum of 384 K in $Ce_2Fe_{14}Al_3$. The $Ce_2Fe_{17-x}Al_x$ solid solutions behave as spin glasses for $x$ greater than 7. The Mössbauer spectra have been fit with a binomial distribution of the near-neighbor environments in terms of a maximum hyperfine field, $H_{max}$, for an iron atom with zero aluminum near neighbors, and a decremental field, $\Delta H$, per aluminum near neighbor. Mössbauer spectral results indicate both that the samples are ferromagnetically ordered in the basal plane for $x$ values between 0.2 and 7 and that a magnetic phase transition occurs from helimagnetic in $Ce_2Fe_{17}$ to ferromagnetic in $Ce_2Fe_{16.8}Al_{0.2}$. However, at 295 K ferromagnetic ordering is observed only for $x$ values between 2 and 5. The average value of $H_{max}$ decreases by about 25 kOe per aluminum atom. The isomer shift increases with aluminum content, an increase which can be explained by the screening of the 4*s* conduction electrons by the 3*d* band electrons. $\Delta H$ decreases by about 1.0 kOe per aluminum atom, a decrease which can be explained by the indirect exchange interaction between iron atoms modified by the presence of non-magnetic aluminum atoms through the 4*s* conduction band. *Note added in proof:* A full account of this work has been published in *J. Appl. Phys. 79*, 3145 (1996). © *1996 American Institute of Physics.* [S0021-8979(96)65208-8]

# Magnetization and coercivity of $Mn_{3-\delta}Ga$ alloys with a $D0_{22}$-type structure

Hiroshi Niida[a] and Tomiei Hori[b]
*Shibaura Institute of Technology, Fukasaku, Oomiya, Saitama 330, Japan*

Hideya Onodera and Yasuo Yamaguchi
*Institute for Materials Research, Tohoku University, Sendai 980, Japan*

Yasuaki Nakagawa
*Department of Electronics, Tohoku Institute of Technology, Yagiyama, Sendai 982, Japan*

The $D0_{22}$-type ($Al_3Ti$-type) phase in the Mn–Ga system is ferrimagnetic; the spin direction is parallel to the tetragonal $c$ axis. The Curie temperature is about 765 K (for $\delta$=0.67), near the decomposition temperature. We have prepared the $D0_{22}$-type alloys by annealing the quenched ingots of the high-temperature phase ($\gamma_{Mn}$ phase) at 400 or 300 °C for a long time. The preparation becomes much easier if the ingots are powdered by filing before the annealing. The single-phase specimens of $Mn_{3-\delta}Ga$ were obtained in the composition range $0.15 \leqslant \delta \leqslant 1.06$. The coercivity of some specimens was so large that we measured the magnetization curve in high magnetic fields up to 150 kOe. The room-temperature values of saturation magnetization, remanent magnetization, and coercivity of the powder sample of the alloy with $\delta$=0.67 are 50 emu/g, 25 emu/g, and 13.5 kOe, respectively. We have also studied the effect of magnetic annealing during the transition from the $\gamma_{Mn}$ phase to the $D0_{22}$-type phase and the effect of the addition of Fe to $Mn_{3-\delta}Ga$ of the $D0_{22}$-type phase. © *1996 American Institute of Physics.* [S0021-8979(96)33408-6]

## I. INTRODUCTION

The $D0_{22}$-type ($Al_3Ti$-type) phase in the Mn–Ga system is known to be ferrimagnetic; the magnetic structure is revealed by neutron diffraction experiments,[1] as shown in Fig. 1. It has also been reported that the $D0_{22}$-type alloy with 74.7 at. % Mn ($Mn_{3-\delta}Ga$ with $\delta$=0.05) shows a large coercivity of 4.5 kOe[2] probably because of a large uniaxial magnetic anisotropy. But, detailed studies on these alloys have not been published to date.

We have made x-ray diffraction experiments and magnetic measurements for the Mn–Ga alloys in a wide composition range. The $D0_{22}$-type phase is unstable at the stoichiometric composition ($Mn_3Ga$), so we have examined $Mn_{3-\delta}Ga$ with appropriate values of $\delta$. We have investigated the composition dependence of the lattice constants, Curie temperature, decomposition temperature, saturation magnetization, remanent magnetization, coercivity, and magnetic annealing effect of these alloys.

## II. EXPERIMENTS

Ingots were prepared by melting gallium (99.9999%) and electrolytic manganese (99.9%) using an argon arc furnace. The ingot was sealed in an evacuated quartz tube with argon gas of $2.2\times10^4$ Pa, annealed for more than 24 h at 900 °C, and quenched into water to obtain homogeneous alloys of the $\gamma_{Mn}$ phase with a fcc structure. Further, powder samples were prepared by filing a small portion of the ingot. We have prepared the $D0_{22}$-type alloys by annealing the ingots or the powder samples at 400 or 300 °C for several days. The preparation is much easier for the powder samples since the stress caused by filing enhances the rate of transition from the $\gamma_{Mn}$ phase to the $D0_{22}$-type phase. We have confirmed by x-ray diffraction experiments that the single $D0_{22}$-type phase specimens of $Mn_{3-\delta}Ga$ are obtained in the composition range $0.15 \leqslant \delta \leqslant 1.06$.

Magnetization measurements were made using a Faraday-type automatic magnetic balance and a Foner-type magnetometer in magnetic fields up to 10 or 20 kOe. Some measurements were extended to 150 kOe using a Bitter magnet.

## III. RESULTS AND DISCUSSION

The 400 °C annealing of $Mn_{3-\delta}Ga$ with $\delta > 1.2$ was found to give the $L1_0$- (CuAu) type phase, which is rather similar to the $D0_{22}$ type, as shown in Fig. 1. Figure 2 shows x-ray diffraction patterns of $Mn_{3-\delta}Ga$ with (a) $\delta$=1.30 and (b) $\delta$=0.97 at 293 K. The pattern (a) exhibits the $L1_0$ type

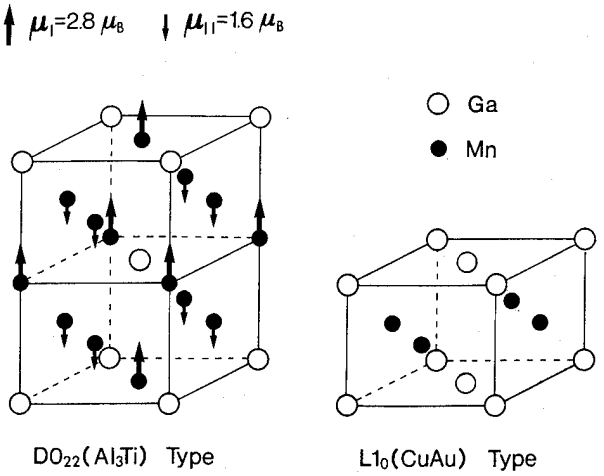



FIG. 1. Crystal structures of $D0_{22}$ type and $L1_0$ type.

[a]Also at Laboratory of Natural Science (Physics).
[b]Also at Department of Electronic Information Systems.

 0021-8979/96/79(8)/5946/3/$10.00 © 1996 American Institute of Physics

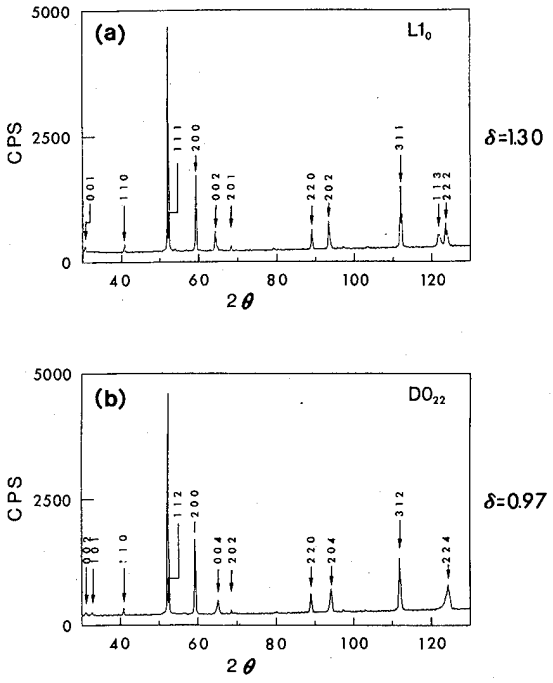



FIG. 2. X-ray diffraction patterns of $Mn_{3-\delta}Ga$ with (a) $\delta=1.30$, and (b) $\delta=0.97$ at 293 K (Fe $K_\alpha$ radiation).

with lattice parameters $a=3.8974$ A and $c=3.6249$ A, while pattern (b) exhibits the $D0_{22}$ type with $a=3.9049$ A and $c=7.1724$ A.

Figure 3 shows the composition dependence of $a$ and $c$ for $Mn_{3-\delta}Ga$. It should be noted that $a$ is constant for both $D0_{22}$- and $L1_0$-type phases while $c$ of $D0_{22}$ type is not so different from $2c$ of $L1_0$ type. The pattern for the alloy with $\delta<0.15$ exhibits the coexistence of the $\beta_{Mn}$ phase with a complex cubic structure.

Magnetic measurements were made only for the $D0_{22}$-type phase. Figure 4 shows the temperature dependence of magnetization $\sigma$ in a magnetic field of 10 kOe for $Mn_{3-\delta}Ga$ with (a) $\delta=0.97$ and (b) $\delta=0.43$. In Fig. 4(a) the magnetization during cooling is larger than that during heating. This is due to the fact that the 10 kOe field is insufficient to saturate the magnetization below the Curie temperature $T_C$ (770 K). In Fig. 4(b), on the other hand, the $D0_{22}$-type phase begins to decompose at about 770 K ($T_{dec}$), resulting in an

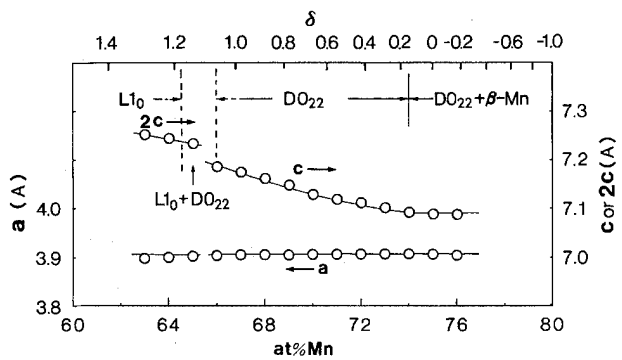



FIG. 3. Lattice constants $a$ and $c$ of $Mn_{3-\delta}Ga$ at room temperature.

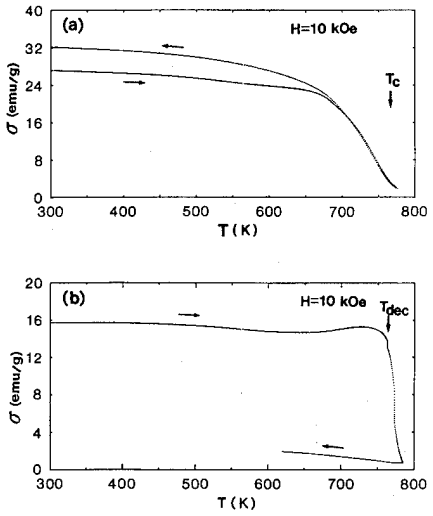



FIG. 4. Temperature dependence of magnetization $\sigma$ for $Mn_{3-\delta}Ga$ with (a) $\delta=0.97$, and (b) $\delta=0.43$.

irreversible decrease in $\sigma$. The Curie temperature of this alloy is evidently higher than $T_{dec}$.

We have also made high-field magnetization measurements since the coercivity of some specimens is so large that we cannot obtain a major hysteresis loop in a conventional field of 20 kOe. As an example, a high-field magnetization curve at room temperature for the powder sample $Mn_{3-\delta}Ga$ with $\delta=0.67$ is shown in Fig. 5. The room temperature values of saturation magnetization $\sigma_s$, remanent magnetization $\sigma_r$, and coercivity $H_c$ are 50 emu/g, 25 emu/g, and 13.5 kOe, respectively. The fact that $\sigma_r=0.5\sigma_s$ suggests the existence of a large uniaxial magnetic anisotropy with random orientation. The large coercivity has not been observed for the bulk samples probably because of the existence of a coarse magnetic domain structure.

Figure 6 shows the composition dependence of $\sigma_s$, $\sigma_r$, and $H_c$ of the powder samples at room temperature. (Instead of $\sigma_s$, the magnetization at 15 T, $\sigma_{15\ T}$, is shown.) With increasing $\delta$, both $\sigma_{15\ T}$ and $\sigma_r$ increase, while $H_c$ decreases. The composition dependence of $\sigma_s$ can be explained on the basis of the spin structure shown in Fig. 1, if we assume that

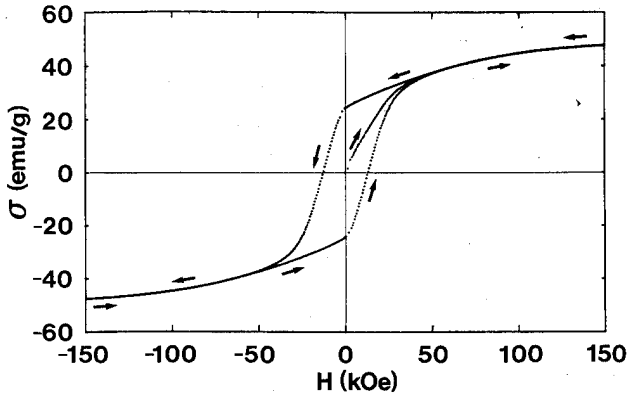



FIG. 5. High-field magnetization curve at room temperature for $Mn_{3-\delta}Ga$ with $\delta=0.67$.

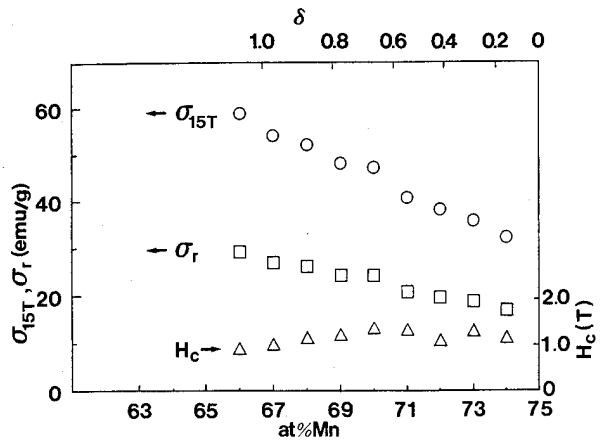



FIG. 6. Composition dependence of the saturation magnetization at 15 T $\sigma_{15\ T}$, the remanent magnetization $\sigma_r$, and the coercivity $H_c$ of the powder samples of $Mn_{3-\delta}Ga$ at room temperature.

the excess Ga in the $D0_{22}$-type structure prefers the $Mn_I$ site to the $Mn_{II}$ site. It should be noted, however, that the $\sigma_s$ value extrapolated to the stoichiometric composition ($\delta$=0) is about 3 times larger than that expected from the spin structure in Fig. 1. Therefore, we are planning to make more detailed neutron diffraction experiments on these alloys.

Because of the rather large values of $\sigma_s$ and $H_c$, we may expect the possibility of $Mn_{3-\delta}Ga$ as a hard magnetic material. The characteristics will be much improved if we can align the magnetic anisotropy axis. For this purpose we have made the magnetic annealing during the preparation of the $D0_{22}$-type (tetragonal) alloy from the $\gamma_{Mn}$ (cubic) phase alloy. Since the annealing temperature is sufficiently lower than the Curie temperature, the $c$ axis of the $D0_{22}$-type structure is expected to align in the direction of the applied field.

As an example, the magnetic annealing of the powder sample of $Mn_{3-\delta}Ga$ with $\delta$=0.67 at 300 °C in a field of 10 kOe is illustrated in Fig. 7, where the magnetization $\sigma$ measured during annealing is plotted against time, together with the temperature $T$. The transition from the $\gamma_{Mn}$ phase to the $D0_{22}$-type phase is almost completed at 360 min (6 h). (A further increase in $\sigma$ in the Fig. 7 corresponds to the temperature dependence of $\sigma_s$ of the $D0_{22}$-type alloy.)

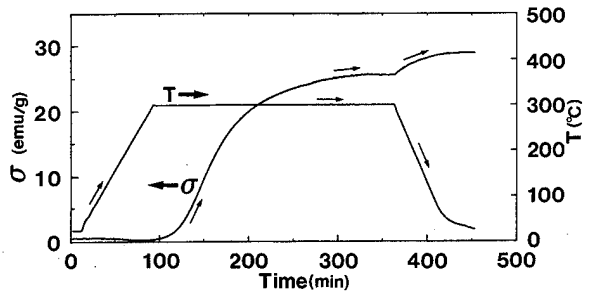



FIG. 7. Magnetic annealing during the transition from the $\gamma_{Mn}$ phase to the $D0_{22}$ phase for $Mn_{3-\delta}Ga$ with $\delta$=0.67. $\sigma$ is the magnetization and $T$ is the temperature. The applied field is 10 kOe.

Unfortunately, however, the alignment of the magnetic anisotropy axis was not so remarkable by this magnetic annealing, probably because the transition from the $\gamma_{Mn}$ (cubic, nonmagnetic) phase to the $D0_{22}$ (tetragonal, magnetic) phase is not direct but through the medium of the $D0_{19}$-type (hexagonal, nonmagnetic) phase, as was confirmed by x-ray diffraction.

A detailed study on this subject is now in progress.

As another effort of the materials research, we have also studied the effect of the addition of Fe to the $D0_{22}$-type $Mn_{3-\delta}Ga$. Single-phase alloys of $(Mn_{1-x}Fe_x)_{3-\delta}Ga$ with $\delta$=0.30 were obtained in the range $0 \leqslant x \leqslant 0.25$. We have made high-field magnetization measurements for the powder samples. For example, the room-temperature values of saturation magnetization, remanent magnetization, and coercivity of $(Mn_{1-x}Fe_x)_{3-\delta}Ga$ with $\delta$=0.30 and $x$=0.25 are 38 emu/g, 18.5 emu/g, and 12 kOe, respectively. In general, no remarkable effect on $\sigma_s$, $T_C$, and $H_c$ was observed by the addition of Fe.

## ACKNOWLEDGMENTS

In conclusion, the authors express their thanks to M. Kudo, K. Sai, and Y. Ishikawa of High-Field Laboratory, Tohoku University, for operation of the Bitter magnet.

[1] E. Krén and G. Kádár, Solid State Commun. **8**, 1653 (1970).
[2] H. Masumoto, K. Watanabe, and M. Mitera, J. Jpn. Inst. Metals **42**, 474 (1978) (in Japanese).

# Magnetic characteristics of $RCo_{13-x}Si_x$ alloys (R=La, Pr, Nd, Gd, and Dy)

M. Q. Huang and W. E. Wallace
*Department of Materials Science and Engineering, Carnegie Mellon University, Pittsburgh, Pennsylvania 15213 and Carnegie Mellon Research Institute, Carnegie Mellon University, Pittsburgh, Pennsylvania 15213*

R. T. Obermyer and S. Simizu
*Carnegie Mellon Research Institute, Carnegie Mellon University, Pittsburgh, Pennsylvania 15213*

M. McHenry
*Department of Materials Science and Engineering, Carnegie Mellon University, Pittsburgh, Pennsylvania 15213*

S. G. Sankar
*Carnegie Mellon Research Institute, Carnegie Mellon University, Pittsburgh, Pennsylvania 15213*

The magnetism of $LaCo_{13}$-type alloys such as $LaCo_{13}$, $PrCo_{13-x}Si_x$, etc., has recently received considerable attention as potentially useful magnetic materials. The present study is concerned with $RCo_{13-x}Si_x$ where R=La, Pr, Nd, Gd or Dy. © *1996 American Institute of Physics.*
[S0021-8979(96)33508-2]

## I. INTRODUCTION

The alloys $LaCo_{13}$ and $La(Co,Fe)_{13}$ have a high content of $3d$ elements. The high concentration of $3d$ elements leads to a large magnetization and, in some cases, a high $T_C$. Because of these properties these alloys have attracted attention as potential high energy permanent magnet materials.[1–6] In earlier studies from this laboratory, Ido *et al.* have studied $La(Co,Fe,Al)_{13}$ (Ref. 1) and Huang *et al.* have studied $PrCo_{13-x}Si_x$.[7] The earlier works have been extended in the present study to include the ternaries $RCo_{13-x}Si_x$, in which R=Nd, Gd, and Dy.

## II. EXPERIMENTAL DETAILS

The ternary alloys were prepared by induction melting under argon, after which they were heat treated at 1273 K for about one week. X-ray diffraction (XRD) with Cu radiation was used to determine crystal structure, lattice parameters, and the phases present.

The magnetic properties ($M$ and $T_C$) were measured using vibrating sample magnetometers (VSM) at temperatures ranging from 10 to 1173 K and fields ranging from 500 Oe to 17 kOe. The TMA measurements were made in such a manner [low applied field (500 Oe) and variable heating rate] to provide the most reliable information about the phases present and the values of $T_C$ and to clearly identify the spin reorientation

## III. RESULTS AND DISCUSSION

A very large body of data was acquired. Due to space limitations, only a few representative data can be presented. The results are exemplified by the data given in Tables I and II and Figs. 1–7.

### A. Phases formed and structural information

Information concerning the phase relationships is obtained by XRD measurements such as those shown in Figs. 1 and 2. The phase relationships are rather similar for the five systems studied: (1) At low Si content, $1.5 \leqslant x \leqslant 2.0$, the alloys form in the fcc $NaZn_{13}$ structure. (2) At high Si content, $3.5 \leqslant x \leqslant 4.5$, they form in the body-centered tetragonal (bct) $Ce_2Ni_{17}Si_9$ structure. (3) At intermediate Si concentrations the systems are a mixture of fcc and bct alloys. There are, however, some exceptions to these generalizations: (1) The fcc phase forms at $x=0$–2 for R=La. (2) The fcc structure begins to form at $x=1.5$ for R=Pr, whereas it forms only for

TABLE I. Phases present and structural information for $RCo_{13-x}Si_x$ alloys (R=La, Pr, Nd, Gd, Dy).

| | | Phases present | | Lattice parameters (main phase) | | | |
|---|---|---|---|---|---|---|---|
| R | $x$ | Main | Minor | $a$ (A) | $c$ (A) | $c/a$ | $V$ (A$^3$) |
| La | 0 | fcc[a] | | 11.340 | | | 1458.27 |
| | 1.0 | fcc | | 11.325 | | | 1452.49 |
| | 2.0 | fcc | | 11.295 | | | 1440.98 |
| | 2.5 | fcc | bct | | | | |
| | 3.0 | bct | fcc | 7.871 | 11.523 | 1.464 | 713.88 |
| | 3.5 | bct[b] | (fcc->0) | 7.851 | 11.551 | 1.471 | 711.98 |
| | 4.0 | bct | | 7.827 | 11.567 | 1.478 | 708.63 |
| | 4.5 | bct | $Co_2Si$ | 7.834 | 11.592 | 1.478 | 711.42 |
| Pr | 2.0 | fcc | | 11.259 | | | |
| | 2.5 | fcc | bct | | | | |
| | 3.0 | bct | fcc | | | | |
| | 3.5 | bct | fcc | 7.821 | 11.500 | 1.470 | 730.43 |
| | 4.0 | bct | | 7.805 | 11.539 | 1.478 | 702.93 |
| | 4.5 | bct | $Co_2Si$ | 7.826 | 11.566 | 1.478 | 708.37 |
| Nd | 3.0 | bct | fcc, 1:11[c] | 7.834 | 11.459 | 1.462 | 703.25 |
| | 3.5 | bct | fcc | 7.828 | 11.489 | 1.470 | 702.22 |
| | 4.0 | bct | | 7.788 | 11.519 | 1.479 | 698.66 |
| | 4.5 | bct | $Co_2Si$ | 7.797 | 11.552 | 1.481 | 702.28 |
| Gd | 3.5 | bct | 1:11 | | | | |
| | 4.0 | bct | fcc, $Co_2Si$ | 7.773 | 11.495 | 1.478 | 694.52 |
| Dy | 3.5 | bct | 1:11 | | | | |
| | 4.0 | bct | $Co_2Si$ | 7.758 | 11.491 | 1.481 | 691.66 |

[a]fcc signifies the $NaZn_{13}$ structure.
[b]bct signifies the $Ce_2Ni_{17}Si_9$ structure.
[c]The 1:11 signifies the $BaCd_{11}$ structure.

TABLE II. Magnetic properties of $RCo_{13-x}Si_x$ (R=La, Pr, Nd, Gd, and Dy).

| R | x | $T_c$ (K) | M (emu/g) 293 K | M (emu/g) 10 K | $M(\mu_B$/f.u.) 10 K | $M$(Co,R) $\mu_B$/atom | $T_{sr}$ (K) | $H_c$ (Oe) 10 K |
|---|---|---|---|---|---|---|---|---|
| La | 0 | 1297 | 126.0 | 131.4 | 21.3 | 1.64 | | |
| | 1.0 | 1050 | 106.0 | 108.0 | 16.9 | 1.41 | | |
| | 2.0 | 880 | 75.9 | 80.2 | 12.1 | 1.10 | | |
| | 3.0 | 295,880 | 26.6 | 41.4 | 6.0 | 0.6 | | |
| | 3.5 | 200,880 | 4.3 | 24.0 | 3.4 | 0.4 | | |
| | 4.0 | 40 | 0.33 | 2.24 | 0.3 | 0.03 | | |
| | 4.5 | ··· | 0.23 | 0.28 | 0.04 | ··· | | |
| Pr | 2.0 | 903 | 78.1 | 92.7 | 14.0 | 1.9 | | |
| | 2.5 | ~295,903 | 54.4 | 73.7 | 11.0 | | ~28 | 900 |
| | 3.0 | ~290,903 | 29.9 | 55.2 | 8.1 | 2.1 | ~28 | 700 |
| | 3.5 | ~70,903 | 10.1 | 37.2 | 5.3 | 1.9 | ~55 | 600 |
| | 4.0 | 20 | 1.7 | 19.2 | 2.7 | 2.4 | ···· | |
| | 4.5 | 20 | 1.4 | 15.8 | 2.2 | 2.2 | | |
| Nd | 3.0 | ~300,908 | 29.6 | 53.9 | 7.9 | 1.9 | ~45 | 500 |
| | 3.5 | 225,908 | 5.8 | 40.7 | 5.8 | 2.4 | ~48 | 400 |
| | 4.0 | 20 | 0.7 | 17.8 | 2.5 | 2.2 | | |
| Gd | 3.5 | 70,483 | 8.6 | 23.1 | 3.4 | 6.8 | | |
| | 4.0 | 50,600 | 7.9 | 26.5 | 3.8 | 4.1 | | |
| Dy | 3.5 | 55,490 | 8.5 | 37.7 | 5.5 | 8.9 | ··· | 750 |
| | 4.0 | 45 | 2.2 | 36.8 | 5.3 | 5.8 | ··· | 240 |

$x$ exceeding 3–3.5 for the heavier rare earths, Nd, Gd, or Dy. Also as noted in Table I, some of the alloys contained minor amounts of other phases: 2:17, 1:11, and $Co_2Si$. The lattice parameters (Table I) show that Si doping causes a shrinkage of the lattice.

In summary, the ternaries (and $LaCo_{13}$) are fcc for low Si content and one bct at high Si content. Further details are given in Table I.

## B. Magnetic properties

Magnetization results are given in Figs. 3–7 and in Table II. From the results presented, it is to be noted that $LaCo_{13}$, which is fcc, is a strongly ferromagnetic material (moment =131 emu/g) with a high $T_C$, 1297 K. It thus satisfies two of the requirements for a high energy permanent magnet material. However, it lacks a third requirement—a uniaxial crystal

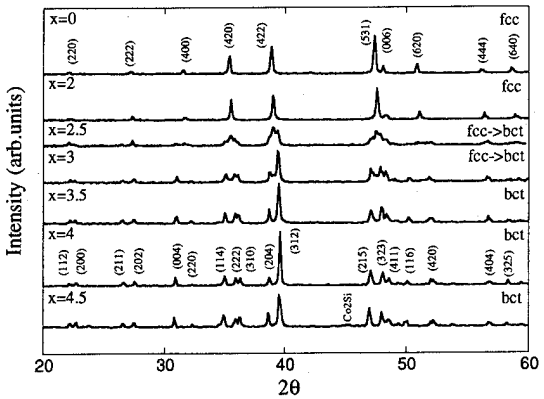



FIG. 1. XRD patterns for $LaCo_{13-x}Si_x$. The splitting of the 422 peak at $2\theta \sim 39°$ is a clear indication of the transformation from cubic to tetragonal symmetry.

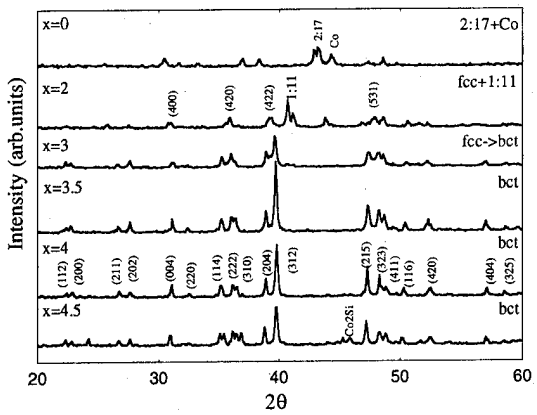



FIG. 2. XRD pattern for $NaCo_{13-x}Si_x$.

structure. The present study (and earlier studies) shows that the third requirement can be induced by Si doping.[1,6,7] Unfortunately, however, as indicated in Figs. 3–7 and in Table II, the tetragonal materials have a low $T_C$—room temperature or below. The fcc alloys have a $T_C$ ranging from 880 K (for $LaCo_{11}Si_2$) to 1297 K for $LaCo_{13}$. For a given Si content, the $T_C$ of the fcc phase is dependent on the nature of R. As expected, the dominant interaction is the Co–Co interaction.

In regard to the magnetic moment, there is a decrease as Si replaces Co, but the decrease is larger than expected due to the simple dilution of the Co sublattices. The decrease begins in the fcc alloys and continues in the bct alloys. The bct alloys have small moments, <10 emu/g, as measured at ~10 K.

The TMA for bct alloys with R=Pr and Nd show clear indications of a spin reorientation when cooled to tempera tures in the liquid hydrogen range (Figs. 4 and 5). As shown in Table II, $T_{sr}$=55 and 48 K for $PrCo_{9.5}Si_{3.5}$ and $NdCo_{9.5}Si_{3.5}$, respectively. No spin reorientation was observed for the La, Gd, and Dy ternaries. This is as expected for $La(Co,Si)_{13}$—since La carries no moment—and for $Gd(Co,Si)_{13}$—in which the rare earth is spherical and hence is isotropic. It is unclear why there is no indication of spin

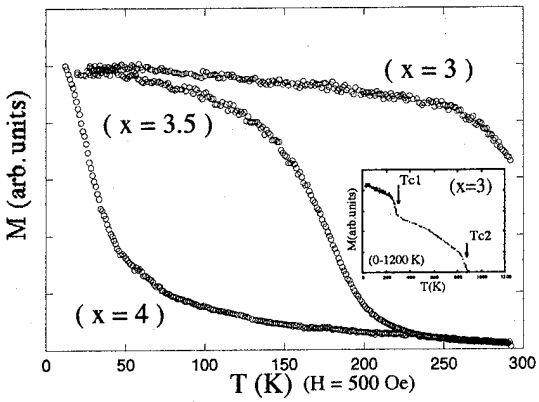



FIG. 3. $M$ vs $T$ for three representative bct $La(Co,Si)_{13}$ alloys. The alloys with $x$=3.5 and 4 are nearly single-phase material. Their Curie temperatures are about 200 and 40 K, respectively. The alloy with $x$=3 is a two-phase system composed of fcc and bct alloys (see Table I). The presence of the fcc impurity phase strongly affects the magnetization of the bct phase.

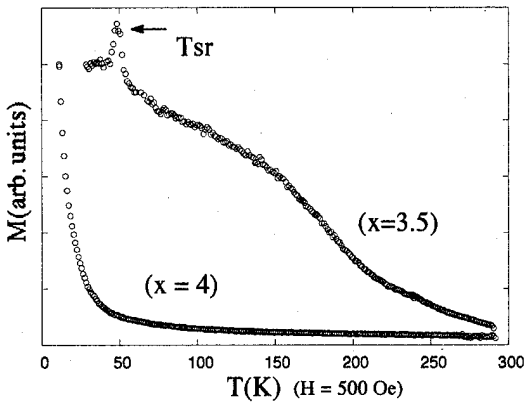



FIG. 4. $M$ vs $T$ for two representative $Nd(Co,Si)_{13}$ alloys. The $T_C$'s for $NdCo_9Si_4$ and $PrCo_9Si_4$ are essentially identical. The spin reorientation at ~50 K is clearly evident.

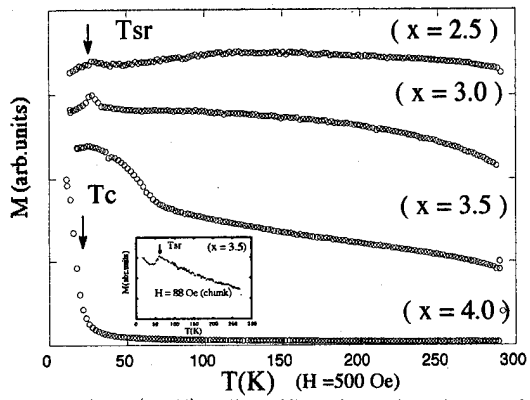



FIG. 5. $M$ vs $T$ for $Pr(Co,Si)_{13}$ alloys. The spin reorientation at ~28 K is clearly evident for $x=2.5$–$3.5$.

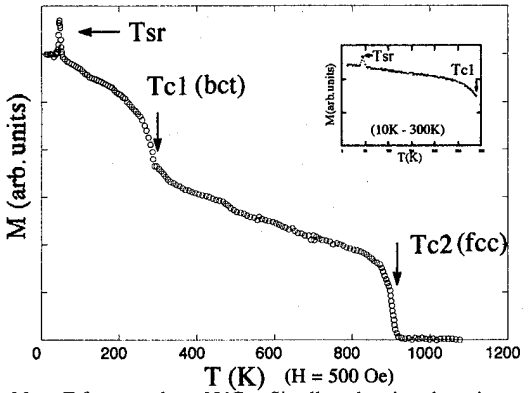



FIG. 6. $M$ vs $T$ for two-phase $NdCo_{10}Si_3$ alloy showing the spin reorientation at ~45 K and the $T_C$'s for the bct and fcc components.

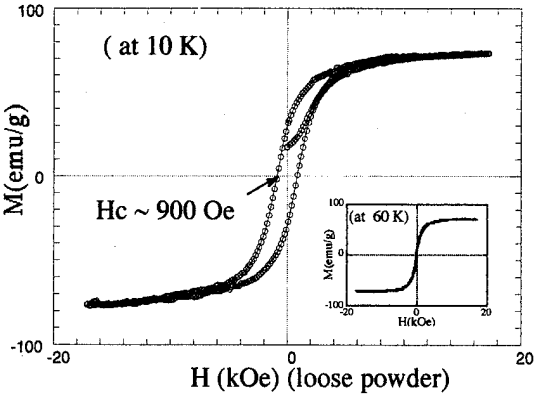



FIG. 7. Hysteretic behavior of $PrCo_{10.5}Si_{2.5}$, showing significant coercivity for $T<T_{sr}$, but not for $T>T_{sr}$.

rotation for the Dy-containing ternaries. Boltich, Pedziwiatr, and Wallace showed[8] some years ago that spin reorientation in rare earth–$d$-transition metal alloys occurs as a result of a complex interplay between the crystal field interaction for the R sublattice and exchange primarily involving the $d$ sublattice. The temperature of the spin reorientation and the shape of the aberration in the TMA depend on the details of this interplay. Perhaps in $Dy(Co,Si)_{13}$ the spin reorientation takes place at a temperature lower than that covered in this study. Interestingly, the Dy alloy exhibits coercivity in its hysteresis loop even though it does not indicate spin reorientation in its $M$ vs $T$ plot.

Hysteresis loops were measured at temperatures above and below $T_{sr}$ for the ternaries in loose powder form. A representative loop (for $PrCo_{10.5}Si_{2.5}$) is shown in Fig. 7. There is negligible coercivity for $T>T_{sr}$ but appreciable coercivity for $T<T_{sr}$. This suggests that magnetization is along the $c$ axis below $T_{sr}$ and shifts to the $ab$ plane above $T>T_{sr}$.

## IV. CONCLUSION

$LaCo_{13}$ exists in the fcc $NaZn_{13}$ structure. The corresponding Pr alloy also forms in the same structure if a small portion of the Co is replaced by Si. At higher Si content, all the systems adopt the bct $Ce_2Ni_{17}Si_9$ structure. The fcc alloys have high $T_C$ and are strongly magnetic. The bct alloys are weakly magnetic with $T_C$ at or below room temperature. $Pr(Co,Si)_{13}$ and $Nd(Co,Si)_{13}$ exhibit spin reorientation at ~60 and 50 K, respectively. Hysteresis results suggest a uniaxial material at temperatures below $T_{sr}$ and $ab$ plane anisotropy for $T>T_{sr}$. Si doping stabilizes the $NaZn_{13}$ structure in $R(Co,Si)_{13}$ alloys. This does not appear to be exclusively a size effect.

## ACKNOWLEDGMENTS

The authors express appreciation to Dr. B. M. Ma of Rhone Poulenc for gifts of rare earth metal for use in this study. This work was supported by U.S. Army Research Office.

[1] H. Ido, J. C. Sohn, F. Pourarian, S. F. Cheng, and W. E. Wallace, J. Appl. Phys. **67**, 4978 (1990).
[2] M. Q. Huang, Y. Zheng, K. Miller, J. Elbicki, W. E. Wallace, and S. G. Sankar, IEEE Trans. Magn. **28**, 2859 (1992).
[3] T. T. M. Palstra, J. A. Mydosh, G. J. Nieuwenhuys, A. M. Van der Kran, and K. H. J. Buschow, J. Magn. Magn. Mater. **36**, 290 (1983).
[4] T. T. M. Palstra, G. J. Nieuwenhuys, J. A. Mydosh, and K. H. J. Buschow, Phys. Rev. B **31**, 4622 (1985).
[5] Z. X. Tang, X. H. Deng, G. C. Hadjipanayis, V. Papatfthmiou, and D. J. Sellmyer, IEEE Trans. Magn. **29**, 2839 (1993).
[6] G. H. Rao, J. K. Ling, Y. L. Zhang, X. R. Cheng, and W. H. Tang, Appl. Phys. Lett. **64**, 1650 (1994).
[7] M. Q. Huang, W. E. Wallace, R. T. Obermyer, S. Simizu, and S. G. Sankar, J. Magn. Magn. Mater. **151**, 150 (1995).
[8] E. B. Boltich, A. T. Pedziwiatr, and W. E. Eallace, J. Magn. Magn. Mater. **66**, 317 (1987).

# First-principles calculation of the 3*d* magnetocrystalline anisotropy energy of $YCo_5$

M. Yamaguchi
*R&D Group for Numerical Experiments, Center for Promotion of Computational Science and Engineering, Japan Atomic Energy Research Institute, Tokai-mura, Ibaraki, Japan*

S. Asano
*Institute of Physics, College of Arts and Sciences, University of Tokyo, Komaba, Meguro-ku, Tokyo, Japan*

The electronic structure of $YCo_5$ was calculated self-consistently by the scalar-relativistic linear muffin–tin orbital method using an atomic sphere approximation within the framework of the local spin density approximation. Using the spin–orbit interaction (SO) and orbital polarization term (OP), magnetocrystalline anisotropy energy due to 3*d*-electrons (3*d*-MAE) was calculated as a function of bandfilling $q$ [Ea($q$)]. At the Fermi level, the calculated Ea($q$), including SO and OP, depended greatly on whether an *f* basis was used for Co. Just below the Fermi level, however, Ea($q$) showed a large and *c*-axial 3*d*-MAE comparable with the experimental data. This behavior of Ea($q$) is closely related to the calculated anisotropy of orbital magnetic moments and the shape of density of states of the 3*d* band. © *1996 American Institute of Physics.* [S0021-8979(96)33608-9]

The magnetocrystalline anisotropy energy (MAE) of rare-earth (or Y) transition metal intermetallics has been studied by many researchers concerning its application to permanent magnetic materials.[1,2] Although the MAE of these compounds is mainly due to the electrostatic interaction between the 4*f* electrons on rare-earth elements and the crystalline field, the spin–orbit splitting of the 3*d* band on the transition metal elements can contribute substantially to the anisotropy energy (3*d*-MAE). For example, the *c*-axial 3*d*-MAE of $YCo_5$ (3.8 meV/f.u.)[3] is smaller than that of $SmCo_5$ (16 meV/f.u.)[4–6] only by a factor of 4. The contribution per Co atom in $YCo_5$—0.76 meV/Co—is by far the largest value among the Y–Co compounds, which is about ten times as large as that of a simple hcp Co (0.065 meV/Co).[7] This large anisotropy of $YCo_5$ is explained from the viewpoint of the localized 3*d* electron model.[3] However, magnetism of the 3*d* electrons is discussed from the viewpoint of band magnetism.

Recently, the 3*d*-MAE of $YCo_5$ was calculated by Daalderop *et al.*[8] and Nordström *et al.*[9] with the linear muffin–tin orbital method with atomic sphere approximation (LMTO-ASA), including both spin–orbit interaction (SO) and an orbital polarization term (OP). They used experimental lattice parameters and *s*, *p*, *d*, and *f* bases for both Y and Co. However, we were not able to obtain the theoretical lattice constant $a_{cal}$ determined so as to minimize the total energy in the region of ±7% of the experimental lattice constant $a_{exp}$ when we used their calculation parameters. On the other hand, we were able to obtain the $a_{cal}$ which is only about 2% smaller than $a_{exp}$ when we did not use an *f* basis for Co. In this work, we calculated the 3*d*-MAE of $YCo_5$ using the LMTO-ASA method under the two different sets of parameters.

Before calculating the 3*d*-MAE, the self-consistent electronic structures were calculated using the LMTO-ASA method based on the local spin density approximation. Here, the parameters of Janak, Moruzzi, and Williams[10] were used and the calculations were carried out in scalar relativistic approximation, neglecting SO interaction. We calculated the self-consistent potential using the two different sets of calculation parameters, in which the most influential difference is whether an *f* basis is used for Co. In set (1), we used parameters similar to Daalderop *et al.*[8] and Nordström *et al.*[9] For atomic positions, lattice constant $a$, and $c/a$ ratio, the experimental data were used. The *s*, *p*, *d*, and *f* bases were used for both Y and Co. The ratio of the atomic sphere radius was chosen as $r_Y/r_{Co}=1.32$. In set (2), we used the following parameters. For atomic positions and $c/a$ ratio, the experimental data were used. The bases we used consist of *s*, *p*, *d*, and *f* for Y, and of *s*, *p*, and *d* for Co. The ratio of the atomic sphere radius was chosen as $r_Y/r_{Co}=1.35$ so that $a_{cal}$ and the spin magnetic moments agreed well with the experimental data. We obtained $a_{cal}$ (4.84 Å), which is only 2% smaller than $a_{exp}$ (4.94 Å). The number of **k** points we used in the irreducible Brillouin zone (IBZ) was 225 in both sets.

Using the self-consistent potential, the full Hamiltonian including only SO or both SO and OP was diagonalized to obtain an energy eigenvalue $\epsilon_i(\hat{\mathbf{n}},\mathbf{k})$, where $i$ was the electronic states, $\hat{\mathbf{n}}$ the direction of quantum axis (magnetization direction). According to the *force theorem*,[11] the total energy difference between the two directions of the quantum axis is given by the difference between the sum of the calculated energy eigenvalues of the occupied states as follows: $\mathrm{Ea}=\sum_{i,k}^{occ}\epsilon_i([0001],\mathbf{k})-\sum_{i,k}^{occ}\epsilon_i([1000],\mathbf{k})$, where [0001] denotes the direction of the $c$ axis while [1000] denotes the direction within the $ab$ plane. The summation on $i$ and **k** was carried out by means of the tetrahedron method. Furthermore, the occupation number of the valence electrons was treated as a variable. Thus, 3*d*-MAE was calculated as a function of bandfilling $q$:Ea($q$). The calculated spin and orbital magnetic moments in the case of [0001] are shown in Table I.

In the case of the [0001] quantum axis, the number of sampling **k** points in IBZ, on which the $\epsilon_i([0001],\mathbf{k})$'s were calculated, were 225. The size of the irreducible part of BZ in the case of the [1000] quantum axis is three times larger than IBZ in the case of [0001]. The variation among the

 0021-8979/96/79(8)/5952/3/$10.00 © 1996 American Institute of Physics

TABLE I. The calculated and experimental magnetic moments ($\mu_B$). The $S$ shows the spin magnetic moment, while the $L$ shows the orbital one.

| | $S^{Co(2c,3g)}$ | $L^{Co(2c,3g)}$ |
|---|---|---|
| (1) SO | 1.36,1.54 | 0.12,0.12 |
| (1) SO+OP | 1.36,1.54 | 0.24,0.25 |
| (2) SO | 1.31,1.51 | 0.10,0.10 |
| (2) SO+OP | 1.31,1.51 | 0.19,0.20 |
| Expt.[a] | 1.31,1.44 | 0.46,0.28 |

[a]Reference 12.

calculated Ea($q$)'s using three sets of 112, 225, and 396 **k** points on a rough bandfilling mesh (0.5 electrons) were within the range of 0.05 meV/Co.

The calculated Ea($q$)'s of $YCo_5$ in four cases are shown in Fig. 1(a). From the left-hand side, the four numbers of bandfilling $q$ correspond to the numbers of valence electrons in a unit cell of Mn, Fe, Co, and Ni compounds, respectively.

Only in the case of (1)SO+OP, the value of Ea($q$) at the Fermi level ($q$=48) agrees well with the experimental data. As can be seen from Table I, the calculated orbital magnetic moments in the case of (1)SO+OP agree with experimental data better than the other results. These results are similar to those of Daalderop *et al.*[8] and Nordström *et al.*[9] However, we mentioned that the $a_{cal}$ could not be determined in set (1). In set (2), we did not use an $f$-basis for Co and were able to obtain the $a_{cal}$ as stated above. In the cases of both (2)SO and (2)SO+OP, however, the Ea($q$) does not agree with the experimental data at the Fermi level. In addition, the values of Ea($q$) at the Fermi level for (2)SO+OP are greatly different from that for (1)SO+OP.

The calculated $3d$-MAEs at the Fermi level depend greatly on the calculation parameters. However, the overall features of the four Ea($q$)'s are similar with one another. All Ea($q$)'s have very large peaks at $q$=46–47, which are comparable to experimental data. This feature can be seen in the anisotropy of orbital magnetic moments calculated in the case of (2)SO, as can be seen from Fig. 1(b). We can see that this feature is mainly due to the Co($2c$).

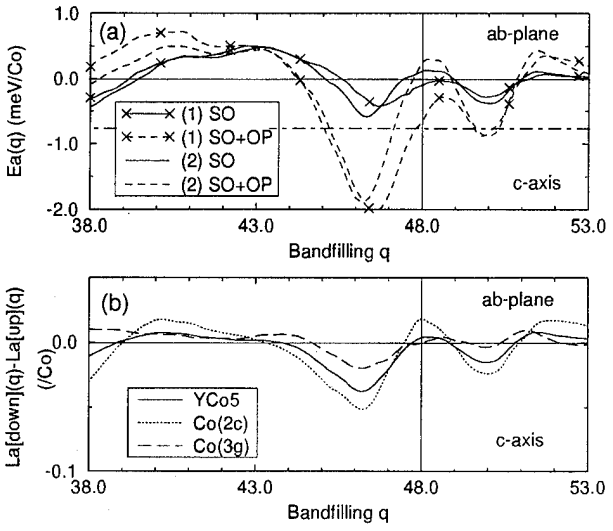



FIG. 1. (a) The calculated $3d$-MAE as a function of bandfilling $q$:Ea($q$) (meV/Co). The vertical line shows the actual Fermi level. The horizontal dot-dashed line shows the experimental data. (b) The calculated anisotropy of orbital magnetic moments of the down-spin band minus that of the up-spin band as a function of bandfilling $q$:La[down]($q$)-La[up]($q$) ($\mu_B$/Co).

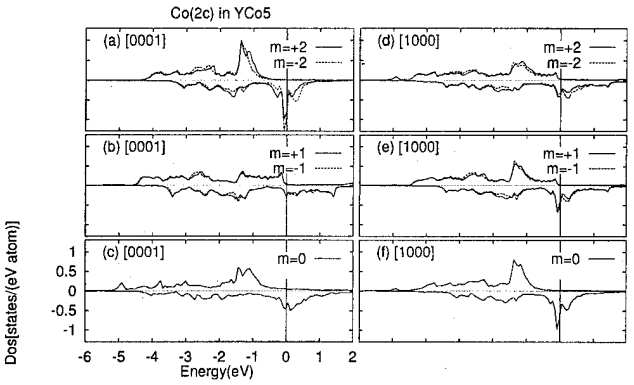



FIG. 2. The density of states of the $3d$ band projected to the $m$ states.

To investigate the behavior of Ea($q$), we show the density of states of the $3d$ band projected to the states of the magnetic quantum number $m=\pm2$, $\pm1$, 0. Those density of states (DOS) were calculated in the case of (2)SO. We found that the DOS of Co($2c$) has a large anisotropy, which is shown in Figs. 2(a)–2(f). This situation cannot be found in the case of Co($3g$). In Figs. 2(a)–2(c) the quantum axis lies in the [0001] ($c$-axis) direction, while in Figs. 2(d)–2(f) they lie in the [1000] ($ab$-plane) direction. Seeing the DOS in Figs. 2(a)–(c), we notice that the shape of the DOS greatly depends on $|m|$. The very large peaks are found near the upper edge of the $3d$ band in the $\pm2$ states in Fig. 2(a). Similar peaks are also found in the $\pm1$, 0 states for [1000] quantum axis in Figs. 2(e) and 2(f). Those large peaks near the upper edge of the $3d$ band for Co($2c$) indicate that there are many electronic states that do not contribute to covalent bonding. In the [0001] quantum axis, the $m=\pm2$ states of the $3d$ band extended in the $ab$ plane. While in the [1000] quantum axis, the states extending in the $ab$ plane are mainly expressed by the $m$=0, $\pm1$ state. The Co($2c$) atom is surrounded by Co($2c$) atoms and Y atoms in the $ab$ plane, which can be seen in Fig. 3. Therefore, the large peaks in the DOS of Co($2c$) indicate that Co($2c$) has a weak bonding with the surrounding Y and Co($2c$) atoms within the same $ab$ plane. This can be understood from the fact that the Co($2c$)—Co($2c$) [Co($2c$)—Y) bonding distance in the $ab$ plane is much longer than the other bonding distances.

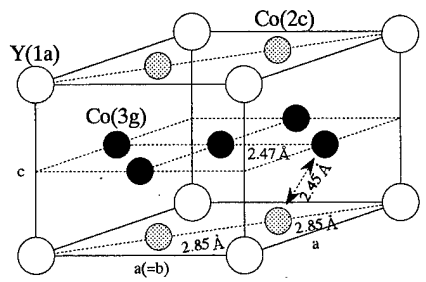



FIG. 3. The crystal structure of $YCo_5$ ($CaCu_5$ type).

The calculated coefficients of the SO interaction of Co are 77.0, 75.0, 77.1, and 74.8 meV for $\xi_d^{\uparrow}(2c)$, $\xi_d^{\downarrow}(2c)$, $\xi_d^{\uparrow}(3g)$, and $\xi_d^{\downarrow}(3g)$, respectively. As can be seen from Figs. 2(a), 2(b), 2(d), and 2(e), this interaction splits the $\pm m(m=2,1)$ states of the $3d$ band. Because of the large difference in the shape of DOS near the Fermi level between the two quantum axes, the large $3d$-MAE and anisotropy of the orbital magnetic moments are expected to be induced.

In conclusion, we showed qualitatively the relation between the experimental large $c$-axial $3d$-MAE and the weak bonding around Co($2c$) within the $ab$ plane through the shape of the DOS of the $3d$ band in Co($2c$).


[1] H. R. Kirchmayr and C. A. Poldy, J. Magn. Magn. Mater. **8**, 1 (1978).
[2] R. J. Radwański and J. J. M. Franse, Int. J. Mod. Phys. B **7**, 782 (1993).
[3] Z. Kakol, H. Figiel, and K. Turek, IEEE Trans. Magn. **MAG-20**, 1605 (1984).
[4] K. H. J. Buschow, A. M. van Diepen, and H. W. de Wijn, Solid State Commun. **15**, 903 (1974).
[5] S. G. Sankar, V. U. S. Rao, E. Segal, W. E. Wallace, W. G. D. Frederick, and H. J. Garrett, Phys. Rev. B **11**, 435 (1975).
[6] R. J. Radwański, J. Magn. Magn. Mater. **62**, 120 (1986).
[7] D. M. Paige, B. Szpunar, and B. K. Tanner, J. Magn. Magn. Mater. **44**, 239 (1984).
[8] G. H. O. Daalderop, P. J. Kelly, and M. F. H. Schuurmans, J. Magn. Magn. Mater. **104–107**, 737 (1992); R. Coehoorn and G. H. O. Daalderop, *ibid.* **104–107**, 1081 (1992).
[9] L. Nordström, M. S. S. Brooks, and B. Johansson, J. Phys. Condens. Matter **4**, 3261 (1992).
[10] J. F. Janak, V. L. Moruzzi, and A. R. Williams, Phys. Rev. B **12**, 1257 (1975).
[11] G. H. O. Daalderop, P. J. Kelly, and M. F. H. Schuurmans, Phys. Rev. B **41**, 11919 (1990).
[12] J. Schweizer and F. Tasset, J. Phys. F **10**, 2799 (1980).

# Magnetic viscosity and microstructure: Particle size dependence of the activation volume

J. M. González, C. de Julián, and Anit K. Giri
*Instituto de Ciencia de Materiales de Madrid, Cantoblanco, 28049 Madrid, Spain*

S. Castro, M. Gayoso, and J. Rivas
*University of Santiago de Compostela, 15706 Santiago de Compostela, Spain*

Ba hexaferrite samples having average particle sizes in the range from the tens up to the thousands of nm have been prepared by using conventional ceramic techniques and the exothermic reaction between Ba and Fe nitrates and oxalic dihydrized acid. The magnetic characterization of these samples included the measurement of the temperature dependence of the high field magnetization, the coercive force, and the evaluation, from thermally activated demagnetization measurements, of the activation volume at different temperatures. From the results of this characterization it was possible to reach conclusions about the occurrence of remarkable differences between the average particle size dependence of the coercive force and that corresponding to the activation volume: whereas the coercive force value increased monotonically with the decrease of the particle size, an activation volume minimum was observed for particle diameters of the order of hundreds of nm. We suggest that this minimum reflects a change of the mechanism ruling the magnetization reversal of the particles forming our samples. © *1996 American Institute of Physics.*
[S0021-8979(96)33708-5]

## I. INTRODUCTION

The existence in ordered magnetic materials of remanence-type states (in which the global magnetization is essentially antiparallel to the applied demagnetizing field) is a direct consequence of the high energy of the states the system should traverse when globally reversing its magnetization. This "energy barrier," having a complex structure due to both the coupling of the local magnetic moments with the microstructure[1] and to the many degrees of freedom of the system,[2] is then of the origin of the coercivity (field induced reversal) and of the magnetic viscosity (thermally activated reversal). Our aim in the present work is to discuss the relationship between coercivity, magnetic viscosity, and particle size in Ba hexaferrite samples covering three orders of magnitude in particle dimensions.

## II. PREPARATION OF SAMPLES AND EXPERIMENTAL TECHNIQUES USED

In order to cover a wide range of particle dimensions our samples were prepared by means of two different procedures. The largest particles were obtained through a ceramic technique consisting of the firing during 12 h in air at 1623 K of a stoichiometric mixture of $BaCO_3$ and $\alpha$-$Fe_2O_3$. The corresponding product was ball milled for different times in the range from 600 to 5400 min. The second preparation method, allowing one to obtain small particles, was based on the exothermic redox reaction of the Ba and Fe nitrates with the dihydrized oxalic acid. In this case, the reaction product was heat treated in air during 10 h at different temperatures in the range from 973 to 1123 K. This treatment allowed us to control the final particle size and to improve the crystallinity of the samples. In this paper we will name the samples obtained via the ceramic method (CE series) and milled for 5400, 1800, and 600 min as CE-3, CE-8, and CE-18, respectively, and those prepared through the exothermic reaction (CA series) and treated at 973 and 1123 K as CA-0 and CA-1, respectively. The phase distribution of the samples was examined by means of x-ray diffraction (Cu $K\alpha$). Transmission and scanning electron microscopies were used in order to obtain information about the morphological characteristics of the particles forming the samples. The magnetic properties study was carried out by measuring pressed powder samples on a superconducting quantum interference device magnetometer.

## III. RESULTS

In Fig. 1 we show two typical diffractograms obtained in samples of both series. In the case of the CE samples the diffraction patterns evidenced the presence of traces of $\alpha$-$Fe_2O_3$ and BaO. No secondary phase reflections were detected in the case of the CA samples. As a general feature the widths of the main Ba hexaferrite reflections were smaller in the CA samples than in the CE ones, indicating that the milling process resulted in the introduction of a large amount of residual stresses. The morphology and particle size of the samples is illustrated in Figs. 2 and 3 where micrographs corresponding to the CA-1 and CE-18 samples are presented.

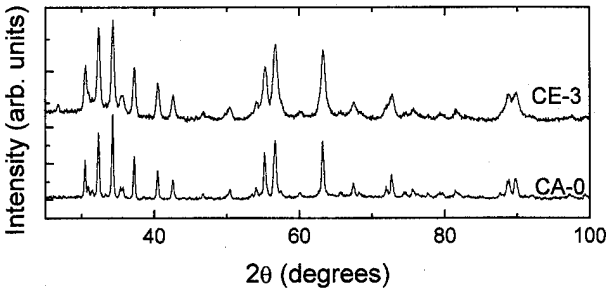



FIG. 1. X-ray diffraction patterns recorded in the CA-0 and CE-3 samples.

 0021-8979/96/79(8)/5955/3/$10.00 © 1996 American Institute of Physics 

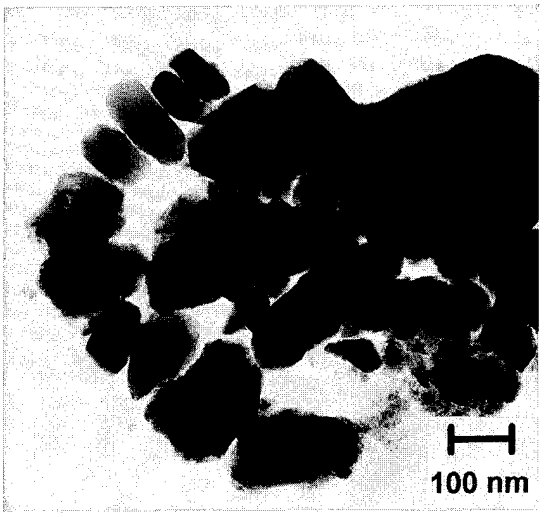



FIG. 2. Transmission electron micrograph (bright field) showing particles of the CA-1 sample.

Both kinds of samples were formed by platelike particles with more or less rounded corners: The particles appeared to be packed at random although in some cases (see Fig. 2) chainlike structures as well as ringlike ones, evidencing interparticle dipolar coupling, were observed. From the micrographs, the average plate diameter was estimated to be 65 $\pm$20, 150$\pm$50, 300$\pm$95, 800$\pm$120, and 1800$\pm$250 nm for the CA-0, CA-1, CE-3, CE-8, and CE-18 samples, respectively. It is interesting to note that the single-domain critical size of Ba hexaferrite particles has been estimated to be 900 nm.[3] The particle size dependence of the specific magnetization of the samples measured under an applied field of 5 T is plotted in Fig. 4. The values obtained in the CA-1 and CE-18 samples are close to the saturation value measured in Ba hexaferrite single crystals (68 A $m^2$ $kg^{-1}$).[3] The differences with this value observed in the CA-0, CE-3, and CE-8 samples are related to incomplete saturation (linked to defects and residual stresses) and/or to the presence of secondary nonmagnetic phases. The hysteresis loops of all the measured samples evidenced the occurrence of some degree of reversible demagnetization. To take this fact into account we measured, in addition to the conventional coercive force, $H_c$, the so-called critical field, $H_{crit}$, defined as that for which the

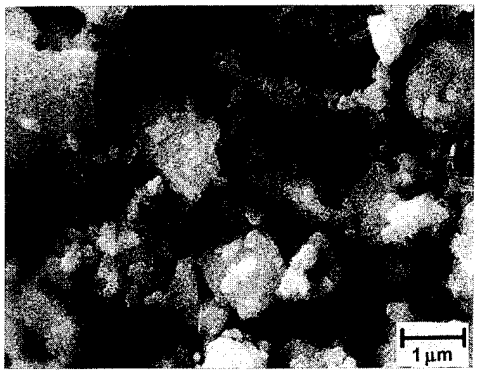



FIG. 3. Scanning electron micrograph showing particles of the CE-18 sample.

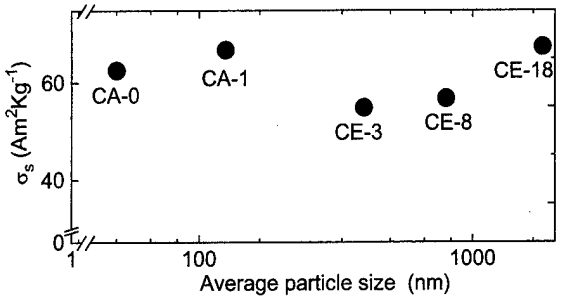



FIG. 4. Particle size dependence of the 5 T specific magnetization of our samples.

maximum of the differential susceptibility measured along the demagnetizing branch of the loop was observed and giving specific information about the irreversible demagnetization processes[1] ($H_c$ and $H_{crit}$ should coincide in a highly textured sample). As is shown in Fig. 5, where we present the room temperature dependence of $H_c$ and $H_{crit}$ on the particle size, both quantities (as well as their difference) increased with a decrease of the particle dimensions. As shown in Fig. 6, where we present the temperature dependence of the critical field of all the samples, this particle size dependence of the coercivity was observed for all the temperatures in the studied range (the weak temperature dependence of the critical field should be linked to that of the anisotropy field, showing a shallow minimum at 100 K).[4]

The study of the magnetic viscosity was carried out, at temperatures in the range from 4.2 to 300 K, by saturating the samples under a field of 5 T and then applying demagnetizing fields (of the order of $H_{crit}$) which were kept constant for 2000 s. During this time the magnetization of the samples was continuously recorded. In all cases, we observed a linear dependence of the magnetization on the logarithm of the time [$M(t)$=constant$-S$ ln $t$] in the range from 200 to 2000 s. The evaluation of the viscosity parameters,[5] i.e., the magnetic viscosity $S_v$ ($S_v=S/\chi_{irr}$, where $\chi_{irr}$ is the irreversible susceptibility) and the activation volume $v_{ac}$ ($v_{ac}=k_BT/\mu_0 M_s S_v$), was carried out following a method compatible with the magnetic equation of state discussed in Ref. 5. Figure 7 presents the temperature dependence of $v_{ac}$ in all our samples. The inset of Fig. 7 presents the particle size dependence, evaluated at 200 K, of the diameter, $d_{ac}$, corresponding to the activation volume (assumed to be

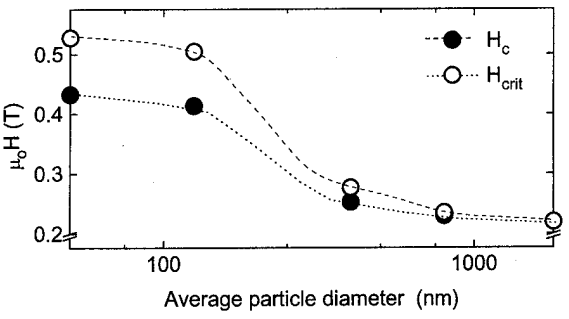



FIG. 5. Particle size dependence at 295 K of $H_c$ and $H_{crit}$.

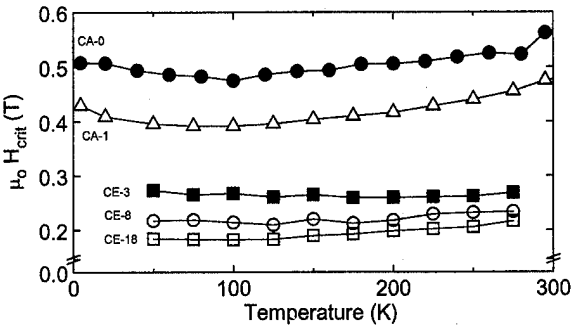



FIG. 6. Temperature dependence of $H_{crit}$ in all the samples.

spherical). Interestingly, that dependence is characterized by the occurrence of a minimum at particle sizes of the order of the hundreds of nm.

## IV. DISCUSSION

We attribute the observed difference between the $H_c$ and the $H_{crit}$ values to the isotropic character of the samples (the reduced remanence of all them was slightly above the 0.5 value corresponding to isotropic systems);[6] the widening, associated with the reduction of the particle size, of the distribution of local reversal fields and the occurrence of some degree of collective demagnetization (which, according to the similar values of $H_c$ and $H_{crit}$ should be particularly relevant in the case of the CE-18 sample). The measured particle size dependence is incompatible with a magnetization reversal ruled by coherent rotation. Two other reversal mechanisms can be consistent with that dependence (there is no microstructural evidence of the occurrence of effective pinning centers in Ba hexaferrite samples): (1) nucleation (coercivity ruled by the energy required to originate the first departure from saturation;[7] this mechanism is conceivable in both the small and the large particles) and (2) propagation (coercivity ruled by the energy associated with the achievement of the conditions of steady propagation of a preexistent wall limiting a reversed nucleus,[1] a mechanism which due to the relative dimension of domain walls and particles is solely conceivable with large particles). For these two mechanisms the increase of coercivity associated with the particle size decrease will be linked to the decrease of the number of defects per particle (these defects located at the surface region could allow a reduction of the field required to form a reversed magnetization nucleus or to propagate a wall).

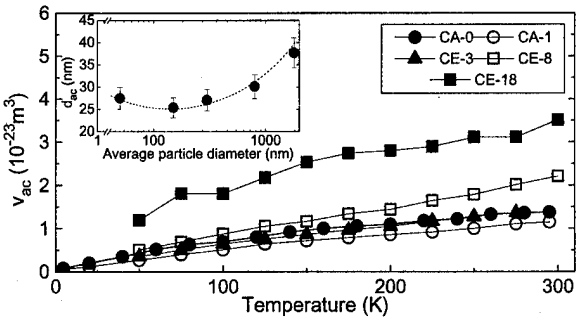



FIG. 7. Temperature dependence of the activation volume measured in all the samples. Inset: particle size dependence, at 200 K, of the diameter ($d_{ac}$) corresponding to a spherical activation volume of the measured magnitude.

The activation volume gives a measure of the size of the region of the samples which is involved in thermally activated demagnetization. It can be identified with the volume of the magnetization inhomogeneity leading to the reversal (nucleation mechanism) and with the reversed area existing prior to wall propagation.[1] In this sense it is interesting to remark that the activation volume measured in all our samples was clearly lower than the average volume of the particles and that, despite the fact that the volume of the CE-18 particles was three orders of magnitude larger than that of the CA-0 ones, the corresponding activation volumes differed by a factor of less than 4. As was already mentioned, a minimum was observed in the particle size dependence of the transverse dimension of the activation volume and, concretely, our estimation of that quantity in the CA-1 (single-domain type) and CE-3 (mixture of single-domain and multidomain particles) samples, yielded very similar values, despite the fact that these two samples were prepared using different methods. Considering this and the differences observed in the critical field values of the CA and CE samples, we propose the occurrence of different demagnetization mechanisms in both kinds of samples. In agreement with the coercivity analysis presented by the authors,[8] where the temperature dependence of the critical field of the CE samples was analyzed, we propose wall propagation as the basic reversal mechanism of the larger (CE) particles and suggest the occurrence of a nucleation ruled process in the smaller (CA) samples.

[1] D. W. Taylor, V. Villas-Boas, Q. Lu, M. F. Rossignol, F. P. Missell, D. Givord, and S. Hirosawa, J. Magn. Magn. Mater. **130**, 225 (1994).
[2] J. M. González, R. Ramirez, and R. Rueda, J. Magn. Magn. Mater. **140–144**, 1847 (1995).
[3] H. Kojima, in *Ferromagnetic Materials*, edited by E. P. Wohlfarth (North-Holland, Amsterdam, 1982), Vol. 3, p. 338.
[4] B. T. Shirk and W. R. Buessem, J. Appl. Phys. **40**, 1294 (1969).
[5] L. Folks and R. Street, J. Appl. Phys. **76**, 6391 (1994).
[6] E. C, Stoner and E. P. Wolfarth. Philos. Trans. R. Soc. London, Ser. A **240**, 599 (1948).
[7] H. Kronmuller, K. D. Durst, S. Hock, and T. Viadieu, J. Phys. **49**, C8 (1988).
[8] J. M. González, A. K. Giri, C. de Julián, M. Reyes, and J. L. Vicent, Europhys. Lett. **28**, 143 (1994).

# High coercivity rare earth–cobalt films

S. S. Malhotra
*Behlen Laboratory of Physics and Center for Materials Research and Analysis, University of Nebraska, Lincoln, Nebraska 68588-0111*

Y. Liu
*Center for Materials Research and Analysis, University of Nebraska, Lincoln, Nebraska 68588-0111 and Department of Mechanical Engineering, University of Nebraska, Lincoln, Nebraska 68588-0656*

Z. S. Shan, S. H. Liou, D. C. Stafford, and D. J. Sellmyer
*Behlen Laboratory of Physics and Center for Materials Research and Analysis, University of Nebraska, Lincoln, Nebraska 68588-0111*

Rare earth–cobalt (RCo, R=Sm, Pr) films with thicknesses from 30 to 700 nm have been prepared with and without a Cr underlayer by dc magnetron sputtering from a $R_2Co_7$ composite target. The as-deposited SmCo films with a Cr underlayer (SmCo‖Cr) have magnetic coercivities of about 500–2800 Oe and the PrCo‖Cr films have coercivities of about 100–300 Oe, but after annealing at 500 °C coercivities as high as 31 kOe for SmCo‖Cr films and 10 kOe for PrCo‖Cr films were observed. The as-deposited PrCo films are composed mostly of an amorphous phase with about 30 vol % of crystallites but after annealing at 500 °C the film is transformed completely to crystallites of about 10 nm diameter as revealed by high-resolution transmission electron microscopy (HRTEM). Nanodiffraction and HRTEM studies show that the crystallites have a closed-packed hexagonal structure. HRTEM study also shows that the annealed SmCo films with a Cr underlayer have grain sizes of about 20 nm and the SmCo films without the Cr underlayer have grain sizes of about 10 nm. The large increase in coercivity for the annealed films is due to the growth of the crystallites. © *1996 American Institute of Physics.* [S0021-8979(96)33808-1]

## INTRODUCTION

Thin films of hard magnetic materials such as rare earth–transition metal alloys are of interest for device applications and magnetic recording media. Among rare earth semi-hard magnetic films, SmCo films with a Cr underlayer prepared at room temperature with high magnetic coercivity ($H_c$) of 3–4 kOe, small grain size and high uniaxial anisotropy have shown good potential for high density recording media.[1–3] Velu *et al.*[4] have shown that $SmCo_4$ films on a Cr underlayer have a coercivity value of 3 kOe at room temperature. Recently, Okumura *et al.*[5] reported $H_c$ of about 3.5 kOe for $Sm_{15}Co_{85}$‖Cr films. Liu *et al.*[6–8] reported systematic studies of the microstructure of SmCo‖Cr films including the Cr underlayer, SmCo layer, and the nanocrystallites in the SmCo layer. The dependence of $H_c$ on the SmCo composition[1–3] is unclear but it has been shown that the $H_c$ strongly depends on the sputtering condition such as substrate temperature and Ar pressure during deposition of Cr and SmCo. This dependence may be related to the microstructure of the films. The Cr underlayer helps to increase the coercivity by controlling the grain size and morphology of the SmCo layer and also improves the in-plane magnetization. Hence if crystallinity and grain growth is promoted in the SmCo layer a much higher value of coercivity can be obtained. This can be achieved by either depositing the film at high substrate temperature or by post-annealing the as-deposited films. A coercivity of 30 kOe was obtained for 4000-Å-thick $Co_{3.65}Cu_{1.35}Sm$ films prepared at substrate temperature of 600 °C by Theurer *et al.*[9] Cadieu *et al.*[10] have shown that $SmCo_5$ films directly crystallized on to a heated substrate have $H_c$ of about 23 kOe. The reason for this high coercivity was associated with the high magnetic anisotropy and the fine grain structure.

In the rare earth–cobalt system the low Co phase adjacent to $SmCo_5$ is in general of the $Sm_2Co_7$ type which has reasonably high anisotropy field $H_A>200$ kOe.[11] The PrCo compounds also feature excellent intrinsic magnetic properties comparable to the SmCo compounds. The $Pr_2Co_7$ phase has $H_A>100$ kOe[11] and the $Pr_5Co_{19}$ phase has $H_A>38$ kOe.[12] In this work we report the effect of post-annealing for $Pr_2Co_7$ and $Sm_2Co_7$ films with and without the Cr underlayer.

## EXPERIMENTAL PROCEDURE

$R_2Co_7$ (R=Sm, Pr) films with thickness from 30 to 700 nm were prepared with and without a Cr underlayer by dc magnetron sputtering from a composite target. All the films have a Cr overlayer of 10 nm to protect the RCo layer. The $Sm_2Co_7$ target was made by pressing the $Sm_2Co_7$ powder and then sintering in vacuum at 1100 °C for 30 min and the $Pr_2Co_7$ target was made by pressing the $Pr_2Co_7$ powder and then sintering in vacuum for 30 min at 1050 °C. The Cr target was obtained commercially and had a 99.9% purity. The base pressure of the sputtering system was $5\times10^{-8}$ Torr and the Ar pressure during sputtering was 20 mTorr. The sputtering rate for $Pr_2Co_7$ and $Sm_2Co_7$ was 1.1 Å/s and for Cr was 5 Å/s.

The magnetic properties of the films were measured with an alternating gradient force magnetometer (AGFM) and SQUID magnetometer. The composition of the films was analyzed by energy dispersive x-ray analysis (EDAX) and was found to be close to the target composition. The structure was studied by x-ray diffraction and high resolution electron microscopy (HRTEM).

 0021-8979/96/79(8)/5958/3/$10.00 © 1996 American Institute of Physics

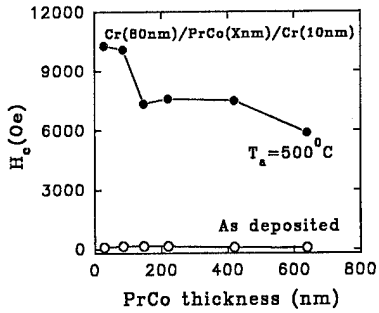



FIG. 1. Coercivity vs PrCo layer thickness for the as-deposited and annealed at 500 °C PrCo‖Cr films with a Cr underlayer of 80 nm.

## RESULTS AND DISCUSSION

We first discuss the magnetic and structural properties for the as-deposited and annealed PrCo films. Figure 1 shows the dependence of the coercivity on the PrCo layer thickness for the PrCo‖Cr films with a Cr underlayer of 80 nm. The as-deposited films show a coercivity of only about 100–300 Oe but after annealing at 500 °C in vacuum for 20 min there is a large enhancement of coercivity. The $H_c$ of the films annealed at 500 °C decreases from about 10 to 5.9 kOe as the film thickness increases from 28 to 640 nm. It was also observed for the 28-nm-thick PrCo‖Cr film that upon annealing up to 350 °C, $H_c$ was nearly unchanged but at 400 °C $H_c$ increased drastically to about 7.7 kOe[13] and at 500 °C the $H_c$ reached about 10 kOe. A bright-field TEM micrograph of the 28-nm-thick PrCo‖Cr film annealed at 500 °C is shown in Fig. 2. The as-deposited films are composed of a mostly amorphous PrCo layer with about 30% volume fraction of crystallites and have small coercivity values because of the mostly amorphous PrCo layer. The film annealed at 500 °C shown in Fig. 2(a) contains nearly 100% crystallites with a grain size of 10 nm resulting in the large increase in the coercivity. The x-ray diffraction pattern of the as-deposited 420-nm-thick PrCo film only shows the (110) diffraction peak of bcc Cr and no PrCo peaks are observed for the films with and without the Cr underlayer. This is due to the large amount of amorphous phase and small crystallites in the PrCo films. After annealing at 500 °C the PrCo layer is crystallized and we observe a few sets of peaks from the x-ray diffraction pattern. The two most intense reflections are observed for $2\theta$=35.5° and $2\theta$=42°. It is difficult to identify the crystal structure unambiguously from the x-ray diffraction pattern because of the limited number of peaks and the several possible phases around the Pr/Co atomic ratio of 3.5, these include the $PrCo_3$, $Pr_2Co_7$ and $Pr_5Co_{19}$ phases. The detailed crystal structure of the annealed 28-nm-thick PrCo‖Cr film was then investigated by nanodiffraction and HRTEM. It was found that the crystallites as shown in Fig. 2(b) have a hexagonal closed packed structure with frequent stacking faults. The nanodiffraction pattern can be well matched to the hexagonal closed packed structure.

In order to investigate whether the Cr underlayer was crucial for the enhancement of coercivity after annealing we compared the magnetic properties of a 420-nm-thick PrCo film with and without a Cr underlayer. It was observed that for the 420-nm-thick PrCo film with no Cr underlayer but

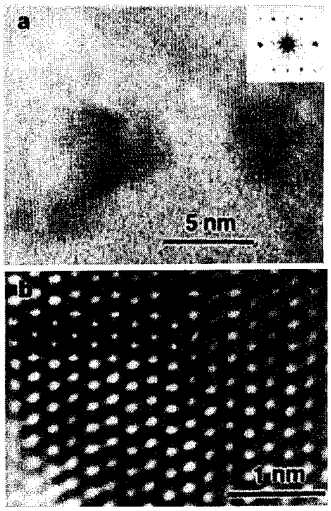



FIG. 2. (a) HRTEM image of Cr(80 nm)/PrCo(28 nm)/Cr(10 nm) film annealed at 500 °C. (b) HRTEM image of a crystallite in (a).

with a Cr overlayer of 10 nm the $H_c$ was about 9 kOe and $M_S \approx 400$ emu/cc after annealing at 500 °C whereas for the 420-nm-thick PrCo film with a Cr underlayer of 80 nm and a Cr overlayer of 10 nm the $H_c$ was about 7.5 kOe and $M_s \approx 300$ emu/cc after annealing at 500 °C. Both the samples have squareness $S(M_r/M_s)=0.8$, but the coercivity squareness $S^*$ for the film with the Cr underlayer was 0.7 and for the film without the Cr underlayer the $S^*$ was about 0.35. Hence we show that if crystallinity and grain growth are promoted a large increase in coercivity can be obtained for the PrCo films with and without the Cr underlayer, except that the films with a Cr underlayer have a better hysteresis loop squareness.

Next we report the magnetic properties of the as-deposited and annealed SmCo films with and without the Cr underlayer. Figure 3 shows the dependence of the coercivity on the SmCo layer thickness for the SmCo‖Cr films with and without the Cr underlayer. The as-deposited films show $H_c$ of about 500–2800 Oe but after annealing at 500 °C for 20 min in vacuum there is a large increase in coercivity. The coercivity of the films with the Cr underlayer of 80 nm and a Cr overlayer of 10 nm annealed at 500 °C varies from 21 to 29 kOe with the maximum coercivity value obtained for 100-nm-thick SmCo film. The $H_c$ of the SmCo film without the

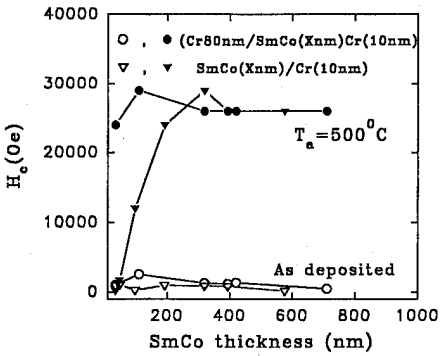



FIG. 3. Coercivity vs SmCo layer thickness for the as-deposited and annealed at 500 °C SmCo films with and without a Cr underlayer.

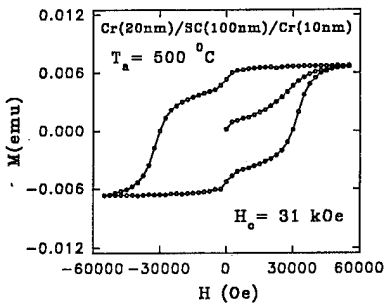



FIG. 4. Hysteresis loop for the 100-nm-thick SmCo film with a Cr underlayer of 20 nm annealed at 500 °C.

Cr underlayer but with a Cr overlayer of 10 nm after annealing at 500 °C shows a large increase in coercivity only for SmCo films with thickness of at least 100 nm and above. A maximum $H_c$ value of 29 kOe is obtained for 300-nm-thick SmCo film. For films without the Cr underlayer and SmCo layer thickness less than 100 nm the reason for no remarkable increase in coercivity after annealing is not clear at this point. This behavior is also observed for the PrCo film with thicknesses less than 100 nm and no Cr underlayer. The $M_s$ of the as-deposited SmCo films is about 400 emu/cc and after annealing at 500 °C the $M_s$ value for the films with the Cr underlayer of 80 nm is about 200 emu/cc and for the films without the Cr underlayer the $M_s$ is about 300 emu/cc. For the SmCo films with a Cr underlayer thickness less than 80 nm there is not a significant change in the coercivity but the $M_s$ value of the films is slightly higher compared to the films with a Cr underlayer of 80 nm. For the 100-nm-thick SmCo film with a Cr underlayer of only 20 nm the $M_s$ was about 250 emu/cc and the $H_c$ was about 31 kOe after annealing at 500 °C. The hysteresis loop for the annealed 100-nm-thick SmCo film with a Cr underlayer of 20 nm measured with a maximum applied field of 55 kOe parallel to the film surface is shown in Fig. 4. The film shows a coercivity of 31 kOe.

Liu *et al.*[6] have observed that for the as-deposited films the Cr underlayer has grain size of about 24 nm and the SmCo layer consist of nanocrystallites about 5 nm diameter embedded in an amorphous matrix. Figure 5 compares the dark field images taken from the SmCo films with and without a Cr underlayer. The film with the Cr underlayer has grain sizes of about 20 nm while the film without the Cr underlayer has grains sizes of about 10 nm. Nanodiffraction and HRTEM study to determine the crystal structure of the annealed films is in progress. The reason for the large enhancement in coercivity after annealing is very likely due to the crystallization of the SmCo grains.

## CONCLUSION

In this work we have shown that 28-nm-thick PrCo films with a Cr underlayer of 80 nm after annealing at 500 °C have in-plane coercivity as high as 10 kOe, $S=0.9$ and $S^*=0.75$. The PrCo‖Cr films have magnetic properties and microstructure which show potential as high density recording media. Nanodiffraction and HRTEM studies show that the crystallites in the annealed film have a hexagonal closed packed

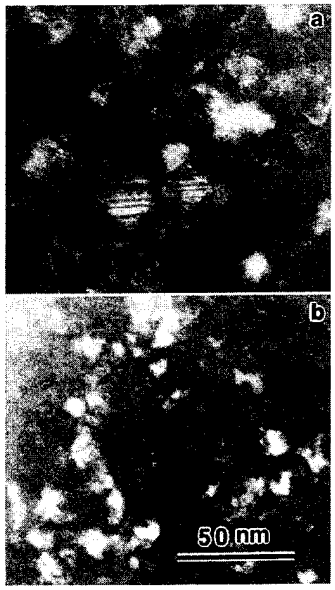



FIG. 5. Comparison of dark field images taken from a SmCo films (a) with the Cr underlayer and (b) without the Cr underlayer.

structure with frequent stacking faults. The enhancement of $H_c$ after annealing is likely due to the crystallization of the PrCo grain.

After annealing at 500 °C $H_c$ as high as 31 kOe was obtained for 100-nm-thick SmCo film with a Cr underlayer of 20 nm and $H_c$ of about 29 kOe for 300-nm-thick SmCo film without the Cr underlayer. By post-annealing the as-deposited films with and without the Cr underlayer, crystallization, and grain growth is promoted for the SmCo films resulting in a large increase in coercivity.

## ACKNOWLEDGMENTS

We are grateful for financial support from the National Storage Industry Consortium (NSIC) and the Advanced Research Projects Agency (ARPA) under Grant No. MDA972-93-1-0009 and from the National Science Foundation under Grants No. DMR-9222976 and No. OSR-9255225.

[1] E. M. T. Velu and D. N. Lambeth, J. Appl. Phys. **69**, 5175 (1991).
[2] Y. Okumura, H. Fujimori, O. Suzuki, N. Hosoya, X. B. Yang, and H. Morita, IEEE Trans. Magn. **30**, 4038 (1994).
[3] D. J. Sellmyer, Z. S. Shan, Y. Liu, S. H. Liou, S. S. Malhotra, and B. W. Robertson, Acta Met. Mater. (in press).
[4] E. M. T. Velu, D. N. Lambeth, J. T. Thornton, and P. E. Russel, J. Appl. Phys. **75**, 6132 (1994).
[5] Y. Okumura, O. Suzuki, H. Morita, X. B. Yang, and H. Fujimora, J. Magn. Magn. Mater. **146**, 5 (1995).
[6] Y. Liu, B. W. Robertson, Z. S. Shan, S. Malhotra, M. J. Yu, S. K. Renukunta, S. H. Liou, and D. J. Sellmyer, IEEE Trans. Magn. **30**, 4035 (1994).
[7] Y. Liu, B. W. Robertson, Z. S. Shan, S. H. Liou, and D. J. Sellmyer, J. Appl. Phys. **77**, 3831 (1995).
[8] Y. Liu, D. J. Sellmyer, B. W. Robertson, Z. S. Shan, and S. H. Liou, IEEE Trans. Magn. (in press).
[9] H. C. Theuerer, E. A. Nesbitt, and D. D. Bacon, J. Appl. Phys. **40**, 2994 (1969).
[10] F. J. Cadieu, T. D. Cheung, and L. Wickramasekera, J. Appl. Phys. **57**, 4161 (1985).
[11] K. H. J. Buschow, J. Less-Common Metals **33**, 311 (1973).
[12] A. E. Ray and K. J. Strnat, IEEE Trans. Magn. **11**, 1429 (1975).
[13] S. S. Malhotra, Y. Liu, Z. S. Shan, S. H. Liou, D. C. Stafford, and D. J. Sellmyer (unpublished).

# High-temperature magnetic properties of $TbCu_7$-type SmCo-based films

H. Hegde, X. R. Qian, Jong-Guk Ahn, and F. J. Cadieu
*Physics Department, Queens College of CUNY, Flushing, New York 11367*

In applications where large remanent moments and energy products are required at elevated temperatures, SmCo-based permanent magnets provide the best properties. In addition to their high Curie points, these SmCo-based ordered phases of 1-5, 2-17, and the disordered 1-7 phase show large uniaxial anisotropies at elevated temperatures. We have now measured the high-temperature hysteresis properties of single-phase $TbCu_7$-type SmCo-based permanent magnet films. Such single-phase samples have the advantage that optimal magnetic properties can be obtained from the as-sputtered films without any subsequent heat treatments. Normally bulk samples in this composition range form the two phase cellular structure whose magnetic properties are very sensitive to heat treatments. Single-phase $TbCu_7$-type films of composition $Sm_{13}Co_{58}Fe_{20}Cu_7Zr_2$ were sputter synthesized such that the crystallite $c$ axes were oriented in the film plane. The net anisotropy field of the films remained larger than the maximum applied field of 18 kOe even at the highest measurement temperature of 460 °C. Thus all measurements were from minor hysteresis loops. The in-plane coercivity showed a monotonic decrease from 6.0 kOe at room temperature to 1.3 kOe at 460 °C. The in-plane remanent flux density decreased from 8.5 kG at 50 °C to 5.8 kG at 460 °C. © *1996 American Institute of Physics.* [S0021-8979(96)33908-8]

Permanent magnets of the rhombohedral-based $Sm_2(CoFeZrCu)_{17}$ type are attractive for high-temperature applications because of their high ferromagnetic Curie point, high saturation magnetization, and high-energy product.[1,2] These magnets exhibit a cellular structure of rhombohedral 2-17 phase and 1-5 type grain boundaries.[3] As a result, the structural and magnetic properties of these magnets are very sensitive to the heat treatments required to develop coercivity. It has been shown that single-phase $TbCu_7$-type film magnets of Sm(CoFeCuZr) can be synthesized by sputtering nonepitaxially so as to exhibit strong in-plane $c$-axis alignment for a wide range of film thicknesses.[4,5] The structural properties of such films are insensitive to thermal treatments below 500 °C, making them extremely suitable for high-temperature applications. $TbCu_7$-type film magnets with magnetic easy axis in the film plane have been shown to be useful in magnetoresistive and magneto-optic devices,[6,7] whereas $Nd_2Fe_{14}B$-type films with magnetic easy axis perpendicular to film plane have been used in a millisize motor.[8] However, in applications at elevated temperatures, as a result of their relatively low Curie points the 2-14-1 type films are intrinsically inferior to the 1-7 type films. While there have been high-temperature studies of the hysteresis properties of bulk multiphase magnets of the type Sm(CoFeCuZr),[9,10] there have been no corresponding studies for single-phase $TbCu_7$-type magnets in either film or bulk form. In this article we present the high-temperature hysteresis properties of single-phase $TbCu_7$-type Sm(CoFeCuZr)-based film magnets.

The films in this study were sputter synthesized from commercially available 2-17 bulk magnets of the type $Sm_2(CoFeCuZr)_{17}$. The films were sputter deposited on polycrystalline $Al_2O_3$ substrates in 80 mTorr of Ar. The film composition was $Sm_{13}Co_{58}Fe_{20}Cu_7Zr_2$. Film deposition temperature was around 350 °C, so that the $TbCu_7$-type phase was formed with the $c$ axis of the crystallites randomly aligned in the film plane. These films needed no post-deposition heat treatments to obtain optimum magnetic hysteretic properties. Further details of film synthesis, crystallographic details, microstructure, and room-temperature magnetic properties have previously been published.[11] The high-temperature magnetic hysteresis measurements were made using a PAR model 151 high-temperature oven attached to a vibrating sample magnetometer. The temperature readings were calibrated against measurements made on a standard Ni sample. While no protective overcoating of the films was used, a positive flow of He gas was used in the high-temperature oven to shield against contamination as much as feasible.

In Fig. 1 hysteresis loops of a film at a temperature of 50 °C for applied field directions in the film plane (solid line) and perpendicular to the film plane (dashed line) are shown. In Fig. 2 similar measurements at a temperature of 250 °C are shown. The in-plane loop measured at 250 °C exhibited a slight shoulder on entering the second quadrant. Such a shoulder was more pronounced in thinner samples. The

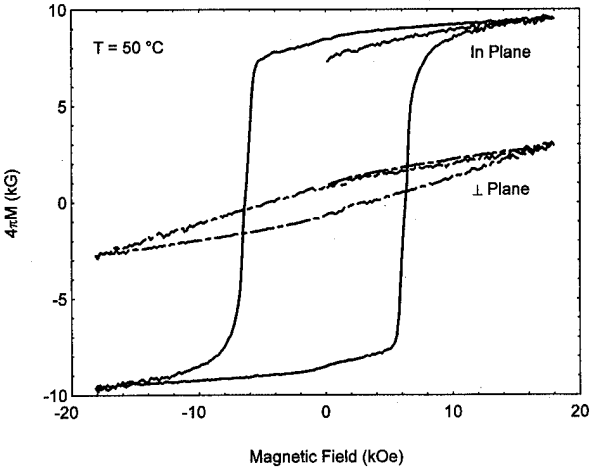



FIG. 1. Magnetic hysteresis loops at 50 °C, for measurements in-plane and perpendicular to film plane.

 0021-8979/96/79(8)/5961/3/$10.00 © 1996 American Institute of Physics 

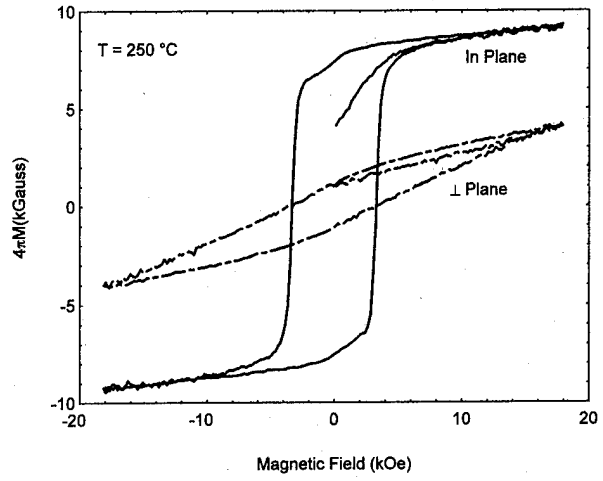



FIG. 2. Magnetic hysteresis loops at 250 °C, for measurements in-plane and perpendicular to film plane.

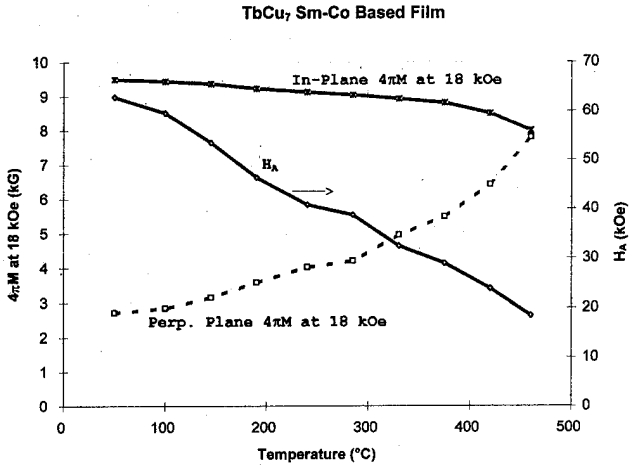



FIG. 4. Temperature dependence of in-plane and perpendicular to film plane flux densities at an applied field of 18 kOe (left axis). Temperature dependence of estimated anisotropy field $H_A$ (right axis).

shoulder is believed due to surface contamination in the high-temperature oven since the film coercivity was unchanged upon thermal cycling to 460 °C. This is shown in Fig. 3 which shows in-plane measurements at room temperature, before and after the sample was subjected to 460 °C high-temperature oven measurements. In films that were subjected to a similar 460 °C thermal cycling in a high vacuum chamber pumped to $\sim 2\times 10^{-7}$ Torr, no hysteresis loop deterioration was observed on remeasuring the loop at room temperature. Instead, such loops only reproduced the before thermal cycling loop. This showed that the high-temperature oven sample deterioration was a result of residual gases causing surface contamination.

Figure 4 shows the magnetic flux density of a SmCo-based $TbCu_7$ film as a function of the temperature, measured in-plane and perpendicular to the plane for an applied field of 18 kOe. Figure 4 also shows the variation of the estimated effective anisotropy field $H_A$ as a function of temperature.

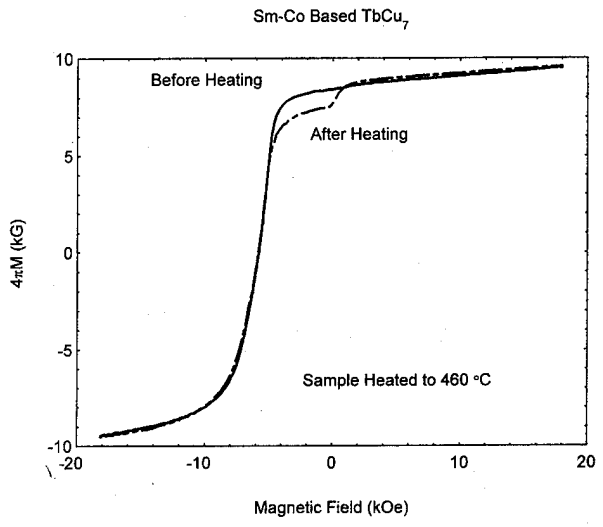



FIG. 3. In-plane hysteresis measurements on a film at room temperature, before and after the sample was subjected to 460 °C high-temperature measurements in the magnetometer oven.

The films were so deposited as to have only crystallites with $c$-axis in-plane orientation, thus making the perpendicular to the plane direction the magnetocrystalline hard axis. In addition, since the planar dimensions are much larger compared to film thickness, the shape anisotropy field in the perpendicular to the plane direction is simply $4\pi M$. Thus, for these films, the effective anisotropy field is the sum of shape anisotropy and magnetocrystalline anisotropy. From Fig. 4, it can be seen that while the effective anisotropy field $H_A$ is around 65 kOe at 50 °C, it drops to around 40 kOe at 250 °C and around 19 kOe at 460 °C. Comparison of temperature variations of the anisotropy field and coercivity as shown in Fig. 4 and Fig. 5 reveals a strong linear correlation between the two. As seen in Fig. 5, the coercivity of the film decreased below 2 kOe above a temperature of 350 °C. Figure 5 also shows the remanent flux density as a function of the temperature, measured in-plane and perpendicular to the plane.

In conclusion, the high-temperature magnetic properties of single-phase $TbCu_7$-type SmCo-based permanent magnet films have been studied. The study shows that after thermal

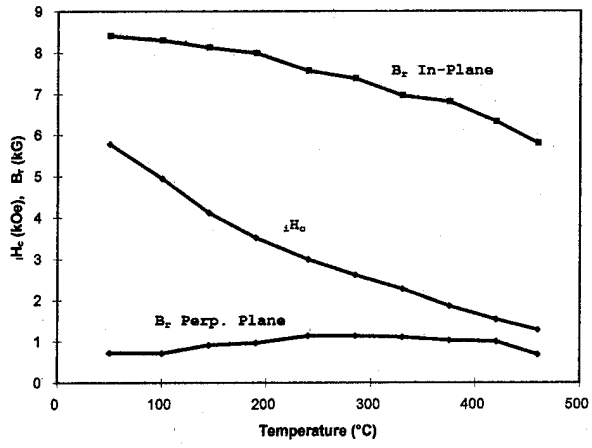



FIG. 5. Temperature dependence of in-plane coercivity $_iH_c$, in-plane $B_r$, and perpendicular to film plane $B_r$.

cycling to 460 °C, these films exhibited no decrease in coercivity. Decreases in room-temperature coercivity following similar thermal cycling has been observed for multiphase cellular structured SmCo-based 2-17 type bulk magnets.[12] Even at a temperature of 350 °C, the inplane coercivity of these films remained in excess of 2 kOe, while at the same temperature, the effective anisotropy was greater than 30 kOe.

This work has been supported by the U.S Army Research Office.

[1] K. Kumar, J. Appl. Phys. **63**, R13 (1988).
[2] R. K. Mishra, G. Thomas, T. Yoneyama, A. Fukuno, and T. Ojima, J. Appl. Phys. **52**, 2517 (1981).
[3] G. C. Hadjipanayis, J. Appl. Phys. **55**, 2091 (1984).
[4] F. J. Cadieu, H. Hegde, and K. Chen, J. Appl. Phys. **67**, 4969 (1990).
[5] F. J. Cadieu, *Permanent Magnet Thin Films*, Physics of Thin Films (Academic, San Diego, 1992), Vol. 16.
[6] M. Levy, R. Scarmozzino, R. M. Osgood, Jr., R. Wolfe, F. J. Cadieu, H. Hegde, C. J. Gutierrez, and G. A. Prinz, J. Appl. Phys. **73**, 5926 (1994).
[7] H. Hegde, S. U. Jen, K. Chen, and F. J. Cadieu, J. Appl. Phys. **73**, 5926, (1993).
[8] S. Yamashita, J. Yamasaki, M. Ikeda, and N. Iwabuchi, J. Appl. Phys. **70**, 6627 (1991).
[9] S. Liu, H. F. Mildrum, and K. J. Strnat, J. Appl. Phys. **53**, 2383 (1982).
[10] H. A. Leupold, E. Potenziani, A. Tauber, and H. F. Mildrum, J. Appl. Phys. **55**, 2097 (1984).
[11] H. Hegde, P. Samarasekara, R. Rani, A. Navarathna, K. Tracy, and F. J. Cadieu, J. Appl. Phys. **76**, 6760 (1994).
[12] A. E. Ray, J. Appl. Phys. **55**, 2094 (1984).

# Nanocomposite $Sm_2Co_{17}$/Co permanent magnets by mechanical alloying

S. K. Chen and J. L. Tsai
*Department of Materials Science, Feng Chia University, Taichung, Taiwan, Republic of China*

T. S. Chin
*Department of Materials Science and Engineering, National Tsing Hua University, Hsinchu, Taiwan, Republic of China*

Mechanically alloyed magnets $SmCo_x$ ($x=6.0-11.0$) have been prepared using starting materials of commercial $SmCo_5$ and Co powders. X-ray diffraction data indicate that the equilibrium $Sm_2Co_{17}$ phase can be achieved in a nanocomposite $Sm_2Co_{17}$/Co system at $x=8.5-11.0$, while a $Sm_2Co_{17}/SmCo_5$ structure occurs at $x=6.0-8.0$. The best magnetic properties obtained at $x=10.0$ are as follows: $(BH)_{max}=10.2$ MGOe, $B_r=9.4$ kG, $H_c=4.0$ kOe, and $S=0.82$. Wohlfarth's remanence analysis indicates that the high remanence can be attributed to the intergranular interaction between neighboring cobalt and $Sm_2Co_{17}$ grains. © *1996 American Institute of Physics.* [S0021-8979(96)34008-2]

## I. INTRODUCTION

Nanocomposite permanent magnetic alloys have been studied extensively. The alloys include $Nd_2Fe_{14}B/\alpha$-Fe,[1–6] $Sm_2Fe_{17}N_3/\alpha$-Fe,[7] and Sm-Co,[8–10] which can be prepared by melt spinning, mechanical alloying (MA), and thin-film processes, etc. The remanence enhancement for the isotropic nanocomposites have been discussed in terms of exchange coupling between two suitably dispersed magnetically hard and soft phases.[11] The two-phase alloys may have potential applications in resin bonded magnets due to the advantages of cost saving and high-energy product. However, the saturation magnetizing field of nanocomposite alloys is still high (close to that of some MQ powders) in spite of the moderate coercivity.

In this article, we will report nanocomposite $SmCo_x$ alloys with high-energy product and acceptable magnetizability. Efforts are focused on the range of $x=8.5-11.0$, because experimental data of the MA powders indicate the existence of the equilibrium $Sm_2Co_{17}$, which is not easy to obtain using melt spinning or thin-film process. The alloys is easy to magnetize because the magnetic anisotropy constant $K_1$ of $Sm_2Co_{17}$ (3.3 $MJ/m^3$) is lower than that of $Nd_2Fe_{14}B$ (5.0 $MJ/m^3$) in the popular $Nd_2Fe_{14}B/\alpha$-Fe system. Moreover, the $Sm_2Co_{17}$/Co alloys should possess the highest magnetization in the binary Sm-Co system.

## II. EXPERIMENT

Commercial powders of cobalt (1.47 $\mu$m) and prealloyed $SmCo_5$ (250 $\mu$m) were used as starting materials. The powders were ball milled in a cylindrical steel container using a planetary vibration mill, which was operated in air. To maintain an inert atmosphere during mechanical alloying, a vacuum valve was mounted into the cover of the container. Through the valve, the container was evacuated to a high vacuum of about $10^{-5}$ Torr, then purged with a positive pressure (2 atm) of high-purity Ar. The vacuum tubes were finally disconnected from the container before ball milling. The MA powders were annealed at 700–900 °C for 20 min in Ar for crystallization. The existing phases of the annealed powders were identified with an x-ray diffractometer.

Vibrating sample magnetometer (VSM) samples were prepared by dispersing the powder in molten wax in a sample capsule. Magnetic properties were measured at room temperature in a maximum field of 20 kOe. Dc− demagnetized samples, as described by Vajda and Torre,[12] were used for Wohlfarth's remanence analysis.

## III. RESULTS AND DISCUSSION

Figure 1 shows the x-ray diffraction patterns of mechanically alloyed powders $SmCo_x$ ($x=6.0-11.0$). The samples were annealed at 900 °C for 20 min. For the cobalt-rich samples with $x=8.5-11.0$, a two-phase $Sm_2Co_{17}$/Co structure appears. A small amount of free Co is still visible in the stoichiometric $Sm_2Co_{17}$ samples. For $x<8.5$, $SmCo_5$ coexists with $Sm_2Co_{17}$. No free cobalt was observed in the high-Sm alloys. The grain sizes of cobalt was estimated to be less than that of $Sm_2Co_{17}$. Both phases have a grain size of

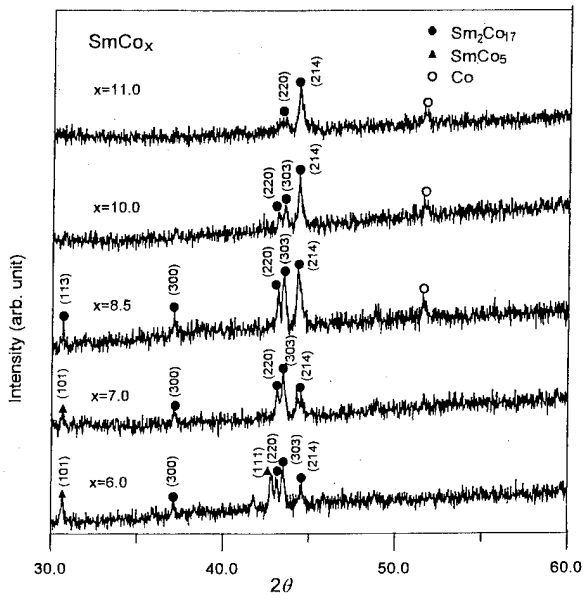



FIG. 1. X-ray diffraction patterns of mechanically alloyed $SmCo_x$ after milling for 16 h and a subsequent annealing at 900 °C for 20 min.

 0021-8979/96/79(8)/5964/3/$10.00 © 1996 American Institute of Physics

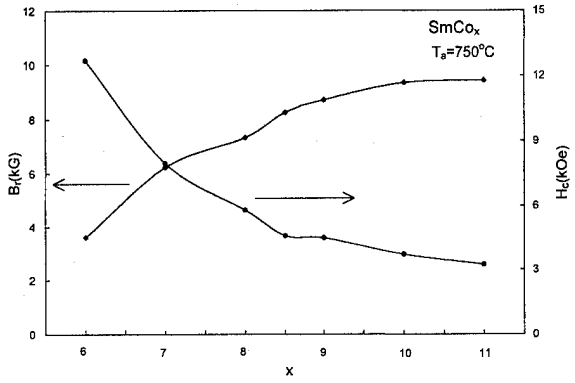



FIG. 2. Composition dependence of coercivity $H_c$ and remanence $B_r$ for mechanically alloyed $SmCo_x$ after milling for 16 h and a subsequent annealing at 750 °C for 20 min.

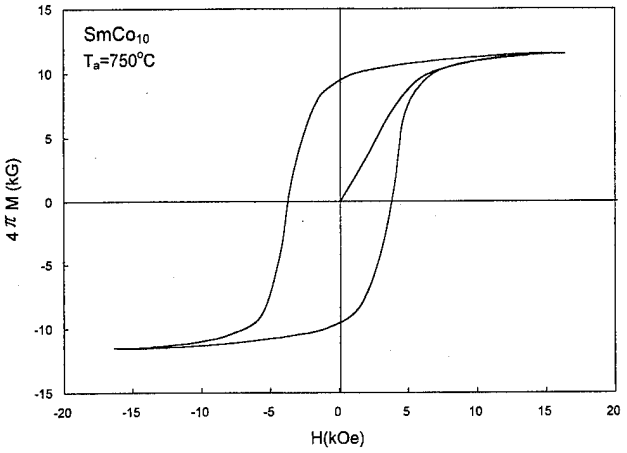



FIG. 3. Magnetic hysteresis loop of mechanically alloyed $SmCo_{10}$.

tens of nanometers, depending on the annealing temperatures. However, the grain sizes are beyond the limit of precise measurements using Scherrer formula.

Composition dependence of the coercivity $H_c$ and the remanence $B_r$ for $SmCo_x$ ($x=6.0-11.0$) is indicated in Fig. 2. The coercivity decreases with increasing $x$. For the low-Sm alloys ($x=8.5-11.0$), the decrease in $H_c$ may be attributed to the change in the morphology of the cobalt phase in the $Sm_2Co_{17}$ phase, which needs further study using a transmission electron microscope (TEM). The measured values of $H_c$ (4–5 kOe) for $SmCo_x$ ($x=8.5-10.0$) is close to some grades of commercial $Sm_2TM_{17}$ magnets, although the Sm-Co alloys contain no precipitation hardening elements, such as Cu and Zr. Coercivity mechanism of this $Sm_2Co_{17}$/Co system can be explained by the domain-wall pinning effect from the cobalt precipitates or the grain boundaries of the $Sm_2Co_{17}$ phase, as studied using Gaunt's model. For the high-Sm alloys ($x=6.0-8.0$), the high coercivity is obviously due to the existence of high-anisotropy $SmCo_5$. Sm-rich system was previously reported by Ding and Wecker *et al.*[8,9]

The variation of $B_r$ values with cobalt contents is also shown in Fig. 2. A maximum value of 9.4 kG was achieved for the samples with $x=10.0$. The high remanence, which is approximately equal to the typical value of some MQ powders, is due to the existence of cobalt phase, of which the $4\pi M_s$ value (18 kG) is about 40% higher than that of $Sm_2Co_{17}$ (13 kG).

The magnetic hysteresis loop of the $SmCo_{10}$ alloys is shown in Fig. 3. The magnetic properties are measured to be as follows: $B_r=9.4$ kG, $H_c=4.0$ kOe, $(BH)_{max}=10.2$ MGOe, and squareness ratio $(M_r/M_s)=0.82$. The alloy is calculated to contain 12 vol. % cobalt and 88 vol. % $Sm_2Co_{17}$. The high remanence and squareness ratio can result from the exchange interaction between neighboring $Sm_2Co_{17}$ and Co grains, so-called exchange-spring magnet.[11] However, the remanence and energy product remain the possibility for further improvement, considering the $SmCo_{10}$ alloy has a theoretical saturation magnetization of 13.6 kG.

To understand if the remanence enhancement is related to the interaction between neighboring grains, we investigate the $SmCo_{10}$ and $Sm_2Co_{17}$ samples using Wohlfarth's well-known remanence relationship[13,14]

$$m_d(H)=1-2m_r(H), \tag{1}$$

where $m_r(H)$ means the isothermal remanence which was normalized by the remanence obtained at a maximum field of 20 kOe, and $m_d$ means the normalized dc demagnetization. The staring samples were dc− demagnetized before $m_r$ and $m_d$ measurements. The plots of $m_r$ vs $m_d$, so-called Henkel plots,[15] were applied to the $SmCo_{10}$ and $Sm_2Co_{17}$ samples, as indicated in Fig. 4. A linear relationship with a slope of $-1/2$, as shown in Eq. (1), should hold for a noninteracting system during magnetization or demagnetization processes.[16] In the case of the $SmCo_{10}$ sample, the Henkel plot shows a large deviation from linear Wohlfarth relationship, which can be the result from the exchange coupling between the neighboring $Sm_2Co_{17}$ and Co grains. For the $Sm_2Co_{17}$ sample, which shows a nearly single-phase structure, the smaller deviation from Eq. (1) can be due to the different nature of interaction arising from different microstructures.

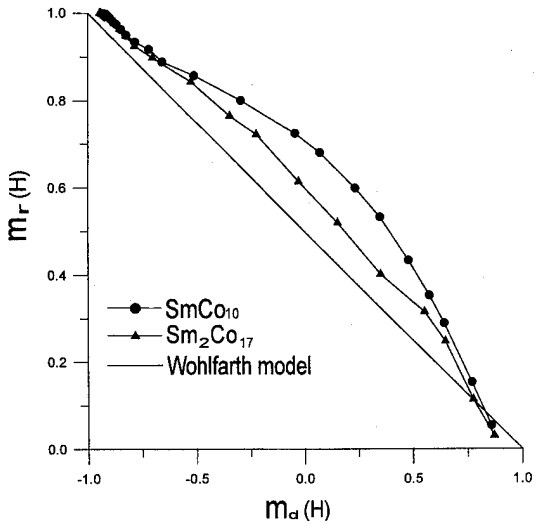



FIG. 4. Wohlfarth's remanence analysis for mechanically alloyed $SmCo_{10}$ and $Sm_2Co_{17}$. The diagonal represents the ideal case according to Eq. (1).

To precisely explain a Henkel plot, the demagnetization states of the sample should be well defined. The effect of demagnetization states (including dc−, dc+, and ac demagnetized states) on Henkel plots have been studied using Preisach models.[12] In our case, a dc− demagnetized state appears to be suitable for the analysis of exchange interaction. Wohlfarth's remanence analysis for various demagnetized Sm-Co samples will be discussed elsewhere.

## ACKNOWLEDGMENTS

The authors are grateful for the support from National Science Council of Republic of China under the Grant No. NSC-83-0208-M-035-008 and No. NSC-85-2112-M-035-002.

[1] R. Coehroon, D. B. De Mooji, J. P. W. B. Duchateau, and K. H. J. Buschow, J. Phys. **49**, C8-669 (1988).
[2] J. Ding, P. G. McCormick, and R. Street, J. Magn. Magn. Mater. **124**, 1 (1993).
[3] A. Manaf, R. A. Buckley, and H. A. Davies, J. Magn. Magn. Mater. **128**, 302 (1993).
[4] J. M. Yao, T. S. Chin, and S. K. Chen, J. Appl. Phys. **76**, 7071 (1994).
[5] L. Withanawasam, A. S. Murphy, G. C. Hadjipanayis, and R. F. Krause, J. Appl. Phys. **76**, 7065 (1994).
[6] S. K. Chen, T. A. Huang, C. S. Duh, T. S. Chin, and J. M. Yao, Intermag Conference 1995, San Antonio, session BD-09.
[7] J. Ding, P. G. McCormick, and R. Street, J. Magn. Magn. Mater. **14**, 1 (1993).
[8] J. Ding, Y. Liu, P. G. McCormick, and R. Street, J. Magn. Magn. Mater. **123**, L239 (1993).
[9] J. Wecker, M. Katter, and L. Schultz, J. Appl. Phys. **69**, 6058 (1991).
[10] F. J. Cadieu, K. Chen, and H. Hedge, IEEE Trans. Magn. **MAG-25**, 3788 (1989).
[11] E. F. Kneller and R. Hawig, IEEE Trans. Magn. **27**, 3588 (1991).
[12] F. Vajda and E. D. Torre, J. Appl. Phys. **75**, 5689 (1994).
[13] G. W. D. Spratt, P. R. Bissel, R. W. Chantrell, and E. P. Wohlfarth, J. Magn. Magn. Mater. **75**, 309 (1988).
[14] F. J. Pinkerton, Mater. Res. Soc. Symp. Proc. **96**, 65 (1987).
[15] O. Henkel, Phys. Status Solidi **7**, 919 (1964).
[16] P. Gaunt, G. Hadjipanayis, and D. Ng, J. Magn. Magn. Mater. **54-57**, 841 (1986).

# Control of the axis of chemical ordering and magnetic anisotropy in epitaxial FePt films

R. F. C. Farrow, D. Weller, R. F. Marks, and M. F. Toney
*IBM Research Division, Almaden Research Center, 650 Harry Road, San Jose, California 95120*

A. Cebollada
*Centro Nacional de Microelectronica, Serrano 144, 28006 Madrid, Spain*

G. R. Harp
*Department of Physics, Ohio University, Athens, Ohio 45701*

Growth of epitaxial films of the $L1_0$ phase of FePt, with the tetragonal $c$ axis along either the film normal or in-plane, is described. Films were grown by coevaporation of Fe and Pt, under ultrahigh vacuum conditions, onto a seed film of Pt grown on MgO or $SrTiO_3$ substrates. The perpendicular or in-plane orientation of the $c$ axis was controlled by selecting the (001) or (110) substrate plane, respectively. Nearly complete chemical ordering was achieved for growth at 500 °C for both orientations. Magnetic and magneto-optical characterization of these films confirmed the huge magnetic anisotropy expected for this phase. In the most highly ordered films, anisotropy fields in excess of 120 kOe were measured. © *1996 American Institute of Physics.* [S0021-8979(96)34108-9]

The magnetic and magneto-optical properties of intermetallic FePt alloy films are of current interest. The magnetic anisotropy, and magneto-optical Kerr rotation of FePt both correlate[1] with the degree of chemical ordering and the magnetic anisotropy energy $K_u$ is predicted[2] to reach a value of $>10^8$ erg/cc for complete ordering. This is one of the highest predicted[2] anisotropy energies of transition metal alloys and results from spin-polarization of the Pt $5d$ bands combined with the large spin-orbit coupling for Pt. Chemically ordered FePt films with their $c$ axis oriented along the film normal have been prepared by annealing sputtered epitaxial films,[3] cosputtering onto heated substrates,[4] and by molecular beam epitaxy (MBE).[1,5] The $c$-axis normal configuration was obtained by growing FePt onto (001) Pt seed films on MgO(001) substrates to symmetry match the fourfold FePt basal plane with the Pt. The lattice misfits for FePt(001)/Pt(001) and Pt(001)/MgO(001) are $-1.8\%$ and $-7.3\%$, respectively. Despite these large misfits FePt grows epitaxially with perpendicular mosaic spreads of only ~1°, as we report in this paper. Up until now, there have been no reports of growth of FePt epitaxy with the $c$ axis in plane. In view of the technological interest[6] in $L1_0$ FePt films for longitudinal magnetic recording media, there is a need to control the orientation of the $c$ axis. In this article we describe the growth and characterization of FePt films with the $c$ axis either perpendicular or in-plane.

The films were grown by coevaporation in a VG Semicon V80M MBE system using $e$-gun sources for both Fe and Pt. The fluxes were controlled by Leybold Inficon Sentinel III rate monitors and film growth rates of Pt and FePt were ~0.1 and 0.2 Å/s, respectively. Film growth was characterized, *in situ* using both reflection high-energy electron diffraction (RHEED) and low-energy electron diffraction (LEED). Following growth, the films were characterized by x-ray diffraction, vibrating sample and torque magnetometry, and magneto-optical Kerr studies. MgO(001) and (110) substrates were supplied by Harrick Inc.; $SrTiO_3$(110) by Marketech Inc. They were polished on one side using a syton finish and prepared as described earlier[7] for sapphire substrates.

We have earlier reported[1] growth of FePt films on 150-Å-thick Pt template films on MgO(001) substrates. Much thinner Pt films also act effectively as templates for FePt(001) growth. Pt films ~7 Å thick, grown at a substrate temperature of 700 °C, exhibited "spotty" RHEED patterns, consistent with transmission electron diffraction through (001)-oriented Pt islands. Overgrowth of FePt[8] resulted in a progressive transition to elongated streaks in the RHEED pattern at ~100 Å consistent with growth of a smooth, con-

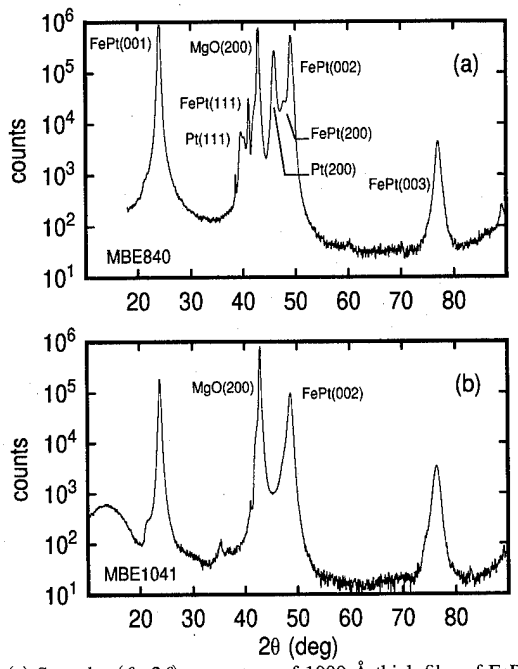



FIG. 1. (a) Specular ($\theta$–$2\theta$) x-ray scan of 1000-Å-thick film of FePt(001)/MgO(001). The complete structure was 18 Å $Pt/Fe_{0.52}Pt_{0.48}$/150 Å Pt/MgO(001). (b) Specular x-ray scan of 943-Å-thick film of FePt(001)/MgO(001). The complete structure was 18 Å $Pt/Fe_{0.50}Pt_{0.50}$/7 Å Pt/MgO(001).

 0021-8979/96/79(8)/5967/3/$10.00 © 1996 American Institute of Physics 

TABLE I. Compositions, long-range order parameters and mosaic spread for FePt(001) films.

| Seed film | FePt (%Fe) | $S_{max}$ | $S_{meas}$ | ⊥ mosaic (°) (001) | ⊥ mosaic (°) (002) | ⊥ mosaic (°) (003) |
|---|---|---|---|---|---|---|
| 150 Å Pt/MgO(001) | 52 | 0.96 | 0.93±0.02 | 1.05 | 0.78 | 0.84 |
| 7 Å Pt/MgO(001 | 50 | 1.0 | 0.92±0.02 | 2.49 | 1.99 | 2.08 |

tinuous epitaxial (001)-oriented film. The RHEED pattern showed little change as the film increased in thickness from 100 to 1000 Å. Specular x-ray diffraction scans for FePt films with thick and thin Pt seed layers are shown in Figs. 1(a) and 1(b). The intense (001) and (003) superstructure peaks in both scans indicate a high degree of chemical ordering with the tetragonal $c$ axis along the film normal. However, structural differences between the two samples are evident from these data. For example, minority structural domains with the tetragonal $c$ axis in plane or inclined to the film plane are indicated by the presence of FePt(200) and (111) specular peaks, respectively, in Fig. 1(a) (thick Pt). For the film of Fig. 1(b) (thin Pt) these minority domains are absent. The long-range order parameter,[1] $s$, for the two samples was quantified using integrated intensities for the (001), (002), and (003) peaks extracted from fits to scans over these peaks using a high-resolution diffractometer. This procedure is described in detail elsewhere.[8] Here we point out that the mosaic spread of each of the peaks was included in the calculation and an experimental Debye–Waller factor ($\sigma$=0.136 Å) was used. Differences in mosaic spread for the superstructure and fundamental peaks are considerable and must be included in the calculation of $S$ for meaningful results. The agreement between $S$ determined from the (001)/(002) and (003)/(002) intensity ratios was within 4%. Table I summarizes film compositions, maximum possible order parameters at these compositions and perpendicular mosaic spreads (FWHM of rocking curves) for the (001), (002), and (003) peaks. The order parameter for both samples is close to the maximum possible values at the compositions stated.

FePt(110) films were prepared in two different ways. Initially, $SrTiO_3$(110) substrates were used with a seed film of 30 Å Pt(110). The growth of this structure has been described earlier.[9] Unfortunately, the cubic perovskite structure of $SrTiO_3$ gives rise to a (110) peak which makes extraction of the FePt(110) superstructure intensity imprecise. MgO has no (110) peak and was used as an alternative substrate. In this case a 7-Å-thick Pt seed film was used. RHEED studies[9] showed facetted Pt(110) film growth on the $SrTiO_3$ and islanded growth of Pt(110) on MgO(110). X-ray specular scans for films grown at 500 °C on $SrTiO_3$ and MgO are

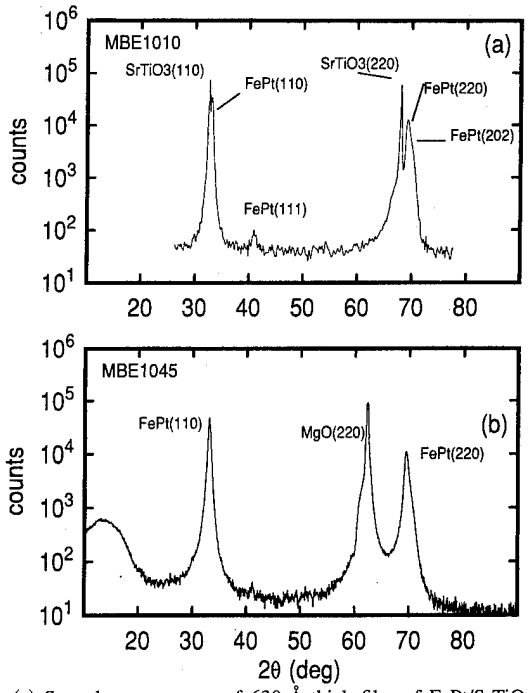



FIG. 2. (a) Specular x-ray scan of 630-Å-thick film of FePt/$SrTiO_3$(110). The complete structure was Pt 18 Å/$Fe_{0.56}Pt_{0.44}$/30 Å Pt/$SrTiO_3$(110). (b) Specular x-ray scan of 830 Å-thick film of FePt(110)/MgO(110). The complete structure was Pt 18 Å/$Fe_{0.58}Pt_{0.42}$/7 Å Pt/MgO(110).

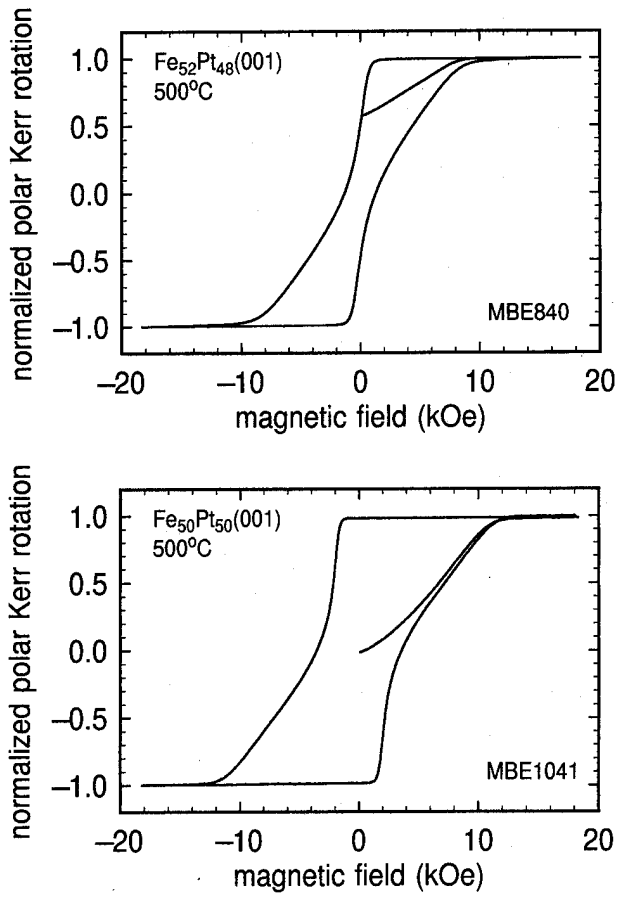



FIG. 3. Magneto-optical polar Kerr loops for FePt(001) films of Figs. 1(a) and 1(b). Laser wavelength 633 nm.

TABLE II. Compositions, long-range order parameters, perpendicular mosaic spread for FePt(110) films.

| Seed film | FePt (%Fe) | $S_{max}$ | $S_{meas}$ | ⊥ mosaic (°) (110) | ⊥ mosaic (°) (220) |
|---|---|---|---|---|---|
| 30 Å Pt/$SrTiO_3$(110) | 56 | 0.88 | 0.78±0.10 | 1.70 | 1.45 |
| 7 Å Pt/MgO(110) | 58 | 0.84 | 0.81±0.02 | 1.64 | 1.22 |

shown in Figs. 2(a) and 2(b), respectively. A high degree of chemical ordering in both samples is evident from the intense FePt(110) peak. However, in the $SrTiO_3$ sample, the FePt(110) peak appears as a shoulder on the $SrTiO_3$ peak. The majority orientation of both FePt films is FePt(110)‖$SrTiO_3$, MgO(110). In this orientation, the $c$ axis of the FePt is oriented in the film plane. Both RHEED and x-ray diffraction confirm that: FePt[001]‖Pt, MgO, $SrTiO_3$[001], and FePt[1$\bar{1}$0]‖Pt, MgO, $SrTiO_3$[1$\bar{1}$0]. The presence of a strong FePt(202) shoulder, for the $SrTiO_3$ sample, reveals a minority structural domain with the tetragonal $c$ axis inclined at ≃44° to the film plane. Peak fitting suggests that ~30% of the film volume is comprised of the minority domain. A small FePt(111) peak in Fig. 2(a) shows that this film also has a very weak (~0.1% of the sample volume) minority (111) orientation. The long-range order parameter for these two samples is given in Table II. Note that for the sample grown on MgO(110) the long-range order parameter is close to the maximum possible value.

Magneto-optical polar Kerr loops and $M$-$H$ loops for the FePt(001) samples of Figs. 1(a) and 1(b) are shown in Fig. 3. For both samples the easy axis is along the film normal. Perpendicular remanence is 60% and 100%, respectively and the saturation Kerr rotations are 0.71 and 0.75°, respectively. In-plane remanence is small for both samples and in-plane $M$-$H$ loops show that the magnetization is not saturated in the maximum applied field of 20 kOe. For these samples the estimated anisotropy fields are ≃75 and 120 kOe, respectively. Figure 4 shows $M$-$H$ loops for the FePt(110) samples with the field applied along the easy axis: FePt[001] (parallel) or along the film normal: FePt[110] (perpendicular). The in-plane remanence is 100% for both samples but there is a large difference in the out-of-plane magnetization data. The FePt/$SrTiO_3$ sample has a much larger remanence than the FePt/MgO(110) sample. The anisotropy fields for the samples are ≃75 and 140 kOe, respectively.

The structural and magnetic data for the FePt(001) films confirm that near-complete chemical ordering is achieved for film growth on Pt(001)/MgO for both 150 and 7-Å-thick Pt seed films at 500 °C. There are, however, significant differences in structural quality of the two samples which probably lead to the observed differences in magnetic properties. For example, the minority (111) and (100) structural domains may provide minority magnetic domains which contribute to the reduced remanence seen in the film with the thicker Pt seed film. Kern microscopy[10] reveals reverse-nucleated domains in zero field for this film. Similarly, for the FePt(110) samples the presence of (111) and (101) minority structural domains, in the film grown on $SrTiO_3$, may contribute to the perpendicular remanence and reduced magnetic anisotropy field for this sample. The huge magnetic anisotropy for the FePt $L1_0$ phase is confirmed by the magnetic data for these films. Torque magnetometry data, to be presented in detail elsewhere,[10] confirms $K_u$ to be ~$10^8$ erg/cm$^3$ for these films.

We acknowledge the work of Sherry Hom in x-ray data collection and peak fitting and are grateful to Andrew Kellock for sample composition and film thickness analysis using Rutherford backscattering.

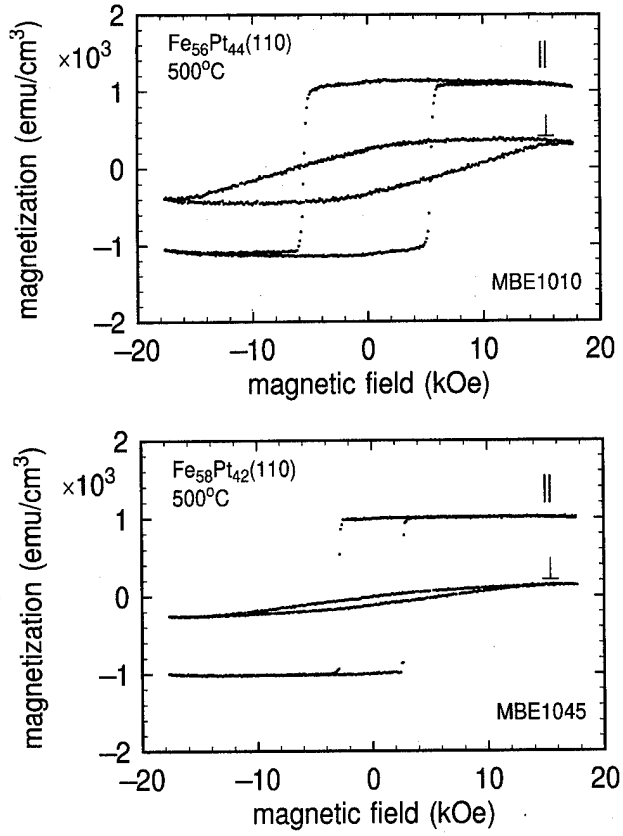



FIG. 4. Magnetization loops for FePt(110) films of Figs. 2(a) and 2(b).

[1] A. Cebollada, D. Weller, J. Sticht, G. R. Harp, R. F. C. Farrow, R. F. Marks, R. Savoy, and J. C. Scott, Phys. Rev. B **50**, 3419 (1994).
[2] G. Daalderop, Phys. Rev. B **44**, 12054 (1991); A. Sakuma, J. Phys. Soc. Jpn. **63**, 3053 (1994).
[3] B. M. Lairson and B. M. Clemens, Appl. Phys. Lett. **63**, 1438 (1993).
[4] M. Visokay and R. Sinclair, Appl. Phys. Lett. **66**, 1692 (1995).
[5] S. Mitani, K. Takanashi, M. Sano, H. Fujimori, A. Osawa, and H. Nakajima, J. Magn. Magn. Mater. **148**, 163 (1995).
[6] K. R. Coffey, M. A. Parker, and J. K. Howard, paper presented at Intermag 1995.
[7] R. F. C. Farrow, G. R. Harp, R. F. Marks, T. A. Rabedeau, M. F. Toney, D. Weller, and S. S. P. Parkin, J. Cryst. Growth **133**, 47 (1993).
[8] R. F. C. Farrow, D. Weller, M. Toney, and S. Hom (unpublished).
[9] G. R. Harp, R. F. C. Farrow, R. F. Marks, and J. E. Vazquez, J. Cryst. Growth **127**, 627 (1993).
[10] D. Weller, J. Heidmann, and R. F. C. Farrow (unpublished).

# Ba ferrite films with large saturation magnetization and high coercivity prepared by low-temperature sputter deposition

K. Noma, N. Matsushita, S. Nakagawa, and M. Naoe
*Department of Physical Electronics, Tokyo Institute of Technology, Meguro, Tokyo 152, Japan*

Ba ferrite films were deposited in a mixture of Xe, Ar, and $O_2$ by using facing targets sputtering apparatus with sintered targets of Fe-excessive BaM ferrite. By using Xe as sputtering gas, the bombardment of energetic Ar atoms recoiled from target to film surface was sufficiently suppressed and Fe content in Ba ferrite crystallites was significantly increased. It was found that the segregation of spinel crystallites among BaM ones were not observed and these BaM crystallites revealed the excellent $c$-axis orientation normal to film plane and clear perpendicular magnetic anisotropy. At substrate temperature $T_s$ of 600 °C, saturation magnetization $4\pi M_s$ of 5.1 kG, which is larger than that of BaM ferrite single crystal, and perpendicular coercivity $H_{c\perp}$ of 2.4 kOe were obtained. BaM ferrite films composed of well $c$-axis oriented crystallites with large perpendicular magnetic anisotropy constant, large saturation magnetization $4\pi M_s$ of 4.7 kG and high perpendicular coercivity $H_{c\perp}$ of 2.4 kOe were obtained at substrate temperature $T_s$ as low as 475 °C. © *1996 American Institute of Physics.* [S0021-8979(96)34208-5]

## I. INTRODUCTION

Ba ferrite films are candidate materials for magnetic recording media, milliwave devices, and permanent magnet components because of their large perpendicular magnetic anisotropy constant and high electric resistivity.

It was already reported that the facing targets sputtering (FTS) system are suitable for depositing the BaM ferrite films composed of well $c$-axis oriented crystallites normal to the film plane at low substrate temperature $T_s$ because the bombardment of energetic particles such as $\gamma$-electrons and negative ions to film surface is negligible.[1] In this study, Fe-excessive BaM ferrite plates with the composition of $BaO \cdot 6.5Fe_2O_3$ were used as sputtering targets for increasing the saturation magnetization $4\pi M_s$.

When the BaM ferrite sintered target was sputtered by Ar ions, neutral Ar atoms recoiled from the target attack the growing film surface resulting in the $4\pi M_s$ as small as 2.1 kG. It has been found that the bombardment of energetic particles to the film surface and incorporation of noble gases in the film interior can be sufficiently suppressed by using Xe instead of Ar as the sputtering gas.[2]

The suppression of the particle bombardment and the increase of kinetic energy of sputtered atoms arriving at film surface caused the significant decrease of critical $T_s$ for forming well $c$-axis oriented crystallites, of 450 °C for Xe sputtering and about 550 °C for Ar sputtering.[1] Films composed of well $c$-axis oriented BaM crystallites were deposited at $T_s$ as low as 475 °C by using mixture of Xe, Ar, and $O_2$ as sputtering gas.

## II. EXPERIMENT

The sintered ferrite plates with Fe-excessive composition of $BaO \cdot 6.5Fe_2O_3$ were used as sputtering targets, where the stoichiometric composition of BaM ferrite is $BaO \cdot 6.0Fe_2O_3$. The mixture of Xe, Ar, and $O_2$ was used as sputtering gas and Xe partial pressure $P_{Xe}$ was varied in the range of 0–0.18 Pa, where the total gas pressure and $O_2$ partial pressure were fixed at 0.20 and 0.02 Pa, respectively. At first, the ZnO underlayer with well $c$-axis oriented crystallites was deposited on the substrate of thermally oxidized $SiO_2$/Si wafer, and then 400-nm-thick Ba ferrite layer was deposited successively on the ZnO underlayer.

Film composition was analyzed by inductive coupled plasma spectrometry (ICPS). Microstructure of BaM/ZnO bilayered films were observed with scanning electron microscope (SEM). Crystallographic and magnetic characteristics were evaluated by x-ray diffraction (XRD), vibrating sample magnetometer (VSM), and torque magnetometer, respectively.

## III. RESULTS AND DISCUSSION

### A. Optimization of Xe partial pressure $P_{Xe}$

The XRD diagrams of all specimen films deposited at $T_s$ of 600 °C revealed the existence of spinel ferrite as well as $c$-axis oriented BaM ones. Figure 1 shows the $P_{Xe}$ dependences of Ba content $x$, ratio in diffraction intensity of spinel

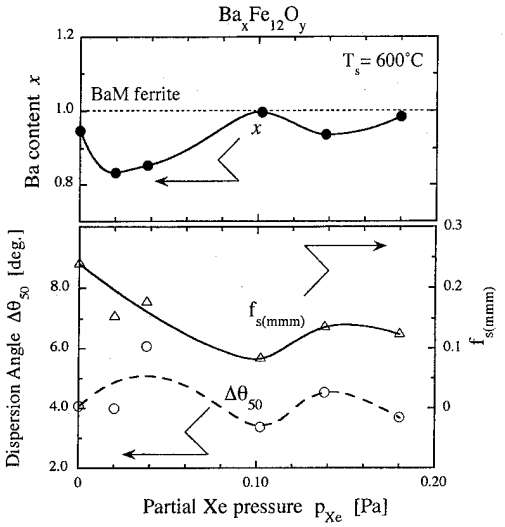



FIG. 1. $P_{Xe}$ dependencies of Ba content $x$, $f_{s(mmm)}$ and $\Delta\theta_{50}$.

 0021-8979/96/79(8)/5970/3/$10.00 © 1996 American Institute of Physics

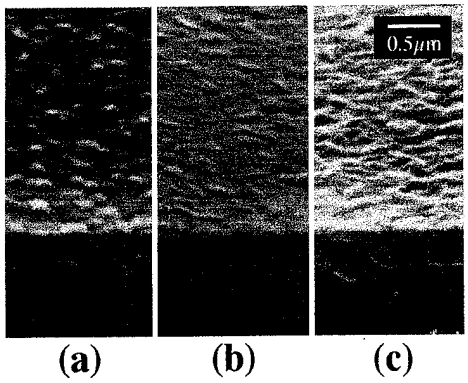



FIG. 2. SEM images of BaM/ZnO bilayered films deposited at $P_{Xe}$ of (a) 0, (b) 0.10, (c) 0.18 Pa.

(mmm) peaks $f_{s(\mathrm{mmm})}$ and dispersion angle of $c$-axis orientation of BaM crystallites $\Delta\theta_{50}$, where $x$ of 1.0 corresponds to the stoichiometric composition of BaM ferrite and the $f_{s(\mathrm{mmm})}$ were defined as follows:

$$f_{s(\mathrm{mmm})}=(\Sigma I_{\mathrm{spinel(mmm)}})/(\Sigma I_{\mathrm{BaM}(00n)}+\Sigma I_{\mathrm{spinel(mmm)}}),$$

where $I_{\mathrm{spinel(mmm)}}$ and $I_{\mathrm{BaM}(00n)}$ are the diffraction intensity of spinel(mmm) and BaM(00$n$).

The maximum value of $x$ of 1.0, the minimum value of $\Delta\theta_{50}$ of 3.4° and that of $f_{s(\mathrm{mmm})}$ of 0.086 were attained at $P_{Xe}$ of 0.10 Pa. The decrease of $x$ and the increase of $\Delta\theta_{50}$ at $P_{Xe}$ below 0.04 Pa seemed to be caused by heavy bombardment of energetic Ar atoms. Figure 2 shows the cross-sectional SEM images of the films deposited at various $P_{Xe}$. The film deposited at $P_{Xe}$ of 0.10 Pa had very smooth surface. Figure 3 shows the $P_{Xe}$ dependencies of the electron temperature ($T_e$) and the electron density ($N_e$) at the anode ring measured by Langmuir's single-probe method. $T_e$ was almost constant but $N_e$ had minimum value at $P_{Xe}$ of 0.10 Pa. The increase of $N_e$ at $P_{Xe}$ below 0.04 Pa and $P_{Xe}$ above 0.14 Pa were caused by enhancement in the degree of ionization of the atmospheric gases which collided with energetic Ar atoms and by an increase in body plasma density originating from the larger collision cross-section coefficient of Xe than

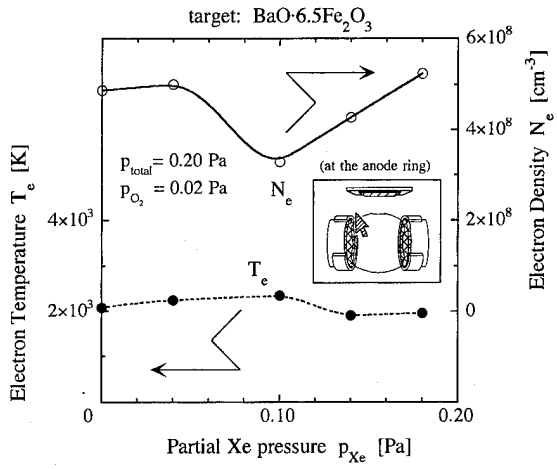



FIG. 3. $P_{Xe}$ dependencies of $T_e$ and $N_e$.

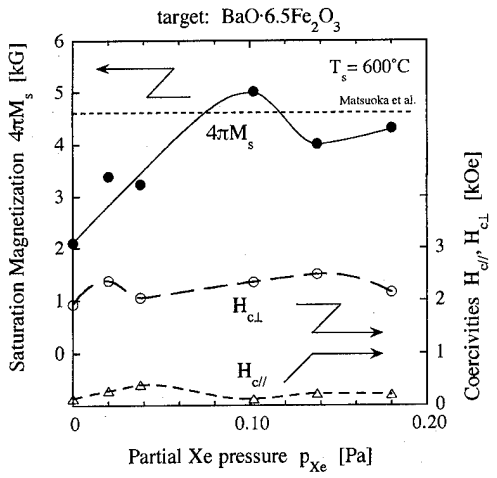



FIG. 4. $P_{Xe}$ dependencies of $4\pi M_s$, $H_{c\parallel}$, and $H_{c\perp}$.

that of Ar, respectively. These results indicate that the damage of film surface during sputtering was minimized at $P_{Xe}$ of 0.10 Pa.

Figure 4 shows the $P_{Xe}$ dependencies of the saturation magnetization $4\pi M_s$, the in-plane and perpendicular coercivities, $H_{c\parallel}$ and $H_{c\perp}$. At $P_{Xe}$ of 0.10 Pa, $4\pi M_s$ took the maximum value of 5.1 kG and $H_{c\parallel}$ took a minimum value of 0.14 kOe and then, $H_{c\perp}$ was 2.4 kOe. The value of $4\pi M_s$ of 5.1 kG was larger than that of 4.8 kG of BaM single crystal with the stoichiometric composition. $4\pi M_s$ of sintered targets used in this study was 3.7 kG, much smaller than that of the specimen films, and that of good crystalline films deposited by using targets with the composition of $BaO\cdot 6.0Fe_2O_3$ and mixture of Ar and $O_2$ as sputtering gas was 4.6 kG,[1] which is rather smaller than that of the specimen films in this study. The increase of $4\pi M_s$ seemed to be caused by the increase of Fe content and the number of layers of spinel blocks in the BaM unit cells. Figure 5 shows the $P_{Xe}$ dependences of the effective uniaxial anisotropy constant $K_\perp$ and the anisotropy field $H_k$. The $P_{Xe}$ dependence of $K_\perp$ corresponds well to that of $f_{s(\mathrm{mmm})}$ as shown in Fig. 1 and $K_\perp$ took the maximum value of $3.3\times10^5$ J/m$^3$ at $P_{Xe}$ of 0.10 Pa.

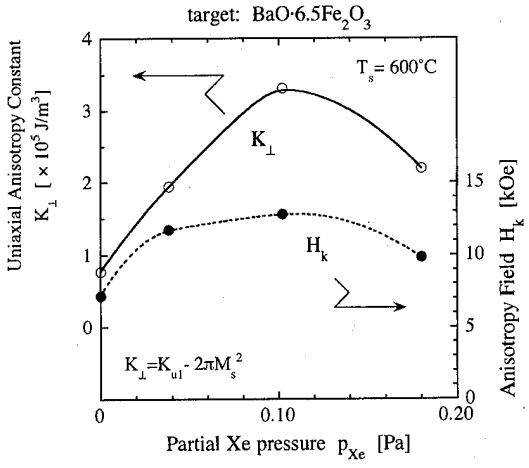



FIG. 5. $P_{Xe}$ dependencies of $K_\perp$ and $H_k$.

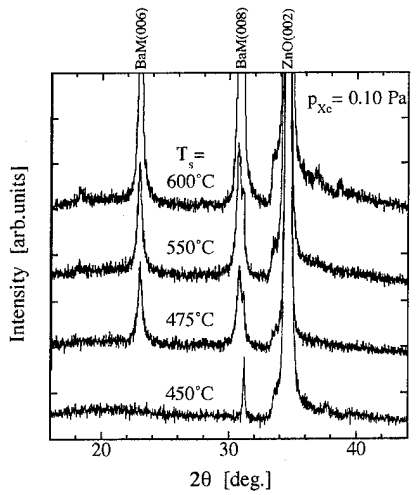



FIG. 6. XRD diagrams of BaM/ZnO bilayered films deposited at $P_{Xe}$ of 0.10 Pa for various $T_s$.

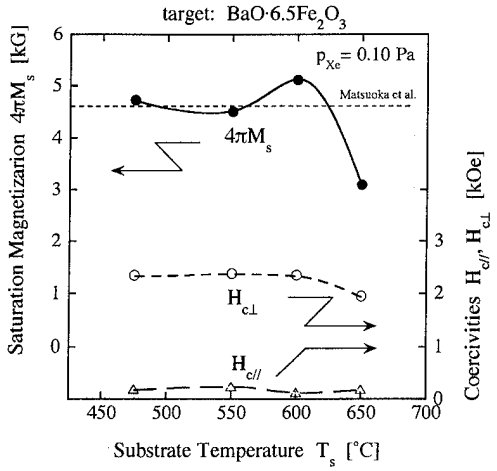



FIG. 7. $T_s$ dependencies of $4\pi M_s$, $H_{c\parallel}$, and $H_{c\perp}$.

It was found that the increase of $K_\perp$ corresponds well to the increase of $4\pi M_s$. These results suggest that the increase in Fe content and number of layers of spinel blocks and the excellent $c$-axis oriented BaM crystallites should increase $4\pi M_s$ and $K_\perp$, significantly. Consequently, BaM ferrite films deposited at $P_{Xe}$ of 0.10 Pa with Fe-excessive targets may be suitable for the perpendicular magnetic recording media.

### B. Deposition at lower substrate temperature $T_s$

Figure 6 shows the XRD diagrams of BaM/ZnO bilayered films deposited at various $T_s$. It was found that the BaM ferrite film composed of well $c$-axis oriented crystallites was obtained even at $T_s$ as low as 475 °C. The decrease of critical $T_s$ for depositing the films seemed to be attributed to the plasma-free film surface and the moderate arrival energy of sputtered atoms at $P_{Xe}$ of 0.10 Pa. Figure 7 shows the $T_s$ dependencies of $4\pi M_s$, $H_{c\parallel}$ and $H_{c\perp}$ of the films deposited at various $T_s$. $4\pi M_s$ of 4.7 kG was obtained even at $T_s$ of 475 °C, of which the value is almost same value as that of BaM ferrite single crystal. These results indicate that the higher Fe content promoted the formation of spinel blocks of several monolayers during the initial growth, which causes the crystallization of Ba ferrites at much lower temperature than pure BaM crystallites, and subsequently results in the decrease of critical $T_s$.

Even at lower $T_s$ of 475 °C, the sufficient magnetic properties seemed to be attained by sputtering of Fe-excessive BaM ferrite targets at $P_{Xe}$ of 0.10 Pa.

## IV. CONCLUSIONS

In this study, BaM ferrite films composed of well $c$-axis oriented crystallites were deposited by using the mixture of Xe, Ar, and $O_2$ as sputtering gas and the Fe-excessive BaM ferrite plates as targets. The obtained results were as follows:

(i) The plasma damage of the growing film surface was significantly suppressed at $P_{Xe}$ of 0.10 Pa.

(ii) The suppression of plasma damage and the formation of spinel block layer in initial growth due to higher Fe content seemed to cause the promotion of excellent $c$-axis oriented crystallites and the decrease of critical $T_s$ for crystallization down to 475 °C.

(iii) The higher Fe content in the films increased $4\pi M_s$. As a result, $4\pi M_s$ of 5.1 and 4.7 kG were obtained for the films deposited at $T_s$ of 600 and 475 °C, respectively.

These results suggest that the further improvements of magnetic characteristics of BaM ferrite films will be achieved by increasing Fe content as high as possible and by adjusting $P_{Xe}$, $P_{Ar}$, and $P_{O_2}$ to optimum values.

[1] M. Matsuoka, Y. Hoshi, M. Naoe, and S. Yamanaka, IEEE Trans. Magn. **MAG-18**, 1119 (1982).
[2] B. Window, J. Vac. Sci. Technol. A **11**, 1522 (1993).
[3] N. Matsushita, K. Noma, and M. Naoe, IEEE Trans. Magn. **MAG-30**, 4053 (1994).

# Characterization of $Fe_{17}R_2$ phases (R=Pr and Sm) oxidized at 200 °C

S. Gama, C. A. Ribeiro, F. A. O. Cabral,[a] C. C. Colucci, E. de Morais, N. L. Sanjurjo, C. Campos, J. D. Ardisson,[b] and A. I. C. Persiano[b]
*Instituto de Física Gleb Wataghin, Universidade Estadual de Campinas-UNICAMP, Caixa Postal 6165, 13 083-970 Campinas, SP, Brazil*

The results of oxygen absorption in temperatures ranging from 200 to 500 °C are reported for the phases $Fe_{17}R_2$, R=Pr and Sm. It was observed that the oxygen saturation limit is temperature dependent, being of 3 at/fu at 200 °C, 12.8 at/fu at 300 °C, 20.3 at/fu at 400 °C, and 28.5 at/fu at 500 °C. This implies that above 200 °C the phase is deeply altered by oxygen absorption. Samples with absorption at 200 °C were studied as prepared and heat treated at 500 °C/40 h. The results show that the heat-treated samples consist of $Fe_{17}R_2$, Fe, and $R_2O_3$. Metallographic examination, susceptibility, and Mössbauer spectroscopy data support the hypothesis that the as-prepared samples consist of a mixture of $Fe_{17}R_2$ and ordered interstitial $Fe_{17}R_2O_x$. © *1996 American Institute of Physics.* [S0021-8979(96)34308-1]

## I. INTRODUCTION

Since Coey's[1] discovery that the $Fe_{17}R_2$ phases (R=rare earths) absorb three nitrogen atoms per formula unit (at/fu), it has been shown that these phases can absorb other interstitials, e.g., hydrogen and carbon. For all these interstitials there occurs a lattice expansion, preserving the same crystallographic structure, but with changes in the magnetic properties.[2] In the nitrogen case, it is observed a direct precipitation of a nitrogen saturated phase, without the formation of any solid solution.[3]

It is expected that oxygen should have the same behavior as nitrogen in regard to absorption by the 17:2 phases. We studied previously oxygen absorption, at 600 °C or higher, by Fe-Pr and Fe-Nd multiphase alloys.[4,5] The results showed only phases that were decomposition products, as mixed oxides or oxides, none of them magnetically ordered. In the present work we describe results obtained for oxygen absorption conducted in the temperature range typical for nitrogen absorption.

## II. EXPERIMENT

The $Fe_{17}Sm_2$ samples were obtained from Goldschmidt Co. (Germany) in powder form. In the case of $Fe_{17}Pr_2$, the samples were arcmelted in argon and heat treated at 1000 °C during ten days, and turned into powder. The samples were sieved to have particle sizes in the range 32–50 $\mu$m. Gas absorption was done in a Sieverts apparatus, with strict temperature control through a type *K* thermocouple inside the reactor chamber. As the absorption is strongly exothermic, gas was admitted in small amounts each time, never allowing the sample temperature to deviate from the reactor temperature. Absorptions were done, from partial to saturation concentrations at 200, 250, 300, 400, and 500 °C. Some of the samples were heat treated at 500 °C/40 h in quartz ampoules under high-purity argon.

Samples were analysed by metallography, by ac thermomagnetic analysis (TMA), by x-ray diffraction using Fe $K\alpha$ radiation, and magnetic measurements at room temperature using a vibrating sample magnetometer (VSM). Also absorption in a Netzsch thermogravimetric analyser (TGA) using heating rate as low as 0.2 °C/min up to 800 °C in flowing oxygen has been done. We did also Mössbauer spectroscopy measurements at room temperature.

## III. RESULTS AND DISCUSSIONS

Our observations show that the $Fe_{17}R_2$ phases (R=Sm and Pr) can absorb large amounts of oxygen. At 200 °C the samples absorb up to 3 at/fu. This is similar to what is observed in the nitrogen case, the difference being that nitrogen absorption takes place at higher temperatures (300 °C). As the temperature increases, the oxygen saturation limit increases dramatically. So, at 300 °C saturation occurs at 12.8 at/fu, at 400 °C at 20.3 at/fu, and at 500 °C at 28.5 at/fu. This last result is confirmed by the TGA experiment, in which the total gas absorbed amounted to 29 at/fu. This indicates that for absorption temperatures above 200 °C the original 17:2 phase is profoundly altered. Similar results were obtained for the Pr case. For this reason, we concentrated this work on the samples of the two materials with absorption temperature of 200 °C. Samples with oxygen nominal contents of 0.5, 1.0, 1.5, 2.0, 2.5 at/fu and saturation were prepared.

The microstructure of a partially oxygenated sample at 200 °C [Fig. 1(A)] is similar to a partially nitrogenated one at 500 °C or higher temperature.[3] It presents a diffusion microstructure of the shell-core type, but it can be clearly seen that diffusion along phase and grain boundaries is competing with bulk diffusion. TMA results (Fig. 2) indicate that for partial absorptions we have the signature of the oxygen-free 17:2 phase and, beginning at 300 °C, a marked susceptibility increase, leading to a maximum at or above 500 °C. We note that this maximum does not appear in the cooling part of the TMA curve.

Comparing visually the samples before and after the TMA runs and after heat treatment, it is seen clearly a remarkable color change. They change from dark gray after oxidation to metallic gray after heat treatment or TMA measurement. Comparing the microstructures of the as-prepared and the TMA samples, we see a big modification of the origi-

[a]Departamento de Física, Centro de Ciências Exatas, UFRN, Natal, RN, Brazil.
[b]Departamento de Física, ICEX-UFMG, Belo Horizonte, MG, Brazil.

 0021-8979/96/79(8)/5973/3/$10.00 © 1996 American Institute of Physics 




FIG. 1. Microstructures of $Fe_{17}Sm_2$ samples, with oxygen absorption at 200 °C (a) as-prepared, (b) TMA measured up to 700 °C.

nal microstructure. The powder particles in the TMA samples are now almost homogeneous [Fig. 1(B)]. This suggests that the heating allows a redistribution of oxygen in the sample, as expected for the case of formation of an oxygen solid solution. To verify this effect, we took the samples and heat treated them at 500 °C/40 h in argon atmosphere.

The microstructures of the heat-treated samples turned out to be very similar to the TMA ones. Thermomagnetic analysis of the heat-treated samples show only the presence of the oxygen-free phase, with no maximum around 500 °C, and the curves are now reversible.

We also obtained x-ray diffraction data for the as-prepared and heat-treated samples. The data show that the

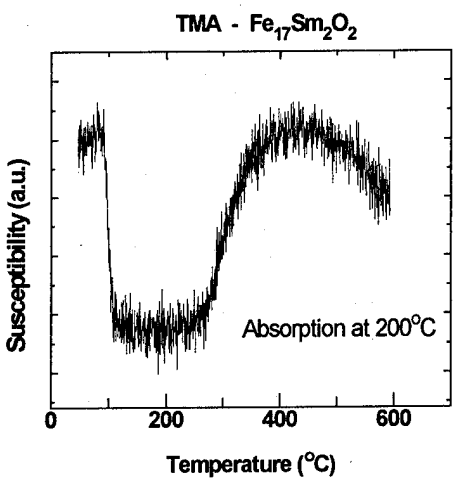



FIG. 2. TMA data for the $Fe_{17}Sm_2O_2$ sample, absorption at 200 °C.

as-prepared samples maintain the same diffraction patterns as the phase not oxidized; no change in peak positions or peak widths are observed, neither the presence of some extra phase. It seems that the oxygen has no noticeable effect in the lattice parameters. The data for the heat-treated samples show that these samples consist mainly of the 17:2 phase, pure Fe and probably $Sm_2O_3$. The x-ray data for the sequence of samples show that, with increasing oxygen content, the Fe amount increases and the $Fe_{17}R_2$ amount decreases. This is also confirmed by Mössbauer measurements.

These results led to the conclusion that holding these samples at high temperatures for long times, as during heat treatments, or for short times, as in a TMA measurement, brings out a decomposition of the phase into pure Fe and $R_2O_3$, which can be described by the reaction:

$$Fe_{17}R_2+3/2\ O_2 \rightarrow 17\ Fe+R_2O_3. \quad (1)$$

We note that in this reaction the number of oxygen atoms per formula unit of the original 17:2 phase is exactly 3. This is also the saturation number for the 200 °C absorption temperature. This observation rises the question: is the oxygen entering interstitially in the phase, or it reacts with the phase at once according to the above reaction? Three observations indicate that there is formation of an interstitial solid solution. First, the radical change in the microstructures after heating the samples. The samples become more or less homogeneous, and this requires that the oxygen is stored interstitially in the lattice of the phase, and, opposite to what happens in the nitrogen case, the oxygen must have high mobility, so that, during the heating, it is able to spread all over the grains, react with the phase and decompose it. The second observation is coming from the TMA curve. It shows a notable increase in the susceptibility, beginning at 300 °C. This has no parallel in the nitrogen case, and can be explained identifying the beginning of the increase in the TMA curves with the beginning of iron precipitation in very fine form in the microstructure. The susceptibility then increases until all oxygen reacts and the corresponding free iron precipitates. This is an irreversible process, and, accordingly, so are the TMA curves for the as prepared samples. The susceptibility decrease observed around 500 °C probably arises from the temperature variation of the Fe susceptibility, or from a phase that is a decomposition product, not yet identified. The uniformity of the observed heat-treated or TMA microstructures is attributed to this Fe and $Sm_2O_3$ precipitation in very fine scale. This same fine precipitation has been observed in the oxidation process for the $Fe_{14}Nd_2B$ phase.[6] These observations imply that if oxygen absorption is increasing the Curie temperature, as happens with the other interstitials (H, C, and N),[2] we can not see it because the very measuring process prevents us from obtaining its value.

The third observation comes from Mössbauer measurements, particularly clear for the case of Pr, in which case the unoxidized phase is paramagnetic at room temperature. The Mössbauer spectra was fitted using the doublet characteristic of the unoxidized phase, plus a broad hyperfine field distribution and a set of four sextets corresponding to an ordered phase (with spectral areas approximately proportional to 6:6:3:2). The existence of the hyperfine field distribution can

be best interpreted as the formation of an oxygen solid solution, distinct from the unoxidized phase. The hyperfine parameters obtained from fitting the four sextets, taking account of the iron present, show hyperfine fields of 35.5, 33.8, 32.0, and 38 T that can be associated with the $6f$, $6h$, $3d$, and $2c$ iron sites, respectively, using the hypothesis that we are dealing with a 17:2 phase. In the moment, there is no firm justification for this supposition, and the data can be interpreted also as belonging to a mixed oxide, as yet not identified.

## IV. CONCLUSIONS

We can conclude that:

(1) The phases $Fe_{17}R_2$, R=Pr and Sm, can absorb oxygen from 200 °C up to 500 °C, with saturation values increasing with the absorption temperatures.

(2) At 200 °C, most probably the oxygen is absorbed interstitially, affecting the magnetic properties as do the other interstitials. At higher absorption temperatures, the original phase is profoundly altered already during the absorption process.

(3) For the 200 °C samples, heating as in heat treatments or TMA measurements homogenizes the microstructures and leads to a very fine scale precipitation of pure Fe and $Sm_2O_3$. This prevents the determination of the Curie temperature for the oxidized phase.

(4) Metallographic analysis, TMA, and Mössbauer spectroscopy measurements all point to the existence of an ordered interstitial phase.

## ACKNOWLEDGMENTS

The authors thank financial support from FAPESP; Fundação de Amparo à Pesquisa do Estado de São Paulo, CNPq, Conselho Nacional de Desenvolvimento Científico e Tecnológico, RHAE, Programa de Formação de Recursos Humanos em Áreas Estratégicas and FAEP, Fundo de Apoio ao Ensino e Pesquisa da Unicamp. They also acknowledge helpful discussions with Dr. H. L. Lukas and G. C. Coelho, Max Planck Institut, Stuttgart, Germany.

[1] J. M. D. Coey and H. Sun, J. Magn. Magn. Mater. **87**, L-251 (1990).
[2] C. N. Christodoulou and T. Takeshita, J. Alloys Compounds **198**, 1 (1993).
[3] C. C. Colucci, S. Gama, and C. A. Ribeiro, J. Alloys Compounds **194**, 181 (1993).
[4] F. A. O. Cabral, S. Gama, and C. A. Ribeiro, J. Magn. Magn. Mater. **75**, L-197 (1988).
[5] E. H. C. P. Sinnecker, S. Gama, and C. A. Ribeiro, J. Appl. Phys. **70**, 6480 (1991).
[6] D. S. Edgley, J. M. le Breton, D. Lemarchand, I. R. Harrys, and J. Teillet, J. Magn. Magn. Mater. **128**, L-1 (1993).

# Magneto-optical properties of (BiGdY) iron garnets for optical magnetic field sensors

O. Kamada
*Department of Electronics, Polytechnic University, 4-1-1 Hashimotodai, Sagamihara, Kanagawa 229, Japan*

The influence of the magnetization process of the stripe domain both on the linearity error and the temperature dependence of the sensitivity in $(BiGdY)_3Fe_5O_{12}$ films for optical magnetic field sensors are studied. By measuring the dc applied field dependence of the light beam diffraction angle by the periodic magnetic domain structure, the domain period and the reduced thickness $\tau$ were determined. The magnetization curves calculated for the measured $\tau$ parameter show good agreement with the experimental results on the output characteristics. The linearity error of the ac Faraday output were within $\pm 1\%$ in the external field ranging of 10–300 Oe. However, a large linearity error was observed in the small field range. It was also found that the sensitivity is not affected by the temperature dependence of the $\tau$ parameter. © *1996 American Institute of Physics.* [S0021-8979(96)28408-1]

## I. INTRODUCTION

With recent developments in optical magnetic field (current) sensors based on Faraday effect, there has been considerable demand for applying these sensors to electric power systems such as power-delivery systems to measure current, and to monitor the condition of these lines.[1] Hence, high sensitivity and high accuracy in a wide magnetic field range are required. It is expected that rare-earth iron garnets, especially Bi-substituted rare-earth iron garnets [hereafter, referred as (BiR) IG] have high sensitivity constants because of a large Faraday rotation angle. But, recently, an attribution of Faraday loops to the light beam diffraction by the stripe magnetic domain structure of garnet films has been demonstrated.[2]

We have previously reported the experimental results on the temperature dependence of the sensitivity in detecting only the zeroth-order diffraction beam from (BiR) IG.[3] And, we have also reported on Gd-substituted (BiY) IG films with a minimal temperature dependence of the sensitivity.

In this work, the influence of the domain-wall-magnetization process both on the linearity error and the temperature dependence of sensitivity in magneto-optical (BiGdY) IG films are studied.

## II. EXPERIMENTS

(BiGdY) IG films were grown on (111)-oriented $(GdCa)_3(MgZrGa)_5O_{12}$ substrates by means of a liquid-phase-epitaxial (LPE) dipping technique with a horizontal-rotation mode. A $PbO–Bi_2O_3–B_2O_3$ system was employed as a solvent and $B_2O_3$-rich melts were used to obtain highly Bi-substituted films.[4] The chemical composition of the prepared films was determined by electron-probe microanalysis.

The applied magnetic-field dependence of the stripe-domain period and its temperature dependence were measured from the first-order diffraction angle of the He–Ne laser beam to determine the reduced thickness $\tau$ which was introduced by Kooy and Enz[5] for the theoretical calculation of the magnetization curves. And, the linearity error measurements in the zeroth-order diffraction beam were made using 850 nm GaAlAs LED light which propagates parallel to the external dc or ac field.

## III. RESULTS AND DISCUSSION

Figure 1 shows the schematic structure of the stripe domain assumed for the (111)-LPE-(BiGdY) IG film. The magnetization $M_s$ inside the domain is indicated by arrows. The stripe domain acts as a binary magnetic grating[6] as shown in Fig. 1. In our case of the zeroth-order diffraction-beam detection, the Jones vector of the electric field of the output light wave according to the domain-wall displacement is given by

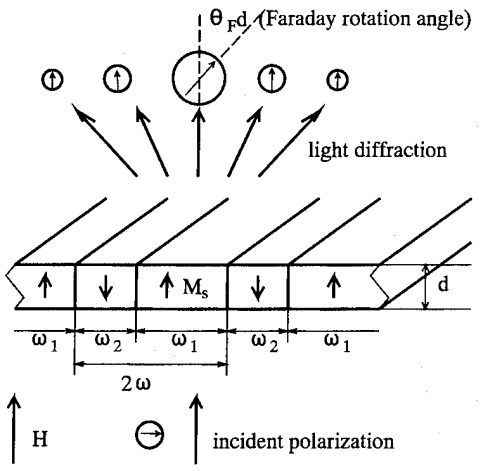



FIG. 1. Model of the stripe domain structure.

 0021-8979/96/79(8)/5976/3/$10.00 © 1996 American Institute of Physics

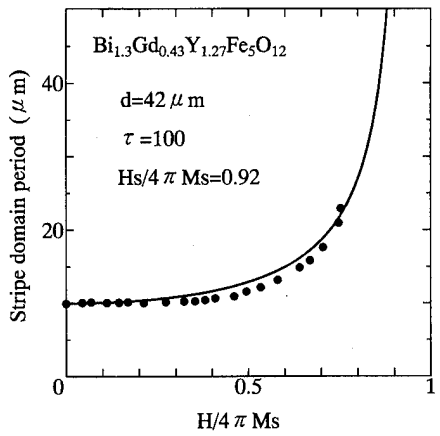



FIG. 2. Calculated curve and measurement results of the stripe domain period as dependent on the normalized external field.

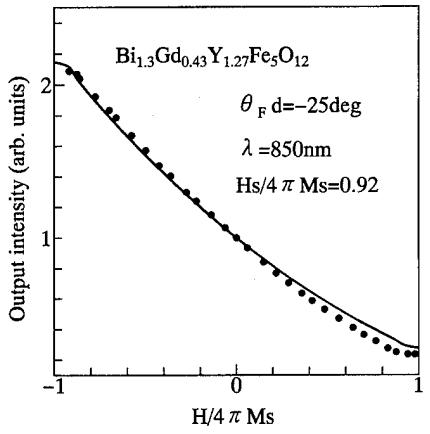



FIG. 4. Sensor output intensity vs normalized dc external field. (●) Show measured results and solid lines show calculated results by Eq. (1).

$$\begin{bmatrix} E_x \\ E_y \end{bmatrix} = \begin{bmatrix} \cos^2 45° & \cos 45° \sin 45° \\ \cos 45° \sin 45° & \sin^2 45° \end{bmatrix} \times \begin{bmatrix} E_0 \cos(\theta_F d) \\ E_0 (M/M_s) \sin(\theta_F d) \end{bmatrix}, \quad (1)$$

where, the action of the analyzer on the polarization state of the zeroth-order diffraction wave is described by 2×2 matrices. And in this case, the analyzer is at an angle of 45° with respect to the polarizer. The Faraday-output intensity, defined by the equation $p=1/2(|E_x|^2+|E_y|^2)$, is given by

$$P(H)/P(0)=[1+(M/M_s)\tan(\theta_F d)]^2, \quad (2)$$

where, $P(H)$ is normalized by $P(0)$. And $M$, $M_s$, $\theta_F$, and $d$ are the magnetic moment induced by the external magnetic field, the saturation magnetization, the Faraday-rotation angle, and the film thickness, respectively. The normalized magnetization of $M/M_s$ in Eq. (2) is given by

$$k=M/M_s=(\omega_1-\omega_2)/(\omega_1+\omega_2), \quad (3)$$

where, $\omega_1$ and $\omega_2$ are widths of the domains, respectively, parallel and antiparallel to the direction of the external field $H$. The domain widths in arbitrary stage of magnetization can be determined from the equilibrium condition to minimize the total magnetic energy $E$ for unit area of the film,[5] and $E$ is

$$E=E_W+E_H+E_d, \quad (4)$$

where $E_W$, $E_H$, and $E_d$ are the wall energy, the potential energy and the demagnetizing energy, respectively. Under these conditions, theoretical magnetization curves for the parameter of the reduced thickness $\tau$ can be obtained, and $\tau$ is defined by

$$\tau=\pi^2(1+\mu^{1/2})^{1/2}M_s d^{1/2}/(26)^{1/2}, \quad (5)$$

where $\sigma$ is the specific wall energy.

The observed external field dependence of the domain periods are plotted in Fig. 2. The theoretical curve is obtained with the parameter values of $\tau=100\pm2$ which can be determined from the domain period at $H/4\pi M_s=0$. And to take account of the $\mu$ effect, $\mu^{1/2}=(1+2\pi M_s^2/K_u)^{1/2}=2.2$ for (BiGdY) IG was used, since the growth induced anisotropy $K_u$ is about $4\times10^4$ erg/cm$^3$,[7] and $M_s=132$ Gauss. The calculated magnetization curves for $\tau=100$ are shown in Fig. 3, and the ratio of $H_s/4\pi M_s=0.92$ is obtained, where $H_s$ is the saturation magnetic field. The cause of the deviation of

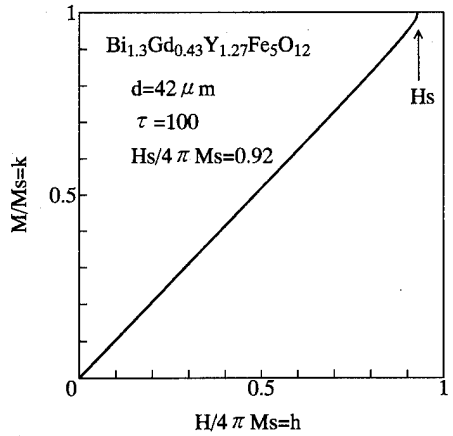



FIG. 3. Calculated magnetization curve for $\tau=100$.

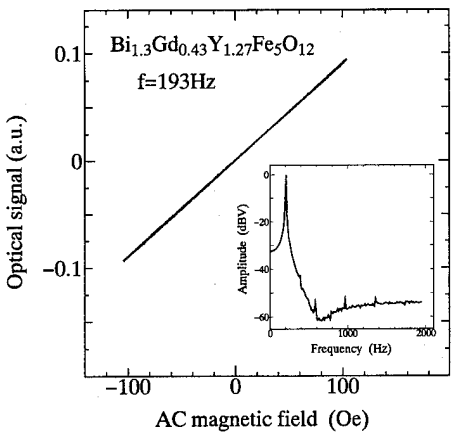



FIG. 5. Minor hysteresis loop. The insets show the result of the spectrum analysis.

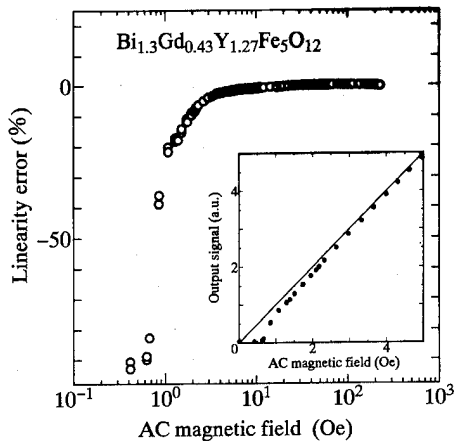



FIG. 6. Linearity error of the Farady output. The insets show the nonlinear ac output characteristics in the small external field region.

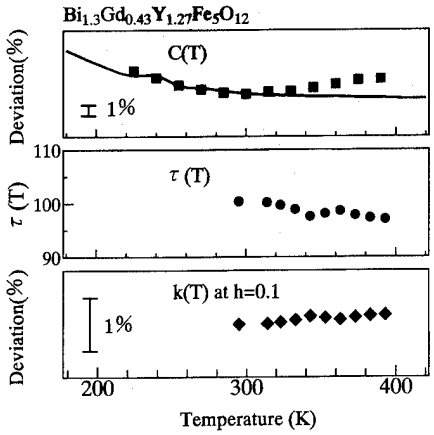



FIG. 7. Experimental results of the temperature dependence of sensitivity $C(T)$ and $\tau$ parameter. Calculated results of $k(T)$ variation related to $\tau(T)$ are also represented.

the experimental results from the calculated results of the domain period is expected to the influence of the small wall coercive force.

The output characteristics as a function of the applied dc field by Eq. (2) is analyzed. The calculated results by Eq. (2) are represented by a solid line in Fig. 4. The measured results are in good agreement with the calculated results and it is experimentally confirmed that the domain wall displacement is the dominant magnetization process in (BiGdY) IG film.

Figure 5 shows the minor hysteresis loop to evaluate the ac output linearity. A good linearity characteristics in (BiGdY) IG films is obtained, and it can also be found from the results of the spectrum analysis which shows the higher-order amplitude is less than −40 dB, as shown in the inset of Fig. 5. Figure 6 also shows the experimental results of the linearity error of less than ±1% over the applied field ranging from 10 Oe to 300 Oe. But a large linearity error at the small external field region is obtained. It is considered that the effect of the domain-wall coercive force of the order of 0.5 Oe appeared sensitively. So to explain this large nonlinearity phenomena quantitatively, it is necessary to calculate the magnetization curves and the minor loops[8,9] which takes the effect of the small wall coercive force into account. The present sensors for power-delivery systems, the higher field range than 10 Oe (for example, 15–150 Oe) is used, but improvement of the large linearity error in the lower field range is necessary to realize the wide range optical magnetic field sensors such as a optical wattmeter.

In previous paper,[3] the temperature dependence of sensitivity $C(T)$ were studied in terms of $\theta_F(T)$ and $M_s(T)$. The experimental results (■) and the calculated results (solid line) are shown in Fig. 7. However, the influence of the temperature dependence of $\tau(T)$ on $C(T)$ have not been taken into consideration. The measured results of $\tau(T)$ and the calculated results of the deviation of $k(T)$ at $h=0.1$ for the obtained $\tau(T)$ values are plotted in Fig. 7 too. From these results it can be found that $k(T)$ has very small temperature dependence within ±0.1% in the temperature ranging of 290–400 k, and the influence on $C(T)$ is very small.

## IV. CONCLUSION

Bi-substituted rare-earth iron-garnet films, (BiGdY) IG for optical magnetic-field sensors were prepared by LPE method.

From the measurement of the applied-field dependence of the domain period, the reduced-thickness parameter, $\tau=100\pm2$ was obtained. Using this value of $\tau$, the magnetization curves were calculated following the stripe-domain theory by Kooy and Enz. These curves show good agreement with the sensor output characteristics. However, in the weak external field region, a large linearity error was observed. It was estimated that the origin of this phenomena is the small coercive force, but more detailed investigations are required.

As another result, it was found that the sensitivity is not affected by the temperature dependence of the $\tau$ parameter.

[1] K. Kurosawa, Proceedings of the 7th International Conference on Optical Fiber Sensors, 1990, p. 67.
[2] T. Numata, H. Tanaike, S. Iguchi, and Y. Sakurai, J. Magn. Soc. Jpn. **14**, 642 (1990).
[3] O. Kamada, H. Minemoto, and N. Itoh, J. Appl. Phys. **75**, 6801 (1994).
[4] C. P. Clages, J. Cryst. Growth **64**, 275 (1983).
[5] C. Kooy and U. Enz, Philips, Res. Repts. **15**, 7 (1960).
[6] H. M. Haskal, IEEE Trans. Magn. **MAG-6**, 542 (1970).
[7] P. Hansen, K. Witter, and W. Tolksdolf, Phys. Rev. **27**, 6608 (1983).
[8] M. Masuda, S. Yoshino, H. Tomita, and S. Uchiyama, Jpn. J. Appl. Phys. **15**, 283 (1976).
[9] H. Hauser, J. Appl. Phys. **75**, 2584 (1994).

# An investigation on the magneto-optical enhancement in Ni-substituted barium ferrites

Xijuan Zhang
*Department of Physics, Nanjing University, Nanjing 210008, and Department of Physics, Teacher's College, Yangzhou University, Yangzhou 225002, People's Republic of China*

You Xu
*CCAST (World Laboratory), P.O. Box 8730, Beijing 100080, Department of Physics, Nanjing University, Nanjing 210008, and National Key Laboratory of Magnetism, Institute of Physics, Chinese Academy of Sciences, Beijing 100080, People's Republic of China*

Mingqian Duan
*Department of Physics, Jiangsu College of Education, Nanjing 210013, People's Republic of China*

Maurice Guillot
*Laboratoire des Champs Magnetiques Intenses, CNRS/MIP, 38042 Grenoble Cedex, France*

The calculation of the contribution of the intraionic electric-dipole transitions between the $3d^8$ and $3d^7\,4p$ configurations of $Ni^{2+}$ ions doped in barium ferrites to the Faraday effect is presented. It is shown that such transition is an important origin of the Ni contribution to the Faraday effect in the Ni-substituted barium ferrite. The energy difference between the mean energies of the $3d^8$ and $3d^7\,4p$ configurations is large. So the 496-nm wavelength (photon energy 2.5 eV) is far from the resonance frequencies. However, since the molecular field upon the $Ni^{2+}$ ions is very large, the Faraday rotation at 496 nm produced by such transition is still large. Other possible origins are discussed briefly. © *1996 American Institute of Physics.* [S0021-8979(96)16108-5]

## I. INTRODUCTION

With new techniques developed to prepare ferrite thin films,[1–3] magnetic oxides again become potential candidates for the magneto-optical (MO) recording material. Barium ferrite films have a marked uniaxial anisotropy and good squareness of in-plane hysteresis loop but the MO response remains quite poor. However it has been reported that the Co or Ni substitution in ferrites enhances the Kerr and Faraday rotations.[4–6] The enhancement factor of specific Faraday rotation (FR) at 496 nm wavelength is as large as $2\times10^4$ deg $cm^{-1}/x$ for $Ba_{1-x}M_xFe_{12-x}Ni_xO_{19}$ films, where M is La or Pr which is substituted for $Ba^{2+}$ ions for charge compensation and enhances no FR in the barium ferrite.[4]

As for the origin of the MO enhancement of the Ni substitution, to our knowledge, up to now there is still a lack of theoretical study. However, the origin of the MO enhancement of the $Co^{2+}$ ions in ferrites has been discussed by some authors.[5–7] They attributed the MO enhancement of the $Co^{2+}$ ions to the $d$–$d$ electric dipole (ED) transitions. They think that a finite transition probability could be produced due to some reasons. First, the $Co^{2+}$ ions in some ferrites have no center of symmetry. The odd-parity crystal potential terms mix higher-lying $p$ orbitals into the $d$ orbitals producing a finite transition probability. Second, the excited-state hybridization with ligands also produces a finite transition probability. Such transition is usually called a charge-transfer transition. However, it is worthwhile to examine if the intraionic ED transitions between the $3d^n$ and $3d^{n-1}4p$ configurations of the $Ni^{2+}$ and $Co^{2+}$ ions have large contribution to the MO effect in magnetic oxides containing cobalt or nickel. In this paper, the calculation of the contribution of such transition in the $Ni^{2+}$ ions to the MO effect in Ni-substituted barium ferrite is presented.

## II. THEORY AND CALCULATION

To calculate the contribution of the intraionic ED transitions between the ground and the parity allowed excited configurations to the MO effect, it is necessary to calculate the splitting of these configurations under the crystal electric field (CF) and superexchange interaction.

The Hamiltonian of the $Ni^{2+}$ ion in the crystal is

$$H=H_0+H_{SO}+H_C+H_{ex}, \tag{1}$$

where $H_{SO}$ is the spin-orbit interaction, $H_0+H_{SO}$ is the Hamiltonian of a free $Ni^{2+}$ ion, $H_C$ is the CF Hamiltonian and $H_{ex}$ is the superexchange interaction. $H_C$ can be expressed as

$$H_C=\sum_i \sum_{kq} A_{kq} r_i^k Y_{kq}(\theta_i,\phi_i), \tag{2}$$

where $A_{kq}$ is the CF parameter. In our calculation, the value of $\langle r^2\rangle_{3d}$, $\langle r^4\rangle_{3d}$, $\langle r^2\rangle_{4p}$ and $\langle r\rangle_{3d4p}$ are determined with the Slater radial wave function. The CF parameters are calculated with the point-charge model and only the contribution of the nearest neighboring $O^{2-}$ ions is considered. In the barium ferrite, the $Fe^{3+}$ ions occupy 2a, 2b, $4f_1$, $4f_2$, and $12k$ crystal sites. The nonzero parameters of the CF upon the $Ni^{2+}$ ion substituting the $Fe^{3+}$ ion at the 2b site are: $A_{20}\langle r^2\rangle_{3d}=-14966$ $cm^{-1}$, $A_{40}\langle r^4\rangle_{3d}=13197$ $cm^{-1}$, $A_{20}\langle r^2\rangle_{4p}=-66386$ $cm^{-1}$. Here the $z$ axis is taken to be along the sixfold symmetric axis of the crystal. The CF-split energy levels and the corresponding wave functions of the ground configuration are obtained by solving the following secular equation,

$$\|\langle JJ_z|H_{SO}+H_C|J'J_z'\rangle-E^0\delta_{JJ'}\delta_{J_zJ_z'}\|=0. \tag{3}$$

 0021-8979/96/79(8)/5979/3/$10.00 © 1996 American Institute of Physics 

TABLE I. The energies and the occupation probabilities at 300 K of the lowest four CF- and exchange-interaction-split levels of the $3d^8$ configuration for the $Ni^{2+}$ ions at the 2b site.

| Energy ($cm^{-1}$) | −3948.3 | −2963.7 | −2909.2 | −2897.0 |
|---|---|---|---|---|
| Probability | 0.976 | 0.009 | 0.007 | 0.006 |

The lowest two terms of the $3d^8$ configuration are $^3F$ and $^3P$. The mean energy of the $^3P$ term is 15 936 $cm^{-1}$ larger than that of the $^3F$ term. So, in solving Eq. (3), only the various multiplets of the $^3F$ term are included. The energies of the lowest five CF-split levels of this term for the $Ni^{2+}$ ion at the 2b site are −3456, −2903.1, −2194.5, 246.8, 1340.8 $cm^{-1}$. Here the energy of the multiplet $^3F_4$ is taken to be zero. All these five levels are doubly degenerate.

The Zeeman splitting of the CF-split levels is calculated by solving the following secular equation:

$$\|\langle\psi_i|H_{SO}+H_C+H_{ex}|\psi_j\rangle-E\delta_{i,j}\|=0. \tag{4}$$

The molecular field acting on the $Fe^{3+}$ ions in YIG estimated by Guillot *et al.* is 4000 kOe.[8] The Curie temperature of barium ferrite is higher than that of YIG. So the molecular field acting on the $Ni^{2+}$ ions in the barium ferrite is taken to be 5000 kOe. Then $2\mu_B H_m$ is about 500 $cm^{-1}$. This is not small compared with the energy differences between the CF levels. Therefore, in general, the mixing of these levels by superexchange interaction is not negligible and it is considered by us. The energies of the lowest four CF- and exchange-interaction-split levels of the ground term of the $Ni^{2+}$ ion at the 2b site are shown in Table I. The occupation probabilities of these levels at 300 K are shown in this table as well.

The $3d^7 4p$ configuration has many terms. Among them the terms allowed by the ED transition from $3d^8$: $^3F$ term are: $3d^7(^4F)4p$: $^3G$, $^3F$, $^3D$; $3d^7(^4P)4p$: $^3D$; $3d^7(^2P)4p$: $^3D$; $3d^7(^2D1)4p$: $^3F$, $^3D$; $3d^7(^2D2)4p$: $^3F$, $^3D$; $3d^7(^2F)4p$: $^3G$, $^3F$, $^3D$; $3d^7(^2G)4p$: $^3G$, $^3F$; $3d^7(^2H)4p$: $^3G$. The lowest three terms are $3d^7(^4F)4p$: $^3G$, $^3F$, $^3D$. Solving the following secular equation:

$$\|\langle JJ_z|H_0+H_{SO}+H_C|J'J'_z\rangle-E^0\delta_{JJ'}\delta_{J_zJ'_z}\|=0, \tag{5}$$

we have obtained the CF-split levels and the corresponding wave functions of these three terms. The differences between the mean energies of these terms are small, so in solving Eq. (5), the bra and ket include various states of these three terms. The values of the diagonal matrix elements $\langle JJ_z|H_0+H_{SO}|JJ_z\rangle$ in Eqs. (3) and (5) are taken from the book by Moore.[9] The energies of the lowest six CF-split levels of these terms are: 96 229, 96 380, 99 027, 99 030, 99 441, 99 699 $cm^{-1}$. Here the energy of the multiplet $3d^8$: $^3F_4$ is taken to be zero. For simplicity, the energies of all other terms are supposed to be 130 000 $cm^{-1}$. The CF splitting of these terms is neglected. Because the CF splitting is small compared with the difference between the mean energies of the $3d^8$ and $3d^7 4p$ configurations, the error due to the above approximation is small. The Zeeman splitting of the $3d^7 4p$ configuration is also neglected.

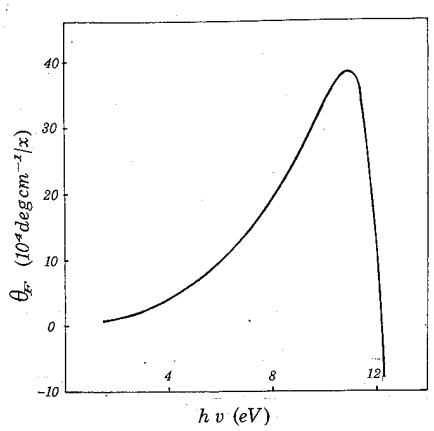



FIG. 1. The specific FR contributed by the $Ni^{2+}$ ions at the 2b site in $Ba_{1-x}M_xFe_{12-x}Ni_xO_{19}$.

The FR per unit length of the medium caused by the ED transitions is (see Refs. 10 and 11 and the references therein)

$$\theta_F=\frac{N\pi(\bar{n}^2+2)^2}{9c\bar{n}\hbar}\times\sum_{ng}A_{ng}\frac{\omega^2(\omega_{ng}^2-\omega^2-\Gamma_{ng}^2)}{(\omega_{ng}^2-\omega^2+\Gamma_{ng}^2)^2+4\omega^2\Gamma_{ng}^2}\rho_g, \tag{6}$$

for each type of ion present in the material, where

$$A_{ng}=|\langle n|V_-|g\rangle|^2-|\langle n|V_+|g\rangle|^2. \tag{7}$$

In Eqs. (6) and (7), $c$ is the velocity of the light in vacuum, $\omega$ the angular frequency of the light wave, $\bar{n}$ an average refractive index, for barium ferrite, $\bar{n}\approx 2.8$,[12] N the number of ions per unit volume, $\Gamma_{ng}$ the half-widths of resonance lines, $|g\rangle$ the CF- and exchange-interaction-split $3d^8$ states with energy $E_g$, $|n\rangle$ the $3d^7 4p$ states with energy $E_n$, and $\hbar\omega_{ng}=E_n-E_g$. $V_\pm$ are the ED moment operators for right- and left-handed circularly polarized light, $\rho_g$ is the occupation probability of the state $|g\rangle$. When $|\omega_{ng}^2-\omega^2|\gg\Gamma_{ng}^2$, Eq. (6) can be reduced to the following formula:[13]

$$\theta_F=\frac{N\pi(\bar{n}^2+2)^2}{9c\bar{n}\hbar}\sum_{ng}A_{ng}\frac{\omega^2}{\omega_{ng}^2-\omega^2}\rho_g \tag{8}$$

Both Eqs. (6) and (8) are accurate at low energies.

The calculated FR contributed by the $Ni^{2+}$ ions at the 2b site at various photon energies is shown in Fig. 1. The FR at 496-nm wavelength is $1.53\times10^4$ deg $cm^{-1}/x$. The FR contributed by the $Ni^{2+}$ ions at the $4f_1$ site is $-1.4\times10^4$ deg $cm^{-1}/x$ at 496 nm. When the $Ni^{2+}$ ions are at the 2a or the $4f_2$ site, the enhancement factor is small. It should be noted that, in our calculation the values of $\langle r\rangle_{3d4p}$, $\langle r^2\rangle_{3d}$ etc. are obtained with the Slater radial wave function of the free $Ni^{2+}$ ions. We think that the extension of the radial wave function of the $Ni^{2+}$ ion in the crystal will make the actual enhancement factor larger than that given above. It is worthwhile to point out that the Slater radial wave function and the point-charge model were used to calculate the magnetocrystalline anisotropy of the barium ferrite[14,15] and $Zn_2W$ ferrite.[16] As we have done in this paper, in calculating the CF parameters only the effect of the nearest neighbors was taken

into account. The calculated results can explain the main experimental results well. However the magnitude of the calculated magnetocrystalline constant $K_1$ is smaller than the measured one. This fact also makes us believe that the actual enhancement factor will be larger than the value given above. According to Machida *et al.*[3] and Gomi *et al.*,[4] the FR induced by a $Fe^{3+}$ ion in the barium ferrite is much smaller than that by a $Ni^{2+}$ ion at the 2b or $4f_1$ site. Therefore, in explaining the enhancement by $Ni^{2+}$ substitution, it has been neglected to a first-order approximation.

## III. CONCLUSION AND DISCUSSION

From our calculation, it is seen that the intraionic ED transition between the $3d^8$ and $3d^7 4p$ configurations is an important origin of the large MO enhancement of the $Ni^{2+}$ ions in the barium ferrite when the photon energy is larger than about 1.5 eV. The $Co^{2+}$ ions have similar characteristic as the $Ni^{2+}$ ions, and the YIG and cobalt ferrite have similar characteristic as the barium ferrite. Therefore we think that the intraionic ED transition between the $3d^7$ and $3d^6 4p$ configurations may be also an important origin of the MO effect contributed by the $Co^{2+}$ ions in such compounds in the wavelength region mentioned above. However, it is found that there is a resonance frequency at about 1500-nm wavelength for Co-substituted garnets[6] and a resonance frequency at about 900 nm for $Co_xCd_{1-x}Cr_2S_4$.[7] They cannot come from the origin mentioned above. Could they come from the $d-d$ transitions induced by the odd-parity crystal field? The environment of the 2b site in the barium ferrite has no center of symmetry. According to our calculation, the odd-parity CF upon the $Ni^{2+}$ ions at the 2b site does produce MO resonance around 2.5 eV. However, the component of the $4p$ orbitals mixed into the $d$ orbitals is so small that the maximum value of the FR near the resonance frequency is about 500 deg $cm^{-1}/x$. In our calculation the value of $\hbar\Gamma$ is taken to be 0.05 eV, which may be too small. The value of the FR near the resonance frequency depends on the value of $\hbar\Gamma$. So the value given above may be larger than the actual value. Therefore, the $d-d$ transitions induced by the odd-parity CF cannot explain the MO resonance phenomenon of the $Co^{2+}$ ions in these compounds at long wavelength region. We think that it might come from the charge transfer between the $Co^{2+}$ ions and the ligands.

As mentioned above, the Zeeman splitting of the excited configuration has been neglected. Therefore, when a plane-polarized electromagnetic wave propagates through the medium, the transition probabilities for the right- and left-handed circularly polarized light between the sublevels of a CF level of the ground configuration and the states of the excited configuration are the same. So there will be no Faraday effect if there is no Zeeman splitting of the CF levels of the ground configuration, but the Zeeman splitting makes the occupation probabilities of these sublevels different. This results in a so called "paramagnetic" type Faraday effect. The Zeeman splitting of the excited configuration will lead to a "diamagnetic" type Faraday effect. However, the energy differences between the CF-split $3d^7 4p$ states and the lowest $3d^8$ states are larger than 99 000 $cm^{-1}$, while the Zeeman splitting is less than 1000 $cm^{-1}$, so the diamagnetic type Faraday effect is very small and is neglected by us.

From the calculated results given above, it could be seen that the value of $\hbar\omega_{ng}$ is larger than 99 000 $cm^{-1}$, so the factor $\omega^2/(\omega_{ng}^2-\omega^2)$ is very small for the wavelengths near 496 nm. However, in barium ferrite, the molecular field upon the $Ni^{2+}$ ions is so large that the occupation probability of the lowest CF- and exchange-interaction-split level of the $3d^8$ configuration is close to 1. Hence, the FR at 496-nm wavelength is still large. By the way, after the estimation of Dionne *et al.*,[17] the molecular field upon the $Fe^{3+}$ ions in YIG is also so large that the occupation probability of the lowest CF- and exchange-interaction-split level is close to 1. Furthermore, for so large a Zeeman splitting, the calculation results do not depend seriously on the exact value of the molecular field. These facts make us believe that our main conclusion is reliable.

## ACKNOWLEDGMENTS

This work is supported partly by the National Natural Sciences Foundation of China and the Natural Sciences Foundation of the Education Commission of Jiangsu Province of China.

[1] M. Naoe, S. Hasunuma, Y. Hoshi, and S. Yamanaka, IEEE Trans. Magn. **17**, 3184 (1981).
[2] M. Matsumoto, A. Morisako, T. Haeiwa, K. Naruse, and T. Karasawa, IEEE Trans. J. Magn. Jpn. **6**, 648 (1991).
[3] H. Machida, F. Ohmi, Y. Sawada, Y. Kaneko, A. Watada, and H. Nakamura, J. Magn. Magn. Mater. **54–57**, 1399 (1986).
[4] M. Gomi, K. Shimai, J. Cho, and M. Abe, J. Appl. Phys. **73**, 6146 (1993).
[5] M. Abe and M. Gomi, J. Appl. Phys. **53**, 8172 (1982).
[6] K. Shinagawa, K. Tamanoi, T. Saito, Y. Aman, K. Sato and T. Tsushima, J. Physique **49**, C8-959 (1988).
[7] R. K. Ahrenkiel, S. L. Lyn, and T. J. Coburn, J. Appl. Phys. **46**, 894 (1975).
[8] M. Guillot and H. Le Gall, J. Physique, **38**, 871 (1977).
[9] C. E. Moore, *Atomic Energy Levels* (Natl. Stand. Ref. Data Ser., 35/VI Nat. Bur. Stand. 1971).
[10] M. Kucera, J. Bok, and K. Nitsch, Solid State Commun. **69**, 1117 (1989).
[11] Y. Xu, J. H. Yang, and X. J. Zhang, Phys. Rev. B **50**, 13428 (1994).
[12] R. Atkinson, R. Gerber, P. Papakonstantinou, I. W. Slater and Z. Simsa, J. Magn. Magn. Mater. **104–107**, 1005 (1992).
[13] W. A. Crossley, R. W. Cooper, J. L. Page, and R. P. van Stapele, Phys. Rev. **181**, 896 (1969).
[14] N. Fuchikami, J. Phys. Soc. Jpn. **34**, 760 (1965).
[15] Y. Xu, G. L. Yang, D. P. Chu, and H. R. Zhai, J. Magn. Magn. Mater. **31–34**, 815 (1983).
[16] Y. Xu, G. L. Yang, C. Heng, and H. R. Zhai, IEEE Trans. Magn. **MAG-20**, 1227 (1984).
[17] G. F. Dionne and G. A. Allen, J. Appl. Phys. **73**, 6127 (1993).

# Second harmonic investigation of ac magnetized in-plane anisotropic garnet film

Sergey V. Lebedev
*Laboratory of Applied Magneto-optics, Moscow Engineering Physics Institute, Kashirskoe shosse 31, 115409 Moscow, Russia*

A magneto-optical method is applied to investigate the influence of external magnetizing on second harmonic signal of magnetic reversal of in-plane anisotropic epitaxial garnet film. The dependencies of the width, slope and amplitude of curves recorded in "amplitude-easy axis magnetic field strength" coordinates versus magnitude of ac longitudinal and dc transversal magnetic fields are obtained and analyzed. It is shown that the slope of transfer function reaches its maximum at 0.7–0.8 Oe ac magnetizing with very slow dependence from transversal magnetic field. The "amplitude vs dc transversal field" dependence appears to have two regions with rapid and slow signal changing corresponded to various magnetization mechanisms. © *1996 American Institute of Physics.* [S0021-8979(96)16208-1]

Thin epitaxial garnet films are the object of investigations during the past 25 years. However available scientific bibliography shows that the major part of investigations is devoted to the films with strong uniaxial anisotropy. As far as in-plane anisotropic garnet films are concerned, there is a sufficient number of articles dealing with their undoubtedly attractive applications—low magnetic fields and electrical currents measurement, nonreciprocal waveguide elements, and nondestructive inspection of various magnetic records. However we know of only a few investigations describing the magnetizing processes of in-plane anisotropic films in dc and ac magnetic fields, the influence of external magnetization on hysteresis loop, and the corresponding mechanisms of magnetic reversal.[1–4] It is noted that the corresponding phenomena in uniaxially anisotropic films are studied many times and in more detail.

The objective here is the investigation of influence of external magnetizing on a second harmonic signal of magnetic reversal of epitaxial garnet film with strong in-plane anisotropy. A high priority of this problem is stipulated on the one hand by complexity of magnetization processes taking place in garnet films with "easy axis in plane" anisotropy[4] as well as the necessity of obtaining additional fundamental information, and on the other hand—by near-term prospect to use them in sensors and fiber optic devices.

All experiments were carried out with previously described 5-$\mu$m-thick epitaxial $(BiLuCa)_3(FeGe)_5O_{12}$ film, grown on a (111)-oriented $Gd_3Ga_5O_{12}$ single-crystal substrate.[4] As is mentioned the film's anisotropy could be characterized more adequately as "easy axis in plane," when there are two mutually perpendicular easy and hard axes of magnetization with saturation fields difference at least by an order of magnitude (f.i. −1 and 10 Oe, respectively). The influence of residual cubic anisotropy results in the appearance of sloped domains.[2,4]

The external fields configuration includes dc transversal field $H_h$ (0–10 Oe), directed along hard axis of magnetization, and a combination of ac field $H_{ac}$ (300–2000 Hz, 0–3 Oe) and slowly changing dc field $H_e$ (−10 to +10 Oe) directed along easy axis of magnetization, as indicated in Fig. 1. The second harmonic of magnetic reversal was recorded in a standard magneto-optical scheme of longitudinal hysteresis registration along the easy axis.[4] The garnet film was placed between two polarizers so that its plane was titled at an angle of 45° from the optical axis to provide the magneto-optical Faraday interaction of light with planar magnetization.

We have used as a light source a previously collimated near infrared LED. The linear output signal detection in balance photodiodes scheme[5] was provided using a 45° deflection of the main axis of the analyzer from that of the input polarizer. Thus the measured optical signal is strongly proportional to the garnet film magnetization averaged over the light aperture. The second harmonic of the magnetic reversal signal from the output of the lock-in amplifier was registered by a two-coordinate recorder with $X$ input coupled to the output of a slow $H_e$ sweeping generator.

Figure 2 shows the recorded amplitude of second harmonic signal as a function of the magnetic field $H_e$. This curve is universal only in external appearance for most ferro- and ferrimagnetic materials. Figure 3 demonstrates the ob-

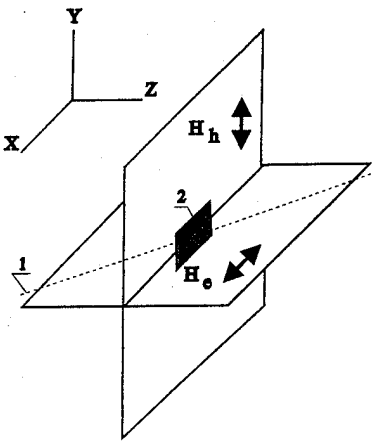



FIG. 1. The geometry of experiments: orientation of magnetic fields and of optical axis relative to garnet film plane: (1) the optical axis; (2) the garnet film.

 0021-8979/96/79(8)/5982/3/$10.00 © 1996 American Institute of Physics

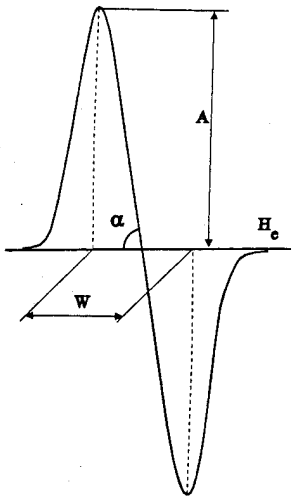



FIG. 2. Typical recorded curve of second harmonic signal.

tained dependencies of the width $W$ (a), slope $Tg\alpha$ (b), and amplitude $A$ (c) of recorded curve vs the amplitude $H_{ac}$ of ac magnetizing along an easy axis corresponding to dc transversal magnetizing of 0, 0.7, and 1.4 Oe (the thin, middle-thick, and thick solid lines, respectively). The greatest peculiarities of these are:

(i) The width and amplitude of the second harmonic signal are monotonously increasing functions of the ac magnetizing field. Moreover the first ones appear to be a nearly linear function with no visible dependence from $H_h$ so that Fig. 2(a) displays the results related only to 0 and 1.4 Oe dc magnetizing.

(ii) The $Tg\alpha$ dependence reaches its maximum at some value of $H_{ac}$ around 0.7–0.8 Oe, slowly varying by changing of transversal field $H_h$. It is noted that the increase of $H_{ac}$ is accompanied by the decrease of slope dependence from $H_h$.

Figure 4 shows the dependencies of $A$ vs $H_h$ measured at 0.4, 0.6, and 0.8 Oe of ac longitudinal magnetizing (the thick, middle-thick, and thin solid lines, respectively). Each curve has the central narrow maximum and the outlying wide and gradually decayed part. The smaller is the value of $H_{ac}$, the sharper is the changeover at 1.2–1.5 Oe from one part of the curve to another. The origin of this inflection may be the correspondent change in magnetization mechanism. The location of amplitude maximum of second harmonic signal in the $H_e$–$H_h$ plane does not fall at great values of $H_h$ outside the limits of the region of horizontal domains motion. However at low values of $H_h$ there is a region where horizontal and sloped domains exist simultaneously. It may result in additional asymmetry of partial hysteresis loops and be responsible for more intensive amplitude increase.

As far as the frequency dependence of presented characteristics is concerned, the magneto-optical response decreases slowly while increasing the frequency of ac magnetizing above 3 kHz. It corresponds qualitatively to the results obtained earlier.[6]

We have used the in-plane anisotropic garnet films in the R&D of the self-calibrated dc current sensor.[7] The possibility of absolute zero determination in a well-known second har-

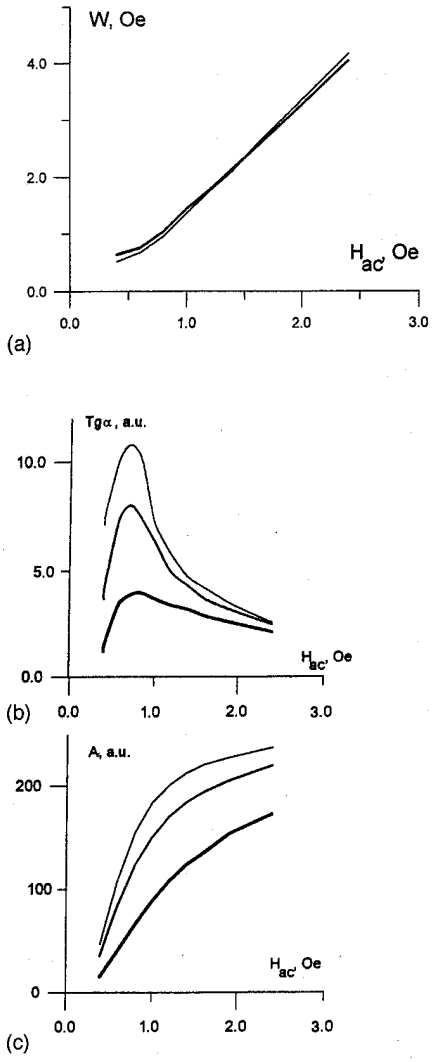



FIG. 3. The dependencies of width (a), slope (b), and amplitude (c) of second harmonic curves vs ac magnetic field oriented along easy axis of magnetization. The thin, middle-thick and thick solid lines correspond to dc transversal magnetizing of 0, 0.7, and 1.4 Oe, respectively.

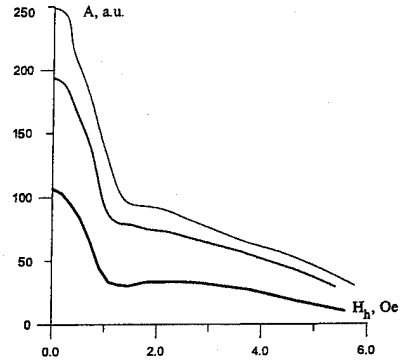



FIG. 4. The dependence of amplitude of second harmonic curves vs dc transversal magnetic field. The thick, middle-thick, and thin solid lines correspond to ac longitudinal magnetizing of 0.4, 0.6, and 0.8 Oe, respectively.

monic magnetometer scheme and the optimized external magnetization regime of our films allow us to increase enormously the sensitivity limit of the conventional magneto-optical sensor as well as to avoid the problems associated with zero drift—very serious ones for all known precise sensors.

The research described in this paper was made possible in part by Grant Nos. M6Q000 and M6Q300 from the International Science Foundation.

[1] M. McGlashan-Powell, R. Wolfe, J. F. Dillon, Jr., and V. J. Fratello, J. Appl. Phys. **66**, 3342 (1989).
[2] A. E. Korsun, S. V. Lebedev, and K. O. Pankratov, Digests of ICF-6, Main Conference in Tokyo, Japan, 1992, p. 149.
[3] A. E. Korsun, S. V. Lebedev, and K. O. Pankratov, Digests of ICF-6, Satellite Conference in Kyoto, Japan, 1992, p. 65.
[4] S. V. Lebedev, J. Tech. Fyz. **63**, 72 (1993) (in Russian).
[5] M. N. Deeter, A. H. Rose, and G. W. Day, J. Lightwave Technol. **8**, 1838 (1990).
[6] O. Jia, Zhang Ying, and He Huahui, Abstracts of MMM'93, p. 343.
[7] S. V. Lebedev (to be published).

# Magneto-optical properties of Sc-substituted holmium iron garnet single crystals

J. Ostoréro
*Laboratoire de Chimie Métallurgique et Spectroscopie des Terres Rares, CNRS, 92195 Meudon Cedex, France*

M. Guillot
*Laboratoire des Champs Magnétiques Intenses, CNRS/MPI, 38042 Grenoble Cedex, France*

The Faraday rotation (FR) of scandium substituted holmium iron garnets single crystals $Ho_3Fe_{5-z}Sc_zO_{12}$ ($z$=0.35, 0.52, 0.56, and 0.73) has been investigated at 1152 nm wavelength in the 6 K $< T <$ $T_{Néel}$ temperature range and magnetic field up to 20 kOe applied along the [111] easy axis. At this wavelength, in a narrow concentration range ($0.5<z<0.6$), in addition to the classic magnetic compensation temperature $T_{comp}$, the spontaneous FR $\Phi_s(T, z=\text{Cte})$ curves present two magneto-optic (MO) compensation points $T^{MO}_{Comp}(1)$ and $T^{MO}_{Comp}(2)$ where the FR vanishes although the ferrite magnetization is different from 0. When $z>0.6$, only $T^{MO}_{Comp}(1)$ remains. These results, due to the influence of the diamagnetic dilution of the octahedral $[a]$ $Fe^{3+}$ sublattice, are interpreted using the one ion FR model of Crossley *et al.* and the Dionne-refined Néel model of garnets. They give an indirect experimental confirmation of the temperature dependence of the MO electric dipole coefficient $C_e(\lambda=1152\text{ nm}, T)$, and of the preponderance of the $(d)-\{c\}$ magnetic interactions compared to the $[a]-\{c\}$ ones. © *1996 American Institute of Physics.* [S0021-8979(96)16308-8]

## I. INTRODUCTION

Nonmagnetic substitutions in iron garnets are of great interest both for fundamental studies and applications in devices such as microwave and magneto-optic (MO) components. We presented recently the results concerning the MO properties of $Al^{3+}$-substituted holmium iron garnet (HoIG:Al) compounds.[1] $Al^{3+}$ ions substitute to $Fe^{3+}$ ions on both tetrahedral $(d)$ and octahedral $[a]$ sites with a large tetrahedral preference.[2] In contrast $Sc^{3+}$ ions substitute almost exclusively to $Fe^{3+}$ on octahedral sites.[3,4] The purpose of this work is thus to study the influence of octahedral Sc substitution on the Faraday-rotation (FR) properties of $Ho_3Fe_{5-z}Sc_zO_{12}$ single crystals ($0.3<z<0.8$). Their formula can be written: $\{Ho_3\}$ $[Fe_{2-z}Sc_z]$ $(Fe_3)$ $O_{12}$ where $\{\}$ represents the rare earth dodecahedral $c$ sublattice. The temperature variation of the magnetic properties of heavy-rare-earth iron garnets presents two different characteristic temperatures: $T_{Néel}$ and $T_{comp}$. $T_{Néel}$ corresponds to the temperature transition to the paramagnetic state governed mainly by the $Fe^{3+}-Fe^{3+}$ interactions.[5] In contrast, the magnetic compensation temperature $T_{comp}$ strongly depends on the nature of the rare earth as the bulk magnetization $M_s=|(M_d-M_a)-M_c|$ vanishes whereas $M_{a,d,c}$ are different from zero ($T_{comp}$=137 K in pure HoIG[6]). At $T_{comp}$ the FR changes its sign, keeping the same absolute value. In some ferrimagnetic garnets ($Gd_3Fe_5O_{12}$, for example), in addition to $T_{Néel}$ and $T_{comp}$, the temperature variation of the FR properties at a fixed wavelength (1152 nm) presents also a MO compensation point $T^{MO}_{Comp}$ where the FR is zero although the ferrite magnetization is different from zero. To our knowledge, in the numerous literature devoted to the MO properties of ferrimagnetic garnets pure or substituted, the presence of at most one $T^{MO}_{Comp}$ is known to occur. We present here the results of the MO properties of HoIG:Sc garnets single crystals with two different $T^{MO}_{Comp}$ at 1152 nm wavelength for the same composition, giving a tentative interpretation based on the one ion FR model of Crossley *et al.*[7] and the Dionne-refined Néel magnetization model of garnets.[8,9]

## II. EXPERIMENT

Using the method of flux growth under 10 bar of oxygen pressure, single crystals of composition $Ho_3Fe_{5-z}Sc_zO_{12}$ with $z$=0.35, 0.52, 0.56, and 0.73 were synthesized. The scandium content was determined by electron microprobe analysis to within ±2% accuracy. Polished platelets ~1 mm thick oriented perpendicular to the [111] axis were obtained from the "as grown" crystals. FR measurements were performed at temperatures between 6 and 600 K, under a magnetic field up to 20 kOe applied parallel to the [111] direction at a wavelength of 1152 nm using a modulation technique. This wavelength is situated in the IR band, in the transparency window of garnets, and the MO properties presented in this paper are mainly dispersive. The FR isotherms $\Phi(H)$ show a linear part when $H>4$ kOe for all compositions and temperatures. A least-squares fit of these isotherms using $\Phi=\Phi_s+\chi_F$ H gives the spontaneous FR $\Phi_s(T,z)$ and FR susceptibility $\chi_F(T,z)$. The experimental accuracy is estimated to ±2% for $\Phi$ and ±1% for $\Phi_s$.

## III. RESULTS AND DISCUSSION

The FR of a three sublattices rare earth iron garnet is given by Refs. 7, 10, and 11 (and references therein):

$$\Phi_s(\lambda,T)=\pm(A_e+A_m)|M_a|\mp(D_e+D_m)|M_d| \pm(C_e+C_m)|M_c|. \quad (1)$$

Upper (lower) signs are valid for $T<T_{comp}$ ($T>T_{comp}$). $A_{e,m}(\lambda)$, $D_{e,m}(\lambda)$, and $C_{e,m}(\lambda)$ are the respective MO electric "$e$" and magnetic "$m$" dipole coefficients of the $[a]$, $(d)$, and $\{c\}$ sublattices with magnetizations $M_{a,d,c}(T)$. The first two terms of Eq. (1) are the contributions from the $Fe^{3+}$ $[a]$

 0021-8979/96/79(8)/5985/3/$10.00 © 1996 American Institute of Physics 

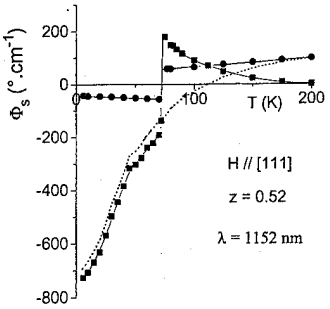



FIG. 1. Low temperature ($T$<200 K) dependence of $\Phi_{\text{HoIG:Sc}}$, $z$=0.52 (■), $\pm\Phi_{\text{YIG:Sc}}$ (●) of same Sc concentration, and $Ho^{3+}$ contribution to FR $\Phi_{\text{Ho}}$ (dotted line) at 1152 nm wavelength.

and ($d$) sublattices which can also be deduced experimentally from the FR at the same wavelength of the corresponding YIG garnet of same composition:[1,10]

$$\Phi_{\text{HolG:Sc}}=\mp\Phi_{\text{YIG:Sc}}\pm(C_e+C_m)|M_c|=\mp\Phi_{\text{YIG:Sc}}+\Phi_{\text{Ho}}, \quad (2)$$

where $\Phi_{\text{Ho}}(\lambda,T)$ is the $Ho^{3+}$ contribution to the spontaneous FR. We plotted in Fig. 1 the temperature variation of $\Phi_s(z=0.52,\ \lambda=1152\ \text{nm})$ when $T$<200 K and $H\|[111]$ for HoIG:Sc and YIG:Sc of same concentration. For HoIG:Sc, the characteristic magnetic compensation temperature $T_{\text{comp}}$ is 72 K where $\Phi_s$ changes its sign. When $T\sim40$ K an inflection in the temperature variation curve is indicative of the onset of the umbrella spin structure in the $Ho^{3+}$ sublattice.[12] The FR of YIG:Sc ($z$=0.52, $\lambda$=1152 nm), positive in the whole temperature range, is plotted in Fig. 1 with the appropriate sign to represent the $Fe^{3+}$ contribution [Eq. (2)] along with the contribution of $Ho^{3+}$ to FR $\Phi_{\text{Ho}}(z=0.52,\ \lambda=1152$ nm).

The high temperature part (100 K $< T <$ $T_{\text{Néel}}$) of the FR of HoIG:Sc and YIG:Sc $z$=0.52 garnets crystals is plotted in Fig. 2. The behavior of $\Phi_s$ is complex and presents two characteristic temperatures $T^{\text{MO}}_{\text{Comp}}(1)$ and $T^{\text{MO}}_{\text{Comp}}(2)$, at which $\Phi_s(\lambda=1152$ nm) changes its sign whereas the bulk magnetization is different from zero. To our knowledge, this is the first time that such a behavior is reported. In order to confirm this situation, we plotted in Fig. 3 the high temperature ($T$ >100 K) variation of $\Phi_s$ for different concentrations of the HoIG:Sc garnets. The presence of two MO compensation temperatures, at 1152 nm, is obtained only for $z$=0.52 and 0.56. At lower concentration ($z$=0.35) there is no MO compensation point but, instead, only an inflection point is observed. When the Sc concentration is higher ($z$=0.73), only the "low" MO compensation point remains. This is evidenced more clearly in Fig. 4 where we plotted the different characteristic temperatures of the HoIG:Sc system. By extrapolating the variation of $T^{\text{MO}}_{\text{Comp}}(1)$ and $T^{\text{MO}}_{\text{Comp}}(2)$, we note that $T^{\text{MO}}_{\text{Comp}}(2)$ is equal to $T_{\text{Néel}}$ for $z\sim0.6$. On the other hand, $T^{\text{MO}}_{\text{Comp}}(1)$ and $T^{\text{MO}}_{\text{Comp}}(2)$ merged together when $z\sim0.5$. Therefore, the limits of the Sc concentration zone where $\Phi_s(T)$ presents two MO compensation temperatures are $0.5<z<0.6$ (dashed area of Fig. 4). The existence of two MO compensation temperatures can be explained by the fact that the Sc substitution decreases at first the total $Fe^{3+}$ contribution to

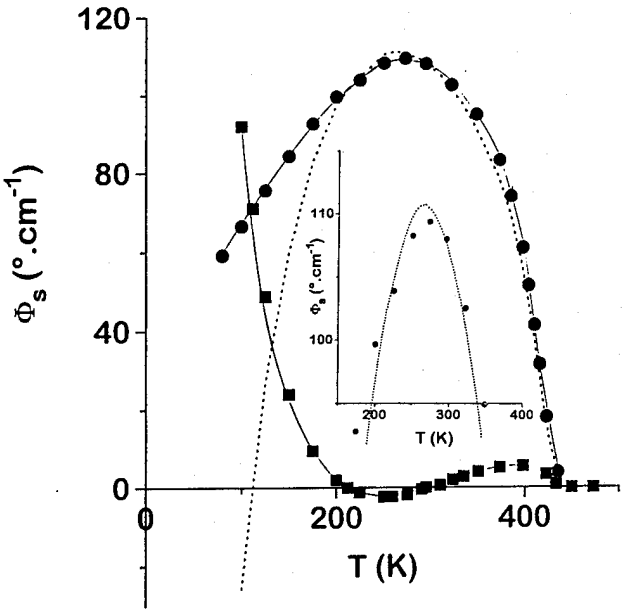



FIG. 2. High temperature (100 K $< T <$ $T_{\text{Néel}}$) dependence of $\Phi_s$ (same legend as Fig. 1). Inset: magnification of the area where the contributions to FR of $Ho^{3+}$ and that of $Fe^{3+}$ intersect twice.

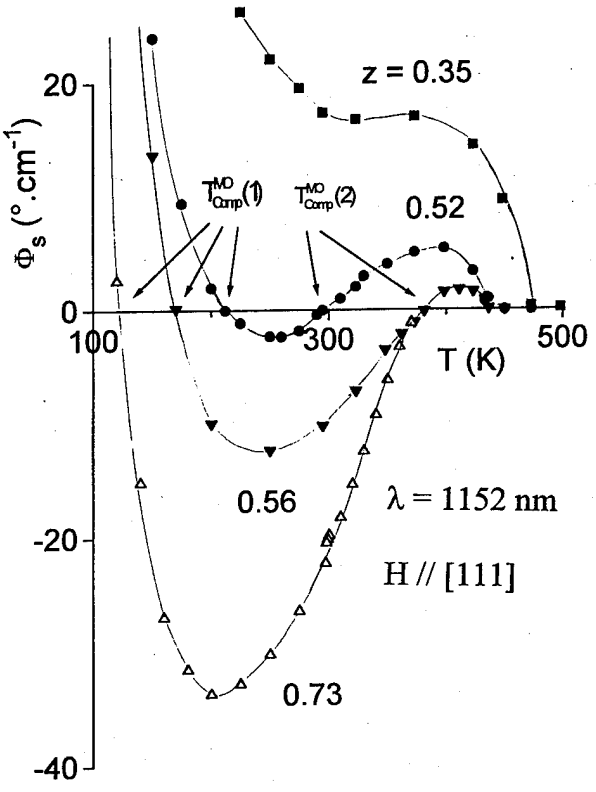



FIG. 3. Temperature dependence ($T$>100 K) of $\Phi_s$ for the different studied compositions at 1152 nm wavelength.

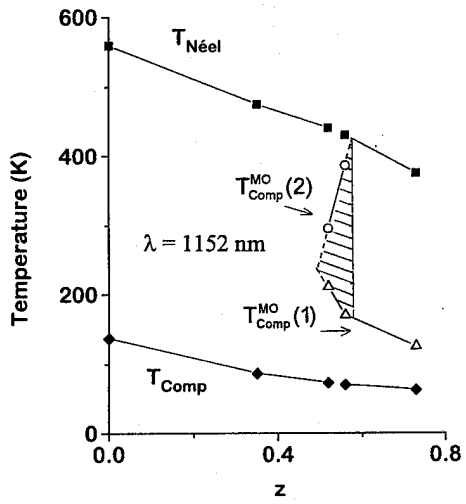



FIG. 4. Concentration dependence of the different characteristic temperatures of the MO properties of the HoIG:Sc system. The dashed area represents the existence zone for two MO compensation points at 1152 nm wavelength.

the FR of the garnet. The temperature variation of this contribution, as represented by the FR of YIG:Sc, presents a maximum in the vicinity of $T=250$ K (Fig. 2). At low temperature ($T<100$ K) the contribution of the $Ho^{3+}$ sublattice is negative and preponderant for all the studied concentrations (Fig. 1). When $T>100$ K, the contributions of $Ho^{3+}$ and $Fe^{3+}$ are of the same magnitude order. In this temperature region, when the substitution is not too high ($z=0.35$), the contribution of $Fe^{3+}$ is always dominant and there is no MO compensation point (Fig. 3). When $z$ increases and $0.5<z<0.6$, the two contributions present a temperature range where they are very similar (Fig. 2) and crosses each other at two temperatures $T^{MO}_{Comp}(1)$ and $T^{MO}_{Comp}(2)$. A slight increase of the Sc concentration rate results principally in a decrease of the $Fe^{3+}$ contributions, leaving the $Ho^{3+}$ one nearly unchanged. As observed in Figs. 3 and 4, this leads to a larger value of the difference $T^{MO}_{Comp}(2)-T^{MO}_{Comp}(1)$: $T^{MO}_{Comp}(1)$ is shifted toward lower $T$, whereas $T^{MO}_{Comp}(2)$ is shifted toward $T_{Néel}$. At higher $z$ ($z=0.73$), only $T^{MO}_{Comp}(1)$ is observed, shifted toward lower $T$ (Figs. 3, 4).

At 1152 nm wavelength, the existence of two different $T^{MO}_{Comp}$ leads thus to a more detailed analysis of the temperature behavior of the Ho contribution $\Phi_{Ho}=\pm(C_e+C_m)|M_c|$. According to Ref. 7, the coefficient $C_m$ is given by $C_m=2\pi(\mu_B/c)ng_{Ho}$, where $\mu_B$ is the Bohr magneton and $g_{Ho}$ the Landé factor of the $Ho^{3+}$ ion. Assuming a refractive index $n=2.2$ and the same $g_{Ho}$ factor as that of free $Ho^{3+}$ ion, $C_m=5.72$ deg .$cm^{-1}.\mu_B^{-1}$.[6] As shown recently in HoIG:Al garnets,[1] $M_c(T,z)$ can be deduced using the Dionne-refined Néel model of ferrimagnetic garnets.[8,9] According to this model, the diamagnetic substitution in one sublattice induces a canting in the opposite sublattice which is taken into account through dilution functions applied to the molecular field coefficients (MFC) $N_{ij}$ ($i, j=a,d,c$). As indicated previously, the $Fe^{3+}-Fe^{3+}$ interactions are well represented by those of YIG:Sc:[9]

$$N_{aa}(z)=N_{aa}(z=0),$$
$$N_{dd}(z)=N_{dd}(z=0)(1-0.43z), \tag{3}$$
$$N_{ad}(z)=N_{ad}(z=0)(1-0.125z).$$

In a first approximation, the MFC related to $Fe^{3+}-Ho^{3+}$ interactions were assumed to be the same as in pure HoIG:[1]

$$N_{ac}(z)=N_{ac}(z=0), \quad N_{dc}(z)=N_{dc}(z=0); \quad N_{cc}\sim 0. \tag{4}$$

The differences between calculated and experimental values of $T_{comp}$ using this model and MFC of Eqs. (3), (4) are systematically greater than 20 K (well outside the experimental accuracy) due to an overevaluation of $M_c(T,z)$. A good agreement can be achieved using MFC of Eq. (4) as a function of $z$, either by increasing $N_{ac}$ or decreasing $N_{dc}$ when $z$ increases. The first solution is not justified because the diamagnetic substitution cannot increase the exchange energy and only the second hypothesis,

$$N_{dc}(z)=N_{dc}(z=0)(1-\alpha z), \tag{5}$$

can be used. The value found for $\alpha=0.32$ is very similar to the coefficients in Eq. (3). This dilution function [Eq. (5)] indicates that Sc substitution in octahedral sites leads to canting in the tetrahedral sublattice which in turn influences the $Ho^{3+}-Fe^{3+}$ interactions. This confirms also that the magnetic rare earth$-Fe^{3+}$ interactions are mainly $(d)-\{c\}$.[5] In effect, in case of tetrahedral substitution (HoIG:Al), the influence of the canting in the $[a]$ sublattice should lead to a dilution function similar to Eq. (5) applied to the MFC $N_{ac}$, which is not the case.[1] This indicates that the $[a]-\{c\}$ interactions have much less influence on the magnetic properties than the corresponding ones $(d)-\{c\}$. Finally, it is to be noted that the temperature variation of $M_c(T)$ is a monotonous decreasing function. As shown in Fig. 2, the Ho contribution $\Phi_{Ho}(\lambda=1152$ nm, $T)=\pm(C_e+C_m)|M_c|$ presents a maximum. $C_m$ being a constant, the MO electric dipole coefficient $C_e$ must be a function of $T$. This confirms the hypothesis of the temperature dependence of the MO electric dipole coefficients in garnets at 1152 nm wavelength.[10]


[1] J. Ostoréro and M. Guillot, IEEE Trans. Magn. **30**, 4422 (1994).
[2] P. Röschmann, J. Phys. Chem. Solids **41**, 569 (1980).
[3] P. Röschmann and P. Hansen, J. Appl. Phys. **52**, 6257 (1981).
[4] G. Ballestrino and S. Geller, Phys. Rev. B **27**, 5807 (1983).
[5] S. Geller in, *Physics of Magnetic Garnets*, edited by A. Paoletti (North-Holland, Amsterdam, 1978).
[6] M. Fadly, P. Feldmann, H. Le Gall, M. Guillot, and H. Makram, IEEE Trans. Magn. **14**, 448 (1978).
[7] W. A. Crossley, R. W. Cooper, J. L. Page, and R. P. Van Stapele, Phys. Rev. **181**, 896 (1969).
[8] G. F. Dionne, J. Appl. Phys. **41**, 4874 (1970).
[9] G. F. Dionne, J. Appl. Phys. **47**, 4220 (1976).
[10] M. Guillot, H. Le Gall, J. M. Desvignes, and M. Artinian, IEEE Trans. Magn. **30**, 4419 (1994).
[11] P. Hansen and J.-P. Krumme, Thin Solid Films **114**, 69 (1984).
[12] M. Guillot, F. Tchéou, A. Marchand, and P. Feldmann, J. Magn. Magn. Mater. **31–34**, 631 (1983).

# Effect of structural irregularity on propagation properties of optical waves in discontinuous magneto-optical media with one-dimensional quasirandom array structures

Mitsuteru Inoue, Takeshi Yamamoto, Keiji Isamoto, and Toshitaka Fujii
*Department of Electrical and Electronic Engineering, Toyohashi University of Technology, 1-1 Hibari-Ga-Oka, Tempaku, Toyohashi 441, Japan*

To elucidate the effect of structural irregularity on propagation properties of optical waves in discontinuous magneto-optical media, theoretical analysis was carried out by employing random matrix technique and a model with one-dimensional quasirandom array structure. The analysis revealed that the effect of structural irregularity was so significant that the dispersion curves of optical waves varied considerably depending on the media structures. However, no matter how the medium structure varies irregularly, dispersion curves of waves always exist within the confines between those of the half (0···01···1) and the alternate (0101···01) structures. This fact suggests that the effect of structural irregularity becomes less significant when the discontinuous media have fine discrete structures, where the dispersion curves of the half and the alternate structures are very close.
© *1996 American Institute of Physics.* [S0021-8979(96)16408-4]

## I. INTRODUCTION

Magneto-optical (MO) properties of discontinuous magnetic media are so unique that they are almost incomparable to those of continuous media. In fact, MO Faraday spectra (MO-FS) of uniformly dispersed or filament-like clustered cobalt particles in plastic films (polymethyl methacrylate) differ considerably from those of continuous media, and can widely be controlled by the concentration and aggregation states of the cobalt particles.[1,2] This suggests positively that the MO-FS can be manipulated artificially by introducing the discontinuous structures in magnetic media, though they are inherently material properties.

To explain the above experimental results theoretically, we analyzed the MO properties of magnetic media with one-dimensional periodic array structures.[3,4] We showed that optical waves in the media were modulated so as to satisfy boundary conditions imposed at every discontinuous plane, which resulted in the unique MO properties of the discontinuous media. However, the actual discontinuous media[1,2] are accompanied by a large number of clusters whose form and size vary irregularly, and thus their discrete structures are more complicated than that of the ideal periodic medium. Then, our previous analysis is still insufficient to elucidate the MO properties of such discontinuous media, because the optical waves will be also affected by the irregularity of the discrete structure.

In order to confirm this, we analyze optical waves in MO media with quasirandom discontinuous structures, and examine the effect of structural irregularity on the propagation characteristics of optical waves. To proceed with analysis, we use the "random matrix technique" which is considered to be an extended method of the matrix approach.[5] As a first step of the analysis, we ignored the change of material properties due to fining of the structures.

## II. MODELING AND RANDOM MATRIX TECHNIQUE

Let us conceive a discontinuous magnetic media with quasirandom array structures which are built up as the following: First, as shown in Fig. 1(a), consider an infinitely wide MO medium with a finite thickness $L$ which is composed of a one-dimensional array of virtual equivalent segments with width $D$. Each segment consists of $N$ subsegments with widths $d_i$ $(i=1,2,\ldots,N)$ which are generally assigned under the condition of $D=d_1+d_2+\cdots+d_N$. Supposing and simplifying our actual discontinuous media, we consider each subsegment is either magnetic material [specific dielectric tensor: $\tilde{\epsilon}_M(\lambda)$ at wavelength $\lambda$] with width $d_M$ or air gap with width $d_G$ [see Fig. 1(b)]. When we signify the magnetic material with "1" and the air gap with "0," sequential arrangement of the subsegments into one virtual segment is expressed by a binary number with $N$ digits like "100101···01." This binary parameter of structure is obtained from a randomized integer generated by a computer. To specify the medium, packing density of the magnetic material in a medium $(P_d)$ is defined by

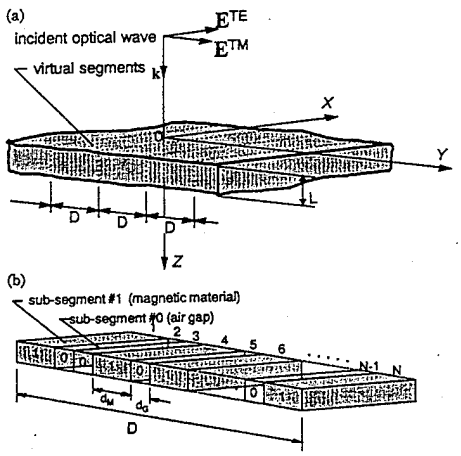



FIG. 1. Model of the discontinuous medium with quasirandom structure; (a) virtual segments in the medium and (b) subsegments in a virtual segment.

 0021-8979/96/79(8)/5988/3/$10.00 © 1996 American Institute of Physics

$P_d = D_M/D = N_M d_M/D$, where $D_M$ and $N_M$ are, respectively, the total width and the number of the magnetic materials in one virtual segment.

All magnetic materials in the medium are assumed to be identical to each other having magnetizations parallel to the propagation direction of optical waves (along the $Z$ axis). When a linearly polarized (TE or TM) optical wave is incident normal to the top surface ($Z=0$) of the medium, fundamental equations of waves propagating in an $i$th subsegment are given by the Maxwell equations (1) and (2):

$$\nabla \times \mathbf{E}(Y,Z;t) = i\omega\mu_0 \mathbf{H}(Y,Z;t), \tag{1}$$

$$\nabla \times \mathbf{H}(Y,Z;t) = -i\omega\epsilon_0 \tilde{\epsilon}_i \mathbf{E}(Y,Z;t), \tag{2}$$

where we assumed that the optical wave had a plane wave form of $\exp[i\omega(n'Z/C_L - t)]$ with a complex refractive index $n' = n + i\kappa$ and an angular frequency $\omega$. Equations (1) and (2) are arranged into the following matrix differential equation:

$$\frac{d}{dY}\mathbf{t}(Y) = \mathbf{A}_i(n',\omega)\cdot\mathbf{t}(Y), \tag{3}$$

in which $\mathbf{t}(Y) = (E_X, E_Z, H_X, H_Z)^t$ is the state vector and $\mathbf{A}_i(n',\omega)$ is the state matrix (4×4 complex matrix) of the $i$th subsegment whose explicit form is given in Ref. 4. Since the state matrix is a constant matrix with respect to $Y$, and the state vector is continuous at all discontinous interfaces between two neighboring subsegments, the state vector at $Y=D$ is given by

$$\mathbf{t}(D) = \Phi_N \cdot \Phi_{N-1} \cdots \Phi_2 \cdot \Phi_1 \cdot \mathbf{t}(0), \tag{4}$$

where $\Phi_i(n',\omega) = \exp\{\mathbf{A}_i(n',\omega)d_i\}$ is the transition matrix of the $i$th subsegment. Periodicity of the virtual segment with width $D$ containing $N$ subsegments imposes $\mathbf{t}(D) = \mathbf{t}(0)$, which yields the dispersion equation of waves with a 4×4 unit matrix $\mathbf{I}$:

$$\det(\Phi_N \cdot \Phi_{N-1} \cdots \Phi_2 \cdot \Phi_1 - \mathbf{I}) = 0. \tag{5}$$

Note that the transition matrices $\Phi_i$ in Eq. (5) are either of the magnetic material or air gap, and the dispersion equation is determined by the products of these matrices whose sequence corresponds to the random binary parameter of structure. The dispersion equation (5) was solved numerically using the combined technique of the steepest descent and the two-variable Newton-Raphson methods.[6]

## III. RESULTS AND DISCUSSION

Numerical calculations were made using the same material parameters as used in the previous analysis, which were those of bismuth-substituted yttrium iron garnet ($Y_{0.25}Bi_{0.5}Fe_5O_{12}$, Bi:YIG hereafter).[7] As for structural parameters, we used $D=500$ nm, $N=2-50$, and $P_d=0-1.0$.

In the discontinuous medium with the one-dimensional periodic array structure, two fundamental eigenmodes of optical waves are $R$- and $L$-mode of waves,[3,4] which degenerate, respectively, into right and left circularly polarized optical waves when $D_M \gg \lambda$ ($D_M$, width of magnetic material; $\lambda$, wavelength of optical wave), while, when $D_M \ll \lambda$, they turn to TE wave (electric field $\mathbf{E}$//$X$-axis) and TM wave ($\mathbf{E}$//$Y$-axis), respectively. By solving Eq. (5), one finds that the $R$- and $L$-modes of waves are also the fundamental eigenwaves for the case of quasirandom array structure. Since the MO properties of the media are mainly prescribed by these waves, we discuss the dispersion characteristics of only these two waves, though the dispersion equation has a number of other solutions corresponding to their higher modes of waves.

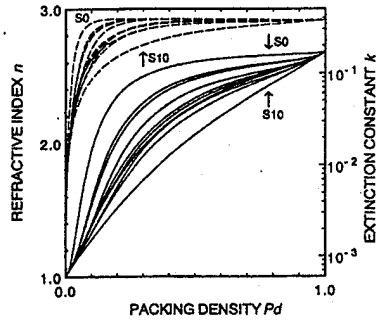



FIG. 2. Dispersion curves of $R$ mode of optical waves in the quasirandom discontinuous media, where S0 and S10 denote the curves for the half and the alternate structures.

Figures 2 and 3 show, respectively, dispersion curves [refractive index $n$ (solid curves) and extinction constants $\kappa$ (broken curves) versus packing density $P_d = D_M/D$] of the $R$- and $L$-modes of waves in the discontinuous media with eleven types of discrete structures when $N=16$ and $\lambda=387.4$ nm. In the figures, curves labeled by S0 and S10 are special cases of periodic subsegment arrangements, where S0 is the curve of half structure of $(0000000011111111)_2=(255)_{10}$ while S10 is the curve of alternate structure of $(0101010101010101)_2=(21845)_{10}$. Subsegment arrangements of the other nine curves are expressed by 1804, 5787, 9195, 11096, 13089, 18571, 19620, 29854, and 54141 in decimal integers. It is seen that the values of $n$ and $\kappa$ of both waves are bounded between those of Bi:YIG (when $P_d \to 1.0$) and air gap (when $P_d \to 0.0$) irrespective of the medium structures. In this range, the dispersion curves vary depending strongly on the media structures, suggesting that the effect of structural irregularity is very large. However,

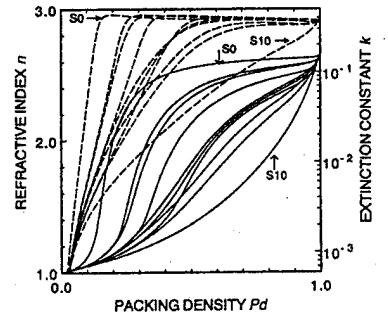



FIG. 3. Dispersion curves of $L$ mode of optical waves in the quasirandom discontinuous media.

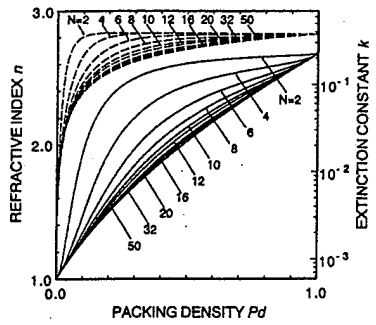



FIG. 4. Dispersion curves of $R$ mode of optical waves in the quasirandom media with the alternate structures, where the number of the subsegments $N$ is taken as a parameter.

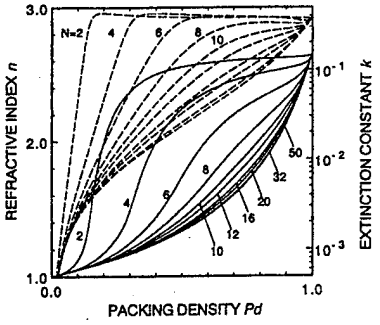



FIG. 5. Dispersion curves of $L$ mode of optical waves in the quasirandom media with the alternate structures.

one should note that all dispersion curves of both waves exist within the confines between the dispersion curves of S0 and S10. This means that, no matter how the medium structure changes irregularly, the properties of optical waves are always within those of the half and alternate structures. Thus, when the dispersion curves of S0 and S10 are close to each other, the effect of structural irregularity should become less significant and can be ignored when describing the optical properties of the discrete media.

It is then worthwhile to examine the situation in which the dispersion curves of the half and the alternate structures are close. We can easily surmise that the dispersion curves of S10 will no longer be changed when the number of subsegments $N$ is sufficiently large, because, for large $N$, the width of each subsegment becomes much smaller than the wavelength of optical waves. This is clearly shown in Figs. 4 and 5, where the dispersion curves for the $R$-mode (Fig. 4) and $L$-mode (Fig. 5) of waves in the discontinuous media with the alternate structures are depicted by taking the number of subsegments $N$ as parameter. The dispersion curves for large $N$ values are indeed almost identical (see the curves of $N=32$ and 50), where the discontinuous medium can be regarded as an effective continuous medium whose properties are solely designated by the packing density of magnetic material.

This indicates that, when the width of magnetic material in the half structure is approximately less than 5% of the wavelength of optical waves (here $\lambda=387.4$ nm), the discontinuous media with the half structure behave as if the effective continuous media. In this case, the dispersion curves of the half and the alternate structures are very close, and hence the effect of structural irregularity on the optical waves can no longer be remarkable.

## IV. CONCLUSION

The analysis shows that the dispersion curves of waves vary considerably depending on the media structures. However, no matter how irregular the media structures are, dispersion curves of optical waves always exist within the region between those of the half and the alternate structures, and hence the more these dispersion curves approach each other, the less the dispersion curves change due to the structural irregularity. Provided that the maximum width of the magnetic material in the media is restricted approximately less than 5% of the wavelength of optical waves, the dispersion curves of the half and the alternate structures are almost identical and the effect of structural irregularity becomes negligible. This situation may correspond to our actual discontinuous media with uniformly dispersed cobalt particles ranging from 5 to 20 nm in diameter whose MO properties were evaluated within the wavelength interval between 400 and 900 nm.[1,2]

Our further calculations suggest that the present results are also applicable for describing the MO properties of the discontinuous media with filament-like clustered cobalt particles whose average size exceeds the limit mentioned above, which will be reported in detail elsewhere.

[1] K. Yamaguchi, T. Imamura, A. Horikawa, M. Inoue, and T. Fujii, Proceedings of the First Magneto-Electronics International Symposium, Nagano, 1994 (unpublished), p. 143.
[2] A. Horikawa, K. Yamaguchi, M. Inoue, and T. Fujii, Proc. International Conference on Nanocrystals and Granular Materials, Sendai, Japan, September, 1995 (in press).
[3] K. Isamoto, T. Yamamoto, M. Inoue, and T. Fujii, IEEE Trans. Magn. **31**, 3286 (1995).
[4] M. Inoue, K. Isamoto, T. Yamamoto, and T. Fujii; J. Appl. Phys. (in press).
[5] A. H. Fhamy and E. L. Adler, Appl. Phys. Lett. **22** 495 (1973).
[6] M. Inoue, N. Fujita, and T. Fujii, J. Appl. Phys. **73**, 6159 (1993).
[7] S. Wittekoek, T. J. A. Popma, J. M. Robertson, and P. F. Bongers, Phys. Rev. B **12**, 2777 (1975).

# Magneto-optic and microwave properties of epitaxial garnet thin film heterostructures and superlattices (abstract)

R. Ramesh, T. Venkatesan, S. Lofland, M. Dominguez, and S. M. Bhagat
*Department of Materials and Nuclear Engineering and Center for Superconductivity Research, University of Maryland, College Park, Maryland 20742*

B. M. Simion and G. Thomas
*Department of Materials Science, University of California, Berkeley, California 94720*

We report on the growth and magnetic characterization of epitaxial garnet thin films and heterostructures by pulsed laser deposition. Thin films and heterostructures consisting of yttrium iron garnet (YIG) interleaved with rare earth substituted bismuth iron garnet (BIG) have been deposited on single-crystal GGG substrates. These heterostructures exhibit strong polar magneto-optic Kerr effects with rotation angles of better than $5 \times 10^4$ °/cm at 533 nm. Microwave measurements at 10 GHz suggest that the Eu-substituted BIG layer has a preferred out-of-plane magnetization while the YIG layer is still magnetized in-plane. The implications of the magneto-optic and microwave results will be discussed in light of the heterostructure periodicity and film microstructure. © *1996 American Institute of Physics.* [S0021-8979(96)47708-4]

 0021-8979/96/79(8)/5991/1/$10.00 © 1996 American Institute of Physics 

# Mössbauer effect and electronic transport studies of icosahedral $Al_{50}Pd_{10}Mn_{25-x}Fe_xB_{15}$ alloys

M. Yewondwossen, J. E. Jagger, Z. Koziol, and R. A. Dunlap
*Department of Physics, Dalhousie University, Halifax, Nova Scotia B3H 3J5, Canada*

The temperature and applied magnetic field dependence of the resistivity of icosahedral $Al_{50}Pd_{10}Mn_{25-x}Fe_xB_{15}$ ($x=0$ and 5) alloys has been measured between 4.2 and 300 K. At low temperature, $T<30$ K, the resistivity showed a rapid decrease with increasing temperature and may be described by a combination of weak localization (WL) and magnetic scattering effects. At higher temperatures the resistivity is adequately described by the temperature dependence of the structural and magnetic effects as described by Boltzmann-type transport. The measured magnetoresistance of both samples is consistent with theoretical predictions based on WL. The room temperature Mössbauer effect spectrum of the $x=5$ sample showed a well resolved doublet with mean isomer shift (relative to room temperature $\alpha$-Fe) and quadrupole splitting of +0.22 mm/s and 0.36 mm/s, respectively. These results indicate that the Fe probe nuclei do not carry a magnetic moment in these alloys. © *1996 American Institute of Physics.* [S0021-8979(96)16508-0]

## I. INTRODUCTION

Quasicrystalline (QC) alloys which contain Mn have shown a wide variety of magnetic behavior and, in some cases have exhibited varying degrees of magnetic order. Typically, these magnetically ordered materials have been characterized by small Mn magnetic moments and low Curie temperatures. Recently, alloys which exhibit high Curie temperatures and substantial Mn moments have been reported[1–5] in the Al-Mn-Pd-B system. The availability of these materials allows for the investigation of the relationship of magnetic order and quasicrystallinity. In the present work we report on magnetotransport and Mössbauer effect studies of $Al_{50}Pd_{10}Mn_{25-x}Fe_xB_{15}$ alloys.

## II. EXPERIMENTAL METHODS

Samples of $Al_{50}Pd_{10}Mn_{25-x}Fe_xB_{15}$ ($x=0$ and 5) were prepared by melt spinning. Resulting ribbons were shown to be single phase icosahedral quasicrystals by x-ray diffraction studies. The transverse magnetoresistance was measured at temperatures from 4.2 to 300 K in applied fields up to 5.5 T. The room temperature $^{57}$Fe Mössbauer effect spectrum of the $x=5$ sample was obtained using a conventional constant acceleration drive system.

## III. RESULTS AND DISCUSSION

The magnetoresistance data of $Al_{50}Pd_{10}Mn_{25-x}B_{15}Fe_x$ QC alloys ($x=0$, 5) are shown in Fig. 1. The most general expression for the magnetoresistance, $\Delta\rho(B)$, due to Fukuyama and Hoshino[6] which includes the effects of spin-orbit scattering, Zeeman splitting, and magnetic impurities is given by;

$$\frac{\Delta\rho}{\rho}=\rho A\sqrt{\frac{eB}{\hbar}}\left\{\frac{1}{2\sqrt{1-\gamma}}\left[f_3\left(\frac{B}{B_-}\right)-f_3\left(\frac{B}{B_+}\right)\right]-f_3\left(\frac{B}{B_2}\right)-\sqrt{\frac{4B_{so}}{3B}}\left(\frac{(\sqrt{t_+}-\sqrt{t_-})}{\sqrt{1-\gamma}}+\sqrt{t}-\sqrt{t+1}\right)\right\} \quad (1)$$

where

$$A=\frac{e^2}{2\pi^2\hbar},$$

$$\gamma=\left(\frac{3g^*\mu_B B}{8eD(B_{so}-B_s)}\right)^2,$$

$$B_\phi=B_i+2B_s,$$

$$B_2=B_i+\tfrac{2}{3}B_s+\tfrac{4}{3}B_{so},$$

$$t=\frac{3B_\phi}{4(B_{so}-B_s)},$$

$$B_\pm=B_\phi+\tfrac{2}{3}(B_{so}-B_s)(1\pm\sqrt{1-\gamma})+2B_s,$$

$$t_\pm=t+\tfrac{1}{2}(1\pm\sqrt{1-\gamma}),$$

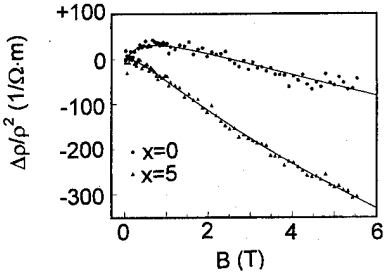



FIG. 1. The magnetoresistivity at 4.2 K of $Al_{50}Pd_{10}Mn_{25-x}B_{15}Fe_x$ plotted as a function of $B$. The solid lines are fits to WL theory.

 0021-8979/96/79(8)/5992/3/$10.00 © 1996 American Institute of Physics

TABLE I. Fitted parameters values for $Al_{70-x}Pd_{15}Mn_{15}B_x$.

| Alloy ($x$) | $1/\tau_i$ ($\times 10^9$ s$^{-1}$) | $1/\tau_{so}$ ($\times 10^9$ s$^{-1}$) | $1/\tau_s$ ($\times 10^9$ s$^{-1}$) | $\rho$(fitted) ($\mu\Omega$ cm) | $\rho$(exp) ($\mu\Omega$ cm) |
|---|---|---|---|---|---|
| 0 | 5.4 | 10 | 0.7 | 870 | 1700 |
| 5 | 7.8 | 0.45 | 0.1 | 1200 | 1400 |

and $D$ is the diffusion coefficient. The characteristic fields are related to electron scattering times through relations of the type

$$B_x=\frac{\hbar}{4eD\tau_x}, \tag{2}$$

where $x=i$, so, and $s$ refer to the inelastic, spin-orbit, and magnetic spin-flip scattering times, respectively. The Kawabata function, $f_3(x)$,[7] has been written in the form proposed by Baxter *et al.*;[8]

$$f_3(x)=2\left(\sqrt{2+\frac{1}{x}}-\sqrt{\frac{1}{x}}\right)-\left[\left(\frac{1}{2}+\frac{1}{x}\right)^{-1/2}+\left(\frac{3}{2}+\frac{1}{x}\right)^{-1/2}\right]+\frac{1}{48}\left(2.03+\frac{1}{x}\right)^{-3/2}. \tag{3}$$

The magnetoresistance due to weak localization, $\Delta\rho_{WL}$, as given by Eq. (1), is negative in the case of weak spin-orbit scattering systems, i.e., $\tau_i<\tau_{so}$. In the case of strong spin-orbit scattering systems the magnetoresistance is positive and $\tau_i>\tau_{so}$.

The fitting procedure adopted for the samples studied is as follows. The WL contribution to the magnetoresistance is fitted with the temperature-dependent inelastic scattering time $\tau_i(T)$, and the temperature independent scattering times $\tau_{so}$ and $\tau_s$ as free parameters. The diffusion coefficient is taken to be 0.075 cm$^2$ s$^{-1}$,[9] from literature values for similar quasicrystals. Quantum corrections to the resistivity predict $\Delta\rho/\rho\propto\rho$. Using $\rho$ as a free parameter in the WL expression allows for a determination of the resistivity in a way that is independent of the sample geometry.[10]

The agreement between WL theory and the experimental data is good over the entire range of fields as illustrated by the fits shown in Fig. 1. The magnetoresistance of $x=0$ sample is positive in region $B<2.5$ T followed by a negative magnetoresistance in the remaining range of field. This feature reflects the moderate spin-orbit scattering case in which $\tau_i\approx\tau_{so}$. For the $x=5$, the magnetoresistance is totally negative and reflects the presence of weak spin-orbit scattering, $\tau_i<\tau_{so}$. The value of the fitted parameters are given in Table I.

The temperature dependence of the resistivity is illustrated in Fig. 2. The resistivity of the $Al_{70-x}Pd_{15}Mn_{15}B_x$ QC alloys is 1700 and 1400 $\mu\Omega$ cm at 4.2 K (for $x=0$ and 5, respectively). Various theories have been proposed to interpret the high values of the resistivity of QC's (e.g., Refs. 11–13). In general, two effects dominate $\rho(T)$ in QCs at low temperature; weak localization and magnetic scattering. The resistivity behavior at low temperature in $Al_{70-x}Pd_{15}Mn_{15}B_x$ is primarily due to magnetic scattering effects. This assertion may be illustrated as follows: The low temperature resistivity can be written as;

$$\rho(T)\approx\Delta\rho_{WL}(\tau_l(T),\tau_{so},\tau_s,D)+\rho_{Kondo}, \tag{4}$$

where $\Delta\rho_{WL}$ and $\rho_{Kondo}$ are the WL and Kondo contributions, respectively. Using the scattering times described above the WL component may be subtracted from the resistivity data. The remaining data exhibit a $\ln(T)$ dependence for all the samples as is expected for Kondo-type scattering. At higher temperatures the resistivity is adequately described by the temperature dependence of Boltzmann-type transport.

The room temperature $^{57}$Fe Mössbauer effect spectrum of icosahedral $Al_{50}Pd_{10}Mn_{20}Fe_5B_{15}$ is illustrated in Fig. 3. This spectrum shows a well defined doublet. The analysis of such spectra has been considered in detail by a number of authors (e.g., Refs. 14–16). In cases where the splitting is quadrupole in nature, spectra may be analyzed on the basis of a quadrupole distribution or a set of discrete splittings. Evidence seems to suggest that in related QC's two distinct classes of transition metal sites exist.[14,17,18] An analysis of

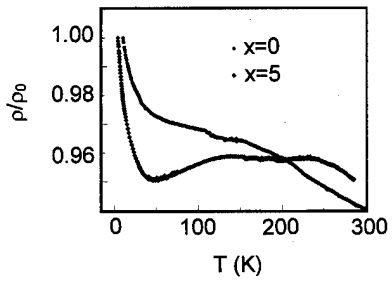



FIG. 2. Temperature dependence of the electrical resistivity normalized to the value at 4.2 K for $Al_{50}Pd_{10}Mn_{25-x}Fe_xB_{15}$ ($x=0$, 5).

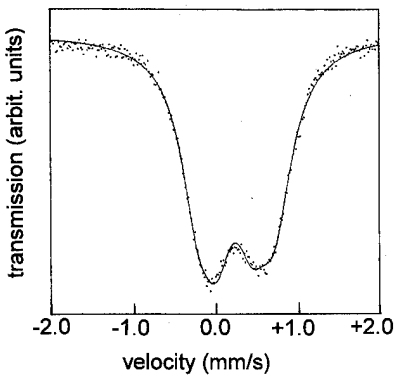



FIG. 3. Room temperature $^{57}$Fe Mössbauer effect spectrum of icosahedral $Al_{50}Pd_{10}Mn_{20}Fe_5B_{15}$. The solid line is a fit to two symmetric doublets.

TABLE II. Room temperature $^{57}$Fe Mössbauer effect parameters for the spectrum of icosahedral $Al_{50}Pd_{10}Mn_{20}Fe_5B_{15}$. Quadrupole splittings, $\Delta$, and isomer shifts, $\delta$, (relative to $\alpha$-Fe) are given for the two doublets as described in the text. Mean parameter values are also given.

| | $\Delta$ (mm/s) | $\delta$ (mm/s) |
|---|---|---|
| doublet No. 1 | 0.233 | +0.219 |
| doublet No. 2 | 0.493 | +0.230 |
| mean value | 0.362 | +0.224 |

Mössbauer spectra in terms of two discrete sites is illustrated in Fig. 3 and are summarized in Table II. In this case the two doublets have been chosen to have similar isomer shifts. Mean quadrupole parameters are consistent with Mössbauer effect results obtained for similar QCs. Spectra have also been fitted on the basis of a combined Zeeman and quadrupole interaction. The quality of fit for this analysis did not show any improvement over the previous analysis, suggesting that the Fe probe atoms do not carry magnetic moments in these alloys. There has been considerable work on Fe moment formation in QCs and evidence seems to suggest that Fe atoms prefer to reside in sites where a moment does not form.[14,19] The present measurements are consistent with this picture.

## IV. CONCLUSIONS

The temperature and applied magnetic field dependence of the resistivity of icosahedral $Al_{50}Pd_{10}Mn_{25-x}Fe_xB_{15}$ ($x=0$ and 5) alloys has been measured. At low temperature results may be explained by a combination of weak localization and Kondo-type magnetic scattering effects. At higher temperatures the resistivity is adequately described by the temperature dependence of Boltzmann-type transport. The room temperature Mössbauer effect spectrum of the $x=5$ sample showed a well resolved doublet. A goodness-of-fit analysis indicated that the spectrum was appropriately described by a combination of two symmetric quadrupole doublets rather than an analysis based on the presence of a Zeeman splitting. This analysis suggests that the Fe probe atoms prefer to reside in sites where they do not carry a magnetic moment.

## ACKNOWLEDGMENTS

This work was supported in part by a grant from the Natural Sciences and Engineering Research Council of Canada. Z.K. also acknowledges support in the form of a Killam Postdoctoral Fellowship.

[1] T. Shinohara, Y. Yokohama, M. Sato, A. Inoue, and T. Masumoto, J. Phys. Condens. Matter **5**, 3673 (1993).
[2] T. Shinohara, Y. Yokoyama, M. Sato, A. Inoue, and T. Masumoto, Mater. Sci. Eng. A **182**, 798 (1994).
[3] M. Yewondwossen, S. P. Ritcey, Z. J. Yang, and R. A. Dunlap, J. Appl. Phys. **76**, 6499 (1994).
[4] Y. Yokoyama, A. Inoue, H. Yamauchi, M. Kusuyama, and T. Masumoto, Jpn. J. Appl. Phys. **33**, 4012 (1994).
[5] Y. Yokoyama, A. Inoue, and T. Masumoto, Mater. Sci. Eng. A **182**, 734 (1994).
[6] H. Fukuyama and K. Hoshino, J. Phys. Soc. Jpn. **50**, 2131 (1981).
[7] A. Kawabata, Solid State Commun. **34**, 431 (1980).
[8] D. V. Baxter, R. Richter, M. L. Trudeau, R. W. Cochrane, and J. O. Strom-Olson, J. Physique **50**, 1673 (1989).
[9] M. A. Chernikov, A. Bernasconi, C. Beel, and H. R. Ott, Europhys. Lett. **21**, 767 (1993).
[10] A. Sahnoune, J. O. Strom-Olsen, and A. Zaluska, Phys. Rev. B **46**, 10629 (1992).
[11] J. C. Phillips and K. M. Robe, Phys. Rev. Lett. **66**, 923 (1991).
[12] S. E. Burkov, T. Timusk, and N. W. Aschcroft, J. Phys. Condens. Matter **4**, 9447 (1992).
[13] T. Fujiwara, S. Yamamoto, and G. Trambly de Laissaridiere, Phys. Rev. Lett. **20**, 4116 (1993).
[14] R. A. Dunlap and D. W. Lawther, Mater. Sci. Rep. **10**, 141 (1993).
[15] M. Miglierini, S. Nasu, and T. Kuwano, Hyperf. Int. **80**, 977 (1993).
[16] Z. M. Stadnik and G. Stroink, Phys. Rev. B **44**, 4255 (1991).
[17] D. Bahadur, C. M. Srivastava, M. H. Yewondwossen and R. A. Dunlap, J. Phys. Condens. Matter (unpublished).
[18] S. Nasu, M. Miglierini, and T. Kuwano, Phys. Rev. B **45**, 12778 (1992).
[19] R. A. Dunlap, R. C. O'Handley, M. E. McHenry, and V. Srinivas, Struct. Chem. **2**, 501 (1991).

# Magnetic and electronic properties of the magnetically ordered quasicrystalline alloys $Al_{70-x}Pd_{15}Mn_{15}B_x$

M. Yewondwossen, Z. Koziol, D. Bahadur,[a] and Z. J. Yang[b]
*Department of Physics, Dalhousie University, Halifax, Nova Scotia B3H 3J5, Canada*

M. Foldeaki
*Institut de Reserche sur l'Hydrogène, Université du Quebec à Trois-Rivières, Trois-Rivières, Québec G9A 5H7, Canada*

R. A. Dunlap
*Department of Physics, Dalhousie University, Halifax, Nova Scotia B3H 3J5, Canada*

The magnetic susceptibility, magnetization and the temperature and field dependence of the Hall coefficient have been measured for the magnetically ordered icosahedral quasicrystals $Al_{70-x}Pd_{15}Mn_{15}B_x$ ($x=0,2,4,6,8,10$). The temperature dependence of the real and imaginary part of the complex ac susceptibility indicates re-entrant magnetic behavior and dc magnetization measurements are interpreted in the context of this behavior. The present Hall resistivity measurement shows the existence of both normal and anomalous Hall effects. The normal Hall coefficient is independent of temperature in all the alloys and changes from negative to positive with increasing boron concentration. This can be explained by the effects of $s-d$ hybridization. The anomalous Hall coefficient is also found to be temperature independent and has a compositional dependence correlated to the spin–orbit scattering rate. © *1996 American Institute of Physics.* [S0021-8979(96)12808-2]

## I. INTRODUCTION

Since the first discovery of quasicrystals in Al–Mn alloys,[1] the electronic and magnetic properties of these materials have been studied extensively. Although early reports indicated that most quasicrystals are weakly magnetic,[2,3] some recently developed materials have shown strong magnetic behavior. Yokoyama *et al.*[4,5] have reported the synthesis and characterization of ferromagnetic $Al_{70-x}Pd_{15}Mn_{15}B_x$ icosahedral alloys. These alloys have Curie temperatures between 300–500 K and exhibit saturation magnetization up to 18 emu/g which disappears after crystallization. In the present work the Hall effect, magnetic susceptibility and magnetization of $Al_{70-x}Pd_{15}Mn_{15}B_x$ have been investigated and these complement our previous transport studies of this series.[6]

## II. EXPERIMENTAL TECHNIQUES

Single phase icosahedral $Al_{70-x}Pd_{15}Mn_{15}B_x$ alloys were prepared in the form of ribbons by the melt spinning method.[7] The quasicrystalline nature of these samples was confirmed from x-ray diffraction patterns. The temperature dependent ac susceptibility was measured by a standard mutual inductance technique[8] at a frequency of 127 Hz in an ac magnetic field of ~80 A/m. dc magnetization measurements were carried out using a conventional superconducting quantum interference device (SQUID) magnetometer. Hall effect measurements were performed using a six-point dc technique in applied magnetic fields up to $4.4\times10^6$ A/m.

## III. RESULTS AND DISCUSSION

Figure 1 shows the room temperature ac susceptibility of $Al_{70-x}Pd_{15}Mn_{15}B_x$ ($x=0-10$). The measured susceptibility increases with increasing $x$ and is consistent with previous magnetization, nuclear magnetic resonance (NMR) and ferromagnetic resonance (FMR)[4,5,9] results for these alloys. This behavior can be described by the model in which the ferromagnetic coupling originates from the Mn–B bonding.[5]

A typical measurement of the real and imaginary parts of the ac susceptibility for the present alloys is shown in Fig. 2. These measurements show a knee in $\chi'(T)$ and, to a lesser extent, in $\chi''(T)$, for $6\leqslant x\leqslant 10$. No anomalous features have been observed for the susceptibility of samples with $x\leqslant 4$. Results may be compared with the previous data of Hattori *et al.*[10] which showed that the ac susceptibility of $Al_{70}Pd_{15}Mn_{15}$ showed a cusp at low temperature which was attributed to the existence of a reentrant spin glass (RSG) transition. There is some ambiguity in the interpretation of features in the ac susceptibility[10,11] which can arise from experimental conditions such as the exciting field frequency

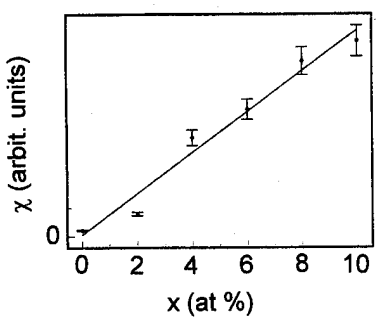



FIG. 1. The room temperature ac susceptibility of icosahedral $Al_{70-x}Pd_{15}Mn_{15}B_x$ alloys as a function of $x$.

[a]On leave from: Department of Metallurgical Engineering and Materials Science, Indian Institute of Technology, Powai, Bombay 400 076, India.
[b]Present address: ET/335, Argonne National Laboratory, Argonne, IL 60439.

 0021-8979/96/79(8)/5995/3/$10.00 © 1996 American Institute of Physics 

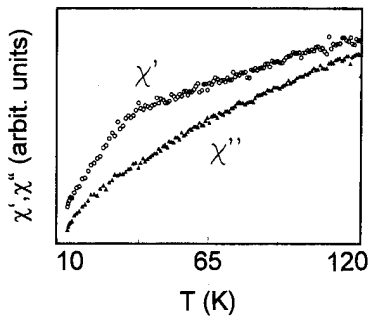



FIG. 2. The temperature dependence of zero-field cooled real and imaginary parts of the ac susceptibility for $Al_{60}Pd_{15}Mn_{15}B_{10}$.

and amplitude. The so-called Hopkinson peak[10] can obscure the characteristic behavior and, as a result, RSG features may be absent or may be shifted to a lower temperature. A comparison with magnetization data is often helpful in understanding the behavior of these materials. In most cases, the transition from ferromagnetism to the RSG state is defined by the onset of deviations from the plateau in the magnetization.[12] Results of these studies are illustrated in Fig. 3 for the present series of alloys. The knee associated with the RSG on lowering the temperature is clear for all alloys with $x \geq 2$. The observed temperature dependence is consistent with the behavior as described above.

In magnetically ordered materials both the ordinary Hall effect (OHE) and spontaneous Hall effect (SHE) are present. The latter is not restricted to ferromagnetic materials, but can appear in any material where strong magnetic interactions are present.[13] These two components combine to give the total Hall resistivity as (SI units):

$$\rho_H = R_0 B + R_s \mu_0 M \tag{1}$$

where $B$ is related to the applied magnetic field by $B = \mu_0(H+M)$, $M$ the magnetization and $R_0$ and $R_s$ are the ordinary and spontaneous Hall coefficients, respectively.

The field dependence of the Hall resistivity $\rho_H(B)$ for $Al_{70-x}Pd_{15}Mn_{15}B_x$ is shown in Fig. 4. This behavior is virtually independent of temperature. The initial slope gives

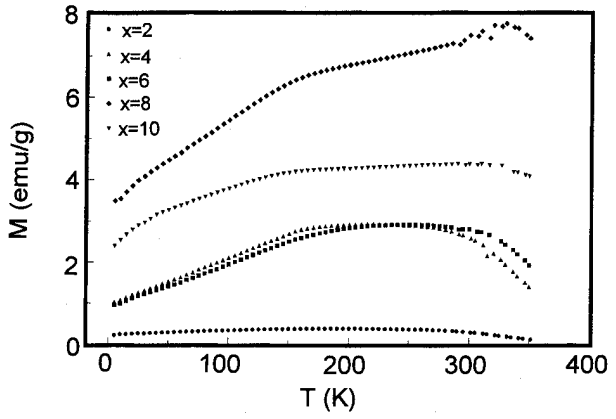



FIG. 3. Temperature dependence of the magnetization of $Al_{70-x}Pd_{15}Mn_{15}B_x$ as a function of $x$ measured in an applied field of $8.0\times10^3$ A/m.

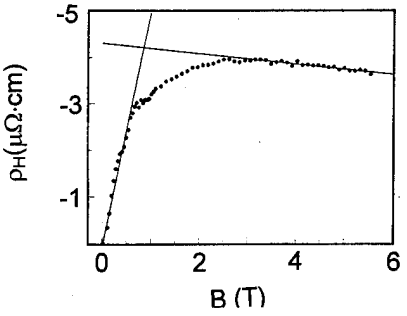



FIG. 4. Hall resistivity as function of field for $Al_{62}Pd_{15}Mn_{15}B_8$ at 4.2 K.

$$R_H = \left(\frac{\partial \rho_H}{\partial B}\right)_{B\to 0} \cong R_s \tag{2}$$

and the slope at high fields, gives:[14]

$$R_H = \left(\frac{\partial \rho_H}{\partial B}\right)_{B\to \infty} \cong R_0 . \tag{3}$$

Figure 5 shows that $R_0$ changes sign as a function of $x$. This behavior can be explained in terms of the effect of $s-d$ hybridization. This mechanism results from a shift of the Fermi energy and has been used to explain Hall effect results in amorphous alloys as it gives rise to regions of negative group velocity leading to positive $R_0$. In the present alloys the substitution of $B$ for Al causes the Fermi level to increase as a result of a reduction in the unit cell volume[7] giving rise to the observed behavior.

In disordered alloys the SHE coefficient may be related to the temperature dependent resistivity, $\rho(T)$, as:

$$R_s(T) = a\rho(T) + b\rho^2(T) \tag{4}$$

where the first term results from quasiclassical skew scattering and the second term results from the quantum mechanical side jump.[13,15] In amorphous alloys, because of the large number of scattering centers, the quadratic term is believed to dominate. In the present alloys $R_s$ is constant in temperature while $\rho(T)$ changes by as much as about 20%.[7] Therefore, at least to first order, there is no measurable correlation between $R_s$ and $\rho$. This has been observed in other systems and has been explained by different scattering mechanisms for $\rho$ and $\rho_H$.[16] The $x$ dependence of $R_s$ is shown in Fig. 6. $R_s$ is negative for all alloys and shows a systematic change

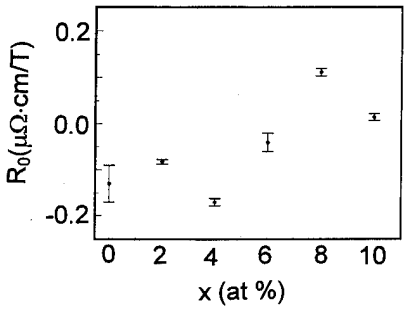



FIG. 5. The ordinary Hall coefficient of $Al_{70-x}Pd_{15}Mn_{15}B_x$ as a function of $x$ at 4.2 K.

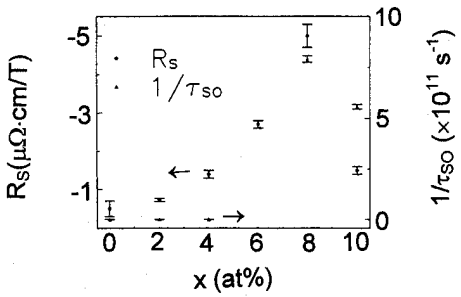



FIG. 6. The spontaneous Hall coefficient and spin–orbit scattering rate of $Al_{70-x}Pd_{15}Mn_{15}B_x$ as a function of $x$ at 4.2 K.

with $x$. These results can be explained in terms of spin–orbit interactions. In Fig. 6 $R_s$ is plotted along with the spin–orbit scattering rate as reported previously.[6,7] The magnitude of $R_s$ increases with the scattering rate showing that the spin–orbit interaction is indeed the important contributor to the Hall resistivity although the mechanism by which the spin–orbit interaction influences the Hall resistivity is not obvious.

## IV. CONCLUSIONS

Magnetic studies of icosahedral $Al_{70-x}Pd_{15}Mn_{15}B_x$ ($x$ =0,2,4,6,8,10) as presented here indicate that these materials are ferromagnetically ordered and show a re-entrant spin glass transition at low temperature. The dc magnetization results indicate a higher transition temperature as expected on the basis of the effects of the Hopkinson peak on ac susceptibility data. The interpretation of these results is consistent with previous magnetic,[4] NMR,[5] and FMR[9] studies.

The data presented show that the Hall resistivity $\rho_H$ is the result of two contributions; the normal term $R_0B$, due to the Lorentz force and anomalous term $\mu_0 M_s R_s$ due to the spin–orbit interaction. $R_0$ is independent of temperature but changes sign as a function of $x$ and can be explained by the effects of $s-d$ hybridization. $R_s$ is also found to be temperature independent and suggests that the scattering mechanisms responsible for $R_s(T)$ and $\rho(T)$ are different. The compositional dependence of $R_s$ is similar to that of the spin–orbit scattering rate and indicates that this is the responsible interaction for the spontaneous Hall behavior in these materials.

## ACKNOWLEDGMENTS

This work was supported by a grant from the Natural Sciences and Engineering Research Council of Canada. Z.K. also acknowledges support in the form of a Killam Postdoctoral Fellowship.

[1] D. Shechtman, I. Blech, D. Gratias, and J. W. Cahn, Phys. Rev. Lett. **53**, 1951 (1984).
[2] S. J. Poon, Adv. Phys. **41**, 303 (1992).
[3] R. C. O'Handley, R. A. Dunlap, and M. E. McHenry, in *Handbook of Magnetic Materials, Vol. 6*, edited by K. H. J. Bushow (North Holland, Amsterdam, 1991).
[4] Y. Yokoyama, A. Inoue, and T. Masumoto, Mater. Trans. JIM **33**, 1012 (1992).
[5] T. Shinohara, Y. Yokoyama, M. Sato, A. Inoue, and T. Masumoto, J. Phys. Condens. Matter **5**, 3673 (1993).
[6] M. H. Yewondwossen, S. P. Ritcey, Z. J. Yang, and R. A. Dunlap, J. Appl. Phys. **76**, 6499 (1994).
[7] M. H. Yewondwossen, Ph.D. thesis, 1995 (unpublished).
[8] L. Koszegi, M. Foldeaki, and R. A. Dunlap, Rev. Sci. Instrum. **62**, 793 (1991).
[9] D. Bahadur, C. M. Srivastava, M. H. Yewondwossen, and R. A. Dunlap, J. Phys. Condens. Matter **7**, 9883 (1995).
[10] Y. Hattori, K. Fukamichi, H. Chikama, H. Aruga-Katori, and T. Goto, J. Phys. Condens. Matter (in press).
[11] J. Nogues and K. V. Rao, J. Magn. Magn. Mater. **135**, L11 (1994).
[12] K. H. Fischer and J. A. Hertz, *Spin Glasses* (Cambridge University Press, Cambridge, 1991), p. 322.
[13] C. M. Hurd, *The Hall Effect in Metals and Alloys* (Plenum, New York, 1972).
[14] R. Malmhall, S. M. Bhagat, K. V. Rao, and G. Backstrom, Phys. Status Solidi A **53**, 641 (1979).
[15] T. R. McGuire, R. J. Gambino, and R. C. O'Handley, in *The Hall Effect and its Applications*, edited by C. L. Chen and C. R. Westgate (Plenum, New York, 1980), p. 137.
[16] D. Muller, J. W. Shunemann, and K. Barner, J. Magn. Magn. Mater. **110**, 161 (1992).

# Structural, magnetic, and magnetocaloric properties of $(Hf_{0.83}Ta_{0.17})Fe_{2+x}$ materials

J. F. Herbst and C. D. Fuerst
*Physics Department, General Motors Research and Development Center, 30500 Mound Road, Warren, Michigan 48090–9055*

R. D. McMichael
*National Institute of Standards and Technology, Gaithersburg, Maryland 20899*

We have investigated the sensitivity of structural, magnetic, and magnetocaloric properties of $(Hf_{0.83}Ta_{0.17})Fe_{2+x}$ alloys ($x=-0.18$, $-0.09$, $-0.02$, 0.00, 0.09, 0.26) to Fe content. As-cast samples for all $x$ consist essentially exclusively of hexagonal $MgZn_2$-type material. Via magnetization and differential scanning calorimetry measurements we find that all the alloys except $x=0.26$ feature both a ferromagnetic→antiferromagnetic (FM→AFM) transition at temperature $T_0$ and a Néel transition. The most abrupt FM→AFM transition occurs in the $x=-0.02$ material which also exhibits the lowest $T_0$ and largest low-temperature moment. We report a magnetocaloric property, the field-induced entropy change $\Delta S$, for the $x=0.00$ and $x=\pm 0.09$ alloys. © *1996 American Institute of Physics.* [S0021-8979(96)12908-9]

## I. INTRODUCTION

Nishihara and Yamaguchi have reported[1] the occurrence of a first order ferromagnetic→antiferromagnetic (FM→AFM) transition with increasing temperature $T$ in the pseudobinary $Hf_{1-y}Ta_yFe_2$ systems having tantalum concentrations in the $0.1<y<0.3$ interval. A reversed (AFM→FM), but otherwise similar first order transition takes place as $T$ increases near room temperature in Fe–Rh alloys, which have been suggested as candidate working materials for magnetic refrigeration.[2] In both systems the FM↔AFM transition is evidently sensitive to preparation conditions as well as composition. Annealed $Hf_{1-y}Ta_yFe_{1.99}$ materials were investigated in Ref. 1, while as-cast $Hf_{0.8}Ta_{0.2}Fe_{1.97}$ was employed in a recent study[3] of thermal and transport properties by Wada, Shimamura, and Shiga, who observed a sharper transition in as-cast, as compared with annealed, samples. Here we explore the sensitivity of the structural and magnetic properties to departures from stoichiometry by focusing on a series of samples with fixed Hf:Ta concentration ratio. For several alloys we also report determination of a magnetocaloric property, the isothermal field-induced entropy change $\Delta S$.

## II. SAMPLE PREPARATION AND STRUCTURAL CHARACTERIZATION

Ingots having nominal compositions specified by $(Hf_{0.83}Ta_{0.17})Fe_{2+x}$ with $x=-0.18$, $-0.09$, $-0.02$, 0.00, 0.09, and 0.26 were prepared by induction melting elemental constituents in BN crucibles under argon. The purity of the iron and tantalum employed was 99.999% and 99.9%, respectively; Zr was the primary contaminant of the hafnium, at a level of 3 at. % for all samples except $x=0.00$, for which it was 5 at. %. Each sample was furnace cooled (~3 min) and not subjected to any additional heat treatment. Phase occurrence and composition were established by x-ray powder diffraction (XRD) measurements and electron beam microprobe (EBM) analyses.

For each sample XRD indicated that the major phase is characterized by the hexagonal $MgZn_2$-type structure (C14; space group $P6_3/mmc$) featuring one Mg site ($4f$) and two Zn sites ($2a$,$6h$). Figure 1(a) displays the pattern observed for the most contaminated material, the $x=-0.18$ specimen, and Fig. 1(b) shows the pattern calculated for $(Hf_{0.83}Ta_{0.17})Fe_2$. It is clear that the sample consists principally of $MgZn_2$-type material; the asterisks indicate the only identifiable impurities, HfN and ZrN, which the EBM results corroborate. Even smaller amounts of nitride impurities were found in the $x=-0.02$, $x=0.09$, and $x=0.26$ samples, and no secondary phases were detected in the $x=-0.09$ and $x=0.00$ materials. The x-ray linewidths and relative intensities exhibited some sample-to-sample variation suggestive of changes

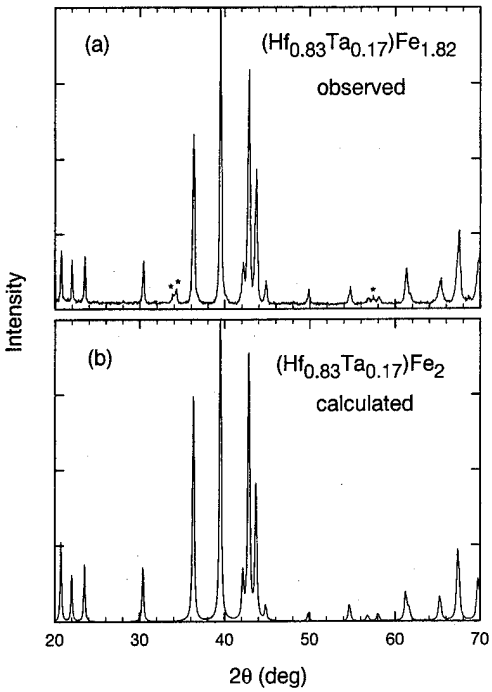



FIG. 1. (a) Cu $K_\alpha$ x-ray pattern observed for C14 $(Hf_{0.83}Ta_{0.17})Fe_{1.82}$ ($x=-0.18$); (b) pattern calculated for $(Hf_{0.83}Ta_{0.17})Fe_2$ using the lattice constants inferred from (a).

 0021-8979/96/79(8)/5998/3/$10.00 © 1996 American Institute of Physics

TABLE I. Compositional, structural, and magnetic information for the materials in this study. The nominal ingot composition is $(Hf_{0.83}Ta_{0.17})Fe_{2+x}$; $x'$ and $y'$ specify the composition $(Hf_{1-y'}Ta_{y'})Fe_{2+x'}$ of the principal $MgZn_2$-type phase as determined by electron beam microprobe analysis; $a$, $c$ are the room-temperature lattice constants of that phase obtained from Rietveld analyses of the x-ray diffraction data; $V$ is volume of the hexagonal unit cell; $M$ (10 K) is the magnetization measured at $T=10$ K, $H=9$ kOe; $\mu_{Fe}$ is the magnetic moment per Fe atom corresponding to $M$ (10 K); and $T_0$, $T_N$, and $T_C$ are temperatures of the FM→AFM, Néel, and Curie transitions, respectively, inferred from differential scanning calorimetry and magnetic measurements.

| $x$ | −0.18 | −0.09 | −0.02 | 0.00 | 0.09 | 0.26 |
|---|---|---|---|---|---|---|
| $x'$ | −0.05 | 0.05 | 0.08 | 0.11 | 0.14 | 0.19 |
| $y'$ | 0.18 | 0.16 | 0.19 | 0.18 | 0.19 | 0.18 |
| $a$ (Å) | 4.9510 | 4.9379 | 4.9301 | 4.9344 | 4.9293 | 4.9309 |
| $c$ (Å) | 8.0869 | 8.0747 | 8.0647 | 8.0715 | 8.0575 | 8.0497 |
| $c/a$ | 1.6334 | 1.6352 | 1.6358 | 1.6358 | 1.6346 | 1.6325 |
| $V$ (Å$^3$) | 171.67 | 170.51 | 169.76 | 170.20 | 169.55 | 169.50 |
| $M$ (10 K) (emu/g) | 49.5 | 51.9 | 55.7 | 49.9 | 46.1 | 49.9 |
| $\mu_{Fe}$ ($\mu_B$) | 1.31 | 1.33 | 1.41 | 1.26 | 1.15 | 1.23 |
| $T_0$ (K) | 260 | 274 | 210 | 230 | 265 | ... |
| $T_N$ (K) | 315 | 323 | 336 | 340 | 323 | ... |
| $T_C$ (K) | ... | ... | ... | ... | ... | 322 |

in effective grain size and at most modest preferred orientation effects.

While the XRD results demonstrate formation of a major C14-type phase over the entire $-0.18 \leq x \leq 0.26$ interval studied here, significant differences between the nominal ingot composition and the actual composition of the major phase in the as-cast samples were revealed by the microprobe work. The second and third rows of Table I specify $x'$ and $y'$ for the $(Hf_{1-y'}Ta_{y'})Fe_{2+x'}$ composition of the principal phase as determined by the EBM analyses. The $y'$ values deviate from the nominal 0.17 Ta content by as much as 12%, outside the ~3% EBM composition accuracy. Furthermore, it is evident that $x'$ undergoes considerably less excursion than $x$, especially on the Fe-poor side where $x'$ reaches its lowest value, $-0.05 \sim 0$, for the $x=-0.18$ material. For all other compositions $x'$ is positive. Despite the narrower range of $x'$, the EBM results confirm that C14-type material forms in a rather broad homogeneity region. Moreover, the $x' \sim 0$ lower limit of the $x'$ interval indicates that the solubility of Hf and Ta on the $2a$ and $6h$ iron sites is negligible compared with the solubility of Fe on the $4f$ sites. This is in qualitative accord with the fact that the metallic volumes of Hf and Ta, 22.4 and 18.0 Å$^3$, respectively, are both much larger than that of Fe, 11.8 Å$^3$.

Lattice parameters $a$ and $c$ determined from Rietveld refinements of the XRD data are included in Table I, as are the unit cell volumes $V$ and the $c/a$ ratios. In general $a$, $c$, and $V$ decline with increasing $x$, aside from a slight deviation for $x=0.00$. The overall trend for $V$ to decrease with Fe content suggests that excess, hyperstoichiometric iron enters substitutionally on the (Hf,Ta) $4f$ sublattice rather than interstitially. The $c/a$ ratio decreases on both sides of a plateau at $x=-0.02$ and $x=0.00$. All the $c/a$ values, however, are remarkably near the ideal ratio $(8/3)^{1/2}=1.6330$ corresponding to the hexagonal closest-packing of spheres; the maximum departure is 0.2%.

## III. MAGNETIC, CALORIMETRIC, AND MAGNETOCALORIC RESULTS

Figure 2 displays magnetization versus temperature curves measured in a maximum applied field of 9 kOe, which in each case was sufficient to saturate the magnetization. The low temperature values $M$(10 K) are listed in Table I, as are the magnetic moments per Fe atom, $\mu_{Fe}$, determined using the $x'$ and $y'$ values. $M$(10 K) spans a substantial range from 46.1 emu/g to 55.7 emu/g and shows no simple relation to the Fe content. For comparison, the magnetization of FeRh alloys is ~130–140 emu/g at low temperature for compositions near the equiatomic stoichiometry.[4,5] It is evident from Fig. 2 that $M(T)$ varies dramatically with $x$. The sharpest variation occurs in the $x=-0.02$ material at a temperature $T_0 \sim 210$ K which we identify with an FM→AFM transition. This result is in agreement with the previous finding[3] that the most abrupt transitions occur in as-cast samples prepared from slightly Fe-deficient starting compositions.

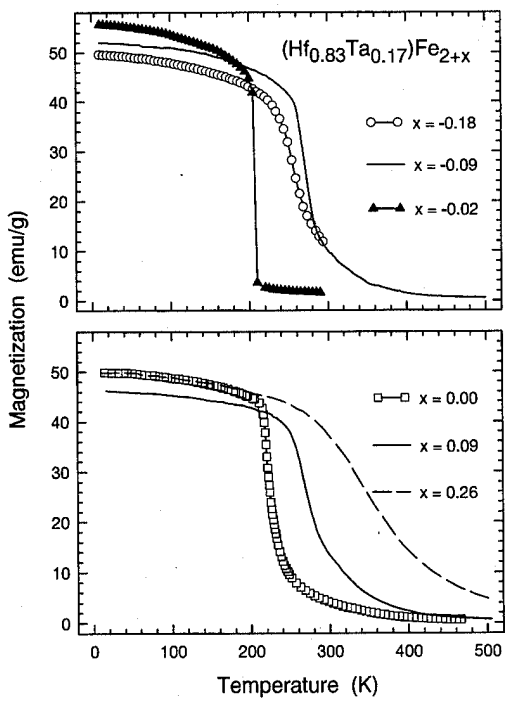



FIG. 2. Magnetization vs temperature for as-cast $(Hf_{0.83}Ta_{0.17})Fe_{2+x}$ materials.

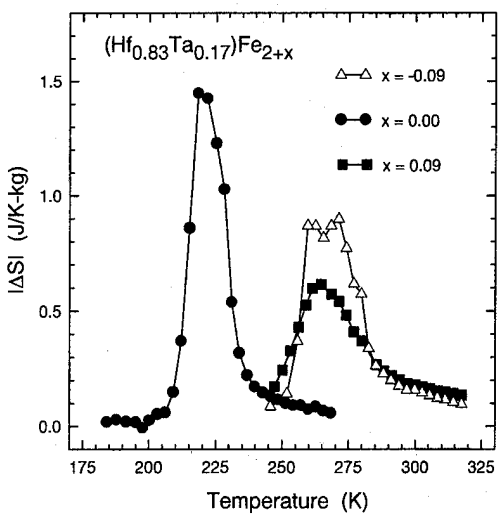



FIG. 3. Entropy change $|\Delta S|$ of $(Hf_{0.83}Ta_{0.17})Fe_{2+x}$ materials after application or removal of a 9 kOe magnetic field.

We identified other FM→AFM, Curie (FM→paramagnetic), and Néel (AFM→paramagnetic) transitions in these samples with the help of differential scanning calorimetry (DSC) measurements performed in the $T>225$ K range; the corresponding transition temperatures, $T_0$, $T_C$, and $T_N$, respectively, are given in Table I. The DSC structures to which we assigned $T_C$ and $T_N$ were characteristically asymmetric, while each peak identified with a FM→AFM transition was considerably more symmetric. We would have been reluctant to make this assignment using the DSC data alone, but our magnetization measurements and the magnetocaloric results derived from them (Fig. 3) make for consistent and credible identification.

Aside from the $x=0.26$ material, each sample is characterized by both a FM→AFM and a Néel transition, with the associated temperatures falling into two distinct groups. For $x=-0.18$ and $x=\pm 0.09$, $T_0\sim 260$–$270$ K and $T_N\sim 320$ K, while for $x=-0.02$ and $x=0.00$, $T_0\sim 210$–$230$ K and $T_N\sim 340$ K. It is interesting to note that the $x=-0.02$ material exhibiting the most abrupt change in $M(T)$ and $T_0$ has the largest low-temperature moment, lowest $T_0$, and largest $(T_N-T_0)$ difference. Only one, asymmetric DSC peak was observed for the Fe-richest sample, $x=0.26$; together with the magnetization curve (Fig. 2), this indicates that the material is ferromagnetic over the entire ordered temperature range.

To make a preliminary assessment of magnetocaloric effects in these systems we determined the field-induced entropy change $\Delta S$ for three of the samples. Using the Maxwell relation $(\partial S/\partial H)_T=(\partial M/\partial T)_H$, which implies

$$\Delta S=\int_0^H\left[\frac{\partial M(H',T)}{\partial T}\right]_{H'}dH', \tag{1}$$

we calculated $\Delta S$ from magnetization data acquired as a function of both applied field $H$ and temperature $T$. Figure 3 displays $|\Delta S|$, corresponding to application or removal of a 9 kOe field, as a function of $T$ for the $x=0.00$ and $x=\pm 0.09$ materials. The maximum entropy change $|\Delta S_{\max}|$ extends from ~0.6 J/K kg to ~1.5 J/K kg and in each case occurs slightly below the $T_0$ value listed in Table I. The sharpness of the transition in the $x=-0.02$ sample precluded an accurate determination of $|\Delta S|$, although we estimate that the peak value exceeds 20 J/K kg. For comparison purposes we note that, in a 9 kOe field and at temperatures in the vicinity of ambient, $|\Delta S_{\max}|\sim 3$ J/K kg for both Gd (Ref. 6) and annealed $Fe_{49}Rh_{51}$ (Ref. 2), while quenched $Fe_{49}Rh_{51}$ features $|\Delta S_{\max}|$ as large as ~17 J/K kg (Ref. 2).

## IV. SUMMARY

We have shown that the magnetic and magnetocaloric properties of $MgZn_2$-type $(Hf_{0.83}Ta_{0.17})Fe_{2+x}$ as-cast alloys are highly sensitive to the Fe level. A FM→AFM transition occurs over a broad range of $x$ and temperature and is most abrupt in materials having slightly substoichiometric Fe content. Magnetocaloric effects in these systems merit further investigation in view of the fact that the effects of preparation conditions as well as composition are still incompletely known.

## ACKNOWLEDGMENTS

We are grateful to E. G. Brewer for assistance in sample preparation, to M. P. Balogh and A. M. Wims for x-ray analyses, to R. A. Waldo for the microprobe work, and to T. S. Ellis for calorimetric measurements.

[1] Y. Nishihara and Y. Yamaguchi, J. Phys. Soc. Jpn. **51**, 1333 (1982); **52**, 3630 (1983); J. Magn. Magn. Mater. **31–34**, 77 (1983).
[2] M. P. Annaorazov, K. A. Asatryan, G. Myalikgulyev, S. A. Nikitin, A. M. Tishin, and A. L. Tyurin, Cryogenics **32**, 867 (1992).
[3] H. Wada, N. Shimamura, and M. Shiga, Phys. Rev. B **48**, 10221 (1993).
[4] B. K. Ponomarev, Sov. Phys. JETP **36**, 105 (1973).
[5] L. I. Vinokurova, A. V. Vlasov, N. I. Kulikov, and M. Pardavi-Horvath, J. Magn. Magn. Mater. **25**, 201 (1981).
[6] C. D. Fuerst, J. F. Herbst, R. K. Mishra, and R. D. McMichael, J. Appl. Phys. **76**, 6301 (1994).

# Magnetic properties of a high $T_c$ superconductivity related system $Y_{1-x}Pr_xBa_2Fe_3O_8$

T. Yuen,[a] M. Seyedahmadian,[b] R. E. Salomon,[b] and G. H. Myer[c]
*Temple University, Philadelphia, Pennsylvania 19122*

G. Cao
*National High Magnetic Field Lab, Tallahassee, Florida 32306*

We studied Pr substitution for Y in a 123 high $T_c$ superconductor related system, $Y_{1-x}Pr_xBa_2Fe_3O_8$ using of x-ray diffraction, magnetization, and $^{57}$Fe transmission Mössbauer spectroscopy. The Fe sublattices are magnetically ordered through the whole system. The Pr substitution, however, suppressed the Fe ordering temperature. The low temperature susceptibility across the system increases with increased Pr concentration $x$, and an additional antiferromagnetic ordering at 24 K is observed for $x=1$, indicating a possible Pr ordering. The averaged magnetic hyperfine field at Fe sites measured at 15 K is also reduced as $x$ increases. The dramatic effect of Pr substitution for Y in this system, which is not observed in studies of Y substitution by other rare-earth elements, is interpreted as the effect of the hybridization between the Pr 4-$f$ electrons and the electrons in the $Fe(2)O_2$ layers, similar to the Pr hybridization in $Y_{1-x}Pr_xBa_2Cu_3O_{7-y}$ system. © *1996 American Institute of Physics.* [S0021-8979(96)16608-7]

The substitution effect has been extensively studied since the 123 high $T_c$ superconductor material $YBa_2Cu_3O_{7-x}$ was discovered. The study of the substitution of Y with most of the rare-earth elements of different concentrations up to 100% shows no or little effect on the superconducting behavior of the material, except with Pr, which suppresses the superconducting transition temperature, $T_c$, to zero at a concentration around 50%.[3] Among the models that explain the suppression of $T_c$ along with other unusual features of the Pr substituted 123 compounds are the hole filling mechanism, which requires tetravalent or mixed valent Pr,[4,1] and the mechanism of hybridization between the 4$f$-electrons of $Pr^{3+}$ and the electrons in the adjacent $Cu(2)O_2$ planes.[5,6,1] Both models are well supported by a large amount of experimental and theoretical data. But the nature of the Pr valence is still inconclusive.[7] The partial replacement of Cu atoms with other transition metals suggests that the two-dimensional $Cu(2)O_2$ layers play a more important role than the Cu(1) chains in the superconducting process.[8,9] It has been thought that the information about the Cu-free 123 compounds could be very important to the full understanding of the 123 high $T_c$ superconductivity, yet relatively few studies on the complete substitution of Cu have been reported in the literature.[10–13] One of the interesting Cu-free compounds is $YBa_2Fe_3O_8$. The neutron diffraction study[1] showed that the crystal structure of the compound is tetragonal with the symmetry of space group p4/mmm. This structure is very similar to the 123 high $T_c$ superconductors, except that the oxygen sites in the Cu(2)-chain layers are fully occupied. The same study also showed that the Fe moments are coupled antiferromagnetically both within each $FeO_2$ layers and along the C axis. The Fe ions at two inequivalent sites, Fe(1) and Fe(2), are interpreted to have same values of the valence and the magnetic moment. The Mössbauer studies on $YBa_2Fe_3O_8$[2,13] showed that the spectrum can be fitted as two sets of subspectra corresponding to Fe(1) and Fe(2). However these two subspectra have the same hyperfine field, and differ only in their quadrupole interactions. It has also been reported[13] that the substitution of Y by a number of rare-earth elements (Ho, Eu, and Er) has essentially no effect on the Fe antiferromagnetic ordering.

In order to further investigate the Cu-free 123 compounds and the nature of the Pr substitution effect, we studied the magnetic properties of $Y_{1-x}Pr_xBa_2Fe_3O_8$ system by means of dc magnetization measurement and $^{57}$Fe Mössbauer experiment. Our study yielded more detailed information at the two different Fe sites. And more importantly, we observed that the Pr substitution has a dramatic effect on the magnetic behavior of the system.

Polycrystalline samples of $Y_{1-x}Pr_xBa_2Fe_3O_8$ for $x=0$, 0.25, 0.50, 0.75, and 1.0 were synthesized by coprecipitation mixing and solid-state sintering techniques. The stoichiometric amounts of 99.9% purity materials $BaCO_3$, Fe metal, $Y_2O_3$, and $Pr(CH_3COO)_3$ were dissolved in dilute nitric acid to form a stock solution with appropriate cation proportions. The solution was then added to a fast stirring concentrated solution containing $Na_2CO_3$ and NaOH with 25% of solvent ethyl alcohol to force the metallic ions to coprecipitate as insoluble carbonates. A better mixing at a microscopic level is therefore achieved without mechanical grinding and shaking. The gel-like precipitates were filtered, washed with mixture of distilled water and ethanol, and dried in an oven at 120 °C for a day. Finally, the dried precursors were fired in tube furnaces at 950 °C with oxygen flow for about 10 days.

The sample purity and their crystal structures were determined by powder x-ray diffraction measurements using a Regaku Diffractometer. A Quantum Design SQUID was used to measure the magnetic susceptibility for 5 K$\leq T \leq$400 K and the isothermal magnetization. In these measurements, the samples were first cooled to the lowest temperature in zero field. The field was then applied and the temperature was increased. The $^{57}$Fe transmission Mössbauer spectra

[a]Physics Department.
[b]Chemistry Department.
[c]Geology Department.

 0021-8979/96/79(8)/6001/3/$10.00 © 1996 American Institute of Physics 

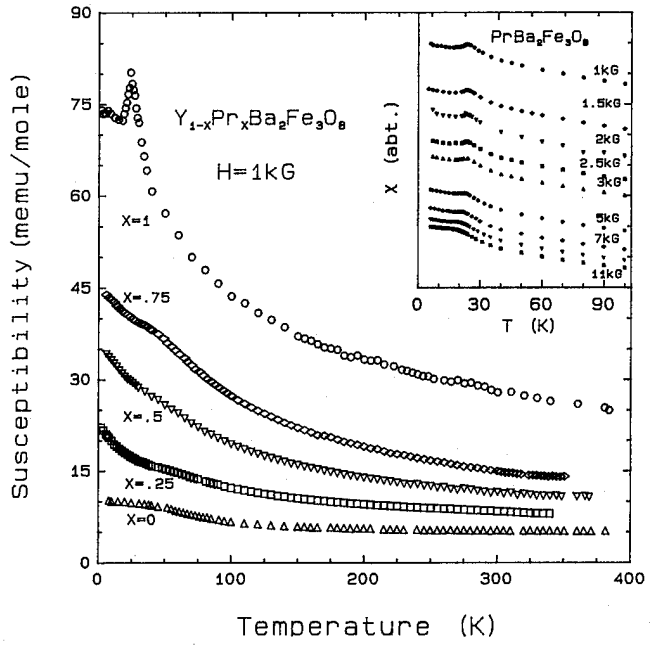



FIG. 1. Magnetic susceptibility of $Y_{1-x}Pr_xBa_2Fe_3O_8$, for $x=0.0$, 0.25, 0.50, 0.75, and 1.0, measured in a field of 1 kG. The insert is the magnetic susceptibility of $PrBa_2Fe_3O_8$, measured in various fields.

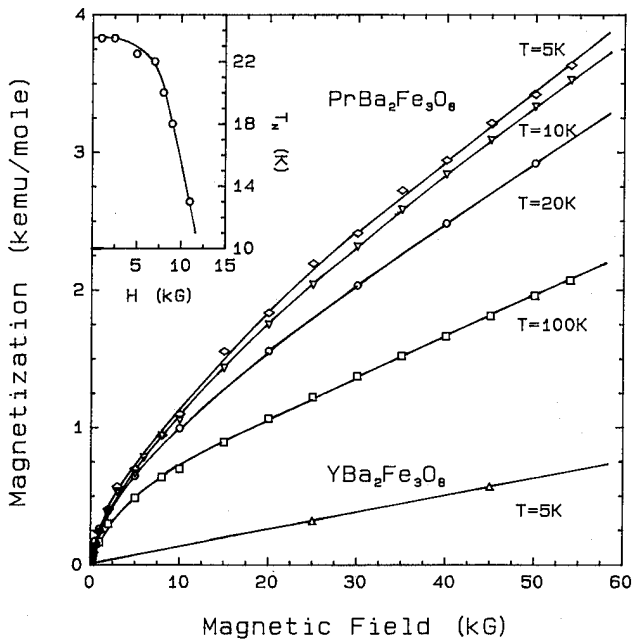



FIG. 2. Magnetization vs field of $PrBa_2Fe_3O_8$, measured at various temperature. The insert is the antiferromagnetic ordering temperature $T_N$ vs field for $PrBa_2Fe_3O_8$.

were measured for 15 K$\leq T \leq$298 K using a conventional constant acceleration Mössbauer spectrometer with a closed cycle refrigerator. A $^{57}$Co:Rh source of 25 mCi was used in the Mössbauer measurements.

Powder x-ray diffraction studies showed clean patterns for all samples with no detectable secondary phase formation. All phases in the system formed a tetragonal crystal structure with space group P4/mmm, which is as reported by other groups for $YBa_2Cu_3O_8$.[1,2] The measured lattice parameters at room temperature are $a=3.916$ Å and $c=11.798$ Å for $YBa_2Fe_3O_8$, and, $a=3.940$ Å and $c=11.817$ Å for $PrBa_2Fe_3O_8$. Across the system the lattice parameters monotonically increase as $x$ increases, but the trend deviates from the Vegard's Law.

Figure 1 shows the temperature dependence of the magnetic susceptibility of $Y_{1-x}Pr_xBa_2Fe_3O_8$, $\chi(T)$, measured in a field of 1 kG. The susceptibility behaves similar to the Curie-Weiss magnetism above $T=50$ K. Below 50 K, for the $PrBa_2Fe_3O_8$ sample, i.e., $x=1$, the susceptibility showed a clear cusp at $T=24$ K, indicating an antiferromagnetic ordering. This ordering is likely originating from Pr moments, which is similar to the Pr ordering in $PrBa_2Cu_3O_7$ at $T=17$ K.[5,1] Shown in the insert of Fig. 1 is the $\chi(T)$ of $PrBa_2Fe_3O_8$ at different fields. The cusp, which determines the Neel temperature, $T_N$, is shifted to lower temperatures as the applied field increases and disappears when the field is larger than 11 kG. The field dependence of $T_N$ is shown in the insert of Fig. 2.

The isothermal magnetization of $PrBa_2Fe_3O_8$ up to 5.4 tesla at various temperatures is shown in Fig. 2. We also plot M(H) for $YBa_2Fe_3O_8$ (data from Ref. 13), which is linear in H, in the same scale for comparison. The deviation of M(H) of $PrBa_2Fe_3O_8$ from the linear dependence suggests a canted magnetic structure of the Fe sublattices. Such a canted structure is expected to be more complicated than the antiferromagnetic structure in $YBa_2Fe_3O_8$, which was determined by the powder neutron diffraction experiment.[1] The difference in the magnetic structures of $PrBa_2Fe_3O_8$ and $YBa_2Fe_3O_8$ might be caused by the effect of hybridization between Pr $f$-electrons and the Fe(2)$O_2$ layers.

The room temperature $^{57}$Fe Mössbauer spectra of $Y_{1-x}Pr_xBa_2Fe_3O_8$ are presented in Fig. 3. The spectra for $x\leq 0.50$ can be very well fitted into a combination of two sextuplets with the intensity ratio 1:2, plus a quadrupole doublet near the center of the spectra, which counts less than 3% of total intensity. The two sextuplets correspond to the two crystallographically inequivalent lattice sites, Fe(1), with an octahedral coordination, and Fe(2), with a square-pyramidal coordination. The additional quadrupole doublet may indicate a small amount of impurity phases in the samples. An important feature shown in this figure is that the spectra of $x=0.75$ and $x=1.0$ samples are significantly different from the spectrum of $YBa_2Fe_3O_8$. Specifically, we did not observe any hyperfine splitting in these two samples. This clearly indicates that the substitution of Y by Pr significantly changes the electronic and magnetic structure of the system. Such an effect, however, was not observed in the substitution of Y by other rare-earth elements, such as Eu, Ho, and Er.[2] In the case of superconducting 123 system, Pr is special because it suppresses $T_c$ when substituted in $YBa_2Cu_3O_7$, while the substitution of other rare-earth elements does not. In our case Pr again singles itself out by affecting the magnetic properties of $YBa_2Fe_3O_8$ by its substitution.

Finally, in Fig. 4 we plot the Mössbauer spectra of $Y_{1-x}Pr_xBa_2Fe_3O_8$ measured at $T=15$ K. The spectra for samples of $x=0.0$ and 0.25 are similar to the room tempera-

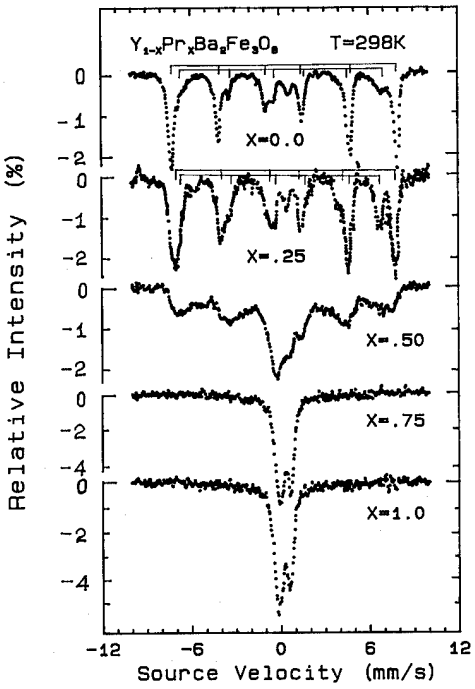



FIG. 3. Mössbauer spectra of $Y_{1-x}Pr_xBa_2Fe_3O_8$, for $x=0.0$, 0.25, 0.50, 0.75, and 1.0, measured at room temperature.

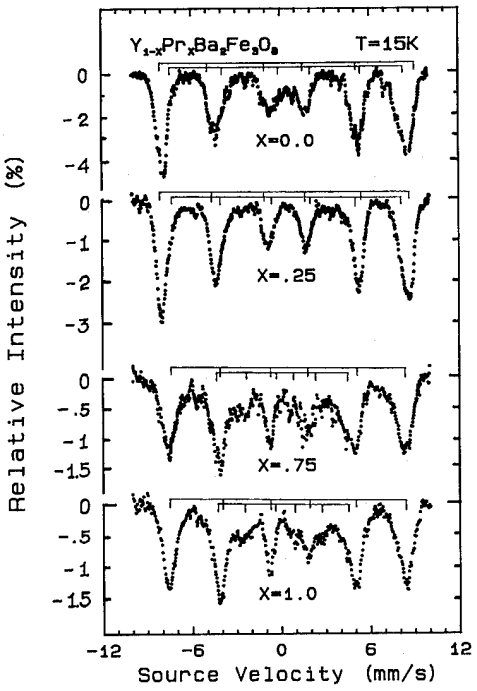



FIG. 4. Mössbauer spectra of $Y_{1-x}Pr_xBa_2Fe_3O_8$, for $x=0.0$, 0.25, 0.75, and 1.0, measured at 15 K.

ture spectra but with larger hyperfine splitting. The spectra of $x=0.75$ and $x=1.0$ samples showed that the Fe(1) and Fe(2) sublattices are magnetically ordered. The averaged hyperfine field reduces its value as $x$ increases. The temperature dependent Mössbauer study on $PrBa_2Fe_3O_8$ indicated that the magnetic ordering temperature is somewhere between 250 K and room temperature. However, we did not see any noticeable anomaly in the susceptibility data. The reduction of the average hyperfine field can be interpreted as the effect of the hybridization between the Pr 4*f*-electrons and the Fe(2)$O_2$ layers. Fitting our Mössbauer data yielded two well-defined parameter sets of isomer shift, quadrupole splitting, and magnetic hyperfine field for all the spectra measured below the magnetic ordering temperature. We find these two sets of parameters are significantly different. This difference is not only due to the Pr substitutions. Even for $YBa_2Fe_3O_8$, the magnetic hyperfine fields at Fe(1) and Fe(2) sites are 428.1 and 471.9 kG at room temperature, and, 496.7 and 523.8 kG at $T=15$ K. This result, along with the result of different isomer shift parameters, clearly indicates that the electronic valence states and the magnetic moments of the Fe ions at the two sites are different. Our result disagrees with the previously reported results[1,2] on $YBa_2Fe_3O_8$, i.e., that the ions at the two different sites have the same electronic valence and the same magnitude of the magnetic moments.

Further studies including the high temperature susceptibility, the specific heat, and the electrical resistivity measurements are being conducted and will be reported later. Neutron study and other complement measurements are required to fully understand this system regarding its magnetic structure.

The authors would like to acknowledge the Center for Materials Research at Temple University for supporting this research. T. Yuen would like to express her appreciation to Dr. C. L. Lin, for his technical help and many valuable discussions.

[1] Q. Huang, P. Karen, V. L. Karen, A. Kjekshus, J. W. Lynn, A. D. Mighell, N. Rosov, and A. Santoro, Phys. Rev. B **45**, 9611 (1992).
[2] O. Cohen, I. Felner, I. Nowik, U. Yaron, and E. R. Bauminger, Hyper. Int. **79**, 897 (1993).
[3] See M. B. Maple, B. W. Lee, J. J. Neumeier, G. Nieva, L. M. Paulius, and C. L. Seaman, J. Alloys Comp. **181**, 135 (1992), and references therein.
[4] J. J. Neumeier, T. Bjornholm, M. B. Maple, J. J. Rhyne, and J. A. Gotaas, Physica C **166**, 191 (1990).
[5] A. Kebede *et al.*, Phys. Rev. B **40**, 4453 (1989).
[6] I. Felner, U. Yaron, I. Nowik, E. R. Bauminger, Y. Wolfus, E. R. Yacoby, G. Hilscher, and N. Pillmayr, Phys. Rev. B **40**, 6739 (1989).
[7] G. Hilscher, E. Holland-Moritz, T. Holubar, H.-D. Jostarndt, V. Nekvasil, G. Schaudy, U. Walter, and G. Fillion, Phys. Rev. B **49**, 535 (1994).
[8] G. Xiao, M. Z. Cieplak, D. Musser, A. Gavrin, F. H. Streitz, C. L. Chien, J. J. Rhyne, and J. A. Gotaas, Nature **332**, 238 (1988).
[9] B. D. Dunlap, J. D. Jorgensen, C. Segre, A. E. Dwight, J. L. Matykiewicz, H. Lee, W. Peng, and C. W. Kimball, Physica C **158**, 397 (1988).
[10] S. Geremia, G. Nardin, R. Mosca, L. Randaccio, and E. Zangrando, Solid State Commun. **72**, 333 (1989).
[11] M. ElMassalami, A. Elzubair, H. M. Ibrahim and M. A. Rizgalla, Physica C **183**, 143 (1991).
[12] P. Karen, P. H. Andresen, and Kjekshus, J. Solid State Chem. **101**, 48 (1992).
[13] I. Felner, I. Nowik, U. Yaron, O. Cohen, and E. R. Bauminger, Phys. Rev. B **48**, 16040 (1993).

# Observation of independent iron and rare-earth ordering in $RFe_6Ge_6$ ($R = Y$, Gd–Lu) compounds

D. H. Ryan[a] and J. M. Cadogan
*School of Physics, The University of New South Wales, Sydney NSW 2052, Australia*

Mössbauer and magnetization measurements have been used to study magnetic ordering in $RFe_6Ge_6$ alloys. The iron sublattice orders antiferromagnetically and $T_N$ remains essentially constant across the series at ~480 K with no evidence of a net magnetization in any of the alloys. For $R$=Gd–Er, the rare-earth sublattice orders ferromagnetically with $T_c$'s that descend from 30 K at Gd to 3 K at Er. This order is established without affecting the order on the iron sublattice. The large difference in ordering temperatures and the unrelated magnetic structures adopted by the two sublattices indicate that the iron and rare-earth moments are effectively isolated from each other and that they order independently. © *1996 American Institute of Physics.* [S0021-8979(96)13008-3]

## INTRODUCTION

Earlier work on $RFe_6Ge_6$ alloys has shown that they order antiferromagnetically below about 480 K, and that $T_N$ (Ref. 1) is insensitive to the rare-earth element present in the alloy. Furthermore, the hyperfine field at the iron sites, $B_{hf}$, does not change when Gd or Tb is substituted for $Y$, nor is any net magnetization observed following these substitutions.[2] These results suggest that either the rare-earth sublattice also orders antiferromagnetically, or that it does not order at all.

In order to investigate this alloy series in more detail, we have extended our previous study[2] to include all of the heavy rare earths. We have used Mössbauer spectroscopy to probe, the effects of the rare-earth substitutions on a microscopic scale, and low-temperature susceptibility and magnetization measurements, to look for evidence of magnetic order at the rare-earth sites.

## EXPERIMENTAL METHODS

The alloys were prepared by arc-melting stoichiometric ratios of the pure elements (Fe: 99.95%, Ge: 99.999%, and rare-earths: 99.9% pure) under Ti-gettered argon to yield ~2 g ingots. To allow for the inevitable loss of Tm and Yb by evaporation during arc melting, excess Tm (10%) and Yb (25%) was added to the starting mixture. Room temperature Mössbauer spectroscopy showed both the magnetic pattern of the 1–6–6 phase with typically a 10%–20% contamination from the nonmagnetic, tetragonal 1–2–2 phase.[3] Annealing at 900 °C for two weeks sealed under vacuum in quartz tubes yielded single-phase 1–6–6 alloys.

Powder x-ray diffraction patterns were obtained using Cu–$K_\alpha$ radiation on an automated Nicolet–Stoe diffractometer. The structures of the annealed alloys were found to be in agreement with those reported by Venturini *et al.*,[1] with the exception of the Gd alloy where we found no evidence for the superlattice structure and Pnma space group they reported. Our $GdFe_6Ge_6$ alloy showed the much simpler hexagonal P6/mmm structure found also in the Yb and Lu alloys.

Mössbauer spectra were obtained at room temperature in transmission geometry on a conventional constant-acceleration drive using a 1 GBq $^{57}$CoRh source. The instrument was calibrated with a natural iron foil and all isomer shifts are given relative to that standard. 60–80 mg samples were hand ground and dispersed in graphite. Resonant absorptions of 7%–10% were obtained.

Thermogravimetric analysis was carried out on a Perkin–Elmer TGA-7 in a small field gradient to look for evidence of ferromagnetic or ferrimagnetic ordering. The Néel temperatures of the alloys were measured on a Perkin–Elmer DSC-7, using the heat capacity peak at $T_N$ as the signature of ordering. Both systems were calibrated using standard alumel and nickel samples. A LakeShore susceptibility system with a closed-cycle refrigerator was used to record $\chi_{ac}$ vs $T$ down to 12 K. Magnetization measurements were carried out on a Quantum Design SQUID down to 2 K in fields of up to 5 T.

## RESULTS AND DISCUSSION

The room temperature Mössbauer spectra of the annealed samples (Fig. 1) show a magnetically ordered, six-line pattern with a splitting of ~15 T, half that found in $\alpha$-Fe, suggesting an iron moment of about 1 $\mu_B$. There is no evidence of either magnetic or nonmagnetic contaminants. Thermogravimetric analysis (TGA) measurements showed no sign of either ferromagnetic or ferrimagnetic order between 300 and 600 K. Given the obvious magnetic order on the iron sites observed by Mössbauer spectroscopy, we conclude, as before,[1,2] that the ordering in all of these alloys is antiferromagnetic. The Mössbauer parameters for the alloys studied here are summarized in Fig. 2. The three crystal structures adopted by the alloys in this series are closely related and is it clear from the absence of any jumps in the hyperfine parameters that the local environment of the iron remains essentially unchanged as the structure passes from Cmcm (Y–Ho) through Immm (Er,Tm) to P6/mmm (Yb,Lu). Furthermore, the easy axis of magnetization must remain in the basal plane at room temperature in all of the alloys since the quadrupole splitting is essentially constant across the series.

[a]On leave from Centre for the Physics of Materials and Department of Physics, McGill University, 3600 University St., Montreal, Quebec, Canada.

 0021-8979/96/79(8)/6004/3/$10.00 © 1996 American Institute of Physics

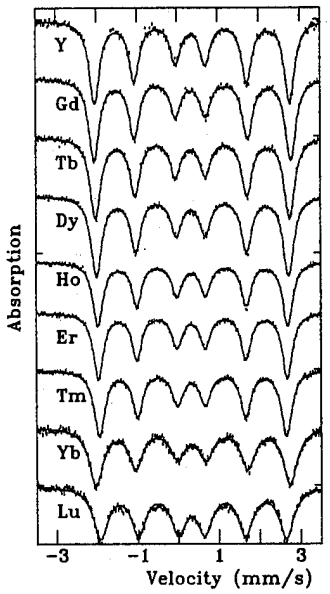



FIG. 1. Room temperature Mössbauer spectra of the annealed $RFe_6Ge_6$ alloys. Solid lines are fits assuming a single, magnetically ordered iron site.

The most surprising feature of this system is the fact that both the hyperfine field at the iron nucleus ($B_{hf}$, Fig. 2) and $T_N$ (Fig. 3) are essentially independent of the rare-earth present. Apart from a gradual decline in $B_{hf}$ (5%) and $T_N$ (2%) there appears to be no significant change in the magnetic properties on going from Gd to Lu. These results suggest that the rare-earth sublattice does not order with the iron at 480 K, furthermore, an earlier study[1] found no evidence of

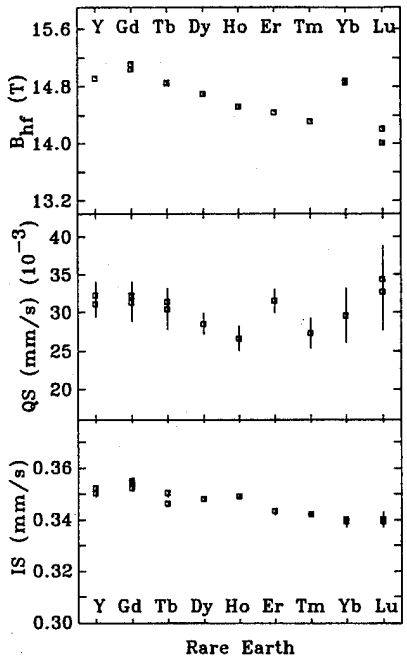



FIG. 2. Summary of fitted hyperfine parameters at room temperature for all of the $RFe_6Ge_6$ alloys studied here. Error bars are derived from statistical uncertainties. Values obtained from samples before and after annealing are shown in several cases, and agree within error. Data on two Gd alloys are included as a consistency check.

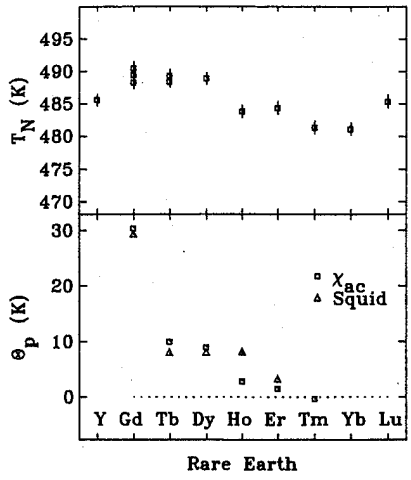



FIG. 3. Top: Néel temperature of the Fe sublattice, derived from DSC measurements. Bottom: Curie–Weiss temperatures for the rare-earth sublattice obtained from fits to $\chi_{ac}$ vs $T$ above 12 K, or SQUID data down to 2 K.

rare-earth ordering down to 90 K. One possible explanation for this behavior could lie in the magnetic structure of the iron sublattice. The ordered state of the binary FeGe compound, from which the 1–6–6 alloys studied here are derived, consists of ferromagnetic Fe planes coupled antiferromagnetically to each other.[4] The 1–6–6 structures are formed by placing rare-earth atoms between the iron planes, and if the magnetic structure of the parent FeGe compound is retained, there could be a net cancellation of the Fe–R exchange at the rare-earth sites, effectively isolating them from the ordering of the iron moments. Since the rare-earth moments do order in $RFe_2Ge_2$ where the iron atoms carry no moment,[5] it seems reasonable to expect order to develop on the rare-earth sublattice at low enough temperatures. Figure 3 shows paramagnetic ordering temperatures ($\theta_p$) derived from Curie–Weiss fits to $\chi_{ac}$ data measured down to 12 K. Except for the case of $GdFe_6Ge_6$, all of the extrapolated ordering temperatures lie below the limit of the closed-cycle refrigerator, while the value for the Tm alloy is in fact slightly negative. $\theta_p$ scales approximately with the deGennes factor for the rare-earths, except for the case of the Tb alloy, where $\theta_p$ is too low.

Our data for $GdFe_6Ge_6$ suggest that it orders ferromagnetically at 30.5±0.2 K, giving a large susceptibility that saturates below $T_c$. This may not be the first observation of ordering in $GdFe_6Ge_6$, as an earlier study of $GdFe_2Ge_2$ showed a susceptibility feature close to this temperature in an off-stoichiometry sample which may have contained some 1–6–6 as an impurity, although no details about phase purity were given.[6] In order to confirm our view of the magnetic structure of the Gd compound, and to determine ordering temperatures for some of the other alloys, we also carried out measurements on a SQUID magnetometer that could be operated down to 2 K. Ordering temperatures, taken from the kink in a plot of $1/\chi$ vs $T$, are also shown on Fig. 3. These are in agreement with the values extrapolated from 12 K except in the case of the Ho alloy whose ordering temperature is somewhat higher than expected. The magnetization at 2 K, converted to $\mu_B$ per formula unit, is shown in Fig. 4

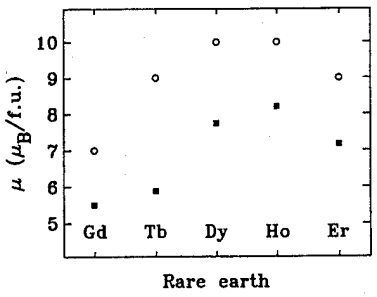



FIG. 4. Ordered moment per formula unit at 2 K (solid symbols) compared with $gJ$ for the corresponding free ion (open symbols) for the $RFe_6Ge_6$ alloys that ordered above 2 K.

along with values of $gJ$ for each of the rare-earths. A difference of about $2\mu_B$ is apparent in each case. Some of this is clearly due to the measurements being carried out rather closer to $T_c$ than ideal, and a further contribution can be attributed to a failure to saturate the magnetization in 5 T for all of the samples other than $GdFe_6Ge_6$. The origin of the discrepancy remains a problem for the Gd alloy, which was measured at 0.15 $T_c$ and had saturated. Two simple explanations would be either a noncollinear ordering of the Gd sublattice, or an Fe–Gd interaction that modifies the antiferromagnetic order on the Fe sublattice so as to yield a net magnetization directed against that of the Gd sublattice. The high capture cross-section of Gd makes neutron diffraction essentially impossible and so direct structural measurements are not available. Preliminary $^{155}$Gd and $^{57}$Fe Mössbauer measurements at low temperatures have confirmed that the Gd moments do order at 30 K and that the iron sublattice does not appear to be affected in any way by this ordering.[7]

## CONCLUSIONS

Mössbauer and magnetization measurements on $RFe_6Ge_6$ alloys with $R=Y$, Gd–Lu, indicate that the antiferromagnetic ordering of the iron sublattice at $T_N \sim 480$ K, is unaffected by changes to the rare-earth element present. Furthermore, the rare-earth sublattice orders ferromagnetically at much lower temperatures, ranging from 30 K for the Gd alloy, to 3 K in the case of Er, without affecting the order on the iron sublattice. The difference in ordering temperature between the iron and rare-earth sublattices, which is never less than a factor of 10, coupled with the unrelated magnetic structures adopted, indicates that the two magnetic species order independently, and that the Fe–R exchange is essentially zero.

## ACKNOWLEDGMENTS

We are grateful to S. J. Collocott and C. Andrikidis at CSIRO, Division of Applied Physics, Lindfield NSW, Australia, who made the SQUID measurements. D.H.R. would like to acknowledge the hospitality of the School of Physics at the University of New South Wales, Sydney, Australia where much of this work was carried out. This work was also supported by grants from the Australian Research Council, the Natural Sciences and Engineering Research Council of Canada and Fonds pour la Formation de Chercheurs et l'Aide à la Recherche, Québec.

[1] G. Venturini, R. Welter, and B. Malaman, J. Alloys Comp. **185**, 99 (1992).
[2] Y. B. Wang, D. Wiarda, J. M. Cadogan, and D. H. Ryan, IEEE Trans. Magn. **30**, 4951 (1994).
[3] J. J. Bara, H. U. Hrynkiewicz, A. Milos, and A. Szytula J. Less-Common Met. **161**, 185 (1990).
[4] O. Beckmann, K. Carrender, L. Lundgren, and M. Richardson, Physica Scripta **6**, 151 (1972).
[5] A. Szytula and J. Leciejewicz, in *Handbook on the Physics and Chemistry of the Rare Earths*, edited by K. A. Gschneider, Jr. and L. Eyring (North Holland, Amsterdam, 1989), Vol. 12, p. 133.
[6] F. M. Mulder, R. C. Thiel, and K. H. J. Buschow, J. Alloys Comp. **202**, 29 (1993).
[7] D. H. Ryan, J. M. Cadogan, and J. D. Cashion (unpublished).

# Cobalt-doped carbon nanotubes: Preparation, texture, and magnetic properties

K. Lafdi, A. Chin, N. Ali, and J. F. Despres
*Southern Illinois University at Carbondale, Carbondale, Illinois 62901, and Laboratoire M. Mathieu, 2 av. du President P. Angot 64000 Pau, France*

The nested carbon nanotubes discovered by Ijima and co-workers as a by-product of fullerene production extended the dimension and geometries of fullerenes into the domain of nanoparticles. These nanotubes are fiberlike structures consisting of concentric graphite sheets nested along the axis extending as long as several micrometers, and diameters of these nanotubes are limited to less than 100 nm. In this paper we report preparation, structural and magnetic properties of cobalt-doped carbon nanotubes. We observed a tubular structure made of coaxial graphite sheets. The inside, of these carbon nanotubes, was filled with cobalt particles. The magnetic properties of the Co-doped nanotubes were measured using a SQUID magnetometer. The undoped (pure) carbon nanotubes exhibit diamagnetic behavior. The Co-doped nanotubes exhibit superparamagnetic behavior with saturation of magnetization at about 0.5 T and coercive field of 750 G. © *1996 American Institute of Physics.* [S0021-8979(96)00908-1]

## I. INTRODUCTION

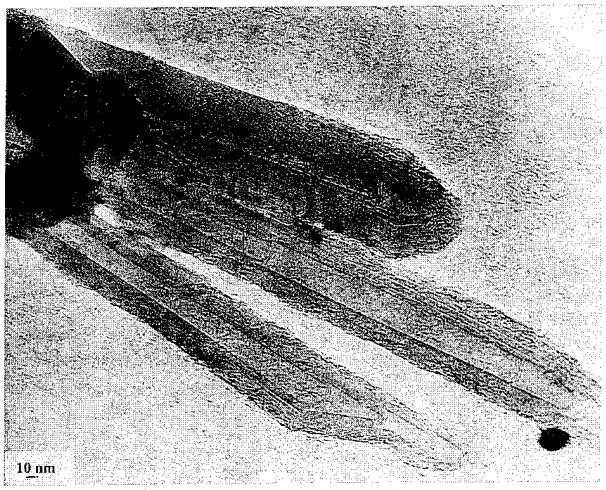
The nested carbon nanotubes discovered by Ijima[1,2] as a by-product of fullerene production extended the dimension and geometries of fullerenes into the domain of nanoparticles and perhaps, to nanowires. Structurally engineered materials with nanometer-sized entities, such as superlattices and granular solids, etc., have attracted much attention in recent years because of their distinctive properties and potential for technological applications. Interest in the unique electrical and thermal properties of these nanotube structures is a result of several theoretical calculations which suggest that the structures might have either metallic or semiconductor properties.[3–6] These nanotubes are fiberlike structures consisting of concentric graphite sheets nested along the axis and extending as long as several micrometers.[1] This type of tubular filament or carbon shell, containing a metal microcrystal less than 100 nm in size, is made by a catalytic reaction.[2,7]

The work of Audier *et al.*[7] emphasizes the role of crystallographic orientation of the metal crystal upon the growth and degree of graphitization of carbon filaments. The objectives of the present study are to fabricate doped carbon nanotubes, to examine the magnetic properties, and to emphasize the textural approach when attempting to understand the observed enhanced magnetic properties of these materials.

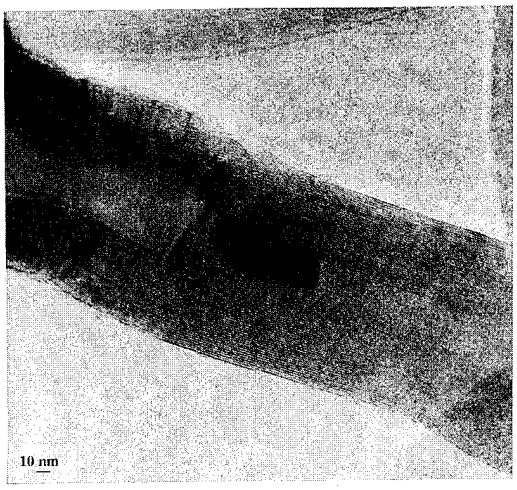
## II. EXPERIMENTAL AND RESULTS

First, a graphite rod doped with cobalt was prepared by mixing "anisotropic" pitch with colloidal cobalt. This mixture produces a homogeneous, two phase dispersed system (sol-gel). After hot pressing, pyrolysis, stabilization, and carbonization, a doped graphite rod is obtained. This rod was used as the anode in an arc discharge process. The Kratschmer–Huffman method was used to prepare nanotubes.[8] During this process the doped graphite evaporates at the anode and a carbon deposit (slag) is formed on the cathode. Samples from the slag collected from the dc electric discharge process were examined using transmission electron microscopy (TEM). We observed a tubular structure made of coaxial graphite sheets. These carbon nanotubes are filled with particles of cobalt. Two samples were made using the arc discharge method. Sample A was produced using pure carbon rods; B was made using cobalt-doped carbon rods. TEM characterization using lattice fringe (LF002) mode shows that the pure carbon nanotubes without cobalt contain several tubes of 100 nm in diameter and about 1 $\mu$m in length. The tube walls consist of at least three or four layers of graphite and resemble the construction of a cardboard tube [Fig. 1(a)]. Sample B, however, as Fig. 1(b) shows, consists of nanotubes containing cobalt particles. The doped carbon nanotube yield seems to be directly related to the homogeneity of the pitch/cobalt powder mixture and the density of the electrode during the fabrication process. In comparison to the catalysis method,[3] the arc discharge process allows us to produce a higher yield of doped carbon nanotubes. The maximum yield obtained is 18%. The magnetization was measured using a SQUID magnetometer (Quantum Design, Inc.) with an applied magnetic field $-2\ \mathrm{T} \leqslant H \leqslant 2\ \mathrm{T}$ in steps of 0.05 T at 10 K. In order to observe clearly the remanence and the coercive field, the measurement step was 0.002 T within 0.05 T range. Figure 2 show the magnetization versus applied magnetic field. It is evident that for pure nanotubes, sample A, the magnetic behavior is diamagnetic with negative magnetic susceptibility. For pure Co powder (sample C), the magnetization curve shows ferromagnetic behavior with hysteresis loop (Fig. 3). The Co powder and carbon nanotube mixture (sample D) show ferromagnetic behavior at low-field range (Fig. 4), however the behavior of sample D changes into diamagnetic behavior with negative magnetic

 0021-8979/96/79(8)/6007/3/$10.00 © 1996 American Institute of Physics 




(a)




(b)

FIG. 1. (a) Lattice fringes LF002 of pure carbon nanotube. (b) Lattice fringes LF002 of cobalt-doped carbon nanotube.

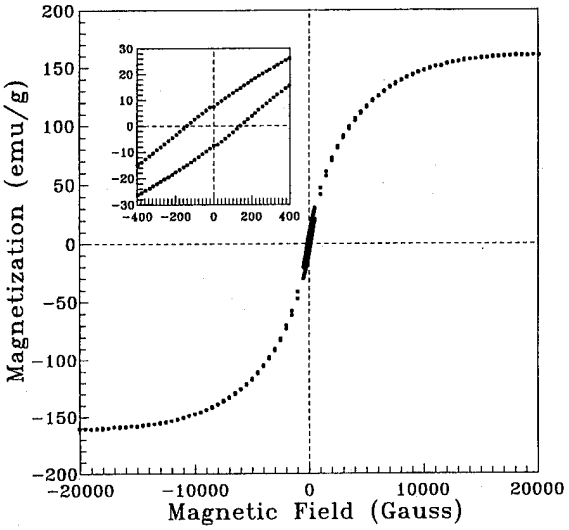



FIG. 3. Magnetization of pure 300 mesh cobalt powder at 10 K.

susceptibility after 1.7 T (inset of Fig. 4). For Co-"doped" nanotube, its magnetization curve shows typical ferromagnetic behavior (Fig. 5) and has a higher coercive force than that of pure Co powder. The values of saturation magnetization, remanence, coercive field, and saturation field of all the specimens are listed in Table 1.

The cobalt-doped nanotubes, sample B, exhibit saturation in magnetization versus field data. This material saturated at about 0.5 T which is approximately half the value exhibited by bulk cobalt.[1] The coercivity of the doped nanotubes was around 0.075 T.

The pure carbon nanotube sample exhibits diamagnetism as one may expect. For the Co powder, the magnetization data show magnetic properties similar to bulk Co. The sample D, which is a mixture of Co powder and pure carbon nanotube, shows the tendency of magnetization saturation up to 1 T (Fig. 4). However, above 1 T one observed a linear decrease in magnetization with increasing applied magnetic

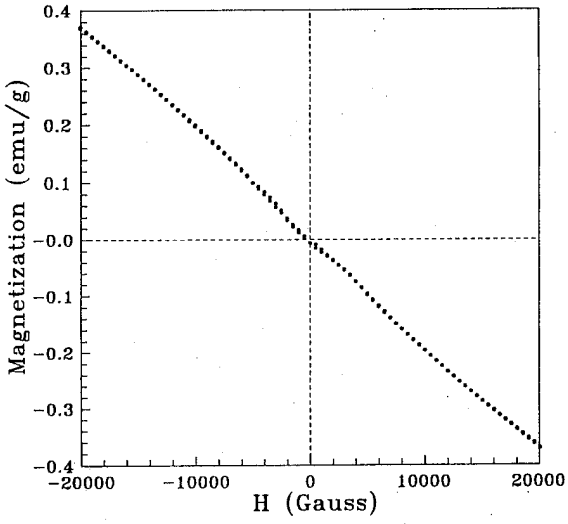



FIG. 2. Magnetization of pure nanotube at 10 K.

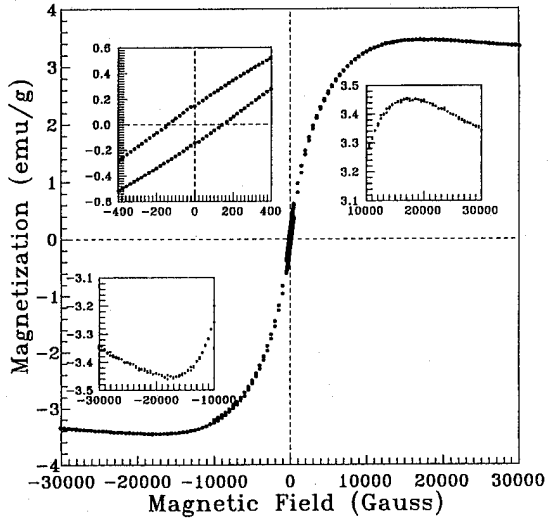



FIG. 4. Magnetization of carbon nanotube and cobalt powder mixture at 10 K.

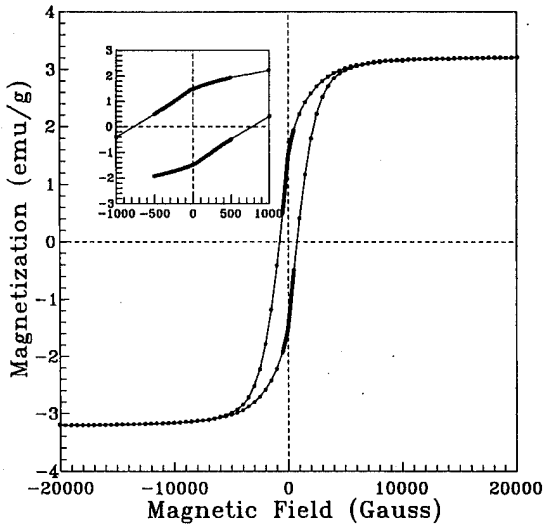



FIG. 5. Magnetization of cobalt-doped carbon nanotube at 10 K.

field. This behavior of magnetization (Fig. 4) can be explained by additive effect of ferromagnetic saturation of Co magnetization and diamagnetic decrease in the magnetization of pure carbon nanotubes with increasing field. The Co-doped nanotube samples show saturation of magnetization much faster (at $-0.5$ T) compared to pure Co powder sample (at $-1.7$ T). In addition we also observe that the coercive field also increases by a factor of more than five. It is estimated that in the Co-doped nanotube samples the size of Co particles inside nanotubes ranges from 7 to 50 nm. The magnetic properties of Co-doped nanotube exhibit most likely superparamagnetic behavior.

## III. DISCUSSION AND CONCLUSION

In summary, the TEM results show clearly that the structure of cobalt-doped carbon nanotubes is similar to that exhibited by pure carbon nanotubes. Also, the Kratschmer–Huffman method produces a higher yield of doped carbon nanotubes than catalysis, but with smaller lengths and diameters.[7] In this work, we observe that the magnetic properties of pure carbon nanotube are diamagnetic, cobalt powder are ferromagnetic, like bulk cobalt, and the magnetic behaviors of the mixture has the results of additive effect. For Co-doped nanotubes the magnetization increases rapidly at low fields, the magnetization saturates faster at lower field and there is no diamagnetic behavior after the saturation. These intriguing magnetic properties are most likely related to the low dimensionality of the cobalt entities. The magnetic properties of cobalt particles can be significantly altered by the nanometric size, their specific surface area and the tubular shape of doped carbon materials. The carbon nanotubes possibly cause the easy magnetization direction of Co particles in the nanotube to align well along the tube axis and lead to fast saturation of the magnetization.

TABLE I. Values of saturation magnetization, remanence, coercive field, and saturation field for all specimens.

| Sample name | A (pure C nanotube) | C (Co powder) | D (Co powder and pure C nanotube) | B (Co-doped nanotube) |
|---|---|---|---|---|
| Magnetization (emu/g) | −0.37 | 160 | 3.45 | 3.2 |
| Remanence (emu/g) | none | 8 | 0.16 | 1.5 |
| Coercive field (G) | none | ∓140 | ∓140 | ∓750 |
| Saturation field (T) | none | 1.7 | 1.7 | 0.5 |


[1] S. Ijima, Nature **354**, 56 (1991).
[2] S. D. Robertson, Carbon **8**, 365 (1970).
[3] J. J. W. Mintmire, B. I. Dunlap, and C. T. White, Phys. Rev. Lett. **68**, 632 (1992).
[4] R. Saito, M. Fujita, G. Dresselhaus, and M. S. Dresselhaus, Phys. Rev. Lett. **64**, 1804 (1992).
[5] J. W. Mintmire *et al.*, *Electrical, Optical and Magnetic Properties of Organic Solid State No. 247* (Materials Research Society, Pittsburgh, PA, 1992), p. 339.
[6] K. Tanaka, K. Okahara, M. Okada, and T. Yamabe, Chem. Phys. Lett. **191**, 469 (1992).
[7] M. Audier, A. Oberlin, and M. Coulon, J. Cryst. Growth **57**, 524 (1982).
[8] W. Kratschmer and D. R. Huffman, Chem. Phys. Lett. **170**, 167 (1990).

# Magnetic properties of nanosized wires

J. Meier, B. Doudin, and J.-Ph. Ansermet
*Institut de Physique Expérimentale, Ecole Polytechnique Fédérale de Lausanne, 1015 Lausanne, Switzerland*

Assemblies of ferromagnetic cylinders made of Ni with diameters ranging from 35 to 250 nm were produced by electrodeposition in nanoporous membranes. The large coercive fields of Ni nanowires at low temperature could be accounted for by the curling mode of magnetization reversal, taking into account the distributions of wire diameters and orientations. The coercive field of the nanowires of the smaller diameter range decreased from 1500 Oe at 20 K to 200 Oe at 300 K nearly linearly.
© *1996 American Institute of Physics.* [S0021-8979(96)40808-X]

## I. INTRODUCTION

Characterization and understanding of the magnetic properties of small particles have been a challenge for decades and prompted intense research activity, motivated in particular by applications in magnetic recording technology. Some simple problems remain unclear.[1] For example, the reversal mode of the magnetization of a perfect cylinder is still the subject of theoretical predictions.[2] Comparison with experiments most often suffered from the difficulty of producing samples with well characterized morphologies. Furthermore, the limited sensitivity of magnetic measurements necessitates the study of a large number of particles. Consequently samples present a dispersion in morphological features. We prepared well defined and reproducible assemblies of ferromagnetic cylinders by electrodepositing ferromagnetic metals in the cylindrical pores of polycarbonate track-etched (PCTE) membranes of thicknesses between 6 and 10 $\mu$m. This method made possible the production of wires as small as 30 nm in diameter. One advantage of this technique is the possibility of changing the composition of the deposit, allowing the comparison of the magnetic properties of various materials in exactly the same morphology. We could also extend the technique to the synthesis of wires with alternating metals, thus opening the study to magnetic grains with controlled shape and separation.[3] The technique of making small wires with diameters under 100 nm has been extensively studied for the case of aluminum oxide porous membranes (alumite).[4–6] Alumite can have a pore density as high as $10^{11}$ pores/cm$^2$. It has been shown that magnetostatic interactions among the wires cannot be neglected.[6,7] In contrast, the highest pore density of commercially available PCTE is $6\times10^8$ pores/cm$^2$ and lower densities can be produced. In this study, we found that the coercive field of nanowires depended on the diameter like in the manner expected of acicular particles or wires, and showed how the distribution of pore orientation of commercially available PCTE change the average magnetic properties of filled membranes.

## II. SAMPLE PREPARATION

We used commercially available nanoporous PCTE membranes.[8] Experimental details on growth and morphological characterization of nanowires have been published.[9] The technique of elctrodeposition in such nanoporous templates has been recently reviewed[10] and initial results about Co and Ni wires have been reported.[11,12]

## III. RESULTS AND DISCUSSION

We used a commercial superconducting quantum interference device (SQUID) magnetometer to measure between 2 and 400 K the magnetic moments of discs of 3 mm in diameter which were cut out of Ni-filled membranes and contained about 1 $\mu$g of Ni. The hysteresis curves were measured with the applied field perpendicular or parallel to the membrane plane (Fig. 1). The anisotropy of the sample ap-

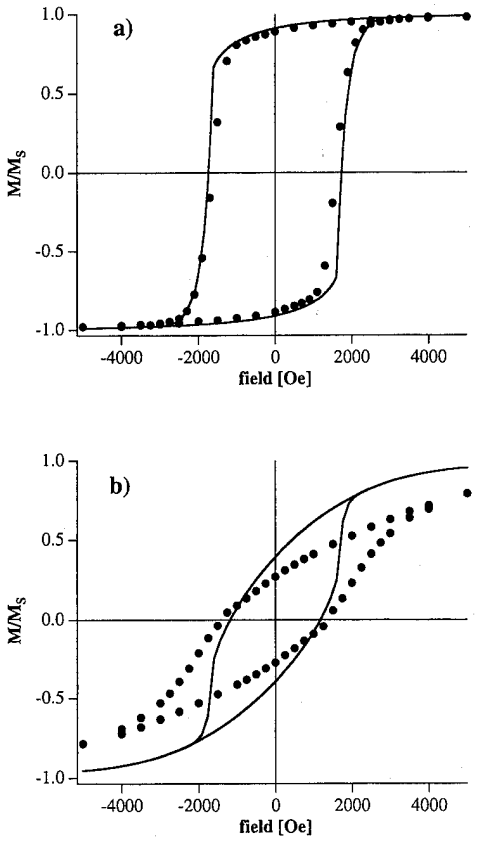



FIG. 1. Hysteresis loops for an assembly of Ni nanowires with a mean diameter of 53 nm at 5 K (dots). The continuous line is the prediction of the Stoner–Wohlfarth model. The wires were oriented predominantly parallel (a) or perpendicular (b) to the applied field.

 0021-8979/96/79(8)/6010/3/$10.00 © 1996 American Institute of Physics

peared clearly. The data can be easily understood in terms of the alignment of the wires. We calculated the hysteresis curves for the Stoner–Wohlfarth (SW) model of uniform rotation with a uniaxial magnetic anisotropy[13] which was taken to be the shape anisotropy only. We took into account the fact that the wires were not perfectly aligned perpendicularly to the membrane by assuming a uniform probability distribution $p(\alpha)$ of the angle $\alpha$ between the wire axis and the normal to the plane of the membrane, ranging from 0 to $\alpha_m$

$$p(\alpha)d\alpha = \frac{1}{1-\cos\ \alpha_m} \sin\ \alpha d\alpha. \tag{1}$$

The value of the maximum angle $\alpha_m$ of 34° was provided by the manufacturer. The hysteresis curves (Fig. 1) were calculated as weighted averages of the prediction of the SW model for the magnetization for all possible orientations of the wires with respect to the applied field.

The influence of the neighboring wires could be estimated as an additional demagnetizing field. In the case where the membrane was perpendicular to the field, it was estimated as the field produced by a uniform film with the same magnetization as that of the filled membranes

$$H_D = 4\pi M p\,, \tag{2}$$

where $M$ is the average magnetization and $p$ is the porosity of the membrane. As the highest density which is commercially available is limited to $6\times10^8$ pores/cm$^2$, the porosity was limited to a few percents. For the sample of Fig. 1, the maximum value of $H_D$ was 85 Oe only. In the case where the membrane was parallel to the field [Fig. 1(b)], the demagnetizing field of a uniform membrane would vanish. The discrepancy between the data and the (SW) model indicates that, in this direction, the magnetostatic interactions among neighboring wires cannot be neglected. Hence the angular distribution of wire orientations accounts correctly for the observed slopes of the hysteresis curve in the orientation of the membranes which corresponds to the greatest alignment of the wires with the field.

The dependence of the coercive field on the average diameter of the Ni wires was measured at 20 K, with the applied field perpendicular to the membranes (Fig. 2). We interpreted the data, as it is customarily done for elongated single domain particles,[14] in terms of curling and uniform rotation. We took into account the angular dependence of the nucleation field for the curling mode of an infinitely long circular cylinder with radius $R$ (Ref. 15)

$$\frac{H_n}{2\pi M_s} = \frac{h_t(1+h_t)}{[(1+h_t)^2-\sin^2\theta(1+2h_t)]^{1/2}}$$

with

$$h_t = -1.08\left(\frac{R}{\sqrt{A}/M_s}\right)^{-2}, \tag{3}$$

where $\theta$ is the angle between cylinder axis and applied field and $A$ is the exchange constant. We used the angular distribution of wire orientations as above and the commonly accepted value of $A$ of $10^{-11}$ J/m ($10^{-6}$ ergs/cm).[16] As each sample had a distribution of wire diameters,[12] a fraction of the wires might undergo uniform rotation and the others curling. The diameter $d_0$ which characterizes the transition from uniform rotation to curling is $d_0 = 2\times A^{1/2}/M_s = 41$ nm. This simple model gave a fair account of the data with no adjustable parameters (Fig. 2). The angular distribution of the wires, which was known and well reproducible in our samples, plays a major role in the outcome of this calculation. The observed coercive field was found somewhat larger than the prediction of the model, by an amount of the order of 200 Oe ($5\times10^3$ J/m$^3$). One can expect a contribution of magnetostrictive effects to the coercivity. The coercive field due to the magnetostrictive energy of elongated particles can be estimated by[17]

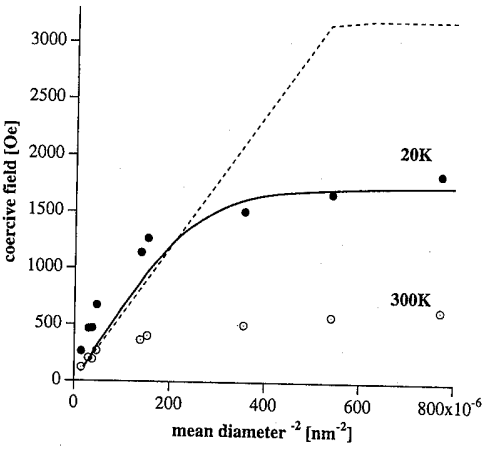



FIG. 2. Coercive field at 20 and 300 K (dots). The full line represents the curling mode for the assembly of misaligned cylinders described in the text. The broken line represents the curling mode for one cylinder aligned with the field.

$$H_c = \frac{3|\lambda\sigma|}{M_s}, \tag{4}$$

where $\lambda$ is the saturation magnetostriction coefficient and $\sigma$ the stress. Taking the value of $\lambda$ of polycrystalline Ni and assuming that the excess coercivity of ~200 Oe was due to magnetostrictive effects, Eq. (4) yields an estimate of the stress of $9\times10^7$ N/m$^2$. Electrodeposited Ni films are known to have indeed internal tensile stresses of $\sim7\times10^7$ N/m$^2$ (Ref. 18). While the data on the low temperature coercive fields can be understood in a commonly accepted view, two observations cast some doubts on this simple interpretation.

First, the temperature dependence of the coercive field was found quite large in wires of the smaller diameters, and nearly linear over a wide temperature range (Fig. 3). This is in contrast with predictions of models of nucleation by thermal activation over an anisotropy barrier, leading to a $T^{1/2}$ variation. Even if a reasonable distribution of barriers is assumed, the temperature dependence is still reminiscent of a $T^{1/2}$ dependence.[19] Linear temperature dependence of the coercive field was observed in acicular $Fe_2O_3$ (Ref. 20) and in percolating granular Fe–$SiO_2$ composites.[21]

Second, the presence of large magnetostrictive effects was observed by taking advantage of our template synthesis to produce assemblies of permalloy wires identical to the Ni wire assemblies. The large temperature dependence vanished

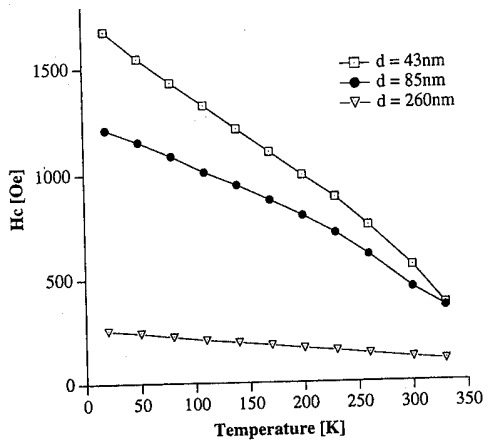



FIG. 3. Temperature dependence of the coercive field for Ni nanowires with different diameters. The lines are a guide to the eye.

in the permalloy wires. Furthermore, when the Ni wires were freed from the membrane by dissolving it, the temperature dependence of the coercive field also disappeared.[12]

These observations suggest that in Ni nanowires, the coercivity is dominated by magnetostrictive effects. Owing to the large mismatch of the thermal expansion coefficients of Ni and polycarbonate, thermal stresses and the resulting magnetrostrictive effects may determine the dependence of the coercive field on both diameter and temperature. Further tests and modeling would be required to ascertain the underlying mechanisms which account for the coercivity of the nanowires.

## IV. CONCLUSION

Assemblies of magnetic nanowires were produced by electrodeposition in nanoporous, track-etched, polycarbonate membranes. This template synthesis allows the production of well reproducible nanowire assemblies. However, the commercially available nanoporous membranes have a distribution of wire orientations which at times precludes conclusive characterization, such as the measurement of the angular dependence of the coercive field in order to test for curling or uniform reversal of the magnetization. The high coercive fields of Ni nanowires at low temperature could be accounted for by a model of curling in the larger wires, and uniform rotation with a shape anisotropy only in the smaller wires. However, the temperature dependence of the coercive field and its disappearance when the wires are freed from the embedding matrix or when Ni is replaced by permalloy indicated that the model of curling and uniform rotation might be too simple a picture.

[1] A. Aharoni, J. Appl. Phys. **63**, 5879 (1988).
[2] J. S. Broz, H. B. Braun, O. Brodbeck, W. Baltensperger, and J. S. Helman, Phys. Rev. Lett. **65**, 787 (1990).
[3] B. Doudin and J.-Ph. Ansermet, Nanostruct. Mater. **6**, 521 (1995).
[4] S. Kawai and R. Ueda, J. Electrochem. Soc.: Electrochem. Sci. Technol. **122**, 32 (1975).
[5] D. AlMawlawi, N. Coombs, and M. Moskovits, J. Appl. Phys. **70**, 4421 (1991).
[6] G. T. A. Huysmans, J. C. Lodder, and J. Wakui, J. Appl. Phys. **64**, 2016 (1988).
[7] L. Cheng-Zhang and J. C. Lodder, J. Magn. Magn. Mater. **88**, 236 (1990).
[8] Poretics Corp., 111 Lindbergh Av., Livermore, CA 94550-9520. Costar Corp. (Nuclepore), One Alewife Center, Cambridge, MA 02140. Whatman SA, 11b Av. Einstein, B-1348 Louvain-la-Neuve, Belgium.
[9] I. Chlebny, B. Doudin, and J.-Ph. Ansermet, Nanostruct. Mater. **2**, 637 (1993).
[10] C. R. Martin, Science **266**, 1961 (1994).
[11] T. M. Whitney, J. S. Jiang, P. C. Searson, and C. L. Chien, Science **261**, 1316 (1993).
[12] J. Meier, A. Blondel, B. Doudin, and J.-Ph. Ansermet, Helv. Phys. Acta **67**, 761 (1994).
[13] E. C. Stoner and E. P. Wohlfarth, Philos. Trans. R. Soc. London, Ser. A **240**, 599 (1948).
[14] A. E. Berkowitz and E. Kneller, in *Magnetism and Metallurgy* (Academic, New York, 1969), Vol. 1.
[15] A. Aharoni, J. Appl. Phys. **30**, 70S (1959).
[16] M. E. Schabes, J. Magn. Magn. Mater. **95**, 249 (1991).
[17] C.-W. Chen, in *Magnetism and Metallurgy of Soft Magnetic Materials* (North-Holland, Amsterdam, 1977).
[18] K. G. Budinski, in *Surface Engineering For Wear Resistance* (Prentice-Hall, Englewood Cliffs, NJ, 1988).
[19] R. W. Chantrell, K. O'Grady, A. Bradbury, S. W. Charles, and J. Popplewell, J. Phys. D. **18**, 2505 (1985).
[20] D. F. Eagle and J. C. Mallinson, J. Appl. Phys. **38**, 995 (1967).
[21] S. H. Liou, C. H. Chen, H. S. Chen, A. R. Kortan, and C. L. Chien, Mater. Res. Soc. Symp. Proc. **132**, 191 (1989).

# Negative remanence in magnetic nanostructures

X. Yan and Y. Xu
*Department of Physics, The Hong Kong University of Science and Technology, Clearwater Bay, Kowloon, Hong Kong*

In nearly percolating magnetic granular (Ni,Fe)-$SiO_2$ films, we observed negative remanence, or a negative remanent magnetization, upon removing the positively applied magnetic field to zero. We propose that there exist both superparamagnetic and ferromagnetic components due to different connectivity of magnetic nanometer scaled particles, as supported by the dark field transmission electron microscopy images. The magnetostatic interaction between them favors an opposite alignment. Moreover, the two-component hypothesis explains satisfactorily the dependencies of the negative remanence on temperature and magnetic volume fraction. © *1996 American Institute of Physics.* [S0021-8979(96)02608-6]

Magnetic granular or nanostructured films, or specifically metal-insulating composite films with nanometer scaled ferromagnetic metal particles, have attracted much attention in the last few decades,[1-3] due to a rich variety of interesting transport, magnetic, and mechanical properties,[4-6] depending strongly on the size of the magnetic particles and its distribution. When $x$ is well below the percolation threshold, or $x<x_p/2$, the ferromagnetic particles are embedded in an insulating matrix and are well isolated, and the collective behavior of the whole system is superparamagnetic with measured magnetic susceptibility inversely proportional to temperature for $T>T_b$, where $T_b$ is the blocking temperature above which the magnetization of the particles can rotate to follow the external magnetic field. The blocking temperature is proportional to the magnetic anisotropic energy and the volume of the particles. Thus when $x>x_p$ where most of the particles are connected, the whole system behaves ferromagnetic globally. In this article, we report the observation of the negative remanence in granular (Ni,Fe)-$SiO_2$ films where the magnetic particles are nearly percolating. The morphologies of the films were illustrated to have both isolated as well as connected magnetic particles, suggesting the coexistence of both superparamagnetic (SPM) and ferromagnetic (FM) components. We further propose that the magnetostatic interaction between the SPM and the FM components, which can favor the opposite alignment.

Granular $(Ni,Fe)_x$-$(SiO_2)_{1-x}$ films were prepared using a Denton magnetron rf sputtering system.[6] It was determined that the magnetic particles are mainly Ni with less than 20% Fe for $x$ above 0.4, and the magnetic volume fraction $x'$ is not too different from the nominal volume fraction $x$, while the matrix is the insulating amorphous $SiO_2$. The average sizes of the magnetic particles are about 3–6 nm, increasing smoothly throughout the percolation threshold ($x_p' \sim 0.6$ according to resistivity[6]). Direct current magnetization was measured for all those films between 5 and 300 K using Quantum Design's SQUID MPMS-5 system for the magnetic field applied parallel to the plane of the films.

Figure 1 shows the $M$-$H$ loop, or the magnetization as a function of magnetic field from 10 kG to −10 kG to 10 kG at 200 K for $x=0.55$. Although no hysteresis is evident in this scale, the magnification of the curve does show some hysteresis as shown in the inset between ±50 G. It is important to note that the remanent magnetization is negative, upon decreasing the magnetic field from the positively saturated field, such as 10 kG, to zero at 200 K. This remanence is as large as −9% compared to the positively saturated value. The dc magnetic susceptibility near zero is about 0.5, or $4\pi\chi\approx 6.3$.

When the same film was cooled to 5 K where the rotation of the isolated particles were frozen, the measured remanent magnetization upon removing positive magnetic field from 10 kG to zero, $M_r$, was positive, similar to the behavior in a conventional ferromagnet. Figure 2 shows $M_r$ and zero-field-cooled dc magnetic susceptibility $\chi$ as a function of temperature for the same film. Note that upon increasing temperature, $M_r$ changes sign, through 0 at about 100 K, to a negative value of a similar amplitude at 200 K as shown in the inset of Fig. 1. The temperature region where $M_r$ becomes negative is not too different from that where $\chi$ reaches maximal and begins to drop very slowly. The drop in $\chi$ clearly indicates that there are isolated particles whose magnetization can follow the external magnetic field like superparamagnetic materials. This indicates that the negative remanence is associated with the presence of the superparamagnetism of the system. However, the drop in $\chi$ does not follow $1/T$ behavior as expected for a superparamag-

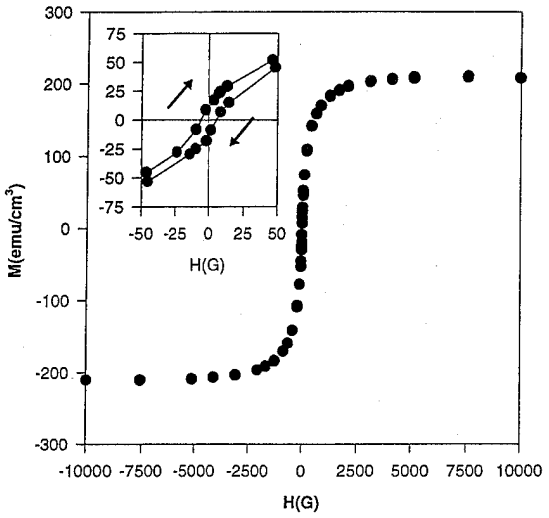



FIG. 1. Magnetization as a function of applied external magnetic field at 200 K for $x=0.55$. Inset shows the $M$-$H$ loop between ±50 G. Arrays indicate the sweep direction of the magnetic field.

 0021-8979/96/79(8)/6013/3/$10.00 © 1996 American Institute of Physics 

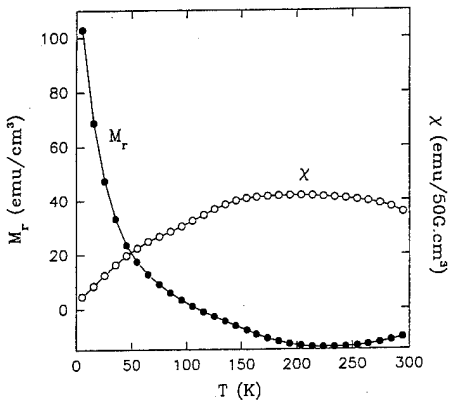



FIG. 2. Remanent magnetization and zero-field-cooled magnetic susceptibility as a function of temperature for $x=0.55$.

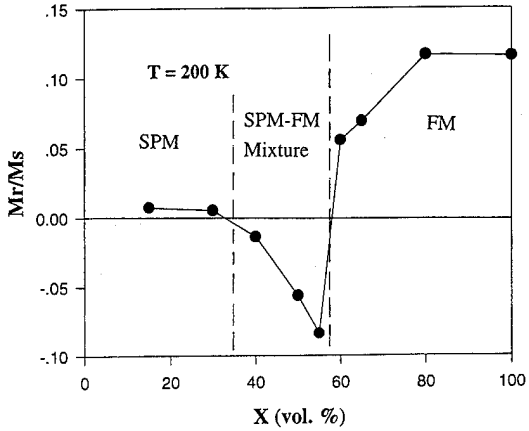



FIG. 3. The remanent magnetization at 200 K, normalized by the saturation magnetization in the positively applied field, vs $x$, the volume fraction of the magnetic particles.

netism with a uniform size distribution, due probably to the existence of a finite distribution of the particle sizes that lead to a finite distribution of $T_b$.[7]

Figure 3 shows the remanent magnetization, $M_r$, normalized by the saturation magnetization at 10 kG, $M_s$, as a function of $x$, at $T=200$ K. Notice that the value of $M_r/M_s$ starts from almost zero for $x\leqslant 0.3$ with a clear SPM behavior, becomes negative only for the nearly percolating films with $x$ between 0.4 and 0.55, and then changes back to a positive value for $x\geqslant 0.6$ with a FM behavior which is also conducting from the resistivity measurement. From the temperature dependence of $\chi$ for various $x$'s, one concludes that both $T_b$ and its uncertainty increase upon increasing $x$,[7] suggesting that the film with $x$ between 0.4 and 0.55 is likely in a SPM–FM mixture. The negative value of the remanence is larger than (the known) experimental error.[8] Thus the negative remanence might be associated with a special geometry of the magnetic nanostructures, in which both isolated and connected particles are present, corresponding to the SPM and FM components, and that the phenomenon disappears abruptly when the magnetic particles are percolated throughout the film. Systematic studies of temperature dependent remanence[9] and zero-field-cooled ac susceptibility at different frequencies[7] support this hypothesis.

The presence of a sizeable remanence signifies the presence of ferromagnetic component in the sample, and the negative value indicates that its magnetization response is in a direction opposite to the external field. One should note that similar phenomena, such as the reverse thermal-remanent magnetization, was observed in geological materials,[10] explained in terms of two components having different Curie temperatures,[11] and the inverted hysteresis loop in amorphous[12] and multilayered materials,[13,14] explained either in terms of interface exchange interaction[13,14] or exchange anisotropy.[15] It is important to note that the negative remanence is forbidden in magnetically homogeneous materials in which the magnetization is the order parameter to describe its thermodynamic state, and is possible only in magnetically inhomogeneous materials.

The nearly percolating granular films are compositionally uniform but magnetically inhomogeneous systems and the inhomogeneous is due to different magnetic responses of the particles of different sizes. From the labyrinth microstructure as displayed by TEM dark field images on nearly percolating films,[9] it is likely that there are connected particles which behave ferromagnetically with a finite coercivity and a finite positive remanence, and isolated particles which behave superparamagnetically with zero remanence and zero coercivity. Contrary to the interface exchange interaction[13,14] or the exchange anisotropy[15] models, we propose that the FM component was aligned antiparallel with respect to the magnetized SPM component due to the magnetostatic interaction.

By considering dipole–dipole interactions, let us demonstrate that such an opposite alignment is plausible if the anisotropically shaped FM particles are embedded in a SPM medium. Consider first the effective field created at the origin by a volume element $dV(=r^2dr\ dW=r^2\times dr\times\sin\theta\times d\theta\times d\varphi)$ at position $(r,\theta,\varphi)$, which has a form $M\times dV\times(1-3\cos^2\theta)/r^3$, where $M$ is the magnetization per unit volume of the uniformly magnetized SPM medium. After the integration in angle $\theta$ from 0 to $\pi$, this will lead to zero in a three dimension (3D). Thus for a uniformly magnetized medium of infinite size, the effective field inside the medium is zero. According to the superposition principle, the effective field in a needle hollow of a uniform medium should have the same value but opposite sign as in a uniform long needle. Here the term "needle" refers to the shape whose length is much larger than its diameter. Thus when there is a needle hollow in a uniformly magnetized medium of magnetization $M$, the effective magnetic field inside it is $-4\pi M$ for the field applied parallel to the needle axis. Placing a FM needle inside the hollow of the SPM medium, the total magnetic field, which is the sum of the effective field and the applied field $H_a$ on a FM needle, will be $-(4\pi\chi-1)H_a$, where $\chi=M/H_a$ is the magnetic susceptibility. For $4\pi\chi>1$, the magnetization of the FM needle can be opposite to the external field provided that the field is applied along the needle axis.

For nearly percolating films, the length of the connected particles is on the order of the percolation correlation length, which diverges when approaching the percolation threshold. Comparing to the diameter of the particle of about 5 nm, it is reasonable to consider the nearly percolating system as a

TABLE I. Local field on the FM component in the nanostructures.

| Type of magnetic nanostructures | Local Field on the FM | | Condition for negative remanence |
|---|---|---|---|
| | Parallel | Perpendicular | |
| 1. Oriented FM needles in a SPM matrix | $-4\pi M$ | $2\pi M$ | $4\pi M > H$, parallel to needles axis |
| 2. Nearly percolating FM particles | $-4\pi M$ | $-4\pi M$ | $4\pi M > H$, isotropic |
| 3. Oriented FM disks in a SPM matrix | $-\pi M$ | $2\pi M$ | $\pi M > H$, parallel to film planes |

composite consisting of FM needles randomly embedded in a SPM matrix. Due to the shape magnetic anisotropy energy, the magnetization direction of each FM needle is likely to be along its needle axis. Hence, needles with different orientations respond to an applied magnetic field independently. Among the FM needles, there are some that are oriented along the applied field with $\theta$ near 0. They will be aligned opposite to the rest of the sample under the applied field. They remain so after the applied field is removed and consequently there is a negative remanence. Thus, when $4\pi\chi > 1$, there could be a net negative remanence in the nearly percolating granular ferromagnetic composites. In this picture, when the FM particles are well connected throughout the system, the FM component starts to response coherently, the negative remanence will disappear abruptly. This hypothesis explains not only the presence of the negative remanence at 200 K but not at low temperatures, but also the dependence of $M_r/M_s$ on the volume fraction.

The local field on the FM component may be calculated in a few specific nanostructures as shown in Table I.[16] This two-component hypothesis predicts that (1) the anisotropically shaped FM particles are important for the observation of the negative remanence, and (2) in oriented FM disks in the SPM matrix where the total magnetization of the SPM is greater than that of the FM, negative remanence should be observed only for the field applied parallel to the disk plane. Subsequent experiments, which will be published elsewhere, show that (1) the negative remanence in these nearly percolating films disappears upon annealing samples for both $x=0.4$ and $x=0.55$, and (2) such a negative remanence was indeed observed predominately for the field applied parallel to the film plane of the SPM/FM multilayers which is the extreme case of oriented FM disks.

There may be a number of possible applications of the negative remanence or the antiparallel alignment of the SPM/FM composite in general. The presence of the antiparallel alignment point out a possible application of the SPM particles as a local magnetostatic shielding element for the FM storage units to achieve ultrahigh density with a controlled media noise. In such a proposed media structure, each FM storage unit is surrounded by the SPM particles whose magnetization may follow the dipole field of the FM unit. The dipole field of these surrounding SPM particles in the long range is in the opposite direction as that of the FM. Hence the effective dipole–dipole interaction in the long range is reduced, resulting in a reduced media noise. The feasibility of this new media structure may depend on the response time of the SPM particles as well as the magnetic ageing of the SPM–FM composite. This feasibility is now being evaluated.


[1] J. I. Gittleman, Y. Goldstein, and Bozowski, Phys. Rev. B **5**, 3609 (1972); B. Abeles, P. Sheng, M. D. Couts, and Y. Arie, Adv. Phys. **24**, 407 (1975); B. Abeles, H. L. Pinch, and J. I. Gittleman, Phys. Rev. Lett. **35**, 247 (1975).

[2] G. Xiao and C. L. Chien, Appl. Phys. Lett. **51**, 1280 (1987); A. Gavrin and C. L. Chien, J. Appl. Phys. **67**, 938 (1990); C. L. Chien, J. Appl. Phys. **69**, 5267 (1991).

[3] See articles in *Physical Phenomena in Granular Materials*, edited by G. D. Cody, T. H. Geballe, and P. Sheng (MRS, Pittsburgh, 1990).

[4] T. E. Schlesinger, R. C. Cammarata, A. Gavrin, John Q. Xiao, C. L. Chien, M. K. Ferber, and C. Hayzelden, J. Appl. Phys. **70**, 3275 (1991).

[5] M. R. Scanlon and R. C. Cammarata, J. Appl. Phys. **76**, 3387 (1994).

[6] A. B. Pakhomov, X. Yan, and B. Zhao, Appl. Phys. Lett. **67**, 3497 (1995); A. B. Pakhomov, X. Yan, and Y. Xu, this conference.

[7] B. Zhao, Y. Chow, and X. Yan, this conference.

[8] A remanent magnetic field is usually positive in a superconductor due to the trapped flux. But this trapped positive field in the superconducting solenoid could lead to a negative field of the order of 10 G in the sample space. This can cause error due to a finite dM/dH. In our experiments, Pd standard was measured subsequently and the results shown in the insert of Fig. 1 was after the field correction. However, we are not absolutely sure if such a correction is sufficient due to the remaining field error of about 1.5 G in our set-up and a large dM/dH for the sample than the Pd standard.

[9] Y. Xu, B. Zhao, and X. Yan, this conference.

[10] T. Nagata, S. Uyeda, and S. Akimoto, J. Geomagn. Geoelec. **4**, 102 (1952); **5**, 168 (1953).

[11] L. Neel, Adv. Phys. **4**, 191 (1955).

[12] G. Gruzalski, Ph.D. Thesis, University of Nabraska, Lincoln, 1978.

[13] C. Cao and M. J. O'Shea, J. Magn. Magn. Mater. **127**, 181 (1993).

[14] M. J. O'Shea and A. L. Al-Sharif, J. Appl. Phys. **75**, 6673 (1994).

[15] A. Aharoni, J. Appl. Phys. **76**, 6977 (1994).

[16] The same results can be obtained by considering bound current density at the interfaces.

# Preparation of Co–Fe–P amorphous fine needles with anodization technique and measurement of demagnetizing factor

A. Tayaoka, E. Tayaoka, and J. Yamasaki
*Department of Electrical Engineering, Kyushu Institute of Technology, Tobata, Kitakyushu Fukuoka 804, Japan*

The amorphous Co–Fe–P and crystalline Co fine needles with diameter 0.1–0.2 $\mu$m aspect ratio more than 100 were prepared successfully by applying the dc electrodeposition to the anodization technique and their demagnetizing factors were measured. It was found that the demagnetizing factor of film with needles decreases with increasing aspect ratio and tends to take low constant values around 0.07–0.08. To obtain the low demagnetizing factor by using the shape anisotropy of needle, it was estimated that the aspect ratio more than 100 is needed. The equivalent demagnetizing factor defined by a ratio of a field needed to achieve saturation to the averaged flux density is estimated around 0.6 for the film with Co–Fe–P amorphous needles with 0.1 $\mu$m diameter.
© *1996 American Institute of Physics.* [S0021-8979(96)05308-2]

## I. INTRODUCTION

Recently, electromagnetic micromachines have been developed and are expected to be applied in various fields. In such a small size machine, a magnetic field in narrow space is used to generate electromagnetic force, so that it is necessary to develop a thin film that can be magnetized with a low field in the direction normal to the surface. It is expected that such a film having the anisotropy perpendicular to the surface can be prepared by the anodization technique. When an aluminum film is anodized in acid solution, a thin aluminum-oxide surface having fine holes with their longitudinal direction normal to the surface is obtained. By depositing magnetic materials into the hole, a magnetic film that has fine magnetic needles with their longitudinal direction normal to the film surface can be prepared. The film thus made has the shape anisotropy with the easy axis normal to the film. So far, the anodizing technique has been applied to prepare the hard magnetic film for perpendicular recording.[1] In the conventional anodization technique, magnetic materials are commonly electrodeposited by using ac current, since Al oxide works as a dielectric material of a capacitor. However, the length of needles obtained by the ac deposition is limited to less than about 2 $\mu$m, because of the decrease in dielectric constant with deposition. On the other hand, films as thick as a few ten microns can be obtained by dc electrodeposition. Therefore, we tried to apply dc electrodeposition technique to anodized film by making an electrical contact through the aluminum oxide layer. In this study, we prepared amorphous Co–Fe–P and crystalline Co fine needles with high aspect ratio and evaluated the dependence of the demagnetizing factor on aspect ratio of needles.

## II. EXPERIMENT

An aluminum plate (99.99% pure, 20×20×0.5 mm) degreased and cleaned in advance was anodized to a depth of 30 $\mu$m in 0.3%-$(COOH)_2$ at a constant dc voltage of 120 V. The plate was anodized again in diluted $H_3PO_4$ at a constant minute current to make fine holes through Al oxide called barrier layer.[2] The expected cross section of thus treated Al plate is shown in Fig. 1. The fine holes in the barrier layer were confirmed by measuring electrical resistivity in ionic solution. Into the holes, Co–Fe–P amorphous alloy and crystalline Co were electrodeposited under the conditions with current density of 10 mA/cm$^2$ and 1 $p$H of solution. For the obtained needles scanning electron microscopy (SEM) observation, electron probe microanalysis (EPMA), and x-ray diffraction measurement were performed. The magnetic properties of the film was measured by a vibrating sample magnetometer (VSM).

## III. RESULTS AND DISCUSSION

Figure 2 shows the SEM views of (a) the top surface, (b) and (c) cross section of the Co–Fe–P needles electrodeposited in fine holes of anodized film. In anodizing technique, diameter and spacing of holes are a function of anodizing current and voltage, respectively. We chose the current and voltage higher compared to those used in conventional deposition to fabricate fine needles with large spacing, so as to give a large shape anisotropy. As seen in Fig. 2(a), the obtained fine needles have fairly good circular cross sections. Their averaged diameter and spacing are about 0.1 and 0.3 $\mu$m, respectively. In the cross section shown in Fig. 2(b), we can see that needles grown straight from the bottom of the Al substrate over 12 $\mu$m in length. The obtained needles have aspect ratio of about 120, which is about six times as large as that of needles fabricated by the ac anodization technique so far. The obtained needles have fairly uniform diameter as

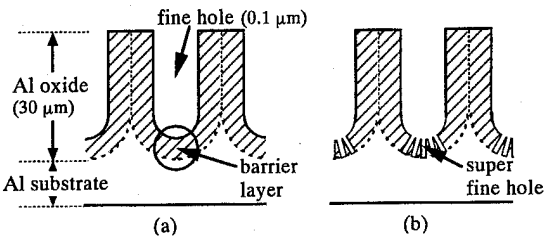



FIG. 1. Schematic diagram showing how super fine holes were made. (a) Before and (b) after making holes.

 0021-8979/96/79(8)/6016/3/$10.00 © 1996 American Institute of Physics

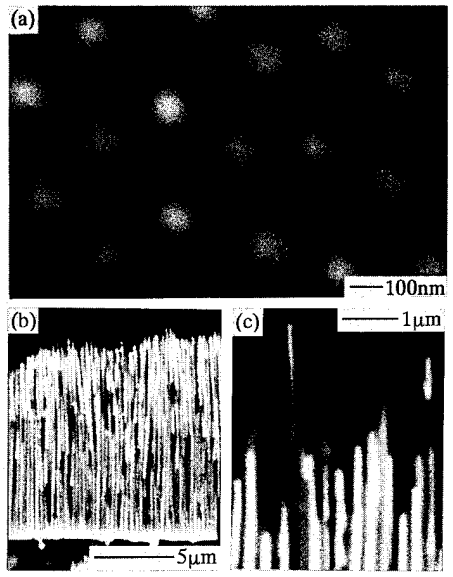



FIG. 2. SEM observation of magnetic needles deposited into holes of anodized films (a) for top surface and (b), (c) for cross section.

seen in enlarged cross section in Fig. 2(c). This was achieved by adjusting the ionic concentration of the solution to keep the resistivity nearly constant.

Figure 3 shows a result of EPMA analysis taken along a needle. The distribution of $P$ is fairly uniform. The EPMA data give a composition of the needle as $Co_{74}Fe_5P_{21}$. Thus, by applying dc deposition technique to anodizing film, it becomes possible to deposit P in fine holes. We tried especially to alloy P around 20% to obtain amorphous phase. This was achieved by keeping $p$H of solution around 1 $p$H. The x-ray diffraction shown in Fig. 4 indicates the obtained needles are amorphous, since there is no sharp peak based on crystalline except those of Al substrate. The magnetostriction of amorphous magnetic material is determined by the concentration ratio of Co to Fe.[3] Though the averaged composition is close to that with zero magnetostriction, the bottom of needles having higher Fe concentration would have positive magnetostriction around $3\times10^{-6}$.

Fine needles with a few microns spacing interact with each other through stray field, so the demagnetizing field of the anodized film would differ from that of a single needle. It is considered that magnetic interaction of fine needles depends on needle diameter so we prepare the needle changing diameter and evaluated the demagnetizing factor as a function of needle aspect ratio. For the evaluation of demagnetizing factor, we used Co fine needles prepared by the dc anodization technique, since the saturation magnetization of Co is strictly known and we do not need to care about compositional variation. Figure 5 shows the magnetization curve for polycrystalline Co needles measured in normal and parallel to the film plane. The Co needle has diameter of 0.1 $\mu$m and length of 12 $\mu$m. The film with needles can be saturated in the direction normal to the film with a field lower than that need to saturate in the parallel direction. To evaluate the demagnetizing field, a straight line was drawn parallel to the magnetization curve as shown in Fig. 5. From the extrapolation of that line to a saturation magnetization, we obtained the demagnetization field approximately. Using the measured demagnetization field and the saturation magnetization of Co of 17.9 kG ($4\pi$Ms), we determined the demagnetizing factor.

Figure 6 shows the demagnetizing factor of the films with Co needles as a function of aspect ratio with needle diameter as a parameter. The diameters of Co needles are 0.1 and 0.2 $\mu$m, respectively, and their spacing is 0.3 $\mu$m. The demagnetizing factor of an anodized film having 0.1 $\mu$m needles calculated by Masuda *et al.* is also shown.[4] The demagnetizing factor decreases with aspect ratio and tends to take a constant value beyond aspect ratio of 100. The constant values of the demagnetizing factor for needles with 0.1 and 0.2 $\mu$m needles are 0.07 and 0.08, respectively. The demagnetizing field that was produced with whole magnetic poles over the surface is not uniform along the length of a needle; it is high near the surface and decreases at the middle region of the needle. When the aspect ratio of a needle increases, it is inferred that the demagnetizing field of the middle region decreases while the demagnetizing field near the surface that has magnetic poles remains high. It seems that nearly constant demagnetizing factor for the aspect ratio beyond 100 is attributable to the high demagnetizing effect near the surface. The calculated demagnetizing factor is the value obtained by averaging the nonuniform demagnetizing

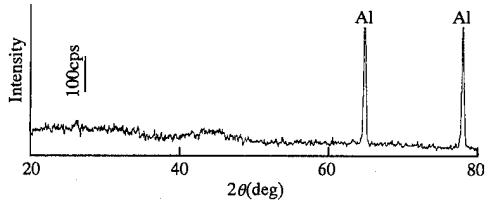



FIG. 4. X-ray diffraction diagrams of $Co_{74}Fe_5P_{21}$ amorphous anodized magnetic film, obtained by a conventional Cu$K\alpha$ diffractometer.

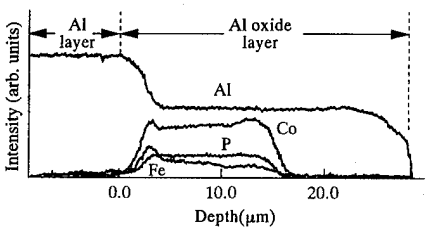



FIG. 3. EPMA line analysis for cross section of Co–Fe–P amorphous anodized magnetic film.

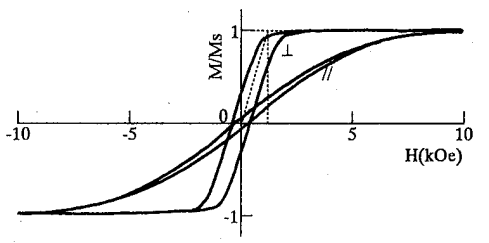



FIG. 5. Magnetization curves for Co anodized magnetic film, when magnetization in the direction normal (⊥) and parallel (||) to the film surface.

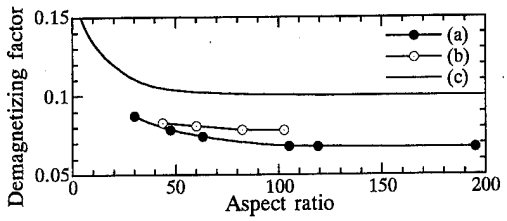



FIG. 6. Dependence of the demagnetizing factor on aspect ratio of Co fine needles (a) for 0.1 $\mu$m, (b) for 0.2 $\mu$m, and (c) for calculated result.

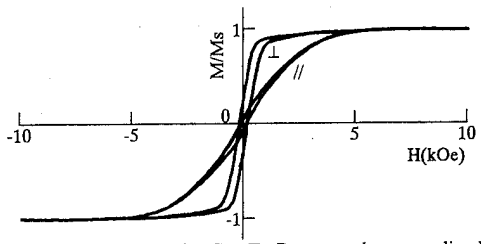



FIG. 7. Magnetization curves for $Co_{74}Fe_5P_{21}$ amorphous anodized magnetic film, when magnetization in the direction normal (⊥) and parallel (||) to the film surface.

field. As shown in Fig. 5, we evaluated the demagnetizing field from the magnetization curves by drawing a straight line. The obtained value corresponds to the demagnetizing field of the middle region of needles that is magnetized easily. This may give the big difference between the experimental and the calculated demagnetizing factors. Thus, the demagnetizing factor takes constant value with increasing aspect ratio. It is considered that the aspect ratio around 100 is enough to decrease the demagnetizing factor of the film using the shape anisotropy of needles.

Figure 7 shows the magnetization curve of the film with $Co_{74}Fe_5P_{21}$ amorphous needles whose cross section is shown in Fig. 2. The diameter and aspect ratio of the needle are 0.1$\mu$m and 120, respectively. The amorphous needles have the coercive force of 170 Oe, lower than that of the Co needles shown in Fig. 5. The needles packed in the fine holes may be highly stressed by the Al oxide. The relatively larger coercive force compared to other amorphous materials would be attributable to the residual stress. The demagnetizing factor of this film is around 0.068, almost the same as that of Co needles because of the same diameter and the aspect ratio. The film prepared by the anodization method partially consists of non magnetic material, so that the flux density averaged over the surface decreases markedly. The portion of magnetic materials of the present film is 12%, which gives averaged flux density of 1.44 kG. An external field of sum of the demagnetizing field of 700 Oe and the coercive force of 170 Oe are needed to obtain the flux density of 1.44 kG, so that the equivalent demagnetizing factor is estimated to be about 0.6. This value is expected to decrease down to 0.15 by the amorphous needle with 0.2 $\mu$m diameter using the demagnetizing factor shown in Fig. 6.

## IV. CONCLUSION

The amorphous Co–Fe–P and crystalline Co fine needles with aspect ratio more than 100 were prepared successfully by applying the dc electrodeposition to the anodization technique and their demagnetizing factors were measured. The results are summarized as follows: (1) The demagnetizing factor of film with fine needles decreases with increasing aspect ratio and tends to take low constant value around 0.07–0.08. (2) To obtain the low demagnetizing factor, the aspect ratio more than 100 is needed. (3) The equivalent demagnetizing factor defined by a ratio of field needed to achieve saturation to the averaged flux density is estimated around 0.6 for the film with Co–Fe–P amorphous needles with 0.1 $\mu$m diameter.

[1] K. Arai, H. W. Kang, and K. Ishiyama, IEEE Trans. Magn. **MAG-26**, 1635 (1990).
[2] Y. Fukuda and T. Fukushima, J. Surf. Finishing Soc. Jpn. **33**, 232 (1982), (in Japanese).
[3] R. C. O'Handley, Proceedings of the Second International Symposium on Amorphous Magnetism, New York, 1976.
[4] M. Masuda, S. Shiomi, and M. Shiraki, Jpn. J. Appl. Phys. **26**, 1680 (1991).

# Nonhomogeneous magnetization reversal in 2D Ising clusters

D. García-Pablos, P. García-Mochales, and N. García
*Física de Sistemas Pequeños (CSIC-UAM), Universidad Autónoma de Madrid, C-IX, Cantoblanco, E-28049-Madrid, Spain*

P. A. Serena
*Depto de Física de la Materia Condensada, Universidad Autónoma de Madrid, C-III, Cantoblanco, E-28049-Madrid, Spain*

We have performed Monte Carlo simulations on 2D circular Ising clusters, studying the distribution of the magnetization within the cluster as well as the magnetization reversal process when an applied external field is suddenly changed. We have shown that for highly anisotropic systems (the Ising-like limit), the magnetization reversal process is not uniform in a wide range of temperatures. Spins having a lower coordination at cluster edges drive the reversal process, acting as nucleation centers. We have found that there is a connection between the roughness transition temperature and the differences in the time evolution patterns of the magnetization. Our simulations agree with experimental results on magnetization reversal of single domain particles. © *1996 American Institute of Physics.* [S0021-8979(96)02708-2]

The study of the reversal magnetization of small particles has received much attention recently due to its broad range of technological applications.[1] Although the theory for the magnetization reversal was initially proposed by Néel,[2] based on the Stonner–Wohlfarth uniform rotation model,[3] recent experimental results[4,5] seem to contradict the basic assumptions of that model.

In the present work we have performed Monte Carlo (MC) calculations[6] in order to understand and characterize the behavior of the magnetization during the reversal process. We have simulated a small ferromagnetic particle by a two-dimensional (2D) circular cluster of radius $R$. Since MC simulations have been shown to be a useful method for describing experimental Ising-like systems,[6] we have considered that interactions among cluster spins are described via the Hamiltonian

$$\mathcal{H}=-J\sum_{\langle i,j\rangle} S_iS_j-H\sum_i S_i, \tag{1}$$

where $S_i$ represents the spin at the site $i$, the sum $\langle i,j\rangle$ is over all nearest neighbor pairs in the cluster, $J$ is the exchange constant, and $H$ is the applied magnetic field. In the present study a 2D square lattice has been considered.

The simulations were carried out following a method very similar to that used for analyzing the relaxation processes of metastable states in 2D infinite Ising systems.[7,8] For a system with radius $R$ and temperature $T$ we follow these steps: (i) Starting from a completely ordered configuration the cluster reaches thermal stabilization (using 2000–15 000 MC steps) in presence of an external magnetic field $H$ pointing out along the positive $z$ direction; (ii) $H$ is reversed (this is the zero of our time scale) and the cluster spins evolve towards a new equilibrium situation (which in general implies the magnetization reversal); (iii) steps (i) and (ii) are repeated $n$ times (in our case $400<n<800$) in order to achieve good statistics; (iv) the time evolution of a given quantity is calculated by averaging it over these $n$ independent runs. In particular we are interested in determining the evolution of the total magnetization $\langle m_z(t)\rangle$ as well as its behavior at different cluster regions. The number of MC steps (MCS) needed for reaching the new thermal equilibrium strongly depends on temperature, and in some cases (large radius and low temperatures) the whole reversal process needed above 60 000 MCS.

We have performed magnetization reversal computer experiments for clusters with $3\leqslant R\leqslant 60$ taking into account a wide range of temperatures ($1.2\leqslant k_BT/J\leqslant 2.3$) for two magnetic fields $H=0.05$ J and 0.1 J. In Fig. 1 we show a typical time evolution curve $\langle m_z(t)\rangle$ for a cluster with $R=25$ at $k_BT/J=1.9$, noticing that the evolution of the outermost crowns is different in magnitude to that of the inner ones, giving rise to a nonhomogeneous magnetization reversal process. It can be seen that when the magnetization of the outermost crown is zero, the inner crowns have not started the reversal process. This edge effect is characteristic of our cluster configuration, and cannot be found in 2D infinite systems.

In order to characterize the magnetization evolution we have studied the lifetime $t_r$, the time at which $\langle m_z(t_r)\rangle=0$. In Fig. 2 we show the dependence of $t_r$ with the temperature $T$ for different radii and for an external field $H=0.1$ J. It can be seen that in the range of temperatures we have considered, there is a well-defined exponential relation between $t_r$ and the temperature

$$t_r\propto\exp(E_a/k_BT), \tag{2}$$

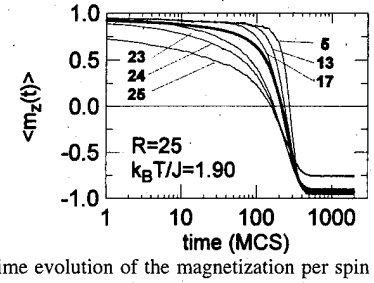



FIG. 1. Time evolution of the magnetization per spin at several distances $r$ from the cluster center ($r=5,13,17,23,24,25$) of a cluster with $R=25$ at $k_BT/J=1.9$. The initial field is $H=0.1$ J. Thick line represents the total magnetization.

 0021-8979/96/79(8)/6019/3/$10.00 © 1996 American Institute of Physics 

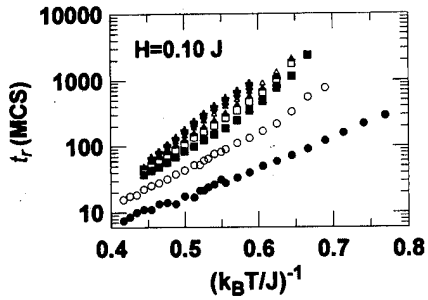



FIG. 2. Reversal lifetime $t_r$ as a function of the temperature for several cluster radii [$R=3$ (full dots), 5 (open dots), 10 (full squares), 15 (open squares), 20 (black triangles), 30 (open triangles), 40 (full diamonds), 50 (open diamonds), 60 (crosses)]. The applied field is $H=0.1$ J.

where $E_a$ is the activation energy. This indicates that we are considering the region where the reversal process is thermically activated.[2] In Fig. 3 we have represented the dependence of the activation energy on the cluster size. For small radii, there is a fast increase of the activation energy, but for $R>10$ the activation energy is almost independent of the cluster size. This behavior is different from that expected for systems described with the Stonner–Wohlfarth[3] model, where the activation energy is proportional to the cluster size. This anomalous dependence can be interpreted in terms of a more complex evolution than that of the uniform rotation, such as it has been shown in Fig. 1.

A second characterization of the reversal process has been done by fitting the average magnetization $\langle m_z(t)\rangle$ to the logarithmic law

$$\langle m_z(t)\rangle \approx A - S\,\log(t), \tag{3}$$

where $A$ is a constant and $S$ is the so-called magnetic viscosity that depends on the magnetic field, the temperature, and the cluster size. This logarithmic behavior is usually associated with a broad distribution of energy barriers.[9] Notice that Eq. (3) is used to represent the evolution of $\langle m_z(t)\rangle$ around $t=t_r$, so that the viscosity $S$ reflects the slope of the magnetization near the transition between positive and negative direction.

In Fig. 4 we have represented the values of $S$ as a function of the temperature for several cluster sizes, and for a fixed field $H=0.1$ J. The first remarkable fact is that $S$ presents a well-defined maximum for clusters with $R>8$, whereas for smaller radii $S$ does not present any structure.

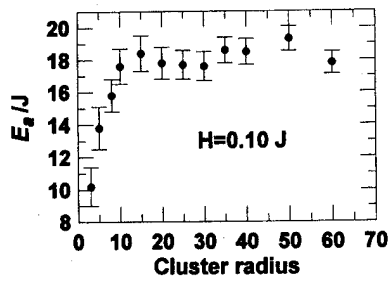



FIG. 3. Activation energy $E_a$ as a function of the cluster radius. The applied field is $H=0.1$ J.

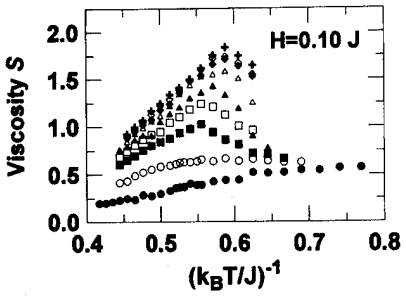



FIG. 4. Magnetic viscosity $S$ as function of the temperature for several cluster radii. Symbols correspond to those of Fig. 2.

We have found that the temperature $k_BT/J\approx 1.75$ represents a critical point separating two regions having different reversal mechanisms. Below this temperature the magnetization reversal is originated by the motion of a domain wall from a point of the cluster edge to another opposite point. Above the critical temperature the reversal is very noisy with a continuous nucleation in all the cluster regions, similar to that happening in infinite systems.[7,8] However, in both cases, spins at the cluster edge play a fundamental role, since the reversal process starts mainly at these points. These sites are nucleation points since they have lower magnetization and stronger fluctuations in comparison with the bulk sites.[10,11] These two different behaviors have been noticed in very thin layers with strong anisotropy with defects and domains mismatching.[12] The critical temperature $k_BT/J=1.75$ limiting these two regions with different time-reversal features is very close to the roughening transition temperature of a 2D Ising system with a free edge having a smaller exchange constant $J$.[13] In our model the exchange constant does not change anywhere, however the effective number of nearest neighbor particles at the cluster perimeter does suffer a considerable decrease with the subsequent decrease of the effective interaction. Therefore, we have found that in a wide range of temperatures the cluster edge acts as a nucleation center, due to the lower magnetization and large fluctuations at the edge particles.

Since the previous simulations can be interpreted as the time evolution of highly anisotropic systems, we have studied whether these 2D clusters satisfy the Néel law[2] which has recently been questioned by experimental results on elongated clusters with large anisotropy.[4,5] We have calculated the probability of not switching $P_{ns}(t)$, as defined in Ref. 4, i.e., the probability of finding at time $t$ the magnetic moment in the direction of the initially applied magnetic field, after a magnetic field inversion at $t=0$. Figures 5(a) and 5(b) show the curves $P_{ns}(t)$ for two radii ($R=5$ and $R=60$) and several temperatures, noticing that the exponential behavior (Néel law[2]) does not correctly describe the cluster reversal process for clusters with $R>10$, in agreement with experiments involving large clusters.[4] In particular, we should remark that the change of the probability is very steep, taking place in a relatively short time.

In conclusion, our simulations show that the magnetization reversal is not homogeneous for the wide range of temperatures we have considered, in good agreement with recent

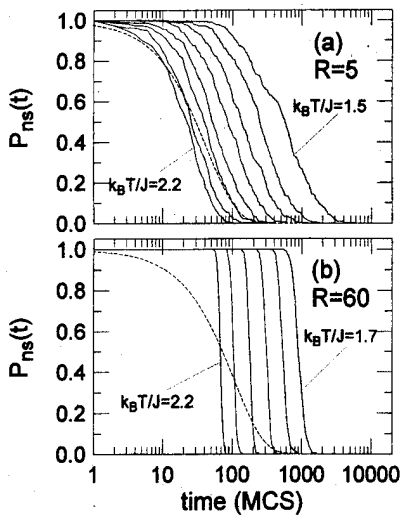



FIG. 5. Probability of not switching $P_{ns}(t)$ vs time, for two clusters with (a) $R=5$ and (b) $R=60$, at several temperatures. Only maximum and minimum $k_BT/J$ values are shown. The temperature change between two subsequent curves is $\Delta k_BT/J=0.1$. Dashed lines correspond to the best fit of the curve with $k_BT/J=2.0$ to the Néel law.

experiments on elongated single-domain particles.[4,5] Thus we can say that the collective motion of spins does not follow a simple path in the configuration space. This fact is reflected by the anomalous behavior of both the activation energy and the notswitching probability. We think that within this perspective, the theory and the interpretation of experiments that claim to have observed macroscopic quantum tunneling (MQT) of the magnetization for small particles,[14,15] on the basis of the coherent rotation model, may need further consideration, incorporating to the theoretical models the nonhomogeneous distribution of magnetization.

This work has been partially supported by the UE through a BRITE Project.

[1] J. L. Dormann and D. Fioriani, eds., *Studies of Magnetic Properties of Fine Particles and their Relevance to Materials Science* (Elsevier, New York, 1992).
[2] L. Néel, Ann. Geophys. **5**, 99 (1949).
[3] E. C. Stoner and E. P. Wohlfarth, Philos. Trans. Soc. London Ser. A **240**, 599 (1948).
[4] M. Lederman, D. R. Fredkin, R. O'Barr, S. Schultz, and M. Ozaki, J. Appl. Phys. **75**, 6217 (1994).
[5] M. Lederman, S. Schultz, and M. Ozaki, Phys. Rev. Lett. **73**, 1986 (1994).
[6] K. Binder and D. Stauffer, in *Applications of the Monte Carlo Method in Statistical Physics*, edited by K. Binder (Springer, Berlin, 1987).
[7] K. Binder and H. Müller-Krumbhaar, Phys. Rev. B **9**, 2328 (1974).
[8] H. Tomita and S. Miyashita, Phys. Rev. B **46**, 8886 (1992).
[9] R. Street and J. C. Wooley, Proc. R. Phys. Soc. London A **62**, 562 (1949).
[10] V. Wildpaner, Z. Phys. **270**, 215 (1974).
[11] K. Binder and P. C. Hohenberg, Phys. Rev. B **9**, 2194 (1974).
[12] J. Pommier, P. Meyer, G. Pénissar, J. Ferré, P. Bruno, and D. Renard, Phys. Rev. Lett. **65**, 2054 (1990).
[13] D. B. Abraham, Phys. Rev. Lett. **44**, 1165 (1980).
[14] P. C. E. Stamp, E. M. Chudnovsky, and B. Barbara, Int. J. Mod. Phys. B **65**, 1355 (1992).
[15] E. M. Chudnovsky and L. Gunther, Phys. Rev. Lett. **60**, 661 (1988).

# Alternating current (ac) susceptibility studies in Ni-$SiO_2$ granular film

B. Zhao, Jeff Y. Chow, and X. Yan
*Department of Physics, Hong Kong University of Science and Technology, Clear Water Bay, Kowloon, Hong Kong*

Alternating current (ac) magnetic susceptibility was measured as a function of frequencies (1 Hz–1 kHz) and temperatures (5–300 K) in nominal Ni-$SiO_2$ granular films for zero field cooled samples. When temperature is well below and well above the blocking temperature $T_b$, the real part of the susceptibility, $\chi'$, remains independent of frequency, while the imaginary part of the susceptibility, $\chi''$, is essentially zero within the experimental error. Near $T_b$, however, both $\chi'$ and $\chi''$ were found to be greatly enhanced, and $\chi'$ decreases with increasing frequency following $\log(f)$ dependence. A scaling method was applied for $\chi'(f,T)$ to determine the distribution of energy barriers and that of particle size. © *1996 American Institute of Physics.* [S0021-8979(96)40908-6]

## I. INTRODUCTION

The peculiar magnetic properties of granular materials attracted much attention in the last few decades.[1–3] The relaxation time $\tau$ of the total magnetic moments for a collective single-domain ferromagnetic particle system was determined by the ratio of anisotropy energy barrier $E_a$ and thermal energy $k_BT$, where $E_a$ is linearly proportional to the volume of the magnetic particle, if the surface anisotropy can be neglected. Many dc magnetic properties such as saturation magnetization, remanence, and susceptibility of granular system have been well investigated.[2,3] Recently, it was found that there is a negative remanence in the nearly percolating system,[4] and a giant Hall effect enhancement when metallic particles are about to percolate.[5] However, a comprehensive understanding of dynamic magnetic properties is still not well established, though some pioneer works have been done in the related system.[6,7] In the present article, we investigate the dynamic susceptibility of $Ni_x$-$(SiO_2)_{1-x}$ granular films with different magnetic volume fraction $x$'s. A scaling method was applied to determine the relaxation energy barrier distributions of samples with different $x$'s.

Using the classical probability of jumping over an anisotropy energy barrier, Neel[8] came up with a simple model where the relaxation time of magnetic moment of an individual granular particle is determined by $\tau=\tau_0\exp(E_a/k_BT)$, $E_a=KV$, where $E_a$, $K$, and $V$ are particle's anisotropy energy barrier, anisotropy constant, and volume, respectively, $k_B$ is the Boltzmann's constant, and $T$ is the absolute temperature. The pre-exponential factor $\tau_0$ is a constant, which is related to the gyromagnetic procession and may be estimated to be on the order of $10^{-10}$ s.[8] The temperature at which the magnetic moment relaxation time $\tau$ with mean volume size of a particle ensemble is equal to the measurement time $\tau_m$ is often called the blocking temperature $T_b$. Following Neel's theory, at high temperature, the magnetic moment relaxation time $\tau$ of the system can be so small that several flips may occur during the measurement time $\tau_m$. Therefore, when $T>T_b$, the magnetization of such an ensemble of particles will be zero in zero applied field, and will behave "superparamagnetically," the same as an ensemble of paramagnetic atoms.

Assuming that the magnetic moment of each particle is $\mu$ for an ensemble of $N$ particles, a time-dependent magnetization will have the following form: $M(t)=\nu(t)N\mu\tan h\{-[1-\exp(-t/\tau)]/k_BT\}$, where, $\nu(t)$ is a unit step function. Through Fourier transformation of the above equation, one can obtain ac susceptibility: $\chi(f)=\chi'(f)+i\chi''(f)=\chi^0(1+i2\pi f\tau)$, where $\chi^0=\mu^2V/3k_BT$ is the dc susceptibility of the system. Considering that the energy barrier has a finite distribution $n(E)$, the real part of ac susceptibility can be written as

$$\chi'(f,T)=\frac{\mu^2V}{3k_BT}\int_0^\infty dEn(E)\left(\frac{(1/\tau)^2}{(1/\tau)^2+(2\pi f)^2}\right).$$

Notice that the temperature differential of the bracket part of the above equation is a sharply peaked function of $E$ about the energy $E=k_BT\ln(1/2\pi f\tau_0)$, with width $\delta E=k_BT$, and can be approximated by a constant Dirac delta function. Thus, if $\chi'(f)$ versus temperature at different $f$'s are measured, the relaxation energy barrier distribution $n(E)$ as a function of scaling parameter $E=k_BT\ln(1/2\pi f\tau_0)$ can be obtained by numerical temperature differential of $T\chi'(f)$.[7] This method is called scaling method, and was considered to be one of the best methods to determine the energy barrier distribution, because (a) the measurement time $\tau_m$ is well defined, (b) the applied field is very weak, so that the modification of the anisotropy energy of individual granular particle and the perturbation to the system may be neglected, to the first approximation. The latter has a clear advantage compared to the analysis based on the remanence studies which perturb the system.[9]

## II. EXPERIMENTS AND RESULTS

Nominal granular $Ni_x(SiO_2)_{1-x}$ films were fabricated using a Denton magnetron rf sputtering system, where nickel and $SiO_2$ targets were mounted on two separate sputtering guns and the rotating silicon substrate was maintained at 150 °C. Films approximately 1 $\mu$m thick with nominal nickel volume fraction $x=0.3$, 0.4, and 0.5 were deposited after presputtering for 30 min. A detailed description of sample characterization can be found in Ref. 9. ac susceptibility $\chi(f)$ measurements (3 Oe zero-to-peak) as functions of frequency $f$(1, 2, 4, 10, 20, 40, 100, 200, 400, and 1000 Hz) and temperature $T$(5–300 K) after cooling samples ($x=0.3$, 0.4, and 0.5) in the zero field were performed using a Quantum Design MPMS-5 SQUID magnetometer. This instrument al-

 0021-8979/96/79(8)/6022/3/$10.00 © 1996 American Institute of Physics

TABLE I. Some parameters for nominal $Ni_x(SiO_2)_{1-x}$. $x$ is nominal nickel volume fraction. $E_0$ is the mean value of energy barrier, $\sigma$ is standard deviation of energy barrier distribution, $D_m$ is the mean particle diameter calculated from energy barrier, $D_{TEM}$ is measured particle diameter from TEM.

| $x$ | $T_b$ (K) | $T_b'$ (K) | $\tau_0$ (s) | $\sigma$ | $E_0$ (eV) | $D_m$ (nm) | $D_{TEM}$ (nm) |
|---|---|---|---|---|---|---|---|
| 0.3 | 27±3 | 26±1 | $0.360\times10^{-11}$ | 1.34±0.05 | 0.054±0.003 | 4.5±0.2 | 3.5±0.7 |
| 0.4 | 40±3 | 40±1 | $0.103\times10^{-10}$ | 1.48±0.06 | 0.083±0.004 | 5.1±0.2 | 5.4±1.1 |
| 0.5 | 80±3 | 82±2 | $0.244\times10^{-8}$ | 1.68±0.06 | 0.170±0.005 | 6.2±0.3 | 6.1±1.2 |

lows the simultaneous measurement of in-phase $\chi'(f)$ and out-of-phase $\chi''(f)$ components with a noise level below $10^{-7}$ emu. Also field cooled (FC) and zero field cooled (ZFC) dc susceptibility were measured to determine dc blocking temperature $T_b$ for different samples using the same magnetometer and the results were listed in Table I.

Figure 1 summarizes the real part of ac susceptibility as a function of temperature for sample with $x=0.3$ at four representative frequencies. In the insert, the real and imaginary part of ac susceptibility, $\chi'(f)$ and $\chi''(f)$, were plotted together at 10 Hz. The data show that both $\chi'(f)$ and $\chi''(f)$ were greatly enhanced near the blocking temperature and as the frequency increases, the peak of $\chi'(f)$ was decreased and was shifted to higher temperature. According to Neel's theory, at $T_b$, the relaxation time $\tau$ of isolated particles with mean particle size $V_m$ is equal to $\tau_m$ taken to be the half period of the applied field, namely, $\tau_m=\tau_0\exp(kV/k_BT_b)$. Thus, from the shift of $T_b$ with increasing measurement frequency, the pre-exponential factor $\tau_0$ was determined as shown in Table I. Since the fitting value of $\tau_0$ is not too different from $10^{-10}$ s for all samples, it may be considered physically reasonable.[7] And the slight increase of $\tau_0$ as increasing $x$ indicates that although the interaction of granular particle became more and more important as increasing $x$, the sample is still in the range in which Neel's theory is applicable. In Fig. 2, the relation between $\chi'$ and $\log(f)$ was plotted at three typical temperatures, namely, well below, well above, and near the blocking temperature $T_b$ for the sample with $x=0.3$. It is clear that (i) when temperature is well above and well below $T_b$, $\chi'$ is essentially frequency independent; (ii) when $T$ is near $T_b$, $\chi'$ decreases with increasing frequency following $\log(f)$ dependence. The reason for (i) is that when temperature is well below $T_b$, the magnetic moment relaxation time $\tau$ of the most particles in the sample were much larger than the measurement time $\tau_m$ which is determined by applied ac frequency. Thus the differences among $\chi'$ at different frequencies were so small that a constant $\chi'(f)$ was observed. When temperature is well above $T_b$, $\tau$ is much smaller than $\tau_m$, there are no differences among $\chi'$ at different measurement frequencies. However, near $T_b$, because $\tau_m$ is in the same order with $\tau$ for most particles, $\chi'$ was found to be much more sensitive to frequency. When frequency is higher, less particles can follow the ac field, hence $\chi'$ is smaller. Physically, $\log(f)$ dependence must be related to particle's energy barrier distribution form, because the broader the distribution, the less particles failed to follow the higher frequency field, leading to a smaller slope in the $\log(f)$ dependence. The inset of Fig. 2 shows $\chi'/\chi_0$ vs $\log(f)$ near the corresponding $T_b$ for different $x$'s. Note that the smaller the $x$, the larger the decreasing rate. Therefore, a sample with $x=0.5$ has the broadest energy distribution, a sample with $x=0.4$ has less, and $x=0.3$, the least. The numerical calculation[6] also indicates that for a broad lognormal distribution in a superparamagnetic system, the low frequency susceptibility can display linear $\log(f)$ behavior, and the broader the distribution, the smaller the slope of the $\log(f)$ dependence, which is in agreement with our experimental results.

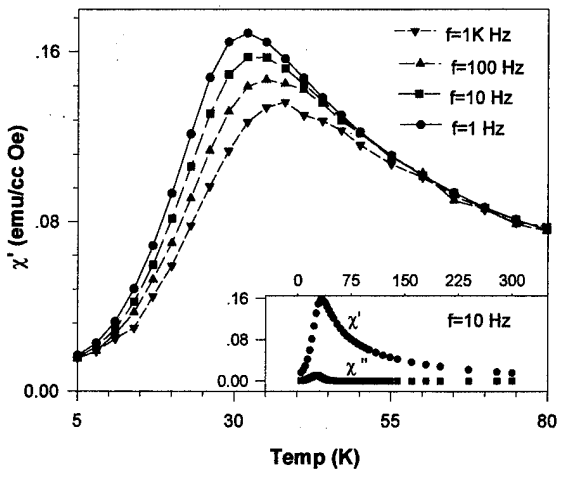



FIG. 1. $\chi'$ vs temperature for different frequencies for sample with $x=0.3$. Inset: $\chi'$ and $\chi''$ vs temperature for the same sample with 10 Hz frequency.

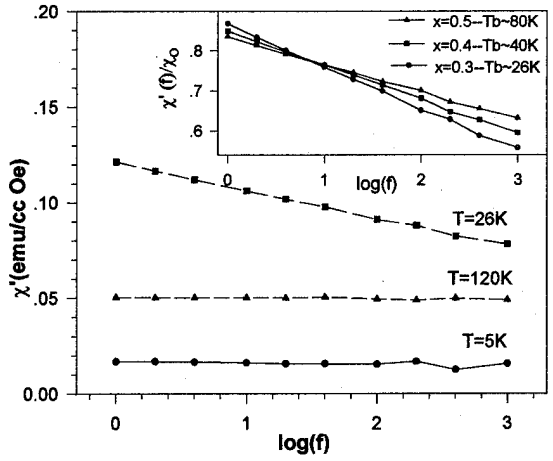



FIG. 2. $\chi'$ vs $\log(f)$ for sample with $x=0.3$, for three different temperatures. Inset: $\chi'/\chi^0$ vs $\log(f)$ at corresponding blocking temperature for samples with different $x$'s.

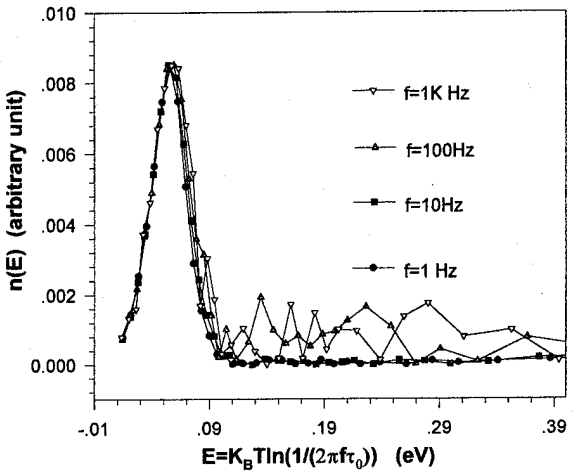



FIG. 3. Master curve of the energy barrier distribution as function of a scaling parameter $E=k_BT\ln(1/2\pi f\tau_0)$ which is obtained by the scaling method for sample with $x=0.3$.

The trend of increasing particles size distribution when increasing $x$ can also be obtained via the scaling method by numerical temperature derivative of $T\chi'(f,T)$ for different $f$'s. Figure 3 shows the master curve of $n(E)$ which describes the energy barrier distribution as a function of scaling parameter $E=k_BT\ln(1/2\pi f\tau_0)$ for magnetic volume fraction $x=0.3$ and the curve was fitted to a lognormal distribution:

$$n(E)=\left(\frac{1}{\sqrt{2\pi}E\ln\sigma}\right)\exp\left(-\frac{[\ln(E)-\ln(E_0)]^2}{2(\ln\sigma)^2}\right).$$

The fitting parameters of mean energy barrier $E_0$ and the standard deviation $\sigma$ were listed in Table I. Assuming that the energy barrier is entirely due to the volume of the particles, the same statement on the energy barrier can be said to the particle size. Taking 100 s as dc measuring time, dc blocking temperature and the mean energy barrier $E_0$ should be related according to $T_b'=E_0/25k_B$. One way to check the validity of this method of determining the distribution is to compare the calculated dc blocking temperature $T_b'$ with that determined by dc susceptibility measurement experiments, $T_b$, as shown in Table I. Note that the calculated $T_b'$ is consistent with experimental $T_b$ surprisingly well. Moreover, the trend of increasing $\sigma$ as $x$ increases is also consistent with the increasing slope in $\chi'$ vs $\log(f)$ near $T_b$. Also, the calculated mean particle diameter is similar to that obtained via TEM,[9] as can be seen in Table I.

## III. CONCLUSION

ac magnetic susceptibility measurement have been performed on $Ni_x(SiO_2)_{1-x}$ granular thin films with different magnetic volume fraction $x$. Near $T_b$, both $\chi'$ and $\chi''$ were found to be greatly enhanced, and $\chi'$ decreases with increasing frequency following a $\log(f)$ dependence. Also, the scaling method was used to obtain the energy barrier distribution.

## ACKNOWLEDGMENTS

The author would like to acknowledge the assistance of Dr. Y. Xu for the sample structure analysis and Dr. Jie Xhie and Mr. Silas Hung for film depositions. This project is supported by HKUST RI92/93.SC07 and HKUST 611/959.

[1] J. I. Gittleman, Y. Goldstein, and Bozowski, Phys. Rev. B **5**, 36009 (1972).
[2] G. Xiao and C. L. Chien, Appl. Phys. Lett. **51**, 1280 (1987).
[3] A. Carl, G. Dumpich, and E. F. Wassermann, Phys. Rev. B **50**, 48002 (1994).
[4] X. Yan and Y. Xu, this conference.
[5] A. B. Pakhomov, X. Yan, and B. Zhao (unpublished).
[6] E. M. Gray and R. Cysinski, J. Phys. Colloq. **C8-1851**, Supplement, Dec (1988).
[7] S. B. Slade, F. T. Parker, and A. E. Berkowitz, J. Appl. Phys. **75**, May (1994); S. B. Slade, Leon Gunther, F. T. Parker, and Ami. E. Berkowithz J. Magn. Magn. Mater. **140–144**, 661 (1995).
[8] L. Neel, Ann. Geophys. **5**, 99 (1949).
[9] Y. Xu, B. Zhao, and X. Yan, this conference.

*Published without author corrections*

# High coercivity single-domain particles in glass matrix

C. Tsang
*Department of Physics, Queens College of CUNY, Flushing, New York 11367*

H. D. Gafney and D. Sunil
*Department of Chemistry and Biochemistry, Queens College of CUNY, Flushing, New York 11367*

M. Rafailovich, J. Sokolov, and R. J. Gambino
*Department of Material Science and Engineering, State University of New York at Stony Brook, Stony Brook, New York 11794*

Impregnating transition metallic compounds into porous glass is a simple way to form ultrafine particles in a glass matrix. In our studies, ultrafine particles were prepared by impregnating Fe compounds into porous glasses (pore size 70±21 Å) and annealing. After annealing, the samples were studied at different temperatures with a vibrating sample magnetometer. In the annealed glasses two types of particles were formed: (a) superparamagnetic particles and (b) ferromagnetic particles with exceedingly high coercivity (Hc=13 kOe at 298 K). The ratio between superparamagnetic and high coercivity particles depends on the annealing temperature and time. In samples annealed at lower temperatures or at high temperature for short times, only superparamagnetic particles were found. In those annealed at high temperatures after certain times, only high coercivity particles were found. It was also found that the blocking temperature $T_B$ of the high coercivity particles depends on the annealing process. Moreover it was found that the Curie temperature of the high coercivity particles is below 520 K. © *1996 American Institute of Physics.* [S0021-8979(96)05408-9]

## I. INTRODUCTION

Decreasing the size of a magnetic particle changes its properties and presents interesting applications for magnetic storage. Nano-sized particles obtained from the decomposition of $Fe(CO)_5$ in porous glass yields superparamagnetic and ferromagnetic particles[1,2] and changing the surface contribution relative to the volume contribution of particles can enhance their coercivity.[3,4] The ratio of superparamagnetic to ferromagnetic particles, which exhibit exceedingly high coercivity (>10 kOe at room temperature), depends on annealing times and temperatures. Superparamagnetic particles are formed at low annealing temperatures, whereas high annealing temperatures results in glass consolidation and ferromagnetic particles.

## II. EXPERIMENTAL SECTION

Samples of Corning code 7930 Vycor glass (PVG) were impregnated with iron pentacarbonyl or iron nitrate by previously described vapor deposition[1,2] or solution adsorption technique. For consistency, the impregnated samples were broken into several pieces, and the individual piece was annealed for different temperatures and times.

The magnetization of the samples were measured with a DMS vibrating sample magnetometer with temperature control and up to a maximum field of 13 kOe.

## III. RESULT

The magnetic properties of iron impregnated PVG after consolidation are dependent on annealing conditions and the temperature (Fig. 1). At high temperatures, ≥150 °C, the coercivity drops to essentially zero at 200 °C (Fig. 1), and the magnetization decreases rapidly as the temperature increases from 200 to 250 °C. The hysteresis loops measured at 150 °C show that coercivity increases with increasing annealing time and temperature. Increasing the annealing time and temperature also reduces the superparamagnetism in the samples.

Previous studies[5] show that the consolidation of PVG begins at 900 °C, and the presence of absorptions at 1300 and 1900 nm, which are overtones of the surface hydroxyl indicate that samples annealed at 1000 °C are not fully consolidated. However, the extent of consolidation increases with annealing time and this affects the magnetic properties of the samples. With the exception of a slightly larger opening in the loop, samples annealed for one minute at 1000 °C exhibit essential identical loops when measured at 30 and −150 °C [Fig. 2(a)]. Increasing the annealing time to 60 min increases the hysteresis in the high-field region [Fig. 2(b)]. The shape of the hysteresis loop could be due to the superposition of a minor loop with high coercivity and a major with little hysteresis. This suggests that two different types of magnetic particles are present in the glass. One possesses a low coercivity, while the other possesses a temperature-dependent high coercivity.

## IV. DISCUSSION

Previous studies[6] show that $\gamma$-$Fe_2O_3$ is formed in a silica matrix when annealed at 900 °C, and Mössbauer spectra of the samples prepared in our experiments are also consistent with the presence of $Fe_2O_3$. This species is assigned to the superparamagnetic material in the glass. The nature of the ferromagnetic particles is not clear, but the Curie temperature indicates it is different from the bulk material. Figure 1 yields a Curie temperature below 250 °C, and in all samples

 0021-8979/96/79(8)/6025/3/$10.00 © 1996 American Institute of Physics 

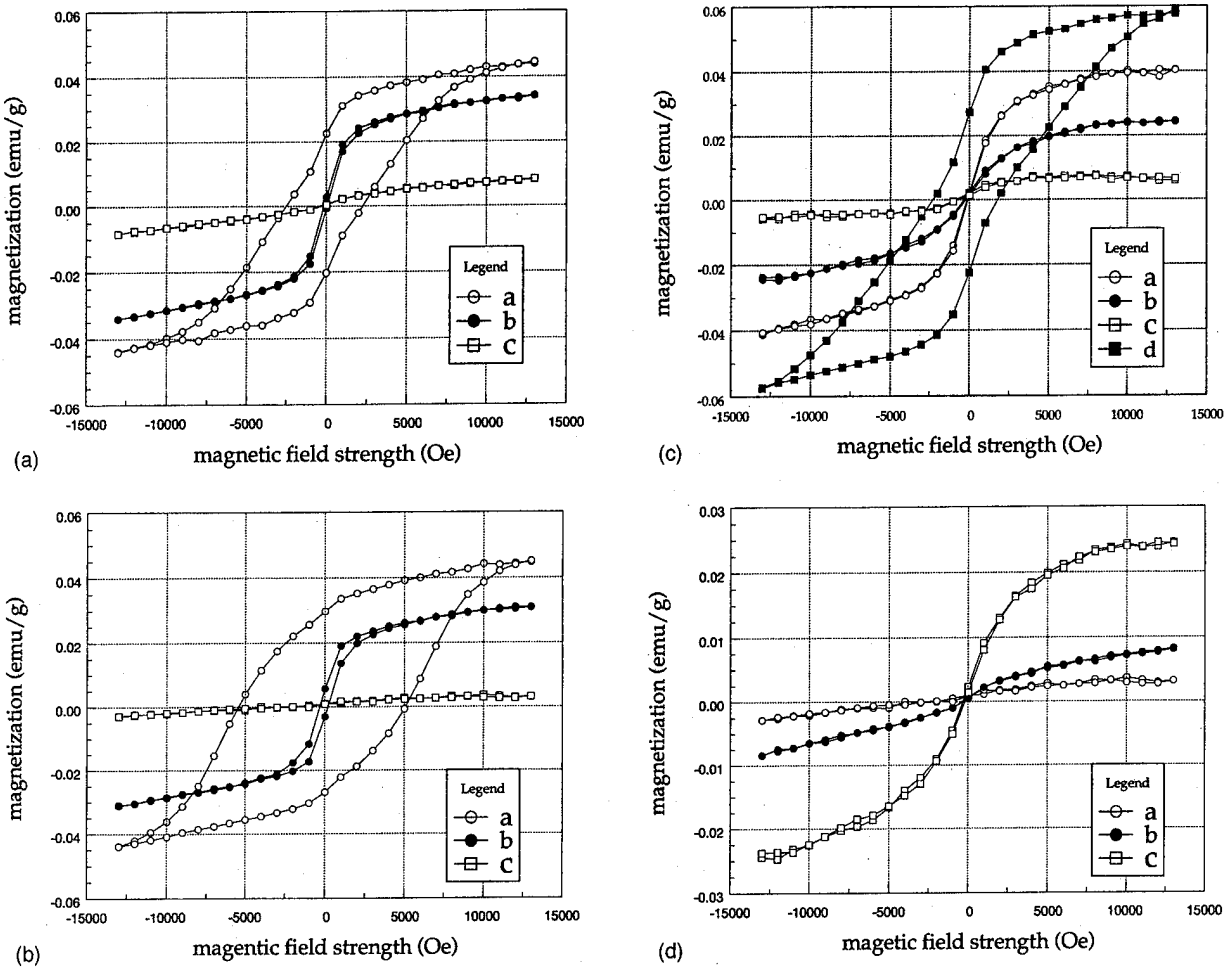



FIG. 1. (a) Magnetization curves of sample annealed at 1200 °C for 15 min at different temperatures: (a) 150 °C, (b) 200 °C, and (c) 250 °C. (b) Magnetization curves of sample annealed at 1200 °C for 90 min at different temperatures: (a) 150 °C, (b) 200 °C, and (c) 250 °C. (c) Magnetization curves of sample annealed at 1100 °C for 120 min at different temperatures: (a) 150 °C, (b) 200 °C, (c) 250 °C, and (d) 30 °C. (d) Magnetization curves at 250 °C of sample (a) annealed at 1200 °C for 90 min, (b) annealed at 1200 °C for 15 min, and (c) annealed at 1100 °C for 120 min.

examined in these experiments, the Curie temperature is below 350 °C. The latter is small in comparison to those reported for bulk iron oxides. The Curie temperature of the $Fe_3O_4$, for example, is 585 °C.

The blocking temperature of the ferromagnetic particle in these glass matrices increase with increasing annealing temperature and time. For a single domain particle, the blocking temperature is given by[7]

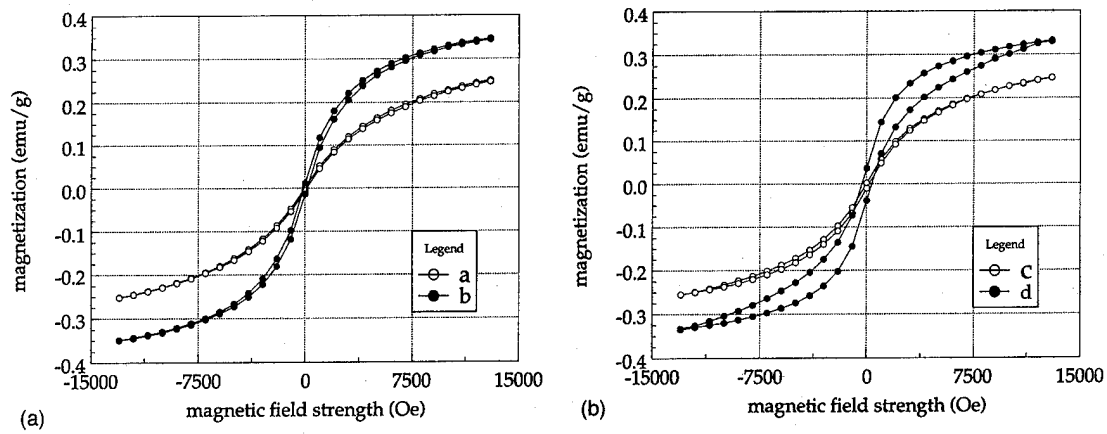



FIG. 2. (a) Magnetization curves of sample annealed at 1000 °C for 1 min at (a) 30 °C and (b) −150 °C. (b) Magnetization curves of sample annealed at 1000 °C for 60 min at (a) 30 °C and (b) −150 °C.

$KV/8 \cong 25 k_B T$,

where $K$ is the magnetic anisotropic constant, $V$ is the volume of the particle, $k_B$ is Boltzmann's constant, and $T$ is temperature. Since the blocking temperature increase with particle size, Figs. 1 and 2 suggest that the size of the ferromagnetic particles increases during the annealing. In addition, the different temperature dependencies of the ferromagnetic and superparamagnetic particles suggest that the consolidation of the matrix changes some of the superparamagnetic particles to ferromagnetic particles.

## V. CONCLUSION

Regardless of the precursor, impregnation of porous Vycor glass and subsequent annealing of the impregnated glass yields superparamagnetic and ferromagnetic particles that exhibit a high coercivity. The temperature dependence of these impregnated glasses suggests applications as magnetic storage materials where the field cooling method could be used to write data onto the material.


[1] D. Sunil, J. Sokolov, M. Rafailovich, B. Kotyuzhanskii, H. D. Gafney, B. J. Wilkens, and A. L. Hanson, J. Appl. Phys. **74**, 2768 (1993).
[2] N. F. Borelli, D. L. Morse, and J. W. H. Schreurs, J. Appl. Phys. **54**, 3344 (1983).
[3] S. Gangopadly, G. C. Hadjipanayis, C. M. Sorensen, and K. J. Klabunde, IEEE Trans. Magn. **MAG-29**, 2602 (1993).
[4] F. E. Spada, A. E. Berkowitz, and N. T. Prokey, J. Appl. Phys. **54**, 4475 (1991).
[5] Thomas H. Elmer, Ceram. Bull. **64**, 513 (1983).
[6] D. Niznansky, J. L. Rehspringer, and M. Drillon, IEEE Trans. Magn. **MAG-30**, 821 (1994).
[7] A. H. Morrish, *The Principles of Magnetism* (Wiley, New York, 1965), Chap. 7.

# Identification of a high-temperature magnetic phase transition in ball-milled and compacted nanocrystalline Fe-Cu alloys

R. D. Shull and J. P. Cline
*Materials Science and Engineering Laboratory, National Institute of Standards and Technology, Gaithersburg, Maryland 20899*

I. Baker and F. Liu
*Thayer School of Engineering, Dartmouth College, Hanover, New Hampshire 03755*

$Fe_x$–$Cu_{100-x}$ alloys ($40 \leqslant x \leqslant 90$) prepared by ball milling nominally pure (99%) Fe and Cu powders and warm compacted (at ~300 °C) were investigated by differential scanning calorimetry, scanning electron microscopy, x-ray diffraction, and magnetic susceptibility measurements. Both fcc and bcc diffraction peaks (indicative of pure Fe and Cu) showed that the mixtures were still two phase even after milling for 400 h, and that they were comprised of 6–10 nm diameter grains. Surprisingly, however, calorimetric measurements indicate the presence of a large endothermic peak for these nanocrystalline composites on heating near 600 °C and an exothermic peak near 400 °C on cooling. Magnetic measurements show that these materials are ferromagnetic at room temperature and remain so (with decreasing saturation magnetization) up to near the Curie point of $\alpha$-Fe, 770 °C. However, near 600 °C on heating (and also near 400 °C on cooling), the magnetic susceptibility indicates the existence of a magnetic phase change. High-temperature x-ray diffraction data show these effects are due to the oxidation of Fe to form magnetite which subsequently decomposes into wustite. The thermal hysteresis observed in the magnetic and thermal data is due to the sluggishness of the latter transformation. Furthermore, heating to temperatures in excess of 600 °C results in the dissolution of Cu into the iron oxides which does not reprecipitate on cooling. © *1996 American Institute of Physics.* [S0021-8979(96)05508-5]

## I. INTRODUCTION

Fine dispersions of magnetic particles in nonmagnetic matrices have been found to possess different magnetic characteristics than the same particles compacted together into a bulk material without the non-magnetic constituent.[1] In fact, the properties may be tailored by proper adjustment of the relative composition of the two species (an easy variable to control) and the thermal-magnetic treatment given the material. Applications of such materials to recording heads, high-density recording media, color reproduction, and magnetic refrigeration have been suggested.[2] One particularly exciting new effect found in multilayers[3] and thin granular metal films[4] of such composites is the "giant magnetoresistance (GMR) effect."[3] In a recent study to prepare bulk GMR-exhibiting Fe–Cu nanocomposites by ball milling and consolidation,[5] the presence of a magnetic transition near 600 °C (on heating) was indicated by magnetization measurements. As there is no equilibrium magnetic (or even crystallographic) phase change in this system at 600 °C,[6] it was suggested that the nanocrystalline morphology had reduced the $\alpha \rightleftarrows \gamma$-Fe transformation temperature in these materials. This effect would be similar to the reduction in the fcc$\rightleftarrows$hcp transformation temperature found in pure Co,[7] when prepared in the nanocrystalline state. In order to clarify the nature of this new magnetic transition in the Fe–Cu system, the present study was initiated.

## II. EXPERIMENTAL PROCEDURE

$Fe_xCu_{100-x}$ composites ($40<x<90$, atomic percents) were prepared by ball-milling powders of pure Fe (99.9% purity; average particle size <9 $\mu$m) and Cu (99% purity; average particle size <8 $\mu$m) in a 318-mm-diam steel tumbler mill using steel balls under a dry-nitrogen atmosphere for 400 h.[5] This method has previously been found successful for preparing fine dispersions of these materials in large quantities.[8] X-ray diffraction of the milled powders indicated the presence of three phases: $\alpha$-Fe, fcc Cu, and a little $Fe_3O_4$ (magnetite). From the widths at half maximum of the (110) and (111) diffraction lines for Fe and Cu, respectively, the average grain sizes were calculated using the Scherrer formula and found to range between 3 and 10 nm.[5]

Prior to measurement of the magnetic and thermal behavior of these composites, 18-mm-tall compacts were prepared by consolidation under a dry-nitrogen atmosphere inside a specially designed 8-mm-diam mold with a steel plunger, sealed with vacuum grease. Typically, the compacts were cold compacted at room temperature in an MTS model 810,[9] followed by warm compaction at 300 °C and 1.5 GPa for 5 h. X-ray diffraction of the compacted samples again only indicated the presence of $\alpha$-Fe, fcc Cu, and a small amount of $Fe_3O_4$. During consolidation the Fe and Cu grains increased to 11–13 nm and 6–9 nm, respectively. Following consolidation, the samples were analyzed using energy dispersive x-ray analysis (EDAXS) in a JEOL JXA-840II scanning electron microscope.[9] Since there were found to be significant variations from the nominal compositions, unless otherwise noted, all compositions in this paper are quoted in their analyzed atomic percentages. Differential scanning calorimetry (DSC) of the consolidated samples was performed in a Perkin–Elmer DSC 7 (Ref. 9) at a heating and cooling rate of 10 °C/min, and magnetization measurements were performed at elevated temperatures under flowing helium gas in a vibrating sample magnetometer using a boron

 0021-8979/96/79(8)/6028/3/$10.00 © 1996 American Institute of Physics

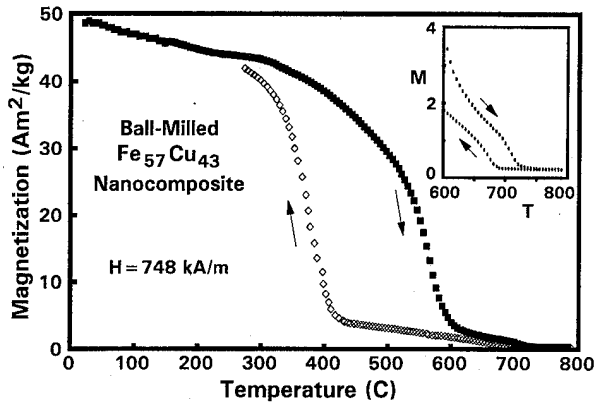



FIG. 1. Magnetization ($M$) vs temperature ($T$) for the ball-milled $Fe_{57}Cu_{43}$ nanocomposite measured during heating (filled symbols) and cooling (open/min symbols) at 2 °C as indicated by the arrows. The highest-temperature data (same units) are magnified in the inset.

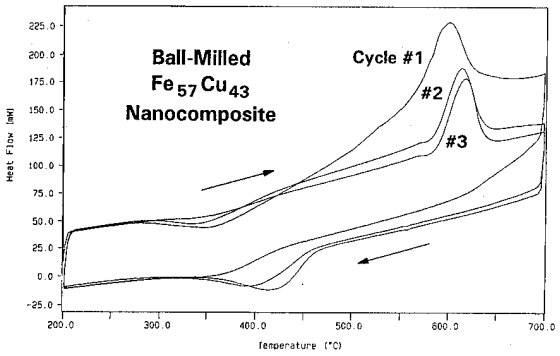



FIG. 3. DSC data vs temperature for the ball-milled $Fe_{57}Cu_{43}$ nanocomposite during heating and cooling (indicated by arrows) for three successive thermal cycles. "Upward" deviations are endothermic events.

nitride sample holder. High-temperature x-ray diffraction (HTXRD) was performed using Cu $K\alpha$ radiation in a Siemens D5000 theta-theta[9] diffractometer equipped with a Buhler 3000 K hot stage,[9] a Braun linear position sensitive detector, and a theta compensating slit. For this latter data, the 1 cm×1 cm×1 mm sample foil was placed on top of an $Al_2O_3$-coated Pt-heater strip surrounded by He gas, and each spectrum measurement took approximately 30 min.

## III. RESULTS AND DISCUSSION

Figure 1 shows the magnetization data measured at 748 kA/m (9.4 kOe) applied field for the $x=57$ nanocomposite. These data are similar to those measured in the earlier study[5] on a different sample. During heating there are two major features: (1) a large broad decrease in $M$ starting at near 400 °C and ending near 600 °C and (2) a smaller sharp decrease in $M$ at near 710 °C. Both features are suggestive of ferromagnetic to paramagnetic transitions. Also, since the magnetization changed by 93% in feature (1), the majority of the sample transformed between 400 and 600 °C. Indeed, the isotherms in Fig. 2 for this sample show that at room temperature the material is ferromagnetic and at 790 °C it is paramagnetic. However, as shown in the phase diagram for the major constituents,[6] Fe and Cu, at this composition there are no magnetic phase changes near 600 °C. Since the lattice constant of Fe in this sample was measured to be only 2.87 Å (only 0.15% larger than that of pure Fe), the 600 °C transition does not come from a Curie temperature ($T_C$) depression of $\alpha$-Fe due to increased solubility of Cu. The smaller sharp decrease in $M$ at near 710 °C, however, probably is due to the Curie point depression of $\alpha$-Fe due to the equilibrium 1% Cu solubility.

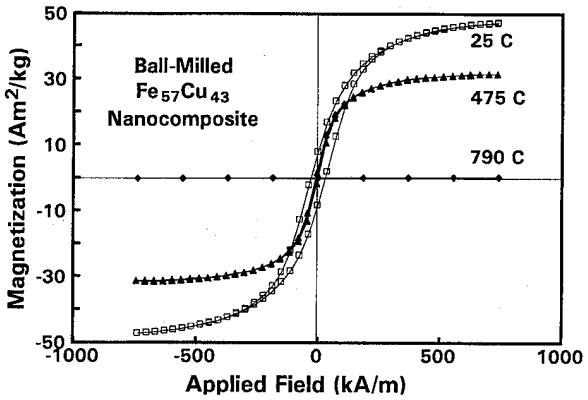



FIG. 2. Magnetization vs applied magnetic field isotherms for the ball-milled $Fe_{57}Cu_{43}$ nanocomposite measured at the indicated temperatures. The central temperature isotherm was measured following the first thermal cycle.

Similar to the magnetization heating data, the cooling data in Fig. 1 also show two prominent features: (1) a small sharp increase in $M$ at near 680 °C and a much larger sharp increase in $M$ beginning at near 400 °C. It is attractive to ascribe both these features to the same phenomena that cause the two drops in $M$ during heating, but with their transition temperatures displaced toward lower temperatures. If this assumption is true, then these features are not likely to be Curie temperatures. Furthermore, the measured hysteresis suggests that the magnetic effect is probably due to a crystallographic change between ferromagnetic and paramagnetic phases.

The DSC data for this sample, Fig. 3, further support the likelihood that the large features in the $M$ vs $T$ data are due to phase transformations. Notable are the endothermic reaction near 600 °C and the exothermic reaction near 425 °C which roughly repeat with thermal cycling. The similarity in the temperatures of these two arrests to the temperatures of the largest magnetic effects is suspiciously coincidental. For a first-order phase transformation between equilibrium crystallographic phases, one would expect these heat effects. However, no heat effect should occur at a Curie point since the ferromagnetic to paramagnetic transformation is of second order. Consequently, the magnetic phenomena occurring at 600 °C on heating and at 400 °C on cooling are unlikely to be Curie point effects. Also notable from the thermal data (and also measured in the magnetometer) is that this phase transformation is repeatable, indicating the transforming phases are stable with respect to the composition and morphology. Consequently, the possible explanation of the above results by a remarkable reduction (by a factor of 2) in the $\alpha \rightleftarrows \gamma'$ transformation of Fe from its equilibrium value of 1100 °C (since these two phases are ferromagnetic and para-

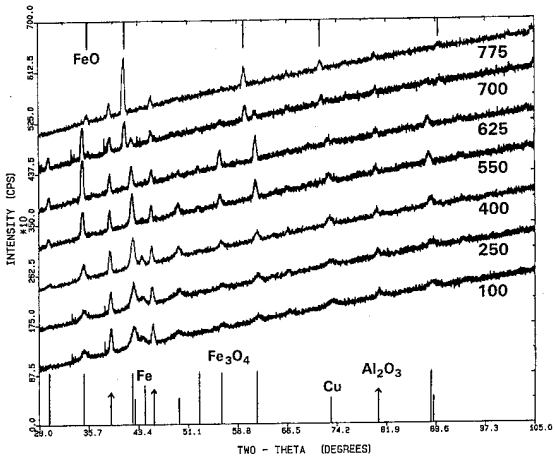



FIG. 4. X-ray diffraction data for the ball-milled $Fe_{57}Cu_{43}$ nanocomposite, measured during heating at the indicated temperatures. The baselines have been shifted for clarity. Peak identification (by length of indicator line) appears at the bottom and top. The arrows refer to peaks from the sample substrate, $Al_2O_3$.

magnetic, respectively) is not likely.

HTXRD data provide the most definitive results on the identification of the unknown magnetic transformations described above. Figure 4 shows that during heating of the 57% Fe nanocomposite, much of the $\alpha$-Fe oxidizes to $Fe_3O_4$ between 550 and 625 °C[10] followed by a dissolution of Cu into the magnetite at temperatures up to 700 °C to form $[Fe(Cu)]_3O_4$. Consequently, the large decrease in $M$ observed near 600 °C is a combination of the $\alpha$-Fe transforming to the less magnetic $Fe_3O_4$ and the subsequent ferromagnetic $\rightleftarrows$ paramagnetic transition of magnetite at its Curie point: 580 °C. Surprisingly, the HTXRD data show that the large endothermic reaction seen in the DSC data at near the same temperatures as the large magnetic transition on heating does not derive from the same cause, but comes from the slightly higher temperature (700 to 775 °C[10]) transformation of the Cu-containing magnetite into a paramagnetic Cu-containing wustite, [Fe(Cu)]O. Without Cu present, this transformation would occur at 570 °C, only 10 °C different from the $T_C$ of magnetite.[11] Cu dissolution, however, does occur in both the magnetite and wustite as indicated by the shift in all the Bragg peaks for these phases to lower angles because of the larger Cu atoms. On cooling, the x-ray data show that the [Fe(Cu)]O does not transform back to $[Fe(Cu)]_3O_4$ until between 625 and 550 °C,[10] i.e., 150–200 °C below that observed during heating. This hysteresis has been observed in the binary Fe-O system,[11] and explains the thermal hysteresis effect observed in the DSC and magnetic data. For the latter data, the large increase in $M$ observed on cooling near 400 °C is due to the creation of the ferromagnetic magnetite from the paramagnetic wustite. In the final transformation of [Fe(Cu)]O to $[Fe(Cu)]_3O_4$ (near 550 °C[10]) during cooling, Cu-containing hematite, $[Fe(Cu)]_2O_3$, is also formed. It is interesting to find that on further cooling, no Bragg peaks for the fcc Cu were observed, indicating that the thermal cycling resulted in all the Cu being contained in the magnetite and hematite.

For an 87% Fe nanocomposite, only a 30 percent magnetic arrest was observed near 600 and 450 °C during heating and cooling respectively while a 60 percent effect was measured during both heating and cooling at near 780 °C. Consequently, it appears that in this more concentrated Fe sample only some of the Fe oxidized to form magnetite during heating, and the two magnetic transitions again reflect the Curie points of magnetite and $\alpha$-Fe, consistent with the data described above for the 57% Fe sample.

## IV. CONCLUSION

Ball-milled and compacted $Fe_xCu_{100-x}$ nanocomposites ($40 \leqslant x \leqslant 90$) are ferromagnetic at room temperature and become paramagnetic at temperatures between 700 and 780 °C depending on their composition. During heating they will oxidize (externally and internally) if all processing (e.g., milling, compaction, and sample transfers) and measurements have not been performed to preclude contact with air and water vapor. The unexpected magnetic transition observed earlier near 600 °C is due to the Curie point of magnetite and its phase transformation into paramagnetic wustite. Heating to temperatures in excess of 600 °C results in the dissolution of Cu into the iron oxides. Furthermore, once the Cu is dissolved in the oxides, it does not reprecipitate on cooling. Care should consequently be taken in the thermal treatment of these and other nanocomposites.

## ACKNOWLEDGMENTS

The authors would like to thank A. J. Shapiro and P. Washington for performing the EDAXS and low-temperature x-ray diffraction measurements, respectively. This work was partially supported by NSF Grant No. DMR-9022824.

[1] *Magnetic Properties of Fine Particles*, edited by J. L. Dormann and D. Fiorani (Elsevier, Amsterdam, The Netherlands, 1992).
[2] J. Q. Xiao, J. S. Jiang, and C. L. Chien, Mater. Res. Soc. Symp. Proc. **286**, 197 (1993); R. D. Shull, U. Atzmony, A. J. Shapiro, L. J. Swartzendruber, L. H. Bennett, W. J. Green, and K. Moorjani, J. Appl. Phys. **63**, 4261 (1988); J. K. Vassiliou, V. Mehrotra, M. W. Russell, E. P. Giannelis, R. D. McMichael, R. D. Shull, and R. F. Ziolo, *ibid.* **73**, 5109 (1993); R. D. McMichael, R. D. Shull, L. J. Swartzendruber, L. H. Bennett, and R. E. Watson, J. Magn. Magnn. Mater. **111**, 29 (1992).
[3] M. N. Baibich, J. M. Broto, A. Fert, F. Nguyen van Dau, F. Petroff, P. Etienne, G. Creuzet, A. Friedrich, and J. Chazelas, Phys. Rev. Lett. **61**, 2472 (1988).
[4] A. E. Berkowitz, J. R. Mitchell, M. J. Carey, A. P. Young, S. Zhang, F. Spada, F. T. Parker, A. Hutten, and G. Thomas, Phys. Rev. Lett. **68**, 3745 (1992); J. Q. Xiao, J. S. Jiang, and C. L. Chien, *ibid*, **68**, 3749 (1988).
[5] I. Baker and F. Liu, J. Nanostructured Mater. **7**, 13 (1996).
[6] *ASM Handbook*, Vol. 3 (American Society for Metals, Materials Park, OH, 1992) p. 168.
[7] A. R. Thölen, *Phase Transitions*, Vols. 24–26 (Gordon & Breach, UK, 1990), p. 375.
[8] J. S. Benjamin, Sci. Am. **234**, 40 (1976); J. Eckert, J. C. Holzer, C. E. Krill, III, and W. L. Johnson, J. Mater. Res. **7**, 1980 (1992); A. R. Yavari, P. J. Desre, and T. Benameur, Phys. Rev. Lett. **68**, 2235 (1992); H. J. Fecht, R. Hellerstern, Z. Fu, and W. L. Johnson, Metall. Trans. A **21A**, 2333 (1990).
[9] Trade names are used for informational purposes only. Their use does not constitute an endorsement by NIST or the US Government.
[10] The increased 100 °C x-ray determined transformation temperatures are felt to be due to the differences between surface and bulk transformation kinetics.
[11] *Phase Diagrams of Binary Iron Alloys* (American Society for Metals, Materials Park, OH, 1993), p. 280.

# Steps in the hysteresis loops of a high-spin molecule

Jonathan R. Friedman and M. P. Sarachik
*Department of Physics, The City College of New York, New York, New York 10031*

J. Tejada
*Facultat de Física, Universitat de Barcelona, 08028 Barcelona, Spain*

J. Maciejewski and R. Ziolo
*Wilson Research Center, Xerox Corporation, Webster, New York 14580*

We report the first observation of steps in the hysteresis loop of a high-spin molecular magnet. We propose that the steps, which occur every 0.46 T, are due to thermally assisted resonant tunneling between different quantum spin states. Magnetic relaxation increases dramatically when the field is in the neighborhood of a step. A simple model accounts for the observations and predicts a value for the anisotropy barrier consistent with that inferred from the superparamagnetic blocking temperature. © *1996 American Institute of Physics.* [S0021-8979(96)41008-0]

## INTRODUCTION

The large-spin molecule $Mn_{12}O_{12}(CH_3COO)_{16}(H_20)_4$, has been the subject of much experimental[1–5,10] and theoretical[6,7] work since it was first synthesized by Lis[8] in 1980. This molecule (often referred to as $Mn_{12}$) contains four $Mn^{+4}$ ($S=3/2$) ions and eight $Mn^{+3}$ ($S=2$) ions. Experiments[1] indicate that it has an $S=10$ ground state. These molecules crystallize into a tetragonal lattice in which magnetic interactions between molecules are thought to be negligible.[3] All experimental work[1–5,10] to date on this system indicates that it has a large magnetocrystalline anisotropy. Superparamagneticlike behavior has been reported.[1–4] Below a blocking temperature of ~3 K, hysteresis is observed[3,5] and slow exponential relaxation of the magnetization has been found[3] with relaxation times that obey an Arrhenius law, $\tau = \tau_0 e^{\Delta E/k_B T}$, down to 2.1 K; studies[4,10] at temperatures down to 175 mK show deviations from this form that have been interpreted as possible signs of temperature-independent quantum tunneling.

In this article, we report the observation of steps in the hysteresis loops of a powdered sample of $Mn_{12}$. We suggest that the steps are manifestations of thermally assisted, field-tuned resonant tunneling through the molecule's anisotropy barrier. We show that the relaxation rate increases dramatically when the applied field is tuned to a field at which one of the steps occurs.

## EXPERIMENTS AND RESULTS

The sample was prepared following the published procedure[8] and was then ground into a powder consisting of submicron-sized crystallites. The powdered sample was mixed into Stycast 1266 and allowed to set in a field of 5.5 T at 300 K. This served to orient the crystallites suspended in the epoxy such that their easy axes aligned with the field due to the anisotropy of the susceptibility tensor. No corrections were made for the diamagnetism of the epoxy, which was considered negligible. The dc magnetization measurements were taken at temperatures between 1.7 and 15 K with a Quantum Design MPMS5 magnetometer equipped with a 5.5-T superconducting magnet.

Figure 1 shows the hysteresis loops taken with the field applied along the easy axis of the oriented sample at six different temperatures from 1.7 to 2.8 K, as indicated. The steps in the loops are clearly visible. In contrast, no steps were seen in a control sample prepared in the absence of a field. It is noteworthy that after the system is saturated and the field is reduced back to zero field, the curve is temperature independent and no steps are apparent. The steps occur only at specific values of magnetic field. The inset to Fig. 1 shows the field at which a step occurs plotted versus step number, where the steps are labeled by integers and the fields plotted are the points in the hysteresis curves where the slope, $dM/dH$, is maximal. The excellent linear fit indicates that a step occurs at approximately every 0.46 T. If data from all temperatures are used, then a total of seven steps, including the one at zero field, are observed and it is quite possible that more would be seen at lower temperatures. We note that as temperature is lowered, steps that were apparent at higher temperatures seem to disappear. These steps can still be observed, however, if the rate at which the field is swept is

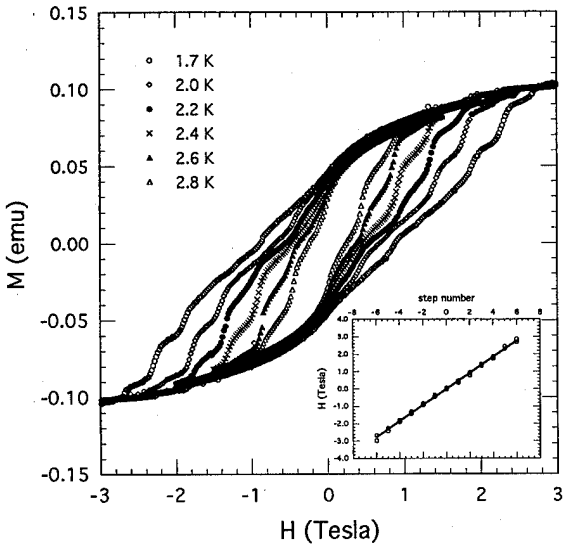



FIG. 1. Hysteresis loops of $Mn_{12}$ for six different temperatures, as shown. The inset shows the fields at which steps occur as a function of step number. The straight line is a least-squares fit.

 0021-8979/96/79(8)/6031/3/$10.00 © 1996 American Institute of Physics 

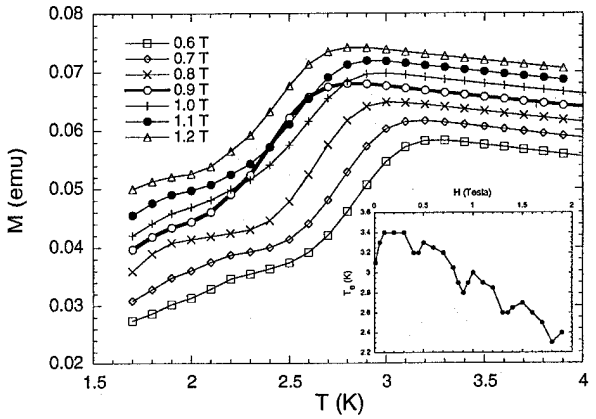



FIG. 2. Zero-field-cooled data for seven different measuring fields. The data for 0.9 T (bold line) is anomalous, shifting abruptly toward lower temperatures. The inset shows the superparamagnetic blocking temperature, $T_B$, as a function of magnetic field. The anomalous dips occur at approximately the same fields as the steps in the hysteresis loops.

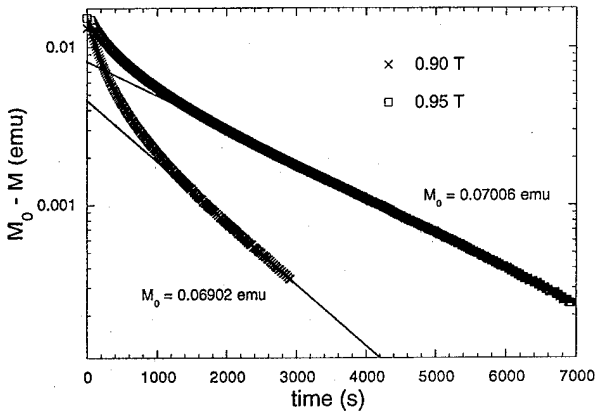



FIG. 3. Magnetic relaxation at 2.4 K plotted on a semilogarithmic scale. After cooling in zero field, a field of 0.9 or 0.95 T was applied, as indicated. $M_0$ is the asymptotic value of the magnetization; the straight lines indicate exponential behavior for $t>2000$ s.

reduced sufficiently. Similar steps have been observed[9] at 0.6 K in $[Fe(OMe)_2(O_2CCH_2\ C1)]_{10}$, a molecular paramagnet comprised of a ring of $Fe^{3+}$ ions which order antiferromagnetically and exhibit no hysteretic effects. Our results appear to be the first observation of such steps in a hysteretic molecular system.

In Fig. 2 we show magnetization data of the $Mn_{12}$ sample after it was cooled from 5 to 1.7 K in zero field and then measured in an applied field as the temperature was raised. Data for seven different measuring fields, as indicated, are shown. (Some curves at other fields were omitted for clarity.) As expected for a superparamagnetic system, the blocking temperature $T_B$ (the temperature of the curve's maximum) decreases systematically as the measuring field is raised. However, the curve at 0.9 T shifts abruptly toward lower temperatures. In the inset, we show the blocking temperature as a function of magnetic field from 0.01 to 1.9 T. Superimposed on the monatonic decrease of these temperatures with increasing field are several sharp dips. These dips occur at approximately the same fields as the steps in the hysteresis loops of Fig. 1. Ignoring these anomalous dips, we extrapolate the zero-field blocking temperature to be ~3.5 K. This corresponds to an energy barrier, $\Delta E$, of 45 $cm^{-1}$.

An interesting feature of the zero-field-cooled curves is that some of them cross: in Fig. 2, one can see that within a certain temperature range the magnetization attains a higher value at 0.9 than at 1 T and sometimes even 1.1 T. This implies that the relaxation rate of the system must be significantly faster at the lower field value than at the higher ones. Direct evidence for this is provided in Fig. 3, where we have plotted the difference between the magnetization and its asymptotic value, $M_0$, as a function of time on a semilogarithmic plot. The curves show the relaxation of the magnetization after the sample was cooled to 2.4 K in zero field and then exposed to a field of 0.9 or 0.95 T, as marked. There is a dramatically faster relaxation rate at 0.9 than at 0.95 T. During the initial ~2000 s, the magnetization decays faster than exponentially. The data for $t \geq 2000$ s can be fitted very well to an exponential, $M = M_0(1 - e^{-(t-t_0)/\tau})$, as shown by the straight lines in Fig. 3. The fit yields time constants, $\tau$, of 1048 and 2072 s at 0.9 and 0.95 T, respectively.

## DISCUSSION

We suggest that the observed steps are due to thermally assisted resonant tunneling between quantum spin states in the $Mn_{12}$ system. In zero field, the molecule has two degenerate ground states, corresponding to the spin being parallel ($m=S$) or antiparallel ($m=-S$) to the easy axis. An anisotropy barrier separates the states and a magnetic field breaks the symmetry, making one state a true ground state and the other a metastable ground state. This model is illustrated in Fig. 4. When an excited level in the right well is resonant with the metastable $m=S$ ground state on the left, transitions across the barrier are induced. Once the system has crossed the barrier, there is presumably a rapid spontaneous decay from the excited state to the ground state. In this way the metastable state is depleted and the system enters the $m=-S$ state.

The simplest Hamiltonian for this system is

$$\mathcal{H} = -DS_z^2 - g\mu_B \mathbf{S}\cdot\mathbf{H}, \tag{1}$$

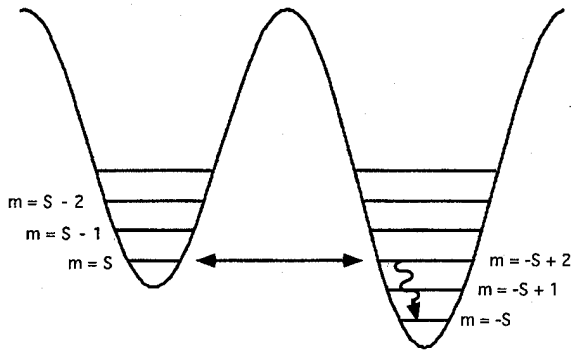



FIG. 4. A schematic representation of the resonant tunneling mechanism proposed to explain the observations. Tunneling from the metastable state $m=S$ to an excited state $m=-S+n$ is followed by a rapid spontaneous decay into the ground state.

where $D$ represents the anisotropy energy that breaks the zero-field Zeeman degeneracy. If the field is applied along the easy axis, then the eigenstates of this Hamiltonian are $|S,m\rangle$. The first term in Eq. (1) implies that the ground state will be $m=\pm S$, as expected; the sign depends on the direction of the field. For clarity, we take $|S,S\rangle$ as the initial state of the system. We propose that a step occurs when the energy of this state is equal to the energy of a state on the other side of the anisotropy barrier. A simple calculation reveals that the field at which the state $|S,S\rangle$ crosses the state $|S,-S+n\rangle$, is

$$H_{S,-S+n}=\frac{-Dn}{g\mu_B}. \tag{2}$$

Thus, steps occur at even intervals of field, as observed. Interestingly, when the field is tuned such that the metastable ground state in the left well is resonant with a state in the right well, all of the excited states in the left well are also resonant with states on the other side of the barrier. Thus, a multiple resonance is set up whenever the field is tuned to a step. Using the fact that a step occurs every 0.46 T, we find $D/g=0.21$ cm$^{-1}$, which is consistent with the published values[1] of $D\sim0.5$ cm$^{-1}$ and $g\sim1.9$ cm$^{-1}$. As a further check of this model, we can estimate the size of the anisotropy barrier: at zero field, the barrier is $g(D/g)S^2\sim41$ cm$^{-1}$, consistent with the estimate of 45 cm$^{-1}$ obtained above from the blocking temperature data. Given that $S=10$ in this system, there should be exactly 21 steps ($n=0$–20), the last corresponding to the elimination of the barrier. Measurements at lower temperatures are needed to observe additional steps.

As noted above, as temperature is reduced, any given step becomes less prominent and the transition rate decreases rapidly. This implies that the resonant tunneling mechanism responsible for the steps is thermally assisted. It is possible that acoustic phonons provide the angular momentum necessary for the transition between different spin states. As temperature is lowered, the population of phonons (or other excitations) drops and the transition rate decreases. More work is needed to understand precisely what role thermal excitations play in this resonant process.

We would like to stress that the above model of field-tuned, thermally assisted resonant tunneling out of a metastable spin state explains many of the observations presented herein. When the field is reduced from saturation, no steps are seen because the system is already in the true ground state $m=S$. It is only when the field is reduced to near zero or reversed that the state becomes metastable allowing resonant transitions and the corresponding steps. The higher-numbered steps have progressively faster magnetic relaxation times since the tunnel barrier is lowered by the applied field.

In summary, we have found steps in the hysteresis curves of $Mn_{12}O_{12}(CH_3COO)_{16}(H_20)_4$ and propose that they result from thermally assisted resonant transitions between spin states. The magnetic relaxation rate of the system increases dramatically when the field is tuned to a step; that is, when there is a level crossing. A simple model has been proposed that accounts for the even interval of field between neighboring steps and is in quantitative agreement with measurements of the anisotropy barrier.

*Note added in proof:* Since we submitted this manuscript, two papers[11,12] have appeared on $Mn_{12}$, reporting anomalously fast relaxation rates at zero field[11,12] and 0.3 T.[12] Novak and Sessoli[12] suggest that these results are due to thermally assisted resonant tunneling. A similar suggestion has been made previously by Barbara *et al.*[10] to explain the zero-field anomaly.

## ACKNOWLEDGMENTS

We would like to thank Dariusz Przybylski for assistance in preparing some control samples and Eugene Chudnovsky, Snezana Bogdanovich, and Dana Calistru for useful conversations. This work was supported by the Air Force Office of Scientific Research under Grant No. F49620-92-J-0190.

[1] A. Caneschi, D. Gatteschi, R. Sessoli, A. L. Barra, L. C. Brunel, and M. Guillot, J. Am. Chem. Soc. **113**, 5873 (1991).
[2] R. Sessoli, H.-L. Tsai, A. R. Schake, S. Wang, J. B. Vincent, K. Folting, D. Gatteschi, G. Christou, and D. N. Hendrickson, J. Am. Chem. Soc. **115**, 1804 (1993).
[3] R. Sessoli, D. Gatteschi, A. Caneschi, and M. A. Novak, Nature **365**, 141 (1993).
[4] C. Paulsen, J.-G. Park, B. Barbara, R. Sessoli, and A. Caneschi, J. Magn. Magn. Mater. **140–144**, 379 (1995).
[5] C. Paulsen, J.-G. Park, B. Barbara, R. Sessoli, and A. Caneschi, J. Magn. Magn. Mater. **140–144**, 1891 (1995).
[6] J. Villain, F. Hartman-Boutron, R. Sessoli, and A. Rettori, Europhys. Lett. **27**, 159 (1994).
[7] P. Politi, A. Rettori, F. Hartmann-Boutron, and J. Villain, Phys. Rev. Lett. **75**, 537 (1995).
[8] T. Lis, Acta Cryst. B **36**, 2042 (1980).
[9] K. L. Taft, C. D. Delfs, G. C. Papaefthymiou, S. Foner, D. Gatteschi, and S. J. Lippard, J. Am. Chem. Soc. **116**, 823 (1994).
[10] B. Barbara, W. Wernsdorfer, L. C. Sampaio, J. G. Park, C. Paulsen, M. A. Novak, R. Ferré, D. Mailly, R. Sessoli, A Caneschi, K. Hasselbach, A. Benoit, and L. Thomas, J. Magn. Magn. Mater. **140–144**, 1825 (1995).
[11] C. Paulsen and J. G. Park, in *Quantum Tunneling of Magnetization*, edited by L. Gunther and B. Barbara (Kluwer, Dordrecht, 1995), pp. 189–207.
[12] M. A. Novak and R. Sessoli, in *Quantum Tunneling of Magnetization*, edited by L. Gunther and B. Barbara (Kluwer, Dordrecht, 1995), pp. 171–188.

# Computer simulation of microstructure and interaction effects in fine particle systems (abstract)

G. N. Coverdale and R. W. Chantrell
*Keele University, Keele, Staffordshire ST5 5BG, United Kingdom*

M. El-Hilo and K. O'Grady
*University College of North Wales, Bangor, Gwynedd, United Kingdom*

The behavior of the magnetization of a fine particle system is partly determined by the interaction effects between the grains. In a previous study by El-Hilo *et al.*,[1] the magnetic particles were considered to be randomly distributed. Many fine particle systems are expected to exhibit a microstructure that has been influenced by intergrain interactions. This effect on the microstructure will be important during the formation of the solid where the magnetic particles exhibit significant mobility. We have developed a 3D Monte Carlo model of a fluid dispersion which after reaching equilibrium is then allowed to "freeze" to produce a fine particle system with microstructures which vary from clusters in the case of zero field to chains of particles in the saturated field case. This provides an excellent model system for the study of interaction effects. Our previous model[1] is then used to study the resulting magnetic properties of the materials. These include the remanence curves in addition to the hysteresis loops. The local microstructure is shown to have a significant effect on the $\delta I$ plots which are often used to characterize interaction effects. The simulation of the systems in a solid matrix exhibits an interaction dependent magnetic after effect. Because of the interaction fields, the magnetic configuration also changes with time following a change in temperature leading to a "waiting time" dependence of magnetic properties, an effect also found in spin glasses. © *1996 American Institute of Physics.* [S0021-8979(96)63308-2]

[1]M. El-Hiro, K. O'Grady, and R. W. Chantrell, J. Appl. Phys. **76**, 6811 (1994).

# Periodic breathing oscillations and instabilities in ferrofluids (abstract)

Weili Luo and Tengda Du
*Department of Physics, University of Central Florida, Orlando, Florida 32816*

Periodic breathing oscillations and instabilities are observed in diffraction patterns of ferrofluids in the presence of a magnetic thermal lens effect. The results crucially depend on (1) the boundary conditions, (2) the strength of external magnetic field, (3) the concentration of magnetic particles, and (4) the thickness of the sample layer. There is a critical field above which instabilities occur. Under a semifree surface boundary condition, the observed oscillation frequency $\omega$ is found to vary with external magnetic field according to $\omega \sim H^{1/2}$ for small field. In the confined geometry, diffraction patterns show random rotation of various shapes between $H_{c1}$ and $H_{c2}$. The mechanisms responsible for these phenomena will be discussed. © *1996 American Institute of Physics.* [S0021-8979(96)63408-7]

The work is partially supported by NSF DMR and the NSF Young Investigator award (Luo).

 0021-8979/96/79(8)/6034/1/$10.00 © 1996 American Institute of Physics

# Effects of Zn ion on magnetic properties of $Fe_3O_4$ magnetic colloids (abstract)

C. H. Lin
*Department of Materials Science, National Tsing Hua University, Hsinchu, Taiwan, Republic of China*

P. C. Kuo and J. L. Pan
*Institute of Materials Science, National Taiwan University, Taipei, Taiwan, Republic of China*

D. R. Huang
*Opto-Electronics and Systems Laboratory, ITRI, Chutung, Hsinchu, Taiwan, Republic of China*

The effects of Zn ion on magnetic properties $Fe_3O_4$ magnetic colloids were investigated in this study. $Fe_3O_4$ magnetic colloids were produced by the chemical coprecipitation method, i.e., mixing an acidic solution containing $FeCl_2 \cdot 4H_2O$, $FeCl_3 \cdot 6H_2O$, $ZnCl_2 \cdot 4H_2O$, with a NaOH alkali solution at 70 °C, and then centrifuging them from the mixed solution. Various reaction times, solution $p$H values, and Zn ion contents were also used. $Fe_3O_4$ magnetic fluid was obtained by adding ammonium oleate into the mixed solution, precipitating the colloids from the solution, neutralizing the colloids by hydrochloric acid, and dispersing the colloids in $n$-hexane. XRD, EDX, TEM, and VSM were used to determine the structure, chemical compositions, particle sizes, and magnetic properties of the colloids and the magnetic fluid. The spinel colloids was easily form at a higher $p$H value in solutions where the $p$H value ranged from 7 to 12. $Fe_3O_4$ colloids were completely formed within the first minute of mixing and the particle size of $Fe_3O_4$ colloids did not increase with time after the first minute. The lattice parameter of $Fe_3O_4$ colloids increased linearly with the Zn ion content because the diameter of Zn ion is larger than that of Fe ions. The particle size of $Fe_3O_4$ colloids was found to be 10 nm by TEM. For an initially fixed Zn content of 8 wt % in solutions, the Zn content in the $Fe_3O_4$ colloids ranged from 3.32 wt % at $p$H=5 to a maximum value of 7.85 wt % at $p$H=10. Later, it reduced to 7.51 wt % at $p$H=12 because Zn ion has the lowest solubility at $p$H=10. At 8 wt % of zinc ion in the solution, the $\sigma_s$ of the $Fe_3O_4$ colloid increase sharply from 0 at $p$H=3 to 92 emu/g at $p$H=8 and then reach a maximum value of 94 at $p$H=10. The $\sigma_s$ value and $H_c$ value of the $Fe_3O_4$ colloid were found significantly improved by adding a suitable amount of Zn ions, e.g., ranging from 70 emu/g and 48 Oe at Zn=0 wt % to a maximum 94 emu/g and 50 Oe at Zn=7.14 wt %. Later they reduced to 70 emu/g and 44 Oe at Zn=12.52 wt % when prepared at $p$H=10. The $\sigma_s$ value of the magnetic fluid was found linearly proportional to the colloid content in the magnetic fluid. For a colloid containing 7.51 wt % of Zn ion, the $\sigma_s$ value of the magnetic fluid is 9.8 emu/g at 25 wt % of colloid. © *1996 American Institute of Physics.* [S0021-8979(96)82708-1]

# Measurements of local magnetization by Kerr effect on Si-Fe nonoriented sheets

S. Defoug and R. Kaczmarek
*SUPÉLEC, Plateau de Moulon, 91192 Gif-sur-Yvette, France*

W. Rave
*Institut für metallische Werkstoffe, I.F.W. Dresden, Postfach, 01171 Dresden, Germany*

Magnetic domains have been visualized by Kerr effect on nonoriented silicon-iron sheets. A simple methodology on how to determine the surface magnetization is proposed. For complex patterns, this method provides interesting results which could not be obtained by any reasoning based on physical principles. © *1996 American Institute of Physics.* [S0021-8979(96)75708-3]

## I. INTRODUCTION

Domain analysis on nonoriented silicon-iron sheets are virtually nonexistent. We found only one picture of magnetic domains visualized by Kerr effect on a Si-Fe sample[1] which may correspond to stress patterns either induced by polishing or by a considerable disorientation of the grain.

Other studies[2,3] forecast complex and hard to interpret magnetic structures due to the disorientation of the grains in nonoriented steels.

For interpretation of such images, an analytic method is necessary to determine the magnetic orientation in each domain. Using the Kerr effect observations, Hubert, Schäfer and Rave[4,5] developed a method that consisted of taking two pictures of the sheet for two different incident polarization, each with the same excitation. This method was successfully tested on materials that show high magnetic contrast such as permalloy and grain-oriented silicon-iron sheets.

However, the method is reliable only if the pictures can be normalized by comparing them with saturated images in several directions. Sometimes the saturation cannot be achieved even in high fields, which introduces inaccuracies. With high field values the Faraday effect can be disturbing. Also, this method is not very fast because about sixteen images must be recorded sequentially, with the polarizers being readjusted in between. This time-consuming procedure can enhance the optical, thermal, and magnetic instability of the measurement bench.




FIG. 1. Magnetic domains on *N.O.* Si-Fe.

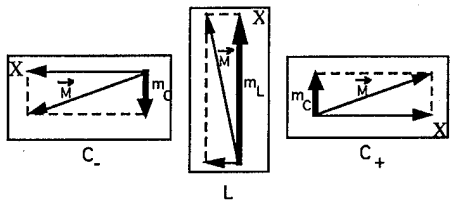



FIG. 2. The different positions of the sample.

In their last relevant study[6] the authors concluded that the method has proven to be of limited usefulness in practice. They proposed a modified method where the calibration procedure was replaced by the interactive assignment of magnetization directions to certain domains (at least to three domains) for which the magnetization directions are known. However, this specific requirement limits the method application.

The drawbacks of both methods have prompted us to look for a simple, reliable, and general strategy. That method would be of more practical application for the nonoriented silicon-iron steels, such as those used in the construction of electrical turning machines. First, however, the regular magnetic domains on this type of material should be visualized.

## II. VISUALIZATION OF MAGNETIC DOMAINS ON NONORIENTED SHEETS

The tests conducted until recently in our lab as well as the bibliography[5,7] have shown that the use of a saturated image as a reference image does not give a satisfying contrast because of the difficulty to entirely saturate the polycrystalline samples and due to the electro-dynamic and optical parasite effects which appear near saturation.

TABLE I. Grey levels on the subtracted pictures.

| Position of the sample s | | |
|---|---|---|
| Lengthwise ($L$) | (1a) | $\Delta n_L = \alpha . I_0 m_L$ |
| Crosswise (+90°) | (1b) | $\Delta n_{c+} = \alpha . I_0 m_C$ |
| Crosswise (−90°) | (1c) | $\Delta n_{c-} = -\alpha . I_0 m_C$ |

 0021-8979/96/79(8)/6036/3/$10.00 © 1996 American Institute of Physics

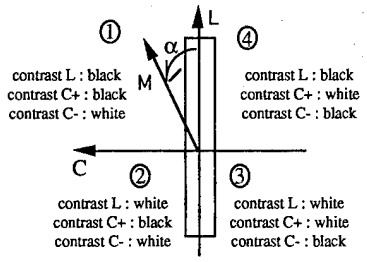



FIG. 3. $(L,C)$ base.

We chose to use the magnetic averaging[8] as the way to obtain the reference images from the samples in a periodically varying excitation field. The utilization of such a reference image enables direct visualization of the domains on nonoriented Si-Fe sheets as shown in Fig. 1.

On this kind of images the different levels of black and white zones correspond to the different orientations of the magnetization. Yet, measurements of the magnetic contrast obtained inform us about only one component of the domain's magnetization. In some easy cases, we can deduce the direction of the magnetization from physical principles (flux closure, minimum magnetic poles) which govern the magnetization of this material.

The visualization of regular domains on Si-Fe sheets being no problem any more we have elaborated an original general method for the determination of the magnetic direction at each point of the acquired images.

## III. DETERMINATION OF THE DIRECTION OF MAGNETIZATION

For soft materials, the calculations prove the polar magnetization component to be negligible. It was also verified experimentally by positioning the aperture diaphragm in the center of the back focal objective, where only the polar Kerr effect should be observable and no contrast was found.

Unlike the cited authors[4,5] who combined the optical information from two different incident polarizations, using both longitudinal and transverse Kerr components to determine the planar magnetization components, we used only the longitudinal effect combined with a 90° rotation of the sample.

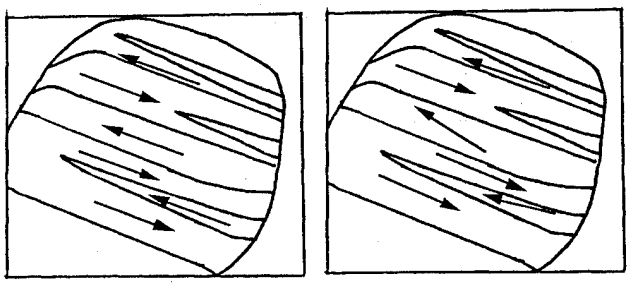


FIG. 5. Classical arrowing (left), magnetization determined by calculation (right). Note: the deviation of the middle arrow is due to the presence of a vertical white band (a problem of the acquisition card) which slightly distorts the values of the grey levels.

The experimental procedure is shown in Fig. 2. The usual positions of the sample holder are lengthwise $(L)$ and crosswise $(C+$ or $C-)$. The figure is a view of the turntable as seen from above, thus illustrating the various positions of the sample. The component drawn in fat line in the figure is the component that is actually detected with the Kerr effect.

With the pure in-plane magnetization and the use of longitudinal effect, the luminous intensity after the analyzer[9] is of the form

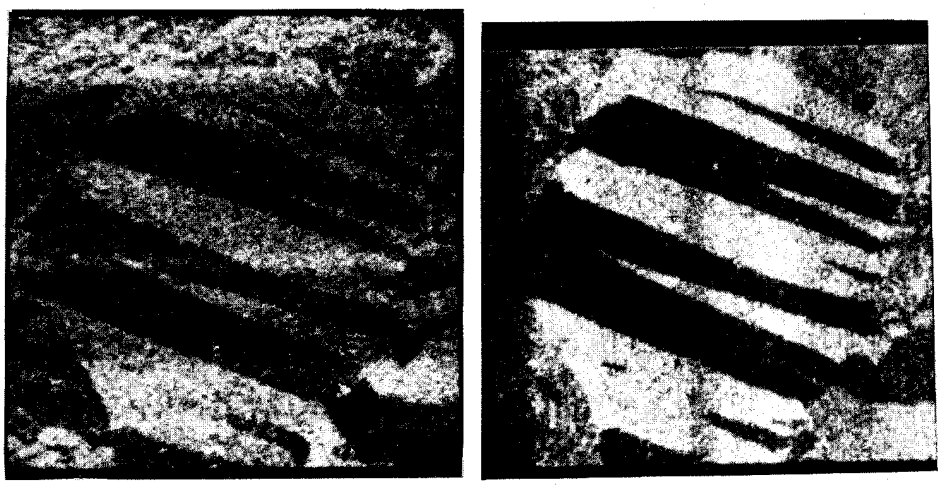
$$I=I_0+I_0Km+D, \tag{1}$$

where the three terms correspond to contributions due to:

(1) the nonmagnetic reflectivity of the metal,
(2) the magneto-optically generated light intensity, and
(3) a quadratic term of the magneto-optical effect, which can be neglected if polarizer and analyzer are uncrossed.

As the acquisition chain is linear, the grey level $\Delta n$ evaluated in our difference images is proportional to the intensity $I$. Different orientations of the sample holder lead to the relations shown in Table I.

Let $(L,C)$ be a base linked to the sheet's surface as shown in Fig. 3. $L$ is parallel to the length of the sheet, and



position L position C+

FIG. 4. Positions $L$ and $C+$, validation in a simple case.

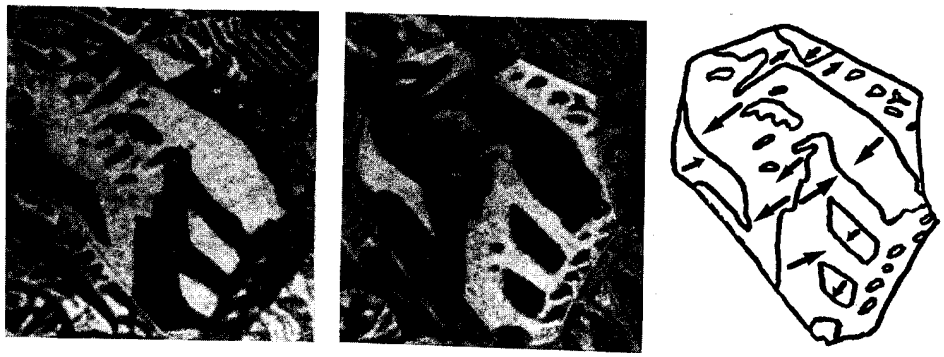



FIG. 6. Example of complex domains analysis.

$C$ to its width. Then let $\alpha$ be the angle between the direction of magnetization $M$- and the $L$-axis.

From the relations $1a-1c$ above, the equation

$$tg\ \alpha = \frac{m_c}{m_l} = \frac{\Delta n_{c+}}{\Delta n_l} = \frac{-\Delta n_{c-}}{\Delta n_l}, \tag{2}$$

follows immediately. Since both signs of the lengthwise and crosswise difference intensities are known, the vector **M** can be unambiguously put into the proper angular quadrant as shown in Fig. 3.

## IV. PRACTICAL IMPLEMENTATION

We applied the following principles:

(1) Since the exact domain structure is nonrepetitive, there should be no variation in the excitation between the different shots of the images with magnetic data;
(2) Since the spatial correspondence of the images to be subtracted is fundamental, both the reference image and the image at a certain level of excitation should be acquired without rotating the turntable in the meantime.

Also, the spatial correspondence between two subtracted images $L$ and $C$ should be carefully treated. The rotation of the sample generates a rotation of the acquired image. The digital image rotation and a correction for residual translations via image processing software has proven to be the best way to cope with the problem.

Although the sampling frequency of the acquisition card was set to get square pixels and the rotation axis of the sample carefully controlled, it was not possible to treat the images pixel by pixel. Consequently, we chose the areas of homogeneous intensity where the magnetization direction was determined locally.

## V. RESULTS OBTAINED

Our method to determine the magnetization vector has been validated on classical examples where the magnetization is well known, as shown in Figs. 4 and 5.

On regions with a certain disorientation, where the material develops complicated branching structures, the method can provide results which are impossible to derive with classical inductive approach based on domains theory. An example of such a structure is given in Fig. 6.

## VI. CONCLUSION

The disadvantage of our approach is the necessity to rotate and align the two images by computer for further quantitative analysis, which slightly limits the resolution. The main advantage is that by using only the longitudinal Kerr effect the measured intensities do not have to be related to the saturated images, what is necessary when using both longitudinal and transverse effects.[4–6] As a matter of fact, the new method assures that the proportionality constants in the contrast transfer function (see Table I) are cancelled by taking the ratio of the signal from the two images $L$ and $C$. Thus the parasite effects like the Faraday effect are avoided and no particular operational limitations are to be taken into account: the new method may be applied to any material, without prior requirements of magnetic saturability or partially known domain structure and without the limitations as to the sample form and size. It is a relatively rapid and memory sparing method that assumes better stability of measurements.

## ACKNOWLEDGMENTS

This work was supported by the Direction des Recherches, Etudes et Techniques of the Ministère de la Défense of France. The authors want also to thank E. Hug and O. Hubert, both of the University of Technology of Compiègne, for annealing the samples and Donald White from Oak Lawn USA for corrections.

[1] F. Schmidt, W. Rave, and A. Hubert, IEEE Trans. Magn. **21**, 1596 (1985).
[2] Brissoneau, "Materiaux Magnetiques pour l'Electrotechnique," edited by INP in Grenoble, France, p. 49.
[3] A. Hubert, R. Schäfer, and W. Rave, Proceedings of the Fifth Symposium on Magn. and Magn. Mater., Taiwan (1989).
[4] W. Rave, R. Schäfer, and A. Hubert, JMMM **65**, 7 (1987).
[5] W. Rave and A. Hubert, IEEE Trans. Magn. **26**, 2813 (1990).
[6] W. Rave, P. Reich, H. Brendel, M. Leicht, J. McCord, and A. Hubert, IEEE Trans. Magn. **29**, 2551 (1993).
[7] P. L. Trouilloud, B. Petek, and B. E. Argyle, IEEE Trans. Magn. **30**, 4494 (1994).
[8] R. Schäfer, B. E. Argyle, and P. L. Trouilloud, IEEE Trans. Magn. **28**, 2644 (1992).
[9] D. B. Dove, J. Appl. Phys. **35**, 1991 (1963).

# The energy loss per cycle in bar domain Si–Fe

Bryen E. Lorenz
*Electrical Engineering Department, Widener University, Chester, Pennsylvania 19013*

Theoretical investigations into the average energy loss per cycle of oriented, bar domain silicon–iron samples, has been typically carried out by treating the static hysteresis and eddy current losses separately. Since all losses ultimately are related to the motion of the domain walls in soft magnetic materials, this differentiation is at best artificial and at worst misleading. A simple model is proposed in this paper, based on the empirical properties of silicon iron, which when incorporated into the loss calculation yields results that predict the presence of both contributions to the total loss. In addition, the model places a limit on the frequency dependence of the domain widths (domain refinement). The implications of this constraint are investigated. © *1996 American Institute of Physics.* [S0021-8979(96)75808-5]

## INTRODUCTION

The energy loss per cycle due to sinusoidal excitation of 180° domain walls in single crystal, oriented, 3%–4% silicon iron has been studied with the hope of understanding the fundamental loss mechanisms involved. By extension, these investigations should shed light on the properties of oriented, silicon iron transformer steels. (An excellent review of this area of research is contained in Ref. 1.)

From the experimental findings contained in the literature, it appears that two types of contributions are associated with the overall loss per cycle (at least for losses below ~100 Hz): the static hysteresis loss and the eddy current loss. The former loss is predominant below 1 Hz and is frequency independent, while the latter becomes prominent above 1 Hz and is linear in frequency. In the theoretical treatment of this behavior, researchers have sought to explain these contributions separately (since, at least on experimental grounds, this expedient seems justified) and then simply assume that these contributions can be added together. On the contrary, since these losses ultimately stem (for magnetization below saturation) from domain wall motion, both types of loss should be handled in a unified manner. The model proposed in this paper seeks to remedy this problem by incorporating the observed characteristics of oriented, silicon–iron material into the appropriate calculations for the energy loss per cycle.

## MODEL

Figure 1 depicts a generalized static characteristic (i.e., where data are obtained under conditions of nearly constant applied field) which relates the domain wall velocity ($\dot{y}_0$) to the applied field ($H$). The literature contains many specific examples illustrating this relationship, most notably in the work carried out by Hellmiss and Storm.[2] By inspection of Fig. 1, one can see that if $H_a$, the amplitude of a given applied magnetic field, is less than some threshold field $H_0$, no domain wall motion is observed. Yet if $H_a > H_0$, $\dot{y}_0$ is linked to $H_a$, to the extent that it exceeds $H_0$, by the constant slope $q$. By extension, if one were to excite this system by a sinusoidal driving force of frequency $f$, then the resulting waveform of $\dot{y}_0$ as it evolves in time would appear as shown in Fig. 2. The output waveform ($\dot{y}_0$ vs $t$) can be analyzed by simple Fourier series techniques to yield the relation:

$$\dot{y}_0(t) = (2/\pi) q H_a \cos^{-1}(a)\cos(\omega t) + \left(\frac{4}{\pi}\right) q H_a \sum_{\substack{n=3 \\ n=\text{odd}}}^{\infty} \left( \frac{\sin((n+1)\cos^{-1} a)}{(n+1)} - \frac{a \sin(n \cos^{-1} a)}{n} \right) \cos(n\omega t), \tag{1}$$

where $a = H_0/H_a$, $\omega = 2\pi f$, and $a \leqslant 1$.

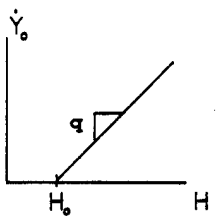



FIG. 1. Typical graph of the domain wall velocity ($\dot{y}_0$) vs the applied magnetic field ($H$).

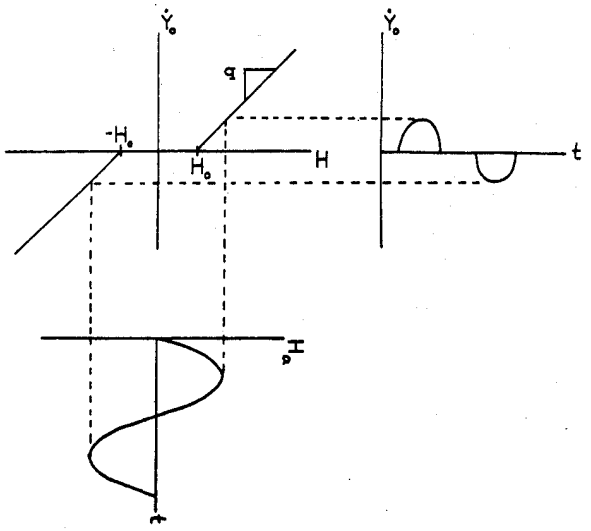



FIG. 2. Input waveform (i.e., $H_a$ vs $t$) subject to the characteristic of Fig. 1 yielding a distorted output waveform (i.e., $\dot{y}_0$ vs $t$).

 0021-8979/96/79(8)/6039/3/$10.00 © 1996 American Institute of Physics 

The average power loss per cycle ($\bar{p}$) can be calculated from the relation:

$$\bar{p}=\left(\frac{1}{T}\right)\int_0^T p(t)dt=\left(\frac{1}{T}\right)\int_0^T \beta(\dot{y}_0)^2\,dt, \tag{2}$$

where $\beta\dot{y}_0$ is the damping force and $\beta$ is the damping coefficient. A further trivial refinement, used in the literature, is to convert these losses into the energy loss per cycle ($\epsilon$) through the relation:

$$\bar{\epsilon}=\bar{p}/f. \tag{3}$$

However, before applying Eqs. (2) and (3) to Eq. (1) to determine $\bar{\epsilon}$, the maximum wall velocity can be described in either of two ways:

$$(\dot{y}_0)_{\max}=q(H_a-H_0), \tag{4}$$

where $H_a>H_0$, which was given in Fig. 1. Equally, one may describe the maximum wall velocity as

$$(\dot{y}_0)_{\max}=2\pi fL(B_m/B_s), \tag{5}$$

where $2L$ is the spacing between the static domain walls, $B_m$ is the mean magnetic induction, and $B_s$ is the saturation magnetic induction.[3] Although Eq. (5) assumes sinusoidal wall velocity and this disagrees to some extent with Eq. (4), we equate the maximum wall velocity and obtain:

$$H_a=(2\pi fL(B_m/B_s)+qH_0)/q. \tag{6a}$$

This result is suggested, if not implied, in Ref. 1:

$$H_0/H_a=qH_0/(2\pi fL(B_m/B_s)+qH_0), \tag{6b}$$

where $H_a>H_0$ and $B_m<B_s$.

Finally, using Eqs. (2), (3), and (6) in Eq. (1) yields

$$\bar{\epsilon}=(2/\pi^2)\beta[4\pi^2L^2(B_m/B_s)^2f+4\pi L(B_m/B_s)qH_0 +q^2H_0^2/f]\left\{(\cos^{-1}a)^2 +4\sum_{\substack{n=3\\ n=\text{odd}}}^{\infty}\left(\frac{\sin((n+1)\cos^{-1}a)}{(n+1)} -\frac{a\sin(n\cos^{-1}a)}{n}\right)^2\right\}. \tag{7}$$

From the expression given in Eq. (7), we note that as $f$ becomes large, $\bar{\epsilon}$ takes on the form

$$\bar{\epsilon}_\infty=2\pi^2\beta L^2(B_m/B_s)^2f +2\pi\beta L(B_m/B_s)qH_0 \quad \text{limit } f\to\infty. \tag{8}$$

The first term in (7) is linear in $f$ and in this regard resembles the Pry–Bean loss or the standard classical loss.[4] The latter term is constant in $f$ and predicts the presence of a frequency independent contribution to the total loss. On the other hand, if $f$ were to go to zero, the energy loss/cycle becomes

$$\bar{\epsilon}_0=(8/\pi)\beta L(B_m/B_s)qH_0 \quad \text{limit } f\to 0 \tag{9}$$

A graphical interpretation of Eqs. (7) and (8), for a small range of frequencies, is given in Fig. 3 in terms of the reduced loss, $\bar{\epsilon}/(2\beta/\pi^2)$ versus the frequency, $f$. The value for $(B_m/B_s)$ and $L$ were taken from Narita and Imamura to be 0.5 and 0.59 mm, respectively, while the product $qH_0$ was taken from the results of Hellmiss and Storm to be 1.22 mm/s.

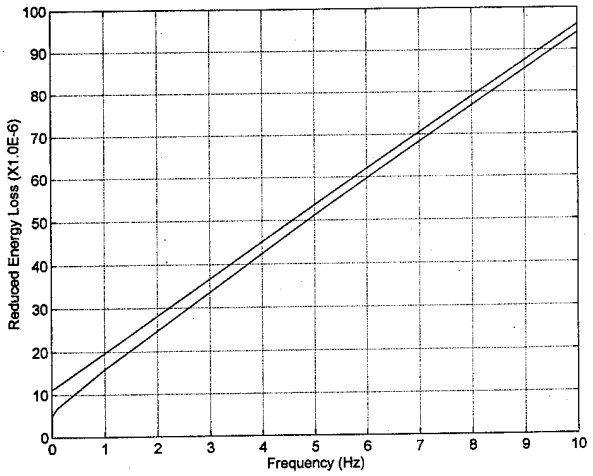



FIG. 3. Reduced energy loss per cycle vs magnetizing frequency. The upper line represents the linear asymptote ($\bar{\epsilon}_\infty$), while the lower curve represents the calculated values ($\bar{\epsilon}$).

At 1 Hz, the discrepancy between the curves, as pictured in Fig. 3, amounts to about 24% of $\bar{\epsilon}$ (the lower curve), while at 50 Hz, a typical power frequency, this difference (not shown in the figure) is slightly less than 1%.

## DISCUSSION

In testing the predictions of the model versus experimental results, we note that in finding the static hysteresis loss, the standard laboratory practice is to extrapolate the approximate linear relationship observed at higher frequencies down to zero. The intercept of $\bar{\epsilon}_\infty$ at zero frequency is considered to be the static hysteresis loss.[3] From Eq. (8), this corresponds to an extrapolated energy loss:

$$\bar{\epsilon}_{\text{ext}}=2\pi\beta L(B_m/B_s)qH_0.$$

However, in the limit as $f$ goes to zero, the actual loss according to Eq. (9) is

$$\bar{\epsilon}_0=(8/\pi)\beta L(B_m/B_s)qH_0.$$

Therefore, the ratio of the extrapolated to the predicted losses, far from being unity (i.e., exhibiting no difference), is $\pi^2/4$. This discrepancy was noted by Bishop[5] in comparing the experimental results of Narita and Imamura and the static hysteresis losses obtained by Hellmiss and Storm. (Both sets of researchers used single crystal, cube-on-side, 3%–4% Si–Fe samples.) Bishop comments that this difference amounts to roughly an order of magnitude.

From (8), the dependence of $\bar{\epsilon}_\infty$ on $L$ comes about through a linear and squared term. However, it is well known that $L$ changes discontinuously through a process of domain refinement with increasing excitation frequency, for instance as shown in the work of Shur and his co-workers,[6] through domain wall nucleation. (Recently reported findings by Kim,

*et al.*[7] indicate that this is also true in very thin, 33–35 $\mu$m, grain-oriented silicon steels.) Haller and Kramer[8] were able to show that domain widths varied, on average, approximately as $(1/\sqrt{f})$. However, if $L=rf^{-0.5}$, where $r$ is some appropriately chosen constant, then the term in $L^2$ in Eq. (8) would be independent of frequency, while the remaining term would vanish as the frequency went to infinity. Saturation in total losses has not been observed experimentally. For this reason, it appears that domain refinement follows the relation, $L=rf^{-\alpha}$ where $0<\alpha<0.5$. If $\alpha=0$, no domain refinement would occur, while the condition $\alpha\geq 0.5$ is physically unrealizable.

Mohri and his fellow researchers,[9] working on samples of grain-oriented, 3% silicon–iron transformer steel, found such a relation where $\alpha=0.4$ and $r$ were dependent upon a fixed power of $B_m/B_s$. More recently, in an article authored by Bishop and Pfützner,[10] reported results seem to indicate that $r$ and $\alpha$ are both functions of $B_m/B_s$ where $\alpha$ assumes a range of allowable values somewhere below 0.5 when domain wall bowing is not significant. The relationship between $L$ and $f$ could be rewritten as $L=L_0(f/f_0)^{-\alpha}$, where $L_0$ is the domain wall spacing in the demagnetized state and $f_0$ is on the order of 1 Hz.

## CONCLUDING REMARKS

The approach, as presented here, allows one to generate both the eddy current loss (i.e., those losses linear in frequency) as well as the hysteresis loss (i.e., residual losses at low frequency) simultaneously from the physical (albeit ideal) properties of silicon iron. As a consequence, the relationship between these losses appear together in a natural way as given in Eq. (7). This model avoids the questionable practice of treating contributions separately and simply adding them together to find the total loss. In addition, the limit placed on the exponent in describing domain wall refinement is less than 0.5 (i.e., $\alpha<0.5$ for $L=rf^{-\alpha}$). This is based on the fact that the energy loss per cycle monotonically increases with excitation frequency.

## ACKNOWLEDGMENT

The author would like to thank Dr. C. Graham of the Materials Science Department, University of Pennsylvania for his many suggestions and insightful comments.

[1] J. W. Shilling and G. L. Houze, Jr., IEEE Trans. Magn. **MAG-10**, 195 (1974).
[2] G. Hellmiss and L. Storm, IEEE Trans. Magn. **MAG-10**, 36 (1974).
[3] K. Narita and M. Imamura, IEEE Trans. Magn. **MAG-15**, 981 (1979).
[4] R. H. Pry and C. P. Bean, J. Appl. Phys. **29**, 532 (1958).
[5] J. E. L. Bishop, IEEE Trans. Magn. **MAG-16**, 1 (1980).
[6] Ya. S. Shur, Ye. B. Khan, and V. A. Zaykova, Fiz. Metal. Metalloved. **31**, 286 (1971).
[7] Y. H. Kim, M. Ohkawa, K. Ishiyama, and K. I. Arai, IEEE Trans. Magn. **29**, 3535 (1993).
[8] T. R. Haller and J. J. Kramer, J. Appl. Phys. **41**, 1034 (1970).
[9] K. Mohri, Y. Satoh, and T. Fujimoto, IEEE Trans. Magn. **MAG-12**, 849 (1976).
[10] J. E. L. Bishop and H. Pfützner, IEEE Trans. Magn. **30**, 46 (1994).

# Correlation between the Barkhausen noise power and the total power losses in 3% Si–Fe

M. Birsan and J. A. Szpunar
*Metallurgical Engineering, McGill University, 3450 University Street, Montreal PQ H3A 2A7, Canada*

T. W. Krause and D. L. Atherton
*Queen's University, Kingston Ontario, Canada*

We present results on Barkhausen noise power in grain oriented 3% Si–Fe samples of different quality (power losses). Barkhausen noise is measured at constant values of the magnetic field applied in the rolling direction of the sheet. The measurements indicate a strong correlation between the Barkhausen noise power and total power losses. A model is proposed to interpret the results according to which the Barkhausen noise power is related to the density of pinning centers per unit coercive field, an intrinsic parameter of the material. It is shown that this parameter characterizes the ability of the external field to increase the number of moving walls. The model and the experiment demonstrate that the power losses in grain oriented 3% Si–Fe are improved either by dynamic homogenization of magnetization, or by decreasing the domain wall spacing in static conditions. © *1996 American Institute of Physics.* [S0021-8979(96)75908-6]

## INTRODUCTION

Grain oriented 3% Si–Fe steel sheets are engineered to minimize power losses arising from magnetic hysteresis and eddy currents during their cyclic magnetization along the rolling direction (RD). The magnetic anisotropy of these materials is associated with a crystallographic {110} ⟨001⟩ texture. The main domain structure consists of two types of domains whose magnetizations are parallel or antiparallel to the rolling direction. When the magnetic field is applied along the rolling direction, the whole magnetization process takes place exclusively by the displacement of domain walls. The most important origin of losses accompanying the magnetization of grain oriented steels is the eddy current. In a material containing many domain walls, the eddy currents are localized at the wall. To reduce eddy current losses accompanying the movement of the walls, these materials are manufactured so that they have a higher number of domain walls,[1] i.e., the magnetic flux is uniformly distributed over the sample. This is accomplished by a uniform domain structure, obtained using a domain refining technique (e.g., mechanical or laser scribing). As a result of domain refinement, the number of walls which move effectively under alternating field increases, and the velocity (eddy current loss) of an individual wall in a constant flux density decreases. We use this information to interpret the experimental data relating the domain wall spacing to the magnetic Barkhausen noise, and to power losses.

Statistical investigation of the microscopic processes contributing to the total power loss can be done through detection and analysis of the magnetic Barkhausen noise (MBN). In the present paper, a method based on the measurement of clustered Barkhausen transitions in grain oriented 3% Si–Fe is proposed and tested to investigate nondestructively the statistical correlation between the Barkhausen phenomenon and the total power losses. The method relates the MBN to power losses through a model based on domain wall displacement after they are released from pinning centers.

## EXPERIMENTAL RESULTS AND DISCUSSION

Magnetic Barkhausen noise (MBN) measurements were performed using the instrument described in Ref. 2. Briefly, the apparatus consisted of a magnetic transducer, a magnetization generator, a preamplifier, and output equipment. The quantity measured in this experiment is the magnetic Barkhausen noise power, defined by the time integral of the squared voltage signal:

$$P_{\mathrm{MBN}}=\int_0^{\infty} V^2(t)dt=\frac{1}{2\pi}\int_0^{\infty} F(\omega)d\omega, \tag{1}$$

where $F(\omega)$ is the power spectrum.

The relationship between the irreversible change in magnetization produced by the sweep field $H$ and the sample magnetic properties has been developed elsewhere.[3] For the case where the macroscopic induction rate is approximately constant for the investigated samples, the MBN power is described by the equation

$$P_{MBN}\propto f_0\,\frac{\langle\tan\gamma\rangle^2}{T}\,H^{1/2}, \tag{2}$$

where $T$ is the thickness of the sample, $\gamma$ is the angle between the magnetic dipole moment and the direction of the magnetizing field, and $f_0$ has the dimension of a density of pinning centers per unit critical field, $dH_0$, which is an intrinsic parameter of material.[4]

The samples used in the present investigation were grain oriented 3% Si–Fe laminates of different quality (power losses) having thicknesses of either 9 mil (≈0.22 mm) or 7 mil (≈0.17 mm). For the quantitative description of material texture, the (110), (200), and (211) pole figures were obtained for each specimen using the x-ray technique (Schulz's reflection method). The material texture was represented using the orientation distribution function (ODF), obtained following the pole figure inversion.[5]

Magnetic measurements were conducted using the conventional Epstein test. The samples were classified as a function of the value of power losses and identified using a combination of numbers and letters. For the materials of the same

 0021-8979/96/79(8)/6042/3/$10.00 © 1996 American Institute of Physics

TABLE I. Power losses and the texture parameter $\langle \sin \gamma \rangle$ for the investigated samples.

| Sample | S-9A | S-9B | S-9C | S-9D | S-9E | S-7A | S-7B | S-7C |
|---|---|---|---|---|---|---|---|---|
| Losses [W/lb] at 1.5 T | 0.376 | 0.404 | 0.408 | 0.432 | 0.438 | 0.362 | 0.369 | 0.390 |
| Losses [W/lb] at 1.7 T | 0.551 | 0.603 | 0.621 | 0.652 | 0.666 | 0.543 | 0.572 | 0.591 |
| $\langle \sin \gamma \rangle$ | 0.14 | 0.07 | 0.19 | 0.09 | 0.11 | 0.09 | 0.14 | 0.07 |

thickness, 9 mil, the letters *A* to *E* indicate the quality of the sample. Power loss increases continuously from sample S-9A through to sample S-9E. The materials with thickness of 7 mil are represented by three specimens of different quality (power losses), identified as *A*, *B*, and *C*, respectively. The values of power losses measured for different samples are listed in Table I.

The results obtained from the MBN experiments performed on these 3% Si–Fe samples are presented in Figs. 1(a) (9 mil samples) and 1(b) (7 mil samples). From these graphs, one can see that the relationship (2) is strongly supported by the experimental data.

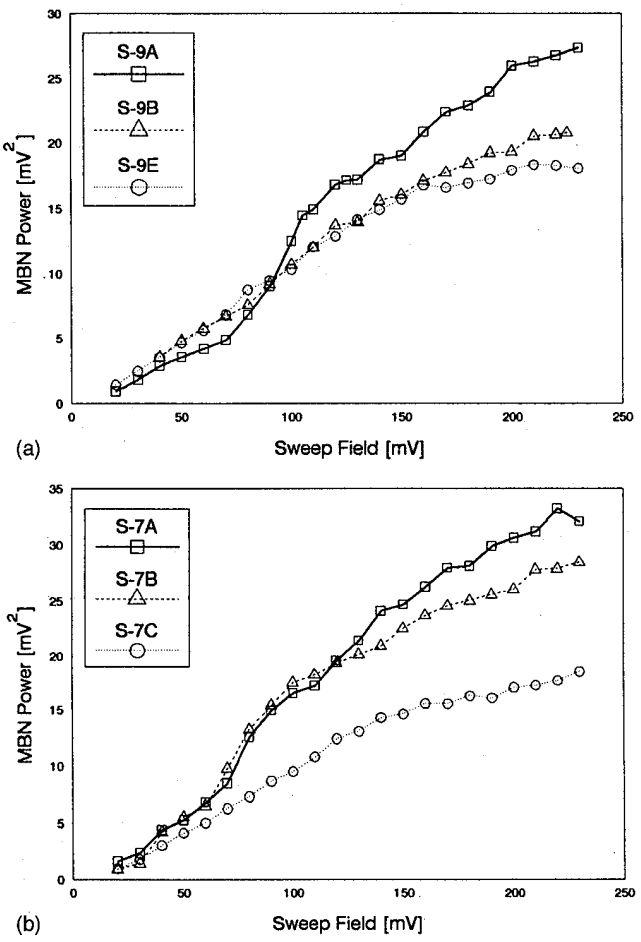



FIG. 1. MBN power versus sweep field in (a) 9 mil samples, and (b) 7 mil samples.

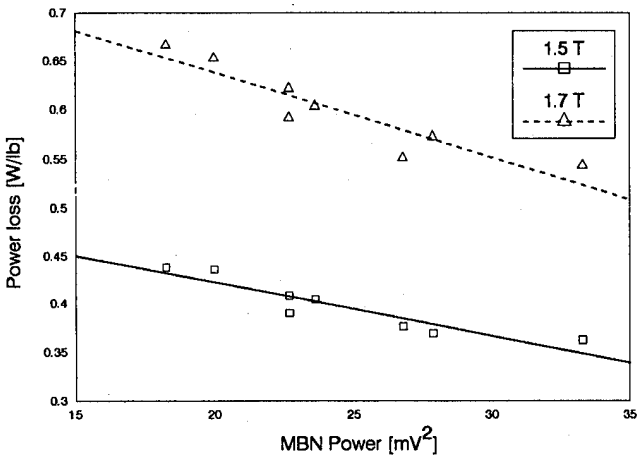



FIG. 2. MBN power versus total power losses in grain oriented silicon steels.

For the samples investigated, the power losses presented in Table I are inversely proportional to the MBN power. The regression of MBN power as a function of power losses is shown in Fig. 2. This graph clearly indicates a correlation between the power loss and the measured Barkhausen noise power, which is explained using Eq. (2). In this expression, there are two terms related to material structure which are analyzed: $\langle \tan \gamma \rangle^2$ is a texture parameter, and $f_0$ is a structural parameter characterizing the material.

The texture parameter is calculated using the averaging over the grain orientation distribution function.[5] If the grain orientation in the sample reference frame is represented by the three Euler angles $(\varphi_1, \phi, \varphi_2)$ and the grain orientation distribution function $f(g)=f(\varphi_1, \phi, \varphi_2)$ is known, the average value of $\tan \gamma \approx \sin \gamma$ (for small values of angle $\gamma$), is given by

$$\langle \sin \gamma \rangle = \frac{1}{8\pi^2} \oint \sin \gamma(g) f(\varphi_1 . \phi, \varphi_2) \sin \phi \, d\varphi_1 \, d\phi \, d\varphi_2, \tag{3}$$

where

$$\sin \gamma(g) = \cos \phi. \tag{4}$$

For the analyzed samples, the values of $\langle \sin \gamma \rangle \approx \langle \cos \phi \rangle$ calculated using Eq. (2) are presented in Table I.

It was demonstrated[6] that, in a single crystal of silicon iron, there is an inverse proportionality between the domain wall spacing $d$ measured in static conditions, and the out-of-plane angle of $\langle 100 \rangle$ easy magnetization direction. Generalizing this relationship to a polycrystalline material, one could write that the average domain wall spacing is

$$\langle d \rangle \propto \frac{\sqrt{T}}{I_s \langle \sin \gamma \rangle}. \tag{5}$$

where $T$ is the sample thickness, and $\langle \sin \gamma \rangle$ is calculated using Eq. (3). The highest value of $\langle \sin \gamma \rangle$ means a lower value of domain wall spacing, or, equivalently, a lower value of eddy current loss.[1] Calculating the domain wall spacing with Eq. (5), we found that there not exists a proportionality

between the calculated values and the values of power losses, which implies that the domain wall spacing is not the only parameter involved in the loss problem.

The other structural parameter in Eq. (2) is $f_0$. The higher value of $f_0$ is equivalent to a higher number of walls contributing to magnetization when the magnetic field increases from $H$ to $(H+dH)$, because the number of moving walls is proportional to $f_0 \cdot dH$. As a result, the magnetization process is more homogeneous in dynamic conditions.

According to the proposed model, the MBN power depends on the product $f_0 \cdot \langle \sin \gamma \rangle^2$. Both parameters contribute to the increase in the active domain wall population. In conclusion, the magnetization process is more homogeneous in samples where the value of the product $f_0 \cdot \langle \sin \gamma \rangle^2$ is higher and, as a result, the corresponding eddy current loss is significantly decreased.

## HOMOGENIZATION OF THE MAGNETIZATION PROCESS

In a series of articles,[7–10] Bertotti found that the number of active domain walls in several iron-based alloys, including grain oriented silicon steels, obeys the linear law:

$$\tilde{n} = n_0 + \frac{H_{\text{exc}}}{V_0}, \tag{6}$$

where $n_0$ is the number of moving walls when the magnetizing frequency $f_m \to 0$, $H_{\text{exc}}$ is a fictional field acting on each domain wall and the field $V_0$ is controlled by the material microstructure.

To move on isolated wall, we must apply a field higher than the coercive field:

$$H = H_c + \Delta H = H_0 + H_{\text{exc}}, \tag{7}$$

where $\Delta H$ represents the excess field required to balance the opposite field produced by eddy currents surrounding the moving wall. Generalizing the above relation to the whole sample, the number of walls which move when the external field is increased with $\Delta H = H_{\text{exc}}$ is

$$\tilde{n} = f_0 H_{\text{exc}} = \frac{H_{\text{exc}}}{1/f_0} = \frac{H_{\text{exc}}}{V_0} \tag{8}$$

and the excess field acting on a single domain wall is decreased accordingly. In this way, the characteristic field $V_0$ is related to a microstructural parameter, $1/f_0$, which represents the critical field per unit pinning center in the interval from $H_0$ to $(H_0 + \Delta H_0)$.

According to the previous discussion [see Eq. (2)], the characteristic field $V_0$ is expected to contain also the texture parameter $\langle \sin \gamma \rangle^2$, so that it has the form

$$V_0 \propto \frac{1}{f_0 \langle \sin \gamma \rangle^2 T}. \tag{9}$$

Bertotti's experimental results[9] prove that $V_0$ decreases with increasing sample cross section ($T$ increases), decreasing grain size ($f_0$ increases), and decreasing degree of magnetic orientation ($\sin \gamma$ increases); no analytical relationship between the characteristic field and these microstructural parameters was suggested.

## CONCLUSIONS

It was found that, in grain oriented 3% Si–Fe, there is an inverse proportionality between the MBN power and the total power loss. A nondestructive method was developed to study the effects of texture and microstructure on the magnetic Barkhausen noise (MBN), and also on the total power losses. The method relates the MBN power to the core loss through a model based on domain walls displacement after they are released from pinning centers. The parameter controlling this process is the characteristic field $V_0$. Even if we are not able to calculate the value of this parameter using the information related to the material structure, it can be directly evaluated from the magnetic Barkhausen noise (MBN) measurements. The basic result of this study is that the lower power losses in grain oriented materials are obtained in samples where the distribution of the magnetic flux is more homogeneous.

Using the MBN measurements, the power losses of different grain oriented silicon steels could be readily compared. Quantitative measurements of power losses are also possible if the instrument is calibrated using the specimens with known values of the power losses.


[1] R. H. Pry and C. P. Bean, J. Appl. Phys. **29**, 532 (1958).
[2] T. W. Krause, L. Clapham, and D. L. Atherton, J. Appl. Phys. **75**, 7983 (1994).
[3] M. Birsan, J. A. Szpunar, T. W. Krause, and D. L. Atherton, IEEE Trans. Magn. (to be published).
[4] S. Chikazumi, *Physics of Magnetism* (Wiley, New York, 1964).
[5] H. J. Bunge, *Texture Analysis in Materials Science* (Butterworths, London, 1982).
[6] M. Imamura, Y. Sasaki, and H. Nishimura, IEEE Trans. Magn. **MAG-19**, 20 (1983).
[7] G. Bertotti, J. Appl. Phys. **55**, 4339 (1984).
[8] G. Bertotti, J. Appl. Phys. **55**, 4348 (1984).
[9] G. Bertotti, J. Appl. Phys. **57**, 2110 (1985).
[10] G. Bertotti, J. Appl. Phys. **57**, 2118 (1985).

# Effects of surface condition on Barkhausen emissions from steel

A. P. Parakka and D. C. Jiles
*Center for NDE, Iowa State University, Ames, Iowa 50011*

H. Gupta
*Center for Grinding Research and Development, University of Conecticut, Storrs, Connecticut 06269*

S. Jalics
*Delphi Chassis, Sandusky, Ohio 44780*

Temperature changes during mechanical processing such as grinding of steel parts can cause phase changes in the microstructure. Thermal shock during the process can give rise to localized surface residual stress. The net result can be reduced wear resistance and fatigue life leading to early failure during service. Effective methods for the detection of such damage are necessary. Barkhausen emissions, which arise from discontinuous motion of domain walls, are sensitive to microstructual changes that affect domain dynamics. Detected Barkhausen signals are predominantly from a surface layer about 200 $\mu$m thick, those from deeper being attenuated due to eddy currents. An analysis of the detected signals can provide an indication of the surface condition of the material. Barkhausen signals from parts ground under controlled conditions were found to be dependent on the grinding process conditions. The signal changes were consistent with residual stress measured by x-ray diffraction and with hardness measurements that are indicative of changes in microstructure. © *1996 American Institute of Physics.* [S0021-8979(96)76008-0]

## I. INTRODUCTION

Surface microstructure plays an important role in determining the mechanical properties of materials.[1] Improper manufacturing process conditions for structural components can adversely affect the microstructure and residual stresses in the material and lead to early fatigue failure.

Barkhausen emissions in steels arise from discontinuous changes in the magnetization and are predominantly the result of spontaneous motion of domain walls in the presence of a changing magnetic field.[2] The Barkhausen emissions, typically detected as voltage pulses in a field coil, appear as a burst of pulses localized in time regions where the magnetization in the material changes polarity as seen in Fig. 1. The signal is influenced by stress, which changes the differential permeability of the material and hence the height of the detected signal, and by microstructure, which determines the defect density in the material and hence the overall shape of the emissions.[3,4] The sensitivity of this technique can also be adjusted to different depths in the material since the higher frequency components of the emissions from deeper inside the material are selectively attenuated due to eddy currents before being detected at the surface.[4]

Grinding involves the removal of material from the surface of a part for the purpose of attaining dimensional tolerance and surface conditioning. A significant portion of the energy used in removing the material results in localized heating.[5] An abnormal rise in temperature during the process can result in detrimental metallurgical phases in the surface microstructure, and the thermal and mechanical shock from the process can introduce localized surface stress.[6]

Damage from improper grinding procedures can arise from several conditions including reduced coolant flow, and is broadly classified by the rise in temperature. Retempering damage occurs when the temperature of the part rises high enough to relieve some of the compressive surface stress, previously introduced by induction hardening for example, leaving regions less resistant to wear. At significantly higher temperatures, rehardening damage occurs which results in a phase change from ferrite to austenite. On quenching by the cooling fluid this produces regions of martensite, a hard and brittle phase, which is prone to cracking.[6] Effective methods are necessary for the detection of such metallurgical changes in the material.

## II. EXPERIMENTAL DETAILS

Automobile wheel bearing components were ground to required dimensional specifications under progressively reduced coolant flow rate (normal flow rate, half, quarter and no coolant) in order to induce different degrees of grinding damage in the surface. Barkhausen measurements were conducted on these components using the Magneprobe.[7] Other measurements using x-ray diffraction, for the determination of the absolute stress level, and Vickers surface microhardness, for the estimation of surface mcirostructure, were conducted on similarly ground components, and correlated with the Barkhausen measurements. Barkhausen signal was detected from regions where most damage was expected using a customized magnetic sensor. Discrimination frequencies for depth were set for maximum sensitivity to physical changes in a region approximately 20 $\mu$m thick.[8]

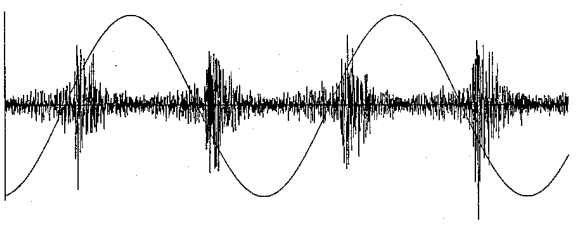


FIG. 1. Magnetizing signal and Barkhausen emissions as a function of time.

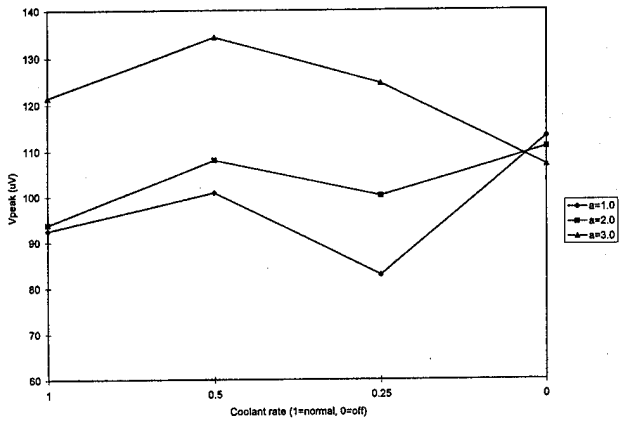



FIG. 2. Change in peak value of smoothed Barkhausen signal from variously ground specimens at different magnetizing amplitudes.

## III. RESULTS AND DISCUSSION

The change in the peak amplitude of the smoothed signal envelope and the width of the peak, (determined simply as the ratio of the envelope area to the peak height) for specimens that had undergone progressively greater surface damage are shown in Figs. 2 and 3. The peak amplitude is an indicator of the local residual stress, since tensile stress in materials with positive differential magnetostriction $d\lambda/dM$ increases the maximum differential permeability and hence the amplitudes of the Barkhausen signal. The peak width on the other hand is an indicator of the distribution and strength of sites pinning the domains walls. The observed decrease in the peak widths is an indication of the altered microstucture. These trends were verified by x-ray measurements of the surface residual stress and the surface hardness for similarly treated specimens.

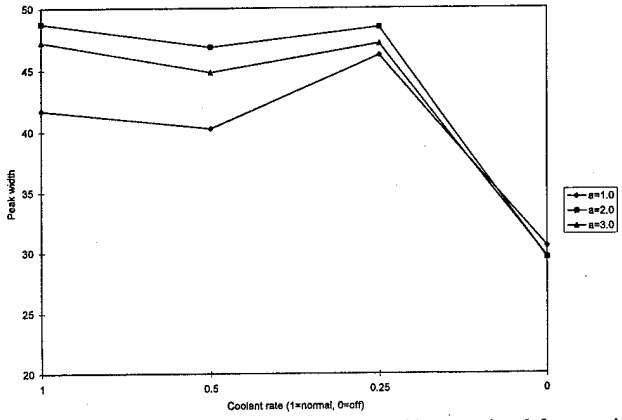



FIG. 3. Change in peak widths of smoothed Barkhausen signal from variously ground specimen at different magnetizing amplitudes.

## IV. CONCLUSION

The Barkhausen technique has been shown to be a viable method for assessing residual stress and microstructural phase changes in steel components and the detection of unfavorable surface conditions. Residual stress, measured by x-ray diffraction, and changes in microstructure, estimated by hardness measurements, verified the measured changes in Barkhausen signals.

[1] S. Weissman, R. N. Pangborn, and I. R. Kramer, Scripta Met. **17**, 807 (1983).
[2] D. C. Jiles, NDT Int. **21**, 311 (1988).
[3] D. C. Jiles, Soumien, IEEE Trans. Magn. **30**, 4294 (1994).
[4] T. Howes and H. Gupta, Proceedings of the AES Conference Procedings, Cleveland, 1990.
[5] K. Neailey, Met. Mater. **93** (Feb. 1988).
[6] K, Neailey, Met. Mater. 141 (Mar. 1988).
[7] A. P. Parakka, D. C. Jiles, J. of Magn. Magn. Mater. **140**, 1881 (1995).
[8] *AST Stressscan-500 Opertors Manual* (American Stress Technologies Inc, Pittsburg, PA).

*Published without author corrections*

# Simultaneous Barkhausen discontinuities of multiple die-drawn Fe-Si-B amorphous wires connected with amorphous ribbons (abstract)

M. Soeda and J. Yamasaki
*Department of Electrical Engineering, Kyushu Institute of Technology, Tobata, Kitakyushu 804, Japan*

In-rotating water quenched Fe-Si-B amorphous wire exhibits the Barkhausen discontinuities (BD) in the as-cast state. Its minimum length to exhibit the BD depends on the demagnetizing effect. The minimum length is around 9 cm for the as-cast wire with 120 $\mu$m diameter. For sensor application of the wire as a pulse voltage generator, small size sensor elements are needed. Die-drawn wires with reduced diameter and minimum length of up to 2 cm exhibit BD1 and are expected for such use. But the pulse voltage induced in the sense coil by the BD decreases because of decreased volume of the wire. In this study, an attempt was made successfully to develop a small size BD sensor element with higher pulse voltage using multiple $Fe_{77.5}Si_{7.5}B_{15}$ die-drawn wires having 30 $\mu$m diameter and 4 cm long. Three die-drawn wires were put together closely in parallel and two pieces of $Co_{74.26}Fe_{4.74}Si_{2.1}B_{18.9}$ amorphous ribbon (5 mm$\times$2 mm$\times$25 $\mu$m) were attached to the wire ends. It was found that the BD of the three wires occur simultaneously at the same threshold field. Domain change of ribbon before and after the BD was observed with a Kerr microscope. It was found that the amorphous ribbons were magnetized by the stray field from the ends of the wires in the direction opposite to the magnetization of the wire and that the magnetization of the ribbon changes discontinuously synchronizing with the magnetization of the wire. So it is likely that the magnetizations of the multiple wires and ribbon form stabilized flux closure and that the simultaneous BD of multiple wires is triggered by the flux jump of the wire having the lowest threshold field. © *1996 American Institute of Physics.* [S0021-8979(96)70008-7]

[1] R. Malmhall *et al.*, IEEE Trans. Magn. **MAG-23**, 3242 (1987).

# The influence of domain activities on MR head performance

Weichun Ye
*Magnetics Technology Centre, National University of Singapore, Singapore 0511*

Jinyue Yu and Bingchu Cai
*Information Storage Research Center, Shanghai Jiao Tong University, 200030, People's Republic of China*

The relation of signal distortion of MR heads to the domain structure and the domain activities was studied in this paper. Several kinds of MR elements were fabricated and a measurement system was set up to measure magnetoresistivity. A large drop near the peak of the output wave form was found for some MR elements. And the magnetic structure of the MR element was investigated by the "Bitter pattern." It was seen that there existed multidomain in the part of the lead without gold coating. Furthermore, it was also found that the multidomain existed in the junction of leads and the MR element, and the new domain looked like a hook. The appearance of this hook-shaped multidomain has not been reported up to now in literature. The design of the MR element was modified to eliminate the drop in the output wave form and the drop was reduced substantially. Our study shows that suitable geometric dimensions and structures of leads are also very important to high performance of MR head in head design in addition to select the optimum biasing conditions.
© *1996 American Institute of Physics.* [S0021-8979(96)76108-7]

## I. INTRODUCTION

The read/write head is a key component in computer disk drives. Due to increasing demands for lower cost and smaller diameter disk drives, large volumes of lower cost heads with high reliability and high areal density, suitable for products even at smaller linear speed between head and media, are required. MR head offers potentially the highest areal density for disk drives and tape recorders. The read back signal of a MR head is velocity independent and is large even for the smaller diameter disk drives. However, the signal response of MR heads is puzzled by the Barkhausen noise which originates from irreversible processes of buckling domains.[1,2] Many studies including longitudinal biasing for suppressing Barkhausen noise have been reported.[3,4] In this paper we studied the relation of signal distortion of MR head to domain structure and the domain activities which appear in some part of leads and in the junction of leads and MR active regions.

## II. EXPERIMENTAL SETUP AND MEASUREMENT

The 81%–19% Ni/Fe permalloy film with 400 Å thickness and 3–4 $\mu$m height was sputtered onto substrate (glass or ferrite) and patterned to MR element with the easy-axis along the longitudinal direction. The reason of putting Ni/Fe film on ferrite substrate was that the ferrite substrate was patterned as a part of shield. As shown in Fig. 1, leads were deposited to the center of the MR element for electrical contacts. Regions I and II were two parts of a lead. The shadowed region I was coated with gold while region II was not. In that case, the Ni/Fe film in region II actually became a part of the MR element.

The measurement system in Fig. 2 was set up by ourselves to measure magnetoresistance. The solenoid was activated by an alternating signal of 50 Hz. There is a uniform magnetic field inside the solenoid which strength ranges between +400 and −400 Oe by changing the activating signal. The MR sample to be measured was placed in this uniform magnetic field of which direction was parallel to the hard axis of the MR bar. A noninductive heater was used to keep the temperature of MR element above the Curie temperature

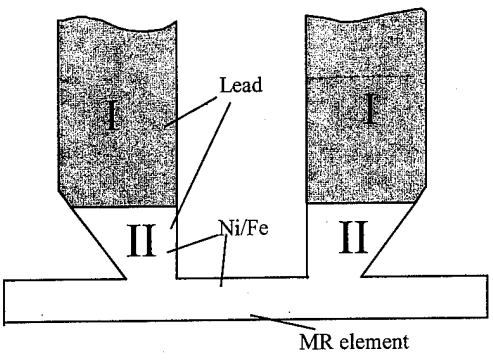



FIG. 1. Original MR element with two deposited leads, each of which consists of two regions, region I—with gold coating and region II—without gold coating.

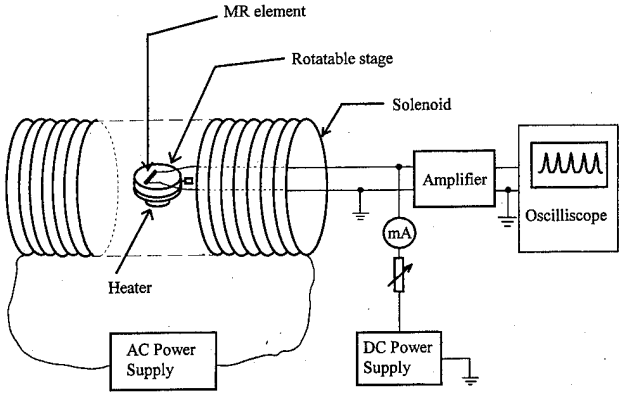



FIG. 2. Measurement system used to measure magnetoresistance.

 0021-8979/96/79(8)/6048/3/$10.00 © 1996 American Institute of Physics

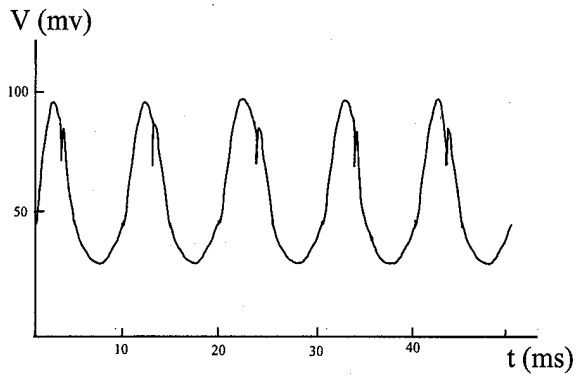



FIG. 3. Output wave form from original MR element.

of ferrite substrate. The ac output signal derived from the MR element could be obtained from an oscilloscope.

## III. RESULTS AND DISCUSSION

Both biased and unbiased Ni/Fe films were studied in our experiments. For simplicity, only output wave forms from unbiased elements were shown as examples in this paper. The frequency of output signals for unbiased film was twice as of the stimulating ac field. In Fig. 3, it could be seen that there existed a large drop near the peak of the output wave form. Obviously, the drop was harmful to the read back signal detection, no matter which type of data detection was adopted, either peak detection or PRML detection. The drop degraded the output signal. The magnetic structure of the MR element under different magnetic field strengths was investigated by "Bitter pattern." The MR element was first covered by a thin layer of ferrofluid, then by a thin layer of glass. The particles of $Fe_3O_4$ were under the influence of the stray fields of magnetic domain walls. Therefore the pattern observed by optical microscope reflects the domain structure. These domain structure patterns were thereafter depicted manually due to equipment limitations.

It was shown in Fig. 4 that there existed multidomain in region II of the lead without gold coating when the field strength was less than 5–6 Oe. The domain structure would

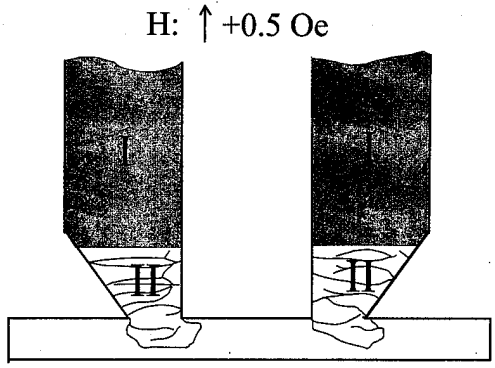



FIG. 4. Magnetic structure showing the existence of multidomain in lead region without gold coating and hook-shaped domain in the junction of lead and MR element.

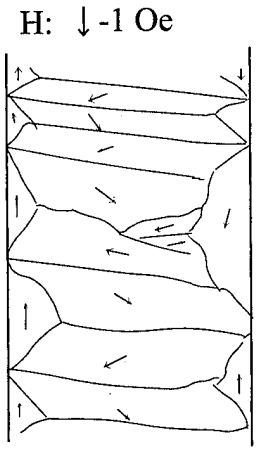



FIG. 5. Multidomain structure in the lead when magnetic field strength $H=-1$ Oe.

change with various field strengths. When the magnetic field strength decreased from the saturation value to about 6 Oe, the multidomain began to appear. As the strength continued to decrease, the domain wall density increased as depicted in Fig. 5. When the field strength decreased to zero and began to increase in the opposite direction, the upward closure domains gradually shrank and disappeared finally, whereas the downward closure domains appeared and grew (Fig. 6). The arrow direction in Figs. 5 and 6 indicates whether its domain is an upward closure domain or a downward one. If the magnetic field strength in opposite direction became more than 6 Oe, the domain walls disappeared and the multidomain state returned to single domain state. The existence of multidomain in region II of the lead in weak magnetic field explains the drop found near the peak of output wave form in Fig. 3.

Furthermore, it was found that the multidomain structure in the leads usually spread into the active region of MR element and the new domain looked like a hook. When the external magnetic field was along the positive direction, the magnetization direction was at the elevation angle. As the positive external magnetic field decreased to zero and thereafter increased in the opposite direction, the magnetization

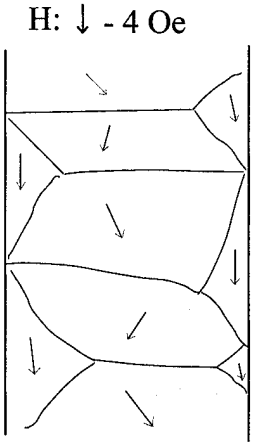



FIG. 6. Multidomain structure in the lead when magnetic field strength $H=-4$ Oe.

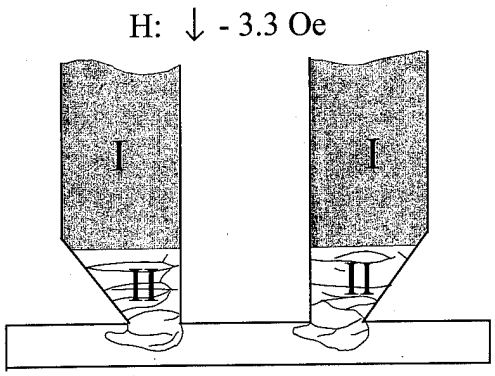



FIG. 7. Magnetic structure change of the "hook-shaped" domain when magnetic field strength $H=-3.3$ Oe, as opposed to its structure in Fig. 4.

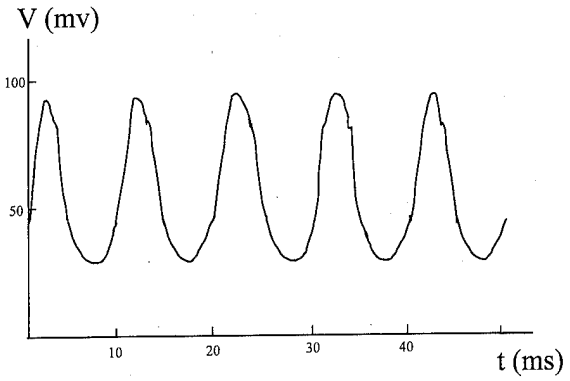



FIG. 9. Output wave form of the improved MR element, in which drops near the peak are substantially reduced.

direction rotated from the elevation angle to depression angle direction and the shape of the domains varied in such a mode that its stretch direction also changed from elevation to depression direction and the direction of the hooks transited from right to left abruptly as in Fig. 7. This phenomenon also leads to the drop found near the peak of output wave form. The appearance of hook-shaped domains has not been reported in any literature yet.

Obviously, the motion of domain walls and the generation of new domains caused Barkhausen noise. The design of MR element was modified, as shown in Fig. 8, in order to eliminate the drop. The region II was also coated with gold as region I. It was discovered that the drop was reduced substantially and the wave form of output signal was improved for this modified MR element (Fig. 9).

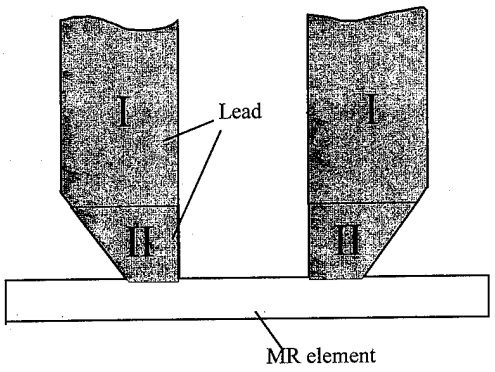



FIG. 8. Improved MR element structure, where two deposited leads are coated entirely and uniformly with gold.

It is one of the explanations that the gold coating shunted current in the Ni/Fe permalloy layer of the leads. Therefore, it reduced the distortion of output signals caused by the multidomain in the Ni/Fe layer.

This observation shows that the multidomains in region II of leads and the hooked domain structure appeared in the junction of leads and MR active regions are related to MR element geometry and structure. The motion and merge of domain walls as well as the generation of new domains cause the noise and the drop of output signals.

## IV. CONCLUSION

The relation of signal distortion of MR heads to domain structure and the domain activities which appeared in part of leads and in the junction of the leads and MR active regions was studied in detail. It was shown that there existed multidomain in some region of leads and in the junction of leads and MR active regions for some MR elements. The motion and merge of domain walls as well as the production of new domains cause the noise and the drop of output signal. Suitable geometric dimensions and structure of an MR element are also very important to its high performance in the head design in addition to select the optimum biasing condition.

[1] Z. Z. Guo and E. D. Torre, IEEE Trans. Magn. **29**, 2521 (1993).
[2] S. K. Decker and C. Tsang, IEEE Trans. Magn. **16**, 643 (1980).
[3] J. K. Howard, M. F. Toney, and C. H. Tsang, U.S. Patent No. 4,809,109 (1989).
[4] J. S. Feng, J. Tippner, B. G. Kinney, J. H. Lee, R. L. Smith, and C. Chue, IEEE Trans. Magn. **27**, 4701 (1991).

# Iron whisker domain patterns imaged by garnet films

J.-G. Lee, S. A. Govorkov, and A. S. Arrott
*Simon Fraser University, Burnaby, British Columbia V5A 1S6, Canada*

Bismuth doped yttrium iron garnet thin films formed on the surfaces of a gadolinium gallium garnet substrate are used as magneto-optical indicators for quantitative studies of the micromagnetics of an iron whisker. The method does not require image processing. A field applied perpendicular to the whisker axis splits a 180° domain wall into two 90° sections slightly separated by a section magnetized in the direction of the perpendicular field. A field along the axis of the whisker has a similar effect. Where the region between the two split 90° sections intersect the surface, there is a magnetic charge that strongly affects the domain pattern of the indicator film. More generally, domain walls become visible because the local internal susceptibility is greater at the walls than in the domains. The magneto-optical indicator can be used to measure both susceptibilities. © *1996 American Institute of Physics.* [S0021-8979(96)76208-3]

## I. INTRODUCTION

Thin films of garnets are useful as magneto-optical indicators.[1] Though they were first used for studying magnetic materials, it is the development of films for studying high temperature superconductors that led us to use domain patterns in garnet films to study the micromagnetics of an iron whisker with current flowing along its axis.[2] The iron whisker is placed on the garnet film as shown in Fig. 1 and viewed between almost crossed polarizers using an optical microscope. An explanation is given for why a 180° wall is visible this way.

The indicator film is a Bi doped yttrium iron garnet formed on the surfaces of a gadolinium gallium garnet substrate of high perfection, flat and smooth on the scale of optical wavelengths.[3] The film is on both sides of the substrate, but because the substrate is 230 $\mu$m thick, only one surface is in focus at a time. The indicator films are several microns thick. Below a characteristic field $H_c \sim 120$ Oe the films exhibit stripe domains and, sometimes, bubbles. The field at the end of a stripe domain depends on whether the applied field is increasing or decreasing. A fully quantitative use of the technique should include calibration of the hysteresis of the films.

The finger pattern seen in Fig. 2 is from the film adjacent to the whisker. There is an applied field $H_p \sim 35$ Oe perpendicular to the film. As shown below, this results in a total field at the film which is ~55 Oe and uniform over most of the surface. The field exceeds 120 Oe at the edges of the whisker (see Sec. II) and in the center at the position of the 180° wall (see Sec. III). The spacing and width of the fringes changes with perpendicular field.[4] There was no applied field $H_0$ parallel to the axis nor is there a current in the whisker for Fig. 2. That the fields are large at the edges follows from the magnetostatics of an ideally soft ferromagnetic material, which is a good approximation for the iron whisker.[5] The large field above the 180° domain wall is the result of $H_p$ separating that wall into two 90° sections joined by a section magnetized in the direction of $H_p$.

Observations and explanations of some effects of $H_0$ and a current in the whisker are given briefly in Secs. IV–VI.

## II. EXTERNAL FIELDS IN RESPONSE TO A PERPENDICULAR FIELD

In a perpendicular field $H_p$ the charges on the surface of an ideally soft ferromagnetic material can be calculated using the Ritz method where a suitable functional form of the charge distribution is assumed. The parameters are adjusted to produce a uniform field in the whisker that precisely cancels the applied field. For a whisker with square cross section and area $d^2$, the charges on the top surface are approximated by the function $M_y(x)$ and the charges on the side surfaces are approximated by the function $M_x(y)$. These functions are shown in Fig. 3(a) along with the fields from the charges, $H'_y(x,y)$ and $H'_x(x,y)$, calculated for the planes just outside the top surface for $y=1.02d, 1.04d$, and $1.06d$. In the center of the surface, the external susceptibility, $1/\chi_{\text{ext}} \sim 0.55\times 4\pi$, was calculated assuming that the local internal susceptibility is infinite. More properly, $1/\chi_{\text{ext}} \sim 1/\chi_i + (0.55\times 4\pi)$, where $\chi_i = M_s/H_k$, which is 3, changing $\chi_{\text{ext}}$ by one part in $3\times 0.55 \times 4\pi = 20$. The present experiment is not quantitative enough to measure the effect of the anisotropy field $H_k$ in the presence of the dominant demagnetizing fields.

For the whisker shown in Fig. 2 $d=320$ $\mu$m. This is a rather fat whisker, but not quite fat enough to favor more than one 180° wall. Its length is $L=6$ mm. There is a one

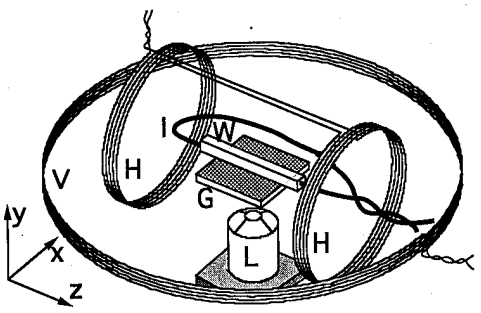



FIG. 1. Perspective sketch of an iron whisker $W$ placed on a garnet magneto-optical indicator $G$ viewed between crossed polarizers using an optical microscope represented by the objective lens $L$. There are three magnetic fields: $H_0$, from a Helmholtz pair $H$ to magnetize the whisker along its axis; $H_p$, from a coil $V$ to bias the indicator; and $H_I$, from the current $I$ along the whisker axis. The coordinate system used here is indicated.

 0021-8979/96/79(8)/6051/3/$10.00 © 1996 American Institute of Physics 

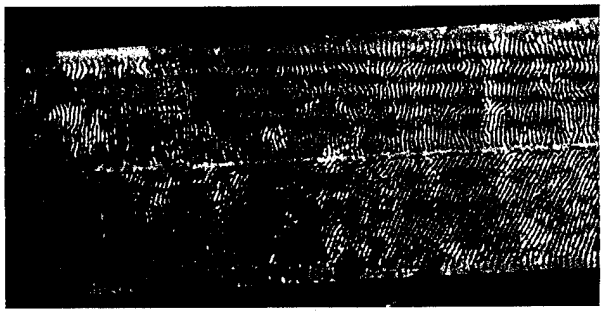


FIG. 2. The striped domain patterns in the garnet film indicate where the fields from the 320 $\mu$m wide iron whisker are less than 120 Oe. The application of $H_p$=35 Oe results in a total field at the film of ~55 Oe, uniform over most of the surface, except at the edges of the whisker and at the position of the 180° wall where it is greater than 120 Oe. The horizontal bands of light and dark background are optical interference fringes.

degree inclination of the indicator film with respect to the whisker surface. This tilt accounts for the optical fringes seen running almost parallel to the edges of the whisker. The surface of the whisker is partially oxidized, but this has negligible effects on the response of either the whisker or the indicator film.

## III. EXTERNAL FIELDS AT A 180° WALL IN A PERPENDICULAR FIELD

The calculation in Sec. II does not account for the visibility of the 180° wall running along the middle of the whisker. In a bulk material with cubic anisotropy a 180° wall is really two 90° walls held together by magnetoelastic forces. Magnetoelastic forces are very long range and depend on the boundary conditions. For the whisker one can make the approximation that the strains, which are different for each of the three cubic axes, are nevertheless uniform. In an internal field greater than $H_{m\text{-el}}$ (for iron $H_{m\text{-el}}$=0.6 Oe) the wall will split into two 90° sections separated by a region magnetized in the direction of $H_p$; that is, the local internal susceptibility at the wall goes through infinity to negative values if the magnetization in the center of the wall was already along $H_p$. The degree of splitting is determined by the magnetic energy of the surface charges generated at the two surfaces in the process. The separation, $t$, of the walls, controlled mainly by the magnetostatic energy, is given by

$$H_p = H_{m\text{-el}} + \frac{4tM_s}{d_y}\left(\log\frac{d_y}{t} + 1\right), \tag{1}$$

where $d_y$ is the thickness of the whisker in the direction of the perpendicular field $H_p$. This relation is shown in Fig. 4 for $d_y$=320 $\mu$m. The separation of the two sets of finger patterns in the garnet indicator is given by the positions where the total perpendicular field is equal to the critical field $H_c$. This occurs at $\pm x_c$. The separation is $2x_c$ given by

$$2x_c = 2\sqrt{\frac{2stM_s}{H_c - 1.55H_p} - s^2}, \tag{2}$$

where $s$ is the vertical distance from the charge at the surface of the whisker to the film. The factor 1.55 multiplying $H_p$ comes from the fields produced by the charges on the entire surface of the whisker; see Fig. 3(a). As $H_p$ approaches $H_c$/1.55=77 Oe, the separation of the finger patterns diverges. Equations (1) and (2) can be used to calculate the dependence of the observed separation, $2x_c$, on $t$ (or $H_p$) for a given $s$. This is shown in Fig. 4. It takes a separation of the walls by a few hundreds of nanometers to produce a separation of the finger patterns by tens of microns. An applied field of 35 Oe gives a splitting of the wall by about 0.2 $\mu$m which for $s$=6 $\mu$m produces an additional 115 Oe at the indicator film just above the wall.

## IV. EXTERNAL FIELDS IN RESPONSE TO A PARALLEL FIELD

There are large fields $H'_\perp$ perpendicular to the surface caused by the magnetic surface charges $\sigma$ that give rise to the demagnetizing field that all but cancels $H_0$ in this magnetically soft material. The charges are proportional to $H_0$ and depend on $z$, the distance along the axis from the center of the whisker. These fields can be assessed from calculations of demagnetizing effects in ideally soft magnetic materials.[6]

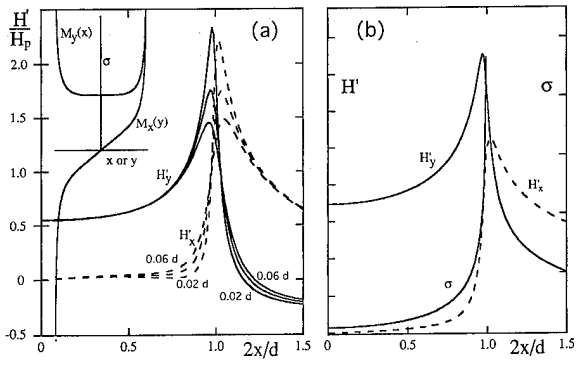



FIG. 3. Calculated components $H'_y$ and $H'_x$ of the external fields from the charges on the whisker surfaces, induced by applied fields: (a) $H_p$; (b) $H_0$. In (a) $H'_y$ and $H'_x$ arise from the charge distributions $\pm M_y(x)$ on the top and bottom surfaces and $\pm M_x(y)$ on the side surfaces. The curves are for three separations ($s$=0.02 $d$,0.04 $d$, and 0.06 $d$) between the top surface and the indicator film. In (b) $H'_y$ and $H'_x$ arise from $\sigma$ ($x$ or $y$,$z$), Eqs. (3)–(4), which is the same on all four surfaces and starts out linearly in $z$ from the midplane.

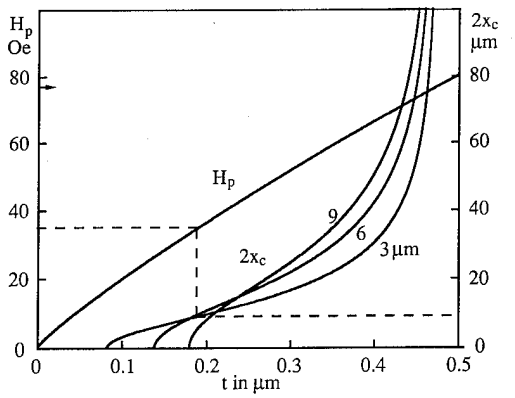



FIG. 4. Relations between the applied perpendicular field $H_p$, the separation $t$ of the two 90° sections of the split 180° wall, and the separation $2x_c$ of the two sets of finger patterns in the indicator film, for 3, 6, and 9 $\mu$m spacings between the indicator film and the top surface of the whisker.

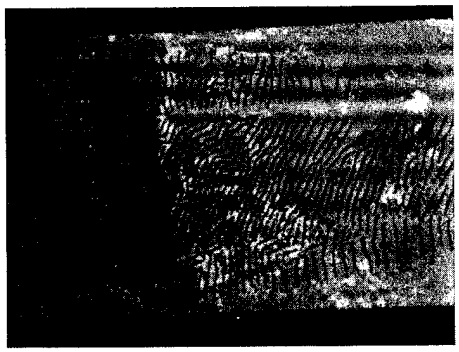


FIG. 5. Striped domain patterns in the indicator film for $H_0 \sim 50$ Oe. This displaces the 180° wall and develops charges on the surfaces as calculated in Fig. 4. The contour of the extremity of the finger pattern is described by $z \propto 1/f(x)$, where $f(x)$ is given by Eq. (4).

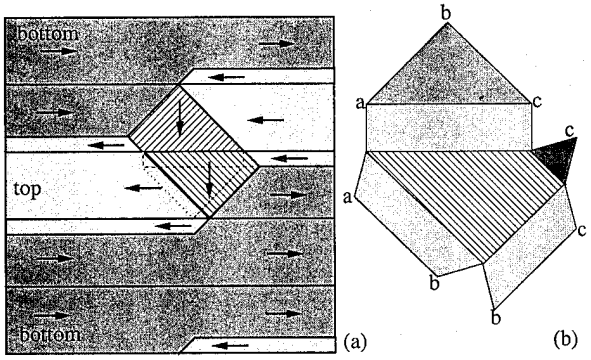



FIG. 6. The transition structure which connects two orthogonal 180° walls, illustrated for an $H_0$ which almost saturates the central cross section. One of the two identical connecting domains is shown from the top in dotted outline in (a) and in cut out form in (b). This structure can be moved by perpendicular fields and by currents along the whisker.

To a crude approximation for $10 < L/d < 100$, in the center of the whisker face at a distance $z$ from the midplane, $H'_\perp(0,z) \cong (3.5+0.2L/d)(2z/L)H_0$. For a whisker with $L/d = 25$ at $z = L/4$, $H'_\perp(0,L/4) = 4H_0$. The profile of the surface charges and the components of the external fields that they produce are shown in Fig. 3(b) as calculated from

$$\sigma(x,z) = \frac{\lambda(z)}{24} f\left\{\frac{2x}{d}\right\}, \tag{3}$$

where

$$f\{x\} = [1.024\{(1-x)^{-1/3} + (1+x)^{-1/3}\} - 0.0913 - 0.036x^2 - 0.066x^4], \tag{4}$$

where $\lambda(z)$ is the charge on all four sides per unit length. For $\lambda(z) \propto z$, contours of constant external field, in the limit of small separation between the indicator film and the top surface of the whisker, are given by $z \propto 1/f\{x\}$ which are approximately ellipses centered on the midpoint of the surface. Figure 5 shows such a contour, distorted slightly by the small angle between the indicator film and the whisker surface.

The wall is visible for moderate values of $H_0$, as shown in Fig. 5, for almost the same reason that the walls are visible for $H_p$. In both cases it is easier to create charge by breaking the 180° wall into two 90° sections than to rotate the magnetization out of the plane in the domains. One could say that the local internal susceptibility is higher at the wall than in the domain. Indeed, the local internal susceptibility for the splitting of the 180° wall goes to infinity when the perpendicular component of the internal field $H_{i\perp} = H_{m\text{-el}}$ and is negative for $H_{i\perp} > H_{m\text{-el}}$.

## V. MOVING DOMAINS WITH PERPENDICULAR FIELDS AND CURRENTS

The position of the 180° wall is determined by $H_0$ and is not affected by $H_p$. For more complicated domain structures and in the presence of the field from the axial current, there can be interactions of the domain configurations with $H_p$. The well-known diamond structure moves under the influence of the perpendicular field. A particularly interesting effect occurs for the transition structure, explained by DeBlois and Graham,[7] shown in Fig. 6, which connects two 180° walls that are orthogonal to one another. This structure can be generated by combinations of $H_0$ and $H_p$. When the structure is near one end of the whisker, it is stable up to a critical current or a critical perpendicular field at which it propagates down the whisker switching the dominate 180° wall from the $xz$ plane to the $yz$ plane.

## VI. PARTIALLY SATURATED IRON WHISKERS

If $H_0 > H_d$, which saturates the center of the whisker, there will be very little charge on the surface for $|z| < z_s$, the limit of saturation. The fringes follow $z_s$ as the field draws the magnetic charge, the sum of which does not change for $H_0 > H_d$, closer to the ends. Then the contours of $H_c$ are observed to be much flatter across the whisker, as predicted[5] for partially saturated whiskers, compared to the case shown in Fig. 5.


[1] A. A. Polyanskii, V. K. Vlasko-Vlasov, M. V. Indenbom, and V. I. Nikitenko, Sov. Tech. Phys. Lett. **15**, 872 (1989).
[2] J.-G. Lee and A. S. Arrott, J. Appl. Phys. **75**, 7006 (1994).
[3] The indicator film, commercially available, was provided by Prof. B. Heinrich, Director of the Surface Physics Laboratory of Simon Fraser University.
[4] A. H. Bobeck and E. Della Torre, *Magnetic Bubbles* (North Holland, Amsterdam, 1975).
[5] T. L. Templeton, A. S. Arrott, and A. Aharoni, J. Appl. Phys. **55**, 2189 (1984).
[6] T. L. Templeton and A. S. Arrott, IEEE Trans. Magn. **MAG-23**, 2650 (1987).
[7] R. W. DeBlois and C. D. Graham, Jr., J. Appl. Phys. **29**, 931 (1958).

# Temperature and field dependence of domain wall dynamics up to the Curie point of EuO

A. Flosdorff, D. Görlitz, and J. Kötzler
*Institut für Angewandte Physik, Universität Hamburg, Jungiusstrasse 11, D-20355 Hamburg, Germany*

Using a broadband vectorial microwave reflectometer, the dynamic susceptibility has been measured on a EuO sphere in the range from 0.3 to 20 GHz. The data taken at zero field between 4.2 K and the Curie temperature $T_c$=69.5 K were analyzed using a phenomenological model of a damped harmonic oscillator for the domain walls, that has been successfully applied to the early investigations on ferrites. Based on the micromagnetic Landau–Lifshitz (LL) model, the temperature variation of the intrinsic resonance and damping frequencies are explained up to $T$=0.98 $T_c$. The resulting LL-kinetic coefficient, $L_\perp = 1.1\times 10^{11}$ s$^{-1}$, remains independent of temperature and is related to the dipolar induced relaxation rate of the longitudinal magnetization fluctuations. In fields along the easy [111] axis and the symmetric [100] direction this wall process prevails for magnetizations smaller than $M_s/4$ and $M_s/\sqrt{3}$, respectively. Above these thresholds, the characteristic frequencies of the dominant process decrease with field, possibly due to rotational dynamics, and for $\mathbf{H}\|[111]$ a second dynamics associated with the paraprocess is contributing.
© *1996 American Institute of Physics.* [S0021-8979(96)76308-X]

## I. INTRODUCTION

Recently, investigations of domain wall (DW) dynamics of the cubic model ferromagnets EuS ($T_c$=16.6 K) and EuO ($T_c$=69.1 K) have been started[1,2] in order to gain a more quantitative understanding of the effects of thermal fluctuations, microscopic damping mechanisms, anisotropy, and domain structure on this collective phenomenon of practical importance. The present work examines in further detail the temperature variations of the wall dynamics of EuO and, in particular, the influence of magnetic fields and of the cubic anisotropy $H_A$=240 Oe ($M_s(T)/M_s(0)$)[5,3] We also try to explain the values of the characteristic frequencies which turn out to be rather high compared to corresponding results for ferrites,[4] garnets,[5] and thin films.[6]

First results obtained by measurements of the dynamic susceptibility $\chi(\omega)$ in zero magnetic field between 4.2 K and $T_c$ of needle-shaped ellipsoids (demagnetization coefficient $N_z \leqslant 0.1$) of EuS (Ref. 1) and EuO (Ref. 2) have been explained assuming a damped oscillator shape for the dynamic wall susceptibility

$$\chi_w(\omega)=(\chi_w^{-1}-(\omega/\Omega_w)^2+i\omega/L_w)^{-1}. \tag{1}$$

This shape derives from the Landau–Lifshitz (LL) equation of motion with the damping term $(L_\perp/M_s^2)(\mathbf{M}\times\mathbf{M})\times\mathbf{M}$ and also follows from a recent more general ansatz[7] in the micromagnetic limit. Instead in terms of the conventional wall-damping and mass,[4] we have represented $\chi_w(\omega)$ by using the kinetic coefficient of the damping,

$$L_w=\frac{(\gamma M_s)^2+L_\perp^2}{L_\perp}\frac{2\delta}{d} \tag{2a}$$

and the resonance frequency of the walls

$$\Omega_w^2=L_\perp L_w, \tag{2b}$$

because these quantities do not depend on the static wall susceptibility $\chi_w$. Basically, they are determined by the ratio of the widths of the walls ($\delta$) and the domains ($d$) and by the LL coefficient $L_\perp$. Note that the kinetic coefficient determines the mobility of the walls $\mu_w \equiv v/\Delta H = L_w d/2M_s$. Effects of sample demagnetization and contributions of other processes to $\chi(\omega)$ have been taken into account by the form

$$\chi(\omega)=\left[\left(\sum_{i=1}^{2}\chi_i(\omega)\right)^{-1}+N_z\right]^{-1} \tag{3}$$

which means that in a first-order approximation[6] the coupling of the walls to the other processes is only provided by the ac-demagnetization field. The results for the less anisotropic EuS [$H_A(T=0)$=24 Oe (Ref. 3)] could be well described by Eq. (3), surprisingly for temperatures extending to $T_c$, i.e., far away from the micromagnetic limit.

Using a broadband microwave reflectometer described elsewhere,[8] we measured the linear complex susceptibility of a single crystalline sphere, ∅=3 mm, between 0.3 and 20 GHz. External fields up to 10 kOe were applied parallel to the ac-field and oriented along either a hard [100] or an easy [111] axis of the crystal. No significant hysteresis effects have been detected in the present range of temperatures and fields which indicates a rather weak DW pinning. This is not inconsistent with the fairly large $\delta/d$ ratios following from the analysis of our data in Sec. III. [Using SQUID magnetization data[9] exemplified by Fig. 3(a), all applied fields $H_a$ have been corrected for demagnetization, $H=H_a-N_zM$.]

Typical frequency scans for dispersion and absorption taken at fixed temperature, $T$=0.43 $T_c$ are shown in Fig. 1. In zero applied field, Fig. 1(a), there is no anisotropy, as expected, and the full curves represent the fit to Eq. (2) considering only $\chi_w(\omega)$. The same single oscillator model describes the dynamic susceptibility measured for $H$=18 Oe applied parallel to the [100] and [111] directions, Fig. 1(b). Though this internal field is small compared to the anisotropy field, $H_A(T=0.43T_c)$=110 Oe, a distinct influence on the dynamic susceptibility is already realized. Before discussing this interesting feature let us consider the effect of temperature at zero field.

 0021-8979/96/79(8)/6054/3/$10.00 © 1996 American Institute of Physics

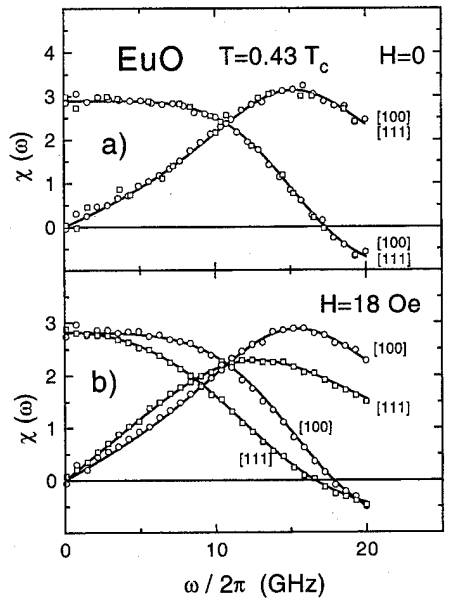



FIG. 1. Dynamic susceptibility of a EuO sphere (a) in zero magnetic field and (b) at internal field 18 Oe applied along the easy [111] and a hard [100] axis. Full lines are fits to Eq. (3) with $\chi_2=0$.

## II. TEMPERATURE VARIATION AT $H=0$

The intrinsic resonance frequencies and the kinetic coefficients of the DWs obtained from fits for data measured in the two crystallographic directions to Eq. (3) are depicted in Fig. 2. Both quantities decrease continuously towards the Curie temperature and the solid lines have been obtained by fits to Eq. (2). Except for temperatures very close to $T_c$, which will be discussed in a future paper,[10] we find excellent agreement using a temperature independent value for the LL parameter, $L_\perp=1.1(2)\times10^{11}$ $s^{-1}$, and for the ratio $\delta/d=0.08(2)m_s^{-\alpha}$, where $\alpha=1.0(1)$. The reduced magnetization $m_s=M_s(T)/M_s(0)$ has been inferred from neutron data.[11] These results agree with those published previously for a EuO needle ($N_z=0.06$)[2] indicating the validity of the dynamic demagnetization, Eq. (3).

Let us first discuss the ratio $\delta/d$ by assuming (i) closure domains at the surface, which give rise to DW period of $d\approx\sqrt{D\,\delta_B}$ in a sample of effective thickness $D$ and (ii) 180°-Bloch walls of width $\delta_B=\chi_A^{1/2}/q_d$ (Ref. 12) to dominate the mobility at low fields. Since the susceptibility associated with the anisotropy field of EuO varies as $\chi_A(T)=M_s/H_A\sim M_s^{-4}(T)$,[3] we find for the ratio, $\delta/d\approx\chi_A^{1/4}/(q_dD)^{1/2}\sim M_s^{-1}(T)$, which corresponds exactly to the temperature variation derived from DW resonance. This gives further evidence for the validity of the micromagnetic approach up to temperatures as high as 0.97 $T_c$ probed here.

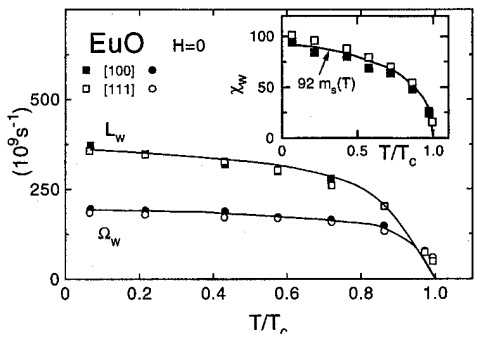



FIG. 2. Temperature variations of the wall resonance $\Omega_w$ and damping $L_w$ defined by Eq. (1) in zero field. Solid curves represent fits to Eq. (3). Inset: static wall susceptibility.

Addressing the magnitude of the LL coefficient, $L_\perp$, we are not aware of any rigorous approach to it. We note here that the analysis of relaxation data in the homogeneously magnetized state of EuO, $H\gg H_A$,[13] revealed a correlation frequency of the torques flipping the magnetization with exactly the same value. There for EuO and also for EuS (Refs. 2 and 14) this (high) frequency could be identified with the decay rate $\Gamma_l(q\to0)$ of longitudinal magnetization fluctuations, $\mathbf{M}(\mathbf{q}\|\mathbf{M})$, which recently has been measured directly by inelastic neutron scattering on EuS.[15] Since this relaxation rate was also in numerical agreement with a prediction of mode coupling work,[16] it remains a challenge to establish the possible relation between $L_\perp$ and $\Gamma_l(\mathbf{q}\to0)$.

Finally we note that the (internal) wall susceptibility shown by the inset to Fig. 2 decays in a rather simple way, $\chi_w(T)=92(4)M_s(T)/M_s(0)$, to zero. If we assume that the static DW response arises from reversible oscillations about local minima of the potential energy $U(x)$ for the walls, then the present finding implies that the restoring force constant $\partial^2U/\partial x^2$ acting on the walls varies with $M_s^2(T)$.

## III. FIELD EFFECTS AT $T=0.43T_c$

The significant effect of an even small internal field parallel to the easy [111] direction on the dynamic response $\chi(\omega)$ is seen in Fig. 1. Whereas for all fields parallel to the [100] axis, $\chi(\omega)$ can be fitted by taking one Lorentzian in Eq. (2), for $\mathbf{H}\|[111]$ there are two processes required for fields $H\geqslant H_1\approx20$ Oe. Interestingly, at this threshold field $H_1$ the magnetization has reached one quarter of the spontaneous value [see Fig. 3(a)], which may be associated with the disappearance of the $[\bar1\bar1\bar1]$ domains due to 180°-wall motion. Above $H_1$, the kinetic coefficient $L_1$ [Fig. 3(b)] and the resonance frequency $\Omega_1$ [Fig. 3(c)] of the process with the dominant static susceptibility $\chi_1$, which is depicted in Fig. 3(a), rapidly decrease with field. The second dynamic process, $\chi_2(\omega)$, contributing $\chi(\omega)$ for $\mathbf{H}\|[111]$ arises from the homogeneous magnetization in the domains, the so called paraprocess with $\chi_2\ll\chi_1$, which is studied in a separate work.[13] This process survives at large fields $H\gg H_A$, where the six unfavorably oriented domains have been turned into the field direction, i.e., parallel to [111]. More details of the dominant process $\chi_1(\omega)$, for which coherent domain rotations have to be considered, will be given in a fuller paper.[10]

For fields along the [100] direction, on the other hand, the kinetic coefficients and resonance frequencies retain their zero field values until a larger threshold field is reached, $H_2=45$ Oe. Looking at the magnetization reached at that field in Fig. 3(a), we find $M(H_2)=M_s/\sqrt{3}$, which suggests that for $H\leqslant H_2$ the four unfavorably oriented (111) domains with magnetization components antiparallel to $\mathbf{H}$ are removed. This would imply, that as for $H=0$, 180° walls are

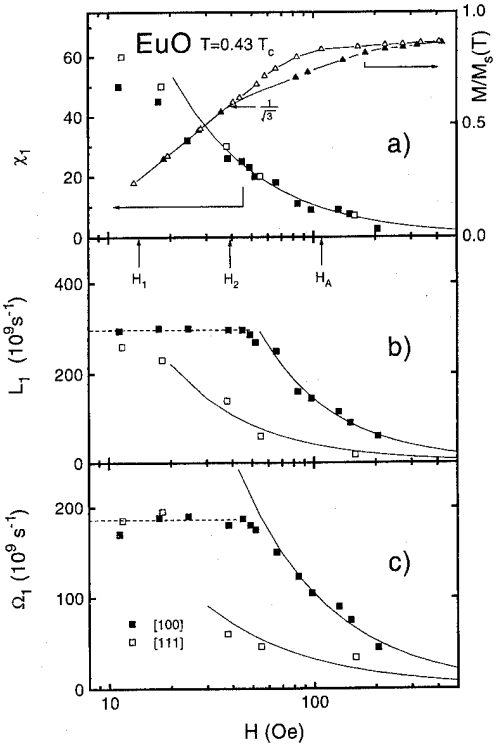



FIG. 3. Field variation of the internal (a) susceptibility, (b) kinetic coefficients of the damping, and (c) resonance frequencies of the dominant dynamic process for two principal orientations of $H$ at $T=0.43T_c$. Full lines represent empirical power laws in $H$. Panel (a) includes magnetization data (Ref. 9).

operative and this conclusion is fully confirmed by the field independence of $L_1$ and $\Omega_1$, so that we identify $\chi_1(\omega)$ with $\chi_w(\omega)$.

Above $H_2$, the characteristic frequencies of the dominant process decrease with field $\mathbf{H}\|[100]$ in qualitatively the same way as for $H>H_1$ when $\mathbf{H}\|[111]$. For the present fully symmetric configuration, the anisotropy field keeps the magnetizations along the easy directions, and for internal fields $H\approx H_A$ [Fig. 3(a)] coherent rotations are expected to dominate, $\chi_1(\omega)=\chi_R(\omega)$. Interestingly, Fig. 3(a) shows that the static susceptibility of this rotation agrees with that associated with the rotation for $\mathbf{H}\|[111]$ $(H>H_2)$, and that we can describe the field variation by an empirical power law, $\chi_R\sim H^{-a_\chi}$ with $a_\chi=0.80(5)$. Such power laws can also explain the decay of the resonance and kinetic coefficients, indicated in Figs. 3(b) and 3(c), with slightly different exponents, $a_L=1.06(9)$ and $a_\Omega=1.00(2)$. More details, in particular on the temperature variation and the interference of all three magnetization processes in the dynamics will be published in the near future.

## ACKNOWLEDGMENTS

We thank M. Baumann for providing us with the magnetization data and the Deutsche Forschungsgemeinschaft for financial support.

[1] D. Görlitz, J. Kötzler, and Th. Lange, J. Magn. Magn. Mater. **104–107**, 339 (1992).
[2] J. Kötzler, D. Görlitz, M. Hartl, and Chr. Marx, IEEE Mag. **30**, 828 (1994).
[3] A. Kasuya and M. Tachiki, Phys. Rev. B **8**, 5298 (1973).
[4] G. T. Rado, R. W. Wright, W. H. Emerson, and A. Terris, Phys. Rev. **88**, 909 (1952); G. T. Rado, Rev. Mod. Phys. **25**, 81 (1953).
[5] J. Morkowski, H. Dötsch, P. E. Wigen, and R. J. Yeh, J. Magn. Magn. Mater. **25**, 39 (1981).
[6] A. A. Parker, M. A. Parker, and P. E. Wigen, J. Appl. Phys. **52**, 2347 (1981).
[7] D. A. Garanin, Physica A **172**, 470 (1991); **178**, 467 (1991).
[8] D. Görlitz, J. Kapoor, and J. Kötzler, J. Phys. E **22**, 884 (1989).
[9] M. Baumann (private communication).
[10] D. Görlitz and J. Kötzler (to be published).
[11] J. Als-Nielsen, O. W. Dietrich, and L. Passell, Phys. Rev. B **14**, 4908 (1976).
[12] M. Grahl and J. Kötzler, Z. Phys. B **75**, 527 (1989).
[13] A. Flosdorff, D. Görlitz, and J. Kötzler, this conference.
[14] R. Dombrowski, D. Görlitz, J. Kötzler, and Chr. Marx, J. Appl. Phys. **75**, 6054 (1994).
[15] P. Böni, D. Görlitz, J. Kötzler, and J. L. Martinez, Phys. Rev. B **43**, 8755 (1991).
[16] E. Frey and F. Schwabl, Z. Phys. B **71**, 355 (1988).

# The dependence of magnetoacoustic emission on magnetizing frequency in nickel and mild steel

D. H. L. Ng,[a] C. C. Yu, and C-D. Qin
*Department of Physics, The Chinese University of Hong Kong, Shatin, Hong Kong*

C. C. H. Lo and J. P. Jakubovics
*Department of Materials, University of Oxford, Parks Road, Oxford OX1 3PH, United Kingdom*

Magnetoacoustic emission (MAE) measurements have been made on nickel and mild steel samples subjected to a magnetizing field of various frequencies $f$. In both samples, the MAE signals are found to increase with increasing $f$. The experimental results are in good agreement with the predictions of a model relating the generation of MAE to domain wall nucleation-annihilation and domain wall motion. When $f$ is large, the contribution of wall motion to the generation of MAE is predicted to be dominant. Conversely, when $f$ is small, MAE is generated mainly by domain wall nucleation-annihilation processes. At high frequencies, the amount of MAE from both nickel and mild steel samples is found to vary linearly with $f^{0.5}$. As $f$ decreases, the MAE deviates from the $f^{0.5}$ relationship for $f<10$ Hz in mild steel, and for $f<2$ Hz for nickel. The results suggest that in nickel, wall motion remains the dominant source of MAE generation over a wider frequency range than in steel. © *1996 American Institute of Physics.* [S0021-8979(96)76408-6]

## I. INTRODUCTION

Magnetoacoustic emission (MAE) is the generation of elastic waves due to changes of magnetostrictive strains during the process of magnetization. It is known that MAE is produced by the motion of domain walls and the processes of domain wall nucleation and annihilation.[1,2] The amplitude of the MAE signal generated is determined by the rate of change of magnetostrictive strain, which depends on (i) the magnitude of the magnetostrictive behavior of the material, and (ii) the rate of change of the magnetic induction, $dB/dt$.[3] In this article we report a study of the dependence of the MAE signals on $dB/dt$, which is determined by the frequency $f$ of the magnetizing field, and the magnetic induction $B$ inside the sample. We formulate a model, in which the MAE signal is expressed explicitly as a function of $f$ by relating the MAE to domain wall motion and the nucleation-annihilation of domain walls. This model provides information about the relative contributions of wall motion and of wall nucleation and annihilation processes involved in the MAE generation. We have calculated the relative MAE output for nickel and mild steel at different frequencies using this model. The result is compared with MAE measurements made on these materials.

## II. EXPERIMENTS AND RESULTS

The dependence of MAE on the frequency of the applied field was investigated on a nickel bar and a mild steel bar, both of thickness about 6 mm. During the measurements, an alternating magnetizing field of triangular wave form and amplitude up to 43 kA $m^{-1}$ was produced by a $c$-core electromagnet placed at the center of the bar as shown in Fig. 1(a). The magnetizing frequency $f$ was varied from 0.5 Hz to 60 Hz. A plastic spacer was inserted between the $c$-core magnet and the sample to minimize the electrical and acoustic noises. The MAE signals detected by a piezoelectric transducer were amplified, rectified and filtered. The mean signals were then plotted as a function of the field over the complete hysteresis cycle. Each measurement was repeated 25 times and averaged in order to improve the signal-to-noise ratio. The MAE profiles for half of the hysteresis cycle usually contain a single central peak for nickel and two outer peaks (initial and final) for mild steel. Typical MAE profiles of both nickel and mild steel are shown in Fig. 1(b). All the MAE profiles obtained are characterized for analysis by their peak heights. Logarithmic plots of the MAE signal (normalized at 0.5 Hz) $V_{tot}$, against $f$ for the nickel bar and the steel bar are

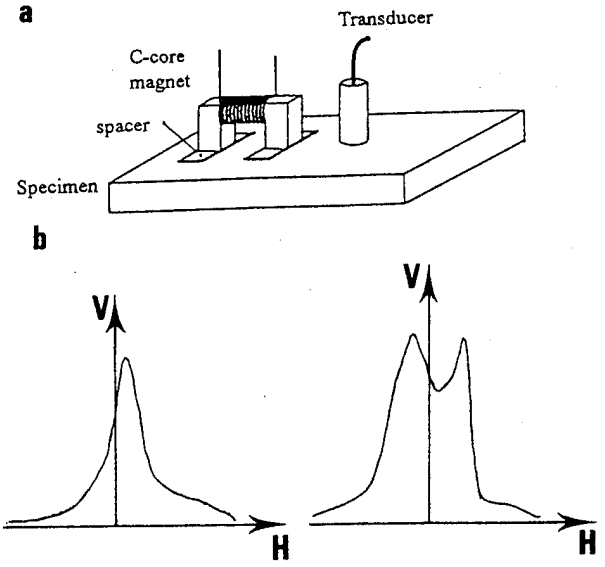



FIG. 1. (a) A diagram to show the experimental arrangement for the MAE measurements. (b) The MAE profiles of nickel (left) and mild steel (right) samples obtained with a magnetizing field frequency of 0.5 Hz. The two profiles are not in the same vertical scale, $V$ is the MAE signal and $H$ is the applied field.

[a]Electronic mail: B108771@vax.csc.cuhk.hk

 0021-8979/96/79(8)/6057/3/$10.00 © 1996 American Institute of Physics 

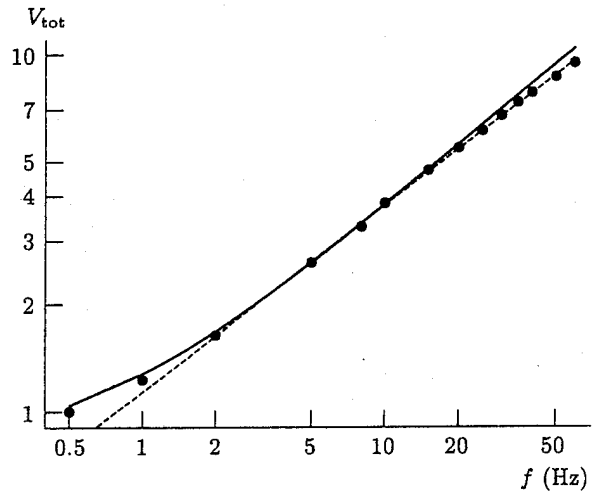



FIG. 2. Logarithmic plot of $V_{tot}$ (normalized at a frequency of 0.5 Hz) against $f$ for the nickel bar. The points (full circles) correspond to experimental results, the dashed line shows the $f^{0.5}$ variation fitted to the points at higher $f$, and the full curve was deduced from the model.

shown in Figs. 2 and 3 respectively. The results show that $V_{tot}$ increases steadily with increasing $f$ when $f$ is large, being a linear function of $f^{0.5}$. However, $V_{tot}$ deviates from the $f^{0.5}$ dependence when $f<10$ Hz in the case of steel (Fig. 3), whereas the $f^{0.5}$ dependence is followed down to $f\approx 2$ Hz for nickel (Fig. 2).

## III. THE MAE MODEL

Based on a classical domain wall motion model,[4] the MAE output $V_{dm}$ within a period of time $\tau$ is given by

$$V_{dm}\sim\frac{1}{\tau}\int \delta E\frac{dH}{dt}n(H)dt, \tag{1}$$

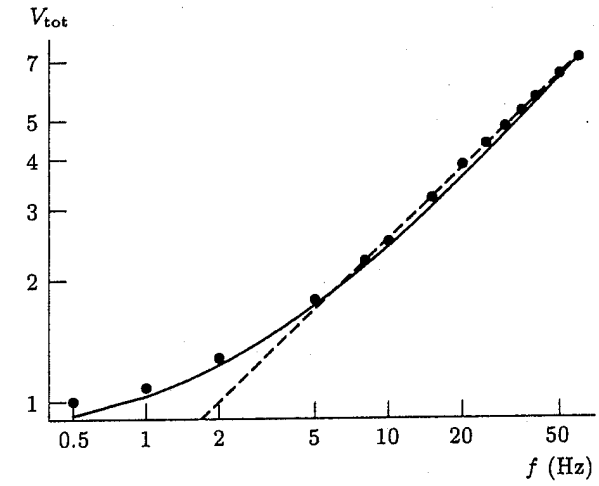



FIG. 3. Logarithmic plot of $V_{tot}$ (normalized at a frequency of 0.5 Hz) against $f$ for the steel bar. The points (full circles) correspond to experimental results, the dashed line shows the $f^{0.5}$ variation fitted to the points at higher $f$, and the full curve was deduced from the model.

where $\delta E$ is the change of elastic energy during the motion of non-180° domain walls, and $n(H)dH$ is the corresponding number of emission sites when the magnetizing field changes from $H$ to $H+dH$. As seen from Eq. (1), the MAE signal is proportional to the rate of change of applied field $dH/dt$. We can therefore write $V_{dm}$ in the form of the rate of change of magnetic induction $B$, which varies as a triangular wave form inside the sample,

$$V_{dm}=C_{dm}\frac{dB}{dt}=C_{dm}B_{max}f. \tag{2}$$

Here $dB/dt$ has been replaced by $B_{max}f$ where $B_{max}$ is the maximum magnetic induction in the sample corresponding to the maximum magnetizing field, and $C_{dm}$ is the proportional constant. Because of the eddy current shielding, significant values of $B$ can only be found within the skin depth, which is proportional to $f^{-0.5}$, and thus the total MAE signal $V'_{dm}$ detected will depend on $f$ in the following way:

$$V'_{dm}=C'_{dm}B_{max}\sqrt{\frac{\rho}{\mu\pi}}f^{0.5}, \tag{3}$$

where $\rho$ and $\mu$ are the resistivity and permeability of the material respectively, and the proportional constant $C'_{dm}$ is equal to $C_{dm}/l_0$ where $l_0$ is the thickness of the sample. In a study of the frequency dependence of the number of domain wall nucleation-annihilation events, it was found that by minimizing the total energy dissipated during the magnetization process with respect to the number of nucleated domain walls,[5] that the total number of domain walls $N_{dw}$ is proportional to $B_{max}f^{0.5}$ when $f$ is above a threshold frequency. When considering the MAE output due solely to the processes of domain wall nucleation-annihilation, the corresponding MAE signal $V_{na}$ is then given by

$$V_{na}=C_{na}B_{max}f^{0.5}, \tag{4}$$

where $C_{na}$ is a constant. When taking the eddy current shielding into consideration, we replace $C_{na}$ by $C'_{na}$ which is equal to $C_{na}/l_0$, the total MAE signal $V'_{na}$ is therefore given by

$$V'_{na}=C'_{na}B_{max}\sqrt{\frac{\rho}{\mu\pi}}, \tag{5}$$

and is independent of the frequency of the applied field. Based on the above results, we can attribute the total MAE signal $V_{tot}$ to a combination of domain wall motion and domain wall nucleation-annihilation processes. We can obtain $V_{tot}$ by combining $V'_{dm}$ and $V'_{na}$ as follows:

$$V_{tot}=(V'^2_{dm}+V'^2_{na})^{1/2}=B_{max}\sqrt{\frac{\rho}{\mu\pi}}(C'^2_{dm}f+C'^2_{na})^{1/2}. \tag{6}$$

The magnetic induction $B_{max}$ inside the sample is not easy to determine. To find $B_{max}$, we have to consider the magnetic circuit formed by the $c$-core magnet, the two spacers (one for each pole), and the specimen. The reluctance of the circuit $\mathfrak{R}$ is given by

$$\mathfrak{R}=\sum_i \frac{l_i}{\mu_i A_i}, \tag{7}$$

where $l_i$, $\mu_i$ and $A_i$ are the length of the flux path, the permeability, and the cross-sectional area respectively of the different sections of the circuit in series. The magnetic induction $B$ which is equal to the flux per unit area, for a given magnetomotive force $NI$ of a coil of $N$ turns carrying a current $I$, is therefore inversely proportional to the product of $\Re$ and $A_s$, the cross-sectional area of the magnetic flux path in the specimen.[6] Therefore Eq. (6) can be written as

$$V_{\text{tot}} \sim \frac{1}{\Re A_s}\sqrt{\frac{\rho}{\mu\pi}}(C'^2_{\text{dm}} f + C'^2_{\text{na}})^{1/2}. \tag{8}$$

It is also difficult to evaluate the constants $C'_{\text{dm}}$ and $C'_{\text{na}}$ appearing in Eqs. (6) and (8), since they depend on various parameters of the samples such as domain dimensions and density of pinning sites, which cannot be found directly from measurements. We therefore introduce a parameter $r = C'_{\text{na}}/C'_{\text{dm}}$ to characterize the relative strength of the MAE output due to the wall motion and the nucleation-annihilation processes. The value of $r$ can be approximated by the ratio of the amplitude of the outer peaks to the amplitude of the central portion of the MAE profile. For the nickel specimen, the MAE profile usually contains a single peak around the coercivity. However, the contribution of wall motion and nucleation-annihilation to MAE can be differentiated by splitting the single peak into three peaks in the same profile by making measurement using thicker spacers.[3] The average values of $r$ was found to be 0.99 for the nickel bar. For steel, the average $V_p$ of the two outer peaks of the MAE profile is attributed to a combination of wall motion and nucleation-annihilation processes, while the central dip of height $V_c$ is a measure of MAE generated only by wall motion. Therefore $r$ can be found from

$$r = \frac{(V_p^2 - V_c^2)^{1/2}}{V_c}. \tag{9}$$

The average value of $r$ was found to be 1.56 for the mild steel bar. A separate experiment was performed to determine the permeabilities of the samples. The values of $\mu$ are 170 and 200 for the nickel and mild steel bars respectively. These values were measured in the low field regions of the magnetization loops of the samples, because in our analysis, the MAE results were characterized by the height of the peaks which usually appeared near the low field regions in the profiles. The values of $r$, $\mu$ and the pre-determined values of $\rho$, $\Re$, and $A_s$ for the nickel bar and steel bar were substituted into Eq. (8), and the normalized $V_{\text{tot}}$ values were then calculated and plotted against $f$. Plots of these calculated values are shown also in Figs. 2 and 3.

## IV. DISCUSSION

Figures 2 and 3 show that the theoretical curves of $V_{\text{tot}}$ are in good agreement with the experimental results over the whole frequency range. According to Eq. (8), when $f$ is small, the constant term $C'^2_{\text{na}}$ is dominant in $V_{\text{tot}}$, and the estimated values of $V_{\text{tot}}$ are therefore larger than those given by the $f^{0.5}$ line at the same $f$. As $f$ increases, the term $C'^2_{\text{dm}} f$ becomes dominant over $C'^2_{\text{na}}$, therefore $V_{\text{tot}}$ increases with $f$ approximately as $f^{0.5}$. It is known that the velocity $v$ of domain walls is proportional to the resistivity, and inversely proportional to the saturation magnetization $M_s$.[7] Therefore a material with a lower $M_s$ such as nickel tends to have a larger $v$ than one with a higher $M_s$ such as steel. The existence of a strong central peak in most of the MAE profiles from Ni suggest that non-180° walls in Ni move faster and are more easily unpinned than in steel, giving rise to more MAE in low fields. Thus in nickel domain wall motion plays a dominant role in the generation of MAE over nearly the whole frequency range. This assumption is supported by the MAE profiles obtained at different values of $f$, in which only a sharp peak around the coercivity can be found. Therefore the $f^{0.5}$ variation fits well with the experimental results except for $f<2$ Hz. In steel, $M_s$ is large and non-180° walls are less mobile, and the wall nucleation process therefore makes a larger contribution than the wall motion process to the generation of MAE ($r$ is larger than in nickel) especially when $f<10$ Hz. There is a greater discrepancy between the $f^{0.5}$ curve and the experimental results for $f<10$ Hz. The predicted $V_{\text{tot}}$ curve, which has taken both wall motion and wall nucleation-annihilation into consideration, however, shows good agreement with the experimental results even in the low frequency range. As $f$ increases, the contribution of the domain wall motion to the MAE signal increases, and the $C'^2_{\text{dm}} f$ term becomes more important, as also indicated by the overall increase of the MAE signal. At very high frequencies, the MAE signals due to the nucleation-annihilation and the wall motion processes tend to merge into a single, broad peak. As a result, the amplitude of the MAE signal is now mainly dominated by wall motion, and the MAE becomes a linear function of $f^{0.5}$.

## V. CONCLUSIONS

It has been shown that the MAE signal increases with $f$ and is a linear function of $f^{0.5}$ if non-180° domain wall motion is the major source of MAE. This happens in nickel over a wide range of frequencies, because nickel has a low $M_s$, the domain walls can easily be unpinned and have a larger velocity. On the other hand, in materials with large $M_s$ such as steel, domain walls have a lower velocity, and the MAE output is mainly due to the domain wall nucleation-annihilation processes. However, as frequency increases, the wall velocity also increases, and both wall motion and wall nucleation-annihilation contribute to the MAE.

This work was funded by the Research Grants Council of Hong Kong (RGC Earmarked Grant 1994/95, Ref:CUHK310/94P).

[1] D. J. Buttle, C. B. Scruby, G. A. D. Briggs, and J. P. Jakubovics, Proc. R. Soc. London Ser. A **414**, 469 (1987).
[2] M. Guyot and V. Cagan, J. Appl. Phys. **73**, 5348 (1993).
[3] D. H. L. Ng, C. C. H. Lo, and J. P. Jakubovics, J. Appl. Phys. **75**, 7009 (1994).
[4] H. Kusanagi, H. Kimura, and H. Sasaki, Proceedings of a Joint Meeting of Acoustical Societies of America and Japan, edited by K. Ono, (Honolulu, 1979), p. 309.
[5] T. R. Haller and J. J. Kramer, J. Appl. Phys. **41**, 1034 (1970).
[6] D. H. L. Ng, C. C. H. Lo, S. C. Cheng, and J. P. Jakubovics, IEEE Trans. Magn. **30**, 4857 (1994).
[7] H. J. Williams, W. Shockley, and C. Kittel, Phys. Rev. **80**, 1090 (1950).

# 180° domain wall with the coordinate dependent azimuthal angle of magnetization

V. L. Sobolev,[a] C. T. Teh, and H. L. Huang
*Department of Physics, National Taiwan University, Taipei 10764, Taiwan, Republic of China*

Structure of 180° one-dimensional domain wall (DW) in a uniaxial ferromagnet in the presence of an external magnetic field arbitrarily oriented with respect to the DW has been investigated. Solutions of the system of equations which describe the behavior of the magnetic moment inside the DW in the case when the magnetization azimuthal angle is dependent upon the coordinate normal to the DW have been obtained and influence of magnetic field on the structure of the DW analyzed. Dependences of the effective widths of the distributions of both the polar and azimuthal angles of magnetization across the DW proper have been obtained. The effective width due to the azimuthal angle variation along the DW normal was found to increase with increasing transverse field.
© *1996 American Institute of Physics.* [S0021-8979(96)76508-2]

## I. INTRODUCTION

Structure of the 180° DW in a uniaxial ferromagnet under the influence of external magnetic field normal to the anisotropy axis (the transverse field) has been already analyzed in a number of papers[1–7] (see Ref. 2 for a review). As a rule, one usually describes the structure of the one-dimensional DW based on the assumption that the azimuthal angle of the magnetization does not depend on the coordinate normal to the DW plane.[2] The only successful attempt which has taken into account the coordinate dependence of the azimuthal angle of magnetization was given in Ref. 8. This paper treated the case of the one-dimensional DW moving at a low velocity.

It was recently shown that new types of one-dimensional solutions of the system of equations for the polar and azimuthal angles of the magnetization $\mathbf{M}=M\{\sin\vartheta\cos\varphi, \sin\vartheta\sin\varphi, \cos\vartheta\}$ which describes the distribution of magnetic moment inside the DW can be obtained in the case when the transverse field is arbitrarily oriented with respect to the DW plane.[6] This new solution for the magnetization azimuthal angle is a function of the transverse field and of the coordinate normal to the plane of the DW. The solution was shown to yield lower value of the DW energy in comparison with the one in which the value of the azimuthal angle was assumed to be constant inside the DW.[6]

The purpose of the present paper is devoted to a detailed further analysis of the structural dependence of the new solutions of both the polar and azimuthal angle of the magnetization inside the one-dimensional DW. The dependence of the new solution on both the coordinate normal to the DW plane and the external field normal to the anisotropy axis arbitrarily oriented with respect to the DW plane will be thoroughly investigated.

## II. EQUATIONS AND METHOD OF SOLUTION

Consider a uniaxial ferromagnet with the anisotropy axis oriented along the $z$ axis of the coordinate frame. For convenience the DW is assumed to be pinned throughout the investigation and the wall plane is chosen to coincide with the $x-z$ plane. The orientation of the external field normal to the anisotropy axis is described by the azimuthal angle $\psi_H$ of the field with respect to the $x$ axis $\mathbf{H}=h(\cos\psi_H, \sin\psi_H, 0)$. In the frames of the uniaxial ferromagnet model we shall consider the so-called uncharged domain walls. The last means that the demagnetization part of the DW energy density can be written as follows:[2]

$$w_m=2\pi M^2\Delta_B(\sin\vartheta\sin\varphi-\mu)^2. \tag{1}$$

Here $4\pi M$ is the saturation magnetization; $\Delta_B=\sqrt{A/K}$ is the Bloch wall width parameter; $K$ is the uniaxial anisotropy constant, $A$ is the exchange stiffness constant, the parameter $\mu$ in (1) is determined by the value of the normal component of the magnetization which exists inside domains in the presence of the transverse field, that is, $\mu=\sin\vartheta_0\sin\psi_H$, where $\vartheta_0$ is the magnetization polar angle inside the domain.

The dimensionless energy density for the DW in a uniaxial ferromagnet may be written as follows:[1,2]

$$w_{\mathrm{DW}}=\frac{\omega_{\mathrm{DW}}}{\sqrt{AK}}=\int d\xi\{\vartheta'^2+\varphi'^2\sin^2\vartheta+\sin^2\vartheta + \epsilon(\sin\vartheta\sin\varphi-\mu)^2-2h\sin)\vartheta\cos(\varphi-\psi_H)\}, \tag{2}$$

where $\xi=y/\Delta_B;\vartheta'\equiv d\vartheta/d\xi,\varphi'\equiv d\varphi/d\xi;\epsilon=Q^{-1}$; the material quality factor $Q=H_K/4\pi M(H_K=2K/M);h=H/H_K$ is the reduced transverse field.

The system of equations from which the distribution of the magnetization inside the DW may be obtained has the form[1–3]

$$\vartheta''-\sin\vartheta\cos\vartheta(1+\varphi'^2+\epsilon\sin^2\varphi + \epsilon\mu\cos\vartheta\sin\varphi+\sin\vartheta_0\cos\vartheta\cos(\varphi-\psi_H)=0, \tag{3}$$

$$(\sin^2\vartheta\varphi')'-\epsilon(\sin\vartheta\sin\varphi-\mu)\sin\vartheta\cos\varphi - \sin\vartheta_0\sin\vartheta\sin(\varphi-\psi_H)=0. \tag{4}$$

The polar angle of the magnetization inside quit is determined by the relation $\sin\vartheta_0=h$, a condition which has been

[a]Current address: Dept. of Physics, National Taiwan Normal Univ., Taipei 117, ROC. Permanent address: Institute for Single Crystals of the Academy of Sciences of Ukraine.

 0021-8979/96/79(8)/6060/3/$10.00 © 1996 American Institute of Physics

properly taken care of in writing down Eqs. (3) and (4). The boundary conditions for the solutions describing the variation of the angles inside the DW have been chosen as follows:

$$\vartheta(\xi)=\vartheta(\xi;h,\psi_H)=\begin{cases}\vartheta_0, & \xi\to-\infty\\ \pi-\vartheta_0, & \xi\to+\infty\end{cases};$$

$$\vartheta'(\xi;h,\chi_H)\to 0, \quad \text{at} \quad \xi\to\pm\infty,$$

$$\varphi(\xi)=\varphi(\xi;h,\psi_H)=\psi_H, \quad \xi\to\pm\infty;$$

$$\varphi'(\xi;h,\psi_H)\to 0, \quad \text{at} \quad \xi\to\pm\infty. \tag{5}$$

The system of Eqs. (3) and (4) along with the boundary conditions (5) has been solved numerically using the adaptive Runge–Kutta–Fehlberg method.[9] The interval of the variation of the coordinate $\xi$ was chosen to be equal to $-15\leqslant\xi\leqslant 15$. The step of the $\xi$ variation was adjusted automatically. We have obtained the set of dependences for $\vartheta(\xi)$ and $\varphi(\xi)$ for several orientation values of the azimuthal angle of the external field $\psi_H$=30°, 35°, 40°, 45°, 50°, 60°, 70°, 80°, and 90° and for several values of the reduced transverse field $h$=0.01, 0.05, 0.1, 0.2, and 0.25. The characteristic value of the material quality factor $Q$ was chosen to be equal to $Q$=2.0 for easy convenience of making comparison with the results obtained in Refs. 6 and 7 where a slightly different method of numerical solution of the system of Eqs. (3) and (4) has been used.

## III. ANALYSIS OF RESULTS

The dependence of the azimuthal angle of magnetization on the coordinate normal to the DW, $\xi$, has the following form: $\varphi(\xi;h,\psi_H)=\psi_H-\psi(\xi;h,\psi_H)$, where $\psi(\xi;h,\psi_H)\to 0$ at $\xi\to\pm\infty$. Such a form of dependence may be easily understood as follows. The external magnetic field applied at an angle $\psi_H$ with respect to the DW plane produces a deviation in the orientation of the magnetization inside the DW which in turn leads to an increase of the demagnetization energy. The type of solution for the azimuthal angle $\varphi(\xi;h,\psi_H)=\psi_H-\psi(\xi;h,\psi_H)$ provides, first, the fulfillment of the condition that the DW is uncharged and, second, it diminishes the increase of the energy of the DW. This is the reason why the energy of the DW with the coordinate dependent azimuthal angle is always lower than the energy of the DW with the constant azimuthal angle $\varphi=\psi_H$.[6] The dependence $\varphi(\xi;h,\psi_H)$ for the case of $\psi_H$=30° for several values of transverse field $h$ is given in Fig. 1. Clearly, it is seen that the maximum value of deviation of the magnetization inside the DW from the orientation of the transverse field located at the center of the DW decreases with increasing transverse field. The dependences of $\varphi(\xi)$ for other orientations of the transverse field are similar to the ones given in Fig. 1. The only difference is that at $\psi_H$=90° the function $\psi(\xi;h,\psi_H)$ becomes identically equal to zero at $h$=0.225.[6] This circumstance is a reflection of the fact that a phase transition from the quasi-Bloch wall to the Néel one has taken place at the value of the reduced field $h$=0.225 when the latter is oriented along the normal to the DW.[2,6]

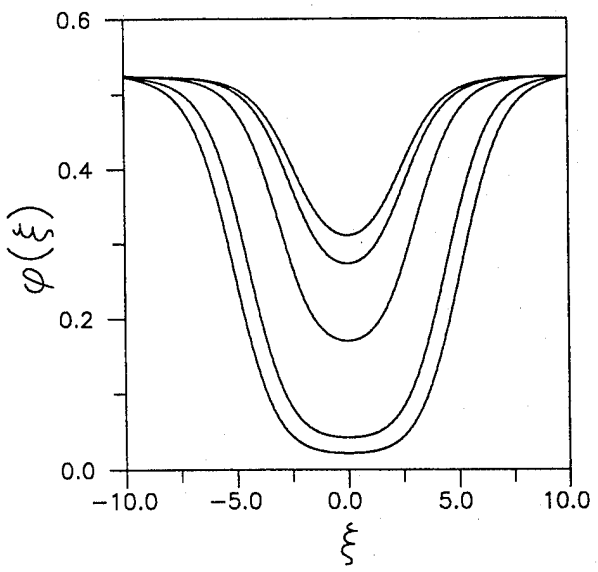



FIG. 1. Variation of the magnetization azimuthal angle $\varphi(\xi)$ along the coordinate $\xi$ normal to the DW plane at $\psi_H$=30° and $h$=0.01, 0.02, 0.1, 0.2, and 0.25 (from bottom to top).

Using the definition of the effective DW width of the distribution of the magnetization angle inside the DW as given in Ref. 10, we have analyzed the transverse field dependences of the effective widths of the distributions of both the polar and azimuthal angles of the magnetization for our solutions of the system of Eqs. (3) and (4). The effective width of the distribution of the azimuthal angle of the magnetization, $\Delta_\varphi(h,\psi_H)$, was found to decrease with increasing transverse field in the region of the reduced fields $0<h\leqslant 0.4\div 0.5$ and then it increases, and tends to infinity as $h\to 1$ when the remagnetization of the sample takes place and it becomes homogeneously magnetized. The transverse field dependences of the effective width of the magnetization azimuthal angle distributions, $\Delta_\varphi(h,\psi_H)$, for several orientations of the transverse field are given in Fig. 2. Note that the curve for $\psi_H$=90° is truncated at $h$=0.225 as remarked above.

It is interesting to compare the transverse field dependences of the effective widths of the distributions of the polar and azimuthal angles inside the DW. Our analysis of the polar angle distributions inside the DW for different orientations of the transverse field showed that this distribution depends weakly on the transverse field orientation.[7] Another result obtained in Ref. 7 was that the numerical solutions of the system of Eqs. (3) and (4) for the polar magnetization angle do not deviate much from the dependence of

$$\sin\vartheta(\xi)=\sin\vartheta_0+\frac{\cos^2\vartheta_0}{\cosh u+\sin\vartheta_0}.$$

Note that the above expression represents the analytical solution of the system obtained under the approximation $\varphi=\psi_H$ inside the DW.[2] In this expression $u=\xi\cos\vartheta_0\sqrt{1+\epsilon\sin^2\psi_H}$. According to Ref. 10, the effective width $\Delta_\vartheta(h)$ of the polar angle distribution described by the above formula is determined by the expression

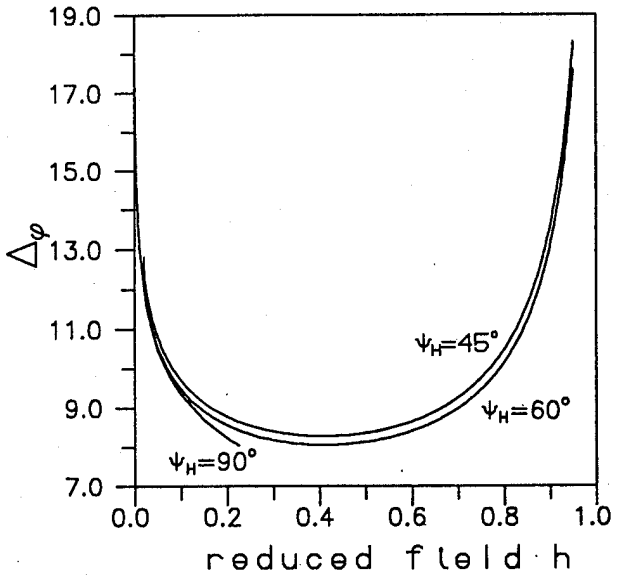



FIG. 2. The transverse field dependences of the effective width of the distribution of the azimuthal magnetization angle inside the DW, $\Delta_\varphi(h)$, for the orientations of the transverse field $\psi_H$=45°, 60°, and 90°.

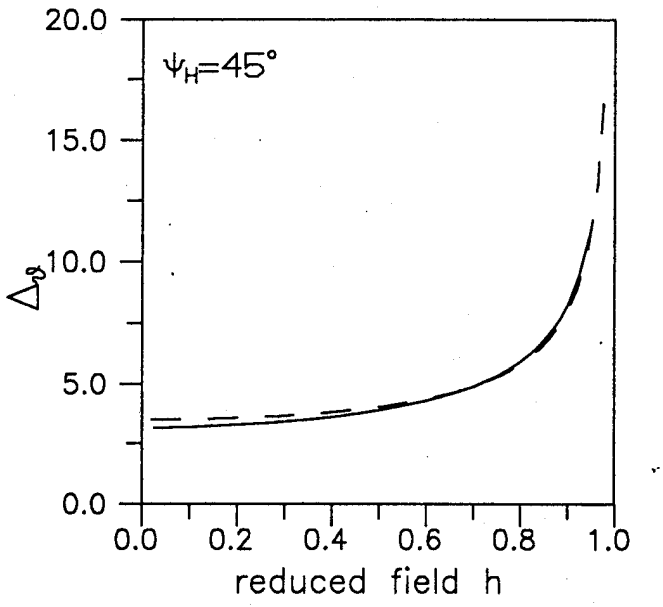



FIG. 3. Comparison of the dependence of the effective widths of the distribution of the polar angles, $\Delta_\vartheta(h)$, on the transverse field $h$ at $\psi_H$=45°. Solid line: numerical result obtained from solving the system of Eqs. (3) and (4); dashed line: analytical result obtained directly from (6).

$$\Delta_\vartheta(h)=\pi\Delta_B[\cos\vartheta_0\sqrt{1+\epsilon\sin^2\psi_H}]^{-1}. \tag{6}$$

It is easy to see from (6) that $\Delta_\vartheta(h)$, increases monotonically with increasing reduced transverse field and, tends to infinity as $h$ approaches to unity. The transverse field dependences of the numerically obtained effective width of the polar angle distribution and the one calculated directly from formula (6) are presented in Fig. 3. One can easily see from this figure that the analytical expression (6) gives a little bit larger values of the effective width in the region of small values of the transverse field but approaches the numerical results when the values of the transverse field approaches unity.

Comparing the dependences given in Figs. 2 and 3, it is clear that the dependence of the effective width of the azimuthal magnetization angle $\Delta_\varphi(h)$, is different from that of polar angle, $\Delta_\vartheta(h)$, and that the absolute value of the effective width for the azimuthal angle distribution is always greater than that of the polar angle.

## ACKNOWLEDGMENT

This research is supported in part by National Science Council through a Contract No. NSC-84-2216-E02-018.

[1] G. A. Jones and B. K. Middelton, Int. J. Magn. **6**, 1 (1974).
[2] A. Hubert, *Theorie der domännenwände in Geordneten Medien* (Springer, Berlin, 1974) (in German).
[3] A. Molozemoff and J. Slonczewski, *Magnetic Domain Walls in Bubble Materials* (Academic, New York, 1979).
[4] C. T. Teh, H. L. Huang, and V. L. Sobolev, J. Appl. Phys. **75**, 7003 (1994).
[5] Yu. A. Dimashko, Sov. Phys.-Solid State **27**, 1274 (1985).
[6] C. T. Teh, V. L. Sobolev, and H. L. Huang, J. Magn. Magn. Mat. **145**, 382 (1995).
[7] C. T. Teh, H. L. Huang, and V. L. Sobolev, J. Magn. Magn. Mat. (in press).
[8] J. Morkowski, H. Dotsch, P. E. Wigen, and R. Y. Yeh, J. Magn. Magn. Mat. **25**, 39 (1981).
[9] D. Kincaid and W. Cheney, *Numerical Analysis* (Brooks/Cole, California, 1990).
[10] B. A. Liley, Philos. Mag. **41**, 792 (1950).

# Modeling MFM images of periodic magnetization patterns (abstract)

R. Madabhushi and R. D. Gomez
*Department of Electrical Engineering, Institute of Advanced Computer Studies, University of Maryland, College Park, Maryland 20742*

E. R. Burke
*Laboratory for Physical Sciences, College Park, Maryland 20740*

I. D. Mayergoyz
*Department of Electrical Engineering, Institute of Advanced Computer Studies, University of Maryland, College Park, Maryland 20742*

Magnetic force microscopy (MFM) is a powerful technique that has gained wide acceptance in the imaging of magnetization patterns. However, MFM images are "raw" images, and they are not necessarily identical to the original images of the magnetization patterns. In an attempt to investigate the relationship between the raw images and the magnetization patterns, we present a theoretical analysis of the MFM images through numerical computations. In this way, we show the dependence of the images on both the orientation of the probe's magnetic moment and the interaction between the probe moment and the sample magnetic fields. For a pure sinusoidal magnetization pattern, a vertical orientation of the MFM probe's magnetic moment will yield images that follow the magnetic charge density distribution, while a horizontal orientation of the probe will yield MFM images that follow the magnetization patterns themselves. We investigate the deviation from this correlation between the images and the magnetization distribution when magnetization patterns are not purely sinusoidal. Computations are performed for periodic patterns with linear and arctangent transitions. To model the interaction of the tip with the sample's magnetic fields, we model the tip as a Stoner–Wohlfarth particle. This allows us to investigate how the tip–sample interaction may distort the MFM image. Our modeling suggests that in general there is no direct correlation between the raw MFM image and the actual magnetization distribution. This makes a strong case for the implementation of image reconstruction techniques. © *1996 American Institute of Physics.* [S0021-8979(96)61008-8]

# Magnetic force microscope study of domain wall structures in magnetite

Taras G. Pokhil and Bruce M. Moskowitz
*Institute for Rock Magnetism, University of Minnesota, Minneapolis, Minnesota 55455*

Domain walls (DW) in a small multidomain grain (≈20 $\mu$m) of magnetite ($Fe_3O_4$) exhibiting a planar domain pattern were studied using a magnetic force microscope (MFM). Most walls were subdivided with one or two Bloch lines and all walls displayed asymmetric MFM responses. Domain walls were observed to have small offsets either at the location of Bloch lines or at other locations without Bloch lines. The experimental data were described by a model in which (1) the easy axis of magnetization is not exactly parallel to the grain surface but is slightly inclined, and (2) there is also some plane dividing the grain in two parts with slightly different inclined easy axis directions. The inclined easy axis produces asymmetric spin distributions across the DW and wall offsets occur to reduce the surface magnetostatic energy of the wall. © *1996 American Institute of Physics.* [S0021-8979(96)54908-7]

## I. INTRODUCTION

The internal structure of domain walls (DW) between two domains with antiparallel magnetization has been intensively investigated both experimentally and theoretically.[1–11] A variety of micromagnetic structures of domain walls in thin films and bulk materials have been observed and predicted including (1) domain walls with asymmetric spin distributions across the wall due to Néel-like structures called Néel caps terminating interior Block walls at surfaces, and (2) vortex-like spin distributions in Bloch lines separating opposite polarity wall segments.[1–5] High spatial resolution imaging of micromagnetic structures using magnetic force microscopy provides experimental data on the structure of domain walls which can be used to test predictions of micromagnetic models.[8–10]

Magnetite is a ferrimagnetic oxide that occurs as a trace mineral in continental and ocean rocks. The magnetic memory in rocks of the ancient geomagnetic field is carried by the remanent magnetization of magnetite particles less than 50 $\mu$m in size.[12] The term pseudo-single domain (PSD) describes magnetic behavior that is intermediate between classical single domain (SD) and multidomain (MD) behavior and is usually attributed to particles containing just a few (<10) domains. The physics of PSD behavior plays a central role in paleomagnetism because most magnetic oxide grains in rocks are too large to be in an equilibrium SD state (<0.1 $\mu$m) and contain domains, yet can carry geologically stable remanence. In this paper we present results of a magnetic force microscope (MFM) study of domain wall structures in a small grain of magnetite containing a few domains.

## II. EXPERIMENTAL METHODS

Small grains (5–50 $\mu$m) of magnetite ($Fe_3O_4$), randomly oriented and dispersed in nonmagnetic matrix, were produced by the glass-ceramic method.[13] The sample was mounted in epoxy and mechanically polished with diamond compounds. Amorphous silica solution was used as a final polish to obtain a smooth surface and to reduce the strained surface layer produced during the initial mechanical polishing.[14] The bulk coercive force of the sample was 15 Oe.

Magnetic force images were obtained with a Nanoscope III scanning probe microscope. The microscope was operated in the "tapping/lift" scanning mode,[15] which combines constant interaction and constant height modes, to separate topographic and magnetic signals. The scanned probes were batch fabricated Si cantilevers with pyramidal tips coated with a CoCr film alloy.[15] All MFM data shown in this paper were collected with the tip magnetized approximately perpendicular to the sample surface ($z$ direction), making the MFM sensitive to the second derivative of the $z$ component of sample stray field. To exclude any influence of the MFM tip on the sample micromagnetic structure, images were taken with various tip-sample orientations and tip-sample separations. Under these experimental conditions we did not observe any noticeable modifications of micromagnetic features during MFM scanning. All MFM images presented in this paper were obtained with tip sample separation of 50 nm and tip vibration amplitude of 20–30 nm. The drive frequency of cantilever was chosen above the resonance frequency of the cantilever near the point of maximum gradient of the cantilever resonance curve.

## III. RESULTS

We concentrated our MFM study on a 20 $\mu$m grain exhibiting a simple planar domain structure. Although the crystallographic orientation of the grain surface was unknown, the simple domain pattern suggested that the direction of magnetization within the domains was approximately parallel to the surface of the grain. Domain walls in this grain were approximately parallel to each other with domain spacing of 2–3 $\mu$m (Fig. 1). The FWHMs of the MFM response profiles across the walls were about 200 nm which is slightly wider than the theoretical Bloch wall width in bulk magnetite (100–150 nm),[16] but similar to MFM results obtained for a large single crystal of magnetite.[10] Surface broadening of the DW can result from the self-demagnetizing field acting on the DW near the grain surface resulting in, for instance, a Néel cap. However, some broadening of the MFM response is expected due to the integrated effect over the tip. Some walls were subdivided into alternating chirality segments separated by Bloch lines. The smallest observed distance between Bloch lines was ≈1 $\mu$m.

 0021-8979/96/79(8)/6064/3/$10.00 © 1996 American Institute of Physics

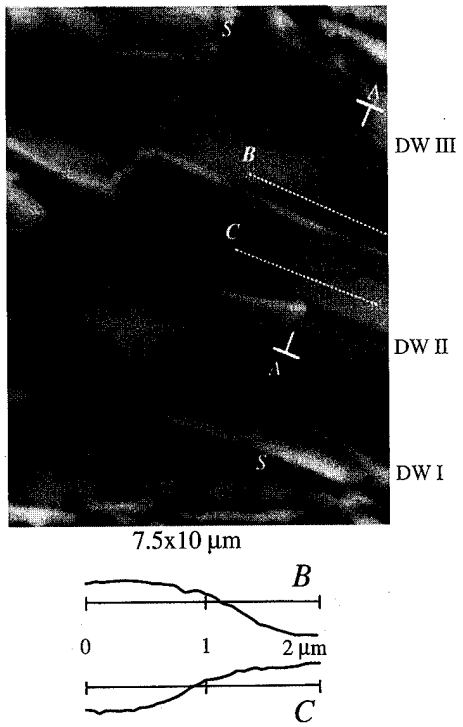



FIG. 1. MFM image of domain walls in a magnetite grain and MFM response profiles along the domains at lines *B* and *C*. Features marked as *S* are stray fields from scratches.

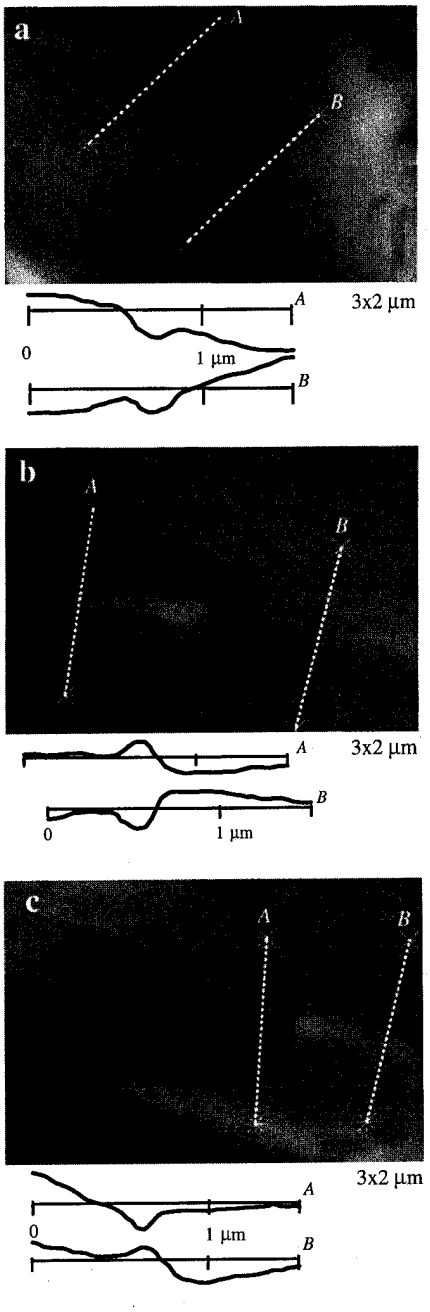



FIG. 2. MFM images of three walls in Fig. 1, DW I, DW II, and DW III and MFM response profiles across the domain walls at lines *A* and *B*. The size of all images is 3×2 μm. (a) DW without a Bloch line; easy axis of magnetization has different directions on different sides of the DW offset point, (b) DW with a Bloch line; easy axis has different directions on different sides of the Bloch line. (c) DW with a Bloch line; easy axis has the same direction on different sides of the Bloch lines.

We found several interesting spin features associated with domain walls. Small offsets of the DW were observed in some walls at the location of Bloch lines [Fig. 2(c)], whereas other walls had offsets without an accompanying Bloch line [Fig. 2(a)]. The size of these offsets varied between 30 and 50 nm. The MFM response profiles across these walls were asymmetric. Moreover, the MFM profiles *A* taken on one side of DW offset point can be transformed into profiles *B* taken on the opposite side of the offset using axially symmetric [Figs. 2(a) and 2(b)] or centrally symmetric transformations [Fig. 2(c)]. We also observed a change of the MFM response within the domains. For example, in Fig. 1, the MFM response changes when the MFM tip crosses line *A-A* and the sign of the change is opposite in neighboring domains resulting in checkerboard contrast pattern. This is seen more clearly in Fig. 2 which shows higher-resolution image scans of the walls labeled DW I, DW II, and DW III in Fig. 1. Here, there is a change in the MFM response within the domains across the wall offset associated with DW III [Fig. 2(a)] and the Bloch line in DW II [Fig. 2(b)], but no change in MFM response associated with the offset at the location of the Bloch line in DW I [Fig. 2(c)].

## IV. DISCUSSION

To explain our experimental data (DW offsets and asymmetric MFM profiles), we proposed the following simple model depicted in Figs. 3 and 4. We assumed that (1) the easy axis of magnetization is not in the plane of the grain surface but is slightly inclined and that the direction of magnetization inside the domains is parallel to the easy axis; and (2) a plane intersecting the domain walls divides the grain in two parts with slightly different inclined easy axis directions (Fig. 4). Under these conditions, the magnetization in each domain will have a small component perpendicular to the surface. Within the same domain, this component is directed out of (into) the surface on one side of the dividing plane and directed into (out of) the surface on the opposite side of the plane. The inclined easy axis relative to the sample surface produces the observed asymmetric spin distribution across the DW. This hypothesis is consistent with the observed change of MFM response within the domains (i.e., the

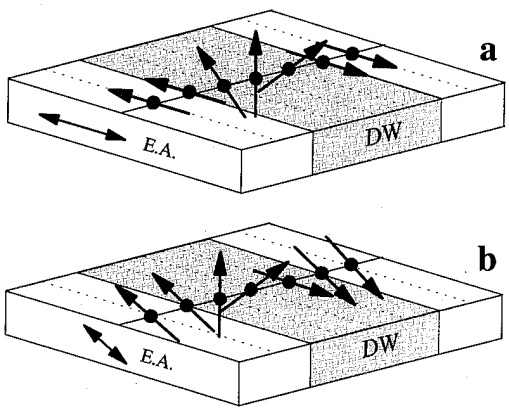



FIG. 3. Distribution of magnetic moments across a Bloch domain wall where (a) the easy axis is in the plane of the surface; and (b) the easy axis makes a small angle with the surface. The MFM response across the wall would be symmetric for (a) and asymmetric for (b).

checkerboard pattern in Fig. 1). Such a change of easy axis direction can result from residual surface stress, or from the formation of subgrain or twin boundaries during crystallization which divides the grain in two parts with slightly different crystallographic orientations.

Spin distributions across a Bloch wall when the easy axes are in plane or inclined are presented in Figs. 3(a) and 3(b), respectively. For the DW shown in Fig. 3(b), the area of the wall with magnetization perpendicular to the surface is shifted toward one side of the wall, while near the other side of the wall, there is an area in which the direction of magnetization is parallel to the surface. The magnetostatic energy of a DW crossing an area where the easy axis changes direction is reduced if the DW is offset and "in-plane" spins in the DW on both sides of this area follow the magnetization in the adjacent domains [Fig. 4(a)]. The stray field distribution above the DW on both sides of wall offset point would be asymmetric as shown in Fig. 4(a). These model field distributions are qualitatively similar to the MFM response profiles in Fig. 2(a). Similarly, it follows that (1) a DW offset is magnetostatically favorable at the location of Bloch line when the easy axis is inclined, but does not change its direction at the Bloch line [Fig. 4(c)]; and (2) no DW offset should occur at the location of a Bloch line if it happens to be located in the plane where the easy axis changes direction [Fig. 4(b)]. The MFM images of domain walls with Bloch lines in Figs. 2(b) and 2(c) agree with this simple interpretation. This model also explains the symmetry relationships exhibited by the MFM response profiles on opposite sides of offset points (Fig. 2). Using the model and measured wall offsets, the angle of the inclined magnetization within the domains with respect to the surface of the grain was calculated to be approximately 20°.

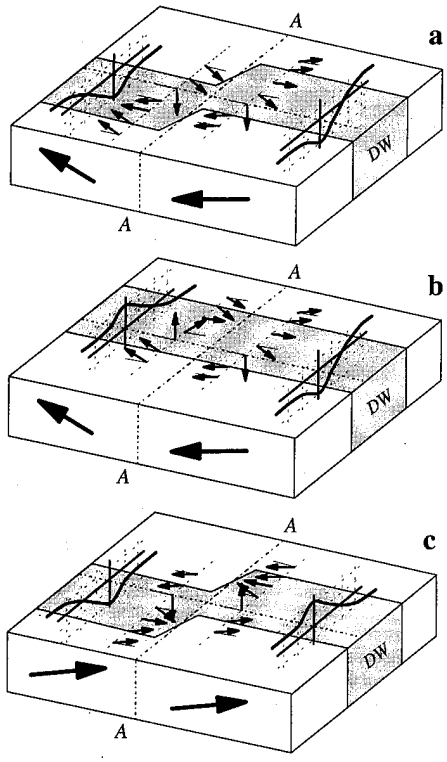



FIG. 4. Schematic drawing of an asymmetric Bloch DW. In (a) the DW has an offset but no Bloch line. The easy axis of magnetization has different directions on different sides of the DW offset point. In (b) the DW has a Bloch line but no offset. The easy axis has different directions on different sides of the Bloch line. In (c) the DW has both a Bloch line and an offset. The easy axis has the same direction on different sides of the Bloch line.

## ACKNOWLEDGMENTS

We thank Sheryl Foss for useful discussions and critical reading of the manuscript and Matthew Dugas (Advanced Research Corporation) for preparation of MFM tips with sputtered CoCr thin films. This work was partially supported by the NSF. This is contribution 9503 of the Institute for Rock Magnetism. The Institute for Rock Magnetism is supported by grants from Keck Foundation and NSF.

[1] A. E. LaBonte, J. Appl. Phys. **40**, 2450 (1969).
[2] A. Hubert, Phys. Status Solidi **38**, 699 (1970).
[3] A. Hubert, IEEE Trans. Magn. **MAG-11**, 1285 (1975).
[4] U. Hartmann, Phys. Status Solidi B **151**, 289 (1989).
[5] M. R. Scheinfein, J. Unguris, R. J. Celotta, and D. T. Pierce, Phys. Rev. Lett. **63**, 668 (1989).
[6] L. Schön and U. Buchenau, Intern. J. Magn. **3**, 145 (1972).
[7] P. Trouilloud and J. Miltad, J. Magn. Magn. Mater. **66**, 1934 (1987).
[8] U. Hartmann, Phys. Rev. B **40**, 7421 (1989).
[9] W. Williams, V. Hoffman, F. Heiden, G. Göddenhenrich, and C. Heiden, Geophys. J. Int. **III**, 417 (1992).
[10] R. B. Proksch, S. Foss, and E. D. Dahlberg, IEEE Trans. Magn. **MAG-30**, 4467 (1994).
[11] M. R. Scheinfein, J. Unguris, D. T. Pierce, and R. J. Celotta, J. Appl. Phys. **67**, 5932 (1990).
[12] D. J. Dunlop, Rep. Prog. Phys. **53**, 707 (1990).
[13] H. U. Worm and H. Market, Phys. Earth Planet. Int. **46**, 84 (1987).
[14] V. Hoffman, R. Schäfer, E. Apple, A. Hubert, and H. Suffel, J. Magn. Magn. Mater. **71**, 90 (1987).
[15] Nanoscope III, Digital Instruments, Santa Barbara, CA.
[16] B. M. Moskowitz and S. K. Banerjee, IEEE Trans. Magn. **MAG-15**, 1241 (1979).

# A scanning microscope using a magnetoresistive head as the sensing element

R. O'Barr, M. Lederman,[a] and S. Schultz
*Department of Physics and Center for Magnetic Recording Research, University of California, San Diego, 9500 Gilman Drive, LaJolla, California 92093-0319*

We have built a scanning probe microscope where a magnetoresistive (MR) head is used as the sensing element. The sensor region of the MR head is about 5 $\mu$m wide and 30 nm thick giving high resolution in one direction and poor resolution in the other. As MR heads with smaller cross-track dimensions are developed, submicron resolution in this direction should also be realizable. The MR head is mounted on a piezoelectric bimorph and vibrated perpendicular to the plane of the sample, and the ac voltage output of the head is detected with a lock-in amplifier. We have imaged pre-recorded bits as a function of scan height, and also imaged bits that were written using the write element of the same MR head. The typical voltage change through a transition is ~4 $\mu$V, two orders of magnitude smaller than signals generated on a spin stand. This is most likely due to the difficulty in setting the slider parallel to within submilliradian accuracy to the plane of the sample. Our positioning system does not have this capability at this time. With modifications in the positioning stage, this device should provide a valuable tool for investigating the recording and playback processes, and for characterizing media and heads at ever decreasing track widths, bit separations, and flying heights. © *1996 American Institute of Physics.* [S0021-8979(96)55008-1]

## I. INTRODUCTION/MOTIVATION

In recent years, a variety of scanning probe microscopes have been developed.[1] These instruments have the common feature of a probe that is raster scanned in close proximity to the surface of a sample. Magnetic force microscopy (MFM) is one form of scanning probe microscopy useful for obtaining spatially resolved information of the magnetic forces or force gradients acting on a magnetic tip as it is passed over magnetic patterns.[2] We have implemented another form of scanning probe microscopy which can be used to directly image magnetic flux patterns. We have used a magnetoresistive (MR) head as the probe which detects the vertical component of magnetic field passing through the MR sensor. The sensor region of present MR heads is typically a few microns wide and ~30 nm thick making such a device capable of imaging magnetic structures with high resolution in one dimension and with poor resolution in the other. As MR heads with smaller cross-track dimensions are developed, submicron resolution in this direction should also be achieved. One application for this device is as a diagnostic tool for characterizing magnetic media and conversely, using known magnetic field patterns to characterize the MR head itself. Since the playback signal generated by an MR head is fundamentally independent of the relative speed between the head and media,[3] diagnostics obtained by the scanning of an MR head over recorded bits should correspond directly with the MR signals in a spin stand or working disk drive device.

## II. SETUP AND PROCEDURE

The apparatus used is a modification of a home-built MFM[4] where the magnetic probe (which in our case is usually an etched Ni wire) is replaced with an MR head. The suspension arm of the MR head is glued onto a piezoelectric bimorph (see Fig. 1). The illumination from an optical fiber (coupled to a laser diode) is positioned incident on the suspension arm in a location directly behind the MR element. By oscillating the bimorph perpendicular to the plane of the sample to be imaged, a time-dependent interference pattern is obtained, allowing one to monitor the oscillation of the MR head. The MR head was typically oscillated at a frequency, $f$=1.85 kHz, which corresponded to the resonant frequency of the bimorph, suspension, and slider assembly. The peak-to-peak vibration amplitude of the MR head perpendicular to the media was typically 50 nm. The sample was mounted on three mutually orthogonal piezoelectric block translators, which were mounted on a mechanical $x,y,z$ positioning stage. The pitch and roll angles that the slider made with the sample were mechanically adjusted so that the slider was approximately parallel to the disk (to less than 1°). When the slider just makes contact with the disk, the amplitude of the interference pattern starts to damp out and then,

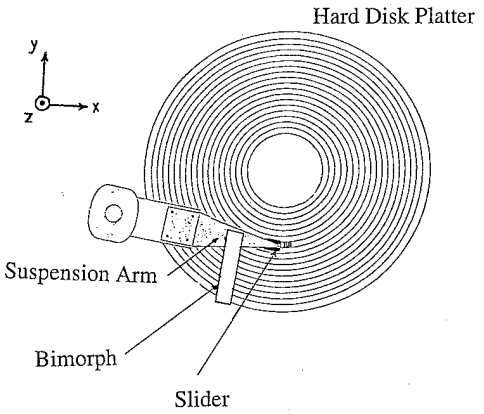



FIG. 1. The experimental setup. An ac voltage is applied to the bimorph causing the MR head to vibrate in the $z$ direction. The sample is scanned in the $xy$ plane.

[a]Currently at Read-Rite Corp.

 0021-8979/96/79(8)/6067/3/$10.00 © 1996 American Institute of Physics 

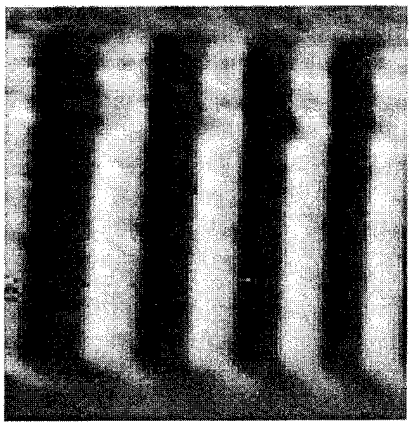


FIG. 2. MFM image of bits. Scan dimensions are 14×14 $\mu$m.

when complete contact is made, disappears altogether. Contact was made with the sample at three points defining the sample plane. The sample was then backed away from the slider a fixed distance, and raster scanned in a plane parallel to the defined sample plane. The MR voltage was fed into a lock-in amplifier with the signal driving the bimorph used as the reference. The dc output of the lock-in was recorded as a function of the coordinate position of the head with respect to the plane of the disk.

## III. IMAGING OF BITS

Bits were prerecorded on a commercial hard disk platter with transitions of alternating polarities. The recorded magnetization patterns were first imaged by MFM (Fig. 2). The bimorph with the MFM etched Ni tip was then removed and replaced with one having an MR head mounted on it. Figure 3 is an image obtained by scanning the MR head over bits written on the same disk (with the same head) as those imaged by MFM. Because the track width of the recorded bits are about twice that of the MR element, the signal is strongest in the central 5 $\mu$m of the track and falls off uniformly toward the edges of the track (see Fig. 4). We initially tried to image the recorded patterns without oscillating the MR

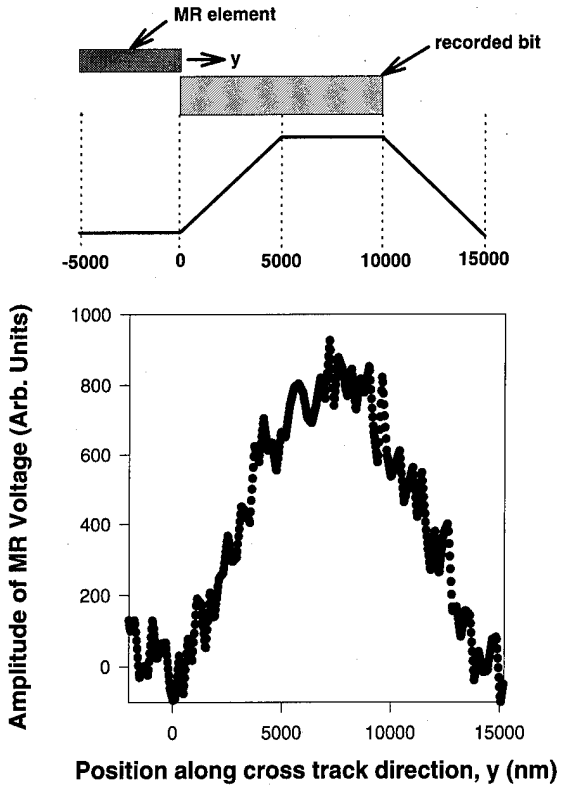



FIG. 4. Cross-track section taken through one of the bits in Fig. 3. The diagram above illustrates the expected MR voltage profile for an element width of 5 m$\mu$ and a track width of 10 m$\mu$. Amplitude of MR voltage is given in arbitrary units.

head (i.e., without lock-in detection) but found insufficient signal to noise to detect the transitions. The peak-to-peak change in MR voltage amplitude between transitions of opposite polarity was approximately 4 $\mu$V when the slider was backed away ~100 nm from the hard disk platter and vibrated with a peak-to-peak amplitude of 50 nm. In Fig. 5, the data of MR voltage change as a function of $d$, the distance between the slider and disk is shown. The data give a good fit to the form expected for square wave recording,

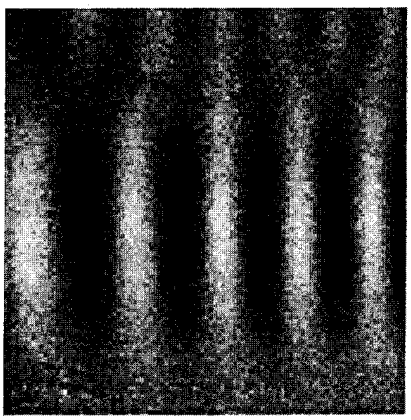


FIG. 3. Bits written on same disk as those in Fig. 2 with the same head but with somewhat lower frequency, as imaged by scanning an MR head. The MR head peak-to-peak amplitude of vibration is 50 nm and the slider-to-disk distance is 250 nm. Scan dimensions are 20×20 $\mu$m.

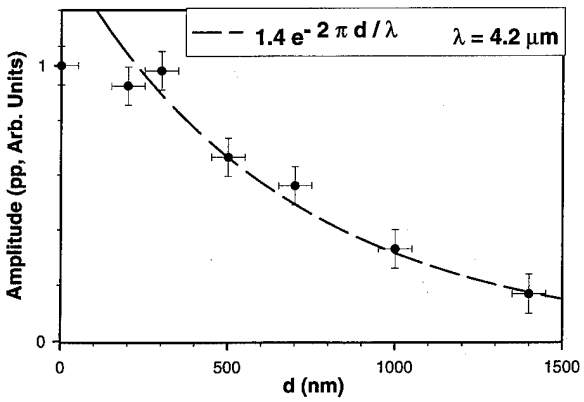



FIG. 5. Change in amplitude of MR head voltage between bits of opposite polarity vs distance to disk peak to peak. Amplitude of vibration of head: 50 nm, $f$=1.85 kHz. Data are fit to the wallace spacing loss formula, where $\lambda$=4.2 is the measured wavelength of the bits imaged.

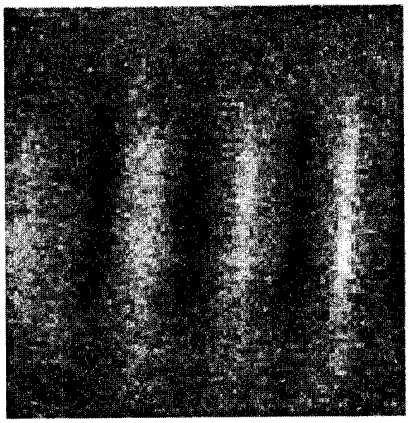


FIG. 6. Image of bits recorded with the write element of the MR head and subsequently imaged by scanning the MR read element. Slider was just in contact during the record process. Imaging was done with a slider to disk distance of 250 nm, pp. Amplitude of vibration of head 100 nm, $f$=1.85 kHz. Scan dimensions are 20×20 $\mu$m.

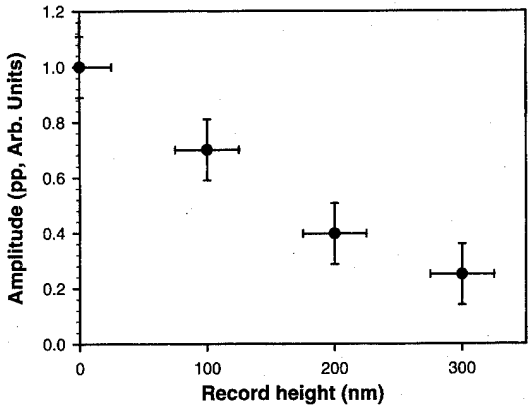



FIG. 7. Change in amplitude of MR head voltage between bits of opposite polarity vs record height. The slider to disk distance is 250 nm, peak-to-peak. Amplitude of vibration of head 100 nm, $f$=1.85 kHz.

$V=V_0\exp(-2\pi d/\lambda)$, where $V_0$ is the voltage at $d_0$, the distance from which $d$ is measured.[5] We have used $\lambda$=4.2 $\mu$m (as measured from the data in Fig. 3).

## IV. WRITING TRANSITIONS

The MR head has an inductive write element which we used to write bits on a nonrecorded region of the hard disk platter. The procedure for writing bits was as follows:

(a) The slider was approached to the platter until contact was made and then backed up a set distance away.

(b) A forward dc current of 40 mA was applied to the write head. The platter was then translated 2 $\mu$m in the recording direction.

(c) A reverse dc current of 40 mA was applied to the write head. The platter was then translated another 2 $\mu$m in the recording direction.

(d) Steps b and c were repeated several times. The current was then turned off.

Figure 6 shows an image taken of bits written with the slider just in contact with the disk. The scan was made with the slider backed up about 250 nm from the surface and with a peak-to-peak oscillation amplitude of ~100 nm. Bits were written at different recording heights and subsequently imaged at the same scan height of ~250 nm. The decrease in peak-to-peak change in MR voltage as a function of record height is given in Fig. 7.

## V. CONCLUSION

We report the implementation of a scanning microscope using an MR head as the scanning probe. As previously mentioned, the signal was too weak to image bits without oscillating the MR head and using lock-in direction. In an actual disk drive, the aerodynamic design of the slider maintains it very nearly parallel to the disk with pitch and roll angles smaller than 100–200 $\mu$rad and 10 $\mu$rad, respectively. These angles are critical because if the pitch angle is only one degree when contact occurs, the MR sensitive element will still be backed almost a half micron away from the disk surface. This is because the MR element on this head is followed by a midshield (shared by the read and write elements), a write gap, a write pole, and an overcoat with a thickness of approximately 25 $\mu$m. The constraint on the roll angle is even more demanding since the slider rail has a width of a few tenths of millimeters with the MR element occupying only a small region near the center of the rail. In our initial setup, we only had coarse mechanical control over the pitch and roll angles. It is likely that the slider was not sufficiently well aligned with the disk and the MR element was always several hundreds of nanometers away from the disk even when one edge or corner of the slider was making contact with the disk. Once modifications permitting fine adjustments over the pitch and roll angles have been implemented, we should be able to align the slider more nearly parallel to the disk. This should allow for imaging without oscillating the MR head, and should generate peak-to-peak dc MR signals of a few hundred microvolts. These changes combined with an improved positioning stage (with feedback control and nm resolution) will provide a valuable tool for investigating the recording and playback processes, and for characterizing media and heads at ever decreasing track widths, bit separations, and flying heights.

## ACKNOWLEDGMENTS

This work was sponsored by the Center for Magnetic Recording Research, NSF Grant No. DMR-90-10908, and NSF Grant No. DMR-94-00439 (MRSEC).

[1] S. Dror, *Scanning Force Microscopy: With Applications to Electric, Magnetic, and Atomic Forces* (Oxford University, New York, 1994).
[2] Y. Martin and H. K. Wickramasinghe, Appl. Phys. Lett. **50**, 1455 (1987); J. J. Saenz, N. Garcia, P. Grutter, E. Meyer, H. Heinzelmann, R. Wiesendanger, L. Rosenthaler, H. R. Hidber, and H. J. Guntherodt, J. Appl. Phys. **62**, 4293 (1987); D. Rugar, H. J. Mamin, G. Guethner, S. E. Lambert, J. E. Stern, I. McFadyen, and T. Yogi, *ibid.*, **68**, 1169 (1990).
[3] H. N. Bertram, *Theory of Magnetic Recording* (Cambridge University, Cambridge, 1994), Chap. 7.
[4] G. A. Gibson and S. Schultz, J. Appl. Phys. **73**, 4516 (1993).
[5] C. D. Mee, *Magnetic Recording Handbook: Technology and Applications* (McGraw–Hill, New York, 1990).

# Surface deformations and domains in Terfenol-D by scanning probe microscopy

A. P. Holden, D. G. Lord, and P. J. Grundy
*Physics Department, Joule Laboratory, University of Salford, M5 4WT, United Kingdom*

This paper reports the first direct measurements of the deformations in the surface of a ferromagnet caused by magnetostrictive lattice strains in neighboring magnetic domains. Observations of the {011} and {112} surfaces of twinned Terfenol-D ($Tb_{0.3}Dy_{0.7}Fe_2$) crystals by atomic force microscopy reveal the deformation domains previously imaged by optical microscopy and predicted by recent theory. The surface topography has been imaged in the remanent and ac demagnetized states and measurements of the deformation gradients have enabled the magnetostriction constant in the ⟨111⟩ direction to be estimated as $1.63\times10^{-3}$ to within 8%. All theoretically predicted deformation domains have been observed and, in particular, the exact compatibility of such deformations across the growth twin boundaries is clearly revealed. The magnetic domains associated with the observed deformations are inferred from magnetic force microscopy observations which yield complex contrast patterns. © *1996 American Institute of Physics.* [S0021-8979(96)55108-8]

## I. INTRODUCTION

The cubic Laves phase compound $Tb_{0.3}Dy_{0.7}Fe_2$ (Terfenol-D) exhibits a large magnetostriction to anisotropy ratio at room temperature, the anisotropic magnetostriction resulting in significant rhombohedral strain within magnetic domains when the magnetization is along the ⟨111⟩ easy axes. Material grown by a free-standing zone (FSZ) technique is known to solidify via a {211} dendritic growth front producing samples composed of dendritic plates which often contain growth twins, the predominant plate and twin boundary plane being the {111} orthogonal to the growth front.[1,2]

The interactions between the magnetic domain structure and both the crystallographic defects and the sample surfaces have been the subject of a number of investigations using x-ray topography,[2] optical differential interference contrast (DIC) microscopy,[3] magnetic colloid,[4] and Lorentz transmission electron microscopy (TEM).[2,5] Such studied have all indicated complex surface domain structures and associated surface deformations which have recently been the subject of theoretical assessment.[6] The application of scanning probe microscopy (SPM) techniques to Terfenol-D surfaces has yielded direct measurements of the deformation gradients for particular domain configurations and data is presented here which has enabled evaluation of the magnetostrictive constant.

## II. EXPERIMENT

Samples used in this investigation were obtained from 8-mm-diam rods prepared by Edge Technologies, Inc., by a FSZ technique. Surfaces parallel to the $(1\bar{1}0)$ plane, orthogonal to the $(11\bar{2})$ growth plane, and surface containing the $(11\bar{2})$ plane were spark eroded from the rods following alignment using the backreflection x-ray Laue technique. The surfaces were polished down to 0.25 $\mu$m diamond finish and then lapped with Syton. Atomic and magnetic force microscopy observations were carried out using a Dimension 3000 (Digital Instruments) SPM employing silicon cantilevers with tips coated with a CoCr film. All observations were carried out at ambient temperature with the tip magnetized normally to the specimen surface. The topography images were obtained in the "tapping" mode and the magnetic force gradient images (hereafter referred to as MFM images) were obtained by phase detection in the "interleave" mode using a typical lift height, above the topography, of either 20 or 30 nm.

## III. RESULTS AND DISCUSSION

Figure 1 illustrates the typical topographic features observed from $(1\bar{1}0)$ surfaces of samples in a remanent state following field application along the $[11\bar{2}]$ growth axis direction. Such images show the chevron-like contrast associated with topography features interacting with the growth twin boundaries (TB) as previously observed by optical DIC microscopy.[3] The exact compatibility of the height changes across the twin boundaries is clearly shown. The nonuniformity of the deformations in the $[11\bar{2}]$ growth direction is thought to be associated with variation in the Tb/Dy ratio resulting in small changes in both anisotropy, and magnetostriction. Figure 2 shows a three-dimensional representation of these data where the angular nature of the deformations is clearly illustrated. An interpretation of the origin of this sur-

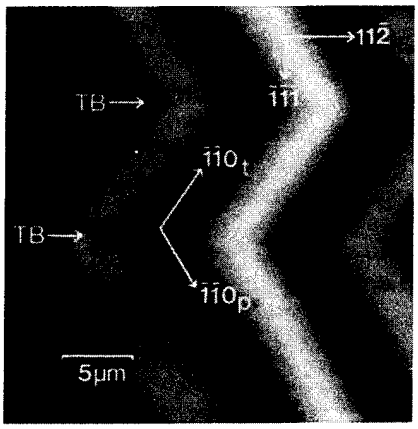



FIG. 1. AFM topographic (height) image of $(1\bar{1}0)$ surface showing surface deformations across two twin boundaries (TB).

 0021-8979/96/79(8)/6070/3/$10.00 © 1996 American Institute of Physics

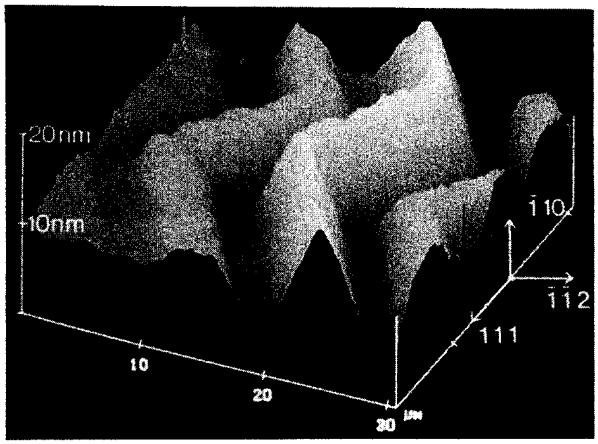



FIG. 2. Three-dimensional representation of Fig. 1 showing the angular deformations.

face relief, generated by internal stress relief at the crystal surfaces, is given in Fig. 3(a) where (001) 109° Bloch walls are shown intersecting the $(1\bar{1}0)$ surface. Such walls lie parallel to the $[\bar{1}\,\bar{1}0]$ direction in this surface and are consistent in their geometry to the deformation domains of the theory of James and Kinderlehrer.[6] Each domain will magnetostrictively strain along its $\langle 111\rangle$ direction as depicted in Fig. 3(a). The magnitude of this strain effect on the surface distortion $\alpha$ is shown in Fig. 3(b) assuming a two-dimensional simplified model. The deformation gradient $\alpha$ can be related to the magnetostriction coefficient such that $\lambda_{111}=\sqrt{2}\alpha/3$. Direct measurements of $\alpha$ have been made on a large number of such topographic images from several specimens, in both $(1\bar{1}0)$ and $(11\bar{2})$ surfaces by the analysis of sections of images such as that shown in Fig. 1. The typical height changes are of the order of 10 nm in 5 $\mu$m and estimates of $\lambda_{111}$ from such data yield a value of $1.63\times10^{-3}$ ($\sigma\sim8\%$) which agrees remarkably well with previous experimental and theoretical evaluations.[7]

Topographic and MFM images of the same area of a $(1\bar{1}0)$ surface across a double growth twin are shown in Fig. 4 and demonstrate the direct relationship between the magnetic and topographic features which is not unduly influenced by the surface scratches in this example. The fine

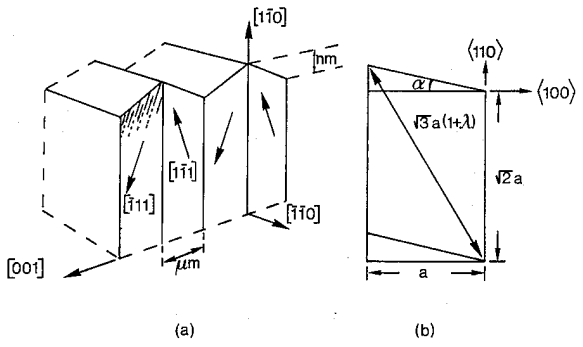



FIG. 3. (a) Magnetization distribution diagram to show origin of surface deformations and closure domains for (001) 109° Bloch walls, (b) simple distortion of a {110} section, where $\alpha$ represents deformation gradient.

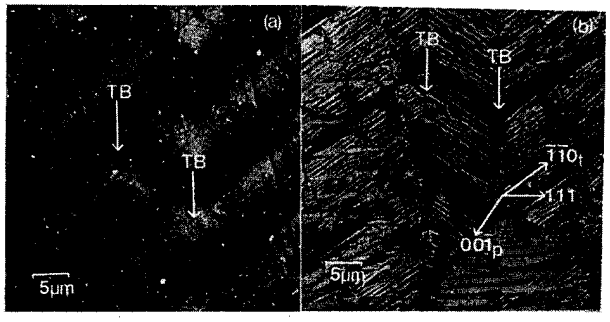



FIG. 4. (a) Topographic and (b) MFM images of a $(1\bar{1}0)$ surface across a double twin (TB). Magnetic contrast can be seen in $\langle 111\rangle$, $\langle 110\rangle$, and $\langle 001\rangle$ directions.

structure associated with the magnetic force gradient image is thought to be associated with closure domains and is symptomatic of the branching structures required to reduce magnetostatic energy. In general these fine structure features, which will not affect the surface distortion as shown in Fig. 3(a), have a separation of about 10% of the major deformation separations. Those lying parallel to the $\langle 110\rangle$ directions in the surface are considered to have {110} 109° Bloch character. Magnetic contrast can also be seen in $\langle 111\rangle$ and $\langle 001\rangle$ directions as predicted[7] and most configurations imply that the growth twin boundaries are associated with domain walls.[2,5] In the few regions of the surface which yield no surface topographical deformation, the MFM images reveal contrast which is considered to arise from in-plane easy axis domain configurations. An example of such contrast is shown in Fig. 5 from a $(1\bar{1}0)$ surface where the [111] and $[11\bar{1}]$ directions lie in the plane. The interpretation of such images however requires further experimental evidence concerning the magnetic state of the tip, since the directionality of the observed contrast will be dependent on the stray field distribution of both tip and sample.

Figure 6 shows the changes in MFM contrast in a $(11\bar{2})$ surface associated with ac field demagnetization of a sample in the in-plane [111] and $[\bar{1}10]$ directions. The surface deformations, and magnetic domain structure, both change consid-

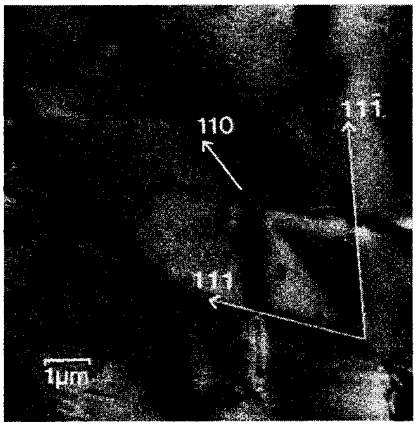



FIG. 5. MFM image from $(1\bar{1}0)$ surface from a region showing no topographic deformation indicating possible in-plane (001) 109° and (112) 180° walls.

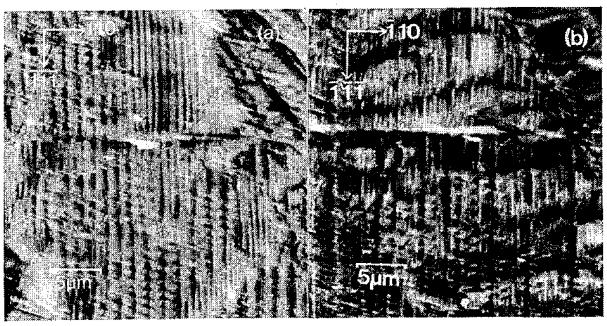



FIG. 6. MFM images from a similar area of a $(11\bar{2})$ surface ac demagnetized (a) along [111] and (b) along $[\bar{1}10]$.

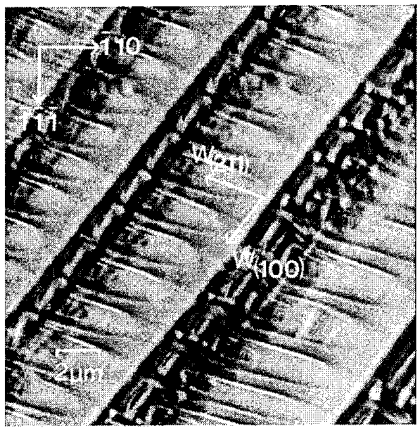



FIG. 7. MFM image from $(11\bar{2})$ surface showing the complex nature of the closure structure ($w_{(hkl)}$ represents the *hkl* plane projection on to the $(11\bar{2})$ plane).

erably under the influence of applied field, and applied external stress, and such observations are the subject of continuing study. The complex nature of the surface closure domain structure on these materials is demonstrated in Fig. 7 obtained from a $(11\bar{2})$ surface. The projections of the (100) and the (211) planes on to this surface are indicated on the figure. Such planes are low-energy Bloch wall planes[8] and geometrically suggest a possible configuration of the magnetic structure in this surface.

## IV. CONCLUSION

The application of SPM techniques to the study of particular crystallographic surfaces of Terfenol-D crystals has yielded the first direct measurements of the deformation gradients associated with magnetostrictively driven lattice strains in neighboring deformation domains. A value of $\lambda_{111}=1.63\times10^{-3}$ has been obtained, with $\sigma\sim8\%$, from such measurements. The complex magnetic force gradient images from observations on both {110} and {112} surfaces are symptomatic of domain branching at surfaces and also illustrate exact compatibility of features across growth twin boundaries. Further work on the effect of magnetic field and applied stress to gain a better understanding of the relation between topography and domain structure is in progress.

## ACKNOWLEDGMENT

The authors wish to thank the UK EPSRC for the support of this work under Grant No. GR\K18665 and No. GR\J31186.

[1] A. E. Clark, J. P. Teter, and O. D. McMasters, J. Appl. Phys. **63**, 3910 (1988).
[2] M. Al-Jiboory, D. G. Lord, Y. J. Bi, J. S. Abell, A. M. H. Hwang, and J. P. Teter, J. Appl. Phys. **73**, 6168 (1993).
[3] D. G. Lord, V. Elliot, A. E. Clark, H. T. Savage, J. P. Teter, and O. D. McMasters, IEEE Trans. Magn. **MAG-24**, 1716 (1988).
[4] A. L. Janio, A. Branwood, R. Dudley, and A. R. Piercy, J. Phys. D. **20**, 24 (1987).
[5] A. P. Holden, D. G. Lord, and P. J. Grundy, these proceedings.
[6] R. D. James and D. Kinderlehrer, J. Appl. Phys. **76**, 7012 (1994).
[7] A. E. Clark, in *Ferromagnetic Materials*, Vol. 1, edited by E. P. Wohlfarth (North Holland, Amsterdam, 1980), p. 531.
[8] G. F. Clarke, B. K. Tanner, and H. T. Savage, Philos. Mag. B **46**, 331 (1982).

# Magneto-optical indicator film (MOIF) microscopy of granular and layer structures (abstract)

V. I. Nikitenko, V. S. Gornakov, L. M. Dedukh, and A. F. Khapikov
*Institute of Solid State Physics, RAS, Chernogolovka, Moscow Distr., 142432, Russia*

L. H. Bennett, R. D. McMichael, L. J. Swartzendruber, A. J. Shapiro, and M. J. Donahue
*National Institute of Standards and Technology, Gaithersburg, Maryland 20899*

V. N. Matveev and V. I. Levashov
*Institute of Microelectronics Technology and High Purity Materials, RAS, Chernogolovka, Moscow Distr., 142432, Russia*

We report on the possibilities of application of magneto-optical indicator film (MOIF) technique for visualization and direct experimental study in real time of the magnetization processes and nondestructive characterization of the quality of magnetic thin granular films and multilayers. The technique utilizes a transparent indicator film, a Bi-substituted iron garnet with in-plane anisotropy, placed on the top of a sample. Polarized light passes through the indicator film and is reflected back by an Al underlayer. Magnetic stray fields with a component perpendicular to the film plane are observed through the magneto-optic Faraday effect created in the garnet film. An investigation of the magnetic moment distribution in granular single films and multilayers was carried out using this method. Some examples of magnetic stray field images of domain walls of different types obtained by MOIF technique and magnetic force microscopy are described. The experimental data are compared with theoretical estimations. The detailed information is obtained on the spin rotation processes as well as on the domain wall nucleation and motion during the remagnetization of these materials. Peculiarities of the magnetization reversal of multilayers with different types of exchange interlayer coupling have been revealed and discussed. © *1996 American Institute of Physics.*
[S0021-8979(96)61108-4]

# High density recorded patterns observed by high-resolution Bitter scanning electron microscope method

O. Kitakami, T. Sakurai, and Y. Shimada
*Research Institute for Scientific Measurements, Tohoku University, Sendai 980-77, Japan*

We have developed a new and versatile method for observation of fine domain structures in ferromagnetic specimens. In this method, which we call here the high-resolution Bitter scanning electron microscope (HRBS) method, ferromagnetic fine particles as small as 20 nm are fabricated by sputtering, and are subsequently deposited on the surface of ferromagnetic samples to be investigated. The particles form very faithful domain patterns reflecting the leakage field distribution from the samples. We have applied this method to several magnetic and magneto-optic high density recording media, and have successfully observed the bit patterns at a recording density of 300 kFCI (bit length ~80 nm). Moreover, we have confirmed that the HRBS method is also effective in investigating the magnetized states within each recording bit. © *1996 American Institute of Physics.* [S0021-8979(96)55608-X]

## I. INTRODUCTION

Recently, we have developed a versatile method for observation of fine domain structures in a ferromagnetic specimen.[1,2] In this method, ferromagnetic fine particles as small as 20 nm are fabricated by sputtering and are subsequently deposited on the surface of magnetic samples to be investigated, resulting in the evolution of the magnetic domain pattern. The method is referred to as the high-resolution Bitter–scanning electron microscope (HRBS) method. The HRBS has the following advantages over the other observation methods. First, this method is applicable to a variety of ferromagnetic specimens without any restrictions on their sample size and shape. Second, it has a high spatial resolution.[3] Third, it is possible to survey domain structures over a very wide area, as large as 100 mm,[2] enabling an easy search and a precise investigation of local points. Finally, high contrast domain images are available without any image processing. Owing to these merits, the HRBS is now widely applied to a variety of ferromagnetic specimens in order to investigate their domain structures.[3–8]

In the present paper, we will demonstrate the usefulness of the HRBS method through observations of magnetic and magneto-optic high density recording media.

## II. EXPERIMENT

The schematic of our dc magnetron sputtering apparatus is shown in Fig. 1. Fine ferromagnetic particles with an average diameter of 20 nm are formed in room B by sputtering the target (in this case, Co or Fe), and they are subsequently transported into room A by a slight pressure difference between the two rooms. The particles are attracted toward the surface of the ferromagnetic sample in accordance with the distribution of the magnetic potential. The domain patterns decorated by the fine particles are observed by a scanning electron microscope (SEM). Samples for pattern observations are a Co-Cr alloy thin-film disk, an obliquely evaporated Co-O thin-film tape and a Tb-Fe-Co magneto-optic disk. In order to enhance the contrast of the domain patterns, an external field of about 100 Oe was applied to the samples along the direction of the recorded magnetization during the formation of the patterns.[1,9,10]

## III. RESULTS AND DISCUSSION

According to the ferrohydrodynamic theory on Bitter pattern evolution by Hartmann and Mende,[11,12] the statistically averaged magnetic potential $\langle U \rangle$ of the ferromagnetic fine particles under the influence of a local field $H$ can be expressed as

$$\langle U \rangle = -kT \ln(\sinh p/p), \tag{1}$$

where $p = \mu_0 mH/kT$, and $m$ denotes the magnetic dipole moment of each fine particle, $k$ the Boltzmann constant, $\mu_0$ the permeability of vacuum, and $T$ the temperature. Using this magnetic potential, the surface density $\rho$ of the ferromagnetic particles on a ferromagnetic specimen is derived as[12]

$$\rho = \Lambda_0 \int \sinh p/p \, dy \quad (\Lambda_0\text{: constant}), \tag{2}$$

where $y$ denotes the distance from the surface of the magnetic specimen. By calculating Eq. (2), we can predict the

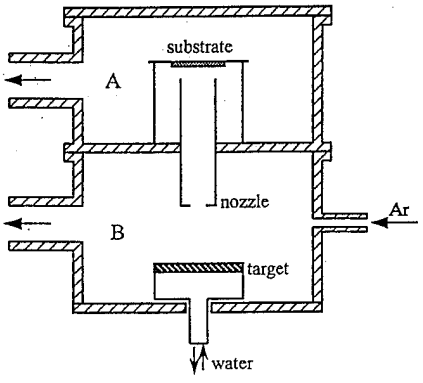



FIG. 1. Schematic draft of a dc magnetron sputtering system for formation of HRBS patterns.

 0021-8979/96/79(8)/6074/3/$10.00 © 1996 American Institute of Physics

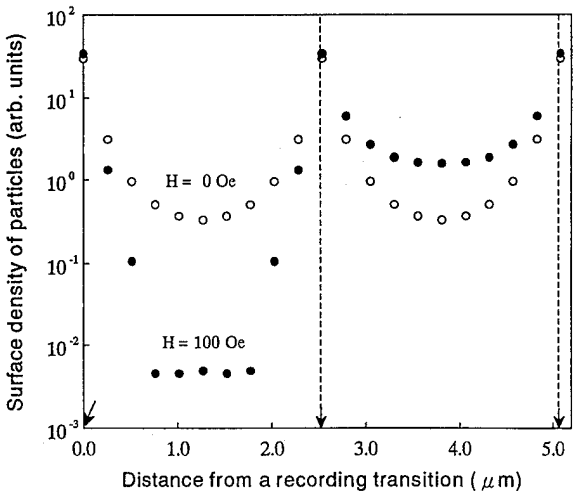



FIG. 2. Calculated surface density of ferromagnetic particles on a recorded thin-film disk at a density of 10 kFCI. Arrows in the figure indicate the positions of recording transitions.

density of ferromagnetic particles at the sample surface if its leakage field distribution can be determined. In the presence of an externally applied field, the magnetic field $H$ used to evaluate $p$ of Eqs. (1) and (2) is the magnitude of the vector sum of both the leakage and the externally applied fields. The detail calculation of the field $H$ is described elsewhere.[10] Figure 2 shows the calculated density of ferromagnetic particles at the surface of a digitally recorded medium, where the thickness and the residual magnetization are assumed to be 25 nm and 350 G, respectively. It is noted that applying a weak external field along the recorded magnetization during the pattern evolution effectively enhances the contrast of the magnetic domain patterns. Such theoretical results are reproduced in the observed HRBS patterns, as shown in Fig. 3, where these patterns were obtained by depositing sputtered Co fine particles onto a longitudinal Co-Cr alloy thin film disk.

In our sputtering apparatus, it is possible to form a HRBS pattern over a sample area as wide as 100 $mm^2$. We have confirmed that very clear magnetic domain patterns can be successfully observed over the whole area by using a conventional SEM. Figure 4(a) shows the SEM micrograph of the HRBS pattern formed on a digitally recorded Co-Cr alloy disk. By merely increasing the magnification of the SEM, we can clearly observe the recording states of 150 kFCI [bit length ~170 nm) as shown in Fig. 4(b)]. In order to roughly estimate the spatial resolution of the HRBS, we

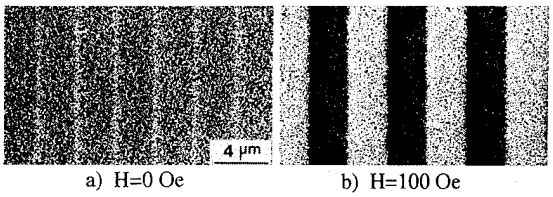



FIG. 3. HRBS patterns of a digitally recorded Co-Cr alloy thin-film disk at a density of 10 kFCI. (a) is formed in zero field and (b) in 100 Oe.

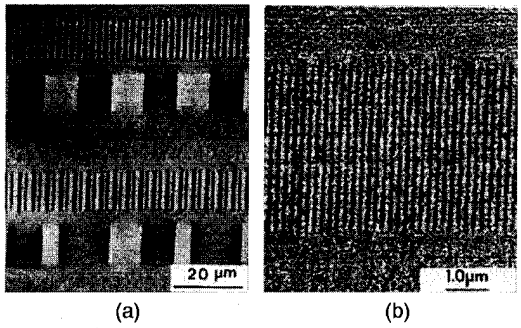



FIG. 4. (a) Several bit patterns recorded on a Co-Cr alloy thin-film disk, and (b) the recording track of 150 kFCI observed with high magnification.

have attempted to observe ultrahigh density recording states of an obliquely evaporated Co-O thin-film tape. Figure 5 is the HRBS pattern at a density of 300 kFCI (bit length ~80 nm). In spite of the extremely small output signals at this density, which are partly due to serious losses in the reproducing process, we can clearly see high density bit patterns, although the neighboring bits having parallel magnetizations are in some places linked to each other across an antiparallel recording bit. Recently, very similar bit patterns have been observed by the spin-SEM method for the same Co-O thin-film tape.[13] According to the above experiments, we believe that the spatial resolution of the HRBS is better than 80 nm. In order to determine the resolution more quantitatively, ideal recording media without any fluctuations of recording transitions are required.

The HRBS method is also effective in observing recording states of magneto-optic media. Figure 6 illustrates the dependence of the recorded bits of a Tb-Fe-Co disk on the input power of a laser source. The circular recording bits drastically shrink from 800 to 400 nm as the input power decreases from 7.5 to 6.8 mW. At present, very small recording bits as small as 200 nm can be clearly observed through a somewhat thick silicon-nitride and aluminum overlayers. By utilizing the HRBS method, intensive studies on the growth mechanisms of the magnetic domains are now in progress.[8]

We will show a typical example to demonstrate the usefulness of the HRBS method. Recently, Takano *et al.* have experimentally confirmed that the recording performance of a thin-film inductive head greatly depends on the electrical resistivity of magnetic materials.[7] According to their results, eddy currents are induced in the magnetic poles, which cause a phase lag of the recording field against the drive current

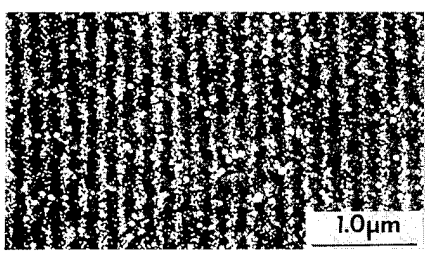
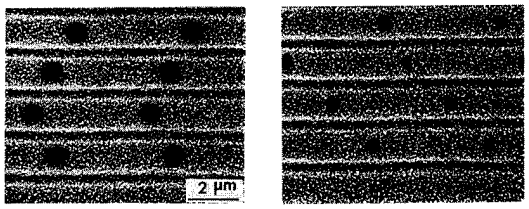



FIG. 5. HRBS pattern of an obliquely evaporated Co-O thin-film tape. Recording density is 300 kFCI (bit length ~80 nm).




a) 7.5 mW b) 6.8 mW

FIG. 6. Recording states of a Tb-Fe-Co magneto-optic disk as a function of the input power of the laser source: (a) 7.5 mW and (b) 6.8 mW.

and deteriorate the recording performance of the magnetic head, especially at high frequencies. In order to investigate their recording states, we applied the HRBS method to Co-Cr alloy thin-film disks which are recorded by using two kinds of thin-film heads. The magnetic poles of head A consist of the polycrystalline films with low resistivity ($\rho$=16 $\mu\Omega$ cm), and the poles of head B are made of the highly resistive amorphous films ($\rho$=90$\mu\Omega$ cm). The observed HRBS patterns are shown in Fig. 7 as functions of recording

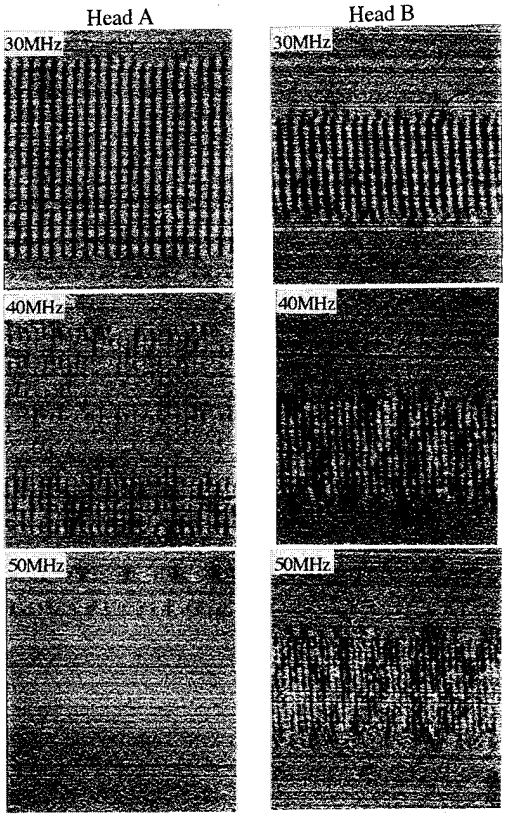



FIG. 7. HRBS patterns of a Co-Cr alloy thin-film disk recorded by two kinds of thin-film heads (heads A and B).

frequency. The relative velocity and the spacing between the head and the disk were maintained at 28 m/s and 100 nm, respectively. Head B exhibits good recording performance over the whole frequency range examined in this experiment. In contrast, head A cannot realize the uniform recording over the whole track width at 40 MHz, and finally no recorded patterns can be seen at 50 MHz. The fact that the fields at the middle of the track are attenuated indicates that the presence of the eddy currents considerably deteriorates the high-frequency performance of head A. Since the distribution of the eddy currents greatly depends on the dimensions of the magnetic poles as well as their electrical resistivity, very careful designing is required in constructing the thin-film heads for high frequency use.

As mentioned above, the HRBS method is one of the most effective measures for the investigation of fine domain structures in a variety of ferromagnetic specimens.

## IV. SUMMARY

Our newly developed high-resolution Bitter SEM is a very versatile method for the observation of magnetic domain structures of various ferromagnetic specimens. Applications of this method to magnetic and magneto-optic high density recording media have revealed that its spatial resolution is better than 80 nm.

## ACKNOWLEDGMENTS

The authors gratefully acknowledge discussions with Y. Sugita, H. Takano, H. Awano, and T. Takayama, and the essential contributions of H. Daimon and M. Kobayashi.

[1] T. Sakurai, O. Kitakami, and Y. Shimada, J. Magn. Magn. Mater. **130**, 384 (1994).
[2] T. Sakurai and Y. Shimada, Jpn. J. Appl. Phys. **31**, 1905 (1992).
[3] T. Sakurai, O. Kitakami, Y. Takeno, Y. Shimada, T. Takayama, H. Awano, and H. Ohlsen, J. Magn. Soc. Jpn. **19**, 89 (1995).
[4] T. Sakurai, O. Kitakami, and Y. Shimada, J. Appl. Phys. **76**, 3177 (1994).
[5] T. Sakurai *et al.*, Bull. Res. Inst. Sci. Meas. Tohoku University **43**, 27 (1994).
[6] H. Takano, M. Suzuki, K. Ito, Y. Maruyama, M. Fuyama, Y. Shiroishi, and Y. Sugita, J. Magn. Soc. Jpn. **19**, 133 (1995).
[7] H. Takano, M. Suzuki, K. Ito, H. Suzuki, Y. Shiroishi, M. Fuyama, and Y. Sugita, presented in INTERMAG'95, HB-01, San Antonio, April, '95.
[8] H. Awano, H. Ohlsen, K. Ando, T. Sakurai, O. Kitakami, Y. Shimada, T. Kohashi, H. Matsuyama, and K. Koike, *19th Annual Conference on Magnetics in Japan*, Tokyo, September '95 (in press).
[9] C. D. Mee, in *The Physics of Magnetic Recording*, edited by E. P. Wohlfarth (North Holland, Amsterdam, 1964).
[10] O. Kitakami, Jpn. J. Appl. Phys. **30**, L739 (1991).
[11] U. Hartmann and H. H. Mende, Z. Phys. B **61**, 29 (1985).
[12] U. Hartmann, J. Magn. Magn. Mater. **68**, 298 (1987).
[13] H. Matsuyama, T. Kohashi, K. Koike, and T. Takayama, *Digests of the 18th Annual Conference on Magnetics in Japan*, 1994, p. 364.

# A new magnetic bar code system based on a magnetic anisotropy detection (abstract)

I. Sasada and N. Watanabe
*Kyushu University 36, Fukuoka 812, Japan*

Magnetic bar codes can be used in unclean environments, where widely used optical bar code systems cannot be applied. Readout system for magnetic bar codes can also be made much simpler than optical ones. A new magnetic bar code system is proposed, in which binary information is coded in the sign of tilted angles of magnetic strips from a given standard direction. This scheme is unique compared to the conventional optical bar code, where width or space of the parallel pattern carries information, or an already reported magnetic bar code,[1] where cross sectional shapes of pattern engraved in a ferromagnetic body carries information. Each of the magnetic strips brings about magnetic anisotropy due to its shape effect, hence angular dependent permeability in the proximity of the strip. The sign of the tilted angle of each magnetic strip is detected inductively through the angular dependent permeability by using a magnetic pickup head with a pair of cross-coupled figure-eight coils,[2] where the sign of mutual inductance between the primary and the secondary figure-eight coil has one to one relationship to the sign of the tilted angle. Because the detection of the tilted angle is independent of scanning speed, variation in the scanning speed of the readout head does not affect the performance. In our preliminary study, the proposed magnetic bar code system was examined using pickup head consisting of a pair of cross-coupled 10-turn figure-eight coils which was embedded in a rectangular ferrite rod with cross-shape groove on the top surface of 6.5×3 mm dimension. The head was made thinner in the scanning direction to allow dense alignment of the pattern. Two kinds of pattern were made: the one was by aligning short amorphous wires (5 mm in length and 120 $\mu$m in diameter) on the plastic film and the other by using a thin (10 $\mu$m in thickness) copper film with tilted slits backed by an amorphous ribbon. These samples of magnetic bar code patterns were scanned with lift-off of 1 mm under the operating condition of 120 kHz and 200 mA. Amplitudes of the positive and the negative peak of the output voltage well exceeded 10 mV. Density of the pattern in the preliminary study was 7 bits for the bar code length of 2.6 cm. We will discuss several factors to make density of the pattern higher. Because the pickup coils can be assembled with planar coils and because the magnetic bar code itself is thin, the total system of this bar code scheme can be realized in thin form. © *1996 American Institute of Physics.* [S0021-8979(96)61208-0]

[1] H. Okada and K. Wakaumi, IEEE Trans. Magn. **26** (1990).
[2] I. Sasada and F. Koga, J. Appl. Phys. **75** (1994).

# Giant magnetoresistance as a probe of interfacial electronic character (invited) (abstract)

S. S. P. Parkin[a)]
*IBM Research Division, Almaden Research Center, 650 Harry Road, San Jose, California 95120-6099*

The giant magnetoresistance (GMR) effect exhibited by magnetic multilayers and related structures is very sensitive to the nature of the interfaces between the magnetic and nonmagnetic layers. We have explored the dependence of GMR on the electronic character of these interfaces by inserting additional thin magnetic layers at the interfaces. Insertion of thin Co layers in Ni–Fe/Cu/Ni–Fe or thin Ni–Fe layers in Co/Cu/Cu exchange biased sandwiches leads to an increase or decrease, respectively, in the magnitude of the GMR effect; the variation is monotonic with thickness of the inserted layer. In contrast, insertion of thin layers of Fe at the Ni–Fe/Cu interfaces in Ni–Fe/Cu/Ni–Fe exchange biased sandwich structure results in a *nonmonotonic* variation of GMR with Fe layer thickness; for intermediate thicknesses in particular the GMR is substantially reduced. The magnetism and structure of the Fe layers is explored in related sputter-deposited single-crystalline Ni/Fe/Cu thin-film structures prepared using thin Fe/Pt seed layers grown at high temperatures on single crystalline polished wafers of MgO(100), MgO(110), and (0001)$Al_2O_3$. The magnetism of the Ni, Fe, and Cu layers is examined using x-ray magnetic circular dichroism (XMCD) and the structure of the Fe is analyzed using extended x-ray absorption fine structure (EXAFS) studies. These experiments show that the Fe moment varies nonmonotonically with thickness resulting from a structural phase transition from fcc to bcc Fe with increasing thickness. The Fe displays a very small magnetic moment for an intermediate range of Fe thickness for which the Fe structure is fcc. This range of thickness depends on the crystalline orientation of the Fe. It is within this same range of thickness that the GMR is suppressed in related exchange biased sandwich structures. Interestingly we find that such nonferromagnetic layers of fcc Fe can be used as spacer layers in magnetic multilayers of, for example, Ni/Fe. These multilayers display both antiferromagnetic interlayer coupling of the Ni layers and giant magnetoresistance, which each oscillate as a function of Fe thickness. © *1996 American Institute of Physics.* [S0021-8979(96)43808-1]

[a)]Electronic mail: parkin@almaden.ibm.com

 0021-8979/96/79(8)/6078/1/$10.00 © 1996 American Institute of Physics

# Nanostructure fabrication via laser-focused atomic deposition (invited)

R. J. Celotta, R. Gupta, R. E. Scholten,[a] and J. J. McClelland
*Electron Physics Group, National Institute of Standards and Technology, Gaithersburg, Maryland 20899*

Nanostructured materials and devices will play an important role in a variety of future technologies, including magnetics. We describe a method for nanostructure fabrication based on the use of laser light to focus neutral atoms. The method uses neither a mask nor a resist, but relies on the direct deposition of atoms to form permanent structures. Since the atomic de Broglie wavelength is of picometer order, the size of structures produced is not significantly limited by diffraction, as in optical lithography. Lines as narrow as 38 nm full width at half maximum spaced by 213 nm have been produced and we have demonstrated the production of a two-dimensional array of dots. The highly parallel process of nanostructure formation and the intrinsic accuracy of the optical wavelength that determines structure spacing suggest a number of interesting applications, including calibration standards for various types of microscopy, lithography, and micromeasurement systems. Possible magnetic applications include the production of arrays of magnetic elements, laterally structured giant magnetoresistive devices, and the patterning of magnetic media.
[S0021-8979(96)22708-X]

## I. INTRODUCTION

The fabrication and use of nanostructures, both as tools to further our understanding of physical principles and to provide novel functionality in devices, continues to expand unabated. Nanostructures are generally understood to possess at least one dimension on the nanometer scale, more typically below 100 nm. Frequently, the near atomic scale of the dimension gives rise to unique properties to be explored or exploited. While this definition includes the area of thin-film research, such work is usually not discussed as nanostructure science. However, multilayer structures of thin films are included within the definition. This general area of research has also been referred to as nanotechnology.

While far more work has been performed on the electronic characteristics of small structures, a growing body of research concerns the fabrication and properties of magnetic nanostructures. A great deal of current research is focused on giant magnetoresistive (GMR) devices generally involving multilayer structures.[1] One recent article reports the fabrication of a GMR device consisting of a series of GMR multilayer structures with all three dimensions in the nanometer range.[2] Another reports the use of a wedge-shaped nanostructure to systematically study exchange-coupled magnetic layers.[3] Others concentrate on fabricating arrays of isolated magnetic elements to study their interactions,[4–7] magnetic properties,[8,9] or magnetic quantum tunneling.[10] Applications include improved MFM tips[11] and high-density magnetic storage.[12]

The production of one-dimensional nanostructures is generally done with molecular beam epitaxy and/or sputter deposition. Structures with two and three dimensions in the nanometer range require a patterning technique, such as optical or electron-beam lithography. Optical lithography, while convenient because of its wide usage and ability to pattern large areas in parallel, is limited because of the diffraction of light to feature sizes of about 180 nm, i.e., just at the upper limit of the nanoscale regime. As a result, electron-beam lithography, which has an insignificant diffraction limit, has generally been the method of choice for fabricating higher-dimensional nanostructures. Features as small as 20 nm can be fabricated with relative ease, and in some special cases, features as small as 1–2 nm have been achieved.[13] Further progress has been made recently by replacing the electron beam with a scanning tunneling microscopy (STM) tip.[14] Despite its popularity and potential for high resolution, there are drawbacks associated with electron-beam lithography. Because patterns are formed by scanning a finely focused beam, structures are generated serially across a substrate. There is also an inherent trade-off between speed and resolution. Since electrons mutually repel each other, high resolution can only be achieved at the expense of beam current. Thus the beam must be scanned relatively slowly across the surface in order to fully expose the resist. Besides introducing problems like sample drift, proximity effects, and stitching errors, this limits the complexity of the pattern to be fabricated: a large array of very small features can require an exposure of many hours, a length of time that rapidly becomes impractical.

## II. LASER FOCUSING OF ATOMS

Neutral atom focusing is a completely different approach to nanostructure fabrication. While still in its infancy, it already addresses several of the stumbling blocks of present methods. The diffraction limit is insignificant, as it is for electron beams, since the de Broglie wavelength of the atom is typically in the picometer range. Unlike electrons, however, the atoms are electrically neutral, so there is no space-charge repulsion limiting the flux in finely focused regions. Furthermore, the focusing scheme can be made massively parallel, allowing large areas to be patterned rapidly. In addition, the focusing schemes generally make use of highly stable optical wavelengths, so highly accurate patterns can be produced over relatively large areas without stitching errors. Still another advantage is that the process can be implemented in a direct-write manner, eliminating the need for a

[a]Current address: School of Physics, University of Melbourne, Parkville, Victoria 3052, Australia.

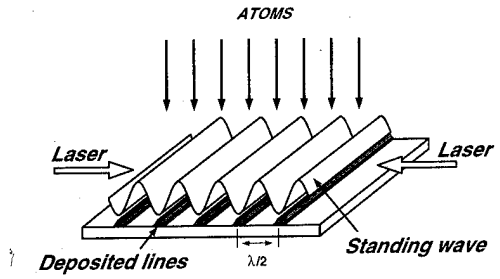



FIG. 1. Schematic of laser-focused atomic deposition process.

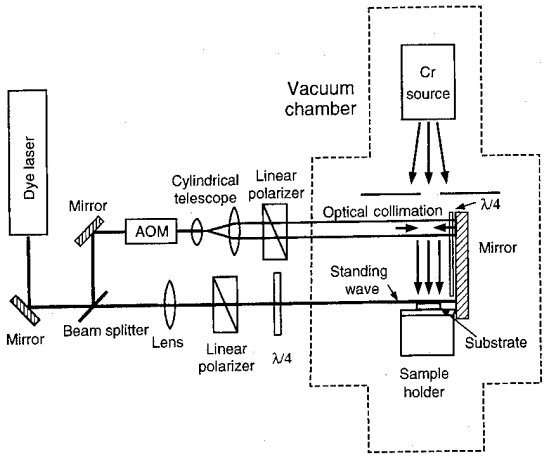



FIG. 2. Schematic of laser-focused atomic deposition apparatus, showing dye laser, acousto-optic modulator (AOM), miscellaneous optics (including quarter-wave plates, denoted by λ/4), vacuum chamber, Cr source, deposition substrate, and sample holder.

physical mask and subsequent processing. Though, so far, no direct application to the fabrication of magnetic nanostructures has been carried out, it appears that many of these advantages could prove useful for such applications.

The focusing of neutral atoms is achieved by configuring electromagnetic fields in such a way as to exert forces on neutral atoms toward an axis. The study of the motion of atoms in electromagnetic fields is a major component of the new field of atom optics,[15] which treats the manipulation of atoms by devices that serve as lenses, mirrors, beamsplitters, and gratings in analogy with light optics. To date, most of the configurations used for focusing atoms have involved the use of laser fields in which the frequency of the laser is tuned very close to an atomic resonance. Some work has been done, however, on the focusing of atoms in a hexapole magnetic field.[16] Laser fields provide an especially good medium for generating the necessary fields for high-resolution focusing of atoms because gradients can be generated over optical-wavelength distances, and tuning near resonance can greatly enhance the interaction. In particular, making use of a laser standing wave allows for massively parallel focusing of atoms in an array of lenses that is spaced with interferometric precision across a substrate (see Fig. 1).

In the presence of a near-resonant laser field, two types of radiation forces are present, the spontaneous force and the dipole force. The spontaneous force is simply the light pressure, i.e., the transfer of momentum that results when an atom absorbs a photon from the direction of the light source and reradiates a photon in an arbitrary direction. After a number of such interactions a beam of neutral atoms will be deflected away from the light source. The dipole force can be thought of as resulting from the interaction between an oscillating electric dipole induced in the atom and any spatial gradient that might be present in the oscillating laser electric field. Over the past 15 years, methods have evolved to use these forces, separately or in combination, to cool and trap,[17] and also focus,[18] atom beams.

The first application of laser focusing of atoms to controlled deposition involved observing the "shadow" of a resonant laser beam traversing a beam of sodium atoms depositing onto a surface.[19] This was followed by observation of optical diffraction from a grating of sodium atoms generated by focusing the atoms with the dipole force generated in the nodes of a standing wave passing across the surface of a substrate.[20] These experiments demonstrated the essential principle of laser focused atomic deposition but, because the deposited atom was sodium, it was difficult to proceed with nanostructure fabrication, or carry out quantitative studies of the process. Sodium was chosen because it was easy to make an atomic beam and easy to tune a laser near the strong resonance at 589 nm. The first permanent laser-focused structures were fabricated using a chromium atomic beam, taking advantage of the atomic resonance at 425 nm.[21] This work has been followed recently by creation of structures in aluminum.[22] Because the use of a hard, fine-grained material such as chromium opens the possibility for precise fabrication and perhaps transfer of the patterns to other materials, and because of the relevance of chromium to magnetic materials, we discuss the results of the chromium research in some detail.

## III. CHROMIUM EXPERIMENT

A schematic of the experimental arrangement[21] is shown in Fig. 2. In this experiment, Cr atoms effuse from a molecular beam epitaxy (MBE)-type evaporator, modified to produce a point source of atoms. They pass through a region where the beam is collimated optically, and then through a second, standing wave region where they are focused to form a pattern on a Si substrate. The optical standing wave, positioned immediately above the Si substrate, is formed by the reflection of a laser beam from a mirror in direct contact with the substrate. The laser wavelength used is 425.55 nm (in vacuum), which corresponds to the energy difference between the Cr $^7S_3$ ground state and the $^7P_4$ excited state, and the spacing between nodes of the resulting standing wave is just half that wavelength, or 212.78 nm. If the correct combination of laser beam size, intensity, wavelength, and position above the substrate is used, the standing wave acts as an array of cylindrical lenses to focus the atoms to form lines on the substrate.[21]

The dipole force is not strong, so the lenses described above are best thought of as weak immersion lenses. In order for their effect to be enough to bring the atoms into a fine focus, the incident atom beam must be highly collimated,

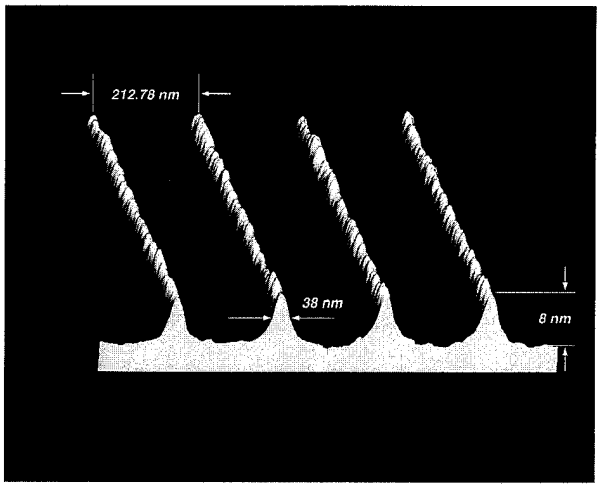



FIG. 3. Atomic force microscope image of Cr lines formed by laser-focused atomic deposition. The lines in this image have a height of 8±1 nm.

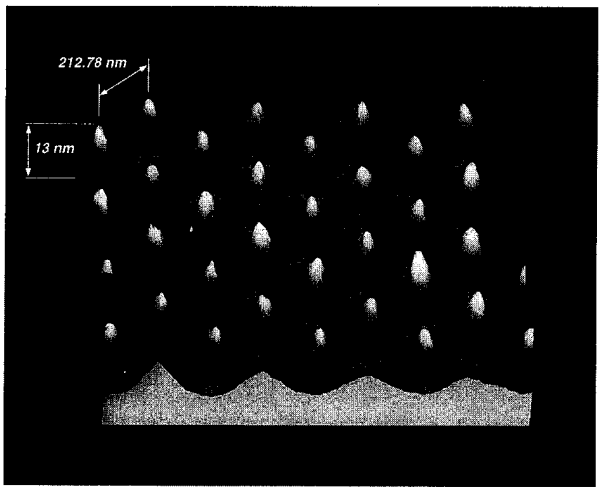



FIG. 4. Atomic force microscope image of a two-dimensional array formed by laser-focused atomic deposition of Cr.

possessing little transverse velocity. To achieve this, a collimation region is used, in which counterpropagating laser beams transverse to the atom beam are tuned to a frequency just below that of the resonant transition. In this process, photons are absorbed only if the transverse velocity of the atoms is large enough to Doppler shift the photon into resonance with the atom. In that case, the atoms will experience a momentum change that moves them closer to an ideally collimated beam. This collimation or laser cooling process, which is sometimes referred to as "optical molasses," has been studied in great depth in one, two, and three dimensions in relation to laser cooling and trapping of atoms.[23] Using a variant of the basic process, which makes use of polarization gradients in the laser beams,[24] an atom beam collimation of the order of one part in 7000 is achieved.

## IV. CHROMIUM RESULTS

Using the apparatus schematically shown in Fig. 2, samples were fabricated with Cr lines covering an area of up to 1 mm×0.40 mm. Figure 3 shows an atomic force microscope (AFM) topograph of one of these samples. The lines are spaced by half the laser wavelength, 212.78 nm. The average height of the lines in Fig. 3 is 8±1 nm,[25] and the full width at half maximum (FWHM) is 38±1 nm, uncorrected for AFM tip shape (which could have an influence in this size range). The evaporation time, using a modest Cr oven, was 10 min. Although the AFM cannot distinguish between bare Si and Cr, we infer that there is a thickness of Cr in the valleys between the lines in this sample, based on measurements of the total atomic flux. We estimate this background to be 10±4 nm thick. A complete understanding of the background is still to be established, however significant contributions include 16% of other isotopes of Cr that do not interact with the laser, about 10% Cr atoms that decay into a metastable $^5D$ level and no longer interact with the laser, and a possible high-velocity tail in the laser-cooled transverse velocity distribution.

In addition to the one-dimensional array of lines shown in Fig. 3, a two-dimensional array has also been created.[26] Figure 4 shows an AFM topograph of a section of a two-dimensional array of Cr "dots" made by first optically collimating in two dimensions and then using two standing waves positioned at right angles to each other. These dots cover an area of approximately 100 μm×200 μm on the sample, have a FWHM of 80±10 nm, and have a height of 13±1 nm.

While the extension of the laser focusing process to two dimensions may seem straightforward, there are some subtleties that must be understood. When two standing waves that are temporally coherent (e.g., originating from the same laser) are superimposed upon each other at right angles, the resulting intensity pattern will, in general, depend on the relative temporal phase. However, for the special situation of orthogonal linear polarizations (one parallel to the substrate, the other perpendicular), this dependence is eliminated, allowing the laser focusing to be carried out without stabilizing the relative phase of the standing waves.

## V. METASTABLE RARE GASES

Although the bulk of the work on laser focusing of atoms has been done with "direct-write" materials such as sodium, chromium, and aluminum, a new possibility has been suggested that makes use of metastable rare gases to exposure a lithographic resist.[27] The potential for this approach lies in the combination of lithography's ability to work with a wide range of materials with the atom optics advantages of high resolution, parallel fabrication, and low substrate damage. Metastable rare gases are both accessible to laser manipulation techniques, and they also have internal energy of up to 20 eV, sufficient to chemically alter a resist, yet not damage a substrate.

The ability of metastable atoms to act as a writing tool on a resist has been demonstrated using self-assembled monolayers (SAMs) of alkanethiolates on gold-coated silicon.[27] The SAM coating acts as a very thin resist, preventing etching of the gold when it is placed in an aqueous

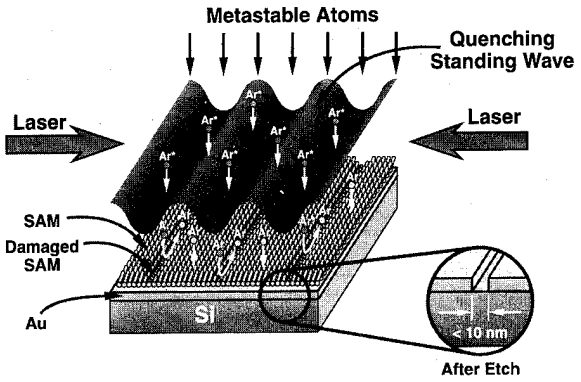



FIG. 5. Schematic of metastable rare gas lithography concept.

solution of ferricyanide. In regions where metastables have been allowed to strike the surface, the SAM is damaged, allowing the etch to penetrate.

So far, an upper bound of around 100 nm has been set for the resolution of this process by examining the edge roughness of a physical mask. The methods of laser manipulation have yet to be applied; however, work is ongoing, and several possibilities exist, using either 1.083 $\mu$m light on the He $(2^3S \rightarrow 2^3P)$ transition or 811 nm light on the Ar $(1s_5 \rightarrow 2p_9)$ transition. Metastable Ar opens a particularly interesting additional possibility in that it is possible to quench the metastable state using laser light at 764 or 801 nm. This allows the spatially selective removal of metastable atoms from the beam as an alternative to focusing (see Fig. 5), suggesting the possibility of significantly less background exposure. Preliminary estimates indicate that this quenching approach may result in features as small as 10 nm, though more work needs to be done to investigate this.

## VI. FUTURE RESEARCH

We have only begun to investigate the application of atom optics to the manipulation of atoms as they impact a surface. There are a large number of possibilities that could lead to exciting new fabrication techniques. Given the current circumstances, a few areas for future improvement can be discussed, though many more may become apparent as the field develops.

Feature size is one area where improvement can be anticipated. Currently features as small as 38 nm FWHM have been created, but calculations of the focusing process, both semiclassical[28] and fully quantum,[29] predict that features as small as 10 nm should be attainable. This reduction in feature size will most probably arise from an improvement in the atomic source: reduction of the velocity spread, and still higher levels of collimation, appear to be the improvements that will help the most in this case.

The ability to create more complex patterns is also highly desirable if the process is to become useful for general nanostructure fabrication. To this end, arrays of complex patterns can be created by using the current two-dimensional process, perhaps with higher resolution, and simply scanning the substrate during deposition. In this way patterns can be "painted" within the unit cell of the standing wave, and these patterns will be repeated with very high accuracy across the substrate. Still more general patterns could be created by designing a more complicated optical field that puts the atoms exactly where they are required.

Another avenue for exploration is the possibility of extending the process to other atomic species. While nanostructures of other materials can be produced by using the metastable rare gas process discussed above or using Cr as a mask for reactive ion etching, it is also of interest to ask what other materials could be used directly. The essential characteristics are that the atomic species be relatively easily evaporated, and that there be a resonance transition accessible to an available laser wavelength. The resonance transition must have as its lower state one that has a significant population of atoms, either naturally or prepared (as in the case of metastable atoms). The full range of materials has not yet been explored, however it appears that many of the metallic species that might be of interest have resonant transitions in the ultraviolet, in the range from 200 to 300 nm. At present these wavelengths are difficult, though not impossible, to access with a laser. Nevertheless, laser technology is improving rapidly, and it is likely that in the future these atoms will become accessible.

The application of these new techniques to the fabrication of magnetic nanostructures remains in the realm of the future. However, the unique capabilities inherent in these new techniques offer several advantages when compared with other lithographic methods, and the length scale of their applicability is an interesting one from a magnetic perspective. We plan to explore the use of this method for magnetic nanostructure fabrication in the near future.

## ACKNOWLEDGMENTS

The authors wish to thank Z. J. Jabbour for contributions to this work, and to R. A. Dragoset for his technical assistance. This work is supported in part by the Technology Administration of the U. S. Department of Commerce, and by the National Science Foundation under Grant No. PHY-9312572.

[1] See, e.g., A. Fert and P. Bruno, in *Ultrathin Magnetic Structures II*, edited by B. Heinrich and J. A. C. Bland (Springer, Berlin, 1994), p. 82.
[2] M. A. M. Gijs, M. T. Johnson, A. Reinders, and P. E. Huisman, Appl. Phys. Lett. **66**, 1839 (1995).
[3] J. Unguris, R. J. Celotta, and D. T. Pierce, Phys. Rev. Lett. **67**, 140 (1991).
[4] A. D. Kent, S. von Molnar, S. Gider, and D. D. Awschalom, J. Appl. Phys. **76**, 6656 (1994).
[5] M. Lederman, S. Schultz, and M. Ozaki, Phys. Rev. Lett. **73**, 1986 (1994).
[6] J. F. Smyth, S. Schultz, D. R. Fredkin, D. P. Kern, S. A. Rishton, H. Schmid, M. Cali, and T. R. Koehler, J. Appl. Phys. **69**, 5262 (1991).
[7] M. S. Wei and S. Y. Chou, J. Appl. Phys. **76**, 6679 (1994).
[8] D. A. Tulchinsky, J. J. Baumberg, D. D. Awschalom, N. Samarth, H. Lou, and J. K. Furdyna, Phys. Rev. B **50**, 10851 (1994).
[9] A. D. Kent, T. M. Shaw, S. von Molnar, and D. D. Awschalom, Science **262**, 1249 (1993).
[10] D. D. Awschalom, D. P. DiVincenzo, and J. F. Smyth, Science **258**, 414 (1992).
[11] S. Y. Chou, M. S. Wei, and P. B. Fischer, IEEE Trans. Magn. **30**, 4485 (1994); S. Y. Chou, M. Wei, P. R. Krauss, and P. B. Fischer, J. Vac. Sci. Technol. B **12**, 3695 (1994).
[12] S. Y. Chou, M. S. Wei, P. R. Krauss, and P. B. Fischer, J. Appl. Phys. **76**, 6673 (1994).

[13] A. Muray, M. Scheinfein, and M. Isaacson, J. Vac. Sci. Technol. B **3**, 367 (1985).
[14] See *Technology of Proximal Probe Lithography*, edited by C. R. K. Marrian (SPIE, Bellingham, WA, 1993), Vol. 10.
[15] See, e.g., C. S. Adams, M. Sigel, and J. Mlynek, Phys. Rep. **240**, 143 (1994).
[16] W. G. Kaenders, F. Lison, A. Richter, R. Wynands, and D. Meschede, Nature **375**, 214 (1995).
[17] See, e.g., J. Opt. Soc. Am. B **2**, 1706 (1985); *ibid.* **6**, 2020 (1989).
[18] See, e.g., J. E. Bjorkholm R. R. Freeman, A. Ashkin, and D. B. Pearson, Phys. Rev. Lett. **41**, 1361 (1978); V. I. Balykin, V. S. Letokhov, Yu. B. Ovchinnikov, and A. I. Sidorov, J. Mod. Opt. **35**, 17 (1988); J. J. McClelland and M. R. Scheinfein, J. Opt. Soc. Am. B **8**, 1974 (1991).
[19] M. Prentiss, G. Timp, N. Bigelow, R. E. Behringer, and J. E. Cunningham, Appl. Phys. Lett. **60**, 1027 (1992).
[20] G. L. Timp, R. L. Behringer, D. M. Tennant, J. E. Cunningham, M. Prentiss, and K. K. Berggren, Phys. Rev. Lett. **69**, 1636 (1992).
[21] J. J. McClelland, R. E. Scholten, E. C. Palm, and R. J. Celotta, Science **262**, 877 (1993).
[22] R. W. McGowan, D. Giltner, and S. A. Lee, Opt. Lett. **20**, 2535 (1995).
[23] See, e.g., C. N. Cohen-Tannoudji and W. D. Phillips, Phys. Today **43**, 33 (1990).
[24] J. Dalibard, C. Saloman, A. Aspect, E. Arimondo, R. Kaiser, N. Vansteenkiste, and C. Cohen-Tannoudji, in *Atomic Physics II*, edited by S. Haroche, J. C. Gay, and G. Grynberg (World Scientific, Singapore, 1989), p. 199; S. Chu, D. S. Weiss, Y. Shevy, and P. Ungar, *ibid.*, p. 633.
[25] Uncertainty estimates are intended to be interpreted as one standard deviation combined random and systematic error, unless otherwise noted. The uncertainty in the line width in this case is dominated by variation in a sample of widths measured from the image in Fig. 3. The height uncertainties are dominated by systematic uncertainties in the calibration of the AFM and the total deposition measurement.
[26] R. Gupta, J. J. McClelland, Z. J. Jabbour, and R. J. Celotta, Appl. Phys. Lett. **67**, 1378 (1995).
[27] K. K. Berggren, A. Bard, J. L. Wilbur, J. D. Gillaspy, A. G. Helg, J. J. McClelland, S. L. Rolston, W. D. Phillips, M. Prentiss, and G. M. Whitesides, Science **269**, 1255 (1995).
[28] J. J. McClelland, J. Opt. Soc. Am. B **12**, 1761 (1995).
[29] P. Marte, R. Dum, R. Taïeb, P. D. Lett, and P. Zoller, Phys. Rev. Lett. **71**, 1335 (1993).

# Perpendicular transport and magnetic properties in patterned multilayer magnetic microstructures (invited)

J. J. Krebs, W. Vavra,[a] and G. A. Prinz
*Naval Research Laboratory, Washington, DC 20375*

S. F. Cheng
*Naval Surface Warfare Center, Silver Spring, Maryland 20910*

Anita Fink
*Nonvolatile Electronics, Eden Prairie, Minnesota 55344*

Using micron-level photolithography, we have prepared a set of patterned multilayer samples which have the form [Co/Cu/NiFeCo/Cu]×10 and which permit perpendicular current transport through the structure. Based on vibrating sample magnetometry, the multilayer stacks show a loss of ≈2 Å of magnetic material at each interface. The magnetoresistance was measured as a function of temperature, magnetic layer thickness, and element size and the $\Delta R/R$ values range up to 8% at 300 K and 18% at 10 K. The thickness dependent data are modeled using an extension of existing methods and can be fit using comparable resistivity, interface resistance, and spin asymmetry parameters. The magnetic fringe fields of the elements have an important effect on the observed $R$ vs $H$ curves. © *1996 American Institute of Physics.* [S0021-8979(96)22808-6]

## I. INTRODUCTION

The strong interest in the giant magnetoresistance (GMR) effect is driven both by the opportunities for technological applications and by purely scientific curiosity about the physical basis of the observed effects. In the work reported here, we have attempted to make a contribution to both of these interests.[1] The perpendicular transport geometry[2] is particularly attractive for understanding the GMR effect because relatively simple theoretical models can be applied to the analysis.[3–5] However, unless one is willing to use superconducting leads and be confined to low-temperature measurements, there is the challenge of fabricating small device structures on the scale of a micron. The fabrication and characterization of these small structures is itself of technological interest for incorporating the GMR effect into electronic circuits with potential use as sensors or information storage. In this article, we report the procedures used in fabrication, the thermal and dimensional dependence of the observed effect and, finally, some physical understanding of the spin-polarized transport results based on the two current models for perpendicular transport through a magnetic multilayered structure containing two different ferromagnetic materials in alternating sequence.

## II. SAMPLE FABRICATION AND MEASUREMENT TECHNIQUES

The samples used in this work were patterned from multilayers having the form (NiFeCo/Cu/Co/Cu)×10. This combination of materials was chosen to achieve simultaneously a sizable intrinsic GMR and distinctly different coercivities for the two types of magnetic layers, maximizing the GMR effect. We chose a NiFeCo permalloy (65% Ni, 15% Fe, 20% Co) and pure Co which have coercivities of 4 Oe and roughly 300 Oe, respectively.

Since we use normal metal (Cu) leads to permit measurements of the temperature dependence of the GMR, the cross sections of the individual elements must be reduced to micron dimensions to achieve adequate element resistances and signal strengths. This requires the use of photolithographic techniques, with careful attention to lead design. This approach was first demonstrated by Gijs *et al.*[6] for the multilayer system $[Fe/Cr]_N$. They found that accurate data could only be obtained using their lithographic pattern if postprocess laser trimming was used to exclude current from the voltage leads.[7,8]

Figure 1(a) is a scanning electron micrograph of a patterned microstructure used in the present study. The multilayer stack is in the center of the "$X$" and in this case is a 2.4 $\mu$m×2.4 $\mu$m square with a 1.2 $\mu$m diam contact area. To prevent current from entering the voltage leads it is essential for all leads approaching the stack to be as narrow as the lithography permits.

Using Si substrates coated with a 2000 Å layer of $Si_3N_4$, the multilayer films were grown by rf sputter deposition. The metal deposition begins with 50 Å NiFeCo for adhesion, then 2500 Å Cu which serves as the bottom Cu electrode in Fig. 1. Next comes the magnetic multilayer [$t$ Å NiFeCo/(100-$t$)Å Cu/$t$ Å Co/(100-$t$)Å Cu]×10 with $t$=10, 20, 40, 50, and 60 for the five wafers studied. Thus the number of ferromagnetic/nonferromagnetic interfaces and the total thickness of each multilayer is held constant throughout the series. Finally, the multilayer is capped with 750 Å of Cu. All metals were sputter deposited at 20 m Torr of Ar with the substrate 1.5 in. from the target.

The samples are then photolithographically processed. Details on this aspect of the sample preparation were presented earlier.[1] Here we only point out that rf sputtered $Si_3N_4$ is used as the insulation between the top and bottom leads and that the top leads consist of 1500 Å of Cu followed 1500 Å of $Al_{0.98}Cu_{0.02}$ (for wire bond adhesion). This last 3000 Å is wet etched to define the top electrical leads, $I+$ and $V+$ in Fig. 1. The minimum contact window diameter achieved was

[a]Now at Honeywell, Inc., Plymouth, MN 55441.

 0021-8979/96/79(8)/6084/6/$10.00 © 1996 American Institute of Physics

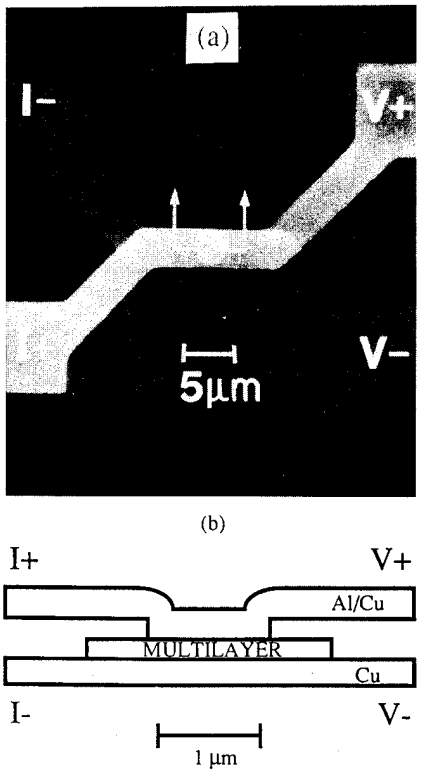



FIG. 1. Perpendicular current sample geometry: (a) Scanning electron micrograph of an element with a multilayer which is 2.4 $\mu$m×2.4 $\mu$m and 0.2 $\mu$m thick. The multilayer stack is located at the center of the "$X$" formed by the leads. (b) A vertical section through the element at the location marked by the arrows in (a). The layer of AlCu on top of the upper Cu lead facilitates wire bonding. The current contact is 1.2 $\mu$m across.

1.2 $\mu$m with a mask alignment tolerance of 0.5 $\mu$m. Other samples with contact window diameters up to 10 $\mu$m were produced simultaneously by the lithography.

The magnetic properties of the multilayers were measured at room temperature using vibrating-sample magnetometry (VSM) to determine the $M$ vs $H$ loops and absolute moments, and 35 GHz ferromagnetic resonance (FMR) to obtain additional anisotropy information. Transport measurements were carried out under computer control using a lock-in amplifier with the internal oscillator serving as the current source. The currents are in the mA range and do not generate fields large enough to effect the data. The magnetoresistance ratios ($MR=\Delta R/R$) found range between 5% and 8% at room temperature and up to 18% at liquid helium temperatures. In terms of magnetoresistance (MR) per magnetic layer, these values compare well with previous studies of perpendicular current magnetoresistance on both sputtered and molecular beam epilaxy (MBE) grown samples.[8]

## III. EXPERIMENTAL RESULTS AND DISCUSSION

### A. Magnetic properties

We will treat the magnetic properties of the samples prior to the magnetoresistance. The $M$ vs $H$ loops of 8 mm square pieces from the wafers containing 10 or 60 Å thick ferromagnetic (FM) layers are shown in Fig. 2. Note that for 10 Å thick layers there is a clear distinction between the

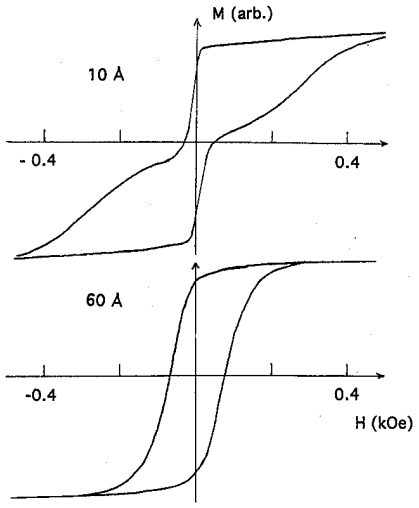



FIG. 2. Magnetization vs applied field loops of 8 mm square pieces taken from multilayer wafers containing ferromagnetic layers either 10 or 60 Å thick.

switching of the NiFeCo at about 5–10 Oe and that of the Co at about 300 Oe as expected. For 60 Å layers, however, no such distinction is apparent. Rather, the two types of FM layers appear to behave as a single or coupled system with an intermediate coercive field. We do not believe that the coupling is via the Cu interlayer because very similar behavior is seen even for 40 Å thick FM layers, in which case there is 60 Å Cu between them. We suggest that this apparent coupling is due to local stray fields associated with the interface roughness of the magnetic layers. Such stray fields would be proportional to the FM thickness which is consistent with increased coupling found for thicker magnetic layers. Note that for such large area samples the stray fields due to edge poles are not significant. This is in contrast to the situation for micron-sized samples, as we will see later.

The magnetic moment of the 8 mm square pieces is shown in Fig. 3 as a function of the total magnetic thickness $20t$ of the stack. The excellent linear fit shows that the magnetization in the interior of each FM layer is constant. Furthermore, the slope agrees quantitatively with that expected from the bulk magnetizations. However, the negative inter-

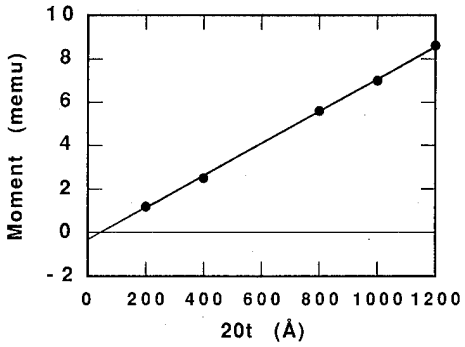



FIG. 3. Total magnetic moment of 8 mm square pieces taken from multilayer wafers as a function of the total magnetic layer thickness $20t$ of the multilayer stack. The solid line is a linear least-squares fit to the data. Note the negative intercept which implies a reduced moment in each layer.

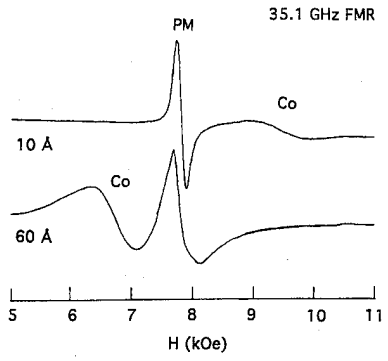



FIG. 4. Ferromagnetic resonance signals from multilayers containing magnetic layers either 10 or 60 Å thick. The signals due to the Co layers are labeled as Co and those due to the NiFeCo permalloy as PM.

cept indicates a net loss of magnetic moment. When the 50 Å seed layer is taken into account, one finds that there is an average loss of about 2 Å of ferromagnetic material at each interface. This is most likely due to the formation of a nonmagnetic interfacial alloy.

The FMR signals from multilayers containing 10 and 60 Å FM layers are shown in Fig. 4. Typical sample areas are about 15 $mm^2$ for these measurements. Note that, while in both cases the NiFeCo and the Co FMR signals are distinct, there is a major change in the resonance field for the Co layer as the magnetic thickness is increased. For in-plane FMR measurements, the principal relevant parameter which influences the resonance field is the sum of $4\pi M$ and the perpendicular anisotropy $2K_\perp/M$. The value of this sum for Co is given for the complete set of layer thicknesses in Table I. Since the data of Fig. 3 indicate that the magnetization of the interior of each magnetic layer has essentially the bulk value, the variation with FM thickness arises entirely from the perpendicular anisotropy. The deduced values of $2K_\perp/M$ are also given in Table I and indicate an out-of-plane anisotropy which increases strongly as the thickness decreases. This is consistent with well-known results for thin films of Co.

### B. Magnetoresistive properties

We define $\Delta R$ as the difference between the maximum and minimum sample resistances $R_{\max}$ and $R_{\min}$ as the magnetic field is swept from positive to negative saturation. The value $R_{\min}$ occurs at saturation and corresponds to the parallel moment resistance $R_p$. Ideally, $R_{\max}$ corresponds to antiparallel resistance $R_{ap}$, although the true antiparallel case seldom seems to be achieved fully in our samples. The temperature dependence of $\Delta R$ and $R_p$ are shown in Fig. 5 for a sample having 60 Å magnetic thickness and the minimum contact area studied. The saturated $R_p$ has a very linear dependence on $T$ over an extended temperature range while $\Delta R$ appears to vary as $R_0(1-aT^2)$. A similar $T^2$ dependence of the quantity $[(R_{ap}-R_p)R_{ap}]^{0.5}$ was found for the Fe/Cr system and ascribed to magnon scattering.[8]

TABLE I. Values of $4\pi M+2K_\perp/M$ and $2K_\perp/M$ deduced from 35.1 GHz ferromagnetic resonance data on multilayer samples with the magnetic layer thicknesses shown. A negative value favors $M$ out of plane.

| $t$ (Å) | 10 | 20 | 40 | 50 | 60 |
|---|---|---|---|---|---|
| $4\pi M+2K_\perp/M$ (kOe) | 4.3 | 7.1 | 12.8 | 13.4 | 14.4 |
| $2K_\perp/M$ (kOe) | −14.0 | −11.1 | −5.4 | −4.9 | −3.8 |

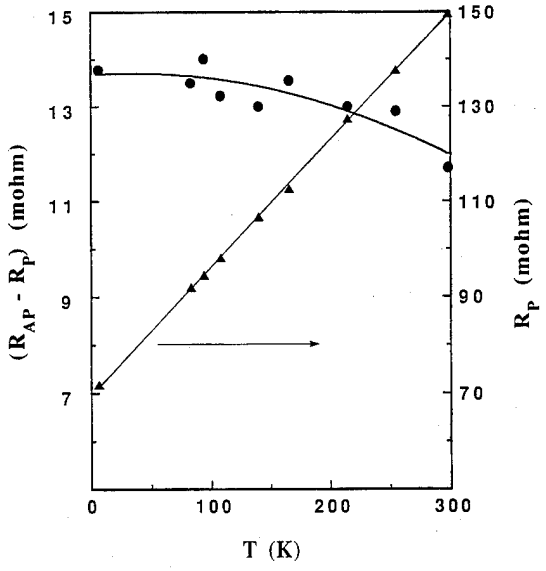



FIG. 5. The temperature dependence of the resistances $R_p$ and $\Delta R=(R_{ap}-R_p)$ for a 1.2 $\mu$m diam multilayer stack. The $\Delta R$ data are fit to the form $R_0(1-aT^2)$ while the $R_p$ data vary linearly with temperature.

The GMR ratio $\Delta R/R_p$ (not shown) decreases nearly linearly as $T$ increases. The only previous CPP temperature-dependent GMR data are for Fe/Cr and Co/Cu.[6–8] Neither of these systems show the linear $T$ dependence found for our NiFeCo/Cu/Co/Cu multilayers, although the fractional change in $\Delta R/R_p$ between liquid helium and room temperature found here, between 2.1 and 3.9 for different stacks, is roughly the same magnitude as for uncoupled multilayers in that earlier work. It is clear that the temperature dependence of $R_p$ dominates the GMR behavior in our samples.

The magnetic field dependence of the sample resistance is shown in Fig. 6 for a set of 2.4 $\mu$m×2.4 $\mu$m square multilayer stack samples for different thicknesses of the magnetic layers. The half-maximum width of these curves shows an approximately linear increase with increasing thickness, with a significant shape asymmetry for 20 and 10 Å thickness. The $R/R_p$ maximum for the thicker layers occurs at ≈100 Oe, and their curves are symmetric about this value. In the absence of any coupling between the magnetic layers, one would expect that at zero applied field $H$ all of the magnetic layers would have their moments parallel, left in remanance in a negative direction after lowering the negative $H_{ap}$ from saturation. Thus $R/R_p$ should remain equal to 1, the saturation value. This condition only begins to be approximated for the thinnest of our magnetic layers when the sample edge fringe fields are a minimum. Since the separation via Cu layers is large enough to preclude exchange coupling, the magnetoresistance-deduced anti-alignment which sets in as the applied field magnitude decreases is due predominantly to fringe-field interlayer coupling.

One can obtain a first-order estimate of these fields by assuming a uniform pole distribution on the edges of the

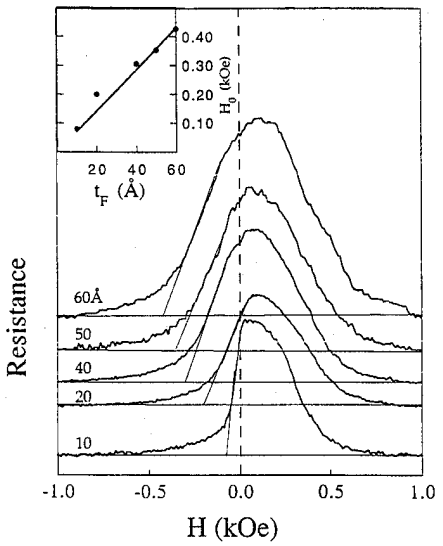



FIG. 6. The magnetic field dependence of the sample resistance for 2.4 $\mu$m×2.4 $\mu$m multilayer stacks. (The magnetic field was swept from negative to positive values.) The ferromagnetic layer thicknesses are indicated on the various traces which are offset vertically. The linear extrapolations of the leading edge of these traces are shown and define the onset fields $H_{on}$. *Inset*: $H_{on}$ plotted as a function of $t_F$. The solid line is calculated from Eq. (2) using bulk ferromagnetic parameters.

magnetic element perpendicular to the magnetization vector. In the two-dimensional approximation, where the magnetic element dimension in the plane perpendicular to the magnetization direction is infinite, the dimension in the plane along the magnetization ($x$ direction) is $\ell$ and the thickness of the magnetic layers (measured in the $y$ direction) is $t$, one obtains for the magnetic field $x$-component at $(x,y)$ due to the poles at $\pm\ell/2$:

$$H_x(x,y)=-4tM\left[\frac{\ell-2x}{4y^2+(\ell-2x)^2}+\frac{\ell+2x}{4y^2+(\ell+2x)^2}\right] \quad (\text{for } t\ll\ell), \tag{1}$$

where (0,0) is at the center of the magnetic film midway between the ends and also its top and bottom surfaces. If the distance $y$ to the neighboring magnetic layer is much less than $\ell$, then one obtains[9]

$$H_x(x,y)=-8M\left(\frac{t}{\ell}\right)\left[\frac{1}{1-4x^2/\ell^2}\right]. \tag{2}$$

In this limit, which corresponds closely to our samples, there is no dependence upon separation, and for $|x|\ll\ell/2$ (i.e., away from the ends), $H_x$ should vary linearly with layer thickness and inversely with the element size. This is exactly what is observed from the inset in Fig. 6, which plots the observed magnetoresistance onset field $H_{on}$ (due to the initial reversal of the permalloy layers) versus magnetic film thickness and compares the data to calculations based on Eq. (2). The agreement is quite good. Quantitatively, the calculated field at a permalloy layer from all 20 magnetic layers (2.4 $\mu$m square, 60 Å thick) is 430 Oe. For the 10 Å layer sample, this field is only 70 Oe and one can begin to see a situation in which an isolated permalloy element would switch (≈10 Oe). The long saturation tail on the 10 Å curve is largely due to the coercive field of the Co layer. These approximate calculations have been verified by two-dimensional finite-element analysis. Both calculations, of course, overestimate the actual field and three-dimensional finite-element analysis will be required for more precise field values.

## IV. EFFECT OF TWO TYPES OF MAGNETIC LAYERS ON THE MAGNETORESISTANCE

One of the principal advantages of measuring perpendicular GMR is the ability to separate the contributions from spin dependent bulk and interface scattering. In this geometry, if the spin diffusion length is much longer than the layer thicknesses, then the currents carried by up and down spin electrons are independent and do not mix. Therefore, the resistance encountered by an up or down spin electron at each layer is simply added in series to determine the total resistance for that spin. The two expressions are then combined as parallel resistors to obtain the total resistance of the multilayer. This technique was initially proposed by Lee *et al.*[3,4] and later justified by Valet and Fert.[5] Given this approach, the expression for the GMR in our samples, which contain two distinct types of magnetic layers, is derived as follows.

Within a ferromagnetic layer F (Co or alloy), the resistivity encountered by an electron whose spin is parallel (antiparallel) to the magnetic moment is $\rho_{\uparrow(\downarrow)}=2\rho_F/(1+(-)\beta_F)$. Here $\rho_F$ is the ordinary resistivity and $\beta_F$ is the bulk scattering asymmetry parameter to be extracted from the data. For Cu interlayers $\rho_\uparrow=\rho_\downarrow=2\rho_{Cu}$ and the corresponding resistance for any layer is just $R=\rho_{\uparrow(\downarrow)}t/A$ where $t$ is its thickness and $A$ the area of the contact window of the multilayer. Similarly, the resistance at each F/Cu interface is $R=2R_{F/Cu}/(1+(-)\gamma_{F/Cu})$ with $\gamma_{F/Cu}$ being the interface scattering asymmetry parameter. One then obtains the rather complex but symmetric expression

$$A(R_{ap}-R_p)=4NX_1X_2/Z, \tag{3a}$$

$$X_1=\rho^*_{Co}t_{Co}\beta_{Co}+2AR^*_{Co/Cu}\gamma_{Co/Cu}, \tag{3b}$$

$$X_2=\rho^*_{al}t_{al}\beta_{al}+2AR^*_{al/Cu}\gamma_{al/Cu}, \tag{3c}$$

$$Z=\rho^*_{Co}t_{Co}+2AR^*_{Co/Cu}+\rho^*_{al}t_{al}+2AR^*_{al/Cu}+2\rho_{Cu}t_{Cu}+AR_{con}/N. \tag{3d}$$

Here al stands for the NiFeCo alloy, $N$ is the number of repeats of the basic four layer unit, $R_{con}$ is the contact resistance between the leads and the stack, and we use the standard abbreviations $\rho^*_F=\rho_F/(1-\beta^2_F)$ and $R^*_{F/Cu}=R_{F/Cu}/(1-\gamma^2_{F/Cu})$.

In the present case, the fortuitous cancellation, which occurred in the earlier derivation[3] of the quantity $[(R_{ap}-R_p)R_{ap}]^{0.5}$ for stacks containing only one type of magnetic layer and which allows the bulk and interface spin scattering to be separated easily, does not occur for GMR stacks containing two types of magnetic layers. Nevertheless, it is still possible to compare Eq. (3) with the experimental

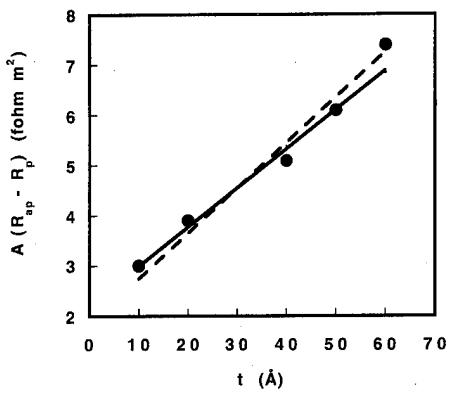



FIG. 7. Thickness dependence of $A(R_{ap}-R_p)$ at 4.2 K for a range of magnetic layer thicknesses $t_F$. Data are from circular shaped multilayers with 2 $\mu$m diam contact windows. The solid and dashed lines are calculated from Eq. (3) using the spin dependent conductivity parameters for Co given in the text plus the following parameters associated with the NiFeCo alloy (al) layers: $\beta_{al}=0.46$, $\gamma_{al/Cu}=0.30$, $AR_{Con}=0.05$ $f\Omega$ m$^2$ (solid line) and $\beta_{al}=0.46$, $\gamma_{al/Cu}=0.17$, $AR_{Con}=0.00$ $f\Omega$ m$^2$ (dashed line).

results. In making this comparison we use the literature values of the Michigan State group:[10] $\rho_{Co}=6.5$ $\mu\Omega$ cm, $\rho_{Cu}=0.7$ $\mu\Omega$ cm, $\beta_{Co}=0.50$, $\gamma_{Co/Cu}=0.76$, $AR_{Co/Cu}=0.21$ $f\Omega$ m$^2$ and our independently measured value of $\rho_{al}=12.9$ $\mu\Omega$ cm. Fits to the $A\Delta R$ data are shown in Fig. 7 using the parameters given in the figure caption and assuming $AR_{al/Cu}=AR_{Co/Cu}$ since the interface resistance in the literature does not vary much from system to system.[10]

The principal conclusion we come to from the data and fits shown in Fig. 7 is that spin dependent bulk scattering is important in the case of the NiFeCo permalloy used in the present samples and is the main cause of the clear thickness dependence observed for $A(R_{ap}-R_p)$. Because our mask set did not allow reliable measurements of the contact resistance between the device leads and the magnetic stacks, we cannot determine $\gamma_{al/Cu}$ accurately but, by determining what combinations of fitting parameters yield reasonable fits, we can conclude that it is no greater than 0.35 (see Fig. 7 caption.) Hence, it appears that the spin dependent scattering at the NiFeCo/Cu interfaces is significantly smaller than is the case for Co/Cu interfaces.

## V. LATERAL SIZE-DEPENDENT EFFECTS

There are two factors dependent on the lateral size of the samples which need brief discussion, viz., current nonuniformity and stray magnetic fields. Because the lateral width of the sample contact windows is always at least several times the thickness of the Cu current leads and the lead thickness is several times the magnetic stack thickness, one cannot avoid some nonuniform distribution of current in the device element. As a result, we have emphasized data only from the samples having the smallest lateral dimensions, typically, 1.2 or 2 $\mu$m. Furthermore, since the temperature dependence of the multilayer stack resistance is much less than that of the Cu leads, the nonuniformity is temperature dependent. Although they lie outside the scope of the present paper, further experimental information on the impact of this nonuniformity can be found in Ref. 1.

Finally, the lateral dimensions of the magnetic stack part of the sample structures affects the stray magnetic fields generated by the edge poles of the stack as is apparent from Eq. (2). Our measurements of the magnetic field dependence of the magnetoresistance of structures with 60 Å thick magnetic layers show that the width at half-maximum of the $R(H)$ vs $H$ traces (similar to those in Fig. 6) decreases with increasing magnetic stack diameter in reasonable agreement with the expectations of Eq. (2). This again emphasizes the necessity of finding a means of controlling the stray fields of the elements before submicron samples can be prepared with reasonable switching fields.

## VI. CONCLUSIONS

In this study of perpendicular transport in lithographically defined devices several important issues have become clear. First, it is possible with standard procedures to fabricate device structures with lateral dimensions of about 1 $\mu$m. Above these dimensions, when using conventional materials (e.g., Cu) for leads, obtaining uniformly distributed currents is a challenge. At these dimensions, however, the magnetic fringing fields from dipoles at the film edges become significant and act to depolarize the magnetic structure. This can lead to an antialigned state at zero field even for nonmagnetic spacer layers more than sufficient to eliminate any exchange coupling. The temperature dependence of the GMR in our samples arises largely from the temperature dependence of the resistance itself, with only small changes in the magnetoresistance. We find some loss of moment in the magnetic layers which we attribute to about 2 Å of alloying at each magnetic interface. Finally, analyzing our data within the framework of the two-current model, we find our results are consistent with the published data on the interface and bulk scattering obtained by others[10] for systems containing two different ferromagnetic layers.

*Note added in proof:* The authors have learned that a version of the magnetoresistance model involving two parallel chains of resistors, one for each spin, was published prior to the work of Refs. 3 and 4 by S. Zhang and P. M. Levy [J. Appl. Phys. **69**, 4786 (1991)].

## ACKNOWLEDGMENTS

The authors thank M.M. Miller for the finite element magnetic modeling. W. Vavra acknowledges support by the National Research Council Postdoctoral Associate Program. This work is supported in part by the Advanced Research Projects Agency.

[1] W. Vavra, S. F. Cheng, A. Fink, J. J. Krebs, and G. A. Prinz, Appl. Phys. Lett. **66**, 2579 (1995). This paper provides added information on the samples studied here.
[2] W. P. Pratt, Jr., S.-F. Lee, R. Loloee, P. A. Schroeder, and J. Bass, Phys. Rev. Lett. **66**, 3060 (1991).
[3] S. F. Lee, W. P. Pratt, Jr., R. Loloee, P. A. Schroeder, and J. Bass, Phys. Rev. B **46**, 548 (1992).

[4]S. F. Lee, W. P. Pratt, Jr., Q. Yang, P. Holody, R. Loloee, P. A. Schroeder, and J. Bass, J. Magn. Magn. Mater. **118**, L1 (1993).
[5]T. Valet and A. Fert, Phys. Rev. B **48**, 7099 (1993).
[6]M. A. M. Gijs, S. K. J. Lenczowski, and J. B. Giesbers, Phys. Rev. Lett. **70**, 3343 (1993).
[7]M. A. M. Gijs, J. B. Giesbers, S. K. J. Lenczowski, and H. H. J. M. Janssen, Appl. Phys. Lett. **63**, 111 (1993).
[8]M. A. M. Gijs, J. B. Giesbers, M. T. Johnson, J. B. F. aan de Stegge, H. H. J. M. Janssen, S. K. J. Lenczowski, R. J. M. van de Veerdonk, and W. J. M. de Jonge, J. Appl. Phys. **75**, 6709 (1994).
[9]R. I. Josephs and E. Schlömann, J. Appl. Phys. **36**, 1579 (1965).
[10]W. P. Pratt, Jr., S.-F. Lee, P. Holody, Q. Yang, R. Loloee, J. Bass, and P. A. Schroeder, J. Magn. Magn. Mater. **126**, 406 (1993).

# Arrays of multilayered nanowires (invited)

B. Doudin, A. Blondel, and J.-Ph. Ansermet
*Institut de Physique Expérimentale, E PFL, 1015 Lausanne, Switzerland*

Multilayered Co/Cu wires with a diameter of 80 nm and a length of 6 $\mu$m were produced by electrodeposition in nanoporous polycarbonate membranes. Their magnetoresistance has been measured in a geometry where the current was perpendicular to the layer plane. The anisotropic part of the magnetoresistance was limited to 1.5%. The study, for layer thicknesses ranging from 3 to 100 nm interpreted in terms of the Valet and Fert model, gave estimates of the spin dependent bulk and interface resistivities and their change with temperature. The large Co bulk resistivity value, caused by a large amount of Cu impurities, limited the magnetoresistance in our samples to 20% at room temperature and 30% at 20 K. The Cu spin flip mean free path was found to be temperature independent and determined by scattering at Co impurities in the Cu layer. It was measured for two sets of samples with different amounts of Co impurities. © *1996 American Institute of Physics.* [S0021-8979(96)22908-2]

## I. INTRODUCTION

The study of the large negative magnetoresistance (MR) in magnetic multilayers in a geometry where the current is perpendicular to the interfaces (CPP-MR) is an experimental challenge, which has been overcome by ultrasensitive voltage measurements at low temperatures[1] or by making pillar structures by lithography.[2] The possibility of making multilayered wires by electrodeposition with a diameter smaller than 100 nm and a length of a few microns opened the possibility of measuring the CPP-MR as a function of temperature on samples with resistance values reaching hundreds of ohms.[3] In contrast to the geometry where the current is parallel to the layer plane, the CPP-MR is expected to be larger[4] and the data can be explained by adding the resistances of the layers and the interfaces in a two-current model.[4,5] This model was improved by Valet and Fert[6] by introducing the concept of spin diffusion lengths (SDL). This quantity is a measure of the length scale over which the spin accumulation at the interfaces relaxes in the ferromagnetic and neutral layers. The experimental results of the Michigan State University (MSU) group on sputtered samples showed that the spin dependent resistivities of the bulk and the interface of the ferromagnetic layers both contributed to the CPP-MR and that the SDL of the neutral layer could be modified by the introduction of impurities.[5,7] We used a similar approach of getting spin dependent scattering parameters although with totally different samples. We made a series of samples with equal Cu and Co thicknesses (constant bulk resistivity) and measured the CPP-MR at low and ambient temperature. We used the two-current model to deduce the spin asymmetry parameters. We also took advantage of the versatility of the electrodeposition technique: we varied the deposition conditions of the Cu to change the amount of Co impurities in the Cu layers. The change of the CPP-MR values revealed that the interface spin asymmetry was also modified. The Co impurities played the role of spin-flip scattering centers, from which the Cu SDL, expressed in a free electron model, corresponded to our observations.

## II. SAMPLE PREPARATION

The technique of electrodeposition of the Co/Cu multilayers in nanoporous membranes has been previously described.[8] In a single bath electrodeposition technique, we apply a large potential difference (with respect to a Ag/AgCl reference electrode) $V_{Co}$ to deposit a majority of Co and a smaller potential difference $V_{Cu}$ to deposit Cu. The concentration of Cu ions in the electrolyte is minimized to limit the amount of Cu co-deposited with the Co. The energy dispersive x-ray spectroscopy (EDS) analysis made by electron microscopy (Hitachi HF200 with Norian Voyager EDS system) revealed that the Co had 15±3% of Cu impurity content. The Cu being more noble than Co, the use of a small potential $V_{Cu}$ should ensure pure Cu layers. In fact, there is some Co co-deposited with Cu. Careful EDS measurements performed on Cu wires deposited at −0.300 V (set 1) and −0.600 V (set 2) showed that some fraction $p$ of Co impurities was present

$$p(-0.3V)=0.50\pm0.15\%, \quad p(-0.6V)=1.0\pm0.3\%.$$

The uncertainties correspond to the variation of the amount of impurities between wires of the same batch. For both sets, we used the same electrodeposition conditions for the Co layers, deposited at 1.000 V. As the voltage transition is less sharp in set 2 than in set 1, it could be expected that the quality of the Co/Cu interface was different in both sets.

The total number of layers in a wire filling a membrane of thickness 6 $\mu$m±0.6 $\mu$m could be estimated by counting

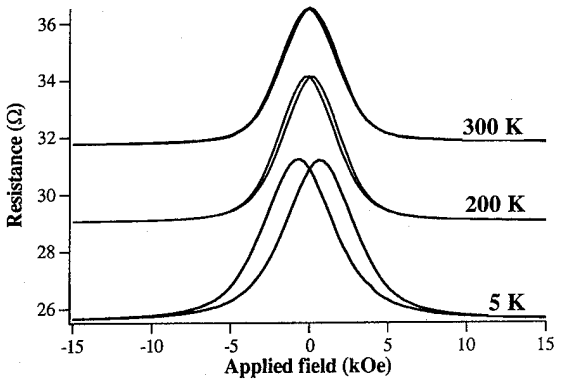



FIG. 1. CPP-MR of Co/Cu wires with Co and Cu thicknesses of 6(±2) nm. The applied field was parallel to the membrane plane.

 0021-8979/96/79(8)/6090/5/$10.00 © 1996 American Institute of Physics

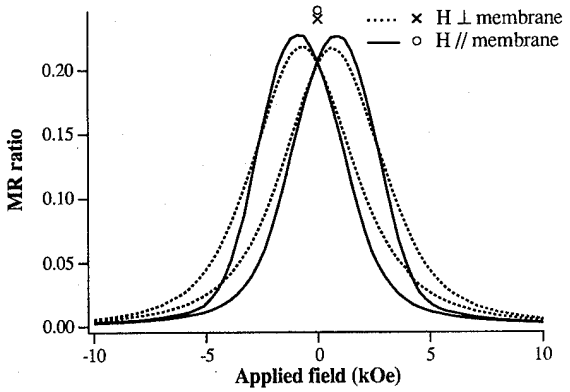



FIG. 2. CPP-MR at 5 K for two orientations of the field with respect to the membrane. The sample was the same as in Fig. 1. The ratio is defined as $\Delta R/R(\infty)$.

the number of voltage cycles until the current would increase when the membrane was filled and a crust would begin to form. An alternative measure of the number of layers and their thickness came from saturation magnetization measurements combined with the relative amount of Co determined by EDS. We estimated the precision in the control of the growth of the layers to be limited to variations of about 2 nm along the wires or between wires of the same membrane. Taking advantage of the roughness of the membrane (100–200 nm), we stopped the deposition at the beginning of the current increase, allowing a small fraction of the wires to reach the surface. We could thus glue gold wires with silver epoxy on a large surface of the sample (a few $mm^2$), keeping a small number of wires connected. We measured samples with resistance values from 1 to 400 Ω, with a current density of typically $10^7$ $A/m^2$. Contacts were formed at the surface of the membranes, to an unknown number of wires connected in parallel. The difficulty of not getting a direct measurement of resistivities was overcome by doing a statistical study of a large number of samples and also by making use of Matthiessen's rule to deduce resistivities from the temperature dependence of the resistances.[8] Furthermore, the data analysis was based on CPP-MR ratios ($\Delta R/R$), since they are independent of the number of wires connected.

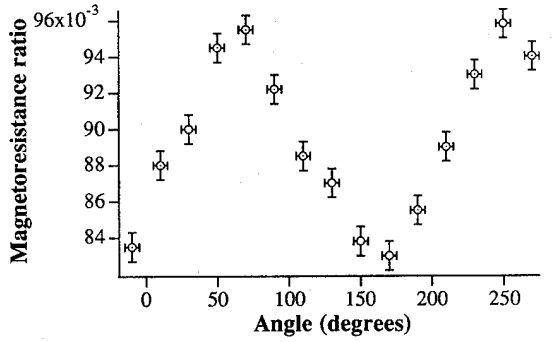



FIG. 3. CPP-MR ratio as a function of the angle between applied field and plane of the membrane, performed at ambient temperature.

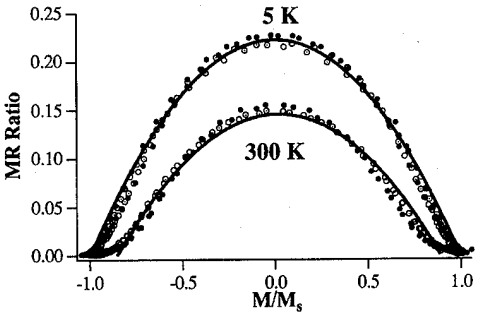



FIG. 4. CPP-MR ratio as a function of the relative magnetization. Applied field parallel to the membrane (filled symbols) and perpendicular to the membrane (open symbols). The curves are the fits to a parabola.

## III. RESULTS

The measurements of CPP-MR were performed as a function of temperature with the applied field parallel or perpendicular to the layers (see Figs. 1 and 2). A larger resistance value was observed when an alternating and decreasing field was applied. The resistance value observed in this "demagnetized" state approached the value observed for virgin samples. The MR curves with field in two directions (see Fig. 2) differ for two reasons. First, the saturation field is anisotropic. Second, there is an anisotropic magnetoresistance (AMR) superposed on the CPP-MR. The AMR was

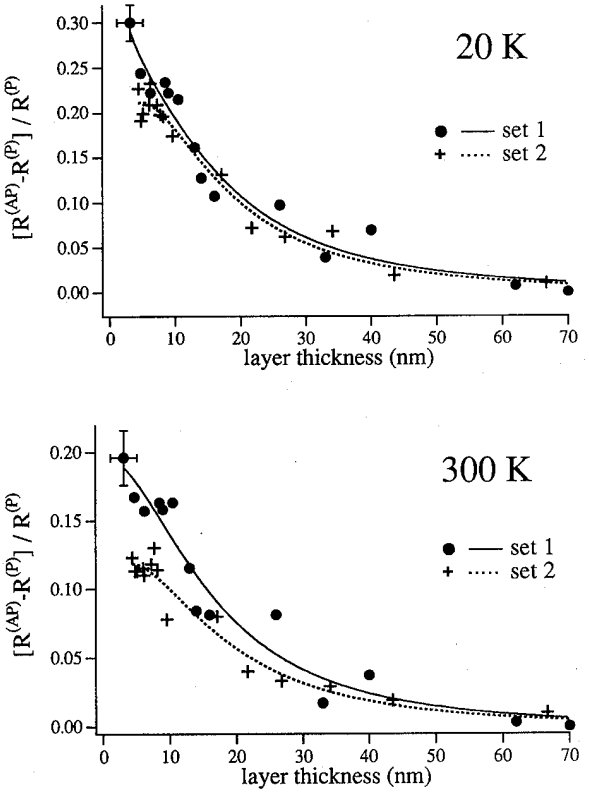



FIG. 5. CPP-MR ratio as a function of equal Cu and Co layer thicknesses. The measurements were performed at two temperatures, for two sets of samples produced under different electrodeposition conditions. The lines correspond to the fit using Eqs. (2)–(4) and the results given in Table I.

deduced from the angular dependence of the CPP-MR (see Fig. 3). This AMR contribution was at most 1.5% and decreased with increasing thickness to 0.5% at a layer thickness of 100 nm. Uniform nanowires produced by deposition at $V_{Co}$ presented an AMR of 1% to 1.5%. In Fig. 3 the angular dependence of the AMR reached a maximum at an angle of 15° between the field and the normal to the membrane. This is consistent with the distribution of wire orientations in the membranes.[9]

The temperature dependence of the field at the maximum MR was that of the coercive field, which changed by one order of magnitude between room temperature and 5 K. The MR measurements, which can be carried out on a very small number of wires, can be seen as a means of measuring coercive fields free of averaging over a large angular distribution of the wire orientations in the membranes.

The relation between CPP-MR and the magnetization is shown in Fig. 4. If the magnetic layers are uncorrelated, the MR can be simply expressed as[10]

$$\frac{\Delta\rho}{\rho(\infty)} \propto \left(\frac{M}{M_s}\right)^2. \tag{1}$$

This relation described well the low-temperature data and only small discrepancies were found at room temperature near the saturation magnetization.

The CPP-MR ratios were measured for two sets of samples produced under different electrodeposition conditions. Samples with equal Cu and Co thicknesses were measured at room and low temperatures (see Fig. 5). The MR increased with increasing density of interfaces, until a limit of layer thickness of approximately 3 nm below which the MR effect vanishes,[8] indicating unreliable layering on this length scale, in agreement with the precision of 2 nm mentioned above.

## IV. DISCUSSION

In the Valet and Fert article,[6] the expression for the resistance per unit area $R^{(P)}$ (all ferromagnetic layers parallel) and $R^{(AP)}$ (magnetic layers antiparallel) of $M$ bilayers is given by

$$R^{(P,AP)} = M(r_0 + 2r_{SI}^{(P,AP)}) \tag{2}$$

with

$$r_0 = (1-\beta^2)\rho_F^* t_F + \rho_N^* t_N + 2(1-\gamma^2) r_b^*, \tag{3}$$

where $t_N$ and $t_F$ are the thicknesses of the nonferromagnetic and ferromagnetic layers. The spin dependent resistivities $r_{SI}^{(P,AP)}$ are given by

$$r_{SI}^{(P,AP)} = \frac{\dfrac{(\beta-\gamma)^2}{\rho_N^* l_{sf}^{(N)}} f^{(P,AP)}\left[\dfrac{t_N}{2l_{sf}^{(N)}}\right] + \dfrac{\gamma^2}{\rho_F^* l_{sf}^{(F)}} \coth\left[\dfrac{t_F}{2l_{sf}^{(F)}}\right] + \dfrac{\beta^2}{r_b^*}}{\dfrac{1}{\rho_N^* l_{sf}^{(N)}} f^{(P,AP)}\left[\dfrac{t_N}{2l_{sf}^{(N)}}\right] \dfrac{1}{\rho_F^* l_{sf}^{(F)}} \coth\left[\dfrac{t_F}{2l_{sf}^{(F)}}\right] + \dfrac{1}{r_b^*}\left\{\dfrac{1}{\rho_N^* l_{sf}^{(N)}} f^{(P,AP)}\left[\dfrac{t_N}{2l_{sf}^{(N)}}\right] + \dfrac{1}{\rho_F^* l_{sf}^{(F)}} \coth\left[\dfrac{t_F}{2l_{sf}^{(F)}}\right]\right\}}, \tag{4}$$

where $f^{(P)}[x] = \tanh(x)$ and $f^{(AP)}[x] = \coth(x)$. The coefficient $\beta$ is a measure of the spin asymmetry of the Co resistivity, which is $2\rho_F^*(1-\beta)$ for the majority spin charge carriers $2\rho_F^*(1+\beta)$ for the minority spins. The Co layers have a bulk resistivity $\rho_F = \rho_F^*(1-\beta^2)$. The Cu (neutral) layers have a bulk resistivity given by $\rho_N^*$. The coefficient $\gamma$ represents the asymmetry of the spin dependent interface resistance, with a resistance per unit area of $2r_b^*(1-\gamma)$ in the majority case and $2r_b^*(1+\gamma)$ in the minority case. The expressions 2–4 are valid under the assumption of a negligible spin mixing and the electronic mean free paths much smaller than the corresponding spin diffusion lengths.

The CPP-MR dependence on layer thickness (see Fig. 5) was analyzed using Eqs. (2)–(4). We could deduce the asymmetry parameters and the spin diffusion length of the Cu layers (see Table I), using set values of the bulk resistivities $\rho_N^*$, $\rho_F^*$ and the interface resistance $r_b^*$. The choice for these values was discussed in Ref. 8. A reasonable range of values was used in Table I.

The predictions of the Valet and Fert model showed that the Co SDL had little influence on the CPP-MR.[11] In our fitting procedure, the Co SDL was fixed at a large value. Any choice of the Co SDL larger than 10 nm would give us similar parameters. In order to bring out the effects of the spin diffusion length of the Co, a set of samples with an increasing Co thickness was produced (see Fig. 6). The Cu layer thickness was fixed at 10 nm. Parameters deduced from the fittings of the more complete sets of data of Fig. 5, with $l_{sf}^{(F)}$ values of 3, 10, and 100 nm, were used to draw the lines shown on Fig. 6. We observed that the CPP-MR was strongly decreased when the layer thicknesses were too different. We consider that our synthesis becomes defective for these types of samples.[8]

The main difference between the two sets of samples is the value of the interface asymmetry parameter $\gamma$. In the samples from the set 2, the lower spin dependent interface resistance is reflected in the lower CPP-MR ratios observed at small thicknesses. The difference in the deposition conditions between the two sets of samples, with a deposition potential gap changed by a factor of 2, appears to be reflected in the spin asymmetry of the interfaces.

The spin asymmetry coefficients $\gamma$ and $\beta$ depend slightly on the original choice of the resistivities. To the contrary, the value of the SDL strongly depends of this choice. We overcame the uncertainty in the resistivity of the Cu layers by

TABLE I. Parameters of the two-channel model. The range of the choice for the resistivity values is given. The uncertainties are those deduced from the fittings, including the indicated variation of parameters $\rho_N^*$, $\rho_F^*$, and $r_b^*$.

| | $\rho_F^*$ $10^{-8}\ \Omega$ m | $\rho_N^*$ $10^{-8}\ \Omega$ m | $r_b^*$ $10^{-15}\ \Omega$ m$^2$ | $\beta$ | $\gamma$ | $l_{sf}^{(N)}$ nm | $l_{sf}^{(F)}$ nm |
|---|---|---|---|---|---|---|---|
| SET 1, 300 K | 60–68 | 2–6 | 0.3–1.1 | 0.44±0.06 | 0.40±0.10 | 38±10 | >10 |
| SET 1, 20 K | 51–57 | 1.3–3.3 | 0.3–1.1 | 0.46±0.05 | 0.55±0.07 | 49±12 | >10 |
| SET 2, 300 K | 60–68 | 2.5–6.5 | 0.3–1.1 | 0.41±0.07 | 0.23±0.15 | 34±14 | >10 |
| SET 2, 20 K | 51–57 | 1.8–38 | 0.3–1.1 | 0.52±0.06 | 0.33±0.11 | 37±11 | >10 |
| MSU 4.2 K Ref. 5 | 8.6±0.4 | 0.7±0.2 | 0.50±0.02 | 0.50±0.10 | 0.76±0.05 | >60 | >20 |

considering the spin flip mean free path. Figure 7 is a plot of the SDL deduced from the fits to the data of Fig. 5, as a function of the choice made for the resistivity $\rho_N^*$. The data at 20 and 300 K of each set of samples are superposed and the SDL of set 2 are systematically smaller than that of set 1. In Fig. 5, no evidence of a contrast between the two sets of samples at large thicknesses (in particular at 20 K) can be seen. However, Fig. 7 took advantage of the statistics from Fig. 5 to exhibit a systematic difference.

A simple physical model can account for the apparent correlation between the resistivity and the SDL of the copper layers. In the free electron model, we can express the SDL as a function of the resistivity as[8]

$$l_{sf}^{(N)} = \sqrt{\frac{m v_F}{6ne^2}}\ \sqrt{\frac{\lambda_{sf}^{(N)}}{\rho_N^*}} = C\sqrt{\frac{\lambda_{sf}^{(N)}}{\rho_N^*}}, \tag{5}$$

where $C = 1.048\times10^{-8}\ \sqrt{\Omega}\ m$ for Cu. Given the dependence of the SDL on $\rho_N^*$ from Eq. (5), the fitted spin-flip mean free paths $\lambda_{sf}^{(N)}$ are

$$\lambda_{sf}^{(N)} = 450\ \text{nm (set 1)} \quad \text{and} \quad \lambda_{sf}^{(N)} = 300\ \text{nm (set 2)}.$$

The spin-flip mean free path can be expressed in terms of the spin flip cross section by

$$\lambda_{sf}^{(N)} = \frac{1}{N\sigma}, \tag{6}$$

where $N$ is the number of impurity per unit volume. The spin-flip cross section $\sigma$ of Co in Cu is known from electron spin resonance (ESR) experiments to be of about $5\times10^{-21}$ m$^2$.[12] Using the impurity contents measured by EDS, Eq. (6) yields

$$\lambda_{sf}^{(N)}(-0.3\ \text{V}) = 470\ \text{nm (set 1)},$$

$$\lambda_{sf}^{(N)}(-0.6\ \text{V}) = 235\ \text{nm (set 2)}.$$

These values are in remarkable agreement with those deduced from Fig. 7. The Cu spin-flip mean free path, due to impurities, is temperature independent. As a consequence, the temperature dependence of the Cu SDL is caused by the variation of the Cu resistivity with temperature. The asymmetry parameters are found to decrease with increasing temperature.

## V. CONCLUSIONS

The magnetoresistance, in a geometry where the current was perpendicular to the layer plane, was measured in samples of resistance values ranging from 1 to 400 Ω, at temperatures of 5–300 K. The two-current model was used to fit the thickness dependence of the CPP-MR of samples with equal Cu and Co layer thicknesses. At low temperatures, we found the Co spin asymmetry parameter to be about the same as found by others for sputtered samples,[5] even though the samples were produced by totally different methods. The spin asymmetry of the interfacial resistance is found to be slightly smaller than for the vacuum deposited samples. Our samples, with a typical area of $10^{-13}$ m$^2$, gave no evidence that the spin accumulation could be hindered by domains in the ferromagnetic layers,[13] a configuration which

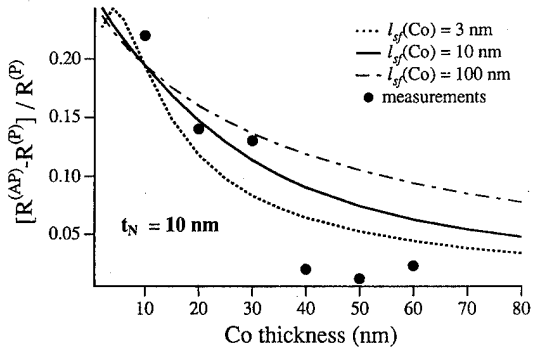



FIG. 6. CPP-MR ratios for samples with a fixed Cu thickness of 10 nm as a function of the Co layer thickness. The drawn lines correspond to different choices in the Co spin diffusion lengths in the fitting of the data of Fig. 5.

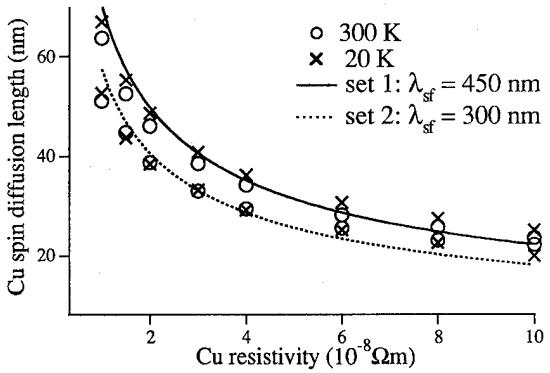



FIG. 7. Cu spin diffusion length found from fitting of the data of Fig. 5 as a function of the choice for the Cu resistivity.

could occur in the vacuum deposited samples of area of $10^{-6}$ $m^2$. The spin diffusion length in the Cu layers was found to be due to Co impurities. The corresponding spin-flip mean free path was found temperature independent and its value corresponded to the one deduced from ESR experiments.

This picture is confirmed by the study of two sets of samples, produced by changing the electrodeposition conditions of the Cu layers. The amount of Co impurities was varied and the corresponding change of the spin-flip mean free path was observed. Furthermore, the interface was changed and its spin dependent resistance modified.

The single bath electrodeposition technique limited the quality of the samples by adding a large amount of impurities of Cu in the Co layers. The resulting large Co resistivity limited the magnetoresistance to 30% at low temperatures.

## ACKNOWLEDGMENTS

The hospitality of the Center for Electron Microscopy of the EPFL (CIME) is gratefully acknowledged. This research was partly financed by the Swiss National Fund, Grant No. 20-42034.94. We thank T. Valet, A. Fert, W. P. Pratt, J. Bass, and W. Schwarzacher for useful discussions.

[1] W. P. Pratt, S.-F. Lee, R. Loloee, P. A. Schroeder, and J. Bass, Phys. Rev. Lett. **66**, 3060 (1991).
[2] M. A. M. Gijs, S. K. J. Lenczowski, and J. B. Giesbers, Phys. Rev. Lett. **70**, 3343 (1993); W. Vavra, W. Cheng, S. F. Fink, A. Krebs, and J. J. Prinz, Appl. Phys. Lett. **66**, 2579 (1995).
[3] L. Piraux, J. M. George, J. F. Depres, C. Leroyx, E. Ferain, R. Legras, K. Ounadjela, and A. Fert, Appl. Phys. Lett. **65**, 2484 (1994); A. Blondel, J. P. Meier, B. Doudin, and J.-Ph. Ansermet, *ibid.* **65**, 3019 (1994); K. Liu, K. Nagodawithana, P. C. Searson, and C. L. Chien, Phys. Rev. B **51**, 7381 (1995); A. Blondel, J. P. Meier, B. Doudin J.-Ph. Ansermet, K. Attenborough, P. Evans, R. Hart, G. Nabiyouni, and W. Schwarzacher, J. Magn. Magn. Mater. **148**, 317 (1995).
[4] S. Zhang and P. M. Levy, J. Appl. Phys. **69**, 4786 (1991).
[5] W. P. Pratt, S.-F. Lee, P. Holody, Q. Yang, R. Loloee, J. Bass, and P. A. Schroeder, J. Magn. Magn. Mater. **126**, 406 (1993); P. A. Schroeder, J. Bass, P. Holody, S.-F. Lee, R. Loloee, W. P. Pratt, and Q. Yang, in *Magnetism and Structure in Systems of Reduced Dimension*, edited by R. F. Farrow *et al.*, (NATO ASI Series Plenum, New York, 1993), p. 129.
[6] T. Valet and A. Fert, Phys. Rev. B **48**, 7099 (1993).
[7] Q. Yang, P. Holody, S.-F. Lee, L. L. Henry, R. Loloee, P. A. Schroeder, W. P. Pratt, and J. Bass, Phys. Rev. Lett. **72**, 3274 (1994).
[8] B. Voegeli, A. Blondel, B. Doudin, and J.-Ph. Ansermet, J. Magn. Magn. Mater. **151**, 388 (1995).
[9] Poretics Corp., 111 Lindbergh Av., Livermore, CA 94550-9520.
[10] S. Zhang and P. M. Levy, J. Appl. Phys. **73**, 5315 (1993); C. L. Chien, J. Q. Xiao, and J. S. Jiang, J. Appl. Phys. **73**, 5309 (1993).
[11] A. Fert, J.-L. Duvail, and T. Valet, Phys. Rev. B **52**, 6513 (1995).
[12] P. Monod and S. Schultz, J. Physique **43**, 393 (1982).
[13] S. Zhang and P. M. Levy, Phys. Rev. B **50**, 6089 (1994).

# Femtosecond near-field spin microscopy in digital magnetic heterostructures (invited)

J. Levy, V. Nikitin, J. M. Kikkawa, and D. D. Awschalom
*Department of Physics, University of California, Santa Barbara, California 93106*

N. Samarth
*Department of Physics, The Pennsylvania State University, University Park, Pennsylvania 16802*

We have designed a low-temperature femtosecond-resolved near-field scanning optical microscope to study spatiotemporal excitonic spin behavior in magnetic semiconductor heterostructures. Local disorder introduced by focused-ion-beam implantation reduces the otherwise large Zeeman splittings in modest magnetic fields, creating a planar spin-dependent energy landscape for diffusing carriers. Near-field polarization-resolved static and femtosecond measurements map out excitonic spin behavior with ~125 nm spatial resolution, revealing spin-dependent diffusion. We demonstrate the applicability of two distinct time-resolved techniques in the near field, and discuss limitations on the measurement of polarized luminescence from semiconductors in the near field. © *1996 American Institute of Physics.* [S0021-8979(96)23008-7]

## I. INTRODUCTION

A detailed understanding of spin scattering in mesoscopic electronic systems remains, for the most part, an open issue in condensed matter physics.[1] To directly investigate the dynamic behavior of electronic spin, one needs to develop both a host material in which the fundamental spin interactions are well understood, and techniques for probing spin scattering on the relevant time and length scales.

Extensive research in recent years has identified II–VI magnetic semiconductor quantum structures as flexible systems in which to study electronic spin interactions in a well-characterized environment.[2] In such systems, the strong exchange coupling between electronic states and paramagnetically aligned magnetic ions results in large effective Landé $g$ factors at low temperatures ($g_{\text{eff}}$~400 at $T=4$ K). Quantum well (QW) confinement enhances by several orders of magnitude the coupling of excitonic states to visible light, enabling a wide array of optical techniques to be used. The Zeeman splittings in recently grown structures can be made much larger than inhomogeneous linewidths,[3] providing model field-tunable two-level systems ideal for magneto-optical studies of spin-dependent phenomena.

Conventional time-resolved optical spectroscopies have successfully probed dynamical spin-dependent phenomena in this class of structures, yielding important information about exciton spin scattering and magnetic relaxation.[3,4] However, to examine directly the role of interfaces, alloy fluctuations, disorder, local magnetic environments, impurities, and defects on excitonic spin *transport*—factors which involve *spatial degrees of freedom*—one requires a technique capable of resolving the relevant physical length scales, from exciton diffusion lengths (~1 $\mu$m) to magnetic correlation lengths (>50 nm in antiferromagnetically ordered MnSe),[5] to the exciton Bohr radius (~4 nm for ZnSe/ZnCdSe).[6] Conventional optical techniques, being diffraction limited, cannot provide sufficient resolution on the length scales of interest. Near-field scanning optical microscopy (NSOM) circumvents the diffraction limit[7] and, combined with femtosecond-resolved spectroscopies, provides a unique capability of interrogating spatiotemporal exitonic spin dynamics in magnetic semiconductors.

Here we present static and time-resolved luminescence studies of excitonic spin behavior in magnetic semiconductor QWs using a low-temperature polarization-resolved NSOM. A series of patterned defects, introduced by $Ga^+$ focused-ion-beam implantation, reduces both the QW luminescence intensity and the local $g$ factor, creating a magnetic-field-driven spin-dependent energy landscape for diffusing excitons. Carrier spin distributions are inferred from the near-field images of the dc luminescence intensity and polarization. Exciton diffusion is found to have a minimal effect on the local magnetic interactions which contribute to Zeeman split states. The incorporation of time resolution, using a luminescence intensity correlation technique, provides additional evidence for spin-dependent exciton diffusion. Time-resolved absorption, another powerful tool, yields direct information about the spatiotemporal evolution of photoexcited excitons. Fundamental limitations on the measurement of polarized luminescence from semiconductors in the near field are demonstrated and discussed.

## II. DIGITAL MAGNETIC HETEROSTRUCTURES

A new class of magnetic semiconductors—Digital Magnetic Heterostructures (DMH)[3]—serve as the host systems that are studied in these experiments. These structures consist of single 12 nm $ZnSe/Zn_{0.80}Cd_{0.20}Se$ MBE-grown quantum wells containing systematic planar distributions of magnetic ions ($Mn^{++}$). Far-field magneto-optical studies show large Zeeman splittings in modest magnetic fields (effective Landé $g$ factor ~430 at 4.2 K), and relatively narrow inhomogeneous linewidths (6 meV).[3] The structures are grown on GaAs(001) substrates with an MBE-deposited 700 nm buffer layer of ZnSe to relieve lattice mismatch strain, and a 100 nm cap layer. Measurements performed in transmission require removal of the GaAs substrate without disturbing the QW or buffer layer. Presently, no stop etch is known for ZnSe; however, preferential etch rates of GaAs vs ZnSe (20:1 selectivity)[8] can be utilized. The GaAs substrate is

 0021-8979/96/79(8)/6095/6/$10.00 © 1996 American Institute of Physics 

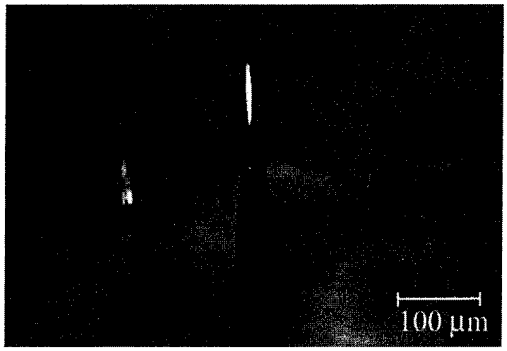



FIG. 1. Micrograph of an NSOM tip between single mode (left) and multimode (right) fibers, used to implement shear-force feedback in a compact microscope design.

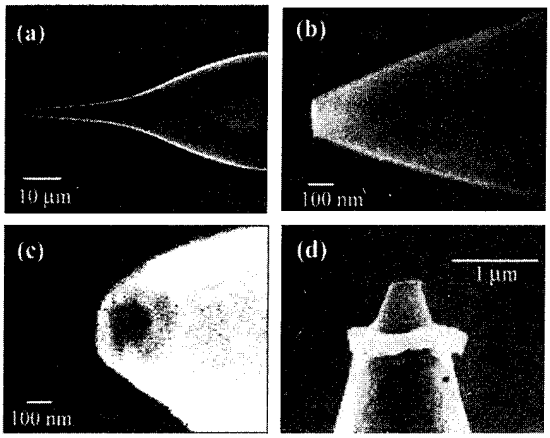



FIG. 2. Scanning electron micrographs of NSOM tips. (a), (b) Pulled fiber tip. (c) Ag-coated NSOM probe viewed at a 45° angle with the dark circle showing the transmitting core. (d) Destroyed coating after coupling 5 mW of HeCd laser light (442 nm) into the fiber.

thinned by polishing to 50–100 $\mu$m to achieve a surface roughness <0.2 $\mu$m, with care taken to keep the thickness uniform. Wet spray etching[8] removes the remaining GaAs on a lithographically patterned circle, leaving smooth (50 nm surface roughness) ZnSe buffer. The processed sample consists of a 300 $\mu$m diam circular film of QW sandwiched between 700 nm buffer and 100 nm ZnSe cap layers, mechanically supported by the surrounding unetched structure. Samples are mounted on a thin (0.2 mm) fused silica slide with the cap layer exposed.

To study the effect of local disorder on exciton spin dynamics, a 140 keV focused (100 nm diam spot size) beam of $Ga^+$ ions is used to implant specific patterns on the processed structure in the plane perpendicular to the growth direction. The small implantation dosage used ($10^4$ $\mu m^{-2}$) introduces lattice defects without destroying the QW. The pattern consists of a series of 100, 200, 400, and 800 nm-wide parallel stripes, each separated by 2 $\mu$m.

## III. LOW-TEMPERATURE NEAR-FIELD SCANNING OPTICAL MICROSCOPY

We have developed a femtosecond low-temperature NSOM, designed to fit in the 30 mm bore of continuous He gas flow optical cryostat, and to operate at temperatures $T=4-300$ K. Measurements are performed in zero and $B=0.2$ T magnetic field in the Faraday configuration, the latter achieved by mounting samples on a permanent annular magnet attached to the microscope sample stage. The stage is kinematically supported and positioned with respect to the near-field probe by three mechanical feedthroughs, allowing coarse (~10 $\mu$m) adjustment of the lateral position as well as fine (~1 $\mu$m) approach toward the near-field probe. Piezoelectric transducers enable the tip to scan the sample surface over a 5 $\mu$m×20 $\mu$m area at $T=5$ K.

Shear-force feedback is employed to measure and control the tip-sample separation.[9] In this technique, the near-field fiber is laterally excited—dithered—a small amount (5–10 nm) at a mechanical resonance, and the damping of that resonance is monitored as the tip approaches the sample surface. To employ shear-force feedback in a compact design of the microscope, the dither amplitude of the near-field fiber is monitored by two side fibers (see Fig. 1). The tip is placed in the small gap between an illuminating single-mode fiber and a collecting multimode fiber, and its position is adjusted so as to partially obstruct the transmitted light. Oscillations of the near-field fiber result in modulations of the detected intensity. The tip-sample separation is determined from an "approach curve," obtained by moving the tip a known amount towards the sample while measuring the lock-in detection signal at the dither frequency. The lock-in signal is fed back to the piezo transducer to keep a constant tip-sample separation.

Near-field probes are manufactured by pulling single-mode optical fibers locally heated by a focused $CO_2$ laser.[10] By varying the laser power and other pull parameters, different near-field probe shapes and tip sizes are obtained [Figs. 2(a) and 2(b)]. Pulled tips are evaporation coated with ~100 nm of a high reflectivity metal to confine the light where the tip diameter $d$ becomes comparable to the wavelength $\lambda$. Silver was found to be a good choice for coating due to its high reflectivity and good adhesion to the fiber surface. As a result, probes are obtained with subwavelength apertures [Fig. 2(c)], through which light is collected and sent up the fiber. An important characteristic of the tip is the throughput $T=I_{tr}/I_{in}$ where $I_{tr}$ the transmitted intensity through the tip aperture, and $I_{in}$ is the intensity of light coupled into the fiber from the other end. Both the tip shape and aperture diameter affect $T$. The tip shape is optimized to obtain the highest possible throughput for a chosen aperture size ($T\sim10^{-5}$ for a $d=100$ nm aperture). Aperture sizes are chosen to balance spatial resolution against photon shot noise and, depending on the type of measurement, are varied between 100–180 nm. High intensity light, coupled through the fiber, can destroy the metallic coating due to the enormous power density at the tip aperture [Fig. 2(d)], thus limiting the maximum incident power to ~5 mW for 100 nm tips. Prolonged exposure to air oxidizes the silver, forming pinholes, so tips are stored in vacuum until use. Samples are excited by focusing a laser beam on one side of the sample, and collecting luminescence with the near-field probe on the opposite side. In this configuration, the sample is uniformly illuminated with-

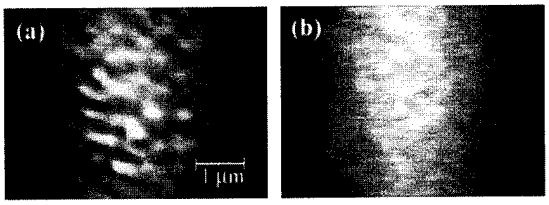



FIG. 3. (a) NSOM image of a tightly focused HeCd laser, transmitted through the etched sample. (b) The NSOM image of the luminescence intensity from the same region at $T=5$ K.

out shadowing from the tip,[11] allowing a variety of optical techniques to be employed.

Despite the care taken to ensure a smooth and flat buffer layer, the laser intensity profile remains highly irregular after passing through the etched nonimplanted sample. Small nonuniformities in the etched buffer layer thickness, exacerbated by the high index of refraction near the absorption edge of ZnSe, produce an interference pattern with sharp features, resolved in the near field [Fig. 3(a)]. Luminescence from the same region, seen in Fig. 3(b), is in comparison more uniform, indicating that photoexcited excitons diffuse on micron length scales within their lifetime.

The processed structures are extremely fragile, consisting only of the buffer, QW and cap layers, with a combined thickness totaling less than 1 $\mu$m. In near-field measurements, the probe is brought close (25–50 nm) to the sample surface using shear-force feedback. It is likely that contact is made when feedback is employed, as prolonged scanning over the same position adversely affects the structure. Figures 4(a)–4(d) show topography and luminescence images from a patterned sample before and after a 24-h line scan. During the scan, the probe is positioned at one point on the line, with the feedback on, while near-field measurements are performed. Despite the lack of apparent topographical changes, a quench in luminescence is observed not only on the scanned line, but also in the surrounding regions along the vertical crystallographic axis, indicating strain-induced destruction of the QW. To prevent damage to the sample, two scan modes are used: raster scan and lift-up scan. In the raster-scan mode, the probe is continuously scanned across the sample, feedback on, while acquiring near-field data. These scans are short (~1 h) and are used mainly for dc

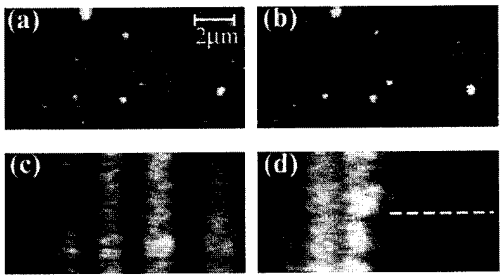



FIG. 4. (a), (b) Shear-force topographic image of a structure before (a) and after (b) a 24-h line scan. (c), (d) Concurrent luminescence intensity images before (c) and after (d) the same scan. The dashed line indicates the scanned path of the NSOM tip. Luminescence quenching occurs in regions above and below the scanned line.

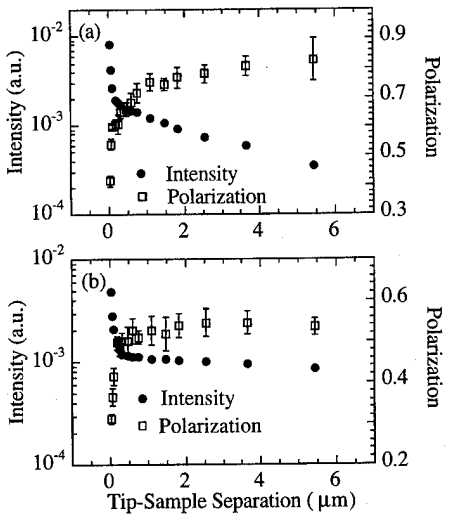



FIG. 5. The dc photoluminescence intensity and polarization of the nonpatterned DMH sample at $T=5$ K in $B=0.2$ T as a function of the sample-probe separation for a tightly focused (5 $\mu$m) (a) and defocused (100 $\mu$m) (b) laser spot.

luminescence measurements. In the lift-up scan mode, the probe position is fixed and the tip lifted ~50 nm from the surface, feedback off, while near-field measurements are taken. Feedback is used only for the short time required to move the tip to a new position; thus, even for long scans, the risk of sample damage is minimized.

### A. Near-field polarization

Polarization analysis in the near-field is complicated by two factors. First, strain-induced birefringence in the single-mode optical fiber "scrambles" the incident polarization. To obtain meaningful results, the polarization must first be "unscrambled" using a variable waveplate and polarizer. The correct parameters are determined in one of two ways. In the first method, circularly polarized luminescence from the magnetic heterostructure is collected in an applied magnetic field. The waveplate angle and retardance are scanned to find a maximum and minimum, corresponding to the two spin states. Alternatively, circularly polarized light from a laser, tuned to the wavelength of interest, is focused onto the near-field tip to find the appropriate waveplate settings. Both methods give identical and consistent values for polarization analysis.

Second, it has been found that polarization from semiconductors, measured under otherwise identical conditions, is significantly reduced in the near field compared to the far field.[12] To investigate the origin of this effect, we have explored the dependence of the sample-probe separation on the measured polarization. A nonpatterned sample in $B=0.2$ T at $T=5$ K, with 80% polarization measured in the far field, is photoexcited by a linearly polarized HeCd laser focused to 5 $\mu$m. Polarized luminescence is collected by the near-field probe, positioned in the laser spot center a distance $d$ over the sample. As the probe approaches the surface, the detected luminescence intensity increases and the polarization decreases [Fig. 5(a)]. The sharp knee in the luminescence in-

tensity curve clearly delineates the near- and far-field regimes.

To explain the loss of polarization in the far-field ($d>\lambda$) regime, we note that the polarization of luminescence from semiconductors depends on the angle $\theta$ between the point of observation and the field direction as $P(\theta)=P(0)\cos\theta$,[13] where $P(0)$ is the polarization measured along the field direction. Luminescence collected over a solid angle $\Omega$ will therefore have an appropriately reduced polarization. An ideal near-field probe collects light from all directions, but its effective numerical aperture is determined by the luminescence spot size and sample-probe separation. As the probe is brought closer to the sample, its effective numerical aperture increases, and the polarization decreases. This contribution to the loss of polarization is seen clearly by comparing Fig. 5(a) with Fig. 5(b), where the same measurements are performed with the laser focused to 100 $\mu$m. In this case, the effective numerical aperture of the probe changes negligibly with distance, and the polarization therefore remains essentially constant over distances $d>\lambda$. This explanation accounts well for the data taken in the far-field regime, but does not explain the near-field data, where the polarization decrease is most dramatic. An intriguing explanation for the loss of polarization in the near field is that the evanescent fields do not propagate angular momentum and hence cannot couple to circularly polarized light in the far field. Regardless of the explanation, the loss of circular polarization in the near field appears to be a general feature associated with NSOM measurements on semiconductors.

### B. Static spin behavior

Static excitonic spin-dependent behavior in the presence of disorder is studied on patterned DMH structures through polarization-resolved dc photoluminescence measurements, performed at $T=5$ K and $B=0.2$ T in the Faraday configuration. Structures are excited with linearly polarized light from a HeCd laser ($E_{ex}=2.807$ eV) with $\sim 1$ kW/cm$^2$ power density. Near-field images are obtained by collecting luminescence at a fixed detection energy in the raster-scan mode. The luminescence intensity [Fig. 6(a)] exhibits maxima in the center of undamaged regions, monotonically decreasing toward the implanted regions. The reduction of luminescence intensity in the implanted regions is attributed to an increase of nonradiative channels created by the focused ion beam. The lack of a sharp interface between intrinsic and implanted areas on the structure, as compared to the sharpness of the polarization image, indicates diffusion of photoexcited excitons. The contrasting interface sharpness of the polarization images [Fig. 6(b)] supports this interpretation, the polarization remaining constant over intrinsic regions and dropping sharply to zero only in the implanted areas. This result suggests that lattice damage, along with increasing the number of nonradiative channels, also destroys the rotational symmetry of the lattice, reducing magnetic interactions responsible for Zeeman splitting. Moreover, the constant polarization over the intrinsic regions implies that exciton diffusion does not result in increased spin scattering.

A more quantitative analysis is obtained by performing a line scan across several interfaces in the lift-up mode.

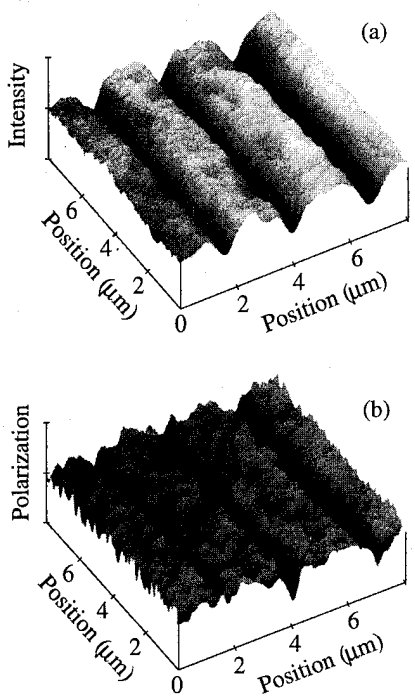



FIG. 6. The dc luminescence (a) and polarization (b) images on a patterned DMH sample at $T=5$ K and $B=0.2$ T.

Polarization-resolved luminescence spectra are collected at points along the line under otherwise identical conditions at $T=9$ K and $B=0.2$ T. The luminescence intensity, polarization, energy of the luminescence peak, and Zeeman splitting profile [Figs. 7(a)–7(d)] are extracted from the collected data. The slow variations in the luminescence intensity and the sharper features of the polarization profiles resemble the 2D images. The luminescence peak energy profile for both spin states [Fig. 7(c)] shows modulations defined by implantation, as well as small (<1 meV) scan-to-scan reproducible fluctuations. Surprisingly, the spatially resolved Zeeman energy splitting shows much smaller fluctuations, but is modulated by implantation much like the polarization. The potential and Zeeman energy variations are attributed mainly to alloy fluctuations.

### C. Femtosecond-resolved NSOM

Femtosecond time resolution is added to the near-field measurements using a luminescence intensity autocorrelation (LIA) technique.[14] By detecting nonlinear photoluminescence corresponding to a certain spin state, the exciton time correlation function $c(\tau)=\langle n(t)n(t+\tau)\rangle$ for that state can be obtained. Measurements are performed using the frequency-doubled output of Ti:Sapphire laser producing 130 fs pulses, tuned 100 meV above the exciton ground state energy. The linearly polarized laser output is split into two equal intensity pulses, separated by a time $\tau$ through a variable delay line. A good spatial overlap of the two beams on the sample is imperative: the beams are coaligned after going through delay optics and their spatial overlap is verified both by examination of the far-field interference pattern and by direct imaging of each beam using the near-field microscope. Optical choppers modulate the two beams at different fre-

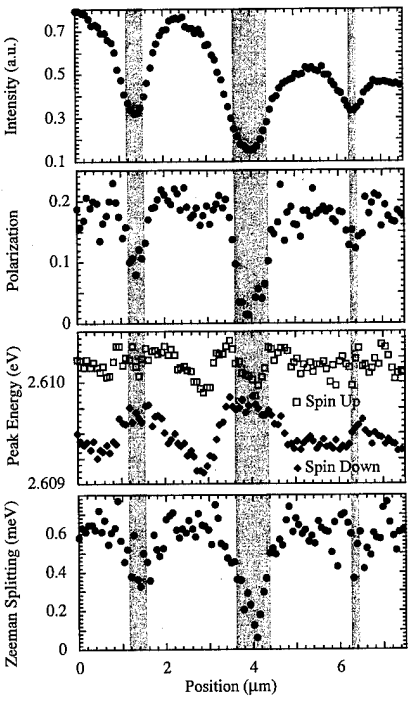



FIG. 7. NSOM data obtained from an energy- and polarization-resolved line scan across a patterned sample at $T=9$ K and $B=0.2$ T. (a) Intensity, (b) polarization, (c) energy of the luminescence peak, (d) Zeeman energy splitting, vs position. Shaded areas indicate regions of ion implantation.

quencies, and phase-sensitive detection at sum frequency yields the LIA signal, whose time decay provides a measure of the exciton lifetime.

Figures 8(a) and 8(b) show the LIA signal as function of position and time delay. Measurements are performed on a patterned DMH sample at $T=9$ K in $B=0.2$ T in the lift-up scan mode. Data is taken by collecting time-varied signal for both polarizations on a line perpendicular to the patterned stripes. For both spin states the initial exciton distribution is

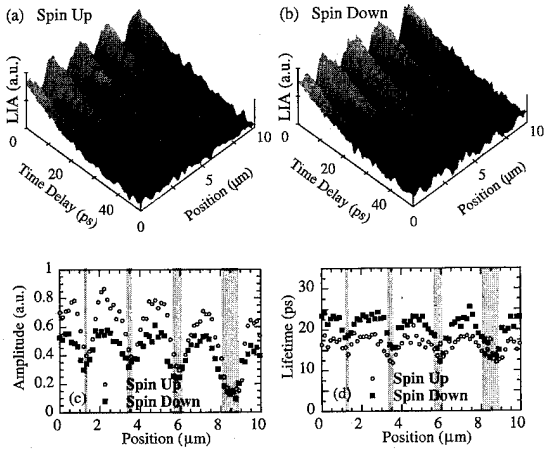



FIG. 8. Time-resolved exciton spin dynamics obtained by LIA measurements in a line scan across four interfaces ($B=0.2$ T, $T=9$ K). (a) Spin up. (b) Spin down. (c), (d) Amplitude and lifetime vs position, extracted by a single exponential fit from the above data. Shaded areas indicate regions of ion implantation.

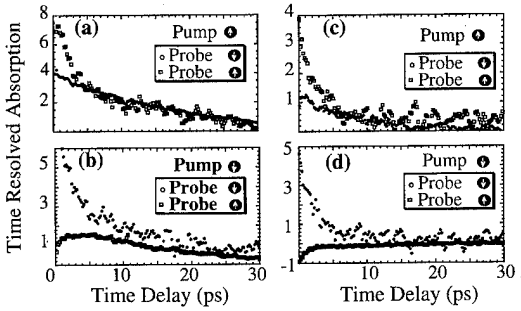



FIG. 9. Time-resolved absorption for both spin up and spin down excitonic states in intrinsic (a), (b) and implanted (c), (d) regions, with the pump pulse initially photopopulating spin up (a), (c) and spin down (b), (d) excitonic states at $T=5$ K and $B=0.2$ T.

spatially modulated, having been suppressed in the implanted areas. The time evolutions for the two spin states, however, are quite different: the spin-up lifetime is significantly shorter than the spin-down lifetime. A more qualitative comparison is made by applying a single exponential fit $A\exp(-t/\tau)$ to the curves at each spatial location. The lifetime of the spin down state [Fig. 8(c)] is decreased almost a factor of 2 in the implanted areas, whereas variations in lifetime of the spin-up state are small. This result indicates preferred diffusion of spin-up excitons from intrinsic into implanted regions.

Similar measurements are performed on a patterned nonmagnetic sample. Exciton lifetimes are several times longer than in the magnetic samples, a fact consistent with far-field measurements performed on unpatterned samples. The $\tau=0$ exciton distribution defined by implantation is smeared out at later times by diffusion. Exciton lifetimes are reduced in the implanted areas, and are smaller for wider implanted stripes.

Another technique employed—time-resolved absorption—provides even more direct information about the time-dependent exciton population. A circularly polarized femtosecond pump pulse resonantly photopopulates an exciton spin state, while a much weaker ($-20$ dB) time-delayed probe measures absorption changes. By choosing the helicity of the probe pulse and the time delay $\tau$, the population of either excitonic spin state can be determined as a function of $\tau$. Both beams are modulated using optical choppers at different frequencies, and lock-in detection occurs at the sum frequency. In far-field measurements the pump beam is blocked at the detection end, allowing only pump-induced changes in the probe beam to be detected. In the near-field this separation is not possible, and photon shot noise from the pump limits the sensitivity attainable using this technique.

Figures 9(a)–9(d) show time-resolved measurements in the intrinsic and implanted regions shown on a patterned sample at $B=0.2$ T and $T=5$ K. The reduced lifetime for both spin states is consistent with LIA measurements. It is also worth noting that when spin-down excitons are optically injected, the number of spin-up carriers increases in the implanted region, but drops down in the intrinsic region, indicating preferential diffusion of spin-up carriers into implanted regions from the nearby intrinsic regions, also in

agreement with LIA measurements. Nonuniformities in both the pump and probe pulse profiles (see Fig. 3), however, make interpretation of spatially resolved images difficult. Smoother etched surfaces may in the future allow this technique to fulfill its promise of providing direct spatiotemporal information on excitonic spin behavior in these systems.

## IV. CONCLUSION

We have demonstrated the unique capability of femtosecond near-field microscopy to optically study spatiotemporal excitonic spin behavior in magnetic semiconductors. The patterned defects introduced by the ion implantation result in locally suppressed magnetic interaction, and create the observed spin-dependent energy landscape for the photoexcited carriers. Time-resolved measurements employing the luminescence intensity autocorrelation technique show that, in the presence of such nonuniform potentials, exciton diffusion acquires a spin component. Both static and time-resolved near-field measurements suggest that exciton diffusion does not affect their interaction with the magnetic matrix and concurrent spin scattering. Time-resolved measurements reveal spin-dependent excitonic lifetimes consistent with the carrier diffusion in nonuniform energy potential.

## ACKNOWLEDGMENTS

This work was supported by Grant Nos. ONR N00014-94-1-0297 and N00014-94-1-0225, NSF DMR 92-07567, the NSF Center for Quantized Electronic Structures DMR 91-20007, AFOSR F49620-93-1-0446, and Digital Instruments, Inc.

[1] G. Bastard, Phys. Rev. B **46**, 4253 (1992); Q. Yang, P. Holody, and S. F. Lee *et al.*, Phys. Rev. Lett. **72**, 3274 (1994); S. S. P. Parkin, *ibid.* **71**, 1641 (1993); Y. Meir and N. S. Wingreen, Phys. Rev. B **50**, 4947 (1994); B. L. Johnson and R. E. Camley, *ibid.* **44**, 9997 (1991); M. A. Blachly and N. Giordano, *ibid.* **51**, 12537 (1995).

[2] D. D. Awschalom and N. Samarth, in *Optics of Semiconductor Nanostructures*, edited by F. Hennenberger and S. Schmitt-Rink (Akademie Verlag, Berlin, 1993), and references within.

[3] S. A. Crooker, D. A. Tulchinsky, and J. Levy *et al.*, Phys. Rev. Lett. **75**, 505 (1995).

[4] J. J. Baumberg, S. A. Crooker, and D. D. Awschalom *et al.*, Phys. Rev. B **50**, 7689 (1994).

[5] N. Samarth *et al.*, Phys. Rev. B **44**, 4701 (1991).

[6] A. Schulzgen, E. Runge, and F. Henneberger *et al.*, Jpn. J. Appl. Phys. **34**, 155 (1994).

[7] The current record for spatial resolution using near-field microscopy is 1 nm. See F. Zenhausern, Y. Martin, and H. K. Wickramasinghe, Science **269**, 1083 (1995).

[8] T. Honda *et al.*, Jpn. J. Appl. Phys. **33**, 1211 (1994).

[9] E. Betzig, P. L. Finn, and J. S. Weiner, Appl. Phys. Lett. **60**, 2484 (1992).

[10] E. Betzig, J. K. Trautman, T. D. Harris *et al.*, Science **251**, 1468 (1991).

[11] H. F. Hess, E. Betzig, T. D. Harris, L. N. Pfeiffer, and K. W. West, Science **264**, 1740 (1994).

[12] J. Levy *et al.*, Phys. Rev. Lett. (in press, 1996).

[13] M. I. Dyakonov and V. I. Perel, in *Optical Orientation: Modern Problems in Condensed Matter Sciences*, edited by F. Meier and B. P. Zakharchenia (North-Holland, Amsterdam, 1984), Vol. 8, p. 27.

[14] A. Olsson, Z. Y. Erskine, and A. Schremer *et al.*, Appl. Phys. Lett. **41**, 659 (1982).

# Nanolithographically defined magnetic structures and quantum magnetic disk (invited)

Stephen Y. Chou, Peter R. Krauss, and Linshu Kong
*NanoStructure Laboratory, Department of Electrical Engineering, University of Minnesota, Minneapolis, Minnesota 55455*

Isolated and interactive arrays of magnetic nanostructures as small as 15 nm are fabricated using nanolithography and related technologies, and are characterized using magnetic force microscopy. It has been demonstrated that manipulating the size, aspect ratio, and spacing of these nanostructures can lead to unique control of their magnetic properties. A quantum magnetic disk based on discrete single-domain nanomagnetic structures with storage density of 65 Gbits/in.$^2$ is demonstrated along with a low-cost method for mass producing such disks. Other impacts that nanofabrication can bring to the development of future magnetic storage are discussed. © *1996 American Institute of Physics.* [S0021-8979(96)41908-8]

## I. INTRODUCTION

In the epic of information and multimedia, there are increasing demands for magnetic storage devices with higher density, faster speed, lower power consumption, smaller size, and lower weight than the current state-of-the-art devices. Presently, most magnetic storage devices are based on the properties of magnetic thin films. Therefore, enormous research efforts have been devoted to the study and control of the key factors that affect magnetic thin film properties.[1–4] These factors include the size and shape anisotropy of the grains in the film, the grain magnetization orientation, the spacing and coupling between the grains, and material compositions.

The advent of nanofabrication technology opens up new avenues to manipulate magnetic materials, thereby leading to unique opportunities in developing innovative ultrahigh density magnetic storage, engineering new magnetic materials and devices, and obtaining better understanding of micromagnetics. Nanofabrication can make magnetic structures with dimensions comparable to or smaller than some fundamental length scales in magnetics, such as domain wall size and exchange interaction length, thus making the behavior different from that of a thin film. Nanofabrication can create arrays of interactive magnetic nanoparticles with precisely controlled interparticle spacing. Nanofabrication can arrange the orientation and position of the nanoparticles at one's will. With such unique manipulation ability offered by nanotechnology, many revolutionary device concepts are no longer regarded as "wild dreams," but become reality.

This article reviews research on nanomagnetic structures fabricated using electron-beam lithography and other fabrication technologies carried out at the NanoStructure Laboratory at the University of Minnesota. Particularly, this article will discuss (1) fabrication and characterization of isolated and interactive single-domain magnetic nanostructures such as bars, pillars, and rings, and (2) properties and low-cost fabrication of a 65 Gbits/in.$^2$ quantum magnetic disk—a new paradigm for ultrahigh density magnetic recording media with a recording density two orders of magnitude greater than current state-of-the-art disks. The work done elsewhere on lithographically defined magnetic structures can be found in Refs. 5–8.

## II. FABRICATION OF MAGNETIC STRUCTURES USING NANOLITHOGRAPHY

A typical fabrication process is illustrated in Fig. 1. In the fabrication, a resist film, polymethylmethacrylate (PMMA), is first spun onto a substrate, typically silicon. A high resolution electron beam lithography system is used to expose patterns in the PMMA.[9] The exposed PMMA is developed in a cellosolve and methanol solution to form a resist template on the substrate. Ferromagnetic materials can be patterned using either a lift-off or electroplating process. In a lift-off process, a ferromagnetic metal film is first deposited onto the entire sample. The sample is then immersed in acetone that dissolves the PMMA template and lifts off the metal on the PMMA surface, but not the metal on the substrate. In an electroplating process, a thin metal plating base is placed between the PMMA and the substrate, and the PMMA template is removed after plating. Besides use for lift-off and plating, the PMMA template also can be used to etch nanostructures into the substrate that will be used later to create magnetic nanostructures.

Figures 2–4 show scanning electron microscope (SEM) images of three magnetic nanostructures fabricated using nanolithography and a lift-off process.[10,11] The nanostructures are a high aspect ratio, isolated Ni bar 15 nm wide and 1 $\mu$m long, an interactive Ni bar array of 20 nm wide and 200 nm long bars, and Ni rings with a 90 nm mean diameter

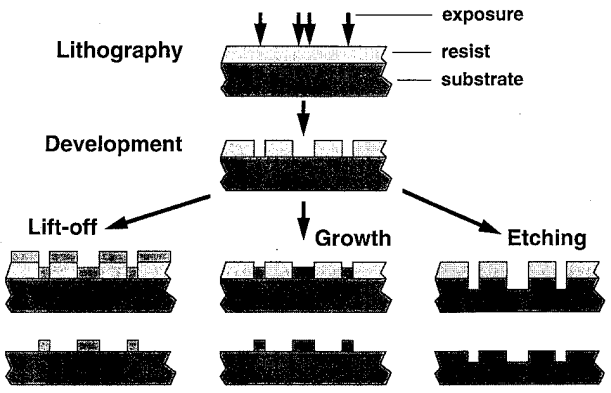



FIG. 1. Schematic of a typical process for fabricating nanomagnetic structures using nanolithography and related technologies.

 0021-8979/96/79(8)/6101/6/$10.00 © 1996 American Institute of Physics 

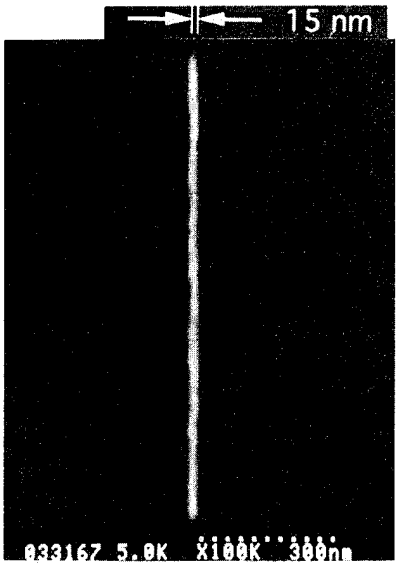



FIG. 2. SEM image of a high aspect ratio isolated Ni bar that is 15 nm wide, 1 $\mu$m long, and 35 nm thick.

and 25 nm ring width. The Ni structures have a thickness of 35 nm and were fabricated on a Si substrate. Figure 5 shows a SEM image of a Ni pillar array with 100 nm spacing, 75 nm average diameter, 700 nm height, and therefore 9.3 aspect ratio fabricated using nanolithography and electroplating.[12]

## III. PROPERTIES OF NANOMAGNETIC STRUCTURES

The first striking property of nanolithographically defined magnetic structures is that without an applied magnetic field, each structure can magnetize itself, making the magnetic moments of all polycrystalline grains in the structure align to the same direction. The single-domain formation is due to the fact that the magnetostatic energy in these magnetic nanostructures is lower than the domain wall energy.

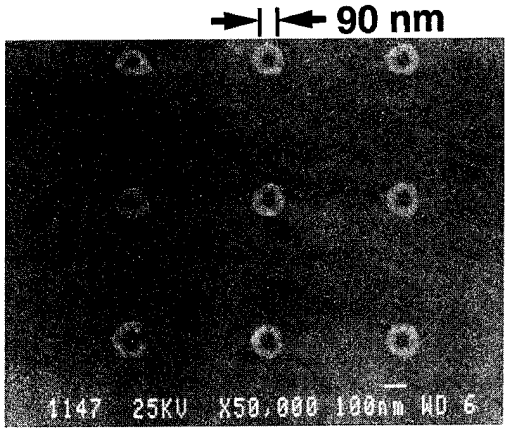



FIG. 4. SEM image of Ni rings of a 90 nm mean diameter, 25 nm ring width, and 35 nm thickness on Si.

Furthermore, the shape anisotropy of the structures forces the magnetization to be aligned along the long axis of the bars and pillars. This single-domain formation and alignment make the magnetic moment quantized with only two stable states, equal in magnitude but opposite in direction. Figure 6 shows that when examined using magnetic force microscopy, each nickel bar, which is 100 nm wide, 35 nm thick, and 1 $\mu$m long, has two opposite magnetic poles at the ends of the bar and no poles in between—a clear picture of a single magnetic domain element.

The second property is that the magnetic field needed to switch the magnetization of a single-domain element from one direction to the opposite direction can be controlled by changing the geometry of the structure, such as bar's width, length, and thickness. Figure 7 shows that the switching field of nickel and cobalt bars with a 1 $\mu$m length and 35 nm thickness increases as the width of the bar decreases. The peak switching fields are 740 Oe for Ni and 3000 Oe for Co, respectively, which are over 30 times larger than the switching field of the as-deposited films.[11,13]

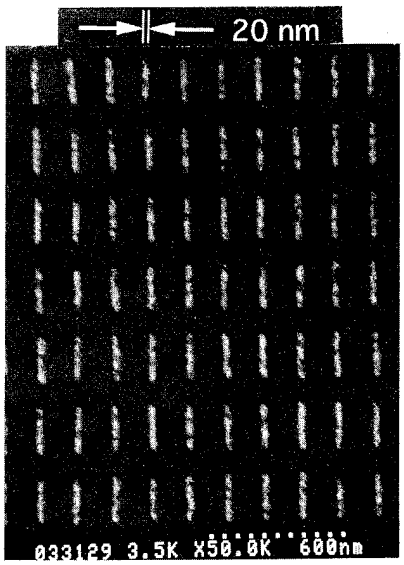



FIG. 3. SEM image of an interactive Ni bar array. Each bar is 20 nm wide, 200 nm long, and 35 nm thick.

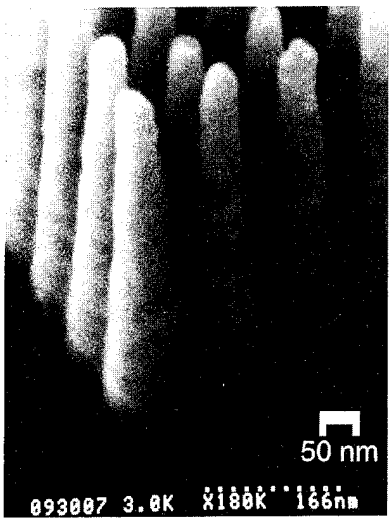



FIG. 5. SEM image of Ni pillar array of a 100 nm spacing, 75 nm average diameter, 700 nm height, and therefore 9.3 aspect ratio.

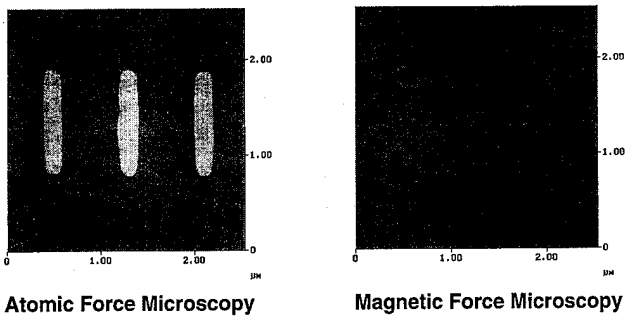



FIG. 6. The atomic force microscopy (a) and magnetic force microscopy (b) of three single-domain nickel bars that are 100 nm wide, 1 $\mu$m long, and 35 nm thick.

The switching field of the single-domain bars can be further controlled by varying the bar length as shown in Fig. 8. It was found that the length dependence is nonmonotonic.[13] The switching field increases with the bar length initially, but then decreases after reaching a peak. For isolated nickel and cobalt bars with a thickness of 35 nm and a width of 100 nm, the peak switching field and corresponding bar length are, respectively, 640 Oe and 1 $\mu$m for Ni, and 1250 Oe and 2 $\mu$m for Co. Moreover, it was observed that the decrease of the switching field with the increase of the bar width is much faster in Ni bars than in Co bars. These results suggest that quasi-coherent switching occurs in short bars and incoherent switching occurs in long bars, and that the exchange coupling is much stronger in Co bars than that in Ni bars.

The effects of the magnetostatic field of a single-domain bar on the crystalline anisotropy and the switching field of its neighbors were studied using nanolithography technology.[14] In this study, pairs of single-domain cobalt bars that were 35 nm thick, 50 nm wide, 1 $\mu$m long and with a spacing from 50 to 1000 nm, were fabricated using electron-beam lithography and a lift-off process. Magnetic force microscopy was used to study the switching behavior of one bar in the presence of another bar and the intrinsic switching field of one bar after the other bar was physically removed. Figure 9 shows the measured switching field for the three cases: (a) only one of the twin bars is switched, $H_{\uparrow\downarrow}$; (b) both bars are switched, $H_{\uparrow\uparrow}$; (c) one bar switched after the other bar was

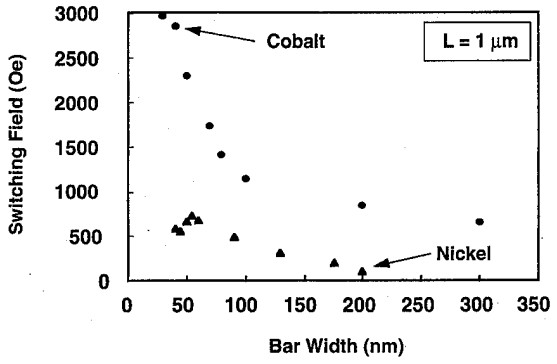



FIG. 7. Switching field of isolated Ni and Co bars vs bar width. The bars are 1 $\mu$m long and 35 nm thick. The actual bar width was measured using SEM.

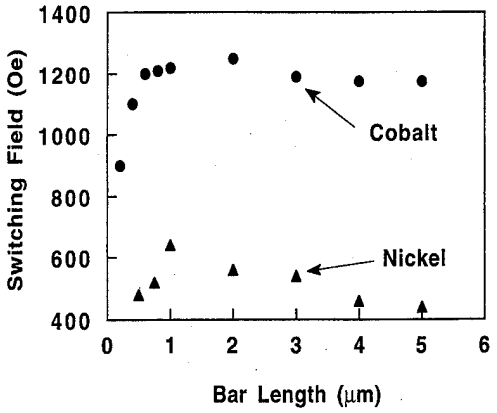



FIG. 8. Switching field of isolated Ni and Co bars vs bar length. The bars are 100 nm wide and 35 nm thick.

physically removed by a nanotechnique, $H_{\uparrow}$. One of the key findings is that even after the neighboring bar was physically removed, the intrinsic switching field of one bar still strongly depends on the original spacing between the bars. Also, the smaller the bar spacing was, the larger the intrinsic switching field. This is attributed to the spontaneous formation of a single-domain region during the Co deposition, whose magnetostatic field enhances the crystalline anisotropy of its neighbors. These results suggest that during the deposition of magnetic media, substrate roughness and large in-plane shape anisotropy of magnetic grains will strongly affect the magnetic properties of neighboring grains and therefore the uniformity of the disk.

Finally, ferromagnetic rings were studied using MFM. It was found that for the rings with a diameter 500 nm or less, no magnetic poles can be observed, indicating the rings are a single domain.

## IV. QUANTUM MAGNETIC DISK

As data storage densities reach 500 MBits/in.$^2$ in commercial magnetic hard disks and 3 Gbits/in.$^2$ in the most advanced laboratory disks, it becomes apparent that one of

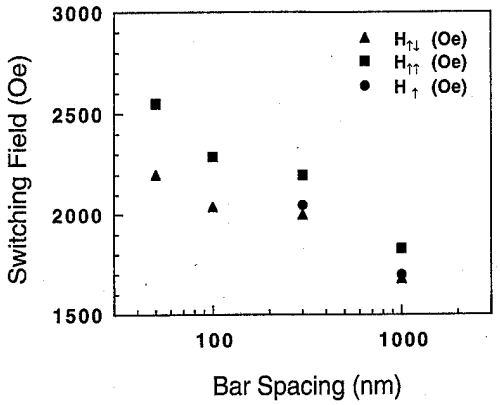



FIG. 9. Switching field of twin single-domain Co bars vs the bar spacing $H_{\uparrow\downarrow}$, only one of twin bars is switched; $H_{\uparrow\uparrow}$, both bars are switched; $H_{\uparrow}$, switching field after one of the twin bars was removed.

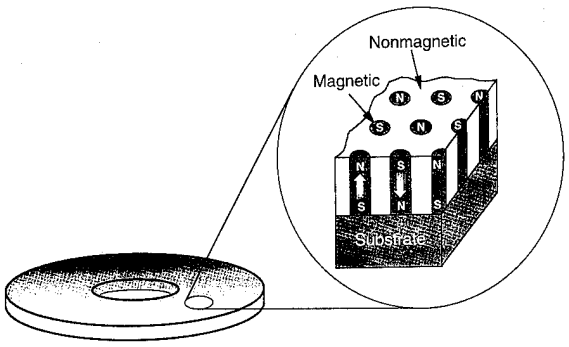



FIG. 10. Schematic of a quantum magnetic disk which consists of prepatterned single-domain magnetic structures embedded in a nonmagnetic disk. Only the vertical magnetization is shown, but the disk can be made with longitudinal magnetization.

the key factors that limit the storage density is the nature of magnetic thin films that are used as the recording media. Many of the limitations can be readily removed if each bit is stored in a discrete magnetic element that is separated from its neighbors by a nonmagnetic material. More advantages can be obtained if each element is made of a single magnetic domain. These ideas are the basis for a new magnetic recording paradigm, the quantum magnetic disk.

A quantum magnetic disk (QMD) completely abandons the continuous magnetic thin film as the recording media used in the conventional disk. Instead, the QMD uses prefabricated discrete single-domain magnetic elements uniformly embedded in a nonmagnetic disk, as shown in Fig. 10.[11] Each element has a uniform and well-defined shape, a prespecified location, and most importantly, a quantified magnetization that has only two states, identical in magnitude but opposite in direction. Each element can store a bit of binary information. The other striking property is that the magnetic field needed for switching the magnetization direction of the elements can be controlled by engineering the elements' geometry.

Before discussing the unique advantages of QMDs in writing, reading, and tracking, let us look at the fabrication process and properties of one QMD embodiment that consists of single-domain nickel (magnetic) nanopillars uniformly embedded in a $SiO_2$ (nonmagnetic) disk.[15,16] In fabrication, electron-beam lithography was used to define the QMD bit's size and location, and reactive ion etching was used to drill holes in the $SiO_2$ layer carried on a Si substrate. Nickel electroplating was used to selectively deposit nickel into the holes and chemical mechanical polishing was used to planarize the surface.

The properties of the QMD have been investigated using scanning electron microscopy (SEM), tapping mode atomic force microscopy (TMAFM), and magnetic force microscopy (MFM).[16] A SEM micrograph of a 3 bit by 3 bit section of the QMD in a top view is shown in Fig. 11(a). The micrograph shows that the nickel pillars of the QMD have a 50 nm diameter and a 100 nm period. The pillars are 200 nm tall and thus have an aspect ratio of 4.

TMAFM and MFM images taken simultaneously on the same area of the QMD are shown in Figs. 11(b) and 11(c), respectively. The TMAFM image of a 3 bit by 3 bit section of the QMD shows that the topology of the nickel pillars is indistinguishable from that of the $SiO_2$. The surface is very smooth with a roughness of 0.5 nm root-mean-squared. The corresponding MFM image, on the other hand, clearly shows that each bit has a quantized magnetization orientation and the magnetic image of each pillar of the 9 bit section can be resolved. Five bits have the south pole (bright) on the top surface and the other four bits have the north pole (dark) on the top. The QMD was demagnetized before imaging, therefore the nearest neighbor bits have opposite magnetic directions. This magnetization configuration is the lowest energy state for the QMD. Our study also showed that the nickel pillar can be switched using a MFM tip with a large magnetic moment. The storage density of the QMD is 65 Gbits/in.$^2$, which is over two orders of magnitude higher than that of state-of-the-art commercial magnetic disks.

The advantages of quantum magnetic disks over the conventional disks are apparent. First, the writing process in the quantum disk is simplified and becomes quantized, resulting in much lower noise and lower error rate and allowing much higher density. Instead of precisely defining the magnetic moment, area, and location of each bit as in a conventional magnetic disk, the writing process in a QMD simply requires flipping the magnetization direction of a discrete single-domain bit. Micromagnetics simulation has shown that even if a writing field is smaller than the size of the bit, the writing field will flip the magnetization direction of the entire bit, leading to a perfect writing.[17] Furthermore, simulation has shown that if the overlap between the writing field and a bit is insignificant, the writing field would only temporarily perturb the magnetic moment distribution of the bit. When the writing field is removed from the bit, the magnetic moment of the bit returns to its original state. In other words, the writing process in a QMD is quantized: a write head either writes perfectly the entire bit, or it does not write the bit at all. The quantized writing process in the QMD will allow the use of a smaller and therefore faster write head. It will avoid errors due to the misplacement and the fringing field of the wire head, and hence is suitable for ultrahigh density storage.

The second advantage of the QMD is near zero transition noise. The transition region between two bits is replaced by a nonmagnetic material and the grains in a QMD bit are tightly coupled and behave like a single large grain. As a result, the noise from the fluctuation of grain magnetization orientation should be greatly reduced, if not completely eliminated. In QMDs, the boundaries between the bits are defined by lithography and etching. They can be very smooth, giving quiet reading signals.

The third advantage of the QMD is reduced cross talk between bits. The cross talk in conventional disks comes from the interbit exchange interaction and magnetostatic interactions. In QMDs, by replacing the ferromagnetic material that is between the bits with a nonmagnetic material, the exchange interaction between the bits gets cut off completely and the interbit magnetostatic interaction is greatly reduced.

The fourth advantage is a solution to the tracking problem. In conventional magnetic disks, the bits do not always have physically recognizable boundaries between them.

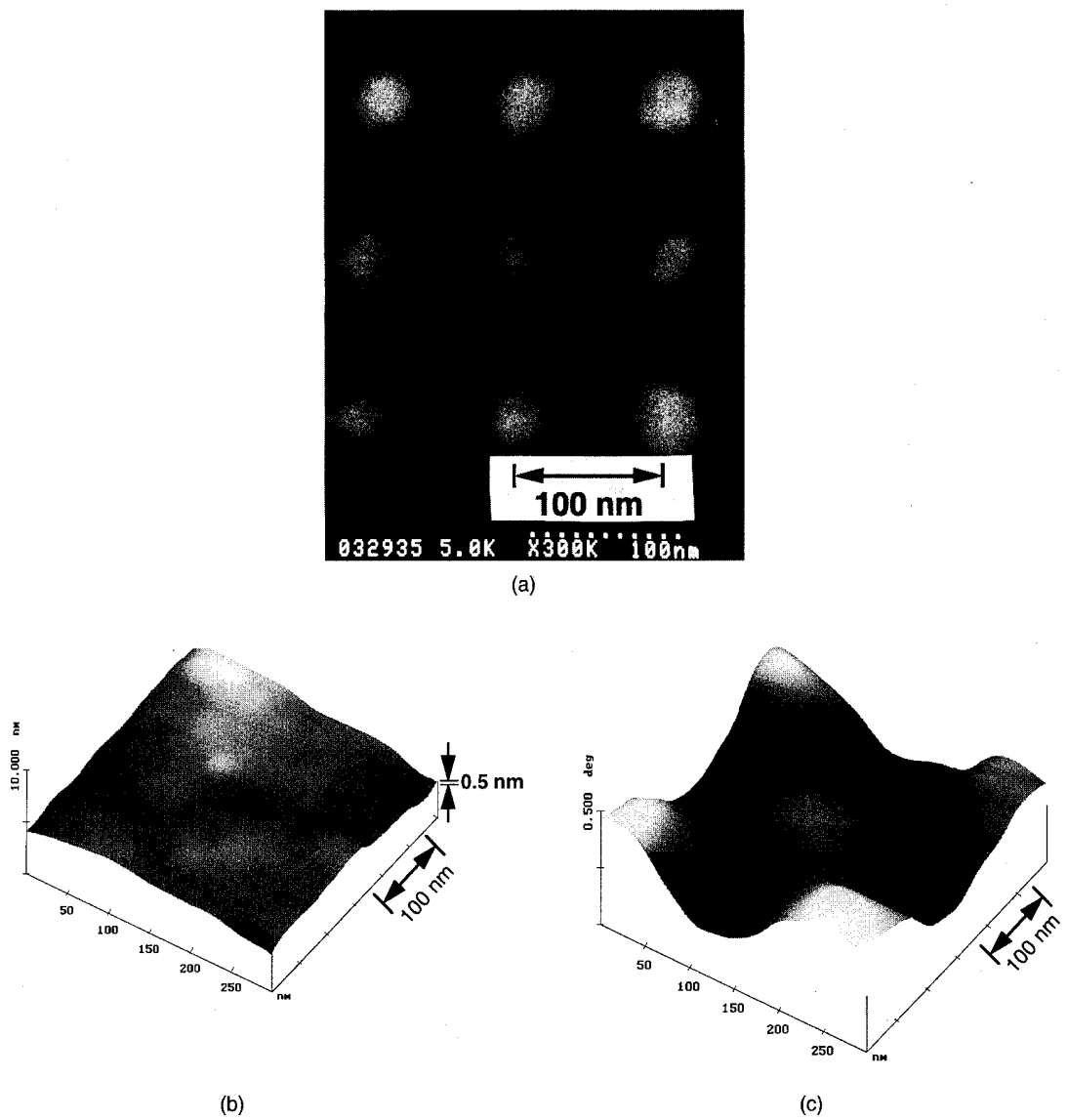



FIG. 11. (a) SEM image, (b) TMAFM image, and (c) MFM image of 3 by 3 bits of a QMD with 65 Gbits/in.$^2$ density. Each bit consists of a nickel pillar uniformly embedded in 200 nm $SiO_2$ with a 50 nm diameter (aspect ratio of 4) and a 100 nm period. The TMAFM image shows a very smooth surface with a roughness of 0.5 nm rms. The MFM image shows an alternating pattern of magnetization directions from each bit.

Tracking depends on the writing of the tracking marks and the ability to rotate the disk the exact amount so that the desired data aligns with the head that writes or reads it. In other words, the tracking is "blind." Furthermore, over 14% of total disk area is used to write the tracking marks in current commercial disks. The area for tracking marks is expected to take up significantly more disk area in future high density disks where more precise tracking is required. In the QMDs, each bit is isolated from one another by nonmagnetic material. Therefore, there is always a variation of magnetic field between the bits (regardless of their magnetization directions) that provides the signal for actual tracking of each bit. Namely, in a QMD drive, each bit can be physically seen before writing or reading.

Clearly, to make the QMDs a competitive technology, low-cost mass production methods must be developed. One of the very promising technologies that we have developed is the nanoimprint lithography which replaces *e*-beam nanolithography.[18] In nanoimprint lithography, a mold is first made with the nanoscale features. Then it is pressed into a resist to create a thickness contrast pattern. After removing the mold, the pattern will be transferred into the entire resist by RIE. A SEM micrograph of 25 nm diam metal dots fabricated by nanoimprint lithography and lift-off is shown in Fig. 12.

From the above discussion, it is clear that the QMD differs from the discrete track disk[19,20] and the discrete segment disk.[21,22]

Finally, we would like to point out that although development of QMDs is still in its infancy, great interest has been generated. Our research shows that with the state-of-the-art nanofabrication technology, the density of QMDs can reach a

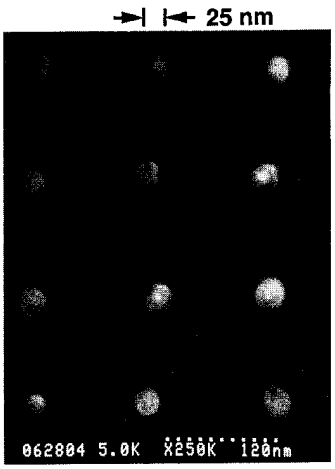



FIG. 12. SEM image of 25 nm diameter metal dots fabricated by nanoimprint lithography and lift-off.

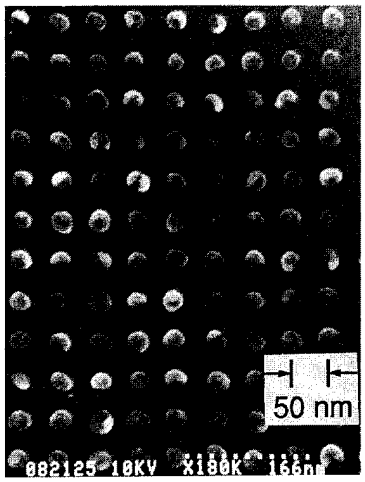



FIG. 13. SEM image of a metal dot array with a density of 0.25 Tbits/in.$^2$

0.25 Tbits/in.$^2$ (Fig. 13) and yet each bit is thermally stable. Besides the QMD media, the future development of the QMDs involves the development of the ultrahigh resolution, high-speed read and write heads as well as new drive systems. The heads will very likely utilize the advanced technologies of nanofabrication and scanning force probes. They will be in the form of large parallel arrays. The disk drive may deviate from the classic circular geometry; instead it may be a linear drive based on state-of-the-art micromechanical elements. Because of the ultrahigh density offered in the QMDs, the total disk area for a 30 Gbit disk can be well less than the size of a penny.

## V. CONCLUSION

Using nanolithography based fabrication technology, magnetic structures can be engineered to have magnetic properties that cannot be achieved by conventional methods. Undoubtedly, the nanofabrication approach opens up new opportunities for engineering novel magnetic materials, understanding the fundamentals of magnetics, exploring limits of magnetic storage, and developing ultrahigh density magnetic storage and innovative magnetic devices such as read and write heads for hard disks, magnetotransport devices, and magneto-optical devices.

## ACKNOWLEDGMENTS

It gives us great pleasure to thank many past and current members of NanoStructure Lab at the University of Minnesota who have contributed significantly to the magnetic nanostructures and quantum magnetic disk projects; in particular, Mark Wei for his study of single-domain elements, Usman Suriono for micromagnetics simulation, Preston Renstrom for his assistance in developing the nanoimprinting technology, and Dr. Paul Fischer and Robert Guibord for their technical assistance in fabrication. We are also grateful to Professor J. G. Zhu for stimulating discussion. This work was partially supported by Office of Naval Research, Advanced Research Program Agency, and a Packard Fellowship. The magnetic force microscope is supported by Army Research Office through a DURIP.

[1] For example, M. Kryder, 40th MMM Conf., 1995 and the proceedings of MMM Conf. and Intrmag.
[2] A. Aharioni, J. Appl. Phys. **63**, 5879 (1988).
[3] Y. Martin and H. K. Wickramasinghe, Appl. Phys. Lett. **50**, 1455 (1987).
[4] Y. Honda, S. Hosaka, A. Kikugawa, S. Tanaka, Y. Matsuda, M. Suzuki, and M. Futamoto, Jpn. J. Appl. Phys. **31**, L1061 (1992).
[5] J. F. Smyth, S. Schultz, D. R. Fredkin, T. Koehler, I. R. McFaydlin, D. P. Kern, and S. A. Rishton, J. Appl. Phys. **63**, 4237 (1988).
[6] G. A. Gibson, J. F. Smyth, S. Schultz, and D. P. Kern, IEEE Trans. Magn. **27**, 5187 (1991).
[7] R. M. H. New, R. F. W. Pease, and R. L. White, J. Vac. Sci. Technol. B **13**, 1089 (1995).
[8] R. M. H. New, R. F. W. Pease, R. L. White, R. M. Osgood, and K. Babcock, 40th MMM Conf.
[9] S. Y. Chou and P. Fischer, J. Vac. Sci. Technol. B **8**, 1919 (1990).
[10] P. B. Fischer, M. S. Wei, and S. Y. Chou, J. Vac. Sci. Technol. B **11**, 2570 (1993).
[11] S. Y. Chou, M. Wei, P. R. Krauss, and P. B. Fischer, J. Vac. Sci. Technol. B **12**, 3695 (1994).
[12] P. R. Krauss, P. B. Fischer, and S. Y. Chou, J. Vac. Sci. Technol. B **12**, 3639 (1994).
[13] L. Kong and S. Y. Chou (unpublished).
[14] S. Y. Chou and L. Kong (unpublished).
[15] P. R. Krauss and S. Y. Chou, J. Vac. Sci. Technol. B **13**, 2850 (1995).
[16] S. Y. Chou and P. R. Krauss, presented at the 40th MMM Conf. Philadelphia, PA, Nov. 1995.
[17] U. Suriono and S. Y. Chou (unpublished).
[18] S. Y. Chou, P. R. Krauss, and P. Renstrom, Appl. Phys. Lett. **67**, 3113 (1995).
[19] L. F. Shew, IEEE Trans. Broadcast Tel. Receivers **BTR-9**, 56 (1963).
[20] S. E. Lambert, I. L. Sanders, A. M. Patlach, and M. T. Krounbi, IEEE Trans. Magn. **MAG-23**, 3690 (1987).
[21] K. A. Belser, T. Makansi, and I. L. Sanders, U.S. Patent No. 4,912,585, March 27, 1990.
[22] S. E. Lamber, I. L. Sanders, A. M. Pattan, M. T. Krounbi, and S. R. Hetzler, J. Appl. Phys. **69**, 4724 (1991).

# Chiral quantum spin solitons

Hans-Benjamin Braun and Daniel Loss
*Department of Physics, Simon Fraser University, Burnaby, British Columbia V5A 1S6, Canada*

The concept of chirality is introduced in the quantum dynamics of spin solitons. For half-integer spin chains we find as universal properties that the Brillouin zone is halved and that two subsequent band minima have opposite chirality. This effect occurs in quasi-one-dimensional (1D) magnets in the semiclassical limit, in anisotropic spin-1/2 chains and for holes propagating in a two-dimensional (2D) antiferromagnetic background. © *1996 American Institute of Physics.*
[S0021-8979(96)76608-9]

## I. INTRODUCTION

Spin solitons leave a wake of reversed spins as they propagate. Such excitations occur in a wide range of systems: Extended domain walls in ferromagnets (FM) or antiferromagnets (AF) whose center tunnels between adjacent lattice sites provide an example of a macroscopic quantum phenomenon (MQP).[1] Solitons rather than spin waves form elementary excitations in AF[2,3] and FM spin-1/2 chains. A prominent example of spin solitons are holes moving through a two-dimensional (2D) antiferromagnetic background in the context of high-$T_c$ superconductors. Such holes flip each spin they pass in order to maintain the local Néel order. In all these cases, solitons tunnel between lattice sites and thus form Bloch bands.[4]

So far, quantum solitons have been considered as compact objects without internal degree of freedom. It is the purpose of this contribution to demonstrate that spin solitons indeed carry an internal degree, the chirality, and that tunneling between chirality states has striking consequences in half-integer spin systems: The Brillouin zone is halved and two subsequent band minima have opposite chirality. This effect is shown to occur in all of above systems and gives rise to a hole dispersion which is in remarkable agreement with recent ARPES (angular resolved photoemission spectroscopy) data on $Sr_2CuO_2Cl_2$ studied in the context of high-$T_c$ superconductivity.[5]

## II. QUANTUM DYNAMICS OF BLOCH WALLS

We describe the spin configuration in a quasi-1D ferromagnetic sample by the unit vector field $\mathbf{n}(x,\tau)$. The energy for $N_0$ coupled spin chains of length $L$ is then given by

$$H=N_0\int_{-L/2}^{L/2}dx\ \{J(\partial_x\mathbf{n})^2-K_y n_y^2+K_z n_z^2\}, \tag{1}$$

with the field conveniently parametrized as $\mathbf{n}=(\sin\theta\cos\phi,\sin\theta\sin\phi,\cos\theta)$. The first term in Eq. (1) represents the exchange interaction with coupling $J$, while the next terms are anisotropies of easy-axis and hard-axis type with strength $K_y, K_z>0$. The hard-axis anisotropy renders the $xy$ plane an easy-plane for the spin configuration. We consider the imaginary time action ($\hbar=1$), $\mathcal{S}_E=\mathcal{S}_B+\int_0^\beta d\tau\, H$, with $\beta$ the inverse temperature. $\mathcal{S}_B$ is the sum of the Berry phases of all individual spins:

$$\mathcal{S}_B=i\frac{sN_0}{a}\int_{-L/2}^{L/2}dx\int_0^\beta d\tau\ \dot{\phi}(1-\cos\theta). \tag{2}$$

The total derivative $\dot{\phi}$ in Eq. (2) is essential.[6] While it does not affect the classical equations of motion, it ensures, e.g., the correct semiclassical quantization of half-integer spins.

As discussed in Ref. 4, the model (1), (2) can also be explicitly derived from a Heisenberg model with on-site anisotropies in the large-$s$ limit. However, it is equally useful to regard it as an effective model which supports solitons and keeps track of the quantum spin phases of the reversed spins as the soliton propagates.

The model (1), (2) exhibits soliton (or Bloch wall) solutions which satisfy $\delta\mathcal{S}_E=0$ and interpolate between the two easy-axis anisotropy minima such that the spins always stay in the easy plane. As a consequence of the symmetries of the energy $H$, there are four degenerate solitons:

$$\phi_s(x)=-QC\frac{\pi}{2}+2\arctan\ e^{\,Cx/\delta},\quad \theta_s=\pi/2, \tag{3}$$

with $Q,C=\pm1$, and $\delta=\sqrt{J/K_y}$ the soliton width. The "chirality" $C=1/\pi\int dx(\mathbf{n}_s\times\partial_x\mathbf{n}_s)_z=1/\pi\int dx\partial_x\phi_s$ reflects the fact that the transition between the anisotropy minima can be accomplished by a right- or left-handed spin rotation in the easy plane as one proceeds along the $x$ axis.

For the moment, we neglect tunneling between different chirality states of the soliton. As discussed in detail in Ref. 4, the effective action for the position $X$ of a moving soliton $\phi_s(x-X)$ then reads as follows

$$\mathcal{S}=\int_0^\beta d\tau\left\{-i\alpha C\dot{X}+\frac{M}{2}\dot{X}^2+V(X)\right\}, \tag{4}$$

where $\alpha=\pi sN_0/a$ and $M=N_0s^2/K_za^2\delta$ is the Döring mass. The first term is a chirality dependent gauge potential and results from insertion of $\phi_s(x-X(\tau)),\theta_s=\pi/2$ into the Berry phase term (2). The second term is the soliton kinetic energy and $V(X)=2V_0\sin^2(\pi X/d)$ is a periodic potential which arises from the crystal lattice or from a superlattice structure. The period $d$ is assumed to be an integer multiple of the lattice constant $a$.

The effective action (4) simply describes a massive particle in a periodic potential. The gauge potential is the only part that reminds of the spin origin of the particle. The action (4) is equivalent to the Hamiltonian $\mathscr{H}=(1/2)M(p-\alpha\sigma_3)^2+V(X)$, where $p=-i\partial/\partial X$ is the soliton momentum, and the Pauli matrix $\sigma_3$ characterizes the chirality pseudospin. The eigenstates are products $|k,C\rangle=|k\rangle|C\rangle$ of chirality states, $\sigma_3|C\rangle=C|C\rangle$, and Bloch states $|k\rangle$ satisfying $\mathscr{H}|k,C\rangle=E(k,C)|k,C\rangle$, where the band index has been suppressed since we are only interested in the lowest band.

We are now in a position to calculate the dispersion of a spin soliton. Consider first the nearly free limit $V_0\to 0$. The spectrum of $\mathscr{H}$ then consists of the pair of parabolas $E(k,C)=(1/2M)(k-\alpha C)^2$ with chiralities $C=\pm 1$, periodically extended by the reciprocal lattice vector $K=2\pi/d$. For $s_0$ half-odd integer, we have $\alpha=(\pi/2d) \bmod K$ and thus the parabolas are separated by $\pi/d$. We thus arrive at the striking result that *the Brillouin zone (BZ) is halved and two consecutive parabolas have opposite chirality*. For $s_0$ integer, the parabolas are separated by $2\alpha=K$, and the BZ is not halved.

The same result is also obtained in the tight-binding limit: An instanton calculation[4] yields for half-integer $s_0$ the dispersion

$$E(k)=-(\Delta/2)|\sin(kd)|. \tag{5}$$

The bandwidth is given by $\Delta=8\omega\sqrt{\mathscr{S}_0/2\pi}e^{-\mathscr{S}_0}$, where $\mathscr{S}_0=(4d/\pi)\sqrt{MV_0}$ the tunneling action and $\omega=(2\pi/d)\sqrt{V_0/M}$ the instanton frequency. Most important, the parts where $\sin(kd)$ is positive (negative) belong to positive (negative) chirality and thus BZ halving and chirality correlation occurs as in the nearly free limit. For integer $s_0$, the band has the simple tight-binding form $E(k)=-(\Delta)/2\cos(kd)$ and is degenerate with respect to the chiralities $Q=\pm 1$.

## III. CHIRALITY TUNNELING

We now investigate how the dispersion (5) is altered due to tunneling between the two degenerate chirality states. To this end we return to the action $\mathscr{S}_E$ and choose angles adopted to describe chirality tunneling, $\mathbf{n}=(\sin\theta\sin\phi,\cos\theta,\sin\theta\cos\phi)$, i.e., the polar angle is now measured from the (easy) $y$ axis. The soliton (3) then reads $\theta_Q=2\arctan e^{Qx/\delta}$ and the two chirality states $\phi_C=CQ\pi/2$ are separated by the barrier of the hard-axis anisotropy. Chirality tunneling thus consists of transitions between $\phi=\pm\pi/2$. Inserting $\phi(\tau)$ into $\mathscr{S}_E$ and integrating out the fluctuations around the (static) soliton we arrive at the effective action for the chirality dynamics

$$\mathscr{S}_{\text{eff}}=\int_0^\beta d\tau\left\{\frac{\mu}{2}\dot{\phi}^2+\kappa\cos^2\phi+\eta\cos\phi+\eta^2/2\kappa\right\}. \tag{6}$$

The fluctuations around the soliton give rise to an effective "mass" $\mu=N_0(s^2\delta/a^2K_y)c_0$ ($c_0>0$ is a numerical constant of order one). The second term is the energy barrier due to the hard-axis anisotropy $\kappa=2N_0K_z\delta$. This barrier between the two chirality states is lowered by an external field $B_z$ along the hard axis which is described by the third term with $\eta=\pi g\mu_B sN_0B_z\delta/a$. The chirality then tunnels between potential minima defined by $\cos\phi_{\min}=-B_z/B_a\equiv\nu-1$ with the anisotropy field $B_a=4aK_z/\pi g\mu_B s$. A standard instanton calculation gives for the tunnel splitting $\epsilon=4\gamma\omega_c\sqrt{\mathscr{S}_c/2\pi}e^{-\mathscr{S}_c}$, where $\gamma>0$ is a constant of order one, and $\mathscr{S}_c=2\pi s N_0(\delta/a)\sqrt{c_0K_z/K_y}\nu^{3/2}$, $\omega_c=(8a/\pi)\sqrt{K_yK_z/c_0}\nu^{1/2}$. Since typically $\epsilon$ can be made quite large (by tuning $B_z$ or small $N_0$) this tunneling scenario is a promising candidate for MQP behavior.

In the presence of chirality tunneling, the effective Hamiltonian becomes $\mathscr{H}_\epsilon=1/2M(p-\alpha\sigma_3)^2+V(X)+(\epsilon/2)\sigma_1$, where $\sigma_1|C\rangle=|-C\rangle$. In the tight-binding limit we have

$$\mathscr{H}_\epsilon=-\frac{\Delta}{4}\sum_{m,l,C}e^{i\alpha Cld}\,|m+l,C\rangle\langle m,C|+\frac{\epsilon}{2}\sigma_1, \tag{7}$$

with $l=\pm 1$, and where $|m,C\rangle$ describes a soliton of chirality $C$ at lattice site $m$. $\mathscr{H}_\epsilon$ is immediately diagonalized and for $s_0$ half-integer we have $E_\epsilon(k)=-(\Delta/2)\{\sin^2 kd+(\epsilon/\Delta)^2\}^{1/2}$, and thus the cusps in Eq. (5) are removed. In our case of interest, $\epsilon\lesssim\Delta$, the explicit form of the eigenfunctions reveals that two adjacent minima belong to opposite chirality. This correlation could be detected as follows. First one measures the chirality in a given ground state, e.g., by optical dichroism techniques or spin polarized neutrons. Then the soliton is adiabatically moved by an external field[7] (applied along the easy axis) until it reaches an adjacent band minimum, and then the chirality is measured again. For half-integer spin solitons the two chiralities are opposite, whereas for integer spins there is no correlation.[8]

Finally, we note that the same chirality effects exist for solitons in AF. In this case the effective action contains the same gauge potential as in Eq. (4) since the total derivative $\dot{\phi}$ in Eq. (2) is *not* affected by the staggering induced by local Néel order (the action contains the term $i(SN/a)/dxd\tau\dot{\phi}$ in addition to the Pontryagin index). The above formulas remain essentially unaltered except that the effective masses are changed into $M=N_0(s^2/J\delta)$ and $\mu=N_0(s^2\delta/J)c_0$, with corresponding changes in the tunneling actions. Note that tunneling is more favorable in AF than in FM since typically $J\gg a^2K_{y,z}$.

## IV. SPIN PARITY TUNING AND EXTERNAL FIELDS

We now discuss some consequences of an applied external field $\mathbf{B}$ which is described by adding a term $N_0\mathbf{h}\cdot\int dx\ \mathbf{n}$ with $\mathbf{h}=g(\mu_B s/a)\mathbf{B}$ to the energy $H$. For large hard axis anisotropy $K_z\gg K_y$ and a field $h_z$ along the hard axis, the soliton solutions are still given by $\phi_s$ as in Eq. (3) but with $\cos\theta=-h_z/K_z$. We then obtain the effective action (4) but with a field dependent gauge potential $\tilde{\alpha}=\alpha(1+h_z/K_z)$. Since the dispersion of the lowest band corresponds in the limit $\epsilon/\Delta\to 0$ to the lower envelope of the two curves $\cos(kd\pm\tilde{\alpha}d)$, an increasing external field $h_z$ changes the dispersion periodically between integer and half-integer behavior with the period $\Delta h_z=(K_z/sN_0)\,d/a$.

If $h_z(t)$ depends on time, then the kinetic part of $\mathscr{H}$ is $(1/2M)(p-\tilde{\alpha}(t)\sigma_3)^2$ and thus $d\tilde{\alpha}/dt$ plays the role of a *force* driving the Bloch wall in positive/negative direction for

positive/negative chirality. Note that this force has its origin in the classical part of the Berry phase $\dot{\phi}\cos\theta$. As shown in Ref. 4 such forces are also induced by a field $h_y$ along the easy axis and lead to Bloch oscillations of the magnetization. Finally, a field $h_x$ gives rise to a bias energy $4\pi N_0 \delta h_x$ between the two potential wells of opposite chirality, or conversely, this field can be used to offset unwanted level detuning between the two chirality states.

## V. SPIN-1/2 CHAINS

In this case the soliton width approaches one lattice constant and it is no longer possible to assign a chirality to a *static* soliton. However, quite surprisingly, we shall see that for both, FM and AF chains, the chirality is generated dynamically. We consider an Ising Hamiltonian with small additional anisotropies, $\mathscr{H}_I = -\Sigma_i [J_z S_i^z S_{i+1}^z + J_y S_i^y S_{i+1}^y + J_x S_i^x S_{i+1}^x]$, where $\mathbf{S}_i$ is a spin-1/2 operator at lattice site $i$ and $|J_z| \geqslant |J_y|, |J_x|$. These inequalities ensure that bands with a different number of solitons are well separated.

Let us first consider the FM case with $J_y > J_x$, and all $J$'s positive. A soliton is characterized by its position and charge $Q = \pm 1$, e.g., $|m, Q=1\rangle = |.\uparrow\uparrow\uparrow\downarrow\downarrow\downarrow.\rangle$ with the last up spin at the $m$th lattice site. The existence of one soliton is enforced by twisted boundary conditions, i.e., $S_{N+1}^{y,z} = -S_1^{y,z}, S_{N+1}^x = S_1^x$. Under the action of $\mathscr{H}_I$, the soliton $|m,Q\rangle$ hops by two lattice constants, $|m \pm 2, Q\rangle$ plus higher energy states with more than one soliton. In the spirit of Villain's approach[2] to the AF, we restrict ourselves to the subspace of one soliton. The energy eigenstates are given by $|k, C_x\rangle = (1/\sqrt{2N}) \Sigma_m e^{ikmd} [|m,1\rangle + e^{ikNd} |m, -1$ with the dispersion $E(k) = \frac{1}{2}(J_y - J_x)\cos(2kd)$, where $k = (\pi/Nd)\, n$, and $n = -N+1, .., N$. Thus, again, the BZ is halved. To investigate the chirality correlation, we consider $\mathbf{C} = \Sigma_i \mathbf{S}_i \times \mathbf{S}_{i+1}$, which displays the chiral character of a magnetic excitation. Clearly, the expectation value of $\mathbf{C}$ vanishes in a static soliton, $\langle m, Q | \mathbf{C} | m, Q \rangle = 0$. However, we easily verify that in the one-soliton subspace, the energy eigenstates are simultaneous eigenfunctions of $C_x$, $C_x |k, C_x\rangle = \sin(kd) |k, C_x\rangle$, and the $x$ component of the total spin, $\Sigma_i S_i^x |k, C_x\rangle = \cos(kd) |k, C_x\rangle$, while $C_z |k, C_x\rangle = 0$. Thus they remain good eigenfunctions in the presence of a uniform external field $B_x$, where they have a dispersion $E_B(k) = E(k) + g\mu_B B_x \cos(kd)$. Similarly, a complete basis can be found in which $C_y$ and $\mathscr{H}_I$ are simultaneously diagonal. Thus, again we find that subsequent band minima have opposite chirality. We note that a field along the $z$ axis can give rise to Bloch oscillations,[7] analogous to the semiclassical limit discussed above.

In the AF case we study the Hamiltonian $\mathscr{H}_I$ with all $J's$ negative and $J_x = J_y = J_t$. (Note the absence of an "easy-plane" anisotropy in this case.) An odd number of lattice sites on a ring then enforces a soliton, e.g., $|m, Q=1\rangle = |.\uparrow\downarrow\uparrow\uparrow\downarrow\uparrow.\rangle$, where $m$ denotes the first spin constituting the soliton. Proceeding as before, we obtain $E(k) = J_t \cos(2kd)$, and again, states differing by $\pi/d$ have opposite chirality $C_x$. While this AF dispersion is theoretically[2] and experimentally[3] well-known, the existence of the chirality and its correlation does not seem to have been noticed before.

In passing we note that for FM spin-1 chains with on-site anisotropies of easy- and hard-axis type we can construct soliton eigenstates in a similar way as above. We then find the dispersion $E(k) = -(K_h/2)\cos kd$ where $K_h$ is the hand-axis anisotropy constant. This is in agreement with the semiclassical approach in Secs. II and III.

We thus have convinced ourselves that the effective Hamiltonian (7) indeed captures (for $\epsilon \lesssim \Delta$) the essential physics also in spin-1/2 chains.

## V. HOLES IN 2D ANTIFERROMAGNET

We now discuss propagating holes in a 2D AF background of spin-1/2. While restoring the spin background, such holes consecutively flip spins as they propagate and thus act as spin solitons in 2D. As they hop, solitons of opposite chirality acquire relative Berry phases of $e^{\pm is\pi} = \pm i$. With this physical picture in mind, we propose a model Hamiltonian for the hole propagation which is a direct generalization of the 1D case, Eq. (7): $\mathscr{H}_h = -(\Delta/4) \Sigma_{\mathbf{m},\mathbf{l},\mathbf{C}}\ e^{i(\pi/2)\,\mathbf{C}\cdot\mathbf{l}}\ |\mathbf{m}+\mathbf{l}, \mathbf{C}\rangle\langle \mathbf{m}, \mathbf{C}| + (\epsilon/2)\,\sigma_1^{(x)} + (\epsilon/2)\,\sigma_1^{(y)}$, where $d=1$, and $|\mathbf{m}, \mathbf{C}\rangle$ describes a hole-soliton at site $\mathbf{m}$ with $\mathbf{l}$ connecting nearest neighbors. $\mathbf{C} = (C_x, C_y)$, $C_i = \pm 1$, characterizes its chirality state along the $x$ and $y$ directions. $\sigma_1^{(i)} |C_i\rangle = |-C_i\rangle$ describes chirality tunneling. While $\Delta, \epsilon$ are, in principle, still free parameters with $\epsilon/\Delta \lesssim 1$, our 1D discussion suggests that $\Delta$ is of the order of the exchange coupling. Next, $\mathscr{H}_h$ is easily diagonalized with the lowest band being simply additive, $E_h = E_\epsilon(k_x) + E_\epsilon(k_y)$, where $E_\epsilon(k)$ as given above. Independent of the values of $\Delta > \epsilon > 0$, this dispersion has three distinct properties in remarkable agreement with recent ARPES data on $Sr_2CuO_2Cl_2$.[5] It exhibits "hole pockets" at $\mathbf{k}_{\pm,\pm} = (\pm(\pi/2), \pm(\pi/2))$, separated by saddle points at $(\pm(\pi/2), 0), (0, \pm(\pi/2))$. And third, in marked contrast[5] to the $t$–$J$ model, $E_h(k_x, k_y = \pi - k_x) = E_h(k_x, k_x)$, and thus the dispersion reaches the *full* bandwidth between $(\pi, 0)$ and $(0, \pi)$. Finally, we see from the exact eigenfunctions that, again, states in different hole pockets are correlated by their chiralities.


## ACKNOWLEDGMENTS

This work has been supported by NSERC of Canada (D.L. and H.B.B.) and the Swiss NSF (H.B.B.).



[1] *Quantum Tunneling in Magnetism*, edited by B. Barbara and L. Gunther, Kluwer ASI Series (Kluwer, Dordrecht, 1995).

[2] J. Villain, Physica B **79**, 1 (1975); F. Devreux and J. P. Boucher, J. Phys. Paris **48**, 1663 (1987); H.-J. Mikesha and M. Steiner, Adv. Phys. **40**, 191 (1991).

[3] S. E. Nagler *et al.*, Phys. Rev. Lett. **49**, 590 (1982).

[4] H. B. Braun and D. Loss, Europhys. Lett. **31**, 555 (1995); Phys. Rev. B **53**, 3237 (1996).

[5] (a) B. O. Wells *et al.*, Phys. Rev. Lett. **74**, 964 (1995); (b) Z.-X. Shen *et al.*, Science **267**, 343 (1995).

[6] D. Loss, D. DiVincenzo, and G. Grinstein, Phys. Rev. Lett. **69**, 3233 (1992).

[7] H. B. Braun and D. Loss, J. Appl. Phys. **76**, 6177 (1994); in Ref.1

[8] The chirality in a ground state can be expressed as $\langle k_\pm | C_x | k_\pm \rangle = (1/2\pi) \int d\omega\ \Sigma q\ e^{-iqd} [S^{yz}(q,\omega) - S^{zy}(q,\omega)]$ where $S^{\alpha\beta}(q,\omega) = \int dx\, dt\, e^{-iqx + i\omega t} \langle k_\pm | S^\alpha(x,t) S^\beta(0,0) | k_\pm \rangle$ is the spin correlation function which can be measured via spin polarized neutron scattering..

# Quantum dynamical calculations in clusters of spin 1/2 particles: Resonant coherent quantum tunneling on the magnetization reversal

D. García-Pablos and N. García
*Laboratorio de Física de Sistemas Pequeños C.S.I.C.-U.A.M., Facultad de Ciencias, S.I.D.I., C-IX, Universidad Autónoma de Madrid, Cantoblanco, 28049 Madrid, Spain*

P. A. Serena
*Dept. Física de la Materia Condensada, Facultad de Ciencias, C-III, Universidad Autónoma de Madrid, Cantoblanco, 28049 Madrid, Spain*

H. De Raedt
*Institute for Theoretical Physics, University of Groningen, Nijenborgh 4, 9747 AG Groningen, The Netherlands*

We investigate the reversal of magnetization and the coherence of tunneling when an external magnetic field is rotated instantaneously in systems of a few ($N$) spin 1/2 particles described by an anisotropic Heisenberg Hamiltonian at $T=0$. The temporal evolution is calculated by a numerically exact solution of the time-dependent Schrödinger equation, and the mean value in time of each spin component is computed as a function of the magnetic field. The correlation function and the spectrum are analyzed in terms of the macroscopic quantum coherence. Our calculations demonstrate that this model for small ($N<11$) magnetic particles exhibit collective tunneling of the magnetization only for some specific resonant values of the applied magnetic field, at variance with the Stoner–Wohlfarth model. © *1996 American Institute of Physics.* [S0021-8979(96)76708-5]

The ability to miniaturize magnetic materials and study the magnetic properties of a single isolated particle has revealed classical and quantum phenomena[1–3] that questions the present understanding of the fundamentals of magnetism. The phenomenon of macroscopic quantum tunneling (MQT)[4,5] has received a lot of attention and consists of the tunneling of a macroscopic variable through the barrier between two minima of the effective potential of a macroscopic system. For small single-domain ferromagnetic clusters,[1,6–8] these minima correspond to the two states of opposite magnetization. When there is a repeated coherent tunneling back and forth between the two wells we have a case of macroscopic quantum coherence (MQC). The Stone–Wohlfarth (SW) model,[9] due to its success in the explanation of many classical magnetic phenomena, provided the idea that the dynamics of small magnetic particles in the single-domain regime would keep its simplicity. However, the SW model has been found inadequate for explaining some details in experimental systems.[3] The quantum mechanical effects have been studied theoretically by the quantization within a path integral formalism of the classical micromagnetic theory of magnetic dynamics.[6–8] Chudnovsky and Gunther[6] showed that in addition to superconducting devices, single-domain magnetic particles represent a rich field for MQT study. In the semiclassical approximation, a uniform and coherent rotation of all spins is imposed, that is, spins are considered to behave dynamically as a single quantum spin. This is known as single spin model (SSM). In experiments with superconductivity quantum interference device microsusceptometers,[10] a well-defined resonance in the frequency-dependent magnetic susceptibility $\chi''(\omega)$ has been found and it is tempting to be associated with a MQC phenomenon although there is some controversy on this interpretation.[11] On the other hand, the process of magnetization reversal in single particles[12,13] is also being studied nowadays with much interest. Recent experimental[13] and theoretical[14] works have studied the mechanism of the nonuniform reversal of the magnetization in this kind of particles.

In the present work we have assumed that there is no dissipation, $T=0$ and we have considered applied magnetic fields for which the energy barrier is present, giving rise to the appearance of tunneling phenomena in the reversal of magnetization. The results we have found calculating the exact quantum evolution of the spins show a qualitatively different landscape to what has been explained above: There is essentially a sharp resonance corresponding to coherent quantum tunneling of the magnetization but only for a particular magnetic field, whereas for lower and larger fields this phenomenon does not appear. Notice that in general, the quantum evolution of the spins is noncoherent. This resonant coherent quantum tunneling occurs at fields much lower than the values corresponding to the vanishing of the barrier in the Stoner–Wohlfarth mode.[9] The former model is at variance with the exact calculations presented in this paper.

We need to introduce the two-time correlation function of the magnetization,[4] which compares the $z$ component of $S$ at one time with its value at a time later: $\langle S^z(t')S^z(t'+t)\rangle$. In the present work, it has been calculated the symmetrized correlation function $C(t)$ defined as $C(t)=1/2\langle\Psi(0)|S^z(0)\times S^z(t)+S^z(t)S^z(0)|\Psi(0)\rangle$. With negligible dissipation present, coherent tunneling back and forth between the two states (magnetization up and down) leads to a sinusoidal oscillation of $C(t)$ at a frequency twice the off-diagonal matrix element. For two measurements of the magnetization separated by the time interval $t$, one should have $\langle S(t')S(t'+t)\rangle=S_0^2\cos(2\Gamma t)$. As the fluctuation–dissipation theorem shows that the frequency-dependent magnetic susceptibility $\chi''(\omega)$ is essentially the Fourier transform of the correlation function, the former equation predicts a resonance at $\omega_R=2\Gamma$ for $\chi''(\omega)$.

 0021-8979/96/79(8)/6110/3/$10.00 © 1996 American Institute of Physics

We have represented a system containing $N$ spin 1/2 particles in presence of an applied magnetic field $\mathbf{H}$ through its Heisenberg Hamiltonian:

$$H=-J_x\sum_{\langle ij\rangle}\sigma_i^x\sigma_j^x-J_y\sum_{\langle ij\rangle}\sigma_i^y\sigma_j^y-J_z\sum_{\langle ij\rangle}\sigma_i^z\sigma_j^z-H_x \times\sum_i\sigma_i^x-H_z\sum_i\sigma_i^z, \quad (1)$$

where $\sigma_i^\alpha(\alpha=x,y,z)$ are the Pauli-spin matrices at site $i$ related to the spin operators by $\mathbf{S}=\hbar\boldsymbol{\sigma}/2$, the sum $\langle ij\rangle$ is over nearest-neighbor pairs, $J_x,J_y,J_z$ are the exchange constants, and $H_x,H_z$ are the components of the external magnetic field. We have limited ourselves to systems with uniaxial anisotropy $\Delta$ along the $z$ direction $[J_x=J_y<J_z=J$, $\Delta=(J_z-J_x)/J]$, containing $N$ particles $(2<N<11)$ with different geometrical forms and to instantaneous rotations of the magnetic field of several angles. The range of the parameters is $0.01J\leqslant\Delta\leqslant 0.1J$ for the anisotropy and $0\leqslant H\leqslant 0.2J$ for the magnetic field. The temporal evolution of the system is calculated by a numerically exact solution of the time-dependent Schrödinger equation (TDSE).[15] This requires the computation of all eigenvalues and eigenvectors of the Hamiltonian. For larger systems $(N>8)$ we use Suzuki's fourth-order fractal product formula[15–17] to solve TDSE.

In our particular model, at $t=0$ there is a field applied along the $z$ direction, $\mathbf{H}_1=(0,0,H_{z1})$ with $H_{z1}<0$. Then the ground state of the ferromagnet has all spins down and we prepare the system in this state. At $t>0$, the magnetic field is rotated instantaneously about the $y$ axis so that $\mathbf{H}_2=(H_{x2},0,H_{z2})$ with $H_{x2},H_{z2}>0$ forms an angle $\theta_f$ with the $z$ axis (notice that nothing happens in the exact propagation for $\theta_f=0°$). We have studied the dependence of $\bar{S}_i^z$, mean value in time of $\langle S_i^z(t)\rangle$ for each different spin $i$, on the size of the second magnetic field $\mathbf{H}_2$:

$$\bar{S}_i^z=\lim_{\tau\to\infty}\left[\tau^{-1}\int_0^\tau dt\langle S_i^z(t)\rangle\right]. \quad (2)$$

The correlation function $C(t)$ for the second Hamiltonian is also analyzed, as well as the eigenvalues, eigenstates and system energy for each magnetic field considered. Depending on the value of the magnetic field the barrier between the two directions of the magnetization can exist or not, and this way we can speak about two regions: (a) tunneling region when there is a barrier between the two wells and (b) non-tunneling region when that activation barrier has vanished.

Let us concentrate on the results for uniaxial anisotropy $\Delta=0.1(J_x=J_y=0.9J_z)$ and a magnetic field forming an angle $\theta_f=45°$ with the $z$ direction, $\mathbf{H}_2=(H_{x2},0,H_{z2})$ with $H_{x2}=H_{z2}$. The result obtained is the following: clusters with $N\geqslant 5$, and with different geometrical forms (chain, ring, and others) present a pronounced resonance in the curve of $\bar{S}_i^z$ in terms of $H_{x2}=H_{z2}$ for a specific magnetic field $H_r$ that clearly falls in the tunneling region (a). In Fig. 1(a) we show this result for an open linear chain of seven spins. We have found that these resonances correspond to pure sinusoidal oscillations in the correlation function $C(t)$ as it must occur when there is MQC. However, for points around these resonances $C(t)$ does not present this sinusoidal shape at all. In

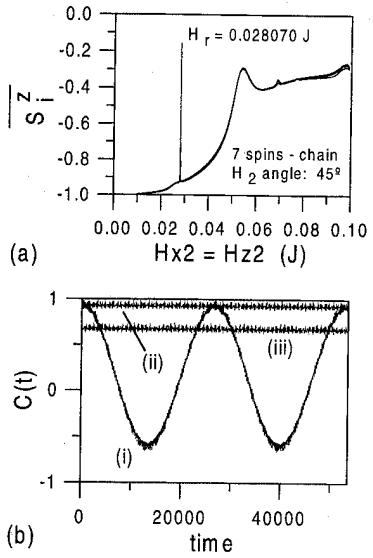



FIG. 1. (a) $\bar{S}_i^z$ for each different spin $i$ as a function of the size of the second magnetic field for a linear chain of seven spins, with $\Delta=0.1$ and $\theta_f=45°$, and (b) symmetrized correlation function for the resonant field $H_r=0.028\,070J$ (i) and two fields around it: (ii) $H=0.0276J$ and (iii) $H=0.0285J$-(iii) curve has been shifted 0.25 in the $y$ axis in order to clarify the picture.

Fig. 1(b) we present $C(t)$ at the resonant field [Fig. 1(b)-(i)] and at two fields around it [Fig. 1(b)-(ii), (iii)] for the same linear cluster. Clusters with $N<5$ do not show this behavior and the reason can be explained in terms of the spectrum and the curve of $H_r$ vs $N$. Clusters with eight and more spins present more than one peak although only one is really sharp.

In order to understand why a particular magnetic field provokes the resonant MQC we have studied the system spectrum calculating its eigenstates energies for each magnetic field applied. For a complete discussion of the spectrum analysis see Ref. 18. This point of view has also been considered for the study of a SSM.[19] To give a slight idea, the specific field that produces the resonance makes practically equal the energies of the second and third eigenstates of the system, which correspond essentially to all spins in one direction and in the opposite, respectively, and which are the only relevant eigenstates in the system state at that field. The system energy for that field is slightly above these two levels of energy. This fact permits a resonant tunneling of the magnetization for a determined field in each case. It must be said that the levels do not cross, there is a small splitting $\Delta E$ between their energies that is related to the tunnel frequency and in consequence to the oscillating period $T$ of the correlation function $C(t)$ by $T=2\pi\hbar\Delta E^{-1}$. The values of $T$ and $\Delta E$ fit very well to this formula.

Other anisotropy values and other directions have been studied and we have also found sharp resonances corresponding to sinusoidal correlation functions.[17] This way it can be said that the resonance found is a general feature of the system considered; it appears for several sizes with any geometrical configuration, different values of the anisotropy and for all the directions of the magnetic field $\mathbf{H}_2$ studied.

In Fig. 2 we show the dependence of the resonant fields $H_r$ and the field $H_b$ that makes the barrier disappear in the

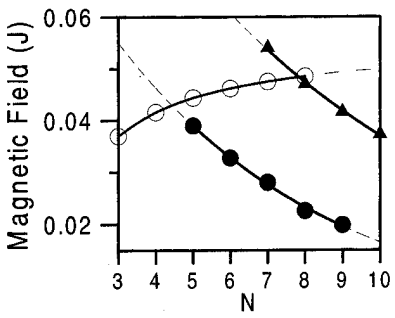



FIG. 2. Dependence of the resonant field $H_r$ (solid circles) and the field needed to vanish the activation barrier $H_b$ (open circles) on the number of spins for a fixed geometrical configuration. The solid triangular symbols correspond to the second peak in the $\tilde{S}_i^z$ curve for clusters with more than seven spins.

single spin model (SSM) on the number of spins ($N<11$) for the same geometrical configuration (chain). As we can see in Fig. 2 $H_r<H_b$ for systems with $N\geqslant 5$. However $H_r$ and $H_b$ have an opposite dependence on the number of spins: while $H_b$ increases with the number of spins since the barrier height is proportional to $N$,$H_r$ decreases with it. The difference between $H_r$ and $H_b$ increases with $N$ and in consequence the resonance is situated further from the region where the barrier vanishes and the semiclassical approaches are applied.[6] The tendency shown by the two curves can explain why clusters with $N<5$ do not present such resonance, as well as the fact that the second and third eigenstates energies do not get close but keep a considerable gap between them. An interesting point is that when $N$ increases and so the separation between $H_r$ and $H_b$ becomes larger, new peaks or resonances appear. We have observed this behavior in clusters with more than seven spins. The field corresponding to the second peak in eight spins cluster is below $H_b$ whereas in seven spins cluster the second peak field is above $H_b$ (see Fig. 2). The sharpness of the peaks is related to the separation between the levels involved. When the repulsion between the levels involved becomes larger the peak gets less important. As $N$ increases and new resonances appear in the tunneling region, those corresponding to very low fields become smaller.

In conclusion, we have studied the reversal of magnetization and the coherence of tunneling when an external magnetic field is rotated instantaneously in systems for a few spin 1/2 particles described by an anisotropic Heisenberg Hamiltonian at $T=0$. Our calculations demonstrate that the model studied for systems with $4<N<11$, for any geometrical configuration and for different anisotropy values exhibits collective tunneling of the magnetization only for some specific resonant values of the magnetic field, at variance with the Stoner–Wohlfarth model that predicts coherent rotation at all fields.

This work has been partially supported by the CICYT of Spain and the European Community.

[1] L. Gunther, Phys. World, **3**, 28 (1990).
[2] D. D. Awschalom, D. P. Di Vincenzo, and J. F. Smyth, Science **258**, 414 (1992).
[3] D. D. Awschalom and D. P. Di Vincenzo, Phys. Today **48**, 43 (1995).
[4] A.J. Legget *et al.*, Rev. Mod. Phys. **59**, 1 (1987).
[5] P. C. E. Stamp, E. M. Chudnovsky, and B. Barbara, Int. J. Mod. Phys. B **6**, 1355 (1992).
[6] E. M. Chudnovsky and L. Gunther, Phys. Rev. Lett. **60**, 661 (1988).
[7] M. Enz and R. Schilling, J. Phys. C **19**, L-711 (1986); G. Scharf, W. F. Wreszinski, and S. L. Van Hemmen, J. Phys. A **20**, 4309 (1987).
[8] E. M. Chudnovsky and D. P. Di Vincenzo, Phys. Rev. B **48**, 10548 (1993).
[9] E. C. Stoner and E. P. Wohlfarth, Philos. Trans. R. Soc. London, Ser. A **240**, 599 (1948), reprinted in IEEE Trans. Magn. **27**, 3475 (1991).
[10] D. D. Awschalom *et al.*, Phys. Rev. Lett. **68**, 3092 (1992); *ibid.* **71**, 4279(E) (1993).
[11] A. Garg, Phys. Rev. Lett. **74**, 1458 (1995); D. D. Awschalom *et al.*, *ibid.* **71**, 4276 (1993); A. Garg, *ibid.* **71**, 4249 (1993).
[12] W. Wernsdorfer *et al.*, J. Magn. Magn. Mater. **145**, 33 (1995).
[13] M. Lederman, D. R. Fredkin, R. O'Barr, S. Schultz, and M. Ozaki, J. Appl. Phys. **75**, 6217 (1994).
[14] P. A. Serena and N. Garcia, in *Quantum Tunneling of the Magnetisation—QTM'94*, edited by B. Barbara and L. Gunther, NATO ASI Series E (Kluwer Academic, Dordrecht, 1995), Vol. 301, pp. 107–120; H. B. Braun. Phys. Rev. Lett. **71**, 3557 (1993); D. García-Pablos *et al.*, these proceedings.
[15] P. de Vries and H. De Raedt, Phys. Rev. B **47**, 7929 (1993).
[16] M. Suzuki, Prog. Theor. Phys. **56**, 1454 (1976).
[17] H. De Raedt, Comp. Rep. **7**, 1 (1987).
[18] D. García-Pablos, P. A. Serena, N. García, and H. De Raedt, Phys. Rev. B **53**, 741 (1996).
[19] A. Garg, Phys. Rev. B **51**, 15161 (1995).

# Frequency mixing phenomena in a bistable system

A. N. Grigorenko, P. I. Nikitin, and G. V. Roschepkin
*General Physics Institute of Russian Academy of Sciences 38 Vavilov Str., Moscow, 117942 Russia*

A response of a bistable system subject to several periodic and random forcing is discussed. It is shown that spectrum components of the response on mixed frequencies demonstrate a noise-induced enhancement typical for stochastic resonance. The quenching of the spectrum harmonics due to an application of a constant force that destroys symmetry of the potential is calculated. The theory is checked on a simple bistable magnetic system: a local part of a domain wall in a thin ferrit–garnet film. © *1996 American Institute of Physics.* [S0021-8979(96)76808-1]

## I. INTRODUCTION

A response of bistable systems subject to periodic and random forcing attracted a lot of interest.[1–7] It was found that a signal, which is a spectrum component of the system response on the frequency of the periodic force, can be enhanced by an application of an additional noise source. As a result, the signal-to-noise ratio $R$ for a bistable system has a peak at some noise strength. This phenomenon is called stochastic resonance (SR). The "quality," $Q$, of SR can be characterized by the ratio of the maximum $R_{\max}$ over the minimum $R_{\min}$ of a SR curve:

$$Q=R_{\max}/R_{\min}, \tag{1}$$

where the SR curve is the dependence of the signal-to-noise ratio (SNR) upon the noise strength $D$. The "canonical" dependence of $R$ upon $D$ is given by[2,3]

$$R=\frac{C}{D^2}\exp\left(-\frac{\Delta U}{D}\right), \tag{2}$$

where $C$ is a constant and $\Delta U$ is the barrier height. One may expect from (1) and (2) that the resonance quality can be arbitrary large. However, this is not true. Equation (2) accounts for transitions between minima and disregards system motion inside the well. Taking this motion into account,[2] we find

$$Q\cong\omega_0/\omega, \tag{3}$$

where $\omega$ is the modulation frequency and $\omega_0$ is the frequency of system vibrations inside the well. Thus, the higher the frequency of the periodic force, the smaller the resonance peak is observed. If the driving frequency is close to the vibration frequency, we see no enhancement of SNR at all.

There is also an experimental problem of conventional SR: an inevitable influence of the driving circuit upon the signal registration circuit.

Both problems can be solved by measurement of spectrum components of the response of a bistable system subject to two different periodic forcing. System motion inside one well is linear for small force amplitudes and does not contribute to spectrum harmonics (signals) on mixed frequencies. So, we can expect to achieve higher values of the resonance quality even for a large driving frequency. In addition, signals shall be measured on frequencies different from those of periodic forcing. This excludes the circuitry problem.

In this paper we show that the spectrum harmonics of the response of a bistable system subject to several periodic forcing in the presence of noise exhibit stochastic resonance behavior. We also discuss the case of an asymmetric bistable potential and check the theory on an isolated magnetic domain wall.

Closing this section, we note that the quality of SR can be characterized by the ratio of signals at the maximum and at the minimum of the noise dependence of the signal: $Q'=S_{\max}/S_{\min}$. This ratio is proportional to $(\omega_0/\omega)^2$ and presents the same feature as $Q$.

## II. THEORY

### A. Model

Let us consider system motion in a symmetric bistable potential $U_0(x)$ exposed to an action of a driving force, $F(t)=f_1\cos(\omega_1 t)+f_2\cos(\omega_2 t)$, a constant force, $h$, and a random force. We use the simple approach to the problem, in which a continuous bistable system is replaced by a discrete system governed by a rate equation.[2] Let $n_+(t)$ be the probability to find the system near the right minimum of the potential and $n_-(t)$ be the probability to find the system near the left minimum. We can write

$$n_+(t)=1-n_-(t)=\int_{x_0}^{+\infty}p(x,t)dx, \tag{4}$$

where $x_0$ is the position of the maximum of the potential and $p(x,t)$ is the probability distribution of the continuous system. The corresponding rate equation is

$$\frac{dn_+}{dt}=-\frac{dn_-}{dt}=W_-(t)n_--W_+(t)n_+, \tag{5}$$

where $W_\pm(t)$ is the transition rate out of the $\pm$ state. The probability density of the discrete system can be found as

$$P(x,t)=n_+\delta(x-x_+)+n_-\delta(x-x_-), \tag{6}$$

where $x_\pm$ is chosen to minimize errors in the calculation of moments.

We consider the case where the noise strength $D$ is not high, so that important integrals, e.g., (4), are concentrated near the minima of the potential. This restriction is given by

$$D\ll a^2\left(\frac{\partial^2 U}{\partial x^2}\right)\Bigg|_{x=x_\pm}. \tag{7}$$

where $2a$ is the distance between minima of the symmetric potential.

 0021-8979/96/79(8)/6113/3/$10.00 © 1996 American Institute of Physics 

In the absence of modulation we have stationary populations

$$n_{\pm 0}=\frac{\exp(\pm ha/D)}{2ch(ha/D)} \tag{8}$$

and $x_{\pm}=\langle x\rangle \pm 2n_{\mp 0}a, \langle x\rangle = a\cdot th(ha/D)$. It is worth noting that $x_+ - x_- = 2(n_{+0}+n_{-0})a = 2a$ even in the presence of the constant force $h$.

We need an expression for transition rates in order to solve time-dependent problem (4). Under the same restriction (7) the rates can be written as[8]

$$W_{\pm}=\frac{\sqrt{U''(x_{\pm})U''(x_0)}}{2\pi}\exp\left[-\frac{U(x_0)-U(x_{\pm})}{D}\right], \tag{9}$$

where $U(x_0)$ is the maximum value of the potential. It is easy to find for the symmetric potential

$$U(x_0)-U(x_{\pm})=\Delta U \pm ha+(h^2/2)([U''(x_0)]^{-1} + [(U''(x_{\pm})]^{-1}), \tag{10}$$

where $\Delta U$ is the barrier in the absence of external forces. We also assume that forces are small ($ha, Fa \ll \Delta U$) and slow ($\omega_1, \omega_2 \ll \omega_0$). Then, the third term in (10) can be neglected and adiabatic approximation can be used, which gives

$$W_{\pm}(t)=\nu \exp\left(-\frac{\Delta U \pm ha \pm F(t)a}{D}\right),$$

$$W_{\pm 0}=\nu \exp\left(-\frac{\Delta U \pm ha}{D}\right). \tag{11}$$

Introducing (11) into (5) and developing all values in series with a small parameter $\epsilon = Fa/D$: $n_+ = n_{+0}+n_{+1}+n_{+2}+\cdots, W_{\pm}=W_{\pm 0}+W_{\pm 1}+W_{\pm 2}+\cdots$, we find

$$\frac{dn_{+0}}{dt}=0=W_{-0}-[W_{+0}+W_{-0}]n_{+0}, \tag{12a}$$

$$\frac{dn_{+1}}{dt}=\frac{W_{-1}W_{+0}-W_{+1}W_{-0}}{W_{+0}+W_{-0}}-[W_{+0}+W_{-0}]n_{+1}, \tag{12b}$$

$$\frac{dn_{+2}}{dt}=-[W_{+1}+W_{-1}]n_{+1}-[W_{+0}+W_{-0}]n_{+2}\cdots . \tag{12c}$$

Equation (12a) gives stationary populations (8), (12b) describes SR in case of nondegenerate minima, (12c) and the following equations describe frequency mixing phemonema. The calculation is straightforward and we present only the results.

### B. A constant force and periodic driving

First, we consider the asymmetric case $h \neq 0$ with only one periodic component $f_1 = f$, $f_2 = 0$. Solving (12b) gives the spectral density $S_1(\omega)$,

$$S(\omega)=\left(4n_{+0}n_{-0}-\frac{2A^2}{B^2+\omega_1^2}\right)\frac{4a^2B}{B^2+\omega^2}+\frac{4\pi a^2A^2}{B^2+\omega_1^2}\delta(\omega_1-\omega) \tag{13}$$

where the coefficients are $A=[2W_{+0}W_{-0}/(W_{+0}+W_{-0})](fa/D)$, $B=W_{+0}+W_{-0}=2\nu_{Kr}ch(ha/D)$, $\nu_{Kr}=\nu_0\exp(-\Delta U/D)$ is the Kramers frequency, and $\nu_0=\omega_0/(2\pi)$. Equation (13) contains all information about SR. It gives the signal

$$S_1=\frac{4\pi f^2a^4}{D^2}\frac{\nu_{Kr}^2}{[4\nu_{Kr}^2ch^2(ha/D)+\omega_1^2]ch^2(ha/D)}, \tag{14}$$

noise

$$N=\frac{8a^2\nu_{Kr}\Delta f}{[4\nu_{Kr}^2ch^2(ha/D)+\omega_1^2]ch(ha/D)}, \tag{15}$$

and the signal-to-noise ratio

$$R=\frac{\pi f^2a^2}{D^2}\cdot\frac{\nu_{Kr}}{2ch(ha/D)\Delta f}=\frac{R_0}{ch(ha/D)}, \tag{16}$$

where $R_0$ is SNR in the absence of the constant force $h$. If $W_{+0}+W_{-0}\gg\omega_1$, then we have $S_1 \cong S_0/ch^4(ha/D)$, where $S_0$ is the signal for the conventional SR.

We draw an important conclusion from Eqs. (14)–(16): SNR and the signal are very sensitive to the symmetry of the bistable potential. Another useful conclusion is connected to the scale of changes of SNR and the signal with $h$. It is clear from Eqs. (14)–(16) that the scale is simply $D/a$. This information can be used to evaluate small constant forces or/and to find parameters of an unknown bistable potential.

### C. A constant force and two periodic drivings

Let us return to the main case where forces $h, f_1, f_2$ are not equal to zero. In order to investigate frequency mixing we should solve linear equations (12.2), (12.3),... subsequently. An analytical solution is possible. However, it is very complicated. For this reason we present the analytical solution for the case $W_{+0}+W_{-0}\gg\omega_1, \omega_2$. Being much simpler, this case contains all essential features of the phenomenon. Then, the signal on the mixed frequencies is

$$S_2(\omega_1\pm\omega_2)=\frac{\pi a^4f_1^2f_2^2}{D^4}\frac{\nu_0^2\exp(-2\Delta U/D)th^2(ha/D)}{4ch^2(ha/D)} \tag{17}$$

and noise is given by (14). Third-order approximation yields

$$S_3(\omega_1\pm 2\omega_2)=\frac{2\pi a^6f_1^2f_2^4}{3D^6}\frac{\nu_0^2\exp(-2\Delta U/D)}{[4\nu_{Kr}^2ch^2(ha/D)+\omega^2]ch^2(ha/D)}. \tag{18}$$

We see that the signals are proportional to $S_n \sim (fa/D)^n\nu_{Kr}^2$, where $n$ is the order of approximation. Consequently, the spectrum harmonics demonstrate typical stochastic resonance behavior. The interesting feature of (17) and (18) is the general property of $S_n$ as a function of $h$. One can see that $S_{2n}, n=1,2,...$ has the minimum at $h=0$, while $S_{2n-1}, n=1,2,...$ has maximum at $h=0$, see also Ref. 4. Moreover, the spectrum components $S_{2n}$ of the response are zero when $h$ is zero. The maximum of second harmonics (17) is reached at $h=D/a$ where the potential is asymmetric.

Again, the scale of signal changes with $h$ is $D/a$. This information can be used for noise evaluation.

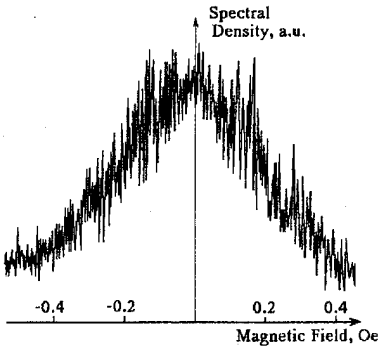



FIG. 1. The signal $S_1(\omega)$ as a function of the constant magnetic field. The sample is ferrit–garnet film with magnetization 50 G, thickness 30 $\mu$m, the anisotropy field 1300 Oe. The frequency is 1 kHz, the length of the studied domain wall part is 5 $\mu$m.

## III. EXPERIMENT

The theory has been checked on an isolated domain wall of a thin ferrit–garnet film. Experimental installations, samples, and adjustment procedures are described in Ref. 9. A position of a local part (5 $\mu$m) of a domain wall pinned between two neighboring microdefects has been measured by means of magnetooptics. The domain wall was subjected to several periodic drivings in the presence of constant and noiselike magnetic fields. The spectrum components of the response were measured by a spectroanalyzer as a function of the noise strength and the constant magnetic field. Figure 1 displays a harmonic of odd order as a function of the magnitude of the constant field. The same dependence for a harmonic of even order is shown in Fig. 2. We note that the function of Fig. 1 has the maximum at zero field, while that of Fig. 2 has the minimum at zero field in agreement with the theory. Figure 3 demonstrates third-order harmonics as a function of $h$ for two different noise strengths. Again, we see qualitative agreement with the theory: the bigger the noise strength, the larger the scale of signal changes. Experiments also confirmed the stochastic resonance dependence of harmonics upon the noise strength.

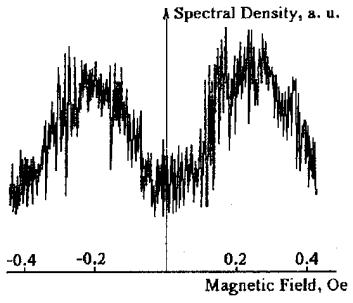



FIG. 2. The signal $S_2(\omega_2-\omega_1)$ as a function of the constant magnetic field. The frequencies are: $\omega_1=3$ kHz, $\omega_2=4$ kHz. The sample is the same as in Fig. 1.

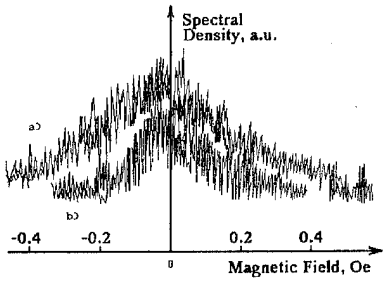



FIG. 3. The signal $S_3(3\omega)$ as a function of the constant magnetic field for two different noise strength. The frequency is 1 kHz, (a) the dimensionless noise strength $D=0.8$ (b) the dimensionless noise strength $D=0.4$. The sample is the same as in Fig. 1.

## IV. CONCLUSION

It has been shown that spectrum harmonics of a bistable system response to periodic driving exhibit noise-induced enhancement. The quality of stochastic resonance has been defined. It has been shown that the quality is larger for harmonics on mixed frequencies. The important dependence of the signals upon the constant force that destroys the symmetry of the potential has been calculated. The theory has been checked on a simple bistable magnetic system—an isolated domain wall pinned between two microdefects.

## ACKNOWLEDGMENTS

This work was supported by International Science Foundation Grant No. M8L000, M8L300, and INTAS Grant No. 94-1720. One author (A.N.G.) thanks the Dzerzhinsky Factory, Makeevka, Ukraine for the help with manuscript preparation.

[1] R. Benzi, A. Sutera, and A. Vulpiani, J. Phys. A **14**, L453 (1981).
[2] B. McNamara and K. Wiesenfelf, Phys. Rev. A **41**, 4854 (1989).
[3] R. F. Fox, Phys. Rev. A **39**, 4148 (1989).
[4] C. Presilla, F. Marchesoni, and L. Gammaitoni, Phys. Rev. A **40**, 2105 (1989).
[5] A. N. Grigorenko, V. I. Konov, and P. I. Nikitin, Sov. JETP Lett. **52**, 593 (1991).
[6] M. Dykman, R. Manella, P. V. E. McClintock, and N. G. Stocks, Phys. Rev. Lett. **68**, 2985 (1992).
[7] S. Vohra and L. Fubiny, Phys. Rev. E **50**, R2391 (1994).
[8] C. W. Gardiner, *Handbook of Stochastic Methods for Physics, Chemistry, and the Natural Sciences* (Springer-Verlag, Berlin, 1983).
[9] A. N. Grigorenko *et al.*, J. Appl. Phys. **76**, 6335 (1994).

# Low temperature magnetic relaxation and quantum tunneling in nanocrystalline particles (abstract)

X. X. Zhang, J. M. Hernandez, E. C. Kroll,[a] R. Ziolo,[a] and J. Tejada
*Department de Fisíca Fonamental, Universidad de Barcelona, Diagonal 647, 08028 Barcelona, Spain*

We report measurements of the magnetic relaxation rate versus temperature for ferrofluid and magnetic-glass samples, which are formed by a modification of nanocomposite material consisting of nanocrystalline $CoFe_2O_4$ and polymer.[1] The magnetic properties of the samples have also been studied by using SHE-SQUID at different temperatures (1.8–300 K) with low and high applied magnetic field (−5 T to 5 T). The magnetic relaxation in two samples show a perfect logarithmic dependence on the time, i.e., $M(t)=M(t_0)[1-S\ \ln(t/t_0)]$, in accordance with the ZFC-FC results which indicate that there is wide energy distribution. The temperature independence of magnetic viscosity $S\equiv[1/M(t_0)dM/d]\ln t$ below several Kelvin for the two samples gives clear evidence of macroscopic quantum tunneling of magnetization, in accordance with current theories of quantum tunneling of magnetization. © *1996 American Institute of Physics.* [S0021-8979(96)70108-6]

---

[a]Also with Xerox Webster Research Center, Xerox Corporation, 800 Philips Rd. 0114-39D, Webster, NY 14580.

[1]R. F. Ziolo *et al.*, Science **257**, 219 (1992).

 0021-8979/96/79(8)/6116/1/$10.00 © 1996 American Institute of Physics

# Annealing and geometric effects in the magneto-impedance of amorphous $Co_{70.4}Fe_{4.6}Si_{15}B_{10}$ alloys

R. L. Sommer[a] and C. L. Chien
*Department of Physics and Astronomy, The Johns Hopkins University, Baltimore, Maryland 21218*

R. Hasegawa
*Allied Signal Inc., Amorphous Metals, 6 Eastmans Road, Parsippany, New Jersey 07054*

Giant magneto-impedance effects in different measuring geometries (longitudinal and transverse) of amorphous $Co_{70.4}Fe_{4.6}Si_{15}B_{10}$ ribbons under different field annealing have been studied at various frequencies (0.1 Hz–2 MHz). For suitably annealed samples, rich peak features have been observed in longitudinal MI measurements. For transverse MI measurements, a large effect magnitude has also been found. These results are discussed in terms of the effects of the magnetic annealing and measurement geometries on the effective permeability. © *1996 American Institute of Physics.* [S0021-8979(96)76908-8]

Recently, frequency and field dependent impedance has been observed in amorphous materials with nearly zero magnetostriction.[1–3] The origin of the pronounced magnetoimpedance (MI) effects appears to be the field dependence of the effective transverse permeability, which is better understood in the case of amorphous wires.[2] Very recently,[4] we reported the effects of field-annealing geometry, highlighting the role of transverse anisotropy on the longitudinal MI (LMI). However, many questions concerning the nature of the MI and the rich spectra of the MI effects remain to be addressed. A key question is the role of the measurement geometry on the MI. Early reports for transverse MI (TMI), describe a very insignificant effect.[1,3] We show in this work that the TMI effects not only exist, they have the same order of magnitude as the LMI. We also report on the effect of the field-annealing and measurement geometries of amorphous $Co_{70.4}Fe_{4.6}Si_{15}B_{10}$ ribbons. The dependency of MI on frequency (up to 2 MHz) is also reported.

Samples from adjacent portions of the same amorphous $Co_{70.4}Fe_{4.6}Si_{15}B_{10}$ ribbon were cut into sections of $10\times1$ mm$^2$. The average thickness of the ribbon was 20 $\mu$m and the resistivity about 115 m$\Omega$ cm. Four-terminal MI measurements with In metal contacts were used in the low frequency range (0.1 Hz$\leqslant f\leqslant$100 kHz). Sinusoidal current (up to 20 mA) was provided by a low noise current source, and the signal detected by a dual-channel lock-in amplifier. The results are expressed in terms of the impedance $Z(I_0,f,H)=R(I_0,f,H)+iX(I_0,f,H)=(V_R+iV_X)/I_0$. In the low frequency range, the dc field was provided by an electromagnet with fields up to 5 kOe. For the high frequency (rf range) measurements (100 kHz$\leqslant f\leqslant$2 MHz), a three-terminal method was used. The rf signal was amplitude modulated in order to allow lock-in detection of the signal proportional to the impedance $Z(I_0,f,H)$. The dc field in rf measurements was provided by a long solenoid with a maximum field of 150 Oe and a field uniformity better than 2%. Magnetic annealing ($T_A=300$ °C) was performed in flowing Ar gas with zero or 2 kOe field oriented either parallel to the long direction of the samples (longitudinal annealing) or along the short direction, but still in the sample's plane (transverse anneal). In what follows, the MI effect will be expressed as $\Delta Z/Z(H_{max})$, $\Delta R/R(H_{max})$, and $\Delta X/R(H_{max})$, where $H_{max}=5$ kOe for the low frequency and $H_{max}=150$ Oe for the high frequency range.

In Fig. 1 the longitudinal magnetoimpedance (LMI) results for the samples subjected to different annealing geometries are shown. These measurements were taken at 100 kHz and 20 mA peak value for the probe current. There is a large LMI effect in the as-produced sample [Fig. 1(a)] with two round peaks. Upon annealing at zero field, the magnitude of the effect decreases significantly [Fig. 1(b)], but the two round peaks can still be observable. Longitudinal annealing produces a very small effect [see Fig. 1(c)] and the overall shape is a wide plateau with no resolvable peak. Transverse annealing recovers the large MI effect [Fig. 1(d)] with very

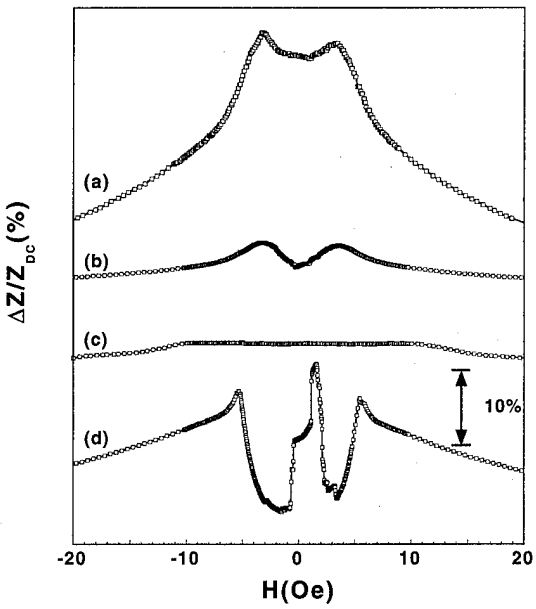



FIG. 1. Longitudinal magnetoimpedance (LMI) results at $f=100$ kHz and 20 mA peak probe current of (a) as-cast sample and samples subjected to different annealing conditions at $T_A=300$ °C: (b) at $H_A=0$, (c) longitudinally annealed at $H_A=2$ kOe, and (d) transversely annealed at $H_A=2$ kOe. The results are expressed as $\Delta R/R(H_{max})$ and $\Delta X/R(H_{max})$. All graphs share the same vertical scale indicated by the 10% mark.

[a]Permanent address: Depto. de Física, UFSM, 97119-900 Santa Maria RS, Brasil.

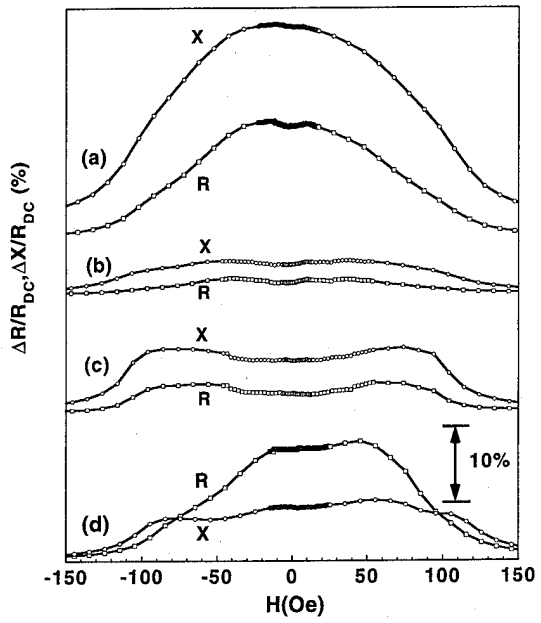



FIG. 2. Transverse magnetoimpedance (TMI) for the same samples shown in Fig. 1.

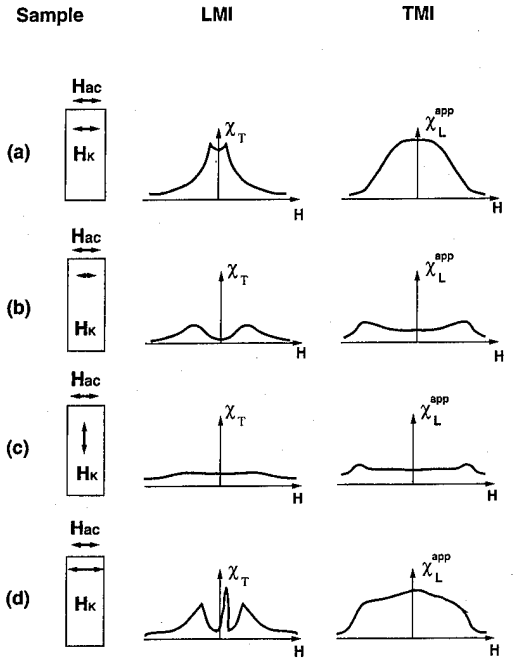



FIG. 3. Schematics showing the effects of annealing, measurement geometries, and induced anisotropies on longitudinal (LMI) and transverse (TMI) magnetoimpedance for (a) as-cast, (b) annealed at zero field, (c) longitudinally annealed, and (d) transversely annealed samples. The relevant transverse susceptibility (second column) for LMI and apparent longitudinal susceptibility for TMI (third column) are also shown. For the LMI the dc field $H$ is parallel to the sample's length and for the TMI the field is parallel to $H_{ac}$.

well-defined peak structure. It may be noted that LMI occurs in very low fields, in the field range of only $\pm 10$ Oe.

It should be mentioned that in Fig. 1(a), 1(b), and 1(c), the decreasing-field curves (not shown) and the increasing-field curves (shown) are essentially the same. In Fig. 1(d) however, the two shoulder peaks at $\pm 6$ Oe are reversible, whereas the central peak is hysteretic; the central peak at 2 Oe in Fig. 1(d) appears at $-2$ Oe in the decreasing field curve.

In Fig. 2, the transverse magneto-impedance (TMI) measurements for the same samples of Fig. 1 are shown. A large effect is again observed in the as-cast sample [Fig. 2(a)] which shows a bell-shaped curve without many of the details present in the LMI. For the sample annealed in a zero field [Fig. 2(b)], the magnitude of the effect is much smaller than the as-cast case, in a way consistent with the LMI. For the longitudinally annealed sample [Fig. 2(c)], the TMI shows broad peaks in the resistance and reactance curves. For the transversely annealed sample [Fig. 2(d)], the large effect in TMI is again retrieved, in a manner similar to that of the LMI. Although still showing bell-shaped curves, the $R$ vs $H$ and $X$ vs $H$ curves indicate some peak structure, which contains as many as four broad peaks. As shown in Fig. 2, regardless of the annealing conditions, the MI effect for the reactance part ($\Delta X/R_{dc}$) is usually larger than that of the resistance part ($\Delta R/R_{dc}$), except for the transversely annealed sample.

It should be noted that the principal difference between LMI and TMI is that the field range in TMI is about one order of magnitude *larger* than those of the LMI. If one were guided by the LMI results shown in Fig. 1 and attempted to measure TMI using only small external fields, one would *not* have observed a large TMI effect. This may explain why TMI, with magnitude similar to that of LMI, was not reported earlier.[1,3]

The differences between the LMI and the TMI measurements can be understood in terms of the effect of the annealing and measurement geometry on the effective differential permeability, the underlying quantity responsible for the MI effects. It is well accepted that in LMI, there are different regimes in high permeability materials, depending on the relative values of the sample thickness $t$ and the skin depth length:[2] $\delta_m = c/\sqrt{2\pi\omega\sigma\mu_{\text{eff}}}$, where $\sigma$ and $\mu_{\text{eff}}$ are the conductivity and the effective differential permeability of the material, $\omega$ the angular frequency, and $c$ is the speed of light. The field and frequency dependence of the permeability $\mu_{\text{eff}}=1+\chi_{\text{eff}}$ play a central role in defining the magnitude of the MI and the peak structure observed.

It is a well-known fact[5] that the as-cast samples already have a small amount of anisotropy induced during the fabrication process, with an effective anisotropy field of $H_K'$, as schematically shown in Fig. 3(a). Upon annealing in the zero field, part of this anisotropy is relaxed, but not eliminated. A perpendicular component of the anisotropy with respect to the probe current is still present in both the LMI and the TMI cases, as indicated in Fig. 3(b). For the longitudinally annealed sample [Fig. 3(c)], a larger part of the anisotropy is parallel to the long direction of the sample, whereas in the case of the transverse-annealed sample [Fig. 3(d)], a larger part of the anisotropy is induced perpendicularly to the long direction of the sample. The geometry of measurement defines which permeability is important for the MI. In all LMI measurements, the field produced by the probe current $H_{ac}$ is perpendicular to the applied dc field $H$. The magnetization

processes produced by the probe current will then be described by the transverse differential susceptibility $\chi_T$.[6] As a consequence, $\chi_T$ will be the relevant susceptibility for the LMI. On the other hand, in TMI, the field generated by the probe current $H_{ac}$ and the applied dc field $H$ are parallel to each other and to the average dc magnetization. In this case the magnetization processes produced by the probe current will be described by the longitudinal differential susceptibility $\chi_L$,[6] which is the relevant one for the TMI.

The details of the field dependence of the susceptibilities, and hence the peak structures in the MI, are the results of the relative orientation of the field generated by the probe current $H_{ac}$, the anisotropy field $H_K$, and the applied field $H$. In the second column of Fig. 3, the expected behavior of $\chi_T$ vs $H$ curve, relevant to LMI, is schematically shown for each annealing geometry. The demagnetization field in LMI has a negligible contribution to the internal field because $H_i = H - 4\pi D_L M$, and $D_L$ is small. For TMI, the longitudinal susceptibility $\chi_L$ is of relevance. Furthermore, in this case, the demagnetization field has a large effect; it not only influences the internal field via $H_i = H - 4\pi D_T M$, but more importantly, it also places a *limit* for the longitudinal susceptibility $\chi_L$.[7] The apparent susceptibility is $\chi_L^{app} = \chi_L/(1 + 4\pi \cdot D_T\chi_L)$, which is $\chi_L$ corrected for demagnetizing effects. In the limit that $\chi_L$ is large, the apparent susceptibility will be given by $\chi_L^{app} \approx 1/4\pi \cdot D_T$, which together with the smaller internal field produce the bell-shaped curves for the transverse measurements over a large range of applied field $H$. The expected apparent differential susceptibility curves for the various samples are schematically represented in the third column of Fig. 3. The demagnetization effects will always be present in the TMI, regardless of the details of the field dependence of the differential permeability or the annealing geometry. The field dependence of the intrinsic $\chi_L$ is therefore masked.

The LMI effects, hardly influenced by the demagnetizing effects, provide the actual field dependence of $\chi_T$, with which one can unravel the processes that contribute to the peak structure of the LMI and $\chi_T$. As mentioned earlier, the as-cast sample already has anisotropy.[5] It is well known that after transverse annealing, the transverse susceptibility ($\chi_T$) develops a peak at $H = H_K$.[6,8] We therefore identify the shoulder peaks in Fig. 1(d), located at $\pm 6$ Oe, as $H_K$.

The central peaks in the transverse-annealed sample can be attributed to a maximum in the permeability associated to the domain wall (DW) motion.[9] This identification is consistent with the fact that the central peaks, located at $\pm 2$ Oe, are hysteretic, as mentioned earlier. The susceptibility can be described as $\chi = \chi_{DW} + \chi_{rot}$, where $\chi_{DW}$ is the susceptibility associated with domain wall motion and $\chi_{rot}$ is the susceptibility associated with the rotation process. This hypothesis can be tested by high frequency measurements, because these susceptibilities ($\chi_{DW}$ and $\chi_{rot}$) have different attenuation constants due to their different nature. In metallic samples, including amorphous materials, DW motion is attenuated at lower frequencies, when compared with the rotation process.

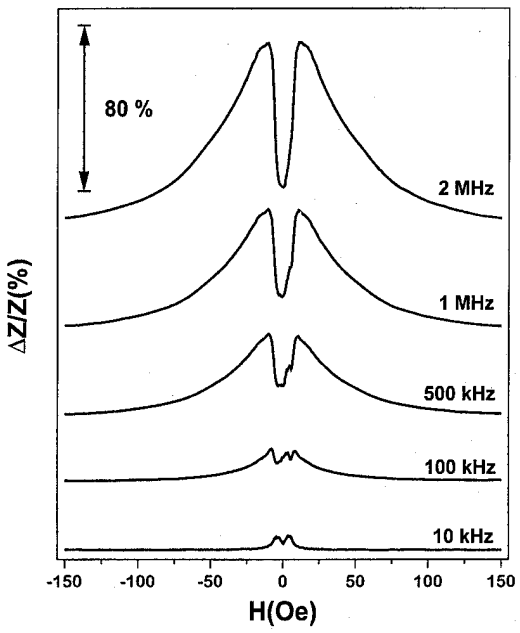



FIG. 4. The results of LMI at 40 mA at various frequencies for the transversely annealed sample.

The LMI vs $H$ curves for the sample annealed under a transverse field are shown in Fig. 4 for various frequencies. Above 100 kHz, while the amplitude of the shoulder peaks increases, the amplitude of the central peaks *decreases* as the frequency increases and vanishes for $f \geq 2$ MHz. Thus the vanishing central peak in this transverse-annealed sample corroborate the assertion that the central peaks are associated with DW motion as proposed[4] and described above. It is also noted that the magnitude of the LMI is very high, increasing as $f^{1/2}$ and reaching more than 150% at high frequencies. The width of the shoulder peaks also broadens with frequency. These results will be described elsewhere.

The support of ONR Grant No. N00014-91-J-1633 and CNPq of Brazil is greatly appreciated.

[1] F. L. A. Machado, C. S. Martins, and S. M. Rezende, Phys. Rev. B **51**, 3926 (1995).
[2] L. V. Panina, K. Mohri, T. Uchiyama, and M. Noda, IEEE Trans. Magn. **31**, 1249 (1995).
[3] R. S. Beach and A. E. Berkowitz, J. Appl. Phys. **76**, 6209 (1994).
[4] R. L. Sommer and C. L. Chien, Appl. Phys. Lett. **67**, 857 (1995).
[5] H. Fujimori, in *Amorphous Metallic Alloys*, edited by F. E. Lubosrky (Butterworths, London, 1983), p. 300.
[6] H. Hoffmann, Phys. Status Solidi **33**, 175 (1969).
[7] R. L. Sommer and C. L. Chien, these proceedings.
[8] W. D. Doyle, X. He, and P. Tang, J. Appl. Phys. **73**, 5995 (1993).
[9] R. Kolano, M. Kuzminski, and W. Gawior, J. Magn. Magn. Mater. **133**, 321 (1994).

# Size dependence of the magnetoresistance in submicron FeNi wires

A. O. Adeyeye, J. A. C. Bland, C. Daboo, Jaeyong Lee, U. Ebels, and H. Ahmed
*Cavendish Laboratory, Madingley Road, Cambridge, CB3 OHE, United Kingdom*

The field-dependent magnetoresistance (MR) characteristic and magnetic hysteresis behavior has been studied in 300–500 Å thickness $Ni_{80}Fe_{20}$ wires of variable width ($w$) in the range from 0.2 to 10 $\mu$m. As the width of the wire decreases, a marked increase in the easy axis coercive field is seen for fields applied along the wire axis and the form of the MR characteristic is markedly modified for the in-plane perpendicular hard axis direction with a large field-dependent MR response observed for applied field strengths exceeding the edge demagnetizing field. The low field hard axis results are discussed in terms of an inhomogeneous spin configuration across the width of the wires arising from the spatial variation of the demagnetizing field. © *1996 American Institute of Physics.* [S0021-8979(96)77008-7]

The size-dependence of the magnetization reversal process in submicron structures provides an important opportunity in testing micromagnetic models and in exploring magnetoresistance effects associated with the modified spin ordering arising from the reduced dimensions. Advances in fabrication techniques based on advanced electron lithography together with recent developments in micromagnetic computational techniques have opened new perspectives in this field. An understanding of the magnetization reversal processes and magnetoresistance (MR) response in small ferromagnetic elements is also important for the design and optimization of miniature MR heads for ultrahigh density data storage applications.[1] Whereas the magnetoresistance properties of micron-range permalloy thin films have already been extensively investigated,[2–4] in the present work we present the results of a systematic study of the magnetization reversal process in submicron $Ni_{80}Fe_{20}$ wires fabricated using advanced lithography techniques. We show that striking new effects are observed in the reversal processes, leading to strong variations in the MR response at large fields.

An ultra high vacuum system with a base pressure of $5\times10^{-10}$ Torr was used to prepare continuous film structures of the form 30 Å Au/t $Ni_{80}Fe_{20}$/GaAs(001) with $t=300$ Å and $t=500$ Å. The $Ni_{80}Fe_{20}$ layers were deposited at a rate of 2.5 Å/min. The pressure during growth was $2.5\times10^{-9}$ Torr while the substrate was held at 30 °C. The film was annealed at 120 °C for 30 min to remove the uniaxial anisotropy induced during growth. $Ni_{80}Fe_{20}$ wire arrays of variable width ($w$) in the range from 0.2 to 10 $\mu$m were fabricated using electron beam lithography and optimized pattern transfer techniques based on a combination of dry and wet etching. The separation ($s$) between wires is 1–10 times the wire width so that the wires are weakly interacting (low $s$) or well isolated (large $s$).

The pattern was first transferred to the Au layer by sputtering. The pattern is further transferred to the underlying $Ni_{80}Fe_{20}$ layer using wet chemical etching with a solution of $HCl:HNO_3:H_2O$(1:25:200). This is made possible because of the high etch selectivity between Au and $Ni_{80}Fe_{20}$. Complete removal of $Ni_{80}Fe_{20}$ in the gap between array structures was confirmed using energy dispersive x-ray analysis (EDX). Details of the fabrication process are described in Ref. 5.

For MR measurements, electrical contacts to the arrays were made using standard optical lithography, metallization and liftoff of 20 nm Cr/300 nm Au. The wires are each of length 250 $\mu$m and extend over a distance of 250 $\mu$m. An initial determination of the device resistance at zero applied field was made and it was found that the resistance scaled approximately inversely with the proportion of metal remaining after etching. A dc current of 1 mA (Ref. 6) was passed along the wires of each grating and the resistance was recorded automatically using a four terminal method as the magnetic field was swept. The magnetic field was applied in the plane of the structures for all the measurements reported since the magnetization of the continuous films lies in plane. MOKE magnetometry measurements were made in the longitudinal geometry using a stabilized HeNe laser source and a focused spot size at the sample of 0.2 mm.

The field-dependent magnetization ($M-H$) loops of the grating structures were measured with the field parallel ($\Theta=0°$) and perpendicular ($\Theta=90°$) to the wire axis in order to investigate the effect of shape anisotropy. Figure 1(a) shows the results of the MOKE measurements on a 300-Å-thick $Ni_{80}Fe_{20}$ grating with $w=0.5$ $\mu$m and $s=0.5$ $\mu$m. This measurement is compared with that of the reference sample (unstructured material) that went through all the processing steps but which displays almost zero anisotropy. The MOKE measurements on the unstructured material display the same $M-H$ behavior in both orientations as that of the original film prior to fabrication. This shows that the magnetic properties of the film are preserved during processing. There is a marked increase in the saturation field of the $M-H$ loop obtained along the hard axis ($\Theta=90°$) in the 0.5 $\mu$m wire, in comparison with the loops obtained along the easy axis ($\Theta=0°$) and for the reference film, due to the magnetic shape anisotropy. A surprising feature of the hard axis MOKE data of Fig. 1(a) is that it is asymmetric with applied field implying that different energy states are explored according to the sense of the field sweep, presumably due to incomplete saturation at the wire edge. Presented in Fig. 1(b) are the easy axis coercive fields derived from experimental hysteresis loops for various wire widths. The increase in the coercive field with reduced width is in qualitative agreement with the results of earlier work.[7,8]

In Fig. 2(a) the magnetoresistance (MR) response to

 0021-8979/96/79(8)/6120/3/$10.00 © 1996 American Institute of Physics

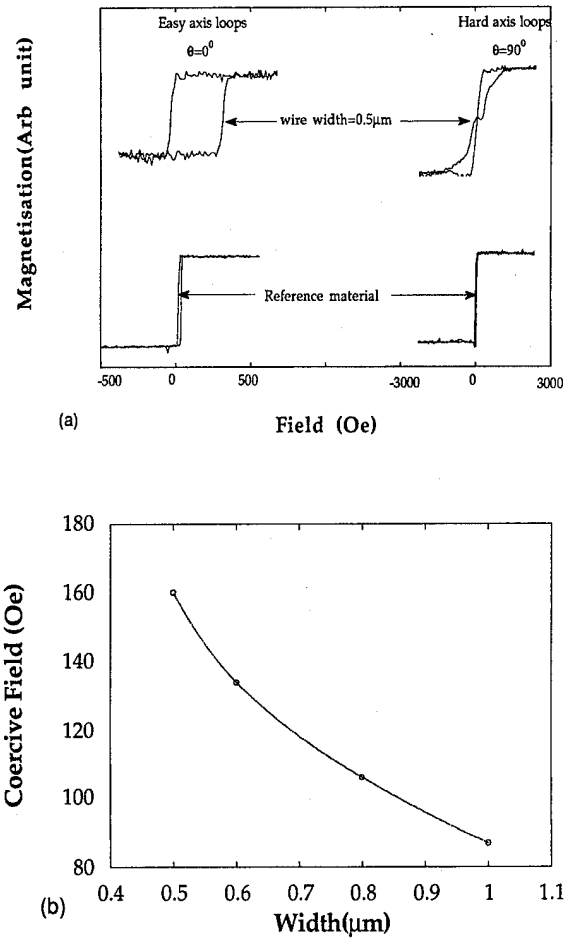



FIG. 1. (a) MOKE loops of a wire array with wire width $w=0.5$ $\mu$m and separation $s=0.5$ $\mu$m (top) and of the unstructured material (bottom). The thickness of the film is 300 Å. (b) The easy axis coercive fields derived from the experimental hysteresis loops for various wire widths.

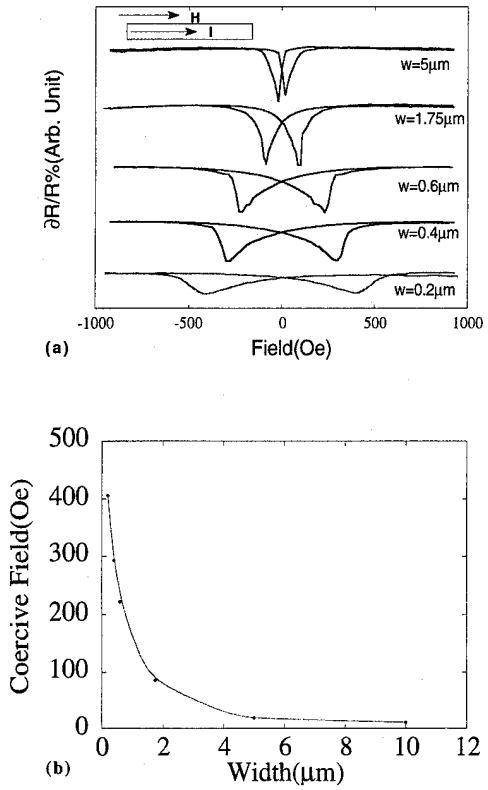



FIG. 2. (a) The magnetoresistance (MR) response to fields applied along the easy axis for a wire grating with film thickness $t=500$ Å and $s=10$ $w$ for various wire widths. (b) The coercive field corresponding to the sharp minima in the MR curves in (a) plotted as a function of the wire width.

fields applied along the easy axis is presented for various wire widths, plotted as a percentage defined as

$$\frac{\partial R}{R}=\left[\frac{R(H)-R(H=0)}{R(H=0)}\right].$$

The sharp minimum in the longitudinal MR curve corresponds to the switching of the magnetization in the wires, and therefore it is taken as the coercive field of the wire. The coercive field corresponding to the minimum of the MR curves is plotted as a function of the wire width in Fig. 2(b). A marked increase in the coercive field $H_c$ with decreasing width is again observed. This has been explained by Kryder[9] as resulting from the buckling of magnetization perpendicular to the length of the wire. This leads to the formation of domain walls perpendicular to the wire. These walls do not move, but block the reverse domain from propagating down the wire because the width of the wire is smaller than the buckling wavelength. Edge wall curling is expected to occur for small $w$. A related result has been obtained by Smyth *et al.*[10] for small particles where a corresponding transition to a spin vortex process is observed with reduced particle size.

Figure 3(a) shows the MR response to a hard axis field for various wire widths. A near reversible behavior, almost symmetric with field strength is now obtained, indicating that spin rotation processes rather than domain wall motion occur. The dependence of the MR curves on the orientation of the applied field will be described elsewhere.[11] The form of the MR–$H$ curve is greatly changed according to the wire width. A striking feature is the large MR response at high fields exceeding the maximum value of the demagnetizing field $M_s$ which occurs at the edge of the wire (approx. 1T). A reduction in the magnitude of the maximum magnetoresistance ratio with reducing wire width is also observed and we note that the easy axis peak MR also reduces with reducing wire width.

The observed behavior can be attributed to the anisotropic magnetoresistance effect[7] at low field (i.e., beneath the maximum demagnetizing field). The change in response with wire width can be partly explained in terms of the inhomogeneous demagnetizing field across the width of the wires resulting from the spatial variation of the dipolar field due to the edge charges.[7] As the wire width is reduced, a greater proportion of the current flows in the regions in the vicinity of the edges of the wires where the demagnetizing field is large, and hence the response extends to larger applied fields. The average hard axis saturation field can be estimated as[12] (SI units)

$$H_s\approx\frac{3}{2}H_d=\frac{3}{2}\left(\frac{t}{w}\right)M_s,$$

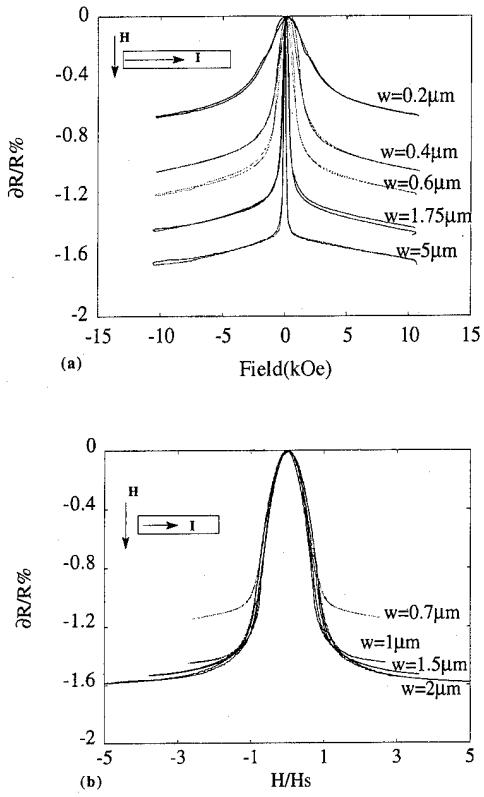



FIG. 3. (a) The MR response to fields applied along the hard axis for various wire widths for a grating structure with $t=500$ Å and $s=10\ w$. (b) MR vs reduced field $h=H/H_s$ as a function of the wire width for a grating structure with $t=500$ Å and $s=w$.

where $H_d$ represents an estimate of the demagnetizing field at the wire center, $t$ is the film thickness, $w$ the wire width, and $M_s$ is the saturation magnetization of the material and the magnetic anisotropy of the constituent film is assumed to be zero. From the results of Fig. 3(a), $H_s$ can be estimated for various values of wire width. Figure 3(b) shows a plot of the MR vs the reduced field ($h$) as a function of the wire width, where $h=H/H_s$. We find that a near universal, parabolic behavior is obtained for $H_a \leqslant H_s$. This result is expected from a simple magnetostatic model of the MR response for fields applied along the hard axis which assumes coherent rotation of the spins. For fields smaller than the average demagnetizing field only the spins in the interior region of the wire rotate significantly with applied field and the average rotation angle will initially scale with $h$. For $H_a > H_s$ a significant deviation of the response from the universal curve with reducing wire width is seen. The deviation from the universal behavior at high fields is clearly associated with the spin configuration at the edge regions of the wire where the demagnetizing field approaches the maximum value given by $M_s$ and a scaling behavior is no longer expected. However for fields larger than the demagnetizing field at the edge, the resistance continues to vary with field in an almost linear fashion. It is possible that the spin configuration at the edge of the wire is greatly modified with reducing width, for example due to an edge pinning effect but it is

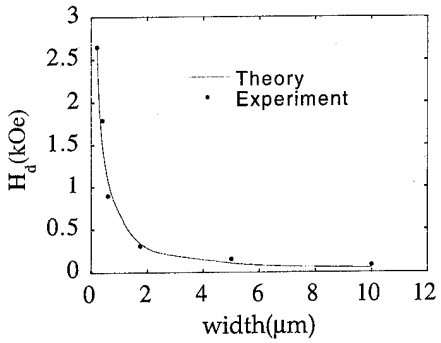



FIG. 4. The experimentally determined and calculated values of the demagnetizing field $H_d$ as a function of the wire width for a grating structure with $t=500$ Å and $s=10\ w$.

also possible that a transverse magnetoresistance effect seen in thick Ni films contributes.[13] The experimentally determined and calculated values of the field $H_d$ are plotted as a function of the wire width in Fig. 4. Reasonable agreement between the calculated and the experimentally determined values is obtained. However in order to understand the origin of the high field behavior, further computational and experimental studies are clearly needed.

In summary, we have studied the magnetization reversal process in submicrometer $Ni_{80}Fe_{20}$ wires of variable width ($w$) in the range from 0.2 $\mu$m to 10 $\mu$m using magnetoresistive measurements and MOKE magnetometry. We have observed a marked increase in the coercive field as the width of the wire decreases, in agreement with earlier studies. A striking feature observed is the large MR response at high fields. The departure from a universal form of the low field MR characteristic may be explained in terms of an inhomogeneous spin configuration across the width of the wires resulting from the spatial variation of the demagnetizing field but the origin of the high field behavior is unclear. We hope that these measurements will stimulate accurate micromagnetic simulations of the edge spin configurations.


[1] S. W. Yuan and H. N. Bertram, J. Appl. Phys. **73**, 6235 (1994).
[2] S. K. Decker and C. Tsang, IEEE Trans. Magn. **16**, 643 (1980).
[3] C. Sang, J. Appl. Phys. **55**, 2226 (1984).
[4] B. W. Corb, J. Appl. Phys. **63**, 2941 (1988).
[5] A. O. Adeyeye, J. A. C. Bland, and H. Ahmed (to be published).
[6] The effect of self fields generated by the applied current has been reported for example in R. W. Cross, S. E. Russek, S. C. Sanders, M. R. Parker, J. A. Barbard, and S. A. Hossain, IEEE Trans. Magn. **30**, 3825 (1994). In the present case the magnetic field generated by the probe current is small compared with all relevant fields for both the easy and hard shape axis direction, even in the smallest wire, and its effect is therefore neglected.
[7] C. Shearwood, S. J. Blundell, M. J. Baird, J. A. C. Bland, M. Gester, H. Ahmed, and H. P. Hughes, J. Appl. Phys. **75**, 5249 (1994).
[8] A. Maeda, M. Kume, T. Ogura, K. Kuroki, T. Yamada, M. Nishikawa, and Y. Harada, J. Appl. Phys. **76**, 6668 (1994).
[9] M. H. Kryder, K. Y. Ahn, N. J. Mazzeo, S. Schwarzi, and S. M. Kane, IEEE Trans. Magn. **16**, 99 (1988).
[10] J. E. Smyth, S. Schultz, D. K. Fredkin, D. P. Kern, S. A. Rishton, H. Schmid, M. Cali, and T. R. Koehler, J. Appl. Phys. **69**, 5262 (1991).
[11] A. O. Adeyeye, C. Daboo, J. A. C. Bland, and H. Ahmed, submitted to Phys. Rev. B.
[12] C. H. Bajorek, C. Coker, L. T. Romankiw, and D. A. Thompson, IBM J. Res. Develop. 542 (1974).
[13] T. T. Chen and V. A. Marsocci, J. Appl. Phys. **43**, 1554 (1972).

# Effect of interstrip gap on the sensitivity of high sensitivity magnetoresistive transducers

Bharat B. Pant
*Solid State Electronics Center, Honeywell Incorporated, 12001 State Highway 55, Plymouth, Minnesota 55441*

For high sensitivity magnetoresistive (MR) transducers, the role of interstrip gap is examined as a design parameter. This is modeled using analytic and numerical approximations. As the gap is narrowed the range of linearity of the MR transducer decreases and the sensitivity increases. For gap/width ratio exceeding 1.8 the strips behave essentially as isolated strips. An example using typical design parameters shows that the minimum detectable field is reduced from 6.3 $\mu$Oe/$\sqrt{\text{Hz}}$ to 3.6 $\mu$Oe/$\sqrt{\text{Hz}}$ as gap/width ratio is reduced from $\infty$ to 0.1. © *1996 American Institute of Physics.* [S0021-8979(96)77108-3]

## I. INTRODUCTION

Magnetoresistive (MR) transducers for low field applications requiring minimum detectable field ($h_{\min}$) in the range of 1 $\mu$Oe–1 mOe are typically made of long strips of thin films of MR material (e.g., NiFe) of thickness $t\sim100$ Å, width $W\sim10$ $\mu$m, and length $L\sim100$ $\mu$m.[1–3] The response of the MR transducer to applied field (sensitivity, range of linearity of the transfer function, etc.) is determined by these dimensional parameters and material parameters—saturation magnetization $M_S$, anisotropy $H_K$, easy axis angle $\gamma$, and exchange constant $A$. For easy axis parallel to the long dimension of the strip the field scale $H_S=H_K+H_D$, where demagnetizing field $H_D\simeq4\pi M_S t/W$, plays an important role in determining the performance parameter[3]—range of linearity $\propto H_S$, and sensitivity $\propto 1/H_S$.

Practical transducers requiring low power consumption must pack several such strips in parallel on Silicon (or other substrates) connected electrically in series to obtain a resistance $\sim1k\Omega$ or higher. A typical interstrip gap $g$ is 1–10 $\mu$m. The effect of proximity is to reduce the effective demagnetizing field[1] in the strips thus reducing the field $H_S$. The response curve of the transducer saturates at a lower value of applied field, and has higher sensitivity compared to an isolated strip.

Other investigators[1,2] have modeled the response of parallel arrays of MR strips as part of a more general set of design parameters. In this paper we elucidate the role played specifically by the interstrip gap. Along with the $t/W$ ratio, the $g/W$ ratio emerges as an important design parameter that can be used to tailor the response of MR transducers. Above a certain value of this ratio a parallel array of strips behaves essentially as an isolated strip. We also calculate the improvement in $h_{\min}$ obtained for realistic transducer designs by narrowing the interstrip gap.

## II. MODEL

Figure 1 shows three parallel strips subjected to an applied field perpendicular to the long dimension of the strips. The material easy axis is parallel to the long dimension. The magnetization rotates toward the applied field. As the magnetization rotates, lines of north (+) and south (−) poles are created at the upper and lower edges, respectively, resulting in demagnetizing field opposite to the direction of rotation.

Focusing on the central strip, the demagnetizing field inside is the sum of fields from its own edges, plus stray field contributions from the edges of other strips. The edges of the three strips are labeled (0,0′), (1,2), and (1′,2′). The stray field from the bottom edge 1 of the strip above and the top edge 1′ of the strip below is, in opposite direction to and lower in magnitude than, the internal demagnetizing field of the central strip. Moving further out, the stray field from the edges (2,2′) is, in opposite direction to and weaker than, the field from edges (1,1′). In the case of an infinite number of strips parallel to each other the demagnetizing field at any strip is given by the sum of an infinite series whose terms are successively smaller in magnitude, and of alternating sign. The total demagnetizing field is smaller than that of an isolated strip for a given rotation of magnetization. This results in a less stiff behavior of a parallel array of strips compared to an isolated one.

As an initial approximation, we treat the magnetization as uniform across the width of the strip, and use the ellipsoidal approximation which has been shown to be adequate for strips of dimensions $t\ll W\ll L$.[3] The demagnetizing field from the two pairs of edges $(2n,2n')$ and $(2n+1)$, $(2n+1)')$, $n=0,1,...$ is

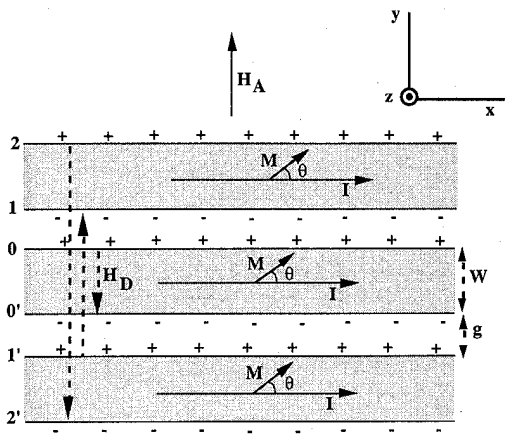



FIG. 1. A parallel array of magnetoresistive strips.

 0021-8979/96/79(8)/6123/3/$10.00 © 1996 American Institute of Physics 

$$H_D = -4\pi M_S \frac{t}{W}\left(\frac{1}{(2n+1)+2nr} - \frac{1}{(2n+1)+(2n+2)r}\right), \quad (1)$$

where $r=g/W$. The sum over infinite array gives

$$H_D = -4\pi M_S \frac{t}{W}\alpha(r),$$
$$\alpha(r) = \frac{2r}{1+2r} + \frac{r}{2(1+r)^2}\left(\frac{\pi^2}{2}-4\right). \quad (2)$$

In arriving at the expression for $\alpha(r)$ the infinite sum over the strips is converted into an integral,[4] which is then expanded to linear order in $r/(1+r)$, ignoring higher order terms.

In the limit of $r\to 0$, the factor $\alpha(r)\to 0$; in the opposite limit of $r\to\infty$, $\alpha(r)\to 1$. The first limit corresponds to the strips coming in physical contact, in which case there is no demagnetizing field, and the second limit corresponds to an isolated strip. In both cases Eq. (2) yields physically sensible limits for the demagnetizing field. Note that for $g/W$ ratio exceeding 3, the proximity effect is negligible; $\alpha(3)=0.94$.

A more exact analysis is performed using numerical methods. In Fig. 1 assume that magnetization **M** varies along the width ($y$ axis) and is constant through the thickness ($z$ axis). We also assume that the strip is infinite along the length ($x$ axis) and the magnetization profile is translationally invariant along this axis. We define a unit length magnetization vector $\mathbf{m}=(m_x,m_y,m_z)$ using $\mathbf{M}=M_S\mathbf{m}$. The strip width is divided into $N$ equal bins. The continuous magnetization profile is approximated by a discrete magnetization profile $\mathbf{m}_i$, $i=1,\ldots,N$. The demagnetizing field in real space is given as the weighted sum over $(m_{yi},m_{zi})$, $i=1,\ldots,N$, the weighting factors being the pairwise interaction kernels between bins.

Two different representations of these interaction kernels are calculated. For an isolated strip the continuous magnetostatic Greens's function[5] is discretized, integrated along the $x$ axis and averaged over the width of the source bin. For the infinite array of parallel strips we employ the FFT method to calculate the demagnetizing field. Magnetization and interaction kernels are expressed in the Fourier space.[6] The FFT method—computationally much faster than the real space method—is well suited to this problem because of its inherent periodicity.

Energy minimization is performed using conjugate gradient method with gradient information.[7] Instead of the $3N$ variables $(m_{xi},m_{yi},m_{zi})$ a nonlinear transformation is used to obtain $2N$ variables for use in the minimization. These are $N$ in-plane angles $\theta_i$, $-\pi<\theta_i\leq\pi$, and $N$ out-of-plane tilt variables $\xi_i$, $-1<\xi_i\leq 1$.

## III. PERFORMANCE TRADEOFFS

We use this formalism to calculate the magnetoresistive response of an array of parallel strips of thickness $t=200$ Å, width $W=10$ $\mu$m, and gap $g=0.5$–$40$ $\mu$m. The exchange constant $A=2\times10^{-6}$ erg/cm, and $4\pi M_S=10$ kG, $H_K=4$ Oe and the applied field is in the range $-60\leq H_A\leq 60$ Oe. Also calculated is the magnetoresistive response of the corresponding isolated strip. The familiar approximately parabolic curve[3] is obtained whose width decreases as the gap becomes narrower. The half width at half height $H_{\text{half}}$ is calculated for all these curves. Figure 2 shows $H_{\text{half}}$ vs $r$ for all these strips and the isolated strip. For $r>1.8$ $H_{\text{half}}$ is within 94% of value for the isolated strip.

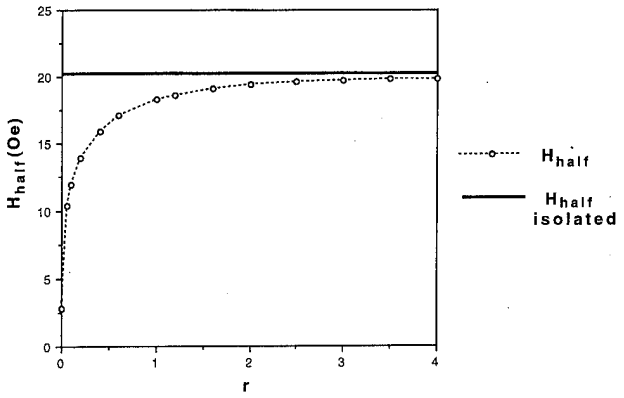



FIG. 2. Half width at half height of the MR response curves as the interstrip gap is varied. The symbols represent actual data points from the numerical calculations, the joining line is used as a guide for the eyes. For comparison the half width for an isolated strip is also shown.

An improved estimate of $\alpha(r)$ than that obtained from the ellipsoidal approximation [Eq. (2)] is made as follows. $H_{\text{half}}=H_K/\sqrt{2}$ for $r=0$. The quantity $H_{D\text{eff}}=H_{\text{half}}-H_K/\sqrt{2}$ is proportional to the demagnetizing field, and is a function of $r$. From this, one obtains $\alpha(r)=H_{D\text{eff}}(r)/H_{D\text{eff}}(\infty)$, i.e., the ratio of $H_{D\text{eff}}$ to the value calculated for the corresponding isolated strip. Figure 3 shows $\alpha(r)$ vs $r$ for $0\leq r\leq 4$. Note that $\alpha(r)=0.94$ for $r=1.8$. For comparison $\alpha(r)$ calculated from the ellipsoidal approximation is also shown. It shows that as $r$ increases the array of parallel strips approaches the response of an isolated strip more rapidly than that calculated from the ellipsoidal approximation.

As an example we calculate the effect of reducing the interstrip gap on $h_{\min}$. If we construct a barberpole transducer[8] of these strips, with a 2/3 ratio of spacing between the shorting bars and the width, the sensitivity is

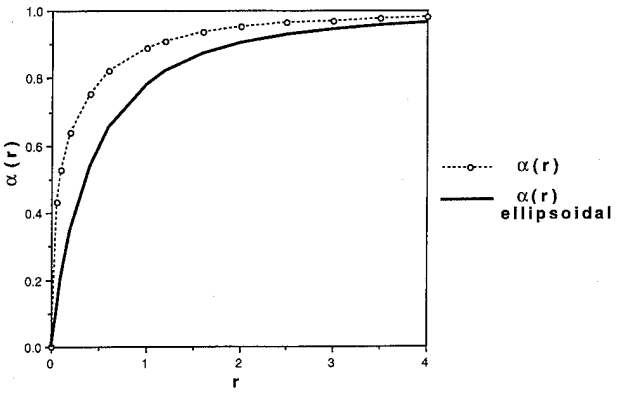



FIG. 3. Demagnetizing field reduction factor $\alpha(r)$ due to the proximity effect. For comparison the ellipsoidal approximation to $\alpha(r)$ is also shown.

$S=0.9(\Delta\rho_{max}/\rho_{ave})(1/H_S)$, where $(\Delta\rho_{max}/\rho_{ave})$ (2.5%) is the total MR effect. For a transducer of resistance $R$ ($1k\Omega$) the rms thermal noise voltage is $V_n=\sqrt{4Rk_BT\Delta f}$, where $\Delta f$ is the bandwidth of signal conditioning electronics. To the thermal noise power must be added any magnetic noise power. For this estimate we assume that the total noise voltage from all sources is twice the thermal noise voltage. For a supply voltage $V_S$ (10 V), $h_{min}$ is calculated using $SV_Sh_{min}/2V_n=6$.

A transducer made of well separated strips of $t=250$ Å, and $W=10$ $\mu$m gives $H_S=29$ Oe, and $S=0.78$ mv/VOe resulting in $h_{min}=6.3$ $\mu$Oe/$\sqrt{\text{Hz}}$. If the transducer is constructed of the same strips separated by a gap $g=1$ $\mu$m, then $\alpha(0.1)=0.5$, $H_S=16.5$ Oe, and $S=1.36$ mV/VOe resulting in $h_{min}=3.6$ $\mu$Oe/$\sqrt{\text{Hz}}$.

## IV. DISCUSSION

The magnetostatic interaction between parallel magnetic strips modifies the magnetoresistive response of these strips compared to an isolated strip. Using analytic and numerical methods, it has been shown that in addition to $H_K$ and $t/W$ ratio, the $g/W$ ratio is an important design parameter affecting the design of magnetoresistive sensors. The FFT method leads to efficient calculation of the demagnetizing field. Because of the inherent periodicity of these structures, FFT method is a natural fit to this problem. The effects of narrowing the interstrip gap are significant in the ranges of design parameters relevant to practical designs. Therefore, these models become useful tools for the design of MR sensors for low field applications.

As $g/W\rightarrow 0$, the range of linearity of the magnetoresistive response curve decreases, and the slope increases. These narrow gaps can be used to advantage in designing high sensitivity transducers. Conversely, for $g/W>1.8$, the effect of the proximity is negligible. Thus, if wide range of linearity is desired it is unnecessary to increase $g/W$ much above 1.8.

An example using typical design parameters demonstrates that reducing the $g/W$ to 0.1 from the isolated strip configuration reduces $h_{min}$ to 3.6 $\mu$Oe/$\sqrt{\text{Hz}}$ from 6.3 $\mu$Oe/$\sqrt{\text{Hz}}$. This shows one means of eking out additional sensitivity from a maturing technology for low field applications.

## ACKNOWLEDGMENTS

The Cray Supercomputer used in this investigation was provided by the Jet Propulsion Laboratory through funding from the NASA Offices of Mission to Planet Earth, Aeronautics, and Space Science. The author gratefully acknowledges programming help from Joseph Glenn.

[1] G. Hoffman and J. Birtwistle, J. Appl. Phys. **53**, 8266 (1982).
[2] G. Hoffman, J. Birtwistle, and E. Hill, IEEE Trans. Magn. **MAG-19**, 2139 (1983).
[3] B. Pant, J. Appl. Phys. **67**, 414 (1989).
[4] I. S. Gradshteyn and I. M. Ryzhik, *Table of Integral, Series, and Products* (Academic, New York, 1980).
[5] J. D. Jackson, *Classical Electrodynamics* (Wiley, New York, 1975), 2nd ed., pp. 192–194.
[6] M. Mansuripur and R. Giles, IEEE Trans. Magn. **MAG-24**, 2326 (1988).
[7] W. H. Press, B. P. Flannery, S. A. Teukolsky, and W. T. Vetterling, *Numerical Recipes*, 1st ed. (Cambridge University Press, Cambridge, 1986).
[8] B. Pant and D. Krahn, J. Appl. Phys. **69**, 5936 (1991).

# Large magnetic Hall effect in ferromagnetic $Fe_xPt_{100-x}$ thin films

C. L. Canedy, G. Q. Gong, J. Q. Wang,[a] and Gang Xiao[b]
*Physics Department, Brown University, Providence, Rhode Island 02912*

We have observed a very large extraordinary Hall effect (EHE) in a series of Fe–Pt thin films with various Fe contents. The origin of this remarkable EHE is the large spin–orbit interaction in the Fe–Pt alloys. At certain Fe content, the Hall resistivity can be saturated with a magnetic field less than 2 kG. The large EHE persists to room temperature with little change in magnitude. The EHE, which to our knowledge is the largest among magnetic transition metals, may find potential applications in magnetic sensors and nonvolatile magnetic random access memories. We will present structural analysis of the Fe–Pt films. © *1996 American Institute of Physics.* [S0021-8979(96)77208-X]

The study of magnetotransport in magnetic solids has received an increasing amount of attention recently.[1] The primary driving force behind this study is the potential applications of various novel magnetic solids in information storage devices and magnetic sensors.[1] Most of the research in this area has focused so far on the magnetoresistance aspect, with relatively little attention being paid to the magnetic Hall effect, often called the extraordinary Hall effect (EHE). The EHE arises from the spin–orbit interaction and it can be substantially larger than the ordinary Hall effect.[2] Currently, a large class of magnetic sensors is the semiconductor Hall sensor which offers good field sensitivity and linearity. However, due to a low carrier concentration, the internal resistance of a semiconductor Hall sensor is large and the frequency response narrow. Metallic solids, though having a high conductivity and a broad frequency response, are not suitable for Hall sensors because of the small Hall coefficient resulting from the inherently high carrier concentration. However, it has been suggested in the past that one may take advantage of the EHE of some magnetic solids and apply it to data storage devices or other types of magnetic sensors.[3] In reality, a large EHE generally occurs in rare-earth based magnetic systems where the spin-orbit interaction is strong,[2] but the rare-earth systems tend to have low magnetic transition temperatures ($T_c$) and are rather susceptible to corrosion.

In this work, we report on a very large EHE uncovered in a transition-metal system of $Fe_xPt_{100-x}$ thin films. The EHE coefficients are roughly three orders of magnitude larger than a typical ordinary Hall coefficient of a metal. The EHE saturates at a couple of kG and remains large at room temperature. We attribute the large EHE to the strong spin–orbit interaction existing in the Fe–Pt alloys.

The Fe–Pt thin films used in this study were deposited on silicon (111) substrates by using the magnetron-sputtering technique. We used the co-sputtering method to obtain samples with varying composition. Two of the collimated cluster guns were loaded, respectively, with an Fe (>99.9%) and a Pt (>99.9%) target. The composition of each sample was controlled by varying the sputtering rates (2–5 Å/s) of the two targets. Before each deposition the background vacuum was better than $7\times10^{-8}$ Torr. The Ar sputtering gas pressure was kept at 4.0 mTorr. All samples were deposited at an ambient substrate temperature. The film thickness was about 2500 Å. The structure of each sample was checked using an x-ray powder diffractometer. The standard photolithography and wet etching were used to pattern samples for transport measurement. The magnetic properties were measured in a superconducting quantum interference device magnetometer.

The equilibrium phase diagram of the Fe–Pt system consists of two face-centered-cubic (fcc) ($FePt_3$ and $Fe_3Pt$), one tetragonal superstructures (FePt) and a continuous solid solution in the $\alpha$-Fe-rich side.[4,5] We have made a series of samples with Fe content ranging from 0 to 50 at. %. The high quenching rate inherent in sputtering allows the formation of metastable Fe–Pt solid solutions. Figure 1 shows the $\theta$–$2\theta$ x-ray diffraction patterns of the $Fe_xPt_{100-x}$ thin films used in our study. Only the (111) and (222) peaks of the fcc structure

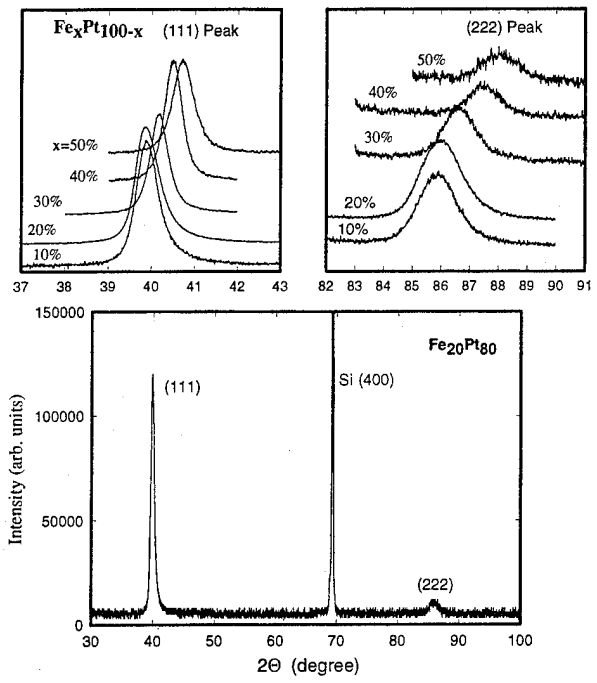



FIG. 1. X-ray diffraction patterns of the $Fe_xPt_{100-x}$ alloys. Only (111) and (222) peaks of the fcc structure are present, indicating textured growth. The details of the (111) and (222) peaks are shown for various samples.

[a]Current address: Applied Physics Department, Yale University, New Haven, CT 06520.
[b]Electronic mail: gxiao@waston.ibm.edu

 0021-8979/96/79(8)/6126/3/$10.00 © 1996 American Institute of Physics

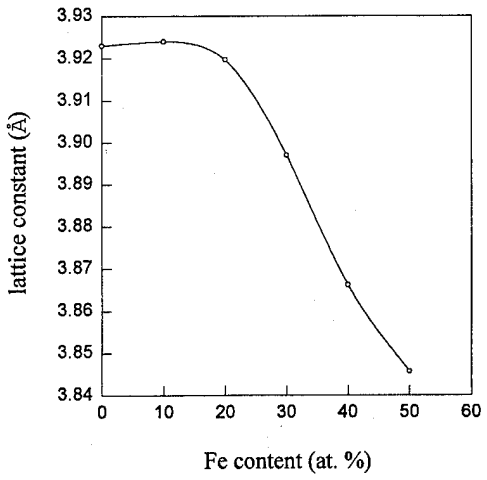



FIG. 2. Lattice constants of the fcc–$Fe_xPt_{100-x}$ alloys, obtained from the (111) and (222) peaks in Fig. 1.

are present, indicating a high degree of (111) textured growth of the thin films. No secondary phases were found in the x-ray patterns. The position of the (111) and the (222) peaks shifts toward high angles as the Fe content is increased (see Fig. 1). The obtained lattice constants ($a$) are shown in Fig. 2. Note that the value of $a$ decreases monotonically with the Fe content.

All of the samples that we studied are ferromagnetic. For samples with an Fe content larger than 20 at.%, $T_c$ is above 300 K. We have also observed giant Fe moments largely exceeding those in pure Fe. The enhanced moment is caused by the narrowing of Fe $d$ band and the polarization of the Pt $d$ states.[5] Detailed study of this phenomenon is underway and will be presented elsewhere.

In the following, we will focus on the EHE observed in the Fe–Pt system. In general the Hall effect is sensitive to the magnetic state of the material.[2] This is clearly revealed in Fig. 3, where we show the Hall resistivity $\rho_{xy}$ as a function of magnetic field $H$ for a representative $Fe_{30}Pt_{70}$ sample measured at 4.2, 77, and 285 K. The value of $\rho_{xy}$ is defined according to $\rho_{xy}=E_y/j_x=V_yt/I_x$, where $E_y$, $V_y$, $j_x$, and $I_y$ are electric field, voltage, current density, and current, respectively, $t$ is the thickness of the Hall bar. The value of $\rho_{xy}$ consists of two components, i.e.,

$$\rho_{xy}=R_0[H+4\pi M(1-D)]+R_s 4\pi M, \tag{1}$$

where the first term is the ordinary Hall effect ($D$ is the demagnetization factor), and the second term is the EHE which is proportional to the magnetization $M$. The dependence of $\rho_{xy}$ shown in Fig. 3 follows the magnetic hysteresis curve closely. The large initial increase in $\rho_{xy}$ with $H$ is due to the EHE. Once $M$ is saturated, so is $\rho_{xy}$. Above the saturation $H$, $\rho_{xy}$ is nearly independent of $H$ at $T=4.2$ and 77 K. The normal Hall effect is too small to be visible in Fig. 3. At $T=285$ K, the increase of $\rho_{xy}$ with $H$ in the high field region is not due to the normal Hall effect, but rather due to the fact that $M$ remains unsaturated up to 6 T.

In Fig. 4, we plot the EHE term at saturation (i.e., $R_s 4\pi M_s$) as a function of Fe content for the $Fe_xPt_{100-x}$ alloys. The values of $R_s 4\pi M_s$ were obtained by extrapolating

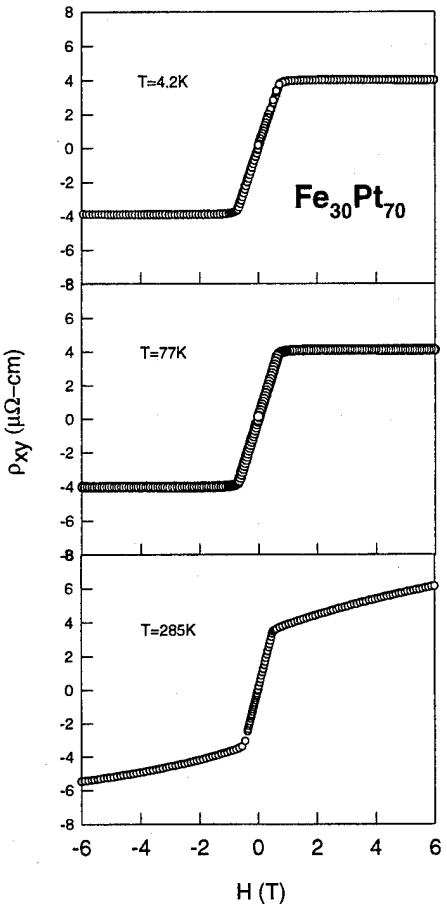



FIG. 3. Hall resistivity, $\rho_{xy}$, as a function of magnetic field measured at 4.2, 77, and 285 K for $Fe_{30}Pt_{70}$.

the $\rho_{xy}(H)$ curve from high field to $H=0$. At $T=4.2$ and 77 K, the quantity $R_s 4\pi M_s$ peaks at the Fe content of 30%. The initial rise of $R_s 4\pi M_s$ with Fe content is simply caused by the increasing concentration of magnetic scattering centers. However, as the Fe content is increased the spin–orbit coupling strength, mostly resulting from the heavy Pt atoms, becomes less effective. This eventually causes the EHE,

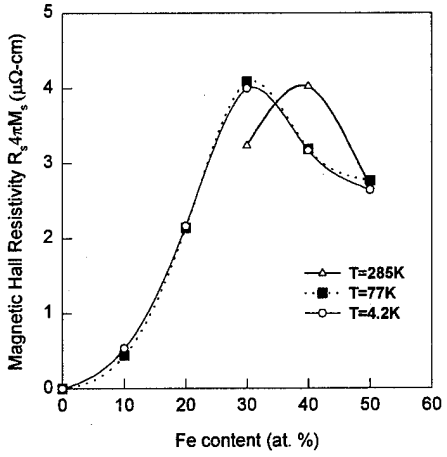



FIG. 4. The extraordinary Hall resistivity, $R_s 4\pi M_s$, measured at 4.2, 77, and 285 K for the $Fe_xPt_{100-x}$ alloys. The lines are guides to the eyes.

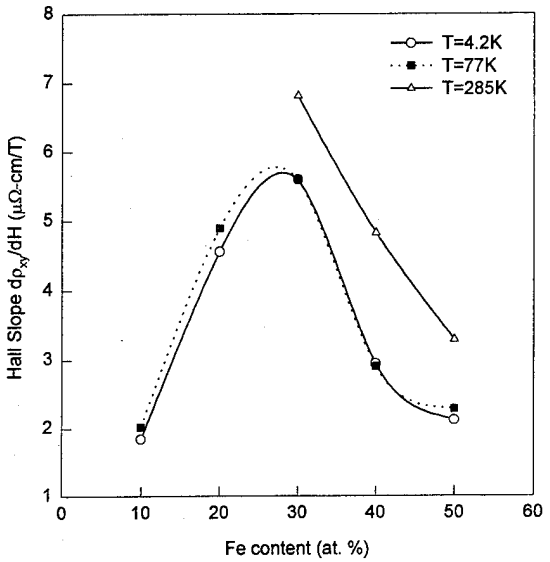



FIG. 5. The initial Hall slope, $d\rho_{xy}/dH$, at 4.2, 77, and 285 K for the $Fe_xPt_{100-x}$ alloys. The lines are guides to the eyes.

originating from the spin–orbit interaction, to weaken when the Fe content exceeds 30%, despite an increasingly larger $M$. The peak value of $R_s 4\pi M_s$ occurring in $Fe_{30}Pt_{70}$ is 5.5 $\mu\Omega$ cm. This is perhaps the largest magnetic Hall coefficient obtained in transition-metal based magnetic systems. The cause for such a large EHE may be twofold: a strong spin–orbit interaction and a strong polarization of the Pt $d$ states induced by Fe. It is noted that the resistivity of these Fe–Pt alloys is in the range of 20–70 $\mu\Omega$ cm. The Hall angle defined by $\tan\theta = \rho_{xy}/\rho_{xx}$ is also very large.

The compositional dependence of $R_s 4\pi M_s$ at 77 K is rather similar to that at 4.2 K. All samples remain ferromagnetic at 77 K. However, at $T=285$ K, the $x=10\%$ and 20% samples are no longer ferromagnetic, thus suppressing the EHE. The peak of $R_s 4\pi M_s$ shifts to $x=40\%$. This is because the $M$ of the $x=40\%$ sample remains appreciable at 285 K, whereas the $M$ of other Fe-poor samples is substantially reduced. Overall, the EHE remains robust at room temperature for samples with Fe content larger than 20%.

In addition to the quantity $R_s 4\pi M_s$, the initial Hall slope ($d\rho_{xy}/dH$) before saturation is also an important quantity (see Fig. 3). As shown in Fig. 3, the initial $\rho_{xy}$ is linear in $H$. To achieve a large Hall slope it is preferred to have a small saturation field, which is equal to $4\pi M$, when the magnetic field is perpendicular to a thin film as required for the Hall measurement. The Hall slope is presented in Fig. 5 as a function of Fe content. The maximum Hall slope, 6.9 $\mu\Omega$ cm/T, is found in the $x=30\%$ sample at $T=285$ K. The Hall slope tends to be smaller at low $T$ because of a larger $M$ at low $T$ and, hence, a larger saturation field. From the maximum Hall slope, we can estimate an effective carrier concentration ("$n$") if the EHE was caused by the normal Hall effect. The value of "$n$" is about $5\times10^{19}/cm^3$. The large Hall slope observed in the Fe–Pt series is, to our knowledge, among the largest in transition-metal based magnetic systems.[2] Compared with a normal metal such as Cu, the Hall slope in the Fe–Pt alloys is enhanced by three orders of magnitude.[6]

The large EHE in Fe–Pt could be potentially important for applications, such as magnetic sensors and nonvolatile magnetic random access memories (MRAM). In one version of MRAM each memory cell consists of a small Hall bar with a large EHE and a magnetic perpendicular anisotropy. The hysteresis loop is squarelike when the field is oriented perpendicular to the Hall bar. A local current loop switches the $M$ to either an up or down direction yielding a Hall voltage with opposite polarity. The Fe–Pt system has both the metallic conductivity and the large EHE. The magnetic perpendicular anisotropy can be achieved by making either sandwich or multilayer structures involving Fe–Pt.[7] The surface or interface magnetic anisotropy may cause the perpendicular anisotropy.

In summary, we have fabricated a series of fcc–$Fe_xPt_{100-x}$ thin films. Due to a large spin–orbit interaction, the Fe–Pt alloys exhibit a very large extraordinary Hall effect which can be saturated with a field of a couple of kG. Optimal magnetic Hall resistivity and Hall slope at room temperature are found in the sample $Fe_{30}Pt_{70}$, which is a good candidate for applications.

This work was supported in part by NSF through the Materials Research program at Brown University, Grant No. DMR-9121747. G.X. is partially support by the NSF Grant No. DMR-9258306.

[1] See, e.g., Reviews in Phys. Today **48**, 58 (April, 1995).
[2] *The Hall Effect and Its Applications*, edited by C. L. Chien and C. R. Westgate (Plenum, New York, 1979).
[3] R. J. Gambino and T. R. McGuire, IBM Tech. Disclosure Bull. **18**, 4214 (1976).
[4] *Iron-Binary Phase Diagram*, edited by O. Kubaschewski (Springer, New York, 1982).
[5] M. Podgorny, Phys. Rev. B **43**, 11300 (1991).
[6] *Solid State Physics*, edited by N. W. Ashcroft and N. D. Mermin (Saunders, Philadelphia, 1976), p. 15.
[7] K. Takanashi, M. Watanabe, and H. Fujimori, J. Magn. Magn. Mater. **104–107**, 1749 (1992).

# Resistivities of sputtered Ag(3.3 nm)/Cu($t_{Cu}$), Ag(3.3 nm)/Au($t_{Au}$), and Ni(4.2 nm)/Co($t_{Co}$) multilayers at 4–5 and 295 K

L. L. Henry, M. Oonk, R. Loloee, Q. Yang, W.-C. Chiang, W. P. Pratt, Jr., and J. Bass
*Department of Physics and Astronomy and Center for Fundamental Materials Research, Michigan State University, East Lansing, Michigan 48824-1116*

To help clarify the sources of the 67% periodic oscillations in the in-plane saturation resistivity, $\rho_S$ ($\rho_S$ varied from 2.5 to 5 $\mu\Omega$ cm at 4.2 K) of molecular beam epitaxy-grown epitaxial Ni/Co multilayers of total thickness, $t_T \approx 100$ nm recently reported by Gallego *et al.* [Phys. Rev. Lett. **74**, 4515 (1995)] we have measured the in-plane resistivities at 4–5 and 295 K of Ag/Cu, Ag/Au, and Ni/Co multilayers with $t_T \approx 100$ nm, dc sputtered nonepitaxially onto (001) Si. In no case do we see reproducible periodic oscillations, and any variations are always similar at 4–5 and 295 K. Our results show that oscillations of the size seen by Gallego are not simply a consequence of an average multilayer resistivity as low as 3.5 $\mu\Omega$ cm. © *1996 American Institute of Physics.* [S0021-8979(96)77308-6]

## INTRODUCTION

Gallego *et al.*[1] recently reported seeing ≈67% periodic oscillations (about the average) in the saturation resistivity, $\rho_S$, ($\rho_S$ varied from 2.5 to 5 $\mu\Omega$ cm) at 4.2 K of molecular beam epitaxy (MBE)-grown epitaxial Ni/Co multilayers of total thickness, $t_T \approx 100$ nm with fixed Ni(Co) thickness and variable Co(Ni) thickness. They ascribed the oscillations to superlattice effects and suggested that prior multilayers did not show them because they did not have mean-free-paths several times longer than the bilayer spacings (evidenced by low enough average resistivities).

To help clarify the source(s) of their oscillations, we have measured the in-plane resistivities at 4–5 and 295 K of Ag/Cu, Ag/Au, and Ni/Co multilayers with $t_T \approx 100$ nm, dc sputtered nonepitaxially onto (001) Si. The Ni or Ag thicknesses were fixed. Ag/Cu and Ag/Au were chosen: (a) to see if oscillations occur in nonmagnetic metal pairs with total resistivities comparable to those of Gallego *et al.*; and (b) to investigate effects of mutual miscibility of the metal pairs; like Ni and Co, Ag and Au are fully miscible, whereas Ag and Cu are nearly immiscible. Ni/Co was chosen to compare the behavior of sputtered samples with the MBE ones of Gallego *et al.* To check for systematic differences between sputtering runs, two independent runs were made for each metal pair. Measurements were made at both 4–5 and 295 K to examine any temperature dependence of the oscillations, a factor not addressed by Gallego *et al.*[1] Subsequently, however, this group indicated[2] that they observe nearly identical oscillations at room temperature and 4 K. Since any variations that we see at 295 K are also very similar to those we see at 4–5 K, for brevity, we omit our 295 K data and focus on those at 4–5 K.

Our samples were dc sputtered onto substrates maintained below room temperature in an ultrahigh vacuum (UHV) compatible four-gun system that has already been described.[3] The system was lightly baked, pumped to a pressure $\leq 2\times10^{-8}$ Torr (after filling of an internal Meissner trap), and then filled with the Ar sputtering gas to a pressure of 2.5 mTorr. The multilayer constituents were sputtered at rates ranging from 0.9 to 1.4 nm/s through masks shaped to give a standard four-probe current-in-plane geometry with sample width 1.6 mm, voltage lead separation of 5.2 mm and current lead separation of 10 mm. Measurements with a traveling microscope showed that the lengths and widths of the different masks were the same to within a few percent, and variations in lengths and widths over one complete set of samples were less than 5%. We will see below that our reproducibility in $\rho$ from completely independent sputtering runs was typically ±10%. Measuring currents of 0.1, 0.5, and 1 mA were used to check that the resistances were current independent. The Ag/Cu and Ag/Au resistances were measured at room temperature (assumed about 295 K) and at 4.2 K in a helium storage dewar. The Ni/Co saturation resistances were measured at room temperature and at 5 K in a Quantum Design MPMS system with the field in the plane of

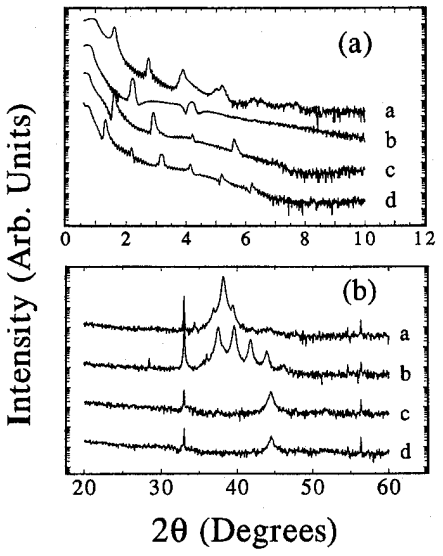



FIG. 1. (a) Low-angle and (b) high-angle Cu $K\alpha$, $\theta$-$2\theta$ x-ray diffraction patterns of representative samples at room temperature. In both graphs, each pattern is offset by a factor of $10^2$ to $10^3$ for clarity. The letters identify the samples: a=[Ag(3.3 nm)/Au(4.5 nm), $N$=15]; b=[Ag(3.3 nm)/Cu(1.2 nm), $N$=26]; c=[(Ni(4.2 nm)/Co(2.4 nm), $N$=15]; and d=[Ni(4.2 nm)/Co(5.0 nm), $N$=11], where $N$=number of bilayers.

 0021-8979/96/79(8)/6129/3/$10.00 © 1996 American Institute of Physics 

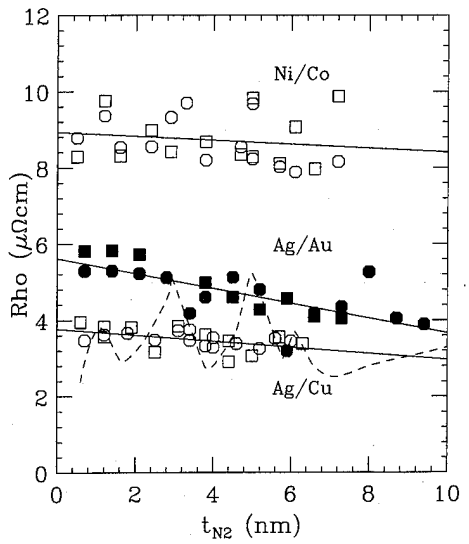



FIG. 2. Resistivity (Ag/Cu—lower open squares and circles—and Ag/Au—filled squares and circles) or saturation resistivity (Ni/Co—upper open squares and circles) vs thickness $t_{N_2}$ for $N_2$=Cu, Au, or Co, for multilayers with total thickness ≈100 nm. For each metal pair, squares and circles are for multilayers made in completely independent sputtering runs. The solid lines are least squares fits to all of the data for a given metal pair. The dashed curve shows the oscillatory behavior reported in Ref. 1.

the layers and parallel to the current direction. In this geometry we see small positive magnetoresistances like those seen by Gallego *et al.*[4] (i.e., the resistance is a maximum at high fields), with saturation fields comparable to theirs.

Figure 1 shows Cu $K\alpha$, $\theta$-$2\theta$ x-ray diffraction patterns of both low-angle superlattice lines and high-angle satellites for representative multilayers. Usually, several low-angle lines are seen, normally with strong Keissic fringes from the top and bottom edges of the films. Rocking curves at the first few lines show very narrow specular spikes (~0.03° in $\omega$ for Ni/Co and ~0.05° for Ag/Au and Ag/Cu, where $\omega$ is the rocking angle) and low fractional diffuse intensities. All of these facets of the data evidence good layering and are quite comparable to the low angle x-ray data of Gallego *et al.*[5] The high-angle satellites for Ag/Cu and Ag/Au demonstrate strong (111) texture in the plane normal to the layers and good coherence (~24 nm). Rocking curves were ~9° in $\omega$. In contrast, our Ni/Co high-angle scans show no clear evidence of superlattice satellites and the high-angle rocking curves are wide (~20°), indicating that our samples have only modest (111) texture.

Figure 2 shows the resistivities at 4–5 K of two independent runs for each metal pair, calculated using the nominal (intended) layer thicknesses. Using the thicknesses derived from x-ray data would make no significant difference for the Ni/Co and Ag/Cu multilayers, or for the Ag/Au ones from the first run, since those thicknesses typically averaged only a few percent lower than the nominal ones, and did not change the patterns of the data. The situation for the second Ag/Au run is more complex; the x-ray bilayer thicknesses averaged about 8% lower than the intended ones, but also did not change the pattern of the data. The cause of the lower x-ray thicknesses in this case is under investigation. The solid straight lines in Fig. 2 are least-square fits for all data points. For comparison, the dashed curve shows the Co/Ni data of Gallego *et al.*[1]

### Ag/Cu

We start with our data for Ag/Cu, which are immiscible and have our lowest average resistivities, similar to those of Gallego *et al.*[1] We see that the reproducibility between our two independent sputtering runs is excellent, with any variations about the average straight line only ±10%, similar to our reproducibility and to that of Gallego *et al.* The peak to peak variation of our data is less than half of theirs, and any reproducible oscillations in our data could not have an amplitude larger than a fourth to a fifth of theirs.

### Ag/Au

For Ag/Au, which like Ni/Co are completely miscible, our average resistivities (solid line) are about 50% larger than both ours for Ag/Cu and those of Gallego *et al.*[1] for Ni/Co. Here, aside from one omitted datum,[6] the data from our first run (filled squares) show little evidence of oscillations beyond our minimum reproducibility of ±10% about the average straight line. The second run, in contrast (filled circles) shows a few larger variations that could be fit with a (not completely periodic) oscillation amplitude almost as large as that seen by Gallego *et al.* We thus have two possible interpretations. (1) That the apparent oscillations in the second run are spurious, in which case we can rule out oscillation amplitudes more than about one-fourth of those seen by Gallego *et al.* in Ni/Co. (2) That the apparent oscillations in the second run are real, and arise from some difference in conditions from the first run not yet under our control. We do not see any strong systematic differences between the x-ray scans from the two runs, aside from the shift in the average bilayer thickness already noted.

### Ni/Co

For Ni/Co, our average $\rho_S \approx 9$ $\mu\Omega$ cm is much larger than those for our other sample sets and for those of Gallego *et al.*[1] The maximum variations in our data (~2 $\mu\Omega$ cm) are almost as large as those seen by Gallego *et al.*, but still within ±10% of our average values. Taken separately, the data for each of our two runs mimics some of the oscillatory structure of the data of Gallego *et al.*, but only their first weak peak at $t_{Co} \approx 1.4$ nm is reproduced in both runs. Taken together, our two data sets do not show reproducible oscillations anywhere near as large as those seen by Gallego *et al.*

## CONCLUSIONS

To summarize, we have measured the resistivities of Ag/Cu, Ag/Au, and the saturation resistivities of Ni/Co, multilayers sputtered onto Si. We do not in any case find reproducible periodic oscillations of amplitude larger than our ±10% reproducibility. Our results indicate that mean-free-paths longer than the multilayer period are not enough to see

oscillations. Rather, our data strongly suggest that any such oscillations require additional constraints including, perhaps, epitaxial growth.

## ACKNOWLEDGMENTS

This research was supported in part by the NSF under Grant No. DMR-94-23795 and by the NSF MRSEC program under Award No. DMR-94-00417. The authors thank D. V. Baxter for use of his XRD facilities at Indiana University.

[1] J. M. Gallego, D. Lederman, S. Kim, and I. K. Schuller, Phys. Rev. Lett. **74**, 4515 (1995).

[2] S. Kim and I. K. Schuller (unpublished).

[3] J. M. Slaughter, W. P. Pratt, Jr., and P. A. Schroeder, Rev. Sci. Instrum. **60**, 127 (1989).

[4] J. M. Gallego, D. Lederman, T. J. Moran, and I. K. Schuller, Appl. Phys. Lett. **64**, 2590 (1994).

[5] J. M. Gallego, S. Kim, T. J. Moran, D. Lederman, and I. K. Schuller, Phys. Rev. B **51**, 2550 (1995).

[6] We have omitted a filled square for a sample of Ag(3.3 nm)/Au(2.8 nm) for which the resistivity at 5 K increased as the sample was remeasured, from an initial value consistent with the other filled squares to later values much larger. We ultimately found this sample to be cracked, and we do not know if the crack was already present when it was first measured. Several other samples were also remeasured, yielding much smaller changes, if any.

# Resonant near-sound reorientation of the domain wall plane in yttrium orthoferrite

M. V. Chetkin, Yu. N. Kurbatova, and A. I. Akhutkina
*Department of Physics, Moscow State University, Moscow, 119899, Russia*

The dynamic orientation of the moving domain wall (DW) inclined at the static at an angle of about 50° to the surface of the plate of the orthoferrite cut perpendicularly to the optical axis was investigated. In the process of the increase of the domain wall velocity a very sharp decrease of the visible thickness of DW takes place near the transversal sound velocity. The moving domain wall changes its orientation plane and becomes almost perpendicular to the plate. This result may be caused by renormalization of anisotropy or dynamic minimization of domain wall energy. The solitary defection wave can propagate along self-organizing structure in the domain wall as a result of supersonic instability. © *1996 American Institute of Physics.* [S0021-8979(96)77408-2]

## I. INTRODUCTION

The canted (weak) ferromagnets—orthoferrites are single magneto-ordered crystals, where the domain wall can move with supersonic velocities.[1,2] The motion of domain walls (DW) with near-sound velocities possesses several interesting peculiarities. During the transition to the supersonic motion, the DW ceases to be one-dimensional object. DW changes its initial plane rectilinear form and becomes tilted to the surface of the sample. The self-organizing periodic structures with singular points are formed on supersonic dynamic DW.[3] The amplitudes of the structures and the visible DW thickness decrease as the DW velocity is approaching the limiting velocity $c$, which is equal to 20 km/s.[4] This velocity is equal to that of spin waves on the linear part of their dispersion law.[4,5] So, the study of the DW dynamics in the orthoferrites can be useful for determining of the magnon dispersion curves.

## II. EXPERIMENTAL PROCEDURE

Most experiments on the domain wall dynamics in the orthoferrites were performed on plates cut perpendicular to the optical axis.[6] In these plates two main types of rectilinear domain walls exist: (1) perpendicular both to the surface of the plate plane and to the $a$ axis, and (2) inclined to the surface of the plate plane at an angle of about 50° and parallel to the $a$ axis. Observed with the help of Faraday rotation, the visible thickness of the domain wall in the last case is equal to 60 $\mu$m in a sample having a thickness of 100 $\mu$m. Such a single DW in the sample exists in the magnetic fields perpendicular to the surface of the sample with a grad $H$=2000 Oe/cm. Magnetic moments of almost all orthoferrites can rotate only in the $ac$ plane which is inclined at an angle of about 50° to the surface of the plate. This paper is devoted to the experimental study of the dynamic orientation of the DW at room temperature. It was shown that the visible thickness of the domain wall initially inclined to the plate surface gradually decreases as the domain wall is approaching the limiting velocity. A very sharp decrease of the visible thickness was observed near the transversal sound velocity. The method of double high speed photography was used in the plates of $YFeO_3$ cut perpendicular to the optical axis at room temperatures. The $N_2$ laser with transversal discharge was used. The thin plate of quartz with a small hole was placed in the discharger of the laser. The discharger was supplied by a sound mutter. These measures provided high temporal stability, a long term and soundless work of the laser. This laser pumped rodamin 6 G dye laser. Pulses of red light of 0.25 ns duration were generated in the same manner as in Ref. 3.

## III. EXPERIMENTAL RESULTS AND DISCUSSION

Twofold high speed photography allows to study the domain wall velocities.[6,7] With an increase of the domain wall velocity the slow decrease of the visible thickness of DW have been observed. Near the transversal sound velocity the very sharp decrease of the visible thickness of the moving domain wall up to 8–10 $\mu$m was observed (see Fig. 1). The plane of the domain wall abruptly leaves the $ac$ plane and at this velocity becomes almost perpendicular to the surface of the sample. This transition takes place in the range of velocities of 200–300 m/s below of the transversal sound velocity. The minimum visible domain wall thickness existed in the magnetic field range $\Delta H$ of about 30 Oe, including the region on the $V(H)$ dependence where domain wall velocity stays at the velocity of the transversal sound. After the transition to the supersonic velocity the visible thickness of moving DW increases again. The non-one-dimensional self-organizing structures arise on the dynamic domain wall of orthoferrite. The similar structures were investigated earlier

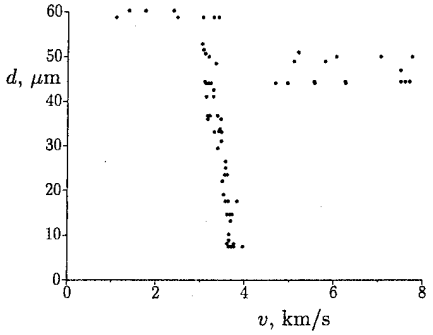



FIG. 1. Dependence of visible thickness of the domain wall of the orthoferrite on its velocity. The static domain wall is tilted with respect to the plate surface.

 0021-8979/96/79(8)/6132/2/$10.00 © 1996 American Institute of Physics



FIG. 2. Twofold high-speed photograph in the contrast of domain wall of self-organizing structure on supersonic domain wall moving at the velocity 12 km/s. The time delay between two light pulses is 4 ns.



FIG. 3. Twofold high-speed photograph in the contrast of the domains of the solitary wave of the domain wall deflection—of the small kink, moving along domain wall. The domain wall moves from down to up. The black region is the area, which the domain wall passes during the time delay between the two light pulses. Two positions of the kink indicated by arrows.

for the domain walls perpendicular both to the $a$ axis and to the surface of the orthoferrite plate cut perpendicular to the optical axis.[3] In Fig. 2 it is easy to see the almost rectilinear parts of the structures. These parts have been observed only for structures with a large period and amplitude. The intersecting semicircular parts of the structure were also observed under certain condition early.[3,6]

In accordance with a magnetoelastic theory[7] an essential renormalization of the magnetic anisotropy (up to the change of the sign of the anisotropy constant) occurs near the transversal sound velocity if the dissipation of sound is small. This fact can account for the observed domain wall reorientation near the sound velocity. The experimental results of Ref. 8 have shown that the moving domain wall really generates a solitary wave of deformation. Its amplitude increases sharply at the sound velocity. This deformation is small and cannot be observed at room temperature. But its amplitude sharply increases at 2 K and this deformation has been observed using the double Doppler shift of frequency with the help of a high-contrast spectrometer based on Fabry–Perrot five-pass interferometer.[8] It is obvious, that in the interpretation of the experimental results it is necessary to take into account the high dissipation of sound, especially at room temperature. If the renormalization of anisotropy really takes place near sound velocity, the generation of the vertical Bloch lines on the domain wall in orthoferrites and its motion under the influence of magnetic field and gyroscopic forces are possible. But this issue is a separate subject. The observed change of DW orientation can also be a result of an increased rigidity of the DW near the sound velocity. The similar situation can also occur near the limiting velocity. Increased rigidity of DW in these cases has also been confirmed by the results of experiments on relaxation of non-one-dimensional disturbance on DW, moving at near-sound and near-limiting velocities.[6] The decrease of the area of DW moving at near-sound and limiting velocities may be caused by dynamical minimization of its energy for domain walls of any orientation in the plate of the orthoferrite.

Small regions of the domain wall perpendicular to the plate surface and regions inclined to the sample surface coexist in the DW during supersonic motion (Fig. 3). The right part of the domain wall in Fig. 3 has not overcome the sound barrier and moves in the initial direction on sound velocity. On almost rectilinear tilted part of the supersonic structure one can see a solitary deflection wave of a small amplitude—a small kink moving along the domain wall. The velocities of the domain wall $v$ and the one of the kink along the DW $u$ are equal to 12 and 16 km/s respectively. So $u^2+v^2=c^2$, is valid in accordance with predictions of quasirelativistic theory of domain wall dynamics in weak ferromagnets.[5,6] This small kink arises on the domain wall after a short-time fast decrease of the amplitude of the pulsed magnetic field driving the domain wall. The small kink has a sharp front, moves along the domain wall from the left to the right and is similar to the one accompanying the VBL in a garnet film moving by a gyroscopic force.[6,9] Instability of the supersonic domain wall motion and the absence of the hysteresis on the dependence of $v$ on $H$ near the sound velocity could be responsible for the generation of the small kink.

## ACKNOWLEDGMENTS

The authors express their deep gratitude to A. F. Popkov for helpful discussions. The research described in this publication was made possible in part by Grant No. M4O300 from the International Science Foundation and Grant No. 95-02-06188a from Russian Foundation for Fundamental Investigations.

[1] C. H. Tsang, R. L. White, and R. M. White, J. Appl. Phys. **49**, 6052 (1978).
[2] M. V. Chetkin, A. N. Shalygin, and A. de la Campa, Fiz. Tverd. Tela (Leningrad) **19**, 3470 (1977) [English translation: Sov. Phys. Solid. State **19**, 2029 (1979)].
[3] M. V. Chetkin, A. K. Zvezdin, S. N. Gadetsky, S. V. Gomonov, V. B. Smirnov, and Yu. N. Kurbatova, Zh. Eksp. Teor. Fiz. **94**, 269 (1988) [English translation: Sov. Phys. JETP **67**, 151 (1988)].
[4] M. V. Chetkin, A. N. Shalygin, and A. de la Campa, Zh. Eksp. Teor. Fiz. **75**, 2345 (1978) [English translation: Sov. Phys. JETP **48**, 1184 (1978)].
[5] A. K. Zvezdin, Pis'ma Zh. Eksp. Teor. Fiz. **29**, 605 (1979) [English translation: JETP Lett. **29**, 513 (1979)].
[6] V. G. Bar'jakhtar, M. V. Chetkin, B. A. Ivanov, and S. N. Gadetskiy, *Dynamics of Topological Magnetic Solitons, 182*, Springer Tracts in Modern Physics, Vol. 129, Berlin, 179 (1994).
[7] A. K. Zvezdin, and A. A. Mukhin, Zh. Eksp. Teor. Fiz. **102**, 577 (1992) [Sov. Phys. JETP **102** (1992)].
[8] S. O. Demokritov, A. I. Kirilyuk, N. M. Kreines, V. I. Kudinov, V. B. Smirnov, and M. V. Chetkin, J. Magn. Magn. Mater. **102**, 339 (1991).
[9] M. V. Chetkin, V. B. Smirnov, I. V. Parygina, S. N. Gadetskii, and A. K. Zvezdin, Phys. Lett. A **140**, 428 (1989).

# Approach to the anhysteretic surface

M. J. Sablik
*Southwest Research Institute, P.O. Drawer 28510, San Antonio, Texas 78228-0510*

R. A. Langman
*University of Tasmania, P.O. Box 252C, Hobart, Tasmania, Australia 7001*

In this paper, we have investigated experimentally the approach to the anhysteretic surface in $M-H-\sigma$ space. In particular, for a 0.5 wt% carbon steel specimen, we have applied 73 MPa tension and a bias field $H$ and determined the end flux density after superimposing an ac field of amplitude gradually decreasing to zero. We find that the point on the anhysteretic curve for 73 MPa tension and field $H$ is not approached unless the initial amplitude of ac field is sufficiently large to overcome domain wall pinning, which restrains redistribution of the domains. A similar experiment in which stress is cycled was also done. Stress was cycled discretely between 0 and 140 MPa, with the discrete changes about 73 MPa eventually decreasing to zero in bias field $H$. It was found that the loci of $(B,H)$ end points did not approach the anhysteretic, suggesting that larger amplitude changes in stress and perhaps more continuous changes are needed to overcome domain wall pinning.
© *1996 American Institute of Physics.* [S0021-8979(96)77508-9]

## I. INTRODUCTION

The magnetic anhysteretic curve is a locus of points giving the $(M,H)$ values which correspond to thermodynamic equilibrium points for a given ferromagnetic material. It has been stated many times[1–3] that the anhysteretic curve can be reached experimentally for a particular magnetic bias field by superimposing an ac field on the bias field and allowing the ac amplitude to decrease to zero. In this work, we shall demonstrate experimentally that whether the anhysteretic is actually reached is dependent upon the initial ac amplitude.

Recently a number of authors[4–7] have suggested or implied that there is more than one anhysteretic curve for a given magnetic material depending on the amount of external stress $\sigma$ that is applied to the material.[5,7] We have observed that the reason for this multiplicity of anhysteretics is that the anhysteretic is actually a surface and not a curve. In particular, the anhysteretic is a surface in $M-H-\sigma$ space where $M$ is magnetization and $H$ is magnetic field intensity. This is the same concept as in $P-V-T$ space, where the ideal gas equation is a locus of thermodynamic equilibrium points that corresponds to a $P-V-T$ surface, where $P$ is pressure, $V$ is volume, and $T$ is temperature.

Figure 1 shows a schematic anhysteretic surface that would be expected in $M-H-\sigma$ space. Three $M-H$ sections are shown for constant stresses $\sigma_0$, 0, and $-\sigma_0$. The anhysteretic curves for the corresponding stresses are shown for each section. These curves are simply sections of the anhysteretic surface. Also shown on the $M-H$ sections corresponding to stress $\sigma_0$ and $-\sigma_0$ are initial magnetization curves to field $H_0$. In the $M-H$ section for constant positive stress is shown a schematic zig–zag path to the anhysteretic followed by the magnetization in response to a decreasing ac magnetic field intensity. We shall see later that the actual picture is not quite so simple.

Jiles and Atherton suggested[8] that similar movement toward the anhysteretic occurs when the stress is changed, regardless of the sign of the stress. Thus, it would seem that application of an alternating stress on a bias stress $\sigma$ and allowing the amplitude of the alternating stress to be decreased to zero also ought to be a way to approach the anhysteretic surface. This would seem to be consistent with the cyclic stress behavior discussed in Refs. 4–7.

Figure 1 shows a schematic path for magnetization at constant field $H_0$ and negative (compressive) bias stress $-\sigma_0$ when an alternating stress is applied with decreasing amplitude about the bias stress. This would be the analog of the other zig–zag path for alternating ac magnetic intensity at a mean $H_0$ and constant $\sigma_0$. Again, we shall show experimentally that the real situation is not quite this simple.

Domain wall pinning is the major reason why the actual approach to the anhysteretic surface is more complicated

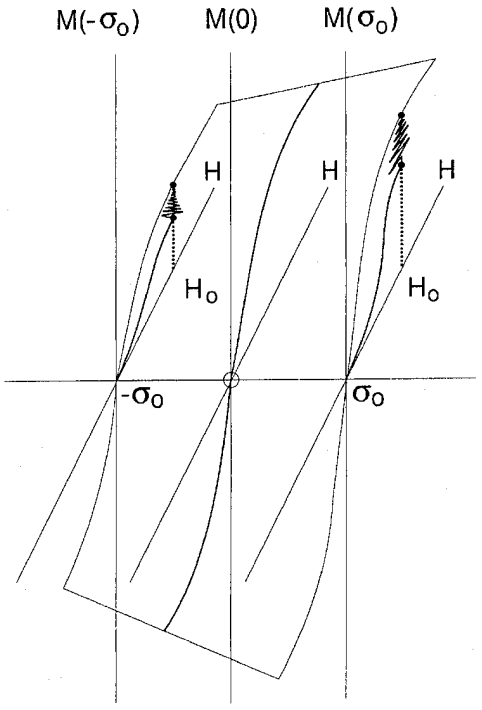



FIG. 1. Depiction of a schematic anhysteretic surface in $M-H-\sigma$ space. Details are discussed in the text.

 0021-8979/96/79(8)/6134/3/$10.00 © 1996 American Institute of Physics

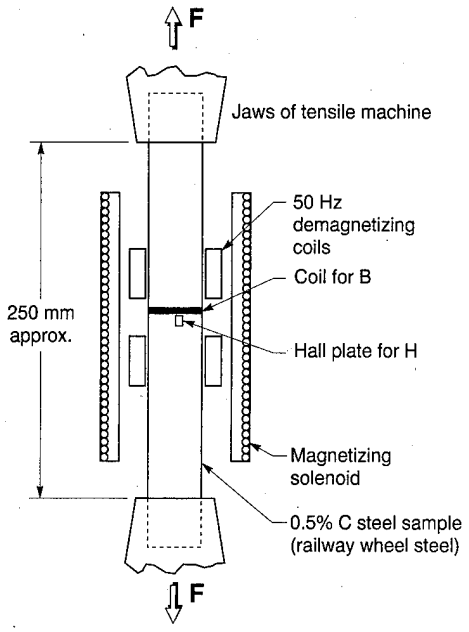



FIG. 2. Diagram of experimental setup.

than in the above description. The pinning must first be overcome in order to sufficiently redistribute the domains so that the anhysteretic is actually approached. The experimental consequences of this will be discussed below.

## II. EXPERIMENTAL RESULTS AND DISCUSSION

Measurements were made on a 0.5% C steel specimen, cut from an Australian railway wheel, with coercivity approximately 1000 A/m. Figure 2 shows the experimental setup. A secondary coil was wrapped about the middle of the specimen, and a ballistic method was used to obtain the flux density when the current in the primary magnetizing coils was reversed. A Hall probe next to the secondary coil measured $H$. Different stresses were applied to the ends of the specimens. Applied force was known from the dial of the testing machine and applied stress was calculated from that. The specimen had a cross section of $40\times8$ mm. Errors of uncertainty were estimated to be $\pm2\%$ for $H$, $\pm2\%$ for $B$, and $\pm5\%$ for stress $\sigma$.

Figure 3 shows $B-H$ curves obtained for a specimen under $+73$ MPa of stress (tension) when different initial amplitudes of 50 Hz decreasing amplitude ac current are superimposed on the quasi-dc bias field $H$. Curve 1 is for when zero ac amplitude is superimposed—i.e., it is the initial magnetization curve. Each other curve is for a different amplitude of ac current and each other curve is the locus of flux densities $B(H)$ obtained for different bias fields $H$ when the superimposed ac field amplitude is allowed to slowly go to zero. Each of the experimental points on curves 2–6 is obtained after a sequence of starting from the demagnetized state, then applying the quasi-dc bias field $H$, then applying the 50 Hz ac field amplitude, then gradually decreasing the 50 Hz field amplitude to zero and measuring the resultant flux density from the emf in the secondary coil at the end of this process to obtain the point $(H,B)$.

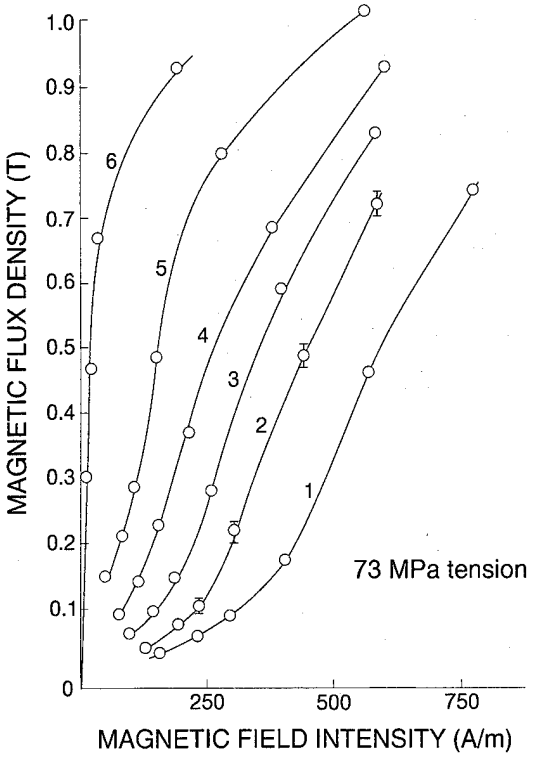



FIG. 3. Loci of $B-H$ points obtained for various bias field $H$ and for 73 MPa of tension $\sigma$ for different initial amplitudes of a 50 Hz ac field decreasing gradually to zero. Curve 1, zero ac field; curve 2, 40 A/m ac; curve 3, 80 A/m ac; curve 4, 160 A/m ac; curve 5, 320 A/m ac; curve 6, 800 A/m ac.

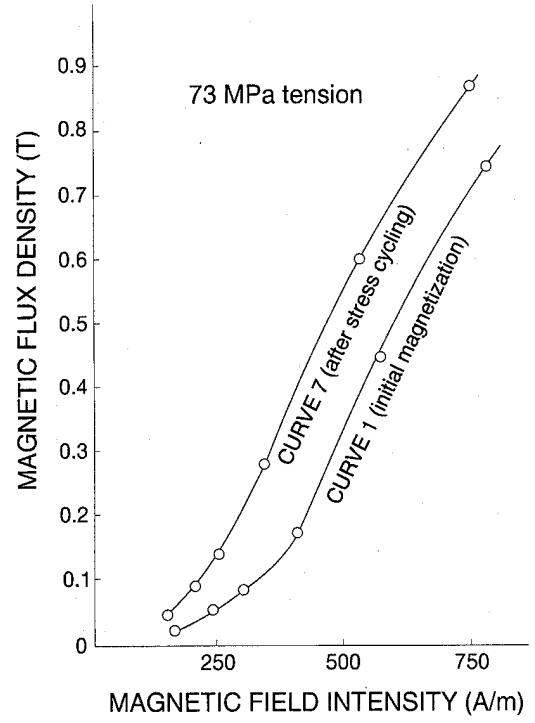



FIG. 4. Loci of $B-H$ points obtained for various bias fields $H$ and for 73 MPa of bias tension. Curve 1 corresponds to curve 1 in Fig. 2. Curve 7 is for a cyclic stress application cycling between 0 and 140 MPa of gradually decreasing amplitude. The stress changes are discrete, rather than continuous.

It will be noted that the end product of decreasing the ac field to zero in a bias field $H$ and under stress $\sigma$ is not necessarily a point on the anhysteretic curve for stress $\sigma$ (see curves 2–5). When the ac amplitude gets large enough the overcome almost all the domain wall pinnings, then the resulting $B-H$ curve has the familiar shape of an anhysteretic curve (curve 6), in this case requiring as much 800 A/m of ac field to approach what is considered to be almost the true anhysteretic.

Figure 4 is the corresponding $B-H$ curve (curve 7) for 73 MPa tension, but after stress cycling 73 MPa→140 MPa→0→120 MPa→20 MPa→100 MPa→40 MPa→80 MPa→60 MPa→73 MPa. Curves 2 and 7 are very similar. One would conclude that a roughly 70 MPa cycling amplitude of stress is not enough to approach the anhysteretic.

Different patterns of stress cycling at a bias field of about 500 A/m were also tried, but generally speaking, there was little difference in the final flux density (falling in a range from 0.54 T to 0.6 T).

Cullity[9] has also discussed the approach to the anhysteretic and has asserted that the initial ac amplitude superimposed on the bias field ought to be enough to saturate the specimen. Our results showing an anhysteretic shape at 800 A/m but not at approximately half that value confirms the conclusion that the initial ac amplitude must be sufficiently large. Whether the ac amplitude must be large enough to saturate the specimen is unanswered by our work, but it would seem that to reach the anhysteretic, the amplitude must be large enough to extend to an $H$ regime where domain wall translation is minimal—i.e., beyond the knee of the initial magnetization curve.

## III. CONCLUSIONS

The results, both of field and stress cycling at constant $(\sigma_0,H_0)$, indicate that the approach to the anhysteretic thermodynamic surface is complicated. Cycling needs to be done with an initially sufficiently large amplitude that domain wall pinning could be overcome sufficiently to redistribute all the domains.

In the case of stress cycling, more work needs to be done to see if a sufficiently large cyclic stress amplitude can be applied so that the anhysteretic can indeed also be approached.

## ACKNOWLEDGMENTS

Work on this project was supported in part by the U.S. National Science Foundation under Grant No. INT-9316679.

[1] D. Jiles, *Introduction to Magnetism and Magnetic Materials* (Chapman and Hall, London, 1991), pp. 94–95.
[2] D. C. Jiles and D. L. Atherton, J. Magn. Magn. Mater. **61**, 48 (1986).
[3] M. J. Sablik and D. C. Jiles, IEEE Trans. Magn. **29**, 2113 (1993).
[4] D. L. Atherton and V. Ton, IEEE Trans. Magn. **26**, 153 (1990).
[5] I. M. Robertson, IEEE Trans. Magn. **29**, 2077 (1993).
[6] M. G. Maylin and P. T. Squire, IEEE Trans. Magn. **29**, 3499 (1993).
[7] D. C. Jiles and M. K. Devine, J. Appl. Phys. **76**, 7015 (1994).
[8] D. C. Jiles and D. L. Atherton, J. Phys. D **17**, 1265 (1984).
[9] B. D. Cullity, *Introduction to Magnetic Materials* (Addison-Wesley, Reading, MA, 1972), pp. 350–351.

# Studies of remanence in granular Ni–$SiO_2$ films

Y. Xu,[a] B. Zhao, and X. Yan
*Department of Physics, The Hong Kong University of Science and Technology, Clear Water Bay, Kowloon, Hong Kong*

We have studied microstructure and remanent magnetization of the granular Ni–$SiO_2$ films. Both analysis of the transmission electron microscope images and that of the particle size distribution via remanence studies support the hypothesis that both superparamagnetic and ferromagnetic components coexists in the nearly percolating films. © *1996 American Institute of Physics.* [S0021-8979(96)77608-5]

## I. INTRODUCTION

For conventional ferromagnetic or ferrimagnetic materials, the remanent magnetization will remain in the same direction as the saturated one, following that of the applied external magnetic field. For antiferromagnetic, superparamagnetic or spin glass materials, there will be a zero or slightly positive remanent magnetization. An opposite magnetic response is often associated with a diamagnetism, which will leave zero response upon removing the applied magnetic field to zero. A clockwise $M-H$ loop is closely related to the negative remanence, or the opposite remanence upon removing the applied field to zero, and is not expected from a magnetic response of a homogeneous system.[1] Related phenomenon such as the reverse thermal-remanent magnetism has been observed in geomagnetic materials[2] and were explained in terms of two components having different Curie temperatures,[3] and a hysterisis loop shifted with respect to the origin has been observed in amorphous[4] and certain multilayered materials[5,6] and was explained either in terms of interface exchange interaction[5,6] or exchange anisotropy.[7] However, a complete understanding of this phenomenon in inhomogeneous materials is still lacking due to the lack of systematic studies of both the microstructure and the remanent magnetization. Recent observation of the negative remanence in systems with nearly percolating magnetic nanostructures[8] provide this opportunity.

In this article, we describe studies of microstructure and remanent magnetization in granular (Ni,Fe)–$SiO_2$ films. Analysis again supports the hypothesis[8] that the negative remanence observed in nearly percolating magnetic nanostructures is likely due to the coexistence of both superparamagnetic (SPM) and ferromagnetic (FM) components, and magnetostatic interactions that can favor the opposite alignment between the two components.

## II. EXPERIMENTS

Granular $(Ni,Fe)_x-(SiO_2)_{1-x}$ films were prepared using a Denton magnetron rf sputtering system, where pure Ni target with a few small Fe pieces and $SiO_2$ target were mounted on two separate sputtering guns. The structure of the films were studied via x-ray diffraction and transmission electron microscope (TEM), and the chemical analysis, via x-ray photoelectron spectroscope and energy dispersive x-ray spectroscope (EDX). dc magnetization was measured for all those films between 5 and 300 K using Quantum Design's SQUID Magnetic Property Measurement System for the magnetic field applied parallel to the plane of the film.

## III. MICROSTRUCTURE CHARACTERIZATION

Figure 1 shows the TEM bright field images (center), electron diffraction patterns (right), and TEM dark field images (left) of the films for (a) $x=0.3$, (b) 0.4, (c) 0.5, and (d) 0.6, respectively. The bright images display microstructure characteristic of typical granular metal films, containing small metallic particles of spherical in shape. From (a) to (d), it is not difficult to see that the average particle size (its diameter) increases smoothly from 3 nm for $x=0.3$ to 6 nm for $x=0.6$, going smoothly through the percolation threshold between 0.55 and 0.6, corresponding to $x'$ of 0.6 according to the resistivity measurements.[9,10] By tilting the sample holder, no preferred orientation of the particles was observed

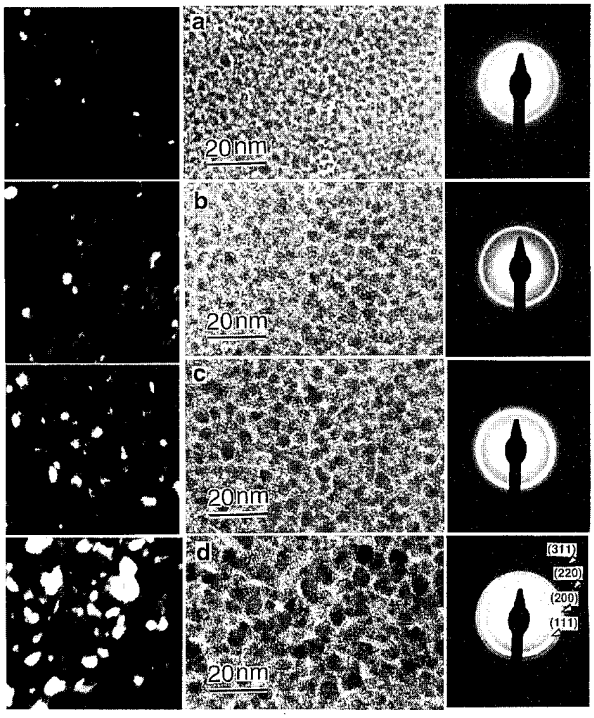



FIG. 1. Bright field TEM images (center), electron diffraction pattern (right), and dark field TEM images (left) of $(Ni, Fe)_x(SiO_2)_{1-x}$ for $x=0.3$ (a), 0.4 (b), 0.5 (c), and 0.6 (d).

[a]On leave from Institute of Physics, Chinese Academy of Sciences, Beijing 100080, People's Republic of China.

 0021-8979/96/79(8)/6137/3/$10.00 © 1996 American Institute of Physics 

TABLE I. Some parameters for $(Ni,Fe)_x(SiO_2)_{1-x}$.

| Nominal magnetic volume fraction, $x$ | 0.3 | 0.4 | 0.5 | 0.6 |
|---|---|---|---|---|
| Measured magnetic volume fraction, $x'$ | 0.336 | 0.427 | 0.518 | 0.650 |
| Fe/Fe+Ni (%) | 29 | 20 | 14 | 11 |
| Mean particle size (nm) from TEM | 3.5 | 5.4 | 6.1 | 7.9 |
| Mr/Ms (%) at $T=200$ K | 0.53 | −1.0 | −4.0 | 5.5 |
| Mr/Ms (%) at $T=5$ K | 34.6 | 36.9 | 36.2 | |

for all of the samples. The electron diffraction patterns were taken from an area of about 0.5 $\mu$m indiameter. The diffraction patterns display rings characteristic of an fcc crystalline structure of a lattice constant closer to that of bulk nickel. Table I shows the magnetic volume fraction $x'$ and the fraction of Fe in Ni–Fe evaluated by EDX, and the granular particle size $d$ as evaluated by TEM bright field images. Note that no diffraction rings of bcc Fe or that of silicides can be revealed in diffraction patterns. Therefore, the system can be considered as fcc Ni–Fe alloy particles of a few nanometer size mixed with the insulating $SiO_2$ amorphous phase.

Dark field TEM images were taken by using one large aperture which covers about a quarter of the major diffraction rings (111, 200, and 220) for films with $x=0.3$, 0.4, 0.5, and 0.6. It is seen from Fig. 1(a) that particles were well separated for $x$ well below the percolation threshold. Starting from (b), some particles are connected with bottlenecks, while others remain isolated separated by amorphous $SiO_2$ bridges. The microstructure with such bottlenecks may be termed "labyrinth structure." Such a bottleneck was evident by a white arrow in Fig. 1(d). As $x$ increases, both the size and the volume fraction of the labyrinth structure increase. Above the threshold ($x\geqslant 0.6$), great number of particles are connected by small bottlenecks, and the size of the labyrinth structure diverges and approaches to the sample size. One can see that particles are getting better connected to each other from (a) to (d) in Fig. 1. Thus, it is reasonable to suggest that as $x$ increases, particles start from well isolated ($x\leqslant 0.3$), through partially isolated and partially connected ($0.4\leqslant x\leqslant 0.55$), to well connected ($x\geqslant 0.6$).

## IV. STUDIES OF REMANENCE

Figure 2 show the thermoremanent magnetization, $Mr(T)$, which was measured at zero field after removing a positive field of 10 kG, for various $x$'s. Upon increasing temperature, $Mr(T)$ decreases sharply from a large positive value and either changes to negative for $x=0.40$, 0.50, and 0.55, or to zero for $x=0.15$ and 0.30. Note that for the film with $x=0.55$, $Mr(T)$ changes to a negative value at about 100 K and reaches the minimum at about 200 K. In the same temperature regions, zero field cooled susceptibility $\chi$ has a broad maximal.[8] Similar negative remanence was also observed in the $M-H$ loop at 200 K for these films with $x=0.4$, 0.5, and 0.55, but not in those with $x=0.15$, 0.3, and 0.6, as shown in Table I for $Mr/Ms$ at 200 K. In contrast, $Mr/Ms$ at 5 K remains to be positive for all films. The

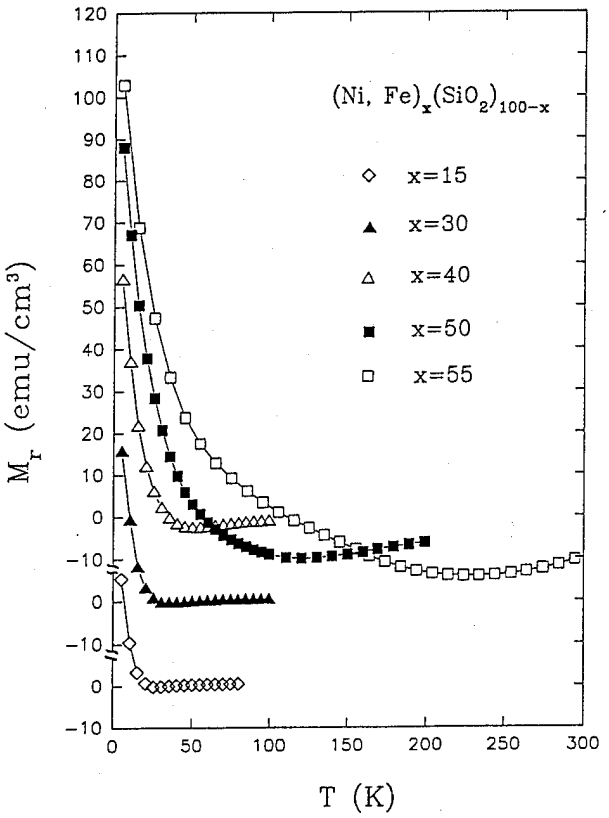



FIG. 2. $Mr(T)$ for $x=0.15$, 0.3, 0.4, 0.5, and 0.55.

appearance of the negative remanence only for the nearly percolating films ($0.4\leqslant x\leqslant 0.55$) indicates the importance of the finite sized labyrinth structure where there are some connected ferromagnetic (FM) particles in addition to the isolated superparamagnetic (SPM) particles.

Let us now examine the hypothesis of the existence of both SPM and FM components in the nearly percolating granular films by studying the remanent magnetization after removing positively saturated field to zero at temperature $T$, $Mr'(T)$, where $'$ is used to defer it from $Mr$. It is known[11] that $Mr'(T)$ is a measure of the relaxed magnetization at a given temperature $T$ in a given measurement time which is in the order of 100 s for our SQUID measurement. Such a relaxation process is thermally activated associated with an energy barrier. When the energy barrier has a distribution function $f(E_a)$, $Mr'$ will decrease gradually as increasing temperature. A positive $Mr'$ thus indicates that a fraction $(Mr'/Ms)$ of the system can not reverse its magnetization with the help of the thermal energy. Following Ref. 11, $Mr'(T) = Ms(T)\int_{E_a^{\rm crit}}^{\infty} f(Ea)dEa$, where $E_a^{\rm crit}$ is a critical energy barrier below which thermal activation may induce magnetization reversal. Since $Ea$ is proportional to $T_b$, $f(E_a)$ is proportional to the blocking temperature distribution $f(T_b)$, which may be obtained by numerical derivative of "$Mr'(T)/Ms(T)$" with respect to temperature. Assuming that the energy barrier is entirely due to the volume dependent anisotropy constant, $f(T_b)$ represents the distribution of the volume of the magnetic particles.

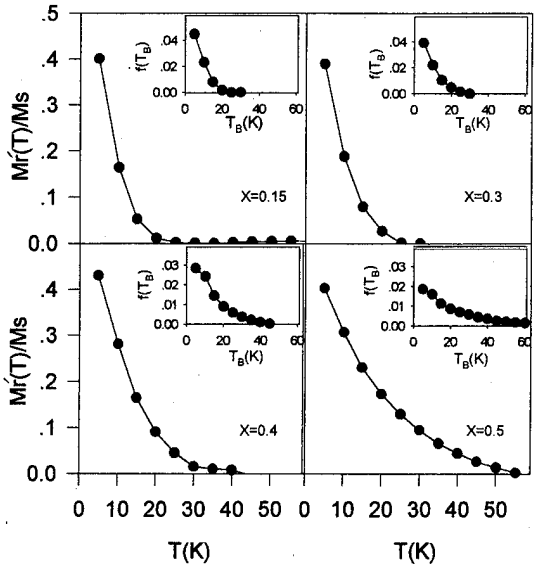



FIG. 3. $Mr'(T)/Ms(T)$ for $x$=0.15, 0.3, 0.4, and 0.5. Inserts show the corresponding blocking temperature distribution function $f$(Tb).

Figure 3 shows $Mr'(T)/Ms(T)$ vs $T$ for samples with $x$=0.15 (a), 0.3 (b), 0.4 (c), and 0.5 (d), respectively. Note that only the temperature region with positive $Mr(T)$ is included due to the difficulty of this method in treating negative remanence.[8] Inserts in Fig. 3 show the blocking temperature distribution $f(T_b)$ which was obtained by numerical derivative of $Mr'/Ms$ with respect to $T$. Note that upon increasing $x$, both the mean value and the uncertainty of the energy barrier increases. The larger uncertainty in the energy barrier for a larger $x$ also indicates a larger uncertainty of the particle volume, which is consistent with more extended labyrinth structure observed in the dark field TEM images. Magnetic particle size distribution was also studied via ac susceptibility as functions of temperature and frequency for different $x$'s.[12] Similar trend of increased particle size distribution with increasing $x$ was concluded.[13] Thus both analysis of the TEM images and that of the particle size distribution via remanence and ac susceptibility studies support the hypothesis of the coexistence of both the superparamagnetic and ferromagnetic components in a given temperature.

## V. SUMMARY

We have studied microstructure and remanent magnetization of the granular Ni–$SiO_2$ films. Both analysis of the TEM images and that of the particle size distribution via remanence studies support the hypothesis that both superparamagnetic and ferromagnetic components coexist in the nearly percolating films at a given temperature.

## ACKNOWLEDGMENT

Authors would like to acknowledge X. Jing, A. Pakhomov, J. Xhie, S. Hung, and J. Zheng for their technical assistance, Dr. K. Y. Szeto and Dr. Z. Zhang for the stimulating discussions, and the financial support from HKUST RI92/93.SC07 and HKUST 611/95P.

[1] R. A. McCurrie, *Ferromagnetic Materials, Structure and Properties* (Academic, New York, 1994), or other textbooks on magnetism.
[2] T. Nagata, S. Uyeda, and S. Akimoto, J. Geomagn. Geoelectr. **4**, 102 (1952); **5**, 168 (1953).
[3] L. Neel, Adv. Phys. **4**, 191 (1955).
[4] G. Gruzalski, Ph.D. Thesis, University of Nebraska, Lincoln, 1978.
[5] C. Cao and M. J. O'Shea, J. Magn. Magn. Mater. **127**, 181 (1993).
[6] M. J. O.'Shea and A. L. Al-Sharif, J. Appl. Phys. **75**, 6673 (1994).
[7] A. Aharoni, J. Appl. Phys. **76**, 6977 (1994).
[8] X. Yan and Y. Xu, these proceedings.
[9] A. B. Pakhomov, X. Yan, and B. Zhao, Appl. Phys. Lett. **67**, 3497 (1995).
[10] A. B. Pakhomov and X. Yan, these proceedings.
[11] K. O'Grady and R. W. Chantrell, in *Magnetic Properties of Fine Particles*, edited by J. L. Dormann and D. Fiorani (North-Holland, Amsterdam, 1992).
[12] B. Zhao, J. Y. Chou, and X. Yan, paper FR-08 of this same conference.
[13] There is a discrepancy between ac and remanence measurements in terms of the particle volume by a factor 5 or so. We feel that this is likely due to a small remanent magnetic field in the remanence measurement due to the past magnetic history, causing error in obtaining particle size distribution. Since ac measurements were done with no prior history for both the magnet and the sample, and is therefore more reliable.

# Observation of giant Hall effect in granular magnetic films

A. B. Pakhomov,[a] X. Yan, and Y. Xu
*Department of Physics, Hong Kong University of Science and Technology, Clear Water Bay, Kowloon, Hong Kong*

The Hall effect in granular co-sputtered ferromagnetic metal–insulator films was found to increase dramatically as the magnetic volume fraction decreases toward the metal–insulator transition. The saturated Hall resistivity is up to 160 $\mu\Omega$ cm at $T=5$ K, that is almost four orders of magnitude greater than that in a pure magnetic metal sample. Close to the metal–insulator transition, both magnetoresistivity and the saturated Hall resistivity decrease with increasing temperature. Correlations of the Hall resistivity with resistivity and magnetoresistivity are discussed. © *1996 American Institute of Physics.* [S0021-8979(96)77708-1]

The discovery of giant magnetoresistance (GMR) in magnetic multilayers[1,2] and granular magnetic—nonmagnetic metal alloys[3] revived the interest to studies of magnetotransport in nanostructured inhomogeneous magnetic solids. Along with GMR, the extraordinary Hall effect was studied for transition metal granular solids. The values of the saturated Hall resistivities $\rho_{xys}$ of up to 1 $\mu\Omega$ cm, that are greater than the typical values for pure ferromagnets, were observed.[4] The granular co-sputtered composite films studied in this work are different from those in Refs. 3 and 4 in that the nonmagnetic component is insulating, so a metal–insulator transition is observed at certain critical volume fraction of metal. Such systems have been widely studied before. Some works on Ni–$SiO_2$ films are listed in Ref. 5. But to the best of our knowledge, no experimental studies of extraordinary Hall effect in magnetic metal–insulator composites have been reported in the literature prior to Refs. 6 and 7. In this work we show that $\rho_{xys}$ as large as 160 $\mu\Omega$ cm can be achieved near the metal–insulator transition. This is a factor of $4\times10^3$ enhancement compared to that in a metallic ferromagnet. By analogy with the "giant" magnetoresistance effect,[1–3] we call the observed phenomenon "giant" Hall effect.

The composite films of about 1 $\mu$m thick, with the different metal volume fractions $x$ in the range $0.5<x\leqslant1$, were prepared on rotating glass substrates in a Denton magnetron co-sputtering system, with magnetic metal [$Ni_{85}Fe_{15}$ (Ref. 8)] and insulator ($SiO_2$) targets mounted on two separate guns. Near the metal–insulator transition, the samples consist of 5–8 nm metal grains imbedded in amorphous insulating matrix.[8] The magnetic metal volume fraction $x$ was determined by energy-dispersive X-ray spectroscopy using a Philips EDAX XL30. The resistance and the Hall resistance were measured in the temperature range between 5 and 300 K, in the fields $|H|\leqslant2.15$ T. Magnetization was measured on a Quantum Design SQUID with magnetic field perpendicular to the film plane.

The Hall resistivity $\rho_{xy}$ of ferromagnetic metals is a sum of two terms, of which the ordinary Hall resistivity, due to the Lorentz force, is proportional to the field. The second, extraordinary part, is attributed to spin–orbit interactions during scattering of the magnetically polarized conduction $d$ electrons on impurities or phonons, and hence is proportional to magnetization.[9] If the extraordinary Hall coefficient is much greater than the ordinary one, the plots of the Hall resistivity against field look like magnetization curves. A small finite slope at fields over saturation is due to the ordinary Hall effect. A qualitatively similar shape was also observed for all our samples with magnetic volume fractions $x>0.53$. Shown in Fig. 1 are the field dependencies of the magnetization $M$, the resistivity $\rho_{xx}$, and the Hall resistivity $\rho_{xy}$ for a sample with $x\approx0.61$, at $T=5$ K [Fig. 1, column (a)] and $T=300$ K [column (b)]. As the ordinary Hall effect is relatively small, the values of $\rho_{xy}$ at $H=2$ T are referred to as the saturated Hall resistivity $\rho_{xys}$ in this work. It can be seen that both $\rho_{xys}$ and magnetoresistivity decrease with increasing temperature.

In Fig. 2 we show $\rho_{xys}$ and $\rho_{xx}$ as functions of $x$, at $T=5$ K. For $x$ in region 1 shown in Fig. 2, the samples are metallic. At high temperatures the temperature coefficient of resistivity (TCR) is positive. However, below certain temperature which depends on $x$, the TCR crosses over to negative, which has been attributed[6,7] to the effect of electron–electron interactions.[10] Below that temperature, the dependence of $\rho_{xx}$

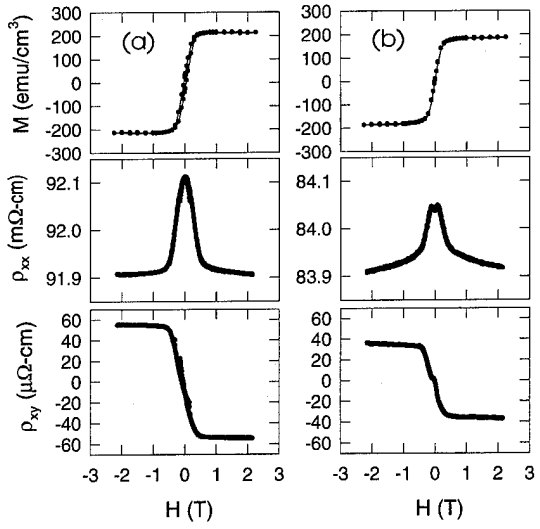



FIG. 1. Field dependencies of the magnetization $M_x$, the resistivity $\rho_{xx}$, the Hall resistivity $\rho_{xy}$ for the sample with $x=0.61$ at (a) $T=5$ K and (b) $T=300$ K. The magnetic field is perpendicular to the sample plane.

[a]On leave from: A F Ioffe Physical Technical Institute, Saint-Petersburg 194021, Russia.

 0021-8979/96/79(8)/6140/3/$10.00 © 1996 American Institute of Physics

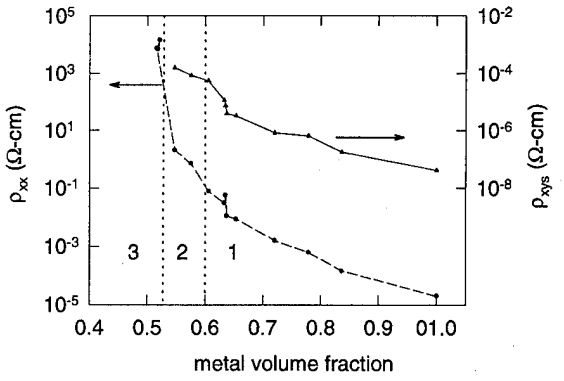



FIG. 2. Resistivity and the Hall resistivity as functions of the metal volume fraction $x$ at $T=5$ K.

on temperature is approximately logarithmic.[10] An example of a $\rho_{xx}$ vs $T$ plot for the same sample as in Fig. 1 ($x=0.61$) is shown in Fig. 3. At the metal–insulator transition (region 2 in Fig. 2), the TCR is negative in the whole temperature range of 5–300 K, and the temperature dependence of resistivity is stronger than logarithmic.[6,7] In the dielectric region 3 conductivity is thermally activated.[6,7] The value of $\rho_{xys}$ increases greatly with decreasing $x$, and reaches a maximum at $x\approx0.55$, which is as large as 160 $\mu\Omega$ cm. The corresponding Hall coefficient defined as $\rho_{xy}/H$ being $\sim-4\times10^{-4}$ Ω cm/T for $H\leqslant0.4$ T, compared to $-7.7\times10^{-8}$ Ω cm/T for $x=1$. Fitting the data for resistivity and Hall resistivity to the percolation relations $\rho_{xx}\propto[(x-x_c)/x_c]^{-t}$, and $\rho_{xys}\propto[(x-x_c)/x_c]^{-g}$,[11,12] was attempted.[7] At any reasonable choice of $x_c$, the fits gave the critical exponents $t$ and $g$ greater than those predicted by discrete percolation models [$t\approx2$ and $g\approx0.4$–0.5 (Refs. 11 and 12)].

To gain insight on the mechanisms of magnetotransport, in Fig. 3 we plot the saturation magnetization $M_s$, the

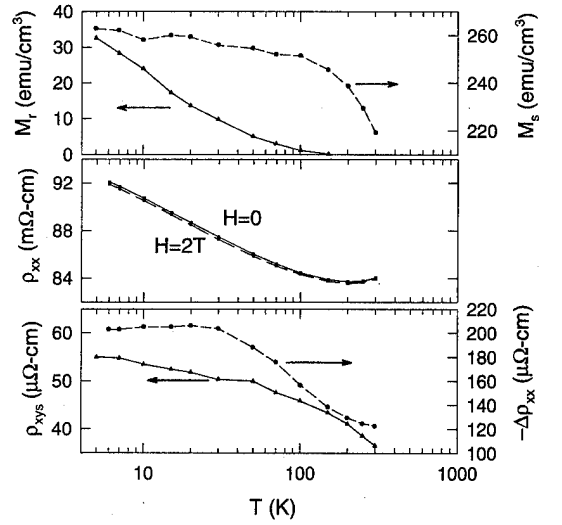



FIG. 3. Saturation magnetization ($M_s$) as defined in the text, remanent magnetization ($M_r$), resistivity $\rho_{xx}$ at $H=0$ (squares and solid connecting line) and at $H=2$ T (triangles and dashed connecting line), magnetoresistivity $-\Delta\rho_{xx}=\rho_{xx}(0)-\rho_{xx}(2\text{ T})$, the Hall resistivity $\rho_{xys}$ at $H=2$ T vs logarithm of temperature for the same sample as in Fig. 1, $x=0.61$.

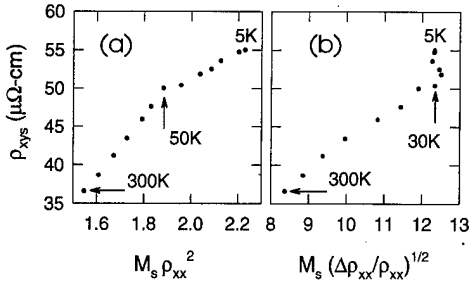



FIG. 4. This figure shows the correlations of the Hall resistivity with $\rho_{xx}^2$, and, at high temperatures, with $(\Delta\rho_{xx}/\rho_{xx})^{1/2}$. Temperature is an implicit parameter.

remanent magnetization $M_r$, as well as the resistivity $\rho_{xx}$ at the fields of both $H=0$ and $H=2$ T, the magnetoresistivity—$\Delta\rho_{xx}=\rho_{xx}(0)-\rho_{xx}(2\text{ T})$, and the Hall resistivity $\rho_{xys}$ defined above as functions of temperature for the same representative sample as in Fig. 1 ($x=0.61$). In this work we use the values of $M$ at $H=2$ T for $M_s$, which was measured at a fixed field with temperature varying from 5 to 300 K. The remanent magnetization was measured by first setting the field to 3 T at 5 K, then setting it to zero and measuring the moment with stepping up temperature from 5 to 300 K. The temperature scale in Fig. 3 is logarithmic, primarily to demonstrate the logarithmic temperature dependence of resistivity at low T. We notice that the difference in resistivity at $H=2$ T and at $H=0$ is very small compared to the temperature dependent logarithmic correction, suggesting that the negative TCR is not associated with the change in spin-dependent scattering rates. The correction due to electron–electron interactions[10] being a probable reason. On the other hand magnetoresistivity, which is of the order of 0.2% of resistivity, was found to be negative for longitudinal, transverse and perpendicular geometries. This appears to suggest that the mechanism is likely to be spin-dependent scattering of conduction electrons on granular boundaries. Scattering decreases at saturation, when the directions of magnetization in different grains are more correlated. The variation of $|\Delta\rho_{xx}|$ below ~30 K is small, while between 30 and 300 K, it drops by roughly a factor of 2 (Fig. 3). We relate the crossover at 30 K to the onset of superparamagnetism,[14,15] corresponding to the blocking temperature determined by a single particle size. From the measurements of $M_s$ and $M_r$ vs T (Fig. 3) all particles are free to rotate above $T\sim100$ K, which is likely to be related to the blocking temperature of the clustered particles.[8]

Only a small change in the slope of the $\rho_{xys}$ vs $\log T$ curve around 50 K can be seen in Fig. 3. The crossover becomes more obvious from a plot of $\rho_{xys}$ vs the product $\rho_{xx}^2M_s$, with $T$ an implicit parameter [Fig. 4(a)]. The scaling predicted by the side jump theory of extraordinary Hall effect[9] seems to hold, but the slopes are different below and above 50 K. Besides, the mechanisms developed for metals may not be valid for the system under investigation. It has been noted in Refs. 13 and 16 that the GMR and the extraordinary Hall effect in a Co–Ag granular system should be correlated. On the other hand, we assume that in a percolating ferromagnet the extraordinary Hall effect is due to scat-

terings of polarized conduction $d$ electrons with spins aligned with the field, the number of these electrons being proportional to magnetization,[9] while magnetoresistance is due to scatterings of all electrons. A scaling in the form $\rho_{xys} \propto (\Delta\rho_{xx}/\rho_{xx})^n M_s$, where $n$ is an unknown exponent, is examined. As shown in Fig. 4(b), the high temperature behavior can be successfully described by the latter relation for $n$ of 1/2, but no correlation is observed at low temperatures. We admit that the particular value of $n$ is not justified, and the choice of $n=1/2$ is arbitrary.

The giant Hall resistivity in the percolating granular magnetic system points out a number of interesting applications for Hall sensors. It may be used as a magnetic field sensing element in a read head of magnetic recording devices, in magnetic switching devices or in a magnetic random memory. The main advantages are that the Hall element will be sensitive to the direction of the magnetic field and will not require a bias field which is necessary in sensors based on the magnetoresistance or spin valve effect. The high resistivity may be a limitation. The initial achievement of the saturation Hall resistivity of over 100 $\mu\Omega$ cm in our best percolating films is already considerably larger than the largest extraordinary Hall effect reported so far for magnetic granular systems which is $\sim 1$ $\mu\Omega$ cm.[4,16]

To conclude, we found a giant enhancement of the extraordinary Hall effect in magnetic metal–insulator granular films, as the metal volume fraction in the composite decreases from 1 to 0.55. The enhancement is greater than that predicted by the percolation theory. Correlations of the Hall resistivity with both resistivity $\rho_{xys} \propto M_s \rho_{xx}^2$ and magnetoresistivity $\rho_{xys} \propto M_s (\Delta\rho_{xx}/\rho_{xx})^{1/2}$ are investigated with temperature being an implicit parameter. The latter relation holds for high temperatures where both magnetoresistivity and the Hall resistivity may be dominated by magnetic disorder via spin-dependent scattering.

Authors would like to acknowledge Jie Xhie for the help with film deposition, Wesley Nieveen for the composition analysis and Bin Zhao for the help in experiment. This work was partly supported by Grant Nos. HKUST RI92/93.SC07 and HKUST 611/95P.

[1] M. N. Baibich, J. M. Broto, A. Fert, F. Nguen van Dau, F. Petroff, P. Etienne, G. Creuzet, A. Friederich, and J. Chazeles, Phys. Rev. Lett. **61**, 2472 (1988).
[2] S. S. P. Parkin, N. More, and K. P. Roche, Phys. Rev. Lett. **64**, 2304 (1990).
[3] A. E. Berkowitz, J. R. Mitchell, M. J. Carey, A. P. Young, S. Zhang, F. E. Spada, F. T. Parker, A. Hutten, and G. Thomas, Phys. Rev. Lett. **68**, 3745 (1992); J. Q. Xiao, J. S. Jiang and C. L. Chien, *ibid.* **68**, 3749 (1992).
[4] J.-Q. Wang and G. Xiao, Phys. Rev. **49**, 3982 (1994).
[5] J. I. Gittleman, Y. Goldstein, and S. Bozowski, Phys. Rev. B **5**, 3609 (1972); J. I. Gittleman, B. Abeles, and S. Bozowski, *ibid.* **9**, 3891 (1974); J. R. Beamish, B. M. Patterson and K. M. Unruh, in *Physical Phenomena in Granular Materials*, edited by G. D. Cody, T. H. Geballe, and P. Sheng (MRS, Pittsburgh, 1990), p. 129; X. Yan and Y. Xu, these proceedings; B. Zhao, Y. Chow, and X. Yan, *ibid.*
[6] A. B. Pakhomov, X. Yan, and B. Zhao, Appl. Phys. Lett. **67**, 3497 (1995).
[7] A. B. Pakhomov and X. Yan (unpublished).
[8] Y. Xu, B. Zhao, and X. Yan, these proceedings.
[9] A. Fert and D. K. Lottis, in *Concise Encyclopedia of Magnetic and Superconducting Materials*, edited by J. Evetts (Pergamon, Oxford, New York, 1992), p. 287, and references therein.
[10] B. L. Altshuler and A. G. Aronov, in *Electron–Electron Interactions in Disordered Systems* (North-Holland, Amsterdam, 1985), p. 1. Electron–electron interactions result in a $T^{1/2}$ correction at low $T$ in $3d$, and a $\log T$ in $2d$. To explain the $\log T$ dependence in the percolating samples, we assume that the fractal dimension of the percolation channels is the relevant dimensionality. See G. Deutscher, B. Bandyopadhyay, T. Chui, P. Lindenfeld, W. L. McLean, and T. Worthington, Phys. Rev. Lett. **44**, 1150 (1980).
[11] D. J. Bergman and D. Stroud, Solid State Phys. **46**, 149 (1992).
[12] M. Sahimi, *Applications of Percolation Theory* (Taylor and Francis, Bristol, PA, 1994).
[13] P. Xiong, G. Xiao, J. Q. Wang, J. Q. Xiao, J. S. Jiang, and C. L. Chien, Phys. Rev. Lett. **69**, 3220 (1992).
[14] B. Abeles, in *Applied Solid State Science*, edited by R. Wolfe (Academic, New York, 1976).
[15] C. L. Chien, J. Appl. Phys. **69**, 5267 (1991).
[16] J.-Q. Wang and G. Xiao, Phys. Rev. B **51**, 5863 (1995).

# Freezing of the extended state in the random local field theory of Ising spin glasses with long range interactions

B. E. Vugmeister[a)]
*Department of Physics, Lehigh University, Bethlehem, Pennsylvania 18015*

D. Nowakowski
*Department of Physics, Harvard University, Cambridge, Massachusetts 02138*

D. L. Huber
*Department of Physics, University of Wisconsin-Madison, Madison, Wisconsin 53706*

The onset of spin glass freezing in dilute Ising systems with long range interactions is investigated within the framework of a random local field approach (previously developed for disordered ferromagnets and ferroelectrics) with the use of numerical simulations. The problem reduces to the diagonalization of an $N\times N$ random matrix, $N$ being the number of spins in the simulation, whose elements depend on the spin–spin interaction and temperature. We identify the onset of spin glass freezing with the temperature at which this boundary eigenvalue separating localized and extended states is equal to one. Numerical simulations give a reasonable value of the freezing temperature for dilute RKKY spin glasses and reproduce its linear concentration dependence in agreement with the scaling relation. © *1996 American Institute of Physics.* [S0021-8979(96)23108-3]

We consider Ising spin glasses with the Hamiltonian

$$H=-\frac{1}{2}\sum_{ij} J_{ij}S_iS_j, \quad S_i=\pm 1, \tag{1}$$

where $J_{ij}$ is the interaction between spins separated by the distance $r_{ij}$. For RKKY interactions

$$J_{ij}=A\,\frac{\cos(2k_Fr_{ij})}{r_{ij}^3}. \tag{2}$$

The goal of the present article is to give an estimate of the spin glass freezing temperature $T_g$ based on Eqs. (1) and (2). In particular, we will show that the dependence of $T_g$ on spin concentration $c$ in a very dilute limit is in agreement with the scaling relation[1] $T_g\sim c$. Until recently there has been no proof given for the validity of the scaling law directly from Eqs. (1) and (2). For example, the approach followed in recent papers leads to $T_g\sim c^{1/2}$ as $c\to 0$.[2]

In its application to dilute Ising spin glasses with RKKY interactions, the present article follows the approach[3] of averaging first over thermal fluctuations before averaging over configurational disorder. First of all, we consider a fixed configuration of the spins and perform the thermal averaging, using the so called random local field approach that has been originally developed for dilute Ising ferromagnets and ferroelectrics, where it was found to be a significant improvement over conventional mean field theory.[4]

In applying the model to dilute systems with long range interactions, additional complications are encountered due to the existence of localized states. In order to find a characteristic boundary (or "mobility edge") between localized and extended states and to estimate the freezing temperature of the extended states, we performed the configurational average of the microscopic equations using computer simulation techniques, numerically diagonalizing random matrices that corresponds to RKKY interactions, between spins randomly occupying sites on a three-dimensional simple cubic lattice. The analogous approach based on local mean field equations has been reported recently.[5]

In the development of random local field approach we start from the identity[6]

$$\langle S_i\rangle=\left\langle \tanh\left(\frac{H_i}{T}\right)\right\rangle, \tag{3}$$

where

$$H_i=\sum_j J_{ij}S_j \tag{4}$$

is the local field acting on every spin due to interaction with its neighbors. Equation (7) can be written in the form

$$\langle S_i\rangle=\int dH\,\tanh\left(\frac{H}{T}\right)f_i(H), \tag{5}$$

where

$$f_i(H)=\langle\delta(H-H_i)\rangle=\frac{1}{2\pi}\int d\rho e^{i\rho H}f_{i\rho}, \tag{6}$$

in which

$$f_{i\rho}=\langle\exp[-i\rho H_i]\rangle=\langle\Pi_k[\cos(\rho J_{ik})-iS_k\,\sin(\rho J_{ik})]\rangle. \tag{7}$$

In order to calculate the spin glass transition temperature, it is sufficient in Eq. (7) to keep only terms linear in $\langle S_i\rangle$. We also neglect correlations between different spins

[a)]Present address: Department of Chemistry, Princeton University, Princeton, New Jersey 08544.

 0021-8979/96/79(8)/6143/3/$10.00 © 1996 American Institute of Physics 

$k,k'\ldots$, interacting with spin $i$, which is equivalent to making a pair approximation. When this is done, the expression for $f_{i\rho}$ assumes the form

$$f_{i\rho}=\Pi_k \cos(\rho J_{ik})-i\sum_j \Pi_{k\neq j}\cos(\rho J_{ik})\sin(\rho J_{ij})\langle S_j\rangle. \tag{8}$$

We make the replacement

$$\Pi_{k\neq j}\cos(\rho J_{ik})\approx\overline{\Pi_{k\neq j}\cos(\rho J_{ik})} \tag{9}$$

based on the fact that the cosine function partially suppresses the effect of fluctuations in $J_{ij}$ that originate from the variable sign interactions. Equation (9) is the exact result for the infinite range SK model with $J_{ij}=\pm J/(N^{1/2})$, $N$ being a number of spins.

In dilute systems in which the randomness in the interaction stems from the random occupation of the lattice sites, the result of the configurational average in Eq. (9) can be written in the form $\exp[-F_1(\rho)]$, where for $c\ll 1$ $F_1(\rho)$ is given by

$$F_1(\rho)=c\sum_j (1-\cos[\rho J(r_{ij})]), \tag{10}$$

where the summation in Eq. (10) is taken over all lattice sites. Using Eqs. (6) and (8) in Eq. (5) we obtain the equation[4(b)]

$$\langle S_i\rangle=\sum_j \phi_{ij}^{\mathrm{RLF}}(T)\langle S_j\rangle, \tag{11}$$

where

$$\phi_{ij}^{\mathrm{RLF}}(T)=T\int_0^\infty \frac{d\rho\,\exp[-F_1(\rho)]\sin(J_{ij}\rho)}{\sinh(\pi\rho T/2)}. \tag{12}$$

Equation (12) is the fundamental equation of the random local field approximation. Note that $\Phi_{ij}^{\mathrm{RLF}}$ remains finite as $T\to 0$.

Before considering the application of Eq. (11) to realistic models, it is worthwhile seeing the consequences for the SK model. Under these conditions, $F_1(\rho)=\rho^2J^2/2$, while $\sin(J_{ij})$ can be approximated by its argument. The matrix $\Phi_{ij}^{\mathrm{RLF}}$ then assumes the form

$$\phi_{ij}^{\mathrm{RLF}}(T)=\left\{T\int_0^\infty \frac{d\rho\,\exp[-\rho^2J^2/2]\rho}{\sinh(\pi\rho T/2)}\right\}J_{ij}. \tag{13}$$

We note that for infinite range interactions all eigenvectors of the random matrix $\Phi_{ij}^{\mathrm{RLF}}$ are delocalized,[3,7] and the transition temperature can be identified with the temperature at which the largest eigenvalue of the matrix $\Phi_{ij}^{\mathrm{RLF}}$ is equal to one. Since the largest eigenvalue of Eq. (13) is equal to the expression in braces multiplied by $2J$,[3] one obtains an expression for $T_g$ by numerically evaluating the integral. The result is $T_g=1.48$ J, which is halfway between the mean field and exact results, and, thus, is a significant improvement over the former. Since the random local field approximation gives a rather good account of the effect of fluctuations in the SK model, it is likely to be a reasonable first step in the estimation of $T_g$ in the RKKY model.

The main difference between the SK model and the model given by Eqs. (1) and (2) is the existence of localized states, the latter associated with small clusters of spins. It is clear, however, that localized states are not responsible for the collective behavior of the system which is the property of delocalized, extended states. The crossover between localized and extended states has been extensively studied (see, for example, Refs. 8–10) in connection with the problem of Anderson localization. It has been shown that the boundary between localized and extended states is usually rather sharp, and the characteristic eigenvalue of the effective interaction matrix for which a relative variance in the distribution of eigenvalues is equal to 1/2 can be considered as a simple criterion determining the crossover between localized and extended states. The relative variance (that is the ratio between the variance and the distribution function) approaches 1 for Poisson statistics, that are a characteristic of localized states, and is much less than 1 for extended states. We have performed the numerical solution of Eqs. (1) and (2) using computer simulation techniques (with $k_F=3$). We randomly distributed approximately $N=900$ Ising spins on a simple cubic lattice with periodic boundary conditions, where the size of the lattice had been adjusted to the spin concentration. We then calculated all eigenvalues $E_k$ $(k=1,\ldots,N)$ of the matrix $\Phi_{ij}^{\mathrm{RLF}}$.

In order to calculate the distribution function of the eigenvalues we divided the interval $[-R,R]$ into 200 subintervals and collected the number $n(E)$ of eigenvalues in each subinterval. This was repeated for 100 different random configurations of the spins and the results averaged. The distribution function was written as

$$\sigma(E)=\frac{1}{M}[n(E)]_{\mathrm{av}}, \tag{14}$$

where $M$ is the normalizing coefficient.

In the same manner we calculated the variance of the eigenvalue distribution

$$\mathrm{var}(E)=\frac{1}{M}([n(E)^2]_{\mathrm{av}}-[n(E)]_{\mathrm{av}}^2). \tag{15}$$

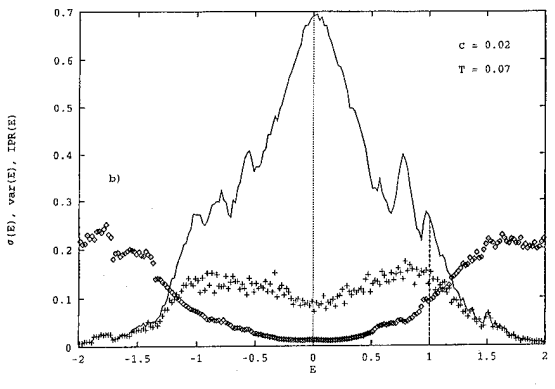



FIG. 1. Eigenvalue distribution function, $\sigma(E)$ (solid line), variance, $\mathrm{var}(E)$ (crosses), and inverse participation ratio $\mathrm{IPR}(E)$ (diamonds) corresponding to matrix $\Phi_{ij}^{\mathrm{RLF}}$ for $c=0.02$ and $T_g=0.07$ (in units $|A|/d^3$).

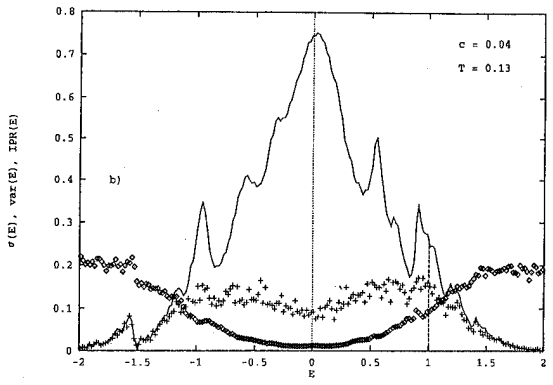



FIG. 2. Eigenvalue distribution function, $\sigma(E)$ (solid line), variance, var($E$) (crosses), and inverse participation ratio IPR($E$) (diamonds) corresponding to matrix $\Phi_{ij}^{\mathrm{RLF}}$ for $c=0.04$ and $T_g=0.13$ (in units $|A|/d^3$).

We have tested the effect of finite lattice size by comparing the results obtained for 900 spins with those for 1300 spins. No noticeable difference in eigenvalue distributions was found.

We have also considered another very common localization measure, the inverse participation ratio, IPR($E$), for the eigenvalue $E$, defined as

$$\mathrm{IPR}(E)=\sum_j \psi_j(E)^4, \tag{16}$$

where $\psi_j(E)$, $j=1,\ldots,N$, are the corresponding eigenvector components. Because $\Sigma_j\psi_j^2=1$, the IPR should be very small, i.e., proportional to $1/N$ for very delocalized states, and approaching one only in the opposite limit of extreme localization.

In order to find the estimate for the $T_g$ we have performed numerical simulations using the values of $\Phi_{ij}^{\mathrm{RLF}}$ matrix at different temperatures and found the temperature for which $E_m=1$.[11] $E_m$ is the crossover eigenvalue separating localized and extended states (see Figs. 1 and 2). This temperature corresponds to the freezing temperature $T_g$ of the extended states. We found $T_g\approx 0.07\pm 0.01$ for $c=0.02$, $T_g\approx 0.1\pm 0.01$ for $c=0.03$, $T_g\approx 0.13\pm 0.01$ for $c=0.04$ (in units $|A|/d^3$, $d$ is the lattice constant). One can see that $T_g$ scales practically linearly with concentration in agreement with scaling relation and can be written as

$$T_g^{\mathrm{RLF}}\simeq 3c\,\frac{|A|}{d^3}. \tag{17}$$

Note that the values of $T_g$ given by Eq. (17) are approximately one-half of the corresponding values for $T_g$ in the mean field approximation.[5]

From a comparison of the numerical values of $T_g$ obtained here with the results of mean field simulations[5] and with the presented above analyses of the SK model one can conclude that the effect of thermal fluctuations on RKKY spin glasses is as crucial as for the SK infinite range interaction model, a result which is consistent with the long range nature of the RKKY interaction. Such a correspondence between the effect of fluctuations in RKKY and SK Ising spin glasses allows us to estimate $T_g$ in RKKY Ising spin glasses as $T_g\simeq 2C|A|/d^3$.


[1] J. A. Mydosh, *Spin Glasses: An Experimental Introduction* (Taylor & Francis, London, 1993).

[2] P. J. T. Eggenkamp *et al.*, Phys. Rev. B **51**, 15250 (1995). In the theory of Shegelski and Geldart [M. R. Shegelski and D. J. Geldart, Phys. Rev. B **46**, 2853 (1992)], $T_g$ is infinite in the absence of electron mean free path effects.

[3] D. J. Thouless, P. W. Anderson, and R. G. Palmer, Philos. Mag. **35**, 593 (1977).

[4] (a) B. E. Vugmeister and V. A. Stefanovich, Solid State Commun. **67**, 323 (1987); (b) Sov. Phys. JETP **70**, 1053 (1990).

[5] B. E. Vugmeister, D. Nowakowski, and D. L. Huber, Solid State Commun. **96**, 711 (1995).

[6] H. B. Callen, Phys. Lett. **4**, 161 (1963).

[7] E. P. Wigner, Ann. Math. **62**, 548 (1955); **67**, 325 (1958).

[8] S. N. Evangelou, J. Stat. Phys. **69**, 361 (1992).

[9] B. L. Al'tshuler, I. Kh. Zharekeshev, S. A. Koshigova, and B. I. Shklovskii, Sov. Phys. JETP **67**, 625 (1988).

[10] Y. V. Fedorov and A. O. Mirlin, Phys. Rev. Lett. **67**, 2049 (1991).

[11] In Ref. 5 a similar analysis has been performed for mean field matrix $J_{ij}T$.

# Criticality of the fully frustrated *XY* model: A study using Monte Carlo hard-spin mean-field theory (abstract)

James E. Tesiero and Susan R. McKay
*Department of Physics and Astronomy, University of Maine, Orono, Maine 04469-5709*

The number and types of phase transitions occurring in the two-dimensional fully frustrated *XY* model have remained controversial in spite of over a decade of attention. In this study, we have developed a Monte Carlo hard-spin mean-field[1] approach for models with a continuous spin variable and applied it to this system. From our calculations of the chirality, helicity modulus, specific heat, and sublattice magnetizations, we find that reflection and rotational symmetries are broken at the same temperature. The chirality, order parameter for the reflection symmetry breaking, exhibits power-law dependence on $T-T_c$ with a critical exponent of $0.246\pm0.006$. This result is decisively different from the mean-field value of 0.500, which would be obtained for a transition in the Ising universality class using this method. This finding enables us to rule out the possibility of two separate transitions, too closely spaced in temperature to be resolved by our calculation. The magnitude of the magnetization on each sublattice also shows power-law behavior as a function of temperature in the critical region, with a critical exponent of $0.126\pm0.002$. © *1996 American Institute of Physics.* [S0021-8979(96)43908-8]

[1]R. R. Netz and A. N. Berker, Phys. Rev. Lett. **66**, 377 (1991).

 0021-8979/96/79(8)/6146/1/$10.00 © 1996 American Institute of Physics

# Magnetization and dynamics of reentrant ferrimagnetic spin-glass $[MnTPP]^{\cdot+}[TCNE]^{\cdot-}\cdot 2PhMe$

W. B. Brinckerhoff and B. G. Morin
*Department of Physics, The Ohio State University, Columbus, Ohio 43210-1106*

E. J. Brandon and Joel S. Miller
*Department of Chemistry, The University of Utah, Salt Lake City, Utah 84112*

A. J. Epstein
*Department of Physics and Department of Chemistry, The Ohio State University, Columbus, Ohio 43210-1106*

We present direct current (dc) magnetization $M(T,H)$ and alternating current (ac) susceptibility $\chi_{ac}(T,H,f)$ data for the quasi-one-dimensional molecule-based ferrimagnet $[MnTPP]^{\cdot+}[TCNE]^{\cdot-}\cdot 2PhMe$ (TPP=*meso*-tetraphenylporphyrinato, TCNE=tetracyanoethylene). Static scaling of the real part $\chi'$ of the ac susceptibility and data collapse of $M(T,H)$ over a limited reduced temperature range above $T_c \approx 13$ K lead to the critical exponents $\gamma \approx 1.6$, $\beta \approx 0.5$, and $\delta \approx 4.2$. Below $T_c$, $\chi_{ac}$ depends sensitively on frequency and exhibits a striking double-peak structure similar to that found in reentrant spin glasses. Possible models for the frequency dependence of the peaks observed in $\chi_{ac}$ are discussed. © *1996 American Institute of Physics.* [S0021-8979(96)23208-X]

## INTRODUCTION

Interest in molecule-based magnets has expanded rapidly as materials with novel physics and technological potential continue to be realized.[1] The first molecular systems possessing bulk magnetization at room temperature were the disordered, organic-based compounds $V(TCNE)_x \cdot y$(solvent) (TCNE=tetracyanoethylene).[2] More recently, magnetism in the vicinity of room temperature has also been observed in the $M[M'(CN)_6]\cdot nH_2O$ Prussian Blue class of materials.[3]

The relative ease of synthesis of molecule-based magnets also yields unique opportunities for studying low-dimensional magnets. In the one-dimensional case, the properties of integral vs half-integral spin chains,[4] alternating quantum-classical ferrimagnetic chains,[5] and low-dimensional spin glasses[6] are currently of great theoretical interest.

The class of metalloporphyrin-TCNE electron-transfer compounds is of interest for its unusual structural and magnetic properties.[7,8] The parent compound, $[MnTPP]^{\cdot+}[TCNE]^{\cdot-}\cdot 2PhMe$ (TPP=*meso*-tetraphenylporphyrinato) is comprised of chains of alternating [MnTPP] ($S_1=2$) and [TCNE] ($S_2=1/2$) molecular units with direct metal-CN bonds similar to those in V(TCNE).

In this paper, we present detailed measurements of direct current (dc) magnetization $M(T,H_{dc})$ and alternating current (ac) susceptibility $\chi_{ac}(T,f,H_{ac},H_{dc})$ for $[MnTPP]^{\cdot+}[TCNE]^{\cdot-}\cdot 2PhMe$. A state of long-range ferrimagnetic order builds up as $T$ is decreased below ~20 K toward a critical temperature of $T_c \approx 13$ K as determined from a static scaling analysis. The broad temperature region of incipient ferrimagnetism above $T_c$ may result from the presence of highly anisotropic coherent clusters of spins and the effects of disorder. At lower temperatures ($T<10$ K), a distinct second peak appears in the out-of-phase ac susceptibility, indicative of the "reentrant" transition to a spin-glass "phase" which coexists with ferrimagnetic order in the field-cooled state. The frequency dependence of this lower-temperature peak, however, is stronger than that observed in the canonical spin glasses[9] as well as known reentrant alloys.[10] The field dependence of the low-temperature state is similar to that of a metamagnet: spins of disordered ferrimagnetic chains reorient coherently over a temperature-dependent critical field range $[\Delta H_c(T)]$ to a state with saturated ferrimagnetic order. These results are compared to the expectations of a model of anisotropic, interacting superparamagnetic clusters.

## EXPERIMENT

The preparation of [MnTPP][TCNE] has been described earlier.[7] The dc magnetization was measured with a Quantum Design MPMS5 superconductory quantum interference device magnetometer in the ranges $2 \leq T \leq 400$ K and $0 \leq H_{dc} \leq 5$ T. The ac susceptibility was measured via the mutual inductance technique with a LakeShore 7225 ac Susceptometer/dc Magnetometer in the ranges $4 \leq T \leq 30$ K and $0 \leq H_{dc} \leq 1$ T. The real and imaginary components of the linear susceptibility were recorded for an ac field of 0.1 Oe and a range of frequencies (5 Hz$\leq f \leq$40 kHz). The dominant source of uncertainty in determining the magnitude of the molar susceptibilities was the sample mass, estimated to be accurate to within 2%.

## RESULTS

The temperature dependence of the zero-field cooled (ZFC) molar magnetization of $[MnTPP]^{\cdot+}[TCNE]^{\cdot-}\cdot 2PhMe$ for different applied fields is shown in Fig. 1. The lowest temperature state is demagnetized ($M$ is near zero at 5 K). The magnetization goes through a broad maximum centered between 8 and 11 K depending on field. As $T$ increases above 15 K, $M$ drops quickly; the intermediate temperature ($100<T<250$ K) $M(T)$ data (not shown) follow Curie–Weiss behavior with $\chi_{dc}=M/H=C/(T-\theta)$, with $\theta=+61$ K. At room temperature, $C \approx 3.1$ emu K mol$^{-1}$, consistent with molecular units with $S_1=2$ (MnTPP) and $S_2=\frac{1}{2}$ (TCNE). The large negative Curie–Weiss temperature $\theta<-100$ K for $T>250$ K indicates antiferromagnetic coupling between adjacent spins. The inset of Fig. 1 shows field cooled (FC) and

 0021-8979/96/79(8)/6147/3/$10.00 © 1996 American Institute of Physics 

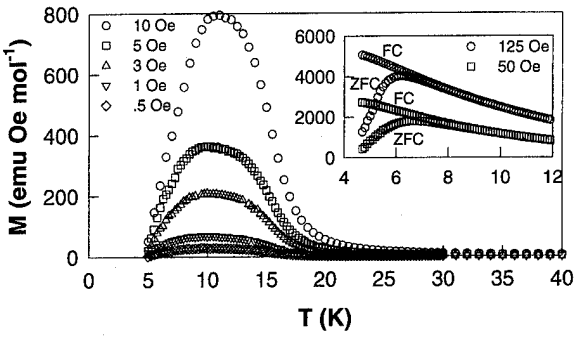



FIG. 1. Temperature dependence of zero-field cooled (ZFC) magnetization at small applied fields. Inset: FC vs ZFC magnetization at 50 and 125 Oe.

ZFC magnetization data at two fields. While the ZFC curves are only obtained on warming, the FC magnetization, which lies above the ZFC magnetization at low temperatures, is reversible at the sweep rate of $\sim 0.1$ K min$^{-1}$. The point where the FC and ZFC data merge is taken as the irreversibility temperature $T_f(H)$.

Isothermal magnetization data were recorded in a ZFC state (initial curves) for several temperatures $2 \leqslant T \leqslant 35$ K (Fig. 2). The saturation magnetization ($H > 4$ T) is $M_S \approx 17\,000$ emu Oe mol$^{-1}$, consistent with the expected value ($M_S = 16\,755$ emu Oe mol$^{-1}$) for a ferrimagnet of net spin $\frac{3}{2}$ per repeat unit. The S-shaped approach to saturation occurs at lower fields as $T$ increases from 2 K.

The zero dc field susceptibility data are presented in Fig. 3. The real $\chi'$ and imaginary $\chi''$ parts of $\chi_{ac}$ were recorded on warming from a ZFC state. An ac field of amplitude $H_{ac} = 0.1$ Oe was applied in a sequence of frequencies (5 Hz $\leqslant f \leqslant$ 40 kHz). Due to the small ac amplitude, a low signal-to-noise ratio was obtained at certain frequencies. A limited frequency range (20 Hz $\leqslant f \leqslant$ 1 kHz) is included in Fig. 3 to maximize clarity. The real part $\chi'$ becomes strongly frequency dependent below $\sim 14$ K. In addition, a distinct shoulder appears in $\chi'$ at lower temperatures. This feature is isolated in the imaginary part $\chi''$ as a separate peak. The "double-peak" structure in these data is discussed below.

## DISCUSSION

The results of the static scaling analysis are presented in Fig. 4. The Kouvel–Fisher[11] scaling function $X_{KF}(T) = -\chi'(d\chi'/dT)^{-1}$ [Fig. 4(a), left axis], obtained from the real zero-field ac susceptibility $\chi'$, has the linear (scaling) form $X_{KF}(T) = (T - T_c)/\gamma$ only above $\sim 16$ K. The critical temperature $T_c \approx 12.5$ K and average susceptibility exponent $\gamma \approx 1.6$ are obtained from the $T$ intercept and inverse slope of $X_{KF}$, respectively. The fact that $\chi'$ does not obey a power law in $|t|$ within $\sim 3$ K above $T_c$ may reflect the presence of strong spatial anisotropy ($J_{inter}/J_{intra} \sim 10^{-2}$)—the buildup of long-range intrachain correlations is particularly sensitive to defects and disorder, possibly leading to the formation of quasi-one-dimensional (1D) "domains" well above $T_c$. Consequently, the "core" (3D) critical region is not probed in this measurement and the observed $\gamma$ is expected[11] to be enhanced over its true value. The effective exponent $\gamma(T) = (T - T_c)/X_{KF}$ [Fig. 4(a), right axis] elucidates the presence of a region ($T < 16$ K) where $\chi'$ does not scale, below an unusually wide range where $\gamma(T)$ is fairly constant, falling off slowly as $T$ increases.

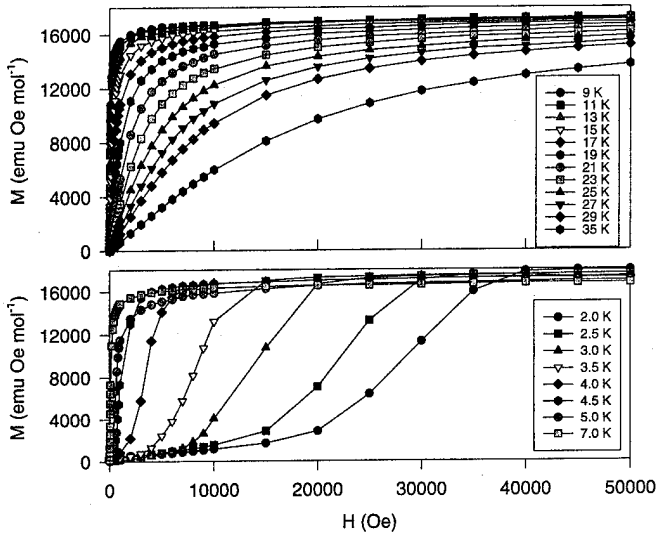



FIG. 2. Zero-field cooled (initial) isothermal dc magnetization.

The value $\gamma \approx 1.6$ is used to restrict the parameter space ($\beta, \delta$) in the scaling of $M(T,H)$ [Fig. 4(b)] through the Griffiths–Rushbrooke relation[12] $\gamma = \beta(\delta - 1)$. The trial critical temperature $T_c^{tr}$ for which the $M(T)$ data appear to coalesce for the three smallest applied fields (over a limited reduced temperature range above $T_c^{tr}$) is independently found to be $T_c \sim 13$–$13.5$ K. It is estimated that $\beta \sim 0.5$ and $\delta \sim 4.2$, though the accuracy and precision are limited by the relative insensitivity of the analysis to the choice of $\beta$ and $\delta$, and that the (possibly enhanced) $\gamma$ is obtained from data above 16 K. The $T_c$ value obtained is significantly lower than that ob-

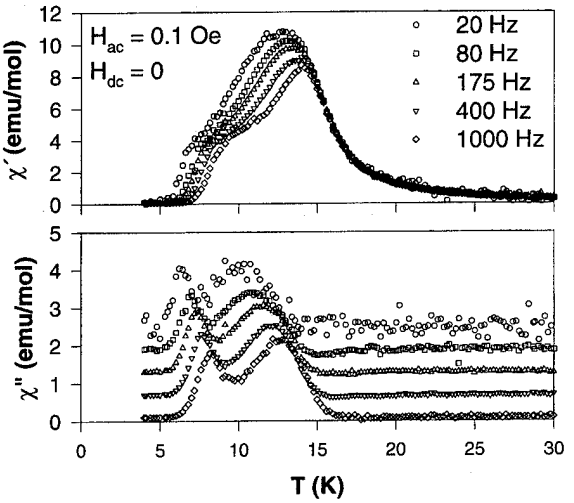



FIG. 3. Real ($\chi'$) and imaginary ($\chi''$) parts of the ZFC ac susceptibility in zero bias field $H_{dc}$ and 0.1 Oe excitation field $H_{ac}$. $\chi''$ data are shifted for clarity; high temperature values show the approximate baseline for each curve.

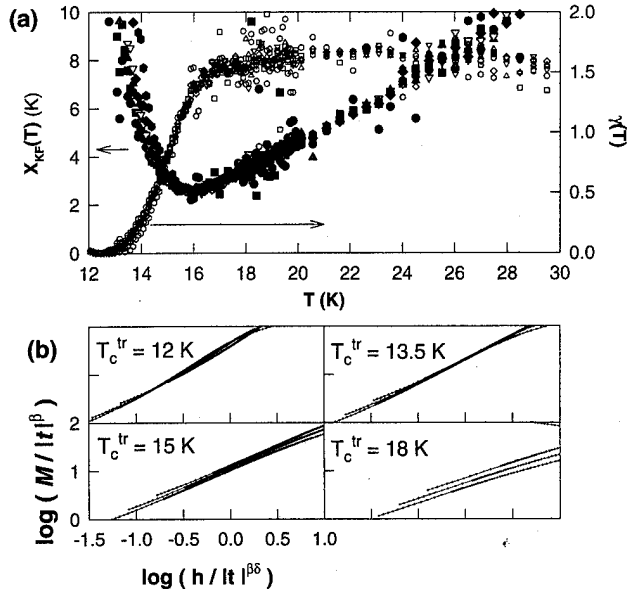



FIG. 4. (a) Kouvel–Fisher scaling function $X_{KF}(T)=-\chi'(d\chi'/dT)^{-1}$ (left axis) and temperature-dependent effective critical exponent $\gamma(T)=(T-T_c)/X_{KF}(T)$ (right axis). (b) Scaling of dc magnetization $M(T,H)$ above $T_c^{tr}$ for $\beta=0.5$ and $\delta=4.2$, where $h=H/T$. See the text.

tained by extrapolating the maximum slope[8] of the low-field $M(T)$ curve to $M=0$, which gives $T_c\approx 18$ K.

As mentioned above, the experimental observation of a "slow" transition to long-range ferrimagnetic order in $[MnTPP]^{\cdot+}[TCNE]^{-}\cdot 2PhMe$ reflects the quasi-1D magnetism in this system. In chainlike magnets, significant long-range longitudinal spin–spin correlations build up well before 3D order is established. For instance, specific heat studies reveal that a very high fraction of the magnetic entropy of quasi-1D magnets lies above $T_c$.[13]

The low-temperature isothermal magnetization $M(H)$ and the appearance of the "reentrant" transition may be interpreted as resulting from the behavior of interacting, anisotropic superparamagnetic clusters. Superparamagnetism (SPM) describes the behavior of well separated, classical (large $S$) spin clusters which behave paramagnetically at high temperatures, but due to internal shape or dipolar anisotropy energy barriers are "blocked" from undergoing global spin flips below a characteristic temperature $T_b$. SPM leads to broad maxima around $T_b$ in $M(T)$ and $\chi_{ac}$, with the latter following an Arrhenius frequency dependence $\omega=\omega_0\exp(-E_a/k_BT)$, where $E_a$ is a characteristic anisotropy energy. In contrast, [MnTPP][TCNE] is a magnetically concentrated system, so intercluster interactions are likely very important, and may be responsible for the spin-glass-like behavior.

The S-shaped crossover in $M(H)$ from low-$M$ to saturation occurs in a range $\Delta H_c(T)$. If $H_c(T)$ is defined as the midpoint of the crossover, it is seen that both $H_c$ and $\Delta H_c$ decrease as $T$ increases from 2 to 7 K. The $\Delta H_c$ trend favors a disordered, spin-glass-like state at low $T$ and $H$ rather than a pure antiferromagnetic one as in the ideal metamagnetic case. Due to a strongly spatially anisotropic exchange $J$, spin clusters in [MnTPP][TCNE] are expected to be elongated. The increase in $\Delta H_c$ as $T$ decreases indicates the presence of a broadening distribution of barriers to the rotation of spin cluster moments.

The appearance of a second, lower temperature peak in $\chi_{ac}$ is similar to that seen in "reentrant" spin-glass (RSG) alloys.[14] However, the frequency dependence of both lower ($T_1$) and upper ($T_2$) peak temperatures is quite strong, suggesting that [MnTPP][TCNE] lies somewhere between traditional RSGs and pure SPM. The fractional shifts in peak temperature per decade of frequency are $(\Delta T_1/T_1)/(\Delta \log f)\approx 0.23$ and $(\Delta T_2/T_2)/(\Delta \log f)\approx 0.14$. Fits to pure Arrhenius behavior give $E_{a1}/k_B\approx 112$ K and $f_{01}\approx 940$ MHz ($\tau_{01}\sim 10^{-9}$ s) for $T_1(\omega)$ and $E_{a2}/k_B\approx 247$ K and $f_{02}\approx 420$ GHz ($\tau_{02}\sim 2.4\times 10^{-12}$ s) for $T_2(\omega)$. ($\tau_0=1/f_0$ is the characteristic limiting relaxation time for a given frequency prefactor $f_0$). The peak positions are relatively close to the "typical" blocking temperatures obtained using $T_b\sim E_a/25k_B$.[10] The applicability of the model of transverse spin freezing[14] to [MnTPP][TCNE] is under investigation.

## ACKNOWLEDGMENTS

The support of the Department of Energy Division of Materials Science (DE-FG02-86BR45271 and DE-FG03-93ER45504) and the National Science Foundation (CHE9320478) is gratefully acknowledged.

[1] J. S. Miller and A. J. Epstein, Angew. Chem. Int. Ed. Engl. **33**, 385 (1994); *Proceedings of the 4th International Conference on Molecule-Based Magnets*, J. S. Miller and A. J. Epstein, eds., Mol. Cryst. Liq. Cryst. **271–274** (1995). *Proceedings of the NATO ASI on Localized and Itinerant Molecular Magnetism* (to be published).

[2] J. M. Manriquez, G. T. Yee, R. S. McLean, A. J. Epstein, and J. S. Miller, Science **252**, 1415 (1991); B. G. Morin, P. Zhou, C. Halm, A. J. Epstein, and J. S. Miller, J. Appl. Phys. **73**, 5648 (1993); P. Zhou, B. G. Morin, J. S. Miller, and A. J. Epstein, Phys. Rev. B **48**, 1325 (1993); W. B. Brinckerhoff, J. Zhang, J. S. Miller, and A. J. Epstein, Mol. Cryst. Liq. Cryst. **272**, 195 (1995).

[3] T. Mallah, S. Ferlay, C. Auberger, C. Helary, F. L'Hermite, R. Ouahes, J. Vaissermann, M. Verdaguer, and P. Veillet, Mol. Cryst. Liq. Cryst. **273**, 579 (1995).

[4] F. D. M. Haldane, Phys. Rev. Lett. **50**, 1153 (1983).

[5] J. Curély, R. Georges, and M. Drillon, Phys. Rev. B **33**, 6243 (1986); M. Drillon, E. Coronado, R. Georges, J. C. Gianduzzo, and J. Curély, *ibid.* **40**, 10992 (1989); J. Curély and R. Georges, *ibid.* **49**, 1146 (1994); **49**, 1158 (1994).

[6] J. A. Lukin, S. A. Friedberg, S. Chadarlapathy, W. W. Brubaker, C. C. Cinquina, and G. C. DeFotis, J. Appl. Phys. **75**, 5529 (1994); A. N. Kocharian and A. S. Sogomonian, *ibid.* **76**, 6186 (1994); E. B. Kolomeisky, Phys. Rev. B **51**, 3047 (1995).

[7] J. S. Miller, J. C. Calabrese, R. S. McLean, and A. J. Epstein, Adv. Mater. **4**, 498 (1992); D. A. Summerville, T. W. Cape, E. D. Johnson, and F. Basolo, Inorg. Chem. **17**, 3297 (1978).

[8] P. Zhou, B. G. Morin, A. J. Epstein, R. S. McLean, and J. S. Miller, J. Appl. Phys. **73**, 6569 (1993).

[9] J. A. Mydosh, *Spin Glasses: An Experimental Introduction* (Taylor and Francis, London, 1993).

[10] T. Eckelt, Ch. Böttger, and J. Hesse, J. Magn. Magn. Mater. **104–107**, 1665 (1992); B. Özçelik, K. Kiymaç, J. C. Verstelle, A. J. van Duyenveldt, and J. A. Mydosh, J. Phys. Condensed Mater. **4**, 6639 (1992); S. Giri, K. Ghoshray, R. Ranganathan, A. Roy, B. Bal, and A. Ghoshray, Solid State Commun. **91**, 273 (1994).

[11] J. S. Kouvel and M. E. Fisher, Phys. Rev. A **136**, 1626 (1964); S. N. Kaul, J. Magn. Magn. Mater. **53**, 5 (1985).

[12] R. B. Griffiths, Phys. Rev. Lett. **14**, 623 (1965).

[13] A. Chakraborty, A. J. Epstein, W. N. Lawless, and J. S. Miller, Phys. Rev. B **40**, 11422 (1989).

[14] B. R. Coles, Philos. Mag. B **49**, L21 (1984); I. A. Campbell and S. Senoussi, Philos. Mag. B **65**, 1267 (1992); M. J. P. Gingras, in *Magnetic Systems with Competing Interactions*, edited by H. T. Diep (World Scientific, Singapore, 1994), p. 238.

# The anhydrous alums: A versatile new series of model triangular lattice magnets (abstract)

S. T. Bramwell, L. Nixon, I. P. Parkin, B. M. Kariuki, and K. D. M. Harris
*University College London, Department of Chemistry, 20 Gordon Street, London WC1H 0AJ, United Kingdom*

S. G. Carling
*The Royal Institution of Great Britain, 21 Albermarle Street, London W1X 4BS, United Kingdom*

C. J. Harding
*Department of Chemistry, The Open University, Walton Hall, Milton Keynes MK7 6AA, United Kingdom*

There is considerable theoretical interest in triangular and stacked triangular lattice antiferromagnets, particularly as regards their phase transitions and the nature of the ground state of quantum systems with spin $S=\frac{1}{2}$. There are, however, no good experimental representatives of the $S=\frac{1}{2}$ triangular lattice antiferromagnet, and indeed there are few good representatives of those with higher spin. Given the diversity of theoretical problems associated with these systems there is a clear need to find appropriate new model materials. We report the discovery of a versatile new series of triangular lattice magnets, the anhydrous alums of general formula $AM(SO_4)_2$, with A=alkali metal, M=Ti,V,Cr,Fe. In these materials the magnetic M ions occupy a regular or very slightly distorted triangular lattice in well-separated layers. All show magnetic ordering effects in the range 2–10 K, the near-neighbor exchange being antiferromagnetic for Ti, V, and Fe and ferromagnetic for Cr. The Ti materials, which we have made for the first time, have $S=\frac{1}{2}$, and may prove to be the best examples of the $S=\frac{1}{2}$ triangular lattice antiferromagnet yet discovered. In general, our ability to control the spin value, spin anisotropy, and exchange anisotropy makes the anhydrous alums a potentially useful series for the investigation of a variety of physical problems. © *1996 American Institute of Physics.* [S0021-8979(96)44008-4]

 0021-8979/96/79(8)/6150/1/$10.00 © 1996 American Institute of Physics

# Finite size effects in thin NiMn spin glass layers

L. Hoines,[a] J. A. Cowen, and J. Bass[b]
*Department of Physics and Astronomy and Center for Fundamental Materials Research, Michigan State University, East Lansing, Michigan 48824*

Measurements of the normalized spin freezing temperatures, $T_f/T_f^b$, ($T_f^b$=bulk spin-freezing temperature) are reported for NiMn/Cu multilayers in which the Mn concentrations are in the spin-glass range and the Cu thickness is held constant at a large enough value ($t_{Cu}$=30 nm) to magnetically decouple the NiMn layers. The variation of $T_f/T_f^b$ with NiMn layer thickness, $t_{NiMr}$, is very similar to the variations previously found for CuMn, AgMn, and AuFe. Quasistatic finite size effects in NiMn spin-glass thus appear to be rather similar to those in the more traditional noble-metal spin glasses. © *1996 American Institute of Physics.* [S0021-8979(96)23308-6]

## I. INTRODUCTION

There has recently been considerable interest in finite size effects (FSE) in magnetic materials.[1–11] In ferromagnets, deviations of the Curie temperature, $T_c$, from its bulk value $T_c^b$ do not become large until the ferromagnetic layer thickness, $t_F$, reaches a few monolayers (ML).[11] In the noble-metal-based spin glasses (SGs), CuMn, AgMn, and AuFe, in contrast, we have shown that the quasi-static spin-freezing temperature, $T_f$, deviates significantly from its bulk value, $T_f^b$, by SG layer thickness $t_{SG}$=100 ML, and reaches 50% of $T_f^b$ by $t_{SG}$~20 ML.[1–3] In this paper, we examine the variation of $T_f$ with $t_{SG}$ for a very different kind of SG, NiMn. The issue of interest is the universality of quasistatic FSE in SGs, previously shown to hold for the noble-metal based SG alloys.[1–3]

The noble-metal based SG alloys consist of dilute magnetic impurities in a nonmagnetic host, in which the impurities interact only with each other, primarily via the RKKY exchange interaction.[12] The NiMn alloys of interest, in contrast, contain two magnetic components, neither of which is dilute. All atoms have magnetic neighbors, and the dominant interaction is short range exchange, with competition between ferromagnetic Ni–Ni and Ni–Mn and antiferromagnetic Mn–Mn interactions.[13] As Mn is added to pure Ni, ferromagnetism persists until the Mn–Mn interactions disrupt the long-range magnetic order. This disruption leads[14] first (Fig. 1) to a rentrant SG (RSG) regime for 24 at.%>$c_{Mn}$>22 at.% Mn, that exhibits paramagnetic (P) to ferromagnetic (F) to disordered SG-like transitions with decreasing temperature, and then, for $c_{Mn}$>24 at.%, to a regime where there is only a P to a more nearly normal-SG transition.[15] It is this latter regime on which we focus in the present paper. Abdul-Razzaq and Wu[16] reported little or no FSE down to $t_{RSG}$=10 nm in a brief study of NiMn thin films in the RSG regime.

## II. SAMPLES AND PREPARATION

To obtain enough SG material for quantitative analysis of FSE, in our previous studies of noble-metal based SG alloys, we sputtered multilayers composed of alternating layers of the SG of interest and one of the nonmagnetic host metals, with the interlayer thickness, $t_{IL}$, thick enough (typically $t_{IL}$=30 nm) to make interactions between the SG layers negligible.[2] We found that different noble metal interlayers yielded essentially the same FSE behavior.[2] Since the two constituents of NiMn are both magnetic, we could not use either for the interlayer material in similar multilayers. Based upon our experience with the noble-metal SG multilayers, and because the noble metals sputter well, we decided to use Cu as the interlayer metal with the NiMn. From previous observations that 30 nm of a wide variety of metals magnetically decouples noble metal SG layers,[17] we assumed the same behavior for NiMnSG layers separated by Cu. To test that this assumption was not strongly violated, we checked for a variation in $T_f/T_f^b$ as the Cu thickness was reduced from $t_{Cu}$=30 to 10 nm for multilayers with $t_{NiMn}$=4 nm, where $T_f/T_f^b$~0.6. The change in $t_{Cu}$ from 30 to 10 nm caused only a small increase in $T_f/T_f^b$, comparable to the measuring uncertainties.

Because Cu is not a constituent of NiMn, it might perturb the NiMn multilayer data due to boundary intermixing. For CuMn and AgMn, non-noble metal interlayers such as Al, Nb, and V, all gave lower values of $T_f$ than those for noble metal interlayers when the SG layer thicknesses fell below about 4 nm.[17] We attributed these reductions to interface mixing that reduced the Mn contribution to SG behavior, since Mn did not give SG behavior in those other metals. The situation in NiMn is more complex. Since CuMn is a

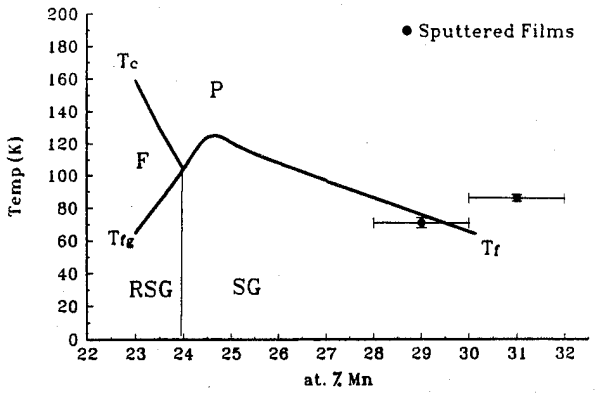



FIG. 1. The spin-freezing temperatures of our sputtered films of thicknesses ≥50 nm compared with the NiMn magnetic phase diagram from Abdul-Razzaq and Kouval (Ref. 14).

[a]Present address: Naval Research Laboratory.
[b]Author to whom correspondence should be sent.

 0021-8979/96/79(8)/6151/3/$10.00 © 1996 American Institute of Physics 

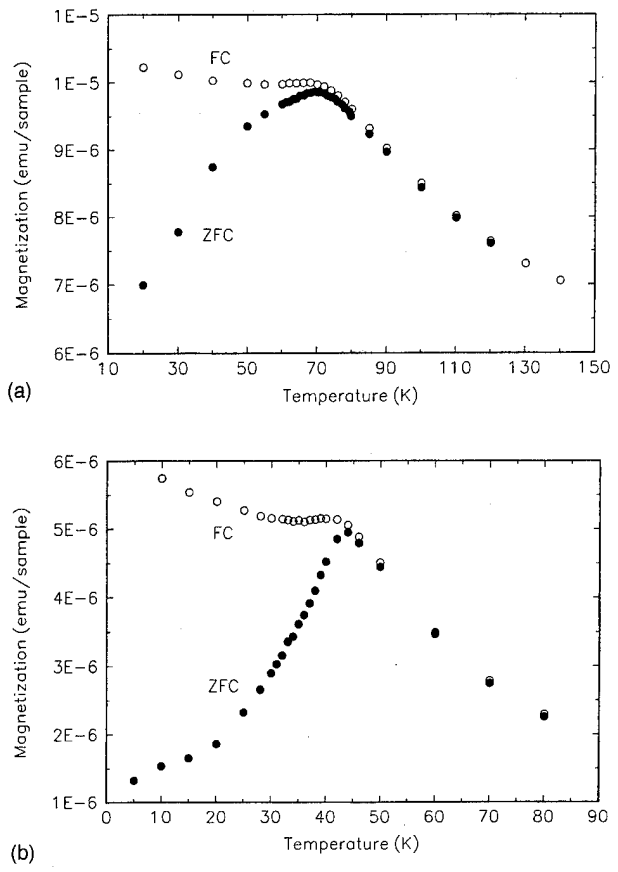



FIG. 2. The field-cooled (FC) (open symbols) and zero-field-cooled (ZFC) magnetizations of (a) a 300 nm thick sputtered single film; and (b) a NiMn [(2 mn/30 nm)×50] multilayer.

SG, dispersal of Mn into the Cu can also lead to SG behavior. Dilute CuNi alloys, in contrast, do not display SG-like behavior.[18] It is thus not clear whether mixing Cu into the edges of a NiMn layer, or spreading some of the Ni and Mn into the Cu interlayer, should drive $T_f$ up or down. In the present study, we assume that the Cu has no net effect on the data. Further studies with interlayers of metals in which both Ni and Mn impurities are nonmagnetic are needed to confirm this assumption.

The multilayers were sputtered in the same system previously used for SG FSE studies in CuMn, AgMn, and AuFe.[2,3] The 1/4 in. thick by 2 in. diam Cu targets were spark cut from 5–9 s pure Cu sheet, while the SG targets were locally fabricated from 3–9 s pure Ni and Mn pellets. Our standard procedure of rf induction melting in a $BN_2$ coated carbon crucible yielded contaminated samples. We thus developed a procedure in which the NiMn alloy was melted inside an alumina crucible that fit snugly into the carbon crucible. This procedure reduced the maximum diameter of the NiMn targets to 1.5 in.

Aside from the use of smaller targets, the only other important change in sample fabrication was adopted because of the instability of NiMn against possible onset of chemical short-range-order at room temperature.[19] To minimize such effects, the substrates were held at temperatures below −20 °C during the entire sputtering run and the sputtering system was opened while still cold so that the multilayers could be quickly transferred into liquid nitrogen for storage until they were measured.

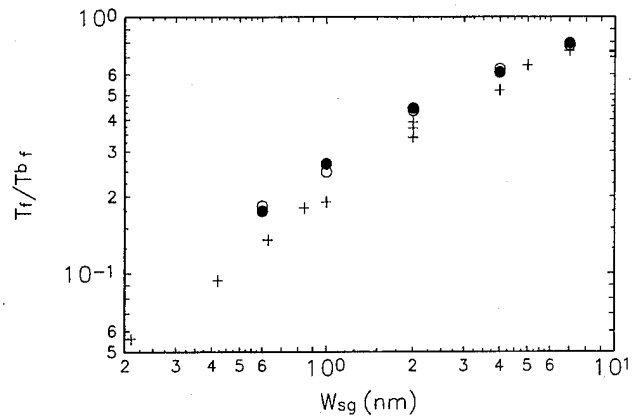



FIG. 3. $T_f/T_f^b$ vs $t_{SG}$ for two sets of (NiMn/Cu) multilayers (open and filled circles) and for CuMn(11 at.%)/Cu and CuMn(14 at.%)/Cu multilayers (crosses).

EDX measurements of the two NiMn targets used in the present study gave Mn concentrations of 29±1 and 31±1 at.% (Fig. 1). These concentrations should be in the SG region.[15] Measurements of $T_f^b$ made on films at least 50 nm thick, that were sputtered alternately with the multilayers, showed that $T_f^b$ was constant to within ±2 K about the average during a single sputtering run.

## III. DATA AND ANALYSIS

Figure 2 shows examples of magnetizations $M$ vs $T$ for: (a) a 300 nm thick NiMn film, and (b) a multilayer with 50 bilayers of NiMn/Cu (2 nm/30 nm). Both samples show typical SG behavior—a peak in the zero-field-cooled (ZFC) data (filled symbols), the location of which we define as $T_f$, and irreversibility between the ZFC and FC (open symbols) data below about $T_f$.

Figure 3 compares the ratio $T_f/T_f^b$ vs $t_{SG}$ for NiMn/Cu multilayers from our two independent NiMn targets with similar data for CuMn(11 at.%)/Cu and CuMn(14 at.%)/Cu multilayers.[2,20] We see that, although the NiMn data display very similar overall behavior, they lie slightly above the CuMn data. Subject to the caveat noted above—that we assume that the Cu interlayer does not perturb the NiMn data—we conclude that the variation of the ratio $T_f/T_f^b$ with $t_{SG}$ is similar for NiMn and CuMn.

This result leads us to the rather surprising conclusion that FSE in the quasistatic freezing temperature do not appear to be sensitive to whether the dominant interaction between the magnetic impurities in the SG is long range RKKY as in CuMn, or shorter range direct exchange as in NiMn.

## ACKNOWLEDGMENTS

This research was supported in part by the NSF under Grant No. 91-21481 and by the MSU Center for Fundamental Materials Research.

[1] G. G. Kenning, J. A. Slaughter, and J. A. Cowen, Phys. Rev. Lett. **59**, 2596 (1987).
[2] G. G. Kenning *et al.*, Phys. Rev. B **42**, 2393 (1990); J. Bass and J. A.

Cowen, *Recent Progress in Random Magnets*, edited by D. H. Ryan (World Scientific, New Jersey, 1992), p. 177.
[3]L. Hoines, J. A. Cowen, and J. Bass, Physica B **194–196**, 309 (1994).
[4]A. Gavrin *et al.*, Phys. Rev. Lett. **64**, 2438 (1990).
[5]J. Vranken *et al.*, Phys. Scr. T **25**, 348 (1989); H. Vloeberghs *et al.*, Europhys. Lett. **12**, 557 (1990).
[6]D. J. Webb and J. D. McKinley, Phys. Rev. Lett. **70**, 509 (1993).
[7]C. Dekker *et al.*, Phys. Rev. B **40**, 11243 (1989); J. A. Mydosh, J. Magn. Magn. Mater. **90&91**, 318 (1990), and references therein.
[8]P. G. N. De Vegvar, L. P. Levy, and T. A. Fulton, Phys. Rev. Lett. **66**, 2380 (1991).
[9]D. S. Fisher and D. A. Huse, Phys. Rev. B **36**, 8937 (1987).
[10]M. J. Thill and H. J. Hilhorst, J. Phys. I France **3**, 2041 (1993), and references therein.
[11]See, e.g., F. Huang *et al.*, J. Appl. Phys. **73**, 6760 (1993).
[12]K. Binder and A. P. Young, Rev. Mod. Phys. **58**, 801 (1986).
[13]H. Tange, T. Tokunaga, and M. Goto, J. Phys. Soc. Jpn. **45**, 105 (1978).
[14]W. Abdul-Razzaq and J. S. Kouvel, Phys. Rev. B **35** (1987).
[15]A. D. Gezalyan and S. V. Shul'pekova have argued that there is an antiferromagnetic RSG regime not far above 31 at.% Mn. From the behaviors of the magnetizations of our samples, we presume that we are still below any such regime.
[16]W. Abdul-Razzaq and M. Wu, J. Appl. Phys. **69**, 5078 (1991).
[17]R. Stubi *et al.*, Europhys. Lett. **19**, 235 (1992).
[18]K. H. Fischer, Landolt–Bornstein New Series, edited by K. H. Hellwege and J. L. Olsen **15a**, 289 (1982).
[19]H. Kunkel *et al.*, Philos. Mag. B **64**, 153 (1991).
[20]L. Hoines, Ph.D. thesis, Michigan State University, 1994.

# A new type of spin glass in spin-density-wave CrMn alloys (abstract)

V. Yu. Galkin and P. C. de Camargo
*Physics Department of Federal University of Parana, Curitiba, Brazil*

Naushad Ali
*Physics Department of Southern Illinois University, Carbondale, Illinois*

J. Schaf
*Physics Department of Federal University of Rio Grande do Sul, Porto Alegre*

E. Fawcett
*Physics Department of University of Toronto, Toronto, Canada*

The temperature dependence of the susceptibility $\chi(T)=M(T)/H$ of $Cr_{1-x}Mn_x$($\ll 0.1<x<8\%$ Mn) alloys in the range $5<T<400$ K and in fields up to 55 kOe, measured with a SQUID magnetometer, and hysteresis of the magnetization $M(H)$ show typical spin-glass (SG) behavior. After zero-field cooling (ZFC), $\chi(T)$ exhibits the low-$T$ maximum typical of a SG, while cooling in the measuring field (FC) gives quite different behavior. In some cases, when measuring at low field, $\chi(5\text{ K})$ is $10\times$ larger in the FC state than in the ZFC state. The temperature of the irreversibility limit decreases with increasing field. All our CrMn alloys show nonlinear field dependence of $M(H)$, with pronounced hysteresis and decay of the remanent $M$ with time. On the other hand, these alloys exhibit properties that are essentially different from those of all other metallic spin glasses: (1) the linear scaling law based on the RKKY interaction between magnetic impurities in a typical SG is not obeyed, and indeed the temperature of the maximum in $\chi(T)$ is essentially independent of Mn concentration, which shows that formation of the SG state does not depend on the distance between the Mn atoms; (2) the maximum in $\chi(T)$ in the alloy containing only a trace of Mn ($\ll 0.1\%$) is at about 40 K, a temperature at least an order of magnitude larger than that in CuMn and other metallic SG with about 0.1% impurity concentration; (3) $\chi(T)$ obeys a Curie–Weiss law above the Neel temperature, but not below, which shows that the Mn moment is frozen in the spin-density-wave (SDW) matrix of Cr. We propose a model to explain this unusual behavior, in which the SG state is formed, not as a result of frustration of the Mn impurity moments, but through the frustration of the moments of the itinerant electrons of the host Cr. At low temperatures the frozen Mn moments pin the SDW, which gives rise to frustration surfaces between adjacent domains having different phase of the SDW. This effect depends only on the $T$-dependent interaction between the Mn moment and its neighbors, and thus is independent of the Mn concentration. © *1996 American Institute of Physics.* [S0021-8979(96)44108-2]

 0021-8979/96/79(8)/6154/1/$10.00 © 1996 American Institute of Physics

# Magnetic phase diagram of the $Fe_xMn_{0.6-x}Al_{0.40}$ alloys series

G. A. Pérez Alcázar, Ligia E. Zamora, and A. Bohórquez
*Departamento de Física, Universidad del Valle. A. A. 25630, Cali, Columbia*

E. González and J. M. González
*Instituto de Ciencia de Materiales de Madrid—CSIC, Serrano 144, 28006 Madrid, Spain*

This work shows preliminary results on the study of $Fe_xMn_{0.6-x}Al_{0.40}$ alloys. It includes measurements of the temperature dependence of the ac susceptibility, zero field cooled magnetization, and Mössbauer spectroscopy. From the results obtained, the occurrence of reentrant spin glass behavior from a spin glass phase to an antiferromagnetic one for $0.2 \leqslant x \leqslant 0.35$ and from a spin glass phase to a ferromagnetic one for the $x=0.55$ sample is proposed. Also, a normal spin glass transition was detected in the Fe range corresponding to $0.35 \leqslant x \leqslant 0.5$. These results allow us to construct a magnetic phase diagram for the alloy series. © *1996 American Institute of Physics.* [S0021-8979(96)23408-2]

## I. INTRODUCTION

Previous theoretical results and experimental works[1–4] on the Fe–Mn–Al system, in particular on the disordered bcc structure of the $Fe_xMn_{0.7-x}Al_{0.3}$ (Ref. 5) series, proved the existence of pure spin glass and reentrant spin glass phases as well as the paramagnetic, ferromagnetic, and antiferromagnetic phases. The competitive ferromagnetic and antiferromagnetic exchange interactions together with the disordered structure make this behavior possible. The transition temperatures for the spin glass phases of the $Fe_xMn_{0.7-x}Al_{0.3}$ alloys are located below 70 K. A study on $Fe_{0.89-x}Mn_{0.11}Al_x$ (Ref. 6) alloys showed a strong dependence of this transition temperature on the aluminum concentration. This series shows reentrant spin glass behavior at $x=0.4$ and $T=50$ K. The concentration of aluminum cannot be too high because the disordered bcc structure and the competing exchange interactions do not occur at higher Al content. In the present work, the $Fe_xMn_{0.6-x}Al_{0.40}$ alloys were selected, and their magnetic alternating current (ac) susceptibility measured, to elucidate the different transition temperatures which characterize the magnetic phase diagram.

## II. EXPERIMENT

Samples were prepared by melting pure elements in an arc furnace under argon, homogenizing the casts in evacuated sealed quartz tubes for one week at 1273 K and quenching them in ice water. Fe content range was $0.2 \leqslant x \leqslant 0.6$. Samples were characterized using x-ray diffraction (XRD), which showed the desired bcc disordered structure.

Magnetic characterization included the measurement of the temperature dependence of the ac susceptibility, and of the zero field cooled and low field cooled magnetization. The ac susceptibility measurements (pressed powder samples) were carried out in a magnetometer/susceptometer with an ac field of 3 Oe, a direct current (dc) field of 10 Oe and a frequency of 175 Hz. Two temperature ranges 5 K$\leqslant T \leqslant$100 K and 80 K$\leqslant T \leqslant$300 K were selected using liquid helium and liquid nitrogen, respectively. The magnetization was measured in a SQUID magnetometer with a magnetic field of 50 Oe.

## III. RESULTS AND DISCUSSION

Figures 1(a) and 1(b) show the ac susceptibility vs temperature curves for 5 K$\leqslant T \leqslant$100 K and 80 K$\leqslant T \leqslant$300 K, respectively. Well defined peaks and also relatively strong changes of curvature can be noted in these curves. Temperatures of the peaks and changes of curvature for the different samples are reported in Table I and are indicated by arrows in Fig. 1.

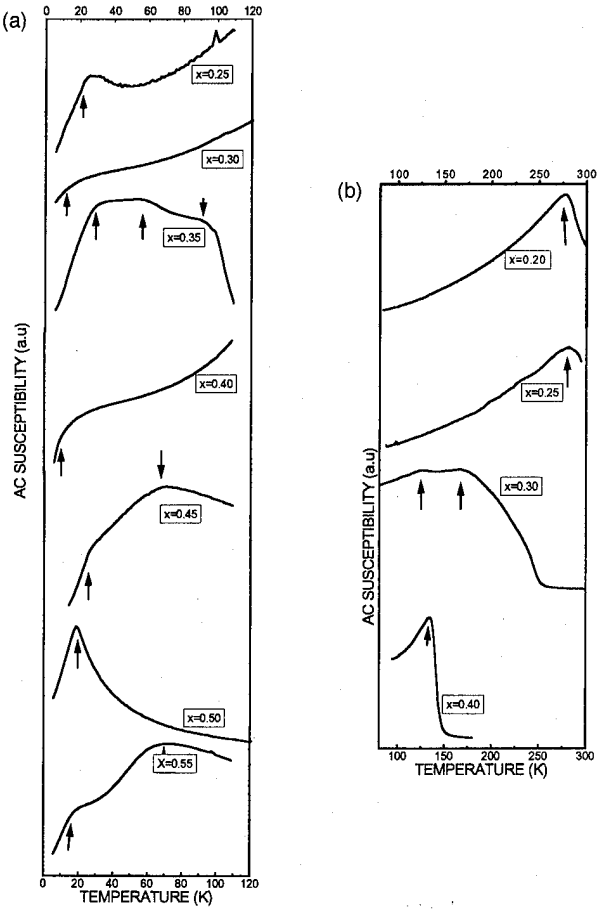



FIG. 1. Alternating current susceptibility vs temperature curves for samples with different Fe content $x$, (a) for 5 K$\leqslant T \leqslant$100 K and (b) for 80 K$\leqslant T \leqslant$300 K.

 0021-8979/96/79(8)/6155/3/$10.00 © 1996 American Institute of Physics 

TABLE I. Different temperatures, of the maxima and the changes of curvature, obtained from the ac susceptibility curves for samples with different Fe concentrations $x$.

| Sample | Temperatures |
|---|---|
| $x=0.20$ | 287 |
| $x=0.25$ | 24 and 282 |
| $x=0.30$ | 17, 120 and 167 |
| $x=0.35$ | 30, 56 and 90 |
| $x=0.40$ | 12 and 135 |
| $x=0.45$ | 17 and 61 |
| $x=0.50$ | 17 |
| $x=0.55$ | 17 and 73 |

The magnetization vs temperature curve for an $x=0.30$ sample obtained, using a SQUID magnetometer, by zero field cooling in a field of 50 Oe is similar to its ac susceptibility curve. It can be noted that the sample appears to be magnetic above 17 K. The magnetization vs temperature curve for this sample, using the SQUID magnetometer, by field cooling in a field of 2 T is showed in Fig. 2. It can be noted that there exist high magnetization values until high temperatures. These results do not agree with those obtained by Mössbauer spectroscopy. Figure 3 shows Mössbauer spectra at 17 and 85 K of the $x=0.30$ sample. It can be noted that at 85 K the sample appears to be paramagnetic and at 17 K there exists a slight broadening which can be attributed to some magnetic behavior.

In order to interpret these results it should be remembered that in this system there are different types of magnetic interactions between atoms due the ferromagnetic, antiferromagnetic, and diluted character of the Fe, Mn, and Al atoms, respectively. Thus, it is possible to have ferromagnetic bonds ($J_{FeFe}$), antiferromagnetic bonds ($J_{FeMn}$ and $J_{MnMn}$) and diluted bonds (Fe, Mn, and Al with an Al atom). Recent theoretical calculations[7] using the mean field renormalization group on a diluted and random-bond Ising model yielded ferromagnetic phase (region rich in Fe), the antiferromagnetic phase (region rich in Mn), spin glass phase (low temperatures and intermediate Fe and Mn contents), and the paramagnetic phase (high temperatures). The relationship between the exchange parameters also makes it possible to derive the reentrant spin glass phase in this system (see Refs. 4 and 7).

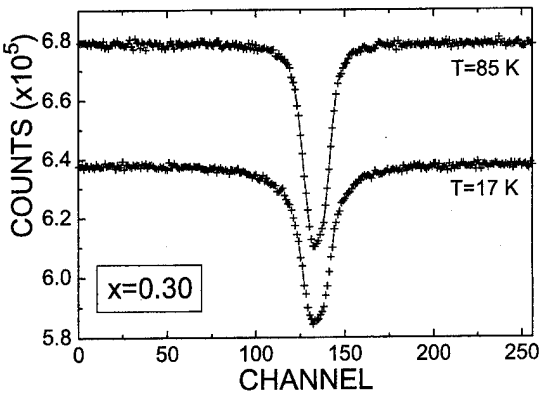



FIG. 3. Mössbauer spectra for the sample with $x=0.30$ for $T=17$ K and $T=88$ K.

According to the previous discussion and the results shown in Figs. 1(b) and 2(b) and Table I, an experimental phase diagram shown in Fig. 4 for the $Fe_xMn_{0.6-x}Al_{0.40}$ series is proposed. In this phase diagram an antiferromagnetic phase appears for $0.20 \leqslant x \leqslant 0.35$ (rich in Mn), a ferromagnetic phase appears for $0.55 \leqslant x \leqslant 0.60$ (rich in Fe), a pure spin glass phase appears for $0.35 \leqslant x \leqslant 0.55$ (intermediate Fe and Mn contents) and a reentrant spin glass phase appears at low temperatures below the antiferromagnetic region. A superparamagnetic region above the spin glass region and near the antiferromagnetic one is proposed. The dashed line represents the variation of the blocking temperature with the composition. The existence of this "superparamagnetic behavior" can be attributed to magnetic clusters of Fe and Mn atoms separated by Al atoms which at very low temperatures behave as a spin glass and for at higher $T$ behave paramagnetic, when the external field is zero, as is shown by Mössbauer spectroscopy. When a little external field is applied, for ac susceptibility or zero field cooling magnetization measurements, the clusters are aligned and thus it is possible to detect the blocking temperature. When high external field is applied, for field cooling magnetization measurement, the clusters are strongly aligned and cannot be detected by the

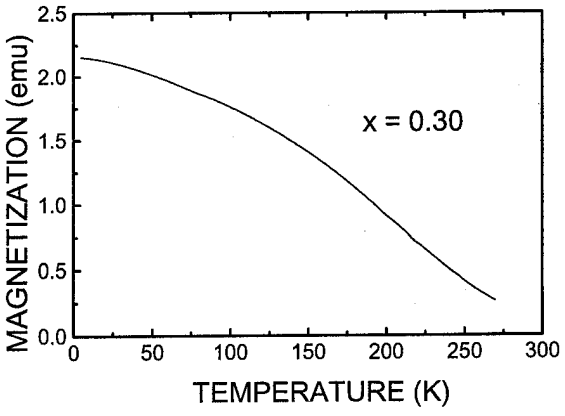



FIG. 2. Field cooling magnetization vs temperature curve using a field of 2 T.

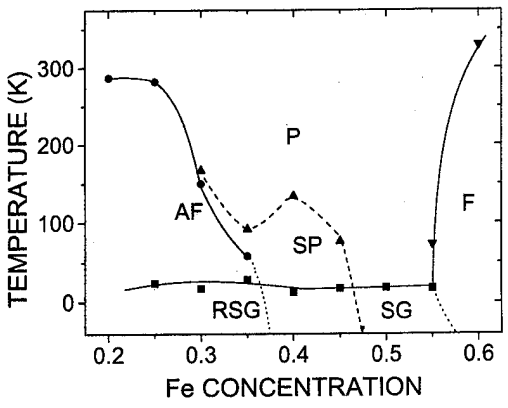



FIG. 4. Proposed magnetic phase diagram according with ac susceptibility curves.

transitions temperatures and the blocking temperature, as can be noted in Fig. 3. It is possible to think that this behavior is due to a ferromagnetic character, but the little Fe content ($x \leqslant 0.45$) is not enough to stabilize this phase as is showed by the Mössbauer spectras in Fig. 2. For alloys rich in Mn, an additional antiferromagnetic region was detected which appears above the spin glass region and below the superparamagnetic region depending on the Mn concentration. The existence of these clusters is possible remembering the structural disorder of the alloy. The experimental point for $x = 0.60$, in the magnetic phase diagram, was obtained by Mössbauer spectroscopy and is reported in Ref. 1.

Additional research work is now in progress in order to take Mössbauer spectra with an applied external field to obtain a confirmation of this superparamagnetic behavior.


## ACKNOWLEDGMENTS

The authors would like to thank Colciencias and the ALAMED Program of the European Community for financial support.



[1] G. A. Pérez Alcázar, J. A. Plascak, and E. Galvão da Silva, Phys. Rev. B **38**, 2816 (1988).

[2] A. Rosales Rivera, G. A. Pérez Alcázar, and J. A. Plascak, Phys. Rev. B **41**, 4774 (1990).

[3] M. A. Kobeissi, J. Phys. Condensed Matter **3**, 4983 (1991).

[4] Ligia E. Zamora, G. A. Pérez Alcázar, A. Bohórquez, and J. A. Tabares, J. Magn. Magn. Mater. **137**, 339 (1994); G. A. Pérez Alcázar, J. A. Tabares, A. Bohórquez, and J. R. Gancedo, Hyp. Int. **83**, 203 (1994).

[5] Ligia E. Zamora, G. A. Pérez Alcázar, A. Bohórquez, and J. F. Marco to be presented in ICAME'95, Rimini, Italy, September 1995.

[6] H. Bremers, Ch. Jarms, J. Hesse, S. Chajivasiliou, K. G. Efthimiadis, and Y. Tsoukalas, J. Magn. Magn. Mater. **140–144**, 63 (1995).

[7] Ligia E. Zamora, G. A. Pérez Alcázar, A. Bohórquez, A. Rosales Rivera, and J. A. Plascak, Phys. Rev. B **51**, 9329 (1995).

# Ferromagnetic critical correlations and dynamics in AuFe reentrant ferromagnets

C. Pappas
*Hahn-Meitner-Institut, Glienickerstrasse 100, 14109 Berlin, Germany*

M. Alba
*CEA/DRECAM, 91191 Gif-sur-Yvette Cedex, France*

A. Brulet
*LLB, CEN-Saclay, 91191 Gif-sur-Yvette, France*

V. Viel[a] and F. Mezei
*Hahn-Meitner-Institut, Glienickerstrasse 100, 14109 Berlin, Germany*

We determined the paramagnetic critical scattering of the reentrant ferromagnets $Au_{1-x}Fe_x$, with $x=0.2$, 0.18, and 0.16, i.e., close to the threshold ($x_c \sim 0.155$), below which ferromagnetism disappears and a spin-glass state sets in. Following the Ornstein–Zernicke formalism, we derived the inverse critical ferromagnetic correlation length ($\kappa=\xi^{-1}$) and the related magnetic susceptibility. The macroscopic susceptibility $\chi_{q=0}$ of the samples was also determined in a separate experiment with a Faraday balance. The neutron results show the same behavior of critical type with $\chi_{q=0}$ for $x=0.18$ but not for $x=0.16$. We interpret this discrepancy as an indication for a non-well-defined ferromagnetic transition for $x=0.16$. A further comparison of our results with those for Fe shows that the amplitude of the correlation length increase with increasing disorder so that, at the same reduced temperature $\tau$, the correlations are much larger in the disordered samples than in Fe. As a consequence of this, the ferromagnetic correlations in the disordered samples persist well above $T_c$ and lead to a much wider critical region than is the case in Fe and in usual ferromagnets. © *1996 American Institute of Physics.* [S0021-8979(96)23508-9]

## INTRODUCTION

Disordered magnetic systems with competing interactions usually show a phase diagram characterized by reentrance: they first undergo a phase transition from the paramagnetic state into a disordered ferro or antiferromagnetic one at a critical temperature $T_c$ and at low temperatures they reenter a magnetic state with spin-glass-like properties. This low temperature spin-glass phase has been the subject of numerous studies in the last twenty years,[1] where strong controversies appeared concerning its nature and the eventual presence of a long range magnetic order. However, little work has been devoted to the influence of the disorder and of the spin-glass phase, which is close in the phase diagram both in concentration and temperature, to the phase transition that takes place at $T_c$.

The above considerations prompted us to investigate the static and dynamic critical behavior by means of neutron scattering of the archetypal reentrant ferromagnetic system $Au_{1-x}Fe_x$ with $x=0.16$, 0.18, and 0.20, i.e., close to the threshold $x_c=0.155$, below which ferromagnetism disappears and spin-glass behavior sets in.[2]

The quasielastic neutron scattering results on $Au_{0.84}Fe_{0.16}$ and $Au_{0.82}Fe_{0.18}$ and the analysis of the critical paramagnetic scattering of $Au_{0.84}Fe_{0.16}$ were presented elsewhere.[3,4] Here we analyze the critical paramagnetic small angle neutron scattering (SANS) of $Au_{0.82}Fe_{0.18}$ and of $Au_{0.80}Fe_{0.20}$ and deduce the inverse correlation length $\kappa=\xi^{-1}$ and the related critical exponents $\nu$. By comparing the SANS results to the macroscopic volumic susceptibility, we determine for $Au_{0.82}Fe_{0.18}$ and $Au_{0.84}Fe_{0.16}$ the dipolar wave vector $q_D$ and the SANS susceptibility. The qualitative agreement between the macroscopic and the SANS susceptibility is a strong indication in favor of a well-defined ferromagnetic transition for $x \geqslant 0.18$. However, for $x=0.16$, the SANS susceptibility is qualitatively different from the macroscopic one. We interpret this discrepancy as an indication of the breakdown of the ferromagnetic phase transition in the vicinity of the percolation threshold.

## SANS RESULTS

Our samples were polycrystalline discs prepared by arc melting of the constituents as described elsewhere.[3] Their homogeneity was tested by microprobe analysis and magnetic susceptibility measurements with a Faraday balance.

The SANS experiments were done with polarized neutrons at the neutron spin echo spectrometer of the LLB (Saclay). The neutron wavelength was 6 Å and the $q$ resolution of spectrometer was equal to $9\times10^{-3}$ Å$^{-1}$.

The transition temperatures were determined from the peaks of the critical scattering of a depolarized neutron beam. The measurements were done at the lowest $q$ value, which was equal to $1.8\times10^{-2}$ Å$^{-1}$. We found $T_c=140$ and 180 K for $Au_{0.82}Fe_{0.18}$ and $Au_{0.80}Fe_{0.20}$, respectively. The SANS peaks were not sharp and we estimate the uncertainty in the determination of the critical temperature to be of the order of one degree. As in Ref. 4 this does not affect our analysis because the data vary smoothly with the temperature.

Three-directional neutron polarization analysis[5] was used to separate the magnetic scattering from the structural

[a]Present address: CERT, 2, avenue E. Belin, 31055 Toulouse, France.

 0021-8979/96/79(8)/6158/3/$10.00 © 1996 American Institute of Physics

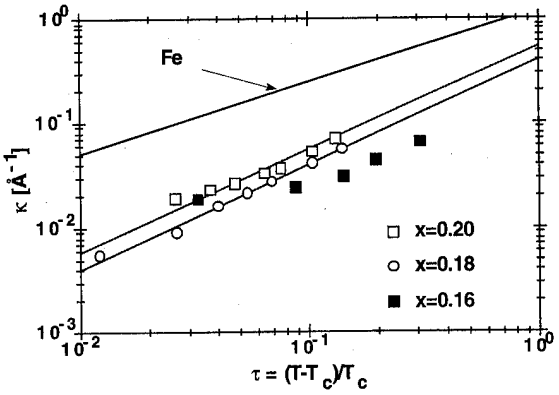



FIG. 1. Log–log plot of the inverse correlation length $\kappa$ vs the reduced temperature for $x=0.20$ (open circles), $x=0.18$ (open squares), $x=0.16$ (closed squares) and Fe ($\kappa=1.22\tau^{0.69}$). The solid lines represent the power law fits for $x=0.20$ and $x=0.18$ given in the text. The characteristic temperatures are: $T_c=180$, 140, and 93 K for $x=0.20$, 0.18, and 0.16, respectively and $T_c=1043$ K for Fe.

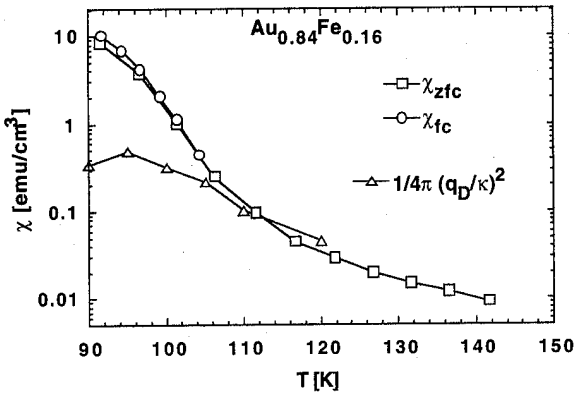



FIG. 2. Zfc (open squares) and fc (open circles) volumic susceptibility of $Au_{0.84}Fe_{0.16}$ measured with a Faraday balance at $H=4$ Oe, as a function of the temperature. The open triangles represent the SANS susceptibility derived by Eqs. (1) and (3). The solid lines are guides to the eye.

small angle contribution. The magnitude of the magnetic guide field at the sample was equal to 4 Oe. The measurements covered the following temperature and $q$ ranges: 203.5 K$\geqslant T\geqslant$184.6 K for $x=0.20$, 159.6 K$\geqslant T\geqslant$141.7 K for $x=0.18$, and for both samples $1.8\times10^{-2}$ Å$^{-1}\leqslant q\leqslant 7.3\times10^{-2}$ Å$^{-1}$.

The $q$ dependence of the SANS intensity $I_q(T)$ was analyzed using the Ornstein–Zernicke formalism, which neglects the Fisher exponent $\eta$ at $T\geqslant T_c$:

$$I_q(T)\propto\chi_q(T)=\frac{C}{q^2+\kappa(T)^2}$$

with

$$C=\frac{q_D^2}{4\pi} \qquad (1)$$

(cgs units), where $\chi_q$ is the $q$-dependent volume magnetic susceptibility and $q_D$ is the dipolar wave vector.

Figure 1 shows on a log–log scale the $\kappa$ values for both the $x=0.18$ and 0.20 samples, as a function of the reduced temperature $(T-T_c)/T_c$. This figure also includes the data of $Au_{0.84}Fe_{0.16}$ (Ref. 4) and Fe (Ref. 6).

According to the predictions of static scaling (the Fisher exponent $\eta$ is neglected),

$$\kappa=\kappa_0\ \tau^{\nu} \quad \text{and} \quad \chi_{q=0}=\chi_0\tau^{-\gamma}$$

with

$$\tau=(T-T_c)/T_c, \quad \nu=2\gamma. \qquad (2)$$

In three-dimensional Heisenberg systems $\nu=0.69$. For both $Au_{0.80}Fe_{0.20}$ and $Au_{0.82}Fe_{0.18}$, $\kappa$ is proportional to $\tau$ with $\kappa_0=0.53$ Å$^{-1}$ for $Au_{0.80}Fe_{0.20}$ and $\kappa_0=0.40$ Å$^{-1}$ for $Au_{0.82}Fe_{0.18}$. We deduce $\nu=1\pm0.1$, where the estimated error in the value of $\nu$ is mainly due to the uncertainty in the determination of the Curie temperatures.

The high value for the exponent $\nu$ agrees with previous findings on $Au_{0.83}Fe_{0.17}$ (Ref. 7) and on other disordered systems[8,9] but is not confirmed by $Au_{0.84}Fe_{0.16}$, which is the most disordered of our samples. As seen in Fig. 1, the variation of $\kappa(\tau)$ is slower in $Au_{0.84}Fe_{0.16}$ than in the other samples.

At the same value of the reduced temperature $\tau$, the inverse correlation length $\kappa$ is significantly smaller in all $Au_{1-x}Fe_x$ samples than in Fe. At $\tau=0.01$, the correlation length of $Au_{0.82}Fe_{0.18}$ is 12.5 times larger than that of Fe and the correlated volumes contain some 350 times more Fe ions in $Au_{0.82}Fe_{0.18}$ than in pure Fe. This astonishing influence of the disorder on the correlations was first seen in $Au_{0.84}Fe_{0.16}$ (Ref. 4) and is confirmed by our susceptibility measurements.

## SUSCEPTIBILITY RESULTS

The susceptibility of $Au_{0.84}Fe_{0.16}$ and $Au_{0.82}Fe_{0.18}$ was measured with the Faraday method on the samples used for neutron scattering. The samples were first either zero field cooled (zfc) or field cooled (fc) down to 4 K. The susceptibility was then recorded by increasing the temperature. The magnetic field was equal to 1.33 Oe, 4 Oe, the magnetic guide field of the SANS experiments, and 12 Oe. At all temperatures covered by the SANS experiments the magnetization was linear to the magnetic field and the absolute value of the volume initial susceptibility $\chi_{q=0}(T)$ could be directly determined from the Faraday method. For the demagnetizing field correction we assumed $N=1.102\times10^{-2}$, the factor calculated for a prolate ellipsoid with $m=70$ (ratio diameter/thickness of the samples).[10] Figures 2 and 3 show the volumic susceptibility above $T_c$ measured at 4 Oe for $x=0.16$ and 0.18, respectively.

The relation between the volumic susceptibility and the SANS results is given by the $q=0$ limit of (1): $\chi_{q=0}=(q_D/\kappa)^2/4\pi$. The numerical value of $q_D$ can therefore be determined from the proportionality factor between $\chi_{q=0}$ and $\kappa^{-2}$, therefore, $q_D=\kappa$ at the temperature where $\chi_{q=0}=1/4\pi$. We found $q_D=0.041$ Å$^{-1}$ for $x=0.18$ and $q_D=0.05$ Å$^{-1}$ for $x=0.16$. These values are very close to $q_D=0.045$ Å$^{-1}$, the value found in Fe (Ref. 11).

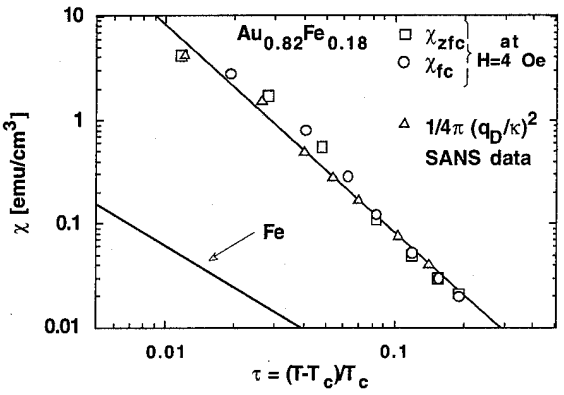



FIG. 3. Zfc (open squares) and fc (open circles) volumic susceptibility of $Au_{0.82}Fe_{0.18}$ measured with a Faraday balance at $H=4$ Oe, vs the reduced temperature. The open triangles represent the SANS susceptibility derived by Eqs. (1) and (3). The solid line represent the power law with $\gamma=2$ (see text). The results on Fe are also included ($\chi=1.35\ 10^{-4}\ \tau^{-1.33}$).

Having determined the proportionality factor between $\chi_{q=0}$ and $\kappa^{-2}$ we could compare the SANS susceptibility to the macroscopic one. The result is shown in Figs. 2 and 3 for $x=0.16$ and 0.18, respectively.

As seen in Fig. 3, the agreement between the Faraday and the SANS susceptibilities is excellent for $x=0.18$. On the other hand, for $x=0.16$, the neutron susceptibility is systematically lower than the bulk one and the discrepancy between the two curves increases when the temperature decreases (Fig. 2).

## DISCUSSION

The behavior of $Au_{0.84}Fe_{0.16}$ is qualitatively different from that of the other two samples, which are more concentrated in Fe. In $Au_{0.84}Fe_{0.16}$, at and above $T_c$, the spin relaxation rate $\Gamma$ is proportional to $q^2$ (Ref. 3), although, in $Au_{0.82}Fe_{0.18}$ (Ref. 3) and in Fe (Ref. 6), $\Gamma \propto q^{5/2}$ as expected for Heisenberg ferromagnets (Ref. 12).

The analysis of the paramagnetic SANS of $Au_{0.84}Fe_{0.16}$ under the assumption of a ferromagnetic phase transition leads to $\nu \sim 0.69$ (Ref. 4) although $\nu=1$ for $x=0.18$ and 0.20. Also the SANS susceptibility deduced in the frame of this analysis is not consistent with the volumic susceptibility measured on the same sample with the Faraday method.

In the light of these results we have to assume that there is no well-defined ferromagnetic phase transition for $x=0.16$. This assumption explains the nonconventional (for ferromagnets) $q$ dependence of the spin-relaxation rate $\Gamma$, the strong $q$ dependence of $T_c$ reported in Ref. 4, the low value of the exponent $\nu$ as well as the inconsistency between the SANS and the Faraday susceptibility. This inconsistency indicates that the $q$ dependence of $I_q$ is not described by the Ornstein–Zernicke formalism. As seen in Fig. 2, the bulk susceptibility is much higher than the SANS one, which implies that the increase of $I_q$ when $q$ is decreased is faster than predicted by Eq. (1). A similar behavior was observed on the spin-glass $Au_{0.87}Fe_{0.13}$ (Ref. 7), where the $1/I_q$ vs $q^2$ plots (Ornstein–Zernicke plots) show a marqued downward curvature. In $Au_{0.87}Fe_{0.13}$ this effect was easily seen in the $q$ range covered by the present measurements. In $Au_{0.84}Fe_{0.16}$, the deviations from the Ornstein–Zernicke formalism were not significant. We therefore expect these deviations to become noticeable at $q<0.02$ Å$^{-1}$.

The qualitative agreement between the SANS and the Faraday susceptibility in $Au_{0.82}Fe_{0.18}$ is a strong argument in favor of a well-defined ferromagnetic phase transition. In the light of the SANS results on $Au_{0.83}Fe_{0.17}$ (Ref. 7) it is reasonable to assume that a ferromagnetic phase transition exists for $x \geqslant 0.17$.

The phase transition that takes place in $Au_{0.82}Fe_{0.18}$ is characterized by different exponents than those found in Fe and more generally in nondisordered 3D Heisenberg systems. This is seen in Fig. 1 but also in Fig. 3. From these plots, we deduce $\nu=1$ and $\gamma=2$ instead of the expected $\nu=0.69$ and $\gamma=1.38$.

Figures 1 and 3 give a consistent picture of the specific features of the phase transition in the disordered ferromagnetic system $Au_{0.82}Fe_{0.18}$. Not only are the exponents different but also the critical amplitudes: at the same reduced temperature the correlation length and the magnetic susceptibility are much higher in the disordered system than in Fe.

Recent results on the insulating system $CdCr_{2(1-x)}In_{2x}S_4$ (Ref. 9) confirmed the existence of larger critical amplitudes $\xi_0(=\kappa_0^{-1})$ in disordered systems than in usual ferromagnets. In Fig. 1 we see that $\kappa_0$ decreases when the disorder in increased, which implies that $\xi_0$ increases with disorder. As a consequence of the large critical amplitudes $\xi_0(=\kappa_0^{-1})$ the ferromagnetic correlations in $Au_{0.82}Fe_{0.18}$ and $Au_{0.80}Fe_{0.20}$ persist well above $T_c$ and lead to a much wider critical region than in Fe and in usual ferromagnets.

## ACKNOWLEDGMENTS

The authors would like to thank S. Pouget for her assistance during the SANS experiments and many fruitful discussions. We would also like to acknowledge W. Mickeley and W. Roennfeld for their help in preparing the $x=20$ sample.

[1] I. Mirebeau, M. Hennion, S. Mitsuda, and Y. Endhoh, *Recent Progress in Random Magnets*, edited by J. H. Ryan (Word Scientific, Singapore, 1992).
[2] B. V. B. Sarkissian, J. Phys. F **11**, 2191 (1981).
[3] C. Pappas, C. Lartigue, M. Alba, and F. Mezei, Physica B **165–166**, 191 (1990).
[4] C. Lartigue, F. Mezei, C. Pappas, and M. Alba, Physica B **180–181**, 359 (1992).
[5] A. P. Murani and F. Mezei, in *Neutron Spin Echo* (Springer-Verlag, Berlin, 1980), p. 104.
[6] F. Mezei, Phys. Rev. Lett. **49**, 1096 (1982).
[7] A. P. Murani, Mater. Sci. Forum **27–28**, 195 (1988), and references therein.
[8] K. Westerhold and G. Sobota, J. Phys. F **13**, 2371 (1989), and references therein.
[9] S. Pouget, M. Alba, and D. Nogues, JMMM **140–141**, 1531 (1995).
[10] J. A. Osborn, Phys. Rev. **67**, 351 (1945).
[11] J. Kötzler, Phys. Rev. Lett. **51**, 833 (1983).
[12] P. C. Hohenberg and B. I. Halperin, Rev. Mod. Phys. **49**, 467 (1977).
[13] J. Als-Nielsen, in *Phase Transitions and Critical Phenomena*, edited by C. Domb and M. S. Green (Academic, London, 1976), Vol. 5a, p. 87.

# Neutron depolarization study of magnetic order in $a$-$Fe_xZr_{100-x}$ ($x$=90–93), $a$-$Fe_{90}Sc_{10}$ and their hydrides

D. H. Ryan[a] and J. M. Cadogan
*School of Physics, The University of New South Wales, Sydney NSW 2052, Australia*

S. J. Kennedy
*Neutron Scattering Group, ANSTO, PMB 1, Menai NSW 2234, Australia*

Neutron depolarization measurements have been used to show that ferromagnetic domains exist in $a$-$Fe_xZr_{100-x}$ alloys for $90 \leq x \leq 93$, and that these domains are not affected by the ordering of transverse spin components at $T_{xy}$. Domain sizes decrease from 1.1 $\mu$m at $x=90$, to 0.08 $\mu$m by $x=93$. Measurements in an applied field set an upper limit of ~50 nm for correlations in the transverse components. By contrast, $a$-$Fe_{90}Sc_{10}$ shows no evidence of ferromagnetic order and is confirmed to be a spin glass. Measurements on deuterium-loaded samples show that all of the $a$-Fe–Zr and $a$-Fe–Sc alloys studied here are ferromagnetic with $T_c$'s in the range 380–400 K, and domains ~1 $\mu$m in size. © *1996 American Institute of Physics.* [S0021-8979(96)23608-5]

## INTRODUCTION

Amorphous iron rich alloys of the form $a$-$Fe_xETM_{100-x}$ (where ETM=Sc, Y, Zr, Hf, and $x \sim 90$) provide a rich testing ground for models of magnetic order in the presence of exchange frustration as their behavior spans the full range of possibilities from ferromagnet to spin glass with increasing frustration. Two magnetic transitions are observed in partially frustrated systems, the first, at $T_c$, to a collinear ferromagnetic state, followed at $T_{xy}$ by the ordering of transverse spin components.[1] Earlier neutron depolarization work on $a$-$Fe_xZr_{100-x}$ ($x=90$–92)[2] confirmed the presence of ferromagnetic order and found large domains for $x \leq 91$, but only weak correlations for $x=92$. However, magnetization and Mössbauer measurements suggest that significant ferromagnetic order persists to $x=93$.[1,3] Our aim here is to extend the neutron depolarization data to $x=93$, to look for possible long-range order in the transverse spin components, and to confirm that the ordering at $T_{xy}$ does not destroy the ferromagnetic order that develops at $T_c$.

For comparison, we have studied $a$-$Fe_{90}Sc_{10}$, which is fully frustrated and exhibits a single transition to a spin glass state with no spontaneous magnetization,[1,4–6] although a large magnetization is readily induced by the application of a modest field (~1 T). Since there should be no long-ranged correlations in a spin glass, we expect no depolarization from this material, and it serves in part as an internal test of our procedures.

Finally, we have also investigated the hydrides of these alloys. The lattice expansion associated with the absorption of hydrogen lifts the exchange frustration in both $a$-Fe–Zr (Ref. 3) and $a$-Fe–Sc (Ref. 4) converting them to soft ferromagnets with ordering temperatures ~400 K. However, it has been suggested that $a$-Fe–Sc–H may remain a spin glass,[6] and depolarization measurements provide a direct way to check for this possibility.

[a]On leave from Centre for the Physics of Materials and Department of Physics, McGill University, 3600 University St., Montreal, Quebec, Canada.

## EXPERIMENTAL METHODS

The alloys were prepared by arc-melting appropriate ratios of the pure elements (Fe: 99.95%, Zr: 99.8%, and Sc: 99.9% pure) under Ti-gettered argon to yield ~2 g ingots. Melt spinning was carried out under a partial pressure of helium onto a copper wheel at 50 m/s. Ribbons were typically 1 mm wide, 20 $\mu$m thick, and several meters long. Thickness variations along the samples used for the depolarization measurements were found to be less than $\pm 1$ $\mu$m. Absence of crystallinity was confirmed using Cu–$K_\alpha$ powder x-ray diffraction and room temperature Mössbauer spectroscopy. A LakeShore susceptibility system with a closed-cycle fridge was used to record $\chi_{ac}$ vs $T$ down to 12 K. The samples were saturated with deuterium using an electrolytic charging method[7] and final deuterium contents were determined from the mass loss on heating to 300 °C in a Perkin–Elmer TGA-7 Thermogravimetric analyzer. This instrument was also used to determine the magnetic ordering temperature of the deuterides by operating with a small field gradient applied. The TGA was calibrated using alumel and nickel standards.

The neutron depolarization measurements were carried out on the long wavelength polarized neutron spectrometer (LONGPOL) at the High Flux Australian Reactor (HIFAR) operated by the Australian Nuclear Science and Technology Organisation (ANSTO). The incident beam, with a wavelength of 0.36 nm, is polarized vertically by scattering from saturated polycrystalline iron sheets. A similar arrangement is used as an analyzer. Typical beam polarizations were in the range 32%–36%. The instrument has been described in more detail elsewhere.[8] A cadmium plate with a 5 mm×5 mm square hole served as the sample holder. Several ribbons were laid side-by-side to cover the opening, with Cd wire covering the gaps between ribbons. One to four layers of ribbon were used, depending on the depolarization expected. The holder was mounted on the cold stage of a closed-cycle fridge which operates down to 12 K. An air-cooled electromagnet was used to apply fields of up to 80 mT in the sample plane, perpendicular to both the beam and the incident polarization.

 0021-8979/96/79(8)/6161/3/$10.00 © 1996 American Institute of Physics 

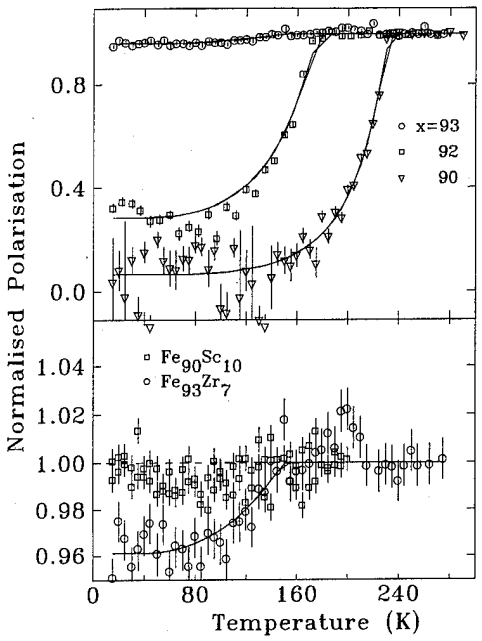



FIG. 1. Normalized depolarization signal for $a$-$Fe_xZr_{100-x}$ (top) and $a$-$Fe_{90}Sc_{10}$ (bottom) measured in a guide field of 1 mT. Solid lines are fits assuming a temperature independent domain size. Notice that the $a$-$Fe_{90}Sc_{10}$ sample does not affect the beam polarization at any temperature.

## RESULTS AND DISCUSSION

On passing through a uniformly magnetized region such as a domain, the neutron moment experiences a torque which causes it to precess about the magnetization direction. The total rotation increases with the internal magnetization, the thickness of the domain, and the wavelength of the neutron. If the neutron now passes through many such domains it will undergo many rotations. If the magnetization direction within each domain can be assumed to be a random vector, and the angle through which the neutron moment turns in each domain is $\ll 2\pi$, then the initial polarization is scrambled and decays according to:[9]

$$P=\exp(-\alpha\lambda^2) \tag{1}$$

with

$$\alpha=\tfrac{1}{2}c^2\langle B_\perp^2\rangle d\,\delta, \tag{2}$$

where $\lambda$ is the neutron wavelength, $\langle B_\perp^2\rangle$ is the mean square domain magnetization perpendicular to the neutron polarization, $d$ is the sample thickness, and $\delta$ is the mean domain size. $c$ is a constant which takes the value $4.63\times10^{14}$ $m^{-2}\,T^{-1}$ in S.I. units.

The depolarization signals for all of the samples studied here are shown in Fig. 1. It is immediately apparent that all of the $a$-Fe–Zr alloys cause a significant depolarization of the beam below their respective $T_c$'s, confirming the presence of ferromagnetic order. The depolarization weakens with increasing iron content as the exchange frustration builds up and the system moves closer to becoming a spin glass. However, even at $x=93$, (shown in the lower half of Fig. 1 on an expanded scale) there is some loss of polarization. By contrast, $a$-$Fe_{90}Sc_{10}$ has no effect on the beam at any temperature, consistent with the spin glass nature of the order in this alloy and the absence of any ferromagnetic correlations. If we assume that the domains, once formed, do not change size, then the observed temperature dependence of the polarization must result from the normal change in spontaneous magnetization with temperature. Taking the estimated magnetization from Ref. 1, and assuming a simple mean-field temperature dependence, then the data in Fig. 1 can be fitted to Eq. (1) to obtain domain sizes and ordering temperatures. These fits (shown as solid lines on Fig. 1, and summarized in Table I) show that large domains persist to $x=92$ but that beyond this point there is a very rapid reduction in domain size. It is not clear that the 80 nm regions suggested by the fit to the $x=93$ sample are large enough to justify the use of the term "domain" but it is clear that some ferromagnetic correlations are present in this material, and that they are not affected by the ordering of the transverse spin components at $T_{xy}\sim80$ K.[1]

TABLE I. Summary of fitted parameters from data shown in Figs. 1 and 3. $T_c(\chi)$ and $T_c$(ndep) are ordering temperatures derived from bulk and depolarization measurements, respectively. $\delta$ is the mean domain size. * Note: $a$-$Fe_{90}Sc_{10}$ is a spin glass, so the value for $T_c$ given here is for $T_{sg}$.

| Alloy | $T_c(\chi)$ K | $T_c$(ndep) K | $\delta$ $\mu$m |
|---|---|---|---|
| $Fe_{90}Zr_{10}$ | 240±3 | 232±4 | 1.1±0.2 |
| $Fe_{92}Zr_8$ | 182±2 | 176±1 | 1.16±0.07 |
| $Fe_{92}Zr_8D_{13\pm2}$ | 376±3 | 362±10 | 1.4±0.1 |
| $Fe_{93}Zr_7$ | 145±2 | 150±5 | 0.077±0.006 |
| $Fe_{93}Zr_7D_{17\pm2}$ | 372±3 | 359±6 | 0.90±0.05 |
| $Fe_{90}Sc_{10}$ | 95* | ··· | 0.0 |
| $Fe_{90}Sc_{10}D_{28\pm0.5}$ | 395±5 | 390±40 | 1.0±0.1 |

The main difference between the results presented here and those of Hadjoudj *et al.*,[2] is that we observe a strong depolarization even at $x=92$ and only the $x=93$ sample shows a weak effect. However, examination of the transition temperatures shown in Ref. 2 allows us to bring the two sets of data into agreement. $T_c$ in $a$-$Fe_xZr_{100-x}$ is a very strong function of $x$, decreasing at ~25 K/at.%,[1,3] and thus provides a sensitive check on sample composition. Using this scale, it is clear that their $x=90$ and 91 samples are consistent with typical values, but the $T_c$ of their $x=92$ sample is below 150 K, a value more often associated with $x=93$. With this modified composition, our data and those of Ref. 2 are in full agreement.

At $T_c$ a ferromagnetic state forms with a substantial fraction of each moment oriented perpendicular to the ordering axis. The moments precess rapidly about the ferromagnetic, $z$, axis, so that the $xy$ components time average to zero, and the system appears to be a collinear ferromagnet. The second transition in $a$-Fe–Zr is associated with the freezing of the transverse degrees of freedom, and as noted above, does not lead to a destruction of the ferromagnetic order. Since the average magnetization does not increase at $T_{xy}$, the $xy$ components cannot be correlated over substantial distances, but no limits have yet been placed on their correlation length. Since the neutrons are only sensitive to $B_\perp$ we can eliminate the ferromagnetic contribution to the depolarization signal by magnetizing the sample parallel to the neutron polarization

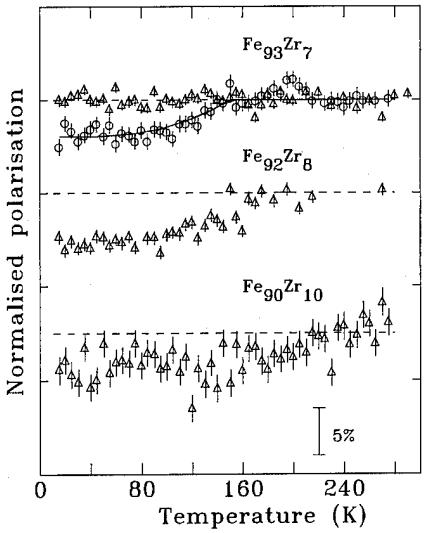



FIG. 2. Normalized depolarization signal for $a$-$Fe_xZr_{100-x}$ measured in a guide field of 80 mT. The 1 mT data for $a$-$Fe_{93}Zr_7$ showing a 4% depolarization of the incident beam are repeated for comparison. Dashed lines indicate the base polarization of the beam.

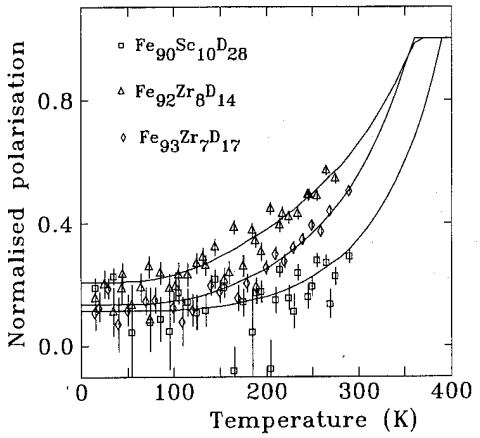



FIG. 3. Normalized depolarization signal for $a$-$Fe_xZr_{100-x}D_y$ and $a$-$Fe_{90}Sc_{10}D_{28}$ measured in a guide field of 1 mT. Solid lines are fits assuming a temperature independent domain size.

direction. A simple ferromagnet would then not depolarize the beam even below $T_c$. In the absence of the ferromagnetic contribution, any correlations in the transverse components should appear as a loss of polarization around $T_{xy}$. However, Fig. 2 shows that while there is some residual effect from the imperfect alignment obtained in the 80 mT field available, no change can be seen in either the $x=92$, $T_{xy}=46$ K, or the $x=93$, $T_{xy}=78$ K (Ref. 1) samples. Since the change in polarization is much smaller than that seen for the ferromagnetic component of the $x=93$ sample, we are able to rule out correlations in the transverse spin components longer than about half of the 80 nm length scale seen there.

Hydrogen loading is known to convert these alloys into soft ferromagnets,[3,4] and the depolarization behavior of the deuterium loaded samples shown in Fig. 3 is as expected. TGA analysis confirmed that they had ordering temperatures well above room temperature, although the values obtained are only lower limits as the samples lose deuterium rapidly as $T_c$ is approached. Neutron depolarization shows that all of the deuterides are ferromagnetic, and fits to the curves yield ordering temperatures in agreement with the TGA data. Values for domain sizes and ordering temperatures are summarized in Table I. The data for $a$-$Fe_{90}Sc_{10}D_{28}$ show that it depolarized the beam more strongly than the two Zr samples, leaving no doubt that this material is ferromagnetic. It is not clear why no critical peaks were observed in the susceptibility of a similar sample.[6]

## ACKNOWLEDGMENTS

D.H.R. would like to acknowledge the hospitality of the School of Physics at the University of New South Wales, Sydney, Australia where much of this work was carried out. The neutron scattering work was supported by a grant from the Australian Institute for Nuclear Science and Engineering. This work was also supported by grants from the Australian Research Council, the Natural Sciences and Engineering Research Council of Canada, and Fonds pour la Formation de Chercheurs et l'Aide à la Recherche, Québec.

[1] H. Ren and D. H. Ryan, Phys. Rev. B **51**, 15885 (1995).
[2] S. Hadjoudj, S. Senoussi, and I. Mirebeau, J. Magn. Magn. Mater. **93**, 136 (1991).
[3] D. H. Ryan, J. M. D. Coey, E. Batalla, Z. Altounian, and J. O. Ström-Olsen, Phys. Rev. B **35**, 8630 (1987).
[4] D. H. Ryan, J. O. Ström-Olsen, W. B. Muir, J. M. Cadogan, and J. M. D. Coey, Phys. Rev. B **40**, 11208 (1989).
[5] H. Ren and D. H. Ryan, J. Appl. Phys. **73**, 5494 (1993).
[6] H. Ma, Z. Wang, H. P. Kunkel, G. Williams, D. H. Ryan, and J. O. Ström-Olsen, J. Magn. Magn. Mater. **104–7**, 89 (1992).
[7] J. M. D. Coey, D. H. Ryan, and Yu Boliang, J. Appl. Phys. **55**, 1800 (1984).
[8] L. D. Cussen, J. C. Osborn, P. Gibbs, and T. J. Hicks, Nucl. Instrum. Methods A **314**, 155 (1992).
[9] S. Mitsuda and Y. Endoh, J. Phys. Soc. Jpn. **54**, 1570 (1985).

# Spin glass behavior of $Zn_{1-x}Mn_xTe$

P. M. Shand and A. D. Christianson
*Physics Department, University of Northern Iowa, Cedar Falls, Iowa 50614*

L. S. Martinson and J. W. Schweitzer
*Physics Department, University of Iowa, Iowa City, Iowa 52242*

T. M. Pekarek, I. Miotkowski, and B. C. Crooker
*Physics Department, Purdue University, West Lafayette, Indiana 47907*

We have performed ac susceptibility and dc magnetization measurements on the diluted magnetic semiconductor $Zn_{1-x}Mn_xTe$. The measurements clearly indicate spin glass behavior. For an $x=0.4$ sample, the data for the imaginary part of the complex susceptibility ($\chi''$) was analyzed according to conventional power-law dynamics and good scaling was obtained with $T_c=13.4\pm0.2$ K, $z\nu = 10.5 \pm 1.0$, and $\beta=0.9\pm0.2$. These values of $z\nu$ and $\beta$ are consistent with results obtained in other spin glass systems. The scaling of the $\chi''$ data was not as good when analyzed within the activated dynamics model. Magnetization measurements of an $x=0.5$ sample also showed a spin glass-like transition. Scaling of the nonlinear magnetization just above the transition gave $T_c = 20.8 \pm 0.2$ K, and the critical exponent values $\beta=0.8\pm0.2$ and $\gamma=4.0\pm1.0$. This confirms the $\beta$ value obtained from the ac measurements and the $\gamma$ value is in fair agreement with reported values for other diluted magnetic semiconductor spin glass systems. We conclude that $Zn_{1-x}Mn_xTe$ and similar systems undergo equilibrium phase transitions to a spin glass state at low temperatures. © *1996 American Institute of Physics.* [S0021-8979(96)23708-6]

## I. INTRODUCTION

Diluted magnetic semiconductors (DMSs) are a class of randomly disordered, insulating Heisenberg antiferromagnets with short-range interactions.[1–3] Recently, the archetypal DMS $Cd_{1-x}Mn_xTe$ has been the subject of continued theoretical and experimental investigations in an attempt to firmly establish that this material undergoes a continuous phase transition to a spin glass state.[4–12] If $Cd_{1-x}Mn_xTe$ is a spin glass, then one is led to the question: Are all DMS alloys spin glasses with the same critical exponents? The aim of this article is to shed some light on this question.

Recent studies of the ac susceptibility $\chi_{ac}$ in $Cd_{1-x}Mn_xTe$ and $Hg_{1-x}Mn_xTe$ show that these materials have zero-frequency transition temperatures $T_c$ which are $>0$ K.[6–8] These data also indicate that the spin relaxation time is a power law function of the reduced temperature $\epsilon = (T-T_c)/T_c$. This behavior (critical slowing down) has been found to give a better description of the dynamics in the critical region above $T_c$ than a process of thermal activation over free energy barriers.[4,6,7] These findings indicate that an equilibrium phase transition to a spin glass state exists at finite temperatures in $Cd_{1-x}Mn_xTe$ and $Hg_{1-x}Mn_xTe$. Further, virtually identical critical exponents were obtained in both materials, which led to the speculation that all DMS alloys belong to the same spin glass universality class.

To further test this hypothesis, we have made ac susceptibility and dc magnetization measurements on $Zn_{1-x}Mn_xTe$ alloys close to the spin freezing transition. The ac susceptibility $\chi_{ac}$ was measured for frequencies 80 Hz$\leqslant f \leqslant$2300 Hz. Both power-law and activated scaling analyses were applied to the data in order to determine which theory provides the better description of the behavior in the vicinity of the transition. Nonlinear magnetization data were also collected in the region of the transition in order to compare the static scaling behavior of $Zn_{1-x}Mn_xTe$ with that $Cd_{1-x}Mn_xTe$.

## II. EXPERIMENTAL DETAILS

The ac susceptibility measurements were performed on a single-crystal sample of $Zn_{1-x}Mn_xTe$, with concentration $x=0.41$. The measurements were carried out with a Lake-Shore susceptometer. Both in-phase ($\chi'$) and out-of-phase ($\chi''$) components were measured in an ac field of 12.5 Oe. For each measurement, the temperature was kept stable to within 0.02 K.

The magnetization measurements were made on another single-crystal sample of $Zn_{1-x}Mn_xTe$, with $x=0.506$. These measurements were made with a Cryogenic Consultants Limited superconducting quantum interference device magnetometer. Measurements were taken for fields between 0 and 100 G and for temperatures between 5 and 300 K. Temperature stability was achieved to within 0.01 K.

## III. RESULTS AND DISCUSSION

The dynamics of the transition are most sensitively probed by the measurement and analysis of $\chi''(\omega,T)$.[7] Figure 1 shows $\chi''(\omega,T)$ for several different frequencies. There is scatter in the data because of the relatively small out-of-phase signal. Smoothing curves were therefore drawn through the data points to enable us to objectively determine the positions of the peaks, which are needed for the data analysis. An examination of the behavior of $\chi''(\omega,T)$ allows us to discern whether critical slowing down or activated dynamics provides a better description of the dynamical characteristics of the freezing transition in DMS systems.

In the critical slowing down description, $\chi''(\omega,T)$ behaves according to the scaling law[7,13]

 0021-8979/96/79(8)/6164/3/$10.00 © 1996 American Institute of Physics

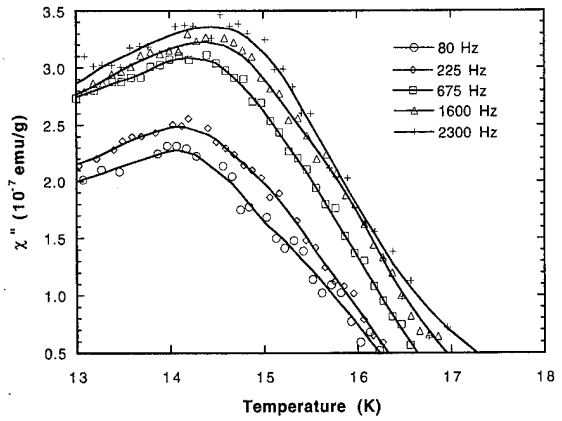



FIG. 1. Temperature dependence of $\chi''$ near the freezing transition. The lines through the data are smoothing curves which enable the positions of the peaks to be reliably ascertained.

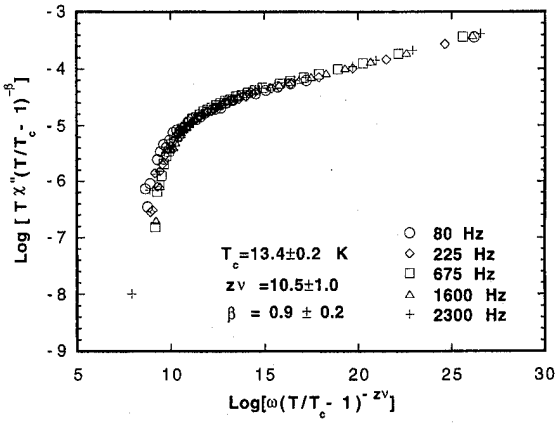



FIG. 2. Power law scaling of $\chi''(\omega,T)$ according to Eq. (1) in the text. The best-fit values of $T_c$ and the scaling exponents $z\nu$ and $\beta$ are also shown.

$$T\chi''(\omega,T)=\epsilon^{\beta}F(\omega\epsilon^{-z\nu}), \tag{1}$$

where $\beta$ is the critical exponent for the order parameter and $F(y)$ is a universal function of $y$. Bertrand *et al.* have argued that the scaling relation Eq. (1) is only valid for temperatures $T > T_p$, where $T_p$ is the temperature at which the peak in $\chi''(\omega,T)$ occurs.[9] We have taken this criterion into account in our analysis of all the $\chi''(\omega,T)$ data, which are shown in scaled form in Fig. 3. The data are well described by a single scaling curve. The best scaling was obtained for the following parameter values: $T_c=13.4\pm0.2$ K, $z\nu=10.5\pm1.0$, and $\beta=0.9\pm0.2$. The uncertainties in these parameters are obtained by ascertaining (by visual inspection) the extremal values of the parameters for which reasonably good scaling is still achieved. The values of the exponents $z\nu$ and $\beta$ obtained here are consistent with previous results obtained for $Cd_{1-x}Mn_xTe$ and $Hg_{1-x}Mn_xTe$, i.e., $z\nu=9\pm1$ and $\beta=0.8\pm0.1$[6–10] Similar values were also obtained in a non-DMS insulating spin glass.[14] One should note that the range of frequencies used in this study is rather limited, and measurements encompassing a larger frequency range need to be made. Nevertheless, our results for $z\nu$ and $\beta$ strongly indicate that the same universal critical exponents indeed describe the spin glass transition in all DMS materials.

We have also attempted to interpret the $\chi''(\omega,T)$ data according to the activated dynamics description of the spin freezing transition. In this picture, the scaling relation governing the behavior of $\chi''(\omega,T)$ near the transition can be written as[15,16]

$$\chi''(\omega,T)=\varepsilon^{P}G[-\varepsilon^{Q}\ln(\omega\tau_0)], \tag{2}$$

where $P$ and $Q$ are scaling exponents. If thermally activated excitations do govern the critical dynamical behavior, then one expects the exponents $P$ and $Q$ to be universal.[7] Figure 3 shows the best scaling plot corresponding to Eq. (2) for our $\chi''(\omega,T)$ data. This was obtained using the values $T_c = 13.4 \pm 0.2$ K, $P = 0.5 \pm 0.1$, $Q = 0.4 \pm 0.1$, and $\tau_0 = 10^{-13}$ s. It is clear from Figs. 2 and 3 that the activated scaling form of Eq. (4) provides a less satisfactory description of the data. Further, the $P$ and $Q$ exponents have quite different values from those obtained in other DMS systems and other systems which show a spin freezing transition ($3.65 \leqslant P \leqslant 4.2$, $Q = 0.8$ for $Hg_{0.7}Mn_{0.3}Te$; $3.65 \leqslant P \leqslant 4.2$, $Q = 1.2$ for $Cd_{0.7}Mn_{0.3}Te$; $P = 0.4 \pm 0.1$, $Q = 0.35 \pm 0.05$ for $BaCo_6Ti_6O_{19}$.[7,14] The different values of these exponents clearly indicate a lack of universality, which makes the activated dynamics description less attractive.

We have also made nonlinear magnetization measurements on a $Zn_{0.5}Mn_{0.5}Te$ sample close to the transition in order to examine the static scaling properties in the critical region. In the immediate vicinity of $T_c$, the universal scaling expression

$$M_{\rm nl}(\epsilon,H)=\epsilon^{(\gamma+3\beta)/2}F(H/\epsilon^{(\gamma+\beta)/2}) \tag{3}$$

applies. Here, $M_{\rm nl}(H,T)=M(H,T)-\chi_{(l)}(T)H$ is the nonlinear magnetization and $\chi_l(T)H$, is the linear contribution near $T_c$.

The magnetization as a function of temperature was measured in several fixed fields. Near $T_c$, $\chi_{\rm nl} = M_{\rm nl}/H$ increases as shown in Fig. 4, as would be expected from the well-known divergence of this parameter at $T_c$ for spin

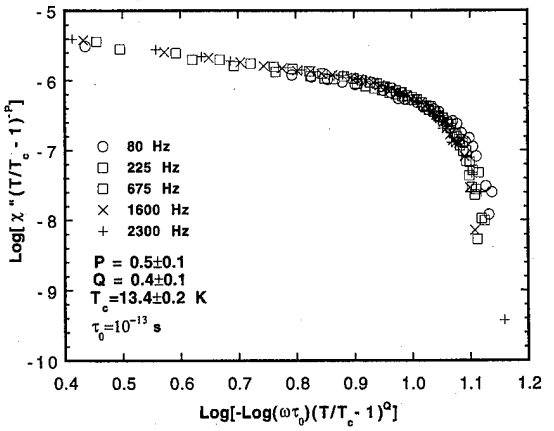



FIG. 3. Activated dynamic scaling of $\chi''(\omega,T)$ according to Eq. (2) in the text. The best-fit values of the $T_c$, $\tau_0$, and the scaling exponents $P$ and $Q$ are shown as well. Notice that the best scaling in this case is significantly worse than that depicted in Fig. 2.

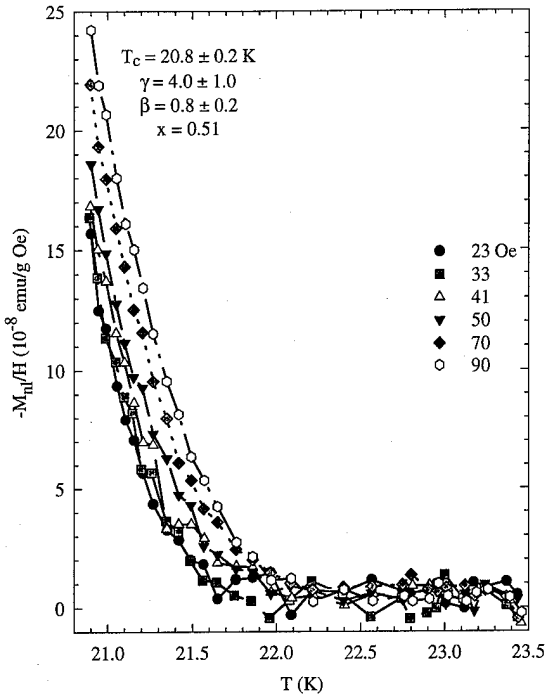



FIG. 4. $M_{nl}/H$ vs temperature $T$ for $Zn_{1-x}Mn_xTe$ for several fixed fields. The data reveal a rapid increase in the nonlinear term near $T_c$.

glasses. In Fig. 5, the data are plotted according to the universal scaling relation of Eq. (3) using values for the parameters $\gamma$, $\beta$, and $T_c$ which produced the best scaling. The parameter values which produced the best scaling were $\gamma=4.0\pm1.0$, $\beta=0.8\pm0.2$, and $T_c = 20.8 \pm 0.2$ K. The data collapse onto the single universal scaling curve which covers many orders of magnitude along both axes. For temperatures significantly greater than $T_c$ (lower part of the curve), the slope approaches three, consistent with the first-order term in the expansion of $M_{nl}$.[11] The scaling plot shows increasing scatter at higher temperatures since the nonlinear magnetization approaches zero as one moves out of the critical region. As $T$ closely approaches $T_c$ from above (upper part of the curve), the slope tends to the proper asymptotic value $(\gamma+3\beta)/(\gamma+\beta)$.[11] These asymptotic limits are shown as solid lines in Fig. 5.

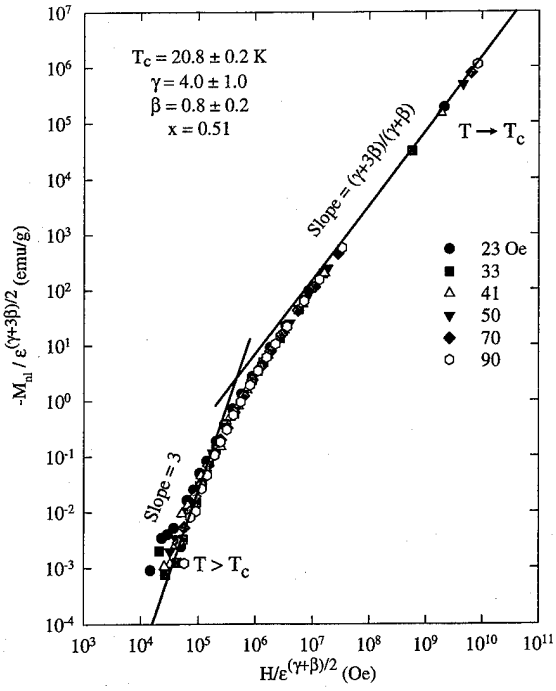



FIG. 5. The nonlinear magnetization data for $Zn_{1-x}Mn_xTe$ analyzed according to a universal scaling model for a spin glass transition. The asymptotic limits, shown by the solid lines, are in agreement with the theory.

The $T_c$ value of $20.8\pm0.2$ K obtained in the static scaling analysis is consistent with that obtained from our zero-field-cooled and field-cooled magnetization data. The value $\beta=0.8\pm0.2$ is in accord with the value obtained from the dynamic scaling analysis discussed above, which reinforces the spin glass picture. Comparing DMS systems, our value of $\gamma=4.0\pm1.0$ for $Zn_{0.5}Mn_{0.5}Te$ is higher than the reported value of $\gamma=3.3\pm0.3$ for $Cd_{1-x}Mn_xTe$ found by Mauger and co-workers.[11] We note that the determination of $\gamma$ via the scaling plot is very sensitive to slight changes in $T_c$ which explains the large error bars which we quote for our $\gamma$ value. One should also note that Geschwind and co-workers using novel linear scaling plots found $\gamma=4.4$ in $Cd_{1-x}Mn_xTe$. We conclude that within our experimental error, there is fair agreement between values for the critical exponent $\gamma$ obtained in $Zn_{1-x}Mn_xTe$ and $Cd_{1-x}Mn_xTe$.

## ACKNOWLEDGMENTS

This research was supported by Research Corporation Grant No. C-3539 and by the National Science Foundation under Purdue University Material Research Group Grant No. DMR-9221390 and by the Purdue Research Foundation.

[1] For a review of diluted magnetic semiconductors, see: J. K. Furdyna, J. Appl. Phys. **64**, R29 (1988).
[2] P. M. Shand, P. A. Polstra, I. Miotkowski, and B. C. Crooker, J. Appl. Phys. **75**, 5731 (1994).
[3] T. M. Pekarek, J. E. Luning, I. Miotkowski, and B. C. Crooker, Phys. Rev. B **50**, 16 914 (1994).
[4] A. Mauger, J. Villain, Y. Zhou, C. Rigaux, N. Bontemps, and J. Ferré, Phys. Rev. B **41**, 4587 (1990), and references therein.
[5] S. Geschwind, A. T. Ogielski, G. Devlin, J. Hegarty, and P. Bridenbaugh, J. Appl. Phys. **63**, 3291 (1988).
[6] A. Mauger, J. Ferré, M. Ayadi, and P. Nordblad, Phys. Rev. B **37**, 9022 (1988-II).
[7] Y. Zhou, C. Rigaux, A. Mycielski, M. Menant, and N. Bontemps, Phys. Rev. B **40**, 8111 (1989-I).
[8] S. Geschwind, David A. Huse, and G. E. Devlin, Phys. Rev. B **41**, 4854 (1990).
[9] D. Bertrand, A. Mauger, J. Ferré, and P. Beauvillain, Phys. Rev. B **45**, 507 (1992-I).
[10] B. Leclercq and C. Rigaux, Phys. Rev. B **48**, 13573 (1993-II).
[11] A. Mauger, J. Ferré, and P. Beauvillain, Phys. Rev. B **40**, 862 (1989).
[12] B. E. Larson and H. Ehrenreich, Phys. Rev. B **39**, 1747 (1989).
[13] M. Continetino and A. P. Malozemoff, Phys. Rev. B **34**, 471 (1986).
[14] X. Batlle, A. Labarta, B. Martinez, X. Obradors, V. Cabañas, and M. Vallet-Regí J. Appl. Phys. **70**, 6172 (1991).
[15] D. S. Fisher, Phys. Rev. Lett. **56**, 416 (1986).
[16] A. P. Malozemoff and E. Pytte, Phys. Rev. B **34**, 6579 (1986).
[17] S. Geschwind, David A. Huse, and G. E. Devlin, Phys. Rev. B **41**, 2650 (1990).

# Observation of spin-glass freezing in the $S=1$ linear-chain Heisenberg antiferromagnet NENP

M. Hagiwara and K. Katsumata
*The Institute of Physical and Chemical Research (RIKEN), Wako, Saitama 351-01, Japan*

S. Sasaki, N. Narita and I. Yamada
*Department of Physics, Faculty of Science, Chiba University, Yayoi-cho, Inage-ku, Chiba 263, Japan*

T. Yosida
*Nakanihon Automotive College, Sakahogi, Gifu 505, Japan*

We have observed spin-glass freezing in a nominally pure single crystal of the $S=1$ linear-chain Heisenberg antiferromagnet $Ni(C_2H_8N_2)_2NO_2(ClO_4)$(NENP) by direct current (dc), linear alternating current (ac), and nonlinear ac susceptibility measurements. A possible origin of this spin-glass freezing is discussed. © *1996 American Institute of Physics.* [S0021-8979(96)23808-4]

Stimulated by Haldane's conjecture,[1] linear-chain Heisenberg antiferromagnets (LCHAs) with spin quantum number ($S$) one have been studied extensively. One of the most interest findings in these systems is the presence of $S=\frac{1}{2}$ degrees of freedom induced at the ends of finite chains. A quasi fourfold degenerate ground state was shown to exist from an exact diagonalization of an $S=1$ LCHA with open boundary conditions.[2] This means that the open chain has a spin $\frac{1}{2}$ degree of freedom at each end. A quantum Monte Carlo calculation on $S=1$ finite LCHAs showed that a staggered moment with $S=\frac{1}{2}$ appears at the ends and decays exponentially with distance.[3] Hagiwara *et al.*[4] demonstrated experimentally the existence of the $S=\frac{1}{2}$ degrees of freedom in the $S=1$ LCHA compound $Ni(C_2H_8N_2)_2NO_2(ClO_4)$, abbreviated as NENP. Many other measurements on $S=1$ LCHA materials have also shown the existence of the $S=\frac{1}{2}$ degrees of freedom.[5–8]

If there is no interaction between the $S=\frac{1}{2}$ degrees of freedom, the system should exhibit paramagnetism down to zero Kelvin. Avenel *et al.*[9] have measured the magnetic susceptibility of a carefully grown single crystal sample of NENP down to 300 $\mu$K and found that the susceptibility obeyed the Curie–Weiss law with a very small Weiss constant (6–12 mK). When an interaction between the $S=\frac{1}{2}$ degrees of freedom exists, we expect that the system will exhibit a magnetic ordering at finite temperature. Recently, we have reported the first observation of a spin-glass transition in NENP.[10] In the present paper, we report additional information on a spin-glass freezing in NENP.

NENP crystallizes in the orthorhombic system and belongs to the Pnma space group with lattice constants $a=15.223$ Å, $b=10.300$ Å, and $c=8.295$ Å.[11] The structure consists of $\cdots Ni-NO_2-Ni\cdots$ chains along the $b$ axis which are well separated from each other by $ClO_4$ anions. The intrachain interaction between $Ni^{2+}$ spins via the nearly 180° Ni–$NO_2$–Ni bond is determined to be antiferromagnetic ($J/k_B=-55$ K).[12] The interchain interaction is much weaker than the intrachain one ($|J'/J|\cong 10^{-4}$).

The single crystals of NENP used in these experiments were grown from a reaction of $Ni(ClO_4)_2 6H_2O$ (99.99%) with ethylenediamine and $NaNO_2$. Usually, the reaction is controlled so as to proceed slowly. When the reaction proceeded quickly by chance, we obtained the crystals of NENP which show a spin-glass behavior described below.

In the following, we present the results of magnetic susceptibility measurements on the single crystal samples of NENP. The direct current (dc) and linear alternating current (ac) susceptibilities were measured with a SQUID magnetometer (Quantum Design's MPMS2). Special care was taken to reduce the magnetic field at the sample position. The nonlinear ac susceptibility was measured with a Hartshorn-type bridge installed at Chiba University.

Figure 1 shows the temperature dependence of the dc susceptibility (magnetization/applied magnetic field) of a single crystal of NENP for zero-field cooled (ZFC) and field cooled (FC) measurements. The susceptibility of this sample is qualitatively different from that of an ideal one reported before.[12] First, no rounded maximum is observed. Instead, the susceptibility continue to increase with decreasing temperature down to about 15 K for both of ZFC and FC measurements. Second, a marked difference between FC and ZFC measurements is observed below about 15 K. From the chemical analysis of the sample used in the measurement, we found that the concentration of transition elements other than Ni is below 0.01 wt. %. Thus, the increase of suseptibility at

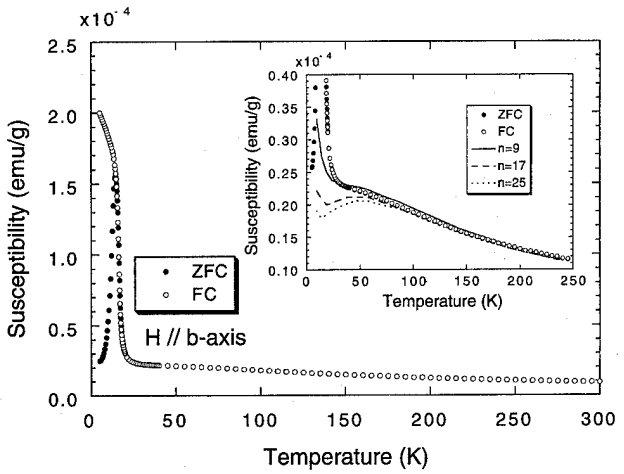



FIG. 1. Temperature dependence of the dc susceptibility in a nominally pure single crystal sample of NENP along the $b$ axis. Inset: Comparison between the experimental data with the result of a Monte Carlo calculation (Ref. 13) in the temperature 20–250 K.

 0021-8979/96/79(8)/6167/3/$10.00 © 1996 American Institute of Physics 

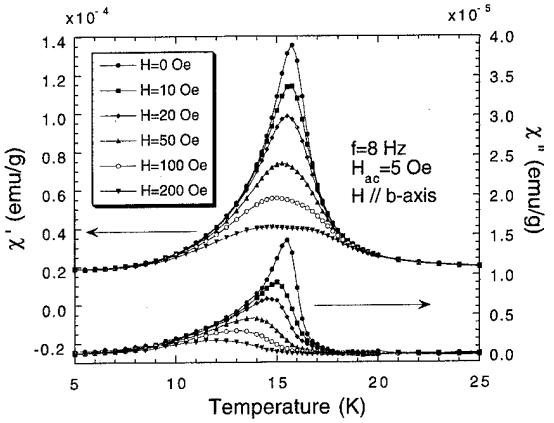



FIG. 2. Temperature dependence of real ($\chi'$) and imaginary ($\chi''$) parts of ac susceptibility in the NENP crystal for various dc fields superposed on the ac field. Solid lines are guides to the eyes.

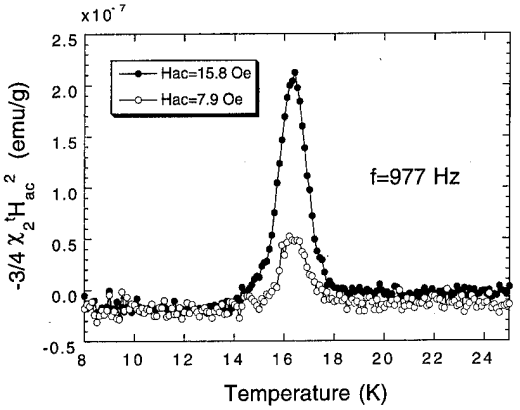



FIG. 3. Temperature vs nonlinear ac susceptibility ($\chi_2'$) of the NENP sample.

the low temperatures must come from the $S=\frac{1}{2}$ degrees of freedom at the chain ends. We have compared our data with the results of the Monte Carlo calculation[13] in the temperature range 20 K$<T<$250 K as shown in the inset of Fig. 1. We found that our results can be reproduced if we take an average chain length between 9 and 17 spins (no data are available for the chains between 10 and 16 spins in the literature). The rapid increase in the susceptibility below about 20 K in Fig. 1 means that an interaction between the $S=\frac{1}{2}$ degrees of freedom exists.

Figure 2 shows the temperature dependence of the real ($\chi'$) and imaginary ($\chi''$) parts of the linear ac susceptibility for different dc bias fields superposed on the ac field. A cusp is seen in the temperature dependence of $\chi'$ in zero dc field as in all the spin-glass materials known to date. The cusp broadens with increasing dc bias field which is commonly seen in spin-glass systems. We have also measured the linear ac susceptibilities for various frequencies.[10] The position of the cusp moves to high temperature side with increasing frequency as commonly seen in spin glasses.

In order to get further evidence for spin-glass transition, we have measured the nonlinear ac susceptibility of this sample. As was predicted theoretically by Suzuki[14] and confirmed experimentally by Chikazawa *et al.*,[15] the second component ($\chi_2'$) of the nonlinear susceptibility in spin glasses diverges to $-\infty$ at the freezing temperature ($T_f$). As is seen from Fig. 3, the temperature dependence of $-\chi_2'$ of our NENP sample shows an anomalous increase when approached to $T_f$ from both sides. From these experimental results, we conclude that a spin-glass transition takes place in the nominally pure single crystal of NENP.

Now we discuss a possible origin of the spin-glass transition in our sample. It is pointed out that the interchain exchange interaction and dipole–dipole interaction alone cannot explain the relatively high freezing temperature. Then, we should take into account the intrachain exchange interaction as an origin of the spin glass. Since our NENP crystals do not contain any detectable magnetic impurities, the moments are induced at the ends of finite chains probably by structural defects. Here, we assume that such defects are created by a displacement of $ClO_4$ molecules towards the chain that pushes away an $NO_2$ molecule. Then, there will be a possibility of having a 90° exchange bond between the neighboring Ni atoms in the chain. We expect that this arrangement will give a ferromagnetic exchange interaction[16,17] between the spins at the ends. These ferromagnetic bonds are distributed randomly in the chains. The randomly distributed ferromagnetic and antiferromagnetic bonds in an open chain do not cause frustration in the system. Then, we propose the following mechanism. At the sites where an $NO_2$ molecule was pushed away, the interchain exchange interaction will be much stronger than that in an ideal sample. Let us consider an example in which frustration is expected to occur. In a short open chain with an even number of spins, the end spins are antiparallel to each other, while they are parallel in a short odd chain. When neighboring even($n$) and odd($n+1$) chains interact at the both ends as shown in Fig. 4, a 90° ferromagnetic exchange bond between the neighboring Ni atoms in the chain and a 180° antiferromagnetic exchange bond between the chains exist. This latter exchange bond causes a frustration as shown in Fig. 4.

In conclusion, the dc, linear ac, and nonlinear ac susceptibility measurements on the nominally pure single crystal of NENP show clearly a spin-glass freezing of the moments at the chain ends created by structural defects.

We would like to thank the Chemical Analysis Unit in RIKEN for the chemical analysis. This work was partially supported by the "MR Science Research Program from RIKEN" and by a Grand-in-Aid for Science Research from the Japanese Ministry of Education, Science, Sports and Culture.

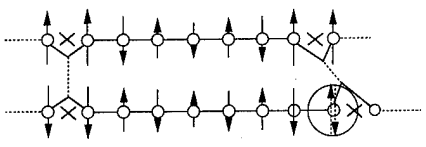


FIG. 4. An example of the arrangement of short chains in which frustration is expected to occur in the NENP crystal. The crosses show the sites where a $NO_2$ molecule was pushed away.

[1] F. D. M. Haldane, Phys. Rev. Lett. **50**, 1153 (1983).
[2] T. Kennedy, J. Phys. Condensed Matter **2**, 5737 (1990).
[3] S. Miyashita and S. Yamamoto, Phys. Rev. B **48**, 913 (1993).
[4] M. Hagiwara, K. Katsumata, I. Affleck, B. I. Halperin, and J. P. Renard, Phys. Rev. Lett. **65**, 3181 (1990).
[5] S. H. Glarum, S. Geschwind, K. M. Lee, M. L. Kaplan, and J. Michel, Phys. Rev. Lett. **67**, 1614 (1991).
[6] M. Hagiwara, K. Katsumata, H. Hori, T. Takeuchi, M. Date, A. Yamagishi, J. P. Renard, and I. Affleck, Physica B **77**, 386 (1992).
[7] H. Deguchi, S. Takagi, M. Ito, and K. Takeda, J. Phys. Soc. Jpn. **64**, 22 (1995).
[8] T. C. Kobayashi, H. Honda, A. Koda, and K. Amaya, J. Phys. Soc. Jpn. **64**, 2609 (1995).
[9] O. Avenel, J. Xu, J. S. Xia, M.-F. Xu, B. Andraka, T. Lang, P. L. Moyland, W. Ni, P. J. C. Signore, C. M. C. M. van Woerkens, E. D. Adams, G. G. Ihas, M. W. Meisel, S. E. Nagler, N. S. Sullivan, Y. Takano, D. R. Talham, T. Goto, and N. Fujiwara, Phys. Rev. B **46**, 8655 (1992).
[10] M. Hagiwara, K. Katsumata, S. Sasaki, N. Narita, I. Yamada, and T. Yosida, J. Phys. Soc. Jpn. **64**, 3647 (1995).
[11] A. Meyer, A. Gleizes, J. J. Girerd, M. Verdaguer, and O. Kahn, Inorg. Chem. **21**, 1729 (1982).
[12] J. P. Renard, M. Verdaguer, L. P. Regnault, W. A. C. Erkelens, J. Rossad-Mignod, and W. G. Stirling, Europhys. Lett. **3**, 945 (1987).
[13] S. Yamamoto and S. Miyashita, Phys. Rev. B **50**, 6277 (1994).
[14] M. Suzuki, Prog. Theor. Phys. **58**, 1151 (1977).
[15] S. Chikazawa, T. Saito, T. Sato, and Y. Miyako, J. Phys. Soc. Jpn **47**, 335 (1979).
[16] J. B. Goodenough, Phys. Rev. **100**, 564 (1955).
[17] J. Kanamori, J. Phys. Chem. Solids **10**, 87 (1959).

# Nonlinear susceptibility measurements at the spin-glass transition of the pyrochlore antiferromagnet $Y_2Mo_2O_7$

M. J. P. Gingras
*TRIUMF, Theory Group, 4004 Wesbrook Mall, Vancouver, British Columbia V6T-2A3, Canada*

C. V. Stager and B. D. Gaulin
*Department of Physics and Astronomy, McMaster University, Hamilton, Ontario L8S 4M1, Canada*

N. P. Raju and J. E. Greedan
*Department of Chemistry, McMaster University, Hamilton, Ontario L8S 4M1, Canada*

We have measured the magnetic field and temperature dependence of the nonlinear dc susceptibility, $\chi_{nl}$, of the frustrated pyrochlore antiferromagnet $Y_2Mo_2O_7$ close to and above the temperature, $T_g \sim 22$ K, where this material exhibits irreversible (spin-glass like) magnetic behavior. Our results suggest that the observed irreversible magnetic properties in this material are due to a thermodynamic spin-glass transition signaled by a divergence of the nonlinear magnetic susceptibility coefficient $\chi_3 \sim (T/T_g - 1)^{-\gamma}$ at $T_g$ with $\gamma = 3.3 \pm 0.5$. $\chi_{nl}$ shows *two* power-law behavior at $T_g$, $\chi_{nl} \sim H^{2/\delta}$, with $\delta \sim 2.8$ for $H < 1000$ Oe and $\delta \sim 4.1$ for $H > 2000$ Oe. These values for $\gamma$ and $\delta$, as well as the crossover behavior of $\chi_{nl}$ at $T_g$, is consistent what is found in common disordered Heisenberg spin glass materials. © *1996 American Institute of Physics.* [S0021-8979(96)23908-4]

The study of magnetic materials with competing, or *frustrated*, antiferromagnetic interactions, inhibiting the formation of a collinear magnetically ordered state, goes back more than forty years.[1,2] However, the past five years have seen considerable increase in the number of systematic experimental, theoretical, and numerical investigations of these systems.[2,3] For example, it has been suggested that the phase transition into a noncollinear spin structure may belong to a "new" chiral universality class different from the universality classes appropriate to collinear magnets.[4] Also, the proposal that large levels of frustration can generate quantum zero-point spin fluctuations sufficient to destroy Néel order at zero temperature even for two and three-dimensional systems, and lead to novel types of magnetic ground states, has attracted much attention.[2,3]

Several families of insulating antiferromagnetic materials with extreme frustration level have been identified.[3] Examples include the kagomé and pyrochlore systems. In the kagomé $SrCr_xGa_{12-x}O_{19}$ (Ref. 5) and $KM_3(OH)_6(SO_4)_2$ (Ref. 6) (M=Cr or Fe) materials, the moment carrying cations (Cr, Fe) reside on stacked, two-dimensional lattices of corner sharing triangles.[5,6] In the $A_2B_2O_7$ pyrochlores (A =Y,Tb; B=Mn,Mo), the $A^{3+}$ and $B^{4+}$ cations, which can be either magnetic or nonmagnetic, sit on two distinct, interpenetrating lattices of corner-sharing tetrahedra.[7–10]

In both the classical kagomé and pyrochlore Heisenberg antiferromagnets, the elementary triangular or tetrahedral plaquettes are highly frustrated, and the classical ground state of the system is determined by the quite unrestrictive condition $\Sigma_{i\in\Delta} \mathbf{S}_{i,\Delta} = 0$ on *each* individual plaquette $\Delta$, where $\mathbf{S}_{i,\Delta}$ is a classical spin on lattice site $i$ of plaquette $\Delta$. The number of states which satisfy this local condition increases exponentially with system size, leading to a finite ground state entropy per spin, and a *collective* paramagnetic ground state.[7] In real systems, however, perturbations such as lattice distortions, crystal-field effects, further nearest-neighbor exchange or dipolar coupling can lead to the selection of a classical Néel ordered ground state.[7,8] A mechanism of order-by-disorder via thermal or quantum fluctuations may also be at play, and lead to long-range order.[8] One may therefore expect two generic scenarios for real kagomé and pyrochlore antiferromagnets. They could display long-range Néel order, possibly with a sizeable quantum reduction of the staggered moment due to the "fragility" of the classical order brought about solely by perturbative effects.[8,11] Alternatively, quantum fluctuations may be sufficiently large to destabilize the otherwise classical ground state, and drive the system to an unconventional quantum ground state.[2,11] It is therefore interesting that a large number of kagomé[3,5,6] and pyrochlore[9,10] antiferromagnets fail to display long-range, or even extended short-range, Néel order. Instead, they exhibit magnetic irreversibilities, i.e., spin-glass like behavior, below a glass temperature, $T_g$.[9,10] This is surprising as a large number of these systems can be prepared with a very high degree of chemical and structural purity.[9,10] The mechanism responsible for this spin-glass behavior is not understood, and is currently the subject of an intense debate.[12] However, irrespective of the origin of the glassiness, one would still like to know: "Does $T_g$ correspond to a true thermodynamic phase transition or, alternatively, is it a dynamical freezing transition?"

$Y_2Mo_2O_7$ is a narrow band gap semiconductor where the $Mo^{4+}$ ions are magnetic, with an antiferromagnetic nearest-neighbor Mo-Mo superexchange, while $Y^{3+}$ is diamagnetic. The 270 mg powder sample of $Y_2Mo_2O_7$ was prepared as described in Ref. 9. Neutron and x-ray powder diffraction studies show that there is no measurable amount of oxygen vacancies or intermixing between the $Y^{3+}$ and the $Mo^{4+}$ sublattices.[9] Any random disorder in that material is therefore below the 1% detectability level. The magnetization was measured using a SQUID magnetometer. The bulk magnetization of $Y_2Mo_2O_7$ becomes hysteretic below $T_g \approx 22$ K: the field-cooled (FC) and zero field-cooled (ZFC) magnetizations measured in fields of 100 Oe show a sharp

 0021-8979/96/79(8)/6170/3/$10.00 © 1996 American Institute of Physics

breakaway below 22 K.[9] This is a characteristic signature of the freezing transition observed in conventional chemically disordered spin glass materials.[13]

To assess whether or not a true thermodynamic spin-glass phase transition occurs in $Y_2Mo_2O_7$, we have measured the nonlinear susceptibility coefficient $\chi_3(T)$, which is expected to show a power-law critical divergence close to $T_g$ of the type $\chi_3 \sim (T-T_g)^{-\gamma}$ ($\gamma>0$). [13] $\chi_3$ is extracted from the temperature, $T$, and field, $H$, dependence of the magnetization, $M(T,H)$,

$$M(T,H)=\chi_1(T)H-\chi_3(T)H^3+\chi_5(T)H^5-\ldots, \qquad (1)$$

where $\chi_1(T)$ is the linear susceptibility. Hence, the temperature dependence of $\chi_3(T)$ allows a determination of $T_g$ and $\gamma$.[13] In fact, all the nonlinear terms $\chi_{2n+1}$ with $n\geqslant 1$ must diverge at $T_g$, since both $M(T,H)$ and $H$ are finite quantities. It is therefore convenient to define a "full" nonlinear susceptibility, $\chi_{\rm nl}$, as

$$\chi_{\rm nl}(T,H)\equiv 1-\frac{M(T,H)}{\chi_1 H}. \qquad (2)$$

Right at $T_g$, $\chi_{\rm nl}$ has a power law dependence on $H$:

$$\chi_{\rm nl}(T_g,H)\sim H^{2/\delta}, \qquad (3)$$

where $\delta$ is a second critical exponent characterizing the spin-glass transition.[13]

The magnetization data were collected using the SQUID magnetometer under field-cooling conditions; the field $H$, in the range 100–7000 Oe was switched on at high temperature (70 K$\sim 3T_g$), and kept constant during subsequent slow cooling at a rate 5 mK/s down to the temperature of interest. Because of the irreversible and time-dependent nature of the system's response below $T_g$ only results in temperature range $T_g<T<3T_g$ are included. Our results on the low-temperature dynamical relaxation of the magnetization in $Y_2Mo_2O_7$ will be reported elsewhere.[14] Three consecutive cooling runs for fixed field were performed, with the magnetization data averaged over the three runs.

Figure 1(a) shows the field cooled susceptibility $\chi(T,H)\equiv M(T,H)/H$ for six different cooling fields. Prior to doing any analysis, we dealt with the fact that the interactions do not perfectly average to zero, as evidenced by the fact that $\chi_1(T)$ does not have a simple $\chi_1\sim 1/T$ Curie law. The *leading* corrections to scaling coming from this nonzero averaging of the interactions can be eliminated by fitting $\chi(T,H)$ in powers of $a_{2n+1}(T)\chi_1[\chi_1 H]^{2n}$ for $n\geqslant 0$, instead of simply $\chi_{2n+1}H^{2n}$, and considering the critical behavior or $a_{2n+1}(T)$ instead of $\chi_{2n+1}(T)$.[13] For each temperature the field dependence of $\chi$ at small field was fitted with $\chi=\chi_1-\chi_3 H^2$, giving $a_3=\chi_3/\chi_1^3$, and varying the upper limit of the field range to determine the limit of validity of this restricted fit beyond which higher $\chi_{2n+1}$ ($n>1$) corrections become significant. The quality of our magnetization data did not allow us to determine the $a_5=\chi_5/\chi_1^5$ coefficient with precision better than 50%–100%, and these $a_5$ data are not included here. We show in Fig. 1(b) the full nonlinear susceptibility, $\chi_{\rm nl}(T,H)$, as defined in Eq. (2), with $\chi_1$ extracted from the fit $\chi(T,H)=\chi_1-\chi_3 H^2$, as a function of $H^2$ for a few temperatures above $T_g$. These results emphasize the

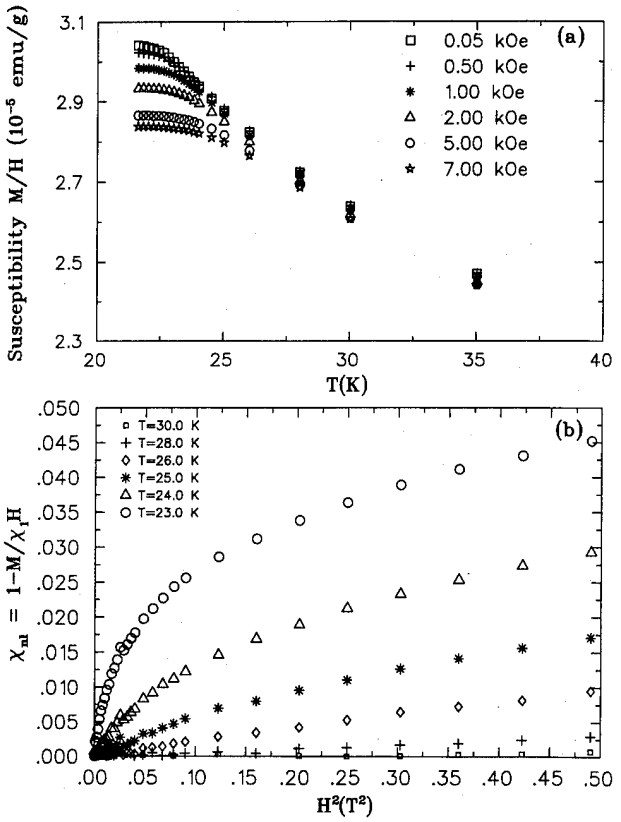



FIG. 1. Panel (a): Raw data, susceptibility $M/H$ vs $T$ for six different cooling fields. Panel (b): net nonlinear susceptibility, $\chi_{\rm nl}=1-M/\chi_1 H$ vs $H^2$ for the six temperatures indicated.

large increase of the nonlinear susceptibility upon approaching $T_g$ in this material. We also notice that the $\chi_{\rm nl}$ is only linear in $H^2$ up to a maximum field $H_+(T)$ whose value is rapidly moving to $H_+(T)=0$ upon approaching $T_g$. This is due to the turning on of the $\chi_{2n+1}$ ($n>1$) corrections which diverge at $T_g$ as $(T-T_g)^{(\beta-n[\gamma+\beta])}$.[13]

Figure 2(a) shows a log-log plot of $a_3$ versus $T/T_g-1$ with $T_g=21.8$ K. There are two sets of data shown on this figure, the squares and the triangles. The two data sets were obtained with the same $Y_2Mo_2O_7$ sample, but from two separate set of experiments separated by four months. The excellent agreement in the absolute value of $a_3$ between the two sets of experiments (i.e., no vertical or horizontal shifting of one set with respect to the other was done) gives us an estimate of the precision of our measurements. A power-law fit to the data with square symbols resulted in a fit with minimum $\chi^2$ value for $T_g=21.9$ K, yielding a critical exponent $\gamma=3.3\pm 0.5$. A fit for the triangles give a best fit for $T_g=21.7$ K with a critical exponent of also $\gamma=3.3\pm 0.5$. The power-law divergence of $a_3$ saturates for $t<0.07$ ($t\equiv T/T_g-1$). A reason for this levelling off of $a_3$ for $t<0.07$ is that the range of dominance of the term $\chi_3(T)H^2$ to $\chi_{\rm nl}$ falls below the smallest field, $H_{\rm min}$ ($H\sim 100$ Oe), for which reliable data are available to us. The increasingly important diverging higher order terms of alternating signs ($\chi_5$, $\chi_7$, etc) contributing to $\chi_{\rm nl}$ then cause $a_3$ to be underestimated when $H_+(T)$ becomes less or equal to $\approx H_{\rm min}$. Another possible effect may be the slow but finite cooling rate inhibits the attainment of

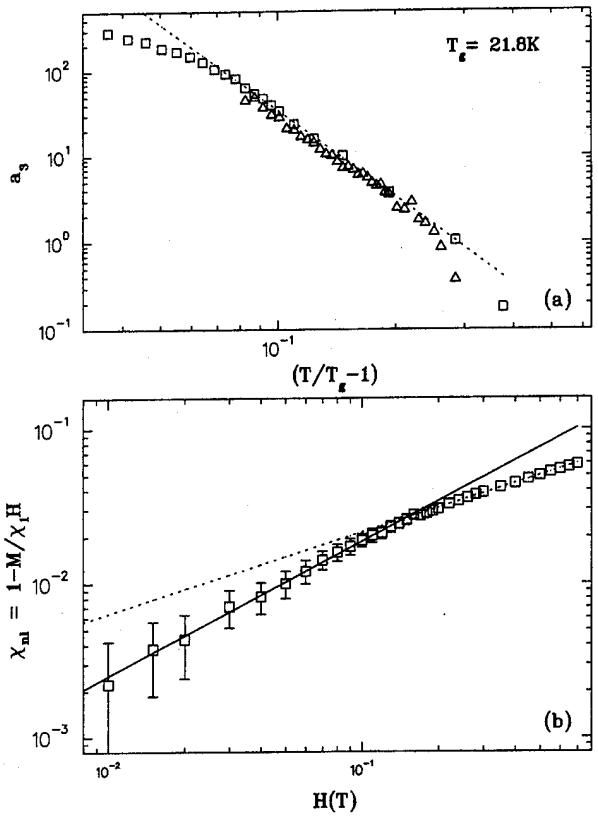



FIG. 2. Panel (a): log-log plot showing the temperature dependence of $a_3(T)$. The square and triangular symbols correspond to two set of independently analyzed experiments. The dashed line shows the power law fit to the square symbols with the average $T_g$=21.8 K. Panel (b): log-log plot of the net nonlinear susceptibility, $\chi_{nl}$, vs applied field $H$ at $T$=21.8 K. The dashed and solid lines correspond to power-law fits for fields $H<1000$ Oe and $H>2000$ Oe, respectively (see discussion in text).

the correct equilibrium value of $\chi_{nl}$ and this effect is compounded with the previous one, saturating $a_3$ for $t<0.07$. Figure 2(b) shows a log-log plot of $\chi_{nl}$ versus $H$ at $T_g$=21.8 K for fields $H$=100–7000 Oe. At criticality, one expects that $\chi_{nl}$ will be given by Eq. (3), with a single value of $\delta$ for fields $H \ll J$, where $J$ is the rms value of the superexchange interactions. Clearly, we observe two trends in Fig. 3(b), one for small fields and one for large fields, with a crossover field between the two regimes of the order of $H_{co} \approx 1500$ Oe. The value of $\delta$ is found to be $2.8 \pm 0.5$ for $H<1000$ Oe (dashed line) and $4.1 \pm 0.1$ for $H>2000$ Oe (solid line). Such field induced crossover, with similar values of $\delta(H<H_{co})$ and $\delta(H>H_{co})$ has also been seen in conventional disordered spin glasses.[13]

It is interesting to compare our results for the $Y_2Mo_2O_7$ pyrochlore with those of the $SrCr_8Ga_4O_{19}$ kagomé system (SCGO),[15,16] and for the site-ordered gadolinium gallium garnet magnet $Gd_3Ga_5O_{12}$ (GGG).[17] Ramirez *et al.*[15] found a power-law divergence of $\chi_3$ in SCGO with $\gamma \approx 2.4$, while Martinez *et al.*[16] recently published results where they argue that the freezing at $T_f \approx 3.5$ K in SCGO is *not* associated with a divergence of $\chi_3$ ($\chi_3$ was found to increase by a factor 5 or so in Ref. 16), and that this material does not exhibit conventional spin glass behavior. Schiffer *et al.*[17] found a large increase of $\chi_3$ in GGG (6 orders of magnitude between 0.2 and 5 K), which they ascribe to a spin glass transition. However, the temperature dependence of $\chi_3$ in GGG is qualitatively different than what is found in conventional spin glasses since $\chi_3$ has two maxima in GGG, while it is a monotonic function of the temperature in conventional spin glasses. Hence, from the point of view of nonlinear susceptibility measurements, it appears that the spin glass behavior observed in $Y_2Mo_2O_7$ resembles much more what is found in conventional spin glasses than what has been found in other topologically frustrated antiferromagnets, such as SCGO and GGG.

We wish to thank D. Huse for useful discussions. This research has been financed by the NSERC under the NSERC Collaborative Research Grant *Geometrically-Frustrated Magnetic Materials.*

[1] J. M. D. Coey, Can. J. Phys. **65**, 1210 (1987).
[2] *Magnetic Systems with Competing Interactions*, edited by H. T. Diep (World Scientific, Singapore, 1994); P. Chandra and P. Coleman, New Outlooks and Old Dreams in Quantum Antiferromagnets, Les Houches Summer School Lectures (August 1991).
[3] A. P. Ramirez, Annu. Rev. Mater. Sci. **24**, 453 (1994).
[4] H. Kawamura, in *Recent Advances in Magnetism of Transition Metal Compounds*, edited by A. Kotani and N. Suzuki (World Scientific, Singapore, 1993); J. Phys. Soc. Jpn. **61**, 1299 (1992) and references therein.
[5] Y. J. Uemura *et al.*, Phys. Rev. Lett. **73**, 3306 (1994).
[6] A. Keren, Ph.D. Columbia University (unpublished, 1994); A. Keren *et al.*, Phys. Rev. Lett. (submitted).
[7] J. Villain, Z. Phys. B **33**, 31 (1978); J. N. Reimers, A. J. Berlinsky, and A.-C. Shi, Phys. Rev. B **43**, 865 (1991); J. N. Reimers, Phys. Rev. B **45**, 7287 (1992); M. Kvale (unpublished).
[8] (a) J. N. Reimers, J. E. Greedan, and M. Björgvinsson, Phys. Rev. B **45**, 7295 (1992); (b) A. Mailhot and M. L. Plumer, Phys. Rev. B **48**, 9881 (1993); (c) S. T. Bramwell, M. J. P. Gingras, and J. N. Reimers, J. Appl. Phys. **75**, 5523 (1994).
[9] J. E. Greedan *et al.*, Solid State Commun. **59**, 895 (1986); J. N. Reimers and J. E. Greedan, J. Solid State Chem. **72**, 390 (1988); J. E. Greedan *et al.*, Phys. Rev. B **43**, 5682 (1991); N. P. Raju, E. Gmelin, and R. K. Kremer, Phys. Rev. B **46**, 5405 (1992).
[10] J. N. Reimers *et al.*, Phys. Rev. B **43**, 3387 (1991); *ibid.* **43**, 5682 (1991); B. D. Gaulin *et al.*, Phys. Rev. Lett. **69**, 3244 (1992).
[11] S. Sachdev, Phys. Rev. B **45**, 12377 (1992).
[12] Disorder-free spin-glassiness in pyrochlores and in the related two-dimensional kagomé Heisenberg antiferromagnet, has been much discussed in the past four years. See Refs. 1–10 and E. F. Shender *et al.*, Phys. Rev. Lett. **70**, 3812 (1993); V. B. Cherepanov (unpublished, 1994).
[13] K. Binder and A. P. Young, Rev. Mod. Phys. **58**, 801 (1986); K. H. Fischer and J. A. Hertz, *Spin Glasses* (Cambridge University Press, Cambridge, 1991).
[14] M. J. P. Gingras *et al.* (unpublished).
[15] A. P. Ramirez *et al.*, Phys. Rev. Lett. **64**, 2070 (1990).
[16] B. Martinez *et al.*, Phys. Rev. B **50**, 15779 (1994).
[17] P. Schiffer *et al.*, Phys. Rev. Lett. **74**, 2379 (1995).

# Magnetic ordering in pyrochlore $Ho_2Mn_2O_7$

N. P. Raju and J. E. Greedan
*Brockhouse Institute for Materials Research, McMaster University, Hamilton, Ontario L8S 4M1, Canada*

J. S. Pedersen
*Department of Solid State Physics, Risø National Laboratory, DK-4000 Roskilde, Denmark*

Ch. Simon and A. Maignan
*Laboratoire CRISMAT, CNRS URA 1318, ISMRa, Université de Caen, Bd du Maréchal Juin, 14050 Caen Cédex, France*

A. M. Niraimathi and E. Gmelin
*Max-Planck-Institut für Festkörperforschung, Heisenbergstrasse 1, 70569 Stuttgart, Germany*

M. A. Subramanian
*Central Research and Development, E.I. DuPont de Nemours and Co., Wilmington, Delaware 19880-0328*

The magnetic susceptibility of $Ho_2Mn_2O_7$ with a spontaneous rise below about 40 K and a paramagnetic Curie temperature of +39 K suggests a ferromagnetic ordering. Indeed neutron diffraction profiles show strongly enhanced Bragg peaks with a temperature dependence which indicates an apparent $T_c \approx 35$ K. Nonetheless, the magnetic diffraction pattern is not consistent with a collinear ferro or ferrimagnetic ordering of the $Ho^{3+}$ and $Mn^{4+}$ sublattices. Furthermore, specific heat and small angle neutron scattering (SANS) show features which are also incompatible with conventional long-range order. © *1996 American Institute of Physics.* [S0021-8979(96)24008-9]

## I. INTRODUCTION

Two necessary but not sufficient conditions for the occurrence of spin-glass-like ordering in a given material are site disorder and magnetic frustration.[1] Recently, some pyrochlore structure materials have been studied extensively as they seem to exhibit spin-glass-like ordering based on magnetic frustration alone, having apparently negligible site disorder.[2–8] The pyrochlore compounds $R_2M_2O_7$ ($R^{3+}$=rare earth; $M^{4+}$=transition metal) crystallize in the face-centered-cubic structure with the space group $Fd3m$.[9] Each of the metal atoms in the these compounds forms a three-dimensional network of corner-sharing tetrahedra. Such a topology leads to a very high degree of magnetic frustration if the nearest neighbor interactions are antiferromagnetic.[10]

The series of pyrochlores $R_2Mn_2O_7$ (R=Dy−Lu, or Y) have been reported to show ferromagnetic ordering based upon the observation of positive $\theta_p$ values and spontaneous magnetization.[3] Further studies of neutron scattering and heat capacity provided no evidence for long-range magnetic ordering in $Y_2Mn_2O_7$.[4] Small angle neutron scattering (SANS) studies indicated the presence of ferromagnetic clusters of finite size in the temperature range 13–20 K.[6] A variety of studies on a related series of compounds $R_2Mo_2O_7$ (R=Sm, Gd, Tb, or Y) demonstrate the presence of spin-glass-like ordering.[5,7,8] In contrast recent studies of magnetic and electrical along with SANS data on $Tl_2Mn_2O_7$ and $In_2Mn_2O_7$ are consistent with the long-range ferromagnetic ordering below about 120 K in both materials.[11]

$Ho_2Mn_2O_7$ has been reported to show spontaneous magnetization below about 40 K with a paramagnetic Curie temperature, $\theta_p$, of +33 K.[3] To understand the nature of this magnetic ordering, a variety of studies, ac and dc magnetic susceptibilities, specific heat, SANS and powder neutron diffraction were performed and the results are discussed in Sec. III.

## II. EXPERIMENT

The polycrystalline powder sample used in the present measurements is the same as that described in Ref. 3. Ac susceptibility, $\chi'$, was determined as function of temperature using a Lake Shore 7000 Susceptometer. Dc susceptibility and magnetization were measured with the help of a SQUID magnetometer (Quantum Design, San Diego). The specific heat of the sample, in the form of powder, was measured in the temperature range 2–90 K using a fully automated quasi-adiabatic calorimeter equipped with a Ge thermometer. The SANS experiments were performed at the instrument at the DR3 reactor at Risø National Laboratory. The powder neutron diffraction data, at different temperatures were obtained at the McMaster Nuclear Reactor with 1.3913 Å neutrons.

## III. RESULTS AND DISCUSSION

Figure 1 shows the temperature dependence of the real part of the ac susceptibility, $\chi'$, of $Ho_2Mn_2O_7$ at 10 G at different frequencies $\chi'$ increases rapidly below about 40 K

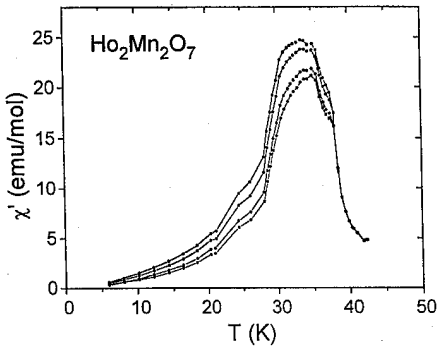



FIG. 1. ac susceptibility, $\chi'$, of $Ho_2Mn_2O_7$ at four different frequencies, from top to bottom: (8, 33, 143, and 222 Hz).

 0021-8979/96/79(8)/6173/3/$10.00 © 1996 American Institute of Physics 

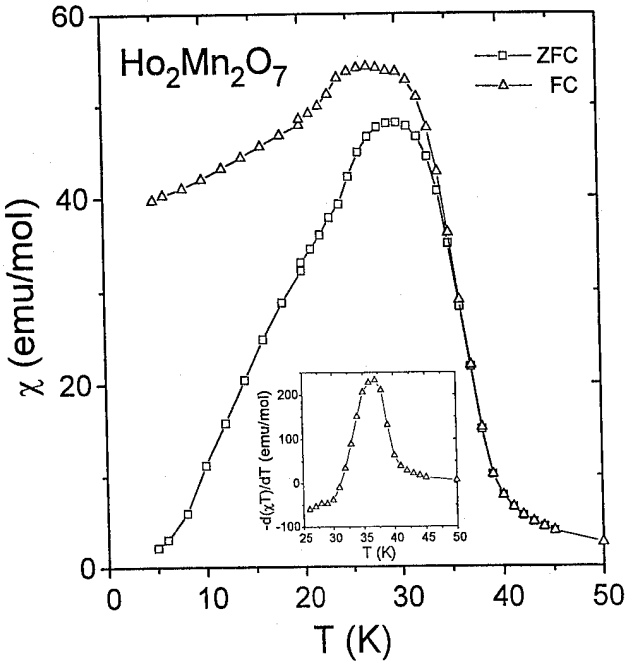



FIG. 2. Zero field cooled (ZFC) and field cooled (FC) dc susceptibility of $Ho_2Mn_2O_7$ measured at 100 G. The inset shows the negative temperature derivative of the product of the FC susceptibility and temperature.

and frequency dependent behavior is seen below 38.0 K with a broad maxima around 33 K. The dc susceptibility, measured at 100 G, is plotted against temperature in Fig. 2. It can be seen that a spontaneous magnetization develops below about 40 K and deviations occur between zfc and fc susceptibilities below 35 K which is expected for a spin-glass transition. A plot of $-d(\chi T)/dT$ against $T$ is generally useful to determine the transition temperature more accurately from the dc susceptibility data. Such a plot given in the inset of Fig. 2 indicates a $T_c$ of $37.1\pm1.0$ K. The magnetization as a function of applied field was measured at 5.0 K. Saturation occurs only above 1.5 T with a value of 12.3 $\mu_B/Ho_2Mn_2O_7$ at 5.0 T. In $Y_2Mn_2O_7$ a magnetic moment of 2.3 $\mu_B$/Mn at 4.0 T was reported.[4] Assuming the same $Mn^{4+}$ sublattice contribution in $Ho_2Mn_2O_7$ leaves a saturation moment of 3.9 $\mu_B/Ho^{3+}$ which is very small compared with an expected value of $gJ=10.0$ $\mu_B$ per $Ho^{3+}$ free ion ($g=1.25$ and $J=8$

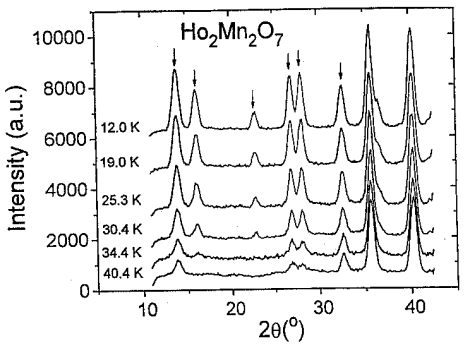



FIG. 3. Powder neutron diffraction profiles at different temperatures for $Ho_2Mn_2O_7$. The base line intensities for different temperatures are shifted arbitrarily for the clarity of the plots.

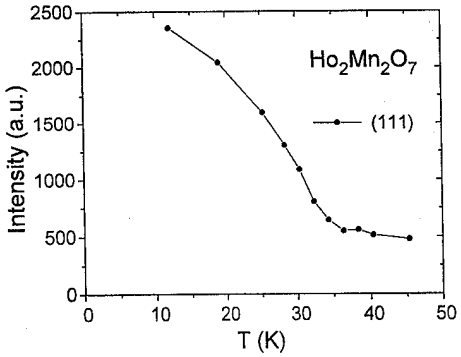



FIG. 4. The intensity of the Bragg reflection (111) against temperature.

for $Ho^{3+}$ with a ground state of $^2I_8$). The significant reduction in $Ho^{3+}$ moment from the expected value suggests the existence of strong crystal field effects. This is consistent with the specific heat data discussed later.

The powder neutron diffraction profiles at different temperatures are plotted in Fig. 3. First, note that the intensity of each nuclear Bragg peak, indicated by the arrows, is enhanced as the temperature is decreased and that there is no apparent change in the peak width. Further the temperature dependence of the intensity of the (111) reflection at 13.85°, as shown in Fig. 4, is consistent with the susceptibility data in suggesting a $T_c$ of about 36 K. The observed magnetic diffraction pattern is not consistent with a collinear ferro or ferrimagnetic structure as found for $Nd_2Mo_2O_7$ or $Yb_2V_2O_7$

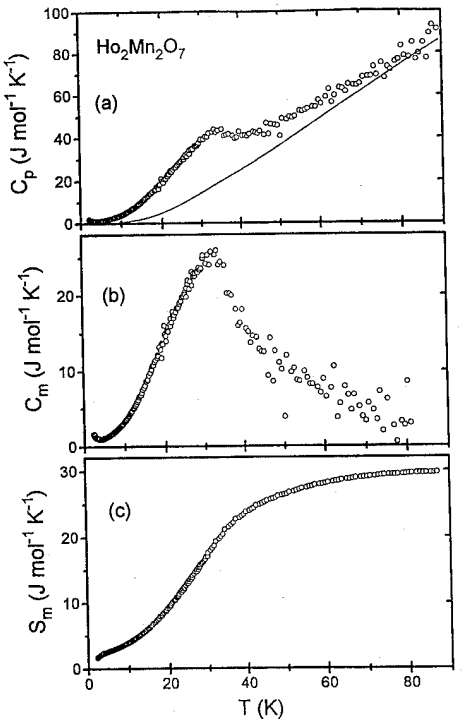



FIG. 5. (a) Measured specific heat, $C_p$, of $Ho_2Mn_2O_7$. The continuous line represents the estimated lattice specific heat, $C_l$. (b) Magnetic specific heat, $C_m$, obtained by subtracting the $C_l$ from the $C_p$. (c) Magnetic entropy, $S_m$, vs temperature.

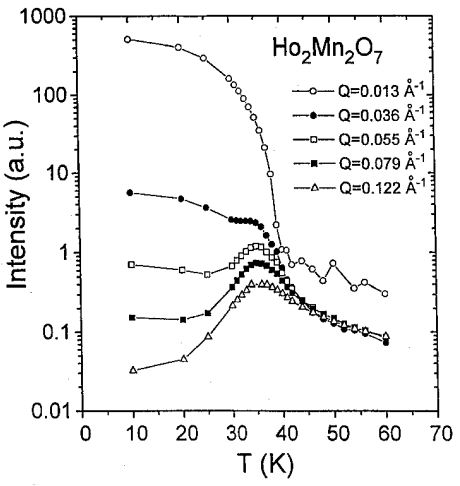



FIG. 6. Small-angle neutron-scattering intensity (in arbitrary units) as a function of temperature at different wave vectors for $Ho_2Mn_2O_7$.

and no solution has yet been found.[5,12] From the resolution of our neutron diffraction data we determine a lower limit for the spin correlation length of ~115 Å.

The measured specific heat, $C_p$, of $Ho_2Mn_2O_7$ in Fig. 5(a) displays an anomaly at about 35 K. The $C_p$ of insulating $Ho_2Mn_2O_7$ consists of contributions from the lattice specific heat, $C_l$, and the magnetic specific heat, $C_m$. The $C_l$ of $Ho_2Mn_2O_7$, represented by continuous line in Fig. 5(a), was evaluated to separate the contribution of $C_m$. The details of this procedure can be found in Ref. 7. The magnetic specific heat, in Fig. 5(b), shows a broad maximum around 33 K. The absence of a sharp λ-type anomaly and the presence of $C_m$ to temperatures much above the apparent $T_c$ suggests the absence of a conventional long-range magnetic ordering and the presence of short-range correlations. At temperatures below about 4 K there is an up turn in $C_m$. The magnetic entropy, $S_m$, involved in the magnetic anomaly is determined as a function of temperature by numerically integrating $C_m/T$ ($C_m/T$ behavior is extrapolated below 2 K). A plot of the magnetic entropy, $S_m$, versus temperature is displayed in Fig. 5(c). It can be seen that $S_m$ reaches a value of 30 J mol$^{-1}$ K$^{-1}$ at 90 K which is far less than the expected magnetic entropy for $Ho_2Mn_2O_7$ with $J=8$ for $Ho^{3+}$ and $S=3/2$ for $Mn^{4+}$, $2R\ln(2J+1)+2R\ln(2S+1)=70.2$ J mol$^{-1}$ K$^{-1}$. This corroborates the reduced saturation moment of $Ho^{3+}$ described above.

Figure 6 displays the temperature dependence of the scattered neutron intensity at different wave vectors, $Q$. For the highest wave vector (i.e., $Q=0.122$ Å$^{-1}$), the SANS intensity shows a broad maximum centering about 36 K, which is close to the $T_c$ observed in the previously described experiments, and decreases with the temperature below the $T_c$. As the $Q$ is reduced down to 0.055 Å$^{-1}$, the broad maximum and persists but the intensity rises towards the lower temperatures. With a further decrease in the $Q$, the intensity does not exhibit any peak but a plateau below 36 K and starts increasing below 30 K. For the lowest $Q$ of 0.013 Å$^{-1}$, the intensity increases sharply below 40 K and continues to increase with the decrease in the temperature. For a long-range ordered material, the SANS intensity observed at low $Q$ as a function of the temperature shows a pronounced cusp at the $T_c$ with a rapid fall off in the intensity both above and below the $T_c$. The SANS intensity of $Ho_2Mn_2O_7$, at the low $Q$ of 0.013 Å$^{-1}$, does not show any cusp at the $T_c$ providing evidence for the absence of long-range magnetic ordering. It is of interest here to mention the SANS intensities of $Tl_2Mn_2O_7$ and $Y_2Mn_2O_7$ against temperature.[11] In $Tl_2Mn_2O_7$, the SANS intensity shows a sharp peak at the transition temperature indicating a long-range ordering and consistent with the other experimental evidence. However, in $Y_2Mn_2O_7$ where long-range order is absent, the SANS intensity rises sharply below the $T_c$. A detailed analysis of SANS data for $Y_2Mn_2O_7$, $Ho_2Mn_2O_7$, and $Yb_2Mn_2O_7$, to be published elsewhere, gives evidence for correlation lengths of the order of 500 Å and greater associated with a random field scattering. It is thus likely that the apparently complex ordering seen in $Ho_2Mn_2O_7$ is not truly long range and thus it is possible to reconcile the neutron diffraction and heat capacity results.

## ACKNOWLEDGMENTS

We thank Professor C. V. Stager for the use of the SQUID magnetometer and McMaster University for direct support of the McMaster Nuclear Reactor. The Natural Science and Engineering Research Council of Canada has provided financial support.

[1] J. A. Mydosh, *Spin Glasses: An Experimental Introduction* (Taylor & Francis, London, 1993), p. 3.
[2] J. E. Greedan, M. Sato, X. Yan, and F. S. Razavi, Solid State Commun. **59**, 895 (1986).
[3] M. A. Subramanian, C. C. Torardi, D. C. Johnson, J. Panetier, and A. W. Sleight, J. Solid State Chem. **72**, 24 (1988).
[4] J. N. Reimers, J. E. Greedan, R. K. Kremer, E. Gmelin, and M. A. Subramanian, Phys. Rev. B **43**, 3387 (1991).
[5] J. E. Greedan, J. N. Reimers, C. V. Stager, and S. L. Penny, Phys. Rev. B **43**, 5682 (1991).
[6] J. E. Greedan, J. Avelar, and M. A. Subramanian, Solid State Commun. **82**, 797 (1992).
[7] N. P. Raju, E. Gmelin, and R. K. Kremer, Phys. Rev. B **46**, 5405 (1992).
[8] B. D. Gaulin, J. N. Reimers, T. E. Mason, J. E. Greedan, and Z. Tun, Phys. Rev. Lett. **69**, 3244 (1992).
[9] M. A. Subramanian, G. Aravamudan, and G. V. Subba Rao, Mater. Res. Bull. **15**, 1401 (1980).
[10] P. W. Anderson, Phys. Rev. **102**, 1008 (1956); R. Liebmann, *Statistical Mechanics of Periodic Frustrated Ising Systems* (Springer, Berlin, 1986), p. 117; J. N. Reimers, A. J. Berlinsky, and A. C. Shi, Phys. Rev. B **43**, 865 (1991).
[11] N. P. Raju, J. E. Greedan, and M. A. Subramanian, Phys. Rev. B **49**, 1086 (1994).
[12] L. Soderholm, C. V. Stager, and J. E. Greedan, J. Solid State Chem. **43**, 175 (1982); G. V. Bazuev, O. V. Makarova, and G. P. Shveikin, Russ. J. Inorg. Chem. **28**, 1088 (1983).

# $\lambda$-$MnO_2$, a new frustrated antiferromagnet with the defect spinel structure (abstract)

J. E. Greedan, Guo Liu, and N. P. Raju
*Institute for Materials Research, McMaster University, Hamilton, Ontario L8S 4M1, Canada*

J. N. Reimers
*Moli Energy, Maple Ridge, B.C. V2X 9E7, Canada*

Zin Tun
*A.E.C.L., Chalk River, Ontario K0J 1J0, Canada*

$MnO_2$ exists in a number of crystalline modifications. $\lambda$-$MnO_2$, prepared by electrochemical delithiation of the spine $Li_2Mn_2O_4$, has $Mn^{4+}$, $S=3/2$, occupying the octahedral (16*c*) sites in $Fd3m$. The magnetic sublattice consists of a pyrochlore-type array of corner-shared tetrahedra and is thus a candidate for frustrated antiferromagnetism. The dc susceptibility data indicate, for very low applied fields of 45 G, a sharp maximum at 32 K but this is smeared to a broad maximum at 25 K for fields as modest as 300 G. Zero-field neutron diffraction data show long range order with $K=(\frac{1}{2}\ \frac{1}{2}\ \frac{1}{2})$ and $T_n=32$ K. Surprisingly, the long range order is robust to applied fields of 1.0 T and higher. Prominent diffuse scattering persists up to greater than 60 K due to short range order which is indicative of frustration. The properties of $\lambda$-$MnO_2$ are compared with those of the spin-glass-like pyrochlore, $Y_2Mn_2O_7$, which has the same magnetic species on the same sublattice. © *1996 American Institute of Physics.* [S0021-8979(96)44208-9]

 0021-8979/96/79(8)/6176/1/$10.00 © 1996 American Institute of Physics

# Theory of nonlinear magneto-optics (invited)

U. Pustogowa, T. A. Luce, W. Hübner, and K. H. Bennemann
*Institute for Theoretical Physics, Freie Universität Berlin, Arnimallee 14, D-14195 Berlin, Germany*

Nonlinear magneto-optics is a very sensitive fingerprint of the electronic, magnetic, and atomic structure of surfaces, interfaces, and thin ferromagnetic films. Analyzing theoretically the nonlinear magneto-optical Kerr effect for thin films of Fe(001) and at Fe surfaces we demonstrate exemplarily how various electronic material properties of ferromagnets, such as the $d$-bandwidth, the magnetization, the substrate lattice constant, and the film-thickness dependence can be extracted from the calculated nonlinear Kerr spectra. Furthermore, we show how the substrate $d$ electrons [Cu(001)] affect the nonlinear Kerr spectra even without being themselves spin-polarized and without film-substrate hybridization. We show that the Kerr rotation angle in second-harmonic generation is enhanced by one to two orders of magnitude compared to the linear Kerr angle and how symmetry can be used to obtain the direction of magnetization in thin films and at buried interfaces from nonlinear magneto-optics. © *1996 American Institute of Physics.* [S0021-8979(96)47808-7]

## I. INTRODUCTION

Nonlinear magneto-optics for metals[1,2] is a new expanding field the significance of which results from extending electrodynamics to the nonlinear case and from applications. Particularly, an important task of theory was to extend the symmetry analysis to an electronic theory[3,4] since this allowed second-harmonic generation (SHG) to be used as an important new tool for the analysis of surface,[5] interface, thin film, and multilayer[6,7] magnetism. The surface sensitivity results since breakdown of inversion symmetry is necessary for SHG. Thus, it is possible to determine with the help of SHG surface magnetic moments, magnetic anisotropy, domains, magnetostriction, and, in particular, properties of buried interfaces.

Using an electronic theory (with a band structure input) we calculate (i) the material specific nonlinear response function $\chi^{(2)}(\omega,\mathbf{M},\lambda_{so},d)$, depending on magnetization $M$, spin-orbit coupling $\lambda_{so}$ and film thickness $d$, (ii) the nonlinear Fresnel formula for the reflected nonlinear fields $E(2\omega)$, and thus finally, (iii) the complex nonlinear Kerr rotation angle $\Phi_K^{(2)}$. The results, presented in the following demonstrate, in particular, what can be learned (a) from an analysis of the frequency dependence and (b) from the symmetry analysis and the Kerr rotation. Some selected general results obtained previously are shown, but also interesting new results indicating important substrate effects. Remarkably, the calculation[8] and recent experiments[9,10] yield that $\Phi_K^{(2)}$ is larger by two orders of magnitude compared to the linear Kerr rotation.

## II. THEORY

### A. Nonlinear susceptibility

Using response theory the nonlinear optical polarization is given by

$$P_i=\chi_{ijm}^{(2)}E_j(\omega)E_m(\omega), \tag{1}$$

where $P_i$ is the $i$th component of the polarizability and where the susceptibility tensor $\chi_{ijm}^{(2)}$ is determined by[1,11]

$$\chi_{ijm}^{(2)}(2q_\parallel,2\omega,\mathbf{M})=\frac{e^3C}{\Omega}\frac{\lambda_{so}}{\hbar\omega}\sum_\sigma\sum_{\mathbf{k},l,l',l''}\left\{\langle\mathbf{k}+2\mathbf{q}_\parallel,l''\sigma|i|\mathbf{k}l\sigma\rangle\langle\mathbf{k}l\sigma|j|\mathbf{k}+\mathbf{q}_\parallel,l'\sigma\rangle\langle\mathbf{k}+\mathbf{q}_\parallel,l'\sigma|m|\mathbf{k}+2\mathbf{q}_\parallel,l''\sigma\rangle\right.$$

$$\left.\times\frac{\dfrac{f(E_{\mathbf{k}+2\mathbf{q}_\parallel,l''\sigma})-f(E_{\mathbf{k}+\mathbf{q}_\parallel,l'\sigma})}{E_{\mathbf{k}+2\mathbf{q}_\parallel,l''\sigma}-E_{\mathbf{k}+\mathbf{q}_\parallel,l'\sigma}-\hbar\omega+i\hbar\alpha_1}-\dfrac{f(E_{\mathbf{k}+\mathbf{q}_\parallel,l'\sigma})-f(E_{\mathbf{k}l\sigma})}{E_{\mathbf{k}+\mathbf{q}_\parallel,l'\sigma}-E_{\mathbf{k}l\sigma}-\hbar\omega+i\hbar\alpha_1}}{E_{\mathbf{k}+2\mathbf{q}_\parallel,l''\sigma}-E_{\mathbf{k}l\sigma}-2\hbar\omega+i2\hbar\alpha_1}\right\}. \tag{2}$$

 0021-8979/96/79(8)/6177/4/$10.00 © 1996 American Institute of Physics 

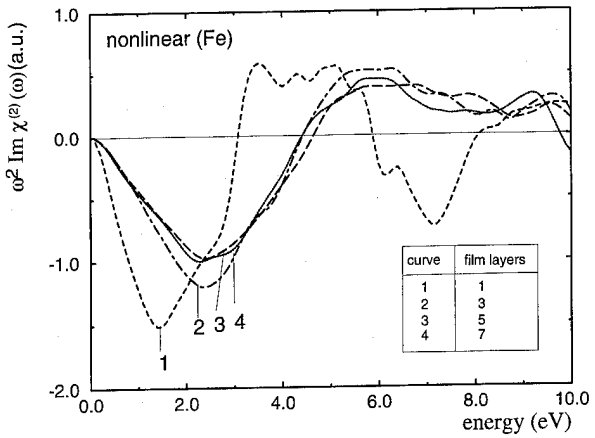



FIG. 1. *Ab initio* calculated nonlinear magneto-optical Kerr spectra of Fe using Eq. (2) for a monolayer (dashed curve—1), and films with 3 layers (dashed-dotted curve—2), 5 layers (long-dashed—3), and 7 atomic layers (dotted curve—4). The second-harmonic response results from the first atomic layer. This SH response is obtained by projecting the wave functions to the first atomic layer yielding the factor $C$.

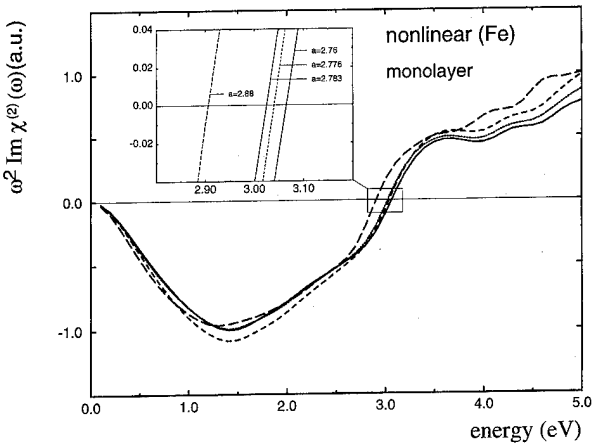



FIG. 2. Film-lattice-constant dependence of *ab initio* calculated nonlinear Kerr spectra of a Fe monolayer. The solid curve refers to the bulk *bcc* Fe lattice constant $a=2.76$ Å, the dashed curve to $a=2.776$ Å (bulk Au), and the dotted curve to $a=2.783$ Å (bulk Ag). The long-dashed curve refers to the experimental $a=2.88$ Å for Fe. Choosing lattice constants $a$ referring to Au and Ag should simulate substrate effects. The inset shows for an enhanced scale the effects of different lattice constants for the zero of Im $\chi^{(2)}$ at $\hbar\omega\approx$ 3 eV and indicate structural effects which should be observable.

Here $E_{\mathbf{k}l\sigma}$ are the electronic energy levels resulting from the band structure calculations, $\langle \mathbf{k}l\sigma|i|\mathbf{k}+\mathbf{q}_\parallel, l'\sigma\rangle$ are the transition matrix elements, which control the symmetry and thus the interface sensitivity. If the matrix elements are treated as constants one has to introduce a cut-off to guarantee the surface sensitivity. This is done by the factor $C$.[12] Typically, magnetic dipole effects are negligible if the electric dipole contribution does not vanish. $\lambda_{so}$ is the key parameter for nonlinear magneto-optics. In particular, for determing the Kerr effect it might be useful to decompose $\chi^{(2)}$ in odd and even contributions $\chi^{(2)}=\chi^{(2)}(\mathbf{M})+\chi^{(2)}(M^2)$.

For the application of the general theory thin films are of particular interest. Then, the layer-dependent contributions to $\chi^{(2)}$ reveal interesting film properties and substrate effects. For the thin film calculations we use $C=W_{\mathbf{k}+2\mathbf{q}_\parallel, l''\sigma} W_{\mathbf{k}+\mathbf{q}_\parallel, l'\sigma} W_{\mathbf{k}l\sigma}$, where $W_\alpha$ denotes the weight of the density of state $|\mathbf{k}l\sigma\rangle$ in the Wigner-Seitz cell of the first monolayer. Note, due to the factor $C$ SHG will always result from the surface layer or from the layer at the interface, however the electronic structure of this layer depends on the film thickness. The band structure $E_{\mathbf{k}l\sigma}$ is calculated employing the full-potential linear muffin-tin orbital method (FP-LMTO)[13] for thin Fe(001) films within a symmetric slab calculation.

Results for one, three, five, and seven layers of Fe are presented in Fig. 1. The depth of the first minimum in the spectra scales linearly with the magnetic moment of the top layer while the energy of this minimum reflects the $d$-band width. As can be seen from Fig. 2, the nonlinear spectra reveal the structural changes induced by different substrates or temperatures. In Fig. 3 we compare the *ab initio* nonlinear Kerr spectrum for the Fe(001) monolayer with tight-binding calculations. From the results of Fig. 3 it becomes obvious that it is necessary to use *ab initio* calculations for the films if only bulk tight-binding parameters are available. However, tight-binding calculations may be adequate if one uses as input parameters those determined from *ab initio* calculations for thin films.

We also generally expect interesting results for $\chi^{(2)}$ at heterogeneous interfaces like Fe/Cu(001). For example, it is of interest to find out how the substrate interferes with the electronic structure of the thin film. For this reason we performed calculations of the Fe/Cu bilayer. Results are shown in Fig. 4. The additional peak structure reveals the electronic influence even of the nonmagnetic Cu on the nonlinear magneto-optic response of thin films. This might be of general significance also with respect to the analysis of quantum well states (tuning of interface properties, $\lambda_{so}$ in substrate, M in films).

From the results of Figs. 1–4 we learn that the nonlinear

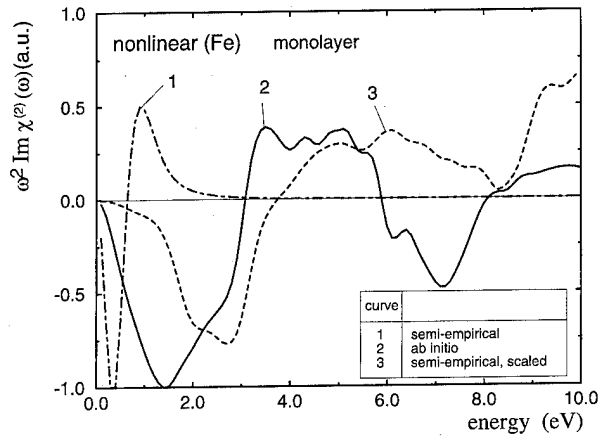



FIG. 3. Comparison of *ab initio* (solid line—2) and semi-empirical calculations of the nonlinear magneto-optical susceptibilities for a Fe monolayer. Semi-empirical calculations are performed for a two-dimensional atomic configuration (dashed-dotted curve—1) and for a three-dimensional one with reduced hopping parameters (dashed curve—3) containing the reduced coordination number of a monolayer compared to the bulk.

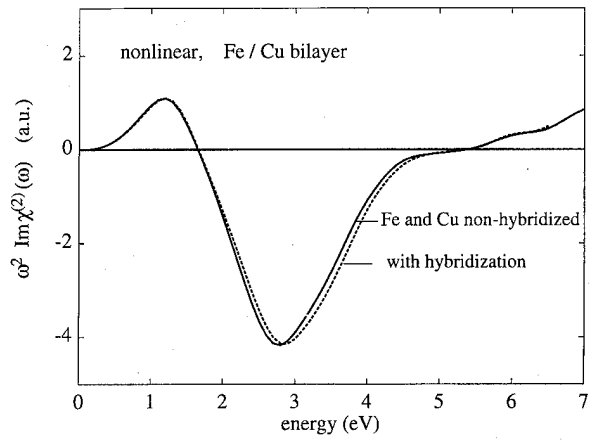



FIG. 4. Nonlinear magneto-optical Kerr-spectrum of a Fe/Cu bilayer system without (solid curve) and with (dashed curve) hybridization between the Fe and Cu layers. Note, the spectrum look rather different from the corresponding one for freestanding monolayers indicating a strong effect of Cu on the optical transitions.

Kerr effect is a sensitive probe of the magnetic and electronic structure at interfaces.

### B. Symmetry and Kerr rotation

That SHG is very symmetry sensitive is furthermore particularly demonstrated by its polarization dependence and by the remarkable enhancement of the Kerr rotation. The latter important result was first theoretically derived by Pustogowa *et al.*[8] and later observed in experiments by Böhmer *et al.*[9] and Koopmans *et al.*[10]

First, we note that due to the symmetry sensitivity SHG exhibits a corresponding polarization dependence, which interestingly is very different for transition and noble metals.[3] The latter results, since $s$ and $d$ electrons feel the breakdown of inversion symmetry at the interface differently. This symmetry dependence mainly results from the matrix elements in $\chi^{(2)}$, see Eq. (2). The different possible optical excitations contributing to $\chi^{(2)}$ for noble and transition metals are illustrated in Fig. 5. Obviously, SHG yields interesting information on the electronic structure even for $M=0$ and when no Kerr effect is present. This area needs further analysis and might offer interesting new results.[3]

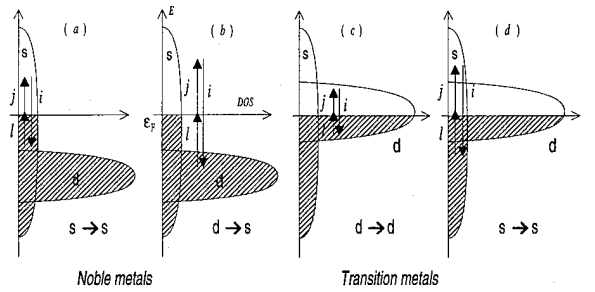



FIG. 5. Illustration of second harmonic generation from noble metals [(a) and (b)] and transition metals [(c) and (d)]. For noble metals, in case (a) no $d$ electrons can be optically excited, which in contrast is possible in case (b). In case (c) for transition metals, predominantly $d$ electrons contribute to the SHG yield, whereas in case (d) the excitation starts from the $s$ band. Note, the cases (a) and (c) refer to low-frequency excitations while (b) and (d) correspond to high-frequency excitation.

Extending the symmetry analysis to the magnetic case we determine the Kerr rotations for different configurations and polarizations. The general analysis can be performed by using for $s$ and $p$ polarization (see Ref. 4)

$$E^{(2\omega)}(\Phi,\varphi)=2i\left(\frac{\omega}{c}\right)|E_0^{(\omega)}|^2\times\begin{pmatrix}A_pF_c\cos\Phi\\A_s\sin\Phi\\A_pN^2F_s\cos\Phi\end{pmatrix}\chi^{(2)}_{ilm}\times\begin{pmatrix}f_c^2t_p^2\cos^2\varphi\\t_s^2\sin^2\varphi\\f_s^2t_p^2\cos^2\varphi\\2f_st_pt_s\cos\varphi\sin\varphi\\2f_cf_st_p^2\cos^2\varphi\\2f_ct_pt_s\cos\varphi\sin\varphi\end{pmatrix},\tag{3}$$

where in the longitudinal configuration the susceptibility tensor is given by

$$\chi^{(2)}_{ilm}=\left(\begin{array}{ccc|ccc}0&0&0&0&\chi^{(2)}_{xzx}&\chi^{(2)}_{xxy}\\\chi^{(2)}_{yxx}&\chi^{(2)}_{yyy}&\chi^{(2)}_{yzz}&\chi^{(2)}_{yyz}&0&0\\\chi^{(2)}_{zxx}&\chi^{(2)}_{zyy}&\chi^{(2)}_{zzz}&\chi^{(2)}_{zyz}&0&0\end{array}\right),\tag{4}$$

and in the polar configuration by

$$\chi^{(2)}_{ilm}=\left(\begin{array}{ccc|ccc}0&0&0&\chi^{(2)}_{xyz}&\chi^{(2)}_{xzx}&0\\0&0&0&\chi^{(2)}_{xzx}&-\chi^{(2)}_{xyz}&0\\\chi^{(2)}_{zxx}&\chi^{(2)}_{zxx}&\chi^{(2)}_{zzz}&0&0&0\end{array}\right).\tag{5}$$

Here, $\Phi$ and $\varphi$ denote the angles of polarization of the reflected frequency doubled and of the incident light, $A_{p,s}$ are the amplitudes, $f_{c,s}$ and $F_{c,s}$ are the Fresnel coefficients, and $t_{s,p}$ are the linear transmission coefficients for the fundamental light. Then, from

$$\phi_K^{(2)}\approx\mathrm{Re}\frac{E_\varphi^{(2\omega)}(s-SH)}{E_\varphi^{(2\omega)}(p-SH)}\tag{6}$$

we determine the Kerr rotation for the polar and longitudinal configuration and for $s$ and $p$ polarized incident light. The following results are obtained: For the longitudinal configuration ($M_\parallel$) and $p$ ($s$) polarized incident light one gets

$$\phi_{K,p}^{(2)M_\parallel}=\mathrm{Re}\frac{E_p^{(2\omega)}(s-SH)}{E_p^{(2\omega)}(p-SH)}=\mathrm{Re}\frac{a_1\chi^{(2)}_{yxx}+a_2\chi^{(2)}_{yzz}}{a_3\chi^{(2)}_{xzx}+a_4\chi^{(2)}_{zxx}+a_5\chi^{(2)}_{zzz}},\tag{7}$$

$$\phi_{K,s}^{(2)M_\parallel}=\mathrm{Re}\frac{E_s^{(2\omega)}(s-SH)}{E_s^{(2\omega)}(p-SH)}=\mathrm{Re}\frac{a_6\chi^{(2)}_{yyy}}{a_7\chi^{(2)}_{zyy}}.\tag{8}$$

For the polar configuration ($M_\perp$) and $p$ ($s$) polarized incident light one gets

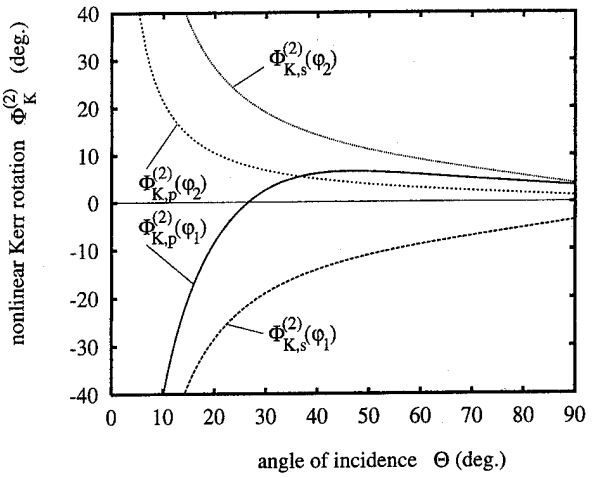



FIG. 6. Nonlinear Kerr rotation angles for $p$ polarized incident light $\phi_{K,p}^{(2)}$ (full and short-dashed curves) and for $s$ polarized incident light $\phi_{K,s}^{(2)}$ (long-dashed and dotted curves) for Fe at 770 nm as a function of the angle of incidence $\theta$ in the longitudinal Kerr configuration. The relative phase between $\chi_{zxx}^{(2)}=\chi_{zyy}^{(2)}$ and $\chi_{zzz}^{(2)}$ is $\varphi_1=0.505\pi$ in the full and long-dashed curves and $\varphi_2=1.505\pi$ in the short-dashed and dotted curves.

$$\phi_{K,p}^{(2)M_\perp}=\mathrm{Re}\frac{E_p^{(2\omega)}(s-SH)}{E_p^{(2\omega)}(p-SH)}$$

$$=\mathrm{Re}\frac{a_8\chi_{xyz}^{(2)}}{a_9\chi_{xxz}^{(2)}+a_{10}\chi_{zxx}^{(2)}+a_{11}\chi_{zzz}^{(2)}}, \tag{9}$$

$$\phi_{K,s}^{(2)M_\perp}=\mathrm{Re}\frac{E_s^{(2\omega)}(s-SH)}{E_s^{(2\omega)}(p-SH)}=\mathrm{Re}\frac{0}{a_{12}\chi_{zxx}^{(2)}}. \tag{10}$$

The coefficients $a_1, \ldots, a_{12}$ contain explicitly the whole information about the Kerr geometry (directions of light incidence and polarization, crystal magnetization) and about the linear transmission and reflection (see Ref. 4).

Summarizing the results, we find that generally $\phi_K^{(2)M_\perp}<\phi_K^{(2)M_\parallel}$ and $\phi_{K,s}^{(2)}>\phi_{K,p}^{(2)}$, which is in agreement with the experiment by Koopmans *et al.*[10] Numerical results of our theory using as input parameters the phase ratio of the various different tensor elements from Ni and linear complex indices of refraction are presented in Fig. 6. These results demonstrate clearly that the nonlinear Kerr angle depends sensitively on the direction of the magnetization and the incident beam, as well as on the light polarization. Depending on the experimental conditions the nonlinear Kerr angle might become even as large as 90°. Moreover, also the ellipticity will yield correspondingly large magnetic effects. From these results we conclude that the enhanced nonlinear Kerr rotation allows for the determination of easy axis and canted-spin configurations due to large magnetic contrast of different interfaces.

This selective discussion demonstrates the usefulness of nonlinear magneto-optics as a promising spectroscopy. Our results show that SHG is a new sensitive tool for determining magnetic interface properties such as the interplay of structure and magnetism, magnetic anisotropy, and magnetic reorientation. In contrast to linear optics, which probes characteristic film-averaged features, the nonlinear Kerr effect originates essentially from the surface and interfaces and thus allows the analysis of buried interfaces.

For future studies on the nonlinear magneto-optical Kerr effect it will be interesting to analyze magnetic anisotropy and easy axis, magnetic structure and domains, multilayers, and magnetostriction effects. Nonlinear optics at interfaces is a bulk-background-free technique and therefore, should yield a pronounced visibility of quantum well states and enhanced nonlinear paramagnetic Kerr oscillations in the presence of an external field.

An important future development of the nonlinear Kerr effect might result from femto-second dynamics which is able to follow the charge and spin dynamics of metallic interfaces in real time without involving the lattice.


[1] W. Hübner and K. H. Bennemann, Phys. Rev. B **40**, 5973 (1989).
[2] R.P. Pan, H. D. Wei, and Y. R. Shen, Phys. Rev. B **39**, 1229 (1989).
[3] W. Hübner, K. H. Bennemann, and K. Böhmer, Phys. Rev. B **50**, 17 597 (1994).
[4] W. Hübner and K. H. Bennemann, Phys. Rev. B **52**, 13 411 (1995).
[5] J. Reif, J. C. Zink, C. M. Schneider, and J. Kirschner, Phys. Rev. Lett. **67**, 2878 (1991).
[6] H. A. Wierenga, M. W. J. Prins, D. L. Abraham, and Th. Rasing, Phys. Rev. B **50**, 1282 (1994).
[7] H. A. Wierenga, W. de Jong, M. W. J. Prins, Th. Rasing, R. Vollmer, A. Kirilyuk, H. Schwabe, and J. Kirschner, Phys. Rev. Lett. **74**, 1462 (1995).
[8] U. Pustogowa, W. Hübner, and K. H. Bennemann, Phys. Rev. B **49**, 10 031 (1994); Appl. Phys. A **59**, 611 (1994).
[9] K. Böhmer, J. Hohlfeld, and E. Matthias, Appl. Phys. A **60**, 203 (1995).
[10] B. Koopmans, M. Groot Koerkamp, Th. Rasing, and H. van den Berg, Phys. Rev. Lett. **74**, 3692 (1995).
[11] W. Hübner, Phys. Rev. B **42**, 11 553 (1990).
[12] U. Pustogowa, W. Hübner, and K. H. Bennemann (unpublished).
[13] M. Methfessel, Phys. Rev. B **38**, 1537 (1988); M. Methfessel, C. O. Rodriguez, and O. K. Andersen, *ibid.* **40**, 2009 (1989); M. Methfessel and M. Scheffler, Physica B **172**, 175 (1991).

# Giant nonlinear magneto-optical Kerr effects from Fe interfaces (invited)

Th. Rasing, M. Groot Koerkamp, and B. Koopmans[a)]
*Research Institute for Materials, University of Nijmegen, Toernooiveld 1, NL-6525 ED Nijmegen, The Netherlands*

H. v.d. Berg
*Siemens AG, D-91052 Erlangen, Germany*

Second harmonic generation from magnetic materials is shown to lead to a nonlinear magneto-optical Kerr effect that can be orders of magnitude larger than its linear equivalent. The origin of this effect can be found in the differences between the linear and nonlinear solutions of the optical wave equations and in the symmetry properties of the corresponding optical tensors. Applications for the study of magnetic surfaces, thin films, and multilayers will be discussed.
© *1996 American Institute of Physics.* [S0021-8979(96)13108-X]

## I. INTRODUCTION

When linearly polarized light is incident on a magnetic material, the reflected beam will be elliptically polarized, with the major axis of the polarization ellipse rotated with respect to the incident plane of polarization. The origin of this magneto-optical Kerr effect (MOKE) lies in the spin-orbit coupling that leads to a difference in the refraction coefficient for left- and right-handed circularly polarized light. This spin-orbit coupling acts like a magnetic field on the current induced by the electromagnetic field of the incident light.[1] This should also hold for the nonlinear contributions of the induced current, that are the origin of optical second harmonic generation (SHG), leading to a nonlinear magneto-optical Kerr effect (NOMOKE). Based on symmetry arguments, Ru-Pin Pan *et al.* indeed showed that the presence of a magnetization would lead to new, nonzero *surface* contributions to the nonlinear optical response.[2] At the same time, Hübner and Bennemann calculated the nonlinear magneto-optical spectrum of Ni, based on a spin dependent band structure calculation.[3] They showed that this should indeed lead to observable effects, with magnetic contributions to the nonlinear tensor coefficients of more than 10%. First experimental evidence for such a NOMOKE was given by Reif *et al.* for an Fe(110) surface,[4] whereas Spierings *et al.* showed the first NOMOKE results from buried Co/Au interfaces.[5] From a SHG study of $Y_{2.5}Bi_{0.5}Fe_5O_{12}$ films, Aktsipetrov *et al.* reported a nonlinear Kerr rotation between 1° and 4°, that was significantly larger than the linear one.[6] These observations triggered much theoretical and experimental research. Reif *et al.* showed the presence of a magnetic circular dichroism in the SHG reflection from the Heussler alloy PtMnSb, as well as a large nonlinear Kerr rotation of 14°,[7] which is an order of magnitude larger than its linear Kerr angle of 1.1°. Interface and monolayer sensitivity was successfully demonstrated by Wierenga *et al.*[8,9] and nonlinear circular dichroism by Fiebig *et al.*,[10] whereas enormous enhancements of the nonlinear Kerr rotation were observed for a thin Fe/Cr film by Koopmans *et al.*[11] Theoretically, these large enhancements appeared to follow from the differences in the solutions for the Maxwell equations for the nonlinear and linear case,[12] and the differences in the symmetry properties of the linear and nonlinear susceptibilities.[11] In combination with the intrinsic surface and interface sensitivity of the SHG response[13] these large NOMOKE effects are particularly interesting for the study of surface magnetism.

SHG arises from the nonlinear polarization $\mathbf{P}(2\omega)$ induced by an incident laser field $\mathbf{E}(\omega)$. This polarization can be written as an expansion in $\mathbf{E}(\omega)$

$$\mathbf{P}(2\omega)=\chi^{(2)}\mathbf{E}(\omega)\mathbf{E}(\omega)+\chi^{(3)}\mathbf{E}(\omega)\nabla\mathbf{E}(\omega)+\cdots . \quad (1)$$

The lowest order term in Eq. (1) describes an electric dipole source. Symmetry considerations show that this contribution is zero in a centrosymmetric medium, thus limiting electric dipole radiation to the interfaces where inversion symmetry is broken. The bulk second harmonic can now be described in terms of the much smaller electric quadrupolelike contributions [second term in Eq. (1)]. However, because of the large volume difference between interface and bulk, this does not necessarily mean that the total bulk second harmonic signal is negligible. Interface sensitivity needs to be verified for any given system. Following the approach of Pan, Wei, and Shen,[2] it is convenient to separate the SH susceptibility into an even ($\chi^+$) and an odd ($\chi^-$) part in the magnetization $\mathbf{M}$. Thus, the induced SH polarization at an interface $\mathbf{P}(2\omega)$ is given by

$$P_i(2\omega)=\chi^{+}_{ijk}(\mathbf{M})E_jE_k+\chi^{-}_{ijk}(\mathbf{M})E_jE_k, \quad (2)$$

where $\mathbf{E}$ is the local excitation field at frequency $\omega$ at the interface, and we implicity assumed a summation over the repeated indices. The introduced susceptibilities fulfill $\chi^{\pm}_{ijk}(-\mathbf{M})=\pm\chi^{\pm}_{ijk}(\mathbf{M})$. In the following we will drop the ex-

TABLE I. The nonzero elements of the SH susceptibility tensor for an isotropic surface in the longitudinal configuration ($\mathbf{M}//\hat{x}$). The two columns list the elements that are even and odd in the magnetization, respectively. The occurrence of the elements in the $p$- and $s$-input configuration is indicated within parenthesis.

| $\chi^+$ | | $\chi^-$ | |
|---|---|---|---|
| $zxx$ | $(p)$ | $yxx$ | $(p)$ |
| $zyy$ | $(s)$ | $yyy$ | $(s)$ |
| $zzz$ | $(p)$ | $yzz$ | $(p)$ |
| $xzx=xxz$ | $(p)$ | $zyz=zzy$ | |
| $yzy=yyz$ | | $xyx=xxy$ | |

[a)]Present address: Max Planck Institut für Festkörperforschung, D-70506 Stuttgart, Germany.

 0021-8979/96/79(8)/6181/5/$10.00 © 1996 American Institute of Physics 

plicit **M** dependence of $\chi^{\pm}_{ijk}$. For a given surface symmetry the $\chi^{+}_{ijk}$ and $\chi^{-}_{ijk}$ can be easily derived (see Table I). In the longitudinal configuration and for pure $p$- or $s$-input polarization we find that all nonzero $\chi^{+}_{ijk}$ elements have $i \epsilon \{x,z\}$, giving rise to $p$-polarized SHG. All nonzero $\chi^{-}_{ijk}$ elements have $i=y$, always resulting in $s$-polarized SHG. From this it follows that the SHG polarization ellipses for $\pm\mathbf{M}$ are each other's mirror image in the plane of incidence, and we can define a nonlinear Kerr angle $\Phi^{(2)}_K$ in correspondence with its linear counterpart $\Phi^{(1)}_K$. Pustogowa and Hübner have shown that for the longitudinal configuration $\Phi^{(2)}_K$ and $\Phi^{(1)}_K$ are given by

$$\tan \Phi^{(2)}_K = i\left[\frac{\chi^{(2),-}}{\chi^{(2),+}} + (h.o.)\right] \tag{3}$$

$$\tan \Phi^{(1)}_K \approx -\frac{\chi^{(1)-}}{\chi^{(1)+}} \frac{\sin\theta_i \cos\theta_i}{\sqrt{\cos^2\theta_i + \chi_0(\omega)}} \tag{4}$$

in which $\chi^{(1),+}$ and $\chi^{(1),-}$ are the nonmagnetic and magnetic contributions to $\chi^{(1)}$. The big difference between the expressions for $\Phi^{(2)}_K$ and $\Phi^{(1)}_K$ is the factor $1/\sqrt{\cos^2\theta_i+\chi_0(\omega)}$ in Eq. (4). This factor causes a small value for $\Phi^{(1)}_K$ but is not present in the nonlinear case. Therefore it is clear that the nonlinear Kerr rotation for all $\theta_i$ is always enhanced by a factor $\sqrt{\cos^2\theta_i+\chi_0(\omega)}$. Above this effect, in the nonlinear case one can select large magnetic $\chi^{(2)}$ contributions by a proper choice of input polarization and angle of incidence. This is in contrast with the linear case where one always deals with small off-diagonal magnetic terms $[\chi^{-}(\omega)]$ relative to large diagonal nonmagnetic terms $[\chi^{+}(\omega)]$.

## II. EXPERIMENTAL RESULTS AND ANALYSIS

The experiments on the nonlinear Kerr rotation from thin, centrosymmetric magnetic films were stimulated by the prediction of large enhancements of $\Phi^{(2)}_K$ by Pustogowa and Hübner.[12] To enable direct comparison with their theoretical results, experiments were performed on Fe thin films and single crystals. All experiments were done *ex situ* and, therefore, required protective cover layers. The first sample consisted of a thin Fe film (thickness 2 nm), covered with a 2 nm Cr film deposited by rf-diode and dc magnetron sputtering, respectively. As a substrate we used a (100) silicon wafer, with a thermal oxide layer of about 525 nm. The substrate was on a rotating table, which moved with a velocity of 0.96 and 3.97 m/min underneath the Fe and Cr targets, respectively. Both targets were equipped with screens for getting uniformity of the layer thickness better than 1%. The base pressure was $2\times10^{-7}$ Torr and the Ar pressure was 5 mTorr. For the second harmonic experiments we used the 770 nm output of a mode-locked (80 MHz) Ti–sapphire laser. The pulse width was 70 fs and the input power was 100 mW focused on a spot diameter of 100 $\mu$m. The experiments were done in the longitudinal configuration, i.e., the magnetization **M** was in the plane of the sample and in the optical plane of incidence (see inset Fig. 1). Figure 1 shows the polarization dependence of the SH signal for an $s$-polarized input at an angle of incidence of 45° and for **M** along $\hat{x}$ and $-\hat{x}$ respectively. The difference between the two minima of

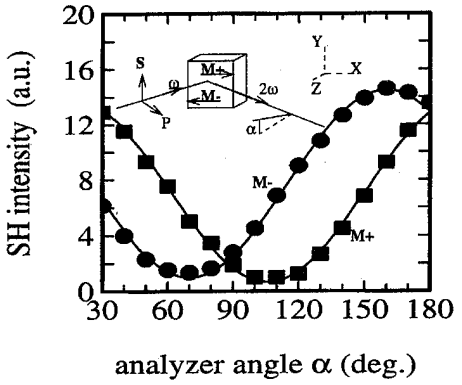



FIG. 1. Output polarization dependence of SHG reflection from an Fe/Cr multilayer, for $s$-polarized input. Squares: $\mathbf{M}\|\hat{x}$, dots $\mathbf{M}\|-\hat{x}$. The inset shows the experimental configuration.

the curves corresponds to $2\Phi^{(2)}_K \approx 34°$, i.e., a nonlinear Kerr rotation $\Phi^{(2)}_K$ of 17°. In this geometry we measured a linear Kerr angle of 0.03°, using the same Ti–sapphire input beam. These observations correspond to an enhancement of almost *three orders* of magnitude for the nonlinear Kerr rotation! The small linear rotation can be compared with the bulk Fe value of 0.1°.

The nonlinear Kerr angle can be expressed in the $s$- and $p$-components of the reflected SH field, denoted by $E_s(2\omega)$ and $E_p(2\omega)$, respectively. The relevant tensor components and their appearance for $s$- and $p$-polarized input are shown in Table I. Defining $R \equiv \mathrm{Re}[E_s(2\omega)/E_p(2\omega)]$, $I \equiv \mathrm{Im}[E_s(2\omega)/E_p(2\omega)]$ and $A^2 = R^2 + I^2$ we get

$$\Phi^{(2)}_K = \tfrac{1}{2}\arctan[2R/(1-A^2)] + \phi_0 \tag{5}$$

with $\phi_0=0$ for $A^2 \leqslant 1$, $\phi_0=90°$ for $A^2>1$ and $R \geqslant 0$, and $\phi_0=-90°$ for $A^2>1$ and $R<0$. Equation (5) is completely analogous to expression (3). It is easily verified that in the limit $A \ll 1$ Eq. (5) reduces to $\Phi^{(2)}_K = R$. However, the nonlinear case generally is far from this limit, since $\Phi^{(2)}_K$ can become as large as 90°.

Inspection of Table I shows that the $s$-input configuration is particularly simple, with only one even, $\chi^{+}_{zyy}$, and one odd, $\chi^{-}_{yyy}$, contributing element per interface. For normal incidence, only the $\chi^{-}_{yyy}$ contribution survives. From $E_p(2\omega)=0$ we then find $\Phi^{(2)}_K = \pm 90°$. Moving away from normal incidence, the ratio $|E_s(2\omega)/E_p(2\omega)|$ and, as a consequence, $|\Phi^{(2)}_K|$ decreases so that $\Phi^{(2)}_K$ is tunable over a wide range while scanning the angle of incidence.

A similar argument for a large $\Phi^{(2)}_K$ close to normal incidence is found for a $p$-polarized input configuration. Table I shows that close to normal incidence, the dominating even tensor components have one $z$ index, and thus vanish at normal incidence, whereas the dominant odd tensor element, $\chi^{-}_{yxx}$, is finite at normal incidence.

Fig. 2 shows the observed nonlinear Kerr rotation for both $s$- and $p$-polarized input as a function of the angle of incidence. We observed a small in-plane anisotropy in our experimental results that is possibly induced by the sputtering process. The plotted data in Fig. 2 have been averaged over this azimuthal anisotropy. The solid curves in Fig. 2 are theoretical fits, based on the multiple reflection model, with

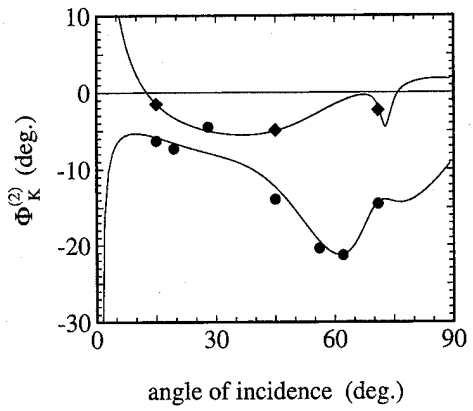



FIG. 2. Nonlinear Kerr rotation $\Phi_K^{(2)}$ for an Fe/Cr multilayer as a function of the angle of incidence. Dots: $s$-input polarization, diamonds: $p$-input polarization. The curves are theoretical fits.

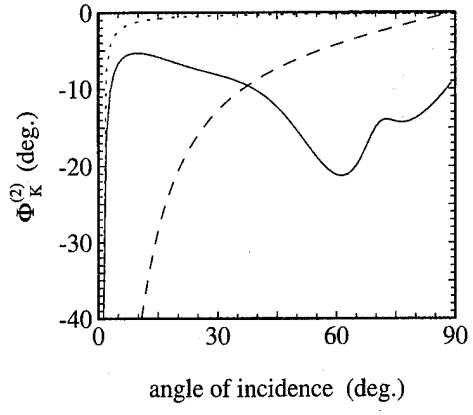



FIG. 3. Nonlinear Kerr rotation $\Phi_K^{(2)}$ for an Fe/Cr multilayer and a bulk Fe surface for $s$-polarized input as a function of the angle of incidence. The bold solid line is the theoretical fit of Fig. 2. The dashed line is a simulation for $\Phi_K^{(2)}$ of a clean Fe surface, based on the multilayer fit. The dotted line is a simulation for $\Phi_K^{(2)}$ for an Fe/Cr multilayer on a silicon wafer with a 10 nm oxide.

the unknown interface tensor elements of Table I as parameters and the following assumptions. Only the Fe is expected to contribute to the magnetic (odd) nonlinear susceptibility because the Cr film is antiferromagnetic. Furthermore, the top Cr layer will be oxidized, so that the major contribution to the nonmagnetic nonlinear susceptibility is also expected to originate from the Fe film. Therefore we assigned effective SH susceptibilities to the Fe and Cr layer together. We verified that the actual position within the Cr/Fe top layer did not significantly change the results of our fits. In addition to these SH sources at the top layer, we incorporate a nonmagnetic SH source at the Si/oxide interface. The bulk optical constants of the metals and silicon were obtained from Refs. 14 and 15, respectively. Because of the limited number of parameters involved in the $s$-polarization configuration ($\chi_{yyy}^{-}$ and $\chi_{zyy}^{+}$ at the top layer, and $\chi_{zyy}^{+}$ at the Si/oxide interface) one finds a unique fit to these experimental data points. The fit in Fig. 2 includes a relative maximum of $|\Phi_K^{(2)}|$ near $\Theta_i \approx 65°$, that is due to an enhancement effect through multiple reflections in the thick silicon oxide layer. Similar, but smaller, enhancement factors due to a substrate are also known for the linear Kerr angle.[16]

For the $p$-polarization, several combinations of tensor elements give satisfying fits. Figure 2 gives one such solution, obtained by choosing fixed values for the relative phase factors and fitting the absolute values of the tensor components. At 45° angle of incidence, we experimentally find for the $p$ input $\Phi_K^{(2)} = 4.9°$.

These results show that for a proper understanding and analysis of the nonlinear response the total electro-magnetic response, linear and nonlinear including multiple reflections, has to be considered. The importance of such substrate effects can be illustrated in the following way. From our thin-film analysis we can simply calculate the response of an Fe surface by letting the thickness of the Fe film go to infinity. Similarly, we can vary the thickness of the silicon oxide layer for the thin-film structure.

Figure 3 shows the results of such simulations. For the thin oxide layer, the enhancement effect around $\theta_i = 60°$ has totally vanished, which demonstrates the importance of the multiple reflections and of the local field effects and thus the role of the substrate.

For the bulk surface, Fig. 3 shows a smooth variation of $\Phi_K^{(2)}$ as a function of the angle of incidence. In accordance with Eq. (5), Fig. 3 shows the $\Phi_K^{(2)}$ can be tuned at will between 0° and 90°, by varying the angle of incidence. This is a direct result of the fact that near normal incidence, the even contribution $\chi_{zyy}^{(2),+}$ vanishes, whereas the odd magnetic term $\chi_{xyy}^{(2),-}$ gives a finite contribution.

The prediction of this large tunable nonlinear Kerr rotation was confirmed by experiments on single crystalline Fe whiskers.[17] The (100) surfaces of the whiskers were capped by molecular beam epitaxy grown Au and Cr layers, while

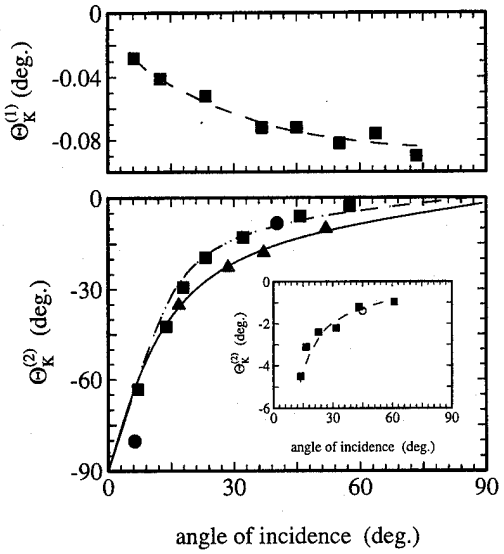



FIG. 4. Linear and nonlinear Kerr rotation for an Fe surface for $s$-polarized input in the longitudinal configuration as a function of the angle of incidence. Triangles: Fe/Cr, Dots: Fe/Au, Squares: uncapped Fe. The solid line is a theoretical fit for the Fe/Cr sample. The dotted line is the theoretical prediction for a clean Fe surface from Ref. 11. The inset shows $\Phi_K^{(2)}$ for $p$-polarized input. The open circle is the calculation from Ref. 12.

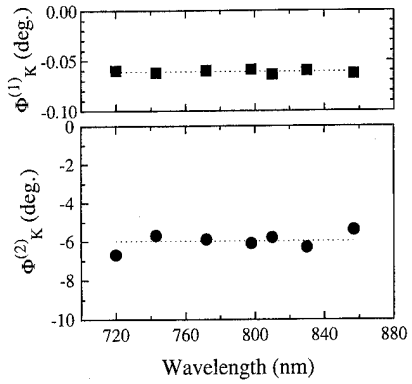



FIG. 5. Experimental wavelength dependence of the nonlinear (dots) and linear (squares) Kerr angle of Fe for the $s$-input longitudinal configuration at an incident angle of 45°.

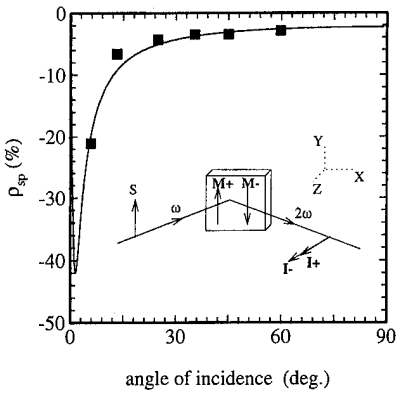



FIG. 6. Magnetic contrast $\rho$ for an uncapped Fe surface for $s$-polarized input in the transversal configuration as a function of the angle of incidence. The solid line is a theoretical fit. The inset shows the experimental configuration.

some experiments were also performed on uncapped, oxidized Fe whiskers. The experiments were done using the 833 nm output of the Ti–sapphire laser. Figure 4 shows the measured angular dependence of the nonlinear Kerr rotation in the longitudinal configuration and $s$-polarized excitation. In Fig. 4 the experimental results can be seen for an Fe sample with a Cr top layer, an Fe sample with an Au top layer, and for an uncapped oxidized Fe sample. We find a maximum Kerr angle of 80° at an angle of incidence of 6°. This corresponds to an enhancement of more than a factor $10^3$, compared with the value for the linear Kerr rotation of 0.03° as obtained in the same experimental setup, using the fundamental incident beam. The solid line in Fig. 4 is a theoretical fit for the Fe/Cr sample based on Eq. (5) and a model for SHG from interfaces.[18] Furthermore, the experimental results are in quite good agreement with the predicted behavior from Fig. 3.

The inset in Fig. 4 shows the experimental results for the longitudinal configuration with $p$-polarized incident light. In Table I it can be seen that now we are dealing with two odd tensor components, both of which give rise to $s$-polarized SHG and three even components which produce $p$-polarized SHG. Therefore it is to be expected that for the same incidence angles the ratio $|E_s(2\omega)/E_p(2\omega)|$ and thus $\Phi_K^{(2)}$ will be smaller compared to the $s$-input configuration. Near normal incidence the influence of the components $\chi_{ijk}$ with a "$z$" for $i$, $j$, or $k$ will again be small. Since all even tensor components have at least one $z$ index the $p$-polarized SHG will then be small. The $s$-polarized SHG, which is now dominated by $\chi^-_{yxx}$, is finite. The result is that for small angles of incidence the Kerr rotation will again increase. This is clearly confirmed by our experiments, but seems in contradiction with the theoretical $\theta_i$ dependence of Ref. 12. However, there one has only considered the odd component $\chi^-_{yzz}$ that also vanishes near normal incidence. At an angle of incidence of 45° the experimental and theoretical configurations should be equivalent. Here we find $\Phi_K^{(2)}=1.2°$ in excellent agreement with the theoretical prediction of 1.4° from Pustogowa and Hübner.[12] In a recent article, the latter authors have included the proper Fresnel dependence in their expression for $\Phi_K^{(2)}$, showing excellent agreement with our experimental findings.[19]

In the longitudinal configuration we also measured the wavelength dependence of both $\Phi_K^{(1)}$ and $\Phi_K^{(2)}$ at an angle of incidence of 45° (see Fig. 5). The average value for $\Phi_K^{(1)}=0.062°$, in excellent agreement with the bulk Fe value of 0.061° of Ref. 20. Figure 5 shows that in the tuning range of the Ti:sapphire laser the Kerr rotations are constant, in agreement with the theoretical prediction of Pustogowa *et al.*[12] From their calculations it follows that for $\Phi_K^{(2)}$ a strong wavelength dependence is expected above 900 nm and below 600 nm. Future experiments in these wavelength ranges are certainly desirable.

In the transversal configuration (**M** along the $y$ axis) for $p$- or $s$-input polarization, $\chi_{ijk}=0$ for $i=y$ (see Table I). This means that the SHG signal will always be $p$ polarized. Changing the direction of the magnetization will not affect the plane of polarization but it has an influence on the total SH signal. The magnetic contrast can be defined as

$$\rho(q_{\text{in}}q_{\text{out}})=\frac{I(2\omega,q_{\text{in}}q_{\text{out}},M^+)-I(2\omega,q_{\text{in}}q_{\text{out}},M^-)}{I(2\omega,q_{\text{in}}q_{\text{out}},M^+)+I(2\omega,q_{\text{in}}q_{\text{out}},M^-)}, \tag{6}$$

where $I(2\omega,q_{\text{in}}q_{\text{out}},M^+)$ and $I(2\omega,q_{\text{in}}q_{\text{out}},M^-)$ are the $q_{\text{in}}q_{\text{out}}$ polarized SH intensities for opposite directions of the magnetization. In Fig. 6 our results for $\rho_{sp}$ from the uncapped Fe sample can be seen while the inset in Fig. 6 shows the experimental configuration. Similar results were obtained for the Fe/Au sample. The dependence of the angle of incidence is again easily understood with the help of Table I. For small incident angles the $z$ component of the $E$ vector of the SH signal will be small. This means that the odd tensor component $\chi^-_{xyy}$ will dominate, resulting in large magnetic effects. However, in the limit of normal incidence there will only be an odd contribution and no magnetic effects will be seen, as $\rho$ depends on the interference between $\chi^+$ and $\chi^-$. The solid line in Fig. 6 is a theoretical fit of Eq. (6) assuming only the Fe surface to contribute to the SH signal.

## III. SUMMARY AND CONCLUSIONS

In this article we have shown how the reflected SHG signal from magnetic surfaces displays nonlinear magneto-optical Kerr effects that are several orders of magnitude larger than their linear equivalents. The reasons for these

enormous enhancements are both the differences in the solutions of the e.m. wave equations as well as the differences in the symmetry properties of the nonlinear and linear optical tensors. The experimental results that have been obtained so far are in excellent agreement with the theoretical predictions (Recently, polar NOMOKE effects have also been measured).[21]

The large, interface sensitive magneto-optical effects offer great possibilities to use this nonlinear technique for studying the magnetic properties of surfaces and interfaces of very thin films and multilayers, an area of intense research nowadays.

## ACKNOWLEDGMENTS

The authors are pleased to acknowledge stimulating discussions with W. Hübner. Part of this work was supported by the Stichting Fundamental Onderzoek der Materie (FOM), which is financially supported by the Nederlandse Organisatie voor Wetenschappelijk Onderzoek (NWO, and by Brite Euram II FFR CT930569.

[1] P. N. Argyres, Phys. Rev. **97**, 334 (1955).
[2] Ru-Pin Pan, H. D. Wei, and Y. R. Shen, Phys. Rev. B **39**, 1229 (1989).
[3] W. Hübner and K. H. Bennemann, Phys. Rev. B **40**, 5973 (1989).
[4] J. Reif, J. C. Zink, C. M. Schneider, and J. Kirschner, Phys. Rev. Lett. **67**, 2878 (1991).
[5] G. Spierings, V. Koutsos, H. A. Wierenga, M. W. J. Prins, D. Abraham, and Th. Rasing, Surf. Sci. **287**, 747 (1993); J. Magn. Magn. Mater. **121**, 109 (1993).
[6] O. A. Aktsipetrov, O. V. Braginskii, and D. A. Esikov, Sov. J. Quantum Electron. **20**, 259 (1990).
[7] J. Reif, C. Rau, and E. Mathias, Phys. Rev. Lett. **71**, 1931 (1993).
[8] H. A. Wierenga, M. W. J. Prins, D. L. Abraham, and Th. Rasing, Phys. Rev. B **50**, 1282 (1994).
[9] H. A. Wierenga, W. de Jong, M. W. J. Prins, Th. Rasing, R. Volmer, A. Kirilyuk, H. Schwabe, and J. Kirschner, Phys. Rev. Lett. **74**, 1462 (1995).
[10] M. Fiebig, D. Frölich, B. B. Krichevtsov, and R. V. Pisarev, Phys. Rev. Lett. **73**, 2127 (1994).
[11] B. Koopmans, M. Groot Koerkamp, Th. Rasing, and H. v.d. Berg, Phys. Rev. Lett. **74**, 3692 (1995).
[12] U. Pustogowa, W. Hubner, and K. H. Bennemann, Phys. Rev. B **49**, 10031 (1994); Appl. Phys. A **59**, 611 (1994).
[13] Th. Rasing, Appl. Phys. A **59**, 531 (1994).
[14] P. B. Johnson and R. W. Christy, Phys. Rev. B **9**, 5056 (1974); Phys. Rev. B **6**, 4370 (1972).
[15] D. E. Aspnes and A. A. Studna, Phys. Rev. B. **27**, 985 (1983).
[16] D. O. Smith, J. Appl. Phys. **36**, 1120 (1965).
[17] M. Groot Koerkamp and Th. Rasing, Surf. Sci. (to be published).
[18] H. A. Wierenga, M. W. J. Prins, and Th. Rasing, Physica B **204**, 281 (1995).
[19] W. Hübner and K. H. Bennemann (to be published).
[20] A. J. Kolk and M. Orlovic, J. Appl. Phys. **34**, 1060 (1963).
[21] M. Groot Koerkamp, A. Kirilyuk, W. de Jong, Th. Rasing, J. Ferré, J. P. Jamet, and P. Meyer, these proceedings.

# Symmetry of the magneto-optic response of the Sagnac interferometer

J. S. Dodge, L. Klein, M. M. Fejer, and A. Kapitulnik
*Department of Applied Physics, Stanford University, Stanford, California 94305*

We demonstrate the application of the Sagnac interferometer to magneto-optic measurements at an oblique angle of incidence. With an appropriate choice of polarization states for the two counter-propagating beams, a wide variety of magneto-optic effects may be measured, in the absence of an external perturbing field, with a sensitivity of a few hundred nanoradians. Using simple symmetry analysis of the conventional Kerr rotation measurement geometry, we may distinguish contributions to the non-reciprocal phase shift due to the polar, longitudinal and transverse Kerr effects, and consequently completely determine the magnetization vector direction, averaged over the probed region. Magneto-optic hysteresis loops were taken on a permalloy film to demonstrate the effectiveness of the new technique. We discuss the relevance of the Sagnac interferometer to magnetic microscopy and to the study of magnetic anisotropies in thin films.
© *1996 American Institute of Physics.* [S0021-8979(96)47908-3]

The Sagnac interferometer (SI) has proven to be a useful instrument for sensitive magneto-optic (MO) measurements.[1–3] Very general arguments based on the Helmholtz reciprocity theorem show that the SI can only be sensitive to effects which break time-reversal symmetry, such as the linear magneto-optic effects.[4] The selective sensitivity of the Sagnac to MO effects is its chief advantage over conventional, polarimetric measurement techniques, as it allows one to perform measurements with a sensitivity of 500 nrad/$\sqrt{Hz}$, in the absence of the perturbing magnetic field which is typically used to ensure that the measured effect has a magnetic origin. This advantage is most apparent in applications such as microscopy and magnetic relaxation measurements, which must be performed in constant magnetic field.[3] In near-field scanning optical microscopy especially, depolarizing topographic features can be difficult to distinguish from magnetic features, a difficulty which the SI overcomes by its very nature.[5–8] In previous work, the application of the SI has been limited to normal-incidence Kerr and Faraday rotation measurements. In this work, we demonstrate the more general application of the SI to magneto-optic Kerr measurements at oblique incidence, and show that symmetry arguments allow us to determine all three vector components of the magnetization by appropriate analysis of the MO response.

The SI measures intensity changes due to interference between counter-propagating waves, from which we can infer the relative phase shift between them.[9] By using only one of the polarization eigenmodes of a single-mode, polarization maintaining fiber to guide the light through most of its path in the interferometer, we ensure that the two counter-propagating waves travel along identical paths. One wave can then be thought of as the time-reversed reciprocal of the other, and consequently any phase shift between them must result from an effect which breaks time-reversal symmetry. To measure magneto-optic effects in reflection, we break the fiber loop and insert collimating optics, together with the bulk optics shown in Fig. (1). We use pairs of $\lambda/2$ and $\lambda/4$ retardation plates to transform the polarization states from the linear eigenmode of the fiber to arbitrary polarization states, $\mathbf{P_1}$ and $\mathbf{P_2}$, which we write as Jones vectors in a cartesian basis.[10] The polarizers at both ends of the optics train serve as polarization filters for the reflected beams. The two beams are reflected from a magnetized sample, and the natural coordinate system for describing the magnetization direction, in which we denote each coordinate by the name of its associated magneto-optic effect, is indicated. The only source of non-reciprocal phase shift in the interferometer is the magnetized sample, so we may neglect the rest of the interferometer and calculate only the relative phase shift between the two beams as they traverse the space between two imaginary observation planes $\mathcal{O}_1$ and $\mathcal{O}_2$, indicated in the diagram.

Conceptually, it is helpful to represent the behavior of the single-mode fibers, polarizers and retardation plates by two pairs of idealized optical elements, a polarized planar source and a coherent, polarization sensitive, spatially filtered detector.[11] One of each is located at each of the observation planes, as indicated in Fig. 2. We denote each monochromatic source field at its plane of origin $\mathcal{O}_i$ by $\mathbf{E_i^{src}}(\mathbf{r},t)=\mathbf{E_i^{src}}(\mathbf{r})e^{-i\omega t}$, and the field which the source generates at its plane of detection by $\mathbf{E_i^{src'}}(\mathbf{r},t)=\mathbf{E_i^{src'}}(\mathbf{r})e^{-i\omega t}$. The field which the coherent detector at $\mathcal{O}_i$ accepts will simply be the reciprocal of corresponding source field, $\mathbf{E_i^{det}}(\mathbf{r},t)=\mathbf{E_i^{s*}}(\mathbf{r})e^{-i\omega t}$. Throughout, we will assume that both the incident and reflected field amplitudes are described by a single polarization state over the whole field profile, so that we may write $\mathbf{E_i^{src'}}(\mathbf{r})=\mathrm{E_i^{src'}}(\mathbf{r})\mathbf{P}_1$. This assumption will not generally hold if the sample is inhomogeneous, but the treatment given here may be extended to such cases by following the standard treatment in Fourier optics of coherent imaging.[2,12] In practice, the optics are aligned so that the scalar part of all of the above fields are identical, described approximately by Gaussian functions $E^0(\mathbf{r})$. We may then represent reflection from a material with magnetization vector $\mathbf{M}$ by a reflectivity matrix $R(\mathbf{M})$ which acts only on the polarization state, so that $\mathbf{E_{1,2}^{src'}}(\mathbf{r})=\mathrm{E}^0(\mathbf{r})R(\mathbf{M})\mathbf{P}_{1,2}$. For fixed source fields, the complex amplitude $\alpha(\mathbf{E_i^{src}}(\mathbf{r}),\mathbf{E_j^{src}}(\mathbf{r}),\mathbf{M})$ which the source at $\mathcal{O}_i$ excites in the detector at $\mathcal{O}_j$ will be given by the overlap integral between the two fields:

$$\alpha(\mathbf{E_i^{src}}(\mathbf{r}),\mathbf{E_j^{src}}(\mathbf{r}),\mathbf{M})=\int_{\mathcal{O}_j}\mathbf{E_j^{det*}}(\mathbf{r})\cdot\mathbf{E_i^{src'}}(\mathbf{r})d\mathbf{r}$$

 0021-8979/96/79(8)/6186/3/$10.00 © 1996 American Institute of Physics

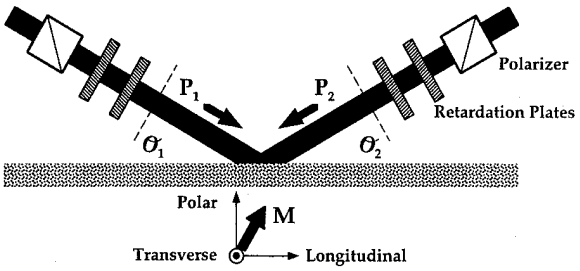



FIG. 1. Bulk optics for measurement at oblique incidence.

$$= \int_{\mathscr{O}_j} \mathbf{E}_\mathbf{j}^{\mathrm{src}}(\mathbf{r}) \cdot \mathbf{E}_\mathbf{i}^{\mathrm{src}'}(\mathbf{r}) d\mathbf{r},$$

$$\propto \mathbf{P_j} \cdot [R(\mathbf{M})\mathbf{P_i}]. \tag{1}$$

The non-reciprocal phase shift between the beams will be

$$\varphi_{\mathrm{nr}}(\mathbf{E}_\mathbf{i}^{\mathrm{src}}(\mathbf{r}), \mathbf{E}_\mathbf{j}^{\mathrm{src}}(\mathbf{r}), \mathbf{M}) = \mathrm{Arg}\left( \frac{\alpha(\mathbf{E}_\mathbf{i}^{\mathrm{src}}(\mathbf{r}), \mathbf{E}_\mathbf{j}^{\mathrm{src}}(\mathbf{r}), \mathbf{M})}{\alpha(\mathbf{E}_\mathbf{j}^{\mathrm{src}}(\mathbf{r}), \mathbf{E}_\mathbf{i}^{\mathrm{src}}(\mathbf{r}), \mathbf{M})} \right). \tag{2}$$

If the sample is nonmagnetic, then by the symmetry of the kinetic coefficients its dielectric tensor $\epsilon_{ij}$ must be symmetric,[13] and the Helmholtz reciprocity theorem holds:[4]

$$\int_{\mathscr{O}_1} \mathbf{E}_\mathbf{2}^{\mathrm{src}'}(\mathbf{r}) \cdot \mathbf{E}_\mathbf{1}^{\mathrm{src}}(\mathbf{r}) d\mathbf{r} = \int_{\mathscr{O}_2} \mathbf{E}_\mathbf{1}^{\mathrm{src}'}(\mathbf{r}) \cdot \mathbf{E}_\mathbf{2}^{\mathrm{src}}(\mathbf{r}) d\mathbf{r}. \tag{3}$$

This implies that the phase shift given by Eq. (2) is zero, as expected. If the sample is magnetized, then the dielectric tensor will develop off-diagonal terms, Eq. (3) no longer holds, and we may detect a non-zero $\varphi_{\mathrm{nr}}$. The SI is dynamically biased to produce a voltage signal which is proportional to the phase shift multiplied by the average optical power at the detector, so the measured signal is roughly proportional to $\varphi_{\mathrm{nr}} \times |\alpha(\mathbf{E}_\mathbf{i}^{\mathrm{src}}(\mathbf{r}), \mathbf{E}_\mathbf{j}^{\mathrm{src}}(\mathbf{r}), \mathbf{M})|^2$. The magnitude of the signal due to this non-reciprocity will depend on the details of the optical constants of the material, the nature of the boundary conditions, the polarization states $\mathbf{P_1}$ and $\mathbf{P_2}$, and the direction of the magnetization. Symmetry considerations will help us choose polarization states which provide useful information about the magnetization state under fairly general circumstances, simplifying our analysis considerably.

We consider the case of an isotropic sample magnetized in an arbitrary direction. Shelankov and Pikus have discussed the constraints which time-reversal symmetry, together with a variety of other crystal symmetries, impose on the reflectivity matrix.[11] Our analysis parallels theirs, and the reader may refer to their work for more details concerning the influence of crystal symmetry and gyrotropy on our results. Neglecting these effects, we can see that there are two transformations which will map the source plane of one beam onto the source plane of the other: (i) $C_2$, a 180° rotation about the film normal, and (ii), $\sigma_v$, a reflection through the plane perpendicular to both the film surface and the plane of incidence. We may choose $\mathbf{P_1}$ and $\mathbf{P_2}$ to satisfy one or both of these symmetries, as shown in Fig. 3. By doing so, we eliminate the contribution of one or more magnetization directions to the magneto-optic response. Consider the case $\mathbf{P_2} = C_2\mathbf{P_1}$. Rotation changes the sign of both the transverse and the longitudinal components of the magnetization, but leaves the polar component unchanged. Thus symmetry requires that a sample magnetized in the polar direction will have the same response to each beam, producing zero relative phase shift between them, while the magnetization along the transverse or longitudinal directions will typically yield a finite shift. In a similar way, by choosing $\mathbf{P_1} = \sigma_v\mathbf{P_2}$ we will observe no longitudinal response. If $\mathbf{P_1}$ and $\mathbf{P_2}$ are linear, p-polarized states, then both symmetries are satisfied and only the transverse component gives a finite response (s-polarized states, due to their symmetry under reflection in the plane of incidence, yield no response whatsoever). Limiting ourselves to the linear response the magnetization, with coupling constants $\alpha$, we may summarize these statements by the following equations:

$$\varphi_{\mathrm{nr}}^{\bar{p}}(\mathbf{M}, \mathbf{E}_\mathbf{1}^{\mathrm{src}}(\mathbf{r})) \equiv \varphi_{\mathrm{nr}}(\mathbf{E}_\mathbf{1}^{\mathrm{src}}(\mathbf{r}), C_2\mathbf{E}_\mathbf{1}^{\mathrm{src}}(\mathbf{r}), \mathbf{M})$$

$$= \alpha_{\bar{p},t} M_t + \alpha_{\bar{p},l} M_l, \tag{4a}$$

$$\varphi_{\mathrm{nr}}^{\bar{l}}(\mathbf{M}, \mathbf{E}_\mathbf{1}^{\mathrm{src}}(\mathbf{r})) \equiv \varphi_{\mathrm{nr}}(\mathbf{E}_\mathbf{1}^{\mathrm{src}}(\mathbf{r}), \sigma_v\mathbf{E}_\mathbf{1}^{\mathrm{src}}(\mathbf{r}), \mathbf{M})$$

$$= \alpha_{\bar{l},t} M_t + \alpha_{\bar{l},p} M_p, \tag{4b}$$

$$\varphi_{\mathrm{nr}}^{\overline{pl}}(\mathbf{M}) \equiv \varphi_{\mathrm{nr}}(\mathbf{E_s}(\mathbf{r}), \mathbf{E_s}(\mathbf{r}), \mathbf{M}) = \alpha_{\overline{pl},t} M_t. \tag{4c}$$

A bar above the magnetization direction indicates that this component is forbidden by symmetry from contributing to the signal. These three phase shifts may all be determined simply by changing the orientations of the retardation plates shown in Fig. 1. By determining the five coupling constants,

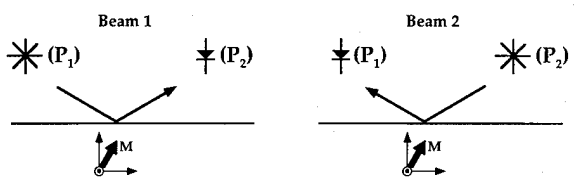



FIG. 2. Idealized schematic of two beams, with planar, monochromatic sources and coherent, polarization sensitive, spatially filtered detectors.

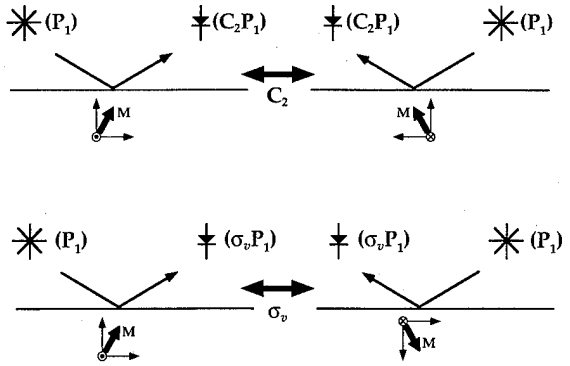



FIG. 3. Symmetries of the experimental apparatus for different choices of the polarization states. When $P_2 = C_2P_1$, the polar effect is not measured. When $P_2 = \sigma_v P_1$, the longitudinal effect is not measured. The operation $\sigma_v$ transforms the magnetization as shown because it is a pseudovector. P-polarized states satisfy both symmetries and measure only the transverse effect.

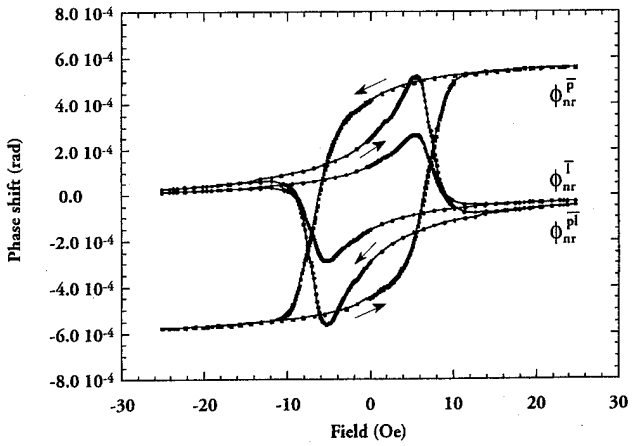



FIG. 4. Raw data from a hysteresis loop in a permalloy film.

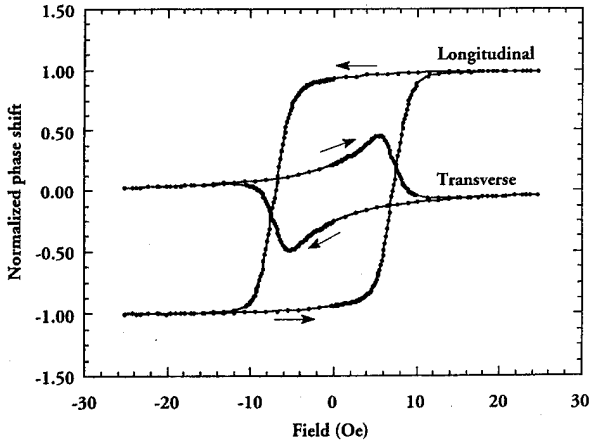



FIG. 5. Normalized magnetization components $M_l$ and $M_t$ calculated from the data in Fig. 4.

we can use Eqs. (4) to calculate the complete magnetization vector from a measurement of the three phase shifts.

To verify this analysis, we have observed hysteresis loops in a permalloy film. Measurements of the three phase shifts described in Eqs. (4) are shown in Fig. 4. In these measurements, the sample was mounted on goniometers for precise alignment to the surrounding optics, and the field was swept with a small horseshoe magnet oriented in the plane of incidence. The field had a small component in the transverse direction, which produced the finite phase shift $\varphi_{\rm nr}^{\bar{p}\bar{l}}$ seen in the saturated part of the loops. All polarizing optics were carefully aligned to satisfy the required symmetry relations; we estimate the error in this alignment to be less than 1 mrad for any one component. In Eqs. (4), the transverse magnetization contributes to all three phase shifts, and must be subtracted. We obtained $\alpha_{\bar{p},t}$, $\alpha_{\bar{l},t}$ and $\alpha_{\bar{p}\bar{l},t}$ directly by rotating the magnet to saturate the magnetization in the transverse direction and measuring each of the three phase shifts. We obtained the constant $\alpha_{\bar{p},l}$ in a similar way. We then scaled the hysteresis loop for $\varphi_{\rm nr}^{\bar{p}\bar{l}}$ accordingly and subtracted it from the other two loops. Demagnetization energy forces the magnetization to lie in the plane of the film, and the curves for $\varphi_{\rm nr}^{\bar{p}\bar{l}}$ and $\varphi_{\rm nr}^{\bar{p}}$ are in fact proportional. We could not easily saturate the permalloy in the polar direction to measure $\alpha_{\bar{l},t}$, but after subtracting the transverse contribution to $\varphi_{\rm nr}^{\bar{l}}$, the remaining phase shift was zero within the noise of the measurement, so we may safely take $M_p=0$. Fig. 5 shows the normalized magnetization components $M_t$ and $M_l$ which we derive from the data in Fig. 4. The data nicely show the effectively coherent rotation of the magnetization during much of the loop. As the field is increased from $-25$ Oe, the magnetization rotates toward the transverse direction. Up to about $+5$ Oe, the magnitude of the magnetization $|\mathbf{M}|$ remains constant as $M_t$ increases. Above 5 Oe, we observe a rounding off of the transverse magnetization, while the longitudinal component switches abruptly. The SI measures the average magnetization in the beam area, so the reduction of $|\mathbf{M}|$ in this field range indicates that the switching occurs by domain formation, preventing $\varphi_{\rm nr}^{\bar{p}\bar{l}}$ from reaching its maximum value. This behavior is similar to that seen in other thin films with uniaxial anisotropy.[14]

We should emphasize that the symmetry properties of the SI allow us to perform these measurements in static or zero applied field as well as for the hysteresis loops shown here. We recently demonstrated the advantage of this capability in normal incidence measurements by correlating the structural domain size in $SrRuO_3$ with the magnetic domain size observed after cooling through the Curie point in zero field.[3] It may be interesting to apply the techniques described here to the study of spin reorientation transitions in epitaxial magnetic films.[15,16] The ability to discriminate clearly between the longitudinal and the polar orientations is an attribute which could be especially useful here. In microscopy with magneto-optic contrast, these capabilities could be useful for characterizing magnetic anisotropy variations in thin films on a microscopic scale.[17] The symmetry considerations are quite general and can be extended to a wide range of experimental geometries.


[1] S. Spielman, K. Fesler, C. B. Eom, T. H. Geballe, M. M. Fejer, and A. Kapitulnik, Phys. Rev. Lett. **65**, 123 (1990).
[2] S. Spielman, J. S. Dodge, L. W. Lombardo, C. B. Eom, M. M. Fejer, T. H. Geballe, and A. Kapitulnik, Phys. Rev. Lett. **68**, 3472 (1992).
[3] L. Klein, J. S. Dodge, T. H. Geballe, A. Kapitulnik, A. F. Marshall, L. Antognazza, and K. Char, Appl. Phys. Lett. **66**, 2427 (1995).
[4] L. D. Landau, E. M. Lifshitz, and L. P. Pitaevskiĭ, *Electrodynamics of Continuous Media* (Pergamon, New York, 1984).
[5] E. Betzig, J. K. Trautman, R. Wolfe, E. M. Gyorgy, P. L. Finn, M. H. Kryder, and C.-H. Chang, Appl. Phys. Lett. **61**, 142 (1992).
[6] T. J. Silva, S. Schultz, and D. Weller, Appl. Phys. Lett. **65**, 658 (1994).
[7] B. D. Terris, H. J. Mamin, D. Rugar, W. R. Studenmund, and G. S. Kino, Appl. Phys. Lett. **65**, (1994).
[8] A. Kapitulnik, J. S. Dodge, and M. M. Fejer, J. Appl. Phys. **75**, 6872 (1994).
[9] H. Lefevre, *The Fiber Optic Gyroscope* (Artech House, Boston, 1993).
[10] M. A. Azzam and N. M. Bashara, *Ellipsometry and Polarized Light* (North-Holland, New York, 1977)
[11] A. L. Shelankov and G. E. Pikus, Phys. Rev. B **46**, 3326 (1992).
[12] S. Spielman, Ph.D. thesis, Stanford University, 1992.
[13] L. D. Landau and E. M. Lifshitz, *Statistical Physics, Part 1* (Pergamon, New York, 1980).
[14] R. Osgood, R. L. White, B. Clemens (submitted).
[15] Z. Q. Qiu, J. Pearson, and S. D. Bader, Phys. Rev. Lett. **70**, 1006 (1993).
[16] A. Berger, A. W. Pang, and H. Hopster, Phys. Rev. B **52**, 1078 (1995).
[17] R. W. Schafer and A. Hubert, J. Magn. Magn. Mater. **65**, 7 (1987).

# Second-order magneto-optic effects in anisotropic thin films (abstract)

R. M. Osgood III, B. M. Clemens, and R. L. White
*Department of Materials Science and Engineering, Stanford University, Stanford, California 94305-2205*

The signal measured in a magneto-optic Kerr effect (MOKE) experiment is normally assumed to be proportional to the component of the magnetization ($M$) along a certain axis.[1] We have observed significant effects from the $M^2$ term in the magneto-optic response (i.e., in the rotation and/or ellipticity, which can be thought of as the real and imaginary parts of the same quantity[2]) from films with in-plane magnetization and in-plane magnetic anisotropy. These films were: epitaxial Fe(110)/Mo(110) bilayers and multilayers, thin Fe films with ion-bombardment induced anisotropy, Co(110) thin films, and NiFe films with anisotropy induced with a field during deposition. In all of these films, the in-plane anisotropy created a coherently rotating magnetization (as evidenced by measurement of the component of the magnetization perpendicular to the applied field) that contributed a large $M^2$ term to the magneto-optic response when an external field was applied close to parallel to the hard axis of the film. The $M^2$ term in the magneto-optic response changed sign as $H$ was rotated through the hard axis and reached a minimum when $H$ was applied nearly parallel ($\pm 0.5°$) to the hard axis, thus providing a sensitive indication of the location of the sample's hard axis. © *1996 American Institute of Physics.* [S0021-8979(96)48008-3]

[1] J. M. Florczak and E. D. Dahlberg, Phys. Rev. B **44**, 9338 (1991).
[2] G. Metzger, P. Pluvinage, and R. Torguet, Ann. Phys. **10**, 5 (1965).

# Spectroscopic Kerr investigations of CoNi/Pt multilayers

W. P. Van Drent and T. Suzuki
*Toyota Technological Institute, 2-12-1 Hisakata, Tempaku-ku, Nagoya 468, Japan*

Q. Meng, J. C. Lodder, and Th. J. A. Popma
*MESA Research Institute, P.O. Box 217, 7500 AE Enschede, The Netherlands*

$Co_xNi_{1-x}$/Pt multilayers with $x=0.4$ and 0.5 were sputtered onto Si substrates. Magnetic and spectroscopic magneto-optic measurements (1.4–5.2 eV) reveal a Kerr rotation up to $-0.48°$ at about 4.5 eV for a sample with rectangular hysteresis loop, about 170 kA/m coercivity, and a Curie temperature of about 300 °C. Pt layers could be made extremely thin (2.9 Å) without loss of perpendicular anisotropy and rectangular hysteresis loop. Simulations show that the Kerr rotation peak shifts back from 4.5 to 3.9 eV with increasing number of bilayers. © *1996 American Institute of Physics.* [S0021-8979(96)13208-6]

## I. INTRODUCTION

The interest in Co/Pt based multilayers as magneto-optical recording material is due to several merits: the high magneto-optical (MO) output at short wavelengths,[1] due to the polarized Pt[2] or alloy layers[3] at the interfaces, the high corrosion resistance, and the high perpendicular anisotropy $K_{\text{eff}}$ in very thin layers. A disadvantage is the relatively high Curie temperature $T_C$, which reduces rewritability. By alloying Co with another element, $T_C$ can be lowered, but the favorable properties of Co/Pt should be preserved in the new material. We tried to alloy Co with Ni,[4] as the magnetic phase diagram[5] indicated that $T_C$ decreases significantly with Ni content. Recently, this was confirmed by a study of CoX/Pt multilayers.[6]

## II. EXPERIMENT

CoNi/Pt multilayers (ML) were prepared by magnetron sputtering from 2 in. sputter guns in argon pressures $8 \leqslant P_{\text{ar}} \leqslant 48$ $\mu$bar. The guns were equipped with shutters and the time between deposition of subsequent layers was about 2 s. The target-substrate distance was fixed at 100 mm, which keeps the substrate relatively plasma free. The samples were prepared on 2 in. Si (111) wafers, which were cleaned in a standard way before insertion. The ML always consisted of a Pt base layer (typically 400 Å) and a stack of 17 or 18 bilayers. Sputter rates were between 1 and 2.5 Å/s. The background pressure before deposition was $<10^{-8}$ mbar. Layer thicknesses were measured by x-ray diffraction (XRD) (low and high angle) and Dektak surface profiler, both on thick layers (of CoNi resp. Pt) and on ML. The bilayer peak was visible up to $P_{\text{ar}}=40$ $\mu$bar. Above that the structure is too distorted to observe.

Kerr rotation $\theta_K$ and ellipticity $\epsilon_K$ of uncoated samples were measured in the range 1.4–5.2 eV by a homemade, automated setup applying the photoelastic modulator principle.[7–9] The accuracy was about 0.001°, and an automatic calibration for *both* $\theta_K$ and $\epsilon_K$ is performed before each measurement. Details of this calibration will be published elsewhere. A sample heater in the Kerr setup served as the $T_C$ measurement stage.

Magnetic measurements were carried out with a vibrating-sample magnetometer (VSM) ($H_{\max}=3$ T, resolution $5\times10^{-9}$ A m$^2$) and a homemade torque meter ($H_{\max}=1.8$ T, resolution $3\times10^{-9}$ Nm).

## III. RESULTS AND DISCUSSION

Perpendicular ($\perp$) anisotropy was found for both $Co_{40}Ni_{60}$/Pt and $Co_{50}Ni_{50}$/Pt ML in the range $4 \leqslant t_{\text{CoNi}} \leqslant 20$ Å, where $t_{\text{Pt}} \approx 15$ Å. The $\perp$ anisotropy was found for very thin Pt layers: a 17×(5.5 Å $Co_{40}Ni_{60}$/2.8 Å Pt) ML still had $K_{\text{eff}}>0$. $K_{\text{eff}}$ can be decomposed in a surface and a volume anisotropy ($K_S$ resp. $K_V$) by[10]

$$t_{\text{magn}}K_{\text{eff}} = 2K_S + t_{\text{magn}}K_V, \tag{1}$$

where $t_{\text{magn}}$ is the thickness of the magnetic layer.

For the 50% (40%) Co multilayers $K_S=0.26$ (0.21) mJ/m$^2$ and $K_V=-257$ ($-185$) kJ/m$^3$ were found. These values are in good agreement with others.[11,12] The maximum $\perp$ anisotropy was found for $5 \leqslant t_{\text{CoNi}} \leqslant 8$ Å in both cases.

Figure 1 displays spectroscopic Kerr measurements of a series of 230 Å Pt+17×(*X* Å $Co_{50}Ni_{50}$/14.7 Å Pt). The thinnest magnetic layer (3.8 Å CoNi) gives the lowest $\theta_K$. In this case $M_{\text{S,CoNi}}$ is also very low, which suggests that the magnetic layers are not continuous. $\theta_K$ increases gradually with increasing $t_{\text{CoNi}}$ to a maximum of about $-0.30°$ at $t_{Co_{50}Ni_{50}}=25$ Å. Thicker CoNi layers did lower $\theta_K$ (not drawn). Enhancement due to more CoNi in the skin-depth region is counteracted by the reduction of the amount of polarized Pt in this region, which is dependent on the number of interfaces.

It is clear that $\theta_K$ at lower photon energies increases with increasing $t_{\text{CoNi}}$ and the features of the Co and Ni spectra (e.g., the peak in $\theta_K$ around 1.5 eV) become more pronounced. The same can be seen for $\epsilon_K$, where the spectrum for the sample with 25 Å CoNi layers resembles a mix of the bulk Co and Ni curves. The MO contribution of polarized Pt at high photon energies is found for thin magnetic layers.

The samples with $t_{Co_{50}Ni_{50}}=5.0$, 6.3, and 8.8 Å have $\perp$ anisotropy and unity squareness. Of these, only the first sample has a rectangular hysteresis loop, and therefore $t_{Co_{50}Ni_{50}}=5$ Å was chosen as the starting point for a Pt thickness variation. Figure 2 displays the spectroscopic Kerr measurements for $t_{Co_{50}Ni_{50}}=5$ Å, and $t_{\text{Pt}}=14.7$, 8.4, and 5.9 Å. Even the 5.9 Å sample is perpendicular, in contrast to Co/Pt ML's with similar layer thicknesses. At high photon energies

 0021-8979/96/79(8)/6190/3/$10.00 © 1996 American Institute of Physics

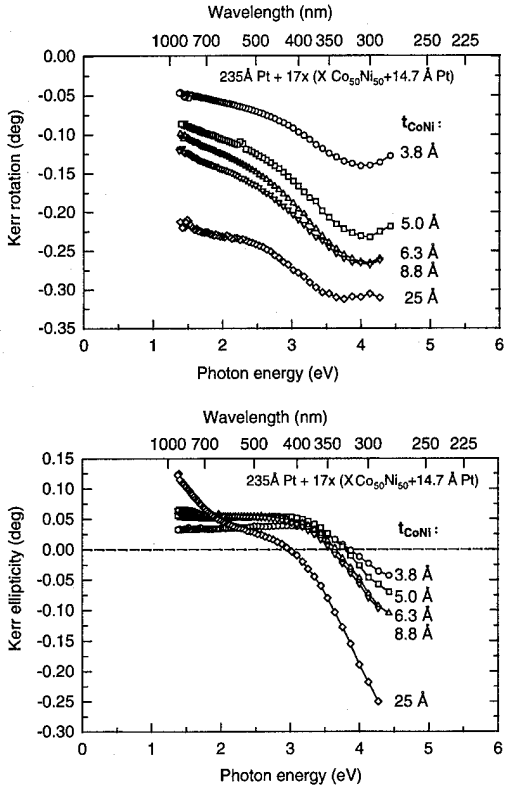



FIG. 1. Spectroscopic Kerr measurements for 230 Å Pt+17 $\times(X$ $Co_{50}Ni_{50}$/14.7 Å Pt). The series ranges from $X=3.8$ to 25 Å.

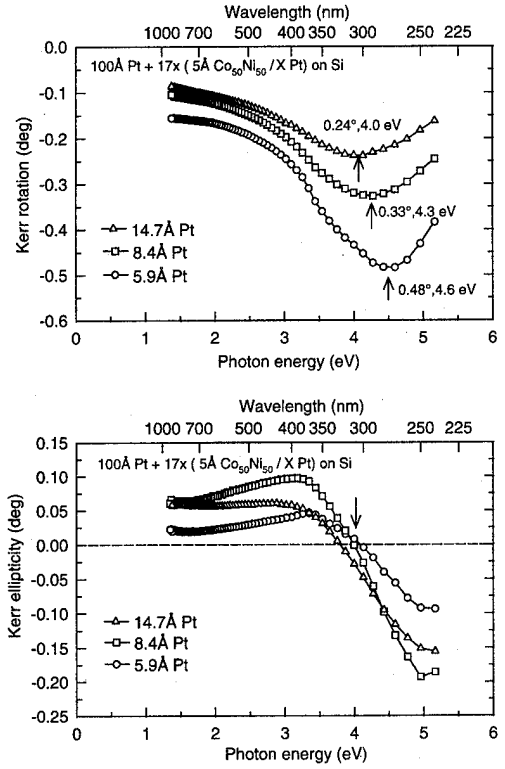



FIG. 2. Spectroscopic Kerr measurements for three samples with decreasing Pt thickness. The samples are 100 Å Pt+17×(5 Å $Co_{50}Ni_{50}$/$X$ Pt) with $X=5.9$, 8.4, and 14.7 Å.

$\theta_K$ increases considerably with decreasing $t_{Pt}$. The maximum value is $\theta_K=-0.48°$ for $t_{Pt}=5.9$ Å, and this is the highest value observed by us for any CoNi/Pt ML. With decreasing $t_{Pt}$ the energy at which the peak occurs shifts up from 4.0 to 4.6 eV. This shift is due to the decreasing total layer thickness, as will be shown by simulations in the next paragraph. Spectroscopic studies of Co/Pt multilayers,[13,14] CoPt alloys,[14,15] and CoNi/Pt multilayers[11] did not reveal such peak shifts, as those results are all taken of ML's that are optically thick.

Figure 3 shows the Kerr hysteresis loop of the sample with a stack of 5 Å CoNi/5.9 Å Pt, taken at 4.13 eV. The loop features unity squareness and high rectangularity. This sample was sputtered at 40 $\mu$bar, which results in a high $H_C\approx 170$ kA/m. Although high $P_{ar}$ is a poor way to introduce a morphology that supports a high $H_C$ (due to the increase in media noise), Fig. 3 demonstrates that it is possible to make a CoNi/Pt multilayer with high rectangularity, high $H_C$, and high $\theta_K$ at short wavelengths.

## IV. SIMULATION OF KERR EFFECTS

Because the thickness of these ML's is of the order of the skin depth[16] (which is between 10.5 and 13.5 nm for Co,Ni and Pt between 1.5 and 4.0 eV), it is of interest to estimate the Kerr effects for an optical thick ML. Using a simulation based on the mathematical approach of Visnovsky[17] the Kerr effects for arbitrary $N$ were calculated using the measurement results for the thin ML as a starting point. In this way it is possible to estimate the Kerr effect of a thick ML from the measurement of a thin one. The approach was as follows:

(1) Calculate the MO Voigt constants $Q(\lambda)$ of either polarized Pt or CoNiPt alloy layers at the interface by fitting these constants in such a way that the calculation gives the same $\theta_K$ and $\epsilon_K$ as the measurement.

(2) These $Q(\lambda)$ are used to calculate the $\theta_K$ and $\epsilon_K$ for a hypothetical $N$ bilayer medium, with arbitrary $N$.

The layer structure of our "best sample," including the Pt seedlayer and 100 nm of the Si substrate, was used as input for the simulation. Now one can either assume that alloyed layers occur at the interface, or that no alloying occurs, and Pt polarizes at the interfaces. For the alloyed layer, a weighted mix of the optical constants of its constituents was taken. Both schemes were applied with several thicknesses of the polarized resp. the alloyed layer, and negligible

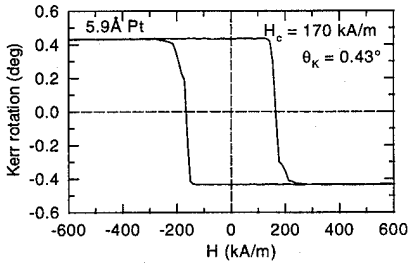



FIG. 3. Kerr hysteresis loop at $E_{photon}=4.13$ eV for 100 Å Pt+17×(5 Å $Co_{50}Ni_{50}$/5.9 Å Pt). The loop has good rectangularity, which is imperative for MO recording.

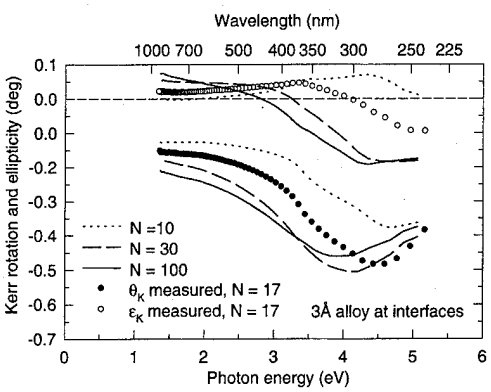



FIG. 4. Simulated Kerr rotation and Kerr ellipticity for several numbers of bilayers $N$. Measurement of 100 Å Pt+17×(5 Å $Co_{50}Ni_{50}$/5.9 Å Pt) (points) was taken as a starting point for the simulations.

differences between these schemes were found. This corresponds to the expectation that such a thin stack behaves as a single optical layer. For the following a 3 Å alloy layer model was taken. In Fig. 4 measurement and simulations are shown for $N=10$, 30, and 100.

According to the simulations the maximum $\theta_{K,\max}$ should be reached at about 30 bilayers. $\theta_{K,\max}$ calculated by simulations of $N=20$, 25, 40, and 50 (not drawn) was lower than in the $N=30$ case. $\theta_{K,\max}$ for $N=30$ occurs at about 4.1 eV, which is in good agreement with reported results for Co/Pt. $\theta_K$ decreases for $N<17$. In the range 1.5–4 eV the simulated optical thick layer has a higher $\theta_K$ than the thin one. The UV peak for $N=100$ occurs at a $E_{\text{photon}}\sim 3.9$ eV. This is slightly lower than the 4.2 eV that is expected for the contribution of Pt in Co/Pt ML's and it is certainly lower than the peak position in the measurement. The simulation for the optical thick layer ($N=100$) gives $\theta_{K,\max}=-0.46°$. This is lower than the measurement for $N=17$ ($\theta_K=-0.48°$), but for application purposes it occurs at a much more favorable photon energy.

The simulated $\epsilon_K$ decreases faster with increasing photon energy and the overall output is larger (both positive and negative) than in the measurement.

## V. CONCLUSIONS

$Co_xNi_{1-x}$/Pt ML's with $x=0.4$ and 0.5 were prepared by magnetron sputtering. Perpendicular anisotropy was achieved up to $t_{\text{CoNi}}=20$ Å for both compositions. A sample of 17×(5 Å $Co_{40}Ni_{60}$/2.8 Å Pt) was still perpendicular. We attribute this to the lower magnetic moment of CoNi compared to pure Co, which on its turn reduces the demagnetizing field. $\theta_K=-0.48°$ was found for 17×(5 Å $Co_{50}Ni_{50}$/5.9 Å Pt). A large $H_C$ (170 kA/m) and high squareness were other features of this sample.


[1] W. B. Zeper, F. J. A. M. Greidanus, and P. F. Carcia, IEEE Trans. Magn. **MAG-25**, 3764 (1989).
[2] E. R. Moog, J. Zak, and S. D. Bader, J. Appl. Phys. **69**, 880 (1991).
[3] J. Nakajima, A. Takahashi, K. Ohta, and T. Ishikawa, J. Magn. Soc. Jpn. **15**, Suppl. S1, 41 (1991).
[4] M. Mes, J. C. Lodder, T. Takahata, I. Moritani, and N. Imamura, J. Magn. Soc. Jpn. **17**, Suppl. S1, 44 (1993).
[5] W. Bendick and W. Pepperhoff, J. Phys. F. **9**, 2185 (1979).
[6] S. Hashimoto, J. Appl. Phys. **75**, 438 (1994).
[7] S. N. Jasperson, D. K. Burge, and R. C. O'Handley, Surf. Sci. **37**, 548 (1973).
[8] K. Sato, Jpn. J. Appl. Phys. **20**, 2403 (1981).
[9] P. Q. J. Nederpel and J. W. D. Martens, Rev. Sci. Instrum. **56**, 687 (1985).
[10] H. J. G. Draaisma, W. J. M. de Jonge, and F. J. A. den Broeder, J. Magn. Magn. Mater. **66**, 351 (1987).
[11] R. Krishnan and H. Lassri, J. Magn. Magn. Mater. **133**, 453 (1994).
[12] R. Krishnan, H. Lassri, M. Seddat, M. Porte, and M. Tessier, Appl. Phys. Lett. **64**, 2312 (1994).
[13] H. Brändle, D. Weller, J. C. Scott, S. S. P. Parkin, and C.-J. Lin, IEEE Trans. Magn. **MAG-28**, 2967 (1992).
[14] D. Weller, W. Reim, K. Spörl, and H. Brändle, J. Magn. Magn. Mater. **93**, 183 (1991).
[15] K. Sato, H. Ikekame, Y. Tosaka, K. Tsuzukiyama, Y. Togami, and M. Fujisawa, J. Magn. Magn. Mater. **126**, 572 (1993).
[16] R. M. A. Azzam and N. M. Bashara, *Ellipsometry and Polarized Light* (North-Holland, Amsterdam, 1977), p. 75, ISBN 0-7204-0694-3.
[17] S. Visnovsky, J. Magn. Soc. Jpn. **15**, Suppl. S1, 67 (1991).

# *In situ* and *ex situ* optical characterization of electro deposited magneto-optic materials

James N. Hilfiker, Darin W. Glenn, Scott Heckens, and John A. Woollam
*Center for Microelectronic and Optical Materials Research, and Department of Electrical Engineering, University of Nebraska, Lincoln, Nebraska 68588*

Kurt W. Wierman
*Department of Physics, University of Nebraska, Lincoln, Nebraska 68588*

Electrodeposition is being investigated as a novel and low-cost method to prepare magneto-optic thin film and nanostructured materials. This deposition method allows precise control over thin-film properties and permits deposition of novel magnetic geometries. Multilayers and alloys can be deposited and controlled by adjusting deposition potentials and ion concentrations in the bath. Nickel/cobalt alloys have been electrodeposited from sulfamate, sulfate, and chloride solutions onto Au substrates. The optical properties were monitored *in situ* with a real-time spectroscopic ellipsometer measuring simultaneously at 44 wavelengths in the 410–750 nm spectral range. *In situ* measurements have the advantage of determining the material microstructural properties (thickness, density, and roughness) before the films are oxidized in the air ambient. *Ex situ* variable angle spectroscopic ellipsometry measurements were taken over the spectral range from 205 to 1000 nm.
© *1996 American Institute of Physics.* [S0021-8979(96)13308-2]

## I. INTRODUCTION

Sputtered Co/Ni and Co/Pt nanometer thick multilayers can exhibit perpendicular magnetization and have previously been investigated as possible recording materials.[1,2] Electrodeposition is investigated as a possible processing technique for similar magneto-optic materials. Alloys can be plated from an electrolyte containing ions of each of the elements to be plated. The ratio of ions in the electrolyte will have a direct effect on the thin-film alloy ratio, and the alloy ratio can be controlled by adjusting the electrolyte constituents. This control is desirable for many magneto-optic materials because of the effects of alloy ratios on Curie temperature, coercivity, optical response, and magneto-optic response. Control of the compensation temperature in TbFeCo is an example.

A full electromagnetic analysis of the multilayer boundary value problem, including dielectric tensor representation for all constituent layers, can provide information about observed optical and magneto-optical phenomena.[3] Predictive modeling with this analysis method allows the optimization of magneto-optic disk performance.[4] Accurate material properties (optical and magneto-optical constants) are necessary to simulate the optical and magneto-optical responses of a disk structure.

In order to accurately model the material thickness and microstructure, *in situ* spectroscopic ellipsometry measurements were taken during the electrodepositions. This allows the materials to be studied before oxidation, and thus the true material optical constants can be used for predictive modeling. The *in situ* measurements also allow diagnostics of time dependent growth effects. Optimization of the thin-film thicknesses and microstructure could be implemented by performing predictive modeling and then controlling the growth.

## II. EXPERIMENTAL PROCEDURE

Electrodeposition of cobalt/nickel multilayers and alloys were carried out from the following electrolyte: 90 g/ℓ nickel sulfamate, 30 g/ℓ boric acid, and $X$ g/ℓ of cobalt chloride (where $X$ is varied). Both potentiostatic and galvanostatic depositions were performed using a Princeton Applied Research (PAR) Model 173 potentiostat/galvanostat. A three electrode cell configuration was used in which the working electrode consisted of the substrate to be plated on, the counter electrode was a platinum foil, and the reference electrode was a saturated calomel electrode. A PAR Model 179 coulometer was used to monitor the charge passing through the sample during the deposition.

An electrochemical cell was designed with optical ports to allow ellipsometry measurements through the liquid. An *in situ* spectroscopic ellipsometer (J. A. Woollam Co., Inc.) was used to study the deposition processes. The *in situ* ellipsometer allowed 44 wavelengths to be measured simultaneously over the spectral range from 410 to 750 nm every 40 ms.

A series of cobalt/nickel multilayers and alloys were electrodeposited on optically thick gold films. The gold substrates were prepared by sputter deposition on silicon wafers. A chromium underlayer was first sputter deposited on the silicon substrate to act as an adhesion layer for the gold. X-ray fluorescence measurements were taken on the series of samples to determine the thin-film cobalt-to-nickel alloy ratio.

*In situ* spectroscopic ellipsometry measurements were also taken on each of these films during deposition. This measurement tool allows the determination of the optical constants and thin-film thicknesses of the deposited layer and their time dependencies. The galvanostatic depositions were modeled with a constant growth rate material model.

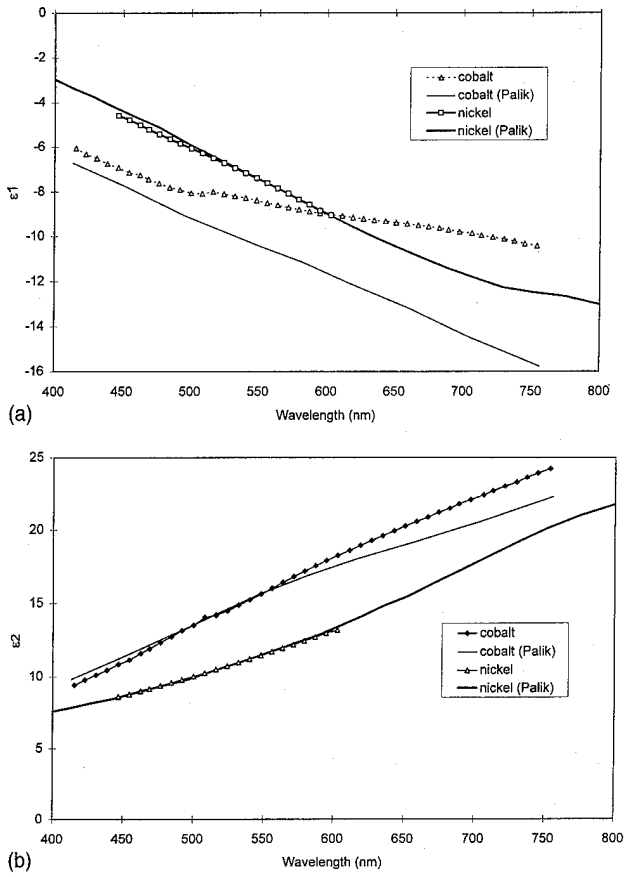



FIG. 1. (a) and (b): Comparison of optical constants determined from *in situ* spectroscopic ellipsometry and those from Palik. (Ref. 5).

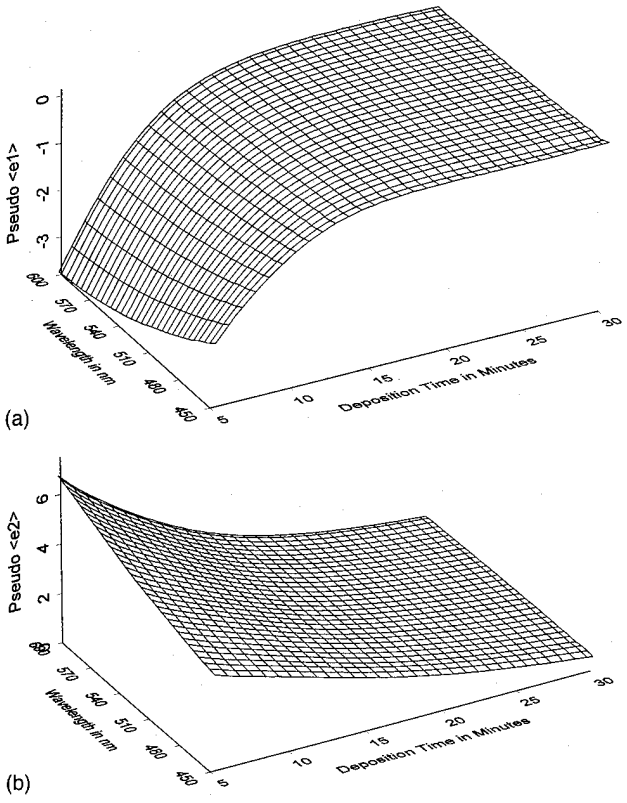



FIG. 2. (a) and (b): Pseudo-dielectric optical constants during the electrodeposition of a cobalt/nickel alloy thin film.

## III. RESULTS

The optical constants and growth rates were determined from *in situ* spectroscopic ellipsometry measurements taken during the electrodeposition process. The optical constants for cobalt and nickel were in reasonable agreement with values from the literature, as shown in Fig. 1, with the differences for cobalt probably due to surface roughness.[5] A comparison between growth rates determined by *in situ* ellipsometry and coulometric calculations was also in good agreement.[6]

*Ex situ* spectroscopic ellipsometry measurements on the optically thick cobalt/nickel alloys showed a basic trend of increasing $\epsilon_1$ and decreasing $\epsilon_2$ as the cobalt ion concentration, $X$, was increased. The pseudo-dielectric constants from *in situ* ellipsometry for one of the cobalt/nickel alloys are shown in Fig. 2. The film is optically thick after 5 min of deposition (time period shown), yet the dielectric constants continue to change with time. A roughness layer from effective medium theory was able to account for the changes during the early stages of film growth, but failed as the films continued to roughen. The *in situ* evidence that the films were roughening with increasing thickness was confirmed by *ex situ* interference microscope measurements. Alloys of cobalt/nickel deposited to the same final thickness were found to have increasing roughness with increasing cobalt concentration. Therefore, in order to predict the optical response of these electrodeposited materials, care must be given to provide the correct optical model. Further calculations using a model without the inclusion of surface roughness would give incorrect results for magneto-optic constants. If the thickness is to be optimized, the theoretical calculations would have to consider the time dependent change in thin-film optical properties during the growth which would give rise to a different optical and magneto-optic response for different thin-film thicknesses.

Lashmore *et al.*, have investigated electrodeposited copper/nickel multilayers for investigation of giant magne-

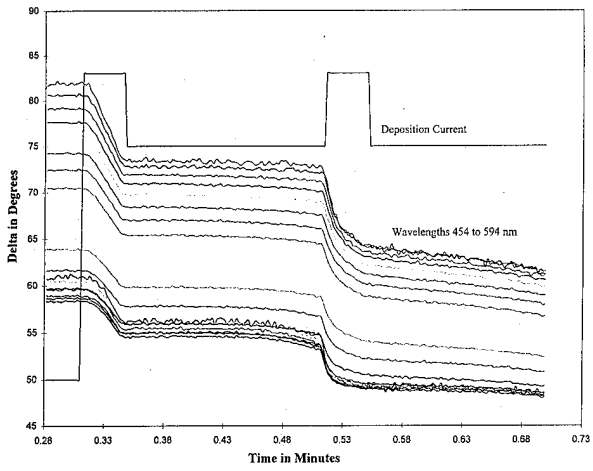



FIG. 3. *In situ* spectroscopic ellipsometry parameter (delta) during a copper/nickel multilayer electrodeposition.

toresistive effects.[7] We have used *in situ* spectroscopic ellipsometry to study the electrodeposition of similar multilayers. For example, the ellipsometric delta parameter during a copper/nickel multilayer deposition is shown in Fig. 3. The multilayers are deposited from the same solution by pulsing to different currents (also shown in Fig. 3).

## IV. CONCLUSION

Electrodeposition is an interesting technique which allows the processing of magneto-optic materials. Both alloy and multilayer thin films have been formed with this technique. *In situ* spectroscopic ellipsometry allowed diagnostics of the electrodeposition process. The optical constants from ellipsometry are in good agreement with those from the literature, and will be needed to optimize any magneto-optic device structures.


## ACKNOWLEDGMENT

Supported by the National Science Foundation, Grant No. NSF-OSR 9255225.



[1] Y. B. Zhang, P. He, J. A. Woollam, J. X. Shen, R. D. Kirby, and D. J. Sellmyer, J. Appl. Phys. **75**, 6495 (1994).

[2] P. He, W. A. McGahan, J. A. Woollam, F. Sequeda, T. McDaniel, and H. Do, J. Appl. Phys. **69**, 4021 (1991).

[3] J. N. Hilfiker, Y. B. Zhang, and J. A. Woollam, IEEE Trans. Magn **MAG-30**, 4437 (1994).

[4] P. He, William A. McGahan, and J. A. Woollam, Proc. SPIE **1499**, 401 (1991).

[5] Edward D. Palik, *Handbook of Optical Constants of Solids* (Academic, Orlando, 1985).

[6] J. N. Hilfiker, D. W. Thompson, J. S. Hale, and J. A. Woollam, Thin Solid Films **270**, 73 (1996).

[7] D. S. Lashmore and M. P. Dariel, J. Electrochem. Soc. **135**, 1218 (1988).

# Theoretical predictions of the polar Kerr effect in Fe and Co

J. M. MacLaren and W. Huang
*Department of Physics, Tulane University, New Orleans, Louisiana 70118*

We present theoretical calculations of the magneto-optic polar Kerr effect in bcc iron, fcc cobalt, and hcp cobalt. The Kerr angle and ellipticity are derived from the optical conductivity tensor, which is computed using wave functions obtained from full potential local spin-density electronic structure calculations. Predicted Kerr angles and ellipticities are computed as a function of magnetization direction. In the case of iron, the calculated Kerr spectra are found to be in good agreement with experimental results and previous calculations. However, in the case of cobalt, the results of previous theoretical studies differ significantly. Our results are in close agreement with experiment and with one of these previous theoretical studies. © *1996 American Institute of Physics.* [S0021-8979(96)13408-9]

The rotation of plane polarized light upon reflection from a magnetic surface, the magneto-optic Kerr effect, has been studied extensively experimentally because of applications in optical data storage.[1,2] In this technology, a large magneto-optic Kerr effect at short wavelengths is desired in order to achieve projected aerial storage densities. Co/Pt and Co/Pd superlattices have been the focus of much research since these materials exhibit large Kerr rotations and the prerequisite perpendicular magnetic anisotropy.[3] In order for electronic structure calculations to be useful in the design of novel magneto-optic materials, they should demonstrate accuracy in simpler systems such as the $3D$ transition metals. There have been several recent theoretical studies of the Kerr effect in Fe and Co, including one which considered the influence of magnetization direction.[4–6] All of the calculated Kerr spectra for Fe are in good agreement with each other and with experiment. However, in the case of Co, there are significant differences between the various calculations.

The magneto-optic Kerr effect is a consequence of an asymmetry in the refractive indices for left- and right-handed circularly polarized light which results from the combined effects of spin polarization and the spin-orbit interaction. In the technologically important polar Kerr effect, both wave vector and magnetization are perpendicular to the surface. A straightforward analysis starting from the Fresnel relations for reflection from a surface leads to the following expression for the complex Kerr angle:

$$\Theta_k = \frac{-\sigma_{xy}}{\sigma_{xx}\sqrt{1+i(4\pi/\omega)\sigma_{xx}}} \tag{1}$$

in terms of the elements of the optical conductivity tensor ($\sigma_{\alpha\beta}$).

An expression for the optical conductivity tensor at frequency $\omega$ in a periodic solid, derived from linear response theory, was given by Wang and Callaway[7]

$$\sigma_{\alpha\beta}(\omega) = \frac{ie^2}{m^2\hbar\Omega}\int d^3k \sum_{\ell\sigma}{}' \sum_{\ell'\sigma'}{}'' \frac{1}{\omega_{\ell'\sigma',\ell\sigma}(\mathbf{k})} \times\left(\frac{\Pi^{\alpha}_{\ell\sigma,\ell'\sigma'}(\mathbf{k})\Pi^{\beta}_{\ell'\sigma',\ell\sigma}(\mathbf{k})}{(\omega-\omega_{\ell'\sigma',\ell\sigma}(\mathbf{k})+i\delta)} + \frac{\Pi^{\beta}_{\ell\sigma,\ell'\sigma'}(\mathbf{k})\Pi^{\alpha}_{\ell'\sigma',\ell\sigma}(\mathbf{k})}{(\omega+\omega_{\ell'\sigma',\ell\sigma}(\mathbf{k})+i\delta)}\right), \tag{2}$$

where $e$ and $m$ are the electronic charge and mass, $\hbar$ Planck's constant, $\Omega$ the unit cell volume, and $\delta=1/\tau$, where $\tau$ is the relaxation time. The integral is over the Brillouin zone. The primed (double primed) summations are over occupied (unoccupied) electronic states. $\hbar\omega_{\ell'\sigma',\ell\sigma}(\mathbf{k})$ is the energy difference, $E_{\ell'\sigma'}(\mathbf{k}) - E_{\ell\sigma}(\mathbf{k})$, between two eigenstates labeled by band index $\ell$ and spin $\sigma$. The matrix elements of the momentum operator $\Pi^{\alpha}_{\ell\sigma,\ell'\sigma'}(\mathbf{k})$ are given by

$$\Pi^{\alpha}_{\ell\sigma,\ell'\sigma'}(\mathbf{k}) = \int d\mathbf{r}\psi^{*}_{\ell\sigma\mathbf{k}}(\mathbf{r})\left(-i\hbar\frac{\partial}{\partial x_\alpha} + \frac{\hbar}{4mc^2} \times[\sigma\times\nabla V(\mathbf{r})]_\alpha\right)\psi_{\ell'\sigma'\mathbf{k}}(\mathbf{r}). \tag{3}$$

In the calculations presented in this article, the spin-flip term $\hbar/4mc^2[\sigma\times\nabla V(\mathbf{r})]$, given in terms of the Pauli matrices $\sigma$ and one-electron potential $V(\mathbf{r})$, is neglected. In addition to the interband conductivity, an intraband Drude term is added

$$\sigma_{\alpha\beta}(\omega) = \frac{\sigma_0}{1-i\omega\tau_D}\delta_{\alpha\beta}. \tag{4}$$

The Drude parameters $\sigma_0$ and $\tau_D$ were taken from the work of Lenham and Treherne.[8] The Drude term is only significant for photon energies less than about 1 eV, and thus has little effect on the Kerr angle in the technologically interesting range of 3–4 eV. In evaluating $\sigma_{\alpha\beta}(\omega)$ using Eq. (2), we have followed the approach suggested by Oppeneer *et al.*, namely to keep a finite value of $\delta$ which we choose to be 0.03 Ry. The other common approach is to evaluate in the sharp limit $\delta\rightarrow 0$ and use Kramers–Kronig relations to reconstruct the full conductivity tensor.[6]

 0021-8979/96/79(8)/6196/3/$10.00 © 1996 American Institute of Physics

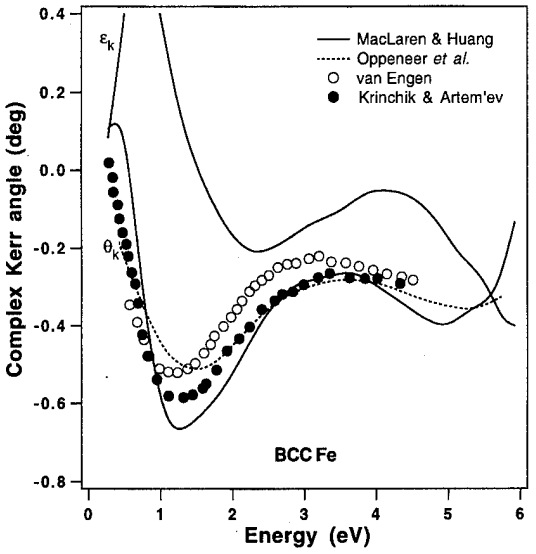



FIG. 1. Kerr angle and ellipticity for bcc Fe. Theoretical data shown are as follows: solid line, this work, dashed line (Refs. 4 and 5). Experimental data shown are open circles (Ref. 15), filled circles (Ref. 14).

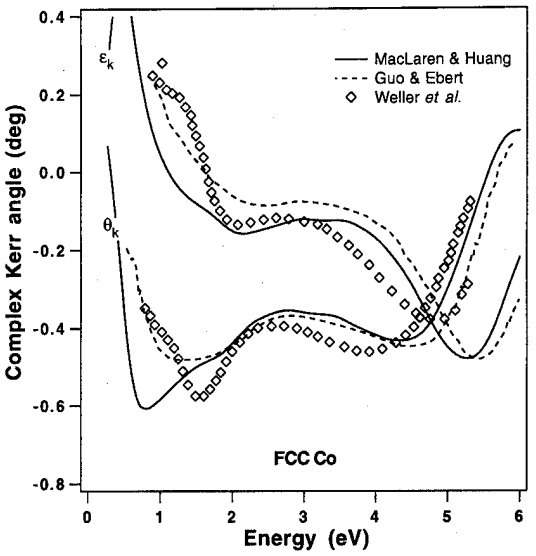



FIG. 2. Kerr angle and ellipticity for fcc Co. Theoretical data shown are as follows: solid line, this work, long dashed line (Ref. 6). Experimental data shown are open diamonds (Ref. 17).

The Bloch states $\psi_{\ell\sigma\mathbf{k}}(\mathbf{r})$ and energy eigenvalues $E_{\ell\sigma}(\mathbf{k})$ are found within the local spin-density approximation using a full potential linearized augmented Slater orbital method (FLASTO). This electronic structure method has been described in detail in other references.[9] Briefly, the method partitions space in muffin-tin spheres and an interstitial region. Within the muffin-tin spheres, the Bloch wave functions are expanded in linear combinations of $\phi$ and $\dot{\phi}$ ($\phi$ is a radial solution to the Schrödinger equation at a fixed energy and angular momentum, and $\dot{\phi}$ its energy derivative), while in the interstitial a linear combination of Slater-type orbitals is formed. In our calculations we used 25 Slater-type orbitals per atom. These were chosen to be the $4s$, $3p$, $3d$, $4f$, $4p$, $4d$, and $5s$ functions. This basis has sufficient variational freedom to yield answers in close agreement with the full-potential linearized augmented plane wave method,[10] but with a significantly smaller matrix size. The exponential decay constant were calculated using the formula given by Davenport.[9] A further benefit of this method is that the matrix elements can be evaluated over the unit cell exactly. In calculations which use the muffin-tin or atomic sphere approximations, the contribution to the matrix elements from the interstitial region is difficult to evaluate, and care must be taken in dealing with the integrals over this region. In the FLASTO approach, the wave function in the interstitial is completely described by its Fourier transform. The matrix elements of the gradient operator are easily evaluated between plane wave states for this region. Within the spheres, matrix elements of gradient operator can be derived from the theory of angular momentum.[11] Details about our technique will be the subject of a forthcoming article.[12] Once self-consistent electronic potentials have been obtained, the wave functions and eigenvalues in the presence of the spin-orbit interaction are formed by diagonalizing the Hamiltonian using the spin-orbitless wave functions as basis functions[13] (the so-called second variation method). Since the spin-orbit perturbation is small, the resulting solutions are sufficiently accurate for conductivity calculations. The spin-orbit interaction lowers the symmetry of the crystal, thus all inequivalent wedges of the Brillouin zone must be sampled.

The Kerr angle and ellipticity for bcc Fe is shown in Fig. 1. As can be seen from this figure, the predictions of the FLASTO calculations are in agreement with those of Oppeneer *et al.*[4,5] and with two experimental studies, one by Krinchik and Artem'ev[14] and the other by van Engen.[15] These calculations assumed the magnetization direction to be

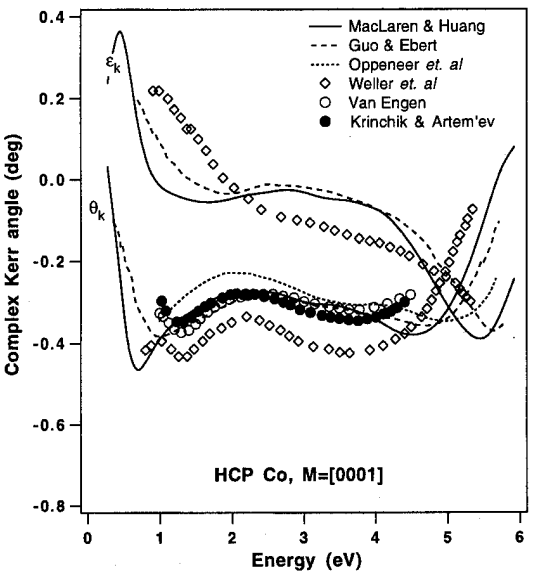



FIG. 3. Kerr angle and ellipticity for hcp Co with the magnetization along the [0001] direction. Theoretical data shown are as follows: solid line, this work, long dashed line (Ref. 6), dashed line *et al.* (Refs. 4 and 5). Experimental data shown are open diamonds (Ref. 17), open circles (Ref. 16), filled circles (Ref. 14).

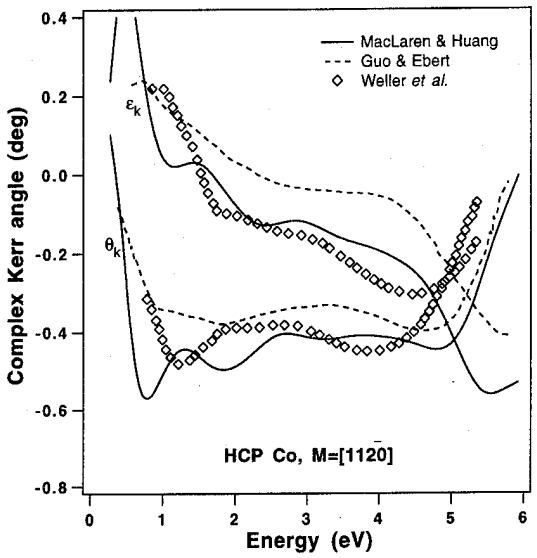



FIG. 4. Kerr angle and ellipticity for hcp Co with the magnetization along the [11$\bar{2}$0] direction. Theoretical data shown are as follows: solid line, this work, long dashed line (Ref. 6). Experimental data shown are open diamonds (Ref. 17).

along the [001] direction. The complex Kerr angle is found to be insensitive to magnetization direction, reflecting the cubic symmetry of the bcc lattice. The anisotropy of the Kerr spectra was discussed by Weller *et al.*[17] These authors concluded that in a cubic lattice the anisotropy in Kerr angle is fourth order in the strength of the spin-orbit coupling, while for an hcp crystal, because of the hexagonal symmetry, the anisotropy should be second order in the spin-orbit coupling strength. Figure 2 shows the Kerr angle and ellipticity for fcc cobalt. Agreement between Guo and Ebert's fully relativistic LMTO calculations,[6] the FLASTO results, and the experimental results for thin-film fcc Co[17] is pretty good. Figures 3 and 4 show the Kerr angle and ellipticity of hcp Co with the magnetization direction along the [0001] and [11$\bar{2}$0] directions, respectively. The anisotropy in the Kerr signal seen experimentally is reproduced in these and Guo and Ebert's calculations.[6] In the case where the magnetization lies along [0001], we see that the FLASTO spectra, and those calculated by Guo and Ebert, agree better with experimental data taken from bulk crystals[14,16] rather than the thin-film data of Weller *et al.*,[17] suggesting that there is some sensitivity to sample preparation. Also, these two calculations are somewhat closer to experiment than either those of Oppeneer *et al.*,[4,5] or those of Gasche.[18] The positions of the minima in the calculated ellipticity and Kerr angle are shifted slightly to higher energy, relecting errors associated with using wave functions obtained from a local spin-density band structure calculation to describe excited states.

In conclusion, we have calculated the Kerr angle and ellipticity for bcc iron, fcc cobalt, and hcp cobalt using the interband conductivity tensor computed from local spin-density band structure calculations. Our approach avoids some of the complications in evaluating matrix elements found in previous studies. The use of calculated ground state wave functions to describe excited states appears to be a good approximation in these metals, at least for energies less than about 6 eV. The level of agreement between theory and experiment is good enough to suggest that this type of calculation is suitable for making predictions of magneto-optical effects in other materials, and work on various Co/Pd and Co/Pt superlattices is in progress.

The authors would like to acknowledge the support of the Louisiana Quality Education Support Fund under Grant No. LEQSF (1991-94)-RD-A-30, the Center for Photoinduced Processes (funded under an NSF EPSCoR Program), and the Eastman Kodak Company.

[1] K. H. J. Buschow, in *Ferromagnetic Materials*, edited by E. P. Wohlfarth and K. H. J. Buschow (North-Holland, Amsterdam, 1988), Vol. 4, p. 493.
[2] W. Reim and J. Schoenes, in *Ferromagnetic Materials*, edited by E. P. Wohlfarth and K. H. J. Buschow (North-Holland, Amsterdam, 1990), Vol. 5, p. 133.
[3] W. B. Zeper, F. J. A. M. Greidanus, and P. F. Carcia, IEEE Trans. Magn. **MAG-25**, 3764 (1989); S. Hashimoto, Y. Ochiai, and K. Aso, J. Appl. Phys. **67**, 2136 (1990); G. A. Bertero and R. Sinclair, Appl. Phys. Lett. **64**, 3997 (1994).
[4] P. M. Oppeneer, T. Maurer, J. Sticht, and J. Kübler, Phys. Rev. B **45**, 10924 (1992).
[5] P. M. Oppeneer, J. Sticht, T. Maurer, and J. Kübler, Z. Phys. B **88**, 309 (1992).
[6] G. Y. Guo and H. Ebert, Phys. Rev. B **50**, 10377 (1994).
[7] C. S. Wang and J. Callaway, Phys. Rev. B **9**, 4897 (1974).
[8] A. P. Lenham and D. M. Treherne, in *Optical Properties and Electronic Structure of Metals and Alloys*, edited F. Abelès (North-Holland, Amsterdam, 1966), p. 196.
[9] J. W. Davenport, Phys. Rev. B **29**, 2896 (1984); G. W. Fernando, J. W. Davenport, R. E. Watson, and M. Weinert, Phys. Rev. B **40**, 2757 (1989).
[10] J. He (private communication).
[11] M. E. Rose, *Elementary Theory of Angular Momentum* (Wiley, New York, 1957).
[12] J. M. MacLaren, W. Huang, and R. H. Victoria (unpublished).
[13] D. J. Singh, *Planewave, Pseudopotentials and the LAPW Method* (Kluwer, Boston, 1994), p. 86.
[14] G. S. Krinchik and V. A. Artem'ev, Sov. Phys. JETP **26**, 1080 (1968).
[15] P. G. van Engen, Ph.D thesis, Technical University Delft, 1983; and reproduced in Ref. 1.
[16] P. G. van Engen, K. H. J. Buschow, and M. Erman, J. Magn. Magn. Mater. **30**, 374 (1983); and reproduced in Ref. 1.
[17] D. Weller, G. R. Harp, R. F. C. Farrow, A. Cebollada, and J. Sticht, Phys. Rev. Lett. **72**, 2097 (1994).
[18] T. Gasche, Ph.D. thesis, Uppsula University, 1994.

# First principles calculations of the Kerr effect in MnBi, MnSb, and $Mn_2BiSb$ (abstract)

W. Huang and J. M. MacLaren
*Department of Physics, Tulane University, New Orleans, Louisiana 70118*

R. H. Victora
*Eastman Kodak Company, Rochester, New York 14650-2017*

First principles electronic structure calculations are used to predict the energy dependence of the polar Kerr effect in MnBi, MnSb, and a $Mn_2BiSb$ alloy. The compounds all have respectable Kerr angles and thus are potential data storage media. The technique used in this work is a full-potential linearized augmented Slater orbital approach. The Kerr angle is obtained from the conductivity tensor that is calculated, within linear response theory, using the Kubo formula. There are several desirable features in this approach. First, unlike methods based upon muffin-tin potentials, open crystal structures present no problems. Second, since the electronic wave functions are defined over the crystal unit cell rather than over space filling overlapping spheres, difficulties in handling the interstitial part of the required matrix elements are avoided. Finally, the small basis set (25 orbitals per atom) leads to reasonable computational times. Results of these calculations show that the Kerr angle in MnBi is above 1° at 1.6 eV and that its variation over 2–4 eV is linear and decreasing. MnSb shows a smaller rotation, about 0.5°, that is almost constant up to 3 eV and then also decreases linearly. The Kerr rotation of $Mn_2BiSb$ is approximately the average of MnBi and MnSb.
This work has been supported in part by the Louisiana Quality Education Support Fund under Grant No. LEQSF (1991–1994)-RD-A-30. © *1996 American Institute of Physics.*
[S0021-8979(96)48108-5]

# Dielectric tensor characterization of $Mn_{0.53}Bi_{0.47}$ and $Mn_{0.52}Bi_{0.44}Sb_{0.04}$ films

Z. Celinski[a] and Zheng Yan
*Optical Sciences Center, University of Arizona, Tucson, Arizona 85721*

We have grown $Mn_{0.53}Bi_{0.47}$ and $Mn_{0.52}Bi_{0.44}Sb_{0.04}$ alloy films on glass substrates under UHV conditions. These films exhibit good magneto-optical (MO) properties. Unfortunately, the measurements of Kerr rotation and ellipticity cannot by themselves provide reliable evaluation of the MO properties of a layer capped with a dielectric SiO film. The purpose of the present work was to determine the dielectric tensor in the $MnBi_{1-x}Sb_x$ films within a multilayer stack, using a combination of ellipsometric, reflection/transmission, and polar MO Kerr effect measurements in the wavelength range of 360–860 nm. We have evaluated the $Mn_{0.53}Bi_{0.47}$ and $Mn_{0.52}Bi_{0.44}Sb_{0.04}$ films based on the intrinsic MO figure of merit (FOM) defined by $\mathrm{FOM}=|\epsilon_{xy}|/(2\ \mathrm{Im}\ \epsilon_{xx})$, where $\epsilon_{xy}$ and $\epsilon_{xx}$ are the diagonal and off-diagonal elements of the dielectric tensor of the MO material. For short wavelengths (360–550 nm) the measured FOM in the $Mn_{0.53}Bi_{0.47}$ and $Mn_{0.52}Bi_{0.44}Sb_{0.04}$ films is significantly larger (≥factor of 2) than that commonly observed in TbFeCo films (~0.01).
© *1996 American Institute of Physics.* [S0021-8979(96)13508-5]

For quite some time, MnBi films have attracted considerable attention as a possible high-density magneto-optical (MO) media.[1] The large Kerr rotation and perpendicular anisotropy have maintained the interest in this material among physicists despite its severe problem, lack of thermodynamical stability. Two phases of MnBi exist, a low-temperature phase (LTP) and high-temperature phase (HTP), which exhibit different MO response. During thermomagnetic writing the HTP phase is quenched and causes a rapid reduction of MO signal. One of the approaches to stabilize the low-temperature phase of MnBi, a phase which exhibits very good MO response, was to substitute a fraction of the Bi atoms with Sb atoms.[2–4]

The aim of the present article is to determine the diagonal and off-diagonal elements of the dielectric tensor for the $Mn_{0.53}Bi_{0.47}$ and $Mn_{0.52}Bi_{0.44}Sb_{0.04}$ films and evaluate the figure of merit (FOM) of these MO layers. To determine the elements of the dielectric tensor of a MO film one must measure thickness and optical constants for all the layers within the structure. To do this, we have performed ellipsometric, reflectance, and polar MO Kerr effect measurements, and analyzed the data using the MULTILAYER computer program. Detailed descriptions of apparatus, measurement procedures, and the computer program can be found in the article by Hong Fu *et al.*[5]

To evaluate the performance of any MO media one should use parameters which do not depend upon the geometry of the studied structures. The intrinsic FOM, introduced for the first time by Mansuripur,[6] provides the best way to compare different media. The FOM, which is solely determined by the dielectric tensor of the MO material, is given by

$$\mathrm{FOM}=\frac{|\epsilon_{xy}|}{2\ \mathrm{Im}\ \epsilon_{xx}}.$$

Frequently, the off-diagonal reflectivity, $r_{xy}$, has been used in the literature to describe the efficiency of a sample in rotating polarization. The incident, linearly polarized beam has only an $x$ component and the reflected beam has both $x$ and $y$ components. The absolute value of the off-diagonal reflectivity is defined by ratio $|E_y^{\mathrm{ref}}/E_x^{\mathrm{inc}}|$, where $E_y^{\mathrm{ref}}$ and $E_x^{\mathrm{inc}}$ are the $E$-field amplitudes of the $y$ component of the reflected light and the $x$ component of the incident light, respectively. The measurements of Kerr rotation $\Theta_k$, ellipticity $\epsilon_k$, and total reflectivity $\mathbf{R}$ can be used to calculate the absolute value of the off-diagonal reflectivity from the following formula:[7]

$$|\mathbf{r}_{xy}|=\sqrt{R(\Theta_k^2+\epsilon_k^2)}.$$

Since values of $\Theta_k$, $\epsilon_k$, and $\mathbf{R}$ strongly depend on the thicknesses of the layers in the studied structure, the value of $|\mathbf{r}_{xy}|$ for the same MO layer may vary significantly. It can be shown,[6] however, that $|\mathbf{r}_{xy}|$ is upper bounded by the FOM. In addition, it is possible to design a structure for which $|\mathbf{r}_{xy}|$ approaches the FOM of the MO material. For these reasons, we will quote both $|\mathbf{r}_{xy}|$ and FOM in our article.

We grew our samples on glass (Corning 7059) substrates under UHV conditions. Sample preparation and systematic studies of the structural, magnetic, and magneto-optical properties of the $MnBi_{1-x}Sb_x$ films have been recently reported elsewhere by Celinski *et al.*[4] The substitution of Bi atoms by Sb does not improve the thermal stability of these MnBi based layers. To avoid ambiguities during analysis of optical measurement data we also grew a single layer of SiO on glass and determined its optical constants independently.

Utilizing a multiwavelength variable-angle ellipsometer we measured the polarization rotation and ellipticity as a function of incident angle $\Theta_{\mathrm{inc}}$ for linearly polarized light with wavelengths $\lambda$ within the range 360–860 nm. The measurements of total reflectance $R$, $\Theta_k$, and $\epsilon_k$ at normal incidence were carried out on a MO Kerr spectrometer. All measurements were taken from the film side. The thickness and diagonal elements $\epsilon_{xx}$ of the various layers were determined by using the ellipsometric and total reflectance $R$ data. Off-diagonal elements, $\epsilon_{xy}$, were determined by using Kerr effect and ellipsometric data.

[a]Present address: Department of Physics, University of Colorado at Colorado Springs, Colorado Springs, CO 80933-7150.

 0021-8979/96/79(8)/6200/3/$10.00 © 1996 American Institute of Physics

TABLE I. The calculated values of diagonal and off-diagonal elements of the dielectric tensor for the $Mn_{0.53}Bi_{0.47}$ and $Mn_{0.52}Bi_{0.44}Sb_{0.04}$ samples. Then $n$ and $k$ values for the SiO layers are presented for the film grown on top of the $Mn_{0.53}Bi_{0.47}$ layer.

| Wavelength (nm) | $Mn_{0.53}Bi_{0.47}$ | | $Mn_{0.52}Bi_{0.44}Sb_{0.04}$ | | SiO | |
|---|---|---|---|---|---|---|
| | $\epsilon_{xx}$ | $\epsilon_{xy}$ | $\epsilon_{xx}$ | $\epsilon_{xy}$ | $n$ | $k$ |
| 360 | $0.01+i2.65$ | $-0.04-i0.09$ | $-1.80+i4.03$ | $-0.09-i0.19$ | 1.735 | 0.109 |
| 400 | $-0.10+i3.19$ | $-0.07-i0.09$ | $-0.84+i4.22$ | $-0.10-i0.11$ | 1.712 | 0.053 |
| 450 | $-0.58+i4.03$ | $-0.09-i0.10$ | $-0.16+i4.71$ | $-0.13-i0.08$ | 1.694 | 0.025 |
| 500 | $-0.86+i5.97$ | $-0.15-i0.12$ | $-0.19+i6.21$ | $-0.18-i0.09$ | 1.719 | 0.014 |
| 550 | $-1.37+i7.53$ | $-0.23-i0.14$ | $-1.26+i7.66$ | $-0.29-i0.12$ | 1.746 | 0.013 |
| 600 | $-2.12+i9.52$ | $-0.34-i0.13$ | $-2.70+i6.71$ | $-0.30-i0.13$ | 1.788 | 0.010 |
| 633 | $-2.75+i10.6$ | $-0.40-i0.11$ | $-4.00+i10.5$ | $-0.54-i0.12$ | 1.805 | 0.007 |
| 650 | $-2.61+i10.9$ | $-0.44-i0.07$ | $-3.19+i10.9$ | $-0.58-i0.03$ | 1.807 | 0.0 |
| 700 | $-4.09+i12.2$ | $-0.57-i0.06$ | $-3.81+i12.2$ | $-0.70+i0.12$ | 1.815 | 0.0 |
| 750 | $-0.89+i16.5$ | $-0.74+i0.35$ | $-5.01+i13.2$ | $-0.843+i0.22$ | 1.835 | 0.0 |
| 780 | $0.48+i16.0$ | $-0.67+i0.52$ | $-5.30+i14.5$ | $-0.92+i0.34$ | 1.814 | 0.0 |
| 820 | $1.38+i15.9$ | $-0.55+i0.63$ | $-1.51+i13.6$ | $-0.61+i0.65$ | 1.827 | 0.0 |
| 840 | $3.71+i17.5$ | $-0.55+i0.96$ | | | 1.830 | 0.0 |
| 860 | $3.91+i17.1$ | $-0.46+i1.02$ | | | 1.835 | 0.0 |

Table I shows results of our analysis of the dielectric tensor elements for both MO layers, $Mn_{0.53}Bi_{0.47}$ and $Mn_{0.52}Bi_{0.44}Sb_{0.04}$. We estimated that the error associated with our analysis does not exceed 5%. The quality of our analysis can be assessed by analyzing Fig. 1 which shows a typical set of ellipsometric data. The open and solid symbols represent rotation and ellipticity, respectively, as a function of incident angle for 400 nm wavelength. The solid lines depict the best theoretical fit to this data. In order to obtain such a good fit at short wavelengths values of $n$ and $k$ for the SiO layer had to be slightly modified from those obtained for a SiO layer grown on glass. Table I also contains the $n$ and $k$ values for the SiO layer grown on top of $Mn_{0.53}Bi_{0.47}$ film.

From our measurements we determined that the $Mn_{0.53}Bi_{0.47}$ film was 70 nm thick and the SiO layer was 65 nm thick. These results are in good agreement with values obtained from the thickness monitor during deposition. The Kerr hysteresis loops are fairly squared with a coercive field of 840 Oe (see inset in Fig. 2). Figure 2 shows the wavelength dependence of the Kerr rotation and ellipticity. The observed extrema in $\Theta_k$ and $\epsilon_k$, at 600 nm, are related to the interference effect due to the SiO overcoating. As expected, we observed a significant decrease in total reflectivity $R$ at this wavelength. For a wavelength of 400 nm, far from the interference condition, the Kerr rotation and ellipticity still have significantly high values, 0.9° and 0.35°, respectively, indicating good MO response at short wavelength. Figure 3 shows the wavelength dependence of $n$ and $k$ for $Mn_{0.53}Bi_{0.47}$ film. The lines were added to guide the reader's eye. Our values of $n$ and $k$ are comparable with those previously reported in the literature.[5] Figure 4 shows the calculated FOM and off diagonal reflectivity, $\mathbf{r}_{xy}$, as a function of the wavelength for $Mn_{0.53}Bi_{0.47}$ film. Determined values of FOM are smaller than those previously reported.[5] This indicates that measured parameters, such as FOM, are not universal for a given compound but strongly depend on the growth conditions, procedure, and small changes in stoichiometry for the MnBi based compounds.

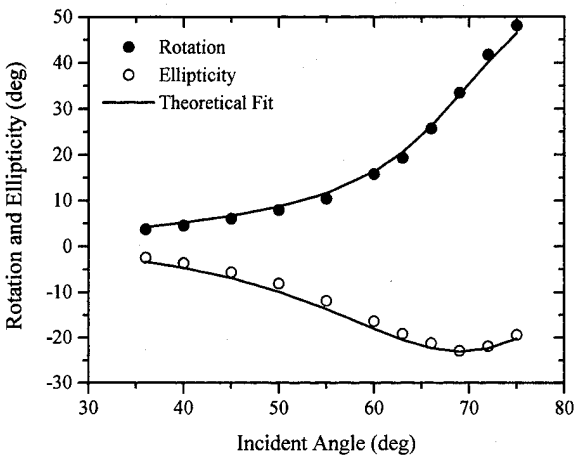



FIG. 1. Measured rotation and ellipticity, open and solid circles, respectively, as a function of incident angle $\Theta_{inc}$ at 400 nm wavelength for the $Mn_{0.53}Bi_{0.47}$ sample. The solid lines represent the best fit.

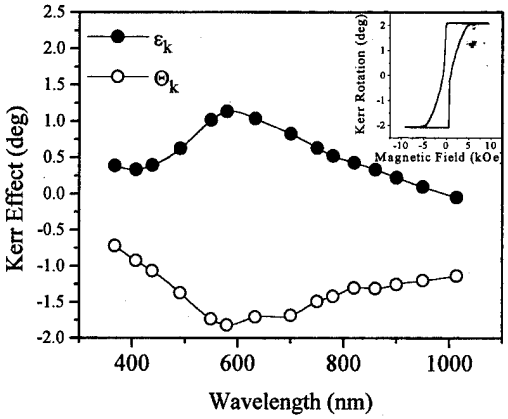



FIG. 2. Measured Kerr rotation $\Theta_k$ and ellipticity $\epsilon_k$, open and solid circles, respectively, as a function of wavelength for the $Mn_{0.53}Bi_{0.47}$ sample. The solid lines were added to guide the reader's eye. Measurements were performed from the film side.

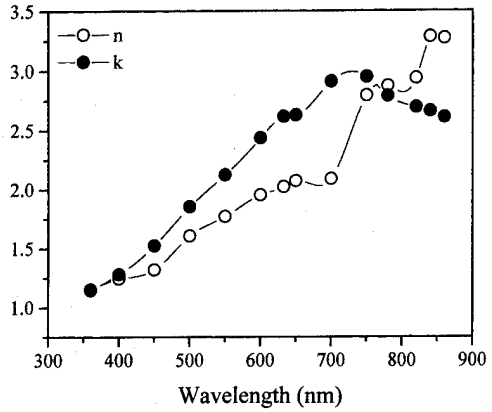



FIG. 3. The best estimate values of $n$ and $k$ as a function of wavelength for the $Mn_{0.53}Bi_{0.47}$ sample.

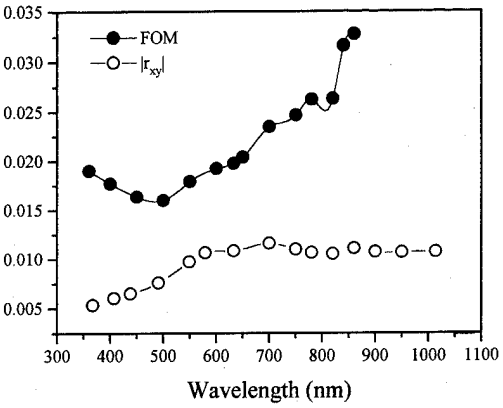



FIG. 4. Measured $|r_{xy}|$ (solid symbols) and the computed FOM (open symbols) for the $Mn_{0.53}Bi_{0.47}$ sample as a function of wavelength.

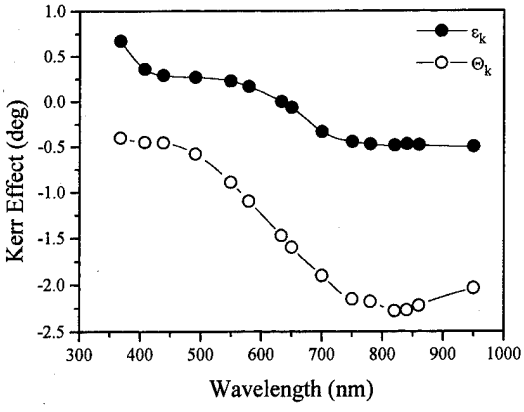



FIG. 5. Measured Kerr rotation $\Theta_k$ and ellipticity $\epsilon_k$, open and solid circles, respectively, as a function of wavelength for the $Mn_{0.52}Bi_{0.44}Sb_{0.04}$ sample. The solid lines were added to guide the reader's eye. Measurements were performed from the film side.

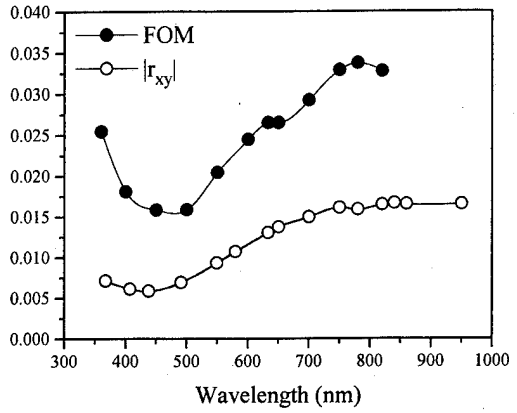



FIG. 6. Measured $|r_{xy}|$ (solid symbols) and the computed FOM (open symbols) for the $Mn_{0.52}Bi_{0.44}Sb_{0.04}$ sample as a function of wavelength.

Our $Mn_{0.52}Bi_{0.44}Sb_{0.04}$ film was also 70 nm thick, capped with a 95 nm SiO layer. The Kerr hysteresis loops are fairly square with a coercive field of 3 kOe. Figure 5 shows the wavelength dependence of $\Theta_k$, and $\epsilon_k$. The observed extreme in Kerr rotation at 800 nm is again related to the interference effect due to SiO overcoating (the total reflectivity also shows a broad minimum at this wavelength). At short wavelengths, the measured values of the Kerr rotation and ellipticity, $-0.4°$ and $0.67°$, respectively, indicate again a good MO response in this material. The determined values of $n$ and $k$ for the $Mn_{0.52}Bi_{0.44}Sb_{0.04}$ film are very similar to that observed for $Mn_{0.53}Bi_{0.47}$ film. This indicates that the presence of Sb atoms does not modify the values of $n$ and $k$. Figure 6 shows the FOM as a function of wavelength for the $Mn_{0.52}Bi_{0.44}Sb_{0.04}$ film. Only for a narrow range, between 400 to 500 nm, the determined values of FOM are equal to those determined for $Mn_{0.53}Bi_{0.47}$. For all other wavelengths the values of FOM are 25% larger than these determined for $Mn_{0.53}Bi_{0.47}$. At 360 nm, the FOM for $Mn_{0.52}Bi_{0.44}Sb_{0.04}$ is equal to 0.025, more than twice the value observed for TbFeCo, which is currently used for MO recording. This would make our films a good candidate for future MO data storage medium if the thermodynamic stability problem could be solved in MnBi based layers.

This work was performed in collaboration with Brad N. Engel, Charles M. Falco, and supported by NSIC/ARPA Contract No. MDA 972-93-1-0009. The authors would like to thank M. Mansuripur for helpful discussions.

[1] D. Chen, J. F. Ready, and E. Bernal, J. Appl. Phys. **39**, 3916 (1968).
[2] M. Takahashi, Y. Kikuchi, and T. Wakiyama, IEEE Trans. J. Magn. Jpn. **4**, 673 (1989); M. Takahashi, Y. Kikuchi, T. Tanaka, and T. Wakiyama, *ibid.* **5**, 998 (1990).
[3] Y. J. Wang, J. X. Shen, and Q. Tang, J. Magn. Magn. Mater. **74**, 365 (1988).
[4] Z. Celinski, Dino Pardo, Brad N. Engel, and Charles M. Falco, IEEE Trans. Magn. **31**, 3233 (1995).
[5] Hong Fu, Zheng Yan, Seh Kwang Lee, and M. Mansuripur, J. Appl. Phys. **78**, 4076 (1995).
[6] M. Mansuripur, Appl. Phys. Lett. **49**, 19 (1986).
[7] M. Mansuripur, *The Physical Principles of the Magnet-Optical Recording* (Cambridge University Press, Cambridge, 1995), p. 206.
[8] A. F. Anderson, J. E. Engebretsen, and J. Refsnes, Acta Chem. Scand. **26**, 175 (1972).

# Influence of Al capping layers on growth, topography, and magnetic properties on MnBi thin films

U. Rüdiger, P. Fumagalli, P. Dworak, A. Schirmeisen, and G. Güntherodt
*Physikalisches Institut, RWTH Aachen, D-52056 Aachen, Germany*

Bi/Mn bilayers have been deposited on fused-quartz substrates at room temperature and annealed at elevated temperatures of 300–380 °C. To investigate the influence of capping layers on MnBi crystallite size and magnetic properties, some of the Bi/Mn bilayers were protected by Al and $SiO_x$ layers. The coercive fields of the resulting MnBi films without a protective layer reach values of up to 1.25 T. In case of depositing an Al capping layers prior to annealing, the coercive fields are decreasing strongly showing coercive fields in the range of 0.6 T. In contrast, using $SiO_x$ as a capping layer, the Kerr hysteresis loops show a nonlinearity near the coercive field indicating an inhomogeneous film. The change in the coercive field is explained by the influence of capping layers on the MnBi crystallite size during annealing. © *1996 American Institute of Physics.* [S0021-8979(96)28208-9]

## INTRODUCTION

As demonstrated in previous work, the crystallite size of MnBi films depends on film thickness, i.e., the number $x$ of deposited $(Bi/Mn)_x$ bilayers.[1] An increasing number of Bi/Mn sequences is accompanied by an increase in MnBi crystallite size after annealing. The preparation of MnBi films deposited without any protective layer on the Bi/Mn sequences causes smaller particle size as compared to films with an $SiO_x$ capping layer[2,3] since the growth of single MnBi particles is not restricted in the direction perpendicular to the surface. Due to the small crystallite size unusual high coercive fields, $H_c$, of values up to 1.25 T were measured. In case of single domain particles $H_c$ achieves high values limited only by the intrinsic anisotropy energy.[4] As the number of Bi/Mn bilayers increases from one to three the reflectivity of the resulting MnBi films decreases from 42% down to 5%.[1] In order to reduce the MnBi crystallite size in thicker films, Bi/Mn bilayers were separated by an Al interlayer from each other.[5] Due to the Al interlayer the reflectivity of MnBi films consisting of two Bi/Mn bilayers could be maintained at 38%.[5] By separating two Bi/Mn bilayers with an Al interlayer, polar Kerr hysteresis-loop measurements show a superposition of two hysteresis loops with different coercive fields. The presence of two different coercive fields could be explained by different granularities of the top and the bottom layer.[5] In this work, we study the influence of Al or $SiO_x$ capping layers on growth and magnetic properties of a single Mn/Bi bilayer.

## EXPERIMENTAL METHODS

The preparation of MnBi thin films was performed according to the method described elsewhere.[1,5,6] By thermal evaporation of Bi and Mn using $Al_2O_3$ crucibles Bi/Mn bilayers have been deposited on clean fused-quartz substrates at room temperature. In order to get MnBi films close to the optimum stoichiometry of $Mn_{55}Bi_{45}$ as reported by Di *et al.*,[7] the thickness of the Bi and Mn layer is adjusted to a constant value of 18 nm and 12 nm, respectively. A 2 nm thick Al capping layer is deposited in the same way as the Bi and Mn layers whereas a 50 nm $SiO_x$ capping layer is deposited by electron-beam evaporation of SiO crystals using a Leybold ESV2. The vacuum during deposition varied between $8\times10^{-7}$ mbar and $5\times10^{-6}$ mbar. Film thickness and deposition rate were controlled by an Inficon thickness monitor. In order to obtain $c$ axis oriented MnBi films after annealing, the Bi-deposition rate has to be lower than 0.4 nm/s. In contrast, the Mn-deposition rate is five times larger. The Bi/Mn and Bi/Mn/capping-layer sandwiches were annealed *ex situ* in a quartz tube for 60 min at a temperature of 300 °C and for 30 min at a temperature of 380 °C followed by a 30 min annealing step at lower temperature down to 300 °C, respectively. The films were characterized by x-ray diffraction analysis (XRD), scanning electron microscopy (SEM) and energy-dispersive x-ray analysis (EDX). The coercive field, $H_c$, was determined by polar Kerr hysteresis-loop measurements at a photon energy of 2.0 eV at room temperature.[1,5]

## RESULTS AND DISCUSSION

### Preparation and characterization

To control the $c$-axis orientation of the Bi layer before and the quality of the alloying process of the MnBi films after annealing x-ray measurements have been carried out. Figure 1(a) shows clearly the Bi(000$l$) peaks, which demonstrate that a Bi layer is highly textured with $c$ axis perpendicular to the film surface, a condition necessary for maintaining the same orientation after annealing.[8] Peaks due to the substrate holder, made of brass, are labeled with an asterisk. Figures 1(b)–1(d) show x-ray pattern after annealing of MnBi films without a protective capping layer, with an Al and a $SiO_x$ capping layer, respectively. The x-ray pattern of MnBi films without and with an Al capping layer are dominated only by the MnBi(000$l$) peaks [see Figs. 1(b) and 1(c)]. The MnBi films exhibit NiAs-type structure. The formation of an additional MnAl $\tau$ phase as reported by Shen can be excluded.[9] In case of depositing a $SiO_x$ protective layer, $Mn_3O_4(h00)$ peaks appear which have intensities of same order of magnitude as the MnBi(000$l$) peaks [see Fig. 1(d)]. The exclusive presence of $Mn_3O_4(h00)$ peaks indicates an $a$-axis orientation of the oxide layer. At room temperature $Mn_3O_4$ exhibits a distorted spinel structure.[10,11]

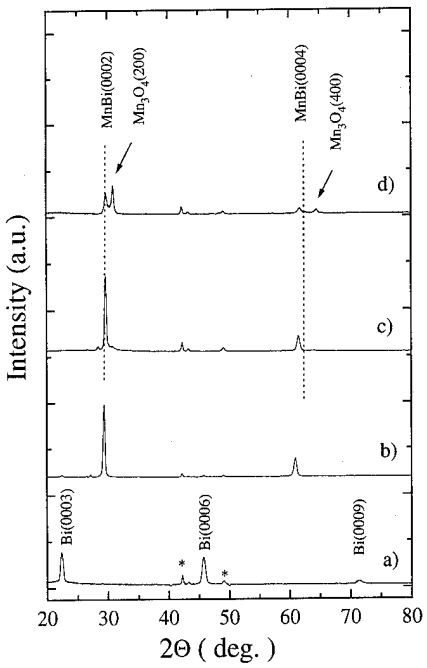



FIG. 1. X-ray analysis of MnBi films (a) before annealing and after annealing, (b) without a capping layer, (c) with an Al capping layer, and (d) with a $SiO_x$ capping layer.

Figures 2(a) and 2(b) show MnBi films after annealing without a protective layer and with an Al capping layer of 2.0 nm thickness, respectively. The topography of the MnBi film with an Al capping layer is smoother than without. The 2.0 nm Al layer covers the MnBi film completely. Nevertheless, it cannot be excluded that a part of the Al diffuse into the bottom MnBi layer during annealing.[5]

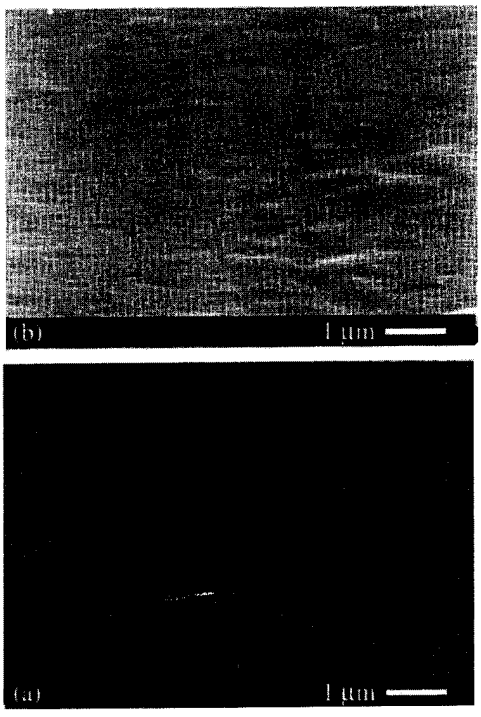



FIG. 2. Topography after annealing of MnBi films (a) without a capping layer, and (b) with an Al capping layer.

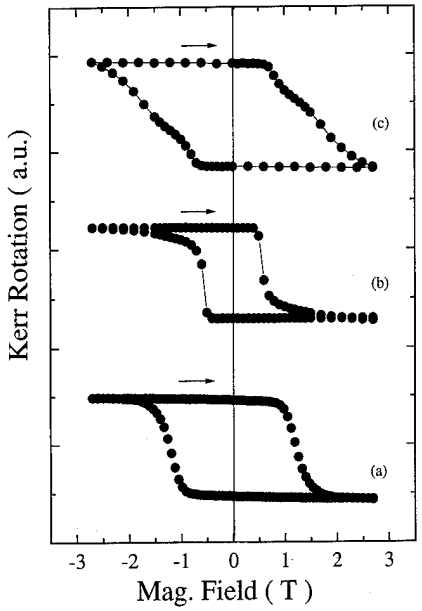



FIG. 3. Polar Kerr hysteresis loops of MnBi films (a) without a capping layer, (b) with an Al capping layer, and (c) with a $SiO_x$ capping layer.

## Magnetic properties

For single domain particles, the coercive field, $H_c$, is limited only by the intrinsic anisotropy energy and decreases linearly as the diameter $d$ of the single domain particles increases.[4] To investigate the influence of different capping layers on crystallite size and hence on the coercive field, polar Kerr hysteresis measurements have been carried out. Hysteresis loops of MnBi films (a) without a capping layer, (b) with an Al capping layer, and (c) with a $SiO_x$ protective layer are plotted in Fig. 3. By covering MnBi films with a 2.0 nm Al capping layer, the coercive field is decreasing from 1.25 T to a value of only 0.6 T. This is in agreement with our previous analysis of Kerr hysteresis loops in MnBi/Al/MnBi multilayers.[5] The preparation of MnBi films with no protective layers on the Bi/Mn sequence causes a smaller particle size since the growth is not restricted in direction perpendicular to the substrate surface which reduces the lateral expansion of the crystallites.[5] In contrast, an Al capping layer reduces the growth perpendicular to the substrate surface which supports the lateral expansion of MnBi crystallites. The influence of an Al capping layer on the MnBi formation process is demonstrated in Figs. 4(a) and 4(b) schematically.

The effect of a $SiO_x$ layer [Fig. 3(c)] is in apparent contradiction with previous literature.[2,3] At a field of 0.7 T, the reversal of magnetization starts but proceeds slowly with increasing field leading to coercive fields of up to 1.5 T. The shape of the hysteresis loop differs from square hysteresis loops of MnBi films without and with an Al capping layer shown in Figs. 3(a) and 3(b), respectively.

An explanation of the unusual hysteresis loops takes into account the close distance (≈20 cm) of the electron beam evaporator to the substrate holder. As a consequence, the

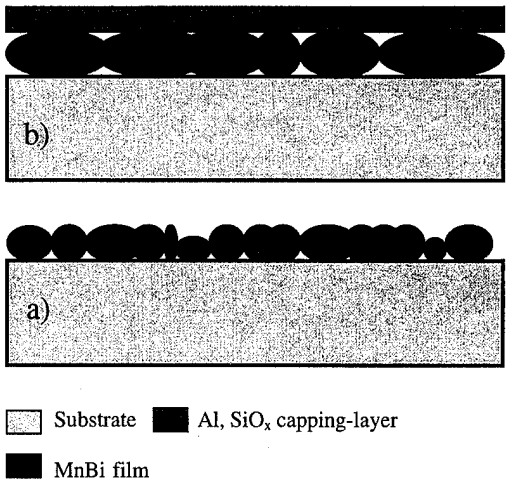



FIG. 4. Model of an annealed MnBi film, originating from a MnBi film (a) without a capping layer, and (b) with an Al or $SiO_x$ capping layer.

$SiO_x$ molecules may impinge onto the substrate at high kinetic energies. This might lead to a very rough Mn/$SiO_x$ interface. After annealing the MnBi crystallite size might be considerably smaller in the interface region due to penetrated $SiO_x$ molecules leading to local regions with increased coercive field.

## CONCLUSION

The influence of Al and $SiO_x$ capping layers on the crystallite size and on the coercive field of MnBi thin films has been investigated. An Al overlayer leads to a pronounced decrease in coercivity from 1.25 T down to 0.6 T. This is explained by a restricted perpendicular growth in conjunction with an extended lateral expansion of MnBi crystallites during annealing. Using $SiO_x$ as a protective layer, leads to unusual Kerr hysteresis loops showing a nonlinear magnetization reversal in contrast to literature. This discrepancy is tentatively explained by the close proximity of the SiO target to the substrate holder. The SiO molecules impinge at high kinetic energies onto the substrate, yielding a very rough Mn/SiO interface influencing locally the MnBi formation process. As a result, local regions may form with smaller grain size and, therefore, increased coercivity.

## ACKNOWLEDGMENTS

The authors wish to thank J. Auge for performing scanning electron microscopy of the samples. This work was supported by the German Federal Ministry of Education and Research 'BMBF' under Grant No. FKZ 13N6178/2.

[1] U. Rüdiger, H. Berndt, A. Schirmeisen, P. Fumagalli, and G. Güntherodt, J. Appl. Phys. **78**, 5391 (1995).
[2] Y. J. Wang, J. Magn. Magn. Mater. **84**, 39 (1990).
[3] C. H. Shang, D. Huang, H. L. Luo, Y. J. Wang, and L. C. König, J. Appl. Phys. **73**, 6118 (1993).
[4] C. Kittel, Phys. Rev. **73**, 810 (1948).
[5] U. Rüdiger, P. Fumagalli, H. Berndt, A. Schirmeisen, and G. Güntherodt, J. Appl. Phys. (to be published).
[6] M. Nakada and M. Okada, IEEE Trans. Mag. **30**, 4431 (1994).
[7] G. Q. Di, S. Iwata, and S. Uchiyama, J. Magn. Magn. Mater. **131**, 242 (1994).
[8] D. Chen, G. N. Otto, and F. M. Schmit, IEEE Trans. Magn., **MAG-9**, 66 (1973).
[9] J. X. Shen and R. D. Sellmeyer, J. Magn. Magn. Mater. **81**, 107 (1989).
[10] Landolt-Börnstein Tables, *Magnetic Properties I* (Springer, Berlin, 1962).
[11] E. P. Wohlfarth, *Ferromagnetic Materials, Vol. 3* (North-Holland, Amsterdam, 1987).

# Magnetic and magneto-optical properties of $Mn_xPt_{1-x-y}Zn_y$

Kurt W. Wierman and Roger D. Kirby
*Behlen Laboratory of Physics and Center for Materials Research and Analysis, University of Nebraska, Lincoln, Nebraska 68588-0113*

In this work we have prepared thin films of the ternary alloy $Mn_xPt_{1-x-y}Zn_y$ by magnetron sputtering onto quartz substrates. We have found a wide range of compositions which are strongly ferromagnetic at room temperature. A transition from a cubic to tetragonal phase with decreasing Pt content is confirmed by x-ray diffraction. X-ray diffraction measurements also show a strong (001) reflection consistent with long range order along the $c$ axis for the tetragonal phase. These films show large complex Kerr rotations (up to 0.7°) in the visible spectrum. This combined with their anisotropic structure suggests that they may be suitable for magneto-optic data storage applications.
© *1996 American Institute of Physics.* [S0021-8979(96)16708-3]

## INTRODUCTION

The ordered alloys of $M_xPt_{1-x}$ (M=Cr,Mn,Fe,Ni,Co) have received considerable attention because of their interesting magnetic and magneto-optic properties.[1–5] For $x=0.25$ these alloys form the $L1_2$ ($Cu_3Au$) cubic structure where the magnetic atoms occupy the cube corners and the Pt atoms the face-centered sites. As $x$ increases from 0.25 there is a continuous change in lattice parameters and by $x=0.5$ the alloys develop the $L1_0$ (CuAu) tetragonal structure with alternating layers of M and Pt atoms along the (001) direction. This appears to result from the geometrical requirements of ordered packing of Pt and M atoms of different sizes and not from electron concentration or Brillouin zone effects, as discussed by Brun *et al.* for M=Mn.[2] $Mn_xPt_{1-x}$ alloys are known to undergo a transition from the cubic to a tetragonal structure for $x>0.38$; unfortunately, the increased number of antiferromagnetic Mn-Mn nearest-neighbor interactions induces a complex noncollinear magnetic structure.[6,7] Kato *et al.*[8] initially observed large Kerr rotation and ellipticity in thin films of $MnPt_3$, but hysteresis loops showed an in-plane anisotropy concordant with its cubic structure. Our goal was to substitute a third nonmagnetic element into the Mn-Pt alloy to develop a ferromagnetic tetragonal structure. Thus, in this study ferromagnetic ternary alloys of $Mn_xPt_{1-x-y}Zn_y$ were produced over a wide composition range ($x=0.17$–$0.29$, $y=0.00$–$0.13$), and their magnetic and magneto-optic properties were studied.

## EXPERIMENT

Mn/(Pt-Zn) multilayers were prepared by dc magnetron sputtering onto room-temperature fused quartz substrates. The base pressure of the sputtering chamber was $4\times10^{-7}$ Torr and the argon sputtering pressure was 2 mTorr. For the series of samples discussed here Pt and Zn were co-sputtered with a layer thickness held constant at 7 Å, while the Mn layer thickness was varied from 3 to 5 Å to obtain the desired $Mn_xPt_{1-x-y}Zn_y$ composition ratios. The compositions of the as-deposited films were measured using x-ray fluorescence and found to be close to the nominal compositions. The total film thickness of each sample was 100 nm and each film was coated with a 100-nm-thick $SiO_x$ protective overcoat. The as-deposited samples were subsequently annealed in vacuum ($6\times10^{-6}$ Torr) at 850 °C for 1 h to form the homogeneous crystalline $Mn_xPt_{1-x-y}Zn_y$ alloy.

The saturation magnetization $M_s$ and coercivity $H_c$ of the $Mn_xPt_{1-x-y}Zn_y$ films were measured at 300 K using an alternating gradient force magnetometer. The polar Kerr rotation and ellipticity spectra were measured in a 10 kOe applied field perpendicular to the film plane using a home-built system based on a photoelastic modulator. The Curie temperatures were obtained from Kerr rotation versus temperature measurements in an applied field of 7.1 kOe.

## RESULTS AND DISCUSSION

Figure 1 shows the x-ray diffraction results for the annealed films of $Mn_{0.25}Pt_{0.75-y}Zn_y$ for several Zn concentrations. The splitting of the (110), (200), and (220) reflections shown in the $y=0.08$ sample indicates the formation of the tetragonal phase. The presence of the superlattice (001) peak is indicative of substantial long range order along the $c$ axis. Figure 2 shows the $a$ axis and $c$ axis lattice parameters as a function of Pt concentration; for these data, $x$ ranges from 0.17 to 0.29 and $y$ ranges from 0.04 to 0.13. For concentrations greater than 69 at. % Pt the cubic phase with an average $a$-axis lattice parameter of 3.83 Å is present. This value is

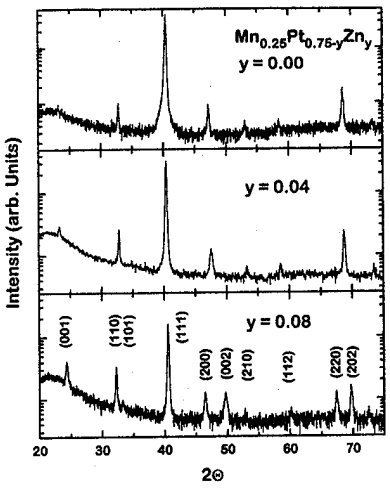



FIG. 1. X-ray diffraction results for $Mn_{0.25}Pt_{0.75-y}Zn_y$ with $y=0.00$, 0.04, and 0.08.

 0021-8979/96/79(8)/6206/3/$10.00 © 1996 American Institute of Physics

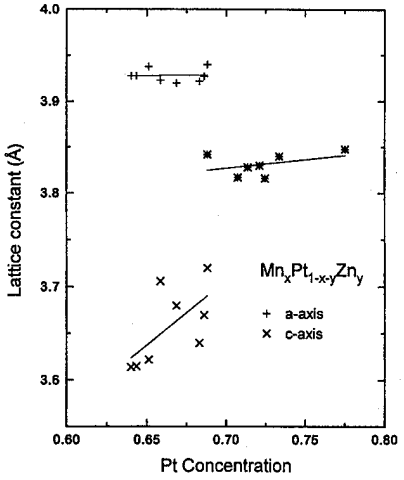



FIG. 2. Lattice parameters for varying Pt concentrations; $x$ ranges from 0.17 to 0.29, $y$ ranges from 0.04 to 0.13. The lines are drawn to aid the eye.

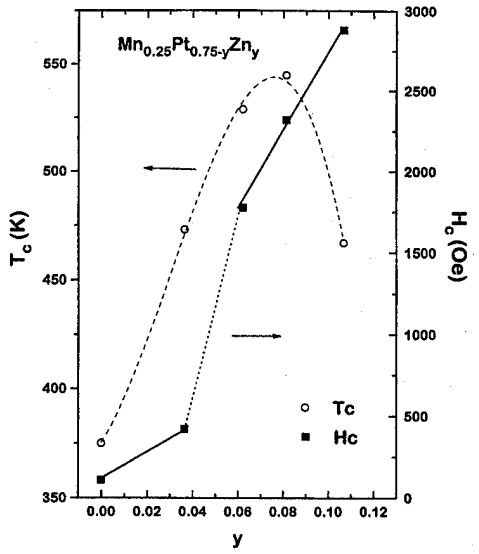



FIG. 4. $T_c$ and $H_c$ vs Zn concentration for $Mn_{0.25}Pt_{0.75-y}Zn_y$. The lines are drawn to aid the eye.

slightly smaller than the reported value of 3.89 Å for bulk $MnPt_3$.[9] Below 69 at. % Pt only the tetragonal phase is present with no indication of the cubic phase. The $a$-axis lattice parameter is 3.93 Å and is independent of Pt concentration, while the $c$-axis lattice parameter diminishes from 3.72 to 3.61 Å. At 69 at. % Pt the tetragonal and cubic structural phases co-exist indicating there is a narrow intermediate phase transition region as reported for bulk $Mn_xPt_{1-x}$.[7]

As Mn-Mn nearest-neighbor interactions are antiferromagnetic the largest possible magnetic moment in the $L1_2$ structure is obtained at Mn concentration of 25%.[7,10,11] For this reason the rest of this discussion will focus on samples with $x=0.25$. Figure 3(a) shows the room temperature in-plane hysteresis loops for $y=0.04$, 0.06, and 0.08. A comparison of the perpendicular (not shown) and in-plane hysteresis loops indicates that the easy axis is not strictly in the plane of the film. Figure 3(b) shows that the saturation magnetization ($M_s$) decreases with increasing Zn content. Figure 4 shows the Curie temperature ($T_c$) and coercivity ($H_c$) as functions of Zn concentration. The initial slope of $T_c$ vs Zn content is nearly the same as the slope found for $T_c$ vs Mn content in $Mn_xPt_{1-x}$.[10,11] This suggests that the increase of $T_c$ in the two systems has the same origin. It may be due to an increase in macroscopic exchange stiffness between Mn atoms due to a larger number of Mn-Mn nearest-neighbor interactions. Note there is a decrease in the $c$-axis lattice parameter for higher levels of Zn content which may contrib-

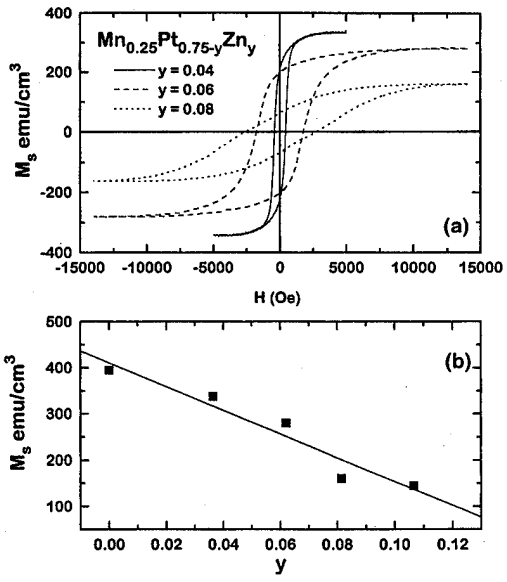



FIG. 3. (a) In-plane hysteresis loops for $Mn_{0.25}Pt_{0.75-y}Zn_y$. (b) $M_s$ vs Zn concentration for $Mn_{0.25}Pt_{0.75-y}Zn_y$. The line is drawn to aid the eye.

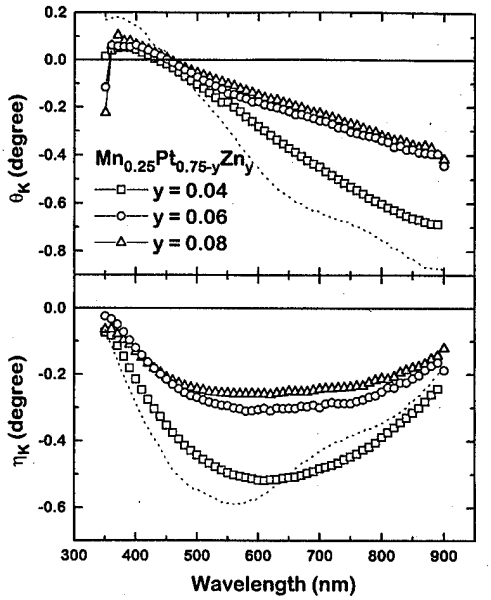



FIG. 5. Kerr rotation and ellipticity wavelength dependence for $Mn_{0.25}Pt_{0.75-y}Zn_y$ measured from the substrate side. Dotted line gives results for $MnPt_3$ measured from substrate side.

ute to the downward trend in $T_c$. The dramatic increase in coercivity appears to be associated with the structural change from cubic to tetragonal since all samples exhibiting the cubic phase have coercivities ranging from 75 to 660 Oe, while the samples with tetragonal phase have coercivities ranging from 1500 to 2900 Oe.

The room-temperature Kerr rotation ($\theta_K$) and ellipticity ($\eta_K$) spectra (measured from the substrate side) for $Mn_{0.25}Pt_{0.75-y}Zn_y$, $y=0.04$, 0.06, 0.08, are shown in Fig. 5. The present spectra are similar to those of pure $MnPt_3$ (shown as dotted line) and the overall decreases in magnitude of $\theta_K$ and $\eta_K$ correlate well with the decrease in $M_s$.

## CONCLUSION

The magnetic and magneto-optical properties of $Mn_xPt_{1-x-y}Zn_y$ alloy films have been investigated. We found that the formation of the tetragonal phase primarily depends on the Pt content, but the addition of Zn influences the formation of a ferromagnetic tetragonal phase with a fairly large saturation magnetization. The crystallographic sites of the Zn atoms have not been determined, but diffraction suggests a preferential layering of the Pt atoms to form alternating (Mn-Zn-Pt)/Pt layers along the (001) direction. No (100) diffraction peak was observed in the tetragonal phases. This together with the rapid decrease in $M_s$ with Zn content seem to indicate a large degree of disorder in the (Mn-Zn-Pt) layer. Such disorder would lead to an increase in the number of Mn-Mn antiferromagnetic exchange interactions.

## ACKNOWLEDGMENTS

We gratefully acknowledge the support of the National Science Foundation under grants OSR-9255225 and DMR-9222976, and support from the Center for Materials Research and Analysis of the University of Nebraska.

[1] A. J. P. Meyer and M. J. Besnus, Phys. Status Solidi B **58**, 533 (1973).
[2] K. Brun, A. Kjekshus, and W. B. Pearson, Philos. Mag. **10**, 291 (1964).
[3] J. Crangle and J. A. Shaw, Philos. Mag. **7**, 207 (1962).
[4] M. C. Cadeville, C. E. Dahmani, and F. Kern, J. Magn. Magn. Mater. **54–57**, 1055 (1986).
[5] D. Treves, J. T. Jacobs, and E. Sawatzky, J. Appl. Phys. **46**, 2760 (1975).
[6] A. F. Andresen, A. Kjekshus, R. Møllerud, and W. B. Pearson, Philos. Mag. **11**, 1245 (1965).
[7] S. K. Sidorv and S. F. Dubinin, Phys. Met. Metalallogr. USSR **24**, 90 (1967).
[8] T. Kato, H. Kikusawa, S. W. Iwata, S. Tsunashima, and S. Uchiyama, J. Magn. Magn. Mater. **140–141**, 713 (1995).
[9] B. Antonini, F. Lucari, F. Menzinger, and A. Paletti, Phys. Rev. **187**, 611 (1969).
[10] M. Auwärter and A. Kussman, Ann. Phys. **7**, 169 (1950).
[11] K. W. Wierman and R. Kirby, these proceedings.

# First principles determinations of magnetostriction in transition metals (invited)

Ruqian Wu
*Department of Physics and Astronomy, California State University, Northridge, California 91330-8268*

A. J. Freeman
*Department of Physics and Astronomy, Northwestern University, Evanston, Illinois 60208-3112*

The mechanism of magnetostriction in transition metal bulk (fcc Co) and thin films [Co/Pd(001) and Co/Cu(001)] is investigated using the *ab initio* full potential linearized augmented plane wave method. With the aid of the state tracking and torque approaches the magnetocrystalline anisotropy energy, the essential ingredient of the magnetostriction, is found to be a linear function of the interlayer distances. The calculated magnetostrictive coefficients and magnetoelastic coupling constants for bulk fcc Co agree very well with experiment. The calculated $\lambda_{001}$ at the Co/Pd(001) interface is much larger in magnitude ($+2.3\times10^{-4}$) and differs in sign compared to that for Co/Cu(001)($-5.7\times10^{-5}$). In these thin films, the hybridization between the Co- $d_{xz,yz}$ and the underlying substrate $d$ states is found to play the key role. © *1996 American Institute of Physics.* [S0021-8979(96)77808-8]

## I. INTRODUCTION

It has been observed that the magnetostriction in transition metal systems is very sensitive to change of environment and can be strongly enhanced in thin film geometries such as at the Co surface[1,2] and at Co/Pd,[3] Co/Cu,[4] and Ni/Ag (Ref. 5) interfaces and multilayers. Due to its intrinsic complexities and difficulties, however, the mechanism of the magnetostriction in these materials still remains as a major challenge today.[6] It is known that the anisotropic magnetostriction (as distinguished from the small volume magnetostriction) is determined by the two key ingredients, namely, the elastic constants and the strain-dependence of magnetocrystalline anisotropy (MCA) energy (so-called magnetoelastic coupling). For a magnetostrictive transition metal thin film, its thickness ($l$) should change when the magnetization turns from the perpendicular direction ($l_\perp$) to the in-plane direction ($l_\parallel$). Since the lattice constant in the lateral plane is fixed by the nonmagnetic substrate, the magnetostrictive coefficient can be determined as

$$\lambda=\frac{4}{3}\frac{l_\perp-l_\parallel}{l_\perp+l_\parallel}. \tag{1}$$

If we focus on the contribution from the interfacial layers, we can interpret $l$ as the equilibrium overlayer/substrate distance. For real transition metal overlayer systems, the difference between $l_\perp$ and $l_\parallel$ is very small so that

$$\lambda=\frac{2}{3}\frac{l_\perp-l_\parallel}{l_0}, \tag{2}$$

where $l_0$ is the equilibrium overlayer/substrate distance for any direction of magnetization and can be obtained by fitting the calculated total energy as a quadratic function of $l$ ($l_0=-b/2a$) as $E=al^2+bl+c$. If we assume that the MCA energy is a linear function of $l$ as $E_{\mathrm{MCA}}=k_1l+k_2$, then we have $l_\perp-l_\parallel=k_1/2a$ and

$$\lambda=-2k_1/3b. \tag{3}$$

Obviously, while the value of $b$ can be easily calculated, the bottleneck for determination of $\lambda$ is the value of $k_1$, i.e., the strain dependence of the MCA energy.

In the present paper, we review our recent developments on the state tracking[7] and torque[8] approaches which enable us to obtain highly stable MCA energies for transition metal thin films, and allow us to report, for the first time, calculated magnetostriction coefficients of transition metals in thin film [Co/Cu(001) and Co/Pd(001)] and bulk (fcc Co) forms. We found that the MCA energy clearly exhibits a good linear relationship with respect to the lattice distortion for each system investigated; this demonstrates the possibility of determining magnetostriction coefficients using modern energy band approaches.

## II. METHODOLOGY

### A. Model

The single particle Kohn–Sham equation is solved self-consistently using the full potential linearized augmented plane-wave (FLAPW) method, which makes no shape approximation for the potential, charge, and wave functions[9] and provides highly precise total energies. For the Co/Cu(001) and Co/Pd(001) thin films, we used a slab model consisting of five Pd (Cu) substrate layers and a pseudomorphic Co overlayers on each side. The ideal fcc structure with a lattice constant of 7.35 a.u. (6.83 a.u.) is assumed for the Pd (Cu) substrate layers while the vertical Co–Pd(Cu) interlayer distance varies as a parameter. When self-consistency for the semirelativistic calculations is achieved, i.e., when

 0021-8979/96/79(8)/6209/4/$10.00 © 1996 American Institute of Physics 

$\sqrt{\overline{\Delta\rho_c^2}}$ and $\sqrt{\overline{\Delta\rho_s^2}}$ are less than $2.0\times10^{-4}$ $e/(\text{a.u.})^3$ (here $\rho_c$ and $\rho_s$ stand for charge and spin densities, respectively), the spin–orbit coupling (SOC) Hamiltonian is invoked as a perturbation in a second variational way.

### B. MCA by state tracking and torque approaches

As is known, the strength of SOC in $3d$ transition metal systems is very weak (30–50 meV, or 100 times smaller than that of the crystalline field) and thus can be well treated using a perturbative framework. As stated in the often-used MCA force theorem,[10,11] the MCA energy can be approximately taken as the band energy

$$E_{\text{MCA}}=E(\rightarrow)-E(\uparrow)$$
$$=\sum_{\text{occ}'}\epsilon_i(\rightarrow)-\sum_{\text{occ}''}\epsilon_i(\uparrow)+O(\delta\rho^n). \tag{4}$$

Very recently, we proved that the order of $n$ goes up to 4 for thin film systems[11] and thus the force theorem should be able to provide sufficient accuracy for MCA energy determinations. However, several numerical uncertainties have been inherent in most previous *ab initio* MCA calculations[12–14] because the sets of occupation, i.e., {occ′} and {occ″}, were determined through the Fermi filling scheme which relies on the very limited information from the eigenvalues, $\epsilon_i$.

Recently, we proposed the state tracking approach[7] in which the {occ′} and {occ″} are determined according to their projections back to the occupied set of the unperturbed states. Since this procedure ensures minimum change in the charge and spin densities as required by the force theorem and excludes the possible randomness in the Brillioun zone (tracking at a given $k$ point),[7] very stable MCA results have been obtained for magnetic thin films such as Fe, Co, and Ni monolayers in free standing case as well as on various substrates (Cu and Pd, etc.) with relatively small number of $k$ points.[15–17] Perhaps more importantly, the behavior of MCA for transition metal thin films can now be related to more fundamental properties such as band structures and wave functions.[17] This enables us to explore the underlying physics and, furthermore, to figure out a way to tune the MCA for transition metal systems: The strong in-plane MCA of a free standing Co monolayer is found to originate from the coupling between the occupied $d_{xz,yz}$ and unoccupied $d_{z^2}$ and $d_{x^2-y^2}$ states at the $\bar{M}$ point.[17] When adsorbed onto the Cu substrate, for example, the $d_{xz,yz}$ state is lowered in energy due to the interfacial hybridization and thus the MCA energy becomes less negative in Co/Cu overlayer systems and even positive in Co/Cu sandwiches.

More recently, we proposed a torque[8] method which can further depress the remaining uncertainties resulting from the SOC interaction between near-degenerate states around the Fermi level (so-called surface pair coupling). To demonstrate the idea of the torque method, recall that the total energy of an uniaxial system can be well approximated in the form of

$$E=E_0+K_2\sin^2\theta+K_4\sin^4\theta, \tag{5}$$

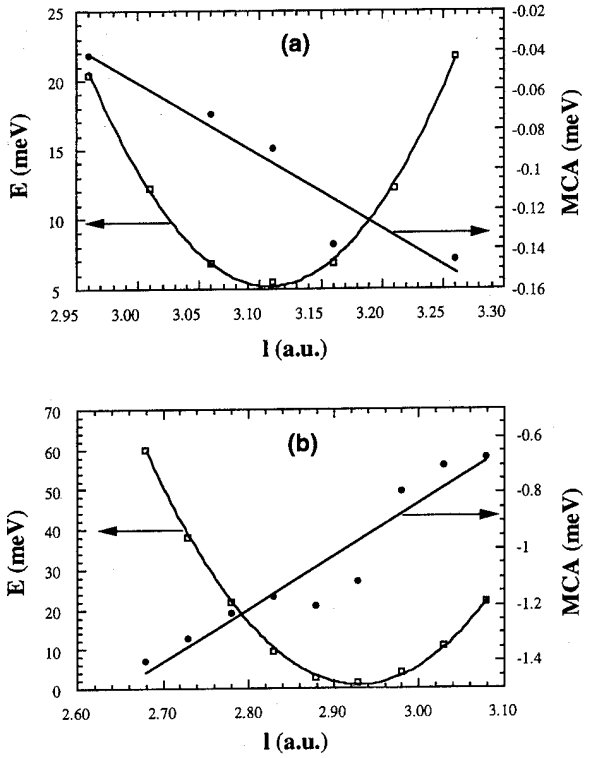



FIG. 1. The calculated change in total energy (left scale) and MCA energy (right scale) as a function of the overlayer/substrate interlayer distance for (a) Co/Cu(001) and (b) Co/Pd(001).

where $\theta$ is the angle between the normal axis and the direction of magnetization. It is easy to find that the MCA energy is equal to the angular derivative of the total energy (torque) at a "magic angle" of $\theta=45°$ as

$$E_{\text{MCA}}\equiv E(\theta=90°)-E(\theta=0°)$$
$$=K_2+K_4=dE/d\theta|_{\theta=45°}. \tag{6}$$

If we apply the Feynman–Hellman theorem, $E_{\text{MCA}}$ finally can be evaluated as (note only $H^{\text{soc}}=\xi\mathbf{s}\cdot\mathbf{L}$ depends on $\theta$ in the Hamiltonian)

$$E_{\text{MCA}}=\sum_{\text{occ}}\left\langle\Psi_i'\left|\frac{dH}{d\theta}\right|\Psi_i'\right\rangle\Bigg|_{\theta=45°}$$
$$=\sum_{\text{occ}}\left\langle\Psi_i'\left|\frac{\partial H^{\text{soc}}}{\partial\theta}\right|\Psi_i'\right\rangle\Bigg|_{\theta=45°}, \tag{7}$$

where $\Psi_i'$ is the $i$th perturbed wave function.

The advantage of the torque method is obvious since in this approach we only have to deal with one particular magnetic orientation and thus only one Fermi surface is required for the $k$ integration. In addition, the MCA energy is expressed as the expectation value of the angular derivative of $H^{\text{soc}}$ and thus it is much more insensitive to the surface pair coupling. With the aid of the state tracking and torque methods, very stable results have been obtained for various transition metal systems and thus we are able to attack the long standing problem of magnetostriction in transition metals.

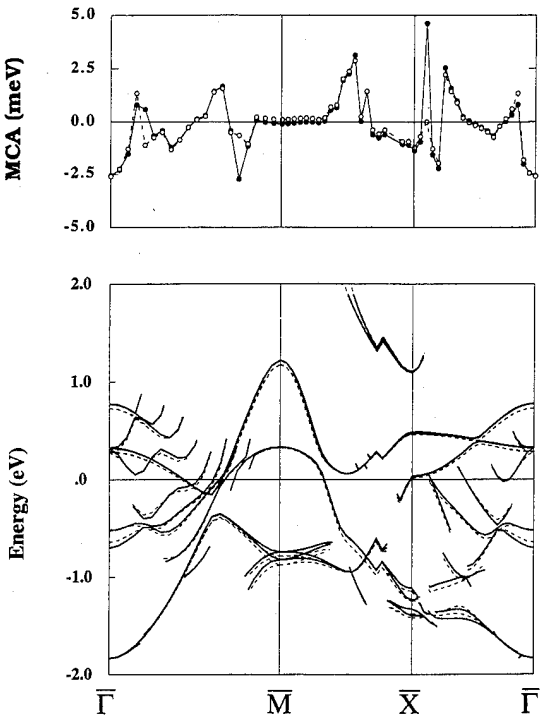



FIG. 2. The calculated band structures (bottom panel) and the distributions of the MCA energies (top panel) along high symmetry directions in the BZ of Co/Cu(001) in the equilibrium (solid lines, $l$=3.11 a.u.) and a reduced geometry (dashed lines, $l$=2.96 a.u.).

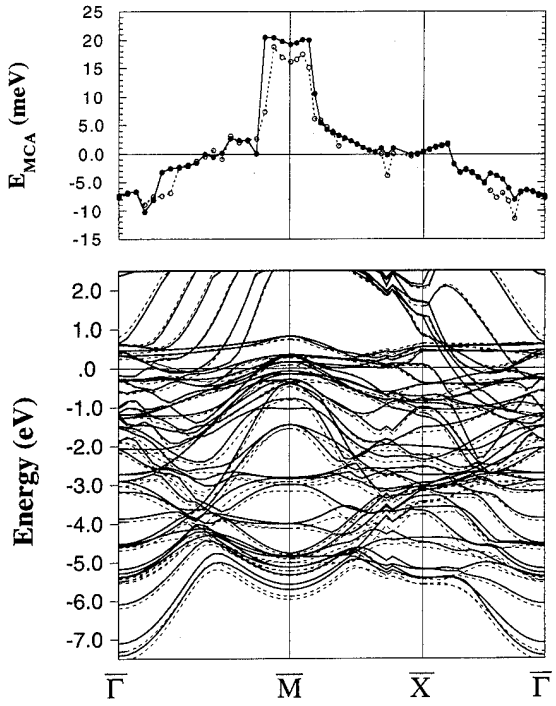



FIG. 3. Same as Fig. 2 but for Co/Pd(001) in equilibrium (solid lines, $l$=2.96 a.u.) and in a reduced geometry (dashed lines, $l$=2.76 a.u.).

## III. RESULTS

To determine values of $k_1$ and $b$ in Eq. (3), we calculated $E$ and $E_{\mathrm{MCA}}$ for Co/Cu(001) and Co/Pd(001) as functions of their overlayer/substrate interlayer distances, $l$. For each system, as shown in Fig. 1, while the total energy curve can be well fitted by a parabola, the MCA energy exhibits a fairly good linearity—indicating the precision of the present calculations and also justifying the huge range of strain ($\Delta l/l \sim 15\%$) used in calculations relative to saturation magnetostrictive strains ($\Delta l/l \sim 10^{-5}$). We found for Co/Cu(001) that $b$ and $k_1$ are equal to $-4390$ and $-0.376$ meV/a.u., respectively; thus, the calculated $\lambda_{100}$ is $-5.7\times10^{-5}$.[18] The negative sign means that the Co–Cu interlayer distance contracts when the direction of magnetization changes from in-plane to normal to the surface. Dramatically, we found that the MCA energy for Co/Pd(001) becomes more *negative* when the Co–Pd distance shrinks and thus $\lambda_{001}$ becomes *positive*, $+2.3\times10^{-4}$, just opposite to those for Co/Cu(001). This result is in reasonable agreement with experiment data currently available.[3]

To reveal the physical background for magnetostriction in transition metal thin films, we need to explain why the MCA energy becomes less (more) negative when the Co–Cu (Co–Pd) distance decreases. As discussed above, the MCA energy can be altered if one increases the energy separation between the $d_{xy}-d_{xz,yz}$ and $d_{z^2}-d_{xz,yz}$ states around the $\bar{M}$ point.[17] Of key importance, we can see from the band structure in the bottom panel of Fig. 2, where only states with weight larger than 50% in the Co muffin-tin (MT) spheres are given, that the Co-$d_{xz,yz}$ states hybridize with the underlying Cu $d$ states and split into a few states (each branch shown in Fig. 2 has only a 54% weight in the Co MT sphere) and thus their energy positions are lowered. As a result, the MCA energy in the top panel of Fig. 2 becomes almost zero around the $\bar{M}$ point and, subsequently, the MCA energy of Co/Cu(001) is only $-0.1$ eV/adatom at the equilibrium geometry. When the Co–Cu interlayer distance is shortened further to 2.96 a.u., as shown by the dashed lines in Fig. 2, the energy position of the Co-$d_{xz,yz}$ states appears very sensitive to the Co–Cu distance and is lowered further by 0.05 eV. As expected, the MCA energy shifts up to be slightly positive around the $\bar{M}$ point. Thus the hybridization between Co-$d_{xz,yz}$ and Cu states is the main driving force for the magnetostriction for Co/Cu(001).

The band structures of Co/Pd(001) are plotted in the bottom panel of Fig. 3, where the solid lines indicate the bands for the equilibrium geometry ($l$=2.96 a.u.) and the dashed lines are for a further contracted case ($l$=2.76 a.u.). Due to the strong Co–Pd interfacial hybridization in both the occupied and unoccupied parts, almost all of the Co states lose their localizations in the Co MT sphere (most of them have less than 40% weighting). Most strikingly, the Co-$d_{xz,yz}$ states are split even into the unoccupied region around the $\bar{M}$ point and, correspondingly, a *positive* contribution to the MCA energy in the $\bar{M}$ neighborhood is found as shown in the top panel in Fig. 3. When the Co–Pd interlayer distance is shortened further to 2.76 a.u., as shown by the dashed lines in Fig. 3, the band broadening enlarges the energy separation between the occupied and unoccupied Co-$d_{xz,yz}$ states and thus their *positive* contributions to the MCA energy is reduced. Again, the most pronounced features happen around the $\bar{M}$ point whereas the contributions from other $k$ points

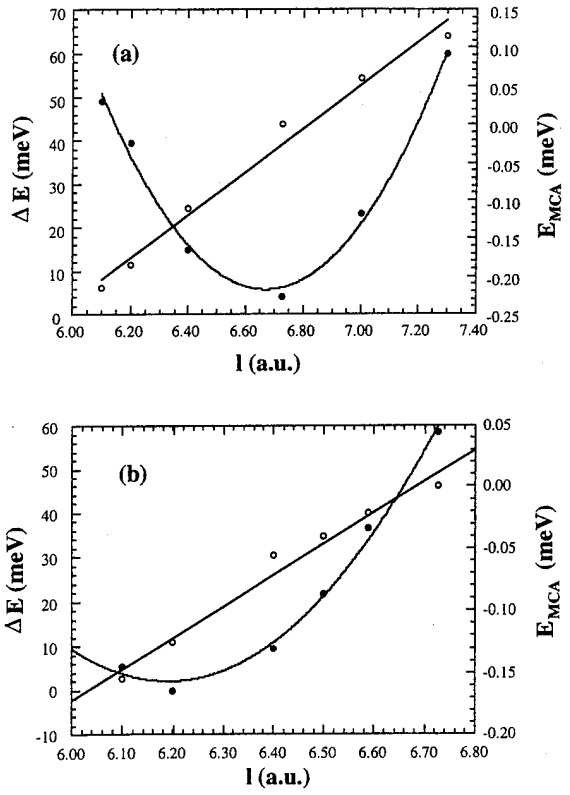



FIG. 4. The calculated change in total energy (left scale) and MCA energy (right scale) as a function of the length of the $c$ axis for fcc Co bulk with distortions that preserve (a) a constant volume and (b) a constant area in the lateral plane.

appear not to be very sensitive to the change of Co/Pd distance.

As a further step, we investigated the magnetostriction for a bulk cubic transition metal. In Fig. 4, the calculated change in total energy (left scale) and MCA energy (right scale) per Co atom for bulk fcc Co with respect to the length of the $c$ axis are given for distortion modes with (a) a constant volume and (b) a constant area in the lateral plane. The linear relationship between $E_{\mathrm{MCA}}$ and $l$ is obvious for both cases—indicating a possibility to determine the magnetostriction even for a cubic transition metal bulk. Quantitatively, for cases (a) and (b) respectively, the calculated $\lambda_{001}$ are $10.2\times10^{-5}$ and $6.8\times10^{-5}$, while the magnetoelastic coupling constants,[19] namely $B_1$, are $-1.6\times10^{8}$ erg/cm$^3$ and $-2.4\times10^{8}$ erg/cm$^3$. The results for the case with a constant volume are surprisingly close to the measured $\lambda_{001}$ [$1.3\times10^{-4}$ (Ref. 20)] and $B_1$ [$-1.6\times10^{8}$ erg/cm$^3$ (Ref. 21)], and appear to validate the present approach for determining magnetostriction in transition metal systems.

## IV. CONCLUSION

In conclusion, with the aid of the state tracking and torque techniques for calculating the MCA energy, the precision of modern first principles approaches appears to be sufficient for the determination of the magnitude, sign and mechanism of the tiny magnetostriction values observed in transition metal thin films. This new capability for making theoretical predictions and, perhaps more importantly, providing meaningful physical insights, appears possible to help guide the search for the right elements and compositions to synthesize thin films with desired magnetostrictive properties.

## ACKNOWLEDGMENTS

We thank Dr. K. B. Hathaway for stimulating discussions and encouragement. Work supported by the ONR (Grant Nos. N00014-95-1-0489 and N00014-94-1-0030) and by a computing grant at the Arctic Region Supercomputing Center and at NERSC, Lawrence Livermore National Laboratory supported by the DOE.

[1] S. W. Sun and R. C. O'Handley, Phys. Rev. Lett. **66**, 2798 (1991).
[2] G. Bochi, O. Song, and R. C. O'Handley, Phys. Rev. B **50**, 2043 (1994).
[3] H. Takahashi, S. Tsunashima, S. Iwata, and S. Uchiyama, J. Magn. Magn. Mater. **126**, 282 (1993).
[4] G. Bochi, C. A. Ballentine, H. E. Inglefield, C. V. Thompson, and R. C. O'Handley, Phys. Rev. Lett. (submitted).
[5] R. Zuberek, H. Szymczak, R. Krishnan, and Tessier, J. Phys. C **8**, 1761 (1988).
[6] J. R. Cullen, A. E. Clark, and K. B. Hathaway, in *Materials Science and Technology*, edited by R. W. Cahn, P. Haasen, and E. J. Kramer (Weinhein, New York, 1991), Vol. IIIB, p. 529.
[7] D. S. Wang, R. Q. Wu, and A. J. Freeman, Phys. Rev. Lett. **70**, 869 (1993).
[8] X. D. Wang, R. Q. Wu, D. S. Wang, and A. J. Freeman, Phys. Rev. B (to be published).
[9] E. Wimmer, H. Krakauer, M. Weinert, and A. J. Freeman, Phys. Rev. B **24**, 864 (1981); M. Weinert, E. Wimmer, and A. J. Freeman, *ibid.* **26**, 4571 (1982), and references therein.
[10] M. Weinert, R. E. Watson, and J. W. Davenport, Phys. Rev. B **32**, 2115 (1985).
[11] X. D. Wang, D. S. Wang, R. Q. Wu, and A. J. Freeman, J. Magn. Magn. Mater. (in press).
[12] J. G. Gay and R. Richter, Phys. Rev. Lett. **56**, 2728 (1986); R. Richter and J. G. Gay, Mater. Res. Soc. Symp. Proc. **151**, 3 (1989).
[13] P. Strange, J. B. Staunton, B. L. Gyorffy, and H. Ebert, Physica B **172**, 51 (1991).
[14] G. H. O. Daalderrop, P. J. Kelly, and M. F. H. Schuurmans, Phys. Rev. B **41**, 11919 (1990).
[15] D. S. Wang, R. Q. Wu, and A. J. Freeman, Phys. Rev. B **47**, 14932 (1993).
[16] D. S. Wang, R. Q. Wu, and A. J. Freeman, Phys. Rev. B **48**, 15883 (1993).
[17] D. S. Wang, R. Q. Wu, and A. J. Freeman, J. Magn. Magn. Mater. **129**, 327 (1994).
[18] A 5%–10% uncertainty may be involved since the MCA energy for $l$=3.16 is away from the trend due to the effects of the surface pair coupling (SPC), i.e., the MCA energy changes from −0.14 meV/adatom to −0.09 meV/adatom when the SPC is dropped. Although these effects also appear to be not negligible for some $k$-points in Fig. 2, we found that the elimination of SPC affects the MCA energies only very slightly (<0.01 eV/adatom) for other geometries for Co/Cu(001).
[19] C. Kittel, *Introduction to Solid State Physics* (Wiley New York, 1996), 7th ed. p. 482.
[20] R. A. Lukaszew and R. Naik, 40th CMMM abstract BC-13, 80 (1995).
[21] R. C. O'Handley (private communication).

# Zero field damping capacity in $(Tb_xDy_{1-x})Fe_y$

J. P. Teter and K. B. Hathaway
*Naval Surface Warfare Center, Silver Spring, Maryland 20903-5640*

A. E. Clark
*Clark Associates, Adelphi, Maryland 20783*

Materials with a large capacity to dissipate mechanical energy are of interest for passive vibration damping. We have measured the zero-field damping capacity of the giant magnetostrictive terbium–dysprosium–iron compounds by quasistatic stress–strain hysteresis loops. The magnetization and strain of the samples were measured for increasing and decreasing compressive stresses, up to 50 MPa. The zero-field, room temperature damping capacity ($\Delta W/W$) was calculated from the stress–strain loops and is plotted against maximum stress. The damping capacity maximum for the alloy with the nominal Terfenol-D composition occurs at 4.1 MPa with the value 1.75 which corresponds to $Q^{-1}=0.28$. The damping is almost independent of stress in a multi-phase sample, $(Tb_{0.6}Dy_{0.4})Fe_{1.4}$, which contains both Laves phase and elemental rare earth. © *1996 American Institute of Physics.* [S0021-8979(96)77908-4]

## I. INTRODUCTION

Magnetomechanical damping of vibrations has been known for many years,[1] but has not been exploited in modern applications of passive damping materials. Magnetic alloys with large magnetomechanical coupling factors, $k$, such as Terfenol-D ($Tb_{0.3}D_{0.7}Fe_2$) with $k=0.7$, transform elastic energy into magnetic energy in each vibration cycle according to the ratio $k^2/(1-k^2)$. If the magnetic system has a high loss factor, less energy is returned to the elastic system and the vibration is damped. In previous work,[2] we extracted the magnetomechanical damping capacity of Terfenol-D from transducer stress–strain hysteresis curves measured with magnetic field at different stresses. The stress–strain hysteresis was related to a Stoner–Wolfarth type magnetic hysteresis caused by magnetic domain jumping between different easy axis directions. Both the data and model indicate that damping should be a maximum for zero field bias conditions.

In this paper we measure the quasistatic stress–strain hysteresis curves for zero field bias for both polycrystalline Terfenol-D rods, as well as for a rare earth rich $(Tb_xD_{1-x})Fe_y$ sample. In the Terfenol sample the maximum damping capacity exceeds unity, suggesting a great potential for this material for high stress applications.

## II. EXPERIMENT AND RESULT

The samples consisted of high purity rare earths and iron melted by rf heating and subsequently poured into a cylindrical mold. The Terfenol-D sample had a nominal composition of $Tb_{0.3}D_{0.7}Fe_2$, a diameter of 1.5 cm, and exhibited a simple polycrystalline morphology with grain size ranging between 0.025 and 0.05 cm. The high rare earth concentration eutectic sample had a nominal composition of $(Tb_{0.6}Dy_{0.4})Fe_{1.4}$, a diameter of 0.9 cm, and exhibited a complex polycrystalline morphology with no feature larger than 0.01 cm.

The samples were placed in an apparatus that could apply incremental quasistatic uniaxial pressure up to 100 MPa and a saturating magnetic field of 2500 Oe. The apparatus was instrumented with an analog pressure gage and a calibrated NIST traceable load cell. Each sample was instrumented with two commercial foil strain gages and a 50 turn pick-up coil. Each stress–strain data acquisition sequence started with the application of a saturating magnetic field being directed along the stress axis. This was done to establish an initial strain state equivalent to the remanent state that would be produced by a saturating tensile stress. Since Terfenol is a brittle intermetallic which is fragile under tensile stress, only the compressive portions of the stress–strain hysteresis loops were obtained by direct application of stress.

In order to determine the damping characteristics of highly magnetostrictive materials, a series of strain data as a function of positive stress was taken, each series started at zero stress and a reproducible initial-state strain, went up to a predetermined maximum stress ($\sigma_m$) and, returned to zero stress. The results of this procedure for the polycrystalline Terfenol-D sample is shown in Fig. 1. The inset details the maximum stress applied for each individual data set. Similar curves were obtained for the sample containing the eutectic. However, for this sample, the enclosed stress–strain area which corresponds to the losses, are smaller.

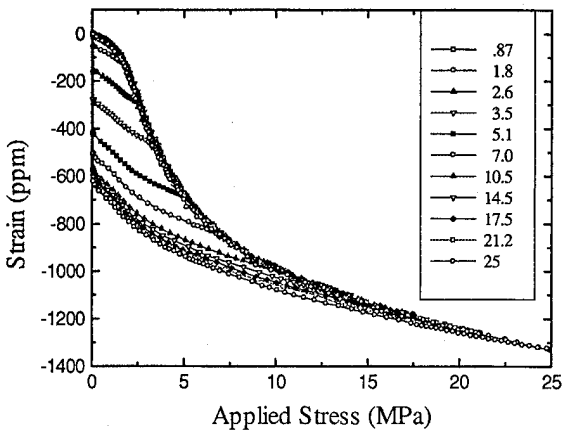



FIG. 1. Stress–strain half loops taken at room temperature on polycrystalline Terfenol-D. The inset shows the maximum applied stress ($\sigma_m$) for each half loop.

 0021-8979/96/79(8)/6213/3/$10.00 © 1996 American Institute of Physics 

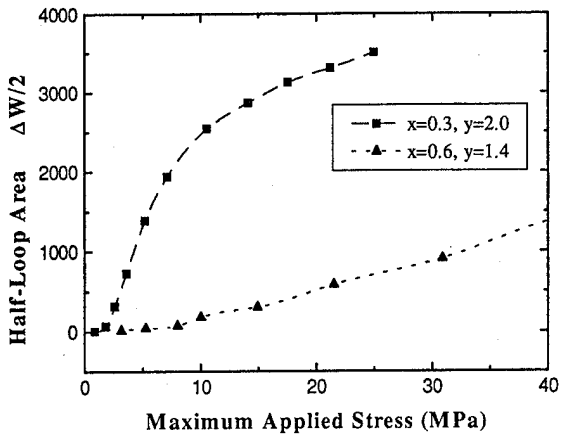



FIG. 2. The half loop enclosed area for polycrystalline Terfenol-D (■) and the high eutectic sample (▲) as a function of maximum applied stress ($\sigma_m$).

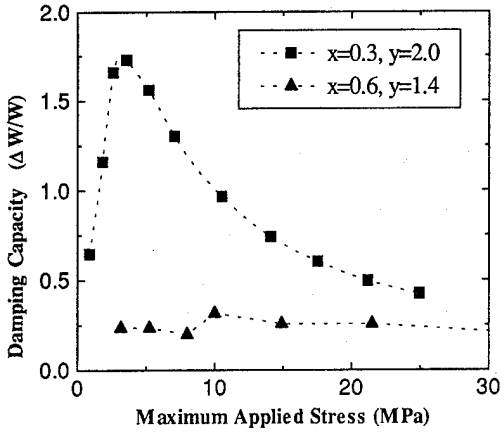



FIG. 3. The damping coefficient $\Delta W/W$ for polycrystalline Terfenol-D (■) and the high eutectic sample (▲) as a function of maximum applied stress ($\sigma_m$).

The damping capacity was calculated from these data sets by integrating the half loop area and applying the formula: $\Delta W/W=(2*\text{half loop area})/[1/2(\sigma_m*\epsilon_m)]$. Here $\epsilon_m$ is the strain corresponding to the maximum stress, $\sigma_m$. The areas for both samples are plotted vs $\sigma_m$ in Fig. 2. The corresponding values of $\Delta W/W$ are plotted in Fig. 3.

Application of a bias magnetic field, ($0<H<500$ Oe), during the damping data acquisition leads to a reduction in the damping coefficient with increasing applied field.

## III. DISCUSSION

In order to understand and tailor magnetomechanical damping we need to relate it to the independently measurable materials parameters: magnetization, $M$, magnetocrystalline anisotropy, $K$, magnetostriction, $\lambda$, and elastic modulus, Y. Stress–strain hysteresis due to magnetoelastic coupling derives from some of the same loss mechanisms that contribute to magnetic hysteresis. However, since the tensor symmetries of a magnetic field and an applied stress are different, their effect on domain wall motion and magnetic domain rotation will be different, depending on the crystal symmetry of the material.[2] Stress cannot discriminate between 180 deg domains and therefore will not produce hysteresis in materials with uniaxial symmetry. In a cubic material such as Terfenol, an applied stress will change the relative energies of the initially equivalent easy axis domain orientations. At some critical stress the magnetization will jump between the now inequivalent directions, and the strain which is coupled magnetoelastically to the magnetization will also change discontinuously. We define the critical stress to be that stress for which the barrier between the energy minima disappears. Steady state oscillations will drive the system cyclically between two different magnetization/strain states. A derivation of stress–strain hysteresis for a stress applied along [001] to a cubic crystal with {100} easy axes ($K>0$) was presented in the appendix of Ref. 2. Critical stresses are found to be proportional to $K/\lambda$ and the peak damping capacity is proportional to $Y\lambda^2K$. Calculations for a Terfenol single crystal with {111} easy axes ($K<0$) proceeds in the same way by finding the minima of the generalized free energy for the single crystal with an externally applied stress, $\sigma$

$$E=K(\alpha_i^2\alpha_j^2+\cdots)-\tfrac{3}{2}\lambda_{100}(c_{11}-c_{12})(\epsilon_{ii}\alpha_i^2+\cdots)$$
$$-3\lambda_{111}c_{44}(\epsilon_{ij}\alpha_i\alpha_j+\cdots)+\tfrac{1}{2}c_{11}(\epsilon_{ii}^2+\cdots)$$
$$+c_{12}(\epsilon_{ii}\epsilon_{jj}+\cdots)+\tfrac{1}{2}c_{44}(\epsilon_{ij}^2+\cdots)-\sigma\cdot\epsilon,$$

where the $\alpha_i$ are the vector components of the magnetization, the $\epsilon_{ij}$'s are the Cartesian strains, and $\lambda_{100}$ and $\lambda_{111}$ are the lowest order cubic magnetostriction constants. For Terfenol, $\lambda_{100}$ is about zero to a good approximation and may be neglected. The $\epsilon_{ij}$'s are eliminated by imposing the equilibrium conditions $\partial E/\partial\epsilon_{ij}=0$, and the equilibrium value of $\alpha$ can then be determined from the condition of zero torque $\boldsymbol{\alpha}(\partial E/\partial\boldsymbol{\alpha})=0$. Solutions of the torque equations, obtained numerically, yield magnetization-stress hysteresis loops. Magnetoelastic strain loops are calculated from them using $\epsilon=3\lambda_{111}(\alpha_i\alpha_j\beta_i\beta_j+\cdots)$, where $\beta$ defines the stress–strain axis.

A series of stress–strain hysteresis loops for stress applied in the $(1\bar{1}0)$ plane at an angle $\theta$ from the [110] direction is shown in Fig. 4. We can approximate the stress–strain hysteresis for a Terfenol polycrystal by an appropriately weighted sum of the hysteresis curves for individual crystallites randomly oriented with respect to the stress axis.

### A. Stress along [111]

Here the two easy axes collinear with the stress ([111] and $[\bar{1}\,\bar{1}\,\bar{1}]$) are inequivalent to the other six easy directions, which are all equivalent to each other. The stress-collinear pair remains stationary but the other six easy directions rotate with applied stress and the magnetization jumps between them and the two stationary easy directions at the critical stresses $\sigma=-0.15K/\lambda_{111}$ and $\sigma=0.44K/\lambda_{111}$ [see Fig. 4(b)].

### B. Stress along [112]

For stresses applied along lower symmetry directions such as [112], all of the easy axes rotate with applied stress. The moment jumps between the easy axis pair nearest to the stress direction ([111] and $[\bar{1}\,\bar{1}\,\bar{1}]$) and the pair ($[11\bar{1}]$ and $[\bar{1}\,\bar{1}1]$) in the same $(1\bar{1}0)$ plane at the critical stresses $\sigma=-0.17\ K/\lambda_{111}$ and $\sigma=0.25\ K/\lambda_{111}$ [see Fig. 4(c)]. The re-

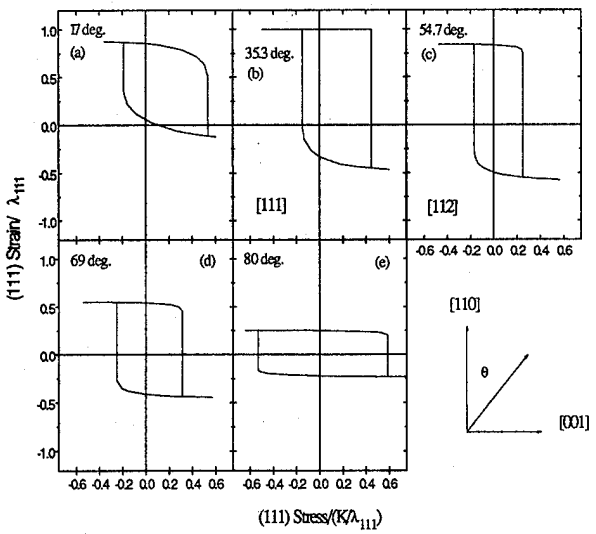



FIG. 4. Calculated stress-strain hysteresis loops for [111] easy material and for stress applied in the $(1\bar{1}0)$ plane at increasing angle, $\theta$, from [110]. Stress in units of $K/\lambda_{111}$, positive values indicate compressive stress. Strain in units of $\lambda_{111}$, negative values indicate compressive strain. Jumps are indicated by vertical lines.

maining four easy axis directions not in the $(1\bar{1}0)$ plane are less strongly affected by the applied stress. The barriers preventing out-of-plane jumping do not disappear until jumping has already occurred in-plane thus out of plane jumping may be neglected to lowest order.

### C. Stress along [001]

In this case all of the easy directions remain equivalent and no jumping occurs. At angles of applied stress close to this hard axis [Fig. 4(e)], the critical stress for jumping approaches infinity and the magnitude of the jumps approaches zero. A similar thing happens for stress applied along or close to [110] [Fig. 4(a)], except that in this case only the four in-plane axes remain equivalent and out-of-plane jumping should be included.

By inspection we see that the maximum hysteresis occurs for crystallites oriented with an easy axis close to the applied stress direction. For Terfenol ($\lambda = 1600E\text{-}6$, $K = 8E4$ J/m$^3$) the maximum damping capacity is predicted for a stress applied along [111] with a peak value of about 5 at 15 MPa stress [see Fig. 4(b) for the stress–strain curve that yields this result). Averaging over crystallites will reduce the hysteresis by a factor of 2–3 depending on the texturing of the sample. This estimate is consistent with the maximum damping capacity as measured in Terfenol and shown in Fig. 3 above. The data for the eutectic sample illustrates both a reduction of damping capacity due to a smaller proportion of magnetostrictive material and the extreme broadening of the damping peak due to the spread of stresses experienced by material in a composite. The measured damping capacity of 0.2, however is still quite large when compared to conventional damping materials.

## ACKNOWLEDGMENT

The authors thank the Carderock division of NSWC Intra-Laboratory Independent Research program office for funding.

[1] A. W. Cochardt, J. Appl. Mech. **20**, 196 (1953).
[2] K. B. Hathaway, A. E. Clark, and J. P. Teter, Metall. Mater. Trans. A **26A**, 2797 (1995).

# Anomolous $\Delta E$ effects in TbDyZn alloys

J. R. Cullen, M. Wun-Fogle, J. B. Restorff, and J. P. Teter
*Caderock Division, Naval Surface Warfare Center, Silver Spring, Maryland 20903-5640*

A. E. Clark
*Clark Associates, Adelphi, Maryland 20783*

The temperature dependence of Young's modulus has been measured for a series of $Tb_{1-x}Dy_xZn$ pseudobinary compounds with $x$ ranging from 0 to 1. From the sharp dips in the modulus vs temperature data, the reorientation transition temperatures have been determined, and the magnetic phase diagram deduced. Magnetization measurements taken on the same samples show less pronounced features at the corresponding temperatures. © *1996 American Institute of Physics.* [S0021-8979(96)78008-3]

## INTRODUCTION

The series of pseudobinary compounds $Tb_{1-x}Dy_xZn$ have several characteristics which make them attractive for scientific and technological reasons. They have simple atomic structures (CsCl), are all ferromagnets with only one magnetic species whose magnetic polarization arises almost exclusively from the localized $4f$ electrons.[1] Easy axis reorientations observed for $x \leq 0.6$ (Refs. 2 and 3) mean low anisotropies at temperatures near the transition points. This, combined with large magnetostrictions leads to strong magnetomechanical coupling, depending on $x$, from 63 K at $x=0$ to 4.2 K near $x=0.6$. The use of fourth- and sixth-order anisotropy constants to describe the magnetic energy has not been adequate for describing related pseudobinary rare earth compounds. In fact, for the low-$T$ portion of the $T-x$ phase diagram there are phases in which the magnetization is directed along nonprincipal axes.[4] One requires at a minimum, eighth-order anisotropy terms to reproduce these phases.[5] The higher-order terms can arise from crystalline electric field contributions to the $4f$-electron wave functions[6] and from local fluctuations in magnetization direction caused by competing terbium and dysprosium anisotropies.[7] The former mechanism is in principle present even in the binary compounds while the latter is expected to vary as $x(1-x)$.

In the past, these magnetic phase diagrams were determined by torque magnetometry on single crystal specimens of $Tb_{1-x}Ho_xFe_2$,[8] and Mössbauer measurements[4] on polycrystalline Laves phase pseudobinaries. At present, only polycrystalline specimens of the $Tb_{1-x}Dy_xZn$ are available. The special feature of the Laves phase, which allowed use of Mössbauer spectra to determine the easy directions, is missing in the CsCl structure. It is still possible, however, to determine the phase boundaries, if not the nature of the phases themselves by measuring the elastic modulus vs temperature. Intuitively, minima or sharp features of some kind would be expected at a magnetization reorientation temperature. We report measurements of Young's modulus as a function of temperature for a series of polycrystalline $Tb_{1-x}Dy_xZn$. Broad minima were found in all the samples. For $x \lesssim 0.5$ sharp dips were seen as well. For $x=0.125$, two such dips were seen. The dips are interpreted as marking second-order transitions between different easy magnetization directions. From these and prior[3] data, a magnetic phase diagram is constructed which predicts the existence of a phase with $[u,v,0]$ easy axis from $x \approx 0.1$ to $x \lesssim 0.5$. Some idea of the $x$ dependence of the ratios of the fourth- and sixth-order anisotropy constants was obtained using this phase diagram. The origin of the broad temperature minima observed in all samples is discussed in terms of a model of competing crystalline and dipolar anisotropies.

## EXPERIMENT

Polycrystalline alloys of $Tb_{1-x}Dy_xZn$ with $0<x<1$ were prepared at Ames Laboratory from stoichiometric proportions of 99.99% pure Tb, Dy, and Zn.[9] Small disks (~100 mg) for magnetization measurements and small transducer rings (~6 mm i.d.×~8.8 mm o.d.×~0.8 mm thick) for magnetoelastic measurements were cut from each alloy composition. To improve sample homogeneity, the samples were then annealed in an inert atmosphere for a period of 18 h up to 1 week at ~900 C. Magnetization as a function of temperature and magnetic field was measured for each disk sample in a vibrating sample magnetometer. The magnetoelastic properties were measured using the ring samples toroidally wound with three coils: (1) a dc bias coil, (2) an ac excitation coil, and (3) an ac pickup coil. The dc bias coil was used to magnetize the samples before each measurement. The complex impedance as a function of frequency was measured to determine resonant frequencies as a function of temperature. The former are related to Young's modulus, $E$, as

$$E=\omega_r^2 \rho a^2, \tag{1}$$

where $a$ is the ring radius [$a=1/4$(o.d.+i.d.)], $\rho$ is the density, and $\omega_r$ is the resonant frequency. Errors in the temperature measurement were on the order of ±1.5%. Further experimental details can be found in Ref. 3.

## RESULTS

Figure 1 shows the modulus vs temperature for samples with $x=0$ and $x=0.075$. The sharp dip in the $x=0$ (TbZn) modulus at $T=63$ K coincides with the reorientation temperature measured in single crystals by magnetization vs temperature curves.[3] Besides the sharp dip in modulus at 53 K in the $x=0.075$ sample, note the drop in modulus at temperatures below 20 K. At larger $x$, the sharp dip is found at lower temperatures, while a second dip at around 13 K is

 0021-8979/96/79(8)/6216/3/$10.00 © 1996 American Institute of Physics

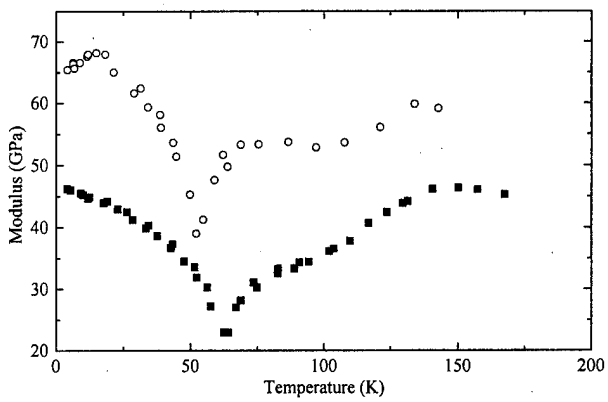



FIG. 1. Young's modulus vs temperature for TbZn (■) and $Tb_{0.925}Dy_{0.075}Zn$ (○).

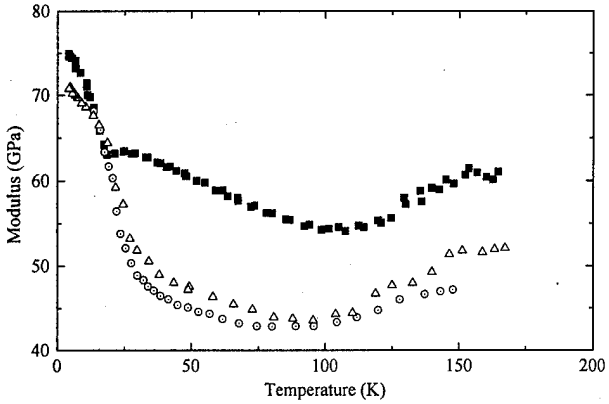



FIG. 3. Young's modulus vs temperature for $Tb_{0.6}Dy_{0.4}Zn$ (■), $Tb_{0.5}Dy_{0.5}Zn$ (△), and $Tb_{0.4}Dy_{0.6}Zn$ (⊙).

apparent in the 0.125 sample (see Fig. 2). Note also that the dip in the 0.150 sample is broader, and is largest at yet a lower temperature than those with smaller $x$. As $x$ is increased beyond 0.15, the dip becomes narrower and moves to lower temperature. By $x=0.4$, the dip, while still clearly visible, represents a relatively small decrease in modulus on a background that is rapidly increasing with decreasing temperature. At $x=0.5$, the dip was seen in some runs and not in others. It is not visible in the data presented in Fig. 3. There is, however, a slight rise in the magnetization between 15 and 5 K. The $x=0.6$ sample does not show any dip in modulus for temperatures down to 4.2 K, although the magnetization does show a small increase around 10 K.

Assuming that the temperatures at which the cusplike dips appear in the moduli mark the boundary between different easy axis magnetization directions, we have constructed the magnetic phase diagram for $Tb_{1-x}Dy_xZn$ depicted in Fig. 4. The facts that the magnetization of TbZn reorients directly from [100] to [110],[2] that there are two cusplike dips in the modulus of the $x=0.075$ sample, and that the modulus dip of the $x=0.15$ sample is relatively broad (which means that this sample is near a phase boundary over a wide temperature range), support the indicated assignments of phases on the $T-x$ diagram.

The magnetization measurements also show a significant coercivity at low temperatures for $x\geq 0.6$ which increases to about 1 kOe for $x=1.0$ and $T\leq 20$ K. Coercive fields of that order of magnitude below 25 K have been reported previously for DyZn.[10]

As we mentioned at the outset, at least three anisotropy constants are required to describe a phase diagram such as that of Fig. 4, in which there exist regions in which the magnetization lies in nonprincipal directions. Writing the anisotropy energy of a particular crystallite in terms of $\alpha_i$, the direction cosines of the magnetization,

$$E=K_4\sum_{i>j}\alpha_i^2\alpha_j^2+K_6\alpha_x^2\alpha_y^2\alpha_z^2+K_8\sum_{i>j}\alpha_i^4\alpha_j^4, \qquad (2)$$

it was shown in Ref. 5 that the $[u,v,0]$ phase is stable for $0\geq K_4/K_6\geq -0.5$, $K_6/K_8>2$. Since the portion of the phase diagram near $x=0$ shows no such phase, it must be that $K_8=0$ for $x=0$. On the other hand, for $x\geq 0.1$, the $[u,v,0]$ phase is stable for all $T<35$ K, so $K_8$ must increase rapidly

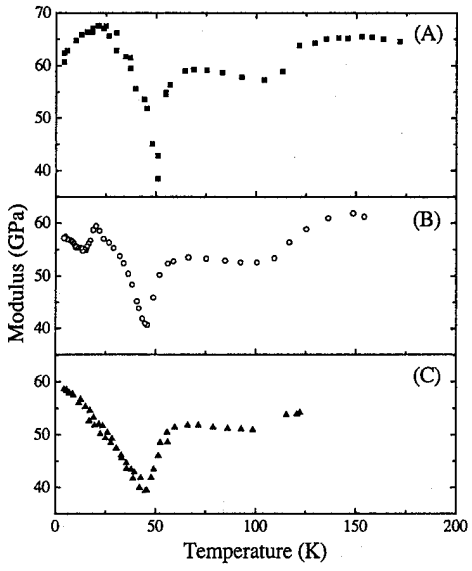



FIG. 2. Young's modulus vs temperature for (A) $Tb_{0.9}Dy_{0.1}Zn$, (B) $Tb_{0.875}Dy_{0.125}Zn$, and (C) $Tb_{0.85}Dy_{0.15}Zn$.

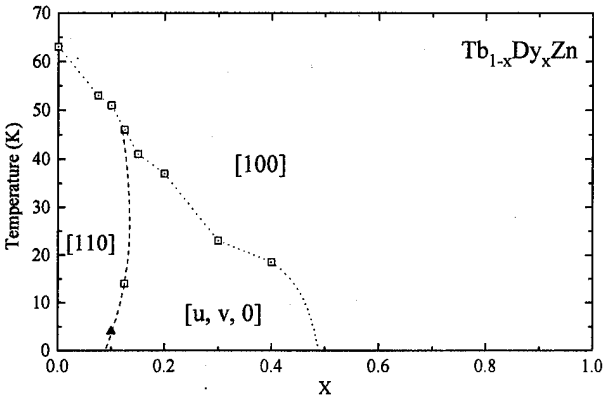



FIG. 4. Easy magnetization phase diagram for $Tb_{1-x}Dy_xZn$. The dashed lines are guides to the eye. The solid triangle is estimated from the drop in the $x=0.1$ modulus as $T\to 0$. The open squares represent the lowest points of the sharp dips in modulus vs temperature.

with $x$, and remain nonzero at least as far as $x=0.6$. These circumstances lead us to conclude that most of the contribution to $K_8$ comes from the Tb–Dy competing anisotropy effect. If this is so, we expect that the $[u,v,0]$ phase is nonuniform; only the direction of the net magnetization is actually along $[u,v,0]$; the local magnetization varies spatially within each domain.

## MAGNETOELASTIC MODULUS SOFTENING

For all the samples, we find a softening of the modulus below the Curie temperature, $T_C$. In contrast to the cusplike features which mark the magnetization reorientations, this softening takes place over a wide temperature range, from just below $T_C$ to as low as 25 K for the $x \geqslant 0.4$ samples. Similar softening has been observed in the shear moduli of $RCo_2$ compounds[11] and in $Tb_{0.3}Dy_{0.7}Fe_2$.[12] The origin of these reductions in the moduli is undoubtedly the magnetoelastic coupling, traceable to the anisotropic rare earth atoms. Schematically, we have the change in modulus as

$$\Delta E \approx -B^2/K_{\text{eff}}, \tag{3}$$

where $B$ is some magnetoelastic coupling coefficient and $K_{\text{eff}}$ is an effective anisotropy. For cubic polycrystals, $K_{\text{eff}}$ is determined by a competition between fourth ($K_4$) and higher-order anisotropy coefficients, which tend to pull the magnetization along easy crystalline axes, and the dipole forces which tend to align the magnetization along the circumferential direction, in the case of our ring-shaped samples. The latter we model as a uniaxial ($K_2$) anisotropy, going as $M^2$. Just below the Curie temperature, the uniaxial anisotropy dominates; $\Delta E \sim -B^2/K_2$. Well below this temperature regime, $\Delta E \sim -B^2/K_4$. In between these extremes, the two anisotropies compete, causing a series of reorientations over a broad range of temperatures at which $K_{\text{eff}}$ is much smaller than either $K_4$ or $K_2$. The result is a broad minimum in $\Delta E$ plotted vs $K_2/K_4$. When mapped onto the temperature axis, using for example $M^4$ for the temperature dependence of the crystalline anisotropy, the result is a broad dip in the modulus vs temperature, as observed. Details of the modelling and more precise comparisons with the data will be published separately.

## SUMMARY

Young's modulus as a function of temperature has been measured for a series of $Tb_{1-x}Dy_xZn$ pseudobinary compounds with $x$ ranging from 0 to 1. From the sharp dips in the modulus vs temperature data, the reorientation transition temperatures have been determined, and the magnetic phase diagram deduced. Magnetization measurements taken on the same samples show less pronounced features at the corresponding temperatures. We note that the model discussed in the previous section, with suitable allowance for different sample shapes and measurement frequencies, should describe the temperature softening of the Young's or shear modulus in any magnetoelastic polycrystal.

## ACKNOWLEDGMENTS

This work was supported by the Materials S & T Division of the Office of Naval Research, the Independent Research Program at the Naval Surface Warfare Center, and the Naval Undersea Warfare Center Detachment, New London, Active Source Technology task, sponsored by the Office of Naval Research. We would like to thank Thu Van Luu for her assistance with some of the measurements.

[1] P. Morin, J. Rouchy, and E. du Tremolet de Lacheisserie, Phys. Rev. B **16**, 3182 (1977).
[2] P. Morin and J. Pierre, Solid State Commun. **13**, 537 (1973).
[3] A. E. Clark, J. P. Teter, M. Wun-Fogle, J. B. Restorff, and J. F. Lindberg, IEEE Trans. Magn. (to be published).
[4] U. Atzmony, M. Dariel, E. Bauminger, D. Lebenbaum, I. Nowik, and S. Ofer, Phys. Rev. B **7**, 4220 (1973).
[5] E. Dublon, U. Atzmony, M. Dariel, and H. Shaked, Phys. Rev. B **12**, 4628 (1975).
[6] U. Atzmony and M. P. Dariel, Phys. Rev. B **13**, 4006 (1976).
[7] J. R. Cullen, J. Appl. Phys. **52**, 2093 (1981).
[8] C. Williams and N. Koon, Phys. Rev. B **11**, 4360 (1975).
[9] Polycrystalline rare earth-Zn compounds were prepared by T. Lograsso at the Materials Preparation Center, Ames Laboratory, Ames, IA 50010.
[10] P. Morin and J. Pierre, Phys. Status Solidi A **17**, 479 (1973).
[11] H. Klimker, M. Rosen, M. Dariel, and U. Atzmony, Phys. Rev. B **10**, 2968 (1974).
[12] K. Hathaway and J. Cullen, J. Appl. Phys. **52**, 2282 (1981).

# Enhancement of piezomagnetic response of highly magnetostrictive rare earth-iron alloys at kHz frequencies

P. P. Pulvirenti and D. C. Jiles
*Ames Laboratory, Iowa State University, Ames, Iowa 50011*

R. D. Greenough and I. M. Reed
*Department of Applied Physics, University of Hull, Hull, United Kingdom*

The effects of Al and Si additions on the frequency response of highly magnetostrictive Tb–Dy–Fe alloys have been studied. These elements reduced the electrical conductivity of the material, thereby increasing the depth of penetration of ac magnetic fields and extending the operational frequency range. Complex permeability measurements were made on doped and undoped polycrystalline samples with the objective of studying the improvement in energy conversion efficiency at kilohertz frequencies as a result of the alloying additions. The resulting complex permeability was compared with the values for single crystal specimens of $Tb_{0.3}Dy_{0.7}Fe_{1.92}$ at a range of frequencies from 10 Hz to 50 kHz. © *1996 American Institute of Physics.* [S0021-8979(96)78108-X]

## INTRODUCTION

The room temperature magnetostriction of rare earth-iron alloys, such as Terfenol-D has a magnitude of typically 1600 ppm.[1] This has stimulated research into their use in sensor and transducer applications. For instance, micropositioning and adaptive vibration control applications require an appropriate high frequency response. Undoped Terfenol-D has a conductivity of $60\times10^{-8}$ Ω m which significantly reduces the magnetic field penetration. For example, the skin depth is typically 1.5 mm in Terfenol-D at 50 kHz. This limits the diameter of a Terfenol-D rod that can usefully be employed and consequently restricts the load bearing capability of an actuator. Doping Terfenol-D with light elements such as aluminum, silicon, or boron could offer a route whereby the electrical resistivity can be increased by providing scattering sites for the conduction electrons, thereby reducing eddy current effects without having a large adverse effect on the magnetoelastic properties.

## EXPERIMENTAL TECHNIQUES

Measurements of complex permeability were taken as a function of frequency for both doped and undoped polycrystalline samples and for twinned single crystal samples of Terfenol-D. Each specimen was approximately 50 mm long and 9 mm in diameter. The voltage signal from an encircling flux coil on the specimen was analyzed using a lock-in amplifier. The lock-in amplifier provided the reference signal driving the solenoid which generated the applied magnetic field. An ac magnetic field amplitude of 240 A/m was applied at frequencies in the range 10 Hz–50 kHz. The variation of complex permeability with frequency is shown in Fig. 1 for single crystal Terfenol and three specimens of polycrystalline Terfenol. Resonance–antiresonance data obtained from the rate of change of magnetic induction are shown in Fig. 2.

The performance of the materials was quantified in terms of the two piezomagnetic coefficients, $d=(d\lambda/dH)_B$ and $g=-(d\lambda/dB)_\sigma$ and the magnetomechanical coupling coefficient $k$. Real and imaginary components of the piezomagnetic strain coefficient $g$, elastic compliance $s$, and complex permeability $\mu$ were determined for the polycrystalline samples.

The magnetomechanical coupling coefficient $k$ is often calculated from resonance-antiresonance data using

$$k^2=\frac{\pi^2}{8}\left[1-\left(\frac{f_r}{f_a}\right)^2\right], \tag{1}$$

where $f_r$ is resonant frequency and $f_a$ is the antiresonant frequency. Another method for calculating $k$ is using the piezomagnetic coefficient $g$, permeability at constant stress $\mu_s$ and compliance at constant induction $s_B$. This is the so-called *three parameter* method. The value of $k$ is obtained from

$$k^2=g^2\frac{\mu_s}{s_B}. \tag{2}$$

Both of these methods for determining $k$ have limitations, however. The resonance method takes no account of the behavior of the material other than the locations of the

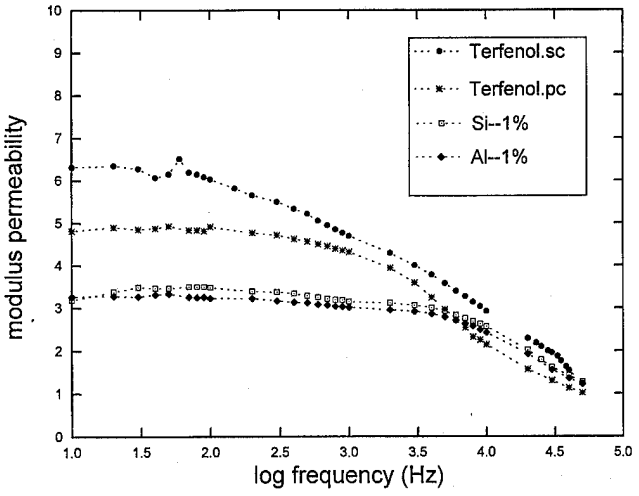



FIG. 1. Complex permeability for (a) single crystal Terfenol, (b) undoped polycrystalline Terfenol, (c) polycrystalline Terfenol +1% Si, (d) polycrystalline Terfenol +1% Al.

 0021-8979/96/79(8)/6219/3/$10.00 © 1996 American Institute of Physics 

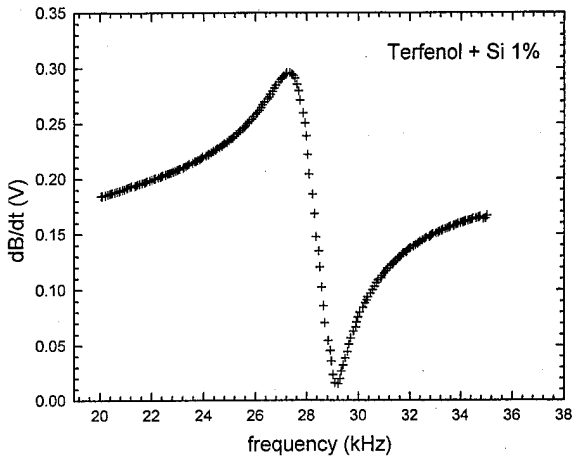



FIG. 2. Resonance–antiresonance peaks for polycrystalline Terfenol +1% Si.

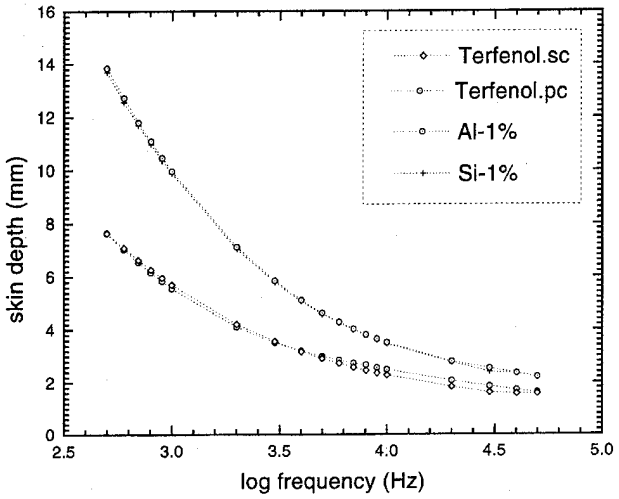



FIG. 3. Calculated skin depth of Terfenol samples as a function of frequency of applied field.

resonance and antiresonance frequencies, and therefore is highly susceptible to slight shifts, or even inaccuracies in the determination of these frequencies.

On the other hand, the analysis leading up to the derivation of Eq. (2) for the three parameter method is flawed because it rests on the assumption of small amplitude, linear and reversible displacements, all three of which are disputable in the case of a ferromagnetic material.

Recently an improved method has been developed for the determination of the coupling coefficient $k$ using plane wave modeling techniques.[2] This allows the shape of the entire frequency response curve of Fig. 2 to be used to determine $k$. Such a calculation is both more robust and more appropriate than the conventional methods used to date.

The coupling factor, $k$ was obtained from the magnetomechanical resonance in rods of different compositions, each approximately 50 mm long and 9 mm in diameter. With no applied prestress, a longitudinal dc bias field of 52 kA/m was sufficient to obtain maximum coupling. The frequency of an oscillatory excitation field of amplitude 80 A/m was swept through a range of frequencies including the resonance and antiresonance. The amplitude and phase of the emf induced in a flux coil wound around the sample were recorded continuously through the whole resonance region. The calculated values of coefficients, $g$, $\mu_s$, and $s_B$ were corrected for the effects of specimen shape and resonant frequency using the plane wave model.[2]

A comparison was made of the measured response with that predicted from a model based on plane acoustic wave propagation in a magnetoelastic medium.[3,4] Values for the piezomagnetic strain coefficient $g$, permeability at constant strain $\mu$, and the elastic compliance at constant induction $s_B$, enabled the magnetomechanical coupling coefficient $k$ to be calculated. The resistivities of the specimens were measured using a standard four probe method.

## RESULTS AND DISCUSSION

Nominal skin depth $\delta$ was calculated for all samples using

$$\delta = \sqrt{\rho/\nu\pi\mu}, \tag{3}$$

where $\rho$ is the resistivity, $\nu$ is the frequency, and $\mu$ is the permeability. Skin depth variation for the different samples as a function of frequency is shown in Fig. 3. The skin depths for the doped specimens were calculated using Eq. (3) together with the measured values of the resistivity $\rho$. The resistivities of the doped samples are an average of 125% greater than the pure Terfenol samples. The skin depths at 1 kHz were found to be 80% greater in the doped specimens than in both the pure polycrystalline Terfenol and the pure single crystal Terfenol.

The polycrystalline unalloyed Tb–Dy–Fe material had $d=1.37\times10^{-9}$ m/A, $g=0.756\times10^{-3}$ A s$^2$/kg, and $k=0.23$. An addition of 1% Al increased $d$ to $1.89\times10^{-3}$ m/A and increased $k$ to 0.287. An addition of 1% Si increased $d$ to $1.92\times10^{-9}$ m/A and increased $k$ to 0.290. These results showed that alloying additions of either 1% Al or Si led to an increase of typically 55% in energy conversion efficiency in the material (see Table I). This improvement arises primarily because of the improved depth of penetration of the magnetic field in the material as shown in Fig. 3.

## CONCLUSION

There is a need to extend the useful operating range of magnetostrictive materials such as Terfenol-D. Presently, material performance is limited by skin depth, which depends on conductivity of the material, and decreases with frequency. The most obvious means to achieve improved performance at high frequency is to limit or reduce the con-

TABLE I. Magnetomechanical coupling coefficients and energy conversion efficiency for various samples.

| Sample | $k$ | $(\Delta k)^2$ |
|---|---|---|
| Polycrystalline Terfenol | 0.232 | ... |
| Terfenol +1% Al | 0.287 | 53% |
| Terfenol +1% Si | 0.290 | 56% |

ductivity. In this work we have alloyed 1% Al or Si with Terfenol to decrease the conductivity. A concomitant reduction in permeability occurs on the addition of Al or Si to Terfenol. This is due to pinning of domain walls by the impurity atoms. Results show that the addition of 1% Al or Si increased the resistivity thus leading to an improvement of field penetration at kHz frequencies and to a 53% or 56% improvement in energy conversion efficiency. However, the addition of higher concentrations of Al or Si resulted in specimens which were extremely brittle and this was recognized as disadvantageous. An alternate method of improving the performance would be through the fabrication of layered specimens consisting of alternate layers of Terfenol and a material of lower conductivity such as silicon.

## ACKNOWLEDGMENTS

This work partially supported by NATO under Grant No. CRG-910275 and by the US Department of Energy Office of Industrial Technology, Advanced Industrial Materials (AIM) Program.

[1] D. C. Jiles, J. Phys. D (Appl. Phys.) **27**, 1 (1994).
[2] I. M. Reed, Ph.D. thesis, University of Hull, United Kingdom, 1994.
[3] I. M. Reed, R. D. Greenough, and M. P. Schulze, IEEE Trans Magn. **29**, 2386 (1993).
[4] I. M. Reed, R. D. Greenough, and A. G. I. Jenner, IEEE Trans. Magn. (to be published).

# Texture in magnetic annealed Terfenol-D films

M. Loveless and S. Guruswamy
*Department of Metallurgical Engineering, University of Utah, Salt Lake City, Utah 84112*

The paper will present an approach to obtaining (111) textured Terfenol-D films suitable for use in magnetostrictive devices. Amorphous thin films of Terfenol-D were rf magnetron sputter deposited on (100) silicon single crystal substrates. A composite target was used to obtain the Terfenol-D films. Samples were subsequently annealed in the range of 300 to 600 °C in the presence of a 2000 Oe magnetic field for times of 15 min to 1 h. X-ray diffraction studies were performed using a Siemens D5000 diffractometer to examine the changes in the preferred crystalline orientation in films with changes in annealing time, annealing temperature, and field orientation. The magnetic properties were examined using a Micromag 2900 alternating gradient magnetometer. Magnetic annealing at 450 °C showed the best combination of magnetic properties. The films exhibited in-plane $H_c$ values in the range of near zero to 350 Oe and $M_s$ values in the range of 200 to 550 emu/cc. © *1996 American Institute of Physics.* [S0021-8979(96)78208-6]

## INTRODUCTION

Large magnetostrictive strains, of the order of 0.1%, make $(Dy_{0.3}Tb_{0.7})Fe_2$ (Terfenol-D) intermetallic bulk alloys and thin films very attractive for use as magnetostrictive sensors and actuators.[1,2] While these alloys have been used in bulk form in a number of commercial and military applications, their use in microactuation and sensing is beginning to be explored. Amorphous and crystalline films of Terfenol alloys have been prepared by several investigators[2–5] and the influence of annealing, composition variations, and sputtering conditions on the magnetostrictive behavior of these films have been examined. Amorphous films deposited without rf bias tend to show perpendicular anisotropy while films deposited with an rf bias have shown in-plane anisotropy.[4] Stresses in the as deposited film also influence the magnetic anisotropy of the film with tensile stresses promoting in-plane easy magnetization. Thermal annealing of amorphous Terfenol films with no applied magnetic field has shown that crystallization was achieved at 450 °C and the magnetic properties and magnetostrictive behavior was inferior to amorphous as deposited films.[4] Magnetic annealing treatments have been shown to modify the magnetostrictive behavior and the magnetic anisotropy in bulk magnetic Terfenol alloys.[6–8] The influence of magnetic annealing has been shown to depend on the stresses present in the film during annealing.[7]

This paper examines the possibility of applying an external magnetic field during annealing of amorphous Terfenol-D films to promote the nucleation of grains with [111] crystallographic axis in the film plane and in the direction of the applied field. The intent of this work is to examine the magnetic properties and the change in crystallographic orientation of magnetically annealed thin films as function of annealing time and temperature.

## EXPERIMENTAL PROCEDURE

A film of Terfenol-D was deposited by rf magnetron sputtering from a mosaic target. The sputtering power was 150 W and the atmosphere was ultrahigh purity argon at a pressure of 5 mTorr. The target itself consists of a 2 in. diameter disk 100 $\mu$m thick of pure iron with pie shaped spokes of pure terbium and dysprosium spot welded to the surface. The nominal composition of a film produced from this target is $Tb_{0.30}Dy_{0.70}Fe_{2.00}$. The substrates used in these experiments were a 2 in. diam (100) silicon wafer and a 10 $\mu$m thick, 2 in. diameter (100) silicon membrane. This film was found to contain more iron than expected so another film was produced which contains less iron. The first film mentioned above will be referred to as the iron rich film and the second will be referred to as the iron deficient film.

Electron probe microanalysis was used to determine the composition of the deposited films.

The substrates were subsequently fractured into strips parallel to the primary flat. Small samples were taken and given magnetic annealing treatments in a high vacuum flash furnace. Annealing temperatures were 300 °C, 450 °C, and 600 °C. Annealing times were 15, 30, and 60 min. Table I shows the conditions for all of the annealing treatments.

Magnetic properties were measured parallel and perpendicular to the film plane of all samples using a vibrating sample magnetometer.

X-ray diffraction experiments were carried out on annealed samples and on the as deposited films.

## RESULTS AND DISCUSSION

Total thickness of the iron rich film was around 2 $\mu$m as measured by an oscillating quartz crystal thickness monitor.

TABLE I. Summary of annealing treatments.

| Sample | Annealing temp. | Annealing time | Field |
|---|---|---|---|
| Iron deficient | 450 °C | 30 min | no field |
| Iron deficient | 450 °C | 30 min | in-plane |
| Iron rich | 300 °C | 15 min | in-plane |
| Iron rich | 300 °C | 30 min | in-plane |
| Iron rich | 300 °C | 60 min | in-plane |
| Iron rich | 450 °C | 30 min | no field |
| Iron rich | 450 °C | 15 min | in-plane |
| Iron rich | 450 °C | 30 min | in-plane |
| Iron rich | 450 °C | 60 min | in-plane |
| Iron rich | 600 °C | 15 min | in-plane |
| Iron rich | 600 °C | 30 min | in-plane |
| Iron rich | 600 °C | 60 min | in-plane |

 0021-8979/96/79(8)/6222/3/$10.00 © 1996 American Institute of Physics

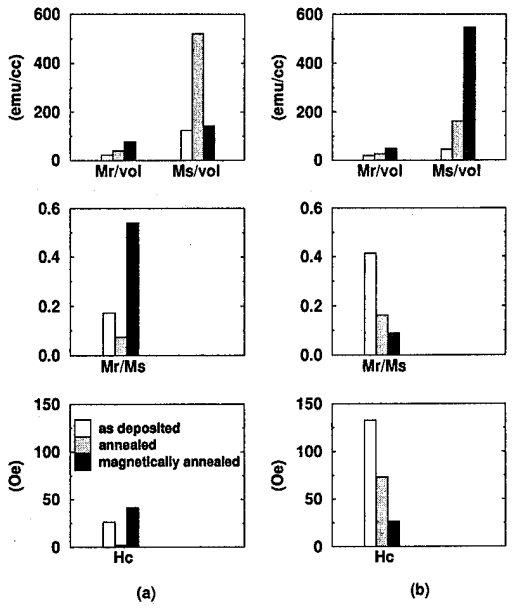



FIG. 1. Comparison of magnetic properties in the as deposited, annealed (450 °C, 30 min) and magnetically annealed (450 °C, 30 min) states of the iron deficient (a) and iron rich (b) films.

Sputtering was stopped when visual inspection of the substrate revealed that it had bulged up in the center. Examination of the target after sputtering showed that the rare earth portions of the target had worn completely through in some areas. The average surface stoichiometry of the film as determined by electron probe microanalysis is $Tb_{0.30}Dy_{0.70}Fe_{2.90}$. The excess iron content is due to the increased surface area of pure iron exposed on the target after the rare earth patches had worn through. After the original film was found to be off composition, a new film was deposited from a new target on a thick silicon wafer as well as the 10 $\mu$m silicon substrate. This new target was found to be intact after sputtering. Compositional analysis of the new film showed it to be $Tb_{0.34}Dy_{0.66}Fe_{1.64}$. Experiments at 450 °C were repeated on this film.

The curvature of both films in the as deposited state was toward the substrate, indicating compressive stresses in the films. Samples magnetically annealed at 300 °C retained this curvature while samples magnetically annealed at 450 °C and 600 °C changed their curvatures to indicate tensile stresses in the film. The sample annealed at 450 °C with no applied field also changed curvature. This result is independent of annealing time. The sample annealed at 600 °C for 60 min developed a rust colored oxide on the surface making the data obtained from this sample suspect.

Magnetic properties are affected profoundly by the presence of a magnetic field during annealing. Figure 1 shows a comparison of magnetic properties measured parallel to the film plane for as deposited, annealed, and magnetically annealed samples of both films. For the iron rich film, a clear trend is visible in the magnetic properties as a result of annealing treatment. The desirable properties of low coercivity ($H_c$), low $M_r/M_s$, and high saturation magnetization ($M_s$) are best achieved by the magnetically annealed sample.

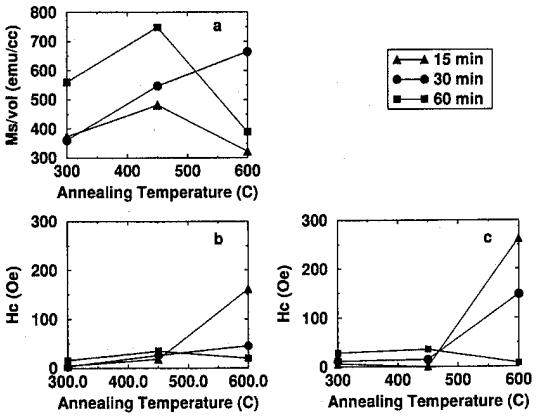



FIG. 2. Temperature dependence of $M_s$(a), and $H_c$ measured parallel (b), and perpendicular (c) to magnetically annealed samples of the iron rich film.

Since strain in Terfenol-D alloys is more closely related to the magnetization than the applied field, the ratio $M_r/M_s$ gives a good indication of the hysteresis that is expected in the magnetostriction. A lower value is desirable because that would indicate less hysteresis. The iron deficient film shows optimum properties in the no field annealed state.

Samples of the iron rich film tend to display maximum $M_s$ when magnetically annealed at 450 °C. Samples magnetically annealed at 600 °C tend to have the largest $H_c$. The only exception to this is the 60 min sample magnetically annealed at 600 °C. This sample developed a rust colored oxide on the surface which possibly affects the coercivity. The coercivity measured parallel and perpendicular to the film plane tend to follow similar trends. Figure 2 shows these

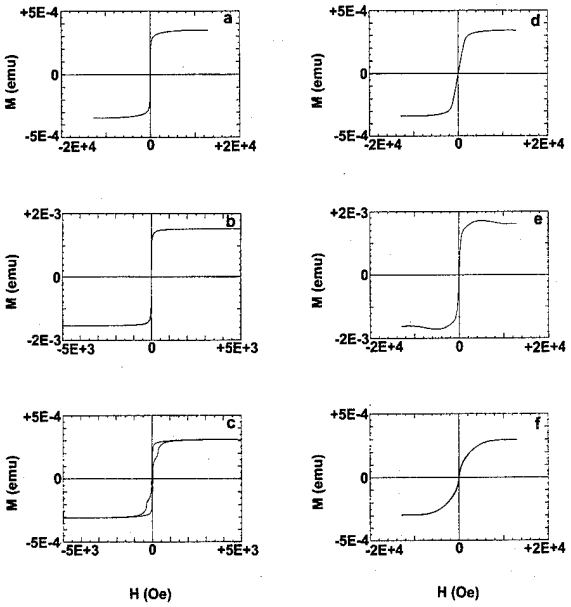



FIG. 3. Hysteresis loops of the iron deficient film measured in-plane for the as deposited (a), annealed (450 °C, 30 min) (b), magnetically annealed (450 °C, 30 min) (c) samples, and perpendicular to the film plane for the as deposited (d), annealed (450 °C, 30 min) (e), and magnetically annealed (450 °C, 30 min) (f) samples. The data shown is not normalized by sample volume.

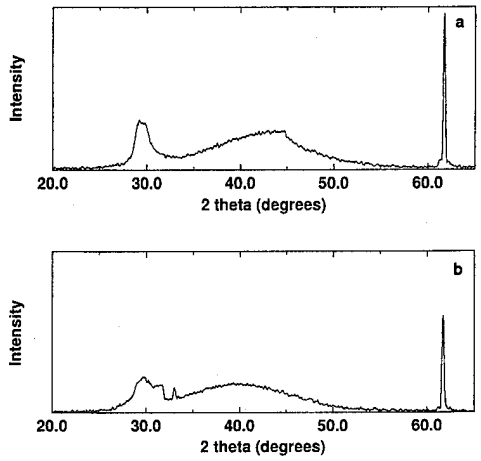



FIG. 4. X-ray spectrum of iron deficient film annealed at 450 °C for 30 min with no magnetic field (a) and with a magnetic field (b) present during annealing.

trends.

Figure 3 shows hysteresis loops of the iron deficient film measured in-plane and perpendicular to the film. Included in the figure are loops from the as deposited, annealed (450 °C, 30 min), and magnetically annealed (450 °C, 30 min) samples. As expected, saturation is achieved at lower fields when measured in-plane.

The properties of the iron deficient film were measured in two in plane directions to look for anisotropy resulting from the magnetic field during annealing. The properties measured parallel and perpendicular to the annealing field were found to be identical. This indicates that there is no in plane anisotropy of the magnetic properties.

X-ray diffraction showed the as deposited iron deficient film to be amorphous. The as deposited iron rich film spectrum has one small peak indicating the presence of some crystalline material. All samples of the iron deficient film showed strong peaks after annealing that could correspond to $Fe_2$(Tb,Dy). There were additional peaks in the magnetically annealed sample spectrum to those in the no field annealed spectrum. Other than the magnetic field present during annealing, these samples were processed identically. This indicates that the magnetic field causes some change in the crystalline nature of the film during annealing. Further investigation is necessary to determine the identity of all phases present. Possibilities include $Fe_2$(Tb,Dy), rare earth oxide, iron oxide, and pure dysprosium. All of these phases have peak positions in common with those found in the experimental diffraction patterns of the iron deficient film annealed at 450 °C for 30 min. Figure 4 shows the diffraction patterns of the iron deficient film annealed with and without a magnetic field at 450 °C for 30 min. Note the extra peaks in the spectrum of the magnetically annealed sample.

## CONCLUSIONS

No preferred in-plane texture was observed as a result of the magnetic field during annealing. One possible explanation for this is the effect of the stresses found to be present in the film. Even though no strong evidence for texture was found, the presence of a magnetic field during annealing of Fe–Tb–Dy thin films does affect the crystal structure and magnetic properties. In the iron rich film, the magnetic field causes lower $H_c$ and higher $M_s$ values than annealing in the absence of a field. For the iron deficient film, the magnetic field causes higher $H_c$ and lower $M_s$ values.

## ACKNOWLEDGMENTS

The authors are grateful for the financial support from the State of Utah through a Mineral Leasing Grant and from NDSEG through a Graduate Research Fellowship to M. Loveless.

[1] A. E. Clark and K. Hathaway, MRS Bull. **XVIII**, 34 (1993).
[2] T. Honda, K. I. Arai, and M. Yamaguchi, J. Appl. Phys. **76**, 6994 (1994).
[3] E. Quant, J. Appl. Phys. **75**, 5653 (1994).
[4] E. Quant, B. Berlach, and K. Seeman, J. Appl. Phys. **76**, 7000 (1994).
[5] P. J. Grundy, D. G. Lord, and P. I. Williams, J. Appl. Phys. **76**, 7003 (1994).
[6] J. D. Verhoeven, J. E. Ostenson, E. D. Gibson, and O. D. McMasters, J. Appl. Phys. **66**, 772 (1989).
[7] N. Galloway, R. D. Greenough, A. G. I. Jenner, and M. P. Schulze, J. Appl. Phys. **76**, 7163 (1994).
[8] J. L. Wallace, J. Appl. Phys. **73**, 5360 (1993).

# Stress dependence of magnetostrictions and strains in ⟨111⟩-oriented single crystals of Terfenol-D

Xuegen Zhao, Guangheng Wu, Jinghua Wang, Kechang Jia, and Wenshan Zhan
*State Key Laboratory for Magnetism, Institute of Physics, CAS, P.O. Box 603, Beijing 100080, People's Republic of China*

Single crystals of $Tb_{0.27}Dy_{0.73}Fe_2$ were prepared successfully by the Czochralski (CZ) method using a magnetic levitation cold crucible first in this laboratory. The Laue x-ray technique and metallography verified its twin-free single crystalline perfection. Weidmanstatten precipitation (WSP) slightly exists in these specimens with WSP platelets parallel to the {111} planes of Terfenol-D. Saturation magnetostriction were measured along three principal crystallographic axes [111], [11 $\bar{2}$] and [1 $\bar{1}$0] of single crystal $Tb_{0.27}Dy_{0.73}Fe_2$ with magnetic field parallel and then perpendicular to the measuring direction, which gives an intrinsic magnetostriction $\lambda_{111}=1640\times10^{-6}$ for ⟨111⟩ easy axis. Stress dependence of magnetostrictions and strains measured along three mutually perpendicular axes, [111], [11 $\bar{2}$], and, [1 $\bar{1}$0] on ⟨111⟩-oriented single crystalline rods of Terfenol-D indicates that apparent magnetostriction for ⟨111⟩ direction increases with increasing applied compressive stress along the rod axis, and reaches $2375\times10^{-6}$ under a stress of 24 MPa and a magnetic field of 20 kOe. Maximum $d_{33}$ decreases with the increment of applied stresses and the amount of WSP, and ranges from $1\times10^{-6}$/Oe to $6\times10^{-6}$/Oe at about 500 Oe. Less hysteresis appears. Magnetizing processes are calculated and compared with the measured changes of magnetostriction. The authors conclude that ⟨111⟩-oriented single crystal of Terfenol-D is suitable for precise displacement actuators although it would be much better to eliminate the WSP precipitation. © *1996 American Institute of Physics.* [S0021-8979(96)78308-2]

## INTRODUCTION

⟨111⟩-oriented single crystals of intermetallic compounds $Tb_xDy_{1-x}Fe_2$ with $x=0.27$ to 0.3, known as Terfenol-D, have been dreamed for more than ten years since Clark and co-workers[1] established that Terfenol-D exhibits very large anisotropic magnetostriction, $\lambda_{111}\gg\lambda_{100}$, and rather low magnetocrystalline anisotropy. It is expected that single crystal rods with a ⟨111⟩ axial orientation and a low defect density posses optimum magnetostrictive properties and find broad applications in vibration emitters such as sonar transducers. Unfortunately, it was only possible to grow crystals along ⟨112⟩ direction and usually occupied by lamellar twins with the plated face parallel to the (111) plane. Much work[2] has been done on such twinned single crystals and it has been found[3,4] such crystals exhibit excellent magnetostrictive properties under compressive stress but twin interfaces, rare earth inclusion and Weidmanstatten precipitates (WSP) and defects inhibit magnetic domain movements by pinning mechanisms. Recently, twin-free ⟨111⟩-oriented single crystals of Terfenol-D have been grown[5] successfully in this laboratory with a cold crucible. The stress dependence of magnetostrictions and elastic strains of single crystals has been investigated.

## EXPERIMENTAL METHODS

Single crystals of $Tb_{0.27}Dy_{0.73}Fe_2$ were grown by using the Czochroaski method with an induction heating magnetic levitation cold crucible. Starting materials of composition $Tb_{0.27}Dy_{0.73}Fe_y$, with $y=1.60$–$1.80$, were prepared from metals of the purity of 99.95%. The metals were alloyed by means of a rf induction heating cold crucible growth system for about 1 h before growth. ⟨111⟩ oriented single crystal bars with dimensions of about $2\times2\times10$ mm$^3$ were used as seeds. X-ray diffraction, Laue back-reflection and metallographical examinations were employed to determine if the samples were single crystals and determine the crystallographic directions. Crystal rods as grown with diameters of 6–12 mm and maximum length of about 80 mm were cut into bars of $5\times5\times15$ mm$^3$ with [111], [11 $\bar{2}$] and [1 $\bar{1}$0] crystal axes perpendicular to their surfaces respectively. Compressive stresses up to 24 MPa were applied along the ⟨111⟩ axial direction by a screw-driven aluminum device fixed between the poles of an electromagnet. The electromagnet with a fixed pole gap of 5 cm can produce a magnetic field up to 20 kOe. Magnetostrictions and strains were measured by strain gauge method.

## RESULTS AND DISCUSSION

X-ray diffraction showed the characteristic diffraction peaks of (111), (222), (333) solely on the transverse sections of the specimens. Laue back-reflection photography confirmed them to be single crystalline with the growth direction along ⟨111⟩ axis. No other phases can be distinguished. However metallographical microscopy shows the existence of slight Weidmanstatten precipitates parallel to {111} planes. WSP can be used as the macro-scale trace of twin interfaces because it always appears parallel to {111}. However WSP traces show no existence of twins in these samples. Zones that are not rare earth rich and without WSP can be found along the rod sometimes. It suggests critical conditions be necessary for growing WSP-and-inclusion-free single crystals of Terfenol-D.

Magnetostrictions were measured at room temperature along three perpendicular crystallographic axes, [111], [11 $\bar{2}$] and [1 $\bar{1}$0].

 0021-8979/96/79(8)/6225/3/$10.00 © 1996 American Institute of Physics 

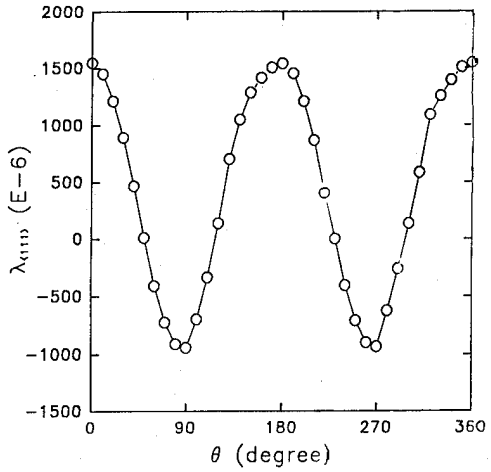



FIG. 1. Magnetostriction vs the relative angles between the [111] measuring direction and applied (1 $\bar{1}$0) magnetic field.

The saturation magnetostrictions measured with applied magnetic field of 20 kOe rotating in (11 $\bar{2}$) and (1 $\bar{1}$0) planes were used to calculate the intrinsic magnetostriction $\lambda_{111}$ by means of the well-known equation

$$\lambda=(3/2)\lambda_{100}(\alpha_1^2\beta_1^2+\alpha_2^2\beta_2^2+\alpha_3^2\beta_3^2)+3\lambda_{111}\times(\alpha_1\alpha_2\beta_1\beta_2+\alpha_2\alpha_3\beta_2\beta_3+\alpha_3\alpha_1\beta_3\beta_1). \quad (1)$$

In which $\alpha_i$ and $\beta_i$ are the direction cosines of magnetization and measuring direction relative to principal ⟨100⟩ crystallographic axes. This method eliminates the influence of prealignments of magnetic domains caused by residual stress or magnetizing history. One of the experimental results is shown in Fig. 1. An intrinsic magnetostriction $\lambda_{111}=1640\times10^{-6}$ for ⟨111⟩ easy axis has been obtained, which is consistent with the previous result.[1]

The magnetostrictions measured with the magnetic field and compressive stress applied in the axial direction of [111] are shown in Fig. 2. The magnetostriction in the axial direction at 3 kOe increases with increasing applied compressive stress until it reaches a maximum of $2200\times10^{-6}$ under 12 MPa, then decreases slightly. The relative change $d_{33}$ of magnetostriction with magnetic field almost be unchanged until 6 MPa, then it becomes smaller with increasing applied compressive stress. $d_{33}$ can range from $1\times10^{-6}$/Oe to $6\times10^{-6}$/Oe at about 500 Oe when the sample is located in a magnetically close circuit. Less hysteresis appears. However the saturation field shifts higher when compressive stress increases, which is true for the stress dependence of magnetostrictions along the [11 $\bar{2}$] and [1 $\bar{1}$0] directions.

It should be noticed that the magnetostrictive behavior under 18 MPa is very different from others. Another magnetization process can be seen clearly in the region of 2.0–2.5 kOe. The [111] magnetostriction changes with a unique slope and the [11 $\bar{2}$] one begins to decrease with increasing magnetic field. This phenomenon also appears in the sample with much fewer defects even under a rather low stress of 3 MPa, as illustrated in Fig. 3.

The elastic strains $\epsilon$ of specimens under different stress and 0, 20 kOe magnetic field were measured and shown in

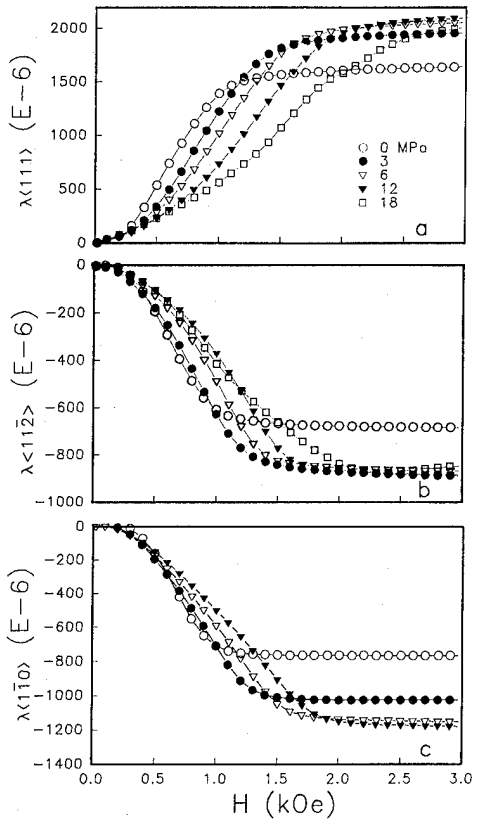



FIG. 2. Magnetostriction curves vs applied magnetic field under different compressive stresses, measured in the direction of (a) [111], (b) [11 $\bar{2}$], and (c) [1 $\bar{1}$0].

Fig. 4. The strains measured in a magnetic field of 20 kOe which is large enough to saturate the specimens, are much smaller than that at 0 kOe due to the large magnetostriction. The change rate of these two strains relative to applied stresses decreases with increasing stresses.

The maximum magnetostrictive strain measured along [111] direction was also shown in Fig. 4. It increases faster under the lower stresses of 0–9 MPa. It is regarded that the

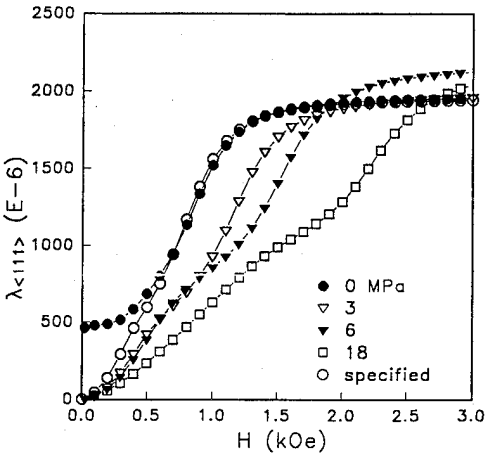



FIG. 3. Magnetostriction curves vs applied magnetic field under different compressive stresses, measured in the direction of [111].

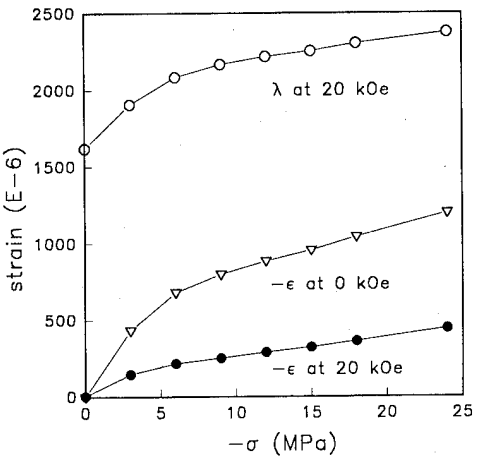



FIG. 4. Magnetostriction λ and elastic strains $\epsilon$ vs applied compressive stress, measured in the direction of [111].

magnetic domains rotate their directions from the axial [111] toward other ⟨111⟩ easy axes under certain stress, which increases the volume of non-180° magnetic domain movements that contribute to magnetostrictive strain. This rotation process seems easy because it proceeds between easy directions. Using Eq. (1) and the magnetostrictions measured in three directions mentioned above, we have calculated the possible arrangement of magnetic domains. We found that when the ⟨111⟩ magnetostriction reaches about $2200\times10^{-6}$ in which the magnetic domains could be assumed to arrange completely along the ⟨111⟩ axes other than the [111] axis at the beginning, the distributions of magnetic domains in other ⟨111⟩ axes are not equal. It might results from the deviation of the applied stress from the axial ⟨111⟩ direction. Under higher stress, the magnetic domains rotate from the ⟨111⟩ easy directions toward ⟨112⟩ directions which are perpendicular to the axial [111] direction. The larger stress is needed to overcome the higher magnetocrystalline anisotropy in the ⟨112⟩ directions. Inclusions and defects hinder all of these rotations.

We can expect that the maximum magnetostrictive strain of $2460\times10^{-6}$ calculated from the measured ⟨111⟩ magnetostriction should be attained when all magnetic moments be forced perpendicular to the axial ⟨111⟩ direction at the beginning. But it is not the case even when the applied stress reaches 24 MPa, a stress enough to overcome the magnetocrystalline anisotropy energy in ⟨112⟩ directions. We can only obtain a maximum magnetostriction of $2375\times10^{-6}$. The mechanical interactions of inclusions and defects with magnetic domains or of magnetic domains with each other may be the reason. It is known that a magnetic heat treatment will improve dramatically the magnetostrictive properties of twinned single crystals with an axial ⟨112⟩ direction and cause a large magnetostrictive jump at low magnetic field. The treatment makes magnetic domains arrange along the same direction just like a single domain and makes the inherent rotation of magnetic domains possible. It also diminishes the mechanical interactions in the sample and reduces the compressive prestress necessary to obtain maximum strain. It would be better if ⟨111⟩-oriented single crystal be annealed in a magnetic field large enough to make all magnetic domains arranged parallel one ⟨112⟩ axis and perpendicular to ⟨111⟩ axial direction, or just only parallel to one ⟨111⟩ axis that is far from the axial ⟨111⟩. Certainly, growth condition should be delicately controlled in order to prevent the formation of rare earth inclusion or WSP.

## CONCLUSION

Twin free ⟨111⟩ oriented single crystals of Terfenol-D, $Tb_{0.27}Dy_{0.73}Fe_2$, have been grown by means of CZ method with an induction heating magnetic levitation cold crucible. The magnetostriction measurements along [111], [11 $\bar{2}$] and [1 $\bar{1}$0] directions with applied magnetic field of 20 kOe rotating in (11 $\bar{2}$) and (1 $\bar{1}$0) planes have confirmed the intrinsic ⟨111⟩ magnetostriction $\lambda_{111}=1640\times10^{-6}$, and $\lambda_{111}\gg\lambda_{100}$. With stress and magnetic field applied in the axial ⟨111⟩ direction, the saturation magnetostriction in this direction and at the field of 20 kOe increases with increasing applied stress, so does the saturation magnetic field. However maximum $d_{33}$ does not change until 6 MPa but decreases with further increase of the applied stresses, and ranges from $1\times10^{-6}$/Oe to $6\times10^{-6}$/Oe. Two magnetizing stages can be observed in these samples under certain stresses, which demonstrates two different inherent magnetic domain movements. The maximum magnetostriction available in ⟨111⟩ direction is $2375\times10^{-6}$, not the calculated value of $2460\times10^{-6}$. The interaction of defects and magnetic domains should be taken into account. No hysteresis can be seen apparently. The authors think that these materials are suitable for vibrating emitters and displacement actuators where the stress can change not too much. Defect-free single crystals would show better magnetostrictive properties.

[1] A. E. Clark, J. E. Cullen, O. D. McMasters, and E. B. Callen, Am. Inst. Phys. Conf. Prof., **29**, 192 (1976).
[2] D. C. Jiles, J. Phys. D **27**, 1 (1994).
[3] A. E. Clark, J. D. Ostenson, and E. D. Gibson, IEEE Trans. Magn. **22**, 973 (1986).
[4] J. D. Verhoeven, J. E. Ostenson, E. D. Gibson, and O. D. McMasters, J. Appl. Phys. **73**, 6168 (1993).
[5] G. Wu, X. Zhao, J. Wang, K. Jia, and W. Zhan, Appl. Phys. Lett., to be published.

# Effects of surface topology and texture on exchange anisotropy in NiFe/Cu/NiFe/FeMn spin valves

C.-M. Park, K.-I. Min, and K. H. Shin
*Division of Metals, Korea Institute of Science and Technology, P.O. Box 131, Cheongryang, Seoul 130-650, Korea*

We have investigated the effects of texture and interfacial roughness on the exchange anisotropy in NiFe/Cu/NiFe/FeMn spin valves with different buffer layers (no buffer, Cu, or FeMn) on Si(100) or Si(111) substrates by magnetron sputtering. The crystalline structure, surface topology, and exchange anisotropy field ($H_{ex}$) were characterized. The exchange anisotropy was established all in (111), (200), and (220) textured samples and there was no systematic relationship between the type of texture and $H_{ex}$. However, it was found that $H_{ex}$ increased as the surface roughness decreased. The results lead us to believe that interfacial roughness rather than crystallographic texture controls the development of the exchange anisotropy. © *1996 American Institute of Physics.* [S0021-8979(96)55308-0]

## I. INTRODUCTION

Giant magnetoresistance of exchange-biased spin valve multilayers of the NiFe/Cu/NiFe/FeMn type has received much attention. The magnetotransport behavior is dependent on unidirectional exchange anisotropy at the interface between the ferromagnetic layer and the antiferromagnetic layer. There has been great interest in the factors that influence the exchange anisotropy.[1,2]

Many reports state that crystalline orientation conditions are important for the establishment of the exchange anisotropy. It has been reported,[1] for example, that the exchange anisotropy field is large when the (111) diffracted intensity of spin valve sandwich is high. Jungblut *et al.*[2] reported that the exchange anisotropy field in NiFe/FeMn couple strongly depends on the crystal orientation. Jungblut *et al.* also tried to account for the orientational dependence of exchange anisotropy field by crystallographic condition, i.e., the compensated or uncompensated nature of ideal NiFe/FeMn interface, but no obvious relation between experimental result and theoretical expectation was observed.

The shortcoming of the interfacial crystallographic condition for exchange anisotropy is that it ignores topological roughness of the ferromagnetic/antiferromagnetic interface. Real interfaces have some roughness and the exchange interaction at the interface is likely to be far more complicated than in the ideal planar case. So far there has been little study on the effects of the interfacial topology on the exchange anisotropy.

The purpose of this study is to examine the effects of preferred orientation and interfacial topology on the exchange anisotropy of spin valves.

## II. EXPERIMENT

Exchange-biased spin valve samples consisting of Si/buffer layer 50 Å/NiFe 80 Å/Cu 28 Å/NiFe 40 Å/FeMn 150 Å/Cu 50 Å were fabricated by three-gun magnetron sputtering with $5\times10^{-3}$ Torr argon pressure during deposition. Ferromagnetic NiFe layers were deposited by rf magnetron sputtering and the other layers (Cu and FeMn) were deposited by dc magnetron sputtering. The base pressure was below $5\times10^{-7}$ Torr. Films of $1\times1$ cm$^2$ were deposited at room temperature in a uniform magnetic field of 300 Oe which determines the direction of exchange anisotropy.

For texture control, FeMn and Cu buffer layers were used with Si(100) or Si(111) substrates, which were precleaned with dilute HF. For Si(111) substrates, the Si[111] axis was off orientation by 4° from the surface normal toward a Si[110] axis. Samples without a buffer layer were also fabricated.

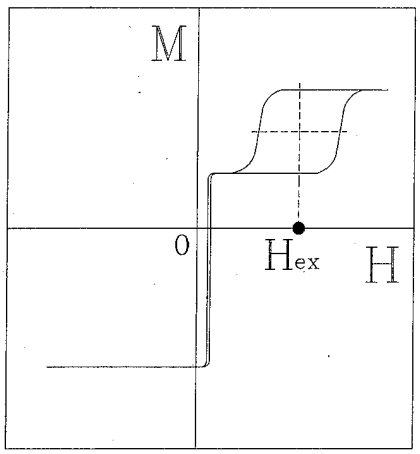



FIG. 1. Typical hysteresis loop of exchange-biased spin valve. The exchange anisotropy field $H_{ex}$ is defined as the horizontal shift of the center of the hysteresis loop of the exchange-biased ferromagnetic layer.

 0021-8979/96/79(8)/6228/3/$10.00 © 1996 American Institute of Physics

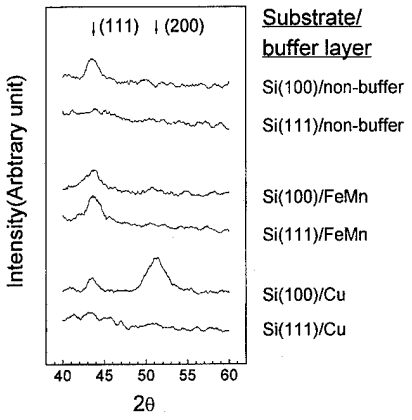



FIG. 2. X-ray diffraction patterns of Si(111 or 100)/NiFe 80 Å/Cu 28 Å/NiFe 40 Å/FeMn 150 Å/Cu 50 Å and Si/(Cu or FeMn 50 Å)/NiFe 80 Å/Cu 28 Å/NiFe 40 Å/FeMn 150 Å/Cu 50 Å.

Crystallographic texture of the samples was assessed by x-ray diffraction. Transmission electron microscopy (TEM) analysis was also performed on selected samples. The exchange anisotropy fields were characterized by a vibrating sample magnetometer (VSM). $H_{ex}$ corresponds to the horizontal shift of the center of the hysteresis loop from the center of whole plot due to the exchange anisotropy of the NiFe/FeMn couple. Figure 1 shows how $H_{ex}$ is determined from an $M$-$H$ curve.

In order to characterize the interfacial topology, surface topology analyses were performed by using PSI AP-200 AutoProbe LS atomic force microscope (AFM). Because multilayers often grow coherently up to considerable thickness when deposited by sputtering, it is reasonable to think that the surface topology is related to the interface topology, if the interface is not too far from the top surface. In our case, they are separated by 200 Å.

## III. RESULTS AND DISCUSSION

X-ray diffraction patterns of six spin valve samples with different buffer layers grown on Si(100) or Si(111) substrates are shown in Fig. 2. For samples with an FeMn buffer layer on Si(100) or Si(111) substrate, a (111) peak is observed. The sample without a buffer layer on Si(100) shows a (111) peak. No sign of peak is seen in the unbuffered sample grown on Si(111). A (200) peak with a weak trace of (111) peak is detected in a sample with a Cu buffer layer on Si(100). The predominant (200) texturing is consistent with previous reports.[3,4] For the sample with a Cu buffer layer on Si(111), no peak is observed. TEM analysis, however, suggested a pseudoepitaxial (220) growth, similar to that reported[5] in NiFe/Cu multilayers with a Cu buffer layer on misoriented Si(111) substrates. No sign of (220) peak was observed near the expected position ($2\theta \sim 75°$), which is not shown in Fig. 2. More detailed description of the TEM analysis will be published elsewhere.

The exchange anisotropy field $H_{ex}$ determined from an $M$-$H$ curve is shown, together with the textures developed, in Table I. The samples with an FeMn buffer layer have larger $H_{ex}$ values by about a factor of 2 than those without a buffer layer. The samples with a Cu buffer layer have intermediate $H_{ex}$ values. It seems from Table I that $H_{ex}$ does not depend on the substrate, whether it be Si(100) or Si(111).

TABLE I. Textures and exchange anisotropy field ($H_{ex}$) values of the samples shown in Fig. 2.

| Substrate and buffer layer | Texture | $H_{ex}$ (Oe) |
|---|---|---|
| Si(100)/nonbuffer | (111) | 80 |
| Si(111)/nonbuffer | untextured | 80 |
| Si(100)/FeMn | (111) | 180 |
| Si(111)/FeMn | (111) | 190 |
| Si(100)/Cu | (200)+weaker (111) | 130 |
| Si(111)/Cu | (220)[a] | 140 |

[a](220) texture is identified from TEM diffraction pattern analysis, not from XRD spectrum.

A prominent feature of the results is that a considerable exchange anisotropy field of about 130 Oe is established for the samples that have the preferred orientations (200) and (220). Also noticeable is the fact that $H_{ex}$'s of 80 Oe at the least are observed for all samples including the untextured one. Nakatani *et al.*[1] have reported that the FeMn layer becomes antiferromagnetic and applies an exchange bias field to the NiFe layer when a sample has a high (111) diffracted intensity. From our study, however, it is found that there is

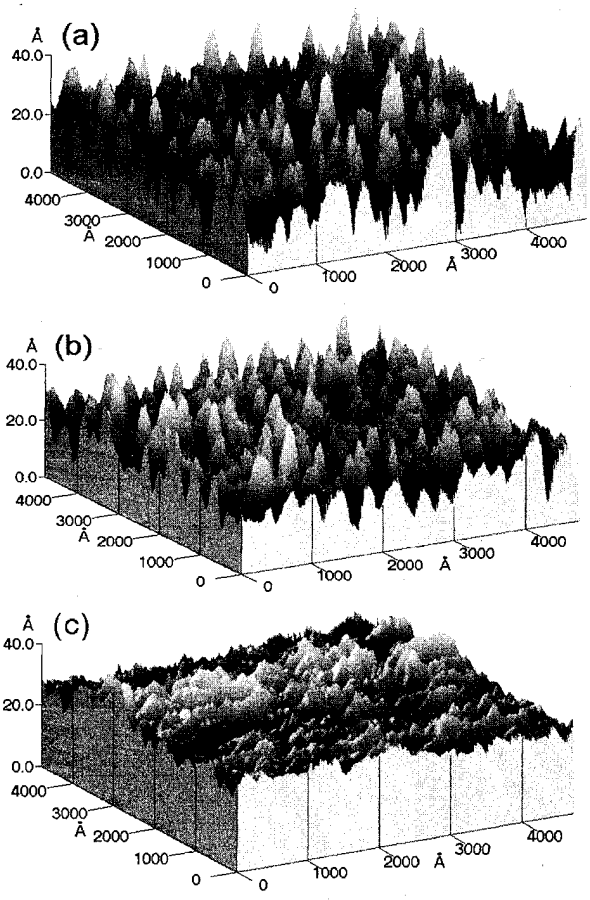



FIG. 3. AFM surface topographs of (a) nonbuffered, (b) Cu buffered, and (c) FeMn buffered NiFe/Cu/NiFe/FeMn/Cu films on Si(111) substrates.

no proportional dependence of $H_{ex}$ on (111) diffracted intensity. Jungblut *et al.*[2] have investigated a dependence of $H_{ex}$ of molecular-beam-epitaxy-grown Cu/NiFe/FeMn samples on the growth orientation and found that there is no obvious relation between the $H_{ex}$ and the compensated or uncompensated nature of the NiFe/FeMn interface. Our results based on texture are consistent with this finding of Jungblut *et al.* Both results suggest that a specific texture is not necessarily a critical factor for establishing an exchange anisotropy, and that preferred orientation alone cannot explain this phenomenon satisfactorily.

No current theoretical model can account for the experimental results of the largest exchange anisotropy field with (111) texturing in FeMn. The discrepancy between expectation and experimental result can be attributed to the assumption that NiFe/FeMn couple has an ideal interface.

The idealized interface does not exist in reality as in the case of multilayers deposited by sputtering. In this case, interfacial roughness can have a great influence on the exchange interaction at the interface by changing the local spin arrangement and the number of antiparallel moments at the interfacial plane. In the naive picture of the uncompensated ideal interface, for example, roughness will cause compensation and thus reduction of $H_{ex}$. The interface topology, therefore, must be examined in addition to the texture.

Surface topographs of films grown on Si(111) substrates taken by AFM are shown in Fig. 3. These figures show peaks and valleys. Valleys are several hundred angstroms apart on the average. This is roughly of the size of the grains, suggesting that this surface topology may be closely related to the nucleation and growth of the initial film layer. It can be seen from Fig. 3 that the surface becomes flatter when a Cu buffer layer is introduced and even flatter in the case of an FeMn buffer layer. In Table II, roughness parameters (median height, mean height, $R_{rms}$, and $R_{ave}$) are given, together with their definitions. It is obvious from this table that roughness decreases in the sequence of nonbuffer, Cu, and FeMn, and $H_{ex}$ increases in this sequence. Therefore, a systematic relationship is found between the surface roughness and $H_{ex}$;

TABLE II. Surface roughness for AFM height profiles shown in Fig. 3, estimated by the parameters defined as follows: $\bar{z}$=mean height $=\frac{1}{N}\sum_{n=1}^{N} z_n$, $R_{rms}=\sqrt{\sum_{n=1}^{N}(z_n-\bar{z})^2/(N-1)}$, $R_{ave}=\sum_{n=1}^{N}|z_n-\bar{z}|/(N)$, where $N$ is the number of data points and $z$ is the height of each data point within the height profile. Median height is the height value which divides the height histogram into two equal areas.

| Si(111)/ buffer layer | Median height (Å) | Mean height (Å) | $R_{rms}$ (Å) | $R_{ave}$ (Å) | $H_{ex}$ (Oe) |
|---|---|---|---|---|---|
| Nonbuffer | 25 | 23 | 6.9 | 5.5 | 80 |
| Cu | 20 | 18 | 5.6 | 4.4 | 140 |
| FeMn | 12 | 12 | 3.2 | 2.4 | 190 |

namely samples with flatter surfaces have larger exchange anisotropy. Summarizing our results, it seems that the exchange anisotropy is more sensitive to surface roughness than to the specific texture of the sputter-deposited film. Our results suggest that the dependence of exchange anisotropy on texture reported in previous works[1,2] might result from changes in NiFe/FeMn interface topology rather than in texture. More sophisticated experiments are required to examine the connection of crystallography with the interfacial exchange interaction.

## IV. CONCLUSION

For exchange-biased spin valves with (111), (200), or (220) textures, no systematic relation between the texture and exchange anisotropy was observed. It was found that the exchange anisotropy increased as the surface roughness decreased. These results lead us to emphasize the role of interfacial roughness rather than texture in the establishment of exchange anisotropy.

[1] R. Nakatani, K. Hoshino, S. Noguchi, and Y. Sugita, Jpn. J. Appl. Phys. **33**, 133 (1994).
[2] R. Jungblut, R. Coehoorn, M. T. Johnson, J. aan de Stegge, and A. Reinders, J. Appl. Phys. **75**, 6659 (1994).
[3] C.-A. Chang, Appl. Phys. Lett. **57**, 2239 (1990).
[4] I. Hashim, B. Park, and H. A. Atwater, Appl. Phys. Lett. **63**, 2833 (1993).
[5] K.-I. Min, S.-K. Joo, and K. H. Shin (in press).

# High sensitivity in magnetoresistance of epitaxial NiFe/Cu/Co (/Cu) (100) superlattices

Y. Kawawake, H. Sakakima, Y. Irie, and M. Satomi
*Central Research Labs., Matsushita Electric Industrial Co., Ltd. 3-4, Hikaridai, Seika-cho, Souraku-gun, Kyoto-fu, 619-02, Japan*

Noncoupled-type [NiFe/Cu/Co(/Cu)] single-crystal-like superlattices were prepared on Si/Cu(100) substrates using ultrahigh vacuum evaporation. Si/Cu (5 nm)/[Co (3 nm)/Cu (6 nm)/NiFe (3 nm)/Cu (6 nm)]×10 multilayers showed 6.1% magnetoresistance (MR) change with 2 kA/m of applied field, which is much higher sensitivity than those of poly-crystalline films. Furthermore, placing a thin Ag layer (0.2 nm) at the midpoint of a Cu layer improved the MR sensitivity of the epitaxial film. Sandwich-type Si/Cu (5 nm)/NiFe (10 nm)/Cu (2.4 nm)/Ag (0.2 nm)/Cu (2.4 nm)/Co (10 nm) superlattice showed sharp switching characteristics of the MR curve between lower and 4.3% higher resistivity. These epitaxial films showed biaxial anisotropy in the film plane with easy axes of [011] and [0$\bar{1}$1] directions. The higher MR sensitivity in the epitaxial films may originate in the square-shaped magnetization curves along the easy axes [011] and [0$\bar{1}$1] of the Co layers. Flatness of interface was also effective to improve the MR sensitivity of the films. © *1996 American Institute of Physics.* [S0021-8979(96)55408-7]

## I. INTRODUCTION

Among a number of systems showing a giant magnetoresistance (MR) behavior, noncoupled-type [NiFe/Cu/Co/Cu] multilayers have been intensively studied because of their low-field operation.[1] In the above system, antiparallel alignment of magnetizations was realized by using the difference of the coercivities of two ferromagnetic layers. Shinjo and Yamamoto reported that glass/[Co (3 nm)/Cu (5 nm)/NiFe (3 nm)/Cu (5 nm)]×15 multilayers showed a resistivity change of 7% in 100 Oe (≅8 kA/m).[1] This sensitivity is lower than that of FeMn/NiFe/Cu/NiFe spin-valve multilayers.[2] In this study, we have tried to improve the sensitivity of NiFe/Cu/Co/Cu multilayers by improving the soft magnetic properties of NiFe layers by reducing the couplings between ferromagnetic layers.

Epitaxial NiFe/Cu/Co(/Cu) superlattices were prepared on Si/Cu (100) substrates to control the crystalline anisotropy of NiFe and Co magnetizations. In the epitaxial [NiFe/Cu] multilayers[3] and Co/Cu/Co sandwich films,[4] the exchange couplings between ferromagnetic layers with the (100) orientation were smaller than those with the (111) orientation.[3,4] Therefore (100) orientation could be thought preferable orientation to improve MR sensitivity in noncoupled type NiFe/Cu/Co(/Cu) films than (111) orientation.

## II. EXPERIMENT

HF etched Si(100) single-crystal substrate was placed in an ultrahigh vacuum chamber. A 5–50 nm thick Cu buffer layer was deposited on Si(100) substrate at room temperature (RT) and NiFe/Cu/Co(/Cu) film was prepared on the Cu buffer layer at RT. Crystal growth was *in situ* monitored by reflection high-energy electron diffraction (RHEED). MR was measured by four-point probe method and magnetization was measured by a vibrating sample magnetometer (VSM). Magnetic field was applied both in [011] and in [001] directions in the film plane. Electric current was along the [001] direction of the film in the film plane. All measurements were performed at RT.

## III. RESULTS AND DISCUSSION

After the deposition of 50-nm-thick Cu buffer layer on Si(100) substrate, a strain-free flat surface of Cu(100) was realized.[3] Figure 1(a) shows RHEED pattern after the deposition of Si/Cu (5 nm)/[Co (3 nm)/Cu (5 nm)/NiFe (3 nm)/Cu (5 nm)]×10 multilayers. Streak pattern of RHEED was maintained during the deposition of the [Co/Cu/NiFe/Cu] multilayers. The orientational relationships of the sample are Si(100)//Cu(100)//Co(100)//NiFe(100) in the stacking direction and Si[011]//Cu[001]//Co[001]//NiFe[001] in the film plane.

Figure 2 shows Cu layer thickness $t$ dependence of MR curve of Si/Cu (5 nm)/[Co (3 nm)/Cu ($t$ nm)/NiFe (3 nm)/Cu ($t$ nm)]×10 multilayers. The MR ratio of the sample with $t=6$ changes from 0.4% to 6.5% in the field range from 0 to 2 kA/m in [011] direction (solid line) while smaller change in MR ratio could be observed in [001] direction (dashed line). These films showed biaxial anisotropy with easy axes of [001] and [0$\bar{1}$1] directions in the film plane. As $t$ increases, the MR ratio decreases owing to shunting effect ($t\geqslant 6$), however, in the $t=10$ sample clear switching characteristics between high and low resistivity could be observed due to free and independent rotations of Co and NiFe magnetizations. Couplings between Co and NiFe layers exist to some extent even in the sample with $t=6$.

To reduce the couplings between ferromagnetic layers, we interposed thin Ag layer at the midpoint of a Cu layer. Figure 3 shows MR curves of Si/Cu (5 nm)/[Co (3 nm)/Cu ($2.5-x/2$ nm)/Ag ($x$ nm)/Cu ($2.5-x/2$ nm)/NiFe (3 nm)/Cu ($2.5-x/2$ nm)/Ag ($x$ nm)/Cu ($2.5-x/2$ nm)]×10 multilayers. The samples with $x=0.1$ and 0.2 show higher sensitivities than the sample without Ag layer ($x=0$). The MR ratio of the sample with $x=0.4$ is lower than those of $x\leqslant 0.2$ and the MR curves of the sample has negligible angular dependence,

 0021-8979/96/79(8)/6231/3/$10.00 © 1996 American Institute of Physics 

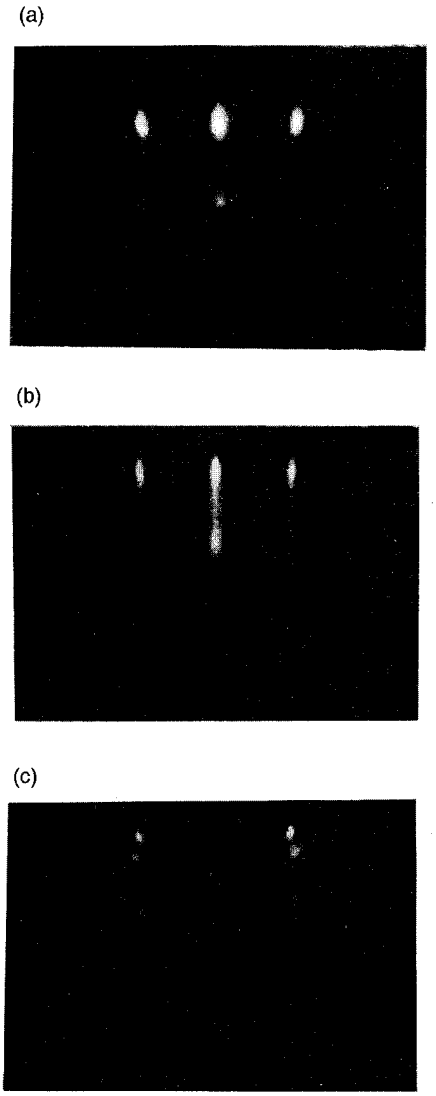



FIG. 1. RHEED patterns of Si/Cu (50 nm)/[Co (3 nm)/Cu (2.5−$x$/2 nm)/Ag ($x$ nm)/Cu (2.5−$x$/2 nm)/NiFe (3 nm)/Cu (2.5−$x$/2 nm)/Ag ($x$ nm)/Cu (2.5 −$x$/2 nm)]×10 multilayers. (a) $x$=0, (b) $x$=0.2, and (c) $x$=0.4.

which is characteristic of poly-crystalline film. RHEED patterns after deposition of the samples with $x$=0, 0.2 and 0.4 are shown in Fig. 1. Figure 1(b) ($x$=0.2) shows a more streaky pattern, which is indicating a flatter surface of the film, than Fig. 1(c) ($x$=0). This result possibly indicates that the interposition of thin Ag layers improves the flatness of the interface between ferromagnetic and nonmagnetic layers.

We have also investigated electric and magnetic properties of sandwich-type NiFe/Cu(/Ag/Cu)/Co films in Si/Cu substrates. In this case, samples were prepared on a thinner buffer layer to increase resistance. Therefore more distortion was induced in these samples, however, they were epitaxially grown on Si/Cu with the same orientational relationships as those of the samples on 50-nm-thick Cu buffer layer. Figure 4 shows (a) MR and (b) magnetization curves of Si/Cu (5 nm)/NiFe (10 nm)/Cu (2.4 nm)/Ag (0.2 nm)/Cu (2.4 nm)/Co (10 nm) film. Figure 4(a) shows clear switching characteristics of resistivity along the [011] direction in the film plane. The MR ratios of the samples are 4.3% and 3.4% in [011]

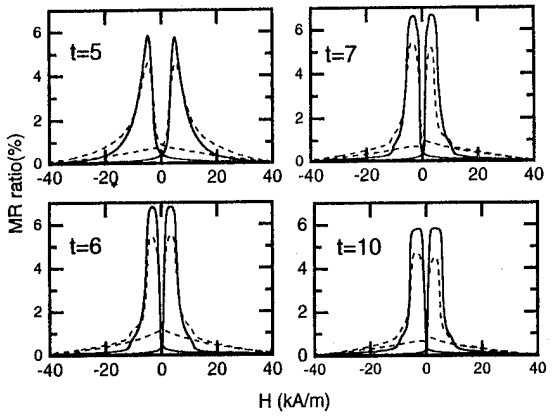



FIG. 2. Room-temperature MR curves for Si/Cu (50 nm)/[Co 3 nm)/Cu ($t$ nm)/NiFe (3 nm)/Cu ($t$ nm)]×10 multilayers with Cu thickness $t$ of 5, 6, 7, and 10 nm. Magnetic field was applied both in the [011] direction (solid line) and in the [001] direction (dashed line).

and [001] directions, respectively. The difference in MR curves between [011] and [001] should come from the difference between magnetization curves of both directions. In Fig. 4(b), the soft layer (NiFe layer) rotates at about 1 kA/m in the same way in both directions, however, only about 70% of the magnetization of the hard layer (Co layer) rotates at about 3.5 kA/m in the [001] direction, while the nearly whole magnetization of the Co layer rotates at the same field in the [011] direction.

In a cubic crystal, magnetocrystalline anisotropy $E_a$ is generally expressed by

$$E_a = K_1(\alpha_1^2\alpha_2^2 + \alpha_2^2\alpha_3^2 + \alpha_3^2\alpha_1^2) + K_2\alpha_1^2\alpha_2^2\alpha_3^2 + \cdots, \quad (1)$$

where $\alpha_1$, $\alpha_2$, and $\alpha_3$ are direction cosines of magnetization from the crystallographic axes and $K_1$ and $K_2$ are cubic anisotropy constants.[5] When the magnetization rotates in the (100) plane, the second term of Eq. (1) is zero and it is expressed as

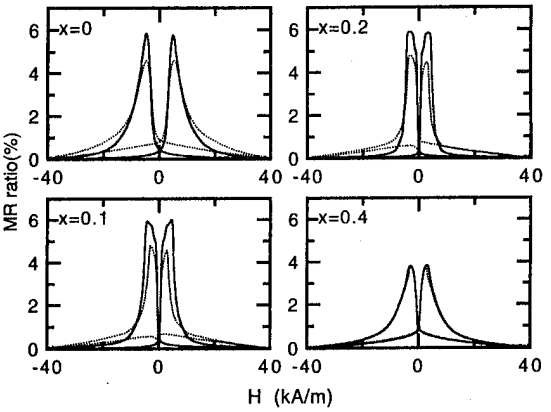



FIG. 3. MR curves of Si/Cu (50 nm)/[Co (3 nm)/Cu (2.5−$x$/2 nm)/Ag ($x$ nm)/Cu (2.5−$x$/2 nm)/NiFe (3 nm)/Cu (2.5−$x$/2 nm)/Ag ($x$ nm)/Cu (2.5 −$x$/2 nm)]×10 multilayers with Ag thickness $x$ of 0, 0.1, 0.2, and 0.4 nm. Magnetic field was applied both in the [011] direction (solid line) and in the [001] direction (dashed line).

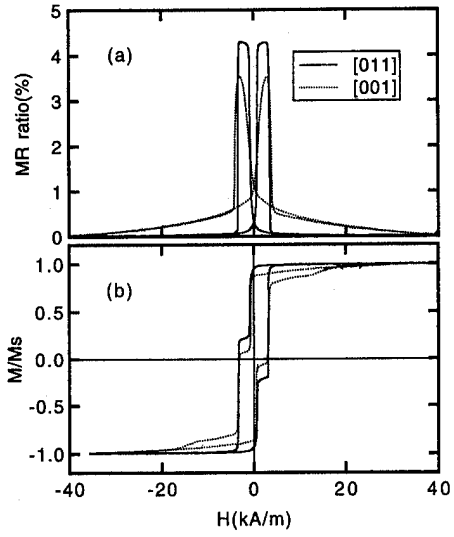



FIG. 4. MR and magnetization curves of Si/Cu (5 nm)/NiFe (10 nm)/Cu (2.4 nm)/Ag (0.2 nm)/Cu (2.4 nm)/Co (10 nm) film with the applied field in the [011] direction (solid line) and in the [001] direction (dashed line).

$$E_a=\frac{K_1}{8}(1-\cos 4\theta)+\cdots, \tag{2}$$

where $\theta$ is an angle between magnetization and [010] axis. In fcc Co, the sign of $K_1$ is minus.[6] Therefore Eq. (2) means biaxial anisotropy with the easy axes of [011] and [0$\bar{1}$1] in the plane. This qualitatively agrees with the results on the epitaxial NiFe/Cu/Co(/Cu) films. The origin of biaxial anisotropy of the films comes from crystalline anisotropy of fcc Co.

Minor MR loop was also measured on the sample along the [011] direction as shown in Fig. 5. In Fig. 5, Co magnetization is fixed to one direction and NiFe magnetization rotates from parallel state to antiparallel state to Co magnetization at $H_2$, and from antiparallel to parallel at $H_1$. Therefore the switching fields, $H_1$ and $H_2$ can be written as follows:

$$H_1=H_{\text{coupling}}-H_{c\text{NiFe}}, \quad H_2=H_{\text{coupling}}+H_{c\text{NiFe}}, \tag{3}$$

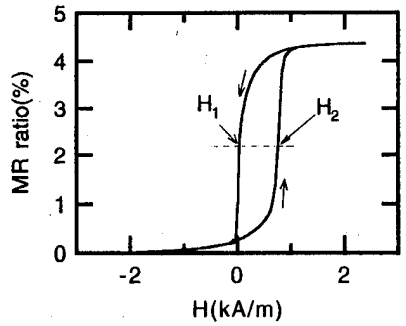



FIG. 5. MR minor loop of Si/Cu (5 nm)/NiFe (10 nm)/Cu (2.4 nm)/Ag (0.2 nm)/Cu (2.4 nm)/Co (10 nm) film with the applied field in the [011] direction.

while $H_{\text{coupling}}$ is the coupling field between Co and NiFe layer and $H_{c\text{NiFe}}$ is the coercivity of NiFe layer.[7] Equations (3) mean $H_{\text{coupling}}=(H_1+H_2)/2$ and $H_{c\text{NiFe}}=(H_2-H_1)/2$. From Fig. 5, the calculated values of $H_{\text{coupling}}$ and $H_{c\text{NiFe}}$ are 0.44 and 0.4 kA/m, respectively. The exchange field of poly-crystalline [Cu (5.5 nm)/Co (2.5 nm)/Cu (5.5 nm)/NiFe (2.5 nm)] multilayers were estimated to be 7 Oe (0.56 kA/m) by Shinjo *et al.*[8] by measuring angular dependence of resistivity in small field. The value of the epitaxial film is roughly the same as that of the poly-crystalline film. Therefore sharp switching characteristics of MR in the epitaxial film are not caused by the reduction of exchange couplings of the film.

Interface roughness should have an effect on exchange couplings between ferromagnetic layers. In [NiFe(Co)/Cu] multilayers, no evidence of a giant MR or antiferromagnetic couplings could be observed in the poly-crystalline films. Oscillations of MR ratio were observed, however, in epitaxial films in which flatter interfaces were observed than in poly-crystalline films.[3] These results suggested that flatter interfaces formed by epitaxial growth promoted the antiferromagnetic couplings between ferromagnetic layers. In the epitaxial [NiFe/Cu/Co/Cu] multilayers, the interposition of thin Ag layer decreased roughness of the interface and improved the MR sensitivity. Interface roughness might generate pinholes and ferromagnetic coupling between ferromagnetic layers. In poly-crystalline [NiFe/Cu/Co/Cu] multilayers, Cr underlayer improve interface flatness and MR sensitivity of the film.[9] Our results on epitaxial films suggests that in noncoupled-type [NiFe/Cu/Co/Cu] multilayers, interface flatness improves MR sensitivity.

## IV. CONCLUSION

In the epitaxial [Co/Cu/NiFe(/Cu)] films on Si(100)/Cu substrates, high MR sensitivity along the [011] and [0$\bar{1}$1] directions in the film plane was realized. Furthermore, interposition of thin Ag layer in a Cu layer improved MR sensitivity of the film. The higher MR sensitivity in the epitaxial films may originate in the square-shaped magnetization curves along the easy axes [011] and [0$\bar{1}$1] of the Co layers. Flatness of interface was also effective to improve the MR sensitivity in the films.


[1] T. Shinjo and H. Yamamoto, J. Phys. Soc. Jpn. **59**, 3061 (1990).
[2] B. Dieny, V. S. Speriosu, S. S. P. Parkin, B. A. Gurney, D. R. Wilhoit, and D. Mauri, Phys. Rev. B **43**, 1297 (1991).
[3] Y. Kawawake, H. Sakakima, Y. Irie, and M. Satomi, Jpn. J. Appl. Phys. **11B**, L1598 (1994).
[4] M. T. Johnson, S. T. Purcell, N. W. E. McGee, R. Coehoorn, J. aan de Stegge, and W. Hoving, Phys. Rev. Lett. **68**, 2668 (1992); M. T. Johnson, R. Coehoorn, J. J. de Vries, N. W. E. McGee, J. aan de Stegge, and P. J. H. Bloemen, *ibid.* **69**, 969 (1992).
[5] Chikazumi and S. H. Charap, *Physics of Magnetism* (Wiley, New York, 1964), p. 129.
[6] J. Fassender, Ch. Mathieu, B. Hillebrands, G. Gruntherodt, R. Jungblut, and M. T. Johnson, J. Magn. Magn. Mater. **148**, 156 (1995).
[7] L. B. Steren, R. Morel, A. Barthelemy, F. Petroff, A. Fert, P. Holody, R. Loloee, and P. A. Schroeder, J. Magn. Magn. Mater. **140–144**, 495 (1995).
[8] T. Shinjo, H. Yamamoto, T. Anno, and T. Okuyama, Appl. Surf. Sci. **60/61**, 798 (1992).
[9] H. Yamamoto, Y. Motomura, T. Anno, and T. Shinjo, J. Magn. Magn. Mater. **126**, 437 (1993).

# Factors affecting performance of NiO biased giant magnetoresistance structures

S. F. Cheng and J. P. Teter
*Naval Surface Warfare Center, White Oak, Maryland 20903-5640*

P. Lubitz, M. M. Miller, L. Hoines, J. J. Krebs, D. M. Schaefer, and G. A. Prinz
*Naval Research Laboratory, Washington, DC 20375-5640*

We have made spin-valve structures of Permalloy/Cu/Co by sputtering or electron-beam deposition onto the antiferromagnetic oxide NiO. The oxides were made either by deposition of the metals and subsequent oxidation or by growing them *in situ* using reactive sputtering. The magnetic properties of the giant magnetoresistance structures were studied by magnetoresistance, vibrating sample magnetometry, and ferromagnetic resonance methods. The oxides were characterized by x-ray diffraction and atomic force microscopy. We studied surface roughness and structure as functions of thickness and oxidation temperature and correlated the oxide properties with the magnetic performance. We found that the metal layer roughened during the postdeposition oxidation process and that the resulting oxide layers were very effective in pinning the direction of the magnetic moment of adjacent metal films. Coercive fields over 500 Oe were obtained for Co overlayers on NiO films but the exchange bias field was generally less than 100 Oe and was not strongly dependent on the roughness. The beneficial effects of this strong pinning were offset to some degree by higher switching fields required in spin-valve structures deposited over the Co. We also made reactively sputtered oxide antiferromagnetic films which had smoother surfaces than those made by postdeposition oxidation. [S0021-8979(96)55508-3]

## I. INTRODUCTION

Properties of antiferromagnetic NiO, CoO, and NiO–CoO mixtures as magnetic bias layers have recently been extensively investigated because of their potential advantages in fixing the orientation of one of the layers in a spin-valve or giant magnetoresistance (GMR) structure.[1–3] The resulting oxide layers are chemically stable, insulating, and can be simply and reproducibly made. Most work has used reactive sputtering to prepare the oxide films; results of using bulk single crystals[2] and molecular-beam-epitaxy (MBE) grown films[4] for magnetic bias have also been reported. While roughness has been identified as a factor increasing both coercivity and exchange bias field, the undesirable effects of roughness on the coercivity of overlying "soft" layers have not been reported. Roughness may increase exchange bias by increasing the amount of interface area available while coercivity is increased by the distribution of dipolar magnetic fields around magnetic defects or structures, which can thus act as traps or barriers for domain walls. The basic aspects of antiferromagnetic oxides in providing exchange bias to adjacent layers were explored by Miekeljohn and Bean[5] and later by Malozemoff;[6] they found that atomic exchange fields of over $10^6$ Oe were drastically reduced by the averaging over random spin orientations in practical materials: In effect, the statistical deviations from zero of the number of surface spins in a given direction, within an exchange correlated region, determine the strength of coupling.

We have made Ni oxide films by postdeposition oxidation of metal films and by reactive sputtering, and observed their effects on the magnetic properties of overlying GMR structures. While our motivation in studying *ex situ* oxidized films was directed toward ease of fabrication, our study of spin-valve structures made on these films, which were found to have varying roughness, has been useful in elucidating the effects of roughness on coercivity and exchange bias and switching fields. The roughness was found to promote large values of the coercivity and moderate exchange bias, both of which are effective in pinning the orientation of magnetic metal overlayers. Systematic relationships of the oxide layer thickness and of the oxidation temperature to roughness, coercivity, and ferromagnetic resonance (FMR) linewidth were found.

## II. EXPERIMENT

Ni metal films were made by either magnetron sputtering or electron-beam evaporation. Metal thicknesses in the range 15–100 nm were deposited, generally on polished Si wafers. Thicknesses were monitored by quartz-crystal oscillator and confirmed by x-ray fluorescence and mass gain. Surface structure was analyzed using an atomic force microscope (AFM) with a depth resolution of about 2 nm. The substrates and the metal films were smooth to at least that level. The oxidation was done in either air or oxygen at temperatures from 400 to 900 °C. During oxidation the film thickness increases by about a factor of 2 in order to accommodate the oxygen; nevertheless, the surfaces remained adherent and crack free. X-ray diffraction showed the films to be the correct structure for antiferromagnetic NiO. The reactively sputtered NiO films were made in various mixtures of O and Ar. Metal overlayers of Co, Cu, and Permalloy of about 5 nm each were deposited on both types of oxides by sputtering or electron-beam evaporation to form GMR structures. These thicknesses were chosen to alloy easy permalloy switching rather than to maximize magnetoresistance.

Magnetic measurements were made using vibrating sample magnetometry (VSM), FMR, and magnetoresistance

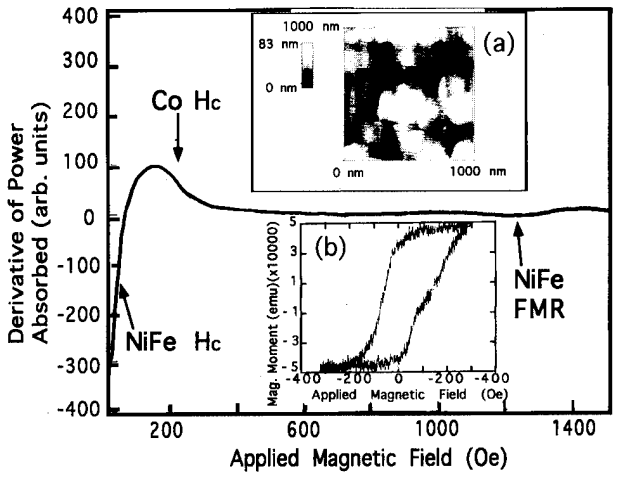



FIG. 1. FMR data of overlying GMR structure. The Co resonance is present but is weak compared to the other features. Insert (a): AFM image of a 200-nm-thick postdeposition-oxidized NiO film; and inset (b): VSM data.

(MR). From the VSM data we found the coercivity of the metal layers and we estimated the exchange field acting on them by the displacement of their loops from the origin. Similar information was obtained from MR data and from the low-field FMR data, in which features of the MR can be seen in the low-field absorptionlike signals.[7]

## III. RESULTS AND DISCUSSION

The AFM images for postdeposition-oxidized Ni films [Fig. 1(a)] show very distinct features with a lateral scale up to 100 nm, and with depths of up to 50 nm, for film thicknesses of about 200 nm of NiO. Apparently considerable migration of the Ni occurs during the oxidation process. Since these features are comparable to domain-wall widths, about 100 nm for Permalloy, it is not surprising that quite large coercivities are seen in both the Co and Permalloy layers deposited on this oxide: Figure 1 shows how the coercivities are reflected in the FMR data observed at 9.78 GHz and the VSM data, inset (b). Exchange bias fields acting on the adjacent layer are about 60 Oe. Significant exchange coupling of the magnetic layers through the Cu is not seen. The Co coercivity fell rapidly for oxide thicknesses much less than 50 nm [Fig. 2(a)] and was largest for the lowest oxidation temperatures used [Fig. 2(b)]. The latter effect may be a result of the finer structure of the low-temperature oxidized material since the size of the features is then closer to the typical domain wall size in Co.

Figure 3 shows the AFM image of a typical reactively sputtered NiO layer. The corresponding VSM and MR curves are also shown. The NiO produced in this way has low roughness except for some isolated features, and results in low coercivities of the overlayer while maintaining moderate exchange bias; thicker NiO becomes rougher and produces large coercivity.

Finally, the correlation of the roughness and coercive fields for GMR structures biased by the reactively sputtered NiO layers is shown in Fig. 4.

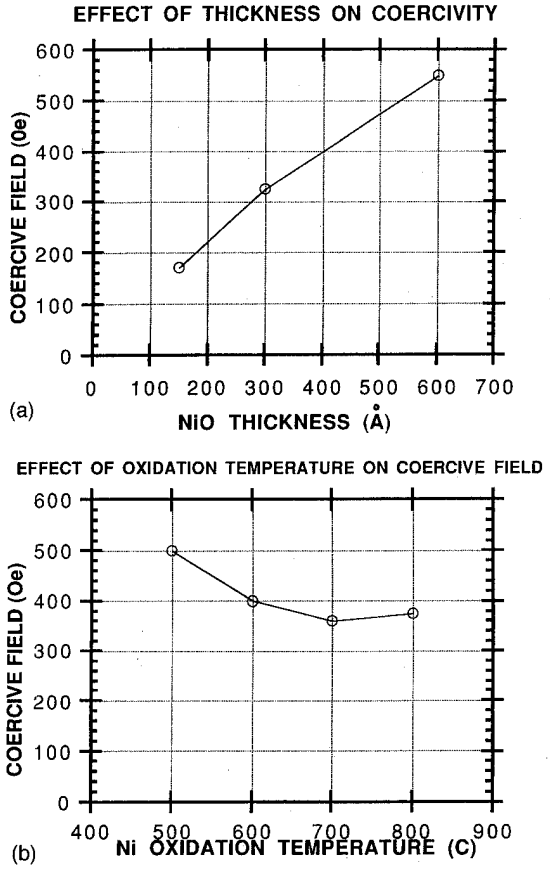



FIG. 2. (a) Effect of NiO film thickness for postdeposition oxidation on the coercive field of an overlying 5 nm Co film. (b) Effect of temperature used for oxidation of the Ni on the coercive field of an overlying 5 nm Co film.

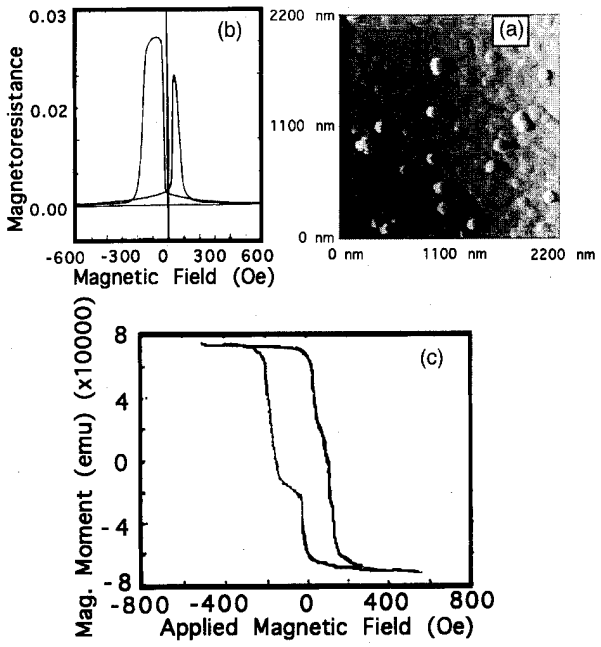



FIG. 3. (a) AFM image of reactively sputtered NiO 170 nm thick, rms roughness in rectangle is 6.2 nm; (b), (c) VSM and MR data, respectively, for this sample.

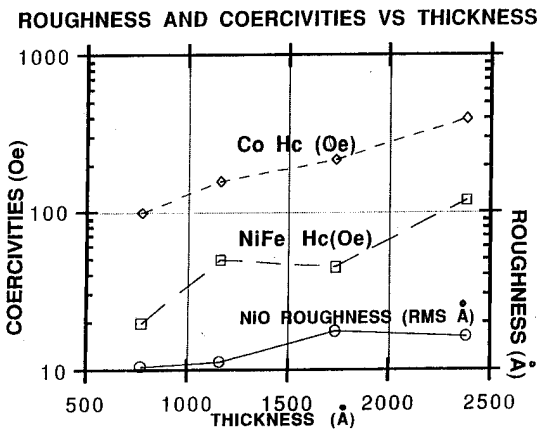



FIG. 4. Effects of increasing thickness on roughness and coercivity for reactively sputtered NiO biased GMR structures.

The effects of the roughness of the thin magnetic films deposited onto rough surfaces on coercivity and linewidth can be understood as arising from the competition between exchange and dipolar energies. The exchange energy can be represented by an effective exchange field of magnitude $H_{\text{exch}}=2A/M(1/L)^2$, where $A$ is the exchange constant, typically $10^{-6}$ erg/cm for Permalloy, $M$ is the magnetization of about 800 G, and $L$ is the scale of spatial variations of $M$, here about 50 nm; the magnitude of $H_{\text{exch}}$ is thus about 100 Oe. This field, favoring local alignment, competes with the demagnetization, which produces fields on the order of $H_d = 4\pi M \sin\theta$, where $\theta$ is the angle of the moment out of the local plane because of the exchange constraint; this field represents a barrier to domain-wall motion, and hence is related to the coercive field. At equilibrium, $H_d$ will thus have the same magnitude as $H_{\text{exch}}$. (This argument suggests that the coercivity becomes very large as $L$ approaches zero. However, for $L$ much less than the wall width, the wall averages over the alternating variations in $H_d$, which are bounded, and becomes insensitive to them; the distribution is therefore "exchange narrowed" to approximately $H_d^2/H_{\text{exch}}$, which approaches zero for short range, e.g., atomic roughness. The lower coercivity of the reactively sputtered films follows from the reduced scale of its roughness relative to the domain-wall widths.) (The variation of $H_d$ will also be the major contribution to the FMR linewidth of the Permalloy.) The above estimates are in good agreement with the observed values of linewidth and coercivity, at least for the choice of $L$ taken above. They also suggest that the relatively larger coercivity of the Co films is related to its larger $A$ value, nearly three times larger than that of Permalloy. Magnetostrictive effects may also play a role in the coercivity of the Co.

Because of the roughness we were not able to image any domain walls using Bitter decoration; traces over regions of Permalloy magnetization reversal made with reflected light, analyzed using crossed polarizers (Kerr imaging) showed a distinctive change of sign, indicating the potential usefulness of this method in evaluating these materials.

## IV. CONCLUSIONS

GMR structures deposited on antiferromagnets grown by oxidation of Ni or Ni–Co metal films produced up to 3% changes in resistance in the range of magnetic fields required to reverse one of the layers with respect to the other. The magnetic fields necessary to reverse the Permalloy are somewhat lower than those required to reverse the Co, leading to a partially anti-aligned state for appropriate field values. For postdepostiion-oxidized NiO bias layers, there is generally an overlap in fields at which some rotation occurs in both magnetic layers, leading to a reduction in the magnitude of the GMR[8] and undesirably large fields of more than 50 Oe to produce the maximum effect. For the smoother NiO produced by reactive sputtering, the switching fields are better separated and the NiFe switching is sharper.

[1] M. J. Carey and A. E. Berkowitz, J. Appl. Phys. **73**, 6892 (1993).
[2] T. R. McGuire, T. S. Plaskett, and R. J. Gambino, IEEE Trans. Magn. **MAG-29**, 2714 (1993); T. R. McGuire and T. S. Plaskett, J. Appl. Phys. **75**, 6537 (1994).
[3] C.-L. Lin, J. M. Sivertsen, and J. H. Judy, IEEE Trans Magn. **MAG-30**, 3834 (1994).
[4] D. M. Lind, S.-P. Tay, S. D. Berry, J. A. Borchers, and R. W. Erwin, J. Appl. Phys. **73**, 6886 (1993).
[5] W. H. Miekeljohn and C. P. Bean, Phys. Rev. **105**, 904 (1957).
[6] A. P. Malozemoff, J. Appl. Phys. **63**, 3874 (1988).
[7] J. J. Krebs, P. Lubitz, A. Chaiken, and G. A. Prinz, J. Appl. Phys. **69**, 4795 (1991).
[8] Y. U. Idzerda, C.-T. Chen, S.-F. Cheng, W. Vavra, G. A. Prinz, G. Meigs, H.-J. Lin, and G. H. Ho, Appl. Phys. Lett. **64**, 3503 (1994).

# Giant magnetoresistance effect and electric conduction in amorphous-CoFeB/Cu/Co sandwiches

M. Jimbo
*Daido Institute of Technology, Nagoya 457, Japan*

K. Komiyama and S. Tsunashima
*School of Engineering, Nagoya University, Nagoya 464-01, Japan*

Giant magnetoresistance (MR) effects have been investigated for spin valve sandwiches using amorphous($a$)-$(Co_{0.9}Fe_{0.1})_{80}B_{20}$ alloy layers. In an $a$-CoFeB/Cu/Co sandwich, a MR ratio as large as 6% was obtained, and a MR curve was found to saturate in a field within 100 Oe. The resistivity is 40–60 $\mu\Omega$ cm. In a CoFeB(4 nm)/Cu(2 nm)/$a$-CoFeB(2 nm)/NiO(10 nm) sandwich, MR ratios as large as 4% were also obtained. The maximum field sensitivity of the sandwich is about 2.5%/Oe.
© *1996 American Institute of Physics.* [S0021-8979(96)68208-2]

## I. INTRODUCTION

Spin valve structures[1] are attracting great interest since the low field magnetoresistive behavior is suitable for the application to magnetoresistive readout heads and magnetoresistance (MR) memory.[2] We have already reported that giant magnetoresistance (GMR) due to the spin-dependent electron scattering appears in amorphous($a$)-CoFeB/Cu/Co sandwiches.[3] In this article, we describe the dependence of the GMR effect and electric conduction on the thickness of magnetic layers for spin valve sandwiches using $a$-$(Co_{0.9}Fe_{0.1})_{80}B_{20}$ layers. We also show that the GMR effect is obtained in $a$-CoFeB/Cu/$a$-CoFeB/NiO sandwiches.

## II. EXPERIMENT

Two types of sandwiches shown in Fig. 1 have been used in this investigation. One is the Co/Cu/$a$-CoFeB sandwiches where the magnetization of the Co layer on the surface side is pinned by the oxidized Co layer.[4] The other is $a$-CoFeB/Cu/$a$-CoFeB sandwiches where the magnetization of the outer $a$-CoFeB layer is coupled with a NiO layer. These sandwiches were prepared using a rf magnetron sputtering system with three targets in a similar manner to that described in a previous article.[3] The composition of the alloy layer is $(Co_{0.9}Fe_{0.1})_{80}B_{20}$, which exhibits nearly zero magnetostriction in an amorphous state.[3] When the $(Co_{0.9}Fe_{0.1})_{80}B_{20}$ layer was deposited to a thickness of 200 nm, the amorphous structure was confirmed with halolike X-ray diffraction patterns. For both sandwiches, a 5-nm-thick SiN layer was deposited first onto a glass substrate as a buffer layer. The SiN layer was sputtered from a $Si_3N_4$ target at 10 mTorr of Ar pressure. The deposition rate is about 0.1 nm/s. The vacuum of the chamber was broken only after the preparation of the SiN layer, otherwise all the layers were grown successively without breaking the vacuum.

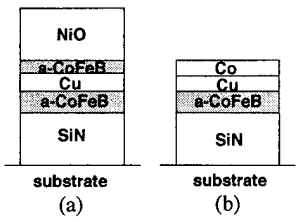



FIG. 1. Constructions of sandwiched films.

## III. RESULTS AND DISCUSSION

Figure 2 is the typical MR curves and MH loops for $a$-CoFeB/Cu/Co sandwiches with CoFeB layers of various thickness. The MR curves were measured with the magnetic field applied in the direction parallel to the easy axis. Large MR ratios were obtained for very thin $a$-CoFeB layers; at CoFeB thicknesses of 2 nm, the MR ratio reaches a maximum of about 6.5%. The maximum field sensitivity of the sandwich is about 2%/Oe.[3] From MH loops, it is seen that the sandwiches which show large MR ratios exhibit a mag-

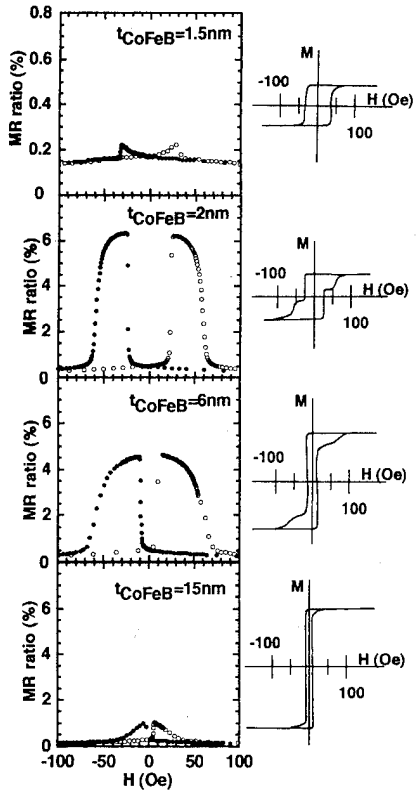



FIG. 2. Typical MR and MH curves for $a$-CoFeB($t_{CoFeB}$)/Cu(2 nm)/Co(2 nm) with various CoFeB layer thicknesses.

 0021-8979/96/79(8)/6237/3/$10.00 © 1996 American Institute of Physics 

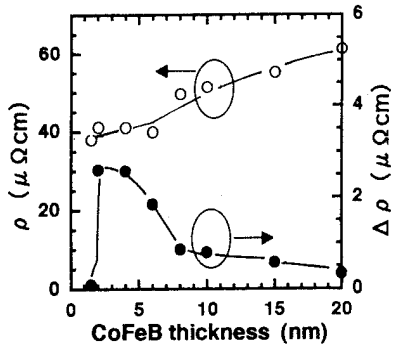



FIG. 3. Dependence of resistivity and resistivity change on CoFeB thickness in $a$-CoFeB($t_{CoFeB}$)/Cu(2 nm)/Co(2 nm) sandwiches.

netization process indicative of the antiparallel alignment of the magnetic layers. Increasing the thickness of an $a$-CoFeB layer, the MR ratio decreased and the two-stage magnetization processes disappeared. Estimating the magnetic moment of Co from the two-stage magnetization loop, the thickness of the Co layer that is still ferromagnetic is presumed to be about 1 nm.

The dependence of $\rho$(resistivity) and $\Delta\rho$(resistivity change) on the thickness of the CoFeB layer is shown in Fig. 3. When the CoFeB layer is thinner than 5 nm, the resistivity is about 40 $\mu\Omega$ cm and almost constant. This may mean that the resistivity is dominated by Cu (and Co) layers. Then with increasing thickness the resistivity increases gradually toward the value of $a$-CoFeB(100 $\mu\Omega$ cm). On the other hand, the resistivity change $\Delta\rho$ shows a peak at around 2 or 4 nm. The abrupt decrease above 5 nm is thought to be due to incomplete antiparallel alignment.

The minor loops of the MR curves of $a$-CoFeB/Cu/Co sandwiches are shown in Fig. 4. The coupling field $H_w$ defined in Fig. 4 is inversely proportional to the thickness of

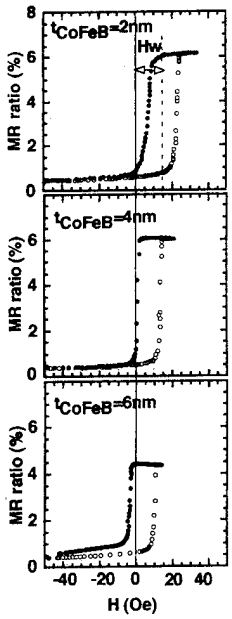



FIG. 4. Minor loops of the MR curves for $a$-CoFeB($t_{CoFeB}$)/Cu(2 nm)/Co(2 nm) sandwiches.

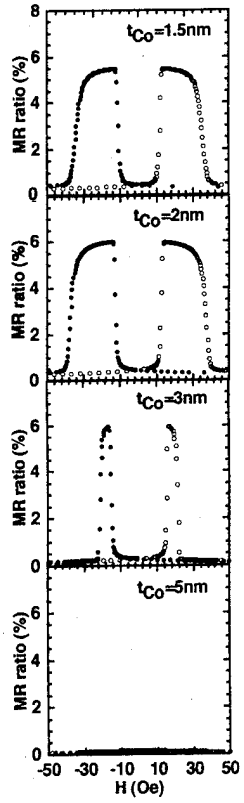



FIG. 5. MR curves of $a$-CoFeB(4 nm)/Cu(2 nm)/Co($t_{Co}$) sandwiches with various Co layer thicknesses.

CoFeB. From the direction of the minor loop shift, the coupling between the magnetic layers is thought to be ferromagnetic.

Figure 5 shows the MR curves of $a$-CoFeB/Cu/Co sandwiches with Co layers of various thicknesses. The MR ratio showed the maximum for a 2-nm-thick Co layer, and decreased with increasing Co thickness, becoming almost 0% for 5-nm-thick Co. From the MR curves, it is also seen that the field for the magnetization reversal of Co layers gradu-

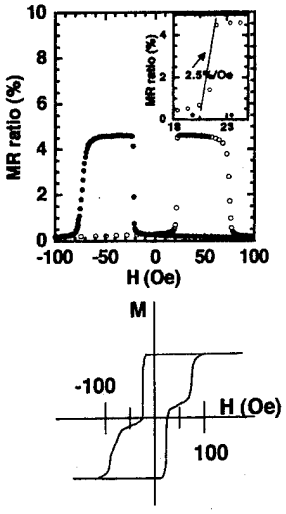



FIG. 6. MR and MH curves for $a$-CoFeB(2 nm)/Cu(2 nm)/$a$-CoFeB(2 nm) sandwich.

ally decrease with increasing thickness of Co layers. In the case of the 5 nm Co layer, the magnetization reversal of both Co and *a*-CoFeB layers seems to occurs almost simultaneously.

For *a*-CoFeB/Cu/*a*-CoFeB sandwiches, the MR curve and the MH loop are shown in Fig. 6, where the thicknesses of Cu and two *a*-CoFeB layers are all 2 nm. The MH loop exhibiting two stages is similar to those of Co/Cu/*a*-CoFeB sandwiches shown in Fig. 2. Comparing the MH loops of these two types of sandwiches, it is found that the *a*-CoFeB/Cu/*a*-CoFeB sandwich shows more complete squareness during the magnetization reversal of the pinned (magnetically hard) layer. The obtained MR ratio of 4.5% is comparable to those of Co/Cu/*a*-CoFeB sandwiches. The maximum field sensitivity of an *a*-CoFeB/Cu/*a*-CoFeB sandwich was estimated at 2.5%/Oe from the slope of the MR curve in soft *a*-CoFeB layer.

In conclusion, the sandwiches using *a*-CoFeB layers exhibit giant MR (GMR) due to spin-dependent electron scattering. Relatively large MR ratios of 4%–6% were obtained even when the thickness of amorphous magnetic layers is as thin as 2 nm. This may be related to the very short electron mean free path in amorphous alloys. From the application point of view, a very thin magnetic layer is favorable to reduce the demagnetizing field and will be useful to reduce the size of magnetic devices operating at low fields. Finally, it is well known that the magnetotransport properties of multilayer materials are very sensitive to structural characteristics. Thus the relationship between layer thicknesses, structural properties, and GMR response in these complex amorphous/crystalline sandwiches is currently being studied and will be presented in forthcoming publications.

[1] B. Dieny, V. S. Sperious, S. Metin, S. S. P. Parkin, B. A. Gurney, P. Baumgart, and D. R. Wilhoit, J. Appl. Phys. **69**, 4774 (1991).
[2] Y. Irie, H. Sakakima, M. Satomi, and Y. Kawawake, Jpn. J. Appl. Phys. **34**, L415 (1995).
[3] M. Jimbo, K. Komiyama, H. Matsue, S. Tsuanshima, and S. Uchiyama, Jpn. J. Appl. Phys. **34**, L112 (1995).
[4] M. Taguchi, Y. Kawano, T. Fukami, and K. Tsutsumi, J. Magn. Soc. Jpn. **17**, 321 (1994) (in Japanese).

# Size effects and giant magnetoresistance in unannealed NiFe/Ag multilayer stripes

S. C. Sanders, R. W. Cross, S. E. Russek, A. Roshko, and J. O. Oti
*Electromagnetic Technology Division, National Institute of Standards and Technology, Boulder, Colorado 80303*

We have observed giant magnetoresistance (GMR) in unannealed NiFe/Ag multilayer thin-film stripes. Rectangular stripes having constant thickness and a constant 11:1 length-to-width aspect ratio, but varying widths down to 0.5 $\mu$m, were measured. Two types of multilayer configurations were tested, a system of five NiFe/Ag bilayers with 5.5-nm-thick Ag spacer layers, and a system of nine bilayers with 4.4-nm-thick Ag layers. In contrast to the characteristic of annealed NiFe/Ag multilayer stripes, the unnannealed stripes produced increasing GMR ratios for decreasing stripe sizes, with the 0.5-$\mu$m-wide stripe of the five-bilayer system exhibiting a $\Delta R/R$ of 2.5%. Barkhausen noise and response broadening also increased with decreasing stripe size, however. The results are discussed in terms of magnetostatic coupling of the NiFe layers within the stripes. [S0021-8979(96)55608-2]

## INTRODUCTION

Studying finite-size effects in giant magnetoresistive (GMR) materials is important both for understanding the micromagnetic phenomena as well as for examining suitability for magnetic sensor applications. The multilayer NiFe/Ag GMR system[1–7] is attractive for potential sensor applications due to its high sensitivity (large change in MR per unit field), especially when annealed to form discontinuous multilayers.[2] In this form, the magnetic NiFe layers are broken up into small grains due to Ag diffusion along grain boundaries.[4] These grains interact magnetostatically to induce antiferromagnetic ordering among neighboring grains in adjacent NiFe layers at low fields. The relatively high degree of antiparallel alignment gives rise to GMR values on the order of 5%. When these annealed multilayers are patterned into micrometer-scale features, however, the magnetoresistive response is significantly suppressed, broadened, and characterized by the presence of distinct "jumps" (Barkhausen noise).[8,9] These characateristics are unsuitable for submicrometer sensor applications.

Recently, GMR in patterned unannealed NiFe/Ag multilayers was reported.[10] The unannealed NiFe/Ag is potentially more attractive for applications since the annealing step is avoided. It may also decrease the noise previously observed in small devices,[8,9,11] if the granular characteristics are eliminated. Hylton *et al.*[10] studied unannealed arrays of 2 $\mu$m dots consisting of two NiFe layers separated by a Ag spacer. MR measurements carried out on the dot arrays, corrected for the continuous Cr overcoat necessary for electrical contact, gave estimated GMR ratios of 2.5% and a 1.6 kA/m (20 Oe) saturation field. The GMR effect was attributed to magnetostatic coupling induced at the edge of the dots, which causes the magnetization in one layer to align antiparallel to the other layer.

In this study we have patterned unannealed NiFe/Ag multilayers into rectangular stripes of various sizes to examine the role of magnetostatics in unannealed NiFe/Ag multilayers. In particular, the goal was to directly test whether individual stripes having widths on a 1 $\mu$m scale could have interlayer magnetostatic coupling sufficiently large to produce GMR, and, if so, whether their MR response contained less noise than their annealed counterparts. Stripes fabricated from five- and nine-bilayer systems both showed increasing GMR amplitude as the stripe width decreased from 16 $\mu$m. In both cases, however, saturation fields and noise also increased with decreasing stripe width.

## EXPERIMENT

NiFe/Ag multilayer films were fabricated by magnetron sputtering onto $SiO_2$-coated Si wafers as reported previously.[6] The films were deposited at room temperature in 0.93 Pa (7 mTorr) of Ar, and no magnetic field was applied during the deposition. NiFe was sputtered from a $Ni_{82}Fe_{18}$ alloy target. Two wafers with varying bilayer number $n$ and Ag thickness $t_{Ag}$ were used: Si/$SiO_2$ (150 nm)/Ta (4.5 nm)/Ag($t_{Ag}$/2)/NiFe(2.0 nm)/[Ag ($t_{Ag}$)/NiFe(2 nm)]$_{n-1}$/Ag ($t_{Ag}$/2)/Ta(11 nm), with $n=5$, $t_{Ag}=5.5$ nm, and $n=9$, $t_{Ag}=4.4$ nm. After deposition the central regions of the wafers were patterned using conventional photolithography and diced into 12.5×12.5 mm$^2$ chips. Several of the chips were annealed in a rapid thermal annealing furnace for 5 min in a 5% $H_2$–Ar ambient. These chips were used for direct comparison with the unannealed chips. Rectangular stripes having nominally 11:1 length-to-width aspect ratios were measured at room temperature using a two-probe MR tester. The active areas defined by the Au contact electrodes were one square. Bias currents were scaled approximately with stripe width, with current density $J\sim5\times10^5$ A/cm$^2$, and the magnetic field was applied in the plane of the stripe. For cross-sectional transmission electron microscopy (TEM) studies, specimens were prepared using standard techniques, including $N_2$-cooled ion milling. Care was taken to prevent heating in excess of 70 °C during all TEM sample preparation steps.

## RESULTS

The central result of this article is illustrated in Fig. 1. Figure 1(a) shows $\Delta R/R$ as a function of applied field for unannealed NiFe/Ag rectangular stripes having $n=5$ and

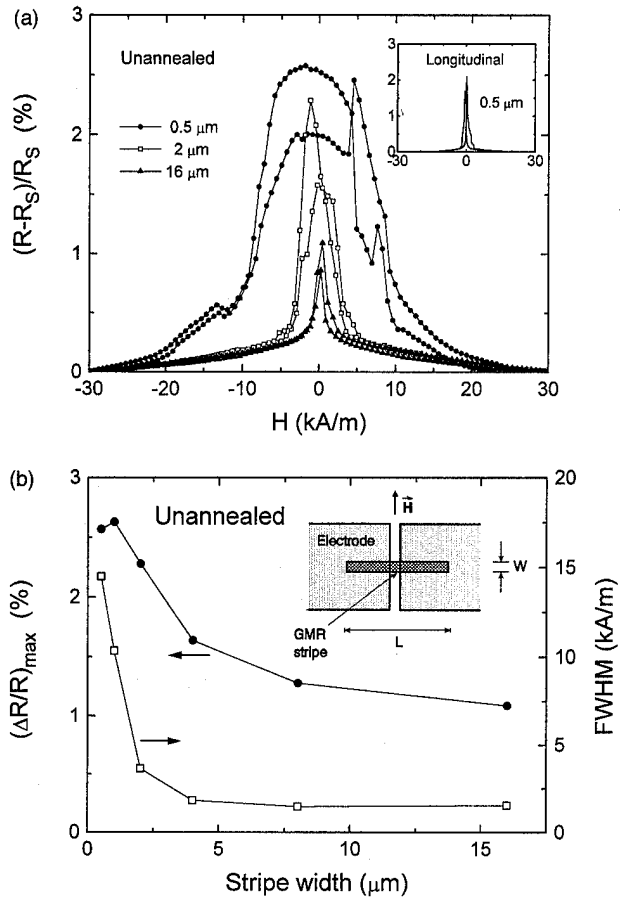



FIG. 1. (a) Magnetoresistive response for unannealed NiFe/Ag multilayer ($n$=5,$t_{Ag}$=5.5 nm) stripes. The field was applied in the plane of the stripe and transverse to the long direction. Inset: longitudinal MR for the 0.5-$\mu$m-wide stripe. (b) Maximum $\Delta R/R$ and full width at half-maximum data for various stripe widths. Inset: schematic of transverse MR measurement.

$t_{Ag}$=5.5 nm. The stripes have nominal widths ranging from 0.5 to 16 $\mu$m. As the stripe width $W$ decreases, the MR response increases in amplitude and broadens. This is seen more clearly in Fig.1(b), where the maximum $\Delta R/R$ and full width at half-maximum (FWHM) data are plotted as functions of $W$. As $W$ decreases from 16 to 0.5 $\mu$m, maximum $\Delta R/R$ increases from 1.1% to 2.6%, and the FWHM increases from 1.6 to 14 kA/m (20 to 180 Oe). The sensitivity $[d(\Delta R/R)/dH]_{max}$ therefore decreases with decreasing $W$. The inset of Fig. 1(a) shows $\Delta R/R$ for the 0.5 mm stripe with longitudinal applied field. Although the longitudinal results show trends similar to the transverse results, the magnitude of the longitudinal broadening is much less (1.2 kA/m as opposed to 14 kA/m for the 0.5 $\mu$m stripe).

We also measured the MR response for unannealed stripes having $n$=9 and $t_{Ag}$=4.4 nm. As in the case of the five-bilayer stripes of Fig. 1, the nine-bilayer samples show the trend of increasing $\Delta R/R$ and broadening with decreasing $W$. For these stripes, the maximum $\Delta R/R$ increases from 0.4% to 1.9% as $W$ decreases from 16 to 2 $\mu$m. The trends that we observe are, therefore, independent of $n$ and $t_{Ag}$ within these ranges.

Noise, in the form of discrete Barkhausen jumps in the MR response, is readily apparent for the smaller stripes in

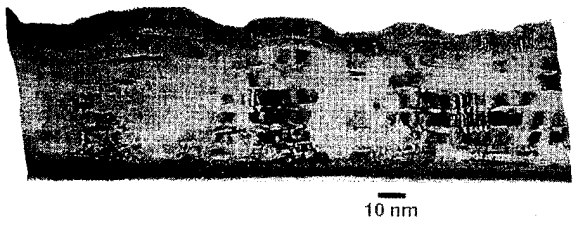



FIG. 2. Cross-sectional TEM micrograph of an unannealed seven-bilayer sample. The GMR multilayer is sandwiched between top and bottom Ta layers. The degree of roughness at the top surface (~5 nm) is typical of the several samples examined.

Fig. 1(a). This may be attributed to a finite granularity (imperfect multilayers), which also produces a nonzero GMR in the larger devices. TEM results on different wafers show a roughening in the unannealed films on the order of a bilayer thickness, as shown in Fig. 2. Previous work has indicated the significance of sputtering gas pressure on film microstructure and properties.[33] The relatively high Ar pressure used during sputtering in this study may introduce some of the observed roughness. Temperatures up to 130 °C are used during photolithography, but these low processing temperatures are not likely to account for the residual granularity and presence of a small GMR component in the larger unnannealed stripes. The Barkhausen noise observed in the response of the small stripes is discouraging for sensor applications. However, processing optimization or biasing optimization, such as increased current density,[9] may diminish the noise problem.

The trend of increasing $\Delta R/R$ with decreasing $W$ for these unannealed stripes is in contrast to annealed stripes. Annealed stripes exhibit decreasing $\Delta R/R$ with decreasing $W$, as illustrated in Fig. 3 for the $n$=5,$t_{Ag}$=5.5 nm configuration (from the same wafer as the unannealed $n$=5 chip) annealed at 340 °C for 5 min in 5% $H_2$–Ar. The maximum $\Delta R/R$ decreases from 3.6% to 3.0% as stripe width decreases from 16 to 0.5 $\mu$m.

## DISCUSSION

In the unannealed stripes, the trend of increasing $\Delta R/R$ with decreasing $W$ is due to the increased thickness-to-volume ratio as $W$ decreases (thickness is constant), and, therefore, the increased relative influence of the stripe edges perpendicular to the layers. As $W$ (and $L$) decreases, the magnetostatic edge charges become closer. If the layers are fully continuous (not granular), the magnitude of magnetostatic energy per unit volume should be greater for the smaller stripes, leading to increased antiparallel alignment in zero applied field, and a larger maximum $\Delta R/R$. In this case, a larger field is required to overcome the magnetostatic energy and align the layers, leading to a broadened response.

The annealed stripes, in contrast, consist of discontinuous layers, so the increasingly strong effect of the stripe edge charges, with decreasing size, increasingly dominates the intergranular, interlayer magnetostatic interaction that occurs

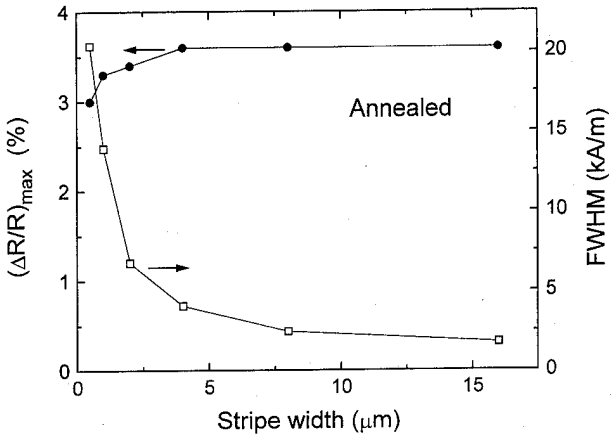



FIG. 3. Maximum $\Delta R/R$ and full width at half-maximum data for various stripe widths in a series of annealed NiFe/Ag stripes having $n=5$ and $t_{Ag}=5.5$ nm. The annealing was carried out in a rapid thermal annealer for 5 min at 340 °C.

due to charges at the grain edges. Some of the zero-field antiparallel orientation is diminished, reducing the maximum $\Delta R/R$ as $W$ decreases.

The increased Barkhausen noise for the smaller samples is attributed to the increased relative contribution of flipping of domains as the domain size becomes an appreciable fraction of the stripe size.

## SUMMARY

We have observed increasing GMR amplitudes with decreasing size in rectangular stripes of unannealed NiFe/AG multilayers. This may be attributed to an increasing significance of magnetostatic charges at the stripe edges as film thickness-to-volume ratio increases, given a constant length-to-width ratio. Noise and response width also increase with decreasing stripe size, however, posing a challenge for technological applications such as highly field-sensitive submicrometer magnetic sensors.

[1] B. Rodmacq, G. Palumbo, and Ph. Gerard, J. Magn. Magn. Mater. **118**, L11 (1993); J. Mouchot, Ph. Gerard, and B. Rodmacq, IEEE Trans. Magn. **MAG-26**, 2732 (1993).
[2] T. L. Hylton, K. R. Coffey, M. A. Parker, and J. K. Howard, Science **261**, 1021 (1993).
[3] T. L. Hylton, K. R. Coffey, M. A. Parker, and J. K. Howard, J. Appl. Phys. **75**, 7058 (1994).
[4] M. A. Parker, T. L. Hylton, K. R. Coffey, and J. K. Howard, J. Appl. Phys. **75**, 6382 (1994).
[5] J. C. Slonczewski, J. Magn. Magn. Mater. **129**, L123 (1994).
[6] Y. K. Kim and S. C. Sanders, Appl. Phys. Lett. **66**, 1009 (1995).
[7] Y. K. Kim, S. C. Sanders, and S. E. Russek, IEEE Trans. Magn. **MAG-31**, 3964 (1995).
[8] R. William Cross, S. E. Russek, S. C. Sanders, M. R. Parker, J. A. Barnard, and S. A. Hossain, IEEE Trans. Magn. **MAG-30**, 3825 (1994).
[9] S. E. Russek, R. W. Cross, S. C. Sanders, and J. O. Oti, IEEE Trans. Magn. **MAG-31**, 3939 (1995).
[10] T. L. Hylton, M. A. Parker, K. R. Coffey, J. K. Howard, R. Fontana, and C. Tsang, Appl. Phys. Lett. **67**, 1154 (1995).
[11] L. S. Kirschenbaum, C. T. Rogers, S. E. Russek, and S. C. Sanders, IEEE Trans. Magn. **MAG-31**, 3943 (1995).

# Effect of sputter gas on the physical and magnetic microstructure of Co/Cu multilayers

D. M. Donnet,[a] K. Tsutsumi,[b] P. de Haan, and J. C. Lodder
*MESA Research Institute and CMO Laboratory, University of Twente, 7500 AE Enschede, The Netherlands*

The physical structure of Co/Cu multilayers, sputtered in different gases (Ar, Kr, and Xe) together with the domain structures that these films support have been investigated using electron microscopy in an attempt to explain the differences in their measured magnetoresistance (MR). Both planar and cross-sectional analyses were undertaken. Due to only partial antiferromagnetic coupling submicron domain structures were observed by Lorentz microscopy in all multilayers. The complex nature of these domain structures made classification difficult, although small magnetic field application allowed wall motion and nucleation to be observed. All films were polycrystalline in nature, although average grains sizes differed. However, smoother interfaces together with less well defined crystal boundaries were observed in the Kr and Xe sputtered films. This trend did not correlate with giant MR (GMR) measurements as the Xe sputtered films had the lowest GMR value of the three. © *1996 American Institute of Physics.* [S0021-8979(96)82808-9]

## I. INTRODUCTION

Giant magnetoresistance (GMR) is a well known phenomenon in Co/Cu multilayers (MLs)[1–3] with $\Delta R/R$ values as high as 65% having been measured at room temperature. Thus far, the critical condition for GMR has not been fully clarified, although it is clear that the morphology of the MLs plays a major role in determining the degree of magnetoresistance present and some recent reports[4–6] have focused on how the growth mechanism [molecular beam epitaxy, epitaxial (111) oriented or sputter-deposited films] affects the structure and orientation of the films and therefore also their GMR value. Since a critical ingredient in the theory of GMR in MLs is spin-dependent electron scattering at the interfaces[7] (as well as in the bulk), it is of particular interest to what extent interfacial roughness is important in determining the GMR value. Recent studies[8,9] have employed a variety of analytical techniques to investigate this property. The ML morphology can be significantly affected by sputtering conditions, such as sputter gas and pressure, and we deposited similar Co/Cu MLs under different sputter gas environments (Ar, Kr, and Xe). A previous study[10] reported upon the initial findings and x-ray diffraction (XRD) measurements. Subsequently, a transmission electron microscopy (TEM) study was undertaken in which we attempted to correlate the measured GMR values with the film structures (and interfaces) observed. Some preliminary domain results are also presented, although space does not allow a full treatment and this will be covered in a future publication.

## II. EXPERIMENT

The Co/Cu multilayers were fabricated by conventional rf-sputter deposition onto Si(100) wafer substrates with a 65 Å Fe buffer layer. The composition of the MLs was typically 15×(14 Å Co+22 Å Cu). Using a nonmagnetic spacer layer at the second peak of the oscillatory coupling region gave reasonably large GMR values with reproducible results.[11] The GMR values were measured by a dc four point method and the MLs were characterized magnetically using a vibrating-sample magnetometer.

Cross-sectional specimens suitable for TEM observation were prepared by the standard method of slicing, polishing, dimpling, and finally Ar ion milling. For planar sections however, specially prepared etched Si wafers with $Si_3N_4$ "TEM windows"[12] were used as the substrate and allowed for direct observation in the microscope. The MLs on TEM windows were deposited at the same time as those on the Si wafers to ensure that they had similar properties. However small differences are to be expected due to the different substrates used. The microscopes used during this study were a Philips CM-30, operated with an accelerating voltage of 300 kV and equipped with a nonimmersion Lorentz "twin" lens, and a JEOL JEM 3010 high resolution electron microscope (HREM), also operated at 300 kV. Typical magnifications used for bright field imaging were 500 000× and selected area electron diffraction patterns allowed any orientation relationships and texturing to be observed.

Lorentz microscopy was carried out (on the CM-30) at significantly lower magnifications (typically 15 000×), due to the position of the twin lens. Small magnetic fields were applied using the objective lens itself. The Fresnel (or defocus) mode was employed as this is easy to implement in a TEM and gives a clear overview of the domain structure.

## III. RESULTS AND DISCUSSION

Ar-sputtered Co/Cu films were deposited at a variety of pressures. The maximum GMR ratio was achieved at $3.1\times10^{-2}$ mbar with deposition rates of 1 and 2 Å/s for Co and Cu, respectively. The deposition rates affect the film morphology and in order to keep both constant during Kr and Xe deposition, different sputtering pressures were used for Kr ($2.2\times10^{-2}$ mbar) and Xe ($8.3\times10^{-3}$ mbar). For this study we then concentrated on the film which gave the largest GMR value for each sputter gas: 16.5% for Ar, 23.5% for Kr, and 7.5% for Xe. Good reproducibility was achieved for the Ar and Kr cases. Poorer reproducibility was achieved

[a]Electronic mail: d.m.donnet@el.utwente.nl
[b]On sabbatical leave from Materials and Electronic Devices Laboratory, Mitsubishi Electric Corporation, Amagasaki Hyogo 661, Japan.

 0021-8979/96/79(8)/6243/3/$10.00 © 1996 American Institute of Physics 

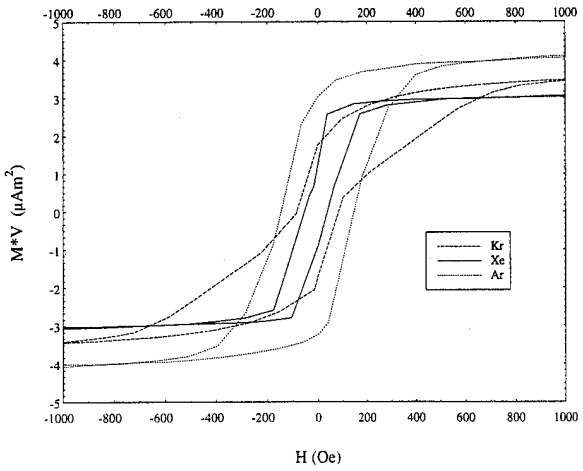



FIG. 1. $M-H$ loops for the three films investigated. Note, differences in saturation values are due to slightly different Co layer thicknesses.

with the Xe films, although it does appear that the maximum GMR measured when sputtering with Xe is significantly lower than when Ar or Kr is used. Figure 1 presents the $M-H$ loops for the three films and it is clear from the shape of the loop for the Kr-sputtered film that it displays the greatest degree of antiferromagnetic behavior ($M_r/M_s=0.5$).

This idea is reinforced when the multilayered structure of the films was observed from cross-sectional TEM images. These are presented in Fig. 2. Due to the similar electron scattering powers of Co and Cu, it is necessary to defocus the objective lens (typically 200 nm) in order to delineate the interfaces. For each film, the individual Co and Cu layers can be distinguished, but it is clear that differences do arise. In particular, the layers in the Ar-sputtered film appear considerably more wavy than in the other two films and there seem to be some areas where the layer thickness is not constant. This could lead to areas where the antiferromagnetic (AF) coupling is not complete and the ML behaves ferromagnetically. In contrast the Kr- and Xe-sputtered layers lie almost perfectly parallel to the substrate surface and only a small amount of waviness is apparent in the Xe case close to the film surface. In all films however, large grains extending throughout the total thickness of the multilayer were observed. Such grains had dimensions of ~20 nm. Planar images (Fig. 3) showed similar differences. Average grain sizes of 20, 15, and 10 nm were measured for the Ar, Kr, and Xe films, respectively. In conjunction with the decrease in grain size, a less distinct grain structure was observed in the Kr and especially the Xe sputtered case. The reduction in crystal size is probably associated with heavier Kr and Xe neutral atoms and the subsequent flatter interfaces as observed in Figs. 2(b) and 2(c). However little or no differences were observed from the planar diffraction patterns: same lattice constant (3.60 Å) measured with only a slight degree of texturing observed in the Xe-sputtered film. HREM images (not shown) of the ML, indicate a highly disordered structure with little or no orientation relationship with respect to the substrate. Large amorphous areas (near the surface of the ML) as well as differently oriented neighboring grains were present. It should be noted however that lattice fringes in

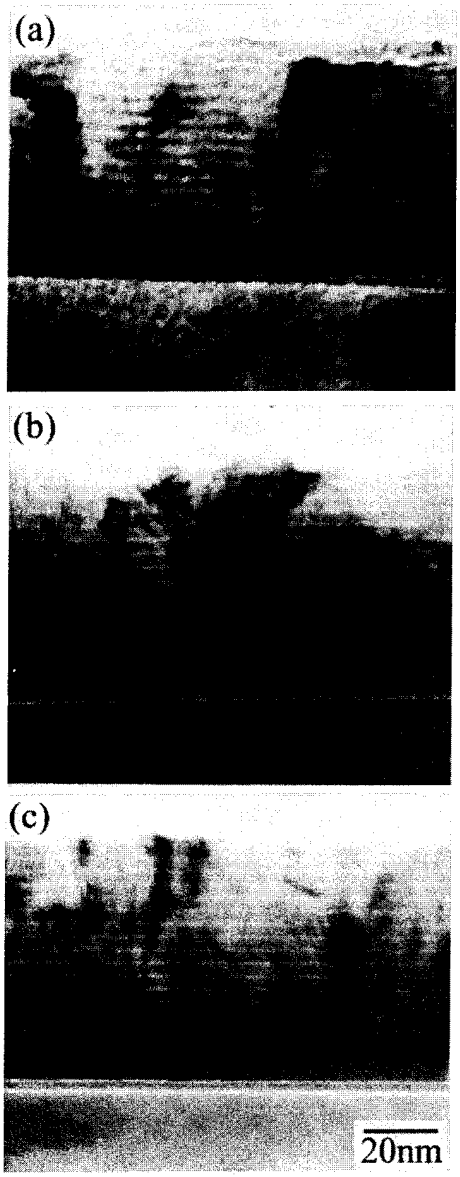



FIG. 2. Cross-sectional TEM images of the Ar (a), Kr (b), and Xe (c) sputtered MLs.

these grains extend through many Co and Cu layers undisturbed. This disorder may have an effect on the degree of GMR found in these films by increasing the number of spin dependent scattering centers.

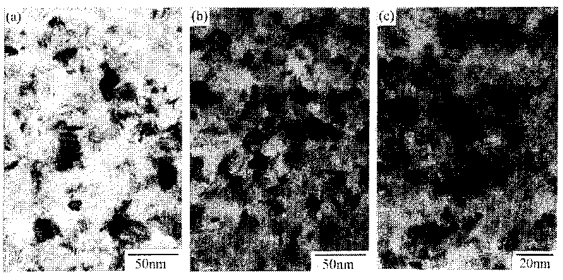



FIG. 3. Planar TEM images of the Ar (a), Kr (b), and Xe (c) sputtered MLs.

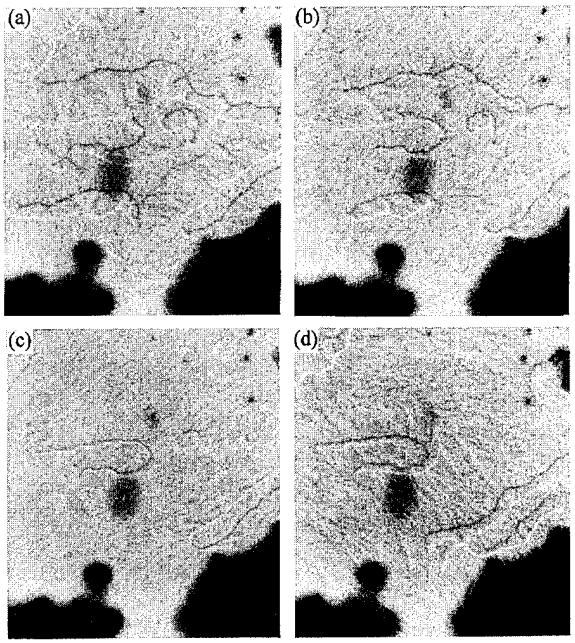



FIG. 4. Domain (Fresnel) images of the Kr-sputtered ML in the ac-demagnetized state (a) and with small fields applied (b)–(d).

These results appear to be in agreement with the earlier XRD experiments which indicated that well oriented films were not required for large GMR values and which revealed a tendency to more amorphous behavior with heavier sputtering gas. To investigate the lower GMR ratio for the Xe-sputtered film we carried out resistance measurements on a Co film grown under similar conditions. This revealed considerably higher resistivity compared to Co films grown in Ar and Kr. We have attributed this high value to the presence of Xe in the film and thus it is also likely that Xe is present in the ML. This would lead to much lower mobility of the atoms and could contribute to the amorphouslike structure in Fig. 3(c). It is also probable that this larger resistivity could lead to a larger number of spin independent scatterings which would have the effect of diminishing the GMR ratio.

With regards to the domain structures that these MLs support, very little qualitative differences were observed. Figure 4 presents Fresnel images of the Kr-sputtered film in an ac-demagnetized state and as magnetic fields were applied. We will concentrate on this film, but the discussion pertains equally well to the Ar and Xe sputtered films. A small (submicron) complex in-plane structure is observed with magnetization ripple present in the domain interiors. The most interesting effects were viewed when small magnetic fields were applied to the film. To do this the film was tilted so that it experienced a small degree of the vertical remanent field from the objective lens (<20 Oe). Thus only very small fields were required for nucleation or domain wall motion. The walls moved with great ease, thus changing the domain dimensions. However, the general shape of the domains remained constant implying that there were a great deal of pinning points available in the ML. Also of interest is the 360° wall nucleated in Fig. 4(c). When the film was finally saturated (not shown) only ripple remained. It should be noted that some of the domain contrast does arise from the Fe buffer layer. A future publication dealing, in more detail, with the domains will investigate MLs deposited on other (or no) buffer layers.

## IV. CONCLUSIONS

We have grown a series of Co/Cu ML films with different sputter gases. In general, good reproducibility was attained, although still some more work is required to find the optimum Xe sputtering conditions. All films are polycrystalline with small grains (10–20 nm) although the Xe case has a significantly less distinct crystal structure which may be explained by the presence of Xe in the film. We have observed that deposition in a Kr environment leads to flatter layers with better AF coupling and a larger GMR ratio with respect to Ar-sputtered MLs. Despite comparable layer smoothness, interfacial sharpness and lattice constant in the Xe-sputtered film, it has significantly diminished AF coupling and GMR and we are currently involved in further research to determine the cause of these differences.

## ACKNOWLEDGMENTS

The authors would like to extend their thanks to Dr. G. J. Sinclair and Professor P. J. Grundy for the use of the HREM facilities at the University of Salford and to CAMST for the provision of funds. We also wish to thank D. Monsma for helpful discussions during the preparation of this article.

[1] S. S. P. Parkin, Z. G. Li, and D. J. Smith, Appl. Phys. Lett. **58**, 2710 (1991).
[2] S. S. P. Parkin, R. Bahdra, and K. P. Roache, Phys. Rev. Lett. **66**, 2152 (1991).
[3] M. E. Tomlinson, R. J. Pollard, D. G. Lord, and P. J. Grundy, J. Magn. Magn. Mater. **111**, 79 (1992).
[4] W. F. Egelhoff and M. T. Kief, IEEE Trans. Magn. **MAG-28**, 2742 (1992).
[5] R. J. Pollard, M. J. Wilson, and P. J. Grundy, J. Magn. Magn. Mater. **146**, L1 (1995).
[6] R. Matteis, W. Andra, L. Fritzsch, A. Hubert, M. Rührig, and F. Thrum, J. Magn. Magn. Mater. **121**, 424 (1993).
[7] P. M. Levy, S. Zhang, and A. Fert, Phys. Rev. Lett. **65**, 1643 (1990).
[8] Z. J. Yang and M. R. Scheinfein, Phys. Rev. B **52**, 4263 (1995).
[9] M. Suzuki and Y. Taga, Phys. Rev. B **52**, 361 (1995).
[10] K. Tsutsumi, P. de Haan, M. Eisenberg, D. Monsma, and J. C. Lodder, Proc. MML '95 (1995).
[11] S. S. P. Parkin, Mater. Lett. **20**, 1 (1994).
[12] F. J. A. M. Greidanus, B. A. J. Jacobs, F. J. A. den Broeder, J. H. M. Spruit, and M. Rosencrantz, Appl. Phys. Lett. **54**, 963 (1989).

# Giant thermopower in 3D-magnetic multilayers. Structural and electron band effects (abstract)

M. M. P. de Azevedo, B. G. Almeida, V. S. Amaral, M. E. Braga, and J. B. Sousa
*Instituto Física Materiais (IFMUP-IMAT) and CFUP, Pr. G. Teixeira, 4050 Porto-Portugal*

P. P. Freitas
*INESC, R. Alves Redol 9, and IST, Av. Rovisco Pais, 1000 Lisboa, Portugal*

R. Krishnan
*Lab. Magnetisme et Mat. Magnétiques, CNRS, Meudon, France*

We report measurements of the thermoelectric power (S) and electrical resistivity ($\rho$) in sputtered multilayers of M(10 Å)/$Au_{25}Cu_{75}(t)$ (with M=Co or Ni) directly grown on Si (100), and in UHV—evaporated Pt 20 Å/Ni($x$) multilayers grown on Si(111). The multilayers have thicknesses $t$=21 Å, 23 Å, and $x$=19.5 Å, 39 Å, and the data spans the temperature range 10–300 K. All the samples exhibit an anomalous thermopower at high temperatures, with a huge maximum in $S$ and a sharp peak in the temperature derivative $dS/dT$ at a characteristic temperature $T^*$, e.g., ~190 K for Ni/Pt and ~260 K for M/$Au_{25}Cu_{75}$ multilayers. In all cases the thermopower decreases abruptly at $T^*$, from a giant positive value ($S \approx 80$ $\mu$V K$^{-1}$ in Ni/Pt and $S \approx 12$–$50$ $\mu$V K$^{-1}$ in M/$Au_{25}Cu_{75}$) to values close to zero below $T^*$. The electrical resistivity also displays an anomaly over the same temperature range, characterized by a rapid resistivity enhancement $\Delta\rho \sim 1$ $\mu\Omega$ cm (within $\Delta T \sim 60$ K) when $T$ decreases below $T^*$. This produces a sharp minimum in the derivative $d\rho/dT$ at $T^*$. The shape of the $S(T)$ anomaly is remarkably similar in all cases (mutatis mutandis) for $\rho(T)$, suggesting a general underlying physical mechanism. We found that a suitable buffer (e.g., 100 Å Pt in Ni/Pt, Fe50 Å in Co/$Au_{25}Cu_{75}$ and 50 Å in Ni/$Au_{25}Cu_{75}$) suppresses the anomalies, indicating a structural-related underlying effect. In this case, $S$ values are small and negative (as occurs with Ni and Co), exhibiting the usual smooth variation over the whole temperature range. At this stage, it is not clear what is the precise physical mechanism responsible for the observed anomalies. Interfacial atomic mixing in the nonbuffered multilayers may cause individual magnetic atoms or clusters to have entirely nonmagnetic environments (Au, Cu, or Pt in our samples). This situation could give an anomalous transport contribution, through conduction electron scattering at virtual bound states (VBS) localized in the (3-D) magnetic atoms. A sharp peak occurs in the local density of states, $N(E)$, at a characteristic energy $E_L$. A giant thermopower may result when the Fermi level is close to $E_L$ ($S \propto dN/dE$; very large). The VBS model successfully explains large $S$ values observed in bulk noble metals diluted with 3-D magnetic impurities such as Co and Ni.[1] However, the standard treatment does not lead to a sharp cutoff-temperature, below which $S(T)$ gets negligible. Another contribution is the usual $s$-$d$ electron transition mediated by phonon scattering. This leads to a thermopower proportional to the energy derivative of the splitted ferromagnetic 3D band density of states at $E_F$, which can be very large when sub-band filling is almost complete. © *1996 American Institute of Physics.* [S0021-8979(96)61308-7]

[1] F. J. Blatt, *Thermoelectric Power of Metals* (Plenum, New York, 1976).

 0021-8979/96/79(8)/6246/1/$10.00 © 1996 American Institute of Physics

# Structural characterization of epitaxial Co–Ag

A. Azizi, L. El Chahal, K. Ounadjela, and J. P. Deville
*IPCMS, 23 rue de Loess, 67073 Strasbourg, Cedex, France*

S. M. Thompson
*Physics Department, University of York, York, YO1 5DD, United Kingdom*

J. F. Gregg
*Clarendon Laboratory, Parks Road, Oxford, OX1 3PU, United Kingdom*

Co–Ag granular films are prepared by molecular-beam epitaxy to enable a detailed structural study to be conducted in conjunction with magnetotransport properties. It is demonstrated that the shape, size, location, and segregation of the magnetic Co grains and the morphology of the surface depend on the growth temperature. Detailed transmission electron microscopy reveals inherent differences between samples prepared at room temperature and those prepared at high temperature. Small clusters of only a few atoms are found to be present in the matrix of the low-temperature samples significantly affecting the spin diffusion length. Well-crystallized regions of both Co and Ag are found in the high-temperature samples, however, the Co grains remain relatively small in size even at the highest growth temperatures. © *1996 American Institute of Physics.*
[S0021-8979(96)55808-2]

## I. INTRODUCTION AND EXPERIMENTAL DETAILS

Giant magnetoresistance (GMR) is caused by the change in spin-dependent scattering in a composite material (either a multilayered film[1] or granular material[2]) when the relative orientation of the magnetic regions is changed by the application of a magnetic field. Both the magnitude and field dependence of the observed GMR in heterogeneous alloys is strongly affected by the structure of the films. The magnetization process of the ferromagnetic regions is controlled by their shape and crystal anisotropy. In addition to the total resistivity of the material being affected by structural defects and grain size, the spin diffusion length in the paramagnetic matrix is greatly reduced by any magnetic impurities present[3] as well as the particle size and distribution due to the jitterbug spin depolarization mechanism.[4] In this study the GMR films were prepared by molecular-beam epitaxy (MBE) in order to complete an integrated study of the structure, magnetic and transport properties. We investigate the effect that growth temperature has on the shape, size, location, and segregation of the magnetic Co grains and the morphology of the surface.

Co–Ag films were coevaporated by MBE at three different growth temperatures: 0 °C (LT), 250 °C (MT), and 450 °C (HT). A Ru buffer layer was first deposited onto the mica substrates at 700 °C, followed by either 640 Å of Co–Ag at LT, 385 Å at MT, or 377 Å at HT and then a capping layer of 30 Å of Ru. A wide range of compositions was prepared, but in this transmission electron microscope (TEM) study we concentrate on a single composition of 45 at. % Co.

The structure of all these samples has been extensively studied by a wide range of techniques both *in situ* by reflection high-energy electron diffraction (RHEED) and *ex situ* by x-ray diffraction, atomic force microscopy (AFM), and TEM. The RHEED patterns for the LT samples indicated that some degree of epitaxy was present throughout the structure with a diffuse single crystal pattern. In contrast at MT and HT two separate sharp diffraction patterns were observed simultaneously indicating a far greater degree of segregation. The results of these measurements and their magnetic and transport properties can be found in previous references.[5,6] Figure 1 shows the x-ray $\theta/2\theta$ scans for the $Co_{45}Ag_{55}$ samples prepared at the three growth temperatures. The Ag

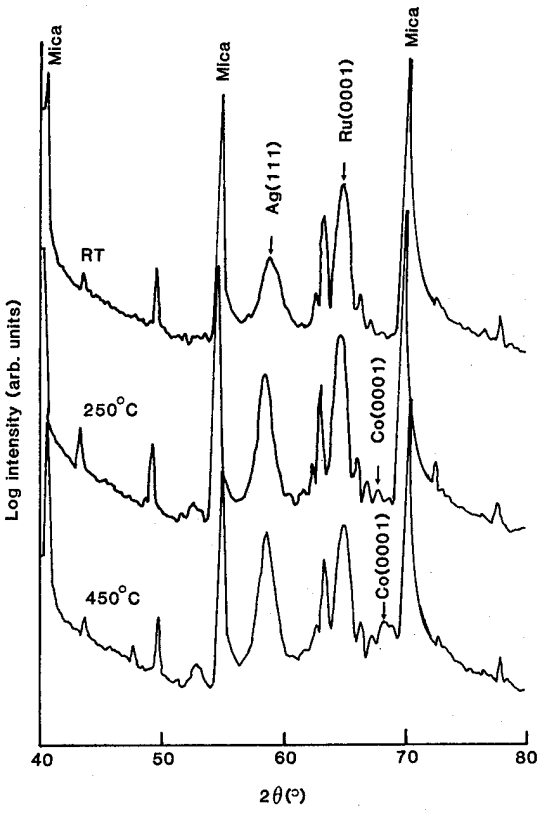



FIG. 1. X-ray $\theta/2\theta$ scans of $Co_{45}Ag_{55}$ prepared at three growth temperatures. The unidentified peaks arise from the mica and are left unindexed for clarity.

 0021-8979/96/79(8)/6247/3/$10.00 © 1996 American Institute of Physics 

peak is relatively broad and less intense at LT and its position slightly shifted from the HT and MT samples. The Co peak is not visible at all at LT, emerging gradually as the deposition temperature and segregation improves. However, even at HT the Co peak is very weak and quite broad which may be a consequence of small grains of Co. This is consistent with the coexistence of high-quality RHEED patterns for HT Co,[5,6] as the RHEED coherence length is 50 Å. These results show the importance of analyzing the samples by TEM in order to quantify the grain size and degree of segregation for the three different growth temperatures. Both in-plane and cross-section TEM studies were made of three 45 at. % Co samples prepared at LT, MT, and HT. A TEM model TOPCON 002B with a point-to-point resolution of 1.8 Å was used. Energy-dispersive x-ray analysis (EDAX) with a probe area of 50–100 Å fitted to the TEM enabled composition analysis in different regions of the samples.

## II. ELECTRON MICROSCOPY

In general the medium-temperature sample had a structure intermediate between the low- and high-temperature samples, but was much closer to the HT one. The MT and HT will therefore be considered together.

### A. Low-temperature sample

Diffraction patterns observed from different areas of the sample indicated that there were two distinct regions. The first is region (1), where there is some segregation between the Ag and the Co. Here, spots related to the fcc structure of both the Co and Ag are visible along with spots deriving from the Ru hcp. Note that the Co is crystallized in its metastable fcc phase at low temperature. This may be due to the reduced mobility of the Co atoms which do not reach their bulk equilibrium position. The resulting strain energy can be minimized in the fcc phase. Region (2) is where only the Ag fcc and Ru hcp spots are visible, but there is nothing from the Co indicating that the Co is still well dispersed. From the coherence length of the beam, the lack of any regions with Co hcp structure is evidence for the fact that there are no significant areas of the sample with this structure.

The presence of a high degree of strain and many areas of dislocations in the plan-view micrographs support the idea that strain is responsible for the stabilization of the fcc Co. Two distinct regions are again observed. Region (1) is clearly two phase with inclusions of the order of 100 Å diameter that EDAX showed to be either Co rich (greater than 80%) or Ag rich. In some cases, as shown in Fig. 2, the contrast surrounding an inclusion is clear evidence of the presence of strain, while in other cases the inclusions are surrounded by a ring of strain relieving dislocations. On close examination it can be seen that the orientation of the lattice planes within the grains is the same as in the matrix. In region (2) EDAX analysis of the matrix indicated that it remained a mixture of Co and Ag with an average composition of 45 at. % Co. A cross section of a region of the matrix is shown in Fig. 3. There is a large scale-wavelike contrast caused by dislocations perpendicular to the well-oriented (111) planes which we do not believe to be due to the Moiré effect. These dislocations may represent a composition variation and their




FIG. 2. TEM plan-view micrograph of $Co_{45}Ag_{55}$ prepared at 0 °C.

arrangement often gives the form of cigar shapes with aspect ratios up to 5:1. The atomic arrangement of the matrix is observed to be primarily fcc although on careful examination small clusters of hcp structure are visible as indicated in the figure. These may be evidence of small Co hcp clusters of order 20–30 Å diameter although it is estimated that these clusters make up only 4%–8% of the matrix so the remaining Co must be in the fcc phase. This result supports previous x-ray analysis of LT samples of varying composition

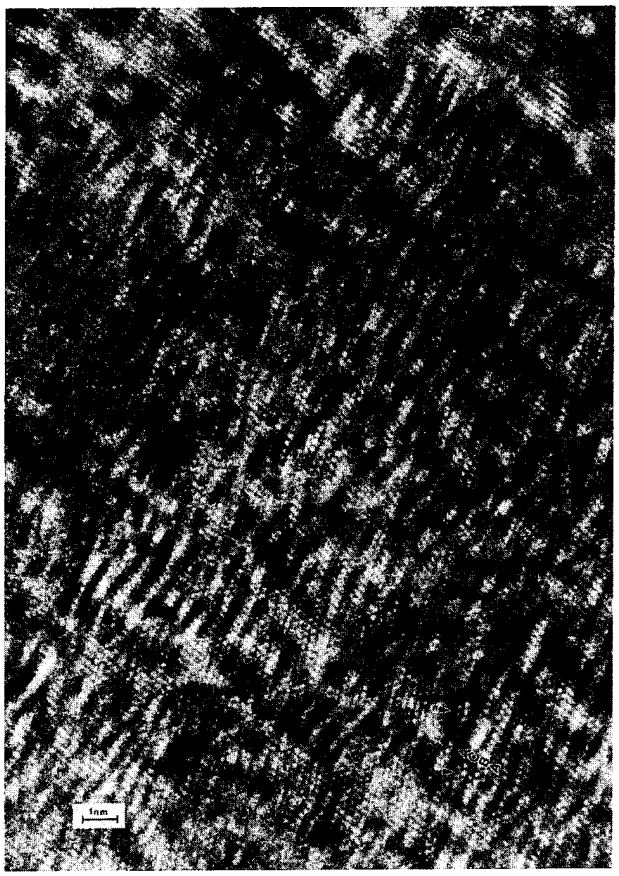



FIG. 3. TEM cross section of $Co_{45}Ag_{55}$ prepared at 0 °C. The letters represent lattice planes and the arrows point to small hcp clusters.

which attributed the divergence of the measured Ag lattice spacing from the bulk value to the presence of up to 8% Co impurities in the matrix.[5,6]

### B. High- and medium-temperature samples

In these cases clear diffraction spots for fcc Ag and hcp Co and Ru are visible. In contrast to the LT sample the plan-view micrographs show little contrast which is a result of the improved crystalline quality with the presence of fewer dislocations. The Co is now stabilized in its hcp phase which is related to the reduced amount of strain in the sample.

Cross-sectional TEM revealed that some areas of the sample consist of pure Ag throughout the thickness, and in other regions where the bulk of the film is Co–Ag there is a layer of pure Co adjacent to the Ru buffer layer. It is also apparent that the thickness of the Ag regions (150 Å) is about half those of the Co–Ag regions (350 Å). Such a thickness variation across the sample was also noted in the AFM scans.[5,6] These AFM images indicated arrays of raised areas 150–200 Å high with flat surfaces about 5000 Å in diameter separated by 1000 Å.

Periodic contract in the CoAg region normal to the film plane was also observed. This may derive from dislocations present due to the composition and hence lattice variation from Co to Ag. The lattice planes do not follow the waves of this modulation but remain well oriented.

The high-crystalline quality of the HT sample can be seen in Fig. 4. Typically there is a very clear array of dislocations between the Ru buffer and a region of pure Co (just out of view of the photograph). The period of the dislocations contrast (32 Å=15 planes) is related to the 8% mismatch in lattice parameter between the Co and Ru. Above the Co region there is a second array of dislocation contrast (shown in the figure), but in this case the period is reduced to seven atomic planes. These upper regions contain CoAg and Ag as determined by EDAX. Here two Co and Ag regions are separated by an array of dislocations. The lattice planes can be counted on either side of the dislocations and here there is a ratio of seven Co atomic planes to six Ag planes which roughly corresponds to the expected lattice mismatch of these materials. This region of the sample is therefore well segregated, but into relatively small areas of Co and Ag.

## III. DISCUSSION

Significant differences were seen between the LT and elevated temperature samples. At LT both the Ag and Co show (111) fcc structure accompanied by strain and dislocations. Cross sections reveal a homogeneous structure broken up by stacking faults with small clusters (10–20 atoms) of Co in a hcp structure. These small Co impurities, too small to be observed in the diffraction patterns, have a significant effect on the spin diffusion length reducing the GMR as discussed in Refs. 5 and 6. In contrast the high-temperature samples display segregated phases of fcc Ag and hcp Co with little evidence of any strain. In addition, cross sections show a step profile regions of the film with pure Ag and




FIG. 4. TEM cross section of $Co_{45}Ag_{55}$ prepared at 450 °C.

mixed CoAg regions which both have the Ag lattice parameter. In the mixed region, there is evidence of small pure Co filaments (23×10 $Å^2$) with the Co bulk lattice parameter. Surprisingly, at the Ru/CoAg interface a pure Co layer 20–30 Å thick was found separated from the CoAg by an array of dislocations.

## ACKNOWLEDGMENTS

The financial support of the EPSRC, Royal Society, Alliance program between the British Council and the Ministère des affaires ètrangères and the EC Human Capital and Mobility program are gratefully acknowledged.

[1] M. N. Baibich, J. M. Broto, A. Fert, F. Nguyen Van Dau, F. Petroff, P. Etienne, G. Creuzet, A. Friederich, and J. Chazelas, Phys. Lett. B **61**, 2472 (1988).
[2] J. Q. Xiao, J. S. Jiang, and C. L. Chien, Phys. Rev. Lett. **68**, 3749 (1992); A. E. Berkowitz, J. R. Mitchell, M. J. Carey, A. P. Young, S. Zhang, F. E. Spada, F. T. Parker, A. Hutten, and G. Thomas, *ibid.* **68**, 3745 (1992); J. A. Barnard, A. Waknis, M. Tan, E. Haftek, M. R. Parker, and M. L. Watson, J. Magn. Magn. Mater. **114**, L230 (1992).
[3] A. Fert, J. L. Duvail, and T. Valen (unpublished).
[4] G. A. Gehring, J. F. Gregg, S. M. Thompson, and M. L. Watson, J. Magn. Magn. Mater. **140–144**, 501 (1995).
[5] A. Azizi, S. M. Thompson, K. Ounadjela, J. F. Gregg, P. Vennegues, A. Dinia, J. Arabski, and C. Fermon, J. Magn. Magn. Mater. **148**, 313 (1995).
[6] K. Ounadjela, S. M. Thompson, J. F. Gregg, A. Azizi, M. Gester, P. Vennegues, and J. P. Deville (unpublished).

# Spin-dependent scattering in the nonmagnetic layers of annealed Co/Cu multilayers

H. Laidler and B. J. Hickey[a)]
*Department of Physics, The University of Leeds, Leeds, LS2 9JT, United Kingdom*

Annealing a multilayer is expected to promote diffusion at the interfaces. We have found that the interface roughness and giant magnetoresistance of Co/Cu (111) multilayers, grown by molecular-beam epitaxy on sapphire substrates, remain unchanged during anneals of up to 320 °C despite the zero-field resistivity having doubled. We explain this large increase in resistivity as due to the formation of an alloy between the top Cu layer of the multilayer and the Au protective cap. We propose that scattering in the AuCu alloy is spin dependent. We discuss this idea in the light of mean free path effects and the density of states of the entire sample. © *1996 American Institute of Physics.* [S0021-8979(96)55908-9]

The origin of the spin-dependent scattering which is the basis of the giant magnetoresistance (GMR) still remains a problem both theoretically[1] and experimentally. In particular, much research has concentrated on the role of interface roughness in magnetic multilayers. Recent growth studies of Co/Cu multilayers by Harp *et al.*[2] and Xu *et al.*[3] have indicated that the highest GMR occurs in samples with the highest degree of structural perfection. Zhang *et al.*[4] annealed sputtered Co/Cu multilayers and found that although the GMR decreased, the effect on the interfaces was too subtle to be deduced from the low-angle specular x-ray data. Without identification of whether the interface roughness had changed, it was difficult to deduce conclusions about the role of interface scattering.

Measurement of the buried interfaces in a multilayer is difficult and we have previously emphasized[5,6] the extreme care needed in interpreting x-ray data, the most widely used technique for analyzing structural changes. Systematic changes in low-angle specular x-ray scattering, which have been reported by other investigators as being interface roughness changes, could be explained by changes taking place in the capping and buffer layers. They can cause phase shifts in the x-ray waves resulting in changes to the Bragg peak height. Interface roughness can only be reliably determined from diffuse x-ray scattering. We have already reported[5] that the annealing of the Co/Cu multilayers discussed here caused no change in interface roughness. In this article we present a discussion of the role that the metallurgical changes in the capping layer play in the spin-dependent scattering.

The (Co 11 Å/Cu 8 Å)$_{20}$ multilayer was grown by molecular-beam epitaxy (MBE) onto a sapphire substrate using buffer layers of Nb (60 Å) and Cu (30 Å) to obtain high-quality growth. A 40 Å Au cap was laid to prevent the top layer of Cu from oxidizing. The sample was cut into identical pieces, checked first for uniformity by resistivity and x-ray measurements, and each annealed in a stream of oxygen-free nitrogen for 45 min at 200, 260, 290, and 320 °C, respectively, while a fifth was left unannealed. Further details of the growth, x-ray, and magnetotransport measurements have been reported elsewhere.[5] Room-temperature magneto-optical Kerr effect (MOKE) measurements were made on all samples in fields up to 2 T.

The resistivity measurements performed at 4.2 K are shown in Table I. Although $\rho_s$, the saturation field resistivity, more than doubled for the highest annealing treatment, $\Delta\rho$ scales with it resulting in little change to the GMR. The saturation field also remained unchanged for each sample at 4 T. Figure 1 shows the longitudinal MOKE curves for the unannealed and 320 °C samples. There is no evidence of any change in magnetization which is consistent with no change in the GMR.

Extensive x-ray measurements have been made on these samples using synchrotron radiation and have been reported elsewhere.[5] They have shown that there is no evidence of any changes in roughness of the Co/Cu interfaces. Thomson, Riedi, and Hickey[7] have performed nuclear-magnetic-resonance (NMR) measurements on these samples and have found that although there is evidence of a small relaxation of the strain in the interior of the Co layers, there is very little change to the interfaces. Also the x-ray rocking curves through the high-angle Co/Cu(111) peak show no discernible differences between any of the samples, which can be seen in Fig. 2.

The low-angle x-ray measurements did indicate that the surface electron density had increased, not possible from oxidation but true if the Au cap had alloyed with the top Cu layer. Figure 3(a) provides further evidence of this. There are significant changes to the shape of the high-angle $\theta$-$2\theta$ x-ray scans between the sapphire and the Co/Cu peak. Simulations of the data have shown that this region depends sensitively on the thicknesses of the Nb and Cu buffers and Au capping layers. The main change on annealing is the disappearance of

TABLE I. Resistivity measurements of the annealed multilayer at 4.2 K.

| Annealing treatment | $\rho_s$ ($\mu\Omega$ cm) | $\Delta\rho$ ($\mu\Omega$ cm) | GMR (%) |
|---|---|---|---|
| Unannealed | 8.2 | 3.0 | 37 |
| 200 °C | 9.0 | 3.4 | 38 |
| 260 °C | 12.0 | 4.4 | 37 |
| 290 °C | 14.4 | 4.7 | 33 |
| 320 °C | 18.6 | 5.8 | 31 |

[a)]Electronic mail: b.j.hickey@leeds.ac.uk

 0021-8979/96/79(8)/6250/3/$10.00 © 1996 American Institute of Physics

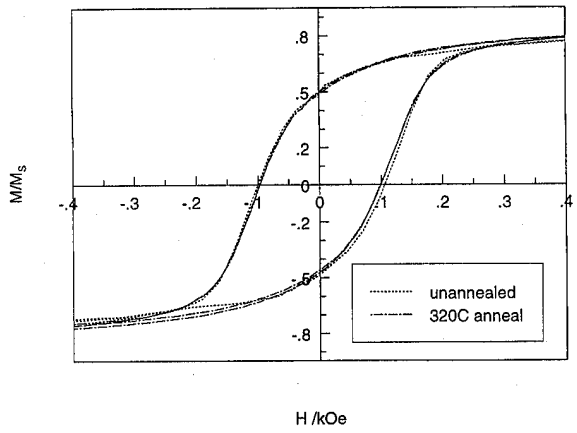



FIG. 1. Room-temperature longitudinal MOKE curves for the unannealed and 320 °C samples showing that the magnetization is unchanged.

the dip at 41° and the appearance of a peak in its place. The peak at 41° corresponds to the lattice constant for a $Au_{35}Cu_{65}$ alloy[8] and the equilibrium phase diagram for the Cu–Au system[9] suggests that an alloy of between 30 and 40 at. % of gold in copper was in fact the most likely to form at the annealing temperatures used. The peak could only be reproduced in this position by a simulation of the multilayer which replaced the top Cu and Au layer with a $Au_{35}Cu_{65}$ alloy.

In order to test the argument that an alloy had formed, a further sample was grown with an extra layer of Co between the multilayer and the Au cap to prevent the Cu and Au alloying. The phase diagram for Co and Au shows that these elements are largely immiscible and there is no stable alloy. This sample was annealed at 320 °C as before and the high-angle x-ray scans are shown in Fig. 3(b). There is very little difference between the two scans, which reinforces the argument that the changes occurring in Fig. 3(a) were due to a CuAu alloy forming.

The conclusion that very little had happened to the Co/Cu interfaces means that these are unusual results compared to many annealing experiments and highlight the importance of choice of substrate, using buffer layers which are immiscible in the multilayer and using nonoxidizing caps.

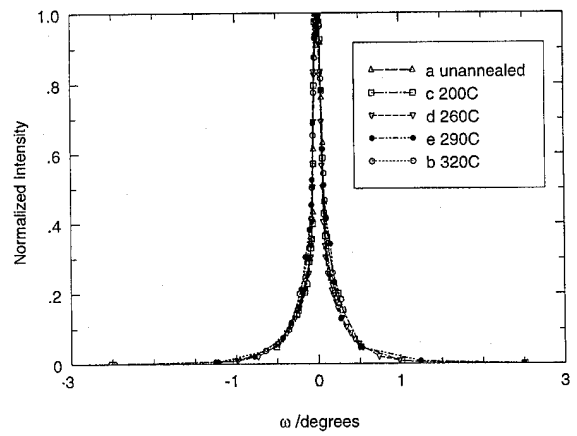



FIG. 2. Rocking curves performed on all samples through the high-angle Co/Cu(111) peak showing that there is no change upon annealing.

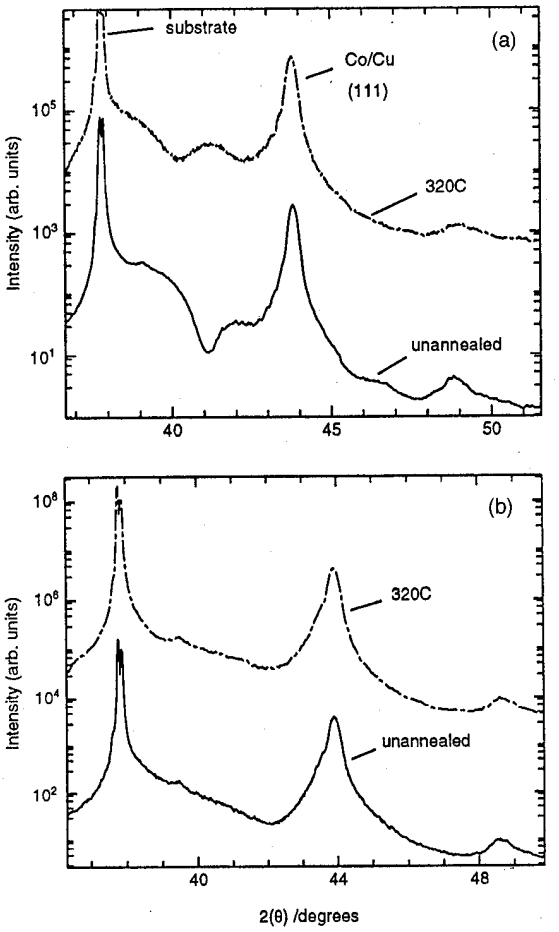



FIG. 3. High-angle $\theta$-$2\theta$ x-ray scans of (a) $Al_2O_3$/Nb 60/Cu 30/(Co 11 Cu 8]$_{20}$/Au 40 and (b) $Al_2O_3$/Nb 30/Cu 30/(Co 15 Cu 8]$_{20}$/Au 15 multilayers (thicknesses in Å) before and after annealing at 320 °C. The shape of the region between the sapphire and Co/Cu peak is due to the Nb and Cu buffers and the Au cap. Scans are offset for clarity.

Additional weight to the argument comes from the magnetometry and transport; there was no observed change in the MOKE curves and the GMR was virtually unchanged. This experiment demonstrates that with careful planning a GMR system can be designed which is impervious to annealing up to temperatures in excess of 300 °C.

It may seem surprising that the alloying of the capping layer which comprises just 20% of the sample could cause such a large increase in resistivity. We have observed that both $\rho(0)$ and $\rho(B_s)$ increase in proportion such that the GMR remains much the same for different annealing conditions. We know that in samples such as these the shorter of the two mean free paths is about 400 Å,[10] which is comparable with the thickness of the sample. Normally capping and buffer layers are considered as low-resistance layers which act as shunts for the current through the sample and thereby reduce the GMR. This interpretation applies when the mean free path is sufficiently short so that the layers can be regarded as resistors acting in parallel.[11] When the mean free path is long, as in this case, the layers effectively act as resistors in series.

Now it can be understood why the cap, which forms only a small part of the total sample, can have a large effect

TABLE II. Comparison of the resistivity at 300 K and the GMR at 4.2 K for the two multilayers described in Fig. 3.

| | $\rho_0$ (300 K)/$\mu\Omega$ cm | GMR % (4 K) |
|---|---|---|
| Cu/Au cap unannealed | 19.3 | 35 |
| 320 °C | 35.7 | 31 |
| Co/Au cap unannealed | 18.8 | 36 |
| 320 °C | 21.9 | 33 |

on the sample resistivity. Previous work on CuAu alloys[12] have found that an increase of 0.3 $\mu\Omega$ cm at. % of Au in Cu is seen. This indicates that an increase of approximately 10 $\mu\Omega$ cm would be expected. Table II summarizes the magnetotransport measurements of the original annealed sample and the Co/Au cap sample before and after annealing at 320 °C. Comparison of the changes in resistivity upon annealing in each sample is consistent with the rise expected for formation of the alloy if the layers act as resistors in series.

Within the two-current model we can find simple expressions for $\rho(0)$, $\rho(B_s)$, and the GMR in terms of the resistivity of the separate spin channels ($\rho_+$ for the up spin and $\rho_-$ for the down spin) and the asymmetry parameter $\alpha = \rho_-/\rho_+$,

$$\rho(0)=\frac{\rho_+}{4}(1+\alpha),$$

$$\rho(B_s)=\rho_+\frac{\alpha}{(1+\alpha)},$$

$$\frac{\Delta\rho}{\rho}=\frac{(1-\alpha)^2}{4\alpha}.$$

The GMR does not change therefore the scattering in the cap must be spin dependent. If the additional scattering were spin independent, the GMR should decrease. The additional resistance due to the alloyed cap is added to the resistance of each spin channel as a factor which multiplies $\rho_+$ and $\rho_-$. In other words, the individual scattering rates have increased by the same proportion. The density of final states, even for scattering in the cap, is asymmetric with respect to spin because it is the density of states of the whole sample which must be considered. The scattering in the cap is therefore spin dependent because it is determined by the density of available states. The increase in the zero-field and saturated-field resistivities is explained by the increase in $\rho_+$ and the constant GMR is a result of a constant $\alpha$. This idea is borne out by the data in Table I where increases in resistivity after annealing are in the same proportion for both $\rho(0)$ and $\rho(B_s)$.

The clear conclusion from the annealing experiments we have performed is that the interface roughness of Co/Cu multilayers does not change significantly despite very large changes being observed in the zero- and high-field resistivities. Provided the multilayer is not destroyed by excessive annealing, the GMR is resistance to the changes in resistivity and it would seem that where large changes are observed, they are likely to be associated with changes in other layers rather than the Co/Cu itself.

Thanks are expressed to M. J. Walker for preparation of the samples and to M. A. Howson, N. Wiser, and B. K. Tanner for useful discussions. Financial support was provided by the Engineering and Physical Sciences Research Council.

[1] J. Barnas, A. Fert, J. Magn. Magn. Mater. **136**, 260 (1994).
[2] G. R. Harp, S. S. P. Parkin, R. F. C. Farrow, R. F. Marks, M. F. Toney, Q. H. Lan, A. Radedeau, and R. J. Savoy, Phys. Rev. B **47**, 8721 (1993).
[3] J. Xu, B. J. Hickey, M. A. Howson, D. Greig, and M. J. Walker J. Magn. Magn. Mater 1996 (in press).
[4] H. Zhang, R. W. Cochrane, Y. Huai, M. Mao, X. Bian, and W. B. Muir, J. Appl. Phys. **75**, 6535 (1994).
[5] H. Laidler, I. Pape, C. I. Gregory, B. J. Hickey, and B. K. Tanner (in press J. Magn. Magn. Mater 1996).
[6] H. Laidler, B. J. Hickey, T. P. A. Hase, B. K. Tanner, and R. Schad J. Magn. Magn. Mater (in press).
[7] T. Thomson, P. Riedi, and B. J. Hickey (these proceedings).
[8] B. E. Warren, *X-Ray Diffraction* (Addison–Wesley, Reading, MA, 1969), pp. 206–250.
[9] B. D. Cullity, *Elements of X-Ray Diffraction* (Addison–Wesley, Reading, MA, 1978), p. 377.
[10] K. P. Wellock and B. J. Hickey (unpublished experiment on varying the number of repetitions of the bilayer in Co/Cu multilayers).
[11] D. M. Edwards, J. Mathon, and R. B. Muniz, IEEE Trans. Magn. **27**, 3548 (1991).
[12] C. H. Johansson and J. O. Linde, Ann. Phys. (Leipzig) **25**, 1 (1936).

# Interfacial roughness of Fe–Cr GMR superlattices (abstract)

W. Dmowski and T. Egami
*Department of Materials Science and Engineering, and LRSM, University of Pennsylvania, Philadelphia, Pennsylvania 19104*

D. Kelly and I. Schuller
*Department of Physics, University of California-San Diego, La Jolla, California 92093*

Fe–Cr superlattices exhibit giant magnetoresistance effect which can be utilized in magnetic recording heads. There are many studies indicating the role of the interfacial structure on the magnetoresistance effect. To elucidate this point we have performed x-ray diffraction study of three $[Fe(30\ Å)/Cr(12\ Å)]_{10}$ superlattices which had been sputtered in 4, 7, and 10 mTorr of Ar. We used position sensitive detector in horizontal setup to collect simultaneously specular scattering intensity ($z$ component of the scattering vector **Q** perpendicular to the film) and off-specular intensity with $Q_y$ parallel to the plane of the sample. This technique[1] allows to evaluate interfacial roughness at various length scales. Short range roughness may be due to interdiffusion, while some medium range roughness is also present, and could have effects on transport phenomena. In conventional low angle diffraction analysis these contributions are intermixed. From the Fourier transform of the scattered intensity distribution in $Q_x - Q_y$ plane the interfacial height fluctuation function $g(r)$ can be obtained ($r$ is a lateral spacing). Figure 1 presents $g(r)$ obtained for three samples of Fe–Cr. It is apparent that 4 mTorr sample is very different than 7 and 10 mTorr in terms of interfacial roughness. We will discuss in detail results of the diffraction studies together with the magnetization and magnetotransport data. © *1996 American Institute of Physics.* [S0021-8979(96)61408-0]

---

Work at University of Pennsylvania supported by NSF DMR 93-0728.
Work at University of California-San Diego supported by DOE.

[1] X. Yan and T. Egami, Phys. Rev. B **47**, 2362 (1993).

# Giant magnetoresistance in evaporated NiFe/Cu and NiFeCo/Cu multilayers (abstract)

A. M. Zeltser and Neil Smith
*Eastman Kodak Company, San Diego Laboratories, San Diego, California 92121*

The magnetic and transport properties of electron beam evaporated $(Ni_{83}Fe_{17}/Cu)_{10}$ and $(Ni_{66}Fe_{16}Co_{18}/Cu)_{10}$ multilayers (ML) were studied as a function of the Cu spacer and magnetic layer thicknesses ($t_{Cu}$ and $t_{NiFe}$), annealing conditions and Ta buffer layer thickness. The ML were evaporated in a magnetic field at deposition rates ~ 2 Å/s and background pressure $<5\times10^{-8}$ mbar on $Si/SiO_2$ substrates at $T_s=200$ °C. These ML exhibited two unique features: (1) $\Delta R/R$ and the interlayer coupling did not show oscillatory behavior as a function of $t_{Cu}$; and (2) after magnetic post annealing, $\Delta R/R$ increased from <0.3% in the as-deposited state, to up to ~6% and 7% in Ta/(NiFe/Cu) and (NiFeCo/Cu), respectively. The coupling between the NiFe layers changed from ferromagnetic in the as-deposited state ($M_r/M_s\sim0.9$) to essentially antiferromagnetic ($M_r/M_s$ <0.2) after appropriate annealing, and the ML became virtually isotropic in-plane. This is quite different from strong oscillatory behavior of giant magnetoresistance (GMR) previously reported in (NiFe/Cu) as-deposited ML made by ion-beam sputtering.[1] After annealing at 300° and 325 °C for 2 h, the $\Delta R/R$ became ~4.5% and ~6.5% in (NiFe/Cu) and (NiFeCo/Cu) ML, respectively, and remained approximately constant for $t_{Cu}=20$ to 40 Å. The coupling field generally decreased with an increase in $t_{Cu}$ and $t_{NiFe}$ and after annealing at 300 °C dropped to as low as ~25 and 45 Oe in (NiFe/Cu) and (NiFeCo/Cu) ML, respectively. The $\Delta R/R$ of Ta/(NiFe/Cu) ML increased with the thickness of Ta buffer layer from 30 to 70 Å. The high-angle $\theta$–$2\theta$ x-ray scans of (NiFe/Cu) ML showed (111) texture, essentially independent of annealing temperature. The low-angle x-ray diffraction did not reveal roughening of the Cu–NiFe interfaces as a result of annealing. In many respects the GMR behavior of these ML is similar to that reported in sputtered "discontinuous" NiFe/Ag.[2] However, in contrast to the latter, the resistivity of NiFe/Cu monotonically increases with annealing temperature. This suggests that lattice interdiffusion is more prominent in the NiFe–Cu system, consistent with a greater equilibrium solubility of Cu in the NiFe matrix compared to that of Ag. It is believed that Cu diffusion along the NiFe grain boundaries creates *intra*-layer magnetic discontinuity in NiFe and promotes *inter*-layer antiferromagnetic coupling between adjacent NiFe layers, which then gives rise to the observed GMR.[3] Evaporated NiFe/Cu ML showed very small hysteresis and uniform GMR properties throughout the thickness, which makes them good candidates for GMR–DMR heads.[4] © *1996 American Institute of Physics.* [S0021-8979(96)61508-X]

The full text of this work will appear in J. Appl. Phys. **79**(11) (1996) (1 June issue).

[1]R. Nakatani, T. Dey, T. Kobayashi, and Y. Sugita, IEEE/Trans. Magn. **28**, 2668 (1992).
[2]T. L. Hylton, K. R. Coffey, M. A. Parker, and J. K. Howard, Science **261**, 1021 (1993).
[3]J. C. Slonczewski, J. Magn. Magn. Mater. **129**, L123-28 (1994).
[4]N. Smith, A. M. Zeltser, and M. R. Parker, IEEE Trans. Magn. **32**, 135 (1996).

 0021-8979/96/79(8)/6254/1/$10.00 © 1996 American Institute of Physics

# Giant magnetoresistance in magnetic granular systems

L. Sheng
*National Laboratory of Solid State Microstructure and Institute of Solid State Physics, Nanjing University, Nanjing 210093, People's Republic of China and Department of Physics, University of Hong Kong, Pokfulam Road, Hong Kong*

R. Y. Gu
*National Laboratory of Solid State Microstructure and Institute of Solid State Physics, Nanjing University, Nanjing 210093, People's Republic of China*

D. Y. Xing
*Chinese Center of Advanced Science and Technology (World Laboratory), P.O. Box 8730, Beijing, People's Republic of China and Department of Physics, Nanjing University, Nanjing, People's Republic of China*

Z. D. Wang and Jian-Xin Zhu
*Department of Physics, University of Hong Kong, Pokfulam Road, Hong Kong*

Based on a semiclassical model, the transport properties in systems of cylindrical or spherical magnetic granules are investigated analytically. It is shown that the conductivities as well as the magnetoresistance of these systems depend strongly on the size of the granules. In particular, there is always an optimum granular size for the magnetoresistance. © *1996 American Institute of Physics.* [S0021-8979(96)79808-0]

Recently, there has been much interest in the study of giant magnetoresistance (GMR) in magnetic inhomogeneous systems[1–7] both experimentally and theoretically. For multilayer structures, almost all the low-temperature features of GMR could be understood by semiclassical models[8–12] or quantum theories[13–15] by including spin-dependent interface scattering and bulk scattering. Previous theoretical investigations[5,16] on the GMR in granular systems are based on the assumption that transport in these systems is quite close to that in multilayered systems with current perpendicular to the layers. However, differing from those in multilayered structures, both the distributions of the electric field and currents are spatially varied in these three-dimensionally inhomogeneous systems. Therefore, it is valuable and interesting to develop a theory which includes spatial variations in the electric field and in the currents.

In this article, we present a semiclassical description of the GMR in magnetic granular systems, in which the spatial variations of the electric fields and the currents are considered. A new formalism of the position-dependent current is developed. In particular, analytical expressions for the resistivity are obtained. We focus our attention on systems of cylindrical magnetic granules. We find that both the GMR and the resistivities depend strongly on the granular sizes and that there is always an optimum granular size for the GMR.

Let us consider a general inhomogeneous system in which charge carriers are scattered by impurities and rough interfaces. For convenience, we do not include the spin degrees of freedom for a while. In the presence of an external electric field, the steady-state transport properties in this system can be described by the following effective Boltzmann equation:[17]

$$\mathbf{v}\cdot\nabla g+g/\tau=e\mathbf{v}\cdot\mathbf{E}^{\mathrm{eff}}, \tag{1}$$

where $\tau$ is the position-dependent relaxation time and $g$ is a function characterizing the deviation of the distribution function $f$ from the equilibrium distribution $f_0$, which satisfies the relation $f=f_0+g(\partial f_0/\partial\epsilon)$. Since interface scattering is also considered as impurity scattering in thin mixing films,[14] the entire scattering effect is included in the position-dependent relaxation time $\tau(\mathbf{r})$. $\mathbf{E}^{\mathrm{eff}}(\mathbf{r})$ is the effective internal field to be determined from the continuity condition of the current.

In general, the position-dependent current is related to the electric-field by a two-point conductivity tensor $\sigma_{\alpha\beta}(\mathbf{r},\mathbf{r}')$, such that

$$J_\alpha(\mathbf{r})=\int d^3r'\,\sigma_{\alpha\beta}(\mathbf{r},\mathbf{r}')E^{\mathrm{eff}}_\beta(\mathbf{r}'), \tag{2}$$

where the summation is indicated by two same coordinate labels. By using the path-integral approach,[12,14] we solve the Boltzmann Eq. (1) and obtain

$$\sigma_{\alpha\beta}(\mathbf{r},\mathbf{r}')=C_e r_{0\alpha}r_{0\beta}\Phi(\mathbf{r},\mathbf{r}'), \tag{3}$$

with

$$\Phi(\mathbf{r},\mathbf{r}')=\frac{1}{4\pi|\mathbf{r}-\mathbf{r}'|^2}\exp\left[-\int_{\mathbf{r}'\to\mathbf{r}}\frac{du''}{\lambda(\mathbf{r}'')}\right], \tag{4}$$

$C_e=3n_e e^2/2mv_F$, $\hat{\mathbf{r}}_0=(\mathbf{r}-\mathbf{r}')/|\mathbf{r}-\mathbf{r}'|$, and $\lambda(\mathbf{r})=v_F\tau(\mathbf{r})$. The integral in Eq. (4) is along the straight line connecting the points $\mathbf{r}$ and $\mathbf{r}'$, and $du''$ is the element of line at the point $\mathbf{r}''$. The effective field $\mathbf{E}^{\mathrm{eff}}$, determined by combining Eq. (2) with the continuity condition for the current, is found to be[17]

$$\mathbf{E}^{\mathrm{eff}}=\mathbf{E}^{\mathrm{ex}}-\nabla\mu, \tag{5}$$

where $\mu = GD_\beta E^{\mathrm{ex}}_\beta$ with

$$G=(1-\Phi\Lambda)^{-1}=1+\Phi\Lambda+\cdots, \tag{6}$$

$D_\alpha(\mathbf{r},\mathbf{r}')=r_{0\alpha}\Phi(\mathbf{r},\mathbf{r}')$, and $\Lambda(\mathbf{r},\mathbf{r}')=\delta(\mathbf{r}-\mathbf{r}')/\lambda(\mathbf{r})$. Here, $GD_\beta$ represents the integral $\int d\mathbf{r}''G(\mathbf{r},\mathbf{r}'')D_\beta(\mathbf{r}'',\mathbf{r}')$. The constant $\mathbf{E}^{\mathrm{ex}}$ in the above expressions is actually the external field, since

 0021-8979/96/79(8)/6255/3/$10.00 © 1996 American Institute of Physics 

$$\mathbf{E}^{\mathrm{ex}}=\langle \mathbf{E}^{\mathrm{eff}} \rangle, \tag{7}$$

where $\langle \cdot \rangle$ means taking the average over the whole system.

Now let us turn to investigate transport in granular systems within the framework of a mean-field treatment. We consider the $N_p$-particle system to be realized by adding one particle to the system of $N_p-1$ particles. The effective field in the system of $N_p-1$ particles is written as $\mathbf{E}^{\mathrm{bc}}$, which is essentially the sum of the applied field and the field produced by the accumulated charge on the $N_p-1$ particles. The $N_p$-particle problem is then treated approximately as that of an isolated particle in the background field $\mathbf{E}^{\mathrm{bc}}$. The above considerations can be explicitly represented as

$$\mathbf{E}^{\mathrm{eff}}=\mathbf{E}^{\mathrm{bc}}-\nabla(G_1 D_{1,\beta} E^{\mathrm{bc}}_{\beta}). \tag{8}$$

A Subscript 1 has been used to indicate that the parameters are associated with the single-particle case. The background field $\mathbf{E}^{\mathrm{bc}}$ will be determined from the boundary condition (7). Equation (8) is highly useful for us to determine the effective electric field in the $N_p$-particle system, because we need only to solve the problem of an isolated particle in the background electric field. We wish to point out that Eq. (8) is appropriate only in the small region near the central particle. Nevertheless, using this equation in the region of every particle, we are able to obtain the field in the whole system.

To obtain the average conductivity analytically, we now take the local limit, i.e.,

$$\sigma^{c}_{\alpha\beta}(\mathbf{r},\mathbf{r}')=\sigma(\mathbf{r})\,\delta_{\alpha\beta}\delta(\mathbf{r}-\mathbf{r}'), \tag{9}$$

where $\sigma(\mathbf{r})=ne^2\lambda(\mathbf{r})/2mv_F$.[18] Since $\nabla\times\mathbf{E}^{\mathrm{eff}}=0$, it is convenient to define an effective scalar potential by

$$\mathbf{E}^{\mathrm{eff}}(\mathbf{r})=-\nabla U^{\mathrm{eff}}(\mathbf{r}). \tag{10}$$

We consider first the system composed of parallel ferromagnetic cylinders of radius $a$ in a nonmagnetic medium. The electric field is assumed to be applied along the $z$ axis and perpendicular to the cylinders. For simplicity, $\lambda(\mathbf{r})$ is taken to be the constant $\lambda_0$ in the medium, $\lambda_F$ in the particles, and $\lambda_I$ in the mixing films, respectively. If we consider all granules to be identical cylinders, the equation of continuity for the current becomes Poisson's equation in all regions. In this case, the effective potential in the $x-y$ plane has the form

$$U^{\mathrm{eff}}(\rho,\varphi)=-\sin(\varphi)\begin{cases} E^{\mathrm{bc}}\rho+D/\rho, & \rho>a+d \\ C_1\rho+C_2/\rho, & a+d>\rho>a. \\ E^{F}\rho, & a>\rho \end{cases} \tag{11}$$

Here $D$, $C_1$, $C_2$, and $E_F$ are constants to be determined from the continuity of the scalar potential and the current at $r=a$ and $r=a+d$. For example, the electric field in the inside region of the particles $E_F$ is found to be $E^F=\gamma_F E^{\mathrm{bc}}$ with $\gamma_F=2\lambda_0/(\lambda_0+\lambda_F+\lambda_0\lambda_F R_I/a)$. We have assumed that $d$ is much less than $a$, so that only the ratio $R_I=d/\lambda_I$ is of significance.

Now, we need to calculate the average of the effective electric field. We emphasize that even when the thickness goes to zero, the contribution from the field in the interlayer cannot be neglected. In terms of Eq. (7), we obtain

$$E^{\mathrm{ex}}=[(1-f)+(\gamma_F+\gamma_I)f]E^{\mathrm{bc}}, \tag{12}$$

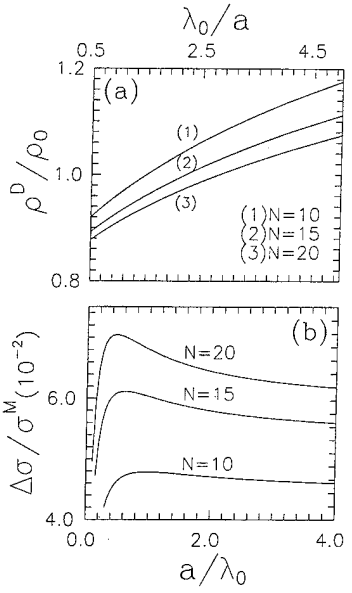



FIG. 1. (a) Resistivity $\rho^D$ as a function of $\lambda_0/a$ and (b) percent of GMR $\Delta\sigma/\sigma^M$ as a function of $a/\lambda_0$ in systems of cylindrical granules for several spin-asymmetry factors $N$. The other parameters are $f=0.3$, $\lambda_F^{\uparrow}=0.6\lambda_0$ and $R_I^{\uparrow}=1.0$.

where $f$ is the volumetric filling factor, and $\gamma_I=\lambda_F R_I\gamma_F/a$. The average conductivity is evaluated from $\langle J\rangle/E^{\mathrm{ex}}$.

In order to elucidate the GMR effect, the spin degrees of freedom need to be included. We focus on the cases where the spin diffusion length is much larger than the mean free path, so that the total conductivity is the sum from the two spin channels, and for each channel the previous formulas can be extended straightforwardly. Let $\lambda_I^s$ and $\lambda_F^s$, with $s=\uparrow$ for the majority spin and $s=\downarrow$ for the minority spin, denote the mean free path of electrons in the mixing films and in the particles,[8] respectively then we arrive at

$$\frac{\sigma^D}{\sigma_0}=\frac{2(1-f)+f(\gamma_F^{\uparrow}\lambda_F^{\uparrow}+\gamma_F^{\downarrow}\lambda_F^{\downarrow})/\lambda_0}{2(1-f)+(\gamma_F^{\uparrow}+\gamma_F^{\downarrow}+\gamma_I^{\uparrow}+\gamma_I^{\downarrow})f}, \tag{13}$$

for the demagnetized state, and

$$\frac{\sigma^M}{\sigma_0}=\sum_{s=\uparrow,\downarrow}\frac{(1-f)+f\gamma_F^s\lambda_F^s/\lambda_0}{2(1-f)+2(\gamma_F^s+\gamma_I^s)f}, \tag{14}$$

for the magnetized state, with $\sigma_0=ne^2\lambda_0/mv_F$.

The GMR effect is measured by $\Delta\sigma=\sigma^M-\sigma^D$, which can be found to be always positive. Its amplitude is defined as $\Delta\rho/\rho^D=\Delta\sigma/\sigma^M$ with $\rho^D=1/\sigma^D$, $\rho^M=1/\sigma^M$, and $\Delta\rho=\rho^D-\rho^M$. For simplicity, we here assume the spin-asymmetry factors in the particles and in the mixing film are of the same value $N=\lambda_F^{\downarrow}/\lambda_F^{\uparrow}=R_I^{\uparrow}/R_I^{\downarrow}$ although they are quite different. In Fig. 1(a), we plot the resistivity as a function of the inverse of radius, which is approximately in linear proportion. The GMR is shown in Fig. 1(b). There is always an optimum radius for the GMR. To understand this feature, we notice that there two factors that determine the GMR. On one hand, since the number of atoms at interfaces is inversely proportional to the radius, the proportion of the spin-dependent interface scattering to the total scattering increases with decreasing size of the cylinders. On the other hand, the

smaller the radius, the more easily the currents pass by the cylinders, an effect which results in the decrease in the spin dependence of the scattering of the electrons. The competition between these two factors leads to a maximum of the GMR.

The above calculations can be extended straightforwardly to the case of spherical granules. We can find that eqs. (13) and (14) are still valid if the parameters $\gamma_F^s$ and $\gamma_I^s$ are represented as

$$\gamma_F^s = \frac{3\lambda_0}{2\lambda_0 + \lambda_F^s + 2\lambda_0 \lambda_F^s R_I^s a}, \tag{15}$$

$$\gamma_I^s = 2\lambda_F^s R_I^s \gamma_F^s / a. \tag{16}$$

In summary, we have presented a new and efficient approach to calculate the conductivity in inhomogeneous systems based on the effective Boltzmann equation. Within a mean-field framework, we employ our formal theory to investigate in detail the GMR effect in cylindrical magnetic granular systems.

This work was supported by the RGC research grant of Hong Kong under No. HKU 262/95P, the CRCG grant at the University of Hong Kong, and in part by a joint grant of the NSFC and NAMCC.

[1] M. N. Baibich, J. M. Broto, A. Fert, F. Nguyen van dau, F. Petroff, P. Etienne, G. Creuzet, A. Friederich, and J. Chazelas, Phys. Rev. Lett. **61**, 2472 (1988).
[2] G. Binasch, P. Grunberg, F. Saurenbach, and W. Zinn, Phys. Rev. B **39**, 4828 (1989).
[3] S. S. P. Parkin, N. More, and K. P. Roche, Phys. Rev. Lett. **64**, 2304 (1990).
[4] W. P. Pratt, Jr., S.-F. Lee, J. M. Slaughter, R. Loloee, P. A. Shroeder, and J. Bass, Phys. Rev. Lett. **66**, 3060 (1992).
[5] A. E. Berkowitz, J. R. Mitchell, M. J. Carey, A. P. Young, S. Zhang, F. E. Spada, E. T. Parker, A. Hutten, and C. L. Chien, Phys. Rev. Lett. **68**, 3745 (1992).
[6] J. Q. Xiao, J. S. Jiang, and C. L. Chien, Phys. Rev. Lett. **68**, 3749 (1992).
[7] J. Q. Wang and G. Xiao, Phys. Rev. B **49**, 3982 (1994).
[8] R. E. Camley and J. Barnas, Phys. Rev. Lett. **63**, 664 (1989).
[9] R. Q. Hood and L. M. Falicov, Phys. Rev. B **46**, 8287 (1992).
[10] T. Valet and A. Fert, Phys. Rev. B **48**, 7099 (1993).
[11] M. Liu and D. Y. Xing, Phys. Rev. B **47**, 12 272 (1993).
[12] L. Sheng and D. Y. Xing, Phys. Rev. B **50**, 1001 (1994).
[13] P. M. Levy, S. Zhang, and A. Fert, Phys. Rev. Lett. **65**, 1643 (1990).
[14] H. E. Camblong and P. M. Levy, Phys. Rev. Lett. **69**, 2835 (1992); J. Magn. Magn. Matter. **121**, 446 (1993); J. Appl. Phys. **73**, 5533 (1993).
[15] H. E. Camblong, S. Zhang, and P. M. Levy, J. Appl. Phys. **75**, 6905 (1994).
[16] S. Zhang and P. M. Levy, J. Appl. Phys. **73**, 5315 (1993).
[17] L. Sheng, Z. D. Wang, D. Y. Xing, and J. X. Zhu, Phys. Rev. B (in press).
[18] Beyond the local limit, only a numerical solution of $\sigma_{\alpha\beta}(\mathbf{r},\mathbf{r}')$ can be obtained in terms of Eqs. (5) and (6). As far as the distance of particles is significantly larger than the mean free path, the conclusion obtained in the following is still expected qualitatively.

# Giant magnetoresistance in granular Fe–$MgF_2$ films

T. Furubayashi and I. Nakatani
*National Research Institute for Metals, Tsukuba 305, Japan*

The giant magnetoresistance effect observed in granular Fe–$MgF_2$ films, which consist of metallic particles embedded in an insulating medium, is reported. Large negative magnetoresistance (MR) with a magnitude up to 7.5% at 78 K was observed in semiconducting films with the Fe composition below the percolation threshold. Field dependence of the MR is well described by the form proportional to the square of the magnetization. The MR effect in this system seems to arise from the tunneling conductance between the Fe particles depending on the relative relation of the magnetization direction. © *1996 American Institute of Physics.* [S0021-8979(96)56008-3]

## I. INTRODUCTION

Much attention has been attracted by granular materials consisting of ferromagnetic metallic particles dispersed in a metallic matrix in view of the giant magnetoresistance (GMR).[1–3] On the other hand, electric conductance of systems consisting of metallic particles in an insulating matrix has been also extensively investigated.[4,5] When the metal content is below the percolation threshold, conductance in such systems is considered to originate in a tunneling current between metallic particles separated by an insulating barrier. Gittleman and co-workers[4] reported negative MR in granular Ni–$SiO_2$ films. They suggested that the MR arises from the effect that tunneling conductance depends on the relative direction of the magnetization between neighboring particles. Although the MR ratio is not large (<1% at room temperature), the sign is independent of the direction of the current to the magnetic field, similarly with GMR effect in granular metal–metal films. Mitani, Ohnuma, and Fujimori recently found large negative MR reaching the amplitude of 8% in granular Co–Al–O films,[6] which consist of Co particles separated by $Al_2O_3$.

Tunneling junctions with ferromagnetic electrodes have been extensively investigated. Miyazaki and Tezuka[7] observed that the conductance of a tunneling junction Fe/$Al_2O_3$/Fe changes with the amplitude reaching 30%, depending on the relative angle of the magnetization of each Fe electrode. Thus, it seems possible to obtain large MR in granular metal–insulator systems by using Fe, although MR effects in granular Fe–insulator systems have not yet been reported so far.

In this work, we investigated MR effects in granular Fe–$MgF_2$ films. It has been shown that the two materials are immiscible and that granular systems consisting of Fe particles in $MgF_2$ can be obtained.[8] The relationship between MR and magnetization curves was examined.

## II. EXPERIMENT

The samples were prepared by coevaporating two sources of Fe and $MgF_2$ in a vacuum better than $5\times10^{-6}$ Pa. The films were deposited onto glass substrates, which were kept at temperatures $T_s$ of 300 or 400 K. The deposited amount of each material was monitored by respective quartz oscillator. The thickness of the films is typically 30–200 nm. Electric resistance was measured by the conventional dc four-terminal method. The magnetization curves were measured by an alternating gradient magnetometer.

From transmission electron microscopy (TEM) observations of the samples with the volume fraction $x$ of Fe studied here, it was found that the films have a granular structure with the Fe grain size of around 3 nm. Figure 1 shows a typical TEM photograph. The electron-diffraction patterns showed the bcc structure of Fe.

## III. RESULTS AND DISCUSSION

Negative MR was observed as typically shown in Fig. 2. Magnetic field was applied in the direction parallel to the film plane. No significant difference was observed between MR curves taken in the longitudinal (current parallel to field) and the transverse (current perpendicular to field) geometry. The MR in this material is isotropic.

The magnetization curve at room temperature in Fig. 2 shows superparamagnetic behavior with no hysteresis. The blocking temperature $T_B$, below which the magnetization curve has hysteresis, was found to be about 200 K for this sample from the magnetization measurements. The MR curves below $T_B$ showed hysteresis correspondingly to the magnetization curves as shown in Fig. 2(b) at 78 K. The MR ratio, $[\rho_0 - \rho(H)]/\rho_0$, where $\rho_0$ is the maximum at each temperature, is 4.0% at 297 K and 7.5% at 78 K with the applied field $\mu_0 H = 0.9$ T.

The resistivity $\rho$ under zero magnetic field and the MR ratio with $\mu_0 H = 0.9$ T, measured in the transverse geometry at room temperature, are summarized in Fig. 3 against the Fe

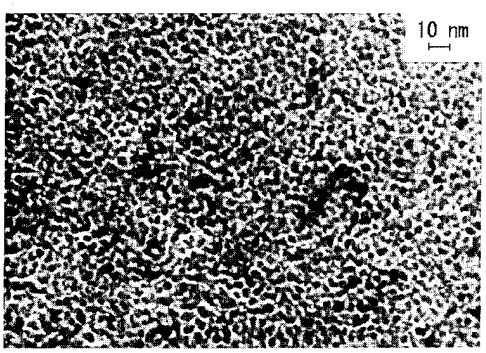



FIG. 1. TEM micrograph of granular $Fe_{0.42}(MgF_2)_{0.58}$ deposited at $T_s$ =400 K.

 0021-8979/96/79(8)/6258/3/$10.00 © 1996 American Institute of Physics

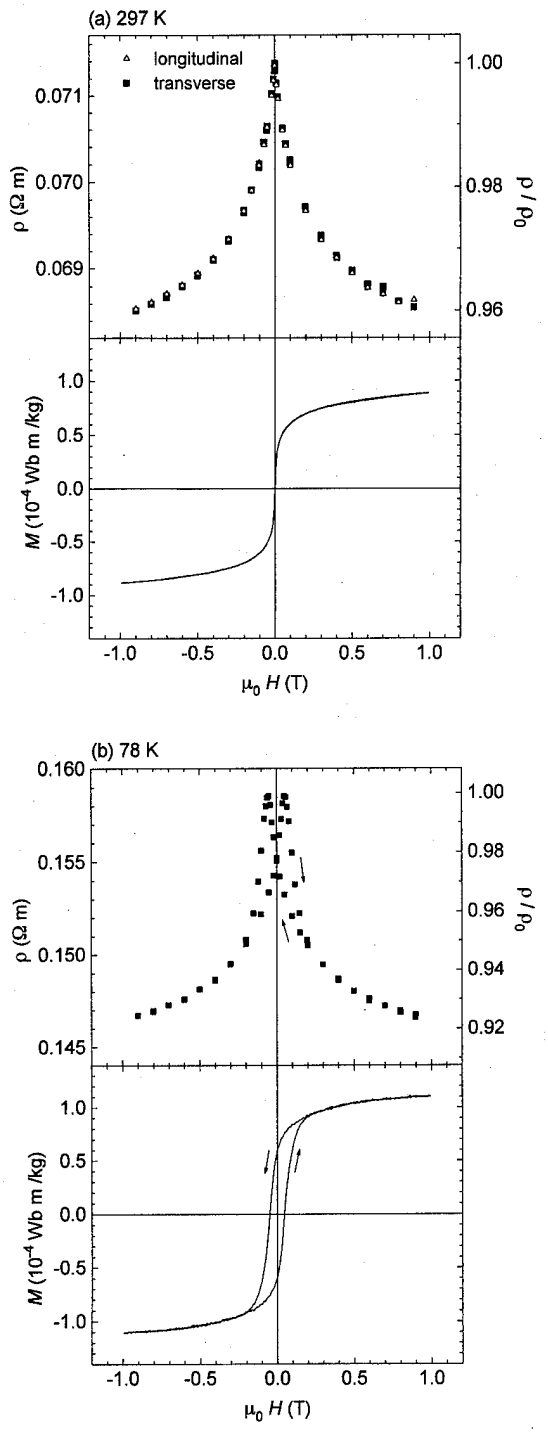



FIG. 2. Electric resistivity and magnetization plotted against magnetic field for the sample with the volume composition $Fe_{0.42}(MgF_2)_{0.58}$ deposited at $T_s$=400 K; measured at (a) 297 K and (b) 78 K. Magnetic field was applied in the direction parallel to the film plane.

volume fraction $x$. The large MR ratio was observed for samples with large resistivity, i.e., small Fe fraction.

Temperature dependence of the resistivity was examined for the samples with large MR. The resistivity increased with decreasing temperature as shown in Fig. 4. The result shows no metallic percolation path in these films. The Fe content in these samples is below the percolation threshold. The electrical resistivity in granular systems consisting of metallic

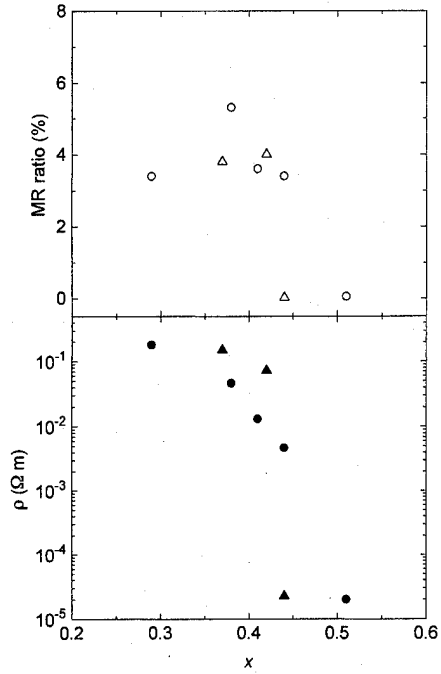



FIG. 3. MR ratio $[\rho_0-\rho(H)]/\rho_0$ with $\mu_0 H$=0.9 T, and zero-field resistivity are shown against the volume fraction $x$ of Fe at room temperature. Circles are for the samples prepared at $T_s$=300 K and triangles are for $T_s$=400 K.

particles separated by an insulating matrix was theoretically investigated in terms of tunneling conductance between particles.[5] It was shown that the temperature dependence is expressed by

$$\rho \propto \exp(T/T_0)^{-\alpha}, \tag{1}$$

with $\alpha$=1/2. It seems in Fig. 4 that log $\rho$ is mostly linear to $T^{-1/2}$ according to the above relation. However, the data can be also fitted to the form (1) with $\alpha$=1/4, which is derived

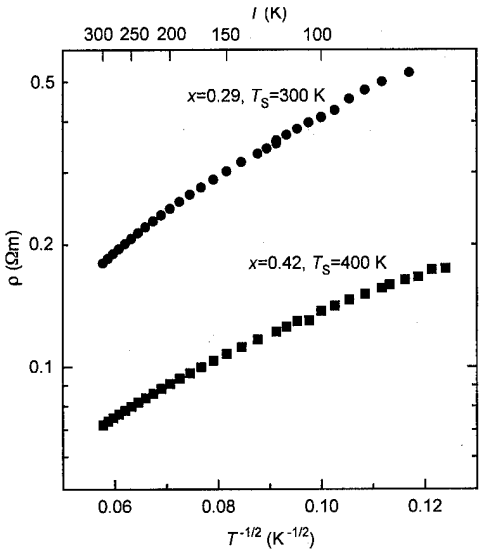



FIG. 4. Resistivity plotted against $T^{-1/2}$, where $T$ is the temperature, for each sample with the Fe volume fraction $x$ prepared at the substrate temperature $T_s$.

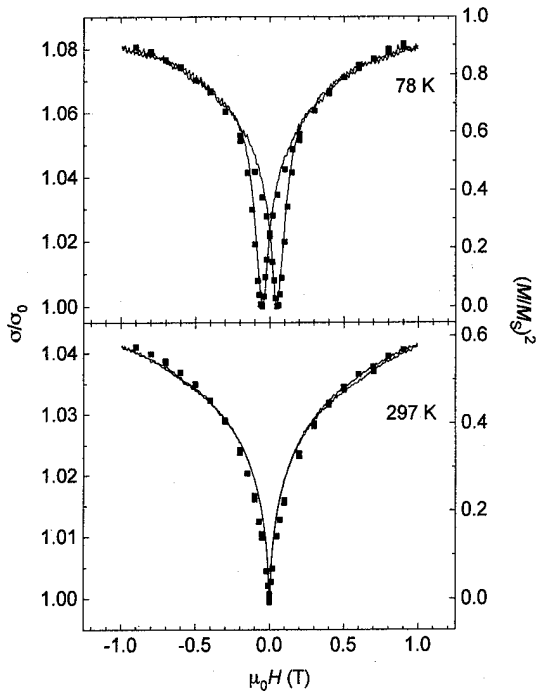



FIG. 5. Solid squares denote conductance $\sigma$ normalized by the minimum value $\sigma_0$ for the same sample as Fig. 2. Solid curves indicate $(M/M_s)^2$, where $M_s$ is the value of $M$ at 10 K with $\mu_0 H=1$ T.

from the theory of variable range hopping[9] for amorphous semiconductors. It is difficult at present to determine the value of $\alpha$. Measurements at lower temperatures would be required.

The field dependence of the MR is discussed in terms of tunneling conductance. The tunneling conductance between two neighboring particles $i$ and $j$ is expressed by[10] $G=G_0[1+\Gamma(\mathbf{m}_i\cdot\mathbf{m}_j/m^2)]$, where $\mathbf{m}_i$ is the magnetization vector and $G_0$ and $\Gamma$ $(>0)$ are constants. If all the particles are uniform and the correlation between $\mathbf{m}_i$ and $\mathbf{m}_j$ can be neglected, we obtain the conductivity $\sigma$ of the film by taking the average of $\mathbf{m}_i\cdot\mathbf{m}_j$ as[3,5]

$$\sigma=\sigma_0[1+A(M/M_s)^2], \tag{2}$$

where $M_s$ is the saturation magnetization. The conductance increases when the magnetization of each particle is aligned in the direction of magnetic field. As shown in Fig. 5, the experimental data are well expressed by the form of Eq. (2).

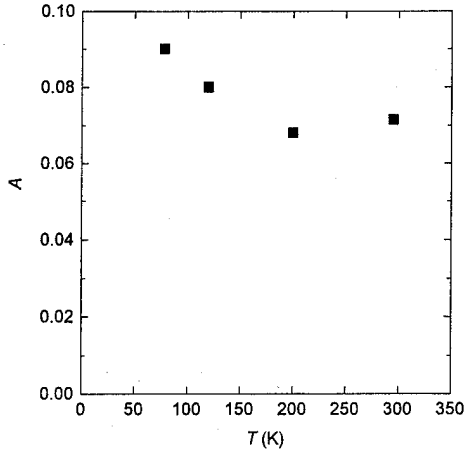



FIG. 6. The coefficient $A$ in Eq. (2) obtained at each temperature for the sample shown in Figs. 2 and 5.

Thus, the field dependence of the MR is understood as the result of tunneling conductance. The coefficient $A$ weakly depends on temperature as shown in Fig. 6.

## IV. SUMMARY

The MR effect in granular Fe–$MgF_2$ films, which consist of metallic particles in an insulating matrix, was investigated. Negative and isotropic GMR with the MR ratio up to 7.5% was observed. The field dependence is approximately proportional to the $(M/M_s)^2$ term. The GMR effect in this system seems to arise from tunneling conductance depending on the relative direction of the magnetization of neighboring particles.

[1] A. E. Berkowitz, J. R. Mitchell, M. J. Carey, A. P. Young, S. Zhang, F. E. Spada, F. T. Parker, A. Hutten, and G. Thomas, Phys. Rev. Lett. **68**, 3745 (1992).
[2] J. Q. Xiao, J. S. Jiang, and C. L. Chien, Phys. Rev. Lett. **68**, 3749 (1992).
[3] C. L. Chien, J. Q. Xiao, and J. S. Jiang, J. Appl. Phys. **73**, 5309 (1993).
[4] J. I. Gittleman, Y. Goldstein, and S. Bozowski, Phys. Rev. B **5**, 3609 (1972).
[5] B. Abeles, P. Sheng, M. D. Coputts, and Y. Arie, Adv. Phys. **24**, 407 (1975).
[6] S. Mitani, S. Ohnuma, and H. Fujimori, (unpublished); H. Fujimori, S. Mitani, and S. Ohnuma, Mater. Sci. Eng. B **31**, 219 (1995).
[7] T. Miyazaki and N. Tezuka, J. Magn. Magn. Mater. **139**, L231 (1995).
[8] T. Furubayashi, J. Magn. Magn. Mater. **140–144**, 393 (1995).
[9] N. F. Mott, Philos. Mag. **19**, 835 (1969).
[10] J. C. Slonczewski, Phys. Rev. B **39**, 6995 (1989).

# The influence of Ni on the microstructure and GMR of the Co–Cu alloy granular films (abstract)

S. Y. Zhang and Q. Q. Cao
*Department of Physics, Nanjing University, Nanjing, Peoples Republic of China*

The microstructure and Giant Magnetoresistance (GMR) in Co–Cu and Co–Ni–Cu alloy granular films prepared by dc magnetron sputtering technique was discussed. The microstructure of Co–Ni–Cu alloy granular films observed by XRD, SEM, and HRTEM examinations showed even microscopic tissue in which nanoparticles of Co–Ni were well-distributed, much different than that of Co–Cu alloy granular films in which full-grown microparticles of Co were embedded in Cu matrix. By Magnetic Hysteresis Measurement and Neel's superparamagnetism theory, the mean size of the Co–Ni particles in Co–Ni–Cu alloy granular films was estimated to be 2 to 4 nm, much smaller than that in Co–Cu alloy granular films. These results indicated that owing to the existence of Ni in Co–Ni–Cu alloy granular films the phase segregation was not a nucleation and growth process as that of Co–Cu alloy granular films but due to spinodal decomposition which was reported for the first time in granular films. It was also found that when samples dropped from room temperature to low temperature, the GMR boomed in Co–Ni–Cu alloy granular films, on the contrary to the behavior of Co–Cu alloy granular films. This fact meant that the Co–Ni–Cu alloy granular films with proper Ni content might have no response to the temperature change. Furthermore, the GMR as a function of magnetic density in Co–Ni–Cu alloy granular films is of much better linearity than that in Co–Cu alloy granular films. © *1996 American Institute of Physics.* [S0021-8979(96)61608-9]

# Real-space analysis of inhomogeneous scattering versus superlattice-potential effects for magnetotransport (abstract)

Horacio E. Camblong
*Department of Physics, University of San Francisco, San Francisco, California 94117*

Spin-dependent scattering has usually been regarded as the basic mechanism for giant magnetoresistance (GMR), following the seminal quasiclassical work of Camley and Barnás. When this mechanism is considered, the correct quantum-mechanical treatment of magnetotransport in multilayers is provided by the real-space Kubo approach.[1] In addition, band-structure effects due to imperfect matching of the Fermi surfaces of the constituent materials of the superlattice have been regarded as another source of GMR.[2] It turns out that a real-space approach to superlattice effects is both straightforward and intuitive. In effect, a solution of this *unified* model of inhomogeneous scattering and superlattice potentials is accomplished by deriving the real-space Green's function, which is a direct generalization of that of Ref. 2, but with a wavevector that is obtained by solving the dispersion relation for a Kronig-Penney model. It is shown that spin-dependent scattering remains the dominant mechanism, even though it is somewhat modified by the presence of superlattice potentials; that is, GRM is mainly due to a "short-circuit effect" rather than due to a "channeling effect." The corresponding "internal quantum size effects" (due to potential barriers) are not easily observable because of, among other factors, the exponential suppression of the one-particle propagator in the presence of the relatively short mean free paths in multilayers; this "geometrical effect" is an outstanding feature of magnetic multilayers as their giant magnetoresistance is governed by strong scattering at the interfaces. Finally, due to interdiffusion, the standard usage of reflection coefficients is shown to be incorrect. © *1996 American Institute of Physics.* [S0021-8979(96)61708-8]

Supported in part by the University of San Francisco Faculty Development Fund.

[1] H. E. Camblong, Phys. Rev. B **51**, 1855 (1995).
[2] R. Q. Hood and L. M. Falicov, Phys. Rev. B **44**, 9989 (1991); P. B. Visscher and H. Zhang, *ibid.* **48**, 6672 (1993); S. Zhang and P. M. Levy, in *Magnetic Ultra-Thin Films, Vol. I: Multilayers and Surfaces*, edited by B. T. Jonker *et al.* (Mat. Res. Soc. Sym. Proc. 1994), Vol. 313.

 0021-8979/96/79(8)/6261/2/$10.00 © 1996 American Institute of Physics 

# Magnetic tunneling effect in $Fe/Al_2O_3/Ni_{1-x}Fe_x$ junctions

N. Tezuka and T. Miyazaki
*Department of Applied Physics, Faculty of Engineering, Tohoku University, Sendai 980-77, Japan*

The dependence of the magnetoresistance ratio, $\Delta R/R_s$, on the Ni content has been studied in $Fe/Al_2O_3/Ni_{1-x}Fe_x$ $(0 \leq x \leq 1)$ tunneling junctions. The value of $\Delta R/R_s$ at 4.2 K increased with increasing $x$ and exhibited a maximum of ~35% at $x=0.8$. The result is discussed by taking into account the spin-polarization of ferromagnetic electrodes. © *1996 American Institute of Physics.* [S0021-8979(96)82908-2]

## I. INTRODUCTION

The pioneering work concerning the magnetic tunneling effect was conducted first by Julliere.[1] He formed Fe/Ge/Co junction and measured the conductance at $T<4.2$ K under different magnetic fields as a function of applied voltage. The relative change of conductance, $\Delta G/G$, was ~14%, where $\Delta G$ is the difference of conductance between the two values corresponding to parallel and antiparallel magnetizations of the two ferromagnetic electrodes, and $G$ is the conductance in the state of antiparallel magnetization. After his report several attempts were made in order to prepare a junction with large conductance (or resistance) ratio. The highest value of $\Delta R/R_s$ at room temperature reported before 1991 was only 2.7%,[2] and far less than the value expected from the theory taking into account of ferromagnetic electrode spin-polarizations. Recently, we have found a giant magnetoresistance (MR) ratio of 30% at 4.2 K and 18% even at room temperature in $Fe/Al_2O_3/Fe$ junction.[3] Also, various junctions with combinations of magnetic electrodes exhibiting a relatively large MR ratio at room temperature were successfully prepared by us[4] and by Moodera *et al.*[5] and it was shown that MR ratio is roughly proportional to the products of spin-polarizations of both ferromagnetic electrodes.[4] However, in these experiments the ferromagnetic electrodes used were pure metals, permalloy and/or 50FeCo alloys, and no experiment for the junctions with the ferromagnetic composition varied systematically is reported.

The spin-polarizations of Fe–Ni binary alloys were measured systematically[6] and their values were relatively large. This article describes the dependence of MR ratio in $Fe/Al_2O_3/Ni_{1-x}Fe_x$ tunnel junctions on $x$, and discusses briefly the results in the light of the spin-polarizations.

## II. EXPERIMENT

The magnetic electrodes were prepared by electron beam evaporation. On the other hand, the aluminum film was prepared by rf sputtering because more smooth Al surface would be obtained by the sputtering than evaporation method. First, 1000 Å thick Fe film was deposited through a mask to form a long narrow strip (1 mm wide 15 mm long) on to a glass substrate. The growth rate was 3–6 Å/s. The pressure during evaporation was $\sim 1\times10^{-6}$ Torr. Next, an aluminum film was sputtered through a mask in a circular form with a 5 mm diameter. The thickness was 55 Å. The system base pressure was lower than $1\times10^{-6}$ Torr and an Ar pressure during sputtering was 1.5 mTorr. The typical growth rate was 5.6 Å/s. Then the sample was taken out from the vacuum vessel and the aluminum was oxidized in air at room temperature for 24 h. Finally, a counter-electrode film was evaporated through a mask to form a cross strip of dimension $1\times15$ mm$^2$. In order to vary the induced magnetic anisotropy and/or coercive force for both electrodes, the substrates temperature were kept at 200 °C for the base electrode and at room temperature for the counter-electrode except $Fe/Al_2O_3/Ni_{0.8}Fe_{0.2}$ junction. In the case of this junction, the substrate was at room temperature for both electrodes. The

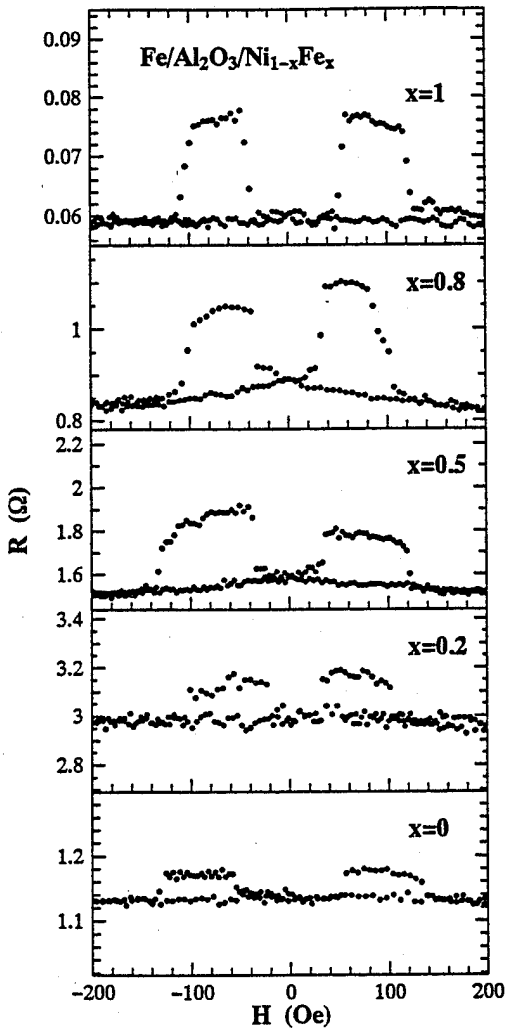



FIG. 1. MR curves for 1000 Å $Fe/Al_2O_3$/1000 Å $Ni_{1-x}Fe_x$ $(0 \leq x \leq 1)$ junctions at 4.2 K.

 0021-8979/96/79(8)/6262/3/$10.00 © 1996 American Institute of Physics

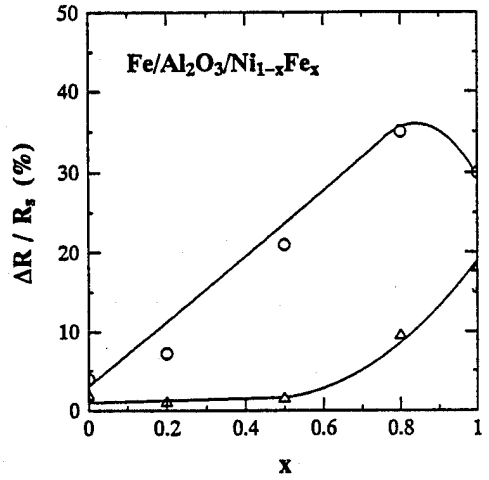



FIG. 2. MR ratio at 4.2 K (○) and 300 K (△) as a function of Fe content in Fe–Ni electrode.

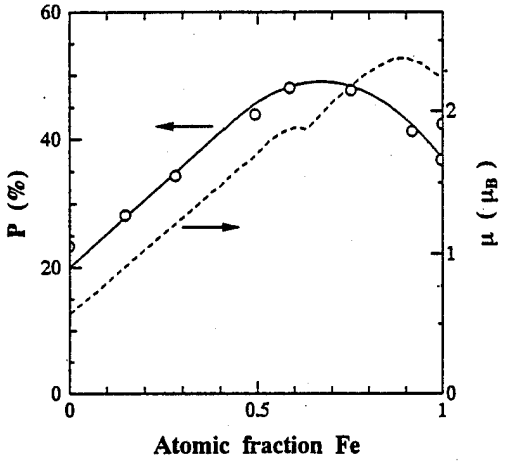



FIG. 3. The spin-polarization (○) and magnetic moment (- - -) at 0 K for Fe–Ni binary alloys (Ref. 6).

MR was measured by a dc four probe method in magnetic fields up to 200 Oe in the temperature range from 4.2 to 300 K. Magnetic hysteresis loop was measured by a vibrating sample magnetometer.

## III. RESULTS AND DISCUSSION

Figure 1 shows the magnetic field, $H$, dependence of the resistance, $R$, measured at 4.2 K for the junctions with different Fe content in the counter-electrode. In these $R$ vs $H$ curves, the sharp change in resistance at smaller magnetic fields corresponds to the coercive force of the first Fe layer for $x=1$, 0.8, 0.5, and 0 junctions. While, in the case of $x=0.2$ junction, the change is due to the magnetization process of $Ni_{0.8}Fe_{0.2}$ (permalloy) layer. All those $R$ vs $H$ curves corresponded well with their magnetic hysteresis loops. Both resistances at parallel and antiparallel magnetizations decreased with increasing temperature.

The values of the tunneling barrier height and width were estimated by the analysis of current–voltage measurement. The current–voltage data at 4.2 K were fitted by Simmons' theory.[7] For all the junctions, the values of the barrier height were 0.1~0.3 eV and the width were ~45 Å. Here it should be noted that the barrier height is much smaller than that expected for $Al_2O_3$ barriers. The reason will be described shortly at the end of this section.

Figure 2 shows the dependence of the MR ratio on $x$ at 4.2 and 300 K. The MR ratio at 4.2 K increases with $x$ and exhibits a maximum around $x=0.8$. Namely, the MR ratio of $x=0.8$ is larger than that of $x=1$ which corresponds the $Fe/Al_2O_3/Fe$ junctions. Since one electrode of the junctions examined in this experiment is always pure Fe, we expect that the dependence of the MR ratio on $x$ is merely due to the counter-electrode of Fe–Ni alloy films. In Fig. 3 we replotted the spin-polarization, $P$, and magnetic moment, $\mu$, reported by Paraskevopoulos *et al.*,[6] as a function of Ni content for Fe–Ni alloy. As seen in Fig. 3, both $P$ and $\mu$ increase with $x$ and exhibit a broad peak at $x=0.7$ and $x=0.9$, respectively. The dependence of MR ratio on $x$ is very similar to that of magnetic moment rather than that of spin-polarization.

We also measured the dependence of MR ratio and the resistance (current at a constant voltage) as a function of temperature between 4.2 and 300 K. The MR ratio at 300 K is much smaller than that at 4.2 K. Furthermore, its dependence on $x$ is quite different from that at 4.2 K.

Stratton[8] has discussed the dependence of the tunneling current on temperature. By fitting our experimental data to the relation obtained by him, we obtained the barrier height. The values are between 0.1 and 0.3 eV for all the junctions, which agree well with those obtained from current–voltage data.

The theoretical treatments of the magnetic tunneling effect have been conducted by also Julliere[1] and successively by Maekawa and Gafvert[9] and Slonczewski.[10] They expressed the conductance ratio instead of the MR ratio by using spin-polarization. If we express the MR ratio in the same manner, it can be expressed as

$$\Delta R/R_s = 2P_1P_3/(1-P_1P_3), \tag{1}$$

where $R_s$ is the resistance in the state of parallel magnetization. $P_1$ and $P_3$ are the spin-polarizations of base and counter electrodes. By using the data on the spin-polarization shown in Fig. 3, we are able to estimate the MR ratio by Eq. (1). In order to confirm this relationship, we plotted MR ratio at 4.2 K as a function of $2P_1P_3/(1-P_1P_3)$ in Fig. 4. In Fig. 4 the data reported by us[2–4] and by others[1,5,9,11] are also plotted. The straight line shows the ideal value expected from the spin-polarizations coefficient. We can see that the junctions with larger spin-polarization electrode exhibits higher MR ratio. However, the experimental value of MR ratio is much lower than that expected from the spin-polarization except for some junctions.

In order to obtain information to understand the reason of smaller value of MR ratio, especially at room temperature, than that expected from spin-polarization and/or low barrier potential, the profile of Auger spectroscopy was examined perpendicular to the surface of the sample. In this

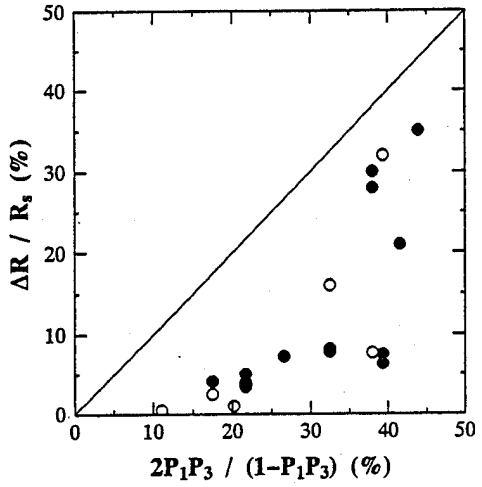



FIG. 4. Experimental and theoretical (straight line) values of MR ratio as a function of $2P_1P_3/(1-P_1P_3)$. ●: reported by us (Refs. 2–4), ○: reported by others (Refs. 1,5,9, and 11).

examination, the sample was prepared separately from that measured magnetic tunneling effect. The preliminary data suggest that the actual barrier is not pure $Al_2O_3$ but a mixture of $Al_2O_3$ and $AlO_x$ or magnetic oxide. Further there exists a remaining metallic aluminum without oxidization. The mixture of oxide may behave as a semiconductor with a small energy gap. Such a phenomenon explains the occurrence of low barrier potential. With lowering the barrier height, the MR ratio decreases as suggested by Slonczewski.[10] The increased barrier width due to the extra oxidization also decreases the MR ratio.[12] Furthermore, the pressure of native oxide can cause spin flipping in the tunneling process giving a low MR ratio.

More detailed structure analysis of the insulator of the tunneling junction is now in progress and will be presented elsewhere in the near future.

## ACKNOWLEDGMENTS

The authors would like to thank Dr. H. Topkins, Dr. S. Tehrani, and Dr. H. Goronkin of Physical Research Laboratory, Motorola for the measurement of Auger spectroscopy. This research was partly supported by Sasakawa Scientific Research Grant from the Japan Science Society and Asahi-garasu foundation.

[1] M. Julliere, Phys. Lett. **54**, 225 (1975).
[2] T. Miyazaki, T. Yaoi, and S. Ishio, J. Magn. Magn. Mater. **98**, 7 (1991).
[3] T. Miyazaki and N. Tezuka, J. Magn. Magn. Mater. **139**, 231 (1995).
[4] T. Miyazaki and N. Tezuka, J. Magn. Magn. Mater. **151**, 403 (1995).
[5] J. S. Moodera, L. R. Kinder, T. M. Wong, and R. Meservey, Phys. Rev. Lett. **74**, 3273 (1995).
[6] D. Paraskevopoulos, R. Meservey, and P. M. Tedrow, Phys. Rev. B **16**, 4907 (1977).
[7] J. G. Simons, J. Appl. Phys. **34**, 1793 (1963).
[8] R. Stratton, J. Phys. Chem. Solids **23**, 1177 (1962).
[9] S. Maekawa and U. Gafvert, IEEE Trans. Magn. **MAG-18**, 707 (1982).
[10] J. C. Slonczewski, Phys. Rev. B **39**, 6995 (1989).
[11] J. Nowak and J. Rauluszkiewicz, J. Magn. Magn. Mater. **109**, 79 (1992).
[12] S. F. Alvarado, Phys. Rev. Lett. **75**, 513 (1995).

# Spin polarized tunneling in half-metallic ferromagnets (abstract)

C. T. Tanaka
*Department of Materials Science and Engineering, Massachusetts Institute of Technology, Cambridge, Massachusetts 02139*

J. S. Moodera
*Bitter Magnet Lab, Massachusetts Institute of Technology, Cambridge, Massachusetts 02139*

We present a study of spin polarized tunneling in tunnel junctions in which one of the conducting layers is a half-metallic ferromagnet (HMF). HMF are unique in that the Fermi level of these materials intersect the majority spin electron band, while the minority band has an energy gap near the Fermi level. Hence, HMF simultaneously have both metallic and semiconducting characteristics, and theory predicts that the conduction electrons are 100% spin polarized. As a result, the magnetoresistance in magnetic multilayers or trilayer tunnel junctions is expected to be significantly higher than with conventional ferromagnetic materials. Two important parameters affecting the performance of these junctions are the smoothness of the HMF surface and its surface composition. Tunnel junctions consisting of a layer of NiMnSb, a barrier layer of $Al_2O_3$, and a layer of aluminum were prepared and studied for their tunneling properties. Surface analysis of HMF films was done using Auger depth profiling and AFM. © *1996 American Institute of Physics.*
[S0021-8979(96)61808-7]

This paper is supported by ONR under Grant No. N00014-92-J-1847 and one of the authors (C. T. T.) was supported by ONR AASERT under Grant No. N00014-93-1-1204.

## Ferromagnetic resonance of sputtered Co/Mn multilayers (abstract)

D. Spoddig, F. Schreiber, and J. Pflaum
*Inst. f. Experimentalphysik III, Ruhr-Universität, 44780 Bochum, Germany*

Q. Wang and H. Zabel
*Inst. f. Experimentalphysik IV, Ruhr-Universität, 44780 Bochum, Germany*

J. Pelzl
*Inst. f. Experimentalphysik III, Ruhr-Universität, 44780 Bochum, Germany*

Co/Mn multilayers were prepared by rf sputtering onto single-crystal MgO and sapphire substrates resulting in, respectively, (001)- and (111)-oriented layers. The structure was thoroughly analyzed by x-ray scattering in various geometries (Q. Wang *et al.* to be published). For the magnetic investigations, ferromagnetic resonance (FMR) was applied. Complementary measurements employed the magneto-optical Kerr-effect (MOKE) and Faraday balance magnetometry. Results for the in-plane anisotropy, the surface anisotropy, the magnetization, and the FMR linewidth are presented. The comparison with other Co-based multilayer systems indicates that both the structural and the magnetic properties of the Co/Mn system are more complicated than in the case of systems with a presumably weaker electronic interaction at the interface [see also K. Ounadjela *et al.*, Phys. Rev. B **49**, 8561 (1994)]. © *1996 American Institute of Physics.* [S0021-8979(96)44408-1]

This work was supported by the Deutsche Forschungsgemeinschaft (SFB 166).

## Thermal effects in magnetization, anisotropy, and interface width in Fe/Cu multilayers (abstract)

Michael J. Pechan
*Department of Physics, Miami University, Oxford, Ohio 45056*

Eric E. Fullerton
*Argonne National Laboratory, Argonne, Illinois 60439*

Ivan K. Schuller
*Physics Department, UC-San Diego, La Jolla, California 92093-0319*

Magnetic properties of Fe/Cu multilayers have been investigated as a function of temperature using dc magnetization and ferromagnetic resonance techniques. The samples were prepared via dc sputtering resulting in equal thickness elemental layers ranging in modulation wavelength from 1 to 30 nm. The interface anisotropy remains nearly constant at 0.32 erg/cm$^2$ through the 4–300 K temperature range, which is in stark contrast to large thermal effects observed in Ni-based systems.[1] Relative increases in magnetization with decreasing temperature range from 3% in the 30 nm sample to 27% in the 1.0 nm sample. This indicates an interface region in which the magnetization is more strongly temperature dependent than the interior of an Fe layer. By plotting magnetization as a function of the inverse layer thickness, we obtain the temperature dependence of the width of this interfacial region. © *1996 American Institute of Physics.* [S0021-8979(96)44508-X]

Supported by US DOE Contract No. DE-FG02-86ER45281 (MU), No. DE-FG03-87ER45332 (UCSD), and No. W31-109-ENG-38 (ANL).

[1]M. J. Pechan, J. Appl. Phys. **64**, 5754 (1988).

 0021-8979/96/79(8)/6266/1/$10.00 © 1996 American Institute of Physics

# Study of magnetic reorientation phenomenon and magnetic properties of Pd/(Pt/Co/Pt) multilayers

Ying Xiao, Jun-Hao Xu, and K. V. Rao
*Department of Condensed Matter Physics, Royal Institute of Technology, S-100 44 Stockholm, Sweden*

Pd/(Pt/Co/Pt) modulated multilayer films have been prepared at substrate temperatures ranging from room temperature to 350 °C by *e*-beam evaporation using various buffer layers. All these films exhibit perpendicular magnetic anisotropy with square polar Kerr hysteresis loops at room temperature. However, we observed a magnetic reorientation from a perpendicular anisotropy to an in-plane anisotropy at temperatures close to the Curie temperature $T_C$. The reorientation temperature $T_R$ is found to depend strongly on the nonmagnetic Pd-spacer thickness in these Pd/(Pt/Co/Pt) multilayers. Over the room temperature to $T_R$ range, we observe a linear temperature dependence of magnetic coercivity. AFM and STM characterization of the role of buffer layers on the microstructure, the dependence of coercivity and squareness of the Kerr hysteresis loops on the buffer layers of Au, Pt, and Al are also presented. © *1996 American Institute of Physics.* [S0021-8979(96)24108-5]

## I. INTRODUCTION

Good thermal stability and ideal square Kerr hysteresis loops of magneto-optical (MO) media are essential to achieve excellent MO device performances. It is well known that with increasing temperature competing anisotropies especially arising from intersurface at layers cause a rotation of the easy axis from a perpendicular to an in-plane magnetic orientation in ultrathin films of Fe/Cu (100), Fe/Ag (100), Co/Au (100), etc.[1–5] This magnetic reorientation also exists in multilayers and may be a source of thermal instability of the multilayered MO media. Thus, it is important to study the magnetic reorientation phenomenon and relate it to thermal stability of MO multilayers like Pt/Co and related multilayers. On the other hand, squareness of the Kerr hysteresis loop is one of the main factors determining the writing speed, and signal to noise ratio of MO recording devices. It is thus of interest to clarify the role of thin film processing parameters and the use of buffer layers in achieving perfect square Kerr hysteresis loops of MO media. There exist very few reports in literature about processing techniques to control squarenesses of the Kerr hysteresis loops of MO thin films and multilayers.

Recently, Pd/(Pt/Co/Pt) modulated multilayer system with enhanced perpendicular anisotropies and magnetic coercivities compared to the Pt/Co and Pd/Co multilayers has been reported.[6,7] In this article we present our recent experimental results of the temperature dependences of the perpendicular magnetic anisotropy, coercivity, and Kerr rotation of some *e*-beam evaporated Pd/(Pt/Co/Pt) multilayers. We also discuss buffer layer effects on the squareness of the Kerr hysteresis loop and influences of grain structures on the coercivity of the multilayers.

## II. EXPERIMENT

The Pd/(Pt/Co/Pt) modulated multilayer films were sequentially deposited by *e*-beam evaporation in a Leybold L560 Universal Deposition System with one electron gun and four crucibles. The deposition rates were kept below 0.5 Å/s for all elements at a base pressure of $1.5\times10^{-6}$ Torr. Glass, Si, and surface oxidized Si were used as substrates. They were mounted on a homemade resistive heater base during deposition. The thickness as well as deposition rate of each metal layer were determined and controlled by means of a computer with a previously calibrated quartz thickness monitor. The thicknesses of the Co and Pt layers were fixed at 3 and 2 Å, respectively, while the Pd layer thicknesses were varied from 3 to 12 Å. Some of the multilayer films were grown on Al, Ag, Au, and Pd/Pt buffer layers. Films and buffer layers were grown at temperatures in a range from room temperature to 350 °C. Before deposition, substrates were heated up to 500 °C under the base pressure to thermally clean substrate surfaces.

The magneto-optical Kerr rotations of the multilayer films were measured over a temperature range from 30 to 250 °C with a Kerr loop tracer at wavelength of 800 nm, in magnetic fields up to 13.5 kOe. The magnetic hysteresis loops of the multilayers were measured at temperatures ranging from 5 to 350 K using a SQUID magnetometer. Low angle and high angle x-ray diffraction (XRD) measurements were carried out to verify the superlattice structures and determine the textures of the multilayered films. Surface microstructures of the films were characterized by the means of scanning tunneling microscopy (STM) and atomic force microscopy (AFM) with a Burleigh Personal SPM.

## III. RESULTS AND DISCUSSIONS

High angle XRD measurements on the Pd/(Pt/Co/Pt) multilayer films grown under different deposition conditions reveal that most of the multilayers exhibit the fcc (111) texture along the film normal. Small angle XRD analyses suggest that these multilayers have the expected periodic structure and reasonable sharp interfaces.

Kerr hysteresis loop measurements indicate that all Pd/(Pt/Co/Pt) multilayers exhibit perpendicular magnetic anisotropy at room temperature. However, with increasing temperature the degree of the squareness of Kerr hysteresis loops decreases continuously, as shown in Figs. 1(a)–1(d). In addition, the magnetic coercivities of the Pd/(Pt/Co/Pt) multilayer films are found to decrease linearly with increas-

 0021-8979/96/79(8)/6267/3/$10.00 © 1996 American Institute of Physics 

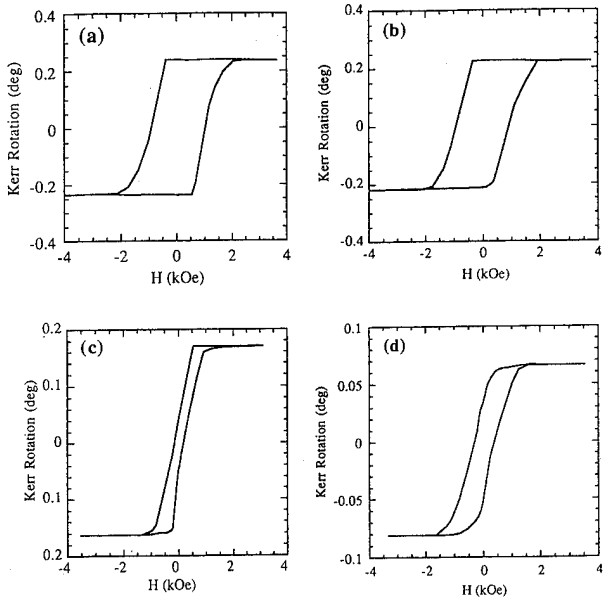



FIG. 1. Kerr hysteresis loops at (a) 30 °C, (b) 100 °C, (c) 180 °C, and (d) 230 °C for a [Pd-3 Å/(Pt-2 Å/Co-3 Å/Pt-2 Å)]$_{15}$ multilayer film deposited at room temperature on oxidized Si.

ing temperatures. In Fig. 2, the determined coercivities for four multilayer films are plotted against temperature. At certain temperatures the multilayers suddenly lose their perpendicular anisotropies. The transition temperature $T_R$ (from a perpendicular anisotropy to an in-plane anisotropy) is found to be a function of the Pd nonmagnetic spacer thickness $t_{Pd}$ of the Pd/(Pt/Co/Pt) multilayers. Figure 3 gives the temperature dependence of remanent magnetization for Pd-3,6,9,12 Å/(Pt-2 Å/Co-3 Å/Pt-2 Å) multilayers. In the inset of this figure the Pd layer thickness dependence of $T_R$ of the multilayers is shown. This indicates that $T_R$ decreases with increasing nonmagnetic spacer thickness. However, the film with $t_{Pd}$ of 3 Å has a slightly lower $T_R$ than that of the film with $t_{Pd}$ of 6 Å. This may be due to a higher degree of interlayer mixing in the film with $t_{Pd}$ of 3 Å which results in a reduction of the perpendicular anisotropy in this film.[7]

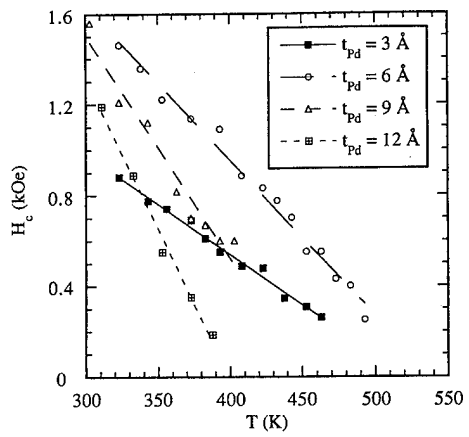



FIG. 2. Temperature dependences of magnetic coercivities for [Pd-3,6,9,12 Å/(Pt-2 Å/Co-3 Å/Pt-2 Å)]$_{15}$ multilayer films deposited at room temperature on oxidized Si.

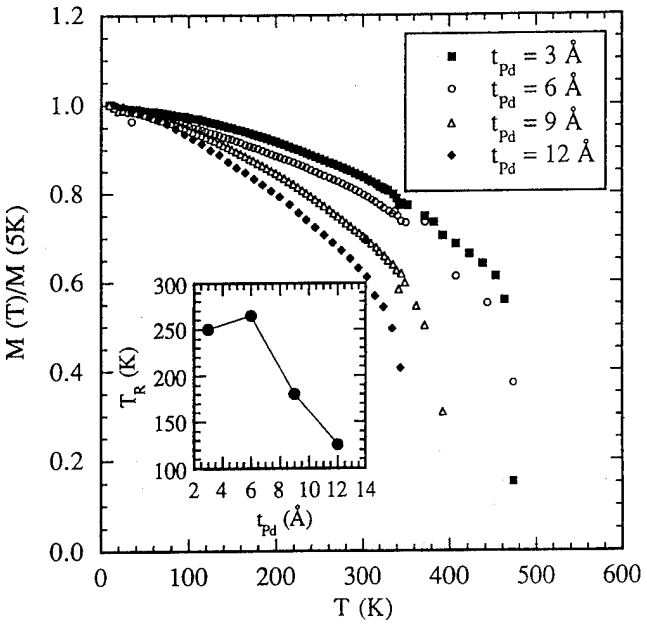



FIG. 3. Temperature dependences of remanent magnetization for [Pd-3,6,9,12 Å/(Pt-2 Å/Co-3 Å/Pt-2 Å)]$_{15}$ multilayer films deposited at room temperature on oxidized Si. Inset: Magnetic reorientation temperature as a function of Pd layer thickness.

The observed magnetic reorientation could arise from the large entropy for the in-plane magnetization which becomes more important at elevated temperatures.[8] The direction of magnetization is also determined by the competition between uniaxial, i.e., surface anisotropy, and shape anisotropy. At a certain temperature, when the temperature dependent perpendicular anisotropy $K_u(T)$ is smaller than the saturation magnetization $2\pi M_s(T)$, the easy axis will turn from the film normal to the plane of the film. If the fourth order anisotropy cannot be neglected as compared to the second order anisotropy at elevated temperatures, a canted orientation of a uniform magnetization could also exist. The observed magnetic reorientation could thus be due to a combination of the above discussed cases. In order to improve the thermal stability of MO media at some temperatures, one needs to tailor the materials to obtain suitably high $T_R$'s. In the case of Pt/Co and related multilayers, an appropriate thin nonmagnetic spacer is essential to enhance the coupling between neighboring Co layers, and thus to achieve a high $T_R$ of the multilayers.

It is found that Pd/(Pt/Co/Pt) multilayers grown on Pd/Pt and Au buffer layers exhibit high coercivities in a range from 5 to 10 kOe, but the squarenesses of these multilayers prepared under various deposition conditions are far from being ideal. However, multilayer films deposited on Al buffer layer under certain deposition conditions exhibit ideal square Kerr hysteresis loops, although the coercivities of these films are relatively low. Figure 4 shows a few Kerr hysteresis loops of some Pd/(Pt/Co/Pt) multilayers deposited on different buffer layers. As seen in Fig. 4, the best square loop is achieved in the multilayer film grown at 250 °C on an Al-100 Å buffer layer deposited at room temperature. High Kerr rotations of

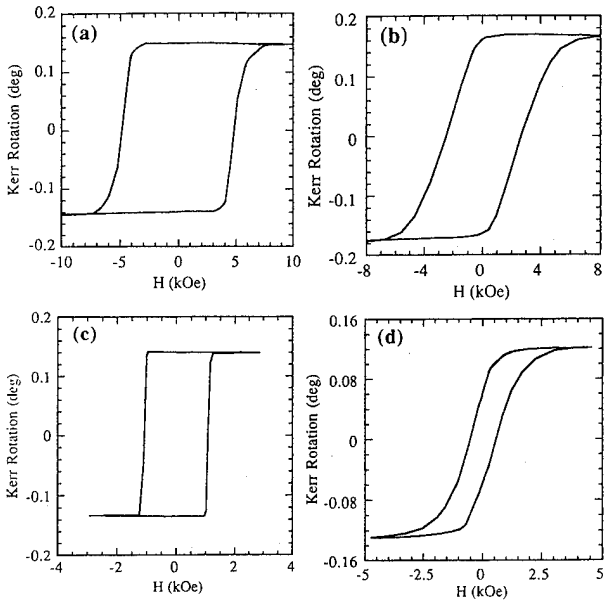



FIG. 4. Kerr hysteresis loops of [Pd-3 Å/(Pt-2 Å/Co-3 Å/Pt-2 Å)]$_8$ multilayer films deposited on oxidized Si with (a) Pd/Pt, (b) Au, (c) Al, and (d) Ag buffer layers.

0.41° in the blue light regime and 0.32° at 800 nm wavelength are observed for the Pd/(Pt/Co/Pt) multilayer film deposited at 350° on an Al-100 Å buffer layer. A detailed study of the wavelength dependencies of the Kerr rotations for films deposited with various kinds of buffer layers will be reported elsewhere.

It is known that not only the crystallographic properties of substrates significantly affect many properties of deposited films, but also the chemical properties of the substrates determine film growth models, such as layer-by-layer growth, island growth and the combination of them. The use of buffer layers can improve both crystallographic and chemical compatibility between films and substrates. Usually ideal square magnetic hysteresis loops reflect a high degree of uniformity of the film structures. In this regard, two extreme cases are amorphous and single-crystal films. Thus, films deposited on Al buffer layers should have superior crystalline quality compared to those films grown on other buffer layers. Since all multilayers grown on glass, Si, and oxidized Si with Al buffer layers exhibit ideal square Kerr hysteresis loops, the chemical properties of Al should play a more important role in promoting the growth of the superlattice structure than its crystallographic properties.

STM and AFM analyses indicate that multilayers grown on Al buffer layers have smooth surface morphologies, while films deposited on Au and Pd/Pt buffer layers exhibit big grain structures and relatively rough surface morphologies. It is noted that those films with large grain structures usually have high coercivities. This observed correlation between large grains and high coercivities is consistent with our previous results.[7]

## IV. SUMMARY

A magnetic reorientation from a perpendicular anisotropy to an in-plane anisotropy has been observed at temperatures close to $T_C$s in the Pd/(Pt/Co/Pt) modulated multilayer films. This magnetic reorientation may be caused by the large entropy for the in-plane magnetization which becomes more important at elevated temperatures or by the competition between uniaxial anisotropy and shape anisotropy. The use of Al buffer layers improves both squareness and Kerr rotation of the Pd/(Pt/Co/Pt) multilayers. This may be due to the suitable chemical and crystallographic properties of Al which promote superior growth of the superlattice structure resulting in an ideal squareness of Kerr hysteresis loop and a high Kerr rotation of 0.41° in the blue light regime.

## ACKNOWLEDGMENT

This work is financially supported by the Swedish funding agencies NUTEK and NFR.

[1] D. P. Pappas, K. P. Kämper, and H. Hopster, Phys. Rev. Lett. **64**, 3189 (1990).
[2] R. Allenspach and A. Bischof, Phys. Rev. Lett. **69**, 3385 (1992).
[3] J. Thomassen, F. May, B. Feldmann, M. Wuttig, and H. Ibach, Phys. Rev. Lett. **69**, 3831 (1992).
[4] Z. Q. Qiu, J. Pearson, and S. D. Bader, Phys. Rev. Lett. **70**, 1006 (1993).
[5] R. Allenspach, M. Stampanoni, and A. Bischof, Phys. Rev. Lett. **65**, 3344 (1990).
[6] G. A. Bertero and R. Sinclair, Appl. Phys. Lett. **64**, 3337 (1994).
[7] Y. Xiao, Jun-Hao Xu, J. Wittborn, Y. Makino, K. V. Rao, and Zuo-Yi Lee, IEEE Trans. Magn. (Sept. 1995).
[8] P. J. Jensen and K. H. Bennemann, Phys. Rev. B **42**, 849 (1990).

# Structural anisotropy of Tb/Fe multilayers

Y. Fujiwara, X. Y. Yu, S. Tsunashima, and S. Iwata
*Department of Electronics, Nagoya University, Nagoya 464-01, Japan*

M. Sakurai and K. Suzuki
*Institute for Materials Research, Tohoku University, Sendai 980, Japan*

We have investigated the local structural anisotropy of Tb/Fe multilayers using linear polarized synchrotron radiation. X-ray absorption measurements were performed at Fe $K$ edge (7.1 keV) using normal and glancing angle incident photon. From the Fe extended x-ray absorption fine structure (EXAFS), the local structural anisotropy was found for all multilayers as a slight difference of oscillation amplitude between the two incident directions. From the Fourier transformed EXAFS spectra, it is found that the local structural anisotropy shows the maximum at bilayer period of about 1 nm, where perpendicular magnetic anisotropy also shows the maximum value in various rare-earth/transition metal multilayers. © *1996 American Institute of Physics.*
[S0021-8979(96)35508-6]

## I. INTRODUCTION

Rare-earth-transition metal (RE-TM) amorphous alloys have been studied for magneto-optical (MO) recording media, and the origin of their perpendicular magnetic anisotropy has been debated with great interest.[1,2] Now, the problem still of the magnetic anisotropy of RE-TM amorphous alloys is still being discussed and several models are proposed.[3,4] But the relationship between the structure and magnetic properties are still unclear because the structural analysis of RE-TM alloys is difficult due to the structural complexity of the amorphous state. Extended x-ray absorption fine structure (EXAFS) spectroscopy is a useful probe providing the informations of short-range atomic structures. In the EXAFS spectroscopy, highly polarized synchrotron radiation gives an opportunity for the angular-resolved analysis of a disordered structure. Recent EXAFS study indicated that the magnetic anisotropy in amorphous RE-TM alloys is correlated with the local structural anisotropy.[5,6]

In our previous work[7–9] as well as in Ref. 10, the magnetic anisotropy of RE/TM multilayers was found to change with the bilayer period showing the maximum at bilayer periods of around 1 nm. In order to study this behavior from the viewpoint of the local structure, we have investigated the local structural anisotropy of amorphous Tb/Fe multilayers, especially its dependence on the bilayer period utilizing the EXAFS spectroscopy with linear polarized synchrotron radiation. In this article preliminary results of EXAFS analysis is presented.

## II. EXPERIMENT

The aim of this study is to confirm the dependence of structural anisotropy on bilayer period. So, multilayers with various bilayer periods and an alloy film for comparison were prepared by rf magnetron sputtering method, where Ar gas pressure and deposition rate were 30 mTorr and about 2.4 Å/s, respectively. The bilayer period was controlled by the rotation speed of the substrate holder. All samples were deposited on the 76.5-$\mu$m-thick polyimide substrate with $Si_3N_4$ under and over layers to prevent the magnetic layers from the oxidation. The total thickness of magnetic layers in all films was about 240 nm. The content of Tb in both alloy and multilayers is 35 at. % and the thickness ratio of Tb to Fe in multilayers is about 1.1:1. Composition analysis was performed by electron probe microanalysis (EPMA), and multilayered structures were confirmed by small-angle x-ray diffraction.

X-ray absorption measurements were carried out utilizing the simple transmission mode with two ionization chambers with a Si(111) double-crystal monochromator. Several sheets of samples were piled up to a suitable absorption length of about 5 $\mu$m. In order to obtain the structural anisotropy, x-ray absorption measurements were performed with two sample directions, where the film plane was put in perpendicular ($E$ in-plane) to or almost parallel (10°, $E$ out-of-plane) to the incident photon. EXAFS measurement were carried out for Fe $K$ edge and Tb $L_3$ edge. Here only results for Fe $K$ edge are reported. It was difficult for Tb $L_3$ edge to analyze the data because of the low S/N ratio.

## III. RESULTS AND DISCUSSION

Compositionally modulated structure was confirmed from the diffraction peaks of the small-angle x-ray diffraction. As shown in Fig. 1, low-angle peaks were observed in the Tb/Fe multilayers with bilayer periods thicker than 1 nm. In the case of glass substrate, higher-order peaks were clearly shown in x-ray diffraction patterns,[9] while in this study, higher-order peaks do not appear even if the bilayer period is as thick as 3.7 nm. This might be due to the difference of flatness of interface of multilayers between glass and polyimide substrates. However, it is supposed that the multilayers grown on polyimide substrates locally keep the multilayered structure in the same manner as those on glass substrates. In high-angle x-ray diffraction patterns, no apparent peak was observed except for the hallow centered at about 25° from the polyimide substrate.

The Fe EXAFS oscillations presented in Fig. 2 are generated by the theoretical background subtraction from the raw absorption spectra and are weighted with $k^3$. $E$ in-plane denotes the film plane structure and $E$ out-of-plane denotes the structure almost perpendicular to the film plane.

 0021-8979/96/79(8)/6270/3/$10.00 © 1996 American Institute of Physics

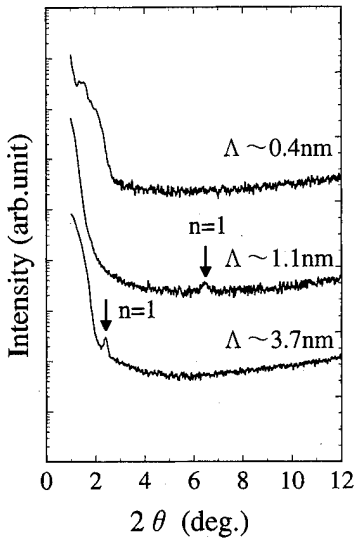



FIG. 1. Small-angle x-ray diffraction patterns of Tb/Fe multilayers, where Δ is bilayer period.

As shown in Fig. 2, the shape of Fe EXAFS oscillations observed for Tb/Fe multilayer and alloy films are similar to each other. In this figure, oscillation amplitudes are found to begin decreasing at $k \sim 8(1/\text{Å})$ in contrast to pure Fe EXAFS which represents strong oscillation up to $k \sim 15(1/\text{Å})$. This suggests that the sample structure is in amorphous state.

It is also found that the frequency of the oscillations for all films is almost the same. This implies that the distances between the absorbing and backscattering atoms are almost the same for all multilayers. Whereas, slight structural anisotropy is seen in all multilayers as the difference in peak to peak amplitude between $E$ in-plane and $E$ out-of-plane oscillations, while no difference is found in the alloy film. This shows that structural anisotropy is induced in the amorphous multilayers.

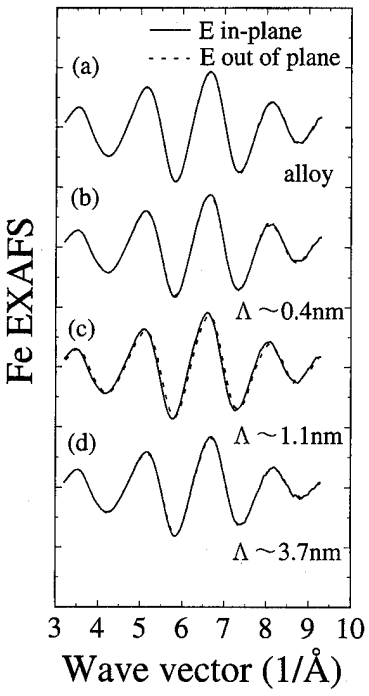



FIG. 2. Fe EXAFS oscillations measured for Tb/Fe multilayer and alloy films.

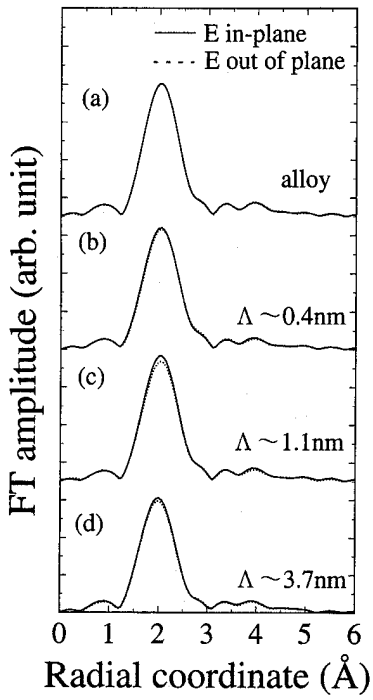



FIG. 3. Fourier transformed Fe EXAFS measured for Tb/Fe multilayer and alloy films.

In this study, structural anisotropy was not found in the alloy film, while considerable structural anisotropy was observed by Harris *et al.*[5,6] This difference may suggest that the anisotropic structure of amorphous RE-TM alloy and multilayers is sensitive to the preparation conditions. We have made the samples of 35 at. % Tb by the rf magnetron sputtering onto polyimide substrates, while Harris *et al.* made experiment on the samples with less than 26 at. % Tb by the ion beam sputtering onto glass substrates, where incident atom energy is much higher than our case and this will strongly affect the film structure.

The Fourier transformed (FT) Fe EXAFS spectra derived from $k$-space Fe EXAFS signals in Fig. 2 are shown in Fig. 3. The FT EXAFS is directly related to the local environment around the central Fe atom in real space. It is seen that a broad nearest-neighbor peak is centered at about 2 Å for all multilayer and alloy films. These peak positions are thought to be shifted 0.4–0.5 Å from the actual distances owing to the effect of the atomic potentials on the photoelectron wave function.[11] In the case of this study, the actual distance between the absorbing atom and nearest neighbors is estimated to be about 2.4–2.5 Å. This means that the nearest neighbors are Fe atoms judging from the atomic radii of constituent atoms, Fe~1.24 Å and Tb~1.78 Å.

We can further estimate from the difference of the shape of FT EXAFS between $E$ in-plane and $E$ out-of-plane spectra. It can be seen in Fig. 3 the peak height is slightly different between the two cases. This difference shows the presence of the structural anisotropy. If we assume the Debye–Waller like factors for each directions are the same, it can be

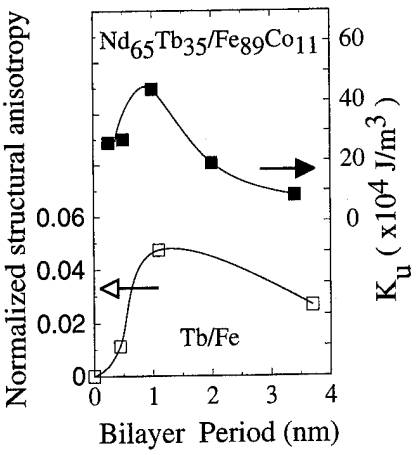



FIG. 4. Normalized structural anisotropy of Tb/Fe multilayers and perpendicular magnetic anisotropy of NdTb/FeCo multilayers as a function of bilayer period.

considered the structural anisotropy is mainly due to the difference of Fe-Fe nearest-neighbor coordination, since both the position and half width are almost the same for each directions. The structural anisotropy is seen to increase up to the bilayer period of around 1 nm and then decrease. This behavior may be explained by the interlayer mixing of about 1 nm thick existing in the multilayers, considering the results of small-angle x-ray diffraction measurement. When the bilayer period is less than the thickness of interlayer mixing, the structural anisotropy increase with increasing bilayer period. While, when the bilayer period become larger than the thickness of interlayer mixing, the each layer approaches pure metal and the local structural anisotropy will go down.

The dependence of the local structural anisotropy on the bilayer period is shown in Fig. 4 together with that of the perpendicular magnetic anisotropy measured in our previous work.[7–9] Here the structural anisotropy is quantitatively expressed as the difference of the peak height of FT EXAFS normalized by those of $E$ in-plane spectra. It is thought that the enhanced perpendicular magnetic anisotropy in RE/TM multilayers is strongly correlated with the enhanced local structural anisotropy.

Comparing the results of EXAFS experiment with those of the small-angle x-ray diffraction, it is noted that both the magnetic and the structural anisotropy become the maximum when the small-angle diffraction peaks become so small that only the first peak is detected.

## IV. CONCLUSION

The dependence of structural anisotropy on bilayer period have been studied for Tb/Fe multilayers. The structural anisotropy shows the maximum at bilayer period of around 1 nm. The dependence of local structural anisotropy on the bilayer period well corresponds to that of the perpendicular magnetic anisotropy. It seems that the structural anisotropy and the perpendicular magnetic anisotropy become their maximum when the bilayer period is roughly equal to the thickness of interlayer mixing.

## ACKNOWLEDGMENT

This work was performed at the beam line 7C of Photon Factory in the National Laboratory for High Energy Physics under the approval of the Photon Factory Program Advisory Committee (accepted No. 93G175).

[1] Y. Miura, N. Imamura, T. Kobayashi, A. Okada, and Y. Kushiro, J. Appl. Phys. **41**, 1208 (1978).
[2] T. R. McGuire, R. J. Gambino, A. E. Bell, and G. J. Sprokel, J. Magn. Magn. Mater. **54-57**, 1387 (1986).
[3] G. S. Cargill III and T. Mizoguchi, J. Appl. Phys. **49**, 1753 (1978).
[4] Y. Suzuki, S. Takayama, F. Kirino, and N. Ohta, IEEE Trans. Magn. **MAG-23**, 2275 (1987).
[5] V. G. Harris, K. D. Aylesworth, B. N. Das, W. T. Elam, and N. C. Koon, IEEE Trans. Magn. **MAG-28**, 2958 (1992).
[6] V. G. Harris, K. D. Aylesworth, W. T. Elam, B. N. Das, and N. C. Koon, Phys. Rev. Lett. **69**, 1939 (1992).
[7] S. Tsunashima, T. Ohtani, X. Y. Yu, and S. Uchiyama, J. Magn. Magn. Mater. **104-107**, 1021 (1992).
[8] Y. Fujiwara, X. Y. Yu, H. Watabe, S. Iwata, S. Tsunashima, and S. Uchiyama, J. Magn. Soc. Jpn. Suppl. **S1**, 161 (1994).
[9] H. Watabe, Y. Fujiwara, X. Y. Yu, S. Iwata, S. Tsunashima, and S. Uchiyama, J. Magn. Soc. Jpn. Suppl. **S1**, 169 (1994).
[10] Z. S. Shan and D. J. Sellmyer, Phys. Rev. B **42**, 10433 (1990).
[11] *X-ray Absorption: Principle, Applications, Techniques of EXAFS, SEXAFS and XANES*, edited by D. C. Koningsberger and R. Prins (Wiley, New York, 1988).

# Occurrence of large perpendicular magnetic anisotropy in bilayered films with nanometer-thick TbFeCo and Al layers

H. Ito
*Corporate R&D Laboratory, Pioneer Electronic Corporation, Fujimi-6, Tsurugashima-shi, Saitama 350-02, Japan*

K. Song and M. Naoe
*Department of Physical Electronics, Tokyo Institute of Technology, 2-12-1, O-okayama, Meguro-ku Tokyo 152, Japan*

For Tb-Fe-Co(MO)/Al bilayered films, dependence of perpendicular magnetic anisotropy constant $K_{u\perp}$ on MO layer thickness $t_{MO}$ of 3–300 nm and Al layer thickness $t_{Al}$ of 5 and 100 nm has been investigated. For either $t_{Al}$, easy magnetization direction was normal to film plane at $t_{MO}$ above 4 nm. $K_{u\perp}$ of films with $t_{Al}$ of 5 nm increased drastically with increasing $t_{MO}$ for $t_{MO}<10$ nm and then assumed a constant value of $4\times10^6$ erg/cm$^3$ which is two times larger than that with $t_{Al}$ of 100 nm. This difference in $K_{u\perp}$ between them may be attributed to stress induced anisotropy. Estimation of rotational hysteresis loss $W_r$ and its integral $R$ suggests that the mechanism of magnetization reversal may be attributed to incoherent curling mode. © *1996 American Institute of Physics.* [S0021-8979(96)24208-1]

## INTRODUCTION

Amorphous films of rare earth-transition metal (RE-TM) alloy such as Tb-Fe-Co and Gd-Tb-Fe are commonly used for magneto-optical storage media. However, high storage capacity and direct overwriting system are required in order to use effectively the magneto-optical disks. For this purpose, the multilayered films composed of many ultrathin layers of these RE-TM alloys are of great current interest for fundamental studies and practical uses.[1–4] In the multilayered films, a large perpendicular magnetic anisotropy constant $K_{u\perp}$ is essential to obtain the minimum size and good regularity of reversed magnetic domains written in the RE-TM alloy films.

There are only a few reports[1,3,4] on the perpendicular magnetic anisotropy in nanometer-thick Tb-Fe-Co films. The authors have found that the strong Kerr rotation enhancement[5,6] was observed at the short wavelength of 400 nm and Tb-Fe-Co(MO) layer of thickness $t_{MO}$ below 10 nm in the MO/Al bilayered films deposited by the facing targets sputtering (FTS) apparatus.

In this study, the perpendicular magnetic anisotropy was investigated for the MO/Al films with various $t_{MO}$ of 3–300 nm and the Al layer thickness $t_{Al}$ of 5 and 100 nm. In addition, the rotational hysteresis loss $W_r$ was measured for the specimen films with $t_{MO}$ of 5–9 nm and was related to the mechanism of magnetization reversal.

## EXPERIMENTALS

The Tb-Fe-Co(MO)/Al bilayered films were deposited on plasma-free glass slide substrates using the facing targets sputtering (FTS) apparatus.[5–7] Both layers were deposited at the Ar pressure $P_{Ar}$ of 0.5 mTorr. Deposition rates of MO and Al layers were 100 and 50 nm/min, respectively. The thickness of MO layer $t_{MO}$ was varied in range from 3 to 300 nm and that of Al layer $t_{Al}$ was 5 and 100 nm. Magnetic measurements were performed using a vibrating sample magnetometer (VSM) and a torque magnetometer with magnetic fields $H_m$ up to 15 kOe. The perpendicular magnetic anisotropy constant $K_{u\perp}$ was determined by the method proposed by Miyajima *et al.*[8]

## RESULTS AND DISCUSSION

The composition of TbFeCo(MO) layer was Fe-Co richer side of the compensation composition. The coercivity $H_c$ of MO layers ranged from 1.08 to 7.8 kOe.

All the MO/Al bilayered films with MO layer thickness $t_{MO}$ above 4 nm showed the rectangular Kerr hysteresis loops.

Figure 1 shows the $t_{MO}$ dependence of $K_{u\perp}$ for the Al layer thickness $t_{Al}$ of 5 and 100 nm. For either $t_{Al}$, $K_{u\perp}$ increased drastically with increasing $t_{MO}$ for $t_{MO}<10$ nm and then assumed almost constant value at $t_{MO}$ above 15 nm. The constant value of $K_{u\perp}$ for $t_{Al}$ of 5 nm was found to be about $4\times10^6$ erg/cm$^3$ which is two times larger than that for $t_{Al}$ of 100 nm. Thus the easy magnetization direction was perpendicular to the film plane at $t_{MO}$ of greater than about 4 nm for either $t_{Al}$. As described in the previous paper,[6] Kerr rotation angle $\theta_k$ at wavelength of 400 nm took a sharp maximum peak at $t_{MO}$ of 5 nm where $K_{u\perp}$ changed drastically. The $t_{MO}$

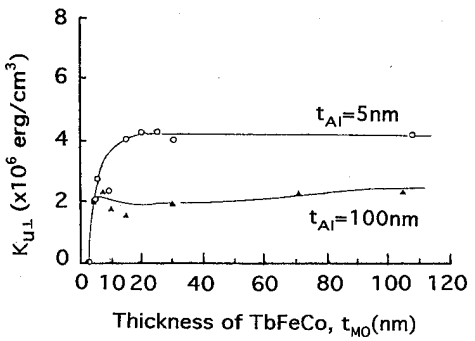



FIG. 1. Thickness ($t_{MO}$) dependence of perpendicular anisotropy constant $K_{u\perp}$ for $t_{Al}$ of 5 and 100 nm.

 0021-8979/96/79(8)/6273/3/$10.00 © 1996 American Institute of Physics 

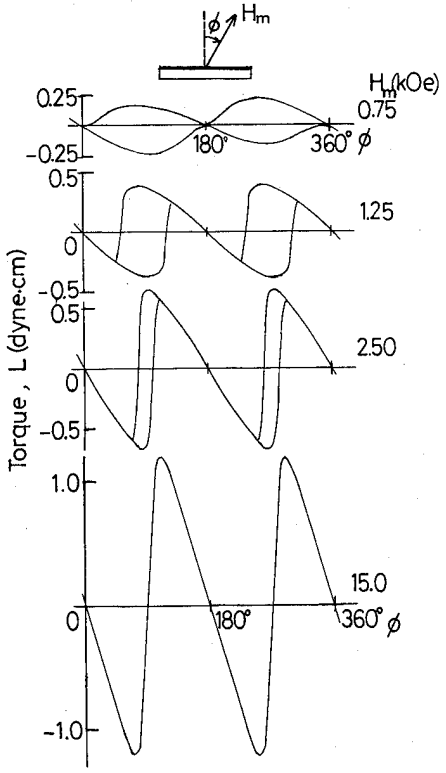



FIG. 2. Torque curves for specimen films with $t_{MO}$ and $t_{Al}$ of 5 nm at various magnetic fields $H_m$.

value of 4 nm is in agreement with the minimum thickness of Tb-Fe layer for which the easy magnetization direction is normal to the film plane in the Tb-Fe/SiO multilayers.[9] Moreover, the $t_{MO}$ value was comparatively close to the grain size (~8 nm) observed in the dense, uniform and columnless Tb-Fe-Co films.[7]

The difference in $K_{u^\perp}$ between the films with $t_{Al}$ of 5 and 100 nm could be attributed to the inverse magnetostriction effect. $K_{u^\perp}$ may be considered to be the sum of $K_{u\ in}$ and $K_u$[ME], where $K_{u\ in}$ is due to the atomic ordering or single-ion anisotropy and $K_u$[ME] is due to magnetoelastic energy. $K_u$[ME][3,4] is defined as $-(3/2)\cdot\lambda\cdot\sigma$, where $\lambda$ is magnetostriction constant[10] and has a positive value of the order of $10^{-4}$, and $\sigma$ is the internal stress of compression or tension. In this study, $\sigma$ for the 50-nm-thick Tb-Fe-Co layers deposited at Ar pressure of 0.5 mTorr was compressive, i.e., negative value of order of $10^9$ dyne/cm$^2$.

When the Al layer with $t_{Al}$ of 100 nm is deposited on the Tb-Fe-Co layer with $t_{MO}$ above 20 nm, the resultant stress may approach close to zero, because the stress in Al layer is tensile,[11] i.e., positive value of $10^9$ dyne/cm$^2$. On the other hand, for $t_{Al}$ of 5 nm, the resultant stress seems to be compressive, i.e., negative, because the stress in Al layer with $t_{Al}$ of 5 nm is negligibly small. Thus, the difference in $K_{u^\perp}$ between the films with different $t_{Al}$ can be attributed to mainly to magnetoelastic energy $K_u$[ME].

In order to determine the rotational hysteresis loss $W_r$,[12] the clockwise and anticlockwise torque curves for several specimen films were measured at various magnetic fields $H_m$.

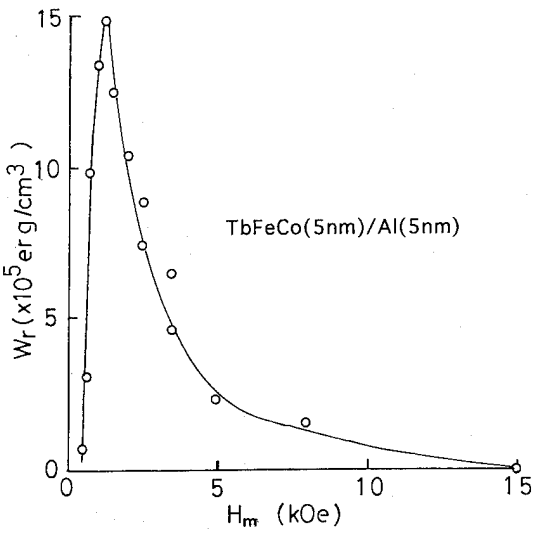



FIG. 3. $H_m$ dependence of rotational hysteresis loss $W_r$ for specimen film with $t_{MO}$ and $t_{Al}$ of 5 nm.

Figure 2 shows the typical different torque curves of the specimen film with $t_{MO}$ and $t_{Al}$ of 5.0 nm. As seen in this figure, the rotational hysteresis loops were observed at $H_m$ of 0.75, 1.25, and 2.50 kOe, while they were not observed at $H_m$ of 15 kOe. $W_r$ is defined as

$$\int_0^{2\pi} L d\,\phi,$$

where $L$ is the torque of the specimen film and $\phi$ is the angle between the magnetic field $H_m$ and the easy magnetization direction normal to the film plane.

Figure 3 shows the $H_m$ dependence of $W_r$ for the specimen film with $t_{MO}$ and $t_{Al}$ of 5 nm. With increasing $H_m$, $W_r$ rose very drastically to a sharp maximum peak at $H_m$ of 1.2 kOe and then decreased gradually and vanished at $H_m$ of about 15 kOe. The $H_m$ corresponding to the peak $H_m$[peak] is close to the coercivity $H_c$ of the specimen film. The field at which $W_r$ reduces to zero was estimated to be about 9.5 kOe. This value is in good agreement with the anisotropy field $H_k$ corresponding to $2K_{u^\perp}/M_s$. $K_{u^\perp}$ and $M_s$ of this specimen film were $1.93\times10^6$ and 408 emu/cm$^3$, respectively.

Similar $W_r$ versus $H_m$ curves were observed in the specimen films with $t_{MO}$ below 10 nm and $H_c$ of about 1–2 kOe.

The rotational hysteresis integral,[12]

$$R\left\{=\int_0^{\infty}(W_r/M_s)d(1/H_m)\right\}$$

was calculated for the specimen films with $t_{MO}$ and $t_{Al}$ of 5 nm. The value of $R$ was evaluated to be 1.46 when the demagnetizing field[13] of $4\pi M_s$ was taken into consideration.

Figure 4 shows the dependence of $W_r/K_u$ on $H_m/H_k$. It revealed a sharp maximum peak at $H_m/H_k$ of about 0.14. These results suggest that the mechanism of magnetization reversal of the bilayered films may be explained based on the incoherent curling mode for aligned and random as-

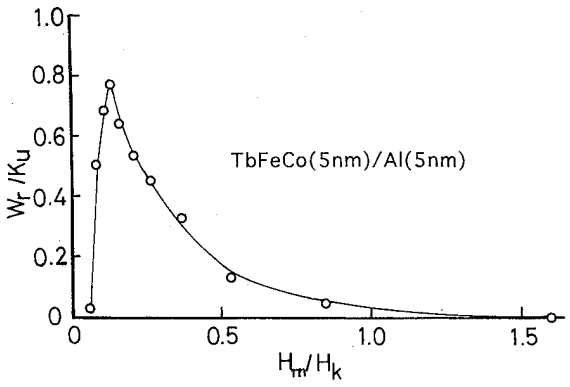



FIG. 4. Dependence of $W_r/K_u$ on $H_m/H_k$ for specimen films with $t_{MO}$ and $t_{Al}$ of 5 nm.

semblies of infinite magnetic cylinders. These results seemed to agree well with those of the Gd-Tb-Fe films.[14]

## CONCLUSION

The Tb-Fe-Co(MO)/Al bilayered films with various MO and Al layers thicknesses, $t_{MO}$ and $t_{Al}$, respectively, have been deposited using the FTS apparatus. The dependence of perpendicular magnetic anisotropy constant $K_{u\perp}$ on $t_{MO}$ and $t_{Al}$ were investigated. At $t_{Al}$ of 5 and 100 nm, the easy magnetization direction was normal to the film plane at $t_{MO}$ above 4 nm. The results of evaluation of the rotational hysteresis loss $W_r$ and its integral $R$ suggest that the mechanism of magnetization reversal in the MO/Al bilayered films with nanometer thick MO layer may be due to an incoherent curling mode.

## ACKNOWLEDGMENT

The authors would like to thank E. Itoh, Toei Industry Co., Ltd. for measurement of rotational hysteresis.

[1] Y. Takeno, M. Suwabe, and K. Goto, J. Magn. Magn. Mater. **93**, 237 (1991).
[2] N. Sato, J. Appl. Phys. **59**, 2514 (1986).
[3] R. Krishnan, M. Porte, and M. Tesier, J. Appl. Phys. **63**, 2447 (1988).
[4] H. Karube, K. Matsumura, and O. Okada, J. Magn. Soc. Jpn. **17**, Suppl. S1, 123 (1993).
[5] K. Song, H. Ito, and M. Naoe, J. Magn. Soc. Jpn. **15**, Suppl. S1, 185 (1991).
[6] K. Song, H. Ito, and M. Naoe, IEEE Trans. Magn. **MAG-29**, 3367 (1993).
[7] H. Ito, M. Yamaguchi, and M. Naoe, Mater. Res. Soc. Symp. **150**, 171 (1989).
[8] H. Miyajima, K. Sato, and T. Mizoguchi, J. Appl. Phys. **47**, 4669 (1976).
[9] K. Saitø, R. Sato, N. Kawamura, and M. Kajiwara, Jpn. J. Appl. Phys. **28**, Suppl. 28-3, 3 (1989).
[10] H. Takagi, S. Tsunashima, S. Uchiyama, and T. Fujii, J. Appl. Phys. **50**, 1642 (1979).
[11] K. L. Chopra, *Thin Films Phenomena* (McGraw-Hill, Florida, 1969), p. 304.
[12] R. A. McCurie and S. Jackson, J. Appl. Phys. **62**, 627 (1987).
[13] E. R. Wuori and J. H. Judy, IEEE Trans. Magn. **MAG-21**, 1602 (1985).
[14] I. M. Song, S. Ishio, M. Ishizuka, T. Tsunoda, and M. Takahashi, J. Magn. Magn. Mater. **119**, 261 (1993).

# Studies of anisotropic and giant magnetoresistance in Co/Cu(111) epitaxial multilayers

J. C. A. Huang, Y. H. Lee, Y. M. Hu, and T. C. Chang
*Physics Department, National Cheng-Kung University, Tainan 701, Taiwan*

Co/Cu(111) multilayers, [Co(17 Å)/Cu(8 Å$<t_{Cu}<$14 Å)]$_{30}$, have been prepared on Co(70 Å) buffer layers on $Al_2O_3$(0001) substrates by molecular beam epitaxy. From the longitudinal and transverse magnetoresistance (MR) measurements, it is observed that MRs consist of two components with a small anisotropic MR (<2%) component at low field sitting on top of the giant MR (up to 22%) component at higher field. The AMR effect strongly correlates with the abundance of hcp stacking of Co, which tends to decrease with the increasing of Cu spacer thickness. The AMR saturation fields (1–3 kOe) coincides with those of the magnetization. It is suggested that the observed AMR effect is due to scattering from the hcp-phase Co layers in the multilayers. This together with the large saturation field (30–40 kOe) obtained from the entire MR curves indicate that the observed GMR effect may result from the Co-Cu interfacial spin-dependent scattering. © *1996 American Institute of Physics.* [S0021-8979(96)24308-8]

## I. INTRODUCTION

Anisotropic MR (AMR≤5%) has commonly been observed in pure ferromagnetic materials for many years.[1,2] Recently, the giant magnetoresistance (GMR) in magnetic multilayers has become the subject of considerable interest both from scientific and advanced technological point of view.[3–6] Note that GMR is quite different from AMR. AMR is basically an effect due to the spin-orbital interaction,[1,7] while GMR effect is related to the spin configuration change of neighboring ferromagnetic layers from the antiferromagnetic (AF) coupling state to the ferromagnetic (F) coupling state.[8] Further, GMR is isotropic with respect to the relative direction between the field $H$ and current $I$, while AMR depends strongly on relative direction of $H$ and $I$.

Giant MR (GMR) was first realized in the Fe/Cr multilayers.[3] Accompanied with the GMR effect, oscillatory exchange coupling phenomena were discovered in many magnetic multilayers.[6] Particularly, Co/Cu multilayers have attracted much attention because of the giant MR values. In addition, Co/Cu is a suitable system to verify the mechanism of oscillatory exchange coupling because of the relatively simple nature of the Cu Fermi surface.[9] Although GMR effect is widely explained in correlation with the spin configuration change of the successive ferromagnetic layers, increasing evidences were shown, however, that scattering from interfacial states between the ferromagnetic and nonferromagnetic layers could be more important for GMR effect in some multilayer systems.[3,10,11]

In this investigation, we report the structural and magnetic characterizations of Co/Cu(111) multilayers prepared by MBE. The effect of structure upon magnetic and magnetotransport properties has been systematically studied.

## II. EXPERIMENTAL PROCEDURES

The epitaxial Co/Cu(111) multilayers presented here were grown on Co buffer layers (70 Å) on $Al_2O_3$(0001) substrates by molecular beam epitaxy (Vacuum Product model MBE-930) system. Pure elements (99.99%) of Co, Cu were evaporated from an $e$-beam evaporator and a Knudsen cell, respectively. The base pressure of the system before deposition was less than $4\times10^{-10}$ Torr. To enable the growth of high-quality samples, polished and epitaxial grade $Al_2O_3$ substrates were chemically precleaned and rinsed in an ultrasonic cleaner. They were then outgassed at 1000 °C for 1 h under ultra-high-vacuum condition in the MBE chamber. Buffer layers of 70 Å Co were deposited on substrates at about 400 °C to initiate the multilayer growth. The deposition rates for Co and Cu were controlled at about 0.1 Å/s. A series of [Co(17 Å)/Cu($t_{Cu}$Å)]$_{30}$ (with the Cu spacer layer thickness $t_{Cu}$ designed to be 8, 10, 12, and 14 Å) multilayers were then prepared at about 150 °C.

The surface structures of the films were *in situ* examined by reflection-high-energy electron-diffraction (RHEED). The bulk structures and the superlattice period were determined by x-ray diffraction (XRD). The magnetic properties and MRs of all the samples were studied by using a commercial (quantum design) SQUID magnetometer in a magnetic field up to 50 kOe with measuring temperature at 10 K. MR measurements were carried out by standard dc four-point probe technique with $I$ and $H$ in the plane of the layers. Transverse and longitudinal MRs were measured with $I\perp H$ and $I\parallel H$, respectively.

## III. RESULTS AND DISCUSSIONS

Figure 1 shows a typical RHEED pattern of fresh Cu(111) surface during the growth of Co/Cu multilayers. Similar RHEED feature was observed on the growing surface of Co. As can be seen from the RHEED pattern, the crystal surface was rather smooth and nice indicating high-quality epitaxial multilayers. Figures 2(a)–2(d) show the high-angle XRD spectra for the Co/Cu(111) multilayers for a fixed Co thickness of 17 Å and variable Cu layer thickness $t_{Cu}$ (in one bilayer). To avoid the enormous $Al_2O_3$(0001) substrate peak at $2\theta\sim41°$, the range of x-ray spectra is limited to above 42.5°. The large peaks located at about $2\theta\sim43.7°$, indexed as fcc(111), lie in between the positions of bulk fcc Cu(111) and bulk fcc Co(111), as illustrated in the inset of Fig. 2. The fcc(111) peaks are likely due to the strain effect between the Cu and Co layers with close lattice parameters

 0021-8979/96/79(8)/6276/3/$10.00 © 1996 American Institute of Physics



FIG. 1. Typical RHEED of Cu(111) surface view along [01$\bar{1}$] direction during the growth of the Co/Cu multilayers.

of 2.087 and 2.051 Å. Similar strain effect was also found in sputtered Co/Cu multilayers in the other work.[12] The fcc(111) peak slightly shifts toward the bulk fcc Cu(111) positions as $t_{Cu}$ increased (see Fig. 2). By average each shift corresponds to an increase of the interatomic spacing of about $2.2\times10^{-3}$ Å. This is quite reasonable since the lattice parameter of fcc Cu is slightly larger than that of the fcc Co.

Shown in Fig. 2 includes the satellite peaks (indexed as $S$) corresponding to the periodicity of the multilayers. In addition, for each XRD spectrum there is a very small yet broad peak around $2\theta\sim51°$, which corresponds to the position of the fcc(200) peak. Interestingly, one can also observe a rather strong peak near the fcc(111) for samples (a) and (b). This peak coincides with the position of bulk hcp Co(0002). The existence of hcp Co(0002) phase is likely due to a large concentration of stacking faults in the multilayers.[12] Furthermore, the Co(0002) peak intensity decreases with the increasing of the Cu spacer layer thickness for the multilayers (see Fig. 2).

Figures 3(a)–3(c) show the magnetization, longitudinal and transverse MRs for the [Co(17 Å)/Cu(10 Å)]$_{30}$ multilayer. Here MR is defined as $[R(H)-R_{min}]/R_{min}$, as usual, where $R_{min}$ is the minimum (at saturated field) of measured electrical resistance. Basically, both longitudinal and transverse MRs possess almost the same curves, saturation field (~30 kOe) and GMR values (up to about 11%) for field larger than 3 kOe. For small magnetic field (≤3 kOe) the longitudinal MR curve exhibits a small dip (~0.5%, negative), while the transverse MR curve displays a sharp spike (~1%, positive). This low field anisotropic behavior together with the obvious hysteresis for both MR curves correlate strongly with the magnetization loops, as shown in the inset of Fig. 3. Note that this AMR phenomenon has a strong link with the hcp phase of Co in the multilayers, as discussed below. In addition, the distinct saturation fields for the magnetization (3 kOe) and the entire MR curves (30 kOe) point to the separate mechanisms between the observed GMR effect and the bulk scattering from the magnetic (Co) layers. The M-H loop shown in Fig. 3 indicates that the magnetic layers are largely ferromagnetically coupled, suggesting that the AF coupling between the magnetic layers may not be responsible for the observed GMR effect. Similar result was also observed by Barlett *et al.* in MBE grown Co/Cu(111) multilayers.[13] It has been proposed that superparamagnetic states at the interface, for the Cu conduction electron band being patially polarized in proximity to the Co layers, are responsible for the high saturation field of GMR curves in MBE grown Co/Cu multilayers.[13,15] We thus believe that interfacial spin-dependent scattering appears to be a dominant factor for the GMR effect in the Co/Cu(111) multilayers.

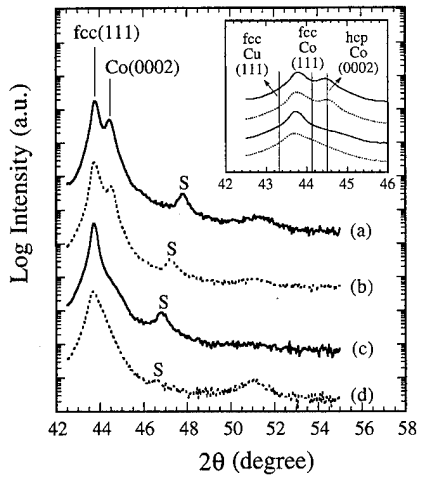



FIG. 2. High angle x-ray diffraction spectra from samples: (a) [Co(17 Å)/Cu(8 Å)]$_{30}$, (b) [Co(17 Å)/Cu(10 Å)]$_{30}$, (c) [Co(17 Å)/Cu(12 Å)]$_{30}$, and (d) [Co(17 Å)/Cu(14 Å)]$_{30}$. The positions corresponding to the bulk fcc Cu(111), fcc Co(111), and hcp Co(0002) are illustrated by the vertical lines.

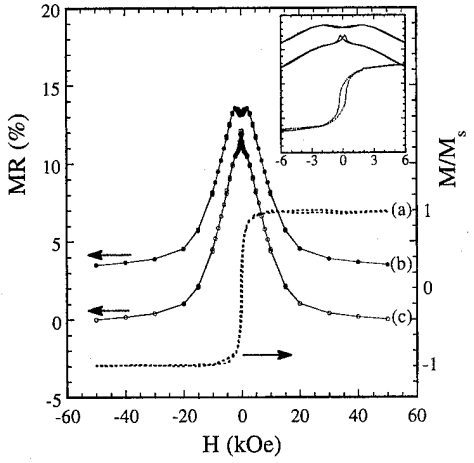



FIG. 3. The magnetization and MR as a function of applied magnetic field $H$ at 10 K for [Co(17 Å)/Cu(10 Å)]$_{30}$ multilayer showing (a) hysteresis loops of magnetization, (b) longitudinal MR ($I\|H$), and (c) transverse MR ($I\perp H$).

Shown in Figs. 4(a)–4(d) are the longitudinal MR curves for sample (a) to sample (d) with increasing $t_{Cu}$. Note that similar features of longitudinal and transverse MRs in sample (b) also exist in sample (a). Compared to sample (b), sample (a) possesses larger GMR saturation field (~40 kOe) and smaller AMR (and magnetization) saturation field (~1 kOe), as shown in Figs. 4(a)–4(b). The AMR effect for sample (a) is slightly stronger [than sample (b)] with the longitudinal dip (see inset of Fig. 4) and transverse spike each of about 1%. On the other hand, the AMR effect completely disappears for sample (d) [see Fig. 4(d)], that is, the

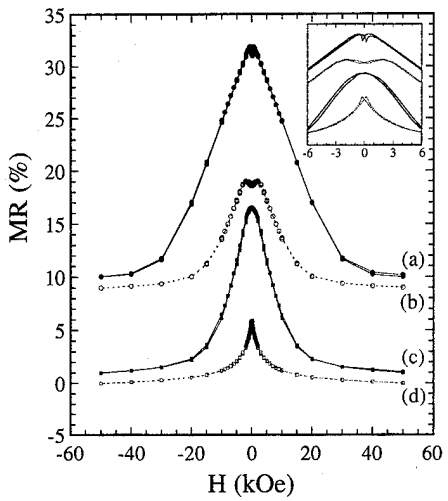



FIG. 4. The longitudinal magnetoresistance as a function of applied field at 10 K from samples: (a) $[Co(17\ Å)/Cu(8\ Å)]_{30}$, (b) $[Co(17\ Å)/Cu(10\ Å)]_{30}$, (c) $[Co(17\ Å)/Cu(12\ Å)]_{30}$, and (d) $[Co(17\ Å)/Cu(14\ Å)]_{30}$.

same longitudinal and transverse MRs at low or high field (isotropic GMR behavior) is found. For sample (c), the MR curve [Fig. 4(c)] appears to be an intermediate configuration between the typical pure GMR effect [like Fig. 4(d)] and the combination of the AMR and GMR effect [like Figs. 4(a) and 4(b)].

Finally we discuss the connection between the observed AMR effect and the hcp phase of Co in the multilayers. By comparison Figs. 4(a)–4(d) with the XRD spectra in Figs. 2(a)–2(d), it is quite easy to see a trend that the AMR effect decreases with the reducing of the hcp Co(0002) intensity. It is suggested that the observed AMR effect could be mainly due to scattering from the hcp Co layers of the multilayers. The strong correlation between the AMR and hcp phase of Co could be owing to the dominance of the anisotropic effect of the hcp phase (uniaxial anisotropy) over than that of the fcc phase.[14] So far, however, we are not able to quantitatively determine the ratio of the fcc and hcp phase of Co in the multilayers.

In summary, we have presented the structural and magnetic characterizations of Co/Cu(111) epitaxial multilayers. A small AMR component at low field sitting on top of a large GMR component extended to higher field has been observed. The AMR effect strongly correlates with the abundance of hcp stacking in the Co layers, which tends to decrease with the increasing of Cu spacer layer thickness. The AMR saturation fields coincides exactly with those of the magnetization. It appears that the observed AMR effect is mainly due to the scattering from the hcp-phase Co layers in the multilayers. This together with the large saturation field obtained from the entire MR curves indicate that the observed GMR effect may result from the Co-Cu interfacial spin-dependent scattering.

## ACKNOWLEDGMENT

We are grateful for the financial support by the ROC NSC under Grant Nos. 84-2112-M-006-017, 84-2112-M-006-018, and 85-2112-M-006-006.

[1] T. R. McGuire and R. I. Potter, IEEE Trans. Magn. **MAG-11**, 1018 (1975).
[2] A. P. Malozemoff, Phys. Rev. B **32**, 6080 (1985).
[3] M. N. Baibich, J. M. Broto, A. Fert, F. Nguyen van Dau, F. Petroff, P. Etienne, G. Creuzet, and J. Chazelas, Phys. Rev. Lett. **61**, 2472 (1988).
[4] E. E. Fullertron, M. J. Conover, J. E. Mattson, C. H. Sowers, and S. D. Bader, Appl. Phys. Lett. **63**, 1699 (1993).
[5] S. S. P. Parkin, Z. G. Li, and D. J. Smith, Appl. Phys. Lett. **58**, 2710 (1991).
[6] S. S. P. Parkin, R. Bhadra, and K. P. Roche, Phys. Rev. Lett. **66**, 2152 (1991).
[7] J. Smit, Physica (Utrecht) **XVI**, 612 (1951).
[8] B. Dieny, J. Magn. Magn. Mater. **136**, 335 (1994).
[9] P. Bruto and C. Chappert, Phys. Rev. Lett. **67**, 1602 (1991).
[10] D. H. Mosca, F. Petroff, A. Fert, P. A. Schroeder, W. P. Pratt, and R. Loloe, J. Magn. Magn. Mater. **94**, L1 (1991).
[11] S. S. P. Parkin, Phys. Rev. Lett. **71**, 1641 (1993).
[12] S. Pizzini, F. Baudelet, A. Fontaine, M. Galtier, D. Renard, and C. Marliere, Phys. Rev. B **47**, 8754 (1993).
[13] D. Barlett, F. Tsui, D. Glick, L. Lauhon, T. Mandrekar, C. Uher, and Roy Clarke, Phys. Rev. B **49**, 1521 (1994).
[14] J. C. A. Huang *et al.*, Phys. Rev. B **52**, R13110 (1995).
[15] S. Pizzini, C. Giorgetti, A. Fontaine, E. Dartyge, G. Krill, J. F. Bobo, and M. Piecuch, Mater. Res. Soc. Symp. Proc. **313**, 625 (1993).

# Effects of discharge pressure on the properties of Ag/Ni superlattices prepared by facing-target sputtering

X. T. Zeng and H. K. Wong
*Department of Physics, the Chinese University of Hong Kong, Shatin, Hong Kong*

Giant magnetoresistance (GMR) effect in magnetic multilayered thin films is strongly affected by interface roughness. We prepared $[Ag/Ni]_{60}$ superlattices on Corning's 7059 glass substrates using a novel facing-target sputtering method and observed that the interface roughness can be controlled by varying the discharge pressure ($P_{Ar}$). The samples prepared at $P_{Ar}\approx 10$ mTorr exhibit sharpest interfaces, good (111) texture, and largest GMR effects ($\Delta\rho/\rho_s=9\%$ at room temperature). Lower $P_{Ar}$ promotes interface mixing while higher $P_{Ar}$ results in much rougher interfaces and emergence of structural defects. Both cases weaken the antiferromagnetic coupling strength and thus reduce the MR effect. When $P_{Ar}\geqslant 30$ mTorr, we observed a further degradation of the multilayered structure. The GMR effects in these samples disappeared. Low-temperature annealing can improve the flatness of the interfaces and film structure, while higher-temperature annealing (>300 °C) decomposes the multilayer structures. © *1996 American Institute of Physics.*
[S0021-8979(96)24408-4]

## I. INTRODUCTION

It is generally believed that the interface roughness in magnetic multilayers plays an important role in the spin-dependent scattering process.[1–8] However the mechanisms involved are still subject to discussions since the scattering processes at the interfaces may lead to an increase or decrease of the giant magnetoresistance (GMR) effects.[1–8] For systems like Ag/Ni or Au/Ni superlattices, the interfaces could be expected to be sharp as the constituents are mutually insoluble even in the liquid state.[9] Recently, Rodmacq *et al.* prepared Ag/Ni multilayers by sputtering and reported some results about their structure and magnetic properties.[4–6] Here, we define $MR=\Delta\rho/\rho_s$, where $\rho_s$ is the resistivity at the saturation field. T. L. Hylton *et al.* reported a GMR value of 6% in weak magnetic field at room temperature in a similar system: $Ag/Ni_{80}Fe_{20}$ superlattices and they attributed the large GMR effect to a discontinuous multilayer structure.[7] However, R. C. Farrow and co-workers have also obtained GMR value of 5.6% in low-field Ag/permalloy multilayers and pointed out that interface roughness can deteriorate the MR effects.[8] Because of this controversy, further experiments to correlate the GMR effects with multilayer microstructure become necessary.

In this article, we prepared the multilayers of Ag/Ni by a facing-target sputtering (FTS) method[10,11] and focused on the effects of the argon discharge pressure ($P_{Ar}$) on the structure and properties of the films. We found that the multilayers with sharp interfaces have large MR values. X-ray diffraction experiments indicate that the crystalline AgNi alloy phase[9] may be formed in our films when prepared at high-Ar pressure.

## II. SAMPLE PREPARATION

The Ag/Ni superlattices were deposited in a sputtering system equipped with four FTS guns.[11] The characteristics of our FTS guns and the sputtering system will be reported elsewhere. Layers of Ag and Ni were alternatively deposited on chemically cleaned Corning's 7059 glass substrates at room temperature. The number of bilayers for each samples was fixed at 60. The discharge current for the FTS guns were maintained at 18 mA. In spite of such a low sputtering power, the deposition rates were not low: about 0.2 nm $s^{-1}$ for Ag and 0.1 nm $s^{-1}$ for Ni. Although the discharge voltage increases at decreasing sputtering pressure, the deposition rate did not vary significantly. Some of the samples were annealed in a vacuum of $4\times10^{-7}$ Torr.

## III. STRUCTURAL STUDY

The Ag/Ni samples were characterized with a four circle x-ray diffractometer using Cu $K\alpha$ x-rays. X-ray diffraction (XRD) $\theta$-$2\theta$ patterns were obtained with the scattering vector perpendicular to the film plane. The surface morphology of these samples was examined by a scanning electron microscope (SEM). Figure 1 shows the high-angle XRD patterns of samples prepared at different $P_{Ar}$ with a nominal composition modulation of [Ag (1.2 nm)/Ni(0.81 nm)]$_{60}$. These patterns have an average Bragg peak $(111)_B$ at $2\theta\sim40°$, flanked by a few satellite peaks. The $(111)_B$ position depends slightly on the discharge pressure. No crystallites with other orientations were observed except for those samples prepared at $P_{Ar}\geqslant 30$ mTorr. For the samples deposited at 5 and 10 mTorr, we observed the second-order satellite peaks in both high-angle and low-angle XRD patterns, clearly indicating that these samples have sharper interfaces. Examination of these samples with an SEM also shows that the films prepared at lower pressures have a smoother surface than those prepared at higher pressures. However it does not mean that the lower the sputtering pressure, the better the sample quality. In fact, the sample prepared at 5 mTorr has a slightly weaker low-angle satellite peak than the 10 mTorr sample indicating that the 5 mTorr sample has a layered structure not as good as the 10 mTorr sample. This can be attributed to large interface mixing induced by the bombardment of the energetic sputtered particles.

For those samples prepared at $P_{Ar}\geqslant 30$ mTorr, only weak first order satellite peaks could be observed. The same characteristics were found in the measurements of the low-angle

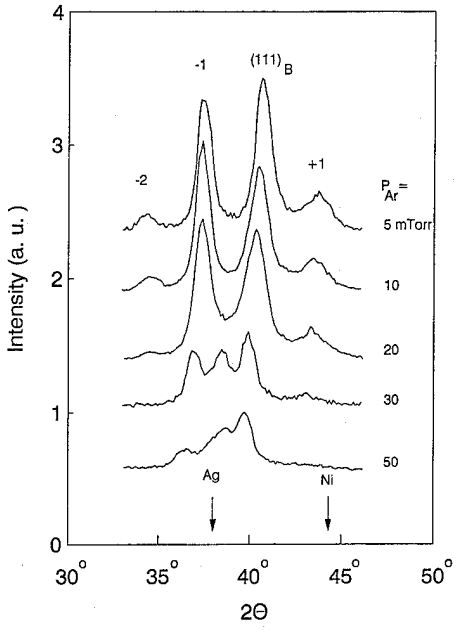



FIG. 1. XRD patterns of $[Ag/Ni]_{60}$ grown at different discharge pressures.

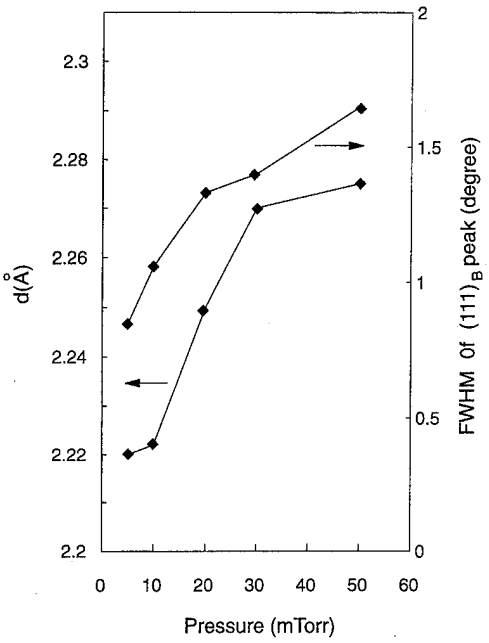



FIG. 2. Dependence of the atomic plane spacing and width of Ag/Ni $(111)_B$ average peaks on the discharge pressure.

satellite peaks. The full-width at half-maximum (FWHM) of these low-angle diffraction peaks for the samples prepared at 5–10 mTorr is much smaller than that for the samples prepared at $P_{Ar}>20$ mTorr. That means that low-pressure samples possess flatter interfaces than the high-pressure samples. The FWHM of the $(111)_B$ is also larger for samples prepared at higher $P_{Ar}$ as shown in Fig. 2. Shown on the same graph is the pressure dependence of the plane spacing $d$.

The roughness of the interfaces mainly results from the dynamics of the sputtered particles on film surface. With the increase of discharge pressure, the sputtered particles scatter more frequently, which results in a kinetic energy loss. The mobility of these particles deposited on the substrate is significantly reduced, which results in increasing disorder in the atomic arrangement and average spacing between atomic planes. This is supported by our experiments using an electric probe to characterize the FTS discharge plasma at different conditions.[12] It is also expected to have misfit dislocation induced by large lattice mismatch between Ag and Ni. Thus we observed that for Ag/Ni superlattices prepared by FTS technique, there exists an optimum pressure for samples with better superlattice structures. We will see later that the pressure dependence of MR has a similar characteristic.

Other than the rough interfaces, we observed a new diffraction peak in the XRD spectra for samples prepared at $P_{Ar}\geqslant 30$ mTorr. This new diffraction peak was found to position between $(111)_B$ peak and Ag(111) peak. It may be attributed as a new phase of $Ag_xNi_{1-x}$ alloy as observed recently by van Ingen *et al.* using pulsed laser deposition (PLD).[9] Because of the complete immiscibility between Ag and Ni, it is not expected to form an AgNi alloy phase by ordinary approach. In order to know the thermal stability of the structure, we annealed samples at different temperatures $(T_a)$ in high vacuum $(4\times10^{-7}$ Torr) for 30 min. Figure 3 shows the XRD patterns for the annealed samples. When annealed at $T_a<280$ °C, both $(111)_B$ peak and satellite peaks gained intensity with slightly decreased widths, but the peak positions remained unchanged. In the words, the crystal quality and the interface flatness were improved. The annealing shifted the new peak gradually to smaller angle. When $T_a=350$ °C, all peaks mentioned above disappeared and pure Ag(111) and Ni(111) peaks appeared as shown in Fig. 4. That means that the alloy phase, if it exists in the samples, is metastable and the high-temperature annealing decomposed it into pure Ag and pure Ni grains. This result is basically in agreement with that obtained by PLD.[9]

## IV. MAGNETORESISTANCE

The magnetoresistance (MR) was measured by the standard 4-point probe method using an ac measurement current of 0.1 mA and a lock-in amplifier. The magnetic field $(B)$ was applied parallel to the film plane and perpendicular to the electric current. The MR of the as-deposited samples was measured at room temperature. Here $MR=[\rho(B)-\rho_s]/\rho_s$. We observed an oscillation of MR with the increase of the Ag layer thickness for samples prepared at 5, 10, and 20 mTorr. The maximal value of MR for all samples was achieved when the thickness of Ag layer was 1.2 nm. The results were reproducible with a deviation of MR value of about 1% for the samples with the same prescribed thickness. Here we focus attention on the effect of the discharge pressure on the MR value. Figure 4 shows the variation of magnetoresistance with discharge pressure. The inset shows the dependence of the magnetoresistance on magnetic field. It is found that the samples prepared at $P_{Ar}=10$ mTorr have the largest MR=9% and the largest saturation field. When $P_{Ar}=5$ mTorr, MR decreases to 6.2%, and the saturation field dropped by about one third. For samples prepared at $P_{Ar}=20$ mTorr, both MR and saturation field rapidly de-

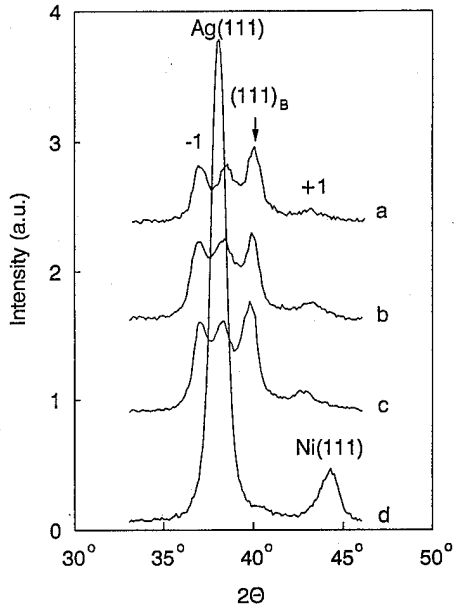



FIG. 3. XRD patterns of the sample grown at 30 mTorr and annealed at different temperatures. (a) As-deposited, (b) 220 °C, (c) 280 °C, and (d) 350 °C.

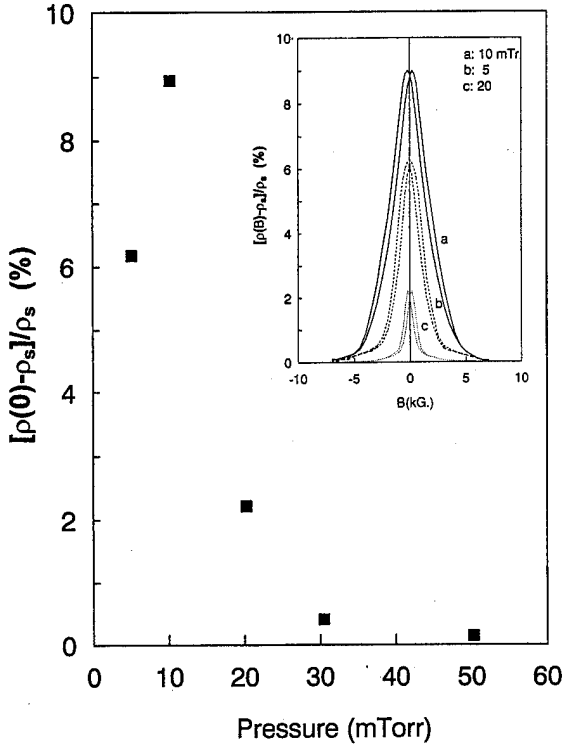



FIG. 4. Variation of the magnetoresistance with discharge pressure. The inset shows the field dependence of the magnetoresistance.

creased. For samples prepared at $P_{Ar}$=30 mTorr, no MR effect could be clearly observed. Fullerton *et al.* studied the Fe/Cr superlattices at $P_{Ar}$=4 and 12 mTorr, and concluded that MR is enhanced by the presence of interface roughness.[2] Our experiment covered a wider pressure range. We found that there exists an optimum pressure for preparation of samples with sharp interfaces and large MR. The decrease of MR at lower pressure was attributed to an increase of the interface mixing due to the higher energy of sputtered particles at lower pressure. The increase of roughness and atomic disorder in the layers cause a large fluctuation of spacing thickness which deteriorates the magnetic coupling properties of the layers and diminishes the MR value. This can be reflected by the sample resistivity. With the increase of the pressure, zero-field resistivity $\rho_0$ varies little, but saturation field resistivity $\rho_s$ obviously increases. This indicates that the samples prepared at high $P_{Ar}$ have many structural defects and rough interfaces which weaken the strength of the antiferromagnetic (AFM) coupling. When no magnetic field is applied, the increasing defect resistance is partially compensated by the decreasing spin-dependent scattering.

## V. SUMMARY

We have prepared Ag/Ni superlattices at different discharge pressures on Corning's 7059 glass substrates by a facing-target sputtering method. Detailed structural and electrical measurements indicate that there exists an optimal discharge pressure (~10 mTorr) at which samples can be prepared with sharp interfaces, good (111) texture, large MR (9% at room temperature) and high saturation magnetic field. Lower discharge pressure causes larger mixing of Ag and Ni atoms at the interfaces, and higher pressure results in much rougher interfaces and emergence of structural defects. Both situations weakened the AFM coupling and decrease MR. Low-temperature annealing can improve the flatness of the interfaces and film structure. Annealing at temperatures higher than 300 °C decomposes the multilayered structures.

## ACKNOWLEDGMENTS

This work was partially supported by grants from the Hong Kong Research Grant Council and Croucher Foundation.

[1] R. Schad, C. D. Potter, P. Beliën, G. Verbanck, V. V. Moshchalkov, and Y. Bruynseraede, Appl. Phys. Lett. **64**, 3500 (1994).
[2] E. E. Fullerton, D. M. Kelly, J. Guimpel, I. K. Schuller, and Y. Bruynseraede, Phys. Rev. Lett. **68**, 859 (1992).
[3] S. Li, C. Yu, W. Lai, Y. Wang, and M. Yan, J. Appl. Phys. **78**, 405 (1995).
[4] C. A. dos Santo, B. Rodmacq, M. Vaezzadeh, and B. George, Appl. Phys. Lett. **59**, 126 (1991).
[5] B. Rodmacq, J. Appl Phys. **70**, 4194 (1991).
[6] V. Pelosin, J. Hillairet, and B. Rodmacq, J. Phys. Condens. Matter **6**, 1099 (1994).
[7] T. L. Hylton, K. R. Coffey, M. A. Parker, and J. K. Howard, Science **261**, 1021 (1993).
[8] R. F. C. Farrow, R. F. Marks, T. A. Rabedeau, M. F. Toney, D. Dobbertin, R. Beyers, and S. S. P. Parkin, J. Appl. Phys. **76**, 3688 (1994).
[9] R. P. Van Ingen, R. H. J. Fastenau, and E. J. Mittemeijer, Phys. Rev. Lett. **72**, 3116 (1994); J. Appl. Phys. **76**, 1871 (1994).
[10] M. Naoe, Y. Hoshi, and S. Yamanaka, IEEE Trans. Magn. **16**, 646 (1980).
[11] X. T. Zeng and H. K. Wong, Appl. Phys. Lett. **66**, 3371 (1995).
[12] X. T. Zeng and H. K. Wong, to be published.

# Influence of the crystal structure on the magnetic property of Co/Cr superlattices

Y. Liou
*Institute of Physics, Academia Sinica, Taipei, Taiwan, Republic of China*

J. C. A. Huang
*Department of Physics, National Cheng-Kung University, Tainan, Taiwan, Republic of China*

Y. D. Yao, W. T. Yang, S. Y. Liao, and C. P. Chang
*Institute of Physics, Academia Sinica, Taipei, Taiwan, Republic of China*

Co/Cr superlattices with Co layer thickness of 15 Å and Cr layer thickness of 10 Å have been successfully grown on different substrates, such as MgO, Si, and quartz, by molecular-beam-epitaxy. The crystal structure of all samples has been characterized by *in situ* reflection high-energy electron diffraction. Both magnetoresistance (MR) and magneto-optical Kerr effect (MOKE) measurements were used to analyze the magnetic properties of these samples. Excellent epitaxial growth of hcp-Co($1\bar{1}00$)/bcc-Cr(211) superlattices grown on MgO(110) was observed. Co/Cr superlattices were polycrystalline when grown on Si and amorphous when grown on quartz. Isotropic MRs of less than 1% were observed for all polycrystalline and amorphous Co/Cr superlattices. For Co($1\bar{1}00$)/Cr(211) superlattices grown on MgO(110), a transverse MR of 14.2% and longitudinal MR of 0.67% were observed. MOKE hysteresis loops show perpendicular magnetization for polycrystalline Co/Cr superlattices grown on Si, and in-plane isotropic magnetization for amorphous Co/Cr superlattices grown on quartz. MOKE hysteresis loops for Co/Cr superlattices grown on MgO(110) show strong anisotropic behavior between the hard and easy directions. The magnetic properties of Co/Cr superlattices are strongly influenced by the crystal structure of Co and Cr which is controlled by the substrate. © *1996 American Institute of Physics.* [S0021-8979(96)24508-0]

## I. INTRODUCTION

Since the discovery of giant magnetoresistance (GMR) phenomena,[1–3] ferromagnetic superlattices have attracted much attention for both fundamental research and industrial applications. Over 50% GMR of Fe/Cr or Co/Cu superlattices have been found, but relatively small magnetoresistance (MR) (<5%) of Co/Cr superlattices was found.[4–6] We have known that the GMR effect mainly comes from the coupling between the ferromagnetic layers. It is different from the anisotropic magnetoresistance (AMR) in ferromagnetic systems,[7] where magnetoresistance depends on the direction of the measurement. It has also been noted that magnetic properties may be influenced by electronic structure, which in turn depends on crystal structure. Since crystal anisotropy is intrinsic to the material, it may effect coupling between the ferromagnetic layers in the superlattice and both MR and magnetization hysteresis loop may have strong anisotropic behavior. The Co/Cr system is suitable for the study of the relationship between the structure and the magnetic property because of its varied structural and magnetic properties. Since Co has a very strong crystal anisotropy, we may also see the strong effect of the magnetocrystalline anisotropy on both MR and magnetization hysteresis loop measurements. For isotropic Co/Cr superlattices, we expect to see isotropic MRs and magnetization hysteresis loops.

In this article, we report measurements of MR and magneto-optical Kerr effect (MOKE) hysteresis loop of different structured Co/Cr superlattices grown on different substrates by molecular beam epitaxy (MBE). These measurements show that Co/Cr superlattices epitaxial grown on MgO(110) are highly anisotropic. Large transverse MR (magnetic field along the in-plane hard axis, Co[$11\bar{2}0$], and current along the in-plane easy axis, Co[0001]) of 14.2% and small longitudinal MR (magnetic field and current both along the in-plane hard axis, Co[$11\bar{2}0$]) of 0.67% were measured, and MOKE hysteresis loops also show strong angular dependence. Isotropic MR of 0.37% and MOKE hysteresis loops were measured on amorphous Co/Cr superlattices grown on quartz. Small MR of 0.13% and perpendicular magnetization were observed on polycrystalline Co/Cr superlattices grown on Si.

## II. EXPERIMENT

The growth of the superlattices was carried out by a molecular beam epitaxy system (Eiko EL-10A), equipped with three independent electron beam evaporators. The base pressure of the system is lower than $1\times10^{-10}$ Torr. During the growth of the superlattices, the pressures were kept below $5\times10^{-9}$ Torr, and the growth rates were kept about 0.1 Å/s. The growth rate and film thickness were monitored by a quartz crystal thickness monitor (Leybold Inficon XTC). A 15 keV reflection high-energy electron diffraction (RHEED) is used to *in situ* examine the crystal structure of the film surface throughout all growth. MR measurements were carried out by the conventional four probe technique in a magnetic field up to 50 kOe in a SQUID magnetometer (Quantum design MPMS-5S). Transverse and longitudinal MRs were measured with current perpendicular to the magnetic field and current parallel to the magnetic field, respectively. Magnetization hysteresis loop observations were carried out at room temperature in the longitudinal configuration in a magnetic field up to 2 kOe by a MOKE system. Two con-

 0021-8979/96/79(8)/6282/3/$10.00 © 1996 American Institute of Physics

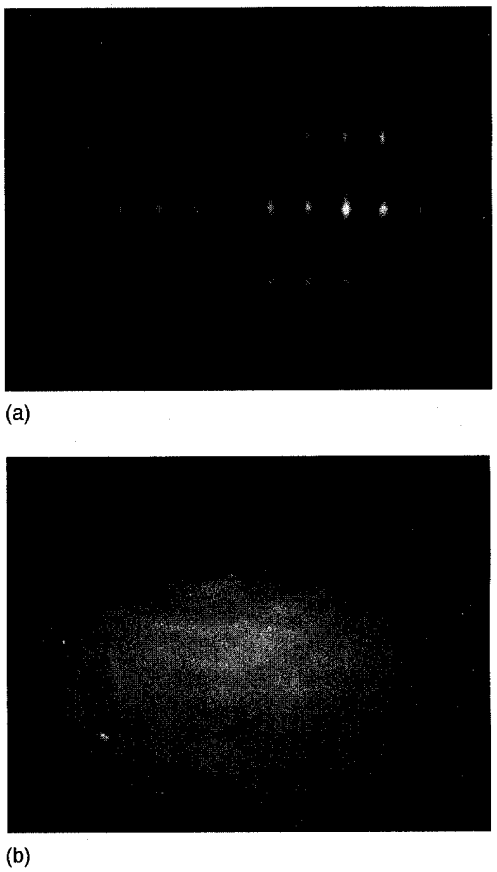



FIG. 1. RHEED patterns of (a) Co($1\bar{1}00$) viewed along [$11\bar{2}0$] of ($Co_{15}$ Å/$Cr_{10}$ Å)$_{40}$ superlattices on MgO(110), (b) Co of ($Co_{15}$ Å/$Cr_{10}$ Å)$_{40}$ superlattices on Si(111).

figurations of MOKE were used: the longitudinal MOKE (LMOKE) in which magnetization lies both in the sample surface and in the incident plane, and the polar MOKE (PMOKE) where magnetization is perpendicular to the sample surface and lies in the incident plane. Prior to the deposition, epitaxial grade substrates were outgassed at 900 °C for at least 1/2 h under ultra-high vacuum in the MBE chamber. The substrate temperatures were kept between 300 and 350 °C during the deposition to reduce the interdiffusion at the interfaces.

## III. RESULTS AND DISCUSSION

The crystal structure and the orientation of epitaxial growth for Co/Cr superlattices with Co layer thickness of 40 Å on MgO(110) have been reported previously.[8–11] The unit cell of Co($1\bar{1}00$), 4.07 Å×2.51 Å, matches perfectly with that of Cr(211), 4.07 Å×2.50 Å. Even though the unit cell of MgO(110) is larger, 4.21 Å×2.98 Å, there still exists the epitaxial relationship:

Co($1\bar{1}00$)‖Cr(211)‖MgO(110),Co[$11\bar{2}0$]‖Cr[$\bar{1}\bar{1}1$]‖MgO[$1\bar{1}0$],

and

Co[0001]‖Cr[$0\bar{1}1$]‖MgO[001].

From RHEED observations, as shown in Fig. 1(a), it was confirmed that ($Co_{15}$ Å/$Cr_{10}$ Å)$_{40}$ superlattices have the same

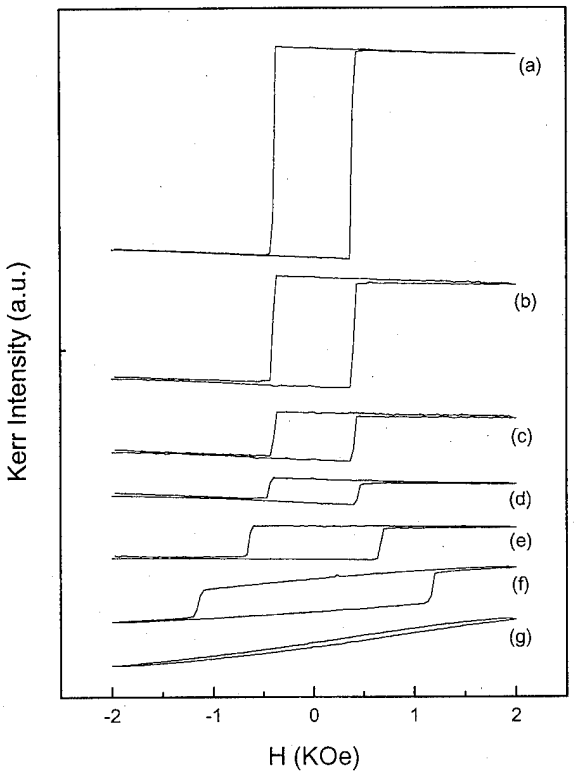



FIG. 2. MOKE hysteresis loops of ($Co_{15}$ Å/$Cr_{10}$ Å)$_{40}$ superlattices on MgO(110) with $\phi$=(a) 0°, (b) 15°, (c) 30°, (d) 45°, (e) 60°, (f) 75°, and (g) 90°.

crystal structure and orientation as ($Co_{40}$ Å/$Cr_{15}$ Å)$_{20}$. Hcp-Co($1\bar{1}00$)/bcc-Cr(211) are the crystal structures and orientations of Co/Cr superlattices grown on MgO(110). Co/Cr superlattices grown on Si were polycrystalline, according to the circle-like RHEED picture shown in Fig. 1(b). Samples grown on quartz were amorphous, with a blur picture with no specific pattern in RHEED (not shown). The strong anisotropic behavior of Co($1\bar{1}00$)/Cr(211) superlattices grown on MgO(110) is shown in Fig. 2. A series of longitudinal MOKE hysteresis loops of the Co/Cr superlattices grown on MgO(110) showed that not only in the shape, but also the

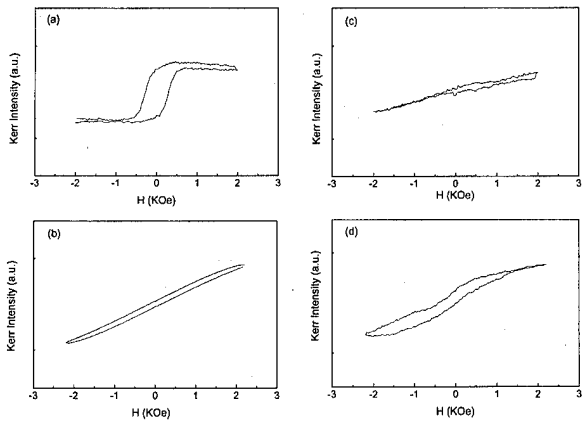



FIG. 3. (a) LMOKE, (b) PMOKE hysteresis loops of ($Co_{15}$ Å/$Cr_{10}$ Å)$_{40}$ superlattices on quartz, (c) LMOKE, (d) PMOKE hysteresis loops of ($Co_{15}$ Å/$Cr_{10}$ Å)$_{40}$ superlattices on Si(111).

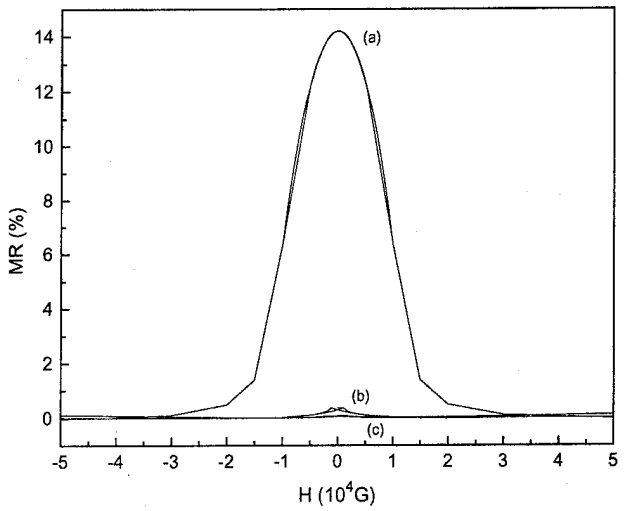



FIG. 4. MRs of $(Co_{15}\ Å/Cr_{10}\ Å)_{40}$ superlattices on (a) MgO(110), (b) quartz, and (c) Si(111).

coercive field of the magnetization hysteresis loop changed with angle $\phi$ from easy axis ($\phi$=0°) to hard axis ($\phi$=90°). The azimuthal angle $\phi$ is the angle between the in-plane crystal axis Co[0001] and the applied magnetic field. The tilt of the baseline slope comes from the background signal. The nonangle-dependent magnetization behavior of Co/Cr superlattices grown on Si and quartz is shown in Fig. 3. From the longitudinal and polar MOKE hysteresis loops in Fig. 3(a) and 3(b), Co/Cr superlattices grown on quartz show an in-plane ferromagnetic magnetization, instead of an out-of-plane magnetization. The Co/Cr superlattices grown on Si show no in-plane magnetization, see Fig. 3(c) (LMOKE), but an out-of-plane magnetization, as shown in Fig. 3(d) (PMOKE). Co/Cr superlattices grown on MgO(110) show strong anisotropic behavior not only in magnetization but also in MR measurements with transverse MR of 14.2%, as shown in Fig. 4(a), and the longitudinal MR of 0.67% at 10 K. This anomalous anisotropic MR has also been reported in epitaxial growth of Co/Cr bilayer films on MgO(110).[12] The crystal anisotropy of the Co layers and the spin flip of the Cr layers may be responsible for those results. Amorphous Co/Cr superlattices grown on quartz with in-plane isotropic magnetization showed a small MR of 0.37%, as shown in Fig. 4(b). Polycrystalline Co/Cr superlattices grown on Si with perpendicular magnetization also showed a small MR of 0.13%. These small MRs for Co/Cr superlattices are similar to those reported previously.[4–6]

## IV. CONCLUSION

We have demonstrated the influence of different crystal structure and orientation on the magnetic properties of $(Co_{15}\ Å/Cr_{10}\ Å)_{40}$ superlattices. Co/Cr superlattices grown on quartz were amorphous with isotropic magnetization and small MR(0.37%). Co/Cr superlattices grown on Si were polycrystalline with perpendicular magnetization and also small MR(0.13%). Anisotropic magnetization and MR were observed on epitaxial Co/Cr superlattices grown on MgO(110). Large transverse MR (14.2%) of Co($1\bar{1}00$)/Cr(211) superlattices may result from the crystal anisotropy of the Co layers and the spin flip of the Cr layers.

## ACKNOWLEDGMENT

We are grateful for the financial support by the National Science Council of the Republic of China under Grant Nos. NSC 85-2112-M-001-019 (Liou), 85-2112-M-006-018 (Huang), and 85-2112-M-001-042 (Yao).

[1] M. N. Baibich, J. M. Broto, A. Fert, F. Nguyen Van Dau, F. Petroff, P. Eitenne, G. Creuzet, A. Friederich, and J. Chazelas, Phys. Rev. Lett. **61**, 2472 (1988).
[2] G. Binasch, P. Grunberg, F. Saurenbach, and W. Zinn, Phys. Rev. B **39**, 4828 (1989).
[3] S. S. Parkin, N. More, and K. P. Roche, Phys. Rev. Lett. **64**, 2304 (1990).
[4] M. B. Stearns, Y. Cheng, and C. H. Lee, J. Appl. Phys. **67**, 5925 (1990).
[5] W. Vavra, D. Barlett, S. Elagoz, C. Uher, and R. Clarke, Phys. Rev. B **47**, 5500 (1993).
[6] S. S. P. Parkin, R. F. Marks, R. F. C. Farrow, G. R. Harp, Q. H. Lam, and R. J. Savoy, Phys. Rev. B **46**, 9262 (1992).
[7] J. Smit, Physica **16**, 612 (1951).
[8] J. C. A. Huang, Y. Liou, H. L. Liu, and Y. J. Wu, J. Crys. Growth **139**, 363 (1994).
[9] Y. Liou, J. C. A. Huang, Y. D. Yao, C. H. Lee, K. T. Wu, Y. Y. Chen, N. T. Liang, C. L. Lu, S. Y. Liao, W. T. Yang, C. Y. Chen, and B. C. Hu, J. Appl. Phys. **76**, 6516 (1994).
[10] Y. D. Yao, Y. Liou, J. C. A. Huang, S. Y. Liao, C. H. Lee, K. T. Wu, Y. Y. Chen, C. L. Lu, and W. T. Yang, Chinese J. Phys. **32**, 863 (1994).
[11] Y. Liou, J. C. A. Huang, Y. D. Yao, S. F. Lee, W. T. Yang, S. Y. Liao, and C. P. Chang, IEEE Trans. Magn. (to be published).
[12] Y. D. Yao, Y. Liou, J. C. A. Huang, S. Y. Liao, I. Klik, W. T. Yang, C. P. Chang, and C. K. Lo (unpublished).

# Magnetoresistance in NiFe/Au multilayers and spin-valve structures (abstract)

K. T. Wu and R. J. Gambino
*Department of Materials Science and Engineering, State University of New York at Stony Brook, Stony Brook, New York 11794*

Permalloy has been widely studied and used in industry for magnetic recording heads and sensors. This article presents a study of the magnetoresistance of $(NiFe/Au)_n$ multilayer films and NiFe/Au/NiFe sandwich structures. Gold is used as the spacer layer because of its low solid solubility in NiFe and the tendency of NiFe and Au to phase separate. Films were grown by dc sputtering with a series of different permalloy and Au thickness. In the multilayer films, the thickness of permalloy varies from 20 to 40 Å and Au varies from 8 to 25 Å. A difference in the sign and magnitude of magnetoresistance for transverse and longitudinal field directions with respect to current indicates the presence of anisotropic magnetoresistance (AMR) effect. The magnitude of $\Delta\rho/\rho$ is small because of shunting by Au layers. In the sandwich structures, the thickness of permalloy layers is different on each side of the Au and varies from 150 to 800 Å. The Au spacer layer varies from 20 to 60 Å. The measurements show mainly anisotropic magnetoresistance. There was a small opposite jump at ~8 Oe on resistivity measurement, which indicates spin valve effect superimposed on the AMR effect. After annealing, the change in magnetoresistance is much more sensitive in low field ~15 Oe, a property which is critical to many applications. © *1996 American Institute of Physics.* [S0021-8979(96)81108-1]

 0021-8979/96/79(8)/6285/1/$10.00 © 1996 American Institute of Physics 

# Temperature dependence of the pinning field and coercivity of NiFe layers coupled with an antiferromagnetic FeMn layer

H. Fujiwara
*Center for Mater. for Information Technology, University of Alabama, Tuscaloosa, Alabama 35487-0209*

K. Nishioka
*Data Storage and Retrieval Systems Division, Hitachi, Ltd., Kozu, Odawara 256, Japan*

C. Hou, M. R. Parker, S. Gangopadhyay, and R. Metzger
*Center for Mater. for Information Technology, University of Alabama, Tuscaloosa, Alabama 35487-0209*

The pinning field $H_p$ (the amount of the shift of the hysteresis loops) and the coercivity $H_c$ of the samples of the form glass/Ta 120 A/(Cu 100 A)/NiFe 75 A/FeMn 150 A/Ta 50 A increase almost linearly with decreasing temperature down to 20 K, below which $H_c$ increases sharply. The observed strong positive correlation between $H_p$ and $H_c$, seems to be reasonably explained by a combination of a newly developed model in which a directional distribution of the pinning field caused by a random distribution of the crystalline orientations in the antiferromagnetic FeMn layer is taken into account and Hoffmann's ripple theory in which the local anisotropy is assumed to be proportional to $H_p$, although the sharp increase in $H_c$ at very low temperatures remains to be explained. © *1996 American Institute of Physics.* [S0021-8979(96)24608-7]

## I. INTRODUCTION

The "spin valve" is now attracting world wide interest because of its high potential to be applied in the most advanced type of magnetic sensors such as read heads for high density magnetic recording. In a spin valve structure in which an antiferromagnetic (AF) layer is employed for pinning the magnetization of one of the two ferromagnetic (F) layers, which lies facing the other F layer via a nonmagnetic metal layer, it is often observed that the pinned F layer exhibits a substantially higher coercivity than its intrinsic coercivity. Although there have been quite a few investigations about the interaction between ferromagnet and antiferromagnet since the late 1950s,[1–6] it still does not seem to be fully understood. Fulcomer and Charap[2] proposed a model to explain the temperature and frequency dependence of the hysteresis loop displacement, the amount of which is to be called a pinning field $H_p$ hereafter, and the coercivity $H_c$. In their model, the switching of the spins in the AF layer which is composed of tiny particles is thought to be responsible for the enhancement of $H_c$. According to this model, the pinning field increases with decreasing temperature, but the coercivity is expected to have a maximum at some temperature and then decreases. This model explained some of the experimental results, e.g., the one on a Co-CoO system,[7] fairly well. Schlenker *et al.*,[3] on the other hand, showed that in a NiFe/FeMn system both $H_p$ and $H_c$ increased monotonically with the decrease of temperature down to 10 K. However, they attributed the enhancement of the coercivity of the NiFe (F) layer in the system to an irreversible rotation of the moments of some parts of the FeMn (AF) layer.

In the course of our investigation on the NiFe/Cu/NiFe/FeMn-type spin valves, the temperature dependence of the pinning field $H_p$ and the coercivity $H_c$ of the NiFe (F) layer coupled with FeMn (AF) layer were examined. The results showed, as was shown by Schlenker *et al.*,[3] that $H_p$ and $H_c$ increased monotonically and almost linearly with decreasing temperature down to 20 K (below which $H_c$ increased drastically), showing a fairly good proportionality between them. It was also observed that $H_p$ and $H_c$ were both enhanced by heating up to 100 °C. These results suggest that there exists some mechanism which gives rise to a strong positive correlation between $H_p$ and $H_c$. This article presents those experimental results and proposes a mechanism to explain this phenomenon, taking into account a ripple structure generated in the F layer through a distribution of the pinning field direction[5,8] which may be attributed to an expected random distribution of the crystalline axes in the AF layer.

## II. EXPERIMENTAL PROCEDURE

The samples were prepared by sputtering on a glass (Corning No. 7059) substrate in a uniform dc field in the form of glass/Ta 120 A/(Cu 100 A)/NiFe 75 A/FeMn 150 A/Ta 50 A [sample-1 (without Cu) and sample-2 (with Cu)]. The sputtering was performed in one continuous process without breaking the vacuum.[9] The crystalline textures were examined by x-ray diffractometry using Cu $K\alpha$ x ray. The hysteresis curves were obtained by means of a vibrating sample magnetometer (VSM) and a SQUID.

## III. EXPERIMENTAL RESULTS

Figure 1 shows the x-ray diffraction patterns obtained for sample-1 and sample-2, respectively. It is seen that sample-1 has a little better perpendicular texturing of [111] direction of the NiFe and/or FeMn layers than sample-2, suggesting that a higher pinning field may be obtained for the former than for the latter.[10]

Figure 2 shows an example of the hysteresis loops obtained for sample-1 at room temperature. $H_p$ and $H_c$ were measured as the shift of the center of the hysteresis loop and a half of the loop width as shown in the figure, respectively.

It was observed by VSM that both $H_p$ and $H_c$ of sample-1 changed almost linearly as a function of temperature, both seeming to become zero at the same temperature which is to be regarded as the blocking temperature $T_B$. In

 0021-8979/96/79(8)/6286/3/$10.00 © 1996 American Institute of Physics

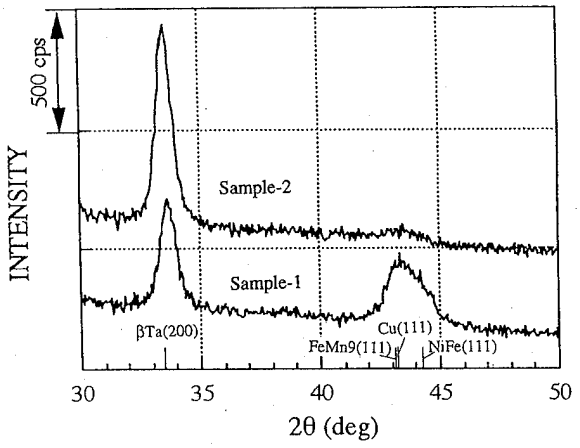



FIG. 1. X-ray diffraction patterns for sample-1 (without Cu) and sample-2 (with Cu) using Cu $K\alpha$.

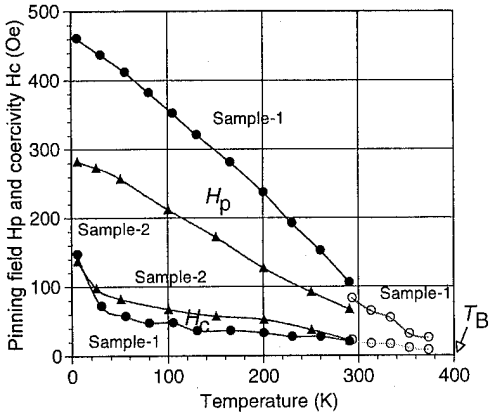



FIG. 3. Temperature dependence of $H_p$ and $H_c$ of sample-1 (circles) and sample-2 (triangles). Solid symbols refer to the data obtained by SQUID. The open circles are the data obtained by VSM for sample-1 by heating from room temperature up to 100 °C (373 K).

order to see to what extent this tendency holds, low-temperature measurement was performed by using a SQUID for both sample-1 and sample-2. Figure 3 shows the results. Solid circles are for sample-1 and triangles, for sample-2. Here, the data obtained for sample-1 which was heated from room temperature up to 373 K are also plotted by open circles. It is seen that both $H_p$ and $H_c$ change almost linearly down to 20 K for both kinds of samples and that below that temperature $H_c$ increases rapidly while $H_p$ is kept almost on the same straight line as at higher temperatures. In Fig. 4, $H_c$'s are plotted as a function of $H_p$.

## IV. DISCUSSION AND CONCLUSION

According to Fulcomer and Charap's model in which the irreversible switching of spins in the AF layer plays a decisive role in enhancing the $H_c$ of the $F$ layer, the $H_c$ should become maximum somewhere around the blocking temperature. Therefore, in order to explain the present results as shown above, some new model seems to be necessary. We have recently proposed a model in which a distribution of the pinning field direction originating from the random distribution of the crystalline orientation of the AF layer is taken into consideration.[11] The model employs an assumption of a checker-board (with a side length $L$) type distribution of the pinning field orientation making angles of plus (+) and minus (−) $\phi_0$ with the average pinning field direction which gives rise to a kind of magnetization ripple structure in the F layer. This assumption is in line with Speriosu *et al.*'s concept of pinning field dispersion[5,7] which was proposed for samples similar to the present ones. According to the model, a substantial enhancement of $H_c$ can be explained by assuming a proper length $L$ and angle $\phi_0$ if some switching mechanism of the magnetizations at the center of the ripple walls (the switching of a kind of Néel wall's polarity) is taken into account. In Fig. 5, the maximum $H_c$ which is attainable through the above mechanism is plotted as a function of the local pinning field $H_{p0}$ in each checker block taking $L$ as a parameter. According to this model, the observable pinning field is expressed as

$$H_p = H_{p0} \cos \phi_0 .$$

Although $H_c$ is not proportional to $H_{p0}$ for each $L$ value, because there may be a wide distribution of $L$ in the actual

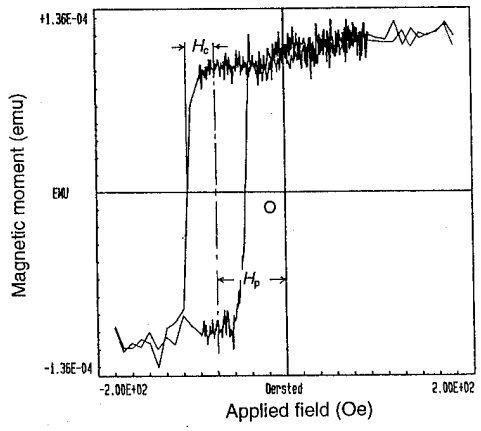



FIG. 2. Hysteresis loop of the as-deposited sample-1 measured at the room temperature by VSM. $H_p$ and $H_c$ were measured as shown in the figure.

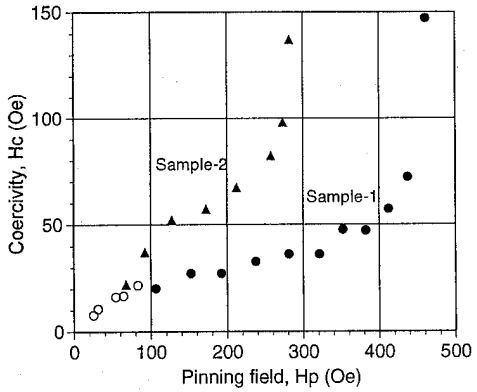



FIG. 4. Coercivity $H_c$ vs pinning field $H_p$ plotted for both sample-1 and sample-2 the data of which are shown in Fig. 3.

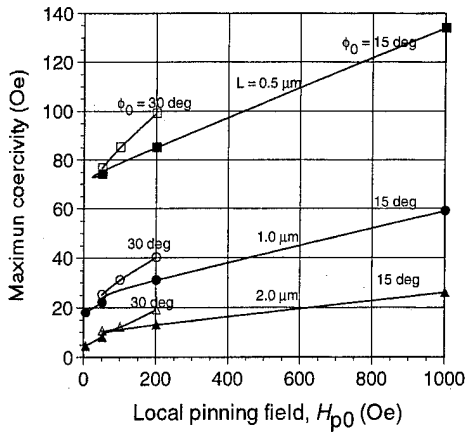



FIG. 5. Calculated maximum coercivity as a function of the local pinning field $H_{p0}$ according to a model proposed recently in which checkerboardlike local distribution of the pinning field direction is taken into consideration (see Ref. 11). $L$ denotes the length of a square of the checker board and $\phi_0$ the deflection angle of the local pinning field direction from their mean direction.

samples, the effective $L$ may decrease with increasing $H_{p0}$ giving rise to a faster increase in the maximum $H_c$ than when $L$ is fixed at a single value. As for the mechanism of the switching of the ripple wall polarity, a direct switching mechanism in which Bloch line creation in the wall takes place has been confirmed unfeasible.[11] Therefore, some macroscopic collective magnetization reversal processes, such as a macroscopic domain wall motion or incoherent rotation should be taken into account. Then, the mechanism explained above will act as a magnetization sustaining one when a reverse field is applied until the average magnetization is switched into the reverse direction. About the $H_c$ of the domain wall motion in the films with a ripple structure, Hoffmann[12] showed that $H_c$ should be proportional to the local anisotropy. This theory will also apply to the incoherent rotation mechanism, although the proof may not be straight forward. In our case, the local anisotropy field in the ripple theory is thought to be proportional to $H_{p0} \sin \phi_0$, which directly leads to the explanation of the observed strong correlation between $H_c$ and $H_p$. The higher coercivity for sample-2 than for sample-1 for the same $H_p$ as is seen in Fig. 4 will be attributed to higher pinning field orientation angle $\phi_0$ for the former than for the latter. The steep increase of $H_c$ observed at very low temperatures, however, is still left to be solved.

## ACKNOWLEDGMENTS

The authors are greatly indebted to Dr. Ping Wong who kindly spared precious time for leading and helping the SQUID measurement of the hysteresis loops. The authors would also like to thank Dr. Kent Howard who kindly offered many published papers concerning the present issue of this article. Thanks are also due to Dr. W. D. Doyle, Dr. J. W. Harrell, and Dr. M. Kief for valuable discussion.

[1] F. B. Hagedorn, J. Appl. Phys. **38**, 3641 (1967).
[2] E. Fulcomer and S. H. Charap, **43**, 4190 (1972).
[3] S. Schlenker, S. S. P. Parkin, J. C. Scott, and K. Howard, J. Magn. Magn. Mater. **54–57**, 801 (1986).
[4] A. P. Malozemoff, J. Appl. Phys. **63**, 3874 (1988).
[5] V. S. Speriosu, D. A. Herman, Jr., I. L. Sanders, and T. Yogi, IBM J. **34**, 884 (1990).
[6] C. Tsang and K. Lee, J. Appl. Phys. **53**, 2605 (1982).
[7] C. Schlenker, Phys. Status Solidi **28**, 507 (1968).
[8] V. S. Speriosu, S. S. P. Parkin, and C. H. Wilts, IEEE Trans. Magn. **23**, 2999 (1987).
[9] K. Nishioka, S. Gangopadyay, H. Fujiwara, and M. R. Parker, IEEE Trans. Magn. (to be published).
[10] K. T.-Y. Kung and L. K. Louie, J. Appl. Phys. **69**, 5634 (1991).
[11] H. Fujiwara, M. R. Parker, K. Nishioka, C. Hou, and S. Gangopadyay, presented at 2nd International Symposium on Metalic Multilayers at Cambridge (1995).
[12] H. Hoffmann, IEEE Trans. Magn. **9**, 17 (1973).

# Magnetic and magnetotransport properties of Ni/Fe multilayers

M. Cai, T. Veres, R. Morel, and R. W. Cochrane
*Département de Physique, Université de Montréal, Montréal, Québec, H3C 3J7, Canada*

We present a study of sputtered Ni/Fe multilayers in order to examine the effect of interfacial mixing and interdiffusion on the magnetic and transport properties. The multilayer structure has been examined by low-angle x-ray reflectivity, which reveals interface mixing of about two monolayers. The magnetization measurements show differences in the anisotropy of multilayers for which the thickness ratio of nickel to iron is changed from 1:1 to 3:1. With the 1:1 composition, multilayers show high permeability with a longitudinal easy axis, while samples with 3:1 composition show lower permeability and a rotated easy axis. By fitting the resistivity and magnetoresistance thickness variation with a semiclassical model, we have determined an interface contribution to the resistivity and a possible contribution to the magnetoresistance. © *1996 American Institute of Physics.* [S0021-8979(96)24708-3]

## I. INTRODUCTION

Since the discovery of new transport and magnetic properties in magnetic/nonmagnetic multilayers, the study of modulated metallic nanostructures has become a very active field of research. On one hand, this interest is driven by the need to design materials with magnetic, magneto-optic and magnetotransport properties suited for high density magnetic recording. On the other hand, these artificially structured materials are also proving to be important for understanding the fundamental physics of interacting magnetic thin films. In multilayers where the individual layers are only a few atomic planes thick, one aspect which needs to be addressed is the nature and the role of the interfaces in the structural, magnetic, and electronic properties of the ensemble. In addition, the structure and properties of individual layers within the multilayers are often different from those of bulk materials, which in turn leads to multilayer properties distinct from those of bulk alloys of the same constituents.

Recently, it has been found that in Ni/Co multilayers this combination of factors produces a relatively large anisotropic magnetoresistance with low saturation fields.[1] Moreover, recent results show oscillations of the magnetoresistance with cobalt and nickel thicknesses, probably due to a superlattice effect.[2] In the case of Ni/Fe multilayers, previous studies have found that for thicknesses below ~20 Å the iron is in an fcc phase,[3] and theoretical calculations predict that this phase may be antiferromagnetic.[4] In the same thickness range, Mössbauer spectroscopy on vacuum deposited Ni/Fe multilayers points to a ferromagnetic fcc iron phase, with an out-of-plane anisotropy.[5] As NiFe alloys are technologically very important due to their magnetoresistive and soft magnetic properties, it is of interest to look at how the magnetic and magnetoresistive properties are influenced by the layering of nickel and iron in a modulated structure.

## II. EXPERIMENTAL DETAILS

We present magnetic and magnetoresistance measurements on $(Ni_xFe_y)_n$ multilayers ($x$ and $y$ are the film thicknesses in Å) deposited by rf magnetron sputtering[6] onto glass (Corning 7059) substrates mounted onto a water-cooled support. With a sputtering pressure of 3 mTorr of argon gas (99.999%) and an rf power of 200 W, the deposition rates were 1.2 Å/s for Fe and 2.1 Å/s for Ni and, hence, the residence time of the substrate above the targets was used to control the layer thickness in the range from 12 to 110 Å. The number of periods was chosen so that the total thickness was kept constant at ~1200 Å. Since two films were deposited simultaneously, the first layer is alternatively iron or nickel. A mask over the substrate in the form of strips, 16 mm long and 4 mm wide with sidearms for electrical contacts defined the sample shape. Finally, pure nickel and iron layers of approximately the same thicknesses were deposited for comparison.

Nominal thicknesses were confirmed by DEKTAK and low-angle x-ray-reflectivity measurements. Coercive fields and remanences were measured at room temperature using a vibrating sample magnetometer. However, due to the large nonsymmetric area of the samples, it was not possible to obtain an absolute measurement of the magnetization. Transport properties under magnetic field were also measured at room temperature, using a high-resolution ac bridge. In order to account for the history-dependent zero-field resistivity, the total anisotropic magnetoresistance (AMR) was measured as the difference in resistivity when the sample is rotated in a saturating field.

## III. RESULTS AND DISCUSSION

Figure 1 shows low-angle x-ray reflectivity spectra of a $(Ni_{60}Fe_{30})_{11}$ multilayer. The spectra exhibit well-developed Bragg superlattice peaks up to the fifth order (not shown), indicating a sharply defined composition modulation in the film growth direction. Note that, in the figure, the third-order peak is suppressed, as expected for a 2:1 ratio of Ni and Fe. Also, finite size oscillations appears between the Bragg peaks due to the eleven bilayers present in the multilayer, suggesting the smooth nature of the films. In addition, high-angle x-ray data reveal a high degree of fcc (111) and bcc (110) texture.

To estimate the interfacial mixing width, the experimental data are fitted using a standard optical model,[6,7] in which the x-ray reflectivity is calculated using a matrix method. In order to include interfacial mixing, a linear composition profile is assumed at the interface. In addition, the global interface roughness and layer thickness fluctuations are included

 0021-8979/96/79(8)/6289/3/$10.00 © 1996 American Institute of Physics 

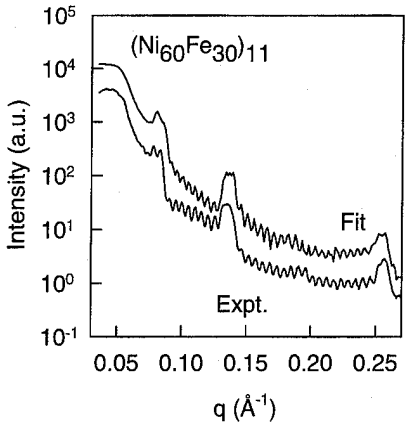



FIG. 1. Low-angle x-ray reflectivity spectra for (Ni 60 Å/Fe 30 Å)$_{11}$. The lower curve is experimental while the upper curve, shifted for clarity, is the fit described in the text.

to simulate a real situation. Further details of the fitting procedure have been described elsewhere.[6] The resulting fitted curve is also presented in Fig. 1 and is clearly in good agreement with the experimental data. An interfacial width of 5 Å is obtained from this fitting, setting an upper limit on the interdiffusion in our samples.

Figure 2 shows magnetization curves for multilayers from two series, measured in longitudinal (along the long axis of the sample) applied field, where the magnetization values are normalized relative to the magnetization of a pure iron layer of equal thickness. On this relative scale, the nickel film gives a saturation magnetization of 0.25 which is slightly less than the ratio of the bulk values for Ni and Fe. Unfortunately, since the absolute values are unknown, it is not possible to determine from these measurements how the Ni and Fe magnetizations depart from their bulk values. Nevertheless, the magnetization of all the multilayers can be fully accounted for using an identical ratio of 0.25 between the magnetizations of the individual Ni and Fe layers. This ratio seems to preclude the possibility of an antiferromagnetic iron phase[4] in our films, even in multilayers with Fe thicknesses below 20 Å.

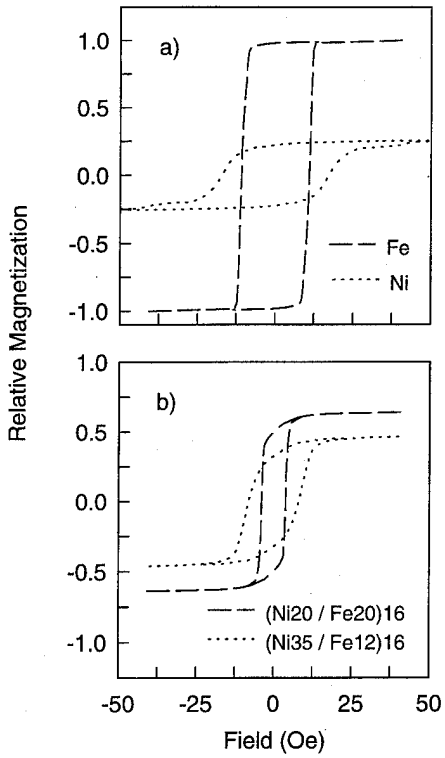



FIG. 2. Magnetization of (a) pure nickel and iron thin films and (b) (Ni 20 Å/Fe 20 Å)$_{16}$ and (Ni 35 Å/Fe 12 Å)$_{16}$ multilayers. In all cases, the applied field is in the longitudinal direction and the magnetizations are normalized relative to that of an iron film of equal thickness.

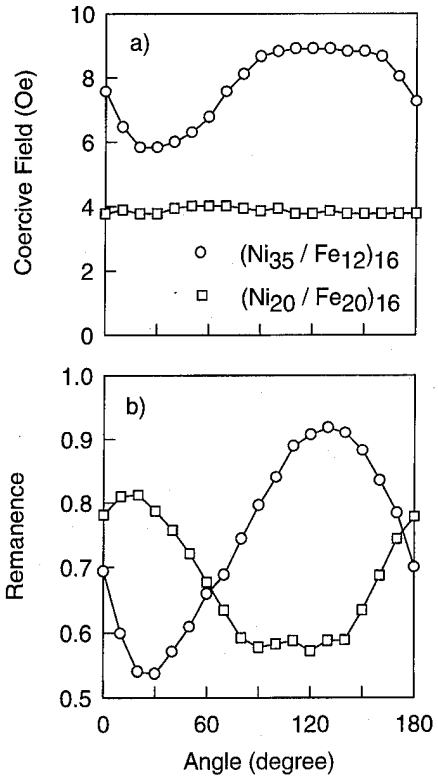



FIG. 3. Coercive field (a) and remanence (b) of (Ni 20 Å/Fe 20 Å)$_{16}$ and (Ni 35 Å/Fe 12 Å)$_{16}$ multilayers as a function of the angle between the applied field and the longitudinal direction of the multilayer strips.

The shape of the magnetization curves of Fig. 2 are reminiscent of those of the pure sputtered films in that the multilayers with greater Ni thicknesses ($x=3y$) have higher coercive fields $H_c$ and reduced remanence $M_r$ than samples with equal Ni and Fe thicknesses ($x=y$). On the other hand, all multilayers show a smaller coercivity and remanence than the elemental films.

In Fig. 3 are presented the angular dependences of $H_c$ and $M_r$ for the multilayers of the previous figure. These curves, representative of all the multilayers within the same series, show that with equal thicknesses of Ni and Fe, the coercive field is almost constant and the remanence is higher when the saturating field is longitudinal, indicating an easy axis in that direction. However, in multilayers where $x=3y$, both $H_c$ and $M_r$ show the presence of an easy axis at some direction varying between 120° and 150° to the sample axis. Since the magnetic field at the substrate position during deposition is only about 1 Oe, this anisotropy is not believed

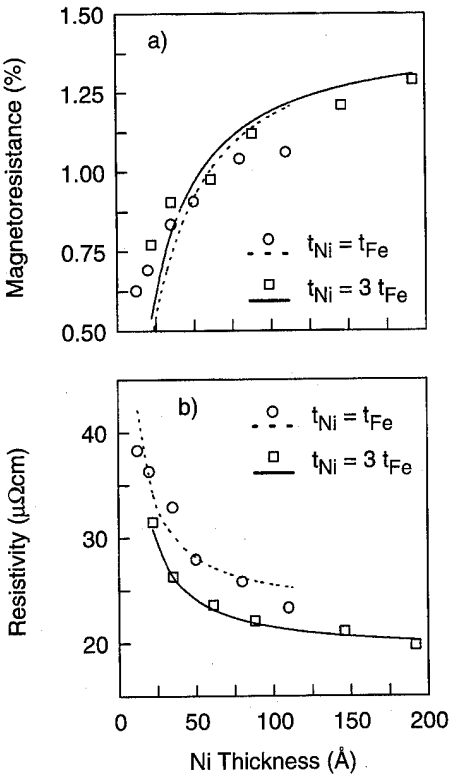



FIG. 4. (a) Anisotropic magnetoresistance (AMR) and (b) resistivity for Ni/Fe multilayers as a function of the nickel layer thickness. The lines have been calculated using the models and parameters described in text.

to be field induced; its precise origin is currently under investigation.

The resistivity and magnetoresistance (AMR) are presented in Fig. 4. The resistance is found to increase and the AMR to decrease as the Ni layer thickness decreases. In single-layer thin films, this behavior is expected when the thickness of the layer becomes of the order of the mean-free path. In multilayers, the thickness variation of the resistivity also depends on the effect of the interface on the conduction electron scattering. To assess this contribution, the results were fitted with a semiclassical model, derived from Carcia and Suna,[8] in which each layer is characterized by its mean-free path $\lambda$ while the interfaces are represented by an angle-dependent transmission coefficient $T$ (details of the model will be presented elsewhere).[9] The fitted resistivity presented in Fig. 4 are obtained with $\lambda_{Ni}=37.5$ Å, $\lambda_{Fe}=15$ Å, and $T=0.8$; these mean-free paths correspond to bulk resistivities of 16 $\mu\Omega$ cm for nickel and 40 $\mu\Omega$ cm for iron, values very close to those measured for the pure films. Moreover, the fit is quite sensitive to the choice of the transmission parameter, which is indicative of the importance of the interface contribution to the resistivity.

In order to calculate the AMR we introduce an asymmetric mean-free path in the form $\lambda=\lambda_0(1+a\cos^2\theta)$, with $a$ the asymmetry parameter and $\theta$ the angle between the electron velocity and the magnetization.[10] Because the bulk magnetoresistance of iron is ten times smaller than that of nickel, we assume that the anisotropy comes solely from the nickel layers. Also, no attempt was made to account for an interface contribution. As can be seen, the fit for AMR obtained with $a=0.05$ in the series with equal thicknesses and $a=0.04$ in the series with $t_{Ni}=3t_{Fe}$ is not as good as that for the resistivity. This observation points to a possible contribution from the interface which could be included in the calculation, for instance by considering for $T$ a dependence on the angle between the electron velocity and the direction of the magnetization.

## IV. CONCLUSION

Low-angle x-ray reflectivity indicates that the sputtered Ni/Fe multilayers have good structural properties, with low roughness and an interface mixing of approximately 2 ML. The magnetization is well described by a simple average of the magnetizations of pure nickel and iron thin films; the remanence and coercivity are reduced from those of the bulk materials, due possibly to the finite width of the interface region. The high permeability of these multilayers leads to an enhanced sensitivity of the magnetoresistance to small field changes (0.1%/Oe), comparable to that found in high sensitivity Ni/Co multilayers.[2] Furthermore, the analysis of the thickness dependence of the resistivity and AMR, based upon a semiclassical model, reveals that the increase in resistivity at low thicknesses and the variation in magnetoresistance cannot be explained without an interface contribution.


[1] J. M. Gallego, D. Lederman, T. J. Moran, and I. K. Schuller, Appl. Phys. Lett. **64**, 2590 (1994); J. M. Freitag, X. Bian, Z. Altounian, J. O. Ström-Olsen, and R. W. Cochrane, MRS Spring Meeting Proceedings, 1995.
[2] J. M. Gallego, D. Lederman, S. Kim, and I. K. Schuller, Phys. Rev. Lett. **74**, 4515 (1995).
[3] N. M. Jennett and D. J. Dingley, J. Magn. Magn. Mater. **93**, 472 (1991); R. Krishnan, H. O. Gupta, H. Lassri, C. Sella, and M. Kaabouchi, J. Appl. Phys. **70**, 6421 (1991).
[4] M. B. Taylor and B. L. Gyorffy, J. Phys. Condens. Matter **3**, 4971 (1991).
[5] E. Colombo, O. Donzelli, G. B. Fratucello, and F. Ronconi, J. Magn. Magn. Mater. **104-107**, 1857 (1992).
[6] Y. Huai, R. W. Cochrane, and M. Sutton, Phys. Rev. B **48**, 2568 (1993).
[7] M. Born and E. Wolf, *Principles of Optics* (Pergamon, Oxford, 1964)
[8] P. F. Carcia and A. Suna, J. Appl. Phys. **54**, 2000 (1983); R. Q. Hood and L. M. Falicov, Phys. Rev. B **46**, 8287 (1992).
[9] T. Veres, M. Cai, R. Morel, and R. W. Cochrane (unpublished).
[10] T. G. S. M. Rijks, R. Coehoorn, M. J. M. de Jong, and W. J. M. de Jonge, Phys. Rev. B **51**, 283 (1995).

# Studies of Fe/Cr multilayer and trilayer films

E. M. Ho, A. C. Daykin, and A. K. Petford-Long
*Department of Materials, University of Oxford, Parks Road, Oxford, OX1 3PH, United Kingdom*

Series of sputter-deposited $Fe_{3\ nm}/Cr_x$ multilayer and Fe/Cr/Fe trilayer films have been analyzed. The small magnetoresistance exhibited by the multilayer films is attributed to very rough interfaces and poor Cr layer quality. The hysteresis loop data show the interlayer exchange coupling to be predominantly antiferromagnetic. *In situ* magnetizing of the trilayer films in a Lorentz TEM showed that for a 1.2 nm thick Cr layer the moments of the Fe layers lie approximately parallel at remanence rotating to antiparallel only when the field is increased. The magnetic moments in an $Fe_{12\ nm}/Cr_{0.6\ nm}/Fe_{12\ nm}$ trilayer film were found to be parallel aligned under an applied field whereas the hysteresis loop for the multilayer films with the same Cr thickness suggest the existence of antiferromagnetic interlayer exchange coupling. © *1996 American Institute of Physics.* [S0021-8979(96)24808-0]

## I. INTRODUCTION

Factors affecting the giant magnetoresistance (GMR) effect in multilayer films (MLFs)[1] have been studied by many groups, both experimentally[2–4] and theoretically.[5–8] It has been established that the GMR oscillates as a function of spacer layer thickness,[9] because the interlayer exchange coupling oscillates with thickness from ferromagnetic (FM) to antiferromagnetic (AFM). For small changes in the spacer layer thickness the interlayer exchange coupling can vary substantially, and as a result interface roughness and microstructure play an important role in determining GMR.

In this work, series of polycrystalline Fe/Cr MLFs and trilayers with a range of Cr layer thicknesses were grown by sputter deposition, and the correlation between the interlayer exchange coupling, magnetoresistance (MR), and microstructure was studied.

## II. EXPERIMENTAL TECHNIQUES

The Fe/Cr layered films were deposited on native-oxide-coated Si(100) wafers using dc (for Fe) and rf (for Cr) magnetron sputter deposition. The base pressure was better than $10^{-5}$ mbar and the argon pressure was $3\times10^{-3}$ mbar. MR measurements were made using the four-point probe method and the hysteresis loops were obtained using an alternating gradient force magnetometer (AGFM) at Bangor University.

A modified JEOL 4000EX transmission electron microscope (TEM) was used to study the magnetic domain structures of the trilayer films in applied fields up to 400 Oe. The large camera length mode of Lorentz microscopy[10] was used. This mode allows the central region of the electron diffraction pattern (DP) to be observed at high magnification. For thin films with low magnetization, the Lorentz deflection angle is very small, and cannot be observed by conventional techniques.

The periodicity of the MLFs was studied by low-angle x-ray reflectometry (XRR), and the interface morphology and crystallographic structure of the film by high-resolution electron microscopy (HREM).

## III. RESULTS AND DISCUSSION

Figure 1 shows MR curves for three $Fe_{3.0\ nm}/Cr_{x\ nm}$, ($0.5<x<1.0$) MLFs measured with the current in-plane and parallel to the applied field. Both the MR and the saturation field $H_s$ increase with decreasing Cr thickness, due to a change in the coupling strength. The magnitude of the MR varies from 0.4% to 1.6%, which is much lower than expected. The hysteresis loops in Fig. 2 for the same films, however, show the presence of a high degree of AFM interlayer exchange coupling, with the characteristic tilting of the curve indicating magnetization rotation rather than domain wall motion. At remanence some of the magnetic moments from the adjacent Fe layers are aligned approximately parallel. They may be pinned in this orientation by microstructural features.

The width of the Bragg peaks visible in the XRR traces (Fig. 3) indicate the presence of some interfacial roughness. For the $(Fe_{3.0\ nm}/Cr_{0.6\ nm})_{55}$ MLF the interference fringes from the top and bottom surfaces of the MLF stack are not visible, suggesting that these surfaces are less well defined than for the other MLFs.

HREM images (Fig. 4) from the $(Fe_{3.0\ nm}/Cr_{0.6\ nm})_{55}$ and $(Fe_{3.0\ nm}/Cr_{0.8\ nm})_{25}$ MLFs confirm both the bilayer spacing and the degree of roughness suggested by the XRR data. In both films the interfaces appear jagged with uneven Cr layer thickness, which is expected to result in nonuniform exchange coupling of the magnetic layers. The MLFs with $x=0.6$ nm show particularly rough interfaces, and the layers

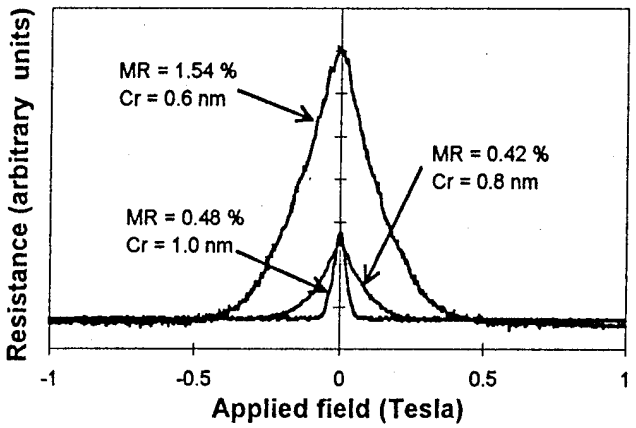



FIG. 1. MR curves for three $Fe_{3.0\ nm}/Cr_{x\ nm}$, ($0.5<x<1.0$) MLFs.

 0021-8979/96/79(8)/6292/3/$10.00 © 1996 American Institute of Physics

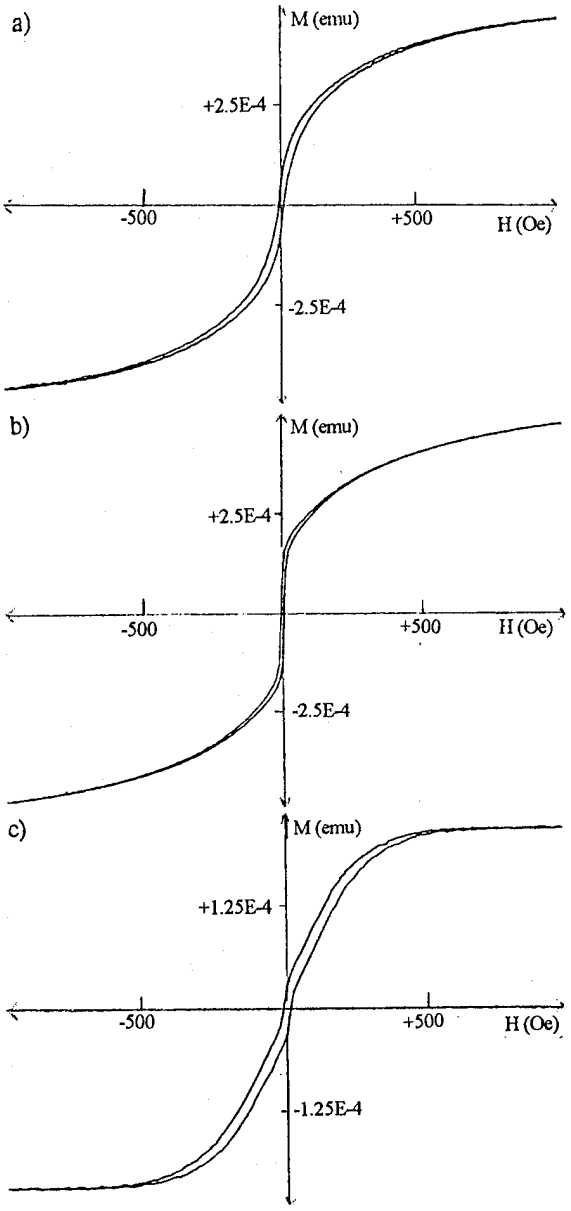



FIG. 2. Hysteresis loops for (a) $(Fe_{3.0\ nm}/Cr_{0.6\ nm})_{55}$ MLFs, (b) $(Fe_{3.0\ nm}/Cr_{0.8\ nm})_{25}$ MLFs, (c) $(Fe_{3.0\ nm}/Cr_{1.0\ nm})_{20}$ MLFs. $H$ is the in-plane applied field and $M$ is the magnetic moments.

appear discontinuous, suggesting that the sputtering conditions used will not allow the growth of continuous Cr layers this thin. In all the MLFs the Cr and Fe layers have a *bcc* structure with strong [100] texture in the growth direction.

The XRR and HREM data suggest that the small MR values obtained may be due to poor layer quality. This will lead to high interfacial scattering which increases the spin independent resistivity of the MLFs. The different layer thicknesses observed suggest that there may be nonuniform coupling throughout the MLF stack.

The trilayer films were chosen for Lorentz microscopy analysis because they contain only two magnetic layers and the domain contrast observed is thus easier to interpret. *In situ* TEM magnetizing experiments were performed on trilayers containing Fe layers of nominal thickness 12 nm

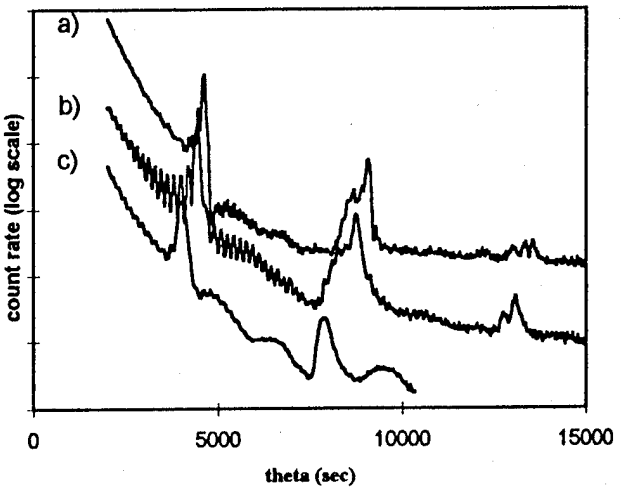



FIG. 3. XRR data for (a) $(Fe_{3.0\ nm}/Cr_{0.6\ nm})_{55}$ MLFs, (b) $(Fe_{3.0\ nm}/Cr_{0.8\ nm})_{25}$, (c) $(Fe_{3.0\ nm}/Cr_{1.0\ nm})_{20}$.

and Cr layers of nominal thickness 1.2 or 0.6 nm. The films were demagnetized *in situ* prior to analysis, and the changes in magnetic structure were monitored around part of the hysteresis cycle starting at remanence. The Lorentz force causes the beam to be deflected if the magnetic moments of the two Fe layers are aligned nearly parallel, whereas the beam is undeflected when the moments of the two Fe layers are aligned antiparallel.

Figure 5 shows an example of an $Fe_{12\ nm}/Cr_{0.6\ nm}/Fe_{12\ nm}$ trilayer which was shown to be FM coupled by *in situ* magnetizing. The magnetic moments in the Fe layers are aligned approximately parallel, and the DP shows a single deflected arc. The presence of an extended arc, as opposed to a sharp spot [Fig. 5(b)] indicates the presence of magnetization ripple, which can be seen in the associated Fresnel mode Lorentz image [Fig. 5(a)]. The saturation field was found to be approximately 55 G. Hysteresis loops from MLFs with a similar Cr layer thickness showed that some AFM interlayer exchange coupling is possible with this thickness of Cr (Fig.

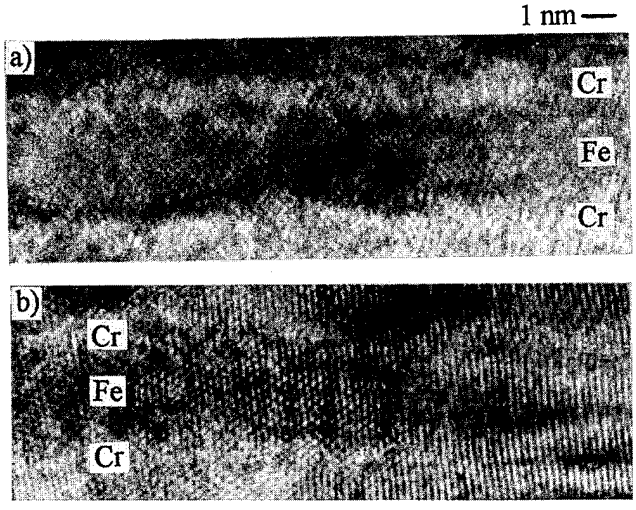



FIG. 4. HREM images of (a) $(Fe_{3.0\ nm}/Cr_{0.8\ nm})_{25}$, (b) $(Fe_{3.0\ nm}/Cr_{0.6\ nm})_{55}$.

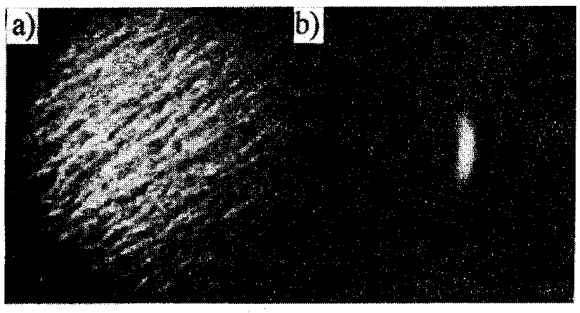



FIG. 5. (a) Fresnel image and (b) DP of an $Fe_{12\ nm}/Cr_{0.6\ nm}/Fe_{12\ nm}$ trilayer film, magnetized at 7.6 G from remanence.

2). The reason why any antiparallel aligned magnetic moments are absent in the trilayers may be that its microstructure affects the interlayer exchange coupling, suggesting the possibility that even with a suitable Cr thickness in a MLF stack some of the magnetic moments can be aligned parallel.

Figure 6 shows a series of DPs and Fresnel Lorentz images of an $Fe_{12\ nm}/Cr_{1.2\ nm}/Fe_{12\ nm}$ film taken during *in situ* magnetizing. At remanence and under a very small applied field most of the magnetic moments are aligned parallel [Fig. 6(a)]. The associated DP shows only a diffuse arc [Fig. 6(b)]. As the applied field increases the magnetic moments begin to align antiparallel, as seen from the changes in the Fresnel image [Fig. 6(c)] and the increase in intensity of the undeflected spot [Fig. 6(d)], until at a field of approximately 72 G

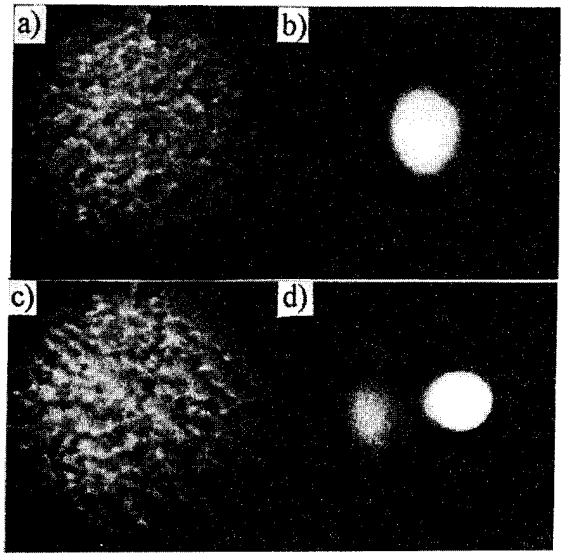



FIG. 6. (a) Fresnel image and (b) DP of an $Fe_{12\ nm}/Cr_{1.2\ nm}/Fe_{12\ nm}$ trilayer film magnetized at 4.2 G. (c) Fresnel image and (d) DP of the same film when magnetized at 23.6 G.

almost all the moments are aligned antiparallel. As the field increases further towards saturation all the magnetic moments align in the direction of the applied field. We believe this to occur because although the coupling is AFM, microstructural features pin the moments in Fe layers in a parallel alignment in zero field. Only on increasing the field slightly is enough energy supplied to allow the moments to relax into an antiparallel state.

XRR data for the two trilayer films shown in Figs. 5 and 6 confirm the nominal layer thicknesses. The FM coupling observed in the $Fe_{12\ nm}/Cr_{0.6\ nm}/Fe_{12\ nm}$ film may be due to the fact that the Cr layer is too thin to be continuous, so that the Fe layers are in direct contact, with no opportunity for their magnetic moments to be aligned antiparallel.

## IV. CONCLUSIONS

The GMR effect was observed in sputtered Fe/Cr MLFs, although the value is considerably lower than expected. This is attributed to poor layer quality and microstructural imperfections as shown by HREM and XRR data. The hysteresis loops show the presence of AFM interlayer exchange coupling in all MLFs, whereas *in situ* magnetizing experiment shows that even for trilayers which have magnetic moments aligned antiparallel under an applied field, the moments are mostly parallel aligned at remanence. In addition even with a suitable Cr layer thickness, the interlayer exchange coupling may not be AFM, as the coupling is affected by the microstructure presence of AFM coupling and low GMR in the MLFs shows the important contribution of microstructure, and further analysis of the trilayer films will be used to assess the relative contributions of interfacial quality and AFM coupling.

## ACKNOWLEDGMENTS

We are grateful to EPSRC, British Gas, and to Royal Society for research support, to Dr. P. Bayle-Guillemaud and to Dr. J. P. Jakubovics for their help. Image processing was carried out using facilities in the Materials Modelling Laboratory.

[1] M. N. Baibich, J. M. Broto, A. Fert, F. Nguyen Van Dau, F. Petroff, P. Etienne, G. Creuzet, A. Friederich, and Chazelas, Phys. Rev. Lett. **61**, 2472 (1988).
[2] S. S. P. Parkin, N. Moore, and K. P. Roche, Phys. Rev. Lett. **64**, 2304 (1990).
[3] S. S. P. Parkin, Phys. Rev. Lett. **67**, 3598 (1991).
[4] J. Unguris, R. J. Celotta, and D. T. Pierce, Phys. Rev. Lett. **67**, 140 (1991).
[5] D. M. Edwards, J. Mathon, R. B. Muniz, and M. S. Phan, J. Phys.: Condens. Matter **3**, 4941 (1991).
[6] J. C. Slonczewski, Phys. Rev. Lett. **67**, 3172 (1991).
[7] J. Barnas, J. Magn. Magn. Mater. **123**, L21 (1993).
[8] Z-P Shi, P. M. Levy, and J. Fry, Phys. Rev. Lett. **69**, 3678 (1992).
[9] Y. Wang, P. M. Levy, and J. L. Fry, Phys. Rev. Lett. **65**, 2732 (1990).
[10] A. C. Daykin, J. D. Kim, and J. P. Jakubovics, these proceedings.

# Spin orientation in an exchange coupled Fe/Cr/Fe trilayer determined by polarized neutron reflection

J. A. C. Bland, H. T. Leung, and S. J. Blundell
*Cavendish Laboratory, Madingley Road, Cambridge CB3 OHE, United Kingdom*

V. S. Speriosu, S. Metin, and B. A. Gurney
*IBM Research Division, Almaden Research Center, 650 Harry Road, San Jose, California 95120*

J. Penfold
*Rutherford-Appleton Laboratory, Chilton 0X11 0QX, United Kingdom*

We have used polarized neutron reflection to determine the layer-dependent spin orientations in an antiferromagnetically coupled 100 Å Cr/50 Å Fe/15 Å Cr/50 Å Fe/Si sandwich structure prepared by sputtering. At low field, the net Fe layer magnetic moments align in an asymmetric canted orientation with a near zero total magnetic moment for the sample. At high fields, a canted state, nearly symmetric with respect to the applied field direction is observed and the magnetization in each layer does not reach the bulk saturation value until the layers are ferromagnetically aligned. The behavior is discussed in the context of current theories of exchange coupling. © *1996 American Institute of Physics.* [S0021-8979(96)24908-6]

Exchange coupling in ultrathin transition metal sandwich structures such as Fe/Cr/Fe has been intensively studied, in part because of the giant magnetoresistance (GMR) behavior which can result.[1–4] In addition to the Heisenberg-like bilinear coupling, an additional biquadratic coupling mechanism, favoring a 90° spin alignment has also been found in several epitaxial systems.[5,6] Theoretical models of biquadratic coupling distinguish between an intrinsic mechanism due to the electronic properties of the perfect structure[7–9] and extrinsic mechanisms which predict a strong dependence on the details of the interface morphology and film structure.[10–12] Neutron scattering studies of biquadratic coupling have been previously performed on both polycrystalline FeNi/Ag[13] and Fe/Cr[14] multilayers. Polarized neutron reflection provides an appropriate tool for probing the spin orientation in polycrystalline single trilayers.

We present in this article the results of a detailed polarized neutron reflection (PNR) study of a polycrystalline Fe/Cr/Fe single-sandwich structure with AF coupling.[15] In an earlier study,[16] we were able to show that the spin orientation for such structures occurring at very low field departed significantly from the purely antiparallel structure expected for pure bilinear coupling. In this article the departure from the antiparallel state is quantified. The 100 Å Cr/50 Å Fe/15 Å Cr/50 Å Fe/Si sandwich structures were prepared by sputtering and the field-dependent magnetoresistance behavior investigated as reported previously.[15] X-ray diffraction studies confirm the polycrystalline structure with a preferred (110) texture. Magnetization measurements obtained using a vibrating sample magnetometer (VSM) indicate the presence of antiferromagnetic coupling with saturation and coercive fields of 1.7 and 0.043 kOe, respectively (solid lines, inset of Fig. 1). The saturation value of the moment agrees with that calculated from the bulk magnetization. Measurements made as a function of the in-plane orientation of the applied field confirm the absence of any significant magnetic anisotropy, as expected for such polycrystalline samples.

PNR measurements[17] were made at 300 K with the sample magnetized in-plane and the total specular reflectivity $R^{\pm}$ was determined as a function of perpendicular wave vector $q$ for incident neutron spin parallel (+) and antiparallel (−) to the applied field direction ($z$ axis). The measurements were made at fixed orientation using the CRISP time of flight reflectometer[17] at the ISIS facility in the UK Rutherford Laboratory. As the field is reduced the magnetic moments of the layers move away from the $z$ axis. Both + and − reflectivities are then dependent upon both of the in-plane compo-

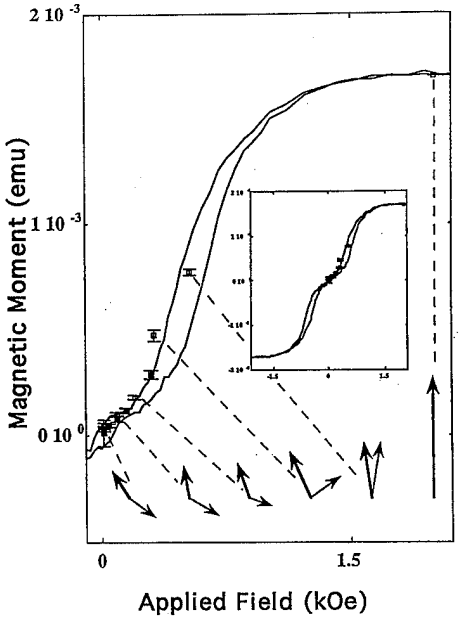



FIG. 1. Magnetization measurements for the positive part of the $M-H$ loop (solid line) for the sputtered 100 Å Cr/50 Å Fe/15 Å Cr/50 Å Fe/Si sample obtained by VSM. The inset shows the full magnetization loop. The net magnetic moment parallel to the applied field deduced from the PNR fits are shown for measurements made upon reducing the applied field from the positive saturation value (open squares) and upon increasing the applied field from the negative saturation value (solid squares). The spin configurations (magnitudes and directions) are drawn to scale as deduced from the coherent multidomain model. The thicker arrow represents the magnetization of the upper Fe layer. The applied field is vertical ($z$ axis).

 0021-8979/96/79(8)/6295/3/$10.00 © 1996 American Institute of Physics 

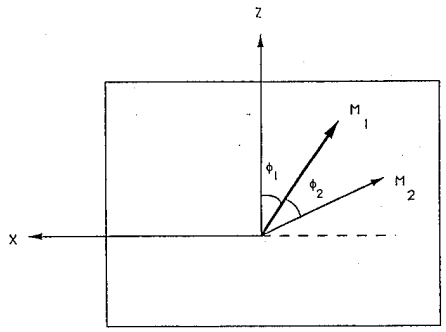



FIG. 2. The sample geometry for a multilayer sample with nonaligned in-plane magnetizations. The first layer magnetization vector $\mathbf{M}_1$ (thick arrow) and the second Fe layer magnetization vector $\mathbf{M}_2$ are constrained to the film plane. The angle $\phi_1$ refers to the orientation of $\mathbf{M}_1$ with respect to the applied field direction (vertical $z$ axis) and the angle $\phi_2$ defines the angular separation of $\mathbf{M}_1$ and $\mathbf{M}_2$ (narrower arrow), with positive angle corresponding to the anticlockwise sense.

nents of the magnetization vector as described by a reflectivity matrix.[18] A similar description has been given by Felcher *et al.*[19] The magnetic configuration of the sample is shown schematically in Fig. 2. An appropriate spatial averaging procedure is also required since beneath the saturation field magnetic domains can develop.[5] If the domains were larger than the coherence length, then each domain would contribute incoherently to the reflected intensity. The coherence length projected in plane is estimated to be about 100 $\mu$m at grazing incidence[17] while Kerr microscopy studies have revealed the existence of an irregular patch domain structure on the scale of a few microns at zero applied field for a trilayer structure with a Cr thickness in the vicinity of the first antiferromagnetic peak (i.e., close to the Cr thickness of our samples) suggesting that coherent averaging applies in our experiment. In a first approximation the net magnetization in each layer then corresponds to the spatial average over the magnetizations of each domain within the coherence area.

The spin asymmetry $S=(R^+-R^-)/(R^-+R^+)$ for $H_a=2$ kOe is consistent with the values calculated for parallel alignment of the two Fe layer moments along the applied field direction.[20] This measurement serves as a check on the experimentally determined layer thicknesses and also on the size of the Fe layer magnetizations which are found to correspond to the bulk value within experimental error. In Fig. 3 we show the spin asymmetry observed evolving as the applied field is reduced from the positive saturation value. The ferromagnetic alignment induces a pronounced peak in the asymmetry at a value of wave vector close to $2.9q_c$ (where $q_c$ is the critical wave vector for the Si substrate). As the applied field is reduced the peak asymmetry at low wave vector diminishes, indicating the expected reduction in the degree of ferromagnetic alignment between the layers, and a second peak close to $6q_c$ increases, as expected from simulations of the spin asymmetry for antiferromagnetic ordering. This peak is related to the antiferromagnetic Bragg diffraction peak that occurs in superlattices,[21,22] although refraction and spin orientation effects must be included in order to accurately fit the position and magnitude of the peak.[18]

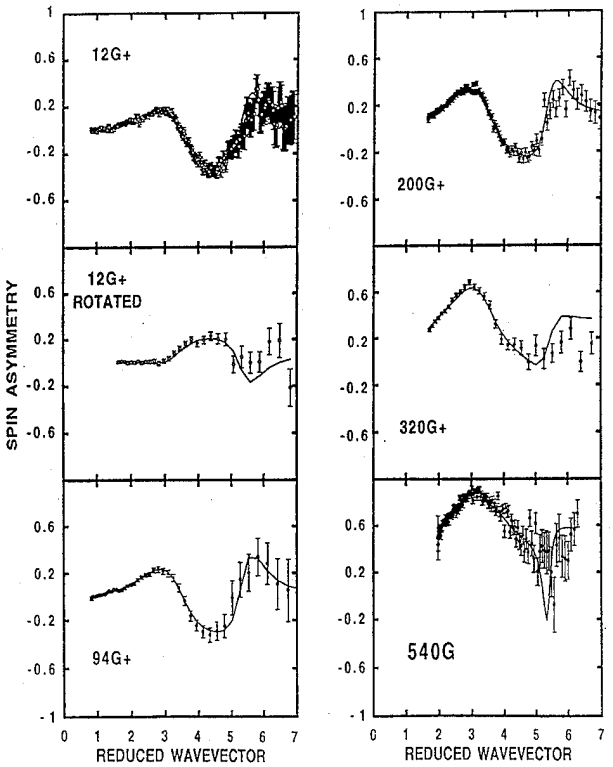



FIG. 3. The spin asymmetry observed for the 100 Å Cr/50 Å Fe/15 Å Cr/50 Å Fe/Si sputtered sandwich structure and the fits (solid lines) predicted by the coherent multidomain model as the applied field is reduced from the positive saturation value to the field strengths indicated. The fit parameters are given in Table I and the resulting spin orientations are shown in Fig. 1.

In fitting the data in the coherent case we relax the requirement that the average magnetization vectors of each layer has the full saturation value $|M_s|$ (corresponding to a single-domain state) and allow both the orientation and size of the magnetization vector in each layer to be determined by the result of a least-squares fit to the asymmetry data. The $S(q)$ curve is computed with the size and orientation of the magnetization vector in each layer treated as independently variable parameters until a close fit (solid line in Fig. 3) is found using a least-squares minimization procedure. This method is found to fit the data very well for the appropriate values of the magnetization vector (magnitude and orientation) in each layer, in contrast to the incoherent averaging method for which no fits could be obtained. The results are summarized in Table I and the resulting spin configurations are shown in Fig. 1. For each configuration shown an alternative symmetry related configuration is also possible corresponding to that obtained by reflecting about the applied field direction. The bold arrow refers to the magnetic moment of the top layer and the thin arrow refers to that of the bottom layer. The resulting component of the magnetization along the applied field ($M_{\|}$ in Table I) fitted using the above procedure is consistent with the magnetometry data on these samples, as shown in Fig. 1. We also find that the angular separation of the magnetic moment vectors is almost exactly preserved under physical rotation of the sample in low-field applied fields (see Table 1 and Fig. 1). This serves as a useful check on our analysis. We see that upon reducing the applied

TABLE I. The result of a least-squares fit to the set of field-dependent spin asymmetry data. The 1st column gives the applied field strength for positive values upon reducing the field from the positive saturation value. The measurement denoted ($R$) indicates that the sample has been rotated by 90° with respect to the applied field. The angles $\phi_1$, $\phi_2$ denote the angular position of the top layer magnetization with respect to the applied field and the angular separation of the layer magnetizations. The 4th and 5th columns show the magnitudes of the top and bottom Fe layer moments. The net components of the magnetization parallel and perpendicular to the applied field $M_{\parallel}$ and $M_{\text{per}}$ are shown in the final two columns.

| $H$ (Oe) | $\phi_1$ | $\phi_2$ | $M_1/M_s$ | $M_2/M_s$ | $M_{\parallel}/M_s$ | $M_{\text{per}}/M_s$ |
|---|---|---|---|---|---|---|
| 12 | −33 | 160 | 0.27 | 0.27 | 0.032±0.004 | 0.034±0.039 |
| 12$R$ | −110 | 170 | 0.26 | 0.26 | 0.021±0.002 | −0.010±0.011 |
| 94 | −11 | 131 | 0.27 | 0.29 | 0.060±0.006 | 0.100±0.293 |
| 200 | −19 | 129 | 0.30 | 0.20 | 0.108±0.005 | 0.045±0.054 |
| 320 | −24 | 79 | 0.42 | 0.30 | 0.278±0.016 | 0.037±0.062 |
| 540 | −8 | 17 | 0.46 | 0.46 | 0.455±0.009 | 0.004±0.087 |
| 2000 | 0 | 0 | 1.00 | 1.00 | 1.000 | 0.000 |

field from the saturation value, the formation of magnetic domains is inferred (i.e., $M_1$, $M_2$ decreases) with, after initial canting away from the applied field direction, the lower Fe layer undergoing a rotation process to attain an overall canted, near AF configuration at low applied fields. Each layer has ~25%–30% of its full saturation magnetization at low fields. We note that from Table I the total magnetic moment of the sample perpendicular to the applied field $|M_{\text{per}}|$ is always zero, within experimental error. This is consistent with the physical requirement that for stability there be no net torque on the layers arising from the applied field since the magnetic anisotropy in the sample is negligible. The magnetization reversal process is clearly inequivalent in the two Fe layers, resulting at low field in an asymmetric magnetic orientation with respect to the applied field direction. This inequivalence may result from the inequivalent interfaces of the two Fe layers (the bottom layer is directly deposited on Si).

The canting observed at low field could suggest that in addition to bilinear coupling favoring antiparallel alignment, biquadratic coupling comparable in strength is also present, since in the absence of anisotropy this configuration would be otherwise unstable. In the fluctuation model[10] biquadratic coupling is expected to occur only for sufficiently large terrace widths and appropriate roughness values. For sputtered structures very sharp interfaces can be achieved on the macroscopic scale but the correlation length is expected to be reduced on a nm scale in comparison with epitaxial structures. On the basis of this model, weaker biquadratic coupling would be expected in sputtered samples in contrast with our findings. Other extrinsic models invoking dipolar coupling[12] and the presence of "loose" spins[11] in the spacer layer are unlikely to result in the large biquadratic coupling strength we observe. It is also possible that the antiferromagnetism of the Cr layer is important in this context. Alternatively, differences between the Fe layers in net moment, pinning sites or local anisotropy variations together with bilinear coupling could explain the canting without invoking biquadratic coupling. This view is supported by the sample rotation results.

In conclusion, the results demonstrate the importance of determining the layer dependent spin orientation in exchange coupled structures, as is possible using PNR.


[1] G. Binasch, P. Grunberg, F. Saurenbach, and W. Zinn. Phys. Rev. B **39**, 4828 (1989).
[2] J. J. Krebs, P. Lubitz, A. Chaiken, and G. A. Prinz, Phys. Rev. Lett. **63**, 1645 (1989).
[3] A. Fert and P. Bruno, in *Ultrathin Magnetic Structures*, edited by B. Heinrich and J. A. C. Bland (Springer, Berlin, 1994), Chap. 2.2.
[4] S. S. Parkin, in *Ultrathin Magnetic Structures*, edited by B. Heinrich and J. A. C. Bland (Springer, Berlin, 1994), Chap. 2.4.
[5] M. Ruhrig, R. Schafer, A. Hubert, R. Mosler, J. A. Wolf, S. Demokritov, and P. Grunberg, Phys. Status Solidi A **125**, 635 (1991).
[6] B. Heinrich and J. Cochran, Adv. Phys. **42**, 523 (1993).
[7] R. P. Erickson, K. B. Hathaway, and J. R. Cullen, Phys. Rev. B **47**, 2626 (1993).
[8] D. M. Edwards, J. M. Ward, and J. Mathon, J. Magn. Magn. Mater. **126**, 380 (1993).
[9] P. Bruno, J. Magn. Magn. Mater. **121**, 248 (1993).
[10] J. C. Slonczewski, Phys. Rev. Lett. **67**, 3172 (1991).
[11] J. C. Slonczewsi, J. Appl. Phys. **73**, 5957 (1993).
[12] S. Demokrtitov, E. Tsymbal, P. Grunberg, W. Zinn, and I. K. Schuller, Phys. Rev. B **49**, 720 (1994).
[13] R. Rodmacq, K. Dumesnil, Ph. Mangin, and M. Hennion, Phys. Rev. B **48**, 3556 (1993).
[14] M. Schäfer, J. A. Wolf, P. Grünberg, J. F. Ankner, A. Schreyer, H. Zabel, and C. F. Majkrzak, J. Appl. Phys. **75**, 6193 (1994); A. Schreyer *et al.*, Europhys. Lett. (1995) (in press).
[15] B. A. Gurney, D. R. Wilhoit, V. S. Speriosu, and I. L. Sanders, IEEE Trans. Magn. **MAG-26**, 2747 (1990).
[16] J. A. C. Bland, R. D. Bateson, N. F. Johnson, S. J. Blundell, V. S. Speriosu, S. Metin, and B. Gurney, J. Magn. Magn. Mater. **123**, 320 (1993).
[17] J. A. C. Bland, in *Ultrathin Magnetic Structures*, edited by J. A. C. Bland and B. Heinrich (Springer, Berlin, 1994).
[18] S. J. Blundell and J. A. C. Bland, Phys. Rev. B **46**, 3391 (1992).
[19] G. P. Felcher, R. O. Hilleke, R. K. Crawford, J. Haumann, R. Kleb, and G. Ostrowski, Rev. Sci. Instrum. **58**, 609 (1987).
[20] J. A. C. Bland, A. D. Johnson, R. D. Bateson, S. J. Blundell, H. J. Lauter, C. Shackleton, and J. Penfold, J. Magn. Magn. Mater. **93**, 513 (1991).
[21] A. Schreyer, K. Bröhl, J. F. Ankner, C. F. Majkrzak, Th. Zeidler, P. Bödeker, N. Metoki, and H. Zabel, Phys. Rev. B **47**, 15334 (1993).
[22] Y. Y. Huang, G. P. Felcher, and S. S. P. Parkin, J. Magn. Magn. Mater. **99**, L31 (1991).

# Superconductivity and magnetic properties of Fe/Nb multilayers (abstract)

Th. Mühge, I. Zoller, K. Westerholt, and H. Zabel
*Institut für Experimentalphysik/Festkörperphysik, Ruhr-Universität Bochum, 44780 Bochum*

Yu. V. Goryunov, N. N. Garif'yanov, G. G. Khaliullin, and I. A. Garifullin
*Kazan Physical–Technical Institute of Russian Academy of Sciences, 420029 Kazan, Russian Federation*

L. R. Tagirov
*Kazan State University, 420008 Kazan, Russian Federation*

The interplay between superconductivity (SC) and ferromagnetism (FM) in dilute magnetic alloys and intermetallic compounds attracted considerable attention during the last 30 years. Usually the ferromagnetic state is more stable and therefore tends to suppress SC. On the other hand, the magnetic state can be changed due to a modification of the RKKY interaction in the SC state. Mutual influence of SC and FM may acquire new peculiarities in such artificial systems as FM/SC multilayers. This work is focused on the study of Fe/Nb multilayered system, prepared on $Al_2O_3(11\bar{2}0)$ substrates by rf-sputtering and by molecular beam epitaxy (MBE) techniques. The Nb thickness $t_{Nb}$ was varied from 150 to 500 Å and the Fe thickness $t_{Fe}$ was changed from 5 to 100 Å. The sputtered samples were highly layered with sharp interfaces as revealed by x-ray reflectivity and were textured in the [110] direction. The epitaxial MBE samples showed (110) growth of Nb and Fe with a coherence lengths comprising the total film thickness. Surface and interface roughnesses were very small. The dependence of the ferromagnetic resonance (FMR) spectra parameters on the direction of the dc magnetic field rotating in the plane of the samples show sixfold anisotropic behavior indicating the well known three-domain in-plane structure of Fe layers on sapphire substrates. FMR and SQUID measurements showed that FM of Fe layers survived down to $t_{Fe}$ = 10 Å. The out-of-plane FMR measurements also showed that the easy axis of magnetization lies in the plane of the samples down to this thickness. The superconducting transition temperature $T_c$ was determined by measurements of the electrical resistivity and by SQUID measurements. It was established that there is a critical thickness of the Fe layer $t_{Fe}^{crit}$ above which SC was not detected for temperatures down to 1.5 K. This value was dependent on $t_{Nb}$. Thus, for example, it was found that for $t_{Nb}$ = 300 Å the value of $t_{Fe}^{crit}$ = 30 Å and for $t_{Nb}$ = 350 Å—$t_{Fe}^{crit}$ = 50 Å. For constant $t_{Fe}$ with increasing $t_{Nb}$ up to a certain thickness, SC was not detected; then $T_c$ started to increase, and, finally, it approached the constant value of the order of 6 K above a certain $t_{Nb}$ which depended on $t_{Fe}$. The critical magnetic field $H_{C2}$ obtained from the resistivity measurements, strongly decreased with increasing $t_{Fe}$ or decreasing $t_{Nb}$. The temperature dependences of $H_{C2}$ were typical for two-dimensional superconductors. For the interpretation of the data obtained, various theories were employed. © *1996 American Institute of Physics.* [S0021-8979(96)44708-8]

 0021-8979/96/79(8)/6298/1/$10.00 © 1996 American Institute of Physics

# A comparison of structure and magnetoresistance in Fe/(Ag–Cu) films (abstract)

S. J. Kwon and S. J. Choi
*Department of Materials Science and Engineering, POSTECH, Pohang, 790-784, Korea*

Films of 12 Fe/(Ag–Cu) bilayers were prepared to have either granular or multilayer structures on glass substrates with a 50 Å Cu buffer layer. A magnetic Fe layer of 15 Å was deposited by e-beam evaporation, and a nonmagnetic Ag–Cu layer of 20 Å by thermal coevaporation with various Ag/Cu ratio. As the nonmagnetic layer composition changed from Ag to Cu, roughness of the film surface varied from more than 100 Å to less than 10 Å, measured with atomic force microscopy. Regularity of multilayer structure was evident in the Fe/Cu film from a superlattice peak at around 2theta=2.5 deg by Cu $K\alpha$ x-ray diffraction. The peak weakened as the Ag content increased in the nonmagnetic layer, and completely disappeared at Ag/Cu>1, which indicated that granular structure became dominant. Pendelloesung peaks at 2theta=1 to 2 deg had a similar composition dependency. The structural change was confirmed with cross-sectional transmission microscopy, too. The deposited structure is explained in terms of surface tension and wettability of each element. Increasing Cu content decreases the surface tension and increases the wettability of the nonmagnetic layer. Heat treated film structures are explained with identical terms. Change of magnetoresistance is discussed in part by connectivity of the nonmagnetic layer. From the discussion, a reasoning is given to the effect of annealing on the magnetoresistance of the films. © *1996 American Institute of Physics.*
[S0021-8979(96)44808-7]

# $^{59}$Co and $^{55}$Mn NMR of CoMn alloys and multilayers

T. Thomson and P. C. Riedi
*Department of Physics and Astronomy, University of St. Andrews, St. Andrews, Fife KY16 9SS, United Kingdom*

Q. Wang and H. Zabe
*Ruhr-Universität Bochum, Institut für Experimental Physik IV, 44780 Bochum, Germany*

$^{59}$Co and $^{55}$Mn NMR measurements have been made on a range of CoMn materials: dilute powder alloy, thin-film alloys, and multilayers. Our results suggest that in dilute alloys isolated atoms of Mn couple both ferro and antiferromagnetically to the Co host, with the latter producing a reduction in the magnitude of the Co hyperfine field of 17%. This reduction of hyperfine field appears similar for both the fcc and hcp phases of Co. NMR on Co/Mn sputtered multilayers shows large changes in the hyperfine field distribution between a film with Mn layers of 10 Å and Mn layers of 30 Å.
© *1996 American Institute of Physics.* [S0021-8979(96)35608-2]

## I. INTRODUCTION

Mn in its elemental state has both complex structural and magnetic properties.[1–3] A total of four-crystal phases are known, dependent on the temperature, with both antiferromagnetic (AFM) and ferromagnetic (FM) alignment possible for the higher-temperature fcc and bcc phases. The various phases of Mn exhibit a wide range of atomic volumes. Multilayer materials containing Mn are therefore likely to show interesting/novel properties, particularly if the high-temperature phases can be stabilized at room temperature. Hence the CoMn system is currently of interest due to the increasing ease with which high quality multilayer materials can be grown by sputtering or molecular beam epitaxy. These growth techniques offer the possibility of stabilizing exotic crystal phases, for example, the stabilisation of bcc Co in Fe/Co multilayers.[4] CoMn also presents some theoretical challenges as recent work[5] on dilute impurities in $3d$ transition metals continues to be inconclusive regarding the orientation of Mn with respect to Co.

In this work we report NMR measurements of thin-film CoMn alloys, Co/Mn multilayers produced by sputtering, and dilute powdered CoMn alloys. The basic problem in dilute alloys is the magnitude of the moment on the Mn atoms and whether such a moment aligns parallel or antiparallel to the Co host. Theoretical work[5] indicates that the change in the Co hyperfine field, and therefore the frequency, should either be quite small (a few percent) for FM alignment of Mn with Co or rather large (~20%) for AFM alignment of an impurity Mn atom in a Co host. These two magnetic orientations are calculated to have only a small difference in energy.[5] In multilayer materials the situation is further complicated by interfacial effects such as the presence of dead layers of Co immediately adjacent to the Mn and the exact structure of the Co fcc, fct, hcp.

## II. EXPERIMENT

The powdered alloy sample was prepared by argon-arc melting Co and Mn. The ingot was filed to a powder and sieved with a 300 mesh sieve to give a $Co_{0.99}Mn_{0.01}$ at. % fine powder. The thin alloy films and the multilayer films were prepared at Bochum by rf sputtering. Base pressures in the sputtering chamber were in the range $1–3\times10^{-7}$ mbar. Sputtering took place at a pressure of $5\times10^{-3}$ mbar in an atmosphere of 99.99% pure Ar gas. The substrates were chemically cleaned in an acetone/ethanol mixture prior to insertion in the chamber, they were then annealed at 500 °C under high vacuum and plasma etched immediately before deposition. Thicknesses were measured *in situ* by a quartz monitor and postdeposition by x-ray reflectivity and x-ray fluorescence.

A total of four thin films were investigated using NMR. Two alloy films with $Co_{0.98}Mn_{0.02}$ were produced simultaneously by cosputtering Mn and Co onto (a) a glass and (b) a MgO substrate. The growth temperature was maintained at 200 °C and the growth rate was 0.12 Å/s. The thickness of the films as measured by the x-ray techniques was 228 Å. Both films were capped with Au=40 Å to inhibit oxidation.

The two multilayer films studied were produced by rotating the MgO(001) substrates between the Co and Mn targets. The growth temperature was 100 °C, and a sputtering rate of 0.1 Å/s was maintained for both Co and Mn. The films were protected by a capping layer of Co=30 Å to inhibit oxidation. The structure of the two multilayers was MgO/[Co 30 Å/Mn 10 Å]$_{\times10}$/Co(30 Å) and MgO/[Co 30 Å/Mn 30 Å]$_{\times10}$/Co(30 Å). Both these films were oriented with the [001] direction normal to the plane of the film.

The NMR spectra were measured in a coherently detected, swept frequency spin echo spectrometer[6,7] using a tuned circuit matched to the 50 Ω line. At each frequency the echo was integrated and measured at phase angles $\varphi$ and $\varphi+\pi/2$. The phase insensitive quantity $S=\sqrt{S_{\varphi}^2+S_{\varphi+\pi/2}^2}$ was then determined and plotted against frequency. In order to accommodate the wide range of frequencies and large differences in the amplitude some changes were made to the spectrometer configuration, in particular two different coils were used. The first coil covered the frequency range 120–280 MHz while the second covered the range 235–400 MHz. The large overlap region ensured good matching between the two parts of the spectrum. A variable gain receiver was used to extract the maximum signal and again a large overlap region ensured good matching between the various parts of the spectrum. Measurements were taken at two temperatures, $T=4.2$ K and $T=1.3$ K. The lower temperature was used for

 0021-8979/96/79(8)/6300/3/$10.00 © 1996 American Institute of Physics

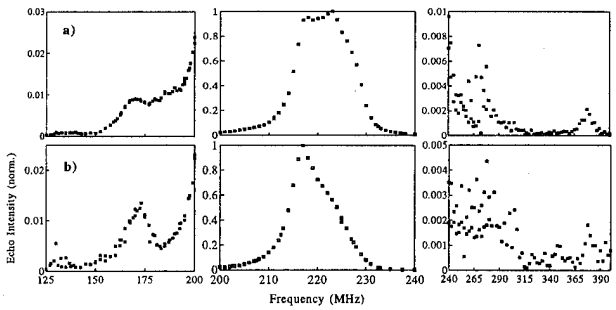



FIG. 1. $^{59}$Co and $^{55}$Mn NMR spectra of $Co_{0.98}Mn_{0.02}$, 228-Å-thick, sputtered alloy films at $T=4.2$ K. The echo amplitude is normalized to the top of the Co fcc line (~217 MHz). No corrections for frequency or $T_2$ have been made. The different scales on the $x$ and $y$ axis are used to show the regions of interest. The films were sputtered simultaneously on to: (a) a glass substrate and (b) a MgO substrate.

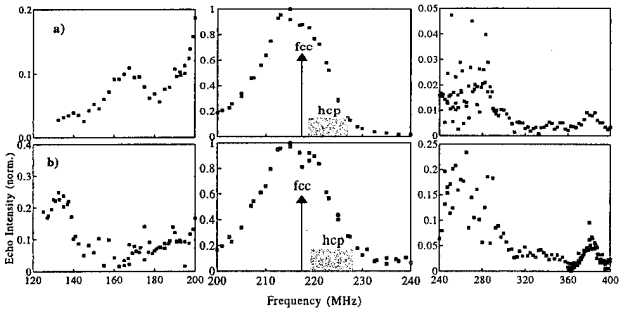



FIG. 2. $^{59}$Co and $^{55}$Mn NMR spectra of Co/Mn multilayers at $T=4.2$ K. The echo amplitude is normalised to the top of the Co fcc line (~217 MHz), no corrections for frequency or $T_2$ have been made. The positions of the free Co fcc and hcp lines at $T=4.2$ K are marked for guidance. The composition of the multilayers are: (a) [Co 30 Å/Mn 10 Å]$_{\times 10}$ and (b) [Co 30 Å/Mn 30 Å]$_{\times 10}$.

the parts of the spectrum with the weakest signal, as the signal-to-noise ratio scales with $1/T$. No corrections were made for either the frequency or relaxation time ($T_2$) dependence of the spectra as these corrections do not alter the positions of the NMR lines and accurate comparison of the relative line intensities was not required for the work undertaken here.

## III. RESULTS AND DISCUSSION

The powdered $Co_{0.99}Mn_{0.01}$ at. % alloy was measured from 70 to 400 MHz. Co was found to exist in both the fcc and hcp phases as demonstrated by a sharp $^{59}$Co resonance line at 217.4 MHz and a broader line extending from 220 to 228 MHz.[8–10] A feature of all the CoMn materials studied, powdered alloys, thin-film alloys, and multilayers was that a significant fraction of the Co was in the hcp phase. A number of sharp, well-defined satellite lines were also identified between 197 and 212 MHz. These satellite lines must either be associated with grain boundaries or with Co atoms with 11 nearest-neighbor (N.N.) Co and 1×Mn N.N. FM aligned to the Co. As the moment on Mn is similar to that of Co, FM alignment of a Mn impurity produces only a small change in hyperfine field. A $^{55}$Mn resonance line was measured at 377.5 MHz, which earlier experimental work[11] ascribes to a single Mn impurity atom FM coupled to 12 surrounding Co atoms.

A line at ~180 MHz was found in all the spectra measured and tentatively identified with the atomic environment where Co is surrounded by 11×Co and 1×Mn N.N. AFM aligned to the Co. This identification is in good agreement with the predictions of Stepanyuk *et al.*[5] for the changes in the Co hyperfine field in the presence of $3d$ impurity atoms. Two much weaker, but still well defined lines were observed at 131 and 114 MHz. The origin of these lines is at present unclear, although the Mn hyperfine field for Mn AFM aligned to 12×Co N.N. is calculated to be about 100 MHz.[5] A paper containing a more comprehensive study of CoMn alloys is currently in preparation.[12]

Figure 1 shows spectra from the two thin-film alloys grown on glass and MgO. The spectra are split into three parts to allow for the difference in amplitude of the various lines. The first point to note is that the film grown on MgO has a significantly smaller fraction of Co in the hcp phase (220–228 MHz) than the film grown on glass. Both alloy films show a clear satellite line at 171 MHz. This line is probably associated with the atomic environment of 11×Co, and 1×Mn AFM aligned N.N., although the frequency of this environment is rather less than that found in the powdered sample (180 MHz). This difference in frequency could be explained in terms of strain, although the reduction in frequency of 9 MHz is rather large compared to the reduction of 0.4 MHz (glass) and 0.8 MHz (MgO) in the Co fcc line from the free-powder value of 217.4 MHz. However as the Mn concentration was double that of the powder it is also possible that Mn in the second nearest-neighbor shell affects the hyperfine field. The Co signal from an environment of 11×Co and 1×Mn FM coupled to Co is contained in the envelope of the main Co line due to the broadening of this line associated with sputtered thin films. Closer inspection of the 180 MHz satellite line reveals that the width and shape of the line are somewhat different between the two samples and that the sample with more hcp Co has a broader line. This indicates that a Mn impurity produces a similar effect in both fcc and hcp Co. A $^{55}$Mn line at 377.5 MHz from FM coupled Mn is observed in both spectra although the signal is quite weak. A rather broad and ill defined peak also appears to exist around 270 MHz, but the interpretation of this feature is unclear.

Figure 2 shows spectra for the two Co/Mn multilayers. The main Co line is similar for both spectra and indicates that a fraction of the Co is in the hcp phase for both samples, as shown by the intensity between 220 and 230 MHz. A qualitative inspection of the data suggests a greater fraction of the Co is in the hcp phase for the sample with thicker Mn layers. This is an interesting result as x-ray work on similar materials[13] did not reveal the presence of the hcp phase. It is possible that fct Co could generate a hyperfine field similar to hcp and hence explain this result. The main line in both spectra is shifted to a lower frequency than is expected for a free fcc powder. In Co/Cu multilayers a frequency shift is usually associated with an extensive strain in the plane of the film,[14] although a distortion of the fcc phase to fct might also explain this result, and would be consistent with the x-ray

data. However, it is unlikely that a distortion of the fcc Co lattice to fct could account for both the apparent contribution from hcp Co and the reduction in the frequency of the main peak. We are currently undertaking further work in order to resolve this point.[12]

Ferromagnetic resonance on *e*-beam evaporated Co/Mn grown on Ru(0001)[15,16] showed, that for Mn layers greater than 12 Å, Co was predominately in the hcp phase. In the region outside the main Co line the two spectra are quite dissimilar which is consistent with work[13] which shows that the stability limit of the fcc/fct Mn structure in these multilayers is about 20 Å. Hence the spectrum of Fig. 2(a) for a [Co 30 Å/Mn 10 Å]$_{\times 10}$ multilayer shows only two well-defined satellite lines one at 172 MHz (11×Co and 1×Mn) and one at 377.5 MHz (Mn with 12×Co). The presence of a substantial intensity in the 172 MHz line and a reduced intensity in the 377.5 MHz line indicates that considerable mixing at the interfaces has occurred with a preferred AFM alignment of Mn.

The spectrum in Fig. 2(b) shows a more complicated behavior with a strong line at 131 MHz. A similar, but much weaker, line was observed in the powder alloy. As the Mn layers in this multilayer are thicker than the stability limit for the fcc/fct phase it is reasonable to assume that an increased amount of alloying has taken place, and with the much larger concentration of Mn it is possible that this line is associated with the 10×Co+2×Mn N.N. atomic environment where both Mn are AFM aligned to the Co. However, it is also possible that the previously reported[13] dead Co layer adjacent to Mn could account for this line. Continuing work on powder alloys should resolve this point. The broad, ill-defined feature at ~270 MHz is clearly visible in this spectrum. The $^{55}$Mn line at 377.5 MHz has a much greater intensity than in the previous spectrum and this re-enforces the argument that more mixing has occurred in the interfacial region.

## IV. CONCLUSIONS

$^{59}$Co and $^{55}$Mn NMR on powder and thin-film CoMn alloys has shown that in the dilute impurity limit (1 or 2 at. %) Mn can exhibit both AFM and FM coupling to its Co nearest neighbors. The AFM alignment of the Mn gives a reduction in the hyperfine field of the N.N. Co atom of 17%. This is in good agreement with the calculations of Stepanyuk *et al.*[5] Thin-film CoMn alloys with different fractions of fcc and hcp Co showed that the substitution of Mn into either of these phases produced a similar reduction in the hyperfine field for this AFM alignment of Mn. In multilayer films the Co hyperfine field associated with both the fcc and hcp phases was observed, although x-ray work on similar samples suggested the absence of hcp Co and the presence of the fct phase. This NMR study confirmed previous work on Co/Mn multilayers which showed that the stability limit for epitaxial growth of Mn on Co is about 20 Å with evidence of substantial interfacial mixing for the [Co 30 Å/Mn 30 Å]$_{\times 10}$ multilayer.

## ACKNOWLEDGMENTS

The support of the U.K. Engineering and Physical Sciences Research Council is gratefully acknowledged as is the support of Deutsche Forschungsgemeinschaft (SFB166).

[1] *Data in Science and Technology, Magnetic Properties of Metals*, edited by H. P. J. Wijn (Springer, Berlin, 1991).
[2] G. Fuster, N. E. Brener, J. Callaway, J. L. Fry, Y. Z. Zhao, and D. A. Papaconstantopoulos, Phys. Rev. B **38**, 423 (1988).
[3] T. Asada and K. Terakura, Phys. Rev. B **47**, 15992 (1993).
[4] P. Boher, F. Giron, Ph. Houdy, F. Baudelet, A. Fontaine, J. M. Ladouceur, E. Dartyge, P. Beauvillain, C. Chappert, P. Veillet, and K. Le Dang, J. Appl. Phys. **71**, 1798 (1992).
[5] V. S. Stepanyuk, R. Zeller, P. H. Dederichs, and I. Mertig, Phys. Rev. B **49**, 5157 (1994).
[6] T. Dumelow and P. C. Riedi, Hyperfine Interactions **35**, 1061 (1987).
[7] J. S. Lord and P. C. Riedi, Meas. Sci. Technol. **6**, 149 (1995).
[8] R. Street, D. S. Rodbell, and W. L. Roth, Phys. Rev. **121**, 84 (1961).
[9] D. Fekete, H. Boasson, A. Grayevski, V. Zevin, and N. Kaplan, Phys. Rev. B **17**, 347 (1978).
[10] H. A. M. de Gronckel and W. J. M. de Jonge, NATO ASI Ser. B **309**, 309 (1992).
[11] M. Kawakami and Y. Koi, J. Phys. Soc. Jpn. **37**, 1257 (1974).
[12] T. Thomson and P. C. Riedi (unpublished).
[13] Q. Wang, N. Metoki, Ch. Morawe, Th. Zeidler, and H. Zabel, J. Appl. Phys. **78**, 1689 (1995).
[14] T. Thomson, P. C. Riedi, and D. Greig, Phys. Rev. B **50**, 10319 (1994).
[15] K. Ounadjela, Y. Henry, M. Farle, and P. Vennegues, J. Appl. Phys. **75**, 5601 (1994).
[16] K. Ounadjela, P. Vennegues, Y. Henry, A. Michel, V. Pierron-Bohnes, and J. Arabski, Phys. Rev. B **49**, 8561 (1994).

# Study of interface structure of Fe/Al multilayers

Ataur R. Chowdhury and Andrea E. Freitag
*Physics Department, University of Alaska-Fairbanks, Fairbanks, Alaska 99775-1320*

Structural and magnetic ordering of the interfaces determines the physical properties of multilayered structures. Interfaces of Fe/Al multilayers were studied using Mössbauer effect spectroscopy. The samples were fabricated by dc planar magnetron sputtering at room temperature on polyester substrates. The observed spectra indicate that the interfaces have a common structural composition and for thin Fe layers, the whole Fe layer forms mixed phases at the interface. For larger Fe layer thickness, the interface is formed using an about 12-Å-thick Fe layer. Besides the hyperfine field component of bcc Fe, six different magnetic components were identified in all samples (with larger Fe layer thickness). The intensities of the components were determined from the area under the absorption peaks of the Mössbauer spectra of the corresponding phases. The average canting angle of the Fe magnetic moments, as obtained from the spectra, indicate parallel magnetic anisotropy for all phases. © *1996 American Institute of Physics.* [S0021-8979(96)35708-9]

## I. INTRODUCTION

There has been a great deal of interest for artificially layered structures for their potential use as new magnetic materials. The fundamental magnetic, electronic, and optical properties of these structures are quite different from their bulk counterparts, and over the last decade, it has been shown that these interesting properties are greatly influenced by the interfaces of the multilayers.[1–3] For a better understanding of the fundamental properties of these multilayers, there is a crucial need for comprehensive studies of the interfaces for their local structures using microscopic techniques.

Multilayers of Fe/Al were chosen for the study of multilayer interfaces using Mössbauer effect spectroscopy. Fe/Al has the potential to be used as thin-film magnetic head for recording media, and it has been shown to possess excellent soft magnetic properties required for such use.[4–6] Structural ordering and magnetic properties of Fe/Al multilayers have been studied in the past.[4–13] Interfacial magnetism of Fe/Al multilayers were studied, in most cases, following either ion beam or thermal mixing of the interfaces using Mössbauer effect spectroscopy.[9–13] Depth selective ion implantation of Al into Fe and Fe into Al was also employed to simulate interfaces of Fe/Al multilayers for studies with Mössbauer effect spectroscopy.[14–16] Results of these Mössbauer investigations clearly reveal a wide variety of magnetic interactions at the interfaces that are characteristic of bcc iron, intermetallic, and nonmagnetic phases. This particular project was initiated to study the structural and magnetic properties of Fe/Al multilayers and correlate these properties with the individual layer thicknesses of Fe and Al.

## II. EXPERIMENT

The samples with the form of ($X$ Å) Fe/($Y$ Å) Al were prepared by dc planar magnetron sputtering at room temperature. The substrate was rotated over the Al and Fe sputtering sources with a constant speed to ensure better uniformity of the samples. The base pressure of the chamber was about $10^{-6}$ Torr and a constant argon pressure of 5 mTorr was maintained during deposition. Individual layer thicknesses were measured with the help of a calibrated quartz crystal thickness monitor. The substrates are polyester films for transmission Mössbauer measurements, and glass slides for x-ray diffraction and other microprobe analysis.

$^{57}$Fe Mössbauer spectra were obtained with a conventional constant acceleration-type spectrometer. A 25 mCi source of $^{57}$Co in rhodium matrix was used, and the velocity was calibrated with a natural Fe foil. Mössbauer spectra of all samples were least-squares fitted with seven sextets.

## III. RESULTS AND DISCUSSION

The room-temperature Mössbauer spectra of four Fe/Al multilayers are shown in Fig. 1. Some of the spectra clearly display the "shoulder" features indicating the presence of more than one magnetic interactions, which, in turn, implies more than one site for $^{57}$Fe isotopes. Mössbauer spectra of three samples (B,C,D) with the same Al layer thickness look quite different. This may imply that the interfaces of Fe/Al multilayers sensitively depend on the layer thickness of both constituent elements and the degree of mixing at the inter-

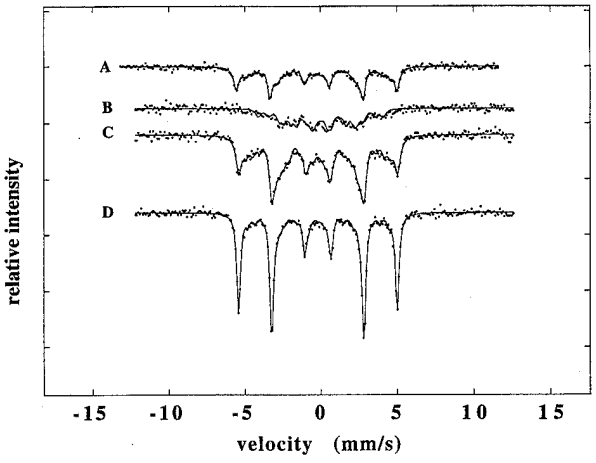



FIG. 1. Room-temperature Mössbauer spectra of Fe/Al multilayer samples: A (19 Å Fe/5 Å Al), B (11 Å Fe/11 Å Al), C (21 Å Fe/11 Å Al), and D (60 Å Fe/11 Å Al).

 0021-8979/96/79(8)/6303/3/$10.00 © 1996 American Institute of Physics 

TABLE I. Sample parameters, hyperfine fields, and corresponding intensities.

| Sample | A | | B | | C | | D | |
|---|---|---|---|---|---|---|---|---|
| $X$ (Å) | 19 | | 11 | | 21 | | 60 | |
| $Y$ (Å) | 5 | | 11 | | 11 | | 11 | |
| | HF (kG) | $I$ (%) | HF (kG) | $I$ (%) | HF (kG) | $I$ (%) | HF (kG) | $I$ (%) |
| site1 | 325 | 49 | 321 | 0 | 321 | 36 | 329 | 77 |
| site2 | 292 | 16 | 288 | 0 | 293 | 15 | 292 | 7 |
| site3 | 263 | 13 | 252 | 23 | 266 | 14 | 258 | 5 |
| site4 | 228 | 7 | 216 | 19 | 234 | 11 | 227 | 2 |
| site5 | 170 | 6 | 168 | 30 | 182 | 8 | 179 | 2 |
| site6 | 130 | 5 | 120 | 7 | 119 | 9 | 122 | 3 |
| site7 | 28 | 4 | 48 | 20 | 33 | 7 | 49 | 4 |
| H avg | 273 | | 169 | | 248 | | 301 | |

Here, $X$ is the Fe layer thickness, $Y$ is the Al layer thickness, HF are the hyperfine fields, and $I$ are the corresponding intensities.

face. Diffusion of Fe into Al and Al into Fe may lead to formation of stable compounds as well as amorphous phases of Fe-Al alloy. This diffusion process may segregate Fe atoms in Al matrix with fcc symmetry and Al atoms in Fe matrix with bcc symmetry. To identify these different interfacial structures and the extent of the interface, Mössbauer spectra were all fitted with seven sextets corresponding to seven dominant $^{57}$Fe sites. Results of these fittings, along with the sample compositions, are provided in Table I. Formation of any Fe clusters in the samples is highly unlikely as none of the spectra show any discernible paramagnetic feature at the center of the spectrum.

As can be seen from Table I, site 1 represents the most dominant Fe phase for samples A, C, and D. Hyperfine field of site 1 of sample D is 329 kG and is typical of bcc Fe, and for samples A and C it is 325 and 321 kG, respectively. This slightly smaller field for site 1 for samples A and C directly scales with the unmixed Fe layer thickness of the respective samples. The size of the interface of the samples studied is about 12 Å, as will be shown later, and hence the thicknesses of unmixed Fe layers for samples A and C are about 7 and 9 Å, respectively. A reduction of hyperfine field compared to bulk bcc Fe is expected for such thicknesses due to the finite size effect. For interpretation of our results, site 1 will be considered as bcc Fe like, and will not be considered as part of the interface. Site 1 is completely absent in sample B, and, therefore, the multilayered structure for this sample is not conserved, and all Fe atoms belong to the interface.

The second sextet, corresponding to site 2, with a hyperfine field of 292 kG is due to stable $Fe_3Al$ phase,[9] and is common for samples A, C, and D. This site is also absent in sample B. The first major site for sample B is the site 3 with a hyperfine field of 252 kG, which is representative of a stable phase of random alloy of the form $Fe_{55}Al_{45}$ with bcc symmetry. Site 3 for samples A, C, D is different from that of sample B, and has an average hyperfine field of 262 kG, which is close to the predicted hyperfine field of a homogeneous Fe-Al alloy having a Fe site with three Al atoms as nearest neighbors.[17] Hyperfine fields of site 4 of all samples are close together with an average field of 226 kG, and this field is close to the predicted hyperfine field of a homogeneous Fe-Al alloy having a Fe site with four Al atoms as nearest neighbors.[17] Although site 4 is small for samples A, C, D; it is quite significant for sample B.

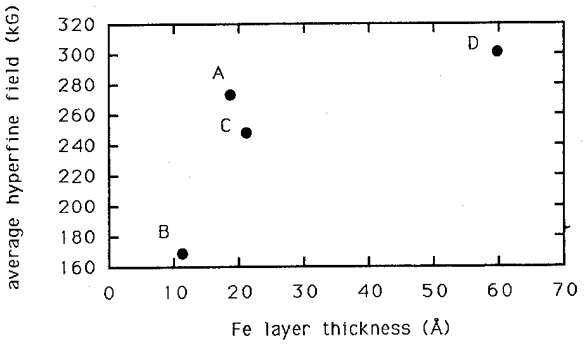



FIG. 2. Plot of the average hyperfine field as a function of Fe layer thickness. For samples B, C, and D the Al layer thickness is 11 Å, and for sample A it is 5 Å.

Aside from the four iron-rich phases that were described above, three aluminum-rich phases were also detected. First one of this is the site 5 with an average hyperfine field of 175 kG. This field is close to the predicted hyperfine field of an aluminum-rich Fe-Al alloy having a Fe site with six Al atoms as nearest neighbors.[9] This site is the most dominant site for sample B. Site 5 is very small for all samples, and has an average field of 122 kG. It has been predicted to be the field of a aluminum-rich Fe-Al alloy with Fe site having eight near-neighbor Al with fcc symmetry.[9] Site 7 is quite small for samples A, C, and D, but significant for sample B with 20% of the Fe atoms belonging to this site. The hyperfine field for this weak magnetic site for samples B and D is about 48 kG, which is close to the predicted field of a metastable homogeneous Fe-Al alloy having a Fe site with eleven Al atoms with fcc symmetry as nearest neighbors.[9] The hyperfine field for site 7 for samples A and C is about 30 kG, and the corresponding Fe site is probably very unstable and not easy to predict.

From the above discussion it is quite clear that the interface of Fe/Al multilayers is composed of a few distinctly identifiable stable and metastable phases, and most of these phases are common to all the samples. This fact indicates that the underlying mechanism for the formation and nucleation of the interfaces of the samples under study is the same. The results show that despite increasing Fe layer thickness the interface is formed by roughly the same number of Fe atoms corresponding to a Fe layer thickness of about 12 Å. It is also clear from above discussion that the diffusion of Fe and Al atoms is greatly influenced by the individual layer thicknesses. When the individual Fe layer thickness is greater than the Al layer thickness, diffusion results in mostly Fe-rich phases, whereas for sample B, for which the Fe and Al layer thicknesses are the same, it results in mostly Al-rich phases.

We find it useful to define an average hyperfine field which is the weighted sum of all hyperfine components. The average hyperfine field of all samples, is listed in Table I, and plotted in Fig. 2 as a function of Fe layer thickness. The average hyperfine field of the three samples (B,C,D) with the

same Al layer thickness decreases with Fe layer thickness. The smaller the Fe layer thickness the larger the fraction of the Fe atoms that belong to the interface where they form stable alloy phases with hyperfine fields less than the bcc Fe phase. This decrease of hyperfine field with Fe layer thickness is very similar to what has been observed in homogeneous $Fe_xAl_{1-x}$ alloys.[18] The decrease of the average hyperfine field of sample A is, however, not consistent with the corresponding decrease of that for samples B, C, D. This is a clear indication that the average hyperfine field sensitively depends on the thickness of both Fe and Al layers. The intensity ratios of the Mössbauer lines (roughly 3:4:1) imply that the average direction of magnetization lies in the plane of the sample, as expected.

## IV. CONCLUSIONS

Results of our Mössbauer experiment with a limited number of samples show that all the interfaces of Fe/Al multilayers are unique and are composed of distinct stable and metastable phases. Seven such phases were detected and identified. Only two of these phases (site 1 and site 2) were previously detected in a similar sample of Fe/Al multilayer.[15] Results establish that the average thickness of the interface is about 12 Å, and the diffusion of Fe and Al atoms depends on the individual layer thicknesses of both elements. The average hyperfine field of the samples with constant Al layer thickness decreases with Fe layer thickness. The observed Mössbauer line intensities indicate an inplane magnetic anisotropy at room temperature for all samples.


[1] Z. S. Shan, S. Nafis, J. Woollam, S. H. Liou, and D. J. Sellmyer, J. Appl. Phys. **73**, 6347 (1993).
[2] C. D. England, W. R. Bennett, and C. M. Falco, J. Appl. Phys. **64**, 5757 (1988).
[3] C. H. Lee, H. He, F. J. Lamelas, W. Vavra, C. Uher, and R. Clarke, Phys. Rev. B **42**, 1066 (1990).
[4] T. Hamaguchi, H. Aida, S. Nakagawa, and M. Naoe, J. Appl. Phys. **73**, 6444 (1993).
[5] M. Nagakubo, T. Yamamoto, and M. Naoe, J. Appl. Phys. **63**, 5751 (1988).
[6] T. Haeiwa, H. Negoro, and M. Matsumoto, J. Appl. Phys. **69**, 5346 (1991).
[7] J. F. Wang, F. Z. Cui, Y. Wang, and Yu-dian Fan, J. Magn. Magn. Mater. **89**, 153 (1990).
[8] Z. Wu, V. Suresh Babu, M. S. Seehra, and W. Abdul-Razzaq, Phys. Rev. B **45**, 2285 (1992).
[9] V. P. Godbole, S. M. Chaudhari, S. V. Ghaisas, S. M. Kanetkar, S. B. Ogle, and V. G. Bhide, Phys. Rev. B **31**, 5703 (1985).
[10] M. Meyer, L. Mendoza Zelis, F. H. Sanchez, and A. Traverse, Hyperfine Interact. **83**, 327 (1994).
[11] G. Principi, Hyperfine Interact. **66**, 149 (1991).
[12] M. Carbucicchio, G. Palombarini, R. Bertoncello, A. Glisenti, E. Tondello, and G. Sberveglieri, Hyperfine Interact. **92**, 1249 (1994).
[13] M. A. Z. Vasconcellos and J. A. T. Borges da Costa, Hyperfine Interact. **66**, 331 (1991).
[14] H. Reuther, O. Nikolov, S. Kruijer, R. A. Brand, W. Keune, D. Liljequist, S. Weber, and S. Scherrer, Hyperfine Interact. **92**, 1367 (1994).
[15] H. Reuther, Hyperfine Interact. **56**, 1637 (1990).
[16] H. de Waard and G. L. Zhang, Hyperfine Interact. **56**, 1569 (1990).
[17] F. H. Sanchez, J. I. Budnick, Y. D. Zhang, and R. Hasegawa, J. Appl. Phys. **61**, 4349 (1987).
[18] J. H. Hsu and C. L. Chien, Hyperfine Interact. **69**, 451 (1991).

# Effect of ion beam mixing on microstructure and magnetic properties of Gd-Co multilayer films

G. Choe[a] and R. M. Walser
*I/UCR Center for Magnetics, The University of Texas at Austin, Austin, Texas 78712*

This work investigated the effect of ion beam mixing on the magnetic and structural characteristics of Gd-Co multilayer films. Multilayer films with bilayer periods (BP) from 10 to 300 Å were mixed by 150 to 300 keV $Ar^+$ ion doses of $10^{16}$ $cm^{-2}$. The magnetizations of the as-deposited multilayers were dominated by oxidation, and by the asymmetric redistribution of Co atoms. Ion beam mixing eliminated much of these effects, but the degree was strongly dependent on the layer thickness. The small BP films were completely mixed, with amorphous nanoparticles, but the large BP films contained small, microcrystals in an amorphous matrix due to incomplete mixing. The magnetic moment of ion beam mixed films were strongly dependent on the ion beam energy and the layer thickness. © *1996 American Institute of Physics.* [S0021-8979(96)25008-0]

## I. INTRODUCTION

Ion beam mixing of layered thin films often results in nonequilibrium amorphous alloys that cannot be obtained by common techniques such as liquid quenching, vapor deposition, and solid state reaction. Ion beam mixing of magnetic multilayers can produce materials with scientifically interesting nonequilibrium structures, and potentially useful magnetic properties.

There has been considerable previous research on ion beam mixing of magnetic multilayers in which the correlation between the microstructure of ion beam mixed films and their magnetic properties has been reported for a wide variety of alloys.[1] In our previous study, ion beam mixed Co-B multilayers were shown to be hetero-amorphous, soft magnetic films, that were ferromagnetic with significantly larger boron concentrations than alloy films.[2] This work investigated the effect of ion beam mixing on the microstructure and magnetic characteristics of Gd-Co multilayers. We report the correlations in the ion induced changes in magnetic properties, and the nanostructural morphological features, as a function of layer thicknesses of the Gd-Co multilayer films, and the ion beam energy.

## II. EXPERIMENTS

Multilayered Gd-Co films with bilayer periods ($BP=T_{Gd}+T_{Co}$, $T_{Gd}/T_{Co}\approx 1$) from 10 to 300 Å were deposited by alternately sputtering Gd and Co in a multitarget, rf diode sputtering system. A background pressure of $5\times10^{-7}$ Torr and argon sputter gas pressure of 10 mTorr were used. The ion mixing of ≈800–900-Å-thick multilayer films was carried out in an ion implanter using $Ar^+$ ions with energies in the range of 150–300 keV, and a dose of $10^{16}$ ions/$cm^2$. The projected ranges and deviations calculated from Lindhard, Scharff, and Schiøtt (LSS) range statistics for these beam parameters (Table I) were selected to ensure that the ions were fully stopped in the films. The substrates of the multilayered films were held at liquid nitrogen temperature during ion beam mixing. The changes in the compositional, structural, and magnetic properties of the ion beam mixed Gd-Co multilayer films were characterized, respectively, by AES (Auger electron spectroscopy) depth profiling, x-ray diffraction, TEM (transmission electron microscopy), Lorentz microscopy, and $B$-$H$ hysteresisgraph.

## III. RESULTS AND DISCUSSION

### A. As-deposited Gd-Co multilayer films

The compositional modulation of Gd and Co layers in Gd-Co multilayer films was observed as a function of layer thickness. The AES depth profiles of the as-deposited Gd-Co multilayer films in Fig. 1 shows the periodic distributions of Gd and Co atoms, and oxygen peaks in the Gd layers. Due to the higher affinity of Gd for oxygen, the Gd layers are selectively oxidized. An asymmetric distribution of Co atoms was also observed, possibly due to a greater diffusion of Co atoms into the Gd layer, compared to the diffusion of Gd atoms into the Co layer.

Cross-sectional TEM micrographs of the multilayered films showed that the growth of Gd and Co grains was limited to within each atomic layer. The Co grains were columnar and grew perpendicular to the film plane. Since Gd-Co alloys readily form amorphous phases, the polycrystalline grain size of Gd-Co multilayer films was strongly dependent on the layer thickness. The change in the grain size of the various Gd-Co multilayer films was determined from the Debye Sherrer equation[3] using the line broadening of the two principal x-ray peaks for hcp Gd(10.0) and Co(00.2). The measured grain sizes agreed well with those obtained from TEM micrographs. As shown in Fig. 2, in all of the films, the grain sizes of Gd and Co were found to be smaller than the Gd and Co layer thickness, suggesting that their growth was

TABLE I. LSS range statistics for ion-implantation of $Ar^+$ ions into $Gd_{25}Co_{75}$.

| Energy (keV) | Range (Å) | Standard deviation |
|---|---|---|
| 150 | 614 | 241 |
| 200 | 821 | 304 |
| 300 | 1242 | 419 |

[a]Presently at Materials Research Corp, Advanced Technology Division, Orangeburg NY 10962.

 0021-8979/96/79(8)/6306/3/$10.00 © 1996 American Institute of Physics

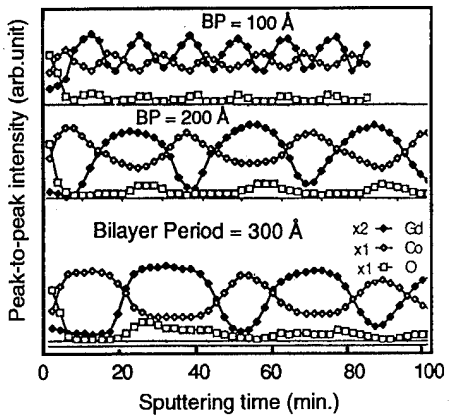



FIG. 1. Auger depth profiles of as-deposited Gd-Co multilayer films as a function of bilayer period.

limited by neighboring different atomic layers. The Co grain growth increased linearly with layer thickness, but the Gd growth increased more slowly, possibly due to the asymmetric diffusion of Co.

The in-plane magnetizations of Gd-Co multilayer films were measured with a thin film hysteresis loop tracer with an applied field of 100 Oe. As shown in Fig. 3, the magnetizations of the Gd-Co multilayer films increased with the BP, and their coercivities were less than 50 Oe. Using their measured total magnetization, we estimated the average magnetic moment per Co atom ($\mu_\beta$) in each film. As the BP increased, the estimated value of the Co magnetic moment increased due to the large magnetic moment of isolated Co grains in films with larger BP. The values of $\mu_\beta$ in Gd-Co multilayer films were lower than those of Co atoms ($\approx$1.7 $\mu_\beta$), possibly due to an antiferromagnetic (AF) coupling at the Gd/Co interfaces. The reduced magnetic moment per Co atom of the small BP films, compared to those of the larger BP films, was ascribed to an enhancement of AF coupling at Gd/Co interfaces.

### B. Ion beam mixed Gd-Co multilayer films

The degree of ion beam mixing was strongly dependent on the layer thickness of multilayer films. As shown in the AES depth profiles of the films mixed with 200 keV $Ar^+$ ions

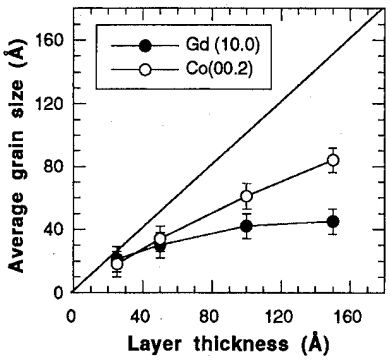



FIG. 2. Change in grain size of Gd-Co multilayer films with layer thickness ($T_{Co}/T_{Gd}\approx1$).

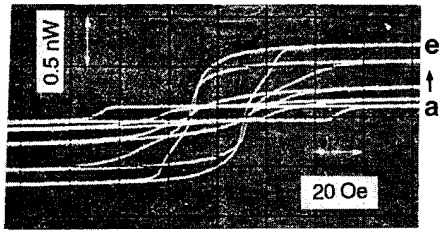



FIG. 3. *B-H* loops of Gd-Co multilayer films as a function of bilayer period: (a) 10, (b) 50, (c) 100, (d) 200, and (e) 300 Å.

(Fig. 4), the small BP film ($\leq$100 Å) was completely mixed throughout the film thickness, but some compositional modulation was observed in the large BP film ($\geq$200 Å) indicating that the ion mixing was incomplete. The principal x-ray diffraction (XRD) peaks observed in the small BP multilayer films (BP$\leq$100 Å) were no longer detected due to the amorphization by ion beam mixing, and the peak intensity of large BP films was also sharply reduced by intermixing of Gd and Co layers.

The morphologies observed in the ion beam mixed films varied with the layer thickness in the multilayer films, and with the beam energy. As shown in Fig. 5, films with a 10 Å BP had a hetero-amorphous morphology with spherical, nanoscale (70 Å) features when mixed by a 150 keV beam, but those mixed at 300 keV had a morphology with a uniform distribution of, amorphous, chainlike features. The change in morphology with ion beam energy is likely associated with the difference in the ballistic displacements of Gd and Co atoms during mixing. The spherical morphologies of the ion-mixed, small BP films was similar to that observed in completely mixed Co-B multilayer films.[2] As the layer thickness increased, the ion beam mixing was incomplete, and the films contained microcrystals embedded in an amorphous matrix. However, the microcrystals of ion beam mixed films were much smaller than those of as-deposited films due to the destruction of microcrystals by the implanted ions. The uniform amorphous matrix seen in the TEM micrographs of Figs. 5(b), 5(c) of large BP (300 Å) multilayers mixed at higher ion energies (300 keV), is similar to the morphology

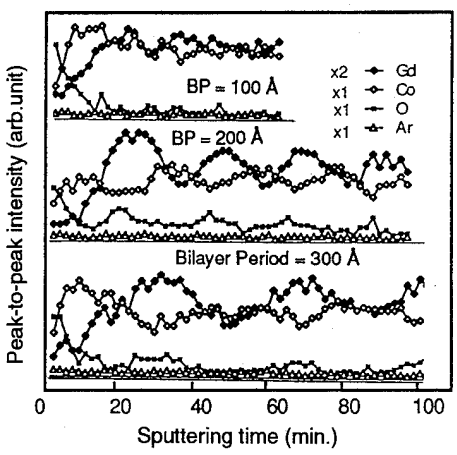



FIG. 4. Auger depth profiles of Gd-Co multilayer films mixed with 200 keV $Ar^+$ ions.

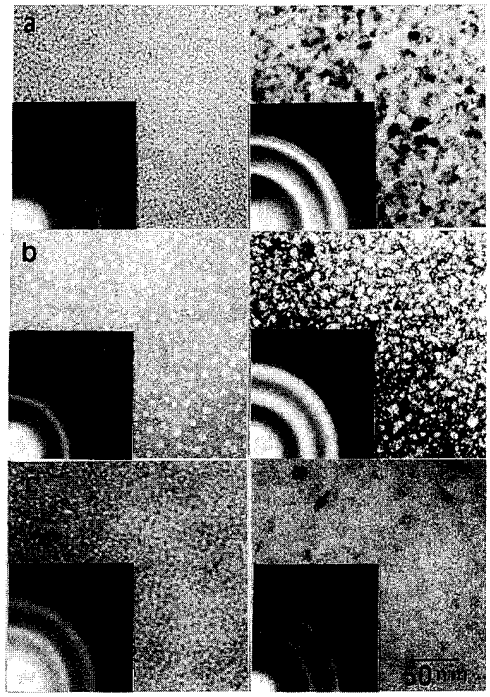



FIG. 5. TEM micrographs of (a) as-deposited Gd-Co multilayer films and ion-mixed films with (b) 150 keV and (c) 300 keV Ar ions: left: BP=10 Å, right: BP=300 Å.

of the as-deposited multilayer. These layers were incompletely mixed because the penetration depth (projected range ≈1240 Å) for the 300 keV ions was comparable to the film thickness.

The domain patterns observed by Lorentz microscopy (Fig. 6) in multilayers with a 300 Å BP, show that the strong ripple pattern associated with the crystalline Co layers in the as-deposited films, was not observed in the ion beam mixed

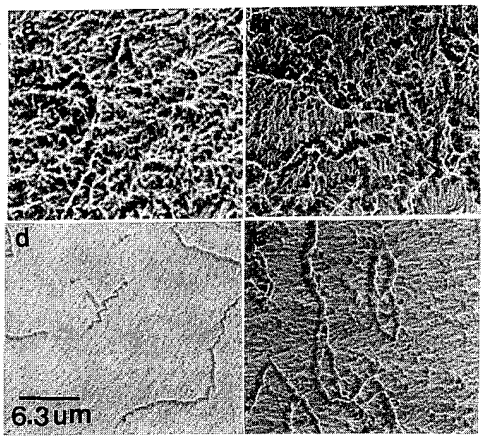



FIG. 6. Lorentz micrographs showing the changes in the magnetization distribution and domain structure of (a) the as-deposited (BP=300 Å) film, and ($b \rightarrow d$) after ion-mixing with increasing dosage of a 200 keV $Ar^+$ beam.

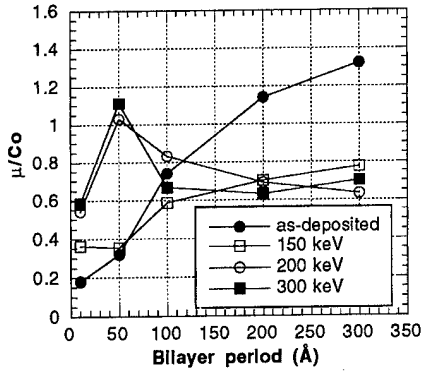



FIG. 7. Change in magnetic moment per Co atom of as-deposited, and ion beam mixed Gd-Co multilayer films with bilayer period.

film. After ion mixing, the irregular submicron domain structure of the as-deposited films was replaced by a single domain with a weak magnetization ripple. Intermediate ion mixing produced domains with a 360° wall structure, and coupled domain walls, similar to those observed in 100 Å BP multilayer films.

The changes in magnetic moments of the ion beam mixed films with ion beam energy are shown in Fig. 7 as a function of BP. After ion beam mixing, the magnetic moments of the larger BP films were greatly decreased due to the destruction of crystalline Co grains and the enhanced AF coupling of Gd/Co pairs, but those of small BP films changed only slightly. When the $Ar^+$ ion energy was increased from 150 to 200 or 300 keV, the magnetic moment of the small BP films was increased but that of large BP films did not change. Since the layered structure of films with large BP was not completely mixed by ion beam energies of 150 or 300 keV, their magnetic moment was nearly independent of ion beam energy. However, the magnetic moment of films with a small BP increased with the ion energy, indicating a change in the nearest-neighbor atomic exchange with ion energy. The energy dependent increase in the magnetic moment of the small BP films is ascribed to the enhancement of interfacial exchange in the hetero-amorphous state. This enhancement is evident in the 2D→3D transition in the TEM morphology (Fig. 5) of the ion-mixed film (10 Å BP).

## ACKNOWLEDGMENTS

This work was supported by the Industry/University of Texas Cooperative Research Center for Magnetics, and by the Texas Advanced Technology Program under Grant No. 257.

[1] (A representative set of references include) M. Van Rossum, M-A. Nicolet, and C. M. Wilts, J. Appl. Phys. **56**, 1032 (1984); G. Suran, R. Krishnan, M. Tessier, and P. Gerard, IEEE Trans. Magn. **20**, 1423 (1984); L. Smardz, J. Baszynski, and B. Rauschenbach, Thin Solid Films **175**, 295 (1989); Y. Kido, M. Tada, J. Mater. Res. **4**, 1151 (1989); M. Kopcewicz and D. L. Williamson, J. Appl. Phys. **74**, 4363 (1993); Z. J. Zhang and B. X. Liu, J. Phys. Conders. Mater. **6**, 2647 (1994).
[2] G. Choe and R. M. Walser, J. Appl. Phys. **73**, 6010 (1993).
[3] B. E. Warren, *X-ray Diffraction* (Addison-Wesley, Reading, MA, 1969).

# Nonlinear dynamics in microwave driven coupled magnetic multilayer systems

S. M. Rezende and F. M. de Aguiar
*Departamento de Física, Universidade Federal de Pernambuco, 50670-901 Recife-PE, Brasil*

Conventional microwave ferromagnetic resonance (FMR) techniques have proven very useful in the investigation of coupled magnetic multilayer systems. Here we show theoretically that with sufficiently high powers, a microwave magnetic field applied either parallel or perpendicular to the dc field, can drive nonlinear effects. The Landau–Lifschitz equation is used to obtain the nonlinear equations of motion for the two normal modes of a coupled two-layer system. In the usual FMR configuration, only the acoustic mode is coupled to the driving field. However, for driving fields above a critical value, energy can be transferred to the optic mode, in a process similar to the subsidiary resonance observed in spin-wave systems. At higher driving the system may display well-known transitions to chaos. © *1996 American Institute of Physics.* [S0021-8979(96)27208-7]

The interlayer exchange coupling between two ferromagnetic films provided by a metallic nonmagnetic spacer gives rise to a variety of phenomena which have attracted considerable interest in recent years.[1–3] The dynamic magnetic excitations in trilayer "sandwich" structures have been studied by ferromagnetic resonance (FMR) and Brillouin scattering techniques.[4] All investigations so far have been restricted to the linear regime of the excitations. However, the equations of motion of the magnetizations in the two coupled films are highly nonlinear. In this article we investigate the conditions under which nonlinear phenomena can be manifest in these systems.

We consider two ferromagnetic layers with uniform magnetizations $\mathbf{M}_1$ and $\mathbf{M}_2$ in a static external field $\hat{z}\,H_0$, applied in the film plane. We assume that the two layers have the same thickness $t$ and are made of the same material, so that they have the same $g$ value and the same saturation magnetization, $M_1=M_2=M$. The exchange energy per unit area is $E=-A_{12}\mathbf{M}_1\cdot\mathbf{M}_2/M_1M_2$, where the interaction constant $A_{12}$ can be positive (ferromagnetic) or negative (antiferromagnetic). In the latter case we assume that $H_0>2|H_{\rm exc}|\equiv 2|A_{12}|/tM$ so that in equilibrium the two magnetizations are parallel to each other. The motion of the magnetization is driven by a microwave oscillating field $h\cos\omega t$, applied either perpendicular to the static field (along $\hat{x}$, in the film plane), as in a FMR experiment, or parallel to the field ($\hat{z}$ direction). The motion of each magnetization is described by the Landau–Lifschitz equation,

$$\frac{d\mathbf{M}_i}{dt}=\gamma\mathbf{M}_i\times\mathbf{H}_i, \tag{1}$$

where the effective field $\mathbf{H}_i$ acting on $\mathbf{M}_i$ is related to the free-energy $E_i$ per unit volume through $\mathbf{H}_i=-\partial E_i/\partial\mathbf{M}_i$ and $\gamma$ is the gyromagnetic ratio (2.8 g/2 GHz/kOe). The damping is introduced by a phenomenological term with relaxation rate $\eta$.

Note that the dynamic demagnetizing energy introduces a uniaxial field perpendicular to the film plane, in the form $H_i^y=-4\pi M_i^y$. As a result the precession of the magnetization has an ellipticity given by

$$e=[(H_0+4\pi M)/H_0]^{1/2}. \tag{2}$$

The linearized equations of motion, obtained with $M_i^x$, $M_i^y\ll M_i^z\simeq M$, yield two normal modes. In the acoustic, or symmetric ($S$) mode, the magnetizations precess parallel to one another with frequency $\omega_S=\omega_0=\gamma[H_0(H_0+4\pi M)]^{1/2}$. In the optic, or antisymmetric ($A$) mode, the two precessions are out of phase and the frequency is $\omega_A=\omega_0+\gamma 2H_{\rm exc}$. In the perpendicular pumping configuration the symmetric mode is linearly coupled to the driving field whereas the antisymmetric mode is not coupled to the driving.

The nonlinearity in the equations of motion arises from the fact that $M_i^z$ is related to the transverse components of $\mathbf{M}$ by higher order terms,

$$M_i^z=[M^2-(M_i^{x2}+M_i^{y2})]^{1/2}\simeq M-(M_i^{x2}+M_i^{y2})/2M. \tag{3}$$

This leads to terms in the equations of motion involving products of three transverse components. In order to obtain the working equations from (1) we proceed with the following steps: (i) elliptically polarized variables are introduced by $M_i^{\pm}=M_i^x\pm ieM_i^y$, where the ellipticity $e$ is defined in Eq. (2); (ii) these variables are then replaced by slowly varying amplitudes in a frame rotating with frequency $\omega$, $\tilde{M}_i=M_i^+\exp(i\omega t)$; (iii) normal mode variables in the rotating frame are introduced through the transformations,

$$\alpha_S=(\tilde{M}_1+\tilde{M}_2)/\sqrt{2}M,\quad \alpha_A=(\tilde{M}_1-\tilde{M}_2)/\sqrt{2}M. \tag{4}$$

The resulting equations of motion for the normal mode variables in the perpendicular pumping configuration are,

$$\frac{d\alpha_S}{dt}=-(\eta+i\Delta\omega_S)\alpha_S+\gamma h(1+e)/\sqrt{2}-iI_1(\alpha_S\alpha_S\alpha_S^*+\alpha_A\alpha_A\alpha_S^*+2\alpha_S\alpha_A\alpha_A^*), \tag{5}$$

$$\frac{d\alpha_A}{dt}=-(\eta+i\Delta\omega_A)\alpha_A-iQ_1\alpha_A\alpha_A\alpha_A^*-iQ_2\alpha_S\alpha_S\alpha_A^*-iQ_3\alpha_S\alpha_S^*\alpha_A, \tag{6}$$

where $\Delta\omega_S=\omega_S-\omega$ and $\Delta\omega_A=\omega_A-\omega$ are the detunings and the nonlinear parameters are

$$Q_1=T_1+2T_2+4T_3,\quad Q_2=T_1+2T_2-4T_3,\quad Q_3=2T_1-4T_2, \tag{7}$$

 0021-8979/96/79(8)/6309/3/$10.00 © 1996 American Institute of Physics 

where

$$T_1=\frac{\gamma 4\pi M}{32e}(1+3/e^2),\quad T_2=-\frac{\gamma H_{\rm exc}}{32}(1-1/e^2)^2,$$
$$T_3=\frac{-\gamma H_{\rm exc}}{32}(1+1/e^2)^2. \tag{8}$$

Note that Eqs. (5) and (6) resemble those describing the nonlinearities in spin wave perpendicular pumping in the two-mode approximation.[5–7] However, whereas the derivation of the spin wave equations involve transformations from spin to magnon operators and lengthy algebraic treatment of the magnon Hamiltonian,[5] here the equations follow in a straightforward manner from the Landau–Lifschitz equation. One also sees in Eqs. (5) and (6) that while the $S$ mode is driven linearly by the oscillating field, the $A$ mode does not couple to the external field. However, the $A$ mode can be excited indirectly by the $S$ mode via the last two nonlinear terms in Eq. (6). This excitation is characterized by an exponential growth of the amplitude $\alpha_A$ when the driving field exceeds some threshold value $h_c$,

$$h_c\sim[(\eta^2+\Delta\omega_S^2)(\eta^2+\Delta\omega_A^2)^{1/2}/\gamma^3|H_{\rm exc}|]^{1/2}. \tag{9}$$

Through this process an absorption peak will appear at the frequency of the $A$ mode at sufficiently high power, similarly to the subsidiary resonance observed in FMR experiments.[7,8] In good crystalline metallic films, such as Fe, Ni, or Co, the FMR linewidths are on the order of 20–40 Oe, as compared to $10^{-1}$ Oe in yttrium iron garnet (YIG). As a result the critical fields in metallic films are at least $10^3$ larger than in YIG films in which nonlinear effects have been widely studied. The detunings also contribute to increase the values of $h_c$. Thus, in order to bring $h_c$ to more reasonable values one should work with sandwiches with large antiferromagnetic exchange coupling near the region where the dispersion relations of the two modes cross[9] [the actual normal modes in the spin-flop configuration yield equations similar to Eqs. (5) and (6)]. As the $h$ field increases further above $h_c$, the $A$ mode reacts back on the $S$ mode through the last two nonlinear terms in Eq. (5). As a result, at some critical value $h_c'$ there is a new bifurcation whereby the fixed point becomes unstable and the system starts to oscillate. The amplitude of the spin precession grows in one mode at the expense of the other, resulting in a dynamic alternating energy shuffling between the two modes. The frequency of this self-oscillation is on the order of $\eta$. In order to study this further one must resort to numerical solutions of Eqs. (5) and (6).

The numerical results presented here were obtained with the following parameters: $\Delta\omega_s/\eta=0.4$, $\Delta\omega_A/\eta=-0.4$, $T_1/\eta=T_2/\eta=1.0$, and $T_3/\eta=3.2$. These are approximately valid for a Ni/Ag/Ni sandwich with AF coupling near the mode-crossing frequency with parameters: $4\pi M\sim 4$ kOe, $H\sim 1.5$ kOe, $\Delta H\sim 30$ Oe, and $H_{\rm exc}\sim -50$ Oe. Figure 1 shows the time record of $|\alpha_A(t)|$ and the phase portrait $|\alpha_A(t)|$ vs $|\alpha_S(t)|$ as the control parameter $R=\gamma h(1+e)/\sqrt{2}\eta$ increases from 0.875 to 0.898. The initial conditions at $t=0$ have been chosen so that the transient response to the limit cycles is negligible. For $R=0.875$ the response is periodic and the frequency in this case is $f\sim 0.3\eta$. Similar to the high-power ferromagnetic resonance in bulk samples, this frequency increases with increasing $R$. Period doubling is shown for $R=0.888$ and a period-4 oscillation is shown for $R=0.893$. Higher-order bifurcations are observed as the driving field is further increased, accumulating at a critical value $R_c=0.8942\ldots$. The lower panel in Fig. 1 shows the strange attractor for $R=0.898$. The overall period-doubling scenario is shown in the bifurcation diagram of Fig. 2, obtained from the local maxima of $|\alpha_A(t)|$ as a function of $R$. There are many periodic windows in the chaotic region ($R>R_c$), the period-3 one being the largest, bearing close resemblance to the behavior of the standard logistic map.[10]

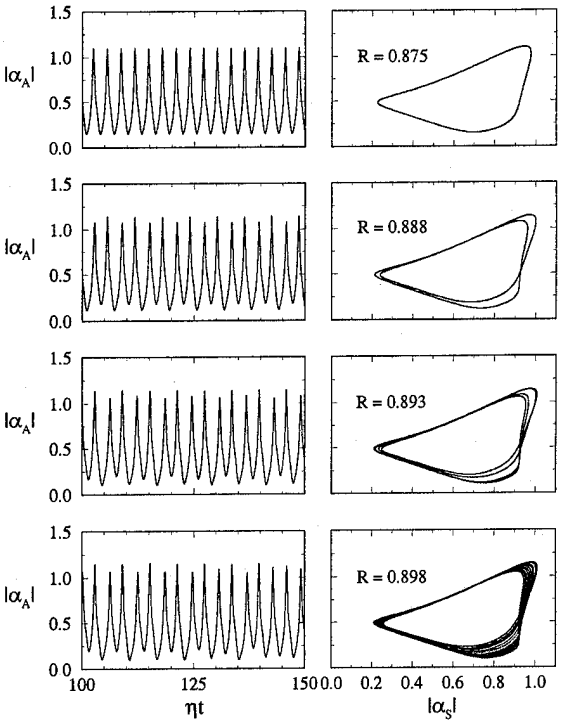



FIG. 1. Time series of $|\alpha_A|$ (left panels) and phase portraits $|\alpha_A(t)|$ vs $|\alpha_S(t)|$ (right panels) in the period-doubling region. Parameters are given in the text.

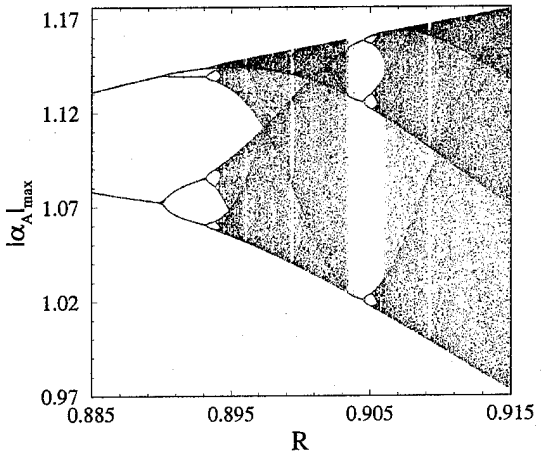



FIG. 2. Bifurcation diagram obtained from the local maxima of $|\alpha_A(t)|$. Parameters are given.

In the case where the driving field is applied parallel to the static field, both modes are driven nonlinearly with a term of the type $h\alpha_\lambda$, where $\lambda=S,A$. In this case each mode grows unstable only when the driving exceeds its critical value. Depending on the parameter values, auto-oscillations, and chaos develop at higher drivings, similar to the perpendicular pumping case.

This work has been supported by the Brazilian federal agencies Financiadora de Estudos e Projetos (FINEP), Conselho Nacional de Desenvolvimento Científico e Tecnológico (CNPq), Coordenação de Aperfeiçoamento de Pessoal de Nível Superior (CAPES), and Programa de Apoio ao Desenvolvimento Científico e Technológico (PADCT), and by the state agency Fundação de Amparo à Ciência e Tecnologia de Pernambuco (FACEPE).

[1] P. Gruenberg, R. Schreiber, and Y. Pang, Phys. Rev. Lett. **57**, 2442 (1986).
[2] M. N. Baibich *et al.*, Phys. Rev. Lett. **61**, 2472 (1988).
[3] S. S. P. Parkin, N. More, and K. P. Roche, Phys. Rev. Lett. **64**, 2304 (1990).
[4] See, for example, in *Linear and Nonlinear Spin Waves in Magnetic Films and Superlattices*, edited by M. G. Cottam (World Scientific, New Jersey, 1994).
[5] S. M. Rezende and F. M. de Aguiar, Proc. IEEE **78**, 893 (1990).
[6] K. Nakamura, S. Ohta, and K. Kawasaki, J. Phys. C **15**, L143 (1982).
[7] *Nonlinear Phenomena and Chaos in Magnetic Materials*, edited by P. E. Wigen (World Scientific, New Jersey, 1994).
[8] H. Suhl, J. Phys. Chem. Solids **1**, 209 (1957).
[9] Z. Zhang, L. Zhou, P. E. Wigen, and K. Ounadjela, Phys. Rev. B **50**, 6094 (1994).
[10] H. G. Schuster, *Deterministic Chaos*, 2nd ed. (VCH, New York, 1989).

# Magnetic interactions in nanocrystalline SmFeCo

D. R. Cornejo and F. P. Missell
*Instituto de Física, Universidade de São Paulo, CP 66318, 05389-970 São Paulo, SP, Brazil*

J. M. González
*Instituto de Ciencia de Materiales-CSIC, Serrano 144, 28006 Madrid, Spain*

Several samples of enhanced-remanence nanocrystalline $Sm_{15}Fe_{19}Co_{66}$ were prepared by mechanical alloying of the elementary powders followed by heat treatments. Sample A had a remanence ratio $\eta=\sigma_r/\sigma_s=0.68$ and $H_c=7.1$ kOe, while, for B, $\eta=0.58$ and $H_c=10.4$ kOe, and, for C, $\eta=0.57$ and $H_c=12.6$ kOe. The isothermal remanent magnetization $M_r(H)$, obtained for different initial demagnetized states (ac, $dc^+$, $dc^-$), and the demagnetization remanence $M_d(-H)$, obtained for an initially saturated state, were determined. The ac-demagnetization Henkel plot showed both magnetizing and demagnetizing interactions as observed in other nanocrystalline magnets. A comparison with the moving Preisach model indicates the importance of both mean-field and random interactions. © *1996 American Institute of Physics.* [S0021-8979(96)34408-8]

## I. INTRODUCTION

Nanocrystalline materials consisting of a hard magnetic rare earth-based intermetallic, exchange coupled to a soft magnetic phase have been the subject of much recent interest. This is due to the possibility of these materials presenting enhanced remanence and large energy products in magnets containing large volume fractions of a soft magnetic phase. Several examples of this phenomenon are known for which the hard magnetic phase is $Nd_2Fe_{14}B$.[1,2] On the other hand, Ding *et al.*[3] reported large energy products in a material consisting of $Sm_2Fe_{17}N_x+\alpha$-Fe, produced by mechanical alloying. Recently Ding *et al.*[4] and Smith *et al.*[5] investigated remanence enhancement in alloys of the SmFeCo system where high-moment $\alpha$-(Fe,Co) is encountered.

Modeling of these exchange-coupled systems by Kneller and Hawig[6] and by Schrefl *et al.*[7] has emphasized the ultrafine-grained microstructure necessary to achieve these "exchange-spring" magnets. However, it is also interesting to study magnetic interactions via remanence measurements using Henkel plots and the Preisach model.[8,9] In this case, an elegant mathematical apparatus can be brought to bear on the problem. The latter approach is adopted here to study magnetic interactions in three SmFeCo alloys presenting different degrees of remanence enhancement. Since the isothermal remanence $M_r(H)$ depends strongly upon the initial demagnetized state, it was obtained for different initial demagnetized states (ac, $dc^+$, $dc^-$). These results were compared to the demagnetization remanence $M_d(-H)$, obtained for an initially saturated state, to determine Henkel plots. The Henkel plot obtained for the ac demagnetization showed both magnetizing and demagnetizing interactions as observed in other nanocrystalline magnets.[2,10] The results were compared with the moving Preisach model.

## II. EXPERIMENT

The starting materials for the samples were high-purity elementary powders: Fe (99.99%, particle size $<40$ $\mu$m), Co (99.99%, particle size $<40$ $\mu$m), Sm (99.99%, particle size $<100$ $\mu$m). The initial composition of the alloys considered here was $Sm_{16}Fe_{10}Co_{74}$. Mechanical alloying was carried out for 30 h with hardened steel balls in a hardened steel vial using a Fritsch Pulverisette-7 mill. The mass of the balls was approximately 25 times the mass of the precursor powders. All powder handling and milling were carried out under a high-purity (99.99%) Ar atmosphere. After milling, the sample compositions were determined by energy dispersive x-ray analysis in a Cambridge Stereoscan 240 SEM. We obtained $Sm_{15}Fe_{19}Co_{66}$, reflecting increased Fe due to milling. As-milled powders were cold pressed into 3-mm-diam cylinders, wrapped in Ta foil, and heated under a $10^{-5}$ mbar vacuum for 15 min at (A) 640 °C, (B) 730 °C, or (C) 750 °C. For this temperature range, Ding *et al.*[4] reported the observation of disordered $Sm(Co,Fe)_7$ with the $TbCu_7$ structure. Our x-ray diffraction, DSC, and Mössbauer measurements will be reported at a later time. Finally, after annealing, the oxygen and nitrogen levels of the samples were measured with a Leco analyzer. Oxygen levels around 5500 ppm and nitrogen levels of 200 ppm were encountered. These levels are comparable to those found in $SmCo_5$ magnets produced in our laboratory.

Sample demagnetizations as well as magnetization measurements were made at room temperature using a vibrating sample magnetometer (VSM) mounted in a 90 kOe superconducting solenoid. Internal magnetic fields were calculated using the demagnetization factors appropriate for the cylindrical geometry of the sample. The $dc^-$ demagnetized state was obtained by saturating the sample to 50 kOe in the positive direction, after which $H$ was decreased to a negative remanent coercive field. Upon increasing $H$ to zero, the specific magnetization $\sigma$ was less than 1% of $\sigma_r$. For the $dc^+$ demagnetization, the sample was first saturated to 50 kOe in the negative direction, after which $H$ was increased to a positive remanent coercive field. Upon decreasing $H$ to zero, $\sigma<0.01\sigma_r$. Finally, the ac demagnetization was carried out

 0021-8979/96/79(8)/6312/3/$10.00 © 1996 American Institute of Physics

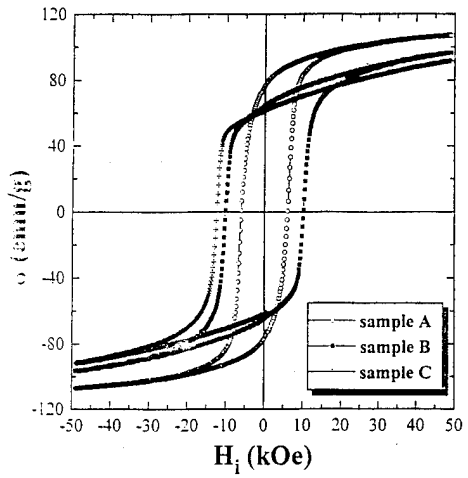



FIG. 1. Specific magnetization $\sigma$ vs internal magnetic field $H_i$ for samples A, B, and C.

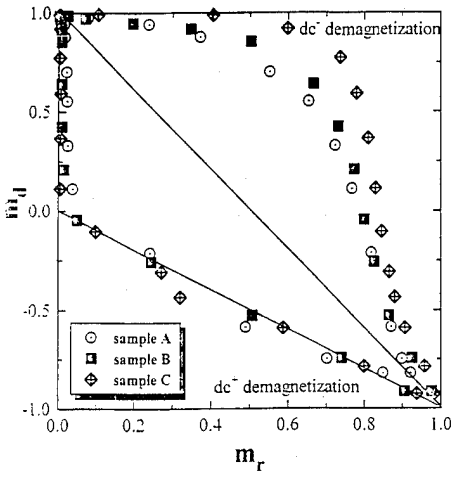



FIG. 2. Normalized demagnetization remanence $m_d$ vs normalized isothermal remanent magnetization $m_r$ for $dc^+$ and $dc^-$ demagnetizations.

by first saturating the sample to 50 kOe, followed by saturation at $-50$ kOe, then to 49 kOe, followed by $-49$ kOe, etc., until $\sigma<0.01\sigma_r$.

## III. RESULTS AND DISCUSSION

In Fig. 1 we show hysteresis curves for samples A, B, and C. The curves did not saturate at the highest fields used (90 kOe), but followed a general trend of higher coercivity values being associated with lower values of $\sigma_s$. The saturation value $\sigma_s$ was calculated by extrapolating the experimental curves to infinite fields using the expression $\sigma=\sigma_s(1-a/H)$. The coercive field $H_c$ was determined from the maximum value of the irreversible susceptibility. We obtained $\sigma_s=114$ emu/g, $\sigma_r=77$ emu/g, and $H_c=7.1$ kOe for sample A, giving a remanence ratio $\eta=\sigma_r/\sigma_s=0.68$. For sample B we obtained $\sigma_s=112$ emu/g, $\sigma_r=65$ emu/g, and $H_c=10.4$ kOe, giving a remanence ratio $\eta=\sigma_r/\sigma_s=0.58$. For sample C we obtained $\sigma_s=109$ emu/g, $\sigma_r=62$ emu/g, and $H_c=12.6$ kOe, giving a remanence ratio $\eta=\sigma_r/\sigma_s=0.57$. Thus, for all three samples we found $\sigma_s$ values which are essentially the same, considering our experimental uncertainty of 2%. Our $\sigma_s$ values are also in excellent agreement with those of Smith *et al.*[5]

For all three samples we observed remanence enhancement above the value $\eta=0.5$ expected for an isotropic magnet. As noted in Ref. 5, the remanence enhancement is lower in samples treated at higher temperatures and this may be due to the increased grain size of the exchange-coupled phases. Furthermore, as reported in Ref. 6 for an "exchange spring" magnet, second quadrant recoil curves show elevated susceptibility. Consistent with the $\eta$ values obtained, it was found that the reversible susceptibility was largest for sample A and smallest for C. Finally, the energy products were calculated for these three materials using the measured densities. Using a density of 6.1 g/cm$^3$, we obtained $(BH)_{max}=6.4$, 5.6, and 5.2 MG Oe for samples A, B, and C, respectively. If these materials had had their full densities (8.5 g/cm$^3$), $(BH)_{max}=10$–12 MG Oe would have been obtained.

Henkel plots were obtained for the three samples by plotting the normalized demagnetization remanence $m_d(-H)=M_d(-H)/M_r(90\text{ kOe})$ as a function of the normalized isothermal remanent magnetization $m_r(H)=M_r(H)/M_r(90\text{ kOe})$. We show the Henkel plots in Fig. 2 for the $dc^+$ and $dc^-$ demagnetizations. Also shown is the line $m_d=1-2m_r$ corresponding to noninteracting, single-domain particles[11] or domain walls in continuous media moving through a fixed distribution of pinning sites. For the $dc^+$ demagnetized state, the Henkel plots for samples A, B, and C are all closely coincident with the curves $m_r=0$ (when $m_d>0$) and $m_d=-m_r$ (when $m_d<0$). This result is predicted theoretically when there is no dispersion in local coercivities.[9] The $dc^+$ demagnetization thus effectively narrows the switching field distributions and allows their representation by some narrow function.

On the other hand, the differences in the switching field distributions have been emphasized by the $dc^-$ demagnetization. In Fig. 2, we see that, for the $dc^-$ demagnetization, the experimental points fall above the Wohlfarth line $m_d=1-2m_r$. In this case, the interactions are said to be magnetizing. In Fig. 2, the points corresponding to sample A are closest to this line, while those of sample C are farthest. Thus, the magnetizing interactions appear to be strongest for sample C, which possesses the highest coercive field $H_c=12.6$ kOe and the lowest remanence ratio $\eta=0.57$. In fact, the Henkel plot measures a combination of effects, and not simply the interaction with neighboring grains.[9] Thus it may be more helpful to consider the results for ac demagnetization.

In Fig. 3, we present $m_d$ vs $m_r$ for samples A and C after these had been subjected to an ac demagnetization. The experimental data for both A and C are close to the Wohlfarth line $m_d=1-2m_r$, being above it (magnetizing) for low fields and below it (demagnetizing) for high fields. This same kind of behavior was observed previously for nanocrystalline $Nd_9Fe_{85}B_6$ ($\alpha$-Fe+$Nd_2Fe_{14}B$) by Liu *et al.*[2] In that case, the dependence of the magnetic properties on applied field was determined for three nanocrystalline NdFeB alloys of very different Nd/Fe ratios. The deviation from the Wohlfarth line

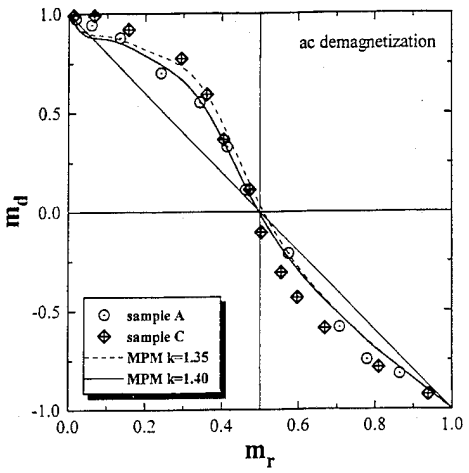



FIG. 3. $m_d$ vs $m_r$ for ac demagnetization of samples A and C. Dashed and solid curves were obtained from the moving Preisach model.

was largest (magnetizing) for the high Nd alloy where the grains were decoupled by the paramagnetic Nd-rich phase. On the other hand, the deviation was small and oscillatory, as we have observed here, for the low Nd alloy where there is believed to be substantial exchange coupling. An oscillatory Henkel plot was observed for thermally demagnetized nanocrystalline $Nd_4Fe_{78}B_{18}$ by Altoé *et al.*[10] This behavior was contrasted to that of MQII which showed strong magnetizing interactions. Thus, an oscillatory Henkel plot has been observed for high remanence materials belonging to the three major systems.

Several authors[8,9] have recently attempted to interpret Henkel plots using variations of the Preisach model. It has been shown using the moving Preisach model (MPM)[8] that Henkel plots exhibiting both magnetizing-like and demagnetizing-like deviations from the line $m_d=1-2m_r$ are an indication of the presence of random interactions and magnetizing-like mean-field effects. We have tried to compare the data of Fig. 3 to the MPM using a probability distribution $p(h_c,h_u)$ such as that of Eq. (14) of Ref. 8:

$$p(h_c,h_u)=\frac{1}{4\pi h_c\sigma_u\sigma_c}\exp\left[-\frac{(\log h_c)^2}{2\sigma_c^2}\right]\exp\left(-\frac{h_u^2}{2\sigma_u^2}\right). \tag{1}$$

The coercive fields have a log normal distribution of width $\sigma_c$ and interaction fields follow a Gaussian distribution of width $\sigma_u$. The MPM differs from the Preisach model in that the field $h=H/H_c$ acting on any elementary loop is

$$h=h_a+ki(h), \tag{2}$$

where $h_a$ is the external field, $ki(h)$ is the mean-field contribution, assumed proportional to the magnetization $i(h)$, and $k$ is the moving parameter. The curves of Fig. 3 represent the predictions of the MPM with $\sigma_c=1$, $\sigma_u=1$, and with the mean-field parameter $k$ assuming the values 1.35 and 1.40. There is general agreement with the shape of the experimental curve, the calculated curves presenting both magnetizing and demagnetizing regions. We have not yet optimized the values of $\sigma_c$, $\sigma_u$, and $k$. However, both the mean-field interactions and random interactions seem to be important in the case of these nanocrystalline materials, as suggested previously.

## IV. CONCLUSIONS

Three samples of nanocrystalline SmFeCo with different degrees of remanence enhancement have been produced. Henkel plots for an ac demagnetization show both magnetizing and demagnetizing regions, as was observed previously in $Nd_9Fe_{85}B_6(\alpha\text{-}Fe+Nd_2Fe_{14}B)$[2] and $Nd_4Fe_{78}B_{18}$.[10] The data were compared to the moving Preisach model. Preliminary calculations indicate the necessity to consider both mean-field and random interactions. It is not yet clear whether this model can account for the different degrees of remanence enhancement observed in our samples.

## ACKNOWLEDGMENTS

This work was supported by FAPESP, CNPq, FINEP, and the CEAM program.

[1] R. Coehoorn, D. B. de Mooij, J. P. W. B. Duchateau, and K. H. J. Buschow, J. Phys. (Paris) **49**, C8-669 (1988).
[2] J. F. Liu, I. Ahmad, H. A. Davies, P. Z. Zhang, S. G. Huo, and R. A. Buckley, *Proceedings of the 8th International Symposium on Magnetic Anisotropy and Coercivity in RE-TM Alloys* (University of Birmingham, Birmingham, UK, 1994), pp. 161–168.
[3] J. Ding, P. G. McCormick, and R. Street, J. Magn. Magn. Mater. **124**, L1 (1993).
[4] J. Ding, P. G. McCormick, and R. Street, J. Magn. Magn. Mater. **135**, 200 (1994).
[5] P. A. I. Smith, P. G. McCormick, and R. Street, *Proceedings of the 13th International Workshop on RE Magnets & Their Applications* (University of Birmingham, Birmingham, UK, 1994), pp. 425–433.
[6] E. F. Kneller and R. Hawig, IEEE Trans. Magn. **27**, 3588 (1991).
[7] T. Schrefl, H. Kronmüller, and J. Fidler, J. Magn. Magn. Mater. **127**, L273 (1993).
[8] V. Basso and G. Bertotti, IEEE Trans. Magn. **30**, 64 (1994).
[9] F. Vajda, E. Della Torre, and R. D. McMichael, J. Appl. Phys. **75**, 5689 (1994); R. D. McMichael, F. Vajda, and E. Della Torre, *ibid.* **75**, 5692 (1994).
[10] M. V. P. Altoé, M. S. Lancarotte, H. R. Rechenberg, F. P. Missell, and J. M. González, IEEE Trans. Magn. **31**, 3614 (1995).
[11] E. P. Wohlfarth, J. Appl. Phys. **29**, 595 (1958).

# Neutron diffraction studies of $Nd_nFe_{m-x-y}V_xAl_y$ [$(n,m)=(1,12)$, (2,17), (3,29)]

Z. Hu and W. B. Yelon
*Research Reactor Center, University of Missouri-Columbia, Columbia, Missouri 65211*

W. J. James
*Graduate Center for Materials Research, University of Missouri-Rolla, Rolla, Missouri 65401*

Several $Nd_nFe_{m-x-y}V_xAl_y$ [$(n,m)=(1,12)$, (2,17), (3,29)] samples were prepared and analyzed using neutron powder diffraction. Rietveld analysis of the neutron diffraction data indicates that the V and Al substituents take those sites with similar environments in all three phases, as observed in our previous study of Ti-substituted compounds. It was confirmed that the diffraction data of the 3:29 compound can be better refined using the $A2/m$ space group than using the $P2_1/c$ space group. The SQUID measurements show that all samples have Curie temperatures well above room temperature. The neutron diffraction results show that the easy direction is along the $a$ axis for the 3:29 compounds, along the $c$ axis for the 1:12 compounds and in the $a$-$b$ plane for 2:17 compounds, respectively. The average site magnetic moments, the metal–metal bond lengths and the unit cell parameters of these compounds are compared with those of the Ti-substituted compounds. © *1996 American Institute of Physics.* [S0021-8979(96)34508-4]

## I. INTRODUCTION

Because the number of known rare-earth-iron phases with high iron/rare-earth ratios is very limited, improving the magnetic properties of the known phases, especially the 2:17, 1:12 and the newly discovered 3:29 phases, to make them practically useful is a focus for research. Addition of some other elements into these phases, such as the interstitial atoms (C or N)[1–5] or substitutional atoms (Al,Ga,Si),[6–14] results in a dramatic enhancement in magnetic properties.

The unit cell of the rare-earth-iron compounds can expand upon the addition of substitutional atoms (Ga,Al)[6–8] or contract upon the addition of Si.[9–14] In both cases the magnetic properties can be enhanced significantly. It is believed that in the expansion case, like the Al-substituted 2:17 compounds, the lattice expansion is sufficient to decrease the antiferromagnetic exchange and to enhance the ferromagnetic exchange.[7] In the contraction case, the enhancement of magnetic properties with Si substitution may be related to the expansion of the bond lengths around the $6c$ and $18f$ sites.[14] However, it appears that the increase in the iron–iron bond lengths is not the only mechanism to improve the magnetic properties of these compounds.[15]

Our previous studies showed that Al and Si have similar site affinities at low Al or Si content and it was found that a combined substitution of Fe by Si and Al (both are nontransition metal atoms), at the appropriate levels, could lead to greater enhancement of the magnetic properties than the singly substituted compounds.[16] It is obviously interesting to study doubly substituted compounds using two substituents of different site affinities. Our previous studies showed that while Al prefers the $18h$ site at low Al contents in 2:17 compounds,[6,7] V atoms strongly prefer the $6c$ sites.[17] Here we report studies of Al+V (a nontransition atom plus a transition atom of different site affinity) substitution compounds, $Nd_nFe_{m-x-y}V_xAl_y$ [$(n,m)=(1,12)$, (2,17), (3,29)].

## II. EXPERIMENT

Samples used in this research were synthesized by rf induction melting of the constituent elements (purity 99.9% or better) in a water-cooled copper boat under a flowing argon atmosphere at the Graduate Center for Materials Research of the University of Missouri-Rolla. The ingots were annealed under vacuum at temperatures of 980 °C for one week. The annealed ingots were then crushed and ground in an acetone bath for neutron diffraction and other studies. Neutron diffraction data were collected using the position sensitive detector (PSD) diffractometer at the University of Missouri Research Reactor. Data collection times for each sample where typically 24 h on about 2 g of the powdered samples in a 3-mm-diam vanadium can at a wavelength of 1.4783 Å.

Neutron diffraction data were analyzed using the program FULLPROF, a program for Rietveld analysis of neutron (nuclear and magnetic scattering) or x-ray powder diffraction data collected at constant steps in the scattering angle $2\theta$ on a conventional instrument. The Curie temperatures $T_c$ were measured using a Quantum Design MPMS system.

## III. RESULTS AND DISCUSSION

It was suggested[18] recently that the structure of the 3:29 phase can be described more accurately by using the space group $A2/m$, a minimal nonisomorphic supergroup of type II of $P2_1/c$ space group which was initially used for solving the structure of this phase.[19–21] Thus, the neutron diffraction data of the 3:29 compounds were refined in both space groups ($P2_1/c$ and $A2/m$). It was found that the fitting factors were only slightly better when the space group $P2_1/c$ was used, in which as many as 91 parameters were refined, compared to 57 parameters refined for the space group $A2/m$. The $R$-factor ratio[22] test leads to the conclusion that the model based on the space group $A2/m$ is more reliable, which confirms the conclusion of Kalogirou *et al.*[18]

Samples with V and Al content ratio changing in a limited range were prepared but only one of each type with the

TABLE I. Refinement results for $NdFe_{10.05}V_{1.38}Al_{0.57}$.

| Space group: $I4/mmm$ | | | Unit cell volume=351.443 Å$^3$ | | | |
|---|---|---|---|---|---|---|
| Atom and site | $x$ | $y$ | $z$ | V (%) | Al (%) | $m$ |
| Nd, 2$a$ | 0 | 0 | 0 | | | 1.8(2) |
| Fe, 8$i$ | 0.2704(3) | 0.5 | 0 | 34.8 | | 2.2(2) |
| Fe, 8$j$ | 0.3586(3) | 0 | 0 | | 14.4 | 2.4(3) |
| Fe, 8$k$ | 0.25 | 0.25 | 0.25 | | | 2.0(1) |
| Lattice parameters: | $a$=8.5691(3) | $c$=4.7861(2) | | | | |
| Fitting factors: | $R_p$=5.80 | $R_{wp}$=7.06 | $R_{mag}$=3.29 | $\chi^2$=1.44 | | |

best phase purity are reported in this paper and the refinement results are given in Tables I, II, and III. Previous work shows that Al and V atoms introduced into $Nd_2Fe_{17}$ compounds will expand the cell of the compounds by 1.44 Å$^3$/V atom[17] and 8.49 Å$^3$/Al atom.[7] The lattice parameters of the V+Al double substituted 2:17 compound are linear combinations of the corresponding singly substituted compounds (Table II). For 1:12 and 3:29 compounds, no data for Al or V single-substitution compounds are available and thus no comparison can be made.

It is not possible to determine the site distributions of the substituents in doubly substituted compounds directly from the neutron diffraction techniques. We use some assumptions based on our previous work to determine the locations of the substituents, as was done for $Nd_2Fe_{17-x-y}Al_xSi_y$.[16] It is found that the V atoms will mostly occupy the 6$c$ sites, which have the fewest rare-earth neighbors and the most transition metal neighbors in $Nd_2Fe_{17-x}V_x$,[17] and it is assumed that the V atoms will occupy the same sites in the $Nd_2Fe_{17-x-y}V_xAl_y$ compound. It was also found that the Ti atoms will occupy sites with similar environments in all 1:12, 2:17, and 3:29 phases.[21] In fact, because the structures of all three compounds are derived from the same parent structure of $RT_5$ with differing degrees of Fe–Fe dumbbell replacement for the rare-earth atoms, it is assumed that a given substituent will occupy those sites with similar environments in all 1:12, 2:17, and 3:29 compounds. Thus, we assume that the V atoms will occupy those sites with the fewest rare-earth neighbors and most transition metal neighbors, while Al atoms will prefer those sites with the most rare-earth neighbors and the fewest transition metal neighbors in all V+Al double-substituted 1:12, 2:17, and 3:29 compounds. Thus, the V atoms occupy the three dumbbell sites in the 3:29 phase, the 6$c$ sites in the 2:17 and the 8$i$ sites in the 1:12 phase, while the substituents found in any other sites are Al atoms. In fact, the neutron data show a strong decrease of the effective scattering length in those sites with the fewest rare-earth neighbors, which indicates substitution of V atoms at those sites because V has a very small scattering length. By using these assumptions, the site occupancies of V and Al in Tables I, II, and III are obtained.

The refined site magnetic moments are also given in Tables I, II, and III. The easy direction is found along the $a$ axis for the 3:29 compounds, along the $c$ axis for the 1:12 compounds and in the $a$-$b$ plane for the 2:17 compounds, respectively. The 1:12 compound has the biggest site moments whereas the 3:29 compound has the smallest site moments. The average Fe site moments are 2.2, 1.81, and 1.5$\mu_B$ for the 1:12, 2:17, and 3:29 compounds, respectively. Compared to the average site moment of $Nd_2Fe_{16.03}Ti_{0.97}$, 1.95$\mu_B$,[21] the average site moment of $Nd_2Fe_{15.66}V_{1.06}Al_{0.28}$ is a little lower, very possibly due to the higher substituent content in the V+Al double-substituted compound. Similarly, the average site moment of $NdFe_{10.05}V_{1.38}Al_{0.57}$, 2.2$\mu_B$, is lower than that of the $Nd_2Fe_{10.9}Ti_{1.1}$ compound, 2.36$\mu_B$.[21] For the 3:29 compounds, the refined average site moment of $Nd_3Fe_{26.97}V_{1.83}Al_{0.20}$, 1.11$\mu_B$, is a little higher than that of the $Nd_3Fe_{27.76}Ti_{1.24}$ compound (1.05$\mu_B$) in spite of the higher substituent content in $Nd_3Fe_{26.97}V_{1.83}Al_{0.20}$. The SQUID measurements give Curie temperatures of 600, 395, and 385 K for the 1:12, 2:17, and 3:29 compounds, respectively. Because the Curie temperatures of the corresponding Al or V single-substitution compounds are not available at present, no comparison between single- and double-substituted compounds can be made. The high $T_c$ and large site magnetic moment of the 1:12 compound suggests that it can be of economic interest even without nitriding or carbiding. Since the substituents and their content ratio can be adjusted in a wide range for doubly substituted compounds, it will not be surprising if doubly substituted compounds with even better properties are discovered.

TABLE II. Refinement results for $Nd_2Fe_{15.66}V_{1.06}Al_{0.28}$.

| Space group: $R-3m$ | | | Unit cell volume=813.306 Å$^3$ | | | |
|---|---|---|---|---|---|---|
| Atom and site | $x$ | $y$ | $z$ | V (%) | Al (%) | $m$ |
| Nd, 6$c$ | 0 | 0 | 0.3439(3) | | | 2.8(2) |
| Fe/V, 6$c$ | 0 | 0 | 0.0949(4) | 37.7 | | 1.6(4) |
| Fe, 9$d$ | 0.5 | 0 | 0.5 | | | 1.4(2) |
| Fe/V, 18$f$ | 0.2902(2) | 0 | 0 | 5.0 | | 2.1(2) |
| Fe/Al, 18$h$ | 0.1691(1) | −0.1691(1) | 0.4907(2) | | 4.6 | 1.8(2) |
| Lattice parameters: | $a$=8.6428(3) | $c$=12.5722(4) | | | | |
| Fitting factors: | $R_p$=4.16 | $R_{wp}$=5.20 | $R_{mag}$=5.18 | $\chi^2$=1.54 | | |

TABLE III. Refinement results for $Nd_3Fe_{26.97}V_{1.83}Al_{0.20}$.

| Space group: $A2/m$ | | | Unit cell volume=886.210 Å$^3$ | | | |
|---|---|---|---|---|---|---|
| Atom and site | $x$ | $y$ | $z$ | V (%) | Al (%) | $m$ |
| Nd1, 2$a$ | 0 | 0 | 0 | | | 1.5(2) |
| Nd2, 4$i$ | 0.5982(16) | 0 | 0.1864(17) | | | 1.5(2) |
| Fe1, 2$c$ | 0.5 | 0 | 0.5 | | | 1.5(2) |
| Fe2, 4$e$ | 0 | 0.25 | 0.25 | | | 1.5(2) |
| (Fe/V)3, 4$e$ | 0 | 0.3578(20) | 0 | 16.4 | | 1.5(2) |
| Fe4, 4$i$ | 0.1138(15) | 0 | 0.7103(16) | | | 1.5(2) |
| (Fe/Al)5, 4$i$ | 0.3055(18) | 0 | 0.0891(20) | | 3.6 | 1.5(2) |
| (Fe/V)6, 4$i$ | 0.2312(24) | 0 | 0.5019(23) | 37.4 | | 1.5(2) |
| (Fe/V)7, 4$i$ | 0.1327(23) | 0 | 0.2901(22) | 37.6 | | 1.5(2) |
| Fe8, 8$j$ | 0.6232(9) | 0.1440(13) | 0.6804(12) | | | 1.5(2) |
| Fe9, 8$j$ | 0.8102(10) | 0.2188(8) | 0.1003(11) | | | 1.5(2) |
| (Fe/Al)10, 8$j$ | 0.4059(9) | 0.2486(14) | 0.0688(8) | | 3.2 | 1.5(2) |
| Fe11, 8$j$ | 0.1998(9) | 0.2545(16) | 0.1577(12) | | | 1.5(2) |
| Lattice parameters: | $a$=10.6576(14) | $b$=8.5937(7) | $c$=9.7508(15) | $b$=96.978(11) | | |
| Fitting factors: | $R_p$=5.77 | $R_{wp}$=7.01 | $R_{mag}$=7.06 | $\chi^2$=3.35 | | |

## IV. CONCLUSIONS

It was confirmed that the diffraction data of the 3:29 compound can be better refined using the $A2/m$ space group than using the $P2_1/c$ space group. All samples have Curie temperatures well above room temperature. The easy direction is along the $a$ axis for the 3:29 compounds, along the $c$ axis for the 1:12 compounds and in the $a$-$b$ plane for the 2:17 compounds. The average site magnetic moments are similar to those of the Ti-substituted compounds.

## ACKNOWLEDGMENT

This work is supported by the Division of Materials Research of the National Science Foundation (Grant No. DMR-9305782) and the Missouri University Research Board.

[1] D. B. de Mooij and K. H. J. Buschow, J. Less-Common Met. **142**, 349 (1988).
[2] R. B. Helmholdt and K. H. J. Buschow, J. Less-Common Met. **155**, 15 (1989).
[3] J. M. D. Coey and H. Sun, J. Magn. Magn. Mater. **87**, 1251 (1990).
[4] H. Sun, J. M. D. Coey, Y. Otani, and D. P. F. Hurley, J. Phys. **2**, 6465 (1990).
[5] Y. C. Yang, X. D. Zhang, L. S. Kong, Q. Pan, J. L. Yang, Y. F. Ding, B. S. Zhang, and C. T. Ye, Solid State Commun. **78**, 313 (1991).
[6] W. B. Yelon, H. Xie, G. J. Long, O. A. Pringle, F. Grandjean, and K. H. J. Buschow, J. Appl. Phys. **73**, 6029 (1993).
[7] G. J. Long, G. K. Marasinghe, Z. Hu, W. B. Yelon, D. P. Middleton, K. H. J. Buschow, and F. Grandjean, J. Appl. Phys. **76**, 5383 (1994).
[8] Z. Hu, W. B. Yelon, S. Mishra, G. J. Long, O. A. Pringle, D. P. Middleton, K. H. J. Buschow, and F. Grandjean, J. Appl. Phys. **76**, 443 (1994).
[9] R. van Mens, J. Magn. Magn. Mater. **61**, 24 (1986).
[10] E. E. Alp, A. M. Umarji, S. K. Malik, G. K. Shenoy, M. Q. Huang, E. B. Boltich, and W. E. Wallace, J. Magn. Magn. Mater. **68**, 305 (1987).
[11] P. C. M. Gubbens, A. M. van der Kraan, T. H. Jacobs, and K. H. J. Buschow, J. Less-Common. Met. **159**, 173 (1990).
[12] C. Lin, Y. X. Sun, Z. X. Liu, H. W. Jiang, G. Jiang, Y. L. Yang, B. S. Zhang, and Y. F. Ding, Solid State Commun. **81**, 299 (1992).
[13] F. Pourarian, R. Obermyer, Y. Zhang, S. G. Shankar, and W. E. Wallace, J. Appl. Phys. **73**, 6272 (1993).
[14] G. J. Long, G. K. Marasinghe, S. Mishra, O. A. Pringle, F. Grandjean, K. H. J. Buschow, D. P. Middleton, W. B. Yelon, F. Pourarian, and O. Isnard, Solid State Commun. **88**, 761 (1993).
[15] C. H. de Groot, F. R. de Boer, K. H. J. Buschow, W. B. Yelon, and Z. Hu (unpublished).
[16] Z. Hu and W. B. Yelon, J. Appl. Phys. **76**, 6147 (1994).
[17] W. B. Yelon, Z. Hu, W. J. James, and G. K. Marasinghe, these proceedings.
[18] O. Kalogirou, V. Psycharis, L. Saettas, and D. Niarchos, J. Magn. Magn. Mater. 145 (1995).
[19] H-S Li, J. M. Cadogan, R. L. Davis, A. Margarian, and J. B. Dunlop, Solid State Commun. **90**, 487 (1994).
[20] Z. Hu and W. B. Yelon, Solid State Commun. **91**, 233 (1994).
[21] Z. Hu and W. B. Yelon, J. Appl. Phys. **76**, 6147 (1994).
[22] *International Tables for X-ray Crystallography* (Kynoch, Birmingham, England, 1974), Vol. IV, p. 288.

# Neutron diffraction structural study of $Ce_2Fe_{17-x}Ga_x$

H. Luo, Z. Hu, and W. B. Yelon
*University of Missouri Research Reactor, Columbia, Missouri 65211*

S. R. Mishra, G. J. Long, and O. A. Pringle
*Department of Physics and Chemistry, University of Missouri-Rolla, Rolla, Missouri 65401-0249*

D. P. Middleton
*Philips Research Laboratories, NL-5656 AA Eindhoven, The Netherlands*

K. H. J. Buschow
*Van der Waals-Zeeman Laboratory, University of Amsterdam, NL-1018 XE Amsterdam, The Netherlands*

Six samples of $Ce_2Fe_{17-x}Ga_x$ with nominal Ga content $x$ equal to 0, 0.3, 0.5, 0.7, 1.0, 2.0 have been studied by powder neutron diffraction at room temperature. Both crystalline and magnetic refinements have been carried out. All six samples adopt the $Th_2Zn_{17}$-type rhombohedral structure. The only additional phase found is $\alpha$-iron. Gallium atoms are found to have high affinity for the iron 18*h* site, and are absent from the 9*d* and 18*f* sites. The Ga substitution for Fe leads to an expansion of both the *a* and *c* axes. The Curie temperature increases from 238 K for $Ce_2Fe_{17}$ to 406 K for $Ce_2Fe_{15}Ga_2$. Magnetic refinements on the samples with $x=0.3$, 0.5, 0.7, 1.0, and 2.0 reveal that the magnetic moments of the four Fe sites are in the basal plane and that their values increase with increasing Ga content. © *1996 American Institute of Physics.* [S0021-8979(96)34608-0]

## I. INTRODUCTION

The studies of high-performance hard magnetic materials consisting of rare-earth (R)-3*d* transition metals have been reinvigorated after the discovery of the ternary $Nd_2Fe_{14}B$ compound[1,2] and the carbided, hydrided, and nitrided compounds based on the $R_2Fe_{17}$ and $RFe_{12}$ phases.[3,4] It is believed that the lengthened Fe–Fe bonds, with enhanced ferromagnetic exchange, play an important role in the increase of Curie temperature ($T_c$). It has been found that some iron site substitutional atoms, such as Al, Si, Ti, and Ga, can also enhance the Curie temperature significantly.[8] Thus, it is of interest to look into the influence of the substitutional atom(s) on the crystallographic structure and the intrinsic magnetic properties of these compounds. Recent studies[7,9,10] of $Tb_2Fe_{17-x}Ga_x$, $Nd_2Fe_{17-x}Ga_x$, and $Tb_2Fe_{17-x}Al_x$ reveal that an increase in unit cell volume and Curie temperature can be achieved through the substitution of gallium or aluminum for iron. For the Tb series, the Curie temperature reaches a maximum between $x=3$ and 4 and the easy magnetization direction changes from planar to axial with increasing Ga concentration. In this article, we report a neutron diffraction structural study of $Ce_2Fe_{17-x}Ga_x$ with gallium nominal composition $x$ up to 2.0. Since Ce is expected to be nonmagnetic, the effect of R-Fe exchange may be ignored.

## II. EXPERIMENT

$Ce_2Fe_{17-x}Ga_x$ samples with nominal gallium contents of $x=0$, 0.3, 0.5, 0.7, 1.0, and 2.0 were prepared by radio-frequency induction melting of the constituent elements of purity 99.9–99.95%. The samples were wrapped in tantalum foil and annealed in argon atmosphere at 950 °C for one week. They were then crushed and ground for later measurements. Neutron diffraction data were collected at the University of Missouri Research Reactor using the high-resolution linear position-sensitive detector diffractometer at room temperature. The neutron wavelength was 1.4783 Å. Approximately 1 g samples were contained in thin wall (0.1 mm) vanadium holders. The data were accumulated in five settings of the detector in 24 h with $2\theta$ values ranging from 5° to 105° in 0.05° steps. The neutron diffraction powder patterns were analyzed by the Rietveld method[11] using the FULLPROF program[12] for multiphase refinement, including magnetic structure refinement.

## III. RESULTS AND DISCUSSION

From the powder neutron diffraction data refinement, all six samples were confirmed to adopt the $Th_2Zn_{17}$-type rhombohedral structure with the R-3*M* space group. The refinement results are given in Table I. Both the *a* and *c* lattice parameters increase as the gallium content increases, approximately 0.45% per substituted Ga for *a* and 0.55% for *c*, as is shown in Fig. 1. The compositional dependence of the unit cell volume is also shown in Fig. 1. The unit cell volume expands from ~775 Å$^3$ for $Ce_2Fe_{17}$ to ~799 Å$^3$ for $Ce_2Fe_{15}Ga_2$. The corresponding Curie temperature rises from 238 K for the parent binary phase to 406 K for $Ce_2Fe_{15}Ga_2$. The compositional dependence of the *c*/*a* ratio is weak; only a very slight rise is observed. $\alpha$-Fe was observed in all samples with a maximum of almost 12% in volume.

Gallium is found to have high affinity for the iron 18*h* site, which is filled by 35% Ga for $x=2$. Some Ga is also found in the iron 6*c* site with less than 10% for the sample with the highest Ga content. However, no gallium is found on either the 9*d* or the 18*f* site. The compositional dependence of the gallium site occupancy is shown in Fig. 2. The 6*c* gallium site occupancy appears to be close to saturation at ~10% for $x>1$. In $Ce_2Fe_{17}$, the iron 6*c* site has the largest Wigner–Seitz cell volume[7] followed by the 18*h* site, while the 9*d* site is the smallest. Gallium's high affinity for the 18*h* site is because this site has the most near-neighbor rare-earth atoms in the coordination shell. The effect of Ga having high

 0021-8979/96/79(8)/6318/3/$10.00 © 1996 American Institute of Physics

TABLE I. Refinement results for the $Ce_2Fe_{17-x}Ga_x$ solid solutions at room temperature. *Data for $Ce_2Fe_{17}$ are from Ref. 13.

| PARAMETER | $x=0$* | $x=0.3$ | $x=0.5$ | $x=0.7$ | $x=1.0$ | $x=2.0$ |
|---|---|---|---|---|---|---|
| $x$ (refined) | 0 | 0.31 | 0.52 | 0.87 | 1.44 | 2.39 |
| $a$ (Å) | 8.4921(2) | 8.5091(2) | 8.5136(2) | 8.5284(3) | 8.5396(3) | 8.5742(2) |
| $c$ (Å) | 12.4060(3) | 12.4354(4) | 12.4394(4) | 12.4641(6) | 12.4887(6) | 12.5425(3) |
| $c/a$ | 1.4608 | 1.4614 | 1.4612 | 1.4615 | 1.4626 | 1.4628 |
| $V$ (Å$^3$) | 774.89 | 779.749 | 780.843 | 785.102 | 788.72 | 798.549 |
| $T_c$ (K) | 238 | ... | ... | ... | 342 | 406 |
| Ce, $6c,z$ | 0.3441(5) | 0.3427(9) | 0.3429(8) | 0.3418(6) | 0.3422(10) | 0.3412(6) |
| Fe/Ga, $6c,z$ | 0.0970(2) | 0.0965(4) | 0.0965(3) | 0.0956(3) | 0.0954(4) | 0.0950(3) |
| Fe, $18f,x$ | 0.2905(1) | 0.2906(3) | 0.2909(2) | 0.2907(2) | 0.2915(3) | 0.2909(2) |
| Fe/Ga, $18h,x$ | 0.1678(1) | 0.1682(2) | 0.1684(2) | 0.1681(2) | 0.1689(2) | 0.1686(2) |
| Fe/Ga, $18h,z$ | 0.4883(1) | 0.4881(2) | 0.4877(2) | 0.4883(2) | 0.4883(2) | 0.4885(2) |
| %Ga, $6c$ | 0 | 1.8 | 4.2 | 7.2 | 8.1 | 9.6(5) |
| %Ga, $18h$ | 0 | 4.6 | 7.4 | 12.8 | 20.1 | 35.2(3) |
| $\mu$, Fe, $6c$ | ... | 0.2 | 0.5 | 0.8 | 2.2(5) | 2.9(4) |
| $\mu$, Fe, $9d$ | ... | 0.2 | 0.5 | 0.8 | 1.1(3) | 1.6(2) |
| $\mu$, Fe, $18f$ | ... | 0.2 | 0.5 | 0.8 | 1.1(3) | 1.6(2) |
| $\mu$, Fe, $18h$ | ... | 0.2 | 0.5 | 0.8 | 1.8(3) | 1.9(3) |
| $\chi^2$ | 2.91 | 2.97 | 3.62 | 2.06 | 4.18 | 4.27 |
| R factor | 5.05 | 7.03 | 6.79 | 5.79 | 7.33 | 6.50 |
| Rw factor | 7.11 | 9.49 | 9.39 | 7.71 | 9.69 | 8.74 |
| Rm factor | ... | 6.13 | 6.81 | 4.79 | 6.06 | 7.71 |
| ALFA-Fe, % $V$ | 5.6 | 5.1 | 3.62 | 0.66 | 11.9 | 5.14 |

affinity for rare-earth atoms surpasses that of the site volume, as is also the case[5,13,14] for Si- and Al-doped samples.

The bond lengths and the site average bond lengths are listed in Table II. Almost all bond lengths increase with increasing Ga concentration, as do the average bond lengths for all four Fe sites. However, two exceptions were observed for $18f-18h$ and $6c-6c$ bond lengths. The $6c-6c$ dumbbell, which is often thought to be responsible for the low Curie temperature of the $R_2Fe_{17}$ compounds, decreases slightly with Ga content despite the increase in the $c$ axis. From this, one would predict a decrease in Curie temperature, which is in contrast with the observations. This phenomenon has also been observed in some other investigations.[13–15] This suggests that it is unlikely that the changes in $T_c$ arise from the changes of the $6c-6c$ bond, but rather, the increase is more likely related to the average bond lengths.

Magnetic refinement has been carried out on samples with $x=0.3$, 0.5, 0.7, 1.0, and 2.0. $Ce_2Fe_{17}$ is not magnetically ordered at room temperature and in all cases cerium is treated as nonmagnetic. The refinement results indicate that the magnetic moments of all four Fe sites lie in the basal plane and the average values of these moments tend to increase with increasing gallium content. The magnetic moments at low gallium contents have been constrained to be equal rather than being refined independently because their moments are too small to give reliable individual values. The refinement results for $x=1$ and 2 samples show that the moments of the $6c$ and $18h$ sites are larger than those of the $9d$ and $18f$ sites, especially that of the $6c$ site. The overall in-

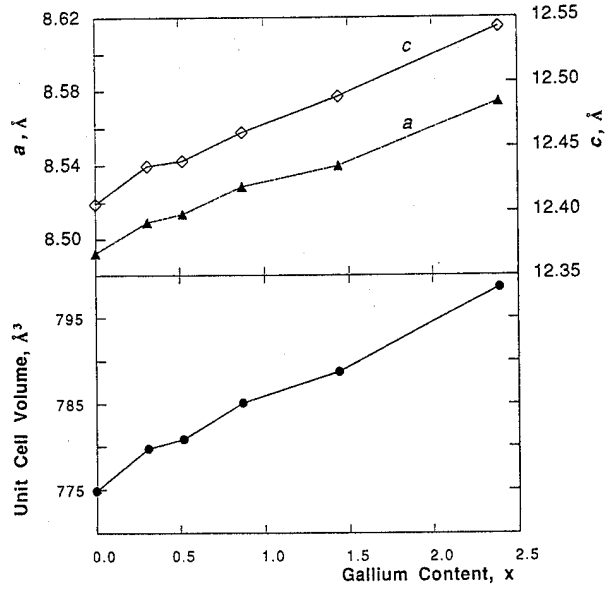



FIG. 1. Compositional dependence of the lattice parameters $a$, $c$, and the unit cell volume of $Ce_2Fe_{17-x}Ga_x$ solid solution.

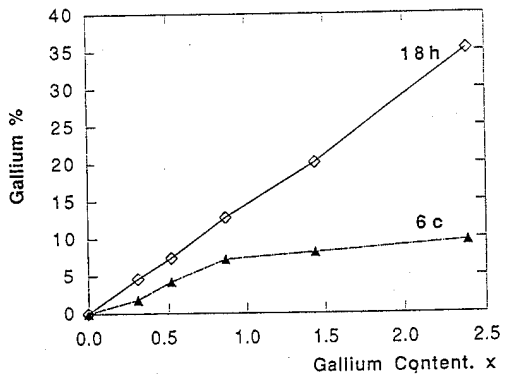



FIG. 2. Compositional dependence of the gallium site occupancy of $Ce_2Fe_{17-x}Ga$ solid solution.

TABLE II. Bond lengths and site averaged average bond lengths for the $Ce_2Fe_{17-x}Ga_x$ solid solutions.

| Bond | $x=0$ | $x=0.3$ | $x=0.5$ | $x=0.7$ | $x=1.0$ | $x=2.0$ |
|---|---|---|---|---|---|---|
| Fe(6*c*)–Fe(6*c*) | 2.4068(35) | 2.3975(70) | 2.4008(53) | 2.3853(53) | 2.3803(71) | 2.3806(53) |
| Fe(6*c*)–Fe(9*d*) | 2.5994(8) | 2.6072(17) | 2.6081(13) | 2.6181(13) | 2.6213(17) | 2.6337(13) |
| Fe(6*c*)–Fe(18*f*) | 2.7448(12) | 2.7495(23) | 2.7537(18) | 2.7525(18) | 2.7584(24) | 2.7645(18) |
| Fe(6*c*)–Fe(18*h*) | 2.5338(12) | 2.6424(27) | 2.6415(22) | 2.6502(19) | 2.6441(28) | 2.6600(24) |
| Fe(9*d*)–Fe(18*f*) | 2.4282(4) | 2.4340(9) | 2.4353(9) | 2.4415(9) | 2.4447(13) | 2.4546(9) |
| Fe(9*d*)–Fe(18*h*) | 2.4475(9) | 2.4506(18) | 2.4506(18) | 2.4565(9) | 2.4532(18) | 2.4651(18) |
| Fe(18*f*)–Fe(18*f*) | 2.4670(6) | 2.4745(12) | 2.4783(12) | 2.4807(22) | 2.4884(18) | 2.4951(12) |
| Fe(18*f*)–Fe(18*h*) | 2.3036(11) | 2.5619(23) | 2.5651(23) | 2.5642(22) | 2.5665(34) | 2.5752(23) |
| Fe(18*f*)–Fe(18*h*) | 2.8394(13) | 2.6189(25) | 2.6165(25) | 2.6321(23) | 2.6306(35) | 2.6457(25) |
| Fe(18*h*)–Fe(18*h*) | 2.4852(13) | 2.4960(21) | 2.5009(21) | 2.5032(11) | 2.5152(22) | 2.5204(26) |
| AVER BL | | | | | | |
| Fe, 6*c* | 2.6377 | 2.6648 | 2.6671 | 2.6696 | 2.6713 | 2.6806 |
| Fe, 9*d* | 2.4702 | 2.4653 | 2.4761 | 2.4828 | 2.4834 | 2.4946 |
| Fe, 18*f* | 2.5566 | 2.5678 | 2.5698 | 2.5742 | 2.5777 | 2.5871 |
| Fe, 18*h* | 2.5211 | 2.5441 | 2.5453 | 2.5513 | 2.5527 | 2.5636 |

crease in site moments is the result of the increase in Curie temperature and the larger degree of magnetic order at room temperature.

## IV. CONCLUSIONS

Both the *a* and *c* lattice parameters show a similar dependence on Ga content in the $Ce_2Fe_{17-x}Ga_x$ solid solutions. The gallium atoms have a high affinity for the iron 18*h* site. The easy magnetization direction is in the basal plane.

## ACKNOWLEDGMENTS

This work was partially supported by the Division of Materials Research of the U.S. National Science Foundation (Grants No. DMR-92142711 and No. DMR-9305782) and the University of Missouri Research Board.

[1] J. J. Croat, J. F. Herbst, R. W. Lee, and F. E. Pinkerton, Appl. Phys. Lett. **44**, 148 (1984).
[2] J. F. Herbst, J. J. Croat, F. E. Pinkerton, and W. B. Yelon, Phys. Rev. B **29**, 4176 (1984).
[3] J. M. D. Coey and H. Sun, J. Magn. Magn. Mater. **87**, 1251 (1990).
[4] D. B. de Mooij and K. H. J. Buschow, J. Less-Common Met. **142**, 349 (1988).
[5] G. J. Long, G. K. Marashinghe, S. Mishra, O. A. Pringle, F. Grandjean, K. H. J. Buschow, D. P. Middleton, W. B. Yelon, F. Pourarian, and O. Isnard, Solid State Commun. **88**, 761 (1993).
[6] W. B. Yelon, H. Xie, G. J. Long, O. A. Pringle, F. Grandjean, and K. H. J. Buschow, J. Appl. Phys. **73**, 6029 (1993).
[7] Z. Hu, W. B. Yelon, S. Mishra, G. J. Long, O. A. Pringle, D. P. Middleton, K. H. J. Buschow, and F. Grandjean, J. Appl. Phys. **76**, 443 (1994).
[8] Z. Hu and W. B. Yelon, J. Appl. Phys. **76**, 6147 (1994).
[9] G. K. Marashinghe, S. Mishra, O. A. Pringle, G. J. Long, Z. Hu, W. B. Yelon, F. Grandjean, D. P. Middleton, and K. H. J. Buschow, J. Appl. Phys. **76**, 6731 (1994).
[10] G. J. Long, G. K. Marashinghe, S. Mishra, O. A. Pringle, Z. Hu, W. B. Yelon, D. P. Middleton, K. H. J. Buschow, and F. Grandjean, J. Appl. Phys. **76**, 5383 (1994).
[11] H. M. Rietveld, J. Appl. Crystallogr. **2**, 65 (1969).
[12] FULLPROF Rietveld refinement code by J. Rodriquez-Carjaval, Institute Laue-Langevin, Grenoble, France.
[13] W. B. Yelon, Z. Hu, E. W. Singleton, and G. C. Hadjipanayis (unpublished).
[14] S. R. Mishra, G. J. Long, O. A. Pringle, D. P. Middleton, Z. Hu, W. B. Yelon, F. Grandjean, and K. H. J. Buschow (unpublished).
[15] S. Miraglia, J. L. Soubeyroux, C. Kohlbeck, O. Isnard, and D. Fruchart, J. Less-Common Met. **171**, 51 (1991).

# Magnetic properties of $DyCo_{10-x}Ni_xSi_2$ compounds

Z. G. Zhao, N. Tang, E. Brück, K. H. J. Buschow, and F. R. de Boer
*Van der Waals-Zeeman Institute, University of Amsterdam, Valckenierstraat 65, 1018 XE Amsterdam, The Netherlands*

The temperature dependence of the magnetization of $DyCo_{10-x}Ni_xSi_2$ compounds with $x=0$, 2, 4, and 6 was measured in fields up to 5.0 T and in the temperature range from 4.2 to 300 K in a SQUID magnetometer. Compensation temperatures were observed for the compounds with $x=4$ and 6. The values of the $R$-$T$ exchange interaction obtained by fitting the $M$-$T$ curves on the basis of two-sublattice molecular-field theory are compared with the values obtained from high-field magnetization measurements on powder particles free to be oriented by the applied field. In all four compounds magnetic transitions are found in the ac-susceptibility measurements which were carried out between 4.2 K and room temperature. The types of magnetic anisotropy were investigated by magnetization measurements on samples that were magnetically aligned at room temperature.
© *1996 American Institute of Physics.* [S0021-8979(96)34708-7]

## I. INTRODUCTION

$RT_{10}Si_2$ compounds (R=rare earth, T=Fe, Co, Ni) form in the tetragonal $ThMn_{12}$-type structure. Like in many other Fe-rich rare-earth intermetallic compounds, the Curie temperature can be strongly increased by partially substituting Co for Fe. This substitution can also be accompanied by changes of the magnetic anisotropy and magnetization of the T sublattices. In $RT_{10}Si_2$ systems, the Fe sublattice, according to the results on $YFe_{10}Si_2$, has an easy-axis magnetic anisotropy,[1,2] and the Co sublattice, according to results on $YCo_{10}Si_2$, has an easy-plane magnetic anisotropy.[3,4] The Curie temperature of $YCo_{10}Si_2$ is about 300 K higher than that of $YFe_{10}Si_2$.[4] To study the influence of the Co sublattice on the magnetic properties of 1:12 compounds, we have investigated the magnetic properties of the series $DyCo_{10-x}Ni_xSi_2$ compounds with $x=0$, 2, 4, and 6.

## II. EXPERIMENTS

$DyCo_{10-x}Ni_xSi_2$ compounds with $x=0$, 2, 4, and 6 were prepared in the same way as the $DyCo_{10-x}Ni_xSi_2$ compounds reported on in Ref. 5. The temperature dependence of the magnetization of samples consisting of powder particles free to be oriented by the applied field was measured from 4.2 K to room temperature in external fields of 2 T.

In order to gather information on the type of magnetic anisotropy of the compounds at room temperature, x-ray-diffraction experiments were carried out both on magnetically aligned samples and on samples consisting of randomly oriented powder particles. Bulk samples were used in ac-susceptibility measurements which were done in the temperature range from 4.2 to 300 K. To study the easy-magnetization direction at different temperatures, the magnetization was measured in a SQUID magnetometer as a function of the angle between the alignment direction of the sample and the applied field of 1.0 T.

## III. RESULTS

The temperature dependence of the magnetization of $DyCo_4Ni_6Si_2$ in a field of 2 T is shown in Fig. 1. A temperature-independent ferromagnetic impurity contribution of $0.53\mu_B$/f.u. has been subtracted in accordance with our former results.[5] From the results on $DyCo_4Ni_6Si_2$, where we were able to study the magnetization fully up to the Curie temperature, we can derive the molecular-field coefficients, $n_{TT}$, $n_{DyT}$, and $n_{DyDy}$ by fitting the curve to the temperature dependence of the magnetization obtained in a two-sublattice molecular-field model. The following relations were used:

$$\mathbf{B}_{Dy}(T)=\mathbf{B}+n_{DyDy}\mathbf{M}_{Dy}(T)+n_{DyT}\mathbf{M}_T(T),$$

$$\mathbf{B}_T(T)=\mathbf{B}+n_{TT}\mathbf{M}_T(T)+n_{DyT}\mathbf{M}_{Dy}(T).$$

The temperature dependence of each sublattice moment is determined by the Brillouin function $B_J(x)$:

$$M_{Dy}(T)=M_{Dy}(0)B_{J_{Dy}}[\mu_{Dy}B_{Dy}(T)/k_BT],$$

$$M_T(T)=M_T(0)B_{J_T}[\mu_TB_T(T)/k_BT].$$

Because the magnetization of the Dy sublattice decreases faster with increasing temperature than does the T-sublattice magnetization, there will be a compensation temperature at which the difference between the two sublattice moments, and therefore also the critical field for breaking the antiparallel configuration, both approach zero.

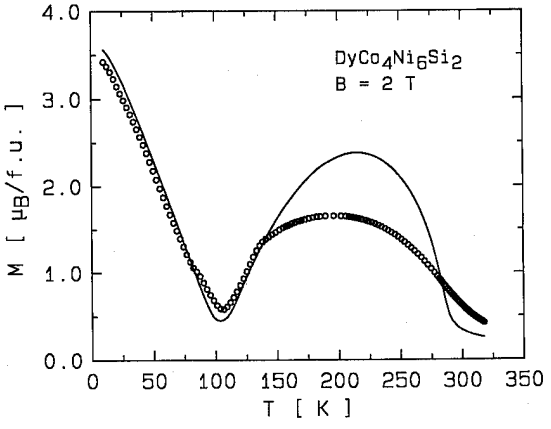



FIG. 1. Temperature dependence of the magnetization of $DyCo_4Ni_6Si_2$ in 2 T. The circles represent the experimental results and the full curve corresponds to the calculated magnetization.

 0021-8979/96/79(8)/6321/3/$10.00 © 1996 American Institute of Physics 

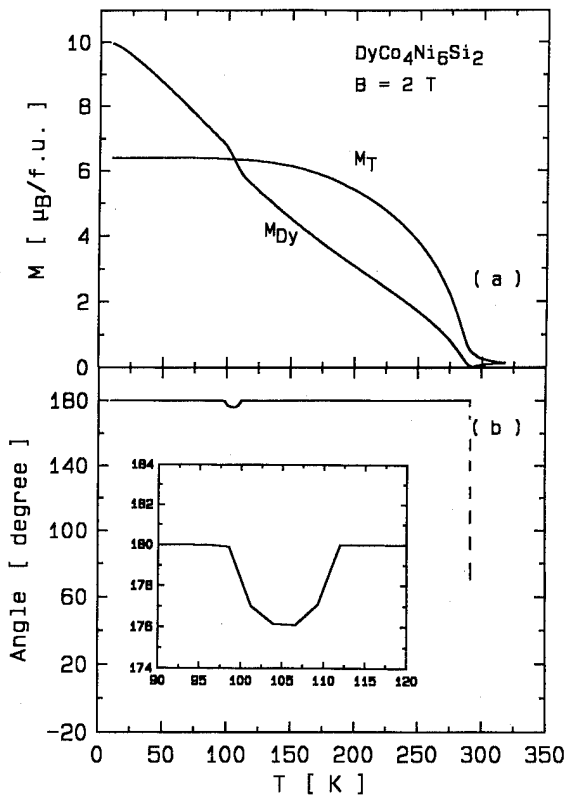



FIG. 2. (a) Calculated temperature dependence of the Dy- and T-sublattice moments in $DyCo_4Ni_6Si_2$. (b) Calculated temperature dependence of the angle between the Dy- and T-sublattice moments in $DyCo_4Ni_6Si_2$.

Therefore, in our calculation the temperature dependence of the angle between the two-sublattice moments has been taken into account. This angle, which determines the value of the magnetization, is found by minimizing the free energy:

$$F(T)=n_{\mathrm{DyT}}M_{\mathrm{Dy}}(T)M_{\mathrm{T}}(T)\cos\,\alpha - B\sqrt{M_{\mathrm{Dy}}^2(T)+M_{\mathrm{T}}^2(T)+2M_{\mathrm{Dy}}(T)M_{\mathrm{T}}(T)\cos\,\alpha}.$$

The fit to the experimental magnetization curve is shown in Fig. 1 as a solid line. The molecular-field coefficients used in the fitting procedure are $n_{\mathrm{DyDy}}=1.1\times10^{23}$ Tf.u./J, $n_{\mathrm{DyT}}=4.9\times10^{23}$ Tf.u./J, and $n_{\mathrm{TT}}=7.8\times10^{24}$ Tf.u./J. The value for $n_{\mathrm{DyT}}$ has been taken equal to the value derived previously from high-field magnetization measurements.[5] One can see in Fig. 1 that the magnetization above 130 K is not fitted very well. This may be due to the change of the magnetic anisotropy around this temperature which will be discussed below and/or to the crystallographic disorder of the T sublattice which may give rise to an inhomogeneous magnetization. In particular, the broadening of the magnetization around $T_C$ may be attributed to this disorder.

The temperature dependences of the Dy- and T-sublattice moments and of the angle between $M_{\mathrm{Dy}}$ and $M_{\mathrm{T}}$ are shown in Fig. 2(b). Around the compensation temperature, the antiparallel configuration between $M_{\mathrm{Dy}}$ and $M_{\mathrm{T}}$ is broken, albeit only slightly [see insert of Fig. 2(b)]. At higher temperatures, the two sublattice moments remain antiparallel until the Curie temperature is reached.

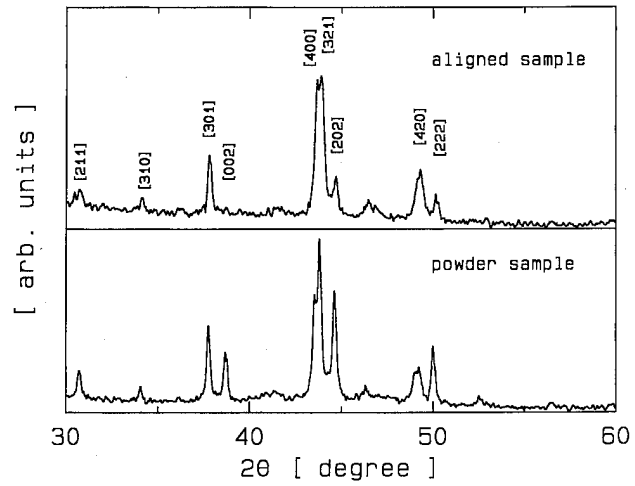



FIG. 3. X-ray diffraction patterns at room temperature on a magnetically aligned $YCo_{10}Si_2$ sample (top) and a randomly oriented powder sample.

The magnetic anisotropy of the Co sublattice is of the easy-plane type. This is demonstrated in Fig. 3 which shows x-ray-diffraction patterns taken on a magnetically aligned $YCo_{10}Si_2$ sample with the alignment direction perpendicular to the surface and on a sample consisting of randomly oriented powder. One can see that for the aligned sample, the [002] reflection has disappeared whereas the [400] reflection is strongly enhanced.

Figure 4 shows the temperature dependence of the ac susceptibility measured on bulk samples between 4.2 and 300 K. All four compounds have clear magnetic transitions. The transition at about 270 K in $DyCo_4Ni_6Si_2$ is related to the Curie temperature which is consistent with the $M$-$T$ measurements. The second transition in this compound is visible as a clear kink but is rather broad in the other compounds. The small anomaly in $DyCo_4Ni_6Si_2$ at low temperatures is probably due to a second phase.

To interpret the ac-susceptibility results, the magnetization of aligned samples was measured as a function of angle between the alignment direction and the direction of the ex-

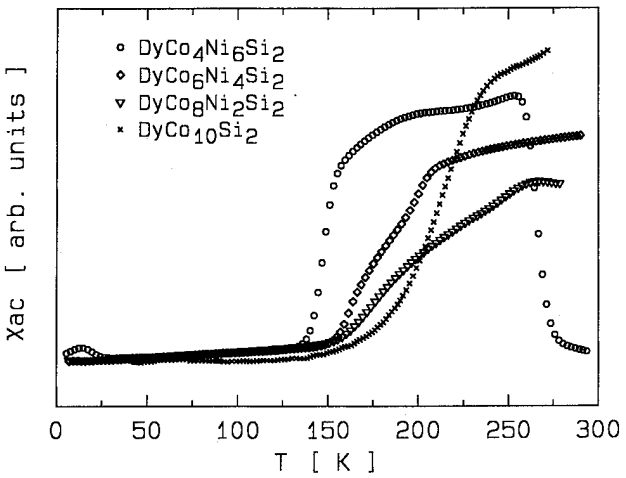



FIG. 4. Temperature dependence of the ac susceptibility of $DyCo_{10-x}Ni_xSi_2$ compounds.

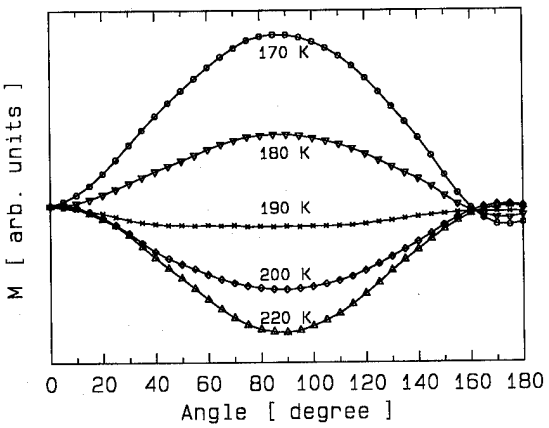



FIG. 5. Dependence of the magnetization of $DyCo_{10}Si_2$ on the angle between the alignment direction and the direction of the external field.

ternal field. The sample was mounted in such a way that the external field is along the direction in which the sample was aligned at room temperature. Therefore, at a certain temperature, the magnetization measured along the external field will get its maximum value when the easy-magnetization direction is in the field direction. The magnetization measured along the external field will get its minimum value when the hard-magnetization direction is in the field direction.

Figure 5 shows the experimental results for $DyCo_{10}Si_2$ measured at 220, 200, 190, 180, and 170 K. The curves have been normalized to the zero-angle magnetization values. The easy-magnetization direction of $DyCo_{10}Si_2$ can be seen to change at 190 K from easy plane above this temperature (established in the x-ray experiment) to easy axis below this temperature. At low temperatures, the magnetic anisotropy of the compound is dominated by the Dy-sublattice anisotropy. At high temperatures, the $3d$-sublattice anisotropy (easy-plane type) becomes most important. Between about 150 and 250 K the two sublattice anisotropies are comparable. The competition between the two sublattices can clearly be seen in Fig. 5. At 190 K, the magnetization is nearly independent of the direction of the external field, indicating that the anisotropy has become very weak.

## IV. DISCUSSION AND CONCLUSIONS

It is shown that Ni substitution for Co in $DyCo_{10}Si_2$ strongly influences the magnetic anisotropy. The ac susceptibility results show that the spin-reorientation temperature decreases with increasing Ni content (see Fig. 4). This may either be due to an increase of the T-sublattice anisotropy upon Ni substitution or to a decrease of the Dy-sublattice anisotropy upon Ni substitution or to both effects. This point will be the subject of further studies.

The molecular-field analysis of the magnetization shows that the Dy-Dy exchange interaction is almost zero in $DyCo_4Ni_6Si_2$ and that $n_{DyT}$ is about one order of magnitude smaller than $n_{TT}$.

The analysis of the temperature dependence of the magnetization presented in this article shows that, in systems with a compensation temperature, when the external field is not very low, the angle between the two sublattice moments has to be taken into account.

## ACKNOWLEDGMENT

The work has been carried out within the scientific exchange program between China and the Netherlands.

[1] K. H. J. Buschow, D. B. de Mooij, M. Brouha, H. H. A. Smit, and R. C. Thiel, IEEE Trans. Magn. **MAG-24**, 1161 (1987).
[2] Q. Li, Y. Lu, R. Zhao, O. Tegus, and F. Yang, J. Appl. Phys. **70**, 1161 (1991).
[3] Q. A. Li, N. Tang, Z. G. Zhao, K. H. J. Buschow, and F. R. de Boer, EMMA'95, to be published J. Magn. Magn. Mater.
[4] F. R. de Boer, Z. G. Zhao, and K. H. J. Buschow, EMMA'95, to be published J. Magn. Magn. Mater.
[5] N. Tang, Z. G. Zhao, K. H. J. Buschow, and F. R. de Boer, EMMA'95, to be published J. Magn. Magn. Mater.

# Magnetic properties of $R(Fe,Mn)_{11}Ti$ compounds

T. Zhao
*Institute of Metal Research, Academia Sinica, Shenyang 110015, People's Republic of China; Van der Waals–Zeeman Laboratory, University of Amsterdam, 1018 XE, Amsterdam, The Netherlands*

X. C. Kou
*Institut für Experimtalphysik, Tecnische Universität Wien, Wiedner Hauptstrasse 8-10, A-1040 Wien, Austria*

Z. D. Zhang, X. K. Sun, and Y. C. Chuang
*Institute of Metal Research, Academia Sinica, Shenyang 110015, People's Republic of China*

F. R. de Boer
*Van der Waals–Zeeman Laboratory, University of Amsterdam, 1018 XE Amsterdam, The Netherlands*

High-field magnetization measurements have been performed on both free-powder samples and magnetically aligned samples of $R(Fe,Mn)_{11}Ti$ (R=Y, Nd, Sm, Gd, Er) compounds at 4.2 K in a step field up to 28 T. The temperature dependence of ac susceptibilities of $R(Fe,Mn)_{11}Ti$ has been measured in a temperature range from 4.2 to 800 K. It has been found that both the magnetic moment of the transition-metal sublattice and the Curie temperature of $RFe_{11-x}Mn_xTi$ compounds decrease with increasing $x$. Spin reorientations occur in $ErFe_{11-x}Mn_xTi$ compounds as the result of competition between the uniaxial anisotropy of the transition-metal sublattice and the planar or conical anisotropy of the Er sublattice. The intersublattice exchange constants $n_{RT}$ of $ErFe_{11-x}Mn_xTi$ compounds have been deduced by the high-field free-powder method. The effect of the substitution of Fe by Mn on the magnetic anisotropies of $R(Fe,Mn)_{11}Ti$ with R=Y, Nd, Sm has been investigated. First-order magnetization processes take place in $SmFe_{11-x}Mn_xTi$ compounds when the external field is applied perpendicular to the alignment direction. © *1996 American Institute of Physics.* [S0021-8979(96)34808-3]

## I. INTRODUCTION

In the early 1980s, many efforts have been made to produce iron-rich compounds with the $ThMn_{12}$ structure by substituting Mn by Fe in $RMn_{12}$ compounds.[1] However, since the solid solubility of Fe in $YMn_{12-x}Fe_x$ limits to $x=8$, this substitution cannot lead to an Fe-rich compound. Recently, the Fe-rich $R(Fe,M)_{12}$ compounds with the $ThMn_{12}$ structure have been obtained by adding a small amount of a third element, such as Ti, V, Cr, Mo, W, and Al.[2] So it is possible to study the effect of Mn substitution on the magnetic properties of Fe-rich rare-earth transition-metal compounds with the $ThMn_{12}$-type structure, in which the Mn is added as a fourth element to substitute part of the iron. In the present work, we have chosen $RFe_{11}Ti$ as the starting compound, and prepared the $RFe_{11-x}Mn_xTi$ compounds with $x=0$, 1, 2, 3, 4. The magnetic properties of these compounds have been investigated by high-field magnetization measurements up to 21 T at 4.2 K and ac-susceptibility measurements from 4.2 to 800 K.

## II. SAMPLE PREPARATION

Polycrystalline $RFe_{11-x}Mn_xTi$ ingots with R=Y, Nd, Sm, Gd, and Er and $x=0$, 1, 2, 3, 4 have been prepared by induction-melting appropriate amounts of pure materials of a purity of at least of 99.99 wt %. The ingots were remelted two times to achieve homogeneity. Weight losses during the melting due to evaporation of the rare-earth element and Mn were compensated for by starting with an excess of 3 wt % R (with respect to the R content) and 5 wt % Mn (with respect to the Mn content). The as-cast ingots were wrapped in Ta foil and sealed in a pre-evacuated and then argon-gas-filled quartz tube, followed by annealing at 1273 K for three weeks and then water-quenched to avoid possible metallographic phase transitions during the cooling process.

The crystal structures of the samples were checked by x-ray diffraction. It was found most of the samples have the $ThMn_{12}$-type tetragonal structure and a small amount of $\alpha$-Fe exists as a second phase.

## III. RESULTS AND DISCUSSION

The high-field measurements at 4.2 K were performed on free-powder samples of $RFe_{11-x}Mn_xTi$ compounds to study saturation magnetization and exchange interaction. For the high-field free-powder (HFFP) measurements,[3,4] fine-powder (<40 $\mu$m) samples were loosely loaded into the sample holders. These particles can be considered as monocrystalline and are free to rotate in the external field so that the total magnetic moment of the samples is always parallel to the external field direction. The values for the saturation magnetization obtained in this way are tabulated in Table I. One can see that, for $RFe_{11-x}Mn_xTi$ (R=Y, Nd, Sm) compounds, the saturation magnetization in these compounds decreases upon Mn substitution. In the $YFe_{11-x}Mn_xTi$ compounds, since Y is nonmagnetic, the magnetic moment of the transition-metal sublattice is equal to the saturation magnetization. In $NdFe_{11-x}Mn_xTi$ and $SmFe_{11-x}Mn_xTi$, if we assume that the $4f$ electrons of rare-earth element are well localized, the moment of the transition-metal sublattice ($M_T$) can be obtained by subtracting the free-ion moment of the rare-earth element ($M_R$) from the saturation magnetization ($M_s$). The obtained $M_T$ values are listed in Table II. In $GdFe_{11-x}Mn_xTi$ and $ErFe_{11-x}Mn_xTi$ compounds, $M_s$ first

 0021-8979/96/79(8)/6324/3/$10.00 © 1996 American Institute of Physics

TABLE I. Saturation magnetization of $RFe_{11-x}Mn_xTi$ compounds.

| $M_s$ ($\mu_B$/f.u.) | Y | Nd | Sm | Gd | Er |
|---|---|---|---|---|---|
| $x=0$ | 20.0 | 21.7 | 19.6 | 12.2 | 10.8 |
| $x=1$ | 15.4 | 17.2 | 16.4 | 9.3 | 6.6 |
| $x=2$ | 12.5 | 15.1 | 10.2 | 4.0 | 2.4 |
| $x=3$ | 7.4 | 13.7 | 7.5 | 2.6 | 1.8 |
| $x=4$ | 4.2 | 6.9 | 4.7 | 2.7 | 4.6 |

TABLE II. Magnetic moments of the transition-metal sublattice in $RFe_{11-x}Mn_xTi$ compounds.

| $M_T$ ($\mu_B$/f.u.) | Y | Nd | Sm | Gd | Er |
|---|---|---|---|---|---|
| $x=0$ | 20.0 | 18.4 | 18.9 | 19.2 | 19.8 |
| $x=1$ | 15.4 | 13.9 | 15.7 | 16.3 | 15.6 |
| $x=2$ | 12.5 | 11.8 | 9.4 | 11.0 | 11.4 |
| $x=3$ | 7.4 | 10.4 | 6.8 | 9.6 | 7.2 |
| $x=4$ | 4.2 | 3.6 | 4.0 | 4.3 | 4.4 |

decreases upon the Mn substitution from $x=0$ to $x=3$, and then increases. This behavior is due to the antiparallel configuration of the moments of the transition-metal sublattice and the heavy-rare-earth sublattice. In $ErFe_{11}Ti$ and $GdFe_{11}Ti$, the magnetic moment of the Fe sublattice is much larger than that of the rare-earth sublattice so that the total magnetic moment equals to $M_T-M_R$. When Fe is substituted by Mn, the moment of the transition-metal sublattice decreases and causes a decrease of the saturation magnetization. If the moment of the transition-metal sublattice becomes smaller than that of the rare earth upon the Mn substitution, the total magnetic moment, which is now $M_R-M_T$, will increase (the case of $x=4$) with decreasing $M_T$. The values of the moments of the transition-metal sublattice are obtained by $M_T=M_R\pm M_s$ accordingly (see Table II).

For all investigated $RFe_{11-x}Mn_xTi$ compounds, $M_T$ decreases monotonically with increasing $x$. If the mean Fe moment were not affected by substitution and the Mn ion were nonmagnetic, $M_T$ would decrease linearly by $M_T(x)=M_T(0)(11-x)/11$, where $M_T(x)$ and $M_T(0)$ are the saturation magnetizations of $RFe_{11-x}Mn_x$ and $RFe_{11}Ti$, respectively. The experimental results obviously deviate from this line, which is similar to the case of $R(Co,Mn)_{11}Ti$ compounds.[5] One possible interpretation for the relatively fast decrease of $M_T$ could be that the magnetic moment of iron is affected by the surrounding of Mn atoms which might be coupled antiferromagnetically with the Fe moment.[1] Another possible reason for this is that the Mn atom which is larger than Fe prefers to substitute the Fe atom on the $8i$ site where Fe has the largest moment in $RFe_{11}Ti$.[1]

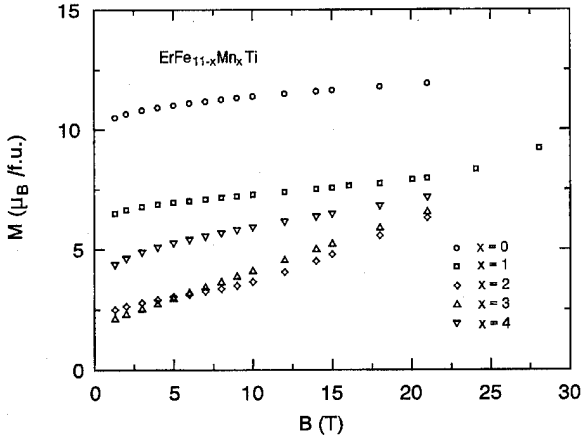



FIG. 1. Magnetic isotherms at 4.2 K of $ErFe_{11-x}Mn_xTi$ compounds measured on powder particles that are free to rotate in the sample holder.

HFFP measurements are usually used to get information about the intersublattice interaction in heavy-rare-earth transition-metal compounds.[3,4] If the external field is so high that the collinear configuration of the magnetic moments of the rare-earth and transition-metal sublattices is broken, the coupling constant $n_{RT}$ can be obtained from the slope of the bending process if the anisotropy of at least one of the sublattices is negligible. In external fields up to 28 T, the bending process can be observed in $ErFe_{11-x}Mn_xTi$ compounds with $x=1$, 2, and 3 (see Fig. 1). Hurley[6] has measured the free-powder magnetization process of $ErFe_{11}Ti$ and its first critical field is 35 T. In the present work, the first critical fields have been determined to be 23, 10.5, and 0 T for $x=1$, 2, and 3, respectively. The coupling constants deduced from the slope in the bending section are 4.5, 4.0, and 4.5 T f.u./$\mu_B$ for $x=1$, 2, and 3, respectively. It seems that Mn substitution has no significant influence on $n_{RT}$. However, no bending process is found in $GdFe_{11-x}Mn_xTi$ compounds. This may be due to the relatively large $n_{RT}$ in Gd compounds.

To investigate the effects of Mn substitution on the anisotropy of $R(Fe,Mn)_{11}Ti$ (R=Sm, Nd, Y) compounds. The high-field magnetization was measured on aligned samples with the magnetic field parallel and perpendicular to the alignment direction. In $YFe_{11-x}Mn_xTi$ compounds, the anisotropy field $B_a$ decreases upon Mn substitution. The values obtained for $B_a$ are 4, 3.5, and 2.5 T for $x=0$, 1, 2, respectively. The Curie temperature for compounds with $x>2$ is

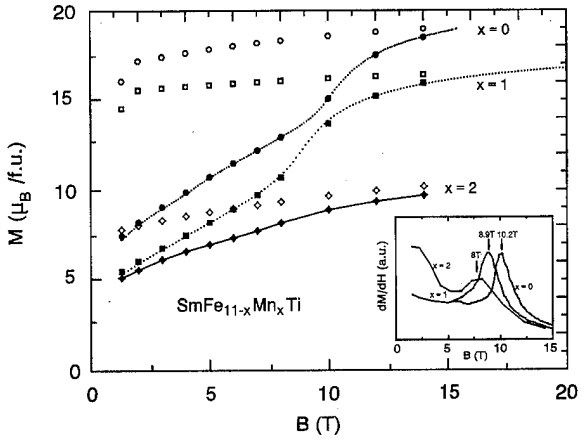



FIG. 2. Magnetic isotherms at 4.2 K of $SmFe_{11-x}Mn_xTi$ compounds measured on magnetically aligned powders. Open marks correspond to the field parallel to the alignment direction and filled marks to the field perpendicular to the alignment direction. The dots correspond to the measurements in a continuously varying field. The solid lines are guides to the eye.

TABLE III. Curie temperatures of $RFe_{11-x}Mn_xTi$ compounds.

| $T_c$ (K) | Y | Nd | Sm | Er | Gd |
|---|---|---|---|---|---|
| $x=0$ | 530 | 550 | 595 | 515 | 605 |
| $x=1$ | 455 | 465 | 510 | 425 | 530 |
| $x=2$ | 370 | 405 | 460 | 305 | 430 |
| $x=3$ | 200 | 285 | 115 | 210 | 330 |
| $x=4$ | 105 | 215 | 85 | 90 | ... |

lower than room temperature, so we cannot prepare well-aligned samples of these compounds at room temperature. For $NdFe_{11}Ti$, the magnetization along the alignment direction is smaller than that perpendicular to the alignment direction. A possible interpretation for this may be that the weak easy-axis anisotropy of $NdFe_{11}Ti$ at room temperature[7] changes to an easy-cone anisotropy with a cone angle larger than 45° at 4.2 K. With increasing $x$, the magnetization parallel to the orientation direction becomes relatively large indicating that Mn substitution decreases the cone angle at low temperature or causes an easy-cone anisotropy at room temperature. Of more interest are the $SmFe_{11-x}Mn_xTi$ compounds in which first-order magnetization process (FOMP)-like anomalies appear in the magnetization curves measured along the direction perpendicular to the orientation direction (Fig. 2). These anomalies are similar to the one found by Hu *et al.*[7] in $SmFe_{11}Ti$. The critical field, corresponding to the maximum of the first derivative of the magnetization curve, decreases upon Mn substitution. The critical fields in $SmFe_{11}Ti$ and $SmFe_{10}MnTi$ are 10.2 and 8.9 T, respectively. In $SmFe_9Mn_2Ti$, the anomaly becomes hard to distinguish because of the poor alignment of the powder at room temperature, and the critical field decreases to about 8 T. These anomalies may be due to field-induced first-order transitions or quasi-FOMPs.[8]

The ac susceptibilities of $RFe_{11-x}Mn_xTi$ compounds were measured in the temperature range from 4.2 to 800 K. The obtained $T_c$ values are listed in Table III. $T_c$ decreases monotonically with increasing $x$. This is similar to the concentration dependence of $M_T$. Spin reorientations from easy axis at high temperature to easy cone or easy plane at low temperature were found in $ErFe_{11-x}Mn_xTi$ compounds. At $T_{SR}$ and above, the uniaxial iron anisotropy usually determines the magnetization direction but at lower temperatures the rare-earth anisotropy may be dominant. The $T_{SR}$ corresponds to the minimum of $d\chi'/dT$. The $T_{SR}$ for compounds with $x=0$, 1, 2, 3 are 48, 50.5, 99.4, and 171.4 K, respectively. The decrease of $T_{SR}$ with increasing $x$ may imply that the uniaxial anisotropy of the transition-metal sublattice decreases upon Mn substitution.

In conclusion, both the magnetic moments of the transition-metal sublattice and the Curie temperatures of the $RFe_{11-x}Mn_xTi$ ($x=0$, 1, 2, 3, 4) compounds decrease with increasing $x$. The introduction of Mn atoms, which are nonmagnetic or possess a magnetic moment antiparallel to the Fe moments, gives rise to a decrease of the mean Fe moment. In $RFe_{11-x}Mn_xTi$, the transition-metal sublattice possesses uniaxial anisotropy which decreases upon Mn substitution. In $RFe_{11-x}Mn_xTi$ (R=Nd, Er), there exists competition between the uniaxial anisotropy of the transition-metal sublattice and the planar or conical anisotropy of the rare-earth sublattice, which gives rise to spin reorientations in the $ErFe_{11-x}Mn_xTi$ compounds. FOMP-like anomalies found in $SmFe_{11-x}Mn_xTi$ compounds indicate that the high-order anisotropies play an important role in the magnetization processes of these compounds.

## ACKNOWLEDGMENTS

This work has been supported by the exchange programma between China and the Netherlands, the National Natural Sciences Foundation of China, the Sciences and Technology Commission of Shenyang, the President Foundation of the Chinese Academy of Science, and the K. C. Wong Education Foundation of Hong Kong.

[1] Y. C. Yang, B. Kebe, W. James, J. Deportes, and W. Yelon, J. Appl. Phys. **52**, 2077 (1981).
[2] H. S. Li and J. D. M. Coey, in *1991 Ferromagnetic Materials*, edited by K. H. J. Buschow and E. P. Wohlfarth (North Holland, Amsterdam, 1991), Vol. 6.
[3] R. Verhoef, F. R. de Boer, J. J. M. Franse, C. J. M. Dennisen, T. H. Jacobs, and K. H. J. Buschow, J. Magn. Magn. Mater. **80**, 41 (1989).
[4] R. Verhoef, R. J. Radwanski, and J. J. M. Franse, J. Magn. Magn. Mater. **81**, 176 (1990).
[5] J. Allemand, C. Bertrand, J. Le Roy, J. M. Moreau, D. Paccard, M. A. Fremy, and D. Givord, in *Concerted European Action on Magnets (CEAM)*, edited by I. V. Harris and R. Hanitsch (Elsevier, London, 1989), p. 98.
[6] D. P. F. Hurley, Ph.D. thesis, The University of Dublin, 1993.
[7] B. P. Hu, H. S. Li, J. P. Gavigan, and J. M. D. Coey, J. Phys. **1**, 755 (1989).
[8] T. Zhao, X. K. Sun, Z. D. Zhang, Q. Wang, Y. C. Chuang, and F. R. de Boer, J. Magn. Magn. Mater. **104**, 2119 (1992).

# Temperature and field-induced spin reorientations in $NdFe_{10-x}Co_xMo_2$ single crystals

W. A. Mendoza and S. A. Shaheen
*Department of Physics and Center for Materials Research and Technology (MARTECH), Florida State University, Tallahassee, Florida 32306*

Single crystals of the $NdFe_{10-x}Co_xMo_2$ alloy system ($x=0,1,3,5,7,10$) have been prepared by the Czochralski technique and studied by x-ray and magnetometry techniques. All of the compounds in this series crystallize in the tetragonal $ThMn_{12}$-type structure. The single-crystal data support the previous findings on polycrystalline samples, namely, that (1) with increasing Co content, the easy direction of magnetization at 300 K appears to deviate from the $c$ axis for $x \leqslant 3$, and becomes axial for $x \geqslant 5$; (2) temperature-induced spin reorientations are observed for $x<3$; and (3) for $x \geqslant 5$, no temperature-induced but field-induced spin reorientations are observed. Single-crystal data also clarify the anomalies observed in the temperature-dependent magnetization data on polycrystalline samples. © *1996 American Institute of Physics.* [S0021-8979(96)34908-X]

## I. INTRODUCTION

Rare-earth-3$d$ transition metal compounds are a fertile area for searching for new materials for permanent magnet applications. In recent years, the attention has been focused on iron-rich ternary compounds of the form $RFe_{12-x}M_x$ (R=rare-earth element, M=Ti, V, Cr, Si, Mo; $x=1$ or 2).[1–7] These compounds crystallize in the $ThMn_{12}$-type structure. The binary $RFe_{12}$ alloys are unstable and 1–2 M atoms are needed to stabilize this structure. The Fe and M atoms occupy the three nonequivalent transition metal sites in this structure. In these compounds, those rare earths with a positive second-order Stevens factor ($\alpha>0$) (e.g., Sm, Er, Tm, Yb) prefer magnetization along the $c$ axis, and so does the Fe. On the other hand, rare earths with $\alpha<0$ (e.g., Nd, Tb, Dy, Ho) prefer magnetization in the basal plane. Nitrogen can be introduced at the interstitial sites in an amount up to one atom per formula unit and causes a lattice expansion. Adding N atoms to the structure enhances the magnetic ordering temperature and changes the easy direction of magnetization (EDM).

The effect of Co substitution on structure and magnetic anisotropy has been studied on a number of systems with the $ThMn_{12}$-type structure, e.g., $RFe_{11-x}Co_xTi$,[8–10] $RFe_{10-x}Co_xV_2$,[11–13] and $RFe_{10-x}Co_xMo_2$.[14–18] From these studies, it has been established that the Curie temperature and magnetic moment initially increase and the EDM goes through a complex cycle of changes, as Fe is gradually substituted by Co in these compounds. In the $RFe_{10-x}Co_xMo_2$ series, temperature and field-induced spin reorientations are observed.[14–18] In this series, the compounds containing R elements with $\alpha<0$ have their EDM (at room temperature) initially slightly deviating from the axial direction ($c$ axis). The EDM turns to the basal direction at the intermediate Co concentrations, and finally returns back to the axial direction at higher Co concentrations. On the other hand, for compounds containing R elements with $\alpha>0$, the EDM (at room temperature) is along the $c$ axis at the Fe-rich end and it starts becoming nonaxial as Fe is substituted by Co and is along the basal direction for Co-rich alloys. Previous studies on polycrystalline samples across the $NdFe_{10-x}Co_xMo_2$ series[16,19] suggested the possibilities of preferential substitution of Co at three nonequivalent sites available for the occupation of 3$d$ metal elements in this lattice structure and canting of the spins. To gain further insight into this system, single-crystal samples have been prepared across the $NdFe_{10-x}Co_xMo_2$ series.

## II. EXPERIMENT

$NdFe_{10-x}Co_xMo_2$ alloys ($x=0$, 1, 3, 5, 7, 10) were prepared by melting together metals of high purity (99.9% or higher) in a water-cooled triarc furnace in a flowing argon gas atmosphere. The alloys were melted several times to ensure homogeneity. The crystals were then pulled from the arc-melted alloys by the Czochralski method. The crystals are typically 2–3 mm in diameter and 10–15 mm in length. The crystals were cut approximately perpendicular to the growth direction and then the cut surface was smoothed for x-ray diffraction studies. A Siemens diffractometer (D500) and Cu $K\alpha$ radiation were used for x-ray examination. Only one line was observed for each sample. For $x=0$, 1, 7, the (101) line was observed, and for $x=3$, 5, 10, the (002) line was observed. The magnetic anisotropy measurements on the samples which showed (002) reflections on x-ray examination showed results identical to those obtained on the aligned powder samples, which in turn confirmed the crystallographic ordering of the crystals and anticipated growth along the $c$ axis. However, these observations do not fully confirm the single-crystal nature of our samples, and the possibility of growth of multiple seeds with axial orientation along the growth direction is not ruled out.

A Quantum Design SQUID magnetometer with external fields up to 55 kOe was used for the measurements of the saturation magnetization ($M_s$). For measurements in fields up to 70 kOe, a Quantum Design SQUID magnetometer at the National High Magnetic Field Laboratory was used. The samples used for magnetic measurement were 2–3 mm in diameter and 5–8 mm in length.

## III. RESULTS AND DISCUSSION

The spin reorientations, described as a change of the EDM from one crystallographic direction to another with

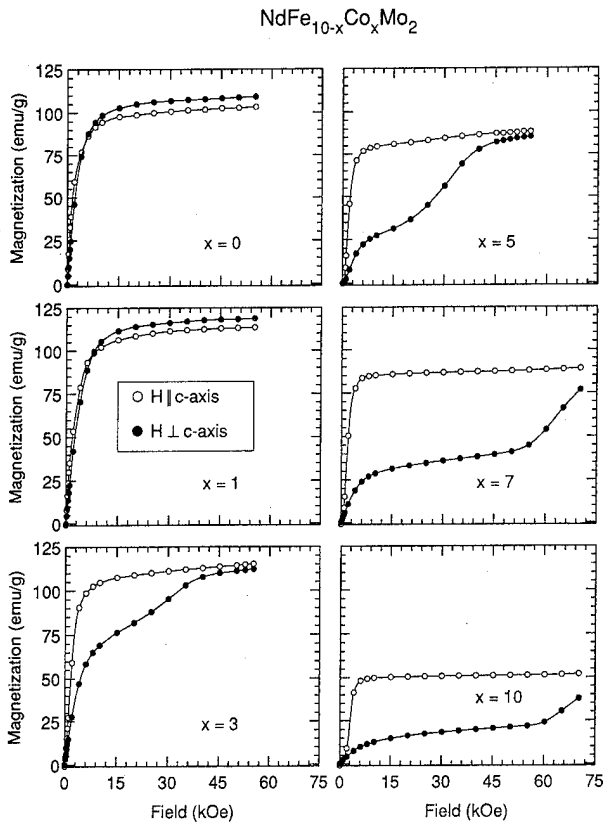



FIG. 1. Magnetization as a function of applied field for the crystals across the $NdFe_{10-x}Co_xMo_2$ series at 5.0 K.

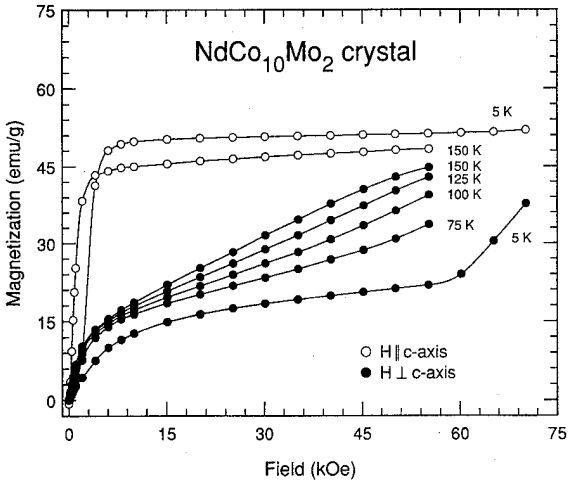



FIG. 2. Magnetization as a function of applied field for the $NdCo_{10}Mo_2$ crystal at different temperatures.

varying temperature, were detected in the ac susceptibility and dc magnetization measurements for $x=0$, and 1 in the $NdFe_{10-x}Co_xMo_2$ series. The observed spin reorientation temperatures of 180 K (for $x=0$) and 190 K (for $x=1$) are in agreement with the published data.[16,20] These spin reorientations appear to be planar to cone type transitions with increasing temperature.

The results of the magnetization versus magnetic field measurements across the $NdFe_{10-x}Co_xMo_2$ series at $T=5$ K in fields up to 70 kOe are displayed in Fig. 1. The samples with small Co content have very little magnetic anisotropy, and measurements with $H$ parallel to the $c$ axis and with $H$ perpendicular to the $c$ axis are nearly identical. On the other hand, for $x=3$, 5, 7, 10, there is a marked difference in magnetization when $H$ is parallel to the $c$ axis and when $H$ is perpendicular to the $c$ axis. For $x=5$, 7, and 10, the magnetization along the hard direction ($H\perp c$ axis) initially increases as a function of field but unlike the spontaneous rise for magnetization along the easy axis, the magnetization along the hard axis does not shoot to its saturation value at low fields. At intermediate field values, the magnetization shows a plateau at a value which is less than half of the saturation magnetization (saturation along the easy axis). At higher field values, there is a spontaneous jump in magnetization and the magnetization value eventually tends to approach the saturation value. These jumps in magnetization along the hard axis occur at about 30, 60, and 65 kOe for $x=5$, 7, and 10, respectively, and are associated with reorientation of spins due to the shift in the EDM from one crystallographic direction to another under the influence of the magnetic field. Therefore, they are referred to as field-induced spin reorientations. They are sometimes also called first-order magnetization processes. There is also some indication of a first-order magnetization process for $x=3$ (see Fig. 1). These data on single-crystal samples are in excellent agreement with measurements on aligned polycrystalline samples in our laboratory[16] and elsewhere.[21]

Figure 2 shows the magnetization versus field data at various temperatures for $x=10$. It is apparent that the field at which the magnetization jump occurs is dependent on the temperature and decreases as the temperature is increased.

During the studies on polycrystalline $NdFe_{10-x}Co_xMo_2$ samples, some observations were made which could not be fully understood and prompted the need for single-crystal samples. One of the observations which was not understood at that time was the unusual temperature dependence of the magnetization at the Co-rich end of the series. The saturation magnetization (in 50 kOe) on randomly oriented chunk samples showed an initial increase on cooling, as expected. However, when cooled below a certain temperature (~200 K), the magnetization started decreasing. Since Nd and Fe (and or Co) spins are expected to align parallel to each other, a decrease in the magnetization at low temperature is not expected. The measurements on single-crystalline samples shed some light on this aspect. Figure 3 shows the temperature dependence of magnetization (in 50 kOe) on various single-crystal samples across the $NdFe_{10-x}Co_xMo_2$ series. For all samples, the magnetization along the easy axis increases monotonically from its room temperature value to 5 K. The noteworthy features are the strong decrease of magnetization for the field along the direction perpendicular to the easy axis for $x=7$ and $x=10$. This decrease in magnetization can be understood in terms of the magnetic anisotropy and field-induced spin reorientations in these samples. The decrease in the magnetization along the hard axis for $x=7$ and 10 is consistent with the corresponding low value of magnetization along the hard axis in magnetization versus field data at 5 K in Fig. 1. It may be noted that for $x=5$, the magnetization in both directions is monotonically increasing

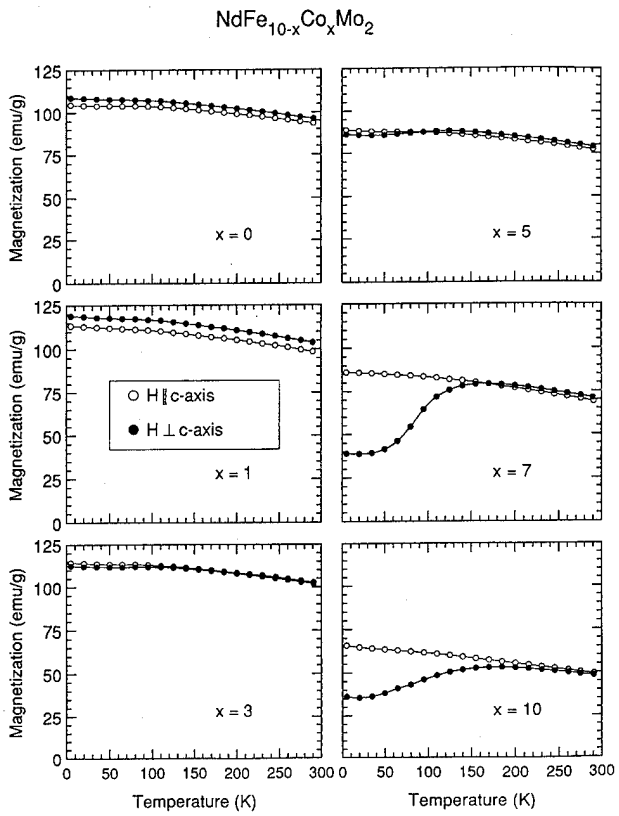



FIG. 3. Temperature dependence of the magnetization in a field of 50 kOe for the $NdFe_{10-x}Co_xMo_2$ crystals.

with the decreasing temperature, even though like $x=7$ and 10, first-order magnetization processes are observed at this composition. The difference lies in the fact that magnetization measurements in Fig. 3 were made in a 50 kOe field that is well above the 30 kOe field at which the spin reorientations for $x=5$ occur and is lower than the field (60–65 kOe) needed to induce the spin reorientations for $x=7$ and 10.


[1] D. B. De Mooij and K. H. J. Buschow, Philips J. Res. **42**, 246 (1987).
[2] K. H. J. Buschow, D. B. De Mooij, M. Brouha, H. H. A. Smith, and R. C. Thiel, IEEE Trans. Magn. **MAG-24**, 1611 (1988).
[3] K. Ohashi, Y. Tawara, R. Osugi, and M. Shimao, J. Appl. Phys. **64**, 5714 (1988).
[4] D. B. De Mooij and K. H. J. Buschow, J. Less Common Met. **136**, 207 (1988).
[5] K. Ohashi, T. Yokoyama, R. Osugi, and Y. Tawara, IEEE Trans. Magn. **MAG-23**, 3101 (1987).
[6] K. Ohashi, Y. Tawara, and R. Osugi, J. Less Common Met. **139**, L1 (1988).
[7] F. R. De Boer, H. Ying-Kal, D. B. De Mooij, and K. H. J. Buschow, J. Less Common Met. **135**, 199 (1987).
[8] S. F. Cheng, V. K. Sinha, Y. Xu, J. M. Elbicki, E. B. Boltich, W. E. Wallace, S. G. Sankar, and D. E. Laughlin, J. Magn. Magn. Mater. **75**, 330 (1988).
[9] V. K. Sinha, S. K. Malik, D. T. Adroja, J. Elbicki, S. G. Sankar, and W. E. Wallace, J. Magn. Magn. Mater. **80**, 281 (1989).
[10] V. K. Sinha, S. F. Cheng, W. E. Wallace, and S. G. Sankar, J. Magn. Magn. Mater. **81**, 227 (1989).
[11] M. Jurczyk and O. D. Chistjakov, J. Magn. Magn. Mater. **82**, 239 (1989).
[12] M. Jurczyk, G. K. Nicolaides, and K. V. Rao, J. Magn. Magn. Mater. **94**, L6 (1991).
[13] M. Jurczyk, G. K. Nicolaides, and K. V. Rao, J. Appl. Phys. **70**, 6110 (1991).
[14] C. Lin, Y.-X. Sun, Z.-X. Liu, G. Li, J.-L. Yang, B.-S. Zhang, Y.-F. Ding, and L. Jin, J. Appl. Phys. **69**, 5554 (1991).
[15] X. Xu and S. A. Shaheen, J. Magn. Magn. Mater. **118**, L6 (1993).
[16] X. Xu and S. A. Shaheen, J. Appl. Phys. **73**, 6248 (1993).
[17] R. Tucker, X. Xu, and S. A. Shaheen, J. Appl. Phys. **75**, 6229 (1994).
[18] X. Xu, R. Tucker, and S. A. Shaheen, J. Appl. Phys. **75**, 6021 (1994).
[19] X. Xu, Ph.D. thesis, Florida State University, 1994.
[20] X. C. Kou, C. Christides, R. Grossinger, H. R. Kirchmayr, and A. Kostikas, J. Magn. Magn. Mater. **104-107**, 1341 (1992).
[21] D. C. Zeng, N. Tang, T. Zhao, Z. G. Zhao, K. H. J. Buschow, and F. R. De Boer, J. Appl. Phys. **76**, 6837 (1994).

# Magnetic anisotropy and spin reorientation transition in a $TbFe_{11}Ti$ single crystal (abstract)

C. Abadía, P. A. Algarabel, M. R. Ibarra, and C. Marquina
*Departamento de Física de la Materia Condensada and ICMA, Facultad de Ciencias, Universidad de Zaragoza-CSIC, 50009 Zaragoza, Spain*

N. V. Kudrevatykh and P. E. Markin
*Institute of Physics and Applied Mathematics, Ural State University, 620083 Ekaterinburg, Russia*

Very large discrepancies exist with regard to the spin reorientation transition in $TbFe_{11}Ti$ (see Ref. 1 for a summary of the different results). In this work, this transition is studied by measuring the angular dependence of the parallel ($M_{\parallel}$) and perpendicular ($M_{\perp}$) components of the magnetization to the applied magnetic field in the temperature range of 4.2–330 K and applied magnetic fields ranging from 2 to 15 kOe. This method allows an accurate determination of the easy magnetization direction to be made, i.e., the maximum value of $M_{\parallel}$ and the zero value of $M_{\perp}$. The experimental results have undoubtedly established that the compound is easy plane below 260 K and easy axis above 320 K. Within this intermediate range of temperature the easy magnetization direction lies along a nonmajor symmetry direction making an angle $\theta$ with the $c$ axis. This angle depends on the applied magnetic field and the magnetic history of the sample. This fact can be understood on the basis of the existence of a first-order spin reorientation transition at $T_{SR} \approx 320$ K from easy axis to easy plane. Within the temperature region 206–320 K both phases (axial and planar) coexist with relative volumes depending on the applied magnetic field and the magnetic history. This gives rise to a macroscopic conical structure. Such behavior has already been observed in $DyFe_{11}Ti$.[2] © *1996 American Institute of Physics.* [S0021-8979(96)65308-4]

[1] A. V. Andreev, N. V. Kudrevatykh, S. M. Razgonyaev, and E. N. Tarasov, Physica B **183**, 379 (1993).
[2] P. A. Algarabel, M. R. Ibarra, J. Bartolomé, L. M. García, and M. D. Kuz'min, J. Phys.: Condensed Matter **6**, 10551 (1994).

 0021-8979/96/79(8)/6330/1/$10.00 © 1996 American Institute of Physics

# Magnetic and structural characteristics of $LaCo_{9+\delta}Si_4$ and $LaCo_{8.5+\delta}Si_{4.5}$ alloys ($\delta$=0–4)

M. Q. Huang, Jason Wolf, and W. E. Wallace
*Department of Materials Science and Engineering, Carnegie Mellon University, Pittsburgh, Pennsylvania 15213*

$LaCo_{9+\delta}Si_4$ and $LaCo_{8.5+\delta}Si_{4.5}$ alloys with $\delta$=0 to 4 have been synthesized and characterized. The stoichiometric alloys ($\delta$=0) have low $T_c$ and small moments, whereas the alloys with $\delta \neq 0$ have larger $T_c$ and magnetization. © *1996 American Institute of Physics.* [S0021-8979(96)35008-4]

## I. INTRODUCTION

The $RCo_{13-x}Si_x$ systems have recently been receiving considerable attention in this and other laboratories as potential high-energy magnet materials.[1–7] Si doping is being extensively employed to generate uniaxial symmetry of the alloys. With extensive Si doping, the cubic symmetry is degraded to tetragonal, allowing the possibility of significant anisotropy. However, $T_c$ and magnetization sharply decrease. In the present study, efforts are made to prepare and characterize alloys that will crystallize in the tetragonal form but will not lose the desirable $T_c$ and $B_{sat}$. Ukranian workers Fedna *et al.*[8] formed about ten years ago a tetragonal phase $Pr_{0.69}(Co,Ge)_{13}$. It can be viewed as a nonstoichiometric (Co,Ge)-rich $Pr(Co,Ge)_{13}$ phase. The work by Fedna *et al.* suggested that the Si counterpart of the Fedna alloy warranted attention. Accordingly, several nonstoichiometric $LaCo_{9+\delta}Si_4$ and $LaCo_{8.5+\delta}Si_{4.5}$ alloys were prepared and studied with $\delta$ ranging from 0 to 4.

## II. EXPERIMENTAL DETAILS

The alloys were prepared by induction melting under high-purity argon, after which they were heat treated at 1273 K for about one week. X-ray diffraction (XRD) with Cu radiation was used to determine the crystal structure, lattice parameters, and phase present. The Hot Stage XRD was performed at temperatures ranging from room temperature to 1023 K under vacuums to determine the structure at high temperature. The relative amount of bct and fcc phases present were established by quantitative XRD measurements.

TABLE I. Phases present and crystal structures of $LaCo_{9+\delta}Si_4$ and $LaCo_{8.5+\delta}Si_{4.5}$ ($\delta$=0–4).

| Si | Co ($\delta$) | Phases present Main | Minor | bct $a$(Å) | $c/a$ | fcc $a$(Å) | $m$*bct [a] (wt %) |
|---|---|---|---|---|---|---|---|
| 4.0 | 0 | bct | | 7.827 | 1.478 | | |
| | 1 | bct | fcc | 7.840 | 1.474 | | ~95% |
| | 2 | bct | fcc | 7.845 | 1.472 | 11.316 | ~94% |
| | 3 | bct | fcc, $Co_2Si$ | 7.850 | 1.470 | 11.327 | ~88% |
| | 4 | bct | fcc, $Co_2Si$ | 7.854 | 1.470 | 11.330 | ~83% |
| 4.5 | 0 | bct | | 7.834 | 1.478 | | |
| | 1 | bct | fcc | 7.840 | 1.475 | | ~95% |
| | 2 | bct | fcc, $Co_2Si$ | 7.843 | 1.472 | 11.295 | ~92% |
| | 3 | bct | fcc, $Co_2Si$ | 7.843 | 1.472 | 11.320 | ~91% |

[a] $m$*bct: mass fraction of bct phase, calculated for the two-phase systems (bct and fcc).

The Jandel Scientific "Peak Fit" and "Desktop Microscopist" computer programs were employed to perform XRD deconvolution and structure factors calculations, respectively. The magnetic properties ($M$ and $T_c$) were measured by vibrating sample magnetometers (VSM) at temperatures ranging from 10 to 1173 K and fields ranging from 100 Oe to 17 kOe. The TMA measurements were made in such a manner—low applied field (500 Oe) and variable heating rate—to provide the most reliable information about phases present and the values of $T_c$.

## III. RESULTS AND DISCUSSION

### A. Phases formed and structural information

The relative amounts of the bct and fcc phases present were established by quantitative XRD measurements;[9] the

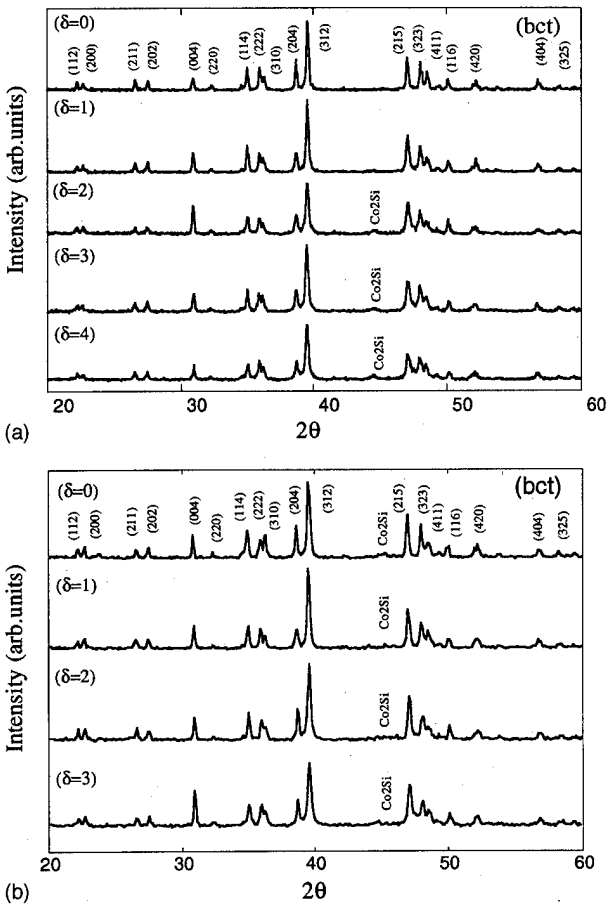



FIG. 1. (A) XRD for $LaCo_{9+\delta}Si_4$ alloys ($\delta$=0–4). (B) XRD for $LaCo_{8.5+\delta}Si_{4.5}$ alloys ($\delta$=0–3).

 0021-8979/96/79(8)/6331/3/$10.00 © 1996 American Institute of Physics 

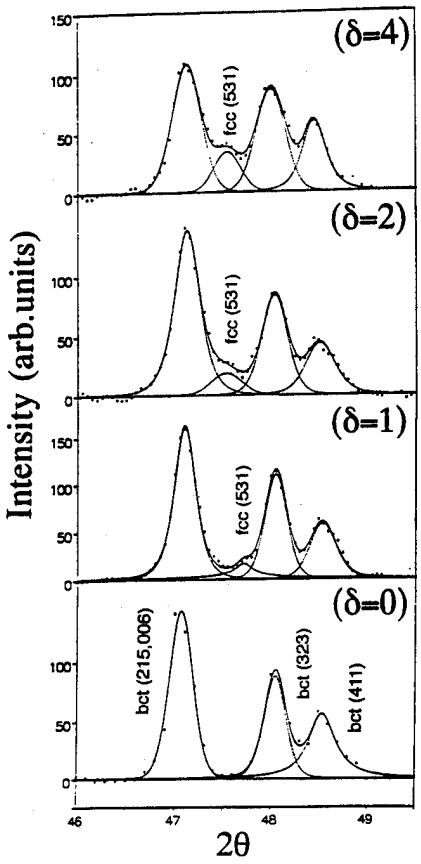



FIG. 2. XRD for $LaCo_{9+\delta}Si_4$ alloys. The lower portion is for a single-phase material (bct). The upper portion is for the two-phase system. As $d$ increases, the fcc phase increases.

$m_{bct}$-mass factor for the bct phase are listed in Table I. Structural information is summarized in Table I. The tabulated results are derived from the data in Figs. 1 and 2. $LaCo_9Si_4$ and $LaCo_{8.5}Si_{4.5}$ may be regarded as the base alloys to which extra Co, $\delta$ is added. The base alloys form in the bct $Ce_2Ni_{17}Si_9$ structure. It is interesting to attempt to ascertain where the extra Co's go. There are at least two possibilities: (1) They may precipitate out as a pure Co phase or (2) they may enter the bct lattice, substituting for La and Si atoms. This issue will be considered shortly.

The similarity of the XRD patterns (Fig. 1) indicates that the main phase for all the alloys ($\delta \neq 0$) has the same structure as the stoichiometric alloys ($\delta=0$). The ratio $c/a$ decrease as $d$ increases, a point that will be returned to later. A minor phase was observed and was found to form in the fcc $NaZn_{13}$ structure. A small amount of $Co_2Si$ was detected in some alloys, as shown in Fig. 1. TMA results, to be discussed below, were consistent with the XRD findings. An important result of the TMAs was that there was no evidence of elemental Co in any of the alloys. This was also indicated by the XRD patterns obtained. The lack of Co lines in the XRD patterns is not unexpected since XRD is less sensitive than TMA.

The location of the extra Co atoms is a matter of considerable interest. The site occupancies in $Ce_2Ni_{17}Si_9$ are as follows: 4 Ce in $4a$; 2 Si+2 Ni in $4d$; 16 Ni in $16k$; 16 Ni in $16l_1$; 16 Si in $16l_2$. The extra Co in the nonstoichiometric alloys is assumed to reside in the $4a$ and $16l_2$ sites. (The $4d$ sites are excluded because they are so much fewer in number than the $16l_2$ sites.) The composition of the main phase of the example alloy $LaCo_{11}Si_4$ accords with site occupancies as follows: $4a$ {3.5 La+0.5 Co}; $4d$ {2 Co+2 Si}; $16k$ {16 Co}; $16l_1$ {16 Co}; $16l_2$ {4 Co+12 Si}. Using $LaCo_{11}Si_4$ as an example, the fraction of the La or Si sites which are occupied by Co is 0.125 and 0.25, respectively. The fraction of the $4a$ sites occupied by Co ranges from 0.067 for $\delta=1$ to 0.223 for $\delta=4$.

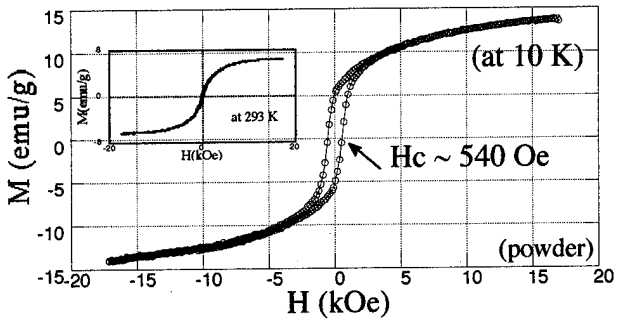



FIG. 3. Hysteresis loop of loose powder for $LaCo_{10}Si_4$ at 10 K.

The site occupancies cited in the preceding paragraph may be substantially overestimated. The surplus Co has been allocated to a portion of the $4a$ and $16l_2$ sites, assuming that one Co atom replaces one La atom. One would expect a decrease in $c$ and $c/a$, since La atom, which located along $c$ axis ($4a$ sites) was replaced by Co atom, the latter is much smaller than the former. Actually, there might exist the situation such as in $R_2Co_{17}$ in which the 2:17 structure is formed by Co pairs (often called dumbbells) replacing R in the $RCo_5$ structure. If R is replaced by pairs of Co, the fraction of the sites not occupied by rare earths will be reduced by about 50% in the nonstoichiometric 1:13 system. If dumbbell Co's are indeed involved, this might also account for the tetragonal structure of the system. If the dumbbell axis lies along the $a$ axis, one would expect expansion of $a$ and $a$ decrease

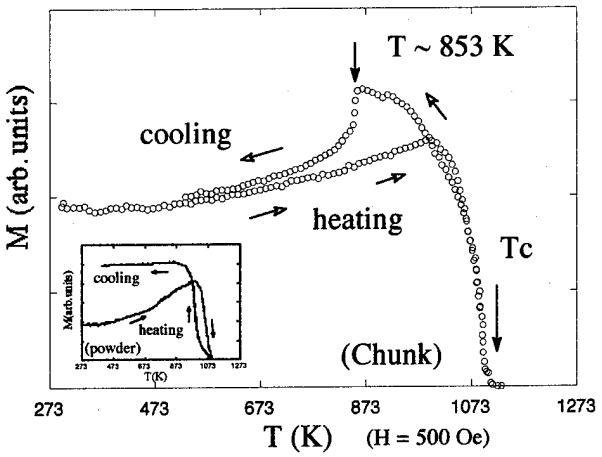



FIG. 4. $M$ vs $T$ for $LaCo_{13}Si_4$ (in chunk and powder form).

TABLE II. Magnetic properties of $LaCo_{9+\delta}Si_4$ and $LaCo_{8.5+\delta}Si_{4.5}$ ($\delta$=0–4). $M_{cal}(bct)=\{M_{ex}(10\ K)-M_{ex}(293\ K)/0.98\}/m_{bct}$. $M_{ex}(10\ K)=M_{fcc}(10\ K)+M_{bct}(10\ K)$, $M_{fcc}(10\ K)=M_{ex}(293\ K)/0.98$.

| Si | Co ($\delta$) | $T_c$ (K) bct | $T_c$ (K) fcc | $M_{ex}$ emu/g 293 K | $M_{ex}$ emu/g 10 K | $M_{cal}$ (bct) [a] $\mu B$/f.u. | $M_{cal}$ (bct) [a] $\mu B$/Co | $H_c$(Oe) 10 K |
|---|---|---|---|---|---|---|---|---|
| 4.0 | 0 | 40 | | 0.33 | 2.24 | 0.27 | $3.0\times10^{-2}$ | |
| | 1 | 50 | 1023 | 6.50 | 14.7 | 1.28 | $12.8\times10^{-2}$ | 540 |
| | 2 | 85 | 1073 | 8.95 | 21.1 | 2.05 | $18.6\times10^{-2}$ | 360 |
| | 3 | 115 | 1083 | 15.4 | 27.9 | 2.37 | $19.8\times10^{-2}$ | 290 |
| | 4 | 125 | 1103 | 28.1 | 39.6 | | | |
| 4.5 | 0 | * | | 0.23 | 0.28 | $0.62\times10^{-2}$ | $0.07\times10^{-2}$ | |
| | 1 | 50 | | 0.44 | 1.51 | $16.5\times10^{-2}$ | $1.74\times10^{-2}$ | |
| | 2 | 65 | 873,1023 | 2.48 | 8.24 | $98.2\times10^{-2}$ | $9.35\times10^{-2}$ | |
| | 3 | 75 | 1023 | 7.89 | 13.3 | | | |

[a] $T_c$ cannot be detected at 10 K.

in the axial ratio. This is in accord with experiment. Although it is tempting to relate the decrease in axial ratio to the substitution of La by Co pairs, other factors are undoubtedly involved. If there is a 1 for 1 Co for La substitution, one should write $LaCo_{11}Si_4$ as $(La_{3.5}Co_{0.5})(Co_{38}Si_{14})$ to emphasize the observance of the 1:13 structure.

The replacement of nonmagnetic La with magnetic Co should profoundly affect the magnetism of the alloy, raising $T_c$, for example.

### B. Magnetic properties

The magnetic properties $T_c$, $M$, and $H_c$ are given in Figs. 3–4 and in Table II.

From the results presented, it is to be noted that the stoichiometric alloys with $\delta$=0, which are bct, have a low moment and low $T_c$. The isostructural La-poor nonstoichiometric alloys with $\delta\neq0$, which are in bct and fcc two-phase mixture, show a higher moment and two Curie temperatures $T_c$. The fcc phase has a $T_c$ above room temperature, up to 1103 K. The bct phase has a lower $T_c$ down to temperature <40 K.

As expected, with increasing Co content, the $T_c$ for both phases increased. In the $LaCo_{9+\delta}Si_4$ case, the bct phase has a $T_c$ ranging from 40 K ($\delta$=0) to 125 K ($\delta$=4), and in the fcc phases $T_c$ is increased from 1023 K ($\delta$=1) to 1103 K ($\delta$=4). In the $LaCo_{8.5+\delta}Si_{4.5}$ case, the $T_c$ of the bct phase with $\delta$=0 cannot detected even at 10 K, but for $\delta\neq0$, $T_c$ increased from 50 K ($\delta$=1) to 75 K ($\delta$=3).

The magnetization observed $M_{ex}$ at 10 K, is contributed by both the weakly magnetic bct phase and the strongly fcc phase. One can estimate the bct main phase's moment, $M_{cal}$(bct), by making use of quantitative XRD measurement,[9] employing "Peak Fit" and "Desktop Microscopist" computer programs to estimate the phases present. As listed in Table II, $M_{cal}$ (bct) increases with increasing Co content $\delta$. In the $LaCo_{9+\delta}Si_4$ case, $M_{cal}$(bct) for $\delta\neq0$ is fourfold to sixfold higher than that of the $\delta$=0 alloy. In the $LaCo_{8.5+\delta}Si_{4.5}$ case, even higher, up to tenfold increases, is observed.

A coercive force of ~540 Oe was observed in loose powder samples of $LaCo_{10}Si_4$ at 10 K (see Fig. 4). Similar behavior was observed in other samples (see Table II). The origin of this behavior may be due to a change in anisotropy or exchange hardening. The latter may occur in a fine mixture of hard and soft phases. It appears to be a consequence of the extra cobalt. Figure 5 shows the $M$ vs $T$ about 293 K in a chunk sample of $LaCo_{13}Si_4$ alloy. The heating curve shows an increase of $M$ with increasing $T$. A puzzling sharp drop in $M$ occurs at $T\sim853$ K during cooling. The XRD patterns before and after this cycle show the main structure did not change. However, Hot Stage XRD patterns show that the intensity for some lines changed when cooling to 773 K, but then returned to normal upon cooling to 373 K. This behavior may be related to some type of order-disorder transformation which affects the Co-Co magnetic interaction. A surprising feature is that the drop is not in powder samples (see insert in Fig. 5). A similar situation was found in other alloys of $LaCo_{9+\delta}Si_4$ ($\delta\neq0$). Further investigation about this unusual behavior and also the odd coercivity behavior cited above is in process.


## ACKNOWLEDGMENT

This work was supported by the U.S. Army Research Office.



[1] F. Weitzer, K. Hiebl, Yu N. Grin, and P. Rogl, J. Appl. Phys. **68**, 350 (1990).
[2] H. Ido, J. G. Sohn, F. Pourarian, S. F. Cheng, and W. E. Wallace, J. Appl. Phys. **67**, 4978 (1990).
[3] M. Q. Huang, Y. Zheng, K. Miller, J. Elbicki, W. E. Wallace, and S. G. Sankar, IEEE Trans. Magn. **MAG-28**, 2860 (1992).
[4] G. H. Rao, J. K. Liang, Y. L. Zhang, X. R. Cheng, and W. H. Tang, Appl. Phys. Lett. **64**, 1650 (1994).
[5] G. H. Rao, J. Magn. Magn. Mater. **139**, 204 (1995).
[6] M. Q. Huang, W. E. Wallace, R. T. Obermyer, S. Simizu, and S. G. Sankar, J. Magn. Magn. Mater. **151**, 150 (1995).
[7] Paper No. FF05 in this Conference.
[8] M. Fedna, V. Pecharski, and O. Bodak, Inorg. Mater. **23**, 504 (1987).

# Magnetic and crystallographic properties of $R_2Fe_{14}Si_2$ ($R$=Y, Gd, Dy, Er, and Tm) compounds (abstract)

K. Konno
*Miyagi National College of Technology, Natori, 981-12, Japan*

H. Ido
*Department of Applied Physics, Tohoku Gakuin University, Tagajo, 985, Japan*

F. Pourarian, R. T. Obermyer, and S. G. Sanker
*Carnegie Mellon Research Institute, Carnegie Mellon University, Advanced Material Corporation, Pittsburgh, Pennsylvania 15213*

In connection with a previous work,[1] magnetic and crystallographic properties of the off-stoichiometric compounds $R_2Fe_{14}Si_2$ of the $R_2Fe_{17}$-type are studied. Magnetization curves at $T$=5 K are observed in a high magnetic field up to 15 T for loose powders as well as for field-aligned powders of the samples expressed in the title. Temperature dependencies of the spontaneous magnetizations are also determined in the temperature region from 5 K to the respective Curie temperature. Detailed x-ray analysis is carried out for $Y_2Fe_{14}Si_2$. Conclusions are as follows: (1) the Si substitution brings about significant displacements of the 12$j$-site Fe as well as the dumbell-site Fe from their original positions, which is discussed in connection with other present experimental data such as the remarkable enhancement of the Curie temperature caused by the Si substitution; (2) averaged Fe moment reduction is strictly determined for the present samples; (3) all the samples have a planer anisotropy at room temperature, taking this fact the magnetization curves for the field-aligned samples are analyzed; (4) exchange interaction between $R$ sublattice and Fe sublattice has been determined for all the samples. © *1996 American Institute of Physics.* [S0021-8979(96)65408-2]

[1] F. Pourarian, R. T. Obermyer, and S. G. Sanker, J. Appl. Phys. **75**, 6262 (1994).

 0021-8979/96/79(8)/6334/1/$10.00 © 1996 American Institute of Physics

# Effect of Fe and/or Cu contents on the intrinsic coercivity of $Sm_2Co_{17}$-type coercive powders for the bonded magnet application

W. L. Liu, Y. L. Liang, D. W. Scott, B. M. Ma, and C. O. Bounds
*Rhône-Poulenc, Rhône-Poulenc Rare Earths and Gallium, CN 7500, Cranbury, New Jersey 08512*

The microstructure of conventionally cast $Sm(Co_{bal}Fe_{0.28}Cu_vZr_{0.022})_{8.0}$ alloys, where $v=0.043$–$0.092$, were examined by optical microscopy and scanning electron microscope with energy dispersed analytical x ray in the as-cast state. In addition to the regular 2:17 matrix phase, the Sm-rich grain boundary phase and the needle-like Zr-rich phases are present in most commercial $Sm(Co,Fe,Cu,Zr)_z$ alloys. A grayish Sm- and Cu-rich grain boundary phase was found in alloys with $v \geqslant 0.07$. Attention was focused on the impact of increasing Cu content to the microstructure and process parameters required to produce coercive powder for bonded magnets. An increase of the Cu content from the $v$ value from 0.043 to 0.092 shifts the liquid+2:17→$TbCu_7$-type transformation temperature from slightly above 1180 to approximately 1140 °C. The $H_{ci}$ of optimally prepared magnet was found to increase significantly while the $B_r$ remained relative constant when the Cu content is increased. When the Cu content was increased to beyond $v=0.07$, a slight decrease in the $BH_{max}$ was noticed. A magnetizing field of 15 kOe and more than 50 kOe were determined to be necessary to charge magnets with a $H_{ci}$ of 12 and 25 kOe, respectively, to about 90% of their full potential. For a composition of $Sm(Co_{bal}Fe_uCu_{0.07}Zr_{0.022})_{8.0}$, a slight increase in Fe concentration from $u=0.22$ to 0.28 was found to increase the $B_r$ of an optimally prepared magnet from 8.07 to 8.28 kG and decrease the $H_{ci}$ from 11.8 to 9.7 kOe. A $BH_{max}$ of 15 MGOe was obtained on a bonded magnet with a composition of $Sm(Co_{bal}Fe_{0.28}Cu_{0.07}Zr_{0.022})_{8.0}$ when the data are normalized to a specific density of 7.0 g/cm$^3$. © *1996 American Institute of Physics.* [S0021-8979(96)35108-0]

## I. INTRODUCTION

Although NdFeB-type permanent magnets have gained most of the attention in the magnet industry in the past decade, outstanding thermal stability and high-energy product ($BH_{max}$) at elevated temperatures make $Sm(Co,Fe,Cu,Zr)_z$ magnets attractive for advanced applications.[1,2] The near net-shape production of $Sm(Co,Fe,Cu,Zr)_z$ bonded magnets make them potentially superior to any magnets made by the sintering route.

In our previous work,[3] we have generally identified the three major phases, namely, the 2:17 matrix phase, the Sm-rich grain boundary phase, and the Zr-rich phases embedded in the grain boundary region, present in the as-cast alloy. The influence of Zr on the solidus curves of liquid+2:17 →$TbCu_7$-type structure transformation, their impact on the selection of processing parameters and, consequently, the $H_{ci}$ of the powders were also discussed.[4] In this article, we discuss the effect of Cu to Fe ratio on the $H_{ci}$ obtained on the coercive powders. We will also try to establish a relationship between the $H_{ci}$ obtained and the magnetizing field required to achieve full potential properties.

## II. EXPERIMENT

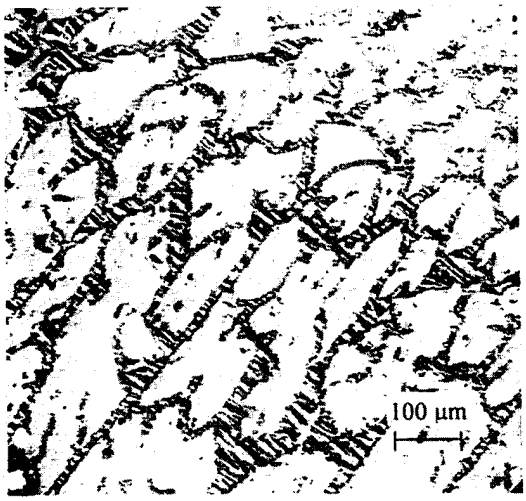
An alloy series with the composition of $Sm(Co_{1-u-v-w}Fe_uCu_vZr_w)_z$, where $u=0.22$–$0.28$, $v=0.043$–$0.092$, and $w=0.02$–$0.029$, and $z$ varied from 7.9 to 8.3, was prepared by vacuum induction melting and conventional mold casting. An isothermal anneal in the temperature range of 1130–1210 °C was applied to cast ingots in order to homogenize the microstructure. At the end of homogenization, ingots were quenched to 200 °C under an argon atmosphere. A precipitation hardening treatment (step aging) was then applied to the homogenized ingots to develop their $H_{ci}$. Alloy ingots were pulverized by a hammer mill to less than 40 $\mu$m. Cylindrical bonded magnets were produced by mixing the alloy powder with a 2 wt % epoxy resin, aligning with a 60 kOe pulse magnetic field and pressing isostatically. After curing, the magnets were demagnetized then sliced to about 10 mm in length for magnetic property measurements. The bonded magnets included in this work all exhibited a specific density of more than 6.1 g/cm$^3$. Samples were then pulse magnetized in a field of 60 kOe prior to magnetic measurement. The magnetic properties, namely, the $B_r$, $H_{ci}$, and $BH_{max}$, were measured by a Walker Hysteresisgraph System model MH-50. The $B_r$ and $BH_{max}$ values reported are normalized to a specific density of 7.0 g/cc, which is the density of most commercial $Sm(Co,Fe,Cu,Zr)_z$ bonded magnets.

The microstructure of alloy ingots at various processing stages was examined by an Olympus PMG-3 microscope under normal mode. A scanning electron microscope (SEM) with energy dispersed analytical x ray (EDAX) was utilized to determine the Cu distribution in the grain boundary region of treated samples.

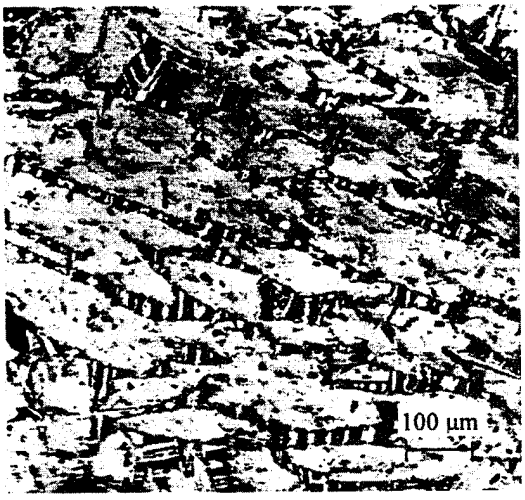
## III. RESULTS AND DISCUSSION

Shown in Fig. 1 are optical micrographs of cast ingots with a nominal composition of $Sm(Co_{bal}Fe_{0.28}Cu_vZr_{0.022})_{8.0}$, where $v=0.043$, 0.056, and 0.092. As in most of the commercially cast $Sm(Co,Fe,Cu,Zr)_z$ alloy, three major phases, namely, the $Sm_2Co_{17}$ matrix phase, the Sm-rich grain boundary phase, and the needle-like Zr-rich phase embedded in the grain boundary phase region, are present in all cast alloys. A grayish phase in the grain boundary region was also detected in alloys of high Cu concentration ($v \geqslant 0.07$). SEM EDAX

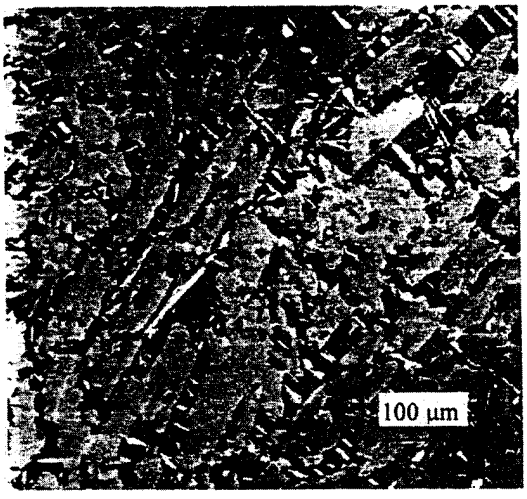
 0021-8979/96/79(8)/6335/3/$10.00 © 1996 American Institute of Physics 




(a)




(b)




(c)

FIG. 1. Optical micrographs of $Sm(Co_{bal}Fe_{0.28}Cu_vZr_{0.022})_{8.0}$, where $v=$(a) 0.043, (b) 0.056, and (c) 0.092, ingots in the as-cast state.

analyses, shown in Fig. 2, reveal significant enhancements on both the Sm/Co and Cu/Co intensity ratios when the Cu content was increased from 0.043 to 0.092. This suggested that the solubility of Sm in the grain boundary region increases with increasing Cu content in the cast alloy. A slight suppression of the Zr peak was also noticed when the Cu

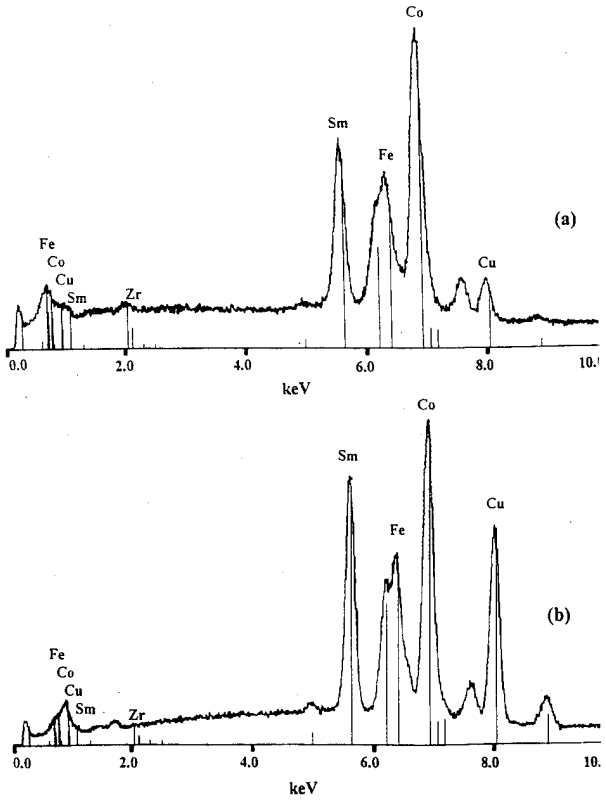
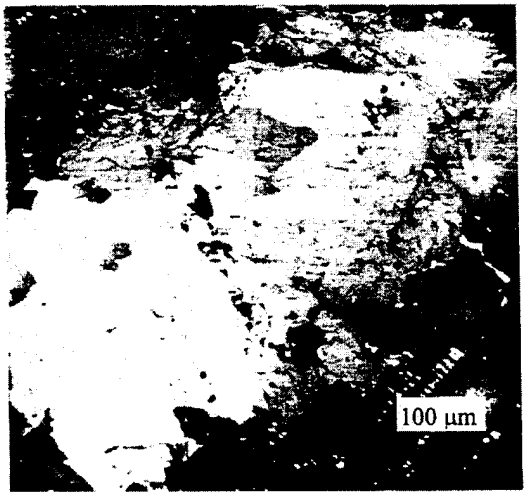



FIG. 2. SEM EDAX analyses of $Sm(Co_{bal}Fe_{0.28}Cu_vZr_{0.022})_{8.0}$, where $v=$(a) 0.043 and (b) 0.092, ingots in the as-cast state.

content ($v$ value in the formula expression) was increased from 0.043 to 0.092. These changes in the Sm, Cu, and Zr distribution in the grain boundary region may also change the position of the solidus line for the liquid+2:17→$TbCu_7$ phase transformation and, consequently, the solid solution treatment temperature required and the magnetic proprieties obtained.

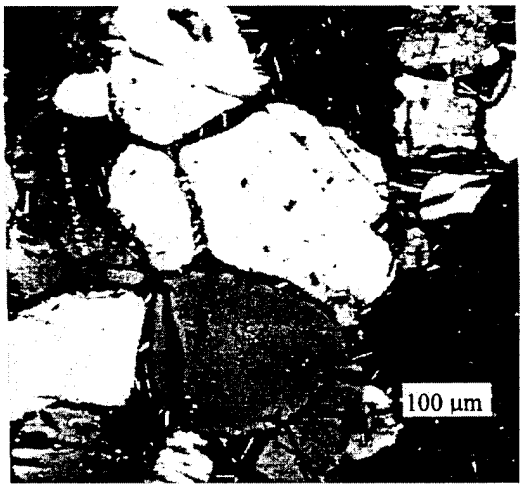
Shown in Figs. 3(a), 3(b), and 3(c) are optical micrographs of three ingots with a nominal composition of $Sm(Co_{bal}Fe_{0.28}Cu_vZr_{0.022})_{8.0}$, where $v=0.043$, 0.056, and 0.092, respectively, after an isothermal annealing at a temperature of 1180 °C. For $v=0.043$ [shown in Fig. 3(a)], the microstructure exhibited a nearly single-phase material with the exception of a few Zr-rich spots scattered in the matrix phase. This relatively uniform microstructure suggests the ingot was annealed at a temperature below the solidus curve.[3] With a slight increase in Cu content [$v=0.056$ shown in Fig. 3(b)], a band-like liquid phase can vaguely be observed around the grain boundary region indicating the ingot was heat treated at a temperature slightly above the solidus curve. When the Cu content was further increased to $v=0.092$ [shown in Fig. 3(c)], the presence of the liquid phase became very pronounced indicating the ingot was treated at a temperature well above the solidus curve. Employing the same technique to a series of alloys, the liquid+2:17→$TbCu_7$ phase transformation temperature was determined to decrease linearly from a temperature slightly above 1180 to approximately 1140 °C when the Cu content $v$ was increased from 0.043 to 0.092. This decrease of the liquid+2:17→$TbCu_7$ phase transformation temperature sug-




(a)




(b)




(c)

FIG. 3. Optical micrographs of $Sm(Co_{bal}Fe_{0.28}Cu_vZr_{0.022})_{8.0}$, where $v$=(a) 0.043, (b) 0.056, and (c) 0.092, ingots after an isothermal annealing at a temperature of 1180 °C for 6 h.

gests that it is necessary to adjust the solid solution treatment for each Cu concentration to obtain the optimum structure and magnetic properties, particularly the $H_{ci}$, desired.

Shown in Fig. 4 are the relationships of the $B_r$, $H_{ci}$, and $BH_{max}$ of bonded magnets to the Cu content for a magnet

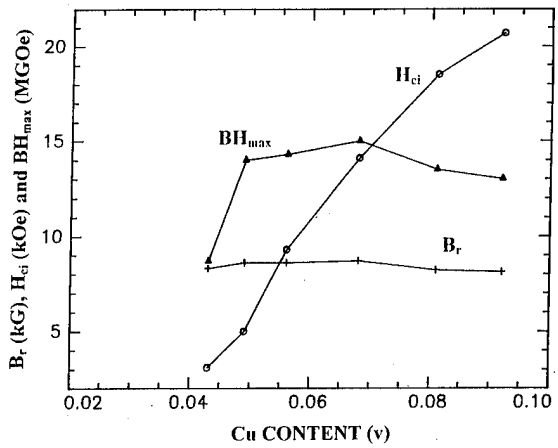



FIG. 4. The variation of $B_r$, $H_{ci}$ and $BH_{max}$ with the Cu content for an alloy series with a nominal composition of $Sm(Co_{bal}Fe_{0.28}Cu_vZr_{0.022})_{8.0}$, where $0.043 \leq v \leq 0.092$.

series with a compositions of $Sm(Co_{bal}Fe_{0.28}Cu_uZr_{0.022})_{8.0}$, where $v$ ranged from 0.043 to 0.092, when optimized with an appropriate solid solution treatment and the corresponding precipitation hardening treatment. The $H_{ci}$ increases sharply while the $B_r$ remains relatively constant with the increasing Cu content. Unlike the $B_r$, the $BH_{max}$ value showed a wide variation with the Cu content. Because of the low $H_{ci}$, a relatively low $BH_{max}$ was obtained at low Cu concentration ($v=0.043$). With a slight increase in $H_{ci}$, a drastic increase in $BH_{max}$ can be observed when the Cu content (the $u$ value in the formula expression) was raised from 0.043 to above 0.05. When the Cu content was increased to above $v=0.07$, a slight decrease in $BH_{max}$ can be observed. This decrease in $BH_{max}$ may be attributed to the fact that either an excessive amount of the nonmagnetic phase is present or a reduction of the magnetization of the 2:17 phase in the final magnet has occurred which would require further investigation.

## IV. CONCLUSIONS

The microstructure of $Sm(Co_{bal}Fe_{0.28}Cu_vZr_{0.022})_{8.0}$, where $v=0.043-0.092$, cast alloys have been examined in the as-cast state. A Sm- and Cu-rich grain boundary phase was found in alloys with $v \geq 0.07$ using SEM EDAX analysis. The liquid+2:17$\rightarrow TbCu_7$ transformation temperature was found to decrease from slightly above 1180 to approximately 1140 °C when the Cu content (i.e., the $v$ value) was increased from 0.043 to 0.092. The $H_{ci}$ of optimally prepared magnets was found to increase significantly while the $B_r$ remained relatively constant with the increasing Cu content.

[1] T. Shimoda, K. Kasai, and K. Teraishi, in the Proceedings of 4th International Workshop on Rare Earth-Cobalt Permanent Magnets and their Applications, Hakone National Park, Japan, 1979, p. 335.
[2] Y. Mortia, T. Umeda, and Y. Kimura, IEEE Trans. Magn. **23**, 2702 (1987).
[3] M. A. Willard, B. M. Ma, D. W. Scott, Y. L. Liang, W. L. Liu, and C. O. Bounds, in the Proceedings of 13th International Workshop on Rare Earth Magnets & Their Applications, Birmingham, UK, 1994, p. 893.
[4] W. L. Liu, Y. L. Liang, D. W. Scott, B. M. Ma, and C. O. Bounds, IEEE Trans. Magn. **31** (1995) (in press).

# $CoFe_2O_4$ thin films grown on (100) MgO substrates using pulsed laser deposition

P. C. Dorsey,[a] P. Lubitz, D. B. Chrisey, and J. S. Horwitz
*Naval Research Laboratory, Washington, DC 20375*

Thin films (≈0.4 $\mu$m) of cobalt ferrite ($CoFe_2O_4$) have been grown on single-crystal (100) MgO substrates using pulsed laser deposition (PLD). The phase, orientation, and microstructure of the as-deposited films were investigated as a function of substrate temperature (i.e., 200–800 °C) at a constant oxygen deposition pressure of 30 mTorr. The as-deposited films were found to be single phase, well oriented, and approximately matching the stoichiometry of the target, but the cubic lattice constant of the films depended on the substrate temperature indicating that the films were strained. The greatest effect of the substrate temperature was on the magnetic properties of the as-deposited films. At 800 °C, $4\pi M_s$ was measured to be 5370 G which is approximately the accepted bulk value for cobalt ferrite. In addition, PLD cobalt ferrite films grown at substrate temperatures of 600 and 800 °C exhibited a uniaxial magnetic anisotropy with an easy direction normal to the film plane. Films grown at 200 and 400 °C also exhibited a uniaxial magnetic anisotropy but possessed a planar easy direction. © *1996 American Institute of Physics.*
[S0021-8979(96)35208-7]

## I. INTRODUCTION

In this study, the potential for growing high quality single-crystal films of Co-ferrite ($CoFe_2O_4$) on (100) magnesium oxide (MgO) substrates using pulsed laser deposition (PLD) was investigated. MgO substrates are a very good lattice match with spinel ferrites and previous success at growing epitaxial MnZn-ferrite films on (100) MgO has already been demonstrated at relatively low substrate temperatures.[1] Most practical applications of Co-ferrite such as magnetic recording and magneto-optic recording require low-temperature processes so PLD may be an attractive alternative to some of the other deposition techniques which have been used to grow Co-ferrite.[2–6] The growth of high quality single-crystal films of Co-ferrite is important since many intrinsic magnetic properties can be investigated using single crystals. The information obtained from the PLD growth of single-crystal films can then be used to understand the PLD processing of Co-ferrite films on amorphous or polycrystalline substrates for more practical applications.

## II. EXPERIMENT

Thin films were pulsed laser deposited from a 5-cm-diam phase-pure polycrystalline $CoFe_2O_4$ target onto 1 cm×1 cm single-crystal (100) MgO substrates. The PLD system was operated for 5000 shots at a laser repetition rate of 5 Hz and an energy density of 2.5 J/cm$^2$. The PLD films were grown at substrate temperatures of 200, 400, 600, and 800 °C in a background of high-purity oxygen at a pressure of 30 mTorr. Substrate heating was provided by attaching the MgO substrate using silver paste to a radiatively heated stainless-steel block which was positioned 4 cm from the target. Substrate temperature and background oxygen pressure were held constant during deposition using a temperature controller with a thermocouple imbedded in the center of the stainless-steel heater block and a capacitance manometer with a controllable needle valve. In order to reduce rutting of the target and to improve film uniformity (e.g., composition and thickness), the focused laser beam was rastered across the face of the target while simultaneously rotating the target.

## III. STRUCTURAL RESULTS

The thickness and microstructure of the as-deposited films were determined using scanning electron microscopy (SEM). The films were first sputtered coated with 100 Å of platinum since the films are insulating. After fracturing the films into two equal halves, cross-section SEM micrographs were taken. The thicknesses of all of the PLD films were measured to be about 0.4 $\mu$m. The surface and cross section of the films were devoid of any visible microstructure at all substrate temperatures. The films were very dense with a smooth surface morphology and very few particulates.

The composition of the as-deposited films was measured using Rutherford backscattering spectroscopy (RBS) and also x-ray fluorescence (XRF). Specifically, RBS was used to measure the oxygen content of the films in terms of the oxygen to iron and cobalt ratio (i.e., O/Co+Fe), while XRF was used to measure the metal ratio of the films (i.e., Fe/Co). The RBS data were collected using 6.2 MeV $He^{2+}$ ions and the analysis was performed using a RUMP simulation which does not require standards.[7] The XRF data, however, were obtained using thin film standards of iron and cobalt which are valid for determining the composition of films up to 1.0 $\mu$m in thickness. The RBS and XRF results for the PLD films are shown in Table I. The PLD process is typically known for producing films whose stoichiometry matches the target even for multicomponent materials. In this specific case, the metal ratios and oxygen to metal ratios are consistent with the target indicating that the films have the nominal composition of $CoFe_2O_4$.

A standard $\theta/2\theta$ x-ray diffraction (XRD) setup was used to determine the phase and orientation of the PLD Co-ferrite films. XRD measurements were performed using a Cu $K_\alpha$ target operating at 20 kV and 30 mA. All of the films, regardless of substrate temperature, exhibited x-ray diffraction

[a]Paul Dorsey is an ASEE postdoctoral fellow.

 0021-8979/96/79(8)/6338/3/$10.00 © 1996 American Institute of Physics

TABLE I. XRF and RBS composition data for PLD films deposited from a $CoFe_2O_4$ target onto (100) MgO substrates in 30 mTorr of $O_2$ as a function of substrate temperature.

| Substrate temperature (°C) | Fe/Co | O/(Co+Fe) |
|---|---|---|
| 200 | 2.11 | 1.58 |
| 400 | 2.17 | 1.61 |
| 600 | 2.16 | 1.60 |
| 800 | 2.14 | 1.46 |

peaks corresponding to the (400) and (800) diffraction lines of the spinel structure. There were no other film diffraction peaks present in the XRD patterns and all of the films exhibited narrow $\omega$ scans about the (400) diffraction plane (see Table II). These results reveal that the films are well oriented and are of high crystalline quality. However, the positions of the (400) and (800) diffraction peaks shifted as a function of substrate temperature indicating a change in the cubic lattice parameter of the films. The accepted literature value for the bulk lattice parameter $a$ of Co-ferrite is 8.38 Å, while the unit cell length for MgO is 4.21 Å.[8,9] The calculated unit cell lengths of the Co-ferrite films, based on the experimentally measured $d$ spacings for the (400) and (800) diffraction peaks, are summarized in Table II. At substrate temperatures of 600 and 800 °C, the PLD Co-ferrite films have a cubic lattice parameter which closely matches the bulk value. At 200 and 400 °C, however, the cubic lattice parameter normal to the film plane is 0.48% larger than the bulk value for $CoFe_2O_4$ which indicates that the PLD Co-ferrite films are under a compressive stress in the film plane.

## IV. MAGNETIC RESULTS

The saturation magnetization ($4\pi M_s$), coercive field ($H_c$), and remanence ratio ($B_r/B_s$) of the PLD Co-ferrite films were measured using a vibrating sample magnetometer (VSM) with a maximum dc magnetic field of 16 500 Oe. The VSM measurements were performed with the dc magnetic field applied normal to the film plane (i.e., parallel to the ⟨100⟩ direction) and in the film plane along both the ⟨001⟩ and ⟨011⟩ crystallographic directions. The $4\pi M_s$ values as a function of substrate temperature are graphed in Fig. 1. The results show that $4\pi M_s$ increases with increasing substrate temperature and then reaches the bulk $4\pi M_s$ value for Co-ferrite, which is 5300 G, at a substrate temperature of 800 °C.[8] The coercive field and remanence ratio are shown in

TABLE II. XRD results for PLD Co-ferrite films summarizing the calculated unit cell length for the films and the full width at half-maximum (FWHM) values for $\omega$ scans about the (400) film plane.

| Substrate temperature (°C) | $\omega$ scan FWHM about the (400) film plane (°) | Cubic lattice parameter (Å) |
|---|---|---|
| 200 | 0.142 | 8.424 |
| 400 | 0.138 | 8.433 |
| 600 | 0.125 | 8.361 |
| 800 | 0.156 | 8.388 |

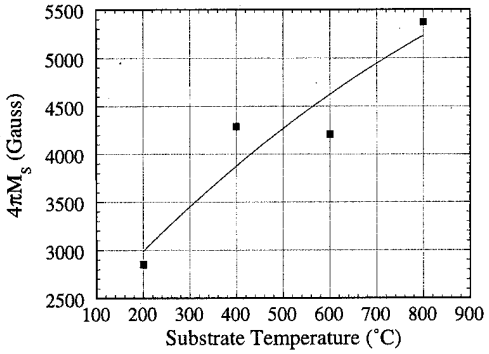



FIG. 1. The saturation magnetization ($4\pi M_s$) as a function of substrate temperature for 0.4-$\mu$m-thick PLD Co-ferrite films grown on (100) MgO in 30 mTorr of $O_2$.

Figs. 2 and 3, respectively. The values in these graphs are the result, in part, of the presence of a large magnetic anisotropy in the PLD Co-ferrite films which changes from a uniaxial to a planar anisotropy as a function of substrate temperature and causes the films to be magnetically anisotropic with respect to the film normal. Films grown at 200 and 400 °C are magnetically easy in the film plane with a hard direction normal to the film. Or, in other words, the uniaxial magnetic anisotropy term $K_u$ is a negative quantity. PLD Co-ferrite films grown at 600 and 800 °C are easy normal to the film plane and magnetically hard in the film plane such that $K_u$ is a positive quantity. At all substrate temperatures, however, the films are nearly isotropic in the plane. Consequently, $H_c$ and $B_r/B_s$ follow similar trends as a function of substrate temperature when measured along the ⟨001⟩ and ⟨011⟩ crystallographic directions. The VSM hysteresis curves for the PLD Co-ferrite films grown at 200 and 600 °C are shown in Figs. 4 and 5, respectively. These hysteresis curves qualitatively demonstrate the change from an easy planar anisotropy to an easy axis normal to the film plane. Only one in-plane hysteresis curve is shown for each substrate temperature, even though two in-plane directions were measured, since the films are nearly isotropic in the plane.

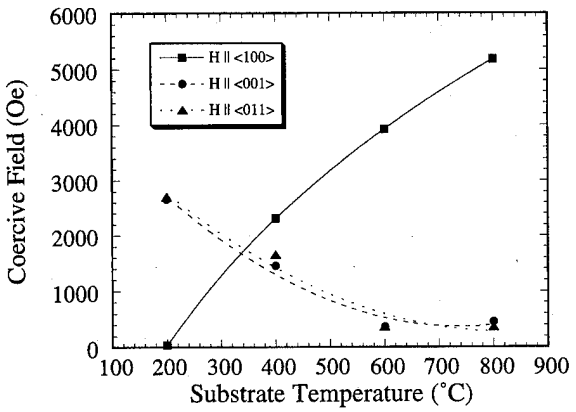



FIG. 2. The coercive field ($H_c$) along the ⟨100⟩, ⟨011⟩, and ⟨001⟩ crystallographic axes as a function of substrate temperature for 0.4-$\mu$m-thick PLD Co-ferrite films grown on (100) MgO.

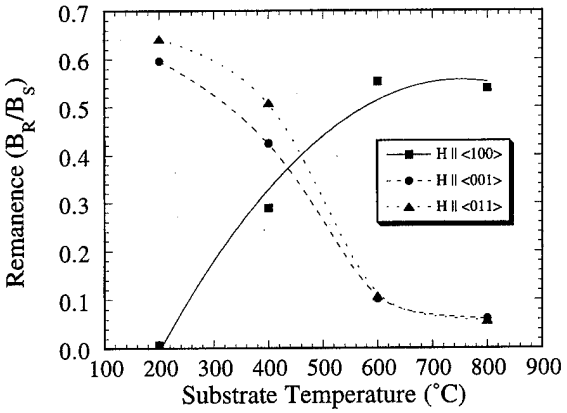



FIG. 3. The remanence ratio ($B_r/B_s$) along the ⟨100⟩, ⟨011⟩, and ⟨001⟩ crystallographic axes as a function of substrate temperature for 0.4-$\mu$m-thick PLD Co-ferrite films grown on (100) MgO.

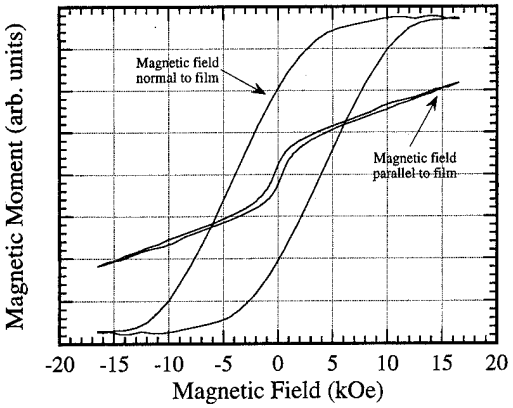



FIG. 5. The VSM hysteresis curves measured normal to the film plane (i.e., magnetic field parallel to the ⟨100⟩ axis) and parallel to the film plane (i.e., magnetic field parallel to the ⟨001⟩ axis) for 0.4-$\mu$m-thick PLD Co-ferrite films grown on (100) MgO at 600 °C.

## V. DISCUSSION AND CONCLUSION

Experimental results from RBS, XRF, and XRD demonstrate that well-oriented (100) $CoFe_2O_4$ films can be grown on (100) MgO substrates using PLD. The PLD Co-ferrite films grown at 200 and 400 °C have a cubic lattice constant normal to the film plane which is larger than bulk value of $CoFe_2O_4$ indicating that the film is compressively stressed. In-plane XRD measurements of the in-plane lattice constant would confirm the existence of a compressive stress since the in-plane lattice constant should show a corresponding reduction in size in order to maintain the unit cell volume at a constant value. This would then rule out other factors, such as compositional variations, which could also cause changes in the lattice constant of the film. Films grown at 600 and 800 °C had nearly bulk cubic lattice constants indicating that the higher substrate temperatures effectively relieve the stress in the films by allowing the film unit cell length to relax to its bulk value.

An estimate of the uniaxial magnetic anisotropy field ($H_u$) and cubic magnetocrystalline anisotropy field ($H_A$) exhibited by the PLD Co-ferrite films can be made based on the VSM hysteresis curves. The estimation can be made using the difference in the applied magnetic fields required for saturation along the hard and easy directions. In the case of $H_u$, the films could not be readily saturated in the hard direction with the available magnetic field, so the hard direction hysteresis curve must be extrapolated to saturation. Extrapolating to saturation for the two cases of the PLD films grown at 200 and 600 °C gives $H_u$ values of 59 and 26 kOe, respectively. The most likely origin of such large uniaxial magnetic anisotropy fields in Co-ferrite would be due to its large magnetostriction terms.[8,10–12] However, the films grown at 600 and 800 °C appear to have little or no uniform stress present so magnetostriction would seem to be an unlikely candidate for producing such a large magnetic anisotropy. In the films grown at 200 and 400 °C, magnetostriction does play a role. The presence of the compressive stress would cause the magnetization to lie normal to the film plane (i.e., normal to the compressive stress) since the sign of the magnetostriction term is negative for Co-ferrite. As was shown, this is the case. Finally, Co-ferrite has a significant cubic anisotropy field of about 6800 Oe which should manifest itself in the in-plane hysteresis curves along the ⟨001⟩ and ⟨011⟩ directions.[8,10–12] There is essentially no difference in the hysteresis curves for these two orientations, however, so the first-order cubic magnetocrystalline anisotropy term ($K_1$) can be considered to be negligible in these PLD Co-ferrite films.

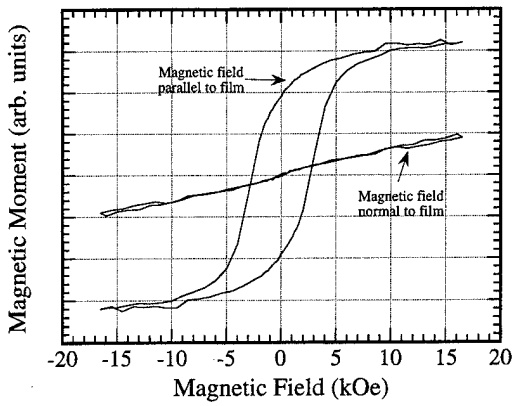



FIG. 4. The VSM hysteresis curves measured normal to the film plane (i.e., magnetic field parallel to the ⟨100⟩ axis) and parallel to the film plane (i.e., magnetic field parallel to the ⟨001⟩ axis) for 0.4-$\mu$m-thick PLD Co-ferrite films grown on (100) MgO at 200 °C.

## ACKNOWLEDGMENT

This work was supported in part by the Office of Naval Research.

[1] C. M. Williams, D. B. Chrisey, P. Lubitz, K. S. Grabowski, and C. M. Cotell, J. Appl. Phys. **75**, 1676 (1994).
[2] N. Matsushita, S. Nakagawa, and M. Naoe, IEEE Trans. Magn. **MAG-28**, 3108 (1992).
[3] S. N. Okuno, S. Hashimoto, and K. Inomata, J. Appl. Phys. **71**, 5926 (1992).
[4] M. Abe and M. Gomi, J. Appl. Phys. **53**, 8172 (1982).
[5] J. W. D. Martens, J. Appl. Phys. **59**, 3820 (1986).
[6] W. L. Peeters and J. W. D. Martens, J. Appl. Phys. **53**, 8178 (1982).
[7] L. R. Doolittle, Nucl. Instrum. Methods Phys. Res. B **9**, 344 (1985).
[8] A. Goldman, *Modern Ferrite Technology* (Van Nostrand Reinhold, New York, 1990), p. 26.
[9] See JCPDS card #4-829.
[10] J. C. Slonczewski, J. Appl. Phys. **32**, 253S (1961).
[11] R. M. Bozorth, E. F. Tilden, and A. J. Williams, Phys. Rev. **99**, 1788 (1955).
[12] G. F. Dionne, Mater. Res. Bull. **6**, 805 (1971).

# Optical and magnetic studies of SmCo and SmFe films (abstract)

K. T. Wu
*Department of Physics, Fu Jen University, Taipei 242, Taiwan*

Y. D. Yao
*Institute of Physics, Academia Sinica, Taipei 115, Taiwan*

T. C. Chen
*Department of Physics, Fu Jen University, Taipei 242, Taiwan*

Permanent magnetic materials based on iron, cobalt, and rare earths have been extensively studied during the past years. It is very interesting to study the physical properties of film type permanent magnet materials. In this investigation, we report the optical and magnetic properties of SmCo, SmFe, Sm, Co, and Fe films as well as the comparison of the electrical resistivity and magnetization behaviors between these films. The optical transmittance and reflectance have been measured as functions of the wavelength and the thickness for all the films with thickness less than 2000 Å. The electrical resistivity and magnetization have been measured below room temperature. The slope of electrical resistivity is decreased with decreasing the thickness of the films. The films are transparent with thickness less than 800 Å for magnetic films. For films with thickness at 200 Å, the values of the transmittance are 50, 48, 38, 18, and 14 for Sm, SmCo, SmFe, Co, and Fe, respectively. This is explained due to the difference of the magnetic permeability of all the films. The oscillatory behaviors of reflection for all the films are qualitatively consistent with that of the theoretical predict for an absorbing surface. Up to now, the best magnetic properties for magnetic films at room temperature are with an intrinsic coercivity of 1450 Oe and an energy product of 4.5 MGOe. © *1996 American Institute of Physics.* [S0021-8979(96)65508-1]

# Aspects of sintering barium hexaferrite with $SiO_2$, $Al_2O_3$, $CaCO_3$, and $Y_6Fe_{10}O_{24}$ additions for microwave applications (abstract)

J. G. Fagan, R. L. Snyder, C. Hach, and L. Jones
*NYS College of Ceramics, Alfred, New York 14802*

J. B. Ings, J. May, and J. J. Simmins
*TransTech., Adamstown, Maryland 21710*

Results are presented regarding the sintering mechanisms of barium hexaferrite ($BaFe_{12}O_{19}$) and modification thereof via secondary phase additions. Additional studies are presented concerning the effect of additives and microstructural development on the resultant microwave frequency magnetic and dielectric loss properties. The increasing demands on materials for microwave application has required development of barium hexaferrites to achieve fine grain size (i.e., $\leqslant 1$ $\mu$m), a high degree of $c$ axis alignment, high density and a minimum in dielectric loss. To accomplish such a task one area of interest is that of incorporating secondary phases. Additions of $SiO_2$, $Al_2O_3$ and $CaCO_3$ are examined in terms of grain size, magnetic, and dielectric loss properties. Thermal analysis methods revealed a redox reaction associated with the sintering process in barium hexaferrite. The use of yttrium iron garnet ($Y_6Fe_{10}O_{24}$) indicated an enhanced densification behavior in comparison to undoped barium hexaferrite which was associated to a decreased redox reaction temperature. The inclusion of the $SiO_2$, $Al_2O_3$, and $CaCO_3$ additions were seen to inhibit the redox reaction as measured via thermal analysis while liquid phase sintering occurred. © *1996 American Institute of Physics.* [S0021-8979(96)65608-3]

# Finite element modeling of powder aligning and multipole magnetizing systems for anisotropic bonded permanent magnets

C. D. Riley, G. W. Jewell, and D. Howe
*Department of Electronic and Electrical Engineering, University of Sheffield, Sheffield S1 3JD, United Kingdom*

The manufacture of anisotropic bonded permanent magnets involves the application of an aligning field during the moulding of the magnet, and in most cases, particularly those involving anisotropic NdFeB powder, the subsequent application of a considerably larger magnitude magnetizing field, which in turn is usually produced by a capacitor discharge magnetizer and a geometry specific fixture. A finite element based method for modeling both of the production stages is presented, and the method is validated by a case study, which includes extensive material characterization on a four-pole anisotropic NdFeB cylinder. © *1996 American Institute of Physics.*
[S0021-8979(96)35308-3]

## I. INTRODUCTION

Bonded permanent magnets based on anisotropic permanent magnet powders are attractive for many applications since they offer significant advantages in terms of flexibility of manufacture compared to sintered magnets, while having magnetic properties which are superior to the isotropic forms of the same material type. However, the manufacture of anisotropic bonded magnets, by either injection or compression moulding, requires that the cavity of the mould is exposed to a magnetic field of the appropriate orientation. The aligning field, which is produced by either an electromagnet or an array of permanent magnets, can be a simple two-pole axial pattern, a homopolar radial pattern, or more complex multipole patterns.

Following the moulding process, the aligned magnet is partially magnetized as a result of the applied aligning field. However, in almost all cases involving NdFeB anisotropic bonded magnets, a secondary impulse magnetization at a considerably higher field level is required in order to establish the full potential properties.

This article is concerned with the electromagnetic finite element modeling of these two coupled production stages, with particular emphasis on modeling the effects of complex and often incomplete alignment and magnetization within a permanent magnet component. Although the material characterization and the case study presented are based on an injection moulded NdFeB anisotropic magnet, the modeling techniques developed are entirely general, and can, with the appropriate material characterization, be equally applied to compression moulding and other materials such as anisotropic ferrite bonded magnets.

## II. MATERIAL CHARACTERIZATION

The finite element modeling of the alignment and magnetization production steps requires extensive characterization of the permanent magnet material, since the remnant properties exhibited by localized regions within the finished permanent magnet component are a function of both the magnitude and orientation of the aligning field and the subsequent impulse magnetizing field.

The extent of the data required for the modeling can be illustrated by considering the characterization of an anisotropic NdFeB injection moulding compound (Dai Nippon Ink and Chemicals Compodic NDA502E, 65% NdFeB volume loading). To characterize the material, a large number of 8 mm cube samples were injection moulded on a small laboratory scale pneumatic injection moulding machine. Each sample was produced under the same moulding conditions, viz., a barrel temperature of 280 °C, a mould temperature of 80 °C, and an injection pressure of 12.4 MPa (1800 psi), conditions which resulted in measured sample densities of ~5.2 g/cc.

To measure the effect of the aligning field on the subsequent properties of the samples, a constant dc uniaxial aligning field was applied throughout the moulding process in an orthogonal direction to the direction of injection. The field was generated by an electromagnet with 40 mm×40 mm pole face, designed to produce a uniform field in the region occupied by the mould cavity. The magnitude of the aligning field was increased from 0 A/m to 800 kA/m (0.0 to 1.0 T), in 80 kA/m uniform increments.

The second quadrant demagnetization curves were measured in an iron yoked dc permeameter, either directly from the mould or following impulse magnetization with a specified magnetizing field strength in a two-pole, air-cored solenoid. The demagnetization characteristics were measured in directions both parallel and perpendicular to the direction of the applied aligning field. In both cases, the impulse magnetizing field was applied in a direction parallel to the direction of measurement. A number of the measurements were systematically repeated in order to ensure that the measured magnetic properties were not significantly affected by the barrel residence time (i.e., the time that the compound remains in the barrel at 280 °C, which in a laboratory scale moulder is not necessarily representative of volume production conditions).

Figures 1 and 2 show the variation of the resultant remanence with the magnitudes of the aligning field and the subsequent impulse magnetizing field. In the absence of an aligning field, a remanence of 0.44 T was measured in three orthogonal directions, which confirms the absence of any significant flow induced anisotropy in the magnet samples.

The surface plots of Figs. 1 and 2 are useful in summarizing the levels of aligning field and magnetizing field required in order to obtain the full potential properties of the

 0021-8979/96/79(8)/6342/3/$10.00 © 1996 American Institute of Physics

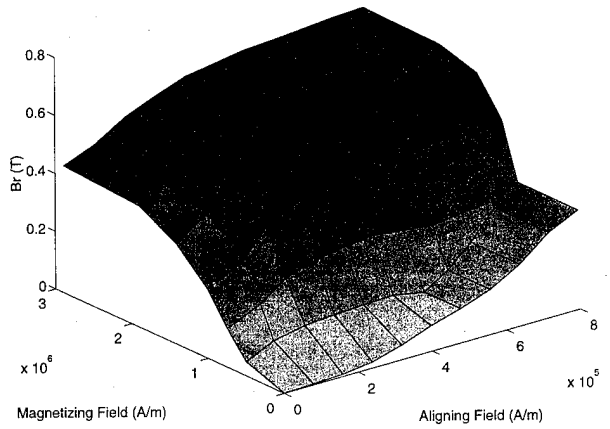



FIG. 1. Remenance of magnet samples measured in the direction of alignment as a function of the aligning field and the subsequent magnetizing field.

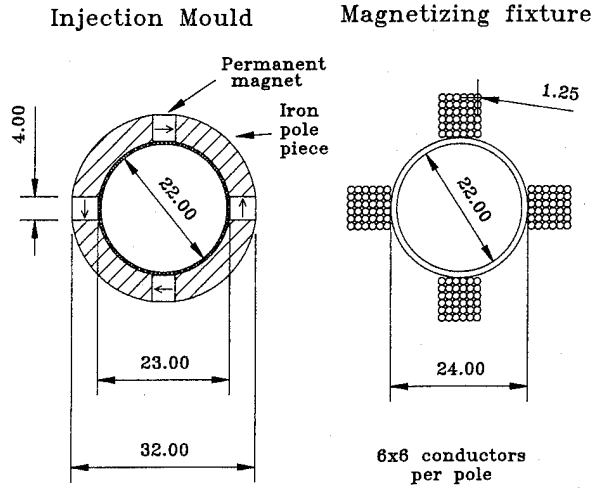



FIG. 3. Leading dimensions of mould and impulse magnetizing fixture.

material. However, to accurately model the behavior of the magnet requires a demagnetization characteristic in a direction both parallel and perpendicular to the aligning field for each combination of aligning field and magnetizing field, a total of 154 curves for the increments chosen in this case.

In order to account for nonlinear behavior of the magnet material in the first quadrant in both the moulding and magnetizing steps, it is necessary to measure the various magnetization curves of the material for each aligning field in directions both parallel and perpendicular to the aligning fields. Magnet samples were moulded in a known aligning field and demagnetized in a dc permeameter, following which the initial magnetization curves were measured.

## III. MODELING METHODOLOGY

Having generated the appropriate material data, the following finite element calculations are performed:

(i) The field distribution in the mould cavity is predicted using an in-house developed magnetostatic nonlinear finite element package. Since the initial magnetization curve of the material during the moulding process is itself a function of the magnitude of the localized aligning field, the initial magnetization curve within each element is iteratively modified to reflect the level of aligning field to which it is exposed. From the resultant field distribution, the direction and magnitude of the aligning field in each individual finite element within the region occupied by the moulded magnet can be determined. The subsequent behavior of the element to externally applied magnetizing fields can then be modeled by reference to the appropriate series of demagnetization curves for the calculated aligning field, with due interpolation between the discrete measured characteristics.

(ii) The model of the aligned magnet is placed in a finite element model of the impulse magnetizing fixture in order to calculate the magnitude and direction of the magnetizing field. In the majority of cases involving the magnetization of the magnet alone, a single nonlinear magnetostatic finite element solution with the calculated peak fixture current will usually suffice. However, in some instances, e.g., the magnetization of a component containing a significant region of solid soft magnetic material such as an assembled rotor for a machine, recourse to a transient, circuit-coupled, finite element simulation may be necessary to include the effect of eddy currents and saturation of the soft magnetic parts on the predicted field distribution and fixture current.[1] The calculated magnetizing field within each element, can be resolved into components along the "preferred" and "nonpreferred" directions of the element, i.e., the direction parallel and perpendicular to the aligning field calculated during the modeling of the moulding process. The resultant second quadrant demagnetization characteristics for this particular element in both its preferred and nonpreferred directions can then be established from the measured material characteristics.

(iii) The model of the magnet, which may well include individual elements which are not fully aligned and/or fully saturated, can be incorporated in a finite element model of the fully assembled device. The resulting predicted field distributions can be used to assess the final device performance, e.g., emf and cogging torque wave forms in the case of a permanent magnet machine.

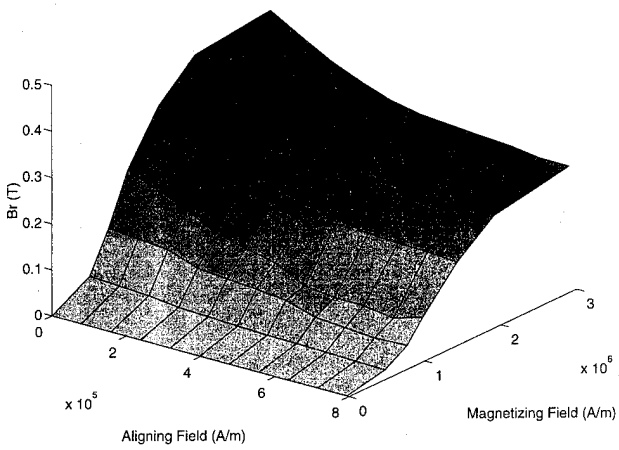



FIG. 2. Remenance of magnet samples measured perpendicular to the direction of alignment as a function of the aligning field and the subsequent magnetizing field.

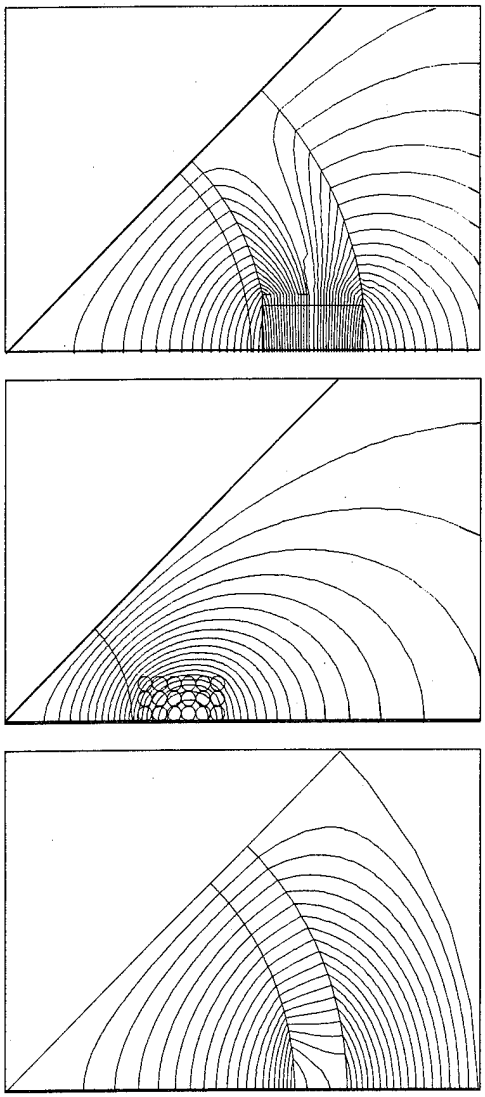


FIG. 4. Predicted magnetostatic field distributions of the aligning system, the impulse magnetizing fixture and the magnet within the mild steel sleeve.

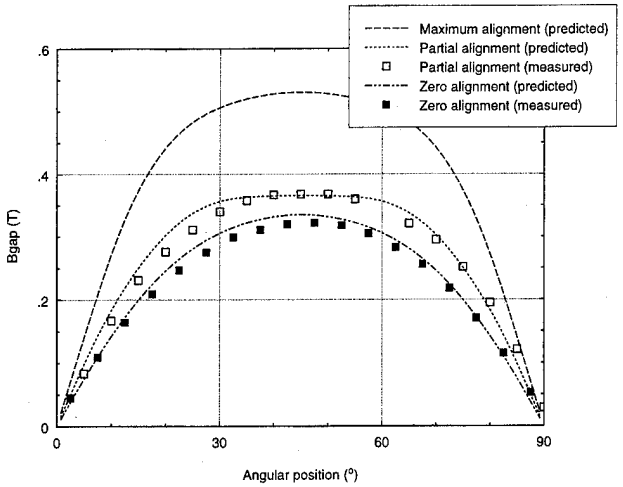



FIG. 5. Measured and predicted airgap flux density wave forms.

## IV. VALIDATION

In order to validate the technique, a mould and fixture to produce a four-pole self-shielding anisotropic NdFeB magnet with a diameter of 22 mm, and an axial length of 25 mm were modeled and constructed for experimental assessment. The leading dimensions of the injection mould and the impulse magnetizing fixture are shown in the cross sections of Fig. 3. The four-pole aligning field in the mould is produced by an array of sintered NdFeB magnets (Ugistab 300H), whose properties were measured at the mould operating temperature of 80 °C for inclusion in the finite element model. The magnetizing fixture draws a current pulse which has a peak magnitude of 3380 A and a time to peak of 0.78 ms when connected to a capacitor discharge magnetizer with a stored energy of 1.72 kJ (7000 $\mu$F at 700 V).

Although the geometry of the aligning system in the mould is in some respects representative of that which would be used in the manufacture of a multipole self shielding rotor, the relative dimensions of the various components were specifically chosen to produce regions within the moulded magnet which are exposed to aligning fields significantly lower than those required to achieve near full alignment, i.e., <800 kA/m (1.0 T). Further, there is a certain degree of misalignment between the orientation of the applied magnetizing field and the orientation of the magnet alignment. In the integrated design of a mould and its associated magnetizing fixture, one would endeavor to avoid both of these situations. However, for the purposes of a general validation, the specified problem is considerably more demanding to model than a well-aligned material with a well-matched magnetizing fixture.

Following the magnetization stage the magnet was located within a 5-mm-thick mild steel sleeve with an air gap of 2 mm. The calculated field distributions during the moulding process, the impulse magnetization, and after incorporation in the mild steel sleeve are shown in Fig. 4. Profiles of the normal component of flux density 1mm from the surface of the magnet were measured by a Hall probe, the location of which was maintained by a precision machined nonmagnetic insert. The process was repeated for a second sample for which the sintered magnets were removed from the mould to give a zero aligning field. Figure 5 shows the measured and predicted profiles of radial flux density in the gap and a predicted profile of a fully aligned sample for comparison. In both cases, there is good agreement between the measured and predicted profiles.

## V. CONCLUSIONS

A finite element based method for modeling both the production stages in the fabrication of an anisotropic injection moulded magnet and the subsequent performance evaluation have been presented. The method has been validated on a four-pole anisotropic NdFeB cylinder for which the aligning system was specifically designed to produce fields sufficient to only partially align the magnet. The method can be utilized in the design of combined alignment and magnetization systems in order to extract maximum leverage from the available injection moulded magnet materials.

[1] G. W. Jewell, D. Howe, and T. S. Birch, IEEE Trans. Magn. **26**, 1638, (1990).

# Metal-insulator transition in the presence of excitonic correlation

Mucio A. Continentino
*Instituto de Física, Universidade Federal Fluminense, Campus da Praia Vermelha, Niterói 24.210-340, RJ, Brazil*

Gloria M. Japiassú
*Instituto de Física, Universidade Federal do Rio de Janeiro, Caixa Postal 68.528, Rio de Janeiro 21.945-970, RJ, Brazil*

Amós Troper
*Centro Brasileiro de Pesquisas Físicas, Rua Dr. Xavier Sigaud 150, Rio de Janeiro 22.290-180, RJ, Brazil*

We study the possibility of an excitonic transition in a two-band model and show that a true phase transition does not occur in the presence of hybridization since the one-body mixing term acts as a conjugate field to the order parameter of the excitonic phase. We suggest an alternative interpretation for recent experiments on rare earth semiconductors based on a metal-insulator transition associated with the opening or closing of a hybridization gap at a critical pressure.
© *1996 American Institute of Physics.* [S0021-8979(96)25108-7]

Recently Wachter and colaborators[1,2] have claimed to observe a transition to an excitonic insulator in a doped narrow-band-gap semiconductor at moderate pressures and in a strongly correlated metal.[2]

With renewed interest in this subject motivated by these challenging experiments[1,2] and the close connection of the materials which have been investigated with Kondo insulators,[3] we study the possibility of this excitonic transition in the presence of hybridization in a two-band model. We point out that no sharp excitonic phase transition occurs, within our model, when external pressure is applied. The reason is that the hybridization, which depends on pressure, acts as a conjugate field to the order parameter of the excitonic phase and destroys this transition.[4] We obtain however that the mixing term is strongly renormalized by excitonic correlations and suggest an alternative interpretation for the experiments of Wachter *et al.*[1,2] on the basis of the appearance of a hybridization gap at a critical pressure. This metal-insulator transition is in the same universality class of the *density-driven transitions* for which the relevant critical exponents have been previously obtained. A characteristic feature of this metal-insulator transition is that the gap opens linearly with pressure close to the critical pressure. This is a direct consequence of the fact that the gap exponent assumes the value $\nu z = 1$.[4]

The Hamiltonian which describes the dynamics of our system is:

$$H=\sum_k \epsilon_k^a a_k^\dagger a_k+\sum_k \epsilon_k^b b_k^\dagger b_k+\sum_k V_k(a_k^\dagger b_k+b_k^\dagger a_k) - \sum_{k,k',q} G(q) a_{k+q}^\dagger a_k b_{k'-q}^\dagger b_{k'}, \tag{1}$$

where $\epsilon_k^a$ and $\epsilon_k^b$ represent the energies for electrons in the narrow *a-band* and in the broad conduction *b-band*, respectively. The operators $a_k^\dagger$, $a_k$ create and destroy electrons in the narrow band and $b_k^\dagger$, $b_k$ are creation and annihilation operators of electrons in the wide conduction band; $V$ is the mixing term, which arises from the crystalline potential and $G$ is the effective attractive interaction between spinless electrons and holes.[5] For the situation we are interested $G$ is the most important interaction and consequently we do not take into account the Coulomb repulsion between the electrons in the narrow band. We shall employ the equation of motion method[6] to calculate the order parameter associated with the excitonic phase, namely, $\Delta = \Sigma_k \langle b_k^\dagger a_k \rangle$. We calculate the frequency-dependent Green's function $\langle\langle a_k ; b_k^\dagger \rangle\rangle_\omega$ and use a convenient mean-field approximation, so that, neglecting the $k$-dependence of $G$, we obtain

$$\langle\langle a_k ; b_k^\dagger \rangle\rangle_\omega = \frac{\tilde{V}_k}{[(\omega-\epsilon_k^a)(\omega-\epsilon_k^b)-\tilde{V}_k^2]}, \tag{2}$$

where $\tilde{V}_k = V + G\Delta_k$, with $\Delta_k = \langle b_k^\dagger a_k \rangle$. The new energies of excitation of the system are given by the poles of the propagator

$$\omega_{1,2}(k) = \tfrac{1}{2}\{\epsilon_k^a + \epsilon_k^b \pm \sqrt{(\epsilon_k^a-\epsilon_k^b)^2+4\tilde{V}_k^2}\}. \tag{3}$$

In order to obtain explicit results for the excitonic order parameter we adopt the homothetic band model[7] which consists in taking $\epsilon_k^b = \epsilon_k$ and $\epsilon_{k\sigma}^a = \alpha\epsilon_k + \beta$. The quantity $\alpha$ ($\alpha<1$) may be interpreted as taking into account the different effective masses of the electrons in the narrow $a$-band and the broad $b$-band, i.e., $(m_b/m_a)=\alpha$. The quantity $\beta$ gives the shift of the narrow band with respect to the broad band.

The energies at the bottom of the hybrid bands are

$$E_B^{2,1} = \tfrac{1}{2}\{\beta \pm [\beta^2+4\tilde{V}^2]^{1/2}\}, \tag{4}$$

and the energies at the top are

$$E_T^{2,1} = \frac{D}{2}\left\{(1+\alpha)+\frac{\beta}{D} \pm \left[\left((\alpha-1)+\frac{\beta}{D}\right)^2+4\left(\frac{\tilde{V}}{D}\right)^2\right]^{1/2}\right\}, \tag{5}$$

 0021-8979/96/79(8)/6345/2/$10.00 © 1996 American Institute of Physics 

where $D$ is the bandwidth of the wide conduction $b$-band.[8]

The expression for the gap $\Delta_G$ between the two bands as a function of the hybridization $V$ and the electron-hole interaction $G$ is given by

$$\frac{\Delta_G}{D}=\frac{1}{2}\left\{\left[\left(\alpha-1+\frac{\beta}{D}\right)^2+4\left(\frac{\tilde{V}}{D}\right)^2\right]^{1/2}+\left[\left(\frac{\beta}{D}\right)^2+4\left(\frac{\tilde{V}}{D}\right)^2\right]^{1/2}-(1+\alpha)\right\}. \tag{6}$$

Consequently for a two-band system the opening of a hybridization gap, contrary to what occurs for the Anderson lattice model,[9] requires a critical value of renormalized hybridization $(\tilde{V}/D)_c$ given by

$$\left(\frac{\tilde{V}}{D}\right)_c=\frac{1}{2}\left[\frac{\left[2\alpha-\frac{\beta}{D}(\alpha-1)\right]^2}{(1+\alpha)^2}-\left(\frac{\beta}{D}\right)^2\right]^{1/2}. \tag{7}$$

Notice that for $\alpha\to 0$, $\tilde{V}_c\to 0$ as expected for a collection of localized levels. In this case[9] also $\Delta_G\propto\tilde{V}^2$ contrary to our two-band problem where close to $(\tilde{V}/D)_c$ we find

$$\frac{\Delta_G}{D}=\left|\left(\frac{\tilde{V}}{D}\right)-\left(\frac{\tilde{V}}{D}\right)_c\right| \tag{8}$$

so that the gap opens linearly close to $\tilde{V}_c$, i.e., $\nu z=1$, as in the non-interacting case.[4] Within the assumption that $|(\tilde{V}/D)-(\tilde{V}/D)_c|\propto|P-P_c|$ where $P_c$ is the critical pressure, this result, i.e., $\Delta_G\propto|P-P_c|$, describes the observed behavior for $Sm_{0.75}La_{0.25}S$[2] and also for the compound $SmB_6$[10,11] (see Fig. 1). We point out that the relevant variable here is $(\tilde{V}/D)$ which can either increase or decrease with pressure, for a given pressure range, depending on the relative pressure dependence of the hybridization and bandwidth.

We give now the scaling results for the properties of the Fermi liquid in the metallic phase close to the metal-insulator transition.[4] We find that the thermal mass $m_T$, defined as the coefficient of the linear term of the specific heat scales as $m_T\propto|P-P_c|^{(d/2)-1}$ and in three dimensions vanishes as $m_T\propto|P-P_c|^{1/2}$. The same scaling is found for the uniform susceptibility $\chi_0$, the compressibility $\kappa$ and the density of states at the chemical potential. The number of carriers $n_c\propto|P-P_c|^{d/2}$. The behavior of the thermal mass obtained above is opposite to that found in heavy fermions,[12] where it is enhanced as the system approaches the critical point. The characteristic or coherence temperature in the metallic phase scales as $T_c\propto(P-P_c)$ since $\nu z=1$.[4] The existence of a small coherence temperature close to the density-driven phase transition gives rise in the presence of electron-electron interactions to a significant $T^2$ term in the resistivity even in wide band materials as Yb.[13] If we write $\rho\approx\rho_0+AT^2$ for $T\ll T_c$, then the coefficient $A$ scales as $A\propto T_c^{-2}\propto(P-P_c)^{-2}$.

At the critical pressure, $P=P_c$, we expect to find non-Fermi liquid behavior with the specific heat vanishing with temperature as $C\propto T^{3/2}$ and $\chi_0\propto T^{1/2}$. In actual systems the states in the tails of the density of states due to impurities or disorder and which are responsible for the saturation of the resistivity in the *insulating phase* may spoil this simple behavior.

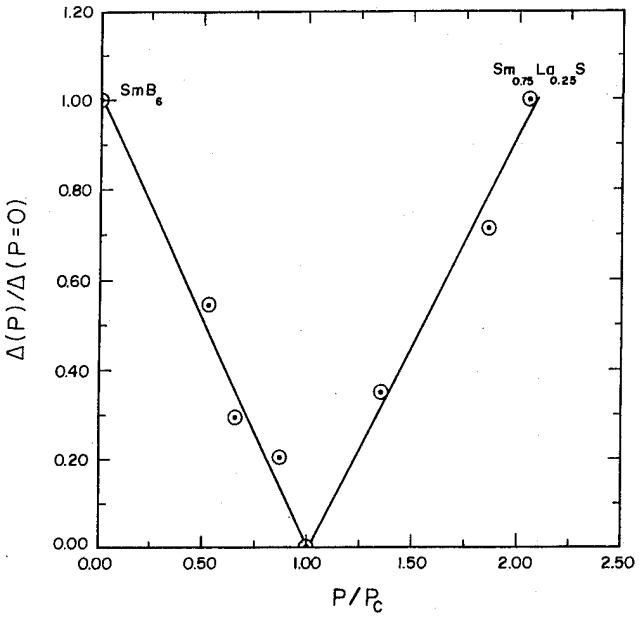



FIG. 1. Normalized gap vs normalized pressure. $P_c$ is the critical pressure where the gap vanishes. The data for $SmB_6$ are collected from Ref. 11 and for $Sm_{0.75}La_{0.25}S$ from Ref. 2. The solid straight lines are a guide to the eye.

In conclusion the possibility of an excitonic phase transition in a two-band model has been investigated. The dominant interaction was taken to be the electron-hole attraction. We argued that a phase transition to an excitonic phase does not occur within this model in the presence of hybridization since the one-body mixing term acts as a conjugate field to the order parameter of this phase. We find however that the hybridization is strongly renormalized by the presence of excitonic correlations.


[1] J. Neuenschwander and P. Wachter, Phys. Rev. B **41**, 12693 (1990); B. Bucher, P. Steiner, and P. Wachter, Phys. Rev. Lett. **67**, 2717 (1991); P. Wachter and A. Jung, IEEE Trans. Magn. **30**, 954 (1994).
[2] P. Wachter, A. Jung, and P. Steiner, Phys. Rev. B **51**, 5542 (1995).
[3] G. Aeppli and Z. Fisk, Comm. Cond. Mat. Phys. **16**, 155 (1992).
[4] M. A. Continentino, Phys. Lett. A **197**, 417 (1995).
[5] R. Ramirez, L. M. Falicov, and J. C. Kimball, Phys. Rev. B **2**, 3383 (1970).
[6] See, for example, A. L. Fetter and J. D. Walecka, *Quantum Theory of Many-Particle Systems* (McGraw-Hill, New York, 1975).
[7] R. Kishore and S. K. Joshi, Phys. Rev. B **2**, 1411 (1970).
[8] M. A. Continentino, G. M. Japiassú, and A. Troper, J. Appl. Phys. **75**, 6734 (1994); M. A. Continentino, G. M. Japiassú, and A. Troper, Phys. Rev. B **49**, 4432 (1994).
[9] C. M. Varma and Y. Yafet, Phys. Rev. B **19**, 2950 (1975).
[10] I. V. Berman *et al.*, JETP Lett. **38**, 477 (1983).
[11] Very recently Cooley *et al.*, Phys. Rev. Lett. **74**, 1629 (1995), through a different analysis of the resistivity curves concluded that the metal-insulator transition as a function of pressure in $SmB_6$ is discontinuous.
[12] M. A. Continentino, Phys. Rep. **239**, 179 (1994).
[13] R. Jullien and D. Jerome, J. Phys. Chem. Solids **32**, 257 (1971).

# Resistivity and $L_{III}$-edge absorption studies in valence fluctuation system $Ce_2Ni_3Si_5$

Chandan Mazumdar[a)]
*Department of Physics, Indian Institute of Technology, Bombay 400 076, India*

R. Nagarajan
*Tata Institute of Fundamental Research, Bombay 400 005, India*

C. Godart
*L.C.M.S.T.R., U.P.R. 209-C.N.R.S., 92195 Meudon, Cedex, France*

L. C. Gupta
*Tata Institute of Fundamental Research, Bombay 400 005, India*

B. D. Padalia
*Department of Physics, Indian Institute of Technology, Bombay 400 076, India*

R. Vijayaraghavan
*Tata Institute of Fundamental Research, Bombay 400 005, India*

From our x-ray ($L_{III}$-edge) absorption (XAS) investigations of $Ce_2Ni_3Si_5$, we show that Ce-valence is temperature dependent; it is 3.07 and 3.11 at 280 and 8 K, respectively. We also report on our resistivity measurements of two related materials $Ce_{2-x}R_xNi_3Si_5$ (R=Y, Gd and $x=0.1$). Absence of any qualitative difference in the resistivities of these two samples suggests that the enhancement of resistivity at low temperature on introduction of impurity atoms is due to Kondo hole scattering implying that $Ce_2Ni_3Si_5$ is a concentrated Kondo system. © *1996 American Institute of Physics.* [S0021-8979(96)25208-3]

Cerium based compounds often exhibit anomalous physical properties, such as Kondo behavior, valence fluctuation (VF), heavy fermion, heavy fermion superconductivity, etc. The close proximity of the cerium $4f$-level *w.r.t.* the Fermi level is responsible for the origin of such behaviors. We had shown earlier that Ce in $Ce_2Ni_3Si_5$ is in the VF state[1] by resistivity, magnetic susceptibility and specific heat measurements. As the resistivity shows a Kondo type behavior at high temperatures and decreases because of onset of coherence at low temperature, it is of interest to study the effect of magnetic and nonmagnetic impurity on the coherence effect. Here we present the results of our investigations on dilute substitution of Ce by Y (nonmagnetic) and Gd (magnetic) in $Ce_2Ni_3Si_5$. We also present the results of x-ray absorption ($L_{III}$-edge) spectroscopic measurements which confirm the VF behavior of Ce ions in this compound.

$Ce_{2-x}R_xNi_3Si_5$ (R=Y, Gd; $x=0$, 0.1) were prepared by melting high purity (>99.9%) constituent elements by standard arc melting procedure.[1] Room temperature powder x-ray diffraction pattern was obtained using Cu $K_\alpha$ radiation on an x-ray diffractometer (JEOL, Japan). X-ray absorption studies at the $L_{III}$-edge, for investigation of valence state of rare earth ions, were carried out at the French synchrotron facility, Laboratoire pour l'Utilisation du Rayonnement Electromagnetique (LURE) at Orsay, France. The details of the experimental setup has been given elsewhere.[2]

The $L_{III}$-edge spectra of the material taken at 280 K and 8 K (Fig. 1) show a double edge structure as expected for a VF system. The two edges correspond to $Ce^{3+}$ and $Ce^{4+}$ states. In order to determine the relative population of the two valence states, the observed spectra were deconvoluted using the procedure given in Ref. 3. The average valency of Ce in this compound thus deduced is 3.07 and 3.11 at 280 K and 8 K, respectively. The *temperature dependence* of the intensity of the two edges confirms that the observed double edge is due to VF phenomenon (and not due to XANES or impurity phases) as, in the case of VF, a change of relative population of the two valence states with temperature is expected. We should point out that x-ray absorption spectroscopy measurement *underestimates* Ce valence. This is due to

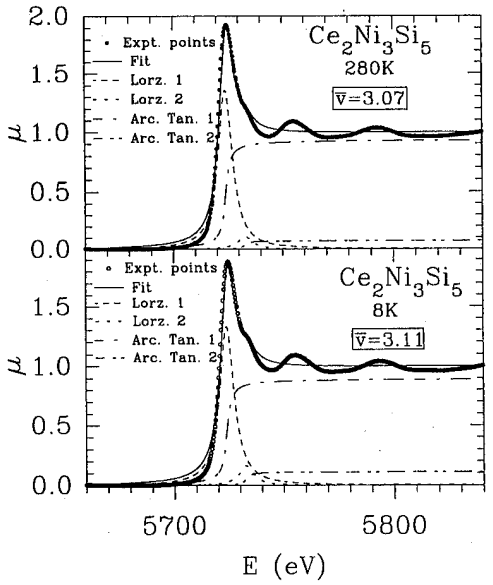



FIG. 1. X-ray absorption spectroscopy ($L_{III}$-edge) measurement of $Ce_2Ni_3Si_5$ at 280 and 8 K.

[a)]Present address: Solid State Physics Group, Tata Institute of Fundamental Research, Bombay 400 005, India.

 0021-8979/96/79(8)/6347/2/$10.00 © 1996 American Institute of Physics 

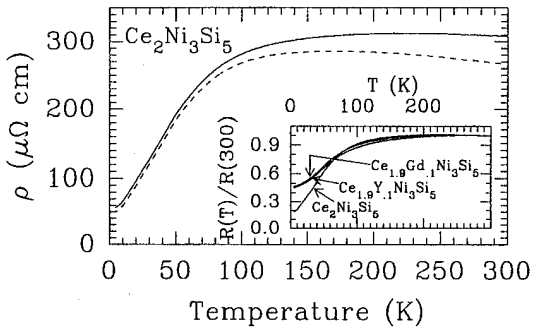



FIG. 2. Resistivity of $Ce_2Ni_3Si_5$ (solid line) as a function of temperature. Dashed line represents the $4f$ contribution of Ce to the resistivity obtained by subtracting the resistivity data of $Y_2Ni_3Si_5$ from the resistivity data of $Ce_2Ni_3Si_5$. Inset: Normalized resistivity of $Ce_{2-x}R_xNi_3Si_5$ (R=Y, Gd; $x=0$, 0.1). The agreement of the resistivity of the three samples in the high temperature region and the resistivity of the substituted samples below ~100 K is to be noted.

the existence of a shake-down satellite located at the same energy as the main peak of $Ce^{3+}$.[4]

Resistivity, $\rho(T)$, of $Ce_2Ni_3Si_5$ (Fig. 2) exhibits anomalous behavior:

(i) Magnitude of $\rho(T)$ in $Ce_2Ni_3Si_5$ is rather high ($\approx$300 $\mu\Omega$ cm at 300 K) than that observed in $Y_2Ni_3Si_5$ and $Gd_2Ni_3Si_5$ ($\approx$40 $\mu\Omega$ cm at 300 K).

(ii) $\rho(T)$ in $Ce_2Ni_3Si_5$ is nearly temperature independent in the interval 100 K $\leq T \leq$ 300 K.

This is to be compared with the temperature dependence of $\rho(T)$ of nonmagnetic $Y_2Ni_3Si_5$ (Ref. 1) and magnetic $Gd_2Ni_3Si_5$ (Ref. 5) which exhibit normal metallic behavior. These considerations suggest that the Kondo scattering dominates the resistivity of $Ce_2Ni_3Si_5$. A similar overall resistivity behavior has been earlier observed in other known VF systems, such as, CeRhIn,[6] $CeIr_2Si_2$,[7] $CePd_3$.[8] $\rho_{4f}(T)$, the $4f$-contribution of Ce to the resistivity, obtained by subtracting the phonon contribution (using the resistivity data of $Y_2Ni_3Si_5$, considering both the materials to have similar phonon contributions) has a negative slope with a broad maximum centered around 150 K and falls relatively sharply below 100 K.[1] Such a behavior is typical of a concentrated Kondo system. The resistivity drop observed at low temperatures, seen in other concentrated Kondo systems also, has been ascribed to the onset of coherence.[1,9] In order to obtain further insight into the behavior, we investigated the effect of impurities on the resistivity behavior. For this purpose, we substituted 5% of Ce by Gd (magnetic) and Y (nonmagnetic) ions in $Ce_2Ni_3Si_5$.

For comparison, considering that effects of dilute substitution may not affect resistivity significantly, the resistivity data of the substituted samples are plotted in inset of Fig. 2, normalized to room temperature value. From the figure we see that the normalized resistivity for all the three sample, viz., $Ce_2Ni_3Si_5$, $Ce_{1.9}Y_{0.1}Ni_3Si_5$, and $Ce_{1.9}Gd_{0.1}Ni_3Si_5$, are similar in the temperature range 70–300 K. This is to be expected because, at high temperatures, there is no coherence and the scattering due to impurity will be negligible compared to scattering by Ce ions. At low temperature end, both the Y and Gd doped samples show a similar increment in the resistivity with respect to undoped material which is remarkable considering that Gd ions are magnetic. That implies that the increase in resistivity at low temperature is due to a *common* effect in $Ce_{2-x}Y_xNi_3Si_5$ and $Ce_{2-x}Gd_xNi_3Si_5$. A similar behavior has also been seen in the system $Ce_{1-x}R_xPd_3$ (R=Y, Gd).[8]

The absence of any qualitative difference in the resistivities of the samples doped with small concentration of a magnetic ion (Gd) and nonmagnetic ion (Y), shows that the impurity-spin scattering does not have much effect on resistivity. We understand this in terms of *Kondo hole* as explained in the case of $CePd_3$ (Ref. 10) where it was shown that coherence is destroyed by the creation of *holes* in an otherwise regular Ce lattice by removing cerium atoms and substituting other atoms in their place. Such removed Ce ions are called *Kondo holes*. The scattering potential due to the impurity is small in comparison to that of the "Kondo hole" term and, as a result, the total resistivity at low temperatures is insensitive to the nature of solute. The total resistivity is primarily controlled by the integrity of the cerium lattice.

In conclusion, we have confirmed here the VF nature of Ce in $Ce_2Ni_3Si_5$ from the temperature dependence of x-ray $L_{III}$ edge results. The alloying of $Ce_2Ni_3Si_5$, by magnetic Gd or nonmagnetic Y, exhibits a Kondo hole pattern in resistivity and strengthens our earlier interpretation of Kondo coherence in resistivity at low temperature in this material.


[1] C. Mazumdar, R. Nagarajan, S. K. Dhar, L. C. Gupta, R. Vijayaraghavan, and B. D. Padalia, Phys. Rev. B **46**, 9009 (1992).

[2] M. Raviso, These de Doctorat d'Etat, Université Paris-Sud, Orsay, 1979.

[3] J. Röhler, J. Magn. Magn. Mater. **47-48**, 175 (1985).

[4] C. Krill, J. P. Kappler, A. Mayer, L. Abadli, and M. F. Ravel, J. Phys. F **11**, 1713 (1981).

[5] C. Mazumdar, R. Nagarajan, L. C. Gupta, R. Vijayaraghavan, C. Godart, and B. D. Padalia, J. Appl. Phys. **75**, 7155 (1994).

[6] D. T. Adroja, S. K. Malik, B. D. Padalia, and R. Vijayaraghavan, Phys. Rev. B **39**, 4831 (1989).

[7] B. Buffat, B. Chevalier, M. H. Tuilier, B. Lloret, and J. Etourneau, Solid State Commun. **59**, 17 (1986).

[8] H. Schneider and D. Wohlleben, Zeit. fur Physik **44**, 193 (1981).

[9] J. M. Lawrence, P. S. Riseborough, and R. D. Parks, Rep. Prog. Phys. **44**, 1 (1981).

[10] J. Lawrence, Y.-Y. Chen, and J. Thompson, in *Theoretical and Experimental Aspects of Valence Fluctuations and Heavy Fermions*, edited by L. C. Gupta and S. K. Malik (Plenum, New York, 1987), p. 169 and references therein.

# Transport, magnetic, and $^{119}$Sn Mössbauer studies on magnetically ordered valence fluctuating compound $SmRuSn_3$

Chandan Mazumdar[a)]
*Department of Physics, Indian Institute of Technology, Bombay 400 076, India*

Z. Hossain and R. Nagarajan
*Tata Institute of Fundamental Research, Bombay 400 005, India*

C. Godart
*L. C. M. S. T. R., U.P.R. 209-C.N.R.S., 92195 Meudon Cedex, France*

S. K. Dhar and L. C. Gupta
*Tata Institute of Fundamental Research, Bombay 400 005, India*

B. D. Padalia
*Department of Physics, Indian Institute of Technology, Bombay 400 076, India*

R. Vijayaraghavan
*Tata Institute of Fundamental Research, Bombay 400 005, India*

$SmRuSn_3$ is a unique compound among the known Sm-based valence fluctuation (VF) systems. Its crystallographic structure has two inequivalent Sm sites and Sm ions at *only* one of them are in VF state while the Sm ions in the other site orders magnetically. Our $^{119}$Mössbauer studies show a quadrupolar splitting at the Sn site, consistent with the noncubic symmetry of the Sn site. A broadening of the Mössbauer spectrum is seen due to magnetic ordering of the material. The transferred hyperfine field at Sn site at 4.2 K is small. © *1996 American Institute of Physics.* [S0021-8979(96)25308-X]

$SmRuSn_3$ was reported to be the first ternary Sm-based valence fluctuating (VF) compound.[1] This compound forms in the cubic (space group $Pm3n$) crystal structure. Sm ions occupy two distinct crystallographically inequivalent sites, i.e., $2a(0,0,0)$ and $6d(\frac{1}{4},\frac{1}{4},0)$.[2] From the lattice constant, transport and magnetic properties measurements, Fukuhara *et al.*[1] concluded that all Sm ions are in VF state. They also showed that $SmRuSn_3$ undergoes a magnetic transition at 6 K. Simultaneous occurrence of VF and magnetic ordering is noteworthy as this is the only Sm based material exhibiting this behavior. Only two Sm-based compounds (both binary), SmS (Ref. 3) and $SmB_6$,[4] are known to exhibit VF phenomena and they do not order magnetically. In view of this unusual behavior, we reinvestigated[5] the physical properties of $SmRuSn_3$. Our magnetic, specific heat and $L_{III}$ edge results of $SmRuSn_3$ established the mixed valence nature of Sm in this system. Here we briefly highlight our earlier work to emphasize the uniqueness of the system and present the results of our investigations of $^{119}$Sn Mössbauer spectroscopy in this system.

Details of sample preparation of $SmRuSn_3$ are given elsewhere.[5] The lattice parameter, $a$, of our sample of $SmRuSn_3$ is 9.666 Å[5] implying that the valence state of Sm ions does not differ significantly from 3+. We may point out that Fukuhara *et al.* reported a value of $a$(=9.73 Å)[1] which deviates from the lanthanide contraction expected for $Sm^{3+}$. Electron microprobe analysis showed that our sample is largely homogeneous having a composition $Sm_{0.98}RuSn_{3.10}$ (normalized to Ru). Small inclusions (≈50 $\mu m^2$), of Sn metal and some inclusions of composition SmRu were observed occasionally.

Our magnetic susceptibility data show a cusp around 6 K (inset Fig. 1), which indicate antiferromagnetic ordering of the material. Since only $Sm^{3+}$ ions carry a magnetic moment, the magnetic order must be due to $Sm^{3+}$ ions. The magnetic susceptibility (Fig. 1) at room temperature is larger than what one would expect for a $Sm^{3+}$ material. Our theoretical calculations[6] showed that the observed susceptibility cannot be accounted by mixing of excited state and/or crystal field contributions. We could account for the observed room temperature susceptibility (also taking into account the temperature independent van Vleck susceptibility) if about 14% of Sm ions are in divalent state (Fig. 1). We note here that

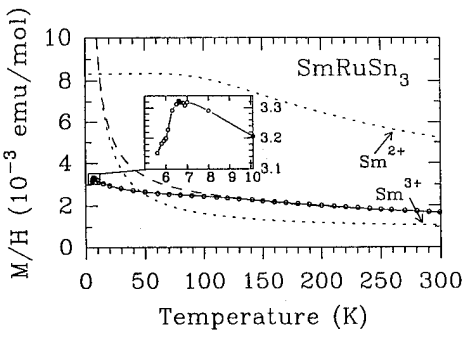



FIG. 1. Temperature dependence of dc magnetic susceptibility (○) of $SmRuSn_3$ (corrected *w.r.t.* dc magnetic susceptibility data of $LaRuSn_3$). Short dashed lines are the calculated susceptibility for free $Sm^{3+}$ and $Sm^{2+}$ ions. Long dashed line represents the susceptibility, $(1-x)\chi(Sm^{3+})+x\chi(Sm^{2+})$, with $x$ having a value 0.14. Inset shows the expanded region near the magnetic ordering temperature.

[a)]Present address: Solid State Physics Group, Tata Institute of Fundamental Research, Bombay 400 005, India.

 0021-8979/96/79(8)/6349/3/$10.00 © 1996 American Institute of Physics 

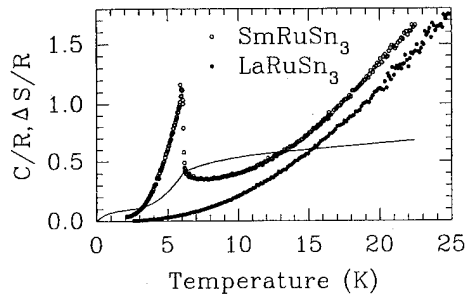



FIG. 2. Specific heat of $SmRuSn_3$ (○) and $LaRuSn_3$ (●). Solid line is the calculated magnetic entropy for $SmRuSn_3$ (obtained by subtracting specific heat data of $LaRuSn_3$ from that of $SmRuSn_3$). $R$ is the molar gas constant.

though $Sm^{2+}$ ions in the ground state do not carry a magnetic moment, it has a relatively large susceptibility due to mixing of low lying excited state. Thus, susceptibility data indicate mixed valence behavior of Sm ions in the material.

A quantitative estimate of the Sm ions taking part in magnetic order was obtained from magnetic entropy estimated from specific heat measurements on $SmRuSn_3$.[5] Specific heat measurements confirmed the magnetic ordering around 6 K (Fig. 2). The presence of strong crystal field effects is evident from the specific heat data of $SmRuSn_3$. If all the Sm ions would have contributed to the magnetic entropy, at the magnetic transition temperature, one would expect a minimum magnetic entropy of $R \ln 2$ ($\approx 0.693R$) as observed for a material having a crystal field doublet ground state. The magnetic entropy at the ordering temperature is much lower ($\sim 0.5R$ at 6 K) and can be accounted for properly, if one assumes that *only* the Sm ions at the $6d$ crystal site (having a crystal field doublet ground state) contribute toward magnetism, resulting a total minimum magnetic entropy of $(3/4)R \ln 2$ at the magnetic transition temperature, which matches very well with the experimental observation. The Sm ions at $2a$ site is nonmagnetic or weakly magnetic and hence do not contribute toward magnetic entropy. The specific heat results in conjunction with the magnetic susceptibility results can be consistently interpreted if Sm ions at $6d$ sites are in stable trivalent state and those at $2a$ sites are not in stable divalent state but are in VF state with an average valency of $\sim 2.6$ at room temperature, making the material a unique one in the field of VF.

Our x-ray absorption ($L_{III}$ edge) spectroscopic measurements on $SmRuSn_3$[7] exhibited a temperature dependent bimodal structure which confirm that some of the Sm ions in the material are in VF state with the average valence varying from 2.88 at 10 K to 2.91 at 300 K. This total average valence is consistent with the above distribution of the valence of Sm at the two sites of the material.

Mössbauer spectroscopy, with a probing time of $\approx 10^{-8}$ s (which is slower than the usually encountered fluctuation time $\approx 10^{-13}$ s) is a complementary technique with respect to $L_{III}$ edge absorption spectroscopy (probing time $\approx 10^{-16}$ s) in the investigation of valence fluctuation phenomenon. This fact has been successfully utilized in the case of Eu-based VF systems using $^{151}$Eu Mössbauer spectroscopy.[8] Although, fluctuation effects primarily take place at the rare earth site,

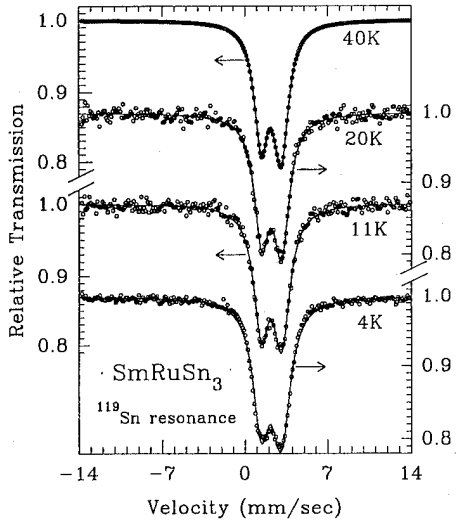



FIG. 3. $^{119}$Sn Mössbauer spectroscopic result on $SmRuSn_3$ at different temperatures. The solid lines are fit to experimental data.

$^{119}$Sn Mössbauer spectroscopy has been fruitfully used in the investigation of certain VF systems.[9–11] One can also obtain information on magnetic ordering of Sm ions through transferred hyperfine interactions at the Sn site. Mössbauer spectra of $SmRuSn_3$ were taken against a $^{119}$Sn source in $CaSnO_3$ matrix in the temperature range 4.2–300 K. A conventional constant acceleration-type spectrometer in conjunction with a home built multiscaler analyzer was used in the studies. Measurements were made with absorbers of different thickness (12 mg/cm$^2$ and 30 mg/cm$^2$) to estimate thickness broadening effects in the line width of the resonance.

Figure 3 shows the $^{119}$Sn Mössbauer spectra on $SmRuSn_3$ at different temperatures. The spectrum at all temperatures is a doublet but the intensities of the two components are not equal. Since there is only one crystallographic site, $24k$, for Sn in this compound, a doublet structure would primarily arise from quadrupole interaction from the presence of electric field gradient at the Sn site. Furthermore, for the same reason, the asymmetry of intensity in the doublet cannot originate from different Sn environments. One may consider the possibility of attributing the asymmetry to fluctuation effects. However, a careful analysis of the spectra reveals that the position of the more intense peak of this doublet is very close to that of pure Sn-metal. It should be noted here, as mentioned earlier, the electron microprobe measurements on $SmRuSn_3$ reveals a few small inclusions of Sn metal in our sample of $SmRuSn_3$. Considering this, we explain the spectrum in terms of a superposition of a doublet, arising out of the non-cubic site symmetry of Sn site, and a single line of small intensity due to Sn metal.

We have analyzed our spectra in terms of a singlet due to Sn metal [(fixed isomer shift (IS) (2.5 mm/s w.r.t. $CaSnO_3$) and fixed width (1.2 mm/s)] and a quadrupole doublet due to $SmRuSn_3$. The fit yields the IS as 2.15 mm/s (w.r.t. $CaSnO_3$), $e^2Qq/2$ (where $e$ is the electronic charge, $Q$ is the nuclear quadrupole moment, and $eq$ is the electric field gradient along the principle axis) as 1.75 mm/s and width of each line as 1.5 mm/s for the Sn-Mössbauer spectra of $SmRuSn_3$. The

result is essentially temperature independent above the magnetic ordering temperature. At 4.2 K, a small broadening of $^{119}$Sn Mössbauer line indicates the magnetic ordering taking place in this compound. However, the transferred hyperfine field, measured at 4.2 K, at the Sn site is very small. Apart from the antiferromagnetic nature of the ordering, the measurement temperature (4.2 K) being very close to magnetic ordering temperature (6 K) may also be one of the reasons responsible for the small transferred hyperfine field. Sm-ions at $2a$ sites, being in non ordered state, do not contribute to the transferred field. Investigations, such as elastic neutron scattering, will be useful to understand the detailed magnetic structure.

To conclude, specific heat and magnetic susceptibility measurements on $SmRuSn_3$ suggest that Sm ions in $2a$ crystallographic site are valence fluctuating, while Sm ions in $6d$ crystallographic site order antiferromagnetically. The valence fluctuating behavior of Sm ions in is confirmed by $L_{III}$-edge spectroscopic measurements. $^{119}$Sn Mössbauer spectroscopy results on $SmRuSn_3$ exhibit a temperature independent isomer shift and electric field gradient (arising due to noncubic site-symmetry). The asymmetry that we observe is not likely to be due to VF. The transferred hyperfine field at Sn site is small at 4.2 K.

We would like to thank S. K. Paghdar in Mössbauer spectroscopy measurements.

[1] T. Fukuhara, I. Sakamoto, and H. Sato, J. Phys. Condens. Matter **3**, 8917 (1991).
[2] B. Eisenmann and H. Schafer, J. Less-Common Metals **123**, 89 (1986).
[3] A. Jayaraman, in *Proceedings of the Eleventh Rare Earth Research Conference*, Traverse City, Michigan, 1974, edited by J. M. Haschke and H. A. Eick (U.S. Department of Commerce, Springfield, VA, 1974), p. 830.
[4] J. C. Nickerson, R. M. White, K. N. Lee, R. Bachman, T. H. Geballe, and G. W. Hull, Jr., Phys. Rev. **3**, 2030 (1971).
[5] C. Godart, C. Mazumdar, S. K. Dhar, R. Nagarajan, L. C. Gupta, B. D. Padalia, and R. Vijayaraghavan, Phys. Rev. B **48**, 16402 (1993).
[6] A. D. Chinchure, C. Mazumdar, V. R. Marathe, R. Nagarajan, L. C. Gupta, and S. S. Shah, Phys. Rev. B **50**, 609 (1994).
[7] C. Godart, C. Mazumdar, S. K. Dhar, H. Flandorfer, R. Nagarajan, L. C. Gupta, B. D. Padalia, and R. Vijayaraghavan, EuroPhys. Lett. **27**, 215 (1994).
[8] R. Nagarajan, in *Theoretical and Experimental Aspects of Valence Fluctuations and Heavy Fermions*, edited by L. C. Gupta and S. K. Malik (Plenum, New York, 1987), p. 307.
[9] G. K. Shenoy, B. D. Dunlap, G. M. Kalvius, A. M. Toxen, and R. J. Gambino, J. Appl. Phys. **41**, 1317 (1970).
[10] J. P. Sanchez, J. M. Friedt, G. K. Shenoy, A. Percheron, and J. C. Achard, J. Phys. C **9**, 2207 (1976).
[11] S. N. Mishra and H. G. Devare, in *Theoretical and Experimental Aspects of Valence Fluctuations and Heavy Fermions*, edited by L. C. Gupta and S. K. Malik (Plenum, New York, 1987), p. 651.

# Kondo behavior in $CeNi_{0.4}Cu_{0.6}$

J. I. Espeso, J. García Soldevilla, J. C. Gómez Sal, and M. Reiffers[a)]
*CITIMAC, Facultad de Ciencias, Universidad de Cantabria, 39005 Santander, Spain*

J. A. Blanco
*Departamento de Física, Universidad de Oviedo, 33007 Oviedo, Spain*

The effect of the substitution of Ni by Cu on the CeNi compound is analyzed by means of susceptibility, magnetization, and magnetoresistance measurements on the pseudobinary $CeNi_{0.4}Cu_{0.6}$ compound. Down to 2 K, the lowest investigated temperature, the compound does not present any magnetic order, but magnetic measurements suggest an ordering temperature ($T_C$) not far below 2 K. Magnetization and magnetoresistance data show an important Kondo interaction leading to a Kondo temperature ($T_K$) higher than $T_C$. The results are discussed considering the Kondo, magnetic exchange, and crystalline electric field interactions. © *1996 American Institute of Physics.* [S0021-8979(96)25408-6]

Cerium ions in a metallic environment give rise to great variety of fascinating many body effects (intermediate valence, heavy fermions or Kondo-type behavior). Among all the different Ce compounds showing these phenomena, $CeNi_xPt_{1-x}$ alloys and their dilutions with yttrium and lanthanum,[1–4] illustrate quite well these different behaviors. In particular the physical properties of this system are well understood from simple ideas concerning Kondo lattice models with "volume effects" playing an important role. Recently, the specific heat of these compounds[4] have been interpreted using a resonant level model, developed in Ref. 5, which accounts for the reduction of the jump of the λ-type anomaly at the Curie temperature in the specific heat when the $4f$-conduction band hybridization increases.

CeNi is a well known intermediate valence compound characterized by an enhanced Pauli paramagnetism.[6] Taking this composition as a starting point, the substitution of Ni by Cu will allow us to investigate the role of conduction electrons in the anomalous properties of these cerium compounds, because the volume effects are expected to be less important. Furthermore, the dilution with Cu have been proved to be particularly attractive, specially in other $RNi_xCu_{1-x}$ pseudobinary compounds.[7,8] Two aspects must be stressed in these systems: On the one hand, the crystalline structure evolves from a CrB type one (Cmcm space group) for Ni rich compounds to a FeB type one (Pnma space group) for largest Cu contents, and on the other hand, from the magnetic point of view, the introduction of Cu yields a change from ferromagnetism to antiferromagnetism which takes place around $x=0.85$ for the $NdNi_{1-x}Cu_x$ compounds.[8] Supporting this evolution, previous results on CeCu[9] report a FeB type structure and an antiferromagnetic behavior ($T_N=3.1$ K) for this compound. In the actual study we present a first survey of the physical properties of the new pseudobinary $CeNi_{0.4}Cu_{0.6}$ compound which is a characteristic representative of the $CeNi_{1-x}Cu_x$ series. The obtained results are discussed under the scope of the main mechanisms of Ce compounds, namely Kondo, RKKY exchange, and crystalline electric field (CEF) interactions.

Polycrystalline $CeNi_{0.4}Cu_{0.6}$ sample has been prepared from stoichiometric amounts of elements using high frequency melting under protective argon atmosphere. The phase purity of the sample has been proved from x-ray diffraction (Cu $K\alpha$ radiation) and its temperature evolution has been followed with neutron diffraction down to 2 K. As expected from the previous $RNi_{1-x}Cu_x$ studies,[7,8] the compound crystallizes in the FeB (Pnma) orthorhombic structure. The cell parameters at 300 K are $a=7.349(2)$ Å, $b=4.493(1)$ Å, and $c=5.648(1)$ Å. This structure remains down to the lowest studied temperature. The relative volume variation from 300 to 2 K is $\Delta V/V$ is around 0.2%. No trace of magnetic intensities was observed in the 2 K neutron diffraction pattern. On the other hand, it is worth mentioning that the volume changes due to dilutions with Cu are much smaller than those coming from dilutions with Pt.

The magnetic and magnetoresistivity measurements have been performed at the Laboratorio de Física de la Materia Condensada of the Universidad de Cantabria using a PPMS (Quantum Design) device. Figure 1 shows the temperature dependence of the magnetic reciprocal susceptibility $\chi^{-1}(T)$ for $CeNi_{0.4}Cu_{0.6}$. A Curie–Weiss behavior is observed at temperature higher than 30 K, giving rise to an effective paramagnetic moment of $\mu_{\text{eff}}=2.1\mu_B$, streakingly small compared with the $\mu_{\text{eff}}=2.54\mu_B$ of the free $Ce^{3+}$ ions.

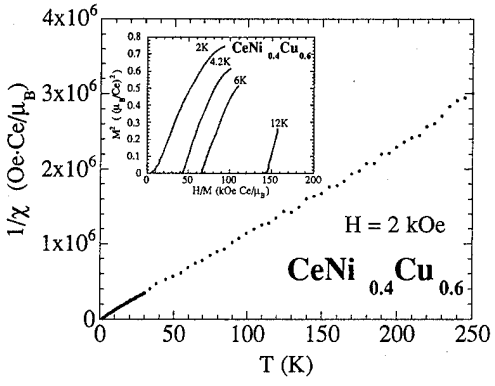



FIG. 1. Temperature dependence of the inverse magnetic susceptibility for $CeNi_{0.4}Cu_{0.6}$. The inset shows the Arrott plots ($M^2$ vs $H/M$) at different temperatures.

[a)]On leave from Inst. of Exp. Physics, 04353 Kosice, Slovakia.

 0021-8979/96/79(8)/6352/3/$10.00 © 1996 American Institute of Physics

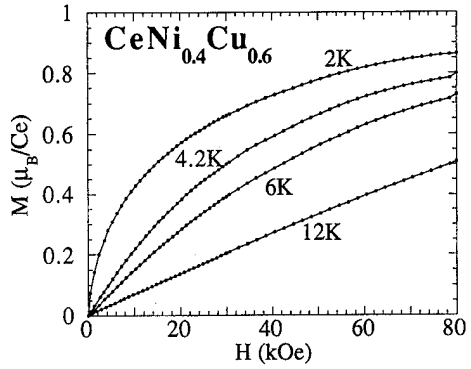



FIG. 2. Isothermal magnetization curves for $CeNi_{0.4}Cu_{0.6}$ at low temperatures.

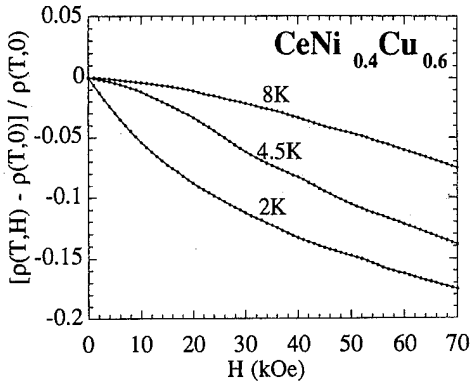



FIG. 4. Field dependence of the magnetoresistivity for $CeNi_{0.4}Cu_{0.6}$ up to 70 kOe at different fixed temperatures.

The extrapolation toward 0 K of $\chi^{-1}$ vs $T$ leads to a negative paramagnetic Curie temperature ($\theta_p$) close to $-10$ K.

The Arrot plots at low temperature (inset Fig. 1) confirm the absence of magnetic order down to 2 K. However the extrapolation of the $H/M$ values vs $T$ indicates a possible magnetic order about 1 K, lower than the minimum temperature experimentally available in our device. The isothermal magnetization curves up to 80 kOe, depicted in Fig. 2, are characteristic of a paramagnetic behavior at all the investigated temperatures, although the magnetization at 80 kOe and 2 K reach $0.86\mu_B$/Ce, which is a similar value than that observed in the CePt ferromagnetic compound.[1] This provides another indication that the magnetic order is not far below 2 K.

Figure 3 shows the temperature dependent electrical resistivity $\rho(T)$ of $CeNi_{0.4}Cu_{0.6}$ at various values of the magnetic field, which has been applied parallelly to the electrical current direction. Qualitative changes in the temperature dependence of $\rho$ are observed under magnetic field: The zero field resistivity $\rho(H=0)$ has a maximum around 4 K and a shallow minimum centered around 15 K, and both of them disappear when the applied magnetic field increases. These features are usually found in Kondo lattice compounds but in $CeNi_{0.4}Cu_{0.6}$ the maximum in $\rho(H=0)$ does not correspond to the ordering temperature as occurs in the $CeNi_xPt_{1-x}$ series.[1–3]

The magnetoresistivity, $\Delta\rho/\rho=[\rho(H,T)-\rho(0,T)]/\rho(0,T)$ of $CeNi_{0.4}Cu_{0.6}$ as a function of the magnetic field is presented in Fig. 4 at different temperatures. This magnetoresistivity is always negative and decreases with the increasing magnetic field. Furthermore, it is worth noting that in the 0–30 kOe range, the $\Delta\rho/\rho$ curves at 8 and 4.5 K have negative curvature while at 2 K in the same range of magnetic field the curvature is positive. At 2 K and 70 kOe $\Delta\rho/\rho$ is 18%, this value is quite large and close to that of $CeNi_xPt_{1-x}$,[10] although this comparison must be taken with caution due to the influence of the residual resistivity. In Fig. 5 $\Delta\rho/\rho$ is represented as a function of the temperature for $H=70$ kOe. From 30 K, when the temperature decreases $\Delta\rho/\rho$ becomes negative and monotonically decreases. However, at low temperatures this variation suddenly reaches the saturation showing a plateau down to 2 K.

From the present results, it is clear that $CeNi_{0.4}Cu_{0.6}$ does not show magnetic order down to 2 K, however some trends suggest the existence of an ordering temperature not far below this temperature. From the shape of the magnetization curves a ferromagnetic order could be expected at lower temperatures. As CeCu has been reported as an antiferromagnet,[9] then the change from ferromagnetism to antiferromagnetism observed in the other $RNi_{1-x}Cu_x$ compounds[7,8] has not taken place in the Ce based com-

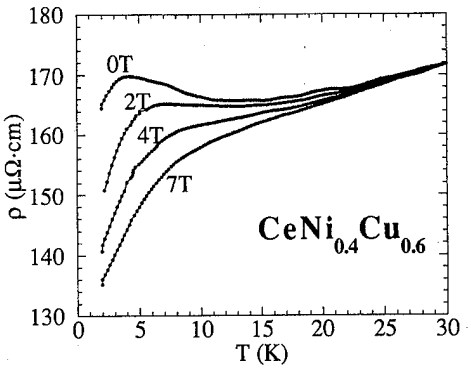



FIG. 3. Temperature dependence of the electrical resistivity for $CeNi_{0.4}Cu_{0.6}$ at various applied magnetic fields.

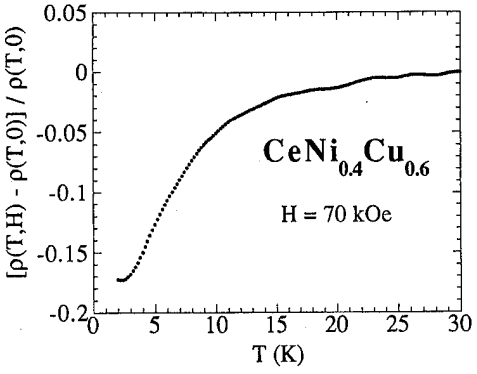



FIG. 5. Temperature dependence of the magnetoresistivity for $CeNi_{0.4}Cu_{0.6}$ corresponding to a 70 kOe applied magnetic field.

pounds at $x=0.6$. On the other hand, the strongly reduced magnetic moment at 80 kOe and 2 K ($0.86\mu_B$/Ce) and the negative value of $\theta_p=-10$ K are clear indications of the existence of a Kondo interaction which seems to be larger than the exchange interactions ($T_K>T_C$). This Kondo behavior is also revealed by the electrical resistivity measurements. The crystalline electric field yields three doublets for these low symmetry orthorhombic structures and then the maximum observed at 4 K is related to the pseudo-Schottky anomaly coming from the splitting of the doublet groundstate due to Kondo interaction. At temperatures just above the maximum a $-\ln T$ law is found. The maximum disappears with the applied magnetic field according to the calculations from Lassailly *et al.*[11] for a doublet groundstate. The fact that the maximum in $\rho(T)$ does not correspond to the ordering temperature as occurs in other Kondo compounds,[1] is commonly observed in systems where $T_K$ is greater than $T_C$, such as $CePd_2Si$.[12] In other cases in which a well defined maximum in $\rho(T)$ exists, such as $CeCu_6$,[13] it can disappear with dilutions [e.g., $Ce(Cu_{1-x}Au_x)_6$[14]] as a consequence of the destruction of Kondo lattice coherence, but this seems not to be the main mechanism in our compound, in which Ni and Cu share the same crystallographic site.

The magnetoresistance variations reflect the competition between Kondo and exchange interactions, and the observed change in the curvature (see Fig. 4) should be a consequence of the greater importance of exchange at low temperatures according to the calculations of Reference 15. From Fig. 5, we see no clear minimum in the $\Delta\rho/\rho$ vs $T$ variation; some theories[13,16] predict the existence of a minimum corresponding to $T_K$. However, these theories do not consider the existence of the molecular field as occurs in our case.

All these features indicate that the dilution with copper introduces new interesting aspects in this low symmetry system. Then, the present results encourage us to complete the study of the magnetic properties of $CeNi_{1-x}Cu_x$ compounds in order to understand the exciting changes of the Ce $4f$ electron properties along this series.

This work was supported by Spanish CICYT (Grant MAT93-0691).

[1] D. Gignoux and J. C. Gómez Sal, Phys. Rev. B **30**, 3967 (1984).
[2] D. Gignoux, J. C. Gómez Sal, J. Rodríguez Fernández, and J. M. Barandiarán, J. Phys. F: Met. Phys. **17**, L295 (1987).
[3] J. A. Blanco, D. Gignoux, J. C. Gómez Sal, J. Rodríguez Fernández, J. Voiron, and J. M. Barandiarán, J. Phys. Condens. Matter **2**, 677 (1990).
[4] J. A. Blanco, J. I. Espeso, J. C. Gómez Sal, C. Lester, K. A. McEwen, N. Patrikios, and J. Rodríguez Fernández, Phys. Rev. B **49**, 15126 (1994).
[5] C. D. Bredl, F. Steglich, and K. D. Schotte, Z. Phys. B **29**, 327 (1978).
[6] D. Gignoux, F. Givord, R. Lemaire, and F. Tasset, J. Less-Common Met. **94**, 779 (1983).
[7] J. A. Blanco, J. C. Gómez Sal, J. Rodríguez Fernández, D. Gignoux, D. Schmitt, and J. Rodríguez Carvajal, J. Phys. Condens. Matter **4**, 8233 (1992).
[8] J. García Soldevilla, J. I. Espeso, J. Rodríguez Fernández, J. C. Gómez Sal, J. A. Blanco, P. Galez, and D. Paccard, these proceedings.
[9] J. Sereni and J. P. Kappler, J. Magn. Magn. Matter. **109**, 349 (1992).
[10] J. I. Espeso, J. Rodríguez Fernández, J. C. Gómez Sal, J. A. Blanco, and M. Reiffers, these proceedings.
[11] Y. Lassailly, A. K. Bhattacharjee, and B. Coqblin, Phys. Rev. B **31**, 7424 (1985).
[12] J. M. Barandiarán, D. Gignoux, D. Schmitt, and J. C. Gómez Sal, Solid State Commun. **59**, 223 (1986).
[13] E. Bauer, Adv. Phys. **40**, 417 (1991).
[14] M. R. Lees and B. R. Coles, J. Magn. Magn. Mater. **76-77**, 173 (1988).
[15] V. V. Gridin, S. A. Sergeenkov, A. M. Strydom, and P. de V. du Plessis, Phys. Rev. B **50**, 12995 (1994).
[16] N. Kawakami and A. Okiji, J. Phys. Soc. Jpn. **55**, 2114 (1986).

# Temperature dependence of the electrical resistivity and thermopower of $U_2Ni_2In$ and $Nd_2Ni_2Sn$

R. P. Pinto, M. M. Amado, M. E. Braga, and J. B. Sousa
*Instituto de Materiais (IFIMUP-IMAT) and CFUP, Pr. Gomes Teixeira, 4050 Porto, Portugal*

B. Chevalier, D. Laffargue, and J. Étourneau
*Inst. Chimie Mat. Conden. Bordeaux, Av. A. Schweitzer, 33600 Pessac, France*

Accurate measurements of the electrical resistivity ($\rho$,$d\rho/dT$) and of the thermoelectric power ($S$,$dS/dT$) were performed in the ternary compounds $U_2Ni_2In$ and $Nd_2Ni_2Sn$ from 4 K to 250 K, and the results are compared with those previously obtained in $U_2Ni_2Sn$. The pair $U_2Ni_2In$/$U_2Ni_2Sn$ enables us to study the influence of the $p$-electron character (and other band effects related to the elements In/Sn) on the transport properties, whereas the pair $Nd_2Ni_2Sn$/$U_2Ni_2Sn$ provides direct information on the role played by the $4f/5f$ electrons. All these compounds order initially in the antiferromagnetic state, exhibiting a characteristic minimum in $d\rho/dT$ at $T_N$. In the $U_2Ni_2In$ compound a drastic reduction is observed in $\rho(T)$ slightly below $T_N$, suggesting the coexistence of the antiferromagnetic state with a coherent Kondo effect when $T \leq 0.8\ T_N$. In $Nd_2Ni_2Sn$ we observe two distinct phase transitions below $T_N$, of first-order character and likely associated with order-order magnetic transitions. The anomalous behavior of $\rho(T)$ in the paramagnetic phase of the $Nd_2Ni_2Sn$ compound can be satisfactorily described in terms of crystal field effects associated with the $4f$-electron levels. © *1996 American Institute of Physics.* [S0021-8979(96)25608-9]

## I. INTRODUCTION

We have shown recently that the tetragonal stannide $U_2Ni_2Sn$ orders antiferromanetically at $T_N$=25 K, exhibiting a cusp in the magnetic susceptibility ($\chi$) and characteristic minima in the temperature derivatives of the electrical resistivity ($\rho/dT$) and thermopower ($dS/dT$).[1] By substituting the Sn element by In one can appreciably change the electronic band structure, since Sn has an extra valence electron and a smaller atomic diameter. In particular one expects significant differences in the degree of hybridization of the uranium $5f$ electron states with the $s$-$p$-$d$ electron states from the transition metal and the $s$-$p$ states from Sn or In. Important changes may then occur in the transport and magnetic properties, reflecting in particular the influence of the transition metal $d$-states on the magnetic behavior of uranium.

The role played by the $5f/4f$ substitution is here analyzed with a comparison of the behavior of the transport properties in $U_2Ni_2Sn$ and $Nd_2Ni_2Sn$, using experimental results on the electrical resistivity ($\rho$) and thermopower ($S$) in the temperature range from 3.7 to 300 K.

Both compounds exhibit antiferromagnetism, enabling us to investigate the possible coexistence of this magnetic phase with a heavy fermion state at sufficiently low temperatures, as recently observed in some compounds of the same series.[2]

## II. RESULTS AND DISCUSSION

All the polycrystalline buttons were prepared by rf levitation melting followed by annealling at 800 °C for one week in evacuated quartz tubes X-ray powder diffraction showed a single phase tetragonal ordered structure derived from the $U_3Si_2$ type structure. Paralelipipedic samples were subsequently cut with a spark machine, for the transport measurements.

### A. $U_2Ni_2In$ versus $U_2Ni_2Sn$

The temperature dependence of the electrical resistivity of $U_2Ni_2In$ and $U_2Ni_2Sn$ is shown in Fig. 1 for the temperature range 4–250 K. A high concentration of internal cracks in these samples hampered the accurate determination of the appropriate geometrical factors, so only relative values of resistivity are displayed.

The $U_2Ni_2Sn$ and $U_2Ni_2In$ compounds order antiferromagnetically at $T_N$=25 K and $T_N$=14 K, respectively, exhibiting the characteristic minimum in $d\rho/dT$ at the transition point, as shown in the inset of Fig. 1. The lower value of $T_N$ for $U_2Ni_2In$ indicates a stronger delocalization of the $5f$ states in this compound. This seems to be a general feature of the In compounds of 2:2:1 type relative to their Sn counterparts.[3]

In the paramagnetic phase $\rho(T)$ in $U_2Ni_2In$ reveals a pronounced increase over a wide temperature range, with a progressive reduction in the curvature towards saturation above ~200 K. This later behavior contrasts with that ob-

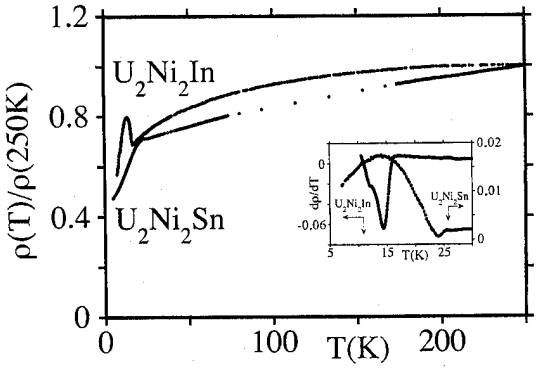



FIG. 1. Temperature dependence of the electrical resistivity ($\rho$) of $U_2Ni_2In$ and $U_2Ni_2Sn$ in the range 4–250 K.

 0021-8979/96/79(8)/6355/3/$10.00 © 1996 American Institute of Physics 

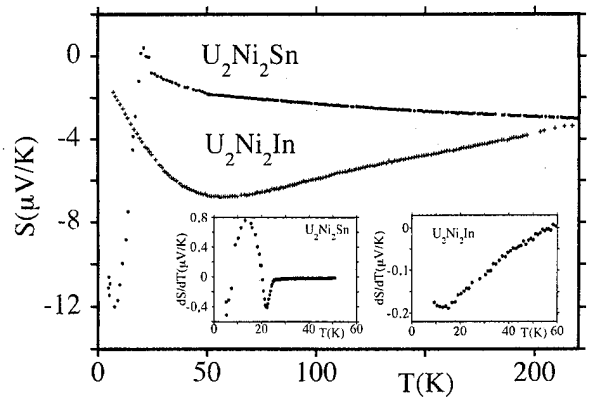



FIG. 2. Temperature dependence of thermopower ($S$) of $U_2Ni_2Sn$ and $U_2Ni_2In$ in the range 4–250 K. In inset is shown the temperature dependence of $dS/dT$ at low temperatures.

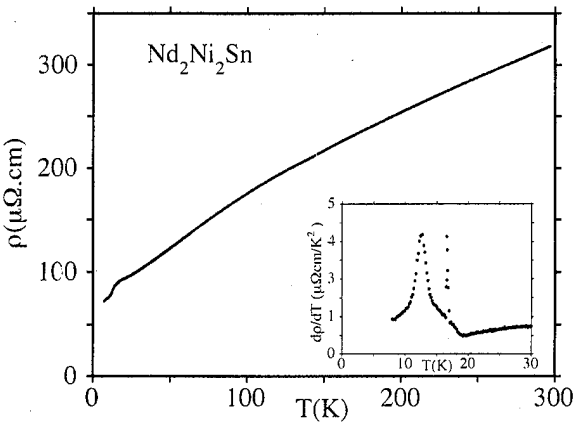



FIG. 3. Resistivity versus temperature for $Nd_2Ni_2Sn$ and its temperature derivative in the inset.

served in $U_2Ni_2Sn$,[1] where $\rho$ exhibits a linear increase with $T$ at sufficiently high temperatures.

The onset of the antiferromagnetic order also produces a much sharper increase in the electrical resistivity of $U_2Ni_2In$ (just below $T_N$) than in $U_2Ni_2Sn$, suggesting in both cases the existence of superzone gap effects associated with the antiferromagnetic periodicity.[4]

Below about 10 K the resistivity of $U_2Ni_2In$ decreases very sharply compared with the usual trend observed in the cooperative phase due to the progressive ordering of the magnetic moments.[5] The enhanced reduction of $\rho(T)$ in $U_2Ni_2In$ can be explained by the rapid decrease in the Kondo scattering in the cooperative state.[6] The same behavior is also observed in $U_2Ni_2Sn$, but with a smaller slope, which is consistent with the smaller Sommerfeld coefficient of the electronic specific heat, $\gamma$=200 mJ/mol $K^2$ for $U_2Ni_2In$ and $\gamma$=172 mJ/mol $K^2$ for $U_2Ni_2Sn$.[3]

The thermoelectric power of $U_2Ni_2In$ (shown in Fig. 2) is negative over the whole temperature range and exhibits a negative minimum near 55 K where $S=-7\ \mu V\ K^{-1}$. For $U_2Ni_2Sn$ a pronounced minima is also observed, but at a much lower temperature, $T\approx 8$ K, where $S=-12\ \mu V\ K^{-1}$. Minima in the $S(T)$ curves have been reported for heavy fermion systems like $U_2Co_3$, $CeCu_2Si_2$ and $CeAl_3$ (at $T$=7, 20, and 4 K, respectively), and explained within the spin fluctuation resonance model.[7,10]

The onset of the magnetic ordering in $U_2Ni_2Sn$ is clearly associated with the upturn in $S(T)$ near $T_N$=25 K (Fig. 2) and with the sharp minimum in $dS/dT$ (inset of Fig. 2; again suggesting the existence of a superzone gap effect below $T_N$). As the magnetic transition in $U_2Ni_2In$ occurs in a temperature range where the thermopower exhibits a rapid decrease with increasing temperature, it is not clearly detected in $S(T)$ but only in $dS/dT$, through a broad minimum near $T_N$ (inset of Fig. 2). This indicates the presence of a background thermopower contribution with a pronounced temperature variation but hardly affected by the magnetic transition.

In the paramagnetic phase and in the temperature range investigated we observe higher thermopower absolute values in $U_2Ni_2In$ than in $U_2Ni_2Sn$, which may be due to a steeper energy dependence of the density states near $E_F$ in $U_2Ni_2In$[2,11] or to enhanced crystal field effects.

### B. $Nd_2Ni_2Sn$ versus $U_2Ni_2Sn$

Figure 3 shows the experimental curves of $\rho(T)$ and $d\rho/dT$ for the $Nd_2Ni_2Sn$ compound. The temperature dependence of $d\rho/dT$ (inset Fig. 3) clearly shows the existence of three magnetic transitions. The initial antiferromagnetic ordering occurs at $T_N$=19.5 K, as revealed by the minimum observed in $d\rho/dT$. At $T$=17.5 K a small discontinuity is seen in $\rho(T)$, with a sharp positive peak in $d\rho/dT$, indicating a 1st order phase transition. At $T\approx 12$ K we observe a positive peak in $d\rho/dT$, approximately symmetric as usually occurs in order-order phase transitions. The physical origins of the underlying magnetic changes are however still unknown.

In the paramagnetic phase the electrical resistivity of $Nd_2Ni_2Sn$ (Fig. 3) is anomalous, showing a pronounced rise which persists up to 150 K ($\Delta\rho$=40 $\mu\Omega$ cm), where the usual linear increase takes over, due to a dominant electron phonon scattering. We associate the extra contribution up to 150 K with a crystal field effect in $Nd_2Ni_2Sn$. Not knowing the exact $4f$-levels scheme, we use a single spacing ($\delta$) crystal field model for an order of magnitude estimate,[12]

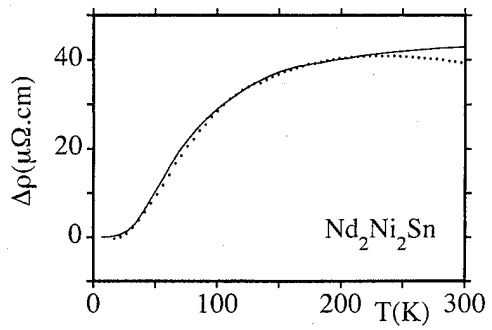



FIG. 4. Theoretical curve (−) and experimental values (●) of the temperature dependence of the electrical resistivity after subtracting the residual, phonon and spin disorder resistivity.

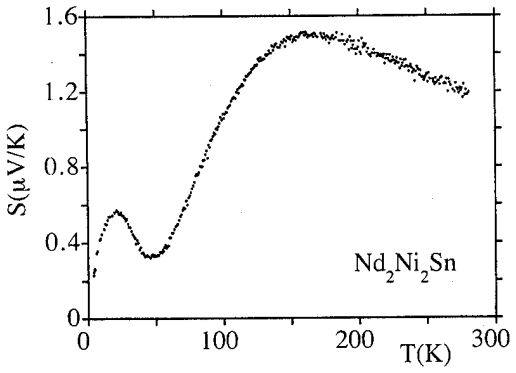



FIG. 5. Temperature dependence of the thermopower $S$ for $Nd_2Ni_2Sn$.

$$\rho_{CF}(T)=\rho_{CF}(\infty)\,\frac{1}{ch^2(\delta/2KT)}\,.$$

A least square fit gives $\rho_{CF}(\infty)=43\ \mu\Omega$ and $\delta=130$ K, providing a good description of the experimental data up to 220 K, as shown in Fig. 4.

Figure 5 gives the $S$ versus $T$ dependence for $Nd_2Ni_2Sn$, exhibiting a double-peak structure as usually observed in heavy fermion materials. The maximum at $T=150$ K is again attributed to the crystal field splitting of the $4f$ ground state configuration. A detailed analysis of $S(T)$ is in progress, with the extension of the measurements to higher temperatures.

A comparison of the transport properties of this compound with those previously measured in $U_2Ni_2Sn$ reveals important differences:

(i) in the paramagnetic phase, the electrical resistivity of the Nd compound increases considerably before reaching the classic linear increase with $T$ (electron-phonon scattering), indicating an appreciable crystal field effect in $\rho(T)$ due to the $4f$ electron levels. The same effect is also present in the $S(T)$ data.

(ii) The Néel temperature is considerably lower in the Nd compound, reflecting the localized character and the indirect exchange coupling (RKKY) of the $4f$ magnetic moments.

(iii) In the cooperative phase of the Nd compound several magnetic transitions are observed below $T_N$, reflecting a subtle competition between different magnetic contributions as usually occurs in $4f$ rare earth elements (e.g., competing anisotropy, crystal field, and exchange effects).

[1] R. Pinto, M. M. Amado, M. A. Salgueiro, M. E. Braga, J. B. Sousa, B. Chevalier, F. Mirambert, and J. Etourneau, J. Mag. Mag. Mat. **140**, 1371 (1995).
[2] M. Divis M. Richter, and H. Eschrig, Solid State Comunn. **90**, 99 (1994).
[3] L. Havela, V. Sechovsky, P. Svoboda, H. Nakotte, K. Prokes, F. R. de Boer, A. Seret. J. M. Winand, J. Rebizant, J. C. Spirlet, A. Purwanto. and R. A. Robinson, J. Mag. Mag. Mat. **140**, 1367 (1995).
[4] R. J. Elliott and F. A. Wedgood, Proc. Phys. Soc. London **81**, 846 (1963).
[5] M. E. Fisher and J. S. Langer, Phys. Rev. Lett. **20**, 665 (1968).
[6] T. Kasuya K. Takegahara, Y. Aoki, T. Susuki, S. Kunii, M. Sera, N. Sato, T. Fujita, T. Goto, A. Tamaki, and T. Komatsubara, *Valence Instabilities*, edited by P. Watcher and H. Bappart (North-Holland, Amsterdam, 1982), p. 359.
[7] F. Steglich, C. D. Bredl, W. Lieke, U. Rauchscchwalbe, and G. Sparn, Physics B **126**, 82 (1984).
[8] F. Steglich, U. Rauchscchwalbe, U. Gottwick, H. M. Mayer, N. Grew, U. Poppe, and J. J. M. Franse, J. Appl. Phys. **57**, 3054 (1985).
[9] S. H. Liu, in *Handbook on the Physics and Chemistry of Rare Earths*, edited by K. A. Schneider *et al.* (Elsevier, Amsterdam, 1993), Vol. 17, p. 87.
[10] R. J. Elliott, Phys. Rev. **94**, 564 (1954).
[11] M. Divis, M. Olsovec, M. Richter, and H. Eschrig, J. Mag. Mag. Mat. **140**, 1365 (1995).
[12] Van Peski, T. Tinbergen, and A. J. Dekker, Physica **29**, 917 (1963).

# Thermal expansion of single-crystalline UNiAl

K. Prokeš, A. de Visser, A. A. Menovsky, E. Brück, and F. R. de Boer
*Van der Waals-Zeeman Institute, University of Amsterdam, 1018 XE Amsterdam, The Netherlands*

V. Sechovský
*Department of Metal Physics, Charles University, 12116 Prague 2, The Czech Republic*

T. J. Gortenmulder
*Kamerlingh Onnes Laboratory, University of Leiden, 2300 RA Leiden, The Netherlands*

Magnetization, magnetic susceptibility, electrical resistivity, and specific heat measurements of UNiAl point to antiferromagnetic ordering below 19.3 K, which is confirmed by neutron-diffraction experiments. The enhanced $\gamma$ value of 167 mJ/mol $K^2$ is reflecting pronounced presence of magnetic fluctuations, which influence also the other electronic properties down to low temperatures. The thermal expansion of UNiAl was measured in the temperature range 1.5–210 K on a single crystal along the $a$ and $c$ axis. Similar to other bulk properties, also the thermal expansion of UNiAl is highly anisotropic. The $a$ axis is monotonously expanding with increasing temperature in the whole temperature range. Along the $c$ axis, the lattice first collapses with increasing temperature up to 35 K. Around this temperature, the thermal expansion coefficient $\alpha_c$ changes sign and continuous expansion with further increasing temperature is then observed. The sharp anomaly of $\alpha$ near 19.3 K present in both directions is consistent with the magnetic phase transition. The results are discussed in terms of the presence of anisotropic magnetic fluctuations. © *1996 American Institute of Physics.* [S0021-8979(96)25708-5]

## I. INTRODUCTION

The study of the formation of U magnetic moments in intermetallic compounds plays an essential role in understanding the electronic properties of $f$-electron-based systems, specially because of possible participation of U $5f$-electrons in the bonding. It has been well established that the variation of the constituent elements in UTX (T=a transition metal, X=a metal from the $p$-block) intermetallic compounds can drastically change the type of ground state due to the influence of the $d$- and $p$-electron states of these elements on the $5f$ electron states, which are principally involved in magnetism.[1] Also when keeping one type of crystal structure (fixed geometry of the surrounding of the U atom) a broad scale of magnetic behavior ranging from Pauli paramagnetism through spin fluctuations towards local-$5f$-moment behavior and magnetic ordering can be observed.

Another essential issue in U intermetallics is the huge magnetocrystalline anisotropy, which originates from the anisotropic bonding of the $5f$ wave functions in the crystal and from considerable $5f$-orbital moments. Among the highly anisotropic UTX compounds crystallizing in the hexagonal ZrNiAl-type of structure (Fig. 1), UNiAl has attracted considerable attention because of the highest $\gamma$ value of 167 mJ/mol $K^2$ in this isostructural group of compounds. In the literature,[1,2] this enhanced $\gamma$ value qualifies UNiAl as a middle-weight heavy-fermion system.

UNiAl becomes antiferromagnetic below 19.3 K as has been inferred from the magnetization, magnetic susceptibility, specific heat and electrical resistivity behavior.[2] It exhibits a strong uniaxial magnetic anisotropy with the easy-magnetization direction along the $c$ axis, which is reflected also in transport properties. The magnetic structure of UNiAl consists of the U magnetic moments oriented along the $c$ axis modulated sinusoidally within the basal planes and coupled antiferromagnetically between these planes. The propagation vector is $\mathbf{k}=(0.1,0.1,0.5)$. The numerous indications of strong involvement of magnetic fluctuations in low-temperature electronic properties[2] make this compound attractive for further experimental investigations and theoretical treatment.

Here, we report the first thermal expansion measurements performed on a single crystal of UNiAl.

## II. EXPERIMENT

A single crystal of UNiAl was grown from a nonstoichiometric melt with a slight excess of U by a modified Czochralski technique in the Center ALMOS at the University of Amsterdam. In order to reduce the mosaicity, the seed was tilted from the easy-growth direction by an angle of about 15°. The quality of the resulting crystal was checked by x-ray diffraction and electron-microprobe analysis. It was

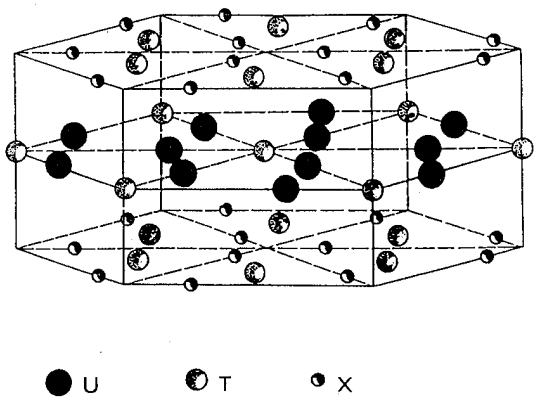



FIG. 1. Schematic representation of the ZrNiAl-type of structure.

 0021-8979/96/79(8)/6358/3/$10.00 © 1996 American Institute of Physics

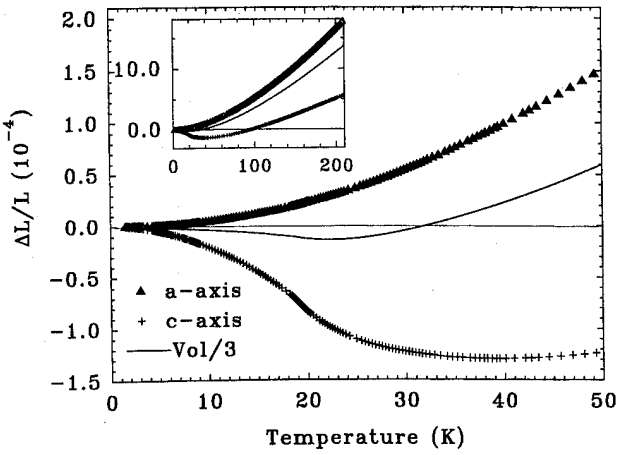



FIG. 2. Temperature dependence of the change of the relative length with respect to 1.5 K measured on a UNiAl single crystal along the $a$ axis ($\Delta$) and the $c$ axis (+), and temperature dependence of the relative volume change (—).

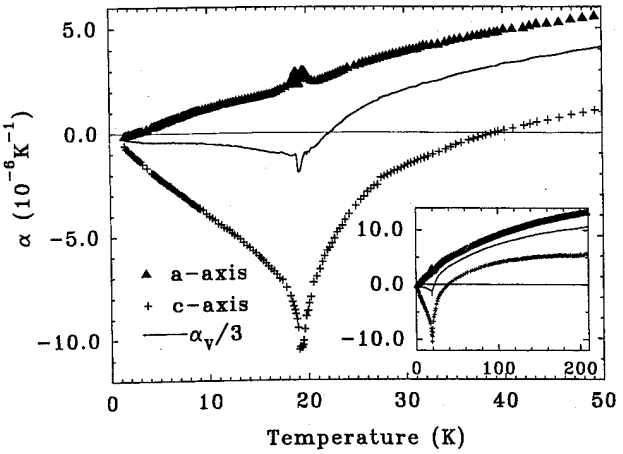



FIG. 3. Temperature dependence of the thermal expansion coefficients along the $a$ axis $\alpha_a$ ($\Delta$) and along the $c$ axis $\alpha_c$ (+) measured on a UNiAl single crystal. The corresponding coefficient of the volume expansion $\alpha_V(T)=2\alpha_a(T)+\alpha_c(T)$ is given by the solid line.

found to be single-crystalline; however, a certain amount of included pure U was detected by the electron-microprobe analysis.

By means of spark erosion a semi-cube with a size of each side of about 3.8 mm was cut perpendicular to the $a$ and the $c$ axes. The temperature dependence of the thermal expansion along the $a$ axis $\alpha_a(T)$ and along the $c$ axis $\alpha_c(T)$ was measured with a parallel-plate capacitance method[3] in the temperature range 1.5–210 K. The temperature was changed in steps and stabilised in order to keep the thermal equilibrium of sample and cell during the measurement. The relative accuracy decreases with increasing temperature, reaching a limit in $\alpha$ of about $3\ 10^{-7}\ \mathrm{K}^{-1}$ around 100 K.

## III. RESULTS AND DISCUSSION

The temperature dependence of the relative length changes, $(\Delta L/L)_i$ with respect to the length of the sample along the particular direction at 1.5 K are displayed in Fig. 2 together with the relative volume change $(\Delta V/V)=2(\Delta L/L)_a+(\Delta L/L)_c$. The temperature dependence of the coefficient of linear thermal expansion, $\alpha_i=L_i^{-1}(dL_i/dT)$, where $i$ refers to the $a$ or the $c$ axis of the hexagonal UNiAl, is shown in Fig. 3. The corresponding coefficient of volume expansion $\alpha_V(T)=2\alpha_a(T)+\alpha_c(T)$ is given by the solid line.

As can be seen, the thermal expansion of UNiAl is highly anisotropic, similar to most of other bulk properties. Along the $a$ axis the lattice monotonously expands with increasing temperature ($\alpha_a$ is always positive). The $c$ axis direction reveals first considerable shrinking with increasing temperature yielding a sharp deep minimum at 19.3 K. Around 35 K, $\alpha_c(T)$ changes sign and the lattice expands at higher temperatures. The sharp anomaly observed at 19.3 K in both $\alpha_a(T)$ and $\alpha_c(T)$ is consistent with the magnetic phase transition. In the case of the $a$-axis direction, the anomaly is doubled. As the absolute value of $\alpha_c(T)$ is considerably larger than $\alpha_a(T)$, the coefficient of volume expansion $\alpha_V(T)$ is negative below 22 K. The maximum anisotropy, corresponding to the maximum difference $\alpha_a(T)-\alpha_c(T)$, is found at $T_N$. At high temperatures, both thermal expansion coefficients can be approximated by a Debye function with distinct Debye temperatures. The best agreement at temperatures above 80–90 K for the coefficient along the $c$ axis is achieved for $\Theta_D=280$ K. For the coefficient along the $a$ axis, a much higher value of $\Theta_D=400$ K is obtained. In this case, the satisfactory agreement is restricted to region above 150 K.

At low temperatures, both $\alpha_a(T)$ and $\alpha_c(T)$ can be approximated by a linear dependence. By fitting in the temperature region 1.5–4 K, the linear coefficients of the thermal expansion $a_a=\alpha_a(T)/T=1.69\times10^{-7}\ \mathrm{K}^{-2}$ and $a_c=\alpha_c(T)/T=-4.57\times10^{-7}\ \mathrm{K}^{-2}$ are obtained, yielding $a_V=2a_a+a_c=-1.19\times10^{-7}\ \mathrm{K}^{-2}$.

The effective Grüneisen parameter $\Gamma_{\mathrm{eff}}(T)$[4]

$$\Gamma_{\mathrm{eff}}(T)=V_m\alpha_V(T)/\kappa c(T), \tag{1}$$

where $V_m$ is the molar volume, $\kappa=-V^{-1}(dV/dp)$ is the isothermal compressibility, and $c(T)$ is the molar specific heat at constant volume, is a parameter which is frequently discussed in the context of heavy-fermion research. The experimental effective Grüneisen parameter $\Gamma_{\mathrm{eff}}(T)$ is in general temperature dependent and consists of several contributions. In the low-temperature limit where the specific heat and thermal expansion vary linearly, the effective Grüneisen parameter $\Gamma_{\mathrm{eff}}(T)$ is driven by the electronic term $\Gamma_e(T)$

$$\Gamma_e=V_m a_V/\kappa\gamma. \tag{2}$$

In the case of UNiAl, the value of the isothermal compressibility is not available and has to be estimated. We have used a value close to that observed for URhAl[5] which amounts to 1.0 $\mathrm{Mbar}^{-1}$. The specific-heat data from Brück *et al.*[2] provide $\gamma=167$ mJ/mol $\mathrm{K}^2$, $V_m=3.18\times10^{-5}$ $\mathrm{m}^3$/mol. Using Eq. (2) we derive for UNiAl $\Gamma_e=-6.8$. This value is about one order of magnitude smaller than for typical heavy-fermion compounds, e.g., $UPt_3$,[4] although it is considerably enhanced with respect to normal metals ($\Gamma_e\sim2$). It also should be noted that the relatively small value of $\alpha_V$ is a consequence

of mutual cancellation of significantly large coefficients $\alpha_a$ and $\alpha_c$, one positive and the other negative. Especially, $\alpha_c$ is very large in absolute value indicating a very strong magnetoelastic coupling along $c$.

It has been pointed out by Brück *et al.*[2] that UNiAl can be classified as an itinerant antiferromagnet with strong indications for the presence of spin fluctuations. Therefore, a partial contribution to $\alpha$ and $\Gamma$ due to the spin fluctuations is most probable to play an important role in UNiAl. For the characteristic temperature of the spin fluctuations in UNiAl, a value of the order of 10 K follows from the specific-heat data. The electrical resistivity and the magnetic susceptibility data strongly support this conclusion. One can perform an analysis of all the bulk data together with thermal-expansion results using the so-called universal relations which couple the magnetic susceptibility, the specific heat or the electrical resistivity with thermal-expansion data.[6] However, to draw clear conclusions, usually inelastic-neutron-scattering experiments are necessary.

Recently, we have performed both, elastic and inelastic-neutron-scattering experiments on a good-quality UNiAl single crystal.[7] Here we summarize only the points relevant to understand the thermal-expansion results. The analysis of the neutron-diffraction results reveals the presence of strong antiferromagnetic fluctuations in UNiAl. The development of the fluctuations with temperature can be followed from low temperatures up to at least $1.5T_N$. However, no particular dispersion can be assigned to magnetic fluctuations. Instead of that, a wide spread in energy transfer of scattering intensity is present in the inelastic spectrum, both, below and above $T_N$.

As the magnetocrystalline anisotropy of UNiAl expressed in values of the paramagnetic Curie temperature reaches 300–400 K, the magnetic fluctuations have entirely different behavior along the $c$ axis and within the basal plane. The onset of magnetic fluctuations is visible around 35–40 K where upon lowering the temperature a deviation from the high-temperature behavior of the thermal-expansion coefficient $\alpha_a$ can be observed accompanied by a contraction along the hexagonal axis. Magnetic fluctuations along the $c$ axis are clearly of antiferromagnetic type. The behavior along the $a$ axis is rather regular, except for the critical region around $T_N$.

## IV. CONCLUSION

We have shown that the thermal expansion of UNiAl which crystallizes in the hexagonal ZrNiAl-type of structure is large and highly anisotropic. The magnetic phase transition at 19.3 K is reflected in both directions by a pronounced anomaly. These findings are in good agreement with other bulk magnetic, transport and thermal properties which reflect the huge magnetocrystalline anisotropy as well. The magnetic structure consists of sine-modulated U magnetic moments within the basal plane with adjacent planes coupled antiferromagnetically.

The value of the electronic contribution to the Grüneisen parameter $\Gamma_e = -6.8$ is relatively small compared to values observed for typical heavy-fermion compounds. This is, however, partially due mutual cancellation of the expansion effects along $a$ and $c$. The large negative expansion along $c$ below 35 K, on the other hand, can be tentatively attributed to the effect of antiferromagnetic fluctuations and to antiferromagnetic ordering in UNiAl below 19.3 K.

## ACKNOWLEDGMENTS

This work was sponsored by the "Stichting voor Fundamenteel Onderzoek der Materie" (FOM), and The Grant Agency of the Czech Republic (project # 202/94/0454). The authors are indebted to Dr. M. Diviš for stimulating discussions on the subject.

[1] V. Sechovský and L. Havela, *Ferromagnetic Materials*, edited by E. P. Wolfarth and K. H. J. Buschow (North-Holland, Amsterdam, 1988), Vol. 4, Chap. 4.
[2] E. Brück, H. Nakotte, F. R. de Boer, P. F. de Châtel, H. P. van der Meulen, J. J. M. Franse, A. A. Menovsky, N. H. Kim-Ngan, L. Havela, V. Sechovský, J. A. A. J. Perenboom, N. C. Tuan, and J. Šebek, Phys. Rev. B **49**, 8852 (1994).
[3] See for instance, N. H. van Dijk, Ph.D. thesis, University of Amsterdam, 1994.
[4] A. de Visser, J. J. M. Franse, and J. Flouquet, Physica B **161**, 324 (1989).
[5] T. D. Cuong, Z. Arnold, J. Kamarád, A. V. Andreev, L. Havela, and V. Sechovský, EMMA'95, J. Magn. Magn. Mater. (in press).
[6] A. de Visser, A. Menovsky, and J. J. M. Franse, Physica B **147**, 81 (1987).
[7] K. Prokeš *et al.* (to be published).

# Electronic properties of $U_2Pt_2Sn$

K. Prokeš and F. R. de Boer
*Van der Waals-Zeeman Institute, University of Amsterdam, 1018 XE Amsterdam, The Netherlands*

H. Nakotte
*MLNSC, Los Alamos National Laboratory, Los Alamos, New Mexico 87545*

L. Havela, V. Sechovský, and P. Svoboda
*Department of Metal Physics, Charles University, 12116 Prague 2, The Czech Republic*

J. M. Winand, J. Rebizant, and J. C. Spirlet
*European Commission, Joint Research Centre, Institute for Transuranium Elements, Postfach 2340, 76125 Karlsruhe, Germany*

X. Hu
*BENSC, Hahn-Meitner Institute GmbH, 14109 Berlin 39, Germany*

T. J. Gortenmulder
*Kamerlingh Onnes Laboratory, University of Leiden, 2300 RA Leiden, The Netherlands*

$U_2Pt_2Sn$ is crystallizing in an ordered version (space group $P4_2/mnm$) of the tetragonal $U_3Si_2$ type of structure. Clear anomalies in the magnetic susceptibility, specific heat, and electrical resistivity around 15 K indicate that $U_2Pt_2Sn$ orders antiferromagnetically below this temperature. As expected for an antiferromagnet, the susceptibility and specific heat anomalies are shifted to lower temperatures upon application of external magnetic field. The specific-heat coefficient $\gamma$=327 mJ/mol f.u. $K^2$ remains unchanged in fields up to 5 T. The antiferromagnetic ground state of $U_2Pt_2Sn$ can be concluded also from the metamagnetic transition around 22 T in the magnetization at 4.2 K and from magnetic reflections in the neutron-diffraction pattern at low temperatures. © *1996 American Institute of Physics.* [S0021-8979(96)25808-1]

## I. INTRODUCTION

Recently, great attention has been given to the isostructural group of $U_2T_2X$ compounds (T=transition metal and X=In, Sn, Al, or Ga).[1–3] The development of their magnetic properties (from Pauli paramagnetism to local-moment behavior) is influenced by the hybridization of the $5f$-electron states with ligand electron states. The $5f$-$d$ hybridization is demonstrated by the evolution of magnetism with respect to the transition metal component.[1,4,5]

$U_2Pt_2Sn$ has been first reported to adopt the tetragonal $U_3Si_2$-type structure (space group $P4/mbm$).[6] More recent studies pointed out a derivative form with the space group $P4_2/mnm$.[7] Both related structures consist of two alternating plane sheets, one containing only U atoms and the other accommodating T and X atoms. The shortest interatomic U-U distance in $U_2Pt_2Sn$ is about 350 pm, which places this compound into a critical region between localized and itinerant $5f$-electron behavior in Hill's classification.[8]

The aim of the present contribution is to investigate the type of the crystal structure, the type of the ground state, as well as to study the magnetic, transport and thermal properties of polycrystalline $U_2Pt_2Sn$.

## II. EXPERIMENT

A polycrystalline sample of $U_2Pt_2Sn$ has been prepared by arc-melting appropriate amounts of the constituting elements under argon atmosphere. The purity and composition homogeneity were checked by x-ray diffraction and by electron-microprobe analysis. The microprobe indicated less than 1 vol. % of UPtSn as a secondary phase. The average composition of the main phase only slightly deviates from the ideal stoichiometric composition of $U_2Pt_2Sn$. A slight U excess and Sn deficiency, both of the order of 1 at. %, were found.

The low-field magnetization and the temperature dependencies of the dc magnetic susceptibility ($\chi=M/H$) were measured between 2 and 300 K in magnetic fields up to 5 T in a Quantum Design SQUID magnetometer on a fine-powder sample with grains fixed in random orientation by diamagnetic glue.

The specific heat was measured by a standard semi-adiabatic method in the temperature region 1.3–50 K in fields up to 5 T.

The electrical resistivity was measured on a small bar-shaped sample by standard ac four-point method. The large error in the geometrical factor (in addition to the expected influence of internal microcracks) makes a reliable estimate of the absolute resistivity values questionable. Therefore, we display the normalized electrical resistivity $\rho/\rho_{300K}$.

Neutron-diffraction data at 2.6 and 24 K were obtained in the neutron powder diffractometer E6 at the Hahn–Meitner Institute using an incident neutron wavelength of 2.386 Å. For these measurements about 10 g of $U_2Pt_2Sn$ was powdered and encapsulated in a vanadium container under He atmosphere. The data were analyzed by means of the Rietveld profile procedure[9] using the program Fullprof.[10] The neutron-scattering lengths were taken from Ref. 11.

## III. BULK MEASUREMENTS

The susceptibility (Fig. 1) above 40 K is nearly field independent, whereas the $\chi$ vs $T$ curves show splitting in the

 0021-8979/96/79(8)/6361/3/$10.00 © 1996 American Institute of Physics 

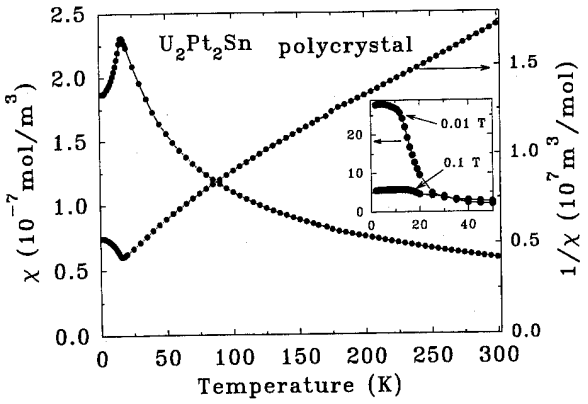



FIG. 1. Temperature dependence of the magnetic susceptibility of $U_2Pt_2Sn$ extrapolated to infinite magnetic field together with its reciprocal value. In the inset the data collected in 0.01 and 0.1 T are shown.

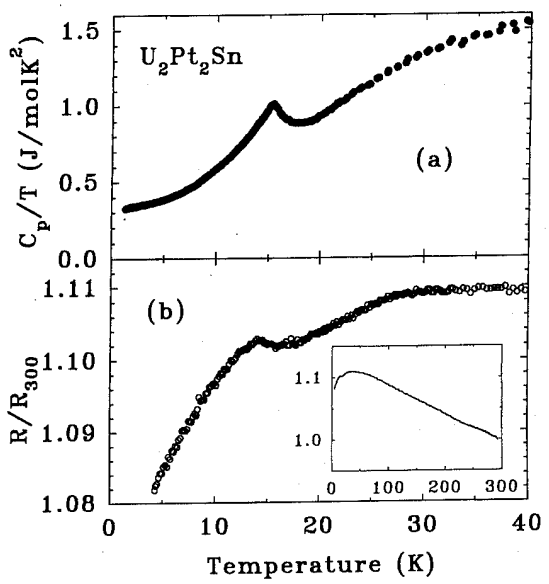



FIG. 2. Temperature dependence of the specific heat of $U_2Pt_2Sn$ in the representation $C_p/T$ vs $T$ (a) and the electrical resistivity (b) in zero magnetic field.

low-temperature region reflecting an increasing amount of a ferromagnetic component with lowering temperature. An upturn becomes progressively pronounced with decreasing magnetic field (the inset of Fig. 1). We tentatively attribute this spurious signal to the UPtSn impurity, which is ferromagnetic below 19 K.[12] In Fig. 1 then the susceptibility data extrapolated to infinite magnetic field are shown. Two regions on the $1/\chi$ vs $T$ above 40 K can be identified: one linear above 160 K, which can be fitted by Curie–Weiss (CW) law

$$\chi = C/(T-\Theta_p), \tag{1}$$

and another strongly curved at lower temperatures which can be approximated only by a modified Curie–Weiss law (MCW)

$$\chi = C/(T-\Theta_p)+\chi_0. \tag{2}$$

In the former case, the fitting parameters are: $C=(2.56\pm0.01)\times10^{-5}$ m$^3$/mol f.u. K ($\Rightarrow\mu_{\rm eff}=2.86\pm0.02$ $\mu_B$/U atom) and a negative paramagnetic Curie temperature of $-141.5\pm1.6$ K. The MCW fit below 160 K is yielding a significantly lower value of $C=(1.11\pm0.01)\times10^{-5}$ m$^3$/mol f.u. K ($\mu_{\rm eff}=1.88\pm0.02$ $\mu_B$/U atom), a fairly less negative $\theta_p=-6.9\pm0.6$ K, whereas $\chi_0=2.9\times10^{-8}$ m$^3$/mol f.u. .

These fits should be taken with caution, because the polycrystalline data on highly anisotropic material as most of the $U_2T_2X$ compounds are, may represent an admixture of very different anisotropic components of the susceptibility. These components may follow the CW law, however, the $1/\chi$ vs $T$ dependence measured on polycrystal is strongly curved especially at lower temperatures. Nevertheless, the high-temperature CW fit provides a good estimate of the upper limit of $\mu_{\rm eff}$ (although, even this value is smaller than the values expected for the localized $f^{3+}$ or $f^{4+}$ configuration). The strikingly different values of $\Theta_p$ from the high-temperature CW fit and the low temperature MCW fit serve rough estimates of paramagnetic Curie temperatures for the hard- and easy-magnetisation direction, respectively. The $\mu_{\rm eff}$ value from the low temperature fit is only a fraction of the genuine effective moment and depends on the multiplicity of the easy axis. The "temperature independent parameter" $\chi_0$ is then an arbitrary value without any deeper physical meaning.

The magnetic phase transition at $T_N=15$ K is reflected by the peak in the $C_p/T$ vs $T$ curve [Fig. 2(a)]. The peak is shifted by $-0.3$ K in 5 T as expected for an antiferromagnet. The linear coefficient of the specific heat $\gamma=327.0\pm0.3$ mJ/mol f.u. K$^2$ follows from the linear extrapolation of $C_p/T$ vs $T^2$ plot in the region 1.3–8.5 K to zero Kelvin. This value which accounts for two U atoms in the formula unit is not affected by magnetic field to 5 T. The value of 163 mJ/mol K$^2$ calculated per one U atom is certainly enhanced with respect to normal nonmagnetic metals.

The onset of antiferromagnetic ordering at $T_N=15$ K is reflected also in the electrical resistivity [Fig. 2(b)]. The electrical resistivity is slightly increasing with lowering temperature and passing a shallow maximum around 35 K. This behavior is commonly observed in strongly hybridized U-based materials. After some precursor behavior around $T_N$ the resistivity drops at lower temperatures. No quadratic temperature dependence is observed down to 4.2 K.

The magnetization curves of $U_2Pt_2Sn$ at 4.2 K show a metamagnetic transition at about 22 T.[13] This result corroborates the conclusion about the antiferromagnetic ground state. The magnetization for the field-aligned (random-oriented) powder sample yields a value of 1.49 (1.23) $\mu_B$/f.u. in 56 T. The magnetization curve is far from saturation even in this very high magnetic field. We cannot exclude that another metamagnetic transition may occur in higher fields and therefore, do not dare making any conclusion about the type of anisotropy from comparison of present data obtained on the field-aligned and random oriented samples.

The low-field magnetization exhibits a small hysteresis loop developing below 20 K, which is believed to be due to the ferromagnetic UPtSn impurity.

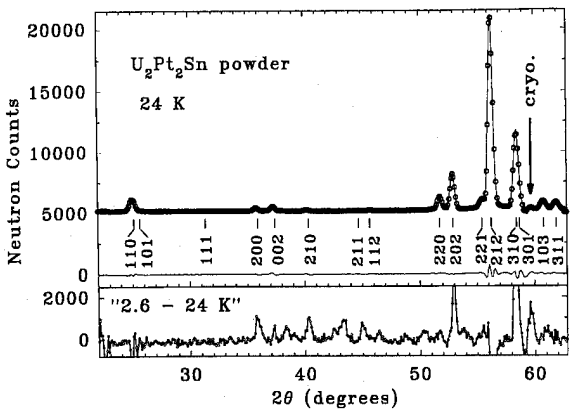



FIG. 3. The neutron-diffraction spectrum of $U_2Pt_2Sn$ recorded at 24 K together with the best fit. The full line at the bottom represents the difference between the experimental data and the fit. The 2.6–24 K spectrum is displayed, as well.

## IV. NEUTRON DIFFRACTION RESULTS

As two possible crystal structures for $U_2Pt_2Sn$ have been reported in the literature, the determination of the exact crystal structure was our first task in the neutron-diffraction experiment. Two tetragonal crystallographic structures were considered: the ideal tetragonal $U_3Si_2$-type of structure (space group $P4/mbm$) and its variant, in which U atoms are forced by relatively large Pt atoms to move from their original positions forming thus zig-zag chains along the $c$ axis (space group $P4_2/mnm$). The pattern recorded (Fig. 3) above the transition temperature, at 24 K, can be fully indexed by using the latter type of structure. The structural parameters are summarized in Table I. Reflections of the very weak UPtSn secondary phase cannot be detected.

In the spectrum recorded at 2.6 K, new—purely magnetic reflections and additional magnetic contributions on some of the nuclear Bragg reflections (see the difference spectrum in Fig. 3) can be resolved. This clearly indicates that the magnetic periodicity is different from the crystallographic one, which is compatible with the antiferromagnetic ordering suggested from bulk experiments. The magnetic structure refinement is difficult from the available powder pattern. In this stage, no magnetic unit cell which would index all observed magnetic peaks could be deduced. Single-crystal data are desirable to choose a proper model out of many, which are roughly satisfying the powder data.

TABLE I. The refined structural parameters of $U_2Pt_2Sn$ at 24 K.

| Space group: | | $P4_2/mnm$, $Z=2$ | | $T=24$ K |
|---|---|---|---|---|
| U1 | $4f$ | $x_{U1}\ x_{U1}0$ | $x_{U1}=0.3414$ (7) | |
| U2 | $4g$ | $x_{U2}\ -x_{U2}0$ | $x_{U2}=0.2044$ (30) | |
| Pt | $8j$ | $x_{Pt}\ x_{Pt}\ z_{Pt}$ | $x_{Pt}=0.1302$ (4) | $z_{Pt}=0.2208$ (8) |
| Sn | $4d$ | 0 1/2 1/4 | | |
| Lattice parameters: | | | $R$ factors: | |
| $a=770.496\pm0.285$ pm | | | $R_p=5.43\%$ | |
| $c=740.760\pm0.296$ pm | | | $R_{wp}=8.16\%$ | |
| | | | $R_B=1.95\%$ | |
| | | $\chi^2=3.30$ | | |

## V. CONCLUSIONS

By means of powder neutron diffraction, we have shown that $U_2Pt_2Sn$ crystallizes in an ordered variant (space group $P4_2/mnm$) of the tetragonal $U_3Si_2$-type of structure and that it orders antiferromagnetically at low temperatures ($T_N=15$ K). The results obtained by means of the magnetic-susceptibility, the specific-heat and the electrical-resistivity suggests that the magnetism in $U_2Pt_2Sn$ is governed by to certain extent delocalized $5f$-electron states in U atoms. However, among the $U_2T_2X$ compounds studied, this material can be considered as an example of a system with rather well-defined U magnetic moments. In order to elucidate the magnetic structure and specific features of magnetic anisotropy, single-crystalline $U_2Pt_2Sn$ are strongly desirable.

## ACKNOWLEDGMENTS

This work was sponsored by the "Stitching voor Fundamenteel Onderzoek der Materie" (FOM), and The Grant Agency of the Czech Republic (project # 202/93/0184). Support to K. P. and J. M. W. given in the framework of the E.C. funded training program HC&M is acknowledged. The work of V. S. and P. S. at HMI Berlin was supported by program PECO.

[1] L. Havela, V. Sechovský, P. Svoboda, M. Diviš, H. Nakotte, K. Prokeš, F. R. de Boer, A. Purwanto, R. Robinson, A. Seret, J. M. Winand, J. Rebizant, J. C. Spirlet, M. Richter, and H. Eschrig, J. Appl. Phys. **76**, 6214 (1994).
[2] F. Bourée, B. Chevalier, L. Fournes, F. Mirambet, T. Roisnel, V. H. Tran, and Z. Zolnierek, J. Magn. Magn. Mater. **138**, 307 (1994).
[3] M. Diviš, M. Olšovec, M. Richter, and H. Eschrig, J. Magn. Magn. Mater. **140–144**, 1365 (1995).
[4] H. Nakotte, K. Prokeš, E. Brück, N. Tang, F. R. de Boer, P. Svoboda, V. Sechovský, L. Havela, J. M. Winand, A. Seret, J. Rebizant, and J. C. Spirlet, Physica B **201**, 247 (1994).
[5] L. Havela, V. Sechovský, P. Svoboda, H. Nakotte, K. Prokeš, F. R. de Boer, A. Seret, J. M. Winand, J. Rebizant, J. C. Spirlet, A. Purwanto, and R. Robinson, J. Magn. Magn. Mater. **140–144**, 1367 (1995).
[6] M. N. Peron, Y. Kergadallan, J. Rebizant, D. Meyer, S. Zwiner, L. Havela, H. Nakotte, J. C. Spirlet, G. M. Kalvius, E. Colineau, J. L. Oddou, C. Jeandey, J. P. Sanchez, and J. M. Winand, J. Alloys Comp. **201**, 203 (1993); F. Mirambet, P. Gravereau, B. Chevalier, L. Trut, and J. Etourneau, J. Alloys Comp. **191**, L1 (1993).
[7] P. Gravereau, F. Mirambet, B. Chevalier, F. Weill, L. Fournes, D. Laffargue, F. Bouree, and J. Etourneau, J. Mater. Chem. **4**, 1893 (1994).
[8] H. H. Hill, *Plutonium and Other Actinides*, edited by W. N. Miner (AIME, New York, 1990), p. 2.
[9] H. M. Rietveld, J. Appl. Cryst. **2**, 65 (1969).
[10] J. Rodrigues-Carvajal, FULLPROF version 2.6 1-Oct94, ILL (unpublished).
[11] V. F. Sears, Neutron News **3**, 26 (1992).
[12] Sechovský and L. Havela, *Ferromagnetic Materials*, Vol. 4, edited by E. P. Wolfarth and K. H. J. Buschow (North-Holland, Amsterdam, 1988), Ch. 4, pp. 309–491.
[13] K. Prokeš, H. Nakotte, F. R. de Boer, T. Fukushima, S. Matsuyama, T. Kumada, K. Kindo, L. Havela, V. Sechovsky, A. Lacerda, J. M. Winand, J. Rebizant, and J. C. Spirlet, Conference Proceedings, Physical Phenomena at High Magnetic Fields-II, Tallahassee, FL, May 6–9, 1995 (in press).

# The spin-glass state of $Y_{1-x}U_xPd_3$

M. A. Lopez de la Torre,[a] J. Rodriguez Fernandez, and K. A. McEwen
*Department of Physics, Birkbeck College, University of London, Malet Street, London WC1E 7HX, United Kingdom*

We have performed a detailed study of the magnetization of $Y_{0.6}U_{0.4}Pd_3$ ($T_f \sim 10$ K), which shows thermal, transport, and magnetic properties typical of a spin-glass system. Strong irreversibility is observed among our zero-field-cooled and field-cooled measurements in fields as large as 30 kOe. Thus, the freezing temperature displays an unusual weak dependence with field. We observe a very slow temporal dependence of the magnetization below the freezing temperature. The nonlinear susceptibility coefficients extracted from our data show an increase by a factor of approximately 20 when approaching the freezing temperature from above, but do not show a true divergence at $T_f$, and a scaling analysis does not seem to be possible. We compare these results with those expected for classical spin glasses, and propose a possible mechanism for the onset of frustration below $x=0.45$ in $Y_{1-x}U_xPd_3$. © *1996 American Institute of Physics.* [S0021-8979(96)25908-8]

## I. INTRODUCTION

The pseudobinary metallic compound $Y_{1-x}U_xPd_3$ has been the subject of intensive study in recent years. For $x=0.2$, anomalous thermal, magnetic, and electrical properties are observed, suggesting a non-Fermi liquid ground state.[1,2] Several theoretical models have been proposed in order to explain the origin of this unconventional behavior, from a multichannel Kondo effect to a $T=0$ phase transition. In this case, the actual character of the magnetic ordering taking place for $x>0.2$ determines whether a non-Fermi liquid ground state develops at low temperature.[3]

Regarding $Y_{1-x}U_xPd_3$, in the U concentration range $0.2<x<0.5$ these materials apparently show clear spin-glass ordering below a freezing temperature ($T_f$) which extrapolates to 0 K in the $x=0.2$ limit.[4] However, close to the upper limit ($x=0.45$), recent experimental evidence indicates the onset of long-range antiferromagnetic ordering,[5] casting some doubts about the spin-glass behavior for all the concentration range. An interesting feature of the spin-glass ordering in these materials is that it develops in a by no means diluted system. On the contrary, canonical spin glasses usually are diluted systems, showing a trend towards long-range magnetic ordering with increasing doping.[6–8]

With the aim of clarifying the actual character of magnetic ordering in this system, we have performed a study of the magnetization of $Y_{0.6}U_{0.4}Pd_3$ ($T_f \sim 10$ K). The results are compared with those expected for classical spin glasses.

## II. EXPERIMENT

The polycrystalline sample of $Y_{0.6}U_{0.4}Pd_3$ was prepared by arc melting in an argon atmosphere, and subsequently annealed at 900 °C for one week. X-ray diffraction studies did not reveal the existence of any secondary phase. Magnetization measurements were performed at Birkbeck College in the temperature range between 2 and 20 K and for fields up to 70 kOe using a Quantum Design SQUID magnetometer.

[a]Departamento de Fisica Aplicada, Universidad de Castilla-La Mancha, c. San Lucas n. 3, 45002-Toledo (Spain).

## III. RESULTS

In Fig. 1 we show results from dc magnetic susceptibility measured on warming, after cooling the sample to the base temperature in zero applied field (ZFC), and measured while cooling to the base temperature in an external applied field (FC). Even for fields as high as 30 kOe, strong irreversibility is observed below a characteristic temperature ($T_{irr}$). For low fields, both ZFC and FC magnetic susceptibilities show a peak ($T_{max}$) at the irreversibility temperature, as it is usually observed in canonical spin glasses. For higher applied fields, both characteristic temperatures are monotonically shifted down, more quickly for $T_{irr}$. It is also clearly observed from Figs. 1 and 2 that the susceptibility maximum becomes progressively smoothed with increasing applied field, which is usually interpreted as a sign of the nonlinear effects. For 50 and 70 kOe, the magnetic susceptibility is practically constant below $T_{max}$, and we were able to observe only a weak irreversibility. Due to experimental difficulties, the starting temperature for these last fields was 4.5 K instead of 2 K. Further experiments down to 2 K are in progress to determine $T_{irr}$ for fields higher than 30 kOe.

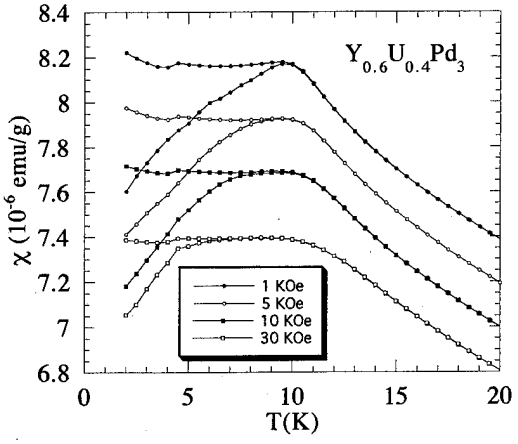



FIG. 1. ZFC and FC magnetic susceptibility of $Y_{0.6}U_{0.4}Pd_3$ as a function of temperature for $H=1$, 5, 10, and 30 kOe. Curves corresponding to 10, 5, and 1 kOe are shifted up for clarity. Solid lines are guides to the eye.

 0021-8979/96/79(8)/6364/3/$10.00 © 1996 American Institute of Physics

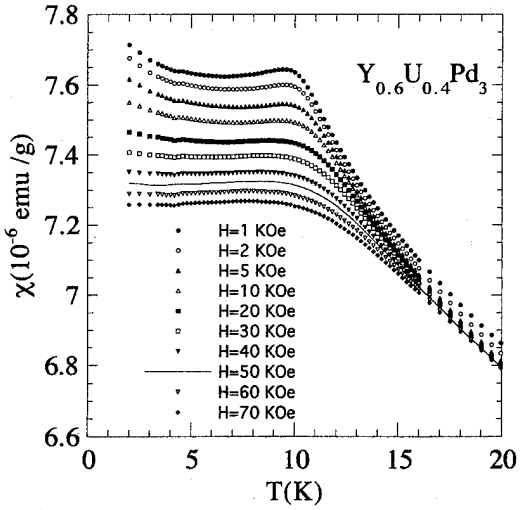



FIG. 2. Field-cooled magnetic susceptibility set of data used for the fits to the nonlinear expression cited in text.

In Fig. 2 we show the results of the FC measurements, from which we extracted $M$ vs $H$ data and performed a classical analysis in terms of nonlinear susceptibility:

$$M=m_0+\chi_0 H-b_3(\chi_0 H)^3+b_5(\chi_0 H)^5. \quad (1)$$

The $m_0$ term is included in order to correct for systematic errors in the low-field data arising from remanent magnetization.[9] In Fig. 3 we show the $b_3$ and $b_5$ coefficients obtained from this analysis. The typical error for the $b_3$ coefficient amounts to 10% of its absolute value, and to 30% for the $b_5$ coefficient. In spite of the significant uncertainty in its absolute values, both coefficients steadily increase by a factor of about 20 when approaching the freezing temperature from above, reaching a maximum around 10.2 K, which can be interpreted as the actual freezing temperature.

We also checked the temporal dependence of the magnetic properties. In Fig. 4, we show the magnetic susceptibility as a function of time, measured at $T=2$ K, well below the freezing temperature, in a 5 kOe applied field and after the sample had been zero-field cooled. A logarithmic law $\chi(t)=M_0+M_1 \ln T$ clearly does not fit our results, nor an

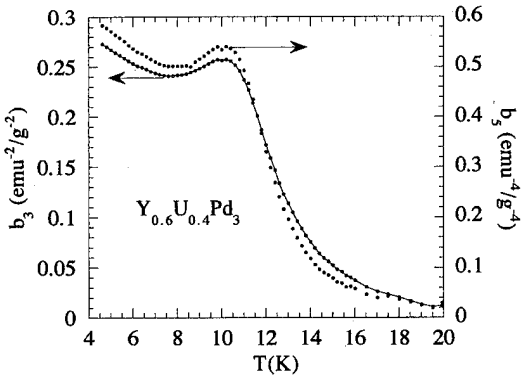



FIG. 3. Temperature dependence of the nonlinear coefficients $b_3$ and $b_5$, showing the peak at the freezing temperature.

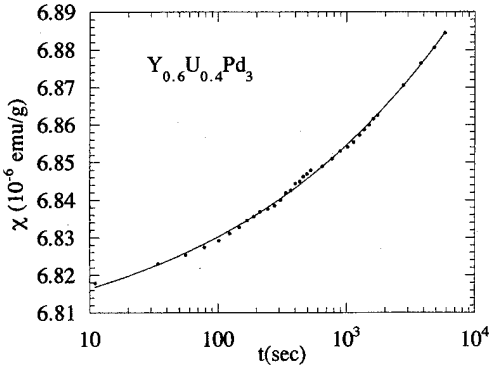



FIG. 4. Magnetic susceptibility as a function of time, measured at $T=2$ K and in 5 kOe applied field after zero-field cooling the sample. Solid line is a fit to the stretched exponential expression cited in text with the coefficients $M_0=7.36\times10^{-6}$ emu/g, $M_1=-5.61\times10^{-7}$ emu/g, $n=0.74$, $t_p=5\times10^6$ s.

algebraic law $\chi(t)=M_0+M_1 t^{-\alpha}$, rather we find that a Kohlrausch law (also called stretched exponential),

$$\chi(t)=M_0+M_1 \exp[-(t/t_p)^{(1-n)}] \quad (2)$$

give us a very good fit, which is a very common behavior for canonical spin glasses. In fact, our value for the coefficient $n$ ($0.74\pm0.01$) is very close to the value obtained by Chamberlin *et al.*[10] for diluted AgMn alloys at temperatures well below $T_f$($n\sim0.69\pm0.01$).

## IV. DISCUSSION

From our results, a first conclusion is readily obtained: most of the features observed in the magnetic susceptibility of $Y_{0.6}U_{0.4}Pd_3$ are reminiscent of those usually observed in canonical spin glasses. We will mention several of them: (a) strong irreversibility, (b) a cusp at $T_{max}$ in the ZFC and FC susceptibilities, which at low fields coincides with the onset of irreversibility at $T_{irr}$, (c) $\chi_{FC}$ almost temperature independent below $T_{max}$, (d) *slow* temporal dependence of the magnetic properties, described by a stretched exponential function.

A remarkable feature that is worth to point out is the magnitude of the fields necessary to destroy the strong irreversibility in the susceptibility ($H>30$ kOe to have $T_{irr}<4.5$ K). For canonical spin glasses, even with freezing temperatures as high as 30 K, 30 kOe would completely destroy the strong irreversibility.[11] However, in our system a weak irreversibility is still present below $T_{max}$ even for 50 and 70 kOe. If we define $T_{max}$ as the actual freezing temperature, then, when applying a field $H=70$ kOe we would have a spin-glass state shifted down 2 K below $T_f(H=0)$, which is only a 20% $T_f$ shift. We have not found in the available literature any material showing such a weak dependence of $T_f$ with magnetic field. Something similar could be pointed out for the temporal evolution of the ZFC susceptibility. Again, we find it quite remarkable that we perform this experiment with an applied field $H=5$ kOe, rather *small* for the frozen state of $Y_{0.6}U_{0.4}Pd_3$ but enormous for any typical spin-glass system.

It is usually stated that conventional spin glasses would show a divergence in $b_3$, $b_5$, the coefficients of the nonlinear expansion for magnetization, if there is a true spin-glass transition at $T_f$.[12] Our results show a substantial increase in both coefficients on approaching the transition from above, but not a strict divergence at $T_f$. Having extracted from the data the nonlinear susceptibility, it is possible, at least in principle, to obtain the so-called critical isotherm, $\chi_{nl} \propto H^{2/\delta}$, computing then one of the critical exponents ($\delta$), and afterwards to follow with a conventional scaling analysis. Due in part to experimental uncertainty at low fields, it is difficult to extract $\delta$ from our results. A log–log plot of $\chi_{nl}$ vs $H$ (not shown) only displays linearity in a restricted range, of less than one decade, at high fields. A system that shows such a weak dependence of $b_3$ and a quite restricted scaling behaviour of the critical isotherm is the *kagomé* system $SrCr_8Ga_4O_{19}$, which is an archetypal highly frustrated system.[9,13] For this material, a nonconventional spin-glass state below $T_f$ has been proposed, which shares an unusual feature with our system: a $T^2$ term in the low-temperature specific heat, which is not generally observed in spin-glass systems. For the *kagomé* system, it has been suggested that this term could arise from finite size antiferromagnetic regions. As it was pointed out before, $Y_{0.55}U_{0.45}Pd_3$ seems to develop long-range antiferromagnetic order below $T_N \sim 20$ K.[5] Otherwise, apart from the almost typical spin-glass-like thermal, magnetic and electrical properties of $Y_{0.6}U_{0.4}Pd_3$, results from $\mu SR$ experiments exhibit features expected for spin-glass ordering developing below the freezing temperature.[14] A possible explanation for this spin-glass state is that frustration develops for U concentrations lower than 0.45. For materials with $x \leqslant 0.45$, like ours, it is tempting to consider that we are close to the percolation limit separating spin glass from long-range magnetic order. In that concentration range, antiferromagnetic clusters play an important role. We want to point out that the percolation limit for antiferromagnetic bonding in a fcc lattice is 45%.[7] Following the common nomenclature, $Y_{0.6}U_{0.4}Pd_3$ should be considered as a cluster glass (also called mictomagnet). Because we are in the high concentration limit, and due to the increasing role of antiferromagnetic clusters, we should observe no scaling of the magnetic properties. If our description is correct, with decreasing U concentration the system would evolve steadily to a more conventional spin-glass behavior, recovering the scaling in the low concentration limit.[7]

Considering the non-Fermi liquid ground state developing for $x=0.2$, it seems to develop right at the concentration limit where the freezing temperature approaches zero. Following our discussion, the $T_f \rightarrow 0$ K limit concentration ($x=0.2$), separates a *canonical* spin-glass region (showing, for example, scaling of the magnetic properties) from the Kondo regime. As far as we know, theories in favor of non-Fermi liquid behavior due to a $T=0$ phase transition consider only long-range magnetic order.[2,3] If such a theory can be applied to a spin glass with $T_f=0$ remains an open question.

## V. CONCLUSIONS

The dc magnetic susceptibility of $Y_{0.6}U_{0.4}Pd_3$ shows most of the features commonly associated with spin-glass order. However, our results show neither a true divergence of the first two coefficients of nonlinear susceptibility ($b_3$,$b_5$) nor scaling of its critical isotherm. This points to a noncanonical spin glass state. Considering the long-range antiferromagnetic ordering reported for the 0.45 compound, we propose that $Y_{0.6}U_{0.4}Pd_3$ should be considered as an example of cluster glass system in the concentration range close to the percolation limit for antiferromagnetic ordering.

## ACKNOWLEDGMENTS

We thank M. Bull, M. Ellerby, and J. G. Park for fruitful discussions. We specially acknowledge M. B. Maple and his group at University of California-San Diego, where the sample was prepared during M. A. Lopez de la Torre's postdoctoral stay, for their kind support and hospitality.

[1] C. L. Seaman, M. B. Maple, B. W. Lee, S. Ghamaty, M. S. Torikachvili, J.-S. Kang, L. Z. Liu, J. W. Allen, and D. L. Cox, Phys. Rev. Lett. **67**, 2882 (1991).
[2] B. Andraka and A. M. Tsvelik, Phys. Rev. Lett. **67**, 2886 (1991).
[3] U. Zülicke and A. J. Millis, Phys. Rev. B **51**, 8996 (1995).
[4] C. L. Seaman, M. B. Maple, B. W. Lee, S. Ghamaty, M. S. Torikachvili, J.-S. Kang, L. Z. Liu, J. W. Allen, and D. L. Cox, J. Alloys Compounds **181**, 327 (1992).
[5] M. Bull and K. A. McEwen (to be published).
[6] K. H. Fischer and J. A. Hertz, *Spin Glasses* (Cambridge University Press, Cambridge, 1993).
[7] J. A. Mydosh, *Spin Glasses: An Experimental Introduction* (Taylor & Francis, London, 1993).
[8] K. Binder and A. P. Young, Rev. Mod. Phys. **58**, 801 (1986).
[9] A. P. Ramirez, G. P. Espinosa, and A. S. Cooper, Phys. Rev. Lett. **64**, 2070 (1990).
[10] R. V. Chamberlin, G. Mazurkevich, and R. Orbach, Phys. Rev. Lett. **52**, 867 (1984).
[11] H. Bouchiat, J. Phys. (Paris) **47**, 71 (1986).
[12] R. Omari, J. J. Prejean, and J. Souletie, J. Phys (Paris) **44**, 1069 (1983).
[13] B. Martinez, A. Labarta, R. Rodriguez-Sola, and X. Obradors, Phys. Rev. B **50**, 15779 (1994).
[14] W. D. Wu, A. Keren, L. P. Le, G. M. Luke, B. J. Sternlieb, Y. J. Uemura, C. L. Seaman, Y. Dalichaouch, and M. B. Maple, Phys. Rev. Lett. **72**, 3722 (1994).

# Search for hybridization gap in the electronic density of states in CeNiSb

Latika Menon, S. K. Dhar, and S. K. Malik
*Tata Institute of Fundamental Research, Homi Bhabha Road, Bombay 400 005, India*

W. B. Yelon
*University of Missouri Research Reactor, Columbia, Missouri 65211*

The compounds CeRhSb and CeNiSn show hybridization gap in the electronic density of states. It is of interest to look for a similar gap in a related compound, CeNiSb. We present here the results of the structural, magnetic, and transport studies on CeNiSb. Rietveld analysis of the room-temperature neutron diffraction data reveals that this compound crystallizes in the hexagonal structure (space group $P6_3/mmc$). Magnetization measurements show that this compound is ferromagnetically ordered with a transition temperature of ~4 K. The magnetic susceptibility of CeNiSb follows Curie–Weiss behavior between 10 and 300 K with effective paramagnetic moment close to that of $Ce^{3+}$ ion. The heat capacity of CeNiSb shows a rise at about 4 K due to the ferromagnetic ordering and a moderately large value of $\gamma$ is obtained. Its electrical resistivity shows a weak shallow minima at 15 K which is a characteristic feature of Kondo lattice systems. However, no rise in the resistivity at low temperatures, as seen in CeRhSb and CeNiSn, is observed in CeNiSb.
© *1996 American Institute of Physics.* [S0021-8979(96)26008-2]

## I. INTRODUCTION

The compound CeRhSb[1,2] is one of the very few Ce-based intermetallic compounds to show an insulating/semiconducting ground state. This compound crystallizes in the orthorhombic $\epsilon$-TiNiSi-type structure (space group *Pnma*). Its susceptibility shows a broad maxima, typical of mixed-valent Ce-based compounds. In such mixed-valent systems, as a result of the strong hybridization between the conduction electrons and the $4f$ electrons, a gap can occur at low temperatures in the electronic density of states. The electrical resistivity of this compound, though metal-like at higher temperatures, indeed shows a sharp rise at low temperature (below 8 K), which is thought to be a manifestation of the gap in the electronic density of states. The gap energy has been estimated to be about 4 K from these measurements. Another Ce-based compound, CeNiSn,[3] isostructural to CeRhSb, also shows similar gap formation.

In view of the above-mentioned results, it is interesting to study the system, CeNiSb, which may be thought to be derived from CeRhSb by substitution of Ni at the Rh site or from CeNiSn by substitution of Sb at the Sn site and to look for gap formation in this compound. We have, therefore, carried out electrical resistivity, magnetic susceptibility, and heat capacity measurements on this compound. Our measurements reveal that the Ce ions in CeNiSb are in a nearly trivalent state. There is a weak Kondo lattice nature and also a ferromagnetic ordering in this compound below 4 K. However, low-temperature resistivity rise is not seen in this compound.

## II. EXPERIMENTAL DETAILS

The RNiSb (R=La and Ce) samples were prepared by arc melting of stoichiometric amounts of the constituent elements under a continuous flow of Argon gas. If the loss in weight is attributed to the volatile nature of Sb, the resulting composition of the Ce compound is $CeNiSb_{0.9}$ (which will be referred to as CeNiSb). We have carried out neutron diffraction measurements on this compound to study its crystal structure and various site occupancies. In order to look for gap formation, heat capacity, resistivity, and magnetic susceptibility measurements were carried out. For heat capacity measurements the adiabatic technique was used in the low temperature range of 2–20 K. (For details on resistivity and susceptibility measurements, see Ref. 4.)

## III. RESULTS AND DISCUSSIONS

Preliminary x-ray measurements had shown that CeNiSb crystallizes in the hexagonal structure unlike CeRhSb while the nonmagnetic analogs, LaNiSb and YNiSb appeared to be isostructural to CeRhSb. However, a more detailed analysis shows that the crystal structure of all the three RNiSb compounds mentioned above can be refined assuming a hexagonal lattice with space group $P6_3/mmc$. The observed and fitted neutron diffraction pattern of CeNiSb is shown in Fig. 1. The GSAS program based on Rietveld analysis was used to refine its crystal structure.[5] The scattering cross sections (in

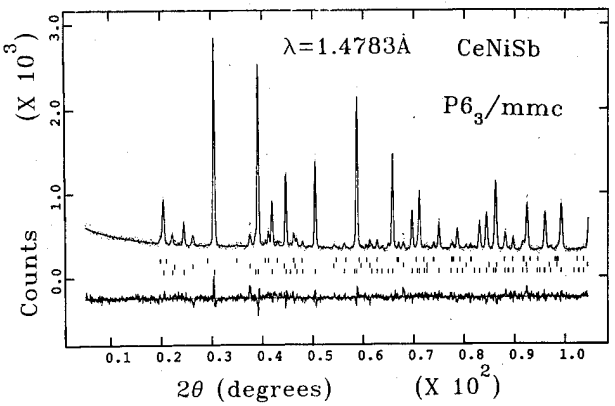



FIG. 1. Observed and fitted neutron diffraction pattern for CeNiSb. The line positions marked below the pattern are for $CeNi_5$, CeSb, and CeNiSb, respectively.

 0021-8979/96/79(8)/6367/3/$10.00 © 1996 American Institute of Physics 

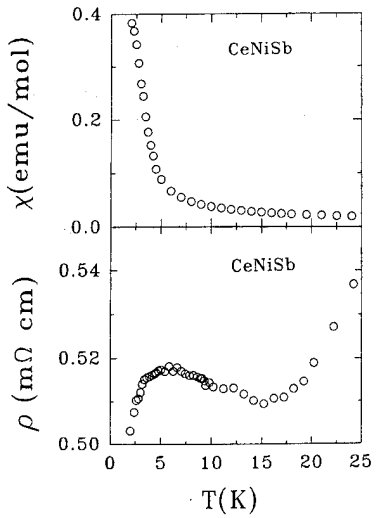



FIG. 2. (a) Plot of magnetic susceptibility $\chi$ vs temperature $T$ for CeNiSb. (b) Plot of electrical resistivity $\rho$ vs temperature $T$ for CeNiSb showing the Kondo minimum.

units of $10^{-12}$ cm) used were Ce(0.484), Ni(1.030), and Sb(0.564). The line shapes were approximated by pseudo-Voigt type function. A reasonably good fit to the data is obtained in the hexagonal structure, (space group $P6_3/mmc$) with two formula units per unit cell in which Ce is at the $2a$ site at (0,0,0), Ni at the $2c$ site at (0.33,0.66,0.25), and Sb at the $2d$ site at (0.33,0.66,0.75). The refinement also included secondary phases CeSb (3%) and $CeNi_5$ (6%). From the refinement, the values of lattice parameters obtained for CeNiSb are $a$=4.3935(1) Å and $c$=8.2375(3) Å. The bond distances obtained are $d_{Ce-Ce}$=4.119 Å, $d_{Ce-Sb}$=3.266 Å, $d_{Ce-Ni}$=3.266 Å, and $d_{Ni-Sb}$=2.536 Å. The reduced $\chi^2$ value for the fit is 1.598, $wR_p$=5.9% and $R_p$=4.6%. The refined fractional site occupancies for the sites are Ce: 1 (fixed), Sb: 1.047(18), and Ni: 0.937(14). Since Ni has a higher neutron scattering cross section than Sb, the obtained site occupancies for Ni and Sb in the context of starting composition may be taken to imply some Ni/Sb disordering.

On fitting the x-ray pattern of LaNiSb and YNiSb to a hexagonal structure with space group $P6_3/mmc$ the following lattice parameters are obtained. For YNiSb $a$=4.312(2) Å, $c$=7.778(3) Å and for LaNiSb $a$=4.385(1) Å, $c$=8.476(1) Å.

Figure 2(a) shows a plot of susceptibility versus temperature for CeNiSb. The rise in susceptibility observed below 5 K is due to impending magnetic ordering. From detailed magnetization measurements on this compound,[4] the ordering is surmised to be of ferromagnetic in nature. Figure 2(b) shows a plot of the electrical resistivity versus temperature. A broad minimum at 15 K is observed which probably indicates Kondo lattice behavior in this system. However, it may be mentioned that this feature in resistivity is somewhat sample dependent but may not be due to impurity phases since no sharp drop is seen. At low temperatures, a sharp drop in the resistivity is observed due to onset of magnetic ordering. No rise in the resistivity is observed at low temperature down to 2 K, unlike that seen in CeRhSb.

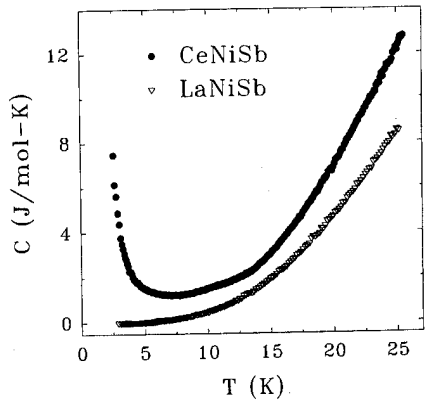



FIG. 3. Plot of heat capacity $C$ vs temperature $T$ for the compounds CeNiSb and LaNiSb in the temperature range 2–26 K.

Figure 3 shows a plot of the heat capacity of CeNiSb and the nonmagnetic analog LaNiSb. The heat capacity of LaNiSb is of the form

$$C=\gamma T+\beta T^3, \tag{1}$$

where $\gamma T$ is the electronic contribution to the heat capacity and $\beta T^3$ is the phonon contribution. The value of $\gamma$ is obtained to be about 1 mJ/mol $K^2$ which is typical of metallic systems.

In the case of CeNiSb, the heat capacity ($C$) shows a sharp rise at about 5 K (Fig. 3) which is due to an approach to magnetic ordering. In order to obtain the magnetic or the $4f$ contribution to the heat capacity in CeNiSb, the nonmagnetic contribution has to be subtracted. As a first approximation, we take the nonmagnetic contribution in CeNiSb to be the same as that of LaNiSb. On subtracting the heat capacity of LaNiSb from that of CeNiSb, the obtained magnetic contribution, $\Delta C$, is plotted in Fig. 4. The sharp rise in $\Delta C/T$ vs $T^2$ plot at 5 K continues to be observed. Above 14 K, the value of $\Delta C/T$ is seen to increase with temperature and on extrapolating $\Delta C/T$ to $T\rightarrow 0$ K, a value of electronic specific heat coefficient, $\gamma$ of about 60 mJ/mol $K^2$ is obtained which is quite high compared to that of normal metallic systems. This behavior of the heat capacity of CeNiSb may be compared with that of Ce-based insulators, $Ce_3Bi_4Pt_3$ (Ref. 6)

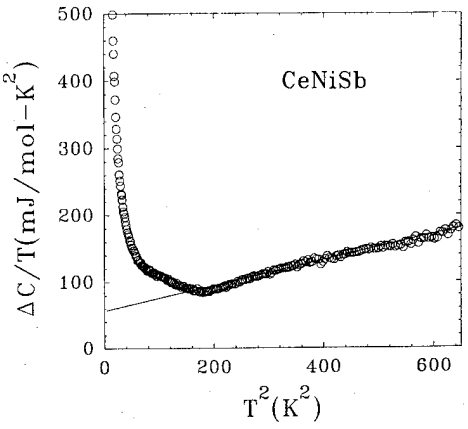



FIG. 4. Plot of $\Delta C/T$ vs $T^2$ for CeNiSb.

and CeRhSb.[7] In the case of $Ce_3Bi_4Pt_3$, the obtained $\gamma$ (~3 mJ/mol $K^2$) is three times smaller than the value for the corresponding La analog. This is indeed expected, since $\gamma$ is directly proportional to the electronic density of states, and hence for a gapped system (where electronic density of states is very small) the obtained $\gamma$ too should be small. In CeRhSb, it is observed that below a temperature of about 8 K (i.e., in the gapped state) the heat capacity, though relatively large in comparison with that of LaRhSb, varies linearly with temperature, due to the linear variation of the electronic density of states with temperature in the insulating state. Thus, a large value of $\gamma$ and the absence of linear variation of $\Delta C/T$ vs $T$ in CeNiSb, suggests that a gap in the electronic density of states of the type seen in CeRhSb and CeNiSn is not observed in this system. This is also consistent with the resistivity behavior of CeNiSb. The large value of $\Delta C/T$ or $\gamma$ above 14 K is most probably due to the Kondo and crystal field effects.

## IV. CONCLUSIONS

In conclusion, CeNiSb is found to crystallize in the hexagonal structure (space group $P6_3/mmc$). Magnetization/susceptibility measurements indicate largely trivalent Ce ions which order magnetically around 4 K. A sharp rise in the heat capacity of CeNiSb is observed at about 5 K consistent with the magnetic ordering in this compound. A moderately large value of $\gamma$~60 mJ/mol $K^2$ is observed, which may be due to the combined effect of crystal field and the Kondo effect. No rise in the low-temperature resistivity is observed, in contrast to the situation in CeRhSb and CeNiSn.


[1] S. K. Malik and D. T. Adroja, Phys. Rev. B **43**, 6277 (1991).
[2] S. K. Malik, L. Menon, K. Ghosh, and S. Ramakrishnan, Phys. Rev. B **51**, 399 (1995).
[3] T. Takabatake, Y. Nakazawa, and M. Ishikawa, Jpn. J. Appl. Phys. **26**, 547 (1987).
[4] L. Menon and S. K. Malik, Phys. Rev. B **52**, 35 (1995).
[5] L. Menon, S. K. Malik, and W. B. Yelon (unpublished).
[6] A. Severing, J. D. Thompson, P. C. Canfield, Z. Fisk, and P. Riseborough, Phys. Rev. B **44**, 6832 (1991).
[7] S. K. Malik, Latika Menon, V. Pecharsky, and K. A. Gschneidner, Jr. (unpublished).

# Anisotropy and angular variation of the giant magnetoresistance in magnetic multilayers (invited)

B. Dieny, C. Cowache, and A. Nossov[a)]
*CEA/Département de Recherche Fondamentale sur la Matière Condensée, 38054 Grenoble Cedex 9, France*

P. Dauguet, J. Chaussy, and P. Gandit
*CNRS/Centre de Recherche sur les Très Basses Températures, 38042 Grenoble Cedex 9, France*

The giant magnetoresistance (GMR) of magnetic multilayers is usually considered as isotropic, i.e., independent of the direction of the sensing current with respect to the applied field. In spin-valve samples of the form NiFe/Cu/NiFe/FeMn it is possible to accurately determine the amplitude of the GMR (without any contribution from the usual anisotropic magnetoresistance) for various direction of the current with respect to the direction of the magnetization of the two ferromagnetic layers, both in the parallel and antiparallel magnetic configurations. In three series of spin-valve samples of the composition F $t_F$/Cu $t_{Cu}$/NiFe/FeMn, we have observed that the GMR amplitude is larger when the current is perpendicular to the magnetizations than when it is parallel to it. This intrinsic anisotropy in the GMR shows a pronounced maximum (relative amplitude of the anisotropy of the order of 10% at the maximum) for a thickness of the ferromagnetic layer of the order of 150 Å. In contrast, this anisotropy depends very weakly on the nonmagnetic spacer layer thickness. The results are compared with semiclassical calculations of Rijks *et al.* [Phys. Rev. B **51**, 283 (1995)]. On another respect, we have measured the in-plane (CIP) and perpendicular to the plane (CPP) giant magnetoresistance of antiferromagnetically coupled (NiFe/Ag) multilayers. Particular attention has been paid on the variation of resistivity with the angle $\Delta\theta$ between the magnetization in the successive magnetic layers. While the CIP GMR varies almost linearly with $\cos(\Delta\theta)$, the CPP GMR shows strong deviations from linearity especially at large NiFe thicknesses. The results are discussed in terms of relative role of *s*-like and *d*-like electrons in CIP and CPP transport. © *1996 American Institute of Physics.* [S0021-8979(96)56108-X]

## I. INTRINSIC ANISOTROPY OF THE GIANT MAGNETORESISTANCE IN MAGNETIC MULTILAYERS

The giant magnetoresistance (GMR) first discovered in (Fe/Cr) multilayers[1] and later observed in a large number of transition-metal-based multilayers or sandwiches[2,3] is often considered as an isotropic phenomenon, i.e., the GMR amplitude is independent on the angle between the applied field and the sensing current.[1] This contrasts to the well-known phenomenon of anisotropic magnetoresistance (AMR)[4] which consists, in single layers of ferromagnetic transition metal, in a variation of the resistivity of the material with the angle between the magnetization and the current. This AMR is ascribed to the spin-orbit coupling which tends to induce an anisotropic spin intermixing of the spin-↓ and spin-↑ *d* subbands. In a previous article, we already reported some preliminary results on spin-valve samples of the composition Si/Co 200 Å/Cu 25 Å/NiFe 50 Å/FeMn 100 Å and on multilayers of the composition Si/(Co 30 Å/Cu 40 Å/NiFe 30 Å/Cu 40 Å)$_{10}$ which clearly demonstrate that the GMR is not isotropic.[5] The GMR amplitude is larger when the magnetizations are perpendicular to the current than when they are parallel to it. In the present experimental study, we measured the anisotropy in GMR (AGMR) on several series of spin-valve sandwiches comprising Co or Ni layers. We studied the variation of the AGMR versus the thickness of the ferromagnetic layers as well as of the nonmagnetic spacer layer. Spin-valve sandwiches are particularly well suited for this type of experiment. In these systems indeed, by applying the field in the direction parallel to the direction of the magnetization in the pinned layer (i.e., NiFe/FeMn), one can change the relative orientation of the magnetic moments in the two ferromagnetic layers from parallel to antiparallel without changing the angle between these moments and the in-plane current, whatever its direction: parallel or perpendicular to the field. A convenient way to proceed is to work on a large sample with a square four-point probe. By permuting the connection of one current and one voltage contact without touching the sample, nor changing the direction of the applied field, it is possible to measure the GMR amplitude both parallel and perpendicular to the current (see the schematic representation of the sample, contacts, and relative orientation of the current, field, and magnetic moments in Fig. 1). In this geometry, one is sure that there is no contribution arising from the usual AMR in the difference of GMR amplitude.

Typical results obtained at room temperature are shown in Figs. 2 and 3 for two spin-valve structures of the composition Si/Co 105 Å/Cu 25 Å/NiFe 50 Å/FeMn 100 Å (Fig. 2)

[a)]Permanent address: Institute of Metal Physics, Ekaterinburg 620219, Russia, CIS.

 0021-8979/96/79(8)/6370/6/$10.00 © 1996 American Institute of Physics

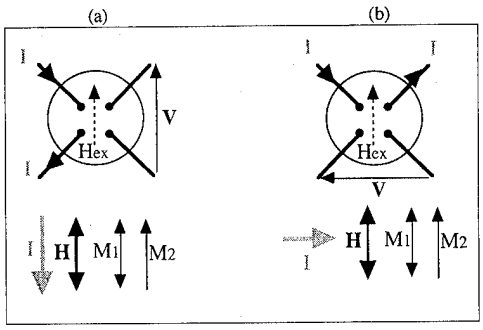



FIG. 1. Schematic representation of the four-point geometry for measurement of anisotropic GMR. The direction of the exchange anisotropy field $H_{ex}$, of the applied field $H$, of the current $I$, of the magnetic moments in the two ferromagnetic layers $M_1$ and $M_2$ are indicated. (a) Magnetic configuration parallel to the current, (b) magnetic configuration perpendicular to the current.

and Si/Co 400 Å/Cu 25 Å/NiFe 50 Å/FeMn 100 Å (Fig. 3). The shape of these curves is normal for spin-valve sandwiches.[5] It consists of two distinct loops associated with the reversal of the free and pinned magnetic layers. In between these loops, flat plateaux of resistance are observed in which the magnetizations of the two magnetic layers are single domain and parallel or antiparallel to each other. The GMR amplitude is determined by the relative difference in resistance between the saturation in the direction parallel to the exchange field created by the FeMn and the first plateau obtained at decreasing field when the magnetization of the free layer ($M_1$) has switched in the direction opposite to the magnetization of the pinned layer ($M_2$). During the reversal of $M_1$, a contribution from the AMR shows up especially when the thickness of the free layer is large (see Fig. 3). This AMR contribution, however, does not affect the determination of the GMR amplitude.

In all measured samples, we observed that the GMR ratio $\Delta R/R_{sat}$ is larger when the magnetic moments are perpendicular to the current as compared to the situation where they are parallel to it. This confirms our previous observation that the GMR is not fully isotropic.

To go further, we have studied the variation of the AGMR versus the thickness of the magnetic and nonmagnetic layers. The results are shown in Figs. 4–6. When the

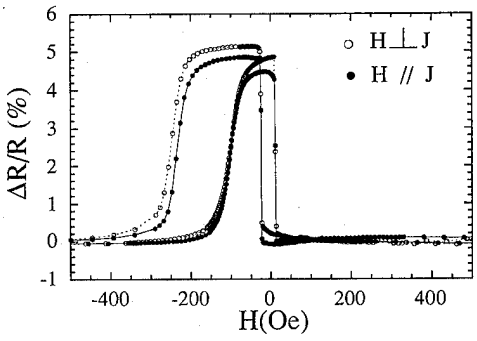



FIG. 2. Magnetoresistance of a spin-valve sample of the composition Si/Co 105 Å/Cu 25 Å/NiFe 50 Å/FeMn 100 Å measured in the two configurations: $H$ parallel to the current [configuration (a) of Fig. 1] and $H$ perpendicular to the current [configuration (b) of Fig. 1].

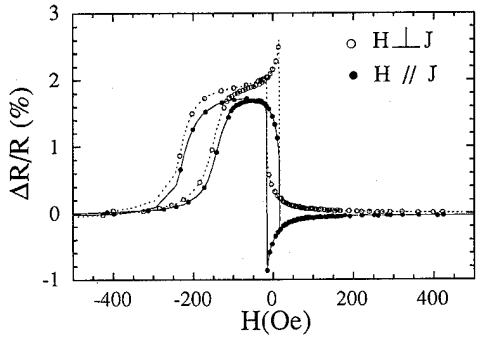



FIG. 3. Magnetoresistance of a spin-valve sample of the composition Si/Co 400 Å/Cu 25 Å/NiFe 50 Å/FeMn 100 Å measured in the two configurations: $H$ parallel to the current [configuration (a) of Fig. 1] and $H$ perpendicular to the current [configuration (b) of Fig. 1].

thickness of the magnetic layers (Co or Ni) is varied (Figs. 4 and 5), the GMR goes through a maximum for an intermediate thickness of the order of 80–100 Å. We define the anisotropy in GMR as

$$\Delta\mathrm{GMR}=\left(\frac{\Delta R}{R_{\mathrm{sat}}}\right)_{\parallel J}-\left(\frac{\Delta R}{R_{\mathrm{sat}}}\right)_{\perp J}$$

(Ref. 6). This quantity is negative for all samples investigated. In absolute value ΔGMR is maximum for an intermediate thickness of the ferromagnetic layers of the same order as the maximum of GMR itself.

In contrast, when the thickness of the nonmagnetic layer is varied, a monotonous decrease in GMR is observed which is usual in this uncoupled sandwich. However, a striking re-

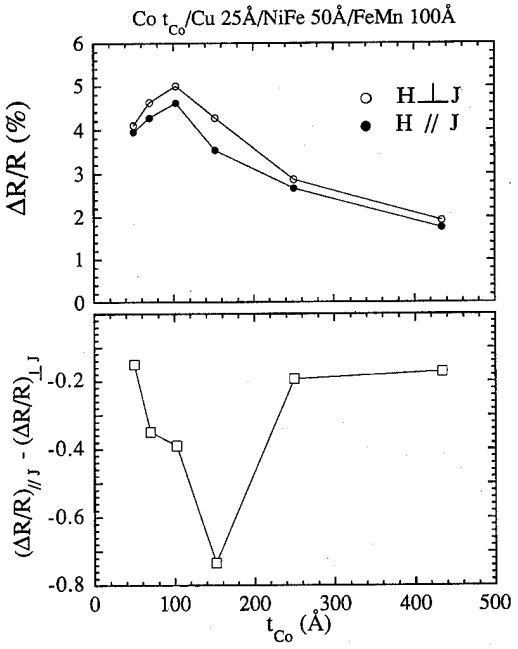



FIG. 4. (a) CIP GMR vs the thickness of the Co layer, measured with the applied field parallel to the current [geometry of Fig. 1(a)] or perpendicular to the current [geometry of Fig. 1(b)] for a series of spin-valve sandwiches of the composition Co $t_{Co}$/Cu 25 Å/NiFe 50 Å/FeMn 100 Å. (b) Difference in GMR amplitude between the two geometries vs the thickness of the Co layer.

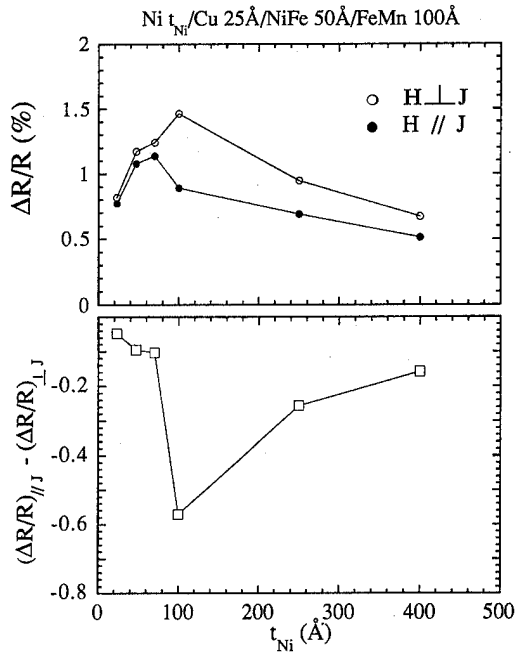



FIG. 5. (a) CIP GMR vs the thickness of the Ni layer, measured with the applied field parallel to the current [geometry of Fig. 1(a)] or perpendicular to the current [geometry of Fig. 1(b)] for a series of spin-valve sandwiches of the composition Ni $t_{Ni}$/Cu 25 Å/NiFe 50 Å/FeMn 100 Å. (b) Difference in GMR amplitude between the two geometries vs the thickness of the Ni layer.

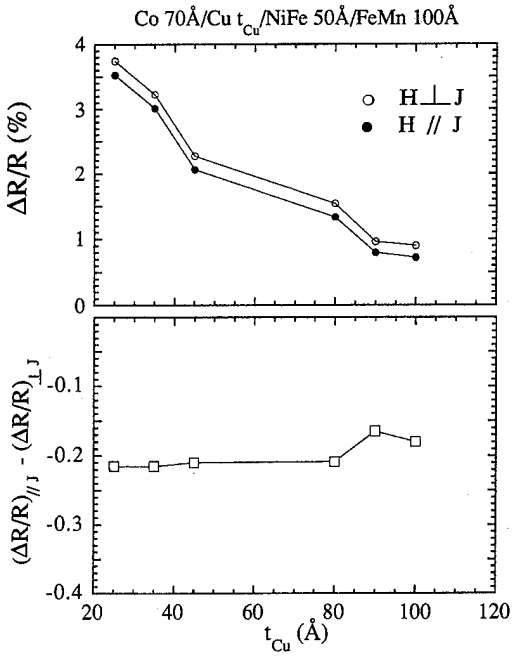



FIG. 6. (a) CIP GMR vs the thickness of the Cu layer, measured with the applied field parallel to the current [geometry of Fig. 1(a)] or perpendicular to the current [geometry of Fig. 1(b)] for a series of spin-valve sandwiches of the composition Co 70 Å/Cu $t_{Cu}$ NiFe 50 Å/FeMn 100 Å. (b) Difference in GMR amplitude between the two geometries vs the thickness of the Cu layers.

sult is that ΔGMR is almost independent of the Cu thickness in the range of thicknesses investigated. These experimental results can be compared with the semiclassical calculations of anisotropic GMR by Rijks *et al.*[6] In these calculations, the authors predicted that the anisotropic GMR could be either negative or positive depending on the thicknesses of the magnetic and nonmagnetic layers. Three effects contribute to the amplitude of this anisotropy,[6] as follows.

(i) It is known that in bulk ferromagnetic transition metals, the resistivity for each spin channel is anisotropic. For instance in $Ni_{80}Fe_{20}$, the resistivities in the direction perpendicular to the current are given by[4] $\rho_{\perp\uparrow}=8.8\ \mu\Omega$ cm, $\rho_{\perp\downarrow}=96\ \mu\Omega$ cm and therefore $\alpha_{\perp}=\rho_{\perp\downarrow}/\rho_{\perp\uparrow}=10.9$, while the resistivities parallel to the current are: $\rho_{\parallel\uparrow}=10.0\ \mu\Omega$ cm, $\rho_{\parallel\downarrow}=93.9\ \mu\Omega$ cm, leading to $\alpha_{\parallel}=\rho_{\parallel\downarrow}/\rho_{\parallel\uparrow}=9.4$. Therefore, an anisotropy in the asymmetry ratio of the resistivities of spin-↓ and spin-↑ electrons exists in these materials. Since the amplitude of the GMR is directly related to this ratio of spin-dependent resistivities, an anisotropy in the $\alpha$ ratio naturally leads to an anisotropy in GMR. To our point of view this effect is certainly the most important one.

(ii) When the magnetizations are parallel to the current, the enhanced scattering of the electrons in this direction results in a relatively larger contribution to the current from electrons with a large velocity component perpendicular to the plane of the layers. This results in a positive contribution to ΔGMR.[6] In our experimental results, we do not see the expected change of sign in ΔGMR which would be caused by this contribution, even at large thicknesses of the magnetic layers. This may be due to diffuse scattering occurring not only at outer boundaries but also at inner interfaces.

(iii) The absolute value of ΔGMR is related to the amplitude of the GMR itself.

Qualitatively, our experimental observations fit rather well with the calculations of Rijks *et al.* in the regime of small thicknesses of the magnetic and nonmagnetic layer (lower-left-hand corner of Fig. 10 of Ref. 6). At small thickness of the nonmagnetic layer, as the thickness of the magnetic layer is varied, a minimum in ΔGMR is expected as observed experimentally. In contrast, at fixed thickness of the magnetic layer (of the order of 40–60 Å in Fig. 10 of Ref. 6), a very weak variation in ΔGMR versus the thickness of the nonmagnetic layer is expected despite a rapid decrease in GMR. This agrees also with our observation.

In conclusion, we have observed the existence of an intrinsic anisotropy in the GMR in several series of spin-valve sandwiches. The GMR amplitude is always larger when the magnetizations are perpendicular to the current than when they are parallel to it. Our results qualitatively agree with the semiclassical calculation of Rijks *et al.*[6] The absence of positive anisotropy in our systems is probably due to some interfacial diffuse scattering.

## II. ANGULAR VARIATION OF THE CIP AND CPP (GMR) IN (NiFe/Ag) MULTILAYERS

So far, most of the experimental studies of the GMR in magnetic multilayers have focused on the influence of various parameters (thicknesses, conditions of preparation, temperature) on the maximum amplitude of the magnetoresistance, i.e., the change of resistance between the parallel and antiparallel magnetic configurations. In contrast, very few

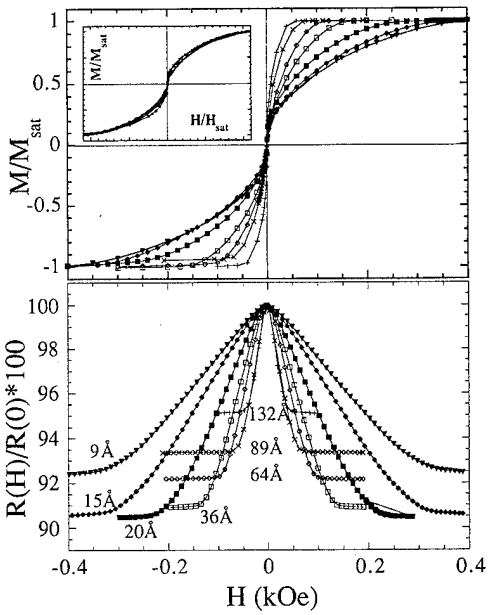



FIG. 7. (a) Magnetization curves at room temperature for a series of multilayers of the composition Si/(NiFe $t_{NiFe}$/Ag 11 Å)$_{20}$. Inset: Magnetization curves in reduced units of $M/M_{sat}$, ($H/H_{sat}$). (b) CIP magnetoresistance for the same set of samples as in (a). The thicknesses of the NiFe layers are labeled in (b).

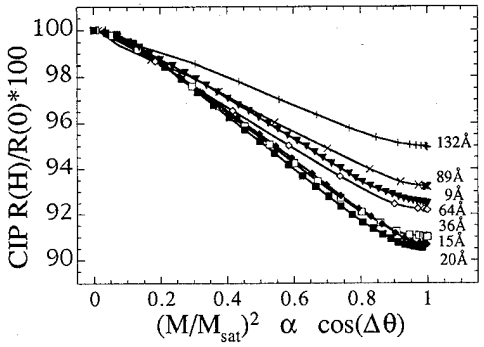



FIG. 8. CIP resistance at room temperature vs $(M/M_{sat})^2$ which is proportional to the cosine of the angle between the magnetization in the successive ferromagnetic layers, for the same series of (NiFe/Ag 11 Å)$_{20}$ multilayers as in Fig. 7.

experimental[7–10] and theoretical studies[11,12] have addressed the variation of resistance versus the angle between the magnetizations in the successive magnetic layers. However, measurements of these angular variations are quite useful since they may provide insights on the role played by the interfacial potential barriers in the GMR mechanism.[11,12] So far, all detailed measurements of the angular variation of CIP GMR have led to a linear variation of resistivity with the cosine of the angle between the magnetizations in the successive magnetic layers.[7–10]

We have carried out a determination of the angular variation of the CIP and CPP GMR in a series of $Si/SiO_2$/(NiFe $t_{NiFe}$/Ag 11 Å)$_n$ multilayers prepared by magnetron sputtering. The substrate temperature was maintained at 77 K during deposition in order to obtain a good structural quality with flat Ag layers.[13] For 11 Å of Ag, the NiFe layers are antiferromagnetically coupled. Figure 7(a) shows the magnetization curves for a series of samples with 20 periods. They are reversible with zero remnant magnetization. The saturation field varies as the inverse of the thickness of the NiFe layers. Such variation results from a balance between the volume Zeeman energy ($M_S t_{NiFe} H_{sat}$) and the interlayer coupling energy which is a surface energy $J$. In reduced units ($H/H_{sat}$, $M/M_{sat}$), all curves fit on a single line [see inset of Fig. 7(a)]. The curvature of this line indicates that a biquadratic coupling exists in these multilayers in addition to the antiferromagnetic bilinear coupling.[14] A detailed analysis of these curves will be published in a forthcoming article.[15] Because the interlayer coupling is predominantly antiferromagnetic, the magnetization process occurs via a coherent rotation of the magnetization of the NiFe layers. Since no significant magnetic anisotropy is observed in these multilayers and neglecting the effect due to the finite number of bilayers, one can consider that the magnetic moments of two successive NiFe layers rotate symmetrically with respect to the field. The cosine of the angle between the magnetizations of two successive layers is then proportional to the $(M/M_{sat})^2$. This relationship will be used further to determine the angular variation of the CIP GMR in these multilayers.

The CIP GMR of this series of multilayers is plotted in Fig. 7(b). The amplitude of the CIP GMR is maximum for an intermediate thickness of the NiFe layers of the order of 20 Å. However, since the saturation field monotonously decreases with the thickness of the NiFe layers, the maximum sensitivity $s=\Delta R/R/H_{sat}$ is obtained at large NiFe thicknesses (above 80 Å).

In Fig. 8 the data of Figs. 7(a) and 7(b) have been combined in order to plot the CIP GMR versus $(M/M_{sat})^2$ which represents $\cos(\Delta\theta)$, i.e., the cosine of the angle between the magnetization in the successive NiFe layers. The AMR is rather small in the present multilayers as compared to the CIP GMR (0.5% in the multilayer with the thickest NiFe layers). Therefore, no correction has been made to subtract the contribution from the AMR to the measured magnetoresistance. Within the accuracy of the measurement, a linear variation of $\Delta R/R$ vs $\cos(\Delta\theta)$ is observed in the interval $0.1<(M/M_{sat})^2<0.9$. The deviation from linearity close to saturation can be ascribed to some paramagnetic or superparamagnetic entities at the interfaces. Once the magnetic moments of the NiFe layers have completed their rotation toward the direction of the applied field, these fluctuations still require higher fields to be saturated. They can, therefore, explain the small tails observed in Fig. 8 close to saturation. On the other side, at low fields, one cannot exclude the existence of a small fraction of ferromagnetically coupled regions which would give large change of magnetization without change in resistance. This would lead to a plateau of $R$ vs $M^2$ as observed in Fig. 8 at low magnetization values; however, the almost linear variation of $R(M^2)$ observed on a large range of angle $\Delta\theta$ means that, according to the theory of Vedyaev *et al.*,[11,12] the electrons which contribute the most to the CIP GMR do not feel interfacial potential barriers and therefore are predominantly $s$-like electrons.

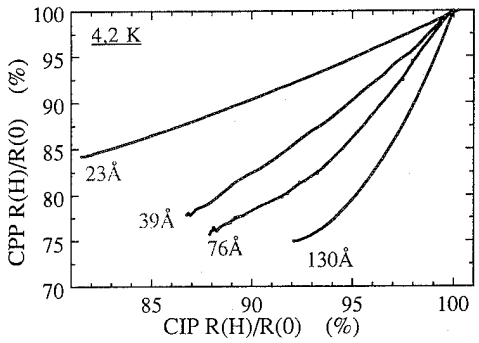



FIG. 9. CPP resistance at 4 K vs the CIP resistance at 4 K for a series of multilayers of the composition (NiFe $t_{NiFe}$/Ag 11 Å)$_{50}$.

We have also measured the CPP GMR of some of these (NiFe/Ag) multilayers. The technique used is based on the measurements of very low resistance on macroscopic samples sandwiched between superconducting Nb leads,[16] described in detail in Ref. 17. The detailed analysis of the results will be published in a forthcoming article.[18] We want here to focus on the angular variation of the CPP GMR as compared to that of the CIP GMR. In order to extract the angular variation of the CPP GMR in these NiFe/Ag multilayers, we measured the CIP and CPP GMR of a series of antiferromagnetically coupled multilayers of the composition Nb/(NiF$e_{t_{NiFe}}$/Ag11 Å)$_{50}$/Nb. The CIP and CPP measurements are carried out on the same samples at 4 K. However, the part of the sample used for CIP measurements does not have the Nb buffer layer while the CPP part has it. This does not seem to affect the magnetic behavior of the samples since exactly the same saturation fields are obtained in CIP and CPP measurements. As already observed in previous CPP measurements on magnetic multilayers,[16] the CPP GMR amplitude is larger than the CIP amplitude. Contrary to the CIP GMR, the CPP GMR increases monotonously with the thickness of the NiFe layers (from 20% for $t_{NiFe}$=23 Å to 50% for $t_{NiFe}$=130 Å). This increase in the CPP GMR can be easily understood in a model of serial resistors which is valid in the present case. The thickness of the Ag layers is indeed much smaller than the spin-flip diffusion length.[19] We then plotted the CPP resistance versus the CIP resistance as a function of the applied field (Fig. 9). According to the discussion of Fig. 8, we assumed that the CIP GMR varies linearly with $\cos(\Delta\theta)$. The plot of Fig. 9 then directly gives a representation of the angular variation of the CPP GMR. It is observed that the angular variation of the CPP GMR is almost linear with $\cos(\Delta\theta)$ at small NiFe thicknesses but shows increasing deviations from linearity at large NiFe thicknesses. These deviations cannot be ascribed to a contribution from the AMR in the CIP measurements since this AMR is quite small as compared to the GMR. The exact meaning of these deviations is not yet clear since no theoretical model of the angular variation of the CPP GMR exists so far. In particular, why are they larger at large NiFe thicknesses than at small thicknesses? This may be related to the role played by the interfacial potential barriers in the CPP transport. Vedyaev *et al.* showed that in CPP transport, a potential step at an interface between two semi-infinite metallic layers leads to spatial oscillations in electric field on both sides of the interface.[20] These oscillations result in an additional interfacial resistance proportional to the square of the barrier height. It may happen that at small NiFe thicknesses, because of the roughness of the layers, interferences between the successive interfaces are smeared out leading to little effect of the potential barriers. In contrast, at large thicknesses, such interferences do not occur so that the potential barriers could play a more effective role.

## III. CONCLUSION

In conclusion, we have demonstrated the existence of an intrinsic anisotropy in the CIP GMR of magnetic multilayers which is due to an anisotropy in the $\alpha=\lambda_\uparrow/\lambda_\downarrow$ ratio. This anisotropy has been measured in several series of spin-valve sandwiches comprising Co, Ni, and Cu layers of various thicknesses. The results qualitatively agree with semiclassical calculations of Rijks *et al.*[6]

On another respect, we have determined the angular variation of the CIP and CPP GMR in (NiFe/Ag) multilayers. The CIP GMR is found to vary linearly with the cosine of the angle between the magnetization in the successive magnetic layers while the CPP GMR shows deviations from linearity especially at large NiFe thicknesses. The linearity observed for the CIP GMR indicates that the electrons which contribute the most to the CIP GMR are not sensitive to interfacial potential barriers. The meaning of the deviations in CPP GMR is not yet clear.

## ACKNOWLEDGMENTS

We gratefully acknowledge A. Granovski, A. Vedyaev, and N. Ryzhanova for stimulating discussions. One of us (A.N.) acknowledges Commissariat à l'Energie Atomique for a fellowship. The spin-valve samples measured in this study were grown at IBM Almaden (V. Speriosu's group) 5 years ago. This work has been partly funded by the European Communities under the BRITE EURAM II program, Grant No. BRE2-0546.

[1] M. N. Baibich, J. M. Broto, A. Fert, F. Nguyen Van Dau, F. Petroff, P. Etienne, G. Creuzet, A. Friederich, and J. Chazelas, Phys. Rev. Lett. **61**, 2472 (1988).
[2] A. Fert and P. Bruno, *Ultrathin Magnetic Structure*, edited by B. Heinrich and A. Bland (Springer, Berlin, 1992).
[3] B. Dieny, J. Magn. Magn. Mater. **136**, 335 (1994).
[4] R. I. Potter, Phys. Rev. B **10**, 4626 (1974); T. R. McGuyre and R. I. Potter, IEEE Trans. Magn. **MAG-11**, 1018 (1975); J. W. F. Dorleijn and A. R. Miedema, J. Phys. F **5**, 1543 (1975).
[5] B. Dieny, V. S. Speriosu, S. Metin, S. S. P. Parkin, B. A. Gurney, P. Baumgart, and D. Wilhoit, J. Appl. Phys. **69**, 4774 (1991).
[6] G. S. M. Rijks, R. Coehoorn, M. J. M. de Jong, and W. J. M. de Jonge, Phys. Rev. B **51**, 283 (1995).
[7] B. Dieny, V. S. Speriosu, S. S. P. Parkin, B. A. Gurney, D. R. Wilhoit, and D. Mauri, Phys. Rev. B **43**, 1297 (1991).
[8] A. Chaiken, P. Lubitz, J. J. Krebs, G. A. Prinz, and M. Z. Harford, Appl. Phys. Lett. **59**, 240 (1991).
[9] T. Shinjo, in *Magnetism and Structure in Systems of Reduced Dimension*, edited by Farrow *et al.*, NATO ASI Series B: Physics, Vol. 309 (Plenum, New York, 1993), p. 323.
[10] A. Barthelemy *et al.*, in Proceedings of the International Workshop on Spin Polarized Electron Transport, Miami, 19–23 February 1995.
[11] A. Vedyaev, B. Dieny, N. Ryzhanova, J. B. Genin, and C. Cowache, Europhys. Lett. **25**, 465 (1994).

[12] A. Vedyaev, B. Dieny, N. Ryzhanova, and J. B. Genin, Phys. Lett. A **185**, 117 (1994).
[13] B. Rodmacq, G. Palumbo, and P. Gerard, J. Magn. Magn. Mater. **118**, L11 (1993).
[14] B. Rodmacq, K. Dumesnil, P. Mangin, and M. Hennion, Phys. Rev. B **48**, 3556 (1993).
[15] C. Cowache *et al.*, Phys. Rev. B (to appear, 1996).
[16] W. P. Pratt, Jr., S.-F. Lee, J. M. Slaughter, R. Loloee, P. A. Schroeder, and J. Bass, Phys. Rev. Lett. **66**, 3060 (1991).
[17] P. Dauguet, P. Gandit, and J. Chaussy, this conference, paper FA-07.
[18] P. Dauguet *et al.* (unpublished).
[19] T. Valet and A. Fert, Phys. Rev. B **48**, 7099 (1993).
[20] A. Vedyaev, C. Cowache, N. Ryzhanova, and B. Dieny, Phys. Lett. A **198**, 267 (1995).

# Theory of the temperature dependence of giant magnetoresistance (invited)

Hideo Hasegawa[a)]
*Department of Physics, Tokyo Gakugei University, Koganei, Tokyo 184, Japan*

The temperature dependence of the giant magnetoresistance (GMR) for currents parallel and perpendicular to the multilayer plane is discussed by taking account of the random exchange potentials, phonon scatterings, and spin fluctuations. The effect of spin fluctuations, which plays an important role at finite temperatures, is included by means of the static functional-integral method developed previously by the present author. Our model calculations well explain the observed features of the parallel and perpendicular GMR of Fe/Cr and Co/Cu multilayers recently reported by Gijs *et al.* [Phys. Rev. Lett. **70**, 3343 (1993); Phys. Rev. B **50**, 16 733 (1994)]. © *1996 American Institute of Physics.* [S0021-8979(96)56208-6]

## I. INTRODUCTION

The giant magnetoresistance (GMR)[1] in magnetic multilayers is one of the most attractive subjects in current solid-state physics. In recent years much progress has been made in understanding the GMR and its related phenomena.[1] One of the important aspects of the GMR is its temperature dependence. A careful study of the temperature dependence of GMR is not only important in understanding its mechanism but also very useful regarding its realistic applications. Most of the magnetic multilayers are fabricated with transition metals such as Fe, Ni, and Co. It would be instructive to briefly discuss the temperature dependence of the resistivity of bulk transition metals, before we study the temperature dependence of the GMR or of the resistivity of transition-metal multilayers. It has been reported that when the temperature is raised from $T=0$ K, the resistivity of Fe (Ref. 2) or Co (Ref. 3) gradually increases up to the Curie temperature, where it has a cusp (see Fig. 1). This characteristic temperature dependence of the resistivity is interpreted as due to the contributions from impurity, phonon, and magnetic terms. The last contribution is classically discussed as spin-disorder scatterings with the use of the $s$-$d$ model.[4] Lately, a modern theory on the itinerant-electron magnetism has accounted for it in terms of spin fluctuations.[5]

It has been well known that $d$ electrons in transition metals show both localized and itinerant character. The Curie–Weiss susceptibility and the large specific heat peak near the Curie temperature are easily explained by the localized spin model whereas the nonintegral ground-state moment and the large linear specific heat coefficient favor the band model. It has been realized that the effect of spin fluctuations plays essential roles to reconcile the duality of $d$ electrons.[6] The finite-temperature band theory, which has been proposed by the author,[7] includes the effect of spin fluctuations by means of the static functional-integral method combined with the coherent potential approximation (CPA). Spin fluctuations including spin waves are shown to yield the $T^2$ contribution to the resistivity at $T\simeq 0$ by several approaches.[8] This type of theory[8] is, however, valid only at very low temperatures. In our finite-temperature theory,[7] spin fluctuations are regarded as localized, static modes with the adopted approximations. This method has proved useful in understanding the overall finite-temperature properties of transition metals, alloy, and multilayers,[9] both below and above the Curie temperature.

By employing the finite-temperature band theory,[7] we discussed in previous articles[10] the temperature dependence of the MR ratio for currents parallel to the multilayer plane. The observed temperature dependences of Fe/Cr (Ref. 11), NiCo/Cu, NiFe/Cu, and CoFe/Cu (Ref. 12) multilayers have been shown to be well explained by our theory. It has been pointed out[10(c)] that a multilayer in which the normal and inverse GMR[13] coexist may have an interesting temperature dependence beneficial for real applications.

One of the purposes of the present article is to generalize our theory[10] to the perpendicular GMR, whose experimental[14–16] and theoretical study[17–19] has been currently performed. The other purpose is to include the phonon contribution to the conductivity calculation, which was neglected in our previous study.[10] The article is organized as follows: In Sec. II, we present our formulation applying our finite-temperature band theory to the GMR. Numerical calculations of the parallel and perpendicular GMR of Fe/Cr and Co/Cu multilayers are reported in Sec. III. Supplementary discussions are given in Sec. IV.

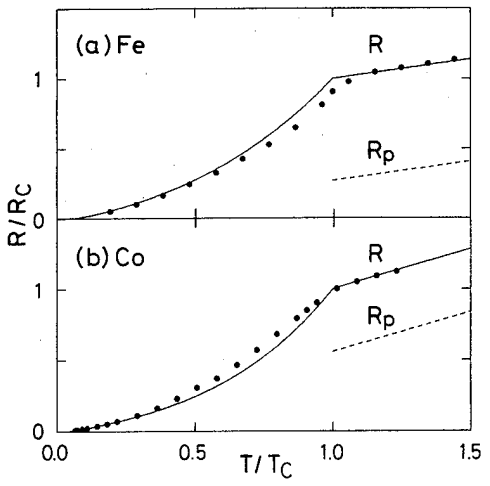



FIG. 1. The temperature dependence of the observed resistivity (circles) of (a) bulk Fe (Ref. 2) and (b) Co (Ref. 3); the calculated resistivity $R(T)$ and its phonon term $R_p(T)$ above $T_C$ are shown by solid and dotted curves, respectively, results being normalized by $R_C=R(T_C)$.

a)Electronic mail: hasegawa@u-gakugei.ac.jp

 0021-8979/96/79(8)/6376/6/$10.00 © 1996 American Institute of Physics

## II. CALCULATION METHOD

### A. An adopted model and the expression of GMR

We adopt an A/B multilayer consisting of magnetic A and nonmagnetic B atoms with the simple-cubic (001) interface. The layer parallel to the interface is assigned by the index $n(=1-N_f)$, $N_f$ being the thickness of the multilayer. It is assumed that atoms A and B are randomly distributed on layer $n$ with the concentrations of $x_n$ and $y_n$, respectively $(x_n+y_n=1)$. The multilayer is described by the single-band Hubbard model, in which the atomic potential (the on-site interaction) is assumed to be given by $\epsilon^{\mathrm{A}}$ and $\epsilon^{\mathrm{B}}$ ($U^{\mathrm{A}}$ and $U^{\mathrm{B}}$) when a given lattice site is occupied by A and B atoms, respectively.

In order to study the finite-temperature properties of the magnetic film, we apply the functional-integral method within the static approximation to the Hubbard Hamiltonian.[7] The partition function is evaluated by calculating the partition function of the effective one-electron Hamiltonian including the random charge and exchange fields with the Gaussian weight. The charge field is included by the saddle-point approximation and the exchange field by the alloy-analogy approximation with the CPA. The energy-dependent coherent potential for an $s$-spin electron $s(=\uparrow,\downarrow)$ on the layer $n$, $\Sigma_{ns}(\epsilon)$, is determined by the CPA condition. The coherent potentials, the average of the magnetic moments on the layer $n$, $\langle M_n\rangle$, and its root-mean-square (rms) value, $\langle (M_n)^2\rangle^{1/2}$, are calculated self-consistently, details having been given in Ref. 7.

When we employ the CPA, the conductivity of the film is given by[19]

$$\sigma_{\xi\eta}=\left(\frac{e}{\hbar}\right)^2\left(\frac{1}{\pi}\right)\int d\epsilon\left(-\frac{\partial f}{\partial\epsilon}\right)\mathrm{Tr}(v_\xi\ \mathrm{Im}\ \mathbf{G}\ v_\eta\ \mathrm{Im}\ \mathbf{G})$$

$$(\xi,\eta=x,y,z), \tag{1}$$

provided the vertex correction is neglected. In Eq. (1) $v_\xi$ is the velocity operator and $\mathbf{G}$ is the Green's-function matrix. The conductivities for currents parallel ($\|$) and perpendicular ($\perp$) to the film layer are given by[10,18,19]

$$\sigma^{\|}=\left(\frac{e}{\hbar}\right)^2\int d\epsilon\left(-\frac{\partial f}{\partial\epsilon}\right)\sum_s\ \nu^{\|}(\epsilon)\left(\frac{1}{N_f}\right)\sum_n\ \sum_m\ \frac{a_{nms}\tau_{nms}}{(\Delta_{ns}+\Delta_{ms})}, \tag{2}$$

$$\sigma^{\perp}=\left(\frac{e}{\hbar}\right)^2\int d\epsilon\left(-\frac{\partial f}{\partial\epsilon}\right)\sum_s\ \nu^{\perp}(\epsilon)\left[\left(\frac{1}{N_f}\right)\sum_n\ \Delta_{ns}\right]^{-1}, \tag{3}$$

with

$$\nu^{\lambda}(\epsilon)=\hbar^2\sum_{k_\|}\ v_\lambda^2\delta(\epsilon-\epsilon_{k_\|})\quad(\lambda=\|,\perp), \tag{4}$$

$$\tau_{nms}=\delta_{nm}+(1-\delta_{nm})\left(\frac{(\Delta_{ns}+\Delta_{ms})^2}{[(\Lambda_{ns}-\Lambda_{ms})^2+(\Delta_{ns}+\Delta_{ms})^2]}\right), \tag{5}$$

where $\Lambda_{ns}=\mathrm{Re}\ \Sigma_{ns}(\epsilon)$, $\Delta_{ns}=|\mathrm{Im}\ \Sigma_{ns}(\epsilon)|$, $\Sigma_{ns}$ is the coherent potential of an $s$-spin electron on layer $n$, and $a_{nls}$ and $\nu^{\lambda}$ are specified by the electronic structure of the film [see Eqs. (19) and (20) in Ref. 10(a)]. Equations (2)–(5) are valid when the thicknesses of the A and B layers are thinner than the mean free path and sufficiently thin compared with the spin diffusion length.[17] Analytic expressions for the conductivity have clear physical meaning. When currents flow parallel to the plane, an $s$-spin electron propagating successively from a site on layer $n$ to a site on layer $m$ is scattered with the strength proportional to $\Delta_{ns}$ and $\Delta_{ms}$, respectively, and its conductivity is given as a sum of such processes with the weight of $a_{nms}\tau_{nms}$.[10] On the contrary, in the case of the perpendicular current, the $s$-spin conductivity is given as of a series circuit of resistivities on successive layers, each of which is proportional to $\Delta_{ns}$.[18] In both cases, the total conductivity is a sum of the up- and down-spin channels. The so-called spin-flip process is implicitly included through the spin-fluctuation term which is responsible to a decrease in layer magnetization, as will be shown shortly. In the following subsection, we employ our formalism in a semiphenomenological way to discuss the temperature dependence of the MR ratio.

### B. A. semiphenomenological study of GMR

We adopt a system consisting of magnetic $(M_1,M_2)$ and nonmagnetic $(N_1,N_2)$ layers, whose thickness are $M$ and $N$, respectively. For a simplicity of calculation, we take into account only the bulk scattering, although the interface scattering is expected to be also important in magnetic multilayers (related discussion is given in Sec. IV). When magnetic moments on $M_1$ and $M_2$ layers are in the antiferromagnetic (AF) configuration, the coherent potentials are assumed to be given by $\Sigma_{ns}=\Delta_s-i\Delta_s$, $\Lambda_{-s}-i\Delta_{-s}$, and $\Lambda_0-i\Delta_0$ for $n\in M_1$, $n\in M_2$ and $n\in N_1$ (or $N_2$), respectively.[10] Using Eqs. (2)–(5), we get the parallel and perpendicular conductivities given by [10]

$$\sigma^{\mathrm{AF}\|}=\sum_s\left[\frac{2c_{MM}}{(\Delta_s+\Delta_{-s})}+\frac{c_{NN}}{\Delta_0}+4c_{MN}\left(\frac{1}{\Delta_s+\Delta_0}+\frac{1}{\Delta_{-s}+\Delta_0}\right)+d_M\left(\frac{1}{2\Delta_s}+\frac{1}{2\Delta_{-s}}\right)+\frac{d_N}{\Delta_0}\right], \tag{6}$$

$$\sigma^{\mathrm{AF}\perp}=\left(\frac{e}{\hbar}\right)^2\nu^{\perp}N_f\sum_s\left(\frac{1}{M\Delta_s+M\Delta_{-s}+2N\Delta_0}\right), \tag{7}$$

with

$$c_{MM}=N_f^{-1}\left(\frac{e}{\hbar}\right)^2\nu^{\|}\sum_{n\in M_1}\ \sum_{m\in M_2}\ a_{nm}\tau_{nm}, \tag{8}$$

$$d_M=N_f^{-1}\left(\frac{e}{\hbar}\right)^2\nu^{\|}\sum_{n\in M_1}\ \sum_{m\in M_1}\ a_{nm}\tau_{nm}, \tag{9}$$

and $c_{NN}$, $c_{MN}$, and $d_N$ are given by similar expressions. We employed the $T=0$ limit of Eqs. (2) and (3) because the relevant temperature is much less than the Fermi energy $\epsilon_F$. In Eqs. (6)–(9) $\nu^{\lambda}=\nu^{\lambda}(\epsilon_F)$, $N_f=2(M+N)$, and the spin dependence in $a_{nms}$ and $\tau_{nms}$ is neglected which can be justified within the Born approximation. Subscripts $MM$, $NN$, and $MN$ denote the contributions from the interlayer scatterings between magnetic layers, between nonmagnetic layers, and between magnetic and nonmagnetic layers, respectively.

On the contrary, the single subscript $M(N)$ expresses the contribution from the intralayer scatterings within magnetic (nonmagnetic) layers.

On the contrary, when magnetic moments on the subsequent magnetic layers are in the ferromagnetic ($F$) configuration, the coherent potentials are given by $\Sigma_{ns}=\Lambda_s-i\Delta_s$ and $\Lambda_0-i\Delta_0$ for $n\in M_1$ (or $M_2$) and $n\in N_1$ (or $N_2$), respectively.[10] We get the parallel and perpendicular conductivities given by[10]

$$\sigma^{F\parallel}=\sum_s\left(\frac{c_{MM}}{\Delta_s}+\frac{c_{NN}}{\Delta_0}+\frac{8c_{MN}}{(\Delta_s+\Delta_0)}+\frac{d_M}{\Delta_s}+\frac{d_N}{\Delta_0}\right), \tag{10}$$

$$\sigma^{F\perp}=\left(\frac{e}{\hbar}\right)^2\nu^{\perp}N_f\sum_s\left(\frac{1}{2M\Delta_s+2N\Delta_0}\right). \tag{11}$$

The MR ratio $\Delta R/R$ is given from Eqs. (6), (7), (10), and (11) by

$$\left(\frac{\Delta R}{R}\right)^{\lambda}\equiv\frac{(R^{\mathrm{AF}}-R^F)}{R^F}=\frac{(\sigma^F-\sigma^{\mathrm{AF}})}{\sigma^{\mathrm{AF}}}$$

$$=\frac{(\alpha-\beta)^2}{4\alpha\beta}X^{\lambda}\quad(\lambda=\parallel,\perp), \tag{12}$$

with

$$\alpha=\Delta_{\uparrow}/\Delta_0,\quad \beta=\Delta_{\downarrow}/\Delta_0, \tag{13}$$

$$X^{\parallel}=\left[1+g_0\frac{(\alpha+\beta)^2}{\alpha\beta}+g_1\left(\frac{N}{M}\right)(\alpha+\beta)\left(\frac{1}{\alpha+1}+\frac{1}{\beta+1}\right)\right.$$

$$\left.+g_2\left(\frac{N}{M}\right)^2(\alpha+\beta)\right]^{-1}, \tag{14}$$

$$X^{\perp}=\left[1+\left(\frac{N}{M}\right)\left(\frac{1}{\alpha}+\frac{1}{\beta}\right)+\left(\frac{N}{M}\right)^2\left(\frac{1}{\alpha\beta}\right)\right]^{-1}. \tag{15}$$

In Eq. (14) $g_0$, $g_1$, and $g_2$ are defined by[10]

$$\frac{d_M}{4c_{MM}}=g_0,\quad \frac{2c_{MN}}{c_{MM}}=g_1\left(\frac{N}{M}\right),\quad \left(\frac{c_{NN}+d_N}{2c_{MM}}\right)=g_2\left(\frac{N}{M}\right)^2. \tag{16}$$

The expression for $(\Delta R/R)^{\perp}$ given by Eqs. (12) and (15) is just the same as that derived by Edwards and co-workers[20] using the resistor network model and has been employed for an analysis of experimental data on the perpendicular GMR.[14]

The temperature dependence of the GMR arises from those of $\alpha$ and $\beta$, which are expressed in terms of the coherent potentials of the film [Eq. (13)]. The imaginary part of the coherent potential in the magnetic ($M_1$ or $M_2$) layer is given within the Born approximation by[10]

$$\Delta_s=\Delta_s^r+\Delta_s^s+\Delta_s^p, \tag{17}$$

with

$$\Delta_s^r=\pi\rho_s xy\left[\tilde{\epsilon}^{\mathrm{A}}-\tilde{\epsilon}^{\mathrm{B}}-s\left(\frac{U^{\mathrm{A}}}{2}\right)\langle M^{\mathrm{A}}\rangle\right]^2, \tag{18}$$

$$\Delta_s^s=\pi\rho_s x\left(\frac{U^{\mathrm{A}}}{2}\right)^2[\langle(M^{\mathrm{A}})^2\rangle-\langle M^{\mathrm{A}}\rangle^2], \tag{19}$$

$$\Delta_s^p=P_m\rho_s Z(T/\Theta_m), \tag{20}$$

where $\tilde{\epsilon}^{\mathrm{A}}$ and $\tilde{\epsilon}^{\mathrm{B}}$ are the spin-independent Hartree–Fock potentials and $\rho_s$ is the density of states of an $s$-spin electron at the Fermi level. The first term ($\Delta_s^r$) in Eq. (17) arises from the scattering due to random Hartree–Fock potentials for an $s$-spin electron; the second term ($\Delta_s^s$) comes from the effect of spin fluctuations; the third term ($\Delta_s^p$) is introduced for phonon scatterings whose explicit form will be given shortly [Eq. (37)].

On the other hand, the imaginary part of the coherent potential in the nonmagnetic ($N_1$ or $N_2$) layer, is given by

$$\Delta_0=\Delta_0^r+P_n\rho_0 Z(T/\Theta_n), \tag{21}$$

where the first and second terms denote the contributions from random potentials and phonons, respectively, and $\rho_0$ is the density of states at the Fermi level of the nonmagnetic metal. In Eqs. (20) and (21) $\Theta_m$ and $\Theta_n$ are Debye temperatures, and $P_m$ and $P_n$ are related with the electron–phonon interactions in magnetic and nonmagnetic metals.

Using Eqs. (13) and (17)–(21), we get $\alpha$ and $\beta$ given by

$$\alpha=A\frac{[1+\gamma(T)]\{xy[B+m(T)]^2+x[\mu(T)^2-m(T)^2]+p_mZ(T/\Theta_m)\}}{[1+p_0Z(T/\Theta_n)]}, \tag{22}$$

$$\beta=A\frac{[1-\gamma(T)]\{xy[B-m(T)]^2+x[\mu(T)^2-m(T)^2]+p_mZ(T/\Theta_m)\}}{[1+p_0Z(T/\Theta_n)]}, \tag{23}$$

with

$$m(T)=\langle M^{\mathrm{A}}\rangle/M_0, \tag{24}$$

$$\mu(T)=\sqrt{\langle(M^{\mathrm{A}})^2\rangle}/M_0, \tag{25}$$

$$\gamma(T)=(\rho_{\uparrow}-\rho_{\downarrow})/(\rho_{\uparrow}+\rho_{\downarrow}), \tag{26}$$

$$A=\pi\rho(U^{\mathrm{A}}M_0/2)^2\Delta_0^r, \tag{27}$$

$$B=(2/U^{\mathrm{A}}M_0)(\tilde{\epsilon}_{\mathrm{B}}-\tilde{\epsilon}_{\mathrm{A}}), \tag{28}$$

$$p_m=P_m/\pi(U^{\mathrm{A}}M_0/2)^2, \tag{29}$$

$$p_0=P_n\rho_0/\Delta_0^r=p_mA(P_n/P_m)(\rho_0/\rho), \tag{30}$$

where $\rho=(1/2)(\rho_{\uparrow}+\rho_{\downarrow})$ and $M_0$ is the ground-state magnetic moment.

At $T=0$ K where $m(0)=\mu(0)=1$ and $\gamma(0)=\gamma_0$, Eqs. (22) and (23) become

$$\alpha_0=\alpha(T=0)=xyA(1+\gamma_0)(B+1)^2, \tag{31}$$

$$\beta_0=\beta(T=0)=xyA(1-\gamma_0)(B-1)^2, \tag{32}$$

from which the coefficients A and B are expressed in terms of $\alpha_0$, $\beta_0$, and $\gamma_0$ as

$$A=\frac{1}{4xy}\left[\left(\frac{\alpha_0}{1+\gamma_0}\right)^{1/2}-\left(\frac{\beta_0}{1-\gamma_0}\right)^{1/2}\right]^2, \tag{33}$$

$$B=\left[\left(\frac{\alpha_0}{1+\gamma_0}\right)^{1/2}+\left(\frac{\beta_0}{1-\gamma_0}\right)^{1/2}\right]\left[\left(\frac{\alpha_0}{1+\gamma_0}\right)^{1/2}-\left(\frac{\beta_0}{1-\gamma_0}\right)^{1/2}\right]^{-1}. \tag{34}$$

The normalized magnetic moment $m(T)$ and its rms value $\mu(T)$ are in principle calculated with the use of the finite-temperature band theory.[9(b)] We here, however, adopt simple, analytic expressions of $m(T)$ and $\mu(T)$ for our model calculation, given by[10]

$$m(T)=\sqrt{1-(T/T_C)^2}, \quad \mu(T)=1. \tag{35}$$

The temperature dependence of the spin asymmetry $\gamma(T)$ defined by Eq. (26) is assumed to be given by

$$\gamma(T)=\gamma_0 m(T). \tag{36}$$

As for the phonon contribution given by $Z(T/\Theta_m)$ in Eqs. (20) and (21), we adopt the simple Grüneisen function,

$$Z\left(\frac{T}{\Theta_m}\right)=\left(\frac{T}{\Theta_m}\right)^5\int_0^{\Theta_m/T}dz\frac{z^5}{(e^z-1)(1-e^{-z})}, \tag{37}$$

which is 124.43 $(T/\Theta_m)^5$ at $T/\Theta_m \ll 1$ and $T/4\Theta_m$ at $T/\Theta_m \gg 1$.

Now we may calculate the MR ratios, $(\Delta R/R)^{\parallel}$ and $(\Delta R/R)^{\perp}$, as a function of temperature with the use of Eqs. (12), (14), (15), (22), (23), (33)–(37), when we treat $\alpha_0$, $\beta_0$, $\gamma_0$, $g_0$, $g_1$, $g_2$, $T_C$, $\Theta_m$, $\Theta_n$, $p_m$, $p_0$, and $y$ as input parameters. Our strategy for calculating the temperature-and layer-thickness-dependent MR ratio is as follows: We first determine the parameters $\alpha_0$, $\beta_0$, and $\gamma_0$ to be consistent with the band calculation, and also $g_0$, $g_1$, and $g_2$ so as to reproduce the $N$ dependence of the observed, ground-state parallel GMR. Then fixing there six parameters thus determined, we calculate the finite-temperature GMR with the additional parameters $T_C$, $\Theta_m$, $\Theta_n$, $p_m$, $p_n$, and $y$, which can be properly chosen as is discussed in the model calculations of the following section.

## III. MODEL CALCULATIONS

### A. Fe/Cr multilayers

Gijs and co-workers have observed both the parallel and perpendicular GMR for a sample of (3 nm Fe+1.0 nm Cr) multilayer, whose results are plotted by circles and squares in Fig. 2, respectively.

First we consider the case of $T=4.2$ K. We determine the value of $\gamma_0=0.4$ from the ground-state band calculation of $\rho_\uparrow/\rho_\downarrow=2.3$.[21] We adopt $\alpha_0=7.9$ and $\beta_0=1.0$, leading to $B=3.38$ [Eq. (34)], which is consistent with the value estimated from Eq. (28) by using the band parameters such as $\tilde{\epsilon}^{\mathrm{Fe}}$, etc. We choose the parameters of $g_0=0.045$, $g_1=0.77$,

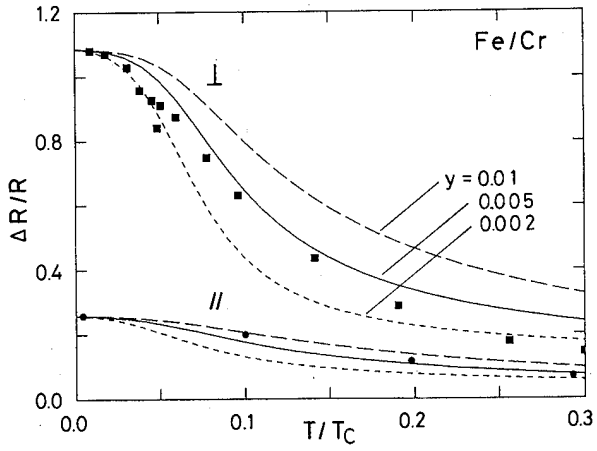



FIG. 2. The temperature dependence of the parallel (∥) and perpendicular $\Delta R/R(\perp)$ of (3 nm Fe+1.0 nm Cr) multilayers. Dotted, solid, and dashed curves denote the calculated results with $y=0.002$, 0.005, and 0.01, respectively, circles (squares) expressing the observed parallel (perpendicular) GMR (Ref. 15).

and $g_2=3.05$, such that we have a good fit to the envelope of the observed layer-thickness ($t_N$) dependence of parallel GMR in (3 nm Fe+$t_N$ Cr) multilayers.[11]

Next we consider the MR ratio at finite temperatures. We assume the Curie temperature of the multilayer of $T_C=1000$ K because the thickness of the Fe layers of the adopted Fe/Cr multilayers[11,15] is sufficiently thick to sustain the Curie temperature of bulk Fe. The Debye temperatures of Fe and Cr are assumed to be $\Theta_m=\Theta_n=460$ K. The phonon parameters $p_m$ and $p_0$ can be determined as follows: The total resistivity, $R$, of a pure, bulk metal is given from Eqs. (2), (3), and (22) by

$$R(T)\propto\left(\sum_s\left\{[1+s\gamma_0 m(T)]\left[\mu(T)^2-m(T)^2+p_m Z\left(\frac{T}{\Theta_m}\right)\right]\right\}^{-1}\right)^{-1}, \tag{38}$$

from which the ratio of the phonon contribution $R_p$ to the total resistivity at $T=T_C$ is given by

$$r_p\equiv R_p(T_C)/R(T_C)=p_m Z(T_C/\Theta_m)/[1+p_m Z(T_C/\Theta_m)].$$

The value of $p_m=0.69$ is chosen from the experimental data of $r_p=0.27$ of bulk Fe [Fig. 1(a)].[2] We calculate $p_0$ by $p_0=p_m A(\rho_0/\rho)$ derived from Eq. (30) with $P_n=P_m$ and $\rho_0/\rho=0.7$.[21] The solid curve in Fig. 1(a) expresses the resistivity $R(T)$ of bulk Fe calculated by using Eqs. (35), (37), and (38) with $\gamma_0=0.4$ and $p_m=0.69$, which well reproduces the observed data.[2]

The last parameter $y$, which expresses a concentration of nonmagnetic atoms in the magnetic layer and which depends on a sample employed in an experiment, is treated as an adjustable parameter. The parallel and perpendicular GMR of the Fe/Cr multilayer calculated with $y=0.002$, 0.005, and 0.01 are shown in Fig. 2. Our calculation with $y=0.005$ well explains both the $(\Delta R/R)^{\parallel}$ and $(\Delta R/R)^{\perp}$ observed by Gijs

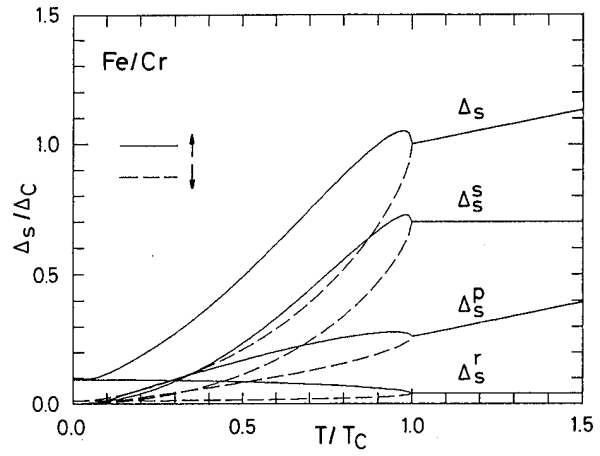



FIG. 3. The temperature dependence of $\Delta_s$ of up-spin (solid curves) and down-spin electrons (dashed curves) calculated with $y=0.005$ for the (3 nm Fe+1.0 nm Cr) multilayer. Also shown are their decomposition to various contributions from the random exchange potentials ($\Delta_s^r$), spin fluctuations ($\Delta_s^s$), and phonons ($\Delta_s^p$), the calculated results being normalized by $\Delta_C=\Delta_s(T_C)$.

and co-workers.[15] The strong temperature dependence of GMRs mainly comes from $(\alpha-\beta)^2/4\alpha\beta$ in Eq. (12); that of $X^{\parallel}$ and $X^{\perp}$ is fairly weak.

In order to study the temperature dependence of the GMR in more detail, we show in Fig. 3, $\Delta_s$ ($s=\uparrow,\downarrow$) as a function of the temperature. When the temperature is raised, $\Delta_\uparrow$ and $\Delta_\downarrow$ increase because of the contributions from spin fluctuations and phonons. Then the ratio $\Delta_\uparrow/\Delta_\downarrow(=\alpha/\beta)$ changes from 7.9 at $T=0$ to unity at $T\geqslant T_C$. Figure 3 also shows the decomposition of $\Delta_s$ to various contributions from random potentials ($\Delta_s^r$), spin fluctuations ($\Delta_s^s$), and phonon ($\Delta_s^p$). We note that at $T=T_C$, $\Delta^s/\Delta=0.70$, $\Delta^p/\Delta=0.26$, and $\Delta^s/\Delta^p=2.65$. This shows a significant spin-fluctuation contribution, as suggested from the resistivity data of bulk Fe.[2]

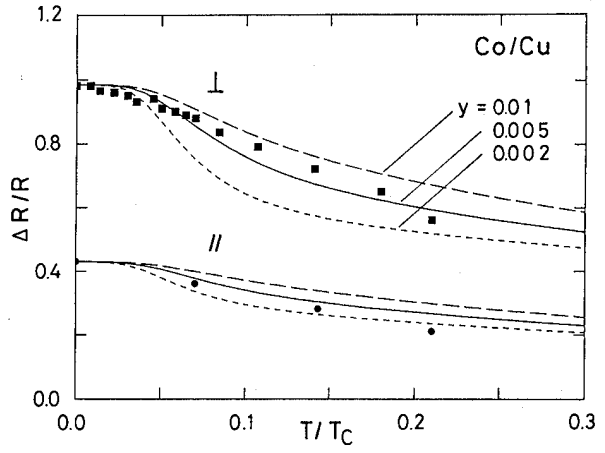



FIG. 4. The temperature dependence of the parallel (||) and perpendicualr $\Delta R/R(\perp)$ of (1.2 nm Co+1.1 nm Cu) multilayers. Dotted, solid, and dashed curves denote the calculated results with $y=0.002$, 0.005, and 0.01, respectively, circles (squares) expressing the observed parallel (perpendicular) GMR (Ref. 16).

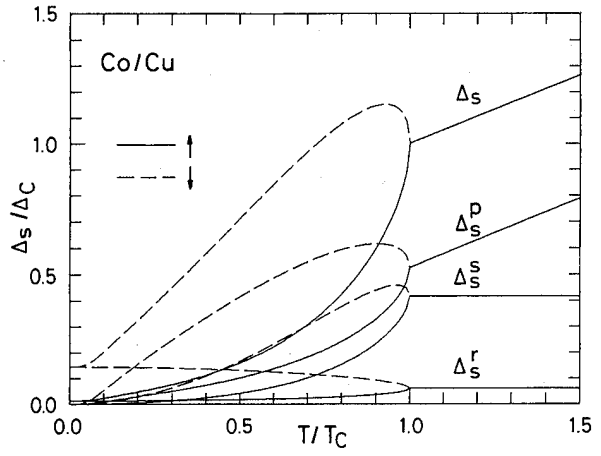



FIG. 5. The temperature dependence of $\Delta_s$ of up-spin (solid curves) and down-spin electrons (dashed curves) calculated with $y=0.005$ for the (1.2 nm Co+1.1 nm Cu) multilayer, (see caption of Fig. 3).

### B. Co/Cu multilayers

We have performed a similar calculation to explain the temperature dependence of parallel and perpendicular GMR of the (1.2 nm Co+1.1 nm Cu) multilayer observed by Gijs *et al.*[16] We adopt $\alpha_0=0.7$, $\beta_0=8.4$ $(\beta_0/\alpha_0=14)$,[16] and $\gamma_0=-0.7$, which comes from the ground-state band calculation of $\rho_\uparrow/\rho_\downarrow\sim0.15$ of bulk Co.[21] We cannot determine the values of $g_0$, $g_1$, and $g_2$ because the layer-thickness dependence of the parallel GMR of this series of samples has not been reported. Then we tentatively adopt $g_0=0.13$, $g_1=0.39$, and $g_2=0.11$ by scaling the data of similar Co/Cu multilayer[22] as to reproduce the observed ground-state value of $(\Delta R/R)^{\parallel}=0.43$.[16] The Curie and Debye temperatures are taken to be $T_C=1400$ K and $\Theta_m=\Theta_n=445$ K. We adopt $p_m=1.62$ from the observed ratio of $r_p=0.56$ for bulk Co [Fig. 1(b)],[3] and $\rho_0/\rho=0.3$.[21] The solid curve in Fig. 1(b) denotes the temperature-dependent resistivity of bulk Co calculated by using Eqs. (35), (37), and (38) with $\gamma_0=-0.7$ and $p_m=1.62$.

The calculated $(\Delta R/R)^{\parallel}$ and $\Delta R/R)^{\perp}$ of the Co/Cu multilayer are shown in Fig. 4, where $y$ is treated as an adjustable parameter. Both the parallel and perpendicular GMR observed by Gijs *et al.*[16] are fairly well explained by our calculation with $y=0.005$.

Figure 5 expresses the temperature dependence of $\Delta_s$ and its components $\Delta_s^r$, $\Delta_s^s$, and $\Delta_s^p$, which shows that at $T=T_C$, $\Delta^s/\Delta=0.42$, $\Delta^p/\Delta=0.53$, and $\Delta^s/\Delta^p=0.79$. Comparing these figures with the corresponding ones of Fe/Cr systems, we note that the spin-fluctuation contribution in Co/Cu multilayer is less significant than in the Fe/Cr multilayer. This fact is expected to be the main reason why the observed temperature dependence of the GMR in Co/Cu multilayer is less considerable than that in the Fe/Cr multilayers.

## IV. CONCLUSION AND DISCUSSION

We have discussed the temperature dependence of the GMR for currents parallel and perpendicular to the multilayer plane, including the random exchange potentials,

spin fluctuations, and phonons. Our model calculations have accounted for the following features of the observed GMR:[11,15,16]

(1) Both the parallel and perpendicular GMR are significantly more temperature dependent than the (average) layer moment;
(2) $(\Delta R/R)^{\perp}$ is larger than $(\Delta R/R)^{\parallel}$;
(3) the temperature dependence of $(\Delta R/R)^{\perp}$ is more significant than that of $(\Delta R/R)^{\parallel}$; and
(4) the temperature dependence of GMR in Co/Cu multilayers is less considerable than that in Fe/Cr multilayers.

The effect of spin fluctuations plays an important role to account for these items whereas phonons play a secondary role. In fact, items (1)–(3) can be explained without invoking phonons.[10] Item (2) can be understood as follows: Setting $N=0$ in Eqs. (12)–(15) for simplicity of explanation, we get

$$\left(\frac{\Delta R}{R}\right)^{\parallel}=\frac{(\alpha-\beta)^2}{4\alpha\beta[1+g_0(\alpha+\beta)^2/\alpha\beta]}, \tag{39}$$

$$\left(\frac{\Delta R}{R}\right)^{\perp}=\frac{(\alpha-\beta)^2}{4\alpha\beta}, \tag{40}$$

and the ratio of the parallel GMR to the perpendicular one is given by

$$(\Delta R/R)^{\parallel}/(\Delta R/R)^{\perp}=[1+g_0(a+1)^2/a]^{-1}\leqslant 1$$

$$(a=\alpha/\beta).$$

When electrons flow perpendicularly to the layer plane, all electrons pass through the adjacent two magnetic layers. On the contrary, this is not the case for currents parallel to the plane; some electrons go through only the one of the magnetic layers without probing the other magnetic layer. The $g_0$ term of the denominator of Eq. (39) [and of Eq. (14)] denotes this contribution. Itoh and co-workers[19] claim that the anisotropy of the velocity operator $v^{\parallel}/v^{\perp}\geqslant 1$ is the main mechanism leading to $(\Delta R/R)^{\parallel}\leqslant(\Delta R/R)^{\perp}$. The factor, $v^{\parallel}$ or $v^{\perp}$, is not, however, relevant because it is cancelled out when the MR ratio given by Eq. (12) is calculated.

In our phenomenological analysis given in Sec. II B we have included only the bulk scattering, neglecting the interface scattering whose importance has been pointed out by several experiments. We can extend our analysis as to take into account both the interface and bulk scatterings.[23] Numerical calculations using the generalized expressions for GMR which evitably include many parameters are in progress and will be reported in a separate article.[23]

## ACKNOWLEDGMENTS

This work is partly supported by a Grant-in-Aid for Scientific Research on Priority Areas from the Japanese Ministry of Education, Science, and Culture.

[1] For a review see, P. M. Levy, *Solid State Physics*, edited by H. Ehrenreich and D. Turnbull (Academic, New York, 1994), Vol. 47, p. 367.
[2] R. J. Weiss and A. S. Marotta, J. Phys. Chem. Solids **9**, 302 (1959).
[3] M. J. Laubitz and T. Matsumura, Can. J. Phys. **51**, 1247 (1973).
[4] P. G. de Gennes and J. Friedel, J. Phys Chem. Solids **4**, 71 (1958); T. Kasuya, Prog. Theor. Phys. **16**, 58 (1956).
[5] H. Hasegawa, Solid State Phys. (Jpn). **14**, 369 (1979); E. A. Turov and V. I. Greenikov, Physica B **149**, 150 (1988).
[6] *Electron Correlation and Magnetism in Narrow-Band Systems*, edited by T. Moriya (Springer, Berlin, 1981).
[7] H. Hasegawa, J. Phys. Soc. Jpn. **46**, 1504 (1979); **49**, 178 (1980).
[8] J. Mannari, Prog. Theor. Phys. **22**, 335 (1959); D. L. Mills and P. Lederer, J. Phys. Chem. Solids **27**, 1805 (1966); A. Fert, J. Phys. C **2**, 1784 (1969).
[9] (a) H. Hasegawa, in *Magnetic Properties of Low Dimensional Systems II*, edited by L. M. Falicov (Springer, Berlin, 1990), p. 175; (b) J. Magn. Magn. Mater. **126**, 384 (1993).
[10] (a) H. Hasegawa, Phys. Rev. B **47**, 15 073 (1993); (b) **47**, 15 080 (1993); (c) **51**, 3655 (1995); (d) J. Phys. Condens. Matter **6**, 21 (1994).
[11] M. A. M. Gijs and M. Okada, Phys. Rev. B **46**, 2908 (1992).
[12] H. Kubota, M. Sato, and T. Miyazaki, Phys. Rev. B **52**, 343 (1995).
[13] J. M. George, L. G. Pereira, A. Bathélémy, F. Petroff, L. Steren, J. L. Duvail, A. Fert, R. Loloee, P. Holody, and P. A. Schroeder, Phys. Rev. Lett. **72**, 408 (1994); J. P. Renard, P. Bruno, R. Mégy, B. Bartenlian, P. Beauvillain, C. Chappert, C. Dupas, E. Kolb, M. Mulloy, P. Veilet, and E. Vélu, Phys. Rev. B **51**, 12 821 (1995).
[14] W. Pratt, Jr., S. F. Lee, J. M. Slaughter, R. Loloee, P. A. Schroeder, and J. Bass, Phys. Rev. Lett. **66**, 3060 (1991).
[15] M. A. M. Gijs, S. K. J. Lenczowski, and J. B. Giesbers, Phys. Rev. Lett. **70**, 3343 (1993).
[16] M. A. M. Gijs, S. K. J. Lenczowski, R. J. M. van de Veerdonk, J. B. Giesbers, M. T. Johnson, and J. B. F. aan de Stegge, Phys. Rev. B **50**, 16 733 (1994).
[17] T. Valet and A. Fert, Phys. Rev. B **48**, 7099 (1993); A. Fert, T. Valet, and J. Barnas, J. Appl. Phys. **75**, 6693 (1994).
[18] H. E. Camblong, S. Zhang, and P. M. Levy, Phys. Rev. B **47**, 4735 (1993).
[19] H. Itoh, J. Inoue, and S. Maekawa, Phys. Rev. B **51**, 342 (1995).
[20] D. M. Edwards, J. Mathon, and R. B. Muniz, IEEE Trans. Magn. **MAG-27**, 3548 (1991).
[21] V. L. Moruzzi, J. F. Janak, and A. R. Williams, *Calculated Properties of Metals* (Pergamon, New York, 1978).
[22] D. H. Mosca, F. Petroff, A. Fert, P. A. Schroeder, W. P. Pratt, Jr., and R. Laloee, J. Magn. Magn. Mater. **94**, L1 (1991).
[23] H. Hasegawa (unpublished).

# Currents at angle to the planes of the layers (abstract)

P. M. Levy and S. Zhang
*Department of Physics, New York University, 4 Washington Place, New York, New York 10003*

T. Ono and T. Shinjo
*Institute for Chemical Research, Kyoto University, Uji 611, Kyoto, Japan*

A new class of *corrugated* multilayers has been grown on silicon substrates which have (111) faceted grooves etched on their surface.[1] These structures can be probed by conventional means with current at an *angle* to the plane of layers (CAP) as well as CIP. This angle is fixed by: the depth to width ratio of the grooves (which determines the angle $\theta$), and the angle $\phi$ of the current probes with respect to the grooves. We have prepared multilayers of [Co(12 Å) Cu($t$)NiFe(12 Å) Cu($t$)]$_y$ with $t$=58 and 116 Å, and $y$=167 and 91 repeats, respectively; and have varied $\phi$ from 0 and 90° while $\theta$ is held fixed at 54.7°. We find the data is very well fit to the theoretical expression for CAP resistivity in terms of the more conventional CIP and CPP resistivities.[2] From measurements of the CIP and CAP–MR's on these corrugated multilayers we are able to *predict* the CPP–MR for these structures. © *1996 American Institute of Physics.* [S0021-8979(96)61908-6]

This work is supported in part by the Office of Naval Research.

[1] T. Ono and T. Shinjo, J. Phys. Soc. Jpn. **64**, 363 (1995).
[2] P. M. Levy, S. Zhang, T. Ono, and T. Shinjo, Phys. Rev. B **52**, 16049 (1995).

 0021-8979/96/79(8)/6382/1/$10.00 © 1996 American Institute of Physics

# Oblique electron transport in the presence of collinear and noncollinear magnetizations

Horacio E. Camblong
*Department of Physics, University of San Francisco, San Francisco, California 94117*

The nonlocal real-space Kubo approach to electron transport in magnetic multilayers is applied to a new geometry, "oblique transport," whose complexity is traced back to a combination of the layering, of the nonlocal character of the linear response, and of the oblique direction transport in this new geometry. The problem is dealt with by applying a condition on the average current density vector or on the average electric-field vector, depending upon the external driving conditions. Its solution exhibits a characteristic anisotropy and it yields the global oblique conductance and magnetoresistance as simple trigonometric expressions in terms of the in-plane and vertical conductances and magnetoresistances, for arbitrary noncollinear-magnetization configurations. © *1996 American Institute of Physics.*[S0021-8979(96)56308-8]

Electrical transport in metallic multilayers is fairly well understood and its applications to giant magnetoresistance have confirmed the validity of the various models that have been used, namely, the quasiclassical approach[1] (based on the Boltzmann equation) and the Kubo approach.[2–5]

Previous theoretical analyses of magnetotransport in multilayers have only dealt with the special cases of in-plane transport (CIP) and vertical transport (CPP). Of course, there is a continuum of alternative geometries with the current neither in the plane of the layers nor perpendicular to the plane of the layers. Any such geometry is referred to as "oblique transport." The electric-field and current patterns for oblique transport are more involved than for CIP or CPP because variations in the local resistivity give rise to changes in the directions of the fields and currents from layer to layer. Actually, a version of this new geometry has been recently explored experimentally[6] using a corrugated metallic multilayered structure.[7]

A typical oblique-transport scenario is shown in Fig. 1, where $z$ is a coordinate along the multilayer axis (or growth direction) and $\zeta$ is a coordinate along the "external driving direction," which I define as the direction of the average "driving field" $\mathbf{V}$. In practice, the driving field $\mathbf{V}$ will be either the current density $\mathbf{j}$ or the electric field $\mathbf{E}$; this leads to two outstanding boundary conditions: a "current-injection condition," when the direction of $\langle \mathbf{j} \rangle$ is externally fixed (for example, by proper insertion of current probes), and a "voltage condition," when the direction of $\langle \mathbf{E} \rangle$ is externally controlled. The parameter $\alpha$, which is defined as the angle between the axes $z$ and $\zeta$ (with $0° \leqslant \alpha \leqslant 90°$) measures the deviation of a particular oblique-transport geometry from either CIP ($\alpha=90°$), or CPP ($\alpha=0°$). These two coordinates are related via $\zeta = z \cos\alpha$, with a suitable choice of origin for both. Correspondingly, unit vectors along the external driving direction $\mathbf{e}_\zeta$, along the growth direction $\mathbf{e}_z$, and along the in-plane direction $\mathbf{e}_x$ satisfy the relations $\mathbf{e}_\zeta \cdot \mathbf{e}_z = \cos\alpha$ and $\mathbf{e}_\zeta \cdot \mathbf{e}_x = \sin\alpha$. In addition, it is clear that averages over $z$ and over $\zeta$ of $z$-dependent quantities are identical, i.e.,

$$\langle f(z) \rangle_z = \langle f(\zeta/\cos\alpha) \rangle_\zeta . \tag{1}$$

As a consequence of the relations above, it follows that the component $A_\zeta(z)$ of any vector $\mathbf{A}(z)$ that is only $z$ dependent (for example, the current densities or the internal fields) has an average [cf. Eq. (1)]

$$\langle A_\zeta(z) \rangle = \sin\alpha A_\parallel + \cos\alpha A_\perp . \tag{2}$$

The analysis presented in this article is based on Eqs. (1) and (2), which are of interest when the relevant physical quantities (fields and currents) are essentially only $z$ dependent. Of course, this assumption breaks down near the external boundaries. Thus, for the computation of global properties, the analysis is valid when edge effects are globally unimportant.

The resulting transport behavior can be described most easily by using the real-space Kubo approach,[3,4] wherein the general nonlocal linear relationship between the currents $\mathbf{j}_{\alpha\beta}(z)$ and the fields $\mathbf{E}_{\gamma\delta}(z')$ can be written as

$$\mathbf{j}_{\alpha\beta}(z) = \int dz' \sigma_{\alpha\beta,\gamma\delta}(z,z') \mathbf{E}_{\gamma\delta}(z'), \tag{3}$$

where the Greek indices label the two spin channels ($\alpha = \uparrow, \downarrow$), $\sigma_{\alpha\beta,\gamma\delta}(z,z')$ is the spin-dependent two-point conductivity, and Einstein's summation convention for repeated indices has been applied. In Eq. (3) the complex structure of

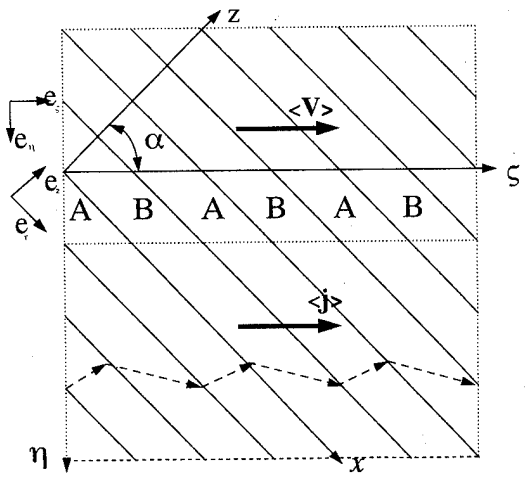



FIG. 1. Schematic representation of the oblique-transport geometry for a binary A/B superlattice grown along the $z$ direction. The dotted lines represent the bounds of a typical region; it is assumed that the system extends to infinity in both directions along the $\eta$ axis and that, if drawn to scale, many more layers would be encountered along the $\zeta$ axis. The lower part of the figure gives a graphical representation in terms of current lines of the current-injection condition (with $\sigma_A < \sigma_B$); the voltage-condition construction is not shown as it is more convoluted.

 0021-8979/96/79(8)/6383/3/$10.00 © 1996 American Institute of Physics 

spin indices is a convenient way of dealing with noncollinear magnetizations. In this framework the internal fields $\mathbf{E}_{\alpha\beta}(z)$ absorb the vertex corrections[4] that correspond to long-range diffusion processes and acquire a spin dependence that can be thought of as arising from electrochemical potentials.[8,9]

The geometries studied so far are simple in that either the current or the fields are essentially uniform: For CIP the external fields $\mathbf{E}_{\gamma\delta}(z)$ are constant (if a uniform external electric field is applied) and for CPP the current densities $\mathbf{j}_{\alpha\beta}(z)$ are constant. Instead, for oblique transport, both the currents and the fields are position dependent (even for a uniform external electric field) and their directions are not fixed in space. This complexity can be tackled by resolving all vector fields into components parallel ($\|$) and perpendicular ($\perp$) to the plane of the layers. This construction is useful due to the fact that geometrical symmetries associated with the multilayered system reduce both the spatial dependence and the vector structure of the two-point conductivity to a simple form. In effect, if edge effects are neglected, the two-point conductivity is only a function of $z$ (twice) and that it admits the resolution into irreducible components: an in-plane or CIP component, $\sigma^{(\|)}_{\alpha\beta,\gamma\delta}(z,z')$, and a vertical or CPP component, $\sigma^{(\perp)}_{\alpha\beta,\gamma\delta}(z,z')$. Explicitly,

$$\sigma_{\alpha\beta,\gamma\delta}(z,z')=\mathbb{1}_{\|}\sigma^{(\|)}_{\alpha\beta,\gamma\delta}(z,z')+\mathbf{e}_z\mathbf{e}_z\sigma^{(\perp)}_{\alpha\beta,\gamma\delta}(z,z'), \tag{4}$$

where $\mathbb{1}_{\|}$ is the unit tensor in the plane of the layers, and $\mathbf{e}_z$ is the unit vector in the $z$ direction. The approach of Refs. 3 and 4 yields the components of the two-point conductivity, $\sigma^{(r)}_{\alpha\beta,\gamma\delta}(z,z')$ (with $r=\|,\perp$), whose nonlocal spatial dependence is governed by the inverse length $\xi(z)$, that is proportional to $\Delta(z)$, the local scattering strength (imaginary part of the self-energy). Then, the resolution of the two-point conductivity into irreducible components, which is expressed by Eq. (4), leads to two independent problems. The CIP problem,

$$j^{(\|)}_{\alpha\beta}(z)=\sigma^{(\|)}_{\alpha\beta,\gamma\delta}(z)E^{(\|)}_{\gamma\delta}, \tag{5}$$

has an apparent local character that is just an artifact generated by the uniformity of the externally applied electric field; in fact, Eq. (5) is formulated in terms of the one-point conductivity[2,3] $\sigma^{(\|)}_{\alpha\beta,\gamma\delta}(z)$, which is the integral of the two-point conductivity with respect to $z'$ and it governs the characteristic CIP exponential size effects (nonlocal effects), a result that is in agreement with experiments [see Eq.(8)]. On the other hand, the CPP problem,

$$E^{(\perp)}_{\alpha\beta}(z)=\rho_{\alpha\gamma}(z)j^{(\perp)}_{\gamma\delta}, \tag{6}$$

is formulated in terms of the local resistivity[4,9] $\rho^{(\perp)}_{\alpha\beta}(z)=C_D^{-1}\xi_{\alpha\beta}(z)$, which is a completely local quantity determined by the local scattering rate; this problem has the remarkable feature that the global conductance has no exponential size effects and is wholly determined by the so-called series resistor model or the average scattering,[9–11] a prediction that has been found to be in impressive agreement with experimental results.[12]

In summary, the problems formulated by Eqs. (5) and (6) solve specifically in-plane and vertical transport. In addition, they can be used as the building blocks for oblique transport, as shown below.

For oblique transport it is necessary to consider the "matching" boundary conditions satisfied by the internal fields and the currents across the interfaces: namely, continuity of the tangential components of the fields $\mathbf{E}^{(\|)}_{\alpha\beta}$ and continuity of the normal components of the currents $\mathbf{j}^{(\perp)}_{\alpha\beta}$. The condition on the internal fields follows from their irrotational character when defined in terms of the vertex corrections to the conductivity,[4] whereas the condition on the currents expresses the independence of the spin channels, i.e., the two-independent current model, an approximation that is valid when the spin-diffusion length is large (compared to the relevant scales for multilayers).[4]

Let us now investigate the variation in the directions of the fields and currents from layer to layer. The relationship between the fields and currents is indeed given by the nonlocal Eq. (3). However, from Eqs. (4)–(6), it follows explicitly that for a uniform externally applied electric field the corresponding internal fields are

$$\mathbf{E}_{\alpha\beta}(z)=\mathbf{e}_z\rho_{\alpha\gamma}(z)j^{(\perp)}_{\gamma\beta}+\mathbf{e}_{\|}\rho^{(\|)}_{\alpha\beta,\gamma\delta}(z)j^{(\|)}_{\gamma\delta}(z), \tag{7}$$

where $\rho^{(\|)}_{\alpha\beta,\gamma\delta}(z)$ is the matrix inverse with respect to $\gamma\delta$ of the one-point conductivity $\sigma_{\alpha\beta,\gamma\delta}(z)$. The interfacial boundary conditions further imply that $j^{(\perp)}$ and $E^{(\|)}$ (second term) are constant. The two terms in Eq. (7) behave very differently because $\rho_{\alpha\gamma}(z)$ is a purely local quantity whereas $\rho^{(\|)}_{\alpha\beta,\gamma\delta}(z)$ has a nonlocal dependence through the local mean free paths. Let us see the limiting forms of $\rho^{(\|)}_{\alpha\beta,\gamma\delta}(z)$: In the local limit (short mean free paths compared with layer thicknesses) it is asymptotically a tensor with components given by various rearrangements of indices of $\rho_{\alpha\gamma}(z)$, whereas in the homogeneous limit (long mean free paths compared with layer thicknesses) it is asymptotically given by $C_D^{-1}\bar{\xi}$. These different limiting behaviors indicate that, in the local limit, $\mathbf{E}$ is locally parallel to $\mathbf{j}$ but globally nonparallel, whereas in the homogeneous limit, $\mathbf{E}$ is globally parallel to $\mathbf{j}$ but locally nonparallel. In other words, the geometrical anisotropy associated with the layering prevents the currents and fields from being parallel to each other; thus, the medium behaves phenomenologically in an anisotropic way both locally and globally, a result that can be understood in terms of charge accumulation: Charges accumulate on the various interfaces to respect the various interfacial boundary conditions.

Averaging Eqs. (5) and (6) over the external-direction axis $\zeta$ gives

$$\langle j^{(\|)}\rangle=\sigma_{\mathrm{CIP}}E^{(\|)} \tag{8}$$

and

$$\langle E^{(\perp)}\rangle=\rho_{\mathrm{CPP}}j^{(\perp)}, \tag{9}$$

where the averages are with respect to either $z$ or $\zeta$ [see Eq. (1)]. In Eq. (8)

$$\sigma_{\mathrm{CIP}}=\langle\sigma^{(\perp)}_{\alpha\alpha,\gamma\gamma}(z)\rangle \tag{10}$$

(with Einstein's summation convention for repeated indices) is the CIP global conductivity[4] and in Eq. (9)

$$\rho_{CPP}=(\sigma_{CPP})^{-1}=C_D^{-1}\,[\mathrm{Tr}(\bar{\xi}^{-1})]^{-1} \tag{11}$$

is the global CPP resistivity, with $\bar{\xi}=\langle\xi\rangle$ being proportional to the average scattering.[4]

The directly measurable quantities are the total voltage per unit length across the sample in the external driving direction,

$$\frac{V}{L}=\frac{1}{L}\int \mathbf{E}\cdot d\mathbf{r}=\langle E_\zeta\rangle=\sin\,\alpha E^{(\parallel)}+\cos\,\alpha\langle E^{(\perp)}\rangle, \tag{12}$$

[where $L$ is the length of the sample along the external-driving direction, see Eq. (2)], and the average current density along the driving direction,

$$\langle j_\zeta\rangle=\sin\,\alpha\langle j^{(\parallel)}\rangle+\cos\alpha j^{(\perp)}. \tag{13}$$

In order to extract a global or measurable resistance from Eqs. (12) and (13), it is necessary to apply the external boundary conditions (see Fig. 1): either the current-injection condition, which is defined by

$$\langle\mathbf{j}\rangle=\mathbf{e}_\zeta\langle j_\zeta\rangle, \tag{14}$$

or the voltage condition, which is defined by

$$\langle\mathbf{E}\rangle=\mathbf{e}_\zeta\langle E_\zeta\rangle. \tag{15}$$

Definition of the global resistivity as

$$\rho=\frac{\langle E_\zeta\rangle}{\langle j_\zeta\rangle} \tag{16}$$

leads to the following results:

$$\rho_1=\rho_{CIP}\,\sin^2\,\alpha+\rho_{CPP}\,\cos^2\,\alpha, \tag{17}$$

for current-injection conditions, and

$$\sigma_2=\sigma_{CIP}\,\sin^2\,\alpha+\sigma_{CPP}\,\cos^2\,\alpha. \tag{18}$$

for external-voltage conditions. Equations (17) and (18) are the main results of this article. They reduce to the familiar expressions $\rho(\alpha=90°)=\rho_{CIP}$ and $\rho(\alpha=0°)=\rho_{CPP}$, and they have the characteristic angular dependence of a quadratic form, i.e., they amount to the existence of a global resistivity tensor

$$\boldsymbol{\rho}_1=\mathbb{1}_\parallel\rho_{CIP}+\mathbf{e}_z\mathbf{e}_z\rho_{CPP} \tag{19}$$

(such that $\rho=\mathbf{e}_\zeta\cdot\boldsymbol{\rho}\cdot\mathbf{e}_\zeta$) for current-injection conditions and to the existence of a global conductivity tensor

$$\boldsymbol{\sigma}_2=\mathbb{1}_\parallel\sigma_{CIP}+\mathbf{e}_z\mathbf{e}_z\sigma_{CPP} \tag{20}$$

(such that $\sigma=\mathbf{e}_\zeta\cdot\boldsymbol{\sigma}\cdot\mathbf{e}_\zeta$) for external-voltage conditions.

The angular dependence of the magnetoresistance with respect to $\alpha$ can be derived straightforwardly from Eqs. (17) and (18). The main consequence stemming from this analysis for the resistivity and magnetoresistance is that the oblique-transport values are in between those for CIP and CPP, with the CPP values being the largest; this is because CPP is exactly self-averaging.[4]

In conclusion, I have calculated the oblique-transport electrical resistivity/conductivity and found that, as a consequence of the layering and if edge effects are unimportant, it is given as a quadratic form in the orientation of the external-driving direction, with an anisotropic resistivity/conductivity tensor composed of the global CIP and CPP resistivities/conductivities, for current-driving/external-voltage conditions. These results may be of help in the implementation of detailed phenomenological analyses of magnetotransport in magnetic multilayers.

## ACKNOWLEDGMENTS

I would like to thank Professor P. M. Levy for providing a copy of his work prior to publication. This work was supported in part by the University of San Francisco Faculty Development Fund.

[1] R. E. Camley and J. Barnás, Phys. Rev. Lett. **63**, 664 (1989); J. Barnás, A. Fuss, R. E. Camley, P. Grunberg and W. Zinn, Phys. Rev. B **42**, 827 (1992).
[2] P. M. Levy, S. Zhang, and A. Fert, Phys. Rev. Lett. **65**, 1643 (1990); S. Zhang, P. M. Levy, and A. Fert, Phys. Rev. B **45**, 8689 (1992).
[3] H. E. Camblong and P. M. Levy, Phys. Rev. Lett. **69**, 2835 (1992); J. Magn. Magn. Mater. **121**, 446 (1993); H. E. Camblong, Phys. Rev. B **51**, 1855 (1995).
[4] H. E. Camblong, P. M. Levy, and S. Zhang, Phys. Rev. B **51**, 16 052 (1995).
[5] A. Vedyayev, B. Dieny, and N. Ryzhanova, Europhys. Lett. **19**, 329 (1992).
[6] T. Ono and T. Shinjo, J. Phys. Soc. Jpn. **64**, 363 (1995).
[7] After completion of this article I have learned that a somewhat similar analysis of oblique transport is presented in P. M. Levy, S. Zhang, T. Ono, and T. Shinjo, Phys. Rev. B **52**, 16 049 (1995).
[8] P. M. Levy, H. E. Camblong, and S. Zhang, J. Appl. Phys. **75**, 7076 (1994).
[9] H. E. Camblong, S. Zhang, and P. M. Levy, Phys. Rev. B. **47**, 4735 (1993).
[10] S. Zhang and P. M. Levy, J. Appl. Phys. **69**, 4786 (1991).
[11] H. E. Camblong and P. M. Levy, J. Appl. Phys. **73**, 5533 (1993).
[12] W. P. Pratt, Jr., S.-F. Lee, J. M. Slaughter, R. Loloee, P. A. Schroeder, and J. Bass, Phys. Rev. Lett. **66**, 3060 (1991); S.-F. Lee, W. P. Pratt, Jr., Loloee, P. A. Schroeder, and J. Bass, Phys. Rev. B **46**, 548 (1992).

# Simulating device size effects on magnetization pinning mechanisms in spin valves[a)]

J. O. Oti, R. W. Cross, and S. E. Russek
*National Institute of Standards and Technology, Boulder, Colorado 80303*

Y. K. Kim
*Quantum Peripherals Colorado, Inc., Louisville, Colorado 80028*

The effects of magnetostatic interactions on the giant magnetoresistive (GMR) response of NiFe/Cu/NiFe spin valves are studied using an analytical model. The model is applicable to devices small enough for the magnetic layers to exhibit single-domain behavior. Devices having lengths in the track-width direction of 10 $\mu$m and interlayer separations of 4.5 nm are studied. Stripe heights are varied from 0.5 to 2 $\mu$m. The magnetization of one magnetic layer is pinned by a transverse pinning field that is varied from 0 to 24 kA/m (300 Oe). GMR curves for transverse fields are calculated. At zero external field the magnetization of the layers shows a tendency to align themselves antiparallel in the transverse direction. This results in an offset from the ideal biasing of the device. Broadening of the curves due to shape anisotropy occurs with decreasing stripe height and increasing magnetic layer thickness, and the magnetization in the pinned layer becomes less stable. © *1996 American Institute of Physics.* [S0021-8979(96)56408-X]

## INTRODUCTION

Spin valves[1] are being actively investigated as promising read-head materials in ultrahigh-denisty magnetic recording. This is because of their relatively simple structure and high sensitivity to external fields. In this work, spin valves are studied using an analytical model that is an extension to two layers of a Stoner–Wohlfarth single-layer model.[2,3] Our model differs from other analytical spin-valve models,[4] by including interlayer magnetostatic interaction effects and the ability to model magnetic layers using general ellipsoidal shapes.

The micromagnetic model is applicable to devices that are small enough in size for the magnetic layers to exhibit single-domain behavior. The transition width of a Néel domain wall in a magnetic thin film increases with decreasing film thickness. For a small enough sample, the transition width exceeds the film dimensions, so that the film is no longer capable of sustaining domain walls. The film then becomes single domain. In Ref. 2, single-domain behavior was observed in magnetoresistive NiFe films having stripe heights less than 2 $\mu$m and film thicknesses less than 10 nm.

Figure 1 shows schematically the three-layer spin-valve structure studied in this work. Two NiFe layers of length $l$, stripe height $w$, and thickness $t$ are separated by a Cu spacer layer of thickness $d$. Current $I$ flows longitudinally through the device. The magnetization **M** of the top NiFe layer is exchange pinned transversely by an antiferromagnetic overcoat layer (not shown in the figure), while the magnetization of the bottom layer is free to rotate. The device is ideally biased if, in the absence of an external field, the magnetization of the layers orient perpendicular to each other in the plane of the film, as shown in Fig. 1(a). Figure 1(b) shows the giant magnetoresistance (GMR) response curve of an ideally biased spin valve. A description of the micromagnetic model is given in the following section. The model is used in a systematic study of the dependence of GMR response on stripe height and pinning-field strength.

## MODEL OF SPIN VALVE

The magnetic layers of a spin valve are treated as single-domain films, and their magnetic behaviors are modeled using the Stoner–Wohlfarth coherent rotation model of the magnetization reversal of a uniformly magnetized ellipsoid. Brown[5] showed that the magnetic behavior of any uniformly

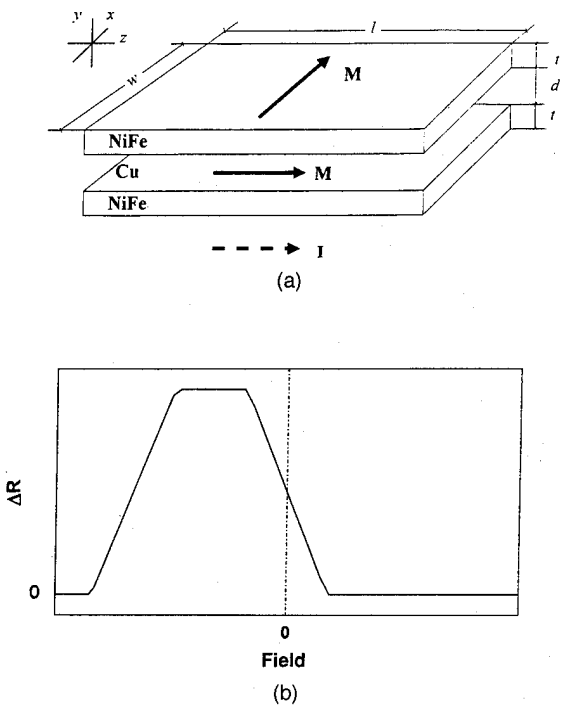
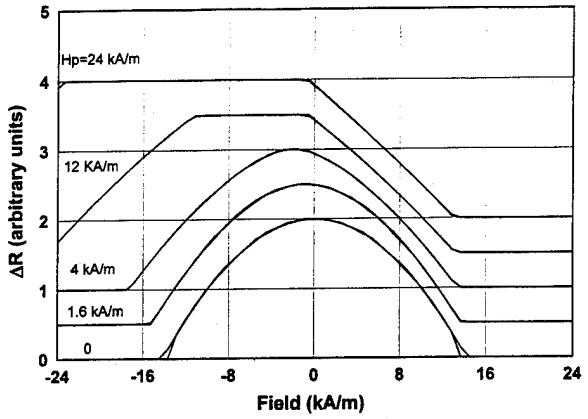


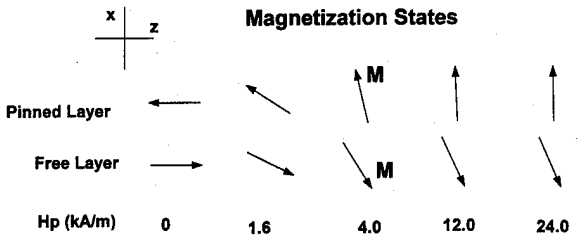

FIG. 1. (a) Schematic of modeled spin valve structure; (b) GMR response of ideally biased spin valve.

[a)]Contribution of the National Institute of Standards and Technology, not subject to copyright.

 0021-8979/96/79(8)/6386/3/$10.00 © 1996 American Institute of Physics




(a)




(b)

FIG. 2. (a) GMR response curves as a function pinning field $H_p$, for devices with stripe height $w=2$ $\mu$m and magnetic layer thickness $t=10$ nm. The curves are displaced vertically from each other for clarity; (b) magnetization states at zero field of the devices in the pinned layer (top arrows) and free layer (bottom arrows).

magnetized body could be modeled as that of an appropriate equivalent ellipsoid, which has the same principal axes and volume as the actual body. For a body in the form of a rectangular film the demagnetizing factors of the equivalent ellipsoid along the principal axes are equal to the magnitudes of the volume-average demagnetizing fields per unit magnetization inside the film, when it is magnetized along its principal axes. The field sources of a uniformly magnetized film are the surface magnetic charges formed on its bounding faces. The field due to such a face can be expressed in closed form.[6]

The free energy density of the pinned magnetic layer, consisting of the self-demagnetization and the applied field terms, is given by the expression

$$W=\tfrac{1}{2}M_s^2(N_x\alpha^2+N_y\beta^2+N_z\gamma^2) - |\mathbf{H_o}+\mathbf{H_p}+\mathbf{H_m}(M_s')|M_s(l\alpha+m\beta+n\gamma), \quad (1)$$

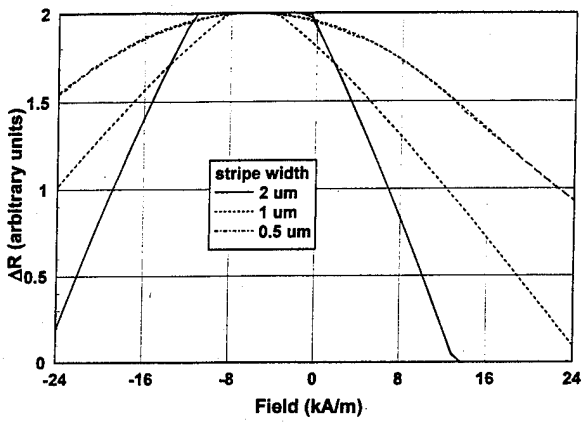
where $\mathbf{H}_o$ is the externally applied field; $\mathbf{H}_p$ is the pinning field; $\mathbf{H}_m(M_s')$ is the interlayer magnetostatic interaction field, and is equal to the volume-average field acting on the film due to the magnetization $M_s'$ of the free layer; $\alpha$, $\beta$, and $\gamma$ are the direction cosines of the magnetization of the film $M_s$; $l$, $m$, and $n$ are the direction cosines of the total field $\mathbf{H}_o+\mathbf{H}_p+\mathbf{H}_m(Ms_s')$, and $N_x$, $N_y$, and $N_z(N_x+N_y+N_z=1)$ are the demagnetizing factors along the three principal axes of the film.

Surface charges on the boundaries of the actual rectangular geometry of the magnetic film are the field sources used in calculating $\mathbf{H}_m$. Other fields, such as the self-field due to current flowing through the device, and possible effective exchange interaction field between the magnetic layers, may be included in the applied-field term in Eq. (1) if needed. These additional field terms were not considered in this work. An expression similar to Eq. (1) follows for the energy density of the free layer, by interchanging the roles of $M_s$ and $M_s'$ and omitting the pinning field term. For the free layer, $\mathbf{H}_m$ is the interlayer magnetostatic interaction field acting on it due to the magnetization of the pinned layer.

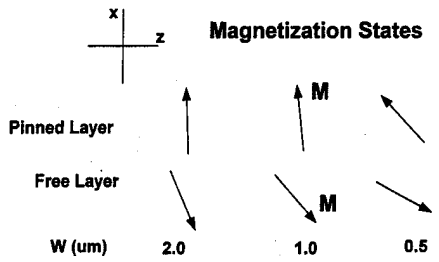
The direction cosines $\alpha$, $\beta$, and $\gamma$ are related to the azimuthal and polar angular coordinates $\theta_M$, $\phi_M$ of the magnetization vector, by $\alpha=\sin\theta_M\cos\phi_M$, $\beta=\sin\theta_M\sin\phi_M$, and $\gamma=\cos\theta_M$. The spin valve is subjected to a uniform external field that is varied step-wise. The magnetization dependence of $\mathbf{H}_m$ necessitates the use of iterative methods in minimizing the energy of the interacting magnetic layers. The expression in parenthesis in the self-demagnetization term of Eq. (1) is precomputed and stored as a function of the angular coordinates. These values are calculated only for one quadrant of space; the values for other quadrants can be found by symmetry. Beginning from an initial magnetization state of the layers, the stored values are used to compute the energy functional $W(\theta_M,\phi_M)$ according to Eq. (1) in each of the magnetic layers. The angular coordinates corresponding to the minima of $W(\theta_M,\phi_M)$ in the magnetic layers are found and used to obtain the first approximations of the magnetization of the layers. These approximations are used to recalculate $\mathbf{H}_m$ and a new energy functional, from which the next approximation to the magnetization is obtained. This procedure is repeated until the magnetization of the layers converges to equilibrium. During iteration, the $(l\alpha+m\beta+n\gamma)$ term continually changes as $\mathbf{H}_m$ changes with the magnetization of the layers. The initial magnetization states used at the beginning of the iteration are the solution states from the preceding external field. The first solution when the external field is initially applied is obtained by assuming that the magnetization of the layers are initially pointing in the positive $z$ direction. The solution space for the magnetization of a single layer depends on the history of the magnetization process, and the search for possible solutions having angular coordinate $\theta_M=0$ requires special treatment. The switching of the magnetization of each layer occurs as its free energy reaches an unstable threshold, changing from a minimum to maximum energy state. These issues are described in detail in Ref. 3. The change in the magnetoresistance of the spin valve is calculated using the expression $\Delta R=1-\cos\theta$, where $\theta$ is the angle between the magnetization vectors of the layers.

## SIMULATION RESULTS

The spin valves simulated in this work have length $l=10$ $\mu$m, nonmagnetic spacer thickness $d=4.5$ nm, and magnetic layers with magnetization $M=800$ kA/m. The GMR response curves for the devices are calculated for an external transverse field (acting along $x$ axis in Fig. 1) that is cycled between $\pm 24$ kA/m (300 Oe). GMR response curves calculated




(a)




(b)

FIG. 3. (a) GMR response curves as a function of stripe width $w$, for devices with magnetic layer thickness $t=10$ nm and pinning field $H_p=12$ kA/m; (b) magnetization states at zero field of the devices in the pinning (top arrows) and free (bottom arrows) layers.

using different pinning fields, for devices having stripe height $w=2$ $\mu$m and magnetic layer thickness $t=10$ nm, are plotted in Fig. 2(a). The zero-field magnetization states of the devices given by the orientations of the magnetization vectors in the pinned and free layers are shown in Fig. 2(b). The shape anisotropy of the magnetic layers causes the magnetization vectors to lie completely in the plane of the magnetic films. For moderately pinned devices ($H_p \leq 4$ kA/m), self-demagnetizing fields in the pinned layer result in considerable canting, away from the transverse direction, of the magnetization vectors at zero field. Pinning is improved as $H_p$ is increased.

Magnetostatic coupling between the magnetic layers favors the antiparallel orientation of the magnetization of the layers. This antiparallel orientation is pronounced in moderately pinned devices. In strongly pinned devices ($H_p=12$ and 24 kA/m), the rotation of the free layer is opposed by the self-demagnetization of the layer. Interlayer magnetostatic interaction thus results in the deviation of the GMR responses of the spin valves from that of the ideal biased state of Fig. 1. The positive saturation fields of the GMR curves decrease slightly as the pinning field is increased. This is due to a reduction in the work required to rotate the magnetization of both magnetic layers toward parallel alignment in the transverse direction against the interlayer magnetostatic interactions opposing this rotation. The peaks of the GMR curves get broader and flatter as the pinning field is increased, and the negative saturation fields increase.

Self-demagnetization effects in the devices increase as stripe heights are made smaller. The effect of decreasing the stripe height on the GMR response and magnetization states of the devices is shown in Fig. 3. The figure was obtained for devices with magnetic layer thickness of 10 nm and pinning field 12 kA/m. Decreasing the stripe height increases the canting of the magnetization of the pinned layers and increases the broadening of the GMR curves.

## DISCUSSION

An analytical micromagnetic model of interacting single-domain films was used in this work to study the dependence on device sizes and pinning field strengths of the GMR responses of spin valves having identical magnetic layers. The calculation of self-demagnetizing and magnetostatic fields can be modified to take into account nonuniform magnetization in the magnetic layers.[7] The simulations show offsets in the ideal biasing of devices due to interlayer magnetostatic interaction. The GMR curves broaden as the self-demagnetization in the magnetic layers increases as the stripe height is decreased. Thus, for moderately pinned devices, self-demagnetization results in the canting of the magnetization of the pinned layers. The behavior of the devices is sensitive to their linear dimensions; the offset in biasing can be corrected by the judicious choice of device dimensions. For example, if the free layer is made thicker than the pinned layer, the self-demagnetization will oppose the antiparallel rotation of the magnetization, resulting in better biasing.

The model can be extended in a straightforward manner to simulate devices with three or more magnetic layers, and to include interlayer ferromagnetic, antiferromagnetic, and biquadratic exchange interactions between adjacent magnetic layers. More exotic devices can thus be simulated and studied both by selectively applying these interactions among the magnetic layers and by making use of magnetic layers with different magnetic properties and linear dimensions. Self-fields due to current flow in the device can be modeled by adding an appropriate field to the applied field free energy density term of Eq. (1).

[1] B. Dieny, V. Speriosu, S. S. P. Parkin, B. A. Gurney, D. R. Wilhoit, and D. Mauri, Phys. Rev. B **43**, 1297 (1991).
[2] R. W. Cross, J. O. Oti, S. E. Russek, T. Silva, and Y. K. Kim, IEEE Trans. Magn. **31**, 3358 (1995).
[3] C. E. Johnson. J. Appl. Phys. **33**, 2515 (1962).
[4] M. R. Parker, H. Fujiwara, S. Hossain, and W. E. Webb, IEEE Trans. Magn. **MAG-31**, 2618 (1995).
[5] W. F. Brown, *Magnetostatic Principles in Ferromagnetism* (North-Holland, Amsterdam, 1962), pp. 49–53.
[6] J. O. Oti, IEEE Trans. Magn. **MAG-29**, 1265 (1993).
[7] H. N. Bertram, *Theory of Magnetic Recording* (Cambridge University Press, Cambridge, 1994), pp. 170–176.

# Exploration of magnetization reversal and coercivity of epitaxial NiO {111}/NiFe films

Chih-Huang Lai, Hideo Matsuyama, and Robert L. White
*Department of Materials Science and Engineering, Stanford University, Stanford, California 94305*

Thomas C. Anthony
*Hewlett Packard Research Laboratories, 1501 Page Mill Road, Palo Alto, California 94304*

Gary G. Bush
*Lockheed Missiles and Space Co., 3251 Hanover Street, Palo Alto, California 94304-1191*

We have grown epitaxial NiO {111} films of thicknesses ranging from 60 to 1200 Å, deposited 45 Å NiFe films on these NiO substrates, and made measurements of exchange field and coercivity, of the effective uniaxial anisotropy, of rotational hysteresis, and of the training effect on these films. We find that the large coercive fields, ~500 Oe, observed in these epitaxial systems can be understood using a model in which the magnetization reversal process is by rotation, with the coercive field determined by the effective uniaxial anisotropy of the system. This effective anisotropy is in turn determined by the anisotropy of the NiO and depends on NiO thickness.
© *1996 American Institute of Physics.* [S0021-8979(96)56508-9]

## I. INTRODUCTION

The anisotropic exchange interaction between Permalloy ($Ni_{0.8}Fe_{0.2}$) and NiO has drawn a lot of attention[1] because of the potential usage of NiO as a biasing layer in magnetoresistance (MR) heads or spin valves.[2] Previous investigations of the NiFe–NiO exchange interaction have involved sputtered polycrystalline NiO and NiFe.[1–3] Generally, it is more difficult to characterize quantitatively the exchange anisotropy interaction in polycrystalline systems because of the random orientations involved. In recent work[4] we demonstrated the epitaxial growth of NiO {111} and {100} by metalorganic chemical-vapor deposition (MOCVD), making a quantitative study of the NiFe–NiO interaction feasible. The coercivity we observed in our NiFe–NiO {111} systems was anomalously large as compared to that observed in polycrystalline systems. We report here further investigation of the physical origins of the large coercive fields observed in the NiFe–NiO {111} films. We have deposited NiFe on NiO {111} films of various thicknesses, and report here the dependence upon the NiO thickness of the exchange field $H_e$, the coercivity $H_c$, and the magnetic training effect. Torque measurements were made to determine magnetic anisotropy and rotational hysteresis observed to help understand the magnetization process. An attempt was made to change the anisotropy of NiO by doping with 2% strontium ($Sr^{2+}$) and the effect of the doping upon $H_e$ and $H_c$ was observed.

## II. EXPERIMENTAL PROCEDURES

Epitaxial NiO films ranging in thickness from 60 to 1200 Å were grown on {0001} $Al_2O_3$ using a solid source MOCVD technique at a growth temperature of about 510 °C. The Sr-doped films were made by putting 2 at. % $Sr^{2+}$ into the solid source $Ni(THD)_2$. NiFe films 45 Å thick were deposited on the epitaxial NiO {111} films by dc magnetron sputtering in the presence of a magnetic field of 275 Oe. 50 Å of Ta was used as a capping layer. Electron probe microanalysis (EPMA) was used to determine the chemical compositions and the thickness of the films. The hysteresis loops were taken at room temperature using the magneto-optical Kerr effect (MOKE). To observe the magnetic training effect, the first five cycles were recorded individually and the stabilized loop was taken after 50 field cycles. The in-plane torque measurements were executed at room temperature from 100 Oe up to 10 kOe after the hysteresis loops had been stabilized.

## III. RESULTS

In Fig. 1 we show the changes in stabilized (after training) $H_c$ and $H_e$ of the NiFe–NiO system as the thickness of NiO is varied from 60 to 1200 Å. As the thickness of the NiO, $t_{af}$, is increased, there is a critical thickness, 150 Å, at which $H_e$ first appears. $H_e$ then increases gradually to a maximum of 70 Oe at $t_{af}$=400 Å. This behavior is to be contrasted with the sharp rise of $H_e$ with $t_{af}$ usual for the NiFe–FeMn system.[5] The coercivity for our NiFe–NiO films rises from about 35 Oe at $t_{af}$=60 Å to a maximum of 510 Oe at 275 Å. $H_e$ and $H_c$ are almost unchanged for thicknesses of NiO between 400 and 1200 Å.

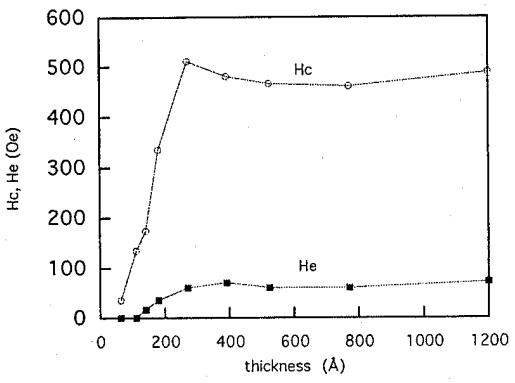



FIG. 1. NiO {111} thickness dependence of the coercivity $H_c$ and the exchange field $H_e$ for 50 Å Ta/45 Å $Ni_{0.8}Fe_{0.2}$/60–1200 Å NiO.

 0021-8979/96/79(8)/6389/3/$10.00 © 1996 American Institute of Physics 

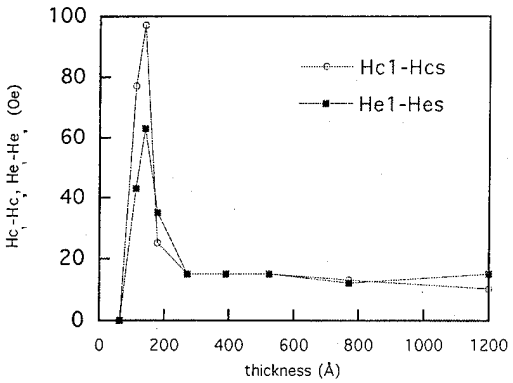



FIG. 2. NiO {111} thickness dependence of the trainable components ($H_{c_1} - H_{c_s}$) and ($H_{e_1} - H_{e_s}$) for 50 Å Ta/45 Å $Ni_{0.8}Fe_{0.2}$/60–1200 Å NiO. $H_{c_1}$ and $H_{e_1}$ ($H_{c_s}$ and $H_{e_s}$) are the coercivity and the exchange field of the first hysteresis loop (of the stabilized hysteresis loop).

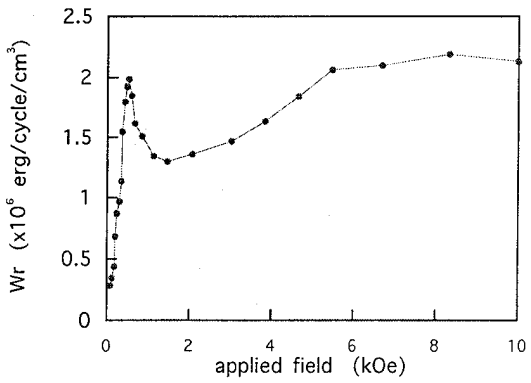



FIG. 4. Field dependence of rotational hysteresis loss $W_r$ for 50 Å Ta/45 Å $Ni_{0.8}Fe_{0.2}$/275 Å NiO.

NiO films having a 2% $Sr^{2+}$ doping with thickness of 400 and 550 Å were prepared. NiFe films deposited on the Sr-doped NiO films showed reductions of $H_c$, 45% and 21%, respectively, and a 20% increase of $H_e$, compared to NiFe deposited on pure NiO of same thicknesses.

The magnetic training effect, the gradual reduction in $H_e$ and $H_c$ during the first several hysteresis loop cycles,[6,7] varies with the thickness of the NiO as shown in Fig. 2. The trainable components of $H_e$ and $H_c$, the difference between the values for the first loop ($H_{e_1}$,$H_{c_1}$) and the stabilized loop ($H_{e_s}$,$H_{c_s}$), are zero at $t_{af}$=60 Å, rise to a sharp peak at the critical thickness of NiO, 150 Å, and return to a small, almost constant, value for $t_{af}$>275 Å.

To determine the anisotropy in the film and to help understand the magnetization process, torque measurements were conducted on each sample. A typical torque curve in this NiFe–NiO system is shown in Fig. 3. A skewed sin $2\theta$ curve indicates that the uniaxial anisotropy dominates in NiFe–NiO films. In addition, a large rotational hysteresis, $W_r=\frac{1}{2}\int_0^{2\pi} L\, d\theta$ ($L$:torque), exists even at a high field. If we assume the energy per unit volume for the NiFe to be $E=-K_e' \cos\theta+K_u \sin^2\theta$ ($\theta$ is the angle between the magnetization and easy axis of the NiFe), $K_u$, the effective uniaxial anisotropy constant, can be deduced from the amplitude of the sin $2\theta$ component. (The cos $\theta$ term arises from the interaction of the anisotropic interfacial exchange with NiO.) The anisotropy field $H_k$ of the NiFe film is equal to $2K_u/M_s$, assuming rotation of a single domain. In this specific sample, 50 Å Ta/45 Å NiFe/275 Å NiO, $K_u=2.2\times10^5$erg/cm$^3$ and $M_s=780$ emu/cm$^3$, giving $H_k$=569 Oe. Comparing this $H_k$ to the $H_c$ measured from MOKE, we find $H_k$ differs from $H_c$ by only 10%. This approximate equality of $H_k$ from torque measurements and $H_c$ from the hysteresis loops held for all our samples with NiO thicknesses greater than 275 Å. This result strongly suggests the magnetization process in the NiFe films coupled to NiO {111} is a pure rotation process.

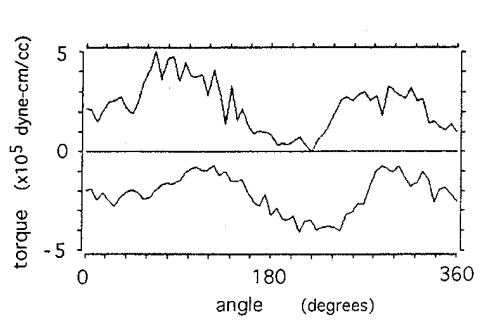



FIG. 3. In-plane torque curve for 50 Å Ta/45 Å $Ni_{0.8}Fe_{0.2}$/275 Å NiO. The applied field is 2000 Oe.

The typical dependence of rotational hysteresis upon magnetic field that we observed is shown in Fig. 4. The nonvanishing rotational hysteresis at a high field is one of the distinguishing characteristics of coupled ferro-antiferromagnetic systems.[8] The rotational hysteresis rises to a sharp peak at the coercive field, 510 Oe, and then increases again at high field.

## IV. DISCUSSION

Following the analysis of Meiklejohn,[9] the magnetic energy of a ferromagnetic layer (f) coupled to an antiferromagnetic layer (af) can be expressed in a simple model. The energy $E$ per unit area of the interface can be written as follows:

$$E=-HM_s t_f \cos(\theta-\theta_f)+K_{af}t_{af} \times \sin^2\theta_{af}-K_e\cos(\theta_f-\theta_{af}), \quad (1)$$

where $M_s$ and $H$ are the saturation magnetization and applied field magnitude, respectively, $t_f$ ($t_{af}$) are the thicknesses of NiFe (NiO), $\theta$ is the angle of the applied field to the anisotropy axis, $\theta_f$ ($\theta_{af}$) is the angle of the magnetization (the sublattice magnetization for the NiO) to the anisotropy axis, $K_e$ is the interfacial coupling constant, and $K_{af}$ is the uniaxial crystalline anisotropy of the NiO.

From this model, the condition

$$K_{af}t_{af}>K_e \quad (2)$$

is required for a shift of the hysteresis loop. In principle, if there are well-defined single values for $K_{af}$ and $K_e$, there should exist a sharp onset of $H_e$. A wide distribution of

blocking temperatures has been reported for the NiFe–NiO system.[10] It was suggested that a variety of exchange paths across the interface existed due to interfacial disorder and fluctuating atomic arrangements. Further, the anisotropy of NiO strongly depends on strain[9] and stochiometry.[11] As a result, it is reasonable to assume a wide distribution of $K_e/(K_{af}t_{af})$ across the films because of local microscopic inhomogeneities. Because of this wide distribution of $K_e/(K_{af}t_{af})$, $H_e$ increases gradually for NiO from 150 to 400 Å thick. When the thickness of NiO is less than 150 Å, there is no loop shift observed; however, nonvanishing rotational hysteresis still appears, which indicates that the exchange interaction between NiFe and NiO exists even for the $t_{af}$ less than critical thickness. The existence of rotational hysteresis below the critical $t_{af}$ implies that the superparamagnetic model[12] is not valid for this system with $t_{af}$ less than the critical thickness.

For simplicity, we can divide the interface area into two categories:

(1) $K_e/(K_{af}t_{af}) \geq 1$ and
(2) $K_e/(K_{af}t_{af}) < 1$.

In the area belonging to the first category, the anisotropy of the NiO is too weak to pin the spins in the NiFe; therefore, this area cannot contribute to loop shift, $H_e$. When the magnetization of the NiFe rotates, the spins of the NiO rotate irreversibly, causing an increase in $H_c$. In the area belonging to the second category, the NiO can effectively block rotation of the spins in the NiFe and contribute to the observed $H_e$. If we can increase the anisotropy of the NiO, we should observe increased $H_e$ and reduced $H_c$. In fact, this was observed in the NiFe coupled to the NiO doped with 2 at. % $Sr^{2+}$. It has been well established that the anisotropy of NiO in the {111} plane is small[13] but sensitive to strain.[9] The large ion, $Sr^{2+}$, probably introduces local strain into the NiO, resulting in a larger local anisotropy and increasing the portion of the film area with $K_e/(K_{af}t_{af}) < 1$.

The torque measurements give us an explanation of the anomalously high $H_c$ observed for the epitaxial NiFe–NiO {111} films. Since the coercive field, $H_c$ is very nearly equal to $H_k$, we believe that the magnetization process is dominated by pure rotation. For normal NiFe films uncoupled to an antiferromagnet, magnetization reversal proceeds by nucleation and propagation of domains of reversed magnetization, with the resulting $H_c$ much smaller than $H_k$. For NiFe films coupled to NiO, coupling through interfacial exchange makes the nucleation of reversed magnetization energetically unfavorable. Further, this coupling makes the effective anisotropy $K_u$ of NiFe films much larger than the intrinsic value for NiFe alone.

Based on Meiklejohn's calculations,[9] the rotational hysteresis loss shows a sharp peak at the threshold field, $H=J_k/M_s$ ($J_k$: anisotropy energy per unit volume) at which the spins of the antiferromagnet rotate. In our samples the field at which the rotational hysteresis loss peaks very nearly equals the coercive field $H_c$. This result reinforces our proposal that the coercivity in the NiFe/NiO {111} system is the field required to rotate the spins in NiO. Further, the existing rotational hysteresis loss at the field less than the threshold field is another indication of distribution of $K_e/(K_{af}t_{af})$. In addition, the increase of the rotational hysteresis loss at high field is probably due to the direct interaction between the applied field and NiO.[14]

We propose also a tentative model of the training effect consistent with the above picture and consistent with the model of Paccard *et al.*[7] in which the training effect is attributed to reorientation of the spins in the antiferromagnet with magnetization reversal in the ferromagnet. For thin NiO films ($t_{af}<60$ Å), the anisotropy resident in the NiO film per unit area is much less than $K_e$, so the NiO spins follow the NiFe spins on all cycles and there is no training effect. For thick NiO films ($t_{af}>200$ Å) the anisotropy per unit area in the NiO is large so that the local spin axes are mostly unchanged after the field cycles; therefore, the training effect is small. For intermediate NiO thicknesses, the local uniaxial anisotropy directions in the NiO are affected through $K_e$ and are shifted during early magnetic cycles to directions favoring the external applied field. The training effect is therefore greatest in this domain of NiO thicknesses.

## V. CONCLUSIONS

We believe we have shown, through measurements of $H_c$ and $H_e$ as a function of the thickness of the NiO and through measurements of torque and rotational hysteresis in epitaxial NiFe–NiO {111} films, that the magnetization process in such coupled film systems is rotational, that the coercive field is determined by the effective uniaxial anisotropy of the system, and that this effective anisotropy is in turn determined by the anisotropy in the antiferromagnetic NiO film. We present also a model of the magnetic training effect consistent with this picture.


## ACKNOWLEDGMENTS

We are grateful to Professor R. S. Feigelson for the MOCVD growth, and to Dr. M. Lu for assistance with the torque measurements.



[1] M. J. Carey and A. E. Berkowitz, Appl. Phys. Lett. **60**, 3060 (1992).
[2] T. C. Anthony, J. A. Brug, and S. F. Zhang, IEEE Trans. Magn. **MAG-30**, 3819 (1994).
[3] S. Soeya, S. Tadokoro, T. Imagawa, and M. Fuyama, J. Appl. Phys. **74**, 6297 (1993).
[4] C. H. Lai, H. Matsuyama, R. L. White, and T. C. Anthony, IEEE Trans. Magn. (to be published).
[5] D. Mauri, E. Kay, D. Scholl, and J. K. Howard, J. Appl. Phys. **62**, 2929 (1987).
[6] C. Schlenker, S. S. P. Parkin, J. C. Scott, and J. K. Howard, J. Magn. Magn. Mater. **54-57**, 801 (1986).
[7] D. Paccard, C. Schlenker, O. Massenet, R. Montmory, and A. Yelon, Phys. Status Solidi **16**, 301 (1968).
[8] W. H. Meiklejohn and C. P. Bean, Phys. Rev. **105**, 904 (1957).
[9] W. H. Meiklejohn, J. Appl. Phys. **33**, Suppl. 1328 (1962).
[10] S. Soeya, T. Imagawa, K. Mitsuoka, and S. Narishige, J. Appl. Phys. **76**, 5356 (1994).
[11] N. Perakis, J. Phys. Radium **23**, 96 (1962).
[12] L. Néel, Ann. Phys. (Paris) **2**, 61 (1967).
[13] W. L. Roth and G. A. Slack, J. Appl. Phys. **31**, Suppl., 352S (1960).
[14] A. E. Berkowitz and J. H. Greiner, J. Appl. Phys. **36**, 3330 (1965).

# Change of magnetoresistance characteristic and crystal structure by ion bombardment to interfaces in [$Ni_{81}Fe_{19}$/Cu] multilayers (abstract)

Y. Miyamoto, T. Yoshitani, S. Nakagawa, and M. Naoe
*Department of Physical Electronics, Tokyo Institute of Technology, Meguro, Tokyo 152, Japan*

Many practical applications using giant magnetoresistance (GMR) have been developed, such as read-out heads and spin valve devices; however, the origin of GMR is not still fully understood. The GMR effect seems to be originated from the spin scattering mechanism whether at the interfaces or at the layer bodies.[1] Therefore, it is necessary to investigate the spin scattering behaviors at the interfaces in GMR multilayers. It is regarded that the mixing and the diffusion of atoms at the interfaces in multilayers can be well promoted by ion bombardment to the interfaces at proper energy in dual ion beam sputtering (DIBS) method. In this study, change of magnetoresistance (MR) and crystallographic characteristics induced by interfacial mixing of atoms were investigated. Specimen films were deposited by DIBS. Additional ion bombardment to the growing surfaces arranges the mixing effect at the interfaces between Ni-Fe and Cu layers. Acceleration voltage of sputtering ion source $V_{mg}$ were set at 500 V and that of bombarding ion source $V_{sg}$ was varied in the range of 0–300 V. Si wafers were used as substrates. Ni–Fe/Cu multilayers with GMR were deposited on 50 Å thick Fe buffer layers. Only two monolayers at the interfaces in Ni–Fe/Cu multilayers were exposed to ion bombardment to cause the local interfacial mixing. X-ray diffraction diagrams, showed that (111) orientations of Ni–Fe and Cu crystallites are obtained at $V_{sg}$ below 200 V and that, on the contrary, (100) orientation became dominant in the films deposited at $V_{sg}$ above 200 V. There is no apparent differences in MR ratio with increase of $V_{sg}$. However, the field sensitivity and saturation field properties were drastically degraded at $V_{sg}$ above 200 V, while the crystal structure seemed to be changed. These results indicate that spin scattering were mainly occurred at the layer bodies in Ni–Fe/Cu multilayers. These results implied that the interfacial mixing is not so effective for changing MR ratio of Ni–Fe/Cu multilayers. However, the behavior of magnetization vectors are much influenced by change of local structure at the interfaces. These results seem to confirm the proposed theory; i.e., the spin scattering in layer bodies is the dominant mechanism on GMR in Ni–Fe/Cu multilayers. © *1996 American Institute of Physics.*
[S0021-8979(96)62008-X]

[1]B. Dieny, Europhys. Lett. **17**, 261 (1992).

 0021-8979/96/79(8)/6392/1/$10.00 © 1996 American Institute of Physics

# Structural comparisons of ion beam and dc magnetron sputtered spin valves by high-resolution transmission electron microscopy

William E. Bailey, Nan-Chang Zhu, Robert Sinclair, Shan X. Wang
*Department of Materials Science and Engineering, Stanford University, Stanford, California 94305-2205*

We have used high-resolution transmission electron microscopy to compare the nanostructures of ion-beam and dc magnetron sputter-deposited giant magnetoresistive (GMR) spin valves and to correlate nanostructure with magnetic properties. Very low coercivities and strong exchange bias (<8 Oe, 125 Oe) were achieved in ion-beam-deposited spin valves of the form NiFe(50)/Co(20)/Cu(>25)/Co(20)/NiFe(50)/FeMn(150)/Ta(30 Å); these were compared with typical dc magnetron deposited structures of the same kind, both with and without a Ta seed layer, which exhibited similar and poorer exchange biasing but superior GMR ratios (to 8%.) Cross-sectional and plane-view samples were prepared of all three structures and examined by high-resolution electron microscopy. Near-perfect (111)-textured fcc metal and *c*-axis hcp Co columnar grains were revealed in the ion beam deposited sample, while some (10°) dispersion of this texture and random grain orientations were observed in the Ta-seeded and unseeded dc magnetron sputter-deposited samples, respectively. No amount of the $\alpha$-FeMn (A12) phase was observed in any of the films. Exchange bias strengths and coercivity of the top Co/NiFe/FeMn layers thus correlate strongly with the degree of (111) texture. © *1996 American Institute of Physics.* [S0021-8979(96)56608-1]

## I. INTRODUCTION

Magnetically soft giant magnetoresistance (GMR) spin value structures of the form $Ni_{80}Fe_{20}/Cu/Ni_{80}Fe_{20}/Fe_{50}Mn_{50}$ are widely recognized to be important to the next generation of magnetic recording systems. Their sensitive change in resistance with applied field[1] is attractive for use in the read element of a recording head; with the addition of thin Co layers at the $Ni_{80}Fe_{20}$/Cu interfaces,[2] resistance changes as great as 9.2% over 50 Oe (Ref. 3) have been demonstrated. Also important among the advantages of GMR spin valves over AMR sensors is the far wider range of applied fields for which the MR response is linear.[4] High coercivities in the pinned ferromagnetic layer can encroach upon this linear range, so the lowest possible pinned-layer coercivities, along with high GMR ratios and strong exchange bias, are sought by developers.

While the overwhelming majority of spin valves have been deposited by rf or dc magnetron sputtering, ion-beam deposition (IBD) is a promising technique, as it offers some greater control over the microstructure of the film and is amenable to *in situ* characterization.[5] Microstructural control and characterization are critical to the properties of these devices, due to the atomic scale of the thin films involved. *Ex situ*, then, high-resolution transmission electron microscopy (HREM) is well suited to characterizing the structure of these thin metallic layers. While HREM has been used to study Co/Cu multilayers[6,7] and some amount of work has been done on the $Ni_{80}Fe_{20}/Fe_{50}Mn_{50}$ couples,[8] there is a lack of HREM data available for full spin valves, with some exceptions.[9] Understanding of structure-properties relations in spin valves remains incomplete.

In the current work we have used HREM to study the microstructure of NiFe/Co/Cu/Co/NiFe spin valves created by ion-beam deposition. These have been compared with spin valves formed by conventional dc magnetron sputtering, and the relationship of microstructure to pinned layer biasing and coercivity has been explored.

## II. EXPERIMENTAL METHOD

A series of nominal Si(111)/$SiO_2$(30 Å)/NiFe(50 Å)/Co(20 Å)/Cu($t_{nm}$)/Co(20 Å)/NiFe(50 Å)/FeMn(150 Å)/Ta(20 Å) spin valve heterostructures, for $t_{nm}$ = 15, 20, 25, 30, and 35 Å, was deposited by IBD. Depositions were carried out on the native oxide of the Si wafer, using 300 V beam voltages and $1 \times 10^{-4}$ Torr working pressures. Permanent magnet biasing was used during deposition and rotated by 90° between ferromagnetic layers; the rotation was carried out in air, with 20 Å of Co sputter-etched back before proceeding. Two comparison structures, nominally [Ta (60 Å)/] NiFe(60 Å)/Co(20 Å)/Cu(28 Å)/Co(20 Å)/NiFe(30 Å)/FeMn(120 Å)/Ta(50 Å) were deposited by dc magnetron sputtering on thermally oxidized (100) Si coated by 1500 Å $Al_2O_3$. To examine the effect on microstructure, one was deposited with and the other without the Ta underlayer. Further information on the sputter-deposition conditions can be obtained elsewhere.[3] The magnetic and magnetotransport properties of the layers were examined using $B-H$ looper magnetometry and four-point probe analysis. These results are summarized in Table I and are discussed in the following section.

Cross-sectional and plane-view TEM specimens were prepared of all three samples using standard methods;[10] low-angle (~6°) ion milling was used on the cross-sectional samples. High-resolution images were obtained using a Phillips EM430 (300 kV) transmission electron microscope, which has ~1.9 Å point-to-point resolution. Additional structural information was gathered using standard bright- and dark-field imaging and selected-area diffraction techniques.

## III. RESULTS

The IBD spin valves show excellent exchange biasing and extremely low pinned layer coercivity (see Table I). Compared by the exchange product $H_E^*(M_s t_f)$,[11] the IBD

 0021-8979/96/79(8)/6393/3/$10.00 © 1996 American Institute of Physics 

TABLE I. Magnetic and magnetotransport properties of the spin valves. Note the extremely low pinned layer coercivity ($H_{c_2}$) and strong exchange biasing ($K_u$) of the ion-beam-deposited sample.

| Deposition method | $(\Delta R/R)$ | $H_{c_2}$ (Oe) | Exchange bias $H_E$ (Oe) | $K_u$ (merg/cm$^2$) |
|---|---|---|---|---|
| Ion beam dc magnetron | 2.8% | 7.7 | 125.0 | 89.3 |
| no Ta seed | 8.1% | 28.5 | 73.4 | 39.8 |
| Ta seed layer | 6.7% | 29.9 | 170.0 | 92.2 |

sample shows only 3% smaller biasing strength than the Ta-seeded sputtered sample. The pinned layer coercivity of the ion-beam-deposited sample, on the other hand, is approximately a factor of 4 less than that of the Ta-seeded sputter-deposited sample: only 8 Oe. This is far lower than values typically found for sputter-deposited spin valves. The exchange biasing of the unseeded sputter-deposited spin valve was weaker than either of the others and about half that of the IBD sample, with coercivity roughly equal to that of the Ta-seeded structure.

The plane-view diffraction patterns of all three samples (Fig. 1) show fcc crystallization of the metals with a range of lattice parameters between 3.54 and 3.66 Å, with differences in texture and the amount of hcp Co present. These lattice parameters are in good agreement with reported bulk values for fcc Co, Cu, $Ni_{80}Fe_{20}$, and thin-film $\gamma$-$Fe_{50}Mn_{50}$ ($a$ = 3.54, 3.62, 3.55, and 3.64, respectively).[9,12]

Highly perfect (111) fcc and (0002) Co textures are observed in the IBD spin valve. In the plane-view diffraction pattern (Fig. 1), note the high intensity of the (220) and (422) fcc and $(3\bar{3}00)$ Co rings, along with the sharp intensity of the innermost $(1\bar{1}00)$ Co ring. Zero diffracted intensity is observed from the (200) or (111) reflections, so no (100)- or (110)-oriented grains are present. The unseeded dc magnetron-sputtered sample shows much weaker diffraction overall, and purely random fcc polycrystalline orientations. No intensity is observed for hcp Co at the $(1\bar{1}00)$ reflection.

With the addition of the Ta seed layer, predominant (111) and $c$-axis texture begins to emerge from dc magnetron deposition, although significant amounts of random orientations are still present. The diffraction rings thus represent a midway point between the textural extremes of the ion-beam-deposited and unseeded dc magnetron-sputtered samples. Strong (220) and weaker (111) and (200) diffracted intensities are present here, as are (111) and (200) fcc orientations. A weak but distinct amount of $(1\bar{1}00)$ Co diffraction discernible inside the fcc (111) ring.

No amount of the $\alpha$-FeMn (A12) phase is observed in any of the samples. In many TEM specimens (not shown here), extra rings appear which index to a fcc phase with $a$ = 4.2 Å. The source of this is uncertain although it may be an artifact of the specimen preparation.

Conclusions about the degree of texturing in the oriented films are supported by the cross-sectional diffraction patterns (insets, Figs. 2 and 3). While the IBD spin valve shows $<1°$ of angular dispersion in the perfect (111) fiber

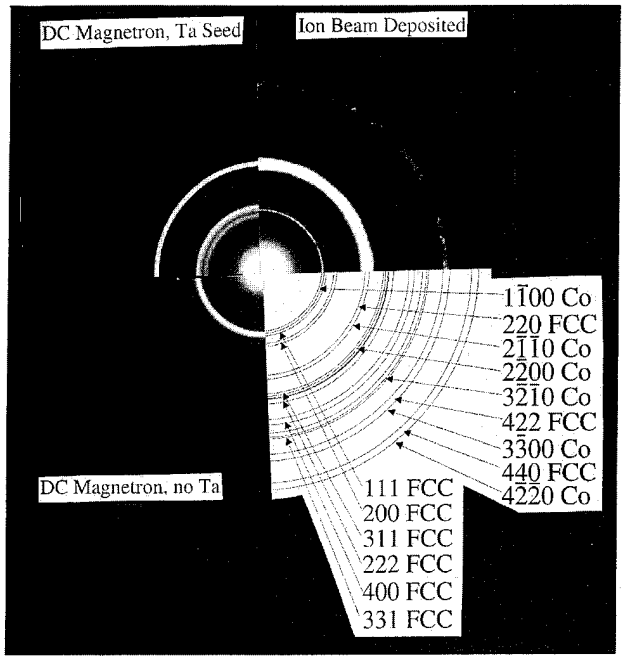



FIG. 1. Selected-area-diffraction patterns of the three plane-view samples. Upper right-hand side: perfect (111) fcc metal and $c$-axis Co texture in the IBD sample. Upper left-hand side: strong (111) and $c$-axis texture, with significant (200) fcc and random grain orientations, for the Ta-seeded sputtered sample. Lower left-hand side: completely random fcc grain orientations for the unseeded sputtered sample.

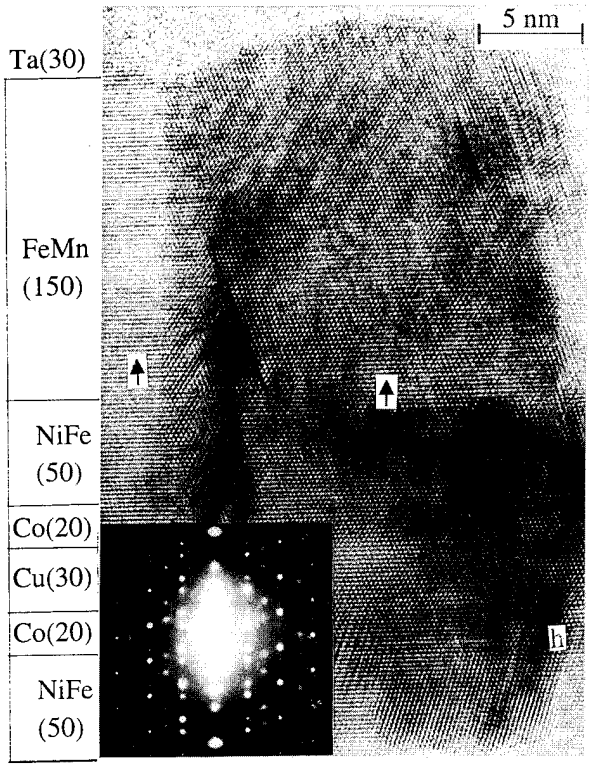



FIG. 2. High-resolution cross-sectional image of the ion-beam-deposited spin valve. Inset: selected-area-diffraction pattern illustrating the $<1°$ variation in (111) texture; arrows indicate the (111) directions on the image. A region of hcp Co is indicated by "h." Nominal interface positions are shown on the left-hand side.

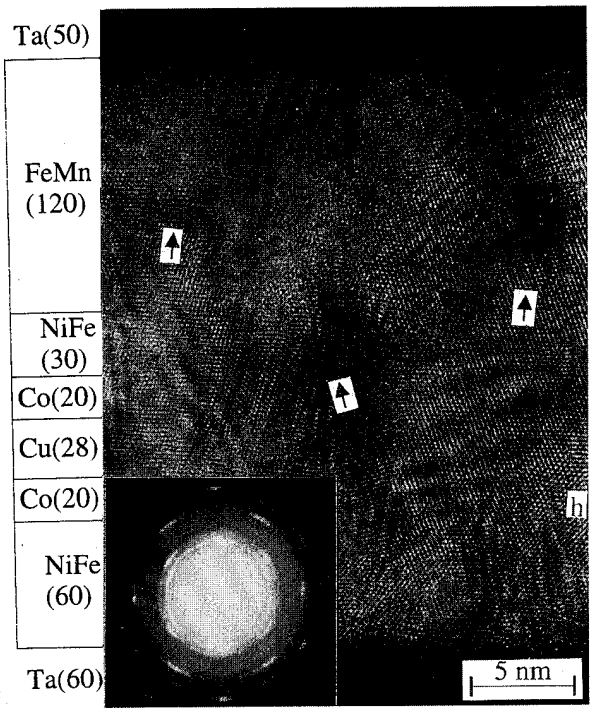



FIG. 3. High-resolution cross-sectional image of the sputtered, Ta seeded spin valve. Inset: selected-area-diffraction pattern illustrating the ~10° variation in (111) texture.

texture, the Ta-seeded, sputter-deposited spin valve shows approximately 10° dispersion. The perfect texturing is apparent from the cross-sectional high-resolution image (Fig. 2) as well. Here, the horizontal (111) stacking planes extend even over distances much greater than the grain size with little undulation. In the dc magnetron-deposited film (Fig. 3), the stacking planes waver by 10° over 50 Å length scales or less. Some regions of $c$-axis-textured hcp Co crystallization, indicated by "h," are visible in both spin valves. These coexist with a great amount of fcc Co, also visible.

The average grain sizes in the spin valves were found from HREM images of the plane-view samples (not shown). Average grain sizes were larger in the IBD films (120 Å) than in the dc magnetron sputtered films and roughly the same size in the seeded as in the unseeded sputtered films (50 Å), though grains in the latter are equiaxed rather than columnar. The cross-sectional images show that full epitaxial growth throughout a grain, typical in the ion-beam-deposited film, is not operative in the Ta-seeded dc magnetron-sputtered film. Thus, the grains tend to extend through all the layers only in the ion-beam-deposited sample, although they may traverse multiple layers in the dc magnetron-sputtered film. Likely related to this difference in growth mode, however, is the development of a convex growth front at the top of the grains of FeMn, on the order of 25 Å, terminating at the grain boundaries. The sputter-deposited samples show a more uniform FeMn surface morphology.

## IV. DISCUSSION

Some relationships between microstructure and spin valve properties can be drawn out from the foregoing results. First, the strength of exchange biasing was seen to depend in large part upon the degree of texture throughout the layers. Strongly textured Co/NiFe(111)/FeMn(111), deposited by either ion-beam or dc magnetron sputtering, provided more than twice the exchange biasing than that of randomly oriented grains. This is in good agreement with studies done on molecular-beam-epitaxy-deposited NiFe/FeMn bilayers in various orientations, in which the (111)-oriented samples were seen to provide some 50% stronger biasing than (100) and (110) orientations.[13] Furthermore, it provides some confirmation for the near-linear relationship between XRD intensity in the (111) peak and $H_E$ found in ion-beam deposited NiFe/Cu/NiFe/FeMn spin valves with various buffer layers.[12]

The pinned layer coercivity is likely to correlate with the homogeneity of crystal orientations at the $F$/AF interface. In our work, the waviness of the (111) planes, clearly visible in the Ta-seeded sputter-deposited sample, is completely absent in the ion-beam-deposited sample and accompanied by a fourfold drop in $H_{c_2}$. A coercivity dependence on textural dispersion may be expected to the extent that variations in texture introduce local inhomogeneities in the energetics of exchange biasing, and is consistent with the similarly low values of $H_{c_2}$ and high values of $H_E$ reached by molecular-beam epitaxial deposition of NiFe(111)/FeMn(111) on Cu(111).[12]

## ACKNOWLEDGMENTS

Thanks are due to Ann Marshall for expert assistance with TEM, Thomas Anthony at Hewlett–Packard for providing the dc magnetron deposited samples, and Stephen Michael at Commonwealth Scientific for assistance with the ion-beam deposition. This work was supported in part by the NSF under Grant No. ECS-9409805, the Stanford Center for Research on Information Storage Materials, and the Center for Materials Research. W.E.B. gratefully acknowledges the support of an ONR Graduate Fellowship; S.X.W. wishes to acknowledge a Terman Faculty Fellowship endowed by W. Hewlett and D. Packard.

[1] B. Dieny *et al.*, J. Appl. Phys. **69**, 4774 (1991).
[2] S. S. P. Parkin, Phys. Rev. Lett. **71**, 1641 (1993).
[3] T. C. Anthony *et al.*, IEEE Trans. Magn. **30**, 3819 (1994).
[4] D. E. Heim, TMRC '93.
[5] H. S. Joo and H. A. Atwater, INTERMAG '95, paper EC-03.
[6] R. J. Pollard *et al.*, J. Magn. Magn. Mater. **146**, L2 (1994).
[7] A. R. Modak *et al.*, Phys. Rev. B **50**, 4232 (1994).
[8] C. Hwang, R. H. Geiss, and J. K. Howard, J. Appl. Phys. **64**, 6116 (1988).
[9] R. Nakatani *et al.*, Jpn. J. Appl. Phys. **33**, 133 (1994).
[10] J. C. Bravman and R. Sinclair, J. Electron. Micro. Technol. **1**, 53 (1984).
[11] A. P. Malozemoff, Phys. Rev. B **35**, 3679 (1987).
[12] JCPDS cards 15-806, 4-836, 23-297.
[13] R. Jungblut *et al.*, J. Appl. Phys. **75**, 6659 (1994).

# Giant magnetoresistance and magnetic phase diagram of UNiGa

K. Prokeš, E. Brück, F. R. de Boer, M. Mihálik, and A. Menovsky
*Van der Waals-Zeeman Institute, University of Amsterdam, 1018 XE Amsterdam, The Netherlands*

P. Burlet
*DRFMC-SPH/LIH CEN Grenoble, 85X-38041 Grenoble Cedex, France*

J. M. Mignot
*Laboratoire Léon Brillouin, CEA/CNRS, CE Saclay, 911 91 Gif-Sur-Yvette Cedex, France*

L. Havela and V. Sechovský
*Department of Metal Physics, Charles University, 12116 Prague 2, The Czech Republic*

As a result of combined magnetization, specific heat, electrical resistivity, and neutron-scattering studies on single crystals, we present a complex magnetic phase diagram of UNiGa that exhibits several antiferromagnetic (AF) phases below $T_N = 39$ K. A relatively low magnetic field (~1–1.5 T) applied along the $c$-axis induces metamagnetic transitions from the zero-field AF structures to an uncompensated AF and/or to a ferromagnetic (F) phase. All the magnetic structures are collinear (uranium magnetic moments parallel to the $c$-axis of the hexagonal structure). They consist of F basal-plane sheets which are coupled along $c$ in various ways. The strongly anisotropic magnetism in UNiGa causes anisotropy of the electrical resistivity. The magnetic phase transitions are reflected in pronounced resistivity anomalies especially for current along the $c$-axis. The metamagnetic transitions are accompanied by giant magnetoresistance (GMR) effects which can be correlated with respective changes of the magnetic periodicity. This implies an important feature of the mechanism responsible for GMR phenomena in UNiGa. The strong resistance enhancement in the paramagnetic range when approaching $T_N$ is connected with AF short-range ordering with propagation along the $c$-axis. © *1996 American Institute of Physics.* [S0021-8979(96)56708-7]

UNiGa is one of uranium ternary compounds UTX (T =transition metal, X=$p$ metal) which crystallize in the hexagonal ZrNiAl-type structure.[1] This structure consists of the U–T and T–X basal-plane layers alternating along the $c$ axis. The huge uniaxial magnetocrystalline anisotropy in these materials locks the uranium magnetic moments along the $c$ axis which leads to an Ising-like behavior. The anisotropy is due to considerable uranium $5f$-orbital moments and in the strong bonding of $5f$-states in the U–T planes.

The bonding implies the anisotropic $5f$-ligand hybridization which mediates anisotropic exchange interactions between the U moments. The strong F exchange interaction within the U–T planes yields magnetic structures built up of F basal-plane sheets (with $\mu_U \| c$). The interaction along the $c$-axis is, as a rule, considerably weaker but it plays an important role in determining the type of magnetic ordering, because it provides the coupling between the F sheets.

We present the magnetic phase diagram of UNiGa deduced from results of magnetization,[2] electrical resistivity and magnetoresistance,[3] specific heat,[4] and neutron-scattering studies performed on single crystals. Results involving application of magnetic fields have been obtained in fields parallel to the $c$-axis, which is the easy magnetization direction. The huge uniaxial anisotropy prevents perpendicular magnetic fields (at least up to 35 T) from affecting the magnetic state of UNiGa.

All experiments were performed on samples originating from two single crystals grown in a Czochralski tri-arc equipment of the FOM ALMOS at the University of Amsterdam. Both crystals were checked by the electron microprobe and found to be stoichiometric within the experimental accuracy of the method. Other details on sample preparation can be found in Ref. 5. The low-field magnetization was measured in the field of 1.2 mT in a SQUID magnetometer. The resistivity, specific-heat,[4] and magnetization[2] results were taken from our previous work where experimental details can be found. Neutron-scattering studies were carried out at temperatures between 2 and 80 K and in magnetic fields up to 2 T on double-axis spectrometers in CEN Grenoble and HMI Berlin. We also present additional neutron-scattering data obtained in zero magnetic on a triple-axis spectrometer at LLB operating in elastic mode.

In Fig. 1 we present the detailed magnetic phase diagram of UNiGa ($B-T$ diagram for $\mathbf{B} \| c$). In zero magnetic field, four antiferromagnetic phases can be observed below $T_N$ within about 5 K. The effects of the magnetic phase transitions on the resistivity, specific heat, magnetization, and peak intensities of characteristic magnetic reflections in the neutron-diffraction experiment are plotted in Fig. 2, from which one can also deduce the temperature ranges of stability of the AF phases.[1–4]

Magnetic ordering in UNiGa appears through a second-order phase transition around 39 K, where the resistivity and low-field magnetization display only faint anomalies. The appearance of satellite reflections $h,k,l+\delta$ with $\delta$=0.36–0.37 gives a clear evidence of an incommensurate antiferromagnetic (IAF) structure with the wave vector $\mathbf{q}=(0,0,\delta)$. The transition temperature can be best defined from the maximum critical scattering anomaly measured for $\mathbf{Q}$=1,1,0.378 (Fig. 3). Since previous estimates[2–4] of $T_N$ from bulk properties had a relatively large scatter due to weakness of the respective anomalies, we consider the present value, $T_N = 39$ K to be the most reliable.

The IAF phase is stable down to 37.3 K (the $\delta$ value is

 0021-8979/96/79(8)/6396/3/$10.00 © 1996 American Institute of Physics

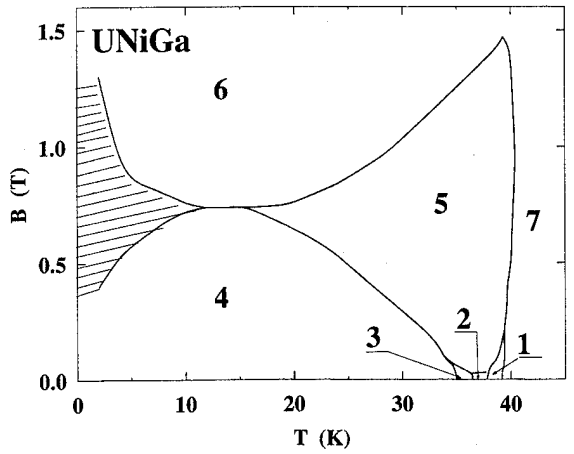



FIG. 1. Magnetic phase diagram of UNiGa for magnetic fields applied along the $c$ axis: (1) incommensurate AF structure, $\mathbf{q}=\pm(0,0,\delta)$,$\delta\sim0.36$; (2) AF phase with $\mathbf{q}=\pm(0,0,1/3)$, e.g., the structure with frustrated "paramagnetic" moments in each third U–T plane, i.e., $(+0-)$; (3) AF phase with the $(++-+--+-)$ stacking, $\mathbf{q}=\pm(0,0,1/8)$, $\pm(0,0,3/8)$; (4) AF phase with the $(++-+--)$ stacking, $\mathbf{q}=\pm(0,0,1/2)$, $\pm(0,0,1/3)$, $\pm(0,0,1/6)$; (5) uncompensated AF phase with the stacking $(++-)$, $\mathbf{q}=\pm(0,0,1/3)$; (6) ferromagnetic phase, $\mathbf{q}=\pm(0,0,0)$; (7) paramagnetic phase.

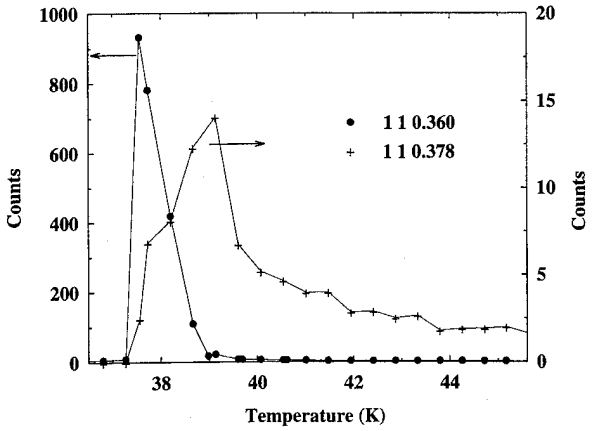



FIG. 3. Temperature dependence of the peak intensity of the magnetic Bragg reflection $\mathbf{Q}=1,1,0.36$ (●) and intensity of the magnetic scattering at $\mathbf{Q}=1,1,0.378$ (+), normalized to the same monitor measured at zero energy transfer on a triple-axis spectrometer.

varying between 0.37 at $T_N$ to 0.36 at 37.5 K), where it transforms to the phase 2 through a first-order transition. This phase has the periodicity $3c$, but zero spontaneous magnetization. This may be conceived with a stacking sequence $+0-$, where 0 means the basal-plane layer of uranium atoms with the zero-ordered magnetic moment. Such a situation can appear in the case of a balanced AF interaction between nearest-neighbor and next-nearest-neighbor uranium planes. The resistivity drops by several percent at this transition.

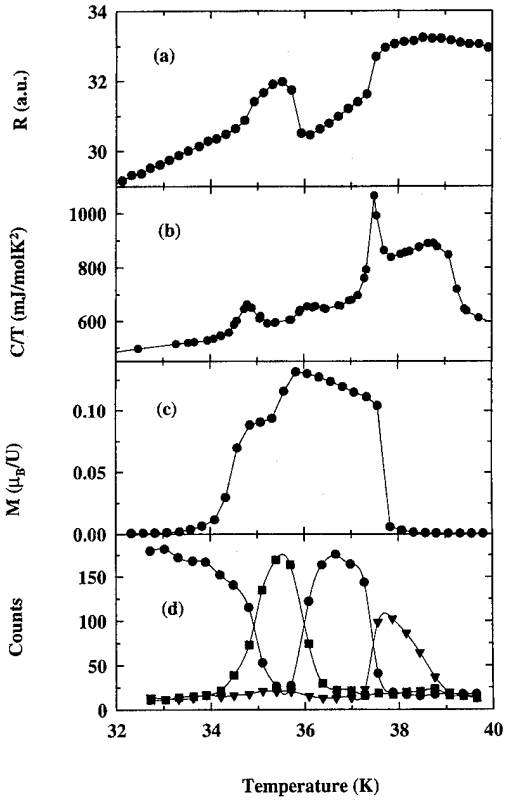



FIG. 2. Temperature dependence of the (a) specific heat, (b) electrical resistivity, (c) magnetization in a field 1.2 mT parallel to the $c$ axis, and (d) the peak intensity of neutron-diffraction magnetic reflections (●) 1,1,4/3, (■) 1,1,11/8, and (▼) 1,1,0.36 in zero magnetic field measured on UNiGa in the temperature range 30–40 K.

With further decreasing temperature, gradual transformation of the magnetic structure to the ground-state AF phase 4 with the stacking $(++-+--)$ via the "intermediate" phase $3(++-+--+-)$ was observed. While the $2\rightarrow3$ is associated with a substantial increase of the resistivity, the other $(3\rightarrow4)$ yields a somewhat smaller decrease. As evidenced by the neutron-diffraction results, both transitions are characterized by a coexistence of neighboring phases over a certain critical region which can be more than 1 K wide (the transition $3\leftrightarrow4$).

The uranium moment, which is $\sim1.4\ \mu_B$ at 2 K, does not decrease substantially with increasing temperature up to almost 35 K, where it retains more than 90% of its low-temperature value. This behavior seems to be more general for the UTX compounds which exhibit high anisotropy yielding an Ising-like behavior.

The line $7\leftrightarrow5$ in fields between $\sim0.2$ and 1 T in Fig. 1 marks the first-order transitions in contrast to the second-order transitions $7\leftrightarrow1$ in lower fields. Also the transitions $4\leftrightarrow5\leftrightarrow6$ above 14 K are second-order transitions. The phases 1, 2, and 3 are stable only in very low fields. The propagation vector $\mathbf{q}$ of the IAF phase gets slightly reduced under application of field (by less than 0.01 in 100 mT).

The hatched area in the magnetic phase diagram below 14 K represents the B–T region in which magnetic history phenomena have been observed by the bulk measurements.[2] These effects are reflected also on the microscopic scale including the relaxation phenomena, as follows.

(a) For $T$=const for sweeping the applied magnetic field the upper (lower) line in Fig. 1. Marks the $4\rightarrow6$ $(6\rightarrow4)$ transition. This fact is well documented by the large hysteresis of the field dependence of the magnetization, magnetoresistance and magnetic reflection displayed in Fig. 4. The hatched region represents the hysteresis, which increases progressively

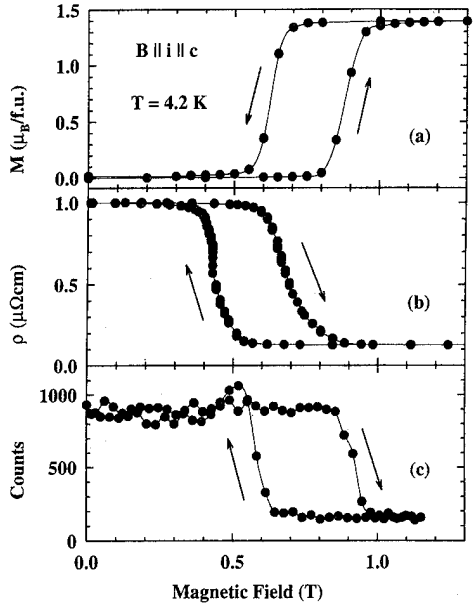



FIG. 4. Field dependence of the (a) magnetization, (b) reduced electrical resistivity, and (c) the peak intensity of the neutron diffraction reflection 1,1,4/3 measured on UNiGa single crystal at 4.2 K in magnetic field applied along the $c$ axis. The offsets in critical fields are due to different demagnetization fields (different sample shapes) in particular experiments.

with lowering temperature. The metamagnetic transitions below 14 K are first order and only one phase (either 6 or 4) is present dependent on the direction of a field sweep. The same holds for the transitions 4→6 and 6→4 with varying temperature.

(b) $B$=const ~0.73 T: By cooling from higher temperatures (phase 5) down to the "hysteresis region" we reach a mixed state consisting of phases 4 and 6. This is clear from the simultaneous observations of magnetic intensities characteristic for each phase (4 and 6), and from bulk properties,[2–4] as well. The 4+6 phase mixture, which we observe also in the magnetoresistance and magnetization, seems to be stable, at least on the time scale of minutes.

As we have mentioned before, the metamagnetic transitions 4↔6 and 4↔5↔6 are inducing giant resistance changes. For example, the effect displayed in Fig. 4 represents almost 90% reduction of the resistance [$\Delta\rho/\rho(0T) \sim -0.9$] when we change from the AF structure with $\mathbf{q}$=0,0,1/6 (magnetic periodicity $6c$) to the F phase 6 ($\mathbf{q}$ =0,0,0; periodicity $1c$). Above 14 K, the transition from the phase 4 to 6 is realized by two steps via the uncompensated AF phase 5 ($\mathbf{q}$=0,0,1/3, magnetic periodicity $3c$) yielding the spontaneous magnetization of $\frac{1}{3}M_s$ ($M_s$ is the magnetization in the F phase). The magnetoresistance also shows two transitions,[3] and the resistivity change between phases 4 and 5 is also approximately 1/3 of that between phases 4 and 6.

All the magnetoresistance changes connected with the metamagnetic transitions between various phases in UNiGa are qualitatively correlating with the change in the periodicity of corresponding magnetic structures. The increase of the magnetic periodicity is followed by a positive resistivity change. This observed systematic behavior points to the possible following scenario based on the high-resistivity state in antiferromagnets appearing due to superzone boundary formation (Fermi-level gapping). Thus, the additional magnetic periodicity yields the reduction of the carrier concentration and consequently enhances the resistivity. In the gapping model of Elliot and Wedgwood,[6] the resistivity in the local-moment AF state can be described by

$$\rho = \frac{\rho_0 + \rho_{e-p} + \rho_{spd}}{1 - g m(T)}, \tag{1}$$

where $m(T)$ is the normalized sublattice (staggered) magnetization, $\rho_0$ the residual resistivity, $\rho_{e-p}$ the contribution of electron–phonon scattering, and $\rho_{spd}$ is the magnetic contribution (spin-disorder scattering). The truncation parameter $g$ characterizes the effective reduction of the number of conduction electrons due to the Fermi-level gapping. The difference between the resistance in the F and AF state depends on the width in the electron energy spectrum, which scales with the exchange coupling parameter between the local moments and conduction electrons. The exchange coupling parameter can be significantly enhanced in case of U local moments connected with the $5f$ states forming a narrow band at $E_F$. A more detailed discussion of magnetoresistance in UTX compounds will be published elsewhere.[7]

The last point we want to discuss is the anomalous temperature behavior of the resistivity for the current along the $c$ axis ($i \| c$), i.e., sensing the AF coupling between uranium moments. Below 80 K, the resistivity starts to increase with decreasing temperature. The increase becomes gradually more pronounced when approaching $T_N$. The fact that this increase can be suppressed by applied fields corroborates the idea that the negative $d\rho/dT$ above $T_N$ is due to incipient AF correlations.[2,5] The fact that a non-negligible neutron scattering (elastic) intensity at $\mathbf{Q}$=1,1,0.378 (see Fig. 3) can be detected far above the Néel temperature indicates that at least part of the enhanced resistance should be due to short-range AF ordering, which probably persists up to 2 $T_N$. A more detailed account of the diffuse scattering at $T_N$ will be a subject of a forthcoming article.

This work was sponsored by the Dutch "Stichting voor Fundamenteel Onderzoek der Materie" (FOM) and the Grant Agency of the Czech Republic (Project No. 202/94/0454). The neutron scattering experiments at HMI Berlin and LLB Saclay were financially supported from the EU programs "Go West" (V.S.) and "HCM–Large Facilities+PECO" (K.P. and V.S.).

[1] V. Sechovský, L. Havela, in *Ferromagnetic Materials*, edited by E. P. Wohlfarth and K. H. J. Buschow (North-Holland, Amsterdam, 1988), Vol. 4, pp. 309–491 and references therein.
[2] L. Havela, V. Sechovský, L. Jirman, F. R. de Boer, and E. Brück, J. Appl. Phys. **69**, 4813 (1991).
[3] V. Sechovský, L. Havela, L. Jirman, W. Ye, T. Takabatake, H. Fujii, E. Brück, F. R. de Boer, and H. Nakotte, J. Appl. Phys. **70**, 5794 (1991).
[4] V. Sechovský, L. Havela, F. R. de Boer, E. Brück, T. Suzuki, S. Ikeda, S. Nishigori, and T. Fujita, Physica B **186–188**, 775 (1993).
[5] E. Brück, Ph.D. thesis, University of Amsterdam, 1991.
[6] R. J. Elliot and F. A. Wedgwood, Proc. Phys. Soc. **81**, 846 (1963).
[7] L. Havela, V. Sechovský, K. Prokeš, H. Nakotte, H. Fujii, and A. Lacerda, Physica B (to be published).

# Giant magnetoresistance and soft magnetic properties of $Co_{90}Fe_{10}$/Cu spin-valve structures

Y. Kamiguchi, K. Saito, H. Iwasaki, and M. Sahashi
*Materials & Devices Laboratories, Toshiba Research and Development Center 1, Komukai Toshiba-cho, Saiwai-ku, Kawasaki 210, Japan*

M. Ouse and S. Nakamura
*Environmental Engineering Laboratory, Toshiba Research and Development Center 1, Komukai Toshiba-cho, Saiwai-ku, Kawasaki 210, Japan*

Spin-valve structures with a magnetic material buffer layer, CoNbZr/NiFe/$Co_{90}Fe_{10}$/Cu/$Co_{90}Fe_{10}$/$Fe_{50}Mn_{50}$, were prepared on a oxidized Si substrate. From x-ray diffraction analysis, it was shown that the CoNbZr/NiFe buffer layer enhances the fcc (111) orientation of the spin-valve structure on oxidized Si. After annealing, the giant magnetoresistance (GMR) ratio of $\Delta\rho/\rho=8\%$ and the soft magnetic properties of $H_c=0.1$ Oe and $H_k=2.8$ Oe were obtained. The sensitivity of GMR, $\Delta(\Delta\rho/\rho)/\Delta H$, of 1.4%/Oe is achieved. © *1996 American Institute of Physics.* [S0021-8979(96)56808-4]

## I. INTRODUCTION

In recent years, the giant magnetoresistance (GMR) in spin-valve structure is attracting much attention.[1–4] In the spin-valve structures, large antiferromagnetic coupling between two magnetic layers across the intervening nonmagnetic layer is not needed, because one of the ferromagnetic layers is biased by exchange coupling from the antiferromagnetic layer. Therefore it is easy to obtain good soft magnetic properties and this makes the spin valve structure very interesting for sensor applications such as the MR head in high-density magnetic recording. For such applications, a high MR ratio and good thermal stability are required. The Co/Cu spin-valve structure satisfies this requirement, but it is difficult to obtain good soft magnetic properties with this structure.

On the other hand, the $Co_{90}Fe_{10}$ film with low magnetostriction is expected to show soft magnetic properties because an fcc phase is, according to its equilibrium phase diagram, stable in the presence of Fe, and an (111)-oriented fcc phase suppresses the softness deterioration due to magnetocrystalline anisotropy. In the previous article, we reported that the $Co_{90}Fe_{10}$/Cu spin-valve structure prepared on the sapphire substrate showed a good (111) orientation and an MR ratio of about 13% with a hysteresis of less than 1 Oe for the magnetization rotation mode.[5] However, the spin-valve structure prepared on the oxidized Si substrate showed a weak (111) orientation and an MR ratio less than 9% with a large hysteresis loop. From technological viewpoints, it is very important to obtain good spin-valve properties on the oxidized Si substrate.

In this article, we investigated a magnetic material buffer layer CoNbZr (100 Å)/NiFe (20 Å). This buffer layer is expected to enhance the (111) orientation of the spin-valve structure, because the surface of this buffer layer is composed of the NiFe (111) plane with high orientation. Moreover, this buffer layer is also expected to enhance soft magnetic properties of the spin-valve structure by its own good soft magnetic properties. We also studied the annealing effect of the proposed spin-valve structure.

## II. EXPERIMENTAL

The spin-valve structure of $Co_{90}Fe_{10}$ (47 Å)/Cu (22 Å)/$Co_{90}Fe_{10}$ (47 Å)/$Fe_{50}Mn_{50}$ (150 Å) was prepared on oxidized Si (hereafter called "$SiO_2$ sample") and $c$-axis oriented sapphire substrates (hereafter called "sapphire sample") by conventional magnetron sputtering. A magnetic field was applied on the film plane during deposition, in order to induce a unidirectional bias field to the CoFe layer in contact with the FeMn layer. The spin-valve structure with a magnetic material buffer layer, CoNbZr (100 Å)/NiFe (20 Å)/$Co_{90}Fe_{10}$ (49 Å)/Cu (28 Å)/$Co_{90}Fe_{10}$ (49 Å)/$Fe_{50}Mn_{50}$ (80 Å), was prepared on oxidized Si substrates (hereafter called "buffer sample"). First, the CoNbZr and NiFe layers were prepared by ion beam sputtering. Then, the prepared sample was exposed to the atmosphere, and brought into another sputtering chamber. The buffer layer was not cleaned by sputter etching after introduction to the deposition chamber, because a sputter etching will cause the surface roughness. So the surface of the buffer layer should be shallow oxidized. Then, the $Co_{90}Fe_{10}$/Cu/$Co_{90}Fe_{10}Fe_{50}Mn_{50}$ layer was prepared on the buffer layer as describe above.

The magnetoresistance ratio was measured by the four-point method at room temperature by applying a magnetic field to the unidirectional bias field. Magnetization curves were measured with a vibrating sample magnetometer. The crystal structure was measured by x-ray diffraction $\theta$-$2\theta$ method with the Cu $K\alpha$ line.

## III. RESULTS

### A. Crystal structure

Figure 1 shows x-ray diffraction patterns around the fcc (111) peak of representative samples. In case of the sapphire sample, some well-separated peaks with large intensity were observed. On the other hand, the patterns of the $SiO_2$ sample show a single broad peak around the (111) peak with small intensity. Figure 1 also shows the patterns of a buffered sample. Some clear peaks are observed and their intensity is larger than the $SiO_2$ sample. This result shows that the buffer layer enhances the (111) orientation of the spin-valve structure.

In order to clarify if these peaks are attributable to the multilayered structure with the preferred (111) orientation, calculations on the x-ray diffraction patterns were carried out by the kinematic theory including interfacial disorder.[6,7] We assume that the spin-valve structure is composed by four

 0021-8979/96/79(8)/6399/3/$10.00 © 1996 American Institute of Physics 

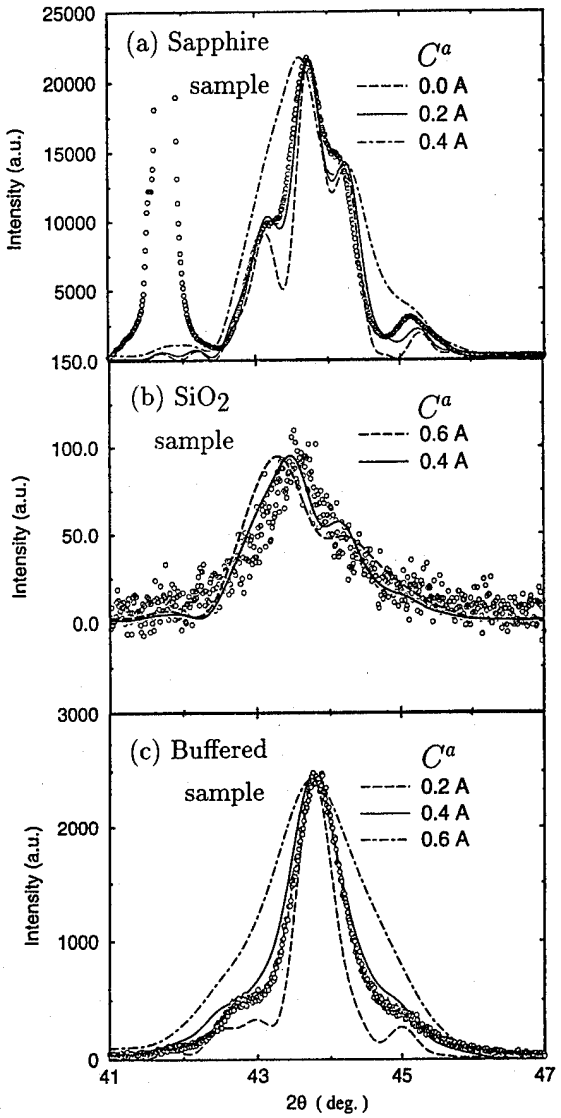



FIG. 1. X-ray diffraction patterns of CoFe/Cu spin-valve structures with calculated x-ray diffraction patterns. Circles and lines represent experimental values and calculation results, respectively. (a) $Co_{90}Fe_{10}$ (47 Å)/Cu (22 Å)/$Co_{90}Fe_{10}$ (47 Å)/$Fe_{50}Mn_{50}$ (150 Å) spin valve prepared on sapphire substrate (sapphire sample). (b) $Co_{90}Fe_{10}$ (47 Å)/Cu (22 Å)/$Co_{90}Fe_{10}$ (47 Å)/$Fe_{50}Mn_{50}$ (150 Å) spin valve prepared on oxidized Si substrate ($SiO_2$ sample). (c) CoNbZr (100 Å)/NiFe (20 Å)/$Co_{90}Fe_{10}$ (49 Å)/Cu (28 Å)/$Co_{90}Fe_{10}$ (49 Å)/$Fe_{50}Mn_{50}$(80 Å) prepared on oxidized Si substrate (buffered sample).

crystalline layers, each layer has materials, lattice stacking $N_i$ with lattice spacing $d_i$ and interfacial distance between the adjacent layers is $a_i$. The $d_i$ and $a_i$ values have Gaussian distribution of widths $c_i^d$ and $c_i^a$, respectively. Then the x-ray profiles are described as

$$I(Q)=\langle F(Q)\cdot F^*(Q)\rangle, \tag{1}$$

where $F(Q)$ is the structure factor and the symbols $\langle\ \rangle$ denote averaging by integrating over all real interface distance. The structure factor $F(Q)$ can be written as

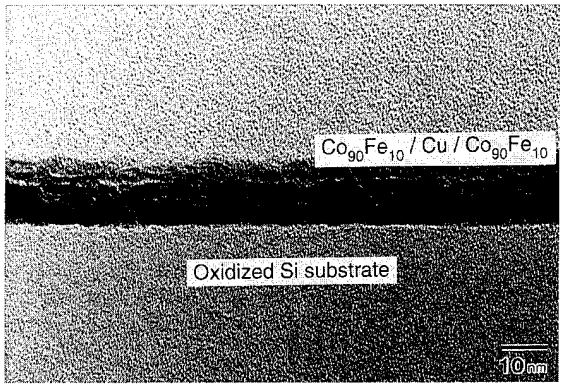



FIG. 2. Cross-sectional view of $Co_{90}Fe_{10}$ (50 Å)/Cu (30 Å)/$Co_{90}Fe_{10}$ (50 Å) sandwich structure prepared on oxidized Si substrate.

$$F(Q)=\sum_l \left[\left\langle \sum_n \left\{ \sum_m M_n^m f_m(Q)\right\} \exp(iQnd_l)\right\rangle \times\left\langle iQ\cdot\sum_{j=0}^{l-1}(a_j+N_jd_j)\right\rangle\right], \tag{2}$$

where $M_n^m$ is atomic density for atom $m$ (Co, Fe, Mn, and Cu) in the $n$th atomic layer and $f_m(Q)$ is the atomic scattering factor of atom $m$.

Fitting was carried out on the following assumptions: (1) the $Fe_{50}Mn_{50}$ layer is oxidized very easily. Therefore we assume a surface oxidized layer having an amorphous structure, and its thickness is determined by fitting. (2) all $c_i^d$ values are equal to zero. This means that all layers have almost the same fluctuation, because the lattice spacing fluctuation value does not affect the shape of the profiles, if all layers take the same $c_i^d$ value. (3) All $c_i^a$ values are equal to $c^a$, and can be determined by fitting.

The fitting does not include the effect of interlayer diffusion or substrate roughness. The values of $c^a$ did not mean the widths of the interfacial region, but mean the interface fluctuation.

Figure 1 shows the experimental and calculated x-ray diffraction profile. The calculated profile of sapphire sample agrees well with the experimental one if $c^a$ is assumed to be 0.2 Å. On the other hand, the calculated profile of $SiO_2$ sample agrees well with the experiment with the assumption $c^a$=0.4–0.6 Å. Further, the best agreement was obtained for the profile of buffered sample with $c^a$=0.4 Å.

These results show that the interface fluctuation of buffered sample is still larger than that of the sapphire sample and at the same level with that of the $SiO_2$ sample, although the preferred (111) orientation is enhanced by the buffer layer.

The x-ray diffraction $\theta$-$2\theta$ method detects the crystal structure perpendicular to the substrate. In order to clarify the in-plane crystal structure, we observed by transmission electron micrography the cross-section view of the $Co_{90}Fe_{10}$ (50 Å)/Cu (30 Å)/$Co_{90}Fe_{10}$ (50 Å) sandwich structure prepared on the oxidized Si substrate. Figure 2 shows that the structure has very rough and undulating interfaces. The sample seems to have the columnar structure.

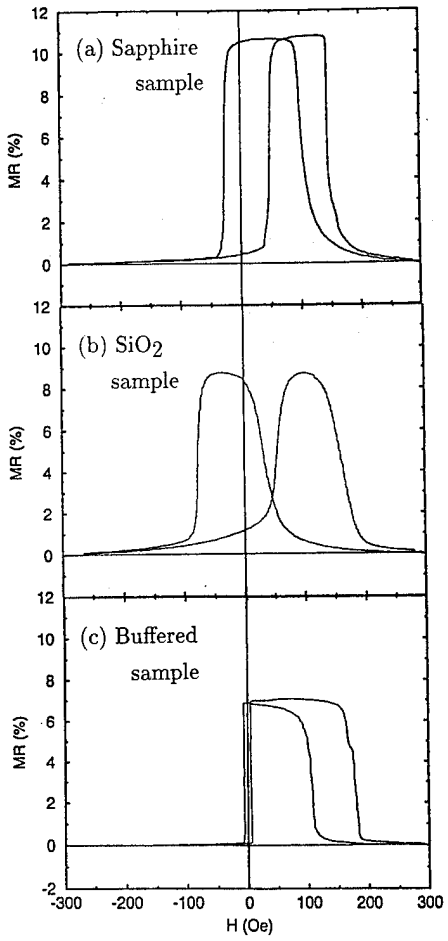



FIG. 3. Magnetoresistance curve of CoFe/Cu spin-valve structures: (a) $Co_{90}Fe_{10}$ (47 Å)/Cu (22 Å)/$Co_{90}Fe_{10}$ (47 Å)/$Fe_{50}Mn_{50}$ (150 Å) prepared on sapphire substrate (sapphire sample). (b) $Co_{90}Fe_{10}$ (47 Å)/Cu (22 Å)/$Co_{90}Fe_{10}$ (47 Å)/$Fe_{50}Mn_{50}$ (150 Å) prepared on oxidized Si substrate ($SiO_2$ sample). (c) CoNbZr (100 Å)/NiFe (20 Å)/$Co_{90}Fe_{10}$ (49 Å)/Cu (28 Å)/$Co_{90}Fe_{10}$ (49 Å)/$Fe_{50}Mn_{50}$(80 Å) prepared on oxidized Si substrate (buffered sample).

## B. GMR characteristics

Figure 3 shows the magnetic field dependence of the MR ratio of three samples. The typical characteristic of spin-valve magnetoresistance is observed. The MR ratio of the sapphire sample is 10.8%. On the $SiO_2$ sample, on the other hand, the MR ratio is 8.5%, and the MR ratio of the buffered sample is 7.0%. Because there is a short current by the buffer layer in buffered sample, the MR ratio of buffered sample is essentially comparable with the $SiO_2$ sample. It is suggested by the x-ray diffraction analysis that buffered sample has the (111) preferred orientation, but the interface coherency is the same as the $SiO_2$ sample. The MR ratio of the spin-valve structure will be affected by interface coherency.

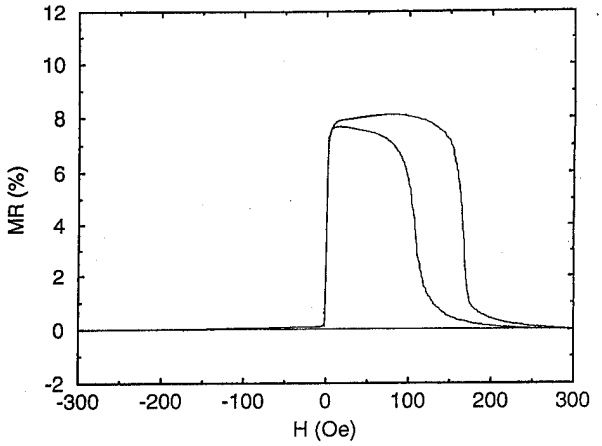



FIG. 4. Magnetoresistance curve of CoNbZr (100 Å)/NiFe (20 Å)/$Co_{90}Fe_{10}$ (49 Å)/Cu (28 Å)/$Co_{90}Fe_{10}$ (49 Å)/$Fe_{50}Mn_{50}$ (80 Å) after annealing.

On the other hand, hysteresis loop of buffered sample is very small. This is a result of the enhancement of (111) preferred orientation. The $H_c$ value was successfully lowered from 66 Oe of $SiO_2$ sample to 5 Oe of buffer sample. This decrease of $H_c$ comes partially from good soft magnetic properties of the buffer layer.

To improve soft magnetic properties, we annealed the buffered sample. In annealing, the temperature was increased to 250 °C and kept in magnetic field. In cooling process, the applied magnetic field was rotated 90°. Because only the unidirectional bias field rotates at low temperatures, the free $Co_{90}Fe_{10}$ layer's easy axis becomes almost orthogonal to that of the exchange-biased $Co_{90}Fe_{10}$ layer. Figure 4 shows the magnetic field dependence of the MR ratio after annealing. The MR ratio were enhanced by annealing and reached 8%. Soft magnetic properties were enhanced and $H_c$=0.1 Oe and $H_k$=2.8 Oe. The sensitivity of GMR, $\Delta(\Delta\rho/\rho)/\Delta H$, became 1.4%/Oe.

[1] B. Dieny, V. S. Speriosu, S. Metin, S. S. P. Parkin, B. A. Gurney, P. Baumgart, and D. R. Wilhoit, J. Appl. Phys. **63**, 4774 (1991).
[2] B. Dieny, V. S. Speriosu, and S. Metin, Europhys. Lett. **15**, 227 (1991).
[3] B. Dieny, V. S. Speriosu, S. S. P. Parkin, B. A. Gurney, D. R. Wilhoit, and D. Mauri, Phys. Rev. B **43**, 1297 (1991).
[4] B. Dieny, J. P. Nozieres, V. S. Speriosu, B. A. Gurney, and D. R. Wilhoit, Appl. Phys. Lett. **61**, 2111 (1992).
[5] H. Iwasaki, Y. Kamiguchi, and M. Sahashi, J. Magn. Soc. Jpn. **18**, Suppl. S1, 359 (1994).
[6] J. P. Locquet, D. Neerinck, L. Stockman, Y. Bruynseraede, and I. K. Schuller, Phys. Rev. B **39**, 13338 (1989).
[7] E. E. Fullerton, I. K. Schuller, H. Vanderstraeten, and Y. Bruynseraede, Phys. Rev. B **45**, 9292 (1992).

# Giant magnetoresistance effect in multilayered wire arrays

Minoru Kume, Atsushi Maeda, Toshio Tanuma, and Kazuhiko Kuroki
*New Materials Research Center, SANYO Electric Co., Ltd, 1-1 Dainichi-higashimachi, Moriguchi, Osaka 570, Japan*

Three wire arrays, each comprised of a different type of giant magnetoresistive (GMR) multilayer, were fabricated by high-resolution electron-beam lithography and lift-off techniques. With a GMR multilayer of the biquadratic-coupling type, a magnetic field applied parallel to the wires produced a larger MR change and higher response than in the corresponding unpatterned multilayered film; however, the wire structures worsened the MR characteristics of two other types of GMR multilayers. © *1996 American Institute of Physics.* [S0021-8979(96)56908-0]

## I. INTRODUCTION

There is considerable interest in the physical properties of microfabricated materials, in which the geometry and spacing are well defined. To date, the authors have observed unique magnetic and microwave absorption characteristics in submicron-size $Ni_{80}Fe_{20}$ or Co wire and box arrays.[1–4] As one application of these laterally artificial structures, the present study looks at multilayered wire arrays prepared with the goal of obtaining superior magnetoresistance (MR) characteristics.

Various multilayered materials display a giant MR (GMR) when the moments of ferromagnetic layers separated by a nonmagnetic layer are turned from parallel to antiparallel.[5–7] However, there is evidence that the magnetization states never reach fully antiparallel and parallel alignments because of the domain structures in the plane.[8] Inducing strong shape anisotropy by fabricating the micron-size magnetic wires is expected to be effective in overcoming the involvement of the magnetic domains. Consequently, the antiparallel and parallel alignments should be improved in the multilayered wires, and therefore the MR should be larger than that of corresponding unpatterned multilayered films. In addition, the shape anisotropy is expected to restrain Barkhausen noise which is a serious problem in device applications. The above-mentioned ideas motivated us to prepare multilayered wire structures.

"Array" samples were considered because they have an advantage in the study of microfabricated materials; using array samples including a large number of wires makes it possible to apply conventional techniques to characterize physical properties.

We report here the results of an investigation on the MR and magnetic characteristics of wire arrays comprised of three types of GMR multilayers.

## II. EXPERIMENT

The wire arrays were fabricated by high-resolution electron-beam lithography and lift-off techniques. Resist films of 1-$\mu$m-thick polymethyl methacrylate (PMMA) coated on Si(100) wafers were directly exposed to an electron beam whose acceleration voltage ranged between 25 and 50 kV. The typical exposure area (equivalent to the sample size) was $8\times8$ mm$^2$. The wire width and spacing were varied from 0.6 to 10.0 $\mu$m. After baking at 473 K under a nitrogen atmosphere for 20 min, the samples were developed using methylisobutyl ketone. Next, various GMR multilayers were prepared on the lithographic resist mask by ion-beam sputtering at room temperature. All the samples possessed only one period. Ar gas pressure was held constant at $4.2\times10^{-5}$ Torr during deposition. The remaining resist material was removed with an acetone lift-off process. A thin Au film was evaporated on both ends of the wires to serve as electrodes. The distance between the Au electrodes was held constant at 1 mm. Thus, the aspect ratio in the multilayered wires ranged from 100 to 1700, resulting in strong shape anisotropy.

The artificial structures of the arrays that were prepared were observed by scanning electron microscopy (SEM). The MR was measured at room temperature in a four-terminal geometry with a direct current. A magnetic field $H$ up to 250 G was applied parallel to the array plane and at a variable angle to the axes of the wires. In the present study the MR ratio was determined as follows:

$$\text{MR ratio}=\Delta R/R(H_{\max}), \tag{1}$$

where $\Delta R$ is the MR change [that is, $R_{\max}-R(H_{\max})$] and $R(H_{\max})$ is the MR at the maximum measuring field. Magnetization $M$ and hysteresis loops were measured at room temperature using a vibrating sample magnetometer.

## III. RESULTS AND DISCUSSION

Figure 1 shows the SEM image of an $Fe_{50}Mn_{50}$ (7.0 nm)/$Ni_{80}Fe_{20}$ (3.4 nm)/Co (0.6 nm)/Cu (2.8 nm)/Co (0.6 nm)/$Ni_{80}Fe_{20}$ (5.4 nm) wire array with widths and spacings of 0.9 $\mu$m. The measured widths were equal to the spacings, as

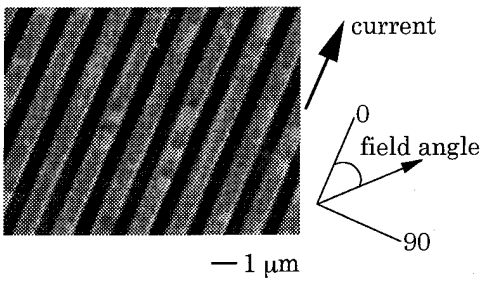



FIG. 1. SEM image of $Fe_{50}Mn_{50}$ (7.0 nm)/$Ni_{80}Fe_{20}$ (3.4 nm)/Co (0.6 nm)/Cu (2.8 nm)/Co (0.6 nm)/$Ni_{80}Fe_{20}$ (5.4 nm) wire array with widths and spacings of 0.9 $\mu$m.

 0021-8979/96/79(8)/6402/3/$10.00 © 1996 American Institute of Physics

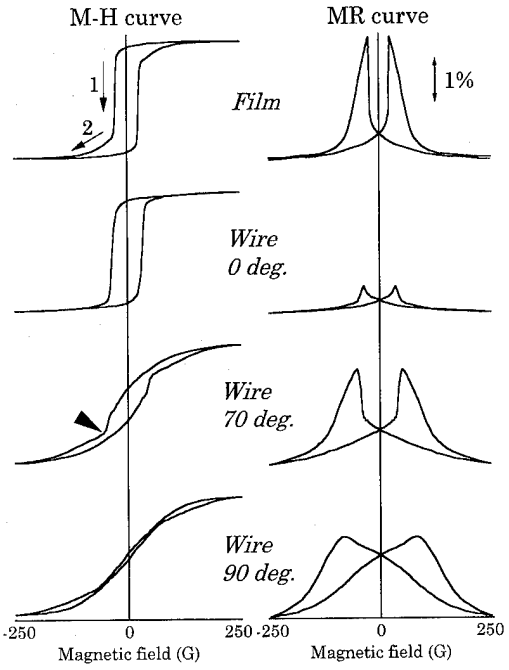



FIG. 2. Angular dependence of magnetization and MR curves for Fe (5.0 nm)/$Ni_{80}Fe_{20}$ (4.0 nm)/Co (0.6 nm)/Cu (4.0 nm)/Co (4.0 nm) multilayered film and wire array with widths of 2.6 $\mu$m and spacings of 1.2 $\mu$m.

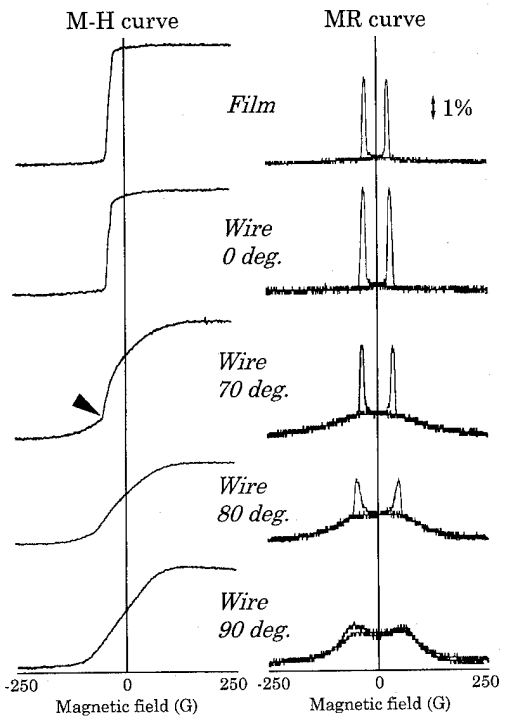



FIG. 3. Angular dependence of magnetization and MR curves for $Ni_{80}Fe_{20}$ (6.0 nm)/Co (0.6 nm)/Cu (4.0 nm)/Co (4.0 nm) multilayered film and wire array with widths of 2.6 $\mu$m and spacings of 1.2 $\mu$m.

designed. The linearity of each wire was good enough to allow for the following meaningful discussion of the physical properties. The other GMR multilayers exhibited similar SEM images.

Figure 2 shows the angular dependence of the $M-H$ and MR curves of an Fe (5.0 nm)/$Ni_{80}Fe_{20}$ (4.0 nm) /Co (0.6 nm)/Cu (4.0 nm)/Co (4.0 nm) multilayered film with no pattern and a wire array with widths of 2.6 $\mu$m and spacings of 1.2 $\mu$m. Here, an ultrathin Co layer was added to the $Ni_{80}Fe_{20}$ layer to enhance the interfacial spin-dependent scattering.[9] In this measurement, we defined the field angle to be 0° when the magnetic field was applied parallel to the stripes. The film sample displayed an isotropic magnetization switching process associated with the different coercive fields $H_c$. Namely, the magnetic moments of Fe/$Ni_{80}Fe_{20}$/Co, with the smaller $H_c$, initially rotated with decreasing field (arrow 1). Next, magnetization switching of the Co layer, with the larger $H_c$, gradually occurred as indicated by arrow 2. In the figure, the features of the MR curve correspond well with those of the $M-H$ curve. The MR ratio was 2.89%, being less than that observed in similar films with a few tens of periods.[6] The $M-H$ curve along the easy axis of the wire array (0°) showed a rectangular loop with indistinct steps. This suggests that strong shape anisotropy reduces the difference in the coercive field between the Fe/$Ni_{80}Fe_{20}$/Co and Co layers. As a result, only partial antiparallel alignment is achieved and the MR was negligibly small. At the field angle of 70° the magnetization process became spread over larger field range. This behavior can be qualitatively modeled by assuming the existence and properties of a demagnetizing field. Here, it is important to note that the step as shown by the arrow is present in the $M-H$ curve, indicating the appearance of the difference in the coercive field. Thus, the MR curves that were observed around this angle possessed the same shape as those of the film sample, though broader. In the hard axis (90°), the magnetic and MR characteristics were strongly affected by a demagnetization field; however, the MR change was large, suggesting that the difference in the coercive field was maintained in the multilayered wires. In summary, the MR characteristics of the Fe/$Ni_{80}Fe_{20}$/Co/Cu/Co multilayered wire arrays along the easy axis were not improved, as expected, because the coercivities are equalized by the shape anisotropy.

Next, we discuss wire arrays fabricated from biquadratic-coupled multilayers. Since the magnetization states of these materials is controlled by "exchange coupling," the effect of the shape on the MR characteristics seems to be small. Figure 3 shows the angular dependence of the $M-H$ and MR curves of a $Ni_{80}Fe_{20}$ (6.0 nm)/Co (0.6 nm)/Cu (4.0 nm)/Co (4.0 nm) multilayered unpatterned film and a wire array with widths of 2.6 $\mu$m and spacings of 1.2 $\mu$m. The film sample displayed a steep MR change. We consider that biquadratic coupling between the $Ni_{80}Fe_{20}$/Co and Co layers is responsible for this behavior.[10–13] The MR ratio was 3.47%, being less than that of similar films with several periods.[14] Along the wire axes of the array sample (0°) it is worth noting that the MR is increased in the wire structure sample compared with the unpatterned sample. The increase in the MR ratio from 3.47% to 4.13% is probably due to the fact that the shape anisotropy improved the magnetic alignments in the multilayers. The improvement in sensitivity is attributable to the steep magnetization switching without the

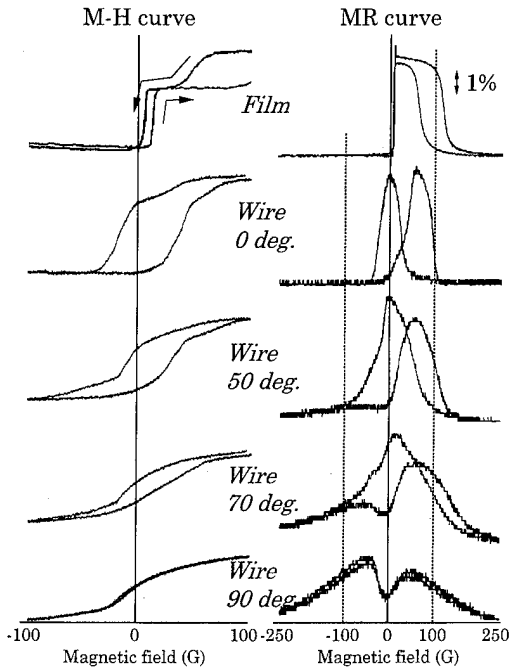



FIG. 4. Angular dependence of magnetization and MR curves for $Fe_{50}Mn_{50}$ (7.0 nm)/$Ni_{80}Fe_{20}$ (3.4 nm)/Co (0.6 nm)/Cu (2.8 nm)/Co (0.6 nm)/$Ni_{80}Fe_{20}$ (5.4 nm) multilayered film and wire array with widths and spacings of 0.9 $\mu$m.

involvement of domain structures in the easy axis. Similar experimental results were observed in the other $Ni_{80}Fe_{20}$ (6.0 nm)/Co (0.6 nm)/Cu (4.0 nm)/Co (4.0 nm) multilayered wire arrays with micron-size widths and spacings. This result indicates that the magnetization states controlled by the biquadratic coupling was maintained in the wire arrays. For multilayered wire arrays of this type, the optimal combination of wire width and spacing to obtain superior MR characteristics is currently under investigation. As shown in Fig. 3, the steep MR change was gradually buried in the broad component with increasing field angle. This is due to the demagnetizing field arising from a narrow width. The step in the $M-H$ curve that was observed at 70° indicates the difference in the coercive field between the $Ni_{80}Fe_{20}$/Co and Co layers. This indicates the coexistence of two kinds of mechanisms that control the magnetization orientation, i.e., biquadratic coupling and different intrinsic coercive fields.

Finally, the physical properties of wire arrays comprised of an exchange-coupled spin-valve multilayer, i.e., $Fe_{50}Mn_{50}$ (7.0 nm)/$Ni_{80}Fe_{20}$ (3.4 nm)/Co (0.6 nm)/Cu (2.8 nm)/Co (0.6 nm)/$Ni_{80}Fe_{20}$ (5.4 nm) are discussed. Figure 4 shows the $M-H$ and MR curves of the film and wire array. Here, the MR curves of the array sample are minor loops measured between $-100$ and 100 G. The wire widths and spacings were both 0.9 $\mu$m. In comparison with the film, the physical properties of the wire array can be characterized as follows:

(1) broader MR curves;
(2) weaker pinning effect by the $Fe_{50}Mn_{50}$ layer; and
(3) weaker coupling between the $Ni_{80}Fe_{20}$/Co and Co/$Ni_{80}Fe_{20}$ layers separated by the Cu layer.

Analyzing the angular dependence, the maximum MR ratio of 4.67% was observed at 50°. This value was larger than that in the unpatterned film and was similar to that in the spin-valve films with a Ta underlayer.[15] In addition, the magnetic response, which is estimated as maximum MR change per 1 Oe, became worse with increasing field angle. Among the results presented in Fig. 4, the MR data obtained in the easy axis (0°) were contrary to our model because the effects of the pinning which control the magnetization states were not expected to be influenced by the shape anisotropy, such as with the biquadratic coupling. To provide further insight into this experimental result, magnetic measurements on samples with various widths and spacings are presently being made.

## IV. SUMMARY

Micron-size multilayered wire arrays comprised of various GMR materials were successfully fabricated by high-resolution electron-beam lithography and lift-off techniques. For some GMR multilayers with biquadratic coupling, when the magnetic field was applied parallel to the stripes, a larger MR and magnetic response were observed in comparison with the corresponding multilayered film having no patterns. These features are attributable to the strong shape anisotropy and provide additional opportunities for technological applications. In contrast, the wire structures worsened the MR characteristics of different-coercive-fields-type and spin-valve-type GMR multilayers.

[1] A. Maeda, M. Kume, T. Ogura, K. Kuroki, T. Yamada, M. Nishikawa and Y. Harada, J. Appl. Phys. **76**, 6667 (1994).
[2] A. Maeda, M. Kume, S. Oikawa, and K. Kuroki, J. Magn. Soc. Jpn. **19**. 309 (1995).
[3] A. Maeda, M. Kume, T. Tanuma, S. Oikawa, and K. Kuroki, J. Magn. Soc. Jpn. **19**, 397 (1995).
[4] A. Maeda and M. Kume (unpublished).
[5] M. N. Baibich, J. M. Broto, A. Fert, F. Nguyen van Dau, F. Petroff, P. Etienne, G. Creuzet, A. Friederich, and J. Chazelas, Phys. Rev. Lett. **61**, 2472 (1988).
[6] T. Shinjo and H. Yamamoto, J. Phys. Soc. Jpn. **59**, 3061 (1990).
[7] B. Dieny, P. Humbert, V. S. Speriosu, S. Metin, B. A. Gurney, P. Baumgart, and H. Lefakis, Phys. Rev. B **45**, 806 (1992).
[8] Y. U. Idzerda, C.-T. Chen, S. F. Cheng, W. Vavra, G. A. Prinz, G. Meigs, H.-J. Lin, and G. H. Ho, J. Appl. Phys. **76**, 6525 (1994).
[9] S. S. P. Parkin, Appl. Phys. Lett. **61**, 1358 (1992).
[10] P. Grunberg, S. Demokritov, A. Fuss, R. Schreiber, J. A. Wolf, and S. T. Purcell, J. Magn. Magn. Mater. **104-107**, 1734 (1992).
[11] H. Fujiwara and M. R. Parker, J. Magn. Magn. Mater. **135**, L23 (1994).
[12] J. Inoue, J. Magn. Magn. Mater. **136**, 233 (1994).
[13] T. Tanuma, S. Takahashi, A. Maeda, M. Kume, and K. Kuroki, in Digests of the INTERMAG Conference, San Antonio, April, 1995.
[14] M. Parker, H. Fujiwara, S. Hossain, J. Yang, M. Kief, and S. Gangopadhyay, J. Magn. Soc. Jpn. **18-S1**, 371 (1994).
[15] B. Dieny, V. S. Speriosu, S. S. S. Parkin, B. A. Gurney, D. R. Whihoit, and D. Mauri, Phys. Rev. B **43**, 1297 (1991).

# Superconductivity and structural transformation in $HfV_2$ and Nb-doped $HfV_2$

F. Chu
*Center for Materials Science, Los Alamos National Laboratory, Los Alamos, New Mexico 87545*

Z. W. Chen,[a] C. J. Fuller, C. L. Lin, and T. Mihalisin
*Department of Physics, Temple University, Philadelphia, Pennsylvania 19122*

The temperature dependence of the specific heat shows that the strong electron-phonon coupling system $HfV_2$ undergoes a structural transformation at 116 K and becomes superconducting around 9 K. The structural instability can be interpreted in terms of a strong electron-phonon coupling and Fermi surface nesting. The structural transformation shifts to lower temperatures with very dilute Nb substitution in $HfV_2$, and completely disappears with only 5 at. % Nb. The low-temperature specific heat of $HfV_2$ shows a large density of states at the Fermi level. These experimental results are consistent with predictions from band-structure calculations. © *1996 American Institute of Physics.* [S0021-8979(96)26108-9]

A15 and C15 compounds have attracted much interest because of a variety of striking phenomena.[1–8] For example, some compounds, e.g., $Nb_3Sn$, $V_3Si$, $HfV_2$, and $ZrV_2$, undergo a structural transformation[1–4] at a low temperature and become superconducting[5,6] at an even lower temperature. These compounds show[5,6] an enhanced electronic specific heat coefficient $\gamma$ which implies a high density of states at the Fermi level. The ratio of $A$, the coefficient of the $T^2$ term in the resistivity, to the $\gamma$ value for these compounds shows a universal behavior[7] which is similar to that of the Ce- and U-based heavy fermion systems. Among the binary C15 Laves phase compounds, $HfV_2$ has the highest superconducting transition temperature ($T_{sc}\approx 9$ K) and undergoes a structural transformation around $T_{st}=116$ K. In addition, it has been shown[9–11] that $T_{sc}$ does not vary significantly with dilute substitution of Ta or Nb for Hf in $HfV_2$ and has nearly the same value for the equi-ternary compounds Hf-V-T with T=Zr, Nb, Ta, and Cr. Some controversial issues remain unresolved. For instance, the specific heat of $HfV_2$ and $ZrV_2$ (Refs. 4 and 9) shows a broad λ-type second-order transition, instead of the more common first-order structural transformation. Moreover, the effects of substitution on the structural transformation have not been studied systematically. To address these issues, we have prepared samples of $HfV_2$, and Nb-doped $HfV_2$, having the C15 Laves phase structure, and have measured the temperature dependence of the specific heat of these compounds. The results are presented and discussed with predictions of theoretical band-structure calculations.[12]

The ternary Hf-V-Nb equilibrium phase diagram has been established recently[13] and shows that the C15 Laves phase exists in a broad region for this ternary system. The binary $HfV_2$ and the Nb-doped ternary with 0.5, 1.0, 2.0, and 5.0 at. % Nb polycrystalline samples having the C15 cubic structure were prepared by melting stochiometric ratios of the constituents in a conventional inert atmosphere arc furnace. The nominal purities of the elemental Hf and V were 99.99 at. % and that of Nb was 99.7 at. %. The samples were annealed under high vacuum at 1200 °C for 120 h. Powder x-ray diffraction studies were used to check the homogeneity and the structure of the samples. No evidence for a second phase was found. The specific heat was measured using a semiadabatic heat pulse method using a $He^4$ probe from 1.2 to 20 K, and using a closed-cycle refrigerator system from 15 to 150 K.

The specific heat of the binary $HfV_2$ for the region from 110 to 125 K is shown in Fig. 1. One can see that in the vicinity of 116 K the specific heat jumps dramatically from about 70 to 250 J/mole K and that the full width at half maximum of this anomaly is very narrow (about 0.5 K). This drastic change in the magnitude and the narrow width of the anomaly may indicate that the transition is in fact first order

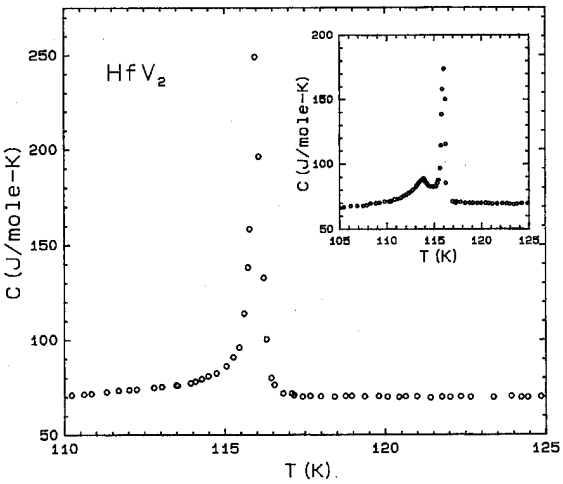



FIG. 1. The temperature dependence of the specific heat of $HfV_2$. Inset: The $C(T)$ data for an off-stochiometric $HfV_2$ sample.

[a]Present address: Department of Materials Science and Engineering, University of Southern California.

 0021-8979/96/79(8)/6405/3/$10.00 © 1996 American Institute of Physics 

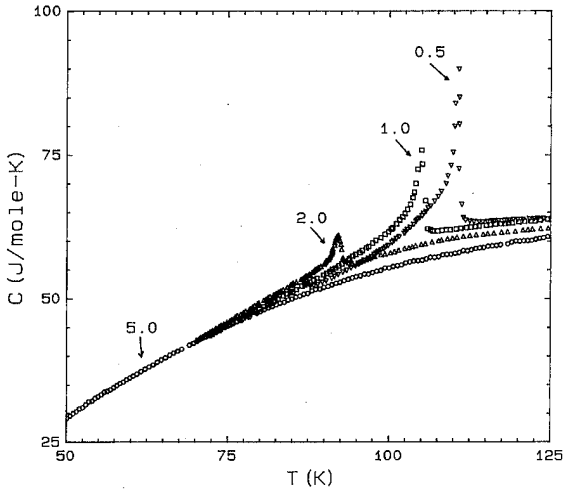



FIG. 2. The $C(T)$ data for the Nb-doped $HfV_2$ ternary system with 0.5, 1.0, 2.0, and 5.0 at. % Nb.

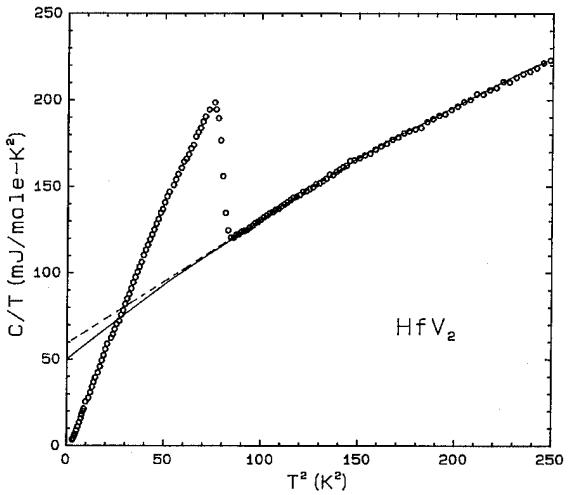



FIG. 3. $C/T$ vs $T^2$ for $HfV_2$ at low temperatures. The dash line is the $C/T=\gamma+\beta T^2$ fit to the experimental data from $T^2$=90 to 120 $K^2$. The solid curve is the $C/T=\gamma+\beta T^2+\alpha T^4+\delta T^6$ fit to the experimental data from $T^2$=90 to 250 $K^2$.

and that a latent heat measurement should be done rather than a specific heat measurement. A first-order structural transformation from a high-temperature cubic structure to a tetragonal structure below 116 K has been reported.[13,14] The value of 116 K is consistent with that previously published by Hafstrom *et al.*[9] and Kimura.[4] However, in both these reports, the specific heat anomaly starts to swing up at about 110 K and reaches a maximum at 118 K. In both cases, the anomaly has a much broader width (about 3 K) and exhibits a λ-type transition. This difference could be due to the limited number of data points taken with large temperature changes $\Delta T$ around the transition temperature and/or samples that were off-stochiometry. We have also measured the specific heat of a $HfV_2$ sample with a slight off-stochiometry Hf to V ratio. The data for this sample are shown in the inset of Fig. 1. The specific heat of this sample starts to increase and deviate from the background at 110 K and shows two anomalies. We believe that the second smaller specific heat anomaly at 114 K can be attributed to a phase separation which follows the structural transformation at 116 K as the sample is cooled to low temperatures.

In order to study the alloying effect on the structural transformation, we have measured the specific heat of the Nb-doped $HfV_2$ ternary system. Shown in Fig. 2 are the specific heat curves for 0.5, 1.0, 2.0, and 5.0 at. % Nb. Note that the magnitude of the specific heat anomaly is significantly reduced from 180 J/mole K for the binary $HfV_2$ to 25 J/mole K for the 0.5 at. % Nb sample and the structural transformation temperature shifts down to 110 K. On careful examination one can see that the shape of the anomaly for the 0.5 at. % Nb sample begins to resemble that of a λ-type transition. The reason for the change from the very narrow transition for the pure $HfV_2$ to a λ-type transition for the case of very dilute Nb doping could be the one alluded to just above. For the 5.0 at. % Nb sample, a specific heat anomaly is not visible for temperatures down to 15 K, implying no structural phase transformation for this sample. The effect of substitution on the structural transformation described above is stronger than that observed previously in similar systems, e.g., $T_{st}$ is about 78 K for 7% Ta doping in $Hf_{1-x}Ta_xV_2$ (Ref. 9) and a structural transformation occurs across the entire series for the case of $Hf_{1-x}Zr_xV_2$.[15] This point is discussed in more detail later.

We have also made measurements of the specific heat at lower temperatures in the region of the superconducting transition. Shown in Fig. 3 is a plot of $C/T$ vs $T^2$ for the binary $HfV_2$. Note that the $HfV_2$ sample undergoes a superconducting transition at $T_{sc}$=9 K which is determined at the midpoint of the specific heat anomaly. The $C/T$ data above $T_{sc}$ exhibit a slight downward curvature (instead of being a straight line), so that it is difficult to extract the electronic specific heat coefficient $\gamma$. We can estimate the $\gamma$ value for the binary $HfV_2$ using two different approaches. First we can use $C/T=\gamma+\beta T^2$ to fit the experimental data for a narrow temperature range from $T$=9.5 to 11 K, i.e., $T^2$=90 to 120 $K^2$. This method gives $\gamma$=60 mJ/mole $K^2$. Or we can use $C/T=\gamma+\beta T^2+\alpha T^4+\delta T^6$ which results from a consideration of the entropy balance between the normal and superconducting states for the wider temperature range from 9.5 to 16 K, i.e., $T^2$=90–250 $K^2$. This method gives $\gamma$=50 mJ/mole $K^2$. These $T_{sc}$ and $\gamma$ values are in good agreement with those previously published.[5,6] Note that either estimate for $\gamma$ is larger than that for a typical weak electron-phonon coupling superconductor or for normal metals. This larger value indicates a large density of states at the Fermi surface in the case of $HfV_2$.

Shown in Fig. 4 is a plot of $C/T$ vs $T^2$ for 5.0% Nb-doped $HfV_2$. Note that this sample does not transform from the cubic to the tetragonal phase at low temperatures. The $T_c$ value increases slightly to 9.6 K. The $\gamma$ values are also 50% higher than those for pure $HfV_2$, i.e., 90 and 75 mJ/mole $K^2$ obtained from using $C/T=\gamma+\beta T^2$ and $C/T=\gamma+\beta T^2+\alpha T^4+\delta T^6$, respectively. The estimated values of $\Delta C/\gamma T_{sc}$ are 1.8–2.0 for both pure $HfV_2$ and 5.0% Nb doping in $HfV_2$. These values are larger than the value of 1.43 given by the BCS theory. The larger $\gamma$ and $\Delta C/\gamma T_{sc}$ values have been explained in terms of strong electron-phonon coupling effects.[5,6]

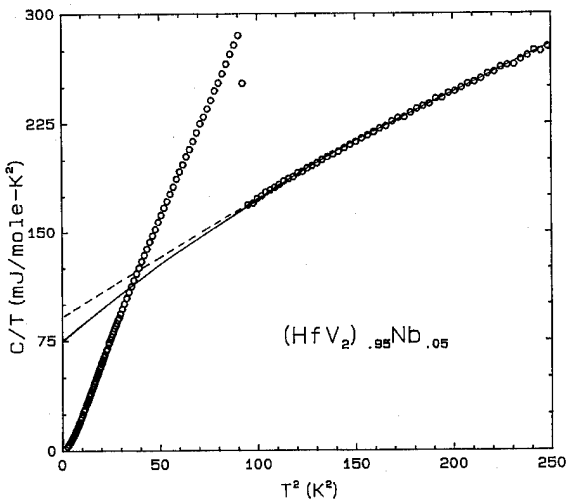



FIG. 4. $C/T$ vs $T^2$ for the 5.0% Nb-doped $HfV_2$ sample. The dash line is the $C/T=\gamma+\beta T^2$ fit to the experimental data from $T^2=90$ to 120 $K^2$. The solid curve is the $C/T=\gamma+\beta T^2+\alpha T^4+\delta T^6$ fit to the experimental data from $T^2=90$ to 250 $K^2$.

The band-structure calculations for the C15 $HfV_2$ have been carried out[12] recently using the linear-muffin-tin-orbital (LMTO) method.[16] The results show a narrow peak close to the Fermi energy, indicating a large density of states $N(E_f)$. This behavior is similar to that calculated for the Ce- and U-based $f$-electron systems.[17] The measured $\gamma$ value of 50 mJ/mole $K^2$ for $HfV_2$ is in qualitative agreement with these calculations. Note that the value of $\gamma$ was measured in the tetragonal phase (at low temperatures) for $HfV_2$ and the cubic phase for 5.0% Nb-doped $HfV_2$, whereas the $N(E_f)$ value was calculated for the C15 cubic phase.

It has been shown previously that a narrow peak at $E_f$, and a large $N(E_f)$, can lead to a very strong electron-phonon coupling,[18–20] which serves as a necessary (but not sufficient) condition for structural instabilities at low temperatures.[9,19,21,22] The band-structure calculations[12] for $HfV_2$ also show that there are large areas of the Fermi surface which are parallel or nearly parallel, leading to a so-called Fermi surface nesting, with a nesting vector $\mathbf{q}$ parallel to $\langle 001\rangle$. This Fermi surface nesting behavior together with the strong electron-phonon coupling effects give rise to the phonon mode $\omega(\mathbf{q})$ softening, and therefore to a lattice distortion.[23] In addition, a nesting vector $\mathbf{q}$ along $\langle 001\rangle$ is expected to give rise to a change in structure from cubic to tetragonal. The transmission electron microscopy measurements at low temperatures[14] are in agreement with these arguments.

The electrons coming from Nb substitution presumably fill unoccupied $d$-$d$ hybrid states[12] and change the Fermi energy $E_f$. The change in $E_f$ could alter the Fermi surface nesting and hence make it difficult to soften the phonon mode $\omega(\mathbf{q})$. Our specific heat data for the Nb-doped $HfV_2$ agree with this argument, i.e., $T_{st}$ shifts to lower temperatures and the size of the anomaly (corresponding to the degree of lattice distortion) becomes much smaller for very low Nb doping in $HfV_2$. For higher Nb substitution, the Fermi surface nesting no longer occurs, and therefore no structural transformation takes place.

As noted earlier Nb doping produces larger depressions of $T_{st}$ than does Zr or Ta doping. The rate at which Zr, Ta, and Nb depress $T_{st}$ are 1.0, 5.4, and 12 K/at. %, respectively. Zr is directly above Hf in the periodic table and has the same number of $4d$ electrons as Hf has $5d$ electrons. Moreover, it has a metallic radius of 1.585 Å which is very close to Hf's value of 1.575 Å. Hence it is not surprising that Zr depresses $T_{st}$ the least of the three dopants since one expects it to have the least effect on the band structure in particular on the Fermi surface nesting responsible for the mode softening. Both Ta and Nb are one column to the right of Hf. But Ta is a $5d$ metal while Nb is $4d$. Moreover, Ta has a metallic radius of 1.462 Å which is closer to Hf's value of 1.575 Å than is Nb's 1.429 Å. Hence it is not surprising that Ta has a less severe effect on $T_{st}$ than does Nb. Thus a qualitative explanation of the differing effects of Zr, Ta, and Nb on $T_{st}$ can be given.

Also mentioned earlier was the fact that both Ta and Nb have surprising small effects on $T_{sc}$. Here we report that the 5.0 at. % Nb sample shows a 50% increase in $\gamma$, while $\Delta C/\gamma T_{sc}$ remains essentially constant but $T_{sc}$ increases by only 6% or 7%. This result is not consistent with the BCS expression for $T_{sc}$ and suggests that further studies may be of interest.


[1] L. J. Vieland and A. W. Wicklund, Solid State Commun. **7**, 37 (1969).
[2] J. E. Kunzler, J. P. Maita, H. J. Levinstein, and E. J. Ryder, Phys. Rev. **143**, 143 (1966).
[3] V. A. Finkel' and E. A. Pushkarev, Sov. Phys. JETP **51**, 422 (1980).
[4] Y. Kimura, J. Phys. Soc. Jpn. **36**, 306 (1974).
[5] Y. Kishimoto, N. Shibata, T. Ohno, Y. Kitaoka, K. Asayama, K. Amaya, and T. Kanashiro, J. Phys. Soc. Jpn. **61**, 696 (1992).
[6] B. Luthi, M. Herrmann, W. Assmus, H. Schmidt, H. Rietschel, H. Wuhl, U. Gottwick, G. Sparn, and F. Steglich, Z. Phys. B **60**, 387 (1985).
[7] T. Matsuura and K. Miyake, J. Phys. Soc. Jpn. **55**, 610 (1986); K. Miyake, T. Matsuura, and C. M. Varma, Solid State Commun. **71**, 1149 (1989).
[8] H. Keiber, C. Geibel, B. Renker, H. Rietschel, H. Schmidt, H. Wuhl, and G. R. Stewart, Phys. Rev. B **30**, 2542 (1984).
[9] J. W. Hafstrom, G. S. Knapp, and A. T. Aldred, Phys. Rev. B **17**, 2892 (1978).
[10] K. Inoue, T. Kuroda, and K. Tachikawa, IEEE Trans. Magn. **MAG-15**, 635 (1979).
[11] K. Inoue and K. Tachikawa, IEEE Trans. Magn. **MAG-13**, 840 (1977).
[12] F. Chu, M. Sob, R. Siegl, and D. P. Pope (unpublished).
[13] F. Chu and D. P. Pope, Scr. Metall. **26**, 399 (1992).
[14] F. Chu and T. E. Mitchell, in *Proceedings of Microscopy and Microanalysis, 1995*, edited by Bailey, Ellisman, Hennigar, and Zaluzec (Jones & Begell, New York, 1995), p. 252.
[15] Y. Kimura, J. Phys. Soc. Jpn. **16**, 517 (1977).
[16] O. K. Andersen, Phys. Rev. B **12**, 3060 (1975).
[17] See, for examples, in *Proceedings of International Conference on Strongly Correlated Electron Systems*, edited by T. Kasuya, A. Yanase, and K. Okuda (Elsevier, North Holland, Amsterdam, 1993); Physica B **186–188**, (1993).
[18] W. L. McMillan, Phys. Rev. **167**, 331 (1968).
[19] S. K. Chan and V. Heine. J. Phys. F **3**, 795 (1973).
[20] H. Krakauer, R. E. Cohen, and W. E. Pickett, in *Atomic Scale Calculations in Materials Science*, edited by J. Tersoff, D. Vanderbilt, and V. Vitek (MRS, Pittsburgh, 1989), Vol. 141, p. 165.
[21] S. K. Sinha and B. N. Harmon, in *Superconductor d- and f-band Metals*, edited by D. H. Douglas (Plenum, New York, 1976), p. 269.
[22] T. Jarlborg and A. J. Freeman, Phys. Rev. B **22**, 2332 (1980).
[23] L. M. Roth, H. J. Zeiger, and T. A. Kaplan, Phys. Rev. **149**, 519 (1966).

# Electronic properties of UCuSn

H. Nakotte, A. Purwanto, and R. A. Robinson
*LANSCE, Los Alamos National Laboratory, Los Alamos, New Mexico 87545*

K. Prokeš and F. R. de Boer
*Van der Waals-Zeeman Instituut, Universiteit van Amsterdam, 1018 XE Amsterdam, The Netherlands*

L. Havela and V. Sechovský
*Department of Metal Physics, Charles University, 12116 Prague 2, The Czech Republic*

I. P. Swainson
*Chalk River Laboratories, Atomic Energy of Canada Limited, Chalk River, Ontario K0J 1J0, Canada*

Crystallographic analysis shows that UCuSn does not form in the hexagonal $CaIn_2$ structure as reported previously, but is an ordered ternary compound and forms in an orthorhombic structure (space group: $P2_1cn$). Bulk and neutron-diffraction measurements reveal that UCuSn orders antiferromagnetically below 62 K. At 4.2 K, high-field magnetization reveals a complex magnetization process with two metamagnetic transitions. Furthermore, bulk investigations show an additional anomaly at 25 K, but a smooth temperature dependence of various magnetic peaks down to the lowest temperature gives no evidence for a second magnetic transition. Possible scenarios responsible for the drastic changes in the electronic properties around 25 K are discussed. © *1996 American Institute of Physics.* [S0021-8979(96)26208-5]

## I. INTRODUCTION

The role of $5f$-ligand hybridization in suppressing local-moment magnetism has been studied extensively in the two largest isostructural groups of UTX compounds (T =transition metal, X=$p$-electron metal), namely, in compounds crystallizing in the hexagonal ZrNiAl and the orthorhombic TiNiSi structures.[1] The aim to search even higher degrees of $5f$-electron localization brings us to compounds reported to crystallize in the hexagonal $CaIn_2$ structure, which is formed for the very late $d$-metals Cu, Au, and Pd.[2]

In this contribution, we concentrate on UCuSn, which was thought to crystallize in this structure.[2–5] For this compound, antiferromagnetic ordering at low temperatures has been reported on the basis of electrical-resistivity,[4,5] magnetic-susceptibility,[4] and $^{119}$Sn Mössbauer studies.[6] In addition, magnetization measurements revealed two metamagnetic transitions at about 12 and 17 T in the ascending field sweep, while in the descending magnetization curve only one transition around 12 T was found.[4] There is also a very unusual temperature dependence of the electrical resistivity: below 60 K, $\rho(T)$ increases suddenly forming a maximum around 25 K, where it drops precipitously.[4,5]

In order to get more insight in the electronic properties of UCuSn, we have checked and extended the study of some basic bulk properties. Here, we briefly describe also the results of additional neutron-diffraction experiments, the details of which will be published elsewhere.

## II. SAMPLE PREPARATION AND CHARACTERIZATION

A polycrystalline sample of UCuSn was prepared by arc-melting stoichiometric amounts of the constituents, with no further heat treatment. The sample was powdered for the neutron diffraction experiments, which were performed on the High-Intensity Powder Diffractometer at LANSCE and on the C2 powder diffractometer at Chalk River. We observed a number of nuclear reflections which could not be indexed in the hexagonal system (e.g., $CaIn_2$ structure type), but we were able to index and refine the whole pattern in the related orthorhombic space group $P2_1cn$. The resultant structure and parameters are given in Fig. 1 and Table I.

## III. BULK PROPERTIES

We also measured the temperature dependences of the electrical resistivity, of the specific heat, and of the magnetization (at 2 and 4 T) and the results are displayed in Fig. 2.

The absolute resistivity values are intermediate between the values published in Refs. 4 and 5 and the overall shape of

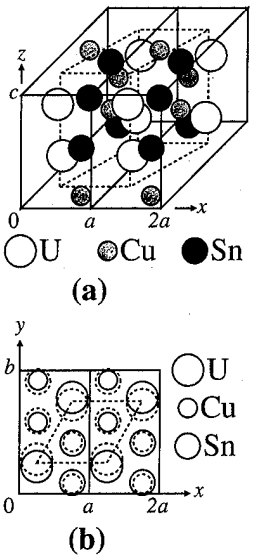



FIG. 1. Crystallographic structure of UCuSn (a) schematically drawn in a doubled cell showing the relation to the "parent hexagonal" cell. For sake of clarity, the $z$ position was shifted by 0.25 with respect to the values given in Table I. In (b), a projection onto the $a$-$b$ plane is shown, where the dashed lines represent the lower $z$ position with respect to the solid lines. The hexagonal cell is indicated by dashed lines.

 0021-8979/96/79(8)/6408/3/$10.00 © 1996 American Institute of Physics

TABLE I. Refined structural parameters for UCuSn at 300 K.

| Space group: $P2_1cn$ | | | |
|---|---|---|---|
| | $x$ | $y$ | $z$ |
| U ($4a$) | 0.25[a] | 0.2788(1) | 0.4982(2) |
| Cu ($4a$) | 0.2597(19) | 0.9168(2) | 0.6958(1) |
| Sn ($4a$) | 0.2586(20) | 0.5835(4) | 0.7762(1) |

(a) fixed to define the origin
Lattice parameters
$a$ (Å)=4.5391(2)
$b$ (Å)=7.8397(2)
$c$ (Å)=7.2203(2)
$R$ factors
$R_{wp}$=4.29%
$R_p$=3.09%
reduced $\chi^2$=3.88

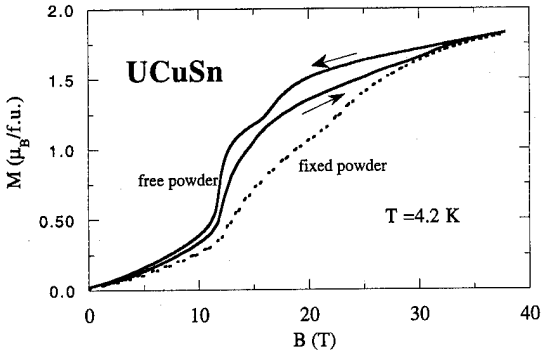



FIG. 3. Field dependence of the magnetization of UCuSn at 4.2 K measured on 'free powder' and 'fixed powder' represented as solid and dotted lines, respectively.

all three results is in good agreement. In our sample, antiferromagnetism sets in around 62 K, which is reflected by a sudden increase of the electrical resistivity. Upon further decrease of the temperature, the electrical resistivity passes a pronounced maximum around 25 K. At both temperatures (62 and 25 K), we observe anomalies in the specific heat and the magnetization. While clear maxima evolve in $C$ and $M/H$ around 62 K, the low-temperature anomaly is far less pronounced. Around 25–30 K, only slight changes in the derivatives are observed. In addition, we find that a small, but significant ferromagnetic component ($\sim 0.02\mu_B$/U atom) evolves below 30 K. At present, we are not sure whether this is intrinsic or due to a small amount of a ferromagnetic impurity phase.

High-field-magnetization studies were performed at the High-Field Facility in Amsterdam on powder, both free to be oriented by the applied field (giving the response of the easy magnetization direction), and in random orientation fixed by frozen alcohol (thereby representing an "ideal" polycrystal). The former ("free powder") result reveals a magnetic moment of $1.82\mu_B$ in 35 T, which is in excellent agreement with the results of Fujii *et al.*[4] The antiferromagnetic ground state is corroborated by metamagnetic transitions. In contrast to the results in Ref. 4, we find metamagnetic transitions around 12 and 30 T in the ascending curve and around 11 and 15 T in the descending curve. We believe that this difference could originate in small differences in the compositions of the samples, which could also account for the slight difference in $T_N$. Two transitions (around 13 and 25 T) are found also in the second (fixed powder) measurement, but no hysteresis was observed. The fact, that both magnetizations are almost equal in the highest field applied, may indicate an anisotropy field only slightly higher than 30 T, which is exceptionally low among U intermetallics.[7]

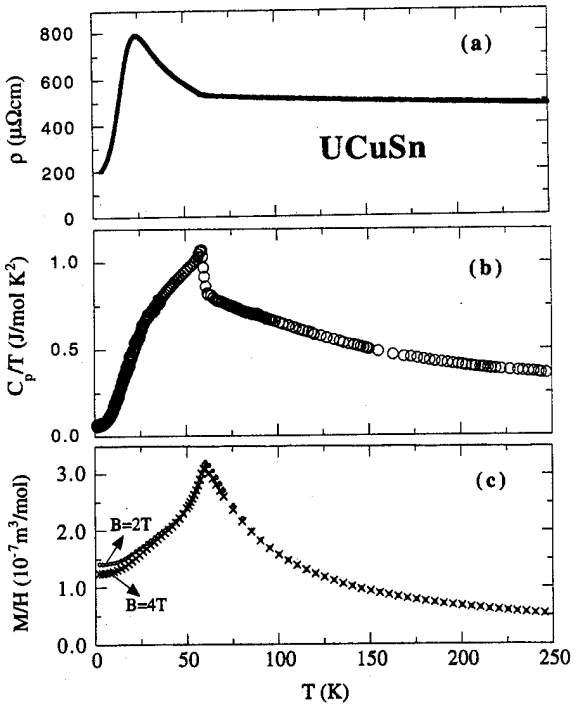



FIG. 2. Temperature dependences for UCuSn of (a) the electrical resistivity, (b) the specific heat, and (c) the magnetization (as $M/H$ for $H$=2 and 4).

## IV. NEUTRON-DIFFRACTION RESULTS

The bulk results above indicate two magnetic transitions in UCuSn at about 62 and 25 K. At low temperatures, the antiferromagnetic ground state was confirmed by the occurrence of additional purely magnetic reflections below 62 K in the neutron data taken at Los Alamos. However, magnetic intensities were found also on some nuclear reflections, and our results indicate that all magnetic contributions can be indexed in the same orthorhombic unit cell.

In order to clarify the (sometimes pronounced) anomalies in the bulk properties around 25 K, we performed additional neutron-diffraction experiments on the C2 powder diffractometer at Chalk River Laboratories. Data were collected at various temperatures, and the temperature dependences of the peak intensities of some "magnetic" peaks are shown in Fig. 4. In all cases, we observe a smooth temperature dependence with no evidence for a second magnetic phase transition around 25 K and no extra magnetic peaks were observed below this temperature.

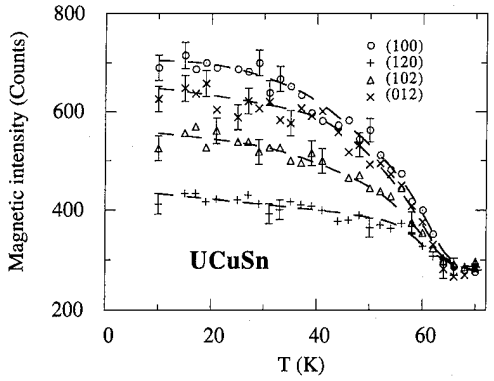



FIG. 4. Temperature dependence of the magnetic intensities of various Bragg reflections. In some cases, the intensities have been corrected for nuclear contributions. The lines are guides to the eye.

## V. DISCUSSION

While the investigations of bulk properties seem to indicate a second magnetic transition around 25 K, any moment reorientation seems to be excluded by the neutron-diffraction results. Clearly, this confusing situation cannot be resolved on the basis of the present data, but we may speculate on scenarios which may account for all observations. A possible explanation may involve temperature-induced changes of the antiferromagnetic gap which ultimately could lead to significant changes in the Fermi surface and therefore strongly affects the bulk properties (without a magnetic phase transition). Such a picture has been suggested by Fujii *et al.*[4]

On the other hand, an alternative explanation arises from the comparison with UPdSn, which forms in an ordered version of the $CaIn_2$ structure. UPdSn exhibits two magnetic transitions which are due to ordering of the $y$ and $z$ components of the magnetic moment at the upper transition temperature, while the $x$ component fluctuates until it also stabilizes at the lower transition temperature.[8] For this compound, single-crystal studies show clear anomalies in the temperature dependence of the intensity for most magnetic peaks, while this transition is "smeared out" in powder diffraction. As a consequence only a broad and featureless temperature dependence was found.[9] It may be that UCuSn behaves in a similar fashion, and one moment component stays fluctuating below $T_N$=62 K, but that its fluctuations gradually slow down until 25 K. In such picture, one may anticipate an enhancement in the resistivity due to fluctuations until they die out, with little or no change in the magnetic moment.

Further high-field magnetization studies at elevated temperature are envisaged to give more insight to the 25 K transition.

## ACKNOWLEDGMENTS

H.N. and A.P. would like to thank the Chalk-River staff for the pleasant stay during the neutron experiments. This work was supported by the U.S.-Czechoslovak Science and Technology Joint Fund under project No. 93039. It was also supported in part by the division of Basic Energy Sciences of the U.S. Department of Energy, by the Grant Agency of the Czech Republic (project nr.: 202/94/0454) and the "Stichting voor Fundamenteel Onderzoek der Materie" (FOM).

[1] V. Sechovský and L. Havela, in *Ferromagnetic Materials*, edited by E. P. Wohlfarth and K. H. J. Buschow (North Holland, Amsterdam, 1988), Vol. 4, pp. 309–491.
[2] T. T. M. Palstra, G. J. Nieuwenhuys, R. F. M. Vlastuin, J. van den Berg, and J. A. Mydosh, J. Magn. Magn. Mater. **67**, 331 (1987).
[3] F. R. de Boer, E. Brück, H. Nakotte, A. V. Andreev, V. Sechovský, L. Havela, P. Nozar, C. J. M. Denissen, K. H. J. Buschow, B. Vaziri, M. Meissner, H. Maletta, and P. Rogl, Physica B **176**, 275 (1992).
[4] H. Fujii, H. Kawanaka, T. Takabatake, E. Sugiura, K. Sugiyama, and M. Date, J. Magn. Magn. Mater. **87**, 237 (1990).
[5] V. H. Tran and R. Troc, Int. J. Mod. Phys. B **7**, 850 (1993).
[6] R. Kruk, K. Latka, K. Tomala, R. Kmiec, R. Troc, and V. H. Tran, J. Alloys Comp. **219**, 256 (1995).
[7] L. Havela, V. Sechovský, H. Nakotte, E. Brück, and F. R. de Boer, J. Alloys Comp. **213/214**, 243 (1994).
[8] R. A. Robinson, J. W. Lynn, A. C. Lawson, and H. Nakotte, J. Appl. Phys. **75**, 6589 (1994).
[9] R. A. Robinson, A. C. Lawson, J. W. Lynn, and K. H. J. Buschow, Phys. Rev. B **45**, 2939 (1992).

# Crystallographic and magnetic structure of $UCu_{1.5}Sn_2$

A. Purwanto, R. A. Robinson, and H. Nakotte
*Los Alamos National Laboratory, Los Alamos, New Mexico 87545*

I. P. Swainson
*Chalk River Laboratories, Atomic Energy of Canada Limited, Chalk River, Ontario KOJ 1JO, Canada*

M. S. Torikachvili
*Physics Department, San Diego State University, San Diego, California 92182*

We report on the crystallographic and magnetic structures of the antiferromagnet $UCu_{1.5}Sn_2$, as determined by x-ray and neutron powder diffraction. It crystallizes in the tetragonal $CaBe_2Ge_2$ structure type, with space group P/4nmm, and we find no site disorder between two different Sn $2c$ sites, in contrast with a previous report. $UCu_{1.5}Sn_2$ orders antiferromagnetically with a Néel temperature of about 110 K. This is unusually high among uranium intermetallics. The uranium moments align along the $c$ axis in a collinear arrangement but alternating along the $c$ axis. The low-temperature uranium moment is $2.01\mu_B$. © *1996 American Institute of Physics.* [S0021-8979(96)26308-1]

## I. INTRODUCTION

In the last decade many studies have been performed on the large family of tetragonal Ce- and U-based ternary intermetallic compounds with stoichiometry $CeT_2X_2$ or $UT_2X_2$ (T =transition metal, X=group IV element), with a view to understanding their magnetic and/or heavy-fermion properties.[1] Those compounds with X=Si or Ge have been studied most extensively, and they include the celebrated heavy-fermion superconductors $CeCu_2Si_2$ and $URu_2Si_2$. Most such compounds form in the body-centered tetragonal $ThCr_2Si_2$ structure (space group I4/mmm), though a significant minority form in the closely related primitive tetragonal $CaBe_2Ge_2$ structure (space group P4/nmm). In some cases, like $UCo_2Ge_2$, both forms can be produced depending on the heat treatment and stoichiometry of the sample.[2] The difference between the two structures is in the stacking sequence of the T and X layers between the layers of Ce or U atoms, as one progresses along the tetragonal axis.

We have recently started to work on $UT_2Sn_2$ compounds, and in this article we report on the crystallographic and magnetic properties of the antiferromagnet $UCu_2Sn_2$, as studied by x-ray and neutron diffraction. $UCu_2Sn_2$ is remarkable among uranium intermetallics for having a Néel temperature of 110 K,[3] while it is more typical for uranium compounds (without Co or Fe) to order magnetically at 50 K or below, if at all. $UCu_2Sn_2$ with a slight copper deficiency had previously been studied by means of x-ray diffraction by Pöttgen *et al.*,[4] and these authors found the $CaBe_2Ge_2$ structure type, but with two interesting features. First, in the stoichiometry $UCu_{1.3}Sn_2$, they found the copper deficiency to be entirely located on the $2c$-type sites, as shown in Fig. 1(a). Second, regarding the tin atoms on the $2c$-type sites in the other half of the unit cell, they found it necessary to use two such sites with significantly different $z$ parameters. Again, this is shown schematically in Fig. 1(a). We have repeated their study on a sample with slightly less copper deficiency using both x-ray and neutron diffraction. While we find the same sort of copper deficiency on the copper $2c$ sites, we find no evidence for a bimodal distribution of Sn atoms over two different sites with different $z$ parameters. In addition, we have used our neutron diffraction data to determine the magnetic structure, the magnitude of the uranium moment and to estimate the Néel temperature.

## II. EXPERIMENTAL METHOD

The polycrystalline sample was prepared by arc-melting stoichiometric (1:2:2) amounts of the constituent elements of at least 99.99% purity. The phase purity was checked by powder x-ray diffraction using Cu $K\alpha$ radiation ($\lambda$=1.54 Å), and the x-ray data were analyzed using the Rietveld refinement program GSAS.[5] A very small amount of impurity scattering was observed. For the neutron experiment, the $UCu_2Sn_2$ powder was sealed in a vanadium tube under a helium atmosphere, and this was in turn mounted in a helium

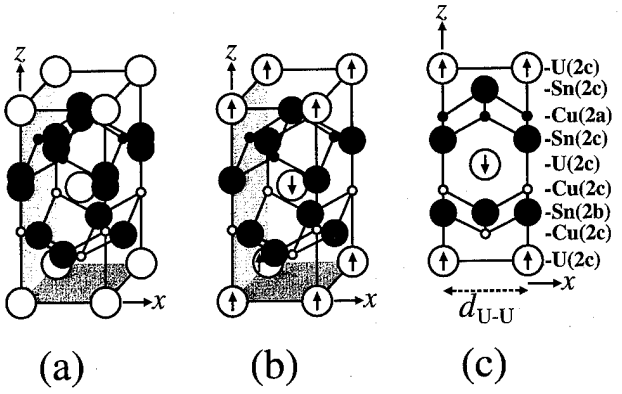



FIG. 1. Schematic diagrams of the structure of $UCu_{1.5}Sn_2$, as reported (a) by Pöttgen *et al.* (see Ref. 4), and (b), (c) in this work. In all cases the tetragonal $c$ axis is shown as vertical. The atomic occupancies are shown in the projection onto the $a$-$c$ plane in (c), with the partially filled Cu $2c$ sites shown by the open circles, while the fully occupied Cu $2a$ sites are represented by filled circles. The closest U-U distance $d_{U\text{-}U}$ is also shown in (c), while the collinear $c$-axis antiferromagnetic structure reported in the text is shown in both (b) and (c). The bimodal distribution of Sn atoms over two different $z$-parameter $2c$ sites reported by Pöttgen *et al.*, but not seen in our work, is shown by the dumbells in (a). The origin in this figure corresponds to (0.25,0.25,0.25) in the coordinates given in Table I.

 0021-8979/96/79(8)/6411/3/$10.00 © 1996 American Institute of Physics 

TABLE I. Refined structural parameters for $UCu_{1.5}Sn_2$ at room temperature (x ray) and at 120 K (neutron).

| Space group P4/nmm | | | | | | |
|---|---|---|---|---|---|---|
| | | | | | % occupancy | |
| U(2c) | 0.25 | 0.25 | z | z=0.2400±0.0006 | 100 | (neutron) |
| | | | | z=0.2435±0.0004 | 100 | (x ray) |
| Cu(2c) | 0.25 | 0.25 | z | z=0.6137±0.0012 | 45.1±1.9 | (neutron) |
| | | | | z=0.6004±0.0021 | 58.1±2.7 | (x ray) |
| Cu(2a) | 0.75 | 0.25 | 0 | | 107.6±2.1 | (neutron) |
| | | | | | 104.3±3.4 | (x ray) |
| Sn(2b) | 0.75 | 0.25 | 0.5 | | 103.7±2.4 | (neutron) |
| | | | | | 100.0±1.7 | (x ray) |
| Sn(2c) | 0.25 | 0.25 | z | z=0.8415±0.0006 | 95.6±2.8 | (neutron) |
| | | | | z=0.8472±0.0006 | 101.5±1.3 | (x ray) |
| Lattice constants (Å) | | | | a=4.3858±0.0003 | | (neutron) |
| | | | | a=4.3920±0.0002 | | (x ray) |
| | | | | c=9.6412±0.0007 | | (neutron) |
| | | | | c=9.6480±0.0004 | | (x ray) |
| R factors (%) | | | | $R_{wp}$=11.06 | | (neutron) |
| | | | | $R_{wp}$=14.52 | | (x ray) |
| | | | | $R_p$=8.50 | | (neutron) |
| | | | | $R_p$=11.12 | | (x ray) |
| | | | | Reduced $\chi^2$=7.821 | | (neutron) |
| | | | | Reduced $\chi^2$=2.163 | | (x ray) |

cryostat. The cryostat was mounted on the C2 powder diffractometer, at the Chalk River Laboratory, in such a way that it could be rotated continuously to give a better powder average over the grains in the sample. A rotating collimator was also used, between sample and the large area detector, to eliminate background peaks from the cryostat tails. We used a Si(531) monochromator with a wavelength of 1.51 Å, and data were recorded between 5° and 85° (for the magnetic scattering) and between 41° and 121° (for the structural analysis). Data were taken at a variety of temperatures between 6 and 120 K, and they were analyzed both by Rietveld refinement using GSAS,[5] as well as by peak-by-peak extraction of integrated intensities for the magnetic structure.

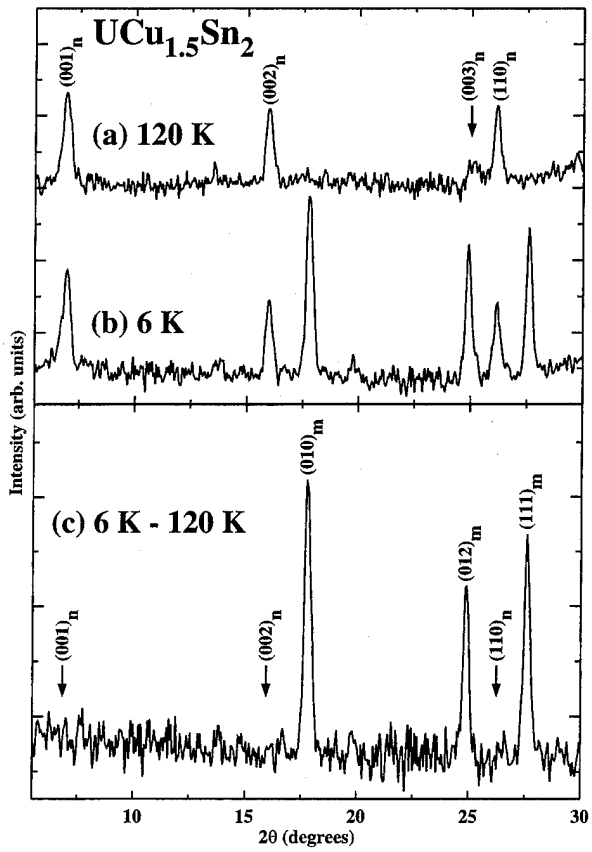



FIG. 2. Low-angle neutron diffraction patterns taken at (a) 120 K, (b) 6 K, and (c) the difference between 6 and 120 K. Note that three magnetic peaks (010), (012), and (111) are observed, but that there is no magnetic contribution to the (001), (002), or (110) nuclear reflections.

## III. RESULTS

The results of the Rietveld refinements using our x-ray and neutron data are listed in Table I. We obtain a good refinement using the $CaBe_2Ge_2$ structure. Second, we find a copper deficiency on the Cu 2c site, as found before by Pöttgen *et al.*,[4] and we deduce a stoichiometry close to $UCu_{1.5}Sn_2$, i.e., slightly less copper deficient than Pöttgen's

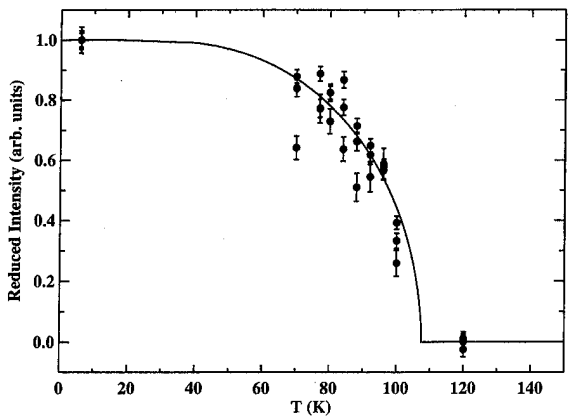



FIG. 3. Variation of the reduced intensity of the (010), (012), and (111) magnetic reflections. The solid line shows a fitted Brillouin function, with $T_N$=107 K.

TABLE II. Observed and calculated intensities for magnetic reflections in $UCu_{1.5}Sn_2$.

| Reflection | Observed intensity at 6 K[a] | Calculated intensity |
|---|---|---|
| 010 | 10.87±0.26 | 10.94 |
| 012 | 10.51±0.58 | 10.55 |
| 111 | 16.96±0.56 | 16.69 |
| Reduced $\chi^2$=0.4 | | |

[a]$I_{hkl} \sin\theta_{hkl} \sin(2\theta_{hkl})$.

sample. However, in contrast with their results, we find no need to invoke two different Sn $2c$ sites. Not only does Pöttgen's model give a worse $\chi^2$ than the model with a single $z$ value for the Sn $2c$ site, but if the occupancies on the two sites are allowed to vary in the refinement, it converges to 100% on the one site and 0% on the other. We therefore believe that our sample has the structure listed in Table I and shown in Fig. 1(b).

Regarding the magnetic structure, some of our low-angle neutron diffraction data are shown in Fig. 2. Three extra peaks, indexed as (010), (012), and (111), are seen at low temperature. We presume that these are magnetic and also note that no extra intensity is seen at the (001), (002), or (110) positions, which would also fall in this angular range. The fact that the observed reflections have no fractional indices implies that the magnetic cell is probably the same as the crystallographic cell, and that there are only two uranium atoms per magnetic cell. If we ignore the Cu and Sn ions, the two uranium atoms lie on a body-centered tetragonal lattice, and the fact that the magnetic reflections obey the $h+k+l=2n+1$ selection rule implies that the two uranium moments are antiparallel to each other. In addition, the fact that no (001) reflection is seen implies that the moments must be parallel to the $c$ axis, giving the simple collinear antiferromagnetic structure shown in Fig. 1(b) and (c). As it happens, a Shubnikov-group analysis of the $2c$ sites (point group 4 mm) shows that this is one of two allowed magnetic extensions to P4/nmm: the other would be a simple $c$-axis ferromagnet, which would only contribute extra magnetic intensity to the existing nuclear reflections. Fitting this model to our data yields a low-temperature uranium moment of $2.01\pm0.05\mu_B$. A comparison of the observed and calculated magnetic intensities is given in Table II.

Finally, the intensities of all three magnetic reflections are shown in reduced units, as a function of temperature, in Fig. 3 along with a fitted Brillouin function. This yields a transition temperature of $T_N$=107 K, which is in good agreement with the value of 110 K extracted from susceptibility data.[3]

## IV. DISCUSSION

A large number of uranium-based intermetallic antiferromagnets have now been studied in a variety of cubic, hexagonal, and orthorhombic structures.[6] Almost invariably, these materials show strong magnetic anisotropies, with the moments aligned perpendicular to planes or chains defined by nearest-neighbor uranium–uranium links. The physical rationale for this is that the $f$ electrons are hybridized more strongly, with ligand $p$ and $d$ electrons, in these directions or planes. They can better support "localized" moments in the directions of weaker hybridization, which are necessarily perpendicular. A second observation is that the coupling within the strongly hybridized planes or chains is usually ferromagnetic. This picture has also recently been shown to apply in several tetragonal $U_2T_2X$ (X=In, Sn) compounds.[7] It is instructive to apply this idea in the present case: in $UCu_{1.5}Sn_2$, the nearest-neighbor U–U distance, $d_{U-U}$ in Fig. 1(c), lies in the tetragonal basal plane along the **a** and **b** directions, with a length $a$=4.39 Å. This is significantly greater than the Hill limit of 3.5 Å, beyond which localized uranium moments might be expected. It also implies that these ordered moments should align perpendicular to the tetragonal basal plane, i.e., along the $c$ axis. This is exactly what we observe. In addition, the moments are also ferromagnetically coupled within the tetragonal sheets, in agreement with the phenomenology in other uranium intermetallics.

In summary, we have shown definitively that $UCu_{1.5}Sn_2$ orders into a simple collinear $c$-axis antiferromagnetic structure below 110 K, with a low-temperature uranium moment of $2.01\mu_B$. This is quite large, indicating fairly localized moments, though still well short of the full Hund's rule moment which would be in excess of $3\mu_B$. We also find the copper deficiency on the $2c$-type sites in agreement with Pöttgen *et al.*, but find no evidence for a bimodal distribution of Sn atoms on different $2c$-type sites with different $z$ parameters.

## ACKNOWLEDGMENTS

We are very grateful to E. Peterson for his assistance in taking the x-ray data and R. Donnaberger for help with the neutron experiment at Chalk River. This work was supported in part by the Office of Basic Energy Sciences of the U.S. Department of Energy.

[1] See, for instance, T. T. M. Palstra, A. A. Menovsky, G. J. Nieuwenhuys, and J. A. Mydosh, J. Magn. Magn. Mater. **54–57**, 435 (1986).
[2] A. Drost, Ph.D. thesis, University of Leiden, 1995.
[3] Unpublished susceptibility data taken by M. S. Torikachvili.
[4] R. Pöttgen, J. H. Albering, D. Kaczorowski, and W. Jeitschko, J. Alloys Compounds **196**, 111 (1993).
[5] A. C. Larson and R. B. Von Dreele, Los Alamos National Laboratory Report LA-UR-86-748.
[6] For a review of the magnetic anisotropy of uranium intermetallic compounds, see R. A. Robinson, A. C. Lawson, V. Sechovsky, L. Havela, Y. Kergadallan, H. Nakotte, and F. R. de Boer, J. Alloys Compounds **213/214**, 528 (1994), and references therein.
[7] A. Purwanto, R. A. Robinson, L. Havela, V. Sechovský, P. Svoboda, H. Nakotte, K. Prokeš, F. R. de Boer, A. Seret, J. M. Winand, J. Rebizant, and J. C. Spirlet, Phys. Rev. B. **50**, 6792 (1994).

# Metal-insulator transition in dirty Kondo insulators

P. Schlottmann and C. S. Hellberg
*Department of Physics, Florida State University, Tallahassee, Florida 32306*

We consider arbitrary clusters of Kondo holes in a Kondo insulator described by the nondegenerate symmetric Anderson lattice with a nearest-neighbor tight-binding conduction band on a simple cubic lattice. The $f$-electron self energy is considered within the local approximation. Each Kondo hole introduces a boundstate in the gap. The quantum interference in the scattering off the impurities gives rise to interactions among the Kondo holes. The spectral weight of the bound states is predominantly localized on the sites neighboring the Kondo holes. Clusters of impurities separated by more than one lattice site are disconnected for boundstates at the Fermi level. On a simple cubic lattice the metal-insulator transition in the impurity band then reduces to the site percolation of Kondo holes with first, second and fourth nearest neighbors. We use the low density mean cluster size expansion and a small cell renormalization to estimate the critical concentration. Hopping in the conduction band beyond nearest neighbors reduces the percolation threshold. Hence, 9.9% of Kondo holes is an upper bound for the insulator to become a metal. © *1996 American Institute of Physics.* [S0021-8979(96)26408-8]

Kondo insulators like $Ce_3Bi_4Pt_3$, CeNiSn, SmS, $SmB_6$, TmSe, $YbB_{12}$, and UNiSn are small-gap semiconductors with properties that strongly depend on strains in the crystal and impurities. The addition of small amounts of impurities gradually destroys the coherence of the ground state of the Kondo insulator. A Kondo hole is the charge neutral substitution of a rare-earth (actinide) ion by a nonmagnetic analog, e.g., La replacing Ce or Th substituting U. Each Kondo hole introduces a $\delta$-function-like bound state in the hybridization gap. The energies of the poles and their spectral weight determine the low-temperature thermodynamic and transport properties of the impure insulator.

We previously reported on the local density of $f$-states ($f$-DOS) in the vicinity of an isolated Kondo hole,[1,2] the formation of impurity bands for a finite concentration of Kondo holes,[3,4] the effects of doping and ligand defects,[5] interaction effects between two Kondo holes,[6] and recently we extended our microscopic theory to study interference effects in arbitrary clusters of impurities.[7] Here, we limit ourselves to the symmetric nondegenerate Anderson lattice with nearest-neighbor (n.n.) tight-binding dispersion for the conduction band on a simple cubic (sc) lattice. The bound state for an isolated impurity pins the Fermi level, and its spectral weight is all located on the n.n. sites to the Kondo hole.[1] This is also the case for a pair of Kondo holes separated by more than one lattice spacing.[6] For two Kondo holes on n.n. sites the spectral weight decreases rapidly with increasing distance from the impurities, the main spectral weight still being located on the n.n. sites to the holes. These results remain valid for an arbitrary cluster,[7] in particular, bound states with Fermi energy have only spectral weight on n.n. sites to a Kondo hole. Hence, the bound states of Kondo holes separated by more than one lattice site are disconnected. Since states at the Fermi level are responsible for the electric transport, the insulator-metal transition is reduced to the site percolation of Kondo holes with first, second, and fourth neighbor bonds.

In this paper, we briefly summarize the properties of the Kondo hole bound states at the Fermi level. Then we estimate the concentration of Kondo holes necessary for the percolation using two methods, the low density mean cluster size expansion and a small cell renormalization. Finally, we argue that hopping in the conduction band beyond n.n. reduces the percolation threshold and briefly address the effects of electron-hole asymmetry, finite temperatures and external frequencies (ac conductivities).

We consider the Anderson lattice $H_0$, and the scattering potential $H_i$, due to the nonmagnetic impurities at sites $\mathbf{R}_j$, $j=1,\ldots,N_i$,

$$H_0=\sum_{\mathbf{k}\sigma}\epsilon_{\mathbf{k}}c^{\dagger}_{\mathbf{k}\sigma}c_{\mathbf{k}\sigma}+\epsilon_f\sum_{i\sigma}f^{\dagger}_{i\sigma}f_{i\sigma}+U\sum_i n_{i\uparrow}n_{i\downarrow}$$
$$+V\sum_{\mathbf{k}\sigma}(c^{\dagger}_{\mathbf{k}\sigma}f_{\mathbf{k}\sigma}+f^{\dagger}_{\mathbf{k}\sigma}c_{\mathbf{k}\sigma}),$$
$$H_i=(\Delta\epsilon_f/N)\sum_{j\mathbf{k}\mathbf{k}'\sigma}e^{i(\mathbf{k}'-\mathbf{k})\mathbf{R}_j}f^{\dagger}_{\mathbf{k}\sigma}f_{\mathbf{k}'\sigma}. \quad (1)$$

Here, $\Delta\epsilon_f$ is large and positive for the impurity to be nonmagnetic,[1–3,6] $N$ is the number of sites and $\epsilon_{\mathbf{k}}=-2t\cos(k_x)-2t\cos(k_y)-2t\cos(k_z)$ with $|k_i|\leq\pi$ is the n.n. tight-binding dispersion on a sc lattice.

Since the impurity potential is a sum of factorizable potentials, the $U=0$ scattering problem can be solved exactly following similar steps as in Refs. 1, 2, and 6. The one-particle Green's function explicitly depends on the space configuration of the Kondo holes. The interaction between Kondo holes arises from the interference in the scattering off the impurities. We introduce a transform of the $f$-electron Green's function of the pure insulator

$$\mathcal{G}^0_\sigma(z,\mathbf{R})=\delta_{\mathbf{R},\mathbf{0}}(z-\epsilon_f)^{-1}+[V/(z-\epsilon_f)]^2$$
$$\times F[z-V^2/(z-\epsilon_f),\mathbf{R}], \quad (2)$$

where $\mathbf{R}=\mathbf{0}$ is the zero vector and $F[z',\mathbf{R}]=(1/N)\Sigma_{\mathbf{k}}e^{i\mathbf{k}\cdot\mathbf{R}}/(z'-\epsilon_{\mathbf{k}})$ is the transform of the spectral function of the conduction band. Denoting $\mathbf{R}_{lj}=\mathbf{R}_l-\mathbf{R}_j$ we define the $N_i\times N_i$ matrix $\tilde{\mathcal{G}}^0_\sigma(z,\mathbf{R}_{jl})$ with entries $l$ and $j$ that correlates the impurity sites. In the limit $\Delta\epsilon_f\to\infty$, the local $f$-DOS at a site $\mathbf{R}_0$ is

 0021-8979/96/79(8)/6414/3/$10.00 © 1996 American Institute of Physics

$$\rho_{f\sigma}(\omega,\mathbf{R}_0) = -(1/\pi)\,\mathrm{Im}\,\mathcal{G}^0_\sigma(z,\mathbf{0}) + (1/\pi)\sum_{jl}\,\mathrm{Im}\{\mathcal{G}^0_\sigma(z,\mathbf{R}_{0j}) \times[\tilde{\mathcal{G}}^0_\sigma(z,\mathbf{R}_{jl})]^{-1}\mathcal{G}^0_\sigma(z,\mathbf{R}_{l0})\}, \quad (3)$$

where $z=\omega+i0$ and Im denotes *imaginary part*. The situations of an isolated[1,2] and of a pair of Kondo holes[6] are contained as special limits.

In the absence of impurities the edges of the hybridization gap are approximately at $\epsilon_f \pm V^2/6t$, and the chemical potential $\mu$ lies within the gap. Correlations within the $f$ band are introduced via the $f$ self-energy $\Sigma_U(z)$ within the local approximation,[8] which neglects the $\mathbf{k}$ dependence. The $\mathbf{k}$ dependence of $\Sigma_U(z)$ is believed to be less relevant in heavy-fermion systems than the energy dependence. The imaginary parts of $\mathcal{G}^0_\sigma(\omega+i0,\mathbf{R})$ and $\Sigma_U(z)$ vanish inside the gap, so the quantities are real.[1,2,6,8] Within the range of interest, $\Sigma_U(z)$ is approximately given by $\Sigma_U(\omega) = Un_f/2-(\gamma-1)(\omega-\mu)$ and just enters the Green's function as a renormalization of $\epsilon_f$. We incorporate the Hartree–Fock shift $Un_f/2$ into $\epsilon_f$. Electron-hole symmetry then requires $\epsilon_f=0$. The Kondo effect is contained in the parameter $\gamma$, which reduces the hybridization gap to $2V^2/\gamma 6t$, i.e., to the size of $T_K$. Within the local approximation $\Sigma_U$ is not calculated selfconsistently, so that the $\mathbf{k}$ dependence induced into $\Sigma_U(\omega)$ via the impurities is neglected.

The local $f$ DOS vanishes identically at any Kondo hole site, since the limit $\Delta\epsilon_f\to\infty$ prevents the occupation of the site by an $f$-electron. With $N_i$ Kondo holes there are $N_i$ boundstates in the gap with energies given by $\det[\tilde{\mathcal{G}}^0_\sigma(\omega+i0,\mathbf{R}_{jl})]=0$, i.e., the poles in Eq. (3). Due to the electron-hole symmetry the bound state energies are symmetrically distributed with respect to the Fermi level at $\mu=0$. Hence, if $N_i$ is odd there is always a bound state at the Fermi level. In general, if $N_i$ is large we expect an accumulation of bound states with energy close to zero, eventually giving rise to the impurity band. These low-energy bound states are the relevant ones for the low-$T$ thermodynamics[3,4] and their mobility (connectivity) determines whether the impure Kondo insulator is a metal or an insulator.

The spectral weights of the bound states follow from the properties of $\mathcal{G}^0_\sigma(z,\mathbf{R})$. For $\mathbf{R}_1$ and $\mathbf{R}_2$ differing by a primitive basis vector of the lattice with $|\mathbf{R}_1|>|\mathbf{R}_2|$, we have that $\mathcal{G}^0_\sigma(z,\mathbf{R}_1)/\mathcal{G}^0_\sigma(z,\mathbf{R}_2)\approx -tz\gamma/V^2$.[7] From Eq. (3) it follows that for low-energy bound states ($|z|$ is small for states close to the Fermi level), the spectral weight at a site dramatically decreases with the distance to the closest Kondo hole. In particular, for states at the Fermi level all the spectral weight is located on n.n. sites to Kondo holes. For $z=0$ all other sites have zero spectral weight. Hence, for clusters separated by more than one lattice site the bound states at the Fermi level are disconnected. A percolating cluster necessarily has a bound state arbitrarily close or at the Fermi level. Hence, the metal-insulator transition on a sc lattice is reduced to the site percolation of Kondo holes with first, second and fourth neighbor bonds.

The critical concentration for the metal-insulator transition is straightforwardly calculated for a Bethe lattice of coordination $\mathcal{Z}$, $c_{\mathrm{cr}}=[\mathcal{Z}(\mathcal{Z}-1)]^{-1}$. For $\mathcal{Z}=6$ this yields $c_{\mathrm{cr}}=0.0333$, which is an underestimate since the lattice connectivity is neglected. For the sc lattice this task is considerably more complicated. We use the low density mean cluster size expansion and a small cell renormalization to estimate the percolation probability.

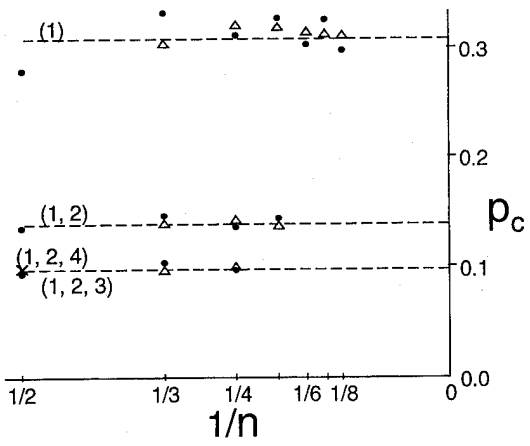



FIG. 1. Estimates of $p_c$ for the low density mean cluster size expansion for the site percolation of (1) first neighbor bonds, (1,2) first and second neighbor bonds, and (1,2,3) first, second, and third neighbor bonds on a sc lattice. The dashed lines are the extrapolated critical concentrations (see Ref. 9). The dots represent estimates using consecutive coefficients $a_n$ and the triangles estimates using $a_{n-2}/a_n$. The cross is the estimate from $a_1/a_2$ for the (1,2,4) problem involving first, second, and fourth neighbor bonds.

The mean size of finite clusters $S(p)$, where $p$ is the probability that a site is occupied, can be expanded in a power series in $p$, $S(p)=1+\Sigma_{n=1}^{\infty}a_n p^n$, by summing over the probabilities of occurrence of all possible clusters up to a desired order. The probability for a class $j$ of clusters of order $s$ is of the form $sb(s,j)p^s(1-p)^r$, where $b(s,j)$ is the number of possible configurations and $r$ is the "perimeter," i.e., the number of unoccupied neighboring sites required for the cluster to be isolated (disconnected from other clusters). The convergence of the series expansion in $p$ is then analyzed with Padé approximants or with the ratio method. In two dimensions the metal-insulator transition corresponds to the site percolation of Kondo holes on a square lattice with first, second, and third neighbor bonds. For this problem all clusters of up to five occupied sites have been computed.[9] Using the ratio method the extrapolated critical percolation probability is $p_c=0.292$.[9]

For the sc lattice the site problem with first neighbor bonds (1) (clusters up to nine occupied sites), first and second neighbor bonds (1,2) (up to six occupied sites), and first, second, and third neighbor bonds (1,2,3) (clusters of fifth order)[9] have been analyzed using the ratio method. The assumption that $S(p)$ diverges as $A(1-p/p_c)^{-(1+g)}$ when $p\to p_c^-$, leads to the large $n$ asymptotic form $a_n\approx An^g/\Gamma(1+g)p_c^n$.[10] We can then determine $p_c$ from the ratio of consecutive coefficients, $p_c=(1+g/n)(a_{n-1}/a_n)$. Critical properties do not depend on the range of the bonds (as long as they are short ranged), so we may use $g=\gamma-1$ $\approx 0.8$ (Ref. 11) for all cases. The dots in Fig. 1 are the

estimates from consecutive coefficients $a_n$. The oscillations present in the estimates for n.n. bonds are suppressed for (1,2) and (1,2,3) due to the higher connectivity of the lattice. The triangles correspond to estimates using $p_c=[(1+g/n)(1+g/(n-1))(a_{n-2}/a_n)]^{1/2}$. This suppresses the oscillations and leads to a monotonic convergence to the extrapolated critical concentrations (dashed lines).

For first, second, and fourth neighbor bonds (1,2,4) we limited ourselves to calculate the first two coefficients of the series are $a_1=24$ and $a_2=342$. This leads to an estimate for $p_c$ of 0.0982 (cross in Fig. 1), a value that is slightly above the corresponding (1,2,3) estimate. Since the estimates for problems with high connectivity do not appear to vary substantially with $n$, we may use this value as an indication that $p_c\approx 0.10$.

Another method to obtain the percolation threshold is the small cell renormalization which, like the block spin renormalization frequently used for thermal critical phenomena, is based on self-similarity under scaling. Scaling assumes that the linear dimension $b$ of the cell is much smaller than the correlation length $\xi$. The $M=b^3$ sites of the cell are replaced by a single supersite. The criterium for such replacement in thermal critical phenomena is the majority rule. For a percolation problem the connectivity is the essential ingredient.[12] We consider a supersite occupied if the bottom and top faces of the cell are connected, and empty otherwise. The renormalization transform yielding the probability of occupation of the supersite $p'$ is then

$$p'=\sum_{r=0}^{M} f_r^M \binom{M}{r} p^r (1-p)^{M-r}, \tag{4}$$

where $f_r^M$ is the fraction of clusters of $r$ sites that are connected from top to bottom. The $f_r^M$ are obtained numerically by considering a representative set of clusters. At the percolation point, $p'=p=p_c$ gives a self-consistent equation with three fixed points, the two stable ones $p=0$ and $p=1$ of attraction basins separated by the desired $p_c$. Figure 2 shows the $p_c(b)$ obtained for the site percolation in the (1,2,4) problem plotted as a function of $b^{-1/\nu}$, where $\nu=0.9$ is the critical exponent of the correlation length. The straight line in Fig. 2 shows the scaling of the data for $b\geq 18$ and extrapolates to $p_c=0.099$ for the infinite system. This value is consistent with the estimate from small cluster expansions.

In summary, the insulator-metal transition for the nondegenerate symmetric Anderson lattice with n.n. hopping for the conduction band on a sc lattice can be reduced to the site percolation of Kondo holes with first, second, and fourth neighbor bonds. We estimated the critical concentration of Kondo holes at about 9.9%. Assuming a constant mean-free path in the vicinity of $p_c$, the electrical conductivity tends to zero proportionally to $(p-p_c)^2$ as $p\to p_c^+$.[11] In the critical region the correlation length diverges as $\xi\propto(p-p_c)^{-\nu}$ with $\nu\approx 0.9$ and the mean size of finite clusters as $S\propto(p-p_c)^{-\gamma}$ with $\gamma\approx 1.8$, while the strength of the infinite network (for $p>p_c$) increases as $P\propto(p-p_c)^{\beta}$ with $\beta\approx 0.4$.[11]

If the tight-binding dispersion extends beyond n.n., also the physical extension of the bound states increases accordingly, e.g., for states at the Fermi level the spectral weight is nonzero on all sites that can be reached by simple hopping from a Kondo hole.

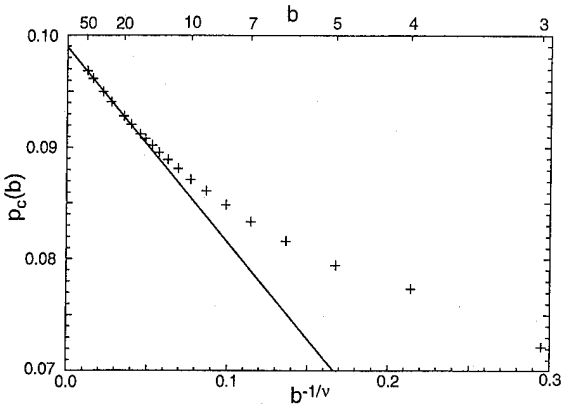



FIG. 2. Small cell renormalization for the (1,2,4) site problem for several cell sizes from $b=3$ up to $b=50$. $p_c(b)$ is obtained as the nontrivial fixed point of the renormalization transformation (4). The extrapolated critical concentration is 0.099. The straight line shows the scaling of the data for $18\leq b\leq 50$ with $b^{-1/\nu}$, where $\nu=0.9$ is the exponent of the correlation length.

For states that are close to the Fermi level or for a small electron-hole asymmetry, also sites beyond n.n. to a Kondo hole have a small spectral weight. The spectral weight decreases very fast with the distance. Hence, electron-hole asymmetry, an ac electric field, a constant magnetic field or a finite temperature increase the connectivity. Two types of connections have to be distinguished: the strong ones we considered in this paper and weak ones induced by the above parameters. Below, the $p_c$ for the strong connections the impure Kondo lattice is expected to behave like a very poor metal or a dirty semiconductor. Although there may be a percolating cluster, the tunneling probability will be very small.

## ACKNOWLEDGMENTS

One of the authors (P.S.) acknowledges the support of the U.S. Department of Energy under Grant No. DE-FG05-91ER45443 and C.S.H. the support of the Office of Naval Research under Grant No. N00014-93-1-0189.

[1] R. Sollie and P. Schlottmann, J. Appl. Phys. **69**, 5478 (1991).
[2] R. Sollie and P. Schlottmann, J. Appl. Phys. **70**, 5803 (1991).
[3] P. Schlottmann, Phys. Rev. B **46**, 998 (1992).
[4] P. Schlottmann, Physica B **186–188**, 375 (1993).
[5] P. Schlottmann, J. Appl. Phys. **75**, 7044 (1994).
[6] P. Schlottmann, Physica B **206&207** 816 (1995).
[7] P. Schlottmann (unpublished).
[8] H. Schweitzer and G. Czycholl, Solid State Commun. **74**, 735 (1990).
[9] J. W. Essam, in *Phase Transitions and Critical Phenomena*, edited by C. Domb and M. S. Green (Academic, London, 1972), Vol. 2, p. 197.
[10] D. S. Gaunt and A. J. Guttmann, in *Phase Transitions and Critical Phenomena*, edited by C. Domb and M. S. Green (Academic, London, 1974), Vol. 3, p. 181.
[11] D. Stauffer, *Introduction to Percolation Theory* (Taylor & Francis, London, 1985).
[12] P. J. Reynolds, H. E. Stanley, and W. Klein, Phys. Rev. B **21**, 1223 (1980).

# Tb impurities in Th: A Kondo system with undercompensated magnetic moment?

J. G. Sereni
*Centro Atómico Bariloche, 8400 Bariloche, Argentina*

P. Schlottmann
*Department of Physics, Florida State University, Tallahassee, Florida 32306*

Dilute $Tb_xTh_{1-x}$ alloys have been thoroughly studied in the light of a possible valence instability and Kondo effect in $Tb^{3+}$ and $Tb^{4+}$ ions. We review the experimental data for the specific heat, magnetic susceptibility, magnetization, magnetoresistivity, and the change of the superconducting properties of Th. In analogy to Tm ($Tm^{2+}$ and $Tm^{3+}$) and Pr ($Pr^{3+}$ and $Pr^{4+}$) impurities in metals, Tb involves two electronic configurations each with a magnetic Hund's rule ground multiplet. Two classes of models for valence admixtures of two magnetic configurations have been investigated in the past. Depending on the form of the hybridization and the $jj$ coupling within the $4f$ shell, the models either have a singlet or a magnetic ground state. As for Tm impurities the latter class of models, related to the undercompensated Kondo effect, appears to describe the system Tb*Th* more appropriately. A qualitative explanation of the data is attempted within a scheme that combines Kondo screening with crystalline field splitting. © *1996 American Institute of Physics.* [S0021-8979(96)26508-4]

The exact solution of the Coqblin–Schrieffer and the degenerate $U\to\infty$ Anderson models in terms of Bethe's ansatz opened the possibility of quantitative comparisons with experimental data for dilute Ce and Yb alloys,[1] i.e., systems with *one* localized electron or hole in the $f$ shell. A remarkably good agreement was obtained for the temperature and magnetic field dependence of the susceptibility, the specific heat, the magnetization, and the valence for impurity systems (see Ref. 1 for a review), alloys[1] and compounds.[1–3]

This analysis has been extended to the transition-metal impurities Fe and Cr in simple metals like Cu and Ag.[4] Realistic models for these impurities, as well as for $Mn^{2+}$ and $Eu^{2+}$ impurities, involve more than one localized electron (hole) and are necessarily more complex. The $n$-channel Kondo model[5] provides a suitable description if one assumes that the orbital degrees of freedom are quenched to an orbital singlet by one or more mechanisms. The low-$T$ properties of such impurity systems are those of a totally compensated impurity spin (spin-singlet ground state), which is realized within the $n$-channel Kondo model if the number of channels $n$ is equal to $2S$.[6]

Two further qualitatively different situations may occur: (a) If $n<2S$, the impurity spin is *undercompensated*, since there are not enough conduction electron channels to yield a singlet ground state, leaving an effective spin degeneracy of $(2S+1-n)$. (b) If $n>2S$, the number of channels is larger than required to compensate the impurity spin. The impurity is said to be *overcompensated* and critical behavior is obtained as both the temperature and the field tend to zero. The overcompensated case for $S=1/2$ and $n=2$ represents the physical situations of the quadrupolar Kondo effect[7] and electron-assisted tunneling of an atom in a double-well potential.[8] An alloy possibly displaying the quadrupolar Kondo effect is $U_xY_{1-x}Pd_3$ (Ref. 9) and an experimental realization for tunneling with multichannel characteristics is the differential resistance of metal point contacts containing structural disorder.[10]

A possible application of the *undercompensated Kondo effect* are dilute alloys of impurities with two magnetic configurations in simple metals. The experimentally most studied case is Tm as dilute impurities,[11] and TmSe and its alloys.[12] For mixed-valent Tm ions the Hund's rule ground multiplets of the two configurations $4f^{12}$ and $4f^{13}$ are $J=6$ and $J=7/2$, i.e., both are magnetic. The experiments seem to point towards a magnetic ground state. Other candidates are Pr ions and Tb impurities. In this paper we explore the possibility of interpreting experiments on dilute TbTh alloys as undercompensated Kondo impurities.

The main experimental results for dilute $Tb_xTh_{1-x}$ alloys can be summarized as follows. (i) The high-$T$ susceptibility for $T>100$ K essentially has the full magnetic moment of $Tb^{3+}$.[13] The magnetic moment is considerably reduced at intermediate $T$,[14] probably as a consequence of Kondo screening and/or crystalline fields. (ii) At low $T$ the susceptibility $\chi$ has a spin-glass-like peak at a $T_{max}$ that monotonically increases with the Tb concentration, $x$.[14] The value of $\chi$ at $T_{max}$ decreases with $x$. (iii) The specific heat in zero field is proportional to $T$ at low $T$ with a $\gamma$ coefficient of about 450 mJ/(K$^2$ mol Tb).[13] As a function of $T$ the electronic specific heat shows a maximum at about 4 K. At higher $T$ the specific heat of Tb impurities follows a $(\gamma T+\beta T^3)$ law with positive $\beta$ (after subtracting the electron and phonon contributions of the host). The sign of $\beta$ is then opposite to that of spin-1/2 Kondo impurities. (iv) The increase of entropy from very low $T$ to about 6 K is approximately $R$ ln(2) but still showing clear tendency to grow.[13] (v) A relatively large magnetic field enhances the specific heat of the alloy at higher $T$, reduces it at intermediate $T$ and an interesting up-turn is observed in-field at low temperatures. This remarkable behavior is displayed in Fig. 1. (vi) The resistivity due to the Tb impurities is only weakly $T$ dependent (if not constant) and independent of the magnetic field (no magnetoresistance). (vii) The magnetization as a function of field has the characteristics of a free spin or Kondoesque impurity.

 0021-8979/96/79(8)/6417/3/$10.00 © 1996 American Institute of Physics 

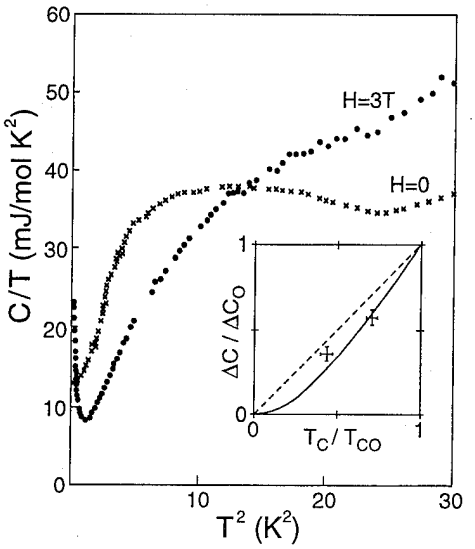



FIG. 1. Specific heat over $T$ as a function of $T^2$ for the alloy $Tb_xTh_{1-x}$ with $x=0.015$ in zero field and a magnetic field of 3 T. For $H=0$ a Schottky-like structure arising from the impurities is seen, which is quenched by the moderate field of 3 T. At low $T$ an up-turn of $C/T$ develops in magnetic field as a consequence of the Tb ions. The inset shows the discontinuity of the specific heat at $T_c$ normalized to the value for the pure superconductor as a function of $T_c/T_{c0}$. The two samples correspond to $x=0.0045$ and 0.0084. The solid curve refers to pure pair breaking (Abrikosov–Gor'kov) and the dashed line to pair weakening (BCS law of corresponding states).

(viii) The Th matrix is a superconductor with $T_{c0}=1.36$ K. Tb impurities reduce $T_c$ approximately linearly with the concentration.[15] The extrapolated critical concentration is roughly 1.5 at. %. The pressure dependence of $T_c$ apparently scales that of the host. The suppression of superconductivity is neither pure pair breaking (Abrikosov–Gor'kov) nor pure pair weakening, but consistent with a Kondoesque mechanism with $T_K \approx 3T_{c0}$.[16] (ix) The discontinuity of the specific heat for the alloy normalized to the value of the pure superconductor is shown in the inset of Fig. 1 for two samples. On one hand, the data lies below the BCS law of corresponding states (pair weakening), but on the other hand, the sample of larger concentration of impurities lies above the Abrikosov–Gor'kov curve (pair breaking). These results could be consistent with a Kondoesque mechanism not displaying reentrance ($T_K > T_{c0}$).[16]

Many of the above properties are not consistent with a singlet ground state for the Tb impurities. Tb ions in a metallic environment are close to a valence instability so that two electronic configurations, namely, $Tb^{3+}$ ($4f^8$) with a Hund's rule ground multiplet of $J=6$ and $Tb^{4+}$ ($4f^7$) ($S$-state isoelectronic to $Gd^{3+}$) with $J=7/2$ are expected to coexist via valence admixture through conduction electrons. The high-$T$ magnetic moment of the susceptibility[13] indicates that the energetically favorable and dominating configuration is $4f^8$. The Hund's rule groundstate for both configurations is magnetic. Two classes of models for valence admixtures of two magnetic configurations were extensively investigated in the past. One class of models involves the hybridization with two (or more) conduction electrons, while the other class only considers the $jj$ coupling with one band state. Neither class decomposes the $f$-shell states using fractional parentage coefficients. We briefly review the main results below.

A representative Hamiltonian of the first class of models (several related variants have been studied) is the following generalization of the Anderson model[17,18]

$$H=\sum_{km}\epsilon_k c^\dagger_{km}c_{km} + E_1\sum_m |1m\rangle\langle 1m| + E_2\sum_{mm'}|2mm'\rangle\langle 2mm'| + V\sum_{kmm'}(|2mm'\rangle\langle 1m|c_{km'}+c^\dagger_{km'}|1m\rangle\langle 2mm'|), \tag{1}$$

where $\epsilon_k$ is the dispersion of the conduction states, $m$ labels the $z$ component of $j(|m|\leqslant j)$, and $|1m\rangle$ and $|2mm'\rangle$ denote $f$ states with *one* and *two* localized electrons (of $z$ components $m$ and $m'$), respectively. Model (1) is formulated for Pr ions ($j=5/2$) or Tm impurities (holes with $j=7/2$ instead of electrons). The reported calculations of the ground state are perturbative in $V$, variational ansatze and selfconsistent diagram summations in the spirit of the $1/N$ expansion,[17–22] and consistently yield a singlet as the state of lowest energy, even if Eq. (1) is modified to include Clebsch–Gordan coefficients to provide a more realistic coupling.

Representative for the second class of models is[23,24]

$$H=\sum_{km}\epsilon_k c^\dagger_{km}c_{km}+\sum_{M_1}E_{J_1M_1}|J_1M_1\rangle\langle J_1M_1| + \sum_{M_2}E_{J_2M_2}|J_2M_2\rangle\langle J_2M_2| + V(2J_2+1)^{1/2}\sum_{kmM_1M_2}(J_2M_{2j}m|J_{2j}J_1M_1) \times[|J_1M_1\rangle\langle J_2M_2|c_{km}+c^\dagger_{km}|J_2M_2\rangle\langle J_1M_1|], \tag{2}$$

where $|J_1M_1\rangle$ and $|J_2M_2\rangle$ denote the states of the Hund's rule ground multiplets of the $4f^{n+1}$ and $4f^n$ configurations, respectively. The relevant conduction states have total angular momentum $j$ and $z$ component $m$. The model corresponds to the $U\to\infty$ limit of an Anderson impurity excluding states other than the $J_1$ and $J_2$ manifolds and a hybridization within a simplified $jj$ scheme. The Clebsch–Gordan coefficient selects $m=M_1-M_2$. This model contains all the relevant mixed valent situations as limiting cases: (1) For $J_2=0$ and $j=J_1=5/2$ it reduces to the Anderson model for Ce. (ii) For $j=J_2=7/2$ and $J_1=0$ we recover the standard picture for Yb. (iii) The case of Pr is obtained for $J_2=j=5/2$ and $J_1=4$, while (iv) Tm ions are parametrized by $J_2=6$ and $J_1=j=7/2$. (v) Mixed-valent Sm impurities are described by $J_2=0$ and $J_1=j=5/2$. (vi) Finally, Eu corresponds to $J_2=0$ and $j=J_1=7/2$.

Several treatments of model (2) (and its generalization to a lattice) have been reported for the situation of two degenerate ground multiplets (i.e., $J_1\neq 0$ and $J_2\neq 0$), e.g., mean-field approaches,[23,25] perturbative summations using Mori's projector formalism,[24,26] the coherent potential

approximation,[27] Wilson's numerical renormalization group,[28] exact solutions via Bethe's ansatz (only $J_2=j=1/2$ and $J_1=1$ is integrable)[29,30] and numerical diagonalizations using Lanczos method.[31] The main result common to all these approaches is a magnetic groundstate.

The magnetic groundstate can be made plausible with the following *Gedanken experiment* based on the fact that an impurity does not undergo a phase transition. Consider model (2) as a function of $\Delta = E_{J_1} - E_{J_2} - \mu$, where $\mu$ is the chemical potential. If $\Delta$ is very large (either positive or negative) compared to $V$, one of the configurations can be projected out by means of a Schrieffer–Wolff transformation. Assume $J_2+j \geqslant J_1$ and $J_1>J_2$ (otherwise interchange electrons with holes). As an example consider first the well-known case of a Ce impurity: If $\Delta \gg 0$ the ground state is the $4f^0$ singlet, while for $\Delta \ll 0$ the impurity spin $J_1$ is Kondo compensated into a singlet via the Coqblin–Schrieffer mechanism. The ground state is a singlet for all values of $\Delta$ and character of the ground-state wave function gradually interpolates between these two limits. The general case can be understood in a similar way. If $\Delta \gg 0$ the ground multiplet is $J_2$, which is coupled to the conduction electrons via a ferromagnetic spin exchange (which includes Clebsch–Gordan coefficients). Under renormalization the model then evolves into a weak coupling fixed point, i.e., asymptotically the impurity is free and decoupled from the host. The impurity has a $J_2$ ground multiplet. $\Delta$ is now continuously decreased from $\Delta \gg 0$ to $\Delta \ll 0$; although the character of the ground state of the impurity changes as a function $\Delta$, it will remain a multiplet of total angular momentum $J_2$. In the limit $\Delta \ll 0$ the exchange coupling of the $J_1$ multiplet with the conduction electrons is antiferromagnetic leading to a strong coupling fixed point under renormalization. Here the conduction electrons of total angular momentum $j$ compensate the $J_1$ multiplet via the Kondo effect into a $J_2$ multiplet. This *undercompensated* Kondo effect picture emerges from all approaches[23–31] for model (2).

We now explore the possibility to qualitatively explain the experimental facts for Tb*Th* with model (2). Via the Kondo effect the $J_1=6$ multiplet of $Tb^{3+}$ is screened to a $J_2=7/2$ multiplet by conduction electrons in the channel $j=7/2$. Assuming that $T_K$ for this undercompensated Kondo effect is large (e.g., about 50 K which is consistent with the drop of the magnetic moment as a function of $T$) compared to the cubic crystalline field, the octet is split into two doublets, $\Gamma_6$ and $\Gamma_7$, and a $\Gamma_8$ quartet. The peak in the specific heat at about 4 K is the Schottky anomaly for the crystalline field splitting between the two lowest levels. The low-$T$ entropy excludes the $\Gamma_8$ from being the ground multiplet; the most likely scenario is that the two lowest levels are the doublets [$\Delta S=R\ln(2)$], but the quartet as the first excited level cannot be excluded [$\Delta S=R\ln(3)$]. The ground doublet opens the possibility of magnetic "order" of the spin-glass type. The specific heat is a superposition (and possible interference of) crystalline field Schottky anomalies and the Kondo effect. The Kondo effect gives rise to the $\gamma T+\beta T^3$ contribution. The numerical value of $\gamma$ associated with $T_K=50$ K is about a factor of two smaller than the experimental one, while the $\beta$ arising from the impurities (phonons have been subtracted) has the correct (positive) sign. The sign of $\beta$ would be the same as for the $J=7/2$ Anderson model in the $U\rightarrow\infty$ limit.[1] The magnetic ground doublet is also consistent with the depression of the superconducting $T_c$ and $\Delta C/\Delta C_0$ deviating from the BCS law of corresponding states. A strong magnetic field would lift the degeneracy of the ground doublet and induce another Schottky anomaly at very low $T$. This Schottky anomaly could be the origin of the up-turn in the specific heat shown in Fig. 1.

In summary, the above speculations are consistent with most of the properties of Tb*Th*. We would like to point out that the above scheme cannot be reconciled with the absence of magnetoresistivity.

One of the authors (P.S.) acknowledges the support of the U.S. Department of Energy under Grant No. DE-FG05-91ER45443.

[1] P. Schlottmann, Phys. Rep. **181**, 1 (1989), and references therein.
[2] J. W. Rasul and P. Schlottmann, Phys. Rev. B **39**, 3065 (1989).
[3] P. Schlottmann, J. Appl. Phys. **73**, 5412 (1993).
[4] P. D. Sacramento and P. Schlottmann, Solid State Commun. **73**, 747 (1990); Phys. Rev. B **42**, 743 (1990); Physica B **171**, 122 (1991).
[5] P. Nozières and A. Blandin, J. Phys. (Paris) **41**, 193 (1980).
[6] P. Schlottmann and P. D. Sacramento, Adv. Phys. **42**, 641 (1993).
[7] D. L. Cox, Phys. Rev. Lett. **59**, 1240 (1987).
[8] K. Vlàdar and A. Zawadowski, Phys. Rev. B **28**, 1564 (1983); A. Muramatsu and F. Guinea, Phys. Rev. Lett. **57**, 2337 (1986).
[9] C. L. Seaman *et al.*, Phys. Rev. Lett. **67**, 2882 (1991); B. Andraka and A. M. Tsvelik, *ibid.* **67**, 2886 (1991).
[10] D. C. Ralph and Buhrman, Phys. Rev. Lett. **69**, 2118 (1992); D. C. Ralph *et al.*, *ibid.* **72**, 1064 (1994).
[11] A. Berger *et al.*, J. Phys. (Paris) Colloq. **40**, C5-364 (1979); E. Holland-Moritz and M. Praguer, J. Magn. Magn. Mater. **31–34**, 395 (1983); E. Holland-Moritz, *ibid.* **38**, 253 (1983).
[12] H. Bjerrum Møller *et al.*, Phys. Rev. Lett. **39**, 1021 (1977); B. Batlogg *et al.*, Phys. Rev. B **19**, 247 (1979); C. Vettier *et al.*, J. Magn. Magn. Mater. **15–18**, 987 (1980); A. Berton *et al.*, Phys. Rev. B **23**, 3504 (1981).
[13] J. G. Sereni *et al.*, J. Magn. Magn. Mater. **63&64**, 597 (1987).
[14] E. Braun *et al.*, Z. Phys. B **70**, 187 (1988).
[15] R. P. Guertin *et al.*, Physica B **102**, 151 (1980).
[16] P. Schlottmann, J. Low-Temp. Phys. **20**, 123 (1975).
[17] Y. Yafet *et al.*, Phys. Rev. B **32**, 360 (1985).
[18] N. Read *et al.*, J. Phys. C **19**, 1597 (1986).
[19] A. C. Nunes *et al.*, J. Phys. C **18**, L873 (1985).
[20] T. Saso, J. Phys. Soc. Jpn. **58**, 4064 (1989).
[21] J. W. Rasul, Phys. Rev. B **42**, 9996 (1990).
[22] H. Lustfeld, Physica B **113**, 69 (1982).
[23] J. Mazzaferro *et al.*, Phys. Rev. Lett. **47**, 274 (1981).
[24] P. Schlottmann, in *Valence Instabilities*, edited by P. Wachter and H. Boppart (North Holland, Amsterdam, 1982), p. 471.
[25] A. A. Aligia *et al.*, J. Magn. Magn. Mater. **40**, 61 (1983).
[26] P. Schlottmann, Phys. Rev. B **29**, 630 (1984); **29**, 4468 (1984).
[27] A. A. Aligia and B. Alascio, J. Magn. Magn. Mater. **43**, 119 (1984); **46**, 321 (1985).
[28] R. Allub *et al.*, Phys. Rev. B **29**, 3098 (1984).
[29] Proetto *et al.*, Phys. Lett. A **107**, 93 (1985); Phys. Rev. B **31**, 6143 (1985).
[30] P. Schlottmann, Z. Phys. B **59**, 391 (1985).
[31] M. Baliña and A. A. Aligia, Europhys. Lett. **13**, 739 (1990).

# Hybridization-induced magnetism in correlated cerium systems

Nicholas Kioussis and J. Thevenot
*Department of Physics and Astronomy, California State University, Northridge, California 91330-8268*

Bernard R. Cooper and Q. G. Sheng
*Department of Physics, West Virginia University, Morgantown, West Virginia 26506*

There is a great change in the nature of the magnetic ordering on going from $CeIn_3$, a local moment antiferromagnetic system, to $CePb_3$, a heavy fermion itinerant antiferromagnetic system, both of which have $Cu_3Au$ crystal structure. We have applied *ab initio* electronic structure calculations, based on the linear-muffin-tin-orbital method, and a phenomenological theory of orbitally driven magnetic ordering, to study the effects of the band-$f$ hybridization-induced interactions and the band-$f$ exchange-induced interactions, pertinent to the magnetic behavior of these systems. The position of the Ce $4f$ energy level relative to the Fermi energy and the intra-atomic Coulomb interaction are obtained from a sequence of three total-energy supercell calculations with two, one and zero $f$ electrons in the Ce $4f$ core. The calculations elucidate the origins in the electronic structure of the variation of the $f$-state resonance width characterizing the strength of the hybridization and the density of states at the Fermi energy characterizing the number and character of band states available for hybridization. We present results for the hybridization potential and the hybridization-induced exchange interactions on going from $CeIn_3$ to $CePb_3$, where the only obvious change is the addition of an anion $p$ electron. © *1996 American Institute of Physics.* [S0021-8979(96)26608-0]

## I. INTRODUCTION

The $CeX_3$ compounds with X=In, Sn, and Pb provide the opportunity to study the competition between different ground states in cerium systems.[1] These compounds are all cubic with the $Cu_3Au$ structure. $CeIn_3$ is a local moment antiferromagnetic system[2] (LMAF) with a Néel temperature of about 10 K and a weak low-temperature moment of $0.4\mu_B$ that shows strong Kondo resistivity.[3] The cerium moments are aligned antiferromagnetically in adjacent (111) ferromagnetic planes. When a small amount of tin is substituted for indium, the magnetic ground state is no longer stable, and the system no longer orders.[1] This indicates that the underlying energy parameters in $CeIn_3$ lie near the values at which a magnetic-nonmagnetic instability of the $4f$ electron occurs. $CeSn_3$ is a mixed valent (MV) system[1] which does not order magnetically. Finally, $CePb_3$ has been shown[4] to be an itinerant antiferromagnet with an extremely small moment and a Néel temperature of 1.2 K. Moreover, several $CePb_3$ properties show heavy fermion-like behavior.[4]

The purpose of the work reported here was to investigate the origins in the electronic structure, of the variation of the $f$-state resonance width characterizing the strength of the hybridization, the density of states at the Fermi energy, characterizing the number and character of band states available for hybridization, the hybridization potential, and the hybridization-induced and exchange-induced interactions on going from $CeIn_3$ to $CePb_3$, where the only obvious change is the addition of an anion $p$ electron. We have employed a unified theory that we have recently developed,[5–11] which involves a synthesis of (i) a phenomenological theory of moderately delocalized $f$-electron systems which includes explicit correlation effects and treats both the band-$f$ hybridization and the band-$f$ Coulomb exchange on an equal footing, and (ii) *ab initio* electronic structure calculations, based on the linear-muffin-tin-orbital (LMTO) method,[12] allowing a first-principles evaluation of the parameters entering the phenomenological theory. The interconfigurational correlation effects, which are important for this class of systems and which are treated explicitly in our theory, are not preserved in band theory and cannot be captured by the exchange correlation potential used in band theory.

The self-consistent one-electron potential is obtained from a warped-muffin-tin LMTO calculation without recourse to the atomic sphere approximation,[12] i.e., using a nonzero tail parameter in the interstitial, which is treated as a variational parameter. Two energy windows are employed to allow coverage of various subbands: the semicore cerium $5p$ states are calculated with a tail parameter about $-0.9$ Ry, and the cerium valence $6s$, $6p$, and $5d$ states and anion In(Pb) $5s(6s)$ and $5p(6p)$ states with a tail parameter, which is the average energy over occupied states in the interstitial. The full potential in the interstitial is used and the only shape approximation to the potential is a spherical averaging in nonoverlapping muffin-tin spheres. The cerium $4f$ electrons are treated as localized rather than itinerant states and thus they are included self-consistently as core states at each iteration, not being allowed to hybridize with band states. The relative magnitude of the muffin-tin radii are chosen so that nearest-neighbor muffin-tin spheres touch at the minimum in the charge density between nearest neighbors. While the basis functions for the band states are scalar relativistic,[13] spin-orbit coupling is included self-consistently. The electronic structure provides the band states and energies, and a self-consistent hybridization potential, thereby allowing determination of the band-$f$ hybridization potential matrix elements, $V_{\mathbf{k}m}$ and the band-$f$ coulomb exchange matrix elements $J_{nn'}(\mathbf{k},\mathbf{k}')$. The $4f$-state energy relative to the Fermi energy $E_f - E_F$, and the intra-atomic correlation energy $U$, are determined from differences of total energy calculations for different $f$ configurations as impurities in a supercell

 0021-8979/96/79(8)/6420/3/$10.00 © 1996 American Institute of Physics

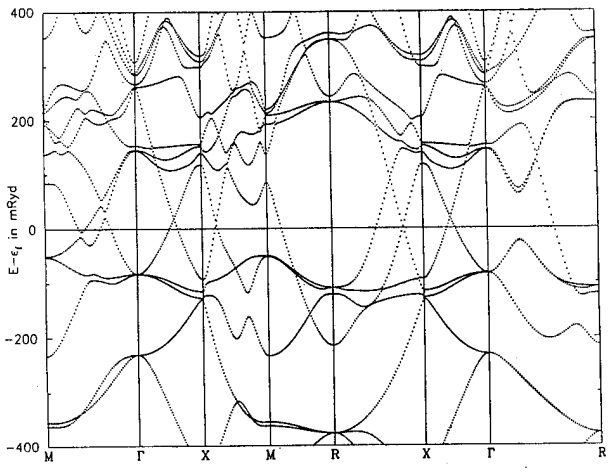



FIG. 1. The band structure of $CeIn_3$, calculated with the cerium $4f$ states treated as core states, along symmetry lines in the Brillouin zone. The band energies are with respect to the Fermi energy.

TABLE I. Summary of LMTO results for the Fermi energy $E_F$, the Ce $4f_{5/2}$ resonance energy, the total density of states $N(E_F)$ at $E_F$, the Ce $d$-derived and anion (In or Pb) $p$-derived partial density of states at $E_F$, the Ce $4f_{5/2}$ resonance width $\Gamma$, and the hybridization potential $v(\kappa_F)$, for $CeIn_3$ and $CePb_3$, respectively. Also listed are the results of the supercell LMTO calculations for the position of the $f$ state relative to the $E_F$, and the intra-atomic Coulomb interaction $U$.

| | $CeIn_3$ | $CePb_3$ |
|---|---|---|
| Lattice constant (a.u.) | 8.859 | 9.210 |
| Ce muffin-tin radius (a.u.) | 2.975 | 3.100 |
| Anion muffin-tin radius (a.u.) | 3.132 | 3.256 |
| $E_F$ (Ry) | 0.487 | 0.453 |
| Ce $4f$ resonance energy (Ry) | 0.503 | 0.442 |
| $N(E_F)$ ($Ry^{-1}$) | 27.3 | 41.5 |
| $N_d^{Ce}(E_F)$ ($Ry^{-1}$) | 5.5 | 7.5 |
| $N_p^{anion}(E_F)$ ($Ry^{-1}$) | 12.3 | 23.3 |
| $\Gamma$ (mRy) | 6.30 | 5.13 |
| $v(\kappa_F)$ (mRy) | −2.55 | −2.21 |
| $E_f - E_F$ (eV) | −3.2 | −3.0 |
| $U$ (eV) | 6.2 | 6.3 |

($f^0$,$f^1$,$f^2$) where all cerium sites but one have the nominal configuration $f^1$. Having determined the phenomenological model Hamiltonian parameters on an absolute basis, one can evaluate[6–11] the hybridization-induced and RKKY (but with the orbital part included) two-ion exchange interactions pertinent to the unusual magnetic ordering in this class of systems.

## II. RESULTS AND DISCUSSION

The band structure of $CeIn_3$ (typical of this class of systems), calculated with the Ce $4f$ states treated as core states, is plotted along symmetry lines in Fig. 1, with the band energies measured with respect to the Fermi energy. We treat the effects of band-$f$ hybridization within the context of the Anderson model Hamiltonian, where the hybridization matrix element $V_{km}$ in the model Hamiltonian is taken to be the matrix element of the muffin-tin Hamiltonian between band states of non-$f$ character and the wave function representing the Ce $4f_{5/2}$ state, $\psi_f$, which is obtained (self-consistently) from the resonance in the potential within the Ce muffin tin.[6,7] The bands dominating the hybridization-induced properties are those lying near the Fermi energy, which are largely derived from anion $p$-derived and cerium $d$-derived bands. Within the context of the model Hamiltonian, anion derived $p$-states hybridize more strongly with the Ce $4f$-resonance states, because the Ce-anion separation is smaller than the Ce–Ce separation. The bands at $\Gamma$ which are 85 mRy below the Fermi energy are indium $p$ bands, whereas those which are 144 mRy above the Fermi energy are Ce $d$ bands. The addition of an anion $p$ electron on going from $CeIn_3$ to $CePb_3$ causes the anion $p$-derived bands at $\Gamma$ to shift at 189 mRy below the Fermi energy, thus suppressing the $p$-$f$ hybridization. This is consistent with the decrease of the $f$-state resonance width listed in Table I, characterizing the strength of hybridization. The partial density of states (DOS) corresponding to the band structure in Fig. 1 is shown in Fig. 2. Plotted are the partial DOS for the Ce $d$-derived (solid curve), the In $s$-derived (dashed curve), and $p$-derived (dotted curve) bands, respectively. The Fermi energy $E_F$, and the DOS at the Fermi energy $N(E_F)$, in $CeIn_3$ are 0.487 Ry and 27.3 states/Ry, respectively, compared to the corresponding values of 0.453 Ry and 41.5 states/Ry in $CePb_3$. On going to $CePb_3$ there is an opening of a gap in the DOS between −0.025 and 0.18 Ry, and there is an increase (by a factor of 2) in the anion $p$-projected density of states at the Fermi energy.

For the purpose of analyzing hybridization effects within the context of our procedure for calculating Anderson model Hamiltonian parameters, band-$f$ hybridization in these compounds may be approximately characterized by two quantities arising from our band structure calculations: $f$-state resonance widths, characterizing the strength of hybridization, and the density of states at the Fermi energy, characterizing the number and character of bands available for

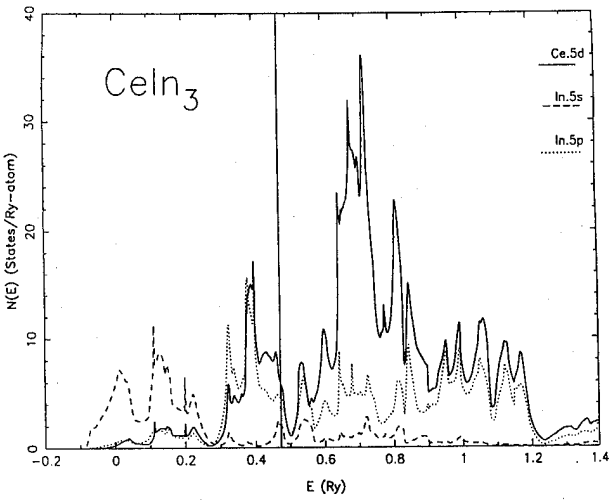



FIG. 2. Calculated partial density of states of $CeIn_3$ corresponding to the band structure of Fig. 1. Plotted are the density of states for the Ce $d$-derived (solid curve), the In $s$-derived (dashed curve), and $p$-derived (dotted curve) bands, respectively.

hybridization.[6,7] Calculated results of the cerium and anion muffin-tin radius, the Fermi energy, the cerium $4f$ resonant energy, the total and partial cerium $d$- and anion $p$-derived density of states at $E_F$, the $f$-state resonance width $\Gamma$, and the hybridization potential $v(\kappa_F)$, are listed in Table I, for $CeIn_3$ and $CePb_3$, respectively. The density of states at $E_F$, $N(E_F)$, are largely derived from anion $p$ states and cerium $5d$ states. It is important to note that the values of $\Gamma$ for both $CeIn_3$ and $CePb_3$ are comparable to that calculated[7] for CeTe ($\Gamma$=5.7 mRy), which was found to be at the *borderline* between magnetic and nonmagnetic behavior in contrast to the almost fully magnetically ordered CeSb. While the total density of states available for hybridization increases on going from $CeIn_3$ to $CePb_3$, the resonance width decreases because of the larger Ce-anion separation in $CePb_3$.

The energy necessary to place the Ce $f$-electron in a band state at the Fermi energy, $E_F-E_f$, and the energy required to change from an $f^1$ configuration to an $f^2$ configuration, $E_f+U-E_F$, have been evaluated for both systems. The values of $E_F-E_f$ and $U$ are then obtained from the $f^0$, $f^1$, and $f^2$ $f$-state eigenvalues by the use[7] of linear transition theory. We find that $E_F-E_f$ and $U$ are 3.2 and 6.2 eV in $CeIn_3$, and 3.0 and 6.3 eV in $CePb_3$, respectively. We have also calculated the 6×6 hybridization-induced exchange interaction matrix, $E_n=E(m,m',\mathbf{R}_n)$,[7] pertinent to the magnetic behavior of this class of systems. We find that the dominant matrix elements involve the $m=m'=\pm 1/2$ states, which correspond to the piling up of charge along the interionic axis. $E_1$, which in the phenomenological treatment,[5] is chosen to match the Néel temperature, is about the same in $CeIn_3$ (2.9 K) and in $CePb_3$ (3.0 K). More importantly, we find that $E_2(E_3)$ are ferromagnetic and large in both compounds, 3.1 K (2.9 K) in $CeIn_3$ and 2.7 K (2.8 K) in $CePb_3$. As for the case of other cerium systems (CeSb,CeTe), Coulomb exchange rather than hybridization was found[10] to be the larger contributor to the highly anisotropic effective two-ion interaction which determines the magnetic ordering behavior. Work currently in progress is aimed at the evaluation of the Coulomb exchange-induced interactions (proportional to $J^2$).[10,11] Having determined the two-ion exchange interactions, the equilibrium magnetic behavior (i.e., the ordered moment and the ordered temperature) of a given magnetic structure will be determined by treating the exchange Hamiltonian [Eq. (3) in Ref. 7] within mean-field theory.

## ACKNOWLEDGMENTS

The research at California State University Northridge (CSUN) was supported through the NSF under Grant No. DMR-89-18887 and the Office of Research and Sponsored Projects at CSUN. The research at West Virginia University was supported through the NSF under Grant No. DMR-91-20333.

[1] S. Rahman, J. Timlin, J. E. Crow, T. Mihalisin, and P. Schlottmann, J. Appl. Phys. **67**, 5209 (1990).
[2] J. Lawrence and S. M. Shapiro, Phys. Rev. B **22**, 4379 (1980).
[3] A. Maury, R. Freitag, J. E. Crow, T. Mihalisin, and A. I. Abou-Aly, Phys. Lett. A **92**, 441 (1982).
[4] C. L. Lin, J. Teter, J. E. Crow, T. Mihalisin, J. Brooks, A. I. Abou-Aly, and G. R. Stewart, Phys. Rev. Lett. **54**, 2541 (1985); C. Vettier, P. Mortin, and J. Flouquet, *ibid.* **56**, 1980 (1986).
[5] B. R. Cooper, R. Siemann, D. Yang, P. Thayamballi, and A. Banerjea, in *Handbook on the Physics and Chemistry of the Actinides*, edited by A. J. Freeman and G. H. Lander (North Holland, Amsterdam, 1985), Chap. 6, pp. 435–500.
[6] J. M. Wills and B. R. Cooper, Phys. Rev. B **36**, 3809 (1987).
[7] N. Kioussis, B. R. Cooper, and J. M. Wills, Phys. Rev. B **44**, 10003 (1991).
[8] N. Kioussis, H. J. Yu, B. R. Cooper, Q. G. Sheng, and J. M. Wills, J. Appl. Phys. **73**, 5424 (1993).
[9] B. R. Cooper, Q. G. Sheng, S. P. Lim, C. Sanchez-Castro, N. Kioussis, and J. M. Wills, J. Magn. Magn. Mater. **108**, 10 (1992).
[10] Q. G. Sheng and B. R. Cooper, Phys. Rev. B **50**, 965 (1994); J. Appl. Phys. **69**, 5472 (1991).
[11] Q. G. Sheng, B. R. Cooper, and S. P. Lim, Phys. Rev. **50**, 9215 (1994); J. Appl. Phys. **70**, 6083 (1991).
[12] O. K. Andersen, Phys. Rev. B **12**, 3060 (1975).
[13] D. D. Koelling and B. N. Harmon, J. Phys. C **10**, 3107 (1977).

# Theoretical interpretation of optical conductivity of $YbCu_4Ag,Au$

A. Continenza and P. Monachesi
*Dip. di Fisica, Universitá dell'Aquila, 67010 L'Aquila, Italy*

M. Galli and F. Marabelli
*Dip. di Fisica A. Volta, Universitá di Pavia, 27100 Pavia, Italy*

E. Bauer
*Institut für Experimentalphysik, Technische Universität Wien, A-1040 Wien, Austria*

We focus on $YbCu_4Ag$ and $YbCu_4Au$ and interpret the optical conductivity, measured from 2 meV to 6 eV at 10 and 300 K, in terms of self-consistent electronic structure calculations. Most of the relevant spectral structures are interpreted as interband transitions from hybridized $f-d$ states below and at the Fermi level at high symmetry points. In particular, the large shoulder at about 2.4 and 2 eV in the spectrum of $YbCu_4Au$ and $YbCu_4Ag$, respectively, can be interpreted in terms of a transition $\Gamma_4 \rightarrow \Gamma_3$ involving mostly $d$ states. We also compare the electronic structure of $YbCu_4Ag$ with that of $LuCu_4Ag$, to ascertain the influence of the $f$ states on the conduction bands and carrier density at $E_F$. This allows us to draw some qualitative considerations on the $f$-band hybridization in these compounds. © *1996 American Institute of Physics.* [S0021-8979(96)26708-7]

Ytterbium, the *hole* counterpart of cerium, is expected to form in several intermetallic compounds with Kondo lattice- and valence fluctuations properties. This has in fact been found in some experiments. In particular, an interesting group of ternary compounds, isostructural to cubic $MgCu_4Sn$, is $YbCu_4M$, where M=Ag, Au, Pd, In. They have been investigated by optical, neutron, Mössbauer, photoemission, and x-ray spectroscopy[1–6] as well as by electrical and magnetic fields[7,8] also performed at high-pressure and high magnetic fields.[9–11]

A new interest towards this series of compounds is raised by the observation of very different ground states reached by decreasing temperature. In fact, $YbCu_4Ag$ displays a Kondo-like behavior below $\simeq 100$ K[2,3,8] that is absent in isovalent $YbCu_4Au$. The latter one, like $YbCu_4Pd$, undergoes a magnetic transition below 1 K. Finally, $YbCu_4In$ exhibits a first-order valence phase transition at $T=40$ K from $Yb^{2+}$ to $Yb^{3+}$ with a sharp volume change.[7] Interestingly, no structural distortions have been detected in any of the above compounds at the transitions. Therefore, since the only ground-state parameters varying through the series are the lattice constant and the electronic charge, a clue to the understanding of all the phenomena could be the interplay between volume and electronic structure.

Optical measurements and electronic band calculations are suitable to test this point. The goal of the present paper is twofold: one is the direct interpretation of the low-temperature conductivity spectra of isovalent $YbCu_4Ag$ and $YbCu_4Au$.[2] The other is to relate, at least qualitatively, the observed Kondo behavior of the Ag compound with the electronic $f-d$ hybridization.

With these aims in mind we have performed self-consistent electronic FLAPW calculations[12] within the LDA approximation for the two isovalent compounds as well as for $LuCu_4Ag$, as the $f$-full analog of $YbCu_4Ag$. Calculations have been performed at the experimental volumes with $a_0=7.0834$ Å for $YCu_4Ag$ and $a_0=7.0519$ Å for $YCu_4Au$. The band structure is displayed in Fig. 1. For the sake of comparison we have labeled the conduction bands at the $\Gamma$ point in Fig. 1 with the irreducible representation of the $T_d$ symmetry in Bethe's notation. The results are consistent with the main features observed in photoemission and x-ray absorption in $YbCu_4Ag$. A peak of Yb $5d$ density is observed at about 4 eV above $E_F$,[6] a Cu $3d$ band appears at 3 eV below $E_F$ and Yb $4f$ states seem located within 2 eV below $E_F$.[5] A slight shift seems to exist for Ag $3d$ states which should be around 6 eV below $E_F$.[5] Anyway, no matrix element analysis has been yet performed on the data.

The bands of the two compounds are quite similar. Differences appear along the lines connecting $\Gamma$ with the points $L$ and $K$ for states at and above $E_F$ with consequences on the optical spectra, as discussed below. In particular, there is in Fig. 1(a) an inversion of the triplet $\Gamma_4$ with the singlet $\Gamma_1$ above $E_F$ with respect to the same bands in Fig. 1(b). In particular we find that the $\Gamma_1$(Au) is 1.5 eV lower in energy

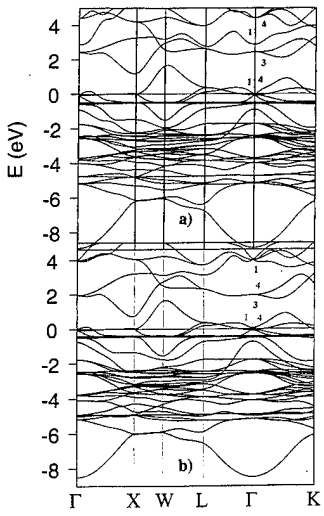



FIG. 1. Calculated band structure of (a) $YbCu_4Au$ and (b) $YbCu_4Ag$. The zero of the energy scale is the Fermi level $E_F$ and some irreducible representation at $\Gamma$ are indicated with the corresponding numerical labels in order of decreasing energy from the top of each panel. Notice the different order of the highest states $\Gamma_4$ and $\Gamma_1$ in the two compounds.

 0021-8979/96/79(8)/6423/3/$10.00 © 1996 American Institute of Physics 

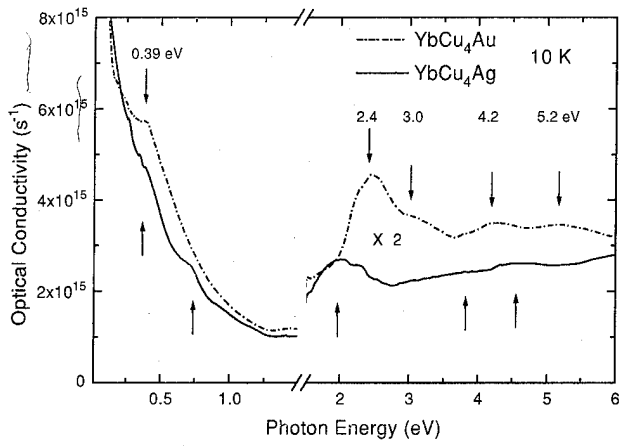



FIG. 2. Optical conductivity of $YbCu_4Au$ and $YbCu_4Ag$ measured at 10 K. The excitations indicated by the arrows are discussed.

than $\Gamma_1$(Ag). Moreover, another singlet $\Gamma_1$ is almost degenerate with the triplet $\Gamma_4$ at $E_F$ in $YbCu_4Au$ and is slightly above it in $YbCu_4Ag$.

In order to test the role of volume as the possible origin of these differences we have calculated the bands of $YbCu_4Au$ with the lattice constant of $YbCu_4Ag$. Practically no changes are introduced by volume expansion, actually quite small, with respect to Fig. 1(a). We are thus led to think that the differences in the band structures of $YbCu_4Ag$ and $YbCu_4Au$ are due to purely electronic effects.

From the analysis of the wave-function composition it results that the higher $\Gamma_1$ singlet is made mainly of $s$ states coming from Ag (34%) and Au (36%), in the corresponding compounds. The doublet $\Gamma_3$ and the triplet $\Gamma_4$ originate from $d$ (Yb, Au/Ag) and $p,d$ states (Yb, Au/Ag, Cu), respectively. The triplet and singlet at $E_F$ ($\Gamma_4$, $\Gamma_1$) show essentially Yb $d$, $f$ and Yb $f$ character, respectively.

From this analysis it seems that the singlet $\Gamma_1$ does not interact with neighboring states but with other $s$ states of much lower energy (e.g., bands bottom). Due to the much larger atomic weight of Au with respect to Ag the energy difference of the atomic valence $s$ states is $E_{6s}(\mathrm{Au})-E_{5s}(\mathrm{Ag})\simeq -1.4$ eV. This is of the same order of magnitude as the energy difference between the highest $\Gamma_1$ singlets in the two compounds. This interpretation is supported by the fact that the order of the excited states in $LuCu_4Ag$ is the same as in the $YbCu_4Ag$.

We have also carried out a symmetry analysis of the allowed optical transitions in the dipole approximation, considering as initial states (i) the narrow $f$ bands at $\simeq -0.5$ eV ($\Gamma_1$, $\Gamma_4$, $\Gamma_5$, not shown) in both compounds and (ii) the states at $E_F$ in Fig. 1. In both cases there are not any symmetry allowed transitions between states $\Gamma_1$ and $\Gamma_3$. In $YbCu_4Ag$ there are allowed transitions from $f$ states at 0.50, 2.3–2.5, 4.2, and 4.5 eV (2) and from the triplet $\Gamma_4$, at $E_F$ as initial state, at 0.16, 2, and 4.1 eV. In $YbCu_4Au$ transitions from $f$ states are at 2.7–2.9 eV (2), 3.7, 4.8–5 eV (2), and from $E_F$ at 2.5, 3 and 4.4 eV.

The optical conductivity, measured at 10 K is shown in Fig. 2. The results at 300 K, not shown, change appreciably only below 0.5 eV. Many structures corresponding to interband transitions may be recognized in the energy range 0.1–6 eV. The arrows in the figure indicate approximately the possible transitions: two shoulders at about 0.35 and 0.7 eV and three broad structures at 2.2, 3.9, and 4.6 eV in $YbCu_4Ag$ and five main transitions at 0.39, 2.4, 3.0, 4.2, and 5.2 eV in $YbCu_4Au$. A very small bump at 1.4 eV in the spectra of both compounds could be related to the spin-orbit splitting of hybridized Yb $4f$ states.[5] Some small anomalies around 1 eV can be noticed in the spectrum of $YbCu_4Ag$. All these structures seem to be relatively independent on the temperature and on the heavy fermion features occurring at the lowest energies and at low $T$.

The most striking differences among the two spectra at low $T$, except for the first one of $YbCu_4Ag$ at 0.35 eV, are the structures at 2 and 2.4 eV in $YbCu_4Ag$ and $YbCu_4Au$, respectively.

Comparing with the excitation energies deduced from the bands in Fig. 1 we can ascribe the broad shoulder at 2 eV (2.4) eV in the Ag(Au) compound to the transition $\Gamma_4 \rightarrow \Gamma_3$, which involves basically $d$ states, as deduced from the analysis of the eigenvectors at this symmetry points. From the same analysis we could ascribe the broadening of the shoulders to transitions from the $f$ states. We notice that, according to our band calculations, the $\Gamma_4 \rightarrow \Gamma_3$ excitation may be predicted in $LuCu_4Ag$ and it would be interesting to check with experimental results. Transitions at other symmetry points may add to those at $\Gamma$. The agreement we find is surprisingly good considering the uncertainties implicit in LDA for the energy of the excited states. We may argue that for transition involving relatively close states of the same symmetry, there could be a common energy shift with respect to $E_F$ not affecting the energy of the transition altogether.

The second goal of this article, i.e., the understanding of the Kondo behavior of $YbCu_4Ag$ can be carried out also on the basis of our electronic calculations. It is known that the Kondo temperature is directly related to the $f-d$ hybridization at $E_F$, a quantity that can be evaluated in an approximated way from electronic calculations.[13] However, it is also possible to have a crude, qualitative estimate of the hybridization from the relative weight of the density of $f,d$ states at $E_F$. In fact, if we roughly assume that, for a given value of the total number of $f$ electrons/Yb, $n_f$, the larger is their DOS($E_F$) the weaker the hybridization,[14] we can draw some qualitative conclusions in the present compounds.

We have calculated the density of states of $YbCu_4Ag$, $YbCu_4Au$,[15] and also $LuCu_4Ag$, to have a reference material where, due to the complete filling of the $f$ states, the $f-d$ hybridization is certainly negligible. The total density of states of $YbCu_4Ag$ and $LuCu_4Ag$, reported in Fig. 3, shows the different $f$ filling: the $f$ peak centered at about $-1$ eV in the Yb compound, shifts to $\simeq -5$ eV in the Lu compound. Its intensity increases with respect to the Yb compound. We have estimated that the $f$ bandwidth in the Lu compound is an order of magnitude smaller than in the Yb compounds. The DOS of $YbCu_4Au$ (not shown) is quite similar to that of the Ag compound. We attribute these facts to the lack of hybridization of the $f$ states with extended states (typically

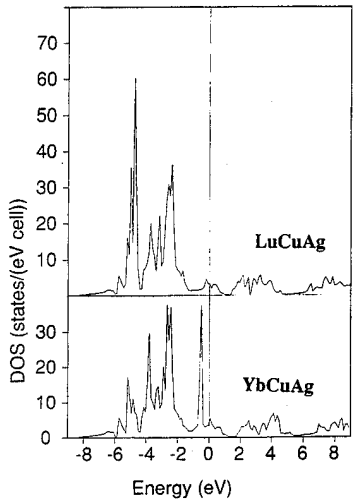



FIG. 3. Calculated total density of states of $YbCu_4Ag$ and $LuCu_4Ag$.

$d$), that keeps the $f$ states very well localized in energy and separated from band states. Nevertheless, the detailed analysis of the partial DOS and $E_F$ gives some quantitative indications on the different degree of hybridization in $YbCu_4Ag$ and $YbCu_4Au$.

In fact, even if $n_f$ is constant in the two compounds, the $f$ DOS at $E_F$ drops from 11.5 states/eV atom in $YbCu_4Au$ to 9.8 states/eV atom in $YbCu_4Ag$, indicating a higher hybridization (i.e., a higher Kondo temperature), in the latter compound. Accordingly, the $d$ component at $E_F$ on Ag drops by about 40% with respect to Au.

In conclusion, the present theoretical calculations agree quite well with the experimental results and explain the main features of the optical conductivity. A clearcut answer about the nature of the observed peaks at 2 and 2.4 eV in $YbCu_4Ag$ and $YbCu_4Au$, respectively, should come from measurements in the corresponding Lu compounds. We have also given qualitative indications of the reason of the observed *heavy fermion* behavior of $YbCu_4Ag$ in terms of a large $f-d$ hybridization. The smaller hybridization found in $YbCu_4Au$ gives rise to a Kondo minimum in the resistivity but this effect is overwhelmed by the onset of intersite magnetic order.[8]

[1] F. Marabelli and E. Bauer, J. Appl. Phys. **73**, 5418 (1993).
[2] M. Galli, F. Marabelli, and E. Bauer, Physica B **206-207**, 355 (1995).
[3] A. Severing *et al.*, Phys. Rev. B **41**, 1739 (1990).
[4] P. Bonville *et al.*, J. Physique I **2**, 459 (1992).
[5] P. Weibel *et al.*, Z. Physik B **91**, 337 (1993).
[6] J. M. Lawrence *et al.*, Phys. Rev. B **49**, 1627 (1994).
[7] I. Felner *et al.*, Phys. Rev. B **35**, 6956 (1987).
[8] C. Rossel *et al.*, Phys. Rev. B **35**, 1914 (1987).
[9] E. Bauer *et al.*, Phys. Rev. B **48**, 15873 (1993).
[10] E. Bauer *et al.*, Phys. Rev. B **50**, 9300 (1994).
[11] T. Graf *et al.*, Phys. Rev. B **51**, 15053 (1995).
[12] H. F. Jansen and A. J. Freeman, Phys. Rev. B **30**, 561 (1984).
[13] P. Monachesi and A. Continenza, Phys. Rev. B **42**, 14622 (1993).
[14] P. Monachesi and A. Continenza, Il Nuovo Cimento **15D**, 307 (1993).
[15] A. Continenza and P. Monachesi, Proceedings of 25$^{emes}$ Journées des Actinides, 7–11 April (1995), L'Aquila, Italy.

# Magnetic dichroism study of the relativistic electronic structure of perpendicularly magnetized Ni/Cu(001)

W. Kuch, M. Zharnikov, A. Dittschar, K. Meinel, C. M. Schneider, and J. Kirschner
*Max-Planck-Institut für Mikrostrukturphysik, Am Weinberg 2, D-06120 Halle, Germany*

J. Henk and R. Feder
*Theoretische Festkörperphysik, Universität Duisburg, D-47048 Duisburg, Germany*

An experimental and theoretical study of magnetic circular dichroism in valence band photoemission from 15 monolayer thick fcc Ni films on Cu(001) is presented. A highly symmetric configuration (light incidence, electron emission, magnetization direction, photon helicity, and surface normal all parallel) allows the illustrative interpretation of the dichroism in terms of the relativistic band structure. Photoemission experiments in the photon energy range of 11–27 eV are compared to fully relativistic one-step photoemission calculations. From this comparison, the dichroic features can be directly related to the double group symmetry of the initial states, which is demonstrated by two examples. © *1996 American Institute of Physics.* [S0021-8979(96)26808-3]

The interplay of spin-orbit and exchange interaction in ferromagnets is of great interest for a variety of effects. Magnetic dichroism in photoemission, which is the change of intensity distribution curves by reversal of the magnetization direction, is exclusively due to this interplay of spin-orbit and exchange interaction.[1] Magnetic circular dichroism in valence-band photoemission (MCDAD), therefore, is an especially well-suited method to study this interaction in the valence states. We want to demonstrate in this contribution that information on the relativistic electronic structure is available by MCDAD which otherwise would have been accessible by spin-resolved photoemission only.

Thin Ni films (10–56 ML), grown epitaxially on Cu(001), have their easy axis of magnetization perpendicular to the film surface.[2] They offer thus the advantage to study the MCDAD in a totally symmetric configuration. Such a configuration, in which the light incidence, electron emission, magnetization direction, and photon helicity are all aligned parallel to the surface normal, allows the illustrative interpretation of the observed dichroism in terms of double-group symmetry of the initial bands along the $\Delta$ axis of the relativistic band structure.

We present an experimental and theoretical MCDAD study of the spin-orbit and exchange split electronic structure of fcc-Ni(001) films. Fully relativistic one-step photoemission calculations were performed. We show that from the comparison between experiment and theory it is possible to determine details of the relativistic band structure such as band dispersion and hybridization between bands of the same double group symmetry.

Ni films of 15 ML thickness were deposited at room temperature by electron bombardment of a high-purity nickel rod. The films were annealed immediately after deposition for 10 min at 450 K in order to minimize the film roughness.[3] Photoemission spectra were taken at the Berlin synchrotron radiation facility (BESSY), with $\approx$ 90% circularly polarized light. The overall energetic resolution was approximately 200 meV, the angular acceptance better than $\pm 2°$. The films were remanently magnetized perpendicular to the surface prior to the acquisition of the spectra. All spectra were collected at room temperature.

Fully relativistic one-step photoemission calculations of the layer Korringa–Kohn–Rostoker (KKR) type were performed using a recently developed Green's function formalism.[4] Details of the calculation procedure will be given elsewhere.[5] The spectra were calculated for a semi-infinite Ni(001) crystal with the lateral lattice constant of bulk Cu, namely, 2.55 Å (compared to 2.49 Å for bulk Ni). The vertical layer spacing was taken as 1.69 Å, which means a 6% tetragonally compressed fcc structure. Such a structure is deduced from our LEED $I(V)$ measurements of the specular beam. Furthermore, we assume $T=0$ K and complete polarization of the incident light.

In a highly symmetric arrangement without the presence of a magnetic field, electronic transitions induced by circularly polarized light are governed by relativistic dipole selection rules.[6] In the presence of a perpendicular magnetization, the electronic states can be classified due to four one-dimensional irreducible representations of the double group, which read $\Delta_6+$, $\Delta_6-$, $\Delta_7+$, and $\Delta_7-$. Their $\Delta^5$ spatial parts can be labeled $\Delta_6^5+$, $\Delta_6^5-$, $\Delta_7^5+$, and $\Delta_7^5-$.[5] The $+/-$ sign should not be attributed to majority or minority spin because the latter is not a "good quantum number" in the presence of spin-orbit coupling.

Figure 1 illustrates the situation. In the bottom panel, the energetic positions of the four bands are depicted schematically. Transitions from this states induced by circularly polarized light depend on the relative orientation of photon spin $\sigma$ and magnetization $\mathbf{M}$. If $\boldsymbol{\sigma}$ is parallel (antiparallel) to $\mathbf{M}$, only states with $\Delta_7^5+$ and $\Delta_6^5-$ ($\Delta_7^5-$ and $\Delta_6^5+$) symmetry contribute to the spectrum.[6] In the center panel of Fig. 1, schematic intensity distribution curves for the two cases are shown. The solid (dotted) lines correspond to parallel (antiparallel) alignment of $\boldsymbol{\sigma}$ and $\mathbf{M}$ [($I(\uparrow\uparrow)$ and $I(\uparrow\downarrow)$, respectively)]. The resulting normalized intensity asymmetry, defined as $A=[I(\uparrow\uparrow)-I(\uparrow\downarrow)]/[I(\uparrow\uparrow)+I(\uparrow\downarrow)]$, is depicted in the top panel. It exhibits a characteristic plus/minus/plus feature, where the minus indentation is evoked by emission from the $\Delta_6^5+$ and $\Delta_7^5-$ bands.

Figure 2 shows a series of intensity spectra for different photon energies. Following the convention of Fig. 1, spectra

 0021-8979/96/79(8)/6426/3/$10.00 © 1996 American Institute of Physics

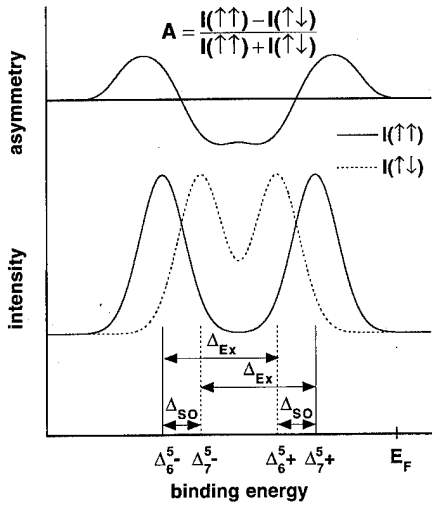



FIG. 1. Bottom: schematic representation of the four bands of $\Delta_7^5+$, $\Delta_6^5+$, $\Delta_7^5-$, and $\Delta_6^5-$ symmetry contributing to the spectra in the totally symmetric geometry. The arrows indicate the splitting due to spin-orbit ($\Delta_{SO}$) and exchange interaction ($\Delta_{Ex}$). Center: schematic intensity distribution curves for parallel (solid lines) and antiparallel alignment (dotted lines) of photon spin and magnetization direction. Top: normalized asymmetry $A$ of the spectra of the center panel.

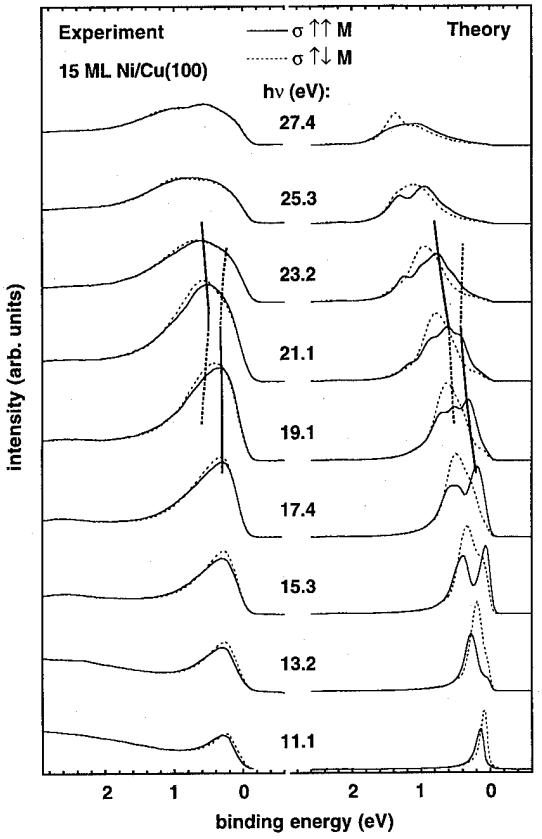



FIG. 2. Series of partial intensity spectra for different photon energies $h\nu$. Shown are spectra for parallel (solid lines) and antiparallel alignment (dotted lines) of photon spin and magnetization direction. Left: experimental spectra, right: theoretical spectra. The vertical lines indicate the occurrence of a hybridization region as explained in the text.

for parallel (antiparallel) alignment of $\boldsymbol{\sigma}$ and $\mathbf{M}$ are reproduced by solid (dotted) lines. Experimental spectra, normalized to the photon flux, are depicted on the left-hand side, the results of the calculation on the right-hand side. The spectra for 11.1 eV photon energy display relatively sharp peaks just below the Fermi energy; with increasing photon energy a dispersion towards higher binding energies and a broadening of the peaks are observed both in the experimental and in the theoretical spectra.

Figure 3 displays asymmetry spectra, corresponding to the intensity spectra of Fig. 2. Again, experimental asymmetries are shown on the left, theoretical curves on the right-hand side. At small photon energies, experimental asymmetries as large as 20% are observed. In order to facilitate comparison with the experimental data, the theoretical asymmetry curves are scaled by a factor of 0.2. The experimental spectra exhibit significantly broader intensity curves and lower asymmetries compared to the calculated ones, which must be attributed to the limited energetic and angular resolution, to possible imperfections in film morphology, and to the background of inelastically scattered electrons not considered in the calculations. Furthermore, the theoretical spectra were calculated for $T=0$ K and 100% circular polarization. A larger broadening of the calculated spectra would lead to a better agreement but impedes the identification of the underlying electronic transitions. Apart from the different size of the dichroic asymmetry, very good qualitative agreement between experiment and theory is seen both in the intensity and in the asymmetry spectra. This enables us to correlate the experimentally observed features to the calculated relativistic band structure.

We will now demonstrate by two examples how this comparison of experiment to theory serves to identify specific details of the electronic states, assuming direct interband transitions. Figure 4 shows the relativistic band structure of Ni along the $\Delta$ axis, calculated with the same parameters as the photoemission spectra. The bands are reproduced with differently dashed and dotted lines according to their double group symmetry, as labeled in the figure.

Let us now as the first example consider the dispersion of the four bands with $\Delta^5$ spatial symmetry which were used for the schematic illustration of Fig. 1. In Fig. 4 these bands are marked by four arrows at both sides of the panel. Starting at the $\Gamma$ point at binding energies between 1.5 and 1.9 eV, these bands jointly disperse upwards, interrupted by hybridization with other bands, to reach the $X$ point at energies between 0.15 eV below and 0.3 eV above the Fermi energy. In the experiment a photon energy of 11 eV corresponds to transitions near the $X$ point, whereas 27 eV corresponds to transitions near the $\Gamma$ point. Comparing experimental spectra to the calculated band structure, off-axis contributions due to the experimental angular resolution have principally to be considered and may contribute to the linewidth of the spectra. At $\pm 2°$, however, these effects are small and affect mainly the relative peak heights.[7] Because of the broadening of the spectra at higher photon energies, it is difficult to obtain the dispersion of the $\Delta^5$ bands from intensity spectra alone. As we see from Fig. 1, the pronounced minus feature in the asymmetry curves is correlated to the energetic posi-

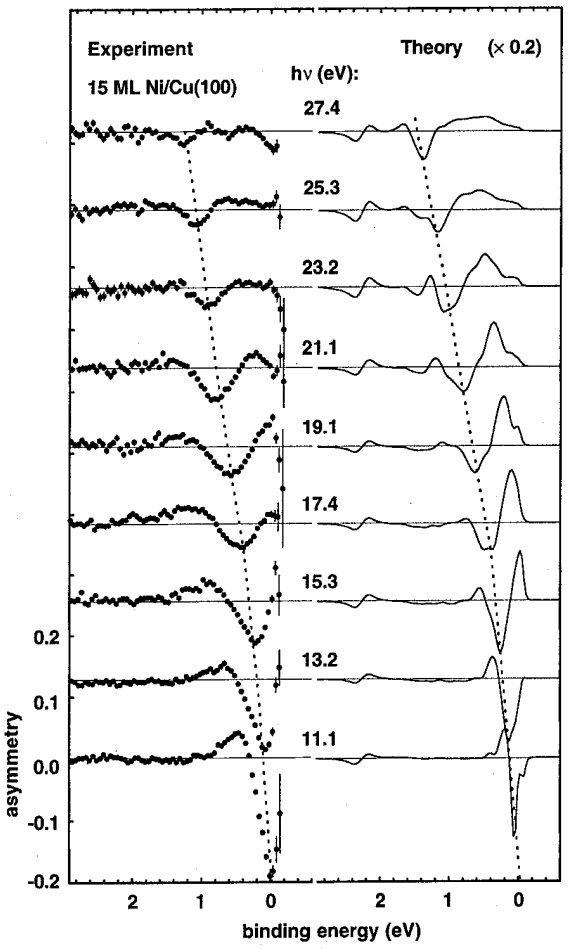



FIG. 3. Series of asymmetry spectra for different photon energies $h\nu$, calculated from the corresponding spectra of Fig. 2. Left: experimental asymmetries, right: theoretical asymmetries. The vertical dotted lines mark the dispersion of the prominent minus peak.

tions of the $\Delta_6^5+$ and $\Delta_7^5-$ bands. The dispersion of this minus peak, marked by vertical dotted lines in Fig. 3, indicates the dispersion of the $\Delta^5$ bands.

As a second example we will consider the hybridization of $\Delta_7+$ bands around 0.5 eV binding energy at about the middle of the $\Delta$ axis. This hybridization is caused by an avoided crossing between a band of $\Delta_7^2+$ symmetry, which is recognized in Fig. 4 by a weak dispersion, and a band of $\Delta_7^5+$ symmetry with a steeper dispersion. As a consequence of the avoided crossing, the bands interchange their symmetry character in the hybridization region and contain both a mixture of $\Delta_7^2+$ and $\Delta_7^5+$ symmetry. This can be seen in the intensity spectra for $\boldsymbol{\sigma}\uparrow\uparrow\mathbf{M}$ (solid lines in Fig. 2). As already mentioned, only bands which contain $\Delta^5$ single group symmetry character contribute to the spectra. This means that the hybridization is observed as an energetic displacement of the corresponding peak towards higher binding energy with increasing photon energy. The vertical lines in Fig. 2 indicate the region of hybridization in the photoemission spectra.

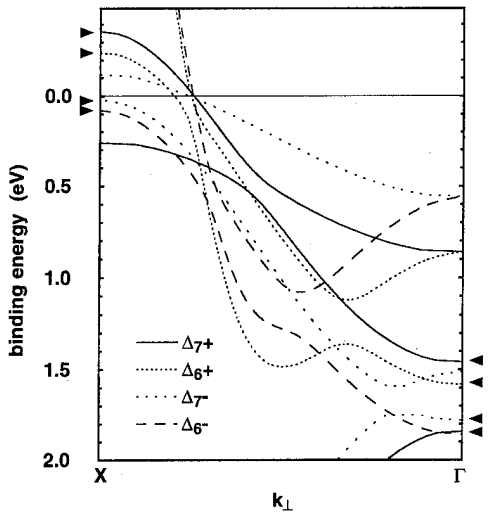



FIG. 4. Relativistic band structure of Ni along the $\Delta$ axis, calculated with the same parameters as the photoemission spectra. Bands with $\Delta_7+$, $\Delta_6+$, $\Delta_7-$, and $\Delta_6-$ double group symmetry are distinguished as labeled in the figure. The arrows indicate bands of $\Delta^5$ orbital symmetry.

They mark the positions of bands containing $\Delta_7^5+$ symmetry, and fade out into dotted lines where the $\Delta_7^2+$ symmetry character in these bands predominates. In the calculated spectra (right-hand side of Fig. 2), both of the hybridizing bands can be distinguished as separate peaks in the solid line spectra. In the experimental spectra (left-hand side of Fig. 2), the hybridization shows up as energetic shift of the intensity weight of the peak for $\boldsymbol{\sigma}\uparrow\uparrow\mathbf{M}$ between 19.1 and 21.1 eV. Whereas at 19.1 eV the peak is asymmetrically shaped with higher weight at the low binding energy side, at 21.1 eV the weight is shifted to the side with higher binding energy.

Both examples demonstrate how the relativistic band structure can be correlated to MCDAD spectra. It has been shown how from the comparison to fully relativistic calculations even fine details of the band structure can be resolved. This demonstrates the capability of magnetic circular dichroism in valence-band photoemission for the investigation of the exchange and spin-orbit split relativistic band structure of ferromagnets.

Financial support by the BMBF under Grants No. 05-621EFA and 05-5PGABB7 is gratefully acknowledged.

[1] L. Baumgarten, C. M. Schneider, H. Petersen, F. Schäfers, and J. Kirschner, Phys. Rev. Lett. **65**, 492 (1990); B. T. Thole and G. van der Laan, Phys. Rev. B **44**, 12 424 (1991).
[2] F. Huang, M. T. Kief, G. J. Mankey, and R. F. Willis, Phys. Rev. B **49**, 3962 (1994); W. L. O'Brien and B. P. Tonner, *ibid.* **49**, 15370 (1994); B. Schulz and K. Baberschke, *ibid.* **50**, 13467 (1994).
[3] J. Shen, J. Giergiel, and J. Kirschner, Phys. Rev. B **52**, 8454 (1995).
[4] S. V. Halilov, E. Tamura, H. Gollisch, D. Meinert, and R. Feder, J. Phys.: Cond. Matt. **5**, 3859 (1993).
[5] W. Kuch, A. Dittschar, K. Meinel, M. Zharnikov, C. M. Schneider, J. Kirschner, J. Henk, and R. Feder (unpublished).
[6] M. Wöhlecke and G. Borstel, Phys. Rev. B **23**, 980 (1981).
[7] S. V. Halilov, J. Henk, T. Scheunemann, and R. Feder, Phys. Rev. B **52**, 14 235 (1995).

# Density functional study of fcc iron and iron particles in copper

Diana Guenzburger
*Centro Brasileiro de Pesquisas Fisicas, Rua Xavier Sigaud 150, 22290-180 Rio de Janeiro, RJ, Brazil*

D. E. Ellis
*Department of Physics and Astronomy and Materials Research Center, Northwestern University, Evanston, Illinois 60208*

The first-principles spin-polarized discrete variational method in the framework of density functional theory was employed to investigate the electronic and magnetic structure of fcc ($\gamma$) Fe and of $\gamma$-Fe particles in copper, represented by 62-atom embedded clusters of cubic geometry. The influence of Al substitutional impurities in $\gamma$-Fe and in the Fe particle in Cu was also investigated. Magnetic moments and hyperfine fields were obtained. © *1996 American Institute of Physics.* [S0021-8979(96)26908-X]

## I. INTRODUCTION

Pure fcc (or $\gamma$) iron cannot be found at room temperature, only between 1183 and 1667 K; however, it may be stabilized at low temperatures as small coherent precipitates in copper or copper alloy matrices, or as thin epitaxial films on Cu or Cu-based alloy substrates.[1,2] Thus the magnetic and hyperfine properties of fcc Fe may be investigated experimentally. Band structure calculations[3,4] have demonstrated the existence of multiple magnetic states, the stability of which depends on the lattice constant. This may be varied experimentally by using pressure or bulkier atoms in the Cu alloys of the matrix or substrate, such as Al or Au.[2]

We report first-principles embedded-cluster electronic structure calculations for pure fcc Fe and for a coherent Fe particle in fcc copper. Magnetic moments, spin density distributions, and magnetic hyperfine fields were obtained. The influence of an Al substitutional impurity in $\gamma$-Fe and in the Fe particle in Cu was also assessed.

## II. THEORETICAL METHOD

$\gamma$-Fe was represented by a 62-atom cubic cluster embedded in the charge densities of several shells of neighboring atoms in the crystal. Several lattice constants were considered, varying from $a=3.38$ to 3.77 Å. For smaller values, an antiferromagnetic (AFM) phase consisting of alternating layers of up and down spins normal to the (001) direction was considered. An AFM spin state is found to be more stable at smaller lattice constants.[2] For larger interatomic distances we studied a ferromagnetic (FM) phase.

A coherent $\gamma$-Fe particle in Cu was represented by a 62-atom cubic cluster, with the 14 innermost atoms representing the Fe particle and the 48 outer atoms being copper ($Fe_{14}Cu_{48}$, see Fig. 1). In the case of Al substitution, two Fe atoms of the particle were substituted for Al, forming the cluster $Fe_{12}Al_2Cu_{48}$. The influence of Al in pure $\gamma$-Fe was also explored, with calculations for the clusters $Fe_{60}Al_2$. The spin-polarized self-consistent numerical discrete variational method,[5,6] in the framework of density functional theory, was employed. The local exchange-correlation potential, which is a functional of the electron density $\rho_\sigma$ for each spin $\sigma$, was that of von Barth and Hedin.[7] A mixed numerical three-dimensional grid of sampling points was employed, consisting of a random Diophantine mesh in the interatomic region and a precise polynomial grid within a sphere of ~2 a.u. around the atoms where the local properties are calculated. A total of ~24 000 points was employed for each cluster. The magnetic moments are defined as the integral of the spin density $\rho\uparrow(\mathbf{r})-\rho\downarrow(\mathbf{r})$ within the Wigner–Seitz sphere of the atom. A multipolar expansion of the charge and spin density, centered at the nuclei of the cluster atoms, is considered to construct the model potential employed, in which only spherical terms were retained. The model density is fitted to the true (eigenvector) density by a least-squares minimization procedure. In determining local properties, such as local densities of states (DOS), magnetic moments, and hyperfine fields, the innermost atoms of the clusters are considered, since they best represent the situation in the bulk.

## III. RESULTS AND CONCLUSIONS

For AFM and FM $\gamma$-Fe, the magnetic moments $\mu$ increase as the lattice constant is increased. The values obtained are not far from those computed by full-potential band structure calculations.[4]

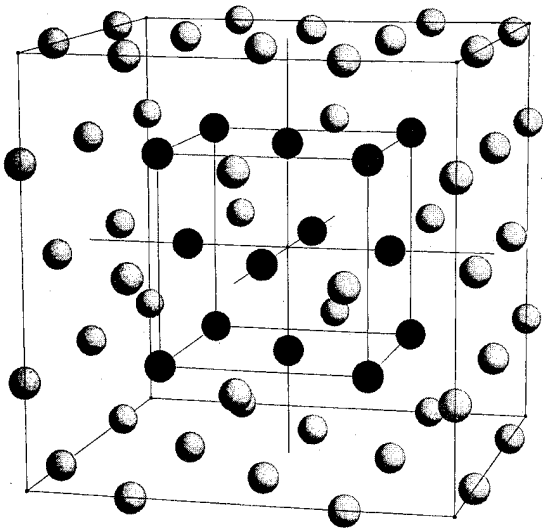


FIG. 1. Schematic of variational cluster, for the Fe particle in copper ($Fe_{14}Cu_{48}$).

 0021-8979/96/79(8)/6429/3/$10.00 © 1996 American Institute of Physics 

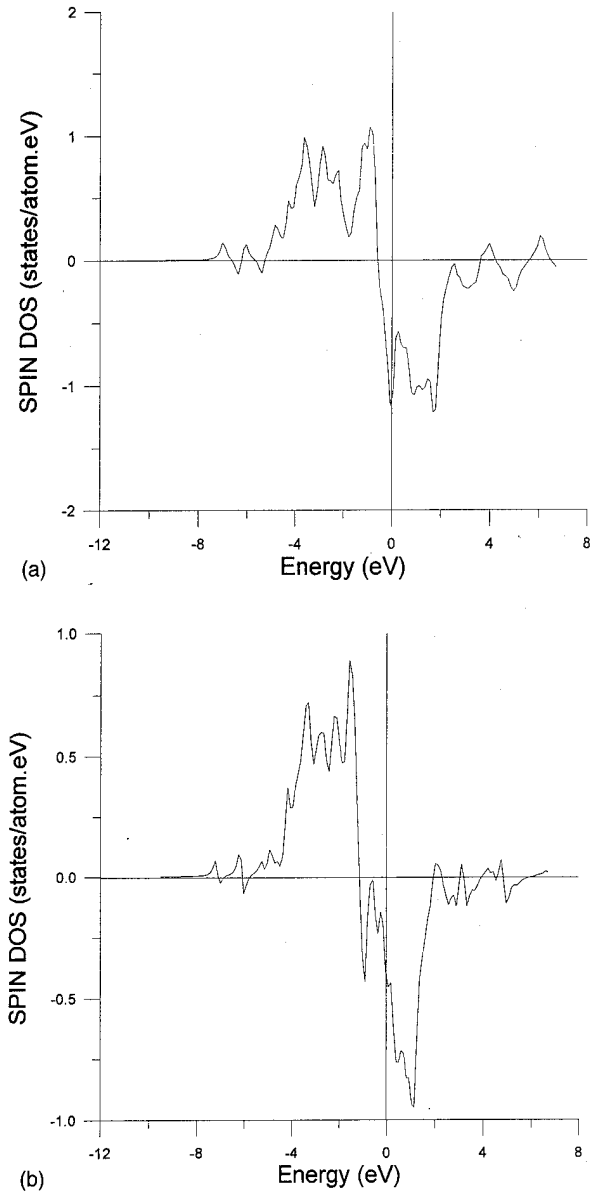



FIG. 2. (a) Valence $(3d+4s+4p)$ spin density of states (DOS $\uparrow$ minus DOS $\downarrow$) for ferromagnetic configuration of fcc Fe. (b) Valence $(3d+4s+4p)$ spin density of states for antiferromagnetic configuration of fcc Fe.

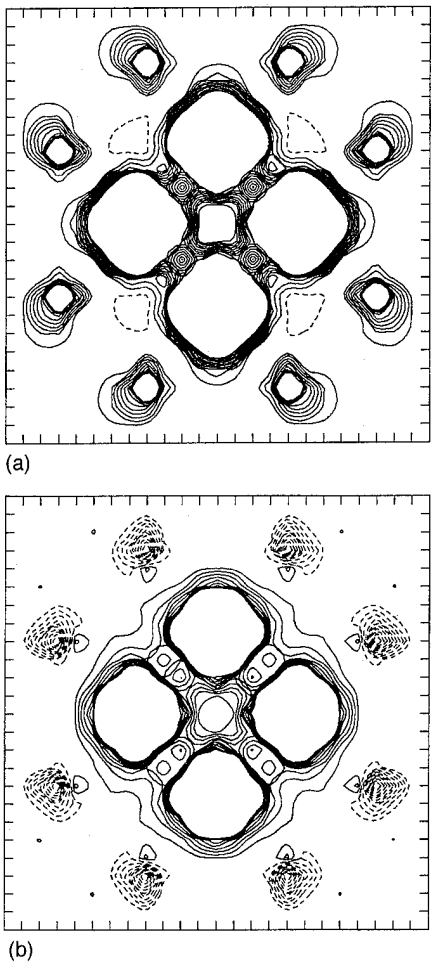



FIG. 3. (a) Spin density contour map, plotted on the $(x,y)$ plane for the ferromagnetic $\gamma$-Fe particle in Cu. Contours range from $-0.01$ to $+0.01$ e/a.u.$^3$ with intervals of 0.001. Full lines are positive values. (b) Spin density contour map, plotted on the $(x,y)$ plane for the antiferromagnetic $\gamma$-Fe particle in Cu. Contours range from $-0.01$ to $+0.01$ e/a.u.$^3$ with intervals of 0.001. Full lines are positive values.

Experimental measurements by Mössbauer spectroscopy show a large gap between the values of the hyperfine fields $H_F$ for AFM $\gamma$-Fe, at smaller lattice constants, and FM $\gamma$-Fe, at larger lattice constants. For the latter, the magnitude of $H_F$ is much larger. However, the calculated values of $\mu$ for both phases do not seem to justify this large discrepancy. In fact, it was found that the large difference observed experimentally in the magnitude of the hyperfine fields of AFM and FM $\gamma$-Fe originates mainly from the different sign of the conduction electrons contribution in both phases. For FM $\gamma$-Fe, the conduction electrons contribution is negative, and adds to the negative core contribution, resulting in hyperfine fields of large magnitude. For AFM, the conduction electrons contribution is positive, thus cancelling part of the negative core contribution and resulting in hyperfine fields of small magnitude.[8] In Figs. 2(a) and 2(b) are shown the valence $(3d+4s+4p)$ spin DOS (spin $\uparrow$ DOS minus spin $\downarrow$ DOS) for FM and AFM fcc Fe, respectively. A larger number of occupied spin down states near the Fermi level for AFM results in smaller values of $\mu$ than for FM. Oscillations at the bottom of the band for both cases are mainly due to polarization of the $4s$ states.

Both FM ($Fe_{14\uparrow}Cu_{48}$) and AFM ($Fe_{4\uparrow}Fe_{10\downarrow}Cu_{48}$) $\gamma$-Fe particles in copper were considered, at interatomic distances typical of the two magnetic phases. In the case of the AFM particle, four spin $\uparrow$ Fe atoms are on the $(x,y)$ plane, with five spin $\downarrow$ atoms on the layers above and below (see Fig. 1). The self-consistent calculations revealed that the $3d$ orbitals of copper tend to polarize parallel to the Fe $3d$ in both cases. As an example, we show in Figs. 3(a) and 3(b) the spin density plotted on the $(x,y)$ plane (see Fig. 1) for the FM and AFM $\gamma$-Fe particles in Cu, respectively. For FM, we see the compact $3d$ spin density on the Cu atoms aligned parallel to the moments on Fe. Dotted lines in Fig. 3(a) represent the spin density of the $(4s,4p)$ conduction electrons which is negative in both Fe and Cu. For the AFM particle [Fig. 3(b)], the $3d$ moments on the Cu atoms are parallel to the negative

TABLE I. Magnetic moments (in $\mu_B$) and hyperfine fields $H_F$ (in kG) of $\gamma$-Fe, $\gamma$-Fe in Cu, $\gamma$-Fe with two Al atoms as first neighbors and the $\gamma$-Fe particle in Cu with two Al neighbors (FM only). Conduction-electron contribution $H^{\text{cond}}$ and core contribution $H^{\text{core}}$ to $H_F$ are given separately. Values given are for AFM and FM states, at typical interatomic distances.

| | | Cluster | $\mu$ | $H^{\text{cond}}$ | $H^{\text{core}}$ | $H^{\text{tot}}=H_F$ |
|---|---|---|---|---|---|---|
| AFM | $\gamma$-Fe | $Fe_{36\uparrow}Fe_{26\downarrow}$ | 1.50 | +44 | −157 | −113 |
| | $\gamma$-Fe+2Al | $Fe_{36\uparrow}Fe_{24\downarrow}Al_2$ | 1.61 | +35 | −171 | −136 |
| $r$=2.63 a.u. | $\gamma$-Fe in Cu | $(Fe_{4\uparrow}Fe_{10\downarrow})Cu_{48}$ | 1.34 | +86 | −130 | −44 |
| FM | $\gamma$-Fe | $Fe_{62\uparrow}$ | 2.44 | −59 | −288 | −347 |
| | $\gamma$-Fe+2Al | $Fe_{60\uparrow}Al_2$ | 2.29 | −60 | −268 | −328 |
| $r$=2.72 a.u. | $\gamma$-Fe in Cu | $(Fe_{14\uparrow})Cu_{48}$ | 2.54 | −23 | −296 | −319 |
| | $\gamma$-Fe in Cu+2Al | $(Fe_{12\uparrow}Al_2)Cu_{48}$ | 2.39 | −23 | −275 | −298 |

moments on the Fe atoms of the particle in the layers above and below, since these are the majority. This result is entirely in agreement with recent measurements with magnetic circular x-ray dicroism at the $K$ edge of copper for Co/Cu and Fe/Cu multilayers, which show that the $3d$ electrons of Cu are polarized parallel to the $3d$ moments of Fe, whereas the $4p$ of Cu are antiparallel.[9]

Finally, the influence of substitutional Al in $\gamma$-Fe and in the Fe particle in Cu was also explored. The results of the self-consistent calculations revealed that the presence of Al substituting for Fe disrupts the AFM spin arrangement: for the AFM $\gamma$-Fe particle in copper, the presence of two Al atoms resulted in nonconvergence for the self-consistent potential (after iteration, the FM state resulted), indicative of the instability of that state. In pure AFM $\gamma$-Fe the two Al impurities caused a tendency to local ferromagnetic arrangement. Details of these calculations will be given in a forthcoming publication.[10]

In Table I are given values of the Fe magnetic moment $\mu$ and hyperfine field $H_F$ for $\gamma$-Fe, $\gamma$-Fe in Cu, pure $\gamma$-Fe with Al neighbors and the $\gamma$-Fe particle in Cu with Al neighbors (FM only). It may be seen in this table that the sign of the conduction-electrons contribution is positive for the AFM state and negative for FM in all cases. The significant influence of the Cu matrix and of Al neighbors in $\mu$ and $H_F$ may be also seen.

## ACKNOWLEDGMENTS

Calculations were performed at the Cray YMP of the Supercomputing Center of the Universidade Federal do Rio Grande do Sul. This work was supported in part by the U. S. National Science Foundation, under the U. S.-Brazil cooperative program, Grant No. INT-9202608 and the MRL program, at the Materials Research Center of Northwestern University, under Award No. DMR-9120521.

[1] T. Ezawa, W. A. A. Macedo, U. Glos, W. Keune, K. P. Schletz, and U. Kirschbaum, Physica B **161**, 281 (1989).
[2] W. Keune, T. Ezawa, W. A. A. Macedo, U. Glos, K. P. Schletz, and U. Kirschbaum, Physica B **161**, 269 (1989).
[3] J. Kübler, Phys. Lett. **81A**, 81 (1981).
[4] C. S. Wang, B. M. Klein, and H. Krakauer, Phys. Rev. Lett. **54**, 1852 (1985).
[5] D. E. Ellis and G. S. Painter, Phys. Rev. B **2**, 2887 (1970); B. Delley and D. E. Ellis, J. Chem. Phys. **76**, 1949 (1982).
[6] D. Guenzburger and D. E. Ellis, Phys. Rev. B **49**, 6004 (1994).
[7] U. von Barth and L. Hedin, J. Phys. C **5**, 1629 (1972).
[8] D. Guenzburger and D. E. Ellis, Phys. Rev. B **51**, 12519 (1995).
[9] S. Pizzini, A. Fontaine, C. Giorgetti, E. Dartyge, J.-F. Bobo, M. Piecuch, and F. Baudelet, Phys. Rev. Lett. **74**, 1470 (1995), and references therein.
[10] D. Guenzburger and D. E. Ellis, Phys. Rev. B (to be published).

# The magnetic response at the metal–insulator transition in $La_{1-x}Sr_xTiO_3$ (abstract)

R. Osborn[a)]
*Materials Science Division, Argonne National Laboratory, Argonne, Illinois 60439-4845*

M. C. Aronson
*Department of Physics, University of Michigan, Ann Arbor, Michigan 48109-1120*

E. A. Goremychkin
*Frank Laboratory of Neutron Physics, JINR, 141980 Dubna, Moscow Region, Russia*

J. E. Greedan
*Institute for Materials Research, McMaster University, Hamilton, Ontario, Canada L8S 4M1*

We report on recent inelastic neutron scattering measurements of the magnetic response close to the metal–insulator transition in $La_{1-x}Sr_xTiO_3$. Specific heat and susceptibility data from Tokura *et al.*[1] give evidence for a divergent effective mass at the critical concentration $x_c = 0.05$ in agreement with recent mean-field theories of the transition. The mass enhancement is believed to arise from the formation of a *d*-electron resonance at the Fermi energy close to the transition. The aim of this investigation is to look for evidence of this resonance in the dynamic magnetic susceptibility. We studied samples with $x = 0$, 0.05, and 0.2 using incident energies between 25 and 200 meV. After correction for the phonon scattering, we observe a broad response above a threshold of 20–30 meV extending to over 100 meV. In addition, the Mott insulating antiferromagnet ($x = 0$) has a peak at 40 meV, consistent with the estimated activation energy derived from resistivity measurements. This feature becomes washed out with temperature and doping. Possible origins for this peak are discussed. © *1996 American Institute of Physics.* [S0021-8979(96)44908-6]

---

[a)]Supported by US-DOE, BES-MS Contract No. W-31-109-ENG-38.

[1] Y. Tokura, Y. Taguchi, Y. Okada, Y. Fujishima, T. Arima, K. Kumagai, and Y. Iye, Phys. Rev. Lett. **70**, 2126 (1993).

 0021-8979/96/79(8)/6432/1/$10.00 © 1996 American Institute of Physics

# On perturbation theory for the three-band model of cuprates

T. A. Kaplan, S. D. Mahanti, and Yen-Sheng Su
*Department of Physics and Astronomy and Center for Fundamental Materials Research, Michigan State University, East Lansing, Michigan 48823*

K. Kubo
*Institute of Physics, University of Tsukuba, Ibaraki 305, Japan*

We raise and discuss the following question. Why does the spectrum for the three-band model of Hybertson, Stechel, Schluter, and Jennison, claimed not to be approachable by perturbation theory because of rather large hopping integrals compared to site energy differences, follow precisely what would be expected by low-order perturbation theory? The latter is, for the insulating case, that the low-lying levels are describable by a Heisenberg Hamiltonian with nearest-neighbor interactions plus much smaller next-nearest-neighbor interactions and $n$-spin terms, $n \geqslant 4$. We first check whether perturbation theory actually does not converge, treating the hopping and $p$-$d$ exchange terms as perturbations. For the crystal, we find that the first three terms contributing to the nearest-neighbor exchange coupling $J$ (which are of third, fourth, and fifth order) *increase* in magnitude, and are not of the same sign, i.e., there is no sign of convergence to this order. We also consider the small cluster, $Cu_2O_7$, for which we have carried out the perturbation series to 14th order; there is still no sign of convergence. Thus the nonconvergence of this straightforward perturbation theory is convincingly established. Yet the apparent perturbative nature of the spectrum suggests the existence of *some* perturbation theory that does converge. The possibility of a particular transformation of the Hamiltonian leading to a convergent perturbation series, thereby answering the above question, is discussed. © *1996 American Institute of Physics.* [S0021-8979(96)27008-4]

## I. INTRODUCTION

Hybertson, Stechel, Schluter, and Jennison[1] (HSSJ) diagonalized the three-band Hubbard model for finite clusters (on a $CuO_2$ plane) using parameter values determined previously[2] for $La_2CuO_4$ by a constrained local density approximation. These values are in essential agreement with those found by others,[3,4] one of which used a different approach; this is a reason these values are considered to be realistic. Because the hopping parameters are not very small compared to on-site energy differences, particularly $\epsilon_{pd}$, it was claimed[2] that usual low-order perturbation theory is not appropriate for the model. We were therefore puzzled by the resulting spectrum, which follows precisely what is expected on the basis of low-order perturbation theory.

In particular for the cluster $Cu_5O_{16}$ with five holes, the low-lying energies were shown[1] to agree with the Heisenberg model (for the five Cu spins) with antiferromagnetic nn (nnn) exchange parameters $J=128$ ($J'=3$) meV. And these levels were separated from the higher ones by an appreciable gap. The puzzling aspects of these results are the smallness of $J'/J$, the apparent negligibility of four-spin terms in the spin Hamiltonian, and the separation of the low-lying levels from the higher ones, since these are just the properties expected from the usual perturbation theory if it is rapidly converging at low orders.

The first step we have taken in trying to sort out this matter is to check the statement that usual perturbation theory is not expected to be appropriate. In fact we go further and consider the possibility that convergence does not appear until fairly high order, so that four-spin terms, which come in rather high order, might be small. Our results indicate strongly that the usual perturbation theory (the hopping and exchange terms are the perturbation) is not convergent at all, and the consideration of a few orders is useless. Discussion of these results constitutes the main body of this paper. We also indicate that a particular change of one-electron basis, to what Anderson[5] termed the exact localized functions, which were actually defined appropriately by others,[6] might lead to a rapidly converging perturbation theory.

## II. HAMILTONIAN AND PERTURBATION THEORY

Because of ambiguities in previous presentations, we write the Hamiltonian explicitly:

$$H = H_1 + H_U + H_K, \tag{1}$$

where

$$H_1 = \epsilon \sum_i n_i^p + t_{pd} \sum_{\langle i,l\rangle,\sigma} (c_{i\sigma}^{d+} c_{l\sigma}^{p} + \text{h.c.}) + t_{pp} \sum_{\langle l,l'\rangle,\sigma} (c_{l\sigma}^{p+} c_{l'\sigma}^{p} + \text{h.c.}), \tag{1a}$$

$$H_U = U_d \sum_i n_{i\uparrow}^d n_{i\downarrow}^d + U_p \sum_l n_{l\uparrow}^p n_{l\downarrow}^p + U_{pd} \sum_{\langle il\rangle} n_i^d n_l^p, \tag{1b}$$

and

$$H_K = K_{pd} \sum_{\langle i,l\rangle} \left( \frac{1}{2} n_i^d n_l^p + 2 \vec{s}_i^{\,d} \cdot \vec{s}_l^{\,p} \right) + K_{pp} \sum_{\langle l,l'\rangle} \left( \frac{1}{2} n_l^p n_{l'}^p + 2 \vec{s}_l^{\,p} \cdot \vec{s}_{l'}^{\,p} \right). \tag{1c}$$

$c_{i\sigma}^{\nu+}$ creates a hole in a Wannier function at site $i$ of type $\nu$, $n_i^\nu = \Sigma_\sigma n_{i\sigma}^\nu$, $n_{i\sigma}^\nu = c_{i\sigma}^{\nu+} c_{i\sigma}^{\nu}$, $s_i^z = (1/2)(n_{i\uparrow} - n_{i\downarrow})$, $s_i^+ = c_{i\uparrow}^+ c_{i\downarrow}$, whose adjoint is the spin lowering operator $s_i^-$. The orbital at a copper site is $d_{x^2-y^2}$; at each oxygen site there is one $p$

 0021-8979/96/79(8)/6433/3/$10.00 © 1996 American Institute of Physics 

orbital, of sigma-bonding character. The parameter values are[7] $\epsilon=3.6$, $t_{pd}=-1.3$, $t_{pp}=-0.65$, $U_d=10.5$, $U_p=4$, $U_{pd}=1.2$, $K_{pd}=-0.18$, $K_{pp}=-0.04$, all in eV. [The signs correspond to orbital phases chosen as follows: if $d_{x^2-y^2}$ exists at a particular Cu, then at the O's immediately to its right and left (along the $x$ axis) the orbitals are $p_x$ and $-p_x$, respectively; similarly, the orbitals at the nearest O's below and above are $p_y$ and $-p_y$, respectively. The remaining phases are determined by having the nearest neighbor $d$-$p$ overlap always negative.]

We choose as the perturbation $V$ the sum of the hopping ($t$) terms and the exchange ($K$) terms, the unperturbed Hamiltonian $H_0$ being $H$-$V$. The unperturbed ground state is then characterized by $n_l^p=0$, $n_i^d=1$, its energy is 0 and its degeneracy is $2^N$, where $N$ is the number of $d$ sites. We define $P$ as the projection operator on to this unperturbed ground state manifold, with $Q=1-P$. Let $\Psi$ be an eigenstate of $H$ with eigenvalue $E$. Then the effective Hamiltonian[8] operating on $P\Psi$ can be shown to equal $EP\Psi$, an equation called the projected Schrödinger equation. Considering that the unperturbed ground state energy $E_0$ is zero, so that $E$ is the change in energy, this projected Schrödinger equation can be expanded in the form[9]

$$P\{VG_0V+VG_0VG_0V+VG_0VG_0VG_0V-(VG_0^2V)\times(VG_0V)+\cdots\}P\Psi=EP\Psi, \tag{2}$$

where $G_0=[Q(E_0-H_0)Q]^{-1}$, Löwdin's inverse of the corner,[8] assumed to exist, and $(A)(B)$ means $APB$.

Using Eq. (2), we calculated the exchange couplings for two cases. One is the infinite crystal; here we found the three leading contributions for the $nn$ coupling to be

$$J_3=\frac{4t_{pd}^2K_{pd}}{\Delta_1^2},$$

$$J_4=\frac{4t_{pd}^4}{\Delta_1^2}\left(\frac{1}{\Delta_4}+\frac{2}{\Delta_5}\right)-\frac{16t_{pd}^2t_{pp}K_{pd}}{\Delta_1^3},$$

$$J_5=4\Bigg[-\left(\frac{4}{\Delta_1^3\Delta_4}+\frac{8}{\Delta_1^3\Delta_5}+\frac{4}{\Delta_1^2\Delta_2\Delta_4}+\frac{16}{\Delta_1^2\Delta_3\Delta_5}+\frac{8}{\Delta_1^2\Delta_2\Delta_3}\right)t_{pd}^4t_{pp}+\left(\frac{2}{\Delta_1^3\Delta_4}+\frac{4}{\Delta_1^3\Delta_5}+\frac{20}{\Delta_1^3\Delta_3}+\frac{12}{\Delta_1^3\Delta_6}+\frac{4}{\Delta_1^3\Delta_7}+\frac{12}{\Delta_1^2\Delta_3^2}$$
$$+\frac{12}{\Delta_1^2\Delta_6^2}-\frac{42}{\Delta_1^4}\right)t_{pd}^4K_{pd}+\frac{8}{\Delta_1^2\Delta_3^2}t_{pd}^4K_{pp}+\frac{1}{\Delta_1^4}t_{pd}^2K_{pd}^2+\left(\frac{12}{\Delta_1^4}+\frac{4}{\Delta_1^3\Delta_2}+\frac{2}{\Delta_1^2\Delta_2^2}\right)t_{pd}^2t_{pp}^2K_{pd}\Bigg]+\frac{8t_{pd}^2t_{pp}K_{pd}^2}{\Delta_1^4}. \tag{3}$$

(The exchange coupling constant $J=J_3+J_4+J_5+\cdots$.) Here,

$$\Delta_1=\epsilon+U_{pd},\quad \Delta_2=\epsilon+2U_{pd},\quad \Delta_3=2\epsilon+U_{pd}+U_{pp},$$

$$\Delta_4=U_d,\quad \Delta_5=2\epsilon+U_p,$$

$$\Delta_6=2\epsilon+2U_{pd}+U_{pp},\quad \Delta_7=2\epsilon+U_{pd}.$$

(We have added $nn$ $p$-$p$ repulsion, $U_{pp}$.) The numerical values of $J_3, J_4, J_5$ are $-0.053$, 0.107, 0.231 eV, respectively. The negative value indicates a ferromagnetic contribution. Clearly these do not show an indication of convergence.

The other case is the small cluster $Cu_2O_7$ with two holes, considered also in HSSJ. In this case there are just singlets and triplets, the lowest singlet-triplet splitting being given by $J$. Equation (2) in the space defined by zero total $z$ component of spin is a $2\times2$ matrix equation. Here we calculated up to 14th order, the contributions $J_n$ to $J$ obtained being, for $n=3,4,\ldots,14$,

$$-.053,\ .107,\ .238,\ .065\ ,\ -.267,$$
$$-.272,\ .153,\ .430,\ .077,\ -.474,\ -.375,\ .349. \tag{4}$$

Obviously there is absolutely no sign of convergence. As a check in this small cluster case, we replaced $V$ by $\lambda V$ and took $\lambda$ small enough to obtain convergence, comparing the result with the exact value (found by directly diagonalizing $H$).

## III. DISCUSSION

The above considerations having given rather convincing evidence that the (standard) perturbation approach used is simply not convergent, we are left with our original question, why then do the *results* of exact calculation show the properties expected from perturbation theory? The following possibility seems promising. The Hamiltonian (1) is written in terms of field operators $c_i$ for some set of Wannier functions, $w_i$. These have been assumed real and to have certain symmetry under point group and translation operations. But such functions are not unique; i.e., there are real linear orthogonal transformations of these functions which preserve this symmetry property. In trying to provide a realization of Anderson's concept[5] of "exact localized or Wannier functions," a simple model of a small cluster and of a linear chain (which can be considered as Cu-O-Cu with two holes and an infinite Cu-O-Cu-O chain with one hole per Cu) were studied.[6] There the general two-band model was treated. In perturbation theory based on arbitrary Wannier functions, there are contributions to $J$ of fourth order in the $d$-$p$ overlap from first through fourth order in formal perturbation theory. It was shown that in a perturbation expansion based on the nonmagnetic localized solutions of the thermal single determinant approximation (TSDA),[10] the convergence through fourth-order perturbation theory is dramatically improved. Higher-order studies were not carried out since the materials of interest at that time, e.g., NiO and $KNiF_3$, are highly ionic and the perturbation expansions were expected to converge

rapidly. Clearly that approach might be very useful in the present case of the cuprates where the degree of covalence is so high that the perturbation theory is nonconvergent. We have made some preliminary calculations along these lines for very small clusters. In particular we were able to convert the nonconvergent series (4) to a convergent series (converging to the exact value of $J$). These ideas will be submitted for publication elsewhere.[11]

We note that if there is a rapidly convergent perturbation approach for the present problem with its presumably realistic parameter values, there is an implication that precise *ab initio* quantum chemical calculations for the solid as a whole might be possible.[12]

We add that after the present work was completed, we became aware of some literature that is quite relevant, namely, Refs. 13 and 14. The approaches of these two groups (Refs. 13 and 14) are very similar to each other, and are in the spirit of our attempts to find a convergent series. But their approach is different from ours. The relationship between the approaches is presently under study, and will be discussed elsewhere.[11]

## ACKNOWLEDGMENTS

The authors thank E. B. Stechel for discussions of her paper HSSJ. They also benefitted from discussions with J. F. Harrison, R. Rencsok and G. Kotliar. This work was partially supported by NSF Grant No. DMR-921-3824.

[1] M. S. Hybertson, E. B. Stechel, M. Schluter, and D. R. Jennison, Phys. Rev. B **41**, 11068 (1991).

[2] M. S. Hybertson, M. Schluter, and N. E. Christenson, Phys. Rev. B **39**, 9028 (1989).

[3] A. K. McMahan, R. M. Martin, and S. Satpathy, Phys. Rev. B **38**, 6650 (1989).

[4] H. Eskes and G. A. Sawatzky, Phys. Rev. Lett. **61**, 1415 (1988).

[5] P. W. Anderson, Solid State Phys. **14**, 99 (1963).

[6] R. S. Tu and T. A. Kaplan, AIP Conf. Proc. No. 24, p. 218 (1974).

[7] These are the same parameter values as those given in HSSJ except that the hopping parameters $t$ are the negatives of those given there. We thank Dr. Ellen Stechel for verifying that these negative values are the values actually used in HSSJ.

[8] P. O. Löwdin, J. Math. Phys. **3**, 969 (1962).

[9] I. Lindgren and J. Morrison, *Chemical Physics* (Springer, New York, 1982), Vol. 13, p. 207.

[10] T. A. Kaplan and P. N. Argyres, Ann. Phys. **92**, 1 (1975).

[11] Yen-Sheng Su, T. A. Kaplan, and S. D. Mahanti (unpublished).

[12] There of course have been other, nonperturbative, approaches to estimating physical properties of the three-band model, e.g., exact studies of very small systems (Ref. 1), Monte Carlo methods for small systems [R. T. Scalletar, D. J. Scalapino, R. L. Sugar, and S. R. White, Phys. Rev. B **44**, 770 (1991); A. Bhattacharya and C. S. Wang, *ibid.* **48**, 13949 (1993)], and a slave-boson saddle point approximation for the infinite system [C. A. Balseiro, M. Avignon, A. G. Rojo, and B. Alascio, Phys. Rev. Lett. **62**, 2624 (1989)]. One hopes that a convergent perturbation theory could allow predictively accurate results to be obtained for large systems, described by more general ($n$ band, $n>3$) models.

[13] H. Eskes and J. H. Jefferson, Phys. Rev. B **48**, 9788 (1993); J. H. Jefferson, H. Eskes, and L. F. Feiner, *ibid.* **45**, 7959 (1992).

[14] V. I. Belenicher and A. L. Chernyshev, Phys. Rev. B **49**, 9746 (1994).

# Magnetic measurements on $Cd_{1-x}Cr_xTe$ and $Zn_{1-x}Cr_xTe$

T. M. Pekarek, I. Miotkowski, and B. C. Crooker
*Department of Physics, Purdue University, West Lafayette, Indiana 47907*

We have investigated the magnetic properties of single-crystal $Cd_{1-x}Cr_xTe$ and $Zn_{1-x}Cr_xTe$ samples. The magnetization is anisotropic (~7% for $Zn_{1-x}Cr_xTe$ and ~0.4% for $Cd_{1-x}Cr_xTe$) with the (111) direction having the greatest value. We have found that the magnetic behavior in fields up to 6 T and temperatures between 1.5 and 324 K for both systems is well described by a theoretical model with crystal field, Jahn–Teller, spin-orbit, and spin-spin terms including ligand field corrections to the spin-orbit and spin-spin parameters. Good agreement was found between the experimental results and the theoretical calculations for a Jahn–Teller splitting of 370 and 320 $cm^{-1}$ and effective spin-orbit parameters of −49.9 and −59.4 $cm^{-1}$ for $Cd_{1-x}Cr_xTe$ and $Zn_{1-x}Cr_xTe$, respectively. The key feature is an orbital singlet, $S=2$ ground state with a small splitting (1.5 K for $Cd_{1-x}Cr_xTe$ and 12.4 K for $Zn_{1-x}Cr_xTe$) of the $m_s$ states. © *1996 American Institute of Physics.* [S0021-8979(96)27108-0]

## I. INTRODUCTION

The class of II–VI diluted magnetic semiconductors (DMS)[1] include the systems of the form $A^{II}_{1-x}M_xB^{VI}$, where $M$ is a transition metal ion (e.g., Mn, Fe, Co, or Cr) and $A^{II}B^{VI}$ is a II–VI semiconductor host. Over the past two decades, much work has been done on the magnetic behavior of Mn,[1] Fe,[2,3] and Co[4–6] based systems. Early work on low concentration Cr-based II–VI semiconductor crystals include optical absorption,[7–10] luminescence,[11] and electron paramagnetic resonance[12] (EPR) experiments. Recently, interest in the chromium based systems has reemerged resulting in the publication of several theoretical[13–17] and experimental[18–21] papers including magnetization measurements for $Zn_{1-x}Cr_xTe$[18] and $Zn_{1-x}Cr_xSe$.[17,19,20] What makes these systems interesting is the presence of a static Jahn–Teller distortion as well as the observation of a ferromagnetic $p$-$d$ coupling in $Zn_{1-x}Cr_xSe$.[17,21]

$Cd_{1-x}Cr_xTe$ is unique among the chromium-based DMS because of its small splitting of the ground multiplet. Early work reported a value of $D=+0.260\pm0.004$ $cm^{-1}$ (=0.374 K) for $Cd_{1-x}Cr_xTe$ which was obtained from EPR measurements.[12] This value of $D$ is approximately an order of magnitude below the other chromium-based DMS which all have a magnitude for $D$ within a factor of 1.4 of each other ranging from 2.6 K in $Cd_{1-x}Cr_xS$ to 3.6 K in $Zn_{1-x}Cr_xSe$.[12] It has been proposed previously that the trend in $D$ in $Zn_{1-x}Cr_xS$, $Zn_{1-x}Cr_xSe$, and $Zn_{1-x}Cr_xTe$ could be accounted for with a model including ligand field corrections to the spin-orbit and spin-spin parameters.

In this article we present magnetization measurements taken on bulk $Cd_{1-x}Cr_xTe$ and $Zn_{1-x}Cr_xTe$ crystals. Using the model Hamiltonian discussed previously,[10,18] we numerically diagonalized the 25×25 matrix to compare the predicted magnetization with our experimental results. We discuss the slight magnetic anisotropy (0.8%±0.9% at 5.2 K in 6 T) in $Cd_{1-x}Cr_xTe$ with the larger anisotropy in the magnetization observed for $Zn_{1-x}Cr_xTe$[18] and $Zn_{1-x}Cr_xSe$[19,20] in the context of the splitting of the ground multiplet. And, the anomalously low value of $D$ in $Cd_{1-x}Cr_xTe$ is compared with the $Zn_{1-x}Cr_xB^{VI}$ series.

## II. EXPERIMENTAL DETAILS

Single-crystal samples of $Cd_{1-x}Cr_xTe$ and $Zn_{1-x}Cr_xTe$ were taken from boules with nominal concentration of $x=0.05$ and 0.005, respectively. Typically, samples grown by the vertical Bridgman method yield actual concentrations less then the nominal value. We report on samples with actual concentrations, which is the only adjustable variable for the magnetization calculated from the 25×25 Hamiltonian, of $x=0.0036$ and $x=0.0031$ for $Cd_{1-x}Cr_xTe$ and $Zn_{1-x}Cr_xTe$, respectively. Both samples were oriented along the (111) and (100) directions using the standard Laue technique.

Magnetic measurements were made between 1.5 and 324 K in fields up to 6 T using a Cryogenic Consultants Limited SQUID magnetometer. A ferromagnetic minority phase was observed in each of our samples which accounts for ~10% of the chromium and is 90% saturated by 0.25 T at 10 K. Above 0.4 T at low temperatures, the ferromagnetic component is nearly saturated. A detailed analysis of the temperature dependence of the ferromagnetic phase will be presented elsewhere.[22] Both the diamagnetic signal from the host II-VI semiconductor and the saturated magnetization from the minority ferromagnetic phase were subtracted to yield the magnetization as a function of field.

## III. EXPERIMENTAL RESULTS AND DISCUSSION

Shown in Fig. 1 is the magnetization versus field data at 5.2 K for $Cd_{1-x}Cr_xTe$ oriented along the (111) and (100) directions. A slight anisotropy of 0.8%±0.9% is observed at 6 T. The solid line in Fig. 1 is a Brillouin fit assuming a pure spin two system with a concentration of $x=0.0037$. If there were a significant splitting of the ground multiplet, we would expect the magnetization to deviate noticeably from the Brillouin response and exhibit a significant anisotropy.[6,18–20] However, as can be seen, the data up to 6 T are well described by this simple model indicating, along with the very slight anisotropy, that the zero-field splitting of the ground multiplet is small. We have also made calorimetric measurements which further confirm the anonymously small value of $D$ in $Cd_{1-x}Cr_xTe$.

 0021-8979/96/79(8)/6436/3/$10.00 © 1996 American Institute of Physics

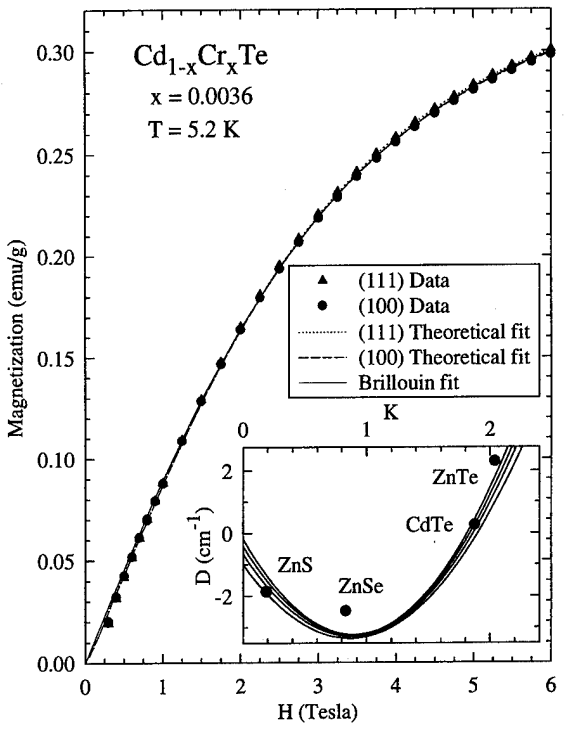



FIG. 1. Magnetization data for $Cd_{1-x}Cr_xTe$ taken at 5.2 K for the (111) and (100) orientations. The theoretical fit obtained from the 25×25 Hamiltonian for each orientation is shown by the dotted and dashed lines. Note that the theoretically predicted anisotropy is negligible on this scale. The solid line is a fit using a Brillouin function. Good agreement is found between the data and a Brillouin function because of the very small splitting of the ground multiplet. The ferromagnetic and diamagnetic contributions have been subtracted. Shown in the inset is a plot of $D$ vs $K$ for several chromium based DMS. The solid lines in the inset show the theoretical prediction for a model including ligand field corrections to the spin-orbit and spin-spin parameters.

However, it is not transparent why the ground multiplet is nearly degenerate. In order to explain our magnetic measurements on $Cd_{1-x}Cr_xTe$, the complete 25×25 complex Hamiltonian for the $^5D$ state was constructed including the crystal field, Jahn–Teller, spin-orbit, and spin-spin effects including ligand field corrections to the effective spin-orbit and spin-spin parameters.[12,18] It has been shown previously[12] that the general trend in $D$ in $Zn_{1-x}Cr_xS$, $Zn_{1-x}Cr_xSe$, and $Zn_{1-x}Cr_xTe$ could be accounted for with a model including ligand field corrections to the spin-orbit and spin-spin parameters using the perturbative result

$$D=\frac{\lambda_1^2}{E_1}-\frac{4\lambda_2^2}{E_2}-3\rho_3, \tag{1}$$

where $E_1=3E_{JT}$, $E_2=E_{JT}+\Delta-2E_{JTE}$, $\Delta$ is the crystal field splitting parameter, and $E_{JT}$ and $E_{JTE}$ are the Jahn–Teller energies for the orbital triplet ($^5T_2$) and doublet ($^5E$), respectively. The corrections due to the ligand field can be reduced to one adjustable parameter $K$ which sets the magnitude of the coupling. The effective spin-orbit and spin-spin parameters are then given by

$$\lambda_1\cong\lambda(1-K),$$

$$\lambda_2\cong\lambda\left(1-\frac{K}{8}\right), \text{ and} \tag{2}$$

$$\rho_3\cong\frac{5}{9E}(-\lambda_1^2+4\lambda_2^2)+\rho,$$

where $E\cong 20\,000$ cm$^{-1}$ is the energy of the next highest $LS$ state of the same symmetry ($3d^4$) and $\lambda$ and $\rho$ are the free-ion spin-orbit and spin-spin parameters, respectively.

Shown in the inset of Fig. 1 is a plot of $D$ vs $K$ for several chromium based DMS which are shown by solid circles. We note that our value for $K=2.0$ for $Zn_{1-x}Cr_xTe$ was determined from numerically diagonalizing the 25×25 Hamiltonian and is lower then the previously reported value of 2.33 determined from a perturbative treatment. The values of $K$ for $Zn_{1-x}Cr_xS$ and $Zn_{1-x}Cr_xSe$ were calculated by scaling our value of $K$ for $Zn_{1-x}Cr_xTe$ by the ratio of the ligand spin-orbit constants $\zeta_S/\zeta_{Te}=1689$ cm$^{-1}$/382.4 cm$^{-1}$ or $\zeta_{Se}/\zeta_{Te}=1689$ cm$^{-1}$/4136 cm$^{-1}$.[12] The four solid lines were calculated using Eq. (2) for the set of parameters for each of the four systems shown.[10,18,22] As can be seen, the general trend is satisfactorily predicted for $Cd_{1-x}Cr_xTe$ ($K=1.9$) as well as the $Zn_{1-x}Cr_xB^{VI}$ series.

The dotted and dashed lines shown in Fig. 1, which are nearly indistinguishable on this scale, are theoretical fits for the (111) and (100) directions which were calculated using the 25×25 Hamiltonian with a Jahn–Teller energy of 370 cm$^{-1}$ and effective spin-orbit and spin-spin parameters within the lower 15×15 ($^5T_2$) state of −49.9 and 0.29 cm$^{-1}$, respectively. These parameters result in a small 1.5 K total splitting ($4D$) of the ground orbital singlet multiplet in agreement with the EPR measurements.[12] The Hamiltonian predicts a 0.44% anisotropy in 6 T which is in good agreement with the data. In our analysis we have assumed that the Jahn–Teller distortions are randomly distributed along the three equivalent crystalline axes as was observed in the $Zn_{1-x}Cr_xTe$ system.[18] As can be seen from Fig. 1 the agreement between the theory and experiment is good with the concentration $x=0.0035\pm0.0005$ being the only adjustable parameter.

Shown in Fig. 2 is the magnetization versus field data at 3.67 K for a $Zn_{1-x}Cr_xTe$ crystal oriented along the (111) and (100) directions which has been presented previously.[18] The solid line is a Brillouin fit assuming a pure spin two system with a concentration of $x=0.0035$. In contrast with the $Cd_{1-x}Cr_xTe$ data, the disagreement between the data and Brillouin fit is obvious indicating a splitting of the ground multiplet. Further magnetic evidence of the splitting of the ground multiplet is the presence of an anisotropy (~7% at 3.67 K in 6 T) in the data. The theoretical response obtained from the Hamiltonian is shown by the dotted and dashed lines for a Jahn–Teller energy of 320 cm$^{-1}$ and effective spin-orbit and spin-spin parameters within the ground $^5T_2$ state of −59.4 and 0.32 cm$^{-1}$, respectively.

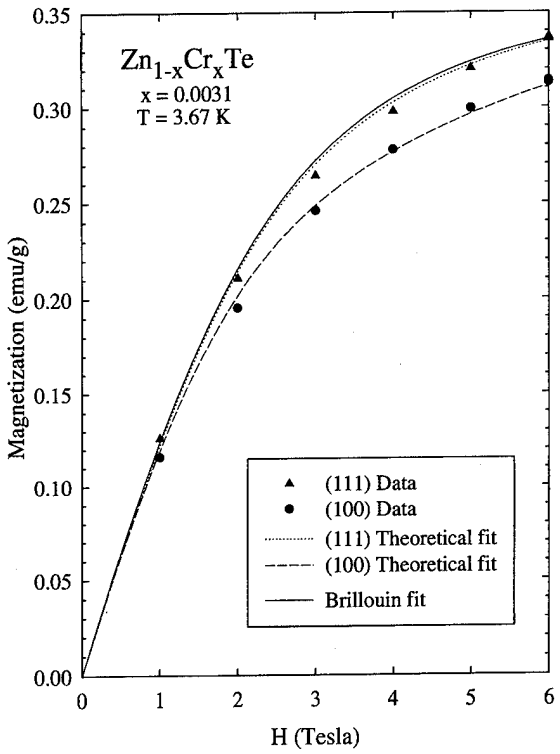



FIG. 2. Magnetization data for $Zn_{1-x}Cr_xTe$ taken at 3.67 K for the (111) and (100) orientations. A theoretical fit obtained from the 25×25 Hamiltonian for each orientation is shown by the dotted and dashed lines. The solid line is a fit using a Brillouin function. An ~7% anisotropy and deviation from the Brillouin fit is evident due to the splitting of the ground multiplet. The ferromagnetic and diamagnetic contributions have been subtracted.

## IV. CONCLUSIONS

We have presented magnetization data on $Cd_{1-x}Cr_xTe$ and $Zn_{1-x}Cr_xTe$. The key feature of these systems is an orbital singlet, $S=2$ ground state with a small splitting (1.5 K for $Cd_{1-x}Cr_xTe$ and 12.4 K for $Zn_{1-x}Cr_xTe$) of the $m_s$ states. The theoretical model we have used provides a good description for the magnetization for both the $Cd_{1-x}Cr_xTe$ and $Zn_{1-x}Cr_xTe$ systems which are the only chromium based II–VI DMS which are reported to have a positive value for $D$. Agreement was found between the experimental results and the theoretical calculations for a Jahn–Teller splitting of 370 and 320 $cm^{-1}$ and effective spin-orbit parameters of $-49.9$ and $-59.4$ $cm^{-1}$ for $Cd_{1-x}Cr_xTe$ and $Zn_{1-x}Cr_xTe$, respectively. The theory correctly predicts the anisotropy and field dependence of the magnetization for both systems and accounts for the anonymously low value of $D$ in $Cd_{1-x}Cr_xTe$.

## ACKNOWLEDGMENT

This work was supported by the National Science Foundation (NSF) under Material Research Group Grant No. DMR-92-21390 and by the Purdue Research Foundation.

[1] See, for example, in *Semiconductors and Semimetals*, edited by J. K. Furdyna and J. Kossut (Academic, Boston, 1988), Vol. 25.
[2] M. Villeret, S. Rodriguez, and E. Kartheuser, Phys. Rev. B **47**, 1228 (1993).
[3] C. Testelin, C. Rigaux, A. Mauger, A. Mycielski, and M. Guillot, Phys. Rev. B **46**, 2193 (1992).
[4] A. Lewicki, A. I. Schindler, J. K. Furdyna, and W. Giriat, Phys. Rev. B **40**, 2379 (1989).
[5] A. Lewicki, A. I. Schindler, I. Miotkowski, and J. K. Furdyna, Phys. Rev. B **41**, 4653 (1990).
[6] A. Lewicki, A. I. Schindler, P. M. Shand, B. C. Crooker, and J. K. Furdyna, Phys. Rev. B **44**, 6137 (1991).
[7] J. T. Vallin, G. A. Slack, S. Roberts, and A. E. Hughes, Phys. Rev. B **2**, 4313 (1970).
[8] J. M. Langer and J. M. Baranowski, Phys. Status Solidi B **44**, 155 (1971).
[9] P. A. Slodowy and J. M. Baranowski, Phys. Status Solidi B **49**, 499 (1972).
[10] M. Kaminska, J. M. Baranowski, S. M. Uba, and J. T. Vallin, J. Phys. C **12**, 2197 (1979).
[11] G. Grebe and H. J. Schulz, Z. Naturforsch. Teil A **29**, 1803 (1974).
[12] J. T. Vallin and G. D. Watkins, Phys. Rev. B **9**, 2051 (1974).
[13] J. Blinowski, P. Kacman, and H. Przybylinska, Solid State Commun. **79**, 1021 (1991).
[14] A. K. Bhattacharjee, Phys. Rev. B **46**, 5266 (1992).
[15] J. Blinowski and P. Kacman, Phys. Rev. B **46**, 12 298 (1992).
[16] G. Goetz, H. Zimmermann, and H. J. Schulz, Z. Phys. B **91**, 429 (1993).
[17] A. K. Bhattacharjee, Phys. Rev. B **49**, 13 987 (1994).
[18] T. M. Pekarek, J. E. Luning, I. Miotkowski, and B. C. Crooker, Phys. Rev. B **50**, 16 914 (1994).
[19] A. Twardowski, T. Fries, Y. Shapira, P. Eggenkamp, H. J. M. Swagten, and M. Demianiuk, J. Appl. Phys. **73**, 5745 (1993).
[20] W. Mac, A. Twardowski, P. J. T. Eggenkamp, H. J. M. Swagten, Y. Shapira, and M. Demianiuk, Phys. Rev. B **50**, 14 144 (1994).
[21] W. Mac, N. T. Khoi, A. Twardowski, J. A. Gaj, and M. Demianiuk, Phys. Rev. Lett. **71**, 2327 (1993).
[22] T. M. Pekarek, I. Miotkowski, and B. C. Crooker (unpublished).

# Specific heat of $R_3Co$ (R: La,Pr, and Nd) (abstract)

I. Umehara, K. Nakano, Q. F. Lu, and K. Sato
*Department of Physics, Faculty of Engineering, Yokohama National University, Yokohama, Japan*

It was reported that $La_3Co$ is an interesting superconductor which has a critical temperature $T_c$ of 4.5 K.[1] $Pr_3Co$ and $Nd_3Co$ are ferromagnetic materials, which have Curie temperatures of 10 and 25 K, respectively. It was claimed that their magnetic structures are associated with the canting moment reflected to the symmetry of their crystal structure.[2] In this paper we present the results of the specific heat measurement in these compounds in the temperature range from 2 to 30 K by a standard adiabatic heat pulse method. Two phase transitions are observed at 8 and 25 K in $Nd_3Co$. One of them at 25 K corresponds to the Curie temperature mentioned above. Another is the transition corresponds to the moment reorientation, which was observed in the thermomagnetic curves and electrical resistivity measurement. This results claim that the moments are canted in this compounds. Magnetic entropy reaches 90% of $R$ ln 2 at 25 K. However, it increases above the Curie temperature because the crystalline electric field effects plays an important role in this compounds. There are two peaks of 10 and 12 K in $Pr_3Co$. The above temperature corresponds the Curie temperature but another was unknown. Thus we performed the specific heat measurement for $Pr_7Co_3$, which is very close to the $Pr_3Co$ in the phase diagram. We could observe the phase transition at 12 K for $Pr_7Co_3$ in the specific heat measurement and electric resistivity measurement. It is clear that the phase transition at 12 K comes from impurity of $Pr_7Co_3$ in our $Pr_3Co$ compound. We prepare the good quality sample of $Pr_3Co$ and try to examine the specific heat measurement. © *1996 American Institute of Physics.* [S0021-8979(96)45008-X]

[1] K. Sato *et al.*, J. Appl. Phys. **73**, 6621 (1993).
[2] K. N. R. Taylor, Adv. Phys. **20**, 551 (1971).

 0021-8979/96/79(8)/6439/1/$10.00 © 1996 American Institute of Physics 

# Submicron characterization of recording media using magnetic force microscopy (invited) (abstract)

K. Babcock, S. Manalis, and V. Elings
*Digital Instruments, Santa Barbara, California 93103*

M. Dugas
*Advanced Research Corporation, Minneapolis, Minnesota 55414*

W. Challener
*3M Corporation, St. Paul, Minnesota 55414*

Magnetic force microscopy is finding widespread use in the analysis of magnetic structure at length scales relevant to modern storage densities. We present a new technique which uses the extremely localized stray fields of MFM tips to probe submicron media characteristics. The tip is brought into contact with the magnetized media, and a uniform external field $H_{ext}$ is momentarily added to the tip's stray field. If the net field exceeds the local media coercivity, the magnetization is reversed locally, and a "bit" is written. High-resolution MFM imaging of the results is done immediately using the same probe. Bit arrays of several Gbit/in$^2$ can be produced with the lithography software of a commercial MFM. Using the external field $H_{ext}$ as a parameter, the threshold for bit writing can be determined, giving a measure of the local, or "point", coercivity of the media on a 100 nm scale. Results for perpendicular Co–Cr and magneto-optical media can deviate significantly from conventional bulk hysteresis measurements, in some cases reversing the bulk coercivity ranking. Intermediate values of $H_{ext}$ reveal spatial variations in the point coercivity due to fluctuations in composition or microstructure. In square media, sufficiently strong fields $H_{ext}$ cause existing bits to grow, leading to bulk reversal via front propagation, and allowing a direct measurement of wall motion coercivity. Possible extensions to longitudinal media will be discussed. In general, combining the imaging and writing capabilities of MFM probes gives a direct assessment of media response to very localized fields, and leads to a powerful method for relating microstructure to bulk hysteresis properties. © *1996 American Institute of Physics.* [S0021-8979(96)62108-9]

 0021-8979/96/79(8)/6440/1/$10.00 © 1996 American Institute of Physics

# Magnetic imaging in the presence of external fields: Technique and applications (invited)

Romel D. Gomez
*Department of Electrical Engineering, University of Maryland, College Park, Maryland 20742 and Laboratory for Physics Sciences, 8050 Greenmead Drive, College Park, Maryland 20740*

Edward R. Burke
*Laboratory for Physics Sciences, 8050 Greenmead Drive, College Park, Maryland 20740*

Isaak D. Mayergoyz
*Department of Electrical Engineering, University of Maryland, College Park, Maryland 20742*

Magnetic force microscopy (MFM) in the presence of an external magnetic field has been developed. This has led to further understanding of image formation in MFM as well as new insights concerning the interaction of magnetic recording media with an external field. Our results confirm that, at low applied fields, image formation results from the interaction of the component by the local surface field along the direction of the probe's magnetization. By reorienting the probe's magnetization by an appropriate application of an external field, it is possible to selectively image specific components of the local field. At higher applied fields, the probe becomes saturated and the changes in the images may be attributed to magnetization reversal of the sample. We have observed the transformations that occur at various stages of the dc erasure of thin-film recording media. This technique has also been applied to conventional magneto-optical media to study domain collapse caused by increasing temperature with an external bias field. The methods, results, and their analysis are presented. © *1996 American Institute of Physics.* [S0021-8979(96)57008-5]

## I. INTRODUCTION

Since the first reports of its development in 1987,[1] magnetic force microscopy (MFM) has emerged as a powerful tool in understanding the micromagnetics of surfaces.[2] Its capability to resolve $\lesssim$100 nm features, combined with lenient requirements on sample preparation and operating environments, has made it a workhorse in technology development as well as fundamental investigations of surface[3] and biological[4] magnetism. Despite its widespread use, however, most MFM images were obtained under ambient magnetic field conditions. As a result, studies have been limited to samples being either in a locally nonmagnetized or remanent states.

Recently, the capability of imaging samples in the presence of an external magnetic field has been developed.[5] This has allowed direct imaging of the microscopic evolution of thin-film recording patterns undergoing dc erasure; and has opened up the possibility of investigating microscopic magnetic properties of surfaces at any point along the magnetization curve. In this paper, we provide the details of our technique and discuss the implications of subjecting both the probe and sample to an external field. We focused our studies on thin-film recording and magneto-optical media, not only because of their importance in the storage industry but because they represent excellent case models for in-plane and out-of-plane magnetization structures.

## II. TECHNIQUE

### A. Background

Magnetic force microscopy generates a two dimensional mapping of the local force-gradient between a magnetic probe and a sample, separated by about a hundred nanometers. The probe is comprised of a cantilever beam with a sharp, magnetic tip at one end that is forced to oscillate at its resonance frequency. It is then rastered across the surface while the changes in the oscillation phase of the cantilever are recorded in an array as a function of its two dimensional lateral position. The change of the oscillation phase is directly proportional to the force gradient, so that the resulting array, by using computer graphics, forms an image of the distribution of the local force gradient.

The technique can be understood by considering the motion of the cantilever probe as a single-point mass $m$ undergoing one-dimensional forced harmonic oscillation along the vertical $z$ axis.[6] The resonance frequency is determined by the intrinsic elastic constant of the cantilever, in combination with a small perturbation due to the probe-surface interaction force $F(z)$. The latter is incorporated by expanding $F(z)$ in a Taylor series and keeping the first order term $F' = \partial F/\partial z_0$. When the driving frequency is near the resonance, $\omega \sim \omega_0$, the local force gradient $F'$ will shift the resonance frequency by an amount $\Delta\omega_0 \approx \omega_0(F'/2k)$. As a consequence, the phase will vary from its nominal 90° out-of-phase condition relative to the driving term by an amount

$$\Delta\phi \approx -2Q\frac{\Delta\omega}{\omega_0} = -\frac{QF'}{k}, \tag{1}$$

where $Q$ is the quality factor of the cantilever. The phase variation at each point is proportional to the local force gradient.

Our commercial device, the Nanoscope III MFM, operates in the so-called lift and phase sensitive detection method.[7] The topography of the surface is first measured by using atomic force microscopy techniques and the contour is retraced with the probe at a preset height above the surface

 0021-8979/96/79(8)/6441/6/$10.00 © 1996 American Institute of Physics 

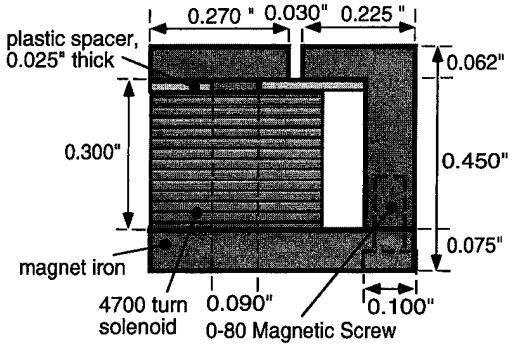



FIG. 1. Electromagnet design for MFM with an external in-plane magnetic field.

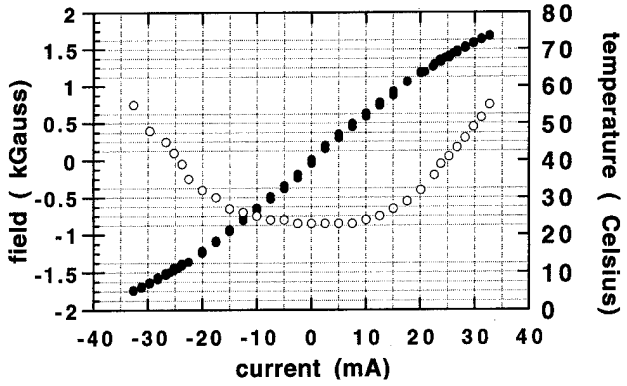



FIG. 2. Magnetic field and temperature calibration vs input current.

as the force-gradient is measured. In this manner, the surface topographical effects are minimized.

Since the probe is coated with a ferromagnetic alloy, the tip-surface force is dominated by the magnetic interaction if short-range adhesion forces[8] are neglected. For simplicity, we describe the tip as a single constant magnetic dipole, $\mathbf{m}_{\text{tip}}$. The force experienced by this dipole in a local magnetic field $\mathbf{H}$ is[2]

$$\mathbf{F}=-(\mathbf{m}_{\text{tip}}\cdot\nabla)\mathbf{H}. \tag{2}$$

Only the $z$ component of the force contributes to the oscillation. By differentiating with respect to $z$ and using $\nabla\times\mathbf{H}=0$, Eqs. (1) and (2) yield an explicit expression for contrast formation in phase-detection MFM:

$$\Delta\phi\approx\frac{Q}{k}\sum_i m_i\frac{\partial^2 H_i}{\partial z^2}. \tag{3}$$

This equation states that as long as the magnetic properties of the sample and the probe are unaffected by their mutual interaction, the contrast in MFM arises from the variations of the second $z$ derivative of the component of the surface field in the direction of the probe's magnetization.

One consequence of Eq. (3) is that it is possible to selectively image specific components of the second derivative of the local surface magnetic field by appropriately orienting the probe magnetization direction. In other words, by a judicious choice of probe magnetization directions, it is feasible to individually map out the $z$ derivatives of the three Cartesian components of the local surface magnetic field vectors. One way, of course, is to prepare probes in a highly controlled manner in order to have the easy axis aligned along definite directions. In principle, specific probes can be used to image particular surface field components. In our experiments, however, the reorientation of the direction of the probe's magnetization is accomplished by applying an external dc magnetic field during imaging. The intention is to orient the probe magnetization by sufficiently low fields which preclude significant effects on the sample.

### B. Magnet design

Adding an external field in MFM involves the incorporation of an electromagnet at the sample stage. Figure 1 shows the critical details of our design which produces magnetic fields primarily oriented along the sample surface plane. The dimensions were constrained by the available space in our device. The materials and coil specifications were chosen to optimize the magnetic field strength generated at the gap location and subject to a heating constraint to prevent temperature-induced problems, such as drifts, depolarization of the piezoelectric scanners, and heat-induced changes in the sample magnetic properties. The magnetic field generated in the gap of length $L_g$ can be estimated as

$$B_g\cong\frac{\mu_0 NI}{L_g}\quad\text{(MKSA units)}, \tag{4}$$

where $N$ is the total number of turns, $I$ is the current, and $\mu_0$ is the permeability of free space. This can be derived from Ampere's law for the case where the permeability of the iron core is large. The relevant parameters are: $N=4700$ turns and $L_g=0.76$ mm. At 30 mA, $B_g=2330$ G and it is expected to reach saturation at $B_g=4500$ G for a current of 56 mA. A measurement of the horizontal component of the field, shown in Fig. 2, was obtained by using a miniature Hall probe (LakeShore HT 2100) which was calibrated against a known field. The data indicate that the magnetic field varies linearly with current from 0 to 30 mA, demonstrating that within this range, the iron yoke is driven at the reversible regime of its magnetization curve. High-frequency fluctuations in the field were found to be about 0.5%. Similarly, the temperature was measured by using a calibrated thermocouple which was spot welded near the gap region. Heating effects, concurrently plotted in Fig. 2, show that a dc current of up to 32 mA elevates the temperature to less than 55 °C.

## III. RESULTS AND DISCUSSION

The samples used in our experiment were obtained from conventional and experimental thin film disks as well as conventional magneto-optic samples. The macroscopic properties of some of these samples were previously measured and reported elsewhere.[5,9]

### A. Probe effect: Component-resolved imaging

Confirming the predictions of Eq. (5), the individual components of the local surface magnetic fields of the thin film in-plane recorded medium are shown in Fig. 3. A diagram representing the expected distribution of the magneti-

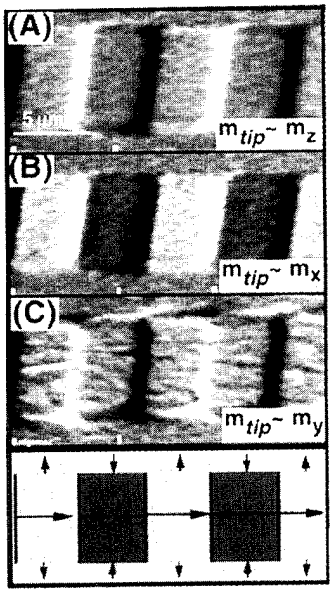



FIG. 3. Component-selective images of a thin-film recording medium. Images obtained with probe nominally oriented along the (A) normal $z$ axis, (B) in-plane $x$ axis, and (C) in-plane $y$ axis, reflecting the contributions of the local surface field at these directions, respectively. Bottom: sketch of the magnetization pattern.

zation distribution is drawn in the bottom of the figure. Figures 3(A) and 3(B) were obtained from the same area of the disk. In Fig. 3(A), the probe was premagnetized by a 3.5 kOe magnet along the vertical direction prior to image acquisition and no external horizontal field was applied to the sample. Neglecting some nonlinear effects due to the probe-sample interaction, the probe magnetization in Fig. 3(A) can be taken as $m \sim m_z$; $m_x, m_y \sim 0$. The contrast formation in Fig. 3(A) arises predominantly from $\partial^2 H_z/\partial z^2$ and it appears as an alternating series of bright and dark strips that are more or less localized along the transition regions. Note that despite the fact that the pattern is a series of alternating in plane magnetizations, very little contrast can be observed within the interior regions of the patterns. In fact, the image contrast in the interior regions is similar to the background areas outside of the patterns. In Fig. 3(B), which was acquired with a 200 Oe field along the track direction, the interior features have emerged and the two opposite magnetization directions are clearly distinguishable. This arises because the external horizontal dc magnetic field produced a nonvanishing $m_x$ component of the probe magnetization which induces a dominant term proportional to $\partial^2 H_x/\partial z^2$.

We offer the following qualitative interpretation of these images in terms of the physical quantities such as the magnetic charges and the magnetization. For illustrative purposes, consider the simple case of a one-dimensional sinusoidal magnetization pattern $M_x = M_0 \sin(kx)$, in a medium of thickness $\delta$. The local surface magnetic field components above the surface for this configuration can be computed,[10] and the corresponding second derivatives with respect to $z$ are

$$\frac{\partial^2 H_z}{\partial z^2} \propto \nabla \cdot M = \frac{\partial M_x}{\partial x} \tag{5}$$

and

$$\frac{\partial^2 H_x}{\partial z^2} \propto M_x . \tag{6}$$

In other words, MFM imaging with the $z$-axis probe orientation yields images that are proportional to the divergence of the magnetization or the volume magnetic charge density while the $x$-axis orientation yields images that are proportional to the distribution of magnetization. In real systems, the images may deviate from this simple interpretation, albeit only slightly. For example, for an in-plane arctangent transition with a transition length of 150 nm, the main difference between the divergence of the magnetization and the second derivative of the field with $z$ is the broadness of the peak. The FWHM widths are 400 nm for $\partial M/\partial x$ and 200 nm for $\partial^2 H_z/\partial z^2$.[11] Once instrumental resolution limits of about 100 nm are taken into account, the distinction becomes less conspicuous. Naturally, in order to obtain quantitative results, one would have to use Eq. (3) to derive the actual image of magnetization from a set of MFM raw images.

By extending this approach, we have selectively imaged the crosstrack or $y$ component[12] as shown in Fig. 3(C). This is obtained by preparing the sample such that the tracks are perpendicular to the direction of the applied field. Note that apart from the contrast at the transition regions, pairs of localized bright and dark areas are visible along both edges of the track. These crosstrack features are distinctive in that a predominantly bright edge structure is paired with a dark edge structure on the opposite edge in any specific "bit." (By a "bit," we mean the entire rectangular area having a constant magnetization direction.) These edge features are clearly distinct from the edges in Fig. 3(A), although both are manifestations of the same magnetic feature. In one case, the transverse component of the edge magnetization (as drawn in the diagram) is detected, and on the other, the $z$ component or the magnetic charges accompanying the edge magnetizations are measured. The intensity of the features are relatively weak in comparison with the main transitions, which explains the higher noise contribution in the image. In general, they depend upon the combined effects of the head geometry and a weakly oriented recording medium.[12]

While the images still show partial mixing between the individual components of the field, they nevertheless clearly support the assertions of Eq. (3). The recurring influence of the $z$ contribution may have resulted from the combination of two effects, namely, the external field having a component along the $z$ direction or the probe having a slight anisotropy favoring vertical alignment.

### B. Probe hysteretic effects

Having established the reorientation of the probe due to the external field, we now study the probe hysteretic behavior along the $x$ direction. Specifically, we focus on the transformation of the images as the horizontal field is cycled between moderately large negative and positive values. The

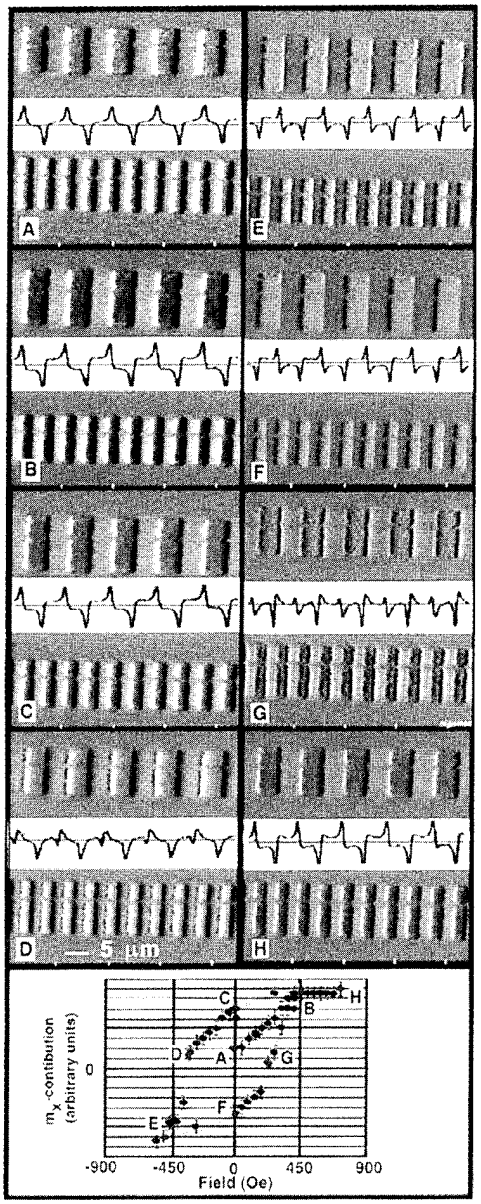



FIG. 4. Hysteretic behavior of MFM probe magnetization along $x$ axis and corresponding images at saturation, remanence, and coercivity.

main goal is to derive, from the images, the changes in the $m_x$ component of the probe under an external bias dc field.

The result is summarized in Fig. 4. The sequence was started by premagnetizing the probe along the vertical direction and acquiring the initial image. The horizontal field was slowly raised up to +500 Oe, ramped back down to −500 Oe, and again reversed direction to +700 Oe. Images were acquired at each field increment all along the cyclic path. The plot at the center of the figure is an actual measurement of the probe's horizontal magnetization component. Each data point along this curve was derived by averaging the line profiles of the upper (long wavelength) track as shown in the images. Since the images were obtained from the same area and the external field was low in comparison with the coercivity of the medium ($H_c$>1600 Oe), then the magnetization component of the probe along the track direction can be derived from the images and Eq. (3). Ideally, this can be done by fitting each of the experimental lineshapes with the modeled response given by Eq. (3) and extracting the relative coefficients $m_x$ and $m_z$. However, since the $z$-component contribution is confined at the transition regions, we simply derived the $m_x$ contribution for each image by measuring the average contrast levels at the midpoints of the "bits" while keeping track of the separate magnetization directions. The resulting plot clearly exhibits the hysteretic property of the probe.

Special points along the probe's magnetization loop are shown in images 4(A)–4(H). They depict how changing the probe magnetization alters the image formation. The contrast mechanism with no applied field is shown in image 4(A), after performing the standard procedure of pre-magnetizing the probe along the $z$ direction. The features are confined exclusively at the transition regions and thus, the horizontal probe magnetization components $m_x$ can be taken to be nearly zero at this initial state. This is a widely used implementation of the MFM and most images of thin-film media in the literature belong in this category.

The contribution of the horizontal component increases linearly with the field until it attains the contrast shown in 4(B). Further increases of the external field do not produce significant variations since the probe's magnetization is saturated along the direction of the field. Once the field has been removed, however, image 4(C) differs only slightly from the saturated state, indicating that horizontally realigned domains maintain their orientation. This large remanent magnetization can be beneficial in being able to premagnetize the probe along the horizontal direction instead of the customary vertical direction, and increase its sensitivity in detecting the local horizontal field contribution. Note, however, that while the horizontal component is large, the contribution from the $z$ component is still quite significant. This implies that the probe contains numerous domains, some of which have strong anisotropy favoring magnetization along the $z$ direction.

The onset of $m_x$ reversal is illustrated in 4(D), which also identifies the coercivity of this specific probe. Note that while $m_x \sim 0$, the image is clearly different from 4(A). Weak dark strips have appeared to the left of the nominally bright areas. This suggests that the process of magnetization reversal in the $x$ direction invariably causes some moments to rotate in the opposite $z$ direction. At negative saturation, image 4(E) shows the complete reversal of the contrast, including the vertical component. Upon removal of the field, the resulting image 4(F), which is at negative remanence, shows a somewhat weaker vertical component. It appears that some of the moments that were oriented along the $-z$ direction have reverted back to $+z$ or to the other orthogonal directions when the field was removed. The amount of $m_z$ retention appearing less in 4(F) than in the positive remanence image 4(C) is due to the fact that the probe was deliberately oriented in the $+z$ direction before application of the field.

At positive coercivity, image 4(G) is analogous to 4(D), with the exception that the dark regions are affected by high-frequency noise. We speculate that since the probe is in a demagnetized state, the influence of local fields at the dark

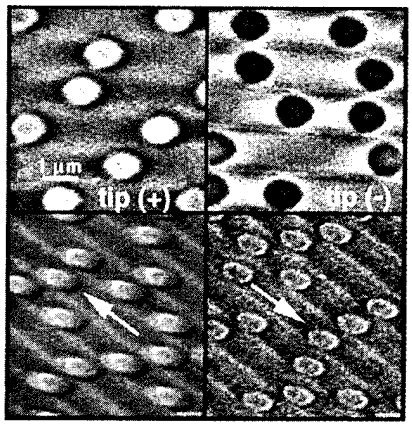



FIG. 5. MFM images of magneto-optic medium at various probe orientations. Tip (+) and tip (−) indicate vertically premagnetized probes, arrows indicate directions of the 600 Oe in-plane external field.

regions may induce transient switching of some magnetic moments of the probe which leads to a noisy image. As the field is brought back to positive saturation, image 4(H) appears identical to 4(B), except that the contrast at the transition areas ($z$ contribution) appears to be less pronounced. In successive experiments, we observed that the $z$ contribution decreases progressively and repeated cycling of the horizontal fields destroys the $m_z$ alignments of the probe.

In the above discussion, the probe orientation was assumed to be perpendicular to the surface. In practice, however, there is a slight angle of about 10° between the main axis of the conical tip and the true vertical direction. This may account for some of the asymmetries between the equivalent points along the ascending and descending branches of the $m_x$-$H$ loop.

Probe reorientation effects for perpendicularly magnetized surfaces are a conventional magneto-optic media are shown in Fig. 5. The upper images, obtained at no bias field, correspond to a vertically oriented $m_{\text{tip}} \approx m_z, m_x, m_y \approx 0$ while the lower images, obtained at $\pm 500$ Oe horizontal applied fields, correspond to a nonvanishing $m_x$ component. The contrast reversals follow directly from the change in sign of Eq. (3).[13] In analogy with the treatment of in-plane magnetization, we assume a simple model for the surface magnetization $M_z = M_0 \sin(kx)$. The interpretation that the $z$-component imaging is sensitive to the distribution of magnetic charges still holds. One distinction, however, is that in this case the volume charge density vanishes and the discontinuity of magnetization at the surface-air interface produces the surface magnetic charges. Hence, the $z$-component images are proportional to $M_z$. From Laplace's equation, it follows that the $x$-component images must be proportional to the discontinuity of surface charges. In other words, the $x$-component images are sensitive to the domain walls.[14] This property is illustrated in the lower images which show the bright and dark features on opposite edges of the marks which follow the direction of the applied field.

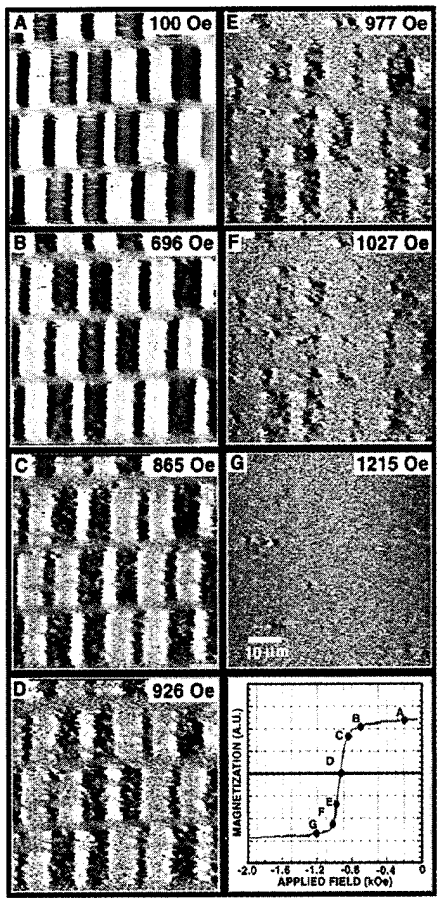



FIG. 6. Erasure of thin-film recording medium with increasing dc field.

### C. Erasure process of a thin-film medium

Once the probe's response to the field is understood, the microscopic characteristics of the sample undergoing gradual dc erasure can be studied. A typical result is shown in Fig. 6. The plot at the bottom is the descending branch of the measured magnetization curve, and the images are labeled according to the positions on this curve. The horizontal field reinforces the magnetization component of the pattern parallel to its direction and at the same time reverses the component in the opposite direction. Thus, the curve represents the magnetization component being reversed by the applied field.

The patterns were unperturbed by relatively weak magnetic fields, and image (A) shows the initial magnetization distribution. The system was stable up to about 700 Oe where changes in the patterns become noticeable. The initial stage occurred over some field range which is characterized by subtle expansion of the bright areas and moderate roughening of the transition regions. By taking the power spectrum of the image at 700 Oe, we obtain an average roughness correlation distance of about 0.4 $\mu$m, which may be related to the average switching volume for this medium. Roughening continued with increasing field and as the field approached coercivity, favorably magnetized areas conglomerated at various spots along the track. Expanding domains

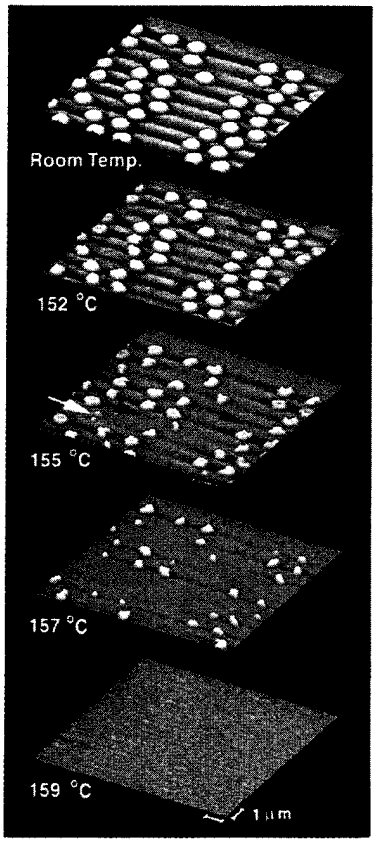



FIG. 7. Erasure of TbFeCo magneto-optic marks with increasing temperature.

adjacent to one another tended to break or percolate through the unfavorable domains. This is best observed at 865 and at 926 Oe where light-intensity streaks can be found in most of the dark contrast bits. At still higher fields, the percolated areas expanded along the crosstrack direction and at 1027 Oe, most parts have reoriented in the direction of the field. The terminal distribution of the remaining clusters appear to be uncorrelated with their previous patterns, and their random distribution may reflect the local fluctuations in the magnetic properties of the medium.

### D. Erasure process of a magneto-optic medium

Since the coercivity of conventional magneto-optic media at room temperature is several kOe, direct imaging of their erasure processes is inaccessible with our device. However, we show the results of a related experiment to elucidate the nature of domain collapse in these systems. These images were obtained at room temperature and under ambient magnetic field after exposure to progressively increasing temperatures in the presence of a 1.8 kOe vertical magnetic field.

The evolution of individual magnetic marks can be seen in Fig. 7, as they were subjected to progressively increasing temperatures in a 1.8 kOe dc external field from a permanent magnet. These images correspond to their final room-temperature configurations after recovering from the elevated temperatures. No visible perturbation of the patterns occurred with heating until about 150 °C where subtle shape variations became evident. The onset of domain movement produced irregular wall boundaries as the marks deviated from their originally circular shapes. This clearly suggests nonuniformity on a local scale and our observations are in qualitative agreement with theoretical simulations of "patchy" amorphous media with voids.[15] This inhomogeneity further resulted in the multidomain character of individual marks and caused the domains to collapse at different rates. The blue and red arrows indicate the locations of marks which disappeared at 155 °C even as most other marks were still intact. The white arrow shows direct evidence of patterns breaking up to microdomains which shrink independently. The microdomains had diameters less than 200 nm wide and were located on opposite grooves. The images at 157 °C and higher exhibit the final states of domain disappearance. In general, there was no correlation between erasure characteristics and the position relative to other marks, i.e., stray magnetic fields did not influence the stability of the marks. Just prior to complete erasure, the image at 157 °C shows that all remaining domains were those attached to the mechanical grooves, providing direct evidence that wall pinning occurred at the mechanical defects. The combination of reduced film thickness, tilted easy axis and increased substrate jaggedness at the side walls of the grooves are believed to be responsible for retarding complete domain collapse at those regions.

## ACKNOWLEDGMENTS

We are grateful to A. Kratz, R. Madabhushi, M. Shih, and F. Lineberger for their assistance in various aspects of this work.

[1] Y. Martin and Wickramasinghe, Appl. Phys. Lett. **50**, 1455 (1987).
[2] P. Grütter, H. J. Mamin, and D. Rugar, in *Scanning Tunneling Microscopy Vol. II*, edited by R. Weisendanger and H.-J. Guntherodt (Springer, Berlin, 1992), p. 151.
[3] U. Hartmann, J. Vac. Sci. Technol. A **8**, 411 (1990).
[4] R. Proksch, T. E. Schäffer, B. M. Moskowitz, E. D. Dahlberg, D. A. Bazylinski, and R. B. Frankel, Appl. Phys. Lett. **66**, 2582 (1995).
[5] R. D. Gomez, I. D. Mayergoyz, and E. R. Burke, IEEE Trans. Magn. **31**, 3346 (1995).
[6] T. Albrecht, P. Grütter, D. Horne, and D. Rugar, J. Appl. Phys. **69**, 668 (1991).
[7] Nanoscope III Multimode SPM, Digital Inst. Inc., Cortuna, CA.
[8] U. Dürig, O. Züger, and A. Stalder, J. Appl. Phys. **72**, 1778 (1992).
[9] R. D. Gomez, A. R. Kratz, E. R. Burke, and I. D. Mayergoyz, IEEE Trans. Magn. **31**, 3265 (1995).
[10] R. L. Wallace, in *Introduction to Magnetic Recording*, edited by R. L. White (IEEE, New York, 1985), p. 226.
[11] D. Rugar, H. J. Mamin, P. Guethner, S. E. Lambert, J. E. Stern, I. McFadyen, and T. Yogi, J. Appl. Phys. **68**, 1179 (1990).
[12] R. D. Gomez, I. D. Mayergoyz, and E. R. Burke, J. Appl. Phys. **75**, 5910 (1994).
[13] S. Foss, R. Proksch, and E. D. Dahlberg, J. Magn. Soc. Jpn. **19**, S1, 135 (1995).
[14] D. Rugar, H. J. Mamin, R. Erlandsson, J. E. Stern, and B. D. Terris, Rev. Sci. Instrum. **59**, 2339 (1988).
[15] M. Mansuripur, R. Giles, and G. Patterson, J. Appl. Phys. **69**, 4844 (1991).

# Domain structure of iron single crystals grown on Si(111) investigated by magnetic force microscopy (abstract)

S. Foss
*Magnetic Microscopy Center and School of Physics and Astronomy, University of Minnesota, Minneapolis, Minnesota 55455*

R. Proksch
*Magnetic Microscopy Center, University of Minnesota, Minneapolis, Minnesota 55455 and Department of Physics, St. Olaf College, Northfield, Minnesota 55057*

K. Moloni and E. D. Dahlberg
*Magnetic Microscopy Center and School of Physics and Astronomy, University of Minnesota, Minneapolis, Minnesota 55455*

Y. Cheng
*General Motors Corporation, Warren, Michigan 48090*

Single-crystal iron films grown epitaxially on (111) silicon were studied using a magnetic force microscope (MFM). The crystalline anisotropy easy axes (⟨100⟩), directed 35° out of the film plane, result in a significant magnetic charge density at the film surface and a sixfold symmetry in the energy minima of the system. To reduce the magnetostatic energy of this configuration, an alternating, stripe domain pattern formed in samples of thickness ranging from 1240 to 315 nm. Because of the wavelike form of the MFM response across the stripes, two-dimensional Fourier transforms of the MFM images were used to give measures at the domain period, i.e., the wavelength of the stripes, as well as the complexity of the patterns. The stripe domain period was found to be approximately equal to the film thickness which is consistent with previous theoretical predictions. The domain patterns of the films in various remanent states and progressive stages of the magnetization process were investigated using the MFM and an *in situ*, variable magnetic field. A MFM tip that is magnetically soft compared to the iron is most suitable for this. Measurements of the domain period and pattern complexity as a funciton of applied field were correlated with bulk hysteresis measurements. © *1996 American Institute of Physics.* [S0021-8979(96)62208-2]

# Force gradient mapping of domain wall structures in magnetite (abstract)

Roger Proksch
*Department of Physics, St. Olaf College, Northfield, Minnesota 55057*

Tilman E. Schäffer
*Department of Physics, University of California, Santa Barbara, Santa Barbara, California 93106*

Sheryl Foss
*School of Physics and Astronomy, University of Minnesota, Minneapolis, Minnesota 55455*

We have used a magnetic force microscope (MFM) in a new imaging mode to study domain walls in magnetite. The oscillation amplitude and phase of a vibrating cantilever were recorded versus cantilever tip-sample separation at each point in an $x$-$y$ raster scan of a conventional MFM image. Amplitude and phase changes of the MFM cantilever depend on the topographic, interferometric, damping, and magnetic force gradients effects the cantilever experiences. For small scan areas, the magnetic force gradient acting between the tip and sample could be separated from the other interactions. This allowed quantitative extraction of the magnetic force gradients into a three-dimensional dataset called a force gradient map (FGM). FGMs were made over a number of samples; the work reported here focuses on domain wall structures in single crystal magnetite. The results of previous conventional MFM images and FGM images will be compared. One result was that the apparent resolution of the MFM tip was strongly dependent on the oscillation amplitude of the cantilever tip, implying that this must be considered when modelling MFM response. The data also suggest that FGMs may provide more sensitive tests of micromagnetic models than conventional MFM imaging of magnetite. This is for two reasons: (i) as mentioned above, FGMs allow the magnetic signal to be separated from the topographic, damping and interferometric effects and (ii) because FGMs sample the interactions between the tip and sample at a variety of well defined separations, it is possible to identify critical micromagnetic structural length scales. © *1996 American Institute of Physics.* [S0021-8979(96)62308-7]

# Superparamagnetic magnetic force microscopy tips

P. F. Hopkins[a] and John Moreland
*NIST, Boulder, Colorado 80303*

S. S. Malhotra and S. H. Liou
*Department of Physics and Astronomy, University of Nebraska, Lincoln, Nebraska 68588*

We report on magnetic force microscopy (MFM) images of a thin-film magnetic recording head taken using batch micromachined silicon tips coated with nanocomposite $Fe_{60}(SiO_2)_{40}$ and $Fe_{70}(SiO_2)_{30}$ films. The small Fe grain size (<10 nm) and dilute Fe volume fraction (0.29–0.4) of these granular films produce tip coatings of low remanence and essentially zero coercivity, reduced by the superparamagnetic properties of these films. We have used these tips to obtain MFM images of the write field of the head with high spatial and magnetic-field resolution. In comparison to images taken using commercial $Co_{85}Cr_{15}$-coated tips, these MFM images show reduced tip memory effects and clearly delineate the gap field from the pole pieces. © *1996 American Institute of Physics.* [S0021-8979(96)57108-8]

Batch fabrication of silicon micromachined cantilevers with integral tips[1,2] coated with thin magnetic films has facilitated the emergence of magnetic force microscopy (MFM) as a qualitative high-resolution magnetic imaging tool.[3] Improvements in magnetic tip coatings are necessary, however, to extend MFM capabilities to imaging stronger stray fields and for quantitative field measurements. Typically, tips coated with 10–50 nm of a magnetically hard material (such as $Co_{85}Cr_{15}$) are used for MFM, providing high sensitivity with an assumed tip magnetic moment **m** which is fixed in direction and magnitude.[2] High-resolution imaging of high-coercivity materials and current-biased magnetic recording heads, however, can subject these tips to fields higher than the coercive field $H_c$ of the tip coating,[2] resulting in a time-dependent **m** and generating images which are difficult or impossible to interpret.

One alternative is to use tips coated with a ferromagnetically soft material such as NiFe.[1,4] The tip moment **m** is assumed to align with the local stray field **B** and have a magnitude equal to the saturated value $m_s$. Unfortunately, the shape and small size of the tip can change the domain structure and greatly enhance the coercivity[1] of these coatings, producing MFM images that also contain artifacts due to hysteresis of the tip moment. To completely eliminate memory effects from MFM images requires tips which have zero hysteresis over the operating field range.

MFM tips coated with granular magnetic films consisting of isolated superparamagnetic particles (<10 nm) would have zero remanence and coercivity, resulting in images with no tip memory effects. Unlike NiFe and other ferromagnetic coatings, the magnetic properties of the individual particles in the superparamagnetic films should not be altered by the shape of the tip, for tip radii larger than the particle size. Sensitivity, determined by **m**, would be orders of magnitude larger than tips coated with paramagnetic films and in strong magnetic fields could approach or exceed that of available ferromagnetic-coated tips. These tips might also be useful for nonperturbative imaging of domain patterns in low coercivity films,[5] due to the lower stray fields emanating from these tips.[1] In contrast to the assumed fixed moment **m** of the ferromagnetic-coated tips, **m** of the superparamagnetic tips can increase with field. This results in a shorter range tip–sample force $\mathbf{F}=\nabla(\mathbf{m}\cdot\mathbf{B})$. In the case of tips of extended geometry where the forces over the tip volume must be summed,[3] the shorter range force means a smaller tip volume contributes to the signal. This leads to improved resolution providing the tip–sample force yields a sufficient signal-to-noise ratio.

We have coated commercial silicon micromachined MFM cantilevers and tips with granular Fe–$(SiO_2)$ films. These nanocomposite films consist of small Fe crystallites (3–7 nm) in an amorphous $SiO_2$ matrix.[6–8] By growing films with dilute Fe volume fractions $p$ of 0.29–0.4 we have manufactured Fe–$(SiO_2)$-coated tips that show no noticeable tip memory effects and which have the following additional advantages for batch MFM tip fabrication: (1) excellent adhesion to silicon; (2) high corrosion resistance and wear resistance; (3) the deposition process can be scaled up for coating entire wafers; and (4) the magnetic properties can be engineered by controlling the film microstructure.[6–8]

Cantilevers with spring constants $k=1-5$ N/m, resonant frequencies $f_0=70-89$ kHz, and quality factors $Q\sim200$ in air were rf magnetron sputter-coated at 300 K using a homogeneously mixed composite Fe–$(SiO_2)$ target of the desired composition.[8] As listed in Table I, one batch of six cantilevers with tips was coated with 40 nm (±10%) of $Fe_{70}(SiO_2)_{30}$ and another batch was coated with 40 nm of $Fe_{60}(SiO_2)_{40}$. A third batch of commercial $Co_{85}Cr_{15}$-coated tips[2] was also used in this study. Variations in the Fe atomic percentages are less than 5%. Scanning electron micrographs of the Fe–$(SiO_2)$-coated cantilevers show tip end radii of 50–100 nm.

The magnetic data in Table I were derived from Figs. 1(a) and 1(b), which show the volume magnetization $M$ versus applied field $H$ (in plane) for the three different films. The Fe–$(SiO_2)$ data were taken at 300 K on films simultaneously deposited with the tips on glass coupons; the data were normalized to the saturation magnetization (1714 kA/m) of pure Fe by multiplying by the volume fraction $p$. For the CoCr data, the actual coated cantilever substrate was

[a]Current address: Quantum Corp., Louisville, CO, 80028-8188.

 0021-8979/96/79(8)/6448/3/$10.00 © 1996 American Institute of Physics

TABLE I. Properties of MFM tip coatings. Listed for the three films are the thickness $t$ and the Fe volume fraction $p$. The measured coercivity $H_c$ and remanence $M_r$ are from Fig. 1.

| Coating | $t$ (nm) | $p$ | $H_c$ kA/m | $H_c$ (Oe) | $M_r$ (kA/m) |
|---|---|---|---|---|---|
| $Fe_{70}(SiO_2)_{30}$ | 40 | 0.39 | 0.08 | (1) | 4 |
| $Fe_{60}(SiO_2)_{40}$ | 40 | 0.29 | 1 | (13) | 6 |
| $Co_{85}Cr_{15}$ | 40 | ··· | 34 | (430) | 300 |

measured after being saturated in plane with a 160 kA/m field; the data were normalized to 400 kA/m (400 emu/cm$^3$).[2] The instrumentation error for $H_c$ is 200 A/m (2 Oe). The measured $H_c$ and remanence for the Fe–($SiO_2$) films in Fig. 1(a) are very small but nonzero. The nonzero values probably occur because a small fraction of the Fe forms clusters larger than the superparamagnetic limit.[6] In the absence of clustering, these films would be completely superparamagnetic. Major and minor hysteresis loops for CoCr are shown in Fig. 1(b), demonstrating a substantial coercivity and remanence.

Figures 2(a) and 2(b) are 10 $\mu$m scans of magnetic force derivative[3] and topography, respectively, of a commercial thin-film inductive magnetic recording head. The images were taken simultaneously as described in Ref. 9 using an $Fe_{70}(SiO_2)_{30}$-coated tip and with the head current biased at 10 mA. The cantilever was vibrated at the resonance frequency $f_0$ with a 30 nm root-mean-square (rms) amplitude. Figure 2(a) was scanned with the tip 100 nm above the air bearing surface (ABS), about twice the designed flying height of the head above the disk. Plotted in Fig. 2(a) is the resonant frequency shift $\Delta f$ of the cantilever, arising from the magnetic force $\mathbf{F}$ between the tip and the write field of the head. For small shifts, $\Delta f$ can be approximated by the expression $\Delta f = -f_0 F'/(2k)$, where $F'$ is the gradient along the tip axis of the axial component of the magnetic force $\mathbf{F}$.[2,3] The strongest feature in Fig. 2(a) occurs at the gap between the two NiFe pole pieces where the field (240–320 kA/m) and its spatial derivatives are the highest, resulting in the strongest attractive tip–sample force and largest decrease in

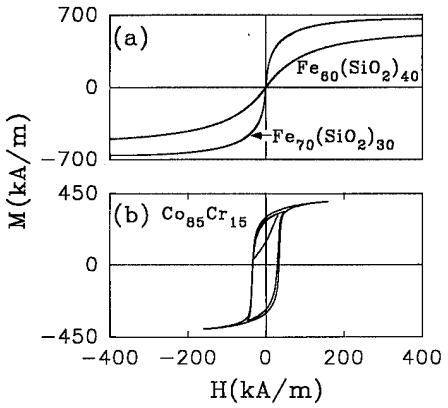



FIG. 1. Magnetization vs applied field H at 300 K with $H$ in the plane of the films: (a) 40-nm-thick $Fe_{70}(SiO_2)_{30}$ and $Fe_{60}(SiO_2)_{40}$ films on glass coupons; (b) commercial cantilever substrate coated with 40 nm of $Co_{85}Cr_{15}$.

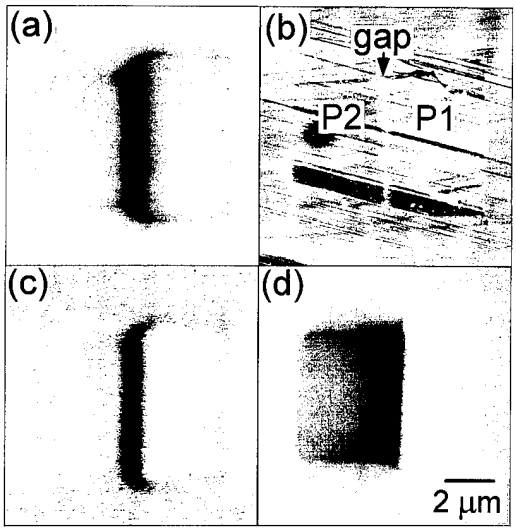



FIG. 2. 10 $\mu$m images of a thin-film inductive magnetic recording head. (a) MFM frequency shift image using a tip coated with 40 nm of $Fe_{70}(SiO_2)_{30}$, a 100 nm tip–sample spacing, and 10 mA current bias of the head; (b) simultaneous topographical image showing the leading (P1) and trailing (P2) pole pieces and the 0.2-$\mu$m-wide gap; (c) MFM image, 40 nm $Fe_{60}(SiO_2)_{40}$-coated tip, 10 mA bias; and (d) MFM image, 40 nm $Co_{85}Cr_{15}$-coated tip, 2 mA bias. The contrast scales are 50 Hz, 50 nm, 10 Hz, and 70 Hz, respectively.

the cantilever resonant frequency. Contrast can also be seen around the edges of the pole pieces where fringing fields are present. There is essentially no frequency shift in the body of the pole pieces. Figure 2(b) is the sample topography and shows polishing scratches across the 0.2-$\mu$m-wide gap and the pole pieces P1 and P2. The contrast between the soft NiFe poles and the surrounding harder alumina material arises from effects due to the polishing process and magnetic forces affecting the topographical force image.

Figures 2(c) and 2(d) are magnetic images taken with $Fe_{60}(SiO_2)_{40}$ and CoCr-coated tips, respectively, under the same imaging conditions as Fig. 2(a). The head was biased at 10 mA for Fig. 2(c) and 2 mA for Fig. 2(d). Figure 2(c) is similar to Fig. 2(a) with contrast centered at the gap; however, the signal has dramatically decreased by roughly a factor of 10. Figure 2(d) was taken immediately after magnetizing the CoCr tip in an external field of 700 kA/m applied along the tip axis. This image is qualitatively different from Figs. 2(a) and 2(c) because of the substantial coercivity of the CoCr tip. One pole piece is darker than the other, and near the center of the gap the contrast changes from dark to light. Unlike Figs. 2(a) and 2(c), Fig. 2(d) is not reproducible, and depends on the prior magnetic history of the tip.

Figure 2 can be better understood by looking at individual MFM line traces taken horizontally across the center of the head using the same three tips, with the head biased at different current levels. Each trace pictured in Fig. 3 is an average of at least 40 line scans and shows the resonant frequency shift $\Delta f$ of the cantilever versus position of the tip over the head. The noise in each line scan was approximately 0.2 Hz rms. The gap center is at $5 \pm 0.1$ $\mu$m. The traces in Figs. 3(a) and 3(b) are essentially flat and featureless except near the gap, where the largest negative frequency shift

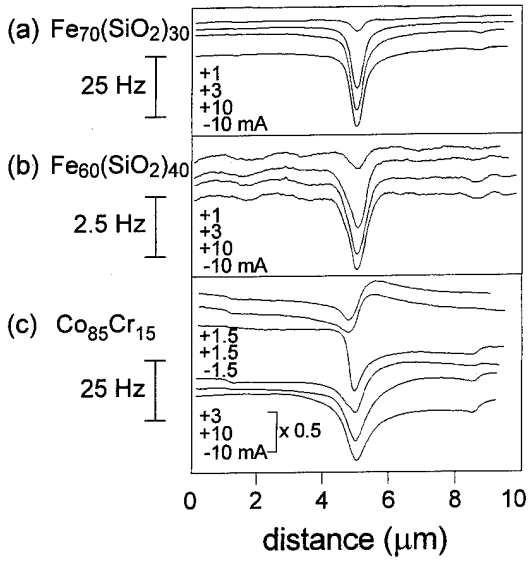



FIG. 3. Line traces taken horizontally across the center of the head, with head biases shown: (a) $Fe_{70}(SiO_2)_{30}$ tip; (b) $Fe_{60}(SiO_2)_{40}$ tip; and (c) $Co_{85}Cr_{15}$ tip previously magnetized to saturation along the tip axis. The gap is located at 5 $\mu$m. Arbitrary offsets were used to display the traces. The bottom three traces in (c) have been reduced by 50% ($\times 0.5$).

($\Delta f_{max}$) occurs. The frequency shifts are primarily negative denoting an attractive tip–sample force, as expected for a soft tip. The response of both Fe–($SiO_2$) tips near the gap increases with increasing current bias and saturates at roughly 4 mA bias, in agreement with the manufacturer's specifications of the head. There is no detectable spatial shift of $\Delta f_{max}$ at different current biases. Also expected for magnetically soft tips, the scans are identical for opposite current polarity as illustrated by the $\pm 10$ mA traces. There is a small feature at $\sim 9$ $\mu$m corresponding to the fringing field on the outside of the P1 pole piece. The smaller features in Fig. 3(b) are due to topography and interface effects in the optical detection. All traces in Figs. 3(a) and 3(b) were reproducible, demonstrating the absence of tip memory effects with the Fe–($SiO_2$)-coated tips. We also imaged bits on longitudinal hard disk media with the $Fe_{70}(SiO_2)_{30}$ tips and found that opposite polarity transitions gave equal response. The sensitivity of the $Fe_{60}(SiO_2)_{40}$ tips was not high enough to image these bits.

Figure 3(c) is illustrative of a CoCr tip while imaging an energized head whose peak field exceeds $H_c$ of the tip coating. After magnetizing the tip as for Fig. 2(d), the second through sixth traces were taken in the order they appear, top to bottom. Finally, the top trace was taken. The two traces at the same current bias of +1.5 mA are not identical due to hysteresis of the tip moment. Traces of opposite current polarity ($\pm 1.5$ and $\pm 10$ mA) are neither identical nor show odd symmetry with respect to the gap. This lack of symmetry along with the predominantly attractive tip–sample response near the gap at higher current biases suggest that the CoCr tip response has both magnetically hard and soft components. This dual nature of the tip makes it difficult to determine important properties of the recording head such as the precise position of the center of the gap, the relative write field strengths at various current biases, and the symmetry of the field near the gap. For example, there is a spatial shift of 0.2 $\mu$m for $\Delta f_{max}$ for the second and third traces ($\pm 1.5$ mA) in Fig. 3(c), a shift comparable to the width of the gap. Differences between prior and subsequent MFM images of bits on a hard disk confirmed that the tip moment **m** was changed (written) by the write head.

Figure 3 shows that the tip response to the gap field is spatially the narrowest for the $Fe_{70}(SiO_2)_{30}$ tip. We can quantify this from the line traces by measuring the full width at half-maximum (FWHM). At +2 and +10 mA biases we measure the FWHM for the $Fe_{70}(SiO_2)_{30}$ tip to be roughly 430 and 500 nm, for the $Fe_{60}(SiO_2)_{40}$ tip 580 and 600 nm, and for the CoCr tip 500 and 600 nm, respectively.

As mentioned above, the presence of magnetic forces can cause an error in the topographical force image and requires that a correction be made to obtain the true tip–sample spacing for the magnetic image. By subtracting the topography of the unbiased head from the image taken at +10 mA bias, we found a maximum correction near the gap of approximately +2, +1, and +30 nm for the $Fe_{70}(SiO_2)_{30}$, $Fe_{60}(SiO_2)_{40}$, and CoCr tips used in Figs. 2 and 3. This correction for the CoCr tip is substantially larger than the true topographical features and is approaching the intended 100 nm tip-sample spacing for the MFM image.

In conclusion, MFM images taken with $Fe_{70}(SiO_2)_{30}$ and $Fe_{60}(SiO_2)_{40}$-coated tips show substantially reduced tip moment hysteresis effects compared to images taken with $Co_{85}Cr_{15}$-coated tips. Given the signal-to-noise ratio of existing commercial MFMs, the higher sensitivity of the $Fe_{70}(SiO_2)_{30}$ tips makes them more appropriate than the $Fe_{60}(SiO_2)_{40}$ tips for imaging the write field above heads. These tips should also be useful for imaging permanent magnet materials and very high-coercivity media. Optimization of the Fe particle size, size uniformity, and interparticle separation in the nonmagnetic $SiO_2$ matrix should produce films that have improved superparamagnetic properties. This will allow thinner coatings with higher Fe concentrations on sharper tips, with the goal of simultaneously improving sensitivity and resolution.

We thank P. Rice, R. E. Thomson, and K. Babcock for advice. The work at the University of Nebraska was supported by NSF Grant No. OSR-9255225.

[1] P. Grütter, D. Rugar, H. J. Mamin, G. Castillo, S. E. Lambert, C.-J. Lin, R. M. Valletta, O. Wolter, T. Bayer, and J. Greschner, App. Phys. Lett. **57**, 1820 (1990).
[2] K. Babcock, V. Elings, M. Dugas, and S. Loper, IEEE Trans. Magn. **30**, 4503 (1994).
[3] See, for example, P. Grütter, H. J. Mamin, and D. Rugar, in *Scanning Tunneling Microscopy II*, edited by R. Wiesendanger and H.-J. Güntherodt (Springer, Berlin, 1992), pp. 151–207.
[4] K. Babcock, M. Dugas, S. Manalis, and V. Elings, in Proceedings of the Material Research Society Meeting, edited by Demczyk *et al.* [Mater. Res. Soc. Symp. Proc. **355**, 311 (1995)].
[5] H. J. Mamin, D. Rugar, J. E. Stern, R. E. Fontana, Jr., and P. Kasiraj, Appl. Phys. Lett. **55**, 318 (1989).
[6] S. H. Liou and C. L. Chien, J. Appl. Phys. **63**, 4240 (1988); C. L. Chien, G. Xiao, S. H. Liou, J. N. Taylor, and A. Levy, *ibid.* **61**, 3311 (1987).
[7] Y. Kanai and S. H. Charap, J. Appl. Phys. **69**, 4478 (1991).
[8] S. S. Malhotra, Y. Liu, J. X. Shen, S. H. Liou, and D. J. Sellmyer, J. Appl. Phys. **76**, 6304 (1994).
[9] V. Elings and J. Gurley, U.S. Patent Nos. 5,266, 801 and 5,308,974.

# Sensitive detection of magnetic field distribution using scanning interference electron microscope (invited) (abstract)

Y. Yajima, Y. Takahashi, K. Kuroda, and Y. Sugita
*Central Research Laboratory, HITACHI, Ltd., Kokubunji, Tokyo 185, Japan*

We have implemented interference imaging mode as well as Lorentz imaging mode on a scanning transmission electron microscope (HITACHI HF-2000 with a scanning option; 200 kV accelerating voltage).[1] In the interference mode, a pair of mutually coherent fine probes scan simultaneously across the region of magnetic induction. By monitoring the relative phase change occurring in the probe pair, the variation of the magnetic flux bound by the probe trajectories can be sensed by the universal unit of $e/h$ ($-|e|$: electron charge and h: Planck's constant). The combined use of this imaging mode with the Lorentz mode which is based on the detection of the probe deflection by Lorentz force facilitates detailed analyses of fringing field around magnetic materials and magnetic induction inside magnetic films. The microscope described above is particularly suited for the study of magnetic storage devices whose microscopic magnetic properties are drawing much attention recently. We show here the results of its application to the observation of field distributions near the MR (magnetoresistive) heads and induction distributions associated with high density longitudinal and perpendicular recording media. © *1996 American Institute of Physics.*
[S0021-8979(96)62408-6]

[1] Y. Takahashi, Y. Yajima, M. Ichikawa, and K. Kuroda, Jpn. J. Appl. Phys. **33**, L1352 (1994).

# Magnetization reversal process in TbCo-biased spin valves

J. N. Chapman and M. F. Gillies
*Department of Physics and Astronomy, University of Glasgow, Glasgow G12 8QQ, United Kingdom*

P. P. Freitas
*INESC, R. Alves Redol 9-1, 1000 Lisbon, Portugal*

The magnetization reversal processes in the free and the pinned layers of TbCo-biased spin valves have been studied in a highly modified transmission electron microscope. Reversal of the free layer in the presence of a field antiparallel to the biasing direction proceeds by a complex domain process with 360° walls forming frequently. In the presence of substantially higher fields, the pinned layer reverses by creep of highly irregular walls through the structure. By studying image grey levels, an estimate of the average orientation of the induction vector in the TbCo layer is made. © *1996 American Institute of Physics.* [S0021-8979(96)57208-2]

## I. INTRODUCTION

Spin valves of the form M1/Cu/M2/TbCo have been grown which display magnetoresistances of 4%–8% and sensitivities of >1%/Oe.[1,2] For the work reported here M1 and M2 were either Permalloy (Py) or Permalloy with approximately 1.5 nm of cobalt (Py/Co) at each interface with the Cu spacer layer. Typical layer thicknesses were 6, 2.5, 6, and 10 nm for the M1, Cu, M2, and TbCo layers, respectively, while the composition of the TbCo layer lay in the range 32–35 at. % Tb. The enhanced magnetoresistance is found when the magnetizations in the free (M1) and pinned (M2) layers are oppositely directed; for our samples this occurred over an applied field range from ≈10 to ≈250 Oe. Here we describe how Lorentz microscopy has been used to study the magnetization reversal process in both the free and the pinned layers. The former relates directly to the noise behavior when the spin-valve material is used as a sensor while the latter provides information on the nature of the coupling between the M2 and TbCo layers. Essential for the experiments undertaken is the ability to form magnetic images at high spatial resolution with the specimen subjected to applied fields where the reversal processes of interest occur. This has been achieved using a highly modified Philips CM20 transmission electron microscope optimized for the study of magnetic materials.[3,4]

## II. REVERSAL OF THE FREE LAYER

Figure 1 shows Fresnel images of the reversal of the M1 layer in a Py/Co spin valve deposited directly onto a $Si_3N_4$ window substrate. Domain walls appear as narrow dark and bright bands while the fact that there is significant dispersion of the magnetization within the domains themselves is revealed by the presence of ripple contrast. The numbers in the top left-hand corner of each image give the applied field in Oe. Note that magnetometry confirms that, over the field range shown in Fig. 1, only one of the magnetic layers reverses. As expected, the zero field state [Fig. 1(a)] is single domain as a result of weak ferromagnetic coupling between M1 and M2. The ripple enables the direction of magnetization, denoted by the white arrow, to be determined and fields in this sequence were applied antiparallel to the bias direction. As the field was increased, so did the magnetization dispersion until at a

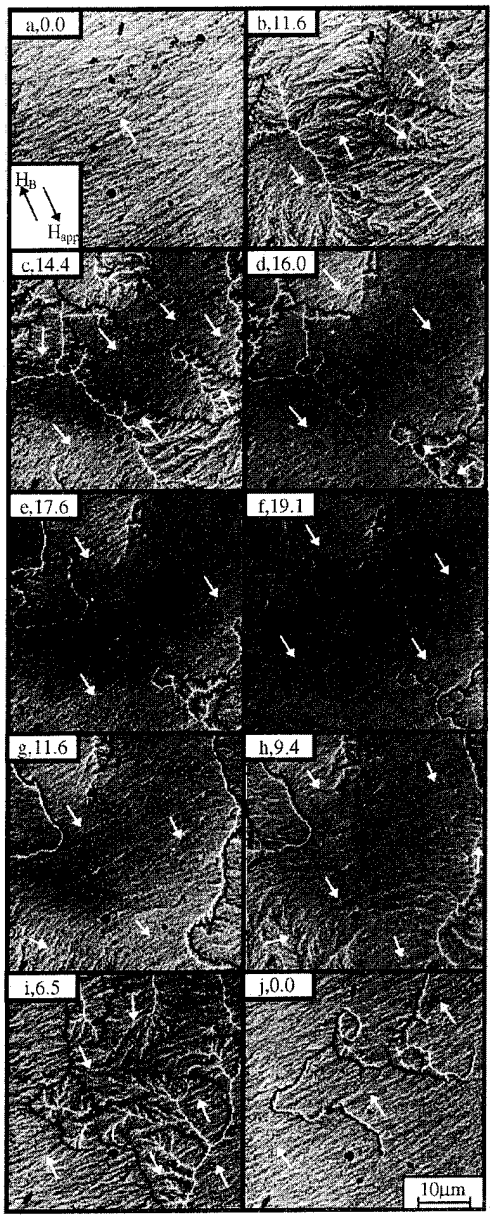



FIG. 1. Fresnel images showing the magnetization reversal of M1. Field values, in Oe, are given.

 0021-8979/96/79(8)/6452/3/$10.00 © 1996 American Institute of Physics

field of ≈11 Oe [Fig. 1(b)] magnetization reversal occurred over a few small areas within the film. Domain boundaries tended to be irregular and observation of the microscope viewing screen showed that they moved jerkily to expand the area of reverse domains [Fig. 1(c)]. Figures 1(d)–1(f), however, show that full antiparallel alignment was difficult to achieve due to the large number of 360° walls which formed in the final stages of the reversal process. These structures proved to be very stable and fields in excess of 100 Oe were required for their annihilation. Reduction of the applied field [Figs. 1(g)–1(j)] led to a return of the magnetization in M1 to its original orientation. It was observed that areas which had been last to reverse under an increasing field tended to be the first to return to their original orientation as the field was reduced. Once again complex erratic domain structures were involved and, while the majority of the spin valve returned to its original parallel state, a number of 360° walls remained when the applied field was removed completely [Fig. 1(j)].

A broadly similar reversal mechanism was observed for Py spin valves, the main differences being that magnetization dispersion and wall irregularity were both markedly reduced. Thus, as with spin valves pinned by FeMn,[5] the reversal of the so-called free layer is very different and much more complex than that of an equivalent isolated magnetic layer of the same composition and thickness. The coupling introduced by the presence of the M2 layer clearly modifies the domain processes involved and acts to stabilize highly charged structures such as 360° walls whose presence is less common in isolated layers.

## III. REVERSAL OF THE PINNED LAYER

At much higher fields (≈250 Oe), where the M1 layer is fully reversed and aligned with the applied field, the reversal of magnetization in the M2 layer has been studied. Figure 2 shows a sequence of Fresnel images recorded at constant field but increasing time. The reversal proceeds by the "creep" of a small number of very irregular domain walls through the M2 layer. Figure 3 shows a higher magnification image from which it is apparent that changes in wall direction occur on a submicron scale. (Note that the fine approximately circular structures are not of magnetic origin.) Wall irregularity on a submicron scale is not usually associated with Py films and is indicative of the strong influence being exerted by the TbCo to which M2 is exchange coupled. Variation of the magnitude of the field changes the rate at which the reversal takes place but not the mechanism. Analysis of image sequences recorded on video under different applied fields suggests that there exists a single well-defined energy barrier which must be overcome.[6] The M2 reversal mechanism is quite different from that of M1 and also from reversal of the pinned layer in FeMn-biased spin valves reported elsewhere.[5]

Further information on the coupling between the M2 and TbCo layers can be gleaned from the use of differential phase contrast (DPC) Lorentz microscopy.[7] The advantage of this technique is its high linearity which allows quantitative information on the induction distribution to be derived. Figure 4(a) shows a DPC image of a spin valve in a remanent

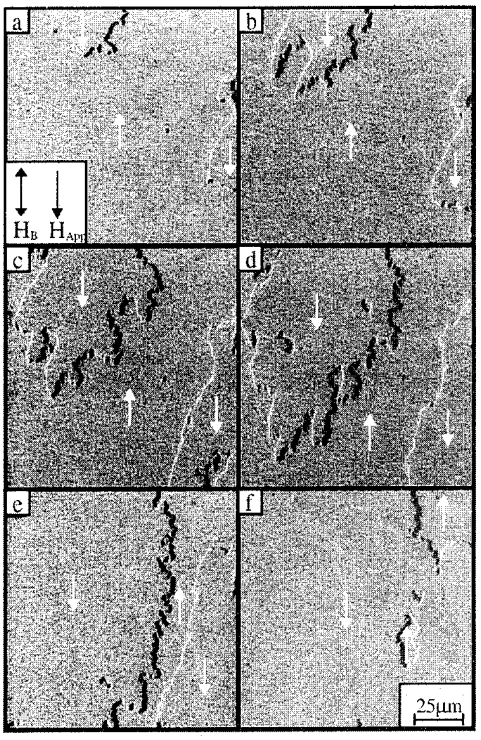



FIG. 2. Fresnel images showing the creep of an irregular domain wall through M2 under constant field (≈250 Oe).

state following the application of a large vertical field. Different grey levels are observed in different parts of the image and these can be interpreted with the help of Fig. 4(b). Note that the orientation of magnetization in the M2 and TbCo layers represents a simplification of models discussed in Refs. 1 and 8.

Following application of the large vertical field, Fig. 4(a) shows that the in-plane component of magnetization in different parts of the pinned layer is oppositely directed. Hence, domain walls are present. Well away from the interface, in

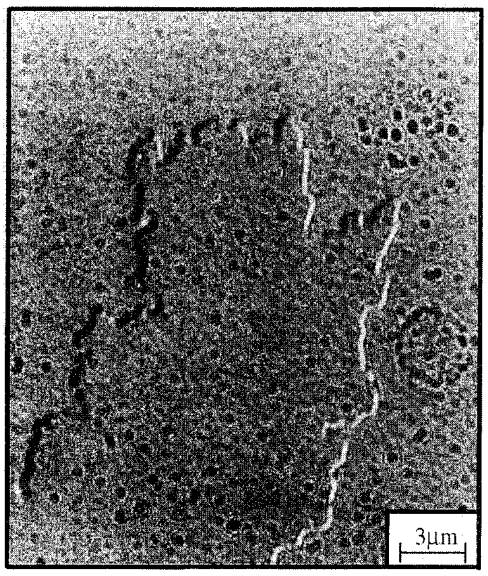



FIG. 3. High-magnification Fresnel image of a domain wall in M2.

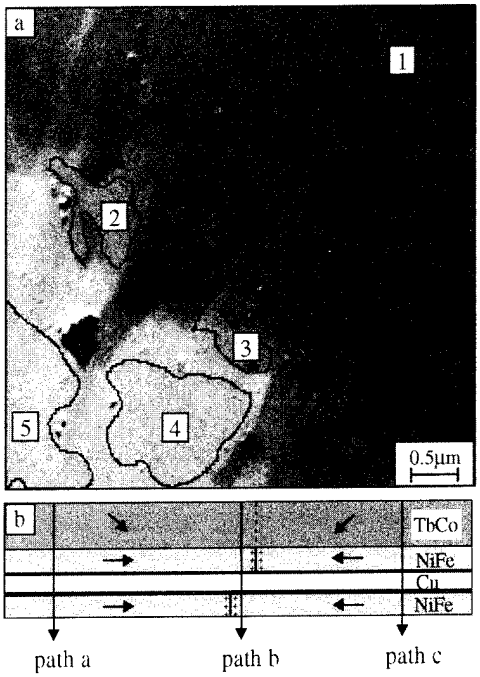



FIG. 4. (a) DPC image of a spin valve following application of a large vertical field; (b) schematic of different electron trajectories through the induction distribution shown in (a).

region 1 and in regions 4 and 5, it is assumed that the electrons follow paths of the kind denoted "a" and "c," respectively, in Fig. 4(b). The grey levels in the DPC image corresponding to these regions are characteristic of the electron having been deflected in the same sense by the magnetization in M1 and M2 and by any in-plane component of magnetization in the TbCo layer; however, in regions close to the domain boundary, such as 2 and 3 of Fig. 4(a), a further grey level is observed. Here we surmize that while there is weak coupling between M1 and M2 it is insufficiently strong for the walls in the two layers to coincide completely, the offset being introduced to reduce the overall magnetostatic energy. Hence the deflection experienced by the electron beam as it passes through such regions (path "b") is reduced in magnitude as the magnetization directions in M1 and M2 are oppositely directed, producing a cancelling effect. Comparison of the mean grey levels from the three different types of region confirms the presence of an in-plane component of induction in the TbCo and allows its magnitude to be calculated. Based on the simplified magnetization distribution of Fig. 4(b) a value of 22° to the vertical is deduced for the orientation of the induction vector in the TbCo layer for a spin valve whose pinning layer contained 32 at. % Tb. More rigorously the analysis provides a measure of the in-plane component of induction throughout the TbCo layer averaged along an electron trajectory. A value corresponding to 38% of the saturation induction is obtained, although no information can be derived about its distribution throughout the layer thickness.

## IV. CONCLUSIONS

The ability to image magnetic structures at high spatial resolution in a magnetic field selected by the experimenter has allowed us to investigate in detail the magnetization reversal mechanisms in the free and pinned layers of TbCo-biased spin valves. Use of different Lorentz imaging modes allows information not only on the domain geometry but also the quantitative distribution of induction throughout the structure to be derived.

## ACKNOWLEDGMENTS

We would like to thank the European Commission (CHRX-CT93-0316) and the EPSRC for financial support.

[1] P. P. Freitas, J. L. Leal, L. V. Melo, N. J. Oliveira, L. Rodrigues, and A. T. Sousa, Appl. Phys. Lett. **65**, 495 (1994).
[2] P. ten Berge, N. J. Oliveira, T. S. Plaskett, J. L. Leal, H. J. Boeve, G. Albuquerque, J. Ferreira, A. R. Morais, A. T. Sousa, L. Rodrigues, and P. P. Freitas, IEEE Trans. Magn. **31**, 2603 (1995).
[3] J. N. Chapman, A. B. Johnston, L. J. Heyderman, S. McVitie, W. A. P. Nicholson, and B. Bormans, IEEE Trans. Magn. **30**, 4479 (1994).
[4] S. McVitie, J. N. Chapman, L. Zhou, L. J. Heyderman, and W. A. P. Nicholson, J. Magn. Magn. Mater. **148**, 232 (1995).
[5] M. F. Gillies, J. N. Chapman, and J. C. S. Kooks, J. Appl. Phys. **78**, 5554 (1995).
[6] R. Street and S. D. Brown, J. Appl. Phys. **76**, 6386 (1994).
[7] J. N. Chapman, I. R. McFadyen, and S. McVitie, IEEE Trans. Magn. **26**, 1506 (1990).
[8] N. Smith and W. C. Cain, J. Appl. Phys. **69**, 2471 (1991).

# Direct observation of domain walls in NiFe films using high-resolution Lorentz microscopy

Bunsen Y. Wong and David E. Laughlin
*Department of Materials Science and Engineering, Carnegie Mellon University, Pittsburgh, Pennsylvania 15213*

A novel approach to observe the interaction between magnetic domain wall and nanoscale microstructural features is demonstrated. The method is based on Focault mode Lorentz microscopy and utilizes a Gatan energy image filter to provide additional magnification. A postexperimental image processing technique was applied to separate lattice diffraction from that induced by magnetic domains. The effect of NiFe thickness on the width of a 180° Néel wall has been studied. It was found that the thickness dependence has a similar profile to the theoretically predicted trend but the actual wall thickness is smaller than the calculated values. © *1996 American Institute of Physics.* [S0021-8979(96)57308-6]

## I. INTRODUCTION

Magnetic properties of materials are closely associated with the magnetic domain configurations and the interaction between domain walls and microstructural features. Techniques such as Lorentz microscopy in both the conventional and scanning transmission mode,[1,2] spin polarized scanning electron microscopy,[3] and magnetic force microscopy[4,5] have been developed to address these issues. However, these techniques are unable to resolve the microstructure-domain interactions on a nanoscale such as those in thin films. In this work, we report on a novel technique utilizing a Gatan energy image filter (GIF) and based on Focault mode Lorentz microscopy which can resolve both fine magnetic domains and microstructural features. A schematic of the GIF unit attached to the transmission electron microscope (TEM) is shown in Fig. 1. In the present study, the function of the GIF is twofold as follows.

(1) Conventional Lorentz microscopy requires a field-free objective lens which generally limits the image magnification to 3000×. The magnetic magnifying lenses (×18.75) and the charge-coupled-device (CCD) camera (~×8) contain within the GIF can provide additional magnification power which helps achieve a theoretical resolution of 1 nm in this technique.

(2) The elastically scattered electrons which have undergone magnetic phase change can be separated from the inelastically scattered electrons by using the energy filter slit. Hence, a higher signal-to-noise ratio in the magnetic image can be obtained. We have applied this technique to study the effect of film thickness on the 180° domain-wall width in sputter-deposited NiFe thin films in order to demonstrate the capacity of this new technique.

## II. EXPERIMENTAL PROCEDURES

$Ni_{81}Fe_{19}$ films of thicknesses ranging from 7 to 35 nm were deposited on NaCl substrates by rf diode sputtering. The Ar sputtering gas pressure was 5 mTorr and a forward power of 50 W was used. The films were then floated off the substrates onto 3 mm Cu TEM grids. The domain-wall profiles and domain structures were studied using Focault mode Lorentz microscopy inside a JEOL 4000EX microscope operating at 400 kV and attached to a GIF unit. Images were recorded with a CCD camera. Postexperimental image analysis was carried out with the interactive data language (IDL) image processing software so that the interference between magnetic and crystalline diffraction contrast can be minimized and an acute domain-wall profile can be determined.

## III. RESULTS AND DISCUSSION

The magnetic domain contrast of two antiparallel domains in a 28-nm-thick NiFe film are shown in Figs. 2(a) and 2(b) along with the corresponding bright-field (BF) image in Fig. 2(c). The location of two reference grains is marked by arrows in the respective images. The average grain size of the lattice diffraction contrast can be clearly observed in the BF image which enables one to discern the grain morphology and other microstructural features. Hence, any interaction between domain boundaries and fine microstructural features can be easily made.

In the Focault mode, the displaced aperture intercepts one of the magnetically diffracted beams and results in black and white contrast within the TEM image. This variation in intensity outlines the local magnetization. In between the magnetic domains, a continuous gray contrast which represents the extent of the domain wall can be observed. In order

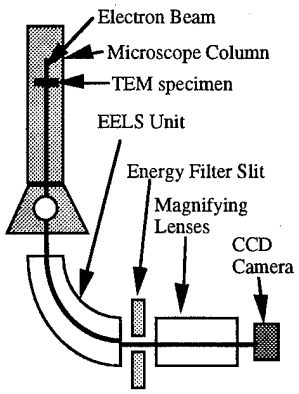



FIG. 1. A schematic of the GIF unit in relation to the TEM.

 0021-8979/96/79(8)/6455/3/$10.00 © 1996 American Institute of Physics 

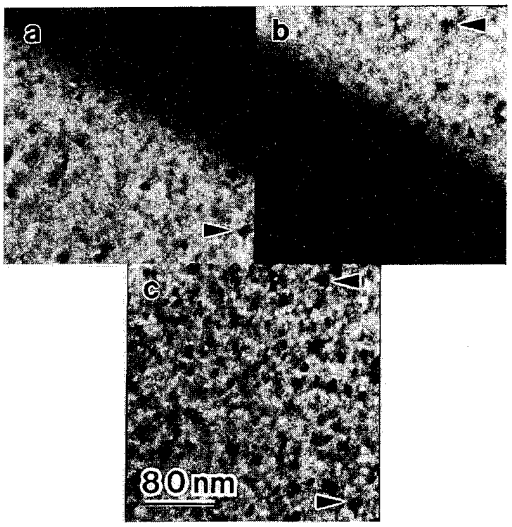



FIG. 2. (a),(b) Lorentz images of antiparallel domains in a 28-nm-thick thin film. (c) Corresponding BF image.

to determine the width of the 180° Néel wall, an integrated intensity profile across the image and perpendicular to the domain wall was obtained and the result is plotted in Fig. 3. This profile consists of three linear regimes and is an indirect representation of the magnetization direction within the image. The wall width is determined by the intercepts of the three linear regions as shown in Fig. 3. Similar Lorentz images for a 90° Néel wall in the same specimen are depicted in Fig. 4 and reference grains are marked with respect to the BF image. The gray regions in each frame represent domains which have half of their magnetization component blocked by the aperture whereas the origin of the black and white domains is similar to that explained above.

The Lorentz images that have been shown so far consist of diffraction contrast of both crystalline, i.e., granular, and magnetic nature. Hence, to assess the most appropriate profile of the domain wall, it is necessary to reduce the contribution from lattice diffraction within the image to a minimum. This is achieved through a postexperimental image processing technique and the path taken is illustrated in Fig. 5. In Figs. 5(a) and 5(b), an as-exposed Lorentz image is accompanied by its BF image, respectively. A negative or inverse of the BF image is shown in Fig. 5(c). In order to curtail the effect of lattice diffraction, intensity from the BF

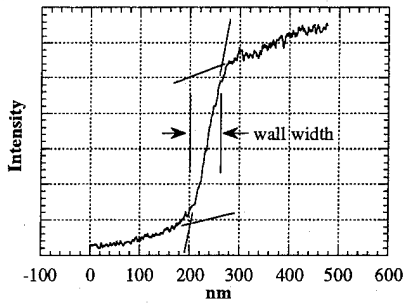



FIG. 3. Intensity trace across the 180° domain wall in 28 nm NiFe film.

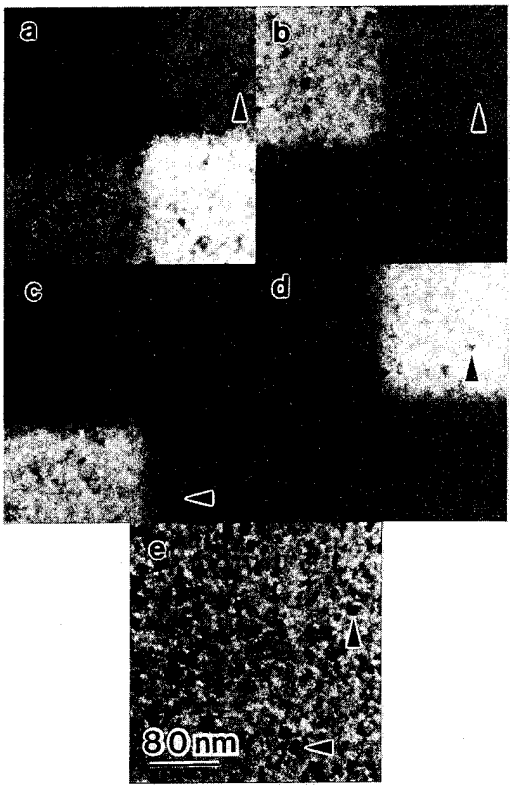



FIG. 4. (a)–(d) Lorentz images of 90° domains in a 28-nm-thick NiFe thin film with different components of the aperture blocked. (e) Corresponding BF image.

negative is added to the Lorentz image to achieve a more uniform contrast and the final processed image is shown in Fig. 5(d). The lattice diffraction within the white domain is reduced but not completely eliminated; however, the contrast in the black domain has deteriorated modestly after the image processing. The intensity profiles across the 180° Néel wall for the as-exposed and processed images are shown in

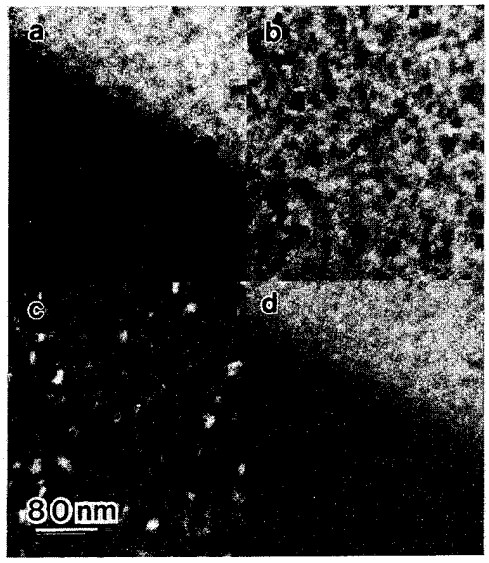



FIG. 5. (a) Lorentz images of a 28-nm-thick NiFe thin film. (b) Corresponding BF image. (c) Inverse of BF in (b). (d) Processed Lorentz image of (a).

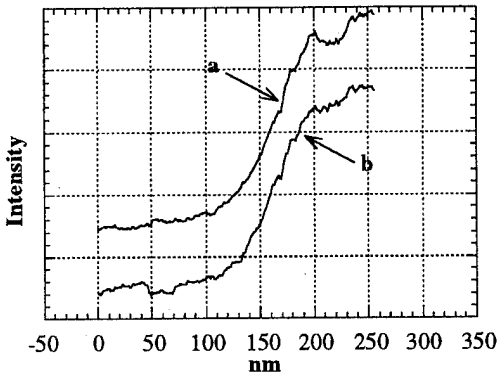



FIG. 6. Intensity profile across a 180° domain wall in a 28-nm-thick NiFe film: (a) as exposed and (b) processed images.

Fig. 6. The reduction in the intensity variation within the white domain has lead to a better definition of the domain-wall width. By combining the two profiles, the 180° Néel wall width in NiFe films of various thicknesses has been measured and the results are plotted in Fig. 7. The dependence of wall width on film thickness is similar to the theoretical profile[6] but the actual measured values are smaller than the calculated ones. They do, however, agree with other experimental observed values.[7]

## IV. CONCLUSIONS

The dependence of 180° Néel wall width on the thickness of NiFe films has been measured by high-resolution Focault mode Lorentz microscopy. This new technique incorporates the magnification capacity of the GIF unit and has been demonstrated to achieve image resolution in the nanometer range. In addition, the lattice diffraction contrast can be reduced by applying postexperimental image processing technique which resulted in better magnetic contrast and a more accurate domain-wall profile.

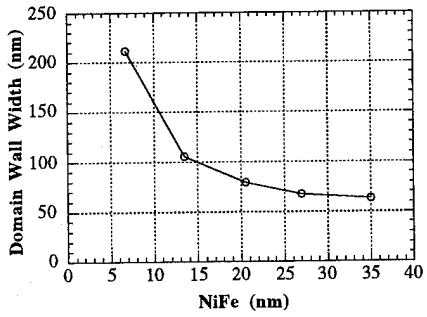



FIG. 7. Plot of 180° NiFe domain-wall width vs film thickness.

## ACKNOWLEDGMENTS

This work was supported by a grant from Hitachi Metals Ltd. The authors would like to thank Elke Fahrmann and Dr. Marc DeGraef for their helpful discussions on image processing techniques.

[1] H. W. Fuller and M. E. Hale, J. Appl. Phys. **31**, 238 (1960).
[2] J. N. Chapman and G. R. Morrison, J. Magn. Magn. Mater. **35**, 254 (1983).
[3] J. Unguris, G. G. Hmebree, R. J. Celotta, and D. T. Pierce, J. Microsc. **139**, SRP1-2 (1985).
[4] Y. Martin, Appl. Phys. Lett. **52**, 244 (1988).
[5] H. J. Mamin, Appl. Phys. Lett. **53**, 1563 (1988).
[6] T. Suzuki and C. H. Wilts, J. Appl. Phys. **40**, 1216 (1969).
[7] S. McVitie and N. J. Chapman, J. Magn. Magn. Mater. **83**, 97 (1990).

# Numerical micromagnetics in hard magnetic and multilayer systems (invited)

T. Schrefl and J. Fidler
*Institut für Angewandte und Technische Physik, Technical University of Wien, Wiedner Hauptstrasse 8-10, A-1040 Vienna, Austria*

Micromagnetic finite element calculations using a magnetic vector potential to treat long-range dipolar interactions describe the interactive magnetization processes which determine the magnetic properties of fine-grained magnetic materials. Micromagnetic models give a quantitative treatment of the correlation between the microstructure and the magnetic properties of melt-spun $Nd_2Fe_{14}B$ magnets and of Co/Pt multilayers. In nanocrystalline permanent magnets, intergrain exchange interactions cause nonuniform magnetic states which increase the remanence and act as nucleation sites. Remanence increases with decreasing grain size. Remanence enhancement of about 15% with respect to noninteracting particles can be achieved for an average grain size $D \leqslant 20$ nm. On the other hand, the nucleation field reduces to about 20% of the anisotropy field. Once a reversed domain has been nucleated, strong internal stray fields cause the expansion of the domain over several grains. The nucleation field of Co/Pt multilayers increases with improving texture. Spatial fluctuations of the magnetocrystalline anisotropy energy create barriers for domain wall motion. The pinning field of reversed domains increases with increasing misalignment and with increasing grain size. The quality of texture and the grain size significantly influence the jaggedness of domains in Co/Pt multilayers. Large grains and strong deviations of the easy directions from the film normal deteriorate the smoothness of domains and increase the transition width. © *1996 American Institute of Physics.* [S0021-8979(96)27308-3]

## I. INTRODUCTION

The macroscopic magnetic properties of a ferromagnetic material result from the microscopic arrangements of magnetic moments. The distribution of the magnetization significantly depends on the microstructure and on interparticle interactions. Since micromagnetism describes magnetization processes on a significant length scale of several nanometers, micromagnetic models provide a quantitative treatment of the correlation between the microstructure and the magnetic properties. During the last decade numerical micromagnetics has become an important tool to investigate the effects of microstructural features on the magnetic properties of modern magnetic materials.[1–5]

Generally, numerical micromagnetic models addressed two basic problems: (i) the calculation of the switching field in particles with nonuniform magnetic ground states, and (ii) calculation of the effects of interparticle interactions on the magnetic properties. The nonlinear micromagnetic energy functional allows a rigorous calculation of nucleation fields only for ellipsoidal particles.[6] Polyhedral particles show nonuniform demagnetizing fields and in turn exhibit inhomogeneous magnetic states. Bertram and Schabes[7] numerically derived nonuniform reversal modes for a ferromagnetic cube. Assuming a uniform magnetization within the individual particles, Zhu[1,2] and Fukunaga[8] studied the effects of interparticle interactions on the magnetic properties in magnetic recording media and in permanent magnets, respectively.

This work reviews micromagnetic concepts for the calculation of interaction effects while taking care of nonuniform magnetic states within single particles. In order to model magnetic inhomogeneities, each particle has to be divided into smaller finite elements. On the other hand, collective processes can only be observed for a sufficiently high number of particles. The concurrent modeling of nonuniform magnetic states and of interparticle interactions requires a considerably high number of variables. For large-scale problems the direct evaluation of the stray field energy becomes impracticable, since the demagnetizing field at a given point depends on the magnetization at all grid points. Introducing a magnetic scalar or a magnetic vector potential eliminates long-range terms from the micromagnetic energy functional.[9]

Section II describes the micromagnetic and numerical background of the simulation model. Section III treats the magnetization reversal process in nanocrystalline $Nd_2Fe_{14}B$ magnets. Section IV presents three-dimensional calculations of the magnetic properties and the domain structures in Co/Pt multilayers.

## II. NUMERICAL MICROMAGNETICS FOR LARGE PARTICLE SYSTEMS

A theoretical treatment of magnetization processes starts from the total magnetic Gibb's free energy. If one neglects magnetoelastic effects, the magnetic Gibb's free energy $\Phi_t$ of a ferromagnetic specimen in an applied field is the sum of the exchange energy, the magnetocrystalline anisotropy energy, the stray field energy, and the magnetostatic energy of the magnetic polarization $\mathbf{J}_s$ in an external field $\mathbf{H}_{ext}$:[10]

 0021-8979/96/79(8)/6458/6/$10.00 © 1996 American Institute of Physics

$$\Phi_t=\Phi_{ex}+\Phi_K+\Phi_s+\Phi_H. \tag{1}$$

For uniaxial magnetic materials, where the direction of $\mathbf{J}_s$ may be described by the angle $\alpha$ between $\mathbf{J}_s$ and the easy axis the energy contributions are given by

$$\Phi_{ex}=\int A\{(\nabla\vartheta)^2+(\nabla\varphi)^2\sin^2\vartheta\}d^3r, \tag{2}$$

$$\Phi_K=\int \{K_1\sin^2\alpha+K_2\sin^4\alpha\}d^3r, \tag{3}$$

$$\Phi_s=-\frac{1}{2}\int \mathbf{J}_s\cdot\mathbf{H}_d\,d^3r=\frac{\mu_0}{2}\int \mathbf{H}_d\,d^3r, \tag{4}$$

$$\Phi_H=-\int \mathbf{J}_s\cdot\mathbf{H}_{ext}\,d^3r. \tag{5}$$

Here $K_1$, $K_2$ are the anisotropy constant, and $A$ is the exchange constant. Using the polar angle $\varphi$ and the azimuth angle $\vartheta$ to represent $\mathbf{J}_s$, automatically fulfils the nonlinear constraint, $|\mathbf{J}_s|=J_s$, during minimization. A second nonlinearity arises from the stray field energy which is the magnetostatic energy of $\mathbf{J}_s$ in its self-demagnetizing field $\mathbf{H}_d$. All energy terms but the stray field energy depend only locally on the magnetic polarization. The long-range terms can be eliminated from the total magnetic Gibb's free energy, introducing a magnetic vector potential $\mathbf{A}$. The micromagnetic energy functional can be written in the following form[11]

$$W[\mathbf{J}_s,\nabla\times\mathbf{A}]=\Phi_{ex}+\Phi_K+\Phi_H+\frac{1}{2\mu_0}\int(\nabla\times\mathbf{A}-\mathbf{J}_s)^2\,d^3r. \tag{6}$$

For any arbitrary continuous vector $\mathbf{A}$ which decays at infinity at least as fast as $1/r$, the last term of Eq. (6) is an upper bound for the stray field energy. The minimization of Eq. (6) with respect to $\mathbf{J}_s$ and $\mathbf{A}$ leads to local minima which are in one to one correspondence to those of the total magnetic Gibb's free energy (1) and makes $\mathbf{A}$ equal to the actual magnetic vector potential.

Since the functional $W[\mathbf{J}_s,\nabla\times\mathbf{A}]$ depends only on local variables and their derivatives, its minimization can be easily performed within the framework of the finite element method. Fredkin and Koehler[12] originally applied a magnetic vector potential in micromagnetic finite element calculations, in order to investigate magnetization processes in irregular shaped particles.

In a similar way, a magnetic scalar potential can be used to eliminate long-range terms from the total magnetic Gibb's free energy. However, introducing a magnetic scalar potential leads to a saddle-point problem. Generally, mixed type finite element methods associated with saddle point problems are numerically unstable unless special discretization schemes are applied.[13]

For the investigation of melt-spun magnets, we assume a geometry where the easy axes of the grains as well as the magnetization are constrained to a plane. The magnetization is taken to be uniform in the direction perpendicular to this plane. Because of translation symmetry along the direction perpendicular to the plane containing the easy axes, only in plane magnetization processes need to be considered. The magnetic polarization and the demagnetizing field depend only on two Cartesian coordinates. Therefore, the vector potential $\mathbf{A}$ reduces to a one component potential. Reference calculations in three dimensions show that this two-dimensional model is valid for nanocrystalline magnets.[14]

The linear interpolation of magnetization angles and of the magnetic vector potential on triangular finite elements gives an algebraic minimization problem. A preconditioned quasi-Newton conjugate gradient method[15] solves for the magnetization and the magnetic vector potential simultaneously at all nodal points of the finite element mesh. The hysteresis properties directly result from subsequent minimum energy solutions for decreasing and increasing applied fields.[16] The last term of Eq. (6) is an integration over the whole space which is evaluated using the "parallelepipedic shell transformation" proposed by Brunotte, Meunier, and Imhoff.[17] This bijective transformation maps the external space into a shell enclosing the parallelepipedic interior domain. Details of the implementation of this transformation in a three-dimensional micromagnetic finite element code are given in Ref. 18. In two-dimensional calculations the vector potential reduces to a one component potential $\mathbf{A}=(0,0,A_z)$ and thus all terms associated with $A_x$, $A_y$, vanish. In order to validate the method, the authors calculated the stray field energy of a uniformly magnetized cube and the nucleation fields of ellipsoidal particles. The relative error in the stray field energy was found to be less than 2%.[18] The same accuracy was obtain for the nucleation fields of ellipsoids in three-dimensional calculations and for the nucleation fields of infinitely extended elliptic cylinders in two-dimensional calculations. Since the nucleation field of ellipsoids depends on the shape anisotropy, these results verify the stray field calculation using a magnetic vector potential and a spatial transformation to treat the external space.

Special finite elements are used to model the multilayer structure in Co/Pt multilayer recording media. Such special elements take into account the energy but have no volume.[19] Thus, ill-conditioned matrices due to poor aspect ratio volume elements can be avoided. Since a Co layer contains only two atomic layers, the magnetization is assumed to be constant in the direction of the film normal. The stray field energy of the Pt layer can described in the very same way as the energy of a thin air gap in magnetostatic finite element calculations.[19] The use of this technique is justified, because the Pt-layer thickness is considerably smaller than the domain width which is in the order 200 nm.[20] Figure 1 summarises the approximations due to the use of special finite elements for modeling Co/Pt multilayer systems. In order to reduce the number of unknowns, the incomplete gauge formulation,[21] $\mathbf{A}\cdot\mathbf{z}=0$ ($\mathbf{z}$ is the film normal), is used. For the calculations periodic boundary conditions are applied at the edges of a quadratic sample. A coordinate transformation in the direction of the film normal maps the exterior space onto some additional layers that account for the stray field energy in the exterior space.

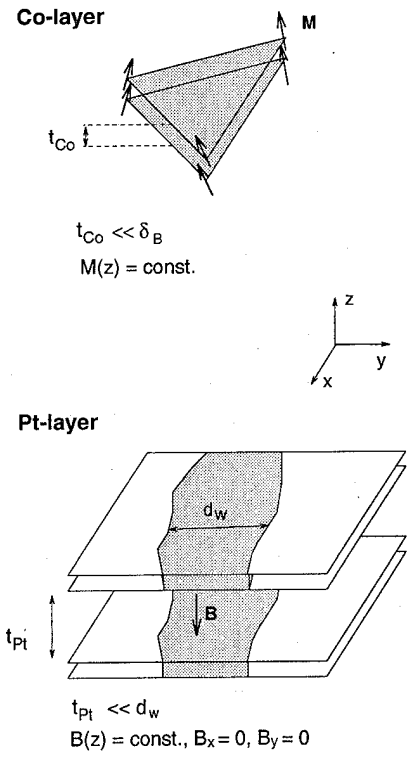



FIG. 1. Special finite elements to model Co/Pt multilayer structures. The Co-layer thickness, $t_{Co}$, and the Pt-layer thickness, $t_{Pt}$, are small as compared to the domain wall width of Co, $\delta_w$, and the extension of domains, $d_w$, respectively.

## III. NANOCRYSTALLINE $Nd_2Fe_{14}B$ MAGNETS

In nanocrystalline permanent magnets the grain diameter approaches the order of the domain wall width. Thus, the magnetization of several grains becomes strongly correlated increasing the remanence with respect to noninteracting particles. Several authors[22–24] reported an enhanced remanence in melt-spun Nd–Fe–B magnets being composed of nanocrystalline homogeneous grains without any nonmagnetic phases separating adjacent grains. Owing to intergrain exchange interactions the remanence considerably exceeds the value

$$J_r = J_s \langle \cos \theta \rangle, \tag{7}$$

given by the Stoner–Wohlfarth theory[6] for noninteracting particles. Here, $\theta$ is the angle between the saturation direction and the easy axes and $\langle\ \rangle$ denotes an ensemble average. According to Eq. (7) $J_r/J_s = 0.5$ for an assembly of noninteracting, randomly oriented particles, whereas $J_r/J_s$ is $2/\pi = 0.64$ for microstructures with in plane random texture.

Modeling of the solidification process yields realistic two-dimensional microstructures of melt-spun Nd–Fe–B magnets.[25] The particles of randomly oriented easy axes are coupled by short-range exchange and long-range magnetostatic interactions. For calculations the material parameters of $Nd_2Fe_{14}B$ at $T = 300$ K [$K_1 = 4.3 \times 10^6$ J/m$^3$, $K_2 = 0.65 \times 10^6$ J/m$^3$, $A = 7.7 \times 10^{-12}$ J/m, $J_s = 1.61$ T (Ref. 26)] have been used. The grain size has been varied between 10 and 40 nm.

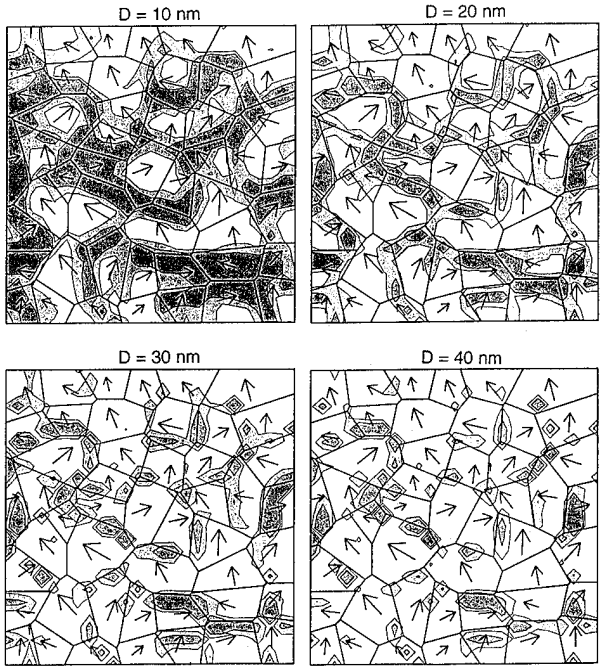



FIG. 2. Nonuniform magnetic states near grain boundaries for different average grain diameter $D$. The shaded areas denote the regions where the magnetic polarization deviates from the local easy axis by more than 10° and more than 20°, respectively.

Figure 2 clearly demonstrates the effect of intergrain exchange interactions on the magnetization distribution in nanocrystalline permanent magnets. The competitive effects of intergrain exchange interactions and magnetocrystalline anisotropy cause the magnetization to deviate from the local easy axis near the grain boundaries. The emphasized areas in Fig. 2 indicate the regions where $\mathbf{J}_s$ deviates from the local easy axes by more than 10° and 20°. The domain wall width $\delta_B = \pi\sqrt{A/K_1}$ restricts the extension of magnetic inhomogeneities. As a consequence the volume fraction of the nonuniform magnetic states becomes smaller for larger grain size. Only magnetic moments which deviate from the local easy

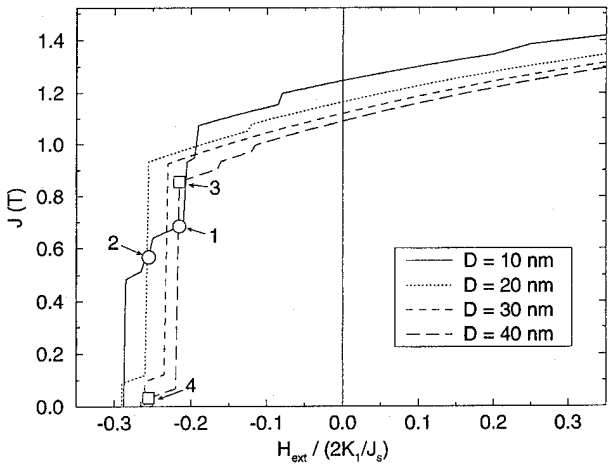



FIG. 3. Demagnetization curves as a function of the average grain diameter $D$. The circles refer to the stable equilibrium states plotted in Fig. 4.

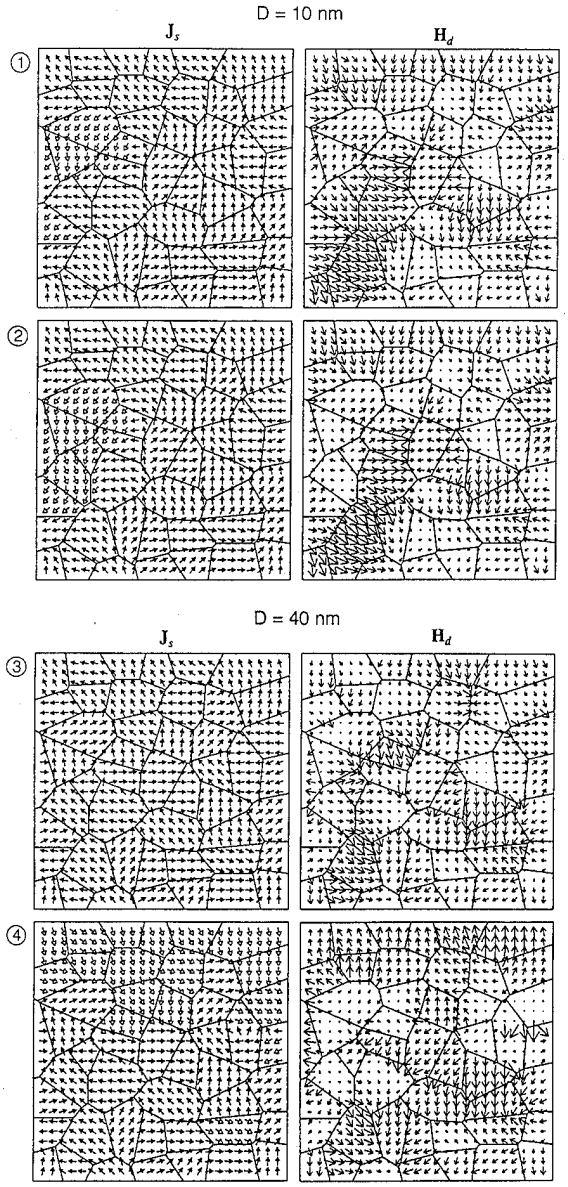



FIG. 4. Spin arrangements (left-hand side) and demagnetizing field (right-hand side) of a stable equilibrium states for different average grain size. (1) $\mu_0 H_{ext}=1.45$ T, $D=10$ nm; (2) $\mu_0 H_{ext}=1.72$ T, $D=10$ nm; (3) $\mu_0 H_{ext}=1.45$ T, $D=40$ nm; (4) $\mu_0 H_{ext}=1.72$ T, $D=40$ nm. The length of the arrows on the right-hand side indicates the absolute value of the demagnetizing field.

axis can increase the remanence. Therefore, the remanence of nanocrystalline permanent magnets deteriorates with increasing grain size. The enhancement of the remanence with respect to noninteracting particles changes from 22% to 6%, as the average grain diameter varies between 10 and 40 nm.

Figure 3 compares the demagnetization curves for increasing grain size. The coercive field varies in the range from $H_c=0.29\times(2\ K_1/J_s)$ to $H_c=0.26\times(2\ K_1/J_s)$ and thus is significantly smaller than the Stoner–Wohlfarth value of 0.48 $(2\ K_1/J_s)$. Whereas the demagnetization curve for a mean grain size of $D=10$ nm shows several small steps, the steps become larger with increasing grain size. Intergrain exchange interactions and strong demagnetizing fields at sharp corners initiate magnetization reversal in the vicinity of the

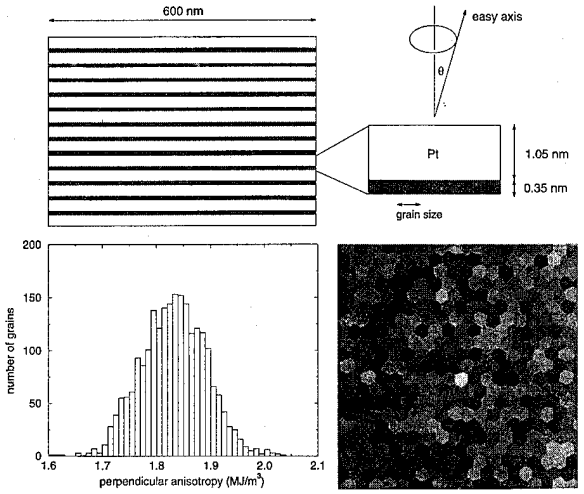



FIG. 5. Cross section of a Co/Pt multilayer structure and distribution of perpendicular anisotropy. The anisotropy constants of the top Co layer are mapped as gray scale with full bright referring to $K_u=1.6$ MJ/m$^3$ and full dark referring to $K_u=2.1$ MJ/m$^3$.

grain boundaries.[27] For an average grain size of 10 nm, the stray field energy and the exchange energy are approximately equal in magnitude. Magnetization reversal remains localised despite strong demagnetizing fields near the boundary of reversed domains, because the reversal of neighboring grains requires to overcome an energy barrier due to the exchange energy. The exchange energy decreases with increasing grain size reaching only 30% of the stray field energy for $D=40$ nm. Magnetization reversal may take place at less expense of exchange energy and thus strong demagnetizing fields easily expand reversed domains. Figure 4 compares stable equilibrium states at different external field for $D=10$ nm and $D=40$ nm.

## IV. Co/Pt MULTILAYERS

Co/Pt multilayer structures are excellent candidates for high-density magneto-optic recording media.[28] Besides Lorentz electron microscopy,[29] micromagnetic modeling reveals the effects of microstructural features on the magnetic properties of Co/Pt multilayers. Figure 5 characterizes the structural properties of the multilayer system used for the calculations. The graphs show the cross section of the multilayer, the distribution of perpendicular anisotropy, and the grain structure. The maximum deviation angle $\theta$ between the easy axis and the film normal is a measure for the texture. The grains in different layers match in the film normal. Both, easy directions and perpendicular anisotropy constants vary from grain to grain and from layer to layer. The shape of each layer is rectangular. Periodic boundary conditions are applied. The polarization of Pt atoms next to the Co layers increases the magnetic polarization per unit volume Co by about 30%.[30] A nonvanishing magnetic polarization in the Pt layers gives rise to weak interlayer exchange coupling in addition to magnetostatic interactions. Table I summarizes the material properties used for the simulations.

Figure 6 presents the numerically calculated demagnetization curves for three different microstructures. The curves

TABLE I. Properties of the Co/Pt multilayer structure used for the calculations.

| Sample | | A | B | C | Ref. |
|---|---|---|---|---|---|
| Number of bilayers | $n$ | 12 | 12 | 12 | |
| Co layer thickness | $t_{Co}$ (nm) | 0.35 | 0.35 | 0.35 | 31 |
| Pt layer thickness | $t_{Pt}$ (nm) | 1.05 | 1.05 | 1.05 | 31 |
| Saturation polarization (Co) | $J_{Co}$ (T) | 1.76 | 1.76 | 1.76 | 32 |
| Exchange constant (Co) | $A_{Co}$ (J/m) | $1.8\times10^{-12}$ | $1.8\times10^{-12}$ | $1.8\times10^{-12}$ | 32 |
| Perpendicular anisotropy (Co) | $K_u$ (MJ/m$^3$) | 1.60–2.04 | 1.60–2.04 | 1.60–2.04 | 32 |
| Texture | $\theta$ | 5° | 10° | 10° | 33 |
| Mean grain size | $D$ (nm) | 20 | 20 | 30 | 33 |
| Effective polarization (Pt) | $J_{Pt}$ (T) | 0.16 | 0.16 | 0.16 | 30 |
| Effective exchange constant (Pt) | $A_{Pt}$ (J/m) | $1.6\times10^{-14}$ | $1.6\times10^{-14}$ | $1.6\times10^{-14}$ | |

show a step decrease at the nucleation field owing to the formation of reversed domains. As the domain wall pinning becomes the governing mechanism, magnetization reversal proceeds with a finite slope of the demagnetization curve. The nucleation field decreases from sample A to C. Both, increasing misalignment and increasing grain size cause a slight reduction of the nucleation field. Spatial fluctuations of the magnetocrystalline anisotropy energy from grain to grain hinder domain wall motion. The pinning field of domain walls increases with decreasing quality of texture and with increasing particle size. Figure 7 compares the domain patterns of samples A, B, and C at different applied fields. Magnetization reversal starts at few nucleation sites. The successive expansion of reversed domains significantly lowers the stray field energy. Numerical calculations for sample B show that an initially reversed domain of about 10 nm diam leads to the growth of an almost circular domain with an extension of 240 nm.

The jaggedness of domain walls significantly depend on the quality of texture and the grain size. Figure 8 shows numerically calculated bubble domains for samples A, B, and C. The equilibrium magnetic states have been calculated starting from an initially reversed magnetization within a cir-

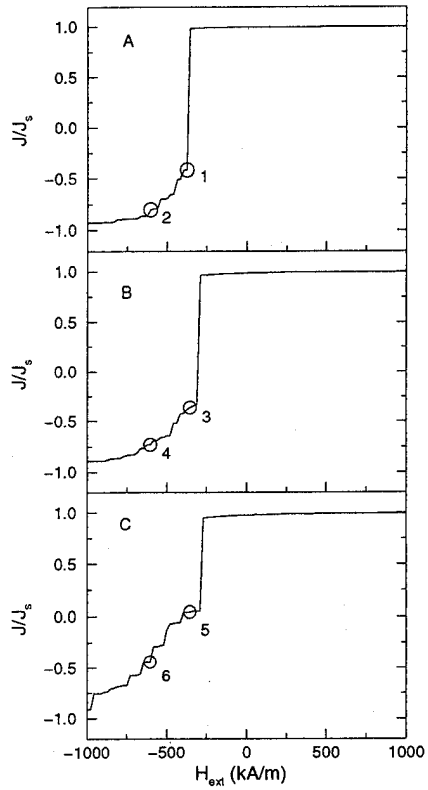



FIG. 6. Demagnetization curves of Co/Pt multilayers with different microstructural properties: (A) $\theta=5°$, $D=10$ nm; (B) $\theta=10°$, $D=20$ nm; (C) $\theta=10°$, $D=30$ nm. The numbers refer to the magnetization patterns given in Fig. 7.

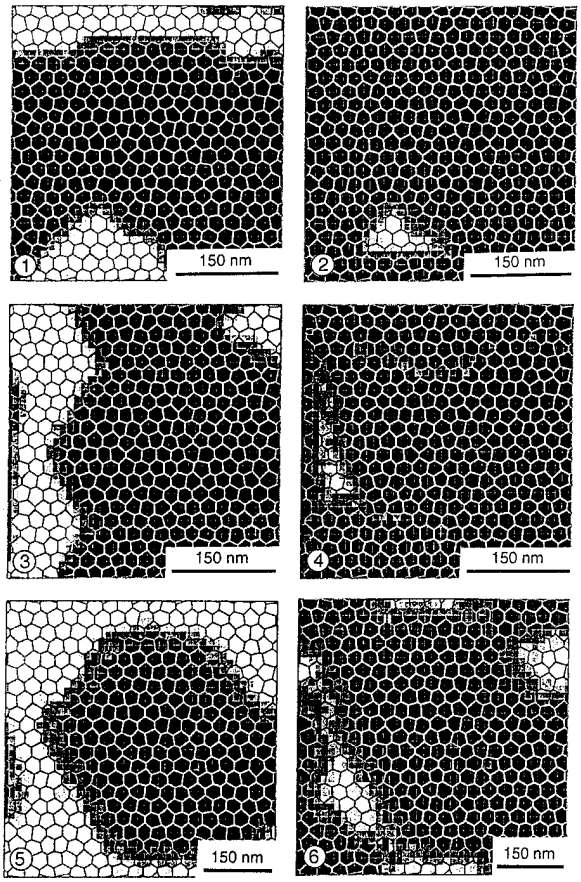



FIG. 7. Domain patterns for different applied fields for the multilayer structures A (top row), B (middle row), and C (bottom row). Full bright refers to $+J_s$ and full dark refers to $-J_s$. The numbers indicating the value of the applied field refer to the demagnetization curves of Fig. 6.

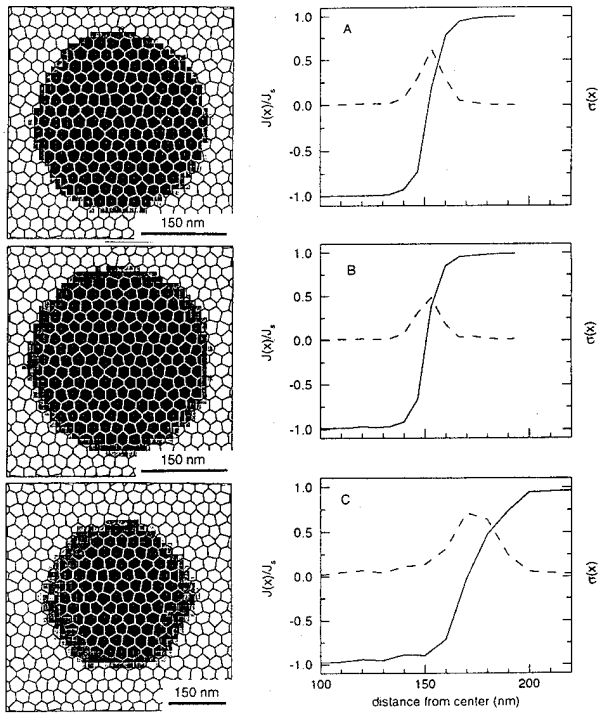



FIG. 8. Microstructural properties and domain jaggedness in Co/Pt multilayers. Left-hand side: calculated bubble domains for the multilayer structures A (top row), B (middle row), and C (bottom row). Right hand side: averaged wall profiles (solid line) and standard deviation of the magnetization (dashed line).

cular region of 300 nm diam. The magnetization component parallel to the film normal has been averaged over 36 radial directions, in order to calculate the wall profiles of Fig. 8. Sharp transitions and smooth domain walls are found in sample A. The transition width and the domain wall jaggedness increase with decreasing quality of texture and increasing grain size.

## V. CONCLUSION

A finite element method using a vector potential to treat long-range dipolar interactions proved to be effective in calculating interactive and cooperative magnetization processes in fine-grained magnetic materials. Nucleation of reversed domains and subsequent domain wall motion determines the hysteresis properties of melt-spun $Nd_2Fe_{14}B$ magnets and Co/Pt multilayers. In nanocrystalline permanent magnets intergrain exchange interactions enhance the remanence and initiate magnetization reversal under the influence of an external field. In Co/Pt multilayers only few nucleation sides are sufficient to form reversed domains with an extension in the order of 300 nm. The pinning field of domains increases with decreasing quality of texture and with increasing grain size.

## ACKNOWLEDGMENTS

This work was supported by the Austrian Science Foundation through Grant No. P10511-NAW and by the BRITE/EURAM EC Project No. BE95-1629.

[1] J.-G. Zhu and H. N. Bertram, J. Appl. Phys. **63**, 3248 (1988).
[2] J.-G. Zhu and H. N. Bertram, J. Appl. Phys. **66**, 1291 (1989).
[3] M. Mansuripur and R. Giles, Comput. Phys. **4**, 291 (1990).
[4] T. Schrefl, J. Fidler, and H. Kronmüller, Phys. Rev. B **49**, 6100 (1994).
[5] J. J. Miles, M. Wdowin, J. Oakley, and B. K. Middleton, IEEE Trans. Magn. **31**, 1013 (1995).
[6] E. C. Stoner and E. P. Wohlfarth, Philos. Trans. R. Soc. **240**, 599 (1948).
[7] M. E. Schabes and H. N. Bertram, J. Appl. Phys. **64**, 1347 (1988).
[8] H. Fukunaga and H. Inoue, Jpn. J. Appl. Phys. **31**, 1347 (1992).
[9] A. Aharoni, IEEE Trans. Magn. **27**, 3539 (1991).
[10] W. F. Brown, Jr., *Micromagnetics* (Wiley, New York, 1963).
[11] P. Asselin and A. A. Thiele, IEEE Trans. Magn. **22**, 1879 (1986).
[12] D. R. Fredkin and T. R. Koehler, IEEE Trans. Magn. **23**, 3385 (1987).
[13] F. Brezzi and M. Fortin, *Mixed and Hybrid Finite Element Methods* (Springer, New York, 1991).
[14] R. Fischer, T. Schrefl, H. Kronmüller, and J. Fidler, J. Magn. Magn. Mater. **150**, 329 (1995).
[15] P. E. Gill, W. Murray, and M. H. Wright, *Practical Optimization* (Academic, New York, 1981).
[16] D. Kinderlehrer and L. Ma, IEEE Trans. Magn. **30**, 4380 (1994).
[17] X. Brunotte, G. Meunier, and J. F. Imhoff, IEEE Trans. Magn. **28**, 1663 (1992).
[18] T. Schrefl, J. Fidler, and H. Kronmüller, J. Magn. Magn. Mater. **138**, 15 (1994).
[19] T. Nakata, N. Takahashi, K. Fujiwara, and Y. Shiraki, IEEE Trans. Magn. **26**, 2379 (1990).
[20] D. M. Donnet, J. N. Chapman, H. W. van Kesteren, and W. B. Zeper, J. Magn. Magn. Mater. **115**, 342 (1992).
[21] R. C. Mesquita, IEEE Trans. Magn. **30**, 2861 (1994).
[22] R. W. McCallum, A. M. Kadin, G. B. Clemente, and J. E. Keem, J. Appl. Phys. **61**, 3577 (1987).
[23] G. C. Hadjipanayis and W. Gong, J. Appl. Phys. **64**, 5559 (1988).
[24] A. Manaf, R. A. Buckley, H. A. Davies, and M. Leonowicz, J. Magn. Magn. Mater. **101**, 360 (1991).
[25] B. Habiger, Diploma thesis, Technical University Vienna, 1995.
[26] S. Hock, Ph.D. thesis, University of Stuttgart, Germany, 1988.
[27] T. Schrefl, H. F. Schmidts, J. Fidler, and H. Kronmüller, J. Appl. Phys. **73**, 6510 (1993).
[28] M. Kaneko, J. Magn. Magn. Mater. **148**, 351 (1995).
[29] D. M. Donnet, V. G. Lewis, J. N. Chapman, K. O'Grady, and H. W. van Kesteren, J. Phys. D: Appl. Phys. **26**, 1741 (1993).
[30] C.-J. Lin, G. L. Gorman, C. H. Lee, R. F. C. Farrow, E. E. Marinero, H. V. Do, and H. Notarys, J. Magn. Magn. Mater. **93**, 194 (1991).
[31] R. Ploessl, J. N. Chapman, M. R. Scheinfein, J. L. Blue, M. Mansuripur, H. Hoffmann, J. Appl. Phys. **74**, 7431 (1993).
[32] W. B. Zeper, H. W. van Kesteren, B. A. J. Jacobs, and J. H. M. Spruit, J. Appl. Phys. **70**, 2264 (1991).
[33] G. A. Bertero and R. Sinclair, J. Magn. Magn. Mater. **134**, 173 (1994).

# Simulation of three-dimensional nonperiodic structures of $\pi$-vertical Bloch line and $2\pi$-vertical Bloch line in magnetic garnet

M. Redjdal and F. B. Humphrey
*Department of ECS Engineering, Boston University, 44 Cummington St., Boston, Massachusetts 02215*

The dynamics of three-dimensional nonperiodic structures in magnetic garnet have been investigated using large scale numerical simulations. The width of a single $\pi$-vertical Bloch line ($\pi$VBL) at equilibrium has been measured to be twice the analytical Bloch line width $\pi(A/2\pi M_s^2)^{1/2}$, where $A$ is the exchange energy constant and $M_S$ the spontaneous magnetization. A $2\pi$VBL has been shown to be 1.5× wider than a $\pi$VBL. A comoving technique is used to track a single domain wall with a single $\pi$VBL when a 5 Oe field is applied perpendicularly to the surface of the film. At dynamic equilibrium, the VBL to wall velocity ratio is equal to ten, smaller than the value found for a simulated loosely spaced chain of $\pi$VBLs. A $2\pi$VBL is split into two single $\pi$VBLs when an in-plane field is applied in the same direction as that of the center spin of the $2\pi$VBL. No motion of the surface spins is observed for the first 10 ns when a 30 Oe field is applied although considerable spin distortion occurs in the wall center. When the field is turned off after 8 ns, the relaxing distortion drives the surface spins apart. The containment due to $2\pi$ horizontal Bloch line formation during the process is demonstrated. © *1996 American Institute of Physics.*
[S0021-8979(96)27408-X]

## I. INTRODUCTION

Domain wall structures in magnetic garnet have been investigated using a large scale simulation method.[1] Bagnérés *et al.* showed that magnetization distortions play a critical role in the dynamics of periodically spaced chains of $\pi$-vertical Bloch lines ($\pi$VBLs) and $2\pi$VBLs.[2–4] Patterson *et al.* investigated horizontal Bloch line (HBL) formation and its effect on wall motion.[5]

Most of the analytical investigations of the static and dynamic characteristics of wall structure have been based on a periodic arrangement of Bloch lines (BLs) in an infinitely long planar wall. Bloch line width was calculated using energy minimization[6] and by balancing exchange and demagnetizing forces.[7,8] The equilibrium distance between Bloch lines is in the order of $\sqrt{\pi A}/M_s$,[7] where $A$ is the exchange energy constant and $M_s$, the spontaneous magnetization. No distinction was made between single $\pi$VBL and $2\pi$VBL. The dynamics of periodic uncompressed Bloch lines in a planar wall with infinite length yielded a VBL to wall velocity ratio equal to $\pi\sqrt{Q}/2\alpha$, where $Q$ is the quality factor and $\alpha$, the damping parameter.[9] Using numerical simulation, Nakatani calculated the static structure of a $\pi$VBL using a very coarse three-dimensional lattice that drastically reduced the effect of the demagnetizing field.[10] Bagnérés used a much larger computer with a finer lattice to show that a $\pi$VBL structure is characterized by in-plane angle twists with a $2\pi$ twist at one surface, a $\pi$ twist through the center line halfway between the surfaces and no twist at all at the other surface.[2]

In this article, the Landau–Lifshitz–Gilbert (LLG) equation is solved numerically to measure the widths of a $\pi$VBL and a $2\pi$VBL in a single domain wall at equilibrium. A $\pi$VBL was moved gyrotropically by applying a field perpendicular to the surface of the film. A co-moving technique is used to track both the domain wall and its structure so as to center the coordinate system on the structure. A $2\pi$VBL is split into two single $\pi$VBLs by applying an in-plane field. It is shown that the distortions drive the VBLs apart. The containment due to HBL formation slows the process.

## II. TECHNIQUE

The simulations were performed by solving the LLG equation numerically in an $xyz$ Cartesian lattice with 32 ×256×32 nodes, or 262 144 grid points. At each grid point, the simulation takes as input a characterization of the phenomenological magnetic parameters exchange, anisotropy, magnetostatic interactions, and saturation magnetization, together with an initial magnetization distribution and prescribed external field. Since free boundary conditions are used, a three-dimensional fast Fourier transform is combined with zero padding to evaluate the demagnetizing field in the isolated sample. The simulations were performed on the Connection Machine system CM5.

Initial magnetization distributions are based on analytical solutions for the azimuthal angle $\Theta$ and in-plane angle $\Psi$. The spin system is relaxed by solving the LLG equation with zero external field. The equilibrium is reached when the angular velocity of the fastest spin is in the order of 0.01 GHz which implies that the highest effective field acting on any spin in the system is no more than 0.2 Oe.

A co-moving technique is applied to the case where the domain wall (in $yz$ plane) with a single $\pi$VBL is subjected to a constant field in the $Z$ direction. A predictor-corrector algorithm is used to align the velocity of the coordinate system with that of the domain wall such that the $\pi$VBL is always kept in the center of the viewing frame. Such a system requires that the wall with the VBL be located accurately in both the $x$ (for the moving wall) and $y$ direction (for the VBL). The instantaneous velocity of the domain wall is directly tied to the total sum of $M_z$ spins in the entire sample. The instantaneous velocity of the $\pi$VBL is calculated using the $M_y$ spin component of the magnetization located in a region that contains the domain wall only. The wall velocity and $\pi$VBL velocity can be accurately calculated. The simu-

 0021-8979/96/79(8)/6464/3/$10.00 © 1996 American Institute of Physics

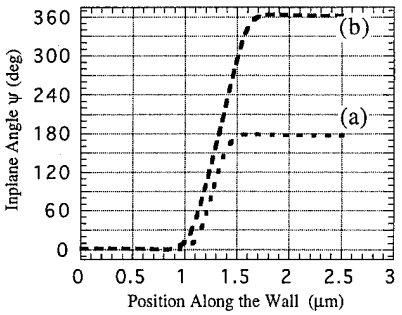



FIG. 1. In-plane angle $\psi$ at the middle of the wall center slice as a function of position along the domain wall; (a) $\pi$VBL and (b) $2\pi$VBL.

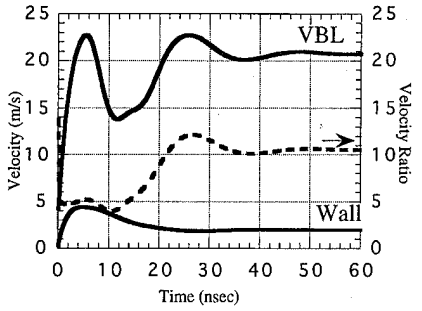



FIG. 2. Instantaneous velocity of a $\pi$VBL and a domain wall when the domain wall is driven by a 5 Oe bias field ($\alpha$=0.2). The dashed curve shows the instantaneous $\pi$VBL to wall velocity ratio.

lation volume is 0.32 $\mu$m×2.56 $\mu$m×1.28 $\mu$m with a nodal ratio of 1:1:4. The maximum integration step is 1 ps. Typically, each nanosecond of simulation time requires about 1 h of CPU time.

The material parameters are exchange constant, $A=3.0\times10^{-7}$ ergs/cm; anisotropy field, $H_k=1860$ Oe; saturation magnetization, $4\pi M_s=452$ G; Gilbert damping constant, $\alpha$=0.2; gyromagnetic ratio, $\gamma=-0.01$ Oe$^{-1}$ ns$^{-1}$.

## III. RESULTS AND DISCUSSION

The equilibrium magnetization configuration for a wall containing a single $\pi$VBL or $2\pi$VBL has been calculated numerically. Figure 1 shows the in-plane angle $\Psi$ along a line in the middle of the sample and the wall center slice. The wall center slice is represented by the wall surface for which the magnetization component $M_z$ is zero. The center spin line is represented by a line of spins midway between the surfaces of the material. For $\pi$VBL, the center spin undergoes a 180° rotation starting at the domain wall with one chirality and ending at the domain wall with the opposite chirality. The $2\pi$VBL starts and ends in domain walls with the same chirality through a 360° rotation of its center spin. The width is determined by extrapolation of the linear portion of the curve to 0° and 180° for the $\pi$VBL and to 0° and 360° for the $2\pi$VBL. The simulated width is 0.41 $\mu$m for a $\pi$VBL and 0.59 $\mu$m for a $2\pi$VBL.

The $\pi$VBL simulated value compares better with the calculated equilibrium distance of 0.27 $\mu$m for the periodic arrangement of Bloch lines[7] and Hayashi's simulated $\pi$VBL (Ref. 10) than with the analytical result based on Bloch line width parameter.[6] According to Thiaville,[11] the measured $\pi$VBL width is 0.45 $\mu$m in a 7 $\mu$m thick sample. These results suggest that the $\pi$VBL width is independent of the thickness of the material.

Figure 2 shows the instantaneous velocity and the velocity ratio of a $\pi$VBL and a domain wall for the first 60 ns of motion under the influence of a 5 Oe field normal to the surface of the material. It can be seen that the wall velocity develops a slight overshoot then settles to a steady state velocity after ~20 ns. However, the $\pi$VBL takes twice as long to reach steady state motion after undergoing a relatively large oscillatory transient state. Finally, a steady state velocity ratio of 10 is reached after 60 ns. For loosely spaced periodic chains of $\pi$VBLs, Bagnérés[4] measured a VBL to wall velocity ratio of 14. We measure a smaller velocity ratio presumably because the motion of a single $\pi$VBL is slowed by the curvature inherent to the presence of the single VBL structure in a plane wall. This makes the velocity ratio even further from the analytically predicted value of 16 for uncompressed BLs in a planar wall.[9]

Figure 3 shows the contours of in-plane angle $\psi$ of the magnetization in the wall center slice. The contour lines correspond to ±15°, ±45°, ±75°, ±105°, ±135°, and ±165° for $\psi$. The in-plane angle $\psi$ is 0° or 180° in the direction perpendicular to the wall. These values are shown by the dotted lines in the shaded areas which represent regions where the magnetization is within ±15° of the direction perpendicular to the wall. In the light shaded areas close to the center along the wall, the magnetization lies within ±15° from the direction parallel to the wall.

Figure 3(A) shows a section of the wall slice center, 2.56 $\mu$m long, with a single $2\pi$VBL at equilibrium. The $2\pi$VBL has a $2\pi$ twist at all levels through the thickness of the material with a notable compression of the twist at both surfaces. For convenience, the distance between the dotted lines is defined as the "half-width." It can be seen that the contours are very regular and symmetric in the surrounding domain walls. The in-plane angle $\psi$ varies at a rate close to 6° per node along the wall and through the thickness of the wall.

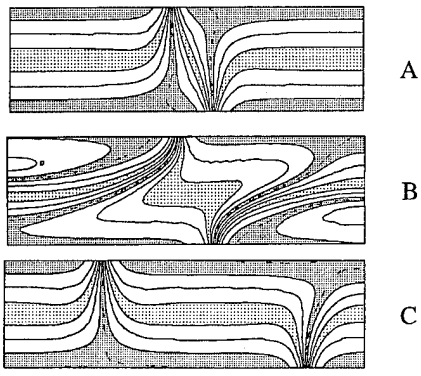



FIG. 3. Contours of the magnetization in-plane angle $\psi$ in the wall containing a $2\pi$VBL for: (A) the initial state, (B) after 8 ns when an in-plane field of 30 Oe has been applied, (C) almost at equilibrium at 100 ns after the field was turned off at 8 ns.

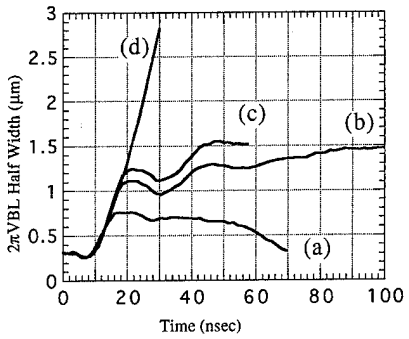



FIG. 4. $2\pi$VBL half-width as a function of time when a 30 Oe pulse field is applied for: (a) 5 ns, (b) 8 ns, (c) 9.5 ns, and (d) 30 ns.

When a 30 Oe in-plane field is applied in a direction opposite to the chirality of the domain walls but in the same direction as that of the center spin of the $2\pi$VBL, the contours become distorted. It can be seen that after 8.0 ns, as shown in Fig. 3(B), most of the distortion takes place at the center of the wall while the compressed twists, weighing down the domain wall at the surfaces, appear not to have moved. Horizontal Bloch lines form in the surrounding domain walls where the spins undergo a supplementary twisting due to the in-plane field. The pulse field is turned off at 8.0 ns. As the structure relaxes toward its equilibrium state, HBLs disappear. Slowly, the $2\pi$VBL structure splits. Figure 3(C) shows the equilibrium configuration at a simulation time of 100 ns or 82 ns after the field is turned off. The separation distance is 1.5 $\mu$m, about three times a $\pi$VBL width. Bagnérés *et al.* measured a separation equilibrium distance equal to 1.2 $\mu$m for a loosely spaced and periodic chain of $\pi$VBLs.[2]

Figure 4 shows the half-width, distance between the center positions of the compressed twists at the surfaces, as a function of time for a $2\pi$VBL when a 30 Oe in-plane field is applied. In curve (a), the pulse field is applied for 5 ns. The compressed twists show no movement during this time or for the first 10 ns. They start moving apart between 10 and 15 ns with no field applied, settle at a plateau of 0.7 $\mu$m until ~65 ns, and finally settle back to the equilibrium configuration at 70 ns without splitting the $2\pi$VBL. Curve (b) shows the results when the pulse field is 8 ns long. It shows similar behavior to case (a) for the first 15 ns but the compressed twists break apart around 19 ns, undergo an oscillatory behavior and then proceed further apart to split the $2\pi$VBL. Again, all motion is observed when no field duration is applied. Similarly, in curve (c), for which the pulse field is 9.5 ns, the compressed twists settle at an equilibrium distance close to 1.5 $\mu$m: the splitting of the structure into two single $\pi$VBLs has taken place. Curve (d) shows the half-width when the in-plane field is applied continuously. It can be seen that curves (b) and (c) are similar to curve (d) between 10 and 20 ns although (d) has a field applied while (b) and (c) have none. The formation of HBLs in the domain walls, on each side of the $2\pi$VBL structure, presumably contributes to the containment of the latter. It implies that the distortions inside the structure are balanced by the formation of HBLs for the duration of the transient phase.

## IV. CONCLUSION

It is shown that equilibrium structures of $\pi$VBLs and $2\pi$VBLs are distinct. The $2\pi$VBL is only 1.5× wider than a $\pi$VBL instead of twice. A velocity ratio of 10 was measured. This ratio is lower than the analytically predicted value of 16 for uncompressed Bloch lines. It was also demonstrated that in splitting a $2\pi$VBL, it is as easy to use the distortions due to a short pulse as using a field. The containment due to horizontal Bloch line formation slows down the process.

## ACKNOWLEDGMENTS

We wish to thank Honeywell Corp., SSEC division, Plymouth, Minnesota for partial support.

[1] R. C. Giles, P. R. Kotiuga, and F. B. Humphrey, J. Appl. Phys. **67**, 5821 (1990).
[2] A. Bagnérés and F. B. Humphrey, IEEE Trans. Magn. **28**, 2344 (1992).
[3] A. Bagnérés, M. Redjdal, and F. B. Humphrey, IEEE Trans. Magn. **29**, 2584 (1993).
[4] A. Bagnérés, M. Redjdal, and F. B. Humphrey, IEEE Trans. Magn. **30**, 4389 (1994).
[5] G. N. Patterson, IEEE Trans. Magn. **29**, 2581 (1993).
[6] A. P. Malozemoff, Appl. Phys. Lett. **21**, 149 (1972).
[7] A. Hubert, J. Magn. Magn. Mater. **18**, 178 (1973).
[8] J. C. Slonczewski, J. Appl. Phys. **45**, 2705 (1974).
[9] A. A. Thiele, J. Appl. Phys. **45**, 377 (1974).
[10] Y. Nakatani and N. Hayashi, IEEE Trans. Magn. **24**, 3039 (1988).
[11] A. Thiaville, J. B. Youssef, Y. Nakatani, and J. Miltat, J. Appl. Phys. **15**, 6090 (1991).

# Simulations of highly anisotropic Co–Cr–Ta thin films

C. Dean and R. W. Chantrell
*Department of Physics, University of Keele, ST5 5BG, United Kingdom*

H. Suzuki and N. Kodama
*Data Storage and Retrieval Systems Division, Hitachi Ltd., Odawara-shi 256, Japan*

P. R. Bissell
*Department of Physics and Astronomy, University of Central Lancashire, Preston PR1 2HE, United Kingdom*

Co–Cr–Ta thin film media produced by transfer deposition are known to be highly anisotropic. Earlier experimental work shows these films achieve the maximum theoretically possible $\delta I$ in the parallel direction but small deviation from zero transverse to the sputtering direction. A thin film micromagnetic model has been extended to simulate this highly anisotropic behavior. It was found that anisotropic exchange coupling was insufficient to account for the anisotropic behavior. Good agreement with experiment has been obtained using an approach which modifies the exchange coupling *and* the magnetostatic interaction. The large values of $\delta I$ are ascribed to difficulties in the production of the ac demagnetized state. © *1996 American Institute of Physics.*
[S0021-8979(96)27508-X]

## I. INTRODUCTION

Transfer deposition has the advantage that it is a continuous method of production. However, sputtered Co–Cr–Ta thin film media prepared by transfer deposition have been shown to be highly anisotropic from the $\delta I$ curves parallel to and transverse to the transfer direction.[1] Furthermore, measurements of modulation of the read/write performance of disks show the anisotropy is strongly dependent upon the track orientation[2] although this has not been related to the magnetization processes within the film. The motion of the substrate past the sputtering target leads to the formation of a "bowed columnar structure" in the transfer direction which leads to the high planar anisotropy.[1]

We have attempted to simulate the anisotropic behavior by studying the effects of the model parameters which are dependent upon the microstructure. The best description of the experimental data is found by introducing a small anisotropy in the microstructure resulting in an anisotropy of both the exchange and the magnetostatic coupling.

## II. MICROMAGNETIC MODEL

A thin film micromagnetic model which includes anisotropy, Zeeman, magnetostatic and exchange energy for $N$ grains on a hexagonal lattice[3] has been extended to study the origins of the difference in remanence properties between the parallel and transverse directions.

In an initial study, "anisotropic exchange coupling" was introduced to account for the anisotropic behavior, but despite giving the correct bulk properties, this was insufficient to account for the maximum $\delta I$.

In the magnetic layer, the bowed columnar structure causes a larger grain area to be in contact with adjacent grains along the transfer direction whereas transverse, the grains will be less affected. In the simulation, this has been interpreted as reduced interactions (both magnetostatic and exchange) in the transverse direction and has been incorporated into the model by expanding the lattice in the transverse direction. We use an exchange coupling term based on that introduced by Zhu and Bertram,[4] modified by Walmsley *et al.*[5] which includes a separation term to allow for irregular structures.

## III. RESULTS

An extensive series of computations has been carried out which cannot be completely reported here because of space limitations. Instead, we report those data which were instrumental in leading to a good theoretical description of the experimental data. Although the fit cannot be considered completely unambiguous, the hypothesis involved seems reasonable and the model predictions lead to experimentally verifiable predictions, particularly the importance of ac erasure in $\delta I$ measurements.

The thin film was represented by $56\times68$ grains on a hexagonal lattice. The grain diameter and thickness are in the range 40–50 nm.

A relatively small expansion ($<10\%$) was required to provide sufficient anisotropy. For a strongly interacting system though, this gave an unrealistic longitudinal squareness ($>0.99$) so 10% of the grains (chosen at random) were considered exchange decoupled to reduce the squareness, which had negligible effect on the co-operative behavior of the film.

Hysteresis loops have been computed for both in-plane orthogonal directions for 5 degrees of exchange coupling, $C^*=0.0,0.1,...,0.4$ and three interaction field parameters, $h_i=0.2$, 0.4, and 0.6. The parameter $h_i$ controls the magnetostatic energy and is defined as $h_i=H_i/H_k$, where $H_i=M_sV/d^3$ with $d$ the grain diameter (prior to expansion). Loops were computed for two expansion factors, $E_y=1\%$ and 5%, but results presented here are with the latter only.

Figure 1 shows the squareness for the parallel and transverse directions for $E_y=5\%$ and the three interaction field parameters as a function of exchange coupling. For each curve there is an increase of squareness with $C^*$, as expected. The small transverse expansion gives rise to a significant anisotropy in the magnetostatic interactions. This is

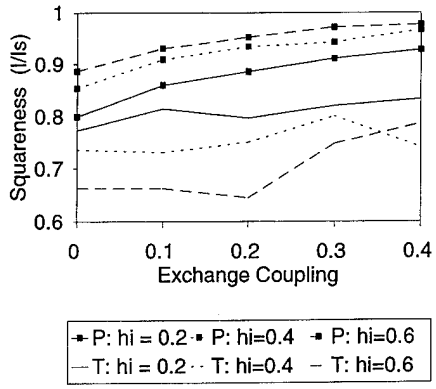



FIG. 1. Effect of exchange coupling on squareness for the two orthogonal directions.

reflected in the squareness which is enhanced parallel and decreased transverse by the magnetostatic interactions. The coercive states from the two orthogonal directions are very different. In the parallel direction, stripe domains dominate along the field direction because of the large exchange coupling and the reduced demagnetizing effect of nearest neighbors. Transverse, the magnetic microstructure consists of vortices which are formed to reduce the stray field.

A high degree of exchange coupling together with a large magnetostatic term is required to give the strong cooperative reversal which occurs experimentally. In fact, with $C^*=0.4$, $h_i=0.6$ and a 5% expansion, the hysteresis loops are in good agreement with experimental data in both parallel and transverse directions.

With these parameters, the dc-demagnetization curves, ac erased states, and IRM curves were computed. Experimentally, samples were demagnetized by rotation in a slowly reducing dc field and further demagnetized by slowly moving across a bulk eraser. If the measured sample moment was too large, the process was repeated a number of times until it fell below 1% of saturation. Difficulty in obtaining a demagnetized state in the simulation was also experienced. We have developed a technique for ac erasure based on simulated annealing, described more fully in Ref. 3, which assumes that the ac erased state is the magnetic ground state. The final ac erased state is strongly dependent upon the rate of annealing. A slow annealing schedule, corresponding to carefully erasure, has previously been followed[3] which leads to a demagnetized state with low system energy which is well correlated, with the formation of large scale structures in the magnetic state. An increased annealing rate leads to a higher system energy, shorter range correlations and less well correlated regions.

The ac erasure was carried out at four rates of erasure. The average grain energy for each erased state for increased annealing rate was −6.9, −6.5, −6.3, and −6.1 kV, the increase in energy being consistent with increasing imperfect demagnetization. A section of the final erased state for the slowly annealed is given in Fig. 2(a) and the most rapidly annealed in Fig. 2(b).

Figure 3 shows the IRM curves for the four ac erased states. The small sample size of 3808 grains causes large changes in the IRM and hence $\delta I$ curves. In order make the

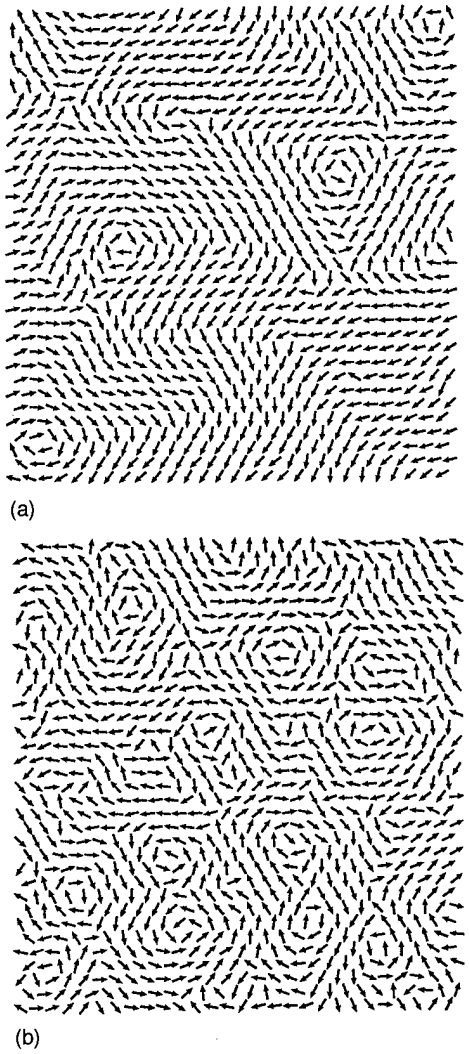



FIG. 2. Section of two ac erased states for (a) slowly (b) rapidly annealed.

interpretation of these curves easier but without changing their form, a moving average over three field steps was performed. The IRM curves are all zero in small fields indicating the stability of the ac erased state. The highest energy erased state reaches saturation remanence at the lowest field

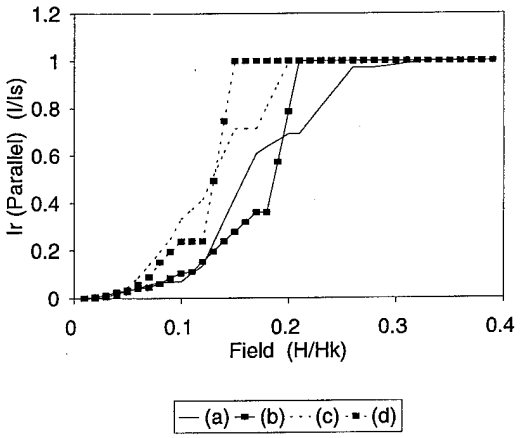



FIG. 3. IRM curves from four ac erased states.

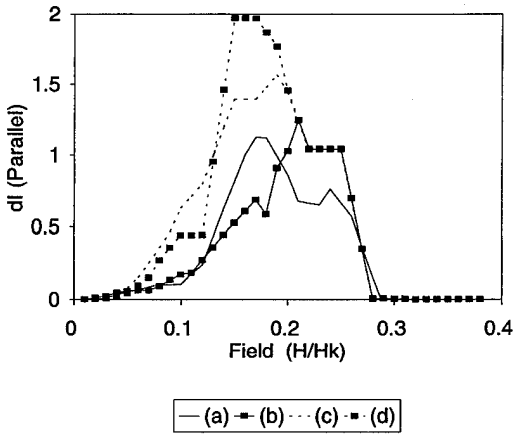



FIG. 4. Corresponding $\delta I$ curves.

with others reaching it at larger applied fields. Using these IRM curves, the $\delta I$ curves were calculated and are given in Fig. 4.

Due to the strong exchange coupling which allows the sample to resist a large negative applied field, all the $\delta I$ curves are positive, but the maximum $\delta I$ of 2 (required for complete agreement with experiment) is achieved only by the highest energy sample. The other samples which are of lower energy, reach saturation remanence at a field below which the sample has started to become demagnetized. This suggests that the form of the IRM curve is central to the $\delta I$ plot. In particular, the erasure process has a strong bearing on the value of $\delta I$, as also stated previously.[6]

## IV. CONCLUSION

The highly anisotropic behavior of sputtered Co–Cr–Ta thin film media prepared by transfer deposition has been simulated by extending a previous thin film model. In order to simulate the effect of the bowed columnar structure on the magnetic properties, the lattice was expanded transverse to the transfer direction. Comparison with experiment showed this to be the most satisfactory and consistent way to simulate the anisotropic magnetic behavior. The latter indicates the effect of disorder in the microstructure on the bulk magnetic properties. A high degree of exchange coupling and magnetostatic interaction was required to give strong cooperative reversal. An expansion factor of 5% gave the high planar anisotropy. It was found that a certain degree of disorder was required to reduce the squareness, and this was introduced by exchange decoupling 10% of the grains at random. These parameters gave the correct bulk hysteresis loop properties. A rapid annealing schedule was followed to simulate the imperfect erasure which is known to occur experimentally and the resulting $\delta I$ curves are in good agreement with the experimental curves, demonstrating the importance of a consistent and reproducible method of ac erasure in $\delta I$ measurements.

## ACKNOWLEDGMENTS

The financial support of the UK EPSRC is gratefully acknowledged. The work was carried out within the framework of the EU CAMST Project.

[1] H. Suzuki, P. R. Bissell, R. W. Chantrell, and N. Kodama, J. Magn. Magn. Mater. **148**, 11 (1995).
[2] K. E. Johnson, J. Appl. Phys. **69**, 4932 (1991).
[3] C. Dean, R. W. Chantrell, A. Hart, D. A. Parker, and J. J. Miles, IEEE Trans. Magn. **27**, 4769 (1991).
[4] J. G. Zhu and H. N. Bertram, J. Appl. Phys. **66**, 1291 (1989).
[5] N. S. Walmsley, A. Hart, D. A. Parker, R. W. Chantrell, and J. J. Miles, J. Magn. Magn. Mater. (in press).
[6] M. El-Hilo, K. O'Grady, P. I. Mayo, and R. W. Chantrell, IEEE Trans. Magn. **28**, 3282 (1992).

# Modeling of permanent magnets: Interpretation of parameters obtained from the Jiles–Atherton hysteresis model

L. H. Lewis
*Department of Applied Science, Brookhaven National Laboratory, Upton, New York 11973*

J. Gao and D. C. Jiles
*Ames Laboratory, Iowa State University, Ames, Iowa 50011*

D. O. Welch
*Department of Applied Science, Brookhaven National Laboratory, Upton, New York 11973*

The Jiles–Atherton theory is based on considerations of the dependence of energy dissipation within a magnetic material resulting from changes in its magnetization. The algorithm based on the theory yields five computed model parameters, $M_S$, $a$, $\alpha$, $k$, and $c$, which represent the saturation magnetization, the effective domain density, the mean exchange coupling between the effective domains, the flexibility of domain walls and energy-dissipative features in the microstructure, respectively. Model parameters were calculated from the algorithm and linked with the physical attributes of a set of three related melt-quenched permanent magnets based on the $Nd_2Fe_{14}B$ composition. Measured magnetic parameters were used as inputs into the model to reproduce the experimental hysteresis curves. The results show that two of the calculated parameters, the saturation magnetization $M_S$ and the effective coercivity $k$, agree well with their directly determined analogs. The calculated $a$ and $\alpha$ parameters provide support for the concept of increased intergranular exchange coupling upon die upsetting, and decreased intergranular exchange coupling with the addition of gallium. © *1996 American Institute of Physics.* [S0021-8979(96)27608-2]

## I. INTRODUCTION

The various relationships between structure and properties in permanent magnet materials are usually explored by experimental methods. With a few notable exceptions,[1,2] these relationships have not yet been extensively explored by theoretical modeling. We present here an inaugural investigation of the results which link model parameters calculated from an algorithm based on the Jiles–Atherton theory[3] with the physical attributes of a set of three related melt-quenched and thermomechanically treated permanent magnets based on the $Nd_2Fe_{14}B$ composition. Interpretations of the information thus yielded provides substantial insight into the hypothesized reversal mechanisms and internal coupling found in these magnets.

## II. THE HYSTERESIS MODEL ALGORITHM

The Jiles–Atherton model[4–6] of hysteresis is based on consideration of the dependence of energy dissipation on change in magnetization, the principal cause of hysteresis in multidomain specimens. Consideration of the underlying mechanisms has produced two differential equations which represent the irreversible differential susceptibility and reversible differential susceptibility. The solution of these differential equations leads to a normal sigmoidal-shaped hysteresis curve, when combined with an appropriate choice of function for the anhysteretic magnetization. The algorithm requires input of nine experimentally measured parameters: The coercivity $H_{ci}$, the remanence $B_R$, the initial normal susceptibility $\chi'_{in}$, the initial anhysteretic susceptibility $\chi'_{an}$, the differential susceptibility at the coercive point $\chi'_{H_{ci}}$, the differential susceptibility at remanence $\chi'_{B_R}$ and the coordinates $(H_m, M_m)$ of the loop tip, as well as the differential susceptibility of the initial magnetization curve at the loop tip, $\chi'_m$.[4] The algorithm yields five computed model parameters, $M_S$, $a$, $k$, $\alpha$, and $c$. The physical interpretation of these five model parameters is given as follows.

$M_S$ is the saturation magnetization of the material, and thus the validity of this parameter is very easy to check, either by experimental means or by obtaining the data from references. The units of $M_S$ are A/m or emu/cc.

The $a$ parameter is sometimes referred to as the "effective domain density." The model parameter $a$ is derived from an analogy to the Langevin expression[7] for the anhysteretic magnetization $M_{an}$ as a function of both temperature $T$ and field $H$ for a paramagnet:

$$M_{an}(H,T)=M_S\times[\coth(H/a)-(a/H)], \tag{1}$$

where $a=k_BT/(\mu_0\langle m\rangle)$; $M_S$ is the saturation magnetization and $k_B$ is Boltzmann's constant. However, in the Jiles–Atherton theory, the spin entity $\langle m\rangle$ is not an atomic magnetic moment $m=n\mu_B$, where $\mu_B$ is the Bohr magneton, as in the original Langevin expression. Rather, it represents the moment from a mesoscopic collections of spins that we refer to as an "effective domain;" each "effective domain" possesses a collective magnetic moment $\langle m\rangle$. These effective domain entities may or may not correspond to actual magnetic domains; the units of $a$ are in A/m or Oe.

$k$ gives a measure of the quasistatic energy dissipation via the expression $k=(1/\mu_0)\times dE/dM$, with $\mu_0$ as the permeability of free space and $dE/dM$ the change in energy per change in magnetization. In the case of a material for which the coercivity is controlled by domain-wall pinning, this expression is related to effect of pinning sites on the progress

 0021-8979/96/79(8)/6470/3/$10.00 © 1996 American Institute of Physics

TABLE I. Sample descriptions and model parameter results calculated from the Jiles–Atherton algorithm.

| Sample identification | Bulk composition | Processing | $M_S$ (emu/cc) | $a$(Oe) | $k$(Oe) | $\alpha$ | $c$ |
|---|---|---|---|---|---|---|---|
| HP1553 | $Nd_{13.75}Fe_{80.25}B_6$ | Hot pressed (MQ-2) | 1080 | 13920 | 8825 | 3.168 | 0.885 |
| DU1418 | $Nd_{13.75}Fe_{80.25}B_6$ | Die upset (MQ-3) | 1000 | 1247 | 4100 | 0.742 | 0.485 |
| DU2162 | $[Nd_{13}(Fe_{0.95}Co_{0.05})_{81}B_6]_{0.996}Ga_{0.004}$ | Die upset (MQ-3) | 1100 | 3748 | 8246 | 1.472 | 0.885 |

of the hysteresis. In soft materials $k$ is approximately equal to the coercivity $H_{ci}$; in hard materials it is equal to a modified form of the coercivity:[8]

$$k=\frac{M_{an}(H_c)}{1-c}\times\left\{\alpha+\frac{1}{\chi'_{max}-\left(\frac{c}{1-c}\right)\times\frac{dM_{an}(H_c)}{dH}}\right\}. \quad (2)$$

$M_{an}$ is the anhysteretic magnetization as defined in Eq. (1); the units of $k$ are A/m or Oe. An explicit expression for $k$ has not been derived for the case where the coercivity is controlled by the nucleation of reversed domains; however, in general it is to be expected that $k$ should increase when the density of domain reversal sites decreases.

$\alpha$ is a dimensionless quantity that describes the mean interaction field experienced by the effective domains, in a manner completely analogous to the Weiss molecular field: $H_{ex}=\alpha M$, where $M$ is the magnetization.

The dimensionless model parameter $c$ gives a measure of the relative magnitude of the reversible magnetization contribution to the total magnetization, and is defined by the expression $\chi'_{in}=c\chi'_{an}$.

## III. RESULTS

The hysteresis loops that provided the experimental inputs to the model algorithm were obtained from three related, melt-quenched and thermomechanically processed magnets obtained from General Motors R. & D. Center. The bulk compositions of the magnets are given in Table I, along with some processing details. The samples were measured at $T=350$ K using a Quantum Design MPMS SQUID magnetometer with the furnace insert. The sample measurement configuration and subsequent data analysis is described in detail in Ref. 9.

Iterations of the parameter-determination algorithm produced the results presented in Table I. In general, the fits between the calculated and the experimental hysteresis loops were very good, being in error by less than 5% of the whole of the hysteresis curve. Figures 1(a)–(c) show the calculated hysteresis loops superimposed upon the measured loops. The calculated saturation magnetization values, $M_S$, agree well with the experimentally determined ones. The model parameters, $a$, $k$, and $\alpha$, show very interesting variations from sample to sample, especially as the sample HP1553 was die upset to become DU1418. The parameters $a$ and $\alpha$, representative of the density of "effective domains" and the operative interdomain coupling, respectively, decreased sharply with die upsetting. These quantities recovered somewhat in the sample DU2162, doped with cobalt and gallium. The value of the $k$ parameter, illustrating the average pinning

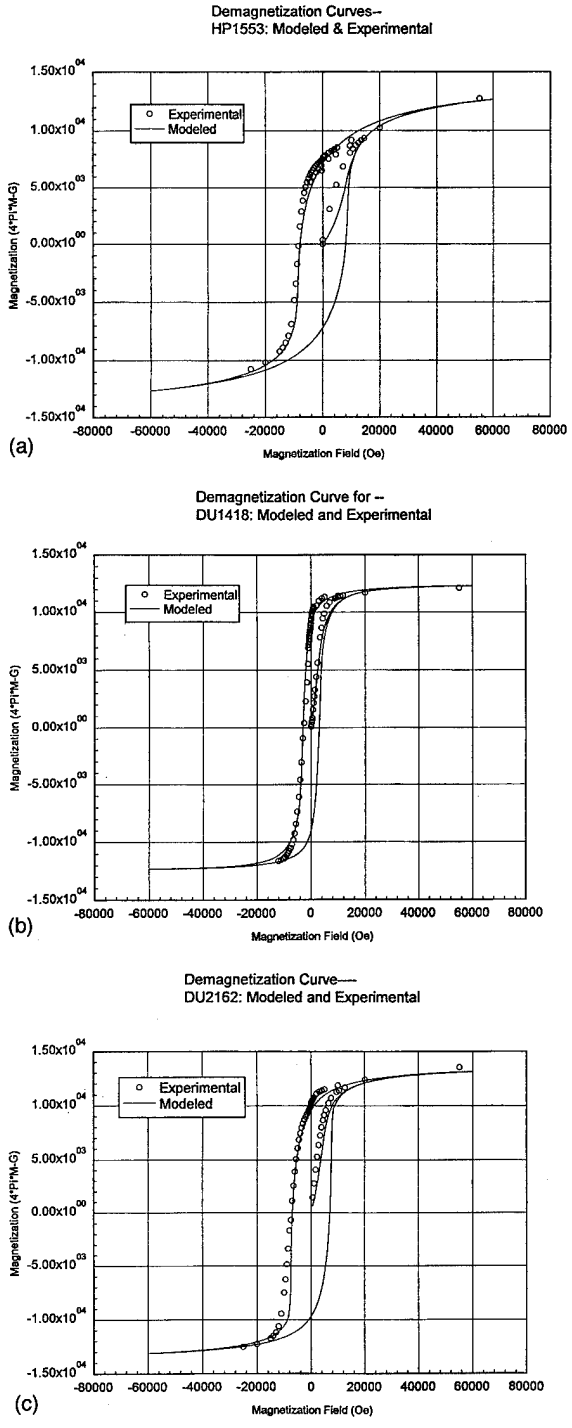



FIG. 1. (a) Hysteresis loops for sample HP1553 ($Nd_{13.75}Fe_{80.25}B_6$), modeled and experimental. (b) Hysteresis loops for sample DU1418 ($Nd_{13.75}Fe_{80.25}B_6$), modeled and experimental. (c) Hysteresis loops for sample DU2162 ($[Nd_{13}(Fe_{0.95}Co_{0.05})_{81}B_6]_{0.996}Ga_{0.004}$), modeled and experimental.

strength of the inhomogeneities in the materials, is roughly the same in HP1553 and DU2162, but is approximately half that value in DU1418.

## IV. DISCUSSION

In order to lend physical insight to the calculated model parameters, a review of recent microstructural and magnetic characterization of the samples is necessary. The process of die upsetting a hot-pressed sample introduces drastic changes within the microstructure. A melt-quenched and hot-pressed sample typically consists of a dense collection of mostly equiaxed grains with dimensions on the order of 100 nm. Preliminary transmission electron microscopy (TEM) investigations performed at Brookhaven National Laboratory indicate that the grain size dispersion of HP1553 is small. Some researchers have found an additional phase in the microstructure, identified by electron diffraction as $Nd_5Fe_2B_5$.[10] An intergranular phase has also been identified at the grain boundaries[11] of hot-pressed samples and is reported to have a composition close to the eutectic composition in the Nd–Fe binary system, $Nd_{70}Fe_{30}$.

With die upsetting, the grains not only increase in size, but they become highly anisotropic. The die-upset structure consists of platelet-shaped grains of the 2–14–1 phase stacked along the press direction, the 2–14–1 tetragonal $c$ axis. A thin intergranular phase has also been identified in these magnets, but the nature and composition of this phase is in dispute. Mishra *et al.*[11,12] report that the intergranular phase is crystalline (fcc), seems to uniformly coat all grains, and has a composition close to $Nd_{70}Fe_{30}$. Recent results, obtained with high resolution TEM methods[9,13] using a nominal 5 Å probe size, have demonstrated the existence of an amorphous grain boundary phase present in DU1418 and a related sample, die-upset PrFeB. Based on a sampling of 30 grain boundaries, the phase clearly shows an enrichment of iron in the grain boundary region relative to the grain itself; it does not evenly wet all surfaces of the deformed 2–14–1 main phase particles, but is found mainly on those boundaries parallel to the $c$ axis.

Magnetic studies performed on DU1418 at elevated temperatures[9] show a linear development of both remanence and coercivity with applied field after thermal demagnetization, consistent with the phenomena of nucleation of reverse domains. The coercivity and remanence in HP1553 and DU2162 also show this same linear dependence. It has been postulated that the iron-rich grain boundary phase may act as a reverse grain nucleation site of lowered anisotropy, as well as providing a means to exchange couple the constituent grains.[9]

The above results lend interpretation to the calculated model parameters. The decrease in the $a$ parameter from the relatively high value of 13920 Oe in HP1553 to the low value of 1247 Oe in DU1418 represents a decrease in the density of effective domains, as described in Sec. II. This decrease is consistent with a change in the microstructure that promotes exchange coupling among the grains in the die-upset sample, as would be expected if a significant portion of intergranular phase changed in composition from rare-earth rich to iron rich. The increase of the $a$ parameter in DU2162, the sample doped with both cobalt and gallium, relative to that of DU1418, is consistent with a certain amount of exchange decoupling between the grains that serves to produce a greater density of "effective domains." Many researchers[14–17] believe that the addition of gallium to 2–14–1-based magnets segregates to the grain boundary phase; such a segregation would be expected to decrease the intergranular coupling by diluting the magnetic properties of the intergranular phase. Consistent with the above discussion, the variation of calculated $k$ parameters can be ascribed to the difficulty in the nucleation of reversed grains. This difficulty may be traced to a dearth of Fe-rich, low-anisotropy rich regions in the microstructures of HP1553 and DU2162 of the proper dimensions to allow nucleation of reverse domains upon the application of a magnetizing field to a thermally demagnetized sample.

The calculated $\alpha$ parameters indicate that the coupling between the "effective domains" in HP1553 is somewhat stronger than that found in DU2162, and is much stronger than that found in DU1418. Such a result may be attributed to differences in the chemistry, thickness and occurrence of the iron poor intergranular and triple-point junction phases found in each material; the iron-rich intergranular phases presumably exist within the volume of the "effective domain" and do not contribute to $\alpha$. Work is presently underway to thoroughly characterize the grain boundary phases in these materials using advanced TEM methods.

## ACKNOWLEDGMENTS

We are grateful to C. D. Fuerst of General Motors R. & D. Center for providing us with samples and for helpful discussions. This research was sponsored by U.S. DOE, Laboratory Directed Research and Development Program, Contract No. DE-AC02-76CH00016.

[1] F. Preisach, Z. Phys. **94**, 277 (1935).
[2] E. C. Stoner and E. P. Wohlfarth, Philos. Trans. R. Soc. London, Ser. A **240**, 599 (1948).
[3] D. C. Jiles and D. L. Atherton, J. Magn. Magn. Mater. **61**, 48 (1986).
[4] D. C. Jiles, J. B. Thoelke, and M. K. Devine, IEEE Trans. Magn. **28**, 27 (1992).
[5] D. C. Jiles, J. Appl. Phys. **76**, 5849 (1994).
[6] D. C. Jiles and M. K. Devine, J. Magn. Magn. Mater. **140**, 1881 (1995).
[7] S. Chikazumi, *Physics of Magnetism* (Krieger, Malabar, FL, 1964).
[8] D. C. Jiles and J. B. Thoelke, IEEE Trans. Magn. **25**, 3928 (1989).
[9] L. Henderson Lewis, Y. Zhu, and D. O. Welch, J. Appl. Phys. **76**, 6235 (1994).
[10] T.-Y. Chu, L. Rabenberg, and R. K. Mishra, J. Appl. Phys. **69**, 6046 (1991).
[11] R. K. Mishra, J. Appl. Phys. **62**, 967 (1987).
[12] R. K. Mishra, T.-Y. Chu, and L. K. Rabenberg, J. Magn. Magn. Mater. **84**, 88 (1990).
[13] Y. Zhu, J. Tafto, L. H. Lewis, and D. O. Welch, Philos. Mag. Lett. **71**, 297 (1995).
[14] V. Panchanathan and J. J. Croat, IEEE Trans. Magn. **25**, 4111 (1989).
[15] M. Tokunaga, Y. Nozawa, K. Iwasaki, M. Endoh, S. Tanigawa, and H. Harada, IEEE Trans. Magn. **25**, 3561 (1989).
[16] C. D. Fuerst and E. G. Brewer, J. Appl. Phys. **73**, 5751 (1993).
[17] I. Ahmad, H. A. Davies, and R. A. Buckley, Mater. Lett. **20**, 139 (1994).

# Superconducting hysteresis and the Preisach model

I. D. Mayergoyz
*Electrical Engineering Department, University of Maryland, College Park, Maryland 20742*

The critical state (Bean) model for superconducting hysteresis is discussed for arbitrary specimen shapes and complex flux distributions. It is demonstrated that this model exhibits the "wiping out" property and "congruency" property of minor hysteresis loops. This leads to the conclusion that the critical state model is a particular case of the Preisach model. For this reason, it is suggested to use the Preisach model for the description of superconducting hysteresis in very general situations.
© *1996 American Institute of Physics.* [S0021-8979(96)41508-2]

High-field (hard) type-II superconductors exhibit magnetic hysteresis. This hysteresis occurs because the motion of flux filaments is pinned by various deffects. The critical state model has been proposed[1–3] to treat the magnetic hysteresis of hard superconductors. This model is based on the assumption of ideal (sharp) resistive transition which is described by a rectangular (step wise) **E** vs **J** relation. This implies that persistent currents up to a critical current density $j_c$ are always induced in superconductors. The critical state model has been further generalized[4] to take into account a dependence of critical current density on magnetic field.

It has been shown[5,6] that the critical state model for superconducting hysteresis is a very particular case of the classical Preisach model which has been traditionally used for the description of hysteresis in magnetic materials. This result has been established for one-dimensional flux distributions and specimens of simple shapes (plane slabs, circular cross-section cylinders). For these cases, explicit analytical expressions for magnetic field distributions within the superconductors are readily available, and they have been instrumental in the discussion presented in the aforementioned references.

The purpose of this article is to demonstrate that the critical state model is a particular case of the Preisach model for specimens of arbitrary shapes and complex flux distributions. For these specimens, analytical machinery for the calculation of magnetic fields within the superconductors does not exist. Nevertheless, it is shown below that the superconducting hysteresis (as described by the critical state model) still exhibits the "wiping out" property and the "congruency" property of minor hysteresis loops. These properties constitute the necessary and sufficient conditions for the applicability of the classical Preisach model.[6,7] This leads to the conclusion that the critical state model is indeed a particular case of the Preisach model. This fact suggests that the "first-order transition curves," which are used for the identification of the Preisach model, may emerge as standard experimental data for the identification of superconducting hysteresis and evaluation of hysteretic losses in superconductors.

To start the discussion, consider a superconducting cylinder of arbitrary cross section subject to the uniform external field $\mathbf{B}_e(t)$ whose direction does not change with time and lies in the plane of superconductor cross section (Fig. 1). We will choose this direction as the direction of axis $x$. As the time varying flux enters the superconductor, it induces screening (shielding) currents of density $\pm j_c$. The distribution of these superconducting screening currents is such that they create the magnetic field which at any instant of time completely compensates for the change in the external field $\mathbf{B}_e(t)$. Mathematically it can be expressed as follows:

$$\delta B_e(t)+B_i(t)=0. \tag{1}$$

Here $\delta B_e(t)$ is the change in $B_e(t)$, while $B_i(t)$ is the field created by superconducting screening currents, and equality (1) holds in the region interior to these currents.

It is clear that $\delta B_e(t)\geqslant 0$ when $B_e(t)$ is monotonically increased, and $\delta B_e(t)\leqslant 0$ when $B_e(t)$ is monotonically decreased. By using this fact and (1), it can be concluded that there is a reversal in the direction (polarity) of superconducting screening currents as $B_e(t)$ goes through its maximum or minimum values.

With these facts in mind, consider how the distribution of superconducting currents is generically modified in time by temporal variations of the external magnetic field. Suppose that, starting from zero value, the external field is monotonically increased until it reaches its maximum value $M_1$ at some time $t=t_1^+$. This monotonic variation of $B_e(t)$ induces a surface layer of superconducting screening currents. The interior boundary of this current layer extends inwards as $B_e(t)$ is increased [see Fig. 2(a)], and at any instant of time this boundary is uniquely determined by the instantaneous values of $B_e(t)$. Next, we suppose that the above monotonic increase is followed by a monotonic decrease until $B_e(t)$ reaches its minimum value $m_1$ at some time $t=t_1^-$. For the time being it is assumed that $|m_1|<M_1$.

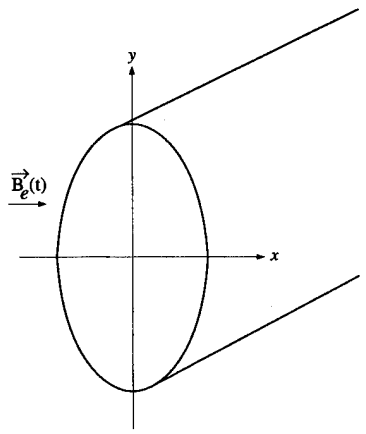



FIG. 1. A superconductor subject to the external magnetic field.

 0021-8979/96/79(8)/6473/3/$10.00 © 1996 American Institute of Physics 

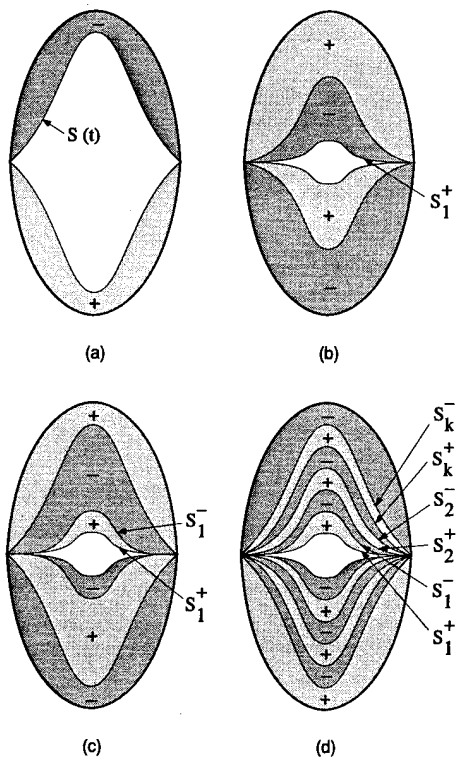



FIG. 2. Superconducting current distributions.

As soon as the maximum value $M_1$ is achieved, the inward progress of the previous current layer is terminated and a new surface current layer of reversed polarity (direction) is induced [see Fig. 2(b)]. This new current layer creates field $B_i(t)$ which compensates for monotonic decrease in $B_e(t)$ in the region interior to this current layer. For this reason, it is clear that the interior boundary of the new current layer extends inward as $B_e(t)$ is monotonically decreased. It is also clear that this boundary is uniquely determined by the instantaneous value of $\delta B_e(t)$, and, consequently, by the instantaneous value of $B_e(t)$ for any specific (given) value of $M_1$. Now, suppose that the above monotonic decrease is followed by a monotonic increase until $B_e(t)$ reaches its new maximum value $M_2$ at some time $t=t_2^+$. For the time being, it is assumed that $M_2<|m_1|$. As soon as the minimum value $m_1$ is achieved, the inward progress of the second current layer is terminated and a new (third) surface layer of superconducting screening currents of reversed polarity is introduced to counteract the monotonic increase of the external field [see Fig. 2(c)]. This current layer progresses inward until the maximum value $M_2$ is achieved; at this point the inward progress of the current layer is terminated. As before, the instantaneous position of the interior boundary of this layer is uniquely determined by the instantaneous value of $\delta B_e(t)$, and, consequently, by the instantaneous value of $B_e(t)$ for a specific (given) value of $m_1$.

By generalizing the previous line of reasoning, the essence of the critical state model can be summarized as follows. Each reversal in the external magnetic field results in the formation of a surface layer of superconducting screening currents. This layer extends inward with time until another reversal value of the external field is reached. At this point, the inward progress of the previous superconducting current layer is terminated and a new inward extending current layer is formed. The previously induced layers of persisting superconducting currents stay still and they represent past history of the temporal variations of the external field. This past history leaves its mark upon future distributions of superconducting currents.

Thus, it can be concluded that at any instant of time there exist several (many) layers of persisting superconducting currents [see Fig. 2(d)]. These persisting currents have opposite polarities (directions) in adjacent layers. The interior boundaries $S_k^+$ and $S_k^-$ of all the layers (except the last one) remain still and they are uniquely determined by the past extremum values $M_k$ and $m_k$ of $B_e(t)$, respectively. The last induced current layer extends inward as the external field changes in time monotonically.

The magnetic moment $\mathbf{M}$ of the superconductor is related to the distribution of the superconducting screening currents as follows:

$$\mathbf{M}(t)=\int\int_S [\mathbf{r}\times\mathbf{j}(t)]ds, \tag{2}$$

where the integration is performed over the superconductor cross section.

In general, this magnetic moment has $x$ and $y$ components. According to (2), these components are given by the expressions:

$$M_x(t)=\int\int_S yj(t)ds, \tag{3}$$

$$M_y(t)=-\int\int_S xj(t)ds. \tag{4}$$

It is clear that if the superconductor cross section is symmetric with respect to $x$ axis, then only the $x$ component of the magnetic moment is present. In the absence of the above symmetry, two components of the magnetic moments exist.

It is apparent from the previous discussion that the instantaneous values of $M_x(t)$ and $M_y(t)$ depend not only on the current instantaneous value of the external field $B_e(t)$ but on the past extremum values of $B_e(t)$ as well. This is because the overall distribution of persisting superconducting currents, $j$, depends on the past extrema of $B_e(t)$. Thus, it can be concluded that relationships $M_x(t)$ vs $B_e(t)$ and $M_y(t)$ vs $B_e(t)$ exhibit *discrete* memories which are characteristic and intrinsic for rate independent hysteresis. It is worthwhile to note that it is the hysteretic relationship $M_x(t)$ vs $B_e(t)$ that is typically measured in experiments by using, for instance, a vibrating sample magnetometer (VSM) with a one pair of pickup coils. By using a VSM equipped with two pairs of orthogonal pickup coils, the hysteretic relation between $M_y(t)$ and $B_e(t)$ can be measured as well.

It is important to stress here that the property of rate independence of superconducting hysteresis can be traced back to the assumption of ideal (sharp) resistive transitions. This connection is especially clear for superconducting specimens of simple shapes (plane slabs or circular cross-section cylinders subject to coaxil and uniform external mag-

netic fields). For such specimens, the explicit and single-valued relations between the increments of the external field and the location of inward boundaries of superconducting layers can be found by resorting only to the Ampere's Law.[1–3] It is also worthwhile pointing here that in the case of gradual resistive transitions, customary described by the "power" law, the property of rate independence of superconducting hysteresis does not hold anymore.[8–10] For this reason, it can be conjectured that the gradual resistive transitions may be at least in part responsible for the rate dependence of hysteresis that has been observed for high-$T_c$ superconductors and that is usually and exclusively attributed to creep.

Now, we return to the above description of the critical state model. It is clear from this description that a newly induced and inward extending layer of superconducting currents will wipe out (replace) some layers of persisting superconducting currents if they correspond to the previous extremum values of $B_e(t)$ which are exceeded by a new extremum value. In this way, the effect of those previous extremum values of $B_e(t)$ on the overall future current distributions will be completely eliminated. According to (3) and (4), the effect of those past extremum values of the external magnetic field on the magnetic moment will be eliminated as well. This is the "wiping out" property of the superconducting hysteresis as described by the critical state model.

Next, we proceed with the discussion of the "congruency" property. Consider two distinct variations of the external field, $B_e^{(1)}(t)$ and $B_e^{(2)}(t)$. Suppose that these two external fields have different past histories and, consequently, different sequences of local past extrema, $\{M_k^{(1)}, m_k^{(1)}\}$ and $\{M_k^{(2)}, m_k^{(2)}\}$. However, starting from some instant of time they vary back-and-forth between the same reversal values. It is apparent from the description of the critical state model and expressions (3) and (4) that these two identical back-and-forth variations of the external field will result in the formation of two minor loops for hysteretic relation $M_x(t)$ vs $B_e(t)$ [or $M_y(t)$ vs $B_e(t)$]. It is also apparent from the same description of the critical state model that these two back-and-forth variations of the external field will affect in the *identical* way the *same* surface layers of a superconductor. Unaffected layers of the persistent superconducting currents will be different for $B_e^{(1)}(t)$ and $B_e^{(2)}(t)$ because of their different past histories. However, according to (3) and (4), these unaffected layers of persistent currents result in constant in time ("background") components of the magnetic moment. Consequently, it can be concluded that the same *incremental* variations of $B_e^{(1)}(t)$ and $B_e^{(2)}(t)$ will result in equal *increments* of $M_x$ (and $M_y$). This is tantamount to the congruency of the corresponding minor loops. Thus, the congruency property is established for the superconducting hysteresis as described by the critical state model.

The experimental testing of the "congruency" and "wiping out" properties has been recently undertaken[11] and it has been found that these properties are in good compliance with experimental data for tested superconductors.

It has been established[6,7] that the "wiping out" property and the "congruency" property constitute the necessary and sufficient conditions for the representation of actual hysteresis nonlinearities by the Preisach model. Thus, the description of the superconducting hysteresis by the critical state model is equivalent to the description of the same hysteresis by the Preisach model. The question can be immediately asked, "What is to be gained from the above result?" The answer to this question can be stated as follows. There is no readily available analytical machinery for the calculation of the interior boundaries of superconducting current layers for specimens of arbitrary shapes. For this reason, the critical state model does not lead to the mathematically explicit results. The application of the Preisach model allows one to circumvent these difficulties by using some experimental data. Namely, for any superconducting specimen, the "first-order transition" curves can be measured and used for the identification of the Preisach model[6] for the given specimen. By using these curves, complete prediction of hysteretic behavior of the specimen can be given at least at the same level of accuracy and physical legitimacy as in the case of the critical state model. In particular, cyclic and "ramp" losses can be explicitly expressed in terms of the first-order transition curves.[6]

The above result can be also useful whenever numerical implementation of the Bean model is attempted. Indeed, the numerical realization of the Bean model can be appreciably simplified by computing only the "first-order transition" curves and then by using these curves for the prediction of hysteretic behavior for arbitrary piece-wise monotonic variations of the external field.

In conclusion, I wish to thank Professor G. Friedman from UIC for many helpful discussions. This research is supported by the U.S. Department of Energy, Engineering Research Program.

[1] C. P. Bean, Phys. Rev. Lett. **8**, 250 (1962).
[2] C. P. Bean, Rev. Mod. Phys. **36**, 31 (1964).
[3] H. London, Phys. Lett. **6**, 162 (1963).
[4] Y. B. Kim, C. F. Hempstead, and A. R. Strnad, Phys. Rev. Lett. **9**, 306 (1962).
[5] I. D. Mayergoyz and T. A. Keim, J. Appl. Phys. **67**, 5466 (1990).
[6] I. D. Mayergoyz, *Mathematical Model of Hysteresis* (Springer, New York, 1991).
[7] I. D. Mayergoyz, Phys. Rev. Lett. **56**, 1518 (1986).
[8] I. D. Mayergoyz, J. Appl. Phys. **75**, 6963 (1994).
[9] I. D. Mayergoyz, J. Appl. Phys. **76**, 7130 (1995).
[10] I. D. Mayergoyz, J. Appl. Phys. **76**, 6956 (1995).
[11] G. Friedman, L. Liu, and J. S. Kouvel, J. Appl. Phys. **75**, 5683 (1994).

# A model for magnetomechanical hysteresis and losses in magnetostrictive materials

A. Bergqvist
*Electric Power Engineering, Royal Institute of Technology, S-10044 Stockholm, Sweden*

G. Engdahl
*Power Engineering, ABB Corporate Research, S-72178 Västerås, Sweden*

A phenomenological hysteresis model for the magnetomechanical constitutive law in highly magnetostrictive materials is proposed. Magnetization and strain are represented using a set of noninteracting particles. Any change in magnetization or strain in individual particles is assumed to be obstructed by a counterforce analogous to mechanical dry friction. Comparisons have been made with experiments performed on Terfenol-D under varying field and/or stress with satisfactory results. © *1996 American Institute of Physics.* [S0021-8979(96)41608-9]

## I. INTRODUCTION

Computer simulations play an increasingly important role in device design. In applications involving highly magnetostrictive materials such as Terfenol-D, it is necessary to have constitutive models relating bulk magnetization $M$ and strain $S$ to magnetic field $H$ and mechanical stress $T$. Such materials exhibit nonlinearity, which is significant except for processes in the small-signal domain, and hysteresis which can contribute considerably to the losses in a device.

In this context, it is more important that a model agrees well with experiments and is computationally simple and efficient rather than giving a detailed description of the microscopic processes involved. Also, in a real device, the waveforms of field and stress in the active material are usually not known *a priori* so a model must allow for both field and stress to be arbitrary functions of time. A model which merely gives for instance the behavior under a fixed mechanical stress is here useless. In this work, we present a phenomenological uniaxial magnetomechanical hysteresis model, using the same approach as in a recent model for magnetic vector hysteresis.[1]

## II. THE MODEL

In the Jiles–Atherton theory,[2] it is reasoned that ferromagnetic hysteresis is due to a friction-like force opposing any changes in magnetization. This notion is adopted here; however the friction is in this work assumed to act analogously to mechanical dry friction, a.k.a. Coulomb friction. We will briefly present the basic properties of Coulomb friction, which is discussed in more detail in standard works on mechanics.[3]

One intuitive formulation of Coulomb friction that emphasizes the parallels with magnetism is as follows: Suppose we have an object on a surface, subjected to gravity, normal force, and a controllable force $P$. Its potential energy $V$ is proportional to its height above the ground and is indirectly a function of the horizontal coordinate $x$. It is straightforward to show that the horizontal component of the sum of gravitational force and normal force is $-\partial V/\partial x$. Without friction, there would be a single-valued relation between applied force $P$ and position $x$ given by the condition that the total force $P-\partial V/\partial x$ is zero. However, if there is Coulomb friction, the object will not move unless $|P-\partial V/\partial x|$ reaches some threshold value, here called $P_F$. In that case, the $P-x$ relation will be a hysteresis curve with a width $2P_F$. Figure 1 shows a typical example. The relation can be formulated more precisely as follows: As long as $|P-\partial V(x)/\partial x|\leqslant P_F$ there is a metastable state. If the force changes to a new value $P'$ such that $|P'-\partial V(x)/\partial x|>P_F$, then the position will change to a new value $x'$ such that $|P'-\partial V(x')/\partial x|=P_F$.

If the force and position are vectors in two or more dimensions, there are a couple of complicating factors. One is that the friction may be anisotropic, so that the threshold value $P_F$ is a function, not necessarily simple, of the direction of the force $(\mathbf{P}-\nabla V)$. We may say that there is no change in position $\mathbf{x}$ as long as $(\mathbf{P}-\nabla V)$ belongs to some metastability region which in the isotropic case is a circle. Another aspect is that when the force does reach the threshold value, it is not apparent in what direction the movement is in, although in the isotropic case, it should be parallel to $(\mathbf{P}-\nabla V)$.

Let us now see how we can adopt Coulomb friction for the description of magnetomechanical hysteresis. Suppose we have a pseudoparticle with magnetization $m$, strain $s$, and a free energy $f$ that depends only on $m$ and $s$. There is a clear analogy between such a particle and a mechanical system with an object on a surface, in that the mechanical system is governed by minimization of $V(\mathbf{x})-\mathbf{P}\cdot\mathbf{x}$, while, due to the principle of entropy maximization, for the particle it is the potential $g=f(m,s)-Hm-Ts$ that strives towards a minimum.[4] We now assume that the relation between $(H,T)$

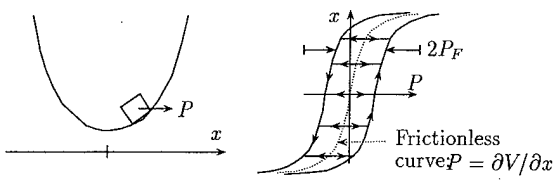



FIG. 1. An object on a surface subjected to an applied force $P$ and Coulomb friction. The figure to the right shows the resulting relation between $P$ and position $x$.

 0021-8979/96/79(8)/6476/3/$10.00 © 1996 American Institute of Physics

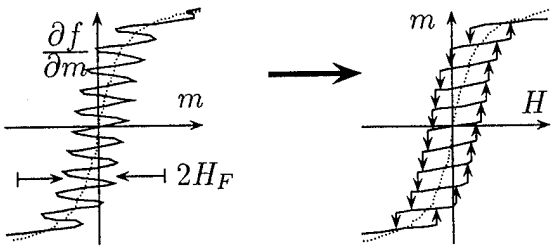



FIG. 2. Relation between $H$ and $m$ when the free energy $f(m)$ contains a small ripple. Dotted curves show behavior without ripple.

and $(m,s)$ is analogous to the relation between **P** and **x** in the presence of Coulomb friction. In other words, for a given $(m,s)$, there exists a region such that as long as $(H,T)$ stay within the region, there is no change in $(m,s)$.

Formally, such behavior can be reproduced by stating that $f$ is the sum of a convex function $f_{an}(m,s)$, corresponding to anhysteretic behavior, and a small ripple $f_F(m,s)$, and then apply the principle of minimization of $g$. The ripple introduces a large number of densely distributed local minima for $g$. As an example we may consider a purely magnetic case with $f_F=-(H_F/N)\cos(Nm)$, where $N$ is large. The relation between $H$ and $m$ can then be derived[4] and is illustrated in Fig. 2. As $N\to\infty$, the magnetization curve asymptotically becomes equivalent to the $P-x$ relation of Fig. 1. Therefore, if $f$ contains a ripple component, Coulomb friction-type behavior emerges naturally. The aforementioned aspects of anisotropic friction can likewise be represented and are then related to the shapes and locations of the small potential wells of $f_F$ in some complicated manner.

We proceed to define the two auxiliary quantities $\tilde{H}=\partial f_{an}/\partial m$, $\tilde{T}=\partial f_{an}/\partial s$. Since without friction we would have $H=\partial f_{an}/\partial m$, $T=\partial f_{an}/\partial s$, it is natural to write

$$(m,s)=[M_{an}(\tilde{H},\tilde{T}),S_{an}(\tilde{H},\tilde{T})], \tag{1}$$

and label $(M_{an}, S_{an})$, which are the inverse of $(\partial f_{an}/\partial m,\partial f_{an}/\partial s)$, the anhysteretic curves.

The shape of the metastability region could conceivably be estimated from experiments. For simplicity however, we here assume it to be elliptical. This can be expressed through the inequality

$$H_F^{-2}(H-\tilde{H})+T_F^{-2}(T-\tilde{T})^2\leqslant 1. \tag{2}$$

$H_F$ and $T_F$ are adjustable parameters corresponding to the half width of purely magnetic hysteresis loops and purely mechanical hysteresis loops, respectively.

Concerning the direction in which changes occur, we again simplify and assume that a change in $(\tilde{H},\tilde{T})$ is parallel to $(H-\tilde{H},T-\tilde{T})$. In other words,

$$(\Delta\tilde{H},\Delta\tilde{T})=\Delta\xi(H-\tilde{H},T-\tilde{T}), \tag{3}$$

where $\Delta\xi$ is adjusted so that after a change in $(\tilde{H},\tilde{T})$, the left-hand side of (2) is exactly 1. It is a straightforward algebraic exercise to show that

$$\Delta\xi=1-[H_F^{-2}(H-\tilde{H})^2+T_F^{-2}(T-\tilde{T})^2]^{-1/2}. \tag{4}$$

An incremental algorithm for determining $(m,s)$ for any variation of $(H,T)$ can now be formulated as follows: Suppose that at some moment we have known values $(H,T)$ and $(\tilde{H},\tilde{T})$ and that $(H,T)$ are then changed by a small amount. With the new $(H,T)$ values and the old $(\tilde{H},\tilde{T})$ values, we check if (2) is fulfilled. If it is, there is no change in $(\tilde{H},\tilde{T})$; otherwise $(\tilde{H},\tilde{T})$ are updated using (4) and (3). Thereafter, $(m,s)$ are found from (1).

We can also determine the energy loss $q$ for arbitrary processes. The change in loss is the difference between changes in work and stored energy, $\Delta q=H\Delta m+T\Delta s-\Delta f$. Noting that $f_F$ is always very small and using Taylor expansions and the definitions of $\tilde{H}$ and $\tilde{T}$, gives $\Delta f\approx\Delta f_{an}\approx\tilde{H}\Delta m+\tilde{T}\Delta s$. Dividing by $\Delta t$ and taking the limit, we find

$$\dot{q}=(H-\tilde{H})\dot{m}+(T-\tilde{T})\dot{s}. \tag{5}$$

It is easy to realize that for any cyclic process, the net loss is the sum of the areas of the closed magnetic and mechanical hysteresis loops $\oint(H\,dm+T\,ds)$. It is also straightforward to show that $\dot{q}\geqslant 0$ at all times. This can be derived from the fact that $f_{an}$ is convex and that $(\tilde{H},\tilde{T})\propto(H-\tilde{H},T-\tilde{T})$. The details are excluded.

The type of pseudoparticle described exhibits basic qualitative properties of magnetomechanical hysteresis. However, the minor loop behavior, which as seen in Fig. 1 consists merely of horizontal lines connecting major loop branches, is too simple to be satisfactory. To get a better agreement, with real behavior, we consider an assembly of such particles, differing only by the magnitude of the friction. Thus they have the same nonhysteretic properties, the same ratio between magnetic and mechanical friction, etc. To express this, we associate each particle with a dimensionless positive scalar $\alpha$. For a given particle, $H_F$ and $T_F$ are multiplied by $\alpha$ in Eqs. (2) and (4). The net magnetization and strain are written

$$M=\int_0^\infty M_{an}[\tilde{H}(\alpha),\tilde{T}(\alpha)]\zeta(\alpha)d\alpha, \tag{6}$$

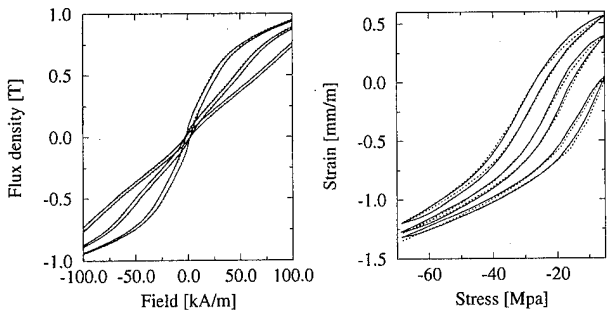



FIG. 3. Flux density vs magnetic field for constant values of $T$ and strain vs stress for constant values of $H$. Solid lines=calculations, dotted lines =experiments.

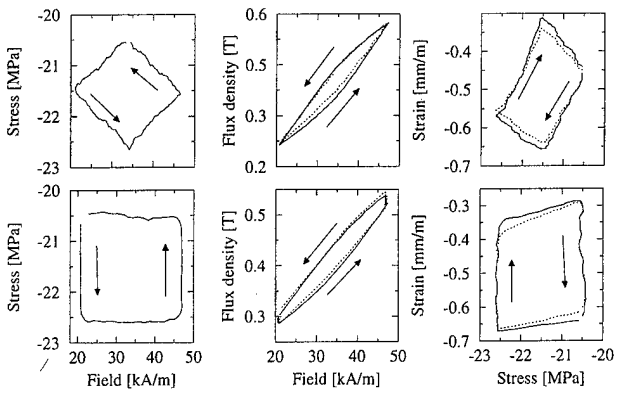



FIG. 4. Magnetic and mechanical work for two processes. Upper row, process A; lower row, process B. Diagrams to the left show controlled stress-field trajectories. Solid lines=calculations, dotted lines=experiments.

$$S=\int_0^\infty S_{\mathrm{an}}[\tilde{H}(\alpha),\tilde{T}(\alpha)]\zeta(\alpha)d\alpha. \tag{7}$$

Here $\tilde{H}(\alpha)$ and $\tilde{T}(\alpha)$ are the values of $\tilde{H}$ and $\tilde{T}$ for a particle with frictional multiplier $\alpha$ and $\zeta(\alpha)$ is a weight distribution giving the volume fraction for the corresponding particle. It satisfies the normalization condition $\int_0^\infty \zeta(\alpha)d\alpha=1$. In a numerical implementation, we must use a finite number of particles and approximate (6) and (7) by sums.

It is straightforward to show that if either field or stress is kept constant, the model behaves like the classical Preisach model[5] (CPM) with a particular configuration of parameters. However, the present work should not be viewed as a mere reformulation of the CPM since the CPM is only defined for a single scalar independent variable and the proper generalization to the case of several variables is far from clear.

## III. DETERMINATION OF PARAMETERS

To use the model, we need a method for determining material parameters from experiments. The parameters involved are the anhysteretic functions $M_{\mathrm{an}}(H,T)$ and $S_{\mathrm{an}}(H,T)$, the distribution $\zeta(\alpha)$, and the friction constants $H_F$ and $T_F$. We will in this work not actually model the anhysteretic curves, but estimate them entirely from experiments in the following manner: If we define $M^+(H,T)$ and $M^-(H,T)$ as the values of $M$ along the upper and lower branches of a saturation loop with respect to $H$ under constant $T$, an approximation that appears to be quite accurate is

$$M_{\mathrm{an}}(H,T)\approx 1/2[M^+(H-H_c,T)+M^-(H+H_c,T)].$$

$S_{\mathrm{an}}(H,T)$ can be similarly estimated.

$\zeta(\alpha)$ is for convenience assumed to be the sum of a Gaussian and a Dirac delta function

$$\zeta(\alpha)=A\ \exp[-(\alpha-1)^2]+\lambda\,\delta(\alpha). \tag{8}$$

Here $A$ is given by normalization and $\lambda$ is an adjustable parameter. The second term in this expression gives a fully reversible contribution since $\alpha=0$ corresponds to the frictionless case. In a small minor loop, any changes are due to this component since particles with $\alpha>0$ then have minor loops that are only horizontal lines as seen in Fig. 1. We can therefore determine $\lambda$ as the ratio between the slope of a small minor loop for some arbitrary $(H,T)$ and the slope of the anhysteretic curve for the same $(H,T)$.

$H_F$ and $T_F$ finally can be found from for instance magnetic and mechanical losses. For a major $M,H$ loop under constant $T$, the loss contribution from a particle is clearly $4\alpha H_F M_s$ where $M_s$ is the saturation magnetization. The total loss of a major loop is therefore $[4H_F M_s\int_0^\infty \alpha\zeta(\alpha)d\alpha]$ which is proportional to $H_F$. In this manner, $H_F$ can be adjusted to fit a measured magnetic loss. Similarly, $T_F$ can be estimated from a measured mechanical loss $\oint T\,dS$ under constant $H$.

## IV. RESULTS AND CONCLUSION

Computations have been compared to experiments done on a sample of Terfenol-D. The experimental equipment has been described in Ref. 6. Parameter values were $\lambda=0.48$, $H_F=2.56$ kA/m, $T_F=1.6$ MPa. Figure 3 shows some results when either field or stress is kept constant. In Fig. 4 are shown two cases, labeled A and B, of simultaneously or alternatively changing field and stress. These are examples of how magnetic energy can be converted to mechanical energy. The supplied positive net magnetic work is $W_H=\oint H\,dB$ giving a negative net mechanical work $W_T=\oint T\,dS$. The net total work $W_H+W_T\geq 0$ is dissipated. The relative loss $(W_H+W_T)/W_H$ was measured to be 65% and 42% for cases A and B, respectively, while model calculations gave 57% and 45%. This shows that hysteresis losses are very significant for these processes and that they are quite well estimated by the model.

It is found that the model shows a fair accuracy for processes when field, stress, or both are changing in time and that this is achieved at a modest cost in terms of computational complexity and experimental characterization of a material.

## ACKNOWLEDGMENT

A.B. is supported by the Swedish Research Council for Engineering Sciences.

[1] A. J. Bergqvist, in Proc. of ISEM 1995, Cardiff, UK, paper D08.
[2] D. C. Jiles and D. L. Atherton, J. Magn. Magn. Mater. **61**, 48 (1986).
[3] J. L. Meriam, *Engineering Mechanics* (Wiley, New York, 1979).
[4] A. Bergqvist and G. Engdahl, IEEE Trans. Magn. **31**, 3539 (1995).
[5] I. D. Mayergoyz, *Mathematical Models of Hysteresis* (Springer, New York, 1991).
[6] L. Kvarnsjö and G. Engdahl, IEEE Trans. Mag. **27**, 5349 (1991).

# On the relaxation of simple magnetic systems

J. M. González, R. Ramírez, and R. Smirnov-Rueda
*Instituto de Ciencia de Materiales de Madrid, Serrano 144, 28006 Madrid, Spain*

J. González
*Facultad de Quimica–UPV/EHU, 20009 San Sebastian, Spain*

The relaxation at constant applied field and temperature of a simple magnetic system is evaluated in the framework of the micromagnetic approximation and using a Monte Carlo algorithm. Our results, and particularly, those corresponding to the time evolution of the probability of magnetic moment reversal, evidence remarkable differences with the classical Arrehnius–Néel predictions. These differences are linked to the fact that relaxation proceeds through the formation of structures involving a large number of degrees of freedom. © *1996 American Institute of Physics.* [S0021-8979(96)28608-4]

## I. INTRODUCTION

The phenomenology of thermally activated demagnetization is discussed by assuming that the magnetic system under consideration can be described in terms of a distribution of noninteracting, local two-level subsystems,[1,2] each one relaxing according to the Arrehnius–Néel kinetics.[3] This assumption is based on the occurrence of energy barriers, linked to the effective anisotropy and preventing the system from evolving from the remanence-type states to reversed ones. In the framework of this approach it could, in principle, be possible to correlate the so-called magnetic viscosity data, that is, the time evolution of the magnetization measured at constant applied field and temperature, with some characteristics of the distribution of energy barriers and eventually with the intrinsic and extrinsic properties originating those barriers.[4]

Nevertheless, the two-level subsystems approach is only acceptable if the process of temperature induced overcoming of the local barriers can be described in terms of a reduced number of degrees of freedom, that is, considering a mechanism of the coherent rotation type.[5] Since with a few exceptions, coherent rotation cannot quantitatively account for the magnetization reversal of real materials, the appropriateness of the approach should then be scrutinized in detail. Also, and importantly, recent experimental[6,7] and simulation[8,9] works have evidenced the occurrence in simple systems of significant departures from the predictions of the two-level Arrehnius–Néel relaxation kinetics.

The aim of the present work is to examine, in the framework of the micromagnetic approximation, a simple magnetic relaxation case: that corresponding to identical, noninteracting individual magnetic entities having many degrees of freedom.

## II. DESCRIPTION OF THE MODEL

An individual relaxing unit (a "particle," see inset in Fig. 1) consists of a chain of 100 parallel infinite planes. This size is, at least, one order of magnitude larger than the different correlation lengths associated with the considered values of the model parameters describing the intrinsic magnetic properties of our system and, therefore, our results are only weakly dependent on the "particle" size. For the sake of simplicity, intraplane and interplane exchange constants are considered infinite and finite, respectively, which makes up our model one-dimensional, although the magnetic moments representing each plane are allowed to orient in three dimensions.

The intrinsic magnetic properties of the "particle" are defined by the exchange-to-anisotropy ratio, $a=Ad^{-2}/K$ (where $A$, $d$, and $K$ are the exchange constant, the interplanar distance, and the anisotropy constant, respectively) and by the square of the magnetization-to-anisotropy ratio, $m=\mu_0 M_s^2/2K$ (where $M_s$ is the saturation magnetization). We considered values for these parameters ($a=5$, $m=0.15$, and $d=2.5\ 10^{-10}$ m) corresponding to highly anisotropic materials. The internal energy of the system included terms corresponding to the anisotropy energy (local, uniaxial), the Zeeman energy (local, unidirectional), the exchange energy (first neighbors) as well as the magnetic energy (many-body interaction although in one dimension it can be reduced to a local form). Explicitly, the total internal energy $E_T$ writes as

$$E_T \propto \frac{1}{2}\sum_{j=1}^{N} \sin^2(\arccos(u_{m_i}\cdot u_z)) + H_{\mathrm{app}}\sum_{j=1}^{N} u_{m_i}\cdot u_z - a\sum_{j=1}^{N-1}(u_{m_i}\cdot u_{m_{(i+1)}}) + m\sum_{j=1}^{N}(u_{m_i}\cdot u_y)^2.$$

Here $u_{mi}$, $u_y$, and $u_z$ are unit vectors along the directions of the moment at the $i$th position in the chain and along the $OY$ and the $OZ$ axes of our reference system, respectively (both

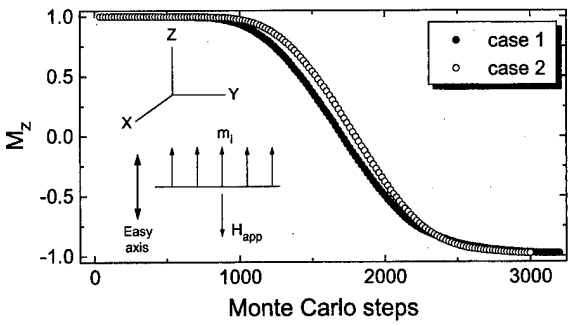



FIG. 1. Evolution with the number of MCS of the reduced total moment corresponding to the relaxation shown in Figs. 2(a) and 2(b).

 0021-8979/96/79(8)/6479/3/$10.00 © 1996 American Institute of Physics 

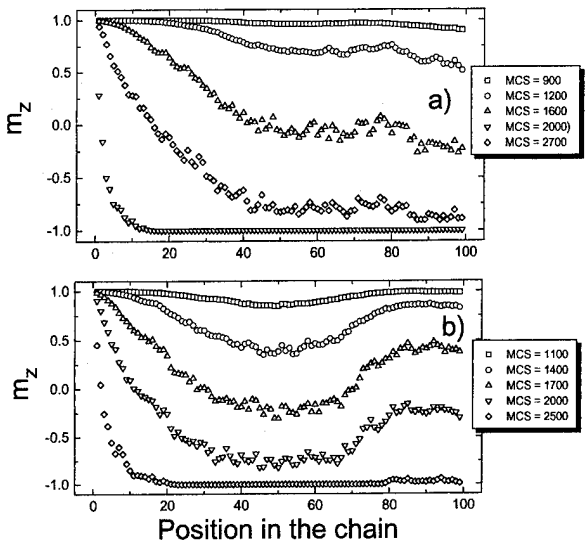



FIG. 2. Two examples of system configurations observed along the relaxation processes and corresponding to (a) case 1 and (b) case 2 (see text).

the easy axis and the demagnetizing field are applied along the $OZ$ axis). The coefficient $H_{app}=\mu_0 M_s H/2K$ gives the applied field, $H$, reduced to the anisotropy field. The evolution of this total internal energy is followed by a Monte Carlo algorithm with Metropolis dynamics[10] in a canonical ensemble at a temperature corresponding to $2\times10^{-4}$ of the maximum anisotropy energy attainable by the system. Regarding the use of this stochastic method, we should remark that we define a Monte Carlo step (MCS) as the process corresponding to the consecutive introduction of random modifications in all the degrees of freedom of the system (the bound for the modification of the two angles defining the direction of every moment in the system was arbitrarily chosen as $9\times10^{-3}$ rads). If the attempt frequency (that is the time rate at which a real system can modify its degrees of freedom) is known (through independent physical arguments) the number of MCS can be converted into time units. In all the cases, the relaxation proceeds from a saturation state in which the magnetization of the "particle" points along the easy axis and antiparallel to the applied field.

## III. RESULTS AND DISCUSSION

In Figs. 2(a) and 2(b) we present two different examples of the evolution with the number of MCS of the configuration of a "particle" during its relaxation at a constant reduced field $H_{app}=1.1$ (we have plotted the component along the easy axis direction of the magnetic moments forming the system as a function of their position in the chain). Relaxation proceeds through the formation of a nucleus of out-from-the-easy axis moments which can be originated either at one of the ends of the chain [case 1, Fig. 2(a)] or in any other position inside it [case 2, Fig. 2(b)]. The moments in those nuclei reverse rapidly their direction forming one (case 1) or two (case 2) structures similar to 180° domain walls which sweep the "particle" leading to the reversal of its total moment.

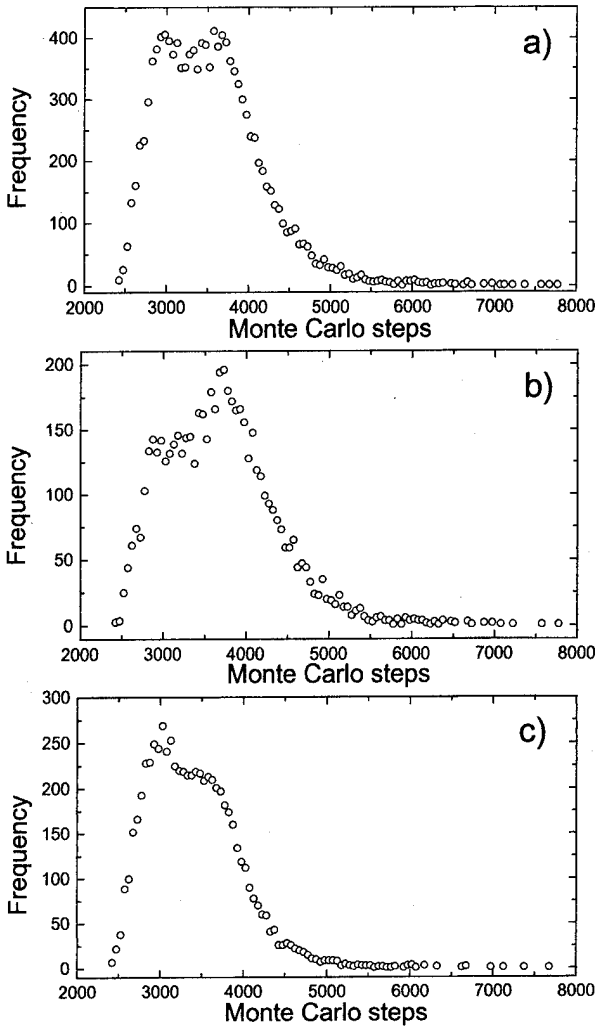



FIG. 3. Distributions of reversal events (a) total; (b) subdistribution corresponding to case 1; and (c) subdistribution corresponding to case 2.

The evolution with the number of MCS of the $OZ$ components of the reduced total moment of the "particle" corresponding to these relaxation processes are shown in Fig. 1. As it is clear from this figure, in both cases, a range of "time" (MCS) exists in which the fluctuations on the orientation of the magnetic moments forming the "particle" do not lead to any change of the macroscopic state of the system. During this "time" range the system is slowly evolving towards the formation of the nucleus which is responsible for the onset of the global reversal but since that nucleus has a domain wall-type structure, its formation cannot be described as a sequential process but as a collective one, requiring the coupling of many degrees of freedom.

In order to get statistical information about the number of MCS required to observe the reversal of the "particle" (or equivalently, to observe a relaxation process in a system formed by many identical, noninteracting particles), we run $1.3\times10^4$ independent relaxations. The results of this simulation are presented in Fig. 3(a) where we show the distribution of reversal events (characterized as corresponding to the achievement of the negative saturation) as a function of the

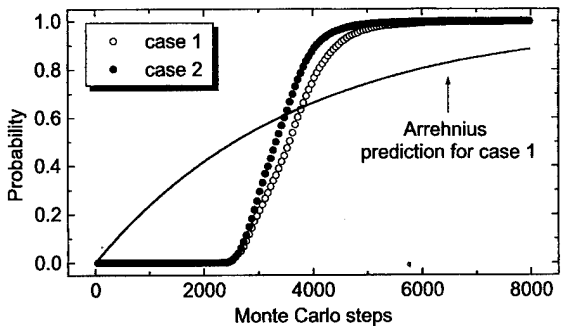



FIG. 4. Probabilities of total moment reversal after a given number of MCS corresponding to cases 1 and 2. The Arrehnius prediction corresponding to case 1 (see text) is also shown.

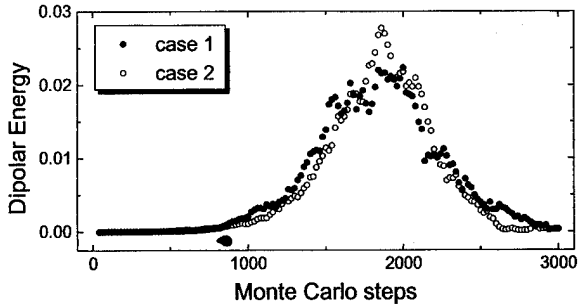



FIG. 5. Two examples of the evolution with the number of MCS of the dipolar energy of the system corresponding to cases 1 and 2.

number of MCS (the data in the figure have been smoothed by adjacent averaging).

As it is apparent from the figure the distribution presents two resolvable peaks. By identifying, during the relaxation process, the nucleation site, we were able to decompose the total distribution of reversal events in the two subdistributions shown in Figs. 3(b) and 3(c) and corresponding to the 1 and 2 nucleation cases, respectively.

In Fig. 4 we have plotted the probabilities of total moment reversal after a given number of MCS corresponding to the two types of nucleation we have detected. These probabilities are obtained, by integration, from the results in Figs. 3(b) and 3(c). In both cases, the reversal probabilities are zero in the initial range of MCS, indicating a remarkable difference with the classical Arrehnius–Néel description of relaxation for which that probability is different from zero for arbitrarily small times[3] {for the sake of comparison with the Arrehnius–Néel predictions, we present in Fig. 4 the curve $[1-\exp(-\mathrm{MCS}/\langle \mathrm{MCS1}\rangle)]$ where $\langle \mathrm{MCS1}\rangle$ is the average value corresponding to the case 1 subdistribution, Fig. 3(b)}. Interestingly, the "waiting time" corresponding to both subdistributions (i.e., the range of MCS for which the reversal probability is zero) seems to be very similar (same probability for both nucleation sites) which allows us to distinguish the observed phenomenology from a real bifurcation (occurrence of inequivalent trajectories linking the initial and final states). Then, we identify the origin of the two maxima in the total distribution of reversal events [Fig. 3(a)] with the presence during relaxation of one or two domain wall-like structures, moving in the last case in opposite sense and requiring a different number of MCS to sweep the system. This point is illustrated in Fig. 5 where we show two particular examples of the evolution with the number of MCS of the dipolar energy stored by the system during relaxations taking place through both modes of nucleation. Accordingly with our idea, the number of MCS required to achieve complete reversal of the total magnetic moment was larger in case 1 (one wall) than in case 2 and the difference of MCS between both relaxation cases is compatible with that observed between the two peaks of the total distribution.

## IV. CONCLUSIONS

From our results we can conclude that thermally activated relaxation proceeds, similarly to hysteresis, through a sequence of the type nucleation-domain wall(s) formation—domain wall(s) propagation. Each one of this events envolves a limited number of the moments in our system but a high number of degrees of freedom. As consequence of this, the evolution with the number of MCS of the orientation of the total magnetic moment of the system cannot be described in terms of the Arrehnius–Néel kinetics since it is characterized by the occurrence of a "waiting time" during which the different degrees of freedom of the system collectively evolve towards the formation of the nucleus which is precusor of the global relaxation.

[1] R. Street and J. C. Wooley, Proc. Phys. Soc. London Ser. A **62**, 562 (1949).
[2] R. W. Chantrell, A. Lyberatos, M. El-Hilo, and O'Grady, J. Appl. Phys. **76**, 6409 (1994).
[3] L. Néel, Ann. Geophys. **5**, 99 (1949).
[4] D. W. Taylor, V. Villas-Boas, Q. Lu, M. F. Rossignol, F. P. Missell, D. Givord, and S. Hirosawa, J. Magn. Magn. Mater. **130**, 225 (1994).
[5] E. C. Stoner and E. P. Wolhfarth, Philos. Trans. A **240**, 599 (1948).
[6] M. Lederman, D. R. Fredkin, R. O'Barr, S. Schultz, and M. Ozaki, J. Appl. Phys. **75**, 6217 (1994).
[7] M. Lederman, S. Schultz, and M. Ozaki, Phys. Rev. Lett. **73**, 1986 (1994).
[8] J. M. González, R. Ramírez, and R. Rueda, J. Magn. Magn. Mater. **140–144**, 1847 (1995).
[9] J. M. González, R. Ramírez, R. Smirnov-Rueda, and J. González, Phys. Rev. B **52**, 16034 (1995).
[10] N. Metropolis, A. W. Rosenbluth, M. N. Rosenbluth, A. H. Teller, and E. Teller, J. Chem. Phys. **21**, 1087 (1953).

# Response of a kinetic Ising system to oscillating external fields: Amplitude and frequency dependence

S. W. Sides and R. A. Ramos
*Center for Materials Research and Technology and Department of Physics, and Supercomputer Computations Research Institute, Florida State University, Tallahassee, Florida 32306-3016*

P. A. Rikvold
*Center for Materials Research and Technology and Department of Physics, and Supercomputer Computations Research Institute, Florida State University, Tallahassee, Florida 32306-3016 and Centre for the Physics of Materials and Department of Physics, McGill University, Montréal, Québec, Canada*

M. A. Novotny
*Supercomputer Computations Research Institute, Florida State University, Tallahassee, Florida 32306-3016 and Department of Electrical Engineering, FAMU/FSU College of Engineering, Tallahassee, Florida 32310-6046*

The $S=1/2$, nearest-neighbor, kinetic Ising model has been used to model magnetization switching in nanoscale ferromagnets. For this model, earlier work based on the droplet theory of the decay of metastable phases and Monte Carlo simulations has shown the existence of a size dependent spinodal field which separates deterministic and stochastic decay regimes. We extend the above work to study the effects of an oscillating field on the magnetization response of the kinetic Ising model. We compute the power spectral density of the time-dependent magnetization for different values of the amplitude and frequency of the external field, using Monte Carlo simulation data. We also investigate the amplitude and frequency dependence of the probability distributions for the hysteresis loop area and the period-averaged magnetization. The time-dependent response of the system is classified by analyzing the behavior of these quantities within the framework of the distinct deterministic and stochastic decay modes mentioned above. © *1996 American Institute of Physics.* [S0021-8979(96)27708-9]

## I. INTRODUCTION

Hysteresis is a nonequilibrium phenomenon characteristic of metastable systems. The kinetic Ising model, for temperatures below its critical temperature $T_c$ and at nonzero external fields $H$, exhibits a metastable phase. If $H(t)$ varies periodically in time, the response of the system, the magnetization $m(t)$, lags behind the forcing field, and hysteresis occurs. Previous studies of hysteresis have been performed, both for mean-field models and for the Ising model.[1,2] In both cases the hysteresis loop area, $A=-\oint m dH$, was found to have a power-law dependence on the frequency and amplitude of $H$ for low frequencies. Also, the mean-field models exhibit a dynamic phase transition in which the period-averaged magnetization, $Q=(\omega/2\pi)\oint m dt$, changes from $Q\neq 0$ to $Q=0$.[3,4] Magnetization reversal in small ferromagnetic grains has been modeled with a kinetic Ising model in static fields.[5] Also, recent experiments on ultrathin ferromagnetic Fe/Au(001) films[6] have considered the frequency dependence of hysteresis loop areas, obtaining exponents that are consistent with those found for the two dimensional Ising model.[1]

The model used in our study is a kinetic, nearest-neighbor Ising ferromagnet on a square lattice with periodic boundary conditions. The Hamiltonian is given by $\mathscr{H} = -J\Sigma_{\langle ij\rangle}s_i s_j - H\Sigma_i s_i$, where $\Sigma_{\langle ij\rangle}$ runs over all nearest-neighbor pairs, and $\Sigma_i$ runs over all $N=L^2$ lattice sites. The dynamic used in this work is the Glauber[7] single spin-flip Monte Carlo algorithm. The system is put in contact with a heat bath at temperature $T$, and each spin can flip from $s_i$ to $-s_i$ with a probability given by[8]

$$W(s_i\rightarrow -s_i)=\frac{\exp(-\beta\Delta E_i)}{1+\exp(-\beta\Delta E_i)},$$

where $\Delta E_i$ gives the change in the energy of the system if the spin flip is accepted, and $\beta=1/k_BT$.

In contrast to earlier studies of hysteresis in Ising models, we have performed simulations in two distinct field regimes. It has recently been observed that the metastable phase in Ising models exposed to a static field $H$ decays by different mechanisms, depending on $H$ and the system size $L$.[9] For fields weaker than a $T$ and $L$ dependent dynamic spinodal field $H_{\mathrm{DSP}}$, the mean lifetime $\tau$ of the metastable phase is comparable to the standard deviation in the lifetime. This field region is termed the stochastic or single-droplet (SD) region because decay of the metastable phase proceeds by random nucleation of a single critical droplet of the stable phase. For fields stronger than $H_{\mathrm{DSP}}$, the mean lifetime of the metastable phase is much greater than the standard deviation in the lifetime. This field region is called the deterministic or multidroplet (MD) region because decay of the metastable phase proceeds by the nucleation, growth, and coalescence of many droplets of the stable phase. The study presented here is, to our knowledge, the first in which the effects of these two different decay mechanisms on hysteresis are considered.

In our simulations, a system of size $L$ at temperature $T$ is prepared with $m(0)=0$ and the up and down spins in random arrangement. Then, a sinusoidal field $H(t)=H_0\sin(\omega t)$ is applied, and the magnetization $m(t)$ is recorded. The field $H(t)$ is changed every attempted spin flip, allowing for a smooth variation. Using the $m(t)$ vs $t$ data, we calculate

 0021-8979/96/79(8)/6482/3/$10.00 © 1996 American Institute of Physics

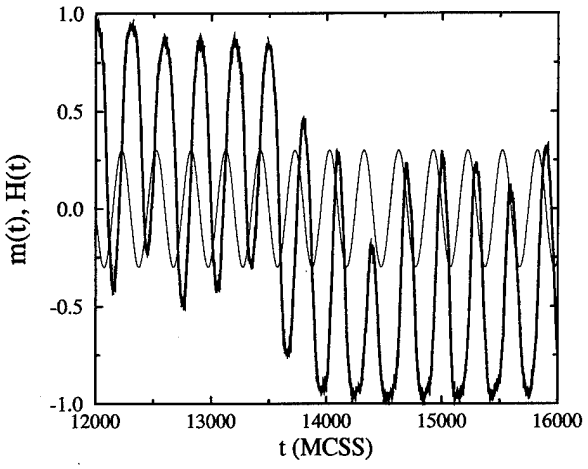



FIG. 1. Magnetization $m(t)$ and external field $H(t)$ vs time $t$ in the MD region with $(2\pi/\omega)\approx 300$ Monte Carlo steps per spin (MCSS), $H_0=0.3J$, and the lifetime in static field $\tau_{\omega=0}\approx 75$ MCSS. The darker line shows $m(t)$ and the lighter line denotes $H(t)$. The total length of the time series is $16.9\times10^6$ MCSS. The ratio of the period of $H(t)$ to $\tau_{\omega=0}$ is $\sim 4$.

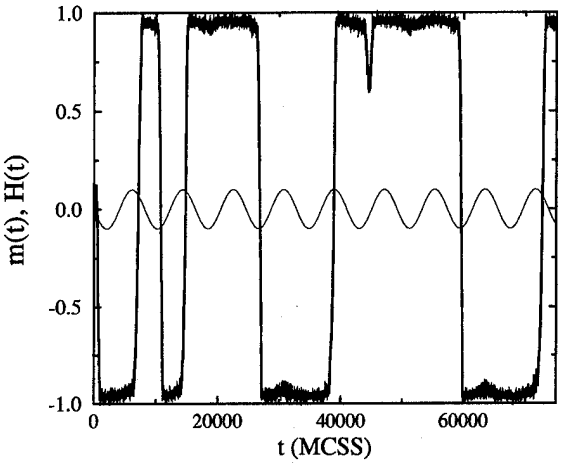



FIG. 2. Magnetization $m(t)$ and external field $H(t)$ vs time $t$ in the SD regime with $(2\pi/\omega)=8192$ MCSS, $H_0=0.1J$, and $\tau_{\omega=0}\approx 2058$ MCSS. The darker line shows $m(t)$ and the lighter line denotes $H(t)$. The total length of the time series as well as the ratio of the period of $H(t)$ to $\tau_{\omega=0}$ are the same as in Fig. 1.

power spectral densities (PSD) and probability distributions for the loop area $A$ and the period-averaged magnetization $Q$ for different amplitudes and frequencies of $H(t)$.

## II. RESULTS

Our results are presented so as to contrast the behaviors of the hysteretic magnetization response in the SD and MD regions. All of the results shown are for $L=64$ and $T=0.8T_c$. The simulations were performed at two field amplitudes $H_0$ and several frequencies $\omega$. One value of $H_0$ was chosen such that for $\omega=0$, the system was clearly in the SD region. Similarly, the other value of $H_0$ was chosen such that the system was definitely in the MD region. While several frequencies were used, here we show results for a value of $\omega$ for which the magnetization switches many times over the course of the entire simulated time series [although not necessarily with the same periodicity as $H(t)$]. Figure 1 shows a portion of the time series in the MD regime, where the system switches over several periods from a state that oscillates with $Q>0$, to a state that oscillates with $Q<0$. In Fig. 2, a portion of the time series in the SD regime shows oscillations with $Q$ near plus or minus the zero-field spontaneous magnetization, punctuated by random switching events that are completed within less than one period of the field oscillation. Here, once a critical droplet forms (in a Poisson process), the stable phase quickly takes over the system.

Figure 3 shows the PSDs for the entire time series of Figs. 1 and 2. The first peak in the MD data is at the driving frequency $f_{\rm MD}=(\omega/2\pi)$ of the external field. The higher-frequency peaks are located at integer multiples of $f_{\rm MD}$. The first peak in the SD data is at the driving frequency $f_{\rm SD}$ of the external field. Here, the higher frequency harmonics are located at odd integer multiples of $f_{\rm SD}$. Both the MD and SD data show large low-frequency components, indicating the slow dynamics of the magnetization reversal in both regimes. In the high-frequency part of the spectrum, the PSDs have slopes on the log–log plot of approximately minus two, corresponding to exponential short-time correlations.

Figure 4 shows the probability distributions of the hysteresis loop areas $A$ for the data of Figs. 1 and 2. The distribution for the MD regime shows a single wide peak, since $m(t)$ lags behind $H(t)$ by a nearly constant phase factor. The distribution in the SD regime has a narrow peak near zero as $m(t)$ oscillates near the positive or negative spontaneous magnetization for most of the length of the run. The narrow peak between the scaled $A$ values of 0.4 and 0.5 corresponds to the rapid switching of $m(t)$ via the nucleation of a single, critical droplet of the stable phase.

Figure 5 shows the distributions of the period-averaged magnetization $Q$ for the data in Figs. 1 and 2. The distributions for both the SD and the MD regions show a double-peaked structure. The two sharp peaks in the SD data are due to $m(t)$ oscillating near the spontaneous magnetization values during most of the run. The distribution for the MD

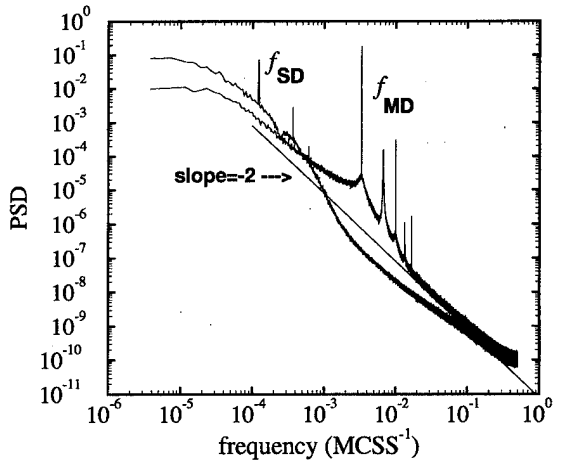



FIG. 3. PSDs for the time series of Figs. 1 and 2. The magnetization is sampled every 1.0 MCSS, so the Nyquist frequency is 0.5 MCSS$^{-1}$. The lowest frequency that can be resolved for both PSDs is $3.8\times10^{-6}$ MCSS$^{-1}$.

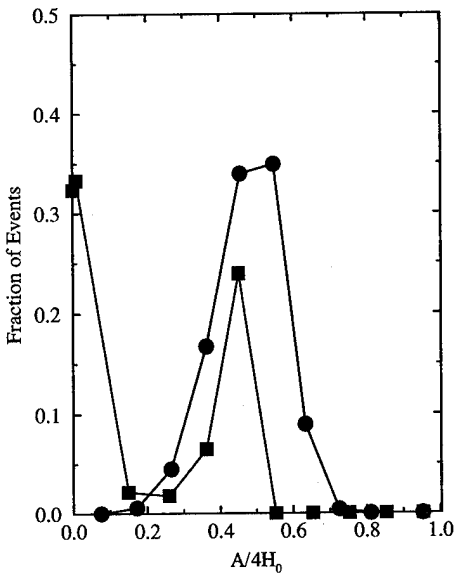



FIG. 4. Probability distributions of the hysteresis loop areas, $A=-\oint mdH$. $A$ is calculated for the MD (●) and SD (□) regions from the data of Figs. 1 and 2. We have used bins of size 0.1 for the area values for both data sets. The value of the area used to plot each of the points is the mean value of the loop areas over a particular bin. Note that the loop areas have been normalized by $4H_0$, the maximum possible loop area. The number of events (periods) for the SD data and MD data is different; the MD distribution uses 56333 events and the SD distribution uses 2062 events.

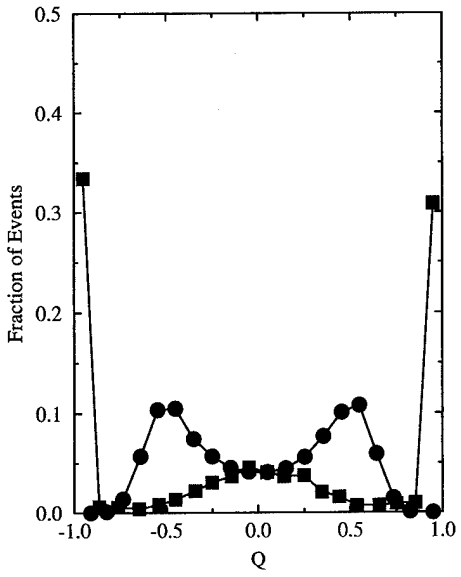



FIG. 5. Probability distributions of the period-averaged magnetization, $Q=(\omega/2\pi)\oint mdt$. $Q$ is calculated for the MD and SD regions from the data in Figs. 1 and 2. The size of the bins used and the quality of the statistics are the same as in Fig. 4.

regime shows two peaks as well, but each peak is much wider than in the SD case. The positions of the peaks in both distributions have been found to be frequency dependent as well as amplitude dependent. In both cases the slight asymmetry of the distribution is an effect of the finite length of the time series.

## III. CONCLUSION

Our results show distinct differences between the multidroplet region and the single-droplet region. This study shows that the nature of the response of an Ising system does not only depend on the competition between the two time scales: the oscillation period of the external field, and the lifetime of the metastable state. It also depends on the mode by which the system switches magnetization states, which depends not only on the field amplitude and frequency, but also on the temperature and system size.

## ACKNOWLEDGMENTS

Supported in part by FSU-MARTECH, by FSU-SCRI under DOE Contract No. DE-FC05-85ER25000, and by NSF Grants No. DMR-9315969 and DMR-9520325.

[1] M. Rao, H. R. Krishnamurthy, and R. Pandit, Phys. Rev. B **42**, 856 (1990).
[2] M. Acharyya and B. K. Chakrabarti, *Annual Reviews of Computational Physics I*, edited by D. Stauffer (World Scientific, Singapore, 1994).
[3] T. Tomé and M. J. de Oliveira, Phys. Rev. A **41**, 4251 (1990).
[4] W. S. Lo and R. A. Pelcovits, Phys. Rev. A **42**, 7471 (1990).
[5] H. L. Richards, S. W. Sides, P. A. Rikvold, and M. A. Novotny, J. Magn. Magn. Mater. **150**, 37 (1995).
[6] Y. L. He and G. C. Wang, Phys. Rev. Lett. **15**, 2336 (1993).
[7] R. J. Glauber, J. Math. Phys. **4**, 294 (1963).
[8] K. Binder and D. W. Heermann, *Monte Carlo Simulation in Statistical Physics* (Springer, Berlin, 1988).
[9] P. A. Rikvold, H. Tomita, S. Miyashita, and S. W. Sides, Phys. Rev. E **49**, 5080 (1994).

# Study of residual magnetization of hard steel samples

M. Saadi, F. Jellali, A. Delmas, and G. Quichaud
*Laboratoire d'Electrotechnique des Universités Paris VI et XI, Université Paris sud, Bât. 214-91405 Orsay, France*

This study forms part of a program trying to determine the position of a train on railway using magnetic spots. In this paper, we investigate the influence of the parameters of the exciting current pulse on the residual magnetization of a hard steel. In the case of a pulse of long duration and small amplitude, we show that the associated hysteresis problem can be reduced to the determination of a magnetic field distribution due to a fixed magnetization. We define this magnetic field distribution by means of a boundary integral equations method. For these conditions, the internal and external induction distributions are of the same order of magnitude. In contrast, for pulses of short duration (millisecond or less) and large amplitude, the eddy currents in hard steel lead to a remanent magnetization loop which is permanently trapped by the hysteresis phenomena. The residual external induction is always small, and is not representative of the large internal magnetization.
© *1996 American Institute of Physics.* [S0021-8979(96)27808-5]

## I. INTRODUCTION

We are interested by the residual magnetism within a conducting ferromagnetic volume $(F)$ in front of a solenoid $(B)$ which carries a pulsed sinusoidal current. In this experiment, the volume $(F)$ is a hard steel ball as shown in Fig. 1.

Practically, this work is related to the use of magnetic spots on railway[1,2] in the aim of localizing a train. For this application, the ball is replaced by a section of a rail. The time duration of the current pulses $T_0$ must be relatively short (less than millisecond) because of the high actual speed of the train (more than 300 Km/h). This leads us to specify the influence of $T_0$ on the residual magnetism of a hard steel.

## II. SLOW MAGNETIZATION

We assume that the current pulse duration $T_0$ is long enough to neglect the induced current in the volume $(F)$. This is equivalent to utilizing an insulating ferromagnetic material. The simplest representative case is the one represented in Fig. 2 where the magnetic induction $\mathbf{b}(t)$ produced by the solenoid is uniform in the absence of the ball. Indeed, the study is made easier by the known uniform internal demagnetizing field $-(1/3)\mathbf{J}$ in the sphere of uniform magnetization $\mathbf{J}$. Thus, the magnetic induction $\mathbf{B}(t)$ and the field $\mathbf{H}(t)$ in the sphere are still uniform and linked by the relation

$$\mathbf{B}(t)=-2\mu_0\mathbf{H}(t)+3\mathbf{b}(t). \tag{1}$$

So we are lead to determine the maximum induction $B_0$ seen by $(F)$ and its residual induction $b_r$ as shown in Fig. 3(a) where we have represented the curve $B(H)$ of a hard steel. This slow magnetization enables us to determine the Frölich's approximation of the ball's first magnetization curve:

$$B=\mu_0 H\left(1+\frac{2}{0.012+\mu_0 H}\right), \tag{2}$$

and the dependence of its coercive field $H_c$ with regard to the applied magnetic induction peak $B_v$ [Fig. 3(b)]. The maximal residual induction in the ball is then nearly $2\mu_0 H_c$. We note that induction values $B_v$ of about 2 T could be obtained with an appropriate magnetic circuit.

In the practical case of a railway section, the residual magnetization is determined using as magnetic characteristic for $t>T_0/2$, the linear law

$$\mathbf{B}=\mathbf{M}_0+\mu\mathbf{H}, \tag{3}$$

where $\mathbf{M}_0$ is the magnetic polarisation at $t=T_0/2$. Yet, the vectorial hysteresis[3] problem becomes an easier permanent magnetization one. It is solved, in a classical way, using a boundary integral method. Then, we calculate a superficial magnetic charges density $\sigma(M)$ at the interface $(s)$ between air and rail which is taken as a solution of the boundary integral equation:

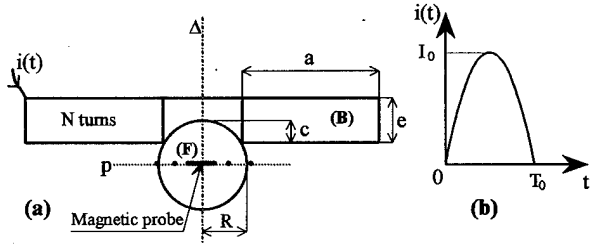



FIG. 1. (a) Experimental device; (b) current shape.

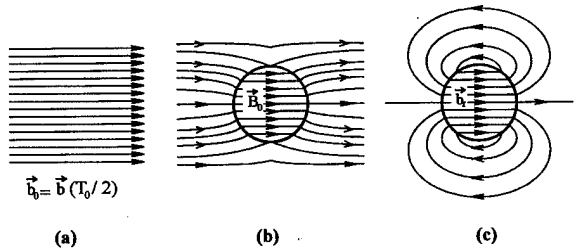



FIG. 2. Distribution of the induction; (a) without ball; (b) with ball at $t=T_0/2$; (c) residual induction at $t\gg T_0$.

 0021-8979/96/79(8)/6485/3/$10.00 © 1996 American Institute of Physics 

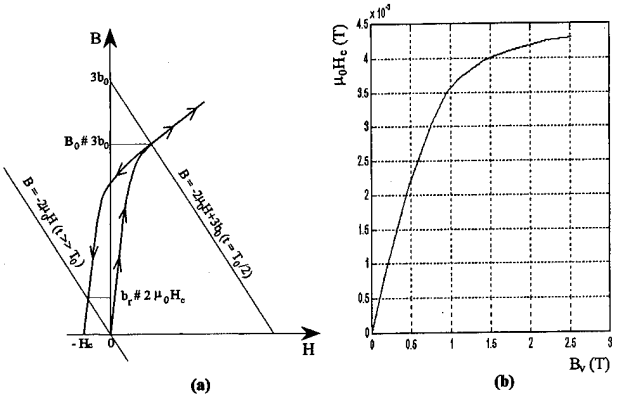



FIG. 3. (a) Determination of magnetization states of the ball; (b) the coercive field as a function of the maximum induction seen.

$$\frac{\mathbf{M}_0\cdot\mathbf{n}}{\mu}+\frac{1}{4\pi}\int_{(F)}\frac{\mathbf{r}\cdot\mathbf{n}}{r^3}\rho_0(M)d\tau + \frac{1}{4\pi}\int_{(S)}\frac{\mathbf{r}\cdot\mathbf{n}}{r^3}\sigma(M)ds-\frac{\sigma(M)}{2}=0, \tag{4}$$

associated with the constraint

$$\int_{(F)}\rho_0(M)d\tau+\int_{(S)}\sigma(M)ds=0, \tag{5}$$

where $\rho_0=-\text{div}\,\mathbf{M}_0/\mu$ is the known volume magnetic charge density in the rail. The residual field distribution in the air $\mathbf{h}_r(M)$ is then given by

$$\mathbf{h}_r=\frac{1}{4\pi}\left(\int_{(F)}\frac{\mathbf{r}}{r^3}\rho_0(M)d\tau+\int_{(S)}\frac{\mathbf{r}}{r^3}\sigma(M)ds\right). \tag{6}$$

We compute this method numerically in the case of a rail section of 60 cm long placed in front of the solenoid as shown in Fig. 4. In the particular conditions where the coercive field is 800 A/m and the peak induction is 1.2 T, we obtained the results shown in Figs. 5(a) and 5(b).

## III. FAST MAGNETIZATION

The geometric parameters of Fig. 1 being as follows: $R=10$ mm, $a=51$ mm, $e=9$ mm, $c=4$ mm, the previous ball is submitted to current pulse of $T_0=400$ $\mu$s duration, and $I_0=3100$ A peak amplitude. The solenoid contains $N=22$ turns. The ball has been previously cut by electroerosion to two hemispheres according to an equatorial plane $p$ (Fig. 1). We are then able to put two magnetic flux probes of axe $\Delta$ (Fig. 1) with respective radius $r_1=4$ mm, $r_2=6$ mm, between the hemispheres, the air gap being reduced to a minimum value. A third probe of radius $r_3=10$ mm has been put at the periphery of the ball.

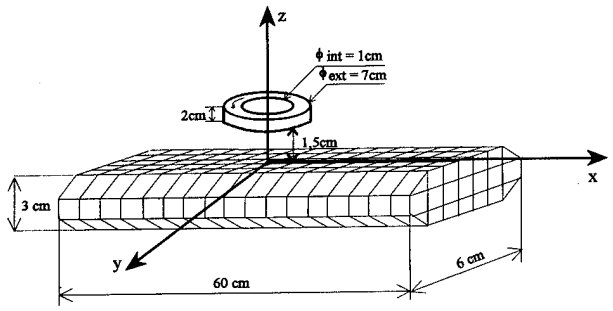



FIG. 4. Simulated model.

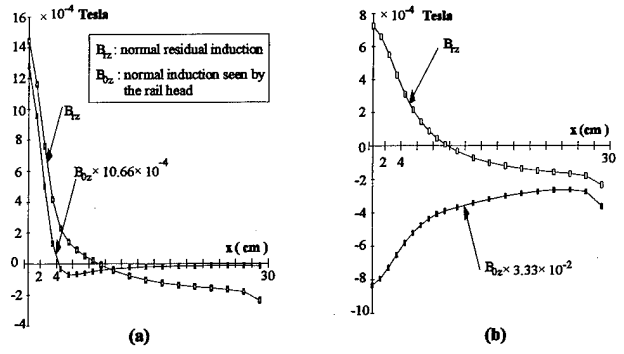



FIG. 5. Normal inductions $B_{0z}$ and $B_{rz}$ as functions of the rail head length $x$ at $y=0.5$ cm for (a) the above face ($z=0$); (b) the bottom face ($z=-3$ cm).

The integration of the induced voltages record $v_1(t)$, $v_2(t)$, and $v_3(t)$ [Fig. 6(a)] in those probes gives, respectively, the flux evolutions $\varphi_1(t)$, $\varphi_2(t)$, and $\varphi_3(t)$ represented in Fig. 6(b). After this magnetization, the residual induction measured around the ball was in agreement with the behavior of the Fig. 2(c). The maximum value on the axe $\Delta$, at the surface of the ball is $25\times10^{-4}$ T. We have also measured a permanent attractive force of 47 N between the two hemispheres. This force would be negligible in the case of a slow magnetization because of the value of the steel's coercive field. The flux evolutions in the Fig. 6(b) show that at $t=300$ $\mu$s, the ball interior peak induction is relatively homogeneous with a value between 2 and 2.3 T.

In the hypothesis of a slow magnetization, this result would give a residual induction of $80\times10^{-4}$ T instead of $25\times10^{-4}$ T measured. This difference is due to the induced current which leads to the formation of a flux loop subsequently trapped in permanence by the magnetic hysteresis. This current is also at the root of the attractive force as well as the $\varphi_1(t)$ and $\varphi_2(t)$ bounds of 41 $\mu$Wb and 75 $\mu$Wb, for

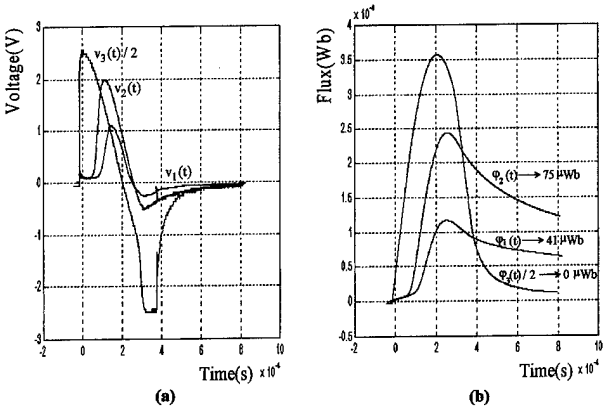



FIG. 6. (a) Induced voltages across the probes; (b) flux.

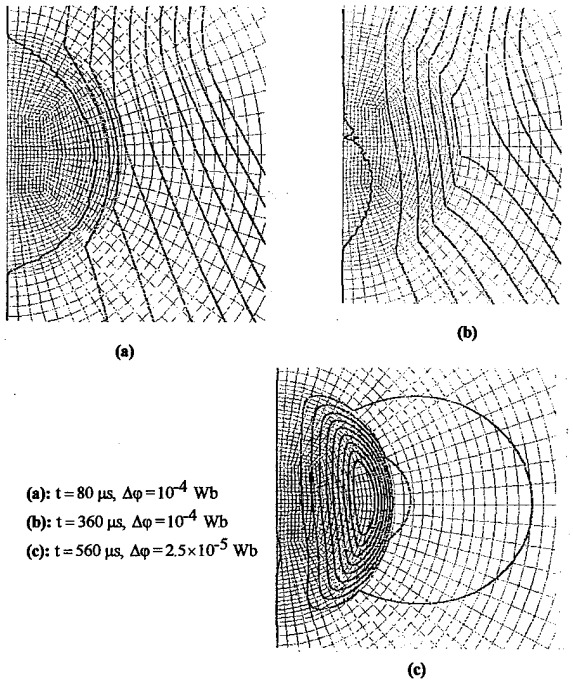



FIG. 7. Progressive penetration of the flux in the ball.

large $t$, than that practically null $\varphi_3(t)$, are representative of that trapped flux. They lead, in the $p$ plane, to a mean residual induction of 0.8 T, in agreement with the 47 N force and the residual induction of a hard steel in taking into account of the parasitic air gap between both hemispheres. Taking into account only the steel's first magnetization curve and its electric conductivity $\sigma=4.17\times10^6(\Omega\,\mathrm{m})^{-1}$, we modeled the transient rating of the induction diffusion[4,5] in the ball for conditions close to the previous experimental ones.

In Fig. 7, we give the equiflux lines with step $\Delta\varphi$ for three instants. One sees the progressive flux penetration until $t=320$ $\mu$s when its distribution is relatively homogeneous and its density is close to 2 T. This result is in agreement with the experimental one shown in Fig. 6(b). Then, after the extinction of the excitation current, that flux is closed up within the ball and attenuates very slowly [Fig. 7(c)]. The induction normal component evolution, in the equatorial plane $p$, shown in Fig. 8, is also in agreement with these results.

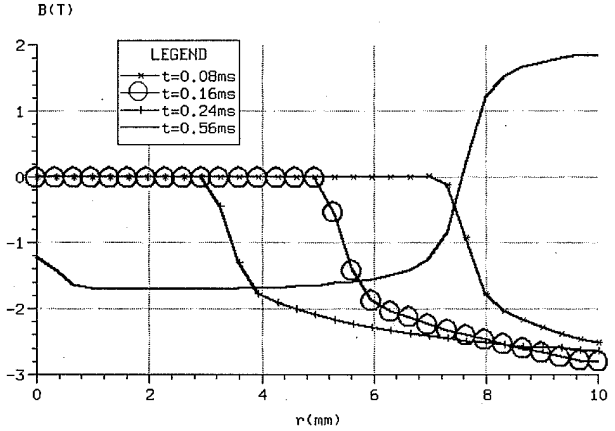



FIG. 8. The normal induction evolution at the plane $p$.

As it is difficult to take into account the vectorial hysteresis,[3,6] even if there are no induced currents, we have used the results of the above global simulation[7] to simulate the case of scalar hysteresis, taking into account the induction tangential component. In these conditions, the complete flux attenuation given by the global simulation does not appear, in agreement with the experiment.

## IV. CONCLUSION

The experiment in conjunction with the modeling process shows the large variation of the internal residual magnetization of a conducting sphere with magnetic hysteresis, according to the excitation current duration. In fact, if for a slow magnetization, the sphere is nearly demagnetized, it has, in contrast, a magnetization close to its remanent one if the excitation peak current is short. We have also investigated[5] the trapped flux phenomena in disks cut out a rail head. Nevertheless, in that case, the comparison of the residual magnetization with the slow magnetization one is more delicate.

[1] M. Saadi, Ph.D. thesis, Paris VI University, 1994.
[2] F. Jellali, Ph.D. thesis, Paris VI University, 1994.
[3] I. D. Mayergoyz, J. Appl. Phys. **63**, 2995 (1988).
[4] B. E. MacNeal, MSC/EMAS, modeling guide, MacNeal-Schwendler Corp., 1989.
[5] F. Jellali, G. Quichaud, and M. Saadi, J. Appl. Phys. **73**, 6796 (1993).
[6] A. Visintin, *Differential Models of Hysteresis* (Springer, New York, 1994).
[7] M. Saadi, F. Jellali, and G. Quichaud, J. Phys. III **5**, 1437 (1995).

# Magnetic reversal in perpendicularly oriented thin films subjected to picosecond magnetic fields (abstract)

Juergen Heidmann
*IBM Storage Systems Division, 5600 Cottle Road, San Jose, California 95193*

Dieter Weller
*IBM Research Division, Almaden Research Center, 650 Harry Road, San Jose, California 95120*

Hans C. Siegmann
*Swiss Federal Institute of Technology, Zurich, Switzerland*

E. L. Garwin
*Stanford Linear Accelerator Center, Stanford University, Stanford, California 94309*

The magnetic reversal mechanism in perpendicularly oriented, premagnetized Co based thin film alloys, induced by ultra short magnetic field exposure of a few picoseconds duration has been studied.[1] Field pulses with a magnitude of several thousand Tesla were generated by the 50 GeV final focus electron beam at the Stanford Linear Accelerator Center (SLAC). Characteristic remanent domain patterns are observed in these films long after field exposure using polar Kerr microscopy.[2] Complete reversal of the magnetization is found to occur during a single spin precession event of 6.0 ps duration where the inplane-field amplitude is greater or equal to the macroscopically determined perpendicular anisotropy field. Further, a wide transition range, dividing the reversed and nonreversed regions is observed which is broken into a quasi periodic stripe domain structure with stripe-width 0.3 $\mu$m. As a main result of this experimental study we find that magnetization reversal on this time scale is solely governed by the intrinsic effective field, i.e., anisotropy- and demagnetization-field contributions, rather then by complex curling and buckling mechanisms.[3] Unique insight into fundamental spin reversal mechanisms and their ultimate speed in thin magnetic recording films is provided by these experiments. © *1996 American Institute of Physics.* [S0021-8979(96)70208-2]

[1]H. C. Siegmann, E. L. Garwin, C. Y. Prescott, J. Heidmann, D. Mauri, D. Weller, R. Allenspach, and W. Weber (unpublished).
[2]W. Rave, R. Schaefer, and A. Hubert, J. Magn. Magn. Matter. **65**, 7 (1987).
[3]E. H. Frei, S. Shtrikman, and D. Treves, Phys. Rev. **106**, 446 (1957).

 0021-8979/96/79(8)/6488/1/$10.00 © 1996 American Institute of Physics

# A theoretical description of magnetic switching experiments in picosecond field pulses

L. He and W. D. Doyle
*Center of Materials for Information Technology and Department of Physics and Astronomy, The University of Alabama, Tuscaloosa, Alabama 35487-0209*

Siegmann *et al.* have reported that the magnetization in a perpendicularly oriented CoPt film with a uniaxial anisotropy field of 20 000 Oe was reversed when the film was exposed to a 20 000 Oe in-plane pulsed field lasting only 6 ps. From a calculation based on the Gilbert form of the Landau–Lifshitz equation (LLG), it is shown that the experimental result is consistent with the LLG model even for values of the damping constant $\alpha$ as larger as 0.5. The dependence of the switching time on the anisotropy field and the applied field are presented as a function of $\alpha$ and the angle $\beta$ between the applied field and the easy axis. Experiments are suggested which could illuminate the damping mechanism at these very short times. © *1996 American Institute of Physics.*
[S0021-8979(96)78408-9]

## INTRODUCTION

Studies of dynamic switching in magnetic materials[1] have been limited for experimental reasons to field pulse widths $\tau_H$ in the nanosecond regime or greater except in a few special cases.[2] Recently, in a beautifully conceived experiment, Siegmann *et al.*[3] demonstrated that the remanent state of a perpendicularly oriented film of CoPt could be switched by an in-plane field with $\tau_H=6$ ps produced by an electron beam focused to a few square microns. The anisotropy field $H_K$ of the CoPt at room temperature was reported to be ~20 000 Oe and the magnitude of the pulsed field in the switched region where thermal effects were felt to be minimal was estimated to be ~20 000 Oe. Because this switching time is more than two orders of magnitude faster than those observed in more conventional systems, it is tempting to speculate that if the spin-lattice relaxation time are $\gg\tau_H$, then the usual damping mechanisms would be effectively inoperative during the field pulse and the magnetization would precess freely in the total effective field. In fact, the authors pointed out that the results were consistent with this assumption.

We have for some time been interested in the high speed switching of high coercivity materials and have studied solutions to the Gilbert form of the Landau–Lifshitz equation (LLG).[4] In this paper we apply that methodology to the present case assuming that in the center of the switched region, the film can be treated as a single domain, switching coherently. For the particular experimental conditions applicable to the CoPt film, we show that the reversal is consistent with LLG even for values of $\alpha$ as large as 0.5. Other experiments are suggested which could illuminate the damping process at these very short times.

## THEORETICAL MODEL

The motion of the magnetization $\mathbf{M}$ with constant magnitude $M_S$ is assumed to be described by the Gilbert form of the Landau–Liftshitz equation:

$$\frac{d\mathbf{M}}{dt}=-|\gamma|(\mathbf{M}\times\mathbf{H}_T)+\left(\frac{\alpha}{M_S}\right)\left(\mathbf{M}\frac{d\mathbf{M}}{dt}\right), \tag{1}$$

where $\gamma=1.76\times10^7$ rad/Oe s is the gyromagnetic ratio, $\alpha$ is the phenomenological damping constant and $\mathbf{H}_T$ is the total effective field acting on $\mathbf{M}$. The easy axis of the uniaxial film is taken to be along the $z$ direction (Fig. 1). At $t=0$, with $\mathbf{M}$ at rest in the $+z$ direction, a pulse field which reaches a constant value $H_A$ in a time $\Delta t$ is applied in the $y-z$ plane at an angle $\beta$ to the $+z$ direction and after a time $\tau_H$ is reduced to zero. The total effective field is $\mathbf{H}_T=\mathbf{H}_A+\mathbf{H}_K$ where $\mathbf{H}_K=H_{KZ}\hat{k}=H_K\cos\theta\hat{k}$ is an effective anisotropy field along the $z$ direction. Following Gillette and Oshima,[5] the motion of $\mathbf{M}$ can be expressed as two coupled differential equations which can be integrated numerically. The fourth-order Runge–Kutta method with double precision was used to find solutions. The accuracy of the calculation was verified by letting $H_K=0$ and comparing the results for various values of step size to the analytical solutions for the isotropic case.[6] For step sizes between $10^{-5}$ and $10^{-3}$ ns, the error in $M_Z/M_S$ was less than $10^{-7}$ for $\alpha=0.1$ over the entire switching time. In all the results described below, the step size was chosen to be $10^{-5}$ ns. The switching time $\tau$ defined as the time at which $M_Z$ changes sign from positive to negative for the last time before the field is shut off, varied by less than 1% for $0\leqslant\Delta t\leqslant1$ ps. For convenience, $\Delta t$ was taken to be zero.

## RESULTS AND DISCUSSION

We first examine the switching process for $H_A=H_K=20\,000$ Oe, $\tau_H=6$ ps and $\beta=90°$, the conditions

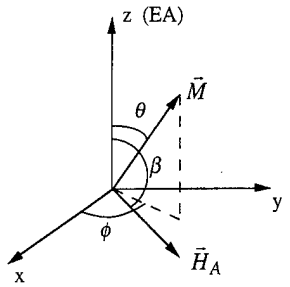



FIG. 1. Definition of the coordinate system used in this calculation. The uniaxial easy axis (EA) is along the $z$ axis.

 0021-8979/96/79(8)/6489/3/$10.00 © 1996 American Institute of Physics 

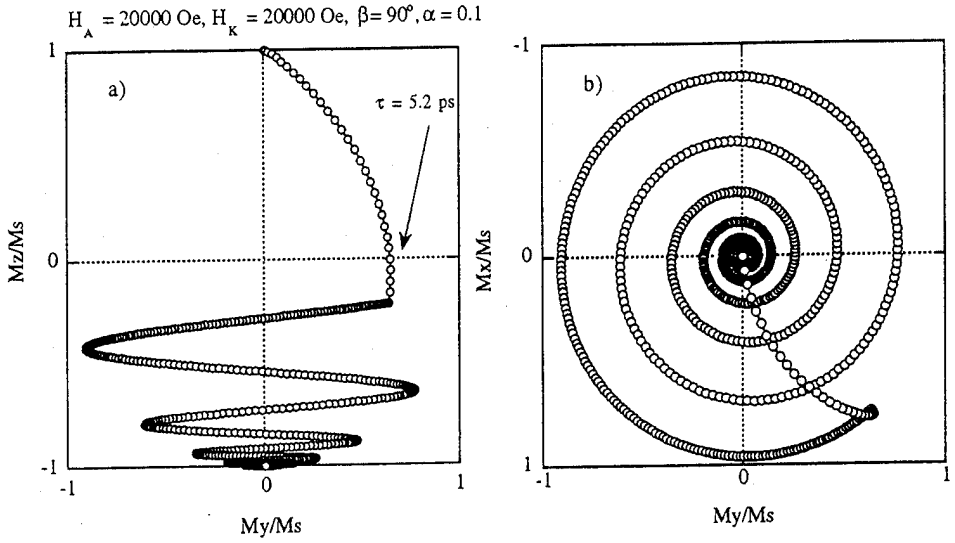



FIG. 2. The locus of the magnetization in terms of its reduced components (a) $Mz/Ms$ vs $My/Ms$ and (b) $Mx/Ms$ vs $My/Ms$ as a function of time for the anisotropy field $H_K$=20 000 Oe, the applied field $H_A$=20 000 Oe, the damping constant $\alpha$=0.1 and the applied field at $\beta$=90° to the easy axis. The full circles are plotted every 0.2 ps.

estimated by Siegmann *et al.*[3] The locus of **M** in terms of its components are plotted every 0.2 ps in Fig. 2 as a function of time for $\alpha$=0.1, a typical value for many materials.[1] Initially since $\mathbf{H}_T$ is at 45° to the $+z$ direction, **M** precesses out of $y-z$ plane. Since the damping torque which tries to align **M** with $\mathbf{H}_T$ is small, **M** precesses at a large angle to $\mathbf{H}_T$ and the polar angle $\theta$ increases rapidly. This reduces the value of the anisotropy field $H_K \cos\theta$ so that the direction of $\mathbf{H}_T$ moves quickly to and passed the $+y$ direction. This, in turn, drives **M** across the hard plane toward the $-z$ direction in 5.2 ps. When $\mathbf{H}_A$ is shut off after 6 ps, **M** continues to precess around $\mathbf{H}_K$ but spirals in slowly toward the $-z$ direction, taking about 82 ps for $M_Z$ to reach $0.95M_S$.

If we test the sensitivity of $\tau$ to the value of $\alpha$ for the same conditions, we find (Fig. 3) that $\tau$ is relatively insensitive to $\alpha$ up to $\alpha\sim0.5$ above which $\tau$ increases rapidly. Thus the results of Siegmann *et al.*[3] in CoPt are consistent with the classical LLG model over a wide range of $\alpha$ and are not inconsistent with the inclusion of normal damping processes.

It should be noted that if $\mathbf{H}_A$ was not terminated after 6 ps, then **M** would continue to precess around the $+y$ direction and after $\sim$18 ps, $M_Z$ would become positive again. If $\mathbf{H}_A$ was then terminated, no change in the remanent state would be observed.

The value of $\tau$ vs the reduced field $h=H_A/H_K$ for several values of $H_K$ with $\beta$=90° and $\alpha$=0.1 are shown in Fig. 4. That the minimum critical field for switching is less than the equilibrium Stoner–Wohlfarth value of $h$=1 when $\alpha<1$ and $\Delta t$=0 had been pointed out previously.[4] For $h$ greater than the minimum switching value, the value of $\tau$ decreases as $H_K$ increases for constant $h$.

When $\beta\neq$90°, the switching time $\tau$ becomes much more sensitive to $\alpha$, suggesting that experiments at other angles could illuminate the damping process more clearly. The de-

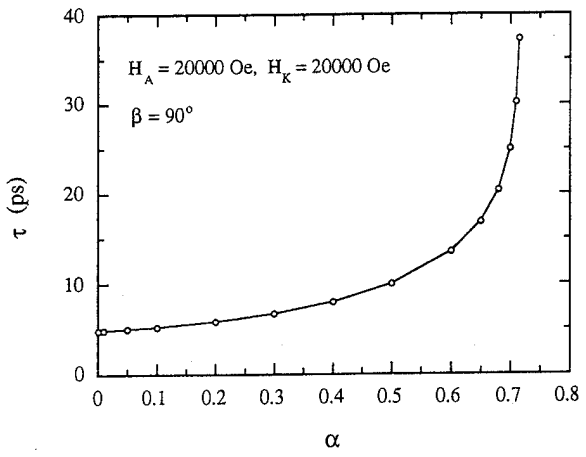



FIG. 3. The switching time $\tau$ vs dampling constant $\alpha$ for $H_A$=20 000 Oe and $H_K$=20 000 Oe with $\beta$=90°.

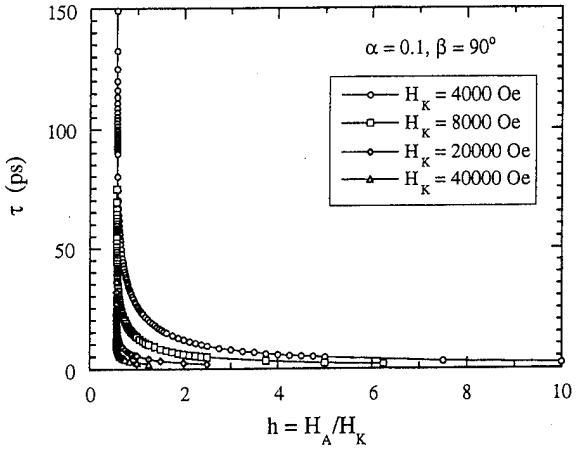



FIG. 4. The switching time $\tau$ vs the reduced field $h$ for several values of the anistropy field $H_K$ with $\alpha$=0.1 and $\beta$=90°.

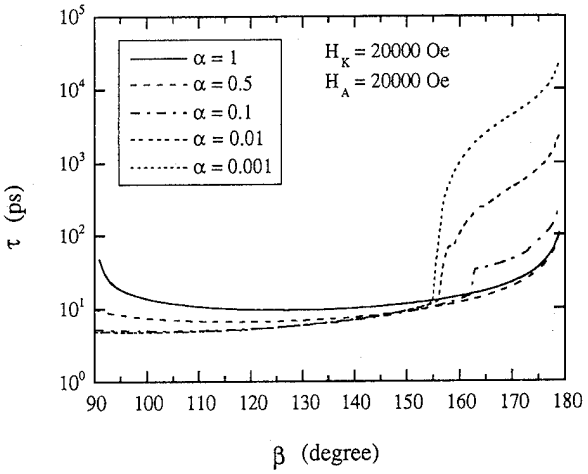



FIG. 5. The switching time $\tau$ vs applied field direction $\beta$ for several values of the damping constant $\alpha$ with the anisotropy field $H_K$=20 000 Oe and the applied field $H_A$=20 000 Oe.

pendence of $\tau$ on $\beta$ for several values of $\alpha$ with $H_A=H_K=20\,000$ Oe is shown in Fig. 5. For $\alpha=1$, $\tau$ approaches 100 ps when $\beta=90°$ or 180°, with a broad minimum at 130°. As $\alpha$ decreases, the minimum value of $\tau$ drops to less than 6 ps and shifts to $\beta=98°$ when $\alpha=0.001$. The values of $\tau$ increase less than 2% when $\beta=90°$ but monotonically to <100 ps as $\beta$ approaches 180°. The increase in $\tau$

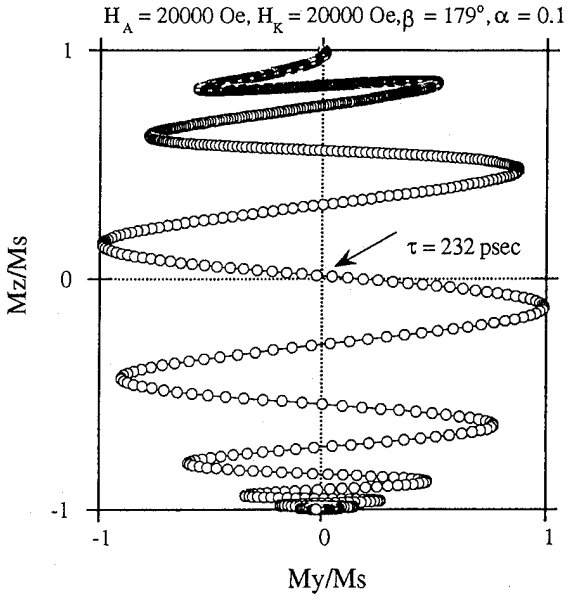



FIG. 6. The locus of the magnetization in terms of its reduced components $Mz/Ms$ vs $My/Ms$ as a function of time for the anisotropy field $H_K$=20 000 Oe, the applied field $H_K$=20 000 Oe and the damping constant $\alpha$=0.1 with the applied field at $\beta$=179°. The full circles are plotted every 0.2 ps.

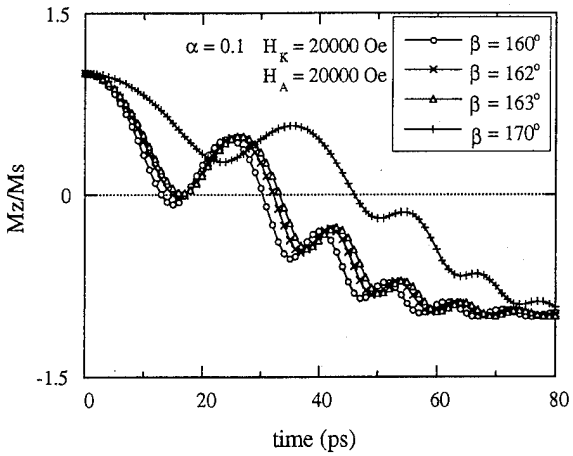



FIG. 7. The normalized component of magnetization $Mz/Ms$ vs time for several values of applied field direction $\beta$ for the anisotropy field $H_K$=20 000 Oe and the applied field $H_A$=20 000 Oe with damping constant $\alpha$=0.1.

at small values of $\alpha$ as $\beta\rightarrow180°$ can easily be understood from Fig. 6 which shows that **M** precesses for several cycles before crossing the hard plane.

In Fig. 5 it can be seen that the switching time $\tau$ is discontinuous between $155°<\beta<165°$ when $\alpha<0.1$. This can be understood from a plot of $M_Z/M_S$ vs time for different values of $\beta$ with, for example, $\alpha$=0.1 (Fig. 7). As $\beta$ changes from 162° to 163°, the time at which the magnetization crosses the hard plane switches discontinuously from the first precession cycle to the second precession cycle.

The experimental beam conditions which determine the amplitude and length of the pulse field are presumably not easily changed. However, if the anisotropy field of the sample could be increased to 40 000 Oe and reliable measurements made nearer to the beam center where the pulse field would be larger, then $\tau$ near $\beta=90°$ would be 2.6 ps. A measurement of $\tau$ vs $\beta$ with $\tau_H$=6 ps should then be able to detect a critical switching angle (Fig. 5) from the effective value of $\alpha$ could be determined.

## ACKNOWLEDGMENTS

We appreciate the consideration of H. C. Siegmann and co-authors who shared their experimental results with us before publication. This work was supported in part by a grant from ARPA administered by the National Storage Industry Consortium.

[1] R. F. Soohoo, *Magnetic Thin Films* (Harper & Row, New York, 1965), Chap. 9.
[2] M. R. Freeman, R. R. Ruf, and R. J. Gambino, IEEE Trans. Magn. **27**, 4840 (1991).
[3] H. C. Siegmann, E. I. Garwin, C. Y. Prescott, J. Heidmann, D. Mauri, D. Weller, P. Allenspach, and W. Weber, to be published in J. Magn. Magn. Mater.; J. Heidmann, D. Weller, H. C. Siegmann, E. I. Garwin, abstract HE-01, Conference on Magnetism and Magnetic Materials, November, 1995, Philadephia.
[4] L. He, W. D. Doyle, and H. Fujiwara, IEEE Trans. Magn. **30**, 4086 (1994).
[5] P. R. Gillette and K. Oshima, J. Appl. Phys. **29**, 529 (1958).
[6] R. Kikuchi, J. Appl. Phys. **27**, 1352 (1956).

# Structural and magnetic studies of heteromagnetic multilayers by reflectivity of circularly polarized soft x rays (abstract)

Y. U. Idzerda, V. Chakarian, C. J. Gutierrez, and G. A. Prinz
*Naval Research Laboratory, Code 6345, Washington, DC 20375*

C.-C. Kao
*National Synchrotron Light Source, Brookhaven National Laboratory, Upton, New York 11973*

J.-H. Park, G. Meigs, and C. T. Chen
*AT&T Bell Laboratories, 600 Mountain Avenue, Murray Hill, New Jersey 07974*

The reflectivity of circularly polarized (CP) soft x rays is a technique which combines the power of x-ray scattering and magnetic circular dichroism and allows the structural *and* magnetic characterization of heteromagnetic multilayers. In this technique, the energy and angular dependence of the differential reflectivity of left- and right-circularly polarized soft x rays at the relevant absorption edges of the constituent elements of the multilayers are measured. As examples the reflectivity curves for single films of Fe, Co, ordered and disordered $Fe_{50}Co_{50}$ alloys, and for a trilayer consisting of two single crystal $Fe_{30}Co_{70}$ films separated by an 8.7 Å Mn spacer layer media utilizing complex dielectric tensors with no free parameters show that the rich reflectivity curves can be used to determine the multilayer magnetic ordering, film thicknesses, interface quality, as well as differentiating between ordered and disordered alloys. © *1996 American Institute of Physics.* [S0021-8979(96)70308-9]

 0021-8979/96/79(8)/6492/1/$10.00 © 1996 American Institute of Physics

# Giant magnetic effects in the *L*-edge extended x-ray absorption fine structure of 3*d* transition metals

V. Chakarian,[a] Y. U. Idzerda, and K. M. Kemner
*Naval Research Laboratory, Code 6345, Washington, DC 20375*

J.-H. Park, G. Meigs, and C. T. Chen
*AT&T Bell Laboratories, 600 Mountain Avenue, Murray Hill, New Jersey 07974*

A systematic extended x-ray absorption fine structure (EXAFS) study at the $L$ edges of ferromagnetic Fe, Co, and Ni thin films has been conducted using circular polarized soft x rays. A very large helicity dependence has been observed in the $L$-edge EXAFS spectra. Surprisingly, in contradiction with prior works, these magnetic EXAFS results indicate a *nonlinear* dependence of this effect on the magnetic polarization of the scattering atom. The data further indicate that the dominant scattering paths responsible for the effect are different from those responsible for EXAFS. A discussion of the results in relation to the present understanding of the underlying mechanism and its ramifications to the existing theoretical frameworks is also presented. © *1996 American Institute of Physics.* [S0021-8979(96)78508-5]

The possibility of adding *magnetic* selectivity to the scope of extended x-ray absorption fine structure (EXAFS) has prompted considerable interest in its spin-dependent counterpart, spin-polarized EXAFS (SPEXAFS) or, more appropriately, magnetic EXAFS (MEXAFS). MEXAFS is the natural extension of x-ray absorption magnetic circular dichroism (MCD) analysis beyond the near-edge region and into the extended fine structure region. Both MCD and MEXAFS are measures of the difference in the absorption of left- and right-circular polarized photons at the absorption edges of the material under investigation.

EXAFS is a mature, chemically selective spectroscopic method for local atomic structure determination.[1] On the other hand, MEXAFS, which is related to the magnetic short-range order, is still in its infancy. The lack of a first-principles theory allowing for the extraction of tangible quantitative material parameters and the added difficulty of the MEXAFS measurements due to the small size of the effect have hampered the generation of a deeper understanding of the underlying mechanism. Its origin is primarily the spin–orbit interaction of the core electrons and the exchange interaction between the spin–polarized photoelectron and the magnetically polarized neighboring atoms. The feasibility of MEXAFS was first demonstrated on $3d$ transition metal $K$-edge and $4f$ rare-earth $L$-edge measurements.[2] In later studies,[2–8] it was almost universally found that, for these edges, the size of the MEXAFS oscillations is linearly proportional to the spin moment of the scattering atom. Finally, in the case of the pure $3d$ metals Fe, Co, and Ni, it was found that the MEXAFS oscillations are in phase with the EXAFS oscillations, further supporting the notion that this effect is due primarily to the scattering from magnetic nearest neighbors.[6–8]

Until now, due to the lack of a suitable circular polarized photon source as well as the lack of an established data reduction procedure, this type of study has not been extended to the lower binding energy $L$ edges of the transition metals. The standard EXAFS analysis is complicated by the small energy separation of the $L_3$ and $L_2$ edges in transition metals, causing the (M)EXAFS oscillations for these edges to overlap. Furthermore, the MEXAFS oscillations for the well separated $L_3$ and $L_2$ edges of rare-earth elements show identical structure, but of opposite sign, prompting prior investigators to suggest that, due to this cancellation, measurements at the overlapping $L$ edges of the $3d$ elements would yield a negligible MEXAFS signal and hence be impractical.[4,6] Nevertheless, due to the strong dipole transition to the magnetically interesting $3d$ states, the MEXAFS effect may be much larger at the $L$ edges of transition metals than their $K$ edges, where the earlier studies were conducted. (Similar arguments apply to the $M$ edges vs $L$ edges of $4f$ rare earths.)

In order to test the above hypotheses and to demonstrate the feasibility of the MEXAFS measurements for the $L$ edges of $3d$ transition metals, transmission MCD measurements extended to the EXAFS region have been performed for Fe, Co, and Ni thin films. Helicity dependent soft x-ray absorption spectra (XAS) were obtained by measuring the relative photon flux transmitted through the magnetic thin films using a photodiode mounted behind the sample. Details of the experimental procedures are described elsewhere.[9,10] Numerous scans were collected over a period of 25–30 h for each sample to improve the signal-to-noise quality of the data.[11]

The films were grown under ultrahigh vacuum conditions by e-beam evaporation from pure-metal sources onto $\sim$1-$\mu$m-thick semitransparent parylene $(C_8H_8)_n$, substrates. The film growth as well as the measurements were conducted at room temperature. The film thicknesses (about 250–300 Å) were independently determined by comparing the measured absorption to the calculated atomic photoabsorption cross sections and by *ex situ* x-ray fluorescence methods. *In situ* element-specific magnetic hysteresis measurements[12,13] show these films to display nearly square magnetization behavior with remnant magnetizations of 90%–100%. The structure of the deposited films can be inferred from the measured $L$-edge EXAFS oscillations. An analysis of the data indicates that the Fe, Co, and Ni films are most likely in the bcc, hcp, and fcc phases, respectively,[14] consistent with structural determinations for the evaporation of these materials on glass slides. In addition, the bcc struc-

[a]Mailing address: NSLS Bldg. 725A/U4B, Brookhaven National Laboratory, Upton, NY 11973.

 0021-8979/96/79(8)/6493/3/$10.00 © 1996 American Institute of Physics 

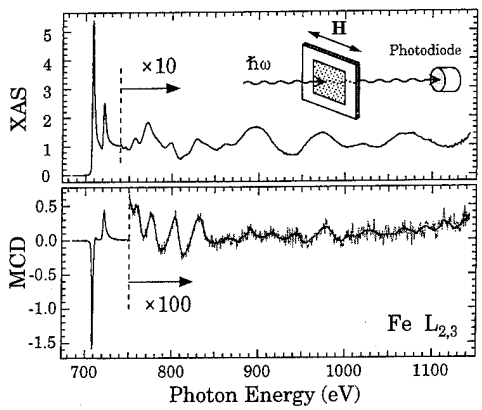



FIG. 1. The $L_{2,3}$ XAS (EXAFS) (top panel) and MCD (MEXAFS) (bottom panel) for the Fe thin film. The solid curve through the MCD data in the EXAFS region is the result of numerical smoothing and is provided as a guide to the eye. The experimental geometry for the acquisition of the helicity-dependent (M)EXAFS spectra is also shown.

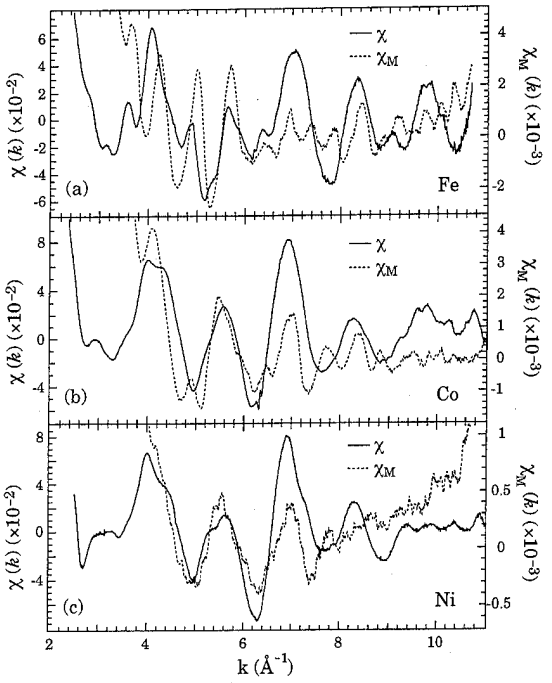



FIG. 2. The $L_{2,3}$ EXAFS, $\chi(k)$, and MEXAFS, $\chi_M(k)$, for Fe (top panel), Co (middle panel), and Ni (bottom panel) thin films. The numerically smoothed $\chi_M(k)$ data are shown for clarity.

ture of the Fe film was verified by $K$-edge EXAFS measurements for a Fe thin film similar to the one used in the $L$-edge work (after capping with a vanadium overlayer to prevent oxidation).[15]

The results for the Fe film are shown in Fig. 1. The figure shows the total absorptivity (XAS), $\mu(\omega)=\mu_+(\omega)+\mu_-(\omega)$, and the dichroic signal (MCD), $\delta\mu(\omega)=\mu_+(\omega)-\mu_-(\omega)$. The MCD spectrum was scaled to correct for the incomplete circular polarization of the photons and the photon incidence angle. A smoothly varying, single cubic-spline spin-independent continuum background function has been removed from the EXAFS region and the data were normalized in the usual way to yield a combined $L_{2,3}$ edge jump of unity after the $L_2$ edge.

A comparison of the results for Fe, Co, and Ni (M)EXAFS is possible after a standard conversion of the data to momentum space, as shown in Fig. 2.[16] Here $\chi(k)=[\mu(k)/\mu_0(k)]-1$ and $\chi_M(k)=\delta\mu(k)/\mu_0(k)$, where $\mu_0(k)$ is the spin-independent high-energy continuum background. Note that the intensity variations of the EXAFS oscillations are about $\pm 6\%$–$7\%$ of the edge jump. Considering that the measurements were made at room temperature and that the films are polycrystalline, this indicates a relatively large coherence length for the crystallites in the films. As is readily apparent in Fig. 2 there is a substantial difference between the detailed shapes of the EXAFS oscillations for Fe and for Co and Ni. This is due, in part, to the differences in the local atomic structure of these films (Fe: bcc; Co: hcp; Ni: fcc). The EXAFS for Co and Ni films are, as expected, strikingly similar. A further source of difference between the detailed shapes of the EXAFS for these films is due to the changes in the interference between the oscillations associated with the $L_3$ and $L_2$ edges (the energy separation between the two edges increases in going from Fe to Ni), which accounts for the minor differences between the Co and Ni EXAFS.

Although the EXAFS oscillations of the Fe, Co, and Ni films are of comparable intensity, the relative amplitude of the MEXAFS oscillations, compared to the EXAFS oscillations, changes dramatically in going from Fe to Ni. The results, summarized in Table I show that $\chi_M(k)/\chi(k)$ is $\pm 5\%$, $\pm 2.5\%$, and $\pm 0.5\%$ for Fe, Co, and Ni, respectively. Noting the magnitudes of the orbital and spin moments of bcc Fe, hcp Co, and fcc Ni, also shown in Table I, these measurements indicate that the size of the effect does *not* scale linearly with the spin (or with the orbital or total) moment of the scattering atom. It is important to note that these oscillations are up to 50 times larger than those observed at the $K$ edge of Fe[2,3,5,8] and Co,[6] demonstrating the enhanced sensitivity of the $L$-edge absorption to the spin-dependent scattering potential of the neighboring atoms. Furthermore, contrary to the $K$-edge measurements, an inspection of the respective EXAFS and MEXAFS spectra readily indicates that the MEXAFS spectra are not in-phase with the EXAFS spectra and display higher frequency oscillations. This clearly indicates that the scattering paths that dominate MEXAFS oscillations are not the same as those which give rise to the EXAFS oscillations. Indeed, the shorter wavelength, higher frequency MEXAFS signal cannot be generated by nearest-neighboring single scattering paths, but is

TABLE I. Summary of experimental results, showing the relative size of the MEXAFS effect ($\chi_M$) as compared to EXAFS ($\chi$) at the $L_{2,3}$ edges of Fe, Co, and Ni thin films. Also shown for reference are the electron orbital ($m_l$) and spin ($m_s$) moments for each of these elements.

| | Fe | Co | Ni |
|---|---|---|---|
| $m_l(\mu_B)$[a] | 0.092 | 0.147 | 0.051 |
| $m_s(\mu_B)$[a] | 2.083 | 1.523 | 0.518 |
| $\chi_M/\chi$ | 5% | 2.5% | 0.5% |

[a]Room temperature Einstein–de Haas gyromagnetic ratio measurements (Ref. 20).

dominated by longer scattering path lengths, most likely from multiple scattering events. Multiple scattering is consistent with both the higher frequency of the MEXAFS, and the nonlinear dependence of the MEXAFS oscillations with the magnetic moment of the scattering center.

In principle, full multiple-scattering EXAFS formalisms which incorporate the appropriate circular polarized selection rules and correct spin-dependent atomic potentials should completely reproduce these spectra, including their amplitude dependence. Theoretical treatments of this type have been attempted,[17] with particularly good agreement for the half-filled shell of Gd.[18] Although variations of the spin-dependent portion of the atomic potential results in only small differences in the individual helicity dependent EXAFS spectra, the *difference* of the two spectra measured with opposite light helicity (the MEXAFS spectra) is quite sensitive to the method of inclusion of the spin–orbit interaction of the core electrons which generate the small energy differences in the spin-dependent potentials. In fact, the detailed comparison of the measured MEXAFS spectra with theoretical spectra can be used to check the accuracy of the calculated spin-dependent potentials, and allow for the refinement of the potential parameters. Combined with the standard EXAFS analysis to determine structural parameters, it is possible to extract meaningful magnetic material properties from the spin-dependent atomic potentials determined from the MEXAFS spectra.

Interestingly, we have found[9] that in extracting the orbital and spin magnetic moments from the near edge MCD spectra of Fe and Co, the best agreement between theory and experiment occurred for *ab initio* calculations which incorporated orbital polarization corrections.[19] This suggests that, to accurately reproduce the MEXAFS oscillations, the inclusion of orbital polarization effects in the spin-dependent atomic potentials may be important.

In summary, we have shown that the $L$-edge soft x-ray absorption spectra of polycrystalline films of bcc Fe, hcp Co, and fcc Ni have a very large helicity dependence, far larger than for their $K$ edges. The relative amplitude of the $L$-edge MEXAFS spectra does not scale linearly with the magnetic moment of the scattering atom and the oscillations are at a higher frequency than the EXAFS oscillations, identifying the dominant scattering paths to be longer than those for the nearest neighbors.

One of the authors (V.C.) is supported by the Office of Naval Research. This work was performed while K.M.K. was a NRL/NRC fellow. Work done at National Synchrotron Light Source was supported by the DOE, under Contract No. DE-AC02-76CH00016.

[1] Many excellent references exist on this topic. For an introduction, see, e.g., B. K. Teo, *EXAFS: Basic Principles and Data Analysis* (Springer, Berlin, 1986). For a more advanced treatment, see, e.g., D. C. Koningsberger and R. Prins, *X-Ray Absorption* (Wiley, New York, 1988).
[2] G. Schütz, R. Frahm, P. Mautner, R. Wienke, W. Wagner, W. Wilhelm, and P. Kienle, Phys. Rev. Lett. **62**, 2620 (1989).
[3] G. Schuütz, M. Knülle, and H. Ebert, Phys. Scripta **T49**, 302 (1993).
[4] G. Schütz, P. Fischer, K. Attenkofer, M. Knülle, D. Ahlers, S. Stähler, C. Detlefs, H. Ebert, and F. M. F. de Groot, J. Appl. Phys. **76**, 6453 (1994).
[5] O. Isnard, S. Miraglia, D. Fruchart, C. Giorgetti, S. Pizzini, E. Dartyge, G. Krill, and J. P. Kappler, Phys. Rev. B **49**, 15692 (1994).
[6] M. Knülle, D. Ahlers, and G. Schütz, Solid State Commun. **94**, 267 (1995).
[7] E. Dartyge, F. Baudelet, C. Brouder, A. Fontaine, C. Giorgetti, J. P. Kappler, G. Krill, M. F. Lopez, and S. Pizzini, Physica B **208–209**, 751 (1995).
[8] K. Kobayashi, H. Maruyama, H. Maeda, T. Iwazumi, H. Kawata, and H. Yamazaki, Physica B **208–209**, 779 (1995).
[9] C. T. Chen, Y. U. Idzerda, H.-J. Lin, N. V. Smith, G. Meigs, E. Chaban, G. H. Ho, E. Pellegrin, and F. Sette, Phys. Rev. Lett. **75**, 152 (1995).
[10] V. Chakarian, Y. U. Idzerda, C. T. Chen, G. Meigs, and C.-C. Kao, in *Applications of Synchrotron Radiation in Industrial, Chemical, and Materials Science*, edited by L. J. Terminello, K. L. D'Amico, and D. K. Shuh (Plenum, New York, in press).
[11] The use of the transmission method offers a significant improvement of signal-to-noise ratio as compared to other methods, e.g., total electron yield, since with the former the entire sample is probed (and hence, samples as thick as 300–500 Å can be used) while with the latter only the top 25–50 Å are probed. The signal-to-noise ratio for partial fluorescence yield measurements, another method for measuring XAS, is always worse than the other methods and hence not suitable for the kind of measurements described in this work.
[12] V. Chakarian, H.-J. Lin, Y. U. Idzerda, G. Meigs, E. E. Chaban, J.-H. Park, C. J. Gutierrez, G. A. Prinz, and C. T. Chen, in *MRS Proceedings: Applications of Synchrotron Radiation Techniques to Materials Science II*, edited by D. L. Perry, N. D. Shinn, K. L. D'Amico, G. Ice, and L. J. Terminello (Materials Research Society, 1995), Vol. 375.
[13] V. Chakarian, Y. U. Idzerda, G. Meigs, E. E. Chaban, and C. T. Chen, Appl. Phys. Lett. **66**, 3368 (1995).
[14] K. M. Kemner *et al.* (unpublished).
[15] K. M. Kemner (private communication).
[16] The Fourier transforms of the data, as is usually done within the standard framework of EXAFS formalism, are not shown. While such conversions are necessary for the subsequent analysis of the data, their interpretation is complicated in this case due to the overlap of the $L_3$ and $L_2$ edges, requiring nontrivial deconvolution of the spectra which is beyond the scope of this manuscript and will be the subject of an upcoming manuscript (Ref. 14). The intention of the present manuscript is to illustrate the nature of the MEXAFS signal rather than presenting a detailed analysis of the (M)EXAFS data to extract bond lengths or Debye–Waller factors.
[17] C. Brouder and M. Hikam, Phys. Rev. B **43**, 3809 (1991).
[18] A. Ankudinov and J. J. Rehr, Phys. Rev. B **52**, 10214 (1995).
[19] P. Söderlind, O. Eriksson, B. Johansson, R. C. Albers, and A. M. Boring, Phys. Rev. B **45**, 12911 (1992).
[20] K. Adachi, D. Bonnenberg, J. J. M. Franse, R. Gersdorf, K. A. Hempel, K. Kanematsu, S. Misawa, M. Shiga, M. B. Stearns, and H. P. J. Wijn, *Magnetic Properties of Metals. Subvolume a: 3d, 4d and 5d Elements, Alloys and Compounds* (Springer, Berlin, 1986), Vol. III/19a, p. 178.

# Magnetic circular dichroism in EELS (abstract)

G. R. Harp
*Department of Physics and Astronomy, Ohio University, Athens, Ohio 45701*

R. F. C. Farrow and R. F. Marks
*IBM Research Division, Almaden Research Center, 650 Harry Road, San Jose, California 95120-6099*

We evaluate the possibility of using dichroic electron energy loss spectroscopy (DEELS) as an alternative to x-ray magnetic circular dichroism (XMCD). It is well known that electron energy loss spectroscopy and x-ray absorption spectroscopy are highly analogous, providing similar information. A simple semiclassical model suggests that DEELS might have a magnetic sensitivity similar to that of XMCD. This sensitivity will be reduced, however, by multiple scattering of the probe electron before and after the energy loss event. Thus it is difficult to predict the magnitude of the DEELS effect. Experiments were performed at the *L*-edge of polycrystalline Fe, Co, and Ni thin film samples with uniaxial in-plane magnetic anisotropy, prepared *in situ* with a magnetic bias field. Even in those most favorable cases, the DEELS effect is seen to be at least 10 times smaller than similar effects in XMCD. © *1996 American Institute of Physics.* [S0021-8979(96)70408-3]

 0021-8979/96/79(8)/6496/1/$10.00 © 1996 American Institute of Physics

# Temperature and field-induced magnetization flips in amorphous Er–Fe alloys evidenced by x-ray magnetic circular dichroism

L. M. Garcia,[a] S. Pizzini, J. P. Rueff, J. Vogel, R. M. Galéra, and A. Fontaine
*Laboratoire L. Néel, CNRS, B.P. 166X, 38042 Grenoble Cedex, France*

J. P. Kappler
*IPCMS, Rue de Loess, 67037, Strasbourg, France*

G. Krill
*LURE, Bat. 209D, 91405 Orsay, France*

J. Goedkoop
*ESRF, B.P. 220, 38042, Grenoble, France*

Magnetic properties of amorphous $Er_{1-x}Fe_x$ alloys with $x \approx 0.7$ have been studied. Macroscopic characterization has been performed by measuring temperature- and field-dependent magnetization. Applying a magnetic field the compensation temperature first decreases, but increases again at larger fields. This "exotic" behavior has been interpreted in terms of the sperimagnetic character of both subnetworks. The suggested scheme has been checked by measuring x-ray circular magnetic dichroism at the Er $M_5$-edge. Using this atom-sensitive technique we have been able to detect temperature-induced as well as field-induced flips of the Er-subnetwork with respect to the direction of the applied field. © *1996 American Institute of Physics.* [S0021-8979(96)78608-1]

## I. INTRODUCTION

Amorphous alloys have received much attention in the last years due to their interesting properties and their applicability for new devices.[1,2] Their magnetic properties are strongly affected by bond and chemical disorder causing a distribution of magnetic moments and exchange interactions. Also, the randomly varying electrostatic fields create, via spin–orbit coupling, locally varying single-site anisotropies giving rise to noncollinear arrangements of the magnetic moments. These sperimagnetic structures have been widely observed in amorphous rare-earth-transition-metals alloys $R_{1-x}T_x (0<x<1)$.[1] The large spin–orbit coupling of non-$S$-state rare earths gives rise to large local anisotropies and therefore to a fan structure in the $R$ subnetwork moment. In the case of $T$=Fe noncollinear structures produced by the $R-T$ exchange have been observed also in the Fe subnetwork.[1]

In the case of heavy $R$, where $R$ and $T$ moments are coupled antiparallel,[3] the different temperature dependence of each subnetwork moment can lead to a vanishing global magnetization at a temperature $T_{comp}$ called "compensation temperature." The fan magnetic structure in amorphous sperimagnets is responsible for a strong dependence of the magnetization of each subnetwork on the applied magnetic field. $T_{comp}$ are therefore strongly dependent on the applied magnetic field.

The objective of the present paper is to characterize the magnetic behavior of an amorphous $Er_{1-n}Fe_n$ ($n \approx 0.70$) compound from a macroscopic point of view and to study independently the magnetic behavior of the Er subnetwork taking advantage of the element selectivity of x-ray absorption spectroscopy. X-ray magnetic circular dichroism (XMCD) measurements were performed at the Er $M$-edge as a function of temperature and applied magnetic field.

[a]On leave from ICMA, CSIC-Universidad de Zaragoza, Spain.

## II. MACROSCOPIC STUDY

Crystalline alloys of $Er_{1-x}Fe_x$ with nominal composition $x=0.60$ were prepared by melting the starting elements in a cold crucible furnace. These alloys were used as targets in a sputtering chamber, using ionized Ar gas as sputter gas. Amorphous films were simultaneously grown on monocrystalline-Si and kapton foils, cooled at 77 K. A Si-deposited sample was used in the XMCD measurements to optimize the thermal contact with the cryostat head, while the kapton-deposited samples were used for macroscopic measurements in order to reduce the diamagnetic contribution of the substrate. The magnetic properties of the samples were shown to be independent of the nature of the substrate. Amorphization was checked by x-ray diffraction. Rutherford backscattering (RBS) with $\alpha$ particles performed on the amorphous films gave us a composition of $x=0.73\pm0.01$ and allowed us to determine the sample thickness. The work presented in this paper is focused on two samples: sample "a," 400 Å thick, and sample "b," 80 Å thick. All the samples were protected against oxidation by Cr 50 Å thick films.

Alternative magnetic susceptibility ($\chi$) was measured in sample "a" with a superconducting quantum interference device from 4.2 to 300 K. The ordering temperature detected by measuring the thermal dependence of susceptibility, $\chi(T)$, is $T_c=190$ K. The macroscopic magnetic behavior of this compound was characterized by isofield-$M(T)$ and isotherms-$M(H)$ measurements from 4.2 K$<T<$300 K and $0<H<6T$ performed in a vibrating sample magnetometer. The Arrott-plots, $M^2(H/M)$, obtained from $M(H)$ measurements show a change of the slope around $T_c$, which is typical for random anisotropy systems.[4] $M(H)$ measurements show, up to $6T$, the characteristic lack of saturation associated with noncollinear magnetic structures. We can therefore assume that our compounds present sperimagnetic structures.

$M(T)$ measurements were performed on the sample "a" for different values of applied magnetic field. At low fields

 0021-8979/96/79(8)/6497/3/$10.00 © 1996 American Institute of Physics 

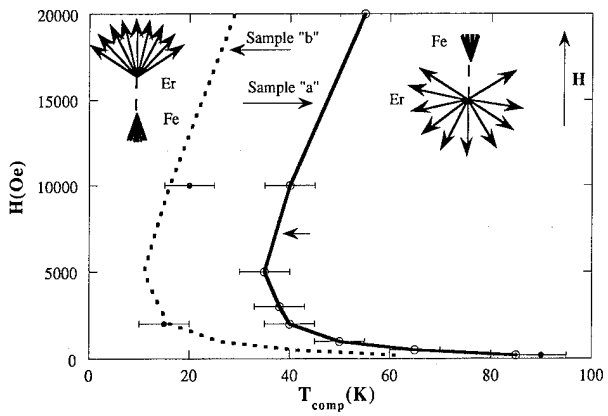



FIG. 1. Configuration phase diagram with respect to the applied field for two samples of $Er_{1-x}Fe_x$ ($x=0.73$): sample "a" (400 Å thick) and sample "b" (80 Å thick).

(around $0.05T$) $M(T)$ shows a compensation temperature at $T_{comp}=65$ K. By increasing $H$, the minimum of the magnetization shifts to lower temperatures and to nonzero magnetization values ($T_{comp}=35$ K at $H=0.5T$). For larger fields this tendency is reversed and the minimum is shifted to higher temperatures. In Fig. 1 we present the evolution of $T_{comp}$ with the applied field.

For each magnetic field, we can identify the minimum in magnetization as a *pseudo*-compensation temperature, although no vanishing of magnetization occurs. As in the case of crystalline compounds, for $T<T_{comp}$ the $R$ subnetwork is parallel to the external applied field. For $T>T_{comp}$ the $T$ subnetwork magnetization dominates and the $R$ moments flip to antiparallel to $H$. The strong evolution of $T_{comp}$ as a function of $H$ is quite unusual for $R-T$ alloys and has to be explained in terms of the sperimagnetic (fan) structure of the amorphous films. As the magnetic anisotropy of Fe is weaker than the Er one, a low magnetic field orients the Fe moments more easily than the Er moments. The reinforcement of the net Fe moment projected along the field gives rise to a decrease of $T_{comp}$. For higher fields this effect saturates, Fe moments are collinear with the applied field and the increase of the field reinforces the collinearity of the Er subnetwork, causing an increase of $T_{comp}$.

The minima detected in the $M(T)$ measurements of sample "b" ($T_{comp}$) show the same tendency of sample "a", but the minimum in the $T_{comp}(H)$ is shifted to lower temperatures. This change in compensation temperature is very likely due to a slight difference in the composition of samples "a" and "b." It has been reported that for $Tb_{1-x}Fe_x$ amorphous alloys a variation of composition of 1 at. % can cause a change of $T_{comp}$ up to 40 K.[1]

The evolution of $T_{comp}(H)$ reported for these samples and the interpretation that we give to this phenomenon suggest that a flipping of Er and Fe subnetworks might be induced by the applied field, if a fixed-temperature slightly higher than the minimum of $T_{comp}(H)$ is chosen (Fig. 1). Macroscopic isothermal measurements performed at these temperatures, $M(H)$ or $\chi(H)$ do not allow us to probe the change of the direction of the two subnetworks. To test the validity of the proposed scheme, we need a technique able to separate the magnetic contribution of each subnetwork and their direction, and suited to amorphous systems.

## III. XMCD STUDY

X-ray magnetic dichroism is the measure of the dependence of the x-ray absorption (XAS) spectra on the helicity of x-ray photons.[5–7] This technique is particularly valuable for our problem since: (a) it is atom selective. By tuning the photon energy to an absorption edge, it allows us to separate the magnetic contributions of the Er and Fe subnetworks; (b) it is sensitive to the direction of the magnetic moments with respect to the applied field and can therefore detect the flipping of the Er or Fe subnetwork upon application of temperature or field; (c) it does not need long-range order and can be applied to any kind of material, crystalline or amorphous, as long as a net magnetic moment exists on each subnetwork.

The XMCD measurements were carried out at SuperACO (LURE) on the SU22 beamline.[8] The calculated circular polarization rate is 12% in the studied energy range.[9] Due to the low XMCD signals at the Er $M_4$ edge[10] only $M_5$-edge absorption spectra ($3d\rightarrow 4f$ transitions) were carried out. Experiments were performed on sample "b" in total electron yield detection for temperatures from 4.2 to 300 K and in magnetic fields up to $5T$. The magnetic field was

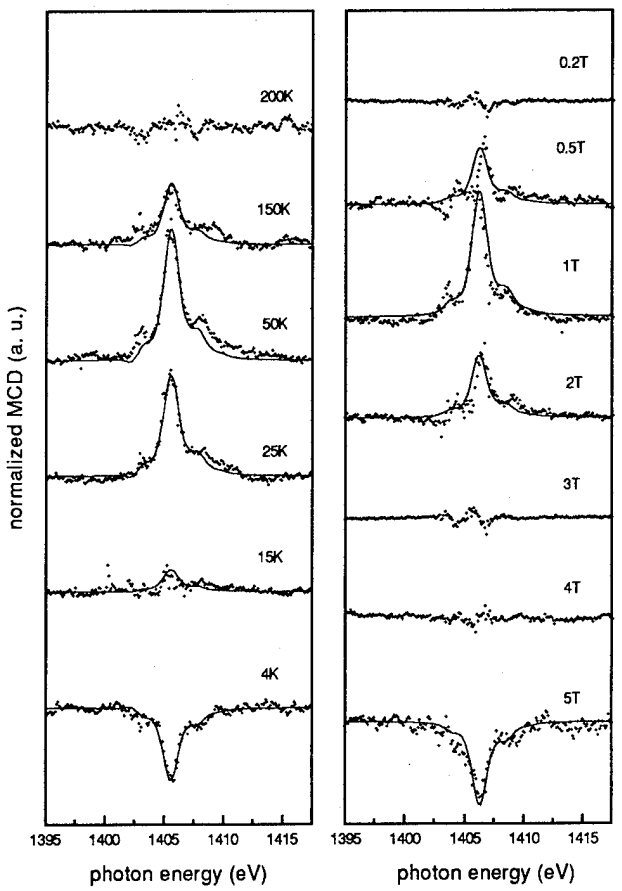



FIG. 2. (a) Temperature evolution of the Er $M_5$-XMCD signal of amorphous $Er_{1-x}Fe_x$ ($x=0.73$) in a magnetic field $H=1T$. (b) Evolution of the Er $M_5$-XMCD signal of the same compound as a function of the applied magnetic field and at a constant temperature of 25 K. The full lines are the theoretical fits to the data.

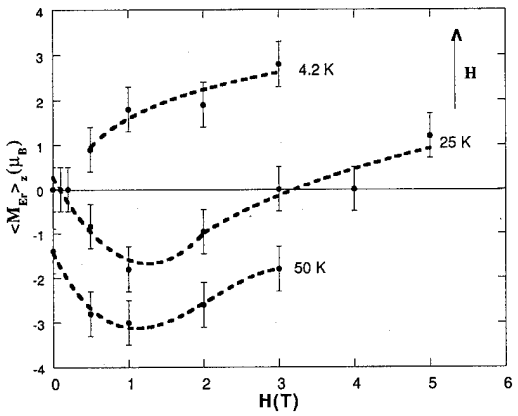



FIG. 3. Field dependence of the Er moment projected along the direction of an applied field at $T$=4.2, 25 and 50 K. Dashed lines are a guide to eye.

applied perpendicular to the sample surface and along the photon propagation direction. XMCD signals are normalized difference of two absorption spectra measured with a fixed helicity and opposite directions of the applied magnetic fields, $\sigma^+(E)$ and $\sigma^-(E)$.

In order to extract an approximate value of $\langle M_J\rangle_{4f}$ of Er from the experimental spectra, the $\sigma^+(E)$ and $\sigma^-(E)$ absorption spectra were calculated using an atomic approach. A combination of a magnetic field[5,11] and an axial crystal field[11] was used to calculate a perturbed level scheme of the $Er^{3+}$ ion which fitted the experimental spectra.

The evolution of the Er $M_5$-XMCD signal as a function of temperature in an applied field of $1T$ is shown in Fig. 2(a). At low temperatures (4.2 K) the signal is negative as expected for Er magnetization parallel to the applied field.[10] At $T$=15 K, we are close to the compensation temperature for this field and the XMCD signal is zero. Above this temperature the signal changes sign, indicating that the Er-subnetwork magnetization is now antiparallel to the external field (flipping). Finally, the decrease of the signal for higher temperature is associated with the approach of the ordering temperature. The Er-$4f$ moments were calculated from a theoretical fit of the experimental data. The largest moment, detected at 50 K, is of the order of $3\mu_B$ which is by far smaller than the saturated $9\mu_B$ Er-moment. Reminding that XCMD gives the average Er-moment projected along the magnetic field, this result suggests a strongly asperomagnetic structure of Er-subnetwork, as proposed in Fig. 1. This result is consistent with the low values of the net projection of the $R$ moment which were extrapolated from macroscopic measurements on other sperimagnetic $R_{1-x}Fe_x$ alloys.[1]

XMCD experiments as a function of the applied field were performed at different temperatures corresponding, in the diagram of Fig. 1, with thermal ranges in which the net moment of the $R$ subnetwork is parallel to the field (4.2 K), antiparallel (50 K) and at a temperature (25 K) in which the isotherm crosses the dashed line of sample "b." In Fig. 3, we show the evolution of the Er-$4f$ moments calculated from the theoretical fit of XMCD for the three isotherms. At 4.2 K, the projection of the Er $4f$-moment along the field is always positive and increases with the field, which agrees with the fan structure proposed in Fig. 1. At $T$=50 K, this projection is always negative and a minimum in its dependence with the field is observed. The net Er $4f$ moment along the field is always antiparallel to the applied field as proposed in Fig. 1, increasing at low $H$ values and decreasing at higher ones. The decrease at high fields is expected, since the field is applied in the opposite direction to the net magnetic moment direction. The increase at low fields can be explained considering the orientation of the Fe subnetwork along the field. Due to antiferromagnetic coupling between Er and Fe subnetworks, the antiparallel projection of the Er subnetwork has to follow the close-up of the angular distribution of the Fe moments.

Figure 2(b) shows selected experimental XMCD spectra measured at $T$=25 K, together with the corresponding theoretical fits. The $H$ dependence of the fitted magnetic moments at 5, 25, and 50 K is shown in Fig. 3. At 25 K the signal is close to zero for low fields ($<0.2T$) since we are very close to the compensation temperature for these fields. For $0.5T$ and $1T$ the signal is positive, i.e., the Er moment is antiparallel to the applied field. For $3T$ and $4T$ the signal is again zero, indicating the approach of a compensation temperature. Increasing the field up to $5T$ induces a further flip of the Er magnetization, as expected on crossing the dashed line of Fig. 1.

In conclusion, the minima detected in the $M(T)$ curves, the Er subnetwork flips with respect to the $H$ direction. This must be correlated with a flip in the Fe subnetwork. The different anisotropy of Fe and Er subnetworks explains the reported $T_{comp}(H)$ behavior in this sperimagnetic compound. This "exotic" behavior gives rise not only to temperature-induced but also field-induced flips of the Er.

## ACKNOWLEDGMENTS

One of us (I.M.G.) acknowledges a FPI grant of the DGICYT (Ministerio de Educacion y Ciencia of Spain). This work has been achieved with the helpful support of the EEC-CHH contract ERBCHRXCT92039.

[1] P. Hansen, in *Handbook of Magnetic Materials,* edited by K. H. J. Buschow (Elsevier, New York, 1991), Vol. 6.
[2] K. Moorjani and J. M. D. Coey, *Magnetic Glasses*, from the Series of Methods and Phenomena in Science and Technology, edited by S. P. Wolsky and A. W. Czanderna (Elsevier, New York, 1984), Vol. 6, Chap 6.
[3] I. A. Campbell, J. Phys. F **2**, L47 (1972).
[4] A. Aharony and E. Pytte, Phys. Rev. Lett. **45–49**, 1583 (1980).
[5] B. T. Thole, G. van der Laan, and G. A. Sawatzky, Phys. Rev. Lett. **55**, 2086 (1985).
[6] G. Schütz, W. Wagner, W. Wilhelm, P. Kienle, R. Zeller, R. Frahm, and G. Materlik, Phys. Rev. Lett. **58**, 737 (1987).
[7] C. T. Chen, F. Sette, Y. Ma, and S. Modesti, Phys. Rev. B **42**, 7262 (1990).
[8] J. Ph. Schillé, J. P. Kappler, Ph. Sainctavit, Ch. Cartier dit Moulin, C. Brouder, and G. Krill, Phys. Rev. B **48**, 9491 (1993).
[9] D. Lefebvre, Ph. Sainctavit, and C. Malgrange, Rev. Sci. Instrum. **65**, 2556 (1994).
[10] J. Goedkoop, B. T. Thole, G. Van der Laan, G. A. Sawatzky, F. M. F. de Groot, and F. C. Fuggle, Phys. Rev. B **37**, 2086 (1988).
[11] M. Sacchi, O. Sakho, F. Sirotti, and G. Rossi, Appl. Surf. Sci. **65–66**, 170 (1993).

# Magnetic circular dichroism at the *K* and *L* edges of Co and Cu in Co/Cu(001)

Ruqian Wu
*Department of Physics and Astronomy, California State University, Northridge, California 91330-8268*

A. J. Freeman
*Department of Physics and Astronomy, Northwestern University, Evanston, Illinois 60208-3112*

The fcc Co/Cu(001) system is investigated using the full potential linearized augmented plane wave method. Through the atomic force approach, large multilayer relaxations (6.5%, 5.3%, and 2.8%) are found between the adjacent Cu layers, which reduces the total energy by 128 meV. The spin and orbital magnetic moments for Co atoms are 1.79 and 0.12 $\mu_B$, respectively. At the interfacial Cu site, we found a sizable induced magnetic moment, 0.05 $\mu_B$, which can be split into $d$ (0.074 $\mu_B$) and $s,p$(0.024 $\mu_B$) contributions. Interestingly, the spin polarization of $d$ and $s,p$ states can be detected separately through the magnetic circular dichroism at the $L$ and $K$ edges, for which the calculated results agree very well with experiments. © *1996 American Institute of Physics.*
[S0021-8979(96)78708-9]

Magnetism in Co/Cu has attracted extensive attention because of its importance in both technical and fundamental aspects, such as the mechanism of magnetic ordering through a Cu spacer and the giant magnetoresistance.[1,2] As a prototype example of layer-by-layer growth, the Co/Cu interface was found to be very sharp with negligible interdiffusion [less than 0.1 monolayer (ML)].[3,4] Recent experimental work has focused on identifying the quantum-well states[5] in the Cu layers and their role in magnetic ordering. However, being overwhelmed by the magnetism of Co, it is very hard to detect the spin polarization of these quantum-well states with usual photoemission techniques.[6] Fortunately, we can solve this problem by using the newly developed magnetic circular dichroism (MCD) technique.[7] Since MCD involves photon-induced excitation from the core levels to the valence states, it has element selectivity. Very recently, strong magnetic signals (from $s$, $p$, and $d$ bands) were detected for Cu in Co/Cu(001) and Fe/Cu(001),[8,9] which challenges theoretical explanation.

In our previous first-principles calculations using the full potential linearized augmented plane wave (FLAPW) method, we found strong proximity effects from the Cu substrate to the magnetic overlayers.[10] For example, the large magnetic moment (2.07 $\mu_B$) of the Co free monolayer is reduced substantially to 1.78 $\mu_B$ when in contact with Cu(001), which is even 5% smaller than that (1.87 $\mu_B$) at the clean fcc Co(001) surface.[11] In this article, the magnetic properties of Co/Cu(001) are scrutinized further by means of discussing the spin and orbital magnetic moments, their angular decompositions, and the calculated $K$-edge and $L$-edge MCD spectra for both the Co and the interfacial Cu atoms. In addition, using the force approach, we reoptimized the atomic structure of the Co/Cu(001) overlayer system and found some significant multilayer relaxations.

Here, the Cu(001) substrate is simulated by a seven-layer slab covered on each side by a pseudomorphic Co layer. The lattice constant in the lateral plane adopts the experimental value of the fcc Cu bulk ($a$=3.615 Å) while the vertical positions of all the atoms are optimized according to their atomic forces. In the FLAPW approach, there is no shape approximation for the charge, potential, and wave functions. The Kohn–Sham equations are solved self-consistently with an energy cutoff of 13 Ry for the variational plane wave basis set. Within the muffin–tin (MT) spheres ($r_{Co}$=$r_{Cu}$=2.20 a.u.), lattice harmonics with an angular-momentum $l$ up to 8 are employed to expand the charge density, potential, and wave functions. Summations over 36 $k$ points in the 1/8 irreducible two-dimensional Brillouin zone are employed for $k$-space integrations. After the mean-root-square differences between the input and output charge and spin densities in the semirelativistic iterations become less than $1.0\times10^{-4}$ $e$/(a.u.)$^3$, the spin–orbit coupling is invoked in a second variational way.

Surprisingly, as listed in Table I, a large multilayer relaxation is found in Co/Cu(001), which lowers the total energy by as much as 128 meV/cell compared to the unrelaxed geometry. The distance between interior Cu layers (e.g., $d_{Cu(C)-Cu(I-2)}$) shrinks 2.8% from that in the ideal fcc Cu lattice, 3.41 a.u. Even larger relaxations are found in the surface and subsurface regions where the $d_{Cu(I)-Cu(I-1)}$ and $d_{Cu(I-1)-Cu(I-2)}$ shrink by 6.5% and 5.3%, respectively. These large multilayer relaxations, however, are mainly due to the fact that the experimental lattice constant used in the lateral plane is too large. Our total energy calculations for the fcc bulk Cu indicate that the equilibrium lattice constant is 6.647 a.u.—a value of 2.7% smaller than the experimental one, 6.831 a.u. Nevertheless, since $d_{Cu(I)-Cu(I-1)}$ is clearly shorter than the interlayer distances between interior Cu layers, the presence of a Co overlayer does not fully restore the relaxation on the Cu(001) surface. The calculated equilibrium dis-

TABLE I. Calculated vertical atomic position, $z$ (in a.u.), the spin and orbital magnetic moments for Co/Cu(001).

| Atom | Cu(C) | Cu(I-2) | Cu(I-1) | Cu(I) | Co |
|---|---|---|---|---|---|
| $z$ | 0.00 | 3.32 | 6.55 | 9.74 | 12.80 |
| $M$ | 0.00 | 0.002 | −0.005 | 0.050 | 1.785 |
| $L_z$ | 0.00 | 0.000 | 0.000 | 0.004 | 0.116 |

 0021-8979/96/79(8)/6500/3/$10.00 © 1996 American Institute of Physics

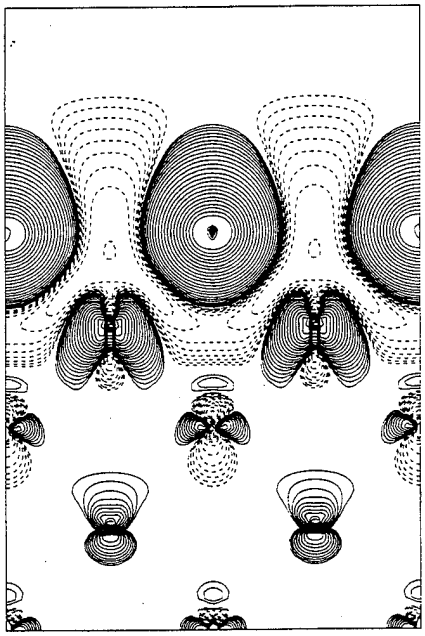


FIG. 1. Calculated spin density for Co/Cu(001). Contours in start from $\pm 1\times10^{-4}$ $e$/a.u.$^3$ and increase successively by a factor of $\sqrt{2}$.

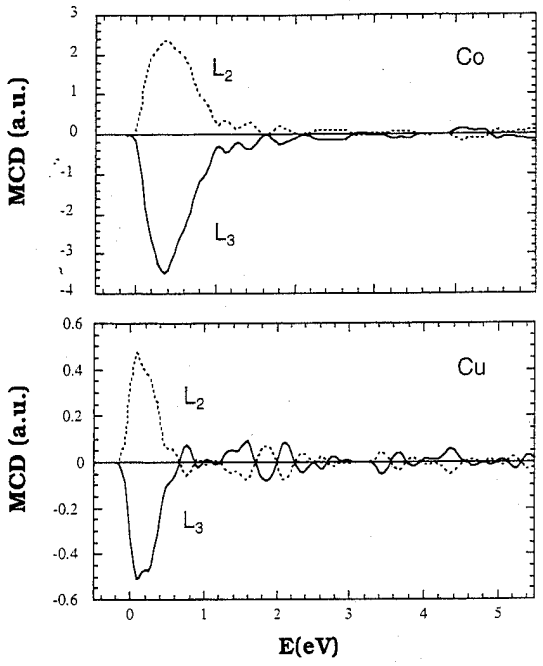



FIG. 2. Calculated $L$-edge MCD spectra for the Co and Cu atoms in Co/Cu(001). Solid and dotted lines stand for the $L_3$ and $L_2$ edges, respectively.

tance between the Co and Cu(I) is 3.06 a.u., which is about 3% smaller than that obtained previously[11] when the relaxations in the Cu substrate were excluded.

In the equilibrium geometry, the spin density shown in Fig. 1 suggests the detrimental effects of the Cu(001) substrate on the spin polarization in the Co overlayer. The area with positive spin density around the Co atom is obviously suppressed in the interfacial direction. As found in most of the magnetic systems,[10] the spin density in the interstitial region (mostly from the $s$, $p$ states) differs in sign from that in the near nuclear region (mainly from the $d$ states). Clearly, the induced magnetization around the interfacial Cu site is parallel to that of Co. Due to the screening effects, the magnetic interference decays very quickly upon going into the interior Cu region. Quantitatively, as listed in Table I, the magnetic moment in the Co MT sphere in Co/Cu(001) is 1.785 $\mu_B$, which can be further decomposed into contributions from the $s$ (0.013 $\mu_B$), $p$ ($-0.002$ $\mu_B$), and $d$ (1.774 $\mu_B$) states. The orbital magnetic moment is also very large, 0.116 $\mu_B$. Both results agree very well with the measured spin and orbital magnetic moments, 1.71 and 0.126 $\mu_B$, respectively.[8]

On the other side, small spin and orbital magnetic moments, 0.050 and 0.004 $\mu_B$, are induced at the interfacial Cu site. The angular decompositions of the spin moment are $-0.006$, $-0.017$, and 0.073 $\mu_B$ for the $s$, $p$, and $d$ states. Corresponding to the weakly spin density, the magnetic moment decreases to almost zero for the interior Cu atoms. However, one should note that both the spin density and the magnetic moment show an oscillative behavior going into the interior Cu layers. This may be somewhat important for the magnetic ordering and transport properties through the Cu spacer layers.

To compare with experimental results,[8] the calculated $L$-edge MCD cross sections for the Co and Cu are presented in Fig. 2. As expected, strong MCD signals can be detected from the Co site. Since the Co atom also possesses a large orbital magnetic moment, 0.116 $\mu_B$, the area of the $L_2$ edge (results from $2p_{1/2}$–$3d$ dipole transition) is obviously smaller than that of the $L_3$ edge (results from the $2p_{3/2}$–$3d$ dipole transition). Interestingly, the Cu-MCD signal is quite strong (1/5–1/8 in amplitude of that for Co) despite the fact that the induced magnetic moment at the Cu site is relatively

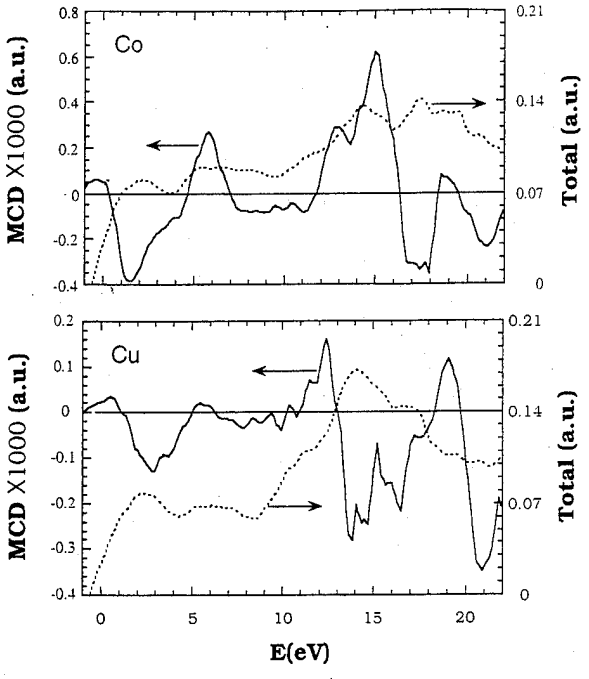



FIG. 3. Calculated $K$-edge MCD (solid lines) and total absorption (dotted lines) spectra for the Co and Cu atoms in Co/Cu(001).

very small. This is partially due to the smaller spatial extension of the Cu-3*d* orbit, which enhances the radial part of the momentum matrix and thus the cross section. We found that the Cu $L_2$ and $L_3$ edges (located at 908 and 928.5 eV) split by 20.5 eV, which agrees well with the measured splitting, 20 eV.[8]

The *K*-edge spectra for both Co and Cu atoms are given in Fig. 3. Strikingly, the profile of the Cu-MCD curve follows very closely that for Co in the lower energy range, which indicates that the spin polarization of the Cu-4*p* states is mainly induced by the Co-4*p* states. As also found experimentally,[9] the MCD signals for both Co and Cu consist essentially of a negative peak in the vicinity of the inflection point of the absorption edge with a small blip at the beginning. Surprisingly, the Co *K*-edge MCD signal is not much stronger than that of Cu. This may be attributed to the weakness of the *p* magnetic moment at the Co site (cf. Table I). Different from the *L* edge, the *K*-edge MCD and even the total absorption spectra show plenty of structures and deserve further investigation since the energy resolution of the currently measured spectra is not high enough to permit detailed comparison. Nevertheless, most of the main features of the Co and Cu *K*-edge MCD and total absorption curves appear to agree fairly well between theory and experiment.[12]

This work was supported by the ONR (Grant Nos. N00014-95-1-0489 and N00014-94-1-0030) and by a computing grant at the Arctic Region Supercomputing Center.

[1] See review papers in J. Magn. Magn. Mater. **100** (1991).
[2] S. S. P. Parkin, N. More, and K. P. Roche, Phys. Rev. Lett. **66**, 2152 (1991).
[3] L. González, R. Miranda, M. Salmerón, J. A. Vergés, and F. Ynduráin, Phys. Rev. B **24**, 3245 (1981).
[4] J. J. de Miguel, A. Cebollada, J. M. Gallego, R. Miranda, C. M. Schneider, P. Schuster, and J. Kirschner, J. Magn. Magn. Mater. **93**, 1 (1991).
[5] F. J. Himpsel, Phys. Rev. B **44**, 5966 (1991); J. E. Ortega and F. J. Himpsel, Phys. Rev. Lett. **69**, 844 (1992); J. E. Ortega, F. J. Himpsel, G. J. Mankey, and R. H. Willis, Phys. Rev. B **47**, 1540 (1993).
[6] N. B. Brooks, Y. Chang, and P. D. Johnson, Phys. Rev. Lett. **67**, 354 (1991).
[7] G. Schütz, W. Wagner, W. Wilhelm, P. Kienle, R. Zeller, and G. Materlik, Phys. Rev. Lett. **58**, 737 (1987); J. Stöhr *et al.*, Science **259**, 658 (1993); Y. U. Idzerda, L. H. Tjeng, H. J. Lin, C. J. Gutierrez, G. Meigs, and C. T. Chen, Phys. Rev. B **48**, 4144 (1993).
[8] M. G. Samant, J. Stohr, S. S. P. Parkin, G. A. Held, B. D. Hermsmeier, F. Herman, M. Schilfgaarde, and R. Nakajima, Phys. Rev. Lett. **72**, 1112 (1994).
[9] S. Pizzini, A. Fontaine, C. Giogetti, A. Dartyge, A. F. Bobo, M. Piecuch, and F. Baudelet, Phys. Rev. Lett. **72**, 470 (1995).
[10] A. J. Freeman and R. Q. Wu, J. Magn. Magn. Mater. **100**, 497 (1991).
[11] R. Q. Wu and A. J. Freeman, J. Magn. Magn. Mater. **116**, 202 (1992).
[12] (i) The calculated spectra have more structures since we used a narrower Gaussian broadening (0.2 eV); (ii) LDA wave functions become less reliable 10 eV above the Fermi level and thus a comparison between theory and experiment does not make too much sense in the high energy region.

# Determination of the energy dependence of the off-diagonal terms of the dielectric tensor by means of $M_{2,3}$ reflection MCD measurements (abstract)

Hartmut Höchst, Dai Zhao, and David Huber
*Synchrotron Radiation Center, University of Wisconsin-Madison, Stoughton, Wisconsin 53589*

We present the first magnetic circular dichroism (MCD) measurements around the $M$ edges of 3d metals utilizing SRCs recently developed quadruple reflection polarizer system.[1] The reflection polarizer converts linearly polarized light by means of the phase shift between $s$- and $p$-reflections into either left or right circular polarized radiation.[2] The concept of the phase shifter has been tested at a bending magnet beam line at the Aladdin storage ring using the $M_{2,3}$ absorptions of magnetically ordered thin films of Fe, Co and Ni. The normalized MCD signal e.g., $(I_R - I_L)/0.5*(I_R + I_L)$ is on the order of several % from peak to peak and scales linearly with the magnetic moments. The shape of the reflection MCD signals has a very pronounced angular dependence with a maximum around a reflection angle of $\theta$=60°–65°. The main trends in the angular dependence of the reflection MCD signal can be verified by model calculations. The model also allows us to extract the energy dependence of the off-diagonal terms in the dielectric tensor from the experimental data. The potential use and high sensitivity to variations in the local magnetic environment will be demonstrated with high resolution measurements of several ferrimagnetic compounds. © *1996 American Institute of Physics.* [S0021-8979(96)70508-2]

[1]H. Höchst, R. Patel, and F. Middleton, Nucl. Instrum. Methods **347**, 107 (1994).
[2]H. Höchst, P. Bulicke, and T. Nelson, Rev. Sci. Instrum. **66**, 1598 (1995).

 0021-8979/96/79(8)/6503/1/$10.00 © 1996 American Institute of Physics 

# Magnetic dichroism in angle-resolved UV photoemission from valence bands, using linearly polarized light

D. Venus
*Department of Physics, McMaster University, Hamilton L8S 4M1, Canada*

W. Kuch, A. Dittschar, M. Zharnikov, C. M. Schneider, and J. Kirschner
*MPI fur Mikrostrukturphysik, D-06120 Halle, Germany*

Magnetic dichroism measurements of the valence bands of films of fcc Co/Cu (001) have been performed using angle-resolved UV photoemission in low-symmetry, off-normal emission geometries, and linearly polarized light. Asymmetries of magnitude 4% are observed upon magnetization reversal. Evidence of both spin-dependent surface transmission and magnetic dichroism in the angular distribution of photoelectrons is seen. The asymmetry spectra indicate sensitivity to both magnetic exchange splitting and to spin–orbit splitting. © *1996 American Institute of Physics.* [S0021-8979(96)78808-3]

Magnetic dichroism in the angular distribution of photoelectrons (MDAD) makes it possible to study the interplay between the magnetic exchange and spin–orbit interactions in solids. To date, it is primarily the deep[1,2] and shallow core[3,4] levels of magnetic materials which have been investigated in this way. Over the course of these studies, a series of findings have overturned expectations, and lead to a better understanding of the technique and its potential. It turns out that the dichroism is sizable not only in the deepest core levels, that circularly polarized light is not required, and a larger dichroism may often be obtained using linearly polarized light;[3,5] and that the dichroism from core levels is not independent of emission angle, but contains significant crystallographic information.[1,6] These findings all suggest the application of MDAD to valence band studies, to see what can be learned about the magnetically important states near the Fermi level without recourse to more complicated spin-resolved experiments, or to monochromators specialized for the production of circularly polarized light. All that is required is a conventional angle-resolved photoemission apparatus, a source of linearly or unpolarized monochromatic light, and a means to reverse the remanent magnetization of the sample.

A few experimental studies which confirm the existence of MDAD in the valence bands have been reported, but most have used circularly polarized light,[7] and all have used normal emission geometries which restrict access to a few regions of the Brillouin zone.[8] Furthermore, a straightforward qualitative model giving an overview of the mechanism by which the dichroism arises in valence band emission is still missing. It is therefore difficult to interpret the measurements without recourse to specialized one-step photoemission calculations with nonperturbative treatments of the exchange and spin–orbit coupling in the surface electronic band structure.[9] These calculations are not yet available for general, low symmetry experimental geometries. The purpose of the present experiments is, in the first place, to observe the magnetic dichroism in the valence bands in off-normal emission geometries, using linearly polarized light. With measurements in hand, it may be possible to better assess how the dichroism can be used in a practical sense to learn about the electronic structure at magnetic surfaces.

An example of the ambiguities which arise in magnetic dichroism experiments in the valence bands, is the question of the conceptual origin of the observed dichroism. For concreteness, consider the experimental geometry in Fig. 1. The remanent magnetization, **M**, is in the surface of the sample crystal, and both the incident light wave vector, **q**, and the photoelectron wave vector, **k**, lie in the $xy$ plane normal to **M**. The light is linearly polarized in this plane. In Fig. 1, **q** and **k** are collinear, but this need not be the case. It is further assumed that the $xz$ plane containing **M** is a mirror symmetry plane of the crystal—a common situation among itinerent ferromagnets.

The experiment involves collecting two angle-resolved photoelectron energy distributions—one for each of the two reversed remanently magnetized states of the sample. The difference in these two energy distributions is the energy- and angle-resolved dichroism. There are two mechanisms which may contribute to the dichroism. The first is spin-dependent transmission.[10] It is most apparent as a "final state effect" in a three-step model of photoemission, where photoexcitation occurs between bulklike electronic states and the photoelectrons are subsequently transmitted to the vacuum. At the surface, the photoelectron states in the crystal (which are not pure spin states, because of spin–orbit coupling) must be matched to those in the vacuum (which are pure

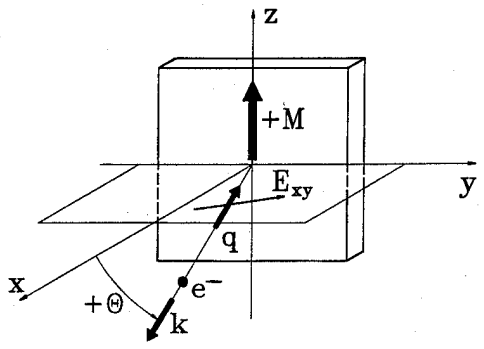



FIG. 1. The Co(001) film has remanent magnetization along $\pm z$, and lies in the $xz$ mirror plane. The incoming light with wave vector **q** (with linear polarization $\mathbf{E}_{xy}$) and the photoelectron wave vector **k** all lie in the $xy$ mirror plane, making an angle $\theta$ with the $x$ axis.

 0021-8979/96/79(8)/6504/3/$10.00 © 1996 American Institute of Physics

spin states). This leads to spin-dependent transmission coefficients. In the above experiment, reversing the magnetization reverses the spin character of the photoelectrons, and the altered transmission coefficient may cause the dichroism. Recent results for Cu show that this mechanism can cause an asymmetry of $\pm 3\%$ in $3d$ metals.[11]

MDAD is typically considered to arise from the photoexcitation step itself.[12,13] The spectra taken with reversed magnetization compare two inequivalent experimental geometries which are related by a mirror reflection—a traditional statement of dichroism. This can be understood with reference to Fig. 1, where reversal of the magnetization is equivalent to reflection in the $xz$ mirror plane of the crystal. However, this operation also alters the experimental quantities $\mathbf{k}$, $\mathbf{q}$, and $\mathbf{E}_{xy}$. In particular, the even and odd parts of $\mathbf{E}_{xy}$ and the photoelectron wave function undergo a relative change in phase, and the resulting photoexcitation matrix element will have both even and odd parts. Upon squaring and subtracting to form the dichroism, only the interference terms between the even and odd parts of the matrix element survive, giving the dichroism.[13] Because of its origin in the transition matrix elements, MDAD is usually classified as an "initial state effect."

The view that magnetic dichroism arises from MDAD when it is an initial state effect and from spin-dependent transmission when it is a final state effect cannot be considered as a rigid classification. However, alternative classifications are worse: In the three-step model of photoemission, spin-dependent transmission exists, but MDAD (with linearly polarized light) does not. In a one-step model, all the dichroism must be assigned to the matrix elements—that is MDAD. These classifications are not as useful for qualitative arguments, and ultimately for the understanding of experiments.

The photoemission experiments were carried out at the BESSY synchrotron storage ring, using a 6.5 normal incidence monochromator, and an angle-resolved photoemission apparatus which is described elsewhere.[14] The samples were 5 or 6 monolayer fcc Co films grown on a Cu(001) substrate. The film growth was monitored using medium energy electron diffraction.[15] Hysteresis loops measured by the magneto-optic Kerr effect confirmed that the films were remanently magnetized in the plane of the surface. The electron energy analyzer had a hole in the back, which allowed the light beam to pass through the entrance lenses, and permitted the experimental geometry with $\mathbf{k}=-\mathbf{q}$, as shown in Fig. 1. This geometry has three important attributes: (a) A wide range of off-normal emission conditions can be reached by a single rotation of the sample about the $\mathbf{z}$ axis. (b) Since $\mathbf{k}$, $\mathbf{q}$, and $\mathbf{M}$ are coplanar, oriented atom models of MDAD predict no dichroism[12]—any observed effects will be related to crystallographic information. (c) The $xy$ plane is a true mirror plane for the magnetic system plus the experiment. This latter point implies that MDAD using either linearly or circularly polarized light measures the same matrix elements, as has been confirmed theoretically[13] and experimentally.[16] A disadvantage of this geometry is that the light passing through the spectrometer creates more secondary electrons than is usual, and this limits the useful energy range of the spectra, particularly at lower photon energies.

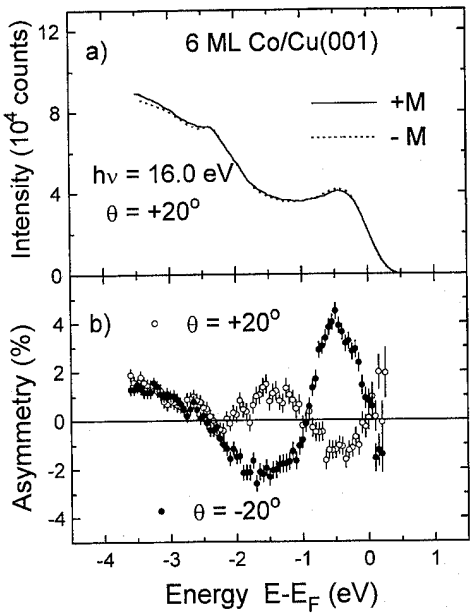



FIG. 2. (a) Photoelectron intensity spectra for two senses of magnetization, with a photon energy of 16.0 eV and emission angle +20°. (b) The resulting intensity asymmetry for the data in part (a) (open symbols), and for data measured at an emission angle of −20° (closed symbol).

Experimental results for a photon energy of 16.0 eV, with $\theta=+20°$ are shown in Fig. 2. Part (a) presents the separate intensity spectra for positive and negative magnetization. The spectra have had a linear background (determined before the Fermi energy) removed, and have been normalized to compensate for changes in the photon flux during the course of the measurements. The open symbols in part (b) show the intensity asymmetry, defined as the difference of the two spectra divided by their sum. It shows clear positive and negative peaks in the energy range down to about −2.5 eV where the Co $d$ bands lie, and a gradual upward slope at lower energy. The asymmetry of a similar pair of data sets collected at $\theta=-20°$ are also plotted in Fig. 2(b). The asymmetry peaks for this angle are reversed in the energy region of the Co bands, as they must be if they are due to either MDAD or spin-dependent transmission. The slope in the region of secondary electrons depends instead on the absolute sign of the magnetization, and probably represents a perturbation of the secondary electrons generated by the light passing through the spectrometer.

It can be seen immediately that the magnitude of the dichroism in off-normal emission is in the range of 2%–4% when secondary electrons are not removed. This is the same approximate size as that seen in previous experiments in normal emission, and is also the same as typical (rather than maximum) values seen in MDAD from core levels when the secondary electrons are not removed. MDAD experiments in the valence bands are not significantly more difficult than those in the core levels. This example also demonstrates the advantage of using a differential spectroscopy such as MDAD—it is possible to display clearly the presence of Co states near −1.5 eV despite the fact that they do not appear

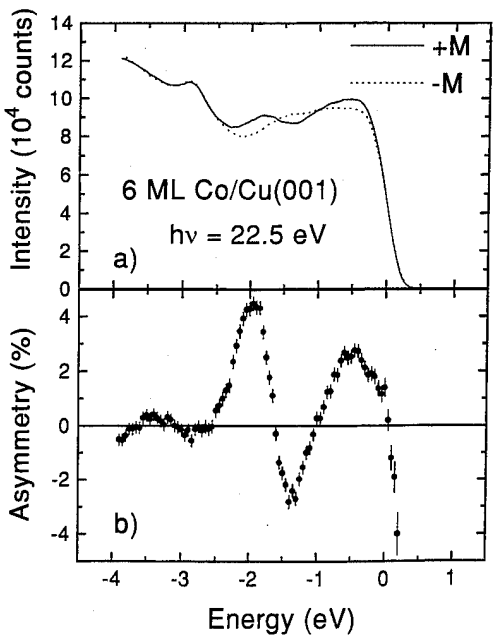



FIG. 3. (a) Photoelectron intensity spectra for two senses of magnetization, with a photon energy of 22.5 eV and emission angle −16°. (b) The resulting intensity asymmetry for the data in part (a).

as peaks in the intensity spectra. The form of the dichroism spectra suggests that, in this instance, the dichroism arises primarily due to spin-dependent transmission at the surface. The first-order perturbation observed in the intensity spectra is a change in the size of the peak—there is no indication that the intensity peak near −0.5 eV is shifted when the magnetization is reversed. This behavior is expected for the final state effect of spin-dependent transmission upon spin reversal. The positive and negative peaks in the asymmetry are then interpreted as being due to separate transitions from states of opposite spin, which are separated by approximately 1.2 eV, in agreement with the exchange splitting found in calculations and spin-resolved photoemission experiments[17] for fcc Co. Note that the absolute sign of the asymmetry is not easily related to the spin of the photoelectrons, since it depends on the surface transmission coefficients.

The data presented in Fig. 3 for a photon energy of 22.5 eV and $\theta = -16°$ show a different behavior. The peak below about −2.5 eV is due to the Cu substrate, and shows no asymmetry. However, a well-resolved peak at −1.8 eV seen with $+\mathbf{M}$ shifts to −1.6 eV when the magnetization is reversed, but the peak intensity is not greatly affected. This is the behavior expected for MDAD. The first-order effect of weak spin–orbit coupling on the initial states is to introduce hybridization between nearly degenerate bands of opposite spin. While the energy of the hybridized states depends on the relative orientation[18] of the spin $\sigma$ and $\mathbf{M}$, as $\sigma+\mathbf{M}$, the transition matrix elements depend as well on the absolute spin direction through the spin–orbit coupling $\sigma \cdot l$. Thus the transition with a given orientation of $\sigma \cdot l$ occurs at a different energy when $\mathbf{M}$ is reversed, leading to the apparent shift in the peak energy in the intensity spectra. A rapid minus/plus variation in the asymmetry results. The experimentally observed energy shift is of the magnitude expected for the spin–orbit interaction for $3d$ metals. These spectra coincidentally demonstrate that MDAD persists in this low-symmetry geometry, where $\mathbf{q}$, $\mathbf{k}$, and $\mathbf{M}$ are coplanar, even though models based on photoemission from oriented atoms predict a null effect. This is a consequence of the crystalline symmetry, rather than atomic symmetry, of the system, and is not surprising for such low photon energies.

The asymmetry close to the Fermi level in Fig. 3 is not as clear cut as the previous two examples, and more a detailed analysis is called for. It is not yet clear whether or not a simple criterion can be found to distinguish MDAD from surface transmission effects. Analysis of the systematics of a more comprehensive data set in underway to determine how widely the present classification of asymmetry features is applicable.


[1] C. M. Schneider, D. Venus, and J. Kirschner, Phys. Rev. B **45**, 5041 (1992).
[2] G. D. Waddill, J. G. Tobin, and D. P. Pappas, Phys. Rev. B **45**, 552 (1992).
[3] Ch. Roth, F. U. Hillebrecht, H. B. Rose, and E. Kisker, Solid State Commun. **86**, 673 (1993).
[4] G. Rossi, F. Sirotti, N. A. Cherepkov, F. Combet-Fornoux, and G. Panacionne, Solid State Commun. **90**, 557 (1994).
[5] D. Venus, Phys. Rev. B **48**, 6144 (1993).
[6] D. Venus, L. Baumgarten, C. M. Schneider, C. Boeglin, and J. Kirschner, J. Phys. Condens. Matt. **5**, 1239 (1993).
[7] C. M. Schneider, M. S. Hammond, P. Schuster, A. Cebollada, R. Miranda, and J. Kirschner, Phys. Rev. B **44**, 12 066 (1991); J. Bansmann, C. Westphal, M. Getzlaff, F. Fegel, and G. Schönhense, J. Magn. Magn. Mater. **104–107**, 1691 (1992).
[8] M. Getzlaff, Ch. Ostertag, F. H. Fecher, N. A. Cherepkov, and G. Schönhense, Phys. Rev. Lett. **73**, 3030 (1994).
[9] N. A. Scheunemann, S. V. Halilov, J. Henk, and R. Feder, Solid State Commun. **91**, 487 (1994).
[10] H.-P. Oepen, K. Hünlich, and J. Kirschner, Phys. Rev. Lett. **56**, 496 (1986); J. Garbe and J. Kirschner, Phys. Rev. B **39**, 9859 (1989).
[11] D. Venus, W. Kuch, A. Dittschar, M. Zharnikov, C. M. Schneider, and J. Kirschner, Phys. Rev. B **52**, 6174 (1995).
[12] B. J. Thole and G. van der Laan, Phys. Rev. B **49**, 9613 (1994).
[13] D. Venus, Phys. Rev. B **49**, 8821 (1994).
[14] H. P. Oepen, Ph.D thesis, Rhenische-Westfälische Technische Hochschule, Aachen, Germany, 1984.
[15] C. M. Schneider, J. J. de Miguel, P. Bressler, J. Garbe, S. Ferrer, R. Miranda, and J. Kirschner, J. Phys. C **8**, 1657 (1988).
[16] F. U. Hillebrecht, Ch. Roth, H. B. Rose, M. Finazzi, and L. Braicovich, Phys. Rev. B **51**, 9333 (1995).
[17] C. M. Schneider, P. Schuster, M. Hammond, H. Ebert, J. Noffke, and J. Kirschner, J. Phys. Condens. Matter **3**, 4349 (1991).
[18] It is assumed that the initial state is not a surface state.

# Spin polarized photoemission studies of the 3*s* core level in ferromagnetic systems[a] (abstract)

Y. Liu, J. Xu, D-J. Huang, and P. D. Johnson
*Physics Department, Brookhaven National Laboratory, Upton, New York 11973*

Spin polarized core level photoemision studies are capable of providing local site specific magnetic information. 3*s* core level photoemission spectra are characterized by a main peak and satellite whose separation reflects the exchange interaction between the core level and the net spin in the valence bands. However, there is currently considerable disagreement as to whether the splitting between these two peaks may be taken as a measure of the local moment. An alternative approach is to examine the intensities of the different peaks in the spectra. Indeed analysis of the multiplet intensities in the final state suggests that it should be possible to obtain a reasonable measure of the local magnetic moment through measurement of the spin dependent intensities in the multiplet structure. In detailed spin polarized photoemission studies of the 3*s* core level of Fe and Co films grown on Ag(001) and Cu(001) substrates, respectively, we find that this is indeed the case. This suggests that studies of the spin polarization of the 3*s* core level photoemission may provide an important new technique for the measurement of magnetic moments in thin films. Lineshape fitting reveals new information about the lifetime of the core holes. Previous studies have suggested that a majority spin core hole will be shorter lived than a minority spin core hole because of the higher density of majority spin electrons in the valence bands. However, our studies indicate that the lifetime is more complicated and that it shows a strong dependence on the LS in the final state. © *1996 American Institute of Physics.* [S0021-8979(90)70668-5]

[a]This work has been supported in part by the Department of energy under Contract No. DEAC02-76CH00016.

# Magnetic dichroism in the soft x-ray regime for magnetic domain imaging by total yield microscopy (abstract)

F. U. Hillebrecht, T. Kinoshita,[a] Ch. Roth, H. B. Rose, D. Spanke, J. Dresselhaus, and E. Kisker
*Institut für Angewandte Physik der Heinrich-Heine-Universität Düsseldorf, Germany*

Among the techniques for studying magnetic materials, methods utilizing magnetic dichroism in the soft x-ray region are receiving particular attention because of the unique feature of chemical specificity introduced by probing core levels. In soft x-ray absorption of linearly polarized light, the dichroism is proportional to the square of the magnetization $M$.[1] The transverse magneto-optic Kerr effect is characterized by a change of the specular reflectivity when $M$ is reversed, thus it is linear in $M$.[2] Due to the relationship between reflected and transmitted radiation, a dichroism may also be expected in the absorption. We confirmed this by quasi-simultaneous measurement of the reflectivity and total yield around the Fe and Co $3p$ thresholds, using $p$-polarized light at oblique incidence:[3] Switching the magnetization between the two directions normal on the plane of incidence indeed shows a magnetic dichroism. The relationship between the dichroisms in total yield and specular reflectivity was investigated as function of incidence angle. In addition to this new form of magnetic dichroism, other forms have been explored for imaging near-surface magnetic domains of elemental and compound materials in a total yield microscope. By using different light polarizations different components of the magnetization are detected. $p$- and circular polarization yield magnetization components parallel to the surface, normal to and in the plane of light incidence, respectively. With linearly $s$-polarized light, images similar to those with circularly polarized light were obtained. This is evidence for a sizeable Faraday rotation, leading to a significant degree of circular polarization before the optical transition takes place. The helicity of the Faraday-induced ellipitical polarization depends on the local sample magnetization, thereby generating the magnetic contrast in an analogous fashion as does circularly polarized light. This mechanism is expected and found to be effective also for $p$-polarized light, however, with contrast smaller than that related to the transverse MOKE. Finally, we report first results for an antiferromagnet, where domains were observed via the $M$-quadratic Voigt effect in the soft x-ray region. © *1996 American Institute of Physics.* [S0021-8979(96)70708-0]

This work was supported by BMFT (Grant No. 05 5PFDAB3) and DFG/SFB 166.

[a]Also with Institute for Molecular Science, UVSOR, Okazaki 444, Japan.

[1]G. van der Laan *et al.*, Phys. Rev. B **34**, 6529 (1986).
[2]C. Kao *et al.*, Phys. Rev. Lett. **65**, 373 (1990).
[3]T. Kinoshita *et al.*, J. Magn. Magn. Mater. **148**, 64 (1995); F. U. Hillebrecht *et al.*, Phys. Rev. Lett. **75**, 2224 (1995).

 0021-8979/96/79(8)/6508/1/$10.00 © 1996 American Institute of Physics

# Spin resolved resonant Raman scattering

W. A. Caliebe, C.-C. Kao, L. E. Berman, and J. B. Hastings
*National Synchrotron Light Source, Brookhaven National Laboratory, Upton, New York 11973*

M. H. Krisch and F. Sette
*European Synchrotron Radiation Facility, F-38043 Grenoble Cedex, France*

K. Hämäläinen
*Department of Physics, University of Helsinki, Siltavuorenpenger 20D, SF-00170 Helsinki, Finland*

Spin resolved resonant Raman scattering measurements in Gd metal made by exciting x-ray resonant Raman scattering with circularly polarized x rays near the $L_{III}$ edge of Gd are presented. The incident photon energy was fixed at the peak of the $2p \rightarrow 4f$ quadrupolar transition, and the scattered photon was energy analyzed around the $3d \rightarrow 2p$ fluorescent energy. Asymmetry ratios in the scattered intensity much larger than that of the $L_{III}$ XMCD effect (x-ray magnetic circular dichroism) were observed upon reversal of the magnetization of the sample or the helicity of the photon. A detailed comparison of these results with XMCD results from both the $M_{IV,V}$ edges and $L_{III}$ edge of Gd metal will be discussed. © *1996 American Institute of Physics.*
[S0021-8979(96)78908-2]

In the last two decades several new techniques to study magnetic phenomena and the fine structure of absorption edges using synchrotron radiation (SR) have been developed.

One of them x-ray magnetic circular dichroism (XMCD), first observed at the Fe $K$ edge,[1] measures the difference in absorption for left and right circularly polarized photons in magnetic materials. In the near edge region the dichroism directly yields information on the magnetic aspects of the electronic structure.

Resonant Raman scattering (RRS), first observed in 1974,[2] is the absorption of a photon with an energy just below the absorption edge and the detection of a photon that is emitted by the electron from an atomic state filling the lower lying core hole.

This technique was used extensively in gas phase studies in the soft x-ray region (<5 keV) by Cowan *et al.* They investigated both atomic systems and small molecules where information about bond orientation was obtained using linear polarized SR.[3]

Later Hämäläinen *et al.* used RRS in dysprosium nitrate in order to overcome the lifetime broadening in absorption and to separate a quadrupolar transition from the dominating dipolar one. The energy of the fluorescence and the available crystal analyzers however prevented a complete study.[4] The simulations[5] where it is possible to calculate the fluorescence signal for different incident energies show a relatively complicated structure. By taking a cut in the right direction of the $E_i - E_i - E_f$ plane, these simulations agree very well with the measured data. Recently, Krisch *et al.* measured, with high resolution, the RRS signal from gadolinium gallium garnet (GGG) near the $L_{III}$ edge.[6] They clearly separated the quadrupolar transition from the dipolar one by measuring, for different incident energies, the $L\alpha_2$ fluorescence. The results for Gd metal, which are shown in Figs. 1 and 2, are very similar to those obtained from GGG. The success of this experiment motivated us to combine RRS and MCD as a means to measure the RRS signal using circularly polarized photons in the incident beam.

The experiment was done at the wiggler-beamline X25 at the National Synchrotron Light Source.[7] The x rays were focused onto the sample using a toroidal mirror and monochromatized with a Si(220) double-crystal monochromator. The energy resolution of the incident beam is about 1 eV and the focal spot size on the sample is about $0.5 \times 0.5$ mm$^2$. The incident beam, which is usually linearly polarized in the plane of the ring, is partially circularly polarized with a diamond (111) quarter-wave plate.[8,9] The degree of polarization is about 50% and was measured using the MCD effect in iron. Due to absorption the efficiency of the quarter-wave plate is only 10%.

In this experiment the sample was a 250-$\mu$m-thick gadolinium foil, mounted on the cold finger of a liquid nitrogen cryostat inside an evacuated beryllium can. The sample temperature was about 200 K so that a magnetization of 80% could be achieved. The sample was magnetized with an external electromagnet. The scattered photons were energy analyzed with a spherically bent Si(333)-analyzer ($R$=890 mm)

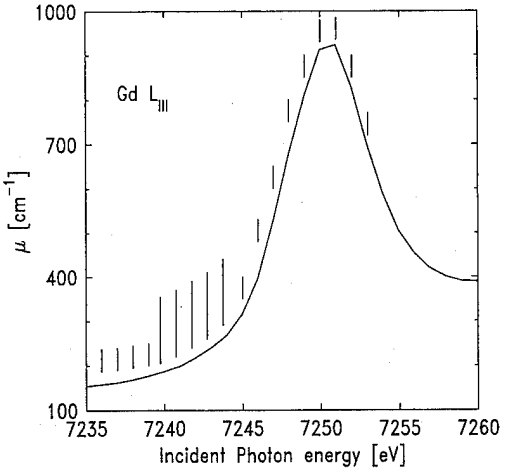



FIG. 1. Absorption coefficient of gadolinium metal around the $L_{III}$ edge. The vertical lines correspond to the incident photon energies at which the high resolution spectra of the inelastically scattered photons were measured. The longer lines indicate the spectra which are shown in Fig. 2.

 0021-8979/96/79(8)/6509/3/$10.00 © 1996 American Institute of Physics 

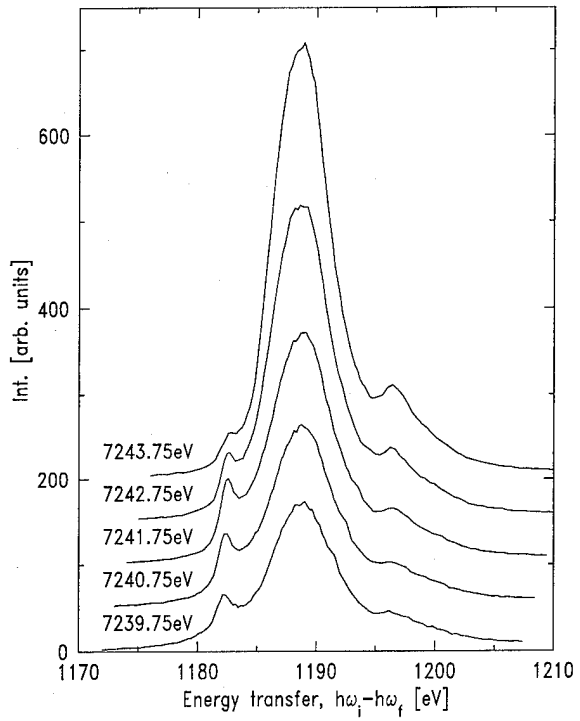



FIG. 2. Inelastic scattering spectra from gadolinium metal. The incident photon energy at which the spectra are taken is given in the figure. These spectra were measured at a different beamline with a better energy resolution so that the pre-edge peak is separated much better from the dipolar transition.

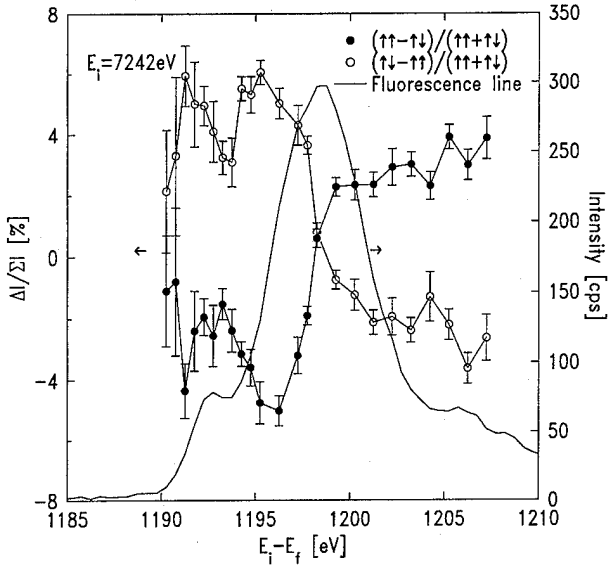



FIG. 4. $\Delta I/\Sigma$ for the different directions of polarization and different orientations of the magnetic field together with the fluorescence line for comparison.

with the sample and the detector on the Rowland circle. The energy resolution of the analyzer was better than 1 eV (see also Fig. 3).

The data were collected in the following mode. The incident and the final energies were fixed and the quarter-wave plate produced one handedness of circularly polarized x rays. After that, the orientation of the magnetic field was flipped with a frequency of 0.1 Hz while the intensity of the scattered photons was measured until about 2000–100 000 counts per orientation of the magnetic field were collected depending on the intensity of the signal. After that the handedness of the circularly polarized x rays was changed by rotating the quarter-wave plate and the same procedure was repeated in order to minimize systematic errors. This was done at several final energies for the incident energy, where the quadrupolar effect is relatively large.

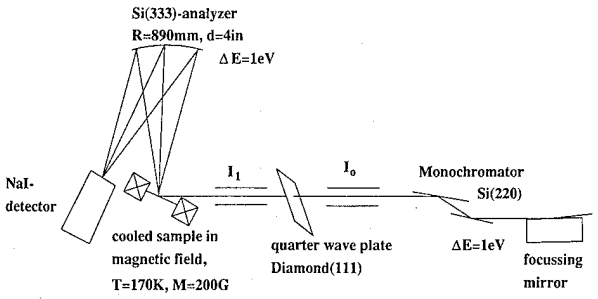



FIG. 3. Experimental setup: The radiation from the X25-wiggler is focused on the sample by a toroidal mirror and monochromatized by a pair of Si(220) crystals. The linearly polarized x rays are partially converted into circularly polarized x rays with the diamond quarter-wave plate. The scattered photons are energy analyzed with a spherically bent Si(333) analyzer and a scintillation counter. The detector and the sample are on the Rowland circle.

In order to process the data we calculate for each energy the ratio $(\uparrow\uparrow-\uparrow\downarrow)/(\uparrow\uparrow+\uparrow\downarrow)$, where $\uparrow\uparrow$ stands for the parallel electron and photon spin and $\uparrow\downarrow$ for the antiparallel orientation (Fig. 4). As we reverse both the magnetic field and the photon spin we obtain two curves which are almost symmetric around 0. The small difference can be explained by the difference in the absorption of the incident photons.

The data show three distinct features: a relatively strong peak (5%–6% effect) at the quadrupolar transition at 1191 eV, a second peak at 1195 eV, which is on the low energy shoulder of the dipolar transition, and then a change of the sign at the peak of the dipolar transition and a positive feature on the high energy shoulder. In the observed region this feature seems not to go back to 0, but the low count rate did not allow us to continue the measurement beyond this region.

The first step is to compare these data with XMCD data in the $L_{III}$ edge obtained by Schütz *et al.*[10] where theoretical calculations[11] agree reasonably well with the measurements. As expected the structure at the quadrupolar transition in our measurement is of opposite sign compared to the XMCD. An unexpected difference is that the sign of the feature on the low energy side of the dipolar transition is the same as the quadrupolar peak. In the one-electron approximation one would expect a different sign in the quadrupolar transition and the lower lying dipolar transition but the interaction of the core hole, in this case now a $3d$ hole in the final state, with the $4f$ electrons might change the states of the $3d$ electrons, so that the exchange splitting of the $5f$ electrons gets canceled by a larger splitting of the $3d$ electrons.

The final state in the quadrupolar peak is $3d^9 4f^{n+1} 5d^0$ and the whole absorption–emission process corresponds to

an $M_{IV,V}$-edge absorption. The final state of the dipolar feature, $3d^9 4f^n 5d^1$, is forbidden in direct absorption and therefore not visible in $M$ edges.

In direct $M_{IV,V}$ MCD the calculations[12] first show a small positive peak and then a very strong negative peak at the maximum of the absorption. The problem in our measurement is that the intensity of the quadrupolar transition itself is already very low so that we cannot see the positive feature. The strong negative feature in direct MCD changes sign in our measurement as expected and is equal in strength to the dipolar transition.

These measurements in general show that an effect can be observed by exciting RRS with circularly polarized x rays and that the results agree to a certain extent with the ones from $L$- and $M$-edge MCD.

However the differences compared to the $L$-edge MCD data show that even simple models do not qualitatively describe the data. This work is one further step toward the so-called complete experiment, where the spin and energy of the incoming photon is fixed and the energy and spin of the scattered photon are determined. We hope that this work will stimulate some theoretical effort in the calculation of spin resolved resonant Raman spectra.

It should be noted that similar experiments on the same system were done at about the same time by Schülke *et al.*[13] and Krisch *et al.*[14] with similar results.

We would like to thank the CMC-CAT, especially R. Hewitt and A. Bommannavar, for loan of the diamond crystal. The National Synchrotron Light Source is supported by the U.S. Department of Energy under Contract No. DE-ACO2-76-CH00016.

[1] G. Schütz, W. Wagner, W. Wilhelm, P. Kienle, R. Zeller, R. Frahm, and G. Materlik, Phys. Rev. Lett. **58**, 737 (1987).
[2] C. J. Sparks, Jr., Phys. Rev. Lett. **33**, 262 (1974).
[3] P. L. Cowan, in *Resonant Anomalous X-ray Scattering Theory and Applications*, edited by G. Materlik, C. J. Sparks, and K. Fischer (Elsevier, Amsterdam, 1994), and references therein.
[4] K. Hämäläinen, D. P. Siddons, J. B. Hastings, and L. E. Berman, Phys. Rev. Lett. **62**, 2850 (1991).
[5] P. Carra, M. Fabrizio, and B. T. Thole, Phys. Rev. Lett. **74**, 3700 (1995).
[6] M. H. Krisch, C. C. Kao, F. Sette, W. A. Caliebe, K. Hämäläinen, and J. B. Hastings, Phys. Rev. Lett. **74**, 4931 (1995).
[7] L. E. Berman, J. B. Hastings, T. Oversluizen, and M. Woodle, Rev. Sci. Instrum. **63**, 428 (1991).
[8] M. Hart, Philos. Mag. B **38**, 41 (1978).
[9] V. A. Belyakov and V. E. Dmitrienko, Sov. Phys. Usp. **32**, 697 (1989).
[10] G. Schütz, M. Knülle, R. Wienke, W. Wilhelm, W. Wagner, P. Kienle, and R. Frahm, Z. Phys. B **73**, 67 (1988).
[11] P. Carra, B. N. Harmon, B. T. Thole, M. Altarelli, and G. A. Sawatzky, Phys. Rev. Lett. **66**, 2495 (1991).
[12] J. Goedkoop, Ph. D. thesis, Katholieke Universiteit te Nijmegen, 1989.
[13] W. Schülke (private communication).
[14] M. H. Krisch (private communication).

# Raman heterodyne detection of magnetic resonance in a phosphate glass

G. K. Liu, C.-K. Loong, James V. Beitz, Ruoxin Cao,[a] Y. H. Chen, and K. Suzuya[b]
*Argonne National Laboratory, Argonne, Illinois 60439-4814*

A Raman heterodyne detection of magnetic resonance has been performed for probing the local structure of a sodium phosphate glass doped with trivalent europium. High resolution rf modulation spectra between 0.5 and 10 MHz were observed without the laser field in resonance with electronic transitions of the glass. The intensity of the observed Raman heterodyne signal depends on the external static magnetic field and sample temperature as well as the intensity of the laser and rf fields. The ability of monitoring the rf resonance spectra with micrometer spatial resolution may offer a potentially important means to probe the variation of local structure in disordered solid state materials. © *1996 American Institute of Physics.* [S0021-8979(96)79008-X]

## INTRODUCTION

The structure of vitreous $P_2O_5$ is thought to consist of a three-dimensional network of corner-sharing $PO_4$ tetrahedra each of which is decorated with a nonbridging P=O bond.[1] A complex structural modification of the parent $PO_4$ network occurs as metal oxides are added into the system. In the glassy $xM_2O\cdot(1-x)P_2O_5$ system where $M^+$ is the network-modifying cation such as $Na^+$, it is expected that the population of the branching configuration (where three O atoms of a $PO_4$ unit are shared with three neighboring $PO_4$) decreases and is replaced by the middle configuration (two bridging O per $PO_4$) as $R=x/(1-x)$ changes from 0 to 1. At the metaphosphate composition ($R=1$), the dominant structural units are believed to be corner-sharing $PO_4$ chains. Details of such intermediate-range (e.g., chain-length distribution, interchain correlations, etc.) are difficult to determine experimentally. Data from conventional diffraction methods provide a reasonable description of the short-range atomic correlations, but interpretation of intermediate-range ordering usually resorts to a comparison with theoretical models. Perhaps the technique of high performance liquid chromatography[2] provides the most substantial information.

Nuclear magnetic resonance spectroscopy, on the other hand, is capable of yielding accurate information regarding the local environments of selective atomic nuclei (e.g., $^{31}P$) in a glass.[3,4] Electronic bonding and interactions among the nuclear spins and electrons give rise to different shielding conditions at nuclear sites which can be detected and analyzed in terms of chemical shifts against a reference compound of known structure. Optically detected nuclear magnetic resonance (ODNMR) is another method for measuring transitions between nuclear sublevels through rf optical double resonance between optically pumped electronic and magnetically split nuclear states. The added advantage of this method is the availability of coherent laser light and noise-reduction techniques of rf wave mixing so that high resolution and high sensitivity can be achieved. In this article we describe a Raman heterodyne detection of nuclear magnetic resonance in a europium-doped sodium metaphosphate glass.

## EXPERIMENTAL DETAILS

A sodium metaphosphate glass, $(Na_2O)_{50}\cdot(P_2O_5)_{50}=NaPO_3$, was prepared from melting and quenching of the appropriate amounts of reagent grade $Na_2CO_3$ and $H_3PO_4$. The glass was then ground into a powder and mixed $Eu_2O_3$ powder in a weight ratio of $NaPO_3$ to $Eu_2O_3$ of 9 to 1. The mixed powder was heated to 1270±5 K in a Pt crucible in air for 30 min and the melt was subsequently quenched on a copper plate. A small amount of undissolved $Eu_2O_3$ powder was found in the Pt crucible, so the dopant concentration of $Eu_2O_3$ is expected to be less than 3 mol %, but the $Na_2O/P_2O_5$ ratio of 1 is unchanged. A piece of the Eu-doped $NaPO_3$ glass was cut with a diamond disk to a rectangular parallelpiped of edges 5–7 mm with two opposite faces polished for the experiment. The sample was kept in a nitrogen purged dry box to minimum exposure of the glass to moist air. No solvent was used during the cutting and polishing.

The schematic layout of the Raman heterodyne detected nuclear magnetic resonance (RHDNMR) apparatus is shown in Fig. 1. A continuous-wave single wavelength laser tunable from 570 to 620 nm was employed. The sample was mounted inside a rf coil with its two polished faces normal to the horizontal laser beam. The sample assembly was placed inside a liquid helium cryostat equipped with a superconducting magnet producing a static magnetic field up to 5 T at

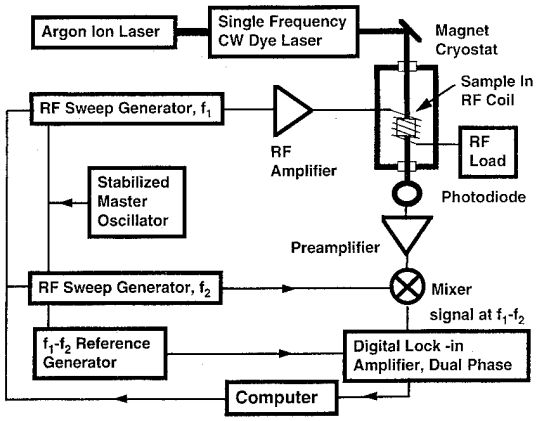



FIG. 1. Apparatus for Raman heterodyne detection of rf-optical resonance in solids.

[a]Current address: Physics Department, Wuhan University, Wuhan, China.
[b]Current address: Japan Atomic Energy Research Institute, Tokai-mura, Naka-gun, Ibaraki 319-11, Japan.

 0021-8979/96/79(8)/6512/3/$10.00 © 1996 American Institute of Physics

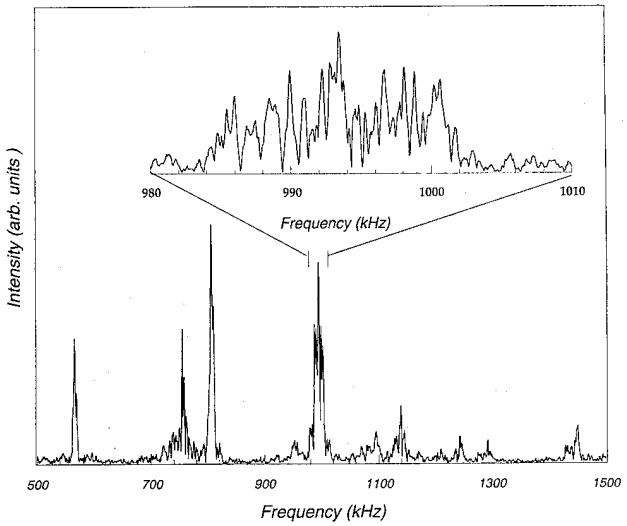



FIG. 2. Observed spectrum of rf resonance in phosphate glass detected via Raman heterodyne method at 3 K and a static magnetic field of 2.26 T. The inset segment from 980 to 1010 kHz is a separate scan. All major features in the spectrum are repeatable and minor variations in the relative intensity are due to laser power fluctuations.

the sample position while the sample was held at temperatures between 2 and 300 K. Two rf generators produced sweeping rf waves, $f_1$ and $f_2$, at a fixed difference ($f_1 - f_2 = 50$ kHz). The output of one rf generator was amplified and sent to the coil inside the cryostat. The other rf generator served as the local oscillator for the frequency mixer. The photocurrent signal from a photodiode intercepting the transmitted laser beam was amplified and mixed with local oscillator signal. The output signal of the mixer was analyzed by a lock-in amplifier using a 50 kHz reference frequency.

The technique of RHDNMR was first introduced by Mlynek and co-workers.[5] It relies on a coherent Raman process being stimulated by resonant rf and laser fields. The method has been applied to investigate the level structure and spin transient properties of an atomic vapor as well as solids doped with impurity ions.[6–8] In the present work, rf resonance in a glassy system was observed *without* optical resonance but requiring the presence of an external magnetic field. This type of modulation was first observed in a lanthanide fluoride crystal,[9] and the mechanism of this novel rf-optical coupling in a solid is not yet understood.

## RESULTS AND DISCUSSION

Sharp modulation of the rf field from 0.5 to 10 MHz in the transmitted laser beam was observed at low temperatures in an applied static magnetic field. Figure 2 shows the spectra of the $NaPO_3$ glass at 3 K in a field of 2.26 T obtained using a rf sweep from 0.5 to 1.5 MHz. It consists of many resonance groups each of which exhibits numerous lines with widths as narrow as 200 Hz. Care has been given to verifying the observed rf resonance. In a series of tests, rf field, laser intensity, sample temperature, and external static magnetic field were varied to confirm our observation and to eliminate possible rf noise from the electronics and the laser. The resonance lines diminished as the magnetic field was reduced. At zero field no resonance was observed. Moreover, the resonance frequencies were independent of the magnetic field strength which was varied from 0.4 to 3 T. Given the energy scale of the rf resonance in MHz and the linewidth in kHz, the observed rf modulation is unlikely to be associated with coupling of the hyperfine split states to phonons such as in coherent Raman or Brillouin scattering. The magnetic-field independence of the resonance frequencies, on the other hand, rules out the possibility of response from noninteracting nuclear spins of $^{31}P$ and $^{23}Na$ in the sample. We believe that magnetic resonance among *spin-coupled* nuclear states of $^{31}P$ ($I=1/2$) and/or $^{23}Na$ ($I=3/2$) under the influence of a magnetic field gives rise to the observed rf spectra. Presumably, the ligand nuclear spin–spin interaction is considerably stronger than the applied field strength. Resonant transitions between the polarized states of the correlated spin moments in an external magnetic field evidently are induced by the rf frequency sweep.

Our initial intent was to observe optical-rf double resonance that involved the electronic and nuclear transitions of the $Eu^{3+}$ ions in the glass. However, rf resonance was observed over the 570–620 nm range of laser wavelengths investigated. Additionally, the observed rf resonance frequencies are lower than those expected for the nuclear quadrupole splitting of $Eu^{3+}$.[10,11] Therefore, we conclude that the optical transition from the $Eu^{3+}$ $^7F_0$ ground state to the $^5D_0$ excited state at 588 nm does not contribute to the rf resonance observed by the Raman heterodyne method. Similar rf resonance spectra were observed also in other phosphate glasses which contain no Eu.

An important feature in our experiment was the spatial distribution of the rf modulation within the transmitted laser beam. In general, variation of the rf resonance pattern as the laser beam traverses the sample suggests structural inhomogeneity in the material. What appears to be a unique capability in our measurements was the fine spatial resolution of the order of 1 $\mu$m. This is achieved by expanding the transmitted laser beam through a lens and monitoring the line intensities as the photodiode (0.5 mm diam) is translated across the expanded beam. The intensity variation presumably reflects the changes in the local structure which contributes to the rf resonance. The combination of high sensitivity and good spatial resolution might be potentially useful for probing the structural variation in a disorder solid.

The rf resonance was observed only at low temperatures. Intensity of the spectrum diminished as the sample was warmed up. At 100 K the resonance was no longer observable. This temperature dependence is consistent with the hypothesis that the observed rf resonance arises from a correlated nuclear spin ensemble. At high temperatures the spin coherency apparently is destroyed by interactions with the surrounding medium (e.g., thermally populated electronic and phonon states).

In summary, the present RHDNMR is highly sensitive to the local structure of the spin–spin coupled nuclear states. Since electronic bonding and ligand field effects affect directly the nuclear spin level structure, this method is useful to probe the local electronic structure, particularly for disorder systems. The observed effect does not require optical resonance with electronic transitions yet the rf resonance exhibits sharp modulations that are immune to inhomogeneous broadening. In the case of a sodium ultraphosphate glass, $NaPO_3$, a richly detailed rf resonance spectrum was observed at low temperatures. Although the spectra are not understood quantitatively, the structure of the resonance patterns seems likely to reflect the complex cross linking of the $Na^+$ cations between different $PO_4$ chains. Such intermediate-range order structure is known to depend on the cation size. Thus it will be instructive to study the systematic of the rf resonance spectra of phosphate glasses with different metal cations. RHDNMR measurements of Ca and Pb phosphate glasses as well as phosphate crystals are currently underway.

## ACKNOWLEDGMENT

This work was performed under the auspices of the Office of Basic Energy Sciences, Division of Chemical Sciences, U.S. Department of Energy, under Contract No. W-31-109-ENG-38.

[1] S. W. Martin, Eur. J. Solid State Inorg. Chem. T **28**, 163 (1991).
[2] B. S. Sales, L. A. Boatner, B. C. Chakoukakos, J. C. McCallum, J. O. Ramey, and R. A. Zuhr, Mater. Res. Soc. Symp. Proc. **321**, 13 (1994).
[3] R. K. Brow, D. R. Tallant, J. J. Hudgens, S. W. Martin, and A. D. Irwin, J. Non-Cryst. Solids **177**, 221 (1994).
[4] P. Hartmann, J. Vogel, and B. Schnabel, J. Non-Cryst. Solids **176**, 157 (1994).
[5] J. Mlynek, N. C. Wong, R. G. DeVoe, E. S. Kintzer, and R. G. Brewer, Phys. Rev. Lett. **50**, 993 (1983).
[6] N. C. Wong, E. S. Kintzer, J. Mlynek, R. G. Devoe, and R. G. Brewer, Phys. Rev. B **28**, 4993 (1983).
[7] M. Mitsunaga, E. S. Kintzer, and R. G. Brewer, Phys. Rev. Lett. **52**, 1484 (1984).
[8] J. Mlynek, Chr. Tamm, E. Buhr, and N. C. Wong, Phys. Rev. Lett. **53**, 1814 (1984).
[9] G. K. Liu and J. V. Beitz (unpublished).
[10] R. M. Shelby and R. M. Macfarlane, Phys. Rev. Lett. **47**, 1172 (1981).
[11] G. K. Liu, R. Cao, and J. V. Beitz, J. Alloys Compounds **225**, 45 (1995).

# Magnetic and Mössbauer studies of hot-pressed MnZnNi ferrites (abstract)

V. K. Babbar
*Applied Physics Department, GND University, Amritsar, India*

R. K. Puri
*Physics Department, Indian Institute of Technology, Delhi, India*

Hot-pressed MnZn ferrites are extensively used for magnetic recording applications. The present work investigates the magnetic properties of MnZnNi ferrites by using the Mössbauer spectroscopy and taking bulk magnetic measurements. Ferrites of the composition $Mn_{0.6}Zn_{0.4-x}Ni_xFe_2O_4$ ($0 \leqslant x \leqslant 0.4$) have been prepared by uniaxial hot pressing technique. The final sintering was performed at 1250 °C for 3 h under a pressure of 35 MPa. The samples exhibit high density (porosity $<0.1\%$) nearly uniform grain size (average grain size=0.01 mm approx.), and large Vickers' hardness (650 approx.). The variations of initial permeability, saturation magnetization, Curie temperature, and coercive field are studied by changing $Ni^{2+}$ content. The initial permeability increases slightly for $x \leqslant 0.05$, attains a maximum value of 5660, and decreases continuously for $x > 0.05$. The saturation magnetization increases for $x \leqslant 0.25$ and decreases for $x > 0.25$. The maximum saturation magnetization obtained for $x=0.25$ is 4825 G. The Curie temperature increases markedly from 431 to 682 K with increasing $Ni^{2+}$ content. The coercive field decreases slightly for $x \leqslant 0.05$, becomes as low as 0.09 Oe, and increases almost linearly thereafter. The results are explained on the basis of sublattice magnetizations, strength of $AB$ exchange interactions and change in magnetocrystalline anisotropy constant. The Mössbauer studies reveal the well-defined hyperfine spectra for $Ni^{2+}$-substituted samples. The isomer shift remains almost unaffected by $Ni^{2+}$ substitution, while the quadrupole splitting is observed to be negligible for all the samples. The hyperfine field decreases continuously as $x$ increases from 0 to 0.4. The occupancy ratio of $Fe^{3+}$ ions on octahedral to tetrahedral sites yields a cation distribution which conforms with the bulk magnetic measurements. The MnZnNi ferrite compositions with $x$ ranging from 0.05 to 0.10 exhibit properties which make them suitable materials for recording head applications. © *1996 American Institute of Physics.* [S0021-8979(96)81208-8]

# Quantum vortex motion in high-$T_c$ superconductors

A. García, X. X. Zhang, and J. Tejada
*Departament de Física Fonamental, Universitat de Barcelona, Diagonal 647, E-08028 Barcelona, Spain*

Magnetic relaxation experiments at low temperatures were performed in different zero-field-cooled (ZFC) and field-cooled (FC) high-$T_c$ superconductors (HTSCs): TlBaCaCuO (2212 and 2223 phases, polycrystalline and thin-film samples), (Hg,Tl)BaCaCuO (1223 phase, polycrystalline material), and (Bi,Pb)SrCaCuO (2212 phase, single crystal). For each system and in the whole temperature range investigated, the relaxation curves obtained after both cooling processes are linear with the logarithm of time. The temperature dependence of the relaxation rate normalized to the first magnetization value, $R=|d(M/M_0)/d\ln(t)|$, follows a trend which is common to all systems: $R$ decreases linearly with decreasing temperature down to a value, which is called the crossover temperature, below which it levels off to a $T$-independent plateau. This behavior gives evidence of a transition in the mechanism responsible for the relaxation process at low temperatures, from thermally activated (linear dependence on $T$) to quantum vortex motion ($T$-independent regime). The experimental values for the crossover temperatures and normalized relaxation rates compare fairly well to numerical estimates in the framework of the theories of quantum vortex motion in layered HTSCs. Finally, the transition from one regime into another was studied in two samples of the TlBaCaCuO, 2223 phase, system in order to investigate the influence of dissipation on the quantum process. A clear conclusion on this point could not be drawn from these kinds of measurements. © *1996 American Institute of Physics.* [S0021-8979(96)57408-0]

During recent years, quantum motion of vortices at low temperatures in high-$T_c$ superconductors (HTSCs) has been extensively investigated in a great variety of systems, mainly by means of the detection of the time evolution of the magnetization.[1,2] At low temperatures this decay with time, which is known as magnetic relaxation, is usually well fitted to a logarithmic law, $M(t)=M_0[1-R(T)\ln(t/t_0)]$, where $M_0$ is the first magnetization point recorded at $t_0$ and $R(T)$ is called the normalized relaxation rate, $R\equiv|d\ln(M/M_0)/d\ln(t)|$. The time-logarithmic law is the natural dependence found in the Anderson–Kim model[3] for thermally activated flux creep and is restricted to the low-temperature regime. As far as a linear dependence is predicted by this model, $R$ should vanish as temperature goes to zero; however, in all reports mentioned above, as the temperature tends to zero, $R$ presents a large, temperature-independent plateau, rather than extrapolating to zero, suggesting a decay of magnetization by quantum motion of vortices through the energy barriers.

Quantum vortex motion in HTSC was first described by Blatter and Geshkenbein in the context of the quantum collective creep (QCC) theory.[4] In this theory, the normalized relaxation rate at $T=0$ in the regime of single vortex pinning is given by $R\simeq -\hbar/S_E^{\rm eff}$, where $S_E^{\rm eff}$ is the saddle-point solution for the effective Euclidean action of the tunneling process in the limit of strong ohmic dissipation, and is given by the following expressions:[5]

$$S_E^{\rm eff}/\hbar\simeq(\hbar/e^2)(L_c/\rho_n) \quad \text{(3D case)}, \tag{1a}$$

$$S_E^{\rm eff}/\hbar\simeq(\hbar/e^2)(d/\rho_n) \quad \text{(2D case)}. \tag{1b}$$

In these equations $\hbar/e^2\simeq 4.1\ \text{k}\Omega$ is the quantum of resistance, $\rho_n$ is the normal state resistivity extrapolated at $T=0$, $d$ is the interlayer spacing, $L_c\simeq(\xi/\gamma)(J_0/J_c)^{1/2}$ is the longitudinal dimension of the tunneling object, $\xi$ is the superconducting coherence length at $T=0$, and $J_0$ and $J_c$ are the depairing and critical current density. All values are taken in the $a-b$ plane.

Because of the layered nature of HTSCs, a flux line in these materials can be pictured as a stack of two-dimensional (2D) pancake vortices lying in adjacent copper oxide layers, connected by Josephson vortices.[6] The dimensionality of the object involved in the tunneling process, however, depends on the strength of the magnetic field applied before or during the measurements relative to a certain dimensional crossover field, $H_{\rm 3D\text{-}2D}\simeq\Phi_0/(\gamma d)^2$, where $\Phi_0$ is the flux quantum, and $\gamma$ is the anisotropy parameter of the material. Below $H_{\rm 3D\text{-}2D}$, 2D pancake vortices are coupled along the $c$ axis and form a three-dimensional (3D) flux line. In this case, the Euclidean action is given by Eq. (1a) and the normalized relaxation rate is represented as $R_{d,\rm 3D}$, where the subscript $d$ stands for the dissipative limit. On the other hand, for fields larger than $H_{\rm 3D\text{-}2D}$, the interaction within one layer is stronger than the interaction between adjacent layers, and 2D pancake vortices become decoupled. In this case, the Euclidean action is given by Eq. (1b) and the normalized relaxation rate is represented as $R_{d,\rm 2D}$.

Very recently, Feigel'man *et al.*[7] suggested that, because of the special values of their superconducting parameters, HTSCs at low temperatures should enter a nondissipative regime in which vortex motion is dominated by the Magnus instead of the friction force acting on it. In this limit, the

 0021-8979/96/79(8)/6516/3/$10.00 © 1996 American Institute of Physics

TABLE I. Superconducting transition temperature $T_c$, lower critical field $H_{c1}$ at 5 K, dimensional crossover field $H_{3D\text{-}2D}$ and applied magnetic field $H_a$ for the different samples. For each $T_c$ the magnetic field at which it has been measured is reported. In sintered samples, only intragranular $H_{c1}$ are listed.

| | Tl-pd | Tl-ps | Tl-f | Hg-ps | Bi-sc |
|---|---|---|---|---|---|
| $T_c$ (K) | 108 (100 Oe) | 116 (50 Oe) | 112 (1 Oe) | 133 (50 Oe) | 85 (10 Oe) |
| $H_{c1}$ (kOe) | 0.3 | 0.7 | 0.03 | 0.14 | 0.08 |
| $H_{3D\text{-}2D}$ (kOe) | 0.007 | 16 | 16 | 10 | 0.2 |
| $H_a$ (kOe) for $M_{ZFC}$ | 1.5 | ··· | 0.5 | ··· | 0.1 |
| $H_a$ (kOe) for $M_r$ | 0.1 | 3, 6 | 0.5 | 3, 10 | ··· |

expressions for the Euclidean action are the following:[7]

$$S_E^H/\hbar \simeq n_s \xi^2 L_c \quad \text{(3D case)}, \tag{2a}$$

$$S_E^H/\hbar \simeq n_s \xi^2 d \quad \text{(2D case)}, \tag{2b}$$

where $n_s$ is the density of superelectrons. The corresponding normalized relaxation rates will be represented as $R_{H,3D}$ and $R_{H,2D}$ for the 3D and 2D cases, respectively, where the subscript $H$ stands for the Hall limit.

The calculations so far reported correspond to the limit of zero temperature. At finite temperatures, however, quantum tunneling is thermally assisted and a gradual transition, instead of the sharp one which characterizes the $T=0$ limit, from thermal to quantum vortex motion occurs,[4]

$$R(T)=R(0)[1+(T/T_0)^2], \tag{3a}$$

$$R(T)=R(0)[1+\exp(-T_0/T)], \tag{3b}$$

corresponding respectively to the strong-ohmic-dissipative and nondissipative limit, which includes the Hall limit. In these equations, $T_0$ is a characteristic temperature. In any case, the quantum rate will be thermally assisted up to a crossover temperature $T_{cr}$ which is given by[4]

$$\hbar/S_E^{(\text{eff})}(0) \simeq k_B T_{cr}/U_c, \tag{4}$$

where $\hbar/S_E^{(\text{eff})}(0)$ is the normalized relaxation rate at $T=0$ and $U_c$ is the energy barrier for thermal activation.

In this article we present experimental evidence of quantum vortex motion at low temperatures in different samples: polycrystalline sintered and epitaxial thin-film $Tl_2Ba_2Ca_2Cu_3O_{10}$ (Tl-ps and Tl-f respectively), polycrystalline sintered $(Hg,Tl)Ba_2Ca_2Cu_3O_8$ (Hg-ps), polycrystalline powder $Tl_2Ba_2CaCu_2O_8$ (Tl-pd), and single-crystal $(Bi,Pb)_2Sr_2CaCu_2O_8$ (Bi-sc). Details on each sample preparation are described elsewhere.[8,9] The magnetic relaxation measurements were performed in a commercial ac superconducting quantum interference device (SQUID) (Quantum Design) magnetometer ($1.8<T<400$ K; $H_{max}=5.5$ T), following two different procedures. In the first one, the sample was cooled from $T>T_c$ in a zero applied field [zero-field-cooling (ZFC) process] down to the working temperature and, after attaining a stable temperature (temperature stability was 0.01 K in the low-temperature range), a magnetic field was switched on and kept constant during the measurement of the time decay of the ZFC magnetization: $M_{ZFC}$ vs $t$. In the second procedure, the sample was cooled with a magnetic field applied on [field-cooling (FC) process] and, after attaining a stable temperature, the field was switched off and the remanent magnetization was recorded as a function of time: $M_r$ vs $t$. After each run was complete the sample temperature was raised well above $T_c$ in order to remove completely the trapped flux lines. Table I summarizes the superconducting transition temperature $T_c$, lower critical field $H_{c1}$, dimensional crossover field $H_{3D\text{-}2D}$, and magnetic procedures performed for each sample.

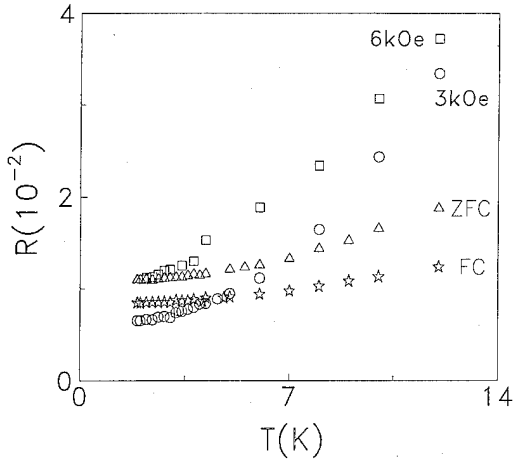



FIG. 1. Temperature dependence of the normalized relaxation rate for the Tl-ps and Tl-f samples. Circles and squares correspond to $M_r$ of Tl-ps obtained with $H_a=3$ and 6 kOe, respectively; triangles and stars represent, respectively, $M_{ZFC}$ and $M_r$ of Tl-f obtained with $H_a=0.5$ kOe.

In the whole low-temperature range investigated ($1.8<T<20$ K), the evolution with time of the remanent and ZFC magnetization of all samples is very well fitted to a time-logarithmic law in the studied time window (the total duration of each measurement was about 1 h). Figure 1 presents the temperature dependence of the normalized relaxation rates corresponding to Tl-f ($M_{ZFC}$ and $M_r$ obtained with 0.5 kOe) and Tl-ps ($M_r$ obtained with $H_a=3$ and 6 kOe). As

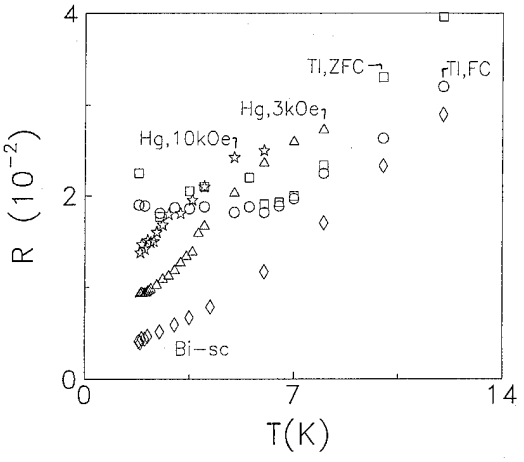



FIG. 2. Normalized relaxation rate vs temperature for Tl-pd, Hg-ps, and Bi-sc. Circles and squares stand, respectively, for Tl-pd $M_r$ obtained with $H_a=0.1$ kOe and $M_{ZFC}$ with $H_a=1.5$ kOe, triangles and stars represent $M_r$ of Hg-ps obtained with $H_a=3$ and 10 kOe, respectively; diamonds are used for Bi-sc.

TABLE II. Experimental and estimated parameters for the samples where quantum tunneling is observed. From top to bottom: experimental value ($R_{0,e}$), dissipative ($R_d$), and Hall ($R_H$) estimate for the plateau; experimental plateau temperature ($T_p$), and estimated crossover temperature ($T_{cr}$). When appropriate, the applied magnetic field or the type of magnetization is reported.

| | Tl-ps | Tl-f | Tl-pd | Hg-ps |
|---|---|---|---|---|
| $R_{0,e}$ (%) | 0.7 (3 kOe), 1.1 (6 kOe) | 0.85 ($M_r$), 1.1 ($M_{ZFC}$) | 2 | 1 (3 kOe) |
| $R_d$ (%) | 1.6 | 1.6 | 2.4 | 2.3 |
| $R_H$(%) | 5 | 5 | 7 | 7 |
| $T_p$ (K) | 2.5–3 | 2.5–3 | 5–6 | 2.1 |
| $T_{cr}$ (K) | 4 | 7–8 | 6–7 | 2.6 |

temperature decreases, all curves show a transition from a more or less linear dependence to a temperature-independent plateau which begins between $T_p \simeq 2.5$ and 3 K, suggesting a crossover from thermal to quantum vortex motion at low temperatures. The experimental plateau values $R_{0,e}$ are similar for both samples: For Tl-ps, $R_{0,e} \simeq 0.7\%$ for $H_a = 3$ kOe and $\simeq 1.1\%$ for $H_a = 6$ kOe; $R_{0,e} \simeq 0.85\%$ and $\simeq 1.1\%$ for the Tl-f FC and ZFC curves, respectively. In order to compare with theoretical values, we must first estimate the dimensional crossover field $H_{3D\text{-}2D}$. Using $\gamma \simeq 20$ (Ref. 10) and $d \simeq 18$ Å (Ref. 11), $H_{3D\text{-}2D} \simeq 16$ kOe is obtained, which is larger than the magnetic fields applied. Thus, quantum vortex motion is of 3D nature in both samples. Substitution of typical HTSC values [$(J_0/J_c)^{1/2} \simeq 15$, $\xi \simeq 30$ Å, $\rho_n \simeq 15$ $\mu\Omega$ cm, $n_s \simeq 10^{21}$ cm$^{-3}$] in Eqs. (1a) and (2a), gives $R_{d,3D} \simeq 1.6\%$ and $R_{H,3D} \simeq 5\%$, which agree qualitatively well with $R_{0,e}$ (an attempt to obtain a quantitative agreement requires the use of more accurate parameters). Finally, good fittings of each gradual transition to Eqs. (3a) and (3b) were obtained, with comparable accuracy in both cases. Therefore, no conclusion can be drawn about the dissipative nature of the quantum process. The temperature up to which each fitting rule varies from 6 to 9 K, depending on the sample and extent of the low-temperature range studied. The crossover temperatures calculated from Eq. (4) are $T_{cr} \simeq 4$ K for Tl-ps (with $U_c \simeq 400$ K, as estimated in the thermally activated regime), and $\simeq 7$–8 K for Tl-f (with $U_c \simeq 700$–1000 K). Both values are larger than, but comparable in order of magnitude to, $T_p$.

The temperature dependence of the normalized relaxation rates corresponding to Tl-pd ($M_r$ obtained with 0.1 kOe and $M_{ZFC}$ obtained with 1.5 kOe), Hg-ps ($M_r$ obtained with 3 and 10 kOe), and Bi-sc ($M_{ZFC}$ obtained with 0.1 kOe) are plotted in Fig. 2. The transition in the Hg-ps curve for $H_a = 3$ kOe and both two Tl-pd curves appear to be very sharp, with no evidence of thermally assisted quantum tunneling. The experimental plateau values are $R_{0,e} \simeq 1\%$ for Hg-ps and $\simeq 2\%$ for both two Tl-pd curves. Using $\gamma \simeq 30$ and $d \simeq 16$ Å for Hg-ps,[9] and $\gamma \simeq 350$ (Ref. 12) and $d \simeq 15$ Å (Ref. 11) for Tl-pd, $H_{3D\text{-}2D} \simeq 10$ and 0.07 kOe are, respectively, obtained. Therefore, Hg-ps is in the 3D quantum creep regime ($H_a < H_{3D\text{-}2D}$), and Tl-pd is in the 2D regime ($H_a > H_{3D\text{-}2D}$). Then, $R_{d,3D} \simeq 2.3\%$ and $R_{H,3D} \simeq 7\%$ are obtained for Hg-ps, while Eqs. (1b) and (2b) give $R_{d,2D} \simeq 2.4\%$ and $R_{H,2D} \simeq 7\%$ for Tl-pd, which are qualitatively comparable to $R_{0,e}$. The plateau temperatures are $T_p \simeq 2.1$ and $\simeq 6$ K for Hg-ps and Tl-pd, respectively, in good agreement with estimates of the crossover temperature from Eq. (4), $T_{cr} \simeq 2.6$ K for Hg-ps, and $\simeq 6$–7 K for Tl-pd. Finally, no plateau can be found in the Hg-ps curve with $H_a = 10$ kOe and Bi-sc curve, suggesting that one must go down to temperatures below 1.8 K to find quantum vortex motion with these magnetic fields. Actually, very low-temperature studies in 2212 Bi-based single crystals present plateaus which begin below 2 K and stretch down to the mK regime.[2] Table II summarizes the relevant parameters for the samples in which quantum motion has been detected.

In summary, we have reported on the detection of quantum relaxation at low temperatures in different HTSCs. In some samples (Tl-pd, Hg-ps) the transition from the thermal to the quantum regime appears to be very sharp, while in some others (Tl-ps, Tl-f) it is more gradual. In the second case, the transition was investigated in order to gain insight on the dissipative nature of the quantum process, but no conclusion could be drawn from the present study. Finally, quantum vortex motion was not detected in a couple of samples (Hg-ps and Bi-sc), suggesting the extension of magnetic relaxation measurements to the regime of ultralow temperatures.

A.G. thanks the Generalitat de Catalunya for a Ph.D. research grant. J.T. acknowledges financial support from the European Community. X.X.Z. thanks the Universitat de Barcelona for financial support.

[1] S. Uji, H. Aoki, S. Takebayashi, M. Tanaka, and M. Hashimoto, Physica C **207**, 112 (1993); S. Moehlecke and Y. Kopelevich, *ibid.* **222**, 149 (1994).
[2] K. Aupke, T. Teruzzi, P. Visani, A. Amann, A. C. Mota, and V. N. Zavaritsky, Physica C **209**, 255 (1993); D. Prost, L. Fruchter, I. A. Campbell, N. Motohira, and M. Konczykowski, Phys. Rev. B **47**, 3457 (1993).
[3] P. W. Anderson and Y. B. Kim, Rev. Mod. Phys. **36**, 39 (1964).
[4] G. Blatter and V. B. Geshkenbein, Phys. Rev. B **47**, 2725 (1993).
[5] G. Blatter, M. V. Feigel'man, V. B. Geshkenbein, A. I. Larkin, and V. M. Vinokur, Rev. Mod. Phys. **66**, 1125 (1994).
[6] J. R. Clem, Phys. Rev. B **43**, 7837 (1991).
[7] M. V. Feigel'man, V. B. Geshkenbein, A. I. Larkin, and S. Levit, Pis'ma Zh. Eks. Teor. Fiz. **57**, 699 (1993) [Sov. Phys. JETP Lett. **57**, 711 (1993)].
[8] A. García, X. X. Zhang, A. M. Testa, D. Fiorani, and J. Tejada, J. Phys. Condens. Matter **4**, 10 341 (1992); X. X. Zhang, A. García, J. Tejada, Y. Xin, and K. W. Wong, Physica C **232**, 99 (1994); A. García, X. X. Zhang, J. Tejada, M. Manzel, and H. Bruchlos, Phys. Rev. B **50**, 9439 (1994).
[9] X. X. Zhang, A. García, J. Tejada, Y. Xin, G. F. Sun, and K. W. Wong, Phys. Rev. B **52**, 1325 (1995).
[10] O. Laborde, P. Monceau, M. Potel, J. Padiou, P. Gougeon, J. C. Levet, and H. Noel, Physica C **162-164**, 1619 (1989).
[11] R. M. Hazen, L. W. Finger, R. J. Angel, C. T. Prewitt, N. L. Ross, C. G. Hadidiacos, P. J. Heaney, D. R. Veblen, Z. Z. Sheng, A. El Ali, and A. M. Hermann, Phys. Rev. Lett. **60**, 1657 (1988).
[12] D. E. Farrell, R. G. Beck, M. F. Booth, C. J. Allen, E. D. Bukowski, and D. M. Ginsberg, Phys. Rev. B **42**, 6758 (1990).

# An ultrasonic study of spin-density-wave effects in a Cr+0.2 at. % Ir alloy single crystal

J. Martynova, H. L. Alberts, and P. Smit
*Department of Physics, Rand Afrikaans University, P. O. Box 524, Auckland Park, Johannesburg 2006, South Africa*

Measurements of the temperature dependences of the second-order elastic constants and attenuation of ultrasonic waves through the magnetic phase transition temperatures of a Cr+0.2 at. % Ir alloy single crystal are reported. The incommensurate–commensurate spin-density-wave transition is marked by steplike decreases, accompanied by hysteresis of width about 16 K, in all the elastic constants on heating through the transition temperature. The attenuation coefficient shows a spikelike peak at this transition. A deep minimum in $c_{11}$ and small peaks in $c_{44}$ and $\frac{1}{2}(c_{11}-c_{12})$ are observed at the Néel transition. © *1996 American Institute of Physics.* [S0021-8979(96)57508-4]

## I. INTRODUCTION

Magnetic interactions in Cr and its dilute alloys are relatively strong,[1] resulting in large anomalies of magnetic origin in the elastic constants at the magnetic phase transition temperatures of these materials. Cr alloys with group-8 nonmagnetic transition metals Ru, Os, Rh, Ir, and Pt are of particular interest[1] in this regard. The magnetic phase diagrams of this group of Cr alloys all contain a paramagnetic (P), an incommensurate (I), and a commensurate (C) spin-density-wave (SDW) phase.[1] Interesting behavior was observed for the polycrystalline elastic constants, Young modulus, the bulk modulus $B$, and shear modulus $G$ of Cr–Ru,[2] Cr–Rh,[3] Cr–Pt,[4] and Cr–Ir (Ref. 5) alloys near the magnetic phase transition temperatures. Magnetoelastic studies on these polycrystalline alloys are, however, of limited value and measurements on single-crystalline alloys are needed for a better understanding of the magnetoelasticity of the above group of Cr alloy systems. Only one of these alloy systems, namely, the Cr–Ru system, was studied[6] up to now for SDW effects on the single-crystal second-order elastic constants $c_{11}$, $c_{44}$, and $c'=\frac{1}{2}(c_{11}-c_{12})$. Remarkable magnetoelastic effects were observed for Cr–Ru alloy single crystals. The longitudinal mode elastic constant $c_{11}$ as well as the shear mode constants $c_{44}$ and $c'$ of Cr–Ru alloy single crystals show steplike decreases, which have the characteristics of a first-order transition, on heating through the ISDW–CSDW magnetic phase transition temperature, $T_{IC}$. The behavior at the CSDW–P transition at the Néel temperature $T_N$ is, on the other hand, quite different. The longitudinal mode constant $c_{11}$ shows a very deep minimum at $T_N$ of Cr–Ru alloys while the shear constant $c_{44}$ and $c'$ show only weak effects in going through $T_N$.

We studied an alloy in another of the above group of alloy systems and report here an investigation of the elastic constants and attenuation of ultrasonic waves in a Cr+0.2 at. % Ir alloy single crystal. This alloy concentration was chosen for preparing a single crystal because it is above the triple-point concentration on the magnetic phase diagram,[1] resulting in the presence of both ISDW–CSDW and CSDW–P magnetic phase transitions on heating the crystal from low temperatures.

## II. EXPERIMENTAL TECHNIQUES

The Cr–Ir single crystal with 0.2 at. % Ir was grown by a floating-zone technique using radio-frequency heating. The starting material was a polycrystalline rod prepared from 99.996% pure Cr and 99.9% pure Ir. The actual concentration was determined, using electron microprobe techniques, to be 0.20±0.05 at. % Ir. Velocity and attenuation of 10 MHz ultrasonic waves were measured by using a standard pulse-echo overlap technique. The distances between parallel sets of (100) and (110) planes on the sample were between 6 and 8 mm. Measurements were done during both cooling and heating runs.

## III. RESULTS AND DISCUSSION

The temperature dependences of the elastic tensor components $c_{11}$, $c_L=\frac{1}{2}(c_{11}+c_{12}+2c_{44})$, $c_{44}$, and $c'=\frac{1}{2}(c_{11}-c_{12})$ are shown in Fig. 1 for heating runs. Figure 2(a) shows the temperature dependence of the bulk modulus $B=\frac{1}{3}(c_{11}+2c_{12})=c_{11}-\frac{4}{3}c'$ of the Cr+0.2 at. % Ir crystal as well as the expected nonmagnetic component taken[7] as $B(T)$ of a Cr+5 at. % V crystal.[7] The magnetic component $\Delta B$ of $B$ for Cr+0.2 at. % Ir is shown as a function of temperature in Fig. 2(b). $\Delta B$ is obtained as $\Delta B=B(Cr_{95}V_5)-B(Cr_{99.8}Ir_{0.2})$, where $B(Cr_{99.8}Ir_{0.2})$ was calculated from the data in Fig. 1.

The data of Fig. 1 show two well-defined anomalies. One of these, in the form of a steplike decrease during heating for all the elastic constants, occurs at a temperature around 270 K. In accordance with the magnetic phase diagram of Cr–Ir alloys,[1] this anomaly is taken to occur at the ISDW–CSDW magnetic phase transition temperature $T_{IC}$. The other anomaly is in the form of a deep minimum around 370 K in both the $c_{11}-T$ and $c_L-T$ curves and in the form of small peaks in the $c_{44}-T$ and $c'-T$ curves. These anomalies are associated with the Néel transition.

Figure 3 shows the temperature dependence of $c_{11}$, $c_L$, $c_{44}$, and $c'$ near the ISDW–CSDW phase transition for measurements taken during both cooling and heating runs. This transition shows large hysteresis effects of width about 16 K for all modes. Above about 280 K the elastic constants in Fig. 3 show no thermal hysteresis between heating and cooling runs, showing that hysteresis effects disappear at

 0021-8979/96/79(8)/6519/3/$10.00 © 1996 American Institute of Physics 

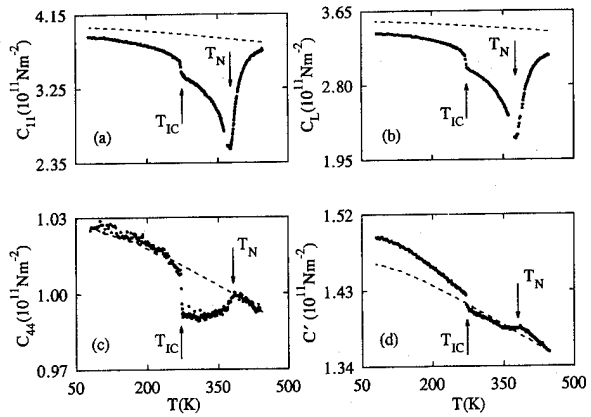



FIG. 1. Temperature dependence of (a) $c_{11}$, (b) $c_L=\frac{1}{2}(c_{11}+c_{12}+2c_{44})$, (c) $c_{44}$, and (d) $c'=\frac{1}{2}(c_{11}-c_{12})$ obtained during heating runs for a Cr+0.2 at. % Ir single crystal. The broken lines represent the temperature dependence of the nonmagnetic component of the corresponding elastic constant of the Cr+0.2 at. % Ir crystal, and are obtained[7] from the corresponding elastic constant of a Cr+5 at. % V crystal that remains paramagnetic at all temperatures.

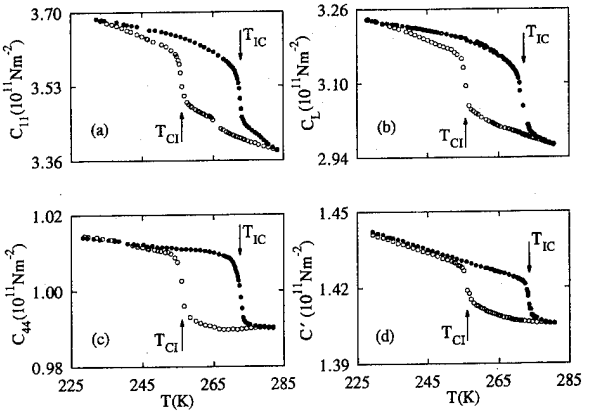



FIG. 3. Hysteresis effects in (a) $c_{11}$, (b) $c_L=\frac{1}{2}(c_{11}+c_{12}+2c_{44})$, (c) $c_{44}$, and (d) $c'=\frac{1}{2}(c_{11}-c_{12})$ near the ISDW–CSDW magnetic phase transition of a Cr+0.2 at. % Ir single crystal for (●) heating runs and (○) cooling runs.

temperatures about 8 K higher than $T_{IC}$ (on heating) for all elastic modes. On the other hand, hysteresis effects are present for the two longitudinal modes, $c_{11}$ and $c_L$, of Fig. 3 down to 232 K, about 24 K below $T_{CI}$ (on cooling), and only to 245 K, about 11 K below $T_{CI}$, for the two shear modes, $c_{44}$ and $c'$. Below 245 K the hysteresis effects for the shear modes are negligible. The observation that hysteresis effects persist in the Cr+0.2 at. % Ir crystal in a much larger temperature range below $T_{CI}$ than above $T_{IC}$ was also noted[8] for a Cr+0.3 at. % Ru single crystal. The difference in behavior between the two crystals is that for the Cr+0.3 at. % Ru crystal[8] this phenomenon was observed for both longitudinal and shear mode elastic constants, while it is observed mainly for the longitudinal mode constants of the Cr+0.2 at. % Ir crystal. All the elastic constants of Fig. 3 show the same first-order character at the I–C or C–I transition as was observed for a Cr+0.3 at. % Ru crystals.[8] No hysteresis effects were observed within the experimental error during cooling and heating runs through the Néel transition.

Figure 4 shows the temperature dependence of the attenuation of 10 MHz ultrasonic waves for the different vibration modes in the Cr+0.2 at. % Ir crystal near the ISDW–CSDW phase transition for both heating and cooling runs. The C–I transition (on cooling) is characterized by a sharp spikelike attenuation peak at a temperature $T_{CI}$. This is also the case for the I–C transition (on heating) that shows a similar peak at $T_{IC}$. The width of the attenuation peak at half amplitude is about 1.5 K or less. An interesting behavior in Fig. 4 is the broad hump in attenuation at temperatures just above the sharp peak for the $c_{11}$ mode of vibration and also the double peak for the $c_L$ mode. At present we do not know the reason for this behavior but note that it is rather small for the two shear vibration modes. From the average temperatures of the peaks in Fig. 4 we obtain $T_{IC}=272.2\pm0.8$ K and $T_{CI}=256\pm1$ K. These temperatures correspond with the temperatures at the inflection points of Fig. 3, identifying the

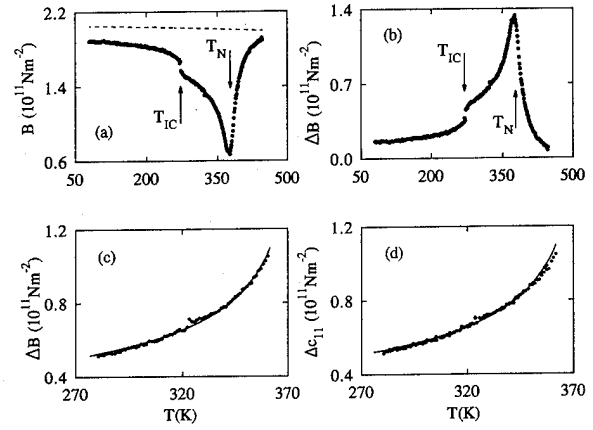



FIG. 2. Temperature dependence of (a) the bulk modulus $B$ and (b) of the magnetic contribution $\Delta B$ to $B$ of Cr+0.2 at. % Ir. (c) and (d) show the best fit (solid line) of Eq. (1) to the experimental data for $\Delta B$ and $\Delta c_{11}$ in the CSDW phase. Results of heating runs are shown.

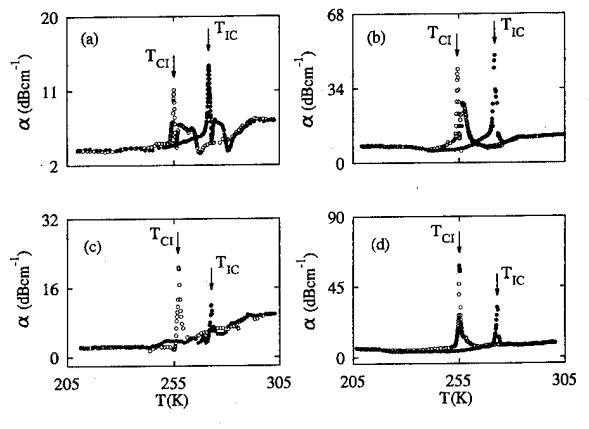



FIG. 4. Ultrasonic (10 MHz) attenuation coefficient $\alpha$ of Cr+0.2 at. % Ir for modes of propagation corresponding to (a) $c_{11}$, (b) $c_L=\frac{1}{2}(c_{11}+c_{12}+2c_{44})$, (c) $c_{44}$, and (d) $c'=\frac{1}{2}(c_{11}-c_{12})$: (●) heating runs and (○) cooling runs.

inflection points as the I–C and C–I SDW transition points on the $c-T$ curves. The ultrasonic attenuation becomes extremely large in the vicinity of the Néel transition and we were unable to measure it reliably around $T_N$ in this study.

$T_N$ for the Cr+0.2 at. % Ir crystal was defined at the minimum point of the $c_{11}-T$ and $c_L-T$ curves of Fig. 1, giving $T_N=377.0\pm0.4$ K. The temperatures $T_{IC}=272.2\pm0.8$ K and $T_N=377.0\pm0.4$ K of the present measurements on single-crystalline Cr+0.2 at. % Ir agree reasonably well with temperatures[9] $T_{IC}=279$ K and $T_N=380$ K as well as with[10] $T_N=371\pm2$ K, determined from electrical resistivity $\rho$ measurements on polycrystalline Cr+0.2 at. % Ir. No hysteresis effects were reported at $T_{IC}$ in the $\rho-T$ measurements of Butylenko and Nevdacha.[9] The $\rho$ anomaly observed by them at $T_{IC}$ is small and weak while such anomalies are absent in the $\rho-T$ measurements of Yakhmi and co-workers[10] on polycrystalline Cr+0.2 at. % Ir. The present measurements show a well-defined and relatively large anomaly in all the single-crystalline elastic constants at $T_{IC}$.

Katsnel'son and Trefilov[11] recently studied the temperature dependence of the elastic constants of dilute Cr alloys near $T_N$ theoretically. Their microscopic theory shows that an anomaly arises for these materials in the temperature dependence of the elastic constants below $T_N$. This anomaly is brought about by the disappearance of the antiferromagnetic gap in the electron spectrum when $T\rightarrow T_N$, resulting in changes in the screening and in the phonon spectrum. The result is a softening of the elastic constants below $T_N$, which explains the observed softening in the Cr+0.2 at. % Ir crystal qualitatively. The theory gives for the magnetic component $\Delta c_{ii}$ of the elastic constant $c_{ii}$ at temperatures not too close to $T_N$

$$\Delta c_{ii}\sim\left(\frac{\partial T_N}{\partial \mu_i}\right)^2 (T_N-T)^{-\gamma}, \tag{1}$$

where $\mu_i$ are components of the deformation tensor. In Eq. (1) $\Delta c_{ii}$ is defined as

$$\Delta c_{ii}=c_{ii}(\text{nonmagnetic Cr alloy})$$
$$-c_{ii}(\text{magnetic Cr alloy}),$$

which is of opposite sign as the definition used by Katsnel'son and Trefilov,[11] but conforms with that used in Fig. 2 for $\Delta B$ and $\Delta c_{11}$. As $T_N$ is particularly sensitive to changes in volume, the bulk modulus $B(T)$ should soften the most from Eq. (1) which explains the softening observed experimentally for $B$ in this study. In Eq. (1), $\gamma=1$ if the density-of-states function in the paramagnetic phase is smooth near the Fermi level and $\gamma=5/4$ if it has a van Hove singularity there.[11]

Equation (1) fits the experimental data for $\Delta B$ and $\Delta c_{11}$ in the CSDW phase of the Cr+0.2 at. % Ir crystal well (see Fig. 2) in the temperature range $280<T<370$ K with $\gamma=0.416\pm0.003$ and $\gamma=0.422\pm0.004$, respectively. This gives a $\gamma$ value different from the theoretically expected values of either 1 or 5/4. A similar analysis of the $\Delta B-T$ data[12] of a Cr+0.3 at. % Ru crystal gives $\gamma=0.280\pm0.002$ over a temperature range of about 120 K, in the CSDW phase, below $T_N$.

## IV. CONCLUSION

In conclusion, Cr alloy single crystals with group-8 nonmagnetic transition metals Ru and Ir show nearly similar temperature dependences of their elastic constants around the ISDW–CSDW and CSDW-P magnetic phase transition temperatures. The only markable difference is in the details of the hysteresis behavior around the ISDW–CSDW transition. Longitudinal and shear mode constants behave differently in this regard for Cr+0.2 at. % Ir while they behave the same for Cr+0.3 at. % Ru. The temperature behavior of the magnetic component of the bulk modulus is different for the two crystals just below $T_N$ in the CSDW phase. The temperature derivative of $\Delta B$ at each temperature in this phase is larger for Cr+0.2 at. % Ir than for Cr+0.3 at. % Ru.


[1] E. Fawcett, H. L. Alberts, V. Yu. Galkin, D. R. Noakes, and J. V. Yakhmi, Rev. Mod. Phys. **66**, 25 (1994).
[2] H. L. Alberts and J. A. J. Lourens, J. Phys. F **18**, L213 (1988).
[3] B. C. Munday, Phys. Status Solidi A **8**, K129 (1971).
[4] H. L. Alberts and J. A. J. Lourens, J. Phys. (Paris) Colloq. **49**, C8-215 (1988).
[5] H. L. Alberts and P. Smit, J. Magn. Magn. Mater. **140-144**, 41 (1995).
[6] A. H. Boshoff, H. L. Alberts, P. de V. du Plessis, and A. M. Venter, J. Phys. Condens. Matter **5**, 5353 (1993).
[7] H. L. Alberts, J. Phys. Condens. Matter **2**, 9707 (1990).
[8] M. Cankurtaran, G. A. Saunders, Q. Wang, P. J. Ford, and H. L. Alberts, Phys. Rev. B **46**, 14 370 (1992).
[9] A. K. Butylenko and V. V. Nevdacha, Dokl. Akad. Nauk Ukr. SSR **5**, 67 (1980) (in Russian).
[10] J. V. Yakhmi, I. K. Gopalakrishnan, and R. M. Iyer, J. Less-Common Met. **91**, 327 (1983).
[11] M. I. Katsnel'son and A. V. Trefilov, Phys. Met. Metallogr. **77**, 362 (1994).
[12] H. L. Alberts and A. H. Boshoff, J. Magn. Magn. Mater. **104-107**, 2031 (1992).

# Hall-effect measurements on Cr films deposited on Ge substrates

Chien-Sheng Hsieh and Klaus Schröder
*Department of Chemical Engineering and Materials Science, Syracuse University, Syracuse, New York 13244*

The Hall effect of Cr films on Ge substrates was measured at room temperature in a high-vacuum system. It was found that the Hall coefficient $R_H$ depends on the pressure in the vacuum system. $R_H$ of films about 1–2 nm thick was about $5\times10^{-11}$ $m^3/C$ for a pressure during Cr evaporation in the $10^{-7}$ Torr range. The Hall coefficient decreased to less than $10^{-11}$ $m^3/C$ if pressure decreased into the $10^{-8}$ Torr range. These $R_H$ values are much lower than found in bulk chromium. They would give in a one-band model about 1 electron hole/atom for the higher-pressure, and about 12 electron holes/atom for the lower-pressure experiments. A two-band model could give the observed low Hall coefficients if the hole current nearly compensated the electron current. Both models cannot be reconciled with presently accepted electron band models for chromium. © *1996 American Institute of Physics.* [S0021-8979(96)57608-3]

## INTRODUCTION

The properties at the Ge–Cr interface are unusual at room temperature. The resistance of ultrathin Cr films on a Ge substrate is much lower than expected, and both Ge or Si overlayers reduce the electrical resistance.[1] These films are strongly diamagnetic, although they should be paramagnetic, just like Cr films on glass substrates.[2] The absolute Seebeck coefficients of an ultrathin Cr film on a Ge substrate is, within experimental accuracy, zero.[3] These results would be expected if the Cr–semiconductor interface region is superconducting; however, the films do not show zero resistance. Therefore, we suggested as a possible model that the interface contains superconducting islands.[1–3]

Hall-effect measurements on superconductors by Dascoulidou *et al.*[4] show that the Hall coefficient $R_H$ of their samples approaches zero if the samples change from the normal to the superconducting state. Their work encouraged us to start $R_H$ measurements on Cr films deposited on Ge substrates.

## EXPERIMENTAL APPROACH

We prepared films in the same high-vacuum system (base pressure close to $10^{-8}$ Torr) described previously.[1,2] First Ge films, about 2–3 nm thick, were deposited by evaporating high-purity germanium (resistivity: 40 Ω cm) on a glass plate ($1.8\times1.8$ $cm^2$) with five electrical silver paint contacts: two for current leads, three for potential leads. Then chromium (99.995% total purity) was evaporated and a Cr film with thickness $t$ formed on the Ge film. The growth rate was of the order of 1 nm/min. Auger spectroscopy studies by Schröder and Walsh[1] showed that this produced clean Cr films. The experimental approach was the same as used for the preparation of films for resistivity[1] and Seebeck coefficient $S$ measurements.[3] For Seebeck coefficient measurements the film was in contact with two Fe wires, forming a differential thermocouple. A second differential thermocouple consisting of two Fe wires and a Constantan wire was placed at the opposite side of the glass plate to measure the temperature gradient. Details are given in Ref. 3. The Hall voltage $V_H$ was measured at a magnetic field $B$ of 0.58 T. Several Cr films were deposited in sequence, and at the end of each Cr-film deposition the Hall voltage was measured at 0.58 T. The main uncertainty in the data is due to the error in the thickness measurements determined with the INFICON XTM/2 thickness monitor. Since the surface of the glass plate and the crystal of the monitor are both initially covered with germanium *in situ*, the sticking probability for chromium should be the same for the films prepared on the glass plate or the crystal of the thickness monitor; however, the glass plate and the thickness monitor crystal are not lined up in the same direction with respect to the Cr source as in previous electrical resistance measurements.[1] We found in our present system, using two thickness monitors, that a few monolayers may form on the glass or quartz crystal substrates first before the films grow on both substrates nearly uniformly. This leads to an uncertainty in the film thickness $t$ which may be as large as 0.5 nm. The resistance per square in our present experiments, shown in Fig. 1, is for sample 3

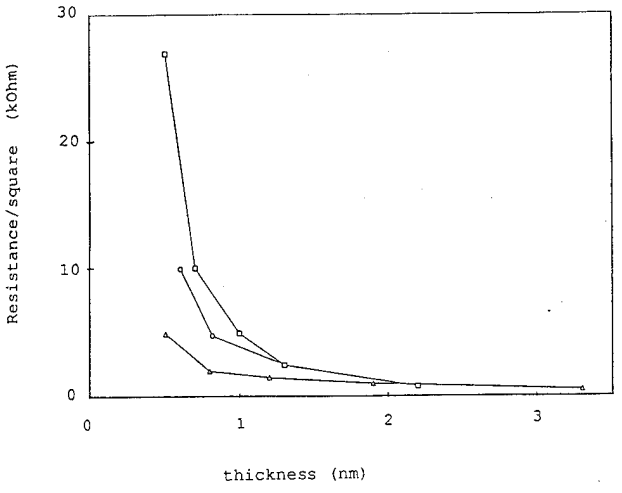



FIG. 1. Resistance per square of sample 1 (circles), 2 (squares), and 3 (triangles) as a function of thickness $t$. The pressure during evaporation was highest for sample 1 (in the upper $10^{-7}$ Torr range), slightly lower in sample 2, and lowest for sample 3 (in the $10^{-8}$ Torr range). Data points are of the size of the error.

 0021-8979/96/79(8)/6522/3/$10.00 © 1996 American Institute of Physics

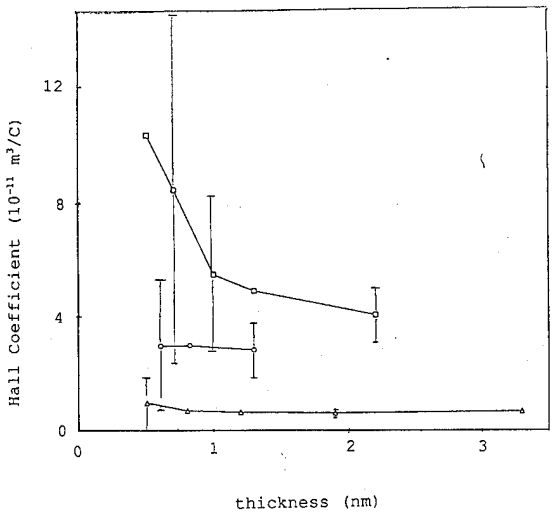



FIG. 2. Hall coefficient of sample 1 (circles), 2 (squares), and 3 (triangles) as a function of thickness.

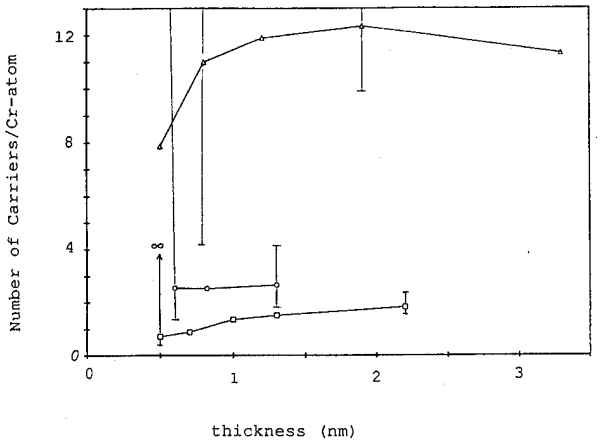



FIG. 3. Number of holes per chromium atom of sample 1 (circles), 2 (squares), and 3 (triangles) as a function of film thickness calculated with the assumption of a one-band model. The length of the error bar extends sometimes above the upper border of the figure. The exact value for the upper error limit is unimportant for the discussion.

very similar to what was found in earlier experiments.[1] Sample 3 was prepared at the same pressure as samples for the earlier tests.[1]

## RESULTS AND DISCUSSION

Figure 2 gives the Hall coefficient $R_H = V_H t/IB$, with $I$ the current flowing through the sample, as a function of the nominal film thickness $t$. $R_H$ is positive. As mentioned previously, the uncertainty in the film thickness is estimated to be 0.5 nm. This means that the $R_H$ values for $t<1$ nm have an error of more than 50%. The error for films with $t>2$ nm is less than 25%. The Hall coefficients for $t>1$ nm are within the experimental accuracy constant. $R_H$ of our films is much smaller than $R_H$ of bulk samples for which the Hall coefficient is about $4\times10^{-10}$ m$^3$/C.[5]

$R_H$ is positive: This suggests that the electric current is carried predominantly by holes. $R_H$ is related to the hole concentration $p$ (number/volume) by

$$R_H = 1/pq, \tag{1}$$

if one can use a one-band model.

Hole concentrations per volume of a Cr atom ($p$/Cr atom) calculated with Eq. (1) are given in Fig. 3. One finds that $p$/Cr atom for films more than 0.7 nm thick is about 1–2 if the pressure during Cr evaporation is in the $10^{-7}$ Torr range. $p$/Cr atom $>10$ if the pressure is in the $10^{-8}$ Torr range, and if one neglects the first data point. (The pressure dependence of the Hall coefficient and $p$ may be due to variations in impurity levels. An increase in base pressure could lead to an increase in the impurity concentration, which in turn modifies the microstructure during growth.) These numbers are, even if one considers the experimental uncertainties, much larger than found for bulk chromium ($p$ =0.2/Cr atom[5]). Values of $p$/Cr atom $>10$ cannot be reconciled with any acceptable electron model for chromium.

One should therefore try to use a multiband model. The Hall coefficient of a multiband system is given by

$$R_H = \sum \left(\frac{\sigma_i}{\sigma}\right)^2 R_{H,i}\,, \tag{2}$$

where $\sigma$ is the electrical conductivity of the sample, $\sigma_i$ the conductivity in subband $i$, and $R_{H,i}$ is the Hall coefficient of subband $i$. This equation shows that if one band carries most of the current it will control $R_H$, and it is therefore usually adequate to use a one-band model. In a system with parabolic energy bands $i$, the Hall coefficient for each subband is $R_{H,i} = -1/n_i q$ for electrons, and $R_{H,i} = 1/p_i q$ for holes.

If one assumes that the current in our thin films is due to one hole and one electron band, then one can explain the small value for $R_H$ with the assumption that the current by electrons is nearly as large as the current by holes. In that case $R_H = (\sigma_h/\sigma)^2 R_{H,h} - (\sigma_n/\sigma)^2 R_{H,n}$. The two terms in the right-hand side of this equation essentially cancel each other. This interpretation of the Hall effect would state that the thin Cr films are compensated, independent of film thickness. This model is not confirmed by other experiments. The absolute Seebeck coefficient is close to zero only for about two monolayers of chromium on germanium and that first decreases to about $-2$ to $-4$ $\mu$V/K for films about 3 nm thick. Such a behavior of $S$ is not expected for a compensated material.

As before we are left with a problem. We have magnetic susceptibility, electrical resistivity, Seebeck coefficient, and Hall coefficient measurements which are unusual. One could try to explain each of the electrical measurements with a conventional model, but the model used to explain the Hall coefficient does not work for the Seebeck coefficient. The strong diamagnetism cannot be explained at all with any standard model. The only model which would explain all results would be the model of disconnected superconducting islands near the surface or the interface with the substrate. This model was already proposed to explain previous measurements.[1–3]

There may be other explanations. Clearly more work is

needed before we understand the electrical transport processes in the Cr–Ge interface.

## ACKNOWLEDGMENTS

The authors appreciate very much discussions with Le Zhang and W.-T. Ger, Syracuse University.

[1] K. Schröder and Le Zhang, Phys. Status Solidi B **183**, K5 (1994); A. N. Aleshin and K. Schröder, Mater. Res. Soc. Symp. Proc. **318**, 465 (1994); K. Schröder and L. Walsh, J. Vac. Sci. Technol. A **9**, 577 (1991).
[2] K. Schröder and S. Nayak. Phys. Status Solidi B **172**, 679 (1992); K. Schröder and H. Hejase, *ibid.* **149**, 685 (1988).
[3] K. Schröder, Le Zhang, and W.-T. Ger, Phys. Status Solidi B **181**, 421 (1994).
[4] A. Dascoulidou, M. Galffy, C. Hohn, N. Knauf, and A. Freimuth, Physica C **201**, 202 (1992).
[5] J. M. Ziman, *Electrons and Phonons* (Clarendon, Oxford, 1960), p. 488.

# Modeling the stress dependence of Barkhausen phenomena for stress axis linear and noncollinear with applied magnetic field (abstract)

M. J. Sablik[a)]
*Southwest Research Institute, San Antonio, Texas 78228-0510*

B. Augustyniak and M. Chmielewski
*Technical University of Gdansk, PL-80-952, Gdansk, Poland*

The almost linear dependence of the maximum Barkhausen noise signal amplitude on stress has made it a tool for nondestructive evaluation of residual stress. Recently,[1] a model has been developed to account for the stress dependence of the Barkhausen noise signal. The model uses the development of Alessandro *et al.*[2] who use coupled Langevin equations to derive an expression for the Barkhausen noise power spectrum. The model joins this expression to the magnetomechanical hysteresis model of Sablik *et al.*,[3] obtaining both a hysteretic and stress-dependent result for the magnetic-field-dependent Barkhausen noise envelope and obtaining specifically the almost linear stress dependence of the Barkhausen noise maximum experimentally.[4] In this paper, we extend the model to derive the angular dependence observed by Kwun[5] of the Barkhausen noise amplitude when stress axis is taken at different angles relative to magnetic field. We also apply the model to the experimental observation that in XC10 French steel, there is an apparent almost linear correlation with stress of hysteresis loss and of the integral of the Barkhausen noise signal over applied field $H$. Further, the two quantities, Barkhausen noise integral and hysteresis loss, are linearly correlated with each other. The model shows how that behavior is to be expected for the measured steel because of its sharply rising hysteresis curve.[6] © *1996 American Institute of Physics.* [S0021-8979(96)70808-X]

[a)]Work supported by U.S. Dept. of Energy Grant No. DE-FG05-9-1ER14180.

[1] M. J. Sablik, J. Appl. Phys. **74**, 5898 (1993).
[2] B. Alessandro, C. Beatrice, G. Bertotti, and A. Montorsi, J. Appl. Phys. **68**, 2901 (1990).
[3] M. J. Sablik, S. W. Rubin, L. A. Riley, D. C. Jiles, D. A. Kaminski, and S. B. Biner, J. Appl. Phys. **74**, 480 (1993).
[4] R. L. Pasley, Mater. Eval. **28**, 157 (1970).
[5] H. Kwun, J. Magn. Magn. Mater. **49**, 235 (1985).
[6] See also M. J. Sablik and B. Augustyniak, J. Appl. Phys. **79**, 963 (1996).

# Magnetovolume and magnetoelastic effects in ternary Cr–Ru–Mo alloys

J. T. Mochele, P. Smit, and H. L. Alberts
*Department of Physics, Rand Afrikaans University, P.O. Box 524, Auckland Park, Johannesburg 2006, South Africa*

The influence of Mo additions on the unusual magnetoelastic properties and Invar-type behavior of a $Cr_{0.997}Ru_{0.003}$ antiferromagnetic alloy was investigated. Measurements were done of the temperature dependence of the thermal-expansion coefficient and bulk modulus of $(Cr_{1-x}Mo_x)_{0.997}Ru_{0.003}$ alloys with $0 \leqslant x \leqslant 0.07$. Well-defined magnetic anomalies were observed at the Néel temperature implying large magnetic contributions to the thermal expansion and the bulk modulus, making these alloys suitable to be analyzed and parameterized in terms of existing theories. The addition of Mo to $Cr_{0.997}Ru_{0.003}$ completely suppresses the presence of the commensurate spin density wave phase for $x \geqslant 0.015$ and does not improve the Invar-type behavior to a desired level that may be useful for practical applications. © *1996 American Institute of Physics.* © *1996 American Institute of Physics.* [S0021-8979(96)57708-4]

## I. INTRODUCTION

Alloying Cr with the nonmagnetic transition metal Ru shows unusual magnetoelastic effects[1] due to strong spin density wave (SDW) interactions with the lattice. The coefficient of thermal expansion $\alpha$ of a $Cr_{0.997}Ru_{0.003}$ alloy shows[1] a deep minimum at the commensurate (C) SDW to paramagnetic (P) Néel transition, observed at the Néel point $T_N$, and a large maximum at the incommensurate (I) to commensurate (C) SDW phase transition temperature $T_{IC}$. One of the remarkable features of $\alpha(T)$ of $Cr_{0.997}Ru_{0.003}$ is the very small value of $\alpha$ ($\alpha \approx 0$) observed[1] at $T_N$ ($\approx$395 K). This behavior indicates antiferromagnetic Invar[2]-type effects to be present in this alloy around $T_N$, making it a candidate for practical application. The temperature region in which $Cr_{0.997}Ru_{0.003}$ displays Invar-type effects is relatively small and occurs well above room temperature, thereby limiting its practical usefulness. In order to eliminate this limitation, $Cr_{0.997}Ru_{0.003}$ should be tailored in such a way that $T_N$, and therefore the temperature where $\alpha \approx 0$, is reduced down to room temperature and that the temperature interval in which $\alpha$ remains close to zero is simultaneously broadened. It was shown[3] that the addition of Mo to Cr acts to weaken the strength of the SDW, thereby decreasing $T_N$ of Cr linearly. Mo is ideally suited for this purpose as it seems from experiment[4] that the magnetic ordering in Cr–Mo alloys is still of a Cr-type SDW ordering, even for relatively high Mo concentrations, up to at least 10 at. % Mo. One can therefore use Mo to adjust the strength of the SDW and study its effects on the Invar-type behavior of the above Cr–Ru alloys. We report in this study on the effects on the thermal expansion and bulk modulus of a $Cr_{0.997}Ru_{0.003}$ alloy when some of the Cr atoms are replaced by Mo.

## II. EXPERIMENTAL TECHNIQUE

Polycrystalline ingots of $(Cr_{1-x}Mo_x)_{0.997}Ru_{0.003}$ with $x=0$, 0.003, 0.007, 0.01, 0.015, 0.03, and 0.07 were prepared from 99.99% Cr and Mo and 99.9% Ru starting materials by means of arc melting. Electron microprobe analyses indicated that the actual concentrations do not differ by more than 5% from the nominal values of $x$ and that the alloys are homogeneous to within less than 5% of the quoted concentrations. Standard strain gauge and ultrasonic (10 MHz) measuring techniques were used[5] to measure the thermal expansion and sound velocity of the alloys as functions of temperature. The thermal-expansion coefficient $\alpha$ was determined for all the alloys, while the bulk modulus $B$, calculated from longitudinal and shear wave sound velocity measurements, was only determined for alloys with $x=0.007$, 0.015, and 0.07. $\Delta L/L$ for the $(Cr_{1-x}Mo_x)_{0.997}Ru_{0.003}$ alloys were measured relative to that of a paramagnetic $Cr_{0.95}V_{0.05}$ alloy in order to obtain the contributions of the magnetic ordering to $\Delta L/L$ of the Cr–Ru–Mo alloys. $Cr_{0.95}V_{0.05}$ remains paramagnetic at all temperatures and simulates the paramagnetic component of $\alpha$ and $B$ of the antiferromagnetic Cr–Ru–Mo alloys.[6] The experimental error in the absolute value of $\Delta L/L$ was about 5% while changes with temperature of the order of $2\times10^{-6}$ could be detected. The error estimated in the absolute value of $B$ is about 2%, while changes in the order of one in $10^3$ with temperature could be observed. All measurements were conducted within the temperature range 77–450 K. Thermal-expansion measurements were carried out during both heating and cooling runs, in order to check for hysteresis effects around $T_{IC}$, since it is known[7] that the ISDW–CSDW phase transition in $Cr_{0.997}Ru_{0.003}$ is first-order like, while sound velocity measurements were done only for heating runs.

## III. RESULTS AND DISCUSSION

The temperature dependence of $\alpha$ is shown in Fig. 1 for different values of $x$. Well-defined anomalies, in the form of a sharp minimum for $x \leqslant 0.03$ and in the form of a relatively steep step for $x=0.007$, are observed in the $\alpha-T$ curves at $T_N$. Minima were also observed at $T_N$ in the $B-T$ curves for $x=0.007$, 0.015, and 0.07 as shown in Fig. 2. The results show that the addition of Mo to binary $Cr_{0.997}Ru_{0.003}$ decreases $T_N$ toward room temperature and below, as expected. This results from the weakening effects of Mo on the SDW in $Cr_{0.997}Ru_{0.003}$. Furthermore, the addition of Mo increases the value of $\alpha$ at $T_N$ making ternary $(Cr_{1-x}Mo_x)_{0.997}Ru_{0.003}$ alloys less suitable for practical applications. It is of interest to note that the $\alpha-T$ curve for $x=0.07$ in Fig. 1 is nearly flat just below $T_N$ in a temperature range of about 50 K, making

 0021-8979/96/79(8)/6526/3/$10.00 © 1996 American Institute of Physics

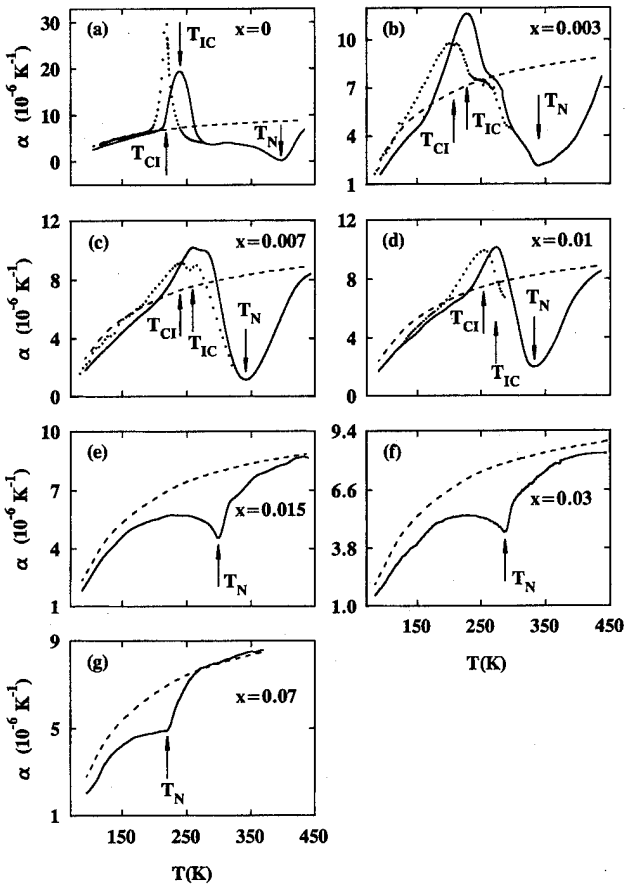



FIG. 1. Temperature dependence of the coefficient of thermal expansion $\alpha=d(\Delta L/L)/dT$ for $(Cr_{1-x}Mo_x)_{0.997}Ru_{0.003}$ where (a) $x=0$, (b) $x=0.003$, (c) $x=0.007$, (d) $x=0.01$, (e) $x=0.015$, (f) $x=0.03$, and (g) $x=0.07$. The solid line and dotted line curves represent the heating and cooling runs, respectively, and they were drawn through the experimental data points which were obtained at 0.1 K intervals. The dashed line curves represent the expected nonmagnetic component of the Cr–Ru–Mo alloys given by $\alpha$ for $Cr_{0.95}V_{0.05}$.

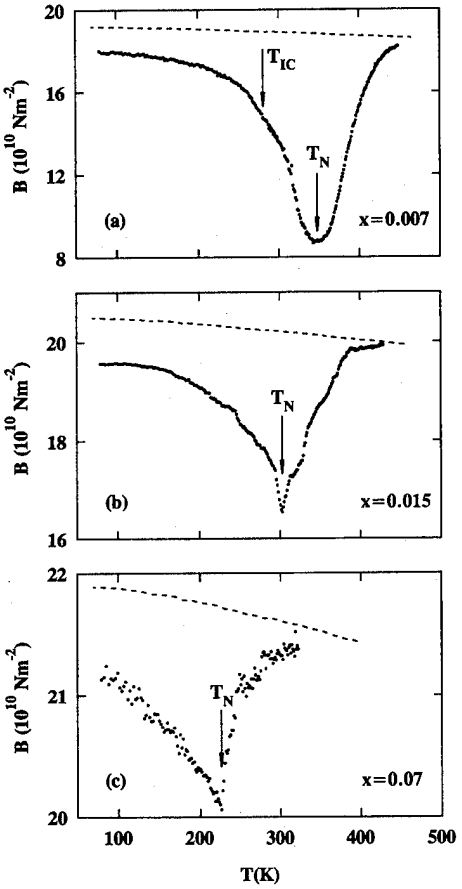



FIG. 2. Temperature dependence of the bulk modulus $B$ for $(Cr_{1-x}Mo_x)_{0.997}Ru_{0.003}$ where (a) $x=0.007$, (b) $x=0.015$, and (c) $x=0.07$. The dashed line curves represent the expected nonmagnetic component of $B$ taken as $B$ for a $Cr_{0.95}V_{0.05}$ alloy that remains paramagnetic at all $T$.

$\alpha$ nearly invariant with temperature. In this temperature range $\alpha$ is however too large to be of any use in practical applications.

The $\alpha-T$ curves are further characterized (Fig. 1) by a large relative maximum at the ISDW–CSDW phase transitions at $T_{IC}$ on heating and a smaller maximum at the CSDW–ISDW transition temperature $T_{CI}$ on cooling. Although hysteresis effects of width $\Delta T\approx 21$ K were clearly observed during heating and cooling runs through the ISDW–CSDW and CSDW–ISDW phase transitions, the ISDW–P phase transition at $T_N$ showed no hysteresis effects, indicative of its second-order nature. The transition temperature $T_{IC}$ (or $T_{CI}$) increases with a progressive suppression of the CSDW phase as the Mo content is increased (Fig. 1), thereby suppressing the CSDW phase completely for $x\geqslant 0.015$. The ISDW–CSDW (CSDW–ISDW) phase transition for $(Cr_{1-x}Mo_x)_{0.997}Ru_{0.003}$ alloys is furthermore also accompanied by a shoulder-hump-type feature on the $\alpha-T$ curve between $T_{IC}$ ($T_{CI}$) and $T_N$ [Figs. 1(a), 1(b), and 1(c)]. The origin of this feature on the $\alpha-T$ curves is presently unknown but it may be mentioned that it was previously also observed in Cr–Pt alloys.[8] This feature progressively moves closer to $T_{IC}$ ($T_{CI}$) as the Mo content is increased up to $x=0.007$ beyond which it disappears. The ISDW–CSDW phase transition was only barely observable as a very weak anomaly on the $B-T$ curve of the sample with $x=0.007$ (Fig. 2). In the case of $x=0.007$, $\alpha(T)$ measurements clearly indicated the existence of both the ISDW–CSDW and the CSDW–P phase transitions, while the measurements of $B(T)$ revealed a large relative minimum at the CSDW–P phase transition, which overshadows the much smaller ISDW–CSDW phase transition that is normally observed on $B-T$ curves of Cr alloys.[1]

The magnetovolume $\Delta\omega(T)$ and $\Delta B(T)$, which are the magnetic contributions to the volume and the bulk modulus, respectively, were determined from the $\Delta L/L$ and $B$ measurements by applying similar calculation techniques as were used previously.[9] For Cr alloys, $\Delta\omega(T)$ and $\Delta B(T)$ are expected[10] theoretically to vary as

$$\Delta\omega(t)/\Delta\omega(0)=a_0+a_1t^2+a_2t^4,$$

and

$$\Delta B(t)/\Delta B(0)=b_0+b_1t^2+b_2t^4,$$

where $t=T/T_N$ and the $a$ and $b$ are fitting parameters, respectively. As shown by the typical examples of Fig. 3, these equations fit the results for those alloys that do not show

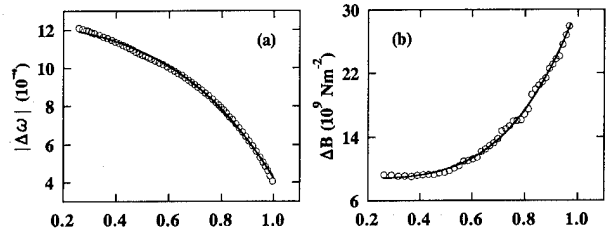



FIG. 3. Temperature dependence of (a) the magnetovolume $\Delta\omega$ and (b) the magnetic contribution to the bulk modulus $\Delta B$ for $(Cr_{1-x}Mo_x)_{0.997}Ru_{0.003}$ where $x=0.015$. The solid line curves in (a) and (b) are best fits of the equations $\Delta\omega=a_0+a_1t^2+a_2t^4$ and $\Delta B=b_0+b_1t^2+b_2t^4$, respectively, to the experimental data.

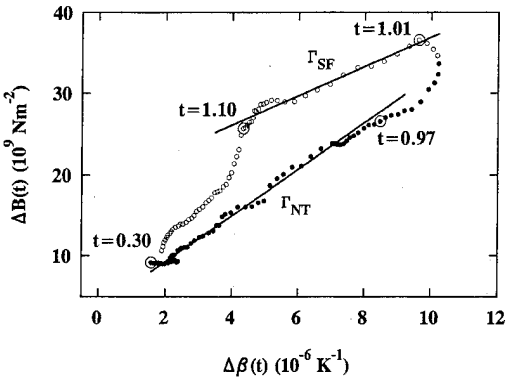



FIG. 4. $\Delta B(t)$ is shown as a function of the magnetic contribution to the volume thermal-expansion coefficient $\Delta\beta(t)$ for $x=0.015$. The solid lines are least-square fits to the data points between and including the encircled points. The values of $t=T/T_N$ ($T_N$=299 K) at the encircled points are shown. The points (●) show the comparison of $\Delta B(t)$ and $\Delta\beta(t)$ for $T<T_N$ and (○) for $T>T_N$.

ISDW–CSDW phase transitions, namely for $0.015\leqslant x\leqslant 0.07$, rather well. This was previously also found to be the case for other Cr alloy systems.[10–12] Theory further predicts[10] that $(a_1/a_0+a_2/a_0)=-1$. For the Cr–Ru–Mo alloys we obtained $(a_1/a_0+a_2/a_0)=-0.66$, $-0.60$, and $-0.84$ for $x=0.015$, 0.03, and 0.07, respectively, which are typical values obtained for other dilute Cr alloys.[10]

The parameterization of the magnetoelastic data of the $(Cr_{1-x}Mo_x)_{0.997}Ru_{0.003}$ alloys was obtained by employing the technique described in Ref. 13. The magnetic Grüneisen parameters $\Gamma_{NT}(t<1)$ and $\Gamma_{SF}(t>1)$, giving, respectively, the volume derivative of the logarithmic Néel temperature function $T_{NT}(\omega)$ and the spin-fluctuation-temperature function $T_{SF}(\omega)$, were calculated from the linear sections of plots of $\Delta B(T)$ vs $\Delta\beta(T)$, where $\beta$ is the volume thermal-expansion coefficient, using the same notations and technique as previously.[13] A typical example of the $\Delta B$ vs $\Delta\beta$ curves for $T>T_N$ and $T<T_N$ is shown in Fig. 4. The parameters $\Gamma_{NT}(t<1)$ and $\Gamma_{SF}(t>1)$ were calculated from the linear parts of these curves for the alloys with $x=0.015$ and 0.07 that exhibit only the ISDW phase for all $T$ below $T_N$. The results are $\Gamma_{NT}=-49$ and $\Gamma_{ST}=-32$ for $x=0.015$ and $\Gamma_{NT}=-39$ and $\Gamma_{SF}=-46$ for $x=0.07$, which are of the same order of magnitude as previously observed in other ternary Cr alloys.[11] For most Cr alloys studied[11,12,14] up to now it was found that $\Gamma_{SF}$ is much smaller (up to three times or more) than $\Gamma_{NT}$. The only exceptions are the members of the $(Cr_{0.97}Mo_{0.03})_{1-y}Si_y$ alloy system, for which[11] $\Gamma_{SF}\approx\Gamma_{NT}$, as is also the case for $(Cr_{1-x}Mo_x)_{0.997}Ru_{0.003}$ with $x=0.015$ and 0.07 of this study.

## IV. CONCLUSION

In conclusion, although the addition of Mo to $Cr_{0.997}Ru_{0.003}$ has the desired effect to decrease the Néel temperature down to room temperature, it simultaneously increases the coefficient of thermal expansion to much larger values. We were therefore not successful in our effort to improve the Invar-type properties of the $Cr_{0.997}Ru_{0.003}$ alloy by the addition of Mo.


[1] H. L. Alberts and J. A. J. Lourens, J. Phys. F **18**, L213 (1988).
[2] E. F. Wasserman, in *Ferromagnetic Materials*, Vol. 5, edited by K. H. J. Buschow and E. P. Wohlfarth (North-Holland, Amsterdam, 1990), Chap. 3.
[3] J. O. Ström-Olsen and D. F. Wilford, J. Phys. F **10**, 1467 (1980).
[4] R. Cywinski and T. J. Hicks, J. Magn. Magn. Mater. **54–57**, 999 (1986).
[5] H. L. Alberts and J. A. J. Lourens, J. Phys. F **13**, 873 (1983).
[6] H. L. Alberts, J. Phys. Condens. Matter **2**, 9707 (1990).
[7] M. Cankurtaran, G. A. Saunders, Q. Wang, P. J. Ford, and H. L. Alberts, Phys. Rev. B **46**, 14 370 (1992).
[8] H. L. Alberts and J. A. J. Lourens, J. Phys. (Paris) Colloq. **49**, C8-215 (1988).
[9] H. L. Alberts and J. A. J. Lourens, J. Phys. F **18**, 123 (1988).
[10] H. L. Alberts and J. A. J. Lourens, J. Phys. Condens. Matter **4**, 3835 (1992).
[11] P. Smit and H. L. Alberts, J. Appl. Phys. **69**, 5789 (1991).
[12] R. A. Anderson, H. L. Alberts, and P. Smit, J. Phys. Condens. Matter **5**, 1733 (1993).
[13] E. Fawcett, H. L. Alberts, V. Yu. Galkin, D. R. Noakes, and J. V. Yakhmi, Rev. Mod. Phys. **66**, 25 (1994).
[14] E. Fawcett and H. L. Alberts, J. Phys. Condens. Matter **2**, 6251 (1990).

# Magnetoelastic energy in domains separated by 90° walls

A. S. Arrott
*Simon Fraser University, Burnaby, British Columbia, V5A 1S6, Canada*

An iron whisker with a current along its axis has four domains in a frame about a central core. The domains in the frame are magnetized perpendicular to the axis. The central core is magnetized along the axis. The magnetoelastic energy and its corresponding effective field, found analytically using the calculus of variations, account for the experimental observation that for each current, below a critical current, there is a narrow range of fields for which there are two stable sizes for the central core. © *1996 American Institute of Physics.* [S0021-8979(96)79908-7]

Iron whiskers make ideal substrates for growing ultrathin films of transition metals by molecular beam epitaxy because of the perfection of their surfaces.[1] They are used also to influence the magnetic response of the ultrathin films, e.g., to measure the coupling to a ferromagnetic film separated from the substrate by a nonmagnetic film.[2] This was the motivation for passing a current along the axis of the whisker, with all surfaces [100], to switch the direction of the magnetization at the surface. The current should produce the domain configuration shown in Fig. 1. The direction of circulation of the magnetization in the four transverse domains (referred to collectively as the *frame*) should be determined by the direction of the current. The size and direction of the central longitudinal domain (referred to as the *core*) should be determined by the strength and direction of a magnetic field applied along the axis. Studies of the ac magnetic response for various applied fields and currents showed that the configuration in Fig. 1 accounts for many of the observations. There were some surprising effects[3] which were eventually traced to magnetoelastic energies, arising because the core elongates in the direction of its magnetization while the frame expands circumferentially.[4]

The dc susceptibility deduced from the ac susceptibility measured with a single turn about the central cross section is also shown in Fig. 1 as a function of the applied field in the presence of a current. This response is determined primarily by the competition between the applied field which expands the longitudinal core and the combined effects of the demagnetizing field and the field from the current which shrink the core.[5] This is shown as the heavy dashed line in Fig. 1. The demagnetizing field is proportional to the area of the core. The effective field from the current is proportional to the width of the core. In a low enough field the dc susceptibility should be proportional to the square root of the applied field. In higher fields it should approach a constant value mainly determined by the demagnetizing factor. It appears that the longitudinal core collapses for fields below a critical field, $H_c \cong 0.7$ G. The problem is to account for this loss of response in small positive fields. The domain wall energy is not responsible for this collapse, rather, it favors the expansion of the central core, as does the applied field.

The effective field from the magnetoelastic energy shrinks the core for small core size and expands it for large core size. The present calculation leads to an effective field of the right sign and magnitude to explain the collapse in positive fields. The aim of this work is to be completely analytical and at the same time to find agreement with experiment with no adjustable parameters. As magnetoelastic problems are not generally familiar to workers in micromagnetics, the exposition below contains some pedagogical elements, Eqs. (2), (5)–(8), and (10), and (11), that might otherwise be skipped.

According to Brown,[6] the Helmholtz free-energy density for the magnetoelastic energy when the magnetization is along one or another of the cube edges is

$$a_{\mathrm{mel}} = k_1\left[e_1\left(\alpha^2-\frac{1}{3}\right)+e_2\left(\beta^2-\frac{1}{3}\right)+e_3\left(\gamma^2-\frac{1}{3}\right)\right] + \frac{1}{2}\sum_{j=1}^{6}\sum_{i=1}^{6} c_{ij}e_i e_j, \tag{1}$$

where the direction cosines of the magnetization are $\alpha$, $\beta$, and $\gamma$ and the six components of the elastic strain are given by the $e_i$'s. In the domain walls the effect of magnetostriction is incorporated into the anisotropy constant; see Brown [Eq. (8-34) in Ref. 6]. Equation (1) is used to find the energy per unit length in the central cross section, where the derivatives of the magnetization with respect to $z$, along the axis, vanish. The full three-dimensional strain problem is treated approximately by assigning an energy to each cross section as if it were a central cross section with a different size core. The

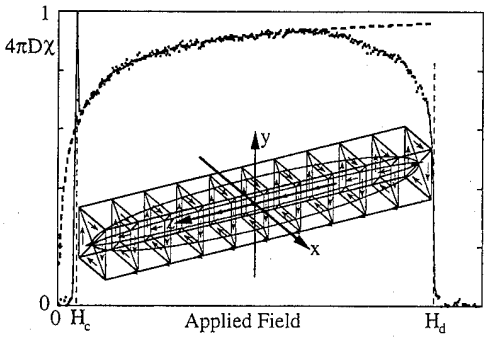



FIG. 1. The field dependence of the dc susceptibility and a schematic drawing of the domain pattern for a [100] whisker with a current along its axis. The calculated response ignoring magnetostriction is shown as the heavy dashed line. Because of magnetoelastic strains, the central core collapses at $H_c$. The hysteresis at $H_c$ is less than the ac driving field used in obtaining this data. The core fills the central cross section at $H_d$. The hysteresis at $H_d$ is less than the ac driving field.

 0021-8979/96/79(8)/6529/3/$10.00 © 1996 American Institute of Physics 

effects of the magnetization in cross sections away from the central cross section are taken into account by assuming that the area $A$ of the central core varies as $A(z)=A(0)[1-(z/L)^2]$ where $2L$ is the length of the whisker.[7] This leads to minor changes in the response compared to assuming that the central cross section applies to the whole whisker.

The simplest, but crude, assumption is that the strains in the central cross section are the same in the core and the frame. This properly maintains the square symmetry. It does not let the lattice planes bow and does not allow for the dependence of the strain on $\log y$ and $1/y^2$, which actually occur for a transverse domain magnetized in the $x$ direction. These terms will be added below after carrying out the uniform calculation for its pedagogical value. In the restricted calculation there are but two unknowns, $\xi$ and $\zeta$ which characterize the displacements of the atoms in both the core and the frame,

$$u_y=y\xi k_1, \quad u_x=x\xi k_1, \quad u_z=z\zeta k_1 \tag{2}$$

and the corresponding strains:

$$e_1=\frac{\partial}{\partial x}u_x=k_1\xi, \quad e_2=\frac{\partial}{\partial y}u_y=k_1\xi, \quad e_3=\frac{\partial}{\partial z}u_z=k_1\zeta, \tag{3}$$

$$e_4=\frac{1}{2}\left(\frac{\partial}{\partial y}u_x+\frac{\partial}{\partial x}u_y\right)=0,$$

$$e_5=\frac{1}{2}\left(\frac{\partial}{\partial z}u_y+\frac{\partial}{\partial y}u_z\right)=0, \tag{4}$$

$$e_6=\frac{1}{2}\left(\frac{\partial}{\partial x}u_z+\frac{\partial}{\partial z}u_x\right)=0.$$

From Eqs. (1) to (4) the energy density in the frame is

$$a_0^f=k_1^2\{\tfrac{1}{2}[c_{11}(2\xi^2+\zeta^2)]+c_{12}(\xi^2+2\zeta\xi)+\tfrac{1}{3}(\zeta-\xi)\} \tag{5}$$

and the energy density in the core is

$$a_0^c=k_1^2\{\tfrac{1}{2}[c_{11}(2\xi^2+\zeta^2)]+c_{12}(\xi^2+2\zeta\xi)+\tfrac{2}{3}(-\zeta+\xi)\}. \tag{6}$$

The total energy per unit volume of the central cross section is

$$a_{\mathrm{mel}}=a_0^f(-r^2+1)+a_0^c r^2, \tag{7}$$

where $r=d_i/d$ is the ratio of the inner, $2d_i$, to outer, $2d$, dimensions of the frame. Minimizing $a_{\mathrm{mel}}$ with respect to $\xi$ and $\zeta$ yields the strains

$$\xi=-\frac{1}{2(c_{11}-c_{12})}\left(r^2-\frac{1}{3}\right), \quad \zeta=\frac{1}{c_{11}-c_{12}}\left(r^2-\frac{1}{3}\right). \tag{8}$$

When the core fills the cross section ($r=1$), the strain $\zeta$ (in the $z$ direction) is the magnetostriction constant $\lambda_{100}$ which for iron is $2.2\times10^{-5}$. In terms of $\lambda_{100}$, given by

$$\lambda_{100}=\frac{2}{3}\frac{k_1}{(c_{11}-c_{12})}, \tag{9}$$

the energy per unit volume depends on $r$ according to

$$a_{\mathrm{mel}}=-\frac{27}{16}(c_{11}-c_{12})\lambda_{100}^2\left(r^2-\frac{1}{3}\right)^2. \tag{10}$$

Note that the energy is lowest when the core fills the cross section. The energy is highest (actually zero) when $r=0.577$ corresponding to the net magnetic moment per unit volume in the central cross section being $M_s r^2=M_s/3$.

The effective field comes from the dependence of the energy per unit volume on the net magnetic moment per unit volume,

$$H_{\mathrm{eff}}(r)=-\frac{\partial}{\partial M}(a_{\mathrm{mel}})$$

$$=-\frac{1}{M_s}\left(\frac{\partial}{\partial r^2}(a_{\mathrm{mel}})\right)$$

$$=\frac{27}{8}\frac{\lambda_{100}^2(c_{11}-c_{12})}{M_s}\left(r^2-\frac{1}{3}\right). \tag{11}$$

The effective field in the limit of vanishing core ($r^2=0$) is

$$H_{\mathrm{eff}}(0)=-(9/8M_s)\lambda_{100}^2(c_{11}-c_{12})\equiv-H_{\mathrm{mel}}. \tag{12}$$

For iron $H_{\mathrm{mel}}=0.30$ G, compared to the experimental collapse fields which are close to 0.7 G. The sign is right and the order of magnitude is right, but in this crude model it is too small. Note that this effective field becomes less negative with increasing magnetization as the core expands. This explains qualitatively the complex behavior seen experimentally. Below a critical current, there are narrow ranges of field for which there are two stable solutions for the area of the central cross section at each field and current. The critical limits of these regions produce interesting and useful magnetic properties.

When calculation is carried out for less restrictive strain fields, $H_{\mathrm{eff}}$ for small $r$ becomes larger. The linear dependence of $H_{\mathrm{eff}}$ on $r^2$ will be joined by a term in $r^2\log r^2$ that amplifies the critical effects. The next order of approximation yields an energy density given by

$$a_{\mathrm{mel}}=\frac{3}{2}M_s H_{\mathrm{mel}}\left(\frac{2(c_{11}-c_{12})(-2r^2\log r^2+r^4-1)}{c_{44}+12c_{11}}-\left(r^2-\frac{1}{3}\right)^2\right) \tag{13}$$

and the corresponding effective field

$$H_{\mathrm{eff}}(r)=3H_{\mathrm{mel}}\left(\frac{2(c_{11}-c_{12})(-\log r^2+r^2-1)}{c_{44}+12c_{11}}-\left(r^2-\frac{1}{3}\right)\right). \tag{14}$$

The energies and effective fields for the two approximate calculations are compared in Fig. 2. Equations (13) and (14) follow from assuming that the strain in a transverse domain

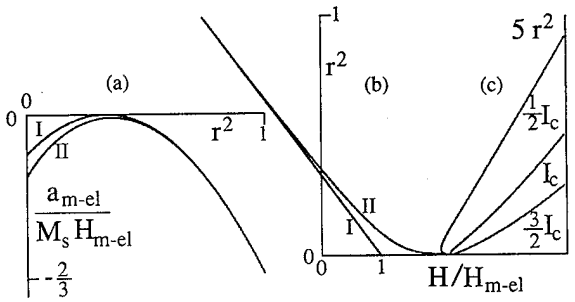



FIG. 2. (a) The dependence of the magnetoelastic energy on the relative area $r^2$ of the core domain for the simple argument I and the more detailed calculation II. (b) The relation between $r^2$ and the effective field from the magnetoelastic energy for I and II. (c) The dependence of $r^2$ on small applied fields for a particular whisker geometry using Eqs. (22) and (23) for the critical current $I_c$, for $I_c/2$, and for $3I_c/2$. For $I_c$, the external dc susceptibility is continuous, reversible, and infinite at the critical applied field.

magnetized in the $x$ direction depends on $y$ while maintaining the walls between transverse domains at 45° with respect to the axes. The displacements are

$$u_x=xg(y)k_1, \quad u_y=yg(y)k_1, \quad u_z=z\gamma k_1. \tag{15}$$

These displacements do not permit bowing of the atomic planes; a more complicated calculation shows this is not important. The corresponding strains are

$$e_1=k_1g(y), \quad e_2=k_1\left(y\frac{\partial}{\partial y}g(y)+g(y)\right),$$

$$e_3=\gamma k_1, \quad e_4=\frac{1}{2}xk_1\frac{\partial}{\partial y}g(y), \quad e_5=e_6=0. \tag{16}$$

By the calculus of variations,

$$g(y)=\frac{\rho}{y^2}-\frac{6}{c_{44}+12c_{11}}\log y+\sigma \tag{17}$$

which introduces the parameters $\rho$ and $\sigma$ which along with $\zeta$ describe the displacements in the frame. (The parameter $\sigma$ could be transferred to the term in $\log y$.) The core is described as before by $\xi$ and $\zeta$, but now $\xi$ is determined by $\xi=g(r)$ by continuity of $e_1$ at the boundary $y=r$. The parameters that minimize the energy are

$$\rho=-\frac{3r^2}{c_{44}+12c_{11}}d^2, \tag{18}$$

$$\sigma=-\frac{r^2-\frac{1}{3}}{2(c_{11}-c_{12})}+\frac{3(r^2+2\log d)}{c_{44}+12c_{11}}, \tag{19}$$

and

$$\zeta=\frac{1}{c_{11}-c_{12}}\left(r^2-\frac{1}{3}\right). \tag{20}$$

Note that $\rho$ vanishes when the core collapses. Also note that $\zeta$ is an expansion along $z$ when $r=1$ and a contraction when $r=0$. With these parameters, Eq. (17) becomes

$$g(y)=\frac{-6\log\frac{y}{d}+3r^2\left(-\frac{d^2}{y^2}+1\right)}{c_{44}+12c_{11}}-\frac{1}{2(c_{11}-c_{12})}\times\left(r^2-\frac{1}{3}\right). \tag{21}$$

The field dependence of the magnetization is found parametrically from

$$M=M_sr^2 \tag{22}$$

and

$$H=4\pi DM_sr^2+C_Ir-\frac{C_\sigma}{r}+3\left(\frac{2(c_{11}-c_{12})}{c_{44}+12c_{11}}\times(\log r^2+1)-r^2+\frac{1}{3}\right)H_{\rm mel}, \tag{23}$$

where $H_{\rm mel}$ is defined in Eq. (12). The first term is the demagnetizing field for demagnetizing factor $D$. The coefficient for the effective field from the current is $C_I=Id/(4\sqrt{\pi c})$. The coefficient for the effective field from the wall energy is $C_\sigma=-(4\sigma_{100}-2\sqrt{2}\sigma_{110})/(dM_s)$ or $C_\sigma=0.9\sigma_{100}/(dM_s)$ for wall energies per unit area $\sigma_{110}=\sqrt{3}\sigma_{100}$. The wall energy restricts the complete collapse of the core at low fields, elsewhere it has negligible effects.

Equations (22) and (23) account for the dc magnetic response of the iron whisker with fields and currents along the $z$ axis. Note the richness of the phenomenology with its dependence on $r^2$, $r$, $\log r$, and $1/r$, e.g., see Fig. 2(c). The full treatment of the ac susceptibility, to be published elsewhere, takes into account the effects of eddy currents and the influence of finite amplitude of the ac driving field at the critical fields. Agreement with experiment is excellent, accounting for the spectacular properties that accompany the existence of a critical point, with a critical field and a critical current. At the critical point the external dc susceptibility is infinite, continuous, and reversible.

The author thanks Dr. Alex Hubert for convincing him that the simple pedagogical argument was not sufficient.

[1] A. S. Arrott, B. Heinrich, and S. T. Purcell, in *Kinetics of Ordering and Growth at Surfaces*, edited by M. G. Lagally (Plenum, New York, 1990), pp. 321–341.
[2] B. Heinrich, Z. Celinski, J. F. Cochran, and M. From, in *Magnetism and Structure in Systems of Reduced Dimension*, edited by R. F. C. Farrow, B. Dieny, M. Donath, A. Fert, and B. D. Hermsmeier (Plenum, New York, 1993), pp. 175–193.
[3] J.-G. Lee and A. S. Arrott, J. Appl. Phys. **75**, 7006-8 (1994).
[4] A. S. Arrott and J.-G. Lee, J. Appl. Phys. **76**, 7031 (1994).
[5] J.-G. Lee, Ph.D. thesis, Simon Fraser University, 1994; A. S. Arrott and J.-G. Lee, J. Appl. Phys. **75**, 5713 (1994).
[6] W. F. Brown, Jr., *Micromagnetics* (Interscience, New York, 1963).
[7] A. S. Arrott, B. Heinrich, and T. L. Templeton, IEEE Trans. Magn. **MAG-25**, 4364 (1989).

# High frequency (1–1200 MHz) magnetoimpedance in CoFeSiB amorphous wires (abstract)

V. P. Paramonov, A. S. Antonov, and A. N. Lagarikov
*Scientific Association IVTAN, Russian Academy of Science, Moscow 127412, Russia*

L. V. Panina and K. Mohri
*Department of Electrical Engineering, Nagoya University, Nagoya 464, Japan*

Magnetoimpedance (MI) in Co-based amorphous alloys has been shown to be a very sensitive, quick-response new method for measurements of magnetic fields. At present, the experimental results on MI in amorphous wires are obtained for frequencies $f<200$ MHz. For quick-response magnetic heads used in high density magnetic recording, the carrier current frequency of the MI element is needed to be increased up to 1 GHz to detect recorded signals of 50–100 MHz. Here we present the experimental data on MI in CoFeSiB amorphous wires for a broad waveband of 1–1200 MHz. The experimental technique is based on the measurement of the complex reflection coefficient from a coaxial waveguide having an amorphous wire as an internal conductor. This method avoids the radiation effects, inevitable at high frequencies, $f>100$ MHz, in simpler techniques utilizing an oscilloscope or an impedance analyzer with a lead wire. From the data on reflection coefficient, the real and imaginary parts of the wire impedance $Z$ and permeability $\mu$ are found as functions of a frequency and an external longitudinal field. The impedance versus field behavior changes with increasing the frequency. For $f<1$ MHz the absolute value of the impedance $|Z|$ decreases with increasing the field. As the frequency is increased, a maximum appears in the impedance-field dependence. In the case of high frequencies, $f>800$ MHz, $|Z|$ increases with the field. For all frequencies, a higher sensitivity is seen in small fields less than 2 Oe. The sensitivity has a maximum of about 100%/Oe at the frequency of 600 MHz, and it is still very high (~20%/Oe) up to $f\sim1$ GHz. These results are in satisfactory agreement with the theoretical ones based on the skin effect in a magnetic wire with a tensor rotational permeability. © *1996 American Institute of Physics.*
[S0021-8979(96)62608-8]

 0021-8979/96/79(8)/6532/1/$10.00 © 1996 American Institute of Physics

# Enhancement of magnetoresistance in Co(1$\bar{1}$00)/Cr(211) bilayered films on MgO(110)

Y. D. Yao[a] and Y. Liou
*Institute of Physics, Academia Sinica, Taipei 115, Taiwan, Republic of China*

J. C. A. Huang
*Department of Physics, National Cheng Kung University, Tainan 701, Taiwan, Republic of China*

S. Y. Liao, I. Klik, W. T. Yang, C. P. Chang, and C. K. Lo
*Institute of Physics, Academia, Sinica, Taipei 115, Taiwan, Republic of China*

Epitaxial Co/Cr bilayered films have been successfully grown on the MgO(100) and MgO(110) substrates by molecular-beam epitaxy. According to the reflection high-energy electron-diffraction and x-ray-diffraction measurements the crystal structure of the film depends on orientation of the buffer and substrate. Epitaxial growth of biaxial Co(11$\bar{2}$0)/Cr(100) on MgO(100) substrate and of uniaxial Co(1$\bar{1}$00)/Cr(211) on MgO(110) substrate has been confirmed. The anisotropy magnetoresistance (AMR) is strongly influenced by the orientation of the Cr buffer. In Co(11$\bar{2}$0)/Cr(100) on MgO(100) AMR is isotropic for all in-plane fields. However, for Co(1$\bar{1}$00)/Cr(211) on MgO(110) we observed enhancement of AMR along the easy axis for temperatures below 150 K, while along the hard axis AMR has a local maximum at about 150 K. The easy axis data suggest that the longitudinal spin density wave of Cr and the crystal anisotropy of Co on Cr(211) plane dominate the enhancement of the AMR. © *1996 American Institute of Physics.* [S0021-8979(96)57808-1]

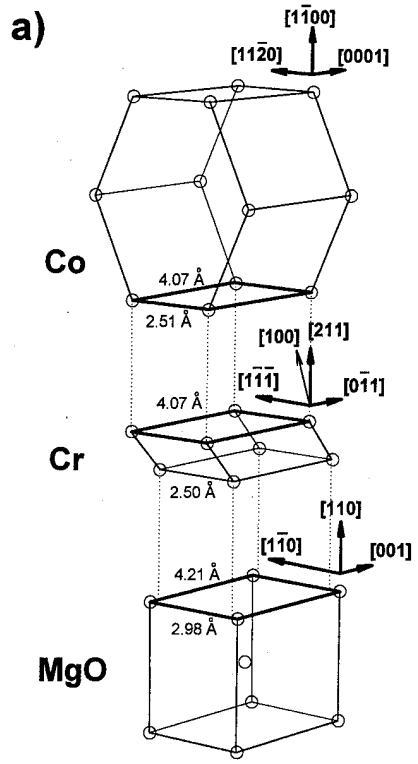
In previous studies of the Co/Cr multilayer system[1–3] its magnetoresistance (MR) was shown to be quite small in comparison with other giant MR (GMR) multilayer systems.[4] Recently it was realized[5,6] that the magnetic properties of the Co/Cr multilayer system are sensitive to anisotropy and to the orientation of the applied magnetic field with respect to crystallographic axes and MR as high as 18% as has been observed in the Co/Cr(211) superlattice system. However, the mechanism of this effect is presently not clear and this motivated us to investigate the simpler case of anisotropy of MR (AMR) in the epitaxial bilayered Co/Cr film system.

Epitaxial Co/Cr bilayer films have been simultaneously prepared on MgO(110) and MgO(100) substrates by using an Eiko EL-10A molecular-beam-epitaxy (MBE) system with base pressure of $2\times10^{-10}$ Torr. To enable the growth of high-quality film samples, polished and epitaxial grade MgO(110) and MgO(100) substrates were chemically precleaned and rinsed in an ultrasonic cleaner. They were then outgassed at 900–1000 °C for at least 0.5 h under ultrahigh vacuum in the MBE chamber. High-purity Co and Cr elements (>99.99%) were evaporated from two independent e-beam evaporators. During deposition of the films, the substrate temperature was kept between 300 and 350 °C, the growth pressure was controlled at below $5\times10^{-9}$ Torr, and the deposition rate kept at ~0.1 Å/s. The film thickness and deposition rate were measured by a quartz-crystal thickness monitor. The crystallographic structure of the surface of the films was *in situ* examined throughout the growth by 15 keV reflection high-energy electron diffraction (RHEED). The crystal orientation was *ex situ* characterized by x-ray diffraction (XRD). The magnetic properties of all samples were studied using a superconducting quantum interference device (SQUID) magnetometer. The AMR measurements were carried out by standard four-probe technique in a magnetic field up to 5 T at temperatures ranging between 10 and 300 K. Typical area of the film sample was roughly $1.5\times6.0$ mm$^2$.

The structure arrangement of both Co and Cr layers in the Co/Cr bilayered films is considerably affected by the choice of the interface direction of the MgO substrate. In this study, the epitaxial Co/Cr bilayer films were simultaneously grown on MgO(100) and on MgO(110) substrates. Their crystalline orientation and quality were determined by RHEED and XRD. Figures 1(a) and 1(b) show schematic diagrams of the 3D geometry of the Co(1$\bar{1}$00)/Cr(210)/MgO(110) and Co(11$\bar{2}$0)/Cr(100)/MgO(100) bilayer films. These epitaxial relationships were also confirmed by both RHEED and XRD studies. Part of the structural analysis related to the Co/Cr superlattice films will be published elsewhere,[5,6] in this study only the bilayer case is discussed. In Fig. 1(a) the lattices of the Co and Cr layers appear to be rectangular, in acccordance with the $4.21\times2.98$ Å$^2$ unit cell of the MgO(110) surface. The unit cell of Co(1$\bar{1}$00), $4.07\times2.51$ Å$^2$, matches perfectly that of Cr(211), $4.07\times2.50$ Å$^2$, and even though the match between Cr(211) and MgO(110) is poorer, we did experimentally observe a twofold symmetry for the whole system and confirmed that the *c* axis of Co is in the film plane and in the Cr[0$\bar{1}$1] direction only. On the other hand, for the Co(11$\bar{2}$0)/Cr(100)/MgO(100) system, because the bcc Cr(100) plane has fourfold symmetry with unit cell of $2.88\times2.88$ Å$^2$, the hcp Co(11$\bar{2}$0) plane possesses only pseudotwofold symmetry with unit cell of $4.34\times4.07$Å$^2$. This suggests that the Co(11$\bar{2}$0) layers behave

[a]Also with: Department of Physics, National Chung Cheng University, Chiayi 621, Taiwan, Republic of China.

 0021-8979/96/79(8)/6533/3/$10.00 © 1996 American Institute of Physics 



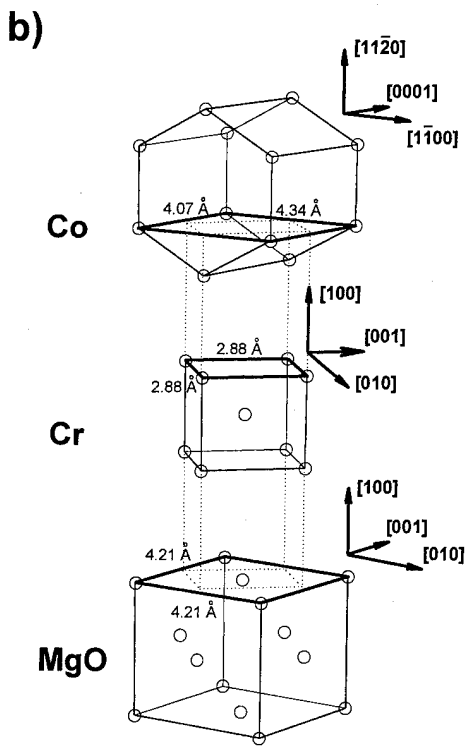




FIG. 1. Schematic diagram of the 3D geometry, unit cell (indicated by bold lines), and epitaxial relationships for (a) Co(1$\bar{1}$00)/Cr(211)/MgO(110) films, and (b) Co(11$\bar{2}$0)/Cr(100)/MgO(100) films.

like a bicrystalline structure; i.e., that the Co[0001] easy axis can either be parallel to MgO[001] or to MgO[010] as shown in Fig. 1(b).

The thickness of the Co layer for all the samples in this study is fixed at 200 Å and the thickness of the Cr layer is

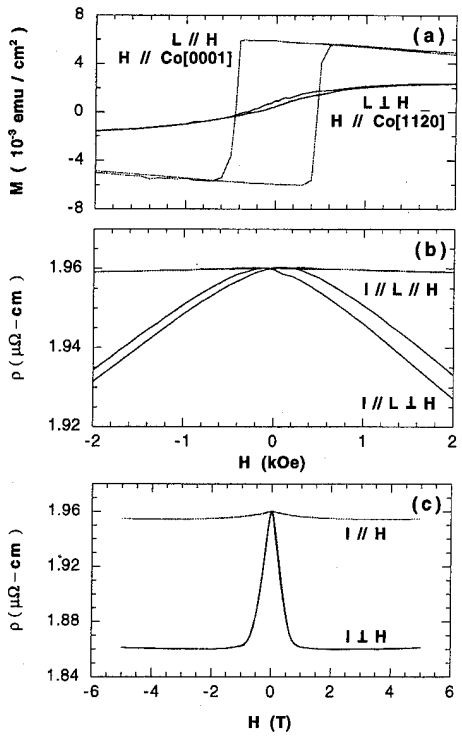



FIG. 2. (a) The magnetization $M$ and (b) and (c) the surface resistivity for $Co_{200\ Å}(1\bar{1}00)/Cr_{6\ Å}(211)/MgO(110)$ films at $T=10$ K as functions of magnetic field applied parallel to the film surface.

varied between 6 and 100 Å. As an example, Fig. 2 shows the magnetic hysteresis loops and the corresponding surface resistivity of the $Co_{200\ Å}(1\bar{1}00)/Cr_{6\ Å}(211)/MgO(110)$ sample at 10 K for field applied parallel to the film surface. For $H$ parallel to the easy axis of the Co layers a square $M-H$ hysteresis loop and small variation of resistivity have been observed. We interpret the magnetization reversal process as being mainly due to domain-wall motion. On the other hand, for $H$ applied parallel to the hard axis of Co layers the magnetization varies slowly with increasing $H$ while electric resistivity decreases very fast below roughly $H=1$ T and saturates then at $H>1$ T. The (very small) values of coercivity deduced from the $M-H$ loop are consistent with the peak positions on the resistivity curve.

In Fig. 3 we plot the magnetization $M$ and surface resistivity as functions of applied field $H$ for a $Co_{200\ Å}(11\bar{2}0)/Cr_{6\ Å}(100)/MgO(100)$ sample at 10 K. According to our structure analysis above, the easy and hard axes of the Co layers are randomly distributed in both MgO[001] and MgO[010] directions. The $M-H$ curves for $H$ applied parallel or perpendicular to the long axis of the sample are roughly the same, apart from a difference due (presumably) to demagnetization factors [see the geometry of Fig. 1(b)]. The coercive force obtained from the $M-H$ curves coincides with the location of a minimum (maximum) of the resistivity with current parallel (perpendicular) to the applied field.

The temperature dependence of the AMR of the saturation magnetization $M_S$ and of the coercive force $H_c$ between 10 and 300 K for both $Co_{200\ Å}/Cr_{6\ Å}/MgO(110)$ and

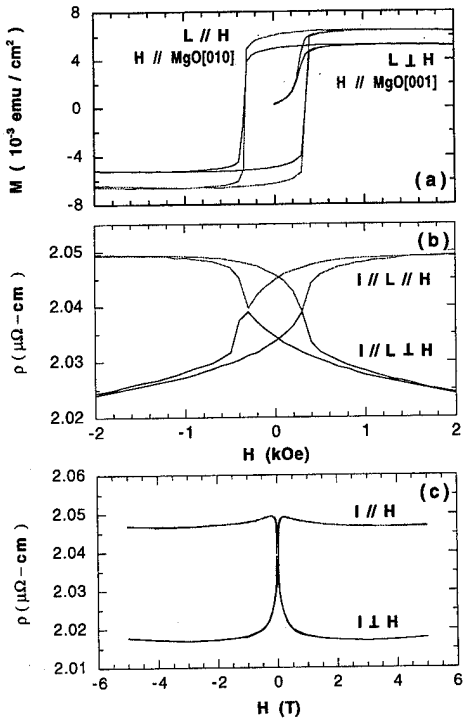



FIG. 3. (a) The magnetization $M$ and (b) and (c) the surface resistivity for $Co_{200\ Å}(11\bar{2}0)/Cr_{6\ Å}(100)/MgO(100)$ films at $T=10$ K as functions of magnetic field applied parallel to the film surface.

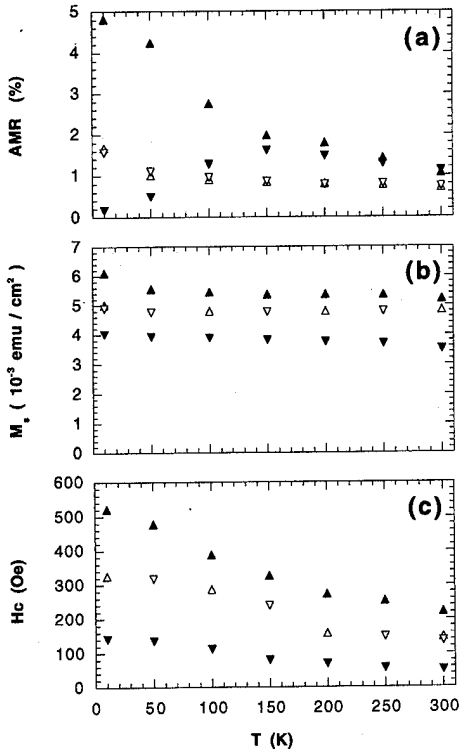



FIG. 4. (a) The AMR, (b) the saturation magnetization, and (c) the coercive force as functions of the temperature between 10 and 300 K for (L: long side of film): (▲) $Co_{200\ Å}/Cr_{6\ Å}/MgO(110)$ with $L\|$ easy axis of Co surface;(▼) $Co_{200\ Å}/Cr_{6\ Å}/MgO(110)$ with $L\|$ hard axis of Co surface; (△) $Co_{200\ Å}/Cr_{6\ Å}/MgO(110)$ with $L\|MgO[001]$ direction; and (▽) $Co_{200\ Å}/Cr_{6\ Å}/MgO(110)$ with $L\|$ MgO[010] direction.

$Co_{200\ Å}/Cr_{6\ Å}/MgO(100)$ are presented in Fig. 4. For samples of $Co_{200\ Å}/Cr_{6\ Å}/MgO(110)$ with their long axis parallel to the easy axis of Co, i.e., in the direction of Co[0001] as shown in Fig. 1(a), we observed a significant enhancement of AMR for temperatures roughly below 150 K [▲ in Fig. 4(a)] while AMR [▼ in Fig. 4(a)] decreases with decreasing temperature below roughly 150 K for samples with long axis parallel to the hard axis of Co, i.e., in the direction of $Co[11\bar{2}0]$ as shown in Fig. 1(a). Our data points between 100 and 150 K are not sufficiently dense, however, this characteristic temperature $T_f$ (~150 K) may be very close to the spin-flip temperature $T_{sf}=123$ K of Cr and we conjecture that magnetization reversal in these samples may be explained by a mechanism similar to that reported for the Fe/Cr system.[7] By contrast, in $Co_{200\ Å}/Cr_{6\ Å}/MgO(100)$ samples the AMR as shown in Fig. 4(a) is almost independent of temperature. The saturation magnetization $M_s$ and the coercive force $H_c$ as functions of temperature between 10 and 300 K are plotted in Figs. 4(b) and 4(c), respectively. Both the $M_s$ vs $T$ and the $H_c$ vs $T$ curves completely coincide for the $Co(11\bar{2}0)/Cr(100)/MgO(100)$ samples; however, a slight shift in these data, perhaps again explainable by the presence of demagnetizing fields, exists in the observed values for the $Co(1\bar{1}00)/Cr(211)/MgO(110)$ samples. All $H_c$ vs $T$ curves show a marked change in their slope at approximately 150 K.

In conclusion, this is the first time that AMR enhancement roughly below the spin-flip temperature was observed in epitaxial $Co(1\bar{1}00)/Cr(211)$ bilayered films on MgO(110), with current in the Co[0001] direction.

We are grateful for the financial support by the National Science Council of the R.O.C. under Grant Nos. NSC85-2112-M-001-020, NSC85-2112-M-001-019, and NSC85-2112-M-006-006.

[1] S. S. P. Parkin, R. Bhadra, and K. P. Roche, Phys. Rev. Lett. **64**, 2304 (1990).
[2] Y. Liou, J. C. A. Huang, Y. D. Yao, C. H. Lee, K. T. Wu, C. L. Lu, S. Y. Liao, Y. Y. Chen, N. T. Liang, W. T. Yang, C. Y. Chen, and B. C. Hu, J. Appl. Phys. **76**, 6516 (1994).
[3] Y. D. Yao, Y. Liou, J. C. A. Huang, S. Y. Liao, C. H. Lee, K. T. Wu, Y. Y. Chen, C. L. Lu, and W. T. Yang, Chin. J. Phys. **32**, 863 (1994).
[4] M. N. Baibich, J. M. Broto, A. Fert, F. Nguyen van Dau, F. Petroff, P. Etienne, G. Creuzet, and J. Chazelas, Phys. Rev. Lett. **61**, 2472 (1988).
[5] Y. Liou, J. C. A. Huang, Y. D. Yao, S. F. Lee, W. T. Yang, S. Y. Liao, and C. P. Chang, IEEE Trans. Magn. **31**, 3927 (1995).
[6] J. C. A. Huang, Y. Liou, Y. D. Yao, W. T. Yang, C P. Chang, S. Y. Liao, and Y. M. Hu, Phys. Rev. B **52**, R 13 110 (1995).
[7] A. Berger and H. Hopster, Phys. Rev. Lett. **73**, 193 (1994).

# Magnetic and electrical properties of CoFeSiB:O thin films near the percolation threshold

R. Banerjee, A. P. Valanju, G. Choe,[a] and R. M. Walser[b]
*I/UCR Center for Magnetics, University of Texas at Austin, Austin, Texas 78712*

Nanocomposite thin films with coexisting magnetic metal and magnetic nonmetal amorphous phases were synthesized by reactively sputtering CoFeSiB:O thin films with a large silicon (15 at.%), and varying oxygen concentrations. The microstructure, magnetization, and hysteresis loops were measured for films with resistivities near the metal–nonmetal transition. These data revealed that, below the metal–nonmetal transition, conductive transport was along the soft magnetic, metallic backbone of the percolation network; the nonmetal phase was a discontinuous, randomly distributed, hard magnetic oxide. The metallic resistivity and exchange anisotropy were both maximized in a nanocomposite with a resistivity at the metal–nonmetal transition. © *1996 American Institute of Physics.* [S0021-8979(96)57908-0]

## I. INTRODUCTION

It is surprising that the metallic resistivities of sputtered, heteroamorphous magnetic thin films can be increased by more than one magnitude by sputtering in reactive gases.[1,2] As the percolation threshold is approached from the metallic side, the resistivity of these metal–nonmetal nanocomposites is determined primarily by electrical transport along the backbone of the continuous metallic network, formed in the growing film by complex reactive processes. It is of scientific and technological interest to understand these processes that permit independent manipulation for the magnetic and electrical properties of these nanocomposites.

Previous studies[2–5] concentrated on obtaining magnetically soft nanocomposite films with a maximum resistivity. To achieve this goal, the reactive gas species (O, F, or N) must preferentially bond with the metalloid (Al, B, or Si) in the film, form a nonmagnetic, insulating complex (e.g., $B_2O_3$), and segregate from the metallic backbone of the Co- or Fe-rich percolation network. In addition to technologically important soft magnetism,[2] giant magnetoresistance tunneling has been observed in these magnetic-metal–nonmagnetic-nonmetal nanocomposites.[6]

Additional interesting behavior could be expected from reactively sputtered magnetic-metal–magnetic-nonmetal nanocomposites. The reactive gas must now substitutionally bond in the film to form a stable nonmetallic magnetic phase. In a previous study[7] we demonstrated that this type of nanocomposite could be produced by reactively sputtering amorphous CoFeSiB alloy thin films in oxygen. A stable, magnetic, nonmetal phase was formed in CoFeSiB:O alloy films with sufficiently large silicon concentrations. The interaction of the two magnetic phases in the nanocomposite gave rise to an exchange anisotropy in the magnetic hysteresis which directly confirmed their existence. The present study was conducted to determine the relative concentrations of incorporated oxygen that produce maxima in the low-field unidirectional hysteresis and metallic resistance of these nanocomposites, and to systematically characterize their magnetic and electrical transport properties.

## II. EXPERIMENT

CoFeSiB:O films were deposited onto glass substrates by oxygen reactive sputtering from a $Co_{70.5}Fe_{4.5}Si_{15}B_{10}$ alloy target in a rf magnetron sputtering system. A partial pressure controller on a residual gas analyzer was used to vary, and feedback control, the partial pressure of reactive oxygen in the argon sputtering gas. The background pressure in the deposition chamber prior to introducing argon and oxygen gases was $5\times10^{-7}$ Torr. The sputtering argon pressure was fixed at 7 mTorr, while the oxygen to argon pressure ratio was varied. The sputter input power was set at 800 W and all the depositions were made in the static mode. The film thicknesses in the 800–900 Å range were measured using a surface profilometer. The film structure and magnetic and electrical properties were studied, respectively, with transmission electron microscopy (TEM/TED), a $B$–$H$ hysteresisgraph and vibrating sample magnetometer (VSM), and a four-point resistivity probe. The low-temperature resistivity measurements were performed using an ac four-point-probe setup with the sample placed on a refrigerator cold stage.

## III. RESULTS AND DISCUSSION

The variations of saturation magnetization $4\pi M_s$, remanence $4\pi M_r$, and resistivity $\rho$ of the CoFeSiB:O thin films are plotted in Fig. 1 as a function of the $O_2$:Ar flow ratio. The oxygen incorporated in the film was not determined, but can be crudely calibrated by noting that the ~8% $O_2$:Ar flow ratio measured at the onset of tunneling (not shown in Fig. 1), would, on the basis of previous research,[2] correspond to a minimum of ~20 at.% oxygen. The incorporated oxygen is not expected, however, to vary linearly with the flow ratio. The metallic region of flow ratio was determined from the temperature coefficients of the film resistivities measured in the 77–300 K temperature range. Figure 2 plots the fractional changes in resistivity measured for CoFeSiB:O films sputtered with $O_2$:Ar flow ratios of 1.4%, 3.5%, and 7%. The resistivities of each film were normalized to their values at 300 K and extrapolated to $T>300$ K. A negative temperature

[a]Present address: Materials Research Corporation, Advanced Technology Div., Orangeburg, NY 10962.
[b]Electronic mail: walser@mail.utexas.edu

 0021-8979/96/79(8)/6536/3/$10.00 © 1996 American Institute of Physics

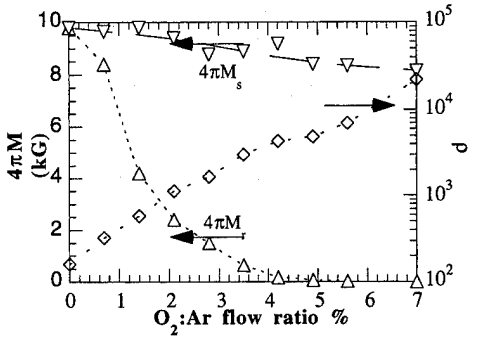



FIG. 1. Variation of $4\pi M_s$, $4\pi M_r$, and $\rho$ ($\mu\Omega$ cm) for CoFeSiB:O thin films deposited at varying $O_2$:Ar flow ratios.

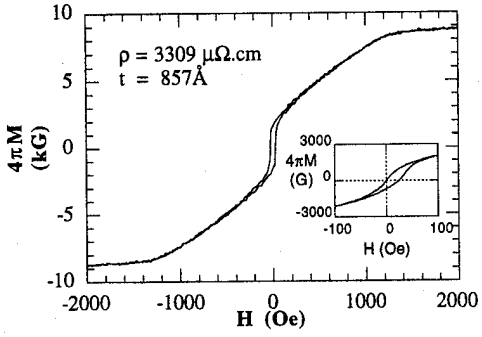



FIG. 3. $B$–$H$ loop of 857 Å CoFeSiB:O thin film. Inset shows low-field $B$–$H$ loop.

coefficient likely indicates that the conduction was dominated by thermally assisted tunneling; a positive coefficient was taken to indicate the dominance of metallic conduction. At 300 K, a crossover from metal to nonmetal conduction occurred at a critical flow ratio of 3.5%, for which a maximum unidirectional exchange shift had been observed previously.[7]

When the flow ratio increased above that at the metal–nonmetal crossover, the resistivity slope was much smaller than observed in granular films produced by cosputtering relatively immiscible metal/nonmetal materials.[8] This behavior indicates that the morphology of the metallic backbone has a large interfacial contact with the nonmetal phase. This morphology could support a large number of thin tunnel junctions and broaden the metal–nonmetal transition.[9]

With increasing $O_2$ content, $4\pi M_s$ decreased as the volume fraction of the oxidized nonmetallic regions grew at the expense of the metallic regions. With increasing flow ratio, $4\pi M_s$ decreased by less than 20% throughout the metallic region, but the magnetic remanence vanished for flow ratios >4%. These changes confirmed that, in the metallic region, the incorporated oxygen substitutionally bonded to form a random, magnetically harder phase in which the total magnetic moment was nearly conserved.

Figure 3 shows the in-plane $B$–$H$ hysteresis loop of an 857-Å-thick critically percolated film, deposited with the 3.5% flow ratio that corresponds to the transition from metal to nonmetal behavior. The inset clearly shows the ~9 Oe exchange shift in the low-field loop. The remanence of the soft magnetic phase was less than 10% of $4\pi M_s$. A dc field of more than 1 kOe was required to saturate the random, magnetically hard phase.

As shown in Fig. 4, the CoFeSiB film sputtered without oxygen had a well-defined uniaxial anisotropy ($H_k$=40 Oe) with coercivity $H_c$ of 6 Oe. Annealing in a rotating field at 350 °C reduced the anisotropy to 28 Oe.[10] Figure 4 also shows that $H_c$ of the low-field hysteresis (associated with the soft magnetic metal phase) initially increased, then decreased with the concentration of incorporated oxygen. These low-field hysteresis loops were observed only after the film was first saturated by a 1 kOe in-plane dc field. The variation of $H_c$ with flow ratio (Fig. 5) shows that a maximum $H_c$ occurred for a 1.5% flow ratio; the minimum flow ratio for which an exchange anisotropy was observed in the CoFeSiB:O films.[7] $H_c$ then decreased to a minimum of ~16 Oe for the 3.5% flow ratio at the metal to nonmetal transition. Only small changes in $H_c$ were observed for films with nonmetal conduction.

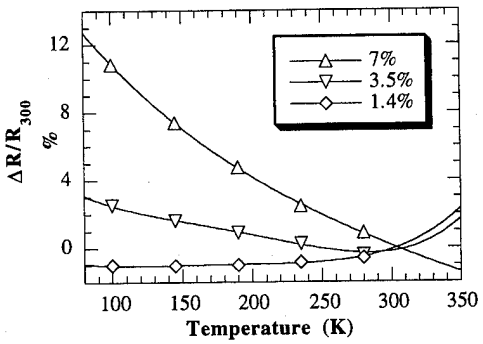



FIG. 2. Variation of resistivity with temperature (77–300 K) for CoFeSiB:O thin films deposited at 1.4%, 3.5%, and 7% $O_2$:Ar flow ratio.

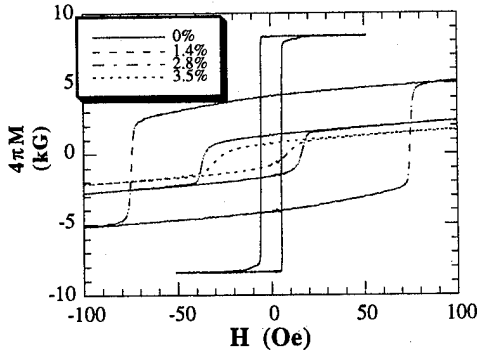



FIG. 4. Low-field $B$–$H$ loops of CoFeSiB:O thin films deposited with varying $O_2$:Ar flow ratio (flow ratios indicated in legend). These low-field $B$–$H$ loops were measured after applying 1 kOe in-plane dc field.

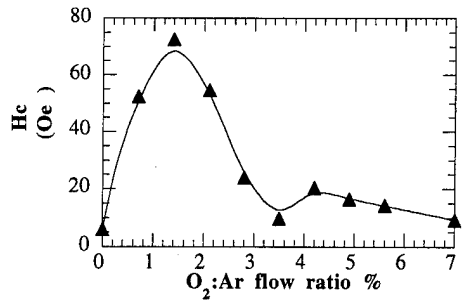



FIG. 5. Variation of coercivity for 800 Å CoFeSiB:O thin films deposited at different $O_2$:Ar flow ratios. The solid line is a guide to the eye.

## IV. SUMMARY AND CONCLUSIONS

The observation of exchange-shifted, low-field hysteresis loops revealed the presence of two magnetic phases in reactively sputtered CoFeSiB:O films. From the temperature coefficients of the film resistivities measured in this study it was shown that, in the range where the exchange anisotropy was observed, the film nanocomposite consists of a continuous metallic backbone in the percolation network. From the changes in the $4\pi M_s$, $4\pi M_r$, and $\rho$ of these films, produced by varying the oxygen flow ratio, the metallic backbone was determined to be the softer of the two magnetic phases. This phase exhibited a low-field, in-plane, uniaxial anisotropy. The harder magnetic phase was determined to be a discontinuous, randomly distributed, nonmetallic, magnetic oxide. The nature of the oxygen bonding in this phase approximately conserved the metallic magnetic moments. Applied magnetic fields of several kOe were required to saturate this phase.

The results also showed that the exchange anisotropy was a maximum when the incorporated oxygen concentration produced the maximum metallic resistivity. The increase in the $H_c$ of the soft metallic phase with small oxygen concentrations was arrested with the initiation of the exchange interaction between the two phases that was responsible for the low-field unidirectional hysteresis observed for flow ratios of approximately 1%–7%.[7] $H_c$ subsequently decreased as the exchange anisotropy increased, and was a minimum at the metal–nonmetal transition. It is reasonable to assume that the interfacial surface area is a maximum at the metal–nonmetal transition and maximizes both properties. This conclusion is supported by the gradual nature of the metal–nonmetal transition which requires a similar morphology.

This study, and those of other investigators,[1–7] indicates that reactive sputtering of amorphous magnetic thin films can be used to synthesize magnetic nanocomposites with a prescribed compositional heterogeneity and morphology. These nanocomposites are expected to exhibit a variety of novel magnetic and electrical properties.

## ACKNOWLEDGMENTS

This work was sponsored in part by the Industry/University of Texas Cooperative Research Center for Magnetics and the Texas Advanced Technology Program under Grant No. 257.

[1] H. Fujimori, S. Mitani, S. Ohnuma, T. Ikeda, T. Shima, and T. Masumoto, Mater. Sci. Eng. **181/182**, 897 (1994).
[2] H. Fujimori, S. Mitani, T. Ikeda, and S. Ohnuma, IEEE Trans. Magn. **30**, 4779 (1994).
[3] E. Sugawara, F. Matsumoto, H. Fujimori, and T. Masumoto, J. Appl. Phys. **73**, 5586, (1993).
[4] S. Ohnuma, H. Fujimori, S. Furukawa, F. Matsumoto, and T. Matsumoto, Mater. Sci. Eng. **181/182**, 892 (1994).
[5] S. Furukawa, S. Ohnuma, F. Matsumoto, H. Fujimori, and T. Masumoto, Mater. Sci. Eng. **181/182**, 1025 (1994).
[6] H. Fujimori, S. Mitani, and S. Ohnuma, Mater. Sci. Eng. B **31**, 219 (1994).
[7] G. Choe, R. Banerjee, W. Win, and R. M. Walser, IEEE Trans. Magn. **31**, 3862 (1995).
[8] B. Abeles, H. L. Pinch, and J. I. Gittleman, Phys. Rev. Lett. **35**, 247 (1975).
[9] J. V. Mantese, W. A. Curtin, and W. W. Webb, Phys. Rev. B **33**, 7897 (1986).
[10] R. Banerjee, G. Choe, B. I. Cho, and R. M. Walser, IEEE Trans. Magn. **31** 3856 (1995).

# Circumferential magnetization processes in CoFeBSi wires

L. Domínguez, J. M. Blanco, P. Aragoneses, and J. González[a)]
*Facultad de Química, Universidad del País Vasco, P.O. Box 1072, 20080 San Sebastián, Spain*

R. Valenzuela,[b)] M. Vázquez, and A. Hernando
*Instituto de Magnetismo Aplicado, UCM, and Instituto de Ciencia de Materiales, CSIC, P.O. Box 155, 28230 Las Rozas, Madrid, Spain*

The total impedance, $Z$, of low magnetostriction wires $(Co_{0.94}Fe_{0.06})_{72.5}B_{15}Si_{12.5}$ was measured at 100 kHz under ac currents of various amplitudes, $i$, for as-cast and current annealed samples. We show that curves $Z$ vs $i$ can represent circumferential permeability curves and that the features observed on these curves as a consequence of annealing can be interpreted due to the induced magnetic anisotropy by the effect of the current annealing. © *1996 American Institute of Physics.* [S0021-8979(96)80008-6]

## I. INTRODUCTION

Giant magnetoimpendance (GMI) has recently been of great interest because of its many potential applications in miniature sensors and devices.[1,2] GMI has been observed in materials with a substantial portion of circumferential domains; it is interesting, from a basic point of view, to elucidate magnetization processes in such magnetic structures.

GMI can be defined as a decrease in the impedance response of a ferromagnetic material, submitted to an ac current, when a dc magnetic field is applied. It is now clear that the impedance response of a magnetic material depends essentially on the interaction between its circumferential domains and the circular field generated by the ac current. At high frequencies, the skin-depth effect plays a central role in GMI by affecting the cross section of the wire where the circular field is concentrated. When the dc field is applied (especially in a longitudinal direction with respect to the material), a rotational component appears in circumferential domains,[1] leading to a decrease in circular permeability, an associated variation in penetration depth, and therefore to a decrease in the interaction. If the dc field is high enough, it can suppress the circular domains and lead to an impedance response as small as that of a nonmagnetic material. GMI is a classical electrodynamics phenomenon.[3,4]

While GMI has been observed in a wide variety of materials, low, negative magnetostriction wires in the as-cast state have been shown to meet the requirements for a particularly strong dependence of impedance on field. Some efforts have been made[4] to improve GMI by annealing various materials under a variety of techniques; to our knowledge, however, the observed changes in impedance response in annealed CoFeSiB wires have not been fully explained. The aim of this article is to contribute to the understanding of changes introduced by current annealings in the domain structure of the wire the analyzing their impedance response.

## II. EXPERIMENTAL TECHNIQUES

Amorphous wires of nominal composition $(Co_{0.94}Fe_{0.06})_{72.5}B_{15}Si_{12.5}$, prepared by in-water-rotation technology,[5] kindly provided by Unitika Ltd. Japan, were cut in pieces of 10 cm. Current-annealing treatments were performed by submitting the wire to dc currents of 360, 400, and 425 mA for a duration of 30 min in air, with no applied stress. Complex impedance measurements were done at various frequencies with a Stanford Research Systems SR 850 lock-in amplifier. Current and voltage leads were made by pasting copper wires with Ag paste. A high-quality resistor was connected in series with the wire, to measure the current amplitude flowing through the wire in all measurements. The current amplitude, $i$, was varied between 0.1 and 40 mA (rms). The impedance was also measured as a function of axial field, $H_z$, which was produced by a solenoid. All measurements were performed with the wire oriented perpendicular to the earth's magnetic field.

## III. EXPERIMENTAL RESULTS

The dependence of total impedance, $Z$, as a function of axial field, $H_z$, at $f=100$ kHz is shown in Fig. 1 for an as-cast sample as well as for a sample annealed at 360 mA. The measurements were made at various values of ac current amplitude, $i$. The as-cast sample exhibits the well-known, decreasing behavior of $Z$ as $H_z$ increasingly produces a rotational component on spins of the circular domains.[1,3,4] For the current-annealed sample, an impedance maximum ap-

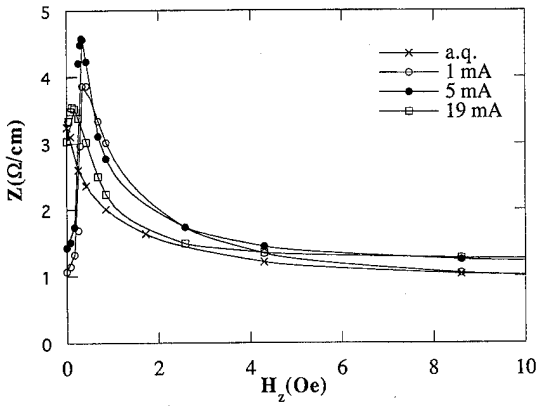



FIG. 1. Dependence of total impedance on the axial dc field, for the as-cast sample, and the sample current annealed at 360 mA. The latter is also shown for several amplitudes of the ac measuring current.

[a)]Author to whom correspondence should be addressed.
[b)]On sabbatical leave from the National University of Mexico.

 0021-8979/96/79(8)/6539/3/$10.00 © 1996 American Institute of Physics 

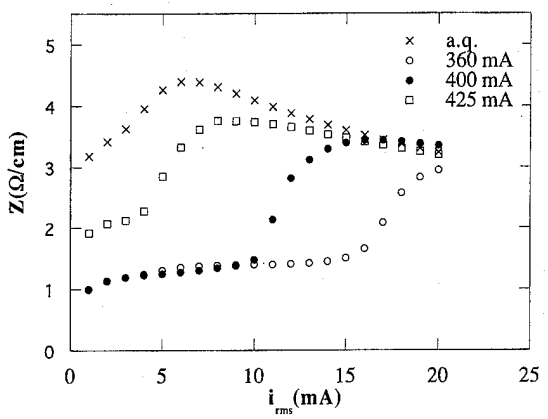



FIG. 2. Total impedance as a function of ac current amplitude at 100 kHz, for samples current annealed under various current values.

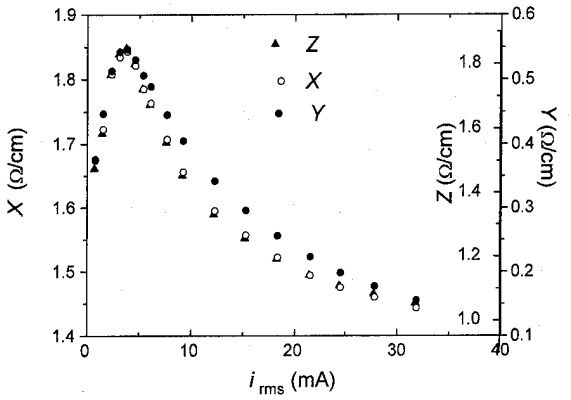



FIG. 3. Real, $X$, imaginary, $Y$, and total, $Z$, impedance measured as a function of ac current amplitude, at 100 kHz, for the as-cast sample.

pears for nonzero axial fields, and a dependence of $i$ is exhibited. For high axial fields, all curves show a tendency to merge into a common behavior. As we have shown elsewhere,[6] the current amplitude, $i$ (and therefore the circular field magnitude), has an important effect on the $Z$ response.

In order to investigate the influence of the circular field, we have measured $Z$ as a function of $i$ at 100 kHz, for all the samples (Fig. 2). All of the curves show a maximum, and except for the as-cast sample, all of them exhibit a propagation field, i.e., a field necessary to initiate domain wall unpinning and displacement. This propagation field is at maximum for the sample annealed at low current (360 mA), and decreases for samples treated at medium (400 mA) and high (425 mA) annealing currents.

## IV. DISCUSSION AND CONCLUSIONS

In order to draw conclusions from these measurements, it is important to establish first whether the total impedance, $Z$, can be associated with a clear physical meaning. Recently, an approach based on equivalent circuits (EC) has been proposed[6] to represent the impedance response of low magnetostriction wires. According to this approach, wire response can be modeled by a $R_sL_s$ series circuit, in series with a $R_pL_p$ parallel arrangement. In short, $R_s$ represents the wires dc resistance, $L_s$ its rotational permeability, $L_p$ the wall permeability of circumferential domains, and $R_p$ the viscous damping of circumferential walls. The EC equations for the real, $X$, and imaginary, $Y$, components of impedance are written as

$$X=R_s+R_pL_p^2\omega^2/(R_p^2+L_p^2\omega^2), \tag{1}$$

$$Y=\omega L_s+R_p^2L_p\omega/(R_p^2+L_p^2\omega^2), \tag{2}$$

where $\omega$ is the angular frequency ($\omega=2\pi f$). While the series circuit is quite insensitive to frequency, the parallel arrangement exhibits a relaxation behavior for a frequency $\omega_x$ where

$$\omega_x=R_p/L_p. \tag{3}$$

For this condition. Eqs. (1) and (2) become, respectively,

$$X=R_s+\omega_xL_p/2, \tag{4}$$

$$Y=\omega_xL_s+\omega_xL_p/2. \tag{5}$$

Since $Z=(X^2+Y^2)^{1/2}$, and both $X$ and $Y$ include the term $\omega_xL_p/2$, total impedance can accurately represent the variations in circumferential permeability. At frequencies close to the relaxation frequency, total impedance measurements can therefore be used to monitor circumferential wall permeability.

Such a relaxation frequency has been found in these wires in the 10–100 kHz range[6] for the as-cast state. A confirmation of this approach is given in Fig. 3 for the as-cast sample, where $X$, $Y$, and $Z$ are measured as a function of $i$. Except for a constant term (note the difference in scales), all of the curves show the same variations as a function of the circular field. At frequencies far from the domain wall relaxation frequency, $X$ is insensitive to circumferential permeability.

Variations in $Z$ at measuring frequencies near the relaxation frequency therefore represent the variations in domain wall permeability of circumferential domains. The curves in Fig. 2 effectively exhibit the basic features of wall permeability behavior as a function of applied field: a practically constant range of low fields (the initial permeability range), followed by a strong increase (propagation of the walls), passage through a maximum (maximum permeability), and finally, a hyperbolic decrease for high fields (approach to saturation). By comparing the curves, we can say that the main difference between them is the propagation field: it is extremely small for the as-quenched sample, increases for the 360 mA sample, and then decreases for the 400 and 425 mA sample.

In order to explain these results, we assume that a directional ordering of Co–Co atom pairs[7] takes place during cooling of the samples. While these pairs are expected to be oriented parallel to the magnetization direction in circumferential domains, they form a complex arrangement in domain walls, where atom pairs tend to follow the spin orientations. The formation of such ordering results in an additional stabilization energy of walls; therefore, an additional energy has to be supplied to initiate wall propagation.

In the stationary state, annealing currents result in well-defined average temperatures in wires; For 360, 400, and 425 mA (leading to current densities of 29.3, 32.6, and 34.6 A/mm$^2$, respectively), the corresponding temperatures[8] are 559, 590, and 610 K, respectively. Crystallization during current annealing is ruled out since the crystallization temperature is substantially higher (810 K).

In the case of the 400 and 425 mA annealings, the observed domain wall pinning seems unrelated to the annealing temperature itself, since these treatments occur at temperatures higher than the Curie point for this alloy ($T_C$=568 K). The low current annealing takes place at $T<T_C$; however, the circular field produced by the current is high enough to eliminate the domain walls and saturate the wire. The domain wall pinning associated with directional ordering can therefore occur only during the cooling process, as the wire cools down through $T_C$ and the domain structure is again formed. No large differences in cooling rate can be expected among the various annealings; therefore, the increase in pinning field exhibited for the low annealing temperature could be ascribed to the formation of a stronger circular anisotropy for this sample. As the annealing current is switched off and the domain structure is formed, the directional ordering created on domain wall sites seems to become stronger as the annealing temperature is lower. This directional ordering could be explained in terms of induced anisotropy.[7]

In conclusion, we say that total impedance measurements can be used as an important tool in GMI investigation, and that for the particular case of current-annealed CoFeBSi wires, directional ordering of atom pairs can explain the observed features in impedance response.

## ACKNOWLEDGMENTS

R.V. thanks DGICyT, Spain, and DGAPA-UNAM, México, for a sabbatical fellowship. Financial support from the Basque Country University (Project No. UPV-057.263-EA149/94) is also acknowledged.

[1] K. Mohri, T. Kohzawa, K. Kawashima, H. Yoshida, and L. V. Panina, IEEE Trans. Magn. **28**, 3150 (1992).
[2] R. Valenzuela, M. Vázquez, and A. Hernando, these proceedings.
[3] R. S. Beach and A. E. Berkowitz, J. Appl. Phys. **76**, 6209 (1994).
[4] L. V. Panina and K. Mohri, Appl. Phys. Lett. **65**, 1189 (1994).
[5] Y. Waseda, S. Ueno, M. Hagiwara, and K. T. Aust. Prog. Mater. Sci. **34**, 149 (1990).
[6] R. Valenzuela, M. Knobel, M. Vásquez, and A. Hernando, J. Appl. Phys. **78**, 5189 (1995).
[7] L. Kraus, M. Vázquez, and A. Hernando, J. Appl. Phys. **76**, 5343 (1994).
[8] C. Gómez-Polo and M. Vásquez, J. Magn. Magn. Mater. **118**, 86 (1993).

# Measurements of magnetization dynamics and magnetoimpedance in FeCoSiB and FeSiB amorphous wires

S. Masuda
*Research and Development Department, Jeco Co. Ltd., 1-4-1 Fujimicho, Gyoda, Saitama 361, Japan*

K. Komatsu, Y. Takemura, T. Yamada, and K. Kakuno
*Division of Electrical and Computer Engineering, Yokohama National University, 156 Tokiwadai, Hodogaya-ku, Yokohama 240, Japan*

A technique to observe magnetization dynamics in amorphous wires is described. When an ac current passes through the amorphous wire, voltages induced between both ends of the wire and in a pickup coil wound around the wire are observed. These voltages indicate circumferential and axial components of magnetization changes in the wire, respectively. Observations in a Co-rich wire having slightly negative magnetostriction and an Fe-rich wire having positive magnetostriction under various bias fields showed quite different wave forms which indicate their domain structure. © *1996 American Institute of Physics.* [S0021-8979(96)58008-7]

## I. INTRODUCTION

Amorphous magnetic wires provide attractive features, including the magnetoelastic wave[1] and the magnetoimpedance effect.[2] The magnetoelastic waves in magnetostrictive Fe-rich amorphous wires are detected usually by a pickup coil wound around the sample wire. Changes of the axial component of the magnetization in the wire induce voltages in the pickup coil.

An ac voltage is also induced in the pickup coil when an ac current passes through the amorphous wire. Ogasawara[3] has reported this phenomenon as "inverse-Matteucci effect." Tekemura *et al.*[4] showed that two signals can be transported individually by the magnetoelastic wave and the ac current passing through the same amorphous wire.

The magnetoimpedance effect in Co-rich amorphous wires, which have slightly negative magnetostriction, has attracted much interest because it has been considered to be applicable as a sensitive method to measure magnetic field. Mohri *et al.*[5] have shown that the magnetoimpedance effect originates from the electromotive force induced between both ends of the wire by changes of the circumferential component of the magnetization, and have described the domain dynamics of the wire based on the domain structure model of the negatively magnetostrictive amorphous wire.

In the present article we discuss magnetization dynamics in FeCoSiB and FeSiB amorphous wires. In order to observe the magnetization process, axial and circumferential components of the magnetization in the wire are simultaneously measured by observation of the wave forms of induced voltages in the pickup coil and between the ends of the sample wire, respectively.[6]

## II. EXPERIMENT

The experimental arrangement is illustrated in Fig. 1. An ac current $i_z$, passing through the sample wire causes a circumferential magnetic field. A voltage $v_c$, induced in a pickup coil (80 turns, 4.8 mm length, 600 $\mu$m inner diameter) turned around the sample wire is proportional to the axial component of magnetization change in the wire. A voltage $v_z$, observed between both ends of the sample wire is considered as a sum of the ohmic voltage and the voltage induced by the circumferential component of the magnetization change in the wire.

Amplitude and frequency of the ac current were chosen as 12 $mA_{p-p}$ (for the Co-rich wire), 30 $mA_{p-p}$ (for the Fe-rich wire), and 500 kHz, respectively. An external dc bias field, $H_{zb}$, was applied along the wire axis using a solenoidal coil.

An amorphous $Fe_{4.3}Co_{68.2}Si_{12.5}B_{15}$ wire having slightly negative magnetostriction and a positively magnetostrictive $Fe_{77.5}Si_{7.5}B_{15}$ wire (both of them are prepared by Unitika Ltd., Japan) were used as samples. The Co-rich wire was cold drawn to its diameter $d_W$=30 $\mu$m, and then annealed at 475 °C with a tension of 40 kg/mm$^2$. The Fe-rich wire was also drawn to $d_W$=90 $\mu$m and annealed at 400 °C with no tension.

## III. RESULTS AND DISCUSSION

Waveforms of $v_z$ and $v_c$ observed in the Co-rich amorphous wire under various bias fields $H_{zb}$ are shown in Figs. 2(a) and 2(b), respectively. These wave forms are shown as Lissajous figures, and abscissas show ac current $i_z$.

The wave forms of $v_z$ are similar to those already reported:[2,7] The frequency of $v_z$ agrees with that of $i_z$; the

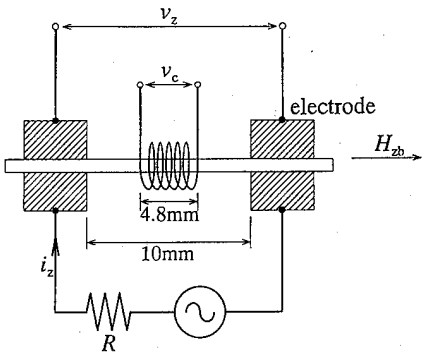



FIG. 1. Experimental arrangement.

 0021-8979/96/79(8)/6542/3/$10.00 © 1996 American Institute of Physics

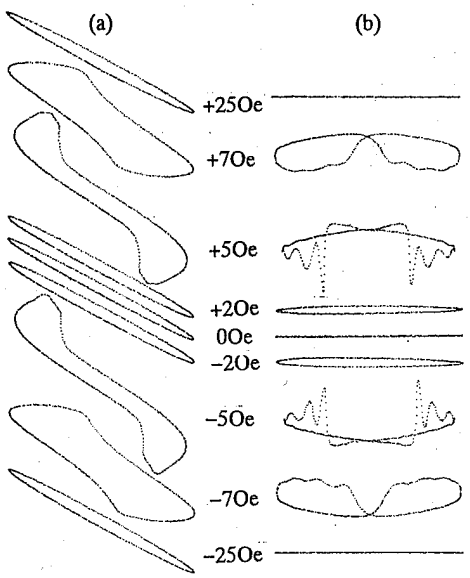



FIG. 2. Wave forms of (a) voltages between both ends of the sample wire $v_z$ and (b) voltages induced in the pickup coil $v_c$, observed in the amorphous $Fe_{4.3}Co_{68.2}Si_{12.5}B_{15}$ wire under various values of the bias field $H_{zb}$ applied to the axis direction of the wire. The wave forms are shown as Lissajous figures and abscissas show the ac current through the wire $i_z$ (500 kHz, 12 $mA_{p-p}$).

amplitude of $v_z$ is markedly influenced by $H_{zb}$ as shown in Fig. 3(a), whereas the polarity of $H_{zb}$ does not affect the wave form of $v_z$.

Observation of $v_c$ provides interesting information of the magnetization dynamics in the sample wire:

(1) The frequency of $v_c$ is double of that of $i_z$ except in a range of $H_{zb}$ near zero;
(2) the polarity of $v_c$ reverses when the polarity of $H_{zb}$ reverses;
(3) in the range of $H_{zb}$, $\pm 4 - \pm 6$ Oe, steep pulses of $v_c$ which indicate jumps of axial component of magnetization are observed.

A domain model for tension-annealed, negatively magnetostrictive amorphous wires, in which circumferential anisotropy is postulated in the whole cross section, has been proposed.[2] The above-mentioned observation seems to support the proposed model, as follows.

(1) During the bias field $H_{zb}$ is zero, magnetization in the wire has no axial component regardless of the circumferential field.

(2) When a small $H_{zb}$ is applied, a reversible magnetization rotation occurs and the axial component of it is observed as $v_c$.

(3) When $H_{zb}$ exceeds an appropriate value, an irreversible magnetization process takes place. Each time the irreversible change occurs, axial and circumferential components of the magnetization induce steep pulses in $v_c$ and $v_z$, respectively.

(4) When $H_{zb}$ becomes sufficiently large, the magnetization vector is restricted to the axial direction and vibrates with a small amplitude;

(5) In the cases of (3) and (4), the magnetization vector vibrates across the axial direction where the axial component of the magnetization has maximum value. Therefore, the frequency of $v_c$ is double of that of $i_z$.

Figures 4(a) and 4(b) show wave forms of $v_c$ and $v_z$, respectively, observed in the Fe-rich amorphous wire. Relationships of these wave forms and $H_{zb}$ are quite different from those observed in the Co-rich wire:

(1) The frequency of $v_c$ and $v_z$ is equal to that of the ac current regardless of $H_{zb}$;
(2) $H_{zb}$ dependence of $v_c$ and $v_z$ has a hysteresis and their polarities are independent of the polarity of $H_{zb}$;
(3) wave forms of $v_c$ and $v_z$ are approximately sinusoidal and noticeable jumps of magnetization are not observed.

In Figs. 5 and 6, phase shift from the ac current and amplitude of $v_c$ and $v_z$ in the Fe-rich wire are shown as functions of $H_{zb}$. $H_{zb}$ dependence of $v_c$ and $v_z$ is quite different from that of the Co-rich wire. The magnetization vector in the Fe-rich wire is most movable when $H_{zb}$ is near zero.

As shown in Fig. 5, magnetoimpedance effect (about

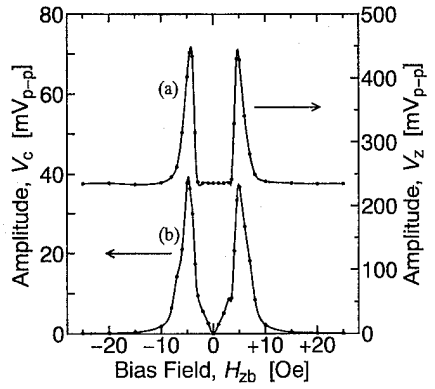



FIG. 3. Amplitude of (a) $v_z$ and (b) $v_c$ observed in the Co-rich amorphous wire as functions of $H_{zb}$.

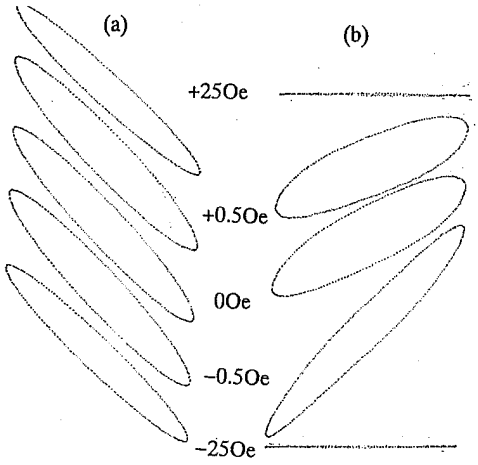



FIG. 4. Wave forms of (a) $v_z$ and (b) $v_c$, observed in the $Fe_{77.5}Si_{7.5}B_{15}$ wire under various values of $H_{zb}$. The wave forms are shown as Lissajous figures and abscissas show the ac current through the wire $i_z$ (500 kHz, 30 $mA_{p-p}$).

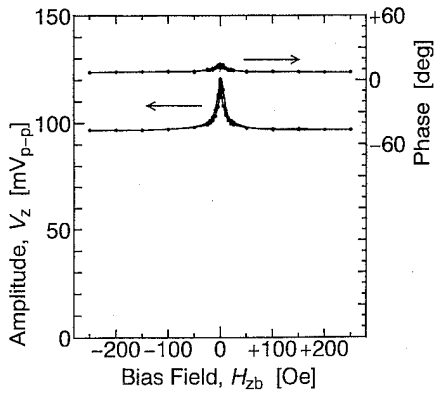



FIG. 5. Amplitude and phase shift of $v_z$ observed in the Fe-rich amorphous wire as functions of $H_{zb}$.

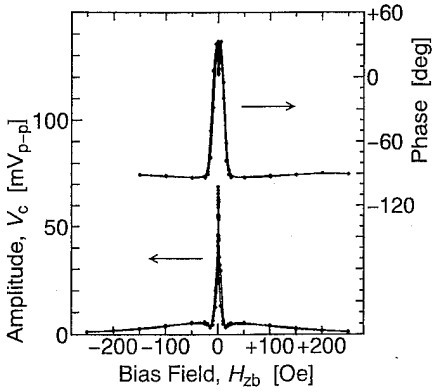



FIG. 6. Amplitude and phase shift of $v_c$ observed in the Fe-rich amorphous wire as functions of $H_{zb}$.

20% amplitude change) is observed. Atkinson *et al.*[8] have reported magnetoimpedance effect in the Fe-rich amorphous wire, and our result is similar to theirs.

Behavior of the magnetization in Fe-rich wire and its relationships to the domain model[5] and to the characteristics of the magnetoelastic wave[1] will be discussed in a future study.

## IV. CONCLUSION

When an ac current passed through an amorphous wire, voltages induced between both ends of the wire and in a pickup coil wound around the wire were observed as functions of bias field applied to the axial direction of the wire. These voltages indicate circumferential and axial components of magnetization change in the sample wire, respectively.

Observations in a Co-rich wire having slightly negative magnetostriction and an Fe-rich wire having positive magnetostriction showed quite different wave forms which indicate the differences between their domain structures.

The goal of our study is to clarify the domain structures and the magnetization dynamics of amorphous wires. Results obtained in the present study show that the proposed method is a powerful way to observe two-dimensional magnetization dynamics.

## ACKNOWLEDGMENT

The authors are grateful to I. Ogasawara, Unitika Ltd., for providing the sample wires.

[1] S. Masuda and K. Kakuno, IEEE Trans. Magn. **MAG-26**, 1801 (1990).
[2] K. Mohri, K. Bushida, M. Noda, H. Yoshida, L. V. Panina, and T. Uchiyama, IEEE Trans. Magn. **MAG-31**, 2455 (1995).
[3] I. Ogasawara, in Technical Meeting on Magnetics in IEE of Japan, MAG-85-97, 1985 (in Japanese).
[4] Y. Takemura, S. Masuda, T. Yamada, and K. Kakuno, IEEE Trans. Magn. (to be published).
[5] K. Mohri, K. Kawashima, T. Kohzawa, and H. Yoshida, IEEE Trans. Magn. **MAG-29**, 1245 (1993).
[6] W. D. Doyle and T. F. Finnegan, J. Appl. Phys. **39**, 3355 (1968).
[7] K. V. Rao, F. B. Humphrey, and J. L. Costa-Krämer, J. Appl. Phys. **76**, 6204 (1994).
[8] D. Atkinson, R. S. Beach, P. T. Squire, C. L. Platt, and S. N. Hogsdon, IEEE Trans. Magn. (unpublished).

# Transport properties of amorphous CoZrNd thin films with very low Nd content (abstract)

C. de Francisco and J. M. Muñoz
*Departamento de Electricidad y Electrónica, Universidad de Valladolid, 47071 Valladolid, Spain*

J. F. Calleja, M. Rivas, and M. C. Contreras
*Departamento de Física, Universidad de Oviedo, 33007 Oviedo, Spain*

The composition and temperature dependence of electrical resistivity were studied for a series of amorphous $(Co_{93}Zr_7)_{100-x}Nd_x$ for $x<3.4$ and for a temperature range between 77 and 300 K. The films were deposited by rf sputtering. Measurements of electrical resistivity were performed by the standard four probe technique with ac currents of 10 mA. The rate of heating and cooling was 1 K/min. The electrical resistivity is very sensitive to the presence of Nd ions, as the resistivity clearly increases with a very slight increase of Nd content. The temperature dependence of resistivity does not obey the $T^2$ law predicted by the diffraction model as proposed by Meisel and Cote[1] but follows very nicely the law $\rho(T)=aT^{3/2}-bT+c$, a result also found for amorphous Gd–Co. The first term corresponds to the electron scattering from the magnetic spin and the second term to the electron scattering from the disordered configuration of atomic potentials. © *1996 American Institute of Physics.* [S0021-8979(96)62708-4]

[1] L. V. Meisel and P. J. Cote, Phys. Rev. B **17**, 4652 (1979).

 0021-8979/96/79(8)/6545/1/$10.00 © 1996 American Institute of Physics 

# Domains and giant magneto-impedance in amorphous ribbons by magneto-optical Kerr effect

A. D. Santos, L. G. C. Melo, C. S. Martins, and F. P. Missell
*Instituto de Física, Universidade de São Paulo, CP 66318, 05389-970 São Paulo, SP, Brazil*

Y. Souche
*Laboratoire de Magnétisme Louis Néel-CNRS, 38042 Grenoble Cedex, France*

F. L. A. Machado and S. M. Rezende
*Departamento de Física, Universidade Federal de Pernambuco, 50739 Recife, PE, Brazil*

By longitudinal magneto-optical Kerr effect microscopy we analyzed the development of the domain structure in $Co_{70.4}Fe_{4.6}Si_{15}B_{10}$ amorphous ribbons for which giant magneto-impedance had been observed. Using transverse and longitudinal magneto-optical Kerr effect magnetometry we measured the magnetization direction around the hysteresis loop. These results allowed us to model the domain structure of the sample during the giant magneto-impedance measurements. © *1996 American Institute of Physics.* [S0021-8979(96)58108-2]

## I. INTRODUCTION

Recently some authors have reported[1,2] observations of giant magneto- impedance (GMI) in amorphous ribbons of composition $Co_{70.4}Fe_{4.6}Si_{15}B_{10}$. Recent literature[3] explains GMI in amorphous wires in terms of classical electromagnetism. For wires, the symmetry of the samples greatly simplifies the theoretical calculations, but makes domain observations very difficult. Thus there is always some doubt as to whether the model describes the actual physical situation. On the other hand, for ribbons, the geometry makes the theoretical modeling somewhat more difficult, but greatly simplifies domain observations. This motivated us to characterize the development of the domain structure of amorphous ribbons under conditions encountered in the GMI measurements. In the present work we employed variations of the magneto-optic Kerr effect (MOKE) to study the evolution of the domain structure and magnetization during GMI measurements.

## II. EXPERIMENT

Samples of composition $Co_{70.4}Fe_{4.6}Si_{15}B_{10}$ were produced by a single-roller melt-spinning technique. For the GMI measurements, they were field-annealed in vacuum at 300 °C for 15 min under an in-plane magnetic field of 3 kOe, perpendicular to the ribbon axis. For the magneto-optical (MO) measurements, the ribbons were mechanically polished using 1 $\mu$m diamond paste and then electrolytically polished using a HCl/methanol solution. Finally, they were covered with a 33 nm ZnS antireflection coating. A transverse and longitudinal magneto-optical Kerr effect (TLMOKE) magnetometer[4,5] allowed the determination of MO signals for different polarization directions. In this system a $p$-polarized incident wave from a diode laser ($\lambda = 670$ nm) is reflected by the sample and detected by a photodiode after passing through an analyzer. Adjusting the analyzer allowed operation in the transverse or longitudinal modes, or in a complex mixture of both.[6]

## III. RESULTS

### A. Magnetization measurements

In Figs. 1(a) and 1(b), we show the hysteresis loops obtained for analyzer positions corresponding to $+45°$ and $-45°$ in relation to the $p$-polarization direction. The frequency of the magnetic field was 0.03 Hz and in both cases, an offset signal was applied to center the loops. From these data, by point-to-point algebraic summation and subtraction,[7] we can reconstruct the hysteresis loops corresponding to the magnetization components parallel ($M_{\parallel}$) and perpendicular ($M_{\perp}$) to the applied magnetic field. The results for $M_{\parallel}$ and $M_{\perp}$ are shown in Figs. 1(c) and 1(d), respectively. As is usual for MO measurements, the vertical axes are in arbitrary units, but, in this case, the scale factor is the same (500) for both magnetization components. Figure 1(c) is similar to results obtained using TMOKE or a hysteresis loop tracer (not shown here) and reflects a transverse in-plane anisotropy. In Fig. 1(d) we have a large signal for $|H| < 2.5$ Oe which goes to zero as the sample is saturated. This indicates that in zero field, the magnetization remains near the direction of the annealing field. From the two components of the in-plane magnetization, we can determine the evolution of the magnetization direction, as shown in Fig. 1(e). We can see in the range 1.3–3 Oe, an almost linear variation of the magnetization direction, corresponding to the rotation of the magnetization in an applied field.

Using the same setup, but synchronizing the lock-in amplifier on an alternating current passing along the axis of the sample, we obtained the magnetic field dependence of the transverse susceptibility ($\chi_t$). We show in Fig. 1(f) the $\chi_t$ vs $H$ loop for a 10 kHz, 10 mA sinusoidal current. This figure is quite similar to Fig. 1 of Ref. 2, and has a peak corresponding to the GMI peak, in the region where the magnetization direction has a linear variation. The low field peaks are due to domain wall motion close to the coercive field.

### B. Domain observations

For the domain observations we used the longitudinal magneto-optical Kerr effect (LMOKE). A Jenapol optical

 0021-8979/96/79(8)/6546/3/$10.00 © 1996 American Institute of Physics

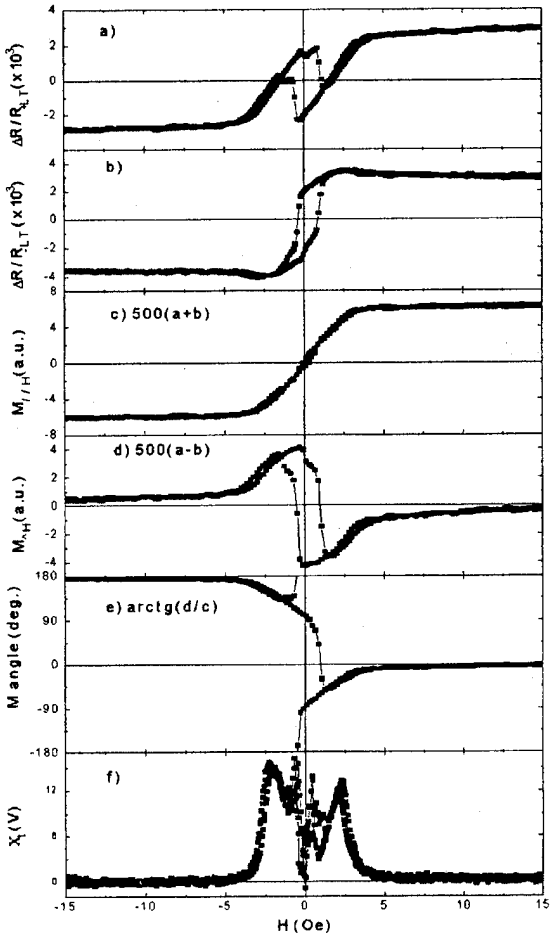



FIG. 1. TLMOKE hysteresis loops for (a) analyzer at 45°; (b) analyzer at −45°; (c) summation of (a) and (b); (d) difference of (a) and (b); (e) magnetization direction; and (f) $\chi_t$.

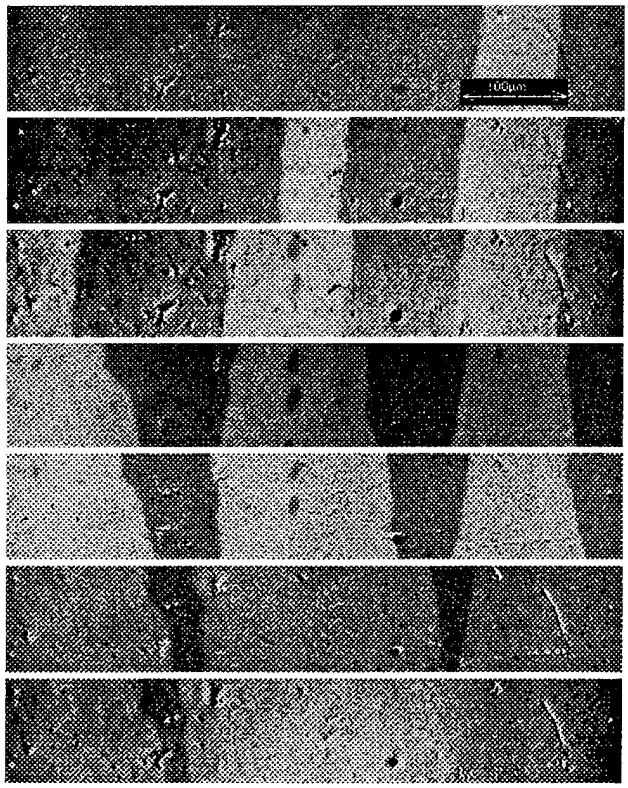


FIG. 2. LMOKE domain observation for the same sample position. From top to bottom, the longitudinal magnetic field is $H=0.08$; 0.11; 0.27; 0.45; 0.57; 0.68; and 0.72 Oe.

microscope coupled to a $10^{-3}$ lux Hamamatsu video camera and a DT2867 Data Translation video board allowed real time image capture and processing, using capabilities such as frame averaging and background subtraction. The sample could be simultaneously submitted to a variable longitudinal magnetic field up to 70 Oe and an alternating current of 10 mA, flowing along the sample axis. In Fig. 2 we present a sequence of images, obtained at the same position on the sample, for applied magnetic fields in the range from 0.08 to 0.72 Oe, after saturation of the sample in the reverse direction. The horizontal direction in the figure is the ribbon axis. We can see the dark domains shrinking as the longitudinal magnetic field grows, and finally disappearing in a field of about 0.8 Oe. Comparing with Fig. 1, this range corresponds to that of strong variation in the magnetization direction, near the coercive field. Thus, for magnetic fields above about 0.8 Oe, only magnetization rotation occurs in the sample.

In Fig. 3 we show, for the same sample position, the variation of the domain structure due to a current having the form of a square wave of amplitude 10 mA and frequency 5 Hz. This low frequency current generates a magnetic field in the sample that is parallel to the surface and perpendicular to the axis of the ribbon. The sense of the field is inverted on either side of the sample. This means that the magnetization is closed upon itself and that the demagnetizing factor in the transverse direction can be neglected. Figures 3(a), 3(b), and 3(c) were obtained with longitudinal fields $H=0.21$, 0.25, and 0.33 Oe, respectively. The images were obtained by averaging 64 frames after the subtraction of the magnetically saturated background. We then obtained a three-level gray image where the bright and dark areas are the regions where

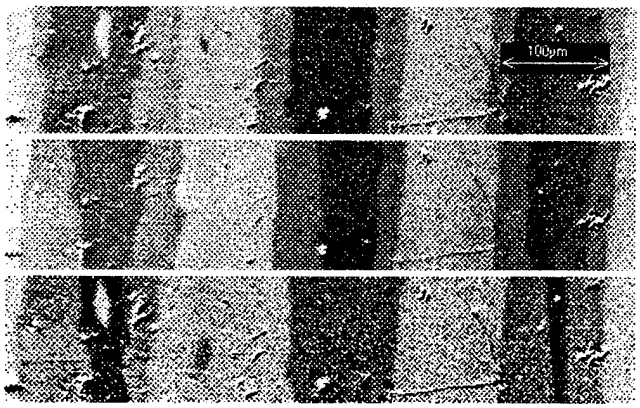



FIG. 3. LMOKE domain observation applying a longitudinal current square wave of amplitude 10 mA. From top to bottom, the longitudinal field is $H=0.21$; 0.25; and 0.33 Oe.

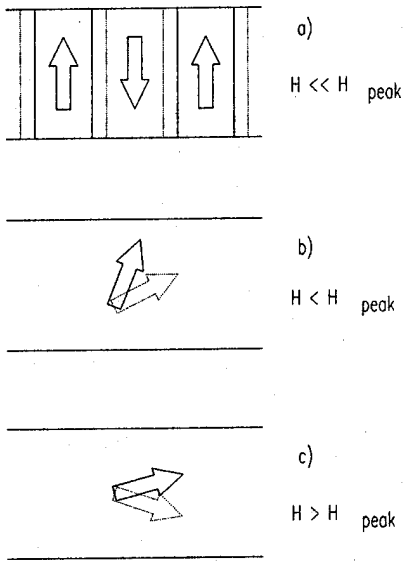



FIG. 4. Model for the domain structure during the GMI measurements.

the magnetization is stable, and the intermediate gray level corresponds to the displacement of the domain walls due to the applied current. The effect of the current is strong: in Fig. 3(a) the displacement of the domain wall is of the order of 30% of the domain dimension. From Fig. 3(c) it is possible to see that, for one sense of the current, the domain structure almost disappears. For larger values of longitudinal field, but certainly below 1 Oe, this side of the sample presents a uniform magnetization.

## IV. DISCUSSION

From the experimental results presented here, we can propose a model for the domain structure for the three different field regions of interest. This model is presented in Fig. 4.

(1) For $H \approx 0$, shown in Fig. 4(a), we have a transverse stripe domain structure, where the effect of the current is to displace the domain walls longitudinally. The dashed and solid lines correspond to the position of the domain walls for peak values of the electric current.

(2) For $0 \ll H < H_{\text{peak}}$, $H_{\text{peak}}$ being the magnetic field of the GMI or $\chi_t$ maximum. In this case, shown in Fig. 4(b), we have a uniform magnetization whose average direction is close to the easy axis. Then the current will produce a small variation of the magnetization direction around this equilibrium direction.

3) For $H > H_{\text{peak}}$, shown in Fig. 4(c), the equilibrium direction is close to the longitudinal one, as the field nears saturation. Then, for both directions of the current, the magnetization direction will alternate between directions symmetrical in relation to the axis of the ribbon.

As the magnetic field generated by the current has a different direction on each side of the ribbon, we can represent the other side by simply reflecting Fig. 4 in a longitudinal plane, perpendicular to the ribbon. Then, for $H \gg 0$, the magnetic behavior of the sample can be represented by an in-plane rotation of the magnetization in a helical domain structure, whose period along the direction of the magnetization is a function of the current and the longitudinal magnetic field. Nevertheless, our measurements do not clarify what happens in the central plane, parallel to the surface of the ribbon. However, we can suppose that the magnetization remains longitudinal, because there is no magnetic field generated by the current in this region.

## V. CONCLUSIONS

From the MOKE measurements we completely characterized the domain structure for the conditions of the GMI measurements. It was possible to demonstrate that the maxima in $\chi_t$ and GMI correspond to a rotation of the magnetization in a longitudinal helical domain structure.

## ACKNOWLEDGMENTS

This work was supported by FAPESP, CNPq, RHAE, and FINEP.

[1] F. L. A. Machado, B. L. da Silva, S. M. Rezende, and C. S. Martins, J. Appl. Phys. **75**, 6563 (1994).
[2] F. L. A. Machado, C. S. Martins, and S. M. Rezende, Phys. Rev. B **51**, 3926 (1995).
[3] R. S. Beach and A. E. Berkowitz, Appl. Phys. Lett. **64**, 3652 (1994).
[4] T. Yonamine, M.Sc. thesis, Universidade de São Paulo, 1995.
[5] T. Yonamine, Y. Souche, and A. D. Santos, J. Appl. Phys. **79** (8) (1996) (to be published).
[6] J. M. Florczak and E. D. Dahlberg, J. Appl. Phys. **67**, 7520 (1990).
[7] A. D. Santos and Y. Souche (in preparation).

# A position sensor based on magnetoimpedance

R. Valenzuela,[a] M. Vazquez,[b] and A. Hernando
*Instituto de Magnetismo Aplicado, UCM, and Instituto de Ciencia de Materiales, CSIC, P.O. Box 155, 28230 Las Rozas, Madrid, Spain*

A magnetic-field sensor based on the giant magnetoimpedance phenomenon is presented. It is shown that a low, negative magnetostriction CoFeBSi amorphous wire can be used to detect the presence or passage of moving pieces or vehicles, simply by pasting a small permanent magnet on the vehicles/pieces. The detection is observed as a decrease in the ac voltage on the wire's ends. A system of such devices can be used to monitor and control a number of industrial processes. © *1996 American Institute of Physics.* [S0021-8979(96)58208-X]

## I. INTRODUCTION

Some ferromagnetic materials subjected to an ac electric current exhibit a strong decrease in their impedance in the presence of a dc magnetic field. This phenomenon is known as giant magnetoimpedance[1–4] (GMI) and is receiving considerable attention because of its applications in magnetic sensors.

GMI is a classical electrodynamics phenomenon[1,2] which depends essentially on the interaction between the magnetic field created by the ac current and magnetic domains of the sample. GMI has been reported for ribbons and wires; however, it has been observed to be more efficient in low, negative magnetostriction wires, which spontaneously form[5] an outer shell with circumferential domains, and still have a weak circular magnetic anisotropy. Since the magnetization direction in such domains has an alternate circumferential orientation, the interaction between magnetization and the magnetic field created by the ac current is strong. At high frequencies, where the impedance response becomes stronger, GMI shows a further complexity[1,2] due to skin effect, which tends to concentrate the ac field on a small cross section near the surface of the wire.

In this article, an application of GMI as a magnetic-field sensor, adapted to monitor the passage of moving pieces or vehicles typical in many industrial processes, is presented. The development of a system of sensors with a feedback loop to monitor and control the process is also discussed.

## II. EXPERIMENTAL TECHNIQUES

We used amorphous wires of composition $(Co_{0.94}Fe_{0.06})_{72.5}B_{15}Si_{12.5}$, of low, negative magnetostriction in the as-cast state, kindly supplied by Unitika Ltd., Japan, prepared by the in-rotating-water technology.[6] A piece of approximately 9 cm was cut, and current and voltage leads were pasted on its ends with Ag paint, after cleaning with a soft acid solution. In order to improve its sensitivity to small, localized magnetic fields, the wire was carefully bent and placed inside a small, acrylic cylinder of 5 and 8 mm inner and outer diameter, respectively, and 4 cm in length. In this way, two sections of the middle part of the wire were exposed to small, localized magnetic fields. The highest sensitivity of wires has been observed[7] to axially applied fields.

To produce an ac current along the wire (in the range up to 20 mA rms), a conventional signal generator (Hameg HM 8030) was used. Voltage measurements were made with a Fluke model 45 multimeter. A dc magnetic field was applied by means of a pair of Helmholtz coils. In other experiments, a small, disk-shaped (5 mm diameter, 2 mm thickness) NdFeB permanent magnet, axially magnetized was used to produce the dc magnetic field on the wire. During all measurements, the wire axis was perpendicularly oriented with respect to the earth's magnetic field.

## III. BASIS OF THE SENSOR

The sensor is based on the dependence of total impedance $Z$ on dc applied magnetic field. As is now well documented,[1–4] $Z$ decreases steeply as $H$ increases, see Fig. 1. This behavior can be explained on the basis of the magnetic domain structure[5] of low, negative magnetostriction wires. It can be described as formed by an inner core with axial magnetization, and an outer shell composed of circumferential domains with alternate magnetization. Evidence showing deviations in magnetization directions in both axial and circumferential domains has been recently reported.[8]

As axial field increases, the inner core is first saturated in the field direction; on further increase, the spins in circumferential domains are deviated toward the axial field direction in a nearly pure rotational process.[9] The circumferential

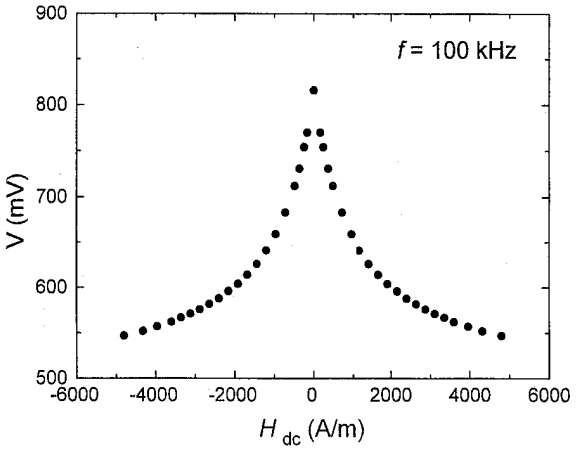



FIG. 1. Voltage response of the CoFeBSi wire, as a function of dc axial field.

[a]On sabbatical leave from the National University of Mexico.
[b]Corresponding author, electronic mail: vazquezV@pinar1.csic.es

 0021-8979/96/79(8)/6549/3/$10.00 © 1996 American Institute of Physics 

component of magnetization is thus decreased, as well as its interaction with the circular field. Therefore, a decrease in impedance response occurs. This process depends both on ac current frequency and amplitude.

At low frequencies ($f<500$ Hz), the decrease in impedance response associated with the presence of axial fields can be extremely small. For as-cast, CoFeBSi wires, a maximum sensitivity to axial fields is observed[10] in the 10 kHz–1 MHz. For $f>100$ kHz, due to the skin-depth effect, field penetration depth becomes smaller than the actual dimensions of the wire. Then, an additional component of impedance appears, which depends on frequency and local permeability values in a complex way.[1,2] Finally, the difference in response due to $H$ becomes unnoticeable[10] for $f>20$ MHz.

In most reported results, the ac current amplitude is kept constant in spite of the impedance variations, by monitoring the current for each $H$ value. Since we are interested in application conditions, particularly in the voltage response, we have measured the voltage decrease on the wire ends at an initial (at $H=0$) constant current amplitude of 10 mA (rms), as a function of magnetic field, Fig. 1. As the dc field increases, the impedance decreases, leading to an increase in current amplitude. A comparison of Fig. 1 with published $Z$ vs $H$ plots shows that variations of $V$ are smaller than variations in $Z$ for similar experimental conditions. This is due to the fact that $Z$ depends also on the ac current amplitude $i$. As we have shown elsewhere[11] circumferential magnetization processes occur in a way similar to any domain-wall magnetization process. Since the imaginary part of impedance is associated with inductance and, in turn, magnetic permeability is proportional to inductance,[11] $Z$ reflects these magnetization processes. $Z$ exhibits, therefore, an increase for small $i$ values (start of wall propagation); as $i$ increases, $Z$ goes through a maximum (corresponding to the maximum value in circumferential permeability; about 5 mA for CoFeBSi wires) and then a hyperbolic decrease, as magnetization approaches the saturation value.

As a summary, the most convenient conditions for a maximum sensitivity in GMI are: frequency work in the range 50–500 kHz; and ac current amplitude $i$ in the 8–15 mA range.

## IV. EXPERIMENTAL RESULTS AND DISCUSSION

In order to test the capability of the device, the wire (bent inside the plastic cylinder, as discussed above) was submitted to an ac current of 10 mA (rms), at a frequency of 100 kHz. A small permanent magnet was then brought near the wire and the voltage response $V$ was monitored, as a function of the distance between the wire and the permanent magnet (see Fig. 2). As can be observed, $V$ decreases from 770 mV for large distances $D$ to 605 mV, for physical contact. For practical purposes, a minimum distance of 2 cm between the sensor and the magnet can be considered, which leads to a threshold voltage of 680 mV. A decrease from 770 to any value $V\leqslant 680$ mV should then be taken as a detection.

The practical application is schematically shown in Fig. 3. In any industrial process involving the detection of moving objects (assembling parts in a fabrication process, moving vehicles in a storage yard, etc.), a precise control of

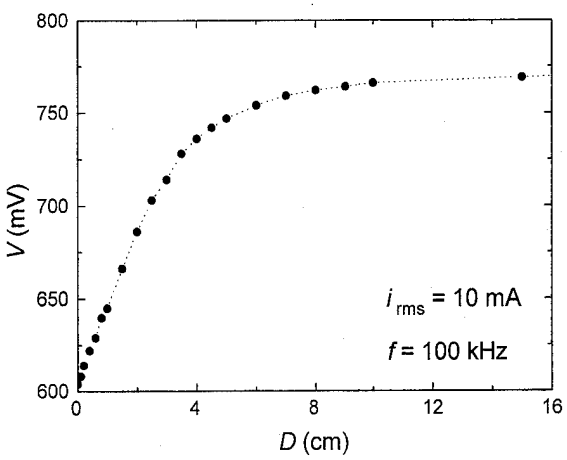



FIG. 2. Voltage dependence on the distance between the sensor and the NdFeB permanent magnet. The magnetic field of the magnet was oriented axially to the wire.

objects passing nearby a sensor can be performed by monitoring the voltage response in the wire. A decrease to or below 680 mV indicates the passage of an object. The ac signal can be easily rectified to a dc signal, which can then be fed to a data acquisition system and, using a simple computer program including a feedback loop, the whole process can be monitored and controlled. In a process involving paths with several bifurcations, for instance, these can be opened or closed after a given number of vehicles have passed.

A variety of magnetic-field sending technologies have been recently reviewed.[12,13] One of the most efficient devices is based on a multivibrator circuit whose tuning frequency depends on the effective permeability of two ferromagnetic cores.[14] The external field is detected by its influence on the core's permeability. A related device,[15] which includes an amorphous wire in a resonant circuit, has also been developed. While these devices are certainly more sensitive than the one presented here, they are also more complex and, presumably, more expensive. For our purposes of position sensing, a well-defined threshold in the voltage response is acceptable, instead of a sensitive detection of the magnitude of the dc field. Concerning other sensing technologies, the magnetic sensor presented here has an advantage over moni-

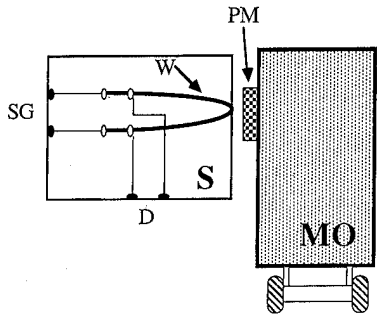



FIG. 3. Layout of the sensor and the moving vehicle, showing the sensor (S), the wire (w), the moving vehicle (MO), the permanent magnet (PM), and the signal generator (SG) and detector circuit (D) contacts, respectively.

toring and control systems based on optical devices in the case of industrial processes involving (nonmagnetic) dusty atmospheres.

As a conclusion, a magnetic sensor based on magnetoimpedance has been presented. Its basic principles, as well as its capabilities have been analyzed.

## ACKNOWLEDGMENTS

This work has been partially supported by the Spanish CICyT under Project No. MAT-95/0273; R.V. thanks DGICyT Spain, and DGAPA-UNAM, Mexico, for a sabbatical fellowship.

[1] R. S. Beach and A. E. Berkowitz, J. Appl. Phys. **76**, 6209 (1994).
[2] L. V. Panina and K. Mohri, Appl. Phys. Lett. **65**, 1189 (1994).
[3] F. L. A. Machado, B. L. da Silva, S. M. Rezende, and C. Martins, J. Appl. Phys. **75**, 6563 (1994).
[4] R. Valenzuela, M. Knobel, M. Vázquez, and A. Hernando, J. Appl. Phys. **78**, 5189 (1995).
[5] J. Yamasaki, K. Mohri, H. Kawamura, F. B. Humphrey, and R. Malmhäll, IEEE Trans. J. Magn. Jpn. **4**, 360 (1989).
[6] Y. Waseda, S. Ueno, M. Hagiwara, and K. T. Aust, Prog. Mater. Sci. **34**, 149 (1990).
[7] K. Mohri, T. Kohzawa, K. Kawashima, H. Yoshida, and L. V. Panina, IEEE Trans. Magn. **28**, 3150 (1992).
[8] H. Theuss, B. Hofmann, C. Gómez-Polo, M. Vázquez, and H. Kronmüller, J. Magn. Magn. Mater. **145**, 165 (1995).
[9] L. Kraus, M. Vázquez, and A. Hernando, J. Appl. Phys. **76**, 5343 (1994).
[10] R. Valenzuela, M. L. Sánchez, M. Vázquez, and A. Hernando, J. Magn. Magn. Mater. (to be published).
[11] R. Valenzuela, M. Knobel, M. Vázquez, and A. Hernando, J. Phys. D: Appl. Phys. **28**, 2404 (1995).
[12] P. T. Squire, D. Atkinson, M. R. J. Gibbs, and S. Atalay, J. Magn. Magn. Mater. **132**, 10 (1994).
[13] T. Meydan, J. Magn. Magn. Mater. **133**, 525 (1994).
[14] K. Mohri, IEEE Trans. Magn. **MAG-20**, 942 (1984).
[15] M. Z. Kozak, E. Misiuk, and W. Kwiatkowski, J. Appl. Phys. **69**, 5023 (1991).

# The field-annealing effect on magnetoimpedance of a zero magnetostrictive metallic glass

S. U. Jen and Y. D. Chao
*Institute of Physics, Academia Sinica, Taipei, Taiwan, 11529 Republic of China*

A commercially made metallic glass, VAC6030, was used for the magnetoimpedance (MI) measurement. Some samples were annealed at a temperature ($T_a$=340 °C) slightly below its Curie point, and cooled in a transverse or longitudinal field. The frequency of the probe current was from 10 kHz to 10 MHz. MI is defined as $\Delta R/R \equiv [R(0)/R(H_s)]-1$ and $\Delta X/X \equiv [X(0)/X(H_s)]-1$, where $H_s$ is the saturating field along sample length, $R$ is the resistance, and $X$ is the reactance. At relatively low frequencies MI is mostly inductive, at relatively high frequencies it is resistive, and a crossover could be defined at a characteristic frequency $f_0$. When the sample is in the as-cast state, $f_0$=890 kHz. If samples have been field annealed, $f_0$ could be shifted either downward or upward; $f_0$ becomes 30 kHz after a transverse anneal, and 8 MHz after a longitudinal anneal. The field annealing would also change the magnitudes of MI. In theory, if $f<f_0$, $\Delta R \propto f^2$ and $\Delta X \propto f$; however, if $f>f_0$, both $\Delta R$ and $\Delta X$ are dominated by the skin-depth effect, and therefore proportional to $f^{1/2}$ instead. © *1996 American Institute of Physics.* [S0021-8979(96)58308-6]

## I. INTRODUCTION

Magnetoimpedance (MI) effect is a high-frequency phenomenon, which describes the changes of impedance (including both resistance $R$ and reactance $X$) in any ferromagnetic sample, when a magnetic field is applied on it. MI is defined as $\Delta R/R \equiv [R(0)/R(H_s)]-1$ and $\Delta X/X \equiv [X(0)/X(H_s)]-1$, where $H_s$ is the saturating field along the long side of the sample. Note, both $\Delta R/R$ and $\Delta X/X$ are dimensionless. However, sometimes it is also necessary to discuss the absolute MI, namely, $\Delta R \equiv R(0)-R(H_s)$ and $\Delta X \equiv X(0)-X(H_s)$. Then, it is self-explanatory that $R$ in $\Delta R/R$ means $R(H_s)$, instead of $R(0)$. The same applies for $X$.

In the past, we have taken some nonzero magnetostrictive metallic glasses (in ribbon forms) as samples, and measured their MI responses.[1,2] Two conclusions were reached:

(i) MI effect ($\Delta R/R$ and $\Delta X/X$) is always positive, as found by others;[3,4] and
(ii) at relatively low frequencies MI is mostly inductive, at relatively high frequencies it is resistive, and a crossover occurs at a characteristic frequency $f_0$ between them.

In this article, a more detailed discussion is given along this line, and the field-annealing effect on MI of a zero magnetostrictive glass is presented as an example.

## II. EXPERIMENTS

Amorphous VAC6030 ribbons, from Vacuumschmelze GmbH, were taken as samples. Although it is not our primary interest to compare the absolute changes of $\Delta R$ and $\Delta X$ due to field annealings, we tried to keep the sizes of all samples roughly the same: $20(l)\times 2(w)$ mm$^2$. The average thickness is $t \cong 23$ $\mu$m. The ribbon could be thinned in a 5% nital solution at a 0.38 $\mu$m/min rate.

The details of a MI measurement were described before.[1,2] The rms magnitude of the ac probe current at frequency $f$ is kept constant, $I$=4.8 mA. In this study, there were two kinds of quasistatic scans:

(i) the field scan ($|H| \leq 300$ Oe) at a fixed $f$ (Fig. 1), and
(ii) the frequency scan (10 kHz$\leq f \leq$10 MHz) either in a zero or saturating field.

Some samples were annealed at a temperature slightly below the Curie point ($T_c$=350 °C) in vacuum. During an anneal, a field of 300 Oe was applied either longitudinally ($\parallel$) or transversely ($\perp$) with respect to sample length. In the end, the samples were field cooled at a rate of 1–3 °C/min.

## III. RESULTS AND DISCUSSION

Since the sample is in a thin sheet form, MI behaviors are classified into two parts: one with $\delta > t/2$ and the other with $\delta < t/2$. $\delta \equiv (2\rho/\omega\mu)^{1/2}$ is the skin depth, $\rho$ is the dc resistivity, $\omega = 2\pi f$, and $\mu$ is the permeability of the material. In the former, since both the current and field penetrate through the sample (for $|z| < t/2$), the current distribution is $J(z)=J_0=I/(tw)$, independent of $z$, and MI is resistance limited. In the latter, as the current and field are attenuated, the current distribution becomes $J(z)=J_1 e^{-|z \pm (t/2)|/\delta}$, and MI is inductance limited. Obviously, when $f$ is scanned, there will exist a transition frequency $f_0$ from the resistance-

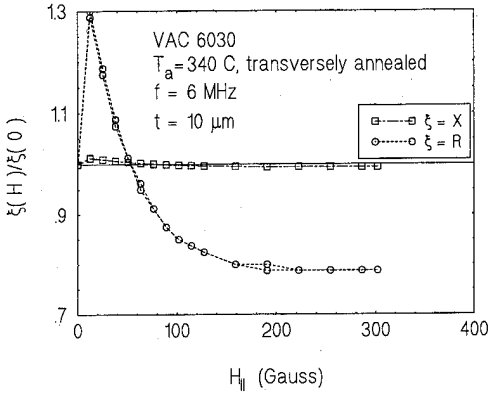



FIG. 1. A typical field dependence of MI in a thinned and field-annealed VAC6030 ribbon. Frequency $f$ of the ac probe current was fixed.

 0021-8979/96/79(8)/6552/3/$10.00 © 1996 American Institute of Physics

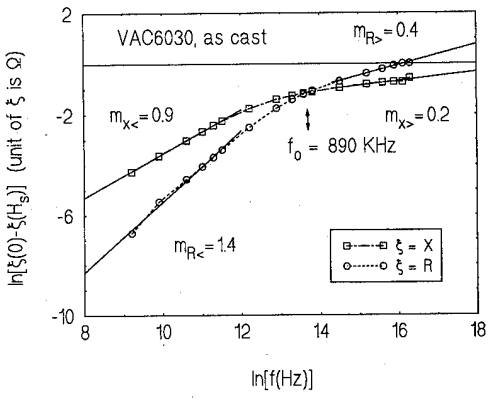



FIG. 2. $\Delta R=R(0)-R(H_s)$ and $\Delta X=X(0)-X(H_s)$, where $H_s$ is the saturation field. $\ln(\Delta R)$ and $\ln(\Delta X)$ are plotted as a function of $\ln f$, respectively, for the as-cast VAC6030. $f$ is the frequency of the probe current. $f_0$ is the characteristic frequency which shows the crossover from a inductive to a resistive MI.

limited to inductance-limited MI region, or vice versa. These features are evident in Fig. 2 and Table I. $f_0$ is equal to 890 kHz, 30 kHz, 8 MHz, and 400 kHz in the as-cast, $\perp$ annealed, $\parallel$ annealed, and $\perp$ annealed plus thinned VAC6030, respectively.

As is well known, MI effect is closely associated with the domain structures in the sample.[4,5] Meanwhile, the field anneal is the most common method used to orient stripe domains either perpendicular ($\perp$ anneal) or parallel ($\parallel$ anneal) to sample length.[6,7] In the $\perp$ annealed case, the circumferential field, generated by $I$, causes an S-shaped distortion for each domain wall.[5] The removal of quenched-in stresses and wall translations (at least the upper or lower part of a wall) would enhance the local $\mu$ value greatly.[8] As a result, $\delta$ is reduced more in $\perp$ annealed sample than in as-cast one for a fixed frequency (note, the small decrease of $\rho$ due to annealing is negligible). This explains why $f_0$ is shifted downward (from 890 to 30 kHz), when the as-cast case is compared with the $\perp$ annealed case; however, for the $\parallel$ annealed sample, the circumferential field acts in a hard-axis direction. The rotational permeability at high $f$ must be the smallest among the three cases (as cast, $\perp$, and $\parallel$).[7] Therefore, $f_0$ of $\parallel$ annealed sample is shifted upward from 890 kHz to 8 MHz. Furthermore, from the criterion $(t/2)=\delta=(2\rho/\omega_0\mu)^{1/2}$, it is easy to find the characteristic frequency $\omega_0=2\pi f_0=(8\rho/t^2\mu)$. Then, the shiftings of $f_0$ stated above are all in agreement with the predictions from the formula of $\omega_0$, and may be estimated quantitatively, if $\mu$ is known exactly. Similarly, in Table I we see that if a sample has been thinned from $t=23$ to 10 $\mu$m, and $\perp$ annealed, $f_0$ could be shifted back from 30 to 400 kHz as expected.

TABLE I. $f_0$ is the characteristic frequency, which separates the resistance-limited from the inductance-limited MI regions. $m_{X<}$, $m_{R<}$, $m_{X>}$, and $m_{R>}$ are the slopes from the fittings of the $\ln\Delta R$ (or $\ln\Delta X$) vs $\ln f$ plot. $<$indicates $t/2<\delta$, and $>$ indicates the opposite.

| VAC6030 | $f_0$(Hz) | $m_{X<}$ | $m_{R<}$ | $m_{X>}$ | $m_{R>}$ |
|---|---|---|---|---|---|
| $t=23$ $\mu$m as cast | 890 k | 0.9 | 1.4 | 0.2 | 0.4 |
| $t=23$ $\mu$m $\perp$ annealed | 30 k | ··· | ··· | 0.3 | 0.4 |
| $t=23$ $\mu$m $\parallel$ annealed | 8 M | 1.0 | 1.4 | ··· | ··· |
| $t=10$ $\mu$m $\perp$ annealed | 400 k | 0.8 | 1.8 | 0.5 | 0.6 |

In regard to the $f$ dependence of $\Delta R$ and $\Delta X$ in the $\delta>t/2$ region, Ref. 5 has shown that if walls are perpendicular to the current, $\Delta R\propto f^2$ and $\Delta X\propto f$. By a similar argument, ac domain rotations (in the $\parallel$ case) would also lead to a result that $\Delta R$ and $\Delta X$ are proportional to $\omega^2$ and $\omega$, respectively. From Fig. 2 and Table I, the slopes $m_{X<}$ and $m_{R<}$ are defined from the $\ln\Delta X$ vs $\ln f$ and $\ln\Delta R$ vs $\ln f$ plots for the as-cast sample. $<$ sign indicates the low-$f$ region to satisfy $t/2<\delta$. Conversely, $m_{X>}$ and $m_{R>}$ could also be found. The ellipses in Table I indicate that the corresponding $f_0$ has been shifted too close to either bound of the frequency measurement and that causes insufficient data for the fitting. For the as-cast sample, although $m_{X<}=0.9$ is close to 1, $m_{R<}=1.4$ is below the value 2, perhaps because the domain structures in the as-cast sample[9] are not all in agreement with the stripe domains assumed in the model. Nevertheless, for the $t=10$ $\mu$m and $\perp$ annealed sample, both the values of $m_{X<}$ and $m_{R<}$ agree with the predicted values respectively. The reasons are threefold:

(i) after $\perp$ anneal stripe domains are oriented properly;
(ii) since the circumferential field is proportional to sample thickness $t$, by thinning $t$ (and/or widening $w$) the wall displacement $\Delta x$ is further reduced for the same magnitude of the probe current; and
(iii) the model calculation in Ref. 5 is valid for small $\Delta x$, i.e., $|I|\ll I_{\text{sat}}=(4\sigma w)/(M_s t)$.

To discuss the skin-depth effect dominant region ($t/2>\delta$), a simple calculation shows that

$$R(f,H)\equiv R_{\text{dc}}(\mathscr{y}/2)[(\sinh\mathscr{y}+\sin\mathscr{y})/(\cosh\mathscr{y}-\cos\mathscr{y})]$$

and

$$X(f,H)=R_{\text{dc}}(\mathscr{y}/2)[(\sinh\mathscr{y}-\sin\mathscr{y})/(\cosh\mathscr{y}-\cos\mathscr{y})]+\omega L_e,$$

where $\mathscr{y}=t/(2\delta)$, $R_{\text{dc}}=\rho/t$, and $L_e$ is the external part of self-inductance of the sample. When $H\geqslant H_s$, the sample behaves like a nonmagnetic conductor; the domain effect has been eliminated. Therefore, no matter if the sample has been field annealed, $R(f,H_s)\simeq$const and $X(f,H_s)\propto\omega L_e$ as shown in Fig. 3. This is true as long as $t\leqslant 4\delta$. However, in the high-$f$ limit, we have

$$R(f,H)=R_{\text{dc}}(kf^{1/2})$$

and

$$X(f,H)=R_{\text{dc}}(k'f^{1/2})+2\pi fL_e,$$

where both $k$ and $k'$ are functions of $t$, $\rho$, and $\mu$, respectively. Since only $\mu$ or $\delta$ is a function of $H$, but $L_e$ is not, we find that in the high-$f$ region

$$\Delta R(f)\equiv R(f,0)-R(f,H_s)\propto f^{1/2}$$

and

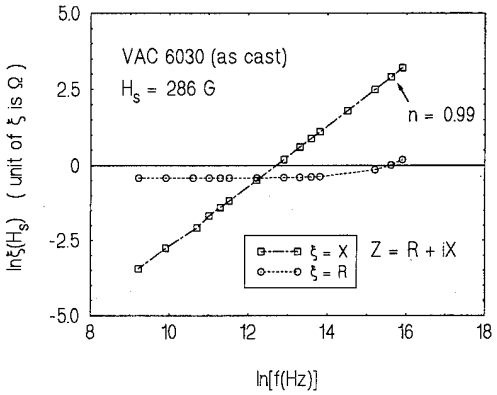



FIG. 3. The frequency dependence of $R(H_s)$ and $X(H_s)$ in an as-cast VAC6030 sample. $n$ is the slope of the $\ln[X(H_s)]$ vs $\ln f$ curve. $R(H_s)$ is almost independent of $f$.

$$\Delta X(f) \propto f^{1/2},$$

also. Hence, in the inductance-limited case, both $m_{X>}$ and $m_{R>}$ approach the same value 1/2. Table I has summarized all $m_{X>}$ and $m_{R>}$. Once again, for the thinner sample ($t$=10 $\mu$m), the agreement between experiment and theory is better.

Finally, Figs. 4 and 5 show the MI effect, $\Delta R/R$ and $\Delta X/X$, plotted as a function of $f$. Here, it is noted that since $l$ and $w$ of each sample were deliberately kept the same sizes, the absolute value of $R$ or $X$ does not vary more than 2% from one sample to another at a fixed $f$. On the other hand, the change of $\Delta R$ or $\Delta X$ due to field annealing is often more than 40%. Therefore, the trends observed in Fig. 2 for $\Delta R$ and $\Delta X$ agree with that in Figs. 4 and 5 for $\Delta R/R$ and $\Delta X/X$ in that a low-$f$ MI is inductive and at high-$f$ MI is resistive. Also, the variations of $\Delta R/R$ and $\Delta X/X$ because of thinning or field-annealing are in proportion to that of $\Delta R$ and $\Delta X$ for each $f$. The explanations have been given in Ref. 2. Since the

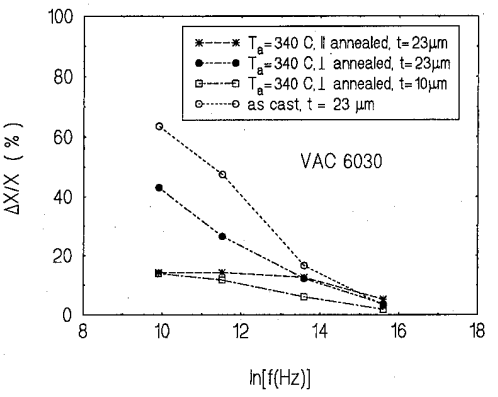



FIG. 4. Field-annealing effects on $\Delta X/X$ at various frequencies $f$. $T_a$ is the annealing temperature. A longitudinal (∥) or transverse (⊥) field was applied with respect to sample's length during annealings. $t$ is the thickness of the sample.

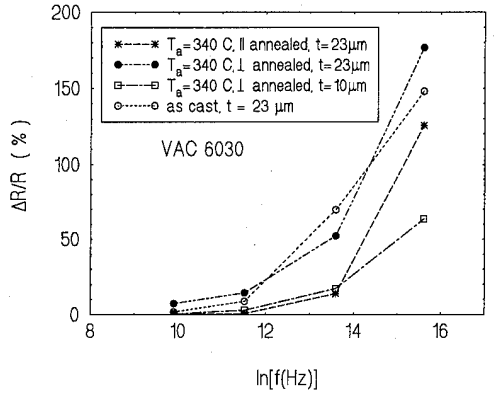



FIG. 5. Field-annealing effects on $\Delta R/R$ at various frequencies $f$. The rest of the notations are the same as in Fig. 4.

precautions have been taken, even if $\Delta R/R$ and $\Delta X/X$ may be a function $(l/w)$ or $(w/l)$, we think Figs. 4 and 5 do reflect the field-annealing effect, rather than other uncertainties from the variations of $l$ or $w$ among different samples.

## IV. CONCLUSION

Zero magnetostrictive VAC6030 samples have been field-annealed at $T$=340 °C. MI measurements were performed for each sample. The field-annealing effects on MI were studied. Those include

(i) how the characteristic frequency $f_0$ is shifted by various field annealings,
(ii) the $f$ dependence of $\Delta R$ and $\Delta X$ in the corresponding two frequency regions ($t/2 < \delta$ and $t/2 > \delta$), and
(iii) the changes of $\Delta R/R$ and $\Delta X/X$ due to different field annealings.

The existing models could partially explain the phenomena observed.

## ACKNOWLEDGMENT

We are thankful for the financial support, Grant No. NSC85-2112-M001-018, from the National Science Council of R.O.C.

[1] S. U. Jen and Y. D. Chao, in International Symposium on Metastable, Mechanically Alloyed and Nanocrystalline Materials, Quebec, Canada, 1995, paper PA-8.10.
[2] S. U. Jen and Y. D. Chao, in Ninth International Conference on Liquid and Amorphous Metals, Chicago, 1995, paper PA4.
[3] L. V. Panina, K. Mohri, K. Bushida, and M. Noda, J. Appl. Phys. **76**, 6198 (1994).
[4] R. S. Beach and A. E. Berkowitz, Appl. Phys. Lett. **64**, 3652 (1994).
[5] A. K. Agarwala and L. Berger, J. Appl. Phys. **57**, 3505 (1985).
[6] J. D. Livinston and W. G. Morris, J. Appl. Phys. **57**, 3555 (1985).
[7] H. J. de Wit and M. Brouha, J. Appl. Phys. **57**, 3560 (1985).
[8] Although we used the word "local" to indicate that the field generated by the probe current does not magnetize the sample globally, the local $\mu$ is equivalent to the conventional $\mu$, as long as the local part of a domain wall is considered.
[9] S. Tsukahara, T. Satoh, and T. Tsuhima, IEEE Trans. Magn. **MAG-14**, 1022 (1978); J. D. Livingston, Phys. Status Solidi A **56**, 637 (1979).

# Giant transversal magnetoimpedance and Hall-effect measurements in $Co_{70.4}Fe_{4.6}Si_{15}B_{10}$

K. C. Mendes,[a] F. L. A. Machado, L. G. Pereira, S. M. Rezende, and F. C. Montenegro
*Departamento de Física, Universidade Federal de Pernambuco, 50670-901 Recife, Pernambuco, Brazil*

M. V. P. Altoé and F. P. Missell
*Instituto de Física, Universidade de São Paulo, 01452-990 São Paulo, São Paulo, Brazil*

We report room-temperature transversal magnetoimpedance (TMI) and Hall-effect measurements performed in ribbons of the zero-magnetostriction soft-ferromagnet $Co_{70.4}Fe_{4.6}Si_{15}B_{10}$ alloy annealed at 587 K for 15 min at a dc magnetic field of 2 kOe. The annealing showed little effect on the magnetostriction of the samples. The frequency $f$ and the amplitude $I_{ac}$ of the current used in the measurements, and the measuring magnetic field $H$ were varied in the intervals $10 \leqslant f \leqslant 10^5$ Hz, $2.5 \leqslant I_{ac} \leqslant 25$ mA, and $-15 \leqslant H \leqslant 15$ kOe, respectively. The magnetic field dependence of the TMI shows a peak which is strongly dependent on $f$ and on $I_{ac}$. It reaches the giant value of 28% at $H=350$ Oe for $f=100$ kHz and $I_{ac}=25$ mA. This TMI giant value is of the same order of the giant longitudinal magnetoimpedance (GLMI) but its peak is positioned in a magnetic field two orders of magnitude larger than the value obtained for the GLMI. The Hall effect yielded a value of $R_S=0.43$ $\mu\Omega$ cm kOe$^{-1}$. Peaks which are also frequency dependent were observed at the Hall voltage. © *1996 American Institute of Physics.* [S0021-8979(96)58408-0]

## I. INTRODUCTION

Recently we showed that annealed amorphous $Co_{70.4}Fe_{4.6}Si_{15}B_{10}$ in an applied magnetic field $H$ exhibits sharp peaks in the longitudinal magnetoresistance.[1] The annealing plays a major role in the shape and size of the magnetoimpedance.[2] The magnitude of these peaks varies strongly with the frequency $f$ and with the amplitude of the ac current $I_{ac}$ used to measure the magnetoresistance. They have their magnitude increased either by increasing $f$ or $I_{ac}$, and reach giant values at low magnetic fields.[3,4] A $f$ and $I_{ac}$ dependence was also observed in the signal phase and the effect was later called giant magnetoimpedance (GLMI). More recently, GLMI was also observed in wires made of amorphous[5–9] and nanocrystalline[10] materials. These phenomena opened interesting questions on electronic transport and its interrelation to magnetic properties and made amorphous materials as strong candidates for applications in magnetic sensor technology.

The transverse field annealing induces an anisotropy which results in a regular pattern of domains aligned antiparallel to each other. This pattern can be seen by, e.g., Kerr-effect spectroscopy.[11] The GLMI in amorphous ribbons has its origin on the combined effect of domain rotation and domain-wall oscillations and the high permeability of this material. These effects are equally important to determine the frequency and magnetic-field dependences of the magnetoimpedance of samples with induced anisotropy. The oscillations are due to the coupling of the domains with the transverse in-plane ac magnetic field $h$ generated by the electrical current. The high permeability leads to a small skin depth even at low frequencies and the experiments essentially measure the surface impedance of the samples. A theoretical model based on this assumption allows one to calculate the magnetoimpedance with a good agreement with the experimental results.[12] Depending on the annealing and measuring conditions one can obtain a regular circular pattern of domain in wires with negative magnetostriction and the skin depth plays also an essential rule in determining the size and shape of the magnetoimpedance in these systems.[5–10]

As far as we know, up to now the giant magnetoimpedance effect has only been observed with the applied magnetic field $H$ parallel to the ac current (longitudinal magnetoimpedance). However, some technological applications require $H$ being applied perpendicularly to the plane of the ribbon. In this article we demonstrate the existence of a transverse magnetoimpedance effect in pieces of ribbons of $Co_{70.4}Fe_{4.6}Si_{15}B_{10}$. The effect of an ac current on the Hall effect and the changes in the magnetostriction due to annealing in samples under an applied magnetic field are also reported. Results for the $I_{ac}$ and $f$ dependencies of the peaks of the GLMI in magnetic field are included for comparison.

## II. SAMPLES AND TECHNIQUES

The samples were prepared by a melt-spinning technique in a He atmosphere. Pieces of a ribbon of $Co_{70.4}Fe_{4.6}Si_{15}B_{10}$ 11 mm long, 1 mm wide, and 40 $\mu$m thick were used throughout the experiments. The samples were annealed in a He atmosphere for 15 min at 587 K in a magnetic field of 2 kOe applied transverse to the length of the samples in the plane of the ribbon.

A modified small angle magnetization rotation technique[13,14] (SAMR) was employed to measure the magnetostriction of samples annealed in the same manner like those used in the magnetoimpedance and Hall-effect measurements.

The magnetoimpedance was measured using an ac four-probe technique. The four leads were attached to samples

[a]Permanent address: Faculdade de Ciência e Tecnologia, Universidade Estadual da Paraíba, 58100-001, Campina Grande, PB, Brazil.

 0021-8979/96/79(8)/6555/3/$10.00 © 1996 American Institute of Physics 

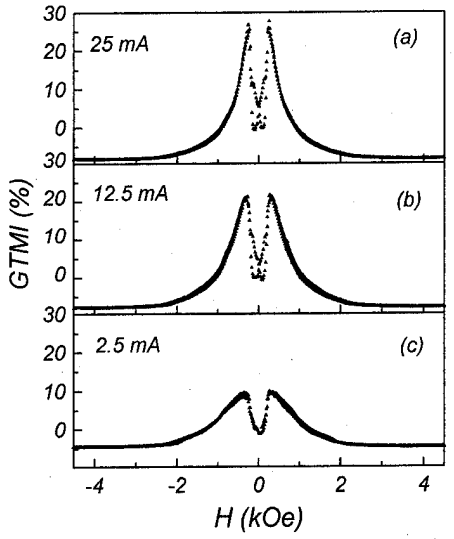



FIG. 1. Transversal giant magnetoimpedance (GTMI) vs applied magnetic field $H$ for three values of $I_{ac}$ and for $f=100$ kHz. The values of the GTMI are given in percent relative to the resistivity at zero applied magnetic field.

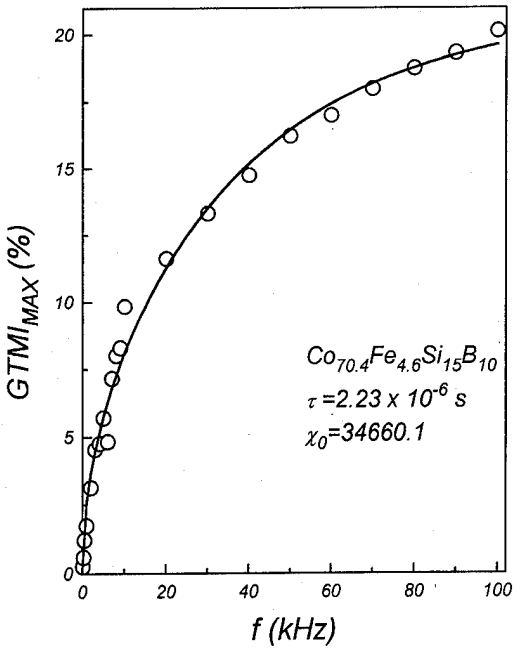



FIG. 2. Frequency dependence of the maximum value of the GTMI vs frequency for $I_{ac}=12.5$ mA. The solid line is a fit to a theoretical model.

cleaned with $HNO_3(10\%)$ using silver paint. Contacts with less than 1 Ω were obtained with this process. The magnitude and the phase of the magnetoimpedance were detected with a lock-in amplifier operating in the $Z$-Θ mode. A pair of Helmholtz coils generated the magnetic field used to measure the GLMI while the giant transversal magnetoimpedance (GTMI) was measured in a conventional magnet.

The Hall effect was measured with the four leads glued directly to the sample using silver paint. The measurements were made using ac current and the Hall voltage was also detected by a lock-in amplifier. The amplitude of the current was kept at 12.5 mA while its frequency was varied from 10 to $10^5$ Hz. The magnetic field was applied perpendicularly to the plane of the ribbon and its amplitude was swept in the interval $-15<H<15$ kOe.

## III. EXPERIMENTAL RESULTS

Figure 1 shows the transversal magnetoimpedance measured as function of the applied dc magnetic field $H$ for three values of current, namely, (a) 25, (b) 12.5, and (c) 2.5 mA, and for $f=100$ kHz. The GTMI is increased by increasing $I_{ac}$. The maximum value of the GTMI as a function of the frequency is plotted in Fig. 2. The solid line is a fit to Eq. (14) reported in Ref. 12,

$$Z=\frac{L}{2lc}\left(\frac{4\pi\rho\omega}{1+\omega^2\tau^2}\right)^{1/2}$$
$$\times[(1+\omega^2\tau^2+4\pi\chi_0)^2+(4\pi\chi_0\omega\tau)^2]^{1/4},$$

where $Z$ is the magnetoimpedance, $\chi_0$ is the static susceptibility, $\tau$ is the dynamical susceptibility relaxation time, $\rho$ is the resistivity, $L$ and $l$ are ribbon length and width, respectively, $c$ is the speed of the light, and $\omega$ is the angular frequency $(=2\pi f)$. The maximum of the GTMI measured as function of $I_{ac}$ for $f=100$ kHz is shown in Fig. 3. The value of the magnetic field where the GTMI reaches it maximum $(H_T)$ also depends on $I_{ac}$. This result is shown in the upper inset of Fig. 3. For small current values $H_T=500$ Oe while for higher currents it is about 350 Oe. The lower inset in Fig. 3 shows the $I_{ac}$ dependence of $H_L$ for the GLMI for three values of $f$. For lower frequencies the dependence on $I_{ac}$ is more pronounced for the GLMI.

Figure 4 shows the Hall resistivity measured for $-15<H<15$ kOe, $f=1$ kHz, and $I_{ac}=12.5$ mA. The lower and

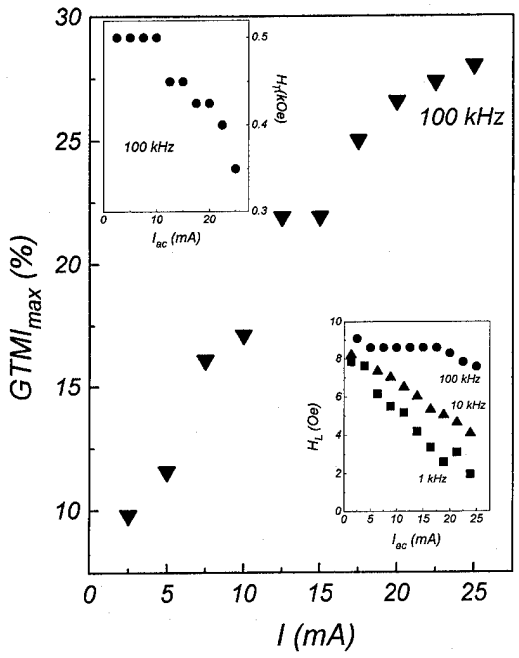



FIG. 3. Maximum value of the GTMI vs $I_{ac}$ for $f=100$ kHz. The values of the GTMI are given in percent relative to the resistivity at zero applied magnetic field. The upper inset shows the $I_{ac}$ dependence of $H_T$ (magnetic field corresponding to the maximum value of the GTMI) while the lower one shows the same dependence for $H_L$ for three values of $f$.

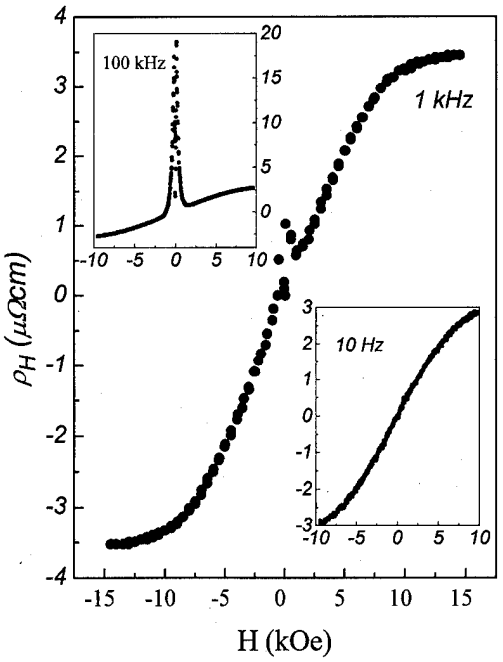



FIG. 4. Magnetic-field dependence of the Hall resistivity for $I_{ac}=12$ mA and $f=1$ kHz. Upper and lower insets show the results for $f=100$ kHz and 10 Hz, respectively. Peaks at the center of the curves are observed for $f=1$ and 100 kHz.

upper insets show the Hall resistivity for $f=10$ and $10^5$ Hz, respectively. Very large peaks which depend on the frequency of the current are also observed in the Hall effect. The Hall resistivity data yields $R_0=-0.02\ \mu\Omega\,\mathrm{cm\,kOe^{-1}}$ and $R_S=0.43\ \mu\Omega\,\mathrm{cm\,kOe^{-1}}$ for the ordinary and spontaneous Hall coefficients, respectively, obtained from the 1 kHz curve.

We also measured the magnetostriction of $Co_{75-x}Fe_xSi_{15}B_{10}$ for samples annealed in a magnetic field and as quenched for $2<x<6$. We found that annealing changes significantly the magnetostriction of the samples with positive or negative values. However, within the experimental resolution ($2\times10^{-8}$) we found no change in the magnetostriction of samples with zero magnetostriction ($x=4.6$).

## IV. DISCUSSION AND CONCLUSIONS

The overall shape and size of the GTMI peaks are quite similar to those observed for the longitudinal magnetoimpedance. Indeed, the $f$ and $I_{ac}$ dependencies for the GTMI maximum and the $I_{ac}$ dependence for $H_T$ show that the same physics is behind both cases. The results do also show that the model proposed in Ref. 12 is also valid for the transverse effect. In the model, the magnetoimpedance increases roughly with the square root of $f$ and the peaks shifts to lower $H$ by increasing $I_{ac}$. The deviation of the fit from the data observed in Fig. 2 for intermediate and high frequencies may be in part due to frequency-dependent contributions not taken into consideration in our model.[15] The main difference among the GTMI and the GLMI is the value of $H$ for which they attain their maximum values. $H_T=500$ Oe for the GTMI while $H_L=10$ Oe for the GLMI. This difference is mainly due to the demagnetizing field which is larger for $H$ applied perpendicular to the plane of the ribbon. These results were confirmed by measuring the magnetization versus $H$ curve in both cases.

Skew scattering and side-jump mechanisms yield a resistivity dependence on the anomalous Hall coefficient ($R_S=a\rho+b\rho^2$). This $\rho$ dependence was investigated in detail in magnetic multilayer systems which show giant magnetoresistance behavior.[16] The anomalous Hall effect in multilayers showed a strong correlation among $R_S$ and $\rho$ as expected from these two scattering processes. In our Hall resistivity results we also observed peaks quite similar to the ones present in the resistivity data. However, from these preliminary results it is quite difficult to distinguish, e.g., if its origin is on a pseudo-Hall effect from a small component of $H$ in the plane of the sample or if it is due to the $\rho$ dependence in $R_S$. In fact, from $R_S$ one would probably expect nonsymmetric peaks around $H=0$ since the magnetization changes sign when $H<0$ and $\rho$ is always positive. More experiments are underway to better clarify these points.

In short, we showed that giant magnetoimpedance can also be observed with $H$ applied perpendicularly to the plane of the ribbon (transverse magnetoimpedance). The $H$, $f$, and $I_{ac}$ dependencies for the GTMI are very similar to those observed for the longitudinal magnetoimpedance reported earlier. These results are somewhat important for magnetic sensor technology.

## ACKNOWLEDGMENTS

We thank C. S. Martins for annealing some of the samples used in this work and Professor Mario Engelsberg for making his high-magnetic-field facility available to us. Work partially financed by PADCT/FINEP, CNPq, FACEPE, and CAPES.

[1] F. L. A. Machado, B. Lopes da Silva, and E. Montarroyos, J. Appl. Phys. **73**, 6387 (1993).
[2] R. L. Sommer and C. L. Chien, Appl. Phys. Lett. **67**, 857 (1995).
[3] F. L. A. Machado, B. L. da Silva, S. M. Rezende, and C. S. Martins, J. Appl. Phys. **75**, 6563 (1994).
[4] F. L. A. Machado, C. S. Martins, and S. M. Rezende, Phys. Rev. B. **51**, 3926 (1995).
[5] R. S. Beach and A. E. Berkowitz, Appl. Phys. Lett. **64**, 3652 (1994).
[6] L. V. Panina, K. Mohri, K. Bushida, and M. Noda, J. Appl. Phys. **76**, 6198 (1994).
[7] K. V. Rao, F. B. Humphreys, and J. L. Costa-Kramer, J. Appl. Phys. **76**, 6204 (1994).
[8] R. S. Beach and A. E. Berkowitz, J. Appl. Phys. **76**, 6209 (1994).
[9] M. Knobel, M. L. Sanchez, J. Velazquez, and M. Vazquez, J. Phys. Condens. Matter **7**, L115 (1995).
[10] M. Knobel, M. L. Sanchez, C. Gomez-Polo, and A. Hernando, Phys. Rev. B (to be published).
[11] J. D. Livingston, W. G. Morris, and T. Jagielinski, IEEE Trans. Magn. **MAG-19**, 1916 (1983).
[12] F. L. A. Machado and S. M. Rezende (following paper at this conference).
[13] K. Narita, J. Yamasaki, and H. Fukunaga, IEEE Trans. Magn. **MAG-16**, 435 (1986).
[14] A. M. Severino, Ph.D thesis, Universidade de São Paulo, São Paulo, Brazil, 1993.
[15] L. V. Panina, K. Mohri, T. Uchiyama, and M. Noda, IEEE Trans. Magn. **MAG-31**, 1249 (1995).
[16] H. Sato, H. Henmi, Y. Kobayashi, and Y. Aoki, J. Appl. Phys. **76**, 6919 (1994), and references therein.

# A theoretical model for the giant magnetoimpedance in ribbons of amorphous soft-ferromagnetic alloys

F. L. A. Machado and S. M. Rezende
*Departamento de Física, Universidade Federal de Pernambuco, 50670-901 Recife-PE, Brazil*

Giant magnetoimpedance (GMI) measured in ribbons of the soft ferromagnet $Co_{75-x}Fe_xSi_{15}B_{10}$ annealed in the presence of a transverse magnetic field exhibits peaks in its field dependence. The GMI is strongly dependent on the magnitude of the longitudinal field and on the frequency of the applied current. We present a theoretical model which explains the existence of the peaks and its frequency dependence. The model is based on the skin depth effect and on the domain-wall motion due to the magnetic field and the ac current. © *1996 American Institute of Physics.* [S0021-8979(96)58508-9]

Amorphous ribbons and wires of soft ferromagnetic alloys have attracted considerable attention in recent years due to their unique physical properties and potential technological applications. One of the most interesting phenomena observed in these materials, is the frequency-dependent giant magnetoimpedance (GMI) exhibited by the low-magnetostriction alloy $Co_{75-x}Fe_xSi_{15}B_{10}$.[1–6] Particularly interesting is the sharp peak in the field dependence of the GMI in transversely annealed ribbons with concentration $x=4.6$.[1,2,6] In this article we present a model which explains the peak in magnetic field and its frequency dependence.

Figure 1 illustrates the experimental geometry used to observe the GMI effect in amorphous ribbons of CoFeSiB prepared by melt spinning techniques. The sample is previously annealed in a field applied in the ribbon plane, perpendicularly to the long direction. This is known to introduce a transverse anisotropy,[7–9] which results in a domain structure consisting of transverse stripe domains. The impedance $\mathbf{Z}=Z\exp(i\theta)$ is measured through an alternating current $I=I_0\exp(i\omega t)$ in the presence of a longitudinal magnetic field $H$. In alloys with composition $Co_{70.4}Fe_{4.6}Si_{15}B_{10}$, which have nearly zero magnetostriction, the variation of $Z$ with $H$ has a pronounced peak at fields of a few Oe. As a result, the magnetoimpedance ratio $\mathrm{MIR}=10^2[Z(H)-Z(0)]/Z(0)$, has a double peak structure. Figure 2(a) shows the peak on the positive $H$ part only. Furthermore, the MIR is a strong function of frequency $f=\omega/2\pi$, increasing continuously with $f$ up to around 100% at about 1 MHz.[6] Notice that in samples with concentration different than $x=4.6$, the MIR is also frequency dependent, but it does not have the double peak structure in field and has a much smaller maximum value.

Since the frequency dependence of the impedance in CoFeSiB with $x\neq 4.6$ has been previously explained by classical electrodynamics,[4] we use here a similar concept. The basic idea is that in a metal with very large initial transverse magnetic permeability $\mu_t$, the ac current is essentially confined to surface layers with thickness given by the skin depth,[10]

$$\delta=c\left(\frac{\rho}{2\pi\omega\mu_t}\right)^{1/2}, \tag{1}$$

where $c$ is the speed of light and $\rho$ the dc resistivity. For typical values $\rho=130\ \mu\Omega$ cm and $\mu_t=10^5$, the skin depth is $10<\delta<2000$ Å for $10^2<f<10^7$ Hz. These values are much smaller than typical ribbon thickness (50 $\mu$m), so that the current flows very near the upper and lower surfaces of the sample. Thus, the impedance of the sample is approximately[10]

$$\mathbf{Z}=(1-i)\frac{\rho L}{2l\delta}=\frac{(1-i)L}{2lc}(2\pi\rho\omega\mu_t)^{1/2}, \tag{2}$$

where $l$ and $L$ are the ribbon width and length, respectively. Equation (2) shows that the behavior of $Z$ with field and frequency is determined by the factor $\sqrt{\omega\mu_t}$, hence, it is dictated by the response of the domains to the longitudinal field $H$ and the ac current $I$.

Field dependence: The motion of the domain walls results from the combined effect of the external longitudinal field $H$ and the transverse field $h$ created by the current, $h=I/2t$, where $t$ is the ribbon thickness.[11] Since the current flows along the two surfaces, we analyze only the behavior of the domains on one surface. Assuming initially quasistatic conditions, the domain-wall displacement $x$ from the equilibrium configuration ($H=h=0$) and the directions of the domain magnetizations are obtained by minimizing the free energy density. This is the sum of the following terms:[12]

$$U_z=M_sH[(\alpha-1)\sin\phi_2-\alpha\sin\phi_1], \tag{3}$$

$$U_A=K[\alpha\sin^2\phi_1+(1-\alpha)\sin^2\phi_2], \tag{4}$$

$$U_{zt}=M_sh[(1-\alpha)\cos\phi_2-\alpha\cos\phi_1], \tag{5}$$

$$U_W=\tfrac{1}{2}kAx^2, \tag{6}$$

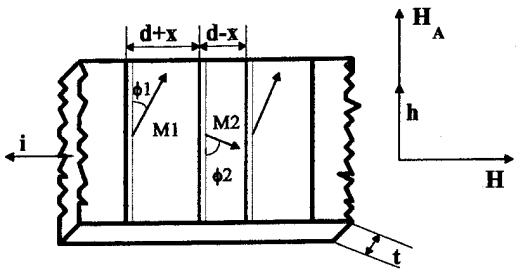



FIG. 1. Illustration of a piece of an amorphous ferromagnetic ribbon used for measuring magnetoimpedance. The magnetizations of the stripe domains, the relevant fields, and the probe current are also shown.

 0021-8979/96/79(8)/6558/3/$10.00 © 1996 American Institute of Physics

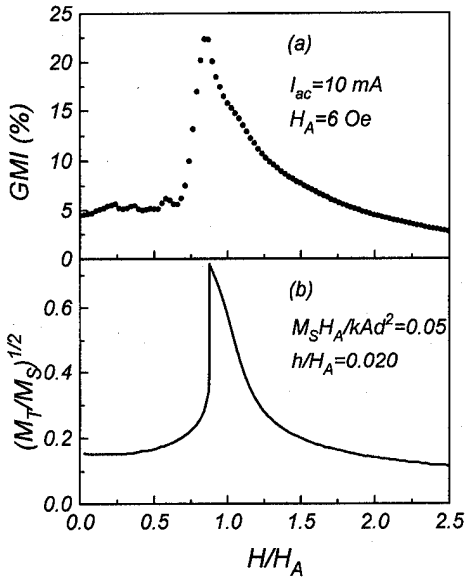



FIG. 2. Comparison between the giant magnetoimpedance ratio measured in Ref. 6 [Fig. 3(c)] in $Co_{70.4}Fe_{4.6}Si_{15}B_{10}$ and the relative impedance calculated with the theoretical model.

where $U_z$, $U_A$, $U_{zt}$, and $U_W$ are, respectively, the Zeeman, anisotropy, transverse Zeeman, and wall energy contributions; $\phi_1$ and $\phi_2$ are the angles between the two domain magnetizations and the easy axis direction induced by the transverse annealing, shown in Fig. 1; $\alpha=1/2+x/d$ is the fraction of the volume occupied by the domains at angle $\phi_1$; $M_s$ is the saturation magnetization; $K$ is the anisotropy constant; $A$ is the wall area per unit volume; and $k$ denotes the mean wall stiffness in a model in which the domain-wall energy is represented by a single parabolic potential. Note that the magnetoelastic energy has been neglected because we are mainly concerned with a nearly zero magnetostriction alloy.

The angles $\phi_1$ and $\phi_2$ and the wall displacement $x$ can be obtained by $\partial U/\partial\phi_1=\partial U/\partial\phi_2=\partial U/\partial x=0$. These equations yield analytical solutions in terms of the variables $H$ and $h$ and the material parameters $K$, $M_s$, $k$, $d$, and $A$. These solutions are

$$\cos^4\phi_1+2b\cos^3\phi_1-(1-g^2)\cos^2\phi_1 -2b\cos\phi_1-b^2=0, \tag{7}$$

$$\cos^4\phi_2-2b\cos^3\phi_2-(1-g^2)\cos^2\phi_2 +2b\cos\phi_2-b^2=0, \tag{8}$$

$$x=\frac{M_s}{kAd}\left(H(\sin\phi_1-\sin\phi_2)-\frac{H_A}{2}(\sin^2\phi_1-\sin^2\phi_2) +h(\cos\phi_2+\cos\phi_1)\right), \tag{9}$$

where $H_A\equiv 2K/M_s$ is the anisotropy field, $b\equiv h/H_A$, and $g\equiv H/H_A$. Solving Eqs. (7)–(9) we obtain $\phi_1$, $\phi_2$, and $x$ which are used to calculate the transverse susceptibility,

$$\chi_t=\frac{M_t}{h}=\frac{M_s}{h}\left(\frac{1}{2}(\cos\phi_1-\cos\phi_2) +\frac{x}{d}(\cos\phi_1+\cos\phi_2)\right). \tag{10}$$

Physically what happens is this: For zero current, $h=0$ and then $\phi_1=\phi_2$. In this case, as the longitudinal field increases, the two domains rotate with the same angle until $\phi_1=\phi_2=90°$ for $H=H_A$. The longitudinal magnetization increases linearly as $H$ varies from 0 to $H_A$, where saturation is reached, whereas the domain displacement and the transverse magnetization are always zero. However, for $h\neq 0$, $\phi_2$ increases more rapidly than $\phi_1$, resulting in $x\neq 0$ and a nonzero transverse magnetization. Figure 2(b) shows the square root of the transverse magnetization versus $H/H_A$ for $h/H_A=0.02$ (which corresponds to a current of 10 mA) and $M_sH_A/kAd^2=0.05$. The jump observed at a field value near $H_A$ is due a flipping of the domains pointing opposite to $h$, made possible by the fact that the anisotropy energy curve is almost flat at $\phi_2\simeq 90°$. Comparing (a) and (b) in Fig. 2 we see that the qualitative agreement between the results of the model and the data is quite good.

Frequency dependence: The frequency dependence of the transverse susceptibility can be obtained from the analysis of the domain dynamics. In a first approximation we assume that the domain dynamics is limited by the wall motion and not by the magnetization rotation. In this approximation the dynamics is not expected to vary with $H$. So we consider $H\ll H_A$, so that $\phi_1\simeq\phi_2\ll 90°$. In this case the force per unit volume acting on the domain walls is $-\partial U/\partial x\simeq 2hM_s/d - kAx$. Thus, the equation of motion for the domain walls is

$$m\frac{d^2x}{dt^2}=\frac{2hM_s}{d}-kAx+\gamma\frac{dx}{dt}, \tag{11}$$

where $m$ is the wall mass per unit volume and the last term is a domain-wall drag force introduced phenomenologically. Assuming an alternating transverse field $h\exp(i\omega t)$ generated by the ac current and neglecting the wall mass we obtain for the displacement

$$x=\frac{2M_s/d}{kA-i\omega\gamma}he^{i\omega t}. \tag{12}$$

Using Eq. (12) in Eq. (10) we obtain the transverse susceptibility

$$\chi_t=\frac{\chi_0}{1-i\omega\tau}, \tag{13}$$

where $\chi_0=4M_s^2/kAd^2$ is the static susceptibility and $\tau=\gamma/kA$ is the relaxation time. Similar expression for the dynamical susceptibility is being used[4,11] for different magnetic field and frequency regimes by choosing the appropriate $\tau$. With this result, the magnitude of the impedance in Eq. (2) becomes

$$Z=\frac{L}{2lc}\left(\frac{4\pi\rho\omega}{1+\omega^2\tau^2}\right)^{1/2}[(1+\omega^2\tau^2+4\pi\chi_0)^2 +(4\pi\chi_0\omega\tau)^2]^{1/4}. \tag{14}$$

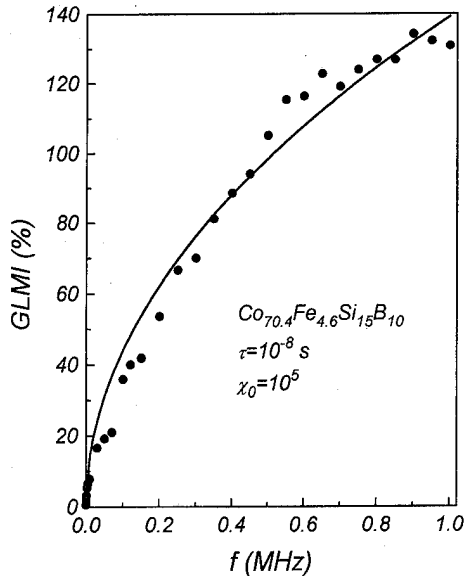



FIG. 3. Fit of the theoretical frequency dependence of the giant magnetoimpedance to the data of Ref. 6.

Figure 3 shows the fit of Eq. (14) to the data obtained for $Co_{70.4}Fe_{4.6}Si_{15}B_{10}$ at the peak of the MIR with the parameters $\chi_0=10^5$ and $\tau=10^{-8}$ s. Thus, the model also accounts very well for the frequency dependence of the GMI observed in this alloy.

The authors acknowledge helpful discussions with Professor A. D. Santos and with C. S. Martins and K. C. Mendes. This work has been supported by the Brazilian federal agencies Financiadora de Estudos e Projetos (FINEP), Conselho Nacional de Desenvolvimento Científico e Tecnológico (CNPq), Coordenação de Aperfeiçoamento de Pessoal de Nível Superior (CAPES), and Programa de Apoio ao Desenvolvimento Científico e Tecnológico (PADCT), and by the state agency Fundação de Amparo à Ciência e Tecnologia de Pernambuco (FACEPE).

[1] F. L. A. Machado, B.L. da Silva, and E. Montarroyos, J. Appl. Phys. **73**, 6387 (1993).
[2] F. L. A. Machado, B.L. da Silva, S. M. Rezende, and C. S. Martins, J. Appl. Phys. **75**, 6563 (1994).
[3] L. V. Panina and K. Mohri, J. Phys. Soc. Jpn. **18**, 245 (1994).
[4] R. S. Beach and A. E. Berkowitz, Appl. Phys. Lett. **64**, 3652 (1994).
[5] J. Ziman, B. Zagyi, and M. Konc, J. Magn. Magn. Mater. **145**, 129 (1995).
[6] F. L. A. Machado, C. S. Martins, and S. M. Rezende, Phys. Rev. B **51**, 3926 (1995).
[7] J. D. Livingston, W. G. Morris, and T. Jagielinski, IEEE Trans. Magn. **19**, 1916 (1983).
[8] J. D. Livingston and W. G. Morris, J. Appl. Phys. **57**, 3555 (1985).
[9] J. D. Livingston, W. G. Morris, and T. Jagielinski, J. Appl. Phys. **55**, 1790 (1984).
[10] J. D. Jackson, *Classical Electrodynamics* (Wiley, New York, 1975).
[11] L. V. Pavina, K. Mohri, T. Uchiyama, and M. Noda, IEEE Trans. **MAG-31**, 1249 (1995).
[12] P. T. Squire, J. Magn. Magn. Mater. **87**, 299 (1990).

*Published without author corrections*

# Superconducting properties of Fe-doped $YNi_2B_2C$

X. Z. Zhou, H. P. Kunkel, P. A. Stampe, and Gwyn Williams
*Department of Physics, University of Manitoba, Winnipeg, MB R3T 2N2, Canada*

The effects of Fe substitution for Ni in the intermetallic superconductor $YNi_2B_2C$ are reported. Samples of nominal composition $Y(Ni_{1-x}Fe_x)_2B_2C$ with $x=0.01$, 0.02, 0.05, and 0.1 have been prepared and subsequently characterized by x-ray diffraction, ac susceptibility, and resistivity/magnetoresistance measurements. A summary of these data is presented, and these are compared and contrasted with both the behavior previously reported for and the conclusions drawn from Fe and Co doping in this system. © *1996 American Institute of Physics.* [S0021-8979(96)41108-7]

Over the past year there have been several studies of the influence of substitutional transition metal replacement of Ni in the quaternary $YNi_2B_2C$ system, in particular by Fe[1] and Co.[1,2] One of the more interesting conclusions drawn from such studies is that Fe carries no moment in this host. Such a conclusion would not be unusual for the Ni sites prior to doping as Ni is unique amongst the $3d$ transition metals in that it never displays a stable moment in the single impurity limit when introduced into nonmagnetic metals.[3] Both Fe and Co are different; they frequently exhibit a long-lived local moment and ordering effects can be important at or below the 1 at. % level.[3]

Samples of nominal composition $Y(Ni_{1-x}Fe_x)_2B_2C$ with $x=0.01$, 0.02, 0.05, and 0.1 were prepared by arc melting appropriate quantities of starting materials [Y (99.9%), Ni (99.95%), Fe (99.98%), B (99%), and C (spec pure)], and the resulting buttons were homogenized by inverting and remelting them several times. Specimens of dimensions $(5\times1\times1)$ $mm^3$ (~30 mg) were cut from these buttons and subsequently annealed *in vacuo* at 1000 °C for 24 h followed by furnace cooling. Powder diffraction measurements on the $x=0.05$ sample confirm that its structure is the same as that of the undoped parent compound, in agreement with Ref. 1. ac susceptibility and (longitudinal) magnetoresistance data were acquired using previously described techniques.[4]

Figure 1 reproduces the ac susceptibility (measured at 2.4 kHz with an ac driving field of 50 mOe rms applied along the largest sample dimension) taken in zero static biasing field; here it can be seen that as the Fe concentration is increased so the superconducting transition temperature $T_c$ is progressively depressed and the width of the transition to the superconducting state broadens. These data—corrected for background and demagnetizing effects[4]—also indicate that these doped samples exhibit no more than about 90% shielding in contrast to the full shielding reported in the parent compound. Furthermore, this shielding decreases as the Fe doping increases, in contrast to the behavior reported[1] for Co doping. The zero-field resistivity data confirm both the depression of $T_c$ and the escalating transition width as the Fe content increases. These data also indicate that Fe substitution increases the residual resistivity (above $T_c$) at a rate of 3–4 $\mu\Omega$ cm/at. % Fe, an estimate that should, however, be regarded with some reservation as it is based on the subtraction of a substantial residual term (~16 $\mu\Omega$ cm) associated with the parent compound; the latter value cannot be attributed to either form factor uncertainties (since these have been calculated from measured lattice parameters)[1] or voids (not detected when cuts on arc-melted buttons were examined with an optical microscope), and while significant strains in polycrystalline specimens appear as a possible source, they do not result in noticeable x-ray line broadening. The residual resistivity quoted above is considerably larger than that (~3 $\mu\Omega$ cm) previously reported[5] for similarly prepared $YNi_2B_2C$ polycrystals; it is, however, comparable with that deduced[6] for $HoNi_2B_2C$ and much smaller than values quoted[6] for $TbNi_2B_2C$, $DyNi_2B_2C$, and[7] $LaRh_2B_2C$. Interestingly, in YPdBC higher residual resistivities have been associated with higher $T_c$ values. The longitudinal magnetoresistance is presented in Figs. 2 ($x=0.02$) and 3 ($x=0.05$); although *initially* not as sharp as the transition in the parent compound ($\Delta H$ for the 10%–90% width is 0.5 T at 10.7 K in the $x=0.02$ specimen, increasing to 0.85 T at 6.1 K in the

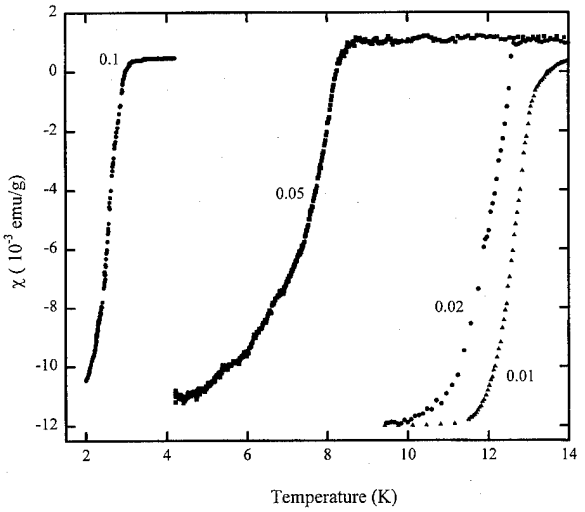



FIG. 1. The zero field ac susceptibility of the doped samples.

 0021-8979/96/79(8)/6561/3/$10.00 © 1996 American Institute of Physics 

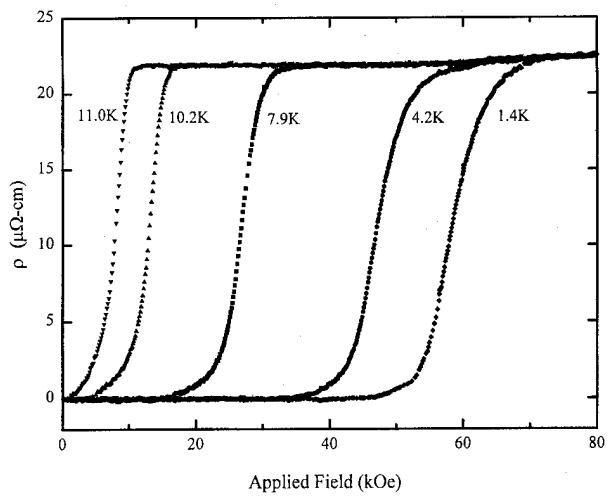



FIG. 2. The longitudinal magnetoresistance of the $x=0.02$ sample at various fixed temperatures.

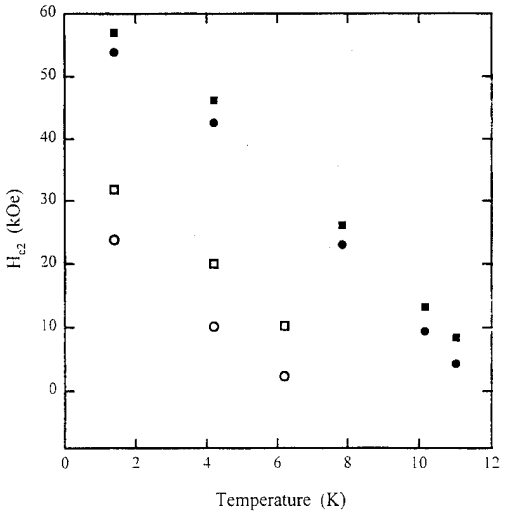



FIG. 4. The temperature dependence of $H_{c2}$ for the $x=0.02$ samples (solid symbols) and $x=0.05$ sample (open symbols) from point of maximum slope of the data in Figs. 2 and 3, respectively (squares) and the field for restoration of 10% of the normal state resistivity (circles).

$x=0.05$ sample, cf. 0.2 T at 13 K in the undoped system[4]), these transitions are sharper at the lowest measuring temperature in the doped specimens (at 1.5 K $\Delta H\sim 1$ T in both doped samples compared with some 2.2 T in the parent)[4]. However, the principal effect of these applied fields is to shift the transition. From these magnetoresistance data it is also possible to estimate the upper (resistive) critical field $H_{c2}$ (here, taken either as the field that restores 10% of the normal state resistivity or as the field at which $d\rho/dH$ is a maximum). Figure 4 summarizes the temperature dependence of these two estimates for the $x=0.02$ and 0.05 samples, respectively; as in the parent compound[4] the unusual feature in this figure is that there is little evidence of a saturation in $H_{c2}(T)$ even at the lowest measuring temperature, a feature that does not depend on the specific criterion used to estimate $H_{c2}(T)$. This behavior resembles that of nonoptimally doped cuprate superconductors.[8] A summary of the dependence of the superconducting transition temperature $T_c$ on Fe concentration from previous[1] and current work is presented in Fig. 5. The present data show less scatter than those of Bud'ko *et al.*,[1] although there is generally good agreement between the estimates for $T_c$ from susceptibility data in Ref. 1 and the present measurements; current data also extend to higher Fe concentration, a point returned to below. The dashed and solid lines in this figure are, respectively, fits to the depression of $T_c$ induced by spin fluctuations[9] and by a stable local moment[10] at the Fe site. The first model, also used to fit the suppression of $T_c$ below that of the host ($T_{c0}$) by Co substitution,[2] predicts that

$$\ln\left(\frac{T_c}{T_{c0}}\right)=-\frac{(\alpha+\beta)c}{g(1-\beta c)}, \tag{1}$$

where $c$ is the Fe concentration, $\alpha=N_i(E_F)/N(E_F)$ is the ratio of the impurity to the host density of states, while

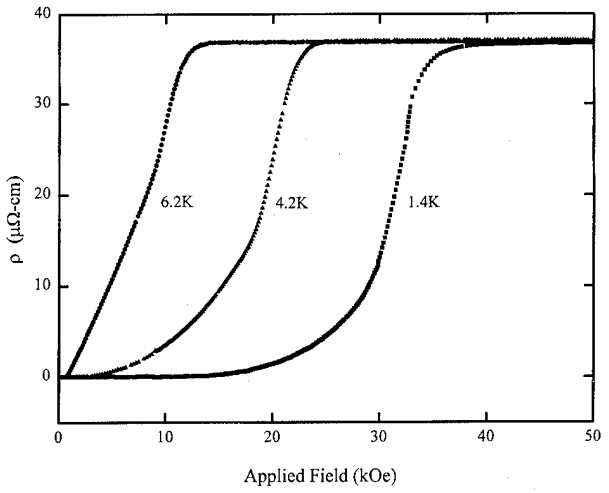



FIG. 3. As in Fig. 2, but for the $x=0.05$ specimen.

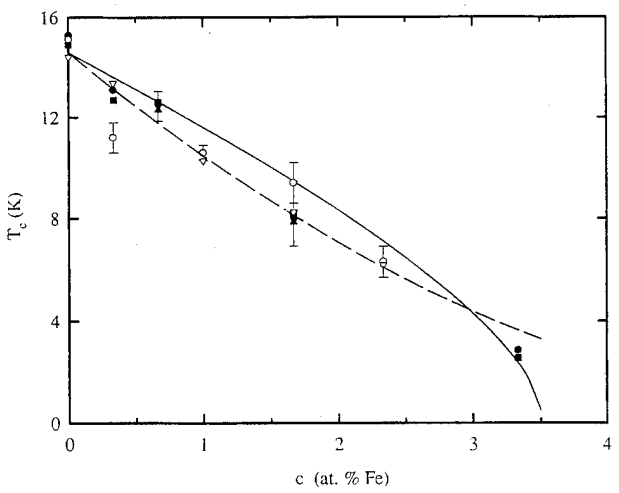



FIG. 5. The superconducting transition temperature [present data estimated from (■) susceptibility onset, (●) maximum in $d\chi/dT$, (▲) resistivity onset, (▼) maximum in $d\rho/dT$, open symbols, Ref. 1] plotted against Fe concentration. The lines are explained in the text.

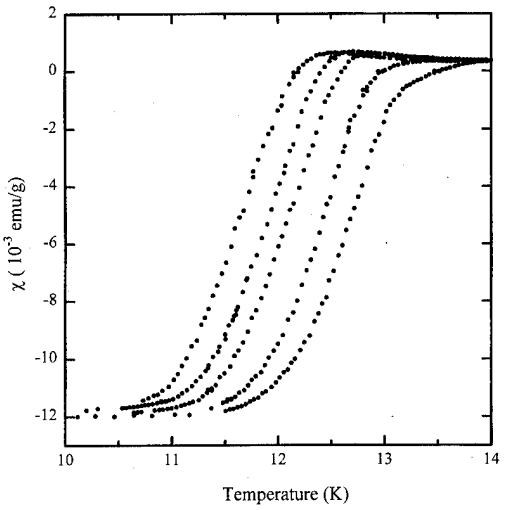



FIG. 6. The ac susceptibility of the $x=0.01$ specimen; the static biasing fields of 0, 100, 500, 750, and 1000 Oe increase from right to left.

$$\beta=\frac{N_i(E_F)^2 U_{\text{eff}}}{N(E_F)(2l+1)g}, \tag{2}$$

in which $U_{\text{eff}}$ is the intra-atomic Coulomb repulsion, $g$ the BCS coupling constant, and $(2l+1)$ accounts for orbital degeneracy. In the second approach

$$\ln\left(\frac{T_c}{T_{c0}}\right)=\Psi\left(\frac{1}{2}\right)-\Psi\left(\frac{1}{2}+\frac{0.14cT_{c0}}{c_0T_c}\right)\cdots, \tag{3}$$

in which $c_0$ is the critical Fe concentration for the complete suppression of superconductivity. $\Psi$ is the digamma function. While neither curve produces a completely convincing fit to these data, the dashed curve displays the opposite curvature to these data at the highest Fe concentration (the latter being associated with data acquired in the present study); this results in the spin-fluctuation model utilizing questionable parameter values of $U_{\text{eff}}\sim 2\times 10^6$ eV and $N_i(E_f)\sim 0.6\times 10^{-5}$ states/eV atom spin [based[11] on $N(E_f)=0.34$ states/eV atom spin and $g=0.27$]; nevertheless $N_i(E_f)\cdot U_{\text{eff}}>1$, so that the static Hartree–Fock criterion for a stable moment *is* satisfied at the Fe site. Recall that the suppression of $T_c$ with Co substitution[2] *is* consistent with the presence of spin fluctuations at the Co site, with $N_i(E_F)\cdot U_{\text{eff}}\simeq 1.06$. The solid line in this figure represents a fit based upon the stable moment model with $c_0=3.5$ at. % Fe ($x=0.105$) and appears to reproduce the curvature evident in the higher concentration data. While these indications that the Fe site supports either persistent spin fluctuations or a stable moment in this environment are admittedly indirect, there is some direct evidence supporting this suggestion; from Fig. 6—a plot of the field dependent ac susceptibility $\chi(H,T)$ in the $x=0.01$ sample—the presence of a small, temperature dependent paramagnetic signal can be seen in the region immediately above $T_c$. As the current indications run counter to those drawn by Bud'ko *et al.*[1] (based primarily on unpublished Mössbauer data), we suggest that there are still unresolved questions concerning the appropriate description of the effects of Fe doping in this host. An investigation of this problem using more sensitive probes is currently under way.

It is a pleasure to acknowledge the input of Professor B. W. Southern on the use of Eq. (1) and support from the Natural Sciences and Engineering Research Council of Canada.

[1] S. L. Bud'ko, M. Elmassalami, M. B. Fontes, J. Mondragon, W. Vanoni, B. Giordanengo, and E. M. Baggio-Saitovitch, Physica C **243**, 183 (1995).
[2] H. Schmidt, M. Muller, and H. F. Braun, Physica C **235-240**, 779 (1994).
[3] K. Fischer, *Landolt-Börnstein New Series Group III* (Springer, Berlin, 1982), Vol. 15, p. 289 et seq; essentially this means that a finite Ni concentration (ranging from a few to a few tens of at. %) is required to form a magnetically ordered ground state.
[4] X. Z. Zhou, H. P. Kunkel, P. A. Stampe, J. A. Cowen, and Gwyn Williams, Physica C **251**, 183 (1995).
[5] H. Takagi, R. J. Cava, H. Eisaki, J. O. Lee, K. Mizuhashi, B. Batlogg, S. Uchida, J. J. Krajewski, and W. F. Peck Jr., Physica C **228**, 389 (1994).
[6] H. Eisaki, H. Takagi, R. J. Cava, B. Batlogg, J. J. Krajewski, W. F. Peck Jr., K. Mizuhashi, J. O. Lee, and S. Uchida, Phys. Rev. B **50**, 647 (1994).
[7] R. J. Cava, T. Siegrist, B. Batlogg, H. Takagi, H. Eisaki, S. A. Carter, J. J. Krajewski, and W. F. Peck Jr., Phys. Rev. B **50**, 12966 (1994).
[8] A. P. Mackenzie, S. R. Julian, G. G. Lonzarich, A. Carrington, S. D. Hughes, R. S. Liu, and D. C. Sinclair, Phys. Rev. Lett. **71**, 1238 (1993); D. J. C. Walker, O. Laborde, A. P. Mackenzie, S. R. Julian, A. Carrington, J. W. Loram, and J. R. Cooper, Phys. Rev. B **51**, 9375 (1995).
[9] A. B. Kaiser, J. Phys. C **3**, 410 (1970).
[10] A. A. Abrikosov and L. P. Gor'kov, Sov. Phys. JEPT **12**, 1243 (1961).
[11] J. I. Lee, T. S. Zhao, I. G. Kim, B. I. Min, and S. J. Youn, Phys. Rev. B **50**, 4030 (1994).

# Magnetic properties of polycrystalline $Sm_{2-x}Ce_xCuO_{4-y}$ at high magnetic fields

R. F. Jardim, C. H. Westphal, and C. H. Cohenca[a)]
*Instituto de Fisica, Universidade de São Paulo, CP 66318, 05389-970, São Paulo, SP, Brazil*

L. Ben-Dor
*Department of Inorganic and Analytical Chemistry, Hebrew University, Jerusalem 91904, Israel*

M. B. Maple
*Institute for Pure and Applied Physical Sciences, UCSD, La Jolla, California 92093-0075*

We have performed measurements of ac magnetic susceptibility $\chi_{ac}$ as a function of temperature and magnetic field on polycrystalline specimens of $Sm_{2-x}Ce_xCuO_{4-y}$ ($0.15 \leqslant x \leqslant 0.18$) prepared from a sol-gel precursor. All the samples studied show a striking double resistive superconducting transition. One of the resistive transitions occurs at a higher temperature $T_{ci}$ and the other one at a lower Josephson-coupling temperature $T_{cj}$. Magnetic measurements reveal the appearance of superconductivity below $T_{cj}$ which is evident from the resistive component $\chi''$ which peaks only at $T_{cj}$. Measurements made on pellets and crushed samples with average grain size $\sim 1$ $\mu$m show essentially the same features. This suggests that Josephson coupling occurs inside physical grains with dimensions close to 5 $\mu$m. We have also utilized the behavior of the peak in the $\chi''$ component as a function of applied magnetic fields to build a $H$ vs $T$ phase diagram for these compounds. Some interesting features were observed in this $H$ vs $T$ phase diagram: (1) a $H^{\alpha}$, $\alpha=2/3$, dependence at low applied magnetic fields ($H \leqslant 2$ kOe) and high temperatures, and (2) an abrupt increase in the magnitude of the exponent at high fields and low temperatures. The behavior at low fields and high temperatures suggests that the magnetic response of the system is mainly controlled by a disordered Josephson network. Possible connections between these two different behaviors are discussed.
© *1996 American Institute of Physics.* [S0021-8979(96)01008-6]

The magnetic response of high-$T_c$ cuprates under applied magnetic fields is still object of some controversy. This seems to be also interesting when the compounds analyzed display the so-called double resistive superconducting transition. This unusual feature has been frequently observed in electrical resistivity $\rho(T)$ measurements carried out on polycrystalline samples of electron-doped superconductors with stoichiometries $Ln_{2-x}Ce_xCuO_{4-y}$; Ln=Nd, Pr, Sm; $0.13 \leqslant x \leqslant 0.20$.[1-6] Such a property is mainly observed when the zero resistance state is attained through two well-defined drops in the magnitude of $\rho(T)$.[1] The first drop, which occurs at an upper transition temperature $T_{ci}$, is attributed to a genuine superconducting phase,[1-6] and usually corresponds to an $\sim$25% fall in the magnitude of $\rho(T)$. Below this temperature, it is believed that the sample is comprised of small superconducting islands embedded in a nonsuperconducting host and $\rho(T)$ exhibits a well-defined plateau until reaching a lower transition temperature $T_{cj}$.[1,2] At this lower temperature, Josephson coupling develops between superconducting islands and a second $\sim$75% sharp drop in $\rho(T)$ is frequently observed. Such a drop ultimately leads the system to a zero resistance state. These features show certain similarities when compared with a disordered network of Josephson junctions.[1-6]

Such an explanation involving superconducting islands embedded in a nonsuperconducting host seems to be a useful tool in separating contributions from inter-and-intragrain properties. In addition, such a separation in these systems can be made by controlling both $T_{ci}$ and $T_{cj}$ by means of Ce doping[1,3,4,6] or oxygen removal.[7]

In this work, we will focus on additional properties of the disordered Josephson-coupled network shown in polycrystalline samples of $Sm_{2-x}Ce_xCuO_{4-y}$ ($0.15 \leqslant x \leqslant 0.18$)[4] obtained from a sol-gel precursor. We have performed measurements of ac magnetic susceptibility $\chi_{ac}$ as a function of temperature and applied magnetic fields in crushed samples, with average grain size $\sim 1$ $\mu$m, and pellets. We found that the resistive $\chi''$ component peaks only at the Josephson-coupling temperature $T_{cj}$ in both crushed and pellets samples, giving further evidence that superconductivity is mostly confined to small islands within grains. In addition, a field dependence of the $\chi''$ peak provided the behavior of the so-called irreversibility line in these compounds. We have found that the irreversibility line inferred from these experiments is characterized by an $\alpha=3/2$ power law near $T_{cj}$, but shows a crossover to a more rapid temperature dependence at low temperatures.

Polycrystalline samples of $Sm_{2-x}Ce_xCuO_{4-y}$ ($0.15 \leqslant x \leqslant 0.18$) were prepared using the sol-gel route. Further details of this chemical route and the reduction processes employed for these samples are given elsewhere.[2,8] All samples were characterized by x-ray diffraction using Cu $K_{\alpha}$ radiation on a Rigaku RU-200B diffractometer and had no additional phases except for the $x=0.18$ sample, which had small amounts of a $Sm_{1-x}Ce_xO_y$ spurious phase.[9]

Alternating current magnetic susceptibility $\chi_{ac}$ measurements, made on both crushed and bar-shaped samples, were performed with a mutual-inductance bridge operating at fre-

[a)]On a FAPESP (Brazil) fellowship Under Contract No. 95/2223-7.

 0021-8979/96/79(8)/6564/3/$10.00 © 1996 American Institute of Physics

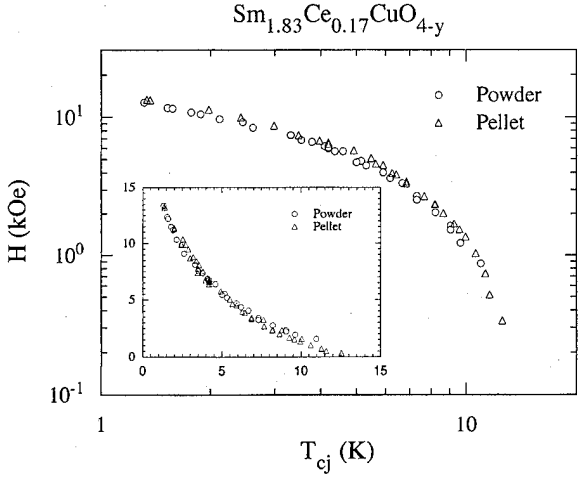



FIG. 1. A log-log plot of magnetic field $H$ vs $T_{cj}$ of a crushed sample and a pellet of polycrystalline $Sm_{1.83}Ce_{0.17}CuO_{4-y}$. The inset shows a $H$ vs $T_{cj}$ plot of the same data.

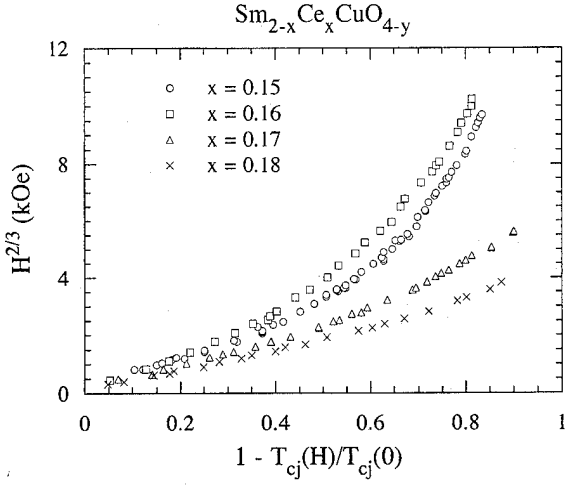



FIG. 2. Magnetic field $H^{2/3}$ dependence of the reduced Josephson-coupling temperature $[1-T_{cj}(H)/T_{cj}(0)]$. We have defined $T_{cj}(0)$ as the temperature at which $\chi''$ peaks in zero applied magnetic field. These measured values of $T_{cj}(0)$ are 17.5, 19.3, 13.5, and 10.6 K for samples of $Sm_{2-x}Ce_xCuO_{4-y}$ with $x=0.15$, 0.16, 0.17, and 0.18, respectively. A change of the exponent at low temperatures and high fields is observed and discussed in the text.

quencies $f$ in the range 17 Hz$\leq f\leq$5555 Hz and modulation fields $H_m$ in the range 0.01 Oe$\leq H_m\leq$17 Oe. External dc magnetic fields were produced with a NbTi superconducting magnet up to 35 kOe. We have defined the Josephson-coupling temperature $T_{cj}$ as the temperature where a peak in the $\chi''$ component is observed. The average grain size of both crushed samples and pellets were $\leq$1 and $\sim$5 $\mu$m, respectively.

It is useful to begin this discussion with the results of Fig. 1 which shows a log-log plot of $H$ vs $T_{cj}$ obtained on both crushed sample and pellet of a polycrystalline sample of $Sm_{1.83}Ce_{0.17}CuO_{4-y}$. As we have discussed previously,[10] the $\chi_{ac}(T)$ data of polycrystalline samples of electron-doped superconductors reveal the total absence of a peak in the $\chi''$ component at $T_{ci}$. Indeed, a well-defined peak in $\chi''$ has been only observed at the Josephson-coupling temperature $T_{cj}$.[10] Such a peak has been widely attributed to the so-called irreversibility line in these cuprates and often used for constructing $H$ vs $T$ phase diagrams. The first interesting feature of these curves is associated with the temperature dependence of the so-called irreversibility line in these compounds. It seems that, within the precision of our measurements, the behavior of the irreversibility line is coincident for both crushed samples and pellets. Such an experimental result has been observed in all samples studied and claims for an additional discussion.

Usually, the ac magnetic response $\chi_{ac}$ of polycrystalline samples of high-$T_c$ superconductors shows two well-defined peaks in the $\chi''$ component.[11] One of these peaks occurs at the temperature where the superconducting order parameter develops, i.e., at the mean-field critical temperature $T_c$ (or more appropriately $T_{ci}$ in samples with the double resistive superconducting transition). The second peak is believed to occur at a lower temperature $T_{cj}$, where the grains become coupled together through Josephson-coupling or proximity effect. Since the average grain size ($\sim$1 $\mu$m) of the crushed samples is significantly smaller than the physical grains ($\sim$5 $\mu$m), the peak in the $\chi''$ component would be mostly associated with Josephson coupling within physical grains. Such an experimental result is also important because it suggests that superconductivity in these polycrystalline samples would occur in small island and that the entire physical grains are not fully superconducting.

The presence of small superconducting islands with average size ranging between 10 and 300 Å in polycrystalline samples of electron-doped superconductors has been proposed recently.[3,4,6] According to Ref. 6, small superconducting islands, closely spaced, are interspersed with occasional large regions resulting in a morphology that accounts for the observed absence of a peak of the $\chi''$ component at $T_{ci}$,[10] and the observed absence of a significant diamagnetism above $T_{cj}$ in these compounds.[1–6] Also, at very low applied magnetic fields, there is no evidence of detectable differences between data taken on the crushed sample and pellet. Such a behavior suggests that, even at very low applied magnetic field, the "irreversibility line" of these compounds should be mainly governed by the intragrain Josephson coupling.

Values of $T_{cj}(H)$ were extracted from curves of $\chi''(T,H)$ and used to construct the $H^{2/3}$ vs $[1-T_{cj}(H)/T_{cj}(0)]$ plots shown in Fig. 2. In the low-field regime ($H\leq$2 kOe) and high temperatures, all the curves display the expected behavior of a disordered Josephson network, i.e., a quasi de Almeida–Thouless boundary line, where $H(T_{cj})=H_0[1-T_{cj}(H)/T_{cj}(0)]^{\alpha}$, $\alpha=1.5$, as discussed in Ref. 10. Careful analysis of the curves also reveals that the data are described well by this general relation. However, a change of exponent is easily observed in all samples studied. Such a change usually takes place at low temperatures and applied magnetic fields higher than $\approx$3 kOe. Fits of the data show that the exponent changes from $\alpha=1.5$ in the low-field regime to 3.5–1.8 in high fields. Indeed, the high-field exponent decreases monotonically with increasing Ce content. We found $\alpha=3.5$, 3.1, 2.4, and 1.8 for samples with Ce concen-

tration $x=0.15$, 0.16, 0.17, and 0.18, respectively. Indeed, no definite correlation between $H_0$ and the concentration of Ce in this series has been found.

Similar crossover or change in the exponent of the irreversibility line has been observed in polycrystalline and single-crystals samples of electron-doped superconductors.[12,13] It was found that such a change in the exponent of the irreversibility line is not only observed in the electron-doped superconductor $Sm_{1.85}Ce_{0.15}CuO_{4-y}$, but also in $Y_{1-x}Pr_xBa_2Cu_3O_{7-\delta}$, oxygen deficient $YBa_2Cu_3O_{7-\delta}$, and $Bi_2Sr_2CaCu_2O_{8+\delta}$.[12] Such an effect has been attributed to the onset of strong correlations in the flux line lattice at high magnetic fields, a universal feature of the irreversibility line of high-temperature superconductors.[12] Similar crossover has been also observed in single crystals of $Nd_{2-x}Ce_xCuO_{4-y}$ with $T_c$ varying from 7 to 19 K.[13]

The results shown in Fig. 2 show different features when compared with the ones described above. While the data seem to be similar to those observed in other high-$T_c$ cuprates, it is important to notice that our results were obtained on samples which exhibit the double resistive superconducting transition.[4] This suggests that, at least for low applied magnetic fields, the macroscopic response of the system would be mainly associated with the response of a disordered array of a Josephson network. The expected irreversibility line of such a system would show a de Almeida–Thouless behavior which is controlled by the intrinsic properties of the junctions, as observed in the experiments.[10]

A reasonable explanation for such a crossover would invoke a competition between inter-and-intragrain properties of these compounds. At low fields all the macroscopic response of these samples are controlled by the disordered array of Josephson junctions. Increasing magnetic field modifies all the properties of the superconducting islands and a crossover of the irreversibility line would be expected.

However, if this were the case, there are few points to be addressed. First of all, there is a change in the exponent of the irreversibility line as a function of Ce content in this series. It decreases from ~3.5 for the sample with $x=0.15$ to ~1.8 for the sample with $x=0.18$. This seems to be in complete agreement with the results obtained in single crystals of $Nd_{2-x}Ce_xCuO_{4-y}$ (Ref. 13) which showed a sample-dependent exponent of the irreversibility line at high magnetic fields. In our case, it seems that a sample dependent exponent would be associated with a different Josephson-coupling temperature. Furthermore, we have not found any systematic correlation between the exponent of the irreversibility line and the Ce content in this series. We plan to explore this point further.

In summary, from the temperature and field dependence of the $\chi''$ peak in pellets and crushed samples of $Sm_{2-x}Ce_xCuO_{4-y}$ ($0.15 \leq x \leq 0.18$), we found evidence that these systems are comprised of small superconducting islands coupled by Josephson junctions. An appropriate $H$ vs $T$ phase diagram reveals that the irreversibility line of these samples, at low fields and high temperatures, shows the expected exponent ($\alpha=1.5$) of a disordered Josephson junction array. Also, we have found a crossover to a more rapid temperature dependence at low temperatures and high magnetic fields. A detailed analysis of the irreversibility line shows no correlation between the exponent at high fields and the Ce concentration of these samples. It has been argued that such a crossover of the irreversibility line would be associated with inter-and-intragrain properties of these polycrystalline samples of electron-doped superconductors.

We have benefited from stimulating discussions with D. Stroud and M. C. de Andrade. This work was partially supported by the Brazilian Agencies FAPESP Under Grant No. 93/4204-4 and the Brazilian National Research Council (CNPq) Under Grant No. 400896/93-1. Work at University of California was supported by the DOE (USA) Under Grant No. DE-FG03-86ER45230. One of us (RFJ) is CNPq research fellow Under Contract No. 304647/90-0.

[1] E. A. Early, C. C. Almasan, R. F. Jardim, and M. B. Maple, Phys. Rev. B **47**, 433 (1993).
[2] R. F. Jardim, L. Ben-Dor, and M. B. Maple, J. Alloys Compounds **199**, 105 (1993).
[3] R. F. Jardim, M. C. de Andrade, E. A. Early, M. B. Maple, and D. Stroud, Physica C **232**, 145 (1994).
[4] R. F. Jardim, L. Ben-Dor, D. Stroud, and M. B. Maple, Phys. Rev. B **50**, 10080 (1994).
[5] R. F. Jardim, E. A. Early, and M. B. Maple, J. Alloys Compounds **221**, 1 (1995).
[6] E. A. Early, R. F. Jardim, C. C. Almasan, and M. B. Maple, Phys. Rev. B **51**, 8650 (1995).
[7] C. Geibel, A. Vierling, P. V. Aken, R. Eichert, A. Gravel, M. Rau, S. Horn, G. Weber, and F. Steglich, Physica C **185–189**, 591 (1991).
[8] P. A. Suzuki, R. F. Jardim, and S. Gama, J. Appl. Phys. **76**, 6585 (1994).
[9] R. F. Jardim, and M. B. Maple, Mater. Lett. **18**, 5 (1993).
[10] R. F. Jardim, C. Westphal, C. H. Cohenca, L. Ben-Dor, and M. B. Maple, J. Appl. Phys. **75**, 6720 (1994).
[11] See, for example, R. B. Goldfarb, M. Lelental, and C. A. Thompson, in *Magnetic Susceptibility of Superconductors and Other Spin Systems*, edited by R. A. Hein, T. L. Francavilla, and D. H. Liebenberg (Plenum, New York, 1992).
[12] C. C. Almasan, M. C. de Andrade, Y. Dalichaouch, J. J. Neumeier, C. L. Seaman, M. B. Maple, R. P. Guertin, M. V. Kuric, and J. C. Garland, Phys. Rev. Lett. **69**, 3812 (1992).
[13] M. C. de Andrade, Y. Dalichaouch, and M. B. Maple, Phys. Rev. B **48**, 16737 (1993).

# Thermal conductivity of $Bi_2Sr_2Ca_nCu_{n+1}O_x$ bulk superconductors in high magnetic fields (abstract)

S. C. Nakamae[a] and J. Schwartz[b]
*National High Magnetic Field Laboratory, Tallahassee, Florida 32306-4005*

The study of the thermal conductivity of high temperature superconductors can provide a theoretical understanding of the nature of the charge carriers, phonons, and scattering processes between them. From the technological point of view, thermal conductivity influences the growth rate of a local hot spot in a superconductor and therefore it is an important parameter in thermal stability analysis. Recently, the magnetothermal conductivity has been considered to be a key factor in the understanding of the vortex mechanisms. Here we report thermal conductivity measurements of bulk $Bi_2Sr_2Ca_nCu_{n+1}O_x$ superconductors in an applied magnetic field up to 20 T. The measurements are taken with field directions both parallel and perpendicular to the *a-b* plane of the samples for a wide range of temperatures. The phonon scattering mechanism at vortex sites, thermal transport mechanism in both *a-b* and *c* directions, as well as across grain boundaries will be discussed. © *1996 American Institute of Physics.* [S0021-8979(96)63508-0]

[a]Also at Department of Physics, Florida State University, Tallahassee, FL 32306.
[b]Also at Department of Mechanical Engineering, Florida State University and Florida A&M University, Tallahassee, FL 32306.

 0021-8979/96/79(8)/6567/1/$10.00 © 1996 American Institute of Physics 

# Cu spin reorientation in $Tl(BaSr)PrCu_2O_7$

W.-H. Li, Y. F. Lin, S. Y. Wu, W. T. Hsieh, and K. C. Lee
*Department of Physics, National Central University, Chung-li, Taiwan 32054, Republic of China*

J. W. Lynn
*Reactor Radiation Division, NIST, Gaithersburg, Maryland 20899*

C. C. Lai and H. C. Ku
*Department of Physics, National Tsing Hua University, Hsinchu, Taiwan 300, Republic of China*

The Cu spins in $TlBa_2PrCu_2O_7$ order at $T_N \approx 370$ K with a spin structure that is collinear and is characterized by the $\{\frac{1}{2}\frac{1}{2}1\}$ wave vector, where the nearest neighbor spins are aligned antiparallel along all three crystallographic directions. If 50% of the Ba atoms are randomly replaced by the smaller Sr atoms to form $Tl(BaSr)PrCu_2O_7$, the $T_N$ of the Cu spins reduces to 350 K but the magnetic structure that forms below $T_N$ is the same. However, at $T \approx 20$ K the Cu spins undergo a change in structure, and the spin arrangement is then characterized by the $\{\frac{1}{2}\frac{1}{2}\frac{1}{2}\}$ wave vector below $T \approx 12$ K. The ground state spin structure of the Cu ions in $Tl(BaSr)PrCu_2O_7$ is hence noncollinear, where the spin directions of the nearest neighbor Cu ions in the $ab$ plane remain collinear and antiparallel while along the $c$ axis they are orthogonal. These results demonstrate that the atoms in the BaO layers are also actively participating in the coupling between the Cu ions. © *1996 American Institute of Physics.* [S0021-8979(96)02808-9]

There are two copper–oxygen layers per unit cell in $TlBa_2PrCu_2O_7$, and both of them are the so-called "$CuO_2$-plane" layers in which O atoms are present between the Cu atoms along both the $a$ and $b$ axes.[1] Neutron diffraction measurements[2] have shown that the magnetic coupling between the Cu spins is antiferromagnetic in nature, and they order at $T_N \approx 370$ K with a spin structure that is identical to the "plane ordering" observed[3] in the 1:2:3 system where the nearest neighbor Cu spins are aligned antiparallel along all three crystallographic directions. The moment direction is in the tetragonal $ab$ plane with a saturated ordered moment $\langle \mu_z \rangle = 0.59\ \mu_B$, and this spin structure of Cu remains unchanged down to $T = 1.36$ K. Specific heat data[4] also show a sizable linear term that is comparable to that found in heavy fermion systems.

To study the role that the atoms in the BaO layers play in the Cu magnetism, neutron diffraction and $ac$ susceptibility measurements have been performed on the $Tl(BaSr)PrCu_2O_7$ compound, where 50% of the Ba atoms in $TlBa_2PrCu_2O_7$ have been replaced by Sr atoms. Structural analysis via high-resolution neutron diffraction has shown that the Ba and Sr atoms in $Tl(BaSr)PrCu_2O_7$ are randomly mixed in such a way that on average there are two $(Ba_{0.5}Sr_{0.5})O$ layers, rather than one BaO and one SrO layer, in a unit cell. The magnetic studies that we are reporting here show that the replacement of Ba atoms by Sr causes only a slight reduction in the ordering temperature of the Cu spins, but increases the saturated ordered moment by 50%, and alters the ground state spin structure of Cu ions.

A polycrystalline sample of $Tl(BaSr)PrCu_2O_7$ was prepared by the solid-state reaction from fine powders, and the details of the preparation procedure can be found elsewhere.[5] Neutron diffraction measurements on the combined powder samples were performed at the Research Reactor at the U.S. National Institute of Standards and Technology. The data were collected using the BT-9 triple-axis spectrometer operated in double-axis mode. A pyrolytic graphite PG(002) crystal was used to extract neutrons of energy 14.8 meV (2.351 Å). A PG filter was also employed to suppress higher order wavelength contaminations, and the angular collimations used were 40′-48′-48′. About a 10 g powder sample was mounted in a cylindrical aluminum can, and a pumped $^4$He cryostat was used to cool the sample.

Neutron diffraction patterns were taken at several different temperatures to study the intensity variations with temperature. Similar to what has been observed[3] in $TlBa_2Cu_3O_7$, the $\{\frac{1}{2}\frac{1}{2}1\}$ magnetic reflection that characterizes the Cu spin ordering is observed below 350 K. However, below $T \approx 20$ K this intensity was found to decrease. Figure 1 shows the difference between the diffraction patterns taken at $T = 15$ K and $T = 50$ K. The solid curve is a fit of the observed Bragg peaks to the Gaussian instrumental resolution function, with the dashed line being the base line, and the indices shown are based on the chemical unit cell. A negative amplitude was obtained for the $\{\frac{1}{2}\frac{1}{2}1\}$ peak, clearly indicating a reduction in the $\{\frac{1}{2}\frac{1}{2}1\}$ intensity as the temperature is reduced from 50 to 15 K, while the intensities of both the $\{\frac{1}{2}\frac{1}{2}\frac{1}{2}\}$ and $\{\frac{1}{2}\frac{1}{2}\frac{3}{2}\}$ reflections increase. Hence there is a change in the magnetic structure, with the magnetic unit cell doubling in size along the $c$ axis.

A more complete temperature dependence of the magnetic intensities is shown in Fig. 2, where the peak intensities of the $\{\frac{1}{2}\frac{1}{2}\frac{1}{2}\}$ and the $\{\frac{1}{2}\frac{1}{2}1\}$ reflections measured over a temperature range of 1.4 to 450 K are presented. Clearly, the $\{\frac{1}{2}\frac{1}{2}1\}$ intensity starts to develop at $T_N \approx 350$ K. This intensity increases on cooling in the usual way, and reaches saturation at $T \approx 220$ K. At $T \approx 20$ K, however, the $\{\frac{1}{2}\frac{1}{2}1\}$ intensity starts to decrease, and at low temperatures no significant magnetic intensity remains. This is accompanied by the development of the $\{\frac{1}{2}\frac{1}{2}\frac{1}{2}\}$ types of peaks, demonstrating that the Cu spins undergo a change in structure.

A half-integer value for the $c$ axis miller's index means that the magnetic unit cell is double the chemical one along that axis direction.[6] We note that in each chemical unit cell

 0021-8979/96/79(8)/6568/3/$10.00 © 1996 American Institute of Physics

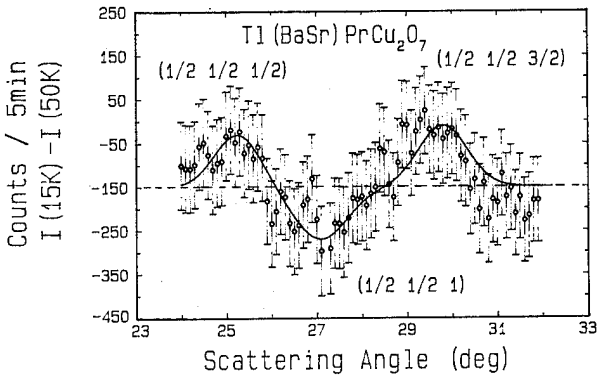



FIG. 1. The difference between the diffraction patterns taken at $T=15$ K and $T=50$ K. As temperature is reduced from 50 to 15 K, the $\{\frac{1}{2}\frac{1}{2}1\}$ intensity decreases while the intensities of the $\{\frac{1}{2}\frac{1}{2}\frac{1}{2}\}$ and $\{\frac{1}{2}\frac{1}{2}\frac{3}{2}\}$ reflections increase. The solid line is a fit to the Gaussian instrumental resolution function with the dashed line indicating the base line.

there is one Cu ion along the $a$ and $b$ axes while there are two along the $c$ axis.[1] The magnetic unit cell for the high-$T$ phase, which is characterized by the $\{\frac{1}{2}\frac{1}{2}1\}$ wave vector, hence contains two Cu ions along each crystallographic direction. The proposed Cu spin structure for the high-$T$ phase is a collinear one, where the nearest neighbor spins alternate in direction along all three crystallographic directions, as shown in Fig. 3(a). The moments lie in the $ab$ plane; however, its specific direction with the $ab$ plane cannot be determined from our powder measurements. In Fig. 3(a) we have simply chosen the moment direction of the Cu spins to be along the $a$ axis for clarity. This is the same Cu spin structure as the one observed for $TlBa_2PrCu_2O_7$,[2] $TlBa_2YCu_2O_7$,[7] and $NbBa_2NdCu_2O_8$.[8] Furthermore, by comparing the $\{\frac{1}{2}\frac{1}{2}1\}$ intensity obtained at $T=50$ K to the $\{001\}$ nuclear intensity, a saturated ordered moment of $\langle\mu_z\rangle=0.89\pm0.05\ \mu_B$ was obtained for the Cu ions. This value of the ordered moment is 50% larger than the 0.59 $\mu_B$ obtained for $TlBa_2PrCu_2O_7$.

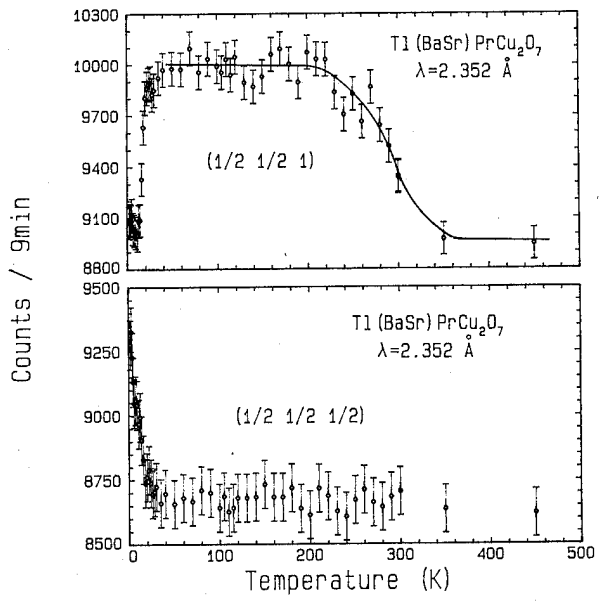



FIG. 2. Temperature dependence of the (a) $\{\frac{1}{2}\frac{1}{2}1\}$ and (b) $\{\frac{1}{2}\frac{1}{2}\frac{1}{2}\}$ intensities observed in $Tl(BaSr)PrCu_2O_7$. The ordering temperature of the Cu spins is determined to be $T_N\sim350$ K, and the solid curve is a guide to the eye only. The downturn in the $\{\frac{1}{2}\frac{1}{2}1\}$ intensity at low temperature is accompanied by the development of the $\{\frac{1}{2}\frac{1}{2}\frac{1}{2}\}$ intensity, and signifies a Cu spin reorientation to a new magnetic structure occurs in this temperature range.

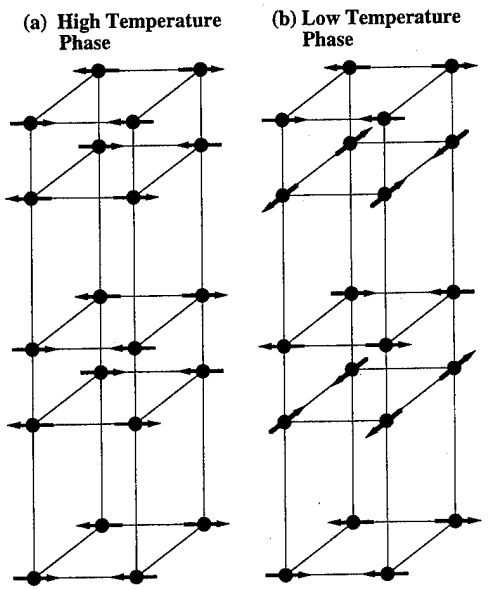



FIG. 3. The Cu spin configurations observed in $Tl(BaSr)PrCu_2O_7$ at (a) high and (b) low temperatures. At high temperatures the nearest neighbor Cu spins alternate along all three crystallographic directions, while at low temperatures the nearest neighbor Cu spins along the $c$ axis are orthogonal.

Below the second magnetic transition at 20 K the magnetic unit cell along the $c$ axis also becomes double the chemical one, which means there are four Cu ions along the $c$ axis in the magnetic unit cell. The simplest Cu spin arrangement along the $c$ axis is the one where the spin directions of the nearest neighbor Cu ions differ by 90°. The nearest neighbor spins along the $a$ and $b$ axes, on the other hand, remain antiparallel. This low-$T$ phase for the Cu spin structure is noncollinear and is shown in Fig. 3(b). The proposed spin structure is supported by the observed relative intensity between the $\{\frac{1}{2}\frac{1}{2}\frac{1}{2}\}$ and $\{\frac{1}{2}\frac{1}{2}\frac{3}{2}\}$ reflections, assuming the magnitude of the moments on the two $CuO_2$ layers are the same. Moreover, the value obtained for $\langle\mu_z\rangle$ using the $\{\frac{1}{2}\frac{1}{2}\frac{1}{2}\}$ intensity observed at $T=1.4$ K is the same value, within experimental accuracy, as the one obtained in the high-$T$ phase. This result further supports the argument that the downturn in the $\{\frac{1}{2}\frac{1}{2}1\}$ intensity together with the development of the $\{\frac{1}{2}\frac{1}{2}\frac{3}{2}\}$ intensity are simply due to Cu spin reorientation.

At intermediate temperatures, i.e., below 20 K and above 12 K, the Cu spin structure may be obtained by superimposing the structures of the high-$T$ and low-$T$ phases, with a weighting which depends on temperature. A noncollinear Cu spin structure such as the one found for the low-$T$ phase is still obtained in this temperature range, but the angle between nearest neighbor Cu spins along the $c$ axis varies continuously with temperature.

The ac susceptibility was measured using a Lake Shore 7221 ac susceptometer. Polycrystalline samples of ~1g were loaded into a cylindrical plastic container which has a height

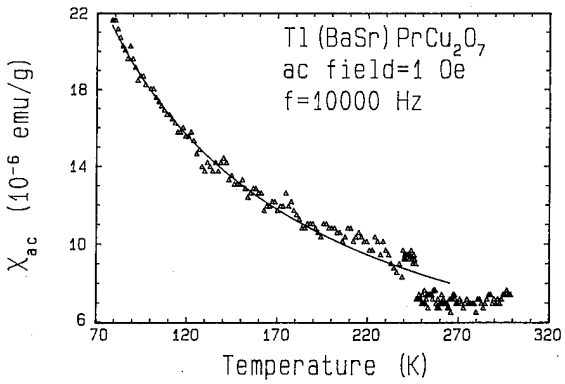



FIG. 4. Portion of the in-phase component of the ac susceptibility measured as a function of temperature. The solid line is a fitted Curie–Weiss curve using the data collected in the temperature range of 30–200 K. The susceptibility shows a sudden drop around 240 K, that signifies the Cu spin disordering.

much greater than its radius, and a conventional $^4$He flow cryostat was used to cool the sample, with a lowest achievable temperature of 4.5 K. Figure 4 shows a portion of the in-phase component of the *ac* susceptibility measured with a driving magnetic field of 1 Oe and frequency $10^4$ Hz. Measurements made using a different field strength or a different frequency generated the same results, indicating the Cu spin relaxation rate is far beyond the frequency used, as expected. The low-temperature portion of the data shown in Fig. 4 may be well described by the Curie–Weiss law, and the solid line shown is a fit of the data to $\chi_0+C/(T+\theta)$ for 30 K$<T<$200 K. This Curie–Weiss behavior signifies the paramagnetic state of the Pr spins, which order at $T\approx5$ K. Around 240 K, the susceptibility is seen to depart from the Curie–Weiss line shown, which is where significant Cu spin disorder begins to occur.

In summary, we have studied the Cu spin ordering in $Tl(BaSr)PrCu_2O_7$ by neutron diffraction and ac susceptibility measurements. By comparing the results obtained in the present study to that obtained previously[2] in $TlBa_2PrCu_2O_7$, it is clear that the atoms in the BaO layer are also actively participating in the magnetic coupling between the Cu ions, especially along the *c* axis. Although both the Ba and Sr ions have a valence state of 2+, replacing $Ba^{2+}$ by the smaller $Sr^{2+}$ should still lead to a modification of the hybridization among the atoms in the unit cell. The present studies show that the coupling between the Cu spins along the *c* axis is affected more strongly by the substitution than those in the *ab* plane. As 50% of the Ba atoms are replaced by Sr atoms, the $T_N$ of the Cu spins is only slightly reduced, while the ground state spin structure is changed from a collinear spin state into a complicated noncollinear spin state. It would be interesting to see how the Cu spin structure is changed by different degrees of substitution.

The research at the NCU was supported by the National Science Council of the Republic of China under Grant No. NSC 84-2112-M-008-021.

[1] T. Manako, Y. Shimakawa, Y. Kubo, T. Satoh, and H. Igarashi, Physica C **156**, 315 (1988).
[2] W. T. Hsieh, K. J. Chang, W.-H. Li, K. C. Lee, J. W. Lynn, C. C. Lai, and H. C. Ku, Phys. Rev. B **49**, 12200 (1994).
[3] W-H. Li, J. W. Lynn, H. A. Mook, B. C. Sales, and Z. Fisk, Phys. Rev. B **37**, 9844 (1988).
[4] P. A. Lee, T. M. Rice, J. W. Serene, L. J. Sham, and J. W. Wilkins, Comm. on Solid State Phys. XII **3**, 99 (1986).
[5] C. C. Lai, B. S. Chiou, Y. Y. Chen, J. C. Ho, and H. C. Ku, Physica C **202**, 104 (1992).
[6] G. E. Bacon, *Neutron Diffraction*, 3rd ed. (Oxford University Press, Oxford, 1975).
[7] J. Mizuki, Y. Kubo, T. Manako, Y. Shimakawa, H. Igarashi, J. M. Tranquada, Y. Fujii, L. Rebelsky, and G. Shirane, Physica C **156**, 781 (1988).
[8] N. Rosov, J. W. Lynn, H. B. Radousky, M. Bennahmias, T. J. Goodwin, P. Klavins, and R. N. Shelton, Phys. Rev. B **47**, 15256 (1993).

# Alternating current susceptibility studies of Tb ordering in $Pb_2Sr_2TbCu_3O_8$

S. Y. Wu, W.-H. Li, and K. C. Lee
*Department of Physics, National Central University, Chung-li, Taiwan 32054, Republic of China*

T. H. Meen and H. D. Yang
*Department of Physics, National Sun Yat-Sen University, Kaohsiung, Taiwan 80424, Republic of China*

The magnetic response of the Tb spins in $Pb_2Sr_2TbCu_3O_7$ to the applied magnetic field have been studied by ac susceptibility measurements. Both the in-phase component $\chi'$ and the out-of-phase component $\chi''$ of ac susceptibility are found to be sensitive to the frequency but not to the strength of the driving field. At high temperatures $\chi'$ exhibits Curie–Weiss behavior, it departs from this behavior as the magnetic correlations between the Tb spins develop, and a cusp which is typical of antiferromagnetic ordering is clearly revealed at lower temperatures. The correlated Tb spins respond "better" to a driving magnetic field which has a lower frequency. The relative maximum of the $d\chi'/dT$ versus $T$ plot matches to the $T_N$ determined using neutron diffraction measurements. This relative maximum continues to occur at the same temperature as the frequency of the driving field is varied. It, however, shifts to a lower temperature as a dc external field is applied, indicating the antiferromagnetic coupling between the Tb spins are weaken by the dc field. Moreover, the thermal behavior of $\chi''$ exhibits a well-defined peak around the transition temperature, and a dc field of strength 5 kOe smears the peak. © *1996 American Institute of Physics.*
[S0021-8979(96)02908-5]

The magnetic interactions between the Tb spins in $Pb_2Sr_2TbCu_3O_8$ are two-dimensional (2D) and antiferromagnetic (AF) in nature. The 2D magnetic correlations between the Tb spins develop below $T\approx 9$ K, and they order two dimensionally at $T_N\approx 5.3$ K. Even at $T=1.36$ K the magnetic correlations are still mainly 2D, with nearest neighbor spins within the $ab$ plane aligned antiparallel.[1] The 2D nature of the Tb spins mainly originates from the crystallographic structure, where the Tb atoms form an orthorhombic sublattice with $a\approx b$ and $c\approx 4a$.[2,3] Highly anisotropic magnetic interactions between the Tb ions are hence anticipated, and 2D magnetic behavior is expected. In comparison to its isostructural compounds $Pb_2Sr_2RECu_3O_8$ (RE=rare earth), the $T_N\approx 5.3$ K for the Tb spins is lower than the $T_N\approx 8$ K for Pr,[4] but is much higher than $T_N\approx 2.4$ K for Gd.[3] It is clear that the $T_N$ for Tb is much higher than expected based on purely dipolar interactions, and likely exchange interactions are responsible for the Tb ordering.

The measurement of ac susceptibility remains one of the most powerful methods in studying the response of spin systems to an applied magnetic field.[5] Both the in-phase component $\chi'$ and the out-of-phase component $\chi''$ of the ac susceptibility characterize the energy exchange between the spin system and the ac field. The in-phase component reflects the response of the system to the ac field, while the out-of-phase component corresponds to the dissipation signal.[6] In this article we present the results of the ac susceptibility measurements performed on polycrystalline $Pb_2Sr_2TbCu_3O_8$ compound with and without an applied external dc field. Our aim is to study the response of the Tb spins to different driving frequencies.

Polycrystalline samples of $Pb_2Sr_2TbCu_3O_8$ were prepared by solid-state reaction from fine powders. The details of the preparation procedure can be found elsewhere.[3] The samples were characterized using x-ray diffraction and the diffraction pattern taken at room temperature is well described by the orthorhombic $Pb_2Sr_2YCu_3O_8$ structure.[2] The ac susceptibilities were measured using a Lake Shore 7221 ac susceptometer, which is capable of measuring both the in-phase and out-of-phase components of the susceptibility driving by ac fields ranging from 0.1 to 25 Oe rms with frequencies from 1 to $10^4$ Hz. A dc magnetic field with strength up to 1 T may also be applied. Powder samples of ~1 g were loaded into a cylindrical plastic container which has a height much greater than its radius, and a conventional $^4$He flow cryostat was used to cool the sample, with a lowest achievable temperature of 4.5 K.

The ac susceptibility was measured over a temperature range of 4.3–320 K using driving fields of strength 1 Oe at various frequencies. Measurements made using a different strength for the driving field generated essentially the same results. At high temperatures, the thermal behavior of $\chi'$ is well described by the Curie–Weiss law $C/(T+\theta)$ that signifies the paramagnetic state of the Tb spins. A small temperature independent term $\chi_0'$, however, is also needed in describing the data, and this term is found to depend weakly on the frequency of the driving field.[7] At low temperatures, on the other hand, a cusp which characterizes the antiferromagnetic ordering[1] of the Tb spins is clearly revealed. A comparison of the response of the Tb spins to different driving frequencies is shown in Fig. 1, where the $\chi'$ measured at three different frequencies with $\chi_0'$ has been subtracted from the data were plotted against temperature.

Above ~16 K, $\chi'-\chi_0'$ obtained at different frequencies agree very well, and this agreement holds up to the highest temperature studied of $T=320$ K. The solid line shown in Fig. 1 is the fitted Curie–Weiss curve using the data obtained at 30 K$\leqslant T\leqslant$320 K (not shown). The effective moment $\mu_{\text{eff}}$ that we obtained using the fitted value for the Curie–Weiss constant $C$ is 8.64(3) $\mu_B$, which is about 10% smaller than the value of 9.72 $\mu_B$ expected for $Tb^{3+}$ free ions. This discrepancy likely originates from crystal field effects. More-

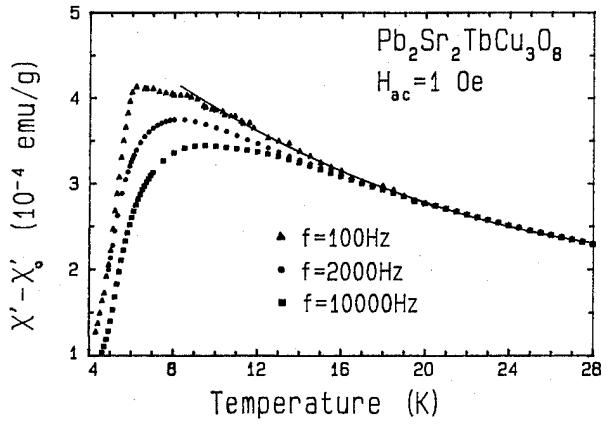



FIG. 1. Frequency dependence of the thermal behavior of $\chi'$ measured at zero dc field. The data were plotted with the temperature-independent term subtracted. The solid line is the fitted Curie–Weiss curve using the data obtained at 30 K$<T<$320 K.

over, a value of $\theta$=21 K was obtained from the fit for Curie–Weiss temperature. This is the temperature at which $\chi'$ departs from the Curie–Weiss behavior, and below which $\chi'-\chi'_0$ measured at different frequencies begin to show discrepancies. The observed frequency-independent character of the Curie–Weiss behavior indicating that the relaxation rate of the paramagnetic Tb spins is far beyond the driving frequency used, as expected. The correlated Tb spins, on the other hand, respond differently to different driving frequency. They respond "better" to a lower frequency, as the cusp goes higher when lower driving frequency was used. This frequency-dependent behavior indicates that the relaxation rate of the correlated Tb spins is somehow far below that of the paramagnetic Tb spins.

Figure 2 shows the effect of dc field on $\chi'$, where the data were taken using a driving field of 1 Oe rms and frequency 100 Hz. At high temperatures, no obvious change on $\chi'$ was found due to the present of dc fields with strength up to 1 T, that indicating 1 T may not be strong enough to alter the paramagnetic Tb spins. At low temperatures, however, the cusp which characterizes the Tb spins ordering is affected by the dc field. Figure 1(a) clearly shows that the cusp shifts slightly upward, its maximum moves to a lower temperature as a dc field was applied. We note that the temperature at which $\chi'$ shows a maximum is not the ordering temperature of the Tb spins, rather it is the temperature at which $d\chi'/dT$ shows a maximum that matches to the ordering temperature determined from neutron diffraction measurements.[8] Figure 2(b) shows the temperature dependence of $d\chi'/dT$ obtained at various dc field, where well-defined peaks are clearly seen. As dc field was increased, however, the peak broadens and its maximum shifts to a lower temperature. The maximum of $d\chi'/dT$ at a zero dc field occurs at $T$=5.3 K, which is consistent with the ordering temperature measured by neutron diffraction.[1] This maximum shifts to 4.8 K as a dc field of 1 T was applied. These behavior suggests that the antiferromagnetic coupling between the Tb spins have been weakened by the dc field.

Portions of the temperature behavior of $\chi''$ measured at different dc fields are shown in Fig. 3, where the data were

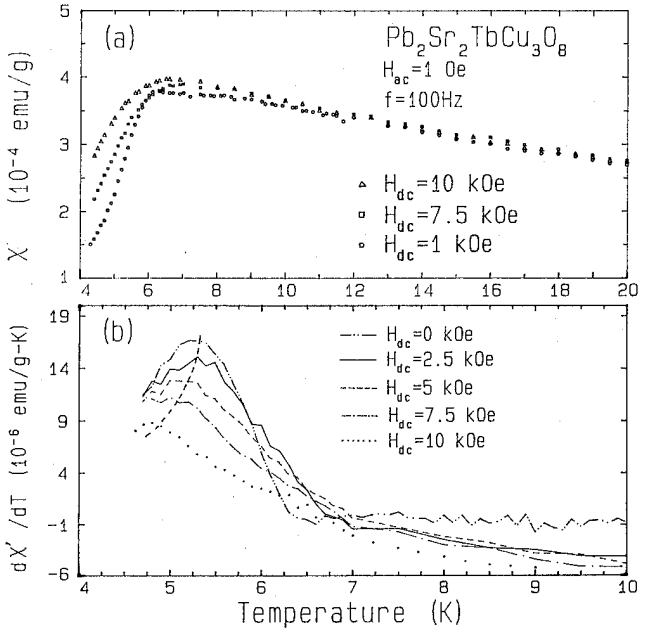



FIG. 2. The low-temperature portion of the thermal behavior of (a) $\chi'$ and (b) its temperature derivative $d\chi'/dT$ measured with dc fields applied. The relative maximum of $d\chi'/dT$ shifts to a slightly lower temperature as dc field was increased.

taken using a driving field of 1 Oe rms and frequency 100 Hz. At high temperatures, where Tb spins are completely disordered, and at low temperatures, where the Tb spin order, $\chi''$ almost remains at constant. Only in the temperature range where transition occurs $\chi''$ departs from the constant value and exhibits a peak in its thermal dependence. The peaks shown in Fig. 3 may be described by Lorentzian functions. At zero dc field, the maximum of $\chi'$ occurs at a temperature slightly above the ordering temperature. As dc field is applied the peak shifts to a slightly higher temperature, the width increases, and the amplitude decreases. A dc field of strength 0.5 T almost washes out the peak. Figure 4 shows the integrated dissipation signal as a function of the applied dc field, where the data were obtained by integrating over the peaks shown in Fig. 3. Clearly, the ac loss over the transition

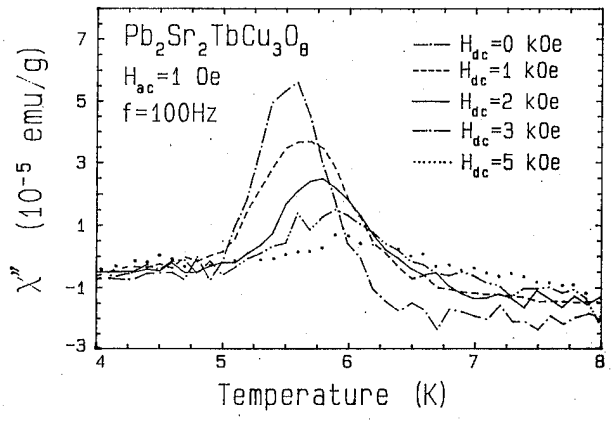



FIG. 3. Temperature dependence of the dissipation signal $\chi''$ measured at different dc fields. At zero dc field, the thermal behavior of $\chi''$ exhibits a well-defined peak; a dc field of 0.5 T then smears the peak.

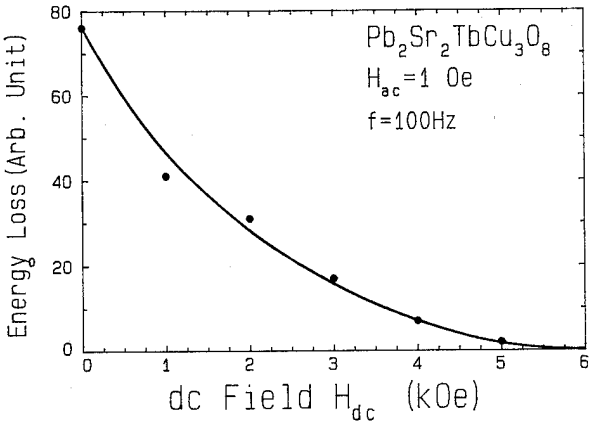



FIG. 4. The integrated ac losses plotted as a function of temperature. The solid curve is a fit to the exponentially decaying function.

decreases with an increasing dc field, and the rate of decrease may be described by an exponentially decaying function. The solid curve shown in Fig. 4 is a fit to $A_0 \exp(-\alpha H_{dc})$.

In summary, we have studied the response of Tb spins in $Pb_2Sr_2TbCu_3O_8$ to a weak ac magnetic field, with and without an additional dc field was applied. The ordered Tb spins are found to be sensitive to the frequency but not to the strength of the driving field, while the paramagnetic Tb spins are not sensitive to the frequency nor to the strength. These results suggesting that the relaxation time of the correlated Tb spins are relatively long in comparison with the uncorrelated Tb spins. The relative maximum of $d\chi'/dT$, which matches to the ordering temperature determined by neutron diffraction, shifts to a slightly lower temperature as a dc field is applied, indicating the antiferromagnetic coupling between the Tb spins has been weakened by the dc field. It would be interesting to see how strong a dc field is needed to flip the correlated Tb spins over to a direction perpendicular to the field.

The research at the NCU was supported by the National Science Council of the Republic of China under Grant No. NSC 84-2112-M-008-022, and the research at the NSYSU was supported by the National Science Council of the Republic of China under Grant No. NSC 84-2112-M-110-005.

[1] S. Y. Wu, W. T. Hsieh, W-H. Li, K. C. Lee, J. W. Lynn, and H. D. Yang, J. Appl. Phys. **75**, 6598 (1994).
[2] J. Cava *et al.*, Nature **336**, 211 (1988).
[3] K.-W. Liaw, T.-H. Meen, Y.-C. Chen, W.-H. Lee, and H. D. Yang, Jpn. J. Appl. Phys. **32**, 1225 (1993).
[4] W. T. Hsieh, W-H. Li, K. C. Lee, J. W. Lynnn, J. H. Shieh, and H. C. Ku, J. Appl. Phys. **76**, 7124 (1994).
[5] See, for example, *Magnetic Susceptibility of Superconductors and Other Spin Systems*, edited by R. A. Hein, T. L. Francavilla, and D. H. Liebenberg (Plenum, New York, 1991).
[6] C. P. Slichter, *Principles of Magnetic Resonance*, 2nd ed. (Springer, New York, 1978).
[7] A 5% increase in $\chi_0'$ was found as the frequency of the driving field was changed from 100 to 10 000 Hz.
[8] S. Y. Wu, W-H. Li, K. C. Lee, J. W. Lynn, T. H. Meen, and H. D. Yang (preprint).

# Field dependence of magnetic relaxation in BiPbSrCaCuO superconductors

V. Raposo, A. G. Flores, M. Zazo, L. Torres, and J. Iñiguez
*Departamento de Física Aplicada, Universidad de Salamanca, E-37071 Salamanca, Spain*

Magnetic relaxation in ceramic cylindrical samples of BiPbSrCaCuO high $T_c$ superconductors has been studied as a function of applied magnetic field for a constant decay rate of that field strength. We have analyzed the variation of the ac susceptibility versus time just after removing the magnetic field. Data have been obtained by means of an inductive technique from 1 to 3600 s, with magnetic fields that range from 10 to 100 Oe, and by switching off the field at a constant rate of 25 Oe/s. The field dependence of the thermally activated parameters has been obtained within the framework of the Anderson–Kim theory and using the so-called box distribution of energies. Anderson–Kim considered a logarithmic decay of the magnetic flux governed by an effective energy $U=U_0-FVX$, where $U_0$ is the pinning energy, $V$ is the activation volume, $X$ the pinning length, and $F$ the driving force density. In this case we have found a field dependence of the form $H^{-n}$ for the pinning energy, with $n$ close to 2 and temperature dependent. However, we have observed that the box distribution, which assumes the existence of a continuous energy spectrum, shows no field dependence for the effective energy. © *1996 American Institute of Physics.* [S0021-8979(96)41208-3]

## I. INTRODUCTION

Magnetic relaxation studies in high $T_c$ superconductors (HTSCs) have received considerable attention from many researchers.[1–6] These studies help us to understand the bulk properties of superconductors and also reveal information about vortex dynamics and flux distribution within these materials. Magnetic relaxation can be studied by analyzing the time evolution of magnetic susceptibility.

The Anderson and Kim theory,[7,8] developed by Beasley *et al.*,[9] shows that the time evolution of the magnetization is logarithmic following a change in the external magnetic field. In conventional type-II superconductors this evolution is related to the decay of persistent currents, caused by the thermally activated jumps of vortices over their pinning barriers.[7] This effect is thought to be small in conventional superconductors, but in HTSCs with higher critical temperatures it can be important. However, initial nonlogarithmic behavior has been found in HTSCs, which is assumed to be caused by the transient diffusion redistribution of the magnetic flux over the sample after the change in the applied magnetic field.[10] This kind of dependence can be represented by introducing a time constant $\tau$ to describe the initial stage.[10] The value of $\tau$ depends on the macroscopic parameters such as geometry and also on the decay rate of the applied magnetic field.

Another way to explain thermally activated processes is to suppose the existence of an exponential decay obeying Debye kinetics. In HTSCs this model is introduced using distributions of activation energies because the theory assumes that a single process is too simple for these kinds of materials.[3] There are several distributions to be used, but a box distribution has proved to give similar results to that of a gaussian distribution and is far simpler.

In this work, we have studied the time evolution of the ac susceptibility in polycrystalline samples of BiPbSrCaCuO HTSCs cooled in different magnetic fields, just after removing the field. We have analyzed the field dependence of the energies involved in relaxation processes for both models. We have fitted our relaxation data to Anderson–Kim's model and we have found a field dependence of the pinning energy $U_0$ of the form $H^{-n}$. In the case of a box distribution, no field dependence for the effective activation energy box has been found.

## II. EXPERIMENT

The ceramic samples of $Bi_{1.7}Pb_{0.3}SrCa_{1.8}CuO_x$ were prepared from the appropriate mixtures of high purity BiO, PbO, SrCO, CaCO, and CuO. The powders were milled and prefired for 14 h in air at 800 °C. The mixture was dry pressed in a cylindrical die, preheated at 845 °C for 72 h and then sintered at 850 °C for 200 h in air. The data reported here were obtained using samples of cylindrical shape, 10 mm in length and 5 mm in diameter.

Susceptibility measurements were performed with the help of a computer-aided system based on the use of an automatic bridge that registers the complex mutual inductance of two coils wound around the specimen under test.[4] The real ($\chi'$) and imaginary ($\chi''$) parts of the complex magnetic susceptibility can be determined from the mutual inductance.[5] The magnetic field is controlled with a programmable dc power supply connected to the computer which allows us to change the field and the decay rate. Although the real and imaginary parts are easily obtained, we have only used the data from the real part for the fits because the signal to noise ratio is better.

Magnetic relaxation takes place when there is a change in the external magnetic field. It can be studied by cooling the sample in a magnetic field and then switching off the field, or cooling without a field and then applying it. In the first case we talk about flux expulsion while in the second case we study flux penetration.[1] Relaxation depends on the magnitude of the magnetic field and the decay rate, and consequently these parameters must be carefully controlled during the experiment. In our measurements the sample was cooled from the normal state under a longitudinal dc field to the chosen temperature, and when the required stability is attained [better than 0.03 K (Ref. 4)], the magnetic field is switched off with a constant decay rate of 25 Oe/s which can

 0021-8979/96/79(8)/6574/3/$10.00 © 1996 American Institute of Physics

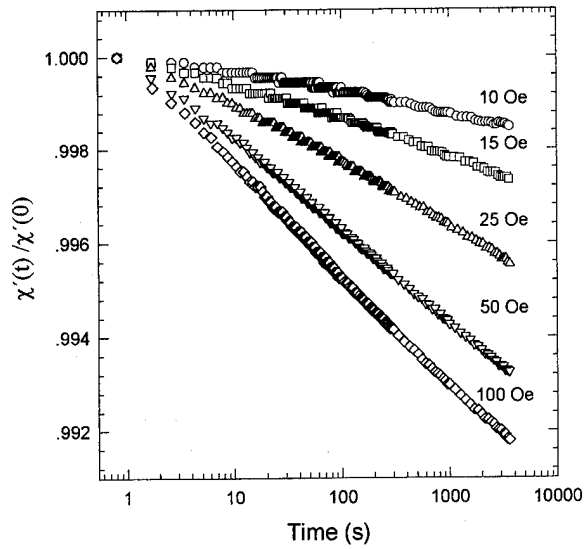



FIG. 1. Time evolution of the real part of the magnetic susceptibility for different magnetic fields at 82 K (frequency=20 kHz and $h_{ac}$=1.2 Oe).

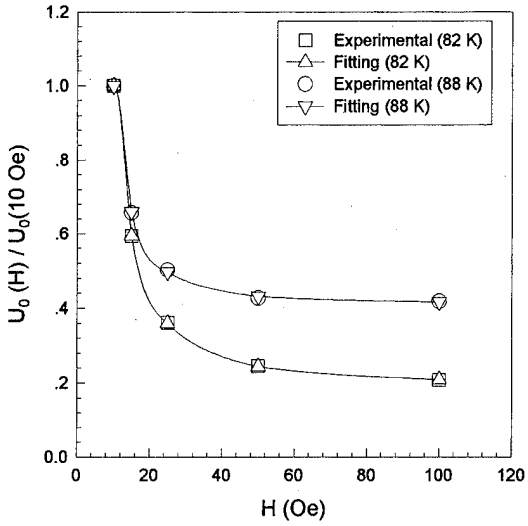



FIG. 2. Field dependence of the pinning energy at $T$=82 K and $T$=88 K. Values are normalized to $U_0$(10 Oe, 82 K) and $U_0$(10 Oe, 88 K), respectively.

be considered an average value in the literature.[10] The first measurement is taken 1 s after the field reaches 0 and data are recorded up to 3600 s. We have measured the relaxation for different temperatures by cooling the samples under magnetic dc fields of 10, 15, 25, 50, and 100 Oe.

## III. RESULTS AND DISCUSSION

The relaxation study in our samples has been carried out by analyzing the time evolution of the ac susceptibility. Figure 1 shows a typical result of the real part of ac susceptibility normalized to the first datum point, versus time when the sample is cooled in different magnetic fields. The variation of the ac susceptibility with time has been analyzed using the Anderson–Kim theory[7,8] that predicts a logarithmic time dependence for the relaxation of the magnetic susceptibility which can be written in the form:

$$\chi(t)=\chi_0\left[1-\frac{kT}{U_0}\ln\left(1+\frac{t}{\tau}\right)\right], \tag{1}$$

where $\chi_0$ is the real part of the magnetic susceptibility at time $t=0$, and $\tau$ is a macroscopic time constant that depends on the sample geometry and the decay rate of the applied magnetic field.[9] $U_0$ is the activation energy of the barrier in the absence of any flux gradient (pinning energy), $T$ is the temperature, and $k$ is the Boltzmann constant. Thermally activated motion of vortices is assisted by the driving force density $F$, which is a function in our cylindrical samples of $|B|$ and $\nabla|B|$.[8] Anderson and Kim used a linear relation $U=U_0-FVX$ between the effective energy ($U$) and the pinning energy in terms of the activation volume $V$ and the pinning length $X$.

In previous measurements we have found that the pinning energy increases with temperature as other researchers have also reported.[10] Fitting the experimental data to this model we have also found that the pinning energy decreases when the applied magnetic field increases (Fig. 2). We have fitted the field dependence of the pinning energy to an experimental law of the form $U_0=\alpha+\beta/H^n$ (Ref. 2) for different temperatures. We have found that the exponent $n$ is close to 2 (i.e., $n=1.7$ at 82 K and $n=2.1$ at 88 K) and the constant $\alpha$ increases with the temperature, as expected. These values are comparable to those obtained by Földeáki *et al.*[2]

Due to the discrepancies founded with the logarithmic fitting for the data close to $t=0$, we tried a nonlogarithmic theory. For this purpose we have also used the Debye theory to describe magnetic relaxation, as it has been used in other magnetic materials.[11,12]

Magnetic relaxation in Debye theory can be described by an exponential law of the form:

$$\chi(t,T)=\chi_0(T)-\Delta\chi\,\exp(-t/\tau), \tag{2}$$

where $\Delta\chi=\chi(0)-\chi(\infty)$ and $\tau$ is the relaxation time. We tried to fit our measurements to this equation, but the fits were not very good. Therefore, to obtain a better description, a distribution of relaxation times was assumed.[3] In this case, we can write the time evolution of the susceptibility in the form:

$$\chi(t,T)=\chi_0(T)-\Delta\chi\int_{U_1}^{U_2}p(U)[1-\exp(-t/\tau)]dU, \tag{3}$$

where $p(U)$ is the normalized distribution of energies, $\tau$ the relaxation time which obeys an Arrhenius expression, $\tau=\tau_0\exp(U/kT)$, and $U_1$ and $U_2$, respectively, the lower and upper limits of the energy distribution. Many distributions can be chosen but, although a gaussian distribution is physically more realistic, a box distribution gives similar results and is mathematically much simpler as other workers have shown.[13] In the case of a box distribution, $p(U)$ takes the form $p(U)=1/(U_2-U_1)$ if $U_2<U<U_1$ and 0 otherwise.

The existence of a box distribution could be explained in this way: if we suppose that there is a pinning energy, the interactions between vortices reduce the effective energy, and when flux expulsion occurs there are less vortices. The

TABLE I. Field dependence of box distributions for $T=82$ K and $T=88$ K, respectively.

| $H$ (Oe) | 10 | 15 | 25 | 50 | 100 |
|---|---|---|---|---|---|
| $U_1$ (eV) | 0.14 | 0.14 | 0.13 | 0.13 | 0.13 |
| $U_2$ (eV) | 0.19 | 0.19 | 0.19 | 0.19 | 0.19 |
| $H$ (Oe) | 10 | 15 | 25 | 50 | 100 |
| $U_1$ (eV) | 0.15 | 0.14 | 0.14 | 0.14 | 0.14 |
| $U_2$ (eV) | 0.21 | 0.20 | 0.20 | 0.20 | 0.20 |

interactions are then smaller and so the effective energy increases with time, because the interaction decreases and the process slows down.[14]

We have fitted our data to this model by means of a nonlinear fitting program which integrates numerically the expression (3). In Table I we present the results of the fits for the different fields. We have also tried an asymmetrical gaussian distribution, finding that the maximum is near to the center of the box distribution. We have chosen $\tau_0=1\times10^{-8}$ s, the pre-exponential factor, as a fixed parameter. The value of $\tau_0$ is comparable to that used in another works.[3] Variations in this parameter of two orders of magnitude increases the value of the energies slightly, as well as the width of the distribution. We can see no field dependence for the effective energies; only a weak dependence of the width of the box on temperature. This temperature dependence can be explained as follows: in a fixed time window, the processes with higher energy only have a reasonable probability of occurrence at higher temperatures and cannot be detected in lower temperatures. The value of the effective energy is smaller than the pinning energy previously obtained because of the influence of the term $FVX$, but the field dependence of $F$ is too complicated to evaluate because it depends on $|B|$ and $\nabla|B|$.[15]

## IV. CONCLUSIONS

We have studied magnetic relaxation by means of measurements of the time evolution of the ac susceptibility of a polycrystalline sample of a BiPbSrCaCuO superconductor for different temperatures and magnetic fields ranging from 10 to 100 Oe. We have analyzed the field dependence of the activation parameters associated with the magnetic relaxation using two theoretical models: the Anderson–Kim model and a box distribution for a superposition of Debye processes. In the case of the Anderson–Kim model we have found a strong field dependence of pinning energy, of the form $U_0=\alpha+\beta/H^n$ with $n\approx2$. However, no sign of a field dependence for the distribution of effective energies has been found.


[1] M. Földeaki, M. E. McHenry, and R. C. O'Handley Phys. Rev. B **39**, 2883 (1989).
[2] M. Földeaki, M. E. McHenry, and R. C. O'Handley Phys. Rev. B **39**, 11475 (1989).
[3] H. Theuss, T. Rieninger, and H. Kronmüller, J. Appl. Phys. **72**, 1936 (1992).
[4] M. Zazo, L. Torres, J. I. Iñiguez, J. M. Muñoz, and C. de Francisco, Appl. Phys. A **57**, 239 (1993).
[5] M. Zazo, L. Torres, J. Iñiguez, C. de Francisco, and J. M. Muñoz, J. Appl. Phys. **76**, 7133 (1994).
[6] L. Fábrega, B. Martínez, J. Fontcuberta, and S. Piñol, Phys. Rev. B **48**, 13840 (1993).
[7] Y. B. Kim, C. F. Hempstead, and A. R. Strnad, Phys. Rev. Lett. **9**, 306 (1962).
[8] P. W. Anderson, Phys. Rev. Lett. **9**, 309 (1962).
[9] M. R. Beasley, R. Labusch, and W. W. Webb, Phys. Rev. **181**, 682 (1969).
[10] A. Gurevich and H. Küpfer, Phys. Rev. B **48**, 6477 (1993).
[11] I. A. Campbell, L. Frutcher, and R. Cabanel, Phys. Rev. Lett. **64**, 1561 (1990).
[12] C. De Francisco, J. I. Iñiguez, and J. M. Muñoz, IEEE Trans. Magn. **25**, 4413 (1989).
[13] M. Földeaki, L. Kószeg, and R. A. Dunlap, Philos. Mag. B **63**, 1101 (1991).
[14] E. D. Dahlberg, D. K. Lottis, R. M. White, M. Matson, and E. Engle, J. Appl. Phys. **76**, 6396 (1994).
[15] S. K. Hasanain, A. Mumtaz, and K. Zaheer, Supercond. Sci. Technol. **5**, 92 (1992).

# Gd concentration dependence of the spin reorientation critical field in $Eu_{2-x}Gd_xCuO_4$

A. Butera, A. Fainstein, and M. Tovar
*Centro Atómico Bariloche and Instituto Balseiro, Comisión Nacional de Energía Atómica, 8400 San Carlos de Bariloche, Río Negro, Argentina*

Z. Fisk
*Los Alamos National Laboratory, Los Alamos, New Mexico 87545*

S. B. Oseroff
*Physics Department, San Diego State University, San Diego, California 92182*

ESR measurements of the microwave absorption signal associated with weak ferromagnetism in single crystals of $Eu_{2-x}Gd_xCuO_4$ are presented for $X$ band (9.5 GHz) and $L$ band (1.2 GHz) as a function of the Gd concentration. The strong absorption observed at low magnetic fields was interpreted, for samples with low Gd concentration, as due to a field-induced spin reorientation transition occurring at a critical field $H_c$, coincident with the in-plane magnetic anisotropy effective field $H_{\text{eff}}^y$. For larger $x$ the Cu-Gd magnetic interaction needs to be considered leading to smaller $H_c$ values. Our measurements show that for Gd concentrations in the range $0 \leqslant x \leqslant 1$ the experimental data can be very well fitted with parameters derived from previous measurements. This fact indicates that these compounds have nearly the same in-plane anisotropy effective field, in spite of the small changes in lattice parameters. For $x=2$ lattice distortions increase causing an $H_c$ larger than the expected one. © *1996 American Institute of Physics.* [S0021-8979(96)03008-X]

## I. INTRODUCTION

The rate earth cuprates $RE_2CuO_4$ (RE=Pr,..., Tm), parent compounds of the so-called $n$-type high $T_C$ superconductors, crystallize in the tetragonal $Nd_2CuO_4$ $T'$ structure.[1] $Pr_2CuO_4$ has the largest $a$ lattice parameter which decreases monotonically for the heavier RE compounds due to the smaller rare earth ion size.[2] This lattice reduction causes a distortion of the $CuO_2$ planes for $Eu_2CuO_4$ ($a=3.910$ Å) and heavier compounds, consisting of a displacement of the in-plane oxygens [called O(1)] from its centrosymmetrical position. These displacements seem to be ordered, and several superstructures have been found in single crystals with diffraction techniques.[2,3] Copper moments order antiferromagnetically (AF) below room temperature for the whole series. However, coincident with the boundary for lattice distortions, a weak ferromagnetic (WF) component in the magnetization develops, that was attributed to a canting of the copper moment away from a perfect AF alignment.[4] Several experimental techniques have been used to characterize the WF behavior. Among them, microwave absorption proved to be very useful to elucidate the magnetic behavior of the compounds near the WF boundary.[5] $X$- and $Q$-band experiments in $Eu_2CuO_4$ single crystals, slightly doped with Gd, have shown that the WF moment lays in the $CuO_2$ plane pointing parallel to an easy axis defined by the field cooling (FC) magnetic field and coincident with a [110] crystallographic direction ($[110]_{FC}$). When the external field is applied perpendicular to this axis a field-induced spin reorientation transition occurs at a critical field $H_c$.[5] More recently[6] it was shown that, for samples with larger amounts of Gd, the interaction between the WF ordered Cu lattice and the Gd paramagnetic (PM) lattice must be taken into account in order to explain several anomalies found in the EPR spectra. In this article we present the Gd concentration dependence of $H_c$ obtained from $X$-band measurements. We also discuss the $L$-band results within the proposed model.

## II. MODEL

The following expression for the magnetic free energy of the coupled PM–WF system was proposed:[6]

$$F_{\text{eff}} = -K_{\text{eff}}^y m_{\text{WF},y}^2 + K_{\text{eff}}^z m_{\text{WF},z}^2 - \mathbf{m}_{\text{WF}} \cdot \mathbf{H}_0 + \left(\frac{1}{2\chi_{\text{Gd}}}\right) M_{\text{Gd}}^2 - \mathbf{M}_{\text{Gd}} \cdot \mathbf{H}_0 - \lambda' \mathbf{m}_{\text{WF}} \cdot \mathbf{M}_{\text{Gd}}, \quad (1)$$

$\mathbf{m}_{\text{WF}}$ and $\mathbf{M}_{\text{Gd}}$ are the Cu-WF and Gd-PM magnetizations, $2K_{\text{eff}}^y m_{\text{WF}} = H_{\text{eff}}^y$ and $2K_{\text{eff}}^z m_{\text{WF}} = H_{\text{eff}}^z$ are in-plane and out-of-plane magnetic anisotropy fields, $\lambda'$ is the Cu-Gd coupling constant and $\chi_{\text{Gd}} = xC/(T+\Theta)$ is the Gd molar magnetic susceptibility. This effective free energy describes the equilibrium and the low-energy excitations of the system. The resonance modes can be obtained solving a $6\times6$ dynamical matrix for $\mathbf{m}_{\text{WF}}$ and $\mathbf{M}_{\text{Gd}}$. Two modes are obtained: a high-energy WF-like mode, and a low-energy PM-like one.

In Fig. 1 we show both modes, as calculated for $\lambda'\chi_{\text{Gd}}=0$ (dashed curves) and $\lambda'\chi_{\text{Gd}}\neq 0$ (solid curves). For $\lambda'\chi_{\text{Gd}}=0$ a softening of the WF mode would occur at a critical field $H_c = H_{\text{eff}}^y$, coincident with the field-induced spin reorientation transition when $\mathbf{H}$ is applied perpendicular to the easy axis (i.e., $\varphi=90°$). Note that for $X$ and $L$ bands a resonance absorption is expected only for $\varphi=90°$. For $\lambda'\chi_{\text{Gd}} \neq 0$ the critical field is reduced by a factor $1+\lambda'\chi_{\text{Gd}}$ giving

$$H_c = \frac{H_{\text{eff}}^y}{1+\lambda'\chi_{\text{Gd}}}, \quad (2)$$

 0021-8979/96/79(8)/6577/3/$10.00 © 1996 American Institute of Physics 

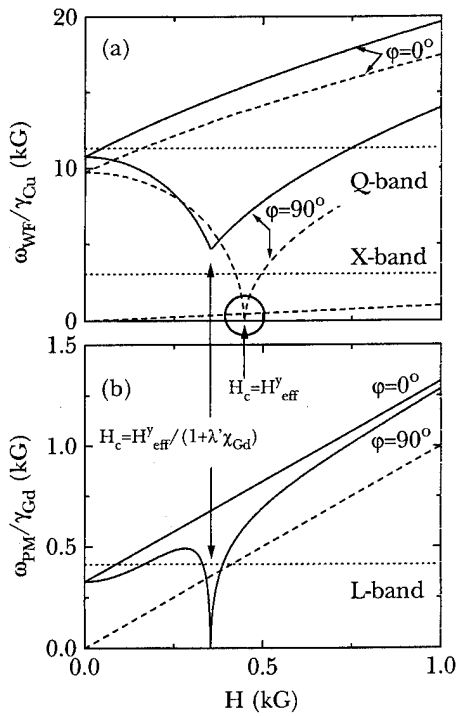



FIG. 1. Magnetic field dependence of (a) the WF-like and (b) the PM-like resonance modes when $H$ is applied within the easy plane (solid curves). The dashed lines, calculated for $\lambda'\chi_{Gd}=0$, illustrate the crossing of modes occurring at $H_c$. Note the shift of $H_c$ to lower fields when $\lambda'\chi_{Gd}\neq 0$.

and the WF mode does not soften to zero. This would imply that no resonance arising from the WF ordered Cu lattice should be observed at $X$ and $L$ bands. However, a maximum in the microwave absorption may be expected due to nonresonant loses as described in Ref. 5. In addition an energy gap opens in the PM-like mode for $H=0$ given by

$$\left(\frac{\omega_{PM}}{\gamma_{Gd}}\right)_{H=0}=\lambda' m_{WF}\sqrt{H^y_{eff}/[\lambda'^2\chi_{Gd}(T)m_{WF}+H^y_{eff}]}. \quad (3)$$

Due to the temperature dependence of $\chi_{Gd}(T)$ the gap tends to zero for $T=0$ K and increases for $T>0$ because other parameters are only weakly temperature dependent.[6] For $T>T_N$ the energy gap becomes zero again. Because of the anticrossing of the coupled modes an "anomaly" is also predicted in the PM-like branch which softens to zero at $H_c$.

## III. RESULTS AND DISCUSSION

$Eu_{2-x}Gd_xCuO_4$ single crystals were grown following standard flux techniques in Pt crucibles.[7] In all cases crystals grew in the shape of small platelets with the $c$ crystallographic axis perpendicular to the axis. EPR measurements were made in a Bruker ESP 300 spectrometer at $X$ band (9.5 GHz) and $L$ band (1.2 GHz) between 120 and 300 K.

Although the softening of the WF mode at $H_c$ is not complete for $\varphi=90°$ (see Fig. 1), originating a strong reduction in the intensity of the WF line at the $X$ band, it could still be clearly detected in all samples due to nonresonant loses.[5] In $L$ band, however, no line was found for samples with low Gd content ($0\leq x\leq 0.2$) indicating that the gap was large enough to prevent even the observation of nonresonant

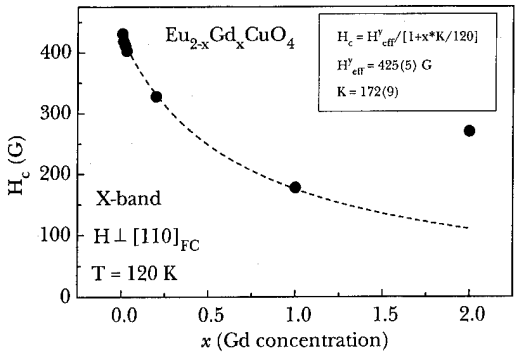



FIG. 2. Spin reorientation critical field, determined from the $X$-band low field absorption, as a function of $x$, the Gd concentration. The dashed line is a best fit of the experimental data in the range $0\leq x\leq 1$ using Eq. (2).

losses. We have determined the Gd concentration dependence of $H_c$, coincident with the $X$-band resonance field of the WF line, at $T=120$ K and with $H\perp[110]_{FC}$. The experimental data, presented in Fig. 2, were fitted using Eq. (2) in the range $0\leq x\leq 1$. We obtain the following values for the in-plane anisotropy effective field and the Cu-Gd coupling constant: $H^y_{eff}=425(5)$ G and $\lambda'=1.2(1)\times 10^5$ G/($\mu_\beta$/Cu-atom). These are consistent with the values found in Refs. 5 and 8 (for samples slightly doped with Gd) and in Ref. 9, respectively. Note that the experimental data can be explained with a single value of the in-plane anisotropy field for all compounds ($0\leq x\leq 1$), although the lattice size varies and consequently the displacement of the oxygen ions might change. We did not include the value measured for $Gd_2CuO_4$ in the fit because it was proposed[10] that for this compound Eq. (2) should be corrected due to the presence of a metamagnetic-like transition at low fields. In Ref. 10 the value of $H^y_{eff}$ for $x=2$ was estimated, from dc magnetization measurements, to be $\approx$1200 G at $T=120$ K. This value is nearly three times larger than the one measured for samples with lower Gd concentrations[8] probably due to the larger lattice distortions. Correspondingly, the measured $H_c$ value is almost three times larger than that predicted assuming a constant $H^y_{eff}$ (see Fig. 2).

In Fig. 3 we show the EPR spectra of $Gd_2CuO_4$ mea-

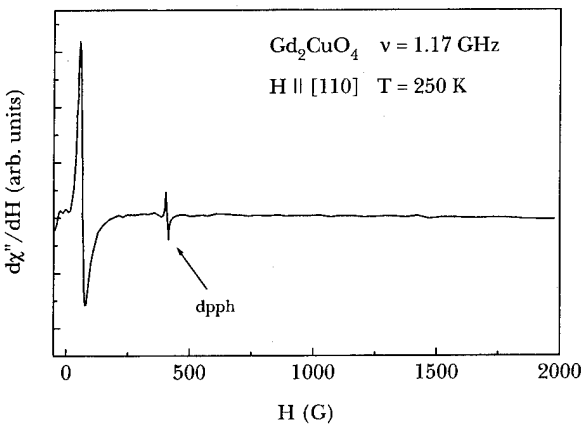



FIG. 3. $L$-band microwave absorption spectra of a $Gd_2CuO_4$ single crystal. Note the shift of the $\omega_{PM}$ line from $g=2$ (dpph).

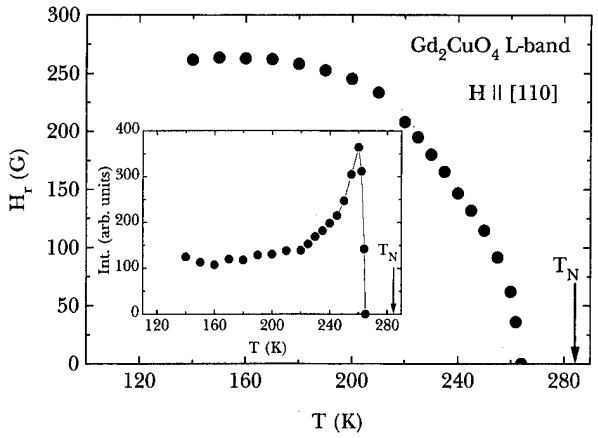



FIG. 4. Temperature dependence of the $L$-band $Gd_2CuO_4$ low field resonance line. Note the sharp decrease of the intensity at $T=260$ K, below the Néel temperature (inset).

sured at $L$ band for $T=250$ K. The PM mode in absence of coupling to the Cu lattice would occur at $\omega_{PM}/\gamma_{Gd}=410$ G. Due to the large linewidth of the $Gd^{3+}$ EPR line in $Gd_2CuO_4$ measured at $X$ band[4] ($\Delta H_{pp}\approx 1500$ G) a superposition of the absorptions occurring at negative and positive fields would cause a strongly asymmetric signal with a broad minimum at $\approx$750 G. Surprisingly a narrow and very intense line is observed at a lower field, $H_r\approx 100$ G. The origin of this absorption may be explained looking at the behavior of the PM-like mode in Fig. 1. From the $X$-band results we estimate the energy gap of the PM-like mode at $T=120$ K, $(\omega_{PM}/\gamma_{Gd})_{H=0}\approx 300$ G, lower than the $L$-band frequency $\omega_L/\gamma_{Gd}=410$ G. Thus the microwave absorption should occur at fields lower than that corresponding to $g=2$. When the temperature is increased $H_r$ moves to lower fields (see Fig. 4) and the line disappears at $T=265$ K, i.e., 20 K below $T_N$. As we have mentioned above, the value of the energy gap of the PM-like mode is expected to increase as $T$ rises and hence $T=265$ K would indicate the temperature where $\omega_{PM}$ equals $\omega_L$.

In this description the reduced linewidth of the PM-like absorption may be associated with coupled excitations. In fact, a strong mixture of modes is expected especially when an anticrossing of modes occurs at $H_c$.

In summary, we have analyzed the variation of the spin reorientation critical field, $H_c = H_{eff}^{y}/(1+\lambda'\chi_{Gd})$, as a function of Gd concentration. We have found that the decrease of $H_c$ for increasing $x$ may be explained (in the range $0\leqslant x\leqslant 1$) in terms of the magnetic coupling between the Cu-WF and the Gd-PM lattices. We have also discussed the origin of the absorption line measured at $L$ band and suggested that it is due to the PM-like branch of the PM-WF coupled modes.

## ACKNOWLEDGMENT

One of us, A. B., acknowledges support from CONICET (Argentina) through a post-doctoral fellowship.

[1] Von B. Grande, H. Muller-Buschbaum, and M. Schweizer, Z. Anorg. Allg. Chem. **428**, 120 (1977).
[2] P. Bordet, J. J. Capponi, C. Chaillout, D. Chateigner, J. Chenavas, Th. Fournier, J. L. Hodeau, M. Marezio, M. Perroux, G. Thomas, and A. Varela, Physica C **193**, 178 (1992).
[3] M. Braden, W. Paulus, A. Cousson, P. Vigoureux, G. Heger, A. Goukassov, P. Bourges, and D. Petitgrand, Europhys. Lett. **25**, 625 (1994).
[4] S. B. Oseroff, D. Rao, F. Wright, D. C. Vier, S. Schultz, J. D. Thompson, Z. Fisk, S.-W. Cheong, M. F. Hundley, and M. Tovar, Phys. Rev. B **41**, 1934 (1990).
[5] A. Fainstein, M. Tovar, and Z. Fisk, J. Phys. Condens. Mater. **4**, 1581 (1992); A. Fainstein, A. Butera, R. D. Zysler, M. Tovar, C. Rettori, D. Rao, S. B. Oseroff, Z. Fisk, S.-W. Cheong, D. C. Vier, and S. Schultz, Phys. Rev. B **48**, 16775 (1993).
[6] A. Fainstein, A. Butera, and M. Tovar, Phys. Rev. B **50**, 16708 (1994).
[7] J. D. Thompson, S.-W. Cheong, S. E. Brown, Z. Fisk, S. B. Oseroff, M. Tovar, D. C. Vier, and S. Schultz, Phys. Rev. B **39**, 6660 (1989).
[8] R. D. Zysler, A. Butera, A. Fainstein, M. Tovar, and Z. Fisk, J. Appl. Phys. **73**, 5680 (1993).
[9] L. B. Steren, M. Tovar, and S. B. Oseroff, Phys. Rev. B **46**, 2874 (1992).
[10] A. Butera, M. Tovar, S. B. Oseroff, and Z. Fisk, Phys. Rev. B **52**, 13444 (1995).

# Magnetization of $HgBa_2CuO_{4+\delta}$ with $0.03 \leqslant \delta \leqslant 0.4$

Q. Xiong, S. Afonso, Y. Q. Tang, F. T. Chan, and G. Salamo
*Physics Department/High Density Electronics Center, University of Arkansas, Fayetteville, Arkansas 72701*

Y. Y. Xue and C. W. Chu
*Physics Department and Texas Center for Superconductivity, University of Houston, Houston, Texas 77204*

$HgBa_2CuO_{4+\delta}$ (Hg1201) samples with $0.03 \leqslant \delta \leqslant 0.4$ have been obtained. The magnetization of the powdered Hg1201 samples was determined using a Quantum Design SQUID magnetometer. It was observed that while the magnetization of Hg1201 increased with $\delta$ in the underdoped region, the magnetization decreased with $\delta$ in the overdoped region. These results suggest an increase of $n_s/m^*$ with oxidation in the underdoped region and a decrease in the overdoped region, similar to that reported in underdoped HTSs and overdoped Tl2201 and Tl1201. © *1996 American Institute of Physics.* [S0021-8979(96)03108-6]

## I. INTRODUCTION

Soon after the discovery of high-temperature superconductivity (HTS), it was realized that the existence of $CuO_2$ layers in HTSs is very crucial and the charge carriers in the $CuO_2$ layers control the physical properties in both the superconducting state and the normal state. $T_c$ is one of the properties that the charge carriers in the $CuO_2$ layers have a marked effect upon. On the one hand, it was found that there are three different regimes in the relationship of $T_c$ to the number of charge carriers $n$ in the $CuO_2$ layers (where $n$ is determined from valence balance or thermoelectric).[1–3] The underdoped region is where the superconducting phase appears near the insulating magnetic phase. $T_c$ increases with increased $n$ in this region. The optimal doping region is where $T_c$ approaches the highest values within the given series. Next, comes the overdoped region. In this region, $T_c$ decreases with further increases in $n$. On the other hand, based on muon spin-rotation ($\mu$SR) measurements,[4–6] it was found that $T_c$ vs $n_s/m^*$ forms a double-valued relation in Tl2201 (where $n_s$ is the superconducting condensate density, $m^*$ is the effective mass). This means that as $n$ increases, $n_s/m^*$ increases in the underdoped region, and decreases in the overdoped region. Until now, most studies have concentrated on the underdoped and optimal region, probably because underdoped and optimally doped samples are fairly easy to synthesize for most HTS systems. On the contrary, the overdoped region has been observed in only a few systems. The $HgBa_2CuO_{4+\delta}$ compound (Hg1201) has been shown to be scientifically significant,[7] because it has the highest $T_c$ among all HTS materials that have one $CuO_2$ plane, and has the widest doping range that can be achieved by changing oxygen content alone.[8] Thus it is a good candidate for studies on charge carrier and doping related properties in the overdoped region.

In this article, we report a study of $T_c$ vs $n_s/m^*$ done by measuring the magnetization volume fluctuation of Hg1201 when oxygen content is varied from 0.03 to 0.4, covering the entire range from $T_c = 0$ K (underdoping region) to $T_c = 20$ K (overdoping region). We observed that the magnetization of Hg1201 increases with $\delta$ in the underdoped region and decreases with $\delta$ in the overdoped region. The results suggest that a double-valued relation of $T_c$ to $n_s/m^*$ also exists in the Hg1201 compound.

## II. EXPERIMENT

All samples were synthesized by a two-step method, i.e., by first forming a precursor of (Ba, Cu) oxides, then reacting HgO with the precursor inside an evacuated quartz tube. Precursor with an initial composition of $Ba_2CuO_y$ was prepared by a solid-state reaction. High-purity powders of BaO (99.95%) were thoroughly mixed in appropriate proportions. The mixed powders were calcined in an alumina crucible at 930 °C for 24 h under a mixed gas of Ar:O=4:1. Three intermediate regrindings were carried out during this period. The composite Hg source used was a prereacted Hg1:2:0:1 pellet made by compacting the thoroughly mixed HgO (99.998%) and pulverized precursor powder. A reactant pellet was sealed in an evacuated quartz tube of fixed volume, together with an extra $Ba_2CuO_y$ precursor pellet. Details were given in Ref. 9. A stainless-steel tube was used to contain the quartz tube as a safety precaution. The whole assembly was then heated to 800–830 °C for 8 h before slow cooling to room temperature. Samples with different oxygen content were obtained by heating as-synthesized samples at different temperatures and oxygen partial pressures for appropriate periods of time.[9] To reach the underdoped region, the sample was heated in a vacuum of $\sim 2\times10^{-6}$ Torr at a temperature between 200 and 450 °C for 20–100 h. For the overdoped samples, the as-synthesized compound was heated in a 1–500 bar O atmosphere between 240 and 400 °C for 10–300 h. Phase characterization was performed by x-ray powder diffraction on a Rigaku DMAX/BIII diffractometer. The magnetization was measured using a Quantum Design SQUID magnetometer. The oxygen content $\delta$ of the samples were measured by thermogravimetric analysis[8] and calibrated using neutron powder diffraction.[10]

## III. RESULTS AND DISCUSSION

Figure 1 shows the x-ray diffraction pattern of one of our as-synthesized samples, which indicated that the Hg1201 sample was nearly single phase. Figure 2 shows the normal state susceptibility as a function of the temperature. The data fits the Curie law, $\chi = \chi_0 + C/T$, very well with $\chi_0 = 1.04\times10^{-6}$ emu/g and $C = 2.45\times10^{-4}$ emu/g. The magnetization in various magnetic fields $H$ has also been measured. As shown in the inset of Fig. 2, the magnetization

 0021-8979/96/79(8)/6580/3/$10.00 © 1996 American Institute of Physics

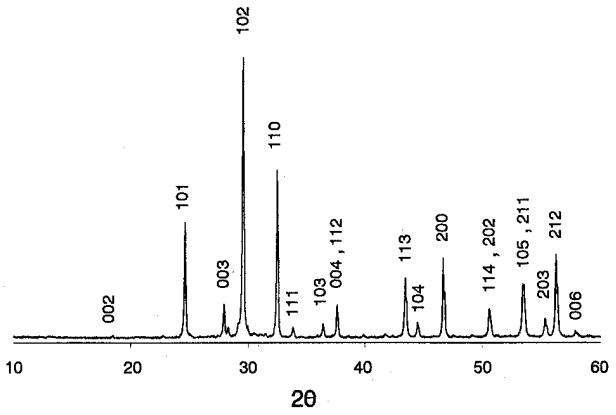



FIG. 1. X-ray diffraction pattern of Hg1201 sample.

changes linearly with $H$ within experimental resolution which suggests negligible ferromagnetic contributions. According to our TEM, SEM, and EDX studies, the paramagnetic contribution results from synthesis related impurities,[11] which were not detectable by x-ray and neutron powder diffraction. Since the magnetization of the samples depends on the percentage of Hg1201 phase inside the samples, we must first be sure all the samples used contain the same percentage of Hg1201 phase if we want to determine how the magnetization of Hg1201 samples change with the oxygen content. To do so, all the samples we used were synthesized at the same time and annealed under differing conditions. So, the samples with different oxygen content should contain similar amounts of impurities. In this study, we were only concerned with the change in magnetization with oxygen content, so these impurities should not effect our results and conclusion.

In an ideal case, the low field magnetization $M$ of superconducting particles is related to $\lambda$ as $M \propto 1-(\lambda/d)^2$, where $d$ is the diameter of the particles and $\lambda$ is the penetration depth. In order to ensure uniformity in particle size among the samples, a large quantity of Hg1201 powder was synthesized and ground at the same time, and then separately annealed under different conditions to obtain samples with different oxygen content. The dc magnetization was measured at 5 Oe for samples that were both zero field cooled (ZFC) and field cooled (FC). The result of the ZFC measurement is an overestimation of the true superconducting volume fraction due to porosity. According to the study by Braunisch *et al.*,[12] the results of FC measurements very badly underestimate the superconducting volume fraction for ceramic HTS samples due to pinning and the large penetration depth in the C direction. The real superconducting volume fraction of the samples $M$ should be between $M_{FC}$ and $M_{ZFC}$. $M_{FC}$ and $M_{ZFC}$ versus oxygen content $\delta$ are shown in the Fig. 3. Both $M_{FC}$ and $M_{ZFC}$ increase with $\delta$, are a maximum for optimally doped Hg1201 and decrease with further increase in oxygen content. The $T_c$ vs $M$ $[M=(M_{ZFC}+M_{FC})/2]$ are shown in Fig. 4. The curve appears to be double valued in nature. Since $n_s/m^* \sim 1/\lambda^2$, $T_c$ vs $n_s/m^*$ follows a "boomerang path" like that in Tl2201 and T1201.

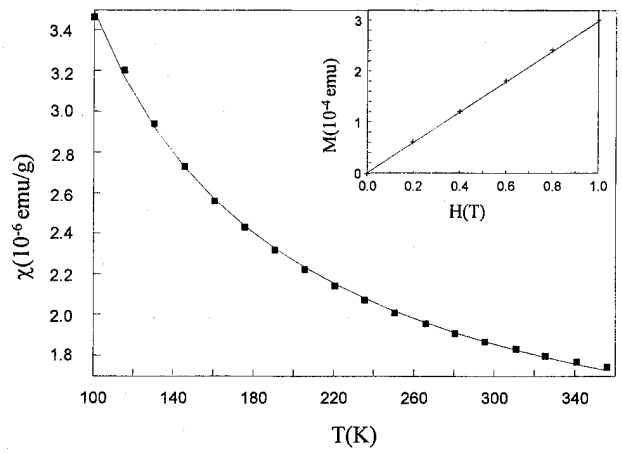



FIG. 2. The normal state susceptibility as a function of the temperature for one of our as synthesized Hg1201 samples [fit of $\chi=1.04\times10^{-6}+2.45\times10^{-4}/T$ (emu/g)]. Inset: Magnetization $M$ as a function of magnetic field $H$.

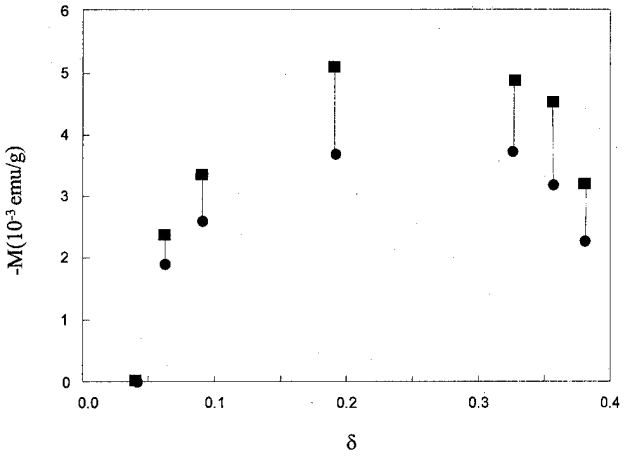



FIG. 3. $M_{ZFC}$ and $M_{FC}$ vs oxygen content $\delta$ (■ $M_{ZFC}$ and ● $M_{FC}$).

## IV. CONCLUSION

The magnetization of Hg1201 with $0.03 \leqslant \delta \leqslant 0.4$ has been studied. The results have shown that the $T_c$ vs $n_s/m^*$ also forms a "boomerang path" in Hg1201, which is similar to that in HTSs in the underdoped region and Tl2201 and Tl1201 in the overdoped region.

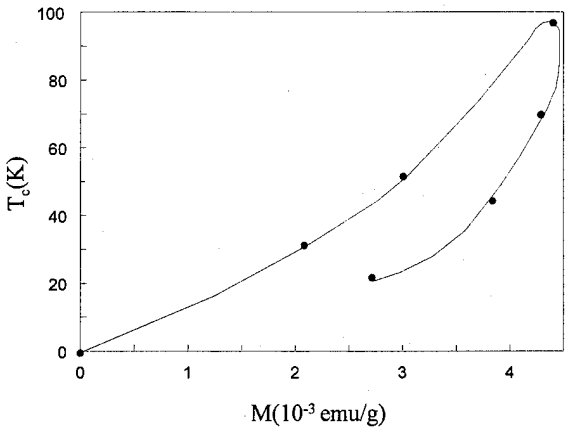



FIG. 4. The $T_c$ vs magnetization $M$.

## ACKNOWLEDGMENTS

This work at the University of Arkansas is supported in part by NSF DMR 9318946, the High Density Electronics Center at the University of Arkansas, DARPA (Contract No. MDA 972-90-J-1001) through Texas Center for Superconductivity at the University of Houston (TCSUH). This work at TCSUH is supported by NSF Grant No. DMR 91-22043, USAFOSR Grant No. F49620-93-1-0310 by BMDO, EPRI RP-8066-04, the State of Texas through TCSUH, and the T. L. L. Temple.

[1] M. R. Presland, J. L. Tallon, R. G. Buckley, R. S. Liu, and N. E. Flower, Physica C **176**, 95 (1991).
[2] H. Zhang and H. Sato, Phys. Rev. Lett. **70**, 1697 (1993).
[3] J. G. Lin, K. Matsuishi, Y. Q. Wang, Y. Y. Xue, P. H. Hor, and C. W. Chu, Physica C **175**, 627 (1991).
[4] Y. J. Uemura *et al.*, Phys. Rev. Lett. **62**, 2317 (1989).
[5] Y. J. Uemura, A. Keren, L. P. Le, Q. M. Luke, W. D. Wu, Y. Kubo, T. Manako, Y. Shimakawa, M. Subramanian, J. L. Cobb, and J. T. Markert, Nature **364**, 605 (1993).
[6] Ch. Niedermayer, C. Bernhard, U. Binninger, H. Glückler, J. L. Tallon, E. J. Ansaldo, and J. I. Budnick, Phys. Rev. Lett. **71**, 1764 (1993).
[7] C. W. Chu, Proceedings of Quantum Theory of Real Materials, Symposium in Honor of Professor Marivin L. Cohen's 60th Birthday, Berkeley, California, August 13, 1994.
[8] Q. Xiong, Y. Cao, Y. Y. Xue, and C. W. Chu, Phys. Rev. B **50**, 10346 (1994); Q. Xiong, Y. Y. Xue, F. Chen, Y. Cao, Y. Y. Sun, R. M. Liu, A. Jacobson, and C. W. Chu, Physica C **231**, 233 (1994).
[9] Q. Xiong, Y. Cao, F. Chen, Y. Y. Xue, and C. W. Chu, J. Appl. Phys. **76**, 7127 (1994).
[10] Q. Huang, J. W. Lynn, Q. Xiong, and C. W. Chu, Phys. Rev. B **52**, 462 (1995).
[11] Q. Xiong, F. T. Chan, Y. Y. Xue, and C. W. Chu, Physica C **253**, 329 (1995).
[12] W. Braunisch, N. Knauf, V. Kataev, S. Neuhausen, A. Grutz, A. Kock, B. Roden, D. Khomskii, and D. Wohlleben, Phys. Rev. Lett. **68**, 1908 (1992).

# Superconducting properties of Hg-1223 prepared by using fluorides

B. J. Jönsson, T. Turkki, and V. Ström
*Condensed Matter Physics, Royal Institute of Technology, S-100 44 Stockholm, Sweden*

Z. Iqbal
*Allied Signal Incorporated, Research and Technology, Morristown, New Jersey 07962*

K. V. Rao
*Condensed Matter Physics, Royal Institute of Technology, S-100 44 Stockholm, Sweden*

A new approach involving the use of fluorides has been adopted to synthesize phase-pure Pb-substituted Hg-1223 superconductors under ambient conditions. A representative sample is characterized using x-ray, SQUID magnetometer, and ac susceptibility techniques. In a measuring field of 1 G, a sharp diamagnetic onset is observed at 132 K and perfect flux screening persists up to 122 K. On approaching $T_c$ the irreversibility li..e follows a power law with exponent $\alpha=2.2$. From the ac susceptibility data, in the context of the Bean critical state model, the critical current density at helium temperatures is estimated to be $1.5\times10^6$ A/cm$^2$. © *1996 American Institute of Physics.* [S0021-8979(96)42008-2]

## I. INTRODUCTION

The discovery by Putilin *et al.*[1] of superconductivity at 94 K in $HgBa_2CuO_{4+\delta}$ and the subsequent report by Schilling *et al.*[2] of superconductivity above 130 K in $HgBa_2Ca_2Cu_3O_{8+\delta}$ initiated intense research in these mercury compounds. They both belong to the homologous series of $HgBa_2Ca_{n-1}Cu_nO_{2n+2+\delta}$ which today has five members ($n=1-5$), with Hg-1223 showing the highest $T_c$. It was observed that $T_c$ of the Hg-1223 phase increases with pressure to 164 K at 30 GPa,[3] indicating that even higher critical temperatures might be obtained at ambient pressure if the internal pressure could be increased by, say, optimizing the doping levels.

A major problem encountered in the synthesis of the Hg compounds is the difficulty in obtaining phase-pure samples. It has been shown that a small amount of Pb facilitates the formation of a single phase.[4] Fluorine doping in Bi-2223 has been shown to enhance the stability and to increase the critical temperature.[5] It is thus of interest to study the effect of fluorine doping in the mercury-based system.

In this work we study the magnetic properties of Pb-substituted Hg-1223 samples synthesized using fluorides.

## II. EXPERIMENT

A precursor of nominal composition $Ba_2Ca_2Cu_4O_x$ was prepared using barium, calcium, and copper nitrates as the starting materials. The nitrates were weighed out and mixed in a dry box and then fired for 6 h at 900 °C under flowing oxygen after a heat-up to 900 °C in 6 h. One mole of the fired precursor was mixed with 0.8 moles of HgO and 0.2 moles of $PbF_2$ in a dry box, pelletized and sealed in a 0.4 mm outer diameter quartz tube after back filling with a tenth of a Torr of oxygen. The quartz tube with the sample is then fired at 850 °C for 25 h after heat-up to the firing temperature in 1 h. The samples are characterized without further annealing.

The x-ray powder diffraction pattern collected within $5°\leqslant 2\theta \leqslant 80°$ using a Siemens D5000 diffractometer shows mainly the lines that belong to the Hg-1223 phase (Fig. 1).

The dc susceptibility measurements were performed using Quantum MPMS$_2$ SQUID magnetometer. All measurements, in fields ranging from 1 G to 10 kG, were performed during the warming scan after zero field cooling the samples to 10 K. The ac susceptibility measurements were performed using a home-built two-position ac susceptometer with a three-coil mutual inductance bridge. Driving fields were varied from 10 mOe to 2 Oe rms at 190 Hz.

## III. RESULTS AND DISCUSSION

Figure 2 shows a typical field cooled (FC) and zero field cooled (ZFC) warming up scan in 1 G. Using the dimensions of the sample ($7.0\times1.5\times0.8$ mm$^3$) a ZFC susceptibility of $-1.02$ (complete flux expulsion) is obtained. The flux expulsion is better than 95% even up to temperatures as high as 122 K. The flux expulsion for FC is only 12%. This big difference is explained by strong pinning—at the thin surface layer during ZFC and in the bulk of the sample during FC.

The magnetic susceptibility was measured at different fields, ranging from 1 to 1000 G. All scans are shown in Fig. 3 together with an ac susceptibility measurement at 10 mG rms. As the field is increased there appear signs of a second

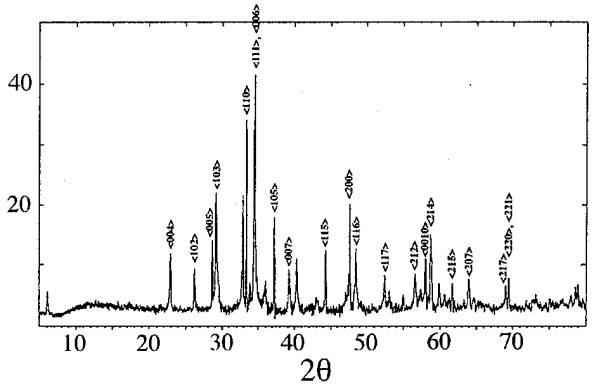



FIG. 1. X-ray powder diffraction pattern identifying intensity peaks that belong to the Hg-1223 phase.

 0021-8979/96/79(8)/6583/3/$10.00 © 1996 American Institute of Physics 

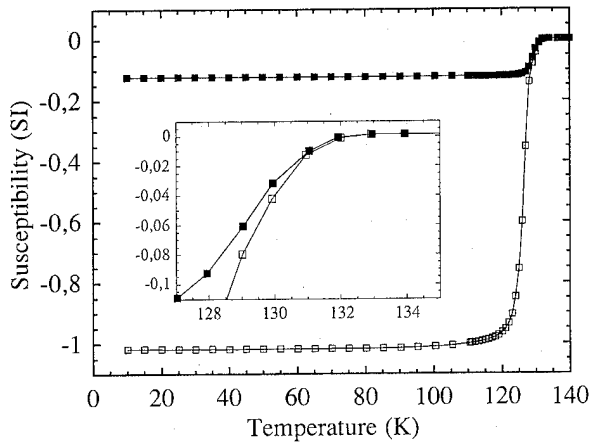



FIG. 2. ZFC and FC dc susceptibility measured in a field of 1 G. In the inset is shown the two curves branching off at the irreversibility point.

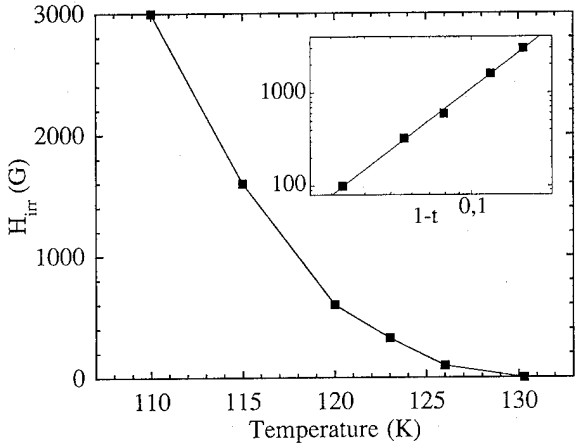



FIG. 4. The irreversibility line. The inset shows a fit to a power law with the exponent $\alpha=2.2$.

phase with a higher critical current. There is almost no change in susceptibility at fields from 300 to 500 G indicating a weaker field dependence of this phase.

The location of the irreversibility line is important from applications point of view. The irreversibility line is obtained from the points in the $T$-$H$ plane where the FC and ZFC curves split. These points can be determined either by measuring FC and ZFC temperature scans in a constant field or measuring $M/H$ loops at a constant temperature. We determined these point by measuring $M/H$ loops at six different temperatures. We chose the criterion for irreversibility as $\Delta M=0.02$ emu/cm$^3$, where $\Delta M$ is the magnetization difference in decreasing and increasing field. On approaching $T_c$ we find a power law dependence $H_{\rm irr}\propto(1-t)^{\alpha}$ with the exponent, $\alpha=2.2$ (Fig. 4).

To get further insight in the magnetic properties we studied the ac susceptibility as a function of temperature and field. The complex susceptibility $\chi=\chi'-i\chi''$ gives additional information since the imaginary part $\chi''$ corresponds to energy dissipation in the material and can be used to deduce various parameters such as the critical current density. The

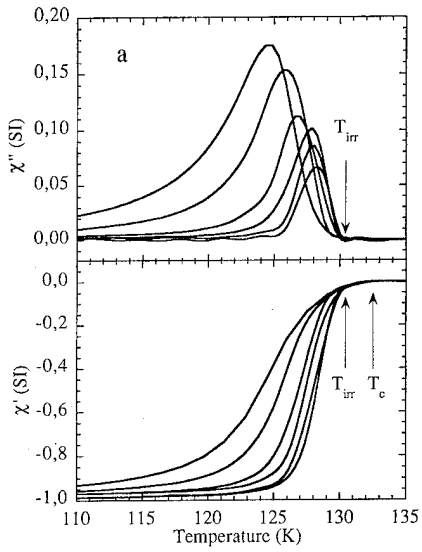



FIG. 5. Imaginary (a) and real (b) part of the complex ac susceptibility measured with driving fields 0.01, 0.03, 0.1, 0.3, 1, and 2 Oe.

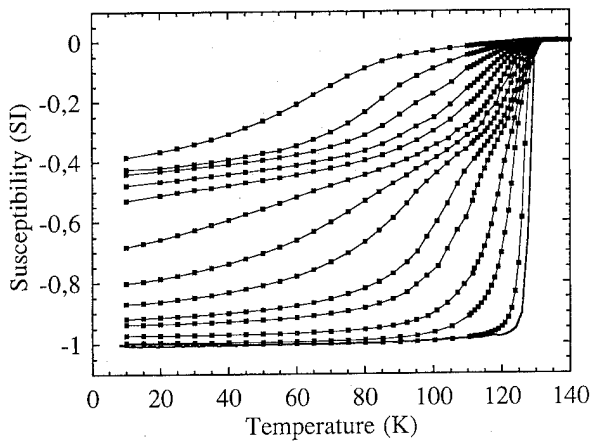



FIG. 3. Susceptibility measured in fields: 1, 5, 10, 20, 30, 50, 70, 100, 150, 200, 300, 500, and 1000 G. Also shown is the real part of the ac susceptibility measured in 10 mG rms.

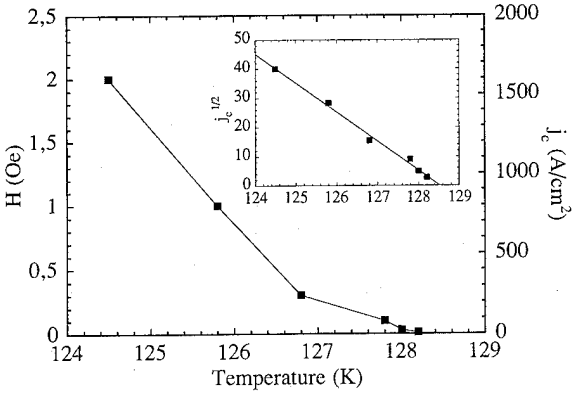



FIG. 6. Peak field and critical current density as a function of temperature. The inset shows a fit $j_c(T)=1.5\times10^6(1-t)^2$ A/cm$^2$.

real part $\chi'$ is approximately equivalent to the ZFC dc susceptibility and can be used to measure ZFC curves at very low field strengths.

We measured the temperature dependence of the complex susceptibility at six different driving fields (Fig. 5). The diamagnetic transition onset is located at 132 K. Below $T_{irr}$, at about 130.3 K, this diamagnetic response becomes field dependent and the dissipation appears.

According to the Bean critical model the peak in $\chi''$ corresponds to the field just penetrating into the center of the sample and at this point there exists a simple relationship between this field $H_p$ (in A/m) and the critical current density:[6]

$$H_p = J_c R.$$

Approximating our sample geometry to a long cylinder of radius 1 mm we can thus calculate the critical current density as a function of temperature (Fig. 6). Assuming a power law dependence we find the critical current density at helium temperatures to be about $1.5 \times 10^6$ A/cm$^2$.

## IV. CONCLUSION

In conclusion we have studied the magnetic properties of phase-pure F-doped Pb-substituted Hg-1223 samples. While it is still premature to claim the important role of fluorine in this system, we observe a high critical temperature and good magnetic properties.


[1] S. N. Putilin, E. V. Antipov, O. Chmaissem, and M. Marezio, Nature **362**, 226 (1993).

[2] A. Schilling, O. Jeandupeux, J. D. Guo, and H. R. Ott, Nature **363**, 56 (1993).

[3] M. Nunez-Reguerio, J.-L. Tholence, E. V. Antipov, J.-J. Capponi, and M. Marezio, Science **262**, 97 (1993).

[4] Z. Iqbal, T. Datta, D. Kirven, A. Lungu, J. C. Barry, F. J. Owens, A. G. Rinzler, D. Yang, and F. Reidinger, Phys. Rev. B **49**, 12322 (1994).

[5] S. Y. Lee, S. Suehara, and S. Horiuchi, Physica C **185-189**, 477 (1991).

[6] C. P. Bean, Rev. Mod. Phys. **36**, 31 (1964).

# Vortex pinning in layered organic superconductors: $\kappa$-(BEDT-TTF)$_2$Cu[N(CN)$_2$]Br

S. Khizroev, F. Zuo, and G. C. Alexandrakis
*Department of Physics, University of Miami, Coral Gables, Florida 33124*

J. A. Schlueter, U. Geiser, and J. M. Williams
*Chemistry and Materials Science Divisions, Argonne National Laboratory, Argonne, Illinois 60439*

Magnetization studies on organic single-crystal superconductors of $\kappa$-(BEDT-TTF)$_2$Cu[N(CN)$_2$]Br with the field $H$ parallel to the $b$ axis (perpendicular to the conducting plane) show anomalous field and temperature dependence of vortex pinning in the mixed state. At high temperatures, the magnetization $M$ decays with increasing field with a power-law dependence. The normalized relaxation rate $S=d(\ln M)/d(\ln t)$ decreases monotonically with $H$. At low temperatures ($T<7$ K), a change of sign in the curvature of $M(H)$ is observed, accompanied by a corresponding change in $S$ as a function of $H$. Measurement of the irreversibility field $H_{rev}$ shows a universal power-law dependence of $H_{rev}$ on $(1-T/T_c)$ in the temperature range investigated. We suggest that the magnetic anomaly observed is due to a dimensional crossover in the nature of vortex pinning.
© *1996 American Institute of Physics.* [S0021-8979(96)03208-2]

The discovery of ambient pressure organic superconductor $\kappa$-(BEDT-TTF)$_2$X family [BEDT-TTF denotes bis(ethylenedithio)tetrathiafulvalene and X a monovalent anion] with $T_c\sim 11$ K has generated considerable interest in the study of anisotropic magnetic properties in the mixed state. The material has an intrinsic layered structure consisting of alternating sheets of metallic (dimerized BEDT-TTF molecules) and insulating (anion X) planes. The anisotropy constant $\gamma$ defined as $\sqrt{M_\perp/M_\parallel}$ has been reported of the order of 100 or more.[1–5] Except the low $T_c$ value, the organic superconductor is very similar to the highly anisotropic $Bi_2Sr_2CaCu_2O_{8+y}$ (BSCCO) and $Tl_2Ba_2Ca_{n-1}Cu_nO_{4+2n}$ (TBCCO) compounds. Moreover, since it is free of secondary phases commonly present in the oxide superconductors, the organic superconductor may prove to be an ideal system to investigate the anisotropic magnetic properties. A careful comparative study in the mixed state in this structurally homogeneous system will contribute to our understanding of the more complex high-temperature oxide superconductors.

We report here magnetization measurements on organic single-crystal superconductors of $\kappa$-(BEDT-TTF)$_2$Cu[N(CN)$_2$]Br with the field $H$ parallel to the $b$ axis (perpendicular to the conducting plane). Our measurements show anomalous field and temperature dependence of vortex pinning in the mixed state. At high temperatures, the magnetization $M$ decays with increasing field with a power-law dependence. The normalized relaxation rate $S=d(\ln M)/d(\ln t)$ decreases monotonically with $H$. At low temperatures ($T<7$ K), a change of sign in the curvature of $M(H)$ is observed, accompanied by a corresponding change in $S$ as a function of $H$. Measurement of the irreversibility field $H_{rev}$, shows a universal power-law dependence of $H_{rev}$ on $(1-T/T_c)$ in the temperature range investigated with $H_{rev}\propto(1-T/T_c)^{3/2}$. We suggest the anomaly observed is due to a dimensional crossover in the nature of vortex pinning.

Single crystals of $\kappa$-(BEDT-TTF)$_2$Cu[N(CN)$_2$]Br superconductors were synthesized by the electrocrystallization technique described elsewhere.[6] Several crystals were used in these measurements with average dimensions of $1\times0.5\times0.1$ mm. Extensive measurements were made on one crystal with $T_c=11$ K. Measurements were performed with the use of a Quantum Design magnetometer with low-field options. A typical hysteresis loop was measured after the sample was zero-field cooled (ZFC) to a set temperature and the magnetization was measured with the superconducting magnet in the persistent mode. Scan length varying from 4 to 6 cm gave similar results. Relaxation measurements were performed in field in ZFC condition. A typical remanent field after quenching the magnet was less than 20 mG. Samples were placed with the field parallel to the $b$ axis.

Figure 1 shows an overlay of the magnetization as a function of field at different temperatures. At high temperatures $T>7$ K, $M$ decreases in a power-law field dependence with $M\propto H^{-n}$ and $n=2/3$. The same exponent is observed for temperature up to 10 K.[7] Below 7 K, a shoulder-like feature is developed in $M(H)$ at $H$ around 200 G, with a corresponding change in the curvature of $M(H)$. The effect is most pronounced at a lower temperature of 6 K. Further decrease in temperature broadens and smears out the change.

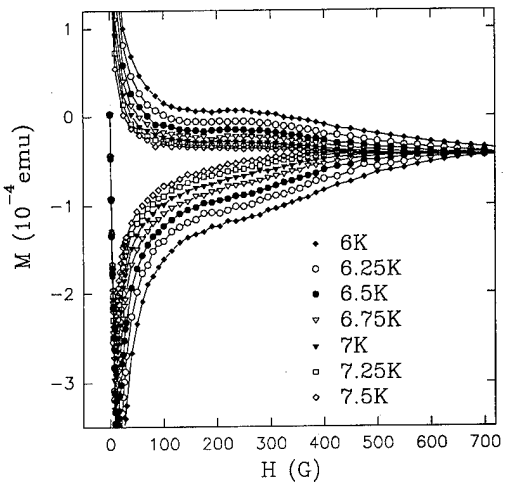



FIG. 1. Magnetization as a function of field at different temperatures.

 0021-8979/96/79(8)/6586/3/$10.00 © 1996 American Institute of Physics

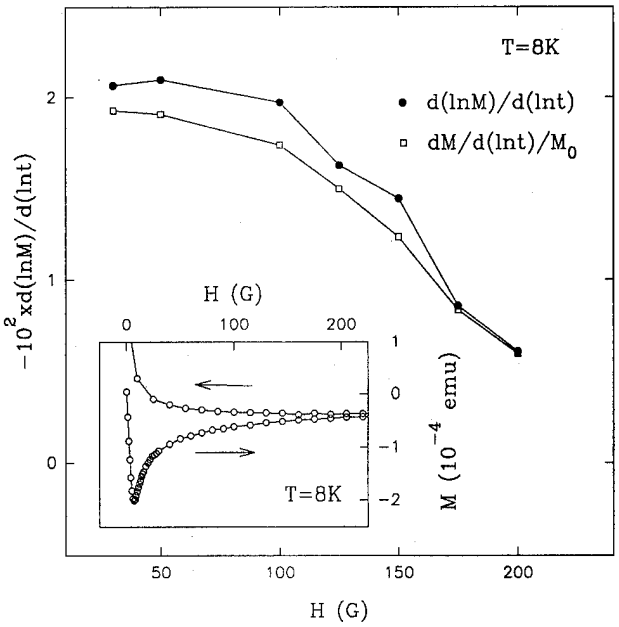



FIG. 2. Normalized relaxation rate as a function of $H$ at 8 K. The inset shows the hysteresis loop at the same $T$.

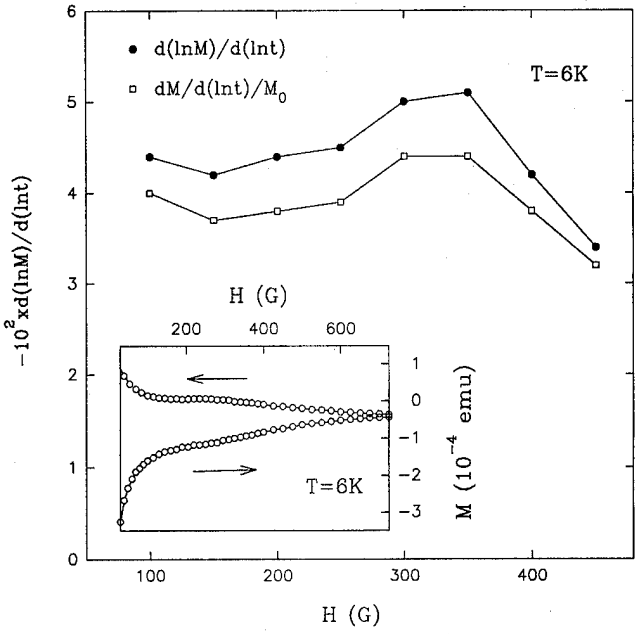



FIG. 3. Normalized relaxation rate as a function of $H$ at 6 K. The inset shows the hysteresis loop at the same $T$.

Figure 2 plots the normalized relaxation rate as a function of field. $S$ is defined as the average slope of $\ln M$ vs $\ln t$. Since the magnetization does not decay strictly with power-law dependence with time nor linear with $\ln t$. We have extrapolated both the average $d(\ln M)/d(\ln t)$ (in solid circles) and the average $dM/d(\ln t)/M_0$, where $M_0$ is the initial magnetization (in open squares). The magnitude of the normalized relaxation rate is similar in both extrapolations, as well as its field dependence. The inset shows the corresponding hysteresis loop at the same temperature of 8 K. The arrows indicate the direction of increasing and decreasing field.

Shown in Fig. 3 is a similar plot of the relaxation rate at a lower temperature of 6 K. Unlike the monotonic field dependence observed at higher temperatures, the normalized relaxation rates as defined by both extrapolations show a slight increase at about 300 G and decrease again at higher field. The peak in $S$ is roughly correlated with the secondary peak field of the corresponding hysteresis magnetization loop, as shown in the inset.

Figure 4 is a semi-log plot of the irreversibility field as a function of temperature. The irreversibility field $H_{\rm rev}$ here is defined as the onset field at which the magnetizations on both ascending and descending directions overlap. The temperature range we had investigated was limited to above 5 K. Measurements of $H_{\rm rev}$ at lower temperatures on the same compound have been reported by Lang *et al.*,[5] as shown by the solid circles. They are consistently higher than ours in the overlapping temperature regime. The difference might be due to different disorders, thus, pinning strengths among samples studied. If we neglect the difference in the magnitude of $H_{\rm rev}$, a change of curvature in $H_{\rm rev}(T)$ with $T$ is clearly visible. The solid line is a fit to $H_{\rm rev}=H_0(1-T/T_c)^{\alpha}$ with $\alpha=3/2$. The inset shows a log–log plot of $H_{\rm rev}$ vs $T$, with the straight line given by the above fit.

The magnetization observed for the $\kappa$-(BEDT-TTF)$_2$Cu[N(CN)$_2$]Br compound is qualitatively similar to the anomalous magnetization reported for the oxide high $T_c$ superconductors,[8–10] especially the BSCCO and TBCCO compounds. Two main similarities are observed. First, a crossover temperature $T_{\rm cr}$ in the magnetization behavior exists in both families. In the case of $Tl_2Ba_2CuO_6$,[10] the anomalous magnetization disappears above a characteristic temperature of about 60 K ($T_c=92$ K). Below 60 K, a second peak in magnetization is developed for field greater than the first penetration field. Second, both families show very similar temperature dependence of the irreversibility

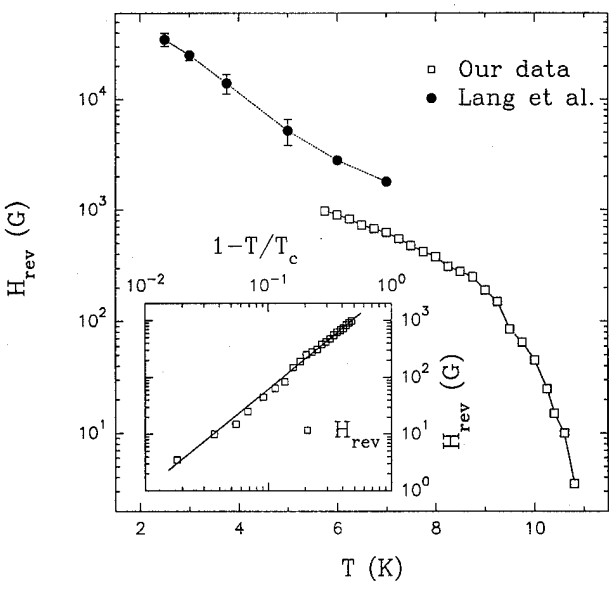



FIG. 4. $H_{\rm rev}$ as a function of $T$. The inset plots the same data in a log–log scale.

field line. At high temperatures, $H_{rev} \propto (1-T/T_c)^{\alpha}$ with the same exponent $\alpha=3/2$. At low temperatures, a change of curvature is observed in $H_{rev}(T)$. For $Tl_2Ba_2CuO_6$, this temperature corresponds to the crossover temperature $T_{cr}$. In the case of organic superconductor, our present data cannot pinpoint the temperature at which $H_{rev}$ changes its curvature. However, results published by Lang *et al.* suggest this temperature is in the range of 5–6 K, very close to the crossover temperature of 7 K.

The mechanism giving rise to the anomalous magnetization in the mixed state has been of recent interest, particularly in the high-temperature oxide superconductors. Various mechanisms have been since proposed to explain the observed effect. In the case of oxides, the understanding of the anomalous secondary peak is complicated by the fact that the system tends to have oxygen inhomogeneities, resulting in superconducting phases with different critical temperatures. Because of this inhomogeneity, one possible explanation is that the increased pinning at high fields is due to the suppression of superconductivity of the lower $T_c$ phases. However, the characteristic peak field should be of the order of $H_{c2}$ of the low $T_c$ phases in this model. Except for YBCO, typical peak field observed for BSCCO and TBCCO is of the order of $10^3$ G or less, much less than the second critical field. In the case of the organic superconductors, to our knowledge, the organic $\kappa$-(BEDT-TTF)$_2$Cu[N(CN)$_2$]Br compound contains no secondary, lower $T_c$ phases.[1] Thus, the enhanced pinning at high fields and low temperatures cannot be due to the secondary phase model.

Other models based on the collective pinning effects, the matching effect, etc., have also been proposed. In the case of collective pinning model,[8] the peak effect is attributed to the slow relaxation of large vortex bundles. The normalized relaxation rate is given by $S=k_BT/[U_0+\mu k_BT \ln(t/t_0)]$, where $U_0$ is the barrier height, $\mu$ is the exponent defined in the $U(j)\propto j^{-\mu}$, $t$ is the measurement time and $t_0$ some attempt time. With increasing field the volume of the vortex bundle increases, resulting in an increase in the magnitude of the pinning barrier and smaller $S$. Unlike most oxide materials, a maximum $S$ in the vicinity of secondary peak is observed in the organic compound, as shown in Fig. 3. This result contradicts sharply the collective pinning model as the mechanism for the enhanced pinning effect. Rather, as will be discussed later, it is consistent with a decrease in the pinning volume due to dimensional crossover from three-dimensional (3D) vortex line to two-dimensional (2D) pancakes. The anomalous field and temperature dependence also excludes a matching effect model in which a peak in critical current is expected when the vortex lattice and the defect structure become commensurate with each other.[9]

The anomalous magnetization in the organic material is consistent with a dimensional crossover model proposed recently for $Tl_2Ba_2CuO_6$.[10] In this model, the secondary peak at high fields is due to the pinning of the 2D vortices. The crossover from 3D vortex line pinning to 2D pancake pinning occurs at the onset of the second peak. The critical field for dimensional crossover for very anisotropic systems has been predicted theoretically and given by[11,12] $H_{cr}\approx\phi_o/\lambda_J^2$, where $\lambda_J=\gamma s$, $\gamma$ is the anisotropy constant, and $s$ is the separation between the superconducting layers. A large anisotropy corresponds to a smaller critical field. In contrast to the collective pinning model, the pinning barrier is expected to decrease at the transition due the smaller volume of the 2D pancakes compared to the 3D lines, resulting in a larger $S$. Experimentally, the critical field is identified by the onset of the rising magnetization. For oxide superconductors, it is associated with the field where $M$ reaches the minimum. For the organic superconductors, the gradual transition in $M(H)$ makes the precise determination of $H_{cr}$ very difficult. For order of magnitude estimate, we take the approximate peak field as the critical field, i.e., $H_{cr}\approx 200$ G. Using the lattice spacing of 15 Å as the separation between the superconducting layers, $\gamma\approx 200$ is obtained. The large anisotropy is consistent with the reported values of similar compounds.

In summary, we have reported detailed magnetization studies on single crystals of a highly anisotropic organic superconductor $\kappa$-(BEDT-TTF)$_2$Cu[N(CN)$_2$]Br. The anomalous magnetization is observed below the crossover temperature of about 7 K. The irreversibility line shows a universal power-law temperature dependence $H_{rev} \propto (1-T/T_c)^{3/2}$ at high temperatures. The normalized relaxation rate shows a maximum near the onset of the magnetic anomaly for temperatures below 7 K. The results are consistent with the model of a dimensional crossover from 3D to 2D pinning. The gradual transition observed is qualitatively in agreement with the weak intrinsic pinning of the organic superconductors.


[1] J. M. Williams *et al.*, *Organic Superconductors* (Prentice-Hall, Englewood Cliffs, NJ, 1992).
[2] D. E. Farrell *et al.*, Phys. Rev. B **42**, 8694 (1990).
[3] Y. Kopelevich *et al.*, Physica C **183**, 345 (1991).
[4] P. Mansky, P. M. Chaikin, and R. C. Haddon, Phys. Rev. Lett. **70**, 1323 (1993); Phys. Rev. B **50**, 15 929 (1994).
[5] M. Lang *et al.*, Phys. Rev. B **49**, 15 227 (1994); **46**, 5822 (1992).
[6] A. M. Kini *et al.*, Inorg. Chem. **29**, 2555 (1990).
[7] F. Zuo *et al.*, Phys. Rev. B **52**, 13 126 (1995).
[8] L. Krusin-Elbaum *et al.*, Phys. Rev. Lett. **69**, 2280 (1992).
[9] G. Yang *et al.*, Phys. Rev. B **48**, 4054 (1993).
[10] F. Zuo *et al.*, Phys. Rev. B **52**, 755 (1995), and references therein.
[11] A. L. Glazman and A. E. Koshelev, Phys. Rev. B **43**, 2835 (1991).
[12] M. V. Feigel'man, V. B. Geshkenbein, and A. I. Larkin, Physica C **167**, 177 (1990); V. M. Vinokur, P. H. Kes, and A. E. Koshelev, *ibid.* **168**, 29 (1990).

# Experimental evidence of a crossover in the vortex dimensionality in high-$T_c$ superconductors

A. García, X. X. Zhang, and J. Tejada
*Departament de Física Fonamental, Universitat de Barcelona, Diagonal 647, E-08028 Barcelona, Spain*

Quantum motion of vortices in high-temperature superconductors (HTSCs) was studied via magnetic relaxation measurements performed with a commercial superconducting quantum interference device magnetometer. At a fixed temperature, the field dependence of the time-logarithmic magnetic relaxation rate normalized to the first magnetization value, $R=|d(M/M_0)/d\ \ln(t)|$, was investigated in different polycrystalline HTSCs: TlBaCaCuO (2212 and 2223 single phases), YBaCuO (123 phase), and (Hg,Tl)BaCaCuO (1223 phase). The results obtained for TlBaCaCuO 2223 phase and (Hg,Tl)BaCaCuO show a common trend: $R$ increases linearly with magnetic field up to a certain value, the dimensional crossover field $H_{3D\text{-}2D}$, above which it becomes field-independent. $H_{3D\text{-}2D}$ is a characteristic field which depends on the anisotropy parameter and the interlayer spacing of the material. The field dependence of $R$ can be ascribed to a crossover in the dimensionality of the object involved in the quantum process: above $H_{3D\text{-}2D}$, the longitudinal dimension of the tunneling object, $L_c$, is smaller than the interlayer distance, so the object is of two-dimensional (2D) nature (2D pancake vortices). Below $H_{3D\text{-}2D}$, 2D vortices in neighboring layers become coupled, so the tunneling object becomes three-dimensional (3D) in nature (3D flux-lines). The field dependences of $R$ obtained for TlBaCaCuO 2212 phase and YBaCuO show only the 2D and 3D vortex regimes, respectively. Well agreement between theoretical estimates and experimental values for the dimensional crossover field and normalized relaxation rates is achieved. © *1996 American Institute of Physics.* [S0021-8979(96)81308-5]

It is well known that, because of their layered structure and the confinement of conductivity in the $CuO_2$ planes, the superconductive properties of high-$T_c$ superconductors (HTSCs) present a very anisotropic behavior. In some cases, this behavior can be described as three-dimensional (3D), whereas in other cases as two-dimensional (2D). The crossover between both dimensionalities takes place when some characteristic length along the $c$ axis is of the order of the interlayer spacing $d$, the physical meaning of this characteristic length being different for each property. Therefore, at the same point in the $H-T$ plane some properties are 2D-like while some others are 3D-like, resulting in a complicated phase diagram. Among these properties, thermal fluctuations, pinning, and creep of vortices are of special interest for the study of the decay of critical currents in HTSCs.

A crossover in the dimensionality of thermal fluctuations at very low temperatures has been independently predicted by Vinokur *et al.*[1] and Feigel'man *et al.*:[2] thermal fluctuations are two-dimensional as long as the vortex lattice spacing in the $ab$-plane, $a_0\simeq(\Phi_0/B)^{1/2}$, remains smaller than the effective Josephson length characterizing the interlayer coupling along the $c$-axis, $R_J=\gamma d$, where $\gamma\equiv(\lambda_c/\lambda_{ab})$ is the anisotropy parameter of the material ($\lambda_c$ and $\lambda_{ab}$ are the London penetration depths along the $c$ axis and $ab$ plane, respectively). This conduction can be equivalently expressed in terms of the magnetic field as $H_a>H_{3D\text{-}2D}$, where

$$H_{3D\text{-}2D}\simeq\Phi_0/(\gamma d)^2 \tag{1}$$

is called the dimensional crossover field. When the opposite inequality holds, thermal fluctuations become 3D.

In the case of pinning, the characteristic length of the problem is the longitudinal dimension of the pinned object, $L_c$. A flux-line in the mixed state of a HTSC can be pictured as a stack of 2D pancake vortices lying in adjacent $CuO_2$ layers, connected by Josephson vortices.[3] Whenever $L_c<d$, 2D pancake vortices are independently pinned in each copper-oxide layer, and pinning is 2D in nature; in the opposite case, 2D pancake vortices lying in adjacent layers are coupled along the $c$-axis and pinning becomes 3D. Although, in principle, the dimensionalities of pinning and thermal fluctuations are independent one from each other, the crossover between 2D and 3D pinning of individual vortices at very low temperatures is predicted[1] to be also ruled by $H_{3D\text{-}2D}$.

As for the dimensionality of creep, the characteristic length in the general case of thermal activation is the perpendicular dimension of the object with respect to the hopping direction.[4] At very low temperatures, however, creep is dominated by quantum motion of individual vortices and the evolution of magnetization with time is essentially logarithmic for very long periods. The expressions for the 3D and 2D quantum relaxation rates normalized to the first magnetization value, $R=|d(M/M_0)/d\ \ln(t)|$, in the limit of strong ohmic dissipation, are given by the QCC theory (the subscript "$d$" stands for "dissipative limit"):[5]

$$R_{d,3D}\simeq(e^2/\hbar)(\rho_n/L_c),\quad \text{for } L_c>d; \tag{2a}$$

$$R_{d,2D}\simeq(e^2/\hbar)(\rho_n/d),\quad \text{for } L_c<d. \tag{2b}$$

In the Hall tunneling limit (zero dissipation), the expressions are the following (the subscript "$H$" stands for "Hall limit"):[6]

$$R_{H,3D}\simeq(n_s\xi^2L_c)^{-1},\quad \text{for } L_c>d; \tag{3a}$$

$$R_{H,2D}\simeq(n_s\xi^2d)^{-1},\quad \text{for } L_c<d\ . \tag{3b}$$

 0021-8979/96/79(8)/6589/3/$10.00 © 1996 American Institute of Physics 

In these expressions, $(e^2/\hbar)\simeq 4.1$ kΩ is the quantum of resistance, $\rho_n$ is the normal state resistivity in the $ab$ plane extrapolated at zero temperature, and $L_c\simeq(\xi/\gamma)(J_0/J_c)^{1/2}$ is the collective-pinning length along the $c$-axis, where the superconducting coherence length $\xi$, deparing current density $J_0$, and critical current density $J_c$, denote in $ab$-plane values. Finally, $n_s$ is the bulk density of superelectrons.

Notice that the criterion that distinguishes the creep dimensionality at very low temperatures is again the relation between $L_c$ and $d$, or, equivalently, $H_a$ and $H_{3D\text{-}2D}$: the 3D quantum rate holds for $H_a<H_{3D\text{-}2D}$, while in the opposite case is valid the 2D quantum rate. Notice also that the 3D quantum rate is directly proportional, through $L_c$ [see (2a) and (3a)], to $\gamma$. Recently, Daemen *et al.*[7] demonstrated that the anisotropy parameter is not a constant in HTSCs, but an increasing function of $H_0$, directly reflecting the field dependence of the penetration depth along the $c$-axis, $\lambda_c(H_a)$. Thus, the 3D quantum rate is expected to increase as $H_a$ increases up to $H_{3D\text{-}2D}$, above which a crossover to the field-independent [see (2b) and (3b)] 2D quantum rate should occur. In this article we show that the study of the field dependence of the normalized relaxation rate at a fixed very low temperature can be a very useful tool for the experimental detection of the dimensional crossover field.

Different polycrystalline systems were investigated: bulk sintered $YBa_2Cu_3O_7$ (Y-123), $Tl_2Ba_2Ca_2Cu_3O_{10}$ (Tl-2223), and $(Hg,Tl)Ba_2Ca_2Cu_3O_8$ (Hg-1223), and powder $Tl_2Ba_2CaCu_2O_8$ (Tl-2212). Details on each sample preparation are described elsewhere.[8] A commerical (Quantum Design) a.c. superconducting quantum interference device magnetometer ($1.8<T<400$ K; $H_{max}=55$ kOe) was used for the experiments. The procedure performed for each magnetic relaxation measurement was the following. The sample was first cooled from well above the superconducting transition temperature $T_c$ down to the target temperature with a magnetic field on [field-cooling (FC) process]. Once the target temperature was stable (the temperature stability in the low temperature range was 0.01 K), the field was removed and the time evolution of the remanent magnetization was recorded. Before each new measurement, trapped flux lines were removed by warming the sample well above $T_c$. At a given temperature, the process was repeated with different magnetic fields applied during the FC process. For each field, the first magnetization point was recorded at 60 s, and subsequent data were taken every 70 s, during a period of ~1 h.

In the whole magnetic field range investigated ($1<H_a<50$ kOe), all relaxation curves are linear with the logarithm of time in the scanned time window, except for an initial nonlinear decay, which could correspond to a reconfiguration of the inhomogeneous flux distribution caused by the sudden suppression of the magnetic field just before the measurement started. The initial nonlinear regime is enhanced in the Tl-2212 system, probably due to sample degration or signal contribution from the powder container. Only the linear regime of each curve was fitted to a time-logarithmic law, with great accuracy for all curves in all the samples.

Figure 1 presents the magnetic field dependence of the normalized relaxation rates of Hg-1223 at $T=2.8$ K and Tl-2223 at $T=2.4$ K. We show elsewhere[9] that the quantum regime manifests itself up to ≃2.5–3 K for $H_a=3$ and 6 kOe in Tl-2223, but only up to ≃2.1 K for $H_a=3$ kOe in Hg-1223. Therefore, while the normalized relaxation rate obtained for Tl-2223 at 2.4 K lies in the quantum regime, that obtained for Hg-1223 at 2.8 K falls off, but near that regime. Thus, in this case, $R$ should be not far from its quantum value, so we will trust the results at 2.8 K as representative of the magnetic field dependence of the actual quantum rate. Let us now turn to the discussion of the results. Both curves appearing in Fig. 1 show a common trend: $R$ increases with $H_a$ up to ≃10–16 kOe, and subsequently reaches a saturation value (≃1.55% for Tl-2223 and ≃1.85% for Hg-1223). As mentioned above, this behavior characterizes a transition in the dimensionality of the pinned object, from 3D to 2D as $H_a$ increases, the experimental dimensional crossover field being $H_{3D\text{-}2D}\simeq$10–16 kOe for both samples. Substitution of $\gamma\simeq 20$ (Ref. 10) and $d\simeq 18$ Å (Ref. 11) in Eq. (1) gives $H_{3D\text{-}2D}\simeq 16$ kOe for Tl-2223, in excellent agreement with the

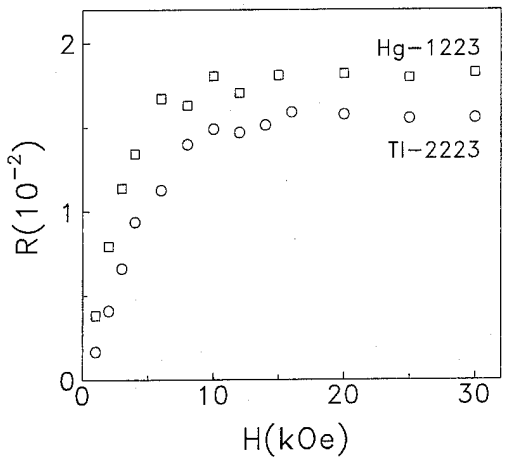



FIG. 1. Magnetic field dependence of the normalized relaxation rates corresponding to the remanent magnetization obtained for Tl-2223 at $T=2.4$ K (circles) and Hg-1223 at $T=2.8$ K (squares).

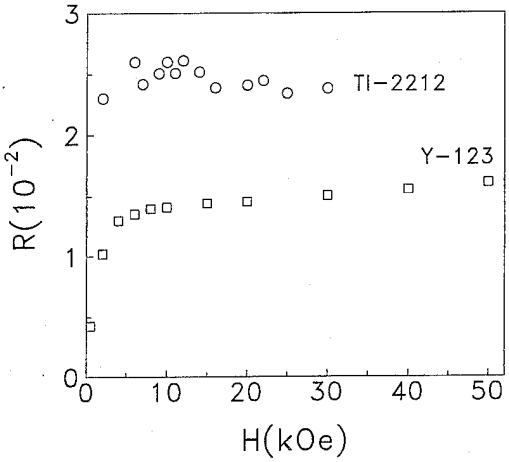



FIG. 2. Normalized relaxation rate as a function of the magnetic field applied during the FC process for Tl-2212 (circles) and Y-123 (squares) at $T=2.4$ K.

TABLE I. Relevant parameters for the different samples. From top to bottom: anisotropy parameter ($\gamma$); interlayer spacing ($d$); experimental (exp $H_{3D\text{-}2D}$) and estimated (est $H_{3D\text{-}2D}$) dimensional crossover field; experimental (exp $R_{2D}$), and dissipatively (est $R_{d,2D}$) and Hall estimated (est $R_{H,2D}$), 2D quantum rate.

| | Tl-2223 | Hg-1223 | Tl-2212 | Y-123 |
|---|---|---|---|---|
| $\gamma$ | 20 | 25–30 | 350 | 8 |
| $d$ (Å) | 18 | 16 | 16 | 12 |
| exp $H_{3D\text{-}2D}$ (kOe) | 10–16 | 10–16 | ··· | ··· |
| est $H_{3D\text{-}2D}$ (kOe) | 16 | ··· | 0.07 | 225 |
| exp $R_{2D}$ (%) | 1.55 | 1.85 | 2.4 | ··· |
| est $R_{d,2D}$ (%) | 2 | 2.3 | 2.4 | 3 |
| est $R_{H,2D}$ (%) | 6 | 7 | 7 | 9 |

experimental result. A similar estimate for Hg-1223 is not available for lack of its anisotropy parameter in the related literature. Nevertheless, from the experimental value of $H_{3D\text{-}2D}$ we can give an estimate of $\gamma$. Using Eq. (1) and assuming a value for $d$ similar to the $c$ axis of the tetragonal unit cell, $d \simeq 16$ Å, $\gamma \simeq 30$ is obtained, similar to that of Tl-2223 ($\gamma \simeq 20$) and Bi-2223 ($\gamma \simeq 30$),[12] and larger than that of the 1223 phase of the Tl-free Hg-based system ($\gamma \simeq 7$).[13] Finally, substitution of typical HTSCs values [$\rho_n \simeq 15\ \mu\Omega$ cm, $n_s \simeq 10^{12}$ cm$^{-3}$, $\xi \simeq 30$ Å] in Eqs. (2b) and (3b) gives an estimate of the 2D quantum plateau. Thus, $R_{d,2D} \simeq 2\%$ and $R_{H,2D} \simeq 6\%$ for Tl-2223, and $R_{d,2D} \simeq 2.3\%$ and $R_{H,2D} \simeq 7\%$ for Hg-1223, are obtained, in good qualitative (in the case of $R_{d,2D}$, also quantitative) agreement with the experimental plateau values.

The magnetic field dependence of the normalized relaxation rates of Tl-2212 and Y-123 at $T = 2.4$ K is shown in Fig. 2. Two different behaviors can be observed. For Tl-2212, the data are scattered around a plateau of $\simeq 2.4\%$, the minimum value of $H_a$ being 2 kOe. In the case of Y-123, $R$ presents an initial fast increase up to $H_a = 10$ kOe, above which slows down but does not reach a constant value. Both dependences can be understood by estimating the dimensional crossover field of each sample. Substitution in Eq. (1) of $\gamma \simeq 350$ (Ref. 14) and $d \simeq 15$ Å (Ref. 11), and $\gamma \simeq 8$ (Ref. 15) and $d \simeq 12$ Å (Ref. 16), gives $H_{3D\text{-}2D} \simeq 0.07$ and $\simeq 225$ kOe for Tl-2212 and Y-123, respectively. This means that in the case of Tl-2212 we are detecting only the 2D regime, while only the 3D regime shows up for Y-123. A more accurate magnetic fields scan of the latter, including extension to fields >55 kOe, is needed in order to clarify the two different increasing regimes which cannot be simply understood in the context of the present work. Finally, the experimental plateau value observed for Tl-2212, $\simeq 2.4\%$, is in excellent quantitative agreement with the 2D dissipative estimate [Eq. (2b)], $R_{d,2D} \simeq 2.4\%$, but compares only qualitatively to the Hall estimate [Eq. (3b)], $R_{H,2D} \simeq 7\%$. Table I summarizes the relevant experimental and estimated parameters of the different samples investigated.

In summary, we have investigated the magnetic field dependence at very low temperatures of the normalized relaxation rate of four different HTSCs. A crossover in the dimensionality of the object involved in the quantum process has been detected in two samples (Tl-2223 and Hg-1223). In the other samples, only 2D (Tl-2212) or 3D(Y-123) behavior could be observed. An exhaustive scan of the whole magnetic field range is needed to obtain more accurate values of the dimensional crossover field $H_{3D\text{-}2D}$.

J.T. acknowledges financial support from the European Community. X.X.Z. thanks the University de Barcelona for financial support. A.G. thanks the Generalitat de Catalunya for a Ph.D. research grant.

[1] V. M. Vinokur, P. H. Kes, and A. E. Koshelev, Physica C **168**, 29 (1990).
[2] M. V. Feigel'man, V. B. Geshkenbein, and A. I. Larkin, Physica C **167**, 177 (1990).
[3] J. R. Clem, Phys. Rev. B **43**, 7837 (1991).
[4] M. V. Feigel'man, V. B. Geshkenbein, A. I. Larkin, and V. M. Vinokur, Phys. Rev. Lett. **63**, 2303 (1989).
[5] G. Blatter, M. V. Feigel'man, V. B. Geshkenbein, A. I. Larkin, and V. M. Vinokur, Rev. Mod. Phys. **66**, 1125 (1994).
[6] M. V. Feigel'man, V. B. Geshkenbein, A. I. Larkin, and S. Levit, Pis'ma Zh. Eks. Teor. Fiz. **57**, 699 (1993) [Sov. Phys. JETP Lett. **57**, 711 (1993)].
[7] L. L. Daemen, L. N. Bulaevskii, M. P. Maley, and J. Y. Coulter, Phys. Rev. Lett. **70**, 1167 (1993); Phys. Rev. B **47**, 11 291 (1993).
[8] A. García, X. X. Zhang, A. M. Testa, D. Fiorani, and J. Tejada, J. Phys. Condens. Matter **4**, 10 341 (1992); X. X. Zhang, A. García, J. Tejada, Y. Xin, and K. W. Wong, Physica C **232**, 99 (1994). X. X. Zhang, A. García, J. Tejada, Y. Xin, G. F. Sun, and K. W. Wong, Phys. Rev. B **52**, 1325 (1995).
[9] A. García, X. X. Zhang, and J. Tejada, *Quantum Vortex Motion in High-$T_c$ Superconductors*, this Conference.
[10] O. Laborde, P. Monceau, M. Potel, J. Padiou, P. Gougeon, J. C. Levet, and H. Noel, Physica C **162–164**, 1619 (1989).
[11] R. M. Hazen, L. W. Finger, R. J. Angel, C. T. Prewitt, N. L. Ross, C. G. Hadidiacos, P. J. Heaney, D. R. Veglen, Z. Z. Sheng, A. El Ali, and A. M. Hermann, Phys. Rev. Lett. **60**, 1657 (1988).
[12] I. Matsubara, H. Tanigawa, T. Ogura, H. Yamashita, M. Kinoshita, and T. Kawai, Phys. Rev. B **45**, 7414 (1992).
[13] M.-K. Bae, M. S. Choi, S. Lee, S.-I. Lee, and W. C. Lee, Physica C **231**, 249 (1994).
[14] D. E. Farrell, R. G. Beck, M. F. Booth, C. J. Allen, E. D. Bukowski, and D. M. Ginsberg, Phys. Rev. B **42**, 6758 (1990).
[15] D. E. Farrell, J. P. Rice, D. M. Ginsberg, and J. Z. Liu, Phys. Rev. Lett. **64**, 1573 (1990).
[16] J. D. Jorgensen, M. A. Beno, D. G. Hinks, L. Soderholm, J. Volin, R. L. Hitterman, J. D. Grace, I. K. Schuller, C. U. Segre, K. Zhang, and M. S. Kleefisch, Phys. Rev. B **36**, 3608 (1987).

*Published without author corrections*

# Vortex gliding between Cu–O planes in an anisotropic high temperature superconductor (abstract)

C. A. Durán
*Phase Metrics, 10260 Sorrento Valley Road, San Diego, California 92121*

P. L. Gammel and D. J. Bishop
*AT&T Bell Laboratories, 600 Mountain Avenue, Murray Hill, New Jersey 07974*

The magnetooptical technique was used to directly observe the magnetic flux penetration in single crystals of the La–Sr–Cu–O superconductor. The large size of the crystals (several millimeters along the three axes) allows for observations to be made along the different crystalline orientations. In a previous study,[1] we reported on direct measurements of critical currents and the dependence of their anisotropy on the amount of Sr doping. When looking at the behavior of vortices which are parallel to the Cu–O planes, we observed that the roughness of the flux fronts was greatly magnified for the highly anisotropic samples. This suggested that the vortices were moving between the planes, as if they were in independent channels. In this communication, we report on observations made when an additional field component is applied along the *c* axis. Our experiments show that this additional component strongly suppresses the vortex penetration, drastically reducing the apparent anisotropy of the critical currents. We argue that this behavior is consistent with a picture in which the vortices easily move ("glide") between the Cu–O planes, and only feel the pinning potential when they are tilted by the additional field component, and thus forced to "puncture" the planes. © *1996 American Institute of Physics.* [S0021-8979(96)63608-X]

---

Experimental work done at AT&T Bell Laboratories, Murray Hill, New Jersey 07974.

[1] C. A. Durán *et al.*, Phys. Rev. B **49**, 3608 (1994).

 0021-8979/96/79(8)/6592/1/$10.00 © 1996 American Institute of Physics

# Magnetic field and temperature dependence of critical current densities in multilayer $YBa_2Cu_3O_{7-\delta}$ films

S. Afonso, F. T. Chan, K. Y. Chen, G. J. Salamo, Y. Q. Tang, R. C. Wang,[a] X. L. Xu,[b] and Q. Xiong
*Physics Department/High Density Electronics Center, University of Arkansas, Fayetteville, Arkansas 72701*

G. Florence, S. Scott, S. Ang, W. D. Brown, and L. W. Schaper
*Electrical Engineering Department/High Density Electronics Center, University of Arkansas, Fayetteville, Arkansas 72701*

In order to build high-temperature superconductor (HTS) multichip modules (MCMs), it is necessary to grow several epitaxial layers of YBCO that are separated by thick dielectric layers without seriously affecting the quality of the YBCO layers. In this work, we have successfully fabricated YBCO/YSZ/$SiO_2$/YSZ/YBCO structures on single-crystal $LaAlO_3$ substrates using a combination of pulsed laser deposition for the YBCO layers and ion-beam-assisted rf sputtering to obtain biaxially aligned YSZ intermediate layers. The bottom YBCO layer had a $T_c \sim 89$ K, $J_c \sim 7.2\times10^5$ A/cm$^2$ at 77 K, whereas the top YBCO layer had a $T_c \sim 86$ K, $J_c \sim 6\times10^5$ A/cm$^2$ at 77 K. The magnetic field and temperature dependence of $J_c$ for the YBCO films in the multilayer have been obtained. The results for each of the YBCO layers within the YBCO/YSZ/$SiO_2$/YSZ/YBCO structure are quite similar to those for a good quality single-layer YBCO film. © *1996 American Institute of Physics.* [S0021-8979(96)03308-9]

## I. INTRODUCTION

In electronic applications of high-temperature superconductor (HTS) thin films, the critical current density ($J_c$) is an important characteristic. One of the potential applications of high-temperature superconducting films is as electronic interconnects on a multichip module (MCM).[1] Since there are a minimum of two HTS thin films, separated by thick dielectric layers required, in HTS multichip modules (MCMs), it is necessary to know if the quality of the HTS layers is still maintained after the entire fabrication process is completed. In addition to the critical temperature ($T_c$) and critical current density at zero field, the dependence of $J_c$ on an externally applied magnetic field and the temperature for the entire multilayer structure is crucial information for electronic applications. The YBCO/YSZ/$SiO_2$/YSZ/YBCO multilayer structure has been fabricated by Reade *et al.*[2] They reported cracking in the top YBCO layer, which limited their investigation of the properties of the multilayered structure.

In this article, we report a study of the temperature and magnetic field dependence of $J_c$ for both YBCO layers in a YBCO/YSZ/$SiO_2$/YSZ/YBCO multilayer structure[3] performed by the magnetization method. Our results show that the temperature and magnetic field dependence of $J_c$ of the YBCO layers of these samples are similar to those of high quality single-layer YBCO thin films.

## II. EXPERIMENT

The YBCO/YSZ/$SiO_2$/YSZ/YBCO multilayer samples investigated here were prepared by using a combination of pulsed laser deposition and ion-beam-assisted magnetron sputtering. Details of the technique will be described elsewhere.[3] In short, a 200-nm-thick $YBa_2Cu_3O_{7-\delta}$ (bottom YBCO, layer 1) film was deposited on a single-crystal $LaAlO_3$ substrate (100 orientation and area $1\times1$ cm$^2$) by pulsed laser ablation at a substrate temperature of ~750 °C. Ion-beam-assisted rf sputtering was used to deposit biaxially aligned 200-nm-thick yttria-stabilized zirconia (YSZ) as a capping layer (layer 2). Next a 1-$\mu$m-thick, amorphous $SiO_2$ layer (layer 3) was deposited on layer 2 at room temperature by rf sputtering. The capping layer (YSZ) is used to prevent diffusion of the third $SiO_2$ layer into the top YBCO layer. A fourth layer (biaxially aligned YSZ) was then deposited on the $SiO_2$ layer to a thickness of 200 nm using the same method as for layer 2. This layer is very important. It not only functions as protection against the diffusion of the third $SiO_2$ layer into the YBCO layer, it also allows good epitaxial YBCO growth if it has a well-aligned structure. Finally, the top YBCO layer (layer 5) was deposited by laser ablation under the same conditions as was used for layer 1.

The orientation of the YSZ and YBCO layers was characterized by x-ray diffraction. The magnetization $M(H)$ loop was measured using a Quantum Design Magnetometer in fields up to 4 T, applied parallel to the $c$-axis direction and at a fixed temperature. This was repeated for different temperatures ranging from 5 to 77 K. The values of $J_c$ were calculated using Bean's model. The electrical resistance was measured using the standard four-lead technique.

## III. RESULTS AND DISCUSSION

X-ray diffraction data showed that all samples investigated here were single-phase highly $c$-axis oriented with very good in-plane epitaxy (Fig. 1). There were no cracks observed in the top YBCO layer. The resistance $R(T)$ and magnetization $M(T)$ of the samples were carefully measured for each YBCO layer. Figure 2 shows the typical resistance as a function of temperature for the top YBCO layer. The

[a]Permanent address: Department of Materials Science, Fudan University, Shanghai, People's Republic of China.
[b]Permanent address: Ion Beam Laboratory, Shanghai Institute of Metallurgy, Chinese Academy of Sciences, Shanghai, People's Republic of China.

 0021-8979/96/79(8)/6593/3/$10.00 © 1996 American Institute of Physics 

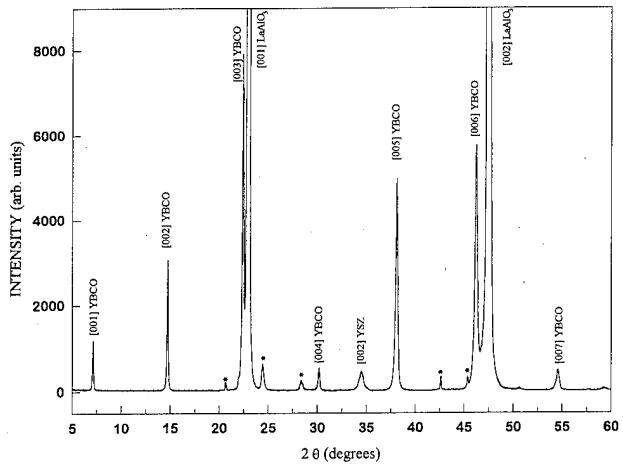



FIG. 1. $\theta$-$2\theta$ x-ray diffractometer pattern for the YBCO/YSZ/$SiO_2$/ YSZ/ YBCO structure on [001] $LaAlO_3$ (*: indicate substrate impurity peaks seen in the bare substrates of the same batch).

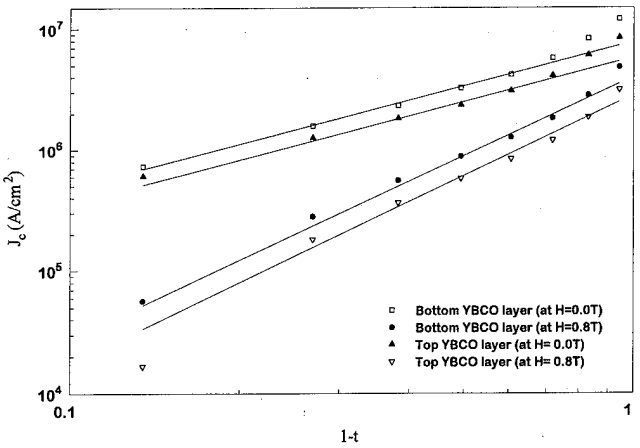



FIG. 3. Logarithmic plots of $J_c$ vs $1-t$ for each of the YBCO layers within the multilayer structure. Straight lines are the curve fits to $(1-t)^n$, where $n\sim1.3$ for $H=0.0$ T and $n\sim2.1$ for $H=0.8$ T.

zero resistance temperature for this YBCO layer is about 86 K with a transition width of about 2 K. The $M(T)$ data for a multilayer sample are shown in the inset of Fig. 2. As can be seen in the inset of Fig. 2, the onset transition of the $M(T)$ curve is about 89 K. A second transition (indicated by the arrow in the inset of Fig. 2) is consistent with the $T_c$ of the top YBCO layer measured by the transport method (Fig. 2). In order to verify this, $T_c$ was remeasured again after the top layer of YBCO was etched away by using a dilute EDTA solution, and the onset transition was found to be about 89 K.

The critical current density $J_c$ of the samples were measured by the magnetization method and calculated using Bean's model. For a rectangular single-layer film, $J_c$ can be calculated from the following formula:[4]

$$J_c=10[M_+(H)-M_-(H)]/L_1[1-(L_1/3L_2)]V. \qquad (1)$$

In Eq. (1), $M_+(H)$ and $M_-(H)$ are the magnetization of the decreasing and increasing field branches in electromagnetic units (emu), respectively; $V$ is the volume of the thin film in cm$^3$; $L_1$ and $L_2$ are the short and long sides of the samples in cm, respectively. We have assumed that $J_c$ is independent of the $B$ field and excluded the anisotropic critical currents in the above calculation. In order to determine $J_c$ of both the top and bottom YBCO layers, the magnetization $M^m_+(H)$ and $M^m_-(H)$ for the multilayer film was measured first, then the magnetization $M^b_+(H)$ and $M^b_-(H)$ for the bottom layer was measured after the top layer of YBCO was etched away. In this article we use superscript $t$ and $b$ for the parameters related to the top and bottom YBCO layer in the multilayer film, then $J_c$ for the bottom layer should be

$$J^b_c=10[M^b_+(H)-M^b_-(H)]/L^b_1[1-(L^b_1/3L^b_2)]V^b, \qquad (2)$$

and for the top layer in the multilayer film,

$$J^t_c=10\{[M^m_+(H)-M^b_+(H)] -[M^m_-(H)-M^b_-(H)]\}/L^t_1[1-(L^t_1/3L^t_2)]V^t. \qquad (3)$$

The $J_c$ of the top YBCO layer was found to be about $6\times10^5$ A/cm$^2$, and a value of $\sim7.2\times10^5$ A/cm$^2$ was obtained for the bottom layer at 77 K under zero magnetic field. $J_c$, as a

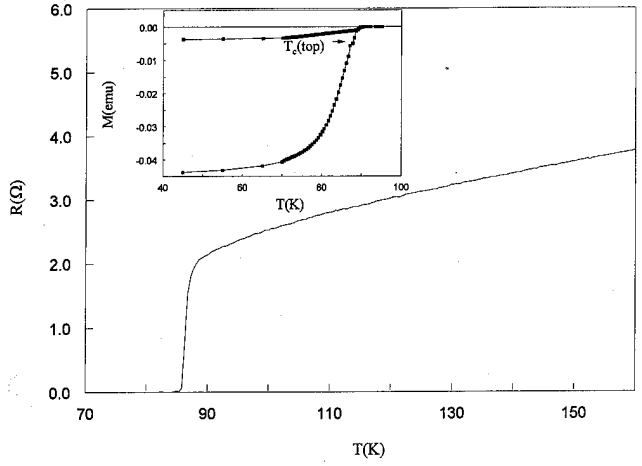



FIG. 2. Resistance vs temperature for the top YBCO layer in the YBCO/ YSZ/$SiO_2$/YSZ/YBCO/$LaAlO_3$ multilayer structure. Inset: magnetization $M$ as a function of $T$ for the entire multilayer structure.

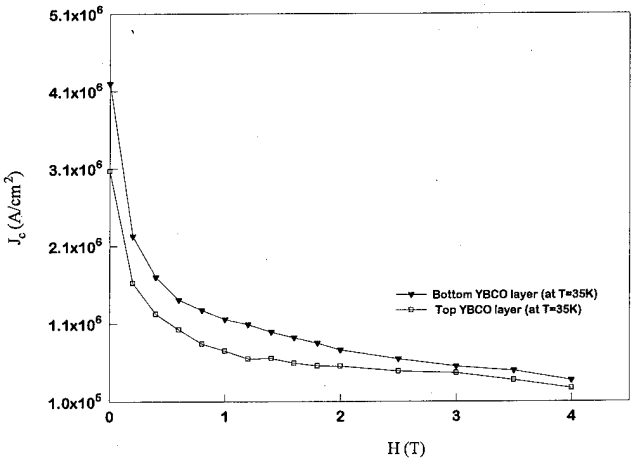



FIG. 4. Magnetic field dependence of $J_c$ for top and bottom YBCO layers at 35 K. Field is applied perpendicular to $a-b$ plane.

function of $(1-t)$, is shown in Fig. 3 for different values of the magnetic field, where $t=T/T_c$. It was found that, for both YBCO layers, the temperature dependence of $J_c$ is similar to that for a good quality, single-layer YBCO film.[5–7] The magnetic field dependence of $J_c$ for both YBCO layers at 35 K are shown in Fig. 4. It clearly shows that $J_c$ for both top and bottom YBCO films essentially has the same magnetic field dependence as that for the high quality, single-layer YBCO film.[5–7]

## IV. SUMMARY

A good quality YBCO multilayer structure has been fabricated using laser ablation and ion-beam-assisted rf sputtering. The dependence of $J_c$ on the temperature and magnetic field for both YBCO layers in the multilayer has been determined. The results suggest that the temperature and magnetic field dependence of $J_c$ of the YBCO layers in the multilayer structure are not altered appreciably by the multilayer growth processes.


## ACKNOWLEDGMENTS

This work was supported in part by NSF DMR 9318946, the High Density Electronics Center at the University of Arkansas, DARPA (Contract No. MDA 972-90-J-1001) and through the Texas Center for Superconductivity at the University of Houston.



[1] M. J. Burns, K. Char, B. F. Cole, W. S. Ruby, and S. A. Sachtjen, Appl. Phys. Lett. **62**, 1435 (1993).
[2] R. P. Reade, P. Beardahl, R. E. Russo, and L. W. Schaper, Appl. Phys. Lett. **66**, 2001 (1994).
[3] S. Afonso, Q. Xiong, K. Y. Chen, F. T. Chan, G. J. Salamo, Y. Q. Tang, G. Florence, S. Scott, S. Ang, W. D. Brown, and L. W. Schaper (unpublished).
[4] E. M. Gyorgy, R. B. van Dover, K. A. Jackson, L. F. Schneemeyer, and J. V. Waszczak, Appl. Phys. Lett. **55**, 283 (1989).
[5] Q. Xiong, W. Y. Guan, P. H. Hor, and C. W. Chu, Chin. J. Phys. **30**, 851 (1992).
[6] D. W. Chung, I. Maartense, T. L. Peterson, and P. M. Hemenger, J. Appl. Phys. **68**, 3772 (1990).
[7] S. B. Ogale, D. Dijkkamp, T. Venkatesan, X. D. Wu, and A. Inam, Phys. Rev. B **36**, 7210 (1987).

# Flux trapping and levitation forces in directionally solidified superconducting $YBa_2Cu_3O_7$ ingots

J. Mora, M. Carrera, X. Granados, J. Fontcuberta, S. Piñol, and X. Obradors
*Institut de Ciència de Materials de Barcelona, CSIC, Campus U.A.B., Bellaterra 08193, Catalunya, Spain*

$YBa_2Cu_3O_7$ cylinders with 10%–20% of $Y_2BaCuO_5$ and 1% $CeO_2$ additions have been directionally solidified under a temperature gradient. It is shown that a steady growth regime of domains, typically 1 cm in diameter, is established after polynucleation at the bottom of the cylinders on the substrate interface. The length of the region where a steady growth proceeds is limited by the liquid loss, which induces an enrichment in unreacted $Y_2BaCuO_5$ in the upper part of the cylinder and a polycrystalline structure. The vertical and lateral magnetic levitation forces and flux trapping profiles have been measured and a direct correlation with the size and location of the domains has been found. © *1996 American Institute of Physics.* [S0021-8979(96)03408-5]

## I. INTRODUCTION

Development of high $T_c$ superconducting materials for levitation and stabilization purposes needs an optimization of bulk electromagnetic properties of relatively large shaped specimens. To this regard the first issue is to obtain single domain ingots, free from large angle grain boundaries. Magnetic levitation applications based in $YBa_2Cu_3O_7$ (YBCO) bulk superconducting materials can nowadays be developed because melt processing techniques allow the fabrication of big tiles with high critical currents.[1,2] The growth process of these big tiles (2–3 cm in diameter) is however complex and several techniques, such as top seeding, have been used to control the nucleation processes.[3,4] Directional solidification under a small temperature gradient is the simplest method to control the growth process and it has been indeed used successfully in the growth of long YBCO bars with small cross sections ($\phi \approx 8$ mm).[5,6] The extension of this methodology to bigger cross sections is not without difficulties and an exhaustive study of the process methodology, in connection with microstructural observations and levitation force measurements, is needed. In this work we present preliminary results concerning the growth process of cylinders having 20 mm in diameter, as well as characterize their texture, flux trapping properties, and magnetic levitation forces.

## II. DIRECTIONAL SOLIDIFICATION

Presintered cylindrical pellets with a typical height of 30 mm and a diameter of 20 mm, and compositions: (A) (123)+10 wt. % (211), (B): 123+15% 211, and (C): 123 +20% 211, are slowly cooled at 1 °C/h from a maximum temperature of 1060 °C in a temperature gradient of 10 °C/cm. All samples contain 1 wt. % $CeO_2$ addition because it allows to optimize the melt viscosity and to refine the resultant 211 precipitate size.[5,6] In this work, only samples nucleated at the bottom are investigated. The alumina substrates are covered by some $CeO_2$ powder in order to avoid reaction with the ceramic block.

From microstructural observations, using polarized light, scanning electron microscopy, and x-ray diffraction pole figures,[7] we can conclude that three regions characterize these cylinders. In region I above the interface with the substrate, a multinucleation process occurs. In region II a few domains remain after a growth competition stage (typically 2–4, depending on the 211 content). No major porosity was observed in the samples and the 211 precipitates were distributed homogeneously in this initial region of the crystallization (about 10 mm in height). However, when advancing vertically along the cylinder, a progressive increase of the concentration of 211 phase is observed due to some liquid loss which perturbs the steady growth of the big domains and, finally, originates new nucleation phenomena (region III). We conclude then that only the central 10–20 mm of the cylinder can be used to investigate the levitation force of these materials.

X-ray pole figures indicated that in zone II the bigger domain has the $c$ axis aligned along the cylinder axis while the $c$ axis of the secondary domains lie 30–45 deg apart. Finally, in region III, where an enrichment in 211 phase occurs, the number of domains is much higher indicating a multinucleation process.[7]

Inductive critical currents of small pieces (few mm) extracted from single domains have been found to be very similar to those previously published on samples with similar concentration of 211 particles (up to $10^5$ A/cm$^2$ at 77 K and zero field).[8]

## III. LEVITATION FORCES

The integral vertical levitation force ($F_z$) and the transversal force ($F_x$) were measured for different samples at 77 K by using a triaxial force sensor based on strain gauges and having a computer controlled movement along two perpendicular ($z$,$x$) axis. All the materials were tested with the same NdFeB (PM) having $\phi=25$ mm, $h=20$ mm, and $B_r=0.3$ T placed above the superconducting cylinders (SCs) of dimensions: $\phi=19$ mm, $h\approx 13$ mm. The relative displacement of the superconductor and the magnet was done quasistatically (1.2 mm/s). Because of the growing conditions it will become important to distinguish between measurements performed approaching the magnet towards the top (Top) or the bottom (Bot) of the samples. In Fig. 1(a) we show a typical levitation force loop obtained, after a zero field cooling (ZFC) procedure, for sample B in the Top configuration. In the figure we also include the hysteresis loop obtained after the first cycle, where it is clear that the trapped flux considerably decreases the vertical force. This effect can be

 0021-8979/96/79(8)/6596/3/$10.00 © 1996 American Institute of Physics

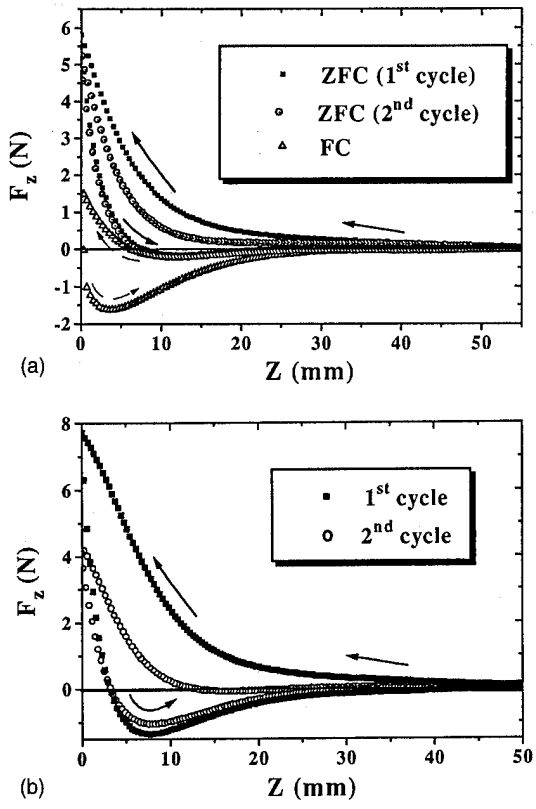



FIG. 1. Axial force vs displacement loops obtained for sample B in the Top (a) and Bot (b) configurations after a ZFC process. In (a) FC measurements are also included.

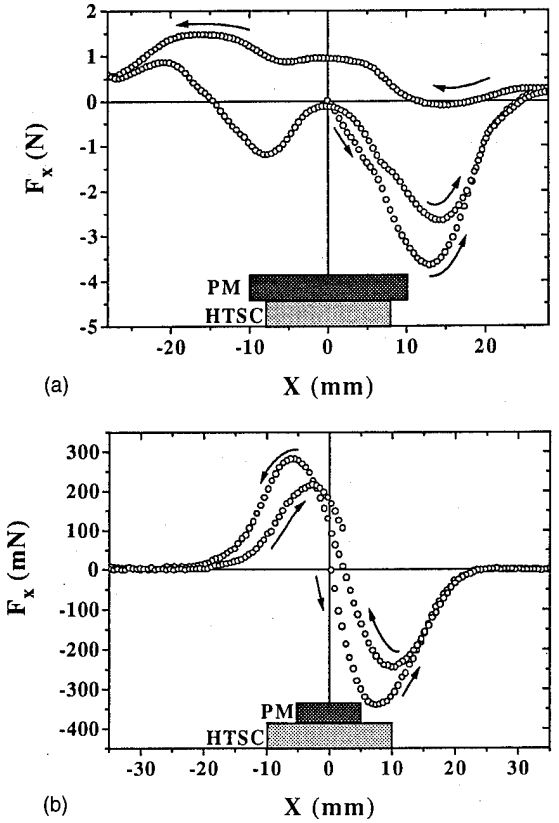



FIG. 2. Transverse force vs lateral displacement after a FC process. (a) and (b) refer to measurements performed with the larger and smaller PM, respectively.

even better appreciated in the hysteresis loop obtained after a FC procedure where trapped flux is greater [see Fig. 1(a)] and the maximal repulsive force is only about 1/4 of the force obtained after a ZFC. This difference arises because of the higher magnetization obtained after a ZFC process in samples having strong flux pinning where the flux front does not penetrate the sample completely. In Fig. 1(b) we show the force versus displacement loops obtained for sample B in the Bot configuration (two domains in the x-ray pole figures). The essential features of this figure are identical to those of the Top configuration, however $F_z(z)$ is significantly lower in the Top case. This result is in agreement with the observation of a multidomain growth in the upper part of the cylinders (near Region III) as discussed above. Similarly, the maximum repulsive force of sample $C$ only achieves 47% of that on B sample, also in agreement with the increase in the number of domains in the x-ray pole figures. The maximal ideal repulsive force for our particular SC/PM geometry assuming a fully shielded state has been evaluated using finite element electromagnetic calculations.[9] We have estimated that the measured maximal $F_z$ is about 45% of the ideal corresponding to a magnetic pressure of 5.7 N/cm$^2$. Similar percentages have been reported recently.[10]

The axial levitation force of a permanent magnet over a superconductor is proportional to the $z$ component of the vector: $d\mathbf{F}=(\mathbf{M}\cdot\nabla)\mathbf{B}_{ex}dV$, where $\mathbf{B}_{ex}$ is the induction generated by the magnet and $\mathbf{M}$ is the magnetization of the superconductor. If large angle grain boundaries exist among the single domains, flux penetration occurs through these boundaries and the critical state is established only within the single domains. In this way $M$ and $F_z$ are reduced even if $J_c$ remains constant within the domains.

Transverse force measurements were also obtained when a lateral displacement was introduced after a field cooling process. A typical hysteresis loop is displayed in Fig. 2(a) where the magnet stays at 1.5 mm above the superconductor B (15% 211). The stiffness constant corresponding to the linear recuperation force observed near the origin was found to be 300 N/m. Although this value is similar to that observed by other authors in similar geometries,[11] we should recall that the shape of the $F_x(x)$ loop is strongly dependent on the particular configuration PM/SC used. As an example, we have performed $F_x(x)$ measurements by using a PM with reduced dimensions ($\phi$=12 mm, $h$=5 mm, and $B_r$=0.12 T). Comparison of Figs. 2(a) and 2(b) strongly emphasizes this important technological point and illustrates that the maximal restoring force is obtained when the PM reaches the edges of the SC. We also note that a clear asymmetry is observed in the transversal force hysteresis loops $F_x(x)$. This anomalous behavior reflects the absence of cylindrical symmetry associated to the two prominent domains observed in the x-ray texture analysis. We suggest that transversal force hysteresis loops can be used as a sensitive tool to detect the existence of a multidomain structure without uniaxial symmetry. Similar measurements performed for sample C have revealed smaller lateral forces.

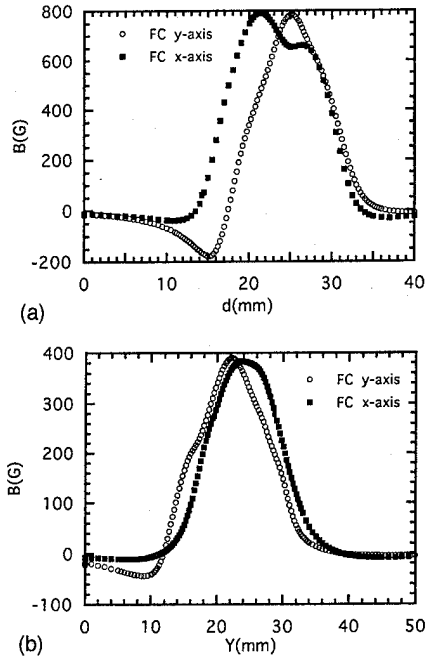



FIG. 3. Remanent induction $B_z(x)$ and $B_z(y)$ flux profiles scanned along two perpendicular directions after a 0.29 T FC process. (a) B sample Bot, (b) B sample Top.

An additional test of the sample homogeneity can be gained by means of remanence magnetic field profiling with Hall microprobes. Measurements have been performed in the remanent state, after cooling the samples in fields of 0.29 T generated by a permanent magnet. In Fig. 3(a) we show $B_z(x)$ and $B_z(y)$ flux profiles in B sample (Bot). A prominent asymmetry, similar to that observed in transverse force measurement, is appreciated. Measurements have also been performed in the Top configuration where a decrease of the remanence is found in agreement with the lower levitation forces [Fig. 3(b)]. This unequal electromagnetic behavior of both faces of the superconducting sample also raises the question of the relevance of the thickness on the final performance of the samples.

Flux mapping measurements can be used to compute the current distribution in the superconducting samples.[12] However the multidomain character of the samples introduces a some uncertainty concerning the definition of the critical state. Further theoretical analysis of these measurements will be reported elsewhere.[9]

In conclusion, we have shown that the directional solidification process allows the fabrication of long cylinders of $YBa_2Cu_3O_7$ for developing big tiles for magnetic levitation applications. The optimization of the performance of these tiles requires to limit the multinucleation process which induces the formation of several domains and reduces the levitation force.

## ACKNOWLEDGMENTS

We are grateful to CICYT (MAT91-0742), Programa MIDAS (93-2331), and EC-EURAM (BRE2CT94-1011).

[1] M. Murakami, ed., *Melt Processed High Temperature Superconductors* (World Scientific, Singapore, 1992).
[2] K. Salama, V. Selvamanicham, and D. F. Lee, in *Processing and Properties of High $T_c$ Superconductors*, edited by S. Jin (World Scientific, Singapore, 1993), Vol. 1, Chap. 5, pp. 155–211.
[3] L. Gao *et al.*, Appl. Phys. Lett. **64**, 520 (1994).
[4] M. Morita *et al.*, in *Advances in Superconductivity III*, edited by K. Kajimura and H. Hayakawa (Springer, New York, 1991), p. 733.
[5] S. Piñol *et al.*, Appl. Phys. Lett. **65**, 1448 (1994).
[6] S. Piñol *et al.*, IEEE Trans. Appl. Supercond. **5**, 1549 (1995); N. Vilalta *et al.* (to be published).
[7] J. Mora *et al.*, Proc. Eur. Conf. Appl. Superc., Edinburgh 1995 (in press), Vol. 1, p. 679.
[8] V. Gomis *et al.*, in *Applied Superconductivity*, edited by H. C. Freyhardt (DGM-I Verlag, 1993), p. 373; B. Martinez *et al.*, Phys. Rev. B (in press).
[9] J. Mora *et al.* (to be published).
[10] T. Strasser *et al.*, Proc. Eur. Conf. Appl. Supercond., Edinburgh 1995 (in press).
[11] H. J. Bornemann *et al.*, Appl. Supecond. **2**, 439 (1995).
[12] W. Xing *et al.*, J. Appl. Phys. **76**, 4244 (1994); F. Frangi *et al.*, Physica C **224**, 20 (1994); T. Schuster *et al.*, Phys. Rev. B **50**, 16684 (1994).

# Magnetostatic effect on magnetic flux penetration in superconducting Nb film covered with a micron–size magnetic particle array

Yukio Nozaki, Yoshichika Otani,[a] Katharina Runge, and Hideki Miyajima
*Department of Physics, Faculty of Science and Technology, Keio University, Hiyoshi 3-14-1, Kohoku, Yokohama 223, Japan*

Bernard Pannetier
*Centre de Recherches sur les Très Basses Températures, CNRS, F-38042 Grenoble, France*

Jean Pierre Nozières
*Laboratoire Louis Néel, F-38042 Grenoble, France*

Magnetostatic effect of the micron-size ferromagnetic particle array on a two-dimensional superconductor was investigated. In the bare Nb film, a sharp drop in magnetization due to the flux rearrangement was observed, whereas this behavior was not observed for the Nb film with the ferromagnetic particles arranged on top. The difference in the magnetization curves may be attributed to the regulated flux penetration process by the ferromagnetic particle array. © *1996 American Institute of Physics.* [S0021-8979(96)01108-2]

## I. INTRODUCTION

The hybrid system is a two-dimensional superconducting film covered with ferromagnetic square particles of micron size. The magnetic particles are arrayed in a square lattice and are uniaxially magnetized along an edge. The array produces a spatially modulated stray field which periodically suppresses the superconducting order parameter of the underlying Nb film. The hybrid system thus exhibits some interesting behaviors. The transition temperature measured in a perpendicularly applied magnetic field to the Nb film surface shows the quantum oscillation[1,2] reminiscent of the Little–Parks oscillation.[3] Moreover, the particle acts as a magnetic flux guide which regulates the flux penetration into the Nb film.[4] Interesting behaviors are also observed in the field dependence of the magnetization. The hysteresis loop of the bare Nb film exhibits an anomalous magnetization drop below 2.5 mT, while that of the hybrid system does not show such a tendency[4] except for the periodical flux jumps. These flux jumps are attributed to the flux quantization into the normal core created by the stray field of the particle.[5]

In this study, we focus our discussion on the origin of the magnetization drop observed in the bare Nb film in relation to the magnetostatic effect observed in the hysteresis loop of the hybrid system.

## II. EXPERIMENT

An array of ferromagnetic amorphous $Sm_{33}Co_{67}$ particles were fabricated on a Nb film of 20 nm thickness by means of high-resolution electron-beam lithography and sputter deposition techniques. The details of the sample preparation are described in Refs. 1 and 5. During the deposition of $Sm_{33}Co_{67}$, the magnetic field of 50 mT was applied parallel to an edge of the particles. This procedure induced the uniaxial magnetic anisotropy of $1\times10^5$ J/m$^3$ along the edge. It is remarked that the magnetic particles are sandwiched by $Si_3N_4$ buffer and protecting layers (20 nm in thickness) in order to avoid the superconducting proximity effect and the oxidation of the particle surface. The array consists of $2\times10^5$ square particles with an edge length of 2 $\mu$m, a thickness of 200 nm, and a separating distance of 4 $\mu$m. The dimensions of the underlying Nb film are 2 mm×2 mm×20 nm. With the aim of clarifying the effect of the

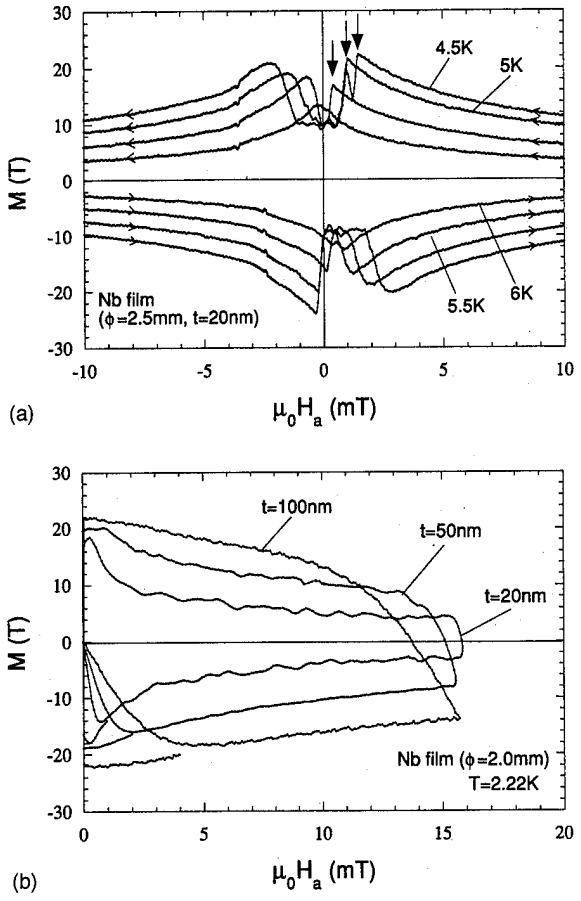



FIG. 1. Magnetic hysteresis loops for Nb films without magnetic particles. (a) and (b) show the variation of the loop with temperature and thickness, respectively. The arrows in (a) indicate the peak field $H_p$.

[a]Present address: Department of Materials Science, Faculty of Engineering, Tohoku University, Sendai 980-77, Japan.

 0021-8979/96/79(8)/6599/3/$10.00 © 1996 American Institute of Physics 

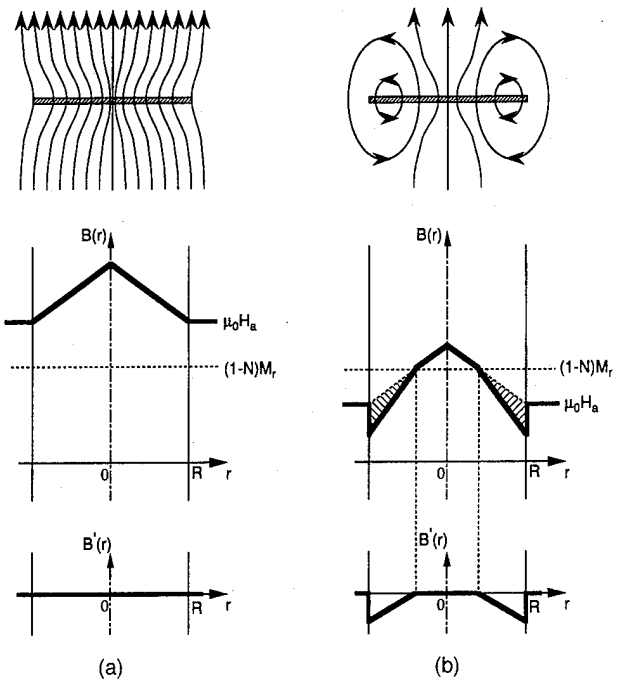



FIG. 2. Schematic view of the flux line profiles and the flux density distributions inside the Nb film in the case of (a) $\mu_0 H_a > (1-N)M_r$ and (b) $\mu_0 H_a < (1-N)M_r$, where $B$ and $B'$ represent the flux density due to the external field and the stray field, respectively.

aspect ratio on the rearrangement of the flux distribution, the following disk-shaped Nb films with different diameters $D$ and thickness $t$ were prepared, denoted as NB1 ($D=2.5$ mm, $t=20$ nm), NB2 ($D=2.0$ mm, $t=20$ nm), NB3 ($D=2.0$ mm, $t=50$ nm), and NB4 ($D=2.0$ mm, $t=100$ nm).

The magnetic hysteresis loop was measured as a function of temperature by using a rotating sample SQUID magnetometer[5] and a vibrating sample magnetometer. Prior to the magnetization measurement, the sample was zero field cooled to the desired temperature, and then the measurement was performed in perpendicularly applied magnetic fields to the Nb film surface between $-20$ and $+20$ mT.

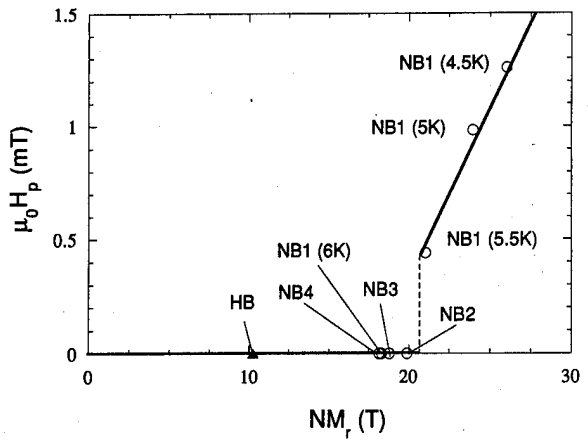



FIG. 3. Relationship between the peak field $\mu_0 H_p$ and the stray field exerting near the edge of the sample $NM_r$ for the Nb films (open circles) and for the hybrid system (closed triangle).

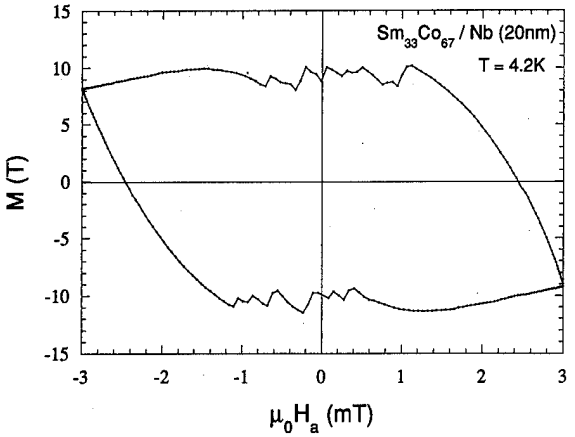



FIG. 4. Magnetic hysteresis loops for the Nb film with ferromagnetic $Sm_{33}Co_{67}$ particles.

## III. RESULTS AND DISCUSSION

The temperature dependence of the hysteresis loops of the NB1 sample is shown in Fig. 1(a), where the arrow indicates the peak field $\mu_0 H_p$ at which the magnetization begins to exhibit a steep fall. The peak field gradually decreases with increasing temperature from 4.5 K and disappears at 6 K. Hysteresis loops as a function of Nb thickness are shown in Fig. 1(b) for the film with a constant diameter of 2.0 mm. As seen in the figure, no magnetization drop is observed. It should be noticed that the drop is not observed in the sample NB2 with the same thickness as the sample NB1, the hysteresis loop of which exhibits the magnetization drops below 5.5 K. This suggests that the aspect ratio $t/D$ may play an important role for the appearance of the magnetization drop. From the fact that the aspect ratio is in proportion to the demagnetizing factor $N$, the magnetization drop is considered to be mainly related to the stray field due to the pinned flux lines in the superconducting Nb film rather than the two dimensionality of the superconductor. In the case of the hybrid film, the magnetostatic effect of the particles must be taken into account because the ferromagnetic particles regulate the flux density distribution inside the superconductor.

Here we limit the discussion to the demagnetizing process in the magnetization curve. The pinned flux lines inside the superconducting Nb film produce a strong stray field near the edge of the film. By using the demagnetizing factor $N$ and the remanent magnetization $M_r$, the stray field is generally expressed as $-NM_r$ which directs opposite to the direction of $M_r$. The magnetic flux density $B$ along the external field $H_a$ inside the superconductor is given by $B=\mu_0 H_a+(1-N)M_r$. When the external field is higher than the demagnetizing field given by $(1-N)M_r$, the whole pinned flux lines are in equilibrium with the external field. Thus, the flux density distribution may have the distribution obtained from the Bean's critical state model, as shown in Fig. 2(a). On the contrary, when the field is lower than $(1-N)M_r$, the number of pinned flux lines is larger than that of the flux lines due to the external field, resulting in the closed-flux loops near the edge. Near the edge, these closed-flux lines are opposite to the flux lines penetrated near the

center of the film. Therefore, the flux density near the edge is reduced from the one expected from the Bean's model [see Fig. 2(b)]. The reduction causes the steep drop in magnetization at the peak field of order $(1-N)M_r$. In reality, similar behaviors of the flux inversion have been observed in high-$T_c$ $Bi_2Sr_2CaCu_2O_{8-\delta}$ single crystal by means of magneto-optical method.[6,7] As the critical current density $J_c$ decreases with an increase of temperature, the remanent magnetization $M_r$ also decreases, and thus the peak field is reduced. At 6 K, the stray field near the edge of the superconducting film may be too small to lead the flux penetration in a negative sense.

The magnitude of the stray field near the edge is nearly equal to $NM_r$. The demagnetizing factor $N$ can be evaluated from the initial susceptibility as $N=1+1/\chi$ if the Nb film is perfectly diamagnetic below $\mu_0 H_{c1}$ (~0.3 mT). The remanent magnetization $M_r$ can be deduced by fitting the hysteresis loops using the conventional critical-state model. Figure 3 shows the relationship between the peak field $H_p$ and the demagnetizing field $NM_r$. Note that the flux rearrangement due to the stray field occurs only when $NM_r>20.5$ T.

Figure 4 shows the magnetic hysteresis loop of the hybrid system consisting of $Sm_{33}Co_{67}$ particles and the Nb film (2 mm×2 mm×2 nm): The system does not exhibit any magnetization drop, and the remanent magnetization is remarkably reduced. The difference between magnetic behaviors of the Nb films with and without the ferromagnetic particles is interpreted as follows. The superconducting order parameter in the Nb film with ferromagnetic particles is periodically modulated by the stray field due to the particles. This reduces the remanent magnetization compared to the bare Nb film. In order to estimate the stray field, the demagnetizing factor $N$ was calculated to be 0.972 by approximating the shape of the 2 mm square Nb film by a 2 mm$\phi$ circle. This yields the stray field $NM_r=10.2$ T, which is smaller than the critical value ($NM_r=20.5$ T). Another feature observed in the hybrid system is the flux guide effect due to the amorphous $Sm_{33}Co_{67}$ particles with high susceptibility. The particles accumulate the external flux lines and guide them into the normal state cores.[4] The presence of the flux guide effect can be proved by the periodical flux jumps as shown in Fig. 4. The periodicity $\Delta B=0.267$ mT gives the area where the flux is quantized as $S=7.79\times10^{-12}$ m$^2$ from the relation $\Delta B=\phi_0/S$. The value coincides well with half of the unit cell area containing a normal core; $(1/2)S_{\text{unit}}=8.0\times10^{-12}$ m$^2$. These ferromagnetic particles act as the artificial flux pinning centers which are homogeneously distributed in the hybrid film. Therefore, the average flux density gradient in the Nb film takes a constant value as expected from the Bean model. This reduces the apparent demagnetizing factor and the stray field near the edge of the Nb film. As a result, the flux rearrangement does not take place in the hybrid film.

## ACKNOWLEDGMENTS

We are grateful to Dr. G. Fillion and Dr. P. Pugnat of the Lab. Louis Néel (CNRS) for their magnetization measurements using the rotating sample SQUID magnetometer.

[1] Y. Otani, B. Pannetier, J. P. Nozières, and D. Givord, J. Magn. Magn. Mater. **126**, 622 (1993).
[2] B. Pannetier, S. Rodts, J. L. Genicon, Y. Otani, and J. P. Nozières, Proceedings of Macroscopic Quantum Phenomena and Coherence in Superconducting Networks, Frascati, Italy, 1995.
[3] W. A. Little and R. Parks, Phys. Rev. A **13**, 97 (1964).
[4] Y. Otani, Y. Nozaki, H. Miyajima, B. Pannetier, M. Ghidini, J. P. Nozières, G. Fillion, and P. Pugnat, Physica C **235–240**, 2945 (1994).
[5] Y. Nozaki, Y. Otani, K. Runge, H. Miyajima, B. Pannetier, J. P. Nozières, and G. Fillion (unpublished).
[6] Th. Schuster, M. R. Koblischka, N. Moser, and H. Kronmüller, Physica C **179**, 269 (1991).
[7] D. Glatzer, A. Forkl, H. Theuss, H. U. Habermeier, and H. Kronmüller, Phys. Status Solidi B **170**, 549 (1992).

# "Standing" diffusion of electromagnetic fields in superconductors with gradual resistive transitions

I. D. Mayergoyz and M. Neely
*Electrical Engineering Department, University of Maryland, College Park, Maryland 20742*

Electromagnetic field diffusion in superconductors with gradual resistive transitions may exhibit a peculiar (anomalous) mode which does not exist in superconductors with sharp (ideal) resistive transitions. This is a "standing" mode. In the case of this mode, the electromagnetic field on a superconductor boundary increases with time, while the region occupied by the electromagnetic field within the superconductor does not expand. In this paper, an exact analytical solution to the appropriate nonlinear diffusion equation is derived. It is demonstrated that this solution can be physically interpreted as the standing mode. The standing mode solution is also obtained by using a "rectangular profile" approximation and these two results are compared. © *1996 American Institute of Physics.* [S0021-8979(96)03508-1]

Models for superconducting hysteresis are based on the analytical study of electromagnetic field diffusion in hard superconductors. In the critical state model,[1–3] this study is usually performed under the assumption of ideal (sharp) resistive transition. This assumption appreciably facilitates the calculation of distribution of electric currents in superconductors of simple shapes (plane slabs, circular cross-section cylinders) and leads to the rate independent models for superconducting hysteresis.

Actual resistive transitions in superconductors are gradual, and they are customarily described by the power law:[4–6]

$$E=\left(\frac{J}{k}\right)^n, \quad (n>1). \tag{1}$$

In the above expression, $E$ is electric field, $J$ is current density, and $k$ is a parameter which coordinates the dimensions in (1). The exponent "$n$" is a measure of the sharpness of the resistive transition and it varies in the range 7–1000.

The above power law can be used as a constitutive equation for hard superconductors. This leads to the following nonlinear diffusion equation for the current density in the case of 1D problems:

$$\frac{\partial^2 J^n}{\partial z^2}=\mu_0 k^n \frac{\partial J}{\partial t}. \tag{2}$$

Previously, the analytical self-similar solutions of Eq. (2) were derived for zero initial condition and the following boundary condition:

$$J_0(t)=J(0,t)=ct^p, \quad (t\geq 0,\ p\geq 0). \tag{3}$$

It has been found that the electromagnetic field diffusion in superconductors with gradual resistive transitions has some features which are very similar to the electromagnetic field diffusion in superconductors with ideal resistive transitions. Namely, it has been found that for $n\geq 7$ the actual profile of electric current density is almost rectangular. This has prompted the suggestion to approximate the actual current density profile by a rectangular one with the height equal to the instantaneous value $J_0(t)$, of the current density on the boundary of the superconductor (see Fig. 1). This "rectangular profile" approximation has led to the following equation for the zero front $z_0(t)$, of the current density:

$$\int_0^t J_0^n(\tau)d\tau=\frac{\mu_0 k^n}{2}[J_0(t)z_0^2(t)-J_0(0)z_0^2(0)], \tag{4}$$

which is valid for any monotonically increasing boundary condition $J_0(t)$.

In this paper, we intend to show that electromagnetic field diffusion in superconductors with gradual resistive transitions may exhibit a peculiar (anomalous) mode which does not exist in superconductors with ideal resistive transitions. This is a standing mode. In the case of this mode, the electromagnetic field on a superconductor boundary increases with time, while the region occupied by the electromagnetic field does not expand. We shall first find the condition for the existence of this mode by using the "rectangular profile" approximation and formula (4). Then, we shall derive the exact expressions for the standing mode through the analytical solution of nonlinear diffusion Eq. (2), that is without resorting to the rectangular profile approximation. Finally, we shall compare these two results.

To start the discussion, we turn to Eq. (4) and try to find such a monotonically increasing boundary condition $J_0(t)$ for which the zero front $z_0(t)$, stands still. To this end, we assume that $z_0(t)=z_0=\text{const}$, and, by differentiating both sides of (4), we arrive at:

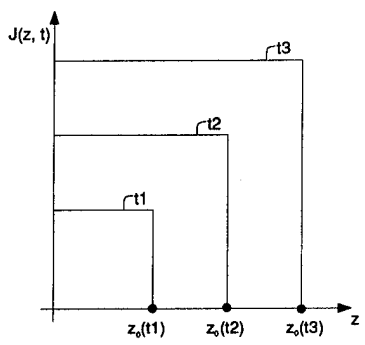



FIG. 1. Rectangular approximation of current density profiles inside the superconducting half-space.

 0021-8979/96/79(8)/6602/3/$10.00 © 1996 American Institute of Physics

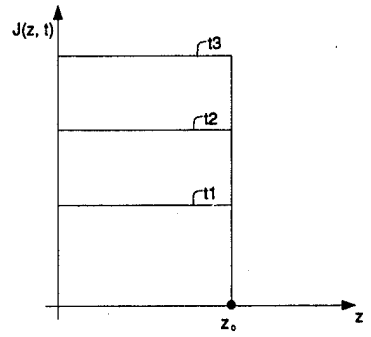



FIG. 2. Rectangular approximation of the standing mode.

$$J_0^n(t)=\frac{\mu_0 k^n}{2} z_0^2 \frac{dJ_0(t)}{dt}. \tag{5}$$

The last expression can be transformed as follows:

$$\frac{2}{\mu_0 k^n z_0^2} dt=\frac{dJ_0(t)}{J_0^n(t)}. \tag{6}$$

By integrating both parts of (6), we obtain:

$$\frac{2}{\mu_0 k^n z_0^2} t=\frac{1}{n-1}\left[J_0^{1-n}(0)-J_0^{1-n}(t)\right]. \tag{7}$$

From (7), we derive:

$$J_0(t)=\frac{1}{\left(J_0^{1-n}(0)-\dfrac{2(n-1)}{\mu_0 k^n z_0^2} t\right)^{1/n-1}}. \tag{8}$$

The last expression can be represented in the form:

$$J_0(t)=\frac{c}{(t_0-t)^{1/n-1}}, \tag{9}$$

where:

$$c=\left(\frac{\mu_0 k^n z_0^2}{2(n-1)}\right)^{1/n-1}, \quad t_0=\frac{\mu_0 k^n z_0^2 J_0^{1-n}(0)}{2(n-1)}. \tag{10}$$

Thus, we have established that, if the current density on the boundary of superconducting half-space varies with time according to the expressions (9)–(10), then the zero front $z_0(t)$, of the current density stands still during the time interval $0 \leqslant t < t_0$. In other words, during this time interval the electromagnetic field diffusion exhibits a standing mode. This mode is illustrated by Fig. 2.

It is desirable to express the boundary condition for the standing mode in terms of magnetic field $H_0(t)$ on the superconductor boundary. This can be easily accomplished by using (9) and Ampere's Law, which leads to:

$$H_0(t)=\frac{c z_0}{(t_0-t)^{1/n-1}}. \tag{11}$$

Our previous derivation has been based on the "rectangular profile" approximation for the electric current density. Next, we shall derive the expressions for the standing mode solution without resorting to the above approximation, but rather through an analytical solution of the nonlinear diffusion Eq. (2). It is remarkable that the standing mode solution can be obtained by using the method of separation of variables. Actually, this is the only solution which can be obtained by this method. According to the method of separation of variables, we look for the solution of Eq. (2) in the form:

$$J(z,t)=\varphi(z)\psi(t). \tag{12}$$

By substituting (12) into (2), after simple transformations we derive:

$$\frac{1}{\varphi(z)}\frac{d^2\varphi^n(z)}{dz^2}=\frac{\mu_0 k^n}{\psi^n(t)}\frac{d\psi(t)}{dt}. \tag{13}$$

This means that

$$\frac{\mu_0 k^n}{\psi^n(t)}\frac{d\psi(t)}{dt}=\lambda, \tag{14}$$

$$\frac{1}{\varphi(z)}\frac{d^2\varphi^n(z)}{dz^2}=\lambda, \tag{15}$$

where $\lambda$ is some constant.

By integrating (14), we easily obtain:

$$\psi(t)=\left(\frac{\mu_0 k^n}{(n-1)\lambda(t_0-t)}\right)^{1/n-1}, \tag{16}$$

where $t_0$ is a constant of integration.

Equation (15) is more complicated than Eq. (14) and its integration is somewhat more involved. To integrate Eq. (15), we introduce the following auxiliary functions:

$$\varphi^n(z)=\theta(z), \quad R(z)=\frac{d\theta(z)}{dz}. \tag{17}$$

From (17) and (15), we derive:

$$\frac{dR}{dz}=\frac{d^2\theta}{dz^2}=\frac{d^2\varphi^n}{dz^2}=\lambda\varphi(z)=\lambda\theta^{1/n}(z). \tag{18}$$

On the other hand

$$\frac{dR}{dz}=\frac{dR}{d\theta}\cdot\frac{d\theta}{dz}=R\frac{dR}{d\theta}=\frac{1}{2}\frac{d(R^2)}{d\theta}. \tag{19}$$

By equating the right-hand sides of (18) and (19), we obtain

$$\frac{d(R^2)}{d\theta}=2\lambda\theta^{1/n}. \tag{20}$$

By integrating Eq. (20), we find:

$$R(z)=\sqrt{\frac{2n}{n+1}}\lambda[\theta(z)]^{n+1/2n}. \tag{21}$$

In (21), a constant of integration was set to zero. This can be justified on physical grounds. Indeed, the magnetic field should vanish at the zero front, that is at the same point where $J(z,t)$ vanishes. By using (12) and (17), it can be shown that the magnetic field and $J(z,t)$ are proportional to $R(z)$ and $\theta^{1/n}(z)$, respectively. This means that the above two functions should vanish simultaneously. This is only possible if the integration constant in (21) is set to zero.

Next, by using (17) in (21), we find:

$$\frac{d\theta(z)}{dz}=\sqrt{\frac{2n}{n+1}}\,\lambda[\theta(z)]^{n+1/2n}. \tag{22}$$

By integrating (22), we derive:

$$[\theta(z)]^{n-1/n}=\frac{(n-1)^2}{2(n+1)n}\,\lambda(z_0-z)^2, \tag{23}$$

where $z_0$ is a constant of integration.

From (17) and (23), we obtain:

$$\varphi(z)=\left[\frac{(n-1)^2\lambda}{2(n+1)n}\,(z_0-z)^2\right]^{1/n-1}. \tag{24}$$

Now, by substituting (16) and (24) into (12), we find the following analytical (and *exact*) solution of nonlinear diffusion Eq. (2):

$$J(z,t)=\left[\frac{(n-1)\mu_0 k^n(z_0-z)^2}{2(n+1)n(t_0-t)}\right]^{1/n-1}. \tag{25}$$

It is remarkable that, as a result of substitution, the constant $\lambda$ cancels out, and the solution (25) does not depend on $\lambda$ at all.

The obtained solution (25) can be physically interpreted as follows. Suppose that at time $t=0$ the electric current density satisfies the following initial condition:

$$J(z,0)=\begin{cases}\left[\dfrac{(n-1)\mu_0 k^n(z_0-z)^2}{2(n+1)nt_0}\right]^{1/n-1}, & \text{if } 0\leq z\leq z_0\\ 0, & \text{if } 0\leq z\leq z_0\end{cases}. \tag{26}$$

Suppose also that the current density satisfies the following boundary condition during the time interval $0\leq t<t_0$:

$$J_0(t)=J(0,t)=\left[\frac{(n-1)\mu_0 k^n z_0^2}{2(n+1)n(t_0-t)}\right]^{1/n-1} \tag{27}$$

Then, according to (25), the exact solution to the initial-boundary value problem (26)–(27) for the nonlinear diffusion Eq. (2) can be written as follows:

$$J(z,t)=\begin{cases}\left[\dfrac{(n-1)\mu_0 k^n(z_0-z)^2}{2(n+1)n(t_0-t)}\right]^{1/n-1}, & \text{if } 0\leq z\leq z_0\\ 0, & \text{if } z>z_0.\end{cases} \tag{28}$$

This solution is illustrated by Fig. 3 and it is apparent that it has the physical meaning of the standing mode. It is also clear from formula (28) (and Fig. 3) that the above solution has the following self-similarity property: the profiles of electric current density for different instants of time can be obtained from one another by dilation (or contraction) along the $J$-axis. In other words, these profiles remain similar to one another. This suggests that solution (28) can be derived by using dimensional analysis. However, we shall not delve further into this matter.

From the practical point of view, it is desirable to express the boundary condition (27) for the standing mode in terms of magnetic field $H_0(t)$ on the superconductor boundary. According to Ampere's Law, we have:

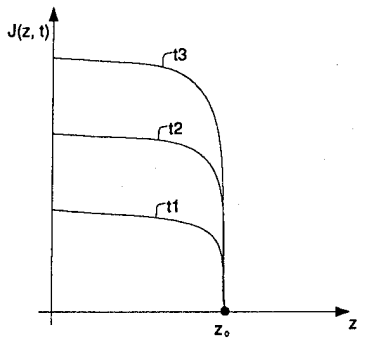



FIG. 3. Current density profiles corresponding to the exact analytical solution of the diffusion equation.

$$H_0(t)=\int_0^{z_0} J(z,t)dz. \tag{29}$$

By substituting (28) into (29) and performing the integration, we obtain:

$$H_0(t)=\frac{n-1}{n+1}\,z_0\left[\frac{(n-1)\mu_0 k^n z_0^2}{2(n+1)n(t_0-t)}\right]^{1/n-1}. \tag{30}$$

It is also instructive to compare the above exact standing mode solution with the standing mode expressions derived on the basis of the rectangular profile approximation. First, it is clear from formula (28) (and Fig. 3) that, for sufficiently large "$n$", the actual current density profiles for the standing mode are almost rectangular. Second, it is apparent that the boundary condition (27) can be written in the form (9) with "$c$" and "$t_0$" defined as follows:

$$c=\left[\frac{(n-1)\mu_0 k^n z_0^2}{2(n+1)n}\right]^{1/n-1},$$

$$t_0=\frac{(n-1)\mu_0 k^n z_0^2 J_0^{1-n}(0)}{2(n+1)n}. \tag{31}$$

By comparing (31) with (10), it can be concluded that for sufficiently large "$n$" these expressions are practically identical. Thus, the rectangular profile approximation is fairly accurate as far as the prediction of the standing mode diffusion is concerned.

The origin of the standing mode can be elucidated on physical grounds as follows. Under the boundary condition (27), the electromagnetic energy entering the superconducting material at any instant of time is just enough to affect the almost uniform increase in electric current density in the region ($0\leq z\leq z_0$) already occupied by the field, but insufficient to affect the further diffusion of the field into the material.

This research has been supported by the U. S. Department of Energy, Engineering Research Program.

[1] C. P. Bean, Phys. Rev. Lett. **8**, 250 (1962).
[2] C. P. Bean, Rev. Mod. Phys. **36**, 31 (1964).
[3] H. London, Phys. Lett. **6**, 162 (1963).
[4] C. S. Nichols and D. R. Clarke, Acta Metall. Matter **39**, 995 (1991).
[5] J. W. Elkin, Cryogenics **2**, 603 (1987).
[6] C. J. G. Plummer and J. E. Evetts, IEEE Trans. Magn. **MAG-23**, 1179 (1987).
[7] I. D. Mayergoyz, J. Appl. Phys. **76**, 7130 (1994).

# Low-temperature specific heat of the degenerate supersymmetric $t$-$J$ model in one dimension

Kong-Ju-Bock Lee
*Department of Physics, Ewha Womans University, Seoul 120-750, South Korea*

P. Schlottmann
*Department of Physics, Florida State University, Tallahassee, Florida 32306*

We consider the one-dimensional SU($N$)-invariant $t$-$J$ model, which consists of electrons with $N$ spin components on a lattice with nearest-neighbor hopping $t$ constrained by the excluded multiple occupancy of the sites and spin-exchange $J$ between neighboring lattice sites. The model is integrable and has been diagonalized in terms of nested Bethe ansatze at the supersymmetric point $t=J$. The low-$T$ specific heat is proportional to $T$. The $\gamma$-coefficient is extracted from the thermodynamic Bethe-ansatz equations and is expressed in terms of the spin wave velocities and the group velocity of the charges for arbitrary $N$, band filling, and splitting of the levels (magnetic and crystalline fields). Our results contain the following special cases: (i) For $N=2$ the traditional spin-1/2 supersymmetric $t$-$J$ model, (ii) for exactly one electron per site the SU($N$)-Heisenberg chain, and (iii) for $N=4$ the two-band supersymmetric $t$-$J$ model with crystalline field splitting.
© *1996 American Institute of Physics.* [S0021-8979(96)03608-8]

One-dimensional (1D) conductors are an active topic of research with experimental realizations in organic (quasi-1D) conductors, polymers, Peierls insulators, and mesoscopic systems. The discovery of high-temperature superconductivity renewed the interest in low-dimensional superconductors and antiferromagnets. Many normal state properties of the 2D high-$T_c$ superconductors cannot be reconciled with the standard Fermi liquid theory and a Luttinger-liquid picture (marginal Fermi liquid) similar to 1D conductors has been proposed to explain some of the features.[1]

Two of the most studied systems of correlated electrons are the Hubbard and $t$-$J$ models. The two models are equivalent to each other for a large on-site repulsion $U$ (small $J$) and a band occupation close to half-filling, but the $t$-$J$ model is by itself an exciting problem for all parameter values. The $t$-$J$ Hamiltonian is given by

$$H=-t\sum_{is} P(c_{is}^{\dagger}c_{i+1s}+c_{i+1s}^{\dagger}c_{is})P$$
$$+J\sum_{iss'} (c_{is}^{\dagger}c_{is'}c_{i+1s'}^{\dagger}c_{i+1s}-n_{is}n_{i+1s'}), \qquad (1)$$

where $t$ is the hopping matrix element between nearest neighbor sites, $P$ is a projector excluding the multiple occupancy of every site, $|s|\leq S$ is the spin index ($N=2S+1$), $J$ is the exchange coupling, and $n_{is}$ is the number operator.

The 1D $t$-$J$ model was found to be integrable at the supersymmetric point $t=J$ by Sutherland.[2] The supersymmetry is related to a graded permutation of $N$ fermionic (spin waves) and one bosonic (holes) degrees of freedom. For $N=2$ the ground state properties, the classification of states and the thermodynamic equations were presented in Ref. 3. These results were used to calculate the spectrum of elemental excitations[4] and the exponents for the long-distance asymptotic of correlation functions.[5] The Bethe ansatz solution was then extended to an arbitrary number of spin components $N$ to obtain the classification of states, thermodynamics,[6] ground state properties,[7,8] the excitation spectrum,[8] and the asymptotic behavior of correlation functions.[9]

Model (1) contains several interesting limiting cases: (i) for $N=2$ the traditional (supersymmetric) $t$-$J$ model,[2,3] (ii) for exactly one electron per site the SU($N$)-invariant Heisenberg chain,[2] and (iii) for $N=4$ the two-band supersymmetric $t$-$J$ model with crystalline field splitting.[10]

In this paper, we calculate the low-temperature specific heat for the supersymmetric $t$-$J$ model for arbitrary band filling, number of components, and splitting between the bands (magnetic and crystalline fields). We first restate some equations of the Bethe ansatz solution,[6,8] then we expand the free energy and the band energies in powers of $T$, and finally we express the $\gamma$-coefficient of the specific heat in terms of the Fermi velocities of the charges and spin waves.

The model is solved in terms of $N$ nested Bethe ansatz. Each Bethe ansatz eliminates one internal degree of freedom and gives rise to one set of rapidities, $\{\xi_{\alpha}^{(l)}\}$, $l=0,\ldots,N-1$, $\alpha=1,\ldots,M_l$, with the set $l=0$ corresponding to the charge rapidities. All rapidities within a given set have to be different, leading to Fermi statistics for the rapidities. The rapidities are self-consistent solutions of the Bethe ansatz equations and have in general, complex values. They are classified[6] into (i) real charge rapidities, (ii) complex spin and charge rapidities, and (iii) strings of complex spin rapidities. States of class (iii) represent excited spin states which are not populated in the ground state and do not contribute to the low-$T$ specific heat. Classes (i) and (ii) are present in the ground state and have Fermi surfaces that contribute to the $\gamma$-coefficient of the specific heat. They correspond to complexes of $n$ electrons ($n\leq N$), sometimes called bound states, defined by strings of the form

$$\xi_p^{(l)}=\zeta^{(n)}+ip/2, \quad l\leq n-1\leq 2S,$$

$$p=-(n-l-1),-(n-l-3),\ldots,(n-l-1),$$

where $\zeta^{(n)}$ is a real rapidity characterizing the center of mass of the cluster.

 0021-8979/96/79(8)/6605/3/$10.00 © 1996 American Institute of Physics 

In the ground state, the real rapidities $\zeta^{(l)}$ are densely distributed in the interval $|\zeta|\geqslant B_l$, while the complementary interval $|\zeta|\leqslant B_l$ corresponds to empty states (holes). A central role is played by linear integral equations of the type[6–8]

$$\begin{aligned} &X_l(\zeta)+\sum_{q=1}^{2S}\int_{|\zeta'|>Bq}d\zeta' X_q(\zeta')K_{l,q}(\zeta-\zeta') \\ &\quad-\int_{-Q}^{Q}d\zeta' X_N(\zeta')F_l(\zeta-\zeta')=Z_l(\zeta), \\ &X_N(\zeta)+\sum_{q=1}^{2S}\int_{|\zeta'|>Bq}d\zeta' X_q(\zeta')F_q(\zeta-\zeta') \\ &\quad-\int_{-Q}^{Q}d\zeta' X_N(\zeta')D_{2S}(\zeta-\zeta')=Z_N(\zeta), \end{aligned} \tag{2}$$

where (2) holds for $l=1,\ldots,2S$, $Q=B_N$, and $Z_l(\zeta)$ are the driving terms. Here, $F_l(\zeta)$, $D_l(\zeta)$, and $K_{l,r}(\zeta)$ are the Fourier transforms of

$$\begin{aligned} &\hat{F}_l(\omega)=\sinh(l\omega/2)/\sinh(N\omega/2), \\ &\hat{D}_l(\omega)=\exp(-|\omega|/2)\hat{F}_l(\omega), \\ &\hat{K}_{l,r}(\omega)=-\delta_{l,r}+\exp(|\omega|/2)\sinh[\min(l,r)\omega/2] \\ &\qquad\times\sinh\{[N-\max(l,r)]\omega/2\}/ \\ &\qquad\sinh(\omega/2)\sinh(N\omega/2). \end{aligned} \tag{3}$$

We introduce a ground state density of states, $\rho_l(\zeta)$, for each set of real rapidities $\zeta^{(l)}$, which for particles (holes) is nonzero only in the interval $|\zeta|\geqslant B_l(|\zeta|\leqslant B_l)$. These densities satisfy integral equations of the type (2) ($X_l=\rho_l$) with driving terms $Z_l(\zeta)=F_{N-l}(\zeta)$ and $Z_N(\zeta)=D_1(\zeta)$. The integration limits $B_l$ and $Q$ are determined by the number of electrons with each component, $n_m N_a=[M^{(m-1)}-M^{(m)}]$, where $N_a$ is the number of sites, $m=1,\ldots,N$, $M^{(0)}=N_e$ is the total number of electrons, $M^{(N)}=0$, and

$$n_m=\sum_{q=N-m+1}^{N}\int_{|\zeta|>B_q}d\zeta\rho_q(\zeta). \tag{4}$$

The thermal population of the states is determined by energy bands $\epsilon_l(\zeta)$, which for low $T$ can be expanded in powers of $T$ by means of a Sommerfeld expansion, $\epsilon_l=\epsilon_l^{(0)}+T^2\epsilon_l^{(2)}+\ldots$. The energy potentials $\epsilon_l^{(0)}$ satisfy equations of the type (2) with[6]

$$\begin{aligned} &Z_l(\zeta)=2\pi F_{N-l}(\zeta)-l(N-l)\Delta_l/N \\ &Z_N(\zeta)=-2-\mu+2\pi D_1(\zeta), \end{aligned} \tag{5}$$

where $\mu$ is the chemical potential and the parameters $\Delta_l$ are the magnetic and crystalline fields determining the splitting of the multiplet. The $\epsilon_l^{(0)}(\zeta)$ are even functions, which monotonically decrease with $|\zeta|$. The conditions $\epsilon_l(\pm B_l)=0$ relate the set of integration limits $\{B_l\}$ and $Q$ to the set of external fields $\{\Delta_l\}$ and $\mu$. The $\epsilon_l^{(2)}$ satisfy Eqs. (2) with

$$\begin{aligned} Z_l(\zeta)&=(\pi^2/6)\partial\epsilon_N^{-1}[F_l(\zeta-Q)+F_l(\zeta+Q)] \\ &\quad+(\pi^2/6)\sum_{q=1}^{N-1}\partial\epsilon_q^{-1}[K_{l,q}(\zeta-B_q)+K_{l,q}(\zeta+B_q)], \\ Z_N(\zeta)&=(\pi^2/6)\partial\epsilon_N^{-1}[D_{2S}(\zeta-Q)+D_{2S}(\zeta+Q)] \\ &\quad+(\pi^2/6)\sum_{q=1}^{2S}\partial\epsilon_q^{-1}[F_q(\zeta-B_q)+F_q(\zeta+B_q)], \end{aligned} \tag{6}$$

where $\partial\epsilon_q^{-1}=|d\epsilon_q^{(0)}/d\zeta|_{B_q}^{-1}$ and $\partial\epsilon_N^{-1}=|d\epsilon_N^{(0)}/d\zeta|_{Q}^{-1}$.

Similarly, the Sommerfeld expansion of the free energy yields the $\gamma$-coefficient

$$\begin{aligned} \gamma/N_a&=(2\pi^2/3)\left[\partial\epsilon_N^{-1}D_1(Q)+\sum_{q=1}^{2S}\partial\epsilon_q^{-1}F_{N-q}(B_q)\right] \\ &\quad+2\int_{-Q}^{Q}d\zeta D_1(\zeta)\epsilon_N^{(2)}(\zeta) \\ &\quad-2\sum_{q=1}^{2S}\int_{|\zeta|>B_q}d\zeta F_{N-q}(\zeta)\epsilon_q^{(2)}(\zeta). \end{aligned} \tag{7}$$

From the structure of (5)–(7) all contributions to $\gamma$ are proportional to $\partial\epsilon_q^{-1}$ for some $q$. We first compute the contributions arising from the internal degrees of freedom ($q<N$) and later those of the charges ($q=N$). Defining

$$\epsilon_l^{(2)}(\zeta)=(\pi^2/6)\sum_{r=1}^{2S}\partial\epsilon_r^{-1}\varphi_l^{(r)}(\zeta), \tag{8}$$

where $\varphi_l^{(r)}(\zeta)$ satisfies (2) with

$$\begin{aligned} &Z_l^{(r)}(\zeta)=[K_{l,r}(\zeta-B_r)+K_{l,r}(\zeta+B_r)],\quad l<N, \\ &Z_N^{(r)}(\zeta)=[F_r(\zeta-B_r)+F_r(\zeta+B_r)], \end{aligned} \tag{9}$$

the coefficient of the term in (7) proportional to $\partial\epsilon_q^{-1}$ is

$$\begin{aligned} &(\pi^2/3)\left\{2F_{N-q}(B_q)+\int_{-Q}^{Q}d\zeta D_1(\zeta)\varphi_N^{(q)}(\zeta)\right. \\ &\left.\quad-\sum_{r=1}^{2S}\int_{|\zeta|>B_r}d\zeta F_{N-r}(\zeta)\varphi_r^{(q)}(\zeta)\right\},\quad q<N. \end{aligned} \tag{10}$$

To show that the curly bracket in (10) reduces to $2\rho_q(B_q)$ we consider the expression

$$\begin{aligned} &\sum_{s=1}^{2S}\int_{|\zeta|>B_s}d\zeta\rho_s(\zeta)[K_{q,s}(\zeta-B_q)+K_{q,s}(\zeta+B_q)] \\ &\quad-\int_{-Q}^{Q}d\zeta\rho_N(\zeta)[F_q(\zeta-B_q)+F_q(\zeta+B_q)], \end{aligned} \tag{11}$$

which by making use of (9) can be rewritten as

$$\sum_{s=1}^{2S}\int_{|\zeta|>B_s}d\zeta\rho_s(\zeta)\Big\{\varphi_s^{(q)}(\zeta)+\sum_{r=1}^{2S}\int_{|\zeta'|>B_r}d\zeta'\varphi_r^{(q)}$$

$$\times(\zeta')K_{s,r}(\zeta-\zeta')-\int_{-Q}^{Q}d\zeta'\varphi_N^{(q)}(\zeta')F_s(\zeta')\Big\}$$

$$-\int_{-Q}^{Q}d\zeta\rho_N(\zeta)\Big\{\varphi_N^{(q)}(\zeta)-\int_{-Q}^{Q}d\zeta'\varphi_N^{(q)}(\zeta')D_{2S}(\zeta-\zeta')$$

$$+\sum_{r=1}^{2S}\int_{|\zeta'|>B_r}d\zeta'\varphi_r^{(q)}(\zeta')F_r(\zeta-\zeta')\Big\}.$$

Using (2) in the second and fifth terms this expression simplifies to

$$\sum_{r=1}^{2S}\int_{|\zeta|>B_r}d\zeta F_{N-r}(\zeta)\varphi_r^{(q)}(\zeta)-\int_{-Q}^{Q}d\zeta D_1(\zeta)\varphi_N^{(q)}(\zeta). \quad (12)$$

On the other hand, using (2), expression (11) can be rewritten as $2F_{N-q}(B_q)-2\rho_q(B_q)$. Equating this to (12) we notice that (10) reduces to $(2\pi^2/3)\rho_q(B_q)$.

We now consider the charge fluctuations, i.e., the terms in (7) that are proportional to $\partial\epsilon_N^{-1}$. Following the same procedure above we define $\epsilon_l^{(2)}(\zeta)=(\pi^2/6)\partial\epsilon_N^{-1}\psi_l(\zeta)$, where $\psi_l(\zeta)$ satisfies (2) with

$$Z_l(\zeta)=[F_l(\zeta-Q)+F_l(\zeta+Q)],\ l<N,$$
$$Z_N(\zeta)=[D_{2S}(\zeta-Q)+D_{2S}(\zeta+Q)], \quad (13)$$

and the coefficient of the term in (7) proportional to $\partial\epsilon_N^{-1}$ is

$$(\pi^2/3)\Big\{2D_1(Q)-\sum_{r=1}^{2S}\int_{|\zeta|>B_r}d\zeta F_{N-r}(\zeta)\psi_r(\zeta)$$

$$+\int_{-Q}^{Q}d\zeta D_1(\zeta)\psi_N(\zeta)\Big\}. \quad (14)$$

To show that the curly bracket in (14) reduces to $2\rho_N(Q)$ we consider the expression

$$\int_{-Q}^{Q}d\zeta\rho_N(\zeta)[D_{2S}(\zeta-Q)+D_{2S}(\zeta+Q)]$$

$$-\sum_{q=1}^{2S}\int_{|\zeta|>B_q}d\zeta\rho_q(\zeta)[F_q(\zeta-Q)+F_q(\zeta+Q)], \quad (15)$$

which using (2) is reduced to $2\rho_N(Q)-2D_1(Q)$. On the other hand, expression (15) is first rewritten with the aid of (13) and (14), and then (2) is used to obtain

$$\int_{-Q}^{Q}d\zeta D_1(\zeta)\psi_N(\zeta)-\sum_{q=1}^{2S}\int_{|\zeta|>B_q}d\zeta F_{N-q}(\zeta)\psi_q(\zeta). \quad (16)$$

Therefore, we have that (14) reduces to $(2\pi^2/3)\rho_N(Q)$.

Elemental excitations from the ground state are obtained by adding (particle excitation) or removing (hole excitation) a rapidity $\zeta_0^{(l)}$ from one of the sets. There are $N$ branches of elemental excitations with energy and momentum given by[8]

$$\Delta E_l(\zeta_0)=|\epsilon_l(\zeta_0)|,$$
$$p_l(\zeta_0)=2\pi\int_{-\infty}^{\zeta_0}d\zeta[\rho_l(\zeta)+\rho_{lh}(\zeta)], \quad (17)$$

with the Fermi surface at $\epsilon_l(\pm B_l)=0$. The respective Fermi velocities are given by the slope of the dispersion at the Fermi points[8]

$$v_F^{(l)}=|d\epsilon_l(\zeta)/d\zeta|_{B_l}/2\pi\rho_l(B_l). \quad (18)$$

Therefore, the $\gamma$-coefficient can be written as

$$\gamma/N_a=(\pi/3)\sum_{l=1}^{N}(v_F^{(l)})^{-1}. \quad (19)$$

In summary, the Fermi statistics of the low-energy excitations gives rise to a low-$T$ specific heat proportional to $T$. In general, there are $(N-1)$ spin wave branches and one branch of charge excitations contributing to $\gamma$. In the absence of external fields all spin wave branches have the same group velocity,

$$v_{sw}=\frac{1}{N}\frac{2\pi+\int_{-Q}^{Q}d\zeta\ \exp(2\pi\zeta/N)\epsilon_N(\zeta)}{1+\int_{-Q}^{Q}d\zeta\ \exp(2\pi\zeta/N)\rho_N(\zeta)}, \quad (20)$$

and (19) reduces to $\gamma/N_a=(\pi/3)[1/v_{ch}+(N-1)/v_{sw}]$. Plots of $v_{ch}$ and $v_{sw}$ for several $N$ as a function of band filling can be found in Ref. 8.

For one electron per site ($Q=0$) model (1) reduces to the SU($N$) Heisenberg chain. The band of $N$-strings is filled in this limit, so that the charge excitations are suppressed (they have a gap) and do not contribute to $\gamma$. Therefore, $\gamma$ consists only of the $2S$ terms of the spin wave branches. In the absence of external fields $v_{sw}=2\pi/N$ for all branches and $\gamma/N_a=N(N-1)/6$, which agrees with previous results for the $S=1/2$ (Ref. 11) and $S=1$ (Ref. 12) Heisenberg chains [note that the Heisenberg exchange in model (1) equals 1/2]. The limits of $T\to0$ and $H\to0$ can be interchanged, contrary to what we claimed previously.[13,14]

Our results are also valid for the supersymmetric two-band $t$-$J$ model, which can be mapped onto model (1) for $N=4$. The four degrees of freedom correspond to charges, the splitting between the bands and the Zeeman splitting of each of the bands. Expressions for the four Fermi velocities (and plots as a function of band splitting for one electron per site and zero magnetic field) can be found in Ref. 10.

We acknowledge the support by the U.S. Department of Energy through Grant DE-FG05-91ER45443, the Ministry of Education of the Republic of Korea under Contract BSRI-95-2428 and the Center of Theoretical Physics of Seoul National University.

[1] P. W. Anderson, Science **235**, 1196 (1987); Phys. Rev. Lett. **64**, 1839 (1990); *ibid.* **65**, 2306 (1990).
[2] B. Sutherland, Phys. Rev. B **12**, 3795 (1975).
[3] P. Schlottmann, Phys. Rev. B **36**, 5177 (1987).
[4] P. A. Bares and G. Blatter, Phys. Rev. Lett. **64**, 2567 (1990).
[5] N. Kawakami and S.-K. Yang, Phys. Rev. Lett. **65**, 2309, 3063 (1990).
[6] P. Schlottmann, J. Phys. CM **4**, 7565 (1992).
[7] K. Lee and P. Schlottmann, J. Phys. (Paris) **49**, C8–709 (1988).
[8] P. Schlottmann, J. Phys. CM **5**, 313 (1993).
[9] N. Kawakami, Phys. Rev. B **47**, 2928 (1993).
[10] P. Schlottmann, Phys. Rev. Lett. **69**, 2396 (1992).
[11] M. Takahashi, Prog. Theor. Phys. **50**, 1519 (1973).
[12] L. Mezincescu, R. I. Nepomechie, P. K. Townsend, and A. M. Tsvelick, Nucl. Phys. B **406**, 681 (1993).
[13] K. Lee and P. Schlottmann, J. Phys. CM **1**, 2759 (1989); (Erratum) *ibid.* **7**, 1959 (1995).
[14] K. Lee, Phys. Lett. A **187**, 112 (1994).

# Magnetic and thermodynamic properties of $Sr_2LaFe_3O_9$

J. T. Wang
*Department of Physics, Southern University and A&M College, Baton Rouge, Louisiana 70813*

C. L. Lin and T. Mihalisin
*Department of Physics, Temple University, Philadelphia, Pennsylvania 19122*

Measurements of the magnetization, specific heat, and $^{57}$Fe Mössbauer spectrum are presented for $Sr_2LaFe_3O_9$. The temperature dependence of the specific heat and magnetization indicates that $Sr_2LaFe_3O_9$ undergoes an antiferromagnetic transition at $T_N$=203 K. The small entropy removal $\Delta S$ and small effective paramagnetic moment $\mu_{\text{eff}}$ suggest an itinerant character for the Fe moment in this compound. In low applied fields, the zero field cooled (ZFC) and field cooled (FC) magnetization below $T_N$ exhibit a hysteretic behavior indicating the existence of some ferromagnetic correlation. This behavior is suppressed by high applied fields. The $^{57}$Fe Mössbauer spectrum measured at 4.2 K for $Sr_2LaFe_3O_9$ indicates two superimposed hyperfine fields of 260 and 450 kOe with area ratios of 1/3 and 2/3, respectively, consistent with previous measurements.
© *1996 American Institute of Physics.* [S0021-8979(96)03708-4]

## I. INTRODUCTION

Since the discovery of high-$T_c$ cuprate superconductors,[1,2] investigations of superconductivity and magnetism of $d$-electron based oxides with the perovskite structure have received renewed interest. Fe based oxides are not superconducting, but have interesting magnetic properties. $CaFeO_3$ and $SrFeO_3$ have antiferromagnetic transitions at $T_N$=115 and 134 K, respectively.[3–6] $T_N$ for both systems decreases when one reduces the oxygen content. The $^{57}$Fe Mössbauer measurements[5,6] below $T_N$ show that $SrFeO_3$ has a single magnetic hyperfine field. However, $CaFeO_3$ shows two kinds of hyperfine fields with nearly equal intensities.[5,6] Takano *et al.*[5,6] were the first to propose a model of charge disproportionation, $2Fe^{4+} \rightarrow Fe^{3+} + Fe^{5+}$, to explain the two distinct hyperfine fields for the $CaFeO_3$ system. They have also studied the $Ca_{1-x}Sr_xFeO_3$ and $Sr_{1-x}La_xFeO_3$ systems[5,6] and found behavior similar to that observed for $CaFeO_3$. Later, Battle *et al.*[7–9] extensively investigated the $Sr_{1-x}M_xFeO_{3+y}$ system with $M$=rare earths and $0 \leqslant y \leqslant 1$ by Mössbauer spectroscopy and neutron diffraction measurements, and observed similar phenomena.

The temperature and magnetic field dependence of thermodynamic and magnetic properties for the $Sr_{1-x}M_xFeO_3$ system has not been investigated. We have measured the specific heat, magnetic susceptibility, and the Mössbauer spectrum at 4.2 K for $Sr_2LaFe_3O_9$.

## II. EXPERIMENT

Polycrystalline $Sr_2LaFe_3O_9$ samples were prepared using the solid state reaction technique. The appropriate amounts of high purity $SrCO_3$, $La_2O_3$, and $Fe_2O_3$ were thoroughly mixed and then pressed into pellets 1/2 in. in diameter. The pellets were reacted in air at 1300–1400 °C for three days and were then very slowly cooled to room temperature. They were again ground to a fine powder and the entire procedure was repeated. After the materials were sintered in air twice, they were annealed in flowing oxygen, at a pressure slightly higher than atmospheric pressure, at 1000 °C for one day. X-ray diffraction and high power, high resolution electron microscopy measurements at room temperature were used to check sample homogeneity and lattice parameters. The results indicated that no detectable amount of second phase was present, and that the sample crystallizes with the cubic perovskite structure with a lattice constant of $a$=3.875 Å. This value is consistent with that previously reported[7,8] and suggests that the oxygen content is close to 9 in this compound. The magnetization was measured from 1.8 to 400 K in applied magnetic fields up to 5.5 T using a commercial SQUID magnetometer. The $^{57}$Fe Mössbauer spectra were measured at 4.2 K using a liquid helium cryostat. The specific heat was measured from 15 to 300 K using the semiadiabatic heat pulse method.

## III. RESULTS AND DISCUSSION

We have measured the temperature dependence of the specific heat for $Sr_2LaFe_3O_9$. The specific heat for this material has not been reported previously. We show the $C(T)$ data from 180 to 220 K in Fig. 1. It can be seen that in the vicinity of the anomaly the specific heat increases significantly from 125 J/mole K at 180 K to 480 J/mole K at 203 K and exhibits a λ type second order magnetic phase transition. This is in contrast to the first order transition proposed previously from Mossbauer measurements.[7] To obtain the magnetic contribution $\Delta C(T)$ to the specific heat, we first fit a smooth curve to the data from 15 to 150 K and from 205 to 250 K, and then subtract this smooth curve from the total specific heat $C(T)$. The entropy removal $\Delta S$ associated with the magnetic transition can be calculated by integrating $\Delta C(T)/T$. We obtain a value of $\Delta S$=2.3 J/mole Fe K for this

 0021-8979/96/79(8)/6608/3/$10.00 © 1996 American Institute of Physics

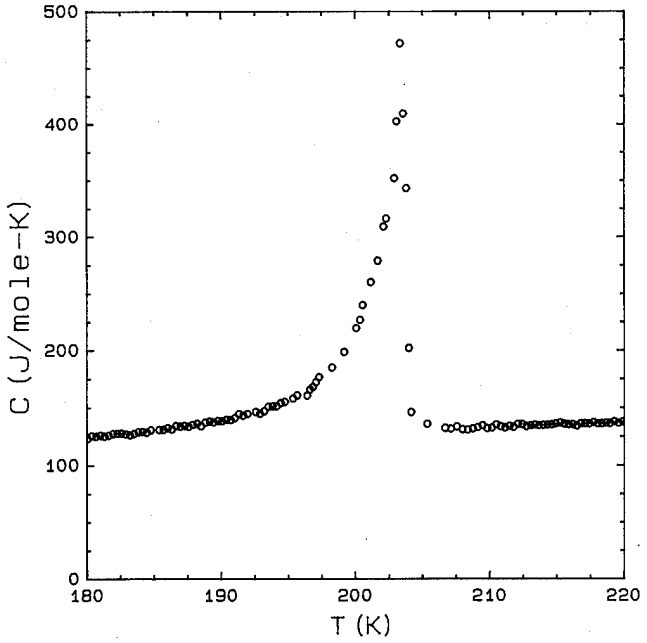



FIG. 1. The temperature dependence of the specific heat of $Sr_2LaFe_3O_9$.

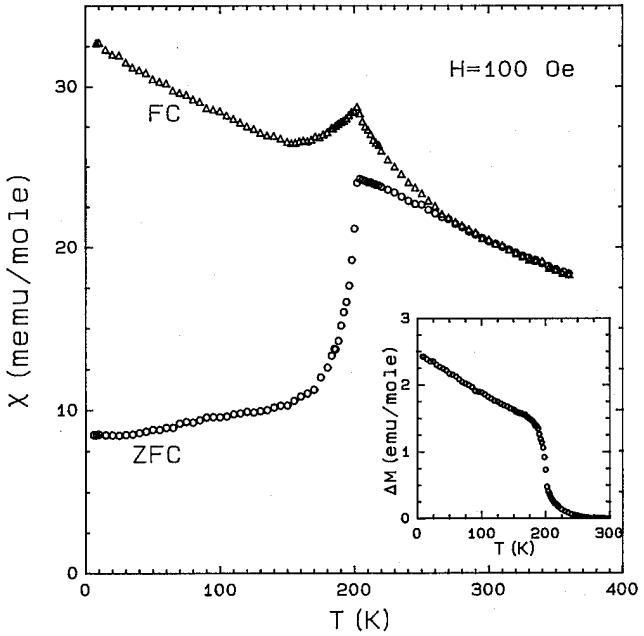



FIG. 3. The temperature dependence of the magnetic susceptibility measured at $H=100$ Oe for $Sr_2LaFe_3O_9$. FC: field cooled data and ZFC: zero field cooled data. Inset: $\Delta M$ vs $T$. (See the definition of $\Delta M$ in text.)

system. This value is much smaller than the value of $R\ln(2s+1)=14.9$ J/mole K which one would expect for localized spin $s=5/2$ Fe atoms.

The $^{57}$Fe Mössbauer spectrum measured at 4.2 K for $Sr_2LaFe_3O_9$ is shown in Fig. 2. It is similar to that previously observed at 78 K by Battle *et al.*[7,8] This spectrum can be fit by two distinct magnetic hyperfine fields 260 and 450 kOe with different isomer shifts. It is interesting that the molar ratio of La to Sr in this compound is the same as the area ratio for the two hyperfine fields, i.e., both ratios are 1/2. Takano *et al.*[5,6] and Battle *et al.*[7,8] have explained two hyperfine fields in terms of a charge disproportionation, i.e., two charge states $Fe^{3+}$ and $Fe^{5+}$ below the magnetic transition. They have also interpreted the room-temperature Mössbauer spectrum, which shows a single dip with no quadruple splitting, in terms of the average valence state. However, it is still not clear why Fe ions in this material occupying identical equivalent sites exhibit two charge states below $T_N$ resulting in two distinct hyperfine fields. Further studies are required to clearly understand this interesting phenomena.

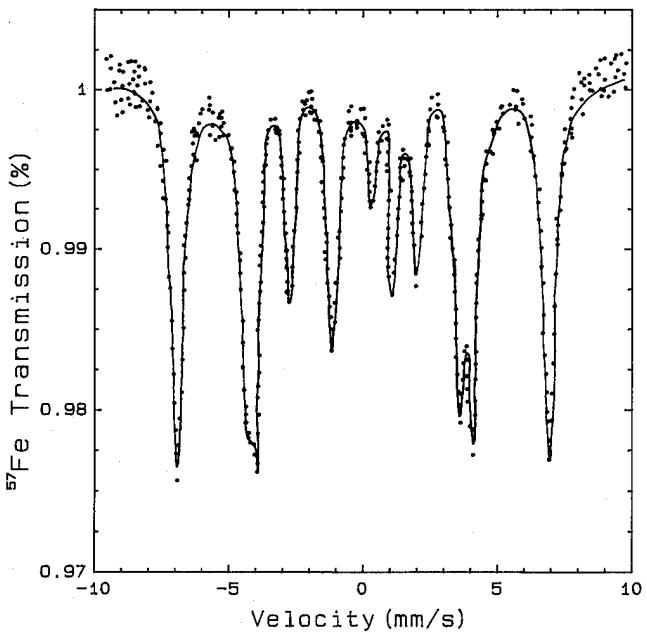



FIG. 2. $^{57}$Fe Mössbauer spectrum measured at 4.2 K for $Sr_2LaFe_3O_9$.

Shown in Fig. 3 is the temperature dependence of the magnetic susceptibility $\chi(T)$ measured at $H=100$ Oe for $Sr_2LaFe_3O_9$. The sample was initially cooled in zero field to 5 K, an applied field of 100 Oe was turned on and the zero field cooled (ZFC) magnetic susceptibility was measured as the sample warmed up to 400 K. Then the field cooled data (FC) were measured at 100 Oe as the sample was cooled from 400 to 5 K. Both ZFC and FC data exhibit a cusp behavior indicating an antiferromagnetic transition at $T_N=203$ K for this material. $T_N$ determined from $\chi(T)$ is in good agreement with that obtained from our specific heat measurement, and from magnetization measurements by another group.[7] It has been shown[8] that $T_N$ decreases with decreasing oxygen content in $Sr_2LaFe_3O_9$. The fact that our sample has a $T_N$ of 203 K suggests that it has an oxygen content very close to 9.

The $\chi(T)$ data above $T_N$ for the FC branch show a Curie–Weiss behavior, i.e., $\chi(T)=c/T-T^*$. By plotting $1/\chi(T)$ vs $T$, we obtain a negative $T^*$ value of $-195$ K consistent with the antiferromagnetic nature of the ordering. From the Curie constant $c$, we obtain a value for $\mu_{\text{eff}}$ of 3.0 $\mu_B$ per Fe atom. This is much smaller than the value of 5.55 $\mu_B$ previously reported.[7] The latter value is close to the theoretical value of 5.9 $\mu_B$ for Fe atoms, and therefore is consistent with a localized electron model. However, our smaller

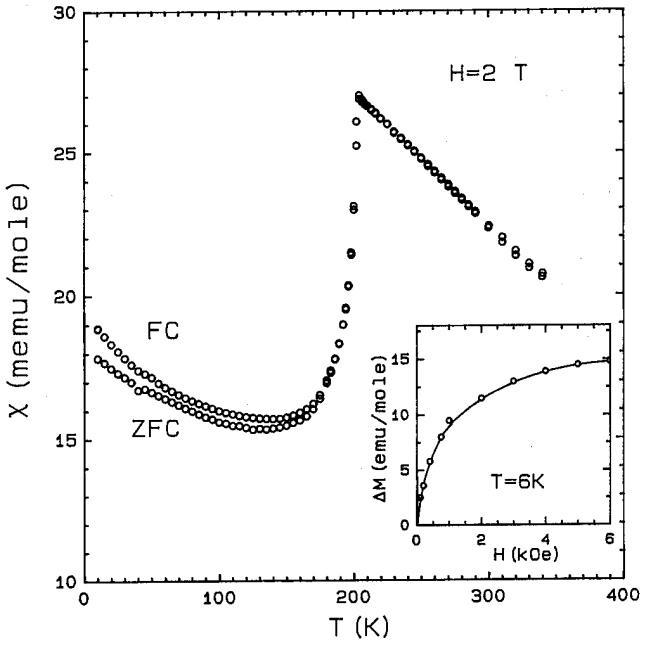



FIG. 4. The temperature dependence of the magnetic susceptibility measured at $H=2$ T for $Sr_2LaFe_3O_9$. Inset: $\Delta M$ vs $H$ measured at $T=6$ K.

values for both $\mu_{\text{eff}}$ and $\Delta S$ indicate itinerant magnetism in the $Sr_2LaFe_3O_9$ system.

It can be seen in Fig. 3 that the ZFC data decrease dramatically just below $T_N$ and then decrease more gradually at low temperatures. However, the FC curve behaves differently below $T_N$. It decreases initially (with decreasing temperature), reaches a minimum, and then increases monotonically at low temperatures. The increase in $\chi(T)$ as one lowers the temperature in the FC branch indicates the existence of a ferromagnetic component in this compound. Shown in the inset of Fig. 3 is the difference in magnetization $\Delta M(T)$ between the FC and ZFC data, that is, the ZFC data subtracted from the FC data. $\Delta M(T)$ exhibits a typical ferromagnetic behavior. This behavior has also been observed in other Fe based oxides, e.g., $YBa_2Fe_3O_8$[10] and annite mica.[11] We have also measured the isothermal magnetization at several low temperatures in applied fields between 5 and $-5$ T for $Sr_2LaFe_3O_9$, and observed a hysteretic behavior, i.e., remanent magnetization (not shown).

Shown in the inset of Fig. 4 is the field dependence of $\Delta M$ at $T=6$ K. $\Delta M$ initially increases significantly and then saturates gradually at high applied fields. Consequently, the difference between the FC and ZFC $\chi(T)$ data will become smaller when one increases the applied field. Shown in the main portion of Fig. 4 are the $\chi(T)$ data measured in a field of 2 T. The difference between the FC and ZFC curves is greatly reduced from that observed at low fields.

Neutron diffraction measurements[9] on $Sr_2LaFe_3O_9$ have shown that the magnetic structure can be described in terms of a spin density wave commensurate with the crystal lattice. The noncubic antiferromagnetic structure might be responsible for a magnetic moment canting in an external field giving rise to a ferromagnetic component for the FC curve.

In conclusion both the specific heat and magnetization measurements indicate that an antiferromagnetic transition occurs at $T_N=203$ K in $Sr_2LaFe_3O_9$. The observed entropy removal and effective paramagnetic moment are much smaller than those that one would expect if the magnetism were due to well-localized moments associated with the Fe atoms. The FC and ZFC magnetic susceptibility curves show hysteretic behavior which is suppressed by applied fields. The $^{57}$Fe Mössbauer spectrum measured at 4.2 K is consistent with two superimposed magnetic hyperfine fields, as previously observed at 78 K.[7,8]

Lin and Mihalisin acknowledge support from the Materials Research Center at Temple University and DOD-AFOSR under Grant No. F49620-93-1-0018.

[1] J. G. Bednorz and K. A. Muller, Z. Phys. B **64**, 189 (1986).
[2] M. K. Wu, J. R. Ashburn, C. J. Torng, P. H. Hor, R. L. Meng, L. Gao, Z. J. Huang, Y. Q. Wang, and C. W. Chu, Phys. Rev. Lett. **58**, 908 (1987).
[3] Y. Takeda, S. Naka, M. Takano, T. Shinjo, T. Takada, and M. Shimada, Mater. Res. Bull. **13**, 61 (1978).
[4] P. K. Gallagher, J. B. MacChesney, and D. N. E. Buchanan, J. Chem. Phys. **41**, 2429 (1964).
[5] M. Takano, N. Nakanishi, Y. Takeda, and S. Naka, J. de Phys. Colloque C **2**, 313 (1979).
[6] Y. Takeda, S. Naka, and M. Takano, J. de Phys. Colloque C **2**, 331 (1979).
[7] P. D. Battle, T. C. Gibb, and S. Nixon, J. Solid State Chem. **77**, 124 (1988); *ibid.*, **79**, 75 (1989).
[8] P. D. Battle, T. C. Gibb, and S. Nixon, J. Solid State Chem. **79**, 86 (1989).
[9] P. D. Battle, T. C. Gibb, and P. Lightfoot, J. Solid State Chem. **84**, 271 (1990).
[10] I. Felner, I. Nowik, U. Yaron, O. Cohen, E. R. Bauminger, T. Kroener, and G. Czjzek, Phys. Rev. B **48**, 16040 (1993).
[11] D. G. Rancourt, I. A. D. Christie, G. Lamarche, I. Swainson, and S. Flandrois, J. Magn. Magn. Mater. **138**, 31 (1994).

# Low-temperature Mössbauer study of the mechanically alloyed $Fe_xMn_{0.7-x}Al_{0.3}$ ($0.4 \leq x \leq 0.5$) series

J. M. González and Anit K. Giri
*Instituto de Ciencia de Materiales de Madrid-CSIC, Serrano 144, 28006 Madrid, Spain*

G. A. Pérez Alcázar and Ligia E. Zamora
*Departamento de Física, Universidad del Valle, A. A. 25630, Cali, Colombia*

Results are presented concerning the magnetic properties at low temperatures of mechanically alloyed samples of the $Fe_xMn_{0.7-x}Al_{0.3}$ ($0.4 \leq x \leq 0.5$) series. According to these results the samples were characterized as having a broad spectrum of relaxation times related to the occurrence of clustering. Also, in the particular case of the $x=0.40$ sample, we were able to detect a reentrant spin glass freezing transition. © *1996 American Institute of Physics.* [S0021-8979(96)03808-0]

## I. INTRODUCTION

The combination[1] of structural disorder and competing ferromagnetic (F) and antiferromagnetic (AF) interactions brings about the possibility of the occurrence of spin glass (SG) behavior in the FeMnAl system. Nevertheless, and despite the amount of already published work,[2–7] both theoretical and experimental, the magnetic properties of this ternary system must still be explored in more detail. To summarize those previously obtained results, let us say that Pérez Alcazar *et al.*[2] showed that disordered bcc samples of this system with Mn and Al contents ranging from 20 up to 35 at. % and from 20 up to 30 at. %, respectively, showed a complex structure for the line in the phase diagram defined by the compositions for which the Curie temperature coincided with the room temperature. This behavior was interpreted by Rosales Rivera *et al.*[3] as related to the occurrence of a SG phase. The presence in the $Fe_{0.50}(Mn_xAl_{1-x})_{0.50}$ series of such a SG phase was reported, on the basis of Mössbauer results, by Kobeissi.[4] A reentrant spin glass (RSG) behavior, linked to the presence in addition to disorder and competing interactions of some paramagnetic sites, has been recently shown to occur in $Fe_{0.45}Mn_{0.30}Al_{0.25}$.[5,6] Finally, Bremers *et al.* presented evidence of RSG in $Fe_{0.49}Mn_{0.11}Al_{0.40}$ samples.

The preparation of samples by means of solid state reaction techniques seems to be specially interesting[8] from the point of view of the study of the influence of the disorder on the magnetic behavior, since these techniques usually have associated control parameters allowing a gradual introduction of both structural (random site occupation) and microstructural (chemical clustering) disorder. In the particular case of the preparation technique used in this work, mechanical alloying, we can mention, among these control parameters, the milling time and intensity and the mass of precursor materials-to-mass of the milling balls ratio.

## II. PREPARATION OF SAMPLES AND EXPERIMENTAL TECHNIQUES USED

In the present work we will report on the preparation and low-temperature magnetic properties of the alloy series $Fe_xMn_{0.7-x}Al_{0.3}$ ($0.4 \leq x \leq 0.5$). Our samples were mechanically alloyed using a planetary ball mill (Fritsch Pulverisette 7). The precursor pure elemental powders (<40 $\mu$m particle size, 99.99% purity) were sealed under inert atmosphere in stainless steel jars together with balls of the same material in a mass of powders-to-mass of the balls ratio of 1:12. That mixture was milled for 72 h. The phase distribution of the as-milled material was examined by means of x-ray diffractometry (XRD, Cu $K\alpha$). The magnetic properties of the samples (measured in the form of pressed powder cylinders) were investigated using a SQUID magnetometer (5 T, 1.7–400 K), an ac susceptometer (4.2–300 K, operated at a dc field value of 10 Oe, ac field amplitude of 3 Oe, and 175 Hz frequency) and a constant acceleration type Mössbauer spectrometer with a $^{57}Co$ source.

## III. RESULTS

In Fig. 1, we present the XRD patterns measured in all the prepared samples. As can be observed, all of the samples exhibited bcc-type reflections exclusively.

In Fig. 2, we have plotted the temperature dependence of the ac magnetic susceptibility measured, after zero field cooling, in the $x=0.50$, 0.475, and 0.45 samples. In all of them we observed a broad plateau which indicated a very wide spectrum of relaxation times. Different from this, the results corresponding to the $x=0.40$ sample (Fig. 3) revealed a well-defined (but still wide) maximum at ~120 K.

In agreement with the former results, the curves corresponding to the temperature dependence of the low field (75 Oe) dc magnetic moment measured after cooling the $x=0.40$

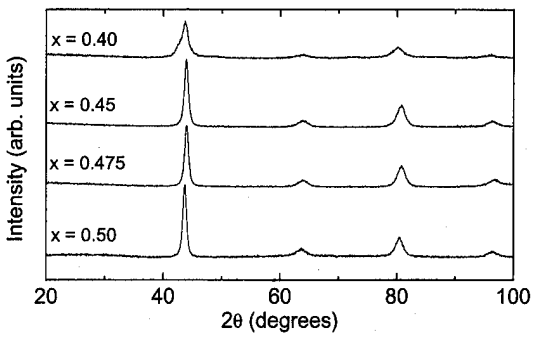



FIG. 1. X-ray diffraction patterns obtained in the different samples under examination.

 0021-8979/96/79(8)/6611/3/$10.00 © 1996 American Institute of Physics 

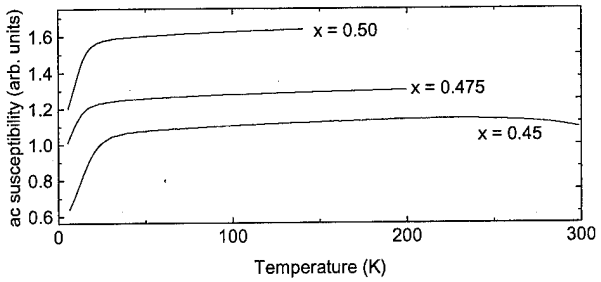



FIG. 2. Temperature dependence of the ac susceptibility measured in the $x=0.50$, 0.475, and 0.45 samples.

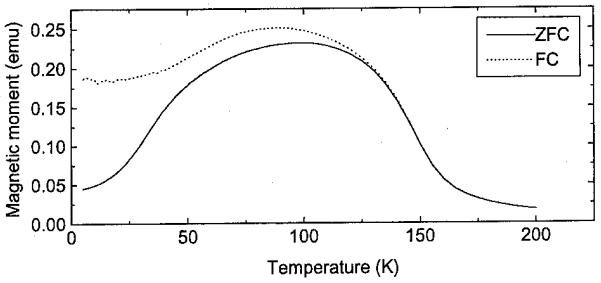



FIG. 4. Temperature dependence of the low field magnetic moment of the $x=0.40$ sample measured after zero field cooling and field cooling.

sample under a field of 75 Oe (shown in Fig. 4) coincided (down to the sensitivity of our magnetometer) for temperatures above 130 K.

The Mössbauer spectra taken in the $x=0.40$ sample at different temperatures in the range from 15 up to 58 K are shown in Fig. 5(a). All the spectra are broad and unresolved, indicating the occurrence of a high degree of disorder in the samples. The best fit of these spectra was obtained using two hyperfine field distributions (HFDs) and a paramagnetic line. The associated hyperfine field probability distributions resulting from the fits are presented in Fig. 5(b). As is apparent from the figure, the HFDs shift towards the low-field range when the temperature is increased.

The average hyperfine field associated with the distributions evolved with temperature as shown in Fig. 6. From the extrapolation to higher temperatures of these data, it is possible to observe that the average hyperfine field should vanish at ~80 K, that is at a temperature clearly lower than that corresponding to the maxima observed in the temperature dependence of the ac susceptibility and the low field zero field cooled magnetic moment. Also and remarkably, a kink was observed in the temperature evolution of the hyperfine field at ~30 K. In agreement with this the temperature dependence of the area of the paramagnetic line considered in the fit of the spectra (see Fig. 7) exhibited a clear increase above 40 K.

## IV. DISCUSSION

From our Mössbauer data obtained in the $x=0.40$ sample two major conclusions can be inferred: on the one side, the order temperature associated to the measured hyperfine field is of the order of 80 K and on the other, following the ideas presented in Ref. 9, the sample exhibits reentrant spin glass behavior. The last point was evidenced by the kink observed in the temperature dependence of the average hyperfine field which can be understood as linked to the appearance (as the temperature is decreased) of an extra contribution to that field coming from the moments which at temperatures higher than that of the kink behaved as paramagnetic and freezed below it. This idea is confirmed by the temperature dependence of the percentage of the total spectral area associated to the paramagnetic line: it peaks at temperatures slightly higher than those of the kink in the average hyperfine field versus temperature curve, indicating an increase, linked to the defreezing process, of the number of moments which behave paramagnetically.

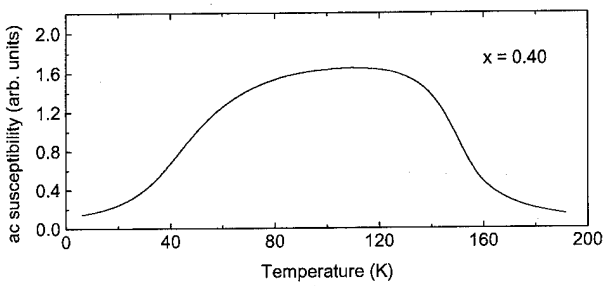



FIG. 3. Temperature dependence of the ac susceptibility measured in the $x=0.40$ sample.

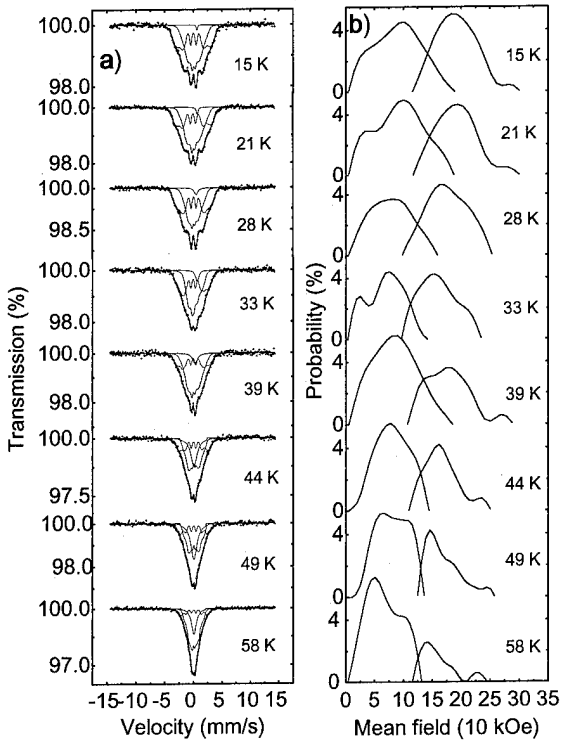



FIG. 5. (a) Mössbauer spectra measured in the $x=0.40$ sample at different temperatures. (b) Hyperfine field probability distributions in the sample with $x=0.40$ evaluated from the fit of the spectra shown in (a). The different subspectra considered are also indicated.

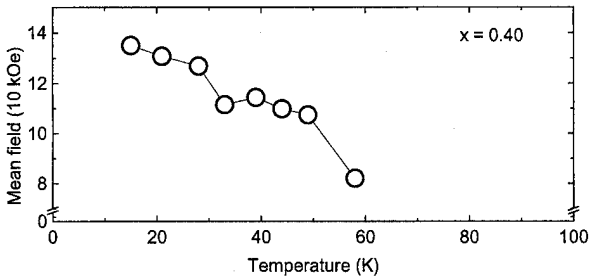



FIG. 6. Temperature dependence of the average hyperfine field of the $x=0.40$ sample.

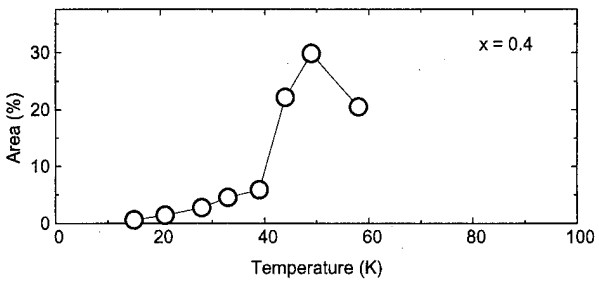



FIG. 7. Temperature dependence of the percentage of the total area associated to the paramagnetic lines used to fit the spectra in Fig. 5(a).

In contrast with the Mössbauer results, magnetometric and susceptometric data obtained in this sample, althoughqualitatively indicating the occurrence of a freezing process, evidenced measurable magnetic moments and susceptibilities at temperatures higher than at which, according to our Mössbauer data, the hyperfine field should vanish. A similar behavior, i.e., the observation in the Mössbauer spectra of broad and unresolved structures at temperatures at which magnetometric techniques are able to detect indications of magnetic order, has been previously reported in a number of different systems[10–14] and is usually related to the occurrence of a range of relaxation times covering many decades, being magnetic field sensitive and linked to the existence of clusters. In our particular case, the broad maxima detected in the susceptibility versus temperature curves of all the examined samples are a further confirmation of the occurrence of clusters.

Regarding the origin of the proposed clusters, let us remember the out-of-equilibrium nature of the preparation process and the fact that the samples were measured in the as-milled state. Then, it is possible to envisage the presence of both chemical (linked to compositional fluctuations) and magnetic (linked to exchange fluctuations) clusters which should result in a wide distribution of local fields. A study of the magnetic properties of structurally relaxed samples is currently being carried out in order to clarify this point.

## ACKNOWLEDGMENTS

This work was supported by the European Union through the ALAMED Program and by COLCIENCIAS, Colombian Agency. G. A. P. A. would like to acknowledge the Spanish Ministry Of Education and Science for a Sabbatical Fellowship.

[1] J. A. Mydosh, *Spin Glasses: An Experimental Introduction* (Taylor & Francis, London, 1993), p. 1.
[2] G. A. Perez Alcazar, J. A. Plascak, and E. Galvao Da Silva, Phys. Rev. B **38**, 2816 (1988).
[3] A. Rosales Rivera, G. A. Perez Alcazar, and J. A. Plascak, Phys. Rev. B **41**, 4774 (1990).
[4] M. A. Kobeissi, J. Phys. Condens. Matter **3**, 4983 (1991).
[5] L. E. Zamora, G. A. Pérez Alcázar, A. Bohorquez, and J. Tabares, J. Magn. Magn. Mater. **137**, 339 (1994).
[6] G. A. Pérez Alcázar, J. Tabares, A. Bohorquez, and J. R. Gancedo, Hyp. Int. **83**, 203 (1994).
[7] H. Bremers, Ch. Jerms, J. Hesse, S. Chadjivasiliou, K. G. Efthimiadis, and I. Tsoukalas, J. Magn. Magn. Mater. **140–144**, 63 (1995).
[8] G. F. Zhou and H. Bakker, Phys. Rev. Lett. **73**, 344 (1994).
[9] J. Hesse, Hyper. Inter. **78**, 247 (1989).
[10] M. Alba, J. Hamman, and M. Nogue, J. Phys. C: Solid State Phys. **15**, 5441 (1982).
[11] D. Bertrand, F. Bensanka, A. R. Fert, I. Gerald, J. P. Redoules, and J. Legrand, J. Phys. C: Solid State Phys. **17**, 1725 (1984).
[12] R. Rodriguez, A. Fernandez, A Isalgue, J. Rodriguez, A. Labarta, J. Tejada, and X. Obradors, J. Phys. C: Solid State Phys. **18**, L401 (1985).
[13] E. Agostinelli, P. Filaci, D. Fiorani, and E. Paperazzo, Solid State Commun. **56**, 541 (1985).
[14] M. Vaidya and P. H. Umadikar, J. Phys. Chem. Solids **52**, 827 (1991).

# Magnetic and crystal phase transitions in $KNiCl_3$

O. A. Petrenko, M. F. Collins, and C. V. Stager
*Department of Physics and Astronomy, McMaster University, Hamilton, Ontario L8S 4M1, Canada*

B. F. Collier
*Institute for Materials Research, McMaster University, Hamilton, Ontario L8S 4M1, Canada*

Z. Tun
*AECL, Chalk River Laboratory, Chalk River, Ontario K0J 1J0, Canada*

Neutron scattering measurements revealed that even a seemingly perfect crystal of $KNiCl_3$ at room temperature may segregate into two phases with different lattice distortions in the basal $ab$ plane at temperatures below $T \approx 270$ K. In phase $A$, distortion leads to an increase of the unit cell size by a factor of 3, giving rise to nuclear Bragg peaks of type $(h/3,h/3,l)$. In phase $B$ the distortion gives rise to Bragg peaks at $(3h/4,0,l)$, with integer $h$ and $l$. Two different magnetic structures have been observed with $T_N = 12.5$ and 8.6 K in phases $A$ and $B$, respectively. Magnetization measurements confirm the values of $T_N$ found by neutron scattering for the two magnetic structures. © *1996 American Institute of Physics.* [S0021-8979(96)00608-2]

The great interest in magnetic properties of the hexagonal $ABX_3$-type compounds is due to the fact that they provide good examples of triangular-lattice antiferromagnets. By varying $A$, $B$, and $X$ (where $A$ is an alkali metal, $B$ is a bivalent metal of $3d$ group, and $X$ is a halogen) one can create systems with different type of magnetic interactions. For example, $CsCoBr_3$ and $CsCoCl_3$ may be described as Ising antiferromagnets,[1] $CsFeBr_3$ and $CsFeCl_3$ are usually referred to as singlet ground state magnets because the $Fe^{2+}$ ion has locally a singlet ground state $(m_s=0)$,[2,3] $CsNiCl_3$ and $CsMnI_3$ are nearly Heisenberg systems with small easy-axis anisotropy,[4,5] while other Heisenberg antiferromagnets $CsMnBr_3$ and $RbMnBr_3$ exhibit strong $XY$-type anisotropy.[6,7] It has been found that a variety of new magnetic properties exists in these types of compounds, such as field-induced phase transitions from the triangular phase to a collinear one, incommensurate–commensurate phase transitions, critical behavior associated with a chiral degeneracy, and unusual phase diagrams. A common feature of all of these systems is that the exchange interactions in the chains of $3d$ ions along the hexagonal axis are much stronger than those in the basal plane.[4]

Here we present the results of elastic neutron scattering measurements and magnetization measurements on $KNiCl_3$, an example of the Heisenberg triangular antiferromagnet. Particular interest in the "$KNiCl_3$ family" of crystals may be attributed to the experimental opportunity to investigate the magnetic properties of the easy-plane triangular lattice antiferromagnets with partially released spin frustration.[8,9] In contrast to the fully frustrated triangular spin systems, such as in $CsMnBr_3$, the crystal distortions in the $KNiCl_3$ family break the symmetry of the interaction between neighboring in-plane magnetic ions. The theory predicts a different type of behavior,[10–12] especially in an applied magnetic field,[13] according to different distortions of the ideal hexagonal packing and consequently of the 120° spin structure.

The neutron scattering measurements were carried out on the $N5$ and $C5$ triple-axis spectrometers at the NRU reactor at the Chalk River Laboratories and on the double-axis spectrometers at McMaster University Nuclear Reactor. A pyrolytic graphite (002) reflection was used for the monochromator, the incident and scattered neutron energy was fixed at 3.52 THz at Chalk River and at 3.36 THz at McMaster. A pyrolytic graphite filter at room temperature and a nitrogen-cooled sapphire filter were installed in the beam to remove higher-order contamination. The collimation was typically 0.47°–0.56°–2.5°. Liquid-helium cryostats with a minimum temperature 1.7 K were used at Chalk River Laboratories, while at McMaster University we used only liquid nitrogen for the sample cooling. The single-crystal samples were aligned in two different ways, so that the horizontal scattering plane contained either $(hhl)$ or $(h0l)$ reflections indexed in the hexagonal cell with $a=11.80$ Å and $c=5.94$ Å.

We investigated three large crystals of $KNiCl_3$ in our neutron scattering experiments. All of them were prepared using the Bridgman method and were cylindrical in a shape with length approximately 10–20 mm and diameter ~10 mm. At room temperature all three crystals gave identical scattering patterns consistent with the space group $P6_3cm$. This structure is distinguished from the undistorted high-temperature structure with space group $P6_3/mmc$ by a shifting of two thirds of the $NiCl_3$ chains along the $c$ axis.[14] Further structural phase transitions just below room temperature have been reported by Machida *et al.*[15] We observe a dramatic difference between crystals after cooling through these transitions at 285 and 274 K.

In crystal number 1 (volume ~0.8 $cm^3$) scans in the $(hhl)$ plane of the reciprocal lattice revealed new Bragg peaks at position $(h/3,h/3,l)$. The intensity of these peaks was small, increasing gradually as the temperature decreases, though even at the lowest temperature it did not exceed half a percent of the intensity of the main reflections. No new nuclear peaks were found for scans in the $(h0l)$ plane. None of the main Bragg peaks change in intensity when passing through the phase transition. From these observations it is concluded that (1) the low-temperature unit cell is rotated through 90° about the $c$ axis from the room-temperature unit cell and enlarged to $\sqrt{3}a$, $\sqrt{3}a$, and $c$, (2) the distortion of the low-temperature structure is small so that the structure does

 0021-8979/96/79(8)/6614/3/$10.00 © 1996 American Institute of Physics

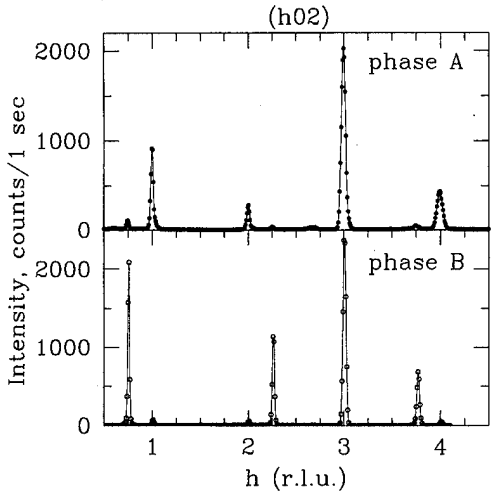



FIG. 1. Bragg-peak intensity of $KNiCl_3$ at $T=4.2$ K observed with $(h02)$ scans. For sample 1 (top), phase $A$ is the majority phase and for sample 2 (bottom), phase $B$ is the majority phase.

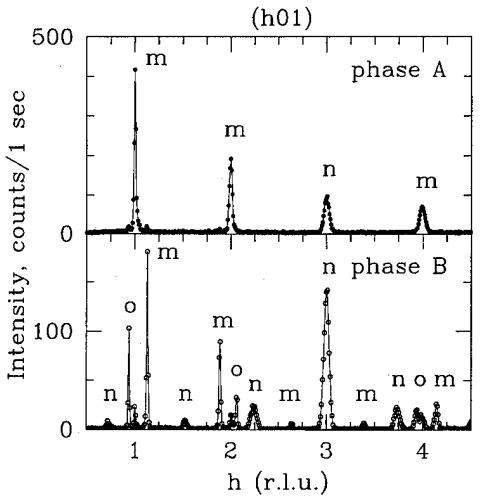



FIG. 2. Bragg-peak intensity of $KNiCl_3$ at $T=4.2$ K for phase $A$ (top) and $B$ (bottom) along the $(h01)$ direction of the reciprocal lattice. Nuclear peaks are designated "$n$," in-plane magnetic peaks "$m$," and out-of-plane magnetic peaks "$o$."

not differ much from the structure at room temperature. This tripling of the unit cell volume is quite common for materials with this crystal structure. Further measurements on a powder sample[16] confirmed this conclusion; the powder neutron scattering pattern looks similar at all temperatures except those where magnetic ordering appeared. We call the low-temperature structure of this crystal phase $A$.

In crystal number 2 (volume $\sim 1.2$ cm$^3$), whose low-temperature phase we call phase $B$, the change of crystal structure below and above the phase transition temperature is less common. Instead of room-temperature peaks at position $(h0l)$, with $l$ even, new peaks appeared at $(h+q,0,l)$ with $q=0$ for $h=3n$ ($n$ integer), $q=-\frac{1}{4}$ for $h=3n+1$ and $q=\frac{1}{4}$ for $h=3n+2$. Figure 1 shows the intensity of nuclear Bragg peaks of $(h02)$ type at $T=4.2$ K for both crystals. Inspection of the scattering patterns from the two crystals shown in Fig. 1 demonstrates that neither crystal is homogeneous; that is a small amount of phase $A$ is present in the second crystal, as well as a small amount of phase $B$ in the first one. Our rough estimation of the phase ratio $A:B$ gives 97:3 for the first crystal and 10:90 for the second one. For each crystal this ratio is repeatable and does not depend upon the cooling rate. To investigate the spatial distribution of phases $A$ and $B$ in the second crystal we restricted the horizontal size of the neutron beam to 2 mm and measured the intensity of the peaks from both phases while moving the beam along the cylindrical sample. This simple experiment showed that phase $A$ in the second crystal is mostly located on the top and bottom of the cylinder, while phase $B$ occurs mostly in the middle.

Crystal number 3 was prepared and studied to investigate the influence of the annealing process on the crystal structure of $KNiCl_3$. A neutron diffraction pattern of this crystal was measured immediately after preparation and again after annealing for 12 days at a temperature of 250 °C. No significant change was found and in both cases the third crystal gave reflections consistent with phase $B$.

As a consequence of the existence of two different crystal modifications, two different magnetic structures have been observed in phases $A$ and $B$ (see Fig. 2). In both cases magnetic reflections $(hkl)$ are only observed for $l$ odd because of the strong antiferromagnetic interactions along the chains.

In phase $A$ the magnetic Bragg peaks are at $(h,0,2l'+1)$ and the magnetic structure is in-plane triangular with the angles between two nearest neighbor spins close to 120°. The nonzero intensity of the reflection (001) (not shown in Fig. 2) shows that there are deviations from 120°. These are brought about by the nonequivalent interchain exchange interaction[17] and correspond to nonzero magnetization in one basal plane. Note, that antiferromagnetic alignment of spins along the chains results in the net magnetization remaining exactly zero for zero external field.

The bottom of Fig. 2 shows the Bragg-peak intensity for phase $B$ along the $(h01)$ direction of reciprocal space. The magnetic peaks are sharper than the nuclear peaks. This might suggest distortions of the nuclear structure to lower symmetry. The magnetic peaks would come from single domains while the nuclear peaks are an unresolved superposition of different domains. Not all of the observed peaks lie in the $(h0l)$ plane, we have seen additional reflections located slightly below and slightly above the scattering plane due to relatively open vertical resolution. The insertion of a vertically focusing monocromator significantly increased the intensity of these peaks, while by decreasing the vertical size of the detector it is possible to decrease the intensity to zero. All magnetic Bragg peaks located in the scattering plane can be indexed as $[\frac{3}{8}(2h+1),0,2l+1]$ and are designated an "$m$" on Fig. 2. The overall magnetic scattering pattern in phase $B$, including peaks above and below the scattering plane, is identical to that observed in another $XY$-like antiferromagnet on a distorted stacked triangular lattice, $RbMnBr_3$, at high magnetic field.[7] The analogy with $KNiCl_3$ may help resolve some unanswered questions about the magnetic properties of $RbMnBr_3$. For example, the presence of

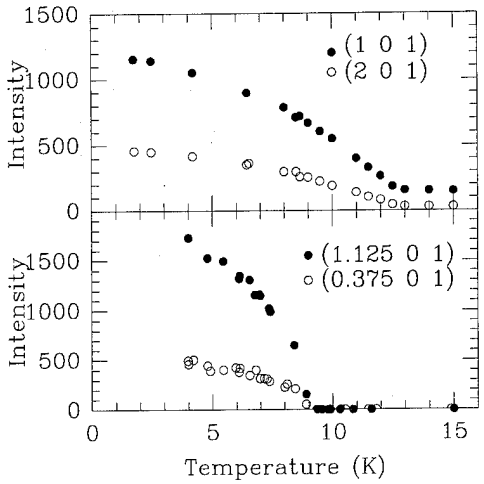



FIG. 3. Integrated intensity of the magnetic Bragg peaks of $KNiCl_3$ vs temperature for phase $A$ (top) and $B$ (bottom).

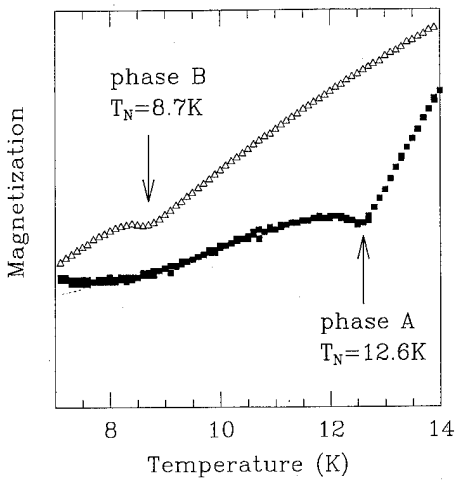



FIG. 4. The temperature dependence of the magnetization of $KNiCl_3$ at $H=0.75$ T, $H\perp c$, in arbitrary units. The arrows at 12.6 and 8.7 K correspond to the ordering temperature for phases $A$ and $B$, respectively.

two magnetic structures with different ordering wave vector and ordering temperatures found in $RbMnBr_3$ by one group of authors[7] and not by another,[18] is likely to be attributed to a different phase ratio $A:B$ in the two samples. Despite the similarity of the crystal structures, the magnetic structure of $RbMnBr_3$ at low magnetic field in phase $B$ differs from phase $B$ of $KNiCl_3$ in that it is an incommensurate ordered structure with magnetic Bragg peaks at $(h/8\pm\delta,\ h/8\pm\delta,\ l)$ with $\delta=0.0183$.

Figure 3 shows the temperature dependence of the integrated intensity of the magnetic Bragg peaks for phases $A$ and $B$. The temperature of magnetic ordering was found to be $T_N=12.5\pm0.1$ K and $T_N=8.6\pm0.1$ K in phases $A$ and $B$, respectively. This result has been obtained both by measurement in a double-axis mode and in a triple-axis mode with zero energy transfer.

It is apparent from the discussion above, that previously reported neutron scattering and magnetization measurements[17] were carried out on a different phase of $KNiCl_3$. Inelastic neutron scattering measurements (Figs. 1 and 2 of Ref. 17) were performed on crystal number 1 with phase $A$, while magnetization measurements (Figs. 3 and 4 of Ref. 17) were performed on a different small crystal corresponding to phase $B$. We remeasured the magnetization of both phases of $KNiCl_3$ using a Quantum Design SQUID magnetometer. A typical example of the temperature dependence of the magnetization at $H=0.75$ T is shown in Fig. 4. Both curves demonstrate well-pronounced changes of slope at the magnetic ordering temperature $T_N=12.6$ K and $T_N=8.7$ K, in good agreement with the neutron scattering results.

In conclusion, we have presented experimental data which unambiguously show the existence of two different low-temperature crystal and magnetic structures in the easy-plane triangular lattice antiferromagnet $KNiCl_3$. Three-dimensional x-ray or neutron diffraction measurements are needed to determine the precise crystal structure of both low-temperature phases.

This work was supported by the Natural Sciences and Engineering Research Council of Canada.

[1] B. D. Gaulin, in *Magnetic Systems with Competing Interactions*, edited by H. T. Diep (World Scientific, Singapore, 1994), p. 286.
[2] B. Dorner, D. Visser, U. Steigenberger, K. Kakurai, and M. Steiner, Z. Phys. B Condens. Matter **72**, 487 (1988).
[3] M. Steiner, K. Kakurai, W. Knop, B. Dorner, R. Pynn, U. Happek, P. Day, and G. McLeen, Solid State Commun. **38**, 1179 (1981).
[4] N. Achiwa, J. Phys. Soc. Jpn. **27**, 561 (1969).
[5] H. W. Zandbergen, J. Solid State Chem. **35**, 367 (1980).
[6] B. D. Gaulin, M. F. Collins, and W. J. L. Buyers, J. Appl. Phys. **61**, 3409 (1987).
[7] L. Heller, M. F. Collins, Y. S. Yang, and B. Collier, Phys. Rev. B **49**, 1104 (1994).
[8] A. Hauser, U. Falk, P. Fischer, and H. Gudel, J. Solid State Chem. **56**, 343 (1985).
[9] H. Tanaka, Y. Kaahwa, T. Hasegawa, M. Igarashi, S. Teraoka, K. Iio, and K. Nagata, J. Phys. Soc. Jpn. **58**, 2930 (1989).
[10] N. Suzuki and M. Shirai, Physica **136B**, 346 (1986).
[11] M. L. Plumer, A. Caille, and H. Kawamura, Phys. Rev. B **44**, 4461 (1991).
[12] W.-M. Zhang, W. M. Saslow, M. Gabay, and M. Benakli, Phys. Rev. B **48**, 204 (1993).
[13] M. E. Zhitomirsky, O. A. Petrenko, and L. A. Prozorova, Phys. Rev. B **52**, 3511 (1995).
[14] D. Visser, G. C. Verschoor, and D. J. W. Ijdo, Acta. Cryst. B **36**, 28 (1980).
[15] K. Machida, T. Mitsui, T. Kato, and K. Iio, Solid State Commun. **91**, 17 (1994).
[16] O. A. Petrenko, M. F. Collins, and Z. Tun (unpublished).
[17] O. A. Petrenko, M. F. Collins, C. V. Stager, and Z. Tun, Phys. Rev. B **51**, 9015 (1995).
[18] T. Kato, T. Ishii, Y. Ajiro, T. Asano, and S. Kawano, J. Phys. Soc. Jpn. **62**, 3384 (1993).

# New spin glass $Fe_{0.67}Cr_{1.33}Sn_{0.67}S_4$ with magnetic ions in tetrahedral and octahedral sublattices (abstract)

L. I. Koroleva, L. N. Lukina, and A. G. Odintsov
*Department of Physics, M. V. Lomonosov Moscow State University, Moscow 119899, Russia*

T. V. Virovets
*Kurnakov Institute of General and Inorganic Chemistry, Moscow 117907, Russia*

To date, spin glass state is observed in chalcogenide spinels with magnetic ions either in tetrahedral $A$ sublattice or in octahedral $B$ sublattice. The possibility of spin glass state in chalcospinels with magnetic ions in both of $A$ and $B$ sublattices is not evident because the intersublattice antiferromagnetic superexhange is more higher than intrasublattice ferromagnetic superexhange. In the present paper the magnetic and electrical properties of first produced spinel $Fe_{0.67}Cr_{1.33}Sn_{0.67}S_4$ are studied. This sample is $p$-type semiconductor. Here $B$ sublattice is diluted of diamagnetic $Sn^{4+}$ ions and $Fe^{2+}$ ions deficiency exists in $A$ sublattice. The isotherms of the magnetization $\sigma$ are not saturated in investigation region of magnetic field $H \leqslant 35$ kOe and of temperatures $4.2 \leqslant T \leqslant 120$ K. At the same time, this sample possesses magnetic properties typical of spin glass. Thus a maximum on the temperature dependence of the magnetic susceptibility measured in a weak ac field is founded at the freezing temperature $T_f$. (The frequency region is $0.3 \leqslant \omega \leqslant 2$ kHz, $H_{\sim}=0.3$ Oe.) The maximum is lowered under a static magnetic field which is applied parallel to the ac field. Low-temperature magnetization in the weak field depends on the cooling process (with or without field). The $T_f(\omega)$ dependence obeys the power law and $T_f(H,T)$ dependence obeys the Almeida–Touless relation; these facts attest that phase transition spin glass–paramagnetic exists in this sample. This is a first spin glass among chalcospinels with magnetic ions in $A$ and $B$ sublattices. © *1996 American Institute of Physics.* [S0021-8979(96)63708-9]

 0021-8979/96/79(8)/6617/1/$10.00 © 1996 American Institute of Physics 

# Scaling of the thermoremanent relaxation in FeNiCr

D. Li and R. M. Roshko
*Department of Physics, University of Manitoba, Winnipeg MB R3T 2N2, Canada*

We present measurements of the relaxation of the low field thermoremanent magnetization of $Fe_{0.65}Ni_{0.24}Cr_{0.11}$ over four decades of observation time 1 s$<t\leqslant 10^4$ s, as a function of temperature $T$ and system age $t_w$. The system orders ferromagnetically at $T_c\cong 110$ K and then, near $T_R\cong 50$ K collapses into a much less responsive low-temperature phase, with glassy, age-dependent dynamics appearing below $T_g\cong 22$ K. We have analyzed the data using a model of random traps developed by Bouchaud, according to which the relaxation curves for different $t_w$ at a given temperature $T$ will scale onto a universal curve when plotted as a function of $t/t_w$, provided that proper account is taken of the distribution of ergodic times $t_{\rm erg}$ possessed by a real system. With the assumption of a log-normal distribution $P(t_{\rm erg})$, we have calculated the nonuniversal correction-to-scaling factor explicitly, and we have shown that the data do indeed collapse remarkably well onto a universal curve, with a suitable choice of values for the two distribution parameters, and for the two relaxation function parameters. © *1996 American Institute of Physics.* [S0021-8979(96)03908-7]

Disordered materials are characterized by a very slow relaxation of their macroscopic observables (typically logarithmic, or stretched exponential, or weak power law) in response to a step-function excitation, and by the aging effect, which means that the relaxation response depends on the time that the system has spent in the glassy state at a temperature $T<T_g$ before it is probed. Recently, Bouchaud[1] has offered a phenomenological explanation for this behavior, which is based on the very general premise that the free energy landscape of a disordered material is very rugged, with many local metastable minima which temporarily trap the system as it evolves towards equilibrium. If the distribution of trapping times $\tau$ has the form $\psi(\tau)\sim\tau^{-(x+1)}$ with $x<1$, then the mean trapping time $\bar{\tau}=\int_{\tau_0}^{\infty}\tau\psi(\tau)d\tau$ diverges ($\tau_0$ is a microscopic time), so that an infinite system will require an infinite time to explore all of its configuration space. Thus, its relaxation response will specifically depend on where it was trapped in configuration space when it was disturbed by the probing field.

In a finite system with $S$ metastable states, a random walk analysis predicts that there will be a most probable longest trapping time encountered by the system, and this plays the role of an ergodic time $t_{\rm erg}=\tau_0 S^{1/x}$, after which the system is assumed to have reached equilibrium. If the wait time $t_w$ between the temperature quench from above to below $T_g$ and the application of the probing field is much less than the ergodic time $t_{\rm erg}$, the relaxation response is nonergodic and given by[1]

$$m(t,t_w)=m_0\exp\left(-\gamma\int_0^t t^{-x}(t+t_w)^{x-1}dt\right). \tag{1}$$

If $t_w\gg t_{\rm erg}$, the system is in equilibrium, and the relaxation response is very nearly the same function,[1,2] but with $t_w$ replaced by $t_{\rm erg}$.

If the response of a real system was purely nonergodic then, for a given temperature $T$, the relaxation data for different $t_w$ should scale onto a universal curve when plotted as a function of $t/t_w$, since the predicted response $m(t,t_w)/m_0$ in Eq. (1) depends only on the reduced variable $t/t_w$. However, if a macroscopic system was actually a collection of independent subsystems, with a distribution of sizes $P(S)$ and of ergodic times $P(t_{\rm erg})$, then departures from universality would be expected, due to that fraction of subsystems with $t_{\rm erg}<t_w$, for which aging has ceased.

In this paper, we present measurements of the relaxation of the low field thermoremanent magnetization in a sample of $Fe_{0.65}Ni_{0.24}Cr_{0.11}$ as a function of observation time $t$, wait

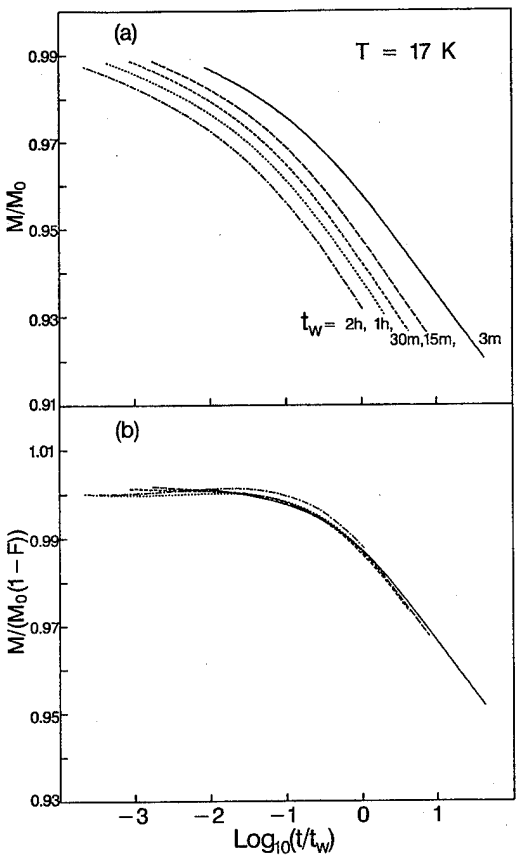



FIG. 1. (a) The thermoremanent relaxation $M(t)/M_0$ measured at $T=17$ K for several different values of the wait time $t_w$, plotted as a function of $\log_{10}(t/t_w)$. (b) The same data in (a) scaled along the vertical axis by the correction factor 1-$F$ as described.

 0021-8979/96/79(8)/6618/3/$10.00 © 1996 American Institute of Physics

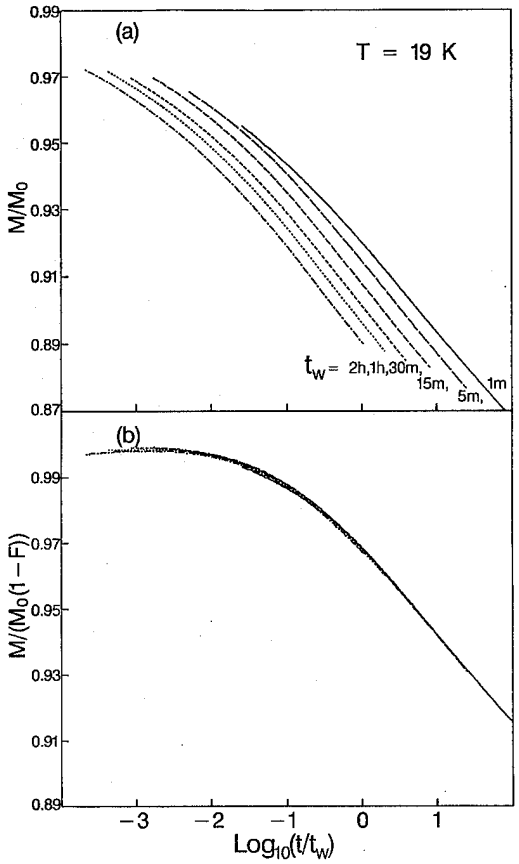



FIG. 2. (a) The thermoremanent relaxation $M(t)/M_0$ measured at $T=19$ K for several different values of the wait time $t_w$, plotted as a function of $\log_{10}(t/t_w)$. (b) The same data in (a) scaled along the vertical axis by the correction factor 1-$F$ as described.

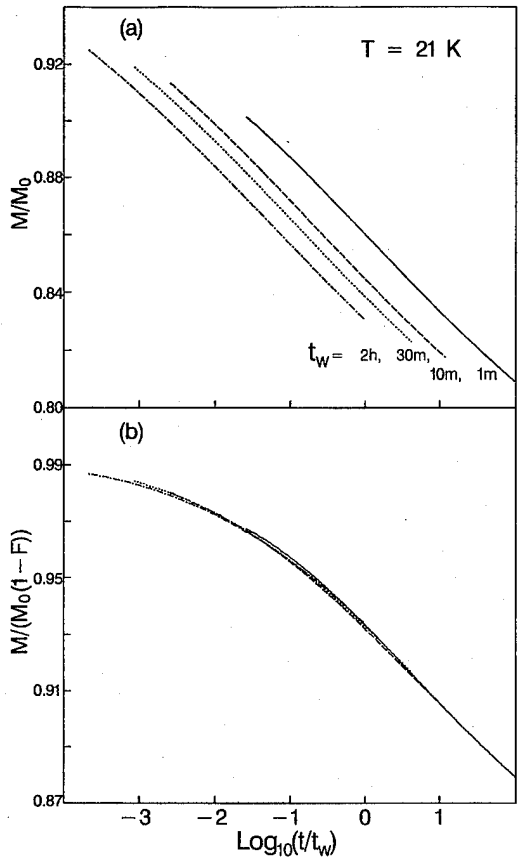



FIG. 3. (a) The thermoremanent relaxation $M(t)/M_0$ measured at $T=21$ K for several different values of the wait time $t_w$, plotted as a function of $\log_{10}(t/t_w)$. (b) The same data in (a) scaled along the vertical axis by the correction factor 1-$F$ as described.

time $t_w$, and temperature $T$, and we show that, with only a few simplifying assumptions, the experimental systematics are remarkably consistent with Bouchaud's model of random traps.

An alloy of $Fe_{0.65}Ni_{0.35-x}Cr_x$ with $x=0.11$ was prepared by melting the appropriate amounts of 99.99% Fe foil, 99.995% Ni foil, and 99.99% Cr chunks, all supplied by Aldrich Chemical Company Inc., on the water-cooled copper hearth of an argon arc furnace, using a tungsten electrode and a titanium getter. The ingot was inverted and remelted several times to ensure homogeneity, then cold rolled into a thin sheet from which a sample of dimensions 10 mm×0.3 mm×0.05 mm was spark cut. The sample was sealed in a quartz tube under a partial atmosphere of argon, annealed for 4 days at 1000 °C, and rapidly quenched into water.

The measurements of the thermoremanent relaxation were performed on a custom-designed SQUID-based susceptometer which has been described in detail elsewhere in the literature.[3]

The system $Fe_{0.65}Ni_{0.24}Cr_{0.11}$ is a reentrant ferromagnet,[4] with a ferromagnetic Curie temperature $T_c \cong 110$ K and a reentrant temperature $T_R \cong 50$ K, the latter identified by a relatively abrupt drop in the low field, frequency dependent differential response function $\chi(\omega) \equiv \partial M/\partial H_a$ as the system is cooled through $T_R$.[4] Below a characteristic temperature $T_g \cong 22$ K, the relaxation response has age-dependent behavior typical of a glass; when the system is cooled in a field $H_c=1.0$ Oe from a paramagnetic reference temperature $T_{\text{ref}}=140$ K above $T_c$ to a temperature $T<T_g$ and held there for a time $t_w$ before turning off the field, the thermoremanent relaxation curves exhibit an inflection point $t_{\text{infl}}$ when plotted on a logarithmic time scale, which propagates towards longer observation times with increasing age $t_w$. The aging rate $d \log_{10} t_{\text{infl}}/d \log_{10} t_w$ is temperature dependent, and decreases as $T \to T_g^-$. Figures 1(a), 2(a), and 3(a) show the measured thermoremanent decay, normalized to its value $M_0$ at $t=0$, and plotted versus $\log_{10}(t/t_w)$, for three temperatures $T=17$, 19, and 21 K, and several wait times $t_w=1$ min, 3 min, 5 min, 10 min, 15 min, 30 min, 1 h, and 2 h. The value of $M_0$ was determined by fitting the data to the superposition of a stretched exponential and a constant, and extrapolating to $t=0$.

If we interpret the decline in the aging rate, and the failure of the data in Figs. 1(a), 2(a), and 3(a) to scale onto a universal curve with $\log_{10}(t/t_w)$, as evidence of interrupted aging, then the magnetization $M(t)$ should be represented as a superposition of independent response functions each weighted according to a distribution $P(t_{\text{erg}})$. If we further assume that the crossover from nonergodic to ergodic behavior occurs suddenly, which is equivalent to assuming that the most probable ergodic time $t_{\text{erg}}=\tau_0 S^{1/x}$ is also the *only* ergodic time which occurs with any appreciable probability for

TABLE I. "Best fit" parameters for Eqs. (3) and (4).

| $T$ (K) | $\overline{\log_{10} t_{erg}}$ | $\sigma_{erg}$ | $x$ | $\gamma$ |
|---|---|---|---|---|
| 17 | 2.0±0.2 | 2.0±0.3 | 0.10±0.05 | 0.0128±0.0010 |
| 19 | 1.0±0.3 | 2.0±0.3 | 0.60±0.10 | 0.0135±0.0010 |
| 21 | 0.0±0.3 | 2.0±0.3 | 0.83±0.10 | 0.0140±0.0010 |

any given subsystem, and that the crossover takes place when $t_w = t_{erg}$ (rather than when $t + t_w = t_{erg}$, as it does in the model), then each term in the superposition is either purely ergodic or purely nonergodic, and the total magnetization is given by

$$M_r(t) = M_0 \left[ \int_0^{t_w} dt_{erg} P(t_{erg}) \exp\left( -\gamma \int_0^t t^{-x}(t + t_{erg})^{x-1} dt \right) + \int_{t_w}^{\infty} dt_{erg} P(t_{erg}) \times \exp\left( -\gamma \int_0^t t^{-x}(t + t_w)^{x-1} dt \right) \right]. \quad (2)$$

By factoring out the purely nonergodic $t_w$-dependent exponential, this equation can be recast as the product of a universal function $f(t/t_w)$ and a nonuniversal correction factor $1\text{-}F$ which describes deviations from $t/t_w$ scaling:

$$M(t) = M_0 \underbrace{\exp\left( -\gamma \int_0^t t^{-x}(t + t_w)^{x-1} dt \right)}_{f(t/t_w)} \cdot \left\{ 1 - \underbrace{\int_0^{t_w} dt_{erg} P(t_{erg}) \left[ 1 - \exp\left( -\gamma \int_0^t t^{-x}(t + t_{erg})^{x-1} dt + \gamma \int_0^t t^{-x}(t + t_w)^{x-1} dt \right) \right]}_{F} \right\}. \quad (3)$$

Thus, a plot of $M(t)/[M_0(1-F)]$ should restore universality. In fact, with the choice of a log-normal distribution of ergodic times:

$$P(t_{erg}) = \frac{1}{\sqrt{2\pi t_{erg}^2 \sigma_{erg}^2}} \exp\left( -\frac{(\log_{10} t_{erg} - \overline{\log_{10} t_{erg}})^2}{2\sigma_{erg}^2} \right), \quad (4)$$

it is possible to explicitly calculate the correction factor in Eq. (3) numerically and, as Figs. 1(b), 2(b), and 3(b) show, to obtain remarkably good universal behavior using the "best-fit" parameters listed in Table I. Inspection of this table shows that (a) the width of the distribution of ergodic times is relatively large ($\sigma_{erg} \cong 2$) and temperature independent, (b) the mean of the logarithm of the ergodic time is relatively small ($\overline{\log_{10} t_{erg}} \leqslant 2$) and decreases with increasing temperature, which is consistent with the observed tendency of the system to age less and thus to approach equilibrium faster as $T$ increases, (c) the parameter $x$, which describes the structure of configuration space, increases with increasing temperature and approaches unity as $T \to T_g^-$, which is more consistent with Derrida's model[5] of random energy levels than with the Sherrington and Kirkpatrick model[6] of random exchange bonds, in agreement with the conclusions reached by Bouchaud and co-workers[2] for more canonical spin glass systems. For our particular choice of distribution, the mean ergodic time $\bar{t}_{erg}$ is given by $\bar{t}_{erg} = \int_0^{\infty} t_{erg} P(t_{erg}) dt_{erg} = \exp(\overline{\log_{10} t_{erg}}/\log_{10} e + \sigma_{erg}^2/2(\log_{10} e)^2)/\log_{10} e$, which yields values of $\bar{t}_{erg}$ ranging from $\bar{t}_{erg}$ (17 K)$\sim 8\times 10^6$ s to $\bar{t}_{erg}$ (21 K)$\sim 5\times 10^4$ s, once again comparable to those deduced in Ref. 2.

This work was supported in part by a grant from the Natural Sciences and Engineering Research Council of Canada.

[1] J. P. Bouchaud, J. Physique I France **2**, 1705 (1992).
[2] J. P. Bouchaud, E. Vincent, and J. Hammann, J. Physique I France **4**, 139 (1994).
[3] H. Kunkel, R. M. Roshko, W. Ruan, and G. Williams, Philos. Mag. B **63**, 1213 (1991).
[4] A. V. Deryabin, A. Yu. Chirkov, and A. V. T'kov, Sov. Phys. JETP **59**, 355 (1984).
[5] B. Derrida, Phys. Rev. Lett. **45**, 79 (1980).
[6] D. Sherrington and S. Kirkpatrick, Phys. Rev. Lett. **35**, 1792 (1975).

# $^7$Li nuclear magnetic resonance spectra and relaxation in $Ni_{1-x}Li_xO$

M. Corti, S. Marini, and A. Rigamonti
*INFM-Department of Physics "A. Volta" and Sezione INFN, University of Pavia, I-27100 Pavia, Italy*

V. Massarotti and D. Capsoni
*Department of Physical Chemistry, University of Pavia, I-27100 Pavia, Italy*

$^7$Li nuclear magnetic resonance (NMR) spectra and relaxation rates in $Ni_{1-x}Li_xO$, for $0.01 \leq x \leq 0.46$ and for $20 \leq T \leq 550$ K are presented. For $x \leq 0.2$ the antiferromagnetic (AF) phase typical of NiO is still observed. The Neel temperatures $T_N(x)$, the temperature dependence of the field at the Li site, and the role of the extra holes in driving the correlated spin dynamics of $Ni^{2+}$ are derived. In particular, from $^7$Li relaxation rates $W$ the hopping frequencies of the holes on the AF background and the energy gaps between itinerant and localized states are extracted. In the mixed regime ($x \geq 0.3$, $LiNiO_2$ structure-type) in which partial ordering on alternate $Li^+$ and $Ni^{3+}$ layers occurs, $^7$Li NMR data display the features typical of disordered paramagnets, consistent with a picture of random distribution of $Ni^{3+}$ ($S=1/2$), $Ni^{2+}$ ($S=1$) and of spin vacancies $Li^+$ ($S=0$). In particular, for $x=0.46$, on cooling, a paramagnetic-like divergence of the width and of the shift of the NMR line is observed while $^7$Li $W$'s indicate slowing down of the spin fluctuations. The fluctuation frequency decreases in the MHz range below a freezing temperature $T_f \simeq 40$ K. © *1996 American Institute of Physics.* [S0021-8979(96)41408-6]

## I. INTRODUCTION

Among the transition metal oxides (TMOs), the antiferromagnetic (AF) NiO and its charge-doped derivates $Ni_{1-x}Li_xO$ play a key role in the studies of the correlated $3d$ electron systems.[1,2] For NiO it seems possible to assess that the holes compensating the $Li^+$ impurity charge are of $O(2p)$ character, with strong AF exchange interaction with localized $Ni^{2+}$ ($S=1$) $d$ electrons. On the basis of general aspects of $t$-$J$ models and by extending the findings in other TMOs, the holes are expected to itinerate, although the impurity potential due to $Li^+$ tends to bind them in localized states.[2] In strongly doped compounds, $x \geq 0.3$, a sizeable distortion of the pseudocubic cell occurs and Li and Ni ions partially order on alternate layers normal to the $\langle 111 \rangle$ directions. The stoichiometric $LiNiO_2$ (thermodynamically unstable), with well separated layers of $Ni^{3+}$ $S=1/2$ on a triangular lattice, has been considered a model system for frustrated AF.[3]

In this article, we report some results of a study carried out in $Ni_{1-x}Li_xO$ by means of pulsed $^7$Li NMR. The NMR spectra convey information on the magnetic field $|\mathbf{h}_{AF}|$ at the Lithium site and on the sublattice magnetization $\langle \mu \rangle_{Ni}$ (average along the local quantization axis). The $^7$Li relaxation rates $W$, due to the time dependent transverse components of the fluctuating part of the field, yield the hopping frequencies of the holes, the energy gap between localized and itinerant states, as it has been shown in $Cu_{1-x}Li_xO$.[4] In the disordered magnetic systems ($0.25 \leq x \leq 0.46$) the relaxation rates probe the cooperative freezing of the magnetic moments. A characteristic spin-fluctuation frequency is measured, leading to the activation energy $E_{eff}$ and to the freezing temperature $T_f$ below which a spin-glass-like phase is present.

## II. EXPERIMENTAL RESULTS

The compounds have been prepared by the reactive system $NiO/Li_2CO_3$ heated up to 800 °C and annealed in alumina.[5] X-ray diffraction indicates a lattice parameter of the pseudo-cubic cell which decreases almost linearly with $x$, up to $x \simeq 0.2$. For $x \geq 0.3$ the quasi-cubic structure is lost and the expected sequence of Li and Ni layers with intercalated close packed oxygen layers is observed. Standard NMR techniques have been used for $^7$Li spectra and to measure the relaxation times $T_1$ from the echo signals.[4] In the AF phases, the shape of the $^7$Li line is controlled by the powder distribution of the field at the Li site of dipolar origin. The line width is $2\gamma |\mathbf{h}_{AF}|$, thus yielding the temperature dependence of the AF field (see Fig. 1). The transferred hyperfine field $\Sigma_i A \langle \mathbf{S}^{(i)} \rangle$ causes a shift $K$. In nominally $LiNiO_2$, the hyperfine field $A$ has been estimated to be equal 350 $G/\mu_B$.[6] It should be stressed that for AF cubic symmetry of $Ni^{2+}$ ions around the reference $^7$Li nucleus, one has $h_{AF}=0$ and $K=0$.

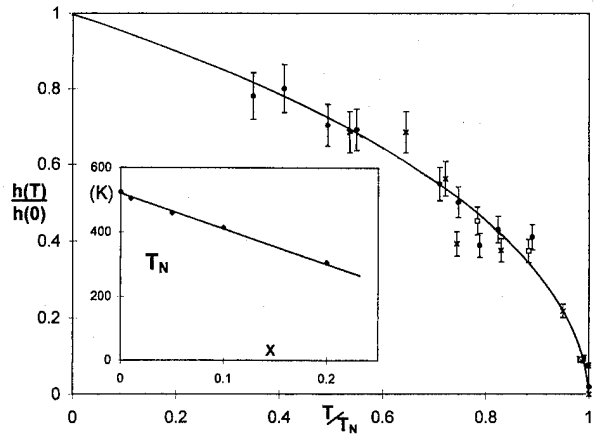



FIG. 1. Temperature dependence of the AF field $|h_{AF}|$ at the Li site for $x=0.05$(□), $x=0.1$(●), and $x=0.2$($X$). The solid line shows the best fit behavior according to the MFA law $h_{AF} \propto (T_N - T)^{\beta}$, with $\beta=0.5$. It is noted that the extrapolated value of the field $h_{AF}(T \to 0)$ equals 800 G for $x=0.05$ and 1400 G for $x=0.1$. In the inset the Neel temperatures $T_N(x)$, as obtained from the extrapolation of the line width and from the concurrent peaks in the relaxation rate (see text) are shown.

 0021-8979/96/79(8)/6621/3/$10.00 © 1996 American Institute of Physics 

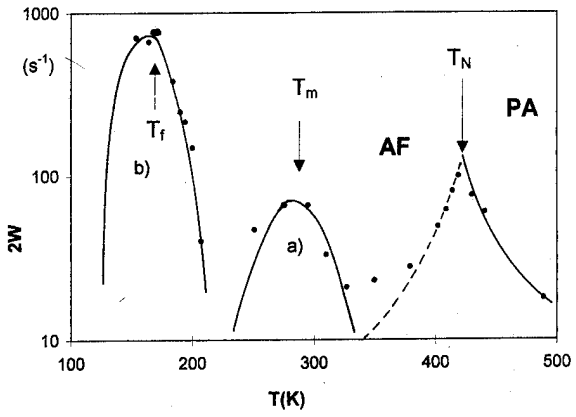



FIG. 2. $^7$Li relaxation rate as a function of temperature in $Ni_{0.9}Li_{0.1}O$. The Neel temperature (Fig. 1) is shown. The curve (a) is the theoretical behavior for the contribution due to hole diffusion [Eq. (2) in the text] and it corresponds to $E_g \simeq 3000$ K and $\tau_0 \simeq 2\times10^{-13}$ s rad$^{-1}$. Curve (b) shows the behavior expected from the freezing of the spin fluctuations for localized magnetic moments superimposed to the AF matrix. The dotted line below $T_N$ is the sketchy behavior of $W$ from two-magnons relaxation in conventional AFs (approximately of the form $W \propto T^3$).

The static and the dynamical effects of the quadrupole interaction on the $^7$Li Zeeman levels can be neglected[4] and the relaxation process is driven by the time dependent part of the electron nucleus Hamiltonian. One has

$$\frac{1}{T_1} = 2W = \frac{\gamma^2}{2} \int \langle h_+(0) h_-(t) \rangle \exp[-i\omega_L t] dt, \qquad (1)$$

where $h_\pm$ are the transverse components of the effective field $\mathbf{h}(t)$ at the Li site. The time dependence of $\mathbf{h}$ is due either to the diffusion of the extra hole that locally destroys the AF order or to the fluctuations of localized magnetic moments (e.g., $Ni^{3+}$) anomalous with respect to the AF matrix.[4] The typical behavior of the $^7$Li relaxation rate observed for $x \leqslant 0.2$, is shown in Fig. 2. The behavior of $W$ in quasistoichiometric $LiNiO_2$ ($x=0.46$) (Fig. 3) is analogous to the one in disordered magnets, with the progressive increase of $W$ on cooling, indicating freezing of spin fluctuations.

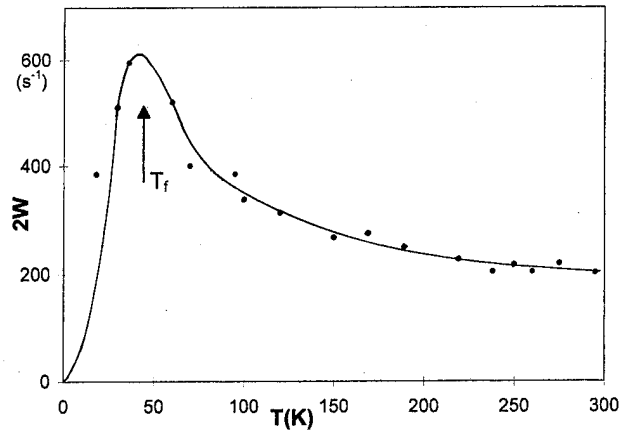



FIG. 3. $^7$Li $2W$ in $Li_{0.92}Ni_{1.08}O_2$ (the sample closest to the fully stoichiometric $LiNiO_2$). The solid line corresponds to the best fit of the data according to a law of the form $2W \propto \Gamma_{SF}/(\Gamma_{SF}^2+\omega_L^2)$, for $\Gamma_{SF}=\Gamma_0 \exp[-E_{eff}/T]$, with $E_{eff}=84$ K and $\Gamma_0 \simeq 10^9$ rad s$^{-1}$. $\omega_L=\gamma H_0$, with $H_0=1.1$ T.

## III. ANALYSIS OF THE RESULTS AND SUMMARIZING REMARKS

For $x \leqslant 0.2$ the Neel temperature decreases (Fig. 1), with initial suppression rate $B=-[T_N(0)]^{-1}(dT_N(x)/dx)$ around $B \simeq 2.2$. This value is about two times larger than the one in Mg-doped NiO.[7] The difference is likely to be due to the fact that while for Mg the spin vacancy is localized, the somewhat equivalent magnetic polaron associated to the extra hole is itinerant in Li-doped NiO. It is noted that in both cases one has a practically linear decrease of $T_N$ on increasing $x$, for $x \leqslant 0.2$. The onset of the order parameter, the sublattice magnetization $\langle \mu \rangle_{Ni}$ to which $h_{AF}$ is proportional, is qualitatively consistent with a critical exponent $\beta=0.5$. The absolute value of $h_{AF}$ for $T \to 0$ is $x$ dependent, since breaking of the AF symmetry is required to have $h_{AF} \neq 0$ (see caption to Fig. 1).

The behavior of $^7$Li $W$ (Fig. 2) for $T \geqslant T_N$ can be justified by considering that the AF symmetry of the critical fluctuations is broken by one or more $Li^+$-induced spin vacancy. Thus transverse components $h_\pm$ [see Eq. (1)] are generated and instead of an antidivergence of $W$, as detected for AF symmetry,[8] on has $W$ diverging for $T \to T_N^+$. The absolute value of $W$ is consistent with the slowing down of dipolar field fluctuations driven by the exchange Heisenberg frequency $\omega_{exch}=[J^2 8zS(S+1)/3]^{1/2}/\hbar$, by using for the exchange constants the values $J_1=-34$ K (for the nearest neighbors, $z=12$) and $J_2=202$ K for the next nearest neighbors.[9]

In the AF phase [region (a) in Fig. 2], instead of the two-magnons relaxation mechanism, a contribution to $W$ approximately of the form

$$W = \gamma^2 C^2 x \frac{\tau_h}{1+\omega_D^2 \tau_h^2}. \qquad (2)$$

and due to the diffusion of the holes,[4] is detected. $C$ is of the order of the dipolar field induced at the Li site when the hole locally anneals the AF spin configuration. $\tau_h$ is the mean time interval between consecutive passages of the holes and it is written $\tau_h=\tau_0/n_h$, $n_h=x \exp[-E_g/T]$ being the fraction of the mobile holes, with $E_g$ gap between itinerant and localized states.

At lower temperatures [region (b) in Fig. 2] the hole is localized and a relaxation driven by the spin fluctuations of extra magnetic moments ($Ni^{3+}$ and the related spin texture in the AF background) occurs. One can write $W=D\Gamma_{SF}/(\Gamma_{SF}^2+\omega_L^2)$ where $D$ is a constant depending on the hole concentration and on the dipolar field and $\Gamma_{SF}$ a characteristic spin fluctuation frequency.

From the analysis of the results along the lines outlined above, one can extract quantitative information, that we summarize in the following. From $W$ in the region (a) of Fig. 2 one derives $E_g \simeq 4000$ K for $x=0.05$ (results not reported) and $E_g=3000$ K for $x=0.1$. $T_m=285$ K corresponds to the temperature at which the hopping frequency $\tau_h^{-1}$ is about $\omega_L=18$ MHz ($2\pi$) and can be considered as freezing temperature for charge fluctuations. The values for $E_g$ are close to the ones estimated for the hopping of the polarons from

resistivity and/or dielectric data.[10] While for isolated polarons the barrier is almost 1 eV, it decreases with increasing $x$.

For $T \ll T_m$ the extra magnetic moments related to $Ni^{3+}$ ions act like magnetic impurities in driving a strong relaxation mechanism. One can extract the barrier for the cooperative freezing: $E_A \simeq 100$ K for $x=0.01$ and $E_A \simeq 300$ K for $x=0.05$ (results not reported). It should be remarked that the divergence of the relaxation rate appears to shift towards higher temperatures on increasing the magnetic field. Thus the increase of $T_1^{-1}$ in the region *b*) of Fig. 2 is likely to reflect a field-induced paramagnetic-like behavior in the $Ni^{2+}$ AF with random $Ni^{3+}$ ions.

In mixed systems ($0.3 \leqslant x \leqslant 0.5$) the relaxation process is a complicated one, in view of nonequivalent Li sites and of the disordered character of the planes with $Ni^{2+}$ and $Ni^{3+}$ ions.[3] $^7$Li $W$'s indicate relaxation mechanism and spin dynamics similar to the ones in spin glass and/or superparamagnetic domains systems. The results are rather well fitted by a temperature activated effective frequency, with barrier $E_{\text{eff}}=84$ K, implying spin fluctuation frequencies in the MHz range below $T_f \simeq 40$ K. Consistency with the occurrence of a frozen spin state, as inferred from neutron diffuse scattering,[11] is thus found.


[1] N. F. Mott, *Metal-Insulator Transitions* (Taylor and Francis, 1990).
[2] G. A. Sawatzky, in *Early and Recent Aspects of Superconductivity*, edited by J. G. Bednorz and K. A. Muller (Springer, Heidelberg, 1990), p. 345.
[3] See, among others, P. Ganguly *et al.*, Phys. Rev. B **46**, 11595 (1992) and J. N. Reimers *et al.*, J. Solid State Chem. **102**, 542 (1993), and references therein.
[4] P. Carretta, M. Corti, and A. Rigamonti, Phys. Rev. B **48**, 3433 (1993); **49**, 7044 (1994).
[5] V. Massarotti, D. Capsoni, and M. Bini, Z. Naturforsch **50a**, 155 (1994).
[6] M. Itah, I. Yamada, K. Ubukoshi, K. Hirokawa, and H. Yasuoka, J. Phys. Jpn. **55**, 2125 (1986).
[7] Zhen Feng and M. S. Seehra, Phys. Rev. B **45**, 2184 (1992).
[8] F. Borsa and A. Rigamonti, in *Magnetic Resonance at Phase Transitions*, edited by F. J. Owens, C. P. Poole, and H. A. Farach (Academic, London, 1979); H. Benner and J. P. Boucher, in *Magnetic Properties of Layered Transition Metal Compounds*, edited by L. J. de Jongh (Kluwer, Dordrecht, 1990), p. 323.
[9] G. Srinivasan and M. S. Seehra, Phys. Rev. B **29**, 6295 (1984).
[10] R. R. Heikes and W. D. Johnston, J. Chem. Phys. **26**, 582 (1957); see also G. F. Dionne, J. Appl. Phys. **67**, 4561 (1990). For dielectric measurements, see E. Iguchi and K. Akashi, J. Phys. Soc. Jpn. **61**, 3385 (1992).
[11] H. Yoshizawa, H. Mori, K. Hirota, and M. Ishikawa, J. Phys. Soc. Jpn. **59**, 2631 (1990).

# Susceptibility and $^{89}Y$ nuclear magnetic resonance in $Y_{1-x}Ca_xVO_3$

F. Cintolesi, M. Corti, A. Rigamonti, and G. Rossetti
*INFM-Department of Physics "A. Volta" and Sezione INFN, University of Pavia, I-27100 Pavia, Italy*

P. Ghigna
*Department of Chemical Physics, University of Pavia, I-27100 Pavia, Italy*

A. Lascialfari
*Department of Chemistry, University of Firenze, I-50144 Firenze, Italy*

Temperature-dependent (10–300 K) field-cooled (FC) and zero-field-cooled (ZFC) susceptibilities, and $^{89}Y$ NMR spectra and relaxation in $Y_{1-x}Ca_xVO_3$ with $0 \leqslant x \leqslant 0.9$ are reported. In the paramagnetic phase (PA) of $YVO_3$ and for $T \geqslant 120$ K the susceptibility $\chi$ is of antiferromagnetic (AF) type, with no field dependence. Around the Neel temperature $T_N^{(1)} = 113 \pm 1$ K a field-dependent ferromagnetic behavior is observed under FC condition. Below $T_N^{(2)} \simeq 77$ K (AF phase with AF interplane coupling) strong difference is present between FC and ZFC $\chi$'s. For $T \rightarrow T_N^{(1)+}$ the $^{89}Y$ NMR line shows marked broadening and no measurable shift, consistent with a dominant dipolar contribution in the nucleus–electrons interaction. The $^{89}Y$ relaxation rate $T_1^{-1}$, related to the correlated spin dynamics of $V^{3+}$ $\mathbf{S}(t)$, seems to indicate that the interplane ferromagnetic symmetry of the spin fluctuations is quenched in strong fields. The peculiar findings for $\chi$ and $T_1$ could result from a field-dependent weak ferromagnetism of Dzyaloshinsky–Moriya character. In $Y_{1-x}Ca_xVO_3$, $\chi$ and $T_1^{-1}$ decrease on increasing $x$, still preserving the qualitative behavior as for $x=0$. For $x \simeq 0.6$ (Ca concentration which drives the transition to the metallic phase) the marks of the PA–AF transition are practically suppressed and behaviors characteristic of correlated metals are observed.
© *1996 American Institute of Physics.* [S0021-8979(96)00708-9]

## I. INTRODUCTION

The magnetic properties of highly correlated $d$-electron systems are presently of great interest, high-temperature superconductivity having recalled attention towards the insulator-metal (IM) transitions driven by carrier doping. $YVO_3$ is a typical Mott–Hubbard antiferromagnetic (AF) insulator, with $V^{3+} 3d^2 S=1$ magnetic ions. As recently observed by neutron scattering,[1] $YVO_3$ undergoes a second-order phase transition ($T_N^{(1)} \simeq 114$ K) to an AF phase, with intraplane AF order and interplane ferromagnetic (FE) order (C type). A first-order phase transition at $T_N^{(2)} \simeq 77$ K leads the system to a G-type phase, with AF order also among planes. $Y^{3+}$ ions can be substituted by $Ca^{2+}$ and for $x \rightarrow 1$ in $Y_{1-x}Ca_xVO_3$ the nominal valence of vanadium is $4^+(3d^1)$. Resistivity measurements and optical spectra[2] have shown that, for $x_C \simeq 0.5$, a hole-doped-induced IM transition occurs.

In this article the main results of a study carried out by means of magnetic susceptibility $\chi$ and $^{89}Y$ NMR and $T_1$ relaxation measurements are presented. $\chi$ has been studied from $x=0$ up to $x=0.9$, under field-cooled (FC) and zero-field-cooled (ZFC) conditions. As regards NMR, $^{51}V$ spectra in the AF phase of $YVO_3$ have been reported, while for $x<0.6$ $^{51}V$ Knight shift and $T_1$ support the picture of a metallic phase.[3] A $^{51}V$ NMR study has been carried out in $La_{1-x}Sr_xVO_3$.[4] No $^{89}Y$ NMR investigations seem to have been performed. $^{89}Y$ is an attractive probe to study magnetic properties and the correlated $V^{3+}$ spin dynamics: the absence of quadrupole interaction ($I=1/2$) and the lattice position makes this nucleus sensitive to the symmetry of the interplane spin correlations and to the wave vector of the critical fluctuations.

## II. EXPERIMENTAL RESULTS AND DISCUSSION

The samples were prepared by heating at 1200 °C in Ar–H atmosphere the stoichiometric mixture of $Y_2O_3$, $V_2O_5$, and $CaCO_3$. X-ray diffraction indicated single phase samples over all the composition range. At $T \simeq 300$ K the resistivity was observed to decrease from $6 \times 10^3$ Ω cm in $YVO_3$ to about $2 \times 10^{-3}$ Ω cm for $x \simeq 0.6$, in agreement with previous results.[2] The dc magnetic measurements were made with a superconducting quantum interference device (SQUID).

In pure $YVO_3$ [see Fig. 1(a)], from the peak in the ZFC $\chi$ in $H=0.1$ T one derives $T_N^{(1)} = 113 \pm 1$ K, in agreement with the estimate from Y NMR in a field of 5.9 T (see below). The FC susceptibility around $T_N$ in a field of 0.1 T is about three times larger than in 0.5 T, an indication of anomalous saturation or of field-induced diamagnetic contribution causing an apparent decrease of the paramagnetic $\chi$. Figure 1(b) shows how the FC temperature behavior of $\chi$ for $H=0.5$ T in $Y_{1-x}Ca_xVO_3$ changes in crossing the IM transition. For $x=0.6$ the ferromagneticlike term around $T_N^{(1)}$ is almost suppressed. Below $T \simeq 50$ K Curie-like terms seem present, possibly due to isolated magnetic defects, or double-exchange ($V^{3+}$–$V^{4+}$) effects.[5] For $x=0.9$ and high temperatures one derives a Pauli-like susceptibility $\chi_P \simeq 2.5 \times 10^{-3}$ cm$^3$/mol, larger than $\chi_P \simeq 1 \times 10^{-3}$ cm$^3$/mol for $x=0.6$, indicating a possible presence oxygen deficiencies. $CaVO_3$, in fact, was shown to become insulating by annealing the sample in air.[6]

The $^{89}Y$ NMR relaxation rates ($H_0=5.9$ T, Fig. 2) are related to the time dependence of the hyperfine field $\mathbf{h}(t)$ at the $Y$ site:

$$T_1^{-1} = \tfrac{1}{4}\gamma^2 [J_+(\omega_L) + J_-(\omega_L)], \tag{1}$$

 0021-8979/96/79(8)/6624/3/$10.00 © 1996 American Institute of Physics

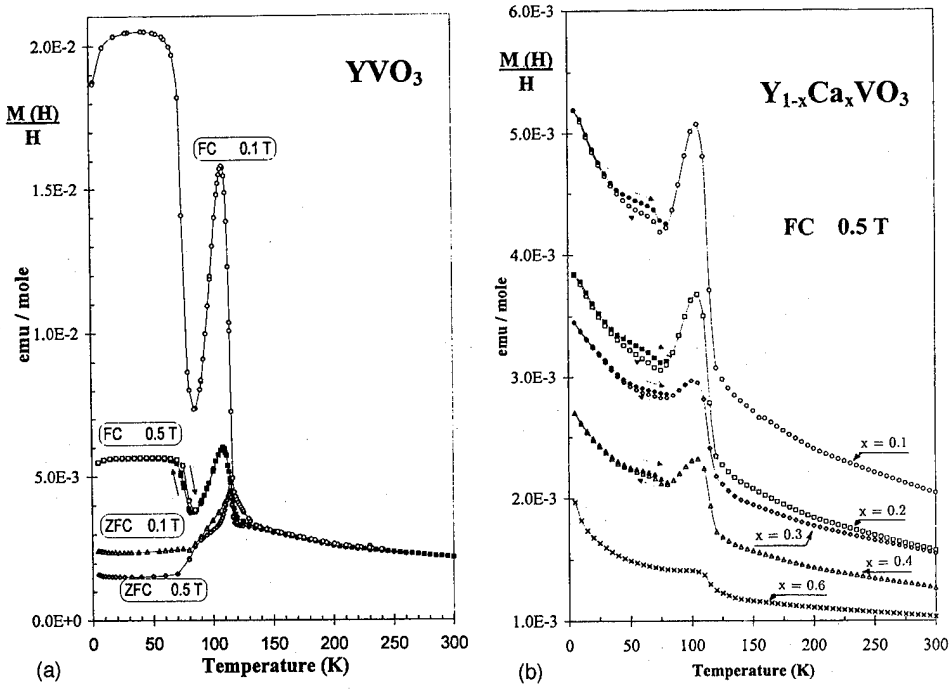



FIG. 1. (a) Field-dependent susceptibility in $YVO_3$ as a function of temperature. The arrows evidence the thermal hysteresis observed below the transition temperature $T_N^{(2)} \simeq 77$ K, in the AF–AF phase (see text). The divergence for FC in 0.1 T is qualitatively of the form predicted for Dzyaloshinsky–Moriya interaction.[8] (b) FC magnetic moment, in $H=0.5$ T, as a function of temperature in $Y_{1-x}Ca_xVO_3$ for $x=0.1$ (○ and ●), $x=0.2$ (□ and ■), $x=0.3$ (◇ and ◆), $x=0.4$ (△ and ▲), and $x=0.6$ ($x$) [where no thermal hysteresis was observed]. For $x \leqslant 0.4$ differences between the values at $H_0=0.1$ and 0.5 T similar to the ones in pure $YVO_3$ are observed.

where $J_\alpha = \int \langle h_\alpha(0) h_\alpha^*(t) \rangle e^{-i\omega t} dt$ $(\alpha = x \pm iy, z)$ are the spectral densities while

$$\mathbf{h} = \sum -A_i \mathbf{S}_i + B_i (\mathbf{r}_i \cdot \mathbf{S}_i) \mathbf{r}_i , \tag{2}$$

where $A_i = \gamma_e \hbar / d_i^3 + C/\gamma$ and $B_i = 3\gamma_e \hbar / d_i^5$. $C$ is the transferred scalar interaction and $d_i$ the distance of the $Y$ nucleus from the $i$-th $V$ ion. On approaching $T_N^{(1)}$ a marked increase in the linewidth is observed. The lack of measurable shift implies that $C$ in Eq. (2) is negligible, the dipolar terms $A$ and $B$ in powdered samples practically causing a broadening proportional to $\langle S \rangle = \chi_A H_0$ and thus tracking the atomic susceptibility. For $x \leqslant 0.5$, the temperature behavior of $T_1^{-1}$ is similar to the one for $x=0$, with decrease of the peak around $T_N^{(1)}$.

The peculiar magnetic properties pointed out in rare-earth (RE) vanadates,[4,7] are evidenced for $YVO_3$ in the data for $\chi$ [see Fig. 1(a)]. While for $T \geqslant 130$ K one has a Curie–Weiss field-independent susceptibility, below $T_N$ $\chi$ depends on the cooling conditions in a way similar to the one in $LaVO_3$,[4,7] attributed to canted spin configuration and/or ferromagnetism. An effect characteristic of $YVO_3$ is the ferromagnetic-type FC divergence for $T \simeq T_N^{(1)}$, possibly due to a Dzyaloshinsky–Moriya interaction $D \cdot \mathbf{S}_i \times \mathbf{S}_j$. In this case, in fact, the susceptibility in a polycrystalline sample, namely $\chi = (2/3)\chi_\perp + (1/3)\chi_\parallel$, near $T_N$ deviates from the Curie–Weiss law. The susceptibility perpendicular to the easy axis displays a divergence of the form[8] $\chi_\perp \propto (T - T_O)/(T - T_N)$ with $T_O = JzS(S+1)/3K_B$, $J$ exchange coupling constant and $z$ number of nearest neighbors. $T_N$ becomes $T_N = T_O[1 + (D/J)^2]^{1/2}$. $T_N$ is slightly affected by charge doping, up to $x=0.4$ (where $T_N$ is around 100 K). In the metallic phase the Pauli-like part of $\chi$ is almost an order of magnitude larger than in other vanadates and for or $x=0.9$, in particular, it appears field dependent. An interpretation of these peculiarities has to be delayed after a complete phase diagram for samples close to $CaVO_3$ is available.

The $^{89}Y$ relaxation rates [see Eq. (1)] can be related to the correlated spin dynamics through the collective spin components $\mathbf{S_q}$ and the decay rate $\Gamma_\mathbf{q}$ of the normal excitations. For localized moments and for fast spin fluctuations ($\Gamma_\mathbf{q} \gg \gamma H_0$) one can write

$$T_1^{-1} = \gamma^2 \sum_\mathbf{q} H_q^2 |S_q|^2 / \Gamma_\mathbf{q} , \tag{3}$$

where $H_q^2$ results from the Fourier transform of the factors $A$ and $B$ in Eq. (2).

For $T \gg T_N$ the correlation functions are $q$-independent and Eq. (3) can be written $T_1^{-1} \simeq \frac{1}{2} n \gamma^2 h_e^2 / \omega_{\text{exch}}$, where $h_e^2 = (h_x^2 + h_y^2)$ comes from the dipolar field at the $Y$ site, $n=8$ is the number of $n.n.$ ions (for which a common distance $d \simeq 3.3$ Å will be assumed), and $\omega_{\text{exch}}$ is the exchange frequency. For $h_e \simeq 3 \times 10^3$ G (for $\mu = 1.6\ \mu_B$)[1] and $\omega_{\text{exch}} = [\frac{3}{2} zS(S+1)]^{\frac{1}{2}} K_B T_N / \hbar \simeq 6 \times 10^{12}$ rad s$^{-1}$, one obtains $T_1^{-1} \approx 12$ s$^{-1}$. The experimental data at $T \simeq 300$ K is likely to reflect a certain degree of AF correlation, which is expected to decrease the relaxation rate. In fact, to analyze $T_1^{-1}$ vs $T$ the complete $q$-dependence should be used. In particular, $H_\mathbf{q}^2$ strongly depends on the symmetry of the critical fluctuations. Here we only emphasize the following. For symmetry corresponding to the AF–AF phase one would have $H_{\text{AF-AF}}^2 = 0$

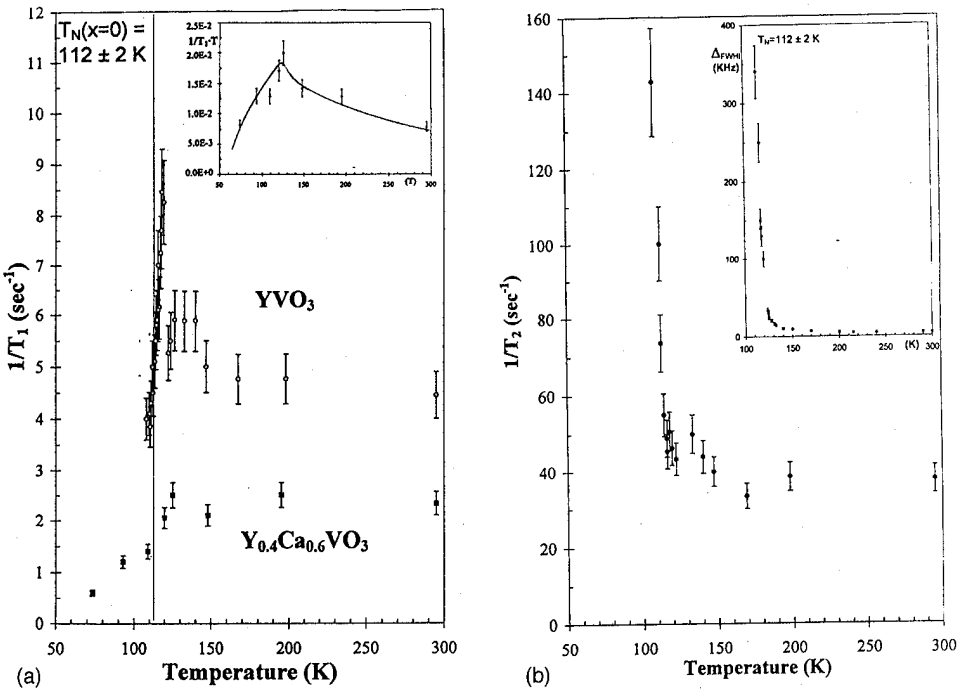



FIG. 2. (a) $^{89}$Y NMR relaxation rate $T_1^{-1}$ as a function of temperature, in $YVO_3$ (○) and in $Y_{0.4}Ca_{0.6}VO_3$ (■), in $H_0$=5.9 T. In the inset the temperature behavior of $(T_1T)^{-1}$ for $x$=0.6 is reported, with the solid line as a guide for the eye. (b) $^{89}$Y spin–spin relaxation rate, from the decay of the echo signal, as a function of temperature in pure $YVO_3$. The decay of the echo amplitude is described by a Gaussian law for $T \geq 150$ K, while it turns to a Lorentzian form for temperature around $T_N^{(1)}$. In the inset the width $\Delta$ of the $^{89}$Y NMR line, in the paramagnetic phase, is shown. No temperature-dependent shift is detected.

and on approaching $T_N^{(1)+}$ from above the relaxation rate would decrease.[9] On the contrary, in correspondence to the interplane FE symmetry $H^2_{\text{AF-FE}}$ in Eq. (3) is different from zero and one should observe a divergent behavior of $T_1^{-1}$ around $T_N$. The lack of a marked divergence in $T_1^{-1}$ indicates that a strong field quenches the ferromagnetic correlations in the spin fluctuations that is somewhat consistent with the finding for $\chi$ in 0.5 [see Fig. 1(a)]. In the ordered phase, for AF–FE configuration, from a lattice sum of the dipolar terms the field at the $Y$ site is evaluated in the form $\mathbf{h}_{\text{AF-FE}} = 1.9S_x - 1.6S_y - 0.23S_z$ (kG/$\mu_B$), $S_\alpha$ being the components of a given $V^{3+}$ spin with respect to the crystalline axes. The random orientation of $\mathbf{h}_{\text{AF-FE}}$ with respect to $\mathbf{H}_0$ causes broadening of the $^{89}$Y NMR line over more than one MHz. The experimental detection of such a broadening (results not reported) confirms that the intermediate phase is of C type.

In $Y_{0.4}Ca_{0.6}VO_3$, just above the carrier concentration driving the IM transition, $T_1^{-1}$ is practically constant down to 130 K and then it decreases. In free-electron metals one should have $T_1^{-1} \propto \chi_P^2 T \propto \rho^2(E_F)T$ [$\rho(E_F)$ density of states at Fermi level] and absolute value decreased with respect to the one for localized spins. These conditions are not verified for $x$=0.6: the Korringa relation is not obeyed and $(T_1T)^{-1}$ shows a maximum at $T^* \simeq 130$ K [see inset in Fig. 2(a)]. These findings indicate strong magnetic correlations among carriers, a situation reminiscent of the one in superconducting cuprates,[10] where $T^*$ is often considered the mark of a spin pseudo-gap opening. In the sample at $x$=0.9, $^{89}$Y $T_1^{-1}$ has been found to decrease and, according to the $^{51}$V NMR data,[3] the Korringa relation is obeyed. However, the role of the oxygen stoichiometry for $x \simeq 1$ has to be clarified.

By summarizing, our susceptibility measurements point out peculiar magnetic properties of yttrium vanadates. In particular, a divergence (of ferromagnetic type) in FC $\chi$ is observed around $T_N$, possibly due to Dzyaloshinsky–Moriya interaction. The divergence is suppressed by increasing the field. $^{89}$Y NMR yields valuable information on the AF's fields and on the symmetry of the critical fluctuations. Again, an effect of the external field in quenching the spin fluctuations of FE symmetry appears to occur. In $Y_{1-x}Ca_xVO_3$ for $x$=0.6, in the metallic state, both susceptibility and $T_1$ measurements indicate the persistence of strong magnetic correlations among carriers.


[1] H. Kawano, H. Hoshizawa, and Y. Ueda, J. Phys. Soc. Jpn. **63**, 2857 (1994).
[2] M. Kasuya, Y. Tokura, T. Arima, H. Eisak, and S. Uchida, Phys. Rev. B **47**, 6197 (1993).
[3] K. Kumagai, K. Kawano, T. Suzuki, H. Takahashi, M. Kasuya, Y. Fujishima, Y. Taguchi, Y. Okada, and Y. Tokura, Physica B **186**, 1030 (1993); J. Kikuchi, H. Yasuoka, Y. Kokubo, and Y. Ueda, J. Phys. Soc. Jpn. **63**, 3577 (1994).
[4] A. V. Mahajan, D. C. Johnston, D. R. Torgeson, and F. Borsa, Phys. Rev. **46**, 10973 (1992).
[5] P. G. De Gennes, Phys. Rev. **118**, 141 (1960).
[6] F. Iga and Y. Nishihara, J. Phys. Soc. Japan **61**, 1867 (1992).
[7] N. Shirakawa and M. Ishikawa, Jpn. J. Appl. Phys. **30**, 755 (1991).
[8] T. Moriya, Phys. Rev. **120**, 91 (1960).
[9] F. Borsa and A. Rigamonti, in *Magnetic Resonance at Phase Transitions*, edited by F. J. Owens, C. P. Poole, and H. A. Farach (Academic, New York, 1979).
[10] See D. Brinkmann and M. Mali, NMR-NQR Studies of High-Temperature Superconductors in *NMR Basic Principles and Progress* (Springer, Heidelberg, 1994), Vol. 31.

# Spin glass behavior of amorphous $Fe_5(InTe_4)_3$

Jian H. Zhang, Damon Williams, and Cuihong Tao
*Department of Chemistry, Xavier University of Louisiana, New Orleans, Louisiana 70125*

Charles J. O'Connor
*Department of Chemistry, University of New Orleans, New Orleans, Louisiana 70148*

The amorphous phases of $Cr_5(InTe_4)_3$ and $Fe_5(InTe_4)_3$ have been prepared via the precipitation reaction of the Zintl polyanion $InTe_4^{-5}$ with $Cr^{3+}$ and $Fe^{3+}$ in aqueous solution, respectively. Their magnetic and conducting properties have been examined as a function of temperature. The high-temperature susceptibility of $Cr_5(InTe_4)_3$ follows the Curie–Weiss law with $\theta = -30.2$ K and $C = 1.65$ emu/mole Cr atom. $Cr_5(InTe_4)_3$ has a conductivity of $1.07\times10^{-3}$ $\Omega^{-1}$ cm$^{-1}$ at 300 K and is a semiconductor with $Ea = 0.20$ eV. $Fe_5(InTe_4)_3$ exhibits relatively high conductivity due to partial delocalization of electrons. Its conductivity is 7.41 $\Omega^{-1}$ cm$^{-1}$ at 300 K, and shows little temperature dependence. $Fe_5(InTe_4)_3$ obeys the Curie–Weiss law at high temperatures with $\theta = -26.3$ K and $C = 1.60$ emu/mole Fe atom, and undergoes a transition to a spin glass state at 6.0 K. The spin glass state has been characterized by an analysis of the field and temperature dependence of the thermal remanent magnetization and isothermal remanent magnetization. The hysteresis loops measured at 2.0 K under field-cooling and zero-field-cooling conditions reveal the presence of a small unidirectional exchange interaction. © *1996 American Institute of Physics.*
[S0021-8979(96)05708-8]

## I. INTRODUCTION

In previous communications, we described the synthesis and characterization of a series of ternary metal chalcogens of the formula $M_5(InTe_4)_2$, where $M$ is a transition metal.[1,2] The preparation of the ternary metal chalcogens involves a metathesis reaction between a Zintl phase material ($K_5InTe_4$) and a divalent transition metal chloride. The Zintl phase of matter can be described as a polar metallic alloy in which the bonds have a substantial amount of ionic character due to the large difference in electronegativity of the metals or metalloids. The ionic character of the Zintl phase, i.e., $K_5InTe_4$ in this case, allows for the solvation of saltlike ions ($InTe_4^{-5}$) in polar solvents such as water. In the presence of a metal cation of sufficient electron affinity, an insoluble intermetallic solid forms due to the transfer of electrons from the active polyanion ($InTe_4^{-5}$) to the transition metal. The rapid precipitation between the polyanion and the transition metal often results in an amorphous product.

These ternary metal chalcogens display a variety of interesting magnetic and electronic conducting properties. For instance, $Fe_5(InTe_4)_2$ undergoes double magnetic transitions: a transition from paramagnetic to weak ferromagnetic at 32 K, and a second transition to a spin glass state at 13 K.[1] It was also observed that the magnetic and conducting properties in this series of intermetallic materials are correlated with the ability of the precursor transition metal cations to be reduced by the Zintl polyanion.[2] To continue the search for the novel magnetic materials, we have extended our study to include trivalent transition metals and rare-earth metals. In this paper, we report the synthesis of two new amorphous phases, $Fe_5(InTe_4)_3$ and $Cr_5(InTe_4)_3$, and a study of their electronic conducting and magnetic propertied, in particular, the spin glass behavior in $Fe_5(InTe_4)_3$ through measurements of ac and dc susceptibility and time-dependent magnetization effects.

## II. EXPERIMENTAL DETAILS

The Zintl phase material, $K_5InTe_4$, was prepared using a solid-state reaction and purified in an argon filled glovebox as described previously.[1] $Cr_5(InTe_4)_3$ and $Fe_5(InTe_4)_3$ were prepared by the reaction of $K_5InTe_4$ with $FeCl_3$ and $CrCl_3$ in degassed water at ambient temperature. In a typical preparation, a 30 mL solution of 0.05 M $K_5InTe_4$ was slowly added to a 25 mL solution of 0.1 M $FeCl_3$ or $CrCl_3$ while stirring. A fine black precipitate was immediately formed, separated by suction filtration, washed with water and acetone, and dried under vacuum. The product was recovered with percent yield greater than 95%. Both solids are amorphous in structure as confirmed by their x-ray diffraction (XRD) patterns obtained with a XDS 2000 Scintag diffractometer.

Resistivity was measured on pressed pellets over the temperature range 100–300 K using the four-probe van der Pauw technique.[3] Magnetic measurements were performed on a Quantum Design MPMS-5S SQUID susceptometer. The temperature dependence of the dc susceptibility ($M/H$) was measured at a fixed field of 1 kG using the temperature cycling, following the usual zero-field cooling (ZFC) and field-cooling (FC) procedures. For $Fe_5(InTe_4)_3$, the thermal remanent magnetization (TRM), isothermal remanent magnetization (IRM), and hysteresis loop were measured. In the TRM measurement, the specimen was cooled in an applied magnetic field to temperatures below the spin glass freezing temperature, then the field was switched off, and the remanent magnetization was measured. In the IRM measurement on the other hand, the specimen was cooled in a zero field to temperatures below the spin glass freezing temperature, exposed to an applied field for a certain time, and then the applied field was quenched and the remanent magnetization was measured.

 0021-8979/96/79(8)/6627/3/$10.00 © 1996 American Institute of Physics 

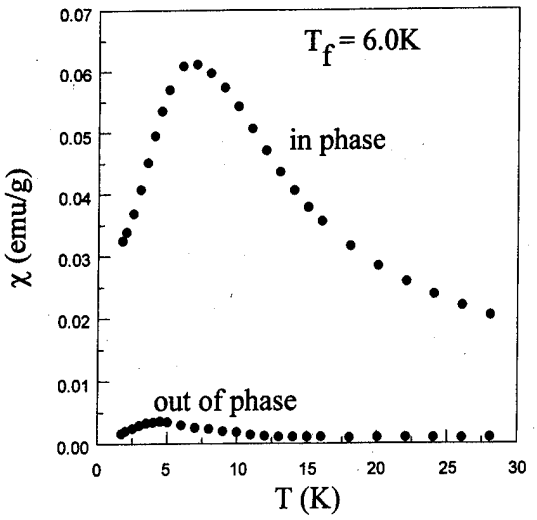



FIG. 1. The temperature dependence of ac susceptibility as determined at 25 MHz for $Fe_5(InTe_4)_3$.

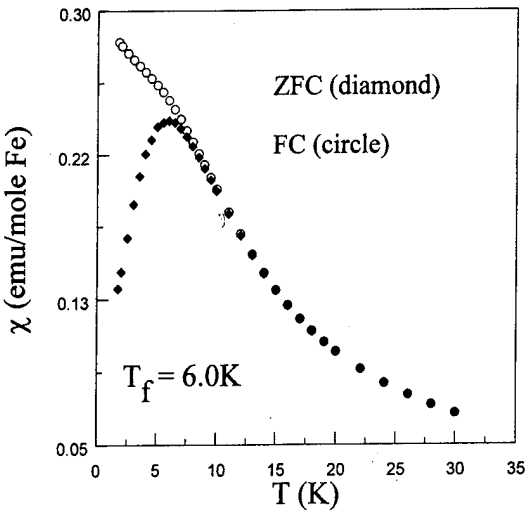



FIG. 2. The temperature dependence of dc susceptibilities as measured at 1.0 kG for $Fe_5(InTe_4)_3$.

## III. RESULTS AND DISCUSSION

The conductivity ($\sigma$) for $Fe_5(InTe_4)_3$ is only slightly affected by temperature and, for example, $\sigma$ is 7.41 $\Omega^{-1}$ cm$^{-1}$ at 300 K and 2.92 $\Omega^{-1}$ cm$^{-1}$ at 100 K. For $Cr_5(InTe_4)_3$, $\sigma$ is $1.07\times10^{-3}$ $\Omega^{-1}$ cm$^{-1}$ at 300 K and highly temperature dependent. A least-squares fit of the linear portion in a plot of $\log\sigma$ vs $1/T$ to the relationship $\sigma = C\exp(-Ea/k_BT)$, where $\sigma$ is specific conductivity, gives an activation energy ($Ea$) of 0.20 eV.

The high-temperature magnetic data indicate that both $Cr_5(InTe_4)_3$ and $Fe_5(InTe_4)_3$ exhibit strong antiferromagnetic interactions. A Curie–Weiss fit of the susceptibilities above 100 K for $Cr_5(InTe_4)_3$ gives $\theta = -30.2$ K and $C = 1.65$ emu K/mole Cr atom. A Curie–Weiss fit of the susceptibilities above 200 K for $Fe_5(InTe_4)_3$ gives $\theta = -46.3$ K and $C = 1.60$ emu K/mole Fe atom. The effective moment at room temperature is $3.64\mu_B$/Cr, that is, close to the spin-only value of $3.87\mu_B$ for $Cr^{3+}$. Thus, the electrons are completely localized in $Cr_5(InTe_4)_3$. The effective moment at room temperature is $3.57\mu_B$/Fe significantly lower than the spin-only value of $5.92\mu_B$ for $Fe^{3+}$, indicating some degree of electron delocalization. This is consistent with its relatively high conductivity.

The susceptibility of $Fe_5(InTe_4)_3$ deviates gradually from the Curie–Weiss law with decreasing temperature due to the development of ferromagnetic correlations between the dominant antiferromagnetic clusters. As a result, the susceptibilities between 10 and 100 K are well fit to the Curie law. The competition between ferromagnetic and antiferromagnetic interactions ultimately gives rise to a spin glass state in $Fe_5(InTe_4)_2$ at low temperatures. Figure 1 shows both in-phase and out-of-phase components of ac susceptibility of $Fe_5(InTe_4)_2$ measured at 25 Hz and zero magnetic field. Usually, a sharp cusp at a well-defined temperature called the freezing temperature $T_f$ is observed in ac susceptibility curve of the classic spin glasses, i.e., the first row transition metals in the noble metal hosts.[4] In our case, a round peak was observed. The reason for the difference might be that the disorder in classic spin glasses is produced only by random occupation of crystal sites by transition metal impurities, and thus the RKKY interaction among the magnetic impurities is solely responsible for the frustration necessary for a spin glass to exist. However, the source of the frustration in the amorphous phase under study is likely due to a combination of bond disorder and topological disorder. The extrapolation around the spin glass transition gives $T_f$ of 6.0 K. From the dc susceptibility shown in Fig. 2, it is seen that the ZFC curve with a maxima at 6.0 K is almost identical to the ac susceptibility curve. The FC susceptibility does not reach a plateau below $T_f$ as seen for many spin glass systems,[4] but instead continue to increase with decreasing temperature. In addition, the FC and ZFC susceptibility curves merge at a temperature higher than $T_f$. These may imply the occurrence of the significant ferromagnetic component in the solid.

Among the most diagnostic experiments for the characterization of a spin glass state is the analysis of the field dependence of the IRM and TRM. The field dependence of both TRM and IRM measured at 2.0 K is illustrated in Fig. 3. The hump at 5.0 kG in the TRM curve is characteristic of a spin glass state and has been observed in many systems.[4] This TRM maximum is time dependent, and may be explained by the cluster model. According to the cluster model, the spins are correlated into "magnetic clusters" of different size at temperatures well above the freezing temperature, and then, the freezing process can be thought of as resulting from a distribution of temperatures at which the different magnetic clusters are no longer able to overcome an energy barrier and are therefore blocked. Aharoni and Wohlfarth[5] have successfully interpreted the anomalous TRM maximum using the physical idea of a blocking process in effective magnetic clusters in the cluster model along with a time delay inherent in the measurement. The cluster model also explains the occurrence of a round peak in the ac curve instead of a sharp cusp. Since a rather sharp cusp is predicted only if all the clusters have the same blocking temperature. A distribution

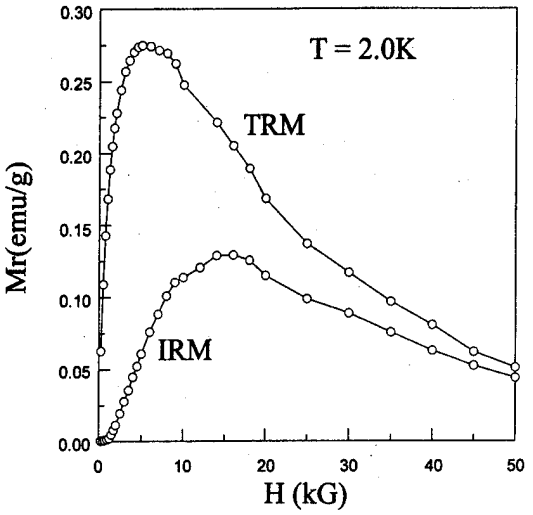



FIG. 3. The field dependence of the remanent magnetizations for $Fe_5(InTe_4)_3$. The solid lines are guides to the eye.

of blocking temperatures results from the distribution of particle size; thus smooths out the sharp cusp.[6]

For a spin glass state at weak fields, the TRM measurements give large remanence relative to the IRM, while at strong fields the TRM and IRM converge to the same saturation remanence as seen in Fig. 3. The effect seen for the TRM is greatly enhanced by performing the experiment at lower temperatures, whereas the IRM is little affected by the temperature as shown in Fig. 4. The TRM and IRM curves merge at a temperature higher than $T_f$. The remanence and irreversible behavior of a spin glass can also be seen in its

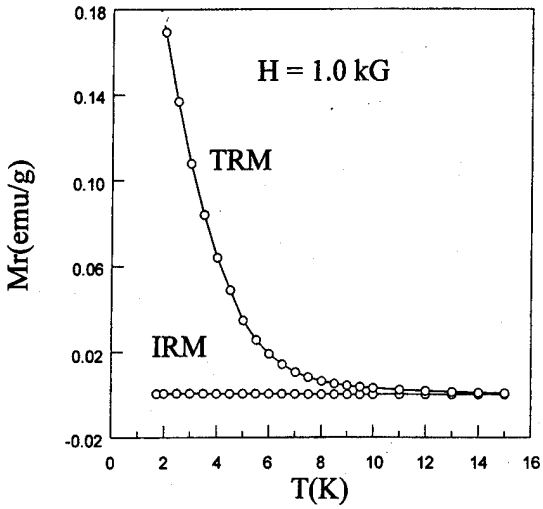



FIG. 4. The temperature dependence of the remanent magnetizations for $Fe_5(InTe_4)_3$. The solid lines are guides to the eye.

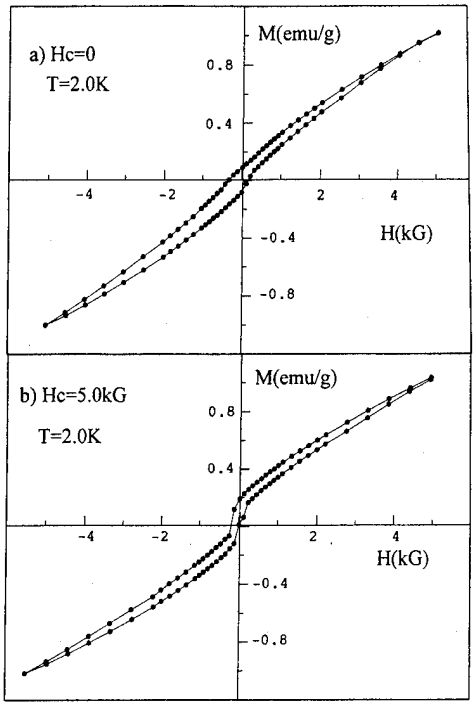



FIG. 5. Hysteresis loops of $Fe_5(InTe_4)_3$ as cooled to 2.0 K (a) at a zero field and (b) at a field of 5.0 kG.

hysteresis loop below the freezing point. Figure 5 shows the hysteresis loops of magnetization between ±5.0 kG obtained after zero field cooling and field cooling to 2.0 K, respectively. For the zero-field-cooled sample, the loop is rather flat and smooth. While for the field-cooled sample the loop consists of sharp steps due to the reversal of the magnetization in a very short time and at a very small oppositely directed field. The field-cooled loop exhibits a small displacement due to the presence of a small unidirectional exchange interaction in the material.

In summary, we have synthesized and characterized the amorphous $Cr_5(InTe_4)_3$ and $Fe_5(InTe_4)_3$. $Cr_5(InTe_4)_3$ is a semiconductor and exhibits strong antiferromagnetic couplings between localized moments. $Fe_5(InTe_4)_3$ exhibits strong antiferromagnetic couplings at high temperatures and undergoes a transition to a spin glass state at 6.0 K.

## ACKNOWLEDGMENT

This work was supported by a grant from the Research Corporation.

[1] J. H. Zhang, A. J. van Duyneveldt, J. A. Mydosh, and C. J. O'Connor, Chem. Mater. **1**, 404 (1989).
[2] J. H. Zhang, B. Wu, and C. J. O'Connor, Chem. Mater. **5**, 17 (1993).
[3] *1986 ASTM Annual Book of Standards*, edited by R. A. Priemon-Storer (American Society for Testing Materials, Philadelphia, 1986), Vol. 10.05, Standard F374-384.
[4] K. Binder and A. P. Young, Rev. Mod. Phys. **58**, 801 (1986).
[5] A. Aharoni and E. P. Wohlfarth, J. Appl. Phys. **6**, 55 (1984).
[6] P. J. Ford, Contemp. Phys. **23**, 141 (1982).

# Order-parameter fluctuations in the frustrated Heisenberg model on the square lattice

Shu Zhang and Gerhard Müller
*Department of Physics, The University of Rhode Island, Kingston, Rhode Island 02881-0817*

The $T=0$ dynamics of the two-dimensional $s=1/2$ Heisenberg model with competing nearest-neighbor ($J_1$) and next-nearest-neighbor ($J_2$) interactions is explored via the recursion method, specifically the frequency-dependent fluctuations of the order parameters associated with some of the known or suspected ordering tendencies in this system, i.e., Néel, collinear, dimer, and chiral order. The results for the dynamic structure factors of the respective fluctuation operators show a strong indication of collinear order at $J_2/J_1 \gtrsim 0.6$ and a potential for dimer order at $0.5 \lesssim J_2/J_1 \lesssim 0.6$, whereas the chiral ordering tendency is observed to be considerably weaker.
© *1996 American Institute of Physics.* [S0021-8979(96)00808-5]

The impact of quantum fluctuations on the zero-temperature phase diagram of a quantum many-body system tends to be strongest if that system contains competing interactions. A particular, sometimes exotic phase may be stabilized by quantum fluctuations in the presence of interactions that frustrate each other's ordering tendencies. The two-dimensional (2D) Heisenberg antiferromagnet with nearest-neighbor ($nn$) and next-nearest-neighbor ($nnn$) coupling on the square lattice,

$$H=J_1\sum_{\mathbf{r}} \mathbf{S}_{\mathbf{r}}\cdot(\mathbf{S}_{\mathbf{r}+\hat{\mathbf{x}}}+\mathbf{S}_{\mathbf{r}+\hat{\mathbf{y}}})+J_2\sum_{\mathbf{r}} \mathbf{S}_{\mathbf{r}}\cdot(\mathbf{S}_{\mathbf{r}+\hat{\mathbf{x}}+\hat{\mathbf{y}}}+\mathbf{S}_{\mathbf{r}+\hat{\mathbf{x}}-\hat{\mathbf{y}}}), \tag{1}$$

has been a prominent object of study in this context.[1]

The Néel long-range order (LRO) present in the ground state of the $nn$ model disappears at some critical coupling ratio, $J_2/J_1 \simeq 0.4$, and is replaced, at sufficiently large $J_2/J_1$, by Néel LRO within each of the two $nnn$ sublattices. The latter is preceeded, at $J_2/J_1 \gtrsim 0.65$, by collinear LRO, which breaks the (discrete) rotational symmetry of $H$ on the lattice but not yet its (continuous) rotational symmetry in spin space. The Néel and collinear order parameters (OPs) are described by the operators

$$O_N=\frac{1}{N}\sum_{\mathbf{r}} (-1)^{x+y}N_{\mathbf{r}}, \quad O_C=\frac{1}{N}\sum_{\mathbf{r}} C_{\mathbf{r}}, \tag{2}$$

where $N_{\mathbf{r}}=S^z_{\mathbf{r}}$, $C_{\mathbf{r}}=\mathbf{S}_{\mathbf{r}}\cdot(\mathbf{S}_{\mathbf{r}+\hat{\mathbf{x}}}+\mathbf{S}_{\mathbf{r}-\hat{\mathbf{x}}}-\mathbf{S}_{\mathbf{r}+\hat{\mathbf{y}}}-\mathbf{S}_{\mathbf{r}-\hat{\mathbf{y}}})$.

At intermediate coupling ratios, $0.4 \lesssim J_2/J_1 \lesssim 0.65$, the Néel and collinear ordering tendencies keep each other at bay and thus make the frustrated ground state susceptible to different kinds of ordering potentialities. Dimer order,[2,3] twist order,[4] and chiral order[5] have been proposed in this context. The dimer and chiral OPs considered here are defined by the following expressions in terms of spin operators:

$$O_D=\frac{1}{N}\sum_{\mathbf{r}} (-1)^{x}D_{\mathbf{r}}, \quad O_\chi=\frac{1}{N}\sum_{\mathbf{r}} \chi_{\mathbf{r}}, \tag{3}$$

where $D_{\mathbf{r}}=\mathbf{S}_{\mathbf{r}}\cdot\mathbf{S}_{\mathbf{r}+\hat{\mathbf{x}}}$, $\chi_{\mathbf{r}} = Z_{\mathbf{r},\mathbf{r}+\hat{\mathbf{x}},\mathbf{r}+\hat{\mathbf{x}}+\hat{\mathbf{y}}} - Z_{\mathbf{r},\mathbf{r}+\hat{\mathbf{x}}+\hat{\mathbf{y}},\mathbf{r}+\hat{\mathbf{y}}}$, $Z_{\mathrm{i,j,k}} = i(S^+_{\mathrm{i}}S^-_{\mathrm{j}}-S^-_{\mathrm{i}}S^+_{\mathrm{j}}+S^+_{\mathrm{j}}S^-_{\mathrm{k}}-S^-_{\mathrm{j}}S^+_{\mathrm{k}}+S^+_{\mathrm{k}}S^-_{\mathrm{i}}-S^-_{\mathrm{k}}S^+_{\mathrm{i}})$. They probe the long-range phase coherence of singlets stacked in columns along the $y$ axis and the handedness of the spin configuration on a plaquette, respectively, in the ground-state wave function $|G\rangle$. Whether any one of these types of LRO is, in fact, realized, or whether a ground state with short-range correlations of the resonating-valence-bond type,[6,7] for example, is stabilized, has not been determined for certain.

The absence or presence of a specific type of LRO determines whether the associated OP correlation function decays to zero or not. In the finite-cluster data, the relevant information on the asymptotic behavior is best captured by the expectation value of the squared OP. The problem here is to find a meaningful reference point for any enhancement in that quantity.[3]

An alternative avenue to comparing the different ordering tendencies in the spin-frustrated ground state of (1) is to explore the dynamic (i.e., frequency-dependent) fluctuations of any proposed OP. The recursion method[8] in conjunction with recently developed techniques of continued-fraction analysis[9,10] is very suitable for that purpose. Here the dynamical information is derived from the finite-size ground-state wave function. No excited states have to be computed. This is an important advantage for the study of systems with complicated spectra and with potential OPs that have widely varying symmetry properties, as is the case here.

We investigate the fluctuations of the four OPs defined in (2) and (3) as they manifest themselves in the dynamic structure factors

$$S_{AA}(\mathbf{q},\omega)=\int_{-\infty}^{+\infty} dt e^{i\omega t}\langle F^A_{\mathbf{q}}(t)F^A_{-\mathbf{q}}\rangle, \tag{4}$$

where $F^A_{\mathbf{q}}=N^{-1/2}\Sigma_{\mathbf{r}}e^{i\mathbf{q}\cdot\mathbf{r}}A_{\mathbf{r}}$ is the fluctuation operator associated with a given OP, and $A_{\mathbf{r}}$ stands for $N_{\mathbf{r}}$, $C_{\mathbf{r}}$, $D_{\mathbf{r}}$, or $\chi_{\mathbf{r}}$, as defined above.

The recursion algorithm in the present context is based on an orthogonal expansion of the wave function $|\Psi^A_{\mathbf{q}}(t)\rangle = F^A_{\mathbf{q}}(-t)|G\rangle$. It produces (after some intermediate steps) a sequence of continued-fraction coefficients $\Delta^A_1(\mathbf{q})$, $\Delta^A_2(\mathbf{q})$, ... for the relaxation function

$$c^{AA}_0(\mathbf{q},z)=\cfrac{1}{z+\cfrac{\Delta^A_1(\mathbf{q})}{z+\cfrac{\Delta^A_2(\mathbf{q})}{z+\ldots}}}, \tag{5}$$

 0021-8979/96/79(8)/6630/3/$10.00 © 1996 American Institute of Physics

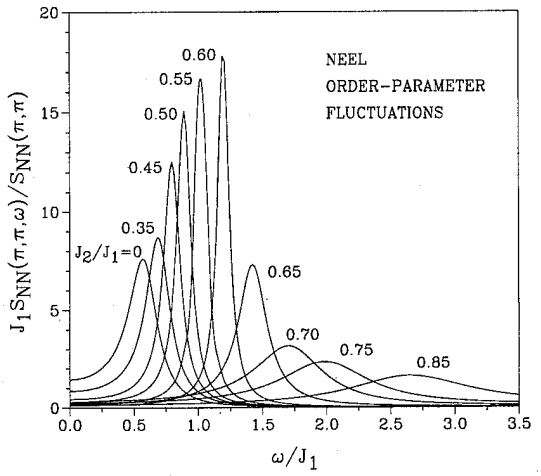



FIG. 1. $T=0$ dynamic structure factor (4) normalized by its integrated intensity for the Néel fluctuation operator $F_{\mathbf{q}}^{N}$ at $\mathbf{q}=(\pi,\pi)$ of the Hamiltonian (1) at various values of the coupling ratio $J_2/J_1$, obtained via strong-coupling continued-fraction reconstruction from the coefficients $\Delta_1,\ldots,\Delta_6$ and a Gaussian terminator as explained in Refs. 9 and 10.

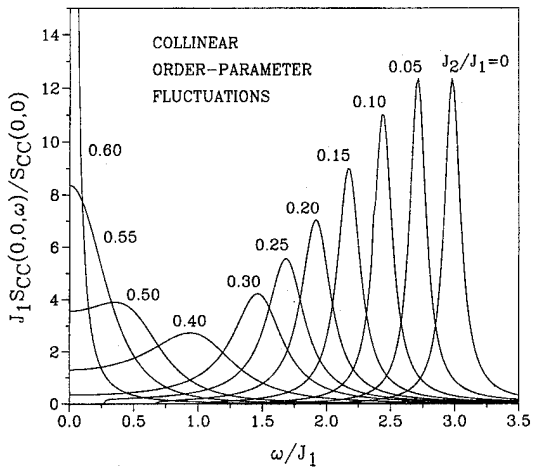



FIG. 2. $T=0$ dynamic structure factor (4) normalized by its integrated intensity for the collinear fluctuation operator $F_{\mathbf{q}}^{C}$ at $\mathbf{q}=(0,0)$ of the Hamiltonian (1) at various values of the coupling ratio $J_2/J_1$, obtained via strong-coupling continued-fraction reconstruction from the coefficients $\Delta_1,\ldots,\Delta_6$ and a Gaussian terminator.

which is the Laplace transform of the symmetrized correlation function $\Re\langle F_{\mathbf{q}}^{A}(t)F_{-\mathbf{q}}^{A}\rangle/\langle F_{\mathbf{q}}^{A}F_{-\mathbf{q}}^{A}\rangle$. The $T=0$ dynamic structure factor is then obtained from (5) via

$$S_{AA}(\mathbf{q},\omega)=4\langle F_{\mathbf{q}}^{A}F_{-\mathbf{q}}^{A}\rangle\Theta(\omega)\lim_{\varepsilon\to 0}\Re[c_0^{AA}(\mathbf{q},\varepsilon-i\omega)], \quad (6)$$

where $\langle F_{\mathbf{q}}^{A}F_{-\mathbf{q}}^{A}\rangle=S_{AA}(\mathbf{q})$ is the integrated intensity.[11]

All the results presented here are for clusters of $N=4\times4$ sites with periodic boundary conditions. Extreme care must be exercised in separating finite-size effects from properties that reflect the physics of the infinite system. This distinction can be made with more confidence for coupling ratios $J_2/J_1\lesssim0.7$ than at $J_2/J_1>0.7$, where the gradual decoupling of the two *nnn* sublattices causes a crossover in the finite-size effects.

The Néel OP fluctuations are probed by the dynamic structure factor $S_{NN}(\mathbf{q},\omega)$ at the wave vector $\mathbf{q}=(\pi,\pi)$. This quantity is shown in Fig. 1 for various coupling ratios. The presence of Néel LRO at $J_2/J_1=0$ implies that $S_{NN}(\pi,\pi,\omega)$ is governed by a zero-frequency peak. Quantum fluctuations split the ground-state level for finite $N$. In a $4\times4$ cluster the finite-size gap is known to be of magnitude $\Delta E/J_1\simeq0.57$.[10] The peak position of the curve for $J_2/J_1=0$ must be interpreted with this fact in mind.

What are the effects of the *nnn* coupling on the Néel OP fluctuations? For $0\leqslant J_2/J_1\lesssim0.4$, i.e., over the estimated range of the Néel phase, we observe only small changes in peak position and line shape. Then the Néel OP fluctuations begin to change rapidly in two stages:

(i) Over the range $0.4\lesssim J_2/J_1\lesssim0.6$, the peak position moves to higher frequencies at an accelerated rate, the linewidth shrinks, and the integrated intensity (not shown) drops to 32% of its value at $J_2/J_1=0$. This signals the presence of some non-Néel type ordering tendency which supports well-defined Néel modes at increasingly high frequencies.

(ii) At $J_2/J_1\gtrsim0.6$ the linewidth of $S_{NN}(\pi,\pi,\omega)$ grows rapidly, while the peak position moves further up and the integrated intensity continues to fade away quickly. As the two *nnn* sublattices begin to decouple, the system ceases to support well-defined Néel modes.

The dynamic structure factor $S_{CC}(0,0,\omega)$, which describes the collinear OP fluctuations, is shown in Fig. 2. At $J_2/J_1=0$, we observe a fairly sharp collinear mode at $\omega/J_1\simeq3.0$. As the Néel ordering tendency weakens with increasing $J_2/J_1$, the collinear mode shifts to lower frequencies, while its line shape broadens considerably. The width reaches a maximum at $J_2/J_1\simeq0.4$. Between here and $J_2/J_1\simeq0.55$, where the competing dimer and chiral ordering tendencies are at their peak, the collinear mode moves to $\omega=0$, and the integrated intensity more than triples in relation to its value at $J_2/J_1=0$. In the interval $0.55\lesssim J_2/J_1\lesssim0.7$, the function $S_{CC}(0,0,\omega)$ transforms into a narrow

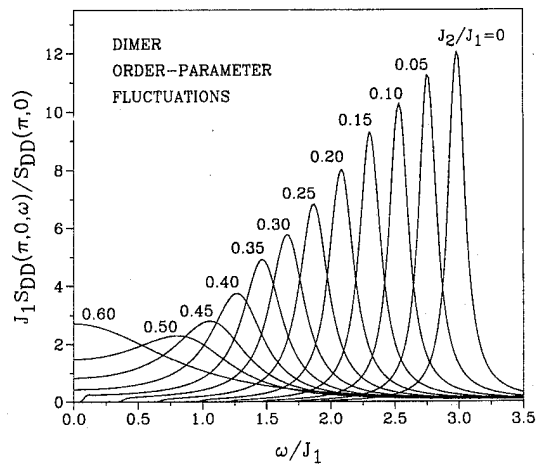



FIG. 3. $T=0$ dynamic structure factor (4) normalized by its integrated intensity for the dimer fluctuation operator $F_{\mathbf{q}}^{D}$ at $\mathbf{q}=(\pi,0)$ of the Hamiltonian (1) at various values of the coupling ratio $J_2/J_1$, obtained via strong-coupling continued-fraction reconstruction from the coefficients $\Delta_1,\ldots,\Delta_6$ and a Gaussian terminator.

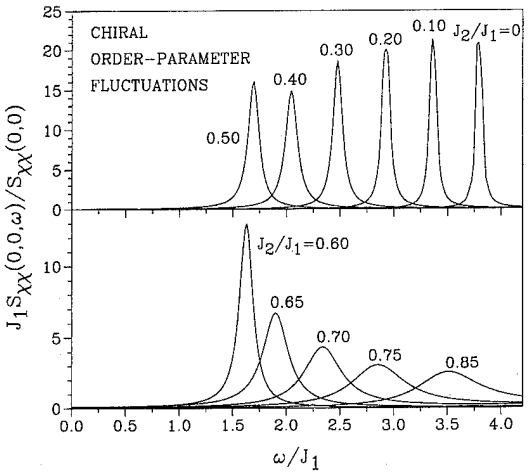



FIG. 4. $T=0$ dynamic structure factor (4) normalized by its integrated intensity for the chiral fluctuation operator $A_{\mathbf{q}}^{\chi}$ at $\mathbf{q}=(0,0)$ of the Hamiltonian (1) at various values of the coupling ratio $J_2/J_1$, obtained via strong-coupling continued-fraction reconstruction from the coefficients $\Delta_1,\ldots,\Delta_6$ and a Gaussian terminator.

central peak, and $S_{CC}(0,0)$ increases by another factor of $\simeq 1.6$. This clearly reflects the onset of collinear LRO in the infinite system.

The dimer OP fluctuations as described by the dynamic structure factor $S_{DD}(\pi,0,\omega)$ and shown in Fig. 3 resemble those of the collinear OP with respect to line shape and peak position for as long as the Néel ordering tendency is perceptible in the ground state ($J_2/J_1 \lesssim 0.4$). Both modes become soft and very broad at $J_2/J_1 \simeq 0.55$, but then they part company. While the collinear mode has been observed to transform into a high-intensity narrow central peak, the dimer mode, which has reached its maximum intensity here ($\simeq$ 1.8 times its value at $J_2/J_1=0$), broadens further and loses intensity very rapidly. It literally dissolves as the inter-sublattice correlations begin to weaken at $J_2/J_1 \gtrsim 0.7$. Nevertheless, the softness of the dimer OP fluctuations at $J_2/J_1 \simeq 0.55$ in the $4\times4$ cluster is consistent with dimer LRO in the infinite system.

The chiral OP fluctuations are based more significantly on intra-sublattice correlations than the dimer OP fluctuations and, therefore, evolve differently. This is illustrated in Fig. 4. At $J_2/J_1=0$ the dynamic structure factor $S_{\chi\chi}(0,0,\omega)$ exhibits a sharp mode at $\omega/J_1 \simeq 3.8$. At $J_2/J_1 \simeq 0.55$, the peak position has moved down to $\omega/J_1 \simeq 1.6$, while the linewidth has increased only slightly, and the integrated intensity has grown to a maximum value of $\simeq 2.3$ times its value at $J_2/J_1=0$. Then the peak position starts to move back out to higher frequencies, the line shape begins to broaden, but less so compared to that of the dimer fluctuations, and the integrated intensity drops rapidly. The minimum gap of the chiral mode is perhaps too large to be entirely attributable to a finite-size effect, which would indicate that the observed chiral ordering tendency does not turn into chiral LRO as $N\to\infty$.

This work was supported by NSF Grant No. DMR-93-12252 and by the NCSA at Urbana-Champaign.

[1] J. Richter, Phys. Rev. B **47**, 5794 (1993). This paper contains many references to pertinent studies.
[2] M. P. Gelfand, R. R. P. Singh, and D. A. Huse, Phys. Rev. B **40**, 10801 (1989); A. V. Chubukov and Th. Jolicoeur, *ibid.* **44**, 12050 (1991).
[3] R. R. P. Singh and R. Narayanan, Phys. Rev. Lett. **65**, 1072 (1990).
[4] E. Dagotto and A. Moreo, Phys. Rev. Lett. **63**, 2148 (1989).
[5] J. Richter, C. Gros, and W. Weber, Phys. Rev. B **44**, 906 (1991); **45**, 10113 (1992).
[6] P. Chandra and B. Doucot, Phys. Rev. B **38**, 9335 (1988).
[7] J. Richter, Z. Phys. B **79**, 403 (1990).
[8] R. Haydock, Solid State Phys. **35**, 215 (1980); M. H. Lee, Phys. Rev. B **26**, 2547 (1982); E. R. Gagliano and C. A. Balseiro, *ibid.* **38**, 11766 (1988).
[9] V. S. Viswanath and G. Müller, *Recursion Method – Application to Many-Body Dynamics*, Lecture Notes in Physics, Vol. 23 (Springer, New York, 1994).
[10] V. S . Viswanath, S. Zhang, J. Stolze, and G. Müller, Phys. Rev. B **49**, 9702 (1994).
[11] A graph of the integrated intensity vs $J_2/J_1$ for each of the four types of OP fluctuations depicted in Figs. 1 through 4 can be found, e.g., in Ref. 1 (with different $N$-dependent factors).

# Mictomagnetism of $\epsilon$-MnZn alloys

T. Hori[a] and H. Shiraishi[b]
*Shibaura Institute of Technology, Oomiya, Saitama 330, Japan*

Y. Nakagawa
*Department of Electronics, Tohoku Institute of Technology, Yagiyama, Sendai 982, Japan*

The $\epsilon$-MnZn alloy (disordered hcp structure) containing 15 at. % Mn seems to be ferromagnetic below about 200 K; the magnetization $\sigma$ in a field $H$ of 9.5 kOe amounts to 26 emu/g at a temperature $T$ of 4.2 K. The $\sigma$ vs $T$ curve in lower $H$, however, shows a maximum, suggesting mictomagnetism. This is verified by the existence of a hump on the ac susceptibility $\chi_{ac}$ vs $T$ curve. The $\sigma$ versus concentration curve shows a maximum at 15 at. % Mn. The $\chi_{ac}$ vs $T$ curves for the 12 at. % Mn alloy show a cusp at 45 K in addition to the hump between 80 and 180 K, suggesting a spin glass state. Both the cusp and the hump are suppressed by a dc magnetic field applied parallel to the ac field. The micromagnetic behavior becomes more pronounced for the Mn richer alloys which show only the hump in the $\chi_{ac}$ vs $T$ curve. The $\sigma$ vs $T$ curves exhibit a magnetic field cooling effect below a freezing temperature $T_f$. The values of $T_f$ for the alloys containing 20, 30, and 45 at. % Mn are 38, 50, and 75 K, respectively. Although the antiferromagnetic interaction predominates in the Mn rich alloys, a long-range antiferromagnetic order may not be expected because of the random distribution of Mn moments. The 25 at. % Mn alloy shows strong ferromagnetism, if the atomic ordering in the hcp lattice is realized. © *1996 American Institute of Physics.* [S0021-8979(96)04008-1]

## I. INTRODUCTION

The $\epsilon$ phase (disordered hcp structure) in the Mn–Zn alloy system is stable at high temperatures in a rather wide composition range (13–55 at. % Mn)[1] and can be retained at room temperature by water quenching. A few decades ago, the ferromagnetism of this phase was found by Nowotny *et al.*[2] The present authors[3] have reported that the magnetic susceptibility of this phase at high temperatures obeys the Curie–Weiss law; the extrapolated Curie temperature is positive for the alloys with less than 20 at. % Mn and negative for those with more than 25 at. % Mn. It has also been clarified[4] that the $\epsilon$-MnZn alloys containing about 25 at. % Mn become strongly ferromagnetic at room temperature if annealed at 100 °C for several days. The ferromagnetism is due to the formation of the ordered hcp structure of $D0_{19}$ type. Since the $D0_{19}$ type phase ($\epsilon'$ phase) is merely metastable, more prolonged annealing gives rise to the transformation to the antiferromagnetic $Cu_3Au$ type phase ($\alpha'$ phase). In the present work, more detailed magnetization and ac-susceptibility measurements for the quenched $\epsilon$-MnZn alloys were made at temperatures down to 4.2 K.

## II. EXPERIMENT

Samples of the Mn–Zn alloys containing 8–50 at. % Mn were prepared by the following procedures. Electrolytic Mn (99.9%) and pure Zn (99.9%) were mixed, sealed in an evacuated quartz tube, melted at about 900–1100 °C, and quenched in water. The ingot was sealed in a quartz tube and annealed at the stable temperature of the $\epsilon$-MnZn phase (about 440–600 °C) for more than 3 days. Powder samples for x-ray diffraction experiments and small pieces (10–500 mg in weight) for magnetization measurements were prepared by filing and cutting, respectively. In order to remove the stress caused by filing and cutting, these samples were annealed again at the stable temperature of the $\epsilon$-MnZn phase for several hours and then quenched in water. The magnetization was measured by a Faraday type magnetic balance in a field up to 10 kOe. The ac-susceptibility measurements were made using a standard double coil in an ac driving field of 3.9 Oe rms and 80 or 160 Hz. Various dc magnetic fields between 0 and 800 Oe were applied parallel to the ac field.

## III. EXPERIMENTAL RESULTS AND DISCUSSION

The x-ray diffraction lines for the well-annealed powder samples are very sharp, indicating that the samples are quite homogeneous and stress-free. No appreciable impurity phases were observed except for the alloys containing less than 10 at. % Mn. The $\epsilon$-phase region is somewhat wider than that of the current phase diagram.[1] The hexagonal lattice constants $a$ and $c$ at 20 °C are shown in Fig. 1(a). Figure 1(b) shows the effective magnetic moment and the extrapolated Curie temperature determined by the magnetization measurement in the paramagnetic region.

Figure 2 shows the temperature dependence of magnetization in various applied fields for the alloys containing 10–15 at. % Mn. These data were taken with increasing temperature after cooling to 4.2 K in zero field. The 15 at. % Mn alloy seems to show a typical ferromagnetism with the Curie temperature of about 200 K and the saturation magnetization of 26 emu/g (1.79 $\mu_B$ per Mn atom). In lower fields, however, the magnetization $\sigma$ vs temperature $T$ curve shows a maximum at about 90 K. The 10 and 12 at. % Mn alloys show a similar behavior. Both the Curie temperature and the saturation magnetization decrease with decreasing Mn concentration. The maximum in the $\sigma$ vs $T$ curve is sometimes

[a]Department of Electronic Information Systems.
[b]Laboratory of Natural Science (Physics).

 0021-8979/96/79(8)/6633/3/$10.00 © 1996 American Institute of Physics 

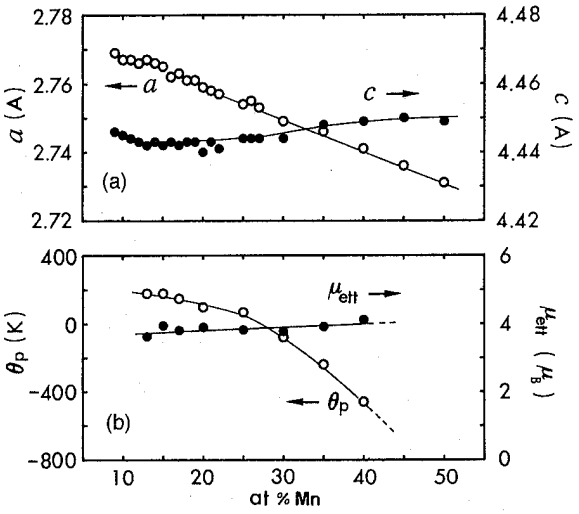



FIG. 1. Concentration dependence of (a) lattice constants $a$ and $c$ at 20 °C, and (b) extrapolated Curie temperature $\theta_p$ and effective magnetic moment per Mn atom $\mu_{\text{eff}}$ for $\epsilon$-MnZn alloys.

observed in mictomagnetism or cluster spin glass owing to the existence of antiferromagnetic interactions.

Figure 3 shows the ac susceptibility $\chi_{\text{ac}}$ vs $T$ curve for these alloys, which was measured during heating after zero-field cooling. A hump is observed between the Curie temperature and 80 K, the latter corresponding to the onset of mictomagnetism or cluster spin glass. In addition to the hump, a cusplike peak is observed at 36 and 45 K for the 10 and 12 at. % Mn alloys, respectively, suggesting the existence of a spin glass state. Both the cusp and the hump are

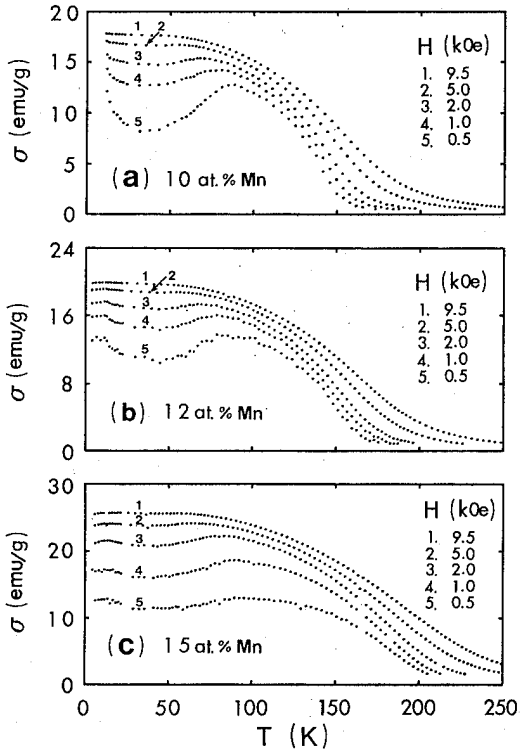



FIG. 2. Temperature $T$ dependence of magnetization $\sigma$ in various magnetic fields $H$ for $\epsilon$-MnZn alloys containing 10–15 at. % Mn.

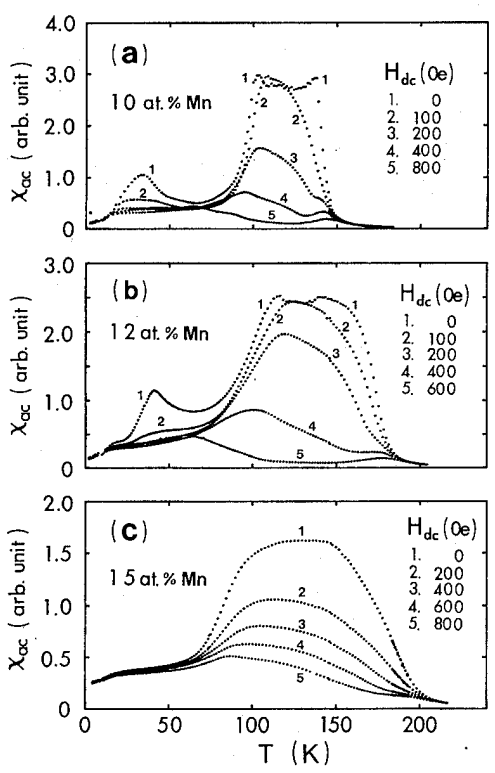



FIG. 3. Temperature $T$ dependence of ac-susceptibility $\chi_{\text{ac}}$ in various dc fields $H_{\text{dc}}$ parallel to the ac field for $\epsilon$-MnZn alloys containing 10–15 at. % Mn.

suppressed by a dc magnetic field applied parallel to the ac field. This effect is more remarkable for the cusp than for the hump. The cusp is not observed for the Mn-richer alloys which, on the other hand, show more pronounced mictomagnetism owing to the enhancement of the antiferromagnetic interaction.

Figure 4 shows the $\sigma$ vs $T$ curves for the alloys containing 20–45 at. % Mn. The magnetization was measured in 9.5 kOe during heating after cooling from about 80 to 4.2 K in 9.5 kOe (curves denoted as I) or in zero field (curves denoted as II). The so-called magnetic cooling effect appears below a freezing temperature $T_f$. The values of $T_f$ for the alloys containing 20, 30, and 45 at. % Mn are 28, 50, and 75 K, respectively. The maximum in the $\sigma$ vs $T$ curve even appears at the field of 9.5 kOe. The maximum values of magnetization are plotted against the Mn concentration in Fig. 5, together with the magnetization values at 4.2 K.

Although the antiferromagnetic interaction predominates in the alloys containing more than 30 at. % Mn, a long-range antiferromagnetic order may not be expected because of the random distribution of Mn moments. Instead, the cluster spin glass may occur.

We have re-examined the strong ferromagnetism of the ordered hcp phase ($\epsilon'$ phase). The $\epsilon$ phase alloys were annealed at 100 °C for a long time. The magnetization of 25 at. % Mn alloy at room temperature showed a maximum (26 emu/g) for the annealing time of 50 h, and then gradually decreased owing to the transformation to the nonferromagnetic $\alpha'$ phase. The results are in qualitative agreement with those of the earlier work.[4]

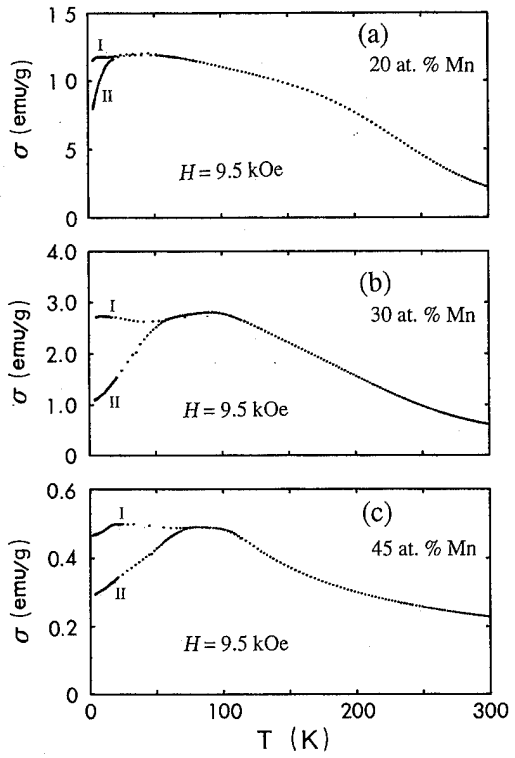



FIG. 4. Temperature $T$ dependence of magnetization $\sigma$ measured during heating in a field of 9.5 kOe for $\epsilon$-MnZn alloys containing 20–45 at. % Mn. Curves denoted as I and II were obtained after the cooling from about 80 to 4.2 K in 9.5 kOe and in zero field, respectively.

Even the 13 at. % Mn alloy is affected by the prolonged annealing at 100 °C. The ferromagnetic Curie temperature of the annealed alloy was about 250 K, being higher than that of the as-quenched alloy. The difference is thought to be caused by an atomic short-range order which may enhance

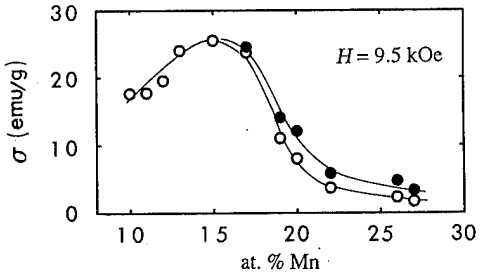



FIG. 5. Concentration dependence of magnetizations $\sigma$ in a field of 9.5 kOe. Open circles show the magnetization at 4.2 K, and closed circles show the maximum magnetization in the $\sigma$ vs $T$ curve.

the tendency to ferromagnetism. Since the short-range order might exist to some extent even in the as-quenched alloy, it would be difficult to determine the Curie temperature of the "ideally disordered" $\epsilon$-MnZn alloys.

## IV. CONCLUSIONS

The $\epsilon$-MnZn alloys containing less than 20 at. % Mn show typical ferromagnetism near the Curie temperature and cluster spin glass at low temperatures. Furthermore, the alloys containing 10–12 at. % Mn show a cusp in the ac susceptibility versus temperature curve at a lower temperature. On the other hand, the Mn-richer alloys show more pronounced mictomagnetism. The so-called magnetic cooling effect is observed even for the alloys containing 45 at. % Mn.

[1] J. Schramm, Z. Metallkde **32**, 399 (1940).
[2] H. Nowotny and H. Bittner, Monatsh. Chemie **81**, 887 (1950).
[3] Y. Nakagawa, S. Sakai, and T. Hori, Suppl. B-I, *Proceedings of the International Conference on Magnetism and Crystallography, Kyoto, 1961* [J. Phys. Soc. Jpn. **17**, 168 (1962)].
[4] S. Tezuka, S. Sakai, and Y. Nakagawa, J. Phys. Soc. Jpn. **15**, 931 (1960).

# Low temperature spin dynamics of geometrically frustrated antiferromagnets $Y_2Mo_2O_7$ and $Y_2Mo_{1.6}Ti_{0.4}O_7$ studied by muon spin relaxation

S. R. Dunsiger
*Department of Physics, University of British Columbia, British Columbia V6T-1Z1, Canada*

R. F. Kiefl
*Department of Physics, University of British Columbia, British Columbia V6T-1Z1, Canada and Canadian Institute for Advanced Research, University of British Columbia, British Columbia V6T-1Z1, Canada*

K. H. Chow
*Clarendon Laboratory, Oxford University, Parks Road, Oxford OX1 3PU, United Kingdom*

B. D. Gaulin
*Department of Physics and Astronomy, McMaster University, Hamilton, Ontario L8S 4M1, Canada*

M. J. P. Gingras
*TRIUMF, 4004 Westbrook Mall, Vancouver V6T 2A3, Canada*

J. E. Greedan
*Department of Chemistry, McMaster University, Hamilton, Ontario L8S 4M1, Canada*

A. Keren, K. Kojima, and G. M. Luke
*Department of Physics, Columbia University, New York, New York 10027*

W. A. MacFarlane
*Department of Physics, University of British Columbia, British Columbia V6T-1Z1, Canada*

N. P. Raju
*Department of Chemistry, McMaster University, Hamilton, Ontario L8S 4M1, Canada*

J. E. Sonier
*Department of Physics, University of British Columbia, British Columbia V6T-1Z1, Canada*

Y. J. Uemura and W. D. Wu
*Department of Physics, Columbia University, New York, New York 10027*

The spin dynamics of geometrically frustrated pyrochlore antiferromagnets $Y_2Mo_2O_7$ and $Y_2Mo_{1.6}Ti_{0.4}O_7$ have been investigated using muon spin relaxation. In $Y_2Mo_2O_7$ a dramatic slowing down of the $Mo^{4+}$ spin fluctuations occurs as one approaches the spin freezing temperature $T_F$ of 22 K from above. At lower temperatures the spins freeze into a disordered magnetic state similar to that found in a spin glass but with a small residual muon spin relaxation rate at low temperatures. This residual relaxation rate is larger in $Y_2Mo_{1.6}Ti_{0.4}O_7$ where $T_F=15$ K. These results suggest that there is a nonzero density of states for magnetic excitations in these systems near zero energy.
© *1996 American Institute of Physics.* [S0021-8979(96)05808-4]

Recently, there has been considerable interest in the behavior of geometrically frustrated antiferromagnets in which the natural antiferromagnetic coupling between ions is uniformly frustrated by the geometry of the lattice. This is unlike the random frustration occurring in conventional disordered spin glasses. In three dimensions, the most well studied systems are pyrochlores, where magnetic ions occupy a lattice of corner sharing tetrahedra. Monte Carlo simulations[1] have shown that Heisenberg spins on a lattice of corner sharing tetrahedra have a classical ground state with a macroscopic degeneracy, since the lowest energy spin configuration requires only that $\Sigma_{i=1}^{4}\mathbf{S}_i=0$ for each tetrahedron. Villain argued the classical ground state is a cooperative paramagnet,[2] with only short range spin-spin correlations and no ordering for $T>0$ K. However, additional factors such as magnetic anisotropy, further nearest neighbor exchange and thermal fluctuations[3] can lift the degeneracy. A variety of magnetic ground states have been observed in different pyrochlores. These include a non-collinear long range order (LRO) in which the spins on each tetrahedron point away from the center and a dense spin glass where the moments are frozen with no LRO.

Bulk magnetic susceptibility measurements on the pyrochlores $Y_2Mo_2O_7$[4] and $Y_2Mo_{1.6}Ti_{0.4}O_7$ show a cusp-like behavior at $T_F$ with strong irreversibilities below $T_F=22$ K and 15 K, respectively, typical of conventional spin glasses. Strong diffuse scattering, indicating the presence of short range correlations, has been observed in wide angle neutron scattering measurements on the isostructural compound $Tb_2Mo_2O_7$.[5,6] No LRO is observed below $T_F$.

We report on the results of an investigation of the low temperature magnetic properties of $Y_2Mo_2O_7$ and $Y_2Mo_{1.6}Ti_{0.4}O_7$ using muon spin relaxation. Below $T_F$ a large static internal magnetic field develops which has a very broad distribution, such that no coherent muon spin precession is observed. At the same time, the muon spin relaxation rate $1/T_1$ decreases according to a power law with decreasing temperature. The most remarkable feature in the data is the

 0021-8979/96/79(8)/6636/3/$10.00 © 1996 American Institute of Physics

presence of a residual spin relaxation rate in both samples at low temperatures, which is evidence for a nonzero density of magnetic states near zero energy. These results may be compared with $\mu$SR experiments on conventional spin glasses AuFe and CuMn.[7]

Pyrochlores crystallize with a fcc structure containing eight formula units per conventional unit cell and space group $Fd\bar{3}m$. The ions on the 16d site form a network of corner sharing tetrahedra; the 16c sites constitute an identical sublattice, displaced by (1/2,1/2,1/2). $Mo^{4+}$ ions occupy the 16c site, while the $Y^{3+}$ ions occupy the 16d site. The $Mo^{4+}$ ion has a magnetic moment of $\sim 1\mu_B$, whereas $Y^{3+}$ and $Ti^{4+}$ are diamagnetic. The oxygen vacancy concentration, which is likely the main source of crystalline disorder in these materials, is below the limit of 1% detectable by neutron and x-ray diffraction.

The $\mu$SR measurements on pressed polycrystalline pellets were made at TRIUMF in a $^4$He gas flow cryostat for temperatures above 2K and in an Oxford Instruments model 400 top loading dilution refrigerator (DR) for lower temperatures. In a $\mu$SR experiment the observed quantity is the time evolution of the muon spin polarization, which depends on the ensemble averaged distribution of internal magnetic fields and their temporal fluctuations. The present measurements were made in a small external field directed along the initial polarization direction (longitudinal field) to reduce sensitivity to small random static nuclear magnetic dipolar fields in the sample, sample holder and cryostat. Details on the $\mu$SR technique may be found elsewhere.[8]

Figure 1(a) shows several typical $\mu$SR spectra of $Y_2Mo_2O_7$ in a longitudinal applied field of 0.02 T. Above $T_F$=22 K the observed spin relaxation is attributed to rapid fluctuations of the internal magnetic field due to $Mo^{4+}$ moments in the paramagnetic phase. When $\nu \gg \Delta$ (defined below) the relaxation function [see $P_z(t)$ in Fig. 1] for each magnetically equivalent site $i$ can be described by a single exponential $e^{-\lambda_i t}$ with a relaxation rate[8]:

$$\lambda_i = \frac{4\pi\Delta_i^2 \nu_i}{\nu_i^2 + 2\nu_L^2}, \tag{1}$$

where $\Delta_i = \gamma_\mu B_i$ is the gyromagnetic ratio of the muon ($2\pi \times 135.54$ MHz/T) times the rms internal magnetic field $B_i$ at site $i$. $\nu_i$ is the fluctuation rate of the internal field, and $\nu_L = \gamma_\mu B_{\text{ext}}$ is the Larmor frequency of the muon in the external magnetic field. Note that $\lambda_i$ is only weakly dependent on the applied field provided $\nu_i \gg \nu_L$; this is consistent with the absence of any observed field dependence above $T_F$. Just above $T_F$, $P_z(t)$ deviates somewhat from a single exponential [see for example T=27.5 K spectrum in Fig. 1(a)] and is better described by a stretched exponential form $e^{-(\lambda t)^\beta}$ with $\beta$ near 0.4. In conventional spin glasses in the limit of rapid spin fluctuations, a square root exponential relaxation is a natural consequence of the large number of magnetically inequivalent sites arising from the broad distribution of distances to the magnetic moments. In a system of dense moments such as $Y_2Mo_2O_7$ it is still possible to have multiple sites and multi-exponential behavior, but the ratio of amplitudes for the various components and the corresponding relaxation rates are temperature independent. The data for $Y_2Mo_2O_7$ near $T_F$ could not be fit with this latter restriction, indicating that the observed non-exponential behavior possibly originates from a distribution of correlation times $\tau_i$ associated with different finite spin clusters. Similar behavior has recently been observed in other dense spin glasses AgMn and AuFe.[9] $\mu$SR spectra for $Y_2Mo_{1.6}Ti_{0.4}O_7$ are shown in Fig. 1(b), where the diamagnetic $Ti^{4+}$ ions are substitutional impurities on the B site, introducing random disorder into the system.

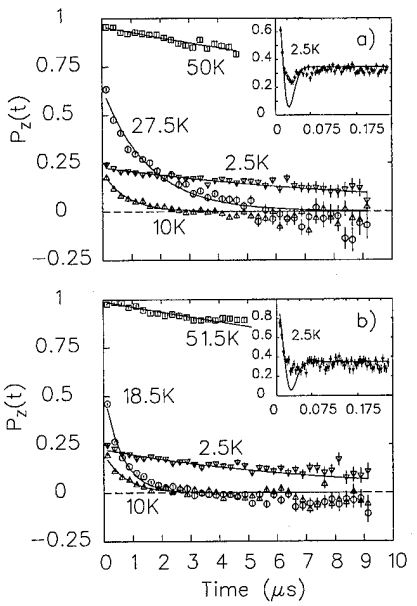



FIG. 1. Long-time dependence of the muon polarization, $P_z(t)$. Solid lines are best fits to the data. The inset shows the short-time behavior at $T = 2.5$ K for (a) $Y_2Mo_2O_7$ and (b) $Y_2Mo_{1.6}Ti_{0.4}O_7$.

The muon spin polarization function below $T_F$ (see insets in Fig. 1) is characterized by rapid depolarization of 2/3 of the initial polarization in the first 0.05 $\mu$s, followed by slow relaxation of the remaining 1/3 component. This is a characteristic signature of a highly disordered magnetic state in which the moments are quasi-static on the timescale of the muon lifetime. For example, the muon polarization function for a single magnetic site with a Gaussian distribution of static internal fields is given by a Kubo-Toyabe function.[8] The curves in the insets of Fig. 1 show a fit of the early time data at 2.5 K to this function, modified slightly to include the small external field of 0.02 T. This does not change the form of the function appreciably provided $B_{\text{ext}}$ is much less than $B_i$. Note that the 2.5 K spectrum for $Y_2Mo_2O_7$ was taken with better statistics. The best fit to the data corresponds to an average field strength $\sqrt{8/\pi}\Delta/\gamma_\mu = 0.105(5)$ T for both compounds. The dip in $P_z(t)$ at 0.032 $\mu$s is not however as deep as predicted by the Kubo-Toyabe function, indicating the distribution of internal fields is more complicated than a single Gaussian.

Muon spin relaxation results from the exchange of energy with magnetic excitations. A first order process, in which the muon absorbs or creates an excitation with an energy equal to the muon Zeeman energy, is normally suppressed in conventional long range ordered systems, since it

requires excitations at energies less than the smallest gap. In a second order process (Raman magnon scattering) involving inelastic scattering of an excitation, application of Fermi's Golden rule gives:

$$1/T_1 \propto \int_0^\infty dE n\left(\frac{E}{k_B T}\right)\left[n\left(\frac{E}{k_B T}\right)+1\right]M^2(E)\rho^2(E), \qquad (2)$$

where the muon Zeeman energy has been neglected, $\rho(E)$ is the density of states and $M(E)$ is the matrix element for inelastic scattering of an excitation of energy E causing a muon spin flip. In a spin glass, $n(E/k_BT)$ is the probability distribution for the intravalley excitations, assumed to be Bose, within one of a macroscopic number of metastable states or "valleys." The power law behavior of $1/T_1$ is primarily determined by the energy dependence of $\rho(E)M(E)$, as intervalley transitions are thought to be important only in the mK range.[10] For example, an energy gap in $\rho(E)$ generally leads to an exponential variation of $1/T_1 \sim T\exp(-E_g/k_bT)$ at low temperatures, where $T$ is much less than $E_g/k_b$. If $\rho(E)$ and $M(E)$ have power law dependences with powers $l$ and $m$, respectively, then Eq. (2) implies $1/T_1$ varies as $T^{2(l+m)+1}$. The low temperature linear specific heat observed in $Y_2Mo_2O_7$ (Ref. 4) suggests $\rho(E)$ is flat or at least weakly dependent on energy.

Figure 2(a) shows the average muon spin relaxation rate in $Y_2Mo_2O_7$ obtained from fits to a single exponential relaxation function over a restricted time interval of 0.05 to 6 $\mu$s. There is a sharp rise in the average $1/T_1$ as one approaches $T_F$=22 K from above. This is attributed to critical slowing down of the $Mo^{4+}$ fluctuations. Below $T_F$, $1/T_1$ decreases gradually as the magnetic excitations freeze out. The curve in Fig. 2(a) shows the best fit of the data below 12 K to a simple power law form, $\lambda = \lambda_0 + AT^n$, with exponent $n$=2.1(3). A similar analysis of the $Y_2Mo_{1.6}Ti_{0.4}O_7$ data below 12 K yields a value of $n$=2.03(6), as illustrated in Fig. 2(b). The spin freezing temperature, as seen by a peak in $1/T_1$, occurs at ~15 K in this sample. The muon spin depolarization rate is roughly temperature independent below 1 K, but at a higher value of ~0.05 $\mu s^{-1}$, as compared to 0.02 $\mu s^{-1}$ in $Y_2Mo_2O_7$. The small but finite residual relaxation at the lowest temperatures implies there is an appreciable density of excitations close to zero energy. We suggest that the mechanism giving rise to temperature independent muon spin depolarization is enhanced by the addition of random disorder. However, the power law behavior is unaffected within the accuracy of the measurements.

Computer simulations by Ching *et al.*[11] on insulating Heisenberg spin glasses $Eu_xSr_{1-x}S$ ($x$=0.54 and 0.40) have indicated the density of states $\rho(\epsilon)$ may be peaked at low energies. The geometrically frustrated kagomé lattice system $SrCr_8Ga_4O_{19}$ has also recently been studied using $\mu$SR. Dynamic spin fluctuations are observed without static freezing, even at 100 mK, well below $T_F$ = 3.5 K.[12]

In summary the data for $Y_2Mo_2O_7$ and $Y_2Mo_{1.6}Ti_{0.4}O_7$ are consistent with spin glass behavior as shown by:

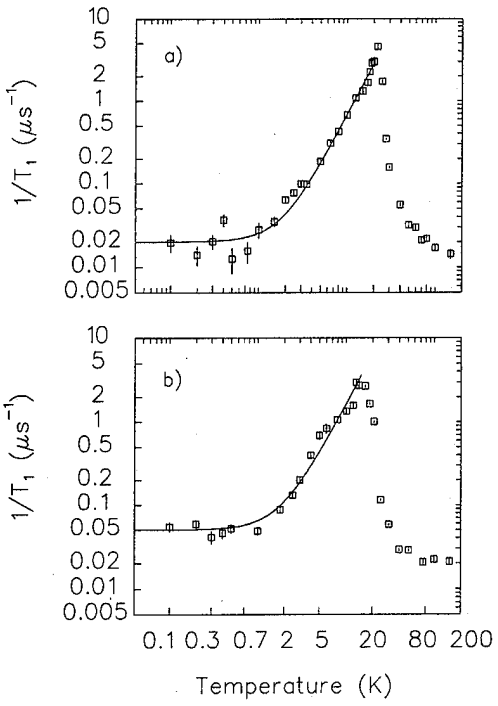



FIG. 2. Dynamical relaxation rate $1/T_1$ vs temperature for (a) $Y_2Mo_2O_7$ and (b) $Y_2Mo_{1.6}Ti_{0.4}O_7$in a longitudinally applied field of 0.02 T. The solid line is the best fit to the data assuming a power law functional form.

(1) the critical slowing down of the spin fluctuations and nonexponential muon spin relaxation near $T_F$,
(2) a broad distribution of static internal fields below $T_F$ and
(3) the weak power law behavior in $1/T_1$ below $T_F$.

In both systems there appears to be a residual relaxation which persists down to very low temperatures. This indicates there is a nonzero density of states for magnetic excitations close to zero energy.

This research has been funded by the NSERC of Canada under the NSERC Collaborative Research Grant *Geometrically-Frustrated Magnetic Materials*.

[1] J. N. Reimers, Phys. Rev. B **45**, 7287 (1992).
[2] J. Villain, Z. Phys. B **33**, 31 (1979).
[3] S. T. Bramwell, M. J. P. Gingras, and J. N. Reimers, J. Appl. Phys. **75**, 5523 (1994).
[4] N. P. Raju, E. Gmelin, and R. K. Kremer, Phys. Rev. B **46**, 5405 (1992).
[5] J. E. Greedan, J. N. Reimers, S. L. Penny, and C. V. Stager, J. Appl. Phys. **67**, 5967 (1990).
[6] B. D. Gaulin, J. N. Reimers, T. E. Mason, J. E. Greedan, and Z. Tun, Phys. Rev. Lett. **69**, 3244 (1992).
[7] Y. J. Uemura, T. Yamazaki, D. R. Harshman, M. Senba, and E. J. Ensaldo, Phys. Rev. B **31**, 546 (1985)
[8] S. F. J. Cox, J. Phys. C **20**, 3187 (1987).
[9] J. A. Campbell, A. Amato, F. N. Gygax, D. Herlach, A. Schenck, R. Cywinski, and S. H. Kilcoyne, Phys. Rev. Lett. **72**, 1291 (1994).
[10] W. Y. Ching and D. L. Huber, Phys. Rev. B **34**, 1960 (1986).
[11] W. Y. Ching, D. L. Huber, and K. M. Leung, Phys. Rev. B **21**, 3708 (1980).
[12] Y. J. Uemura, A. Keren, K. Kojima, L. P. Le, G. M. Luke, W. D. Wu, Y. Ajiro, T. Asano, Y. Kuriyama, M. Mekata, H. Kikuchi, and K. Kakurai, Phys. Rev. Lett. **73**, 3306 (1994).

# Quarternary giant magnetoresistance random access memory

Zhigang Wang and Yoshihisa Nakamura
*Research Institute of Electrical Communication, Tohoku University, Sendai 980, Japan*

We designed a quarternary memory using weakly coupled giant magnetoresistance (GMR) multilayers based on the fact that there are four stable states when the applied field is zero. Compared with conventional binary memory, the major advantage of the quarternary GMR memory is that we can simply double its capacity. This design's feasibility has been proved by experiments.
© *1996 American Institute of Physics.* [S0021-8979(96)13608-1]

## I. INTRODUCTION

The discovery of giant magnetoresistance (GMR) in magnetic multilayers has led to a large number of studies[1–3] on the giant magnetoresistance system for application. Usually, devices exhibiting giant magnetoresistance are under consideration and development as magnetic field sensors, for instance, in read-back magnetic heads used in magnetic recording technology. Differing from these studies for sensing purposes, we found a storage mechanism in GMR materials and succeeded in fabricating a binary GMR memory.[4] Moreover, the fact that the magnetizations in two ferromagnetic layers of weakly coupled multilayer act independently makes it possible to realize a quarternary data storage by making use of the four combinations of magnetizations. The different coercivities between the two ferromagnetic layers can be just employed to magnetize or remagnetize the two layers, respectively. In this article, we will discuss the mechanism, design, and experimental results of the quarternary GMR memory.

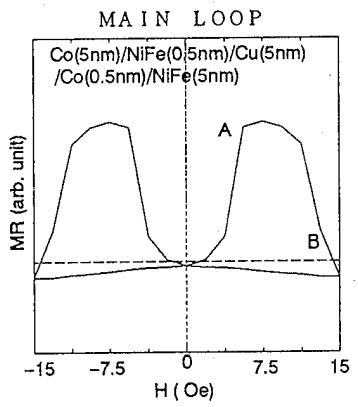
## II. QUARTERNARY STORAGE MECHANISM

From the viewpoint of application, weakly coupled GMR multilayer,[5,6] with two ferromagnetic components possessing different coercivities, is a hopeful candidate because of its low switching field (smaller than 10 Oe) and relatively large magnetoresistance (MR) ratio (4%–17%). We made samples of Co (5 nm)/NiFe (0.5 nm)/Cu (5 nm)/Co (0.5 nm)/NiFe (5 nm) by rf sputtering. The thinner NiFe and Co layers were formed to enhance interfacial scattering, which increases the MR ratio two times as large as that of Co (5 nm)/Cu (5 nm)/NiFe (5 nm), and the sandwich structure is comprised of two ferromagnetic components: the hard component Co (5 nm)/NiFe (0.5 nm) and the soft component Co (0.5 nm)/NiFe (5 nm). Uniaxial anisotropy, important both for memory storage and for the way that a bit is selected, is induced by a magnetic field of 15.5 Oe applied in the plane of the films during sputtering. Thereafter, an ac magnetic field anneal (300 °C×80 Oe×2 h) was executed and it was found that the ac magnetic thermal treatment helps to increase the slope of the $R(H)$ curve.

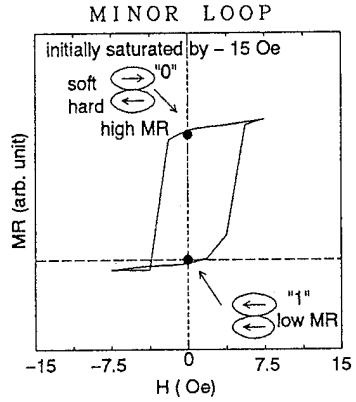
The resistance-field transfer curves $R(H)$ of these samples under exciting field of various strength were investigated. The applied magnetic field is along the plane of the samples. The switchings of the double ferromagnetic layers with different coercivities gives rise to the "double-hump" shaped curve of the main loop depicted in Fig. 1(a), where the applied field is between ±15 Oe. From Fig. 1(a) we can observe two obvious switching points: point A corresponds to the switching field (about 5.5 Oe) of the soft component and point B corresponds to the switching field (about 14 Oe) of the hard component. Figures 1(b) and 1(c) illustrate the $R(H)$ response's minor loop for the same sample operating in the mode in which only the soft component is switched by limiting an applied field between ±7.5 Oe. In Fig. 1(b) the element is initially saturated to the "negative" direction by a field of −15 Oe, while in Fig. 1(c) it is initially saturated to the "plus" direction by +15 Oe.

Theoretical analysis[7] indicates that the minor loop is primarily determined by the hysteresis of the soft component. But we found that these minor loops were shifted since the initially polarized hard component blocks the spins of the soft component through the ferromagnetic exchange interaction. In this case, the exchange field is about 1.5 Oe, smaller than the coercivity (4 Oe) of the soft component. So that the remanent state of the soft component cannot be influenced, although the exchange field is present. For this reason this type of GMR material is called weakly coupled. It is apparent that the soft component will act independently as long as the exchange field is smaller than its coercivity, and the lower the exchange field becomes the more stable the working point is. In fact, the exchange field will decrease with increasing Cu's thickness but, unfortunately, the MR ratio will also decrease with increasing Cu's thickness. We have to balance these two requirements and we found that for a Cu thickness of about 5 nm, the MR change ratio stays large and the exchange field is still relatively small. As a result, there are four stable states for the sample we used when the applied field is zero, which correspond to four combinations of

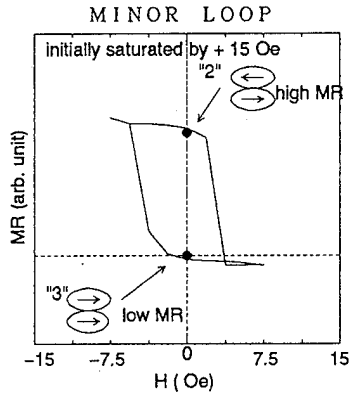
 0021-8979/96/79(8)/6639/3/$10.00 © 1996 American Institute of Physics 




(a)Main loop in which the applied field is between ±15 Oe.




(b)Minor loop in which the applied field is between ±7.5 Oe but the sample is initially saturated by the field of −15 Oe.




(c)Minor loop in which the applied field is between ±7.5 Oe but the sample is initially saturated by the field of +15 Oe.

FIG. 1. Quarternary storage mechanism.

magnetizations, as shown in Fig. 1. In GMR multilayers the resistance is lower when alternate magnetizations are parallel than when they are antiparallel. This rule is also shown in the same figure.

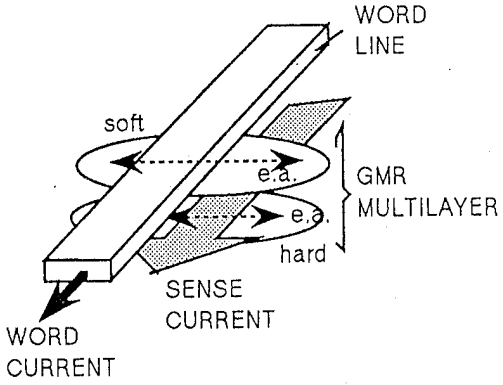



FIG. 2. Schematic diagram for quarternary memory cell.

The above description gives a quarternary storage mechanism. For any uniaxial anisotropic ferromagnetic film, there are two stable states: the magnetization will tend to point in one of two easy directions, and the fact that the magnetizations in two ferromagnetic layers act independently in weakly coupled sandwiches makes it possible to use these directions to represent a quarternary data.

## III. EXPERIMENTAL RESULTS

We have fabricated a one-bit quarternary GMR memory cell with a storage/sense line and a word line on to neoceramic substrate. Its schematic diagram is illustrated in Fig. 2. A brief outline of the fabrication method is given in the following. The material of the storage/sense line was the GMR multilayer, as described in the above section. This sandwiches were patterned into a rectangular shape whose size is 5 $\mu$m×10 $\mu$m by optical lithography and ion milling techniques. The storage/sense line was covered with a 0.5 $\mu$m thick $SiO_2$ layer, which served as an insulator, and a Cr (10 nm)/Cu (1000 nm)/Cr (30 nm) multilayer was deposited onto the $SiO_2$ and patterned into the word line. Contact holes were etched in the $SiO_2$ by a lift-off technique, followed by the structuring of electrodes for the storage/sense line. The use of the Cr/Cu/Cr structure was to make mechanically strong contacts. The word line was parallel to the storage/sense line, and both of them were orthogonal to the easy axis because the preferred easy axis is chosen to lie along the transverse direction of the GMR stripe. A combination of a sense current flowing along the GMR line itself (the sense current is assumed to pass primarily through the intermediate layer Cu because of its high conductivity), together with an exciting current flowing along the word line, make it possible for a 2D selective storage/sense function to be realized.

The different coercivities of the two ferromagnetic layers can be used to polarize the two layers, separately. In our experiments, we first use a strong magnetic field of 15 Oe to polarize the hard component whose switching field is 14 Oeand then use a weak field of 7.5 Oe to polarize the soft

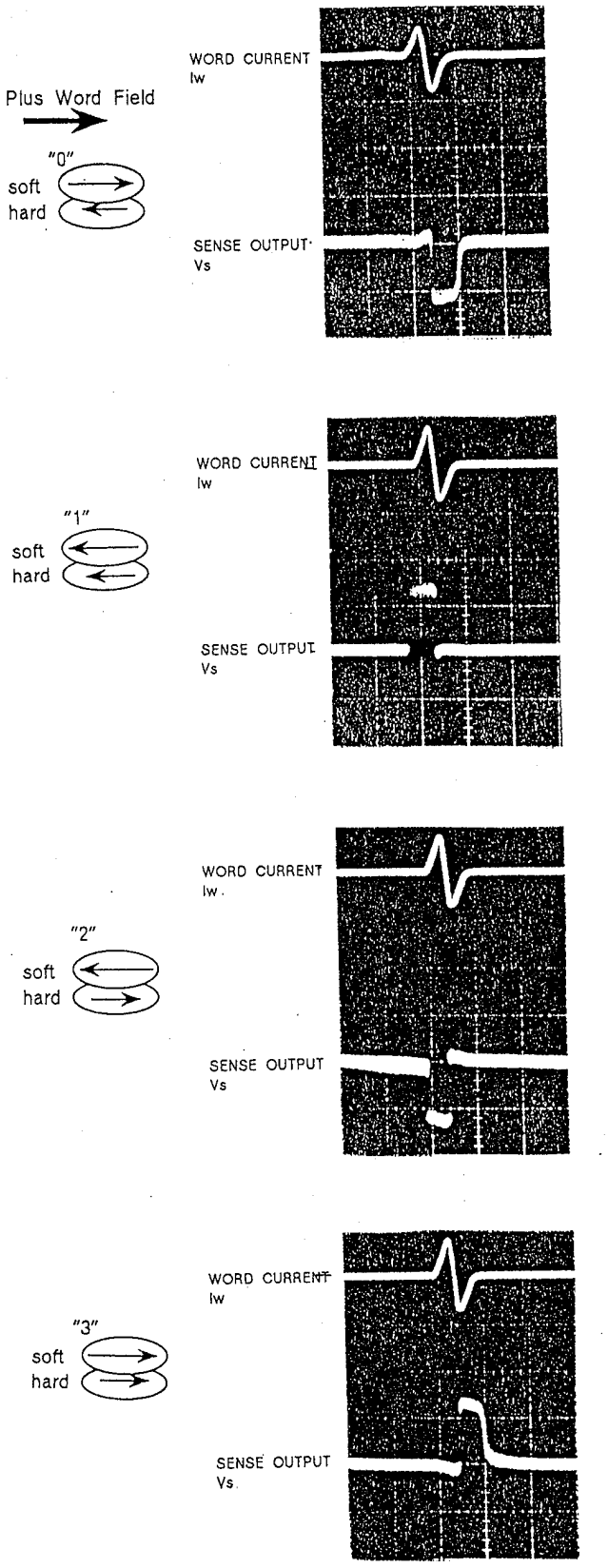



FIG. 3. Reading timing sequences. The vertical scale for sense voltage output Vs is 5 mV/div.

component. (In this mode the remanent magnetization of the hard component cannot be altered but the soft component can be switched since its switching field is about 5.5 Oe.)

For reading method, a bipolar excitation pulse current was used, and the strength of the corresponding magnetic field is limited to be smaller even than the coercivity of the soft component to confirm a nondestructive readout (NDRO) capability. It is easy to understand that the magnetization parallel to the excitation field could not rotate while the magnetization anti-parallel could. When a bipolar pulse word current Iw passes through the word line, a voltage-pulse combination should appear across the GMR line, in which a plus pulse corresponds to increasing resistance, and a minus pulse corresponds to decreasing resistance, and zero voltage corresponds to no resistance change. Figure 3 is the measured result, in which four kinds of pulse combinations corresponding to the remanent states arise, and therefore data readout can be performed by monitoring these pulse combinations against the plus–minus word current (field). The word current Iw is 15 mA and the sense current is 5 mA. The voltage difference between plus and minus pulses is 12 mV. Furthermore, the continuous test indicates that a stable readout waveform can be held for a long time. That is to say, this element has NDRO ability, and an additional rewrite operation after reading is not needed.

## IV. CONCLUSIONS

We succeeded in fabricating a quarternary memory cell. In this structure, the multilayer is used not only for data storing but also for data sensing. The major advantage of the quarternary GMR memory is that we can simply double its capacity compared with conventional binary memory. NDRO capability was also confirmed.

## ACKNOWLEDGMENTS

It is a pleasure to thank Dr. H. Muraoka and Dr. K. Takano for their helpful interest and criticism.

[1] W. Folkerts, J. Kools, and R. Coehoorn, INTERMAG'94, BB-01, Albuquerque, NM, 1994.
[2] E. Y. Chen, A. V. Pohm, J. M. Daughton, J. Brown, and W. C. Black, INTERMAG'94, BB-02, Albuquerque, NM, 1994.
[3] J. M. Daughton and Y. J. Chen, IEEE Trans. Magn. **29**, 2705 1993.
[4] Z. Wang and Y. Nakamura, IEICE General Conference Proceedings, C-502, Fukuoka, Japan, 1995 (unpublished).
[5] A. Chaiken, G. Prinz and J. Krebs, MMM-Intermag Proceedings, 1991 (unpublished), p. 5864.
[6] T. Shinjo and H. Yamamoto, J. Phys. Soc. Jpn. **9**, 3061 (1990).
[7] Z. Wang and Y. Nakamura, these proceedings.

# Important factors included in nondestructive readout of GMR MRAM (abstract)

Y. Nakamura and Z. Wang
*Research Institute of Elect. Communication, Tohoku University, Sendai 980, Japan*

We proposed a new type of magnetoresistive random access memory (MRAM) using a weakly coupled GMR effect. It operates on the general principle of storing a binary digit in hard component and sensing its remanent state by switching the soft component in such a way that the magnetic state of the hard component is unaltered.[1] It is believed that this structure could have nondestructive readout (NDRO) characteristics. However, in experiments we found that NDRO was not always achieved; i.e., NDRO was dependent on the polarity of the excitation field. We take an example for mode "0" (corresponding to a + remanent state). Although tests involving $3\times10^8$ plus excitation pulses indicated that the element was still stable, stability against minus disturb pulses could not be expected. The remanent state of 0 was degrading gradually and was finally destroyed after nenormous numbers of readout switching. An analytical model, in which the hard component follows the Rayleigh law, can explain the above phenomenon. It is because the irreversible magnetization processes cause disturbed states (0′ or 1′). Obviously the worst case for mode 0 is being excited by continous minus pulses whereas the worst case for mode 1 is being excited by continous plus pulses. We think that two methods will be effective to eliminate the unstability. One is to obtain a rectangular hysteresis loop for the hard component. The other is to imporve the excitation method, for example, to employ bipolar pulses for excitation signals. © *1996 American Institute of Physics.* [S0021-8979(96)46708-4]

[1]Z. Wang and Y. Nakamura, J. Magn. Magn. Mater. (to be published).

# Domain collapse in grooved magnetic garnet material (abstract)

J. C. Peredo and G. N. Patterson
*Jet Propulsion Laboratory, California Institute of Technology, Pasadena, California 91109-8099*

Y. N. Fedyunin
*Department of Electrical, Computer, and Systems Engineering, Boston University, Boston, Massachusetts 02215*

Material grooving has been proposed as a possible technique for stabilizing magnetic domains in a thin film. Grooving changes the local properties of the material, and can change the stability range of domains in the vicinity of a groove.[1] In this work, the effects of material grooving on the collapse fields of magnetic domains were simulated, measured, and interpreted magnetostatically for thin, epitaxial $(YBiGdHoCa)_3(FeGeSi)_5O_{12}$ and $(YBiSmLuCa)_3(FeGaSi)_5O_{12}$ garnet films which were 2 $\mu$m thick. The domain collapse field ($H_{co}$) was simulated with a recently developed computer code based on a simplified model of domain structure.[2] Simulation results indicated that $H_{co}$ varied linearly with groove depth ($\delta$) increasing for groove widths ($\omega$) $<20$ $\mu$m, and decreasing for $\omega>20$ $\mu$m. As groove widths increased, $H_{co}$ is a maximum when $\omega$ is near the domain diameter. These trends correspond to the effect induced by the demagnetizing fields from the groove bottom and edges, respectively. The grooved film is modeled as an ungrooved film of reduced film thickness upon which were placed two semi-infinite magnetized film layers separated by $\omega$. Experimental measurement of $H_{co}$ was performed by magneto–optic observation on an array of grooves at pitches of 4–8 $\mu$m. $\delta$ from 0.2–0.6 $\mu$m, and $\omega$ from 1.2 to 2.6 $\mu$m. The experimental data were in good agreement with the simulated values and magnetostatic interpretation. © *1996 American Institute of Physics.* [S0021-8979(96)46808-8]

The research described in this article was performed in part by the Center for Space Microelectronics Technology, Jet Propulsion Laboratory, California Institute of Technology, and was jointly sponsored in part by the Ballistic Missile Defense Organization/Innovative Science and Technology Office and the National Aeronautics and Space Administration, Office of Space Access and Technology.

[1]R. R. Katti, J. A. Dooley, and A. Meng, IEEE Trans. Magn. **MAG-29**, 2578 (1993).
[2]N. Hayashi and K. Abe, Jpn. J. Appl. Phys. **15**, 1683 (1976).
[3]A. H. Eschenfelder, 2nd ed. (Springer, Berlin 21, 1981).

 0021-8979/96/79(8)/6642/1/$10.00 © 1996 American Institute of Physics

# Fundamental studies of stripe-domain chopping in the presence of magnetic fields

K. J. Fogarty, K. Matsuyama, and H. Asada
*Electrical Engineering Department, Kyushu University 36, Fukuoka, Japan*

W. W. Clegg
*Electrical Engineering Department, Manchester University, Manchester, United Kingdom*

The effects of externally uniform applied orthogonal and parallel in-plane magnetic fields on the stripe-chopping characteristics and negative vertical Bloch line replication probability have been studied experimentally and by numerical simulation on a 5 $\mu$m bubble film. The orthogonal and parallel in-plane fields on the stripe domain were varied from $-50$ to 50 Oe and $-9$ to 9 Oe, respectively, to represent actual working device parameters. The numerical simulation results agree with the experimental data, confirming the suppression of horizontal Bloch line nucleation by the external-uniform in-plane fields and the in-plane field components of the chopping conductor.
© *1996 American Institute of Physics.* [S0021-8979(96)13708-8]

The chopping detection of vertical Bloch lines (VBL) is the major impediment for all of the VBL memory processes, yet full fundamental studies have never been performed in terms of large uniform-orthogonal in-plane fields and the probability of the chopped parts of an $S=0$ stripe domain still being an $S=0$ state for positive and negative in-plane fields. Nakada *et al.*[1] showed that the cause and the reproducibility can be understood in the relation of the in-plane wall magnetization to the in-plane field components of the chopping conductor (CC). The in-plane field parallel to the in-plane wall magnetization increases the Bloch line (BL) nucleation velocity,[2] effectually reducing the presence of the horizontal Bloch lines (HBLs). However, the in-plane field orthogonal to the stripe domain wall changes the critical velocity for BL instability and the actual position of the critical point itself.[2,3] The critical points are Bloch-line nucleation centers. It is this changing of the critical point that should aid the suppression of the HBLs in the chopping process.

The film characteristics are as follows: $4\pi Ms=187$ G, $\alpha=0.11$, $Ku=8200$ erg/cm$^3$, $\gamma=1.76\times10^7$/(Oe s), $A=1.88\times10^{-7}$ erg/cm, and $h=4.12$ $\mu$m. Figure 1 shows a schematic of the chip configuration. The stripe domain is stabilized in a loop conductor field of 6.4 Oe and a mid-range external bias field of 58 Oe.[4] The CC is 1.8 $\mu$m above the bubble garnet with a gap, width, and thickness of 4, 6, and 1.01 $\mu$m, respectively. The externally applied orthogonal, $Hy$, and parallel, $Hx$, in-plane field ranges applied to the stripe domain are $-50$ to 50 Oe and $-9$ to 9 Oe, respectively. The stripe domain is chopped with a triangular pulse of fixed rise and fall times of 100 ns, and at the threshold current value (100–110 mA) that successfully chops the stripe domain for each in-plane field value. The chopped parts of the initial $S=0$ stripe domain to the left and to the right of the CC are rocked[5] and their rocking states determined as being $S=0$, positive or negative. The minimum number of repetitions that were made to show the probability of specific chopping characteristics was 30.

The simulation method used is that used by Fujita *et al.*[6] which is a $(q,\phi)$ model of a side view through the film thickness. To show the physical effects of the in-plane field components of the CC on the wall structure, the wall structures at 0, $\pm1$, and $\pm2$ $\mu$m, from the center of the CC were simulated. The material parameters for the simulation are the actual physical characteristics of the 5 $\mu$m $(YSmLuCa)_3(GeFe)_5O_{12}$ garnet film as given above.

Considering the positive $(+ve)$ $Hx$ simulation conditions (with reference to Fig. 1), generally the dynamic HBLs are formed at the bottom and the top surface of the left-hand side (LHS) and the right-hand side (RHS) Bloch walls, respectively. This is due to the gyrotropic force induced by the chopping field, as shown in Fig. 2, for curves 3a and 3b. Lines 3a and 3b, etc., in Fig. 2, are the magnetization structures of the RHS and LHS Bloch walls, respectively. However, due to the CC being located on the bottom surface, HBLs will normally be formed from here, and the HBL will generate more easily on the LHS of the CC as the in-plane field component here is opposite to the in-plane wall magnetization, reducing the Bloch line nucleation velocity, as suggested in curves 2a and 2b. The application of the $Hy$ field to the stripe domain changes the static wall profiles as reported by Kosiński *et al.*,[3,7,8] but the wall profiles are different for each wall as their surface magnetizations are opposite to each other, therefore their respective critical points will change, as in curves 1a and 1b. The critical points for lines 1a and 1b, are the two depths from each film surface at which, because of the planar components of demagnetizing or external fields, the wall structure changes from truly

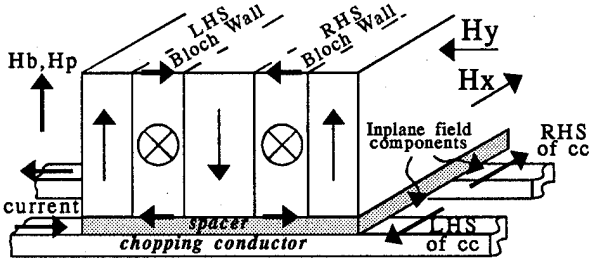



FIG. 1. Schematic of stripe domain and chopping conductor configuration.

 0021-8979/96/79(8)/6643/3/$10.00 © 1996 American Institute of Physics 

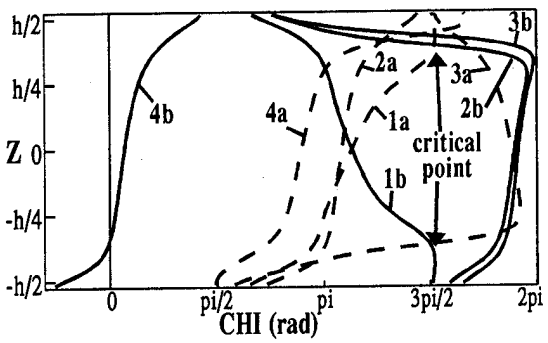



FIG. 2. Wall-magnetization distributions for the RHS and LHS Bloch walls. For all of the curves, $Hx=3$ Oe. $Hy=10$ Oe, curves 1a and 1b: $t=0$ s, at the center of the CC. $Hy=10$ Oe, curves 2a and 2b and curves 3a and 3b: $t=135$ ns, $-1$ $\mu$m and $-2$ $\mu$m from the center of the CC, respectively. $Hy=-50$ Oe, curves 4a and 4b: $t=135$ ns, $-2$ $\mu$m from the center of the CC.

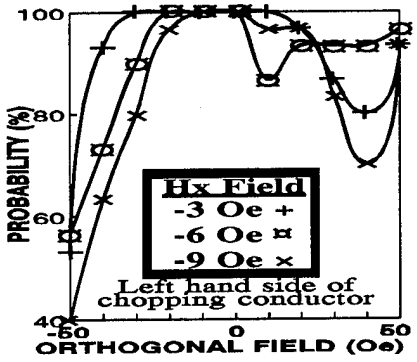



FIG. 4. Bubble $S=0$ probability for $-ve$ $Hx$ field range on the good side.

Bloch wall to Néel type. A $+ve$ $Hy$ field will push the critical point on the bottom surface of the LHS Bloch wall away from the surface, whereas on the upper surface the critical point will be pushed into the top surface. The opposite effect occurs in the RHS Bloch wall, and vice-versa for the negative $(-ve)$ $Hy$ field. It is the movement of the position of the critical point into and away from the surface magnetization that causes the suppression and the acceleration of the HBL generation, respectively. Also, if the $\pm\pi/2$ magnetization around the Bloch loop is parallel to $Hy$, the Bloch loop should effectively sweep its area out faster. Curve 4b shows punch through from the top surface to the bottom surface due to the wall's stored momentum and the critical point's position.

Bearing in mind the above, the simulations show that at the time when the chopping current is at its peak from the start of the simulation (relaxation time of 10 ns+100/0.8 =135 ns),[12] a $-ve$ $Hy$ field causes a complete HBL suppression even on the LHS of the CC. At $Hy=0$ Oe and $Hx=3$ Oe, HBLs are formed only on the LHS of the CC due to the gyrotropic force and the in-plane field components, but as $Hy$ becomes more positive, the HBL nucleation is accelerated and slowly sweeps out from the LHS to the RHS of the CC, though the HBL does not actually punch through. A HBL does not appear on the RHS until $Hy=30$ Oe. As $Hx$ increases, it reduces the effective in-plane field component of the LHS of the CC causing a slight HBL suppression at the lower $Hy$ field values. Therefore, with a HBL being present, it will change the chopping characteristics and the $S$ states of the bubbles. For $-ve$ $Hx$ fields, which would invert the Bloch wall in-plane magnetization due to the $-ve$ VBLs switching their stripe domain head positions, the shape and principal behavior of the wall structure is the same for opposite $Hy$ field values.

Figure 3 shows the simulated threshold values of $Hy$ for the presence/absence of HBLs as a function of distance from the center of the CC for six values of $Hx$, showing all of the physical characteristics of the above explanation. For the $+ve$ $Hx$ field values, below each line, there are no HBLs and vice-versa for the $-ve$ $Hx$ field values. Point symmetry is shown in the figure for $+ve$ and $-ve$ $Hx$.

Referring to Fig. 1, the RHS of the CC, the in-plane wall magnetization and the direction of $Hx$, this is referred to as the "good" side where no errors should occur[1] and the LHS is the "bad" side. The reverse is realized for the $-ve$ $Hx$ field.

Figures 4 and 5 show the percentages of success for the LHS and RHS $S=0$ bubbles after chopping, for the $-ve$ and $+ve$ $Hx$ fields, respectively. The best of the error-free

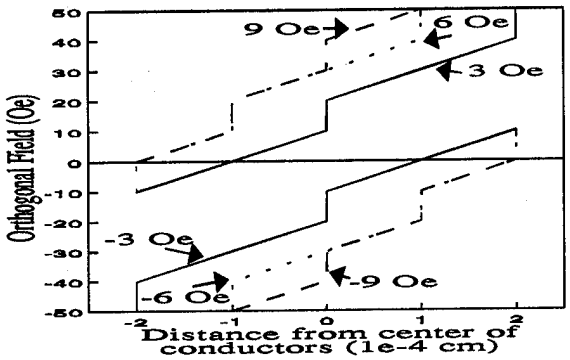



FIG. 3. Simulated threshold values of $Hy$ for the presence/absence of HBLs as a function of distance from the center of the CC for six values of $Hx$.

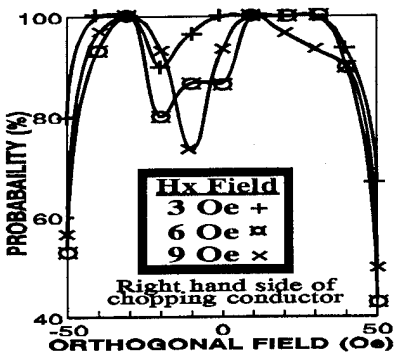



FIG. 5. Bubble $S=0$ probability for $+ve$ $Hx$ field range on the good side.

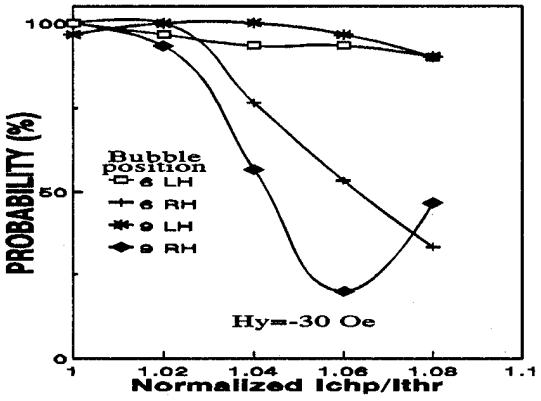



FIG. 6. Effects of larger currents on bubble probability on the LHS and RHS of the CC at $Hy=-30$ Oe for $Hx=6$ Oe and 9 Oe.

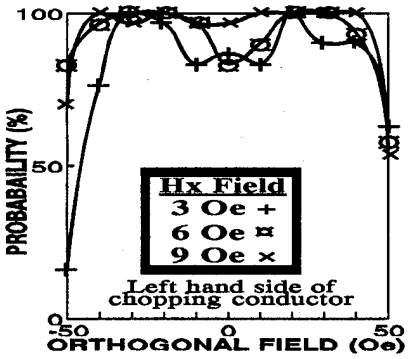



FIG. 7. Bubble $S=0$ probability for $+ve$ $Hx$ field range on the bad side.

chopping is seen in the $Hy$ ranges $-30$ to 10 Oe for $Hx$ equal to $-3$ Oe, and 0 to 30 Oe for $Hx$ equal to $+3$ Oe, due to the suppression of the dynamic HBL formation by the in-plane field components of the CC. Figures 4 and 5 also show a mirror symmetrical effect for the opposite in-plane fields. In Fig. 5, in the $Hy$ range 0 to $-20$ Oe, they form various minimums but, at $-30$ and $-40$ Oe, the bubble percentages are between 90% and 100%, indicating HBL suppression. For the $-ve$ $Hx$ and $-ve$ $Hy$ field values, as $Hx$ increases in magnitude, the $S=0$ bubble percentage starts to decrease. Similarly, Fig. 5 depicts the same effect for the $+ve$ $Hy$ and $+ve$ $Hx$ field values. Iwata *et al.*[9] also found that as $Hx$ is applied, the experimental results gradually deviate from the theory, but we are unable to propose a cause of this. The origin may be due to the cubic anisotropy of the garnet. The large minimums in the figures occur for the current being too large, but these are the threshold values which consistently chop the stripe domain. Figure 6 shows these effects on the $S=0$ bubble percentage at $Hy=-30$ Oe and $Hx=6$ Oe and 9 Oe as a function of current. The minimum threshold currents ($I_{\text{thr}}$) at $Hy=-30$ Oe and 30 Oe, are 100 and 108 mA, respectively. The simulations showed total HBL suppression for the different currents for the RH bubbles (the good side), but experimentally the $S=0$ bubble percentage decreases drastically as the current increases. The experimental and simulation results are comparable at $Hy=30$ Oe for the RH bubbles, since the simulation showed no HBLs on the RHS, and yet the LH $S=0$ bubble percentage is greater than that for all of the RH bubbles. The reason may be that as the chopping current increases, increasing the effective $+ve$ $Hx$ in-plane field at the RHS part of the CC, it induces the same errors that are due to a large $Hx$. Also, a larger chopping current would increase the wall velocity and the gyrotropic force causing the HBLs to generate faster, though the simulations did not show this. The strong effective $Hx$ field and the large $Hy$ field could flip the VBL magnetization, or Bloch point (BP) injection might occur after chopping. An analogy for the BP injection can be made with the experiment of Beaulieu *et al.*[10] on the contracting movement of the domain heads of the chopped parts of the stripe domain to the $Hy$ field. The experiment in Ref. 10 has the in-plane field applied perpendicular to the gradient drive field that is rocking the bubble and induces bubble state conversion via BP injection. The velocities of the stripe domain heads are not known, and therefore a relation with the Bloch line nucleation velocity[11] cannot, at this stage, be made. Figure 7 shows a very good $S=0$ bubble percentage for the supposedly bad side of the CC for increasing $Hx$ and $Hy$ fields, confirming the suppression of the HBLs as shown by the simulations.

Although there remain discrepancies at high values of planar fields, thus requiring further work, the broad results of numerical simulations are borne out by experimental results.

The Japanese government is thanked for the award of a Monbusho scholarship to enable K.F. to further his research studies in Japan.

[1] S. Nakada, M. Kohno, and K. Watanabe, IEEE Trans. Magn. **MAG-24**, 3042 (1988).
[2] A. P. Malozemoff and J. C. Slonczewski, *Magnetic Domain Walls in Bubble Materials*, (Academic, London, 1979), Chap. 8, pp. 196–197.
[3] R. A. Kosiński and J. Engemann, J. Appl. Phys. **55**, 3732 (1984).
[4] Unpublished results.
[5] B. R. Brown, AIP Conf. Proc. **29**, 69 (1975).
[6] E. Fujita, H. Kawahara, S. Sakata, and S. Konishi, IEEE Trans. Magn. **MAG-20**, 1144 (1984).
[7] R. A. Kosiński, J. Heidmann, D. Krumbholz, and J. Engemann, IEEE Trans. Magn. **MAG-20**, 1150 (1984).
[8] R. A. Kosiński and J. Engemann, J. Magn. Magn. Mater. **50**, 229 (1985).
[9] S. Iwata, S. Isomura, S. Shiomi, and S. Uchiyama, IEEE Trans. Magn. **MAG-18**, 1343 (1982).
[10] T. J. Beaulieu, B. R. Brown, B. A. Calhoun, and T. Hsu, AIP Conf. Procs. **34**, 138 (1976).
[11] P. Pougnet, L. Arnaud, M. Poirier, L. Zimmermann, M. H. Vaudaine, and F. Boileau, IEEE Trans. Magn. **27**, 5492 (1991).
[12] The significance of "10 ns+100/0.8=135 ns" is as follows; The "10 ns" is the simulation relaxation time of the stripe domain. The "100/0.8" is to convert the 10% and 90% rise time to a 100% transition time.

# Micromagnetic study on write operation in submicron magnetic random access memory cell

H. Asada, K. Matsuyama, and K. Taniguchi
*Department of Electrical Engineering, Kyushu University 36, Fukuoka 812, Japan*

In a spin-valve random access memory, the binary bit states of the storage cell are determined by the magnetization direction in the free magnetic layer. The write operation of a submicron memory cell element has been studied by a micromagnetic computation based on an energy minimization scheme, which aids in the chip design. The magnetization of the binary bit states in the element was found to take a single domain structure having the opposite direction of the long-axis component. The mean long-axis component of magnetization of each binary state was $\pm 0.97$ without external fields. The selective switching of the bit state in the element was performed by the write currents applied into the two level conductors overlying the element for various conditions. The influence of the write currents to the neighboring element on a two-dimensional memory array with a $1\times1$ $\mu$m pitch was also simulated, in order to confirm the selective switching of the memory element. It was found that the selective write current amplitude decreased with an increasing assist current amplitude and the range was extended by the large difference of the transverse magnetic field between the selected and neighboring element. The effect of the exchange interaction from the pinned magnetic layer on the write operation was also discussed. © *1996 American Institute of Physics.* [S0021-8979(96)16808-X]

## I. INTRODUCTION

Using a giant magnetoresistance material, a nonvolatile random access memory has been proposed.[1,2] In the memory cells proposed by D. D. Tang *et al.*,[2] the binary states of the storage cell are determined by the magnetization direction in the free magnetic layer, which offer a static signal depending upon the magnetoresistive variation caused by the parallel and antiparallel states between both the pinned and the free magnetic layers. The write operation of the bit information is performed by applying the pulse currents into the two-dimensional array of conductors overlying the storage cell. Micromagnetic simulation is useful to investigate the bit states before and after applying the write currents, which aids in the chip design and development of the memory operation. Two-dimensional micromagnetic simulation results of the bit state change performed by the uniform in-plane fields have been reported.[3]

In the present work, the write operation of a submicron memory cell element has been studied by the micromagnetic computation representing a three-dimensional magnetization direction, based on an energy minimization scheme, for various cases. The effect of an uniform in-plane field, which corresponds to the exchange interaction from the pinned magnetic layer, on the write operation has also been studied.

## II. RESULTS AND DISCUSSION

A schematic memory bit cell configuration assumed in the simulation is illustrated in Fig. 1. Since the storage cell was constituted with a noncoupled spin valve film, the magnetization state in the free layer was computed by the micromagnetic simulation representing a three-dimensional magnetization direction. A memory cell element of $0.5\times0.25$ $\mu m^2$ size was discretized into a two-dimensional array ($32\times16\times1$) of a tetragonal grid, assuming that the magnetization distribution was uniform through the thickness of the material due to the negligible film thickness. For calculating the magnetization distribution of each grid, the total magnetic energy, written as the sum of the exchange, anisotropy and demagnetizing energy terms, was minimized by using the conjugate gradient method.[4] The following standard material parameters for permalloy were assumed as the free magnetic layer; saturation induction $4\pi M = 10^4$ G, uniaxial anisotropy $K_u = 10^3$ erg/cm$^3$ ($H_k = 2.5$ Oe), exchange constant $A = 10^{-6}$ erg/cm and film thickness $h = 50$ Å. The selective write operation was performed by applying the pulse currents into the two level conductors overlying the element, which consist of the write and assist conductors located along the short- and long-axis direction of the element, respectively. The magnetization direction in the free magnetic layer is determined by the direction of the longitudinal component of the magnetic field generated by the write current, $I_w$. The write conductor width and thickness were 0.7 and 0.3 $\mu$m, respectively, and the assist conductor width and thickness were 0.5 and 0.3 $\mu$m, respectively. The spacer thickness between the free magnetic layer surface and the conductors were 0.1 $\mu$m for the first layer and 0.5 $\mu$m for the second layer. The switching of the bit state is performed by the magnetization rotating towards the opposite state by the longitudinal magnetic field from the write current, $I_w$, with the assistance of the transverse magnetic field from the assist current, $I_a$.

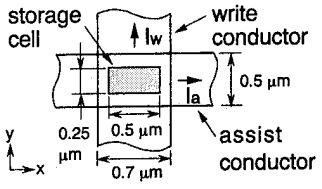



FIG. 1. Schematic memory cell element.

 0021-8979/96/79(8)/6646/3/$10.00 © 1996 American Institute of Physics

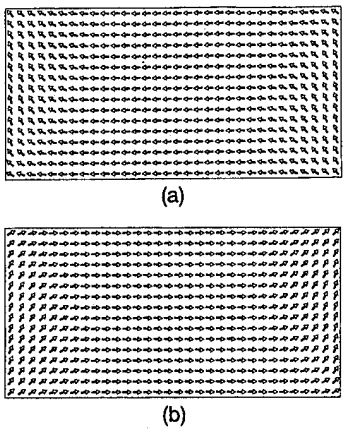



FIG. 2. Magnetization states in the free magnetic layer of each binary state after applying the (a) positive and (b) negative write currents.

Figure 2 shows the simulation results of the magnetization direction in the element without external magnetic fields after applying (a) positive and (b) negative currents into the write conductor. The arrows indicate the magnetization direction on each calculation grid. The easy axis direction of anisotropy was along the long-axis direction of the element. As shown in the figures, though the magnetization around the long-axis edges inclines due to the demagnetizing field, the long-axis component of each magnetization for (a) and (b) are opposite to each other. Both magnetization states take the single domain structure, which is suitable for the binary bit states of the storage cell. The relative amount of the exchange energy compared to that of the magnetostatic energy becomes dominant in the fine pattern with the thin film thickness. The mean long-axis component of each binary state, which contributes to the magnetoresistive variation, is $\pm 0.97$.

For estimating the amplitudes of the write currents, the bit state switching from the magnetization direction as shown in Fig. 2(a) to that in Fig. 2(b) by the uniform transverse and longitudinal fields were computed. Figure 3 shows the threshold amplitude of the longitudinal field, $H_l$, with various transverse fields, $H_t$. The $H_l$ value, needed to switch the bit state, decreases with increasing $H_t$, which enables the selective switching. However, the gradient of the threshold

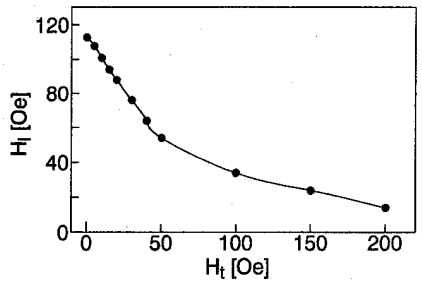



FIG. 3. Threshold amplitude of the longitudinal magnetic field, $H_l$, for the state switching as a function of the transverse field, $H_t$.

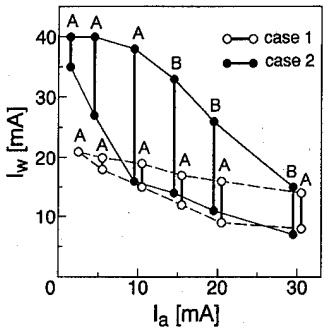



FIG. 4. Dependence of the write current range, $I_w$, of the selective switching upon the assist current, $I_a$, for both the case 1 (first layer, write conductor; second layer, assist conductor) and case 2 (first layer, assist conductor; second layer, write conductor).

curve, $H_l/H_t$, decreases with increasing $H_t$. The gradients are 1.2 at $H_t=30$ Oe and 0.2 at $H_t=100$ Oe.

The selective write operation was studied by calculating the bit state switching under the application of the write currents. We also simulated the influence of the write currents to a neighboring element on a two-dimensional memory array with $1\times1$ $\mu$m pitch, which achieves a density of $10^8$ bit/cm$^2$, in order to confirm the selective switching of the memory element. The dependence of the selective write current range, $I_w$, upon the assist current, $I_a$, is shown in Fig. 4. Open circles connected with the line indicate the selective switching range when the write and assist currents were applied into the first and second conductor layers (case 1), respectively. In this case, the averaged longitudinal magnetic fields due to $I_w$ over the different memory elements are 5.2 Oe/mA in the selected element and 0.55 Oe/mA in the neighboring element aligned in the long-axis direction. The averaged transverse magnetic fields due to $I_a$ are 2.9 Oe/mA in the selected element and 0.94 Oe/mA in the neighboring element aligned in the short-axis direction. Closed circles also indicate the selective switching range when the write and assist currents were applied into the second and first conductors (case 2). The marks A and B in the figure indicate the error modes of the upper threshold for the selective switching, which were limited by the occurrence of the switching in the neighboring element aligned in the short-axis (mark A) and long-axis (mark B) directions, respectively. For case 1, the lower threshold of $I_w$ decreases and the current range increases with increasing $I_a$. Below $I_a=20$ mA, though the lower threshold of $I_w$ for case 2 is higher than that for case 1, the current range for case 2 is fairly larger due to the improvement of the upper threshold. These results show that the selective switching current range is extended by the large difference of the transverse component of the magnetic field between the selected and neighboring elements. For case 2, however, the abrupt degradation of the upper threshold was observed for $I_a$ greater than 15 mA caused by the occurrence of error B, where the large amplitude of the transverse magnetic field was generated. The obtained current ranges are $I_w=15-19$ mA at $I_a=10$ mA and $I_w=9-16$ mA at $I_a=20$ mA for case 1, and $I_w=16-38$ mA at $I_a=10$ mA and $I_w=11-26$ mA at $I_a=20$ mA for case 2.

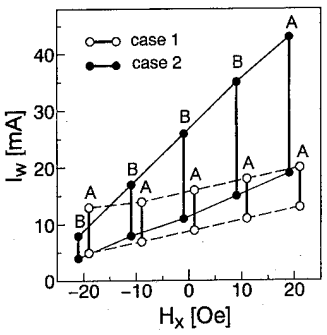



FIG. 5. Dependence of the write current range, $I_w$, of the selective switching upon the uniform longitudinal magnetic field, $H_x$, for both the case 1 (first layer, write conductor; second layer, assist conductor) and case 2 (first layer, assist conductor; second layer, write conductor).

We also investigated the influence of the direction and amplitude of the anisotropy to the selective switching. It was found that the $I_w$ amplitude can decrease without any degradation of the range for each $I_a$, when the easy axis direction of the anisotropy was assumed along the short-axis direction of the element. Furthermore the amplitude of anisotropy increased.

In order to study the effect of the exchange interaction from the pinned magnetic layer on the write operation, we simulated the bit state switching by the write currents under the conditions of an uniform in-plane field, $H_x$, along the long-axis direction for simplification of the exchange interaction. Simulation results are as shown in Fig. 5. The open and closed circles connected with the line indicate the selective switching range of $I_w$ for case 1 and case 2, respectively, which are the same as in Fig. 4. The assist current, $I_a$, was 20 mA. When the magnetization directions of the free and pinned layers are parallel to each other, this defines the positive $H_x$ field direction, which suppresses the bit state switching. And for the negative $H_x$ field direction, the magnetization directions are antiparallel to each other, which supports the switching. For case 1, the $I_w$ amplitude varied as 2 mA per 10 Oe, and the current ranges for each $H_x$ are the same. The influence of $H_x$ to the bit state switching in the neighboring element aligned in the long-axis direction is significantly larger than that in the neighboring element aligned in the short-axis direction. Therefore, for case 2, the effect of $H_x$ on the upper threshold of $I_w$, which is limited by the occurrence of error B, is much stronger, as clearly seen in the figure. The most serious case for the selective switching is the parallel state in the selected element and the antiparallel state in the neighboring element. The selective current ranges decrease to $I_w = 11-14$ mA for case 1 and $I_w = 15-17$ mA for case 2 with the exchange interaction field of 10 Oe, which corresponds to the common $I_w$ ranges at $H_x = \pm 10$ Oe as in the figure.

## III. CONCLUSIONS

The write operation in a submicron memory cell has been investigated by the micromagnetic computation. The magnetization of the binary bit states in the free magnetic layer was found to take a single domain structure having the opposite long-axis component. The selective switching was performed by write currents applied into the two level conductors overlying the element. It was found that the selective write current amplitude decreased with increasing assist current amplitude and the range was extended by the large difference of the transverse field amplitude between the selected and neighboring elements. However, the large amplitude of the transverse magnetic field from the assist current caused the abrupt degradation of the upper threshold for the selective switching. The effect of the exchange interaction from the pinned magnetic layer on the write operation was studied and clarified.

[1] K. T. M. Ranmuthu, A. V. Pohm, J. M. Daughton, and C. S. Comstock, IEEE Trans. Magn. **29**, 2593 (1993).
[2] D. D. Tang, P. K. Wang, V. S. Speriosu, and S. Le, Digests of INTERMAG'95 Conference, AP-03 (1995).
[3] R. S. Beech, A. V. Pohm, and J. M. Daughton, Digests of INTERMAG'95 Conference, AP-02 (1995).
[4] B. B. Pant, and K. Matsuyama, Jpn. J. Appl. Phys. **32**, 3817 (1993).

# Analytical model in a weakly coupled sandwich for memory purposes

Zhigang Wang[a] and Yoshihisa Nakamura
*Research Institute of Electrical Communication, Tohoku University, Sendai 980, Japan*

A simple analytical model explains giant magnetoresistive properties in a weakly coupled sandwich with two magnetic components. The model describes in detail a new storage mechanism in which the minor loop's slope depends on its past magnetic histories. A new type of solid-state giant magnetoresistance memory based upon this mechanism has been realized by experiments. Furthermore, some important factors included in nondestructive readout capability are also analyzed by this model. © *1996 American Institute of Physics.* [S0021-8979(96)13808-4]

## I. INTRODUCTION

Results obtained on giant magnetoresistance (GMR) materials show increases in magnetoresisce of a factor of 10 over conventional anisotropic magnetoresistance materials. Many devices based on giant magnetoresistance are under consideration and development for reproductive heads for use in magnetic tape and disk devices. In addition, a storage mechanism in GMR materials itself has been found recently and the feasibility of a new type of solid-state memory using weakly coupled GMR effect has been examined by experiments.[1]

The present study presents a simple analytical model for the field dependence of the GMR effect in both full-field and small-field cases. The model permits a determination of the ferromagnetic coupling energy through conducting spacers. The model is essentially an extension of Stoner–Wohlfarth theory with an included small-field hysteresis property for the hard magnetic component in the form articulated by Rayleigh. The model also simply presents a description of the above-mentioned new storage mechanism. The so-called "distortion" phenomenon, which can be observed in the experimental transfer curves, can be explained confidently with the present model.

## II. MODEL DESCRIPTION

We established an engineering model to demonstrate the giant magnetoresistive properties in a weakly coupled sandwich. The model is based on the coherent rotation and uniaxial anisotropy assumptions. Because of the flux closure configuration of the sandwich, the demagnetizing field perpendicular to the length is strongly reduced compared to those obtained from a single layer structure. As a result, multiple magnetic domain formation could be reduced and the sandwich structure will behave more in the manner of a single domain ferromagnetic layer. Hence the consideration that the switching characteristics of the films behave like a single domain is reasonable. We consider two ferromagnetic components of identical thickness having the uniaxial anisotropy ($Ku_1$ and $Ku_2$) with easy axes parallel to each other, as shown in Fig. 1. The angles of the magnetizations with respect to the easy axis are $\theta_1$ and $\theta_2$, and the angle of applied field is $\phi$. In this calculation the applied field was held constant at an angle of 45° for the consideration of 2D memory cell selection application.[1,2] The parameters are taken as experimentally measured:[3] the anisotropic fields of the soft and the hard magnetic component are assumed as 8 and 28 Oe, respectively; the exchange coupling between the two components is assumed as ferromagnetic (parallel) coupling and its value is 2 Oe (in fact the exchange field is a function of spacer thickness and the exchange field of 2 Oe corresponds to the spacer thickness=4 nm according to the experiments). Please note that the coupling's value is so weak that it is even less than the soft component's coercivity (theoretical value is 4 Oe). For this reason this type of GMR is named as a weakly coupled one. The angles of the magnetizations in two layers are chosen such that they minimize the energy function[4] which covers the anisotropy and external field terms in the two components, respectively, and the ferromagnetic exchange term between the two components. The total energy per unit volume may then be expressed as

$$E=(\tfrac{1}{2})(E_1+E_2)+A_{12}\cos(\theta_1-\theta_2), \tag{1}$$

where $E_i=Ku_i\sin^2\theta_i-M_iH\cos(\phi-\theta_i)$, $i=1$ for the soft component and $i=2$ for the hard. $A_{12}$ is the exchange constant and $Mi$ is the saturation magnetization ($M_1=1000$ emu/cm$^3$ and $M_2=500$ emu/cm$^3$).

The resistance is calculated by

$$GMR(H)=G^*\sin^2\frac{\theta_1(H)-\theta_2(H)}{2}, \tag{2}$$

where $G$ is the coefficient of the GMR effect.

We calculated the resistance versus applied field $R(H)$ transfer curves under excitating field with various strength. The switching of the double ferromagnetic layers with different coercivities gives rise to the "double-hump" shaped

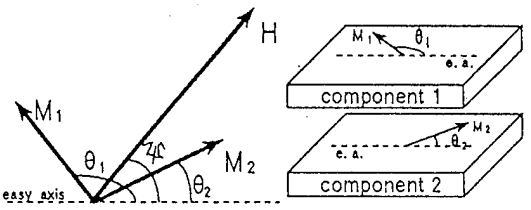
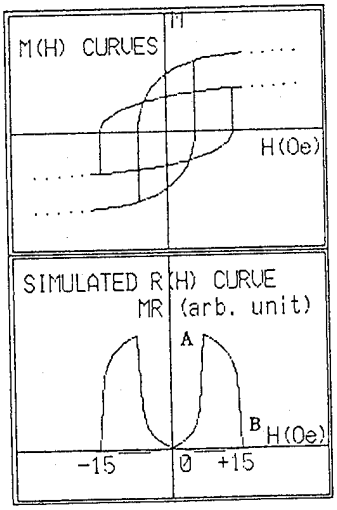


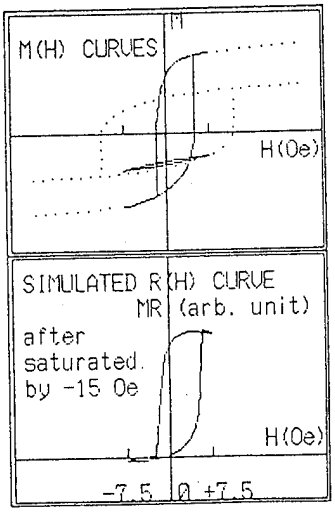

FIG. 1. The analytical model is based on the coherent rotation and uniaxial anisotropy assumptions. The angles of the magnetizations with respect to the easy axis are $\theta_1$ and $\theta_2$, and the angle of applied field is $\phi$.

[a]Address communications to Dr. Z. Wang, Nakamura Laboratory, Research Institute of Electrical Communication, Tohuko University, Katahira 2-1-1, Sendai 980, Japan.

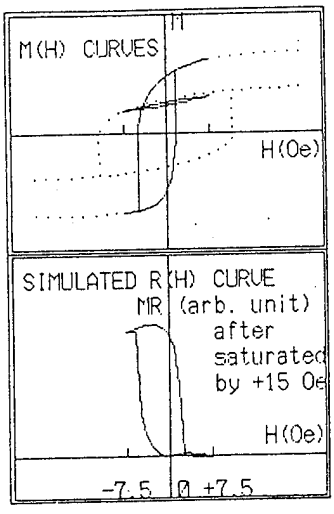
 0021-8979/96/79(8)/6649/3/$10.00 © 1996 American Institute of Physics 




(a) main loop

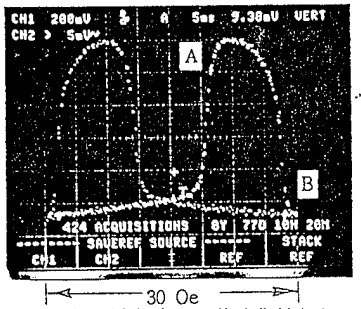



(b) minor loop

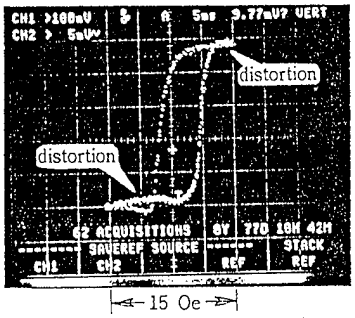



(c) minor loop

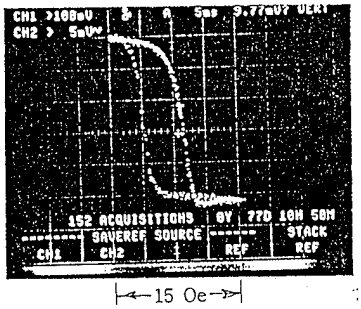
FIG. 2. The calculated resistance vs applied field $R(H)$ transfer curves under excitating field with various strength. In main loop of (a), the applied field was varied between ±15 Oe. In minor loops of (b) and (c), only the soft component is switched by applying a field between ±7.5 Oe. The initial saturated states in (b) and (c) are different as indicated in the figure.




(a)Main loop in which the applied field is between ±15 Oe.




(b)Minor loop in which the applied field is between ±7.5 Oe but the sample is initially saturated by the field of −15 Oe.

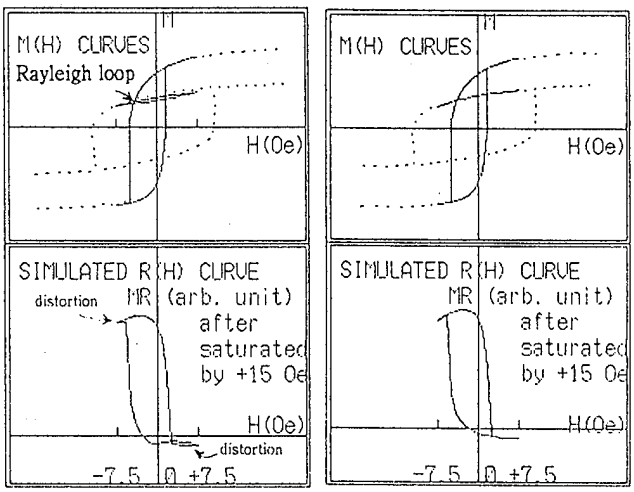



(c)Minor loop in which the applied field is between ±7.5 Oe but the sample is initially saturated by the field of +15 Oe.

FIG. 3. Experimental results of Co (5 nm)/NiFe (0.5 nm)/Cu (4 nm)/Co (0.5 nm)/NiFe (5 nm). The measurement conditions are indicated in the figure.

main loop depicted in Fig. 2(a), where the applied field was varied between ±15 Oe. The two switching thresholds at point A and point B correspond to the magnetization reversals of the soft and the hard component, respectively. The magnetization in the soft component rotates in weak field below point A while that of the hard is not saturated up to point B. The sharp increase of resistance starts when the magnetization of the soft component begins to rotate (below A). The maximum of resistance is observed at the A where the direction of the soft component's magnetization has just reversed. With further increasing of the field (exceeding A), the direction of the hard component's magnetization also turns to the field direction and subsequently the resistance gradually decreases.

Figures 2(b) and 2(c) illustrate the $R(H)$ response's minor loops operating in the mode in which only the soft component is switched by applying a field between ±7.5 Oe. In




(a) with Rayleigh loop. (b) without Rayleigh loop.

FIG. 4. Comparison of $R(H)$ curves with and without Rayleigh loop. The calculation conditions are indicated in the figure.

Fig. 2(b) the element is initially saturated to the "negative" direction by a field of $-15$ Oe while in Fig. 2(c) it is initially saturated to the "plus" direction by $+15$ Oe. In these minor loops of small-field GMR response one can expect a shift since the initially saturated hard component blocks the spins of the soft component through the ferromagnetic exchange interaction. Figures 2(b) and 2(c) also illustrate a possible storage mechanism. The slope of the small-field response $R(H)$ (minor loop) depends on its past magnetization history. After being magnetically saturated to the negative direction the response's slope will be positive, whereas after being saturated to the plus direction the slope will be negative. Based on this property, data readout will be performed by monitoring the polarity of the voltage signal against the unipolar excitation field.

## III. DISCUSSIONS

The above calculated $R(H)$ curves gives a good agreement with the experimental results shown in Fig. 3. The sample is Co (5 nm)/NiFe (0.5 nm)/Cu (4 nm)/Co (0.5 nm)/NiFe (5 nm), in which the thinner NiFe and Co layers were formed to enhance interfacial scattering.

The measured $R(H)$ curves shown in Fig. 3 illustrate the phenomenan known as distortion. It can be explained confidently with the present model. Under small-field excitation, the soft component is switched but the magnetization in the hard component should rotate along a loop in the following form articulated by Rayleigh:[5]

$$M_1 = a_1 H^2 + b_1 H + c_1, \tag{3}$$

$$M_2 = a_2 H^2 + b_2 H + c_2, \tag{4}$$

where $a_i$, $b_i$, and $c_i$ are Rayleigh constants. As shown in Fig. 4(a), the distortion happens to the simulated $R(H)$ as expected. On the other hand, if neglecting the hysteresis,

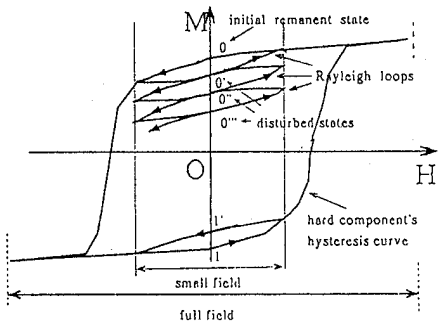



FIG. 5. The hard component's hysteresis curve with small-field Rayleigh loops. The remanent state will be degrading gradually along a series of half Rayleigh loops, whereas the rehabilitation function will be achieved along the whole Rayleigh loop.

simulations without the Rayleigh loop could not give rise to the distortion phenomenon, as shown in Fig. 4(b). In conclusion, the hard component's small-field response should be characterized by Rayleigh law.

The existence of Rayleigh loop in the hard component will be harmful to our memory design. This memory operates on the general principle of storing a binary digit in the hard component and sensing its remanent state by switching the soft component in such a way that the magnetic state of the hard component is unaltered. Initially, it was believed that this design should have a nondestructive readout (NDRO) characteristic. However, experiments indicated that NDRO was not always achieved; i.e., NDRO was dependent on the polarity of the excitation field. Consider the mode of "0" (corresponding to the + remanent state). Experimental tests involving $3\times10^8$ plus excitation pulses indicated that the readout wave form was still stable. However, stability against minus disturb pulses could not be achieved. We can use our model to explain the reason. Because irreversible magnetization processes (Rayleigh loop) exist, a disturbed states ($0'$ or $1'$) will possibly be caused, as shown in Fig. 5. For the mode of "0," the worst case is being excited by continuous minus pulses, whereas for "1" the worst case is being excited by continuous plus pulses. The remanent state will be degrading gradually along a series of half Rayleigh loops and finally destroyed after enormous numbers of readout switching. We think that two methods will be effective to eliminate the unstability. One is to select the hard materials with rectangular hysteresis loop. The other is to regrade the excitation method, for example, to employ bipolar exciting pulses with rehabilitation function. As shown in Fig. 5, stability against bipolar disturb pulses could be achieved because the hard component should rotate along the whole Rayleigh loop.

[1] Z. Wang and Y. Nakamura, IEICE General Conference Proceedings C-502, Fukuoka, Japan, 1995 (unpublished).
[2] J. M. Daughton, Thin Solid Films **216**, 162 (1992).
[3] Z. Wang and Y. Nakamura, *2nd MML Abstract Book* (Cambridge University Press, England, 1995), p. 242.
[4] H. Fujiwara and M. Parker, J. Magn. Magn. Mater. **L23**, 135 (1994).
[5] L. Neel, Cah. Phys. **12**, 1 (1942).

# AUTHOR INDEX


Abadía, C.–(8) 6330
Abarra, E. N.–(8) 5919
Abe, M.–(8) 4561
Abe, S.–(8) 4611
Abele, M. G.–(8) 5199
Achutharaman, V. S.–(8) 4553
Adachi, K.–(8) 4905
Adamashvili, G. T.–(8) 5727
Adenwalla, S.–(8) 4524
Adeyeye, A. O.–(8) 6120
Adly, A. A.–(8) 4675
Aeppli, G.–(8) 5023, 5391
Afonso, S.–(8) 6580, 6593
Aguiló, M.–(8) 5439
Ahern, Brian–(8) 4759
Ahmed, H.–(8) 6120
Ahn, Jong-Guk–(8) 5961
Ahn, Y. M.–(8) 5696
Akagi, K.–(8) 4905
Akeura, K.–(8) 4957
Akhsakhalyan, A. D.–(8) 4625
Akhutkina, A. I.–(8) 6132
Akiba, Etsuo–(8) 5126
Akiyama, J.–(8) 5655
Alba, M.–(8) 6158
Alberts, H. L.–(8) 6519, 6526
Albuquerque, E. L.–(8) 5736
Albuquerque, M. R. M. L.–(8) 5736
Alexandrakis, G. C.–(8) 6586
Algarabel, P.–(8) 5175
Algarabel, P. A.–(8) 4656, 4659, 5178, 6330
Ali, N.–(8) 6007
Ali, Naushad–(8) 5233, 5398, 6154
Allen, W.–(8) 5593
Allenspach, P.–(8) 5869, 5869
Almeida, B. G.–(8) 6246
Al-Omari, I. A.–(8) 4590
Alonso, J.–(8) 5182
Altoé, M. V. P.–(8) 4846, 6555
Altounian, Z.–(8) 4605, 4619, 4769, 4833, 5519, 5536
Amado, M. M.–(8) 6355
Amaral, V. S.–(8) 6246
Ambert, G.–(8) 5384
Ambrose, T.–(8) 5920
Anane, A.–(8) 4554
Anderson, G. W.–(8) 4954, 5641
Andou, T.–(8) 4884
Ang, S.–(8) 6593
Ankner, J. F.–(8) 4762, 4775, 4782
Ansermet, J.-Ph.–(8) 6010, 6090
Anthony, T. C.–(8) 4491, 5277
Anthony, Thomas C.–(8) 6389
Antonov, A. S.–(8) 6532
Antropov, V. P.–(8) 4799, 5409
Appino, C.–(8) 4575
Arabski, J.–(8) 5068
Aragoneses, P.–(8) 6539
Arai, K. I.–(8) 4574
Ardisson, J. D.–(8) 5973
Arnold, Z.–(8) 4656, 5178
Aronson, M. C.–(8) 6432
Arrott, A. S.–(8) 4570, 4635, 4973, 5752, 6051, 6529
Artinian, M.–(8) 5932
Artman, J. O.–(8) 4787
Arvanitis, D.–(8) 4983
Asada, H.–(8) 5318, 6643, 6646
Asamitsu, A.–(8) 5288
Asano, H.–(8) 5507
Asano, S.–(8) 5952
Atherton, D. L.–(8) 6042
Atlan, D.–(8) 4518
Atzmony, U.–(8) 5456
Augustyniak, B.–(8) 6525
Awschalom, D. D.–(8) 5296, 5324, 6095
Axtell, S. C.–(8) 5263
Ayres, A. M.–(8) 5680
Azizi, A.–(8) 6247

Babbar, V. K.–(8) 6515
Babcock, K.–(8) 5296, 5851, 6440
Baberschke, K.–(8) 4983
Back, Young R.–(8) 5788
Bader, S. D.–(8) 4524, 5838
Badia, F.–(8) 5605
Baggio-Saitovitch, E.–(8) 5256
Bahadur, D.–(8) 5995
Bailey, William E.–(8) 6393
Baker, I.–(8) 6028
Bakonyi, Imre–(8) 4811
Baldomir, D.–(8) 4674
Ball, A. R.–(8) 5103
Ballentine, C. A.–(8) 5845
Ban, S.–(8) 5452
Banerjee, R.–(8) 6536
Bao, W.–(8) 4558, 5023
Bao, Xiaohua–(8) 4866, 4869
Barandiarán, J. M.–(8) 5146
Bardou, N.–(8) 5068, 5848
Barmak, K.–(8) 5330
Barnard, J. A.–(8) 5005, 5606, 5904
Barnard, John A.–(8) 5779
Barquín, L. Fernández–(8) 5146
Barry, Walter–(8) 5733
Bartenlian, B.–(8) 5068, 5270, 5848
Basak, A.–(8) 4753
Bass, J.–(8) 5811, 6129, 6151
Basso, V.–(8) 5764
Batlle, X.–(8) 5605
Batlogg, B.–(8) 4541
Bauer, E.–(8) 6423
Bayreuther, G.–(8) 4509
Beauvillain, P.–(8) 5270
Becerra, C. C.–(8) 5236
Beech, R. S.–(8) 5889
Beers, K. L.–(8) 4644
Beitz, James V.–(8) 6512
Bellesis, G. H.–(8) 4496, 5011
Belorisky, E.–(8) 4698
Ben-Dor, L.–(8) 6564
Bennemann, K. H.–(8) 6177
Bennett, B. R.–(8) 5125
Bennett, L. H.–(8) 4712, 5315, 5456, 6073
Bensch, F.–(8) 4509
Berg, H. v.d.–(8) 6181
Berger, A.–(8) 4524, 5619
Bergqvist, A.–(8) 4689, 6476
Berkowitz, A. E.–(8) 5071, 5072, 5277, 5504, 5919
Berkowitz, Ami E.–(8) 4932
Berman, L. E.–(8) 6509
Berry, S. D.–(8) 5102
Bertero, G.–(8) 5342
Bertotti, G.–(8) 4575, 5142, 5764
Bertram, H. N.–(8) 5658
Bertram, H. Neal–(8) 4916, 5661, 5883
Bessho, K.–(8) 5057
Bhagat, S. M.–(8) 5165, 5166, 5292, 5991
Bhatia, C. S.–(8) 5327
Bhatt, R. N.–(8) 5096, 5196
Bhattacharyya, M.–(8) 4491
Bhushan, Bharat–(8) 5791, 5794, 5798, 5799, 5802, 5916
Biagini, Cristiano–(8) 4638
Bian, X.–(8) 4769, 4980
Biner, S. B.–(8) 5453
Binesti, D.–(8) 4575
Binninger, U.–(8) 5530
Biringer, P. P.–(8) 4671
Birsan, M.–(8) 5202, 6042
Bishop, D. J.–(8) 6592
Bissell, P. R.–(8) 4746, 6467
Bitoh, T.–(8) 5472
Blanco, J. A.–(8) 6352
Blanco, J. M.–(8) 5465, 6539
Bland, J. A. C.–(8) 4987, 6120, 6295
Blasco, J.–(8) 5175, 5178
Blondel, A.–(8) 6090
Blundell, S. J.–(8) 6295
Blyakhman, Yuri–(8) 4625
Boardman, A. D.–(8) 5365
Bochi, Gabriel–(8) 5609, 5845
Bohórquez, A.–(8) 6155
Borchers, J. A.–(8) 4762, 5102
Bornfreund, R. E.–(8) 5191
Borsa, F.–(8) 5084
Bottauscio, O.–(8) 4575
Bottoni, G.–(8) 4872, 5469
Bouarab, S.–(8) 5834
Boucher, J. P.–(8) 5384, 5395
Boumaiz, E.–(8) 5381
Bounds, C. O.–(8) 4830, 5501, 6335
Bourez, A.–(8) 5336
Brabers, V. A. M.–(8) 5936
Braga, M. E.–(8) 6246, 6355
Bramwell, S. T.–(8) 4976, 6150
Branagan, D. J.–(8) 4847, 5510
Brand, R. A.–(8) 5582
Brandon, E. J.–(8) 6147
Braun, Hans-Benjamin–(8) 6107
Bresowar, J.–(8) 4766
Brewer, M. A.–(8) 5321
Brinckerhoff, W. B.–(8) 6147
Britel, M.–(8) 5136
Broholm, C.–(8) 5023, 5391
Brown, W. D.–(8) 6593
Brubaker, W. W.–(8) 4644
Brück, E.–(8) 5221, 6321, 6358, 6396
Brucker, C. F.–(8) 5704
Brug, J. A.–(8) 4491, 5277
Brulet, A.–(8) 6158
Bruno, P.–(8) 5270
Brunsman, E. M.–(8) 5293
Brusca, T. E.–(8) 5185
Bucher, J. P.–(8) 5068
Bud'ko, S. L.–(8) 5256
Budnick, J. I.–(8) 4596, 5530
Buehler, C. J.–(8) 5746
Burke, E. R.–(8) 6063
Burke, Edward R.–(8) 6441
Burlet, P.–(8) 6396
Buschow, K. H. J.–(8) 4593, 4599, 4626, 5221, 5945, 6318, 6321
Bush, Gary G.–(8) 6389
Butera, A.–(8) 5269, 6577
Butler, W. H.–(8) 5282
Byers, Jeff M.–(8) 4553

Cabral, F. A. O.–(8) 5973
Cadieu, F. J.–(8) 4614, 5425, 5961
Cadogan, J. M.–(8) 4622, 5149, 5713, 6004, 6161
Cagan, V.–(8) 5472
Cai, Bingchu–(8) 4998, 6048
Cai, M.–(8) 6289
Cain, G.–(8) 5324
Cain, Jason L.–(8) 4860
Caliebe, W. A.–(8) 6509
Calleja, J. F.–(8) 5472, 6545
Camblong, Horacio E.–(8) 6261, 6383
Cambril, E.–(8) 5068
Camp, F. E.–(8) 4840, 5035
Campos, C.–(8) 5973
Candolfo, D.–(8) 4872, 5469
Canedy, C. L.–(8) 4538, 4546, 6126
Canova, A.–(8) 5554
Cao, G.–(8) 4567, 4821, 5876, 6001
Cao, Lei–(8) 5045
Cao, Q. Q.–(8) 6261
Cao, Ruoxin–(8) 6512
Cao, Wei–(8) 4932
Capsoni, D.–(8) 6621
Carbucicchio, Massimo–(8) 4869
Carcenac, F.–(8) 5068
Carl, A.–(8) 4990
Carley, L. R.–(8) 4485
Carling, S. A.–(8) 4644
Carling, S. G.–(8) 6150
Carrera, M.–(8) 6596
Carroll, T. L.–(8) 5377
Castro, S.–(8) 5955
Cava, R. J.–(8) 5856, 5923
Cavalleri, A.–(8) 5406
Cebollada, A.–(8) 5967
Cecchetti, A.–(8) 4872, 5469
Celinski, Z.–(8) 6200
Celotta, R. J.–(8) 6079
Cervantes-Lee, F.–(8) 4715
Chacko, Antony P.–(8) 4863
Chaiken, A.–(8) 4772, 4775
Chakarian, V.–(8) 4558, 5345, 6492, 6493
Chakoumakos, B. C.–(8) 5398
Chakraborty, A.–(8) 5011
Challener, W.–(8) 6440
Challener, W. A.–(8) 5693
Chan, F. T.–(8) 6580, 6593
Chan, K.–(8) 4715
Chandarlapaty, S.–(8) 4644
Chandramouli, M.–(8) 4846
Chang, C. P.–(8) 4790, 6282, 6533
Chang, C. R.–(8) 4919
Chang, Ching-Ray–(8) 4960
Chang, H. S.–(8) 5357
Chang, S. P.–(8) 5699
Chang, T. C.–(8) 6276
Chang, W. C.–(8) 4843, 5159, 5533

Chantrell, R. W.–(8) 4915, 5703, 5767, 6034, 6467
Chao, Y. D.–(8) 6552
Chapman, J. N.–(8) 6452
Chappert, C.–(8) 5068, 5270, 5848
Charap, S.–(8) 5671
Châtel, P. F. de–(8) 4626
Chaussy, J.–(8) 5823, 6370
Chavan, S. A.–(8) 5260
Cheeks, T. L.–(8) 5072
Chen, C. H.–(8) 5923
Chen, C. J.–(8) 5159, 5432
Chen, C. M.–(8) 5557
Chen, C. T.–(8) 4558, 6492, 6493
Chen, E. Y.–(8) 5889
Chen, Ga-Lane–(8) 5782
Chen, K. Y.–(8) 6593
Chen, L. H.–(8) 5599
Chen, L. Y.–(8) 4949
Chen, Liang-Yao–(8) 5193
Chen, Lujun–(8) 4783
Chen, P. J.–(8) 5277
Chen, S. K.–(8) 5533, 5964
Chen, T.–(8) 5342
Chen, T. C.–(8) 6341
Chen, Y. H.–(8) 6512
Chen, Y. J.–(8) 4878
Chen, Yinchao–(8) 5733
Chen, Z. W.–(8) 4812, 6405
Cheng, S. F.–(8) 6084, 6234
Cheng, Y.–(8) 6447
Cheng, Zhao-Hua–(8) 5528, 5709
Cheong, S.-W.–(8) 4558
Cheong, S-W.–(8) 4541
Cherry, H. B.–(8) 5169
Chetkin, M. V.–(8) 6132
Chevalier, B.–(8) 6355
Cheyne, Douglas–(8) 4711
Chiampi, M.–(8) 4575
Chiang, Donyau–(8) 5560
Chiang, W.-C.–(8) 5811, 6129
Chien, C. L.–(8) 5139, 5306, 5309, 5615, 5920, 6117
Chilamakuri, Sameera–(8) 5794
Chin, A.–(8) 6007
Chin, T. S.–(8) 5964
Ching, W. Y.–(8) 4602, 5545
Chmielewski, M.–(8) 6525
Cho, B. I.–(8) 5482, 5696
Cho, C. Peter–(8) 5548
Choe, G.–(8) 4923, 6306, 6536
Choi, G.–(8) 5873
Choi, S. J.–(8) 6299
Chou, C. H.–(8) 5866
Chou, Stephen Y.–(8) 5066, 5066, 5067, 5855, 6101
Chow, Jeff Y.–(8) 6022
Chow, K. H.–(8) 6636
Chowdhury, Ataur R.–(8) 6303
Chrisey, D. B.–(8) 6338
Christianson, A. D.–(8) 6164
Christodoulides, J. A.–(8) 5152, 5302
Chu, C. W.–(8) 6580
Chu, F.–(8) 6405
Chuang, Y. C.–(8) 6324
Chui, S. T.–(8) 4951
Cintolesi, F.–(8) 6624
Ciureanu, P.–(8) 5136
Clark, A. E.–(8) 6213, 6216
Clausen, K. N.–(8) 5078
Clavel, M.–(8) 4571
Clegg, W. W.–(8) 6643
Clemens, B. M.–(8) 6189
Cline, J. P.–(8) 6028
Cochran, J. F.–(8) 4518
Cochrane, R. W.–(8) 6289
Coffey, G. A.–(8) 4644
Coffey, K. R.–(8) 4762, 5330
Cohenca, C. H.–(8) 6564
Coker, G. S.–(8) 4644
Collier, B. F.–(8) 6614
Collins, M. F.–(8) 6614
Colucci, C. C.–(8) 5973
Continentino, Mucio A.–(8) 6345
Continenza, A.–(8) 6423
Conto, C. R.–(8) 4756
Contreras, M. C.–(8) 4936, 5217, 5472, 6545
Cooper, Bernard R.–(8) 6420
Corlett, John–(8) 5733
Cornejo, D. R.–(8) 6312
Corrales, J. A.–(8) 5217
Corti, M.–(8) 5084, 6621, 6624
Cottam, M. G.–(8) 5371, 5724
Courtois, D.–(8) 4622
Coverdale, G. N.–(8) 6034
Cowache, C.–(8) 6370
Cowen, J. A.–(8) 6151
Crooker, B. C.–(8) 5401, 6164, 6436
Cross, R. W.–(8) 5820, 6240, 6386
Crow, J. E.–(8) 4567, 4821, 5876
Cuccoli, Alessandro–(8) 4638
Cullen, J. R.–(8) 6216
Currie, J. F.–(8) 5136

Dabkowska, H.–(8) 5081
Daboo, C.–(8) 4987, 6120
da Cunha, S. F.–(8) 5220
Dahlberg, E. D.–(8) 6447
Dahlberg, E. Dan–(8) 5758
Dail, R.–(8) 5826
Dalton, J. J.–(8) 4753
Das, B. N.–(8) 4890
d'Assunção, A. G.–(8) 5736
Daughton, J. M.–(8) 5889
Dauguet, P.–(8) 5823, 6370
Davidson, R.–(8) 5671
Day, P.–(8) 4644
Daykin, A. C.–(8) 6292
de Aguiar, F. M.–(8) 6309
Dean, C.–(8) 4915, 6467
de Azevedo, M. M. P.–(8) 6246
De Boeck, J.–(8) 4957
de Boer, F. R.–(8) 4626, 5221, 6321, 6324, 6358, 6361, 6396, 6408
de Camargo, P. C.–(8) 6154
Decanini, D.–(8) 5068
Dederichs, P. H.–(8) 5129, 5638
Dedukh, L. M.–(8) 5315, 6073
DeFotis, G. C.–(8) 4644, 4718
Defoug, S.–(8) 6036
de Francisco, C.–(8) 5436, 6545
de Haan, P.–(8) 6243
de Jong, W.–(8) 5632
de Julián, C.–(8) 5955
de Leon Guevarra, A. M.–(8) 4554
Della Torre, Edward–(8) 5773
Delmas, A.–(8) 6485
del Moral, A.–(8) 5175
Demangeat, C.–(8) 5834
de Morais, E.–(8) 5973
Dempsey, N. M.–(8) 5045
Dender, D.–(8) 5391
Deng, Hong–(8) 5779
Denlinger, J. D.–(8) 5626
Dennis, K. W.–(8) 4847
De Raedt, H.–(8) 6110
Despres, J. F.–(8) 6007
Desvignes, J. M.–(8) 5932
De Teresa, J. M.–(8) 5175
Deville, J. P.–(8) 6247
Devine, M. K.–(8) 5493
de Visser, A.–(8) 6358
Dey, Subrata–(8) 5916
de Zhang, Yi–(8) 5709
Dhagat, P.–(8) 4695, 5652
Dhalenne, G.–(8) 5099, 5384, 5395
Dhar, S. K.–(8) 6349, 6367
Díaz, F.–(8) 5439
DiBari, R. C.–(8) 5102
DiBari, Rebecca C.–(8) 5841
Dieny, B.–(8) 6370
Diep, H. T.–(8) 5087
Dimitrov, D. V.–(8) 5106
Ding, Juren–(8) 5892
Dionne, Gerald F.–(8) 5172
Disselnkötter, Rolf–(8) 5208
DiStefano, Sal–(8) 5776
Dittschar, A.–(8) 5618, 6426, 6504
DiTusa, J. F.–(8) 5023
Dmowski, W.–(8) 6253
Dodge, J. S.–(8) 6186
Doerner, M. F.–(8) 5327
Doerner, Mary–(8) 4916
Doerner, Mary F.–(8) 5348
Doi, M.–(8) 5583
Doi, T.–(8) 4699, 4884, 4887, 5214
Domínguez, L.–(8) 6539
Dominguez, M.–(8) 5165, 5991
Donahue, M. J.–(8) 4712, 5315, 6073
Donnet, D. M.–(8) 6243
Dorsey, P. C.–(8) 6338
Doudin, B.–(8) 6010, 6090
Douglas, T.–(8) 5324
Dowben, P. A.–(8) 5838
Doyle, W. D.–(8) 4995, 6489
Dresselhaus, J.–(8) 6508
Dreyssé, H.–(8) 5834
Drouhin, H.-J.–(8) 4734
Drumheller, John E.–(8) 5094, 5368
Du, Tengda–(8) 6034
Duan, Mingqian–(8) 5979
Ducreux, J. P.–(8) 4575
Dugas, M.–(8) 6440
Duk Choi, Seung–(8) 5489
Dulcie, L. L.–(8) 5358
Duncombe, P. R.–(8) 4549
Dunlap, R. A.–(8) 4662, 4679, 5992, 5995
Dunn, J. Hunter–(8) 4983
Dunsiger, S. R.–(8) 6636
Dupas, C.–(8) 4554, 5270
Dupre, L. R.–(8) 5496
Durán, C. A.–(8) 6592
Durin, G.–(8) 5142, 5764
Durlam, M.–(8) 5889
Durst, A. C.–(8) 5196
Dworak, P.–(8) 6203
Dykes, J. W.–(8) 4775, 5584

Earl, J.–(8) 5703
Eastham, J. F.–(8) 4685, 5554
Ebels, U.–(8) 6120
Egami, T.–(8) 6253
Egelhoff, W. F., Jr.–(8) 5277
Elam, W. T.–(8) 5345
El Chahal, L.–(8) 6247
El-Hilo, M.–(8) 6034
Elings, V.–(8) 6440
Ellerbrock, R. D.–(8) 5582
Ellis, D. E.–(8) 6429
Elmers, H. J.–(8) 4984
Eloot, K.–(8) 5496
El-Shall, M. S.–(8) 5063
Engdahl, G.–(8) 4689, 6476
Epstein, A. J.–(8) 6147
Ercole, A.–(8) 4987
Erickson, R. P.–(8) 4808
Eriksson, O.–(8) 4983, 5837
Erwin, J. K.–(8) 5687
Erwin, R. W.–(8) 4762, 5102
Escorcia-Aparicio, Ernesto J.–(8) 4532, 4964
Espeso, J. I.–(8) 6352
Étourneau, J.–(8) 6355
Ezekwenna, Peter C.–(8) 4587

F.-Calleja, J.–(8) 4936, 5217
Fagan, J. G.–(8) 6341
Fainstein, A.–(8) 6577
Fang, T. M.–(8) 5739
Fang, Ta-Ming–(8) 4759
Fang, W. W.–(8) 4790
Farrow, R. F. C.–(8) 5967, 6496
Fawcett, E.–(8) 6154
Fawcett, Eric–(8) 4802
Feder, R.–(8) 6426
Fedyunin, Y. N.–(8) 6642
Feiner, L. F.–(8) 5103
Fejer, M. M.–(8) 6186
Felcher, G.–(8) 4524
Felder, R. J.–(8) 5923, 5926
Feng, Y. C.–(8) 5345
Fernandez, J. Rodriguez–(8) 6364
Fernandez-Baca, J. A.–(8) 5398
Ferré, J.–(8) 5632
Fetisov, Y. K.–(8) 5721, 5730
Fidler, J.–(8) 5029, 6458
Figge, M.–(8) 4531
Filipkowski, M. E.–(8) 4525
Filoti, G.–(8) 5257
Fink, Anita–(8) 6084
Fiorillo, F.–(8) 4575
Fisch, Ronald–(8) 5088
Fisher, A. S.–(8) 5185
Fisher, Kevin D.–(8) 4502
Fishman, R. S.–(8) 4824
Fisk, Z.–(8) 6577
Florence, G.–(8) 6593
Flores, A. G.–(8) 5422, 6574
Flosdorff, A.–(8) 4641, 6054
Flynn, C. P.–(8) 4779
Fogarty, K. J.–(8) 6643
Folan, L. M.–(8) 5716
Foldeaki, M.–(8) 5995
Foner, S.–(8) 4740, 5071
Fontaine, A.–(8) 6497
Fontcuberta, J.–(8) 5182, 6596
Fontes, M. B.–(8) 5256
Fontijn, W. F. J.–(8) 5936
Foss, S.–(8) 6447
Foss, Sheryl–(8) 6447
Franklin, D. R.–(8) 5390
Fredkin, Donald R.–(8) 5755, 5762
Freeman, A. J.–(8) 4805, 5827, 5831, 6209, 6500
Freeman, M. R.–(8) 5898
Freibert, F.–(8) 4567, 4821, 5876
Freitag, Andrea E.–(8) 6303
Freitas, P. P.–(8) 6246, 6452
Friedman, Jonathan R.–(8) 6031
Friedmann, A.–(8) 5658, 5661
Fruchart, D.–(8) 4584, 4608, 5542
Fuerst, C. D.–(8) 4656, 5539, 5998
Fuest, A.–(8) 5582
Fujii, Toshitaka–(8) 5988
Fujimori, A.–(8) 5707, 5708
Fujimori, H.–(8) 4733, 5130
Fujita, E.–(8) 5351
Fujita, J.–(8) 4999
Fujiwara, H.–(8) 6286
Fujiwara, Hideo–(8) 4970
Fujiwara, Shuzo–(8) 4721
Fujiwara, Y.–(8) 6270
Fukutani, H.–(8) 5707, 5708
Fuller, C. J.–(8) 6405
Fullerton, Eric E.–(8) 4524, 6266
Fulmek, Paul L.–(8) 5761
Fumagalli, P.–(8) 5929, 6203
Furlani, E. P.–(8) 4692
Furubayashi, T.–(8) 6258
Fussell, Barry K.–(8) 5548

Futamoto, M.–(8) 5354, 5359

Gadetsky, S.–(8) 5667, 5687
Gadetsky, S. N.–(8) 5700
Gafney, H. D.–(8) 6025
Gago-Sandoval, P. A.–(8) 5590, 5605
Gair, S.–(8) 5554
Galéra, R. M.–(8) 6497
Gallagher, W. J.–(8) 4538, 4546, 4549
Galli, M.–(8) 6423
Gama, S.–(8) 5973
Gambino, R. J.–(8) 5253, 5929, 6025, 6285
Gambino, Richard J.–(8) 5776
Gammel, P. L.–(8) 6592
Gandit, P.–(8) 5823, 6370
Gandra, F. G.–(8) 5462
Gangopadhyay, S.–(8) 6286
Ganguly, R.–(8) 5260
Gao, J.–(8) 6470
Gao, Z.–(8) 5510
García, A.–(8) 6516, 6589
Garcia, F.–(8) 5220
García, J.–(8) 5175, 5178
Garcia, L. M.–(8) 6497
García, N.–(8) 6019, 6110
García-Mochales, P.–(8) 6019
García-Pablos, D.–(8) 6019, 6110
García Soldevilla, J.–(8) 6352
García Tello, P.–(8) 5479
Garifullin, I. A.–(8) 6298
Garif'yanov, N. N.–(8) 6298
Garshelis, I. J.–(8) 4756
Garwin, E. L.–(8) 6488
Gaspard, P.–(8) 5936
Gaulin, B. D.–(8) 4769, 5081, 6170, 6636
Gautier, F.–(8) 5834
Gavrin, A.–(8) 5306, 5309
Gayoso, M.–(8) 5955
Gehring, G. A.–(8) 5593
Gehring, P. M.–(8) 4762
Geiser, U.–(8) 6586
Geisler, H.–(8) 4765
Ghigna, P.–(8) 6624
Gider, S.–(8) 5324
Giles, R. C.–(8) 4685
Giljer, P.–(8) 5327
Gill, B. L.–(8) 5696
Gillies, M. F.–(8) 6452
Gingras, M. J. P.–(8) 6170, 6636
Giri, Anit K.–(8) 5479, 5955, 6611
Girt, Er.–(8) 4833
Girvin, S. M.–(8) 5096
Gjoka, M.–(8) 5539
Glavinas, E.–(8) 4695, 5652
Glenis, S.–(8) 5873
Glenn, Darin W.–(8) 6193
Gmelin, E.–(8) 5869, 5869, 6173
Godart, C.–(8) 5857, 6347, 6349
Goedkoop, J.–(8) 6497
Göktürk, H.–(8) 4857
Goldman, A. M.–(8) 4553
Gomez, R. D.–(8) 6063
Gomez, Romel D.–(8) 6441
Gómez Sal, J. C.–(8) 4815, 6352
Gong, G. Q.–(8) 4538, 6126
Gong, X. G.–(8) 5162
González, A. C.–(8) 5242
González, E.–(8) 6155
González, J.–(8) 5465, 5479, 6479, 6539
González, J. M.–(8) 5465, 5479, 5955, 6155, 6312, 6479, 6611
González-Calbet, J. M.–(8) 5182
Goodey, J. R.–(8) 4718
Goodman, K. W.–(8) 5626
Gorelik, S. S.–(8) 5500
Goremychkin, E. A.–(8) 6432
Görlitz, D.–(8) 4641, 6054
Gornakov, V. S.–(8) 5315, 6073
Gorría, P.–(8) 5146
Gortenmulder, T. J.–(8) 5221, 6358, 6361
Goryunov, Yu. V.–(8) 6298
Gotaas, J. A.–(8) 4746
Goto, T.–(8) 4647
Gouzerh, J.–(8) 5932
Govindaraju, M. R.–(8) 5453
Govorkov, S.–(8) 4518
Govorkov, S. A.–(8) 6051
Gradmann, U.–(8) 4984
Granados, X.–(8) 6596
Grandjean, F.–(8) 4584, 4587, 5945
Gray, S. J.–(8) 4987
Greedan, J. E.–(8) 6170, 6173, 6176, 6432, 6636
Greene, R. L.–(8) 4545, 4552, 4552, 5165, 5166, 5292
Greenough, R. D.–(8) 6219
Gregg, J.–(8) 4528
Gregg, J. F.–(8) 5593, 6247
Grigorenko, A. N.–(8) 6113
Grimes, Craig A.–(8) 4581, 5497
Grishin, A. M.–(8) 5860
Grünberg, P.–(8) 4782
Grundy, P. J.–(8) 4650, 4939, 6070
Gu, R. Y.–(8) 6255
Guenzburger, Diana–(8) 6429
Guilfoyle, S. J.–(8) 4939
Guillot, M.–(8) 4608, 5542, 5932, 5985
Guillot, Maurice–(8) 5979
Guimarães, A. P.–(8) 5468
Güntherodt, G.–(8) 6203
Güntherodt, H.-J.–(8) 5609
Gupta, A.–(8) 4538, 4546, 4549
Gupta, D.–(8) 5179
Gupta, H.–(8) 6045
Gupta, L. C.–(8) 5857, 6347, 6349
Gupta, R.–(8) 6079
Gupta, S.–(8) 5018, 5446, 5584
Gurney, B. A.–(8) 6295
Guruswamy, S.–(8) 4851, 6222
Gusev, S. A.–(8) 4625
Gutierrez, C. J.–(8) 4525, 5826, 6492
Gutiérrez, M. O.–(8) 4936
Guyot, M.–(8) 5472
Gyorgy, E. M.–(8) 5923, 5926

Hach, C.–(8) 6341
Hadjipanayis, G. C.–(8) 4590, 4616, 4827, 4837, 5106, 5152, 5302
Hafner, J.–(8) 4963, 5051
Hagiwara, M.–(8) 5245, 6167
Hajnal, J. V.–(8) 4685
Halada, Gary–(8) 5776
Hamacher, K.–(8) 4779, 4782
Hamaguchi, T.–(8) 5797
Hämäläinen, K.–(8) 6509
Hamdeh, H. H.–(8) 5431, 5435
Hammar, Philip R.–(8) 5392
Hanf, M. C.–(8) 4954
Hara, M.–(8) 5664
Harbison, J. P.–(8) 4967
Harding, C. J.–(8) 6150
Hardner, H. T.–(8) 4980
Harmon, B. N.–(8) 4799, 5409
Harp, G. R.–(8) 5967, 6496
Harris, K. D. M.–(8) 6150
Harris, V. G.–(8) 4561, 4890, 5345, 5431
Hart, A.–(8) 4915
Hasan, M. K.–(8) 5879
Hasegawa, Hideo–(8) 6376
Hasegawa, R.–(8) 6117
Hashi, S.–(8) 4574
Hashimoto, S.–(8) 5057
Hastings, J. B.–(8) 6509
Hatamura, Y.–(8) 5797
Hathaway, K. B.–(8) 6213
Hatwar, T. K.–(8) 5704
Hauschild, J.–(8) 4984
Hauser, Hans–(8) 5761
Hautot, Dimitri–(8) 4584
Havela, L.–(8) 6361, 6396, 6408
Hayano, S.–(8) 4699, 5214
Hayashi, K.–(8) 5907
Hayes, Alan–(8) 5776
He, L.–(8) 6489
Heagy, J. F.–(8) 5377
Heckens, Scott–(8) 6193
Heenan, R.–(8) 5146
Heffner, R. H.–(8) 4535
Hegde, H.–(8) 4614, 5961
Hehn, M.–(8) 4528, 5068
Heidmann, Juergen–(8) 6488
Heim, K. R.–(8) 5056
Heimel, J.–(8) 4922
Heinrich, B.–(8) 4518, 4954
Hellberg, C. S.–(8) 6414
Hellman, F.–(8) 5854, 5919
Hembree, G. G.–(8) 5056
Henk, J.–(8) 6426
Henning, P.–(8) 4567
Henry, L. L.–(8) 5811, 6129
Herbst, J. F.–(8) 5998
Hernandez, J. M.–(8) 6116
Hernàndez, J. M.–(8) 4686
Hernandez, Laura–(8) 5087
Hernandez, P.–(8) 5436
Hernando, A.–(8) 4815, 6539, 6549
Hicken, R. J.–(8) 4987
Hickey, B. J.–(8) 5119, 5816, 6250
Hiebl, K.–(8) 5241
Hikosaka, T.–(8) 5655
Hilfiker, James N.–(8) 6193
Hill, J. P.–(8) 4802
Hill, Peggy–(8) 5398
Hill-Cottingham, R. J.–(8) 4685
Hillebrands, B.–(8) 4531
Hillebrecht, F. U.–(8) 6508
Hines, W. A.–(8) 4596, 5530
Hirai, T.–(8) 4611
Hirayama, Y.–(8) 5359, 5664
Hiroki, Tomoyuki–(8) 5683
Hirota, Noriyuki–(8) 4721
Hjortstam, O.–(8) 4983, 5837
Ho, E. M.–(8) 6292
Ho, J. C.–(8) 5431, 5435
Höchst, Hartmut–(8) 6503
Hoines, L.–(8) 6151, 6234
Holden, A. P.–(8) 4650, 6070
Holdsworth, P. C. W.–(8) 4976
Holody, P.–(8) 5811
Homma, Takuro–(8) 4721
Honda, Naoki–(8) 5362, 5913
Honig, J. M.–(8) 5401
Hono, K.–(8) 5907
Hopkins, P. F.–(8) 6448
Hopster, H.–(8) 5619
Hori, T.–(8) 6633
Hori, Tomiei–(8) 5238, 5946
Horrocks, D. H.–(8) 4753
Horwitz, J. S.–(8) 6338
Hoshi, Y.–(8) 4945
Hosoe, Y.–(8) 5351, 5354
Hossain, S. A.–(8) 5817
Hossain, Z.–(8) 5857, 6349
Hou, C.–(8) 6286
How, H.–(8) 5739
How, Hoton–(8) 4759
Howard, J. K.–(8) 4762, 5330
Howe, D.–(8) 6342
Hsieh, Chien-Sheng–(8) 6522
Hsieh, W. T.–(8) 6568
Hsieh, Yung-Chieh–(8) 5700
Hsing, D. M.–(8) 4843
Hsu, Y. Y.–(8) 5863, 5866
Hu, Bo-Ping–(8) 5713
Hu, S. B.–(8) 5649
Hu, X.–(8) 5221, 6361
Hu, Xiao–(8) 5842
Hu, Y. M.–(8) 4790, 6276
Hu, Z.–(8) 4587, 5522, 5939, 5945, 6315, 6318
Huang, D. R.–(8) 5557, 5699, 6035
Huang, Der-Ray–(8) 5560
Huang, D-J.–(8) 6507
Huang, H. L.–(8) 6060
Huang, Huei Li–(8) 5415
Huang, J. C. A.–(8) 4790, 6276, 6282, 6533
Huang, M. Q.–(8) 5949, 6331
Huang, M.-Q.–(8) 5293
Huang, Ming-Zhu–(8) 4602, 5545
Huang, Q.–(8) 5857
Huang, W.–(8) 6196, 6199
Huang, Xiaohua–(8) 5742
Huang, Y. H.–(8) 5674
Huber, D. L.–(8) 6143
Huber, David–(8) 6503
Hubert, O.–(8) 4571
Hübner, W.–(8) 6177
Hug, E.–(8) 4571
Hug, Hans J.–(8) 5609
Humphrey, F. B.–(8) 6464
Hundley, M. F.–(8) 4535
Hung, John Y.–(8) 5548
Hurben, M. J.–(8) 5390
Hwang, H. Y.–(8) 4541
Hylton, T. L.–(8) 4762
Hyman, R. A.–(8) 5096

Iannarella, L.–(8) 5468
Ibarra, M. R.–(8) 4656, 4659, 5175, 5178, 6330
Ibsen, K. B.–(8) 4546
Ichihara, T.–(8) 5910
Ido, H.–(8) 4647, 5507, 6334
Ido, Hideaki–(8) 5224
Idzerda, Y. U.–(8) 4558, 5345, 5622, 6492, 6493
Igarashi, Masukazu–(8) 5576
Iglesias, I.–(8) 5217, 5472
Iguchi, Yasuo–(8) 5238
Iijima, Makoto–(8) 5602
Iio, K.–(8) 5707, 5708
Imura, Ryo–(8) 5576
Inaba, N.–(8) 5354
Inagaki, J.–(8) 5351
Inami, T.–(8) 4802
Indeck, R. S.–(8) 4695, 5652
Inglefield, H. E.–(8) 5845
Ings, J. B.–(8) 6341
Iñiguez, J.–(8) 5422, 5436, 6574
Inoue, A.–(8) 4836, 5149, 5472
Inoue, J.–(8) 4730
Inoue, Mitsuteru–(8) 5988
Inturi, V. R.–(8) 5904
Iqbal, Z.–(8) 6583
Irie, Y.–(8) 6231
Isamoto, Keiji–(8) 5988
Ise, Kazuyuki–(8) 5913
Iseki, Takayuki–(8) 4970
Ishii, Osamu–(8) 5483
Ishikawa, A.–(8) 5351
Ishiyama, K.–(8) 4574
Ishizaki, O.–(8) 4905
Isnard, O.–(8) 4584, 4608, 5542
Ito, H.–(8) 6273
Ito, T.–(8) 5507
Itoh, H.–(8) 4730

Itoh, K.–(8) 5452
Iwasaka, M.–(8) 4705, 4708
Iwasaka, Masakazu–(8) 4721
Iwasaki, H.–(8) 6399
Iwasaki, Shun-ichi–(8) 5362, 5913
Iwasaki, Y.–(8) 5057
Iwata, S.–(8) 6270

Jagger, J. E.–(8) 5992
Jain, V. K.–(8) 5260
Jakubovics, J. P.–(8) 6057
Jalics, S.–(8) 6045
James, W. J.–(8) 4587, 5522, 5939, 6315
Jamet, J. P.–(8) 5632, 5848
Jander, A.–(8) 4491, 5652
Japiassú, Gloria M.–(8) 6345
Jardim, R. F.–(8) 6564
Jarratt, J. D.–(8) 5606
Jaswal, S. S.–(8) 5942
Jayasekara, W. P.–(8) 5880
Jee, Chan-Soo–(8) 5403
Jeffers, F.–(8) 5658
Jellali, F.–(8) 6485
Jen, S. U.–(8) 6552
Jensen, J. H.–(8) 5199
Jewell, G. W.–(8) 6342
Jhon, Myung S.–(8) 5785, 5788
Jia, Kechang–(8) 4665, 6225
Jia, Q. X.–(8) 4535
Jiaand, Kechang–(8) 4668
Jiang, E. Y.–(8) 5440
Jiang, J. Samuel–(8) 5615
Jiang, Q.–(8) 5122
Jiles, D. C.–(8) 4749, 5453, 5493, 5510, 6045, 6219, 6470
Jimbo, M.–(8) 6237
Jin, Cai-Xia–(8) 5193
Jin, Q. Y.–(8) 4949
Jin, S.–(8) 5599
Jin, Zhi-qiang–(8) 5525
Jin Yang, Choong–(8) 5489
Jo, S.–(8) 5670
Johansson, B.–(8) 4983, 5837
Johnson, D.–(8) 5299
Johnson, P. D.–(8) 6507
Johnston, D. C.–(8) 5084
Jones, L.–(8) 6341
Jonker, B. T.–(8) 5125, 5195
Jönsson, B. J.–(8) 5063, 6583
Ju, H. L.–(8) 4552, 5165, 5166
Judy, J. H.–(8) 5277, 5327
Judy, Jack–(8) 4912
Judy, Jack H.–(8) 5782

Kabos, P.–(8) 5367
Kaczmarek, R.–(8) 6036
Kadin, A. M.–(8) 5179
Kaiser, H.–(8) 4775, 4779, 4782
Kakudate, Yozo–(8) 4721
Kakuno, K.–(8) 4653, 6542
Kalogirou, O.–(8) 5539
Kamada, O.–(8) 5976
Kamarád, J.–(8) 4656
Kambe, Takashi–(8) 5576
Kamenev, K.–(8) 5178
Kamiguchi, Y.–(8) 6399
Kamimura, T.–(8) 5707
Kaminski, D. A.–(8) 4749
Kamishima, K.–(8) 4647
Kaneko, T.–(8) 4611
Kanematsu, K.–(8) 5449, 5452
Kanematsu, Kazuo–(8) 5238
Kang, Soo-Choon–(8) 5785
Kao, C.-C.–(8) 5345, 6492, 6509
Kapitulnik, A.–(8) 6186
Kaplan, T. A.–(8) 6433
Kappler, J. P.–(8) 6497
Kapusta, Cz.–(8) 4599
Karis, Thomas E.–(8) 5788
Kariuki, B. M.–(8) 6150
Kasai, M.–(8) 5288
Katayama, T.–(8) 5708
Katsumata, K.–(8) 5245, 6167
Käufler, A.–(8) 4765
Kaul, S. N.–(8) 5146
Kawabe, H.–(8) 5707, 5708
Kawakami, R. K.–(8) 4532, 4964
Kawakita, Shinya–(8) 5339
Kawamura, Mitsutaka–(8) 4721
Kawana, Takahiro–(8) 4875
Kawawake, Y.–(8) 6231
Kawazoe, Yoshiyuki–(8) 5842
Kazmi, A. S.–(8) 4685
Keimer, B.–(8) 5022
Kelley, M. H.–(8) 5306
Kelly, D.–(8) 6253
Kemmler-Sack, S.–(8) 5257
Kemner, K. M.–(8) 5345, 5622, 6493
Kennedy, Robin J.–(8) 4570
Kennedy, S. J.–(8) 6161
Keren, A.–(8) 6636
Keszei, B.–(8) 5742
Keune, W.–(8) 5582
Khaliullin, G. G.–(8) 6298
Khapikov, A. F.–(8) 5315, 6073
Khater, M.–(8) 5826
Khizroev, S.–(8) 6586
Kida, A.–(8) 5583
Kief, M. T.–(8) 4766, 5008
Kiefl, R. F.–(8) 6636
Kikkawa, J. M.–(8) 5296, 6095
Kikuchi, Akira–(8) 5339
Kim, A. S.–(8) 4840, 5035
Kim, C.–(8) 5468
Kim, C. S.–(8) 5516
Kim, Chul Sung–(8) 5428, 5459, 5516
Kim, K. S.–(8) 5153, 5860
Kim, K. Y.–(8) 5153
Kim, M. J.–(8) 5696
Kim, Miyoung–(8) 5831
Kim, S. G.–(8) 5670
Kim, S. S.–(8) 5696
Kim, Sung Baek–(8) 5459
Kim, T. W.–(8) 5253
Kim, Won Tae–(8) 5476
Kim, Y. B.–(8) 5516
Kim, Y. K.–(8) 5446, 5584, 5596, 6386
Kinder, Lisa R.–(8) 4724
Kinoshita, T.–(8) 6508
Kioussis, Nicholas–(8) 4783, 6420
Kirby, R. D.–(8) 4786
Kirby, Roger D.–(8) 6206
Kirilyuk, A.–(8) 5632
Kirschner, J.–(8) 5618, 6426, 6504
Kisker, E.–(8) 6508
Kisker, H.–(8) 5143
Kiss, László F.–(8) 4811
Kitakami, O.–(8) 6074
Kitakami, Osamu–(8) 5250
Kitazawa, Koichi–(8) 4721
Klebanoff, L. E.–(8) 4796
Klein, Barry M.–(8) 4776
Klein, L.–(8) 6186
Kleinefeld, Th.–(8) 4531, 4922
Klicznik, A.–(8) 5609
Klik, I.–(8) 4919, 6533
Kneedler, E.–(8) 5125
Knobel, M.–(8) 5462
Kobayashi, H.–(8) 4999
Kobayashi, Kazuo–(8) 5602
Kobayashi, T.–(8) 5907
Kodama, N.–(8) 6467
Kodama, R. H.–(8) 5071
Koerkamp, M. Groot–(8) 5632, 6181
Koide, T.–(8) 5707, 5708
Koinkar, Vilas N.–(8) 5798
Kojima, A.–(8) 4836
Kojima, K.–(8) 6636
Kojima, Naomi–(8) 5602
Koknaeva, M.–(8) 4833
Kolb, E.–(8) 5270
Komatsu, K.–(8) 6542
Komiyama, K.–(8) 6237
Komoda, O.–(8) 4905
Komuro, Matahiro–(8) 5576
Kondo, Akio–(8) 5677
Kong, Linshu–(8) 5067, 5855, 6101
Konno, K.–(8) 6334
Koon, N. C.–(8) 4561, 4890
Koon, Norman C.–(8) 5841
Koopmans, B.–(8) 6181
Korenivski, V.–(8) 5923, 5926
Koroleva, L. I.–(8) 6617
Kos, A. B.–(8) 5820
Koshimoto, Yasuhiro–(8) 5483
Kottler, V.–(8) 4509
Kötzler, J.–(8) 4641, 6054
Kou, X. C.–(8) 6324
Koubouros, I.–(8) 5563
Kouvel, J. S.–(8) 5879
Kowalewski, M.–(8) 4954
Koziol, Z.–(8) 4662, 5992, 5995
Kozioł, Z.–(8) 4679
Krajewski, J. J.–(8) 5923
Kramer, M. J.–(8) 4847
Krasko, Genrich L.–(8) 4682
Kraus, P. A.–(8) 4553
Krause, T. W.–(8) 6042
Krauss, Peter R.–(8) 5066, 6101
Krebs, J. J.–(8) 4525, 5125, 5622, 6084, 6234
Krill, G.–(8) 6497
Krisch, M. H.–(8) 6509
Krishnan, Kannan M.–(8) 4848, 5169, 5321
Krishnan, R.–(8) 4936, 5472, 6246
Kroll, E. C.–(8) 6116
Kronmüller, H.–(8) 5143
Kryder, M. H.–(8) 4485, 4878, 4890, 5011, 5880
Ku, H. C.–(8) 5863, 5866, 6568
Kubo, K.–(8) 6433
Kuch, W.–(8) 5618, 6426, 6504
Kudrevatykh, N. V.–(8) 6330
Kume, Minoru–(8) 6402
Kunkel, H. P.–(8) 6561
Kuo, P. C.–(8) 6035
Kurbatova, Yu. N.–(8) 6132
Kurisu, H.–(8) 4884, 4896
Kuroda, K.–(8) 6451
Kuroki, Kazuhiko–(8) 6402
Kuwabara, M.–(8) 5564
Kuwahara, H.–(8) 5288
Kwon, S. J.–(8) 6299

Labarta, A.–(8) 5605
Lafdi, K.–(8) 6007
Laffargue, D.–(8) 6355
Lagarikov, A. N.–(8) 6532
Lai, C. C.–(8) 6568
Lai, Chih-Huang–(8) 6389
Laibowitz, R. B.–(8) 4549
Laidler, H.–(8) 6250
Lal, Brij B.–(8) 5336
Lam, T. T.–(8) 5645
Lam, Terence–(8) 4906
Lam, Terence T.–(8) 4909
Lambeth, D. N.–(8) 4496, 5011
Lambeth, David N.–(8) 4902, 5348
Lampel, G.–(8) 4734
Lang, P.–(8) 5129, 5638
Langman, R. A.–(8) 6134
Lascialfari, A.–(8) 6624
Lassailly, Y.–(8) 4734
Laughlin, D. E.–(8) 4496, 5345
Laughlin, David E.–(8) 4902, 5348, 6455
Lavers, J. D.–(8) 4671
Lebedev, Sergey V.–(8) 5982
Le Dang, K.–(8) 4554, 5099
Lederman, D.–(8) 5112
Lederman, M.–(8) 5303, 6067
Lee, B. H.–(8) 5482
Lee, C. S.–(8) 5649
Lee, Chan Young–(8) 5710
Lee, Choong Sub–(8) 5710
Lee, J.-G.–(8) 5752, 6051
Lee, J. S.–(8) 5459
Lee, Jaeyong–(8) 6120
Lee, K. C.–(8) 6568, 6571
Lee, K. G.–(8) 5696
Lee, Kong-Ju-Bock–(8) 6605
Lee, L. L.–(8) 4496
Lee, Li-Lien–(8) 4902
Lee, S.-H.–(8) 5023
Lee, S. K.–(8) 5670
Lee, Seung Wha–(8) 5428, 5516
Lee, T. D.–(8) 5357
Lee, W.-T.–(8) 4802
Lee, Y. H.–(8) 6276
Lee, Y. P.–(8) 5699
Lee, Young Jong–(8) 5516
Lee, Young-sook–(8) 5870
Lefmann, K.–(8) 5078, 5391
Le Gall, H.–(8) 5932
Leithe-Jasper, A.–(8) 5241
Leng, Q.–(8) 4766
Leslie-Pelecky, Diandra L.–(8) 5312
Letyuk, L. M.–(8) 5500
Leung, H. T.–(8) 6295
Leupold, H. A.–(8) 5551
Levashov, V. I.–(8) 5315, 6073
Levy, J.–(8) 6095
Levy, P. M.–(8) 6382
Lewis, L. H.–(8) 5513, 6470
Lewis, Laura Henderson–(8) 4848
Li, A. S. K.–(8) 4854
Li, D.–(8) 6618
Li, Dongqi–(8) 5838
Li, Fa-shen–(8) 5709
Li, Feiyue–(8) 4866, 4869
Li, Hong-Shuo–(8) 4622, 5713
Li, Lin–(8) 4578
Li, Q.–(8) 5165
Li, Qi–(8) 4552
Li, W.-H.–(8) 6568, 6571
Li, Yiqun–(8) 4998
Li, Youlin–(8) 5791
Li, Zisen–(8) 5188
Liang, Y. L.–(8) 4830, 5501, 6335
Liao, C. P.–(8) 5557
Liao, S. Y.–(8) 4790, 5599, 6282, 6533
Liechtenstein, A. I.–(8) 4805
Lin, C.–(8) 5440
Lin, C. H.–(8) 6035
Lin, C. L.–(8) 4812, 5403, 5873, 6405, 6608
Lin, C.-L.–(8) 5277
Lin, J. C.–(8) 5159
Lin, M. S.–(8) 5863
Lin, Y. F.–(8) 6568
Lind, D. M.–(8) 5102
Lind, David M.–(8) 5841
Liou, S. H.–(8) 5060, 5958, 6448
Liou, Y.–(8) 4790, 6282, 6533
Lipp, D.–(8) 5609
Lisyansky, A. A.–(8) 5091
Liu, B.–(8) 5649
Liu, C. S.–(8) 5432
Liu, F.–(8) 6028
Liu, Francis H.–(8) 5895
Liu, G. H.–(8) 4984
Liu, G. K.–(8) 6512

Liu, Guo–(8) 6176
Liu, J.–(8) 4753
Liu, Qingxia–(8) 4702
Liu, R. L.–(8) 4790
Liu, S. H.–(8) 4824
Liu, W.–(8) 5525
Liu, W. L.–(8) 6335
Liu, X.–(8) 5387
Liu, Y.–(8) 5060, 5333, 5958, 6507
Liu, Ying–(8) 5094
Liu, Z. J.–(8) 4678
Livne, Z.–(8) 5456
Lizzi, T.–(8) 4840
Lo, C. C. H.–(8) 6057
Lo, C. K.–(8) 4790, 6533
Lochner, E.–(8) 5102
Lochner, Eric–(8) 5841
Lodder, J. C.–(8) 6190, 6243
Lofland, S.–(8) 5991
Lofland, S. E.–(8) 5165, 5166
Lois, P.–(8) 4674
Loloee, R.–(8) 6129
Long, G. J.–(8) 6318
Long, Gary J.–(8) 4584, 4587, 5945
Loong, C.-K.–(8) 6512
Lopez de la Torre, M. A.–(8) 6364
López-Quintela, M. A.–(8) 5269
Lord, D. G.–(8) 4650, 6070
Lord, J. S.–(8) 4599
Lorenz, Bryen E.–(8) 6039
Lorenz, R.–(8) 4963, 5051
Lorenz, T.–(8) 4765
Loss, Daniel–(8) 6107
Lounasmaa, O. V.–(8) 5078
Loveless, M.–(8) 6222
Low, T. S.–(8) 4678, 5674
Lu, Feng–(8) 4759
Lu, Q. F.–(8) 6439
Lu, S. L.–(8) 5533
Lubitz, P.–(8) 6234, 6338
Lucas, C. A.–(8) 5169
Luce, T. A.–(8) 6177
Lukaszew, R. A.–(8) 4787
Luke, G. M.–(8) 6636
Lukina, L. N.–(8) 6617
Lumpp, Janet K.–(8) 5497
Lumsden, M. D.–(8) 5081
Luneau, D.–(8) 4698
Luo, C. P.–(8) 4899
Luo, H.–(8) 6318
Luo, Weili–(8) 6034
Luo, Y.–(8) 5645
Luo, Yansheng–(8) 4906, 4909
Luse, C. N.–(8) 4942
Lyberatos, A.–(8) 5703
Lynn, J. W.–(8) 5857, 6568

Ma, B. M.–(8) 4830, 5501, 6335
Ma, P.–(8) 5641
MacFarlane, W. A.–(8) 6636
Machado, F. L. A.–(8) 6546, 6555, 6558
Maciejewski, J.–(8) 6031
MacLaren, J. M.–(8) 5282, 5828, 6196, 6199
Madabhushi, R.–(8) 6063
Maeda, Atsushi–(8) 6402
Maekawa, S.–(8) 4730
Mahanti, S. D.–(8) 6433
Mahía, J.–(8) 5269
Maignan, A.–(8) 6173
Majetich, S. A.–(8) 5293
Majkrzak, C. F.–(8) 4762, 4782
Maki, K.–(8) 4857
Makino, A.–(8) 4836, 5472
Makovkin, A. V.–(8) 5721
Maletta, H.–(8) 5221
Malhotra, S. S.–(8) 5060, 5958, 6448
Malik, S. K.–(8) 6367
Mamin, H. J.–(8) 5644
Manago, Takashi–(8) 5126
Manalis, S.–(8) 6440
Mankey, G. J.–(8) 5626, 5635
Mann, S.–(8) 5324
Mansuripur, M.–(8) 5667, 5687, 5700
Mao, Ming–(8) 4769
Mao, Ming-xi–(8) 5709
Mao, O.–(8) 4605, 4619, 5536
Mao, Ou–(8) 5519
Maple, M. B.–(8) 4926, 6564
Mar, D. J.–(8) 5377
Marabelli, F.–(8) 6423
Maradudin, A. A.–(8) 5727
Maraner, A.–(8) 5406
Marasinghe, G. K.–(8) 4587, 5939
Marchon, B.–(8) 4508
Marezio, M.–(8) 4541
Marinero, E. E.–(8) 5680
Marini, S.–(8) 6621
Markin, P. E.–(8) 6330
Marks, R. F.–(8) 5967, 6496
Marmorino, J. L.–(8) 4644
Marquina, C.–(8) 4659, 5175, 5178, 6330
Martínez, B.–(8) 5182
Martinez, G.–(8) 5395
Martins, C. S.–(8) 6546
Martinson, L. S.–(8) 6164
Martynova, J.–(8) 6519
Marx, D.–(8) 5018
Massarotti, V.–(8) 6621
Masuda, S.–(8) 4653, 6542
Masumoto, T.–(8) 4836, 5130, 5149, 5472
Mathieu, Ch.–(8) 4531
Matsuda, T.–(8) 5075
Matsuda, Y.–(8) 5351
Matsuguma, I.–(8) 5318
Matsui, M.–(8) 5583
Matsumoto, Mitsunori–(8) 4881
Matsumoto, Morihiko–(8) 5486
Matsushita, N.–(8) 5247, 5910, 5970
Matsuura, M.–(8) 4884, 4896
Matsuyama, Hideo–(8) 6389
Matsuyama, K.–(8) 5318, 6643, 6646
Matveev, V. N.–(8) 5315, 6073
May, F.–(8) 4983
May, J.–(8) 6341
Mayergoyz, I. D.–(8) 5746, 6063, 6473, 6602
Mayergoyz, Isaak D.–(8) 6441
Mazumdar, Chandan–(8) 6347, 6349
McCall, S.–(8) 4567, 4821, 5876
McCallum, R. W.–(8) 4847, 5510
McCarter, M. K.–(8) 4851
McClelland, J. J.–(8) 6079
McEwen, K. A.–(8) 6364
McGuire, T. R.–(8) 4549
McHenry, M.–(8) 5949
McHenry, M. E.–(8) 5293
McIlroy, D. N.–(8) 5838
McKay, Susan R.–(8) 5087, 6146
McMichael, R. D.–(8) 5277, 5315, 5456, 5998, 6073
McNiff, E. J., Jr.–(8) 5071
Medeiros-Ribeiro, G.–(8) 5296
Medina, A. N.–(8) 5462
Meen, T. H.–(8) 6571
Mégy, R.–(8) 5270, 5632, 5848
Mehta, H.–(8) 5365
Meier, J.–(8) 6010
Meigs, G.–(8) 4558, 6492, 6493
Meinel, K.–(8) 6426
Melkebeek, J. A.–(8) 5496
Melo, L. G. C.–(8) 6546
Menard, D.–(8) 5136
Mendes, K. C.–(8) 6555
Mendoza, W. A.–(8) 6327
Meng, Q.–(8) 6190
Meng-Burany, X.–(8) 5152
Menon, Latika–(8) 6367
Menovsky, A.–(8) 6396
Menovsky, A. A.–(8) 6358
Mertig, I.–(8) 5276
Messner, W.–(8) 4485
Metin, S.–(8) 6295
Metz, A.–(8) 5078
Metzger, R.–(8) 6286
Metzger, Robert M.–(8) 4866, 4869
Meyer, P.–(8) 5632, 5848
Mezei, F.–(8) 6158
Michel, R.–(8) 5169
Michel, R. P.–(8) 4772, 4775
Michel, Steve–(8) 5826
Micklitz, H.–(8) 5256
Middleton, D. P.–(8) 4593, 5945, 6318
Mignot, J. M.–(8) 6396
Mihálik, M.–(8) 6396
Mihalisin, T.–(8) 4812, 5403, 5873, 6405, 6608
Miller, Joel S.–(8) 6147
Miller, L. L.–(8) 5084
Miller, M. M.–(8) 6234
Millot, F.–(8) 4554
Miloslavsky, Lena–(8) 5011
Milosvlasky, Lena–(8) 5895
Min, Byung G.–(8) 5788
Min, K.-I.–(8) 6228
Minor, M. K.–(8) 5005
Minvielle, Timothy J.–(8) 5116
Miotkowski, I.–(8) 6164, 6436
Mira, J.–(8) 5269
Miraglia, S.–(8) 4584, 4608, 5542
Mishra, S. R.–(8) 6318
Mishra, Sanjay R.–(8) 5945
Missell, F. P.–(8) 6312, 6546, 6555
Mitani, S.–(8) 4733, 5130
Mitchler, P. D.–(8) 5758
Mitsis, A.–(8) 5563
Miyajima, H.–(8) 4659, 5075
Miyajima, Hideki–(8) 5126, 6599
Miyajima, T.–(8) 5452
Miyamoto, Y.–(8) 6392
Miyashita, E.–(8) 5770
Miyata, Yoshimori–(8) 5486
Miyauchi, H.–(8) 5707, 5708
Miyazaki, T.–(8) 4977, 6262
Mochele, J. T.–(8) 6526
Modak, A. R.–(8) 5169
Modlin, Cory S.–(8) 4502
Mohri, K.–(8) 6532
Molins, E.–(8) 5182
Moloni, K.–(8) 6447
Momiji, H.–(8) 4905
Monachesi, P.–(8) 6423
Montenegro, F. C.–(8) 6555
Moodera, J. S.–(8) 6265
Moodera, Jagadeesh S.–(8) 4724
Moon, Ki-Seok–(8) 4991
Moon, R. M.–(8) 5022
Mora, J.–(8) 6596
Moran, Timothy J.–(8) 5109
Morchenko, A. T.–(8) 5500
Morel, R.–(8) 6289
Moreland, John–(8) 6448
Morellon, L.–(8) 4656
Mori, Toshinori–(8) 5483
Morimoto, K.–(8) 5040
Morin, B. G.–(8) 6147
Morisako, Akimitsu–(8) 4881
Moritani, Isao–(8) 5677
Moritomo, Y.–(8) 5288
Moschel, A.–(8) 4994
Moser, A.–(8) 5609
Moses, A. J.–(8) 4753
Moske, M.–(8) 4765
Moskowitz, Bruce M.–(8) 6064
Mountfield, K. R.–(8) 4787, 5011
Mryasov, O. N.–(8) 4805
Mühge, Th.–(8) 6298
Mulder, F. M.–(8) 4593
Müller, Gerhard–(8) 4629, 4632, 5227, 6630
Müller, K.-H.–(8) 5045
Muller, M. W.–(8) 4695, 5652
Mulloy, M.–(8) 5270
Muñoz, J. M.–(8) 5436, 6545
Muraoka, Hiroaki–(8) 5002
Murillo, N.–(8) 5465
Murthy, A. S.–(8) 4616, 4827, 5106, 5152, 5302
Myer, G. H.–(8) 6001
Myrtle, K.–(8) 4518, 4954

Na, J. G.–(8) 4893
Nagai, N.–(8) 5686
Nagarajan, R.–(8) 5857, 6347, 6349
Naik, R.–(8) 4787
Nakagawa, S.–(8) 5247, 5910, 5970, 6392
Nakagawa, Shigeki–(8) 5015, 5156
Nakagawa, Y.–(8) 6633
Nakagawa, Yasuaki–(8) 5946
Nakai, Junichi–(8) 5339
Nakajima, K.–(8) 4977
Nakajima, N.–(8) 5707, 5708
Nakajima, Tetsuo–(8) 5205
Nakamae, S. C.–(8) 6567
Nakamura, A.–(8) 5354
Nakamura, S.–(8) 6399
Nakamura, Y.–(8) 6642
Nakamura, Yoshihisa–(8) 5002, 6639, 6649
Nakano, K.–(8) 6439
Nakao, M.–(8) 5797
Nakatani, I.–(8) 5067, 6258
Nakaya, Y.–(8) 4699
Nakotte, H.–(8) 6361, 6408, 6411
Namjoshi, K. V.–(8) 4671
Nan Lin, I.–(8) 5432
Naoe, M.–(8) 4945, 5247, 5910, 5970, 6273, 6392
Naoe, Masahiko–(8) 4881, 5015, 5156
Narducci, A. A.–(8) 4718
Narita, N.–(8) 6167
Nash, J. M.–(8) 5367
Nashi, H.–(8) 5564
Nashima, O.–(8) 4647
Neely, M.–(8) 6602
Nelson, D. J.–(8) 4715
Neumeier, J. J.–(8) 4535
New, R. M. H.–(8) 5851
Ng, D. H. L.–(8) 4750, 4854, 6057
Nguyen, S. H.–(8) 4769
Nguyen, T.–(8) 5358
Nguyen, Tai D.–(8) 4848
Niarchos, D.–(8) 5539, 5563
Nicholson, D. M. C.–(8) 5282
Nickel, J. H.–(8) 4491
Nicolaides, D.–(8) 5091
Nicolaides, G. K.–(8) 5563
Niida, Hiroshi–(8) 5946
Nikitenko, V. I.–(8) 5315, 6073
Nikitin, P. I.–(8) 6113
Nikitin, V.–(8) 6095
Nikitov, S. A.–(8) 5365
Nikles, David E.–(8) 4860, 4863
Niraimathi, A. M.–(8) 5869, 5869, 6173
Nishimura, Naoki–(8) 5683
Nishinaga, T.–(8) 4957
Nishioka, K.–(8) 6286
Nishioka, Koichi–(8) 4970
Nixon, L.–(8) 6150

Nogués, J.–(8) 5112
Noh, T. H.–(8) 5153, 5459
Nolan, T. P.–(8) 5359
Noma, K.–(8) 5247, 5970
Nordman, C. A.–(8) 4553
Nordquist, K.–(8) 5889
Nordström, L.–(8) 5638
Nordström, Lars–(8) 4515
Norton, P. R.–(8) 4954, 5641
Nossov, A.–(8) 6370
Novak, M.–(8) 4698
Novo, J. M.–(8) 4815
Novotny, M. A.–(8) 6482
Novotny, Mark A.–(8) 5749
Nowakowski, D.–(8) 6143
Nozaki, Y.–(8) 5075
Nozaki, Yukio–(8) 6599
Nozières, Jean Pierre–(8) 6599
Numazawa, J.–(8) 5770
Nummila, K. K.–(8) 5078
Núñez-Regueiro, J. E.–(8) 5179

O'Barr, R.–(8) 5303, 6067
Obermyer, R. T.–(8) 5949, 6334
Obradors, X.–(8) 5182, 6596
O'Brien, W. L.–(8) 5623, 5629
O'Connor, Charles J.–(8) 5870, 6627
O'Connor, Teresa M.–(8) 5788
Odintsov, A. G.–(8) 6617
Ogale, S. B.–(8) 4545, 4552, 5292
O'Grady, K.–(8) 5590, 6034
Oh, Young Jei–(8) 5428
O'Handley, R. C.–(8) 5468, 5609, 5845
Ohashi, Masayoshi–(8) 5238
Ohinata, Y.–(8) 5655
Ohkubo, N.–(8) 5449, 5452
Ohmori, H.–(8) 5907
Ohnuki, S.–(8) 5686
Ohnuki, T.–(8) 4905
Ohnuma, S.–(8) 4733, 5130
Ohta, Masayuki–(8) 4721
Ohta, N.–(8) 4905, 5686
Okada, Takeshi–(8) 5683
Okamoto, Satoshi–(8) 5250
Oliver, S. A.–(8) 5431, 5435
Ono, T.–(8) 6382
Onodera, Hideya–(8) 5946
Onodera, Seiichi–(8) 4875
Oonk, M.–(8) 6129
Ortiz, C.–(8) 5321
Osborn, R.–(8) 6432
Oseroff, S. B.–(8) 5269, 6577
Osgood, R. M.–(8) 5851
Osgood, R. M., III–(8) 6189
O'Shea, M. J.–(8) 5299, 5435
Ostoréro, J.–(8) 5985
Ostrovskaya, N. V.–(8) 5730
O'Sullivan, J. A.–(8) 4695
Otani, Y.–(8) 4659, 5075
Otani, Yoshichika–(8) 5126, 6599
Oti, J. O.–(8) 5596, 6240, 6386
Ouchi, Kazuhiro–(8) 5362, 5913
Oudet, Xavier–(8) 5416
Ounadjela, K.–(8) 4528, 5068, 6247
Ouse, M.–(8) 6399

Padalia, B. D.–(8) 6347, 6349
Padovani, S.–(8) 5068
Paduan-Filho, A.–(8) 5236
Pakhomov, A. B.–(8) 6140
Palacio, F.–(8) 5236
Palme, W.–(8) 5384
Palstra, T. T. M.–(8) 4541
Pan, C. Y.–(8) 5162
Pan, J. L.–(8) 6035
Panagiotopoulos, I.–(8) 4616, 4827, 4837
Panchanathan, V.–(8) 4851
Panina, L. V.–(8) 6532
Pannetier, B.–(8) 5075
Pannetier, Bernard–(8) 6599
Pant, Bharat B.–(8) 6123
Pappas, C.–(8) 6158
Parakka, A. P.–(8) 6045
Paramonov, V. P.–(8) 6532
Parashikov, I.–(8) 5609
Pardavi-Horvath, M.–(8) 5742
Parekh, J. P.–(8) 5718
Park, C.-M.–(8) 6228
Park, J.-H.–(8) 4558, 6492, 6493
Park, J. K.–(8) 5357
Park, Jae Yun–(8) 5428
Park, K.–(8) 5195, 5357
Park, Ki-Ook–(8) 5785
Park, M. C.–(8) 4967
Park, S. J.–(8) 5879
Park, Seung Iel–(8) 5428
Park, Y.–(8) 4967
Parker, D. A.–(8) 4915
Parker, F. T.–(8) 5504
Parker, M. A.–(8) 4762, 5330
Parker, M. R.–(8) 5817, 6286
Parker, Martin R.–(8) 4970
Parkin, I. P.–(8) 6150
Parkin, S. S. P.–(8) 4980, 6078
Parra, R. E.–(8) 5242
Patterson, G. N.–(8) 6642
Patton, C. E.–(8) 5367, 5390
Patton, Steven T.–(8) 5802, 5916
Paul, D. I.–(8) 5609
Pavlovic, A. S.–(8) 5230
Pearson, J.–(8) 5838
Pease, R. F. W.–(8) 5851
Pechan, Michael J.–(8) 6266
Peck, Paul R.–(8) 5785
Peck, W. F., Jr.–(8) 5923
Pecora, L. M.–(8) 5377
Pedersen, J. S.–(8) 5146, 6173
Pekarek, T. M.–(8) 5401, 6164, 6436
Pelzl, J.–(8) 4929, 6266
Penfold, J.–(8) 6295
Peng, Liang-Ping–(8) 5718
Peng, Qingzhi–(8) 4916
Peredo, J. C.–(8) 6642
Pereira, L. G.–(8) 6555
Perera, P.–(8) 5299
Pérez Alcázar, G. A.–(8) 6155, 6611
Persiano, A. I. C.–(8) 5973
Peterman, D. W.–(8) 5378
Petford-Long, A. K.–(8) 6292
Petrenko, O. A.–(8) 6614
Petroff, P. M.–(8) 5296
Pflaum, J.–(8) 4929, 6266
Philips, D. A.–(8) 5496
Phillips, J. M.–(8) 5926
Phillips, Julia M.–(8) 5923
Piñol, S.–(8) 5182, 6596
Pinsard, L.–(8) 4554
Pinto, R. P.–(8) 6355
Pirkle, B. H.–(8) 5817
Pizzagalli, L.–(8) 5834
Pizzini, S.–(8) 6497
Platt, C. L.–(8) 5072
Pohm, A. V.–(8) 5889
Pokhil, Taras G.–(8) 6064
Pollard, R. J.–(8) 4939
Polushkin, N. I.–(8) 4625
Poon, Chin Y.–(8) 5799
Popkov, A. F.–(8) 5730
Popma, Th. J. A.–(8) 6190
Popović, Zoran S.–(8) 4555
Porter, D. G.–(8) 4695, 5652
Potenziani, E., II–(8) 5551
Pourarian, F.–(8) 5513, 6334
Powell, C. J.–(8) 5277
Prabhakar, A.–(8) 5374
Pratt, W. P., Jr.–(8) 5811, 6129
Prieur, J.–(8) 5270
Pringle, O. A.–(8) 4587, 5945, 6318
Prinz, G. A.–(8) 4525, 5387, 5622, 6084, 6234, 6492
Prokeš, K.–(8) 5221, 6358, 6361, 6396, 6408
Proksch, R.–(8) 6447
Proksch, Roger–(8) 6447
Psycharis, V.–(8) 5539
Pugh, V. J.–(8) 4644
Pulvirenti, P. P.–(8) 6219
Puri, R. K.–(8) 6515
Purwanto, A.–(8) 6408, 6411
Pustogowa, U.–(8) 6177
Putris, F. F.–(8) 5504

Qian, X. R.–(8) 4614, 5961
Qian, Y. H.–(8) 4949
Qian, You-Hua–(8) 5193
Qin, C-D.–(8) 4750, 4854, 6057
Qiu, Z. Q.–(8) 4532, 4964
Quichaud, G.–(8) 6485

Rachford, F. J.–(8) 5377
Radaelli, P. G.–(8) 4541
Rafailovich, M.–(8) 6025
Raju, N. P.–(8) 6170, 6173, 6176, 6636
Ramesh, A.–(8) 5453
Ramesh, R.–(8) 4545, 5292, 5935, 5991
Ramírez, R.–(8) 6479
Ramos, R. A.–(8) 6482
Rani, R.–(8) 5425
Ranjan, R.–(8) 5342
Rao, K. V.–(8) 5063, 5112, 5153, 5860, 6267, 6583
Raposo, V.–(8) 5422, 6574
Rasing, Th.–(8) 5632, 6181
Rasmussen, F. B.–(8) 5078
Rastelli, E.–(8) 5745, 5745
Rave, W.–(8) 6036
Ravet, M. F.–(8) 5068, 5848
Ravipati, Durga–(8) 5011
Rebizant, J.–(8) 6361
Redjdal, M.–(8) 6464
Reed, I. M.–(8) 6219
Regnault, L. P.–(8) 5099
Reich, D. H.–(8) 5391
Reich, Daniel H.–(8) 5392
Reiffers, M.–(8) 6352
Reimers, J. N.–(8) 6176
Renard, J. P.–(8) 4554, 5099, 5848
Renard, J.-P.–(8) 5270
Rengarajan, S.–(8) 5482
Repetto, M.–(8) 4575
Restorff, J. B.–(8) 6216
Revcolevschi, A.–(8) 4554, 5099, 5384, 5395
Rey, P.–(8) 4698
Rezende, S. M.–(8) 6309, 6546, 6555, 6558
Rhyne, J. J.–(8) 4779
Ribeiro, C. A.–(8) 5973
Richards, Howard L.–(8) 5749
Riedi, P. C.–(8) 4599, 5119, 6300
Rieke, Reuben D.–(8) 5312
Rigamonti, A.–(8) 6621, 6624
Rikvold, P. A.–(8) 6482
Rikvold, Per Arne–(8) 5749
Riley, C. D.–(8) 6342
Ripka, P.–(8) 5211
Ristau, R. A.–(8) 5330
Ritley, K. A.–(8) 4779
Ritter, C.–(8) 5869
Rivas, J.–(8) 4674, 5269, 5955
Rivas, M.–(8) 4936, 5217, 5472, 6545
Ro, M. D.–(8) 5696
Robertson, B. W.–(8) 5333
Robertson, J. L.–(8) 4524
Robinson, R. A.–(8) 6408, 6411
Röder, Heinrich–(8) 4632
Roderick, J. M.–(8) 5453
Roig, A.–(8) 5182
Rojdestvenski, I. V.–(8) 5724
Rojo, J. M.–(8) 4815
Rooney, P. W.–(8) 5854
Roschepkin, G. V.–(8) 6113
Rose, H. B.–(8) 6508
Rosenberg, M.–(8) 5257
Roshko, A.–(8) 5358, 6240
Roshko, R. M.–(8) 5758, 6618
Ross, C. A.–(8) 5342
Rossetti, G.–(8) 6624
Rotenberg, E.–(8) 5626
Roth, Ch.–(8) 6508
Rothberg, G. M.–(8) 4967
Rothman, J.–(8) 4976
Rottmayer, R.–(8) 5645
Rottmayer, Robert–(8) 4909, 5012, 5886
Rousseaux, F.–(8) 5068, 5848
Rudee, M. L.–(8) 5072
Rüdiger, U.–(8) 6203
Rudkowska, G.–(8) 5136
Rudkowski, P.–(8) 5136
Rueff, J. P.–(8) 6497
Rugar, D.–(8) 5644
Ruiz, X.–(8) 5439
Runge, K.–(8) 5075
Runge, Katharina–(8) 6599
Rupp, M.–(8) 4549
Russak, Michael A.–(8) 5336
Russek, S. E.–(8) 6240, 6386
Ryan, D. H.–(8) 6004, 6161

Saadi, M.–(8) 6485
Sabirianov, R. F.–(8) 5942
Sablik, M. J.–(8) 6134, 6525
Sá de Melo, C. A. R.–(8) 5412
Saeki, T.–(8) 5318
Sager, R. E.–(8) 4926
Saha, Shibaji–(8) 5233
Sahajwalla, V.–(8) 5149
Sahashi, M.–(8) 4611, 6399
Saito, K.–(8) 6399
Saito, Y.–(8) 4699, 5214
Sakakima, H.–(8) 6231
Sakuma, Akimasa–(8) 5570
Sakurada, S.–(8) 4611
Sakurai, M.–(8) 6270
Sakurai, T.–(8) 6074
Sal, J. C. Gómez–(8) 5146
Salamanca-Riba, L.–(8) 5195
Salamo, G.–(8) 6580
Salamo, G. J.–(8) 6593
Salashchenko, N. N.–(8) 4625
Salem-Sugui, S.–(8) 5462
Salomon, R. E.–(8) 6001
Samarasekara, P.–(8) 5425
Samarth, N.–(8) 6095
Samwer, K.–(8) 4765
Sánchez, D.–(8) 5256
Sanders, S. C.–(8) 5584, 6240
Sanjurjo, N. L.–(8) 5973
Sankar, S. G.–(8) 5949
Sanker, S. G.–(8) 6334
Santos, A. D.–(8) 5266, 6546
Sarachik, M. P.–(8) 6031
Sasada, I.–(8) 5490, 6077
Sasaki, S.–(8) 6167
Sato, K.–(8) 4896, 6439
Satomi, M.–(8) 6231
Satpathy, S.–(8) 4555
Schabes, M. E.–(8) 5342
Schaefer, D. M.–(8) 6234

Schaefer, H.-E.–(8) 5143
Schaf, J.–(8) 6154
Schäfer, M.–(8) 4782
Schäffer, Tilman E.–(8) 6447
Schalek, R.–(8) 5263
Schaper, L. W.–(8) 6593
Schatz, A.–(8) 5582
Scheidt, R.–(8) 4531
Scheinfein, M. R.–(8) 5056
Scherer, A.–(8) 5303
Schirmeisen, A.–(8) 5929, 6203
Schlottmann, P.–(8) 5419, 6414, 6417, 6605
Schlueter, J. A.–(8) 6586
Schmidlin, F.–(8) 4746
Schmidt, K. E.–(8) 5056
Schmidt, R.–(8) 5739
Schneider, C. M.–(8) 5618, 6426, 6504
Scholten, R. E.–(8) 6079
Schrefl, T.–(8) 5029, 6458
Schreiber, F.–(8) 4793, 4929, 6266
Schreyer, A.–(8) 4782
Schröder, Klaus–(8) 6522
Schroeder, P. A.–(8) 5811
Schuller, I.–(8) 6253
Schuller, Ivan K.–(8) 5109, 5112, 6266
Schulthess, T. C.–(8) 5282
Schultz, S.–(8) 5303, 6067
Schumann, F. O.–(8) 5635
Schwartz, J.–(8) 6567
Schweitzer, J. W.–(8) 6164
Scipioni, L.–(8) 4976
Scott, D. W.–(8) 4830, 5501, 6335
Scott, J. H.–(8) 5293
Scott, S.–(8) 6593
Sechovský, V.–(8) 5221, 6358, 6361, 6396, 6408
See, A. K.–(8) 4796
Seehra, M. S.–(8) 5185
Seehra, Mohindar S.–(8) 5230
Seffar, A.–(8) 5182
Selestino, R.–(8) 5826
Sellmyer, D. J.–(8) 4590, 4786, 4827, 4899, 5060, 5333, 5958
Semenov, V. G.–(8) 4625
Senda, Masakatsu–(8) 5483
Serena, P. A.–(8) 6019, 6110
Sereni, J. G.–(8) 6417
Sette, F.–(8) 6509
Seyedahmadian, M.–(8) 6001
Shaheen, S. A.–(8) 5425, 6327
Shan, Z. S.–(8) 4786, 4899, 5958
Shanabrook, B. V.–(8) 5125
Shand, P. M.–(8) 6164
Shapiro, A. J.–(8) 5315, 6073
Shapiro, A. L.–(8) 5854
Sharma, R. P.–(8) 4545, 4552
Shaw, K. A.–(8) 5102
Shaw, Kimberly A.–(8) 5841
Shen, Bao-Gen–(8) 5528, 5713
Shen, Bao-gen–(8) 5709
Shen, J. X.–(8) 4786, 5008
Shen, N. X.–(8) 5530
Sheng, L.–(8) 6255
Sheng, Q. G.–(8) 6420
Shepard, M.–(8) 4567, 4821, 5876
Shevchenko, N. B.–(8) 5152, 5302
Sheverev, V. A.–(8) 5716
Shi, Jing–(8) 5296
Shi, Zhu-Pei–(8) 4776
Shidara, T.–(8) 5707, 5708
Shieh, J. H.–(8) 5863, 5866
Shield, J. E.–(8) 4851
Shih, Tom I.-P.–(8) 5785
Shimada, K.–(8) 5707
Shimada, Y.–(8) 6074
Shimada, Yutaka–(8) 5250
Shimatsu, Takehito–(8) 5339
Shimazaki, K.–(8) 5686
Shimizu, Yutaka–(8) 5602
Shin, K. H.–(8) 5357, 6228
Shin, Sung-Chul–(8) 4991
Shin, T.–(8) 4967
Shinjo, T.–(8) 6382
Shiraishi, H.–(8) 6633
Shiraishi, Hiroshi–(8) 5238
Shirane, G.–(8) 4802
Shiroishi, Y.–(8) 5648
Shoji, H.–(8) 5564
Shoji, M.–(8) 5907
Shull, C. G.–(8) 5021
Shull, R. D.–(8) 6028
Sides, S. W.–(8) 6482
Sides, Scott W.–(8) 5749
Siegmann, Hans C.–(8) 6488
Siemensmeyer, K.–(8) 5078
Silver, Richard N.–(8) 4632
Silversten, John M.–(8) 5782
Simion, B. M.–(8) 5935, 5991
Simizu, S.–(8) 5949
Simmins, J. J.–(8) 6341
Simmons, R.–(8) 5671
Simon, Ch.–(8) 6173
Sin, Kyusik–(8) 5901
Sinclair, Robert–(8) 6393
Singer, B.–(8) 5102
Singer, Brian–(8) 5841
Singh, David J.–(8) 4515, 4818
Singleton, E. W.–(8) 4590, 4827
Sinha, S. K.–(8) 5857
Sinkovic, B.–(8) 4976
Sinnemann, Th.–(8) 5257
Sivertsen, J. M.–(8) 5277, 5327
Sivertsen, John–(8) 4912
Slavin, A. N.–(8) 5366, 5371, 5724
Smirnov-Rueda, R.–(8) 6479
Smit, P.–(8) 6519, 6526
Smith, Neil–(8) 6254
Smyth, J. F.–(8) 5898
Snowman, Daniel P.–(8) 5087
Snyder, J. E.–(8) 4890
Snyder, R. L.–(8) 6341
Sobolev, V. L.–(8) 5415, 6060
Soeda, M.–(8) 6047
Sohn, J. W.–(8) 5670
Sokoloff, J. B.–(8) 4564
Sokolov, J.–(8) 6025
Solé, R.–(8) 5439
Somasundaram, P.–(8) 5401
Sommer, R. L.–(8) 5139, 6117
Song, K.–(8) 6273
Song, Xing–(8) 4912
Sonier, J. E.–(8) 6636
Sooryakumar, R.–(8) 5387
Souche, Y.–(8) 5266, 6546
Sousa, J. B.–(8) 6246, 6355
Sowers, C. H.–(8) 4524
Spagna, S.–(8) 4926
Spanke, D.–(8) 6508
Speriosu, V. S.–(8) 6295
Spirlet, J. C.–(8) 6361
Spoddig, D.–(8) 4929, 6266
Srinivasan, G.–(8) 5185
Stafford, D. C.–(8) 5958
Stager, C. V.–(8) 6170, 6614
Stampe, P. A.–(8) 6561
Stamps, R.–(8) 4528
Stamps, R. L.–(8) 5387
Stancil, D. D.–(8) 5374
Stashkevich, A. A.–(8) 5371
Staudinger, R.–(8) 5367
Steiner, M.–(8) 5078
Stepanyuk, V. S.–(8) 5129
Sternlieb, B. J.–(8) 4802
Stiefel, B.–(8) 5609
Stiles, M. D.–(8) 4994, 5277, 5805
Stoeffler, D.–(8) 5834
Stolze, Joachim–(8) 4632, 5227
Stoyanov, Plamen–(8) 5841
Stoyonov, P.–(8) 5102
Ström, V.–(8) 5063, 5153, 6583
Ström, Valter–(8) 5860
Ström-Olsen, J. O.–(8) 4605, 4619, 4769, 5136, 5536
Su, Yen-Sheng–(8) 6433
Subbaraman, Kala–(8) 5368
Subramanian, M. A.–(8) 6173
Suemitsu, Katsumi–(8) 5156
Sugawara, Hiroharu–(8) 4721
Sugita, Y.–(8) 5648, 5664, 6451
Sugita, Yutaka–(8) 5576
Sugiyama, S.–(8) 5797
Sugiyama, Y.–(8) 5907
Suh, B. J.–(8) 5084
Suharyana, –(8) 5713
Sui, X.–(8) 4890
Sui, Y. C.–(8) 5525
Sui, Y. X.–(8) 4949
Sun, D. C.–(8) 5440
Sun, J. Z.–(8) 4538, 4546, 4549
Sun, Ji-jun–(8) 5709
Sun, Kunquan–(8) 5733
Sun, X. K.–(8) 5525, 6324
Sundaram, Ramesh–(8) 5916
Sunil, D.–(8) 6025
Suran, G.–(8) 5381
Suresh Babu, V.–(8) 5185, 5230
Suriono, Usman–(8) 5066
Suzuki, E.–(8) 4945
Suzuki, H.–(8) 6467
Suzuki, K.–(8) 5149, 6270
Suzuki, M.–(8) 5648
Suzuki, T.–(8) 4647, 5143, 5327, 5687, 6190
Suzuki, Takanobu–(8) 5224
Suzuki, Takao–(8) 5677
Suzuki, Y.–(8) 5708, 5923, 5926
Suzuya, K.–(8) 6512
Svoboda, P.–(8) 5221, 6361
Swainson, I. P.–(8) 6408, 6411
Swann, C. P.–(8) 5106
Swanson, R.–(8) 5658
Swartzendruber, L. J.–(8) 5315, 6073
Szpunar, J. A.–(8) 5202, 6042

Tagirov, L. R.–(8) 6298
Taguchi, T.–(8) 5655
Takahashi, H.–(8) 5564
Takahashi, Hiromasa–(8) 5576
Takahashi, Koyata–(8) 5677
Takahashi, M.–(8) 5700
Takahashi, Migaku–(8) 5339, 5564
Takahashi, Y.–(8) 6451
Takano, H.–(8) 5648
Takano, K.–(8) 5277, 5919
Takano, Ken-ichi–(8) 5002
Takano, Kentaro–(8) 4932
Takeda, Tsutomu–(8) 4875
Takei, Koji–(8) 5483
Takemura, Y.–(8) 4653, 6542
Takeshita, T.–(8) 5040
Takeuchi, A.–(8) 4836
Takeuchi, A. Y.–(8) 5220
Tako, K. M.–(8) 5767
Talyansky, V.–(8) 4545
Tamari, K.–(8) 4884, 4887
Tan, Minshen–(8) 5012
Tan, Swie-In–(8) 5012
Tanabe, S.–(8) 4999
Tanaka, Atsushi–(8) 5602
Tanaka, C. T.–(8) 6265
Tanaka, M.–(8) 4957, 4967
Tanaka, Satoshi–(8) 5156
Tanaka, Y.–(8) 5655
Tang, F. C.–(8) 4790
Tang, Jinke–(8) 5870
Tang, Li–(8) 5348
Tang, N.–(8) 6321
Tang, Y. Q.–(8) 6580, 6593
Taniguchi, K.–(8) 5318, 6646
Tanuma, Toshio–(8) 6402
Tao, Cuihong–(8) 6627
Tassi, A.–(8) 5745, 5745
Tayaoka, A.–(8) 6016
Tayaoka, E.–(8) 6016
Teh, C. T.–(8) 6060
Tehrani, S.–(8) 5889
Tejada, J.–(8) 4686, 5406, 5439, 6031; 6116, 6516, 6589
Templeton, T. L.–(8) 4635
ter Haar, L. W.–(8) 4715
Terris, B. D.–(8) 5644
Tesiero, James E.–(8) 6146
Teter, J. P.–(8) 6213, 6216, 6234
Tezuka, N.–(8) 6262
Theis-Bröhl, K.–(8) 4531, 4779
Theuss, H.–(8) 4990
Thevenot, J.–(8) 6420
Thibado, P. M.–(8) 5125
Thiel, R. C.–(8) 4593
Tholence, J. L.–(8) 4698
Thomas, G.–(8) 4846, 5935, 5991
Thomas, Gareth–(8) 4932
Thompson, C. V.–(8) 5845
Thompson, J. D.–(8) 4535
Thompson, S. M.–(8) 5593, 6247
Thomson, T.–(8) 5119, 6300
Tian, M. B.–(8) 5440
Tiberto, P.–(8) 4575
Tiefel, T. H.–(8) 5599
Tilak, A. S.–(8) 5551
Tischer, M.–(8) 4983
Tobin, J. G.–(8) 5626
Tognetti, Valerio–(8) 4638
Tokura, Y.–(8) 5288
Tomida, Toshiro–(8) 5443
Tomioka, Y.–(8) 5288
Tomiyama, F.–(8) 5648
Tomka, G. J.–(8) 4599
Toney, M. F.–(8) 5967
Tong, H.-C.–(8) 5645
Tong, Hua-Ching–(8) 4909, 5011, 5012, 5886, 5895
Tonner, B. P.–(8) 5623, 5629
Tonomura, A.–(8) 5075
Tonucci, R. J.–(8) 5303
Torgeson, D. R.–(8) 5084
Torikachvili, M. S.–(8) 6411
Torres, L.–(8) 5422, 5436, 6574
Totland, K.–(8) 4518
Tovar, M.–(8) 5269, 6577
Tran, L.–(8) 4491
Tran, M. Q.–(8) 5854
Tristan, L.–(8) 5826
Troper, Amós–(8) 6345
Trygg, J.–(8) 4983, 5837
Tsai, J. L.–(8) 5964
Tsamakis, D.–(8) 5563
Tsang, C.–(8) 6025
Tsifrinovich, V. I.–(8) 5716
Tsoukatos, A.–(8) 5018, 5446, 5584
Tsuda, H.–(8) 4708
Tsunashima, S.–(8) 6237, 6270
Tsunashima, Shigeru–(8) 5683
Tsutai, A.–(8) 4611
Tsutsumi, K.–(8) 6243
Tuan, H. S.–(8) 5718
Tun, Z.–(8) 4769, 6614
Tun, Zin–(8) 6176
Tuoriniemi, J. T.–(8) 5078
Turkki, T.–(8) 5063, 6583
Tyagi, S.–(8) 5166

Uchizawa, M.–(8) 4999
Uemura, Y. J.–(8) 6636
Ueno, S.–(8) 4705, 4708
Ueno, Shoogo–(8) 4711, 4721
Umehara, I.–(8) 6439

Vaia, Ruggero–(8) 4638
Vajda, Ferenc–(8) 5773
Valanju, A. P.–(8) 6536
Valenzuela, R.–(8) 6539, 6549
van der Heijden, P. A. A.–(8) 5103, 5936
van der Sluijs, A. J.–(8) 4734
van der Zaag, P. J.–(8) 5103, 5936
van de Straat, D. A.–(8) 4593
van de Veerdonk, R. J. M.–(8) 5936
Vandlik, J.–(8) 5742
van Dover, R. B.–(8) 5923, 5926
Van Drent, W. P.–(8) 6190
van Loosdrecht, P. H. M.–(8) 5395
van Schilfgaarde, M.–(8) 4799
Varga, L.–(8) 4995
Varga, Lajos K.–(8) 4811
Vas'ko, V. A.–(8) 4553
Vavra, W.–(8) 6084
Vazquez, M.–(8) 6549
Vázquez, M.–(8) 6539
Vázquez-Vázquez, C.–(8) 5269
Vega, A.–(8) 5834
Veillet, P.–(8) 4554, 5099, 5270, 5848
Vélu, E.–(8) 5270
Velu, E. M. T.–(8) 4496
Venkatesan, T.–(8) 4545, 4552, 4552, 5165, 5166, 5292, 5991
Venus, D.–(8) 4518, 6504
Veres, T.–(8) 6289
Verrucchi, Paola–(8) 4638
Viala, B.–(8) 5005
Victora, R. H.–(8) 6199
Viel, V.–(8) 6158
Vijayaraghavan, R.–(8) 6347, 6349
Virovets, T. V.–(8) 6617
Vitale, S.–(8) 5406
Vittoria, C.–(8) 5739
Vogel, J.–(8) 6497
Vugmeister, B. E.–(8) 6143
Vukajlović, Filip R.–(8) 4555
Vuorinen, R. T.–(8) 5078

Wakiyama, T.–(8) 5564
Waldfried, C.–(8) 5838
Wall, M. A.–(8) 4775
Wallace, W. E.–(8) 5949, 6331
Walmsley, N. S.–(8) 4915
Walser, R. M.–(8) 4933, 4948, 5482, 6306, 6536
Wan, H.–(8) 5504
Wang, C. T.–(8) 4772
Wang, D. S.–(8) 5827
Wang, Dingsheng–(8) 5831
Wang, Fang-Wei–(8) 5713
Wang, G.-C.–(8) 5122
Wang, Geng–(8) 5782
Wang, Guiqin–(8) 5473
Wang, J. Q.–(8) 6126
Wang, J. T.–(8) 4812, 6608
Wang, Jian-Qing–(8) 5587
Wang, Jie–(8) 5193
Wang, Jinghua–(8) 4665, 4668, 6225
Wang, Lien-Chang–(8) 5776
Wang, P. S.–(8) 4712
Wang, Q.–(8) 4929, 6266, 6300
Wang, R. C.–(8) 6593
Wang, S.–(8) 5880
Wang, Shan X.–(8) 5901, 6393
Wang, Shyh-Jier–(8) 5560
Wang, X. Q.–(8) 4812, 5873
Wang, Xindog–(8) 5827
Wang, Xindong–(8) 5831
Wang, Xue-Qin–(8) 5403
Wang, Xun–(8) 5193
Wang, Y.–(8) 4949
Wang, Y. D.–(8) 4949
Wang, Ya-Dong–(8) 5193
Wang, Yu–(8) 5193
Wang, Z.–(8) 6642
Wang, Z. D.–(8) 6255
Wang, Zhigang–(8) 5525, 6639, 6649
Warwick, A.–(8) 5626
Watanabe, K.–(8) 5797
Watanabe, N.–(8) 6077
Watson, M. L.–(8) 5590, 5593, 5605
Weerasooriya, S.–(8) 5674
Wei, D.–(8) 5658
Wei, Dan–(8) 5661
Weinberg, Harold–(8) 4711
Welch, D. O.–(8) 5513, 6470
Welch, David O.–(8) 4848
Welch, M. H.–(8) 4718
Weller, D.–(8) 4922, 4990, 5967
Weller, Dieter–(8) 6488
Wellock, K. P.–(8) 5816
Wendhausen, P. A. P.–(8) 5045
Werder, D. J.–(8) 5923
Werner, S. A.–(8) 4802
Wesseling, E.–(8) 5758
Westerholt, K.–(8) 6298
Westphal, C. H.–(8) 6564
White, R. L.–(8) 5851, 6189
White, R. M.–(8) 5113
White, Robert L.–(8) 5116, 6389
Whitman, L. J.–(8) 5125
Wierman, Kurt W.–(8) 6193, 6206
Wigen, P.–(8) 4528
Wigen, P. E.–(8) 5191, 5378
Wiggins, J.–(8) 5590, 5605
Wildberger, K.–(8) 5129
Willey, R. J.–(8) 5435
Williams, C. M.–(8) 4561
Williams, Damon–(8) 6627
Williams, Gwyn–(8) 6561
Williams, J. M.–(8) 6586
Willis, R. F.–(8) 5626, 5635
Wills, J. M.–(8) 4983, 5837
Wilmers, K.–(8) 5582
Wilson, Robert J.–(8) 5116
Win, W.–(8) 4933, 4948
Winand, J. M.–(8) 6361
Withanawasam, L.–(8) 4827, 4837
Wittborn, J.–(8) 5153
Woicik, J. C.–(8) 5345
Wolf, J. A.–(8) 5622
Wolf, J. K.–(8) 5658
Wolf, Jason–(8) 6331
Wolf, R. M.–(8) 5103, 5936
Wolff, P. A.–(8) 5196
Wong, Bunsen Y.–(8) 6455
Wong, H. K.–(8) 5188, 6279
Wong, K.–(8) 5324
Wongsam, M. A.–(8) 5767
Woollam, John A.–(8) 6193
Wu, Bingyao–(8) 5473
Wu, D. C.–(8) 5159
Wu, Guangheng–(8) 4665, 4668, 6225
Wu, J. M.–(8) 5432
Wu, K. T.–(8) 6285, 6341
Wu, M. D.–(8) 5557
Wu, R.–(8) 5827
Wu, Ruqian–(8) 4783, 6209, 6500
Wu, S. Y.–(8) 6568, 6571
Wu, S. Z.–(8) 5635
Wu, W. D.–(8) 6636
Wu, X. D.–(8) 4535
Wu, Xiaohua–(8) 5473
Wun-Fogle, M.–(8) 6216

Xiao, Gang–(8) 4538, 4546, 4549, 5587, 6126
Xiao, J. Q.–(8) 5306
Xiao, John Q.–(8) 5309
Xiao, Q. F.–(8) 5525
Xiao, Ying–(8) 6267
Xie, K.–(8) 5365
Xing, D. Y.–(8) 6255
Xing, Xinzhi–(8) 5883
Xiong, G. C.–(8) 4545, 4552, 4552, 5165, 5166
Xiong, Q.–(8) 6580, 6593
Xu, Dong–(8) 4998
Xu, J.–(8) 6507
Xu, Jun-Hao–(8) 6267
Xu, Weihua–(8) 5303
Xu, X. L.–(8) 6593
Xu, Y.–(8) 6013, 6137, 6140
Xu, You–(8) 5979
Xu, Zhenghe–(8) 4702
Xue, Y. Y.–(8) 6580

Yahisa, Y.–(8) 5351
Yajima, Y.–(8) 6451
Yakhmi, J. V.–(8) 5260
Yamada, I.–(8) 6167
Yamada, M.–(8) 5507
Yamada, T.–(8) 4653, 6542
Yamada, Y.–(8) 5583
Yamaguchi, M.–(8) 5952
Yamaguchi, Y.–(8) 5452
Yamaguchi, Yasuo–(8) 5238, 5946
Yamakawa, Kiyoshi–(8) 5913
Yamamoto, S.–(8) 4884, 4896
Yamamoto, T.–(8) 5354, 5490, 5907
Yamamoto, Takeshi–(8) 5988
Yamasaki, J.–(8) 6016, 6047
Yamashiro, Y.–(8) 4574
Yamauchi, T.–(8) 5490
Yan, X.–(8) 6013, 6022, 6137, 6140
Yan, Zheng–(8) 6200
Yanagida, Y.–(8) 4611
Yanase, Satoshi–(8) 5362
Yang, Bo–(8) 5755
Yang, C. L.–(8) 5866
Yang, D. P.–(8) 4596
Yang, H. D.–(8) 6571
Yang, H.-N.–(8) 5122
Yang, J.–(8) 4605, 4619, 5536, 5817
Yang, Jun–(8) 5519
Yang, Kun–(8) 5096
Yang, Q.–(8) 5811, 6129
Yang, W. T.–(8) 4790, 6282, 6533
Yang, Z. J.–(8) 5995
Yao, Y. D.–(8) 4790, 4919, 5533, 5599, 6282, 6341, 6533
Ye, M.–(8) 5378
Ye, Weichun–(8) 6048
Ye, Xiao-Guang–(8) 4906, 5886
Yelon, A.–(8) 5136
Yelon, W. B.–(8) 4587, 5522, 5939, 5945, 6315, 6318, 6367
Yewondwossen, M.–(8) 5992, 5995
Yi, J. Y.–(8) 5072
Ying, T. F.–(8) 5557
Yogi, T.–(8) 5358
Yokoi, Hiroyuki–(8) 4721
Yonamine, T.–(8) 5266
Yoneda, Y.–(8) 5770
Yonesu, A.–(8) 4574
Yoo, Yong Goo–(8) 5476
Yoon, Do Y.–(8) 5788
Yoshida, Hideki–(8) 4711
Yoshida, K.–(8) 5664
Yoshida, S.–(8) 4699
Yoshihiro, M.–(8) 5686
Yoshitani, T.–(8) 6392
Yoshizawa, Masami–(8) 5205
Yosida, T.–(8) 6167
You, Y. B.–(8) 5863, 5866
Young, I. R.–(8) 4685
Youssef, J. Ben–(8) 5381
Yu, C. C.–(8) 4750, 6057
Yu, Jinyue–(8) 6048
Yu, M.–(8) 5060
Yu, S. C.–(8) 5153
Yu, Seong Cho–(8) 5476
Yu, X. Y.–(8) 6270
Yu, Yongmin–(8) 4629
Yu. Galkin, V.–(8) 6154
Yuan, Samuel W.–(8) 5886
Yuasa, S.–(8) 4659
Yuen, T.–(8) 6001
Yun, E. J.–(8) 4933, 4948, 5482

Zabe, H.–(8) 6300
Zabel, H.–(8) 4782, 4793, 4929, 6266, 6298
Zamora, Ligia E.–(8) 6155, 6611
Zangwill, A.–(8) 4942, 4994
Zaspel, Craig E.–(8) 5368
Zazo, M.–(8) 5422, 5436, 6574
Zeidler, Th.–(8) 4531, 4782, 4793
Zeller, R.–(8) 5129, 5638
Zeltser, A. M.–(8) 6254
Zeng, X. T.–(8) 5188, 6279
Zeng, Xianglin–(8) 4998
Zhan, Wen-Shan–(8) 5713
Zhan, Wenshan–(8) 4665, 4668, 6225
Zhang, J.–(8) 5113
Zhang, Jian H.–(8) 6627
Zhang, Jianqiang–(8) 5473
Zhang, Jun-Xian–(8) 5528, 5709
Zhang, Kezhao–(8) 5762
Zhang, Q.–(8) 4561
Zhang, S.–(8) 6382
Zhang, S. Y.–(8) 6261
Zhang, Shu–(8) 5227, 6630
Zhang, Shufeng–(8) 4542
Zhang, X.–(8) 5406, 5522
Zhang, X.-G.–(8) 5282
Zhang, X. Q.–(8) 5312
Zhang, X. X.–(8) 4686, 5439, 5440, 6116, 6516, 6589
Zhang, Xijuan–(8) 5979
Zhang, Y. D.–(8) 4596, 5530
Zhang, Z. D.–(8) 5525, 6324
Zhao, B.–(8) 6022, 6137
Zhao, Dai–(8) 6503
Zhao, Jiwan–(8) 5473
Zhao, T.–(8) 6324
Zhao, Wei–(8) 5870
Zhao, X. G.–(8) 5525
Zhao, Xuegen–(8) 4665, 4668, 6225
Zhao, Z. G.–(8) 4626, 6321
Zharnikov, M.–(8) 5618, 6426, 6504
Zheng, Guobao–(8) 5742
Zheng, Qing-Qi–(8) 5162
Zheng, Y.–(8) 4590
Zheng, Y. X.–(8) 4949
Zheng, Yu-Xiang–(8) 5193
Zhong, Lieping–(8) 5831
Zhou, Li–(8) 4528
Zhou, S. M.–(8) 4949
Zhou, Shi-Ming–(8) 5193

Zhou, X. Z.–(8) 6561
Zhu, J.-G.–(8) 5645
Zhu, Jian-Gang–(8) 4906, 4909, 5886, 5892
Zhu, Jian-Xin–(8) 6255
Zhu, Nan-Chang–(8) 6393
Zhu, T.–(8) 5889
Zhu, Yimei–(8) 4848
Ziolo, R.–(8) 6031, 6116
Zoller, I.–(8) 6298
Zou, Liang-Jian–(8) 5162
Zuo, F.–(8) 6586
Zvyagin, A. A.–(8) 5419

AIP

# AMERICAN INSTITUTE OF PHYSICS

**500 Sunnyside Boulevard, Woodbury, NY 11797-2999**

Under United States copyright law, a transfer of copyright from the author(s) must be explicitly stated in writing to enable the publisher to disseminate the work to the fullest extent. The following transfer agreement must be completed, signed and returned to the Editor's office before the manuscript can be accepted for publication. Further information is available from the Office of Rights and Permissions, American Institute of Physics (AIP), 500 Sunnyside Boulevard, Woodbury, NY 11797-2999; Tel: (516) 576-2268; Fax: (516) 576-2327; Internet: rights@aip.org.

## TRANSFER OF COPYRIGHT AGREEMENT

Copyright in the unpublished and original article, including the abstract forming part thereof, entitled _____

_____

_____

Title of Article

(the "Article"), submitted by the following author(s) [the "Author(s)"] _____

_____

_____

Names of all Authors

is hereby assigned and transferred to the American Institute of Physics ("AIP") for the full term thereof throughout the world, subject to the terms of this Agreement and to acceptance of the Article for publication in _____

_____

Name of Journal

AIP shall have the right to publish the Article in any medium or form, or by any means, now known or later developed.

AIP shall have the right to register copyright to the Article in its name as claimant whether separately or as part of the journal issue or other medium in which the Article is included. The Author(s) reserve all proprietary rights other than copyright, such as patent rights. If the Article was prepared under a United States Government contract, the Government shall have rights in the copyright to the extent required by the contract, and the Author(s) shall notify AIP of any such rights. The Author(s) represent and warrant: (1) that the Article is original with them; (2) that the Article does not infringe any copyright or other rights in any other work, or violate any other rights; (3) that the Author(s) own the copyright in the Article or are authorized to transfer it; and (4) that all copies of the Article the Author(s) make or authorize will include a proper notice of copyright in AIP's name. If each Author's signature does not appear below, the signing Author(s) represent that they sign this Agreement as authorized agents for and on behalf of all the Authors, and that this Agreement and authorization is made on behalf of all the Authors.

_____ _____

Name (print) Date

_____

Signature

If the manuscript has been prepared as a work for hire, this Agreement should be signed by the employee (or commissioned party) **(above)** and by the employer (or commissioning party) **(below).** In such event, the employer (or commissioning party) agrees to be bound by all of the obligations of the Author(s) under this Agreement.

_____

Name of Employer (or Commissioning Party) (print)

_____ _____ _____

Signature Title Date

A work prepared by a U. S. Government officer or employee as part of his or her official duties is not eligible for U. S. copyright; however, foreign copyright laws may differ. Thus this form should be signed even by U. S. Government officers or employees. Signing of this form will not affect U. S. Copyright law provisions in the case of works of the U. S. Government.

**If all the authors are in this category, check the box here and return the signed form.** ☐

*See page 2 (over) for rights granted by AIP to authors.*

AIP hereby grants to the Author(s) a nonexclusive license to do the following:

(a) After publication of the article by AIP, to publish all or part of the Article in any compilation or publication limited to the Author(s)' own works, or in any compilation or publication approved by AIP, and to make copies of the Article for the Author(s)' own use for lecture or classroom purposes;

(b) To make an oral presentation of the Article;

(c) If the Article was prepared as a work made for hire, to allow the employer or commissioning party to make copies of the Article for its own internal use.

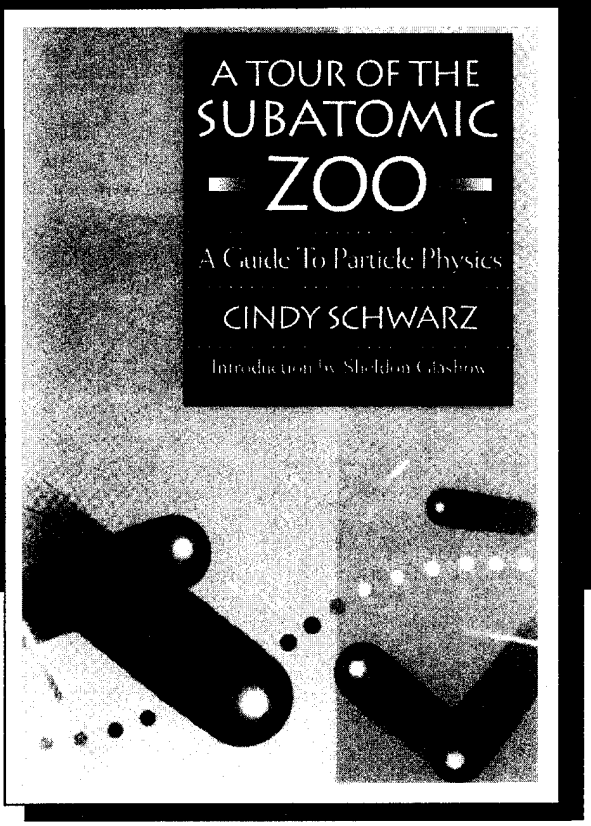
AIP and the Author(s) further agree that, after publication of the Article by AIP, third parties wishing to republish the Article must obtain written permission from both the Author(s) and AIP; provided, however, that only AIP's permission is necessary with respect to republication of entire journal issues which contain the Article.

**Please sign the applicable portion of the form and return it promptly to the Editor's Office. We cannot begin the production process until this signed form has been received. Please help us to expedite the publication of your paper with your immediate response.**

# A TOUR OF THE SUBATOMIC ZOO

## A Guide to Particle Physics

Cindy Schwarz, *Vassar College*




"A great little book, and if every physics textbook were like this, physics classrooms would be crowded."

**—Scitech Book News**

With hardly a mathematical formula, Ms. Schwarz clearly explains the substance of elementary particle physics. The book guides readers through the subatomic "zoo," populated by some of the most dramatic discoveries of modern science—notably, quarks, leptons, and the basic forces that govern their interactions.

Most important, this tour is conducted in terms that are easily understood—even by those who have no prior particle physics background. Each chapter in this book begins with an overview of concepts and ends with a summary and self-tests to help readers gauge their understanding.

If you're involved in teaching science to the non-scientist, think about using this book. It's been used successfully to introduce future lawyers, politicians, and parents to the ideas, terminology, and techniques of high energy physics and it's given them a unique historical perspective on the field.

1992, 128 pages, illustrated
ISBN 0-88318-954-2, paper
$25.00 ***Members $20.00**

*Members of AIP Member Societies are entitled to a 20% discount.

## ORDER FORM

❑ **Yes!** Please send me ___ copy(ies) of ***A Tour of the Subatomic Zoo*** by Cindy Schwarz (ISBN 0-88318-954-2) at **$25.00 per copy ($20.00 for Members.)**

**Shipping:** $2.75 first book ($7.50 foreign), $.75 each additional book.

### METHOD OF PAYMENT

❑ Check enclosed (payable in U.S. dollars to the **American Institute of Physics** and drawn on a bank in the United States).

❑ Charge my credit card: ❑ AMEX ❑ VISA ❑ MasterCard

Cardholder name (please print)_____

Acct. No. _____ Exp. Date _____

Signature _____

(Credit card orders not valid without signature)

Name_____

Organization_____

Address_____

City/State/Zip_____

**☎ FOR FAST SERVICE, CALL TOLL-FREE:**

**1-800-488-BOOK (2665)**

**In Vermont: (802) 862-0095**

**Or mail to:**

**American Institute of Physics • c/o AIDC**
**P.O. Box 20 • Williston, VT 05495**

AIP PRESS

**American Institute of Physics**
**500 Sunnyside Boulevard**
**Woodbury, NY 11797-2999**

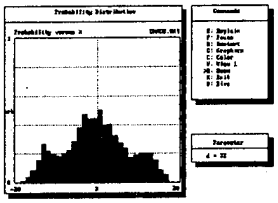
9472

# We Put the World of Physics Right at your Fingertips

*Explore the science of physics with interactive educational software*

## Chaos Data Analyzer

by J. C. Sprott
University of Wisconsin,
G. Rowlands
University of Warwick



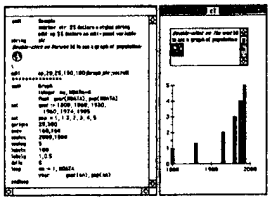
Pc

Fourteen analytical tools search for chaotic behavior in real world data and determine the properties of the underlying equations. Performs time series analysis.

**$99.95; $299.95 (10-copy lab pack)**

## cT

by D. Andersen,
B. Sherwood,
J. Sherwood,
K. Whitley
Carnegie Mellon



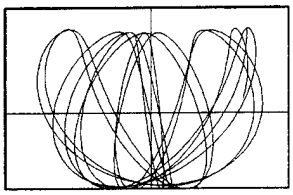
Pc Mac

cT programming language offers instant portability between Macintosh and MS-DOS computers. For expert and novice programmers.

**$175 (PC or Mac), $525 (10-copy lab pack); $275 (PC/Mac combo), $825 (lab pack)**

## ODE Workbench

by Juan Aguirregabiria
University of the
Basque Country



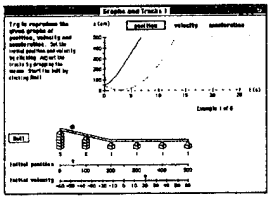
Pc

Computational tool for solving ordinary differential equations. Features user-defined graphical output for extended exploration and visualization.

**$54.95; $164.95 (10-copy lab pack)**

## Graphs & Tracks

by David Trowbridge
Microsoft
Corporation



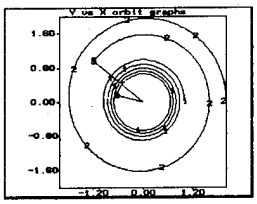
Pc Mac

Goal-oriented simulation underscores the connection between animated motion and graphs using an inclined track and ball scenario.

**$79.95; $239.95 (10-copy lab pack)**

## Dynamic Analyzer

by Roger Sipson
Moorhead State
University



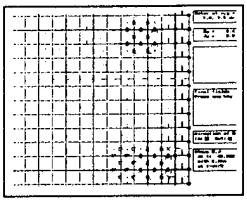
Pc

Interact with 22 common linear and nonlinear physical systems and view the results simultaneously in graphs and animations. Over 30 different scenarios are included.

**$74.95; $224.95 (10-copy lab pack)**

## Maxwell

by Pieter Visscher
University
of Alabama



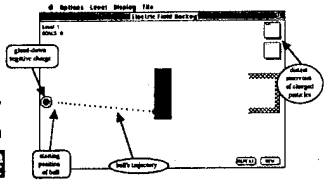
Pc

Displays time evolution of electromagnetic fields. Helps create an intuitive understanding of electrodynamics with a variety of configurations and devices.

**$69.95; $209.95 (10-copy lab pack)**

## Electric Field Hockey

by Ruth W. Chabay
Carnegie Mellon



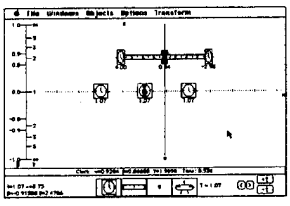
Pc Mac

Unique simulation game instills intuitive understanding of the Coulomb force, the superposition of forces, and frictionless motion.

**$59.95; $179.95 (10-copy lab pack)**

## Spacetime

by Edwin F. Taylor
Massachusetts
Institute of
Technology



Pc Mac

Introduction to the study of special relativity. Explore time dilation, Lorentz contraction, the twin paradox, and the Doppler shift.

**$59.95; $179.95 (10-copy lab pack)**

**PAS offers a diverse selection of more than 30 peer-reviewed titles, so there is something for everyone—students, teachers, and scientists!**

PHYSICS ACADEMIC SOFTWARE

**Act Now Order Today!**

Order by check, credit card (MC, Visa, AmEx), or institutional purchase order. Just call or write:

**The Academic Software Library**
**Box 8202**
**North Carolina State University**
**Raleigh, NC 27695–8202**

For shipping & handling in the U.S., Mexico, & Canada add $3.50 for first package and $.75 for each additional package. All other foreign orders will be shipped air mail. Add $12.50 for first package and $4.00 for each additional package. Allow 2 weeks for delivery.

**Satisfaction Guaranteed**

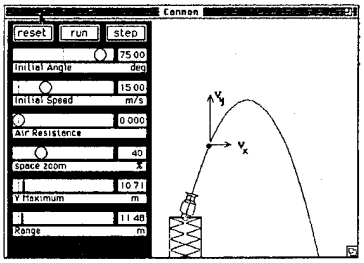
**Call Toll Free**
**(800) 955-TASL**
**(919) 515-7447**
**Fax 515-2682**

A publishing project of the American Institute of Physics in cooperation with the American Physical Society and the American Association of Physics Teachers

# Make an Introduction That Leaves a Lasting Impression

*Introductory Physics Software for your Classroom and Lab*

## Objects In Motion



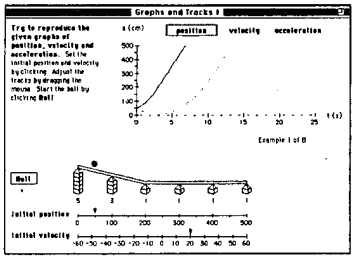

**Peter Cramer**

**Case Western Reserve**

Your students will learn the notion behind the motion with Objects In Motion, a collection of six interactive simulations—Cars, Cannon, River, Planet, Circle, and Collider—that focuses on the physics of moving objects and teaches the concepts underlying kinematics, rotational motion, uniformly accelerated motion, conservation laws, Galilean relativity, Kepler's laws, scattering, and vector superposition.

**$84.95; $254.95 (10-copy lab pack)**

## Graphs & Tracks



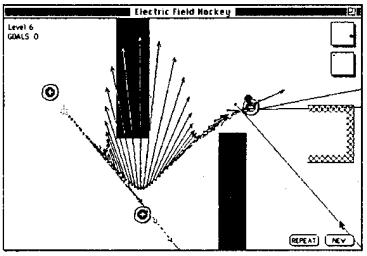

**David Trowbridge**

**Microsoft Corporation**

Put your students on the right track with Graphs & Tracks, a goal-oriented simulation tutorial that underscores the connection between animated motion and graphs. In Part I, students set up a ball on an inclined set of tracks and try to reproduce the motion indicated on a given set of graphs. In Part II, they roll the ball on the tracks and sketch the subsequent motion with a graph-drawing editor.

**$79.95; $239.95 (10-copy lab pack)**

## Electric Field Hockey



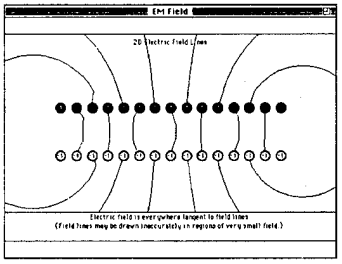

**Ruth Chabay**

**Carnegie Mellon**

By combining serious learning with serious fun, Electric Field Hockey instills an intuitive understanding of the Coulomb force, the superposition of forces, and frictionless motion. This computer-simulated game challenges students to move a charged ball around various barriers and into a goal. Because you can show the resultant force acting on the ball, Electric Field Hockey is a powerful tool for demonstrating the superposition of forces.

**$59.95; $179.95 (10-copy lab pack)**

## EM Field




**David Trowbridge**

**Microsoft Corporation**

**Bruce Sherwood**

**Carnegie Mellon**

Get your students charged up about electricity and magnetism with EM Field! This interactive software will help them visualize electric fields produced by point and line charges and magnetic fields produced by current-carrying wires and gain an intuitive, physical feel for fields. Unique features include the ability to explore Gauss's law and Ampere's law.

**$69.95; $209.95 (10-copy lab pack)**

**Mention this ad and receive a free one-year subscription to the *Physics Courseware Communicator* with any order!**

PHYSICS ACADEMIC SOFTWARE

### Act Now Order Today!

Order by check, credit card (MC, Visa, AmEx), or institutional purchase order. Just call or write:

**The Academic Software Library**
**Box 8202**
**North Carolina State University**
**Raleigh, NC 27695–8202**

For shipping & handling in the U.S., Mexico, & Canada add $3.50 for first package and $.75 for each additional package. All other foreign orders will be shipped air mail. Add $12.50 for first package and $4.00 for each additional package. Allow 2 weeks for delivery.

### Satisfaction Guaranteed

**Call Toll Free**
**(800) 955-TASL**
**(919) 515-7447**
**Fax 515-2682**

A publishing project of the American Institute of Physics in cooperation with the American Physical Society and the American Association of Physics Teachers

AMERICAN INSTITUTE OF PHYSICS 500 Sunnyside Boulevard, Woodbury, NY 11797-2999

The American Institute of Physics (AIP) is a not-for-profit membership corporation chartered in New York State in 1931 for the purpose of promoting the advancement and diffusion of the knowledge of the science of physics and its application to human welfare. In order to achieve our purpose, we serve the sciences of physics and astronomy by serving the member societies, by serving individual scientists, and by serving students and the general public.

As leading scientific publishers, the American Institute of Physics and its Member Societies publish more than one-quarter of the world's research literature in all areas of physics including: general physics, applied physics, chemical physics, geophysics, plasmas and fluids, medical physics, nuclear and particle physics, astronomy, electronics, engineering, crystallograhy, instrument science, materials science, mathematics, acoustics, rheology, optics, and vacuum science. AIP publishes its own archival and translation journals, and provides publishing services to member and other organizations.

## Member Societies

The American Physical Society
Judy Franz, Executive Officer
One Physics Ellipse
College Park, MD 20740-3844

Optical Society of America
David W. Hennage, Executive Director
2010 Massachusetts Avenue, N.W.
Washington, DC 20036

Acoustical Society of America
Charles Schmid, Executive Director
500 Sunnyside Blvd., Woodbury, NY 11797-2999

The Society of Rheology
Andrew M. Kraynik, Secretary
Department 1512
Sandia National Labs.
Albuquerque, NM 87185

American Association of Physics Teachers
Bernard V. Khoury, Executive Officer
One Physics Ellipse
College Park, MD 20740-3845

American Crystallographic Association
William L. Duax, Executive Officer
P.O. Box 96, Endicott Station
Buffalo, NY 14205-0096

American Astronomical Society
Peter B. Boyce, Executive Officer
1630 Connecticut Avenue, N.W.
Washington, DC 20009

American Association of Physicists in Medicine
Sal Trofi, Executive Director
One Physics Ellipse
College Park, MD 20740-3846

American Vacuum Society
William D. Westwood, Secretary
Bell–Northern Research, Ltd.
P.O. Box 3511, Station C
Ottawa, Ontario K1Y 4H7, Canada

American Geophysical Union
A. F. Spilhaus, Jr., Executive Director
1630 Connecticut Avenue, N.W.
Washington, DC 20009

## Affiliated Societies

American Institute of Aeronautics and Astronautics, American Meteorological Society, American Nuclear Society, ASM International, Astronomical Society of the Pacific, Division of Physical Chemistry of ACS, Engineering Information, Inc., The Geological Society of America, Instrument Society of America, International Association of Mathematical Physicists, International Centre for Diffraction Data, Materials Research Society, Microscopy Society of America, Nuclear and Plasma Sciences Society of IEEE, Physics/Astronomy Section of the Council on Undergraduate Research, Physics Section of AAAS, Society for Applied Spectroscopy, SPIE—The International Society for Optical Engineering.

**Corporate Associates:** Approximately 175 leading corporations, by their membership, participate in and contribute to the support of AIP.

## Publications

Physical Review A · Bernd Crasemann, *Editor,* Physics Dept., University of Oregon, Eugene, OR 97403
Physical Review B · P.D. Adams, *Editor,* The American Physical Society, 1 Research Rd., Box 1000, Ridge, NY 11961
Physical Review C · Sam Austin, *Editor,* Cyclotron Labs., Michigan State University, E. Lansing, MI 48824
Physical Review D · Lowell S. Brown and D.L. Nordstrom, *Editors,* APS, 1 Research Rd., Box 1000, Ridge, NY 11961
Physical Review E · Irwin Oppenheim, *Editor,* Dept. of Chemistry, Massachusetts Institute of Technology, Cambridge, MA 02139
Physical Review Abstracts · Reid Terwilliger, *Editor,* APS, One Physics Ellipse, College Park, MD 20740-3844
Physical Review Letters · J. Sandweiss, G. Basbas, S.G. Brown, and G.L. Wells, *Editors,* APS
APS News · Brian Schwartz, *Editor,* APS, One Physics Ellipse, College Park, MD 20740-3844
Bulletin of The American Physical Society · Brian Schwatz, *Editor,* APS, One Physics Ellipse, College Park, MD 20740-3844
Reviews of Modern Physics · David Pines, *Editor,* Loomis Lab. of Physics, 1110 W. Green St., Urbana, IL 61801
The Journal of the Acoustical Society of America · Daniel W. Martin, *Editor-in-Chief,* 7349 Clough Pike, Cincinnati, OH 45244
American Journal of Physics · Robert H. Romer, *Editor,* 222 Merrill Science Bldg., Box 2262, Amherst College, Amherst, MA 01002
The Astronomical Journal · Paul W. Hodge, *Editor,* Astronomy Dept.FM-20, University of Washington, Seattle, WA 98195
Publications of the Astronomical Society of the Pacific · Howard E. Bond, *Editor,* Space Telescope Science Institute, Baltimore, MD 21218
Bulletin of the American Astronomical Society · Peter B. Boyce, *Editor,* AAS
The Astrophysical Journal · Helmut A. Abt, *Managing Editor,* Kitt Peak National Observatory, Box 26732, Tucson, AZ 85726
The Journal of Chemical Physics · J.C. Light, *Editor,* James Franck Institute, The University of Chicago, Chicago, IL 60637
Journal of Mathematical Physics · Roger G. Newton, *Editor,* Indiana Univ., The Poplars, Rm. 324, Bloomington, IN 47405
Physics of Fluids · A. Acrivos, *Editor,* The Levich Institute, Steinman 202, CCNY, Convent Ave. at 140 St., New York, NY 10031
Physics of Plasmas · Ronald C. Davidson, *Editor,* Plasma Phys. Lab., Princeton Univ., P.O. Box 451, Princeton, NJ 08543
Journal of Applied Physics · Steven J. Rothman, *Editor,* Argonne Natl. Lab., Box 8296, Argonne, IL 60439-8296
Applied Physics Letters · Hartmut Wiedersich, *Editor,* Argonne Natl. Lab., Box 8296, Argonne, IL 60439-8296
Review of Scientific Instruments · Thomas H. Braid, *Editor,* Argonne Natl. Lab., Box 8293, Argonne, IL 60439-8293
Journal of Physical and Chemical Reference Data · Jean W. Gallagher, *Editor,* NIST, MS221/A3223, Gaithersburg, MD 20899
Physics Today · Gloria B. Lubkin, *Editor,* AIP, One Physics Ellipse, College Park, MD 20740-3843
Computers in Physics · Lewis Holmes, *Editor,* One Physics Ellipse, College Park, MD 20740-3843
Chaos · David K. Campbell, *Editor*, Dept. of Physics, University of Illinois–UC, Urbana, IL 61801
Journal of Vacuum Science and Technology A · Gerald Lucovsky, *Editor,* Dept. of Physics, N. Carolina State Univ., Raleigh, NC 27650
Journal of Vacuum Science and Technology B · Gary E. McGuire, *Editor,* MCNC, Research Triangle Park, NC 27709
Surface Science Spectra · C. E. Bryson, *Editor*, Surface/Interface, Inc., Mountain View CA 94041; Gary McGuire, *Editor*, MCNC, NC 27709
Medical Physics · J.S. Laughlin, *Editor,* Memorial Sloan-Kettering Cancer Center, 1275 York Ave., New York, NY 10021
Noise Control Engineering Journal · Alan H. Marsh, *Editor-in-Chief,* DyTec Engineering, Inc., 5092 Tasman Dr., Huntington Beach, CA 92649
Powder Diffraction · Deane K. Smith, *Editor-in-Chief,* Dept. of Geosci. and Mineralogy, Penn State Univ., University Park, PA 16802
AAPT Announcer · Bernard V. Khoury, *Editor,* AAPT, One Physics Ellipse, College Park, MD 20740-3845
The Physics Teacher · Clifford E. Swartz, *Editor,* Phys. Dept., State University of New York, Stony Brook, NY 11794
Journal of Rheology · Arthur B. Metzner, *Editor,* Dept. of Chemical Engineering, University of Delaware, Newark, DE 19716
Journal of the Optical Society of America A · Bahaa E. A. Saleh, *Editor*, 2010 Massachusetts Ave., N.W., Washington, DC 20036
Journal of the Optical Society of America B · Paul F. Liao, *Editor,* 2010 Massachusetts Ave., N.W., Washington, DC 20036
Applied Optics · William T. Rhodes, *Editor-in-Chief,* Dept. of Electr. & Computer Eng., Univ. of Colorado, Boulder, CO 80309-0425
Optics Letters · Peter W. E. Smith, *Editor,* Bellcore, 331 Newman Springs Rd., Red Bank, NJ 07701
Optics and Photonics News · Andrea Pendleton, *Editor,* 2010 Massachusetts Ave., N.W., Washington, DC 20036
Journal of Lightwave Technology · Donald B. Keck, *Editor,* Corning Glass Works, Sullivan Park FR29, Corning, NY 14830
The Journal of Undergraduate Research in Physics · R.E. Adelberger, *Editor,* Physics Dept., Guilford College, Greensboro, NC 27410

AIP Conference Proceedings

| | | | |
|---|---|---|---|
| Acoustical Physics | JETP Letters | Physics of Atomic Nuclei | Semiconductors |
| Astronomy Reports | Low Temperature Physics | Physics of the Solid State | Journal of Optical Technology |
| Astronomy Letters | Optics and Spectroscopy | Plasma Physics Reports | Technical Physics |
| Crystallography Reports | Physics-Doklady | Physics of Particles and Nuclei | Technical Physics Letters |
| JETP | | | |

Current Physics Index (CPI), quarterly and annual subject index with abstracts to all the above journals.
General Physics Advance Abstracts (GPAA), semimonthly advance abstracts of AIP-published physics literature.
Searchable Physics Information Notices (SPIN), monthly computer-readable tape of abstracts.
Current Physics Microform (CPM), monthly microfilm edition of all the above journals.
Current Physics Reprints (CPR), on-demand copies of any article in any of the above journals.
Physics Briefs (PB), semimonthly comprehensive index with abstracts to the world literature of physics.
PINET, an online physics information network.


## Governing Board 1994–1995

Roland W. Schmitt, *Chair**
Reuben E. Alley
Benjamin Bederson
Roger A. Bell
Marc H. Brodsky *(ex officio)**
Robert L. Beyer*
Patricia E. Cladis
Charles Counselman, III
G. Brent Dalrymple*
Robert L. Dixon
William L. Duax
Judy R. Franz
Roderick M. Grant *(ex officio)**
Joseph E. Greene
David Hennage
David W. Hoffman*
Karen L. Johnston
Frank J. Kerr
Bernard V. Khoury*
Carl Kisslinger
Patricia K. Kuhl
Donald N. Langenberg
Tingye Li
Harry Lustig*
Christopher H. Marshall
Gregory B. McKenna
Duncan T. Moore
Norman F. Ness
C. Robert O'Dell
C. Kumar N. Patel
Burton Richter
Barrett H. Ripin
J. William Rogers, Jr.
Charles E. Schmid*
Benjamin Snavely
A. F. Spilhaus, Jr.
Hugo Steinfink
Richard Stern
Howard G. Voss*
Martin Walt
* executive committee

## AIP Officers

Marc H. Brodsky, *Executive Director and CEO*
Roderick M. Grant, *Secretary*
Arthur T. Bent, *Treasurer and CFO*
Theresa C. Braun, *Director of Human Resources*
Darlene Walters, *Vice President, Publishing*
John S. Rigden, *Director of Physics Programs*

## Publishing Services

James J. Donohue, *Director Publishing Services*
Edward P. Greeley, *Director Business Development and Society Services*
Douglas LaFrenier, *Director of Marketing*
Peggy Judd, *Director of Information Technology*
Maria Taylor, *Publisher AIP Press*
Carol Fleming, *Manager Publishing II Branch*
Doreene A. Berger, *Manager Journal Production I Division*
Maya Flikop, *Manager Translation Program Division*
Richard Kobel, *Manager Advertising Division*
John T. Scott, *Manager Editorial Operations Division*
Brian Schmitt, *Manager Circulation and Fulfillment Division*
Cheryl Taub, *Manager Composition I Division*
Denise Weiss, *Manager Books and Special Projects*
Janice Wilmot, *Manager Production II Division*

# American Institute of Physics

## A TRADITION IN PHYSICS PUBLISHING

### AIP and Member Society Journals

Acoustical Physics
APS News
*Applied Physics Letters
Applied Physics Letters Online
Astronomical Journal
Astronomy Letters
Astronomy Reports
Bulletin of the American Astronomical Society
Bulletin of the APS
Chaos
Computers in Physics
Crystallography Reports
Current Physics Index
General Physics Advance Abstracts
*Journal of the Acoustical Society of America
*Journal of Applied Physics
*Journal of Chemical Physics
Journal of Experimental and Theoretical Physics
JETP Letters
*Journal of Mathematical Physics
Journal of Physical and Chemical Reference Data
Journal of Rheology
Low Temperature Physics
*Medical Physics
*Physical Review A: Atomic, Molecular and Optical Physics
*Physical Review B: Condensed Matter
*Physical Review C: Nuclear Physics
*Physical Review D: Particles and Fields
*Physical Review E: Statistical Physics, Plasmas, Fluids and Related Interdisciplinary Topics
Physical Review Abstracts
*Physical Review Index
*Physical Review Letters
Physics of Atomic Nuclei
*Physics of Fluids
*Physics of Plasmas
Physics of Particles and Nuclei
Physics of the Solid State
Physics–Doklady
*Physics Today
Plasma Physics Reports
*Powder Diffraction
*Review of Scientific Instruments
*Reviews of Modern Physics
Semiconductors
Surface Science Spectra
Technical Physics
Technical Physics Letters

*available on microfiche

### Also Available:

**Sample Copies**
Sample copies are available to institutions considering a subscription.

**Back Volumes**
Back volumes are available in print, microfilm or microfiche.

**Microform**
Journals marked with an asterisk are available on microfilm and microfiche.

**Special Discount Rates**
Reduced rates are available for a variety of combination subscriptions. For details, contact AIP Circulation and Fulfillment.

**Document Delivery**
Obtain full-text copies of individual articles from core journals in physics – plus AIP and Member Society books and conference proceedings – through **Articles in Physics.** Documents are sent to you within 24 hours of your order via fax, mail or overnight express. For more information or to order call 1-800-480-PHYS or 415-259-5002. FAX: 415-259-5044. E-Mail: articles@aip.org

**Online Access**
Abstracts of journals published by AIP and Member Societies are available online in the SPIN database via the commercial service Dialog as well as on PINET, the AIP online information service. PINET also offers a current awareness database, Advance Abstracts, offering abstracts up to three months prior to their journal publication dates. Please call 516-576-2262 for additional information.

**Book Program**
AIP publishes a full line of monographs, proceedings, texts, and references. For further information in the U.S. and Canada contact William Phillips, Books Customer Service, at (516) 576-2411. Elsewhere, contact Susan Harrison, Oxford University Press, at +44 865-56767

**Send orders and inquiries to:**
American Institute of Physics
Circulation and Fulfillment
500 Sunnyside Boulevard
Woodbury, NY 11797-2999
Tel. (516) 576-2270
or (800) 344-6902
Fax (516) 576-9704
E-Mail: elecprod@pinet.aip.org

AMERICAN INSTITUTE OF PHYSICS